

AD \_\_\_\_\_

Award Number: W81XWH-10-1-0128

TITLE: Prosthetic Hand Technology-Phase II

PRINCIPAL INVESTIGATOR: S. Subbaram Naidu

CONTRACTING ORGANIZATION: Idaho State University  
Pocatello, ID 83209

REPORT DATE: February 2013

TYPE OF REPORT: Final Report

PREPARED FOR: U.S. Army Medical Research and Materiel Command  
Fort Detrick, Maryland 21702-5012

DISTRIBUTION STATEMENT: Approved for public release; distribution unlimited

The views, opinions and/or findings contained in this report are those of the author(s) and should not be construed as an official Department of the Army position, policy or decision unless so designated by other documentation.

REPORT DOCUMENTATION PAGE				Form Approved OMB No. 0704-0188	
Public reporting burden for this collection of information is estimated to average 1 hour per response, including the time for reviewing instructions, searching existing data sources, gathering and maintaining the data needed, and completing and reviewing this collection of information. Send comments regarding this burden estimate or any other aspect of this collection of information, including suggestions for reducing this burden to Department of Defense, Washington Headquarters Services, Directorate for Information Operations and Reports (0704-0188), 1215 Jefferson Davis Highway, Suite 1204, Arlington, VA 22202-4302. Respondents should be aware that notwithstanding any other provision of law, no person shall be subject to any penalty for failing to comply with a collection of information if it does not display a currently valid OMB control number. <b>PLEASE DO NOT RETURN YOUR FORM TO THE ABOVE ADDRESS.</b>					
1. REPORT DATE (DD-MM-YYYY) February 2013		2. REPORT TYPE Final, Phase II		3. DATES COVERED (From - To) 21 April 2010 - 20 November 2012	
4. TITLE AND SUBTITLE Prosthetic Hand Technology-Phase II				5a. CONTRACT NUMBER	
				5b. GRANT NUMBER W81XWH-10-1-0128	
				5c. PROGRAM ELEMENT NUMBER	
6. AUTHOR(S) Dr. Subbaram Naidu  E-Mail: naiduds@isu.edu				5d. PROJECT NUMBER	
				5e. TASK NUMBER	
				5f. WORK UNIT NUMBER	
7. PERFORMING ORGANIZATION NAME(S) AND ADDRESS(ES) Idaho State University Pocatello, ID 83209				8. PERFORMING ORGANIZATION REPORT NUMBER	
9. SPONSORING / MONITORING AGENCY NAME(S) AND ADDRESS(ES) U.S. Army Medical Research and Materiel Command Fort Detrick, Maryland 21702-5012				10. SPONSOR/MONITOR'S ACRONYM(S)	
				11. SPONSOR/MONITOR'S REPORT NUMBER(S)	
12. DISTRIBUTION / AVAILABILITY STATEMENT Approved for Public Release; Distribution Unlimited					
13. SUPPLEMENTARY NOTES					
14. ABSTRACT  The present Phase II of Smart Prosthetic Hand Technology focuses on the four closely connected areas of EMG signal identification and estimation, hand motion estimation, intelligent embedded systems and control, robotic hand and biocompatibility and signaling. The developed identification algorithm using a new sensor array, a proposed hybrid estimation algorithm provides for the decomposition and inference of multiple signals. Different categories of amputation level are simulated and the identification of EMG signals is tested and adapted to these different cases. Next, the proposed sensing and actuation system for the artificial hand overcomes the limitations on dexterous manipulation of the prosthetic hands. Strategies on grasping and manipulation are developed to complement the myoelectric signals. The proposed fusion of soft and hard embedded control systems strategy alleviates the present problems associated with prosthetic devices. Finally, by investigating into the issues of the inflammatory responses of cells/tissues in response to an artificial implant and the interference with signaling of the artificial implant, the design of our in-vitro model ultimately improves the design and construction of a functional and biocompatible artificial limb.					
15. SUBJECT TERMS Smart Prosthetics, Bio-Robotics, Intelligent EMG Signal Processing, Embedded Systems and Intelligent Control, Inflammatory Responses of Cells, Toxicity of Nano Materials					
16. SECURITY CLASSIFICATION OF:			17. LIMITATION OF ABSTRACT	18. NUMBER OF PAGES	19a. NAME OF RESPONSIBLE PERSON
a. REPORT	b. ABSTRACT	c. THIS PAGE			USAMRMC
U	U	U	UU	1069	19b. TELEPHONE NUMBER (include area code)



## Table of Contents

	<u>Page</u>
Introduction.....	1
Body.....	2
Key Research Accomplishments.....	289
Reportable Outcomes.....	293
Conclusion.....	310
References.....	315
Appendices.....	329

## INTRODUCTION

Over 1.2 million people in America have missing limbs resulting from combat (e.g., wars and other conflicts) and non-combat (e.g., accidents, birth defects) operations. Thus, availability of artificial limbs will help these people to lead a more normal life. Although artificial devices have been around for the last 30 years, there are no artificial hands that fully simulate the various natural/human-like operations of moving, grasping, lifting, and twisting. Moreover, prosthetic devices still pose significant biocompatibility problems, that need to be addressed and tissues surrounding implants develop “inflammatory reactions”.

The present Phase II of Smart Prosthetic Hand Technology focuses on the four closely connected areas of EMG signal identification and estimation, hand motion estimation, intelligent embedded systems and control, robotic hand and biocompatibility and signaling. The developed identification algorithm using a new sensor array, a proposed hybrid estimation algorithm will provide for the decomposition and inference of multiple signals. Different categories of amputation level will be simulated and the identification of EMG signals will be tested and adapted to these different cases. Next, the proposed sensing and actuation system for the artificial hand overcomes the limitations on dexterous manipulation of the prosthetic hands. Strategies on grasping and manipulation will be developed to complement the myoelectric signals. The proposed fusion of soft and hard embedded control systems strategy will alleviate the present problems associated with prosthetic devices. Finally, by investigating into the issues of the inflammatory responses of cells/tissues in response to an artificial implant and the interference with signaling of the artificial implant, the design of our in-vitro model will ultimately improve the design and construction of a functional and biocompatible artificial limb.

## **BODY**

## **Goal 1: EMG Signal Identification and Estimation**

### **Spatial filter Isolation of Motor Unit Sets and Simulation of Degree of Amputation:**

Nonlinear force-sEMG modeling, Hybrid PSO-TS, Optimization of nonlinear filters, Spatial filtering and Optimization, Zone Classification

### **EMG-hand motion model integration and optimization for degree of amputation using sensor fusion strategies:**

Force Modeling, Force fatigue Modeling, System Identification, Data Fusion Algorithms, Finger Motion Modeling

## **Abbreviations and Acronyms**

AI	Artificial Intelligent
AIC	Akaike's Information Criterion
ANFIS	Adaptive Neuro Fuzzy Inference System
ANN	Artificial Neural Networks
AR	Autoregressive
ARIMA	Autoregressive Integrated Moving Average
ARMA	Autoregressive Moving Average
ARMAX	Auto Regressive-Moving Average with eXogenous Terms
ARX	Auto Regressive with eXogenous Term
ATP	Adenosine Triphosphate
BIC	Bayesian Information Criterion
BJ	Box-Jenkins
BSS	Blind Source Separation
CNS	Central Nervous System
CMAP	Compound Muscle Action Potential
Cov.	Covariance
CrP	Creatine Phosphate
DRNN	Dynamic Recurrent Neural Networks
EIG	Eigenvector
FDS	Flexor Digitorum Superficialis
FFT	Fast Fourier Transforms
FIS	Fuzzy Inference System
FL	Fuzzy Logic
FPE	Final Prediction Error
FSR	Force Sensing Resistor
GA	Genetic Algorithm
HOS	Higher Order Statistics
HW	Hammerstein-Wiener
IIR	Infinite Impulse Response
IPFAM	Integral Pulse Frequency and Amplitude Modulation

IPI	Interpulse Interval
ISEK	International Society of Electrophysiology and Kinesiology
JASA	Joint Analysis Using EMG Amplitude and Spectrum
KIC	Kullback Information Criterion
MDL	Minimum Description Length
MF	Median Frequency
Mcov.	Modified Covariance
MU	Motor Unit
MUAP	Motor Unit Action Potential
MUSIC	Multiple Signal Classification
NMT	Neuromusculoskeletal Tracking
OE	Output-Error
PAM	Pulse Amplitude Modulation
PDF	Probability Density Function
PEM	Prediction Error/Maximum Likelihood Method
PFM	Pulse Frequency Modulation
$P_i$	Inorganic Phosphate
PIP	Proximal Interphalangeal
PSD	Power Spectral Density
RMS	Root Mean Square
sEMG	Surface Electromyographic
SFT	Short Fourier Transforms
SI	System Identification
SR	Sarcoplasmic Reticulum
TKE	Teager–Kaiser Energy
US	United States
WF	Wavelet Function
WT	Wavelet Transform
WVD	Wigner-Ville Distribution
Y-W	Yule-Walker

## **CHAPTER ONE**

### **Spatial filter Isolation of Motor Unit Sets and Simulation of Degree of Amputation**

This chapter describes the signal processing techniques used for post-processing of the sEMG signal and the modeling methods used to determine sEMG-Force relation.

#### **1.1 Experimental Setup**

The experiments were carried out on a healthy male subject in order to collect sEMG and force data, with the objective to extract dynamical models describing the relationship among these two quantities. The motor point of the subject was located using a Muscle Stimulator, manufactured by Rich-Mar Corporation; model number HV 1100. The motor location of the ring finger was identified and chosen for the experiments. The EMG detection system used was the Delsys, Bagnoli-16 channel EMG, DS-160, S/N-1116, which has an internal amplification and noise reduction technology built into it. The sensors used for measuring the surface EMG action potentials were two pronged DE 2.1 differential surface electrodes. The material for the contacts of the electrode is 99.9% pure silver, while the contacts are 10mm long, 1mm in diameter and spaced 10mm apart. The subjects' skin was prepared before the sensors were placed over the motor point location of the forearm musculature being measured. Hair around the area was shaved and an alcohol swab was used to clean the skin. The Delsys Electrode Interface SC-FO2-3 was used, which promotes a quality electrical connection between the electrode and the skin, minimizing motion artifacts and line interference. The electrodes were placed along the muscle fibers (Flexor Digitorum Superficialis) for recording surface EMG. The force was recorded using a force sensitive resistor (FSR). The data acquisition for the force and the EMG signal was done at 2000 samples per second. NI DAQ 6024 E Series boards were used.

The procedure mentioned in this section was used for all of the experiments, which involved modeling of the sEMG from a single motor point, of a particular finger, to the corresponding force the finger generated.

The most widely accepted standard for filtering and recording surface EMG signals is published by the International Society of Electromyography and Kinesiology (ISEK), [1]. Other filtering methods commonly include low-pass or band-pass filtering. Some researchers have also employed notch filtering to remove power line noise from the recorded EMG signal, [2]. Whitening filters have also been employed in order to increase the quality of the amplitude estimates of the surface EMG signals, [3]. Many signal processing methods can be found in the literature to extract useful information from surface EMG signals. Some of these include using Markov models, [4] and fuzzy logic control, [5] – for classification of EMG, wavelet processing [6], and Bayesian estimators, [7].

In our initial work, nonlinear system identification was used to extract dynamical models relating the force generated by an individual finger from measured surface EMG signals. The surface EMG signal is measured in milli-volts and is a function of the muscle activity. In particular, investigation of the optimal Bayesian filter parameter settings were carried out aimed at identifying a dynamical model. Bayesian filters were utilized for processing the measured surface EMG signals, as done by T. D. Sanger, [8]. The filter parameters of the Bayesian filters were optimized using elitism based Genetic Algorithm to search for the optimal values. Since, changes in the processed EMG signal, with respect to the expected rates in sudden shifts and gradual drift have direct implication on the expected extraction of the underlying dynamics, the optimal setting was found by defining an objective function that is directly related to the nonlinear model fit obtained from system identification results. Also, GA is used to find the optimal parameters for the Hammerstein-Wiener models used for system identification.

#### **1.2 Bayesian Filtering**

In [8] T. D. Sanger proposed using a nonlinear recursive filter based on Bayesian estimation. The desired filtered signal was modeled as a combined diffusion and jump process and the measured electromyographic (EMG) signal was modeled as a random process with a density in the exponential

family and rate given by the desired signal. The rate is estimated on-line by calculating the full conditional density given all past measurements from a single electrode. The Bayesian estimate gives a filtered signal that best describes the observed EMG signal. This estimate yields results with very low short-time variability but also with the capability of very rapid response to change. The estimate approximates isometric joint torque with lower error and higher signal-to-noise ratio than current linear methods. Use of the nonlinear filter significantly reduces noise compared with current algorithms, and it may therefore permit more effective use of the EMG signal for prosthetic control, biofeedback, and neurophysiology research. This filtering technique was adopted for modeling the relation between the sEMG and the finger force produced. As sEMG is plagued by a multitude of non-physiological and physiological factors as investigated by Farina *et al.* in [9], the Bayesian filtering technique described was investigated to determine its usefulness and to investigate if it would help in reducing the inherent variability of sEMG signals and facilitate dynamic modeling of the sEMG and force relation using system identification. A brief outline of the Bayesian filtering procedure is mentioned here. The variables used in the theory of Bayesian filtering are given below.

$B_{j,i}(s), F_{j,i}(s)$	Polynomials in the linear block.
$C$	Constant chosen so that the density integrates to 1.
$F$	Nonlinear Regression command.
$N$	Number of events.
$P[x(t)]$	Probability density for .
$f(rpc)$	Fitness function for each chromosome.
$f_i()$	Input nonlinearity function.
$f(\bullet)$	Static nonlinear function
$h()$	Output nonlinearity function.
$n$	Integer proportional to the magnitude of the rectified EMG signal.
$q(t)$	Regressors
$rpc$	random population of chromosomes.
$s$	Backward shift operator.
$u(t)$	Input of a system.
$v(t), w(t)$	Internal variables.
$x$	Measured surface EMG signal.
$y(t)$	Output of a system.
$\hat{y}(t)$	Predicted or Estimated output.
$\alpha$	Expected rate of gradual drift.
$\beta$	Expected rate of sudden shifts in surface EMG.
$\varepsilon$	Width of discretizing bin.
$\theta$	Finite dimensional vector used to parameterize the mapping.
$\eta$	Physical parameters of non-linear function $f(\bullet)$ .

The instantaneous relation between the measured surface EMG – represented by the variable ‘x’ and the resulting sEMG – represented by EMG after filtration can be described by a conditional probability density function  $P(EMG|x)$ . Under the assumption that the rectified EMG signal results from random depolarization events of multiple muscle fibers, then the average amplitude in a small time window will be proportional to the number of depolarization events during that time, [8]. The number of events  $N$ , can be modeled as a Poisson process given by Equation 1.1. The rectified  $emg = |EMG|$  is used in most of the equations from here on forth and  $n$  is an integer proportional to the magnitude of the rectified EMG signal.

$$P(emg | x) \approx (x^n e^{-x}) / N! . \quad (1.1)$$

However, empirical observations of EMG signals have led to the common assumption that it can be described as amplitude modulated zero-mean Gaussian noise [10], [11]. For rectified EMG signals i.e.  $emg > 0$  the expression is:

$$P(emg | x) = 2 \times \exp(-emg^2 / 2x^2) / (2\pi x^2)^{1/2} . \quad (1.2)$$

Also, under close observation of EMG signals, the density function can be better approximated using a Laplacian density, which for a rectified EMG signal is as follows:

$$P(emg | x) = \exp(-emg / x) / x. \quad (1.3)$$

Say,  $emg(t)$  is a single measurement of the rectified EMG signal at a given time  $t$ , and  $x(t)$  is the measured surface EMG at time  $t$ , then the function  $P[emg(t) | x(t)]$  specifies the likelihood of each possible value of  $x(t)$ . Bayes rule gives the posterior density as,

$$P[x(t) | emg(t)] = P[emg(t) | x(t)] \times P[x(t)] / P[emg(t)], \quad (1.4)$$

Where,  $P[x(t)]$  is the probability density for  $x(t)$  immediately before the measurement of  $emg(t)$ . In general, the prior  $P[x(t)]$  will depend on the entire past history of the measurements. Estimation of  $P[x(t)]$  can be performed using a recursive algorithm based on discrete time measurements.

Using Bayes' rule the expression can be rewritten as,

$$P[x(t) | emg(t), emg(t-1), \dots] = P[emg(t) | x(t)] P[x(t) | emg(t-1), emg(t-2), \dots] / C \quad (1.5)$$

$C$  is a constant chosen to make the density integrate to 1. From equation 1.5, an estimate of  $P[x(t) | emg(t), emg(t-1), \dots]$  can be obtained which is written as  $p(x, t-1)$ . Also, the estimate of the conditional density of  $x$  at time  $t$ , immediately before the measurement of  $emg(t)$  is written as  $p(x, t-)$ , which is calculated by propagating the density of  $p(x, t-1)$  forward in time by one sampling interval. The recursive algorithm (numerical integration of Fokker-Planck equation in [8]) is utilized for the filtration of the recorded EMG signal. The mathematical form of the derived probability density function is given by:

$$p(x, t-) \approx \alpha P(x - \varepsilon, t-1) + (1 - 2\alpha) p(x, t-1) + \alpha p(x + \varepsilon, t-1) + \beta + (1 - \beta) p(x, t-1). \quad (1.6)$$

The recursive algorithm follows the same steps as in [8]. But in the case of [8], the values of  $\alpha$  and  $\beta$  are chosen empirically. Using an elitism based Genetic Algorithm (GA), the probability of choosing the optimum values of  $\alpha$  and  $\beta$  was increased, with the cost function in GA being the percentage of the model fits that are returned by the system identification model between the surface EMG and the force data.

The following sections discuss GA and System Identification (SI).

### 1.3 Genetic Algorithm:

Genetic Algorithm is a class of evolutionary methods for solving both constrained and unconstrained optimization problems that are based on natural selection. This is the same rule that governs biological systems. In GA, the population of individual solutions is modified repeatedly. Each step or iteration in GA selects individuals (chromosomes) in some fashion that may include some randomness, from a given population, as parents and uses them to produce offspring for the next generation. Over successive iterations or generations, the population evolves and finally reaches an optimal solution.

The steps that make up GA are as follows: 1) Generate a random population of chromosomes 'rpc'; these chromosomes carry information of the population and are confined in the feasible solution space. 2) Evaluate the objective or fitness function  $f(rpc)$  for each chromosome. 3) Create a new population or offspring from the initial population by using certain rules. This step includes a) *Selection* – selection of two parent chromosomes from the population according to their fitness. b) *Crossover* – crossover the parents to form new offspring, if no crossover is performed then the offspring is an exact copy of the parents. c) *Mutation* – involves the changing of a variable in a chromosome or some other change in the original chromosome as defined by the user. d) Acceptance Condition – if offspring satisfies the acceptance condition, include offspring in the new population or else discard. 4) Use the offspring as the parents for the generation of a new population.



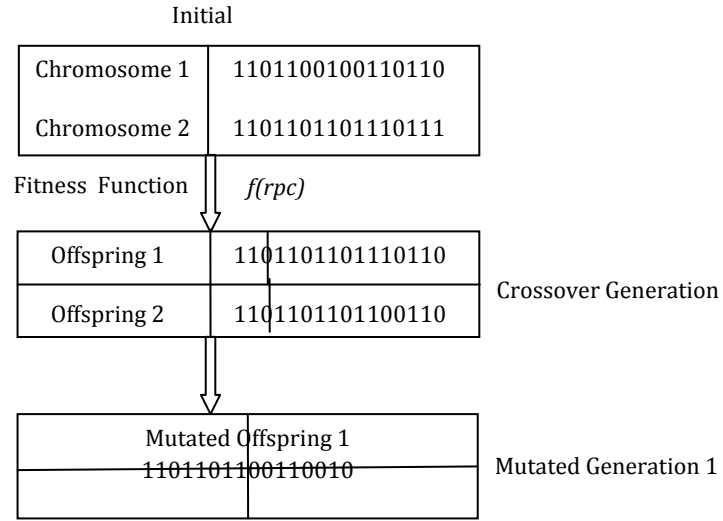


**Figure 1.1:** Steps in a Genetic Algorithm

5) Continue until the end condition is satisfied i.e. the number of iterations specified. Refer Figure 1.1 for an example of the GA steps. Here, GA is used to find the optimal values of  $\alpha$  and  $\beta$  for the filtration of the surface EMG signal using the Bayesian filter. The cost function that GA tries to minimize is the model fit obtained from the system identification of the surface EMG and the corresponding force data collected.

#### 1.4 System Identification: [12]

System Identification (SI) has its roots in standard statistical techniques, such as least squares and maximum likelihood methods. SI helps the user to build mathematical models of a dynamic system based on measured data. This is done by adjusting the parameters within a given model until its output emulates the measured input in some minimum fashion, [13]. System identification is especially useful for modeling systems that cannot be easily represented in terms of first principles or known physical laws. In this case, one can use SI to perform black-box modeling, where the measured data determines the model structure.

Black-box modeling has the following advantages; 1) the structure and the order of the model need not be known, and 2) many model structures can be estimated and compared, and the best among them can be selected to suit the measured data sets. Systems that can be represented using ordinary difference or differential equations can be modeled using grey-box models. Grey-box models have a known mathematical structure and unknown parameters and they have the following advantages over black-box models; 1) known constraints can be imposed on the model characteristics, 2) there are fewer model parameters to estimate, 3) coupling between parameters can be defined in the model structure, and 4) in the non-linear case the dynamic equations can be specified dynamically.

The most common system identification models in engineering are Auto-Regressive with exogenous input (ARX) and Auto-Regressive Moving Average with exogenous input (ARMAX). The more recent additions to system identification have been black-box models with a non-linear structure such as Artificial Neural Networks, Fuzzy models and so on.

The most basic relationship between the input and the output of a system can be given by a linear difference equation, [13] such as:

$$y(t) + a_1 y(t-1) + \dots + a_n y(t-n) = b_1 u(t-1) + \dots + b_m u(t-m), \quad (1.7)$$

where,  $u(t)$  and  $y(t)$  are the input and output of the system at time  $t$  respectively, and  $a_n$  and  $b_m$  are the parameters of the system.

$$\theta = [a_1, \dots, a_n, b_1, \dots, b_m]^T, \quad (1.8)$$

where,  $\theta$  is the parametric vector with coefficients  $a_n$  and  $b_m$ .

$$\varphi(t) = [-y(t-1) \dots -y(t-n) u(t-1) \dots u(t-m)]^T,$$

where,  $\varphi(t)$  is the regression vector, then we can write:

$$y(t) = \varphi^T(t) \theta. \quad (1.9)$$

Generally, a model structure is a parameterized mapping from past inputs and outputs  $Z^{t-1}$  to the space of the model outputs, [14]:

$$\hat{y}(t | \theta) = g(\theta, Z^{t-1}), \quad (1.10)$$

Where,  $\hat{y}(t)$  is the predicted output.

In the real world, almost all systems are nonlinear and the output is a non-linear function of the input variables. However, linear models often sufficiently and accurately describe system dynamics. While modeling a system using grey-box models, the linear and the nonlinear structures can be set using its differential or difference equations. Since linear models are adequate for many situations, it should be tried first to see if the results of the model fit are satisfactory.

Figure 1.2 shows a general flow chart of the system identification procedure.

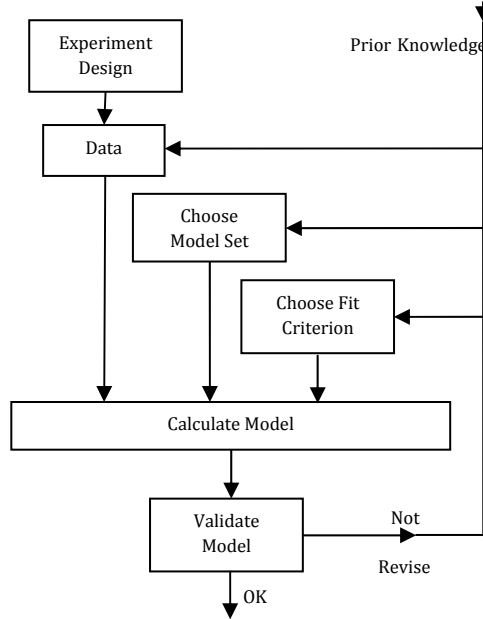


**Figure 1.2:** System Identification Loop Flowchart

### 1.5 Nonlinear ARX Models:

Nonlinear ARX models use a parallel structure to combine linear and nonlinear blocks. Figure 1.3 shows the structure of a nonlinear ARX model. The nonlinear and linear functions are called regressors.

The predicted output of a nonlinear model  $\hat{y}$  at any given time  $t$  can be described by,

$$\hat{y}(t) = F(q(t)) \quad (1.11)$$

$F$  can include linear or nonlinear functions of  $q(t)$ . Where  $F$  is a non-linear regression command which is approximated by nonlinearity estimators, and  $q(t)$  represents the regressors.

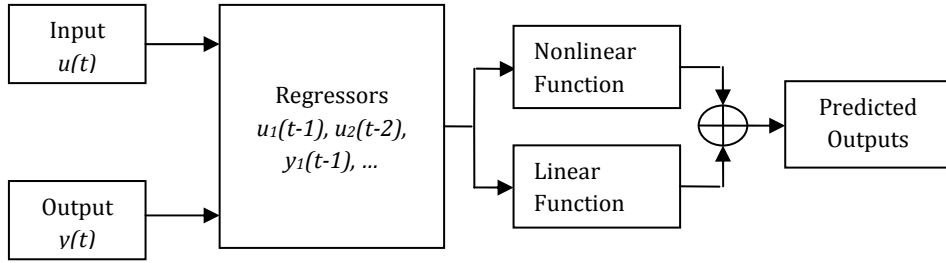


**Figure 1.3:** Nonlinear ARX Model Structure

There are different types of regressors for nonlinear ARX models. Standard Regressors – for specified model orders, the past input and output signals are computed automatically as delay transformations. Custom Regressors – input and output variables that can be specified for example as products, powers *etc.* Nonlinear ARX model regressors can be computed by specifying the following orders;  $n_a$  - the number of past output terms used to predict the current output,  $n_b$  - the number of past input terms used to predict the current output and  $n_k$  - the delay from input and output in terms of the number of samples. The various nonlinearity estimators that can be used for nonlinear ARX models are, a) Sigmoid Network, b) Tree Partition, c) Wavelet Network, d) Neural Networks and d) User defined custom networks.

### 1.6 Hammerstein and Wiener Models:

It is a possible and quite a common situation, where the dynamics of the system can be well-described using linear models, but they do not account for any static nonlinearities at the input and/or at the output. This might be the case if the actuators are nonlinear. For example, when saturation occurs, or when the sensors employed have nonlinear characteristics. A model with a static nonlinearity accounted for at the input is called a Hammerstein model. When the nonlinearity is at the output a Wiener model is more appropriate. The combination of the two is then the Hammerstein-Wiener model, [15]. Refer Figure 1.4(a) and (b) for Hammerstein and Wiener models. Consider the Hammerstein case where the static nonlinear function  $f(\bullet)$  can be parameterized, either in terms of physical parameters, such as saturation point and saturation level, or in black-box terms such as spline-function coefficients. This defines  $f(\bullet, \eta)$ , [15]. If the linear model is given by  $G(q, \theta)$ , the predicted output model will be in the following form:

$$\hat{y}(t | \theta, \eta) = G(q, \theta) f(u(t), \eta). \quad (1.12)$$

The Hammerstein-Wiener representation allows us to model the dynamic system using one or two static nonlinear blocks in series with a linear block. The static non-linearity could represent saturation or dead-zone behavior. Figure 1.5 represents the Hammerstein-Wiener model structure, while Equation 1.13 describes the Hammerstein-Wiener model structure:

$$w(t) = f_i(u(t)), \quad v(t) = \frac{B_{j,i}(s)}{F_{j,i}(s)} w(t), \quad y(t) = h(v(t)), \quad (1.13)$$

Where  $w(t)$  and  $v(t)$  are internal variables,  $w(t)$  has the same dimensions as  $u(t)$ , and  $v(t)$  has the same dimensions as  $y(t)$ .

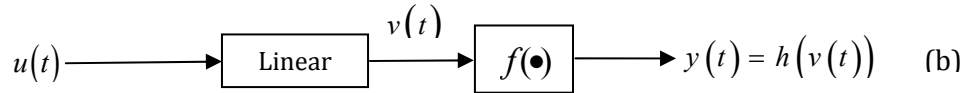
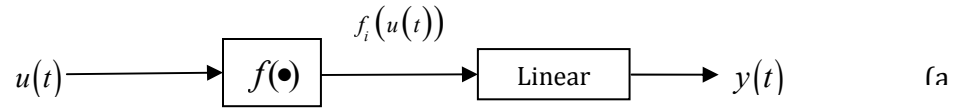


**Figure 1.4:** a) Hammerstein Model, b) Wiener Model

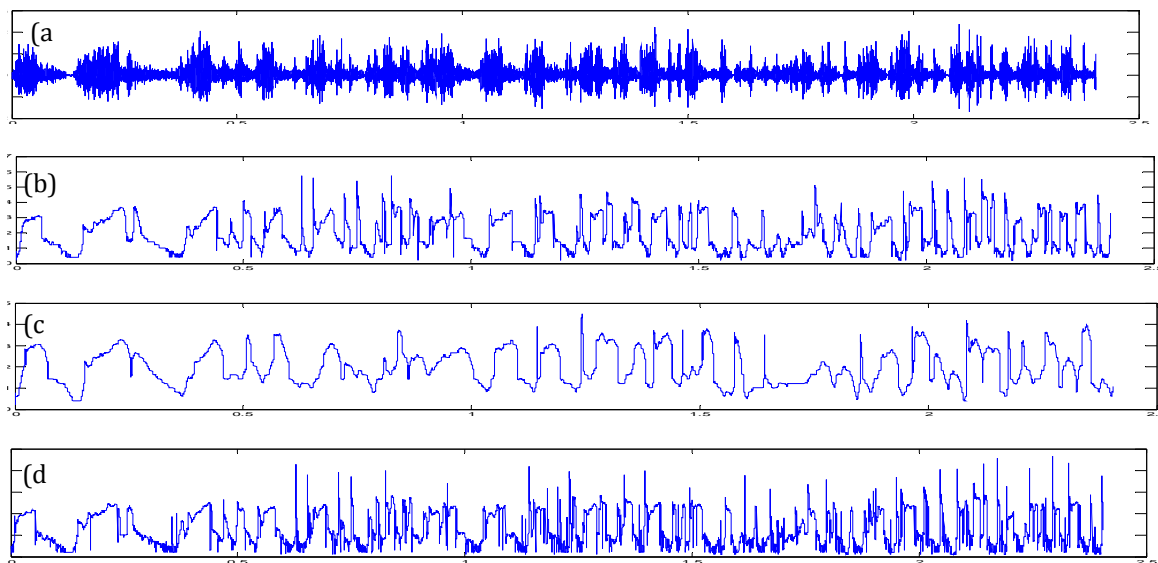


**Figure 1.5:** Hammerstein-Wiener Model

The linear block is specified using the terms  $n_b$  - the number of zeros plus one,  $n_f$  - the number of poles and  $n_k$  - the delay from the input to the output in terms of the number of samples. The commonly used nonlinear estimators for Hammerstein-Wiener model are, a) Dead Zone, b) Piecewise Linear, c) Saturation, d) Sigmoid Network, and e) Wavelet Network, [16-18].

The results presented in this section are for the implementation of Bayesian filters with optimized filter parameters for the Bayesian filters and optimized Hammerstein-Wiener model parameters for the experiments, where the subject performed a random series of flexion's of the ring finger.

Figure 1.6 shows the output of the raw, filtered sEMG, and also the raw and filtered force data. The x-axis in the figure is the number of samples and the y-axis is the amplitude of the sEMG and the force signal in milli-volts. The randomness – as depicted in Figure 1.6(e) – was necessary in order to ensure that the system is excited at all modes. During the experiment all fingers were flexed in order to generate the force and sEMG signal. A result of this, there was substantial cross talk in the measurement.



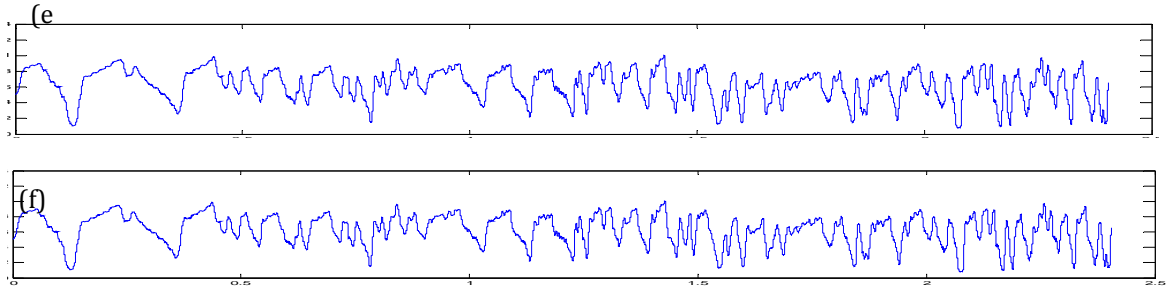


**Figure 1.6:** a) Raw EMG Signal, b) Bayes' Exponential Filtered EMG, c) Poisson Filtered EMG, d) Half-Gaussian Filtered EMG, e) Raw Force Signal, f) Filtered Force Signal

Besides Hammerstein-Wiener models, nonlinear ARX models were also tested with the recorded sEMG-force data with varying model properties for system identification. The results were very poor as compared to the Hammerstein-Wiener models.

Table 1.1 lists the system identification results using nonlinear ARX models with random parameter settings. To compute the model fit using the models extracted from the SI algorithm, the following relationship was used:

$$fit = 100 * (1 - norm(\hat{y} - y) / norm(y - mean(y))) \quad (1.14)$$

It can be seen from Table 1.1, the variation in the model fits that were obtained for the nonlinear ARX models with various combinations of  $n_a$  and  $n_b$  was very large and also the majority of the model fits that were obtained were very poor.

**Table 1.1:** Results of nonlinear ARX Model Estimations

	$n_b$ (range)	$n_f$ (range)	$n_k$	Model Fit % (range)
Non Linear ARX Models	2-10	3-20	1	-157700 – 63.51

The force and the sEMG data collected were imported to MATLAB<sup>R</sup>. The results of the experiments are shown in Tables 1.2 and 1.3. The steps for running the nonlinear filter algorithms were the same as in [8]. The values for  $\alpha$  and  $\beta$  used in [8] were deduced empirically. Here, the filter parameters are chosen from among a large search space, thereby allowing the optimization routine to find the best settings within a large range.

An elitism continuous GA based optimization algorithm was run for 10, 30, and 80 generations. The various GA parameters set were: a) Maximum number of Iterations – 10, 30, 80, b) Initial Population size – 98, c) Population size for the first generation – 48, d) Number of chromosomes used for mating – 24, e) Mutation rate – 4%. The data shown in Table 1.2 is for the parameters of the nonlinear filtration of the raw sEMG data with the three different types of filters: namely the Bayes Exponential, the Half-Gaussian and the Poisson. The values of  $\alpha$  and  $\beta$  were chosen as given in [8]. The subject performed the experiment for 60 sec, while only but the first 10 sec of the recorded data was used for model estimation. This was done in order to avoid the onset of fatigue which would influence the modeling of the system.

As can be seen from Table 1.2, the range of model fit values obtained for  $\alpha=0.001$  and  $\beta=1e-24$ , with Nonlinear Hammerstein-Wiener SI was between 39 – 72%. We have a range of values here, as the models parameters were randomly chosen and 25 different combinations of  $n_b$  and  $n_f$  were tested for the same values of  $\alpha$  and  $\beta$ . The best fit was obtained for the Half-Gaussian filtration of the sEMG signals of 72.61%. With GA as the optimum search algorithm, the range of  $\alpha$  (0.005 – 0.009) and  $\beta$  (10e-24 – 10e-23) for the

different filters could be expanded and correspondingly the nonlinear Hammerstein-Wiener SI fit obtained also increased to around 85%.

The values in Table 1.2 are read as, number of GA iterations – 10, 30 and 80 – the corresponding  $\alpha$  values obtained for Bayes Exponential filter were 2.2e-23, 3e-23 and 4e-23. Similarly the  $\beta$  values obtained for 10, 30 and 80 GA iterations, for Bayes Exponential filter, were 8.2067e-23, 1.5924e-23 and 1.4987e-23 correspondingly. The model fits obtained for the combination of  $\alpha$  and  $\beta$  values after 80 GA iterations were 68.18%, 83.65% and 85.05%. The results shown in Table 1.3 row 1, indicates the range for which  $n_b$  and  $n_f$ . The range of the fits obtained for the nonlinear Hammerstein-Wiener SI was between 22.73 – 70.22%.

The force signal used for modeling purposes, was filtered using a low pass Butterworth filter using a cutoff frequency of 15Hz. The EMG signal was filtered using a Chebyshev Type II high pass filter with the following filter parameters,  $F_{\text{stop}}=60\text{Hz}$ ,  $F_{\text{pass}}=70$ ,  $A_{\text{stop}}=80$ ,  $A_{\text{pass}}=1$ , match=stopband, to remove any line frequencies and followed by a low pass Chebyshev Type II high pass filter with the following filter parameters,  $F_{\text{stop}}=600\text{Hz}$ ,  $F_{\text{pass}}=650$ ,  $A_{\text{stop}}=80$ ,  $A_{\text{pass}}=1$ , match=stopband. This was done since EMG signals have an effective frequency content of not more than 500Hz, according to the ISEK standards, [1]. Random combinations of  $n_b$  and  $n_f$  were used for the Hammerstein-Wiener SI models.

**Table 1.2:** Model outputs after Pre-processing sEMG data using Bayesian Filtering and Filtered force data

<b><math>\alpha</math> and <math>\beta</math> used from [6]</b>					
	<b>Parameter Setting</b>		<b>[1] Bayes Exponential Model Fit Range %</b>	<b>[2] Half- Gaussian Model Fit Range %</b>	<b>[3] Poisson Model Fit Range %</b>
	<b><math>\alpha</math> x1e-3</b>	<b><math>\beta</math> x1e-23</b>			
<b>Nominal</b>	1	1	46.61 - 68.42	39.91 - 72.61	54.61 - 60.39
<b>GA-Based Iteration Results</b>					
<b>Nonlinear Filter</b>	<b>GA Iterations</b>	<b><math>\alpha</math> x1e-3</b>	<b><math>\beta</math> x1e-23</b>	<b>Model Fit %</b>	
<b>Bayes Exponential</b>	10	2.2	8.2067	68.187	
	30	3	1.5924	83.657	
	80	4.9	1.4987	85.050	
<b>Half-Gaussian</b>	10	6.1	1.1413	74.236	
	30	8.7	7.9649	80.791	
	80	6.3	1.3240	86.359	
<b>Poisson</b>	10	6.8	5.312	51.389	
	30	5.1	7.3887	61.589	
	80	8.4	7.8648	72.582	

On executing the GA based optimization, for the model parameters, the results obtained improved to 78.22% from 70.22%, the best fit obtained for  $n_b=5$ ,  $n_f=9$  and  $n_k=1$ . The final row in Table 1.3 shows the model fit obtained using the optimized filter parameters for the Half-Gaussian, with the GA optimized model parameters for Hammerstein-Wiener, which resulted in a fit of 81.64%.

**Table 1.3:** Optimization of Nonlinear Hammerstein-Wiener Model Parameters using GA

	$n_b$	$n_f$	$n_k$	Model Fit %	
Nominal	2 – 22 (range)	3 – 24 (range)	1	22.73 – 70.22	
GA-Based Iteration Results					
	GA Iterations	$n_b$	$n_f$	$n_k$	Model Fit %
Non-linear Hammerstein- Wiener Model	10	15	8	1	65.4
	30	5	9	1	78.224
	80	5	9	1	78.224
Optimal Half-Gaussian Filter Parameters [ $\alpha$ =6.3e-3, $\beta$ =1.3240e-23] and Model Parameters Results		5	9	1	81.64%

In this section, a set of filtering approaches were investigated for the explicit use of system identification, which is a new approach in the field of sEMG processing. The results indicate robust improvements in the SI outcomes for each of the filters used when optimized. In addition, we explored nonlinear model structures to describe the sEMG-force relationship for finger forces. SI results, for relating sEMG signals to force applied by individual digits of the hand, were improved using an elitism based GA to find the optimal parameter setting for Hammerstein-Wiener models.

In the next section, analysis of the sEMG signals, obtained from specific Motor Unit locations corresponding to the index, middle and ring finger, and the corresponding force data is presented. This is a continuation of the analysis methods that were used in the previous section, i.e. employing system identification and various filtering techniques to glean useful information from the sEMG and the corresponding force data. Also, one of the shortcomings of our previously used method was the speed of estimation and optimization of model parameters with GA. GA is inherently slow as compared to most of the optimization schemes available in literature. In this section, replacing GA with another suitable but faster optimization technique was investigated. The technique that was tested is called Particle Swarm Optimization (PSO). Before the results of the optimization technique applied to the modeling of sEMG-force relation are presented a brief background of PSO is provided in section 1.7

### **1.7 Particle Swarm Optimization (PSO)**

In 1995, a new evolutionary algorithm was developed by J. Kennedy, a social psychologist, and R. Eberhart, known as Particle Swarm Optimization (PSO). This method is computationally less expensive and has been used in this section to optimize the Bayesian filter parameters  $\alpha$  and  $\beta$ . Other well established optimization algorithms are; a) Genetic Algorithm (GA) – inspired by biological evolution, is at its core, survival of the fittest. The main drawback of GA being that it is computationally very expensive especially for large search spaces. GA has been paired with many other search methods in order to improve its overall performance. b) Tabu Search on the other hand – which has a set of tabu balls and promising balls or a tabu list which helps it to reduce the search space is not very computationally expensive. Particle swarm optimization has a simple procedure; 1) Defining the input parameters: This includes the swarm size (number of particles of the swarm), maximum number of iterations, the limiting velocity of the particles, the upper and lower bounds of the search space and the stopping tolerance. 2) Initializing the position of the particles – can be randomly assigned using a uniform or normal distribution, [1]. 3) Evaluating the fitness

function  $fn$  (objective function) for the  $j^{th}$  particle. This depends on the cost function, e.g. the local best and the global best values are compared and suitably updated. Moreover, the difference between  $|fn^*(t) - fn^*(t-1)|$ , i.e. the current ( $t$ ) and ( $t-1$ ) is compared to the tolerance  $\mathcal{E}$ . If  $|fn^*(t) - fn^*(t-1)| < \mathcal{E}$ , then stop the loop; otherwise continue. Figures 1.7 and 1.8 show the particles of the PSO in the search space and the flow chart of the PSO algorithm respectively.

Experiments were conducted for three fingers, the index, middle and the ring finger. The motions simulated were a) pad to pad grip and b) a power grip, while measuring the force developed by individual fingers. For the ring finger, the motion to generate the force signal was randomized (the levels of force signal generated by the subject varied significantly over one experiment, in all six experiments were carried out). This was done in order to have poor correlation between the sEMG-Force signals analyzed for various time windows. For the index and the ring finger four experiments were conducted for each. The motion to generate the force signal was made cyclic in order to have high correlation between the sEMG-Force signals. Cyclic motion was considered, in this case, to study the effects of fatigue as time progressed on system identification and the Hammerstein-Wiener modeling. Data, for the ring finger (random motion), was collected for 30, 45 and 60 seconds.

- $x_i^j(t)$  The  $i^{th}$  component position of the  $j^{th}$  particle in time  $t$ .
- $x_i^{j,lbest}(t)$  The local best position of the  $j^{th}$  particle in generation  $t$ .
- $x_i^{j,gbest}(t)$  The global best position of the  $j^{th}$  particle in generation  $t$ .
- $V_i^j(t)$  The  $i^{th}$  component velocity of the  $j^{th}$  particle in time  $t$ .
- $t$  time.

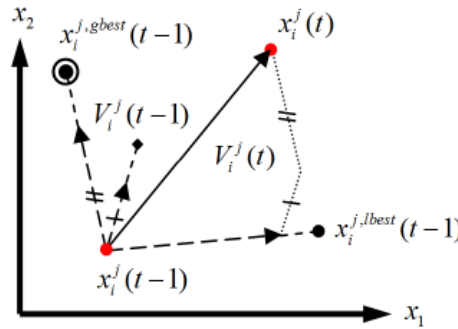


**Figure 1.7:** Previous & Updated Position of particles [19]

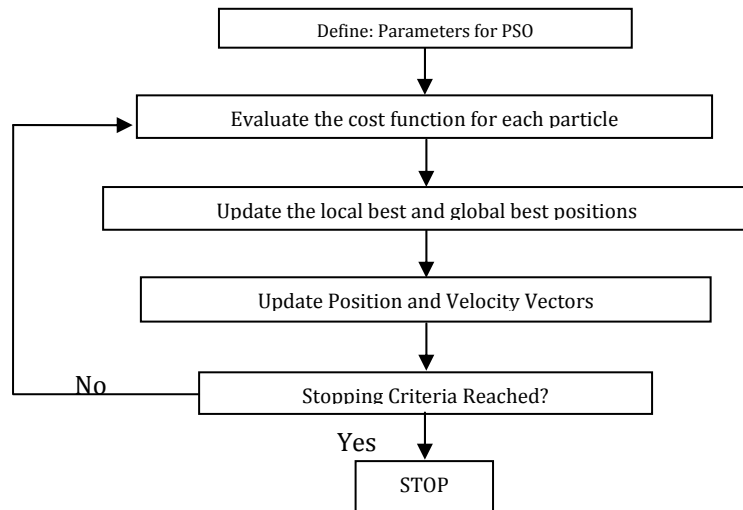


**Figure 1.8:** Particle Swarm Optimization Algorithm Loop



Data for the middle and index fingers was collected for 30 and 45 seconds. The subject performed a cyclic and random series of flexion's and contractions with the ring finger at constant and random speeds. Again, the randomness was necessary in order to ensure that the system is excited at all modes. During the experiment all fingers were flexed in order to generate the force and sEMG signal. As a consequence of which there was substantial cross talk in the measurements.

*Cyclic and Random Data Analysis:*

As mentioned earlier, experiments were carried out a) in a cyclic motion, to have a cyclic change in the sEMG and force signal so that the effects of fatigue could be studied and b) in a random manner (with fatigue induced by repetition) to investigate how the Hammerstein-Wiener model parameters (model order) change with time. For the cyclic case, experiments were conducted on the index and the middle finger, while the ring finger was used for the random case. In all, for the cyclic case four experiments each were conducted on the index and middle finger and the data analyzed. The sEMG data was filtered using a Chebyshev filter and a Half-Gaussian filter. Hammerstein-Wiener models were tested by varying  $n_b$  and  $n_f$  values for both the cases. The data sets for the cyclic variation were collected for 30 seconds. This data set was then split into smaller windows; an example of the windows used for estimation and validation of the modeling is shown in Table 1.4, where 'ze' is the time interval that was used for the model estimation and 'zv' is the time interval used for model validation. A small overlapping time window, with the estimated model is used for the validation model.

**Table 1.4:** Modeling Time Windows Cyclic Motion (Index & Middle Fingers)

ze (sec)	zv (sec)
0.5-6.5	2.5-8.5
6.5-13.5	9.5-16.5
13.5-19.5	16.5-22.5
17.0-23.0	20.0-26.0

In all, the total time intervals for which models and fits were computed for the index finger alone, were  $4(\text{time intervals per experiment}) \times 4(\text{experiments}) \times 49 (\text{models per window by varying } n_b \text{ and } n_f) \times 2 (\text{filtering methods}) = 1,568$  different models. This was also repeated for the middle finger (1,568 different models). For the random motion/force variation scenario;  $8(\text{time intervals per experiment}) \times 7(\text{experiments}) \times 49 (\text{models per window by varying } n_b \text{ and } n_f) \times 2 (\text{filtering methods}) = 5,488$  different models were analyzed. It is not feasible to show all the results of all the models here, but examples are provided along with some of the results in the following tables as to how the modeling was affected for the various time intervals and motion/force variations. Also, for the random scenario, PSO was used to investigate a relation between the filter parameters  $\alpha$  and  $\beta$  and also to investigate the effect of fatigue on the model outputs. The results of the PSO optimization are summarized in Figure 1.9. From the results it can be concluded that  $\alpha$  values between  $1.5$  to  $2.9\text{e-}6$  and  $\beta$  values between  $2.6\text{-}3.7\text{e-}26$  are more likely to give better fits for nonlinear Hammerstein-Wiener models. The fits are not very conclusive, as the fit values for experiment 1 are not very high (probably the search space for  $\alpha$  and  $\beta$  would need to be expanded) as compared to the other experiments for the initial time windows, where one would not expect any fatigue.

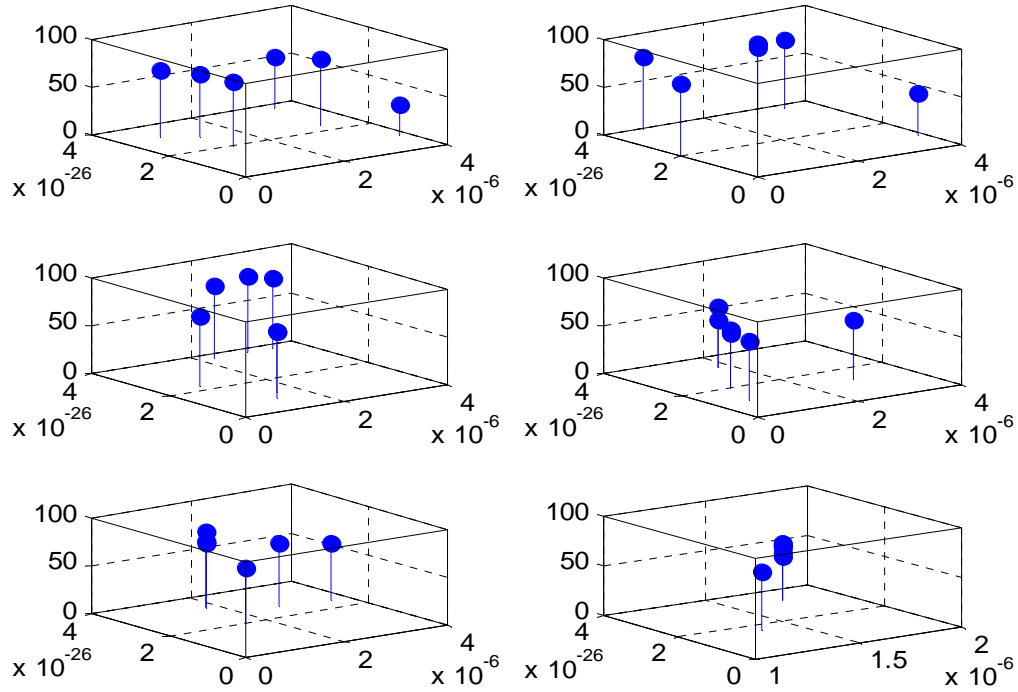


**Figure 1.9:** Results of PSO for six experiments. Axes are Alpha, Beta and Fit values

But a trend could be observed, as fatigue sets in towards the last time window of almost all the experiments, the fit % dropped, except for experiments 5 and 6 where the fit values remained high. This indicates that as the muscle fatigue increases, it directly deteriorates the input sEMG signals relation to force. This casts a doubt on the effectiveness of the nonlinear blocks in the Hammerstein-Wiener models investigated. From these results, it could be concluded that a thorough investigation into the nonlinear block would be needed to capture the dynamics of fatigue and to compensate for the detrimental effects it has on modeling the sEMG-force signals. Figure 7 shows some of the results for the index finger, nonlinear Hammerstein-Wiener models investigated for the experiments. The red plot is of the signal used for model estimation, the green plot is of the signal used for validation of the model and the blue plot is of the entire data spectrum for that experiment for Figure 1.10 (a) & (b). Figure 1.10(a) captures the data spectrum of the input and output signal, 1.10(b) is of the amplitude and the frequency content of the data sets, 1.10(c) plots the model residuals and the autocorrelation and the cross-correlation of the signals, 1.10(d) shows the model outputs to the original signal, 1.10(e), (f) and (g) are the input nonlinearities, the linear block and the output nonlinearity blocks of the Hammerstein-Wiener models. 1.10(h) represents a contour plot of the fit values for the various models.

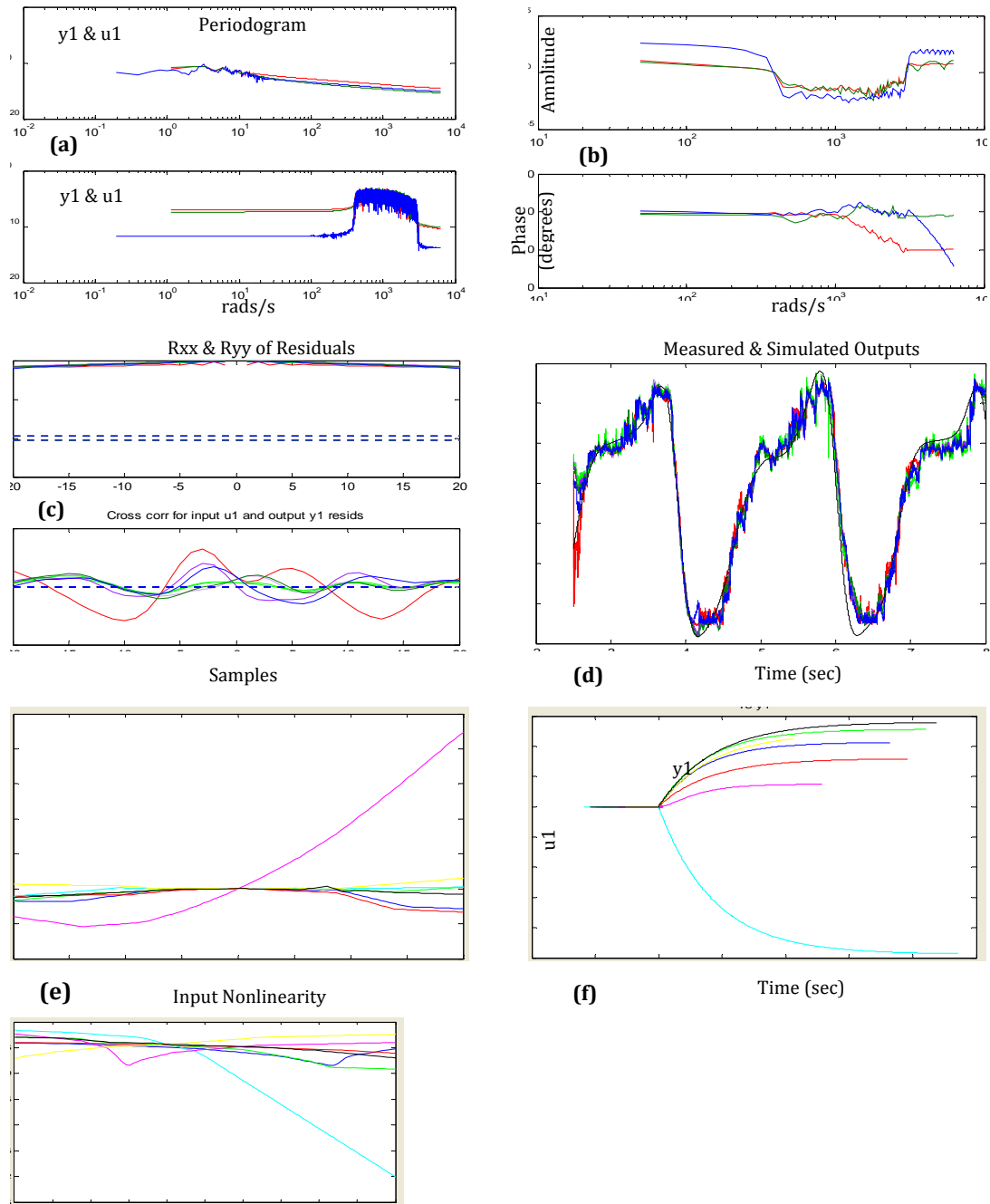


**Figure 1.10:** a) EMG Index Finger Data Spectrum, b) Frequency content of signals c) Model Residuals & Auto-correlation and Cross-correlation of signals, D) Model outputs, e) Input nonlinearity, f) Linear block, g) Output nonlinearity

The description given previously is applicable to Figure 1.11. The results shown in Figure 1.11 are for the Middle finger.

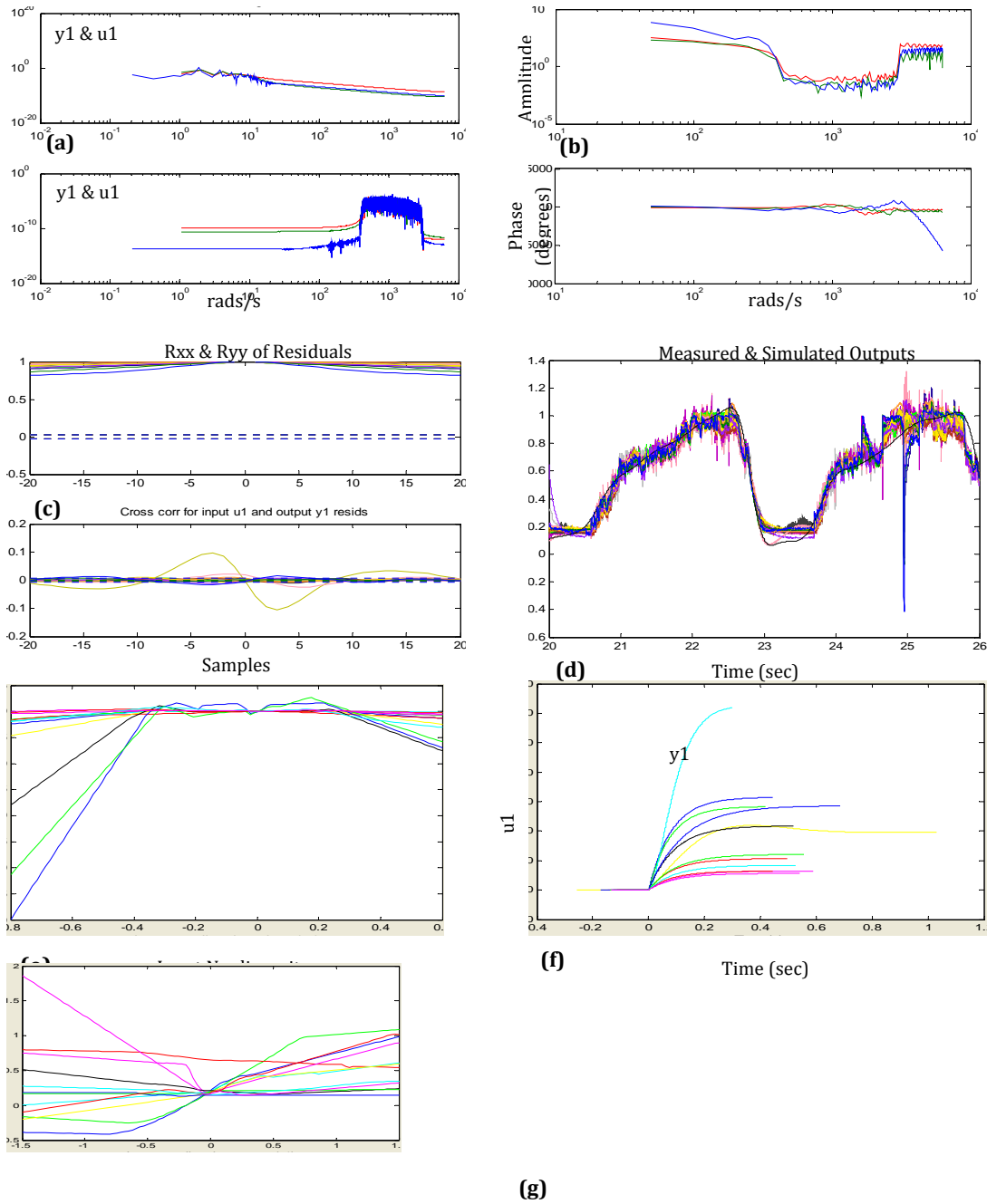


**Figure 1.11:** a) EMG index Finger Data Spectrum, b) Frequency content of signals. c) Model residuals & Auto-correlation and Cross-correlation of signals, D) Model outputs, e) Input nonlinearity, f) Linear block, g) Output nonlinearity

From the experiments and the Hammerstein-Wiener modeling it was concluded that, a) the Hammerstein-Wiener models do capture the dynamics of the sEMG-Force data, very well, for all the three fingers tested (in the range of 65 to 82% model fits). This statement holds true for all the initial time windows in the experiments. But the model fits deteriorate (between 17-25%) as fatigue in the muscle increases b) The Half-Gaussian filtering of the sEMG signal, used for modeling, yielded better results than the Chebyshev filtering of sEMG (about 7-12% more). c) A change in the piecewise linearity function in the Hammerstein-Wiener modeling did have a significant effect on the model fit value. d) Although the

PSO did not offer concrete results about the effect of fatigue on the filter parameters  $\alpha$  and  $\beta$ , it did throw some light on the possibility of expanding the search area for these parameters, which could assist in modeling the sEMG-force signals, especially with muscle fatigue.

One of the results of this study was further expanded; the optimization scheme of PSO. A hybridized PSO and Tabu Search (TS) algorithm was developed and tested for unconstrained and optimization problems. This hybrid algorithm was tested for some commonly used benchmark problems from literature. The next section 1.8 presents a brief background of the hybrid PSO-TS algorithm developed and the results obtained for various benchmark problems.

### 1.8 Hybrid PSO-TS Algorithm

Meta-heuristic approaches such as Particle Swarm Optimization (PSO) and Tabu Search (TS) algorithms have been around for a few years. They present alternative approaches to find optimality for a diverse set of optimization problems, such as estimation and system identification, among others. PSO and TS based approaches stand in contrast to hard computing methods such as gradient based methods by vastly reducing the computational complexity, especially for higher dimensional problems. A key motivation for using these soft-computing algorithms is the ability to escape local optimal points in pursuit of the global optimum during the search process. The PSO algorithm searches the cost-surface with a set of individual particles, each representing a solution to the optimization problem. The particles orient themselves via influence components such as inertia, current best solution found by the entire flock, and the particle's best position. TS was presented by Glover, [20], as an iterative optimization procedure that attempts to avoid the shortfalls of the Local Search (LS) algorithm. TS is a single agent algorithm that progresses through the cost surface by creating a set of neighbors (which are potential new locations) and moves to a new location by evaluating these neighbors and comparing them to a list of previously visited locations. This list, the tabu list, ensures that no cycling will occur and local optimal points are overcome.

Recent efforts in improving PSO and TS have led to a number of propositions that include concepts from other optimization philosophies. In [21] the authors proposed a TS-Genetic Algorithm based scheme to find best parameter estimates in colored noise environments. Higashitani *et al.*, [22] proposed a predator-prey based PSO. The Constriction Factor Method (CFM) proposed by Clerc [23] reduces the velocity of the particles with duration of the search process in order to facilitate the intensification over the diversification mission with time. Combinations of PSO and TS have also been investigated, such as in [24], where PSO and TS are switched at each step to explore the vicinity of the particles, and in [25] where TS and PSO and sequential quadratic programming are combined. In [26] concepts of TS are used to create two swarms in PSO, one responsible for intensification, the other for diversification.

In this hybrid algorithm, various elements of the TS algorithm were applied to the PSO scheme. In particular, the TS concept is used to adapt the PSO parameters to the given problem using a parallel scheme of hybridization. The optimization problems addressed in this section are of the unconstrained type.

The problem statement is as follows:

Consider a real valued objective function  $f(\mathbf{x})$  defined on a set  $\mathbf{x} \in S$  in  $R^n$ . We are tasked to find a point  $\mathbf{x}^*$  corresponding to the value of  $f(\mathbf{x}^*)$  such that

$$f(\mathbf{x}^*) = \min \{f(\mathbf{x}) | \mathbf{x} \in S\} \quad (1.15)$$

The difficulty of finding such a point arises when  $f(\mathbf{x})$  or the feasible domain  $S$  is non-convex. For such problems, gradient based methods will result in local optimums. Soft computing methods such as PSO and TS allow for an escape from local optimums and the continued search for a better optimum, in the extreme case the global optimum. For PSO algorithms, we consider a set of particles  $p$  and their associated location  $\mathbf{x}^i$  where  $i$  is the index for the particles. The particles explore  $S$  in an incremental fashion. Their position is altered at each step by the following update rule:

$$\mathbf{x}^i(k+1) = \mathbf{x}^i(k) + \mathbf{v}^i(k+1), \quad (1.16)$$

where,  $k$  is the increment number and  $\mathbf{v}^i$  the velocity associated with the particle, which can be computed

as follows:

$$\mathbf{v}^i(k+1) = w\mathbf{v}^i(k) + c_1 r_1 [\mathbf{b}_p^i - \mathbf{x}^i(k)] + c_2 r_2 [\mathbf{b}_g^i - \mathbf{x}^i(k)]. \quad (1.17)$$

In the velocity update formula,  $\mathbf{b}_p^i$  and  $\mathbf{b}_g^i$  represent the best ever position of the particle  $i$  and the global best position of the swarm up to iteration  $k$ , respectively.  $r_1$  and  $r_2$  are uniformly distributed random numbers between 0 and 1, while  $w$ ,  $c_1$  and  $c_2$  are weighting coefficients that manage the three tendencies of Equation (1.17). These tendencies as given by the three terms in the velocity equation are characterized as: audacious for following your own way; conservative, for going back towards your best previous position; and sheep-like, for being pulled to the best overall position. The weighting coefficients help the balancing act of combining these tendencies in order to be globally efficient. The PSO scheme described so far is rather simple and computationally very efficient, especially when compared to a GA or any gradient based methods. To further this algorithm, a limitation on the maximum value of  $\mathbf{v}$  can be imposed, say  $v_{\max}$ . This type of velocity clamping balances the exploration and intensification and also avoids excessive velocities that are responsible for particles overshooting their targets, [27]. Also, the CFM method can be employed, where the velocity update is modified – reduced – as the search progresses.

For this, Equation (1.17) is altered as follows:

$$\mathbf{v}^i(k+1) = K \times [\mathbf{v}^i(k) + c_1 r_1 (\mathbf{b}_p^i - \mathbf{x}^i(k))] + K \times [c_2 r_2 (\mathbf{b}_g^i - \mathbf{x}^i(k))] \quad (1.18)$$

Where,  $K = \frac{2}{2 - \varphi - \sqrt{\varphi^2 - 4\varphi}}$  and  $\varphi = c_1 + c_2$ , as given by [23].

The inertia weight  $w$  has a competing purpose to the velocity clamping method [28], and is responsible for balancing the exploration and intensification part of the PSO. In [29] it is also shown that  $w$  is problem dependent. Here we investigate the option of adapting  $w$  using a TS based scheme such that the PSO algorithm becomes less problem dependent. Besides  $w$ ,  $c_1$  and  $c_2$  control the stochastic influence, analogous to the mutation operator in GA. In [30], it is stated that for most problems the popular choice in literature is,  $c_1 = c_2$ , but the ratio is also problem dependent, i.e. for unimodal problems with smooth surfaces, usually one selects  $c_2 > c_1$ , while for multimodal problems these coefficients are chosen to be  $c_1 > c_2$ . Also the optimization of these coefficients is implemented using TS scheme in parallel to the PSO.

The TS algorithm has the same objective as PSO- given by Equation 1.15. A TS algorithm employs one candidate point, which moves incrementally on  $S$ . The moves between increments are defined by selecting the best update from a set of candidate points. This set is created by forming  $R$ ,  $n$ -dimensional spheres about the current position, and randomly place a point in each section (sphere). These points are evaluated on  $f(\mathbf{x})$  and then compared to a list  $T \in R^{n \times q}$  of previously visited places. The list length  $q$  basically represents the memory of the algorithm. Around each element in  $T$  a  $n$ -dimensional sphere is created serving as a tabu-ball, where no new solution can be located. The best performing candidate point not violating the restricted spaces given by the  $q$  tabu balls is selected as the new position of the search. An aspiration criterion can be formulated as an escape clause to circumvent the restrictions imposed by the tabu-balls, often in the form of having an improved cost to the current solution. All of the past best solutions are stored in a new list – the promising list, which is assembled as the TS algorithm processes. The optimum of the entries of that list will be used as the final optimal value of the algorithm.

Usually,  $q$ ,  $R$ , and the dimension of the individual  $R$ 's are considered the control parameters of the TS algorithm, which are all problem dependent.

The selection of  $w$ ,  $c_1$ , and  $c_2$  have rather large implication on the update of the new velocity vector  $\mathbf{v}^i(k+1)$ , as is illustrated in Figure 1.12. Here, the three influence vectors with regard to the global best solution,  $\mathbf{b}_g^i - \mathbf{x}^i(k)$ , and with regard to the particles best solution  $\mathbf{b}_p^i - \mathbf{x}^i(k)$  as well as the inertia vector

$\mathbf{v}^i(k+1)$  are depicted for an instant  $k$  and a single particle  $i$ . Each of these vectors are pre-multiplied by  $w$ ,  $c_1$ , and  $c_2$  respectively, resulting into some variation of the vectors, denoted by  $\Delta$  in Figure 1.12.

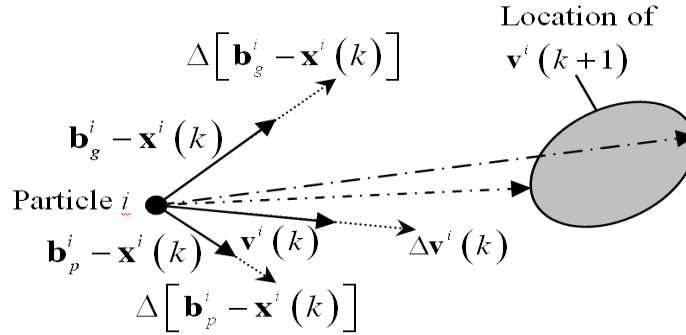


**Figure 1.12:** Adaptation of proposed PSO-TS Algorithm

As stated earlier, these three influence coefficients are problem dependent. Here the optimal coefficients are found by utilizing TS. This is accomplished by using the variation of the influence vectors to describe a new search area, in which the original cost function  $f(\mathbf{x})$  is prescribed. In Figure 1.12, this area is symbolized in the shaded ellipsoid. The best combination of coefficient along with the influence vectors will then determine the velocity update  $\mathbf{v}^i(k+1)$ . This optimization is repeated at each increment. TS lends itself well for this purpose, since it is computationally very efficient. Since  $r_1$  and  $r_2$  are superimposed to the influence coefficients, we will investigate an option where this randomization is suppressed.

Parameter estimation is an important concept in engineering where a mathematical model of a system is identified with the help of input and output signals. The classical Least-Squares (LS) algorithm gives an unbiased estimate of the parameters when the system noise is white. A bias result may occur if the residual  $\varepsilon(k) = y(k) - \hat{y}(k)$  is not white, where  $y$  is the system output,  $\hat{y}$  is the estimated output, and  $k$  is the discrete time index. For such instances, one can use a whitening filter, i.e.  $C(q^{-1})\varepsilon(k) = e(k)$ , where  $C(z^{-1})$  is the coefficient polynomial of the whitening filter and  $z^{-1}$  is the backward shift operator. The corresponding cost function for the estimation becomes, [21]:

$$J = \sum_k e^2(k) = \sum_k [C(z^{-1})A(z^{-1})y(k) + C(z^{-1})B(z^{-1})u(k)]^2 \quad (1.19)$$

where,  $u(k)$  is the input sequence,  $A(z^{-1})$  and  $B(z^{-1})$  are the numerator and denominator polynomials of the system transfer function, respectively. As the signal to noise ratio becomes large, the cost function  $J$  may become multimodal. This was shown by Söderström et al. [31]. In order to obtain the global minimum an intelligent optimization technique needs to be employed. Here the proposed hybrid PSO-TS algorithm is also tested against such a parameter estimation problem with a colored noise environment and compared to the traditional LS method.

The proposed hybrid algorithm was tested on a set of standard optimization benchmark problems, which are listed below:

**Spherical:**  $f(\mathbf{x}) = \sum_{j=1}^n x_j^2$  (also known as De Jong's function) and

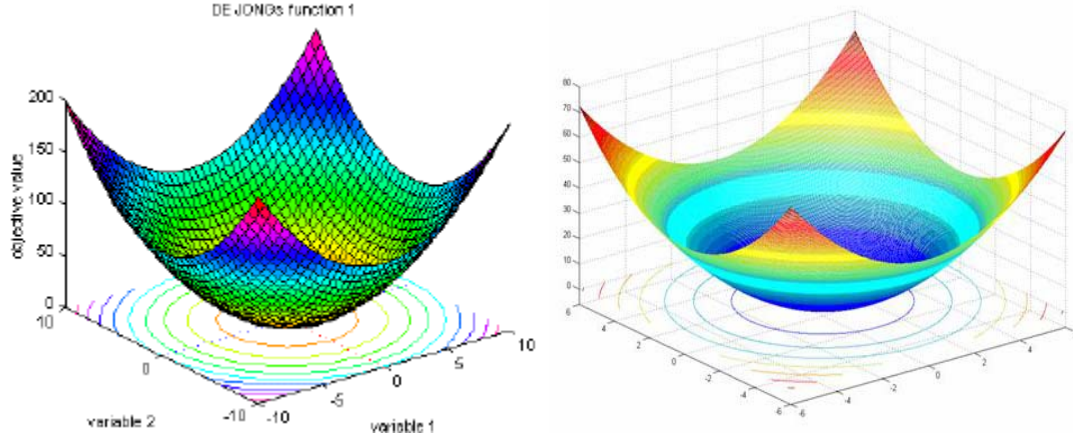


**Figure 1.13:** Plot of the Sphere or De Jong's Function, [32-33]

**Quadratic:**  $f(x) = \sum_{j=1}^n \left\{ \sum_{i=1}^j x_j \right\}^2$ ,

Where  $x_j \in [-100, 100]$  and  $f(\mathbf{x}^*) = [0, 0]$ .

**Hyperellipsoid:**  $f(\mathbf{x}) = \sum_{j=1}^n j^2 x_j^2$  where  $x_j \in [-1, 1]$  and  $f(\mathbf{x}^*) = [0, 0]$ .

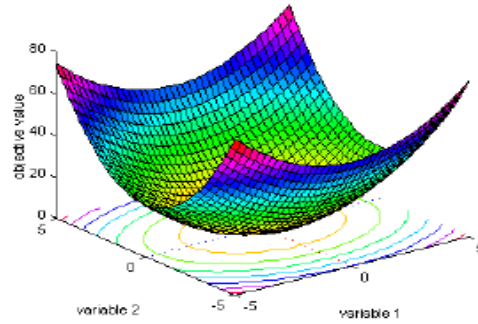


**Figure 1.14:** Plot of the Hyper-Ellipsoid Function, [32]

**Bohachevsky 1:**

$f(\mathbf{x}) = x_1^2 + 2x_2^2 - 0.3 \cos(3\pi x_1) - 0.4 \cos(4\pi x_2) + 0.7$  where  $x_j \in [-50, 50]$  and  $f(\mathbf{x}^*) = [0, 0]$ .



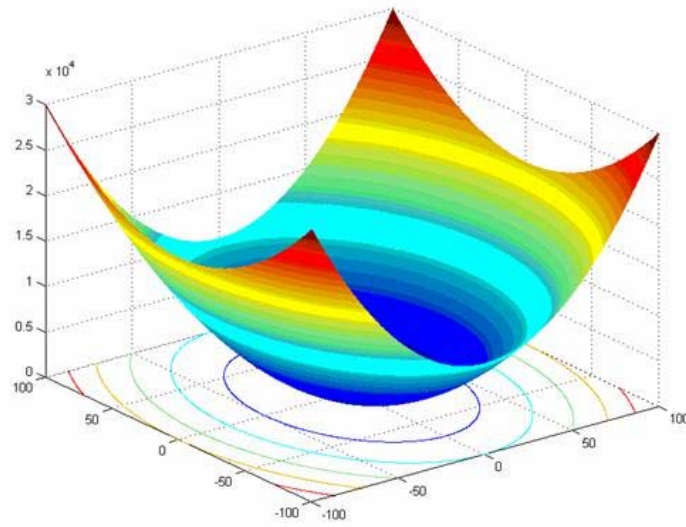


**Figure 1.15:** Plot of the Bohachevsky I Function, [33]

**Rastrigin:**  $f(\mathbf{x}) = \sum_{j=1}^n (x_j^2 - 10 \cos(2\pi x_j) + 10)$  where  $x_j \in [-5.12, 5.12]$  and  $f(\mathbf{x}^*) = [0, 0]$ .

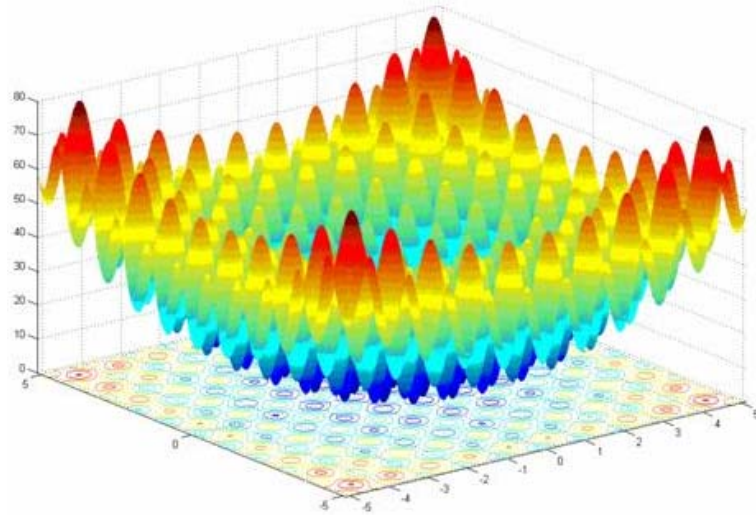


**Figure 1.16:** Plot of the Rastrigin Function, [33]

**Rosenbrock:**  $f(\mathbf{x}) = \sum_{j=1}^{n/2} \left[ 100(x_{2j} - x_{2j-1}^2)^2 + (1 - x_{2j-1})^2 \right]$  , where  $x_j \in [-2.048, 2.048]$  and  $f(\mathbf{x}^*) = [1, 1]$ .

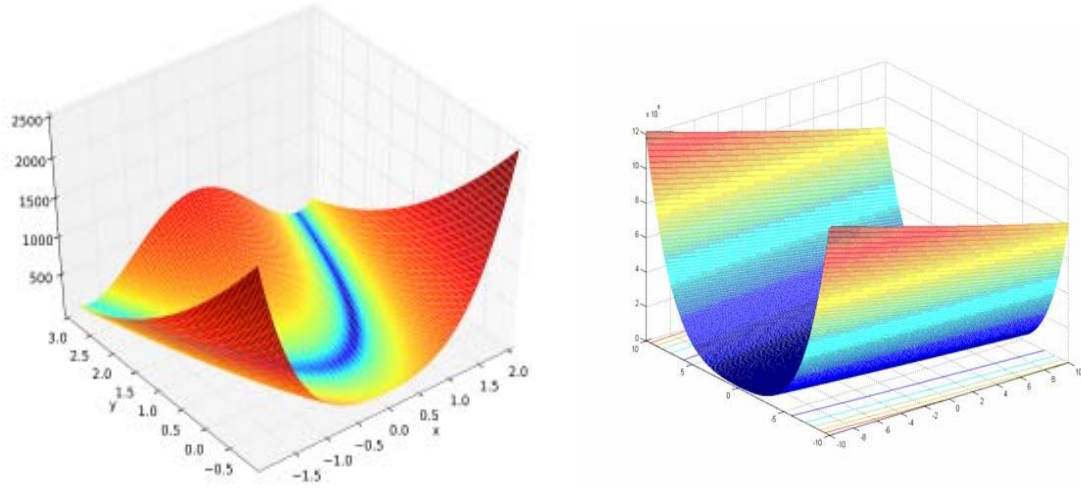


**Figure 1.17:** Plot of the Rosenbrock Function, [32]

**Haupt & Haupt:**  $f(\mathbf{x}) = x_1 \sin(4x_1) + 1.1x_2 \sin(2x_2)$  , where  $x_j \in [0, 10]$  and  $f(\mathbf{x}^*) = [9.0389, 8.6674]$ .

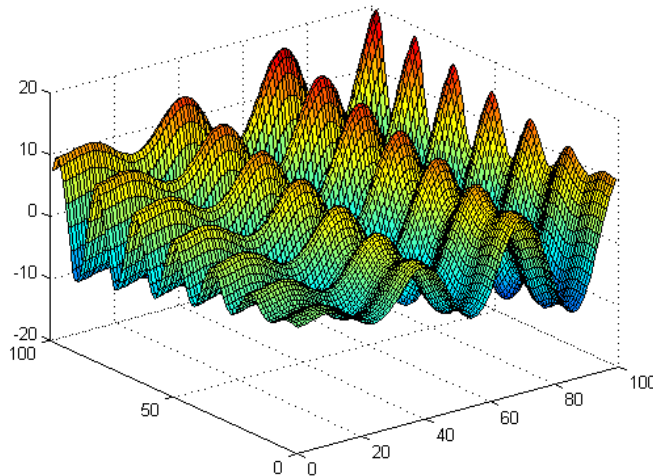


**Figure 1.18:** Plot of the Haupt & Haupt Function

In addition to these benchmark problems, the proposed algorithm was also tested for a parameter estimation problem with a colored noise environment. In particular the simple parametric model given by Equation (1.20):

$$y(k) = 0.5y(k-1) - 0.5y(k-2) + u(k) + \varepsilon(k) \quad (1.20)$$

The simulation was carried out by using the following set of parameters and conditions: uniformly distributed initial locations of particles, number of neighborhoods created at each step for each particle  $R = 25$  , uniform initial velocity of magnitude 1 for all particles,  $p = 40$  ,  $q = 5$  , radius of the  $n$  dimensional Tabu balls:  $r = 0.025(x_{\max} - x_{\min})$  , where  $x_{\max}$  and  $x_{\min}$  are the dimensions of  $S$  , radius of neighborhood  $r_N = 0.5r$  , and radius of promising balls  $r_p = 0.5r_N$  . The PSO portion utilized 100 iterations, while the embedded TS section used 10 iterations. Since randomness is a factor in the used and

proposed algorithms, and in order to gain some kind of understanding of consistency, the simulations were carried out 100 times for each cost function listed above.

**Table 1.5:** Simulation results for Benchmark Problems using Hybrid PSO-TS Algorithm (Random  $r_1$  and  $r_2$ )

Cost Function	PSO	Hybrid PSO-TS		
		w	w, c1	w, c1c2
Spherical	0.55135	<b>0.17214</b>	<b>0.0555</b>	<b>0.2216</b>
Quadratic	0.50718	<b>0.25637</b>	<b>0.12497</b>	<b>0.1347</b>
Bohachevsky	0.80852	<b>0.17689</b>	<b>0.15473</b>	<b>0.01617</b>
Hyperellipsoid	0.03252	<b>0.00436</b>	<b>0.00745</b>	<b>0.00069</b>
Rastrigin	<b>0.07168</b>	0.16678	0.16728	0.16021
Rosenbrock	1.4261	1.43255	1.47011	1.44042
Haupt	12.4736	<b>10.5563</b>	<b>10.5329</b>	<b>11.5222</b>

Table 1.5 lists the results for the unconstraint optimization problems in comparison with the original PSO algorithm. In this set of simulations,  $r_1$  and  $r_2$  were selected to be uniform random between 0 and 1.

Table 1.6 lists the results for the unconstraint optimization problems in comparison with the original PSO algorithm. In this set of simulations,  $r_1$  and  $r_2$  were set equal, at all times, to 1. It is interesting to note that for almost all the cases, the proposed hybrid optimization algorithm, regardless of which set of coefficients are optimized, performs significantly better in comparison to the standard PSO for the Hyperellipsoid, the Bohachevsky cost function. For this case too, the spherical and the quadratic functions produced better results. In both the cases there was no improvement in the Rosenbrock function values and the Rastrigin still showed poor results as compared to the standard PSO algorithm.

The distinction between the characteristics of the cost function and the performance of the proposed algorithm can be made by associating the presented results with unimodal and multimodal cost functions. As listed above, the improved performance given by the proposed hybrid algorithm is found for unimodal cost functions. While the proposed algorithm does work well for multimodal cost functions, it does excel in comparison to the standard PSO algorithm with regard to unimodal functions.

**Table 1.6:** Simulation results for Benchmark Problems using Hybrid PSO-TS Algorithm ( $r_1 = r_2$ )

Cost Function	PSO	Hybrid PSOTS		
		w	w, c1	w, c1c2
Spherical	0.55135	<b>0.08975</b>	<b>0.19801</b>	<b>0.81325</b>
Quadratic	0.50718	<b>0.31023</b>	<b>0.14124</b>	<b>0.07529</b>
Bohachevsky	0.80852	<b>0.13091</b>	<b>0.20773</b>	<b>0.15158</b>
Hyperellipsoid	0.03252	<b>0.01464</b>	<b>0.01736</b>	<b>0.00278</b>
Rastrigin	<b>0.07168</b>	0.13648	0.23206	0.4902
Rosenbrock	1.4261	1.44026	1.44147	<b>1.39044</b>
Haupt	12.4736	<b>10.6342</b>	<b>10.8366</b>	<b>10.8408</b>

The hybrid algorithm was also tested to estimate the parameters of the system given by equation (1.20). The estimated system parameters are given in Table 1.7 for the two cases a) Random  $r_1$  and  $r_2$  and b) Fixed  $r_1$  and  $r_2$  to unity. In addition, we distinguished two cases where we either computed the instantaneous optimum value of the influence coefficients and the accumulated “averaged” optimum. The variance in the noise was set at 1%, while the input sequence was a white noise sequence with variance of 30%.

**Table 1.7:** Simulation results for Estimation Problem

<b>Random</b>			
<i>Accumulative</i>			
<b>w</b>	0.5898	-0.4583	1.0425
<b>w,c1</b>	0.5319	-0.3717	1.1217
<b>w,c1,c2</b>	0.4704	-0.4666	0.8921
<i>Just Optimum</i>			
<b>w</b>	0.5340	-0.5159	1.0025
<b>w,c1</b>	0.5339	-0.5234	1.0550
<b>w,c1,c2</b>	0.4820	-0.4622	1.0110
<b>Fixed</b>			
<i>Accumulative</i>			
<b>w</b>	0.5289	-0.3794	1.0061
<b>w,c1</b>	0.5018	-0.3799	1.0777
<b>w,c1,c2</b>	0.478	-0.4917	0.9182
<i>Just Optimum</i>			
<b>w</b>	0.4707	-0.4827	1.0515
<b>w,c1</b>	0.4797	-0.4397	1.0260
<b>w,c1,c2</b>	<b>0.5074</b>	<b>-0.5164</b>	<b>0.9794</b>

The hybrid algorithm gave the best estimated values of the system parameters for the following combination; Fixed  $r_1$  and  $r_2$ , just optimum,  $w$ ,  $c_1$ ,  $c_2$  optimized, and 40 particles. Table 1.7 is giving the average values based on 10 sample points. This combination was then used to compare the results of the hybrid algorithm with Least Squares (LS). Table 1.8 shows the comparison between LS and the proposed hybrid algorithm for various variances in the noise level. The hybrid PSOTS again outperforms the LS method in almost all the cases and in some estimated values. These cases are highlighted in bold italics. Simulation runs, for the hybrid algorithm, for variances 0.05, 0.09, 0.1 and 0.2 were increased from 10 to 30 which gave slightly better results once again in comparison to the LS.

**Table 1.8:** Comparison of Hybrid PSOTS & Least Squares

<b>Simulation Options: Optimized w,c1,c2, Fixed <math>r_1</math> and <math>r_2</math> and Just Optimum, Simulation Runs :10</b>	
Hybrid PSOTS	Least Squares
<i>Variance: <b>0.001</b></i>	
<b>[0.5265,-0.4688,0.9695]</b>	[-0.00640,-0.4238,0.8794]
<i>Variance: <b>0.005</b></i>	
<b>[0.5256,-0.5206,1.0531]</b>	[0.0005,-0.5050,0.8703]
<i>Variance: <b>0.009</b></i>	
<b>[0.5289,-0.4394,0.9640]</b>	[0.0640,-0.5395,0.8626]
<i>Variance: <b>0.01</b></i>	
<b>[0.5074,-0.5164,0.9794]</b>	[0.0208,-0.4711,0.8592]
<i>Variance: <b>0.05</b></i>	
<b>[0.4183,-0.3988,0.9539]</b>	[0.1354,-0.5345,0.8100]
<i>Variance: <b>0.09</b></i>	
<b>[0.3300,-0.2699,0.9840]</b>	[0.0981,-0.7102,0.9573]

<i>Variance: 0.1</i>	
<b>[0.4035,-0.3056,1.0322]</b>	[0.1276,-0.6684,0.8821]
<i>Variance: 0.2</i>	
<b>[0.2952,-0.1684,0.9861]</b>	[0.0418,-0.7096,0.9323]
<i>Variance: 0.05, Simulation runs:30</i>	
<b>[0.4476,-0.3844,1.0049]</b>	[0.1354,-0.5345,0.8100]
<i>Variance: 0.09, Simulation runs:30</i>	
<b>[0.3852,-0.3505,0.9672]</b>	[0.0981,-0.7102,0.9573]
<i>Variance: 0.1, Simulation runs:30</i>	
<b>[0.4129,-0.3550,0.9922]</b>	[0.1276,-0.6684,0.8821]
<i>Variance: 0.2, Simulation runs:30</i>	
<b>[0.3072,-0.2769,0.9970]</b>	[0.0418,-0.7096,0.9323]

A key objective of this hybridization was to make the proposed algorithm adaptive in nature to the subjected problem, i.e. cost function. As discussed earlier the choice of the influence coefficients is dependent on the characteristics of the cost surface. The proposed hybrid algorithm optimizes these coefficients as well as the inertia coefficient  $w$  at each iteration. Hence we can plot these coefficients in order to determine if they show adaptation and consistency. This is done in Figure 1.19.

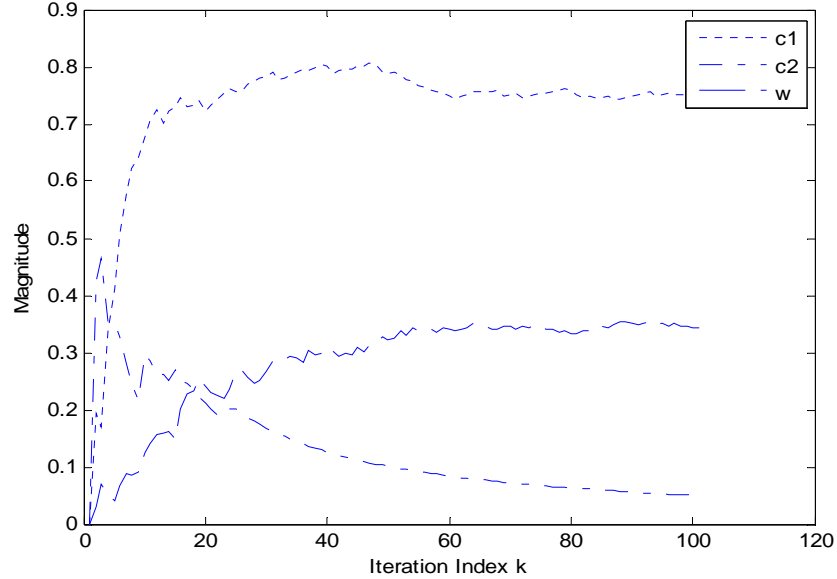


**Figure 1.19:** Plot of the Optimized Influence Coefficients

The plot is a representative characterization of the simulation results obtained for the tested multimodal cost functions. It can be observed from the plot that the proposed algorithm adapts fast to the cost function and selects  $c_1 > c_2$  as determined in the literature, indicating that each particle is dominated by its own personal best, and the algorithm is searching wider ranges. The rather non-smooth convergence plot is due to the fact that  $r_1$  and  $r_2$  are kept random and impose a perturbation to the optimal location of the influence coefficients. In comparison, the same plots are generated for some multimodal cost functions, i.e. the Hyperellipsoid in Figure 1.20 and Spherical as depicted in Figure 1.21. In both cases for the unimodal cost functions, the coefficients move quickly to the case where  $c_2 > c_1$  as given in the literature, but after a few iterations, the weighting is switched and  $c_1 > c_2$ .

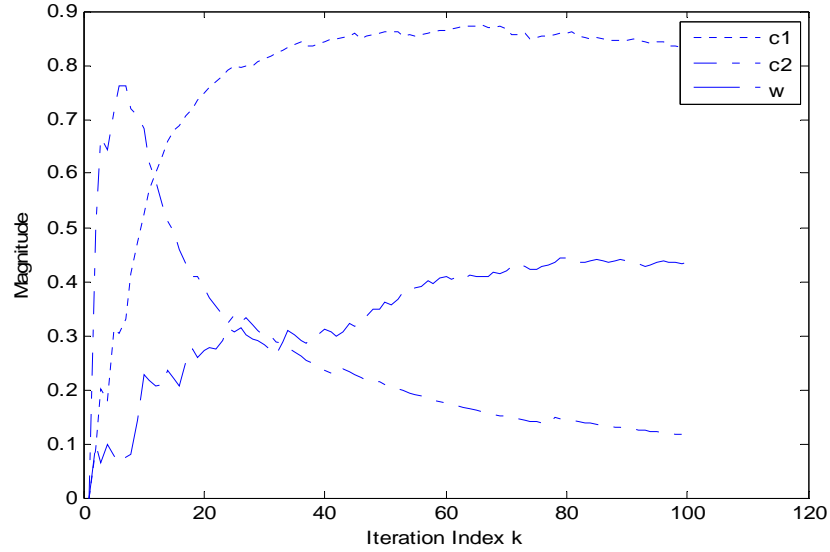


**Figure 1.20:** Plot of the Optimized Influence Coefficients for the Hyperellipsoid Cost Function

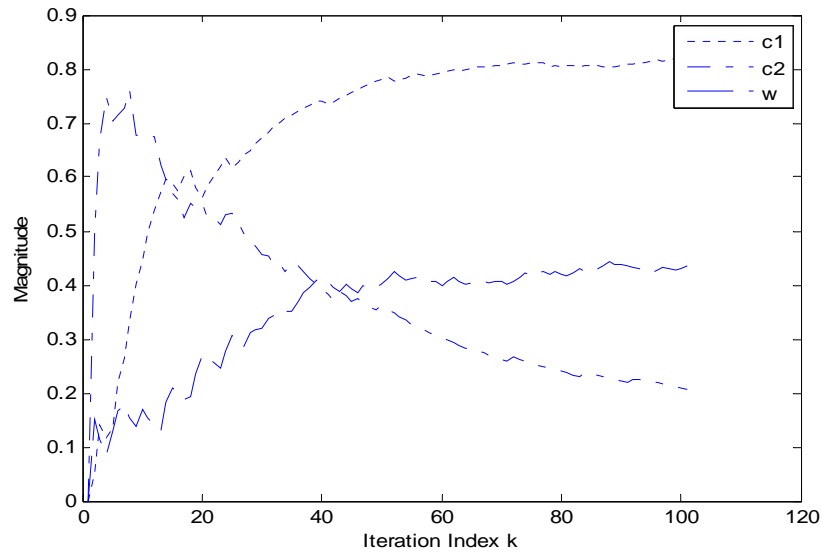


**Figure 1.21:** Plot of the Optimized Influence Coefficients for the Spherical Cost Function

This implies that the particles are no longer are dominated by the global optimum, but rather by their own personal best performance and try to improve their performances. An explanation for this is found by considering the convergence plot, as detailed in Figure 1.22. Here we can see that most of the convergence is achieved after the first few iterations.

Once not much improvement is found, the algorithm tries to spread out and search larger regions rather than concentrating to the area dominated by the current global best solution. This adaptation may explain the cause for the improved performance of the proposed algorithm for unimodal functions compared to standard PSO algorithms.

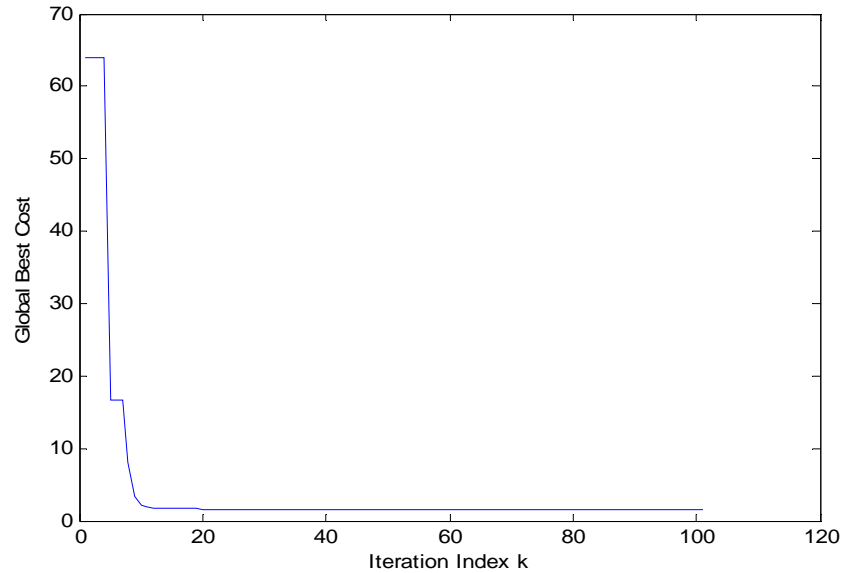


**Figure 1.22:** Plot of the Global Best Cost vs. Iteration Index for the Spherical Cost Function

The algorithm developed here adapts to the underlying cost surface by adjusting the influence coefficients at each step. The proposed algorithm was tested on a series of benchmark problems and showed improved performance for the unimodal cost functions. In addition, the hybrid PSO-TS algorithm was tested on a parameter estimation problem where colored noise influence causes bias estimates when the LS algorithm is used. The simulations indicate an improved estimate when the proposed PSO-TS algorithm was used.

Another area of research focused on the use of spatial filters, applied to an array of sEMG sensors, to look at the distribution of the sEMG signal on the hand near muscles of interest and also develop or modify the currently existing spatial filters to extract useful information from the setup we were using. The objective was to obtain an insight into the ideal placement of the sensor array over the arm. And if a sensor array, in the form of a glove is developed, this research could be expanded to accommodate the desired sensor array density and would also help in computing the spatial filter masks to be applied to the array. The next section provides a detailed description of the spatial filters used, comparison of the seven linear and 4 nonlinear spatial filters to 4 IIR filters, and the optimization of the filter masks to the setup that we are using.

### **1.9 Spatial Filtering:**

"Spatial filtering" is broadly defined as methods, which compute spatial density estimates for events that have been observed at individual locations. This type of filtering describes a set of tools for displaying functions estimated from these data points, which are generally distributed in two-dimensional space. Spatial filtering can also be thought of as a form of data smoothing method, which is designed to give us a clearer view of the general underlying information.

Spatial filtering is a non-parametric analysis method, which belongs within the field of exploratory spatial analysis, which relies, to a large degree, on graphical methods of analysis. Spatial filters are used when there is no a priori curve to fit to a data series. Instead, it relies on nearby or adjacent, values to estimate the value at a given point. These filters take out variability in a data set while retaining the local features of data. By varying the size of the filter, features in the data that vary at different spatial scales can be differentially removed. Spatial filtering is useful as an exploratory technique for identifying areas that are homogeneous or areas that have larger or smaller values than which generally occurs.

Spatial filtering is principally associated with digital image processing. This method may be applied to almost any type of grid/data set or image (which contains the gray scale values or pixel data in the form of a grid). This term can also be used, in a related manner, in the area of spatial statistics. The most commonly

provided functions of spatial filtering are the so-called low-pass and high-pass spatial filters. These are focal functions whose operation is determined by a kernel or neighborhood of  $N \times N$  cells around each pixel or grid position, [34]. Grid cells “covered” by a kernel are multiplied by the matching kernel entry and then the weighted average is calculated and assigned as the value for the central cell,  $G$ . For example, asymmetric  $3 \times 3$  kernel may look like the one shown in (20), or any combination of the weights. Typically  $a, b$  are positive integers. If  $a=b=1$ , then the kernel provides a simple smoothing or averaging operation. The weights in the kernel can be modified for specific cases or data sets. In any case the weighted average is divided by the sum of the elements of the kernel. Filters of this type are sometimes referred to as low-pass filters.

$$\text{Symmetric Kernel} = \begin{bmatrix} a & a & a \\ a & b & a \\ a & a & a \end{bmatrix} \quad (1.21)$$

If the weights in the kernel looks like the one in (1.21) and  $a, b$ , and  $c$  are positive integers.

$$\text{Symmetric Kernel with different weights} = \begin{bmatrix} c & a & c \\ a & b & a \\ c & a & c \end{bmatrix} \quad (1.22)$$

And if the following,  $b > a > c$ , is true then the kernel is described as a Gaussian filter which is symmetric but center-weighted.

The filtered grid value ‘ $G$ ’ of an  $m = N \times N$  kernel matrix, with  $C_i$  set of coefficients and  $P_i$  - set of source grid values, is calculated as;

$$G = \frac{\sum_{i=1}^m C_i P_i}{\sum_{i=1}^m C_i} + B \quad (1.23)$$

Where,  $B$  is often set to 0.  $B$  is a bias term to increase or decrease the resulting value of ‘ $G$ ’

There are many different forms of spatial filters depending on the weights and the symmetry associated with the kernel. This kernel is also sometimes referred to as the ‘*filter mask*’. Some of the other examples are given in Table 1.8.

### **Linear Spatial Filtering:**

Linear spatial filtering modifies an image ‘ $f$ ’ by replacing the value at each pixel with a linear function of the values of nearby pixels (This same analogy can be applied to data set in a grid format; similar to the case of multiple sEMG sensors placed in grid). Moreover, this linear function is assumed to be independent of the pixel's location  $(k, l)$ , where  $(k, l)$  are the indices of the pixels in  $f$ , which is represented by a data matrix. This kind of operation can be expressed as convolution or correlation. For spatial filtering, it's often more intuitive to work with correlation.

The filtered result  $g(k, l)$  is obtained by centering the mask over pixel  $(k, l)$  and multiplying the elements of  $f$  with the overlapping elements of the mask and then adding them up. A special case exists when the special when the center of the mask is on the boundary of  $f$ . The common assumption in this case is that the data matrix is periodic. But this assumption does not always hold true. In such cases the non-existing entries assumed to be zero.

### **Application of Spatial Filters to sEMG data Array:**

Recording and analysis of Surface EMG (sEMG) has been around for almost a century now. Surface electrodes have been routinely used to record the gross electrical activity of skeletal muscles. However, when specific information about individual motor unit discharge rates or recruitment needs to be extracted, sEMG signal have been treated with some reservation. So previously, in most cases, intramuscular EMG



recording using fine wire or needle electrodes were employed to selectively record the single motor unit activity. Invasive recordings of sEMG are inconvenient, do induce pain to the subject and may potentially damage muscle tissues and nerves. In recent years, considerable efforts have been directed towards effectively recording single motor unit activity noninvasively *i.e.* using surface EMG sensors.

The principle underlying this approach is to be increasingly selective in recording the information using surface EMG electrodes. In other words, the objective is to amplify the activity of motor unit/s located closest to the recording site (generally the actual motor location for the particular limb) and reducing the EMG signal generated by other motor units located further away.

**Table 1.8:** Linear Spatial Filters

Filter Type	Filter	Kernel	Description
Low-pass (symmetric)	Averaging	$\begin{bmatrix} a & a & a \\ a & b & a \\ a & a & a \end{bmatrix}, \begin{bmatrix} 0 & a & 0 \\ a & b & a \\ 0 & a & 0 \end{bmatrix}$	Smoothing, Noise Reduction or Blurring Filter (focal mean)
	Gaussian	$\begin{bmatrix} c & a & c \\ a & b & a \\ c & a & c \end{bmatrix}$	Smoothing, Noise Reduction or Blurring Filter (focal weighted mean)
High-pass (symmetric)	Sharpening	$\begin{bmatrix} -a & -a & -a \\ -a & +b & -a \\ -a & -a & -a \end{bmatrix}$ $\begin{bmatrix} 0 & a & 0 \\ -a & b & -a \\ 0 & -a & 0 \end{bmatrix}$	Mean effect removal/sharpening filter (focal sum). Provides limited edge detection. Typically entries sum to 1 but may be greater.
Gradient (asymmetric)	Edge Detection	$\begin{bmatrix} a & b & a \\ 0 & 0 & 0 \\ -a & -b & -a \end{bmatrix}, \begin{bmatrix} -a & 0 & a \\ -b & 0 & b \\ -a & 0 & a \end{bmatrix}$	Kernel highlights vertical and horizontal edges. Typically $a=1$ , and $b=1$ or 2 and entries sum to 0.
	Embossing	$\begin{bmatrix} 0 & +a & +a \\ -a & +a & +a \\ -a & -a & 0 \end{bmatrix}$	Enhance edges in a selected direction to provide embossed effect.
	Directional	$\begin{bmatrix} -1 & 1 & 1 \\ -1 & -2 & 1 \\ -1 & 1 & 1 \end{bmatrix}, \begin{bmatrix} 1 & 1 & 1 \\ 1 & -2 & 1 \\ -1 & -1 & -1 \end{bmatrix}$ $\begin{bmatrix} 1 & 2 & 1 \\ 0 & 0 & 0 \\ -1 & -2 & -1 \end{bmatrix}$	

Many types of linear and nonlinear spatial filters have also been studied in the past [35]. In this section comparison of a few linear and non-linear spatial filters is presented.

Experiments were performed using multiple sEMG sensors in the array configuration as shown in Figure 1.23. Nine different experiments were conducted and the corresponding sEMG was measured simultaneously from all the different sensors. Information regarding the various experiments is given below;

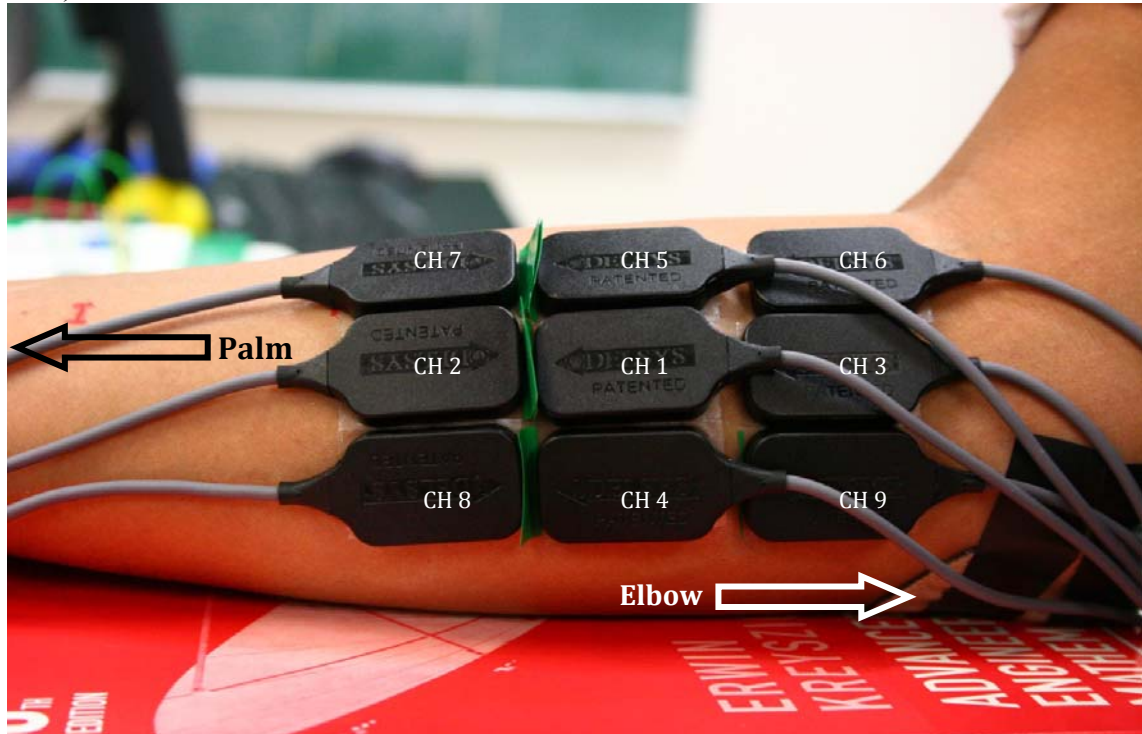


**Figure 1.23:** Experimental Setup – Location of sEMG sensors (3x3 Array)

- Experiment 1 – Baseline – 30 sec – No Motion/ Force – Red Stress ball
- Experiment 2 – Baseline – 30 sec – No Motion/ Force – Red Stress ball
- Experiment 3 – 30 sec – Ring Finger Grasping Motion – Red Stress ball
- Experiment 4 – 30 sec – Ring Finger Grasping Motion – Red Stress ball
- Experiment 5 – 45 sec – Ring Finger Grasping Motion with Thumb Restrained – Red Stress ball
- Experiment 6 – 45 sec – Ring Finger Grasping Motion with Thumb Restrained – Red Stress ball
- Experiment 7 – 45 sec – Ring Finger Grasping Motion with Thumb Restrained – Yellow Stress ball
- Experiment 8 – 45 sec – Ring Finger Grasping Motion with Thumb Restrained – Yellow Stress ball
- Experiment 9 – 60 sec – Ring Finger Grasping Motion with Thumb Restrained – Red Stress ball

The sensors used for measuring the sEMG action potentials were three pronged DE 3.1 differential surface electrodes. The electrodes were placed along the muscle fibers (Flexor Digitorum Superficialis) for recording sEMG. Multiple sEMG sensors in an array configuration were mounted on and around the identified motor unit, as shown in Figure 1.23. The subjects' hand was placed on a flat surface; the reference electrode was placed on the elbow where there is no sEMG signal. Sensor *CH1* was placed on the identified motor unit location. *CH2* and *CH3* were placed along the muscle fiber in front and behind *CH1* respectively. Channels 4-9 were placed in the orientation as shown in Figure 1.23.

Experiments 1 and 2 were conducted to give an insight into the sEMG generated by the subject's hand, in the absence of any motion or force. Also, a thumb restrain was used to limit the influence of thumb while application of force to the stress ball. A Force Sensitive Resistors (FSR) was mounted on the stress ball to record force levels for different grasping force levels.

Figure 1.24 shows the variables associated with the various sEMG locations. Figure 1.25 shows the thumb-restrain in use during various contraction experiments. Figure 1.25 also shows the location of the FSR. Figure 1.26 shows the sEMG data acquisition 16 channel Bagnoli system.

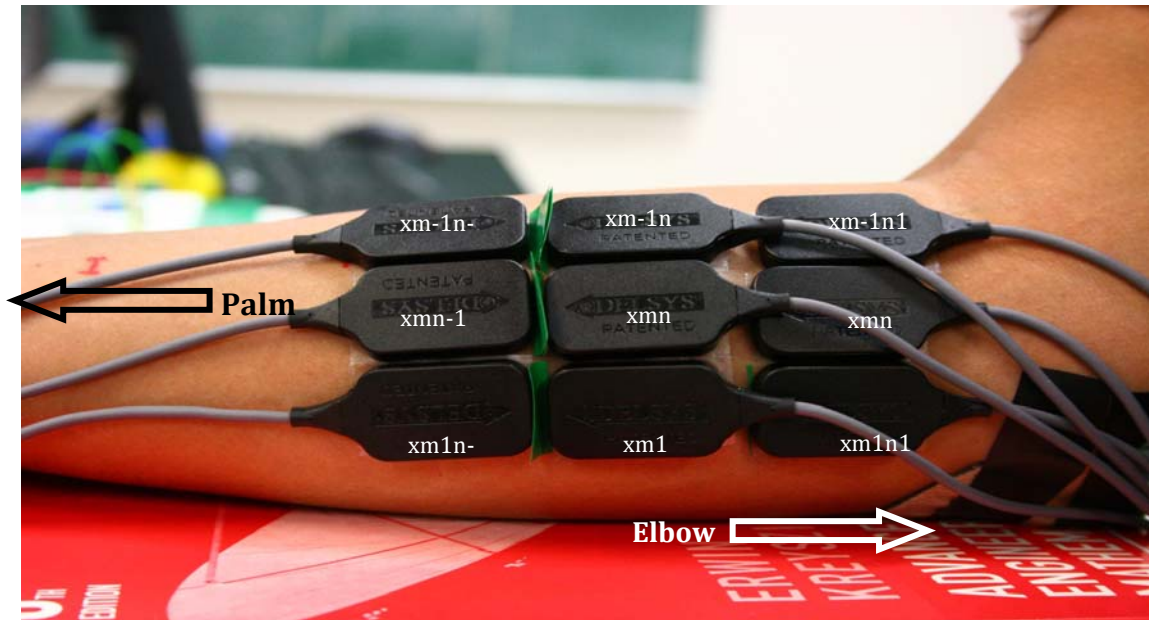


**Figure 1.24:** Experimental Setup – Variables associated with the sEMG channels

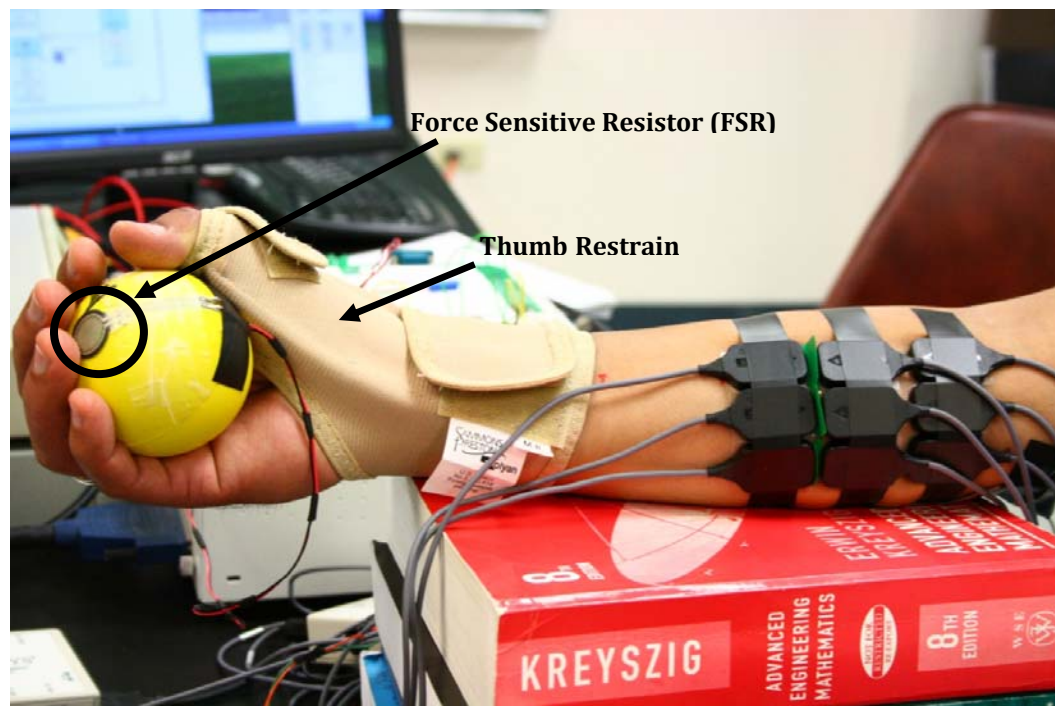


**Figure 1.25:** Experimental Setup – Location of Force Sensitive Resistor (FSR) and Thumb Restrain

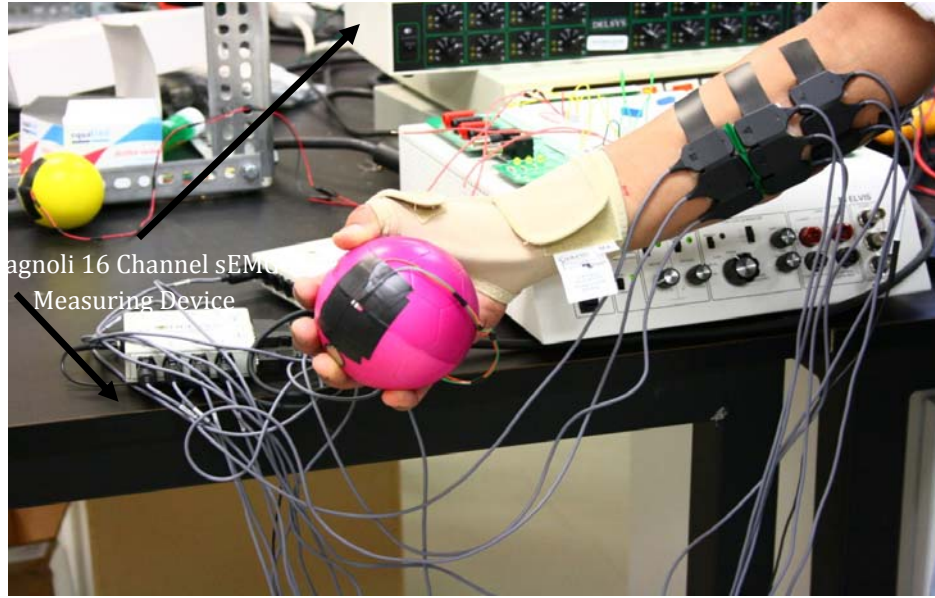


**Figure 1.26:** Experimental Setup – Bagnoli 16 Channel sEMG Measuring Device

The most commonly used Linear Spatial filters for isolating the motor unit action potentials (MUAPs) are;

- 1) Longitudinal Single Differential (LSD)
- 2) Transverse Single Differential (TSD)
- 3) Longitudinal Double Differential (LDD)
- 4) Transverse Double Differential (TDD)
- 5) Normal Double Differential (NDD)
- 6) Inverse Binomial (IB2) and the
- 7) Inverse Rectangular (IR) Filter.

The mask of these filters and the corresponding resultant equations on application of the mask to the grid data obtained from the sEMG array arrangement are given below.

### **CASE 1**

#### **Longitudinal Single Differential (LSD)**

EMG array Information

Spatial Filter Mask

$$\begin{bmatrix} sEMG 7 & sEMG 5 & sEMG 6 \\ 0 & 0 & 0 \\ sEMG 2 & sEMG 1 & sEMG 3 \\ -1 & 1 & 0 \\ sEMG 8 & sEMG 4 & sEMG 9 \\ 0 & 0 & 0 \end{bmatrix}$$

$$\text{Result Equation: } -sEMG 2 + sEMG 1 \quad (1.24)$$

### CASE 2

#### Transverse Single Differential (TSD)

EM G array Information

Spatial Filter Mask

$$\begin{bmatrix} sEMG\ 7 & sEMG\ 5 & sEMG\ 6 \\ 0 & -1 & 0 \\ sEMG\ 2 & sEMG\ 1 & sEMG\ 3 \\ 0 & 1 & 0 \\ sEMG\ 8 & sEMG\ 4 & sEMG\ 9 \\ 0 & 0 & 0 \end{bmatrix}$$

$$\text{Result Equation: } -sEMG\ 5 + sEMG\ 1 \quad (1.25)$$

### CASE 3

#### Longitudinal Double Differential (LDD)

EM G array Information

Spatial Filter Mask

$$\begin{bmatrix} sEMG\ 7 & sEMG\ 5 & sEMG\ 6 \\ 0 & 0 & 0 \\ sEMG\ 2 & sEMG\ 1 & sEMG\ 3 \\ -1 & 2 & -1 \\ sEMG\ 8 & sEMG\ 4 & sEMG\ 9 \\ 0 & 0 & 0 \end{bmatrix}$$

$$\text{Result Equation: } -sEMG\ 2 + 2 * sEMG\ 1 - sEMG\ 3 \quad (1.26)$$

### CASE 4

#### Transverse Double Differential (TDD)

EM G array Information

**Spatial Filter Mask**

$$\begin{bmatrix} sEMG\ 7 & sEMG\ 5 & sEMG\ 6 \\ 0 & -1 & 0 \\ sEMG\ 2 & sEMG\ 1 & sEMG\ 3 \\ 0 & 2 & 0 \\ sEMG\ 8 & sEMG\ 4 & sEMG\ 9 \\ 0 & -1 & 0 \end{bmatrix}$$

$$\text{Result Equation: } -sEMG\ 5 + 2 * sEMG\ 1 - sEMG\ 4 \quad (1.27)$$

#### **CASE 5**

##### **Normal Double Differential (NDD)**

EM G array Information

**Spatial Filter Mask**

$$\begin{bmatrix} sEMG\ 7 & sEMG\ 5 & sEMG\ 6 \\ 0 & -1 & 0 \\ sEMG\ 2 & sEMG\ 1 & sEMG\ 3 \\ -1 & 4 & -1 \\ sEMG\ 8 & sEMG\ 4 & sEMG\ 9 \\ 0 & -1 & 0 \end{bmatrix}$$

Result Equation:

$$-sEMG\ 5 - sEMG\ 2 + 4 * sEMG\ 1 - sEMG\ 3 - sEMG\ 4 \quad (1.28)$$

#### **CASE 6**

##### **Inverse Binomial 2-D (IB2)**



EM G array Information

Spatial Filter Mask

$$\begin{bmatrix} sEMG\ 7 & sEMG\ 5 & sEMG\ 6 \\ -1 & -2 & -1 \\ sEMG\ 2 & sEMG\ 1 & sEMG\ 3 \\ -2 & 12 & -2 \\ sEMG\ 8 & sEMG\ 4 & sEMG\ 9 \\ -1 & -2 & -1 \end{bmatrix}$$

Result Equation:

$$\begin{aligned} & -sEMG\ 7 - 2 * sEMG\ 5 - sEMG\ 6 - 2 * sEMG\ 2 + 12 * sEMG\ 1 \\ & -2 * sEMG\ 3 - sEMG\ 8 - 2 * sEMG\ 4 - sEMG\ 9 \end{aligned} \quad (1.29)$$

#### **CASE 7**

##### **Inverse Rectangle Filter (IR)**

EM G array Information

Spatial Filter Mask

$$\begin{bmatrix} sEMG\ 7 & sEMG\ 5 & sEMG\ 6 \\ -1 & -1 & -1 \\ sEMG\ 2 & sEMG\ 1 & sEMG\ 3 \\ -1 & 8 & -1 \\ sEMG\ 8 & sEMG\ 4 & sEMG\ 9 \\ -1 & -1 & -1 \end{bmatrix}$$

Result Equation:

$$\begin{aligned} & -sEMG\ 7 - sEMG\ 5 - sEMG\ 6 - sEMG\ 2 + 8 * sEMG\ 1 \\ & -sEMG\ 3 - sEMG\ 8 - sEMG\ 4 - sEMG\ 9 \end{aligned} \quad (1.30)$$

#### **Non-Linear Spatial Filtering [35]:**

The Nonlinear Spatial Filters use the Teager-Kaiser Energy (TKE) Operator [36], [37]. This operator is derived from Teager's experiments in 1983. This technique is a threshold 'energy' based approach where outliers are first detected and then replaced by their estimated values. Based on Newton's law of motion, a nonlinear quadratic operator called Teager-Kaiser (TK) operator was first introduced by Teager and Kaiser [36], [37] to measure the real physical energy of a system. This nonlinear operator differs from the common way to calculate the energy of a discrete-time signal as the average sum of its squared magnitudes. The energy of a generating system of a simple oscillation signal was computed as the product of the square of the amplitude and the frequency of the signal. It was found that this nonlinear operator exhibits several

attractive features such as simplicity, efficiency and ability to track instantaneously-varying special patterns. Since its introduction, several applications have been derived for one-dimensional [38], [39], and two dimensional signal processing [40].

Before the Teager-Kaiser operator was introduced, various filtering methods were proposed both linear and nonlinear alternatives. Filtering is often a trade-off between different features, such as performance in Gaussian and non-Gaussian environments, ability to adapt in case of non-stationary signals, edge preservation and computational complexity. Two typical methods were running mean and median filters, which exploit a sliding fixed length window. Mean filters are known to remove the additive Gaussian noise very well, but they tend to soften edges and cannot fully cope with impulsive noise. Median filters on the other hand are nonlinear, which involve sorting of the data, and are able to eliminate impulses at the expense of some streaking and edge jittering [41]. De-noising deals with the same problem of estimating the underlying signal from the noisy observations, but now the data is not needed to process online or is not time-dependent at all. De-noising is not restricted to the methods acting in time domain, the signal is often processed in some transform domain. Wavelet transform has recently gained research interest in several fields of signal processing, using thresholding of (orthogonal) wavelet coefficients and taking the inverse wavelet transform has been proposed to solve de-noising problem.

The nonlinear spatial filters with the TKE operator incorporated are given as follows;

- a) General Form of Nonlinear Spatial Filter using the Teager-Kaiser (TKE) operator

$$\Psi[x(n)] = x^2(n) - x(n+1)x(n-1) \quad (1.31)$$

- b) 1-D Nonlinear Transverse Spatial Filter

$$\Psi_{d,m}[x(m,n)] = x^2(m,n) - x(m-1,n)x(m+1,n) \quad (1.32)$$

- c) 1-D Nonlinear Longitudinal Spatial Filter

$$\Psi_{d,n}[x(m,n)] = x^2(m,n) - x(m,n-1)x(m,n+1) \quad (1.33)$$

- d) Nonlinear Spatial Filter in Two Orthogonal Directions

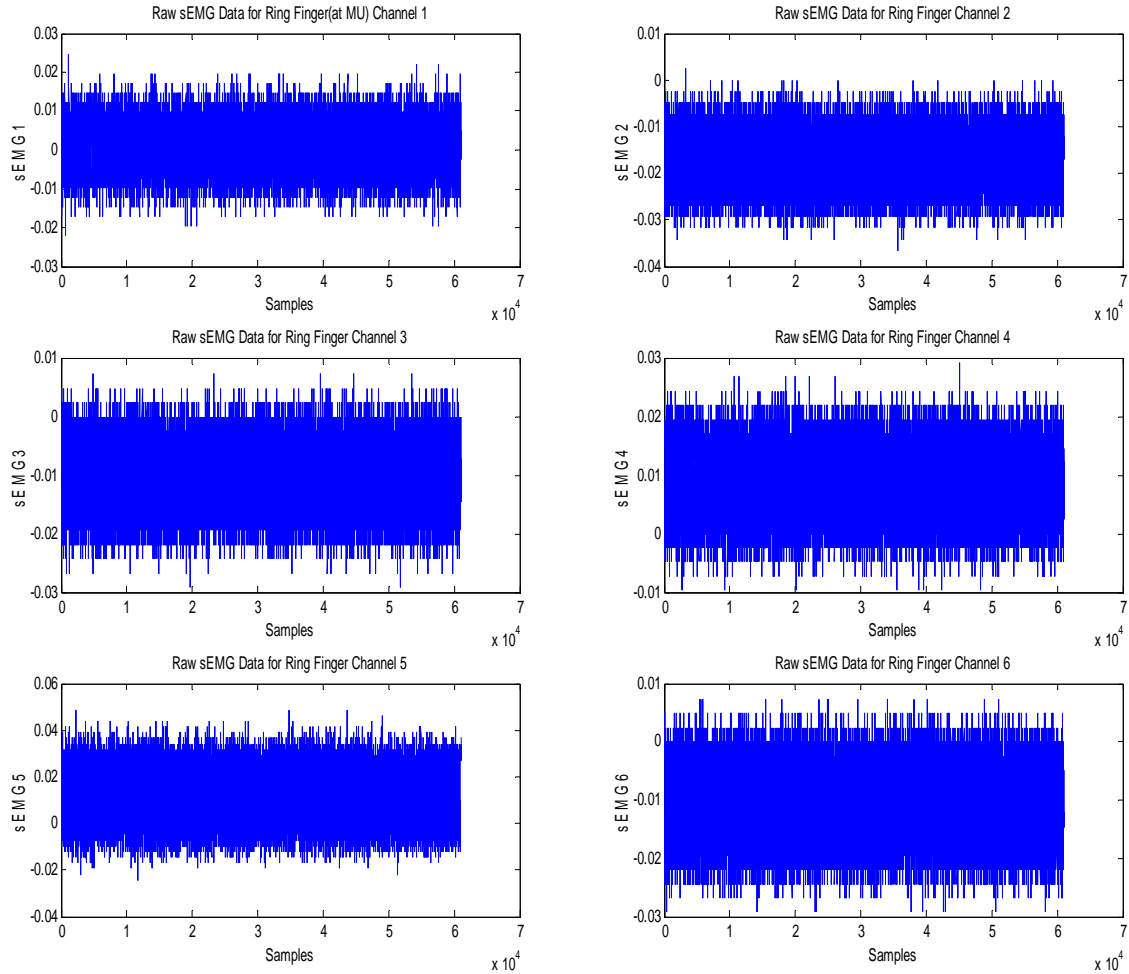
$$\begin{aligned} \Psi_{d,2}[x(m,n)] &= \Psi_{d,2m}[x(m,n)] + \Psi_{d,n}[x(m,n)] \\ &= 2x^2(m,n) - x(m-1,n)x(m+1,n) - x(m,n-1)x(m,n+1) \end{aligned} \quad (1.34)$$

- e) Nonlinear Spatial Filter in all Four Directions

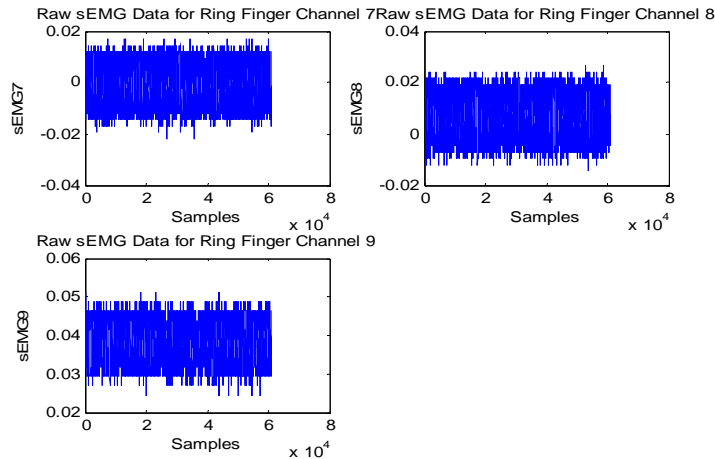
$$\begin{aligned} \Psi_{d,4}[x(m,n)] &= 4x^2(m,n) - x(m-1,n)x(m+1,n) \\ &\quad - x(m,n-1)x(m,n+1) \\ &\quad - x(m-1,n+1)x(m+1,n-1) \\ &\quad - x(m-1,n-1)x(m+1,n+1) \end{aligned} \quad (1.35)$$

Figure 1.27 and 1.28 show the plots of the raw sEMG signal for the experiment without any force being applied.





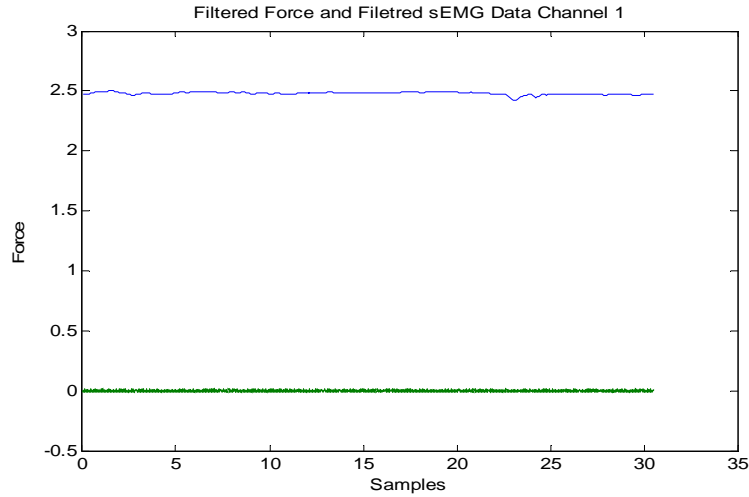
**Figure 1.27:** Raw sEMG Data Plots Channels 1 to 6



**Figure 1.28:** Raw sEMG Data Plots Channels 7 to 9

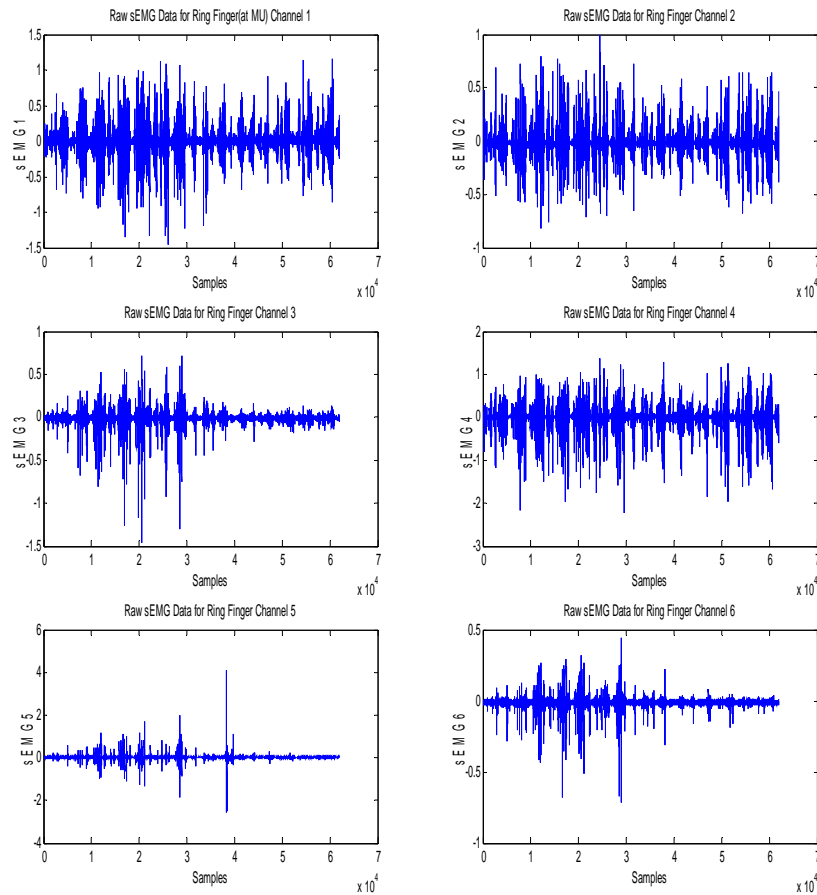
The sEMG data was then filtered using four (4) IIR filters; 1) Bessel 2) Butterworth, 3) Chebyshev Type I and 4) Chebyshev Type II with a pass-band frequency of 60-450 Hz. The force data was also filtered using a 3rd order Low-pass Butterworth filter with cutoff frequency of 10 Hz. The same filtering was carried out for all the experiments conducted. An example plot of the filtered force and sEMG data are

given in Figure 1.29. Figure 1.29 shows the baseline sEMG and force levels generated by the subject where no contractions were performed.

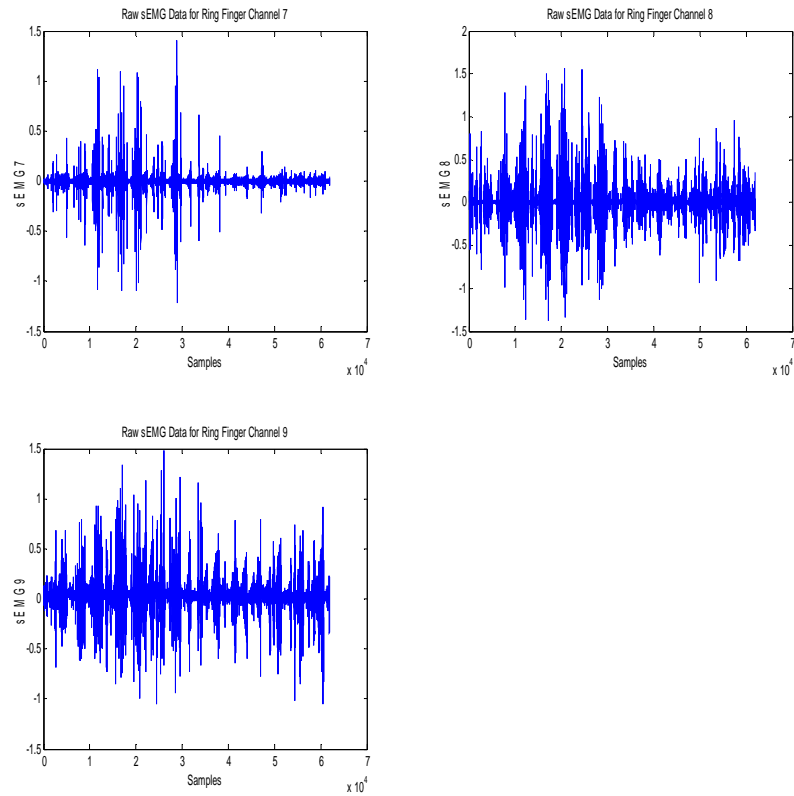


**Figure 1.29:** Filtered sEMG and Force Data – No Force Generated

Figure 1.30 and 1.31 plots the raw sEMG of all the channels (1-9) for another experiment where the subject was performing the action of squeezing the force ball with a force sensor attached to the ball.

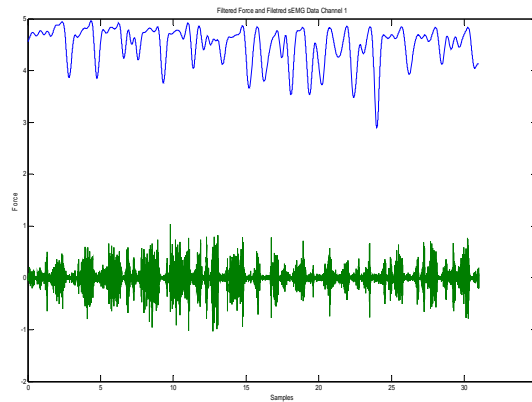


**Figure 1.30:** Raw sEMG Data Plots Channels 1 to 6



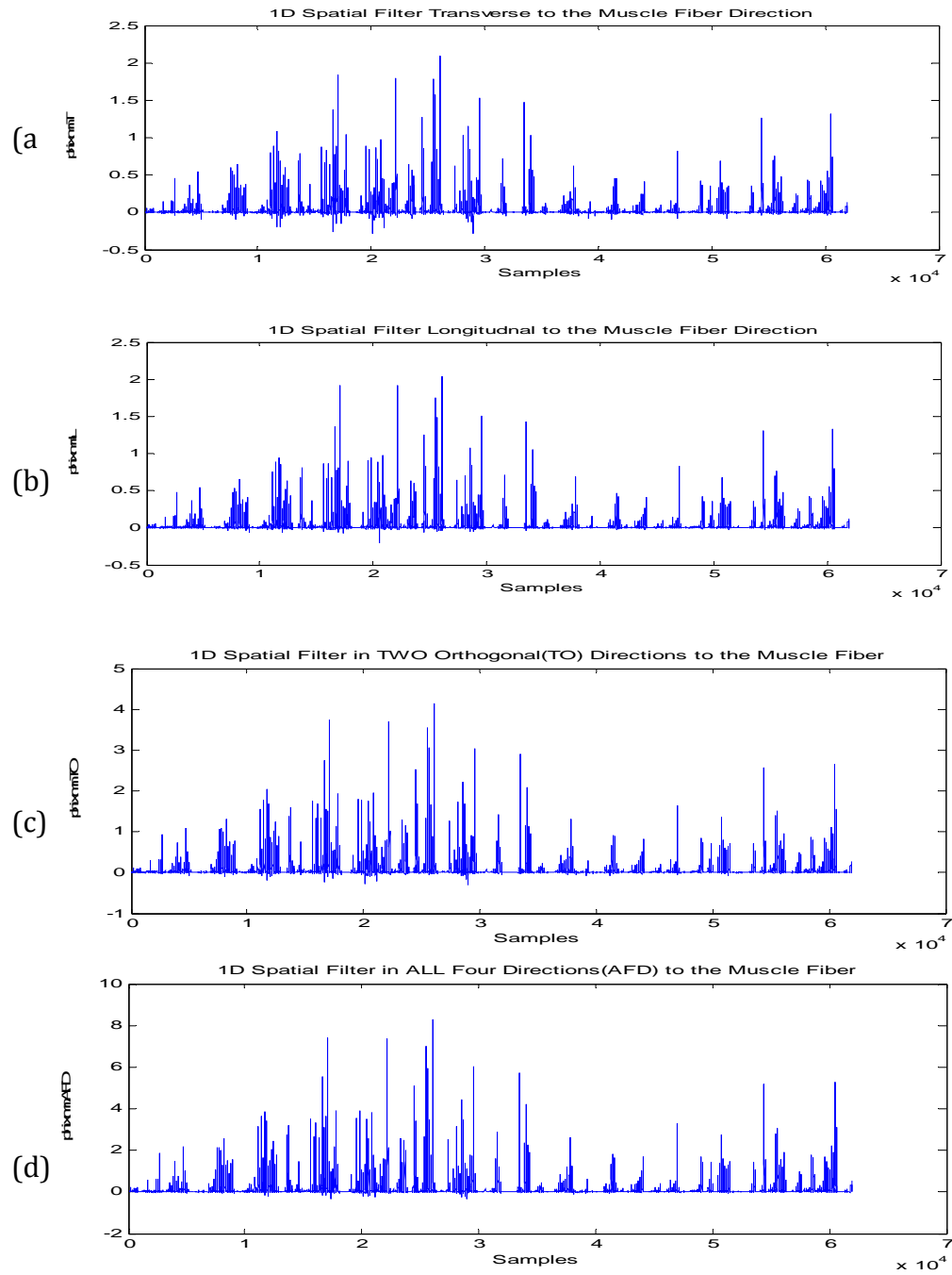
**Figure 1.31:** Raw sEMG Data Plots Channels 7 to 9

Figure 1.32 shows the sEMG and the force signal generated by the subject where the subject performed random variation of force by squeezing the stress ball.



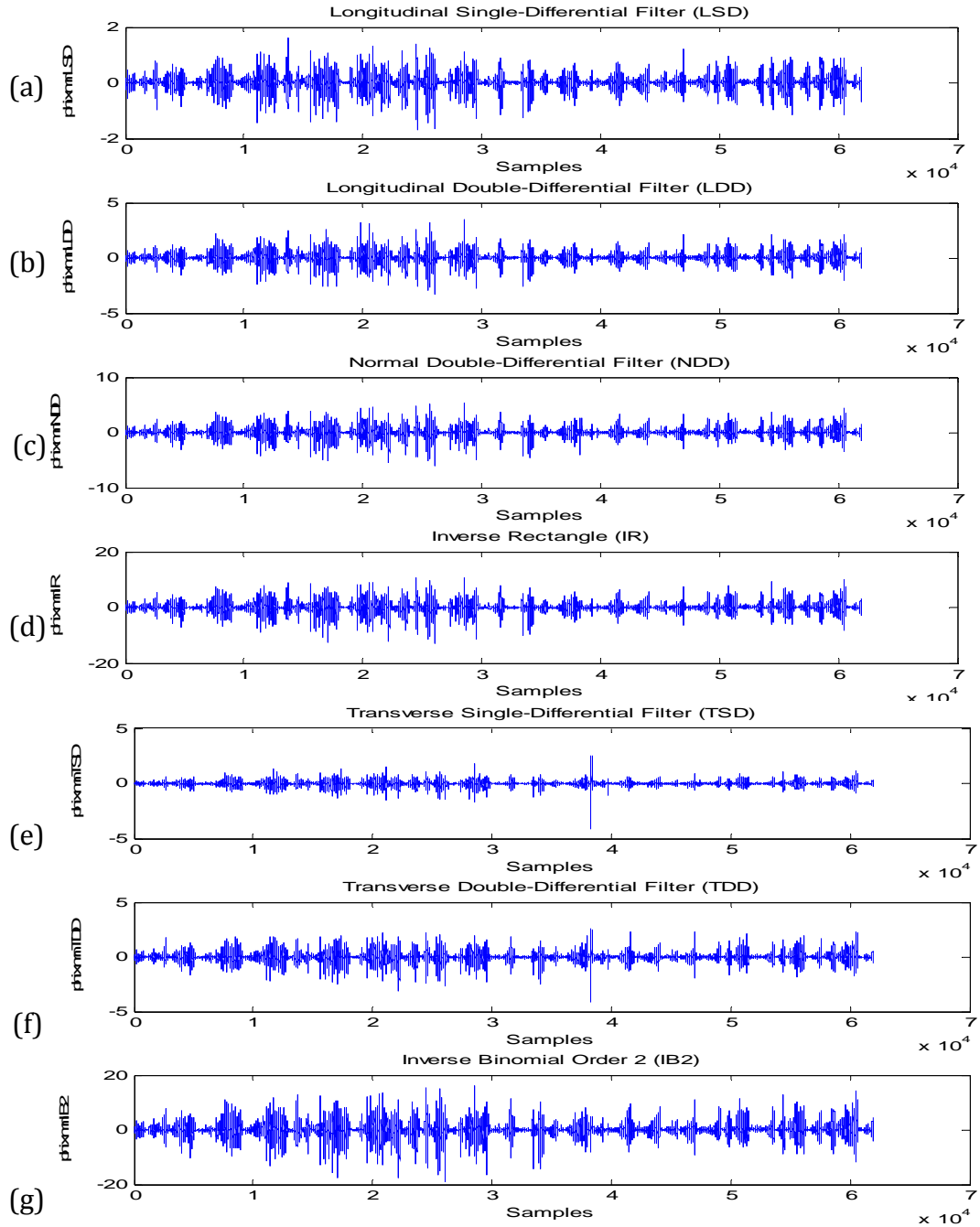
**Figure 1.32:** Filtered sEMG and Force Data (Generated Force Level)

Figure 1.33 a, b, c and d show the results of the Non-linear Spatially Filtered sEMG data for the multi-sensor array setup shown in Figure 1.23.



**Figure 1.33:** Spatially Filtered sEMG a) 1-D Nonlinear Transverse Spatial Filter, b) 1-D Nonlinear Longitudinal Spatial Filter, c) Nonlinear Spatial Filter in Two Orthogonal Directions, d) Nonlinear Spatial Filter in All Four Directions

Figure 1.34 shows the results of the various Linear Spatially Filtered sEMG data for the multi-sensor array setup shown in Figure 1.23.



**Figure 1.34:** Spatially Filtered sEMG a) Longitudinal Single Differential (LSD), b) Longitudinal Double Differential (LDD), c) Normal Double Differential (NDD), d) Inverse Rectangular (IR) Filter, e) Transverse Single Differential (TSD), f) Transverse Double Differential (TDD), g) Inverse Binomial (IB2)

For this analysis too, the time windows used for estimation and validation of the models were ‘ze’ and ‘zv’ respectively. ‘ze’ contained 8000 sample points and ‘zv’ contained data points shifted by 2000 sample points. For example, if ‘ze’ was a time window between 2-6 seconds i.e. samples 4000-12000, then ‘zv’ was between 3-7 seconds i.e. 6000-14000 samples. Thus the Hammerstein-Wiener method uses ‘ze’ to estimate the model structure and based on this information predicts the next 2000 sample points. The data was filtered using the various filters mentioned in the previous sections. Once again the experiments were performed such that the force was varied randomly and the subject was not trying to achieve maximum

voluntary contractions during each cycle. A cycle is defined as the subject starting without any force on the stress ball, squeezing it (to any force level) and then going back to no force. A plot of the variations in force achieved for 6 different experiments is shown in Figure 1.35.

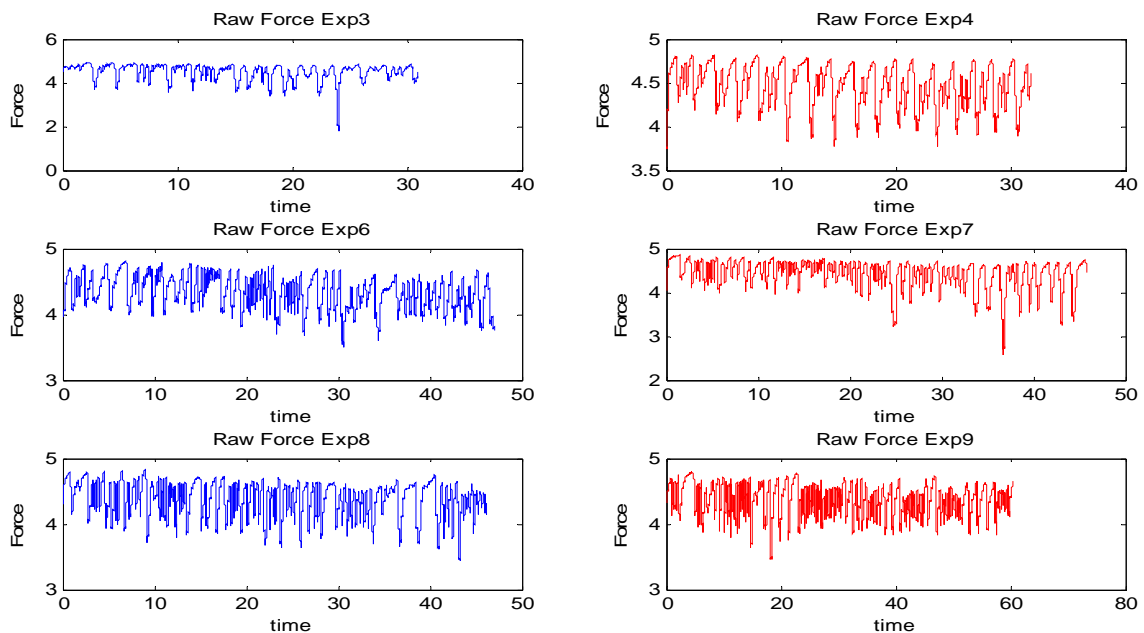


**Figure 1.35:** Variations in Force levels; Experiment 3, 4, 6, 7, 8 & 9

For this analysis too, 42 models with variations in  $n_a$  and  $n_b$  were tested while the value of  $n_k$  was kept as 1. The total number of models estimated were 15 (filter types) x 4 (time windows) x 42 models per time window x 4 experiments = 10,080 models. As an example, for experiment 3, for time window of 2-7 sec, the fit values obtained by varying  $n_a$  between 2-7 and  $n_b$  between 3-9, are shown in Figure 1.36. Figure 1.36 contains a lot of information as it shows 49 models fit percentages for each of the IIR and spatial filter types tested. The large variation in the model fit values can be attributed to the fact that the two data sets have poor correlation between one another. The significant result for this time duration was noted for the Bessel and NLTO filters, these are plotted in Figure 1.37. The predicted model output plots for these values are shown in Figure 1.38

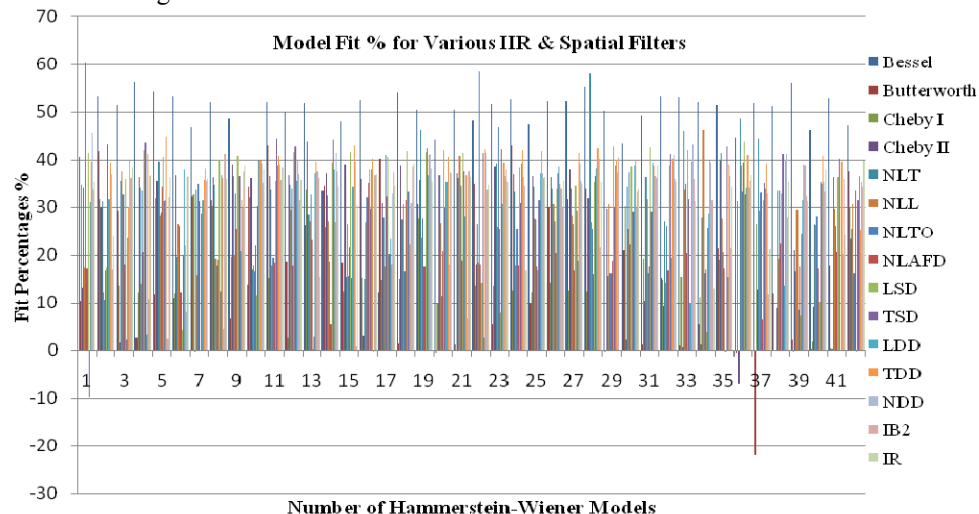


**Figure 1.36:** Fit % for Hammerstein-Wiener Models – Various IIR & Spatial Filters (time window 2-7 sec,

Exp. 3)

### Model vs Fit %

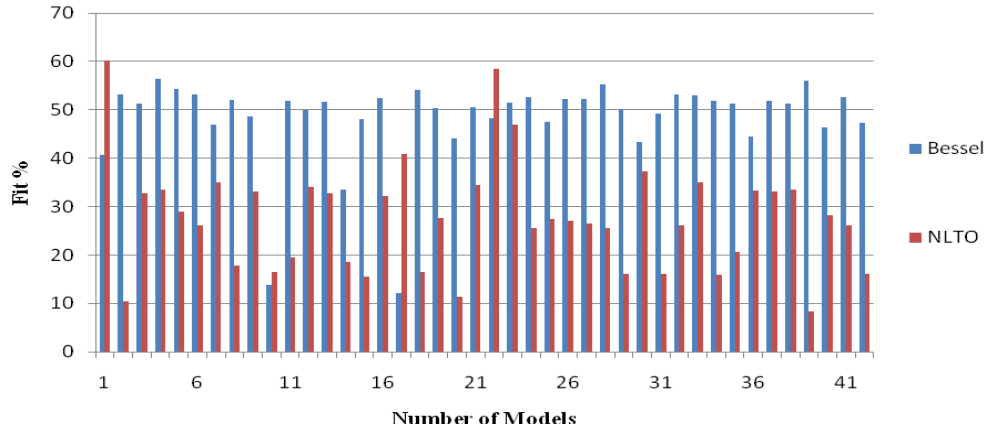


**Figure 1.37:** Fit % for Hammerstein-Wiener Models – Bessel & NLTO (time window 2-7 sec, Exp. 3)

The other filters used also predict the future variations in force but the fit percentages were in the range of 30-48%. A key objective of this analysis is to help develop a control regime, which is not based on threshold values of force can incorporate the dynamics in the force. This would help to control the response of the artificial limb to be closer to that of the actual hand. Similarly we tested various models for the other experiments too. Another set of results which gave very high values of fit was for the later time windows. This case was especially interesting as the subject had fatigued due to the repetitive experiments, but the Hammerstein-Wiener models did successfully capture the variations in the sEMG signal. The Hammerstein-Wiener models performed very well even as the sEMG signal changed and we obtained fit values in the high sixties.

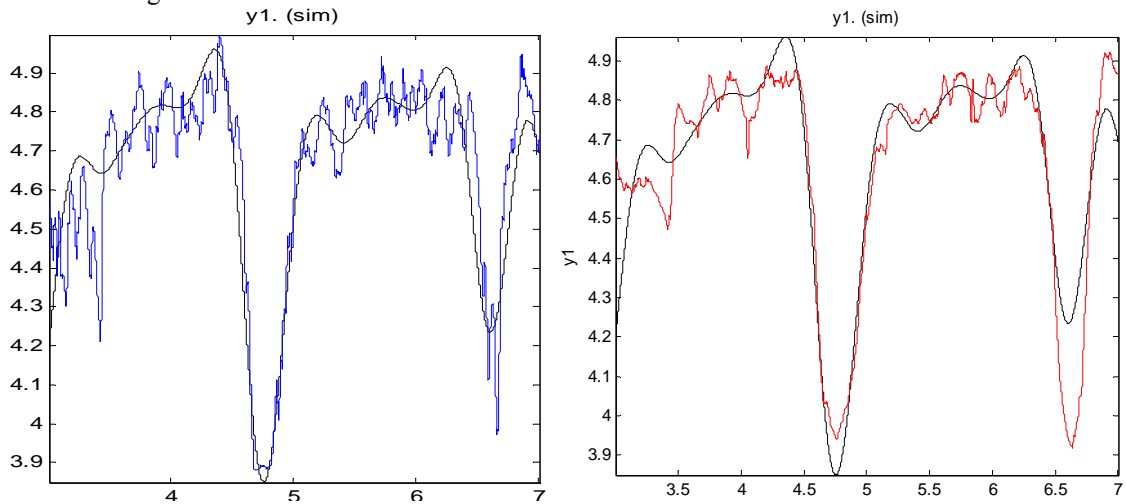


**Figure 1.38:** Measured data (black) a) Bessel (blue) 56.36% and b) NLTO (red) 60.13% for Exp. 3 time window 2-7seconds

Figure 1.39 shows the model fit values obtained for these later data windows. As can be seen from the plots, contrary to our expectations the Hammerstein-Wiener Models performed very well and produced very good fit values.

Figures 1.40, 1.41 and 1.42 show the model output plots for some of the filters mentioned in Figure

1.38. The only IIR filter whose performance matched, and in a few cases exceeded, the performance of the linear and the non-linear spatial filters was the Bessel filter. As can be seen from Figure 1.38 the Bessel filter modeled the sEMG-force relation to 52.85 % though this is a slightly lower value than the Butterworth filter mentioned, the spread of the model fit values was more consistent in the range of 45-50% as compared to the Butterworth filter which had a far more spread out distribution.

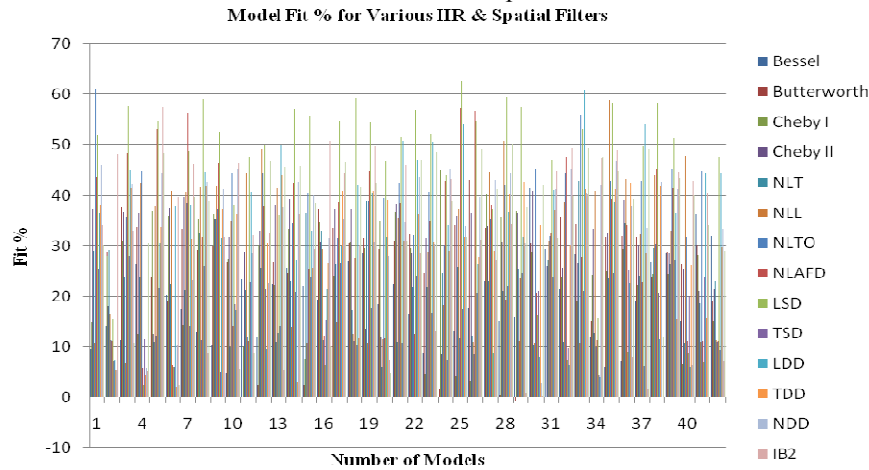


**Figure 1.39** Fit Values Obtained for Different Hammerstein-Wiener Models – Bessel, NLTO NLT, TDD, NDD, NLAFD Filters (time window 20-25 sec, Exp. 5)

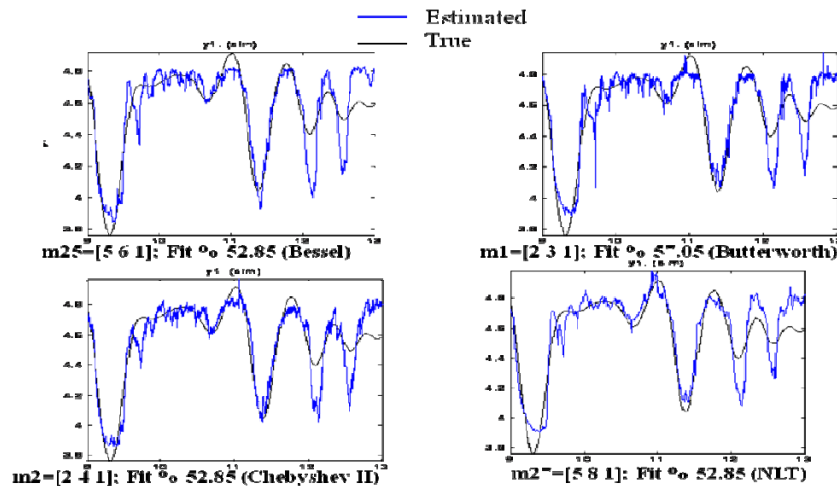


**Figure 1.40** Measured Data (Black) & Estimated Data (Blue)

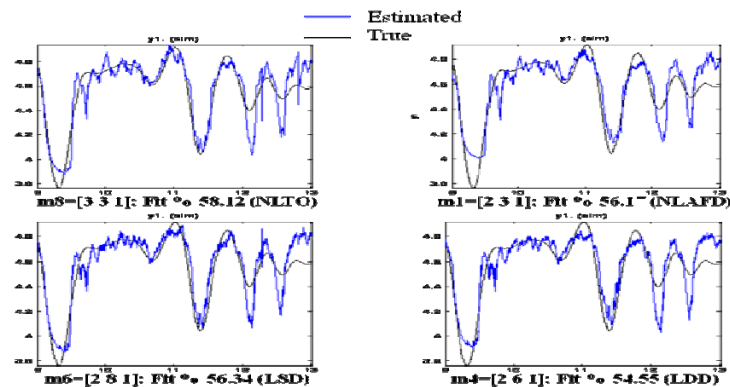


**Figure 1.41:** Measured Data (Black) & Estimated Data (Blue)



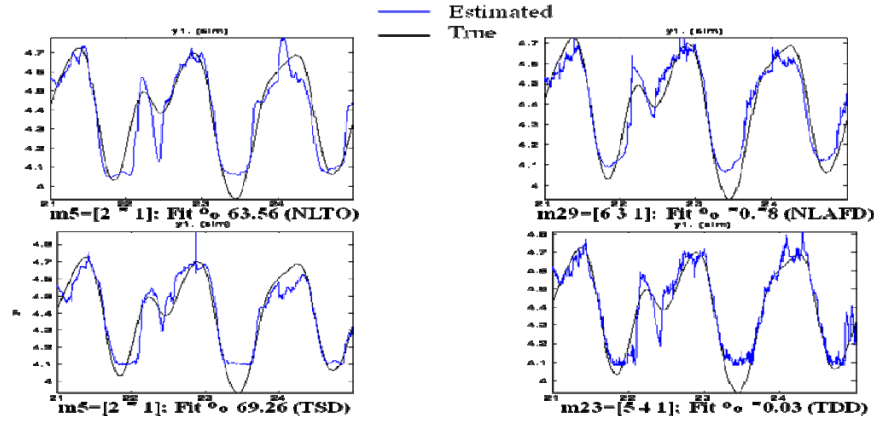


**Figure 1.42:** Measured Data (Black) & Estimated Data (Blue)

The Hammerstein-Wiener models worked very well in capturing the dynamics of the force levels for the various experiments conducted. This method of modeling could help in improving the control over the motors used in prosthetic devices to mimic the actual changes force levels in a real hand. This method also performed very well in the scenarios where the subject did fatigue but the affects were successfully modeled by the Hammerstein-Wiener models. The nonlinear and linear spatial filters (TDD, NDD and NLT, NLTO and NLAFD) did outperform the other filtering methods used especially for the later time windows. The only other filter which had a comparable performance to the spatial filters was the Bessel filter. Further investigation into reducing the wide range of the fit values obtained needs to be performed. One of the possible methods to pursue would be to use Genetic Algorithm to optimize the model parameters and also the number of iterations used for the modeling of sEMG-force levels. One of the possible reasons for poor fit values could also be attributed to the model trying to over-fit the data sets.

In the next section the spatial filter masks available in the literature were compared to the optimized masks for our setup and experiments. Figure 1.43 provides an overview of the entire procedure followed for this analysis. Analysis of the kurtosis improvement of these filters before optimization was also performed.

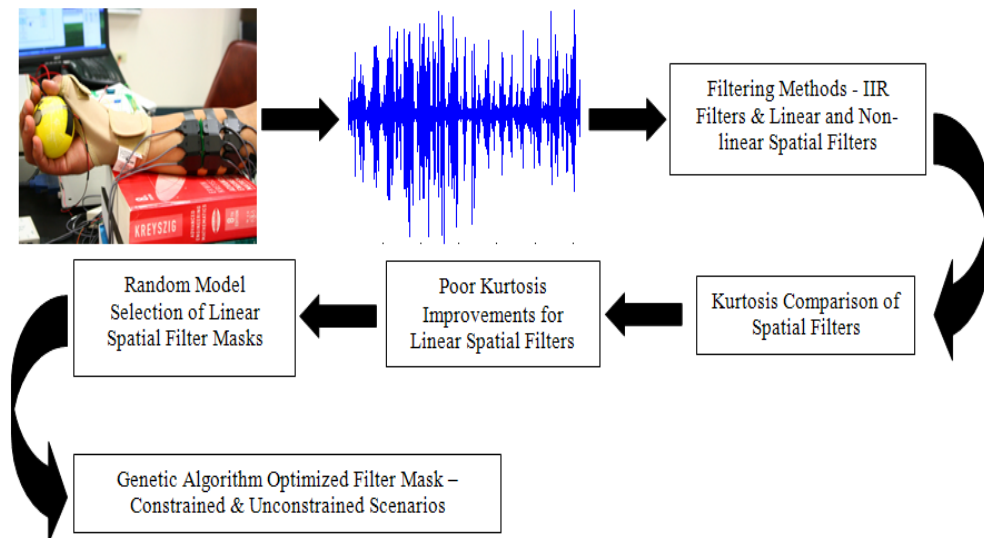


**Figure 1.43:** Overview of the methodology used

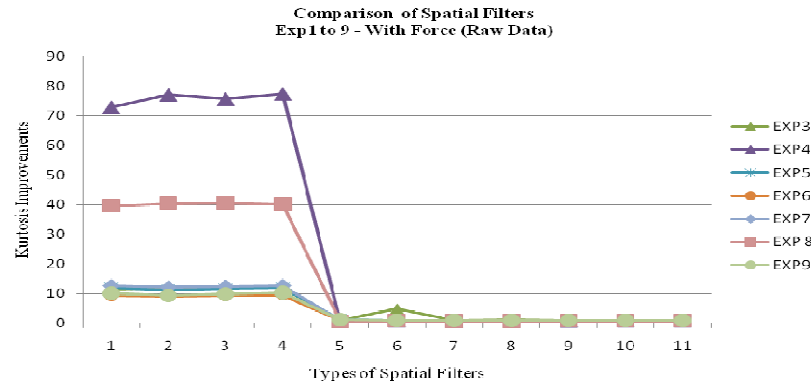
The results of spatially filtered data for the linear and the nonlinear spatial filters were first compared

based on the “*Kurtosis*” criteria, [35 & 36]. ‘*Kurtosis*’ is a measure of whether the data sets are peaked or flat relative to a normal distribution. That is, data sets with high kurtosis tend to have a distinct peak near the mean, decline rather rapidly, and have heavy tails. Data sets with low kurtosis tend to have a flat top near the mean rather than a sharp peak. A uniform distribution would be the extreme case. The mathematical expression for kurtosis is given in Equation 34.

$$Kurt = \frac{E[x^4] - 3(E[x^2])^2}{E[x^2]^2} \quad (1.36)$$

Figure 1.44 shows the plot obtained for the various filters based on the *kurtosis* measure. The y-axis is the *kurtosis improvements* which is the ratio of the *output* to the *input kurtosis*. It is evident from the plot that the NLT, NLL, NLTO and the NLAFD spatial filters performed very well as compared to the linear spatial filters under investigation. The best *kurtosis improvements* were obtained for experiment 4 (approx.)  $\approx 44$  for the nonlinear spatial filters. The x-axis in Figure 1.42 shows the numbers allotted to the various spatial filters investigated.

Based on these results we focused our attention to the linear spatial filter masks for experiment 3, which exhibits poor model fit percentages and also low *kurtosis* values. This section does not investigate the reason for the low *kurtosis* values of the linear spatial filters but only investigates the use of GA to improve the low model fit percentages obtained for experiment 3. The filters were compared based on the model fit values obtained from various Hammerstein-Wiener models.



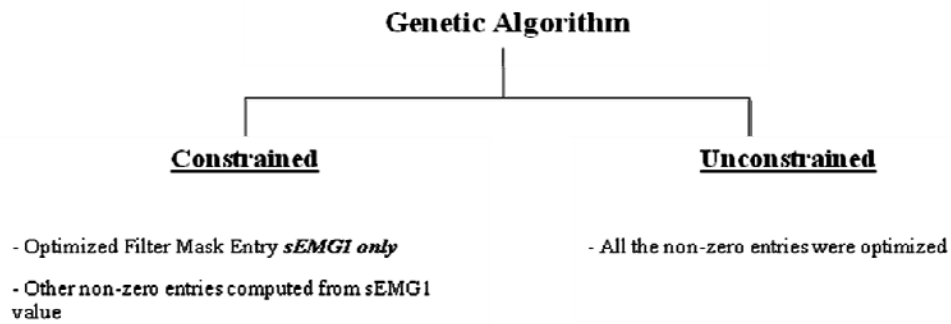
**Figure 1.44:** Kurtosis plots of various filters for exp3 – 9; y-axis numbers are for the various filters tested 1-NLT, 2-NLL, 3-NLTO, 4-NLAFD, 5-LSD, 6-TSD, 7-LDD, 8-TDD, 9-NDD, 10-IB2, and 10- IR

Table 1.9 shows an example of the fits that were obtained on varying the parameters of the Hammerstein-Wiener model. The highlighted models (and a few other models) were selected randomly to be optimized using Genetic Algorithm (GA). We had two scenarios under GA –1) GA Constrained and 2) GA – Unconstrained. The first scenario GA constrained optimized only the mask entry  $a_{22}$  (location of the sEMG sensor on the motor unit). The other entries of the filter mask were then computed from this optimized value. In the second scenario, GA unconstrained we let GA optimize all the entries for various masks. The GA parameters for optimization were as follows: number of iterations: 50; initial population size Generation 0: 96; population size Generation 1: 48; Number of Chromosomes kept for mating: 24; and mutation rate was set to 4%. Figure 1.45 shows the difference between the two GA scenarios.

**Table 1.9:** Example of System Identification Results Using Filter Mask from Literature – Highlighted Models Optimized using GA

Model Number	$n_a$	$n_b$	$n_k$	LDD	LSD	TDD	TSD	ND D	IB2	IR
m1	2	3	1	31.06	41.39	39.53	-9.685	45.5	33.7	35.38

								5	9	
<b>m2</b>	2	4	1	31.86	17.4	39.36	43.19	36.8 4	16.8 8	23.89
<b>m3</b>	2	5	1	23.54	35.94	30.09	2.247	39.7 8	36.1 7	38.16
<b>m4</b>	2	6	1	3.266	41.99	41.28	43.46	10.8 3	36.4 1	36.7
<b>m5</b>	2	7	1	31.58	40.55	44.65	31.28	2.59 3	32.2 6	36.34
<b>m6</b>	2	8	1	37.84	4.259	21.89	20.08	8.03 6	36.2 2	36.57
<b>m7</b>	2	9	1	31.42	-0.188	35.78	28.71	38.1 1	35.5 4	35.82
<b>m8</b>	3	3	1	36.59	40.04	36.17	12.33	4.47 8	41.0 9	35.81
<b>m9</b>	3	4	1	20.74	40.72	31.53	36.57	29.7 6	37.4 3	38.76
<b>m10</b>	3	5	1	39.87	11.53	39.83	30.24	39.2 5	35.1 5	37.9
:	:	:	:	:	:	:	:	:	:	:
:	:	:	:	:	:	:	:	:	:	:
<b>m40</b>	7	7	1	34.91	10.18	40.79	35.21	35.2 4	33.4 2	37.92
<b>m41</b>	7	8	1	- 0.112	36.28	39.68	40.26	20.2 7	35.8 8	24.32
<b>m42</b>	7	9	1	36.55	-0.412	25.24	31.31	35.4	34.2 6	39.82



**Figure 1.45:** Two genetic algorithm scenarios tested

**Table 1.10:** Results of constrained and unconstrained GA of highlighted models from Table 1.9

Longitudinal Double Differential (LDD)			
	Fit %		
	From Literature	GA Constrained	GA Unconstrained
m1	31.06	42.8291	61.3475
m6	37.84	53.3134	63.7240
m12	35.54	44.2513	51.7942
m31	39.44	47.0034	60.6489

Longitudinal Single Differential (LSD)			
	Fit %		
	From Literature	GA Constrained	GA Unconstrained
m1	41.39	48.9135	57.9136
m4	41.99	41.5731	60.2369
m8	40.04	40.5924	46.3310
m9	40.72	45.2322	45.4538

Transverse Double Differential (TDD)			
	Fit %		
	From Literature	GA Constrained	GA Unconstrained
m1	39.53	41.5297	59.8055
m5	44.65	49.4667	68.4191
m10	39.83	41.307	63.8523
m15	43.01	43.3466	56.5113

Transverse Single Differential (TSD)			
	Fit %		
	From Literature	GA Constrained	GA Unconstrained
m2	43.19	44.0017	65.9038
m4	43.46	43.0529	58.2755
m11	44.24	39.7867	44.8431
m31	29.1	43.5787	47.6688

Normal Double Differential (NDD)			
	Fit %		
	From Literature	GA Constrained	GA Unconstrained
m1	45.55	53.1512	57.9496
m3	39.87	47.1084	60.7374
m7	38.11	51.8065	60.5535
m11	39.01	46.881	56.1193

Inverse Binomial 2 (IB2)			
	Fit %		
	From Literature	GA Constrained	GA Unconstrained
m1	33.79	38.6076	58.2365
m3	36.17	38.9074	58.1653
m4	36.41	38.9957	55.5179
m8	41.09	47.2971	55.0537

From the results in Table 1.10 we can see that the optimization of the filter mask using GA worked in almost all the cases chosen. GA without constraints performed significantly better, in most cases, than the filter masks reported in literature and also the mask which we computed using GA, which only optimized the entry ( $a_{22}$ ) i.e. the weight associated with the sEMG signal at the motor unit. This restriction on GA would leave the filter mask symmetrical. But looking at the results of the GA, we can conclude that the filter mask need not always be symmetrical for analysis of sEMG, especially for data recorded using an array. All the filter masks, with the individual entries of the masks that were obtained after optimization along with the respective fit values are provided in Table 1.11.

**Table 1.11:** Optimized filter masks for constrained and unconstrained GA

Linear Spatial Filter Type	Mask in Literature	GA Optimized Spatial Filter Mask - Constrained	GA Optimized Spatial Filter Mask - Unconstrained
<b>LDD m1</b>	$\begin{bmatrix} 0 & 0 & 0 \\ -1 & 2 & -1 \\ 0 & 0 & 0 \end{bmatrix}$ Fit 31.06 %	$\begin{bmatrix} 0 & 0 & 0 \\ -6.5 & 13 & -6.5 \\ 0 & 0 & 0 \end{bmatrix}$ Fit 42.8912 %	$\begin{bmatrix} 0 & 0 & 0 \\ -64.2686 & 23.5033 & -20.8633 \\ 0 & 0 & 0 \end{bmatrix}$ Fit 61.3475 %

<b>LSD m4</b>	$\begin{bmatrix} 0 & 0 & 0 \\ -1 & 1 & 0 \\ 0 & 0 & 0 \end{bmatrix}$ Fit <b>41.99</b> %	$\begin{bmatrix} 0 & 0 & 0 \\ -2 & 2 & 0 \\ 0 & 0 & 0 \end{bmatrix}$ Fit 41.5731%	$\begin{bmatrix} 0 & 0 & 0 \\ -52.7866 & 54 & 0 \\ 0 & 0 & 0 \end{bmatrix}$ Fit <b>60.2369</b> %
<b>TDD m5</b>	$\begin{bmatrix} 0 & -1 & 0 \\ 0 & 2 & 0 \\ 0 & -1 & 0 \end{bmatrix}$ Fit <b>44.65</b> %	$\begin{bmatrix} 0 & -27 & 0 \\ 0 & 54 & 0 \\ 0 & -27 & 0 \end{bmatrix}$ Fit <b>49.4667</b> %	$\begin{bmatrix} 0 & -41.5561 & 0 \\ 0 & 54.7329 & 0 \\ 0 & -22 & 0 \end{bmatrix}$ Fit <b>68.4191</b> %
<b>TSD m2</b>	$\begin{bmatrix} 0 & -1 & 0 \\ 0 & 1 & 0 \\ 0 & 0 & 0 \end{bmatrix}$ Fit <b>43.19</b> %	$\begin{bmatrix} 0 & -28.5 & 0 \\ 0 & 57 & 0 \\ 0 & 0 & 0 \end{bmatrix}$ Fit <b>44.0017</b> %	$\begin{bmatrix} 0 & -74 & 0 \\ 0 & 89.6214 & 0 \\ 0 & 0 & 0 \end{bmatrix}$ Fit <b>65.9038</b> %
<b>NDD m3</b>	$\begin{bmatrix} 0 & -1 & 0 \\ -1 & 4 & -1 \\ 0 & -1 & 0 \end{bmatrix}$ Fit <b>39.87</b> %	$\begin{bmatrix} 0 & -6.75 & 0 \\ -6.75 & 27 & -6.75 \\ 0 & -6.75 & 0 \end{bmatrix}$ Fit <b>47.1084</b> %	$\begin{bmatrix} 0 & -11.5790 & 0 \\ -46.7773 & 36.9276 & -11.8061 \\ 0 & -70.0491 & 0 \end{bmatrix}$ Fit <b>60.7374</b> %
<b>IB2 m1</b>	$\begin{bmatrix} -1 & -2 & -1 \\ -2 & 12 & -2 \\ -1 & -2 & -1 \end{bmatrix}$ Fit <b>33.79</b> %	$\begin{bmatrix} -0.42 & -0.83 & -0.42 \\ -0.83 & 5 & -0.83 \\ -0.42 & -0.83 & -0.42 \end{bmatrix}$ Fit <b>38.6076</b> %	$\begin{bmatrix} -9.3405 & -85.0222 & -53.7102 \\ -95.4633 & 42 & -30.7811 \\ -28.6087 & -8.2511 & -10.0189 \end{bmatrix}$ Fit <b>58.2365</b> %

The linear spatial filter masks as reported in the literature have poor model fit percentages and poor kurtosis improvements. The linear spatial filter masks were optimized using GA and compared them based on the model fit values achieved. The selected model structure for characterizing the sEMG and finger force data is a Hammerstein-Wiener model. The fit values did improve significantly in the two GA scenarios – GA with and without constraints. The GA without constraints performed better than the GA with constraints, which brings into focus the possibility that the sEMG signal distribution over the entire grid cannot be assumed to be symmetrically distributed and that the weights associated with the sEMG signal at various locations need to be modified depending on probably the subject and also based on the experimental design. This is in contrast to the reported filter mask in the literature, which are all symmetric. Almost all the filter masks optimized resulted in a significant improvement over the masks reported in literature.

#### 1.10 Zone Classification of Amputation [42]

This section emphasizes the need for classification of amputation. The smart prosthetic hand being developed would use the sEMG signals as a control signal to compute the necessary force and joint angles. In order to extract suitable sEMG signals for the corresponding finger force and joint angles, we initially conducted experiments in which external stimulation was used to identify motor points. These experiments helped us understand, with a fairly high degree of accuracy, the ideal location on the hand where the sEMG sensors could be placed. These experiments were carried out on individuals without amputations. But with individuals with amputations we would need an alternate method to identify the useful locations, depending on the degree of amputation. In order to ascertain the ideal locations on a residual limb we set out to map the major muscles in both the flexor and extensor compartments of the forearm, which control the hand motion and could be targeted for sEMG monitoring.

Residual limb length classification in patients with upper extremity amputations is important to identify the useful part of the remaining skeletal muscle groups for definitive prosthetic control in both body powered and myoelectric prosthesis. Approximately 30-50% of the individuals with upper extremity amputations are non-compliant in the use of their prosthesis secondary to control issues. The purpose of the study undertaken was to determine a length multiplier that can be used to facilitate decision making about what type of myoelectric prosthesis to prescribe for a given upper extremity (trans-radial) amputation residuum length.

Three female and five male cadaver arms (16 arms) were used in this study. The mean height of the specimens was 171.175 cm ( $\pm 9.114$ ).

Eight cadavers were dissected to expose the muscles of both upper extremities and shoulder girdles. Length measurements were obtained using digital Vernier® calipers as shown in Figure 1.46. Muscle belly length measurements were obtained from six wrist and hand flexor muscles, ten wrist and

hand extensor muscles and six arm muscles. Muscle belly lengths from the 16 forearm muscles were averaged into a single combined muscle belly length for each subject, which was then divided by the subject's arm length to yield a single forearm muscle belly:humerus ratio for each subject. A second ratio was similarly calculated using the arm muscle belly length and the arm length. Means and standard deviations for both ratios and for arm length and muscle belly length for all specimens were determined. A coefficient of variation was calculated to assess inter-subject variability for the ratios.

The calculated mean forearm muscle belly: humerus ratio was  $.636 \pm .053$ , while the arm muscle belly ratio was  $.505 \pm .041$ . Table 1.12 shows results of measurements from AC joint to humeral condyles. Table 1.13 shows data from all MTJ measurements of forearm muscles. Figure 1.47 indicates Zone 1 and 2 delineations.

The coefficients of variation in measurements ranged from 7.87 - 10.35%. Analysis of the measurements taken by the three researchers produced a Pearson product-moment inter-tester correlation of  $r = .866$ .



**Figure 1.46:** Example of measurement taken of Extensor carpi ulnaris in the extensor compartment of the forearm [42]

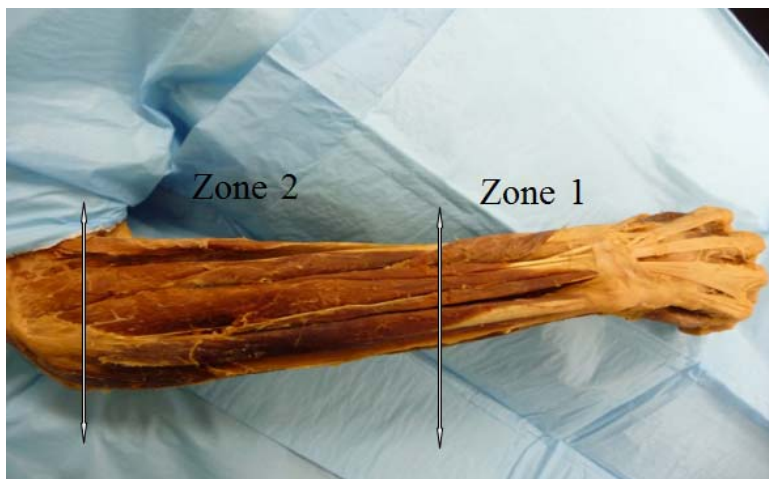


**Figure 1.47:** Zone delineations on a specimen using calculated ratios [42]

**Table 1.12:** Measurement of Acromioclavicular joint to medial and lateral epicondyles [42]

	Mean	SD
<b>Medial Condyle</b>	31.780 cm	2.118 cm
<b>Lateral Epicondyle</b>	32.638 cm	2.205 cm
<b>Combined</b>	32.209 cm	2.165 cm

**Table 1.13:** Muscle mean measurements of Forearm and Upper Arm Muscles [42]

	Mean	SD
<b>Extensor Grouping</b>		
Brachioradialis	17.873	3.221
Extensor carpi radialis longus	18.477	2.650
Extensor carpi radialis brevis	15.683	2.205
Extensor digitorum	18.306	2.598
Extensor digitorum minimi	16.776	2.705
Extensor carpi ulnaris	17.820	2.854
Anconeus	6.960	1.872
Supinator	6.856	1.598
Abductor policis longus	15.545	2.111
Extensor policis longus	13.820	1.896
Extensor policis brevis	7.631	1.601
<b>Flexor Grouping</b>		
Pronator teres	15.040	1.705
Flexor carpi radialis	17.942	3.050
Flexor carpi ulnaris	21.030	3.339
Flexor digitorum superficialis	20.726	3.201
Flexor digitorum profundus	18.308	1.211
Flexor policis longus	15.438	2.063
<b>Upper Arm</b>		
Biceps brachii long head	25.821	2.603
Biceps brachii short head	23.832	3.126
Brachialis	24.765	2.652
Deltoid	16.272	2.212
Triceps long head	22.578	3.226
Triceps short head	16.671	2.176

Multiplying the forearm muscle belly length:humerus length ratio by the patient's humerus length after a forearm amputation will yield a reference length against which a decision about the type of myoelectric prosthesis can be determined. The low coefficient of variation values derived in this study suggests the ratio can be safely applied in clinical situations as a convenient multiplier to determine reference lengths for most cases. We identified two length 'zones' to help focus the decision. Zone 1 includes any residuum length that is longer than the reference and Zone 2 includes any length shorter than the reference length. If an amputation results in a residuum in Zone 1, forearm muscle bellies have been spared and a prosthesis that employs sEMG signals from forearm musculature to operate the prosthesis can be prescribed.

This study was used as the basis for analysis of the sEMG signal obtained from the two zones that were identified. Fifteen healthy subjects: 14 male and 1 female were tested for sEMG obtained for various motions and force levels from the two zones. Figure 1.48 shows the experimental setup for the experiments conducted. The experiments were carried out on the Noraxon Myosystem. As shown in Figure 1.48 we have 3 pairs of sensors in each zone. For this analysis, we did not perform any identification of the ideal motor point by using the external stimulator, but referring to published anatomical drawings of known sEMG sites [43], we arbitrarily placed the sEMG sensors on the most favorable location on the subjects' hand. The placement of the sensors also incorporates the findings from the zone classification study presented earlier in this section. A series of experiments were conducted and model fit values were estimated to compare the sEMG signals from the two zones.

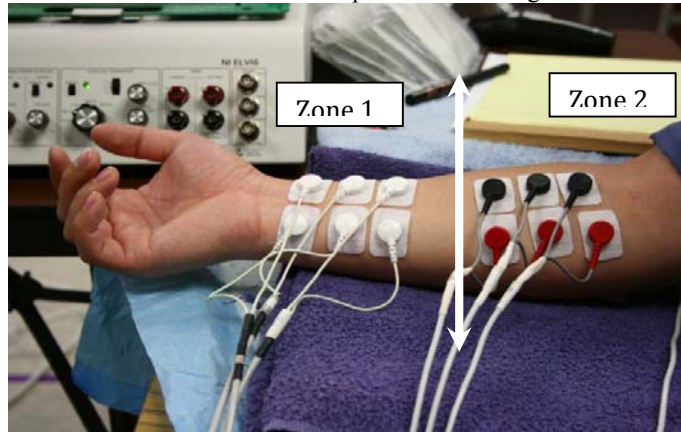


**Figure 1.48:** Experimental Setup for Zone Classification

**Table 1.14** (a) & (b) provide a list of experiments that were conducted on 15 subjects, 14 male and 1 female

(a)

(2)

Zone 1		<u>Motion</u>		
		Devices for Angle Measurement	Data Glove (DG)	
			Finger Device (FD)	
		Experiments to be performed with Stress Balls – two types of Balls/FSR's		
		Planned Experiments		
		Description		Duration
	Exp. 1	Random motion with DG w/stress ball 1 (fast)		30-45 sec
	Exp. 2	Random motion with FD w/stress ball 1		30-45 sec
	Exp. 3	Cyclic motion with FD w/stress ball 1		30-45 sec
	Exp. 4	Cyclic Motion with DG only w/stress ball 1 (slow)		30-45 sec
Exp. 5	Constant Force Level with DG w/stress ball 1		>30 sec	
Exp. 6	Random motion with DG w/stress ball 2		30-45 sec	



		<b>(fast)</b>		
	<b>Exp. 7</b>	Random motion with <b>FD</b> w/stress <b>ball 2</b>		30-45 sec
	<b>Exp. 8</b>	Cyclic motion with <b>FD</b> w/stress <b>ball 2</b>		30-45 sec
	<b>Exp. 9</b>	Cyclic Motion with <b>DG</b> only w/stress <b>ball 2 (slow)</b>		30-45 sec
	<b>Exp. 10</b>	Constant Force Level with <b>DG</b> w/stress <b>ball 2</b>		>30 sec
<b>Zone 2</b>		<b>Description</b>		<b>Duration</b>
	<b>Exp. 1</b>	Random motion with <b>DG</b> w/stress <b>ball 1(fast)</b>		30-45 sec
	<b>Exp. 2</b>	Random motion with <b>FD</b> w/stress <b>ball 1</b>		30-45 sec
	<b>Exp. 3</b>	Cyclic motion with <b>FD</b> w/stress <b>ball 1</b>		30-45 sec
	<b>Exp. 4</b>	Cyclic Motion with <b>DG</b> only w/stress <b>ball 1 (slow)</b>		30-45 sec
	<b>Exp. 5</b>	Constant Force Level with <b>DG</b> w/stress <b>ball 1</b>		>30 sec
	<b>Exp. 6</b>	Random motion with <b>DG</b> w/stress <b>ball 2(fast)</b>		30-45 sec
	<b>Exp. 7</b>	Random motion with <b>FD</b> w/stress <b>ball 2</b>		30-45 sec
	<b>Exp. 8</b>	Cyclic motion with <b>FD</b> w/stress <b>ball 2</b>		30-45 sec
	<b>Exp. 9</b>	Cyclic Motion with <b>DG</b> only w/stress <b>ball 2 (slow)</b>		30-45 sec
	<b>Exp. 10</b>	Constant Force Level with <b>DG</b> w/stress <b>ball 2</b>		>30 sec

(b)

Zone 1				
		Devices for Angle Measurement	Data Glove (DG)	
			Finger Device (FD)	
		Experiments to be performed with Stress Balls – two types of FSR's		
		Planned Experiments		
		Description		Duration

	<b>Exp. 1</b>	Random motion with <b>DG</b> w/stress <b>ball 1 (fast)</b>		30-45 sec
	<b>Exp. 2</b>	Random motion with <b>FD</b> w/stress <b>ball 1</b>		30-45 sec
	<b>Exp. 3</b>	Cyclic motion with <b>FD</b> w/stress <b>ball 1</b>		30-45 sec
	<b>Exp. 4</b>	Cyclic Motion with <b>DG</b> only w/stress <b>ball 1 (slow)</b>		30-45 sec
	<b>Exp. 5</b>	Constant Force Level with <b>DG</b> w/stress <b>ball 1</b>		>30 sec
	<b>Exp. 6</b>	Random motion with <b>DG</b> w/stress <b>ball 2 (fast)</b>		30-45 sec
	<b>Exp. 7</b>	Random motion with <b>FD</b> w/stress <b>ball 2</b>		30-45 sec
	<b>Exp. 8</b>	Cyclic motion with <b>FD</b> w/stress <b>ball 2</b>		30-45 sec
	<b>Exp. 9</b>	Cyclic Motion with <b>DG</b> only w/stress <b>ball 2 (slow)</b>		30-45 sec
	<b>Exp. 10</b>	Constant Force Level with <b>DG</b> w/stress <b>ball 2</b>		>30 sec
<b>Zone 2</b>				
	<b>Exp. 1</b>	Random motion with <b>DG</b> w/stress <b>ball 1(fast)</b>		30-45 sec
	<b>Exp. 2</b>	Random motion with <b>FD</b> w/stress <b>ball 1</b>		30-45 sec
	<b>Exp. 3</b>	Cyclic motion with <b>FD</b> w/stress <b>ball 1</b>		30-45 sec
	<b>Exp. 4</b>	Cyclic Motion with <b>DG</b> only w/stress <b>ball 1 (slow)</b>		30-45 sec
	<b>Exp. 5</b>	Constant Force Level with <b>DG</b> w/stress <b>ball 1</b>		>30 sec
	<b>Exp. 6</b>	Random motion with <b>DG</b> w/stress <b>ball 2 (fast)</b>		30-45 sec
	<b>Exp. 7</b>	Random motion with <b>FD</b> w/stress <b>ball 2</b>		30-45 sec
	<b>Exp. 8</b>	Cyclic motion with <b>FD</b> w/stress <b>ball 2</b>		30-45 sec
	<b>Exp. 9</b>	Cyclic Motion with <b>DG</b> only w/stress <b>ball 2(slow)</b>		30-45 sec
	<b>Exp. 10</b>	Constant Force Level with <b>DG</b> w/stress <b>ball 2</b>		>30 sec

The results presented here include data analysis of 4 subjects was performed, for the two zones and 4 different filter types were used. The data analysis also included modeling for static force measurements and comparison of the two zones. An excerpt of the results obtained is presented in the following section.

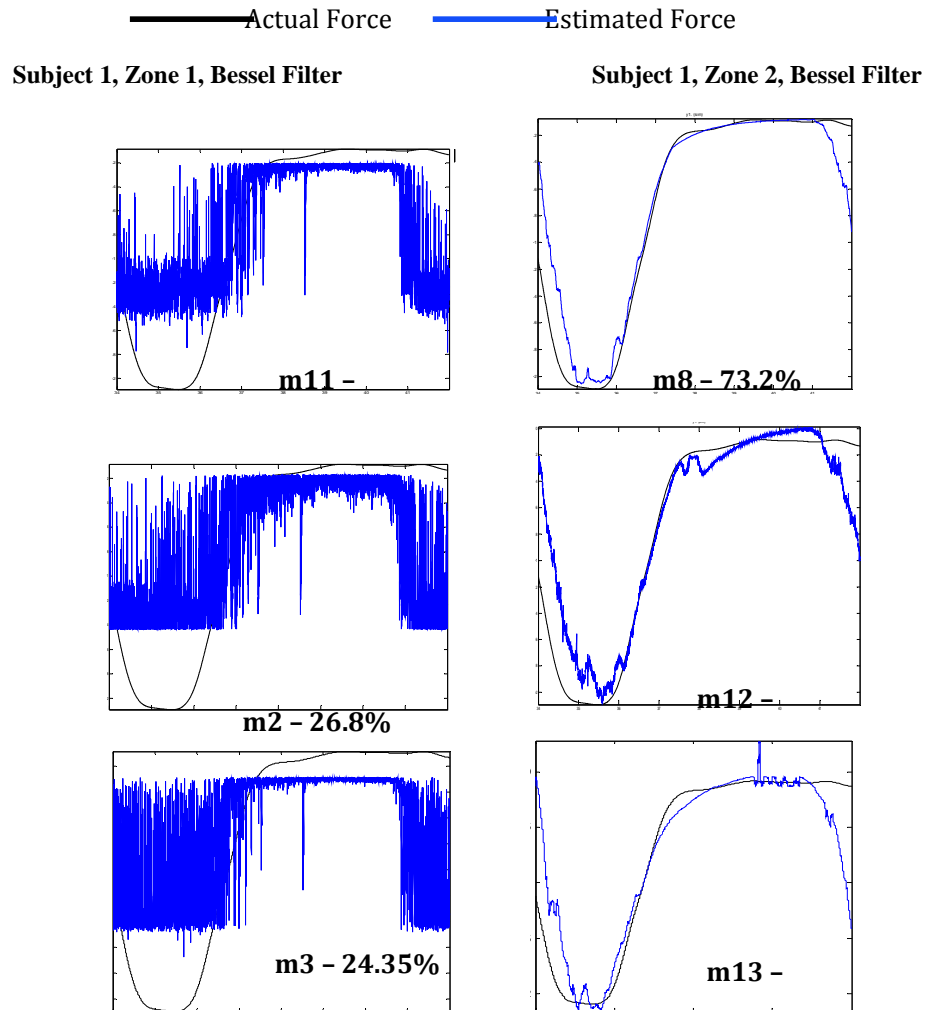


**Figure 1.49:** Zone Classification Results – Subject 1, Bessel, Band-Pass filter 60-450Hz, Zone 1 & 2

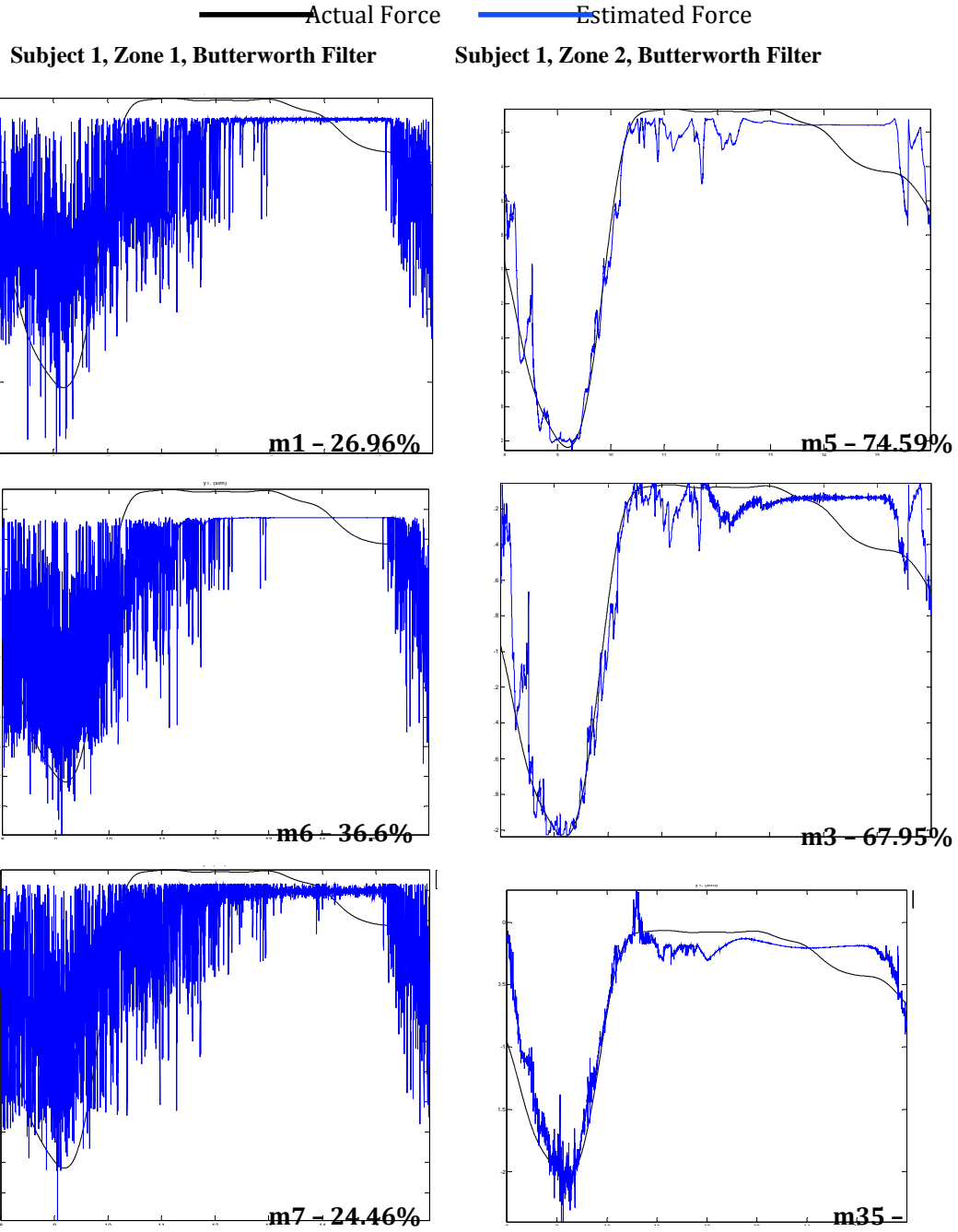


**Figure 1.50:** Zone Classification Results – Subject 1, Butterworth, Band-Pass filter 60-450Hz, Zone 1 & 2

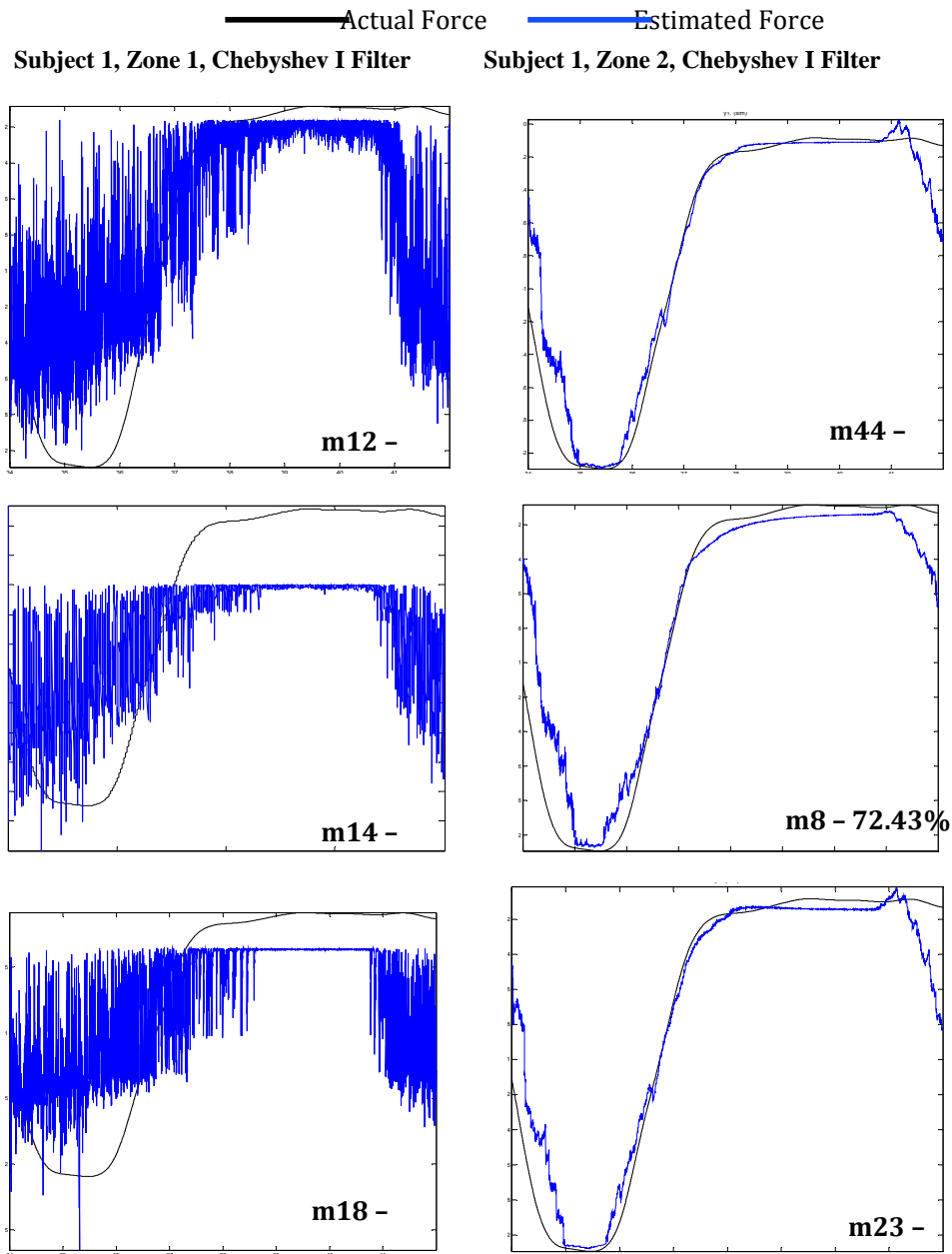


**Figure 1.51:** Zone Classification Results – Subject 1, Chebyshev Type I, Band-Pass filter 60-450Hz, Zone 1 & 2

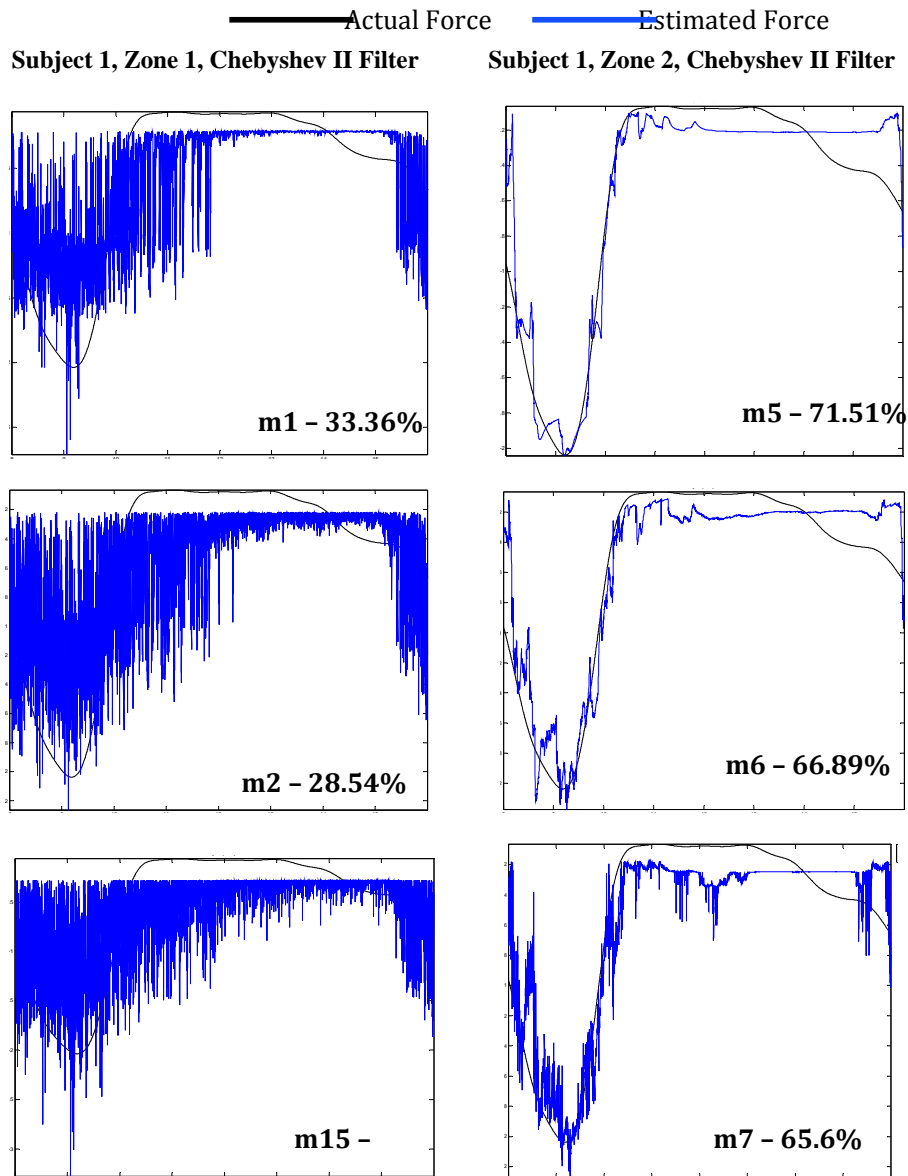


**Figure 1.52:** Zone Classification Results – Subject 1, Chebyshev Type II, Band-Pass filter 60-450Hz, Zone 1 & 2

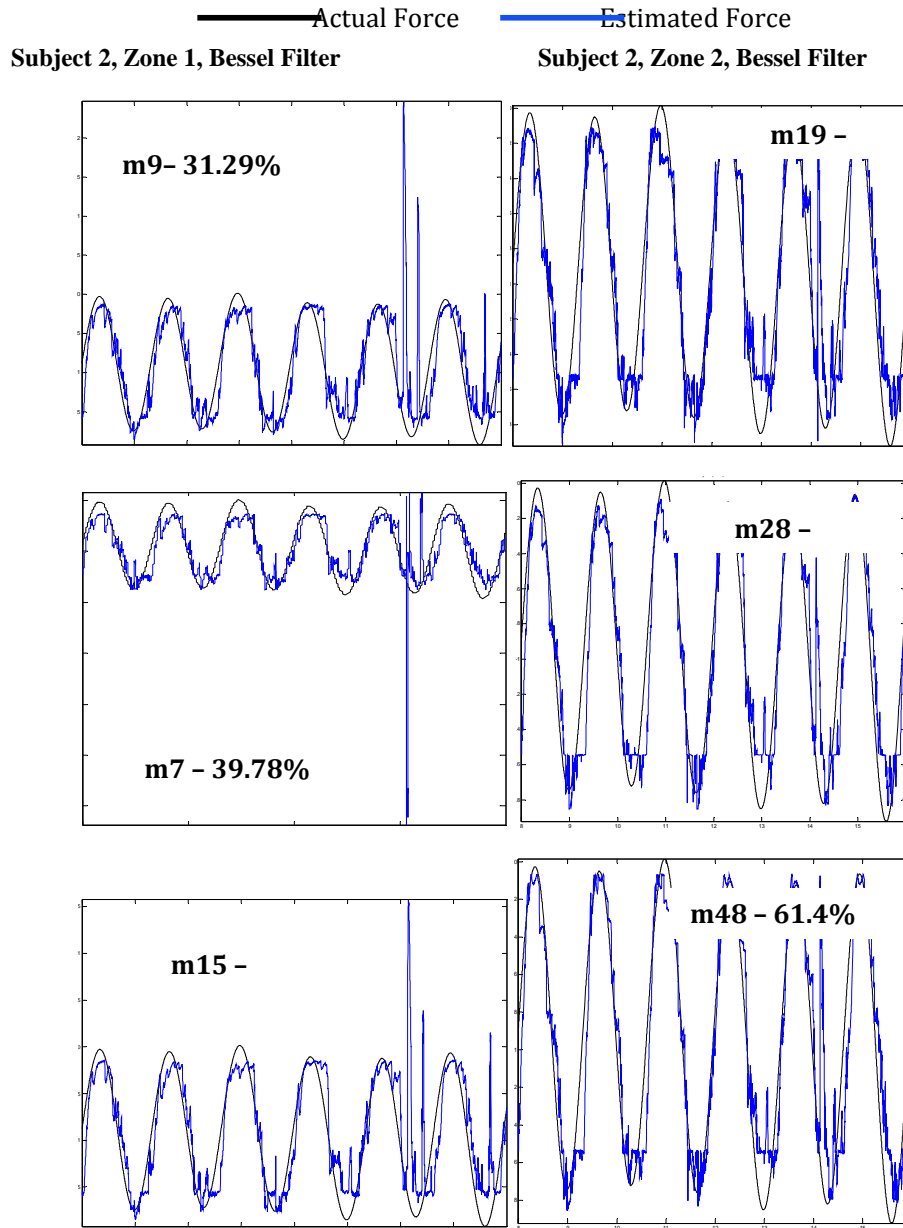


**Figure 1.53:** Zone Classification Results – Subject 2, Bessel, Band-Pass filter 60-450Hz, Zone 1 & 2

From the figures 1.49 to 1.53, for 4 types of filters and 2 subjects, we see that the sEMG-force relation modeled by the nonlinear Hammerstein-Wiener models, using the Adaptive Gauss-Newton algorithm, results in the best fit values for data (sEMG) collected in zone 2. This outcome is in good agreement with the ideal locations to measure the sEMG signals indicated in the published anatomical drawings of known sEMG sites [43]. Also, zone 2 contains the majority of the muscles which are responsible for the generation of force and finger motion.

## CHAPTER TWO

### EMG-hand motion model integration and optimization for degree of amputation using sensor fusion strategies

This chapter describes force modeling, force fatigue modeling, system identification, data fusion algorithms, and finger motion modeling.

#### 2.1 Introduction

This section reviews techniques of EMG signal analysis, sEMG-skeletal muscle force relationships, sEMG-skeletal-muscle fatigue and introduces the System Identification approach to dynamic modeling.

##### 2.1.1 Techniques of EMG Signal Analysis

Literature shows that there are numerous mathematical and Artificial Intelligent (AI) techniques available for the EMG signal detection and analysis [6]. In the category of mathematical models, there are Fourier transform, statistical measures, time-frequency approaches, wavelet transform, Wigner-Ville Distribution (WVD), and higher-order statistics. However, on the other hand in AI approaches, there are Artificial Neural Networks (ANN), dynamic recurrent neural networks (DRNN), fuzzy logic (FL) systems, and Genetic Algorithm (GA).

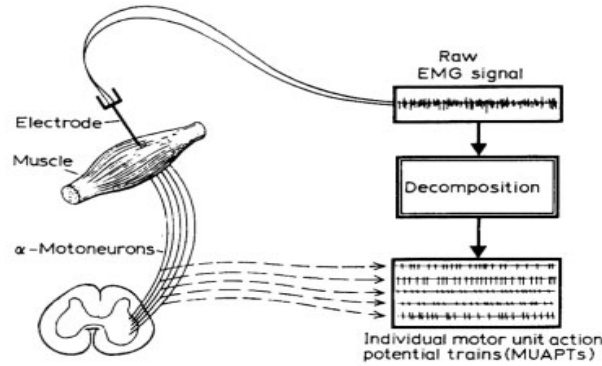


**Figure 2.1.** Detection and decomposition of intramuscular EMG signal. Adapted from [48].

The motor unit action potential (MUAP) is the combination of the muscle fiber action potentials from all the muscle fibers of a single motor unit [47]. The two detection methods of MUAP are a skin surface electrode (non-invasive) located near this field, and a needle electrode (invasive) inserted in the muscle. In general the EMG signal can be modeled as given in Equation (1), [6].

$$x(n) = \sum_{r=0}^{N-1} [h(r) * e(n-r) + w(n)]. \quad (1)$$

In Equation (1),  $x(n)$  is the modeled EMG signal,  $e(n)$  is the point processed, representing the firing impulse,  $h(r)$  is the MUAP,  $w(n)$  is the zero mean additive white Gaussian noise, and  $N$  is the number of motor units firing [6]. Figure 2.1 illustrates the detection and decomposition of intramuscular EMG Signal [48].

Following are the various signal processing methods that have been studied and applied to raw EMG for its better and precise interpretation [6].

#### Wavelet Analysis

A very appropriate method for the classification of the EMG signal is the wavelet transform (WT), which can be implemented by means of a discrete time filter bank [6].

- Wavelet analysis is one of the best techniques to match the shape of the MUAP, which results in the best possible energy localization in the time-scale plane [49].
- Work of [49] was followed further and wavelet analysis was used to match the shape of the MUAP [50]. Wavelet analysis is linear, gives a multi-resolution representation and does not get altered by cross-terms, for instance, in the instance of multicomponent-signal analysis, which makes the WT an alternative to other time-frequency representations [50].
- Mexican hat wavelet is a second-order derivative of a Gaussian distribution, which is an



appropriate option to estimate the shape of MUAP for a unipolar recorded signal with underpinning assumptions [51].

- In contrast to the non-stationary nature of the EMG signal, with the assumption that the EMG signal is stationary, the fast- and short-term Fourier transforms (FFT and SFT) are commonly used to compute the frequency spectrum of the EMG signal [52].
- WT is also an appropriate method for multi-resolution analysis, which is basically analyzing the signals at different resolution levels [53].
- ‘Wavelet function’ (WF) is a basis function used in the WT to decompose the signal into several multi-resolution components [54]. In one side, the Short Fourier Transform (SFT) with relatively short-time windows track the spectral variations with time; however, this method does not work well for the non-stationary signal [54].

### ***Time-Frequency Approach***

Some of the time-frequency methods for EMG signal processing are Cohen-class transformation, Wigner-Ville distribution (WVD), and Choi-Williams distribution [6]. EMG signals for dynamic contractions represent non-stationary stochastic processes and can be modeled with the Cohen-class transformation, which is a class time-frequency representation [55]. The mathematical representation of the Cohen-class time-frequency spectrum is given by Martin and Flandrin [56], Amin [57] and Syeed and Jones [58].

### ***Autoregressive Model***

EMG signals have been modeled with the autoregressive (AR) time-series models where EMG signals are assumed with the delayed intramuscular input [6]. EMG signals were modeled by Graupe and Cline in 1975 with the autoregressive moving-average (ARMA) model [59], where they considered the EMG signal as stationary over sufficient short time intervals. In [60], Sherif stated that the electrical behavior of the medical deltoid is non-stationary and proposed a replacement with AR, integrated moving-average (ARIMA) representation where the non-stationary nature of the EMG during different phase of muscle activity was characterized. The surface EMG signal with delayed intramuscular EMG signal as the input was modeled with AR model by Zhou et al. [61]. Heftner et al. suggested that the AR model was a good choice with better computational speed [62]. A static nonlinear element with time-varying ARMA model and a non-stationary identifier of time-varying AR parameters were proposed by Bernatos et al. [63], and Moser and Graupe [64]. Research work by Tohru suggested that the AR model which computationally economical was better than the more precise ARMA or ARIMA models for dynamic muscle movements [65].

### ***Artificial Intelligence***

The EMG signal recording and analysis is a real-time application and Artificial Intelligence techniques mainly based on Neural Networks (NN) have been proposed for this application [6]. Del and Park proposed a real-time application of artificial neural network which can solve problems with acceptable cost and performance criteria that conventional statistical methods cannot [66]. Neural-network architectures are a fast way of system customization to the patient, but also provide better patient adoption to the system [6].

In addition, artificial dynamic recurrent neural networks (DRNN) were used to model the muscle EMG activity and the arm kinematics, where the simulated movements were the result of the interaction between raw EMG signals, without invoking any theoretical assumptions for the control strategy [67].

Fuzzy-logic systems have a reasoning style similar to humans and emulate human decision-making more closely than the artificial neural network (ANN); one of the properties of the Fuzzy logic (FL) systems is that, FL deals with contradictions nicely, which makes FL a good choice for EMG signal processing and classification [68].

Another NN based method is the blind source separation (BSS) method proposed in 2001 by Belouchrani et al. [69]. EMG signals generated by different muscles may overlap in the time and frequency domain; therefore, spatial time-frequency distributions based approach was a solution for source separation rather than the classical linear filtering [70].

### ***Higher-Order Statistics***

Higher-order statistics (HOS) is a technique based on probability theory, which can be used to study the characteristics and nature of a random process. In 1974, Kanosue et al. [71] proposed a statistical method to estimate the amplitude and the number of newly MUAPs, after this there are some more methods proposed by some other researchers.

### ***Other Methods***

Some of the other models proposed by researchers for the EMG signal processing are briefly discussed in this section.

- The experimental works of Ludin [72] on the intercostal muscles was the bases of Rosenfalck's mathematical model in 1969. The model is given below in Equation (2).

$$g(z) = 96z^3e^{-z} - 90, \quad (2)$$

where  $g(z)$  is intracellular action potential in mV, and  $z$  is nerve or muscle measurements in mm. To match with better experimental data, Nandedkar and Stalberg [73] suggested a modified expression as  $e(z) = g(2z)$ , which is intracellular formulation for the single fiber action potential modeling and given by Equation (3).

$$e(z) = 768 * z^3 * e^{-2z} - 90. \quad (3)$$

- Previous studies in 1990 by Slawnych, Laszlo, and Hershler [74] suggested that the MUAP amplitude adds algebraically to results into the compound muscle action potential (CMAP), which is not valid because the occurrence of MUAP waveforms is not synchronous. In 1992, Nandedkar and Barkhaus proposed a model, which gives the phenomena of phase cancellation, where the MUAP contributes less than its amplitude to CMAP amplitude [74], Equation (4).

$$A_{12}^2 = A_1^2 + A_2^2 - 2 * A_1 * A_2 * \alpha. \quad (4)$$

Here,  $A_1$  and  $A_2$  are the two MUAPs with phase angle  $\alpha$ , and  $A_{12}$  is the CMAP.

- Englehart and Parker considered two interpulse interval (IPI) probability density function (pdf) models, the Gaussian density function model (Equation (5)) and the Gamma density function model (Equation (6)) [75].

$$f_x(x) = \frac{1}{\sigma_x \sqrt{2\pi}} * \exp\left(-\frac{(x-\mu_x)^2}{2\sigma_x^2}\right). \quad (5)$$

Here,  $\mu_x$  is the mean and  $\sigma_x^2$  is the variance.

$$f_x(x) = \frac{1}{\beta * \Gamma(\rho)} \left(\frac{x-\alpha}{\beta}\right)^{\rho-1} * \exp\left(-\frac{x-\alpha}{\beta}\right); x < \alpha. \quad (6)$$

Here,  $\alpha$  is the location parameter,  $\beta$  is the scale parameter,  $\rho$  is the shape parameter, and  $\Gamma()$  is the gamma function.

- In 1995, Zhang et al. [76] derived a model for the myoelectric signal with the integral pulse frequency and amplitude modulation (IPFAM). The three main components of the pulse amplitude modulation (PAM), the pulse frequency modulation (PFM) and the linear system explains the characteristics of the EMG signals with change in muscular force, rates of nerve firing, and the compound motor unit action potential including effects of propagation dispersion and tissue filtering. The IPFAM model includes the key aspects for the EMG signal generation, where the potential increases up to a threshold resulting in an event [76].
- In 1995, Karlsson and Nystrom developed a real-time system for the EMG signal analysis for clinical applications, where a signal is represented in time-frequency domain with the short-time Fourier transform [77]. The limitation of this system is that in contrast to the inherent characteristic of the EMG signal, this method assumes the signal to be stationary.
- In 2000, Duchene and Hogrel produced an efficient surface EMG simulation model, which was useful for assessing algorithms related to surface EMG features description [78]. The model allowed the surface EMG simulation in both voluntary and elicited contractions; considered all transformations from intracellular potential to surface recordings, and exhibited a fast implementation of the extracellular potential computation.
- In 2005, Hamilton and Stashuk proposed an EMG signal model, which was designed to resemble the physiology and morphology of skeletal-muscle closely, incorporated the line source models of commonly used needle electrodes positioned in alignment with the clinical studies [79].

### 2.1.2 sEMG – Skeletal-Muscle Force Relationship

Bouisset surveyed the relationship between the EMG signal and muscle-force relationship in normal motor activities [80]. The EMG is a measure of the level of nervous excitation, and the skeletal-muscle force during the contraction depends on the nervous excitation, therefore, the EMG can be used to measure the skeletal-muscle force [81]. There is a necessity to develop a good means of quantification of skeletal-muscle force using the EMG signal, and there have been numerous research efforts in this direction. Perry and Bekey in [81] present a review on the mathematical models for the EMG signal and muscle-force relationship. Those authors concluded that some of the results are experimental in nature, no detailed mathematical models with the physiological properties and parameters exist, the model provides only a steady-state relationship, and the model is only algebraic in nature with no information about the transient behavior. The EMG signal processing is a viable option

to study the “active state,” which depends on the internal change of the muscle. Numerous dynamic linear and nonlinear modeling approaches were proposed with integrated EMG signal to study the “active state” of the muscle. These mathematical models do not have any parameter for physiological properties and hence are of very limited use. The conclusion of the study in [81] include:

- a) At the middle of the operating force range and for some electrode configurations during the isometric contractions, the EMG signal and muscle-force has linear relationship.
- b) For the EMG signal and force relationship, the joint position affects the constant of proportionality.
- c) The EMG signal and muscle-force relationship is not linear in the presence of joint movements.
- d) The EMG signal and muscle-force relationship estimate highly depends on the type of electrode, location of electrode placement, and the signal processing method.
- e) There is no good, verified and validated mathematical model for the EMG and muscle-force relationship in the presence of joint movements.

In 1993, research by Fuglevand A. J. et al. [82] presented a muscle-force model for a pool of 120 motor units, which gave an exponential function for the distribution of twitch forces for the motor units. Equation (7) gives the model of twitch force in terms of the impulse response of a critically damped, second order system.

$$f(t) = \frac{P \cdot t}{T} * e^{1 - (\frac{t}{T})}. \quad (7)$$

Here,  $T$  is contraction time to peak force of the twitch and  $P$  is its peak amplitude. Twitch contraction times are inversely proportional to twitch amplitudes, which were determined by the rank in the recruitment order. The total force of the muscle was determined as a linear summation of all the individual MU forces, where MUs followed the sigmoidal relationship of MU force and firing rate [82].

A study in 2007 develops a neuromusculoskeletal tracking (NMT) method, which estimates muscle-forces from observed motion data [83]. Skeletal motion tracking calculates the joint torques needed to actuate a skeletal model and track observed segment angles and ground forces in a forward simulation of the motor task; optimal neuromuscular tracking resolves the muscle redundancy problem dynamically and finds the muscle excitations (and muscle-forces) needed to produce the joint torques calculated by the skeletal motion tracker. NMT method can estimate muscle-forces using experimentally obtained kinematics and ground force data in a fast and accurate way [83].

The relationship between the EMG signal and the force produced by a muscle and the complicated and associated factors influencing this relationship are discussed in [46]. For proper use, the understanding the EMG signal is important, conversely it is complicated because of the difficulties in quantifying factors and processes that affect the EMG signal. The anisotropy and non-homogeneity of the tissues between the muscle membranes and the detection electrode, and the uniqueness of the microanatomical structures of each detection location further complicates this issue. Carlo J. De. Luca in [46] states that, “It is conceivable that in the future, elegant and complex models will be used in conjunction with means for describing the anatomy, physiology, and electrical field properties to allow a direct consideration of this problem.” The factors that influence the EMG signal can be causative, intermediate, and deterministic. The causative factors can be extrinsic, those associated with the electrode structure and its placement on the surface of the skin above the muscle, and intrinsic, the physiological, anatomical, and biochemical characteristics of the muscle. The extrinsic causative factors as listed in [46] are:

- a) Electrode configuration -- the shape and the surface area of the electrode and the inter electrode surface distance.
- b) The relative position of the electrode and the motor points in the muscle.
- c) Crosstalk detected by the electrode: Surface location of the electrode on the muscle.
- d) The electrode detection surface orientation with respect to the muscle fibers.

The intrinsic factors as listed in [46] are given as:

- a) The amplitude of the detected signal depends on the number of active motor units at any instance of the contraction.
- b) Fiber type composition of the muscle; fiber diameter; Depth and location of the active fibers within the muscle with respect to the electrode detection surfaces.
- c) Blood flow in the muscle.
- d) “The amount of tissue between the surface of the muscle and the electrode, which affects the spatial filtering of the signal.”
- e) Some other un-identified factors: the length of the depolarization zone and ionic fluxes across the membrane.

Figure 2.2 shows the influence of the location of the electrode on the amplitude and frequency spectrum of the EMG signal (top electrode), the myotendinous junction (bottom electrode) and the lateral edge of the muscle (middle right electrode). The EMG signal has maximum amplitude at the midline of the belly of the muscle between the nearest innervation zone and the myotendinous junction [46].

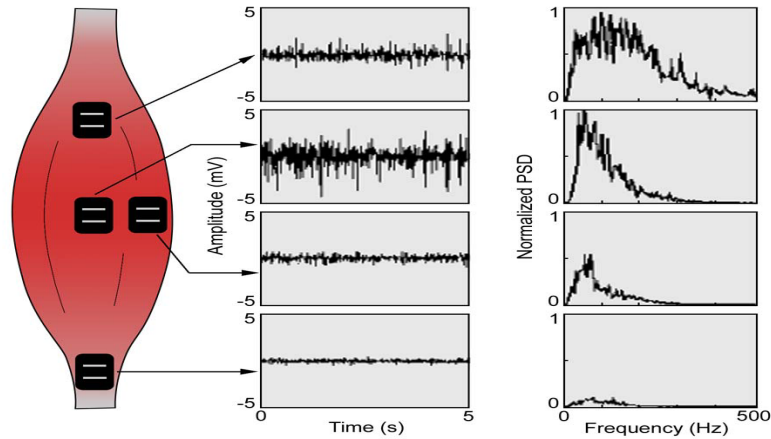


**Figure 2.2:** The influence of the electrode location on signal amplitude. Adapted from [46].

The intermediate factors are: The implicit characteristics of a differential electrode configuration such as band-pass filtering aspects of the electrode; detection volume of the electrode; superposition of action potentials in the detected EMG signal; crosstalk from nearby muscles; conduction velocity of the action potentials that propagate along the muscle fiber membrane; and the relative position of the electrode and the active muscle fibers affects the spatial filtering [46].

The deterministic factors for the relationship of the EMG and the muscle-force are: the number of active motor units; motor unit force-twitch; mechanical interaction between muscle fibers; motor unit firing rate; the number of detected motor units; amplitude, duration, and shape of the MUAPs; and recruitment stability of motor units [46].

At present, we do not have an equation that can represent the relationship between the surface EMG signal and the muscle-force during muscle contraction. The increase in the muscle-force generally results in the increase of the amplitude of the EMG signal. This knowledge gives us only the qualitative information and lacks in the quantitative part in it [46].

As discussed previously, there are many causative, intermediate, and deterministic factors, which make this relationship to be non-rigid. If the electrode is placed firmly, and there is no relative distance between the electrode and the active muscle fibers, normalization of the amplitudes of the EMG signal and the force among contractions will neutralize the effect of all these factors [46].

The surface EMG signals are affected by the issue of crosstalk and stationarity [46], [84]. The stability of the electrode position with respect to the active muscle fibers and the stability of the motor unit activation pattern have the greatest effect on signal stationarity [46], [84]. For natural movements and to interact with our environment, we need concentric (CC: shortening of muscle) or eccentric (EC: lengthening of muscle) contractions, whereas isometric contraction is the most studied contraction even though it is less physiologically interesting [46].

The EMG signal and muscle-force relationship primarily depends on a CC/EC contraction, which entails various mechanical, physiological, anatomical and electrical modifications during the contraction. To obtain a quantitative relationship between the EMG signal and muscle-force, the signals must be acquired during an isometric contraction. Considering the absence of the technical factors and crosstalk, the EMG and muscle-force relationship is not always linear, which change as the type of muscle change. Figure 2.3 shows the relationship between the normalized EMG and joint Force signals for three types of muscles, where the smoothed data window is of 2 seconds duration [46].

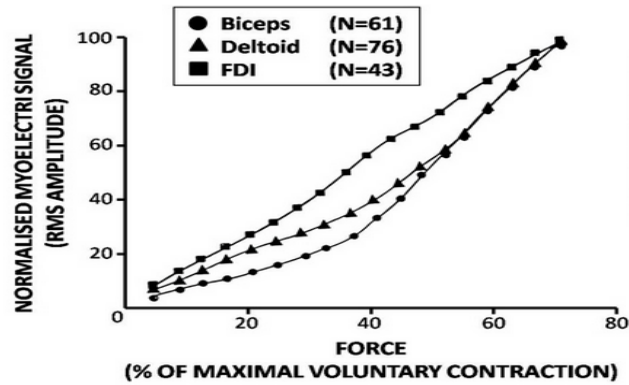


**Figure 2.3:** Normalized EMG signal vs. joint force. Adapted from [46].

The random nature of the surface EMG signal, intrinsic anatomical and physiological factors results in the nonlinear relationship between the EMG and the muscle-force signal [46]. Other reasons for the nonlinear relationship are:

- 1) For most of the available electrode types, the detection volume of the electrode is less than the muscle volume, which implies that the number of MUAPs detected by the electrode is less than the active MUAPs in the corresponding muscle.
- 2) The firing rate of the recruited motor units will increase with the increase in the muscle-force. Each MUAP, however, will continue to provide energy to the EMG signal, while the force contribution saturates. This results in the nonlinear relationship between the EMG signal and the muscle-force signal. The central nervous system (CNS) also affects the EMG-force relationship by controlling the motor units firing rate dynamics, and motor unit recruitment range [46].

### 2.1.3 sEMG – Skeletal-Muscle Fatigue

The energy consumption of skeletal-muscle cells may increase to 100-fold when going from rest to high-intensity exercise. The aerobic capacity of the muscle cells falls short with the energy demand during high-intensity exercise, and anaerobic metabolism supplies a major portion of the required adenosine triphosphate (ATP). Skeletal-muscle fatigue (i.e. a decline in contractile function is also an outcome of high-intensity exercise). Muscle-fatigue and anaerobic metabolism likely are correlated, and the decrease in contractile function results as a consequence of anaerobic metabolism [85]. Lactic acid is the main part of inorganic acids, and intracellular accumulation of inorganic acids results from anaerobic breakdown of glycogen [85], [86]. Lactate and  $H^+$  are the products of the dissociation of the lactic acid, which is a strong acid. Muscle contraction is not affected greatly by lactate ions [86]; but, the buildup of  $H^+$  or moderation of pH is the typical reason of the skeletal-muscle fatigue. Several recent studies illustrate that the decreased pH may have small effect on the contraction in mammalian muscle [85], [87], [88], [89], [90]. In addition to acidosis, anaerobic metabolism in skeletal-muscle also entails hydrolysis of creatine phosphate (CrP) to creatine and inorganic phosphate ( $P_i$ ). Several mechanisms may justify the decrease of contractile function as an outcome of increased  $P_i$ , but creatine has small effect on contractile function. So, during high-intensity exercise the buildup of  $P_i$ , rather than acidosis seems to be the chief cause of muscle-fatigue [90], [91], [92], [93], [94], [95]. Failure of action-potential propagation and other similar elements become critical with even more intense activation such as continuous maximal contraction [85].

The breakdown of CrP is the main reason for increase of the  $P_i$  concentration during intense skeletal-muscle activity. The release of  $P_i$  in the transition from low-force (weakly attached states) to high-force (strongly attached state) is proposed by most cross-bridge action models. So, the transition to high-force states is constrained by  $P_i$  buildup. This outcome indicates that during fatigue development there will be less cross-bridges in high-force states and increased  $P_i$  would cause decrease in force production [85].

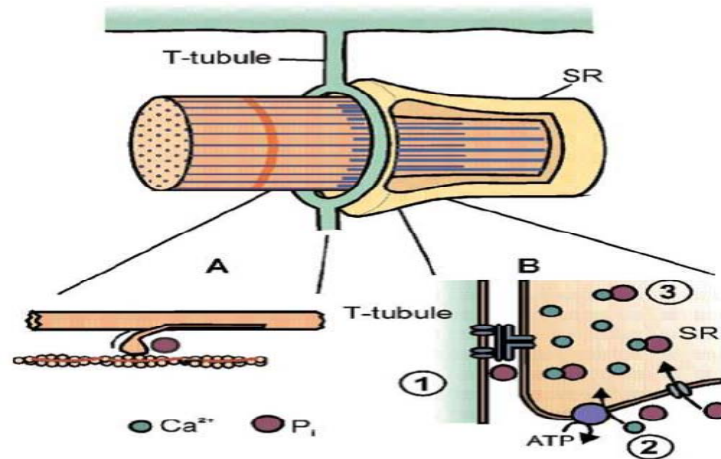


**Figure 2.4:** Various mechanisms of  $P_i$  effect on muscle function during fatigue. Adapted from [85].

Increased  $P_i$  also affects fatigue development by acting on sarcoplasmic reticulum (SR)  $Ca^{2+}$  handling. In this respect, there are several mechanisms by which increased  $P_i$  may exert its effect, and the result may be both increased and reduced tetanic  $[Ca^{2+}]_i$ . Figure 2.4 illustrates the various mechanisms by which  $P_i$  may affect muscle function during fatigue. It shows that increased  $P_i$  may depress force production by acting directly on the myofibrils or on sites in the excitation-contraction pathway within muscle cells. The depressive effect of increased  $P_i$  may, like the effect of acidification described above, diminish as the temperature is increased to that prevailing in mammalian muscles in situ. Increased  $P_i$  may act directly on the myofibrils and decrease cross-bridge force production and myofibrillar  $Ca^{2+}$  sensitivity (A). By acting on SR  $Ca^{2+}$  handling (B), increased  $P_i$  may also increase tetanic  $[Ca^{2+}]_i$  in early fatigue by stimulating the SR  $Ca^{2+}$  release channels (1); inhibit the ATP-driven SR  $Ca^{2+}$  up-take (2); and reduce tetanic  $[Ca^{2+}]_i$  in late fatigue by entering the SR, precipitating with  $Ca^{2+}$ , and thereby decreasing the  $Ca^{2+}$  available for release (3), [85].

Muscle-force output has been used as a muscle fatigue-index in the study of human biomechanics [46]. The muscle is assumed to be fatigued at the failure point, which is the point at the muscle contraction, can no longer be maintained. Use of failure point as an indication of muscle-fatigue has some practical disadvantages, where fatigue would be detected only after it had occurred, which is not desirable for clinical and ergonomics applications. Moreover, there are three other critical factors:

- 1) The measured torque may not truly represent the force of the muscle of interest, because for a voluntary contraction the force of an individual muscle is not directly accessible.
- 2) The physiological and biochemical processes are microscopic in nature, and change the means for generating force during a sustained submaximal contraction at constant torque.
- 3) Either both or any one of physiological and psychological factors can be the reason for the failure, which is almost impossible to determine accurately. An alternative and preferable method to detect the muscle-fatigue is the spectral analysis of the EMG signal during a sustained contraction. The fatigue-index is a means for monitoring and quantifying the spectral modification during sustained contractions, which results in the fatigue-related changes in the physiological and biochemical processes.

During the fatigue progression, both the EMG spectral modification and muscle-force changes; this result indicates that there is a relationship between the two variables. Although the causal nature of this relationship has yet to be demonstrated, the spectral fatigue-index is useful to study muscle-fatigue [46]. Mean or mode frequency, and median of the spectrum are some of the characteristic indicators of the frequency spectrum, which can be used to monitor and compute the spectral modification. Median frequency is the best choice for fatigue-index, because it is less sensitive to noise and signal aliasing, and more sensitive to the biochemical and physiological factors within the muscles during sustained contractions [46], [96]. A diagrammatic representation of the spectral modification during muscle-fatigue is shown in the Figure 2.5.

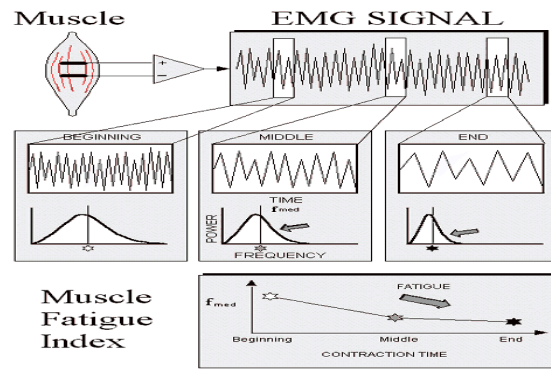


**Figure 2.5:** The muscle fatigue-index is represented by the median frequency of the spectrum of the EMG signal during sustained contraction. Adapted from [46].

#### 2.1.4 System Identification (SI) a Dynamic Modeling Approach

System Identification (SI) is the interface between the real world of applications and the mathematical world of control theory and model abstractions, where the dynamic mathematical models of natural phenomena are designed from observed input-output data [97]. System identification is a very large topic with many facets and there are many approaches and methods in SI [97].

Thermodynamics and electromagnetism in physics, chemical processes and adaptation in biology, control systems in engineering, and decision making in macro-economics, finance, and business economics are some of the phenomena with a dynamical evolution over time [98]. These dynamic processes can be studied with mathematical models; we require stability, uncertainty reduction, and optimal decision making for these models. These models need to have model parameters that can be estimated from available data. In the process of SI to estimate a system, we need an observed data set, a model structure with specifications, compute the unknown model parameters, and finally validation of the obtained model. Modeling of dynamical phenomena from observed data can be used for numerous fields such as engineering, astronomy, microbiology, psychology, management, and many others. SI application flow chart is given in Figure 2.6.

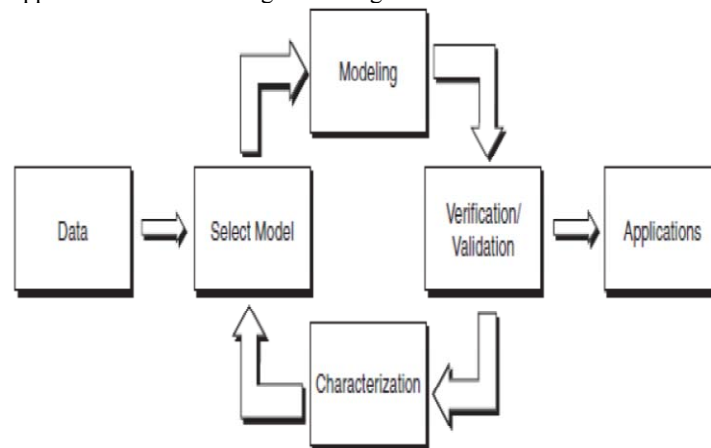


**Figure 2.6:** Flow chart: System Identification application. Adapted from [99].

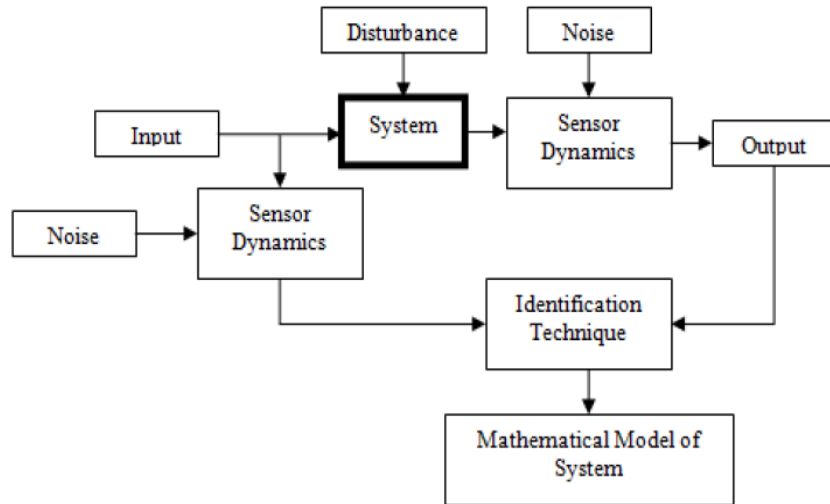


**Figure 2.7:** Schematic block diagram of SI components. Adapted from [99].

In a real world environment a system is subjected to disturbances and noise influences. In parallel to the regular measured input the disturbance also plays a role in the excitation of the system modes. Noise and internal dynamics of the system is part of the data collected with input/output sensors [99]. Figure 2.7 illustrates the typical SI components in order to extract a mathematical model from experimental data.

#### Non Parametric System Identification Techniques

Non-Parametric System Identification uses the direct estimation of the response of the system and does not require system parameters. Table 2.1 shows a set of nonparametric SI methods [99].

**Table 2.1:** Non-Parametric SI Methods

Method	Domain	Principle	Characteristics
Correlation	Time	Correlation of output with input, and solve for the impulse response	Approximation of the covariance matrix
Frequency Response	Frequency	Apply a sine wave, and determine amplitude and phase graphically	»Sinusoid inputs only » Long experiment periods necessary
Frequency Response and correlation	Frequency	Apply a sine wave, correlate with sine and cosine to suppress noise	»Sinusoid inputs only » Long experiment periods necessary
Fourier Analysis	Frequency	The empirical transfer function estimate = DFT of the output divided by the discrete Fourier transform of the input	» Fast » Noise-sensitive



## Parametric System Identification

Parametric System Identification methods require a model that fits the given system. The models of this method are in parametric form, hence the name of this SI method. Some of the parametric model structures are covered in the following section [99].

### General - Linear Polynomial Model

A general-linear polynomial model, also known as general-linear model, can describe many different types of systems. These models are used for discrete systems only. Equation (8) gives a discrete system model, which is known as the general-linear polynomial model.

$$y(k) = z^{-n}G(z^{-1}, \theta)u(k) + H(z^{-1}, \theta)e(k), \quad (8)$$

where  $u(k)$  is the system input,  $y(k)$  is the system output,  $e(k)$  is a zero-mean white noise or the disturbance of the system,  $G(z^{-1}, \theta)$  is the transfer function of the deterministic part of the system, and  $H(z^{-1}, \theta)$  is the transfer function of the stochastic part of the system. The deterministic transfer function describes the relation between the output and the input signal. Effects of random disturbances on the output signal can be explained by the stochastic transfer function. System dynamics are associated with the deterministic and stochastic dynamics with stochastic parts of a system [99]. The term  $z^{-1}$  is the backward shift operator, which is given by Equation (9).

$$z^{-1}x(k) = x(k-1).$$

$$z^{-2}x(k) = x(k-2).$$

...

$$z^{-n}x(k) = x(k-n). \quad (9)$$

$z^{-n}$  defines the number of delay samples between the input and the output.  $G(z^{-1}, \theta)$  and  $H(z^{-1}, \theta)$  are rational polynomials and are given by Equation (10) and (11) respectively:

$$G(z^{-1}, \theta) = \frac{B(z, \theta)}{A(z, \theta)F(z, \theta)}, \quad (10)$$

$$H(z^{-1}, \theta) = \frac{C(z, \theta)}{A(z, \theta)D(z, \theta)}, \quad (11)$$

The vector  $\theta$  is the set of model parameters. To simplify the equations  $\theta$  is not used in the following sections.

Defining  $A(z)$ ,  $B(z)$ ,  $C(z)$ ,  $D(z)$ , and  $F(z)$  as follows:

$$A(z) = 1 + a_1z^{-1} + a_2z^{-2} + \dots + a_{k_a}z^{-k_a}, \quad (12)$$

$$B(z) = b_0 + b_1z^{-1} + b_2z^{-2} + \dots + b_{k_b-1}z^{-(k_b-1)}, \quad (13)$$

$$C(z) = 1 + c_1z^{-1} + c_2z^{-2} + \dots + c_{k_c}z^{-k_c}, \quad (14)$$

$$D(z) = 1 + d_1z^{-1} + d_2z^{-2} + \dots + d_{k_d}z^{-k_d}, \quad (15)$$

$$F(z) = 1 + f_1z^{-1} + f_2z^{-2} + \dots + f_{k_f}z^{-k_f}, \quad (16)$$

where  $k_a$ ,  $k_b$ ,  $k_c$ ,  $k_d$ , and  $k_f$  are the model orders.

Equation (17) represents the general-linear polynomial model.

$$A(z)y(k) = \frac{z^{-n}B(z)}{F(z)}u(k) + \frac{C(z)}{D(z)}e(k) = \frac{B(z)}{F(z)}u(k-n) + \frac{C(z)}{D(z)}e(k). \quad (17)$$

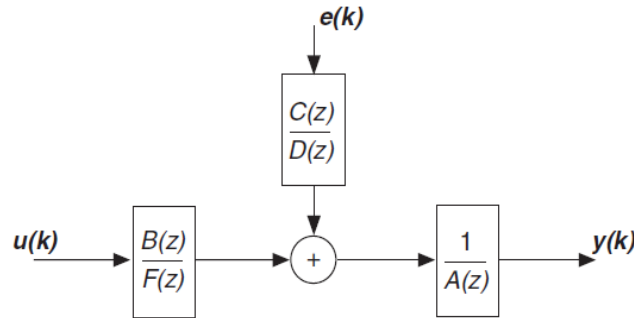


**Figure 2.8:** Signal flow of a General-Linear polynomial model. Adapted from [99].

Schematic of the signal flow of the general-linear polynomial model is given in Figure 2.8. This model structure is good for both system and stochastic dynamics. The estimation of the general-linear model is done using a nonlinear optimization method. Nonlinear optimization methods need intensive computations, and they do not guarantee global convergence [99].

Assigning one or more of  $A(z)$ ,  $C(z)$ ,  $D(z)$ , and  $F(z)$  equal to 1 will result simpler models such as Auto Regressive with eXogenous terms (ARX), Auto Regressive-Moving Average with

exogenous terms (ARMAX), Output-Error (OE), and Box-Jenkins (BJ) models, which are suitable for real-world dynamic modeling problems and used very commonly [99].

Considering Equation (17) and setting  $C(z)$ ,  $D(z)$ , and  $F(z)$  equal to 1, the general-linear polynomial model gives an ARX model. Considering  $D(z)$  and  $F(z)$  equal to 1, the general-linear polynomial model reduces to the ARMAX model. Considering  $A(z)$ ,  $C(z)$ , and  $D(z)$  equal to 1, the general-linear polynomial model gives an Output-Error (OE) model. Considering  $A(z)$  equals to 1, the general-linear polynomial model gives a Box-Jenkins (BJ) model. Considering  $C(z)$ ,  $D(z)$ , and  $F(z)$  equal to 1 and  $B(z)$  equals to 0, the general-linear polynomial model gives an Auto Regressive (AR) model [99]. In linear models, AR, ARX, ARMAX, OE, BJ, and State-Space models; in nonlinear models, nonlinear ARX and nonlinear Hammerstein-Wiener models; Adaptive Neuro Fuzzy Inference System (ANFIS); Curve fitting are discussed in details as used in the later part of this section.

### Prediction Error Method Parameters Determination

The prediction error method is used as an identification method for the work done in this section. Use of a trial-and-error process is necessary to determining the delay and model order for the prediction-error method. Following steps can be used to find a suitable model [99].

- I. Observe the number of resonance peaks in the nonparametric frequency response function and find some insight about the model order. (The number of peaks in the magnitude response equals half the order of  $A(z)F(z)$ .)
- II. Observe the impulse response or test reasonable values in a medium sized ARX model and find the delay that provides the best model fit based on prediction errors or another criterion.
- III. Choose the model order corresponding to the best fit of the various ARX models with this delay.
- IV. "Reduce the model order by plotting the poles and zeros with confidence intervals and examining potential cancellations of pole-zero pairs. The resulting model might be unnecessarily high in order because the ARX model describes both the system dynamics and noise properties with the same set of poles. The ARMAX, Output-Error, and Box-Jenkins models use the resulting orders of the poles and zeros as the  $B$  and  $F$  model parameters and the first- or second-order models for the noise characteristics [99]."
- V. If a suitable model is not selected at this stage then examine whether additional signals influence the output, which can be incorporated as extra input signals.

If after following previous steps, if a suitable model cannot be obtained, additional physical insight into the problem might be necessary. From the prediction error standpoint, the higher the order of the model, the better the model fits data because of the large degree of freedom. It is wise to pick a model with smallest degree of freedom or number of parameters. Therefore, the model-order assessment criteria must rely on the prediction error and at the same time targets low model order. There are three standard criteria for model-order estimation that is Akaike's Information Criterion (AIC), Akaike's Final Prediction Error Criterion (FPE), and the Minimum Description Length Criterion (MDL).

#### Akaike's Information Criterion

Akaike's Information Criterion (AIC) is a subjective estimation error. Equation (18) is minimized by an optimal model order.

$$AIC = V_n \left( 1 + \frac{2p}{N} \right), \quad (18)$$

where the number of data points are given by  $N$ , an index related to the prediction error by  $V_n$ , and the number of parameters in the model by  $p$  [99].

#### Final Prediction Error Criterion

As the name suggests Final Prediction Error (FPE) Criterion estimates the model-fitting error. It is used mainly during new output prediction with the model order [99]. Equation (19) is minimized by an optimal model order.

$$FPE = V_n \left( 1 + \frac{2p}{N-p} \right). \quad (19)$$

#### Minimum Description Length Criterion

For the Minimum Description Length (MDL) Criterion, Equation (20) is minimized by an optimal model order [99]. Equation (20) is given below.

$$MDL = V_n \left( 1 + \frac{p \ln N}{N} \right). \quad (20)$$

The basis for the MDL depends on  $V_n$  and the number of terms used.

#### Analyzing, Validating, and Converting Models

Once the plant model is estimated, we can analyze and observe its characteristics. To verify that the model replicates the true plant dynamics, we need to run validation tests. A linear system can

be expressed by different models, but none of these will yield a fit with the dynamics of the real system. “Certain model representations are more suitable for certain analysis techniques [99].”

## **2.2 Skeletal-Muscle Force**

### **2.2.1 Adaptive Multi Sensor Based Nonlinear Identification of Skeletal-Muscle Force**

Skeletal-muscle force and surface electromyographic (sEMG) signals are closely related. Hence, the later can be used for the force estimation. Usually, the location for the sEMG sensors is near the respective muscle motor unit points. EMG signals generated by skeletal-muscles are temporal and spatially distributed which results in cross talk that is recorded by different sEMG sensors. This research focuses on modeling muscle dynamics in terms of sEMG signals and the generated muscle-force. Here, an array of three sEMG sensors is used to capture the information of the muscle dynamics in terms of sEMG signals and generated muscle-force. Optimized nonlinear Half-Gaussian Bayesian filters and a Chebyshev Type-II filter are used for the filtration of the sEMG signals and the muscle-force signal, respectively. Genetic Algorithm is used for the optimization of the filter parameters. The sEMG and skeletal-muscle force is modeled using multi nonlinear Auto Regressive eXogenous (ARX) and Hammerstein-Wiener models with different nonlinearity estimators/classes using System Identification (SI) for three sets of sensor data. An adaptive probabilistic Kullback Information Criterion (KIC) for model selection is applied to obtain the fusion based skeletal-muscle force for each sensor first and then for the final outputs from each sensor. The approach yields good skeletal-muscle force estimates.

An EMG signal recorded on the surface of the limb is expressed as an electric voltage ranging between -5 and +5 mV. This method is known as surface electromyography (sEMG). The sEMG is utilized as an input to the controller to realize the movements of the prosthesis and force control [44], [45]. Past research results show that EMG signal amplitude generally increases with skeletal-muscle force. However, this relationship is not always rigid; various factors affect this relationship. EMG signals are a result of the varying motor unit recruitments, crosstalk, and biochemical interaction within the muscular fibres. This makes EMG signals random, complex and dynamic in nature and the control of the prosthesis difficult. Moreover, it changes continuously due to the onset and progression of muscle-fatigue which results because of continuous high frequency stimulation or because of titanic stimulation [96]. Synchronization of active motor units along the muscle fibres, and a decrease in conduction velocity are reflected in the EMG signal as an increase of amplitude in time domain and a decrease of medium frequency in frequency domain [96]. All these factors make the relationship between the EMG and force nonlinear. Correct interpretation of EMG signal is vital to achieve precise motion and force control of prosthesis.

The present work presents a novel approach to estimate skeletal-muscle force using an adaptive multi-sensor data fusion algorithm with hybrid nonlinear ARX and Hammerstein-Wiener models as summarized in Figure 2.9. Here, an array of three sEMG sensors is used to capture the information of muscle dynamics in terms of sEMG signals. The recorded sEMG signals are filtered utilizing optimized nonlinear Half-Gaussian Bayesian filter parameters, and the skeletal-muscle force signal is filtered by using a Chebyshev Type-II filter. A simple Genetic Algorithm code is used to optimize the Bayesian filter parameters. Using an input/output approach, the EMG signal measured at the skin surface is considered as input to the skeletal-muscle, whereas the resulting hand/finger force constitutes the output. Multi nonlinear ARX and Hammerstein-Wiener models with different nonlinearity estimators/classes are obtained using SI for three sets of sensor data obtained from the vicinity of a single motor unit. Different nonlinearity estimators/classes are used for nonlinear modeling as they capture the dynamics of the system differently. The outputs of estimated nonlinear models are fused with a probabilistic Kullback Information Criterion (KIC) for model selection and an adaptive probability of KIC. First, the outputs are fused for the same sensor and for different models and then the final outputs from each sensor. The final fused output of three sensors provides good skeletal-muscle force estimates.

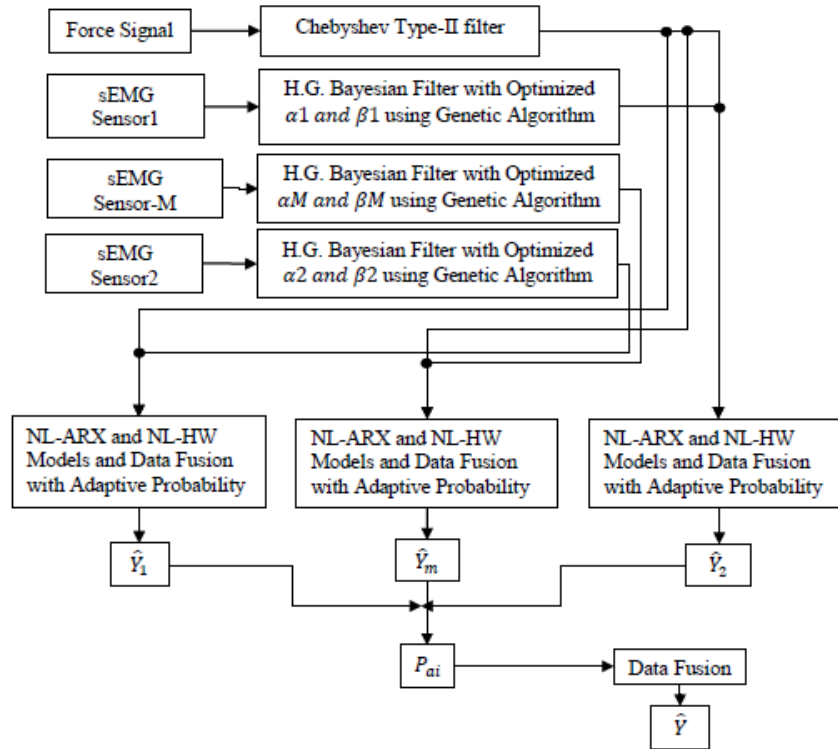


**Figure 2.9:** The flow chart for skeletal-muscle force estimation.

Figure 2.9 shows the flow chart for skeletal-muscle force estimation. This section is structured as follows. First, the experiment design, pre-processing and filter parameter optimization for sEMG signals are discussed. Second, nonlinear ARX and Hammerstein-Wiener modeling are covered. Third, the fusion of various nonlinear model outputs using KIC and adaptive probability of KIC is covered. Finally, the results, discussion and future work are provided followed by a conclusion to summarize the importance of this work.

### Experiment Design and Pre-Processing

The experiment design is shown in Figure 2.10. Both sEMG and muscle-force signals are acquired simultaneously using LabVIEW™ at a sampling rate of 2000 Hz. The sEMG data capturing was aided by a DELSYS® Bagnoli-16 EMG system with DE-2.1 differential EMG sensors. The corresponding force data was captured using Interlink Electronics Force Sensing Resistor (FSR) 0.5” circular force sensor. One sEMG sensor is placed on the motor point of the ring finger and two adjacent to the motor point of a healthy subject. Prior to placing the sEMG sensors, the skin surface of the subject was prepared according to International Society of Electrophysiology and Kinesiology (ISEK) protocols.

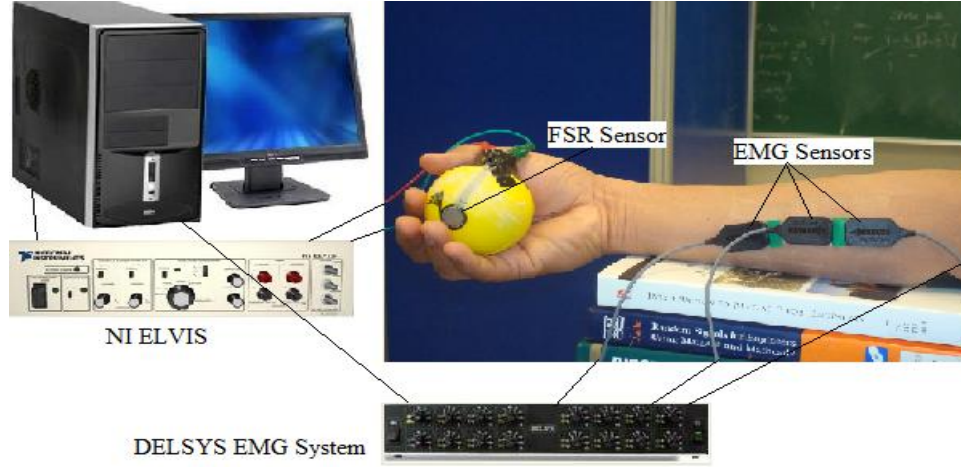


Figure 2.10: Experiment design.

According to previous research, the Bayesian based filtering method yields the most suitable sEMG signals [100]. The nonlinear filter significantly reduces noise and extracts a signal that best describes EMG signals and may permit effective use in prosthetic control. An instantaneous conditional probability density  $P(EMG|x)$  provides the resulting EMG for the latent driving signal  $x$  [100]. The model for the conditional probability of the rectified EMG signal  $emg = |EMG|$  is used in this current estimation algorithm. EMG signals are usually described as amplitude-modulated zero mean Gaussian noise sequence [6]. For the rectified EMG signal, the “Half-Gaussian measurement model” in [100] is given by Equation 21.

$$P(emg|x) = 2 * \exp(-\frac{emg^2}{2*x^2}) / (2 * \pi * x^2)^{1/2}. \quad (21)$$

The EMG signal is modeled for the conditional probability of the rectified EMG signal as a filtered random process with random rate. The likelihood function for the rate evolves in time according to a Fokker–Planck partial differential equation [100]. The discrete time Fokker–Planck equation is given by Equation 22.

$$p(x, t - 1) \approx \alpha * p(x - \varepsilon, t - 1) + (1 - 2 * \alpha) * p(x, t - 1) + \alpha * p(x + \varepsilon, t - 1) + \beta + (1 - \beta) * p(x, t - 1). \quad (22)$$

Here,  $\alpha$  and  $\beta$  are two free parameters,  $\alpha$  is the expected rate of gradual drift in the signal, and  $\beta$  is the expected rate of sudden shifts in the signal. The unknown driving signal  $x$  is discretized into bins of width  $\varepsilon$ . These two free parameters of the non-linear Half-Gaussian filter model are optimized for the acquired EMG data using elitism based GA. GA belongs to a class of optimization algorithms that are based on observing nature and its corresponding processes to imitate solving complex problems, most often optimization or estimation problems [101], [102], [103]. A Chebyshev Type II low pass filter with a 550 Hz pass frequency is used to filter the force signal. Figs. 2.11 (a), and (b) depict the raw and Chebyshev Type-II low pass filtered force signals. Figs. 2.12, 2.13 and 2.14 show the rectified EMG and Half-Gaussian Filtered EMG signal for three sensors.

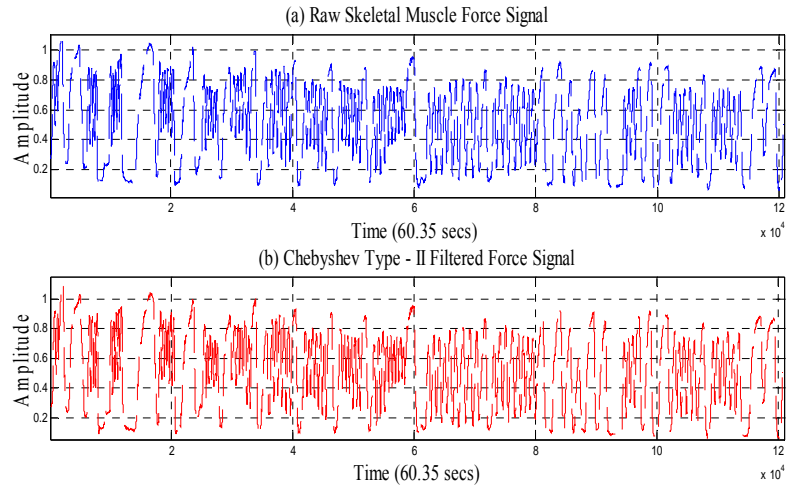


**Figure 2.11:** (a) Raw and (b) Chebyshev Type-II filtered skeletal-muscle force signals.

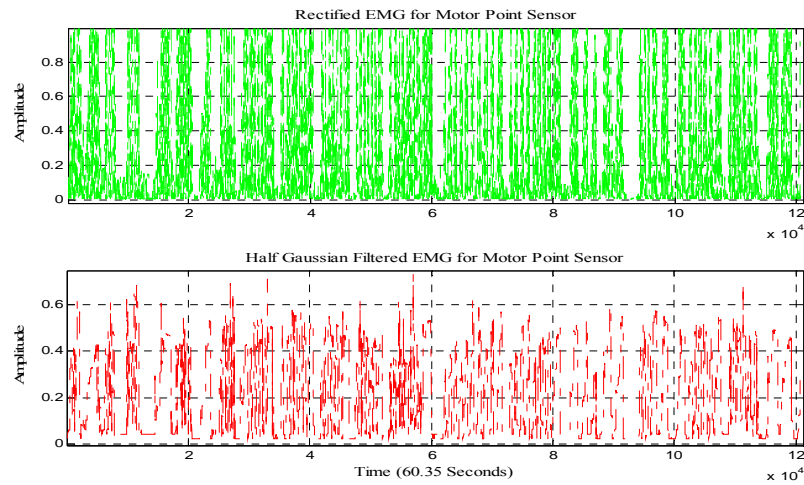


**Figure 2.12:** Rectified EMG and Half-Gaussian filtered EMG signal for motor point sensor.

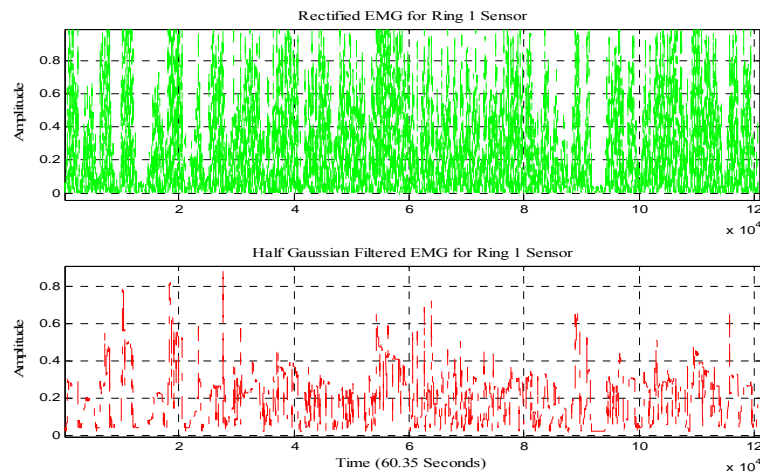


**Figure 2.13:** Rectified EMG and Half-Gaussian filtered EMG signal for ring1 sensor.

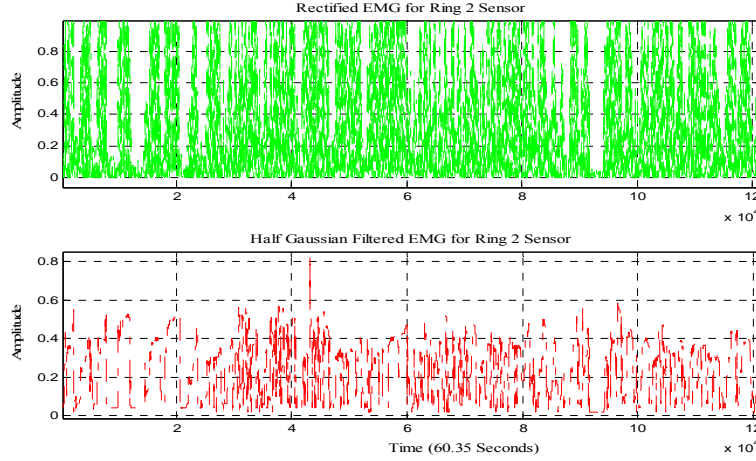


**Figure 2.14:** Rectified EMG and Half-Gaussian filtered EMG signal for ring2 sensor.

### Nonlinear ARX and Hammerstein-Wiener Modeling

In this section, we are using nonlinear ARX and Hammerstein-Wiener models with different nonlinearity estimators/classes to model three sEMG sensors data as input and skeletal-muscle force data as output. The nonlinear ARX model uses a parallel combination of nonlinear and linear blocks [104].

Figure 2.15 shows the nonlinear ARX model structure. The nonlinear ARX model uses regressors as variables for nonlinear and linear functions. Regressors are functions of measured input-output data [104]. The predicted output  $\hat{y}(t)$  of a nonlinear model at time  $t$  is given by the general Equation 23:

$$\hat{y}(t) = F(x(t)), \quad (23)$$

where  $x(t)$  represents the regressors,  $F$  is a nonlinear regressor command, which is estimated by nonlinearity estimators/classes [104].

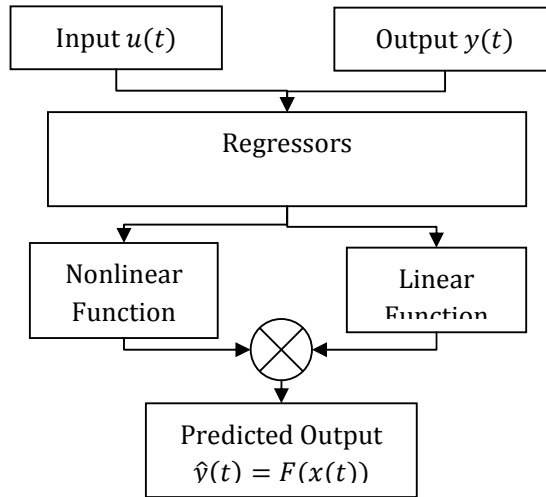


**Figure 2.15:** Structure: nonlinear ARX model.

As shown in Figure 2.15, the command  $F$  can include both linear and nonlinear functions of  $x(t)$ . Equation 24 gives the description of  $F$ .

$$F(x) = \sum_{k=1}^d \alpha_k \kappa(\beta_k(x - \gamma_k)) \quad (24)$$

where  $\kappa$  is the unit nonlinearity command,  $d$  is the number of nonlinearity units, and  $\alpha_k$ ,  $\beta_k$  and  $\gamma_k$  are the parameters of the nonlinearity estimators/classes [104].

The Hammerstein-Wiener model uses one or two static nonlinear blocks in series with a linear block. Structural representation of a nonlinear Hammerstein-Wiener is shown in Figure 2.16 [104].

The general Equations (25), (26), and (27) can describe the Hammerstein-Wiener structure [104].

$$w(t) = f(u(t)) \quad (25)$$

$$x(t) = \frac{B_{j,i}(q)}{F_{j,i}(q)} w(t) \quad (26)$$

$$y(t) = h(x(t)). \quad (27)$$

Here,  $u(t)$  and  $y(t)$  are input and output of the system, respectively.  $f$  and  $h$  are nonlinear functions, which corresponds to input and output nonlinearity, respectively.  $w(t)$  and  $x(t)$  are internal variables, where  $w(t)$  has the same dimensions as  $u(t)$  and  $x(t)$  has the same dimensions as  $y(t)$ , and  $B(q)$  and  $F(q)$  corresponds to the linear dynamic block, as polynomials in the backward shift operator.

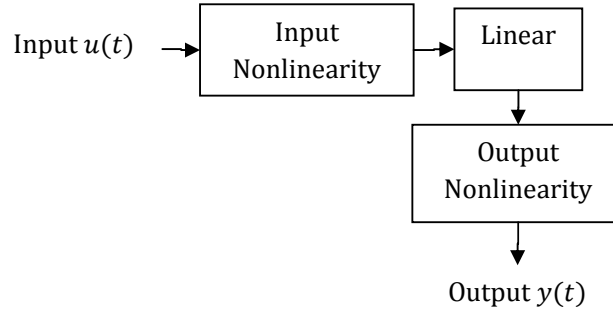


**Figure 2.16:** Structure: nonlinear Hammerstein-Wiener model.

The nonlinearity classes used in this work are Wavenet, Treepartition, Sigmoidnet, Pwlinear, Saturation, and Deadzone. For motor point and ring1 sensors, three nonlinear ARX and four nonlinear Hammerstein-Wiener models with different nonlinearity estimators/classes are obtained. For ring2 sensor, three nonlinear ARX and five nonlinear Hammerstein-Wiener models with different nonlinearity estimators/classes are obtained. Tables 2.2, 2.3 and 2.4 give the nonlinearity estimators/classes for different sensors and their corresponding model fit values.

**Table 2.2:** Different Nonlinearity Estimators and Model Fit Values for Motor Point Sensor (WSEAS 2010)

S. No.	Model	Nonlinearity Class	Model Fit
1.	<i>nlarx1</i>	Wavenet	24.78 %
2.	<i>nlarx2</i>	Treepartiton	40.46 %
3.	<i>nlarx3</i>	Sigmoidnet	48.75 %
4.	<i>nlhw2</i>	Wavenet	32.38 %
5.	<i>nlhw3</i>	Pwlinear	26.27 %
6.	<i>nlhw4</i>	Saturation	55.16 %
7.	<i>nlhw5</i>	Deadzone	42.45 %

**Table 2.3:** Different Nonlinearity Estimators and Model Fit Values for Ring1 Sensor (WSEAS 2010)

S. No.	Model	Nonlinearity Class	Model Fit
1.	<i>nlarx31</i>	Wavenet	-60.76 %
2.	<i>nlarx32</i>	Treepartiton	-52.64 %
3.	<i>nlarx33</i>	Sigmoidnet	-39.36 %
4.	<i>nlhw31</i>	Pwlinear	31.06 %
5.	<i>nlhw32</i>	Sigmoidnet	10.05 %
6.	<i>nlhw33</i>	Saturation	31.57 %
7.	<i>nlhw35</i>	Wavenet	32.36 %



**Table 2.4:** Different Nonlinearity Estimators and Model Fit Values for Ring2 Sensor (WSEAS 2010)

S. No.	Model	Nonlinearity Class	Model Fit
1.	<i>nlarx21</i>	Wavenet	-25.12 %
2.	<i>nlarx22</i>	Treepartiton	-22.31 %
3.	<i>nlarx23</i>	Sigmoidnet	-33.65 %
4.	<i>nlhw21</i>	Pwlinear	34.69 %
5.	<i>nlhw22</i>	Sigmoidnet	34.76 %
6.	<i>nlhw23</i>	Saturation	33.3 %
7.	<i>nlhw24</i>	Deadzone	34.94 %
8.	<i>nlhw25</i>	Wavenet	34.89 %

**Data Fusion and Adaptive KIC Probability**

Data fusion of multiple outputs of nonlinear ARX and Hammerstein-Wiener models is done by assigning a particular probability to each individual model [105]. First, the adaptive fusion algorithm is applied to the outputs of different nonlinear ARX and Hammerstein-Wiener models for each sensor obtained using different nonlinearity estimators. Second, the adaptive fusion algorithm is again applied to the final fusion based outputs of each sensor; this gives good force estimate. SI model fit value gives the probability for each model, which is given by  $\left[1 - \frac{|Y - \hat{Y}|}{|Y - \bar{Y}|}\right] * 100$ . The model selection criterion used is KIC. The sum of two directed divergences, which is the measure of the models dissimilarity, is known as Kullback's symmetric or J-divergence [106], as given by Equation 28.

$$KIC(p_i) = \frac{n}{2} \log R_i + \frac{(p_i+1)n}{n-p_i-2} - n\psi\left(\frac{n-p_i}{2}\right) + g(n), \quad (28)$$

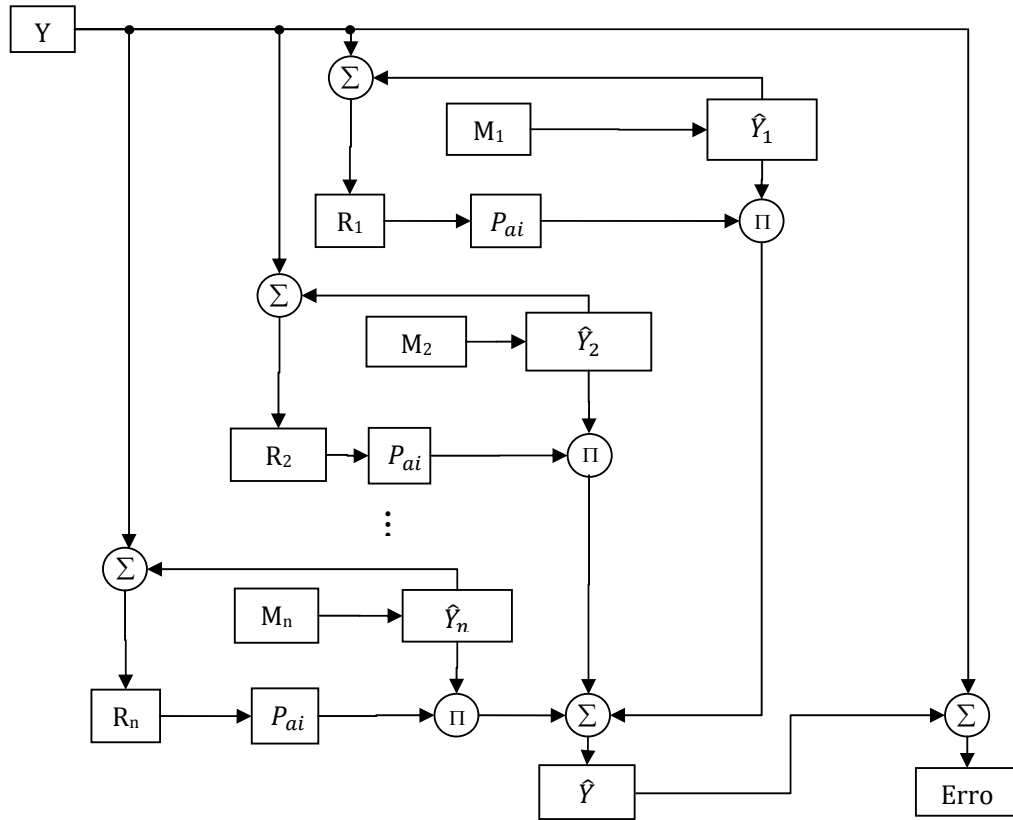
where  $g(n) = n * \log(n/2)$ .

The following adaptive fusion algorithm given by [105] is applied for data fusion of the outputs of different nonlinear ARX and Hammerstein-Wiener models:

- 1) Identify models  $M_1, M_2, \dots, M_k$  using sEMG data ( $u$ ) as input and force data ( $Y$ ) as output, for  $k$  number of sensors collecting data simultaneously.
- 2) Compute the residual square norm  $R_i = \|Y - \Phi_i \hat{\Theta}_i\|^2 = \|Y - \hat{Y}\|$ ,  
where  $\hat{\Theta}_i = \{\Phi_i^T \Phi_i\}^{-1} \Phi_i^T Y$ , and  $\Phi = \begin{bmatrix} Y_p^T & u_p^T & Y_{p-1}^T & \dots & u_1^T \\ Y_{p+1}^T & u_{p+1}^T & Y_p^T & \dots & u_2^T \\ \vdots & \vdots & \vdots & \ddots & \vdots \\ Y_{n-1}^T & u_{n-1}^T & Y_{n-2}^T & \dots & u_{n-p}^T \end{bmatrix}$ .
- 3) Calculate the model criteria coefficient using Equation 28.
- 4) Compute the model probability  $p(M_i|Z) = \frac{e^{-l_i}}{\sum_{j=1}^k e^{-l_j}}$ , where  $l$  is model selection criterion, i.e.  $KIC(p_i)$ .

- 5) Compute the data fusion based model output  $\hat{Y}_f = \sum_{i=1}^k p(M_i|Z) \hat{Y}_i$ .

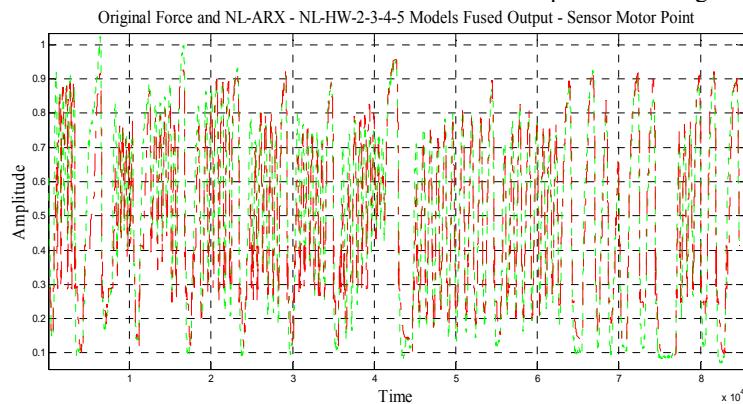
Here all the computation from step 2) to 5) is adaptive i.e. the residual square norm,  $KIC(p_i)$ , model probability  $p(M_i|Z)$ , and fused model output  $\hat{Y}_f$  are being updated with time or for each data point. Figure 2.17 shows the flow chart for fusion of outputs and adaptive probability of KIC.



**Figure 2.17:** Data fusion and adaptive KIC probability.

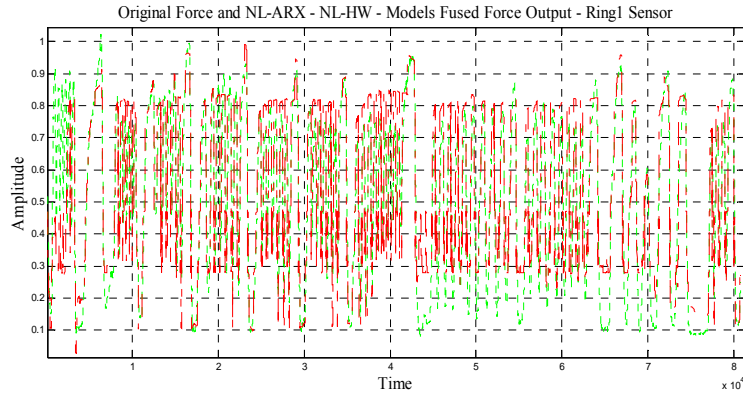
### Results, Discussion, and Future Work

This section deals with the results, discussion and future work. The following plots show the nonlinear (ARX and Hammerstein-Wiener) model and adaptive fusion algorithm based estimated force output for each sensor first and then finally combined adaptive fusion based output for all three sensors. Figure 2.18 shows the overlapping plot of the original and adaptive fusion based force output for the motor point sensor. The output is the result of the adaptive fusion algorithm on three nonlinear ARX and four nonlinear Hammerstein-Wiener models for the motor point sensor signal.

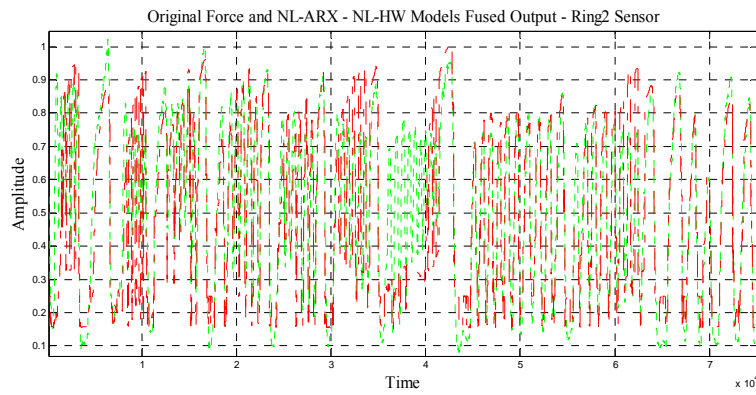


**Figure 2.18:** Measured vs. adaptive data fusion based output for motor point sensor.

Figure 2.19 shows the overlapping plot of the original and adaptive fusion based force output for ring1 sensor. This output is the result of adaptive fusion algorithm of three nonlinear ARX and four nonlinear Hammerstein-Wiener models for ring1 sensor signal.

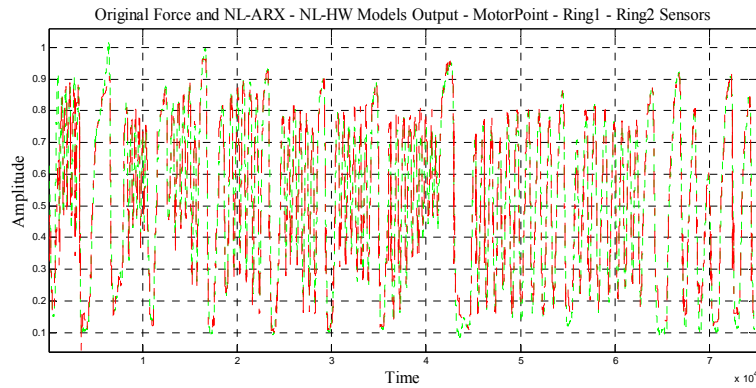


**Figure 2.19:** Measured vs. adaptive data fusion based output for ring1 sensor.



**Figure 2.20:** Measured vs. adaptive data fusion based output for ring2 sensor.

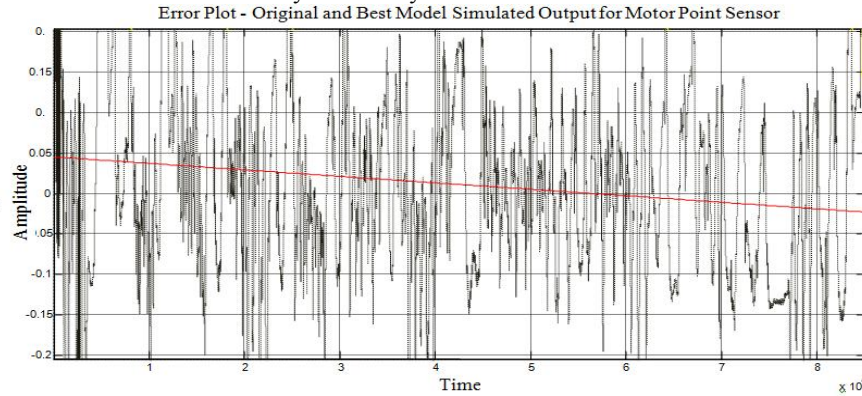
Figure 2.20 shows the overlapping plot of the original and adaptive fusion based force output for ring2 sensor. This output is the result of adaptive fusion algorithm on three nonlinear ARX and five nonlinear Hammerstein-Wiener models for ring2 sensor signal.



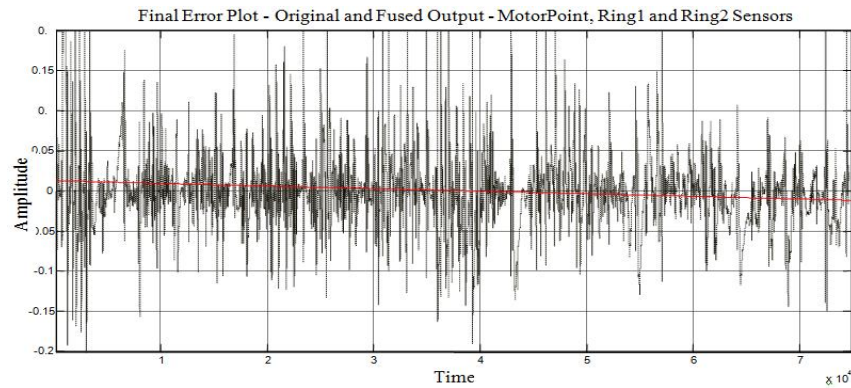
**Figure 2.21:** Final plot – measured vs. adaptive data fusion based output for all three sensors.

Figure 2.21 shows the overlapping plot of the original and final combined adaptive fusion based force output for motor point, ring1 and ring2 sensors. The output is the result of adaptive fusion algorithm on the final outputs of three sensors i.e. motor point, ring1 and ring2 as shown in Figs. 24 to 26. Also, Figure 2.21 shows the best skeletal-muscle force estimate, which is the result of the multi nonlinear ARX and Hammerstein-Wiener models and an adaptive hybrid data fusion on these nonlinear models. Figure 2.22 shows the error plot of the original and best-estimated model output for the motor point sensor. Figure 2.23 shows the error plot of original and final multi nonlinear modeled

and adaptive hybrid data fusion based force estimate (results from three sensors, nonlinear modeling and adaptive data fusion algorithm). If we compare Figs. 28 and 29, it is very clear and conspicuous that the error has decreased remarkably and is very close to zero.



**Figure 2.22:** Error plot – measured vs. best-estimated model output for motor point sensor.



**Figure 2.23:** Final error plot – measured vs. adaptive data fusion based output for motor point, ring1 and ring2 sensors.

Future work will focus on the improvement of the data collection techniques and experiment design. By using the combination of linear and nonlinear modeling, and adaptive hybrid data fusion, the skeletal-muscle force estimate can be improved further. Furthermore, the authors believe that by using different model selection criteria such as Akaike Information Criterion (AIC), Kullback Information Criterion (KIC) and the Bayesian Information Criterion (BIC) together to obtain final skeletal-muscle force estimate will give improved results.

sEMG and force data acquired using three EMG and one common FSR force sensor is modeled using nonlinear SI. Using different nonlinearity estimators/classes, multi nonlinear ARX and Hammerstein-Wiener models are obtained for each sensor. First, the outputs of different models for each sensor are fused with a data fusion algorithm and an adaptive KIC probability. Finally, the fused outputs from each sensor are again fused with same algorithm and adaptive KIC probability. The final estimated force using this technique gives the best estimate. The presented approach can be utilized for controlling prosthetic hands [107].

### **2.2.2 A Hybrid Adaptive Data Fusion with Linear and Nonlinear Models for Skeletal-Muscle Force Estimation**

Position and force control are two critical aspects of prosthetic control. Surface electromyographic (sEMG) signals can be used for skeletal-muscle force estimation. In this section, skeletal-muscle is considered as a system and System Identification (SI) is used to model sEMG and skeletal-muscle force. The recorded sEMG signal is filtered utilizing optimized nonlinear Half-Gaussian Bayesian filter, and a Chebyshev Type-II filter prepares the muscle-force signal. The filter

optimization is accomplished using Genetic Algorithm (GA). Multi- linear and nonlinear models are obtained with sEMG as input and skeletal-muscle force of a human hand as an output. The outputs of these models are fused with a probabilistic Kullback Information Criterion (KIC) for model selection and an adaptive probability of KIC. This approach gives good estimate of the skeletal-muscle force.

The present work presents a novel approach to estimate skeletal-muscle force using an adaptive data fusion algorithm with hybrid multi linear and nonlinear models as shown in Figure 2.24. The recorded sEMG signals are filtered utilizing Genetic Algorithm (GA) based optimized nonlinear Half-Gaussian Bayesian filter parameters, and the skeletal-muscle force signal is filtered by using a Chebyshev Type-II filter. Using an input/output approach, the EMG signal measured at the skin surface is considered as input to the skeletal-muscle, whereas the resulting hand/finger force constitutes the output.

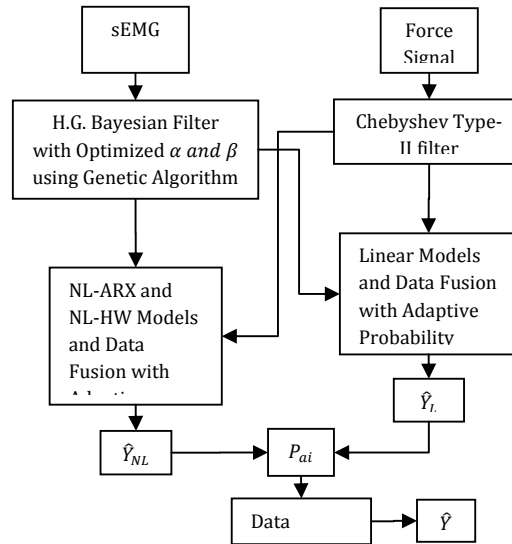


**Figure 2.24:** Flow chart for estimation of skeletal-muscle force using an adaptive data fusion algorithm.

Multi linear and nonlinear models are obtained using System Identification (SI) for the motor point signals as they capture the dynamics of the system differently. The outputs of estimated linear and nonlinear models are fused with a probabilistic Kullback Information Criterion (KIC) for model selection and an adaptive probability of KIC. First, the outputs are fused for the linear models and then for nonlinear models and finally the resultant outputs of linear and nonlinear models are fused together. The final fused output of different linear and nonlinear models results in good skeletal-muscle force estimates.

### Experiment Design and Pre-Processing

Experiment design and signal preprocessing is discussed in the ‘Experiment Design and Pre-Processing’ section of ‘Adaptive Multi Sensor Based Nonlinear Identification of Skeletal-muscle Force’ in ‘Chapter 2: Skeletal-muscle Force.’ Please refer to Figure 2.10 in this section.

### System Identification – Linear and Non-Linear Modeling

System Identification (SI) is based on the acquired experimental data and is an alternative to physically based mathematical modeling [110]. A dynamical model such as the Auto Regressive with eXogenous input (ARX) or Output Error (OE) gives the system in mathematical form which is the outcome of parametric SI process. In this work, the SI approach is used with the myoelectric signal as the input to the system and as the output is the intended finger/hand force. In this work, multi- linear and nonlinear  $y(t)u(t - n_k)e(t)$  models are obtained for modeling of EMG and hand/finger force signals. Six linear and three nonlinear models are obtained for the motor point sEMG signal.

For the linear models Output Error model of order 6, ARX model of order 6, ARMAX model of model order 5, Box-Jenkins model of order 18, State-Space model with subspace method of order 12 and a State-Space model with prediction error/maximum likelihood method of order 12 are obtained using SI as given in Table 2.5. In Table 2.5  $y$  is output,  $t$  is time,  $B(q)$ ,  $F(q)$ ,  $A(q)$ ,  $C(q)$ ,  $D(q)$ , are

polynomials,  $q$  is a backward shift operator,  $u$  is input,  $n_k$  is delay and  $e$  is error [104]. For State-Space models:-  $x$  is state,  $t$  is time,  $Ts$  is sampling time,  $u$  is input,  $e$  is error,  $A, B, K, C$ , and  $D$  are system matrices, and  $y$  is output [104].

In contrary to six linear models as given in Table 2.5, nonlinear ARX with nonlinearity estimator as ‘sigmoidnet’ and nonlinear Hammerstein-Wiener models with nonlinearity estimators as ‘piecewise linear - pwlinear’ and ‘saturation’ are obtained, as given in Table 2.6.

**Table 2.5:** Linear Models and Their Structures (CIBEC 2010)

Linear Model Name	Linear Model Structure
Output Error	$y(t) = \frac{B(q)}{F(q)}u(t - n_k) + e(t)$
ARX	$A(q)y(t) = B(q)u(t - n_k) + e(t)$
ARMAX	$A(q)y(t) = B(q)u(t - n_k) + C(q)e(t)$
Box-Jenkins	$y(t) = \frac{B(q)}{F(q)}u(t - n_k) + \frac{C(q)}{D(q)}e(t)$
State-Space – subspace method	$\begin{aligned} x(t + Ts) &= Ax(t) + Bu(t) + Ke(t) \\ y(t) &= Cx(t) + Du(t) + e(t) \end{aligned}$
State-Space – prediction error/maximum likelihood method	$\begin{aligned} x(t + Ts) &= Ax(t) + Bu(t) + Ke(t) \\ y(t) &= Cx(t) + Du(t) + e(t) \end{aligned}$

**Table 2.6:** Nonlinear Models and Their Structures (CIBEC 2010)

Nonlinear Model Name	Nonlinear Model Structure
Nonlinear ARX – Sigmoidnet	$y_p(t) = f(y(t-1), y(t-2), y(t-3), \dots, u(t-1), u(t-2), \dots); f(z) = \frac{1}{e^{-z} + 1} \text{ is sigmoid function.}$
Nonlinear HW – Piecewise Linear – pwlinear	$w(t) = f(u(t)), x(t) = \frac{B_{ji}(q)}{F_{ji}(q)}w(t), y(t) = h(x(t));$
Nonlinear HW – Saturation	$w(t) = f(u(t)), x(t) = \frac{B_{ji}(q)}{F_{ji}(q)}w(t), y(t) = h(x(t));$

In Table 2.6  $f$  is a nonlinear function for the nonlinear ARX model. Inputs to  $f$  are model regressors.  $y_p(t)$  is the predicted output as a weighted sum of past output values and current and past input values. For the nonlinear Hammerstein-Wiener model  $u(t)$  and  $y(t)$  are the inputs and outputs for the system, respectively.  $f$  and  $h$  are nonlinear functions that corresponds to the input and output nonlinearity, respectively.  $w(t)$  and  $x(t)$  are internal variables.  $w(t)$  has the same dimension as  $u(t)$ .  $x(t)$  has the same dimension as  $y(t)$ .  $B(q)$  and  $F(q)$  in the linear dynamic block are polynomials in the backward shift operator. If only the input nonlinearity is present, the model is called the Hammerstein model. If only the output nonlinearity is present, the model is called the Wiener model [104].

### Fusion of Outputs and Adaptive Probability of KIC

Fusion of outputs is achieved with an adaptive probability of KIC, as given in the subsection ‘DATA FUSION AND ADAPTIVE KIC PROBABILITY,’ of the previous section ‘ADAPTIVE MULTI SENSOR BASED NONLINEAR IDENTIFICATION OF SKELETAL-MUSCLE FORCE’ of this chapter.

### Results, Conclusion, and Future Work

Adaptive KIC probability based data fusion algorithm is applied to linear and nonlinear models separately and then combined. Figs. 2.25 and 2.26 show the results for the linear and nonlinear models respectively. Finally, both linear and nonlinear models are combined and adaptive KIC probability based data fusion algorithm is applied to obtain the final output that is given by Figure 2.27. Validation of this technique is confirmed with a separate data set. Figure 2.28 depicts the validation of the proposed technique. Future work will focus on the improved data collection techniques, use of spatial filters for sEMG signals filtration, and use of multi sensor data with this technique.

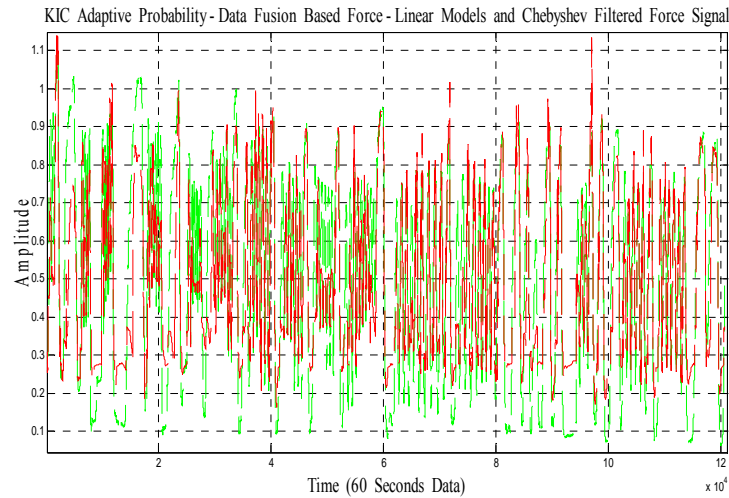


**Figure 2.25:** For linear models: KIC adaptive probability data fusion based force vs. Chebyshev Type II filtered force.

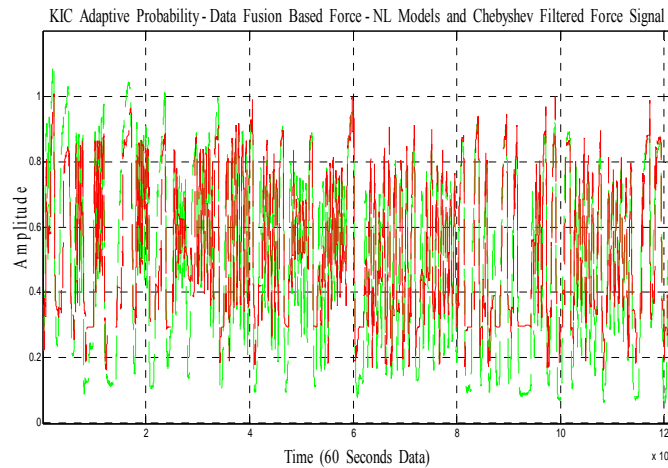


**Figure 2.26:** For nonlinear models: KIC adaptive probability data fusion based force vs. Chebyshev Type II filtered force.

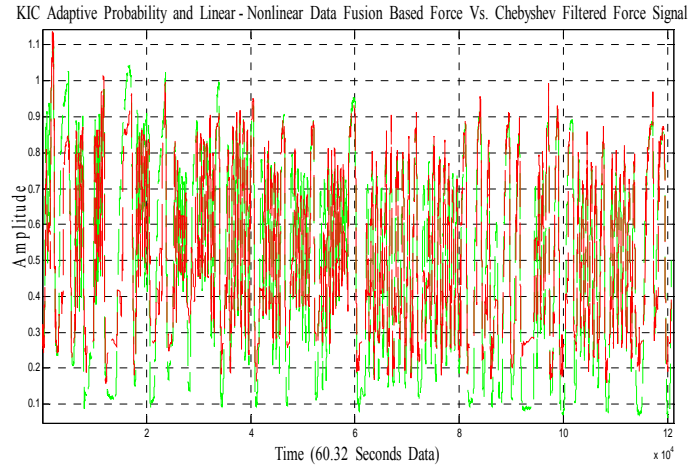


**Figure 2.27:** For linear and nonlinear models combined: KIC adaptive probability data fusion based force vs. Chebyshev Type II filtered force.

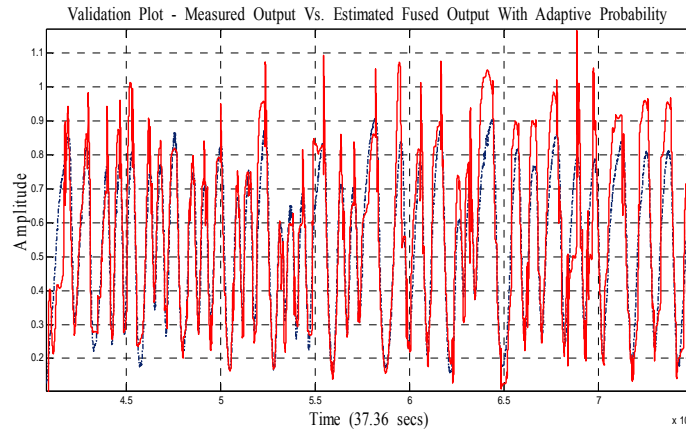


**Figure 2.28:** Validation plot - for linear and nonlinear models combined: KIC adaptive probability data fusion based force vs. Chebyshev Type II filtered force.

### **2.2.3 A Hybrid Adaptive Multi Sensor Data Fusion for Estimation of Skeletal-Muscle Force for Prosthetic Hand Control**

Effective use of upper-extremity prostheses depends on the two critical aspects of precise position and force control. Surface electromyographic (sEMG) signals can be used as a control input for the position and force actions related to the prosthesis. In this section, we use the measured sEMG signals to estimate skeletal-muscle force. Further, we consider skeletal-muscle as a system and System Identification (SI) is used to model multi-sensor sEMG and skeletal-muscle force. The sEMG signals are filtered utilizing optimized nonlinear Half-Gaussian Bayesian filter, and a Chebyshev Type-II filter provides the muscle-force signal. The filter optimization is accomplished using a Genetic Algorithm (GA). Multi- linear and nonlinear models are obtained with sEMG data as input and skeletal-muscle force of a healthy human hand as an output for three sensors. The outputs of these models for three sensors are fused with a probabilistic Kullback Information Criterion (KIC) for model selection and an adaptive probability of KIC. The final fusion based force for multi-sensor sEMG gives improved estimate of the skeletal-muscle force.

The present work is an extension of our previous work [111] where we proposed estimation of the skeletal-muscle force using an adaptive data fusion algorithm with hybrid multi linear and nonlinear models. In [111] the sEMG data was based only from measuring the motor point sEMG signal, whereas in the present work we extend this to three sensors for the ring finger of the dominant



hand of a healthy male subject. Figure 2.29 presents the flow chart of the work done in this section. The sEMG signals are acquired from the forearm of a healthy subject and filtered utilizing Genetic Algorithm (GA) based optimized nonlinear Half-Gaussian Bayesian filter. On the other hand, the skeletal-muscle force signal is filtered using a Chebyshev Type-II filter. The sEMG is considered as input whereas force signal is considered as an output. Since each model captures the dynamics differently, we obtained multiple linear and nonlinear models using System Identification (SI) for the sEMG data corresponding to the three sensors. First, the outputs of all the linear and nonlinear models from the three sensors are fused separately and then the resultant three outputs are fused with a probabilistic Kullback Information Criterion (KIC) for model selection and an adaptive probability of KIC. The final fused output using this approach gives improved skeletal-muscle force estimates.

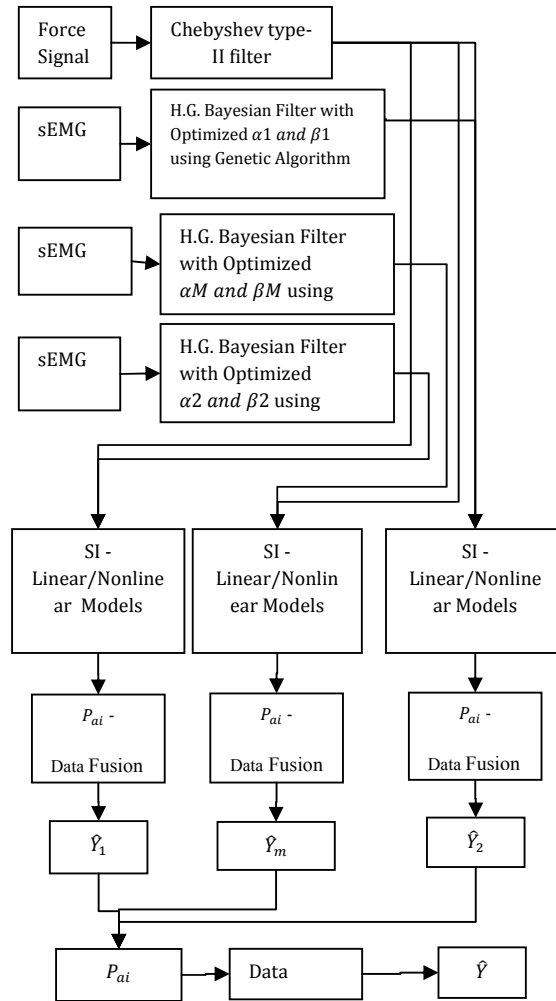


**Figure 2.29:** Flow chart for estimation of skeletal-muscle force using an adaptive data fusion algorithm.

## Experiment Design and Pre-Processing

Experiment design and signal preprocessing is discussed in the ‘Experiment Design and Pre-Processing’ section of ‘Adaptive Multi Sensor Based Nonlinear Identification of Skeletal-Muscle Force’ in ‘Chapter 2: Skeletal-Muscle Force.’ Please refer to Figure 2.10 in this section.

### System Identification – Linear and Nonlinear Modeling

A system can be modeled either by using physics based mathematical models or by System Identification (SI) [110]. Parametric SI gives a dynamic model such as the Auto Regressive with exogenous input (ARX) or Output Error (OE) of the system in mathematical form. In this research, we

use the SI approach to model the two signals. The sEMG is the input to the system and the intended finger/hand force is output. In this work, mutli- linear and nonlinear  $y(t)u(t - n_k)e(t)$  models are obtained for modeling of sEMG and hand/finger force signals for three sensors for the ring finger of the dominant hand of a healthy subject. Six linear and three nonlinear models are obtained for the motor point sEMG signal, three linear and five nonlinear models are obtained for the ring1 sensor, and six linear and five nonlinear models are obtained for ring2 sensor data. Table 2.7 and VIII give the structures of linear and nonlinear models respectively.

The model order of the various models used in this work are as follows: linear models for the motor point data, OE model of order 6, ARX model of order 6, ARMAX model of model order 5, Box-Jenkins (BJ) model of order 18, State-Space model with subspace method (N4SID) of order 12 and a State-Space model with prediction error/maximum likelihood method (PEM) of order 12 are obtained using SI. For ring1 sensor (sensor adjacent to the motor point sensor) data OE model of order 17, ARMAX model of order 35 and BJ model of order 11 are obtained. For ring2 sensor (sensor on opposite side of ring1 sensor) data OE model of order 45, ARX model of order 12, ARMAX model of order 17, BJ model of order 14, N4SID model of order 13 and PEM model of order 22 are obtained. Table 2.7 gives the structure of all the linear models. In Table 2.7  $y$  is output,  $t$  is time,  $B(q)$ ,  $F(q)$ ,  $A(q)$ ,  $C(q)$ ,  $D(q)$ , are polynomials,  $q$  is a backward shift operator,  $u$  is input,  $n_k$  is delay and  $e$  is error [104]. For State-Space models:-  $x$  is state,  $t$  is time,  $T_s$  is sampling time,  $u$  is input,  $e$  is error,  $A$ ,  $B$ ,  $K$ ,  $C$ , and  $D$  are system matrices, and  $y$  is output [104].

Table 2.8 gives the structures of nonlinear models. The nonlinear models for the motor point data are obtained as, the nonlinear ARX with a sigmoidnet nonlinearity estimator, nonlinear Hammerstein-Wiener models with a piecewise linear nonlinearity estimator, and a saturation based estimator. For each ring1 and ring2 signal data sets, five nonlinear Hammerstein-Wiener models with nonlinearity estimators as ‘piecewise linear – pwlinear,’ ‘sigmoidnet,’ ‘saturation,’ ‘deadzone,’ and wavelet network’ are obtained.

In Table 2.8  $f$  is a nonlinear function for the nonlinear ARX model. Inputs to  $f$  are model regressors.  $y_p(t)$  is the predicted output as a weighted sum of past output values and current and past input values. For the nonlinear Hammerstein-Wiener model  $u(t)$  and  $y(t)$  are the inputs and outputs for the system, respectively.  $f$  and  $h$  are nonlinear functions that corresponds to the input and output nonlinearity, respectively.  $w(t)$  and  $x(t)$  are internal variables.  $w(t)$  has the same dimension as  $u(t)$ .  $x(t)$  has the same dimension as  $y(t)$ .  $B(q)$  and  $F(q)$  in the linear dynamic block are polynomials in the backward shift operator.

For nonlinear Hammerstein-Weiner model with deadzone nonlinearity estimator,  $F$  is a nonlinear function of  $x$  with the properties given in the Table 2.8. For nonlinear Hammerstein-Weiner model with wavelet network as nonlinearity estimator,  $\kappa(s)$  as a wavelet function, and  $\beta_k$  is a row vector such that  $\beta_k(x - \gamma_k)$  is a scalar. If only the input nonlinearity is present, the model is called the Hammerstein model. If only the output nonlinearity is present, the model is called the Wiener model [104].

**Table 2.7:** Linear Models and Their Structures (ICAI 2011)

Linear Model Name	Linear Model Structure
Output Error	$y(t) = \frac{B(q)}{F(q)}u(t - n_k) + e(t)$
ARX	$A(q)y(t) = B(q)u(t - n_k) + e(t)$
ARMAX	$A(q)y(t) = B(q)u(t - n_k) + C(q)e(t)$
Box-Jenkins	$y(t) = \frac{B(q)}{F(q)}u(t - n_k) + \frac{C(q)}{D(q)}e(t)$

State-Space – subspace method

$$\begin{aligned}x(t + Ts) &= Ax(t) + Bu(t) \\ &\quad + Ke(t) \\ y(t) &= Cx(t) + Du(t) + e(t)\end{aligned}$$

State-Space – prediction error/maximum likelihood method

$$\begin{aligned}x(t + Ts) &= Ax(t) + Bu(t) \\ &\quad + Ke(t) \\ y(t) &= Cx(t) + Du(t) + e(t)\end{aligned}$$

**Table 2.8:** Nonlinear Models and Their Structures (ICAI 2011)

Nonlinear Model Name	Nonlinear Model Structure
Nonlinear ARX – Sigmoidnet	$y_p(t) = f(y(t-1), y(t-2), y(t-3), \dots, u(t-1), u(t-2), \dots);$ $f(z) = \frac{1}{e^{-z} + 1} \text{ is sigmoid function.}$
Nonlinear HW – Piecewise Linear – pwlinear	$w(t) = f(u(t)), x(t) = \frac{B_{ji}(q)}{F_{ji}(q)} w(t),$ $y(t) = h(x(t));$
Nonlinear HW – Sigmoidnet	$y_p(t) = f(y(t-1), y(t-2), y(t-3), \dots, u(t-1), u(t-2), \dots);$ $f(z) = \frac{1}{e^{-z} + 1} \text{ is sigmoid function.}$
Nonlinear HW – Saturation	$w(t) = f(u(t)), x(t) = \frac{B_{ji}(q)}{F_{ji}(q)} w(t),$ $y(t) = h(x(t));$
Nonlinear HW – Deadzone	$y = F(x); a \leq x < b, \quad F(x) = 0$ $x < a, \quad F(x) = x - a$ $x \geq b, \quad F(x) = x - b$
Nonlinear HW – Wavelet Network	$g(x) = \sum_{k=1}^n \alpha_k \kappa(\beta_k(x - \gamma_k))$

### Adaptive Data Fusion Algorithm

Fusion of outputs for different linear and nonlinear models is achieved with an adaptive probability of KIC, as given in the subsection ‘DATA FUSION AND ADAPTIVE KIC PROBABILITY,’ of the previous section ‘ADAPTIVE MULTI SENSOR BASED NONLINEAR IDENTIFICATION OF SKELETAL-MUSCLE FORCE’ of this chapter.

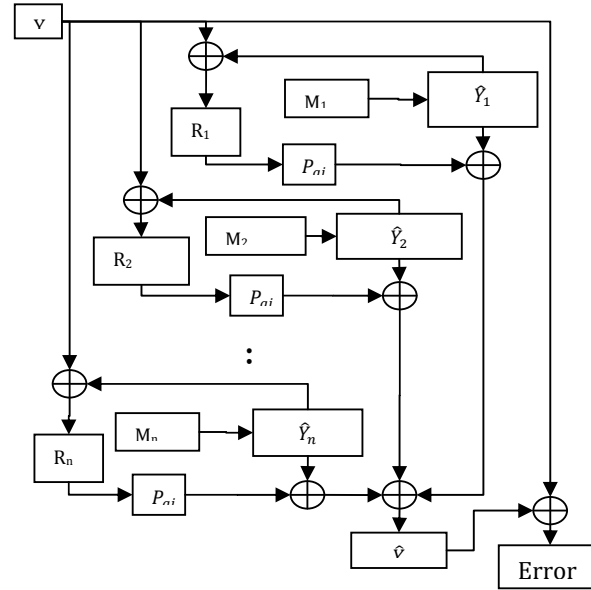


**Figure 2.30:** Adaptive KIC probability based data fusion.

In this research work, we are obtaining multi-linear and nonlinear models using SI for the sEMG sensor for the ring finger motor unit, and two adjacently placed sensors, ring1 and ring2. The fusion of outputs and adaptive KIC probability is shown in Figure 2.30, which is followed by the adaptive data fusion algorithm.

### Results and Discussion

An adaptive KIC probability based data fusion algorithm is applied to linear and nonlinear models separately for the models obtained using three sets of input and output data for three sEMG sensors. First the fusion based output for each sensor is obtained and then the three fusion based outputs from three sEMG sensors are fused to get the improved estimates of the skeletal-muscle force. The following plots show the improvement in the force estimates in succession with different sensors separately and then combined. All the plots have the measured skeletal-muscle force signal in green and the estimated force signal in red color.

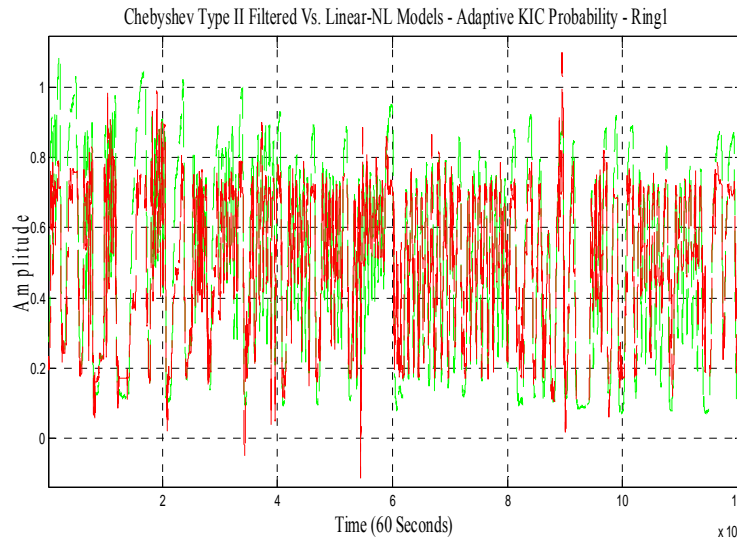


**Figure 2.31:** Chebyshev Type II vs. adaptive KIC probability based force from linear and nonlinear models for ring1 sensor.

Figure 2.31 is a plot of measured and Chebyshev Type II filtered finger force data with the adaptive KIC probability fusion based force for the first sensor named as ring1. The two signals are very clear and the estimated signal shows good follow up of the measured signal. Figure 2.32 and 2.33 show the measured and Chebyshev Type II filtered skeletal-muscle force with the adaptive KIC probability fusion based force signals for the second sensor named as ring2, and motor point sensor. It is evident to us that the measured signal has a very close follow up by the estimated signal.

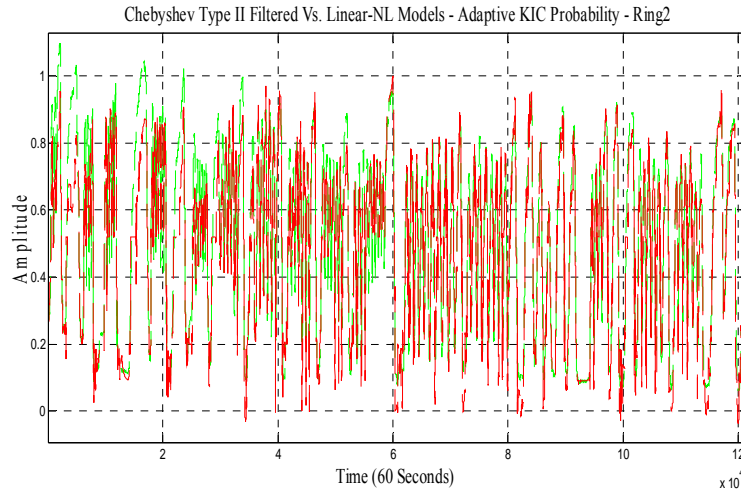


**Figure 2.32:** Chebyshev Type II vs. adaptive KIC probability based force from linear and nonlinear models for ring2 sensor.

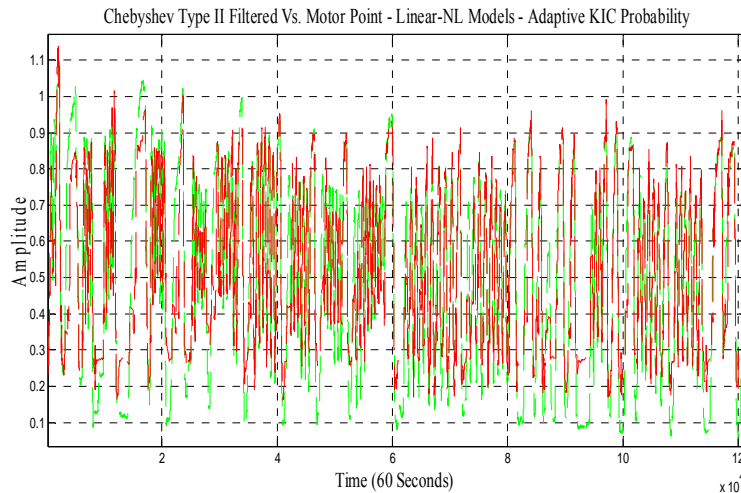


**Figure 2.33:** Chebyshev Type II vs. adaptive KIC probability based force from linear and nonlinear models for motor point sensor.

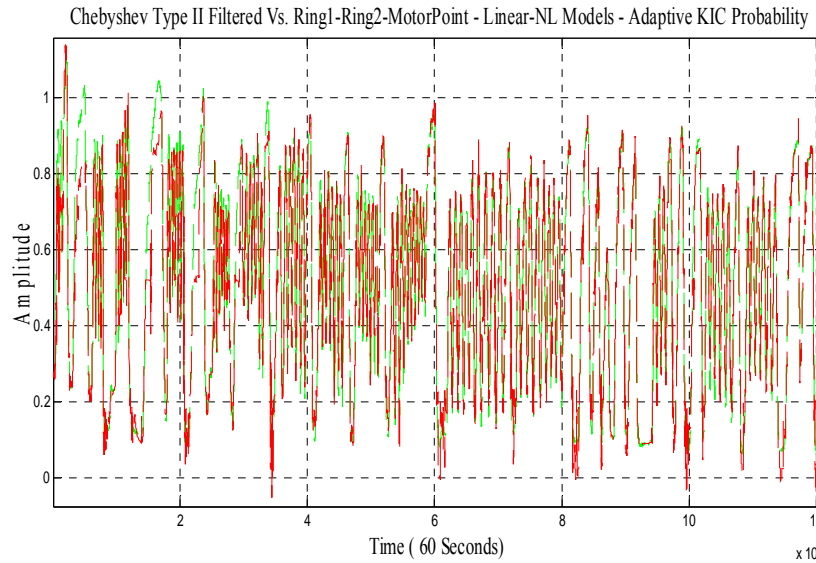


**Figure 2.34:** Chebyshev Type II vs. adaptive KIC probability based force from linear and nonlinear models for ring1, ring2 and motor point sensor combined.

Finally the estimated skeletal-muscle force from three sEMG sensors is further fused with adaptive KIC probability based data fusion algorithm. Figure 2.34 shows the comparison of the measured and Chebyshev Type II filter with the final adaptive KIC probability based fusion skeletal-muscle force estimate using three sEMG sensors. The final result for three sensors is the best estimate of skeletal-muscle force and it is evident to us that the measured signal has a very close follow up by the estimated signal.

The results show that there is a decrease in the percentage error from the linear and nonlinear models adaptive fusion based separate outputs to the adaptive fusion based combined output of linear and nonlinear models combined for all three sensors. However, these results show that there is a 16% improvement in the mean fit value of the motor point signal models with the adaptive KIC probability based data fusion algorithm for multi-sensors (three in this case). Figure 2.35 and 2.36 show the validation plots of this approach for two separate sets of sEMG and skeletal-muscle force data, where green signal is the Chebyshev Type II filtered measured force signal and the blue signal is estimated using this approach.

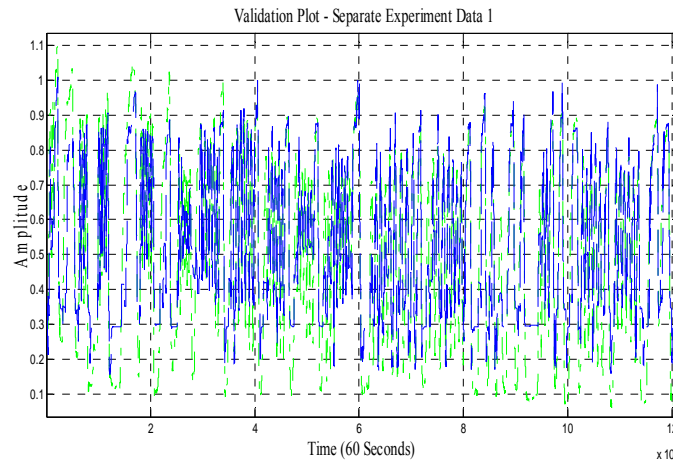


**Figure 2.35:** Validation plot 1 - Chebyshev Type II vs. estimated force signal using adaptive KIC probability.

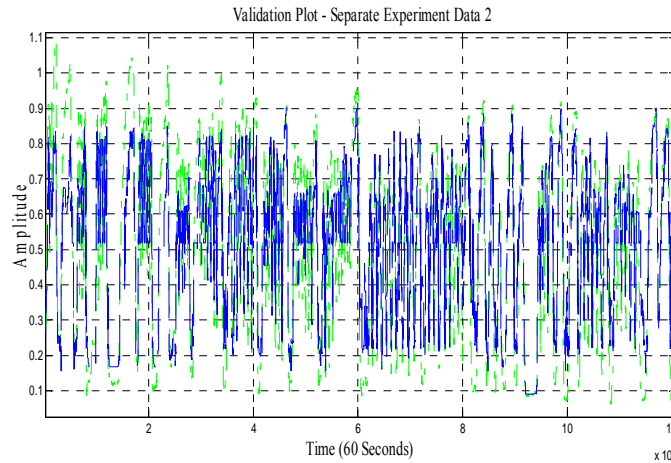


**Figure 2.36:** Validation plot 2 - Chebyshev Type II vs. estimated force signal using adaptive KIC probability.

Different linear and nonlinear models are obtained using system identification (SI) for three sets of data. Linear and nonlinear models' outputs are fused separately for each sensor and then fused together to get the final force estimate for each sensor. The net force estimates for each sensor is then applied with adaptive KIC probability based data fusion algorithm. The final estimates of the skeletal-muscle force gives improved results. Future work will focus on the improved data collection techniques and capturing data at higher sampling rate (6000 samples per second). Also, we would design new model selection criteria using different model selection criteria such as Akaike Information Criterion (AIC), Kullback Information Criterion (KIC) and the Bayesian Information Criterion (BIC).

#### **2.2.4 An Adaptive Hybrid Data Fusion Based Identification of Skeletal-Muscle Force with ANFIS and Smoothing Spline Curve Fitting**

Precise and effective prosthetic control is important for its applicability. Two desired objectives of the prosthetic control are finger position and force control. Variation in skeletal-muscle force results in corresponding change of surface electromyographic (sEMG) signals. sEMG signals generated by skeletal-muscles are temporal and spatially distributed that result in cross talk between adjacent sEMG signal sensors. To address this issue, an array of nine sEMG sensors is used with a force sensing resistor to capture muscle dynamics in terms of sEMG and skeletal-muscle force. The sEMG and skeletal-muscle force are filtered with a nonlinear Teager-Kaiser Energy (TKE) operator based nonlinear spatial filter and Chebyshev Type-II filter respectively. Multiple Takagi-Sugeno-Kang Adaptive Neuro Fuzzy Inference Systems (ANFIS) are obtained using sEMG as input and skeletal-muscle force as output. Outputs of these ANFIS systems are fitted with smoothing spline curve fitting. To achieve better estimate of the skeletal-muscle force, an adaptive probabilistic Kullback Information Criterion (KIC) for model selection based data fusion algorithm is applied to the smoothing spline curve fitting outputs. Final adaptive fusion based output of this approach results in improved skeletal-muscle force estimates.

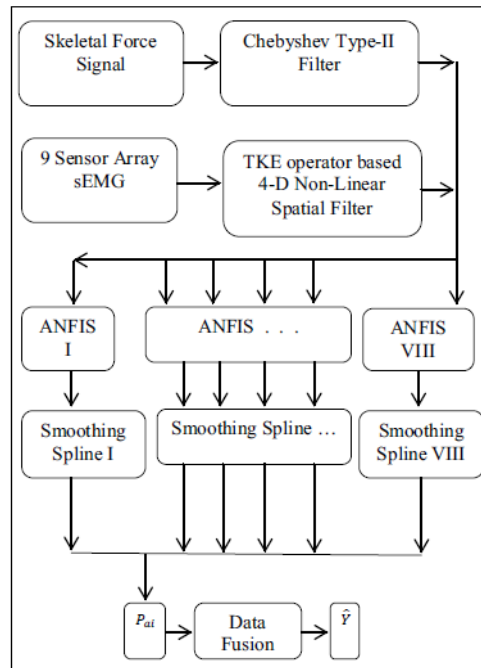


**Figure 2.37:** Flow chart of the approach used in this research work.

### Experiment Design

Based on the arrangement of the sEMG sensor array in [113], an experiment design was developed using DELSYS® Bagnoli-16 EMG system with nine DE-3.1 sEMG sensors to capture sEMG signals from skeletal-muscles. Here, the array involves nine sensors covering four directional spatial distributions of the sEMG signal. The middle three sEMG sensors were attached directly on the skin surface above the motor point of the flexor digitorum superficialis (FDS) muscle which controls the flexion of the ring finger. Appropriate sEMG electrode attachment point for the flexion of the ring finger was identified using a wet probe muscle stimulator at the FDS (RICH-MAR, HV 1000).

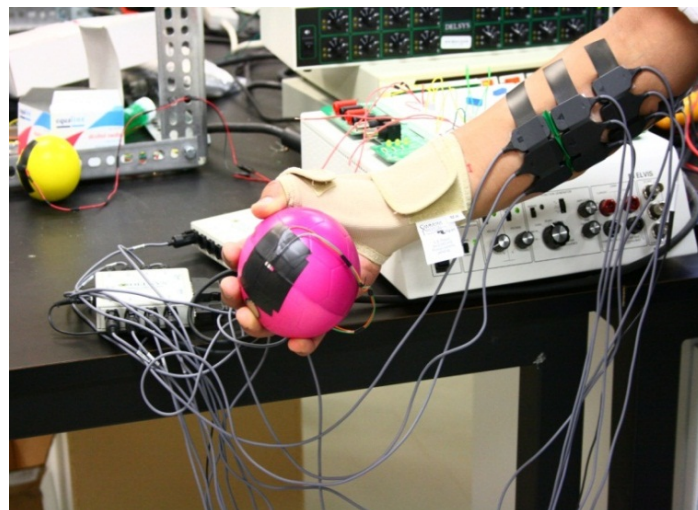


**Figure 2.38:** Experiment design: 9 sEMG sensors.

Prior to placing the sEMG sensors, the skin surface of the subject was prepared according to International Society of Electrophysiology and Kinesiology (ISEK) protocols. The thumb movement was restricted in this experiment using a thumb splint. However, the corresponding force data was captured using NI ELVIS™ with Interlink™ Electronics FSR 0.5" circular force sensor. Experiment design is shown in Figure 2.38, where 9 sensors are shown on a healthy subject forearm, holding a



stress ball for force measurements. The sEMG and finger force data was collected at a sampling rate of 2000 Hz using LabVIEW™ in conjunction with DELSYS® Bagnoli-16 EMG and NI ELVIS™. With this experiment design we conducted several experiments of 30 seconds, 45 seconds and 60 seconds durations.

### Signal Processing

The recorded sEMG signal is filtered using nonlinear spatial filtering for multichannel surface EMG. As given in [113], this nonlinear spatial filter is derived from “Nonlinear Teager-Kaiser Energy (TKE) Operator.” As given in [113], the TKE operator in the time domain on sEMG signal is defined by Equation 29.

$$\Psi[x(n)] = x^2(n) - x(n+1) * x(n-1). \quad (29)$$

Here,  $\Psi$  is the TKE operator and  $x(n)$  is the time domain sEMG signal. Based on the TKE operator, the four-dimensional nonlinear spatial filter is given by Equation 30.

$$\Psi_{d,4}[x(m,n)] = 4 * x^2(m,n) - x(m-1,n) * x(m+1,n) - x(m,n-1) * x(m,n+1) - x(m-1,n+1) * x(m+1,n-1) - x(m-1,n-1) * x(m+1,n+1). \quad (30)$$

Figure 2.39 shows a comparison between the measured and nonlinear spatial filtered sEMG signals. A Chebyshev Type II infinite impulse response (IIR) low pass filter with a 550 Hz pass band frequency is used to filter the skeletal-muscle force signal. Figure 2.40 shows the comparison between the measured and Chebyshev Type II filtered skeletal-muscle force signal.

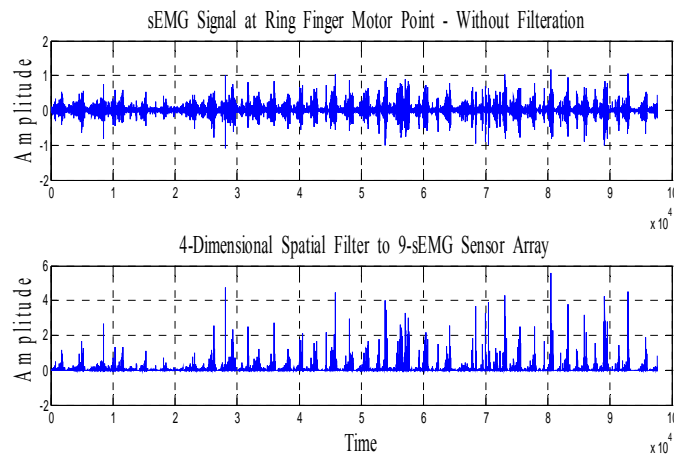


**Figure 2.39:** sEMG: ring finger motor point signal vs. filtered 9 sensor array signal.

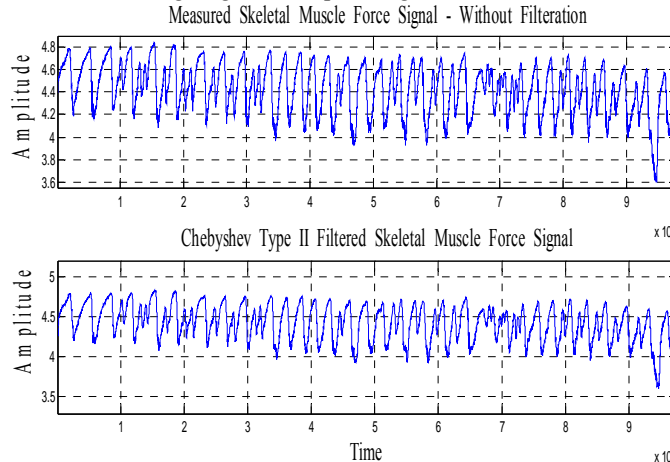


**Figure 2.40:** Skeletal-muscle force signal from ring finger.

## ANFIS Modeling

In 1965 professor Lofti A. Zadeh introduced the concept of “*Fuzzy Sets*”, which are sets with imprecise amplitudes [114]. Dr. Zadeh stated that the “*membership*” in a fuzzy set is a matter of degree and not a matter of affirmation or denial. For last four decades, this proposal has gained recognition as an important point in the evolution of modern concept of imprecision and uncertainty [114]. This innovation represents a paradigm shift from the classical sets or the crisp sets to “*Fuzzy Sets*” [114].

Fuzzy set and fuzzy logic theory can be used to capture the natural phenomenon of the imprecision and uncertainty [114]. The membership function is the characteristic of fuzzy set, which is a function whose range is an ordered membership set within the closed unit interval [114].

A crisp set which is a collection of distinct objects is defined in a way to partition objects in a given domain of discourse into two groups: members and non-members [114]. On the other hand, a fuzzy set can be formed by assigning a membership value (which represents the degree to which an object belongs to a fuzzy set) to each object in the interval of 0 to 1 [114]. Fuzzy membership functions can be of different forms such as triangular, trapezoidal, pi, bell and Gaussian form.

Fuzzy Inference System (FIS) in fuzzy logic can be used to model a system which is an inference system based on empirical knowledge based linguistic rules [115]. The fuzzy inference system is composed of five steps: fuzzification of the input variables, application of the fuzzy operator (AND or OR) in the precedent, implication from the precedent to the subsequent, aggregation of the subsequents across the rules, and defuzzification. In the fuzzification process, the membership values coming from quantitative measurements are converted to linguistic values based on the membership functions [115].

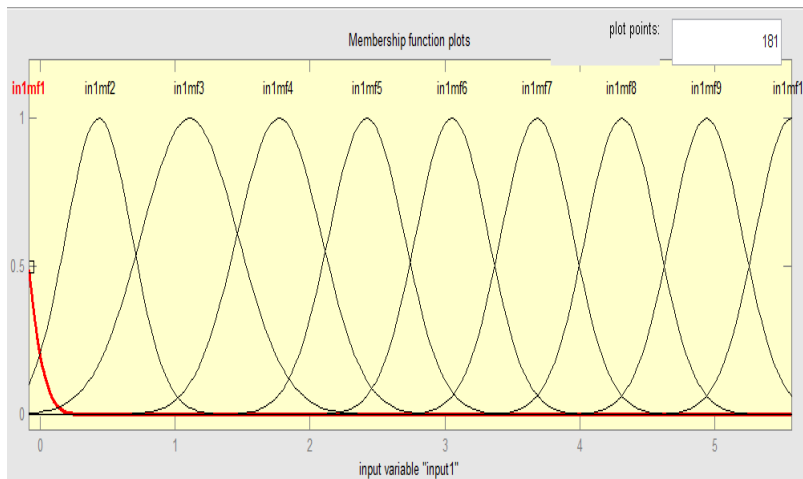
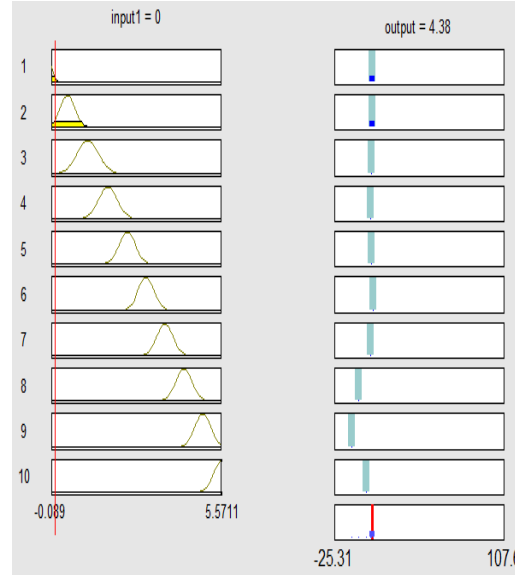


Figure 2.41: Gaussian membership functions for the sEMG.

Figure 2.41 shows the plot of Gaussian membership functions for fuzzification of the sEMG. The process of fuzzification followed by IF .. AND.. THEN ..OR ELSE type control or relation/estimation rules [115]. The output of the rules is computed as a max-min composition [115]. In the defuzzification process, the output of the rules has to be converted to a crisp value [115].

Using eight different membership functions types we designed eight single-output Sugeno-type adaptive neuro-fuzzy inference systems (ANFIS) using a grid partition on the data. The output membership function in each of these is linear. Each ANFIS has ten rules and connection type is ‘And’ with a weight of 1. For the ‘And’ method ‘product’ and for ‘Or’ method ‘probabilistic’ types are used for each ANFIS. Defuzzification is achieved using weighted average (wtaver) from each rule. Figure 2.42 shows the rules for ANFIS with Gaussian membership functions and illustrate the ANFIS inference mechanism. The membership functions used are tabulated in Table 2.9.



**Figure 2.42:** Illustration of ANFIS inference mechanism.

**Table 2.9:** Membership Functions (FUZZ-IEEE 2011)

S. No.	Membership Function
1.	Gaussian (GAUSSMF)
2.	Gaussian combination (GAUSS2MF)
3.	Difference between two sigmoidal membership functions (DSIMF)
4.	Generalized bell-shaped (GBELLMF)
5.	II-shaped (PIMF)
6.	Product of two sigmoidally shaped membership functions (PSIMF)
7.	Trapezoidal-shaped (TRAPMF)
8.	Triangular-shaped (TRIMF)

A Gaussian function is given by  $f(x; \sigma, c) = e^{-\frac{(x-c)^2}{2\sigma^2}}$  for some real constants  $c$  and  $\sigma > 0$ , and  $e = 2.718$ . Gaussian combination membership function (GAUSS2MF) depends on the  $c$  and  $\sigma$  parameters [116]. The sigmoidal membership function is given as  $f(x; a, c) = \frac{1}{1+e^{-a(x-c)}}$  and depends on the two parameters  $a$  and  $c$ . The difference between two sigmoidal membership function (DSIMF) which is the difference between two sigmoidal functions depends on the four parameters  $a_1, c_1, a_2$ , and  $c_2$  [116]. Generalized bell-shaped membership function (GBELLMF) is given as  $f(x; a, b, c) = \frac{1}{1+|\frac{x-c}{a}|^{2b}}$  and depends on three parameters  $a, b$ , and  $c$  where parameter  $a$  and  $b$  decide the width of the curve and parameter  $c$  locates the center, usually  $b > 0$  [116]. Pi-shaped membership function (PIMF) is given by

$$f(x; a, b, c, d) = \begin{cases} 0, & x \leq a \\ 2 \left( \frac{x-a}{b-a} \right)^2, & a \leq x \leq \frac{a+b}{2} \\ 1 - 2 \left( \frac{x-b}{b-a} \right)^2, & \frac{a+b}{2} \leq x \leq b \\ 1, & b \leq x \leq c \\ 1 - 2 \left( \frac{x-c}{d-c} \right)^2, & c \leq x \leq \frac{c+d}{2} \\ 2 \left( \frac{x-d}{d-c} \right)^2, & \frac{c+d}{2} \leq x \leq d \\ 0, & x \geq d \end{cases}, \text{ and evaluated at the points given by vector } x.$$

The “feet” of the curve is determined by parameters  $a$  and  $d$  whereas parameters  $b$  and  $c$  decides its “shoulders” [116]. The Product of two sigmoidally shaped membership functions (PSIMF) is simply

the products of two sigmoidal functions as given before. The trapezoidal shaped membership function (TRAPMF) is given by

$$f(x; a, b, c, d) = \begin{cases} 0, & x \leq a \\ \frac{x-a}{b-a}, & a \leq x \leq b \\ 1, & b \leq x \leq c \\ \frac{d-x}{d-c}, & c \leq x \leq d \\ 0, & d \leq x \end{cases}$$

which depends on four scalar parameters  $a, b, c$ , and  $d$ . The

triangular shaped membership function (TRIMF) is given by

$$f(x; a, b, c) = \begin{cases} 0, & x \leq a \\ \frac{x-a}{b-a}, & a \leq x \leq b \\ \frac{c-x}{c-b}, & b \leq x \leq c \\ 0, & c \leq x \end{cases}$$

which depends on the scalar parameters  $a, b$  and  $c$  [116].

### Smoothing Spline Curve Fitting

MATLAB® Curve Fitting Toolbox™ is a useful tool for fitting curves and surfaces to acquired data [117]. It can be used to do exploratory data analysis, preprocessing and post-processing of the data, comparing candidate models, and for removing outliers [117]. Weights for each smoothing spline curve fit are calculated by subtracting the ANFIS output from the measured skeletal-muscle force output. A graphical user interface is used to fit the smoothing spline curve to each output from eight ANFIS with respective weights. Smoothing spline which is a piecewise polynomial computed from a smoothing parameter ( $p$ ) of 0.92 is fitted to each of eight outputs of ANFIS. Smoothing parameter ( $p$ ) is a number between 0 and 1. Change in the value of  $p$  from 0 to 1 results in the change in smoothing spline. For  $p = 0$  the smoothing spline is a least-square straight-line approximation to the data whereas for  $p = 1$  it gives the "natural" cubic spline interpolant to the data [117].

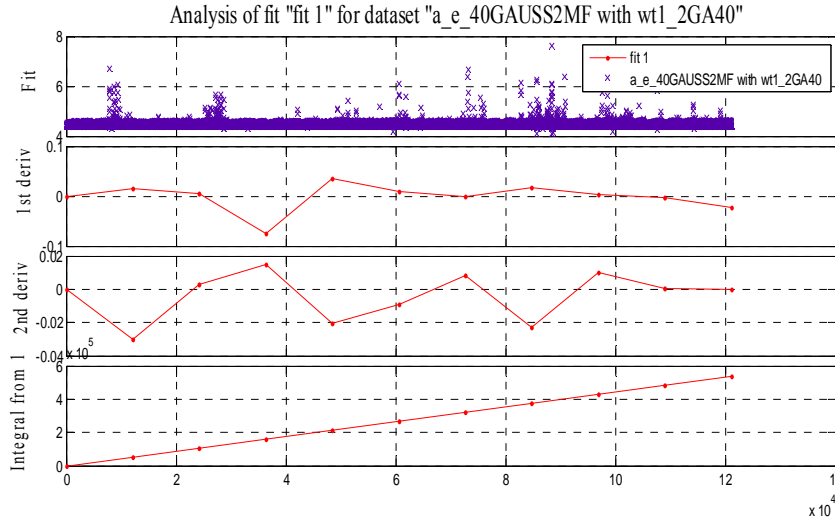


**Figure 2.43:** Analysis results for smoothing spline curve fitting to the output of ANFIS with Gaussian membership function.

For the specified weight ( $w_i$ ) and smoothing parameter ( $p$ ) a smoothing spline  $s$  is formed which minimizes the parameter  $J$  given by Equation (31).

$$J = p \sum_i w_i (y_i - s(x_i))^2 + (1 - p) \int \left( \frac{d^2 s}{dx^2} \right)^2 dx, \quad (31)$$

where  $x_i$  and  $y_i$  are predictor and response data respectively. The smoothing parameter  $p$  should be chosen to make the error  $E(s) = \sum_i w_i (y_i - s(x_i))^2$  and roughness  $\int \left( \frac{d^2 s}{dx^2} \right)^2 dx$  small. In this work the smoothing parameter  $p$  is chosen as 0.92 [117]. Figure 2.43 shows the analysis results for smoothing spline curve fitting to the output of ANFIS with Gaussian membership function.

### Adaptive Data Fusion

Fusion of outputs for different linear and nonlinear models is achieved with an adaptive probability of KIC, as given in the subsection ‘DATA FUSION AND ADAPTIVE KIC PROBABILITY,’ of the previous section ‘ADAPTIVE MULTI SENSOR BASED NONLINEAR IDENTIFICATION OF SKELETAL-MUSCLE FORCE’ of this chapter. Figure 2.44 shows the flow chart for fusion of outputs and adaptive probability of KIC.

### Results and Discussion

The proposed method gives good estimation of the skeletal-muscle force. A data set of 45 seconds is used to estimate the output. Figure 2.45 shows the measured and estimated skeletal-muscle force using this method.

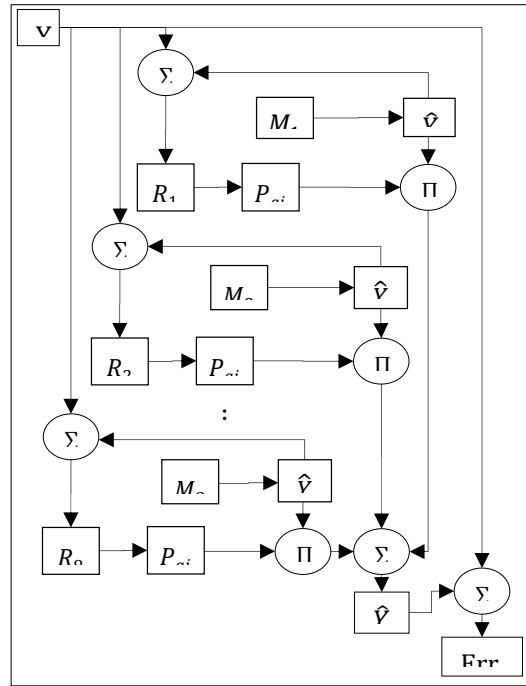


**Figure 2.44:** Flow chart for fusion of outputs and adaptive probability.

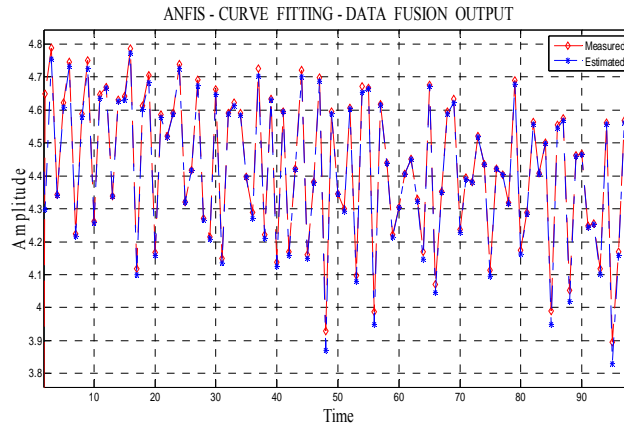


**Figure 2.45:** Plot of measured and proposed method estimated skeletal-muscle force.

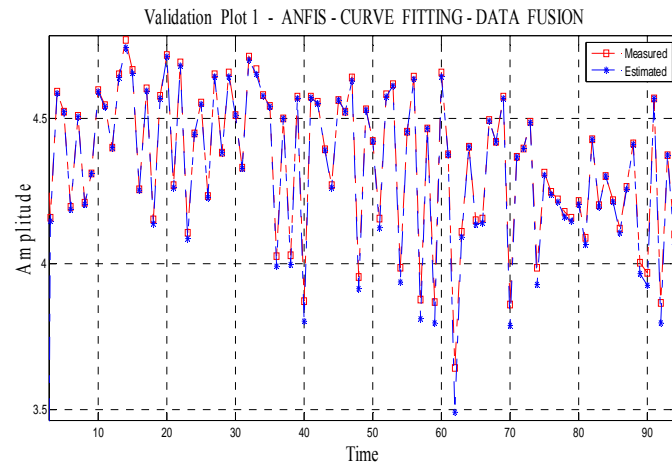


**Figure 2.46:** Validation plot 1 using different data set.

Figs. 2.46 and 2.47 are the validation plots for 45 seconds and 60 seconds of data sets respectively. All of these three plots show a very close follow up of the measured signal by the estimated signal using this approach.

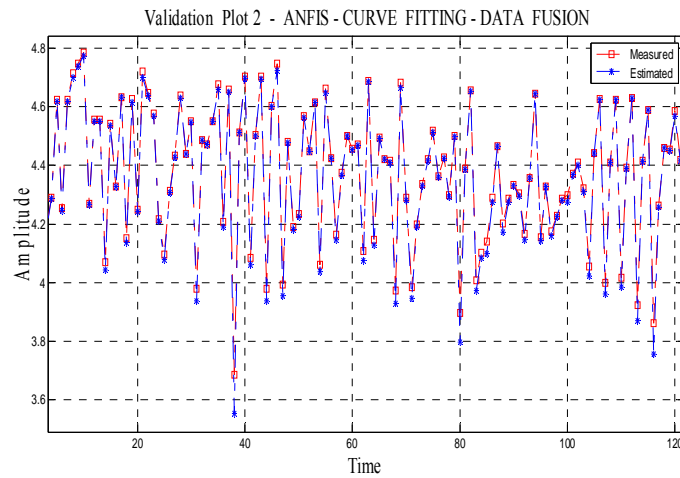


**Figure 2.47:** Validation plot 2 using different data set.

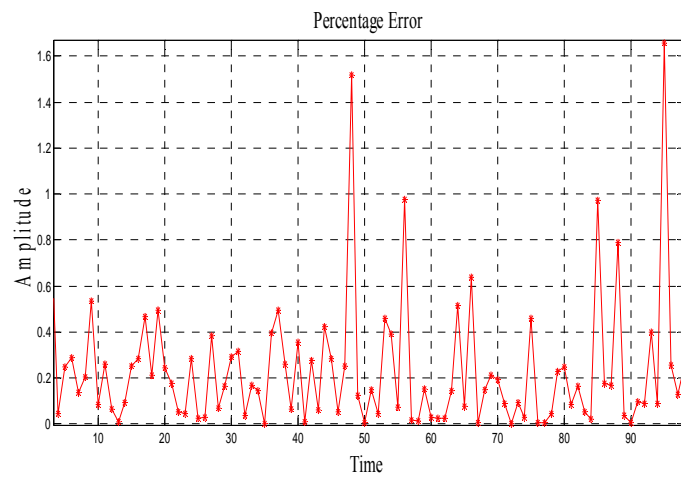


**Figure 2.48:** Percentage error plot.

Figure 2.48 shows the percentage error between the measured force signal and estimated finger force signal for 45 seconds of data set. The percentage error reduced to the lower values and the maximum percentage error value is 1.7 percent. The mean fit value between the measured and estimated output is 91.3 percent.

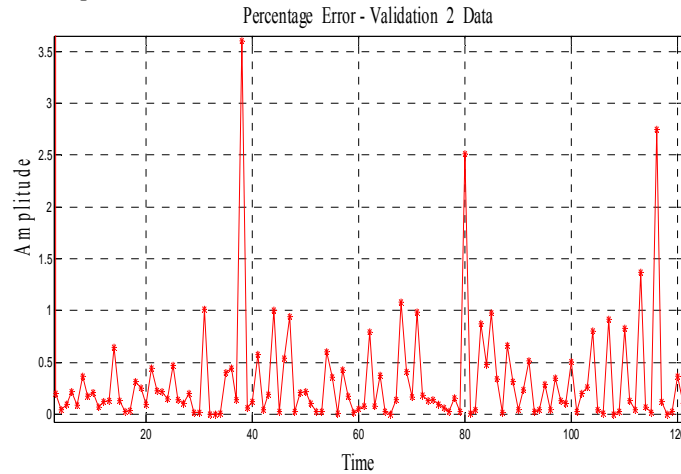


**Figure 2.49:** Percentage error plot for 60 seconds data set.

Figure 2.49 shows the percentage error plot for different data set of 60 seconds duration. Percentage error reduced to lower values and the maximum percentage error value is 3.7 percent. The mean fit value between the measured and estimated output is 40 percent. The mean fit value for another 45 seconds of data set is 73 percent.

Using the sEMG and skeletal-muscle force as input and output data, eight ANFIS were designed and tested. Outputs of these ANFIS were fitted with smoothing spline curve fit and resultant outputs were fused using a KIC based adaptive data fusion algorithm. This approach has been validated using two separate data sets. Results are promising and show good estimation of skeletal-muscle force which can be applied to design, application and improvement of prosthetic hands for amputees.

Future work will address the improvement of data collection techniques, the sEMG sensor design, use of this approach for finger angles and stiffness estimation from sEMG signals. Different modeling techniques with this approach and combined probability of different model selection criteria such as Akaike Information Criterion (AIC), Kullback Information Criterion (KIC) and the Bayesian Information Criterion (BIC) together will give improved results.

## 2.3 Skeletal-Muscle Fatigue

### 2.3.1 Towards Smart Prosthetic Hand: Adaptive Probability Based Skeletal-Muscle Fatigue Model

Skeletal-muscle force can be estimated using surface electromyographic (sEMG) signals. Usually, the surface location for the sensors is near the respective muscle motor unit points. Skeletal-muscles generate a spatial EMG signal, which causes cross talk between different sEMG signal sensors. In this study, an array of three sEMG sensors is used to capture the information of muscle dynamics in terms of sEMG signals. The recorded sEMG signals are filtered utilizing optimized nonlinear Half-Gaussian Bayesian filters parameters, and the muscle-force signal using a Chebyshev Type-II filter. The filter optimization is accomplished using Genetic Algorithms. Three discrete time state-space muscle-fatigue models are obtained using system identification (SI) and modal transformation for three sets of sensors for single motor unit. The outputs of these three muscle-fatigue models are fused with a probabilistic Kullback Information Criterion (KIC) for model selection. The final fused output is estimated with an adaptive probability of KIC, which provides improved force estimates.

This section addresses the issue of skeletal-muscle fatigue that is a dynamic phenomenon. The Flow Chart of the work in this section is shown in Figure 2.50. The modeling is based on system identification, where mathematical relations are inferred from experimental data. The data consists of sEMG signals and hand/finger force generated by healthy subjects. The recorded three-sEMG signals

are filtered using nonlinear Half-Gaussian Bayesian filters with optimized filter parameters, whereas the skeletal-muscle force signal is pre-processed using a Chebyshev Type-II filter [118], [100].

A simple Genetic Algorithm code is used to optimize the Bayesian filter parameters. Using an input/output approach, the EMG signal is the input to the skeletal-muscle, and the produced hand/finger force constitutes the output. Three discrete time state-space models are obtained using system identification and modal transformation for three sets of sensors. One sensor is placed at the motor unit of the ring finger of the dominant hand and two sensors are located in its vicinity as shown in Figure 2.51. The extracted models from the data sets are fused with a probabilistic Kullback Information Criterion (KIC) for model selection. The final fused output is estimated with an adaptive probability of KIC that gives improved skeletal-muscle force estimates.

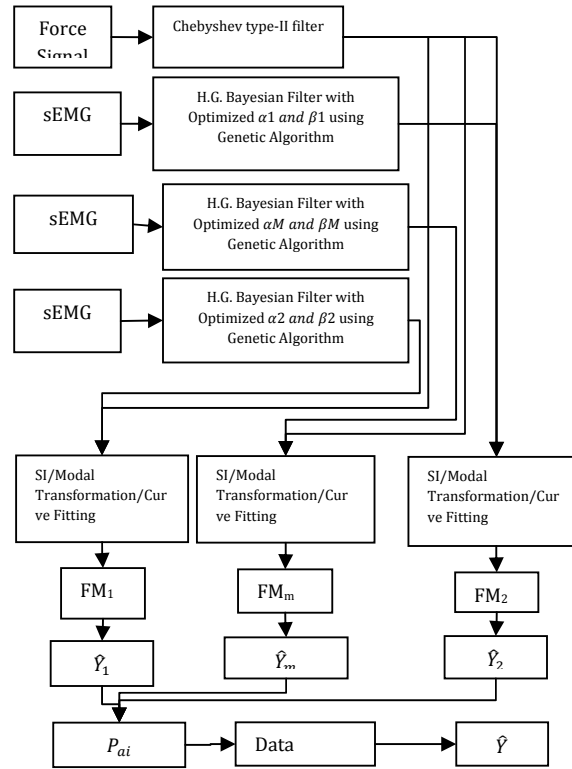


**Figure 2.50:** The flow chart of the work in this section.

### Experiment Design and Pre-Processing

Both sEMG and muscle-force signals were acquired simultaneously using LabVIEW™ 8.2 at a sampling rate of 2000 Hz. The sEMG data capturing was aided by a DELSYS® Bagnoli-16 EMG system with DE-2.1 differential EMG sensors. The corresponding force data was captured using NI ELVIS with Interlink Electronics FSR 0.5" circular force sensor. The experiment design is shown in Figure 2.51. One sEMG sensor was placed on the motor point of ring finger and two adjacent to the motor point of a healthy subject. Prior to placing the sEMG sensors, the skin surface of the subject was prepared according to International Society of Electrophysiology and Kinesiology (ISEK) protocols [1].



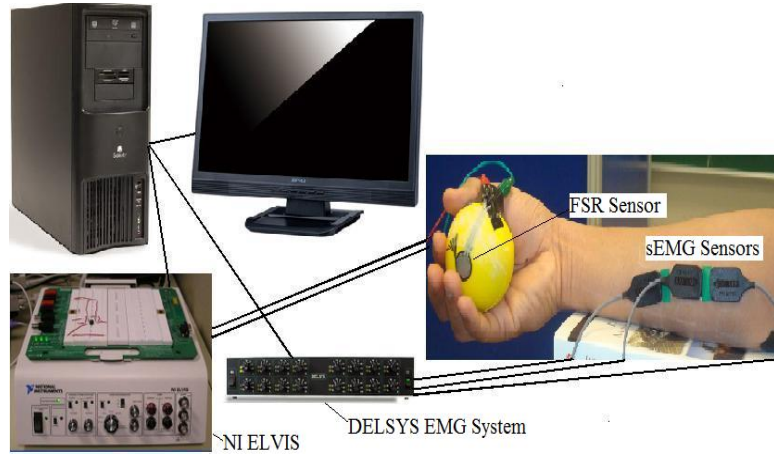


**Figure 2.51:** Experiment set-up.

The EMG signal is modeled for the conditional probability of the rectified EMG signal as a filtered random process with random rate. The likelihood function for the rate evolves in time according to a Fokker–Planck partial differential Equation [100]. Here,  $\alpha$  and  $\beta$  are two free parameters,  $\alpha$  is the expected rate of gradual drift in the signal, and  $\beta$  is the expected rate of sudden shifts in the signal. These two free parameters of the non-linear “Half-Gaussian filter model” are optimized for the acquired EMG data using elitism based Genetic Algorithm. A Chebyshev Type II low pass filter with a 550 Hz pass frequency is used to filter the force signal.

### System Identification and Modal Transformation

An alternative to physically based mathematical modeling is data based -‘system identification (SI)’- that can be applied to different systems where it needs sufficient experimental data [110]. The parametric system identification process yields a dynamical model such as the Auto Regressive with eXogenous input (ARX) or Output Error (OE) model, this model gives us the system in mathematical form. In this work, the SI approach is used with the myoelectric signal as the input to the system and as the output is the intended finger/hand force. In this work, we are using an output error (OE) model structure for the modeling of EMG and hand/finger force signals, which has been documented in the literature to perform well for EMG signals among linear parametric models [118]. Each OE model takes the form of Equation (32),

$$y(t) = \frac{B(q)}{F(q)}u(t - n_k) + e(t), \quad (32)$$

where  $t$  is time index,  $y(t)$  is output,  $u(t - n_k)$  is input,  $n_k$  is the delay,  $e(t)$  is the error, and  $B(q)$  and  $F(q)$  are polynomials.

A common OE model is obtained for each sensor data set using one set of model parameters (polynomial order). The OE models then are converted into a state-space formulation. By doing this, the identification properties of the OE model formulation are preserved and represented in the state-space form. A modal form is computed by using state-space matrices and following transformation:

$$\Lambda = T^{-1}AT, \Omega = T^{-1}B, \Gamma = CT, \quad (33)$$

where  $T$  is the matrix composed of the eigenvectors of  $A$ ,  $\Lambda$ ,  $\Omega$  and  $\Gamma$  are corresponding transformations for matrix  $A$ ,  $B$ , and  $C$ . Matrix  $D$  came out to be a zero matrix for the cases treated in this work. Equation 33 refers to the continuous representation of the identified models. Using the modal form representation for each corresponding data set, the influence of fatigue can be observed by charting the modal coefficients in time for each matrix. For example, the coefficients contained in the transformed matrix  $\Lambda$  can be plotted in the complex  $s$ -plane. This tracking can then be used as the basis for constructing polynomials that connect each element of each matrix in time with the corresponding time stamp. Hence, a fatigue model in state-space description is constructed, where the input is the recorded EMG signal and the output the expected force generated by the hand motion all as a function of time.

### Fusion of Outputs and Adaptive Probability of KIC

Multiple model fusion is done by assigning a particular probability to each individual model [105]. These models are obtained using SI for three sEMG sensors for single motor unit. SI model fit value is used to compute the probability for each model. The fit value is given by  $\left[1 - \frac{|Y - \hat{Y}|}{|Y - \bar{Y}|}\right] * 100$ .

The model selection criterion used in this section is Kullback information criterion (KIC), which is an asymmetric measure. The sum of two directed divergences, which is the measure of the models dissimilarity, is known as Kullback's symmetric or J-divergence [106], as given by Equation 34.

$$KIC(p_i) = \frac{n}{2} \log R_i + \frac{(p_i+1)n}{n-p_i-2} - n\psi\left(\frac{n-p_i}{2}\right) + g(n), \quad (34)$$

where  $g(n) = n * \log(n/2)$ .

Following fusion technique is applied for sEMG – force identification models, which is based on [105].

- 1) Identify OE models  $M_1, M_2, \dots, M_{k1}$  using sEMG data ( $u$ ) as input and force data ( $Y$ ) as output, for  $k1$  number of sensors collecting data simultaneously.
- 2) Compute the residual square norm  $R_i = \|Y - \Phi_i \hat{\Theta}_i\|^2 = \|Y - \hat{Y}\|^2$ ,

$$\text{where } \hat{\Theta}_i = \{\Phi_i^T \Phi_i\}^{-1} \Phi_i^T Y, \text{ and } \Phi = \begin{bmatrix} Y_p^T & u_p^T & Y_{p-1}^T & \dots & u_1^T \\ Y_{p+1}^T & u_{p+1}^T & Y_p^T & \dots & u_2^T \\ \vdots & \vdots & \vdots & \ddots & \vdots \\ Y_{n-1}^T & u_{n-1}^T & Y_{n-2}^T & \dots & u_{n-p}^T \end{bmatrix}.$$

- 3) Calculate the model criteria coefficient using Equation 34.
- 4) Compute the model probability  $p(M_i|Z) = \frac{e^{-l_i}}{\sum_{j=1}^{k1} e^{-l_j}}$ , where  $l$  is model selection criterion, i.e.

$$KIC(p_i).$$

- 5) Compute the data fusion based model output  $\hat{Y}_f = \sum_{i=1}^{k1} p(M_i|Z) \hat{Y}_i$ .

Here all the computation from step 2) to step 5) is adaptive i.e. the residual square norm,  $KIC(p_i)$ , model probability  $p(M_i|Z)$ , and fused model output  $\hat{Y}_f$  are being updated with time or for each data point.

## Results and Discussion

Based on previous research results and after trying different model orders for sEMG/Force data, an optimal model order of  $n_b = 2, n_f = 2, n_k = 1$  is used in this work. Equation 35, 36, and 37 give three resulting discrete time state-space sEMG-Force-Fatigue models for motor point sensor, sensor-1 and sensor-2 respectively.

$$\begin{aligned} x_m(h+1) &= A_m x_m(h) + B_m EMG_m(h); \\ \hat{Y}_m(h) &= C_m x_m(h) + D_m EMG_m(h). \end{aligned} \quad (35)$$

$$\begin{aligned} x_1(h+1) &= A_1 x_1(h) + B_1 EMG_1(h); \\ \hat{Y}_1(h) &= C_1 x_1(h) + D_1 EMG_1(h). \end{aligned} \quad (36)$$

$$\begin{aligned} x_2(h+1) &= A_2 x_2(h) + B_2 EMG_2(h); \\ \hat{Y}_2(h) &= C_2 x_2(h) + D_2 EMG_2(h). \end{aligned} \quad (37)$$

In these case matrices  $D_m, D_1$ , and  $D_2$  are zero matrices, whereas matrices  $A_m, B_m, C_m, A_1, B_1, C_1, A_2, B_2$ , and  $C_2$  are given as:

$$A_m = \begin{bmatrix} a_{m1}(t) & 0 \\ 0 & a_{m2}(t) \end{bmatrix}; B_m = \begin{bmatrix} b_{m1}(t) \\ b_{m2}(t) \end{bmatrix}; C_m = [c_{m1}(t) \ c_{m2}(t)]; A_1 = \begin{bmatrix} a_{11} & 0 \\ 0 & a_{12} \end{bmatrix};$$

$$B_1 = \begin{bmatrix} b_{11} \\ b_{12} \end{bmatrix}; C_1 = [c_{11} \ c_{12}]; A_2 = \begin{bmatrix} a_{21}(t) & 0 \\ 0 & a_{22}(t) \end{bmatrix}; B_2 = \begin{bmatrix} b_{21}(t) \\ b_{22}(t) \end{bmatrix}; \text{ and } C_2 = [c_{21}(t) \ c_{22}(t)];$$

where the elements of matrices  $A_m, B_m, C_m, A_2, B_2$ , and  $C_2$  are function of time and the elements of matrices  $A_1, B_1$  and  $C_1$  are constants for this particular data set. The time variables  $a_{m1}(t), a_{m2}(t), b_{m1}(t), b_{m2}(t), c_{m1}(t), c_{m2}(t), a_{21}(t), a_{22}(t), b_{21}(t), b_{22}(t), c_{21}(t)$ , and  $c_{22}(t)$  are given by quadratic polynomials obtained by curve fitting the tracked modal transformed coefficients. These time variables are given as:

$$\begin{aligned} a_{m1}(t) &= 0.00026t^2 - 0.033t - 11; a_{m2}(t) = -0.0018t^2 + 0.24t - 33; \\ b_{m1}(t) &= -0.002t^2 + 0.33t + 42; b_{m2}(t) = -0.0017t^2 + 0.33t + 25; \\ c_{m1}(t) &= (3.2 * 10^{-7})t^2 - (4.2 * 10^{-5})t + 0.71; \\ c_{m2}(t) &= (4.6 * 10^{-8})t^2 - (5.8 * 10^{-6})t - 0.71; \\ a_{21}(t) &= -(1.2 * 10^{-5})t^2 + 0.0013t - 0.47; a_{22}(t) = 0.001t^2 - 0.037t - 35; \\ b_{21}(t) &= (6.4 * 10^{-6})t^2 - 0.001t + 0.3; b_{22}(t) = 0.0023t^2 - 0.12t - 75; \end{aligned}$$

$c_{21}(t) = -(1.8 * 10^{-7})t^2 + (6.4 * 10^{-6})t + 0.71$ ; and  $c_{22}(t) = -(2.1 * 10^{-9})t^2 + (2.4 * 10^{-7})t - 0.71$ .

Elements of matrices  $A_1, B_1$ , and  $C_1$  are constants for this particular data set, they are given as:  
 $a_{11} = -0.0159$  ;  $a_{12} = -43.1883$  ;  $b_{11} = 0.0090$  ;  $b_{12} = -72.1875$  ;  $c_{11} = 0.7147$  ; and  $c_{12} = -0.7071$ .

The discrete models have a sampling time of  $\Delta t = 0.0005$  seconds. The duration of the final estimated and fused output for three sensors is 37.36 seconds. Figure 2.52 depicts the probability and 10<sup>th</sup> degree curve fitting for motor point, ring2 and ring1 sensor signals.

Figure 2.53 and 2.54 shows the measured and estimated fused output, depending on the error between the two later follows the measured signal very closely. This approach identifies a fused fatigue model and estimates an adaptive probability based output that follows the measured output very closely. The outcome of this research can be used to estimate the skeletal-muscle force of a human hand for prosthetic hand design, application and improvement.

In future work improvement of the data collection techniques and sEMG sensor design, may lead to improved force estimation.

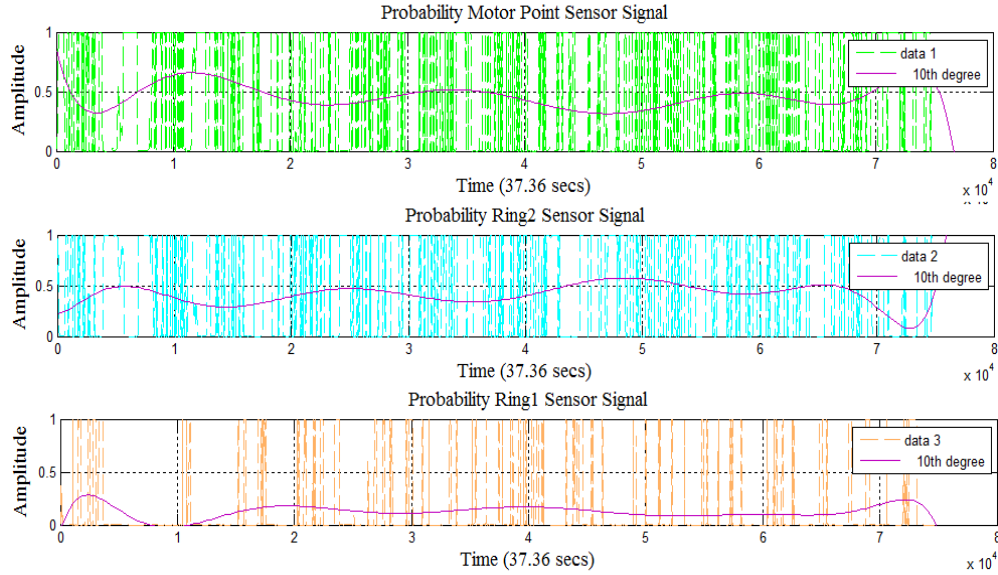
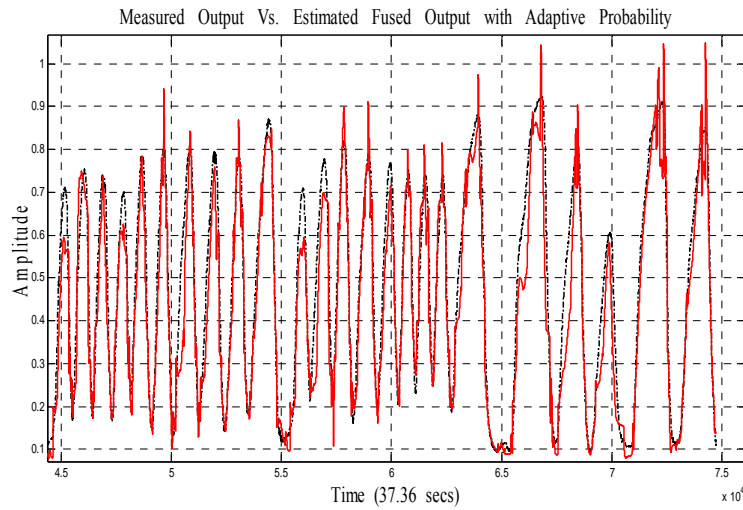
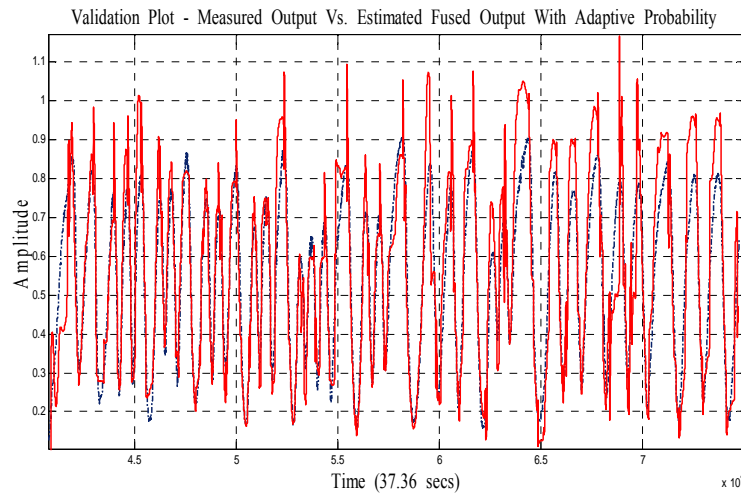


Figure 2.52: 10<sup>th</sup> degree curve fitting – probability motor, ring2 and ring1 sensor signals.



**Figure 2.53:** Measured output vs. fusion based estimated output with adaptive probability.



**Figure 2.54:** Validation plot - measured vs. fusion based estimated output with adaptive probability.

### **2.3.2 Spectral Analysis of sEMG Signals to Investigate Skeletal-Muscle Fatigue**

Our recent investigations are focused to develop dynamic models for skeletal-muscle force and finger angles for prosthetic hand control using surface electromyographic sEMG as input. Since the sEMG is temporal and spatially distributed and is influenced by various factors, muscle-fatigue and its related sEMG becomes of importance. This study is an effort to spectrally analyze the sEMG signal during progression of muscle-fatigue. The sEMG is captured from the arms of healthy subjects during muscle fatiguing experiments for dynamic and static force levels. Filtered sEMG signal is segmented in five parts with 75% overlap between adjacent segments. The analysis is done using different classical (fast Fourier transform, Welch's averaged modified periodogram), model-based (Yule-Walker, Burg, Covariance and Modified Covariance autoregressive (AR) method), and eigenvector methods (Multiple Signal Classification (MUSIC) and eigenvector spectral estimation method) in frequency domain. Results show that the classical and eigenvector based methods are more sensitive than the model-based methods to fatigue related changes in sEMG signals.

The present work investigates the change in sEMG in frequency domain during skeletal-muscle fatigue. sEMG signals are acquired for multiple subjects for dynamic and static force experiments to induce skeletal-muscle fatigue. sEMG signals are filtered with a nonlinear Teager-Kaiser Energy (TKE) operator-based nonlinear spatial filter [113]. Two sets of dynamic force data are segmented into three and five parts and two sets of static force data are segmented into five parts each. There is a 75% overlap between the two adjacent segments. A number of classical, model-based and eigenvector based spectral estimation techniques are used to study the change in sEMG signals as a result of muscle-fatigue. In classical methods Fast Fourier transform (FFT) and Welch's averaged modified periodogram methods are used. In case of model-based methods, Yule-Walker (Y-W), Burg, Covariance (Cov.), and Modified Covariance (Mcov.) Autoregressive (AR) methods are applied. For eigenvector methods Multiple Signal Classification (MUSIC) and Eigenvector (EIG) spectral estimation methods were selected for processing sEMG signals. Using these spectrum analysis techniques, Power Spectral Density (PSD) estimates and detailed documentations of sEMG signals were obtained. These methods were compared in terms of their frequency resolution and the effects in determination of skeletal-muscle fatigue.

### **Experiment Design and Pre-Processing**

An experiment design was developed using DELSYS<sup>®</sup> Bagnoli-16 EMG system with nine DE-3.1 sEMG sensors to capture sEMG signals from skeletal-muscles as given in [113]. This arrangement involves nine sensors covering four directional spatial distributions of the sEMG signal. The appropriate motor point of the flexor digitorum superficialis (FDS) muscle, which controls the flexion of the ring finger, was identified using a wet probe muscle stimulator at the FDS (RICH-MAR, HV 1000). The middle three sEMG sensors were attached directly on the skin surface above the motor point of the ring finger. Prior to placing sEMG sensors, the skin surface of the subject was prepared according to International Society of Electrophysiology and Kinesiology (ISEK) protocols [119]. Two different sets of fatigue inducing experiments were conducted using this experiment design of sEMG

sensors, one experiment by varying the force dynamically, and second with 50 pounds of static force. For the dynamic force variation we used an Interlink™ Electronics FSR 0.5” circular force sensor on a stress ball and for the static force experiment we used a cable tensionmeter (T5166) by ‘Pacific Scientific Company.’

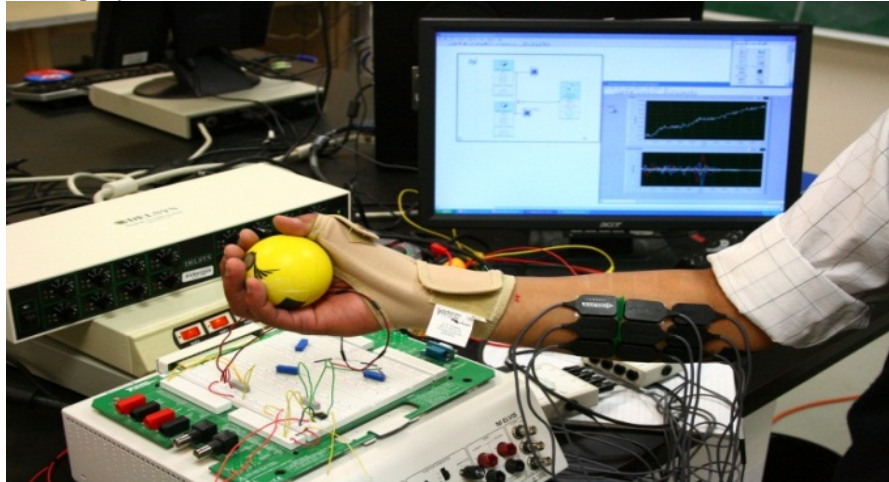


**Figure 2.55:** Experiment design for dynamic force levels.

For the dynamic force experiment we restricted the thumb movement using a thumb splint. For the static force experiment we held the force of the dynamometer at 50 pounds and tried to maintain this force level to induce fatigue in skeletal-muscles. Force data for dynamic force experiments was captured using NI ELVIS™ with Interlink™ Electronics FSR 0.5” circular force sensor. Experiment design is shown in Figure 2.55 and 2.56, where 9 sensors are shown on a healthy subject forearm, holding a stress ball and a grip tension dynamometer, respectively. sEMG and finger force data were collected at a sampling rate of 2000 Hz using LabVIEW™ in conjunction with DELSYS® Bagnoli-16 EMG and NI ELVIS™. With these experiment designs, we conducted several experiments of 30 seconds, 45 seconds and 60 seconds durations.

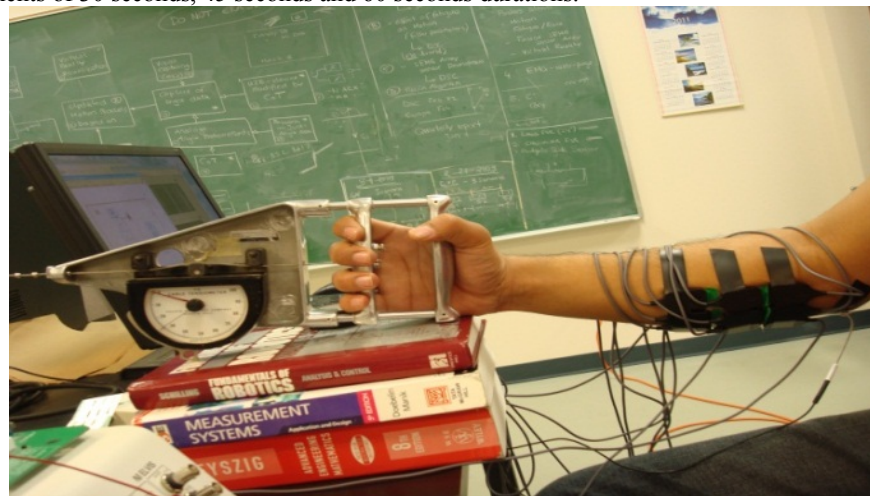


**Figure 2.56:** Experiment design for 50 pounds static force levels.

### Spectral Estimation Methods

Signals can be analyzed in the time and frequency domains and in some instances the frequency content of the signal is more useful than the time domain characteristics [120]. Various bio signals such as the heart rate, EMG, EEG, ECG, eye movements, and other motor responses, acoustic heart sounds, and stomach and intestinal sounds, show much richer information in the frequency domain [120]. Spectral analysis is a mathematical prism which finds the frequency content of a waveform by decomposing the signal into its constituent frequencies [120], [121]. There is a wide range of methods for spectral analysis, each having its own benefits and drawbacks. In this research we

are using classical methods based on the Fourier transform, modern methods based on the estimation of model parameters, and eigenvector based methods [120] in order to characterize the muscle-fatigue occurring in skeletal human muscles, in particular muscles of the forearm. To use the spectral analysis wisely, we need to have an understanding of the spectral features of interests and the best methods to accurately determine those features [120].

#### A. Discrete Fourier Transform (DFT)

DFT which is the computational basis of the spectral analysis transforms the time or space domain data into frequency domain data [122]. The DFT of a vector  $x$  of length  $N$  is given by Equation (38).

$$X(k) = \sum_{j=1}^N x(j) \omega_N^{(j-1)(k-1)}, \quad (38)$$

where  $\omega_N = e^{(-2\pi i)/N}$  is the  $N_{th}$  root of unity [122].

#### B. Welch's averaged modified periodogram method

As the name suggests, the 'Welch's averaged modified periodogram method' depends on the periodogram of the signal  $\{x(n)_n^N\}$  which is given by Equation 39, [122].

$$\hat{S}_{per}(f) = \frac{1}{N} |\sum_{n=1}^N x(n) \exp(-j2\pi f n)|^2. \quad (39)$$

In Welch method, the signal is segmented into eight parts of equal length with an overlapping ratio of 50% and each part is segmented using a Hamming window as given by Equation 40, [122].

$$w(n) = 0.54 - 0.46 \cos\left(2\pi \frac{n}{N}\right), 0 \leq n \leq N. \quad (40)$$

#### C. Yule-Walker (Y-W) autoregressive (AR) method

The Yule-Walker autoregressive method, also called the autocorrelation method, estimates the power spectral density (PSD) of the input. This method fits an autoregressive (AR) model to the windowed input data by minimizing the forward prediction error in the least-squares sense. This formulation leads to the Yule-Walker equations, which are solved by Levinson-Durbin recursion [122].

#### D. Burg autoregressive (AR) method

The Burg autoregressive (AR) method is a parametric spectral estimation method of the signal,  $x$ . The power spectral density is calculated in units of power per radians per sample. This method is based on the minimization of the forward and backward prediction error and on estimation of the reflection coefficients [122].

#### E. Covariance (Cov.) autoregressive (AR) method

The covariance autoregressive (AR) method uses the covariance algorithm to estimate the parametric spectral density of the signal,  $x$ . Based on causal observation of the input signal, the covariance method minimizes the forward prediction error and fits an AR linear prediction filter model to the signal [122].

#### F. Modified covariance (Mcov.) autoregressive (AR) method

Modified covariance autoregressive (AR) method estimates the PSD of the signal using the modified covariance method. Based on the causal information of the input signal, the modified covariance method fits an autoregressive (AR) linear prediction filter model to the signal by simultaneously minimizing the forward and backward prediction errors. The spectral estimate returned by this method is the magnitude squared frequency response of the AR model [122].

#### G. Multiple Signal Classification (MUSIC) spectral estimation method

The MUSIC algorithm estimates the pseudospectrum (in rad/sample) at the corresponding vector of frequencies for the input signal  $x$  [122]. This algorithm uses the estimates of the eigenvectors of a correlation matrix associated with the input signal using Schmidt's eigenspace analysis method [123]. The MUSIC pseudospectrum estimate is given by Equation (41),

$$P_{music}(f) = \frac{1}{e^H(f) (\sum_{k=p+1}^N v_k v_k^H) e(f)} = \frac{1}{\sum_{k=p+1}^N |v_k^H e(f)|^2}, \quad (41)$$

where  $N$  is the dimension of the eigenvectors and  $v_k$  is the  $k$ -th eigenvector of the correlation matrix [122]. The signal subspace has a dimension  $p$  and the eigenvectors  $v_k$  used in the sum corresponds to the smallest eigenvalues and also spans the noise subspace [122]. The vector  $e(f)$  consists of the complex exponentials, so the inner product  $v_k^H e(f)$  amounts to a Fourier transform. To estimate the pseudospectrum, the squared magnitudes are summed for FFT computed for each  $v_k$  [122].



#### H. Eigenvector (EIG) spectral estimation method

The eigenvector spectral estimation method estimates the pseudospectrum (in rad/sample) at the corresponding vector of frequencies using estimates of the eigenvectors of a correlation matrix associated with the input signal  $x$  [122]. This method estimates the pseudospectrum from a signal or a correlation matrix using a weighted version of the MUSIC algorithm derived from Schmidt's eigenspace analysis method [123], [124]. To find the frequency content of the signal the algorithm performs eigenspace analysis of the signal's correlation matrix. Singular value decomposition is used to compute the eigenvalues and eigenvectors of the signal's correlation matrix [122]. This method computes the pseudospectrum estimate as given by Equation (42).

$$P_{ev}(f) = \frac{1}{(\sum_{k=p+1}^N |v_k^H e(f)|^2) / \lambda_k}, \quad (42)$$

where the eigenvectors have a dimension of  $N$  and  $v_k$  is the  $k$ -th eigenvector of the correlation matrix [122]. The signal subspace has a dimension  $p$  and the eigenvectors  $v_k$  used in the sum corresponds to the smallest eigenvalues and also spans the noise subspace [122]. The vector  $e(f)$  consists of the complex exponentials, so the inner product  $v_k^H e(f)$  amounts to a Fourier transform and to estimate the pseudospectrum, the squared magnitudes are summed for FFT computed for each  $v_k$  [122].

#### I. Selection of Model Orders for Model-Based and Eigenvector Based Methods

Model-based and eigenvector-based methods need to have a specific model order which is an important aspect of the use in these methods. Using sEMG and force data as input and outputs for three and five sets of the segments for different data sets, we created model structure matrices using 'struc' function in MATLAB<sup>®</sup>, using 'arxstruc' we compared a model order of 1 to 50<sup>th</sup> with varying delay of 1 to 50 using cross-validation on the second half of the data set. With this approach, it was possible to select the order that gives the best fit for the validation data set.

### Results and Discussion

sEMG signal changes as a consequence of muscle-fatigue, the amplitude of the PSD of the signal increases and the median frequency shifts towards the lower frequency range. In this study, PSDs of the different segments of each sEMG data set were obtained using FFT, Welch's averaged modified periodogram, Yule-Walker, Burg, Covariance, Modified Covariance autoregressive (AR), Multiple Signal Classification (MUSIC), and Eigenvector spectral estimation methods. The objective of this study was to determine preferred methods of signal processing that elevates the sensitivity of muscle-fatigue as represented in the PSD of the sEMG signal. An increased sensitivity allows for better modeling of the fatigue phenomena and hence more accurate sEMG models. Ultimately this may lead to better prosthetic control.

Data of two experiments for dynamic force variations was segmented in three and five parts respectively. Each segment is with an overlap of 75% with its adjacent segment. Using different methods, we computed the PSDs for each segment. For the dynamic force experiments, the maximum value of PSDs of sEMG signal increases with muscle-fatigue as time or segment number is increased. The classical methods (FFT and Welch) and eigenvector based methods (MUSIC and Eigenvector (EIG.)) are representing this change well in case of maximum PSD values and show a clear difference.

Table 2.10 lists the peak values of the PSDs of five segments using classical and eigenvector based methods for a dynamically varying force experiment. Figure 2.57 shows the overlapping plot of PSDs for five segments using the MUSIC algorithm based spectral estimation method. The increase in the maximum PSD value is evident from the 1st to the 5th segment of the data.

**Table 2.10:** Maximum Value of PSD for Classical Methods and Eigenvector Based Methods – Dynamic Varying Force – Experiment 2 (IEEE-CDC 2011)

Segment No.	Classical-Methods		Eigenvector-Methods	
	FFT	Welch	MUSIC	EIG
1 <sup>st</sup>	4.1e+6	0.0082	371.59	1.0819
2 <sup>nd</sup>	5.09e+6	0.0100	424.43	1.3892
3 <sup>rd</sup>	5.74e+6	0.0111	480.71	1.4132
4 <sup>th</sup>	6.79e+6	0.0133	508.64	1.4936
5 <sup>th</sup>	2.13e+7	0.0379	695.08	10.2118

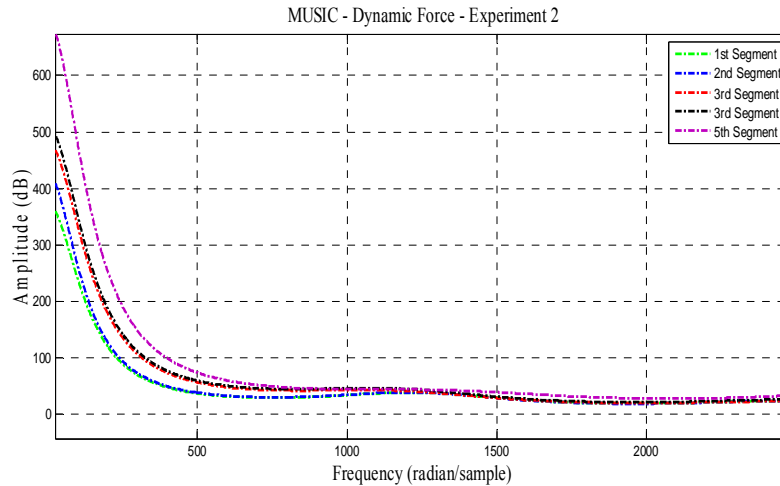


**Figure 2.57:** PSD vs. frequency plot for MUSIC algorithm – dynamic force experiment.

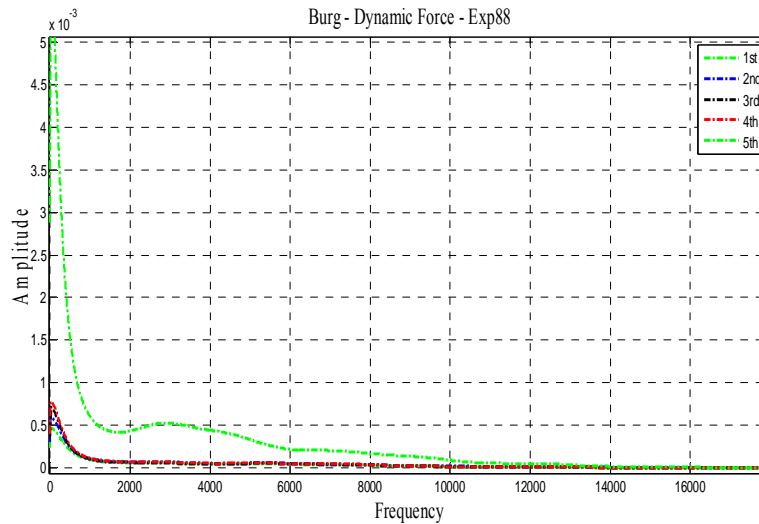


**Figure 2.58:** PSD vs. frequency plot for Burg method – dynamic force experiment.

Figure 2.58 shows the resulting PSD using the Burg method. Comparing Figs. 63 and 64, the progression of fatigue influence shift in PSDs is evident in both plots. However, the MUSIC algorithm not only shows larger amplitudes, but also a greater relative sensitivity to fatigue. The rather equal spacing between the lines of the PSD for the MUSIC algorithm compared to the Burg method indicates a rather more linear relationship of the fatigue progression.

sEMG data of two experiments for static force (50 pounds) were processed and the maximum PSDs of five segments using classical, model-based, and eigenvector based methods were computed. Data from both the experiments show similar results as the dynamic case. Table 2.11 lists the peak values of the PSDs of five segments using classical and eigenvector based methods for static force (50 pounds) for one experiment. Table 2.12 lists the maximum values of the PSD for model-based methods: Y-W, Burg, Covariance, and modified covariance.

**Table 2.11:** Maximum Value of PSD for Classical Methods – Static Force – 50 Pounds - Experiment 1 (IEEE-CDC 2011)

Segment No.	Classical-Methods		Eigenvector-Methods	
	FFT	Welch	MUSIC	EIG
1 <sup>st</sup>	1.03e+5	6.81e-5	1413	9.93e-4



2 <sup>nd</sup>	1.80e+5	1.12e-4	1793	16e-4
3 <sup>rd</sup>	3.21e+5	1.80e-4	2296	28e-4
4 <sup>th</sup>	4.25e+5	2.62e-4	3102	37e-4
5 <sup>th</sup>	6.23e+5	3.58e-4	7723	104e-4

**Table 2.12:** Maximum Value of PSD for Classical Methods – Static Force – 50 Pounds - Experiment 1 (IEEE-CDC 2011)

Segment No.	1 <sup>st</sup>	2 <sup>nd</sup>	3 <sup>rd</sup>	4 <sup>th</sup>	5 <sup>th</sup>
Model-Based Methods	7.7e-7	1.3e-6	2.3e-6	3.1e-6	7.81e-6

All of these methods resulted in the same maximum values for each segment. Comparing Table 2.11 and XII, we recognize the large difference in maximum value between the model-based methods and the corresponding values from the FFT and MUSIC method. Figure 2.59 shows the overlapping plot of PSDs for five parts using eigenvector algorithm based spectral estimation method. The increase in the maximum PSD value is evident from the 1<sup>st</sup> to the 5<sup>th</sup> segment of the static force sEMG data.

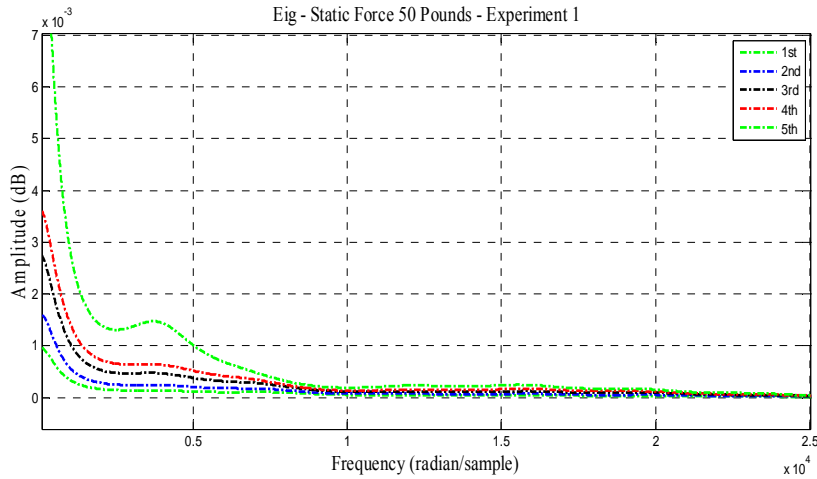


**Figure 2.59:** PSD vs. frequency plot for Eigenvector method – static force of 50 pounds.

The eigenvector method produces a similar characteristic as the MUSIC algorithm and distinguishes itself by also providing a more linear characteristic of the fatigue progression and a greater relative sensitivity. Figure 2.60 depicts the PSD generated by using FFT method for the 1<sup>st</sup> and 5<sup>th</sup> segments of a static force experiment. While providing a large maximum value, the FFT method is limited by its own spectral resolution ( $1/N$ ) and, due to windowing of the finite data set, results into spectral leaking.

All the model-based methods for both dynamic and static force levels produce the same peak values and the same PSD for the corresponding experiment. Since Burg and Y-W methods guarantee stability while the covariance and modified covariance methods have conditions for stability to be satisfied (i.e. min. order must be of certain length of the input frame size), Burg and Y-W should be the preferred methods for sEMG analysis. However, the Burg method is to be preferred if short data sets are used.

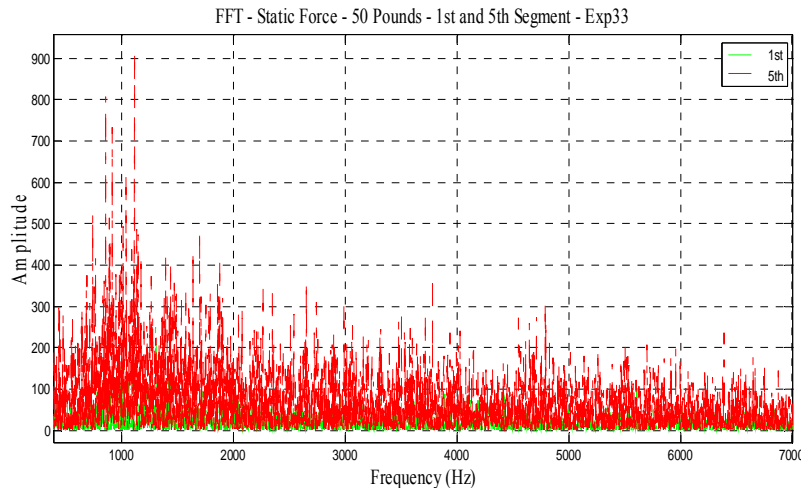


**Figure 2.60:** PSD vs. frequency plot for FFT method – static force of 50 pounds.

Comparing the eigenvector based methods (MUSIC and Eigenvector), both of these methods are frequency estimator techniques based on eigenanalysis of the autocorrelation matrix where the resulting estimate has sharp peaks at the frequencies of interest. The eigenvector method uses inverse eigenvector weighting whereas the MUSIC method uses unity weighting, implying that the eigenvector method gives fewer spurious peaks than the MUSIC algorithm [125]. As seen from the dynamic experiment results, the MUSIC method provides for a better spacing between the segments based PSDs compared to the Burg and eigenvector method. From static experiments, we conclude that all three (MUSIC, Burg, and Eigenvector) methods perform similarly if a linear relationship of the fatigue progression is desired.

This research characterizes muscle-fatigue using a PSD representation of different segments of sEMG data. Classical (fast Fourier transform and Welch's averaged modified periodogram), model-based (Y-W, Burg, Cov., and Mcov. autoregressive (AR) method) and eigenvector based methods (MUSIC and EIG. spectral estimation method) are used to compute the PSDs. Classical and eigenvector based methods are more sensitive than the model-based methods for analyzing the fatigue related changes in the sEMG signal. However, the MUSIC algorithm provides good maximum value in the PSD as well as a clear distinction between the segmented sEMG data. The latter point is indicative of a relative linear fatigue progression in time for the same case when the MUSIC algorithm is utilized. In the future work these results can be used to design and improve the skeletal-muscle 'Force-sEMG-Fatigue' based models [108] for prosthetic design and other rehabilitation research.

## **2.4 Hand Finger Motion**

### **2.4.1 A Novel Adaptive Hybrid Finger Angle Estimation from sEMG Data with Multiple Linear and Nonlinear Model Data Fusion**

This section presents a novel approach to estimate the finger joint-angles for smart prosthetic control using surface electromyographic (sEMG) signals. All currently available prostheses use a motion control strategy that utilizes pre-programmed commands upon reaching some threshold value of the measured sEMG signal for a particular motion set. In this work we use a novel approach to model the finger joint-angle with the help of System Identification (SI) techniques. The dynamic model obtained allows the instantaneous control of the finger motions. sEMG data is acquired using an array of nine sensors and the corresponding finger angle data is acquired using a finger angle measuring device and a data glove. A nonlinear Teager-Kaiser Energy (TKE) operator based nonlinear spatial filter is used to filter sEMG data whereas the angle data is filtered using a Chebyshev Type-II filters. The filtered signals are resampled and smoothed using a smoothing spline curve fitting method. Using SI techniques, a set of linear and nonlinear models are obtained with the smoothed sEMG data as input and the respective smoothed finger angle data as output. An adaptive probabilistic Kullback Information Criterion (KIC) based data fusion algorithm is applied to the outputs of the linear and

nonlinear models to achieve better estimates of the finger angles. The resulting adaptive fusion based output of this approach gives improved estimates of the finger joint-angles.

Present research focuses on the dynamic modeling and estimation of the angles of the proximal interphalangeal (PIP) joint of the index and the middle finger with the corresponding sEMG signal. Two different systems and experiment designs are used to acquire the data for the index and middle finger angles and the corresponding sEMG signals. For the index finger data an array of nine sEMG sensors is used to record sEMG signals and joint-angles are recorded using a wheel potentiometer from the arm of a healthy subject. For the middle finger data an array of three sensors is used to record sEMG signals and joint-angles are recorded using a NODNA X-IST DataGlove. Both experiment designs are explained in the following section. Both signals are filtered and smoothing-spline-curve fitted with 0.993 as smoothing parameter. The dynamic modeling is achieved using System Identification (SI) where smoothed sEMG data is the input and the smoothed joint-angle data is the output. Multiple linear and nonlinear models are obtained. To achieve better estimate of the finger angles, an adaptive probabilistic Kullback Information Criterion (KIC) for model selection based data fusion algorithm is applied to the linear and nonlinear models outputs. In all the cases, the final fusion based output of this approach results in improved estimates of finger angles.

## Experiment Design

### A. First Experiment Design

The first experiment design is designed to simultaneously acquire the sEMG from the motor point of the flexor digitorum superficialis (FDS) of the index finger and the joint-angle of the PIP joint of the finger. The motor point was identified by the use of a wet probe muscle stimulator at the FDS (RICH-MAR, HV 1000). Nine DE-3.1 sEMG sensors of the DELSYS® Bagnoli-16 EMG system are placed in a three-by-three array [113]; the arrangement covers the four directional spatial distributions of the sEMG signal. The middle three sEMG sensors were attached directly on the skin surface above the motor point of the index finger of a healthy subject. Using a 10k- $\Omega$  wheel potentiometer, an angle measurement device is designed to measure the joint-angles of the PIP joint of the index finger of a healthy subject. An Interlink™ Electronics FSR 0.5" circular force sensor on a stress ball is used to press with the movement to introduce some resistance to the movement of the PIP joint of the index finger.

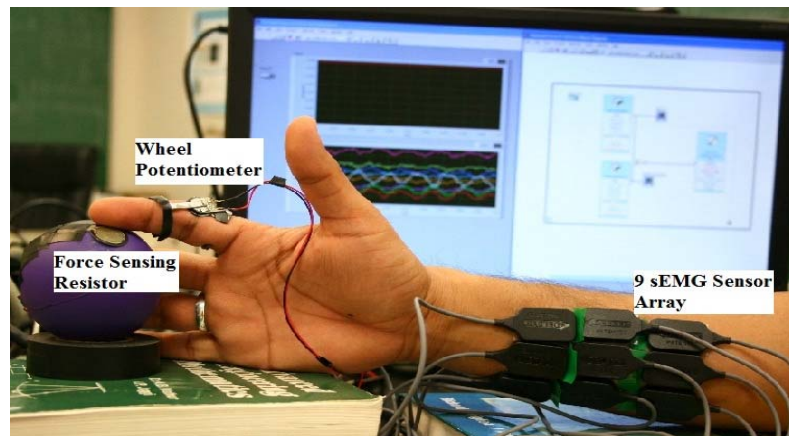


**Figure 2.61:** First experiment design.

Experiment design is shown in Figure 2.61. Here nine sensors are shown on a healthy subject forearm, with an angle measurement device on the PIP joint of the index finger and having a stress ball for force measurements. The various signals are sampled at a rate of 2000 Hz using LabVIEW™ in conjunction with DELSYS® Bagnoli-16 EMG and NI ELVIS™.

### B. Second Experiment Design

For the second experiment design different sEMG sensors and angle measuring DataGlove was used. In this case the PIP joint-angle of the middle finger was acquired using a NODNA X-IST DataGlove. The sEMG system is a NORAXON MyoSystem 2000 and sEMG electrodes are dual electrodes which are disposable, self-adhesive Ag/AgCl dual snap electrodes for surface EMG

applications. Data acquisition rate for the sEMG is 1000 Hz and for the corresponding angle data on the DataGlove is 60~62 Hz. Several experiments were conducted with sEMG sensors on the extensor and flexion side of the arm. In this work the data captured from the flexion side is used for the simulations. The experiment design is given in Figure 2.62.



**Figure 2.62:** Second experiment design.

Prior to placing sEMG sensors, the skin surface of the subject was prepared according to International Society of Electrophysiology and Kinesiology (ISEK) protocols [119]. With these set-ups we conducted several experiments of 30 seconds, 45 seconds and 60 seconds durations.

### Signal Pre-Processing

The recorded sEMG signal for the index finger is filtered using nonlinear spatial filtering using the “Nonlinear Teager-Kaiser Energy (TKE) Operator,” [113]. Equation (43) gives the TKE operator in the time domain of the sEMG signal [113].

$$\Psi[x(n)] = x^2(n) - x(n+1) * x(n-1). \quad (43)$$

Here,  $\Psi$  is the TKE operator and  $x(n)$  is the time domain sEMG signal at location  $n$ . Data from first experiment design was filtered with four-directional spatial filter whereas the data from the second experiment design is filtered with one-directional spatial filter. Both of the filters, the one-directional and the four-directional nonlinear spatial filters, can be derived from the TKE operator. Equations (44) and (45) give the one-directional and four-directional nonlinear spatial filters, respectively.

$$\Psi_{d,1}[x(m,n)] = x^2(m,n) - x(m-1,n) * x(m+1,n). \quad (44)$$

$$\Psi_{d,4}[x(m,n)] = 4 * x^2(m,n) - x(m-1,n) * x(m+1,n) - x(m,n-1) * x(m,n+1) - x(m-1,n+1) * x(m+1,n-1) - x(m-1,n-1) * x(m+1,n+1). \quad (45)$$

Figs. 2.63 and 2.65 show the comparison between the measured and four and one directional nonlinear spatial filtered sEMG signals from the first and second experiment designs, respectively. A Chebyshev Type II infinite impulse response (IIR) low pass filter with a 550 Hz pass band frequency is used to filter the PIP joint-angle data for both first and second experimental data sets. Figs. 2.64 and 2.66 show the comparison between the measured and Chebyshev Type II filtered PIP joint-angle data for first and second experimental data sets respectively.

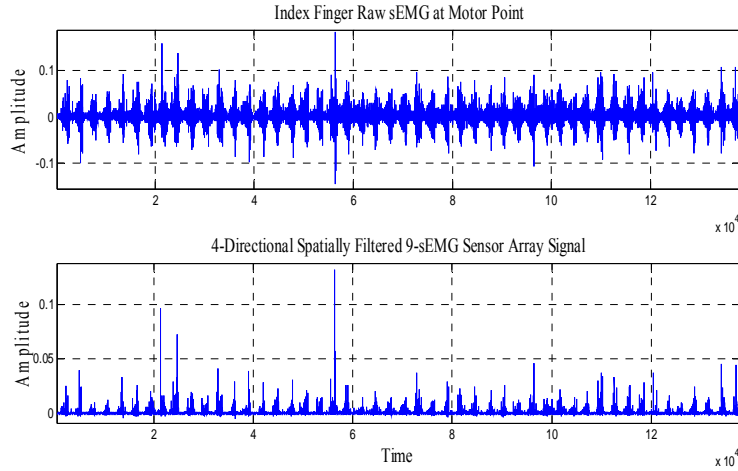


**Figure 2.63:** Raw and spatially filtered sEMG signal from Index finger – first experiment design.

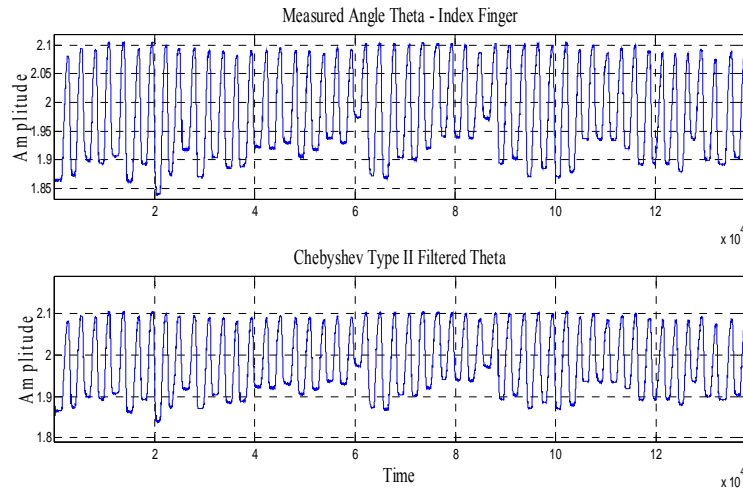


**Figure 2.64:** Raw and Chebyshev Type II filtered PIP joint-angle for Index finger – first experiment design.

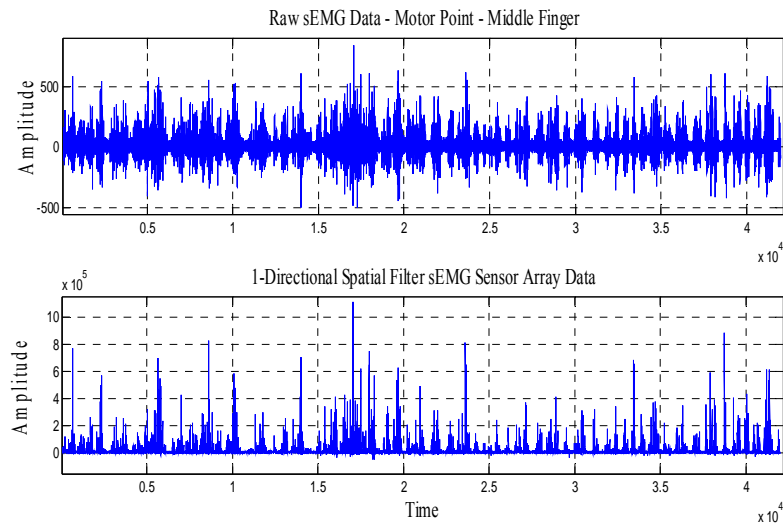


**Figure 2.65:** Raw and spatially filtered sEMG signal from Index finger – second experiment design.

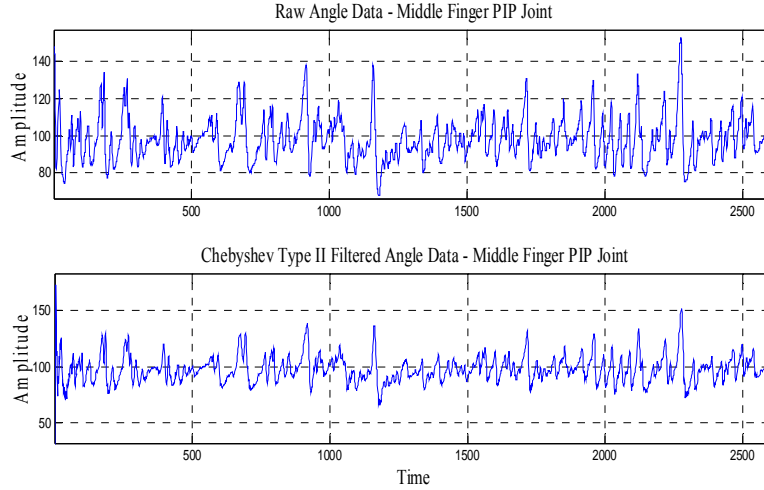


**Figure 2.66:** Raw and Chebyshev Type II filtered PIP joint-angle for Index finger – second experiment design.

### Smoothing Spline Curve Fitting

The input and output data from both the experiment designs i.e. the first and the second are fitted with a smoothing spline which is a piecewise polynomial computed from a smoothing parameter ( $p$ ) of 0.993. Smoothing spline can be changed by changing the smoothing parameter ( $p$ ) which is a number between 0 and 1. For  $p = 0$  the smoothing spline is a least-square straight-line approximation to the data, whereas for  $p = 1$  it gives the "natural" cubic spline interpolant to the data [117].

For the specified weight ( $w_i$ ) and smoothing parameter ( $p$ ), a smoothing spline  $s$  is formed that minimizes the parameter  $J$  given by Equation (46).

$$J = p \sum_i w_i (y_i - s(x_i))^2 + (1 - p) \int \left( \frac{d^2 s}{dx^2} \right)^2 dx, \quad (46)$$

where  $x_i$  and  $y_i$  are predictor and response data respectively.

The smoothing parameter  $p$  should be chosen to make the error  $E(s) = \sum_i w_i (y_i - s(x_i))^2$  and roughness  $\int \left( \frac{d^2 s}{dx^2} \right)^2 dx$  small. Here in this work the smoothing parameter  $p$  is chosen as 0.993 [117].

### System Identification

System Identification (SI) is a tool to model a dynamic system based on input-output data [110]. In this research, we use SI to model two sets of signals from two different experiment designs which are smoothing-spline-curve fitted. For both the experimental data the sEMG is the input to the system and the intended PIP joint-angle is the output. PIP joint-angle data from the index and the middle finger are processed with the corresponding sEMG signals. Multiple linear and nonlinear models are obtained for modeling of sEMG and PIP joint-angle signals of the dominant hand of a healthy subject. For the data from the first experiment design, five linear and three nonlinear models are obtained for the input and output data set. For the data from the second experiment design, six linear and six nonlinear models are obtained. Tables XIII and XIV give the structures of the linear and nonlinear models, respectively.

For the data from the first experiment design, the model order of the various models used are as follows: linear models for the input and output data set, OE model of order 16, ARX model of order 18, ARMAX model of order 16, state-space model with subspace method (N4SID) of order 18 and a State-Space model with prediction error/maximum likelihood method (PEM) of order 12 are obtained using SI. For the data from the second experiment design, the model order of the various models used are as follows: linear models for the input and output data set, OE model of order 46, ARX model of order 73, ARMAX model of order 36, Box-Jenkins model of order 12, state-space model with subspace method (N4SID) of order 40 and a state-space model with prediction error/maximum likelihood method (PEM) of order 40 are obtained using SI.

Table 2.13 gives the structure of all the linear models. In Table 2.13,  $y$  is output,  $t$  is discrete time,  $B(q)$ ,  $F(q)$ ,  $A(q)$ ,  $C(q)$ ,  $D(q)$ , are polynomials,  $q$  is a backward shift operator,  $u$  is input,  $n_k$  is delay and  $e$  is error [104]. For State-Space models:-  $x$  is state,  $t$  is discrete time,  $T_s$  is sampling time,  $u$  is input,  $e$  is error,  $A$ ,  $B$ ,  $K$ ,  $C$ , and  $D$  are system matrices, and  $y$  is output [104]. Table 2.14 gives the

structures of nonlinear models. The nonlinear models for the input and output data set from the first experiment design are obtained as, the nonlinear Hammerstein-Wiener models with nonlinearity estimators of ‘piecewise linear – pwlinear,’ ‘sigmoidnet,’ and ‘wavelet network.’

**Table 2.13: Linear Models and Their Structures (IEEE-TBE 2011)**

Linear Model Name	Linear Model Structure
Output Error	$y(t) = \frac{B(q)}{F(q)}u(t - n_k) + e(t)$
ARX	$A(q)y(t) = B(q)u(t - n_k) + e(t)$
ARMAX	$A(q)y(t) = B(q)u(t - n_k) + C(q)e(t)$
Box-Jenkins	$y(t) = \frac{B(q)}{F(q)}u(t - n_k) + \frac{C(q)}{D(q)}e(t)$
State-Space – subspace method	$x(t + Ts) = Ax(t) + Bu(t) + Ke(t)$ $y(t) = Cx(t) + Du(t) + e(t)$
State-Space – prediction error/maximum likelihood method	$x(t + Ts) = Ax(t) + Bu(t) + Ke(t)$ $y(t) = Cx(t) + Du(t) + e(t)$

The nonlinear models for the input and output data set from the second experiment design are obtained as, the nonlinear ARX models with nonlinearity estimators of ‘wavelet network,’ and ‘tree partition,’ the nonlinear Hammerstein-Wiener models with nonlinearity estimators of ‘piecewise linear – pwlinear,’ ‘sigmoidnet,’ ‘deadzone,’ and ‘wavelet network.’ In Table 2.14, for the nonlinear ARX model with wavelet network as nonlinearity estimator,  $\kappa(s)$  as a wavelet function, and  $\beta_k$  is a row vector such that  $\beta_k(x - \gamma_k)$  is a scalar. For the nonlinear ARX model with the nonlinear estimator as ‘treepartition,’ the output  $y$  is a nonlinear function, where  $F$  is piecewise linear (affine) function of  $x$ ,  $y$  is scalar, and  $x$  is a 1-by- $m$  vector.  $F$  is a local linear mapping, where  $x$ -space partitioning is determined by a binary tree. In  $F$ ,  $L$  is 1-by- $m$  vector,  $C_a$  is 1-by- $(m + 1)$  vector and  $d$  is scalar [104].

**Table 2.14: Nonlinear Models and Their Structures (IEEE-TBE 2011)**

Nonlinear Model Name	Nonlinear Model Structure
Nonlinear ARX – Wavelet Network	$g(x) = \sum_{k=1}^n \alpha_k \kappa(\beta_k(x - \gamma_k))$
Nonlinear ARX – Tree-partition	$y = F(x)$ $F(x) = x * L + [1, x] * C_a + d$
Nonlinear HW – Piecewise Linear – Pwlinear	$w(t) = f(u(t)),$ $x(t) = \frac{B_{ji}(q)}{F_{ji}(q)}w(t),$ $y(t) = h(x(t));$
Nonlinear HW – Sigmoidnet	$y_p(t) = f(y(t - 1), y(t - 2), y(t - 3), \dots,$ $u(t - 1), u(t - 2), \dots);$ $f(z) = \frac{1}{e^{-z} + 1}$ is sigmoid function.
Nonlinear HW – Deadzone	$y = F(x);$ $a \leq x < b, \quad F(x) = 0$ $x < a, \quad F(x) = x - a$ $x \geq b, \quad F(x) = x - b$
Nonlinear HW – Wavelet Network	$g(x) = \sum_{k=1}^n \alpha_k \kappa(\beta_k(x - \gamma_k))$



For the Hammerstein-Wiener model,  $u(t)$  and  $y(t)$  are the inputs and outputs for the system, respectively.  $f$  and  $h$  are nonlinear functions that corresponds to the input and output nonlinearity, respectively.  $w(t)$  and  $x(t)$  are internal variables.  $w(t)$  has the same dimension as  $u(t)$ .  $x(t)$  has the same dimension as  $y(t)$ .  $B(q)$  and  $F(q)$  in the linear dynamic block are polynomials in the backward shift operator. For the nonlinear Hammerstein-Wiener model with nonlinear estimator as ‘sigmoidnet,’  $f(z)$  is the sigmoid function [104]. The nonlinear Hammerstein-Wiener model with nonlinear estimator as ‘deadzone,’ defines a nonlinear function  $y$ , where  $F$  is a function of  $x$ , and,  $y$  and  $x$  are scalars [104]. For the nonlinear Hammerstein-Wiener model with wavelet network as nonlinearity estimator,  $\kappa(s)$  is a wavelet function, and  $\beta_k$  is a row vector such that  $\beta_k (x - \gamma_k)$  is a scalar. If only the input nonlinearity is present, the model is called the Hammerstein model. If only the output nonlinearity is present, the model is called the Wiener model [104].

### Adaptive Data Fusion

Data fusion of multiple outputs of the linear and nonlinear models is done by assigning a particular probability to each individual output [105]. This method gives good estimation of the PIP joint-angles. The goodness of the fit of each linear and nonlinear model output can be computed using SI model fit value, which is given by Equation (47).

$$FIT = [1 - |Y - \hat{Y}| / |Y - \bar{Y}|] * 100. \quad (47)$$

In Equation (47),  $Y$  is measured,  $\hat{Y}$  is estimated and  $\bar{Y}$  is mean output signal. The model selection criterion used in this section is Kullback Information Criterion (KIC) which has shown to perform well for sEMG sensor data fusion [109], [108], [112], [111], [126]. The sum of two directed divergences, which is the measure of the models dissimilarity, is known as Kullback’s symmetric or J-divergence [106], as given by Equation (48).

$$KIC(p_i) = \frac{n}{2} \log R_i + \frac{(p_i+1)n}{n-p_i-2} - n\psi\left(\frac{n-p_i}{2}\right) + g(n), \quad (48)$$

where  $g(n) = n * \log\left(\frac{n}{2}\right)$ , and  $\psi$  is known as digamma function which is logarithmic derivative of

$$\text{the gamma function. } \psi(x) = \text{digamma}(x) = \frac{d(\log(\Gamma(x)))}{dx} = \frac{d(\Gamma(x))}{\Gamma(x) dx}.$$

The adaptive fusion algorithm as given in [105] is applied for data fusion of the outputs of the linear and nonlinear models obtained using SI:

- 1) Estimate the linear and nonlinear models outputs  $M_1, M_2, \dots, M_k$  for  $k$  number of outputs.
- 2) Compute the residual square norm  $R_i = \|Y - \Phi_i \hat{\Theta}_i\|^2 = \|Y - \hat{Y}\|^2$ ,  
where  $\hat{\Theta}_i = \{\Phi_i^T \Phi_i\}^{-1} \Phi_i^T Y$ , and

$$\Phi = \begin{bmatrix} Y_p^T & u_p^T & Y_{p-1}^T & \dots & u_1^T \\ Y_{p+1}^T & u_{p+1}^T & Y_p^T & \dots & u_2^T \\ \vdots & \vdots & \vdots & \ddots & \vdots \\ Y_{n-1}^T & u_{n-1}^T & Y_{n-2}^T & \dots & u_{n-p}^T \end{bmatrix}.$$

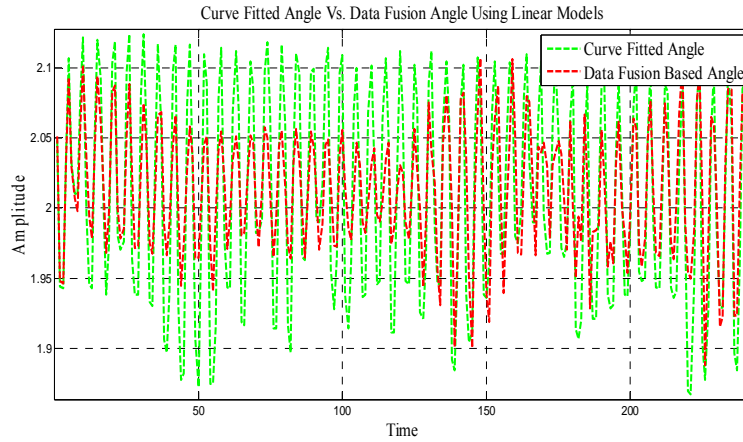
- 3) Calculate the model criteria coefficient using Equation (48).
- 4) Compute the model probability  $p(M_i|Z) = \frac{e^{-l_i}}{\sum_{j=1}^{k_1} e^{-l_j}}$ , where  $l$  is model selection criterion, i.e.  $KIC(p_i)$ .
- 5) Compute the data fusion based model output  $\hat{Y}_f = \sum_{i=1}^{k_1} p(M_i|Z) \hat{Y}_i$ .

In this algorithm, the computation from step 2) to 5) is adaptive i.e. the residual square norm,  $KIC(p_i)$ , model probability  $p(M_i|Z)$ , and fused model output  $\hat{Y}_f$  are being updated with time or for each data point.

### Results and Discussion

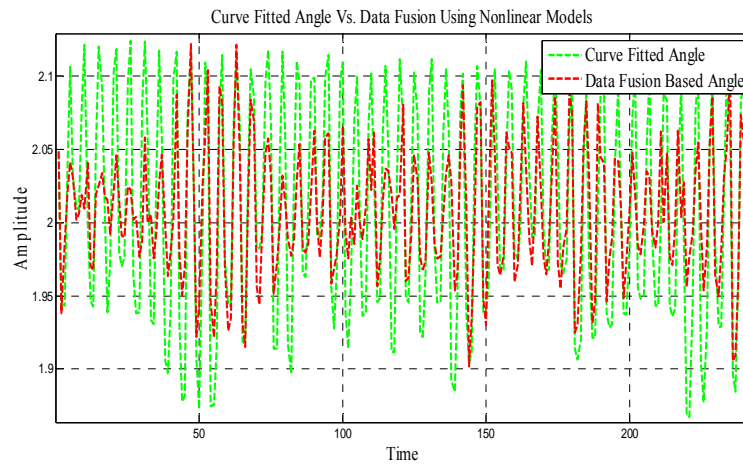
Two different experiment designs are designed to capture the sEMG and PIP joint-angles of index and middle finger. For the index finger an angle measuring device was designed whereas for the middle finger a DataGlove was used to capture the joint-angle data. The first and second experiment designs in Figs. 67 and 68 are for the index and middle finger experiments, respectively. For both cases, sEMG signals from the sensor array and angle signals of PIP joint of index and middle finger are filtered; smoothing spline curve fitted and modeled using multiple linear and nonlinear models. In each case, first, the outputs of linear and nonlinear models are fused separately and then the resultant outputs are fused using an adaptive KIC based probability.





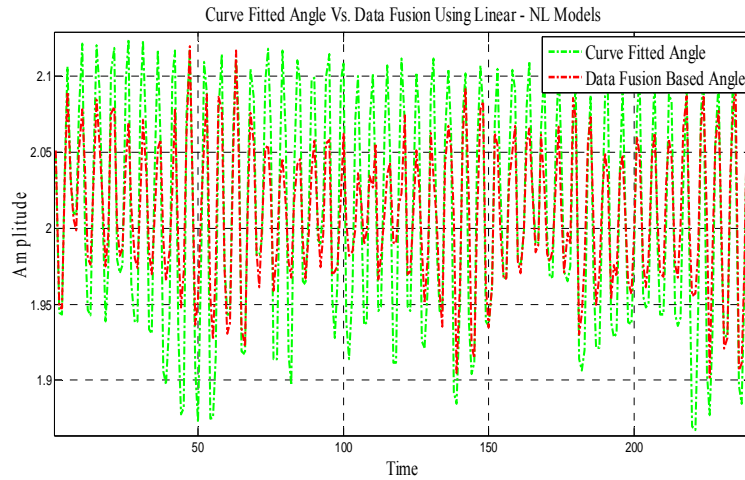
**Figure 2.67:** Curve fitted vs. adaptive data fusion based angle using linear models – first experiment design data.

This approach gives improved estimates of the finger angles of the PIP joint of the index and middle finger of the dominant hand of a healthy subject. Results are presented in the following figures. For the first experiment design: Figure 2.67 shows the overlapping plot of the measured-curve fitted angle vs. adaptive data fusion based angle using linear models.



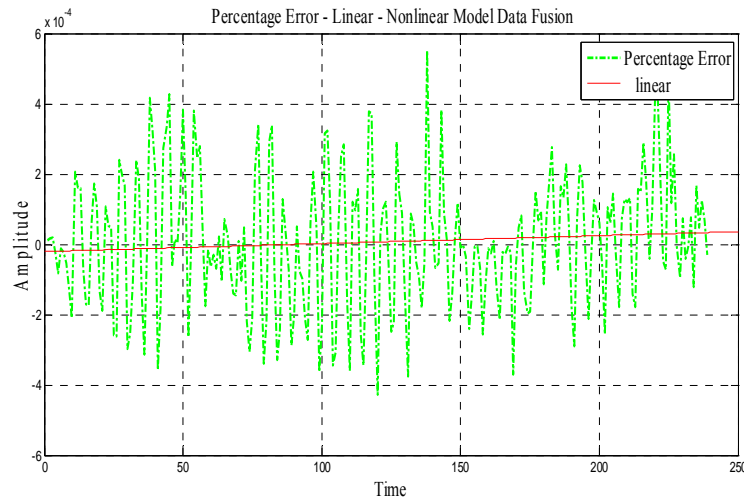
**Figure 2.68:** Curve fitted vs. adaptive data fusion based angle using nonlinear models – first experiment design data.

Figure 2.68 shows the overlapping plot of the measured-curve fitted angle vs. adaptive data fusion based angle using nonlinear models. Figure 2.69 shows the overlapping plot of the curve fitted angle vs. adaptive data fusion based angle using linear-nonlinear models. It is clearly evident to us that the adaptive data fusion based output follows the measured-curve fitted output. Standard deviation can be computed as,  $s = (\frac{1}{n-1} \sum_{i=1}^n (x_i - \bar{x})^2)^{1/2}$ , where  $\bar{x} = \frac{1}{n} \sum_{i=1}^n x_i$  and  $n$  is the number of elements in the sample. Percentage error can be computed using the formula;  $\% \text{ error} = \frac{|P-Y|}{Y} * 100\%$ .

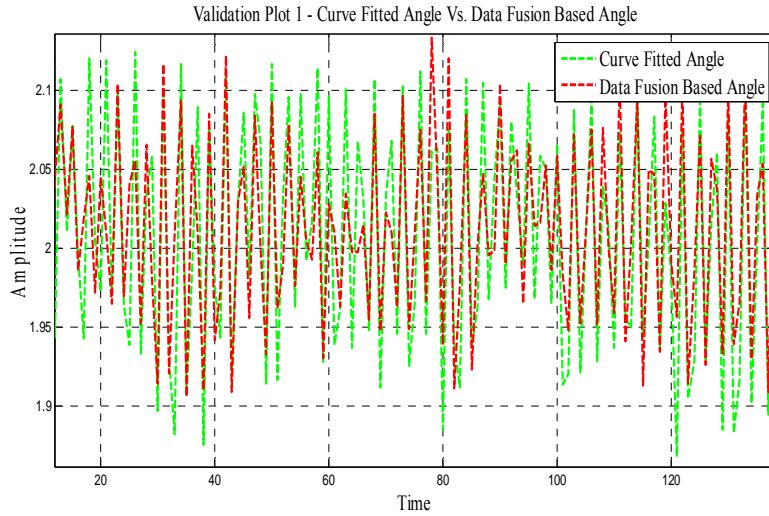


**Figure 2.69:** Curve fitted vs. adaptive data fusion based angle using linear-nonlinear models – first experiment design data.

The mean value and the standard deviation of the measured angle data is 2.0074 and 0.0756, respectively. The mean value of the adaptive data fusion based estimated angle for linear, nonlinear and linear-nonlinear models combined is 2.0131, 2.0075 and 2.0102, respectively. The respective standard deviations are 0.0450, 0.0448 and 0.0467. Mean percentage error of the linear, nonlinear and linear-nonlinear models data fusion based angles are  $2.0060 \times 10^{-4}$ ,  $2.1128 \times 10^{-4}$ , and  $1.5067 \times 10^{-4}$  respectively. Figure 2.70 shows the percentage error plot for the final estimated output based on linear-nonlinear models.



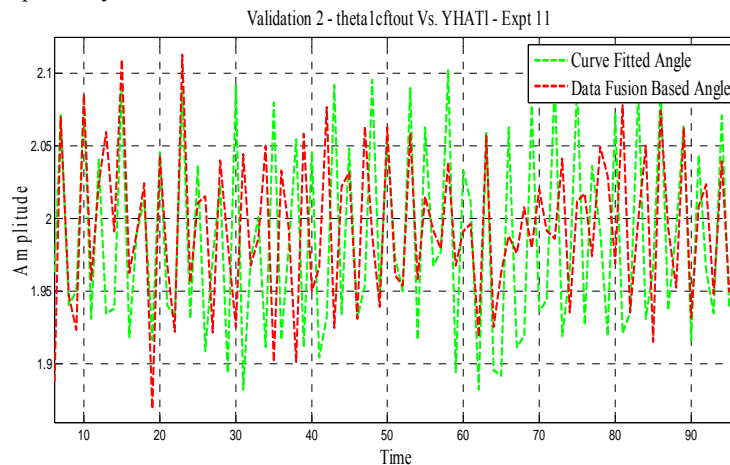
**Figure 2.70:** Percentage error plot for the final estimated output based on the linear-nonlinear model – first experiment design.



**Figure 2.71:** Validation plot - curve fitted vs. adaptive data fusion based angle using linear-nonlinear models – first experiment design data.

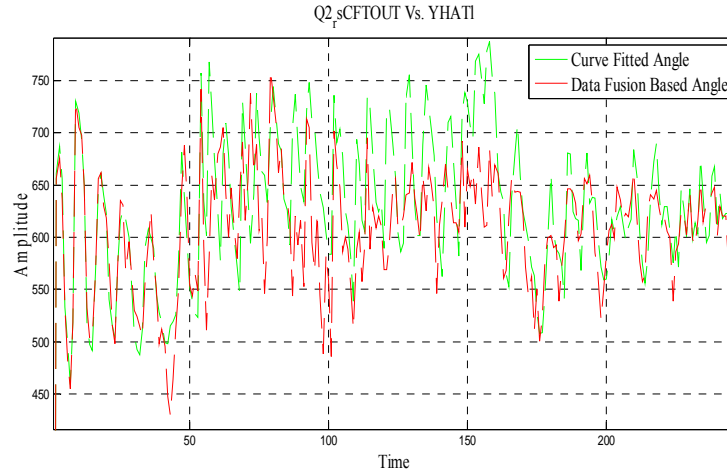
Figure 2.71 shows the first validation plot for a different experimental data where the measured-curve fitted and the linear-nonlinear modeled data fusion based angle signal shows a close follow up. The mean value and the standard deviation value of the measure angle data in this case is 1.9655 and 0.1840, respectively. The mean value of the adaptive data fusion based estimated angle for linear, nonlinear and linear-nonlinear models combined is 1.9718, 1.9729 and 1.9642, respectively. The respective standard deviations are 0.1767, 0.0653 and 0.1727. Mean percentage error of the linear, nonlinear and linear-nonlinear models data fusion based angles are  $2.8653 \times 10^{-4}$ ,  $4.3135 \times 10^{-4}$ , and  $2.9251 \times 10^{-4}$  respectively.

Figure 2.72 shows the second validation plot for a different experimental data where the measured-curve fitted and the linear-nonlinear modeled data fusion based angle signal shows a close follow up. The mean value and the standard deviation value of the measured angle data in this case is 1.9720 and 0.1832, respectively. The mean value of the adaptive data fusion based estimated angle for linear, nonlinear and linear-nonlinear models combined is 1.9767, 1.9728 and 1.9652, respectively. The respective standard deviations are 0.1811, 0.0677 and 0.1784. Mean percentage error of the linear, nonlinear and linear-nonlinear models data fusion based angles are  $2.4654 \times 10^{-4}$ ,  $3.6941 \times 10^{-4}$ , and  $2.2478 \times 10^{-4}$  respectively.



**Figure 2.72:** Validation plot - curve fitted vs. adaptive data fusion based angle using linear-nonlinear models – first experiment design data.

For the second experiment design: Figure 2.73 shows the overlapping plot of the measured-curve fitted angle vs. adaptive data fusion based angle using linear models.



**Figure 2.73:** Curve fitted vs. adaptive data fusion based angle using linear models – second experiment design data.

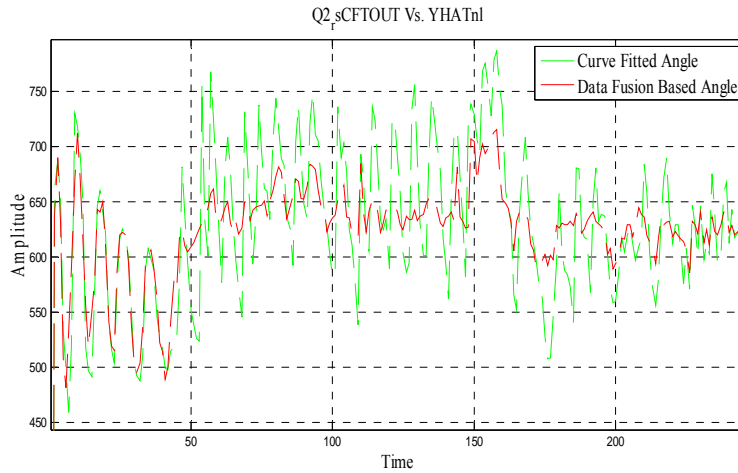


**Figure 2.74:** Curve fitted vs. adaptive data fusion based angle using nonlinear models – second experiment design data.

Figure 2.74 shows the overlapping plot of the measured-curve fitted angle vs. adaptive data fusion based angle using nonlinear models. Figure 2.75 shows the overlapping plot of the curve fitted angle vs. adaptive data fusion based angle using linear-nonlinear models. It is clearly evident to us that the adaptive data fusion based output follows the measured-curve fitted output. The mean value and the standard deviation of the measured angle data in this case is 627.1338 and 78.6537, respectively. The mean value of the adaptive data fusion based estimated angle for linear, nonlinear and linear-nonlinear models combined is 604.8511, 623.6136 and 615.8080, respectively. The respective standard deviations are 68.1358, 53.6293 and 62.4144. Mean percentage error of the linear, nonlinear and linear-nonlinear models data fusion based angles are  $6.0430 \times 10^{-4}$ ,  $5.3726 \times 10^{-4}$ , and  $4.2376 \times 10^{-4}$  respectively. Figure 2.76 shows the percentage error plot for the final estimated output based on linear-nonlinear models.

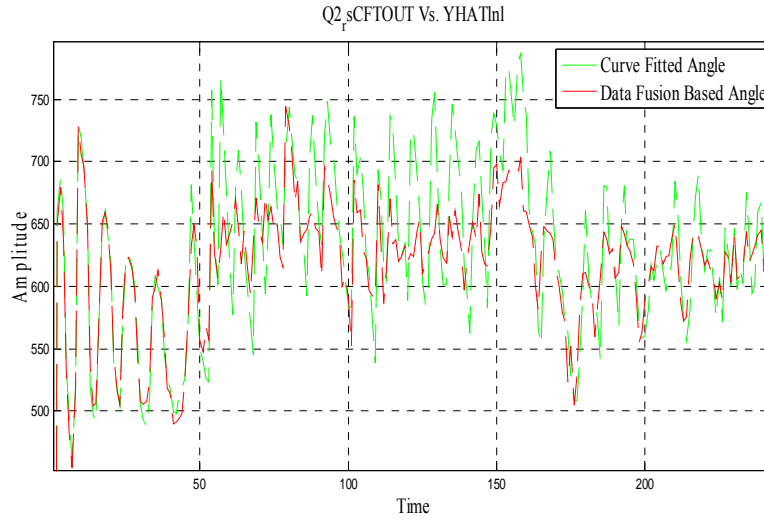


**Figure 2.75:** Curve fitted vs. adaptive data fusion based angle using linear-nonlinear models – second experiment design data.

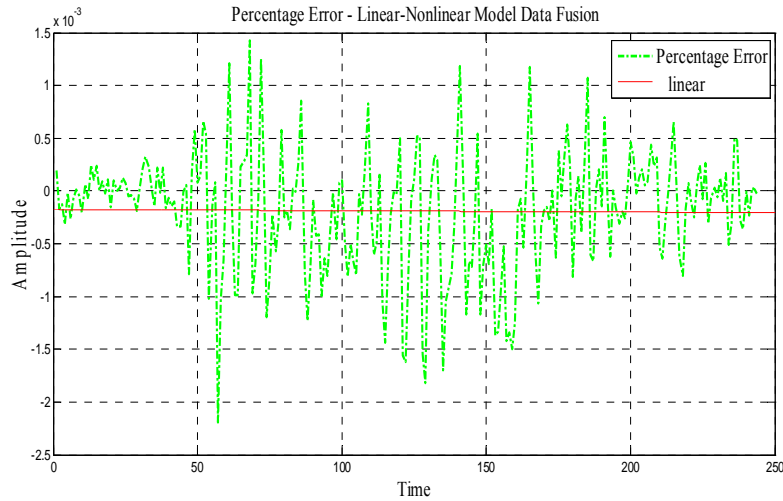


**Figure 2.76:** Percentage error plot for the final estimated output based on the linear-nonlinear model – second experiment design data.

Figure 2.77 shows the first validation plot for a different experimental data where the measured-curve fitted and the linear-nonlinear modeled data fusion based angle signal shows a close follow up. The mean value and the standard deviation value of the measure angle data in this case is 853.1549 and 70.7298, respectively. The mean value of the adaptive data fusion based estimated angle for linear, nonlinear and linear-nonlinear models combined is 313.6785, 635.6205 and 614.6949, respectively. The respective standard deviations are 245.3495, 40.8147 and 76.6001. Mean percentage error of the linear, nonlinear and linear-nonlinear models data fusion based angles are 0.0058, 0.0023 and 0.0026, respectively.

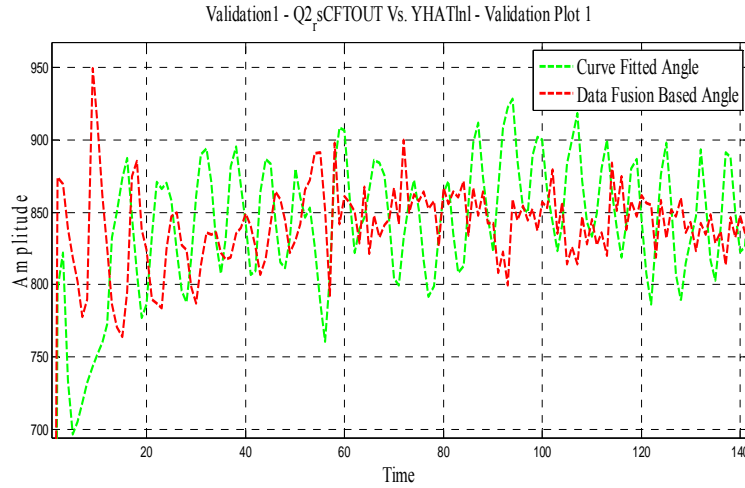


**Figure 2.77:** Validation plot 1 - curve fitted vs. adaptive data fusion based angle using linear-nonlinear models – second experiment design data.

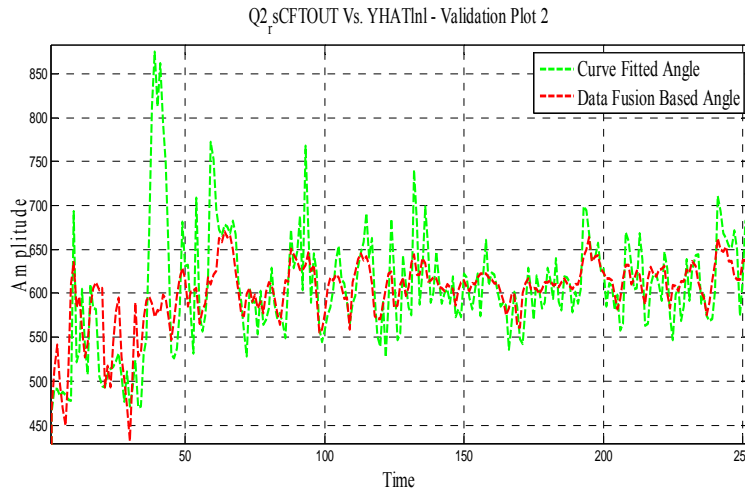


**Figure 2.78:** Validation plot 2 - curve fitted vs. adaptive data fusion based angle using linear-nonlinear models – second experiment design data.

Figure 2.78 shows a second validation plot for a different experimental data where the measured-curve fitted and the linear-nonlinear modeled data fusion based signal shows a close follow up. The mean value and the standard deviation value of the measure angle data in this case is 602.3498 and 75.0967, respectively. The mean value of the adaptive data fusion based estimated angle for linear, nonlinear and linear-nonlinear models combined is 367.2863, 606.6189 and 599.6719, respectively. The respective standard deviations are 121.4799, 39.6640 and 49.22210. Mean percentage error of the linear, nonlinear and linear-nonlinear models data fusion based angles are 0.0042, 5.9129e-004 and 5.4813e-004, respectively. The dynamic modeling of the filtered and smoothed sEMG and PIP joint-angle of the index and middle finger is achieved using SI with sEMG as the input and the joint-angle as the output. Multiple linear and nonlinear models are obtained for the input and output data. To achieve a better estimate of the finger angles, an adaptive probabilistic Kullback Information Criterion (KIC) for model selection based data fusion algorithm is applied to the linear and nonlinear models outputs. For both the cases, the final adaptive fusion based output of this approach results in improved estimates of PIP joint-angles of the index and middle finger. The approach is validated using different sets of experimental data. As this initial study shows good potential for controlling an artificial hand in real time, we will implement the recent control strategies developed in [107], [127], [128], [129], [107] to control a hand prototype. We will further investigate on improving the data collection techniques and optimizing the experimental procedure as well as optimizing the smoothing parameter for the smoothing-spline-curve fitting.

## Goal 2A: Intelligent Control

The overall research is accomplished under four goals: Goal 1: EMG Signal Identification and Estimation, Hand Motion Estimation, Goal2: Intelligent Control of Prosthetics, Goal 3: Robotic Hand and Goal 4: Biocompatibility and Signaling. The schematic diagram of the proposed work is shown in Figure 1 (see the works of Light et al. (2002); Rodriguez-Cheu and Casals (2006); Zhao et al. (2006)). The overall system, in brief, consists of electromyographic (EMG) signal acquisition from user arm for surface or implanted electrodes (in the implanted case we focus on biocompatibility based on nano-materials research). The EMG signal is then processed for feature extraction and classification or identification of EMG signal to correspond to different motions of the prosthetic hand. The classified signal is then used to control the prosthetic hand using actuators and driving mechanisms.

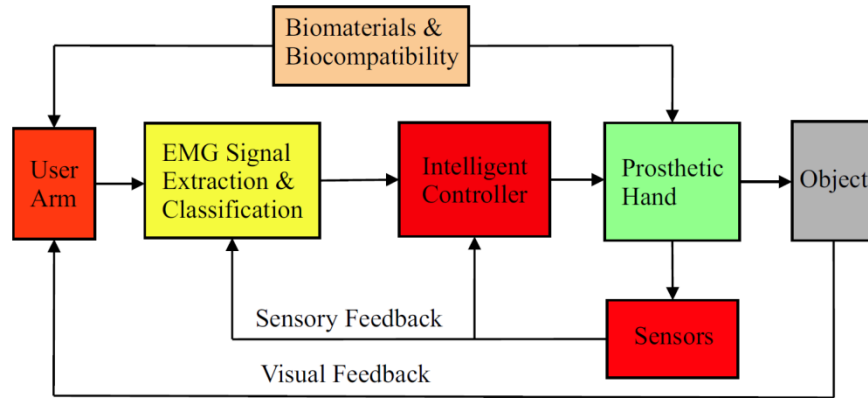


Figure 1: Schematic Diagram of Prosthetic Hand Technology

Soft computing (SC) or computational intelligence (CI) (Konar (2005)) is an emerging field based on synergy and seamless integration of neural networks (NN), fuzzy logic (FL) and genetic algorithms (GA) (Karray and De Silva (2004)). The previous works on prosthetic hand used artificial neural networks by Hudgins (1991); Christodoulu and Pattichis (1999); Light et al. (2002), fuzzy logic by Weir and Ajiboye (2003); Chan et al. (2000); Ajiboye and Weir (2005), genetic algorithms in (Fernandez et al. (2000)) etc mostly for EMG signal classification for various movements or functions of the prosthetic hand.

## Kinematics, Dynamics and Control of Prosthetic Hand with Extended Degrees of Freedom

### Abstract

It is obvious to all that the human hand represents a mechanism of the most intricate fashioning and one of great complexity and utility. Its ability to adapt to different surfaces and shapes, touch and grasp objects has made it a versatile tool. But beyond this, it is ultimately correlated with the brain both in the evolution of the specie and the development of the individual.

In this report, we present a virtual hand that closely mimics the human hand. Based on the anatomy of the hand, we designed a hand with 22 degrees of freedom (DOF), with each of the carpometacarpal joints (CMC) having 2 degrees of freedom each and metacarpal joints (MP) and inter-phalangeal (IP) joints having one each. The two degrees of freedom at the CMC joints are non-intersecting and are responsible for the flexion and extension (FE) motion as well as the abduction and adduction motion.. It is important to note that because of the constraint in the range of the abduction adduction motion in the index, middle, ring and small fingers, the workspace is limited.

In our approach, the problem of forward kinematics using the Denavit-Hartenberg (D-H) method was applied to compute the position of the end-effector (fingertip) given the joint variable. This followed by the inverse kinematics which is a little more difficult problem. The inverse kinematics calculates the joint variables given the position of the hand. Based on the kinematic structure, a mathematical model that describes the dynamics of the hand was calculated. These dynamic models were calculated using the Lagrangian and Newton Euler formulations. Hard control strategies such as feedback linearization and proportional integral derivative (PID) control were applied to control the hand based on the kinematic and dynamic models.

## 1.1. Introduction

In robotics terms, the hand can be said to be the end-effector of the human form. Because of its correlation or connection with the brain, it is able to perform tasks like grasping, touching, lifting and so on. Attempts have been made in the past by various researchers to build a prosthetic hand that closely mimics the human hand and various propositions have been made as to the numbers of degrees of freedom the human hand has. Our own virtual model is a 22 degree of freedom smart prosthetic hand that will work with Myo-electric signals from the hand muscles.

## 1.2. Literature

The Human hand consists of connected parts composing kinematic chains so that the hand is highly articulated. At the same time, many constraints among fingers and joints make the hand motion even hard to model. Over the years, there has been an increasing interest in the area of prostheses which lead to the creation of various models. Vardiy proposed a 26 degree of freedom (DOF) hand model based on the Denavit-Hartenberg methodology [5]. The model from [5] is incomplete because the wrist was not incorporated and the palm was modeled as a seven DOFs articulation whereas in our model, all fingers have the same essential structure, so that the D-H methodology is applied to all fingers. The wrist was modeled as a 2 DOF articulation made up of flexion/extension (FE) and abduction and adduction motion (AA) motions. We placed the global reference frame on the wrist so that the forward kinematics of the finger-tip frame is calculated with respect to the reference frame at the base of the wrist.

In similar model to ours is [6], where the thumb was modeled as two DOFs and the rest of the fingers 3 DOFs. In [6], they assumed a serial link planar manipulators for all fingers.

## 2. Kinematics

Kinematics being the science of geometry is restricted to a pure geometrical description of motion by means of position, orientation and their time derivatives [1]. The kinematic study of manipulators and their various roles is fundamental to the formation of the equations of motion (dynamics) and control of the manipulator. The manipulator may be thought as a set of bodies connected in a chain by joints [2]. However, for the purpose of deriving the kinematic description of a robot hand, a link is considered as a rigid body which defines the relationship between two neighboring joint axes of a manipulator. To develop a systematic kinematic description and representation of the location of the arms of a robot with respect to a global fixed reference frame  $G$ , we utilize the matrix algebra or the Clifford algebra

### 2.1 Robot kinematics using matrix algebra

We model any mechanical system, including robots as a series of rigid link connected by joints. The joints restrict the relative movements of adjacent links and are generally powered and equipped with sensors to control the movements. To apply number synthesis to hand mechanisms, we first define mobility and connectivity. The degrees of freedom of a robot also called mobility are defined as the number of independent parameters needed to specify completely (or within a finite set) the position of everybody in the system at the instant of concern [3]. In order to compute the mobility, we employ the following version of Grubler's formula (Hunt 1978).

$$M \geq \sum f_i + \sum g_j - 6L \quad (2.1)$$

$$M' \geq \sum g_j - 6L \quad (2.2)$$

Where;

$M$  - Mobility of system with finger joints free to move.

$M'$  - Mobility of system with finger joints locked.

$g_j$  - Degrees of freedom of motion at the  $j$ th contact point.

$L$  - Number of independent loops in the system

However, for a serial robot, the degrees of freedom are equal to the number of joints multiplied by the mobility allowed by each joint. Once the mobility is defined and the active joints of the hand identified, the two main problems of kinematic analysis of robot are forward kinematics and inverse kinematics. In the forward kinematics also known as direct kinematics, we define the position of the end-effector as a matrix which is a function of the angles or slides at each joint. If the joint angles are known, the position of the end-effector is completely specified. The inverse kinematic problem which is a more difficult problem is: given the desired position and orientation of the hand relative to the station, how do we compute the set of joint angles which will achieve this result [2].



The solution of forward kinematics defines the workspace of the individual fingers of the hand as well as the hand in general. The workspace can be defined as a set of all possible positions of the end-effector (finger-tip), constructed using all possible values of the joint variables within the range. Note that the position means location plus orientation; the workspace of the robot hand is a six-dimensional subset of the six-dimensional space of rotations and translations.

Several workspace have been defined [4]

Reachable workspace ( $W_R$ ): Set of all locations of the origin of the fingertip/ hand frame that the robot can reach. It is a three-dimensional subset of the workspace.

Dexterous workspace ( $W_D$ ): Set of all location of the origin of the end-effector frame that the robot can reach with any orientation. It is useful because the robot has full dexterity in this subspace, which ensures that any task can be performed within it.

Workspace with constant orientation ( $W_\theta$ ): Set of all locations of the origin of the finger-tip frame that the robot can reach with a specified orientation for the finger-tip.

## 2.2 Forward Kinematics Equations

Consider a rigid body with a fixed reference frame {A} specified as X, Y & Z and another moving body {B}. A possible description of frame {B} with respect to frame {A} is to start with the frame coincident with a known frame {A}. First rotate {B} about  $\hat{Z}_B$  by an angle  $\alpha$ , then rotate about  $\hat{Y}_B$  by an angle  $\beta$  and then rotate about  $\hat{X}_B$  by an angle  $\gamma$ . In this representation, each rotation is performed about an axis of the moving frame {B}, rather than the fixed reference frame {A}. These sets of three rotations are called Euler angles [2]. The Euler angle rotation matrix for XYZ axes are as follows:

$$R_X = \begin{pmatrix} 1 & 0 & 0 \\ 0 & \cos \alpha & -\sin \alpha \\ 0 & \sin \alpha & \cos \alpha \end{pmatrix} \quad (2.2.1)$$

$$R_Y = \begin{pmatrix} \cos \beta & 0 & \sin \beta \\ 0 & 1 & 0 \\ -\sin \beta & 0 & \cos \beta \end{pmatrix} \quad (2.2.2)$$

$$R_Z = \begin{pmatrix} \cos \theta & -\sin \theta & 0 \\ \sin \theta & \cos \theta & 0 \\ 0 & 0 & 1 \end{pmatrix} \quad (2.2.3)$$

We can represent local transformations from joint to joint using a 4 x 4 homogeneous matrices. The composition of these displacements is given as a result of the displacement from the base to the end-effector. In order to create the local transformations along any chain, we identify the line locating the joint axes,  $S_i$ , and we compute the common normal line  $A_{i,i+1}$  between  $S_{i+1}$ . We consider that the link joining two consecutive joints extends along the common normal line, regardless of its real shape.

We assign local coordinate frames with the z axis along the joints axes and the x axis along the common normal line. Local displacements will take us from local coordinate frame to local coordinate frame, from the base to the end-effector.

### 2.2.1 Denavit-Hartenberg Parameters

In 1995, Denavit and Hartenberg introduced the methodology of 4 x 4 homogeneous matrix transformations to analyze robotic systems, which became a standard tool in robotics [11, 12, 1]. The shaped the local transformations

along the chain as screw displacements about z and x axes, dependent on only four parameters. Although a few modifications has been made over the years. The D-H notations we used are similar to Craig [3].

We locate the first local frame with the x axis along the common normal  $A_{12}$ . The origin of the frame is located at the intersection of these two lines. Assume that a general displacement [G] locates the first local frame with respect to the fixed frame, as shown in fig. 2.1.

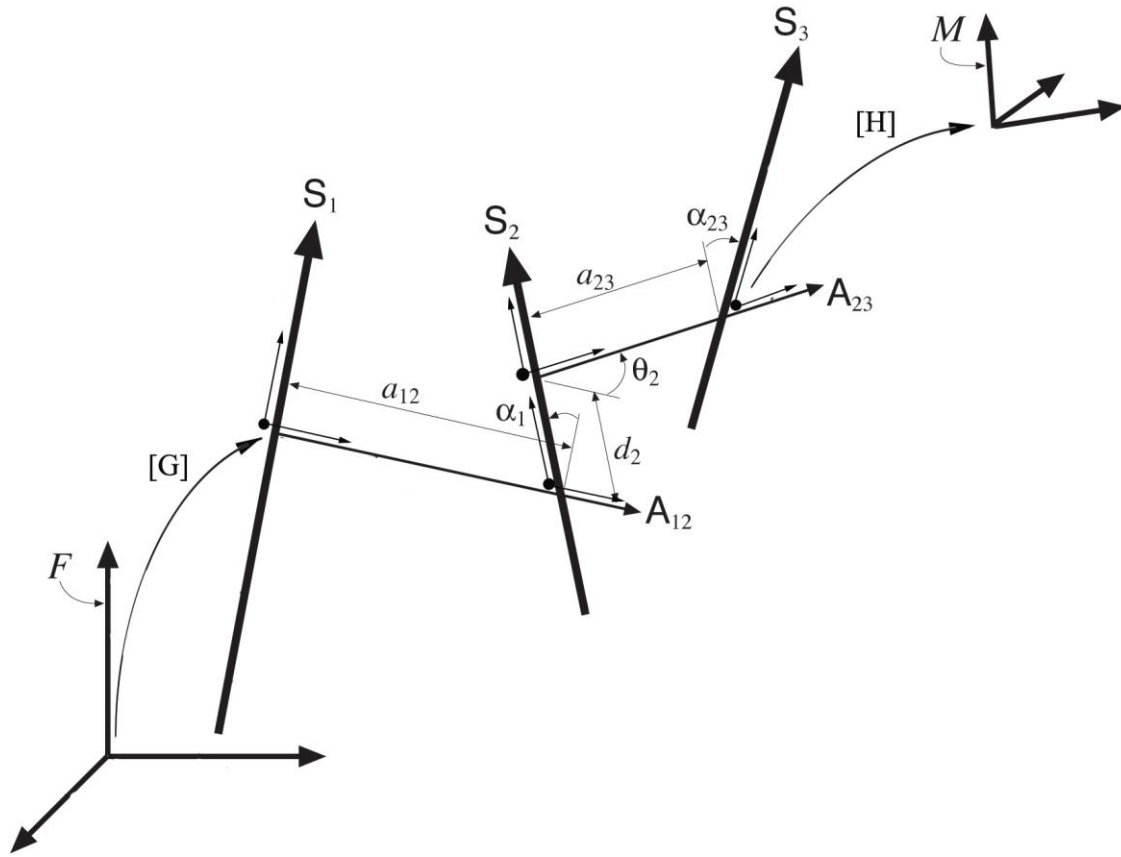


Figure 2.1: Local transformations along the links of a robot

The second local frame has the same x axis but now the z axis is aligned with  $S_2$ , with its origin at the intersection point of these two lines, while the third local frame has same z axis as the second and the line  $A_{23}$  as its x axis. From the local frame attached. Two parameters are needed to transform from local frame to local frame along links: Link twist and link length. This is X-screw displacements. Link twist,  $\alpha_{i-1,i}$ : This defines the relative location of two axes, whose common normal lines are mutually perpendicular and it is measured along this line. Link length,  $a_{i-1,i}$ : This is the distance measured along a line that is mutually perpendicular (common normal) to two axes. Also, links that are next to each other have a common joint axis between them. The first parameter describes the distance along the common axis from one link to the next. This parameter is called the link offset,  $d_i$ . A second parameter describes the amount of rotation about this common axis between one link and the next. This parameter is called joint angle,  $\theta_i$ .

The human hand consists of connected parts composing kinematical chains so that the hand motion is highly articulated. Various models of the human hand have been created with varying degrees of freedom. The aim of this research is to obtain a model that closely mimics the human hand, as natural as possible. The Kinematical scheme was considered to be consisting of 22 revolute joints linking together the palm and the phalanges as rigid bodies. The Denavit-Hartenberg methodology becomes necessary because we have four open-loop kinematic structure and a high number of degree of freedom (DOF).

### 2.2.2 KINEMATIC SCHEME OF THE HUMAN HAND

The kinematic scheme of the human hand contains the palm and the phalanges as rigid bodies linked by 22 revolute joints. The joint variables for all the fingers are  $q_1$ ,  $q_2$ ,  $q_3$  and  $q_4$ . The kinematic chain structure is the same for the little, ring, middle and index fingers.

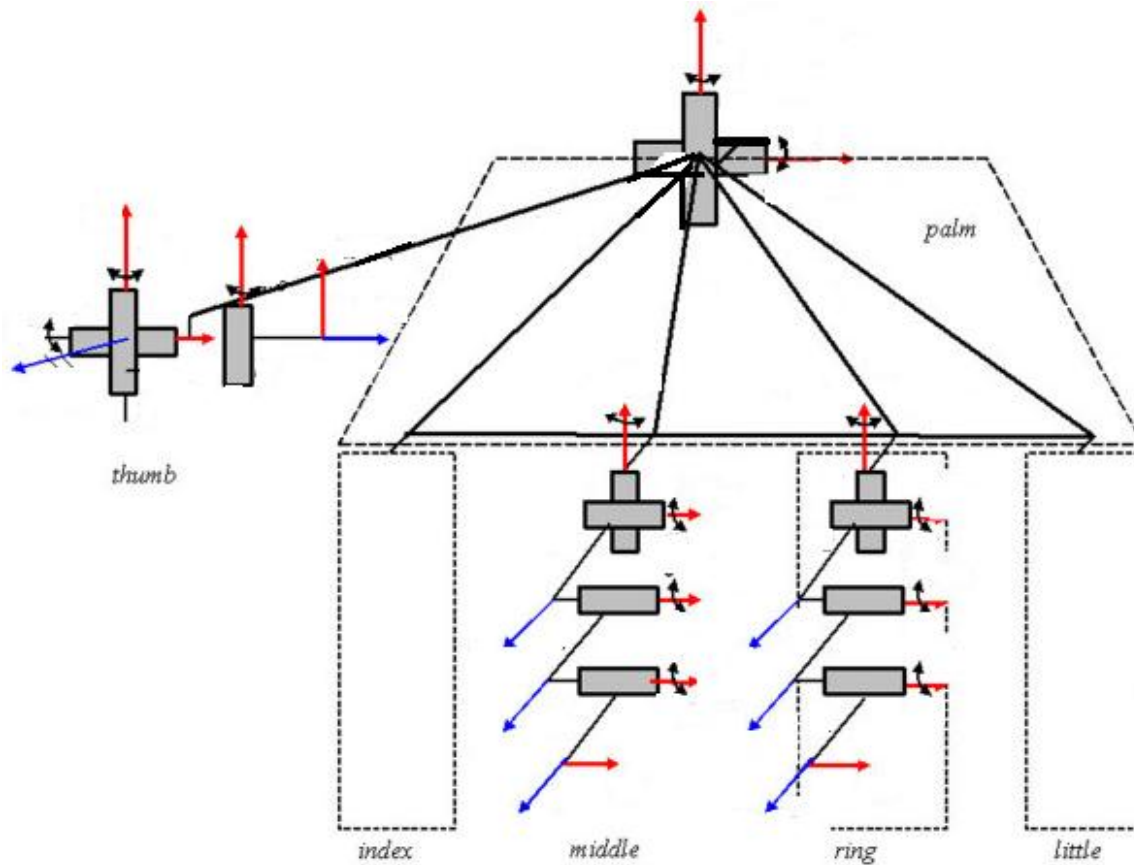


Fig. 2.3 Kinematic scheme of the human hand

### 2.2.3 KINEMATIC MODEL OF THE THUMB

The kinematic properties of the thumb should mimic those of a human thumb. Matching the robotic thumb joints to the anatomic thumb joints creates the proper relative motion between the bones. Working from the wrist up to the thumb tip, the four bones of the thumb are the trapezium carpal, the metacarpal, the proximal phalanx, and the distal phalanx. The three thumb joints are named the carpometacarpal (CMC), metacarpophalangeal (MCP), and interphalangeal (IP) joints, as shown in fig. 1.

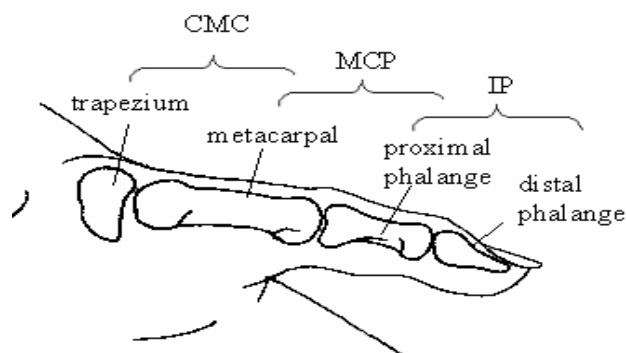


Figure1. Bones and joints of the thumb [11]

Based on the kinematic model described above the resulting location of the axes within the thumb bones are shown in fig. 2.

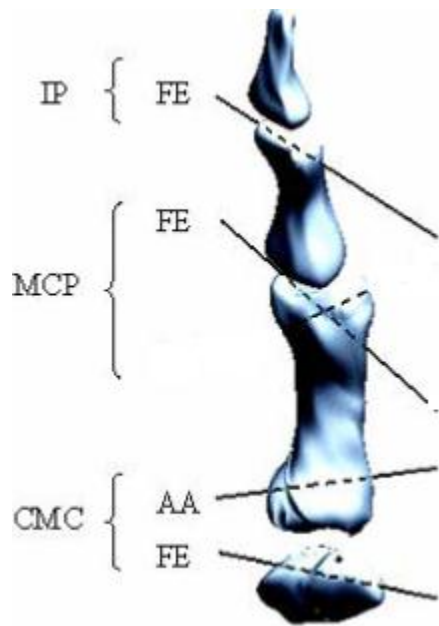


Fig. 2 Kinematic Model of the thumb with four rotational degrees of freedom thumb. [11]

The resulting locations of the axes within the thumb bones are shown in fig. 2. The IP joint FE axis passes through the distal end of the proximal phalanx and is not perpendicular to the sagittal plane of the thumb. The flexion-extension (FE) and the adduction-abduction (AA) rotational degrees of freedom (DOF) at the CMC joint are non-orthogonal and non-intersecting, as shown in figure 2. The FE axis is fixed relative to the trapezium bone at the base of the thumb. However, the anatomy of the interfacing bone surfaces of the trapezium and the thumb metacarpal bones suggests a saddle joint model with two axes that are non-intersecting and non-orthogonal (skew)

### **The Four degrees of freedom Thumb**

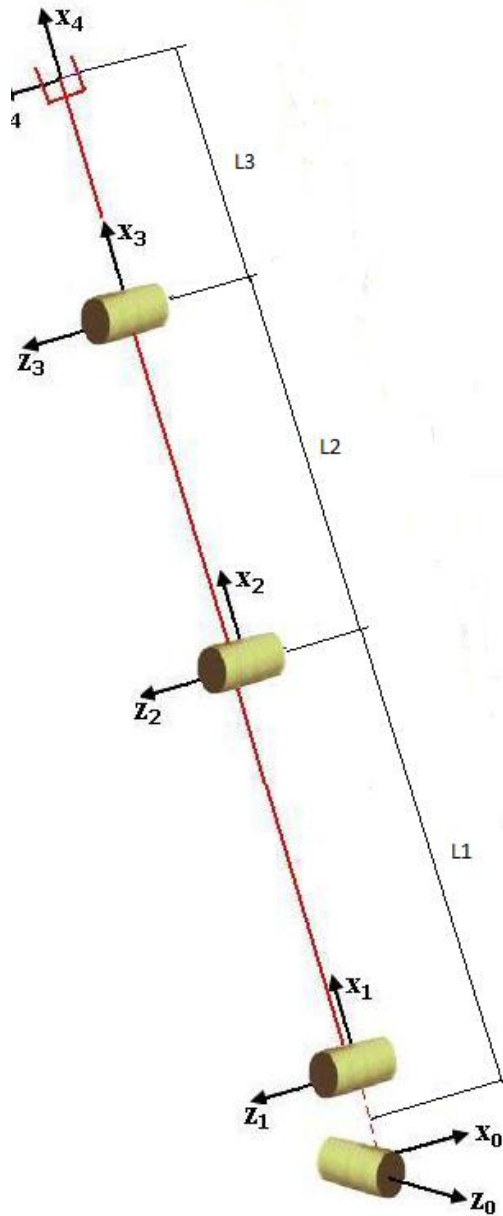


Fig.3 Four-DOF thumb illustration

Figure 1.0 shows the illustration of a four-link thumb. L1, L2, L3, L4 and L5 are the link lengths of the respective links; S1, S2, S3 AND S4 are the joint axis of the respective joints;  $q_1, q_2, q_3, q_4$ , and  $q_5$  are the twist angles of the respective joints. The orientation of the fingertip (end-effector),  $P(x, y)$  can be obtained using the Denavit-Hartenberg Method. The Denavit-Hartenberg, D-H matrices are obtained by the by the product of the transformations from the origin (fixed frame) to the various local frames and the finger-tip (end-effector frame)

Table 1.0: DH Parameter Table for Four-link shown In Figure 1.1

Link No.	$a_{i-1,i}$	$\alpha_{i-1,i}$	$d_i$	$\theta_i$
1	0	$-\pi/2$	0	$q_1 + \pi/2$

2	L 2	0	0	q 2
3	L 3	0	0	q 3
4	L 4	0	0	q 4

$\alpha_{i-1,i}$  : Twist angle between  $S_{i-1}$  to  $S_i$   
 $a_{i-1,i}$  : Link length from  $S_{i-1}$  to  $S_i$   
 $d_i$  : offset  
 $\theta_i$  : Joint angle between  $A_{i-1,i}$  and  $A_{i+1,i}$

From the DH table for four-link thumb shown in Table 2.0, the transformation matrices  ${}^G T_0^t$ ,  ${}^0 T_1^t$ ,  ${}^1 T_2^t$ ,  ${}^2 T_3^t$  and,  ${}^3 T_4^t$  can be written as

$${}^G T_0^t = \begin{pmatrix} 1 & 0 & 0 & 0 \\ 0 & 1 & 0 & 0 \\ 0 & 0 & 1 & 0 \\ 0 & 0 & 0 & 1 \end{pmatrix}$$

$${}^0 T_1^t = \begin{pmatrix} \cos(q_1^t) & -\sin(q_1^t) & 0 & L_1^t \cos(q_1^t) \\ \sin(q_1^t) & \cos(q_1^t) & 0 & L_1^t \sin(q_1^t) \\ 0 & 0 & 1 & 0 \\ 0 & 0 & 0 & 1 \end{pmatrix}$$

$${}^1 T_2^t = \begin{pmatrix} 1 & 0 & 0 & 0 \\ 0 & \cos(q_2^t) & -\sin(q_2^t) & L_2^t \cos(q_2^t) \\ 0 & -\sin(q_2^t) & \cos(q_2^t) & L_2^t \sin(q_2^t) \\ 0 & 0 & 0 & 1 \end{pmatrix}$$

$${}^2T_3^t = \begin{pmatrix} \cos(q_3^t) & -\sin(q_3^t) & 0 & L_3^t \cos(q_3^t) \\ \sin(q_3^t) & \cos(q_3^t) & 0 & L_3^t \sin(q_3^t) \\ 0 & 0 & 1 & 0 \\ 0 & 0 & 0 & 1 \end{pmatrix}$$

$${}^3T_4^t = \begin{pmatrix} \cos(q_4^t) & -\sin(q_4^t) & 0 & L_4^t \cos(q_4^t) \\ \sin(q_4^t) & \cos(q_4^t) & 0 & L_4^t \sin(q_4^t) \\ 0 & 0 & 1 & 0 \\ 0 & 0 & 0 & 1 \end{pmatrix}$$

Here  ${}^G T_0^t$  is the transformation matrix from thumb local base frame (zero) to Global frame.  ${}^0 T_1^t$  Is the transformation matrix from frame 1 to base frame (zero),  ${}^1 T_2^t$  is the transformation matrix from frame 2 to frame 1,  ${}^2 T_3^t$  is the transformation matrix from frame 3 to frame 2 and  ${}^3 T_4^t$  is the transformation matrix from frame 4 to frame 3. The transformation matrix from thumb local frame 4 to global frame  ${}^G T_4^t$  can be written as

$${}^G T_4^t = {}^G T_0^t {}^0 T_1^t {}^1 T_2^t {}^2 T_3^t {}^3 T_4^t$$

#### 2.2.4 The Four degrees of freedom Index finger

The Index, the middle, the ring and the little fingers can be considered to be made up of four links as against the human hand configuration which is made up of three links and three bones (Metacarpal phalangeal MP, Proximal interphalangeal and Distal interphalangeal).

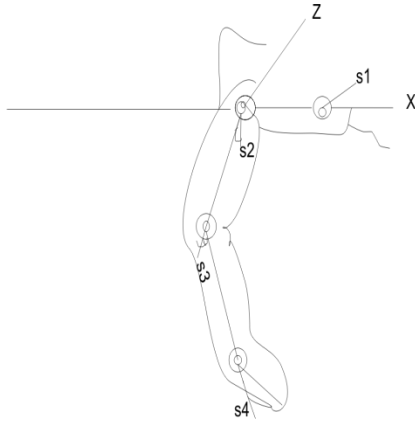


Fig. 4 Configuration of the joints of the index finger

The coordinate of the fingertip,  $P^t(X^t, Y^t)$  and the orientation  $\phi^t$  of the thumb finger (t) can be written as

$$X^t = L_1^t c(q_1^t) + L_2^t c(q_{12}^t) + L_3^t c(q_{123}^t) + L_4^t c(q_{1234}^t)$$

$$Y^t = L_1^t s(q_1^t) + L_2^t s(q_{12}^t) + L_3^t s(q_{123}^t) + L_4^t s(q_{1234}^t)$$

$$\phi' = q_1' + q_2' + q_3' + q_4'$$

The Homogeneous transformation matrix  ${}^G T_t$  to transform the thumb Local coordinate frame base  $x_0^t - y_0^t - z_0^t$  to the global frame  $x^G - y^G - z^G$  is expressed as a product of two basic homogeneous transformations  $R(X^G, \alpha)$  and  $R(Y^G, \beta)$ .

### 2.3 Inverse Kinematics of 4-Link thumb

As presented in the previous section, the forward kinematics problem of a robot manipulator is to determine the configuration (position and orientation) of the end-effector of the manipulator as a function of the manipulator joint angles. The inverse kinematics problem is to determine the joint angle. The inverse kinematics problem is to determine the joint angles given a desired end-effector configuration. Different approaches to solving the inverse kinematics problem has been studied [10]. The method adopted requires that the number of unknown is the same as that of equations and finally it solves a set of highly non-linear equations. The Newton-Raphson (N-R) method is Implemented for 4 DOFs, 5 DOFs and 6 DOFs, but for some configuration the system of equations will not converge.

The thumb has 4DOFs and to solve the inverse kinematics, we use the theory of robotics [11], where

$${}^G T_4^t = {}^0 T_1^t \bullet {}^1 T_2^t \bullet {}^2 T_3^t \bullet {}^3 T_4^t \quad (2.3.1)$$

and from equation,

$${}^G T_4^t =$$

Where the vector  $d = [d_x d_y d_z]^T$  is a known vector position of the fingertip and each element of the right hand form the equation of transformation matrix:

$${}^G T_4^t = \begin{pmatrix} n_x & 0_x & P_x & d_x \\ n_y & 0_y & P_y & d_y \\ n_z & 0_z & P_z & d_z \\ 0 & 0 & 0 & 1 \end{pmatrix} \quad (2.3.2)$$

$${}^0 T_1^t = \begin{pmatrix} \cos q_1' & -\cos(\frac{\pi}{2})\sin(q_1' + \frac{\pi}{2}) & \sin(-\frac{\pi}{2})\sin(q_1' + \frac{\pi}{2}) & 0 \\ \sin(q_1' + \frac{\pi}{2}) & \cos(-\frac{\pi}{2})\cos(q_1' + \frac{\pi}{2}) & -\sin(-\frac{\pi}{2})\cos(q_1' + \frac{\pi}{2}) & 0 \\ 0 & \sin(-\frac{\pi}{2}) & \cos(-\frac{\pi}{2}) & 0 \\ 0 & 0 & 0 & 1 \end{pmatrix} \quad (2.3.3)$$

$${}^1 T_2^t = \begin{pmatrix} \cos q_2' & -\cos(0)\sin(q_2') & \sin(0)\sin(q_2') & L_2 \cos(q_2') \\ \sin(q_2') & \cos(0)\cos(q_2') & -\sin(0)\cos(q_2') & L_2 \sin(q_2') \\ 0 & \sin(0) & \cos(0) & 0 \\ 0 & 0 & 0 & 1 \end{pmatrix} \quad (2.3.4)$$



$${}^2T_3^t = \begin{pmatrix} \cos q_3^t & -\cos(0)\sin(q_3^t) & \sin(0)\sin(q_3^t) & L_3 \cos(q_3^t) \\ \sin(q_3^t) & \cos(0)\cos(q_3^t) & -\sin(0)\cos(q_3^t) & L_3 \sin(q_3^t) \\ 0 & \sin(0) & \cos(0) & 0 \\ 0 & 0 & 0 & 1 \end{pmatrix} \quad (2.3.5)$$

$${}^3T_4^t = \begin{pmatrix} \cos q_4^t & -\cos(0)\sin(q_4^t) & \sin(0)\sin(q_4^t) & L_4 \cos(q_4^t) \\ \sin(q_4^t) & \cos(0)\cos(q_4^t) & -\sin(0)\cos(q_4^t) & L_4 \sin(q_4^t) \\ 0 & \sin(0) & \cos(0) & 0 \\ 0 & 0 & 0 & 1 \end{pmatrix} \quad (2.3.6)$$

The unknown angles are  $q_1^t, q_2^t, q_3^t$  and  $q_4^t$ . We can pre-multiply the equation on both sides for the inverse  $({}^0T_1^t)$  and the equation is now

$$({}^0T_1^t)^{-1} {}^G T_4^t = {}^1T_2^t \bullet {}^2T_3^t \bullet {}^3T_4^t \quad (2.3.7)$$

With the convenient operation, we can see that from the left matrix the element  $[3,4]_L$  is  $-d_x \cos q_1^t - d_y \sin q_1^t$  and for the right hand the element  $[3,4]_R$  is 0. We can assume that  $[3,4]_L = [3,4]_R$  and we calculate the first unknown with

$$\tan q_1^t = -\frac{d_x}{d_y} \quad (2.3.8)$$

The tangent has two solutions with a variation of  $\pi$ , but the thumb has constrained the movement, the range of motion is between  $-13/180\pi$  and  $7/30\pi$  and we only accept one solution within the range of motion. Note that this equation is only for this four DOFs system and its D-H table. We need three more independent equations to find the three unknowns. Following a similar method, the equation can be pre-multiplied for  $({}^1T_2^t)^{-1}$  on both sides and

$$({}^0T_1^t)^{-1} ({}^1T_2^t)^{-1} {}^G T_4^t = {}^2T_3^t \bullet {}^3T_4^t \quad (2.3.9)$$

For this equation,  $[1,4]_L = [1,4]_R$  and  $[2,4]_L = [2,4]_R$ ; from this, we have two equations and three unknowns.

$$d_y \cos q_1^t \cos q_2^t - d_x \cos q_2^t \sin q_1^t - d_z \sin q_2^t - L_1 = L_2 \cos q_3^t + L_3 \cos q_3^t \cos q_4^t - L_3 \sin q_3^t \sin q_4^t \quad (2.3.10)$$

and

$$d_y \cos q_1^t \sin q_2^t + d_x \sin q_2^t \sin q_1^t - d_z \sin q_2^t - L_1 = L_2 \sin q_2^t + L_3 \sin q_3^t \cos q_4^t + L_3 \cos q_3^t \sin q_4^t \quad (2.3.11)$$

We need more equations to pre-multiply for  $({}^2T_3^t)^{-1}$ . The next equation is

$$({}^0T_1^t)^{-1} \bullet ({}^1T_2^t)^{-1} \bullet ({}^2T_3^t)^{-1} \bullet {}^G T_4^t = {}^3T_4^t \quad (2.3.12)$$

With the new equation, we can extract for  $[1,4]_L = [1,4]_R$ , as follows

$$\begin{aligned}
& -L_1 \cos q_3' - L_2 - d_z ((\cos q_3' \sin q_2' + \cos q_2' \sin q_3' + d_y \cos q_1' ((\cos q_2' \cos q_3' - \sin q_2' \sin q_3')) \\
& -d_x \sin q_1 \cos q_2 \cos q_3' - \sin q_2' \sin q_3' = L_3 \cos q_4
\end{aligned} \tag{2.3.13}$$

We have one system of equations with three unknowns. This is a system of non –linear equations and to solve this system of equations, we need some iteration method or applied optimization.

## 2.4. DIFFERENTIAL KINEMATICS

Differential Kinematics establishes the relationship between the linear and angular velocities and accelerations of fingertips and the angular velocities and accelerations of joints by the manipulator geometric Jacobian.

### 2.4.1. Four-link thumb

If we only consider the linear velocities of the fingertip, then the angular velocities and angular accelerations of joints can be obtained by taking the first derivative and second derivative on the finger-tip co-ordinate  $P^t(X^t, Y^t)C_i$  of the thumb

$$\begin{bmatrix} \dot{X} \\ \dot{Y} \end{bmatrix} = \begin{bmatrix} -L_1' S(q_1') - L_2' S(q_{12}') - L_3' S(q_{123}') - L_4' S(q_{1234}') \\ L_1' C(q_1') + L_2' C(q_{12}') + L_3' C(q_{123}') + L_4' C(q_{1234}') \end{bmatrix}$$

### 2.4.2. Jacobians

The jacobians, J is a multidimensional form of the derivative. Suppose, for example we have four functions, each of which is a function of four independent variables:

$$\begin{aligned}
Y_1 &= f_1(q_1, q_2, q_3, q_4), \\
Y_2 &= f_2(q_1, q_2, q_3, q_4), \\
Y_3 &= f_3(q_1, q_2, q_3, q_4), \\
Y_4 &= f_4(q_1, q_2, q_3, q_4).
\end{aligned}$$

Now if we wish to calculate the differentials of  $y_i$  as a function of differentials of  $x_j$ , we simply use the chain rule to calculate and we get

$$\begin{aligned}
\partial y_1 &= \frac{\partial f_1}{\partial x_1} \delta x_1 + \frac{\partial f_1}{\partial x_2} \delta x_2 + \frac{\partial f_1}{\partial x_3} \delta x_3 + \frac{\partial f_1}{\partial x_4} \delta x_4, \\
&\vdots \\
\partial y_4 &= \frac{\partial f_4}{\partial x_1} \delta x_1 + \frac{\partial f_4}{\partial x_2} \delta x_2 + \frac{\partial f_4}{\partial x_3} \delta x_3 + \frac{\partial f_4}{\partial x_4} \delta x_4
\end{aligned}$$

This again might be written more simply using vector notation as

$$\partial Y = \frac{\partial F}{\partial X}$$

The 6x6 matrix of partial derivatives is what we call the Jacobian, J.

The differential derivative of the coordinate of the points of the finger-tip can be written as

$$\dot{P} = J_p^t(q^t) \dot{q}$$

The matrices  $\dot{p}^t, \dot{q}^t$  and  $J_p^t(q^t)$  as follows

$$\dot{p}^t = \begin{bmatrix} \dot{X}^t \\ \dot{Y}^t \end{bmatrix} \quad \dot{q}^t = \begin{bmatrix} \dot{q}_1^t \\ \dot{q}_2^t \\ \dot{q}_3^t \\ \dot{q}_4^t \end{bmatrix} \quad q^t = \begin{bmatrix} q_1^t \\ q_2^t \\ q_3^t \\ q_4^t \end{bmatrix}$$

$$J_p^t(q^t) = \begin{bmatrix} -L_1^t S(q_1^t) - L_2^t S(q_{12}^t) - L_3^t S(q_{123}^t) - L_4^t S(q_{1234}^t) \\ {}^t C(q_1^t) + L_2^t C(q_{12}^t) + L_3^t C(q_{123}^t) + L_4^t C(q_{1234}^t) \end{bmatrix}$$

The matrix  $J_p^t(q^t)$  is called a sub-matrix of the geometric jacobian of the thumb. We will only consider the geometric jacobian for the planer location  $P^t(X^t, Y^t)$  and not the orientation, that is, a sub-matrix of the geometric jacobian.

The angular velocities  $\dot{q}_1^t, \dot{q}_2^t, \dot{q}_3^t$  and  $\dot{q}_4^t$  of the joints 1, 2, and 3 are

$$\dot{q}^t = J_p^t \left( \dot{q} \right)^{-1} \dot{P}^t$$

Similarly, the angular accelerations  $\ddot{q}_1^t, \ddot{q}_2^t, \ddot{q}_3^t$  and  $\ddot{q}_4^t$  of the joints 1, 2 and 3 are obtained as

$$\ddot{q}^t = J_p^t \left( \dot{q} \right)^{-1} \left( \ddot{P}^t - \frac{dJ_p^t(q^t)}{dt} \dot{q}^t \right)$$

Where  $\ddot{P}^t$  is the linear acceleration vector of the fingertip.  $\ddot{P}^t, \dot{q}^t$ , and  $\frac{dJ_p^t(q^t)}{dt}$  are denoted as

$$\ddot{P}^t = \begin{bmatrix} \ddot{X}^t \\ \ddot{Y}^t \end{bmatrix}, \quad \ddot{q}^t = \begin{bmatrix} \ddot{q}_1^t \\ \ddot{q}_2^t \\ \ddot{q}_3^t \\ \ddot{q}_4^t \end{bmatrix}$$

$$\frac{dJ_p^t(q^t)}{dt} = \begin{bmatrix} -L_1^t \cos(q_1^t) \dot{q}_1^t - L_2^t \cos(q_{12}^t) \dot{q}_{12}^t - L_3^t \cos(q_{123}^t) \dot{q}_{123}^t - L_4^t \cos(q_{1234}^t) \dot{q}_{1234}^t \\ -L_1^t \sin(q_1^t) \dot{q}_1^t - L_2^t \sin(q_{12}^t) \dot{q}_{12}^t - L_3^t \sin(q_{123}^t) \dot{q}_{123}^t - L_4^t \sin(q_{1234}^t) \dot{q}_{1234}^t \end{bmatrix}$$

### 2.4.3. Finger-tip Workspace

The solutions of the direct kinematics define the workspace of the finger. The workspace can be defined as the set of all possible positions of the finger-tip, constructed using all possible values of joint variables within their range.

Because of the difficulty in visualizing the workspace, several subspaces have been defined

- Reachable workspace: This is a set of all locations of the origin of the finger-tip frame that the robot finger can reach. It is a three dimensional subset of the workspace.
- Dexterous workspace: Set of all locations of the origin of the finger-tip frame that the robot finger can reach with any orientation. This useful because the robot has full dexterity in this subspace, which ensures that any task can be performed within it
- Workspace with constant orientation: Set of all locations of the origin of the end-effector frame that the robot can reach with a specified orientation for the end-effector.

### 2.4.4. Three-link thumb

The three-link thumb with four degree of freedom is shown in the figure. The red region is the reachable workspace of the thumb. The first, second and third positions (joint angles) are constrained in the ranges of  $[0,90]$ ,  $[-80,0]$  and  $[60,0]$  respectively.

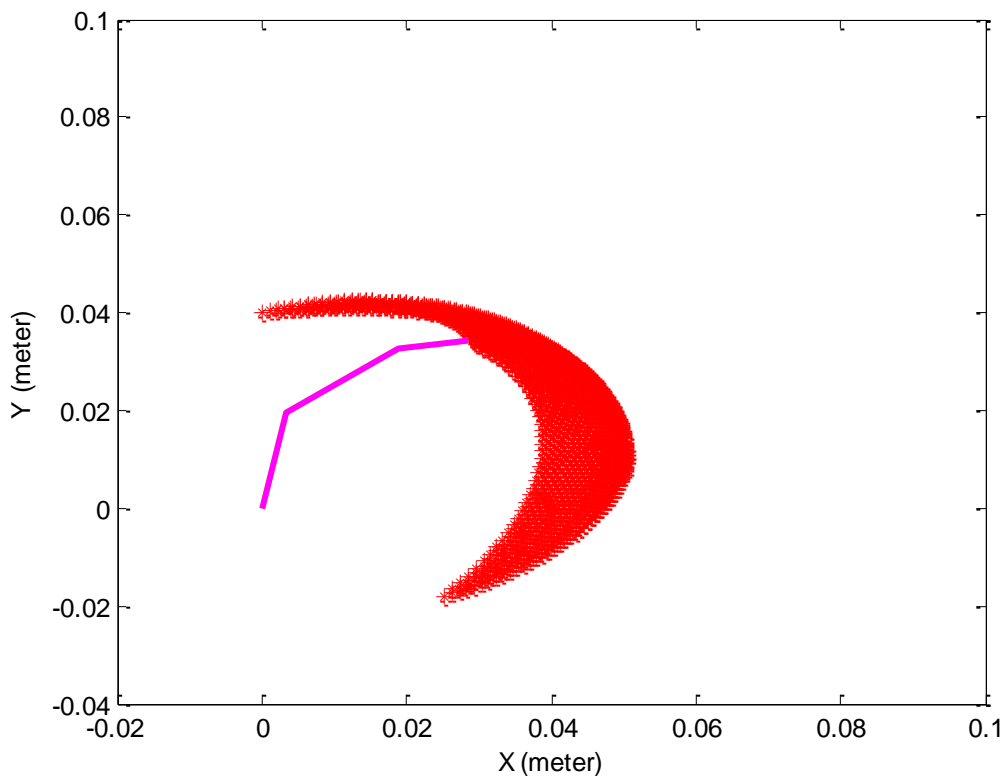


Figure 2.0. Workspace of thumb in Flexion and extension motion

Also for the combined workspace of the thumb and index finger during extension and flexion is show in the figure. The Index finger is constrained within the range  $[0, 90]$ ,  $[0,110]$  and  $[0, 80]$ . In the figure a square shaped object is within the reachable workspace of the thumb-index fingers motion.

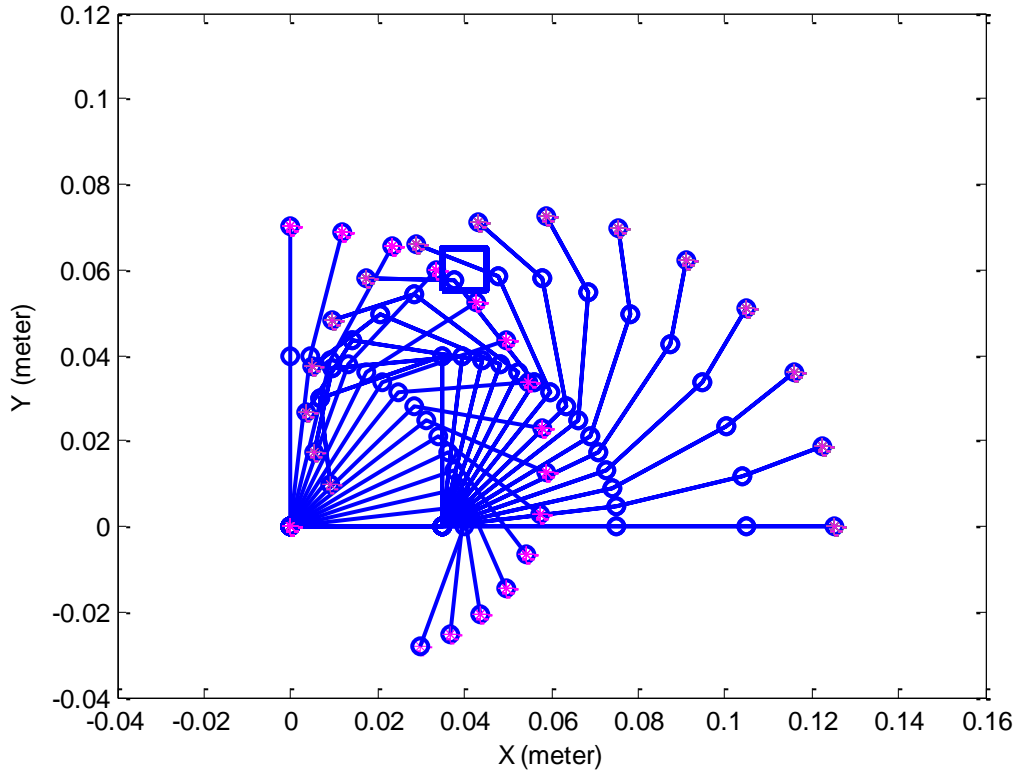


Figure 2.1. Configuration of a Square shaped object within the workspace of a thumb-index finger

### 3. Dynamics

In order to derive a control technique for the prosthetic hand, a mathematical model that describes the dynamic behavior of the hand must be calculated. An ideal model of a 4-link with 4-R finger is studied in this section. It is called ideal because it is assumed that the links are massless and there is no friction. The equation of motion that describes the dynamic behavior of systems can be obtained via Newton's equation of motion or Lagrange's approach. We will use the Lagrange's form of Newton's equation of motion to derive the dynamic equations.

The Lagrangean form of Newton's equation are given by

$$\frac{d}{dt} \left( \frac{\partial L}{\partial \dot{q}} \right) - \frac{\partial L}{\partial q} = Q_r \quad r=1, 2, \dots, n \quad (3.00)$$

Where

$$L = K - V \quad (3.10)$$

Equation (3.10) is called the Lagrangean of the system,  $Q_r$  is the non-potential generalized force; K and V are the potential energy of the n degree of freedom prosthetic hand respectively.

#### 3.1. Four-link index finger

The Lagrangean equation of the index finger can be expressed as

$$L^i = K^i - V^i. \quad (3.20)$$

Where

$$K^i = \sum_{m=1}^{n=4} \frac{1}{2} m_m^i (\dot{X}_m^2 + \dot{Y}_m^2) \quad (3.30)$$

$$V^i = \sum_{m=1}^{n=4} V_m^i = \sum_{m=1}^{n=4} M_m^i g Y_m \quad (3.40)$$

Here,  $n$  is the number of links of the index finger;  $m_m^i$  is the mass of link  $m$ ; we take the absolute angle  $\theta_1$  and the relative angles  $\theta_2, \theta_3$  and  $\theta_4$  as the generalized coordinates to express the configuration of the index finger.

The global position of  $m_1, m_2, m_3$  and  $m_4$  are

$$\begin{bmatrix} X_1 \\ Y_1 \end{bmatrix} = \begin{bmatrix} l_1 \cos \theta_1 \\ l_1 \sin \theta_1 \end{bmatrix} \quad (3.50)$$

$$\begin{bmatrix} X_2 \\ Y_2 \end{bmatrix} = \begin{bmatrix} l_1 \cos \theta_1 + l_2 \cos(\theta_1 + \theta_2) \\ l_1 \sin \theta_1 + l_2 \sin(\theta_1 + \theta_2) \end{bmatrix} \quad (3.60)$$

$$\begin{bmatrix} X_3 \\ Y_3 \end{bmatrix} = \begin{bmatrix} l_1 \cos \theta_1 + l_2 \cos(\theta_1 + \theta_2) + l_3 \cos(\theta_1 + \theta_2 + \theta_3) \\ l_1 \sin \theta_1 + l_2 \sin(\theta_1 + \theta_2) + l_3 \sin(\theta_1 + \theta_2 + \theta_3) \end{bmatrix} \quad (3.70)$$

$$\begin{bmatrix} X_4 \\ Y_4 \end{bmatrix} = \begin{bmatrix} l_1 \cos \theta_1 + l_2 \cos(\theta_1 + \theta_2) + l_3 \cos(\theta_1 + \theta_2 + \theta_3) + l_4 \cos(\theta_1 + \theta_2 + \theta_3 + \theta_4) \\ l_1 \sin \theta_1 + l_2 \sin(\theta_1 + \theta_2) + l_3 \sin(\theta_1 + \theta_2 + \theta_3) + l_4 \sin(\theta_1 + \theta_2 + \theta_3 + \theta_4) \end{bmatrix} \quad (3.80)$$

The global velocities of the masses are the time derivative of the global position of the masses.

$$\begin{bmatrix} \dot{X}_1 \\ \dot{Y}_1 \end{bmatrix} = \begin{bmatrix} -l_1 \dot{\theta}_1 \sin \theta_1 \\ l_1 \dot{\theta}_1 \cos \theta_1 \end{bmatrix} \quad (3.90)$$

$$\begin{bmatrix} \dot{X}_2 \\ \dot{Y}_2 \end{bmatrix} = \begin{bmatrix} -l_1 \dot{\theta}_1 \sin \theta_1 - l_2 \dot{\theta}_{12} \sin \theta_{12} \\ l_1 \dot{\theta}_1 \cos \theta_1 + l_2 \dot{\theta}_{12} \cos \theta_{12} \end{bmatrix} \quad (3.91)$$

$$\begin{bmatrix} \dot{X}_3 \\ \dot{Y}_3 \end{bmatrix} = \begin{bmatrix} -l_1 \dot{\theta}_1 \sin \theta_1 - l_2 \dot{\theta}_{12} \sin \theta_{12} - l_3 \dot{\theta}_{123} \sin \theta_{123} \\ l_1 \dot{\theta}_1 \cos \theta_1 + l_2 \dot{\theta}_{12} \cos \theta_{12} + l_3 \dot{\theta}_{123} \cos \theta_{123} \end{bmatrix} \quad (3.92)$$

$$\begin{bmatrix} \dot{X}_4 \\ \dot{Y}_4 \end{bmatrix} = \begin{bmatrix} -l_1 \dot{\theta}_1 \sin \theta_1 - l_2 \dot{\theta}_{12} \sin \theta_{12} - l_3 \dot{\theta}_{123} \sin \theta_{123} - l_4 \dot{\theta}_{1234} \sin \theta_{1234} \\ l_1 \dot{\theta}_1 \cos \theta_1 + l_2 \dot{\theta}_{12} \cos \theta_{12} + l_3 \dot{\theta}_{123} \cos \theta_{123} + l_4 \dot{\theta}_{1234} \cos \theta_{1234} \end{bmatrix} \quad (3.93)$$

The kinetic energy of the finger is made up of the kinetic energy of the masses and is equal to

$$K = K_1 + K_2 + K_3 + K_4$$

$$\begin{aligned}
K := & \frac{m1 \left( L1^2 \sin(\theta1(t))^2 \dot{\theta1}(t)^2 + L1^2 \cos(\theta1(t))^2 \dot{\theta1}(t)^2 \right)}{2} \\
& + \frac{1}{2} \left( m2 \left( L1^2 \sin(\theta1(t))^2 \dot{\theta1}(t)^2 - L2^2 \sin(\theta1(t) \right. \right. \\
& + \theta2(t))^2 \left( \dot{\theta1}(t) + \dot{\theta2}(t) \right)^2 + L1^2 \cos(\theta1(t))^2 \dot{\theta1}(t)^2 \\
& + L2 \cos(\theta1(t) + \theta2(t))^2 \left( \dot{\theta1}(t) + \dot{\theta2}(t) \right)^2 \left. \right) \left. \right) \\
& + \frac{1}{2} \left( m3 \left( L1^2 \sin(\theta1(t))^2 \dot{\theta1}(t)^2 - L2^2 \sin(\theta1(t) \right. \right. \\
& + \theta2(t))^2 \left( \dot{\theta1}(t) + \dot{\theta2}(t) \right)^2 - L3^2 \sin(\theta1(t) + \theta2(t) \\
& + \theta3(t))^2 \left( \dot{\theta1}(t) + \dot{\theta2}(t) + \dot{\theta3}(t) \right)^2 + L1^2 \cos(\theta1(t))^2 \dot{\theta1}(t)^2 \\
& + L2^2 \cos(\theta1(t) + \theta2(t))^2 \left( \dot{\theta1}(t) + \dot{\theta2}(t) \right)^2 \\
& + L3^2 \cos(\theta1(t) + \theta2(t) + \theta3(t))^2 \left( \dot{\theta1}(t) + \dot{\theta2}(t) + \dot{\theta3}(t) \right)^2 \left. \right) \left. \right) \\
& + \frac{1}{2} \left( m4 \left( L1^2 \sin(\theta1(t))^2 \dot{\theta1}(t)^2 - L2 \sin(\theta1(t) \right. \right. \\
& + \theta2(t))^2 \left( \dot{\theta1}(t) + \dot{\theta2}(t) \right)^2 + L3^2 \sin(\theta1(t) + \theta2(t) \\
& + \theta3(t))^2 \left( \dot{\theta1}(t) + \dot{\theta2}(t) + \dot{\theta3}(t) \right)^2 + L4^2 \sin(\theta1(t) + \theta2(t) \\
& + \theta3(t) + \theta4(t))^2 \left( \dot{\theta1}(t) + \dot{\theta2}(t) + \dot{\theta3}(t) + \dot{\theta4}(t) \right)^2 \\
& + L1^2 \cos(\theta1(t))^2 \dot{\theta1}(t)^2 + L2^2 \cos(\theta1(t) + \theta2(t))^2 \left( \dot{\theta1}(t) \right. \\
& + \dot{\theta2}(t) \right)^2 + L3^2 \cos(\theta1(t) + \theta2(t) + \theta3(t))^2 \left( \dot{\theta1}(t) + \right. \\
& \left. \dot{\theta2}(t) + \dot{\theta3}(t) \right)^2 + L4^2 \cos(\theta1(t) + \theta2(t) + \theta3(t) \\
& + \theta4(t))^2 \left( \dot{\theta1}(t) + \dot{\theta2}(t) + \dot{\theta3}(t) + \dot{\theta4}(t) \right)^2 \left. \right) \left. \right)
\end{aligned}$$

The Potential Energy of the manipulator  $V=v1+v2+v3+v4$

$$\begin{aligned}
& = m_1 g Y_1 + m_2 g Y_2 + m_3 g Y_3 + m_4 g Y_4 \\
& m_1 g l_1 \sin \theta + m_2 g (l_1 \sin \theta_1 + l_2 \sin \theta_{12}) + m_3 g (l_1 \sin \theta_1 + l_2 \sin \theta_{12} + l_3 \sin \theta_{123}) \\
& + m_4 g (l_1 \sin \theta_1 + l_2 \sin \theta_{12} + l_3 \sin \theta_{123} + l_4 \sin \theta_{1234})
\end{aligned} \tag{3.96}$$

Here  $l_m^i$  is the length of link k;  $\theta_m$  is the angle at joint m and a function of time; g is the acceleration due to gravity.

Therefore the Lagrangean is obtained from equations (3.95) and (3.96) by substituting it in (3.20) . Here  $l_m^i$  is the length of link k;  $\theta_m$  is the angle at joint m and a function of time; g is the acceleration due to gravity.

$$L = K - V$$

$$\begin{aligned}
L := & \frac{m_1 (L_1^2 \sin(\theta_1(t))^2 \dot{\theta}_1(t)^2 + L_1^2 \cos(\theta_1(t))^2 \dot{\theta}_1(t)^2)}{2} \\
& + \frac{1}{2} (m_2 (L_1^2 \sin(\theta_1(t))^2 \dot{\theta}_1(t)^2 - L_2^2 \sin(\theta_1(t) \\
& + \theta_2(t))^2 (\dot{\theta}_1(t) + \dot{\theta}_2(t))^2 + L_1^2 \cos(\theta_1(t))^2 \dot{\theta}_1(t)^2 \\
& + L_2^2 \cos(\theta_1(t) + \theta_2(t))^2 (\dot{\theta}_1(t) + \dot{\theta}_2(t))^2)) \\
& + \frac{1}{2} (m_3 (L_1^2 \sin(\theta_1(t))^2 \dot{\theta}_1(t)^2 - L_2^2 \sin(\theta_1(t) \\
& + \theta_2(t))^2 (\dot{\theta}_1(t) + \dot{\theta}_2(t))^2 - L_3^2 \sin(\theta_1(t) + \theta_2(t) \\
& + \theta_3(t))^2 (\dot{\theta}_1(t) + \dot{\theta}_2(t) + \dot{\theta}_3(t))^2 + L_1^2 \cos(\theta_1(t))^2 \dot{\theta}_1(t)^2 \\
& + L_2^2 \cos(\theta_1(t) + \theta_2(t))^2 (\dot{\theta}_1(t) + \dot{\theta}_2(t))^2 \\
& + L_3^2 \cos(\theta_1(t) + \theta_2(t) + \theta_3(t))^2 (\dot{\theta}_1(t) + \dot{\theta}_2(t) + \dot{\theta}_3(t))^2)) \\
& + \frac{1}{2} (m_4 (L_1^2 \sin(\theta_1(t))^2 \dot{\theta}_1(t)^2 - L_2 \sin(\theta_1(t) \\
& + \theta_2(t))^2 (\dot{\theta}_1(t) + \dot{\theta}_2(t))^2 + L_3^2 \sin(\theta_1(t) + \theta_2(t) \\
& + \theta_3(t))^2 (\dot{\theta}_1(t) + \dot{\theta}_2(t) + \dot{\theta}_3(t))^2 + L_4^2 \sin(\theta_1(t) + \theta_2(t) \\
& + \theta_3(t) + \theta_4(t))^2 (\dot{\theta}_1(t) + \dot{\theta}_2(t) + \dot{\theta}_3(t) + \dot{\theta}_4(t))^2 \\
& + L_1^2 \cos(\theta_1(t))^2 \dot{\theta}_1(t)^2 + L_2^2 \cos(\theta_1(t) + \theta_2(t))^2 (\dot{\theta}_1(t) \\
& + \dot{\theta}_2(t))^2 + L_3^2 \cos(\theta_1(t) + \theta_2(t) + \theta_3(t))^2 (\dot{\theta}_1(t) + \\
& \dot{\theta}_2(t) + \dot{\theta}_3(t))^2 + L_4^2 \cos(\theta_1(t) + \theta_2(t) + \theta_3(t) \\
& + \theta_4(t))^2 (\dot{\theta}_1(t) + \dot{\theta}_2(t) + \dot{\theta}_3(t) + \dot{\theta}_4(t))^2)) \\
& - m_1 g L_1 \sin(\theta_1(t)) - m_2 g L_1 \sin(\theta_1(t)) - m_2 g L_2 \sin(\theta_1(t) \\
& + \theta_2(t)) - m_3 g L_1 \sin(\theta_1(t)) - m_3 g L_2 \sin(\theta_1(t) + \theta_2(t)) \\
& - m_3 g L_3 \sin(\theta_1(t) + \theta_2(t) + \theta_3(t)) - m_4 g L_1 \sin(\theta_1(t)) \\
& - m_4 g L_2 \sin(\theta_1(t) + \theta_2(t)) - m_4 g L_3 \sin(\theta_1(t) + \theta_2(t) \\
& + \theta_3(t)) - m_4 g L_4 \sin(\theta_1(t) + \theta_2(t) + \theta_3(t) + \theta_4(t))
\end{aligned}$$

$$\frac{\partial L}{\partial \theta_1} = -(m_1 + m_2 + m_3 + m_4) g l_1 \cos \theta_1 - (m_2 + m_3 + m_4) g l_2 \cos(\theta_1 + \theta_2) + (m_2 + m_3 + m_4) g l_2 \cos(\theta_1 + \theta_2) + m_4 g l_4 \cos(\theta_1 + \theta_2 + \theta_3)$$

$$\frac{\partial L}{\partial \dot{\theta}_1} = (m_1 + m_2 + m_3 + m_4) l_1^2 \dot{\theta}_1 - (m_2 + m_3 + m_4) l_2^2 (\dot{\theta}_1 + \dot{\theta}_2) + (m_3 + m_4) l_3^2 (\dot{\theta}_1 + \dot{\theta}_2 + \dot{\theta}_3) + m_4 l_4^2 (\dot{\theta}_1 + \dot{\theta}_2 + \dot{\theta}_3 + \dot{\theta}_4)$$

### 3.2. Dynamics for a 3R Planar Index finger

We can derive a set of recursive equations to relate each link in the coordinate frame attached to the previous link based on the velocity and acceleration kinematics. We may generalize the method of analysis to be suitable for a robot index finger any number of links. The Newton-Euler's equations of motion application in robot dynamics enables us to calculate the joint forces one link at a time starting from the end-effector (finger-tip) link.

The backward Newton-Euler equations of motion for the link (i) in the local coordinate frame  $B_i$  are

$$F_{i-1} = \sum^i F_{ei} + m_i {}^i_0 a_i$$



$$M_{i-1} = {}^iM_i - \Sigma {}^iM_{ei} - ({}^id_{i-1} - {}^ir_i) \times {}^iF_{i-1} \\ + ({}^id_i - {}^ir_i) {}^iF_i + {}^iI_{i0} {}^i\alpha_i + {}^i\omega_i \times {}^iI_{i0} {}^i\omega_i$$

$${}^in_i = {}^id_{i-1} - {}^ir_i$$

$${}^im_i = {}^id_i - {}^ir_i$$

Translational acceleration of link (i) is denoted by  $a_{0i}$  and is measured at the mass center  $C_i$ . Angular acceleration which is the same for all points of a rigid link (i) is denoted by  $\alpha_{0i}$  and is usually shown at the mass center  $C_i$ . The forces,  $F_{i-1}$  and moment  $M_{i-1}$  are the resultant force and moment that link (i) applies to link (i+1) at joint i+1. When the driving force system ( $F_{i-1}$ , and  $M_{i-1}$ ) is found in frame  $B_i$ , we can transform them to the frame  $B_{i-1}$  and apply the Newton-Euler equation for link (i-1).

$${}^{i-1}F_{i-1} = {}^{i-1}T_i {}^iF_{i-1}$$

$${}^{i-1}M_{i-1} = {}^{i-1}T_i {}^iM_{i-1}$$

The negative of the converted force system acts as the driven force system ( $F_{i-1}$ , and  $M_{i-1}$ ) for the link (i-1).

### 3.3. Three-link Index finger Dynamics

Fig.

The Torques of the actuators are parallel to the z-axis and are shown to be  $Q_0$ ,  $Q_1$  and  $Q_3$ .

The Newton Euler equations of motion for the first link are

$$F_0 - F_{01} + M_1 \hat{g} = M_1 a_{01} \\ Q_1 - Q_2 + n_{01} \times F_0 - m_{01} \times F_{01} = I_{01} \alpha_{01} \quad (3.2.1)$$

Equations of motion for the second link are

$$F_{01} - F_{02} + M_2 \hat{g} = M_2 a_{02} \\ Q_1 - Q_2 + n_{02} \times F_{01} - m_{02} \times F_{02} = I_{02} \alpha_{02} \quad (3.2.2)$$

Equations of motion for the third link are

$$F_{02} + M_3 \hat{g} = M_3 a_{03} \\ Q_2 + n_{03} \times F_{02} = I_{03} \alpha_{03} \quad (3.2.3)$$

There are six equations with six unknowns;  $F_0$ ,  $F_1$ ,  $F_2$ ,  $Q_0$ ,  $Q_1$  and  $Q_2$

However in robot dynamics, actuator torques is usually applied in the control not the joint forces. So we do not necessarily need to find the joint forces. We may eliminate  $F_0$ ,  $F_1$  and  $F_2$  and reduce the number of equations by half.

Eliminating  $F_2$  in equation (3.2.3)

$$Q_2 = I_{03} \alpha_{03} - n_{03} (m_3 a_{03} - m_3 \hat{g}) \quad (3.2.4)$$

Eliminating  $F_1$  and  $F_2$  in equation (3.22)

$$Q_1 = Q_2 + I_{02} \alpha_{02} + m_{02} \times m_3 (a_{03} - \hat{g}) - n_{02} (m_2 (a_{02} - \hat{g}) - m_3 (a_{03} - \hat{g})) \quad (3.2.5)$$

Eliminating  $F_0$  and  $F_1$  in equation (3.2.1)

$$Q_0 = Q_1 + I_{01} \alpha_{01} + m_1 \times m_3 (a_{03} - \hat{g}) - n_{01} (m_1 (a_{01} - \hat{g}) - m_2 (a_{02} - \hat{g}) - m_3 (a_{03} - \hat{g})) \quad (3.2.6)$$

Using MAPLE, the position of  $C_i$  and the links' angular velocity and acceleration are calculated. The translational acceleration,  $a_{01}$  at the center of mass of each link is also calculated. Substituting these results in equations (3.2.1), (3.2.2) and (3.2.3), provides the dynamic equations for the 3R robotic finger in appropriate form.

$$\begin{aligned}
Q2 := & \left[ \left[ \frac{1}{2} \left( L3 \cos(\theta1(t) + \theta2(t) + \theta3(t)) m3 \left( \right. \right. \right. \right. \\
& - \frac{L1 \cos(\theta1(t)) \dot{\theta}1(t)^2}{2} - \frac{L1 \sin(\theta1(t)) \ddot{\theta}1(t)}{2} \\
& - \frac{L2 \cos(\theta1(t) + \theta2(t)) (\dot{\theta}1(t) + \dot{\theta}2(t))^2}{2} \\
& - \frac{L2 \sin(\theta1(t) + \theta2(t)) (\ddot{\theta}1(t) + \ddot{\theta}2(t))}{2} \\
& - \frac{L3 \cos(\theta1(t) + \theta2(t) + \theta3(t)) (\dot{\theta}1(t) + \dot{\theta}2(t) + \dot{\theta}3(t))^2}{2} \\
& \left. \left. \left. - \frac{L3 \sin(\theta1(t) + \theta2(t) + \theta3(t)) (\ddot{\theta}1(t) + \ddot{\theta}2(t) + \ddot{\theta}3(t))}{2} \right) \right) \right] \\
& + \frac{1}{2} \left( L3 \sin(\theta1(t) + \theta2(t) + \theta3(t)) m3 \left( \right. \right. \\
& - \frac{L1 \sin(\theta1(t)) \dot{\theta}1(t)^2}{2} + \frac{L1 \cos(\theta1(t)) \ddot{\theta}1(t)}{2} \\
& - \frac{L2 \sin(\theta1(t) + \theta2(t)) (\dot{\theta}1(t) + \dot{\theta}2(t))^2}{2} \\
& + \frac{L2 \cos(\theta1(t) + \theta2(t)) (\ddot{\theta}1(t) + \ddot{\theta}2(t))}{2} \\
& - \frac{L3 \sin(\theta1(t) + \theta2(t) + \theta3(t)) (\dot{\theta}1(t) + \dot{\theta}2(t) + \dot{\theta}3(t))^2}{2} \\
& + \frac{L3 \cos(\theta1(t) + \theta2(t) + \theta3(t)) (\ddot{\theta}1(t) + \ddot{\theta}2(t) + \ddot{\theta}3(t))}{2} \\
& \left. \left. - g L3 \cos(\theta1 + \theta2 + \theta3) \right) \right] \right], \\
& \left[ \begin{array}{c} 0 \end{array} \right], \\
& \left[ \begin{array}{c} I3 (\ddot{\theta}1(t) + \ddot{\theta}2(t) + \ddot{\theta}3(t)) \end{array} \right] \Bigg]
\end{aligned}$$

#### 4. Hard Control of the Prosthetic Hand

Control is the science of desired motion. The prescribed motion of a robot is related to the dynamics and kinematics by control. In applying controls, certain optimal indices should be considered to enable the system (device) function

optimally. For example performance of task by the prosthesis in the shortest possible time. This is where the concept of path planning for the robotic finger comes into play.

An integral part of robot control is planning the path (path planning) the robot should follow in carrying out specific tasks. Task compliance or constrained motion is critical in situations where the robot comes in contact with obstacles. This could be done in either Cartesian or joint space. Path planning in the joint space appear to be easier compared to Cartesian space.

There are number control algorithms that can be used to control the robotic hand, each of which is best applicable to particular class of robots in a particular task. Some of these control methods are: Feedback linearization or computed torque control, linear control technique, adaptive control, robust control, gain scheduling and also the proportional controls (PI, PD, and PID).

#### 4.1. Feedback Linearization

In feedback linearization or computed torque approach, a control law is defined to obtain a linear differential equation for error command and then use the linear control design technique. An alternate dynamics of a robot finger can be written in the form.

$$Q = D(q)\ddot{q} + H(q, \dot{q}) + G(q) \quad (4.1.1)$$

Where  $q$  is the joint variable vector and  $Q(q, \dot{q}, t)$  is the torques applied at joints. Assume a desired path in joint space is given by twice differentiable function  $q = q_d(t) \in C^2$ . From the dynamics, the desired time history of joints' position, velocity and acceleration are known. Hence, by introducing a computed torque control law, we can control the robot fingers to follow desired path.

$$Q = D(q)(\ddot{q}_d - K_D e - K_P \dot{e}) + H(q, \dot{q}) + G(q) \quad (4.1.2)$$

Where  $e$ , the tracking error is defined as

$$e = q - q_d \quad (4.1.3)$$

$K_D$  and  $K_P$  are constant gain diagonal matrices. The control law is stable and applied as long as all the eigen values of the matrix below have negative real parts.

$$[A] = \begin{pmatrix} 0 & I \\ -K_P & -K_D \end{pmatrix}$$

The idea behind the introduction of a feedback signal is to make the robot fingers' actual path track the desired path. Unlike in the open loop approach, there is always a difference between the robot finger's actual path and the desired path. This is due to non-modeled parameters and also errors in adjustment.

#### 4.2. PID CONTROL

The proportional-integral-derivative (PID) control has simple structure and clear physical meanings for the gain. It's a widely accepted control strategy in most industrial robot design. In most cases, feedback loops are controlled using PID algorithm. The main reason why feedback is very important in systems is to be able to attain a set point irrespective of disturbance or any variation in characteristics of any form. The PID control is always designed to correct error(s) between process values and particular desired set point in a system.

Consider the characteristic parameters- Proportional (P), integral (I) and derivative (D) controls as shown in the diagram below is to be applies to the robotic hand (system). The system,  $S$  is to be controlled using a controller,  $C$ ; where  $C$  depends on the P, I and D parameters.

Considering the nonlinear equation that are derived from Euler-Lagrange equation (), the control input variable  $F$  which represents the torque applied to the robot, is unknown, ( assumed that the considered robot actuators were ideal sources of torques and forces). However it requires a control in the joints to reach a final position. Therefore we use the classical PID law as shown below;

$$F = K_p e + K_i \int_0^t e(\tau) d\tau + K_d \dot{e} \quad (4.2.1)$$

Where  $e = q^d - d$ ,  $q^d$  is the desired joint angle,  $K_p$ ,  $K_i$  and  $K_d$  are the proportional, integral and derivative gains respectively.

#### 4.2.1. 4 DOF Index finger

For this experiment, what we want to control with PID is the force applied to the robot to take it to a desired position using as parameter the error between the actual and the desired coordinate. To develop the dynamic model we will consider the index finger configuration shown in figure 3.

Considering the nonlinear equation that are derived from Euler-Lagrange equation (), the control

From equation 4.1.1 we can describe the motion of the system as follows;

$$q = \begin{bmatrix} \theta_1 \\ \theta_2 \\ \theta_3 \\ \theta_4 \end{bmatrix} \quad D(q) = \begin{bmatrix} M_{11} & M_{12} & M_{13} & M_{14} \\ M_{21} & M_{22} & M_{23} & M_{24} \\ M_{31} & M_{32} & M_{33} & M_{34} \\ M_{41} & M_{42} & M_{43} & M_{44} \end{bmatrix} \quad (4.2.2)$$

The matrix entries for D (q), C (q,q) and g(q) can be are obtained from the dynamic equation of a 4DOF thumb obtained in section 3.

Where

$$M_{11} =$$

$$b11=(M1+M2+M3+M4)*L1^2+(M2+M3+M4)*L2^2+(M3+M4)*L3^2+M4*L4^2+2*(M2+M3+M4)*L1*L2*\cos(x(4))+2*(M3+M4)*L1*L3*\cos(x(6)+x(7))+2*(M3+M4)*L2*L3*\cos(x(7))+2*M4*L1*L4*\cos(x(6)+x(7)+x(8))+2*M4*L2*L4*\cos(x(7)+x(8))+2*M4*L3*L4*\cos(x(8))$$

$$M_{22} =$$

$$(M2+M3+M4)*L2^2+(M3+M4)*L3^2+M4*L4^2+2*(M3+M4)*L2*L3*\cos(x(7))+2*M4*L2*L4*\cos(x(7)+x(8))+2*M4*L3*L4*\cos(x(8))$$

$$M_{33} = (M3+M4)*L3^2+M4*L4^2+2*M4*L3*L4*\cos(x(8))$$

$$M_{44} = M4*L4^2$$

$$M_{12} = M_{21} = (M2+M3+M4)*L1*L2*\cos(x(6))+ (M3+M4)*L1*L3*\cos(x(6)+x(8))+2*(M3+M4)*L2*L3*\cos(x(7))+M4*L1*L4*\cos(x(6)+x(7)+x(8))+2*M4*L2*L4*\cos(x(7)+x(8))+2*M4*L3*L4*\cos(x(8))$$

$$M_{13} = M_{31} = (M3+M4)*L1*L3*\cos(x(6)+x(7))+ (M3+M4)*L2*L3*\cos(x(7))+M4*L1*L4*\cos(x(6)+x(7)+x(8))+M4*L2*L4*\cos(x(7)+x(8))+2*M4*L3*L4*\cos(x(8))$$

$$M_{14} = M_{41} = M4*L1*L4*\cos(x(6)+x(7)+x(8))+M4*L2*L4*\cos(x(7)+x(8))+M4*L3*L4*\cos(x(8))$$

$$M_{23} = M_{32} =$$

$$(M3+M4)*L2*L3*\cos(x(7))+M4*L2*L4*\cos(x(7)+x(8))+2*M4*L3*L4*\cos(x(8))$$

$$M_{24} = M_{42} = M4*L2*L4*\cos(x(7)+x(8))+M4*L3*L4*\cos(x(8))$$

$$M_{34} = M_{43} = M4*L3*L4*\cos(x(8));$$

The Centrifugal force,  $C_i(q, \dot{q})$  are as follows

$$C_1(q, \dot{q}) =$$

$$((M2+M3+M4)*L1*L2*\sin(x(6))+ (M3+M4)*L1*L3*\sin(x(6)+x(7))+M4*L1*L4*\sin(x(6)+x(7)+x(8)))*(2*x(9)*x(10)+x(10)^2)+((M3+M4)*L1*L3*\sin(x(6)+x(7))+ (M3+M4)*L2*L3*\sin(x(7))+M4*L1*L4*\sin(x(6)+x(7)+x(8))+M4*L2*L4*\sin(x(6)+x(8)))*(2*(x(9)*x(11)+x(10)*x(11))+x(11)^2)+(M4*L1*L4*\sin(x(6)+x(7)+x(8))+M4*L2*L4*\sin(x(7)+x(8))+M4*L3*L4*\sin(x(8)))*(2*(x(9)*x(12)+x(10)*x(12)+x(11)*x(12))+x(12)^2)$$

$$\begin{aligned}
\dot{C}_2(q, q) &= -((M3+M4)*L2*L3*\sin(x(7))+M4*L2*L4*\sin(x(7)+x(8)))*(2*(x(9)*x(11)+x(10)*x(11))+x(11)^2)- \\
& (M4*L2*L4*\sin(x(7)+x(8))+M4*L3*L4*\sin(x(8)))*(2*x(9)*x(12)+x(12)^2)- \\
& (M4*L2*L4*\sin(x(7)+x(8))+M4*L3*L4*\sin(x(8)))*2*(x(10)*x(12)+x(11)+x(12)) \\
\dot{C}_3(q, q) &= ((M3+M4)*L2*L3*\sin(x(7))+M4*L2*L4*\sin(x(7)+x(8)))*(2*x(9)*x(10)- \\
& x(10)^2)+(M4*L3*L4*\sin(x(8)))*(2*x(9)*x(12)+2*x(10)*x(12)+2*x(11)*x(12)+x(12)^2)+(M3+M4)*L2*L3*\sin(x( \\
& 7))+(M3+M4)*L1*L3*\sin(x(6)+x(7))+(M4*L1*L4*\sin(x(6)+x(7)+x(8))+M4*L2*L4*\sin(x(7)+x(8)))*x(9)^2); \\
\dot{C}_4(q, q) &= (M4*L2*L4*\sin(x(7)+x(8))+M4*L3*L4*\sin(x(8)))*(2*x(9)*x(10)+x(10)^2)+(M4*L3*L4*\sin(x(8)))*( \\
& 2*(x(9)*x(11)+x(10)*x(11))+x(11)^2)+(M4*L1*L4*\sin(x(6)+x(7)+x(8))+M4*L2*L4*\sin(x(7)+x(8))+M4*L3*L4* \\
& \sin(x(8)))*x(9)^2;
\end{aligned}$$

The Vector of gravity torques are as follows

$$\begin{aligned}
g_1(q) &= -(M1+M2+M3+M4)*g*L1*\sin(x(5))-(M2+M3+M4)*g*L2*\sin(x(5)+x(6))- \\
& (M3+M4)*g*L3*\sin(x(5)+x(6)+x(7))-M4*g*L4*\sin(x(5)+x(6)+x(7)+x(8))
\end{aligned}$$

$$\begin{aligned}
g_2(q) &= -(M2+M3+M4)*g*L2*\sin(x(5)+x(6))-(M3+M4)*g*L3*\sin(x(5)+x(6)+x(7))- \\
& M4*g*L4*\sin(x(5)+x(6)+x(7)+x(8))
\end{aligned}$$

$$g_3(q) = -(M3+M4)*g*L3*\sin(x(5)+x(6)+x(7))-M4*g*L4*\sin(x(5)+x(6)+x(7)+x(8))$$

$$g_4(q) = -M4*g*L4*\sin(x(5)+x(6)+x(7)+x(8))$$

From the system equation, 4.1.1 we can have

$$\ddot{q} = D(q)^{-1}[-C(q, \dot{q}) - g(q)] + \hat{F} \quad (4.2.4)$$

With

$$\hat{F} = D(q)^{-1} F \Leftrightarrow M(q)\hat{F} \quad (4.2.5)$$

The error signals of the system are

$$e(\theta_i) = \theta_{if} - \theta_i \quad (4.2.6)$$

Where i = joint angle 1 to 4 and f is the final positions of the joint angles.

Where  $\theta_{if}$  is the final position of joints i = 1, 2, 3 and 4. For the control, the final positions are given by

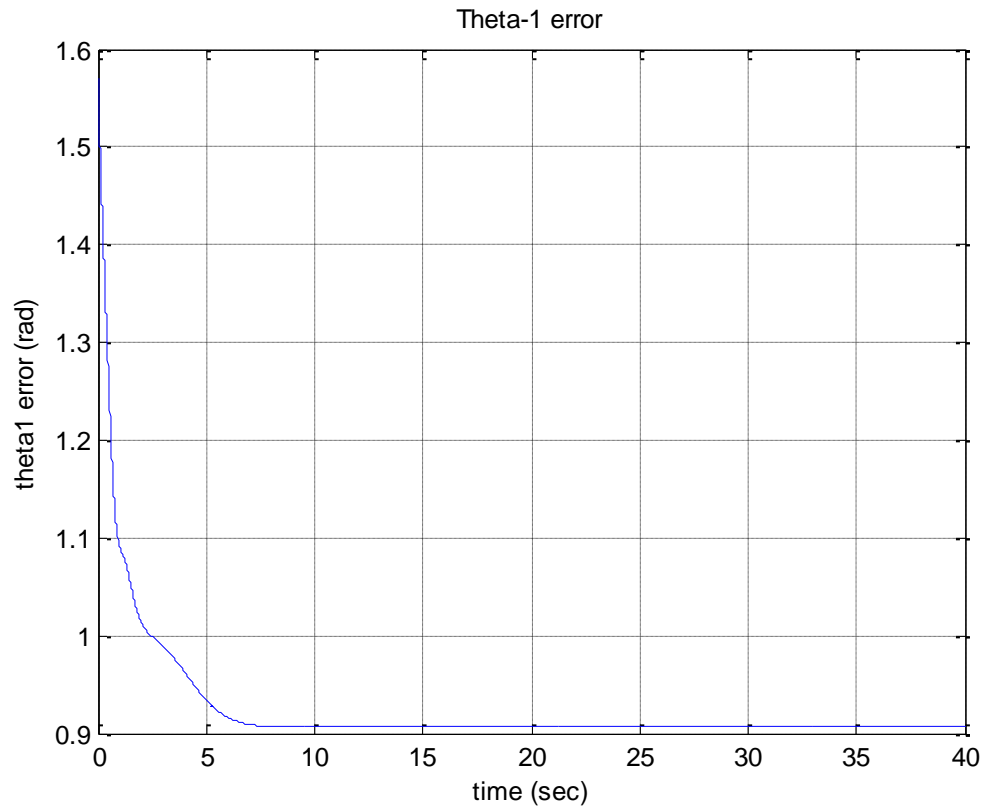
$$\begin{bmatrix} \theta_{1f} \\ \theta_{2f} \\ \theta_{3f} \\ \theta_{4f} \end{bmatrix} = \begin{bmatrix} \pi / 2 \\ \pi / 2 \\ \pi / 4 \\ \pi / 6 \end{bmatrix} \quad (4.2.7)$$

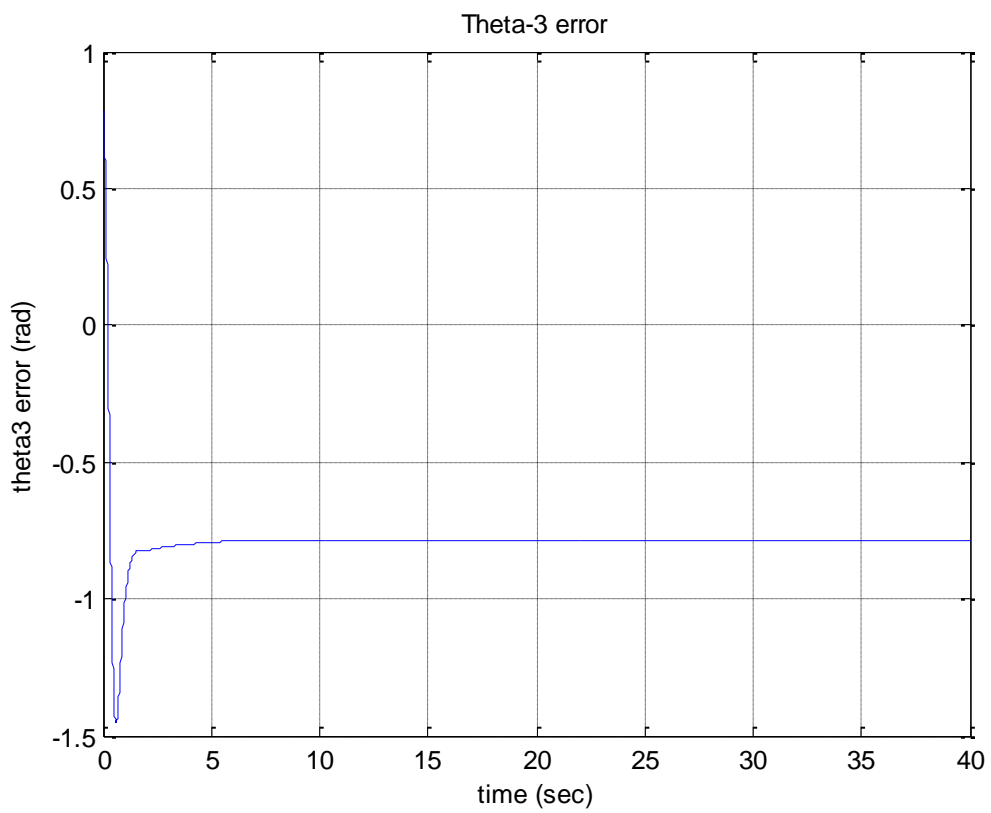
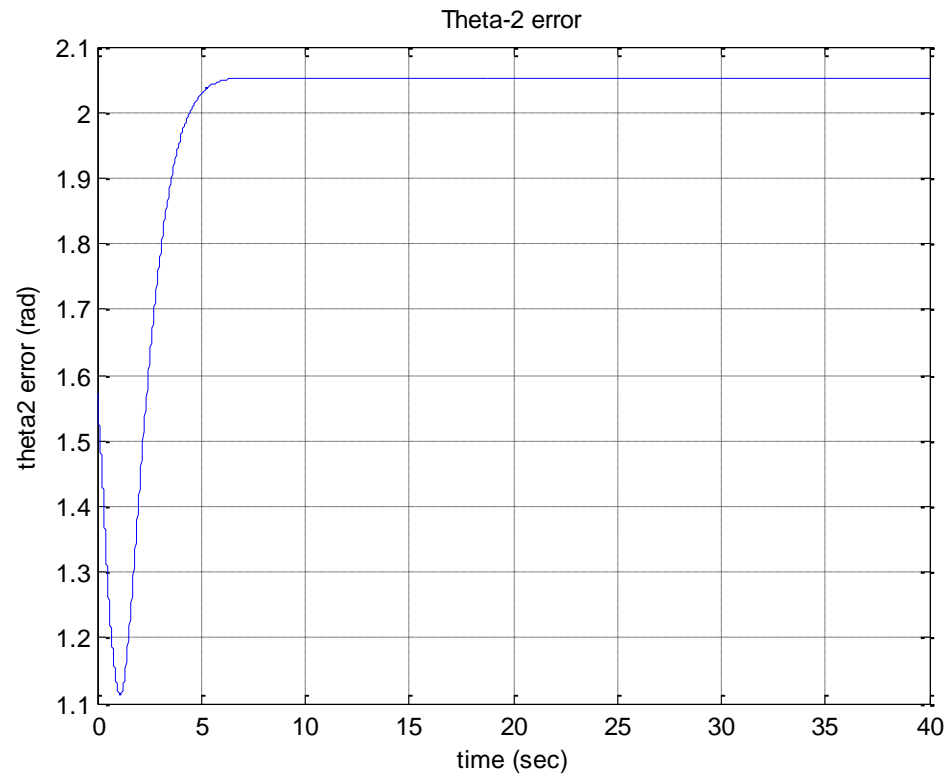
The index finger is considered to be parallel to the x-axis so all initial positions are zero

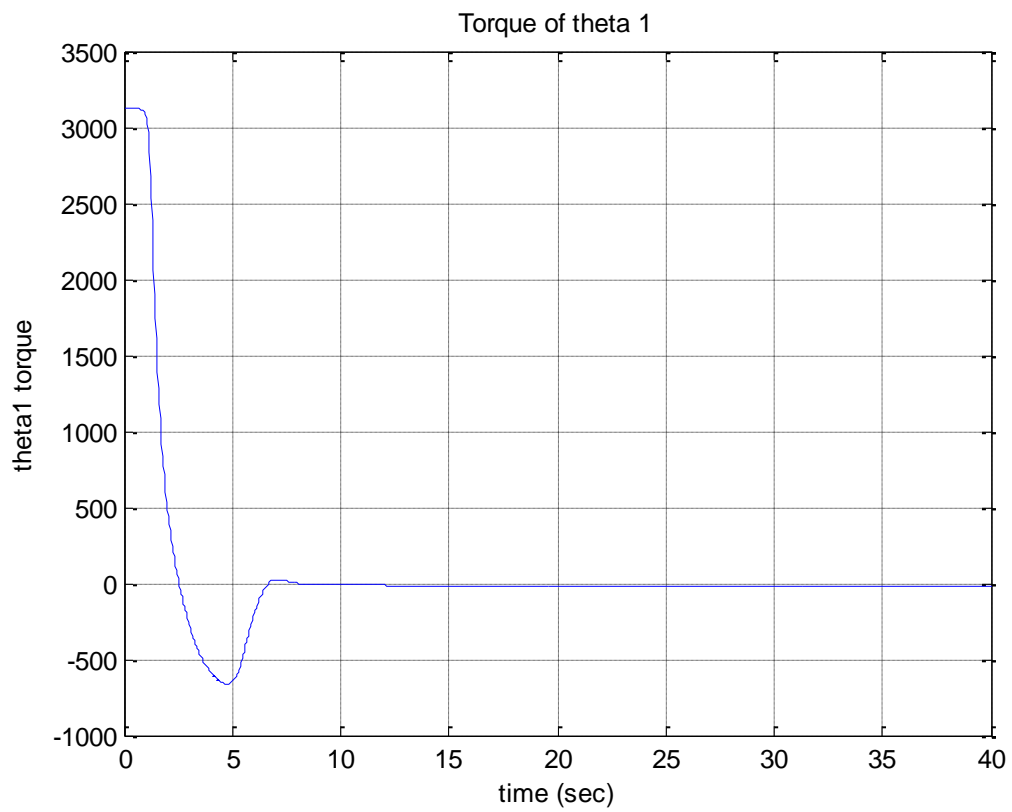
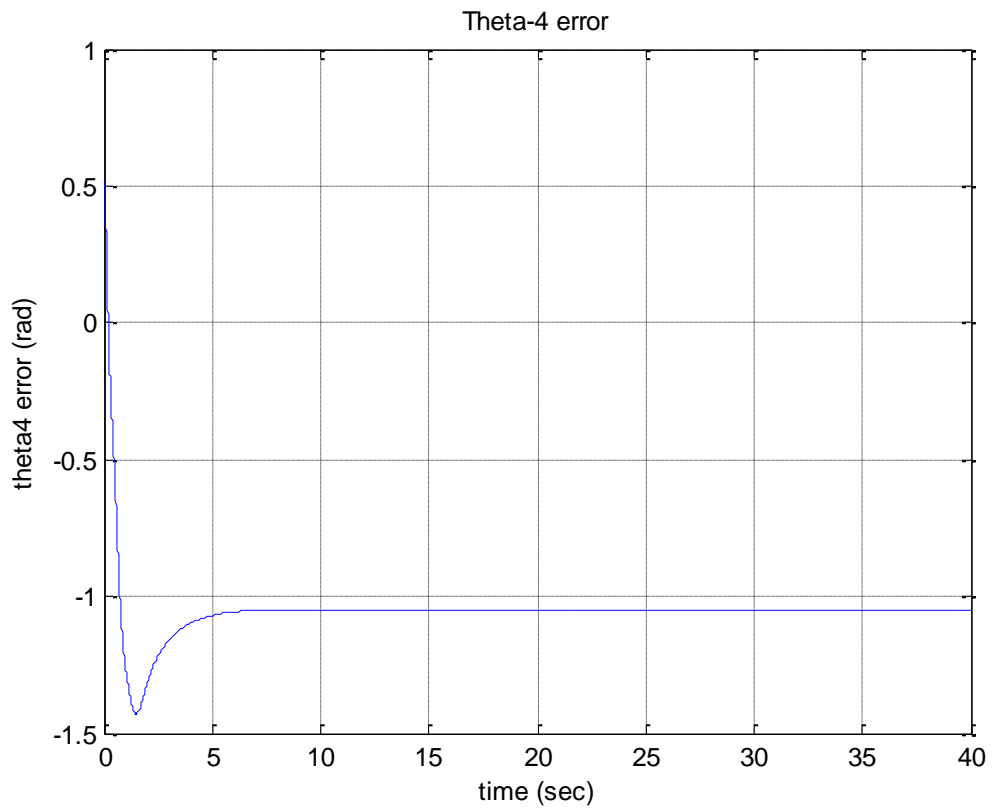
Figures 4.1 and 4.2 are the simulations obtained using the PID controller for a 3DOF thumb. The best performance of the controller parameter where obtained with the following values after considering 3 cases of different PID combinations.

PID PARAMETERS	CASE1	CASE2	CASE3
$K_p$ (1, 2, 3, & 4)	35, 35, 35 & 35	25, 25, 25 & 25	50, 50, 50 & 50
$K_I$ (1, 2, 3, & 4)	10, 13, 17 & 20	20, 23, 27 & 30	15, 20, 35 & 40
$K_D$ (1, 2, 3, & 4)	25, 25, 25 & 25	20, 20, 20 & 20	45, 45, 45 & 45

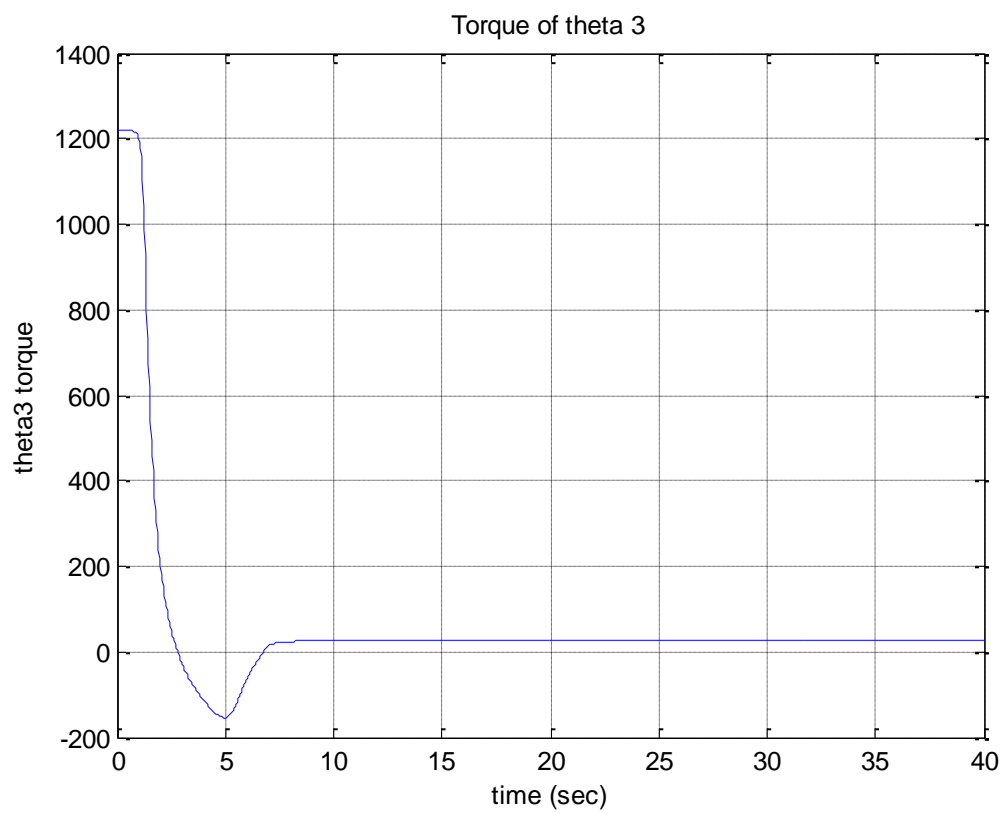
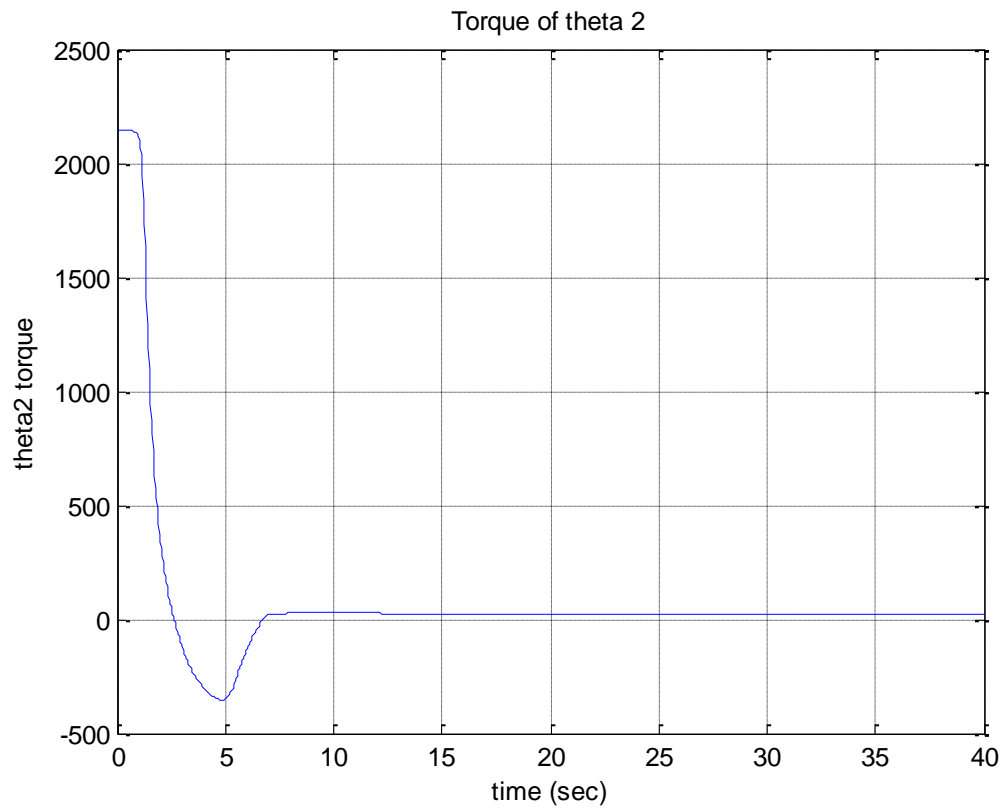
Table 4.1. Three cases of best performance of PID parameters

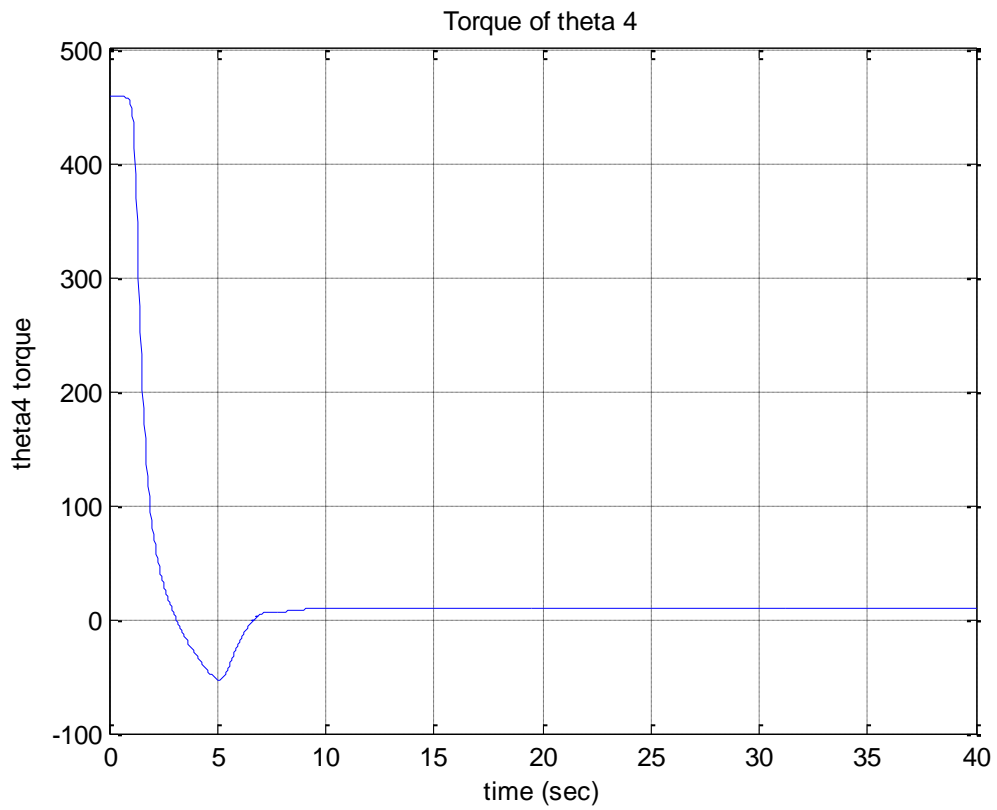




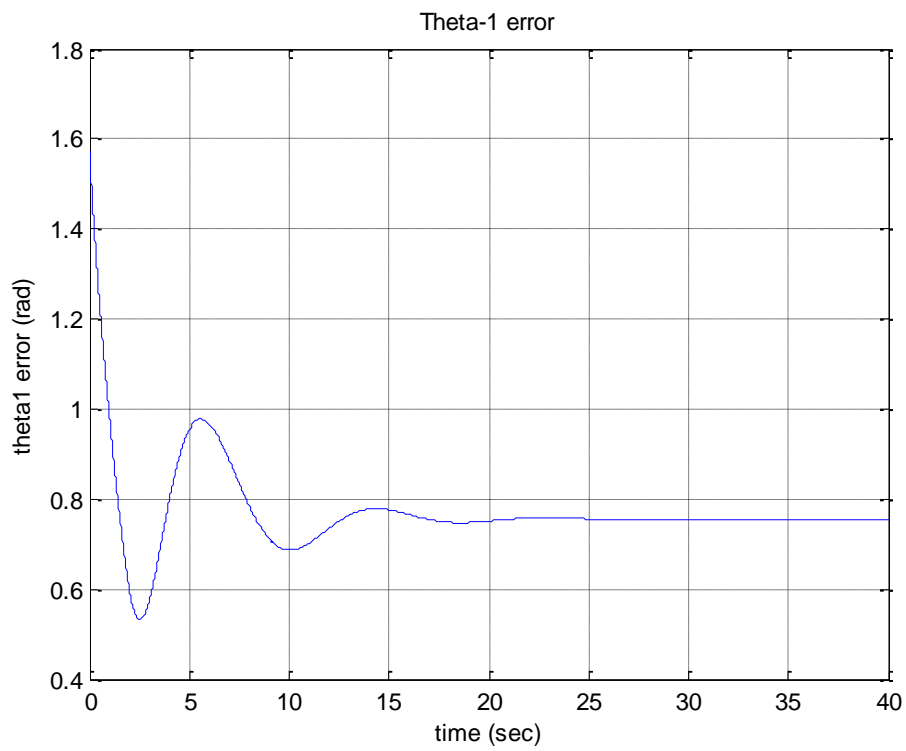


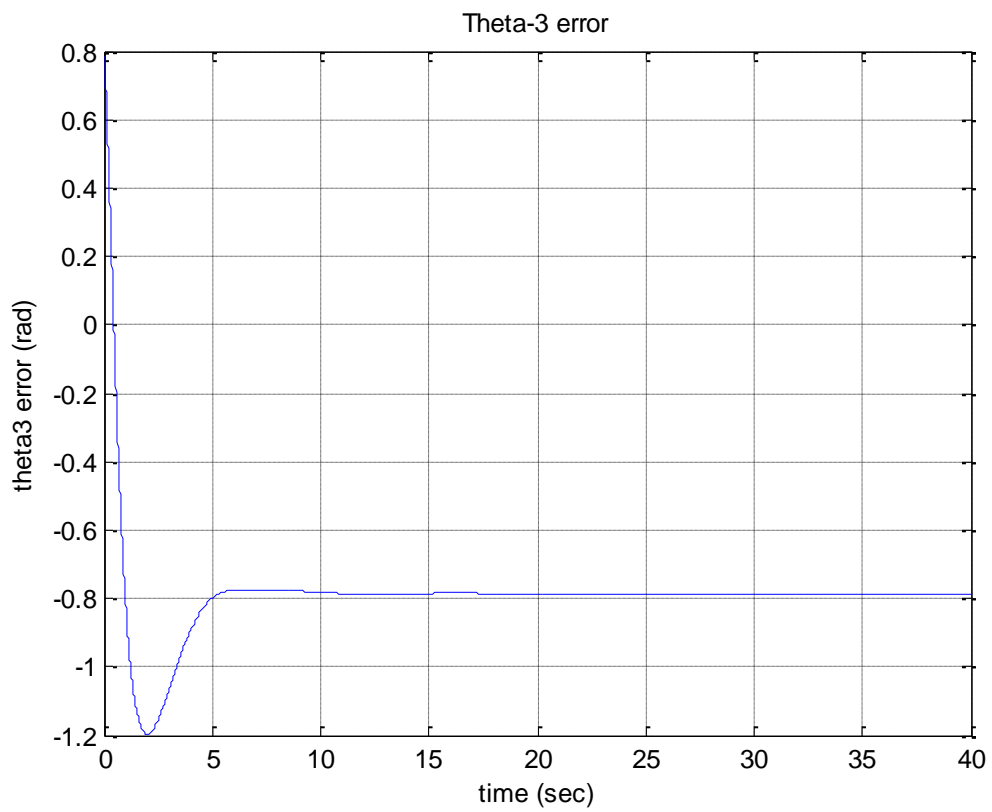
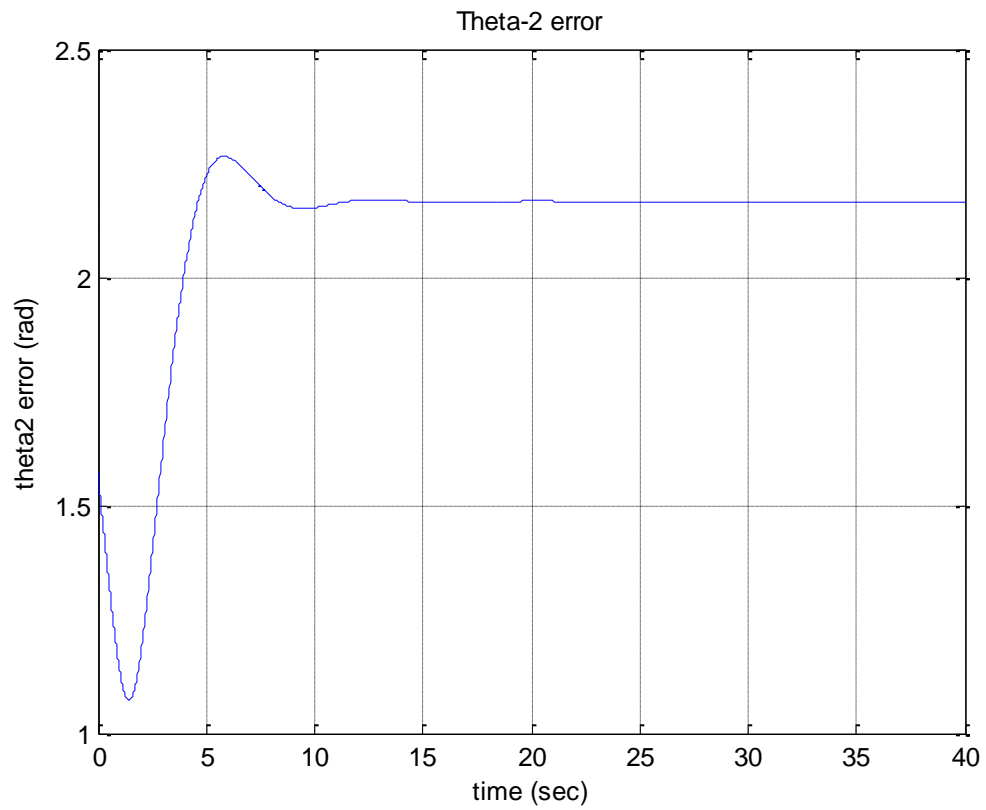


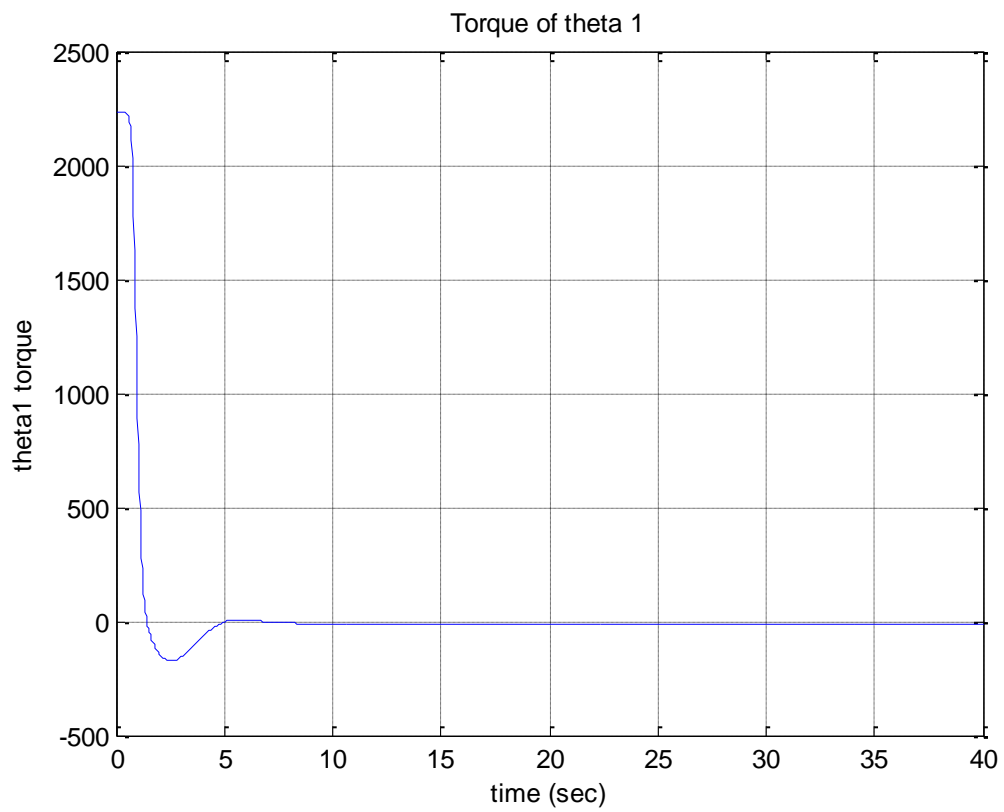
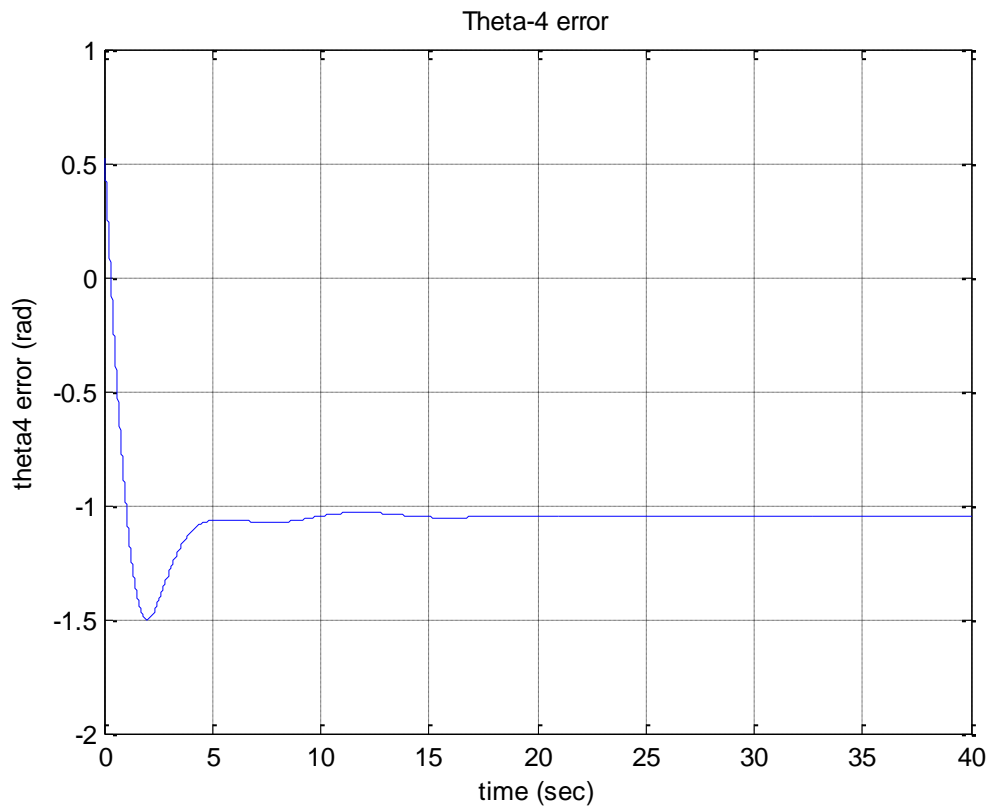


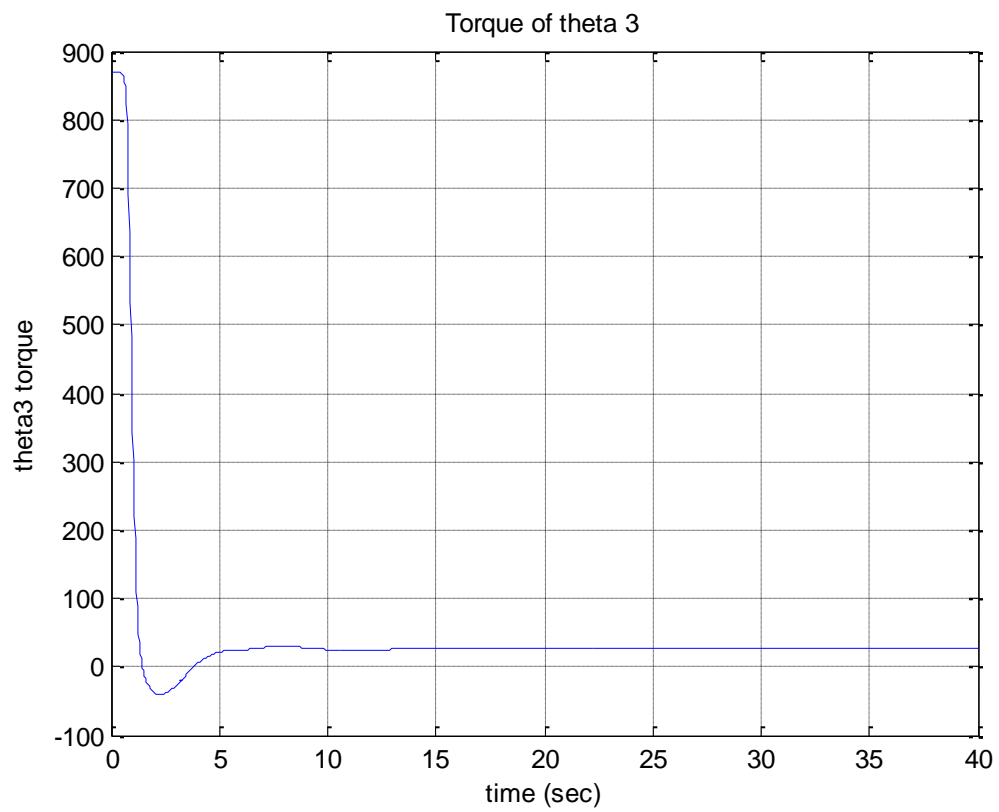
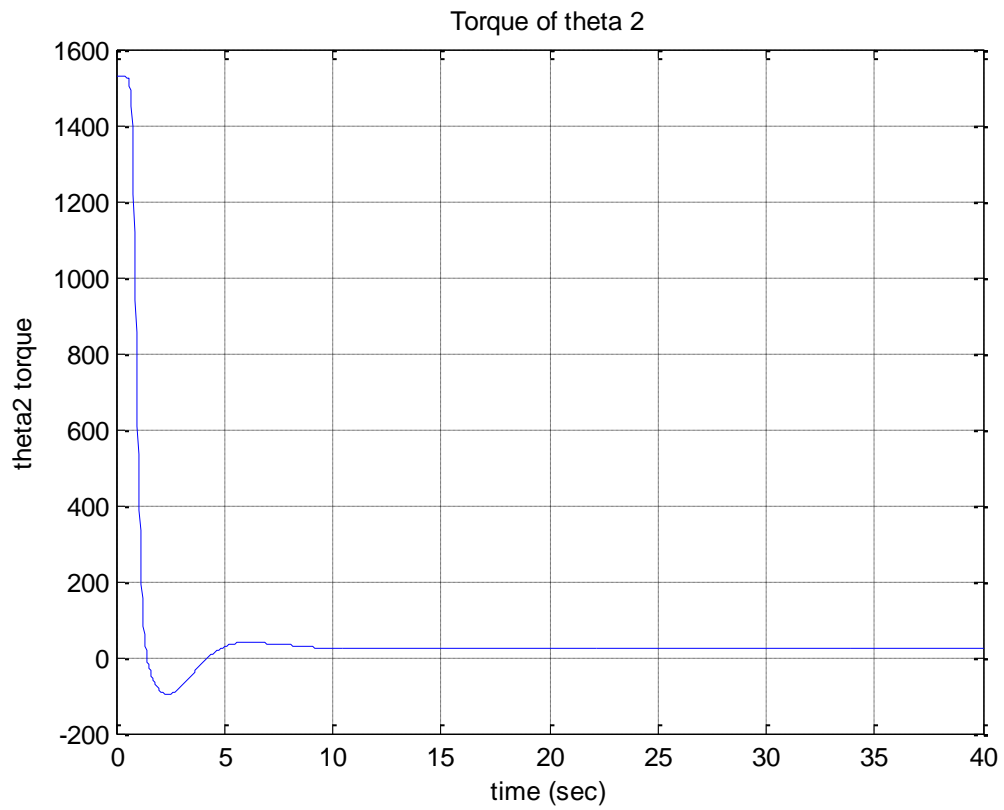


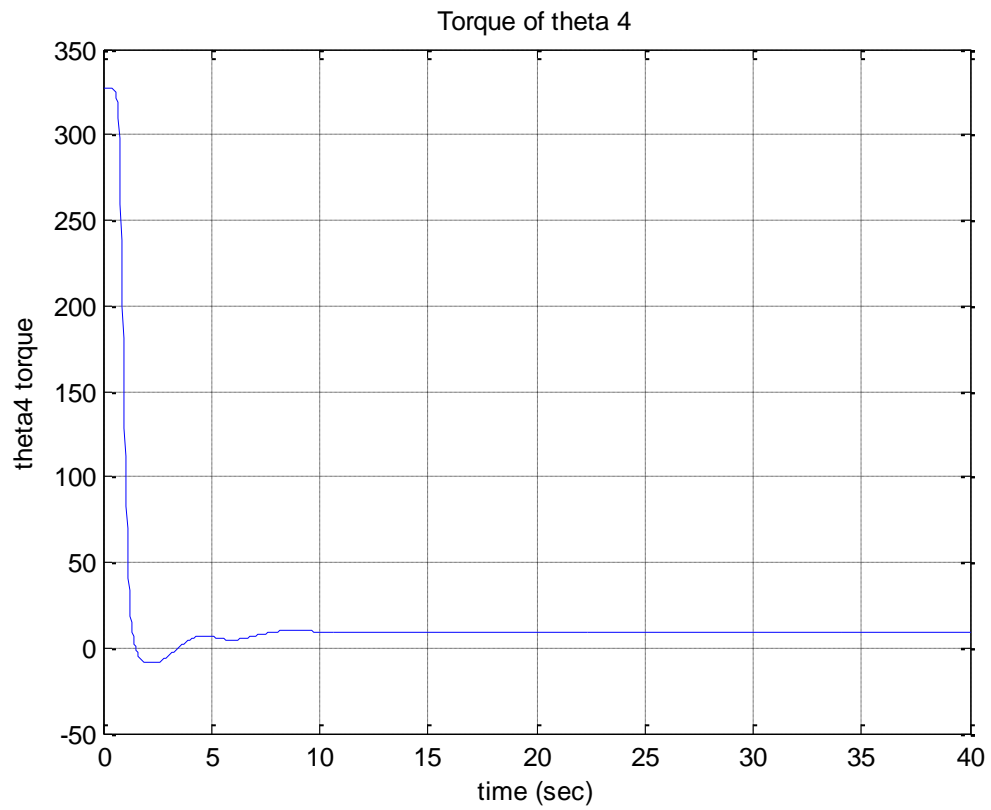
### Graphs of Case 2



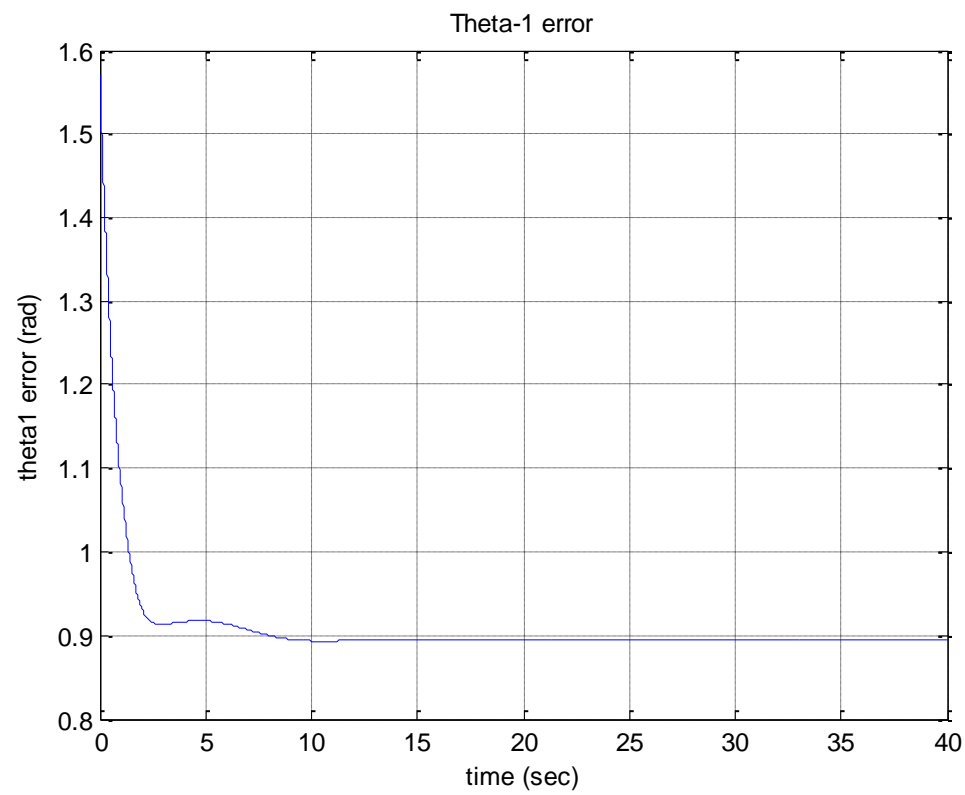


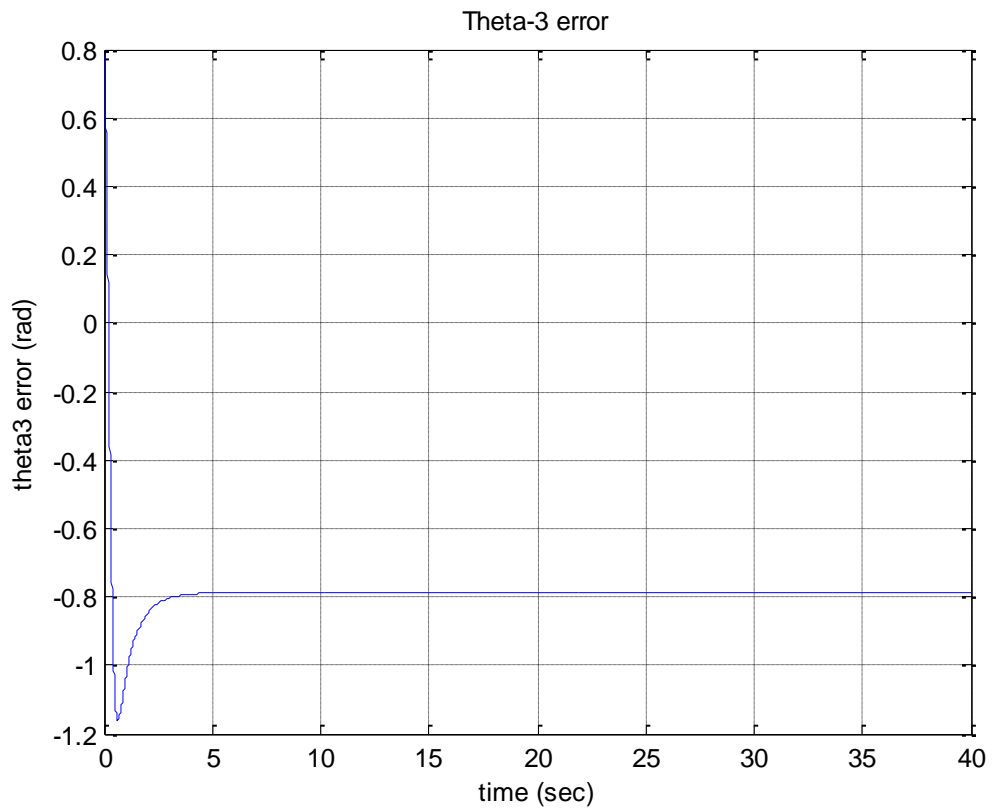
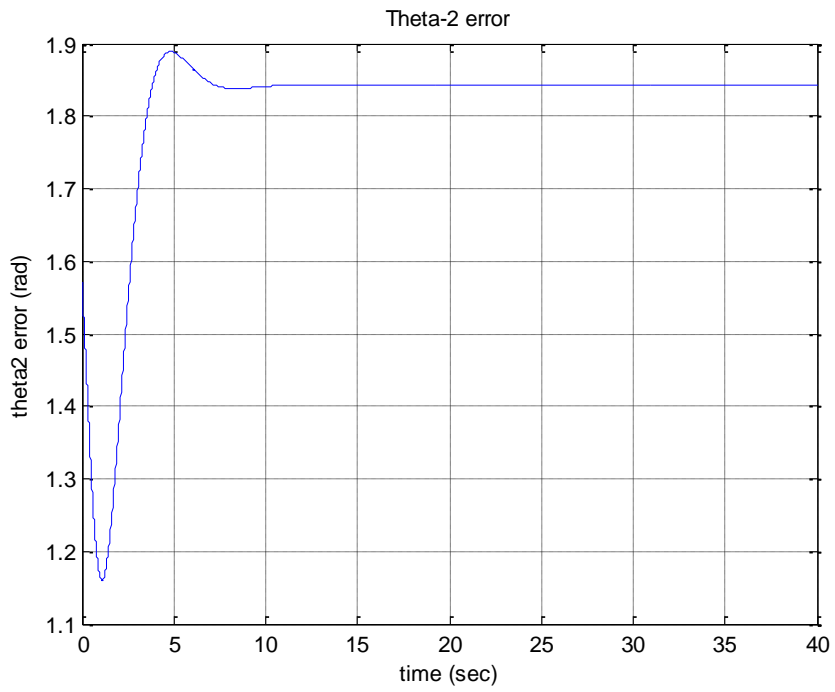


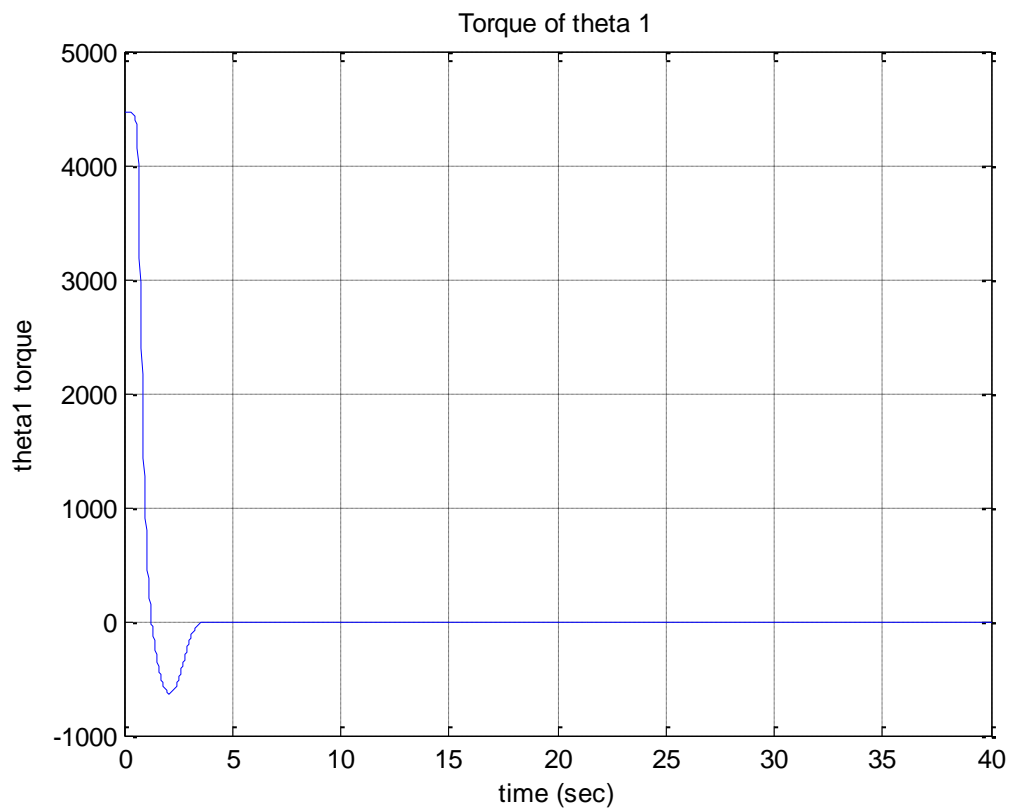
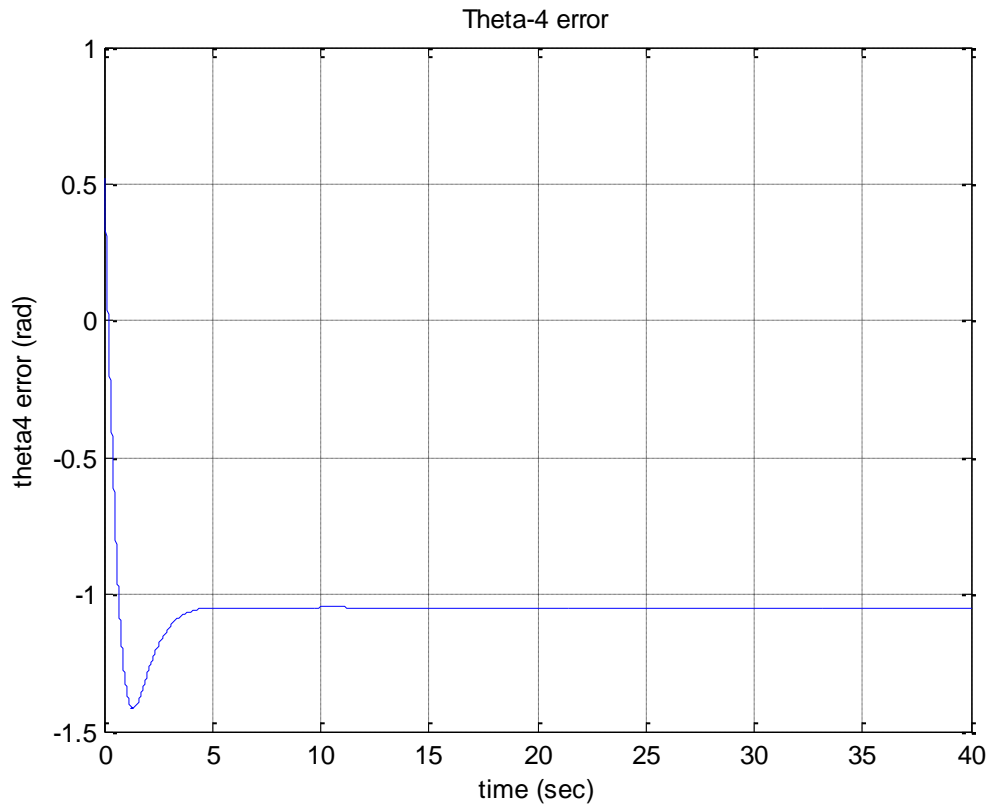




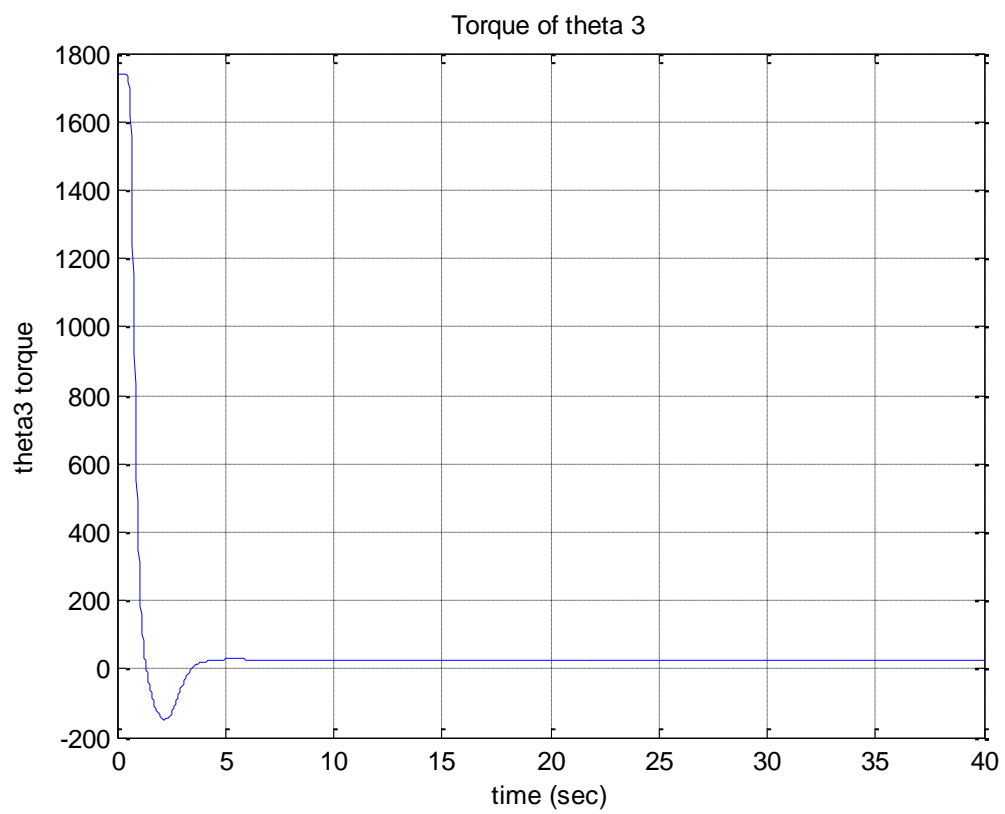
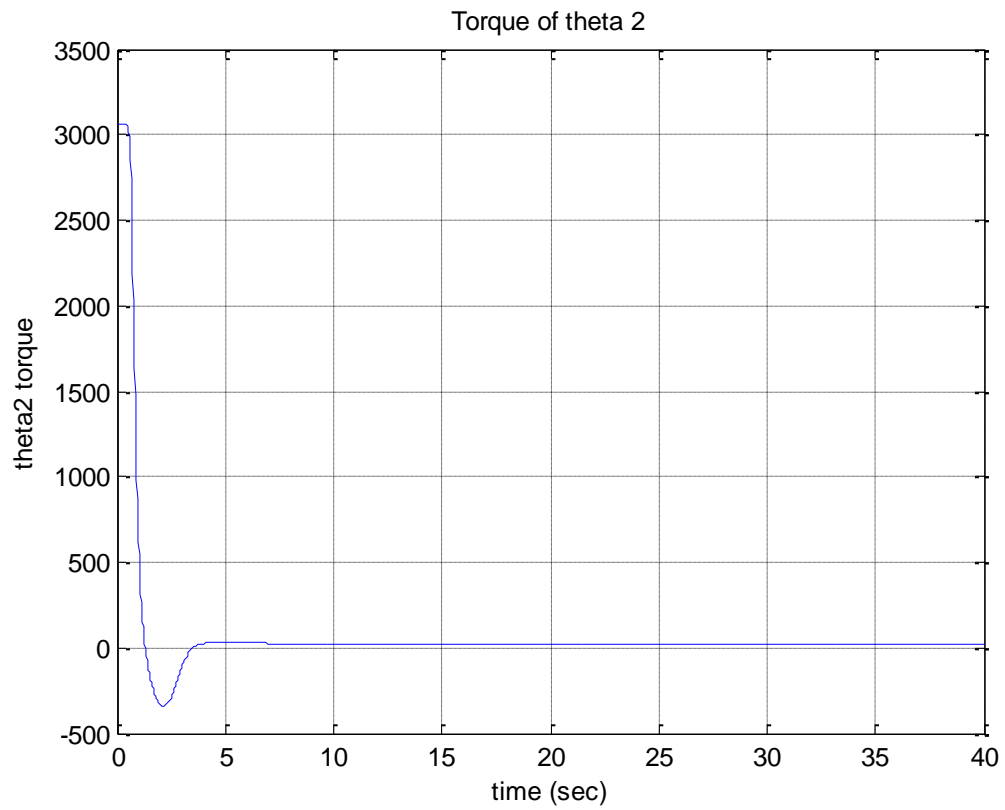
**Graphs of Case 3**

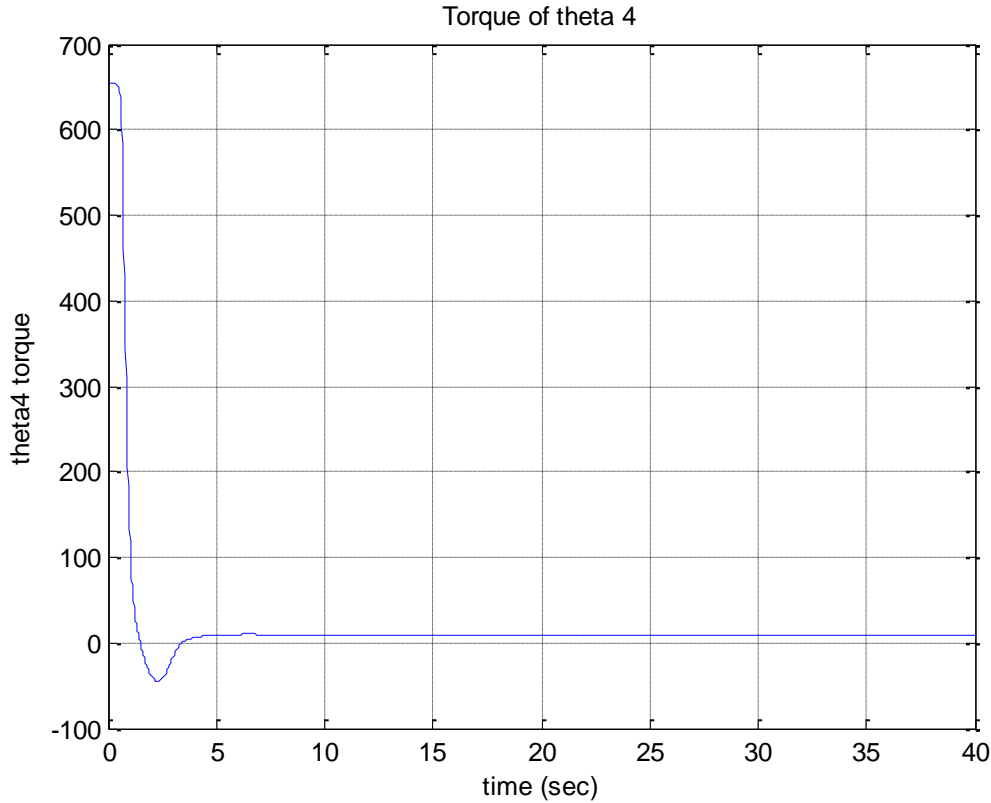












## 5. Conclusion

In this report, section 1 addressed the problem of kinematics, inverse kinematics and Differential kinematics of the thumb and index finger of a prosthetic hand. These kinematic structures could be applied to the rest of the fingers to form a complete prosthetic hand. In Section 3, we derive the dynamic models for a 4 DOFs finger via the Lagrangian convention and the Newton Euler postulations. A Proportional Integral Derivative control strategy was applied to the parameters from the dynamics and simulation results gotten. Our first approach to control the robotic finger arm is by trial and error, the two parameters of the controller will be tuned manually to obtain the best results. The best performance of the controller parameters values were shown in table 4.1 in three different cases.

## **Optimal Control Strategy for Smart Prosthetic Hand**

### **Summary**

Optimization is a very desirable feature in day-to-day life. We like to work and use our time in an optimum manner, use resources optimally and so on. The subject of optimization is quite general in the sense that it can be viewed in different ways depending on the approach (algebraic or geometric), the interest (single or multiple), the nature of the signals (deterministic or stochastic), and the stage (single or multiple) used in optimization.

This report presents a control technique of finite-time linear quadratic optimal control for five-fingered smart prosthetic hand. The optimal control is used for feedback linearized dynamics to minimize tracking error. This work is different than the work done in [2] as in this work the reference input can be chosen to be constant, ramp, sinusoidal values etc. The simulations of this optimal controller showed good performance.

### **Introduction**

Optimal control theory is a mature mathematical discipline with numerous applications in both science and engineering. It is emerging as the computational framework of choice for studying the neural control of movement, in much the same way that probabilistic inference is emerging as the computational framework of choice for studying sensory information processing. Despite the growing popularity of optimal control models, however, the elaborate mathematical machinery behind them is rarely exposed and the big picture is hard to grasp without reading a few technical books on the subject.

The main objective of optimal control is to determine control signals that will cause a plant to satisfy some physical constraints and at the same time (maximize or minimize) a performance index or cost function. We are interested in finding the optimal control  $u^*(t)$  (\* indicates optimal condition) that will drive the plant P from initial state to final state with some constraints on controls and states and at the same time extremizing the given performance index J.

The formulation of optimal control problem requires:

1. a mathematical model of the process to be controlled (generally in state variable form),
2. a specification of the performance index, and
3. a statement of boundary conditions and the physical constraints on the states and/or controls.

We can describe a physical plant by a set of linear or nonlinear differential equations.

Classical control design techniques have been successfully applied to linear, time-invariant, single-input, single output (SISO) systems. Typical performance standards are system time response to step or ramp input characterized by rise time, settling time, peak overshoot, and steady state accuracy; and the frequency response of the system characterized by gain and phase margins, and bandwidth.

In modern control theory, the optimal control problem is to find a control which causes the dynamical system to reach a target or follow a state variable (or trajectory) and at the same time extremize a performance index. Performance index in general can be in the form as

$$J = \mathbf{x}'(t_f)\mathbf{F}\mathbf{x}(t_f) + \int_{t_0}^{t_f} [\mathbf{x}'(t)\mathbf{Q}\mathbf{x}(t) + \mathbf{u}'(t)\mathbf{R}\mathbf{u}(t)]dt$$

Where, R is a positive definite matrix, and Q and F are positive semi definite matrices, respectively. Note that the matrices Q and R may be time varying. The particular form of this performance index is called quadratic (in terms of the states and controls) form.

In tracking (trajectory following) systems, we require that the output of a system track or follow a desired trajectory in some optimal sense. Thus, we see that this is a generalization of regulator system in the sense that the desired trajectory for the regulator is simply the zero state.

The optimal control  $u_*(t)$  is given by

$$\mathbf{u}^*(t) = -\mathbf{R}^{-1}(t)\mathbf{B}'\mathbf{P}(t)\mathbf{x}^*(t) = -\mathbf{K}(t)\mathbf{x}^*(t)$$

Here, K(t) is called Kalman gain and P(t), the symmetric positive definite matrix is the solution of the matrix differential Riccati equation (DRE)

$$\dot{\mathbf{P}}(t) = -\mathbf{P}(t)\mathbf{A} - \mathbf{A}'\mathbf{P}(t) - \mathbf{Q}(t) + \mathbf{P}(t)\mathbf{B}\mathbf{R}^{-1}(t)\mathbf{B}'\mathbf{P}(t)$$

Satisfying the final condition:

$$\mathbf{P}(t = t_f) = \mathbf{F}(t_f)$$

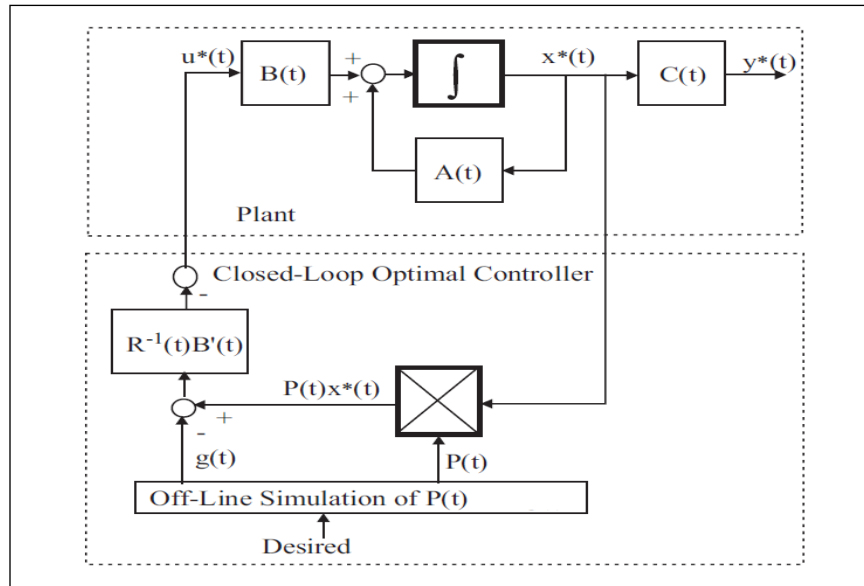
The optimal state  $\mathbf{x}^*$  is the solution of:

$$\dot{\mathbf{x}}^*(t) = [\mathbf{A} - \mathbf{B}\mathbf{R}^{-1}(t)\mathbf{B}'\mathbf{P}(t)] \mathbf{x}^*(t)$$

And the optimal cost  $J^*$  is

$$J^* = \frac{1}{2} \mathbf{x}^{*'}(t) \mathbf{P}(t) \mathbf{x}^*(t)$$

The optimal tracking system can be summarized in the next figure.



Modeling:

It is necessary to have a mathematical model that describes the dynamic behavior of prosthetic hand for the purpose of designing the control system. Hence, in this section the dynamic equations of hand motion are derived via Lagrangian approach using kinetic energy and potential energy. from Lagrangian approach, dynamic equations of thumb can be obtained as below.

$$\mathbf{M}(\mathbf{q})\ddot{\mathbf{q}} + \mathbf{C}(\mathbf{q}, \dot{\mathbf{q}}) + \mathbf{G}(\mathbf{q}) = \boldsymbol{\tau} - \mathbf{F}_v\dot{\mathbf{q}} - \mathbf{F}_s\text{sign}(\dot{\mathbf{q}}) - \mathbf{J}'\mathbf{F}_{\text{ext}}$$

Where  $\mathbf{M}(\mathbf{q})$  is the inertia matrix;  $\mathbf{C}(\mathbf{q}, \dot{\mathbf{q}})$  is the Coriolis/centripetal vector and  $\mathbf{G}(\mathbf{q})$  is the gravity vector;  $\mathbf{F}_v$  denotes the diagonal positive definite matrix of viscous friction coefficients;  $\mathbf{F}_s$  is a diagonal positive definite matrix and  $\text{sign}(\dot{\mathbf{q}})$  is a vector whose components are given by the sign functions of the single joint velocities;  $\mathbf{J}$  is the Jacobian and  $\mathbf{F}_{\text{ext}}$  denotes the vector of external forces in each direction. It can also be written as:

$$\mathbf{M}(\mathbf{q})\ddot{\mathbf{q}} + \mathbf{N}(\mathbf{q}, \dot{\mathbf{q}}) = \boldsymbol{\tau}$$

Where

$$\mathbf{N}(\mathbf{q}, \dot{\mathbf{q}}) = \mathbf{C}(\mathbf{q}, \dot{\mathbf{q}}) + \mathbf{G}(\mathbf{q}) + \mathbf{F}_v\dot{\mathbf{q}} + \mathbf{F}_s\text{sign}(\dot{\mathbf{q}}) + \mathbf{J}'\mathbf{F}_{\text{ext}}$$

Represents nonlinear terms in  $\mathbf{q}$  and  $\dot{\mathbf{q}}$ .

This work is different than the work done in [2] as in this work the reference input can be chosen to be constant, ramp, sinusoidal values,...etc.

In obtaining the linear system from the original nonlinear system, there has been no state-space transformation. Further, the difficult design of a controller for the original nonlinear system has been transformed into a simple design of a controller for the linear system. If we select the control function  $u(t)$  to stabilize the linear system and make the tracking error zero, then the nonlinear torque-control will command the prosthetic hand to follow the desired trajectory. The original robotic hand system becomes:

$$\mathbf{M}(\mathbf{q}(t)) \ddot{\mathbf{q}}(t) + \mathbf{N}(\mathbf{q}(t), \dot{\mathbf{q}}(t)) = [\mathbf{M}(\mathbf{q}(t))] [\ddot{\mathbf{q}}_d(t) - \mathbf{u}(t)] + \mathbf{N}(\mathbf{q}(t), \dot{\mathbf{q}}(t))$$

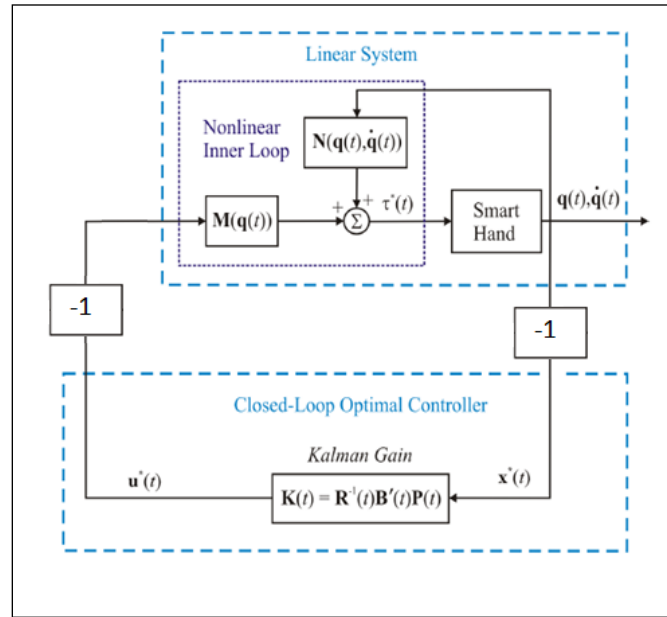
Where

$$\ddot{\mathbf{e}}(t) = \mathbf{u}(t)$$

Therefore, the required torque can be calculated by the optimal control  $\mathbf{u}^*(t)$ .

$$\boldsymbol{\tau}^*(t) = \mathbf{M}(\mathbf{q}(t))(\ddot{\mathbf{q}}_d(t) - \mathbf{u}^*(t)) + \mathbf{N}(\mathbf{q}(t), \dot{\mathbf{q}}(t))$$

The next figure shows the block diagram of a hybrid finite-time linear quadratic optimal controller



Simulation Results:

Optimal control coefficients,  $A$ ,  $B$ ,  $F(tf)$ ,  $R(t)$  and  $Q(t)$  of all fingers are chosen as:

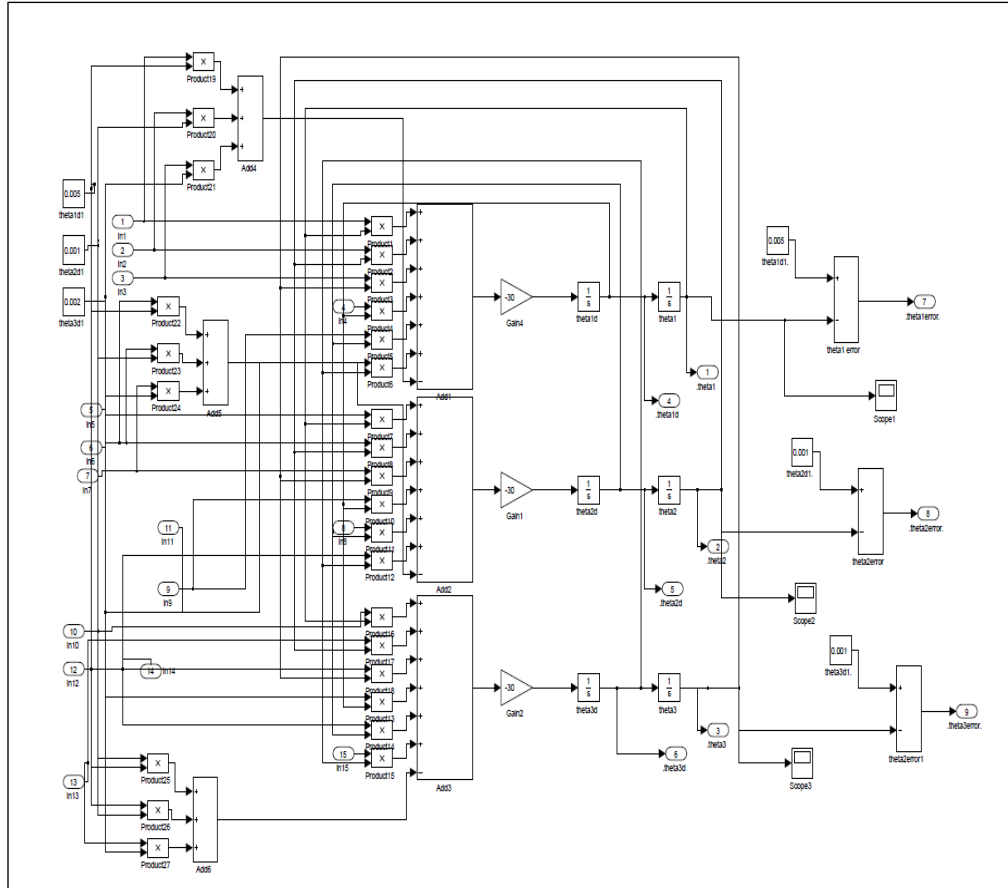
$$A = \begin{bmatrix} 0 & I \\ 0 & 0 \end{bmatrix}, \quad B = \begin{bmatrix} 0 \\ I \end{bmatrix}, \quad F(t_f) = 0, \quad R(t) = \frac{1}{30}I,$$

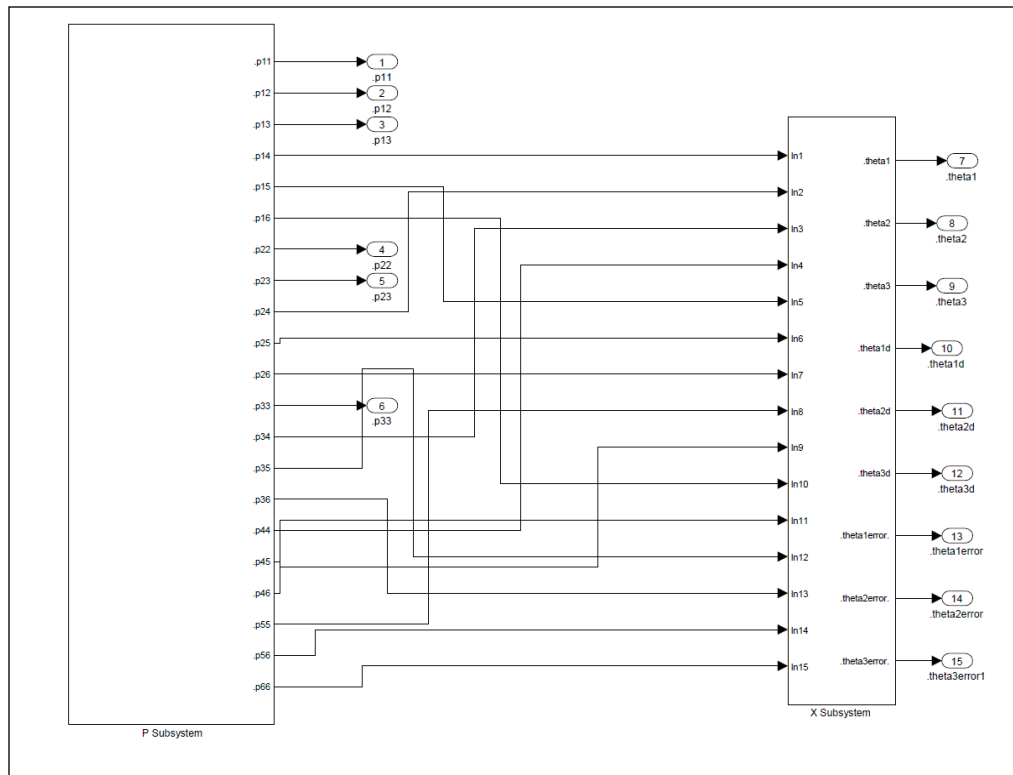
$$Q^i(t) = \begin{bmatrix} Q_{11} & Q_{12} \\ Q_{12} & Q_{22} \end{bmatrix}, \quad Q^j(t) = \begin{bmatrix} Q_{11} & Q_{12} & Q_{13} \\ Q_{12} & Q_{22} & Q_{23} \\ Q_{13} & Q_{23} & Q_{33} \end{bmatrix},$$

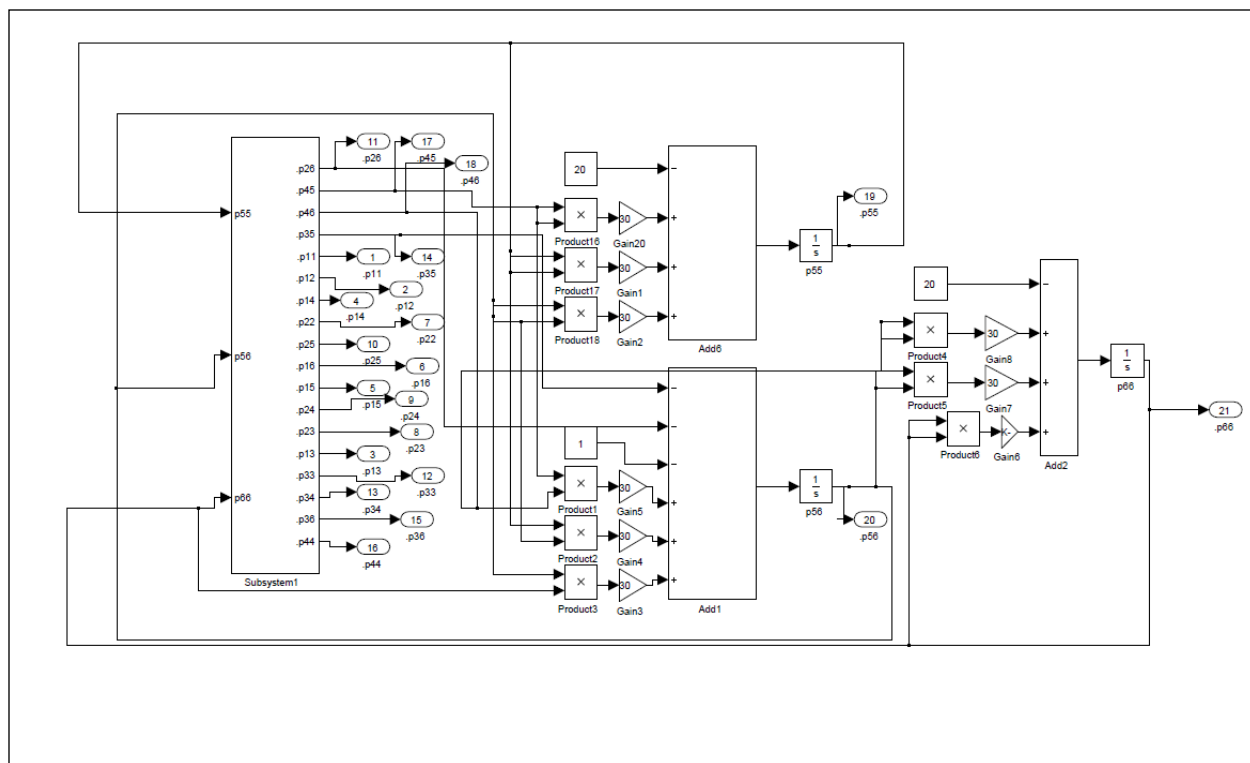
$$Q_{11} = \begin{bmatrix} 10 & 2 \\ 2 & 10 \end{bmatrix}, \quad Q_{22} = \begin{bmatrix} 30 & 0 \\ 0 & 30 \end{bmatrix}, \quad Q_{33} = \begin{bmatrix} 20 & 1 \\ 1 & 20 \end{bmatrix},$$

$$Q_{12} = \begin{bmatrix} -4 & 4 \\ 3 & -6 \end{bmatrix}, \quad Q_{13} = \begin{bmatrix} -4 & 4 \\ 3 & -6 \end{bmatrix}, \quad Q_{23} = \begin{bmatrix} -4 & 3 \\ 4 & -6 \end{bmatrix}.$$

The model that is built in Simulink is shown:

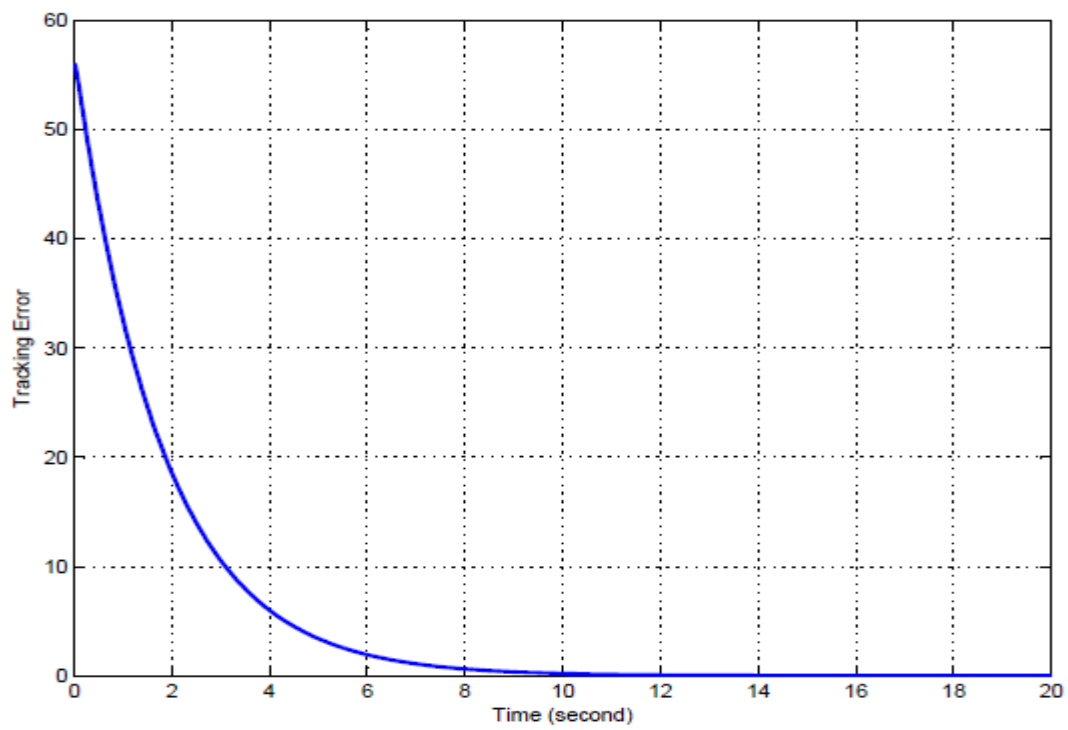




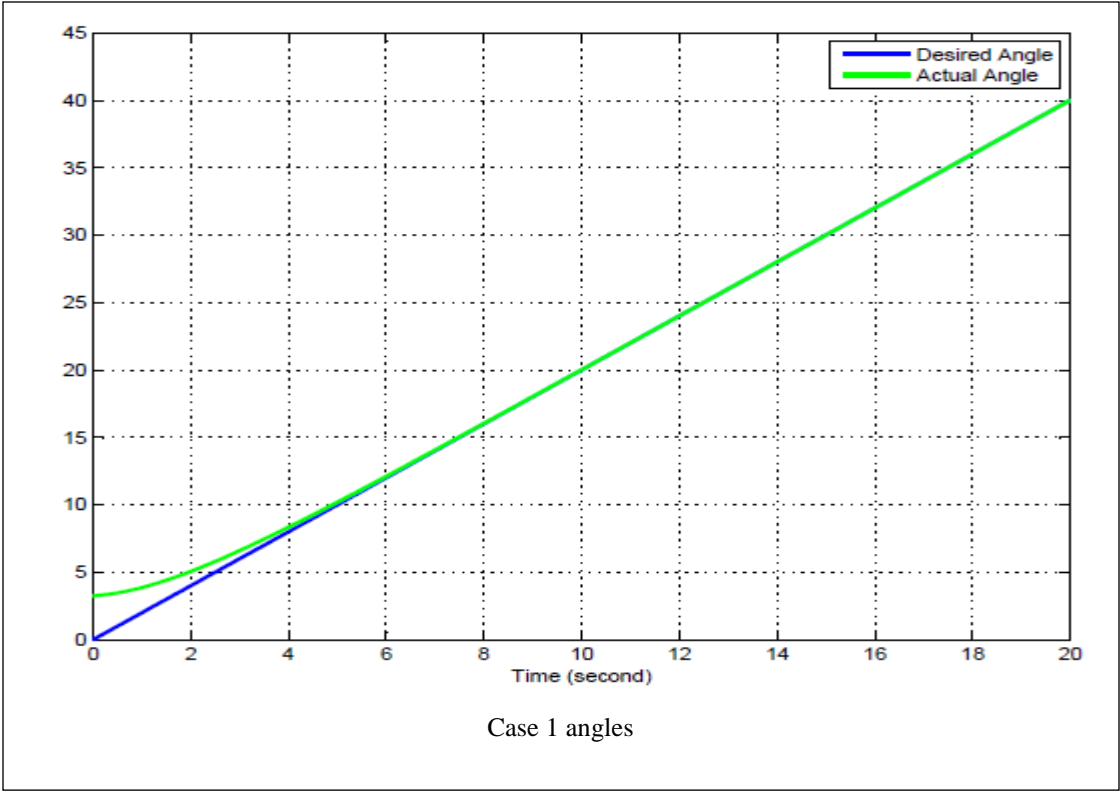


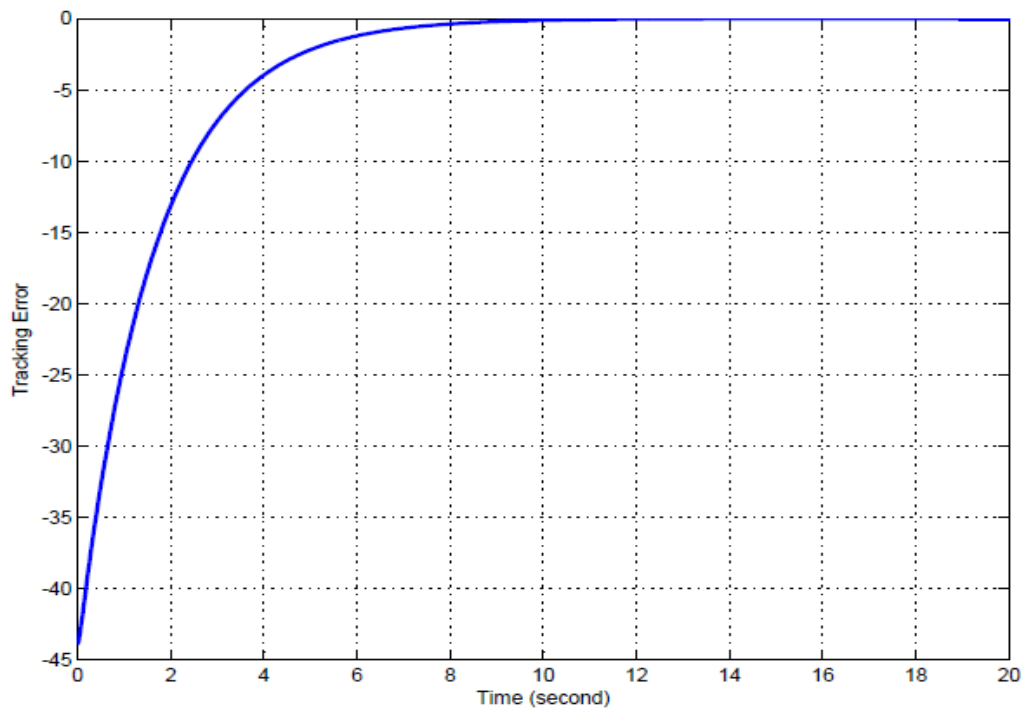
And the next figures shows some study cases to show the designed control method affectivity:



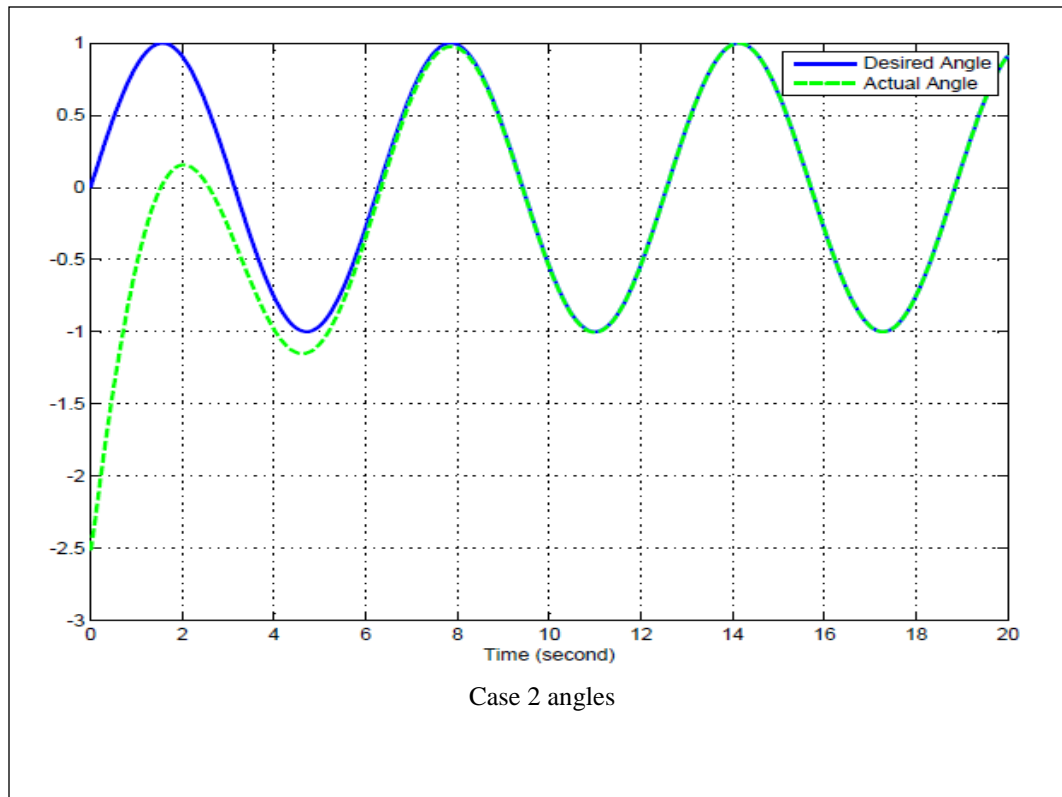


Case 1 tracking error





Case 2 tracking error



### **Conclusion:**

This report presented a control technique of finite-time linear quadratic optimal control for five-fingered smart prosthetic hand. The optimal control used for feedback linearized dynamics to minimize tracking error. This work is different than the work done in [2] as in this work the reference input can be chosen to be constant, ramp, sinusoidal values etc. The simulations of this optimal controller showed good performance. This work can be expanded to five fingers hand with 22 degree of freedom

- [1] D. Naidu, Optimal Control Systems. Boca Raton, FL: CRC Press, 2003.
- [2] C.-H. Chen, "Hybrid control strategies for smart prosthetic hand," Ph.D. dissertation, Measurement and Control Engineering, Idaho State University, May 2009.
- [3] D. S. Naidu, C.-H. Chen, A. Perez, and M. P. Schoen, "Control strategies for smart prosthetic hand technology: An overview," in Proceedings of the 30th Annual International IEEE EMBS Conference, Vancouver, Canada, August 20-24 2008, pp. 4314–4317.

## Goal 2AB: Real-Time Control

In this research different strategies for controlling a smart prosthetic hand will be investigated. The aim of the controller is to define how the fingers should move considering the amputee's intention and an appropriate grasp shape. Two major kinds of plants will be covered: fully actuated and underactuated hands. In fully actuated hands all the joints of the are active and they have separate actuators, while in an underactuated hand the number of actuators are less than degrees of freedom. Besides grasp formation strategies, control techniques that allow accurately following command signal from EMG analysis in real-time will be investigated. These commands can be in the form of position (angle) or force signals. All the purposed control strategies are designed for real-time implementation.

Human hand is one of the most important and complex parts of the body, which has the ability to handle different tasks. The ultimate goal of a robotic hand is to achieve the functionality of a human hand. In the past three decades, there have been numerous investigations to achieve dexterity and ability of human hand, especially in the fields of humanoid robotics and prosthetic hand [1-6]. In spite of all these advances in this field, the current state of research on prosthetic hands is far from that objective of achieving the functionality of human hand. Commercially available prosthetic hands have very limited functionality and they are just simple grippers. The present research on prosthetic hands involves complex control schemes to achieve the most important functions of the hand [7-8].

Grasping can be categorized into two main groups: precision and power grasping. In precision grasping the object is held by tips of the fingers, while in power grasping, the whole the finger is active and in contact with the object [9].

Many control methods require the knowledge of the shape of the object. For humans this information is available by visual feedback from eyes, while in case of a prosthetic hand this visual information is not directly available for hand controller, and the only available information is electromyographic (EMG) signal related to patient's arm muscle activities. However, normally the EMG signal is not available for all individual joints and besides, due to measurement noise, accessing high quality EMG signal is hard [10]. Moreover, using EMG signal to control all the movements requires lot of attention during grasping and leads to fatigue for the amputees [11]. Hence it is required for prosthetic hand to be semi-autonomous which means a part of command information will be provided by the EMG signal and the rest of the required command should be provided automatically by hand controller.

Defining finger trajectory without the knowledge of shape of object to be grasped is a challenging task for many path planning techniques. For multi DOFs robots there are two common methods for trajectory planning which are "inverse kinematic" and "inverse dynamic" [12-15]. Both these methods require object shape and are based on solving optimization problem which requires high computation, hence they are hard to implement for real-time applications.

To avoid solving the path planning problem for prosthetic hands, many researchers advocated under-actuated mechanisms, which are capable of adapting to object shape mechanically and without additional computation [16-18]. In these mechanisms, the number of actuators is less than the DOFs, and because of less actuators they have less weight. However fewer actuators result in less functionality, because fingers joints can't move independently. In this research the control methods for both underactuated and fully actuated hands will be covered.

In this repot, in section 2 power grasping control for fully actuated hand based on virtual spring damper hypothesis is investigated. Section 3 focuses on precision grasping of fully actuated hand. Section 4 discusses the underactuated hand position and force control method. Section 5 covers robust control method to follow accurately angle command signal from EMG analysis in presence of plant uncertainty. Section 6 concludes current works and presents considered future works and corresponding time table.

## 2. Power Grasping Control for fully actuated prosthetic hand

Arimoto et al. [19] used “virtual spring-damper hypothesis” for control of robotic arm-hand systems. A similar method called “virtual model control” is also suggested by J.Pratt et al. [20] used for walking robots, and it is based on defining virtual forces between two points. Both methods are based on the use of Jacobian matrix to relate task space movement to joint space. In [20] it is shown that any kind of force can be defined between two points and the other study [19] shows that use of spring-damper forces will result in human like movement. From physiological point of view, human skilled multi-joint reaching movement has these characteristics that 1) endpoint trajectory become a quasi-straight line and less variable, 2) velocity profiles of the endpoint has a bell-shape, and 3) joint trajectories are rather variable from trial to trial [19].

In this research, a new control scheme is proposed that can efficiently address the problem of power grasping without complete knowledge of the shape of the object which may be called “blind power grasping” for prosthetic hand. The proposed method is based on the works by Arimoto et al. [19] using virtual spring-damper (VSD) hypothesis used for control of robotic arm-hand systems. In our research, we use the above mentioned hypothesis, in particular for the power grasping of a prosthetic hand. In this method, we define a virtual spring-damper between finger tip and desired point for control of movement of fingers. Further, in this method there is no need to introduce any performance indices to solve inverse kinematics uniquely and Jacobian pseudo-inverse or inverse dynamics which are common methods to define trajectories of redundant DOFs robots. Besides, in the present method, there is no need for any information on tactile or force sensing.

### 2.1. Modeling of Prosthetic Hand

In this control method, controller is not derived directly from dynamic model of the system. Kinematics equation and Jacobian matrix are the required for controller design.

A model of a robotic hand system is shown in Fig.1. The model consists of a finger with 3DOF which represents three joints of a finger and palm.

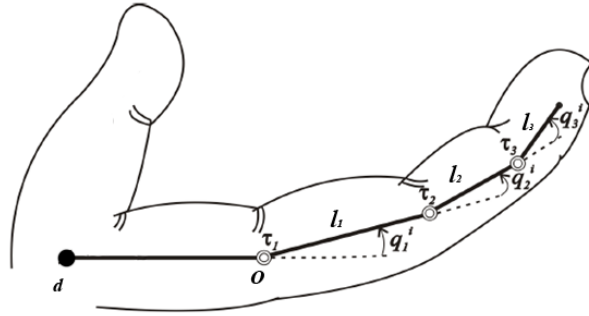


Fig. 1: Model of a Robotic Hand System.

In this research we assume the following:

- 1- Movement of both finger and object are confined to a two dimensional horizontal plane, and therefore there is no gravity effect.
- 2- The object is assumed to be initially stable in its position.
- 3- The initial movement toward object is handled by amputee, so the hand is close enough to the object before grasping.

The position of the tip of the finger is evaluated as (see Figure 1):

$$x = l_1 \cos q_1 + l_2 \cos(q_1 + q_2) + l_3 \cos(q_1 + q_2 + q_3) \quad (1)$$

$$y = l_1 \sin q_1 + l_2 \sin(q_1 + q_2) + l_3 \sin(q_1 + q_2 + q_3) \quad (2)$$

where,  $l_1$ ,  $l_2$ , and  $l_3$  are lengths of each finger and  $q_1$ ,  $q_2$ , and  $q_3$  are angles of each corresponding joint.

Based on above equation the Jacobian matrix is as:

$$J = \begin{bmatrix} j_{11} & j_{12} & j_{13} \\ j_{21} & j_{22} & j_{23} \end{bmatrix}, \quad (3)$$

$$j_{11} = -l_1 \sin q_1 - l_2 \sin(q_1 + q_2) - l_3 \sin(q_1 + q_2 + q_3), \quad (4)$$

$$j_{12} = -l_2 \sin(q_1 + q_2) - l_3 \sin(q_1 + q_2 + q_3), \quad (5)$$

$$j_{13} = -l_3 \sin(q_1 + q_2 + q_3), \quad (6)$$

$$j_{21} = l_1 \cos q_1 + l_2 \cos(q_1 + q_2) + l_3 \cos(q_1 + q_2 + q_3), \quad (7)$$

$$j_{22} = l_2 \cos(q_1 + q_2) + l_3 \cos(q_1 + q_2 + q_3), \quad (8)$$

$$j_{23} = l_3 \cos(q_1 + q_2 + q_3). \quad (9)$$

$$j_{33} = l_3 \cos(q_1 + q_2 + q_3). \quad (10)$$

### 2.3. Virtual Spring-Damper Method

“Virtual model control” is a motion control scheme that uses simulations of virtual components to generate desired joint torques [20]. These joints produce the same effect that the virtual elements placed on robot would have created; hence they create the illusion that these virtual elements are connected to the real robot. Virtual elements can be any kind of real physical elements such as springs, dampers, gravity fields, nonlinear fields or any other components.

Virtual model control was proposed by J. Pratt et al [20] for biped walking robot. In a study by Arimoto [19] on robotic hand arm system, it is shown that using a virtual spring damper between robot end effector and desired point, and virtual dampers at each joint, human like movement can be achieved.

For power grasping by a prosthetic hand, one of the best options is the use of Virtual Spring-Damper (VSD) hypothesis. Some benefits of VSD control scheme are that it has a simple structure and requires relatively less computation. Besides, it doesn't need inverse dynamics to precisely define the robot movement. Thus, we use spring set points instead of commanded movement and robot automatically adapts its shape. Since finger joints at prosthetic hand work as virtual dampers, which is sensitive to velocity and not to position, they don't have a forced shape, instead just finger tip follow a defined path as will be discussed more in control strategy section.

The joint torques to virtual forces is given by:

$$\tau = J^T F, \quad (11)$$

where  $\tau$  is the torque, and  $F$  is the force due to virtual spring damper given as

$$F = -(\xi\sqrt{k}\dot{x} + k\Delta x), \quad (12)$$

and

$$\tau_{spring-damper} = -J^T(\xi\sqrt{k}\dot{x} + k\Delta x), \quad (13)$$

where  $k$  represents the stiffness of the virtual spring,  $\Delta x$  is distance between finger tip and desired point, and  $\xi$  is the damping ratio. The damping force is defined at each joint as

$$\tau_{joints\ damping} = -C\dot{q}, \quad (14)$$

where,  $C$  denotes a diagonal positive definite matrix as follows:

$$C = \xi_0 \text{diag}(c_1, \dots, c_n). \quad (15)$$

Hence control signal would be sum of these two terms

$$u = -C\dot{q} - J^T(q)(\xi\sqrt{k}\dot{x} + k\Delta x). \quad (16)$$

Higher values of  $k$  result in more accurate and faster response to the desired point and higher  $C$  provides more stability. Thus  $k$  and  $C$  are chosen as design variables.

#### 2.4. Control Strategy

Virtual spring-damper hypothesis is suitable for point to point control. Defining the desired trajectory as a semicircle (in order to have a full grasp of the object) given by,

$$x_d = (l_1 + l_2 + l_3) \cos(t), \quad (17)$$

$$y_d = (l_1 + l_2 + l_3) \sin(t), \quad (18)$$

Where  $t$  is proportional to EMG signal which is scaled to change between  $0 < t < \pi$ .

As shown in Fig. 2, after passing this semi-circle, finger tip goes toward center to make a tighter grasping. This is achieved by defining a desired point close to center.

As mentioned earlier, the goal is not exactly following the defined path. If the object is big, due to contact of hand and object, it would be impossible to follow exact path and following this path is just to achieve grasping.

Fig. 3 illustrates the physical counterparts of the virtual forces for control strategy and Fig. 4 shows structure of the proposed control system. As shown, the command force comes from EMG signal, and controller provides the movement for hand which has dynamic interaction with the object.

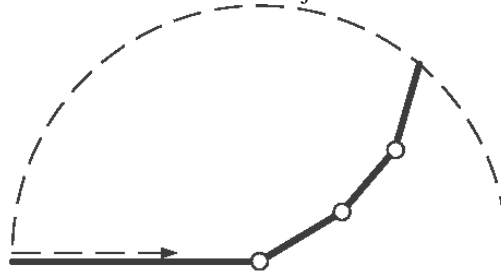


Fig. 2: Semi-Circle Path of Finger Tip

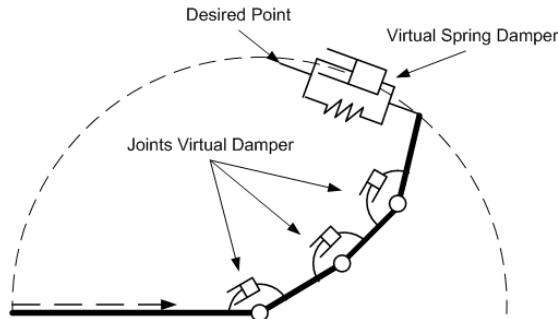


Fig 3: Physical Counterparts of the Virtual Forces



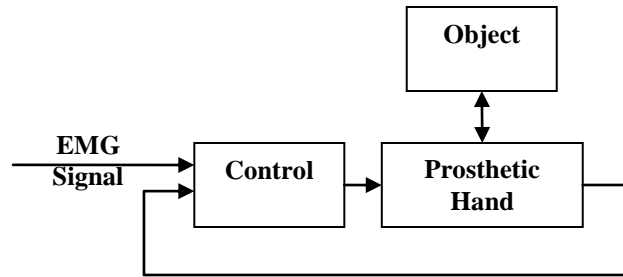


Fig. 4: Control Diagram of Prosthetic Hand System

## 2.5. Numerical Simulation

In order to show the effectiveness of the proposed control strategy, numerical simulations were conducted to grasp three different objects, based on the physical parameters of a hand system and objects summarized in Table 1.

In order to simulate dynamics of the hand and interaction with object, Adams software is used. This software is a multi-body analysis simulation program that solves the rigid body dynamic equilibrium equations and directly interfaces with Matlab/Simulink software in order to implement controller. The contact between object and hand is modeled and three sets of simulations with different objects are performed. In all three simulations the same control strategy is used which shows controller can handle grasping without information about physical parameters of object. Fingers and objects are assumed to be rigid. In these simulations the EMG signal is assumed to increase linearly with time.

Table 1. Parameters used for simulation

Index finger link 1	5 cm
Index finger link 2	2.5 cm
Index finger link 3	2.5 cm
Damping at joints	0.01 kg/s
Virtual damping ratio ( $c$ )	1
Virtual spring stiffness ( $k$ )	50 N/m
Rectangular object width	3 cm
Circular object radius	3 cm
Star shape object outer radius	2 cm

### 2.5.1 Simulation One

For first simulation a rectangular (cubic) object is used, and as mentioned earlier the movement is restricted to 2D movement. Object is not moving initially. Hand starts movement from open finger configuration. The hand positions at 1 second time interval are shown. Fig. 5 shows finger tip angle with respect to palm.

As it is shown in Fig. 6 the grasping is accomplished successfully.

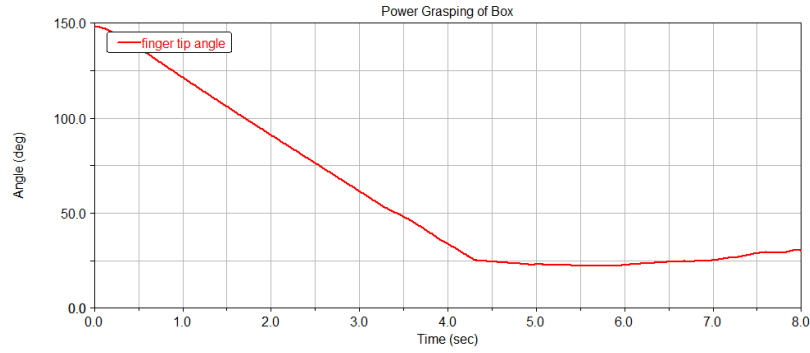


Fig. 5: Finger's Tip Angle at Rectangular Object Grasping

### 2.5.2 Simulation Two

For the second simulation a glass (circular object) is used. The control parameters are identical to previous simulation.

As shown in Fig. 7 the grasping is done successfully and the hand positions for 1 second time interval are depicted. Similarly the finger tip angle respect to palm is shown in Fig. 8.

Regardless of object shape, by use of proposed control scheme the hand can successfully grasp objects.

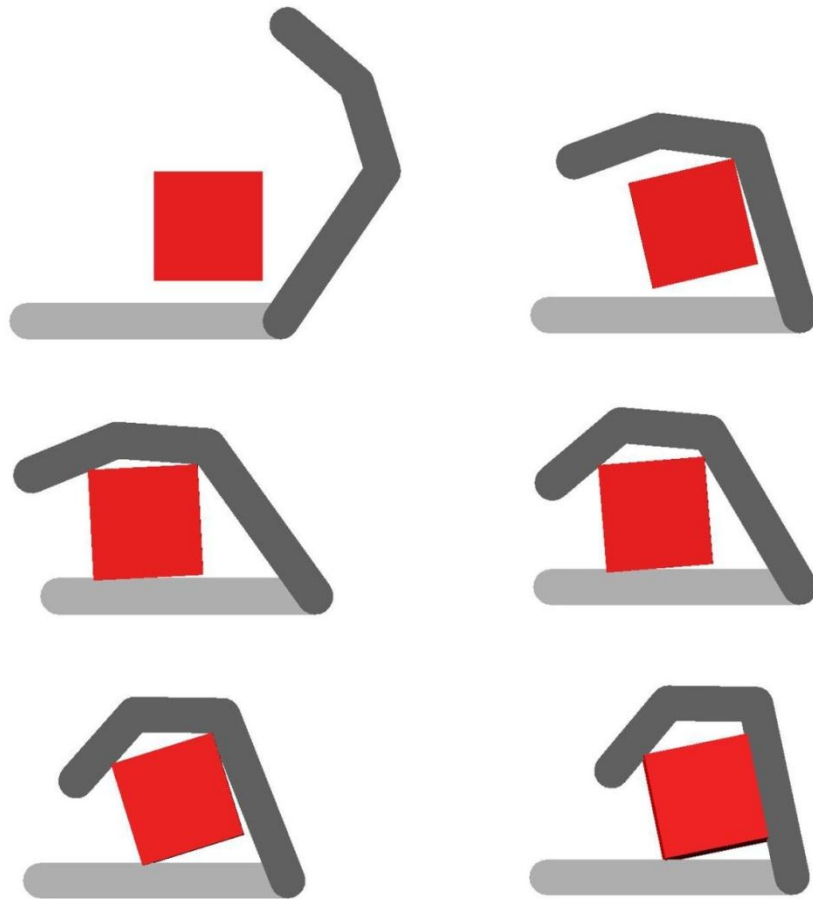


Fig. 6: Rectangular Object Grasping (1 Sec Intervals)

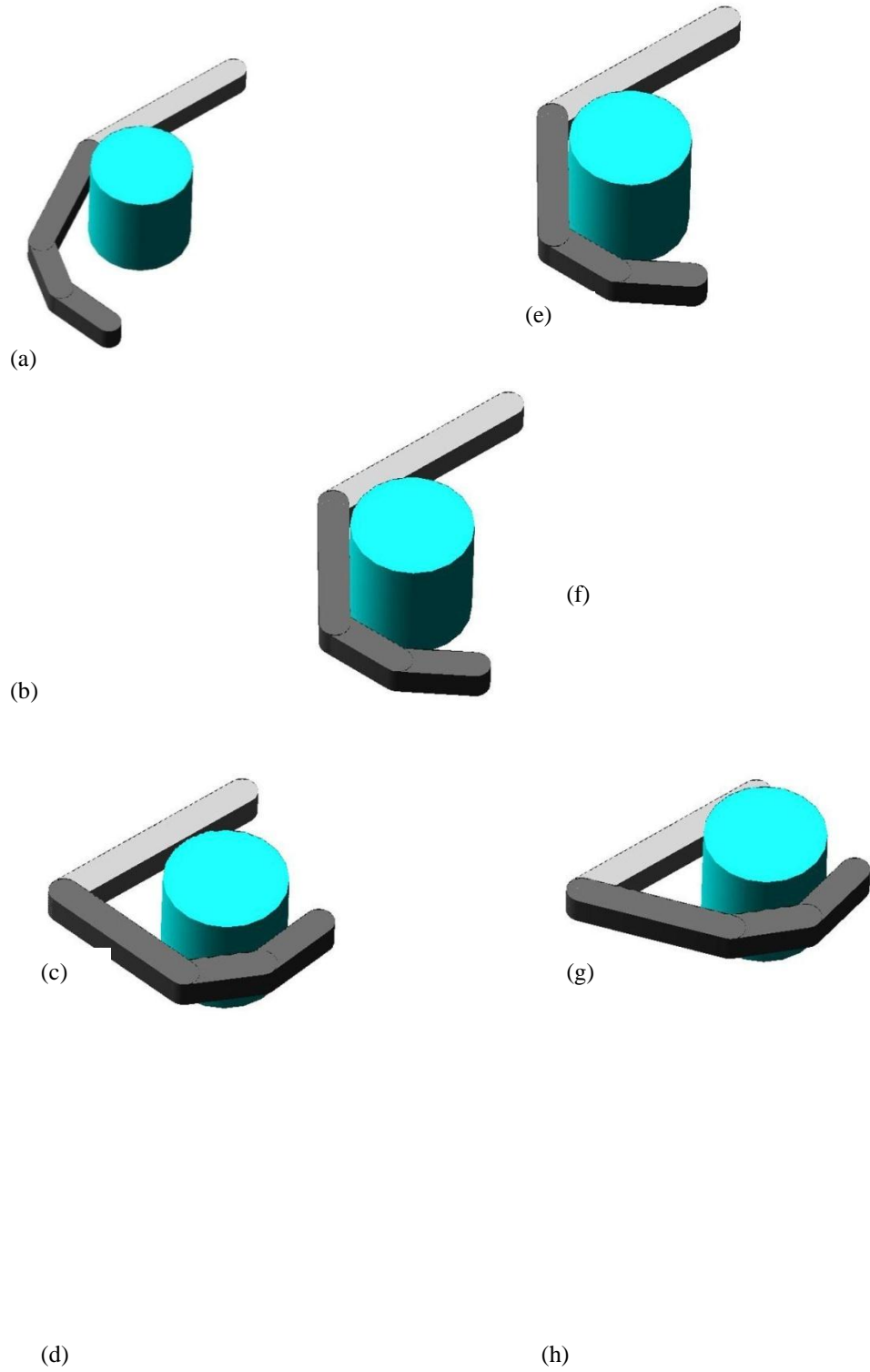
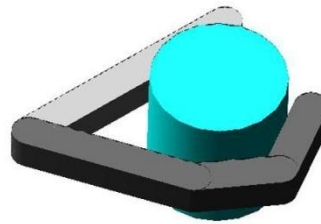
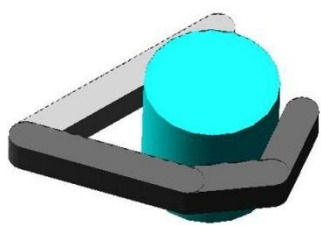
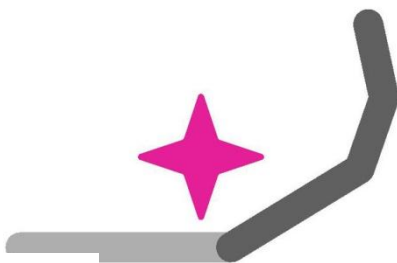
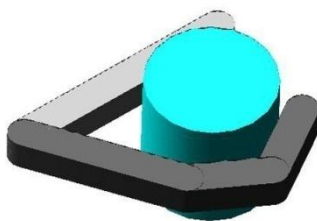


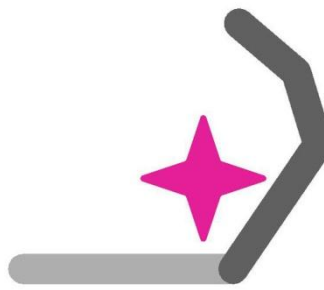
Fig. 7 (a-h) : Grasping of a Glass (1 sec. Intervals)



(d)



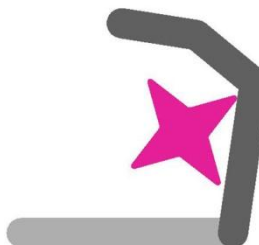
(a)



(e)



(b)



(f)

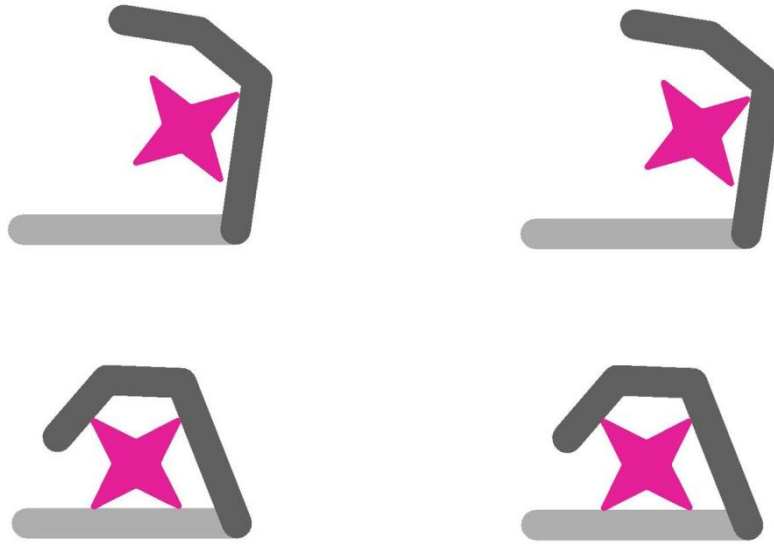


Fig. 9 (a-h) : Grasping of Star Shape Object (1 sec. Intervals)

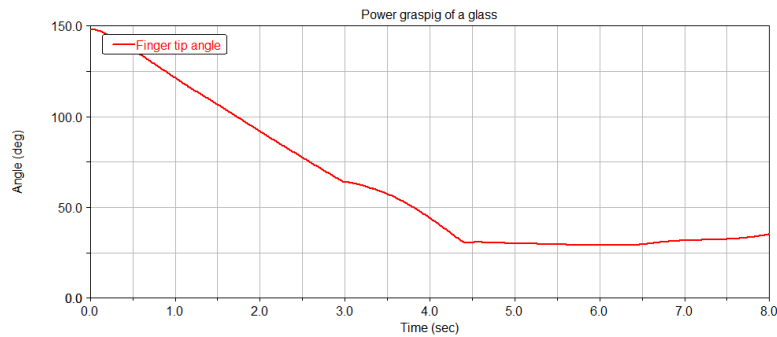


Fig. 8: Finger's Tip Angle at Grasping a Glass

### 2.5.3. Simulation Three

For the third simulation a star shape object is used. The control parameters are identical to previous simulation.

As shown in Fig. 9 the grasping is done successfully and the hand positions for 1 second time interval are illustrated. Similarly the finger tip angle respect to palm is shown in Fig. 10.

The complicated shape of object shows that controller is able to handle grasp for wide variety of objects, without information of object shape.

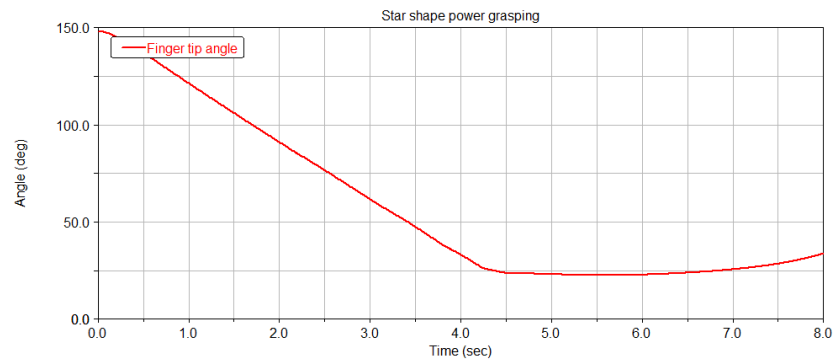


Fig. 10: Finger's Tip Angle at Star Shape Object Grasping

### 3. Precision grasping control for fully actuated prosthetic hand

Using the similar technique discussed in previous section for power grasping which is virtual spring damper hypothesis a control strategy is developed for precision grasping. In precision grasping the object is held by tips of the fingers, while in power grasping, the whole finger is active and in contact with the object. First a model is derived for kinematic of the hand, then the control strategy and numerical simulations are provided.

#### 3.1. Modeling of Prosthetic Hand

In this control method, controller is not designed based on dynamic model of the system. Instead, kinematics equation and Jacobian matrix are used for controller design.

A model of a robotic hand system is shown in Fig.1. The model consists of a finger with 3DOF which represents three joints of index finger, palm and a finger with 2DOF which represents thumb.

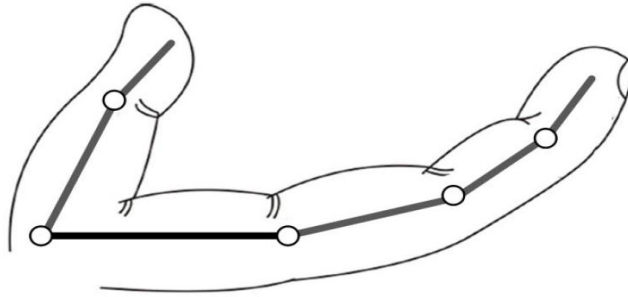


Fig. 1. Schematic of a robotic hand system

In this research we assume the following:

- Movement of both finger and object are confined to a 2 dimensional horizontal plane, and therefore there is no gravity effect.
- The object is assumed to be initially stable in its position.
- The initial movement toward object is handled by amputee, so the hand is close enough to the object before grasping.

The position of the tip of index fingers is evaluated as (see Fig. 1):

$$x_i = l_{i1} \cos q_{i1} + l_{i2} \cos(q_{i1} + q_{i2}) + l_{i3} \cos(q_{i1} + q_{i2} + q_{i3}), \quad (1)$$

$$y_i = l_{i1} \sin q_{i1} + l_{i2} \sin(q_{i1} + q_{i2}) + l_{i3} \sin(q_{i1} + q_{i2} + q_{i3}), \quad (2)$$

where,  $l_{i1}$ ,  $l_{i2}$ , and  $l_{i3}$  are lengths of index finger and  $q_{i1}$ ,  $q_{i2}$ , and  $q_{i3}$  are angles of each corresponding joint. Similarly the position of thumb finger is evaluated as:

$$x_t = l_{t1} \cos q_{t1} + l_{t2} \cos(q_{t1} + q_{t2}), \quad (3)$$

$$y_t = l_{t1} \sin q_{t1} + l_{t2} \sin(q_{t1} + q_{t2}), \quad (4)$$

where,  $l_{t1}$  and  $l_{t2}$  are lengths of thumb finger and  $q_{t1}$  and  $q_{t2}$ , are angles of corresponding joints.

Based on above equation the Jacobian matrix for index finger is as:

$$J_i = \begin{bmatrix} \frac{\partial x}{\partial q_{i1}} & \frac{\partial x}{\partial q_{i2}} & \frac{\partial x}{\partial q_{i3}} \\ \frac{\partial y}{\partial q_{i1}} & \frac{\partial y}{\partial q_{i2}} & \frac{\partial y}{\partial q_{i3}} \end{bmatrix}, \quad (5)$$

and Jacobian for thumb finger is as:

$$J_t = \begin{bmatrix} \frac{\partial x}{\partial q_{t1}} & \frac{\partial x}{\partial q_{t2}} \\ \frac{\partial y}{\partial q_{t1}} & \frac{\partial y}{\partial q_{t2}} \end{bmatrix}. \quad (6)$$

### 3.2. Control Strategy

Virtual spring-damper hypothesis is suitable for point to point control. In precision grasping two approaches can be considered. 1) Defining a virtual spring damper between fingers tip and geometrical center of the object, which requires information about the object position and shape, and this information is not available in case of a prosthetic hand for the controller which is used in [13] 2) Defining a virtual spring damper between tips of two fingers, then fingers attract together and grasp the object in between, without exact knowledge of object position and shape. In this case the amputee should place the hand close to the object and in appropriate position. Besides, a virtual damper force is considered at each finger joint. The latter method is used and physical counterpart of virtual forces are depicted at Fig. 2.

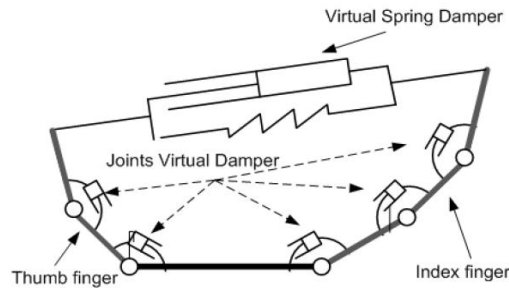


Fig. 2. Physical counterparts of the virtual forces

Higher values of  $k$  (virtual spring stiffness) results in faster movement of fingers as well as, higher grasping force. Thus by defining  $k$  proportional to EMG signal, amputee have control over speed of movement and grasping force. The damping coefficient of finger joints, can change the final shape of fingers. The joints with lower damping tends to move more, while higher damped joints move more. The appropriate values of damping are evaluated based on trial and error to reach positions close to normal hand and they are held constant for further simulations.

### 3.3. Numerical Simulation

In order to show the effectiveness of the proposed control strategy, numerical simulations were conducted to grasp two different objects, based on the physical parameters of a hand system and objects summarized in Table I.

The Adams software which is multi-body dynamic simulation software is used for numerical analysis. The software is capable to conduct information between Matlab/ Simulink software environment, hence the plant is modeled by Adams and controller is implemented in Matlab/Simulink.

TABLE I  
PARAMETERS USED FOR SIMULATION

Parameter	Value
index finger link 1 length	5 cm
index finger link 2 length	2.5 cm
index finger link 3 length	2.5 cm
thumb finger link 1 length	4 cm
thumb finger link 2 length	3 cm



distance between thumb and index	6 cm
damping at joints	0.01 kg/s
virtual damping ratio	1
virtual spring stiffness	50 N/m
rectangular object width	2 cm
circular object radius	2 cm

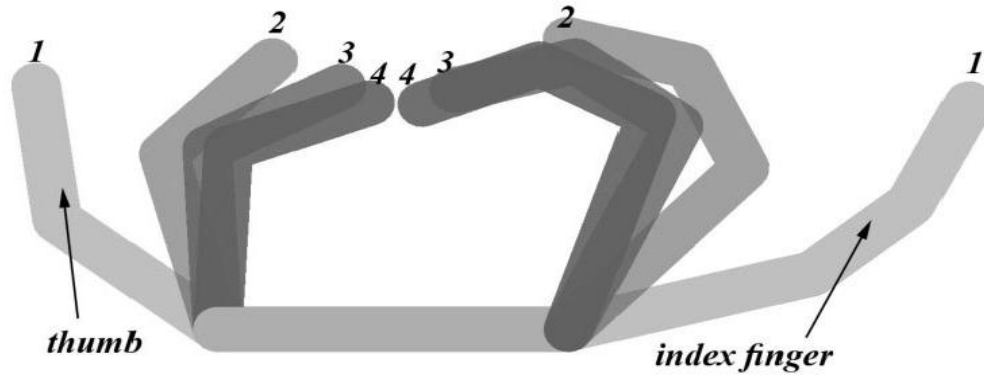


Fig. 3. Finger movements in 4 different position (0.25 sec. intervals)

For first simulation, two fingers are modeled without any object in between. As shown in Fig. 3, two fingers come together, and final position is close to normal hand coordination.

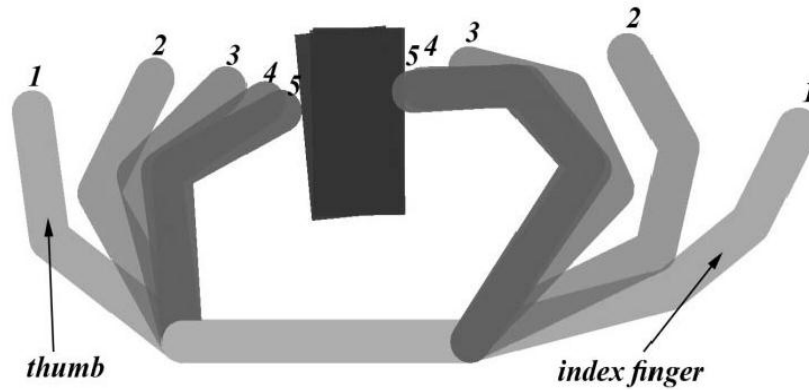


Fig. 4. Rectangular object grasping (0.25 sec intervals)

For the second simulation, a rectangular object is chosen to be grasped. The object is free to move in 2 dimensional plane, and contact and friction force are simulated between finger tip and the object. The object is placed at arbitrary final position of previous experiment. The finger movement at 0.25 sec time intervals and finger tip angles relative to palm are shown respectively in Figs. 4 and 5.

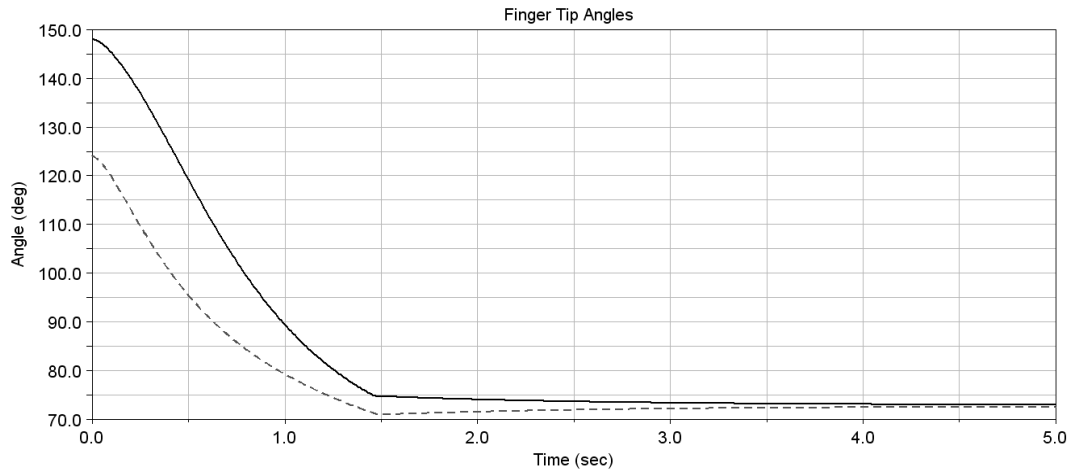


Fig. 5. Finger tips angle at rectangular object grasping (index finger solid line and thumb finer dashed line)

As it is shown after contact with object at approximately 1.5 second the angles are not changing much. The small changes are due to object movements toward left.

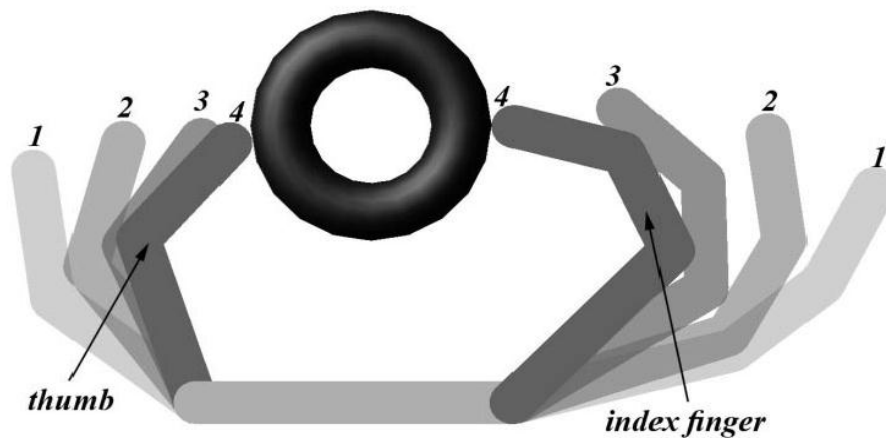


Fig. 6. Circular object grasping (0.25 sec intervals)

For third simulation a round object is selected. The object is not subjected to any constrain in 2 dimensional plane. The contact and friction force are defined between object and finger tip. The virtual spring coefficient which is proportional to EMG signal is assumed to be constant. Almost after 1 sec, the fingers contacted with the object. The finger movement at 0.25 sec time intervals and finger tip angles relative to palm are shown respectively in Figs. 6 and 7.

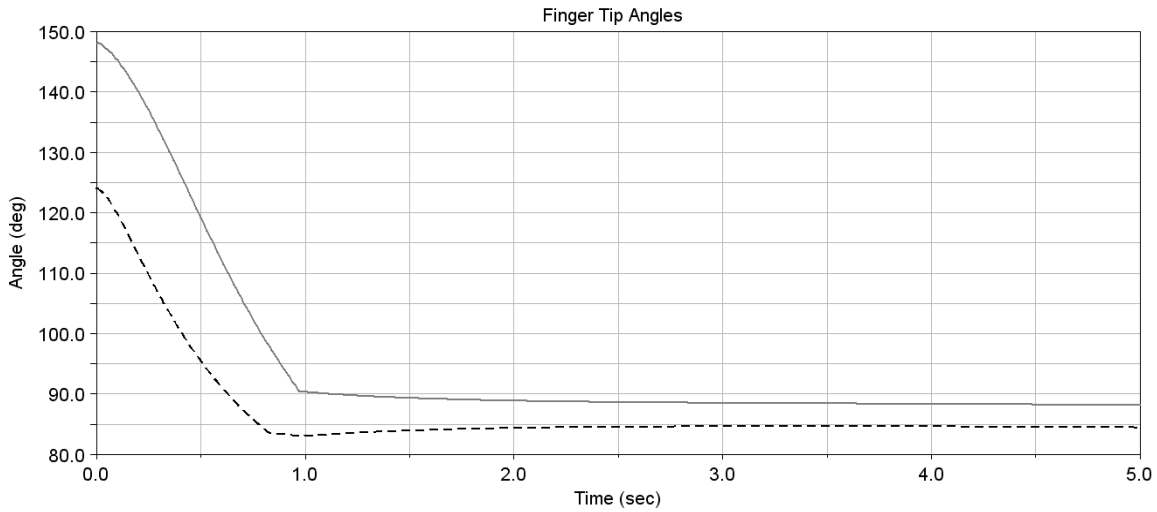


Fig. 7. Finger tips angle at circular object grasping  
(index finger solid line and thumb finer dashed line)

Appropriate object position and friction force between fingers and object are important parameters that help successful grasping. For the case of a round object if the object has inappropriate position or friction is not enough, the grasping might be unstable, but guaranteed successful grasping under all conditions require information about object shape and position which are not available for case of a prosthetic hand hence this control strategy is appropriate for most of the daily activities.

#### 4. Underactuated prosthetic hand

In underactuated mechanisms the number of actuators is less than their degree of freedom. These mechanisms are widely used in prosthetic hands because of two useful properties: the first advantage is less weight due to less actuator which is used in their design and the second advantage is easier control method.

Underactuation can be implemented through the use of passive elements like mechanical limits and springs leading to a mechanical adaptation of the finger to the shape of the object to be grasped. Underactuated robotic hands are the intermediate solution between fully actuated robotic hands for manipulation and simple grippers. It takes advantage of the mechanical intelligence embedded into the design of the hand allowing the shape adaptation of the fingers. In an underactuated finger, the actuation torque (or more generally wrench) is applied to the input of the finger and is transmitted to the phalanges through suitable mechanical design, e.g. linkages, pulleys and tendons, gears, etc.

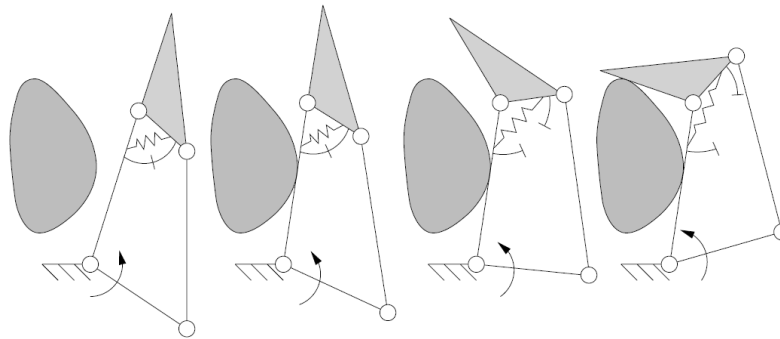


Fig 1. Closing sequence of a two-phalanx underactuated finger

An example of underactuated two-phalanx finger using linkages performing a typical closing sequence is illustrated in Fig. 1. The finger is actuated through the lower link, as shown by the arrow in the figure. Since there are two DOFs and one actuator, one (two minus one) elastic element is used. In the first two steps of the Figure, the finger behaves as a single rigid body in rotation about a fixed pivot. When the proximal phalanx makes contact with the object, the second phalanx is rotated away from the mechanical limit, and the finger is closing on the object since the proximal phalanx is constrained. During this phase, the actuator has to produce the force required to extend the spring. Finally, both phalanges are in contact with the object and the finger has completed the shape adaptation phase. The actuator force is distributed among the two phalanges in contact with the object. It should be noted that this sequence occurs with a continuous motion of the actuator. Notice also the mechanical limit that allows a pre-loading of the spring to prevent any undesirable motion of the second phalanx due to its own weight and/or inertial effects, and to prevent hyperextension of the finger. Springs are useful for keeping the finger from incoherent motion, but when the grasp sequence is complete, they still oppose the actuator force. Thus, they should be designed with the smallest stiffness possible, however sufficient to keep the finger from collapsing.

The basic property of the transmission system of an underactuated finger is to offer  $n > 1$  DOF produced with fewer than  $n$  actuators. In Figure 2, the transmission stage consists of a five-bar linkage (the base joint is a double pivot) with two DOFs but one angle is initially constrained to a particular value with the spring and the mechanical limit.

##### 4.2. Force analysis of underactuated finger

A two phalanx finger is considered in Fig.2. The input torque  $T_i$  is applied to the link  $a$  which transmits the torque to the whole finger through phalanges. A rotational spring with force  $T$  is located at  $O$  which moves the phalanx back to its original position in absence of external force. The closing process is shown in Fig 2. Providing a mechanical limit can help in order to make pre-tension for the spring to prevent undesirable motion of the second phalanx and also hyper-flexion of the finger.

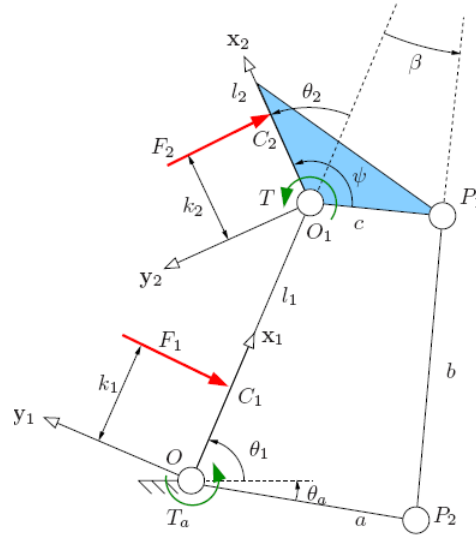


Fig.2. Underactuated hand model and exerted forces

To obtain the static model between inputs and outputs of the finger the virtual work principle is used. Equating the input and output virtual powers results

$$t^T \omega_i = f^T v \quad (1)$$

Where  $t$  is the input torque vector exerted by the actuator and the spring,  $\omega_i$  is the rotational velocity vector,  $f$  is the vector of contact forces, and  $v$  is the velocity of the contact points along the normal vector of each phalanx. Contact forces are assumed to be normal to the phalanges and without friction. Each element in the above equation can be expressed as

$$t = \begin{bmatrix} T_i \\ T = -k\Delta\theta_2 \end{bmatrix} \quad (2)$$

$$\omega_i = \begin{bmatrix} \dot{\theta}_1 \\ \dot{\theta}_2 \end{bmatrix} \quad (3)$$

$$f = \begin{bmatrix} f_1 \\ f_2 \end{bmatrix} \quad (4)$$

$$v = \begin{bmatrix} v_{C1}^T y1 \\ v_{C2}^T y2 \end{bmatrix} \quad (5)$$

The normal velocities of the contact point can be expressed as a Jacobian matrix  $J_T$  and the derivatives of the phalanx joint coordinates which is a natural choice, as  $v = J_T \dot{\theta}$  or

$$\begin{bmatrix} v_{C1}^T y1 \\ v_{C2}^T y2 \end{bmatrix} = \begin{bmatrix} k_1 & 0 \\ k_2 + l_1 \cos \theta_1 & k_2 \end{bmatrix} \begin{bmatrix} \dot{\theta}_1 \\ \dot{\theta}_2 \end{bmatrix} \quad (6)$$

Through differential calculus, one also can relate vector  $\omega_i$  to the derivatives of the phalanges joint coordinates defined previously with an actuation Jacobian matrix  $J_A$  as  $\dot{\theta} = J_A \omega_a$  or

$$\begin{bmatrix} \dot{\theta}_1 \\ \dot{\theta}_2 \end{bmatrix} = \begin{bmatrix} X & Y \\ 0 & 1 \end{bmatrix} \begin{bmatrix} \dot{\theta}_1 \\ \dot{\theta}_2 \end{bmatrix} \quad (7)$$

Where  $X=1$  and

$$Y = \frac{c[l_1 \sin(\theta_2 - \psi) - a \sin(\theta_1 - \theta_a + \theta_2 - \psi)]}{a[l_1 \sin(\theta_1 - \theta_a) + c \sin(\theta_1 - \theta_a + \theta_2 - \psi)]} \quad (8)$$

Finally, one obtains

$$f = J_T^{-T} J_A^{-T} t \quad (9)$$

which is the equation that provides a practical relationship between the actuator torque and contact forces. If the spring contribution is neglected the analytical expression are rather simple linear functions of the actuator torque,

$$f_1 = \frac{(k_2 - h \cos \theta_2) l_1}{a k_1 k_2 (\cot \beta \cos \alpha_1 + \sin \alpha_1)} T_a \quad (10)$$

$$f_2 = \frac{h}{a k_2 (\cot \beta \cos \alpha_1 + \sin \alpha_1)} T_a \quad (11)$$

where  $h = c(\cos(\theta_2 - \psi) - \sin(\theta_2 - \psi) \cot \beta)$  is the distance between point  $O_1$  and the intersection of lines  $(OO_1)$  and  $(P_1P_2)$ . Also,  $\alpha_1$  is the angle between link  $a$  and the first phalanx. It can be shown that

$$\cot \beta \cos \alpha_1 + \sin \alpha_1 = \frac{\sin X}{\sin \beta} \quad (12)$$

where  $X$  is the angle between links  $a$  and  $b$ .

### 4.3. Design optimization

After obtaining the forces equation two consideration form the guidelines for design parameters selection: first grasp should be stable which means ejection should be prevented and differences between the phalanx forces should be minimum possible value. In Ejection phenomena the finger slide and push the object out instead of a secure grasping. To prevent ejection the exerted forces by each phalanx to the object should be positive. It is also desirable that forces at each phalanx to be close to their mean value and force distribute evenly between phalanxes which is referred to as force isotropy. So the conditions which should be satisfied can be expressed as:

$$\begin{cases} f_1 = f_2 \\ f_1 > 0 \text{ and } f_2 > 0 \end{cases} \quad (13)$$

In order to have force isotropy it is necessary that forces by each phalanx are equal, but forces are function of contact position and  $\theta_2$  angle hence it is a local property. Therefore if the object moves these conditions are not true anymore. However in this case, another step is necessary since  $h$  is a function of the design parameters and the angle  $\theta_2$ . Furthermore, many design variables are available to satisfy the latter equation, namely  $a$ ,  $b$ ,  $c$ , and  $d$ .

For instance, if one chooses  $a = b$ , a known  $c$  (e.g. resulting from minimal distance considerations) and  $\psi = \frac{\pi}{2}$ ,  $a$  is completely defined as

$$a = \frac{2 l_1 c \sin \theta_2 + c^2 + l_1^2 \sqrt{A}}{B} \quad (14)$$

with ,

$$A = (C - 1)((C - 1)c^2 + 2cCl_1 \sin \theta_2) + C^2 l_1^2 \quad (15)$$

$$B = -c^2 + Cc^2 - l_1 c \sin \theta_2 + 2Cl_1 c \sin \theta_2 + Cl_1^2 \quad (16)$$

$$C = -K\theta_2 + \frac{k_2}{k_2 + l_1 \cos \theta_2 + k_1} \quad (17)$$

The above mentioned relationship can be used in order achieving isotropic design. However, the isotropic property is not very robust with respect to design parameters, so it suggests using the following method.

If one obtains an isotropic and therefore stable design for a particular contact set  $(k_1, k_2, \theta_2)$ , it may be of interest that the finger is also robust with respect to ejection around this isotropic point, in order to ensure that a deviation from this configuration does not lead to an unstable grasp. The final aim is to guaranty stability for all grasps if possible and satisfy certain “quality” based indices like the isotropy. An index that can be used to ensure the grasp stability, even if the proximal contact is lost, is:

$$\mu = \frac{\int_W \delta(k_2, \theta_2) dk_2 d\theta_2}{\int_W dk_2 d\theta_2} \quad (18)$$

Where  $\delta(k_2, \theta_2)$  is a Kronecker-like symbol for characterizing the stability of the contact situation:

$$\delta(k_2, \theta_2) = \begin{cases} 1 & \text{if the final grasp is stable} \\ 0 & \text{otherwise} \end{cases} \quad (19)$$

This index is the ratio between the stable and unstable areas in the grasp-state plane of the finger. Contour plots of the index  $\mu$  is illustrated in Fig 3. for a mechanically actuated finger. The optimal design parameter values can be obtained using the following plot. In our design equal lengths are considered for both phalanxes ( $l_2/l_1=1$ ), so the optimal value for  $c/a$  is around 0.6.

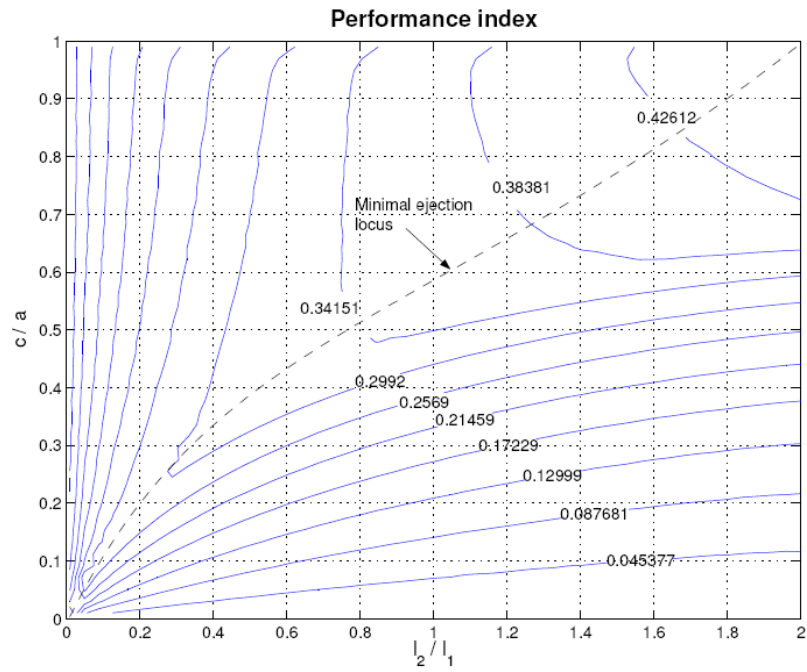


Fig 3. Performance index for linkage driven 2 phalanx underactuated hand

#### 4.4. Control system

The control is aimed at exploiting the main properties of underactuation to perform motion tasks close to reference angles obtained by EMG signal. The ordinary task considered for design and development of the motion control law is the finger preshaping for the palmar grasp of a cylindrical object. Kinematic coupling among the joints is related by the relation

$$x_s = l_1\theta_1 + l_2(\theta_1 + \theta_2) \quad (20)$$

$$\dot{x}_s = l_1\dot{\theta}_1 + l_2(\dot{\theta}_1 + \dot{\theta}_2) \quad (21)$$

The dynamic relation among the joints are derived in equations (10) and (11).

##### 4.4.1. PD Control in the joint space with elastic compensation

Dynamic relation (20) and (21) is used to actively control the first joint and passively move the second joint. The proposed control law is a modified version of the standard PD control in the joint space with gravity compensation and is expressed as

$$T_i = K_p\tilde{\theta} - K_D\dot{\theta} + g(\theta) + T_e \quad (22)$$

Where  $\tilde{\theta} = \theta_D - \theta$  is the joint position error defined as the difference between the reference set point  $\theta_D$  and the current joint angle  $\theta$ ,  $g(\theta)$  is the estimation of joint gravitational torque, and  $K_p$  and  $K_D$  are the diagonal gain matrices for the proportional and derivative control actions, respectively. In addition to the standard PD control plus gravity compensation, an elastic term is introduced in order to compensate for the preload spring located between phalanxes joint.

The joint elastic torque is expressed as  $T_e = k\Delta\theta_2$ .

#### 4.5. Numerical simulation

Based on results of optimal design a model of two phalanx finger is made in Adams software linked with Matlab/Simulink, which is shown in Fig. 3. Both phalanxes has the equal length and c/a ratio is 0.6 based on optimal design analysis. Torsion spring is located between two phalanxes. The revolute joint is located at joints and a motor is moving the finger which is shown by round arrow. A circular object is chosen to be grasped and the proposed controller is used to control finger movement.

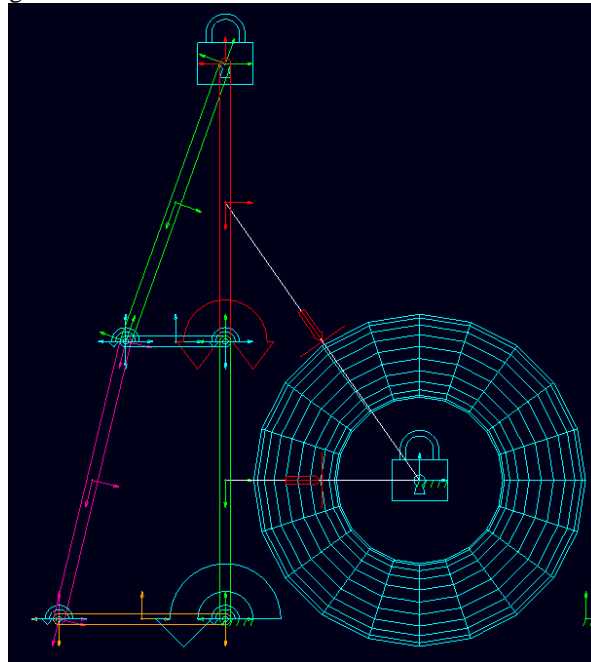


Fig.3. The two phalanx finger modeled in Adams software



By applying the control algorithm to the mechanism the finger can grasp the object. The grasping sequence is shown in Fig. 4 .

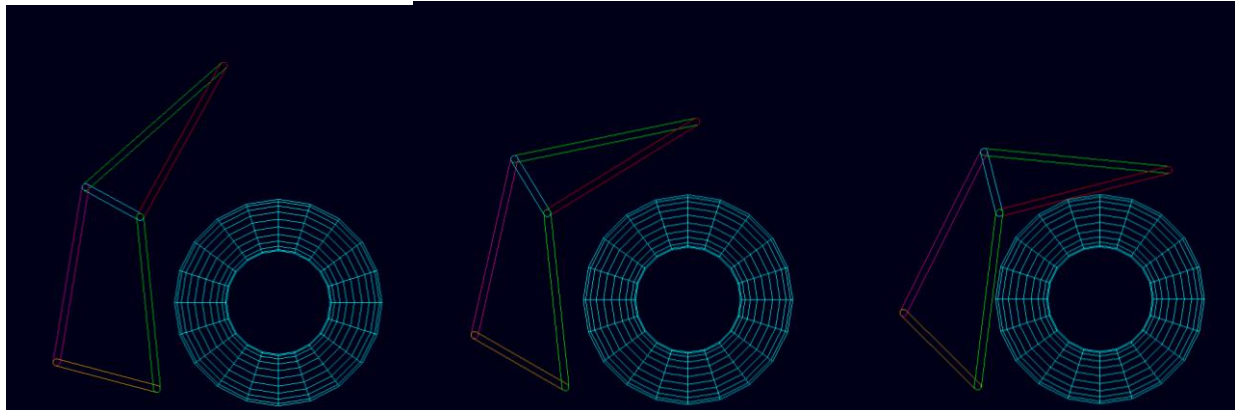


Fig. 4. The grasping sequence of a circular object by underactuated hand

The finger tip angle respect to horizontal plane is shown in Fig. 5. It starts from 90 degree and after first phalanx has contact with the object the rate of change of angle is changed.

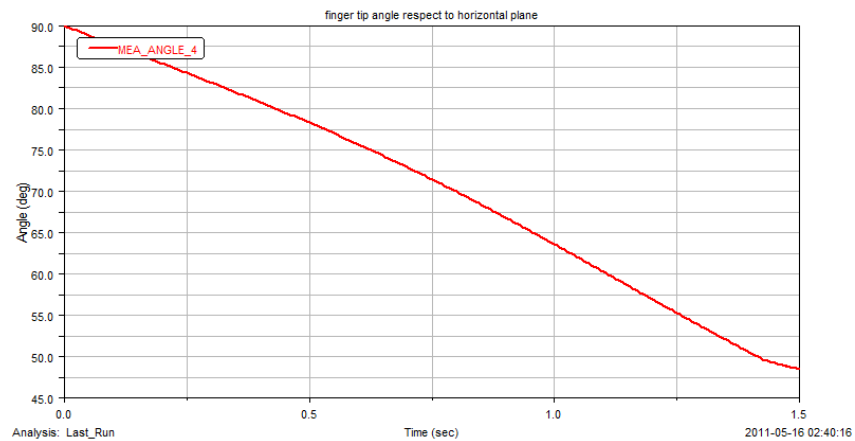


Fig. 5. Finger tip angle respect to horizontal plane for underactuated hand

Angle between two phalanxes is shown in Fig. 6. The angle starts from 180 degree and gradually changes until second phalanx touches the object.

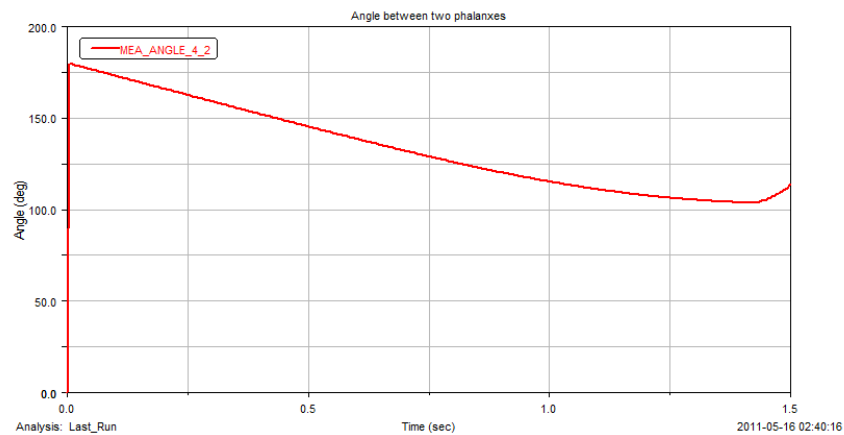


Fig.6. Angle between two phalanxes for underactuated hand

#### 4.6. Comparison study between fully actuated and underactuated hand

Two general design which are fully actuated and underactuated and appropriate control methods for each of them are provided for prosthetic hand. In order to compare the functionality of these two methods a fully actuated finger with the same dimension and with a similar object to grasp is simulated. Power grasping algorithm which described before is used in order to control the movement. The sequence of movement is shown in Fig. 7. The finger tip angle respect to horizontal plane is shown in Fig. 8 and the angle between two joints is shown in Fig. 9.

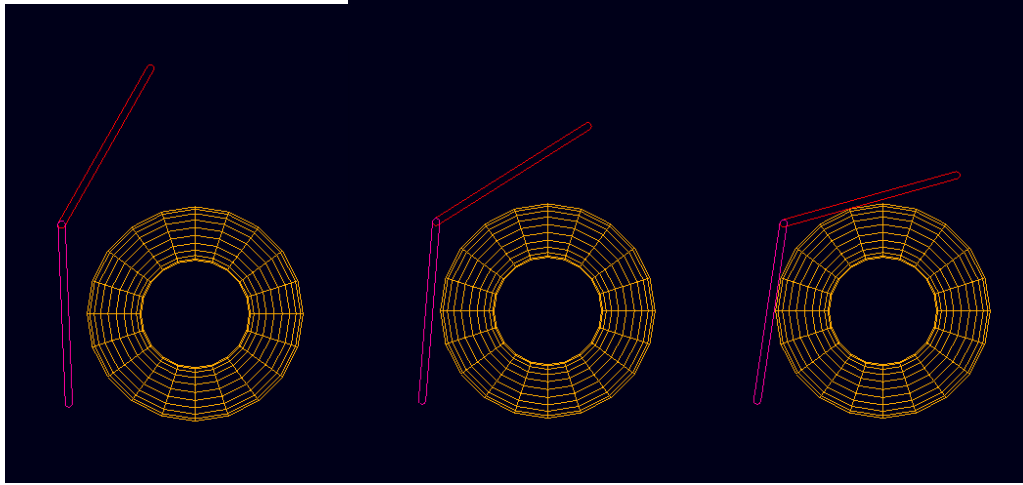


Fig. 7. The grasping sequence of a circular object by a fully actuated hand

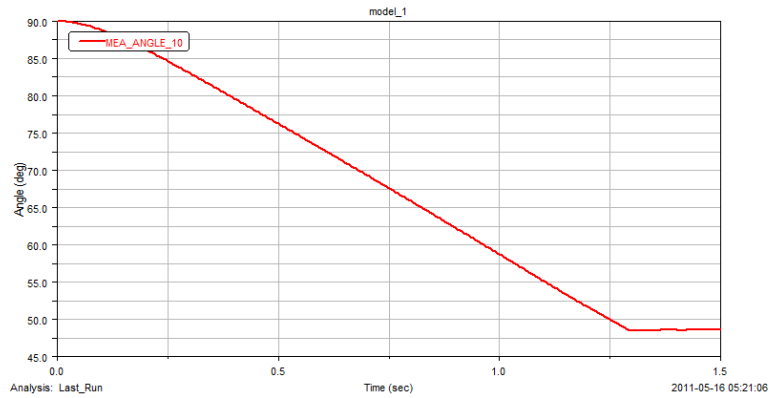


Fig.8. Finger tip angle respect to horizontal plane for fully actuated hand

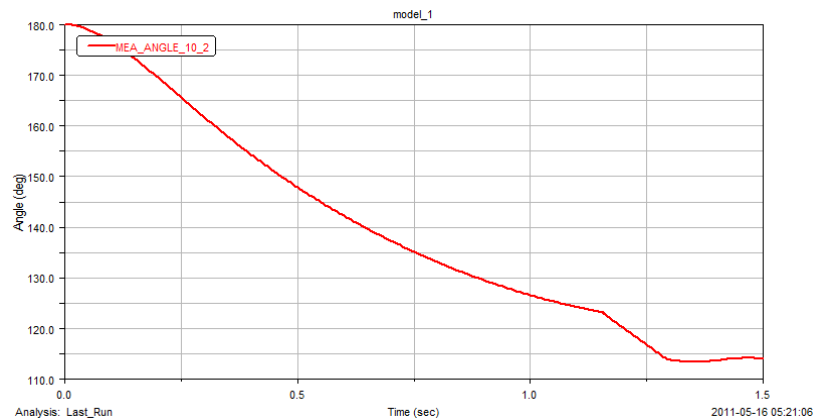


Fig.9. Angle between two phalanxes for fully actuated hand

As we can see both methods are capable to perform grasping and the graphs are very similar for both methods.

## 5. Robust Control of a Prosthetic Hand

A finger can be considered as a 3 link robot, while in extracting the model for angle estimation, the PIP joint (the second) angle is considered, the third link angle normally has about 70% of the second joint angle and the first link angle is not considered in this research. As a result a two-link planar robot is considered as a plant to investigate the control approach performance.

A dynamic model can be derived from the general Lagrange equation method. The modeling of a two-link planar nonlinear robotic system with assumption of only masses in the two joints can be found in the literature, e.g., [3, 4]. However, in practice, the robot arms have their mass distributed along their arms, not only masses in the joints as assumed. Thus, it is desired to develop a detailed model for two-link planar robotic systems with the mass distributed along the arms. We present a new detailed consideration of any mass distributions along robot arms in addition to the joint mass. Moreover, it is also necessary to consider numerous uncertainties in parameters and modeling. Thus, robust control, robust adaptive control and learning control become important when knowledge of the system is limited. We need robust stabilization of uncertain robotic systems and furthermore robust performance of these uncertain robotic systems. Robust stabilization problem of uncertain robotic control systems has been discussed in [21-23, 24-26] and many others. Also, adaptive control methods have been discussed in [21,27] and many others. Because the closed-loop control system pole locations determine internal stability and dominate system performance, such as time responses for initial conditions, papers [26,28] consider a robust pole clustering in vertical strip on the left half splane to consider robust stability degree and degree of coupling effects of a slow subsystem (dominant model) and the other fast subsystem (non-dominant model) in a two-time-scale system. A control design method to place the system poles robustly within a vertical strip has been discussed in [26, 28-30], especially [26] for robotic systems. However, as mentioned above, for accurate prosthetic hand control there is a need of a detailed and practical two-link planar robotic system modeling with the practically distributed robotic arm mass for control.

Therefore a practical and detailed two-link planar robotic systems modeling and a robust control design for this kind of nonlinear robotic systems with uncertainties considered for robust control approach with both  $H_\infty$  disturbance rejection and robust pole clustering in a vertical strip. The design approach is based on the new developing two-link planar robotic system models, nonlinear control compensation, a linear quadratic regulator theory and Lyapunov stability theory.

### 5.1. MODELING OF PROSTHETIC HAND SYSTEMS

The dynamics of a rigid revolute robot manipulator can be described as the following nonlinear differential equation [21, 22, 26, 30]:

$$\mathbf{F}_c = \mathbf{M}(\mathbf{q})\ddot{\mathbf{q}} + \mathbf{V}(\mathbf{q}, \dot{\mathbf{q}})\dot{\mathbf{q}} + \mathbf{N}(\mathbf{q}, \dot{\mathbf{q}}) \quad (4)$$

$$\mathbf{N}(\mathbf{q}, \dot{\mathbf{q}}) = \mathbf{G}(\mathbf{q}) + \mathbf{F}_d\dot{\mathbf{q}} + \mathbf{F}_s(\dot{\mathbf{q}}) \quad (5)$$

where  $\mathbf{M}(\mathbf{q})$  is an  $n \times n$  inertial matrix,  $\mathbf{V}(\mathbf{q}, \dot{\mathbf{q}})$  an  $n \times n$  matrix containing centrifugal and coriolis terms,  $\mathbf{G}(\mathbf{q})$  an  $n \times 1$  vector containing gravity terms,  $\mathbf{q}(t)$  an  $n \times 1$  joint variable vector,  $\mathbf{F}_c$  an  $n \times 1$  vector of control input functions (torques, generalized forces),  $\mathbf{F}_d$  an  $n \times n$  diagonal matrix of dynamic friction coefficients, and  $\mathbf{F}_s(\dot{\mathbf{q}})$  an  $n \times 1$  Nixon static friction vector.

However, the dynamics of the robotic system (4,5) in detail is needed for designing the angle control, i.e., especially, what matrices  $\mathbf{M}(\mathbf{q})$ ,  $\mathbf{V}(\mathbf{q}, \dot{\mathbf{q}})$  and  $\mathbf{G}(\mathbf{q})$  are.

Consider a two-link planar robotic system representing the prosthetic hand finger in Fig. 8, where the system has its joint mass  $\mathbf{m}_1$  and  $\mathbf{m}_2$  of joints 1 and 2, respectively, robot arms mass  $\mathbf{m}_{1r}$  and  $\mathbf{m}_{2r}$  distributed along arms 1 and 2 with their lengths  $\mathbf{l}_1$  and  $\mathbf{l}_2$ , generalized coordinates  $\mathbf{q}_1$  and  $\mathbf{q}_2$ , i.e., their rotation angles,  $\mathbf{q} = [\mathbf{q}_1, \mathbf{q}_2]$ , control torques (generalized forces)  $\mathbf{f}_1$  and  $\mathbf{f}_2$ ,  $\mathbf{F}_c = [\mathbf{f}_1, \mathbf{f}_2]$ .

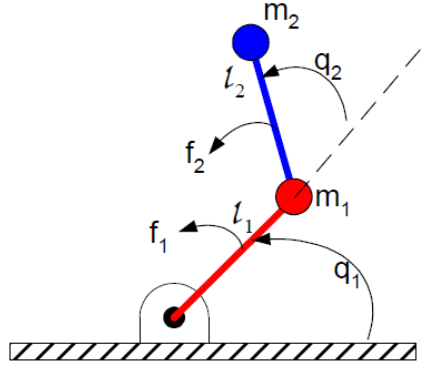


Fig 8- A two link robot system representing prosthetic hand

## 5.2. ROBUST CONTROL

In view of possible uncertainties, the terms in (4,5) can be decomposed without loss of any generality into two parts, i.e., one is known parts and another is unknown perturbed parts as follows [22, 26]:

$$\mathbf{M} = \mathbf{M}_0 + \Delta\mathbf{M}, \mathbf{N} = \mathbf{N}_0 + \Delta\mathbf{N}, \mathbf{V} = \mathbf{V}_0 + \Delta\mathbf{V} \quad (6)$$

where  $\mathbf{M}_0, \mathbf{N}_0, \mathbf{V}_0$  are known parts,  $\Delta\mathbf{M}, \Delta\mathbf{N}, \Delta\mathbf{V}$  are unknown parts. Then, the models in previous section can be used not only for the total uncertain robotic systems with uncertain parameters, but also for a known part with their nominal parameters of the systems.

Following [26], we develop the torque control law as two parts as follows:

$$\mathbf{F}_c = \mathbf{M}_0(\mathbf{q})\ddot{\mathbf{q}}_d + \mathbf{V}_0(\mathbf{q}, \dot{\mathbf{q}})\dot{\mathbf{q}} + \mathbf{N}_0(\mathbf{q}, \dot{\mathbf{q}}) - \mathbf{M}_0(\mathbf{q})\mathbf{u} \quad (7)$$

where the first part consists of the first three terms in the right side of (7), the second part is the term of  $\mathbf{u}$  that is to be designed for the desired disturbance rejection and pole clustering,  $\mathbf{q}_d$  is the desired trajectory of  $\mathbf{q}$ , however, the coefficient matrices are with all nominal parameters of the system. Define an error between the desired  $\mathbf{q}_d$  and the actual  $\mathbf{q}$  as:

$$\mathbf{e} = \mathbf{q}_d - \mathbf{q} \quad (8)$$

From (4) and (6)–(8), it yields:

$$\ddot{\mathbf{e}} = \mathbf{M}^{-1}(\mathbf{q})[\Delta\mathbf{M}(\mathbf{q})\ddot{\mathbf{q}}_d + \Delta\mathbf{V}(\mathbf{q}, \dot{\mathbf{q}})\dot{\mathbf{q}} + \Delta\mathbf{N}(\mathbf{q}, \dot{\mathbf{q}}) + \mathbf{M}_0(\mathbf{q})\mathbf{u}] = \mathbf{w} + \mathbf{E}\dot{\mathbf{e}} + \mathbf{F}\mathbf{u} + \mathbf{u} \quad (9)$$

$$\mathbf{E} = -\mathbf{M}^{-1}(\mathbf{q})\Delta\mathbf{V}(\mathbf{q}, \dot{\mathbf{q}}), \quad \mathbf{F} = -\mathbf{M}^{-1}(\mathbf{q})\Delta\mathbf{M}(\mathbf{q}), \quad \mathbf{w} = -\mathbf{F}\ddot{\mathbf{q}}_d - \mathbf{E}\dot{\mathbf{q}}_d + \mathbf{M}^{-1}\Delta\mathbf{N} \quad (10)$$

From [26], we can have the fact that their norms are bounded:

$$\|\mathbf{w}\| < \delta_w, \|\mathbf{E}\| < \delta_e, \|\mathbf{F}\| < \delta_f \quad (11)$$

Then, it leads to the state space equation as:

$$\dot{\mathbf{x}} = \mathbf{A}\mathbf{x} + \mathbf{B}\mathbf{u} + \mathbf{B}[0 \ \mathbf{E}]\mathbf{x} + \mathbf{B}\mathbf{F}\mathbf{u} + \mathbf{B}\mathbf{w} \quad (11)$$

$$\mathbf{x} = \begin{bmatrix} \mathbf{e} \\ \dot{\mathbf{e}} \end{bmatrix} = [\mathbf{e}_1 \ \mathbf{e}_2 \ \dot{\mathbf{e}}_1 \ \dot{\mathbf{e}}_2]', \quad \mathbf{A} = \begin{bmatrix} 0 & \mathbf{I} \\ 0 & 0 \end{bmatrix}, \quad \mathbf{B} = \begin{bmatrix} 0 \\ \mathbf{I} \end{bmatrix} \quad (12)$$

The last three terms denote the total uncertainties in the system. The desired trajectory  $\mathbf{q}_d$  for manipulators to follow is to be bounded functions of time. Its corresponding velocity  $\dot{\mathbf{q}}_d$  and acceleration  $\ddot{\mathbf{q}}_d$ , as well as itself  $\mathbf{q}_d$ , are assumed to be within the physical and kinematic limits of manipulators. They may be conveniently generated by a model of the type:

$$\ddot{\mathbf{q}}_d(t) + \mathbf{K}_v\dot{\mathbf{q}}_d(t) + \mathbf{K}_p\mathbf{q}_d(t) = \mathbf{r}(t) \quad (13)$$

where  $\mathbf{r}(t)$  is a 2-dimensional driving signal and the matrices  $\mathbf{K}_v$  and  $\mathbf{K}_p$  are stable.

The design objective is to develop a state feedback control law for control  $\mathbf{u}$  in (7) as

$$\mathbf{u}(t) = \mathbf{K}\mathbf{x}(t) \quad (14)$$

such that the closed-loop system:

$$\dot{\mathbf{x}} = (\mathbf{A} - \mathbf{BK} + \mathbf{B}[0 \ \mathbf{E}] - \mathbf{BFK})\mathbf{x} + \mathbf{B}\mathbf{w} \quad (15)$$

has its poles robustly lie within a vertical strip  $\Omega$ :

$$\lambda(\mathbf{A}_c) \in \Omega = \{s = x + jy \mid -\alpha_2 < x < -\alpha_1 \leq 0\} \quad (16)$$

and a  $\delta$ -degree disturbance rejection from the disturbance  $\mathbf{w}$  to the state  $\mathbf{x}$ , i.e.,

$$\|\mathbf{T}_{xw}(s)\|_\infty = \|(s\mathbf{I} - \mathbf{A}_c)^{-1}\mathbf{B}\|_\infty \leq \delta \quad (17)$$

$$\mathbf{A}_c = \mathbf{A} - \mathbf{BK} + \mathbf{B}[0 \ \mathbf{E}] - \mathbf{BFK} \quad (18)$$

we derive the following robust control law to achieve this objective is discussed in [20,26].

Consider prosthetic hand uncertain system (15) with (4)–(18) where the unstructured perturbations in (10) with the norm bounds in (11), the disturbance rejection index  $\delta \geq 0$  in (17), the vertical strip  $\Omega$  in (16) and a matrix  $Q > 0$ .

With the selection of the adjustable scalars  $\varepsilon_1$  and  $\varepsilon_2$ , i.e.,

$$(1 - \delta_f)/\delta_e > \varepsilon_1 > 0, (1 - \delta_f - \varepsilon_1 \delta_e)\delta > \varepsilon_2 > 0 \quad (19)$$

there always exists a matrix  $P > 0$  satisfying the following Riccati equation:

$$A'_{\alpha 1}P + PA_{\alpha 1} - \left(1 - \delta_f - \varepsilon_1 \delta_e - \frac{\varepsilon_2}{\delta}\right)PBB'P + \left(\frac{\delta_e}{\varepsilon_1}\right)I + \left(\frac{1}{\varepsilon_2 \delta}\right)I + Q = 0 \quad (20)$$

where

$$A_{\alpha 1} = A + \alpha_1 I = \begin{bmatrix} \alpha_1 I_2 & I_2 \\ 0 & \alpha_1 I_2 \end{bmatrix} \quad (21)$$

Then, a robust pole-clustering and disturbance rejection control law in (7) and (14) to satisfy (17) and (18) for all admissible perturbations  $E$  and  $F$  in (11) is as:

$$u = -Kx = -rB'Px \quad (22)$$

if the gain parameter  $r$  satisfies the following two conditions:

$$(i) \quad r \geq 0.5 \text{ and} \quad (23)$$

$$(ii) \quad 2\alpha_2 P + A'P + PA - \left(\frac{\delta_e}{\varepsilon_1}\right)I - [2r(1 + \delta_f) + \varepsilon_1 \delta_e]PBB'P > 0 \quad (24)$$

Proof for the approach is provided in [26, 28].

It is also noticed that:

$$BB' = \begin{bmatrix} 0 & 0 \\ 0 & I_2 \end{bmatrix} \quad (25)$$

It is evident that condition (i) is for the  $\alpha_1$  degree stability and  $\delta$  degree disturbance rejection, and condition (ii) is for the  $\alpha_2$  degree decay, i.e., the left vertical bound of the robust pole-clustering.

There is always a solution for relative stability and disturbance rejection in this form. It is because the Riccati equation (20) guarantees a positive definite solution matrix  $P$ , and thus there exists a Lyapunov function to guarantee the robust stability of the closed loop uncertain robotic systems. The nonlinear compensation part in (7) has a similar function to a feedback linearization.

### 5.3. NUMERICAL SIMULATION

Based on the proposed control approach, a two link robot is modeled considering uncertainties. Then the input signal from sEMG-Angle estimation model is used as reference signal to the plant and the performance is evaluated.

The system parameters are: link mass:  $m_2 = m_2 = 0.05\text{Kg}$ , lengths  $l_1 = l_2 = 0.03\text{m}$ , angular positions  $q_1, q_2$  (rad), applied, torques  $f_1, f_2$  (Nm).

The initial states are set as  $q_1(0) = q_2(0) = 0$ , and  $\dot{q}_1(0) = \dot{q}_2(0) = 0$ . The parametric uncertainties are assumed to satisfy (11) with  $\delta_f = 0.05$ ,  $\delta_e = 0.4$ ,  $\delta_n = 0.1$ . Select the adjustable parameters  $\varepsilon_1 = 0.01$ ,  $\varepsilon_2 = 0.01$  from (19), disturbance rejection index  $\delta = 0.1$ , the relative stability index  $\alpha_1 = 0.1$ , and the left bound of vertical strip  $\alpha_2 = 2000$  since we want a fast response. We solved the Riccati equation (20)

to get the solution matrix  $P$  and the gain matrix as:

$$P = \begin{bmatrix} 12693I_2 & 1584I_2 \\ 1584I_2 & 1643I_2 \end{bmatrix}$$

$$K = rB'P = [950I_2 \ 985I_2]$$

Numerical simulation is done in Matlab software. For the plant the above mentioned parameters is used. Two sets of simulation are done. In the first simulation nominal plant is used and for the second simulation the perturbed model considering uncertainty is tested. The input signal for both simulations is measured angles from the above mentioned experiments from PIP joint. For the third joint the 70% of the measured angle of PIP joint used which is a good estimate of that signal.

The system response with nominal plant and perturbed plant to the input signal respectively are shown in Fig. 9 and Fig. 10. As it is shown the input and output signals are close and system is capable of following the command signal with sufficient accuracy. Obviously the system has a better performance in case of nominal plant compare to the perturbed model in which the uncertainties are applied.

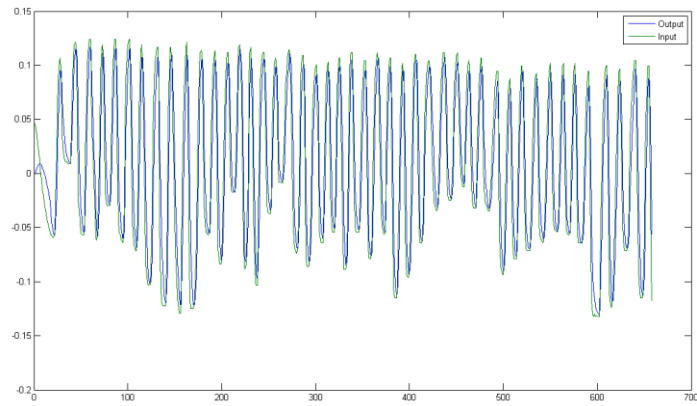


Fig. 9- System response to the nominal plant

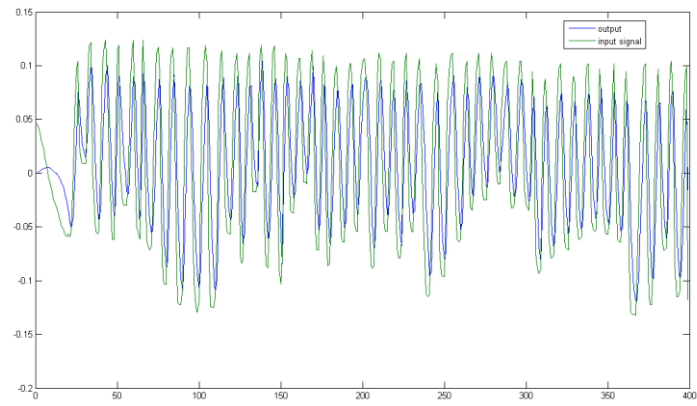


Fig. 9- System response to the perturbed plant

## 6. Stable Grasping by Prosthetic Hand Using Tactile Feedback and Hand Kinematics

Grasp planning is a fundamental problem in the field of robotics that has been attracting an increasing number of researchers [4], [15], [9], [13], [12]. One fact about many existing grasp planning algorithms is that they all require some information about the object to be grasped, i.e. either a 2D image as required in [15], [12] or a full 3D geometric model as in [4]. In case of a prosthetic hand although visual information might exist by amputee but the data regarding object shape is not directly available for prosthetic hand controller.

As human beings, it is intuitive and straightforward for us to grasp objects even when we cannot see them. Lederman and Klatzky have shown [8] that humans have the ability to “blindly” recognize objects with a high degree of accuracy. Humans can also create stable grasps on unknown objects in the total absence of any visual feedback. This ability is sorely lacking with current robots that are performing grasping tasks. Using tactile sensing for object recognition has been explored by many researchers. Some recent work includes [16], [7], [11], [19] using tactile exploration for grasping, Bierbaum *et al.* proposed a method to generate grasp affordances based on reconstructed faces of an object through tactile exploration [1]. In this report, we are attempting to use non-visual tactile and kinematic feedback to predict stable grasps on an unknown object for a 3 fingers prosthetic hand which is capable of expanding to a 5 fingers hand.

We take a machine learning approach to this problem. A problem with this approach is to generate datasets of reasonable size that encode tactile and kinematic information on robotic grasps. To overcome this, we use a tactile simulator on a large database of objects to be grasped.

The Columbia Grasp Database (CGDB) [6] consists of over 300,000 stable grasps over 7,256 objects and for several robotic hands, including Barrett hands of different surface materials and a simulated human hand. It provides us with a pool of robotic grasp data from which we can simulate a tactile sensor system and collect useful tactile feedback. It then allows us to use this simulated tactile feedback data to learn the stability of a prosthetic hand grasp.

In Section II, we describe a soft finger contact model used to simulate tactile feedback. In Section III, we describe the procedure to collect simulated tactile feedback from grasps in CGDB. In Section IV, we talk about the feature vectors we used to represent each grasp and build an SVM that accepts these feature vectors as input to predict the stability of the corresponding grasp. Simulations are described and discussed in Section V, followed by conclusions in Section VI.

### 6.1. SOFT FINGER CONTACT MODEL

Tactile sensors play an important role in representing the contacts between the surface of the hand and the object that are touching each other. The output of the tactile sensors around each contact is characterized by the forces applied at each sensor cell. So, a reasonable contact model that approximates the contact region and the pressure distribution is necessary for simulating a reasonable tactile feedback. Pezzementi *et al.* [18] used a point spread function model to simulate the response of a tactile sensor system. In our approach, we build our tactile simulation system based on a soft finger contact model proposed by Ciocarlie *et al.* [3]. We briefly introduce this model as follows.

#### A. Contact Region Approximation

In *GraspIt!* each contact is initially considered as a point contact since the two bodies, i.e. the hand and the object, are assumed as rigid bodies. In the real world, however, the hand and the object in contact are actually deformable to some extent, resulting in an area in contact rather than a point. A point contact assumption then no longer holds reasonably. To simulate the contact region between the two bodies touching each other, we use a soft finger contact model as is developed in [3]. This model takes into account the local geometry and structure of the objects in contact and captures frictional effects such as coupling between tangential force and frictional torque. It locally approximates the surfaces of the two touching bodies as

$$z_i = A_i x^2 + B_i y^2 + C_i xy, \quad i \in \{1, 2\} \quad (1)$$

where the local contact coordinate system has its origin at the center of the contact and the  $z$  axis aligned with the contact normal. The subscript  $i$  distinguishes the contacting bodies from each other.

Table I Configuration of Sensor Pads on a Prosthetic Hand			
Location	Num. of Cells	Res.(mm)	Grid
Palm	24	10*10	4*6
Mid-Digit	24	6*6	8*3
Fingertip	22	6*6	7*3+1 tip

Table II TEST ACCURACY ON 5641 GRASPS (%)		
Classification Accuracy	False Neg. Predct.	False Pos. Predct.
70.4	19.4	10.2

The separation between the two surfaces  $h$  is

$$h = (A_1 - A_2)x^2 + (B_1 - B_2)y^2 + (C_1 - C_2)xy \quad (2)$$

By choosing the orientation of the  $x$  and  $y$  axes so that the term in  $xy$  vanishes, we can end up with the separation  $h$  between the two surfaces in the form of

$$h = \frac{1}{2R}x^2 + \frac{1}{2R}y^2 \quad (3)$$

where  $R$  and  $R$  are the relative radii of curvature of the objects in contact, depending only on their local geometry.

## B. Pressure Distribution

After a contact region is determined, we consider how the forces are formed within the contact region so that the response of the corresponding tactile sensor cells can be analyzed and evaluated. To express the pressure distribution inside a contact region using non-planar models that take into account the local geometry of the objects involved, we choose a Hertzian model as used in [3]. In this model, the ratio of frictional torque to contact load which is used to compute the eccentricity parameter of the friction ellipsoid can be obtained from

$$\frac{\max(\tau_n)}{P} = \frac{3\pi}{16} \mu \sqrt{ab} \quad (4)$$

where  $\mu$  is the frictional coefficient,  $\tau_n$  is a frictional moment about the contact normal,  $P$  is the contact load, and  $a$  and  $b$  are the lengths of the semi-axes.

## 6.2. TACTILE SENSOR SIMULATION

### A. Tactile Sensor Configuration of a Prosthetic Hand

In prosthetic hand simulation the tactile sensors attached on the surfaces of the palm, the mid-digit links and the fingertip links. The tactile sensor system contains seven major sensor pads which cover many possible hand-object contact points of the hand. Each pad has 22 to 24 tactile sensor cells which results in a 162-cell sensor system. The configuration of these sensor pads and sensor cell arrangement is described in Table I.

#### Algorithm 1: Computing tactile feedback

**Input:** A robotic grasp with a list of point contacts between the hand and the object

**Output:** Seven 2D arrays that carry the simulated tactile sensor values of the corresponding sensor cells

1. Initialize the output tactile sensor cell arrays to zero's
2. foreach point contact do
3.   Calculate the relative radii at the contact
4.   Calculate the contact region
5.   Discretize the contact region to 10 \* 10 sub-regions
6.   Calculate the forces within each discretized sub-region according to the pressure distribution



```

7.  foreach discretized contact sub-region do
8.    foreach tactile sensor cell do
9.      if the discretized contact sub-region overlays on the tactile sensor cell
10.     then
11.       Accumulate the force of the discretized contact sub-region onto the overlaying tactile sensor cell
12.     end
13.   end
14. end
15. end
16. Return the sensor cell arrays

```

### B. Generating Tactile Feedback from the CGDB

Based on the soft finger contact model, we can compute the contact region for a hand-object contact as well as the pressure distribution within the contact region. Since a tactile sensor cell performs as an atomic sensing unit, we discretized the soft finger contact region so that we can accumulate the total forces within each discrete part and use this to compute the forces sensed on each corresponding tactile sensor cell.

We summarize the procedure to generate the tactile feedback of a robotic grasp in Algorithm 1. Figure 2 shows an example of a simulated tactile feedback.

### 6.3. LEARNING THE STABILITY OF A ROBOTIC GRASP

Following the explanation of the simulation process, we now discuss the way we built an SVM classifier that predicts the stability of a given robotic grasp. Once trained, this classifier can be used efficiently to estimate the stability of a robotic grasp without even knowing the geometric or visual information about the object to be grasped.

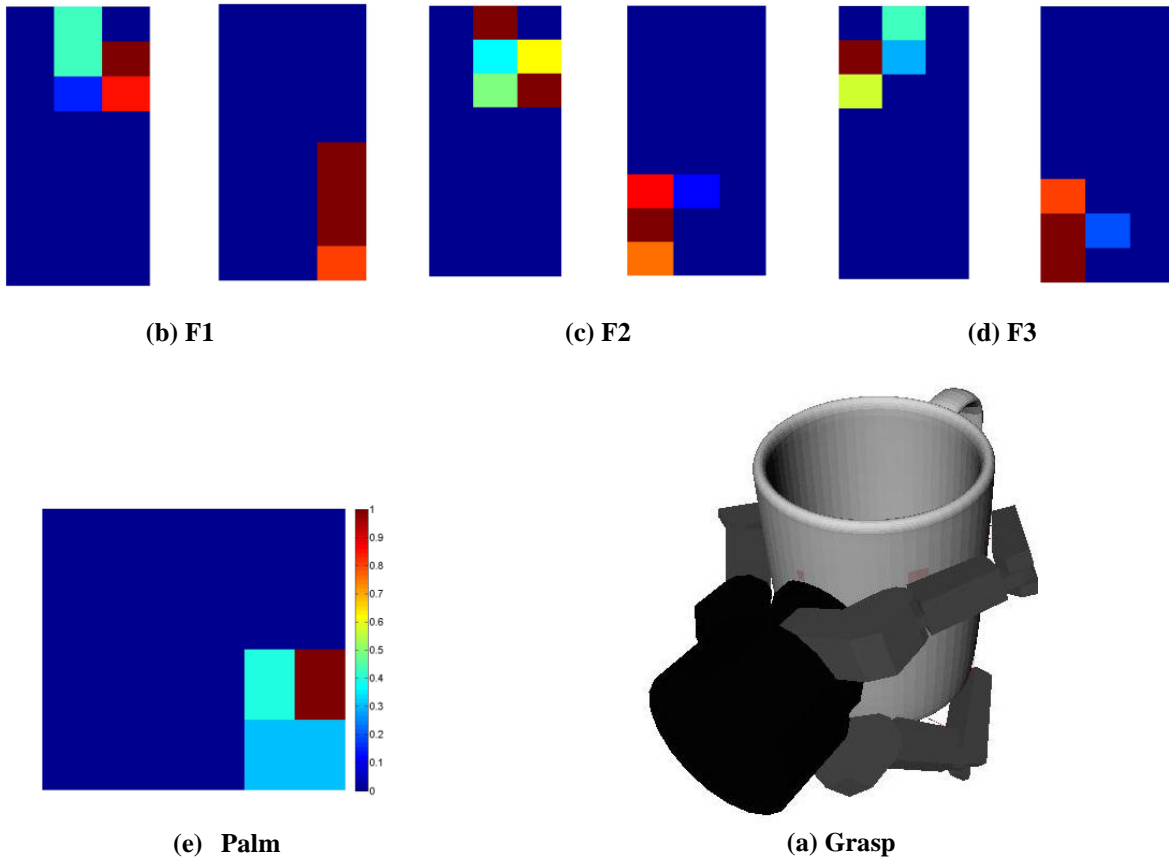


Fig. 2. Tactile Sensor Simulation, Figure 2(a) show a robotic grasp of a Barrett hand on a mug, Figure 2(b), 2(c), and 2(d) show the tactile responses on finger F1, F2, F3 respectively. In each group, the left one is the tactile pad on the finger tip and the right one is the tactile pad on the mid finger. Figure 2(e) shows the tactile readings on the palm. The 8-bit scale (0 - 255) goes from blue (no response) to red (saturation).

### A. Grasp Dataset

Our grasp data is from the CGDB database. This database contains hundreds of thousands of grasps constructed from several robotic hands and thousands of object models. Object models used in the CGDB are from the Princeton Shape Benchmark (PSB) [17]. The PSB provides a repository of 3D models which span across many objects that we encounter everyday. One fact about the PSB model set is that the models were not originally selected with an eye towards robotic grasping or prosthetic grasping, and so some of the models are not obvious choices for grasping experiments. For example, the model set contains insects, which are often outside our everyday grasping range. Although the CGDB provides grasps for all these object models in the PSB, instead of using the full set of grasps in the CGDB, we choose to select grasps computed on a smaller set of objects that are more frequently grasped and manipulated by us in our everyday life. In total, we collected about 15,000 robotic grasps from 936 objects across 23 different classes.

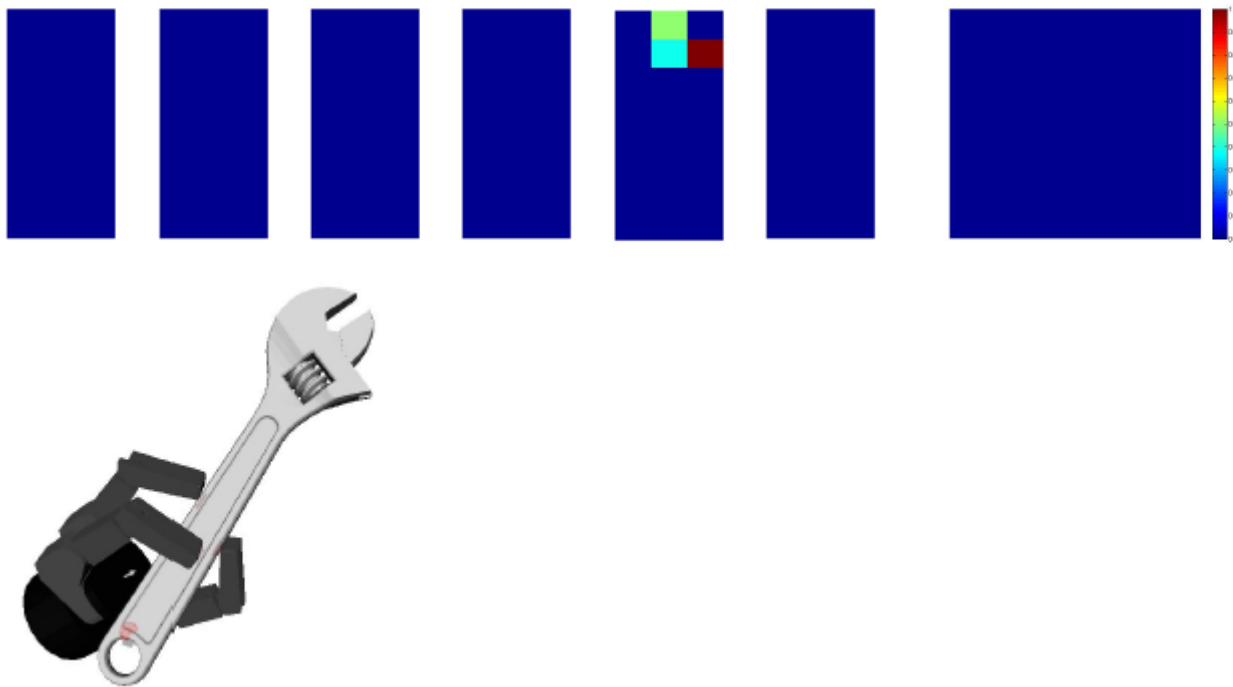


Fig. 3. A robotic grasp whose contacts are not fully captured by the current tactile sensor system. Figure 3(b) to 3(e) show the tactile sensor outputs in each of the seven sensor pads. Only contacts on the tip of the Finger3 are captured in the system as shown in 3(d). Contacts that are on the other two fingers, Finger1 and Finger2, are not captured by the tactile system.

### B. Labeling Grasps

In the CGDB, all of the grasps are good in terms of their physical properties, i.e. they either have good Ferrari-Canny grasp metric volume qualities or good epsilon qualities [5]. The epsilon quality,  $\epsilon$ , measures the minimum relative magnitude of the outside disturbances that could destroy the grasp. So, when we take into account the limit of the maximum forces a prosthetic hand can apply, a grasp would be less stable if it has a smaller epsilon quality. This is because the smaller epsilon quality indicates that a relatively smaller outside disturbance can break this grasp even when the robotic hand has already applied the maximum forces it supports.

Another consideration is from the perspective of the environment uncertainty. Due to the uncertainty of the environment, objects may move away slightly from their original position during a grasp execution. A fragile grasp may fail to fully grasp the object in this situation while a stable one may display its robustness and still succeed in

grasping the object in the perturbation. We have experimentally found a strong correlation between this robustness and the epsilon quality.

We have found that grasps with epsilon quality  $\epsilon > 0.07$  tend to be more robust in uncertain object perturbations. Based on the above two considerations, for grasps that are form-closure, they may also differ from each other in the sense of being more stable or less stable. So, we treat those more stable grasps as good grasps and the less stable

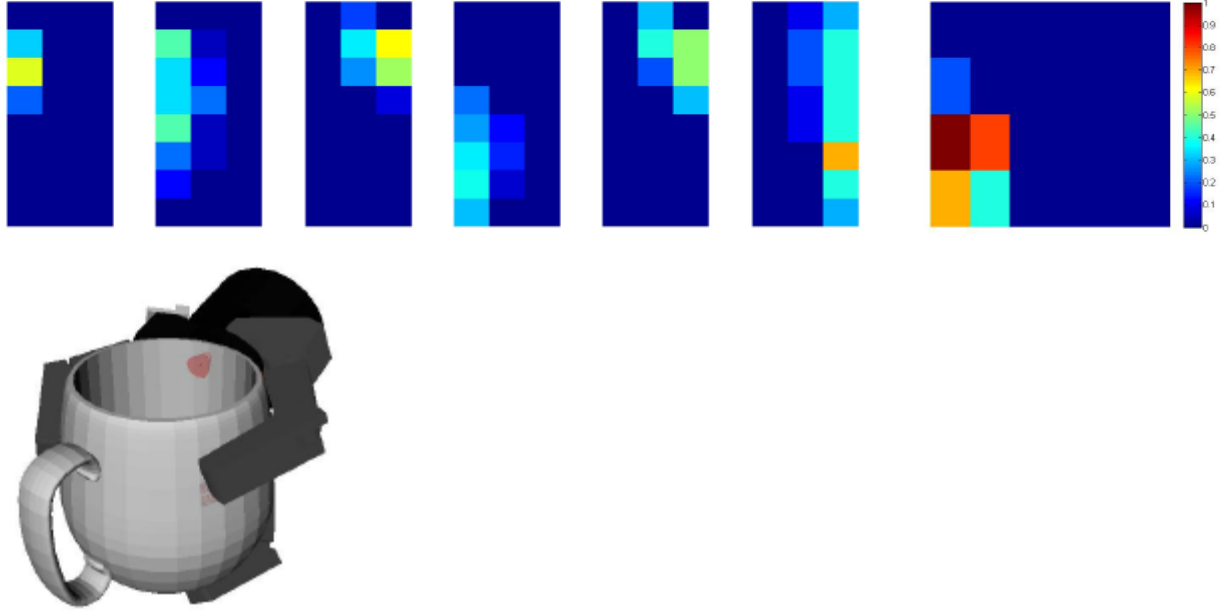


Fig. 4. A good robotic grasp which is classified correctly. Figure 4(b) to 4(e) show the tactile sensor outputs in each of the seven sensor pads. All of those contacts are captured by the seven tactile sensor pads.

ones as bad grasps. Using a threshold  $t_\epsilon = 0.07$  as the boundary, we label grasp  $i$  as a good (1) or a bad (0) grasp as follows:

$$label(grasp_i) = \begin{cases} 0 & \text{if } \epsilon(grasp_i) \leq t_\epsilon \\ 1 & \text{if } \text{otherwise} \end{cases} \quad (5)$$

### C. Feature Vector

For a normal human grasp, two properties are usually perceived by us. One is the tactile sensing which specifies the contact configuration between our hands and the object. The other is the hand kinematics which indicates how our hands are shaped around the object for the manipulation. These two pieces of information help us predict whether this is a stable grasp. In the prosthetic hands, we use the same idea to synthesize a feature vector for a robotic grasp: we use tactile and kinematic information to characterize a grasp.

Given a robotic grasp, the output of the simulated tactile sensor system is a group of seven 2D arrays. Each array is corresponding to one sensor pad. Each element of an array stores the value of the force sensed in the corresponding sensor cell. We vectorize each of these 2D arrays into one dimensional vectors and concatenate them together. This gives us a 162-dimensional vector. In addition to the tactile feedback, we also obtain the values of the seven joint angles of a prosthetic hand when a grasp is applied and append them to the end of the 162-dimensional tactile feedback vector. This makes the final feature vector 169-dimensional.

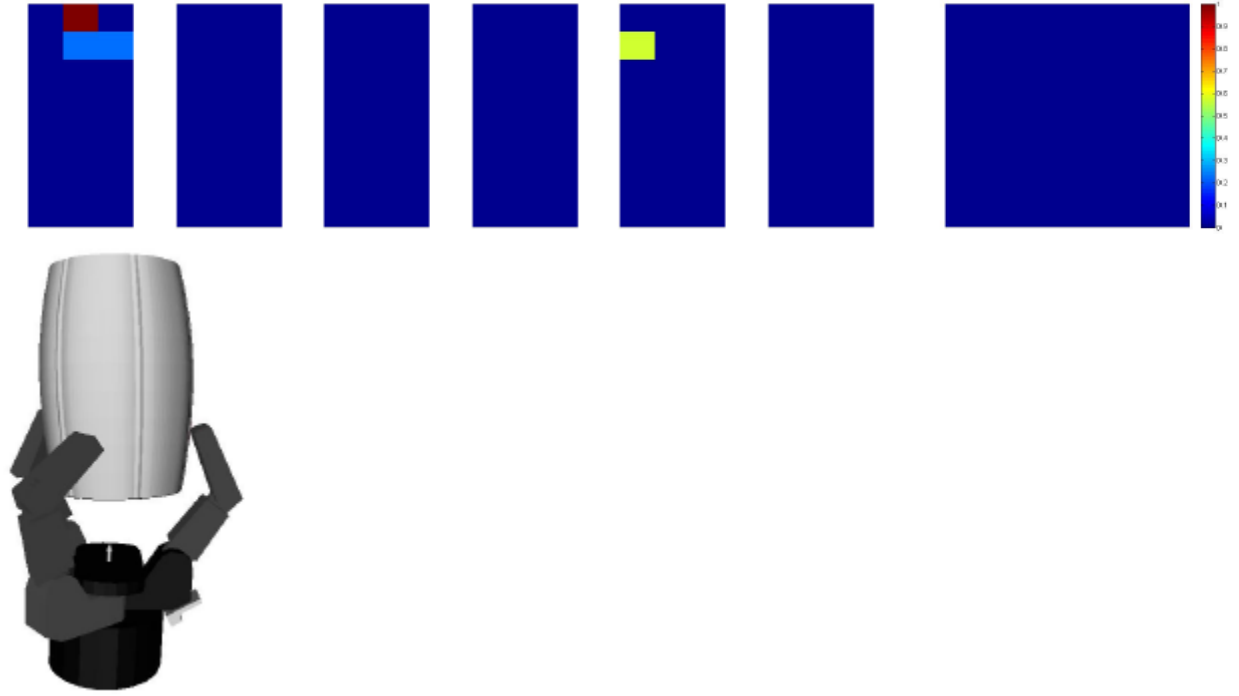


Fig. 5. False negative: A good robotic grasp which is classified incorrectly as a bad one. Figure 5(b) to 5(e) show the tactile sensor outputs in each of the seven sensor pads. The problem here is that the contacts on the edges of the fingers are not fully captured.

#### D. Scaling

A feature vector contains both the 162-dimensional tactile feedback and the 7-dimensional joint values. They are from two totally different domains and of two different dimensions. Instead of feeding them directly into a training algorithm which will treat each dimension in both the tactile feedback and the joint angle equally, we scale each dimension of the tactile data and the joint data differently so that these two major parts can be weighted equally on the whole.

For each tactile feedback  $T_i$ , we first normalize the 162- dimensional tactile feedback such that they sum up to one. Specifically we write it down as follows,

$$\bar{T}_i = \frac{T_i}{\sum_{j=1}^{162} T_i^j} \quad (6)$$

Then, for a feature vector, the scaling approach we used is to scale the dimensions of the tactile part such that the standard deviation across all the samples is one while to scale the dimensions of the joint angle part such that the standard deviation is  $\omega$ , where  $\omega$  is considered as a weight factor that balances the weights between the tactile feedback and the joint angle values. More specifically, a feature vector  $x = [T \ J]$ ,  $T \in R^{162}$ ,  $J \in R^7$  is scaled as follows:

$$\hat{x}^i = \begin{cases} \frac{x^i}{std^i} & \text{if } 1 \leq i \leq 162 \\ \omega \frac{x^i}{std^i} & \text{if } 163 \leq i \leq 169 \end{cases} \quad (7)$$

where  $x^i$  denotes the  $i^{th}$  dimension of the feature vector.  $std^i$  denotes the standard deviation in the  $i^{th}$  dimension. In our scaling process, we used the same  $std^i$  computed from the training set to scale the test data.

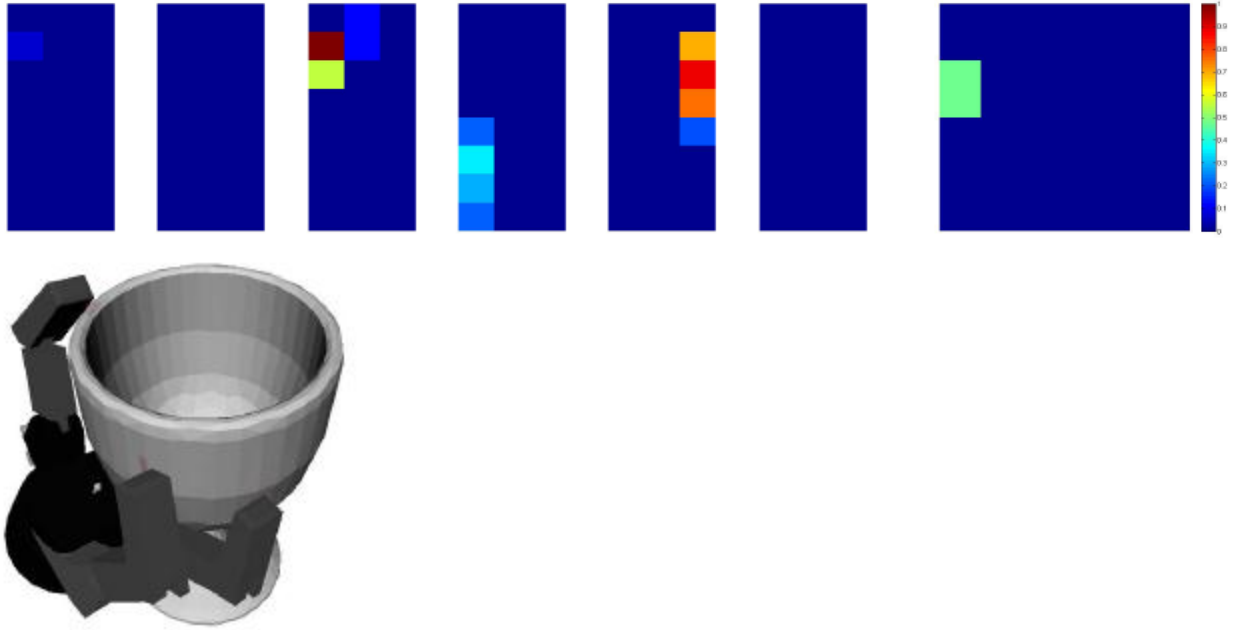


Fig. 6. False positive: A bad robotic grasp which is classified incorrectly as a good one. Figure 6(b) to 6(e) show the tactile sensor outputs in each of the seven sensor pads. All of those contacts are captured by the seven tactile sensor pads. However, they are on the edges of the fingers and the dramatic surface normal differences between the object and the robotic hand at the contact location may confuse the classifier.

## 6.4. Simulation and Results

### A. Training and Testing Dataset

Tactile feedback is a core component in our feature vector. Inside *GraspIt!*, the physical simulation system is able to capture all the possible contacts between a robotic hand and the object. Although the current PPS tactile sensor system captures many possible hand-object contacts, there are still locations the system does not cover. For example, Figure 3 shows a grasp when a prosthetic hand is grasping a wrench. The contacts on the edges of the fingertips, F1 and F2, cannot be captured by the current tactile sensor system. However, it is detected and considered in the physical simulation system inside *GraspIt!* for the computation of the epsilon quality. For such kind of grasps which involve contacts in uncovered regions, they cannot be fully represented by the tactile sensor system, either the simulated or the real one. Therefore, there is an inconsistency in these grasps between the physical simulation and the real world and this inconsistency may influence the performance of the classification.

Since grasps with fewer number of non-zero tactile responses have more potential to contain un-captured contacts, we first filter out grasps from the grasp dataset,  $D$ , obtained in Section IV-A based on the number of sensor pads that have non-zero responses. Since each sensor pad is a flat plane, a stable grasp must have at least two sensor pads in contact with the object being grasped, resulting in at least two sensor pads with non-zero responses. In our experiment, we first divide the grasp dataset  $D$  into two subsets,  $D1$  and  $D2$ .  $D1$  contains all the grasps that have only one tactile sensor pad with non-zero responses, while  $D2$  contains all the grasps with at least two tactile sensor pads having nonzero responses.

We then choose  $2/3$  grasps from  $D2$  that evenly distributed among all the objects to generate our training set. We put the remaining  $1/3$  of the grasps from  $D2$  into the test set. Although contacts of grasps in  $D1$  are not fully captured by the simulated tactile system, their tactile feedback would be realistic considering a real prosthetic hand with a real tactile system. In order to keep this potential considered as in a real working environment, we do not want to rule them out for testing. Thus, we put all the grasps from  $D1$  in the testing set, and the test set is a union of  $D1$  and  $1/3$  of  $D2$ .

## B. Results

During scaling, we tried different  $\omega$ 's.  $\omega = \sqrt{\frac{162}{7}}$  worked best in our experiment. To train an SVM classifier, we used libsvm [2]. We used a RBF kernel with 5-fold cross validation to determine the best cost parameter  $C$  and RBF parameter  $\gamma$ .

After we trained our SVM classifier, we fed the grasps in the testing set to the classifier. Experiment results are shown in Table II. In total, the best overall accuracy we get is 70.38% with  $\omega = \sqrt{\frac{162}{7}}$ . In this experiment, only 10.2% grasps are incorrectly classified as positive. This means that a grasp will be classified incorrectly as a good one with only a small probability. It also indicates the conservativeness of this classifier which is very necessary in a blind grasping context. Because usually we can just keep searching for another grasp if we mis-classify a good grasp to be a bad one, but the cost or risk is usually too high to tolerate if we execute a grasp that is actually bad but mis-classified as a good one.

In Table III, we show more detailed statistics on the accuracy in each object class based on our best result. In the context of blind grasping, the false positive predictions are more important in our consideration because of the high cost we have to pay for a false positive prediction. We summarized the percentages of false positive predictions of each object class.

In Figure 4, 5, and 6, we show some example test grasps. Based on these test results, we find some interesting points.

**For grasps whose contacts are fully captured, they have more potential to be classified correctly.** Figure 4 shows an example grasp whose contacts are fully captured by the tactile sensor system. This is an example grasp that is classified correctly. In contrast, Figure 5 is a false negative prediction. As is shown in the tactile sensor response, the contacts on the fingers are not fully captured by the current tactile sensor system. This makes the tactile feedback incapable to carry enough information to represent the grasp. Thus, losing tactile information increases the potential of a false prediction.

**Contacts on the edges of the finger may confuse the classifier and result in more false predictions.** Figure 6 shows a false positive example. Although all the tactile pads have non-zero responses, many of the contacts are on the edges of the fingers. In this situation, the contact normals on the object surface differ dramatically from that of the surface of the finger. But a tactile sensor can only record the normal forces leaving the tangential forces uncaptured. The tactile sensor representation does not fully capture the grasp feature.

**When contacts are not fully captured, hand kinematics may confuse the classifier.** As we can see in Figure 6, two of the three fingers of the Prosthetic hand are shaped towards the other one. In general, a grasp with a set of contacts that are facing each other is more likely to be a good one and having fingers facing towards each other increases the potential of such contacts. In this sense, without further distinction obtained from the tactile sensor feedback, the hand kinematics may confuse the classifier to make it consider this grasp as a good one.

## 7. Conclusion and future works

In this report, power grasping control for fully actuated hand based on virtual spring damper hypothesis is investigated. This method is applicable in real time and does not rely on information about object shape to be grasped. Besides it can follow command line from EMG model.

Using the virtual spring damper precision grasping of fully actuated hand is covered in section 3. Similarly the method is applicable for real-time implementation and independent of information about object shape.

Section 4 discussed the underactuated hand design and optimization. Furthermore, position and force control method are presented and the results are compared with power grasping technique of fully actuated hand.

Section 5 covered robust control method to follow accurately angle command signal from EMG signal analysis in presence of plant uncertainty. In this part the EMG model is mixed with control technique and overall performance of the hand is analyzed.

Future works will be focused on other control strategies to follow command signal from EMG for both force and position models and mixing EMG model and control strategies. The fuzzy control is a powerful technique which

will be studied to this aim. Sliding mode control is another option which is robust and also appropriate for nonlinear plants. This technique can be used for both force and position control of the prosthetic hand. Any other control technique which fits to this problem might be considered too.

Moreover, the precision grasping and power grasping techniques based on virtual spring damper, requires improvement to follow more precisely command signal from EMG signal. Current method is based on impedance control and it should be relate to force and position reference signal more accurately.

For underactuated hand, simple PID controller were studied which can be improved by more powerful control techniques like fuzzy control, neural networks, nonlinear control and any other applicable technique.

## Goal 2B: Embedded Hierarchical Real-Time Systems

**INTRODUCTION:** The annual work under this Goal involved the following key tasks: (1) the construction of a test bed that integrates the software tool chain and prototype hardware (test bed); (2) the study on design and Implementation of the real-time control strategies on the embedded test bed, and the study and experimental set up of a real-time operating system on the embedded processor used in (1); (3) the study of integrating sEMG acquisition, filtering techniques and models on the embedded test bed for real-time control, signal processing and acquisition. The primary purpose of this work is to develop an embedded control system by researching, designing, testing, and prototyping the hardware and software for the system.

### System Design

#### Test Bed for Embedded Systems Prototyping

A test bed based on a 32-bit embedded processor (a.k.a. programmable intelligent controller, or PIC) was built. Figure 3 depicts the test bed, where Stage 1 represents the (micro-level) signal processing circuitry composed of the processor, its I/O expansion board, and the wiring needed to receive input sEMG signals and produce output actuation signals for the plant (the controlled one-finger device). Stage 2 consists of circuit elements and wiring for motor powering, actuation, and isolation of the motor circuit from the Stage 1 circuit for protection of the embedded processor against power surge.

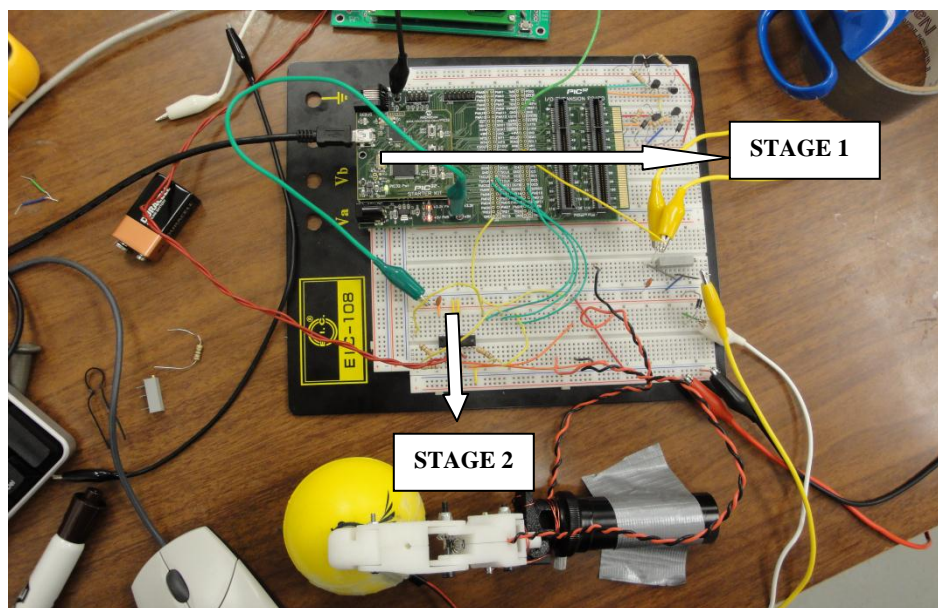


Figure 3. Overview of the test bed (omitting the software tool chain computer)

For Stage 1, a Microchip PIC32-I was used to implement our system. Based on this processor, we selected the dsPIC block set to generate the C code for PIC32-I from Simulink. The intent of this approach for the tool chain is due to the fact that our controller designs are being specified in Matlab models; and Simulink, along with its Real-Time Workshop toolbox, provides a logical and efficient path from model to prototype implementation and testing, for a given controller design. The processing flow of the various elements of the tool chain is shown in Figure 4, which builds and releases the executable of the controller to the PIC.



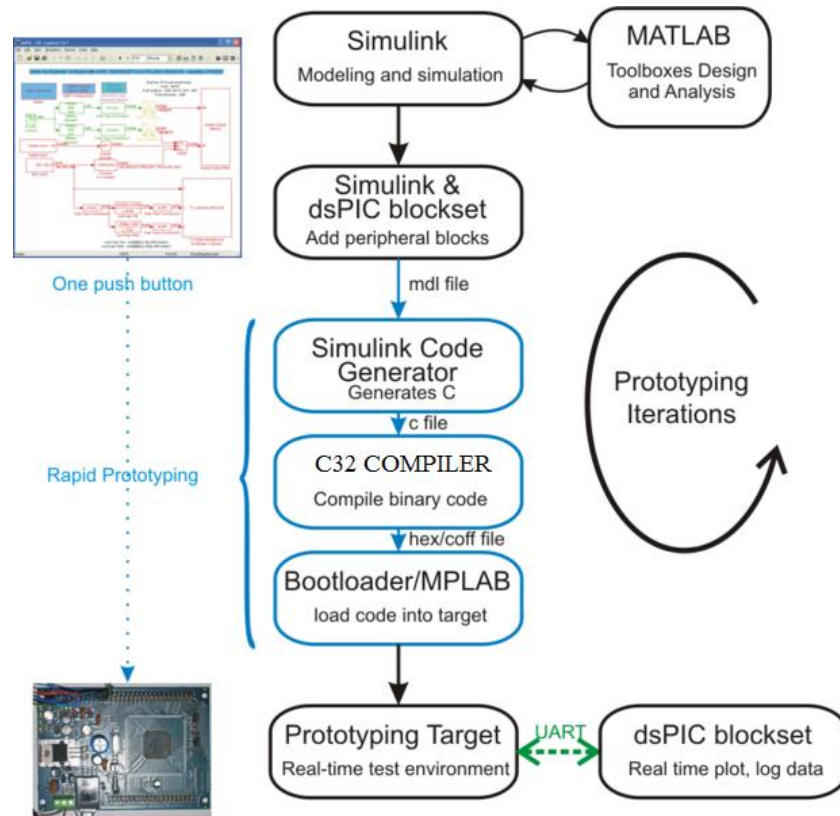


Figure 4. Processing flow for generating code to the processor

Several hardware modules within the PIC32-I were also used, including the Analog Input module, the Digital Output module, the Output Compare module, and the UART module. The Analog Input module was used for reading the input sEMG as well as sensory feedback data from the prototype hand. PIC32-I has an internal analog to digital converter. A real-time control strategy uses the data from the Analog Input module as a reference signal or the set point. Based on the control strategy, the Digital Output module generates digital control signals. The Output Compare module then generates a pulse width modulated (PWM) waveform with a specific duty cycle, based on the input analog signal (i.e. the sEMG). The UART module is used to transmit the signals from PIC32-I to a personal computer via the serial (i.e. RS-232) communication. This interface enabled us to debug and evaluate the performance of control strategies.

For Stage 2, we used the SN754410 quadruple half-H driver to actuate the motor with the control signal. The pin configuration for the H-driver is shown in Figure 5. The PWM signal from the Output Compare module is connected to pin1 (labeled “1,2EN”) of the H-driver. The digital outputs of the PIC32-I are connected to the direction pins of the H-driver (pins 2 and 7). By switching the digital outputs to 0 and 1 between the direction pins, the motor will rotate clockwise or counter-clock wise.  $V_{cc1}$  and  $V_{cc2}$  are connected to the 5-volt DC supply of the PIC32-I I/O expansion board.

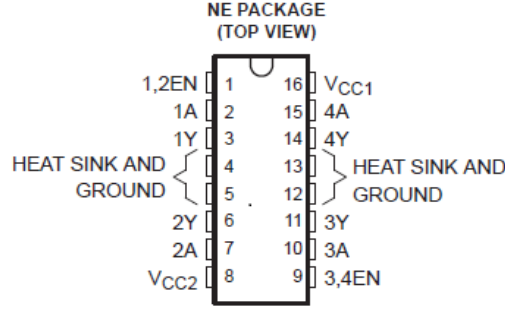


Figure 5. Pin configuration of the quadruple half-H driver.

The test bed and its operation was demonstrated, in the form of recorded video, to the researchers at the Applied Physics Laboratory of Johns Hopkins University, a major collaborator on the TATRC project with which ISU is a part of. The JHU APL researchers expressed their interest in further collaboration with ISU in several areas including this and the validation/verification of sEMG signal processing algorithms.

### Design and Implementation of Real-Time Control Strategies:

In this work [1], the threshold values establish a correlation between the sEMG and the corresponding force required for the power grasp of an object. C.Potluri *et. al* [2] explained the correlation between sEMG entropy threshold values and skeletal muscle forces. These threshold values are fed as the reference or a set point to the controller. The signal flow is depicted as a block diagram in Figure 6.

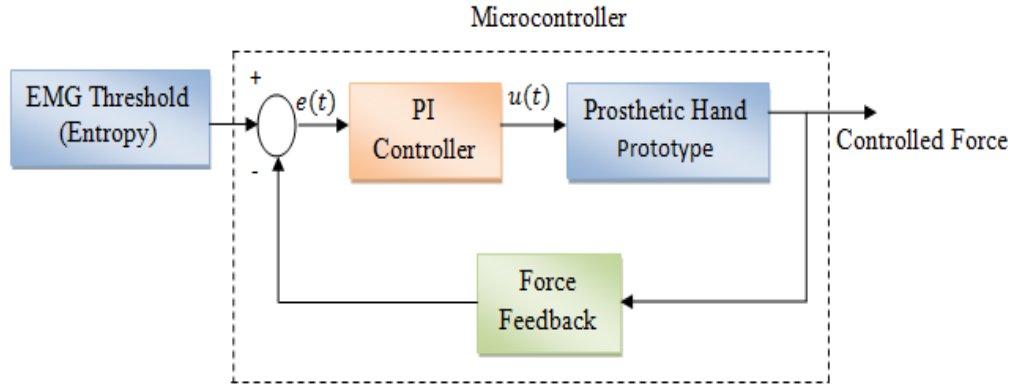


Figure 6. Block diagram of the real-time control signal flow.

The force feedback signal is acquired by a force sensitive resistor (FSR). The FSR is mounted on the fingertip of the prosthetic hand prototype as shown in Figure 8. The error  $e(t)$  is computed as the difference between the reference value and the actual force from the FSR. A proportion-integral (PI) controller is employed to generate the actual force from the FSR, and make it equal to the reference force in order to reduce the error  $e(t)$  to zero. The PI control action is given below in Equation (1).

$$u(t) = K_p * e(t) + K_i \int_0^t e(\tau) d\tau, \quad (1)$$

In Equation (1),  $u(t)$  is the control signal,  $K_p$  is the proportional gain, and  $K_i$  is the integral gain,  $e(t)$  is the error, and  $\tau$  is the dummy integration variable. Gain parameters  $K_p$  and  $K_i$  are tuned using the Ziegler-Nichols method in MATLAB®.

Our proposed design was implemented on a PIC32-I microcontroller in two stages: “Signal Processing” and “Motor Actuation.” The Signal Processing stage facilitates the implementation of real-time control strategies. A dsPIC

blockset was used to generate the C code for the PIC32 from Simulink<sup>®</sup>. The dsPIC blockset generates a .hex file, and this file is imported by MPLAB<sup>®</sup> to program the PIC.

### Signal Processing Stage

We used the following modules of the PIC32 as a part of implementing our control strategies: the Analog Input module, the Digital Output module, the Output Compare module, and the UART module. The Analog Input module was used for reading the sEMG and sensory feedback data. The PIC32 has an internal analog to digital converter (ADC) which has a 10-bit resolution so that it can distinguish up to 1024 different voltages, usually in the range of 0 to 3.3 volts, and it yields 3mV resolution. A real-time control strategy was developed using the threshold value of the entropy of sEMG data as a reference or set point. The difference between the threshold of the sEMG entropy and the FSR feedback was fed in to the PI control loop to reduce the error to zero. The Digital Output module of the PIC32 was used to generate digital control signals. Depending on the error, a pulse width modulated (PWM) wave with a specific duty cycle was generated in the Output Compare module. The UART module in the PIC32 was used to transmit the signals from the microcontroller to the PC via serial communication. In this design, a virtual com port was created to feed the data via USB cable to the computer. MATLAB<sup>®</sup> was used to read the signals from the ports. This enables the user to troubleshoot and see the performance of the designed control strategy. The design is consistent with our initial system design and the embedded test bed.

### Motor Actuation Stage

A SN754410 quadruple half-H driver is used to actuate the motor with the corresponding control signal. Fig. 3 shows the schematic of the pin configuration of the half-H driver. The PWM signal from the Output Compare module was connected to pin1 (1, 2EN) of the H driver. The PWM wave enables this H driver. The speed of the motor depends on the duty cycle of the PWM wave from the Output Compare module, which is a function of  $e(t)$ . The digital outputs of the PIC32 microcontroller are connected to the direction pins of the Hdriver (pins 2 and 7). Switching the digital outputs to 0 and 1 between the pins will makes the motor rotate in clockwise and counter-clockwise directions.  $V_{cc1}$  and  $V_{cc2}$  are connected to the 5V supply of the PIC32 I/O board. This proposed design was tested on an index finger of a prosthetic hand prototype. This part of the work made use of the embedded test bed as previously described.

### Mechanical Structure of Hand Prototype

The robotic hand prototype finger has three degrees of freedom, and is actuated by two Pololu 35:1 mini metal gear motors and a bevel gear transmission system. The main characteristic of this prototype is its biologically-inspired parallel actuation system based on the behavior/strength space of the "Flexor Digitorum Profundus (FDP)" and the "Flexor Digitorum Superficialis (FDS)" muscles as explained in Figure 7. However this research work focuses on the "Region 1" actuation system and it is interfacing with a microcontroller. Region 1 is populated by the more frequent dexterous tasks.

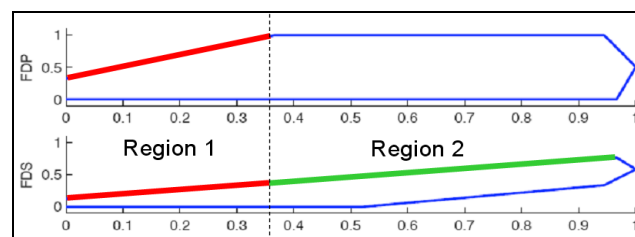


Figure 7. Strength space of FDS and FDP muscles

In our design, the movements associated with Region 1 are achieved by 2 DC motors. The motor in the metacarpal phalange of the finger actuates the PIP (Proximal Inter Phalangeal) joint and the motor at the base of the finger actuates the MCP (Meta Carpo Phalangeal) joint, as shown in Figure 8. As the main objective of this work is to

interface and control the two motors with a microcontroller, we have not considered the belt transmission system which is designed to drive the DIP (Distal Inter Phalangeal) joint as well.

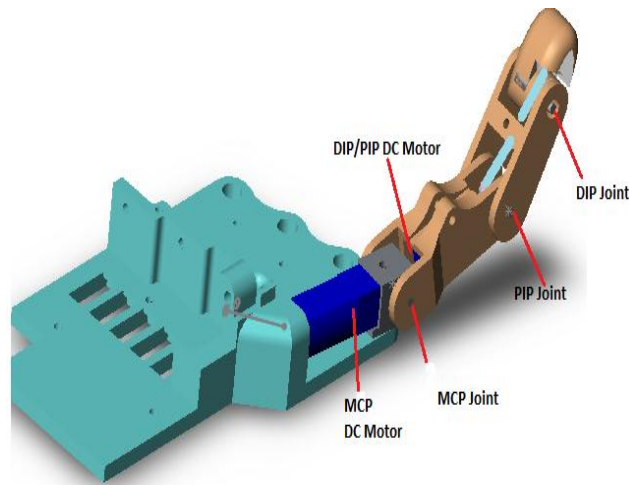


Figure 8. Region 1 actuation scheme for the finger

### **Reportable Outcomes**

Results are acquired from the microcontroller through UART channel 2 of the PIC32 by a virtual com port via USB at 57600 baud rate. The data from the microcontroller is converted into unit16 data before it is transmitted through the UART. The PIC32 microcontroller is running 80 million instructions per second (MIPS) with its phase lock loop (PLL) activated. It is running at an external clock frequency of 8MHz with internal scaling enabled.

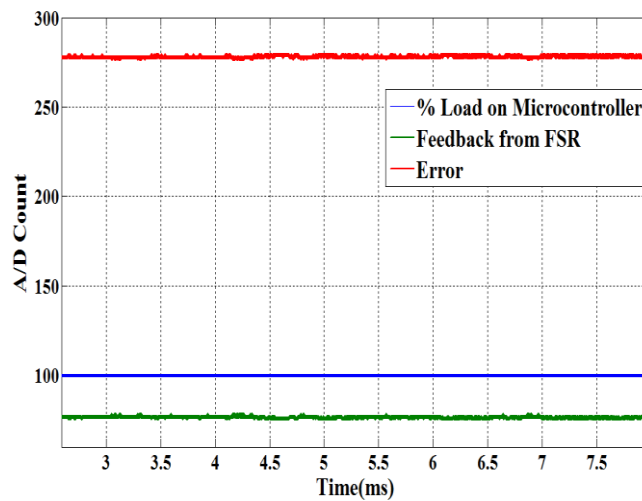


Figure 9. Feedback force and error before grasp

Figure 9 depicts the feedback force from the FSR and the error  $e(t)$ , before the grasp. As there is no contact between the object and the hand, the force is low and ideally should be zero. However, because the PIC32's ADC module has a high resolution, it shows some values even when the object is not in contact.

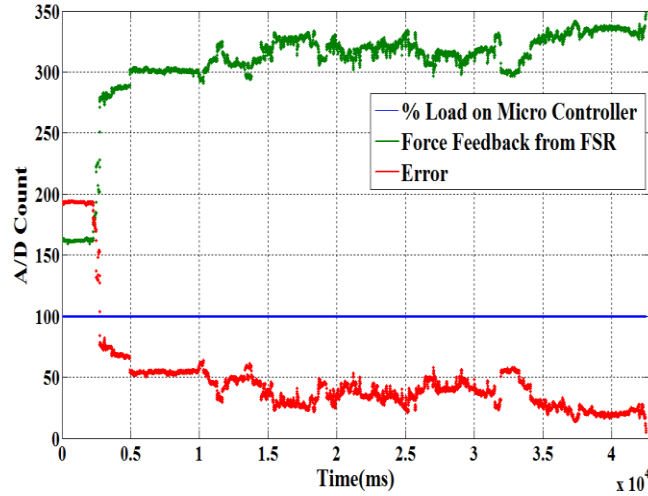


Figure 10. Feedback force and error after grasp

Figure 10 depicts the feedback force from the FSR plotted against the error  $e(t)$  after the grasp. The error  $e(t)$ , i.e. the difference between the reference force from the sEMG threshold value and the actual force feedback from the FSR, is almost zero. From Figure 10, it is also evident that the actual force from the FSR is almost equal to the reference force value that is established from the sEMG threshold value, as the error approaches zero. Figure 11 shows the computational load on the PIC32 while performing this grasp. It indicates that the microcontroller completed the computation in approximately 12ms. The rest is handed over to the I/O blocks of the microcontroller and to the motor actuation stage.

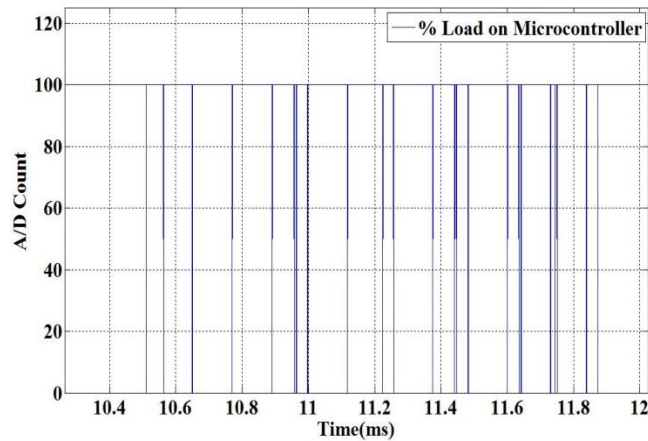


Figure 11. Computational load on the PIC32 during the grasp.

These results suggest an extensible design for increased load on the processing by the embedded system.

#### Real-Time Operating System for Embedded Control

For our work FreeRTOS is used to schedule several tasks that the microcontroller needs to do, based on their priority levels. These tasks include sEMG analysis, high-level control (i.e. the control strategy), low-level control (i.e. the motor control), receive data from contact sensors, receive data from force sensors, and receive data from encoders, among others. All these tasks need not be done at the same frequency. Some of them might happen only occasionally. In case of contact an interrupt might happen and the controller algorithm might change, based on the event driven structure. Control load for each situation might be different. A task is an independent thread of execution that contains a sequence of independently schedulable instructions. Multitasking is the ability of the operating system to handle multiple activities within set deadlines. The Free RTOS multitasks in such a way that

many threads of execution appear to be running concurrently; however, the OS is actually interleaving executions sequentially, based on a preset scheduling algorithm. The scheduler ensures that the appropriate task runs at the right time. FreeRTOS supports up to 256 priority levels, in which 0 is the highest and 255 the lowest. With a preemptive priority-based scheduler, each task has a priority, and the highest-priority task runs first. If a task with a priority higher than the current task becomes ready to run, the kernel immediately saves the current task's context and switches to the higher-priority task. When that is done, the control is returned to the original task.

An experimental setup similar to the one shown in Figure 3, but with Free RTOS installed on the PIC32-I, was built. For proof of concept, the embedded processor running a Free RTOS kernel was connected to two different sets of components: a DC motor and a group of LED's. An application program was built and released onto the PIC32-I, which drove the DC motor and flashed the LED's by way of interleaving the two separate tasks, with equal priority levels assigned to both tasks. The application performed as designed without any noticeable delay. While the computational loads of these tasks are insignificant, this experiment demonstrated the value of Free RTOS and its potential use at least in the low-level control, where multiple motors or sensing devices will likely be employed.

### I. Proposed Design using Model reference adaptive controller (MRAC)

The objective of the embedded system design is for the prosthetic hand fingers to track a force signal as closely as possible. Here, the force signal is inferred from surface EMG (sEMG) signals obtained from the array of the three sEMG sensors located at the arm. The sEMG data is processed by filtering and using a sensor fusion algorithm to facilitate the extraction of the best finger force estimates. Sensor fusion is done in the frequency domain for the sEMG data using a simple elitism based Genetic Algorithm (GA). The data from the three sensors is collected around the corresponding individual motor unit location at the transradial arm location (flexor digitorum superficialis) and before fusing are rectified and filtered using a Half -Gaussian filter, as given by (1).

$$p(EMG|x) = 2 \times \frac{\exp\left(-\frac{EMG^2}{2x^2}\right)}{\sqrt{2\pi x^2}}, \quad (1)$$

where  $p(EMG|x)$  is a conditional probability density function,  $x$  is a latent driving signal.

System identification (SI) is used to identify the dynamical relationship between the sEMG data from the three sensors  $u_1$ ,  $u_2$ , and  $u_3$  and the corresponding finger force of a healthy male subject. In this fusion algorithm, Output Error (OE) models are used and are constructed for each individual data set. The OE model is given as follows.

$$y(t) = \frac{B(q)}{F(q)} u(t - nk) + e(t), \quad (2)$$

Where  $B$ , and  $F$  are the polynomials,  $q$  is shift operator,  $e(t)$  is output error,  $y(t)$  is system output,  $u$  is input,  $nk$  is the system delay and  $t$  is time index.

Using the three resulting OE models and the fusion algorithm given by [12] a corresponding continuous-time model is constructed as given by the transfer function as

$$G(s) = \frac{B(s)}{F(s)} = \frac{b_{nb}s^{(nb-1)}b_{nb-1}s^{(nb-2)}+\dots+b_1}{s^{nf}+f_{nf}s^{nf-1}+\dots+f_1}, \quad (3)$$

Similar to the discrete-time case  $nb$  and  $nf$  determine the orders of the numerator and denominator. For multi-input systems,  $nb$  and  $nf$  are row vectors.  $b, f$  are the coefficients of the numerator and denominator polynomials respectively.

A MISO transfer function is constructed based on the poles of three individual OE models corresponding to each sensor. GA is used to find the corresponding zeros. The search area is limited to the unit circle, because a discrete time model is used (and the resulting MISO model is decreased to minimum phase). The number of zeros is at most

the number of poles. The number of potential zeros is set to the order of the corresponding denominator. The error squared of the resulting MISO system  $H(s)$  (see Appendix) and the recorded force signal was set as an objective function. The objective function  $f$  is constructed as follows,

$$f = \int_{t_0}^{t_f} (\hat{Y}(t) - Y(t))^2 dt = \int_{t_0}^{t_f} \varphi^2(t) dt, \quad (4)$$

where  $t_0$  and  $t_f$  are the initial and final time values,  $\hat{Y}(t)$  is the fusion model estimated force and  $Y(t)$  is the actual force from the FSR. The MISO system  $H(s)$  is constructed as follows,

$$H(s) = \begin{pmatrix} \frac{Z_{1,1}s^n + Z_{1,2}s^{n-1} + \dots + Z_{1,n+1}}{P_{1,1}s^n + P_{1,2}s^{n-1} + \dots + P_{1,n+1}} \\ \frac{Z_{2,1}s^n + Z_{2,2}s^{n-1} + \dots + Z_{2,n+1}}{P_{2,1}s^n + P_{2,2}s^{n-1} + \dots + P_{2,n+1}} \\ \frac{Z_{3,1}s^n + Z_{3,2}s^{n-1} + \dots + Z_{3,n+1}}{P_{3,1}s^n + P_{3,2}s^{n-1} + \dots + P_{3,n+1}} \end{pmatrix}, \quad (5)$$

where  $Z$ 's and  $P$ 's are the zeros and poles respectively of the individual transfer function and  $n$  is the order of the system.

Feeding the new data sets to the MISO transfer function ( $H(s)$ ) results in an estimated fusion based force  $\hat{Y}$ .

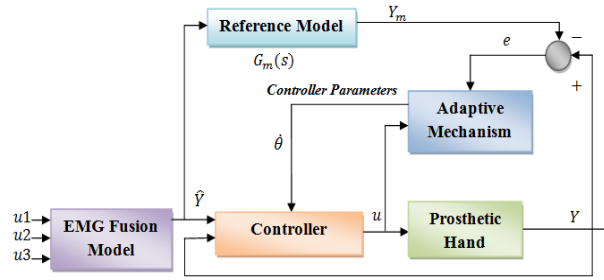


Fig. 1. Block Diagram of Model Reference Adaptive Control (MRAC).

The controller utilized for compensating the dynamics of the prosthetic hand is based on a simple MRAC scheme. During the development of the artificial hand, changes are being undertaken to the mechanical design and drive trains of the hand that affect the dynamics of the finger motion of the prosthesis. In addition, the uncertain characteristics of the kinematic and actuator interaction may lead to different performance than expected. Hence, a simple MRAC controller is devised in order to maintain some performance stability. The controller is given by Fig. 1 where the MIT rule is used for updating the controller parameter  $\theta$ ,

$$\frac{d\theta}{dt} = -\gamma e Y_m. \quad (6)$$

The gain  $\gamma$  is chosen to be 3.0 and the error  $e = Y - Y_m$  is computed by the difference of the model reference output  $Y_m$  and the true output (force generated by the prosthetic hand). The model reference is chosen to be of first order to suppress overshoot and facilitate fast response time, given by

$$G_m(s) = \frac{2}{2s+1}. \quad (7)$$



## II. Proposed Design using LQG Controller

The same reference force [2, 3] input in equations (1-5) is fed to the LQG controller. The controller design is tested and validated theoretically and implemented on the embedded test bed. The prosthetic hand dynamics for the theoretical verification of the proposed controller is given as follows.

### DYNAMICS OF PROSTHETIC HAND

The dynamic equations of motion for the hand are obtained from the Lagrangian approach as

$$\frac{d}{dt} \left( \frac{\partial \mathcal{L}}{\partial \dot{q}} \right) - \frac{\partial \mathcal{L}}{\partial q} = \tau, \quad (5)$$

where  $\dot{q}$  and  $q$  represent the angular velocity and angle vectors of joints respectively;  $\mathcal{L}$  is the Lagrangian;  $\tau$  is the given torque vector at joints. The Lagrangian  $\mathcal{L}$  is given as

$$\mathcal{L} = T - V, \quad (6)$$

where  $T$  and  $V$  are denoted as kinetic and potential energies respectively. Substituting (6) into (5), we get the following dynamic equations

$$M(q)\ddot{q} + C(q, \dot{q}) + G(q) = \tau, \quad (7)$$

where  $M(q)$  describes the inertia matrix;  $C(q, \dot{q})$  is the coriolis/centripetal vector and  $G(q)$  is the gravity vector. (7) can be written as

$$M(q)\ddot{q} + N(q, \dot{q}) = \tau, \quad (8)$$

where  $N(q, \dot{q}) = C(q, \dot{q}) + G(q)$  represents nonlinear terms.

Feedback linearization technique is used to convert the nonlinear dynamics represented by (8) into a linear state-variable system [8]. In order to obtain the alternative state-space equations of the dynamics, the position/velocity state  $x(t)$  of the joint is defined as

$$x(t) = [q'(t) \ \dot{q}'(t)]', \quad (9)$$

and rewriting (8) as,

$$\frac{d}{dt} \dot{q}(t) = -M^{-1}(q(t)) [N(q(t), \dot{q}(t)) - \tau(t)] \quad (10)$$

Therefore, from (9) and (10), a linear system in Brunovsky canonical form is obtained and represented as

$$\dot{x}(t) = \begin{bmatrix} 0 & I \\ 0 & 0 \end{bmatrix} x(t) + \begin{bmatrix} 0 \\ I \end{bmatrix} u(t). \quad (11)$$

The control input vector  $u(t)$  given by

$$u(t) = -M^{-1}(q(t)) [N(q(t), \dot{q}(t)) - \tau(t)]. \quad (12)$$

As the prosthetic hand is required to track the desired force profile  $q_d(t)$  described under the reference force model, the tracking error  $e(t)$  is defined as

$$e(t) = q_d(t) - q(t). \quad (13)$$



Here,  $q_d(t)$  is the desired angle vector of the joints and can be obtained by the reference force model [6];  $q(t)$  is the actual angle vector of the joints. Differentiating (13) twice, we get,

$$\dot{e}(t) = \dot{q}_d(t) - \dot{q}(t) , \quad \ddot{e}(t) = \ddot{q}_d(t) - \ddot{q}(t). \quad (14)$$

Substituting (10) into (14) gives

$$\ddot{e}(t) = \ddot{q}_d(t) + M^{-1}(q(t))[N(q(t), \dot{q}(t)) - \tau(t)]. \quad (15)$$

From (15) the control function  $u(t)$  can be defined as

$$u(t) = \ddot{q}_d(t) + M^{-1}(q(t))[N(q(t), \dot{q}(t)) - \tau(t)]. \quad (16)$$

This is often called the feedback linearization control law, rewriting (16) as,

$$\tau(t) = M(q(t))[\ddot{q}_d(t) - u(t) + N(q(t), \dot{q}(t))]. \quad (17)$$

Using (14) and (16), the state vector  $x(t) = [e'(t) \ e''(t)]'$ , the state-space model can be represented as

$$\dot{x}(t) = \begin{bmatrix} 0 & I \\ 0 & 0 \end{bmatrix} x(t) + \begin{bmatrix} 0 \\ I \end{bmatrix} u(t). \quad (18)$$

Now, (18) is in the form of a linear system such as

$$\dot{x}(t) = Ax(t) + Bu(t). \quad (19)$$

## **LOG CONTROLLER DESIGN**

Given the prosthetic hand model as

$$X_{k+1} = F_k x_k + G_k u_k + B_{wk} w_k \quad (20)$$

The observation of the state as

$$y_k = H_k x_k + v_k \quad (21)$$

The conditions as

$$\begin{aligned} \mathcal{E}\{w_k w_k'\} &= Q_k, i = k, \text{ and } 0, i \neq k \\ \mathcal{E}\{v_k v_k'\} &= R_k, i = k, \text{ and } 0, i \neq k, \\ \mathcal{E}\{w_k w_k'\} &= 0 \forall i \text{ and } k \end{aligned}$$

The performance index is given by

$$J(x_{k_0}, k_0) = \mathcal{E} \left\{ \frac{1}{2} x_{k_f}' F_{k_f} x_{k_f} + \frac{1}{2} \sum_{k=k_0}^{k_f-1} [x_k' Q_k x_k + u_k' R_k u_k] \right\} \text{ To find the best estimator}$$

Step 1: Enter the prior estimate  $\hat{x}_k^-$  and its error covariance  $P_k^-$ .

Step 2: Compute Kalman estimator (filter) gain

$$K_{ek} = P_{ek}^- C_k' [H_k P_{ek}^- C_k' + R_k]^{-1} = P_{ek}^- C_k' (R_k')^{-1} \quad (22)$$

Where

$$P_{ek} = [I - K_{ek} H_k] P_{ek}'$$

Step 3: Update estimates with measurement  $y_k$

$$\hat{x}_k = \hat{x}_k^- + K_{ek} [y_k - H_k \hat{x}_k^-] \quad (23)$$

Step 4: Project ahead the state and the error covariance as

$$\hat{x}_{k+1}^- = F_k \hat{x}_k + G_k u_k \quad (24)$$

$$P_{e(k+1)}^- = F_k \hat{x}_k + G_k u_k, \quad (25)$$

$$P_{ek}^- - K_{ek} [H_k P_{ek}^- H_k' + R_k] K_{ek}' \quad (26)$$

Step 6: goto step 2 and repeat

To find the best optimal control

Step 7: Solve the matrix difference Riccati equation

$$P_k = F_k' [P_{k+1} - P_{k+1} G_k [G_k' P_{k+1} G_k + R_k]^{-1} G_k' P_{k+1}] F_k + Q_k \quad (27)$$

With the final condition  $P(k = k_f) = F_{kf}$

Step 8: Using the solution of  $P_k$  from step 7, obtain the optimal Kalman controller gain as

$$K_k = [G_k' P_{k+1} G_k + R_k]^{-1} G_k' P_{k+1} F_k \quad (28)$$

Step 9: then the optimal control  $u_k$  is given by

$$u_k = -K_k \hat{x}_k + r_k \quad (29)$$

### Implementation:

The force feedback signal is acquired by a Force Sensitive Resistor (FSR). The FSR is mounted on the fingertip of the prosthetic hand prototype as shown in Fig. 3. A simple MRAC is employed to generate the actual force from the FSR, and make it equal to the model reference output in order to impose a desired dynamical response. The proposed control design is implemented on a PIC 32MX360F512L microcontroller in two stages: "Signal Processing" and "Motor Actuation". The Signal Processing stage facilitates the execution and implementation of real-time control strategies. A dsPIC block set is used to generate the C code for the PIC 32 from Simulink®. The dsPIC block set generates a .hex file, and this file is imported in MPLAB® to program the PIC 32.

### Signal Processing Stage:

The following modules of the PIC 32 are used for the implementation of the signal processing stage.

- The Analog Input module
- The Digital Output module
- The Output Compare module
- The UART module

The Analog Input module is used for acquiring the sensory feedback force data from the FSR. The PIC 32 has an internal analog to digital converter (ADC) which has a 10-bit resolution so that it can distinguish up to 1024 different voltage values, usually in the range of 0 to 3.3 volts, and it yields 3mV resolution. The Digital Output module of the PIC 32 is used to generate digital control signals based on the selected control strategy to the motor actuation stage. This module detects the changes in the reference/command signal and flips the direction bits between 0 and 1. The motors switch direction accordingly. Depending on the error, a pulse width modulated (PWM) wave with a specific duty cycle is generated by the Output Compare module. The UART module in the PIC 32 is used to transmit the force data from the microcontroller to the PC via serial communication. In this design, a virtual com port was created to feed the data via USB cable to the computer. MATLAB® is used to read the signals from the ports. This enables the user to troubleshoot and see the performance and accuracy of the designed control strategy.

#### *Motor Actuation Stage:*

In this stage, a SN754410 quadruple half-H driver [14] is used to actuate the motor with the corresponding control signal. The PWM wave from the Output Compare module is connected to the pin1 (1, 2EN) of the H driver. The PWM wave enables this H driver. The speed of the motor depends on the duty cycle of the PWM wave from the Output Compare module which is a function of error  $e(t)$ . Therefore the speed of the motor is adjusted based on the error to achieve desired performance and accuracy. The digital outputs of the PIC 32 microcontroller are connected to the direction pins of the H driver (pins 2 and 7). Switching the digital outputs to 0 and 1 between the pins makes the motor rotate in clockwise and counter-clockwise directions. This controls the finger to maintain the force levels based on the control strategy.  $V_{cc1}$  and  $V_{cc2}$  are connected to the 5V supply of the PIC 32 I/O board. This proposed design was tested on an index finger of a prosthetic hand prototype. Fig. 2 shows the test bed for the proposed design. The Mechanical design of the robotic hand prototype is explained in the following section.

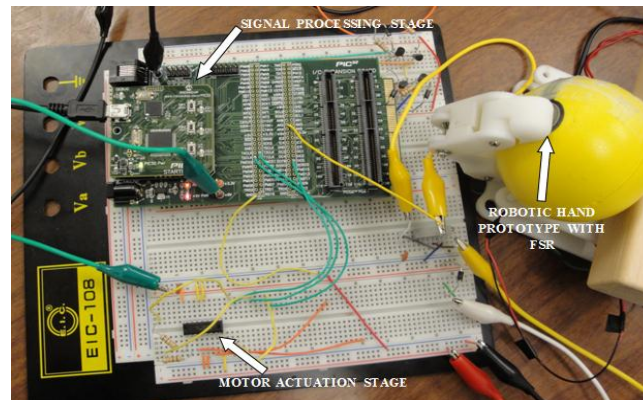


Fig. 2. Embedded Test bed for the proposed design

## **Results and Discussion**

### *Results for MRAC*

Data is acquired from the microcontroller through UART channel2 of the PIC 32 micro controller by a virtual com port via USB at 57600 baud rate. The data from the microcontroller is converted into unit16 data type before it is transmitted through the UART. The PIC 32 microcontroller is running at 80 million instructions per second (MIPS) with its phase lock loop (PLL) activated. It is running at an external clock frequency of 8MHz with internal scaling enabled. Fig. 3 depicts the experimental results of the proposed design. The prosthetic hand prototype mathematical model is used instead of the actual hand to obtain the simulation based force output to validate the controller performance. The simulation based force output converges to the fusion model estimate  $\hat{F}$  in approximately 0.9 ms. The simulation based force output exactly matches the fusion model estimated force  $\hat{F}$  after the convergence. The actual force output from the FSR (i.e.  $Y$ ) closely follows the fusion model estimated force  $\hat{F}$ . In Fig. 3 there are some instances where the FSR lost contact with the object, as indicated by a sharp drop in the force curve.

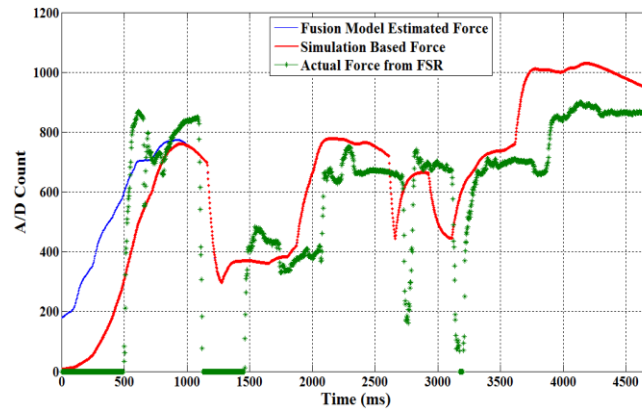


Fig. 3. Fusion based force estimate, simulation based force and actual force from FSR during the grasp.

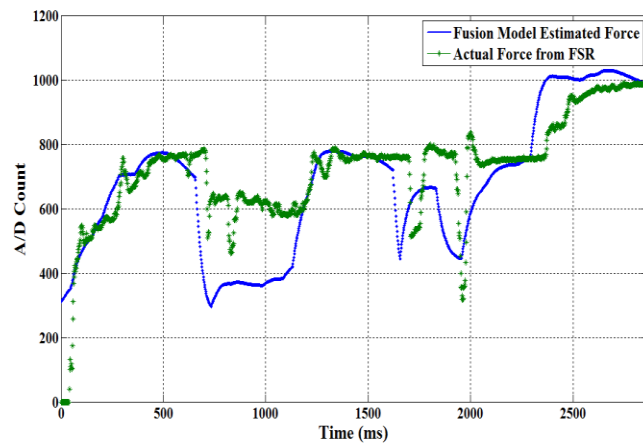


Fig. 4. Fusion based force estimate and actual force from FSR during the grasp (separate experiment).

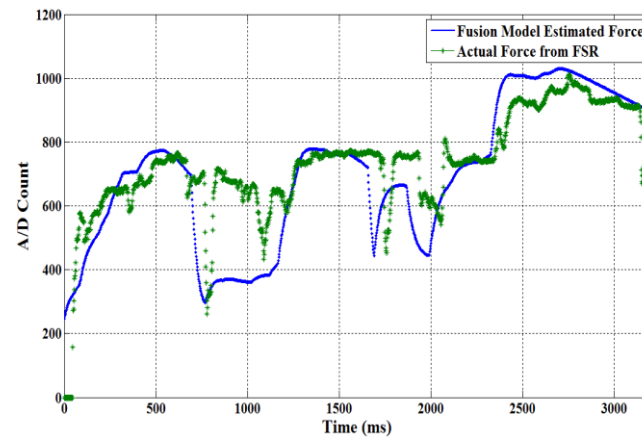


Fig. 5. Fusion based force estimate and actual force from FSR during the grasp (for a repeated experiment).

Fig. 4 shows the fusion model estimated force  $\hat{Y}$  and actual force from the FSR ( $Y$ ) plotted for a separate experiment. In this case, the prosthetic hand prototype is made to maintain a minimum constant force so that the contact between the FSR and the object will not be lost. The same experiment is repeated to test the consistency, and to make sure that the object is in contact with the FSR throughout the experiment.

Fig. 5 shows the repeated experimental results. The proposed control strategy is tracking the force profile and matching the actual force with the model estimated force ( $\hat{Y}$ ). While conducting the experiments, the following observations were made. The DC motors currently employed have the primary task of moving the prosthetic fingers. As the project is ongoing research, the SMA actuation scheme is not yet implemented because of the slow response of the SMA's, and also SMA's have high relaxation time. Therefore it is difficult to track a randomly changing force profile with a slowly responding actuation system. However, as the hand is designed to use the parallel actuation of these DC motors and SMA's, the DC motors alone cannot produce fusion model estimated force. In this work, the DC motors are solely responsible for the motion and force actuation. Since the DC motors have small gear heads, the usual characteristic of gear driver actuation cores occurs: gear backlash. In addition, the DC motors employed were slow in responding to the changes in the force profile. Hence some gaps were observed in the measured force signal. This indicates that there are instances in which the fingertip loses contact due to backlash and vibration problems. However, the profile of the measured force from the FSR has a similar pattern as the fusion model estimated force ( $\hat{Y}$ ). Thus we can conclude that apart from those mechanical transmission problems the implemented control scheme produced promising results. These problems will be considered in a new prototype design that we are currently developing. It is also evident from Figs. 4 and 5 that the minimum constant force is needed to obtain better contact with the object and to accomplish accuracy in tracking the reference force profile. In order to test the precision of the proposed control strategy, 15 different experiments were conducted. The mean of the Pearson's correlation coefficient (see Appendix) for fusion model estimated force ( $\hat{Y}$ ) and the actual force from the FSR ( $Y$ ) in all the 15 experiments is 0.86. Because of the above mentioned transmission problems and the slow response of the gears, slight variability is observed in the correlation coefficients for the 15 experiments. Hence the difference in tracking the force profile is observed in Figs. 4 and 5. Fig. 6 depicts the validation plot with a different fusion based force estimate  $\hat{Y}$  obtained by feeding a different sEMG signal to the MISO transfer function ( $H(s)$ ). The fusion based force estimate, simulation based force and the actual force from the FSR are all shown in Fig. 9. The same mechanical transmission problems and the slow response of gears are observed in this experiment as well. However, the controller is tracking the force profile and the Pearson's correlation coefficients for fusion model estimated force ( $\hat{Y}$ ) and the actual force from the FSR ( $Y$ ) is 0.84, which is close to other experiments.

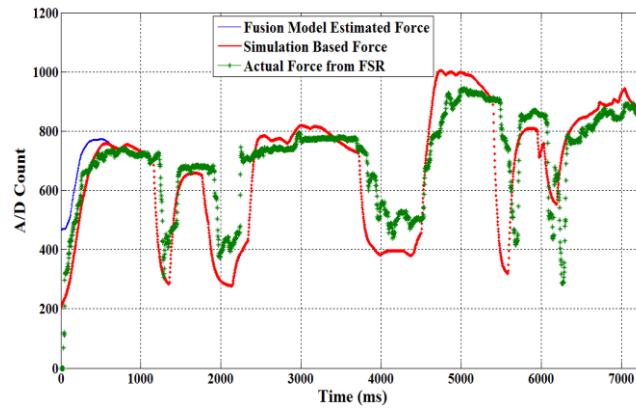


Fig. 6. Validation plot for different model estimated forces.

#### Results for LQG Controller

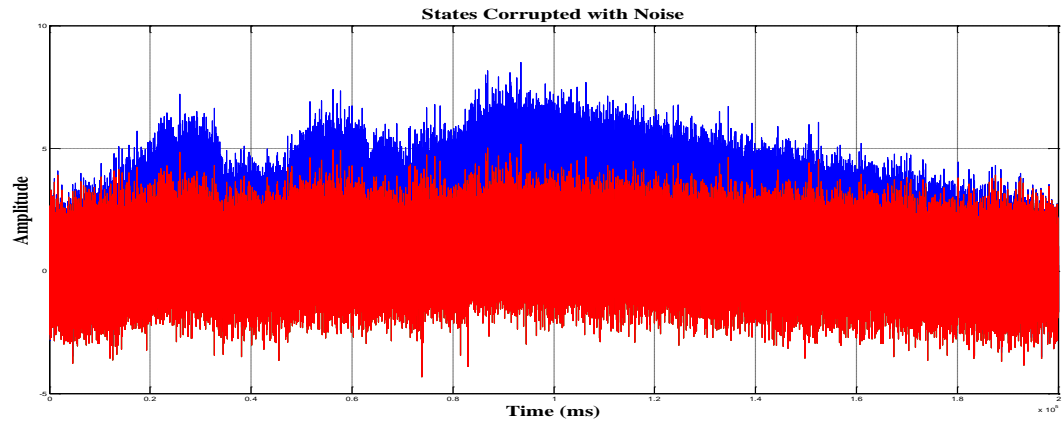


Fig. 7. States corrupted with white noise.

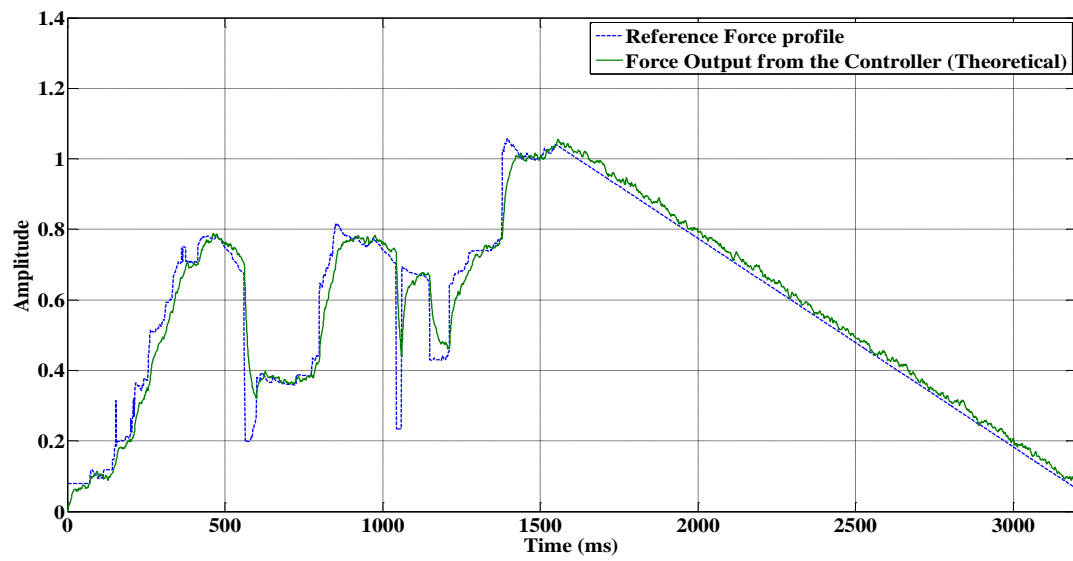


Fig. 8. Fusion based force estimate, simulation based force (force output from the LQG controller)

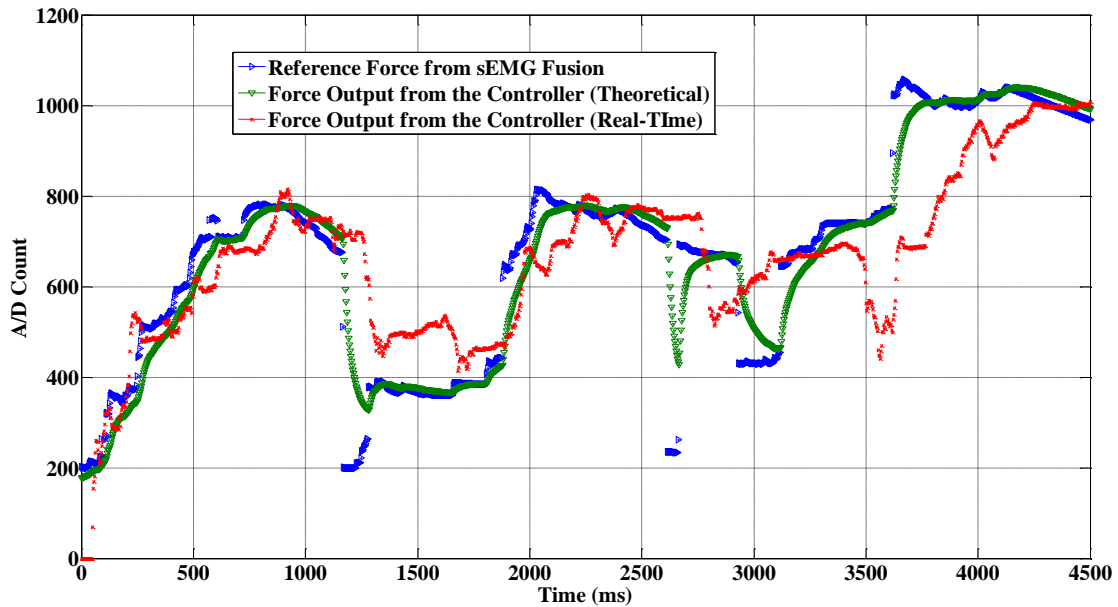


Fig. 9. Fusion based force estimate and actual force from FSR during the grasp

Figs 7 and 8 are useful to validate the controller performance. The plot states are manually corrupted with white noise. It is evident from the two figures that the controller is able to clean out all the white noise and estimate the states. A correlation of 89% is achieved between the reference and the actual force, using the theoretical controller design. Fig. 9 shows the performance of the controller on the real prosthetic hand after prototyping it on embedded test bed. In the real time implementation a correlation of 82% is achieved due to the above mentioned mechanical design problems.

## Position Control

### EXPERIMENTAL SETUP

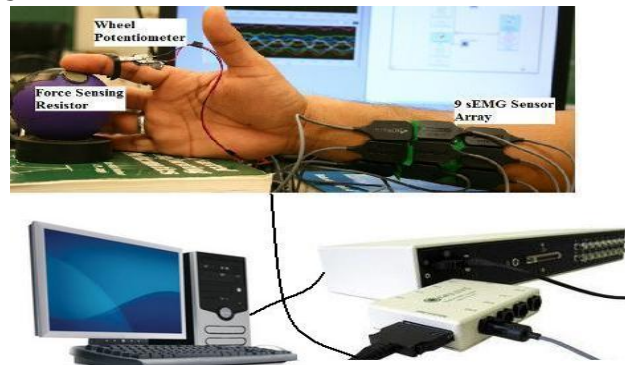


Fig.1: Experimental set-up.

Fig.1. illustrates the experimental design used in this for capturing the sEMG signal and the corresponding joint angle of the PIP joint of the index finger. Prior to placing the sEMG sensors on the skin surface, the test subject was prepared according to the ISEK standards. The motor point is identified by using a wet probe muscle point stimulator (Richmar HV-1000). Nine DE-3.1 sEMG sensors of the DELSYS Bagnoli-16 EMG system are arranged on the skin surface in a three-by-three array. The middle rows of sensors are placed on the motor point of the index finger. An angle measurement device is designed using a 10k-Ohm wheel potentiometer shown in Fig.1. It is used to measure the PIP joint angle.

Force Sensitive Resistor (FSR) is mounted on the stress ball and it is used to measure the force. All the data is acquired at a sampling rate of 2000 samples/sec.

## PROPOSED DESIGN

The objective of the proposed design is to track a joint angle of the prosthetic hand as closely as possible. Here, the joint angle signal is inferred from the sEMG signals obtained from the array of the sEMG sensors located at the arm.

Sensor fusion is done in the time domain for the sEMG data using a probability based Kullback information criterion (KIC) fusion algorithm. The data from the nine sensors are collected around the corresponding individual motor unit location at the transradial arm location (flexor digitorum superficialis) and before fusing the SEMG are rectified and filtered using a Half -Gaussian filter, as given by (1).

$$p(EMG|x) = 2 \times \frac{\exp\left(-\frac{EMG^2}{2x^2}\right)}{\sqrt{2\pi x^2}}, \quad (1)$$

where  $p(EMG|x)$  is a conditional probability density function,  $x$  is a latent driving signal.

System Identification (SI) tool is used to determine the dynamic relationship between the input-output data. The sEMG signal is used as input and the corresponding PIP joint angle as output. In particular, nonlinear Wiener Hammerstein one-dimensional polynomial models are obtained for sEMG/joint angle data.

The mathematical representation of the modeling is given by,

$$w(t) = f(u(t)), \quad (2)$$

$$x(t) = \frac{B_{j,i}(q)}{F_{j,i}(q)} w(t - nk) + e(t), \quad (3)$$

$$y(t) = h(x(t)), \quad (4)$$

where  $u(t)$  is the sEMG signal and  $y(t)$  is the PIP joint angle.  $f$  and  $h$  are nonlinear functions,  $w(t)$  and  $x(t)$  are internal variables,  $B_{j,i}(q)$  and  $F_{j,i}(q)$  are polynomials,  $q$  is the back shift operator, and  $e(t)$  is the output error. From (3), the WH model structure utilizes a linear OE model, which is given by,

$$y(t) = \frac{B(q)}{F(q)} u(t - nk) + e(t) \quad (5)$$

where  $nk$  is the system delay and  $t$  is time index

The resulting nine WH models are fused together by using a probabilistic the KIC algorithm .It assigns a particular probability to each model.The overall estimated model output and the individual models outputs are compared by using the Pearson's correlation coefficient.

From the previous research, it was shown that the KIC algorithm performs better than the other criterions [12, 14]. KIC is a asymmetric measure of the models dissimilarity which can be obtained by the sum of the two directed divergences known as J-divergence or kullback's symmetric [15]. It is given by

$$KIC(p_i) = \frac{n}{2} \log R_i + \frac{(P_i + 1)n}{n - p_i - 2} - n\psi\left(\frac{n - p_i}{2}\right) + g(n) \quad (7)$$

Where  $g(n) = n \cdot \log(n/2)$ ,  $\psi$  - digamma function.

The probability based fusion algorithm given is applied to the nonlinear models obtained by using SI technique with the following steps:

1: The WH models are obtained by considering the sEMG data  $u(t)$  as input and joint angle  $Y$  as output,



2: Calculate the residual square norm i.e.,  $R_i = Y - \Phi_i \hat{\theta}_i = \|Y - \hat{Y}\|$

where  $\hat{\theta}_i = \{\Phi_i^T \Phi_i\}^{-1} \Phi_i^T Y$ , and

$$\Phi = \begin{bmatrix} Y^T & u_{p-1}^T & Y_{p-1}^T & u_1^T \\ Y_{p+1}^T & u_{p+1}^T & Y_p^T & u_2^T \\ \dots & \dots & \dots & \dots \\ Y_{n-1}^T & u_{n-1}^T & Y_{n-2}^T & u_{n-p}^T \end{bmatrix}$$

3: Compute the model criteria coefficients using (7).

4: The model probability can be computed using

$$p(M_i(t) | Z) = \frac{e^{-l_i}}{\sum_{j=1}^k e^{-l_j}}$$

5: The fused model output can be calculated using

$$\hat{Y}_f = \sum_{i=1}^k p(M_i(t) | Z) \hat{Y}_i.$$

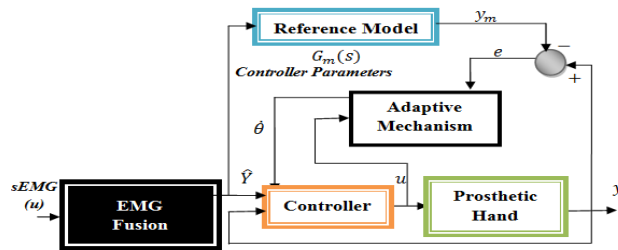


Fig.2: Block diagram representation of Model Reference Adaptive Controller (MRAC)

A simple MRAC based scheme (Fig. 2) is utilized for compensating the dynamics of the prosthetic. During the development of the artificial hand, changes are being undertaken to the mechanical design and drive trains of the hand that affect the dynamics of the finger motion of the prosthesis. In addition, the uncertain characteristics of the kinematic and actuator interaction may lead to a different performance than expected. Therefore, a simple MRAC controller is developed in order to maintain some performance stability. For updating the controller parameter  $\theta$ , the MIT rule is used.

$$\frac{d\theta}{dt} = -\gamma e Y_m. \quad (8)$$

According to the MIT rule [16] the gain parameter  $\gamma$  is selected to achieve the desired performance. In this  $\gamma$  is taken as 3.0 and the error  $e = Y - Y_m$  is calculated by the difference of the model reference output  $Y_m$  and the actual output (joint angle generated by the prosthetic hand).

#### Reference Model Derivation

The dynamic equations of motion for the hand are obtained from the Lagrangian approach as

$$\dot{x}(t) = \begin{bmatrix} 0 & 1 \\ 0 & 0 \end{bmatrix} x(t) + \begin{bmatrix} 0 \\ 1 \end{bmatrix} u(t). \quad (15)$$

The control input vector  $u(t)$  given by

$$u(t) = -M^{-1}(q(t)) [N(q(t), \dot{q}(t)) - \tau(t)]. \quad (16)$$

As the prosthetic hand is required to track the desired angle profile  $q_d(t)$  described under the reference angle model, the tracking error  $e(t)$  is defined as

$$e(t) = q_d(t) - q(t). \quad (17)$$

Here,  $q_d(t)$  is the desired angle vector of the joints and can be obtained by the reference angle model [20];  $q(t)$  is the actual angle vector of the joints. Differentiating (17) twice, we get,

$$\dot{e}(t) = \dot{q}_d(t) - \dot{q}(t), \quad \ddot{e}(t) = \ddot{q}_d(t) - \ddot{q}(t). \quad (18)$$

Substituting (14) into (17) gives

$$\ddot{e}(t) = \ddot{q}_d(t) + M^{-1}(q(t))[N(q(t), \dot{q}(t)) - \tau(t)] \quad (19)$$

From (19) the control function  $u(t)$  can be defined as

$$u(t) = \ddot{q}_d(t) + M^{-1}(q(t))[N(q(t), \dot{q}(t)) - \tau(t)]. \quad (20)$$

This is often called the feedback linearization control law, rewriting (20) as,

$$\tau(t) = M(q(t))[\ddot{q}_d(t) - u(t) + N(q(t), \dot{q}(t))] \quad (21)$$

Using (17) and (20), the state vector  $x(t) = [e'(t) \dot{e}'(t)]'$ , the state-space model can be represented as

$$\dot{x}(t) = \begin{bmatrix} 0 & I \\ 0 & 0 \end{bmatrix} x(t) + \begin{bmatrix} 0 \\ I \end{bmatrix} u(t). \quad (22)$$

Now, (22) is in the form of a linear system such as

$$\dot{x}(t) = Ax(t) + Bu(t). \quad (23)$$

#### Implementation:

The proposed control design is implemented on a PIC 32MX360F512L microcontroller in two stages: “Signal Processing” and “Motor Actuation”. The Signal Processing stage enables the execution and implementation of real-time control strategies. A dsPIC block set is used to generate the C code for the PIC 32 from Simulink<sup>®</sup>. The dsPIC block set generates a .hex file, and this file is imported in MPLAB<sup>®</sup> to program the PIC 32.

#### Signal Processing Stage:

In spite of many modules available on PIC 32, the following four modules are utilized for the implementation of the signal processing stage: Analog Input Module, Digital Output module, Output Compare module, URAT module.

The sensory feedback position data from the wheel potentiometer is acquired through the Analog Input module. Based on the selected control strategy to the motor actuation stage, the digital control signals are generated by Digital Output module of the PIC 32. The changes in the reference/command signal are detected by this module. A pulse width modulated (PWM) wave with a specific duty cycle is generated by the Output Compare module based on the error. The position data from the microcontroller to the PC is transmitted by the UART module via serial communication. In this particular design, the data was fed to the computer by a virtual com port via USB cable. The signals from the ports are read by MATLAB<sup>®</sup>.

### *Motor Actuation Stage:*

In this stage, the motor is actuated with a SN754410 quadruple half-H driver [21] with the corresponding control signal. This proposed design was tested on an index finger of a prosthetic hand prototype. Fig. 3 shows the test bed for the proposed design.

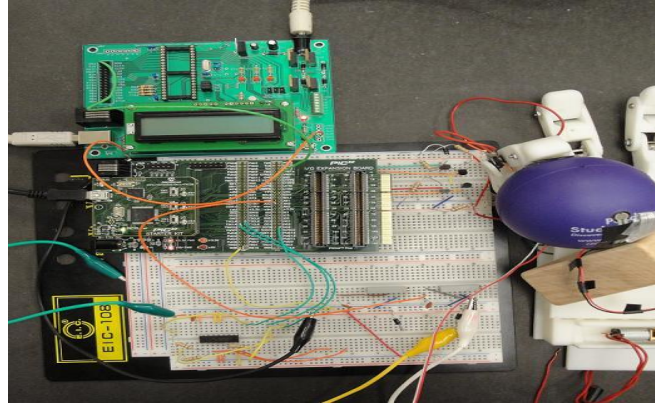


Fig. 3. Embedded Test bed for the proposed design

### ***1. Mechanical structure of the robotic hand prototype:***

The prosthetic hand prototype finger has three degrees of freedom stimulated by two Pololu 35:1 mini metal gear motors. Biologically inspired parallel actuation is the main characteristic of this robotic hand prototype. It is based on the behaviour/strength space of the Flexor Digitorum Profundus (FDP) and the Flexor Digitorum Superficialis (FDS) muscles [22]. Based on the belt transmission system, the DC motor in the metacarpal phalange of the finger triggers the Proximal Inter Phalangeal (PIP) joint. It also drives the DIP (Distal Inter Phalangeal) joint. The Meta Carpo Phalangeal (MCP) joint is actuated by the DC motor located at the base of the finger as shown in Fig. 4.

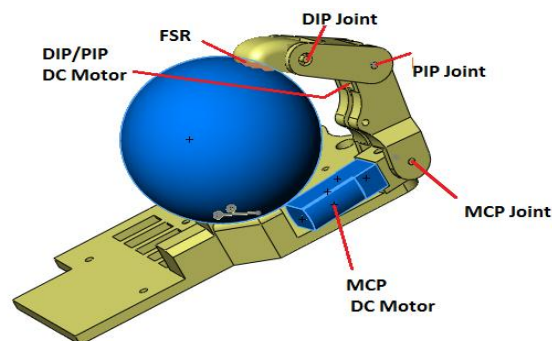


Fig. 4. Actuation scheme for the finger

## **RESULTS AND DISCUSSION**

Data is acquired from the microcontroller through UART channel2 of the PIC 32 micro controller by a virtual com port via USB at 57600 baud rate. The data from the microcontroller is converted into unit16 data type before it is transmitted through the UART. It is running at an external clock frequency of 8MHz with internal scaling enabled. Fig. 5 depicts the experimental results of the proposed design. The actual position output from the position sensor (i.e.  $\hat{Y}$ ) closely follows the fusion algorithm estimated position  $\hat{Y}$ . Fig. 7 shows the fusion estimated position profile  $\hat{Y}$  and actual position from the position sensor ( $\hat{Y}$ )

plotted for a separate experiment. Fig. 7 shows the repeated experimental results. The proposed control strategy is tracking the position profile and matching the actual position profile with the model estimated position ( $\hat{Y}$ ).

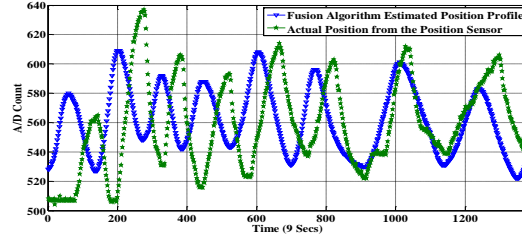


Fig. 6. Fusion based position estimate and actual position from position sensor during the grasp action.

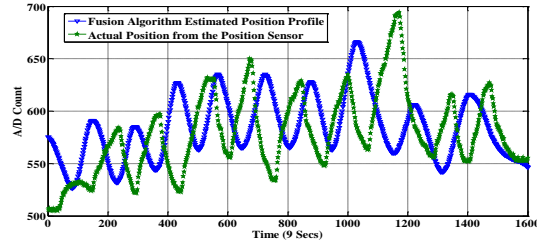


Fig. 7. Fusion based position estimate and actual position from position sensor during the grasp action (for experiment-2).

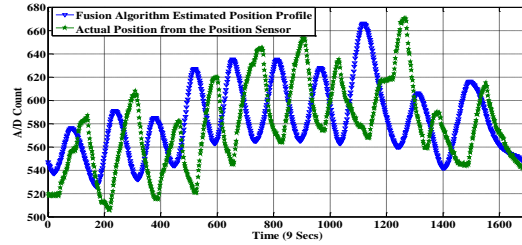


Fig. 8. Fusion based position estimate and actual position from position sensor during the grasp action (for experiment-3).

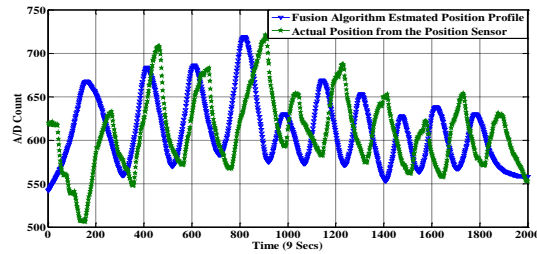


Fig. 9. Validation Plot.

While conducting the experiments, the following observations were made. The DC motors currently employed have the primary task of moving the prosthetic fingers. As the project is an on-going research, the SMA actuation scheme is not yet implemented because of the slow response of the SMA's, and also SMA's have high relaxation time. Therefore it is difficult to track a randomly changing position profile with a slowly responding actuation system. However, as the prosthetic hand prototype is designed to use the parallel actuation of these DC motors and SMA's, the DC motors alone cannot produce fusion algorithm estimated position profile.

In this, the DC motors are solely responsible for the motion actuation. Since the DC motors have small gear heads, the usual characteristic of gear driver actuation cores occurs: gear backlash. In addition, the DC motors employed were slow in responding to the changes in the force profile. Hence some gaps and

delay were observed in the measured position signal. However, the profile of the measured position from the position sensor has a similar pattern as the fusion algorithm estimated position ( $\hat{Y}$ ). Thus we can conclude that apart from those mechanical transmission problems, the implemented control scheme produced promising results. These problems will be considered in a new prototype design that we are currently developing. It is also evident from Figs. 6, 7 and 8 that the controller is tracking very well the slow changes in the position profile where as a small delay was observed while tracking the position profile. In order to test the precision of the proposed control strategy, 15 different experiments were conducted. The mean of the Pearson's correlation coefficient for fusion algorithm estimated position ( $\hat{Y}$ ) and the actual position from the position sensor ( $Y$ ) in all the 15 experiments is 0.86. Because of the above mentioned transmission problems and the slow response of the gears, slight variability is observed in the correlation coefficients for the 15 experiments. Hence the difference in tracking the position profile is observed in Figs. 7 and 8. Fig. 9 depicts the validation plot with a different fusion algorithm position estimate  $\hat{Y}$  obtained by feeding a different sEMG.

## CONCLUSION AND FUTURE

In this work, based on sEMG signals, we proposed a two-stage real-time embedded MRAC strategy for a prosthetic hand prototype. The proposed design was tested on a prosthetic hand prototype, based on tracking a reference position profile and it gives good performance. This design enables the transmission of the data from the microcontroller to the computer. This design facilitates the control engineer to increase the accuracy and performance of the design by implementing various novel control strategies and also enables fast trouble shooting.

For the future, we are planning to use the above mentioned embedded platform to implement online model-based skeletal muscle angle estimation along with controller designs that address the above listed mechanical shortcomings. It will be stimulating to acquire the sEMG signal directly from the arm of a healthy subject and transmit to our embedded system rather than using pre-recorded sEMG signals, which will be investigated as well in the future.

## PIC 32 MICROCONTROLLER BASED sEMG ACQUISITION SYSTEM AND PROCESSING USING WAVELET TRANSFORMS

### II. EXPERIMENTAL SET-UP

Using a muscle stimulator (Richmar HV 1100) the motor point for the ring finger of the dominant hand of a healthy male subject is identified. Prior to affixing the sEMG sensors, the skin surface of the subject was prepared according to International Society of Electrophysiology and Kinesiology (ISEK) protocols. Different sets of experiments were conducted with DE 2.1 and DE 3.1 DELSYS® Bagnoli sEMG sensors. One sensor was placed on top of the motor point location and two sensors were placed next to the motor point. The subject was asked to squeeze the stress ball with the ring finger which has a 0.5 inch force sensing resistor from Interlink™ Electronics mounted on it. The sEMG and skeletal muscle force signals were acquired using the 16-channel DELSYS® Bagnoli sEMG and NI ELVIS™ respectively. Using a PIC 32 embedded platform. A similar experimental set-up was designed where the sEMG and the force data was acquired. In both the cases, data was captured at a sampling frequency of 2000Hz. Fig. 1 and 2 show the two experimental set-ups.

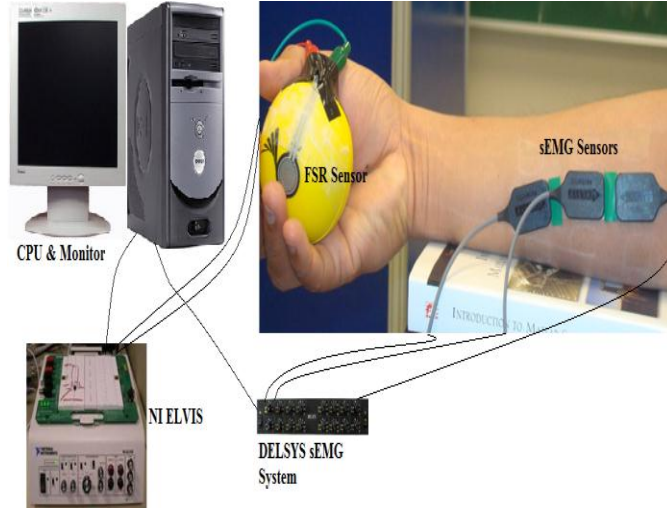


Fig. 1. Experimental Set-Up with NI ELVIS and DELSYS® EMG System.

### III. SIGNAL PRE-PROCESSING

From the authors' previous research shows that the Bayesian based filtering method yields the most suitable sEMG signals. These nonlinear filters extract a signal by significantly reduces the noise. The latent driving signal  $x$  results in the EMG which can be computed using an instantaneous conditional probability  $P(EMG|x)$ . Research describes the EMG signal as an amplitude-modulated zero mean Gaussian noise sequence. This estimation algorithm uses the model of the conditional probability of the rectified EMG signal  $emg = |EMG|$ ,

Equation (1) gives an “Exponential Measurement Model” for the rectified EMG signal

$$P(emg|x) = \frac{\exp(-\frac{emg}{x})}{x}. \quad (1)$$

Equation (2) gives a “Poisson Measurement Model” for the rectified EMG signal [15].

$$P(emg|x) \approx x^n \frac{\exp^{-x}}{n!}. \quad (2)$$

In equation (2)  $n$  is the number of events. Equation (3) presents the “Half-Gaussian measurement model” for the rectified EMG signal [17].

$$P(emg|x) = \frac{2 \cdot \exp(-\frac{emg^2}{2x^2})}{\sqrt{(2\pi x^2)}}. \quad (3)$$

The model for the conditional probability of the rectified EMG is a filtered random process with a random rate. The likelihood function for the rate evolves in time according to a Fokker–Planck partial differential equation. The discrete time Fokker–Planck Equation is given by Equation (4).

$$p(x, t-) \approx \alpha * p(x - \varepsilon, t - 1) + (1 - 2 * \alpha) * p(x, t - 1) + \alpha * p(x + \varepsilon, t - 1) + \beta + (1 - \beta) * p(x, t - 1) \quad (4)$$

In Equation (4)  $\alpha$  and  $\beta$  are two free parameters, where  $\alpha$  is the expected rate of gradual drift and  $\beta$  is the expected rate of sudden shift in the signal. The latent driving signal  $x$  is discretized into bins of  $\varepsilon$ . These free parameters of the nonlinear Half-Gaussian filter model are optimized by a simple elitism based Genetic Algorithm (GA). GA is an optimization algorithm which is based on observing nature and its



corresponding processes to imitate solving complex problems, most often optimization or estimation problems. A wavelet transform is used with a Daubechies mother wavelet (filter). The order of the wavelet is chosen as 44 at 8 levels of decomposition [21]. Continuous wavelet transform of a signal is computed by

$$\begin{aligned} CWT(t, \omega) &= \left( \frac{\omega}{\omega_0} \right)^{1/2} \int_{-\infty}^{+\infty} s(t' - t) dt \\ &= \langle s(t), \psi(t) \rangle \end{aligned} \quad (4)$$

The inner product of the signal  $s(t)$  and  $\psi \in L^2(\mathcal{R}) \setminus \{0\}$  is the mother wavelet function. It must satisfy the following condition:

$$0 < C_\psi = 2\pi \int_{-\infty}^{+\infty} |\hat{\Psi}(\xi)| \frac{d\xi}{|\xi|} < +\infty \quad (5)$$

Skeletal muscle force signal from FSR is filtered utilizing a Chebyshev type II low pass filter with a 550 Hz pass band frequency.

#### IV. METHODOLOGY

The acquisition and transmission of the sEMG signals are done by using Analog Input (ADC Module) and the UART module of the PIC 32. The outputs from the DELSYS<sup>®</sup> Bagnoli system are connected to the analog input channels of the PIC 32 micro controller. In this the signal from the motor unit (middle sensor) is acquired and pre-processed. A C code is generated by a dsPIC block set for the PIC32 from SIMULINK<sup>®</sup>. The dsPIC block set generates a '.hex' file, and this file is imported by MPLAB<sup>®</sup> to program the PIC32. The sEMG and the corresponding skeletal muscle force data is read by using analog Input module. There is an internal analog to digital converter (ADC) in the PIC 32. It has a 10-bit resolution so that it can differentiate up to 1024 different voltages, usually in the range of 0 to 3.3 volts, and it gives 3mV resolution. The signals from the microcontroller are transmitted to the PC through the UART module in the PIC32 using serial communication. In this design, a virtual 'com port' is created to feed the data via USB cable to the computer. The signals from the ports are read by MATLAB<sup>®</sup>. Fig 2 depicts the acquisition system using the PIC 32 micro controller

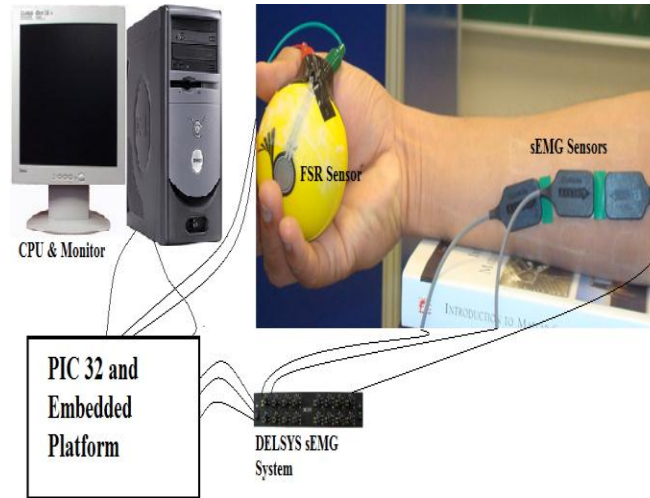


Fig. 2. Experimental Set-Up with PIC 32 Embedded Platforms and DELSYS<sup>®</sup> EMG System.

#### V. RESULTS AND DISCUSSION

Surface Electromyography (sEMG) and the corresponding skeletal muscle force data was acquired from the microcontroller through UART channel 2 of the PIC32MX360F512L by a virtual com port via

USB at 57600 baud rate. The data from the microcontroller was converted into uint16 data before it was transmitted through the UART. The PIC32 microcontroller is running at 80 million instructions per second (MIPS) with its phase lock loop (PLL) activated. It was running at an external clock frequency of 8 MHz with internal scaling enabled. Fig. 3a shows the sEMG signal acquired by the proposed acquisition system using DE 2.1 electrodes. Fig3b. shows the filtered sEMG signal using a wavelet transform Daubechies 44 filter. Fig. 4a and 4b shows the raw EMG and wavelet transform based Daubechies 44 filtered sEMG signals at 5 levels of decomposition acquired by the proposed acquisition system using DE 3.1 electrodes.

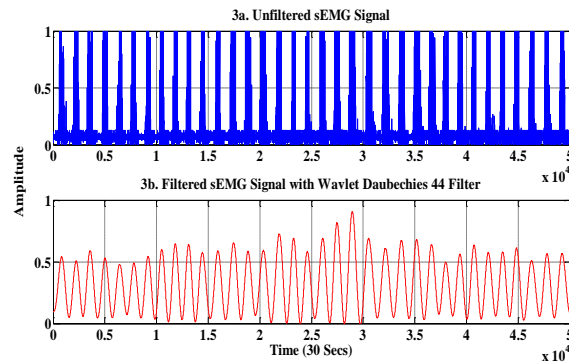


Fig. 3. 3a. Unfiltered sEMG Signal from the Proposed Acquisition System Using DE 2.1 Electrodes, 3b. Filtered sEMG signal with Wavelet Daubechies 44 Filter.

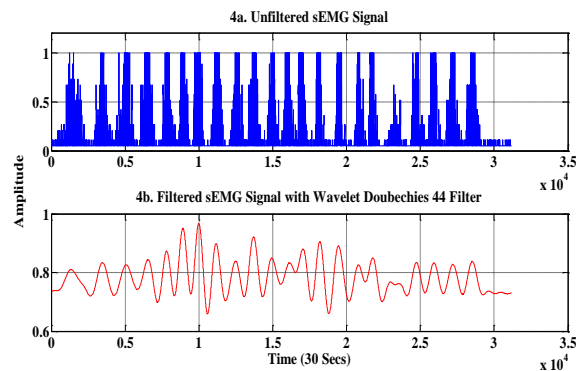


Fig. 4. 4a. Unfiltered sEMG Signal from the Proposed Acquisition System Using DE 3.1 Electrodes, 4b. Filtered sEMG signal with Wavelet Daubechies 44 Filter

The following experiment was repeated several times to check the consistency and the accuracy of the proposed acquisition system. Fig. 5 and 6 show the validation for the proposed acquisition system for repeated experiments using DE 2.1 and DE 3.1 electrodes.



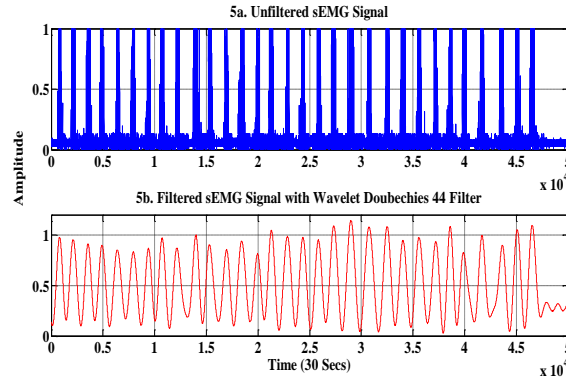


Fig. 5. 5a. Unfiltered sEMG Signal from the Proposed Acquisition System Using DE 2.1 Electrodes, 4b. Filtered sEMG signal with Wavelet Daubechies 44 Filter.

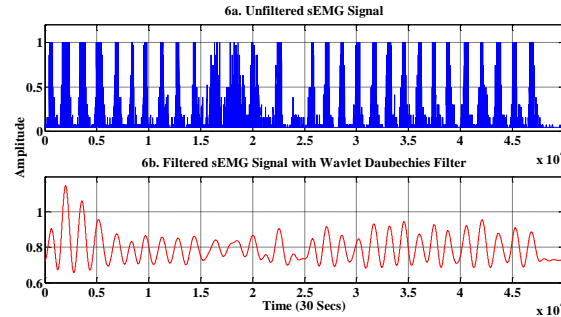


Fig. 6. 6a. Unfiltered sEMG Signal from the Proposed Acquisition System Using DE 3.1 Electrodes, 6b. Filtered sEMG signal with Wavelet Daubechies 44 Filter.

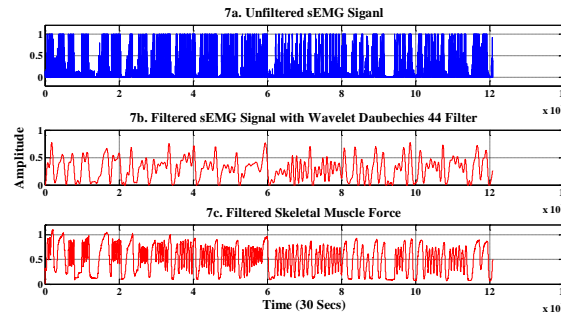


Fig. 7. 7a. Unfiltered sEMG Signal from the Standard Acquisition System, 7b. Filtered sEMG signal with Wavelet Daubechies 44 Filter, 7c. Filtered Skeletal Muscle Signal from Chebyshev Type II Filter.

The sEMG signals and the corresponding skeletal muscle force acquired from the standard acquisition system are given in Fig. 7a, 7b and 7c. Since the sEMG is a random signal corrupted with noise it is hard to achieve the same correlation every time. This proposed acquisition and filtering system is ing better than the Half-Gaussian filtering that was previously developed by the authors [22].

## VI. CONCLUSION AND FUTURE

In this work, a real-time sEMG acquisition and processing system was designed for the control of a prosthetic hand prototype. The proposed design shows the same performance when compared with the standard EMG acquisition system. The DE 2.1 electrodes are giving good results when compared to the

DE 3.1 electrodes of the Delsys® Bangnoli 16 system. This proposed acquisition system miniaturizes the size and helps the transmission of the data from the microcontroller to the computer. This helps the user to compare the accuracy, precision and real-time performance of the acquisition system.

For future, we are planning to implement a real-time online model-based force estimation along with controller design for position and force control, based on this embedded platform [22]. It will also be interesting to do the wavelet Daubechies 44 filtration online instead of post processing. Finally, we expand this sEMG acquisition to all the five fingers of the prosthetic hand prototype.

### **III. Intelligent Classification of Surface Electromyographic (EMG) Signals Based on Entropy for the Control of a Robotic Hand**

#### ***sEMG Electrode Placement***

For the purpose of this research [4] the forearm can be broken into 2 zones. Zone 1 is in the area closest to the wrist. Zone 1 contains mostly the tendons that are connected to the fingers and the muscles in the adjacent zone. Zone 2 where the sensors are placed in Figure 1 is the proximal part of the forearm or the zone closest to the elbow. Zone 2 has the majority of the muscle bellies which contain the main motor units that drive the function of the hand.



**Figure 1: Array of Sensors Placement**

Motor units, such as those in zone 2, are made up of motor neurons and all the connected muscle fibers. Motor units use motor neurons to carry impulses from the spinal cord or central nervous system to the muscles fibers. When the electrical signals for the motor neurons reach the muscles it innervates, the muscles contract.

Actions that require fine motor skills have smaller motor units than gross or rough motor actions. For example, surgeons need fine motor skills to make precise incisions with their hands whereas walking does not require as precise movements. The motor units for people's hands are much smaller than motor units for their thighs.

Motor units are not isolated in one specific area. Each unit is spread throughout the muscle. External stimulation can be used to activate the motor unit of a muscle, but this generally causes weak contractions. In a past experiments [5] and [10] a muscle stimulator, the Rich-Mar HV 1000, was used to find motor points and then the sEMG signal was taken from those points. The points where the motor units are located are difficult to isolate and only contain part of the entire motor unit. Finding the best spot for muscle contraction is difficult due to variations in individuals. This method can be used to find motor units of all fingers for some people to no motor units for others. This variation depends on the subject's muscle mass, sex and other anatomical factors.

On a subject with an amputation, finding motor units is difficult because the only indication of muscle stimulation of a motor unit is movement or twitching of the muscle from the skin's surface since the contraction of the muscle no longer results in finger movement. The severity and type of amputation can also play a factor in finding the correct locations of motor units. If an amputation was planned, it allows the physician to leave more of the motor units. If an accident occurred, the amputation could destroy or damage the motor units for the hand. As time goes on the motor units can weaken in an amputation.

The electrodes were placed parallel with the muscles of the forearm. Zone 1 contains the tendons of the muscles, and past experiments verified that this area contained significantly fewer sEMG signals than zone 2. Zone 2 was over the general muscle bellies, where higher concentrations of motor units are located. An array of 6 electrodes was placed over the muscles in zone 2. The electrodes were used to measure the sEMG signals while conducting the experiments. Surface electrodes are less evasive and do not have to be implanted. For these reasons surface electrodes were used for the experiments.

## Experimental Setup

Experiments were conducted on the forearm of healthy subjects. All subjects volunteered for the experiments. The sEMG electrodes used were dual GS27 ECG & EMG disposable silver/silver chloride pre-gelled surface electrodes. The electrodes measure the voltage on the skin's surface created by the actuation of the motor units which cause muscle to contract. The gel helps the sensors attach to the skin. The gel also is conductive which allows for a better connection to the skin. Before sensors were placed the subject's skin was prepared according to International Society of Electrophysiology and Kinesiology (ISEK) protocols [11]. The arm was also shaven prior to electrode placement to allow for better contact with the skin surface.

The sEMG data acquisition device used was a NORAXON MyoSystem 2000. The data was acquired at a 1,000 Hz frequency (or 1,000 samples a second). The system outputs that information into an output file with 3 signal columns.

The electrodes were placed in an array of 2 by 3. See Figure 2 for the sensor array setup. The six sensors were placed in the back portion of the forearm, towards the elbow. The array was centered between the elbow and 11 cm from the wrist. The 2 sensors were placed perpendicular to the muscle fibers and centered at the halfway mark. Then two sensors were placed towards the wrist and two towards the elbow. They were all evenly spaced with enough space so that the sensors didn't overlap each other. A reference electrode was placed on the elbow where no significant sEMG signal can be measured. See Figure 1 for the electrode placement on forearm. The sensor closest to the wrist is the 1st electrode, the middle one is the 2<sup>nd</sup> and the 3<sup>rd</sup> is the electrode closest to the elbow.



Figure 2: Electrode Array

## Experiment

The experiments that were ran with the subjects were: a baseline test, power grasp of a ball, pad to pad pincer grasp of the middle fingers, and key grip. These experiments were chosen because there would be common task that a person does thought there day.

The baseline was used for the remainder of the signals to be compared to. The baseline consisted of the test subjects holding their hands in a still, relaxed position for approximately 30 seconds. The rest of the experiments were conducted in about 5 seconds allow time for the patient to preform one motion. The power grasps the ball; a stress ball was used to provide resistance to the patient. The next test was a pad to pad pincer grip. This grip was done by touching the thumb and the middle finger pad to pad, not fingertip to fingertip. The subjects would start with their hand open and then close their finger pad to pad tightly against the thumb and then release the grip. The final test is a key grip test. This test simulated the common task of a person grasping a key. Patients would start with their hands open and then close their thumbs on the key tightly and then release the key.

## Data Processing

For the experiment of test results for: baseline tests, power grasp of a ball, pad to pad pincer grasp middle finger, and key grip the overall results can be seen in Table 1. Spectral entropy of unfiltered sEMG signals yielded the best results. Normal entropy and wavelet entropy were both tested but did not give as consistent and accurate results. Also pre-filtering the data by rectifying the signals actually made the entropy calculation more inconsistent.

Table 1: Entropy Results

Baseline		Ball Close & Open	
Average $z^2$		Average $z^2$	
Average	0.7159	Average	0.2682
Range	0.494 to 0.9378	Range	0.1863 to 0.35

Pad to Pad Middle Finger Close & Open		Key Grip	
Average $z^2$		Average $z^2$	
Average	0.4645	Average	0.4172
Range	0.397 to 0.532	Range	0.3518 to 0.4825

From Table 1 the baseline has a much higher average than the rest of the experiments. This tells us that the sEMG signals of people arms in a relaxed position are more random than when they are going a task. This true since most of the signal in a relaxed position is random noise which has a high entropy value and helps support that these results have meaningful information. The ball grasp was around 0.26. The pad to pad pincer grip of middle finger entropy was about 0.46. The key grip was around 0.42 which close to the pad to pad test. This will test the classifier to see if it can differentiate the difference between these motions.

### ***Intelligent Controller***

With the ranges of entropy determined from the experiments an intelligent controller can be created. The controller developed using a fuzzy controller with parameters based on the information in Table 1. sEMG signals of know hand motions were then input into the controller. This was done to test the controller to see how well it can distinguish between different hand gestures. Table 2 is the summary of the results. This table shows that the controller is able to distinguish between a when a person's hand is held still and when they are doing they are power grasping a ball. Hand motions such as pad to pad and key grip are close enough to each other that the controller has more difficulty determining the motion. Some of the time the controller would mix up the two motions.

**Table 2: Experiments Classification of Hand Motions**

	Electrode	Correctly Characterized
Baseline	1 <sup>st</sup>	66.7%
	2 <sup>nd</sup>	66.7%
	3 <sup>rd</sup>	66.7%
Power Grasp Ball	1 <sup>st</sup>	100.0%
	2 <sup>nd</sup>	100.0%
	3 <sup>rd</sup>	100.0%
Middle Finger Pad to Pad	1 <sup>st</sup>	33.3%
	2 <sup>nd</sup>	33.3%
	3 <sup>rd</sup>	66.7%
Key Grip	1 <sup>st</sup>	0.0%
	2 <sup>nd</sup>	33.3%
	3 <sup>rd</sup>	66.7%

**Table 3: Summary of Controller Classification of Signals**

Electrode	Correctly Characterized
1 <sup>st</sup>	50.0%
2 <sup>nd</sup>	58.3%
3 <sup>rd</sup>	75.0%
Total Electrode Accuracy	61.1%

In Table 3 the results are show of the different electrodes. The 1<sup>st</sup> electrode has the lowest accuracy of characterization a signal with 50%. The 3<sup>rd</sup> electrode has the highest accuracy with 75%. The overall successful characterization of the gestures was 61.1%. Some of this variation can be from having male and female subject. It states that sex causes variability in electromyographic amplitudes. Entropy calculation may also be affected by gender. With these promising result of this controller could be used to control a robotic or prosthetic hand. This controller could be loaded onto an embedded platform and use the output to control the prosthetic hand that had sEMG sensor connected to a patients arm.

### Goal 3: Robotic Hand

The main goal for Phase II regarding the prosthetic device is to have a final prototype that fulfills the requirements, one that can be tested with the developed EMG control signals and control strategy, and that can be used as a base for the embedded system.

In order to do so, two deliverables were proposed within Goal 3 for Phase II, which were divided in three objectives.

The first objective was the implementation and testing of the hand prototype developed in Phase I (Hand 1 Prototype I). It had as main characteristic its parallel actuation system, which followed the force / motion division of EMG signals. However this turned out to be difficult to implement. The main disadvantages were the discontinuity of affordable commercial SMA actuators, and the time delay and hysteresis in the SMA actuation. In Prototype II and Prototype III, the parallel SMA actuation was disabled in order to obtain a functional hand, while keeping a very similar hand structure.

The second objective is the design of the new hand prototype (Hand 2 prototype I), combining the experiences of Hand 1 with the results of the testing, newly developed kinematic synthesis results, and with the results from the EMG signal identification. For Hand 2, we introduce a very different design, with remote actuation, which is explained below. In addition, the theoretical developments in kinematic synthesis have allowed us to apply the same strategy for the design of exoskeletons.

The third objective is to explore the manipulation of grasped objects from a theoretical point of view; this benefits both the design and the implementation of path planning algorithms. In order to do so, we continued with the research activity on human hand motion identification, including the design of new motion sensors.

Find in the Body section the detailed report of work and findings for each of these objectives.

#### Goal 3, Objective 1: Implementation and testing of Hand 1, Prototype II-III.

Hand 1 Prototypes II and III are similar in structure, having 5 fingers each with independent actuation and motors embedded within the fingers-palm. It is a good hand for experimentation but it does not meet the requirements regarding size and force output, if a reasonable price is set for it. The main limitation is the size/torque of the small electric actuators that power each degree of freedom. Previous testing gave an average force of about 15N. Currently, no reasonably-priced actuators exist that can power this hand for a force comparable to the human hand. In addition, no realistic-motion actuation was accomplished for the thumb. See CAD model for Hand 1 in Figure 1.

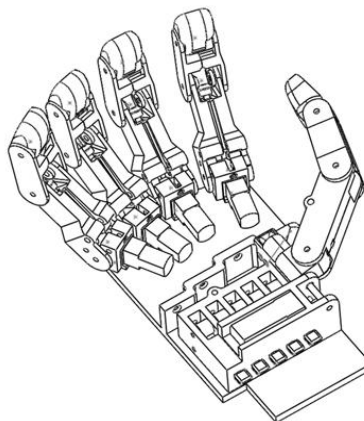
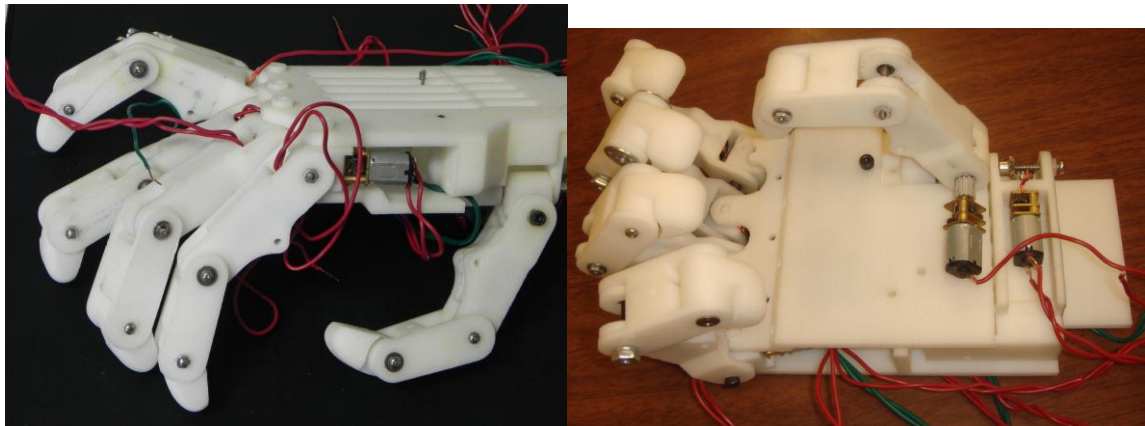


Figure 1: Hand CAD model

Because of this, limited new effort has been devoted to keep refining Hand 1. However, it is a good test bed for the EMG and control testing. Rapid-prototypes of this hand are available for the team to test their different algorithms and results, and individual fingers and combination of fingers are being tested in this way. See Prototype II in Figure 2.



**Figure 2: Prototype II**

The testing performed using this prototype includes some rough EMG controllers using threshold signal and the experimental setup for checking the grasping ability of the hand.

EMG signal capturing capability was added to control the DC motors. The raw signals were processed by taking the maximum absolute value over a 100 sample interval and generating a new data set. In order to get the full flex and extend ability of the finger from this new data set two threshold levels were introduced. Above one threshold the motor would spin in one direction (flex) and below another the motor would spin in the opposite direction (extend). The deadzone was implemented as a buffer area to transition between the flexion and extension zones.

The EMG signal was acquired from the digit III FDP muscle and supplied as an analog voltage from a separate PC incorporating a Delsys Bagnoli EMG system. The analog voltage was sampled through a National Instruments data acquisition card installed in the motor control PC. The analog signal was then filtered and scaled using LabVIEW to a value representing the amplitude of the EMG signal, which was then used to control the direction of the motors. A sample of the filtered and scaled signal with thresholds is shown in Figure 3.

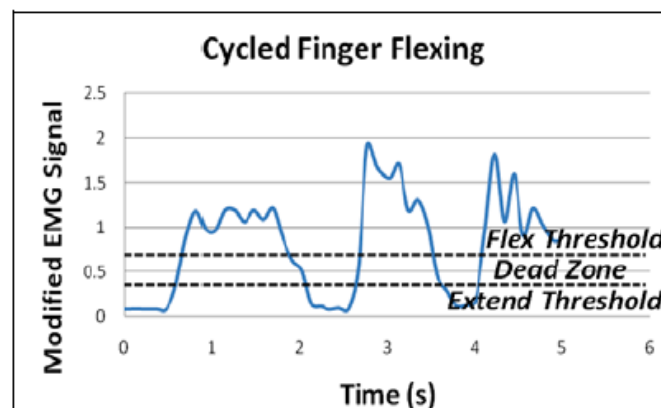


**Figure 3: Thresholds used in the EMG driving signal**



The controller was applied to the DC motors of finger and thumb only, in their close grip configurations. The objective of these tests is to obtain some preliminary data in order to setup the EMG-testing platform.

The EMG voltage and current outputs for both the finger and thumb were consistent with that of the direct power supply inputs. The EMG thumb test resulted in a DC motor force of 0.95N which agreed with the  $1.24\text{N} + 0.35\text{N}$  generated by the direct power supply tests presented in the Final Report of Phase I.

The grasping ability and the reaching of each finger have been analyzed in the real prototype. There are two main patterns in prehensile grasping, the precision grip (or grasp), between the terminal digital pad of the opposed thumb and the pads of the fingertips, and the power grip (or grasp). Holding large objects involve all the digits, while small objects require only the thumb, the index, and the middle digits. Smaller objects may be pinched specifically between the thumb and index (or middle) finger, which should be adapted to perform fine control. The power grip is executed between the surface of the fingers and the palm, which acts as a buttressing and reinforcing agent. All these grasping actions have been visually checked in the prototype, see Figure 4.

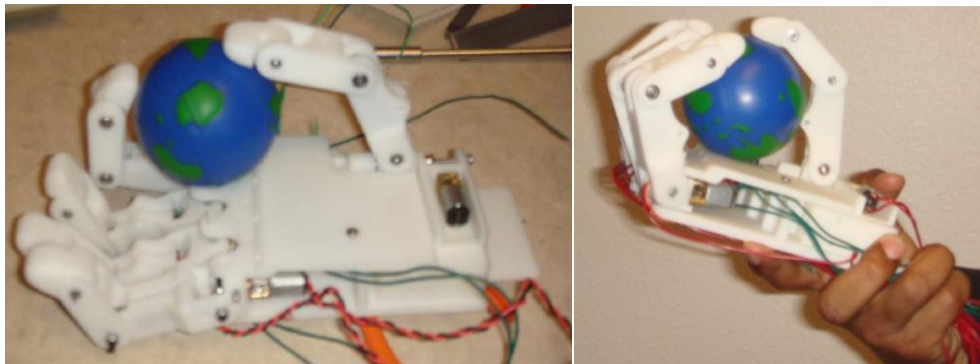


**Figure 4: Hand 1 holding a spherical object**

### **Goal 3, Objective 2: Design of Hand 2, Prototype I**

In Hand 2, the design strategy has been radically changed in order to fulfill the force, weight, size and function requirements. The main requirement for the prosthetic hand is the matching between the kinematic and mechanical design and the driving signals and control laws. These last ones need to be flexible in order to adapt to individuals and environmental changes in signal acquisition, identification and transmission, while this flexibility is hard to implement in a mechanical system without compromising some of the capabilities of the hand, usually the full actuation. Another important problem when designing fully actuated hands is the placement and weight of actuators. With this hand, we aim to create a prosthetic design with the advantages of both under actuated and fully actuated robotic hands, using a simple method to switch from one configuration to the other and placing most of the actuators outside of the hand. Given the complexity associated with the human hand, with its many actuators and sensors, which makes use of forearm muscles, nervous system, and body's energy generation systems, fitting all needed components within the physical size of the hand requires a degree of miniaturization that is still to be achieved at a reasonable price.

In this hand, all actuators are remotely located (it can be in the arm or in the back of the user) and the actuation is performed via cables. Given the variability of amputees, for this hand we are interested in a design that is a hybrid fully-actuated / underactuated [Dollar 2010; Birglen 2008; Hirose 1978] hand.

The human hand has an average weight of 400 grams [Balasubramanian 2011] (distal to the wrist and not



including the forearm extrinsic muscles). However, prosthetic terminal devices of similar weight have been described as being too heavy by users [Chandler 1975]. This is primarily because the attachment methods between the prosthesis and the user compound the effects of the weight in the terminal device. Although researchers are currently working to alleviate attachment problems through the use of integrated attachment mechanisms, the weight of the prosthesis is a key contributor to interface discomforts and user fatigue [Pylatiuk 2007].

A key performance of this hybrid design is to produce power grasps that passively make contact at multiple points, thereby providing the user the ability to apply the desired force on the object from multiple contact points. Due to the limited number of actuators and the uncertainty in object location and shape, the coupled actuation must be designed to minimize situations in which not all links make contact with the object. It is expected that the flexibility associated with this design will allow for a better adaptation to the many different types of amputees.

### ***Hand Structure***

The overall shape and size of the hand is based on the average human hand. This includes five fingers and a thumb that are attached to a fixed palm. Revolute joints make up the 10 degrees of freedom for the interphalangeal (IP) joints of the fingers and IP and MCP joints of the thumb. Universal joints are used in the Metacarpals of each finger (MCP joints) and the CMC joint of the thumb, as well as the combination of flexion-extension and abduction-adduction of the wrist. These joints make up the other 12 degrees of freedom in this design. Joint actuation is created by a cable system that converts actuator rotational motion to linear motion and that back to rotational motion in the joint.

To achieve the desired motion in a lightweight, durable construction, the hand components are made from thin gauge stainless steel. Individual links that make up each finger and the thumb are created by bending thin gauge sheet metal into a tube like section that allow the finger pulleys, cables, and cable conduit to be discreetly hidden inside.

The palm of the hand is constructed in a similar fashion using shaped sheet metal as an external shell. Consecutive links are connected with 3 mm axle shafts that pass through ball bearings creating the revolute and universal joints. To drive the joint motion, 0.039 diameter Teflon-coated cables pass through 0.100 diameter cable conduit as it is roughed through each finger to the palm and then out to actuators located away from the hand. **Figure 5** shows the joint arrangement.

### ***Joint Actuation***

The linear actuation design for Hand 2 operates with the use of a pull-pull cable system. Each joint is controlled by two cables that pass through cable conduits, from the actuator to the joint pulley. The actuator's rotational motion causes the pulley on the actuator to release cable on one side and draw cable in on the other. This results in a rotation of the joint pulley and ultimately a rotation of the joint. In reverse fashion when the actuator rotates in the reverse direction the opposite cable is drawn or pulled in causing a tension in the cable and a reverse rotation of the joint pulley and the joint.

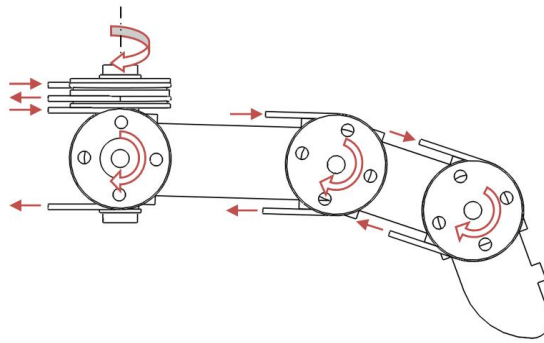


**Figure 5: Finger Pulleys**

This simple design is repeated for the Distal, Proximal, and Metacarpal joints of each finger and the thumb. However the metacarpal joints on each finger and the thumb are universal joints and add a second degree of freedom and a second pull-pull actuation cable system to the joint, see **Figure 6**.

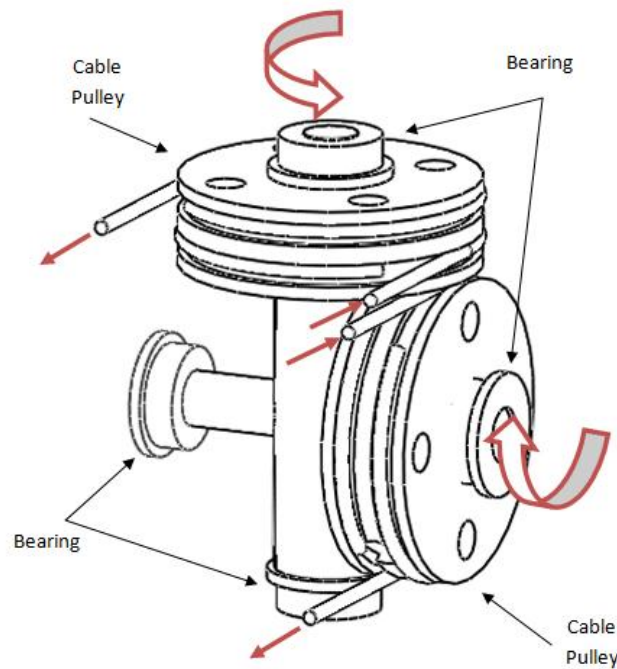


**Figure 6: Metacarpal Universal Joint**

The 2-dof wrist joint is also a universal joint, but a third rotational degree is added to allow hand pronation/supination. This results in 23 degrees of freedom. Because of the fact that the distal IP joints of a human hand on average are 70% coupled to the Proximal IP joints, the distal joint and the proximal joint of this design are actuated with one actuator resulting in a coupled motion for each finger. This coupling reduces the total independent degrees of freedom down to 19.

## Actuation

To minimize the overall weight seen by the user, the actuators that control the hand motion are to be placed remotely, in an operational backpack. This allows actuators to be sized based on output power instead of overall dimensions. The power unit that is used to power both the control system and the actuators can also benefit from this design.



**Figure 7: Faulhaber Gearmotor and Encoder**

For each degree of freedom a Faulhaber Gear Motor and Encoder (**Figure 7**) will be used to drive the 19 active degrees of freedom. The windings have an overall resistance of 11 ohm, which means the motor will draw 0.55 amps at 6V if stalled. The motor has a peak efficiency of 74%. The no-load motor speed is 13,400 RPM at 6V but will be slower with a gearhead attached.

The dual-channel encoder is similar to an HEM encoder that accepts a 4.5v to 15v. To measure only RPM or distance, the encoder has two channels, one of them providing one high pulse per revolution of the motor. There will be 141 high pulses per revolution of the gearshift, or about 2.55 degrees of final output rotation per pulse. To increase resolution or to measure rotation direction, the microcontroller can watch both channels A and B. The output of the encoder is very clean, see **Figure 8**.

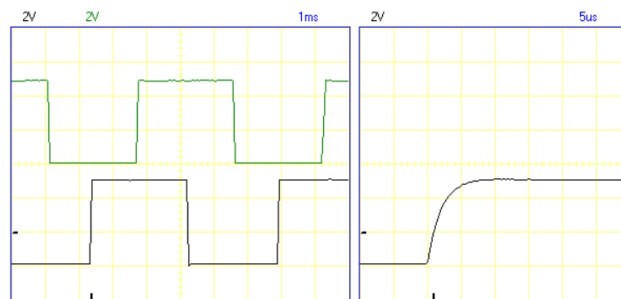


**Figure 8: Oscilloscope trace of two channel encoder**

To connect the gear motors to the individual finger pulleys, the pull-pull system described above is to be utilized. The routing of the individual cable conduits is yet to be developed.

## Pressure Sensing

To provide tough/strength of grasp sensing in the hand, the actuator utilizes a variable resistance sensor. This sensor provides feedback to the controller of the torque being applied by the actuator to the finger. In simple control layouts the input voltage for the motor would pass through the variable resistor controlling the speed and stopping signal based on the spring constant. In more complicated controls this resistive signal would provide the force input that will allow one finger to provide more force than another and possibly create motion of object that have already been grasp.

This sensor is constructed by connecting a variable resistor to the drive hub and the motor pulley. A torsion spring connects the motor pulley to the drive hub. When force increased due to object contact, this force is carried through the actuation cables to the motor pulley and then into the torsion spring. As the spring stores this energy it allows the motor pulley to rotate on the drive hub and change the resistance in the variable resistor. This change in resistance provides feedback to the motor controller on the strength of grasp that the robot is producing. This sensor also provides a buffer to jerk that would otherwise be produced in the actuation system during grasp contact. A diagram of this sensor is shown in Figure 6.

One of the main benefits of using this type of touch/strength sensing is it allows for contact to be sensed no matter where it occurs on the robotic hand. Pressure sensors located at the tips of each finger have been used to provide similar sensing however if object contact does not happen in the unit normal direction this force can be misinterpreted by the sensor.

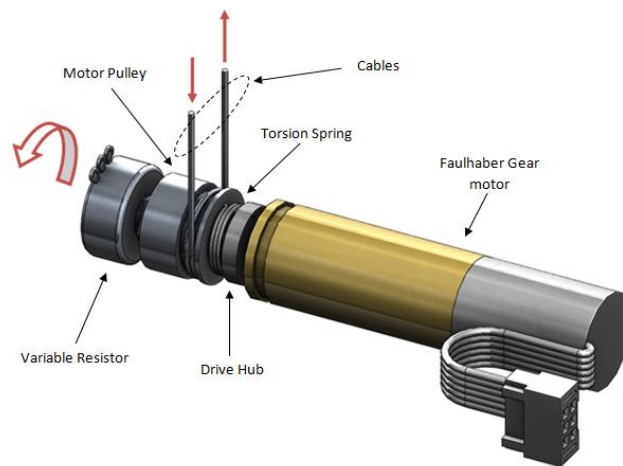


**Figure 9: Pressure Sensor**

### ***Prototype***

The prototype is to be created using a sheet metal laser. Thin gauge stainless and sheet metal flat patterns created in Solidworks® CAD software (**Figure 10**) will allow each link in the hand to be created with an interlocking design that minimizes weight and maintains strength. This design also allows for simple maintains on the joint pulleys, cables, and cable conduits by allowing access to these areas without major disassembly.

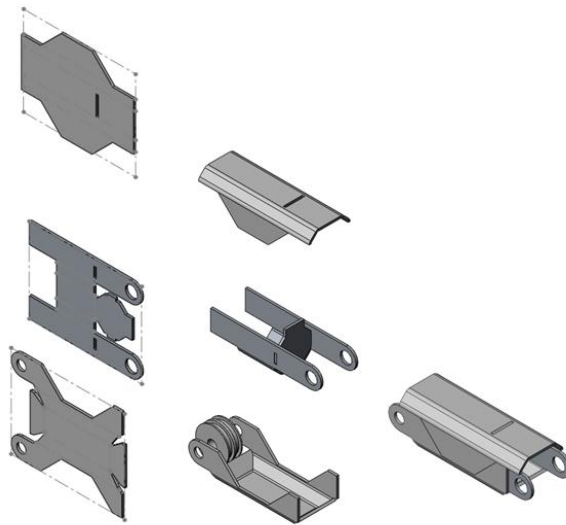


**Figure 10: Sheet Metal Construction**

The remaining palm and wrist of the hand will be constructed in similar fashion. Formed sheet metal stainless steel plates are joined together to form the bearing carrier for each metacarpal universal joint. The thumb of the hand is constructed the like each finger and connected to the palm plates with internal sheet metal bearing carriers. Structural strangle of the system is achieved after all components are connected. This included the access plates that are used to maintain the actuation cables. Actuators for each degree of motion are mounted to a common mounting plate that is located in an operational backpack. A general layout of the actuators can be found in **Figure 11**.



**Figure 11: Remote Actuation**

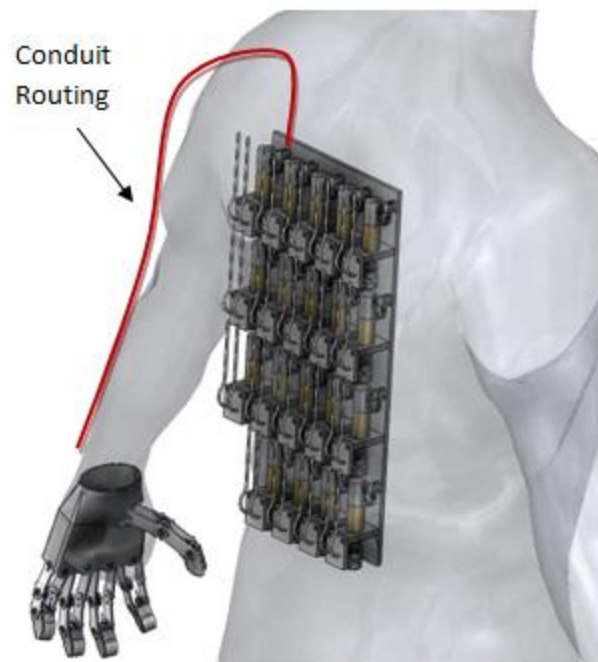


**Figure 12: Conduit Layout**

Cable conduit runs connect the robotic hand to the remote actuators that are located in the operational backpack. These conduit runs will attach the outside of the operators arm and follow the arm down to the hand similar to the sleeve on a shirt. That gives much more flexibility for the design of the hand.

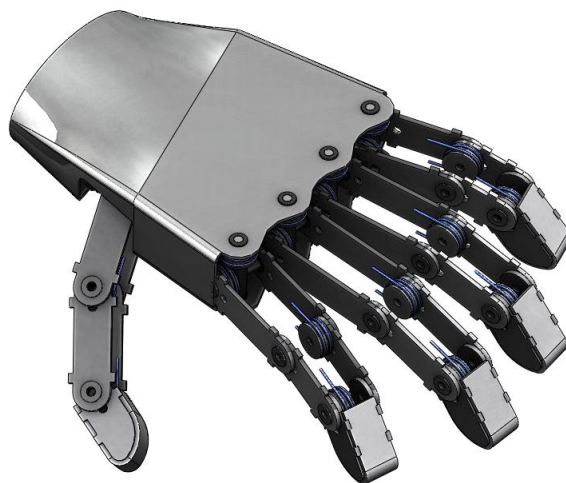


**Figure 13: General Layout**

Because of its flexible design, several actuation schemes are being considered. In this first prototype (Prototype 1), we are not planning to implement parallel actuation. We will compare its performance with Hand 1 regarding the EMG control and will decide whether to add the parallel actuation for a final

prototype of this hand model. Another actuation scheme is the possibility of combining the actuation from several motors in order to create an underactuated hand. This may be needed depending on the limitations of the amputee.

### ***Implementation***

Fabrication of the MS-3 hand has been completed for all fingers and joints during construction of the hand, according to the final model of Figure 14.

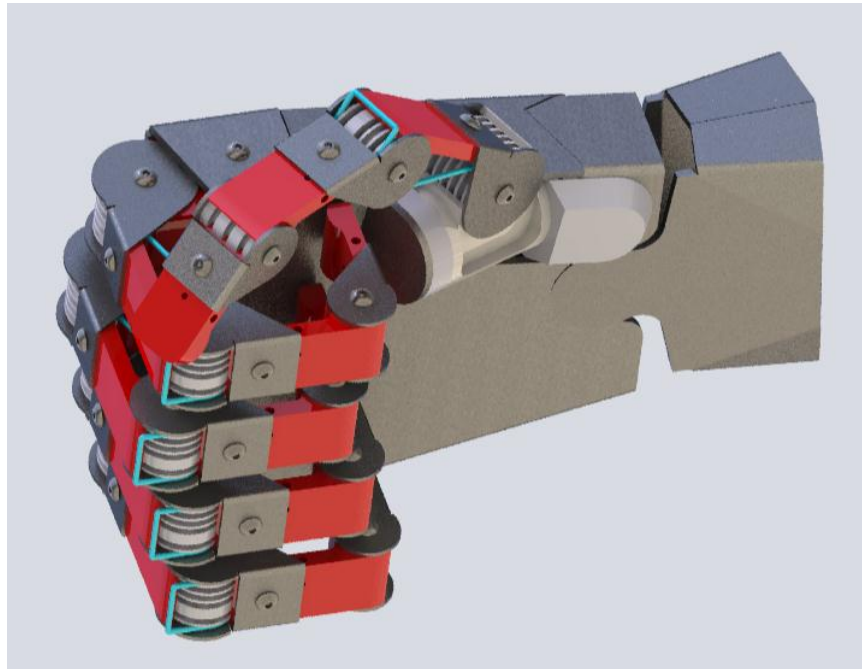


Figure 14: Final design of Hand 2

The hand is being assembled and then tested for compliance to functionality. The hand is based on the overall size constraints of a woman or large child, this was chosen due to scalability. Figure 15 shows the comparison with a human finger.

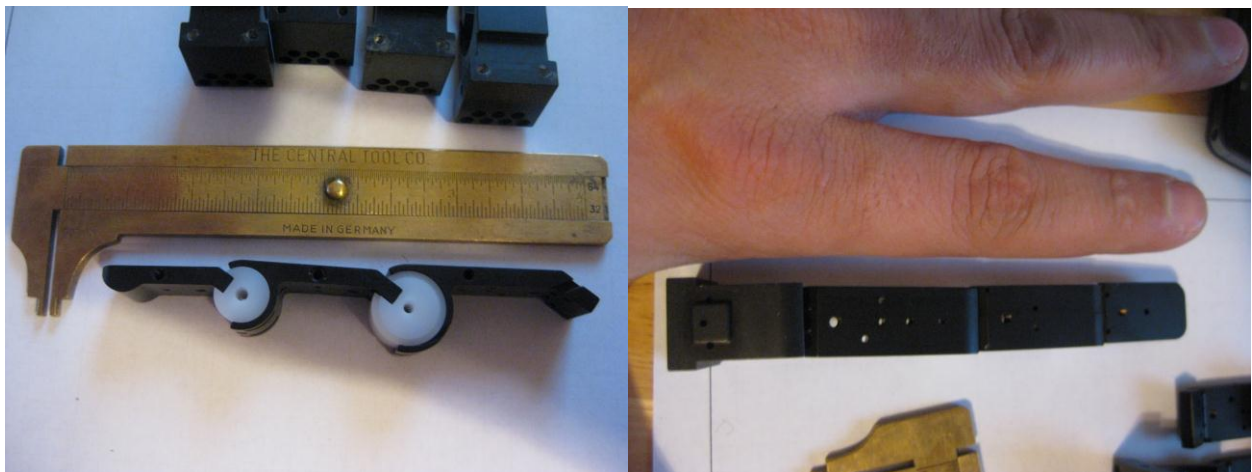


Figure 15: Finger dimensions for Hand 2



In the final design, distal and intermediate phalanges are coupled, resulting in a single degree of freedom for the each finger and thumb. Proximal to metacarpal joint add a second degree of freedom to each finger and thumb. The thumb adds a second degree of freedom in the carpal to metacarpal joint, this results in 11 degrees of freedom. Servo motors provide the torque and rotation motion required for each degree of freedom. This is transferred from the servo motor to the desired joint with the use of Bowden cables. For each servo motor two cables are required and act as a pull-pull configuration. All servos are controlled by a mini maestro 12-channel USB servo controller. Figure 16 shows some of the expected actions of the hand, and the table below shows some of the final dimensions.

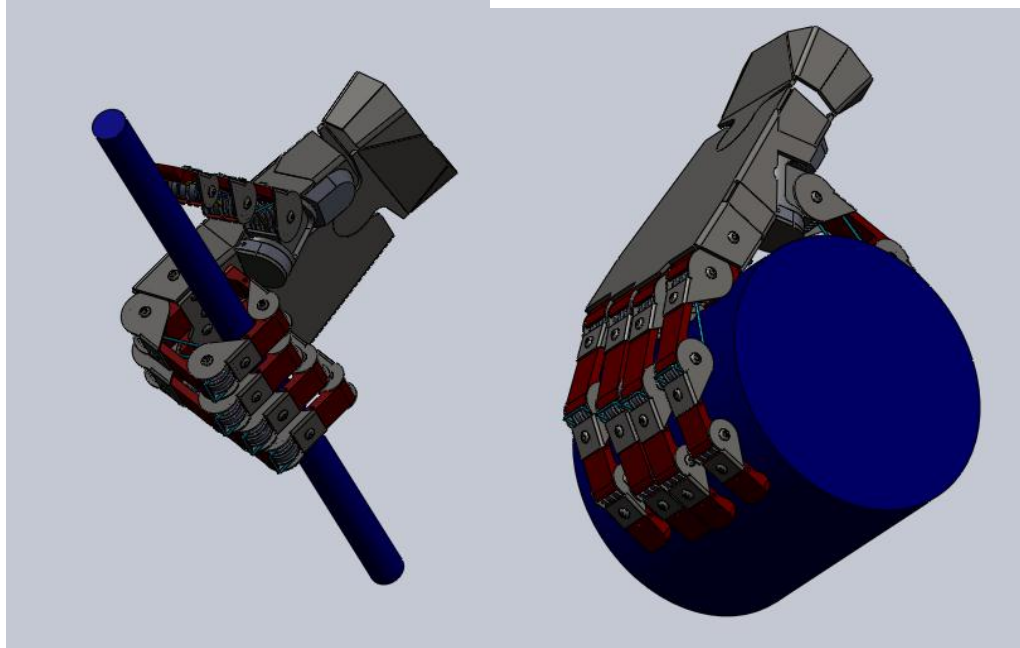


Figure 16: Grasping actions of Hand 2

### HAND DIMENSIONS

Distal Phalanges	Intermediate Phalanges	Proximal Phalanges	Metacarpal	Finger Width
1.0"	1.125"	1.375"	3.25"	0.5"

### Goal 3, Objective 3: Theoretical hand grasping and manipulation results

Within this goal we have been exploring the theoretical relation between the hand structure and the hand motion and force transmission. This relations are key in design decisions, which are limited by this lack of knowledge. In order to explore these issues, we have created a design methodology, which uses visual hand trajectories as an input and returns mechanical structures able to follow those trajectories. We apply this to each finger in order to design optimal structures, while the human aspect of the hand can be imposed as additional constraints (for standard prostheses) or just not considered, for innovative prostheses and exoskeletons. For capturing the hand motion we use video cameras together with some image processing techniques and 3D pose recovering techniques, as well as newly-developed exoskeleton sensors.



We have applied this methodology to other problems related to human hand motion, such as design of exoskeletons for rehabilitation. We have also created mechanical sensors for the finger joints that are to be used in the EMG signal identification techniques. The idea of these ones is that, while we cannot exactly measure the finger joint angle, we can follow its motion with precision using a mechanical device, and then we can relate the angular position of the device to the angle of the finger joint. For the prosthetic hand, the most interesting design is that of the thumb with its complex motion.

### ***General kinematic synthesis solver for tree-like articulated system***

A theoretical framework has been developed to allow the kinematic synthesis of tree-like articulated systems with variable number and type of joints. This is the outcome of the job being developed in (Simo-Serra, Moreno-Noguer and Perez-Gracia 2011 ). The kinematic synthesis problem is again expressed equating the forward kinematics in Clifford algebra form to a set of finite positions. Using a mixed solver, based on genetic algorithms and paired with a local Levenberg-Marquardt algorithm, multiple solutions can be found. This has been applied to recover an anthropomorphic skeleton, as well as to create new designs.. However, the huge number of solutions of the problem poses an additional difficulty if we want to select something for prosthetic applications. Future research includes adding additional constraints for anthropomorphism for this application.

The raw application of the solver to fingertip trajectories from human hands leads to a big number of articulated structures, which could be highly non-anthropomorphic. Figure 17 shows one of these results. In order to get anthropomorphic solutions, we are working on adding additional geometric constraints to the model. One important theoretical result out of this research is the proof that, despite common belief, the hand/wrist complex is not a redundant kinematic structure when the tasks of more than one fingertip are considered simultaneously.

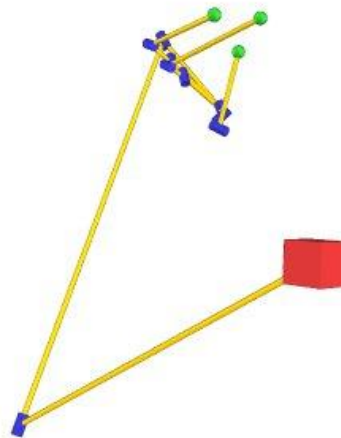


**Figure 17: One hand design from the kinematic solver**

The actual model of the hand that the solver is working with has 26 degrees of freedom and handles 27 discrete poses of the hand for finding a solution set of dimension zero (that is, discrete number of solutions). This implies a system with more than 800 variables and more than 1000 equations, all highly nonlinear. The solution time for this model is about 60 hours on a single computer; the algorithm can be parallelize and is able to work on a computer cluster.

This solver is an important tool to test different chain topologies in order to find new designs for some of the components of the hand. It has been implemented so that it can be applied to the design of any articulated system.

### *Kinematic Synthesis: Application to Thumb Exoskeleton for Pinching and Grasping motion*

A single-degree-of freedom mechanisms has been selected for following the trajectories of the thumb during simple pinch and grasping movements. The linkage to perform the thumb motion was selected among several single-degree-of-freedom spatial closed linkages with four to six links, with a single end-effector for controlling the orientation and position of the proximal phalanx of the thumb. In this approach, the mechanism will be actuated by a single actuator, and so the design of the mechanism is responsible for appropriately shaping the thumb motion. In addition, the designed mechanism is confined to the back of the hand, so as to minimize sensory feedback interference, and to allow the mechanism to be manufactured with minimal size. This combined with the intended location of the actuators will allow the device to be constructed with low apparent inertia. This application was done in collaboration with University of Idaho and University of California, Irvine. Figure 18 shows the process of the design, from the data capture to the prototyping.

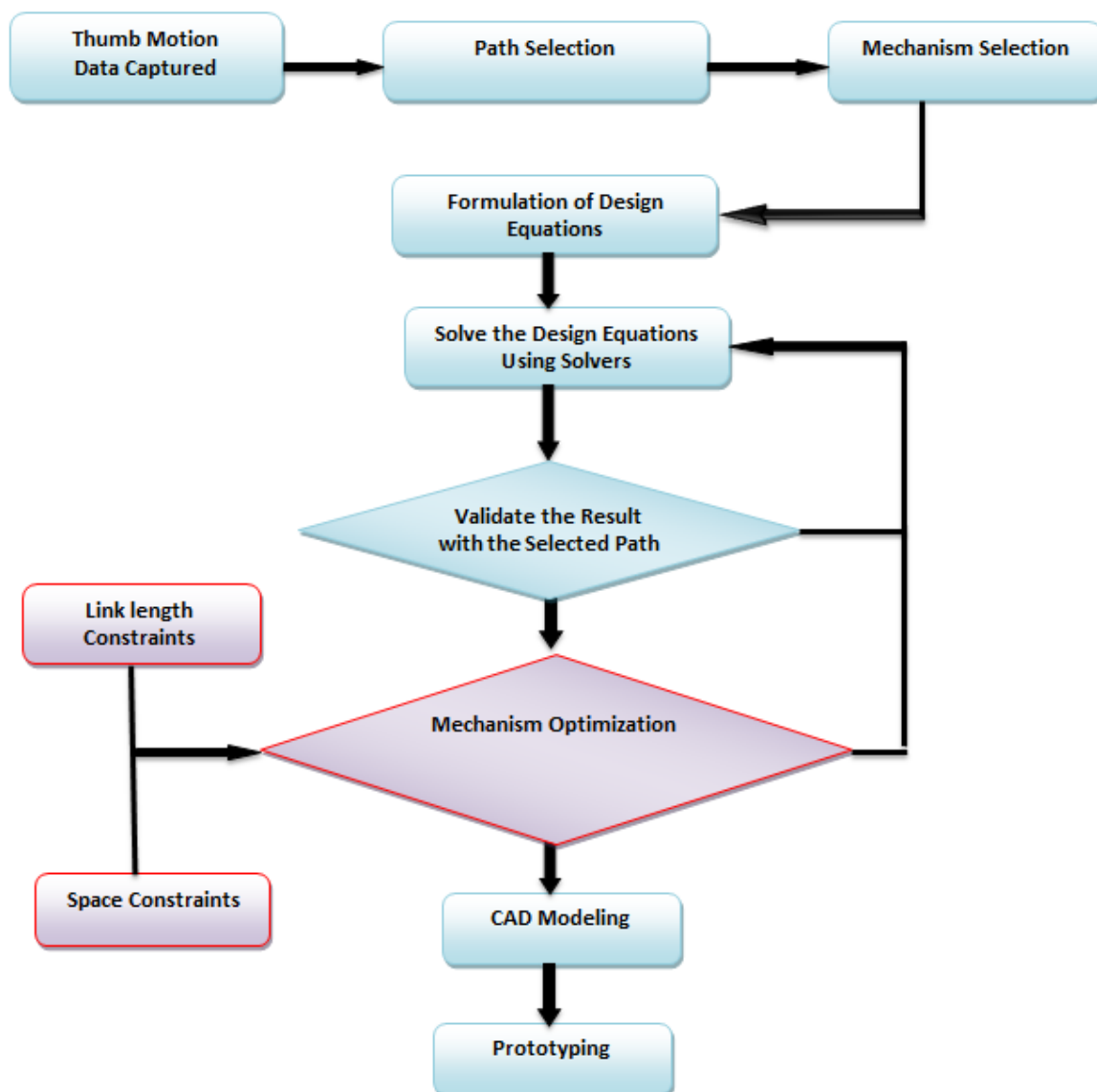


Figure 18: Design framework for exoskeletons

The thumb data were acquired using a Vicon motion tracking system at the University of Idaho. The set up we used had eight infrared cameras set around the room, primarily for larger applications. The markers that are used in the system are small white balls that reflect the infrared light. Arrays with the markers placed 1.25 inches apart were used, making it easy to collect data in the three dimensions, see Figure 19.



**Figure 19: Markers placed in the thumb and data capture setup**

Figure 20 shows one typical point trajectory. For the design of spatial motion, it is sometimes advantageous to work with relative displacements. Each relative displacement expresses a motion of the thumb from a reference configuration, taken as the thumb position at the first frame. Each displacement can be modeled as an axis, plus a rotation about and a translation along the axis. We encode this information as a *screw*, where the screw axis is the axis of the displacement and the pitch is the ratio of translation to rotation for that displacement.

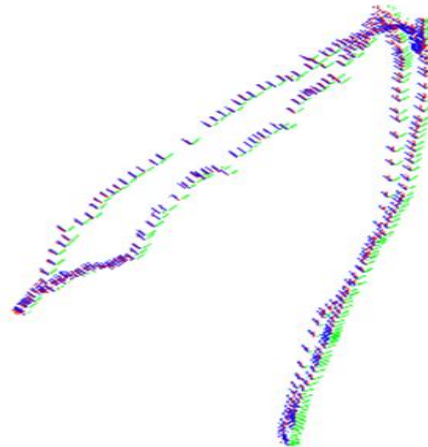


**Figure 20: Thumb's proximal phalanx point trajectory**

In order to accomplish simplicity together with spatial motion under a one-degree-of-freedom system, the first step is to select the closed linkage that better adjusts to this trajectory. Among the properties of these linkages that are useful for our application we can cite the 1-dof motion, requiring only one actuator, and topological simplicity while creating a complex motion. In addition, overconstrained linkages have other advantages, such as inherent structural rigidity. As an example, Figure 21 shows the topology of the spatial CCCC and CCC-CCC linkage; candidate linkages with four and six links are particular cases of this one, obtained by making some of the joint variables ( $\theta_i, r$ ) constant.

Out of the several candidate linkages selected, and after examining their workspaces (see Figure 22), the CRR-RRR linkage has been selected.

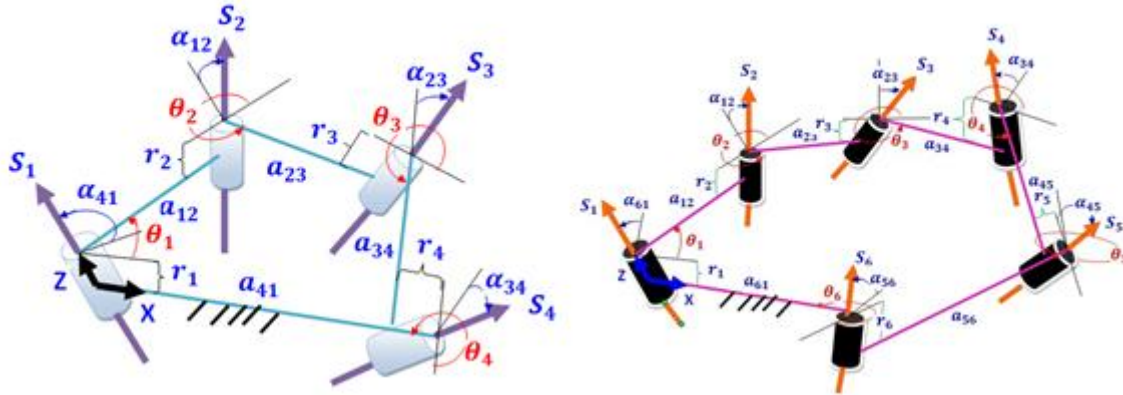


Figure 21: A spatial 4-bar CCCC and 6-bar CCCCCC linkage

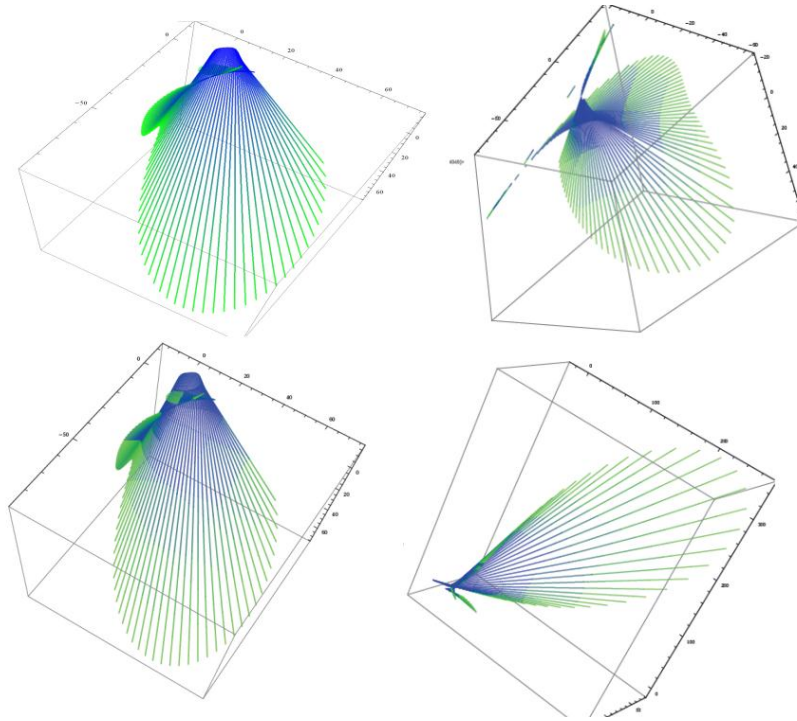


Figure 22: Some of the approximate screw systems for the motion of the CCCR

linkage

Let us consider the closed CRR-RRR linkage as two serial chains, CRR and RRR, joined at their end-effectors. The axes are labeled as shown in Figure 5, starting at the fixed C joint and going around up to the final fixed R joint. For every joint  $i$ , let  $S_i = \mathbf{s}_i + \mathbf{s}_i^0$  be the joint axis, with rotation  $\theta_i$ , and slide (for the C joint only)  $d_i$ . We express the forward kinematics equations of the CRR and RRR chains using dual quaternions [3],

$$\hat{Q}_{CRR}(\Delta\hat{\theta}_1, \Delta\theta_2, \Delta\theta_3) = \prod_{i=1}^3 \left( \cos \frac{\Delta\hat{\theta}_i}{2} + \sin \frac{\Delta\hat{\theta}_i}{2} S_i \right)$$

$$\hat{Q}_{RRR}(\Delta\theta_6, \Delta\theta_5, \Delta\theta_4) = \prod_{i \in \{6,5,4\}} \left( \cos \frac{\Delta\theta_i}{2} + \sin \frac{\Delta\theta_i}{2} S_i \right)$$

where  $\Delta\hat{\theta}_i = \Delta\theta_i + \epsilon\Delta d_i$  is the dual angle, and all  $d_i = 0$  except  $d_1$  corresponding to the cylindrical joint. The forward kinematics so expressed represent the set of relative displacements of the chain with respect to a reference configuration.

In order to create the design equations, we minimize the distance between the displacements captured and the displacements of the candidate chain. We perform dimensional synthesis, that is, the goal is to find the location and dimensions of the mechanism performs approximately the task. The design equations are created by equating the forward kinematics of the mechanism to each of the discrete positions obtained  $-1$ , to yield design equations

$$\hat{Q}_{CRR}(\Delta\hat{\theta}_1^i, \Delta\theta_2^i, \Delta\theta_3^i) = \hat{P}^{1i},$$

$$\hat{Q}_{RRR}(\Delta\theta_6^i, \Delta\theta_5^i, \Delta\theta_4^i) = \hat{P}^{1i}, \quad i = 2, \dots, m.$$

In these equations, the variables we are interested in are what we call the *structural variables*, which are the Plucker coordinates of the joint axes  $S_i = s_i + \epsilon s_0 i$  at the reference configuration. In addition, the optimization process outputs the angles of the chains in order to reach the thumb displacements.

Seventeen positions were selected from the thumb trajectory, and the first frame was taken as the reference configuration, which yield a high number of nonlinear equations. The equations were solved using a Levenberg-Marquardt nonlinear, unconstrained solver implemented in Java. This is based on public domain MINPACK routines, translated from FORTRAN to Java by Steve Verrill [Verrill 2000].

One of the sets of positions can be seen in Figure 24. The equations were run 14 times for three different sets of positions chosen from the thumb frames. The overall error of the function was smaller than 0.04, and it took a variable amount of time, from a few minutes to a few hours, to find solutions. For these 14 runs, 14 considerably different solutions were found. Out of these 14 solutions, 3 linkages were selected because of their overall dimensions and placement on the hand. Figure 23 shows the SolidWorks model of those solutions, named candidate I, II and III. As overall solution, we selected the mechanism with the best combination of fit to the trajectory and smoothness of motion. Figure 24 presents some of the early prototypes of the exoskeleton; rapid prototypes have been built in order to assess the manufacturing and to better design the hand attachment and compatibility with the finger exoskeleton.

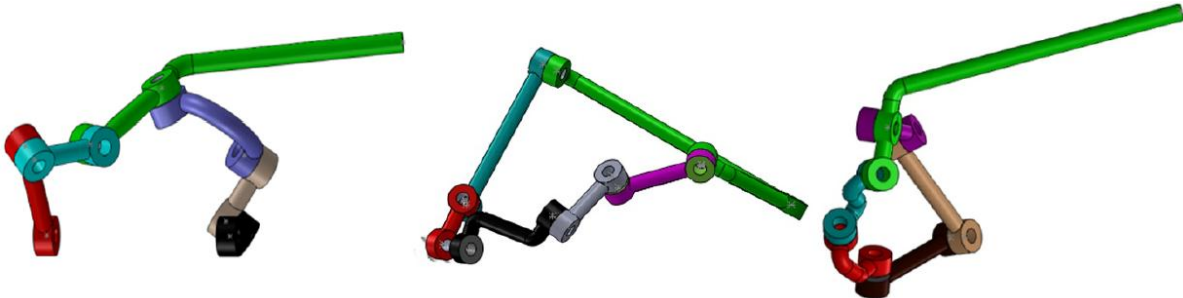
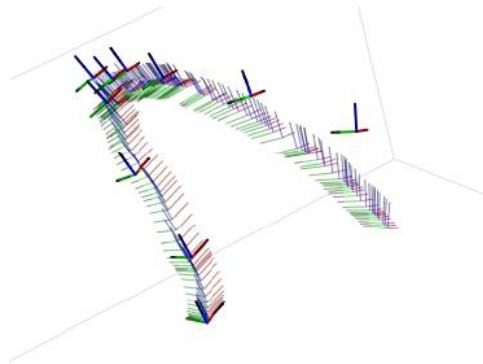


Figure 23: The three solutions selected for prototyping

The main advantage of this method with respect to previous exoskeleton designs is that it does not need any assumption about the location and type of joints in the subject; the exoskeleton is going to follow the

trajectory that is selected as task regardless of the skeletal structure that generates it. This allows for the creation of new and innovative exoskeleton designs.



**Figure 24: One of the thumb trajectories (thin frames) with superimposed linkage trajectory (thick lines)**

The high number of solutions obtained mean more choices for the designer regarding placement, size, and inertia of the exoskeleton for the desired trajectory and the results seem to be acceptable. The placement of the mechanism on the lower arm and close to the wrist is also according to specifications.

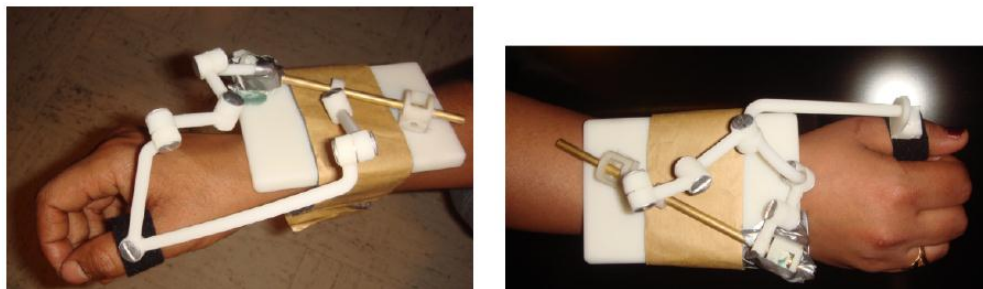


**Figure 25: Two different prototypes, attached to the thumb**

The mechanism obtained by joining the common normal of these axes is then optimized in terms of size and interference with a constrained region.

The design solution of **Error! Reference source not found.** -where the cylinder represents the hand with which the mechanism should not interfere- shows interference and large and uneven link sizes. Both of them are not acceptable in terms of compactness, manufacturability and assembly point of view.

A CAD model for manual adjustment has been created as shown in **Error! Reference source not found.**, in which the links can be changed by sliding along the joints. This procedure can give a mechanism that is out of the constrained region; however, the manual procedure is time consuming and does not give the optimized solution in general.

The optimization problem is solved using genetic hybrid optimization algorithm. The procedure and the technique implemented here can also be applied to other problems too.



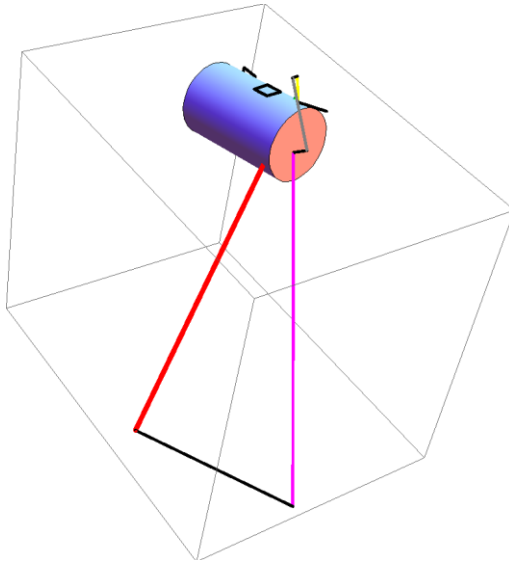


Figure 26: Raw mechanism from synthesis

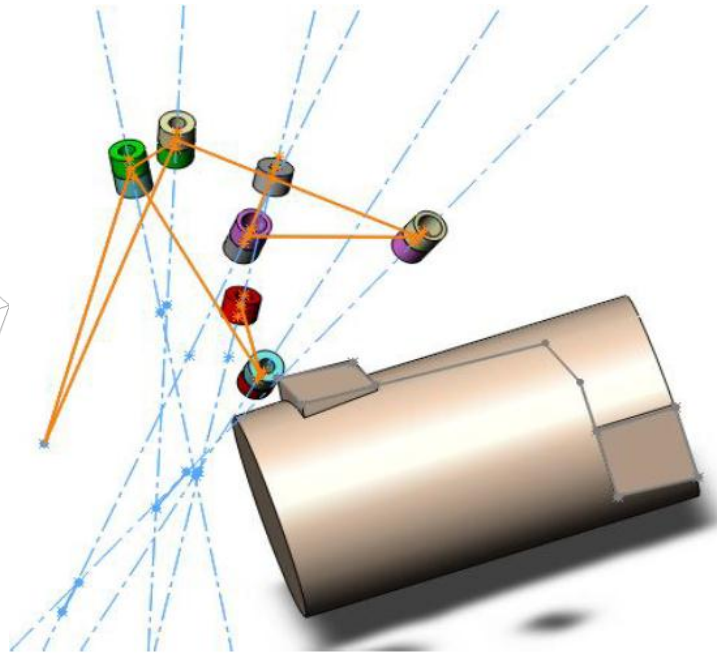


Figure 27 : CAD model for manual optimization

The design objective considered is the minimization of the total link length needed for the mechanism. In this stage, the link dimensions were optimized by converting them into a single combined objective. The problem has a number of geometrical constraints:

*Minimizing the overall length of the mechanism:* the mechanism is required to be compact while preserving its function. To formulate the objective function, the parameters as shown in **Figure 28** ,are used.

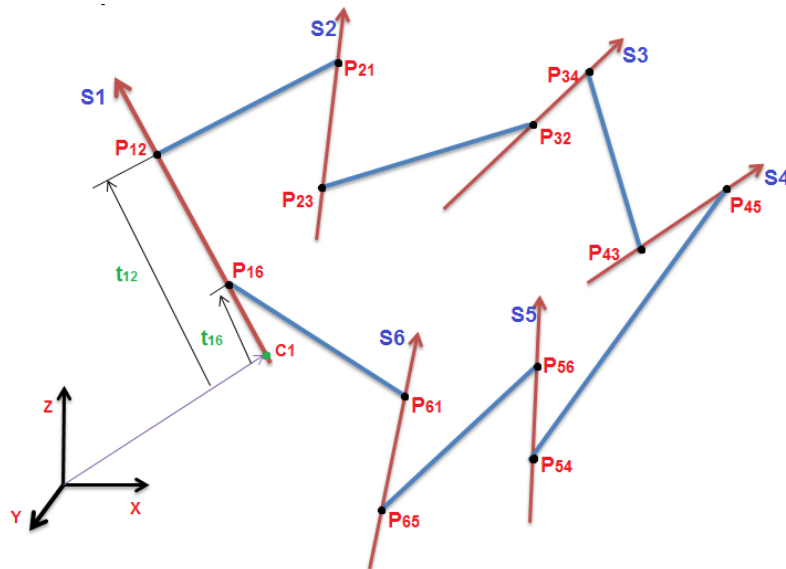


Figure 28: The screw axis of the CRR-RRR mechanism

The objective function was then formulated to minimize the distance between points in the same axis as well as the links between each axis using the formula below, together with inequalities on maximum and minimum length.

$$F = \sum [(P_{i(k+1)} - P_{ik}).(P_{i(k+1)} - P_{ik}) + (P_{(i+1)k} - P_{i(k+1)}).(P_{(i+1)k} - P_{i(k+1)})]$$

$$(P_{i(k+1)} - P_{ik}) \geq 20$$

$$(t_{i(k+1)} - t_{ik}) \geq 20$$

As an additional requirement, the mechanism should not interfere with the hand. For the convenience of analysis, the hand has been represented or modeled as a cylindrical region with radius  $R_c$  and the axis of the cylinder through points  $P_{C1}$  and  $P_{C2}$  as shown in the **Figure 29**. The constraint functions are defined in such a way that the 3D points of the mechanism joint should stay out of the cylinder. The unit vector along the cylinder axis is defined as follows

$$V_C = (P_{C2} - P_{C1}) / \sqrt{[(P_{C2} - P_{C1}).(P_{C2} - P_{C1})]}$$

If any of the mechanism joint points represented by “ $P_{mi}$ ”, the distance of “ $P_{mi}$ ” with respect to the point  $P_{C1}$  along  $V_C$  is the dot product of  $(P_{mi} - P_{C1})$  and  $V_C$

$$L_{mc} = (P_{mi} - P_{C1}).V_C$$

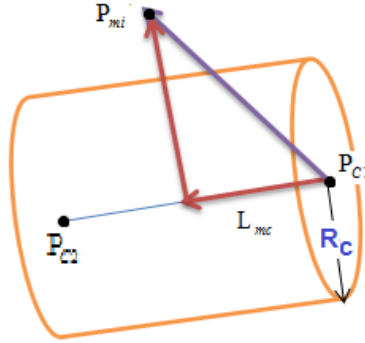


**Figure 29: The cylindrical surface to represent the constrained region of the hand**

Since the CRR\_RRR mechanism has six axes and twelve points (joints) we have a total of twelve nonlinear constraint functions for this space constraint, each of them defined as follow:

$$(P_{mi} - P_{C1}).(P_{mi} - P_{C1}) - L_{mc}^2 \geq R_C^2$$

This gives a total of twelve nonlinear constraints.

Considering all the constraints and the objective function, the optimization problem involves twelve decision variables, one nonlinear objective functions, six linear inequality constraints and twenty four nonlinear constraints. Each variable also bounded within a lower and an upper limit. The nonlinearity in the objective function over the constraints provide the main difficulty in solving the problem. A set of randomly generated solutions over the above mentioned variable bounds indicate that about only one in 105 solutions is feasible. Such a severity of the feasible region makes the problem even more difficult to solve. In the following section the optimization method and simulation results are presented.



For instance , let us consider one of the solution obtained through the synthesis of CRR\_RRR, **Figure 31**. The Black colors are the links of the mechanism, whereas the colored lines represent the screw axes i.e red=S1, blue=S2 etc.

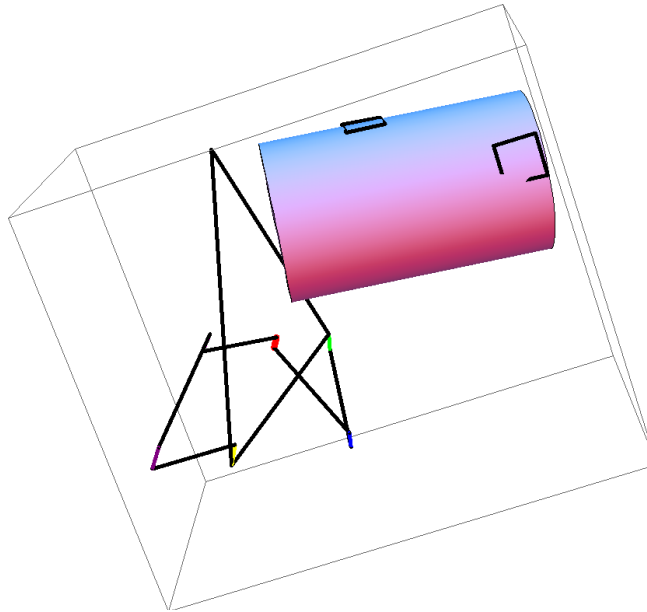


**Figure 30: The optimized mechanism using genetic algorithm**

The result obtained was refined further by using hybrid genetic algorithm. Here the above solution was used as an input to the gradient nonlinear optimization algorithm and the result found more optimized as shown in **Figure 32**. Here all the constraints are met and a more compact mechanism is obtained.

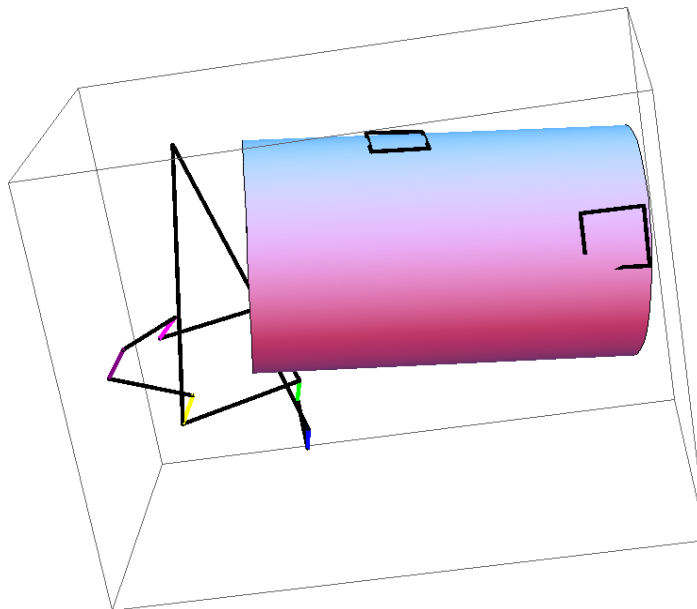


**Figure 31: The optimized mechanism using a hybrid genetic algorithm**

Based on the data , the exoskeleton has been redesigned and prototyped

**Figure 33.** In the testing of the mechanism we also observed a little resistance at the joints which are caused by the rough surface resulted from the prototyping machine . To overcome this problem , smooth and light weighted mechanical bushes are used, and future optimizations will include transmission angles for all joints.

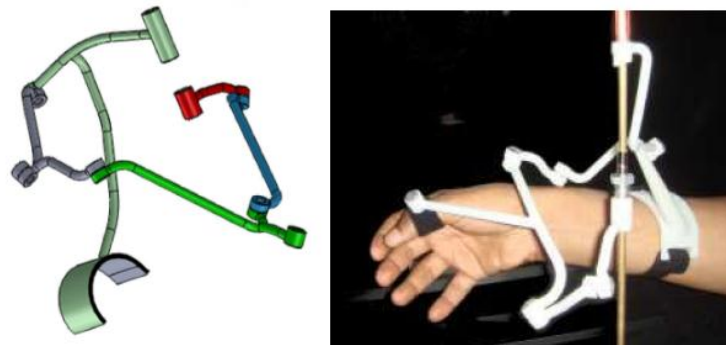


**Figure 32: The CAD and the prototyped model of the exoskeleton**

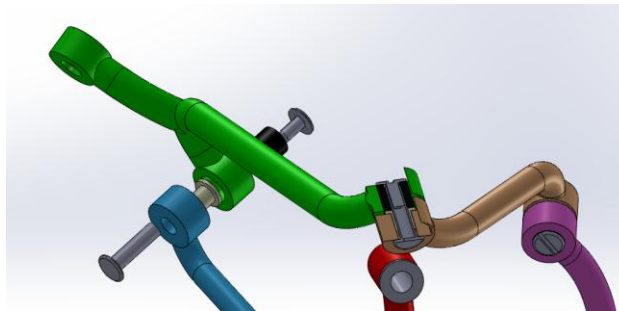


**Figure 33 : Joint connections**

#### ***Kinematic Synthesis: Application to the design of a Finger-joint angular sensor***

Estimation of joint angles for human joints is important for many applications in Bioengineering. Most of the existing angular joint sensors rely on the approximate assumption of the knowledge of the type of motion and location of the joint. Using the kinematic synthesis methodology, a new design for the measurement of finger joint angular motion has been developed. The design presented here consists of an exoskeleton, designed to fit the finger motion, in which we can relate the angular displacement of its links to the change in orientation of the phalanx under consideration. Unlike other designs, the exoskeleton does not need any information about the actual anatomy and the dimensions of the hand in order to provide with the angular information. The design is to be used in myoelectrical signal identification.

For this application, the desired mechanism is required to do two things: firstly, it should follow the trajectories described by the collected data; and secondly, there should be a one-to-one correspondence between the orientation of the MIP joint of the finger to one of the joints of the mechanism. It seemed that a six-bar linkage was the simplest closed, planar linkage able to follow the collected trajectories

accurately. On the other hand, being a simple, one-dof linkage, the relationships between all its angles are well known and can be related to the angle of the coupler and the MIP joint. The topology to be used is shown in Figure 34.

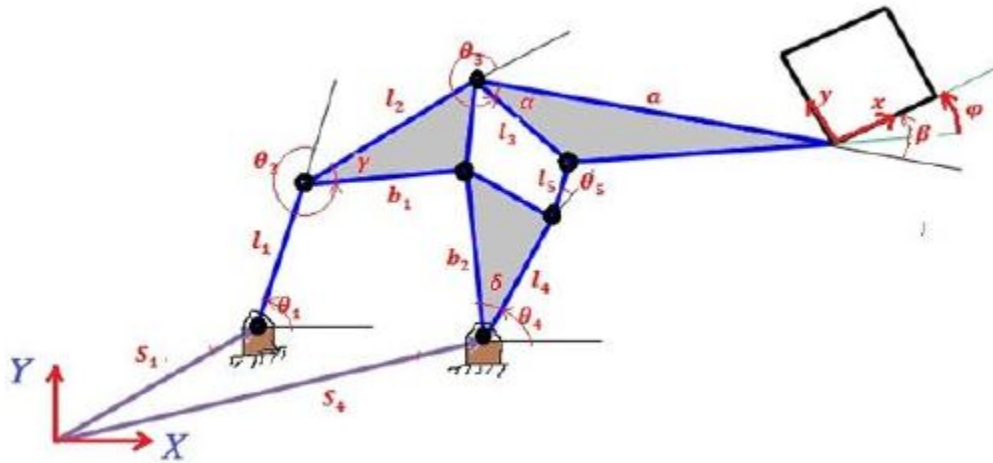


Figure 34: The six- bar linkage with variables used

A set of equations are created to determine the trajectory that point  $P$  would follow through the operation of the mechanism. In this case we have a total of 63 nonlinear equations and 61 unknowns. The equations were solved using a Levenberg-Marquardt nonlinear, unconstrained solver implemented in Java.

From the design of the mechanism it is shown that the angle  $\phi$  corresponds to the orientation of the MIP joint of the finger. Thus, we can get the value of  $\phi$  for every finite displacement of the finger in terms of 1. Since the objectives is to come up with a cost effective sensing device, a resistive potentiometer is 1 ratio or the rate is less by which we can reduce noise and sensitivity issue for the sensor and the other reason is the accessibility or the orientation of the linkage is also suitable to mount the sensor.

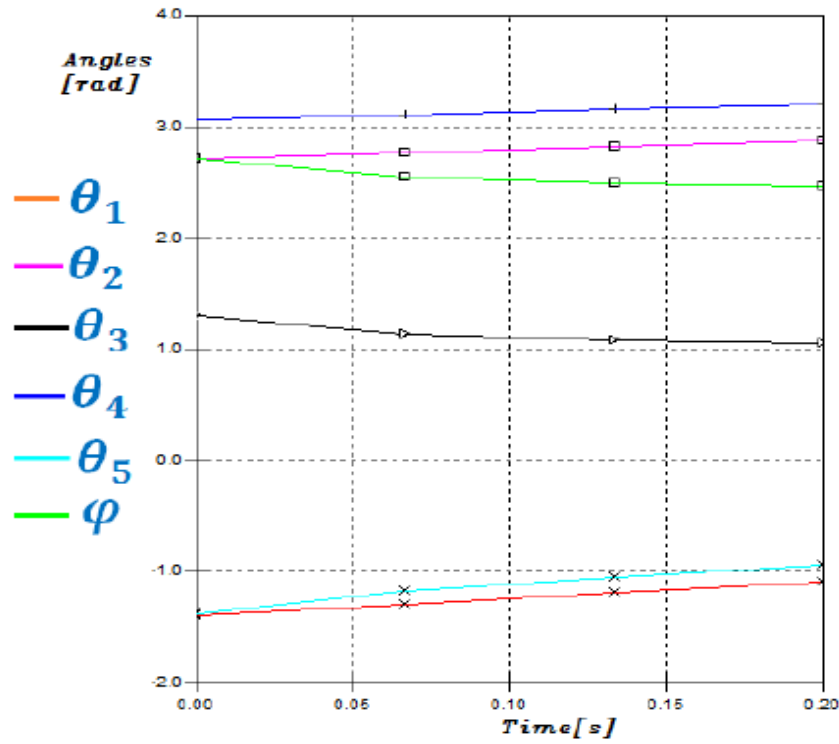


Figure 35 :Angular positions as a function of time

The candidate designs were ranked considering size, mechanism placement and overall structure. The selected design, optimized to fit the user's hand, is shown in Figure 36. Figure 37 shows an earlier version at two different configurations.

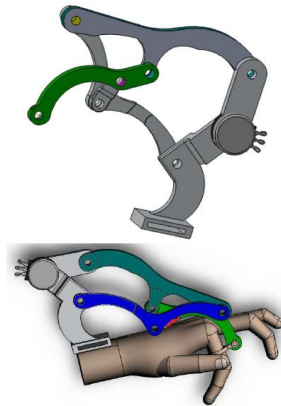
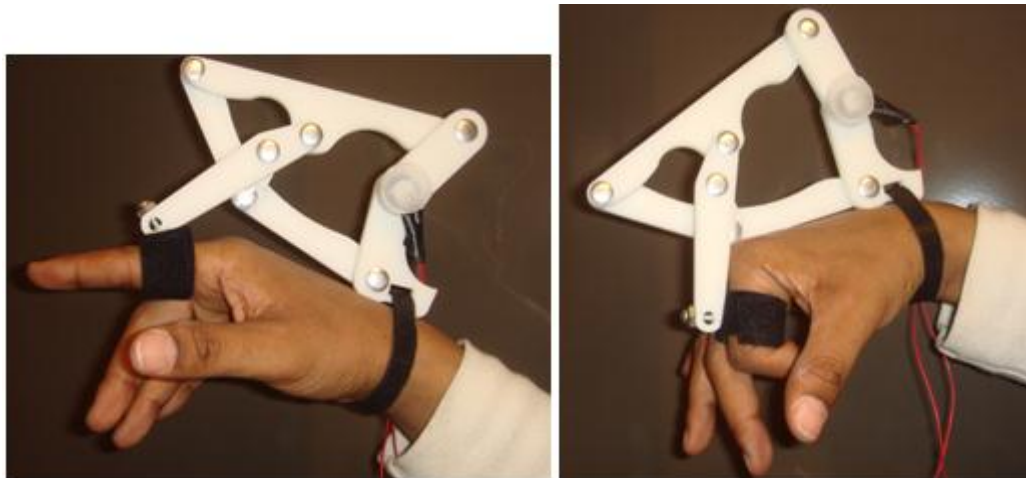
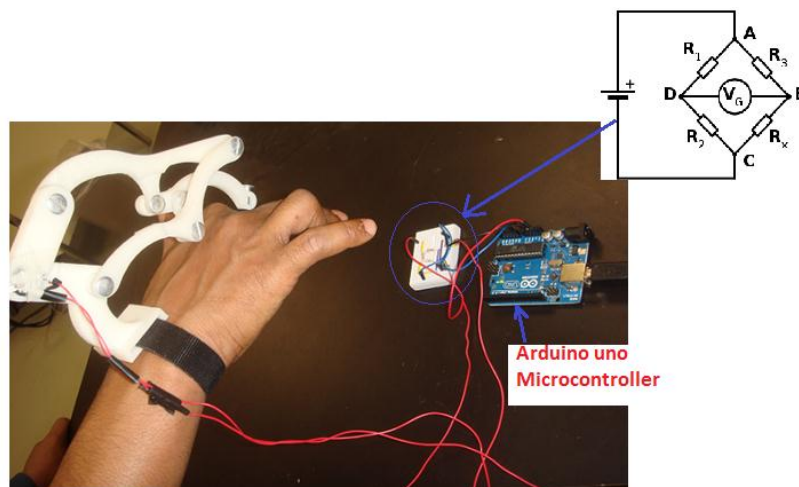


Figure 36: CAD model of the exoskeleton and the sensor on the hand,



**Figure 37: Exoskeleton and sensor on the hand, at two different configurations**

The sensor has been prototyped and tested. Figure 38 shows the experimental setup and the prototyped sensor. In order to increase the sensitivity of the sensor a Wheatstone bridge has been built ; the potentiometer on the exoskeleton is used as the variable resistor in the bridge. And for the convenience of recording and monitoring the sensor value, the microcontroller and Labview have been used. Using this labview model we can monitor the analog signal change due to the position change of the potentiometer on the sensor. Once we have recorded the data, the angle relation obtained from the kinematic analysis will be applied to relate the real change of the MCP joint angle.



**Figure 38: Experimental setup**

In order to assess the effect of the sensor on the EMG signal, an experiment with and without the sensor have been performed. The result shown in Figure 39 (left) indicates the EMG signal without having the sensor whereas the right plot shows the EMG signal of the same subject taken with the sensor on the hand . Observing these two figures it can be said that the sensor doesn't have a significant effect on the EMG signal.

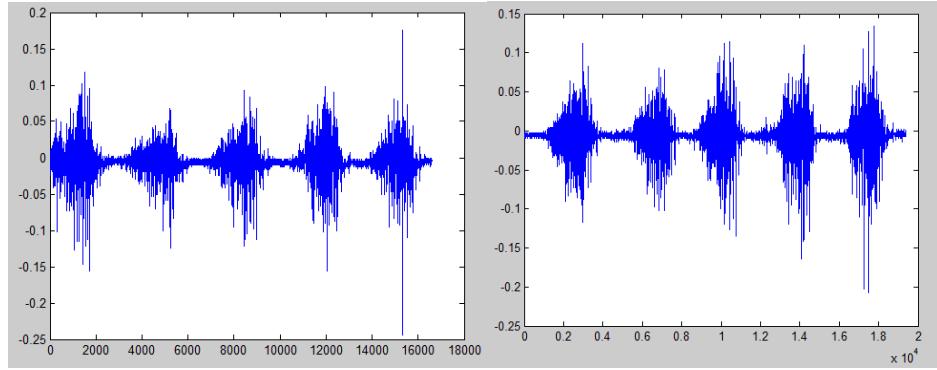


Figure 39: EMG signal, without and with finger sensor

These results also confirm that this simple and cost-effective mechanism for the estimation of the angles of the Metacarpal interphalangeal (MIP) joint is more attractive in many ways. The design strategy includes vision system and image processing coupled with kinematic synthesis techniques. The main advantage of this method is that it does not need any assumption about location and type of joints in the subject; the exoskeleton is going to follow the trajectory that is selected as task regardless of the skeletal structure that generates it. This allows for the creation of new and innovative exoskeleton-based position sensors which can help for EMG and position modeling in the grasp and control study. The application of image-processing techniques and use of a six-bar mechanism and a simple potentiometer grants a less-cost, effective sensing device.

#### *Kinematic data acquisition system*

The experimental approach to get the data is based on the principle that the pose of a calibrated camera can be uniquely determined from a minimum of four coplanar but noncollinear points. Thus, two squares attached to the proximal phalanges and to the dorsal part of the carpal are used. Then the index finger is moved to its different positions/reaches. While moving the index finger, different frames are captured using a Dragonfly 2 camera from GreyPoint, with a Fujinon 1:1.4/9mm lens, interfaced with a computer using LabVIEW. The LabVIEW program captures and saves multiple images into the hard disk [Ahsan 2008]. Once the frames are saved, sample frames from different orientation of the index finger are selected for processing. See schematic diagram of the process.

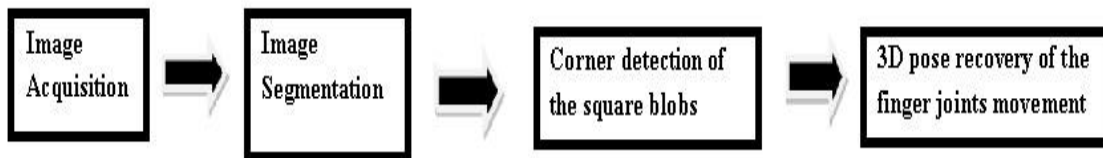
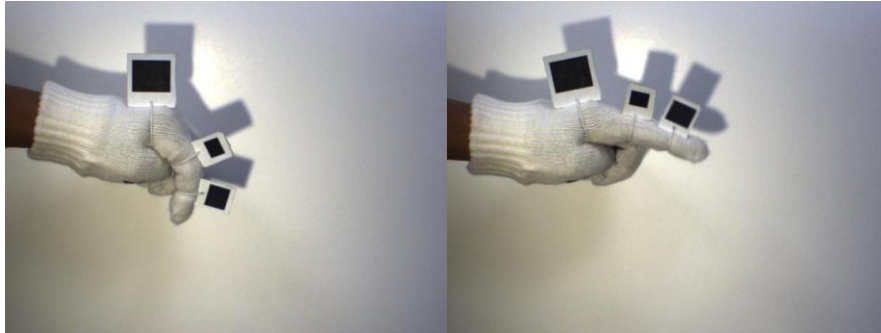


Figure 40: Image acquisition and processing

In order to compute pose for 3D to 2D correspondences of a planar target, the algorithm used is based on Hager and Schweighofer [Schweighofer 2006]. The algorithm is customized to obtain a set of task positions from a video stream of a hand moving with markers.

Some squares are used as a reference position, as the relative position between this square and the fixed joint of the mechanism is always constant while the hand is moving. The markers are used to estimate the pose, which consists of the position and orientation of each finger. An important aspect of this setup is the geometry of the markers. The geometry of a marker affects directly its performance and usability in computer vision applications. The design used by this project is a simple white square with a smaller black square inside as shown in Figure 41. In order to segment the squares properly, three different square sizes are used. This provides four sharp visible corners which form a perfect square that can be used to find the 3D pose of the marker.



**Figure 41: Images of the hand with the squares**

It is important for these markers to be completely rigid for accurate pose estimation. For detection of the candidate points the Harris corner and edge detector algorithm is used. To get a better result both in the detection and pose recovery image segmentation is also performed so that the square corners are visible enough to be detected.

The images showing in Figure 42 are two of the images we acquire for the image processing of the finger joints movements. After the image segmentation, based on blob size, we get some images with only blobs of attached with the finger joints.

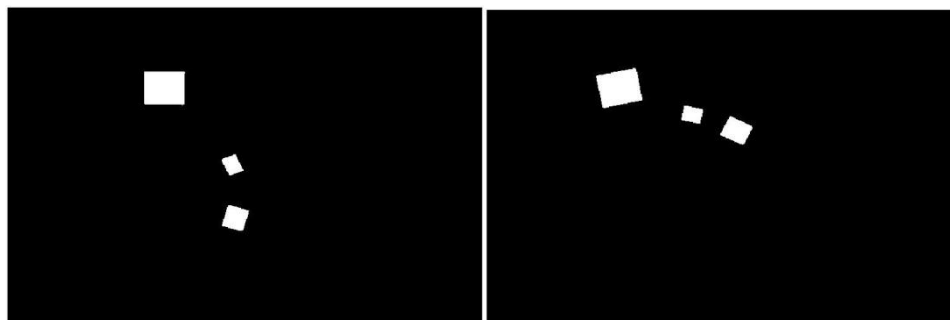


**Figure 42: The detected blobs for the squares**

The image segmentation algorithm for detecting the square blobs, separates the square blobs from the images. The rgb images were made as binary images then the allowable area of the image and red channel pixels were

changing for the detecting and separation of the square blobs. We used the red channel thresholds as less than 70x70 pixels and the allowable area as 430x430 pixels.

The square blob separation algorithm worked perfectly for all the sample images we used and it was easier to run the Harris corner detection algorithm on these images to get the perfect corners of the squares..

After the separation of the square blobs we compute the corners of the squares. The 2D position of the corners is to be converted in a 3D pose, which will be the position of the squares for the design of the finger movement. We got the position of the 12 corners after running this algorithm. See **Figure 43**.

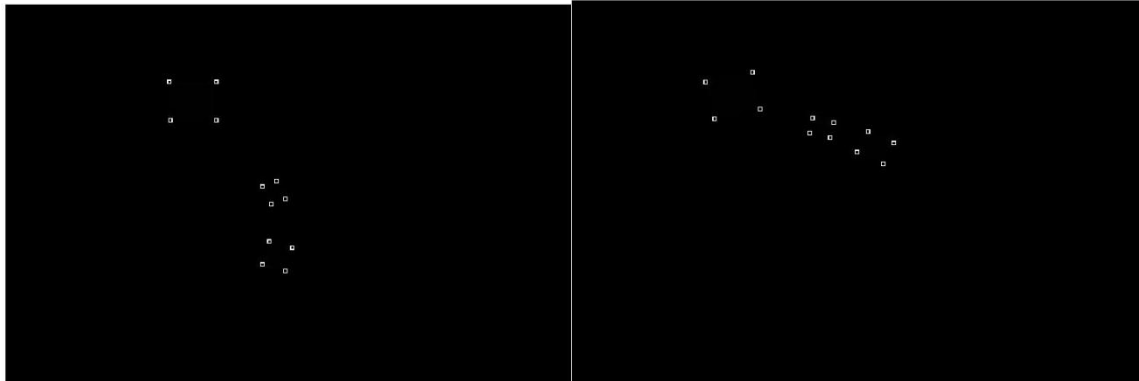


Figure 43: Corners detected from the square blobs

After detecting the corners of the squares we got the 2D position of the squares, which is given below:

#### Image 1

X	88	131	88	131	206	294	268	226	200	220	301	275
Y	186	187	239	239	291	291	299	301	307	317	317	325

#### Image 2

X	92	133	81	122	149	132	154	137	170	147	183	160
Y	150	160	202	211	266	269	289	293	319	331	348	360

Next step is to use a clustering algorithm on the 12 points to separate the three squares. **Figure 44** shows the results of the clustering, separating all three squares. It is easy then to identify the square belonging to each limb by computing its size using the points.



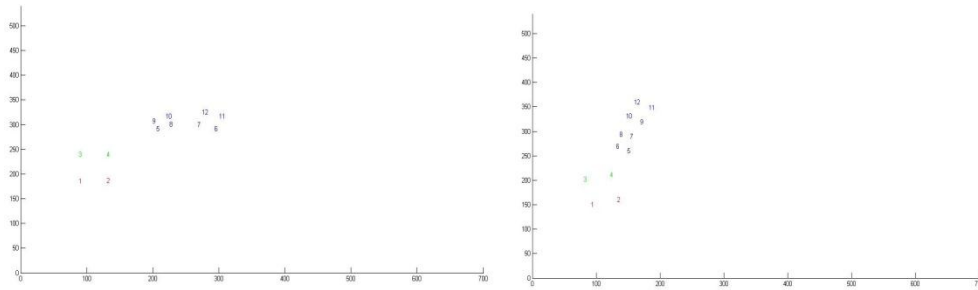


Figure 44: Results of the clustering algorithm

The 3D pose recovery algorithm (Hager and Schweihofer) can map 3D reference points from the 2D  $t_i = 1, \dots, n, n \geq 3$ .

These points can be expressed in an object-centered reference frame. The corresponding camera space  $\mathbf{p}_i$ . These points are related by rigid transformation as,  $\mathbf{p}_i = \mathbf{R} \mathbf{p}_i + \mathbf{t}$

$\mathbf{p}_i$ ).

$\mathbf{p}_i$  for each position of the target point (the point from the square at the  $\mathbf{p}_i$  (the point from the square at the carpal) with respect to the camera. In order to refer all the movements of the target point locally we use  $\mathbf{p}_i$ .

$\mathbf{p}_i$ , the transformation from the reference frame at the carpal to the proximal phalange, the design equations are formulated based on the candidate mechanism.

This methodology in theory provides results for an arbitrary motion of the fingertips, which it is used both as an input for the design and as a way to collect hand motion information and synergies. However, it is difficult to apply successfully this methodology to motion that is highly non-planar, especially the segmentation and clustering parts. As a conclusion, other methods for data capture, such as combining vision with infrared detection, are going to be studied. The vision system may be used in the future to capture information about velocity using a direct method. Current method, which calculates the finite differences, is prone to having high error from noise.

## Goal 4: Biocompatibility and Signaling

Abstract of this section:

A major unresolved biocompatibility issue pertains to how tissue and cellular inflammatory responses are elicited by artificial implant material(s). We are developing a “Sensor on Cells on Skin Model” to facilitate the investigation of this biocompatibility issue. We have made significant progress in cell model development. We have developed new cell models of peripheral nervous system consisting of dorsal root ganglion neurons and Schwann cells. The new models are suitable for elucidating nerve degeneration and regeneration. We are characterizing these new models further. We have developed several “smart” biosensors for tissue engineering and biocompatibility studies and related biomedical engineering applications. In parallel with cell model and sensor development, we have investigated the molecular mechanisms underlying the cytotoxicity of silicon dioxide and magnesium oxide nanoparticles in neural cells. Our extensive literature survey indicates that our studies are truly novel and will lead to further ground-breaking discoveries because the whole important issue of how tissue and cellular inflammatory responses are elicited by implant material(s) have not been resolved and is poorly understood.

### INTRODUCTION:

Current artificial organ and tissue engineering research (e.g., artificial bone and joint implants) reveals that over time the artificial implants fail to function even though over a short initial period after they were implanted, such devices appear to function as the biomedical engineers, who had designed them, expected. The findings of numerous studies indicate that the failure of the implants (despite their initial success) were attributed to the fact that, over time, the cells/tissues immediately surrounding and/or in contact with the implants appear to develop “inflammatory reactions” to the implants thereby compromising the implants’ performance (see Lai et al., 2007a & ref. therein). Furthermore, if the implants act as sensors, the “inflammatory reactions” exhibited by the cells/tissues surrounding the implanted sensors induce interference of the signal transmission of the implants. However, “inflammatory reactions” exhibited by the cells/tissues surrounding the implanted sensors are poorly understood and remain to be major challenges for tissue engineers and other biomedical engineers who design such implant devices. Moreover, our extensive searching in the literature reveals that there is a paucity of literature on robotic implants and tissue inflammatory responses (Lai et al., 2007a). Nevertheless, nanoparticles and other nanomaterials have been increasingly employed to manufacture implants and biosensors. There is emerging concerns that some nanomaterials may pose health hazards to humans because of recent findings of nanotoxicology (Lai et al., 2007a,b). Consequently, in order to circumvent such biocompatibility issues in the design of robotic implants, it is imperative to elucidate the mechanisms by which such “inflammatory reactions” exhibited by the cells/tissues surrounding the implants arise and elucidate the putative nanotoxicity of nanomaterials employed to fabricate implants and biosensors. Thus, our *in vitro* model (see Fig. 1 below) allows us to address these physiologically and pathophysiologically important mechanistic issues. For phase II of our projects, the goals are to: (1) Continue to develop the “sensor on cells on skin model,” especially stages two and three of the model development (see Addenda of Full Proposal); (2) Further characterize the putative nanotoxicity of nanoparticles and other nanomaterials commonly employed to fabricate biosensors and implants; (3) Detect signal mechanisms that influence cell growth and suppression such as apoptosis; (4) Couple enzymes on sensors for signal identifications and amplifications; and (5) Detect signals for biological growth and interferences with quantifiable parameters such as current, voltage, pH, etc. between various cell types of different organs of origin.

The following are the deliverables:

- 1) Continue to develop the “sensor on cells on skin model,” especially stages two and three of the model development (see Addenda of Full Proposal);
- 2) Further characterize the putative nanotoxicity of nanoparticles and other nanomaterials commonly employed to fabricate biosensors and implants;
- 3) Detect signal mechanisms that influence cell growth and suppression such as apoptosis;
- 4) Couple enzymes on sensors for signal identifications and amplifications; and
- 5) Detect signals for biological growth and interferences with quantifiable parameters such as current, voltage, pH, etc. between various cell types of different organs of origin.

We have continued to make progress in studies outlined in Goal 4 of our proposal and have summarized the results obtained during this period in the following sections. We have been productive despite the gap in funding between the ending of Phase I and initiation of funding of Phase II: we have presented **40** papers at national and international meetings and have **9 journal articles, 3 reviews, 20 conference proceedings papers and 40 abstracts** published or in press (see **Publications** below).

#### A. Set up of the “Sensor on Cells on Skin Model”:

Based on our extensive experience in working with mammalian (including human) cells in culture (Dukhande et al., 2006; Hertz et al., 1998; Isaac et al., 2006; Isaac et al., 2007; Lai et al., 2008, 2010; Malthankar et al., 2004; Puli et al., 2006), we envisaged that we will undergo three stages to develop our “sensor on cells on skin model:” (i) stage one involves the development of different human and other mammalian cells (including nerve, muscle, and skin cells) in co-culture; (ii) stage two requires the juxtaposition of cells in relation to the membrane as illustrated in Figure 1. below (this figure was included in our proposal); and (iii) stage three involves designing the sensor(s) and fitting them into the “sensor on cells on skin model” (as shown in Fig. 1).

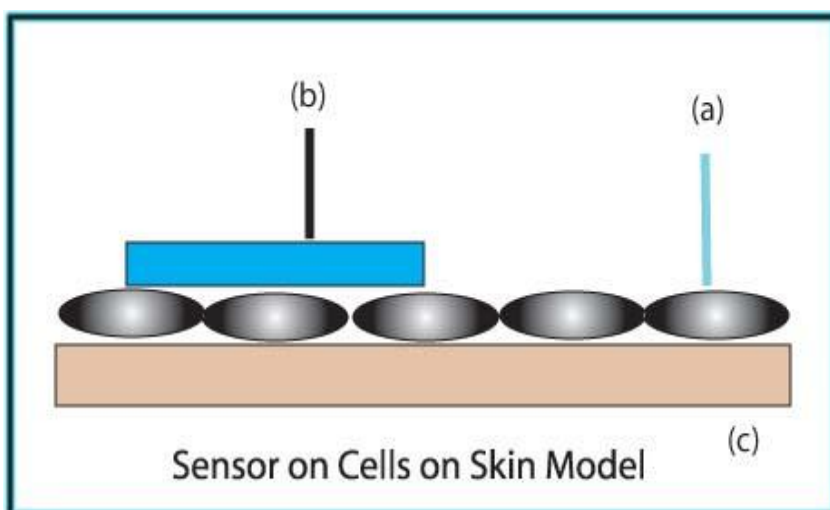


Fig. 1 “Sensor on Cells on Skin Model.” The sensor (or implant: blue rectangle) is in contact with a monolayer of muscle or nerve cells (gray ovals), which are in contact with the artificial skin (an artificial membrane with specified pores: brown rectangle). (a) stimulating electrode; (b) sensor signal pick-up; (c) alternative position of sensor.

We successfully completed (i) stage one of setting up the model as depicted above. More recently, we have begun developing new cell models employing dorsal root ganglion neurons and Schwann cells, both are neural cells from the peripheral nervous system (see Appendices 2 & 6). Both dorsal root ganglion neurons and Schwann cells are important and relevant cell types for investigating biocompatibility of biomaterials. We have therefore characterized these cell types and test their ability to respond to inflammatory assaults.

As shown in Figure 2, the population of dorsal root ganglion neurons showed exponential growth *in vitro* as a function of initial seeding density. Similarly, as shown in Figure 3, the S16 Schwann cells also showed exponential growth *in vitro* as a function of initial seeding density. Once we have established their growth patterns in culture, we are now in a position to further characterize them in terms of other physiological and cell biological functions.

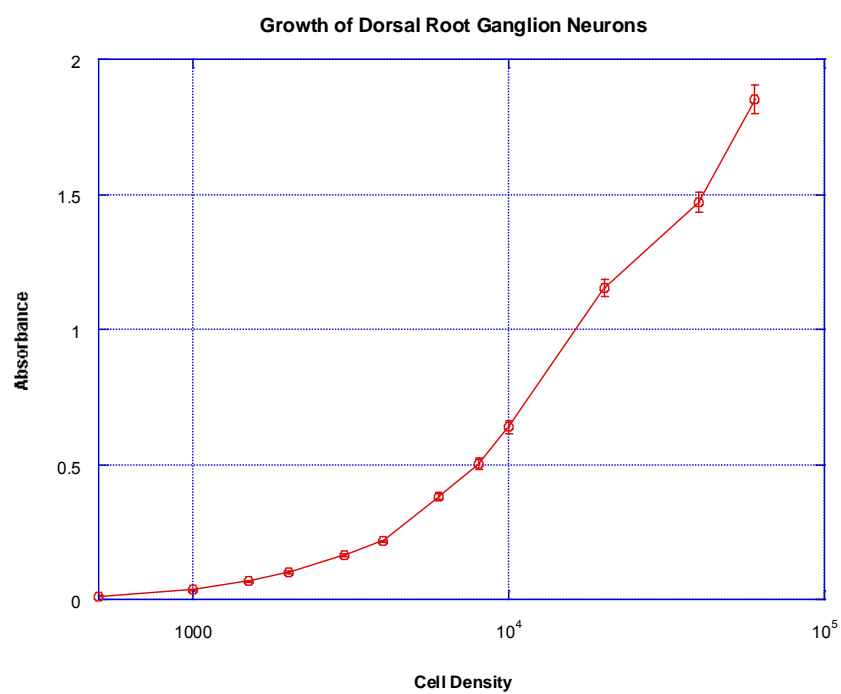


Figure 2. Growth of Dorsal Root Ganglion Neurons in Culture.

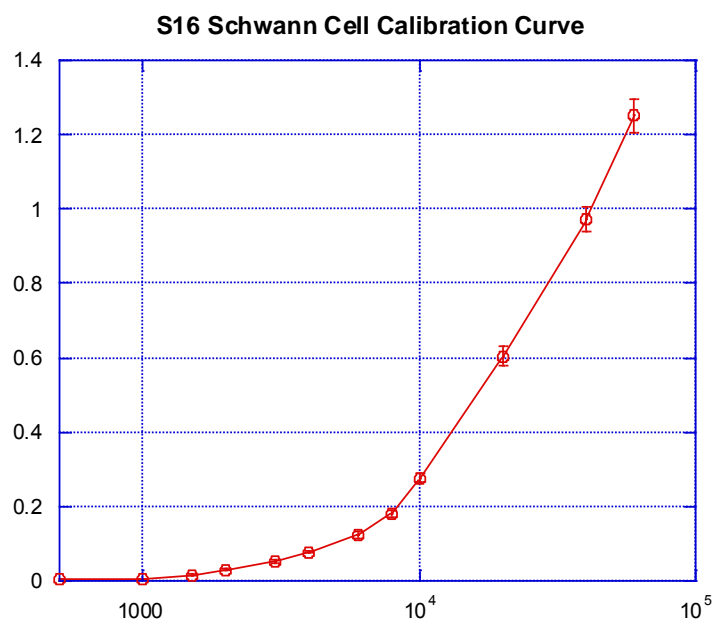


Figure 3. Growth of S16 Schwann Cells in Culture.

Various biocompatible materials in tissue engineering have been employed to construct artificial skin. One such material is chitosan, a polysaccharide biopolymer derived from chitin. We have employed chitosan as a tissue-engineered model of skin and investigated how this artificial skin can interact with other mammalian neural and non-neural cell types. Because the amount of acetylated monomer (i.e., N-acetyl-D-glucosamine) in chitosan influences the surface and other properties of chitosan, the “artificial skin,” we considered it important to characterize and compare the degree of deacetylation of chitosan prepared and/or purified by several methods.

### Purification of Chitosan

Chitosan was further purified by dissolving it in 1% acetic acid, followed by filtration and precipitation with 5% (w/v) NaOH. The alkaline precipitate was then washed with deionized water until the water pH was ~ 7.0. The resultant material was then freeze-dried or oven-dried at 60 °C.

### Preparation Chitosan from Chitin

Chitin (~1.5g) was immersed in 75 ml of 45% aqueous NaOH, and the mixture was heated at 130 °C for 0.5, 1, 2, or 5 hours (h). The deacetylated material was washed with deionized water until the water pH was ~ 7.0. The residue was then dried at 60 °C for 24 hours.

### Determination of the Degree of Deacetylation (DD) of Different Preparations of Chitosan

The DD of chitosan, purified chitosan, and chitosan from chitin prepared with different duration of heating was assessed by determining the amount of acetylated monomer (N-acetyl-D-glucosamine) in the sample using first derivative UV-spectroscopy with maximum at 201 nm. Samples (0.1 mg/ml in 0.01M acetic acid) prepared by the methods depicted above were analyzed. Standards of N-acetyl-D-glucosamine at concentration between 5 and 50 µg/ml in 0.01M acetic acid were used to construct the standard curve used to determine the amount of N-acetyl-D-glucosamine in the samples. The degree of deacetylation (DD) of the chitosan in the samples was calculated using the following equation:

$$\text{DD} = (1 - \text{ratio of acetylation}) * 100$$

$$= (1 - \text{concentration of N-acetyl-D-glucosamine in sample} / 100) * 100.$$

### Calibration Curve

As shown in Fig. 4, in the range from 5 to 50 µg/ml, there was a linear relationship between N-acetyl-D-glucosamine concentration and its first derivative absorbance. Its first derivative UV-spectra are shown in Fig. 5.

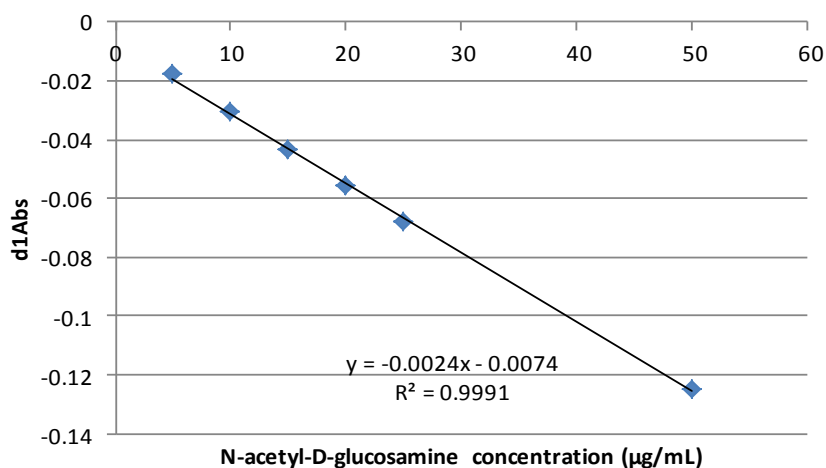


Figure 4. Calibration curve for N-acetyl-D-glucosamine.

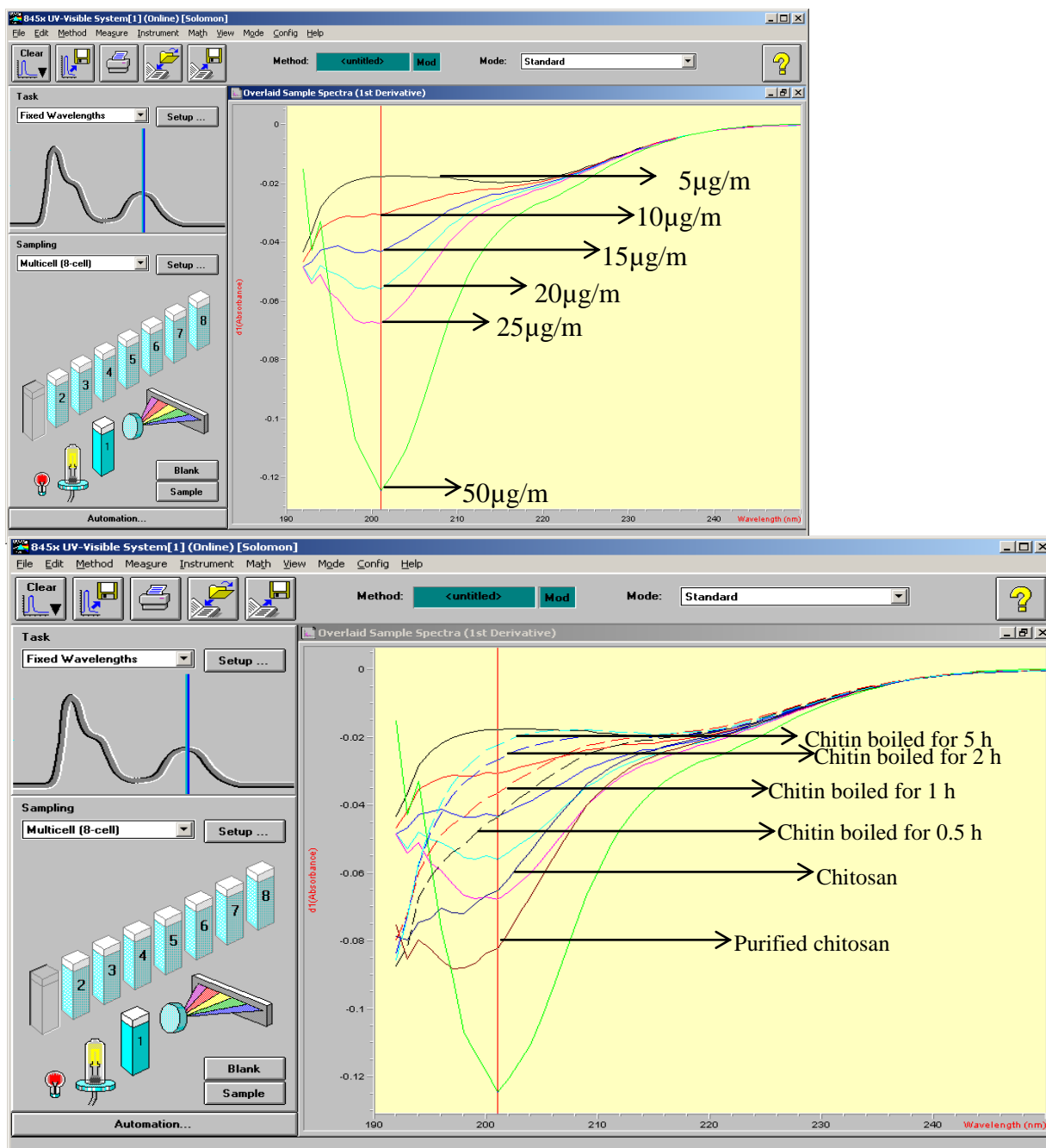


Figure 6. First derivative UV-Spectra of Various chitosan/chitin samples.

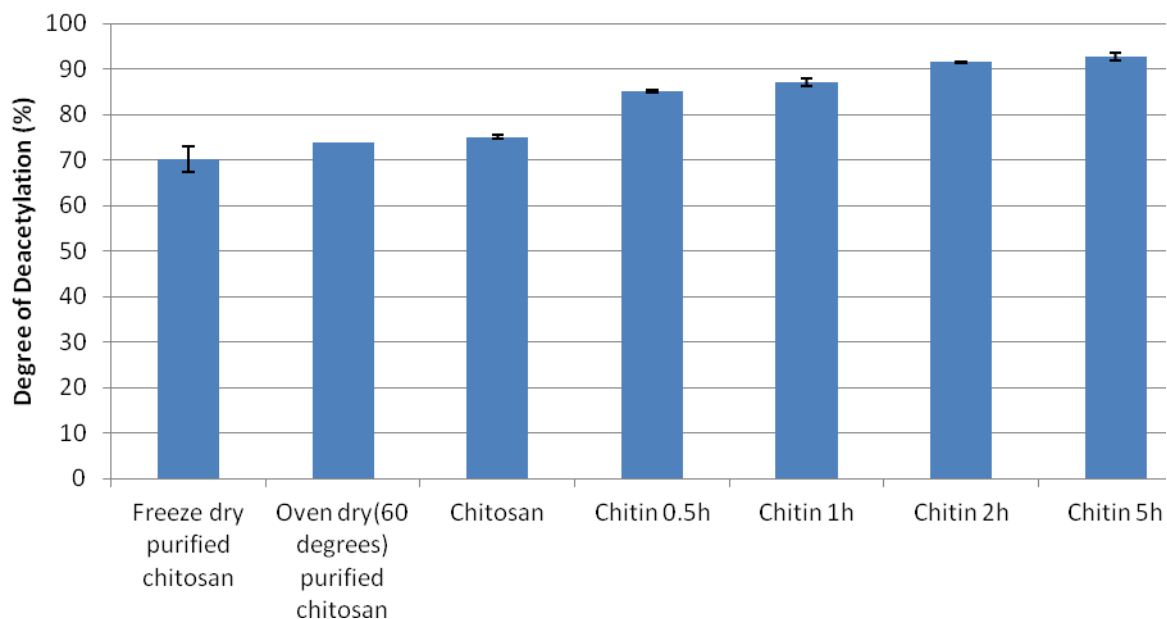


Figure 7. Degree of deacetylation of purified chitosan, chitosan, and chitin boiled for different times.

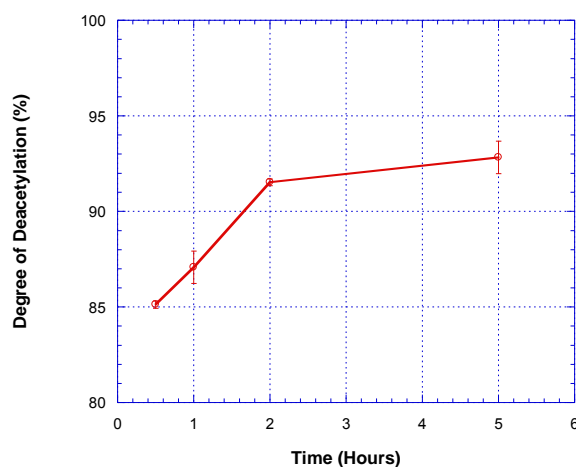


Figure 8. Effect of heating on the degree of deacetylation of chitin.

The first derivative UV-spectra for chitosan, purified chitosan, and chitin boiled for different times are shown in Fig. 6. As shown in Fig. 7, the DD of chitosan without purification was 75.08% while that for the purified chitosan was 70.18%. After being oven-dried, the DD of purified chitosan was 73.81%. These results strongly suggested that purification of chitosan led to decreases in its DD because the concentration of N-acetyl-D-glucosamine in purified chitosan is higher than that in non-purified chitosan.

Heating at 130 °C only exerted a modest effect on the DD of chitosan (Fig. 8): the DD only increased to a small extent with increases in heating time up to 5 hours (Fig. 8). Thus, the results of our ongoing studies indicate that the deacetylation of chitosan can be modified by physico-chemical modification(s) during the purification process. This property of chitosan can be exploited further in the tissue engineering of “artificial skin.” Additionally, we are continuing to investigate the properties of chitosan membrane in combinations with nanoparticles.

We have continued the studies to address (ii) stage two of setting up the model and (iii) stage three of designing and characterizing the biosensors. We have summarized below our progress in developing and characterizing the biosensors.

### Sensor Development:

During Phase I of this project, we studied the development of biosensor platform that are capable of measuring biometabolites and environmental sensitive species, such as peroxide and nitrate/nitrate, to concentration in the order of ppb (parts per billion) or lower.

In our more recent development, we modified our platform with dendrimers to enhance its performance. Zero and second generation of dendrimers were coated on the surface of a carbon glassy platform electrode modified with GDH (glutamate dehydrogenase) and it was used to measured ammonium, a common biometabolite, at near neutral pH that is common for normal bioactivities. The resulting electrode was tested with ammonium concentrations ranged from 0.002 to 0.3  $\mu\text{M}$  with satisfactory results. Figure 9 shows the cyclic voltammograms of various ammonium concentrations measured by the modified glassy carbon electrode, the lowest concentration was 2 nM. As indicated in the voltammogram in the reductive curves (upper lines), there was a big gap (current difference) between the blank (of buffer solution) and the first reductive curve (2 nM). Therefore, it is possible that the modified electrode can measure ammonium concentrations down to subnanomolar levels.

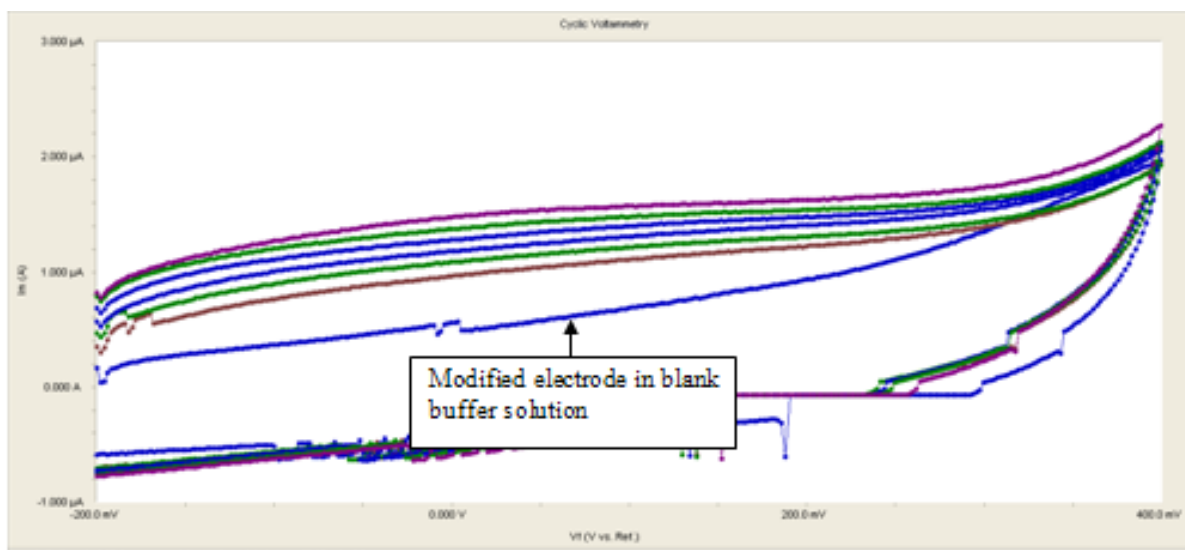


Figure 9. Cyclic voltammograms (i/v) of gold colloid-cysteamine/PAMAM<sub>2</sub><sup>ND</sup>-modified glassy carbon electrode measured from -0.2 to 0.4 V for the measurement of  $\text{NH}_4^+$ , the lowest concentration was 2 nM.



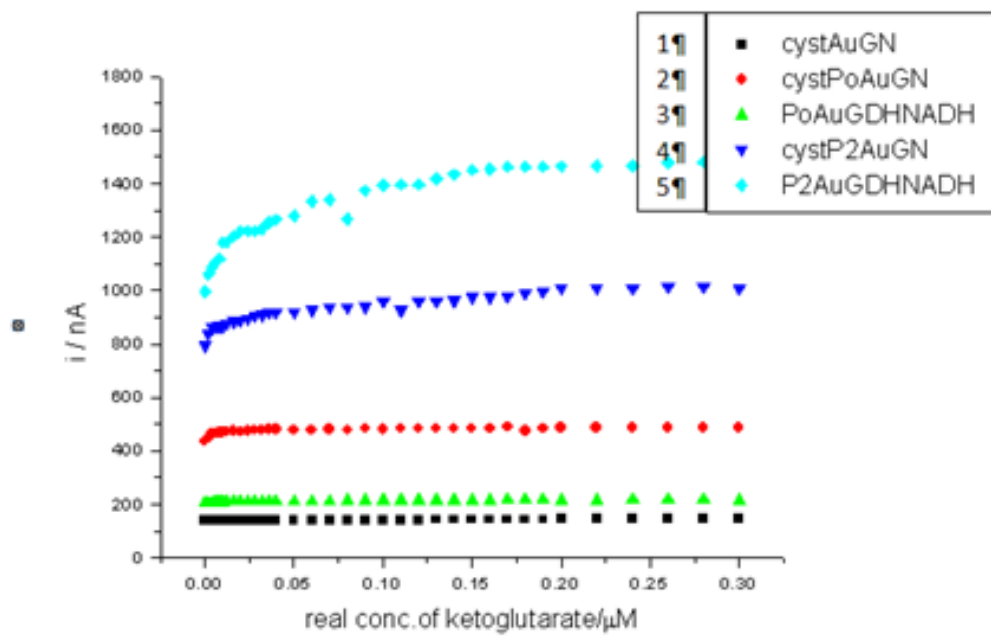


Figure 10. Performance differences of the glassy carbon electrode modified by different materials: 1. Modified with cysteamine-Au-GDH/NADH; 2. Cysteamine /PAMAM\_0-Au-GDH/NADH; 3. PAMAM\_0-Au-GDH/NADH; 4. Cysteamine /PAMAM\_2<sup>nd</sup>-Au-GDH/NADH; 5. PAMAM\_2<sup>nd</sup>-Au-GDH/NADH.

Figure 10 shows that there were distinctive current differences for the reaction of ammonium and  $\alpha$ -ketoglutarate when the electrode was modified by different materials. From the stand point of detection, within the five modifications, sensor coated with second generation of PAMAM would have the highest sensitivity (current vs. concentration). The results were conceivably due to the higher branching property of PAMAM\_2<sup>nd</sup>.

As shown in Figure 11, PAMAMs can be attached to cysteamine to enhance the available sites for the electrons transfer between reactions, in this case, ammonium and  $\alpha$ -ketoglutarate, therefore increase the detection lower limit.

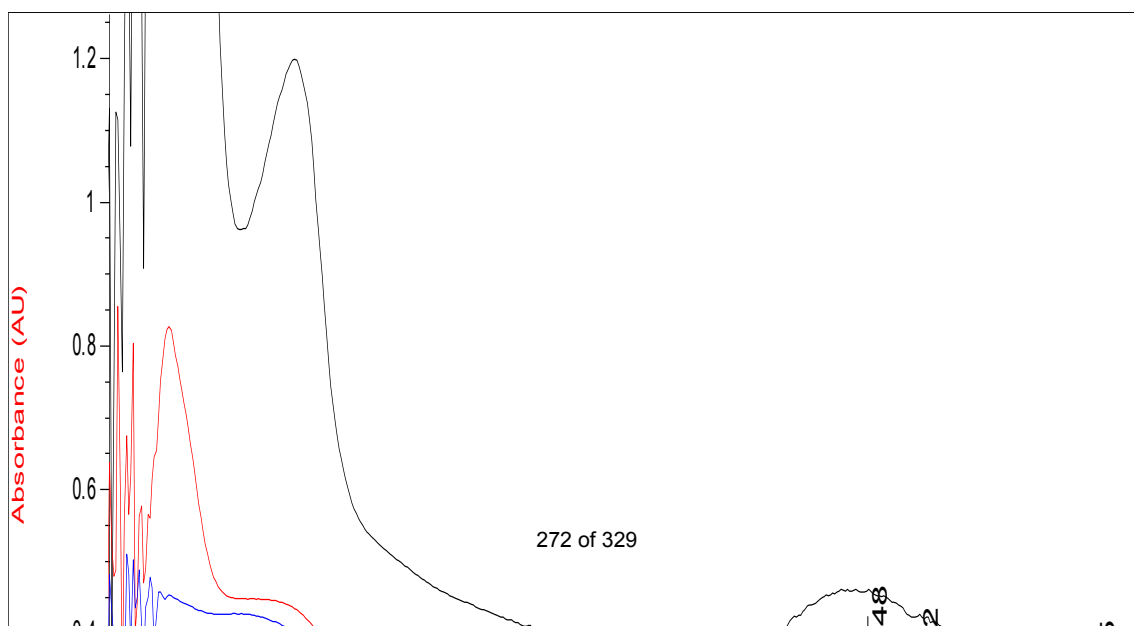


Figure 11. Cysteamine-PAMAM-Au-GDH coated on plastic UV-VIS cell with permanent absorption peak at 278 nm. Various lines indicated concentration differences.

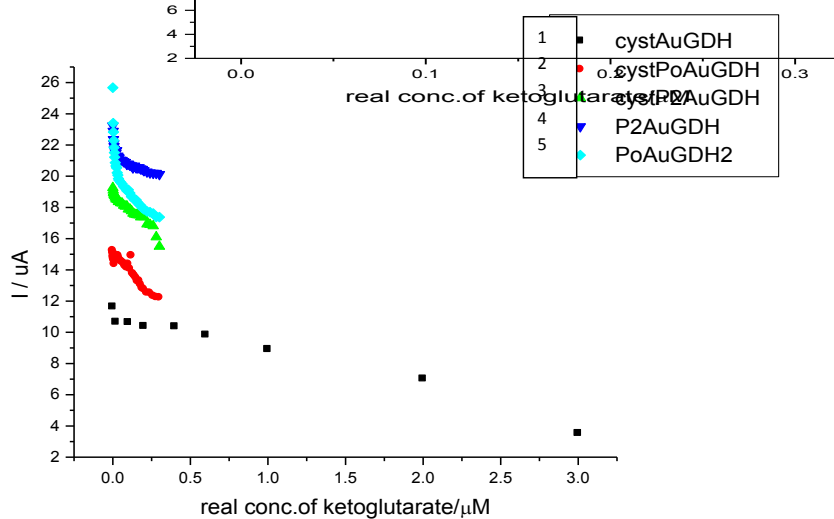
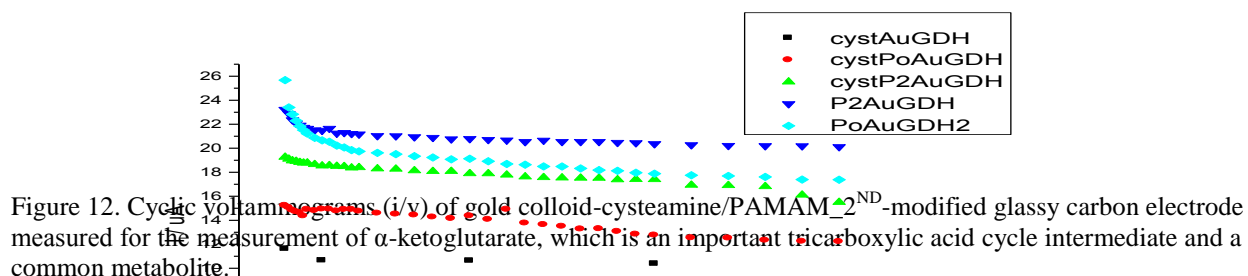


Figure 13. Cyclic voltammograms of GDH/NADH modified glassy carbon electrode (at low and high voltage range) for current vs. real concentration of  $\alpha$ -ketoglutarate at low and high voltage for GDH and NADH modified electrodes. 1. Glassy carbon electrodes modified with cysteamine -Au-GDH. 2. Glassy carbon electrodes modified with cysteamine /PAMAM\_0 -Au-GDH. 3. Glassy carbon electrodes modified with cysteamine /PAMAM\_2<sup>nd</sup> -Au-GDH. 4. Glassy carbon electrodes modified with PAMAM\_2<sup>nd</sup> -Au-GDH. 5. Glassy carbon electrodes modified with AMAM\_0 -Au-GDH.

Figures 12 and 13 show that there were distinctive current differences for the reaction of ammonium and  $\alpha$ -ketoglutarate when the electrode was modified by different materials. Because  $\alpha$ -ketoglutarate is an important tricarboxylic acid cycle intermediate and a common metabolite, the modifications as indicated in the two figures suggested that the biosensor has good capacity for detecting a range of concentrations of this metabolite. However, the current-voltage relationship is nearly linear after the initial extreme low concentrations. Thus, one should be cautious in selecting for the  $i/v$  ratio depending on the applications (for detection of extreme low and higher concentrations).

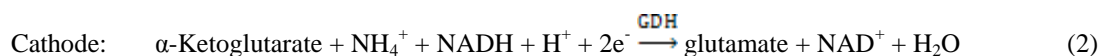
In our more recent development, we modified our platform to include the parallel development of biosensors and fuel cells. As in most biosensors, the detection principles are based on redox reactions of enzymatic reactions, which is the same principle used in most biofuel cell and how biological systems obtain energy to sustain live functions. For the sensors we previously developed that utilize the enzymes, LHD and GDH, for detections of various metabolites, biochemical reactions that involved these two enzymes can also be converted to a biofuel cell system:

For the biofuel cell system, the anodic half-cell was made by an Au electrode coated with lactate dehydrogenase (LDH) submerged in solution containing lactate and nicotinamide adenine dinucleotide (NAD<sup>+</sup>), thus, for the anodic half reaction:



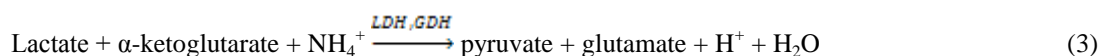
As lactate was oxidized into pyruvate in the anode, the oxidative potential,  $E_0'$ (25 °C), would be 0.19 V.

The cathodic half-cell was made by a glassy carbon electrode (GCE) coated with glutamate dehydrogenase (GDH) submerged in solution containing ammonia and reduced nicotinamide adenine dinucleotide (NADH), the cathodic half reaction was:



As  $\alpha$ -ketoglutarate was reduced into glutamate in the cathode, it generated a reductive potential,  $E_0'$ (25 °C), of -0.14 V.

Combining Equation (1) and (2), the total potential for the fuel cell with the anode and cathode above was 0.05 V (per mole). In general, biological reactions in nature do not release large amount of energy for each reaction step to preserve energy utilization efficiency. The overall reaction for the biofuel cell in our system was:



Since the  $\Delta E_0'$  of Equation (3) was greater than 0, the reaction was spontaneous and would proceed as written from left to right.

#### A. Anodic half-cell

Figure 14 shows the oxidative responses of the modified Au electrode with nanogold particles, cysteamine and LDH. As seen, the characteristic peak of lactate conversion to pyruvate was detected at 250 mV and the accumulative current increased linearly with added lactate instantaneously. It verified that the modified anodic electrode was functioning as expected in Equation (1).

#### B. Cathodic half-cell

Figure 15 is the reductive response of a GCE modified with 2<sup>nd</sup> generation of PAMAMs, nanogold particles, and GDH. The cathodic half-cell reaction functioned more efficiently at lower concentrations of  $\alpha$ -ketoglutarate and became less effective as the accumulative concentration of  $\alpha$ -ketoglutarate was higher (>0.025 mM).

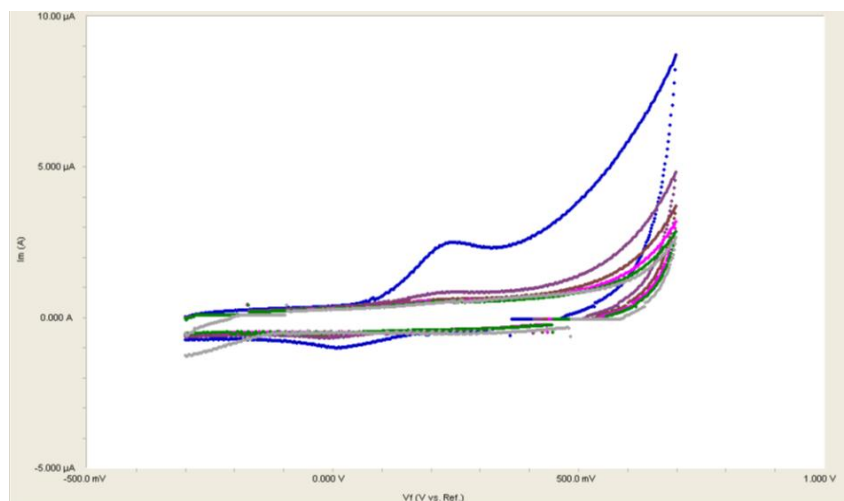


Figure 14. Voltammetric responses of an Au electrode coated with cysteamine, Au nanoparticles, and LDH at pH 8. Responses were stepwise additions of lactate at  $1.0 \times 10^{-4}$  mol/ml with linear current increments (oxidative peaks) at 250 mV.

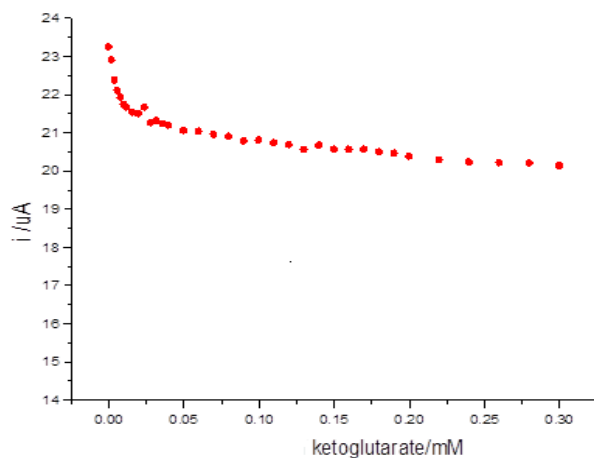


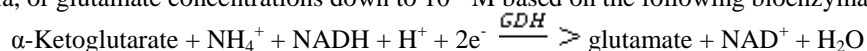
Figure 15. Reductive responses of a glassy carbon electrode modified with PAMAM, Au nanoparticle and GDH measured at 0.7 V in solution of ammonia and  $\alpha$ -ketoglutarate.

Our biofuel cell system would generate a relative low potential (0.05V), but the reactants are all readily available from our body which make it closer to reality for the system to be implanted into our body as power source for biomedical devices. A similar approach can be used to explore enzymatic reactions within human body that can produce higher energy output. This biofuel cell can be used potentially to power the prosthetic hand this grant is developing.

The biosensor platform thus far was proven to be versatile and can be used in many biomedical and environmental applications. We continue to work on the development of these smart sensors: we are particularly focusing on the development of bionanosensors for tissue engineering and biocompatibility studies and related biomedical engineering applications (see Appendices 9 &13).

#### Further Development of Nanobiosensors

We previously have successfully developed a glassy carbon electrode (GCE) biosensor that could detect ammonia, or glutamate concentrations down to  $10^{-9}$  M based on the following bioenzymatic reaction:



Currently, we have used the same platform of electrode sensor system to explore the ultimate limit of concentration detection for the system: down the  $1 \times 10^{-11}$  M, that is at least 6 orders of magnitude lower than any wet chemical methods or electrode(s) available in the commercial market (Figs 16-17).

The significance of the research is not only to develop a sensitive method for chemical speciation, but also to develop a viable method to detect signals between organs and cells that are reactions-specific, and a sensor that can differentiate the chemical signals sent from different cells or organs, a very important step for prosthetic applications and development.

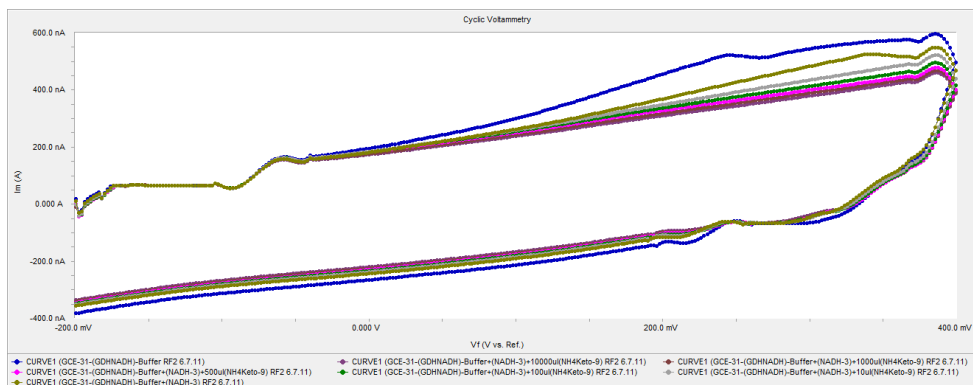


Figure 16. Detection of ammonia concentrations from  $10^{-11}$  M to  $10^{-7}$  M with a glassy carbon electrode (GCE) that was coated with PAMAM-Au-GDH/NADH by a potentiometer from 0.2 to 0.4 V, species specific measurements located (peaks) at about 0.01 V. A coating of PAMAM (*Dendrimer*) appears to enhance performance of the sensor compared to cysteamine that was used as a linker for the electrode and bioenzyme.

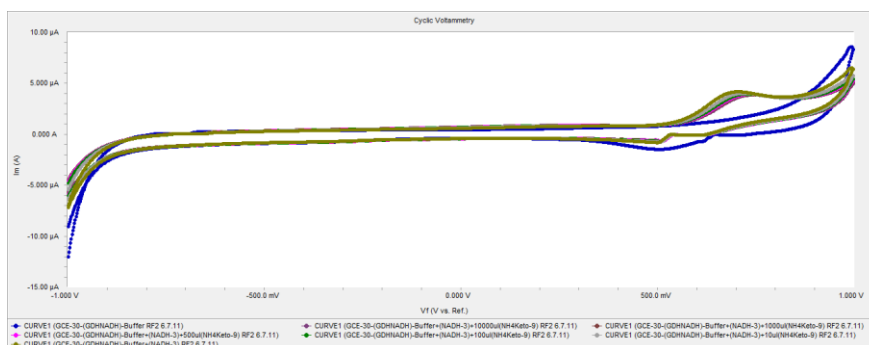


Figure 17. Similar measurements with the same electrode from -1 to 1 V that give the characteristic peaks at about 0.75 V.

Further research will be concentrating on sensor stability and selectivity in a multi-ionic matrix.

## Comparison of Anchoring Materials of High Performance Sensors Modified with Nanoparticles and Enzymes

We previously tested the efficacy of various combinations of composite materials used to construct the high performance sensors that were able to detect target species (signals) concentrations to levels below ppb. These materials included various polymer and dendrimers used to link between the anchoring electrode and bioenzymes, and different bioenzyme couplings used for selective detection of target species (signals).

We have been investigating how the anchoring materials used to fabricate the electrode (surface) may affect the overall performance of the sensors/electrodes, otherwise the electrodes were all fabricated with the same procedures and materials; the anchoring materials investigated included Pt, Glass carbon, Au, and Ag. These anchoring materials are important because of the following factors. 1. The sensor/electrode detection is based on redox

chemistry and anchoring materials easily oxidized are expected to alter the linkage surface. Thus, one important parameter to be ascertained is stability issue in detection. 2. The anchoring materials must be able to bond well with the linking materials (polymers as linker) and the coupling bioenzymes: weak bonding between the conducting electrode and the linker would weaken the detection signal thereby rendering the sensor ineffective. 3. Cost can be a factor if the electrode is put into commercial production. The cost factor for the electrodes in descending order is: Glossy carbon > Pt > Au > Ag.

Among the 4 tested anchoring materials, as expected and shown in Fig. 18, Ag gave the most noise. It was the most unstable because when the electrode was used multiple times (cycles), the electrode characteristic peak deteriorated rather fast compared to those of other materials used in this study.

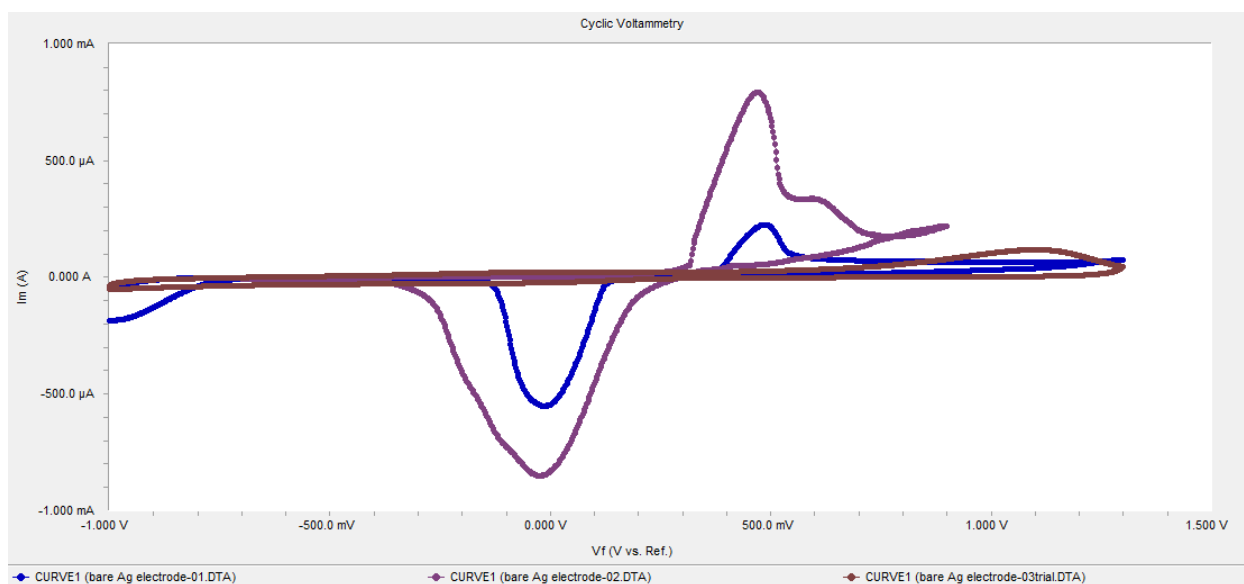
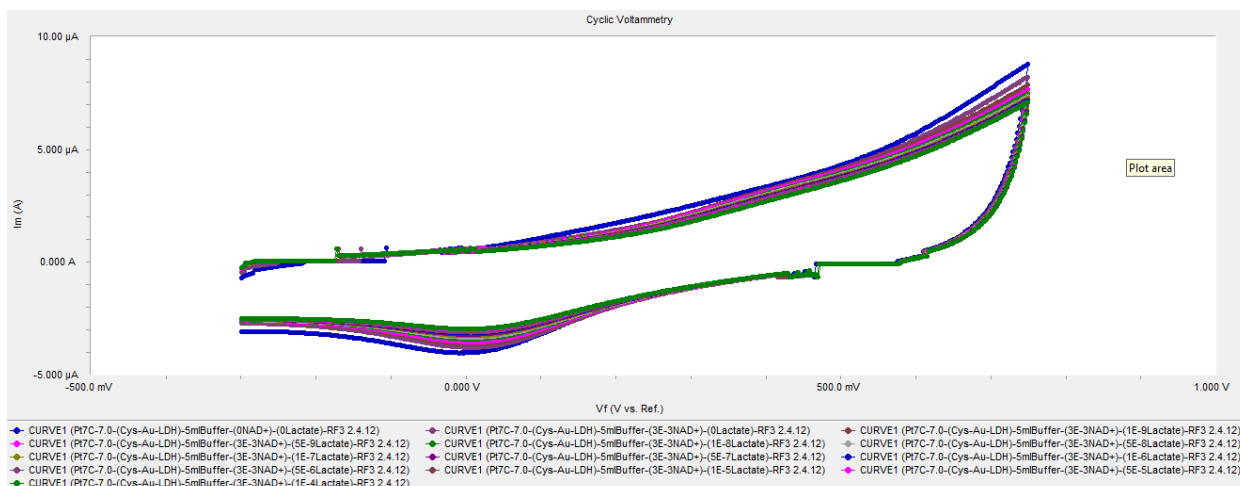
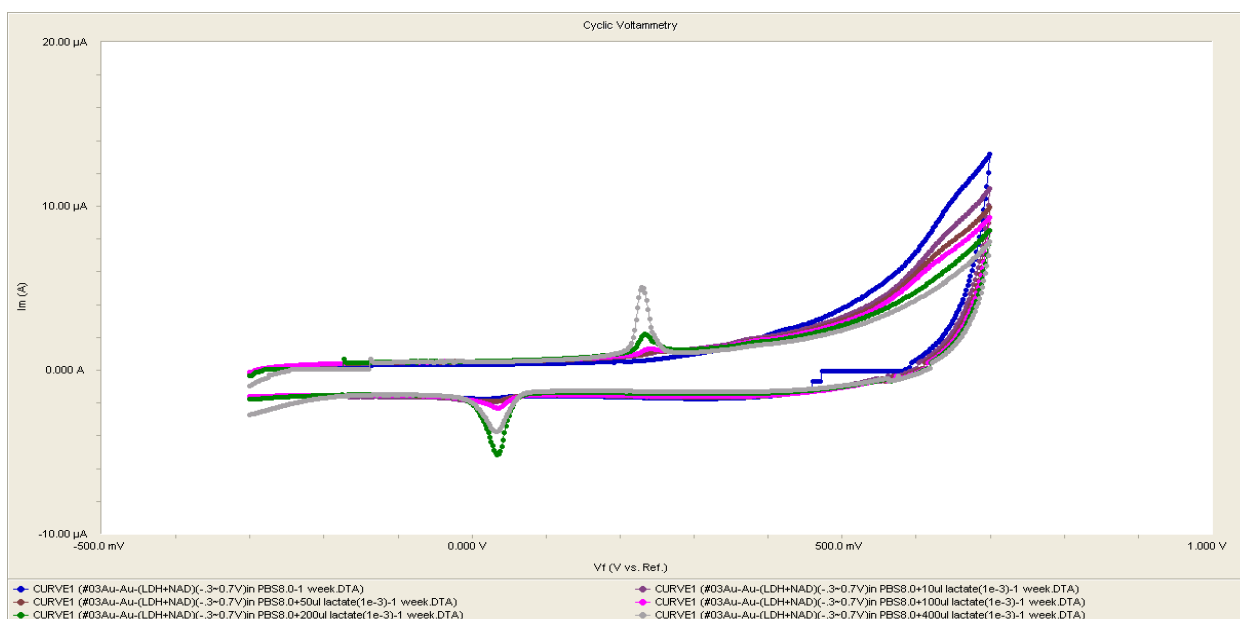


Figure 18. Ag bare electrode in 0.1 M of phosphate buffer solution, test runs in different voltages and repeated run of same voltage. Current signals showed high signal fluctuations with repeated runs.

Out of the 3 metals used in the testing of anchoring materials, Pt was thought to be the most ideal metal due to its inertness to chemical reactions. However, Pt appeared not to bind with our linkers well and thus did not provide characteristic signals as strong as other metals for at least 2 of the coupling enzymes, namely, lactate dehydrogenase (LDH) and glutamate dehydrogenase (GDH): this low signal was particularly obvious for the measurement of lactate with LDH as coupling enzyme. Despite this observation, Pt anchored electrode appeared to be functioning competitively with the GDH coupling and corresponding reactions (Fig. 19). Glassy carbon worked competitively with the metal electrodes, but is the most expensive among all electrodes tested.



a.



b.

Figure 19. Performance comparison of Pt and Au electrodes in similar lactate concentrations: a. Pt electrode coated with biocomposite materials; b. Au electrode coated with the same materials. Note that characteristic peaks at about 260 mV for Au electrode are more distinctive, although Pt electrode also produced peaks that are function of lactate concentrations.

### Further and Current Development of Biosensors:

We have highly modified our glassy carbon electrode (GCE) with glutamate dehydrogenase (GDH) for  $\text{NH}_4^+$  detection (Fig. 20). This  $\text{NH}_4^+$  sensor (GCE) was based on the sensor platform that can be used for the detection of many chemicals and metabolites that are generated in natural environment or by human body. When electrodes are coated/modified with different biocomposite materials, they can be grouped together to form an **array sensor** that can detect different chemicals and metabolites simultaneously. The measured current (in  $\mu\text{A}$ ) was near linear with concentration (in M) (Fig. 21). These ultra-high performance sensors showed that they could measure

concentrations down to  $5 \times 10^{-20}$  M, that are at least 10 orders of magnitude better than the current ammonia electrodes available in the public domain. Clearly this innovative and productive area merits further research and development.

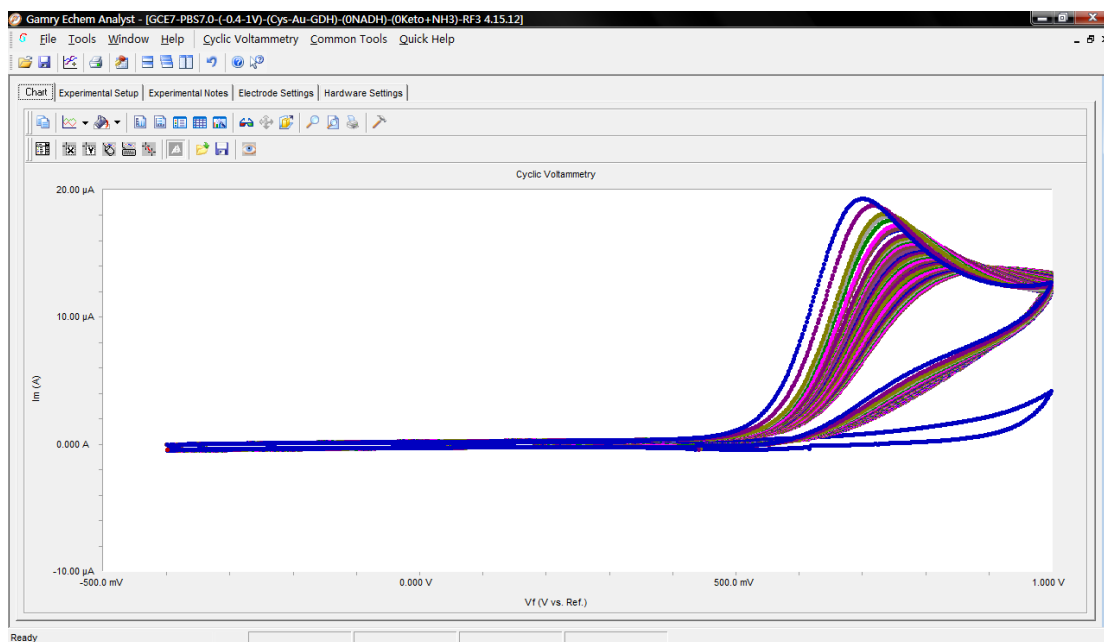


Figure 20. Cyclic voltammogram responses of using highly modified glassy carbon electrode (GCE) with Glutamate dehydrogenase (GDH) for  $\text{NH}_4^+$  detection.

#### Voltammogram outputs of Au electrode and GCE with concentrations for ammonia detection

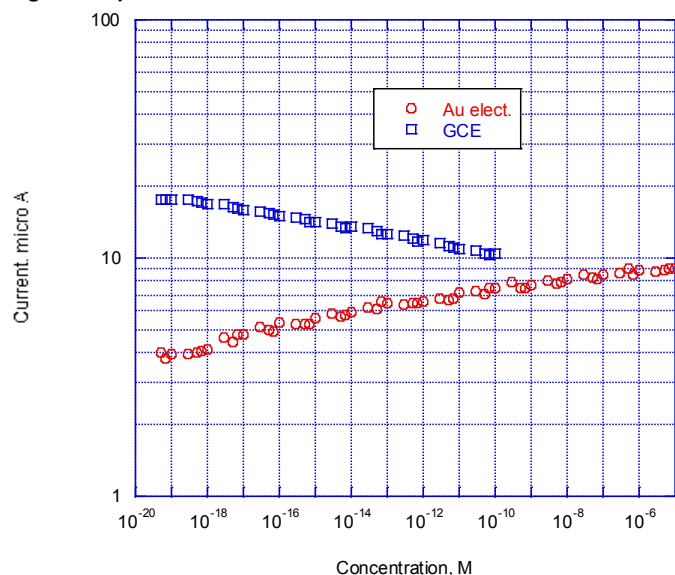


Figure 21. Results of the same sensor platform (Fig. 20) that was anchored by different materials (Au and glassy carbon) for  $\text{NH}_4^+$  detection.

The biosensor platform thus far was proven to be versatile and can be used in many biomedical and environmental applications. We continue to work on the development of these smart sensors: we are particularly



focusing on the development of bionanosensors for tissue engineering and biocompatibility studies and related biomedical engineering applications (see Appendices 9 &13).

## B. Investigate the biocompatibility of materials that are commonly used to fabricate sensors:

**Introductory remarks.** One established approach to investigate the biocompatibility of materials is to determine whether or not such materials exert cytotoxic effects on mammalian cells (Lai et al., 2008, 2010). Two nanomaterials that are commonly used to fabricate nanobiosensors are silicon dioxide nanoparticles and titanium oxide nanoparticles (Lai et al., 2008, 2010).

**Molecular and Signaling Mechanisms underlying the Cytotoxic Effects of Metallic Oxide Nanoparticles.** Nanomaterials have been increasingly used in industrial applications (e.g., drug delivery, additives to drugs and cosmetics). Because of their wide use, occupational exposure to nanomaterials and nanoparticles may pose as health risks. Recent studies have suggested that exposure to nanoparticles may induce cytotoxic effects in some mammalian cell types (Lai et al., 2010; Puli et al., 2006) although these effects have not been systematically investigated.

In these studies, we have begun to systematically investigate the molecular and signaling mechanisms underlying the cytotoxic effects of nanomaterials, especially nanoparticles, on human neural and non-neural cell types. Here we report on some of the mechanisms responsible for the cytotoxic effects of silicon dioxide ( $\text{SiO}_2$ ) nanoparticles on human astrocytoma U87 cells that are astrocytes-like.

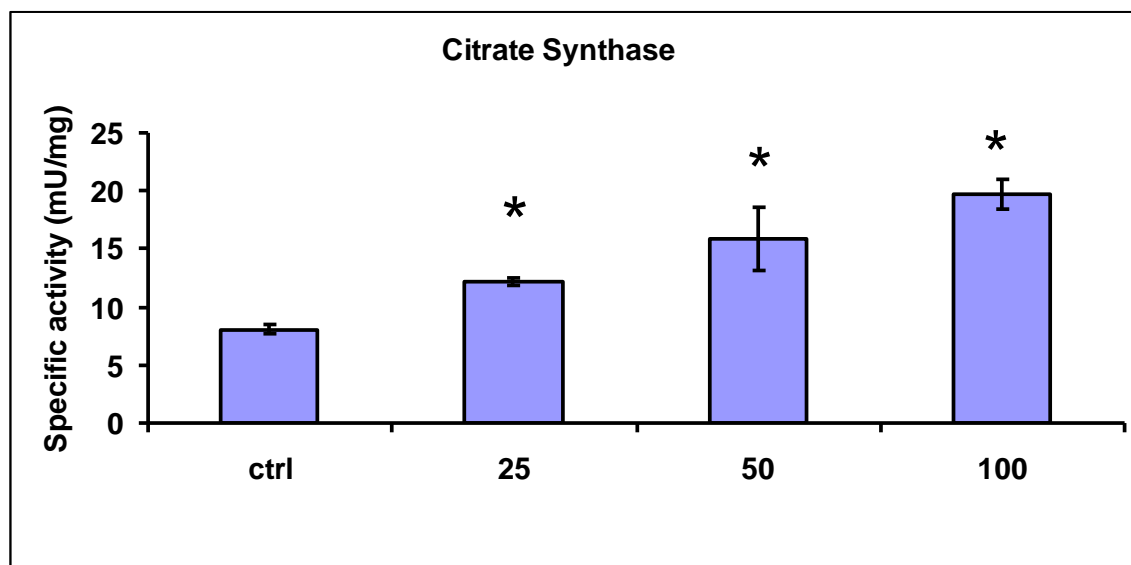


Figure 22. Effect of treatment with silicon dioxide nanoparticles on specific activities of citrate synthase in human astrocytoma U87 cells. U87 cells were treated at specified concentrations of silicon dioxide nanoparticles for 48 hours. Then the activities of citrate synthase in the homogenates of treated and untreated (i.e., control, ctrl) U87 cells were determined as described in Materials and Methods; the activities of citrate synthase were expressed per mg of homogenate protein as specific activities. The specific activities values were the mean  $\pm$  SEM of at least three separate experiments; ctrl represented the value in untreated U87 cell homogenate; \* $p < 0.05$  versus that of control cells.

Because cell survival critically depends on mitochondrial functions maintained at a normal physiological level, we determined the effect of  $\text{SiO}_2$  nanoparticles on mitochondrial function in U87 cells by monitoring the activities of one key enzymes of the tricarboxylic acid (TCA) cycle namely, citrate synthase (CS). As shown in Figure 22, at treatment concentrations of 25-100  $\mu\text{g/mL}$  for 48 hours,  $\text{SiO}_2$  nanoparticles induced dose-related increases in CS activities in U87 cells.

Treatment of U87 cells with SiO<sub>2</sub> nanoparticles could also lower the survival of U87 cells through altering cell signaling pathway(s) that regulate(s) cell survival and proliferation (7). We therefore investigated this possibility by examining the effect of these nanoparticles on expression of ERK and phospho-ERK proteins. We observed that when U87 cells were treated with 1-50 µg/mL of SiO<sub>2</sub> nanoparticles for 48 hours, their protein expression of phospho-ERK showed a dose-related decrease while that of ERK protein remained essentially unchanged (Fig. 23), suggesting that a lowering of this cell survival/proliferation signaling mechanism could, at least in part, account for the dose-related decrease in U87 cell survival induced by these nanoparticles.

The results of our ongoing studies on the molecular and signaling mechanisms underlying the cytotoxic effects of silicon dioxide (SiO<sub>2</sub>) nanoparticles indicate that alterations of mitochondrial bioenergetics and cell survival signaling underly the cytotoxic effects of these nanoparticles. Moreover, they suggest there may be other such mechanisms present. We are therefore continuing to pursue this interesting line of investigation.

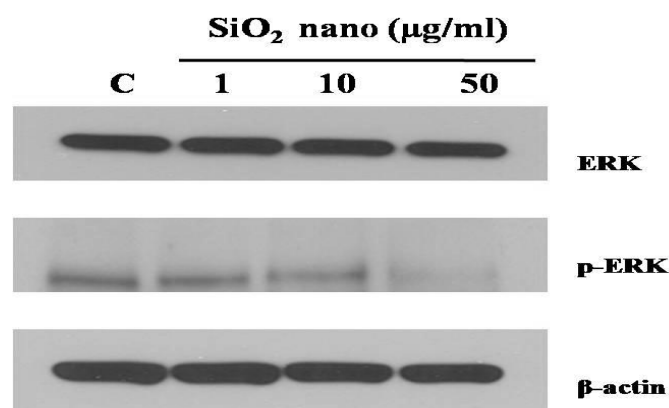


Figure 23. Effect of treatment with silicon dioxide nanoparticles on expression of ERK and phosphor-ERK in human astrocytoma U87 cells. U87 cells were treated at specified concentrations of silicon dioxide nanoparticles for 48 hours. Then cell lysates of treated and untreated (i.e., control) U87 cells were prepared as described in Materials and Methods. The expression of ERK and phosphor-ERK (p-ERK) was determined by Western blot analysis using β-actin as the loading control: Lane marked C, lysate of untreated or control U87 cells; lane marked 1, lysate of U87 cells treated with silicon dioxide nanoparticles at 1 µg/ml; lane marked 10, lysate of U87 cells treated with silicon dioxide nanoparticles at 10 µg/ml; lane marked 50, lysate of U87 cells treated with silicon dioxide nanoparticles at 50 µg/ml. The blots were from a typical experiment. Two other experiments yielded essential the same trend of results.

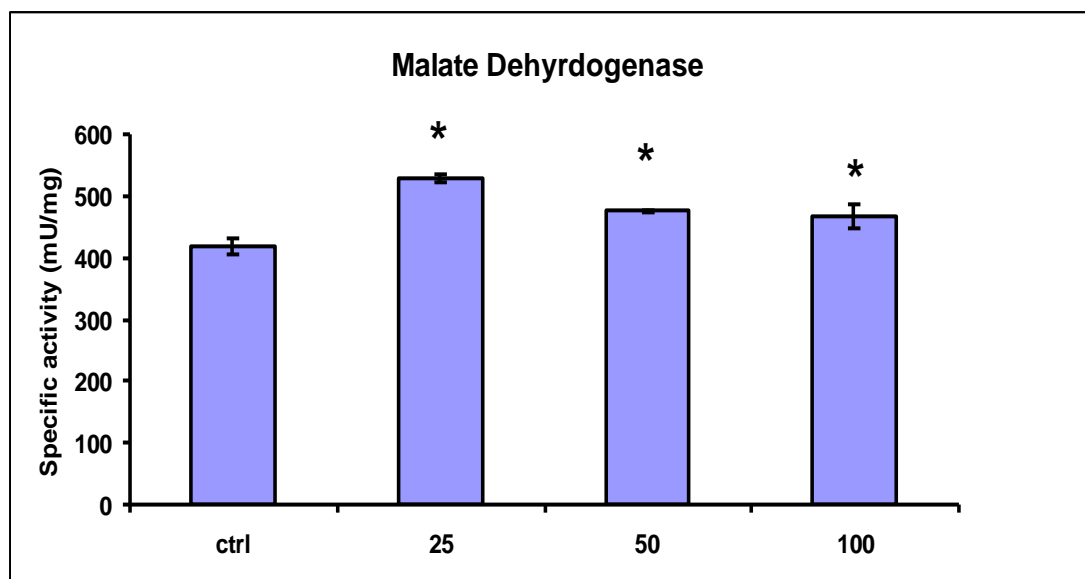


Figure 24. Effect of treatment with silicon dioxide nanoparticles on specific activities of citrate synthase in human astrocytoma U87 cells. U87 cells were treated at specified concentrations of silicon dioxide nanoparticles for 48 hours. Then the activities of malate dehydrogenase in the homogenates of treated and untreated (i.e., control, ctrl) U87 cells were determined as described in Materials and Methods; the activities of malate dehydrogenase were expressed per mg of homogenate protein as specific activities. The specific activities values were the mean  $\pm$  SEM of at least three separate experiments; ctrl represented the value in untreated U87 cell homogenate; \* $p < 0.05$  versus that of control cells.

Because cell survival critically depends on mitochondrial functions maintained at a normal physiological level, we determined the effect of SiO<sub>2</sub> nanoparticles on mitochondrial function in U87 cells by monitoring the activities of one key enzymes of the TCA cycle namely, malate dehydrogenase (MDH). As shown in Figure 24, at treatment concentrations of 25-100  $\mu\text{g/mL}$  for 48 hours, SiO<sub>2</sub> nanoparticles induced dose-related increases in MDH activities in U87 cells.

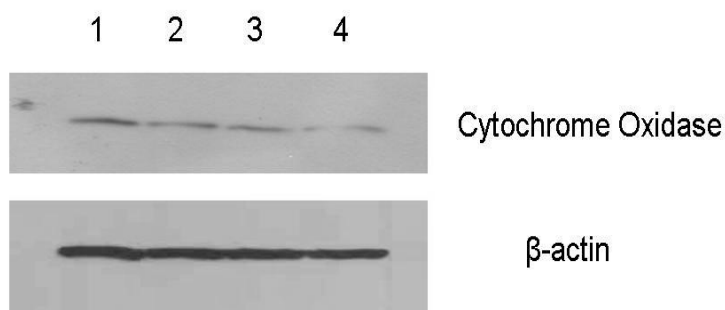


Figure 25. Effect of treatment with silicon dioxide nanoparticles on expression of cytochrome oxidase subunit II in human astrocytoma U87 cells. U87 cells were treated at specified concentrations of silicon dioxide nanoparticles for 48 hours. Then cell lysates of treated and untreated (i.e., control) U87 cells were prepared as described in Materials and Methods. The expression of cytochrome oxidase subunit II, encoded by mitochondrial DNA, was determined by Western blot analysis using  $\beta$ -actin as the loading control: Lane 1, lysate of untreated or control U87 cells; lane 2, lysate of U87 cells treated with silicon dioxide nanoparticles at 25  $\mu\text{g/ml}$ ; lane 3 lysate of U87 cells treated with

silicon dioxide nanoparticles at 50 µg/ml; lane 4, lysate of U87 cells treated with silicon dioxide nanoparticles at 100 µg/ml. The blots were from a typical experiment. Two other experiments yielded essential the same trend of results.

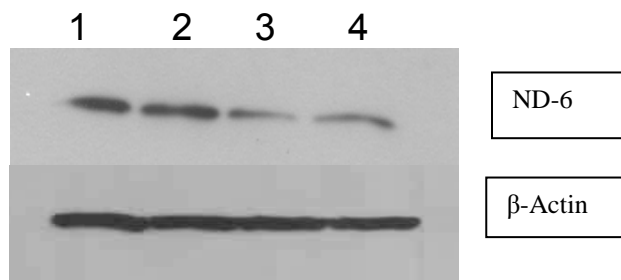


Figure 26. Effect of treatment with silicon dioxide nanoparticles on expression of NADH dehydrogenase subunit 6 (ND-6) in human astrocytoma U87 cells. U87 cells were treated at specified concentrations of silicon dioxide nanoparticles for 48 hours. Then cell lysates of treated and untreated (i.e., control) U87 cells were prepared as described in Materials and Methods. The expression of NADH dehydrogenase subunit 6 (ND-6), encoded by mitochondrial DNA, was determined by Western blot analysis using  $\beta$ -actin as the loading control: Lane 1, lysate of untreated or control U87 cells; lane 2, lysate of U87 cells treated with silicon dioxide nanoparticles at 25 µg/ml; lane 3 lysate of U87 cells treated with silicon dioxide nanoparticles at 50 µg/ml; lane 4, lysate of U87 cells treated with silicon dioxide nanoparticles at 100 µg/ml. The blots were from a typical experiment. Two other experiments yielded essential the same trend of results.

On the other hand, at treatment concentrations of 25-100 µg/mL for 48 hours, SiO<sub>2</sub> nanoparticles induced dose-related decreases in the expression of cytochrome C oxidase subunit II (a mitochondrial DNA-encoded peptide) in U87 cells (Fig. 25). These results strongly suggested treatment with SiO<sub>2</sub> nanoparticles altered the normal functioning of the mitochondrial genome in U87 cells.

At treatment concentrations of 25-100 µg/mL for 48 hours, SiO<sub>2</sub> nanoparticles induced dose-related decreases in the expression of NADH dehydrogenase subunit 6 (ND 6) (a mitochondrial DNA-encoded peptide) in U87 cells (Fig. 26). These results strongly suggested treatment with SiO<sub>2</sub> nanoparticles altered the normal functioning of the mitochondrial genome in U87 cells. A likely consequence of this effect of the nanoparticles is the impairment in the electron transport chain of the mitochondria in U87 cells: indeed, the nanoparticle-induced disruption of mitochondrial respiratory chain structure and function may be one cause of energy failure that ultimately led to the death of U87 cells.

Taken together, the results of our ongoing studies on the molecular mechanisms underlying the cytotoxic effects of silicon dioxide (SiO<sub>2</sub>) nanoparticles indicate that alterations of mitochondrial bioenergetics underlying the cytotoxic effects of these nanoparticles. Moreover, they suggest there may be other such mechanisms present. Consequently, we are continuing to pursue this interesting line of investigation.

Our previous and ongoing studies have demonstrated that nanoparticles of metallic and non-metallic oxides exert differential cytotoxic effects in neural cells derived from the central nervous system. Nonetheless, as the putative toxic effects of such nanoparticles in neural cells derived from the peripheral nervous system (PNS) are largely unknown, we have initiated studies to systematically investigate the putative cytotoxicity of nanoparticles of metallic and non-metallic oxides in neural cells derived from the PNS (see Appendices 19, 21-23, 27, 28). Here we report on some of the mechanisms responsible for the cytotoxic effects of silicon dioxide (SiO<sub>2</sub>) nanoparticles on Schwann cells and dorsal root ganglion (DRG) neurons.

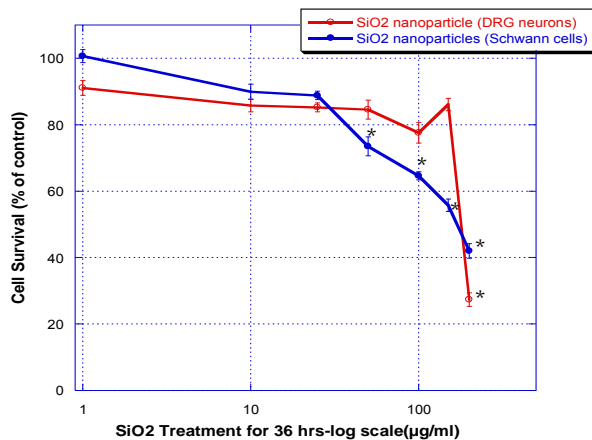


Figure 27. Effects of SiO<sub>2</sub> nanoparticles on DRG neurons and Schwann cells. Values are mean  $\pm$  SEM of 12 determinations and replicate experiments show the same trend. DRG neurons and Schwann cells treated with SiO<sub>2</sub> nanoparticles for 36 hours are marked red and blue, respectively.

Treatment of Schwann cells (R3) with SiO<sub>2</sub> nanoparticles induced a dose-related decrease in their survival when we progressively increased the concentrations of the nanoparticles from 1 to 200  $\mu$ M. The IC<sub>50</sub> for SiO<sub>2</sub> nanoparticles in lowering the survival of Schwann cells (R3) was  $\sim$ 150  $\mu$ M and at the highest concentration employed, only  $\sim$ 40% of the cells survived (Fig. 27).

When we exposed dorsal root ganglion (DRG) neurons to SiO<sub>2</sub> nanoparticles, we did not detect significant decreases in their survival at lower treatment concentrations (0.1-150  $\mu$ g/ml) but their survival was significantly decreased only at the highest concentration employed (i.e., 200  $\mu$ g/ml; Fig. 27). Moreover, DRG neurons did not appear to internalize SiO<sub>2</sub> nanoparticles in large amounts (data not shown). Nevertheless, the DRG neurons treated with the nanoparticles did show some cytoplasmic swelling (data not shown).

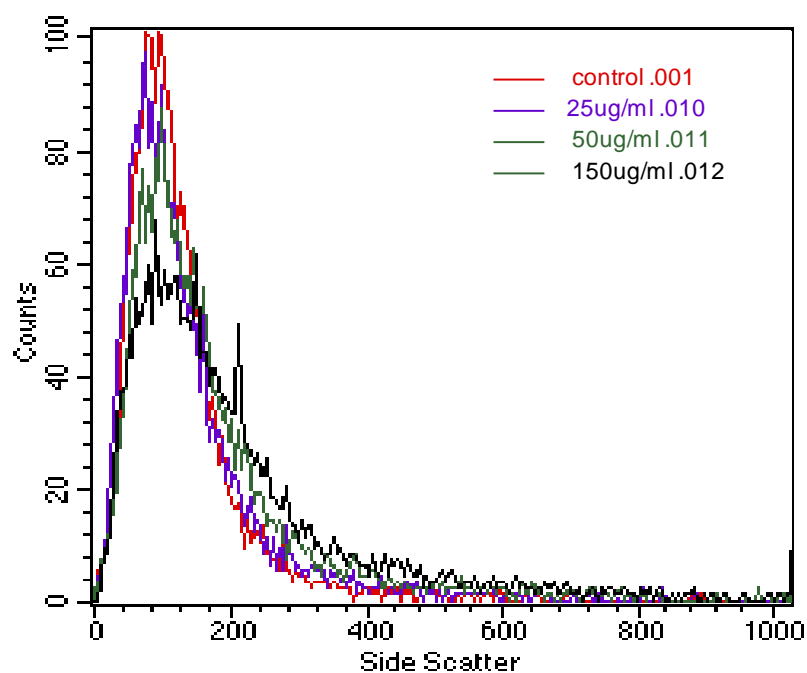


Figure 28. Uptake of silicon dioxide nanoparticles as determined by flow cytometry.

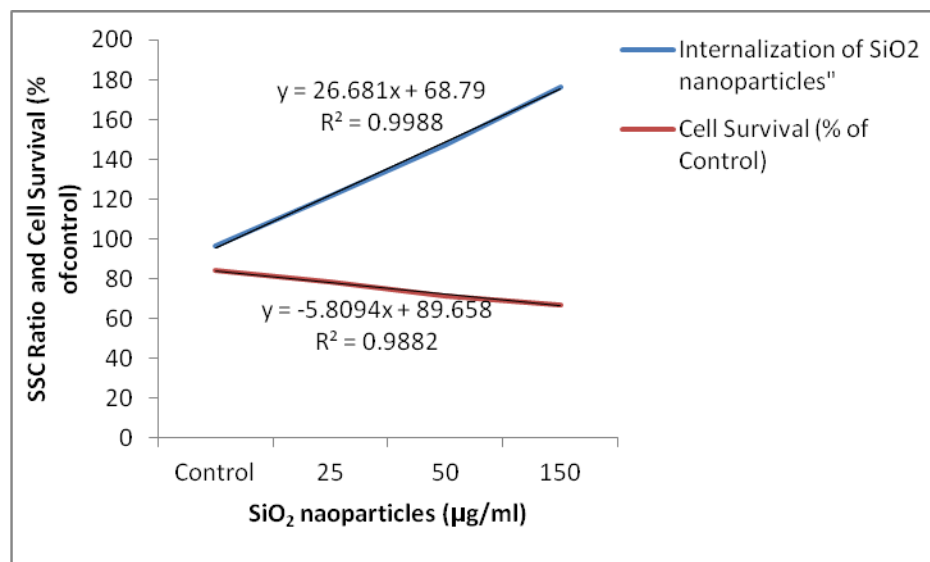


Figure 29. Uptake of  $\text{SiO}_2$  nanoparticles by Schwann cells compared with their survival.

Cellular uptake of SiO<sub>2</sub> nanoparticles were studied using FACSCalibur™ flow cytometer and dark field microscopy. The side scatters increase and forward scatters decrease sequentially, presumably due to substantial light reflection by the internalization of nanoparticles particles. Schwann cell showed internalization of SiO<sub>2</sub> nanoparticles in a dose-related manner (Figs. 28-29).

Nanoparticles gradually sediments onto Schwann cells and Schwann cells appeared to internalize them. Once the nanoparticles entered a cell, they showed a tendency to aggregate around the nucleus (data not shown). However, the nanoparticles did not appear to penetrate into the nucleus; rather, at higher treatment concentrations, the nuclei appeared to be swollen and their morphology changed. At higher treatment concentrations, the cell bodies of the Schwann cells appeared to be much more oval, presumably due to swelling; this altered morphology was distinctly different from the spindle-shaped cell bodies of untreated (i.e., control) Schwann cells (data not shown). Thus, in general, the photomicrographs revealed that treatment with the nanoparticles induced dose-related changes in cellular morphology, a finding that appeared to correlate with the nanoparticle-induced, dose-related progressive decrease in cell survival of the treated cells.

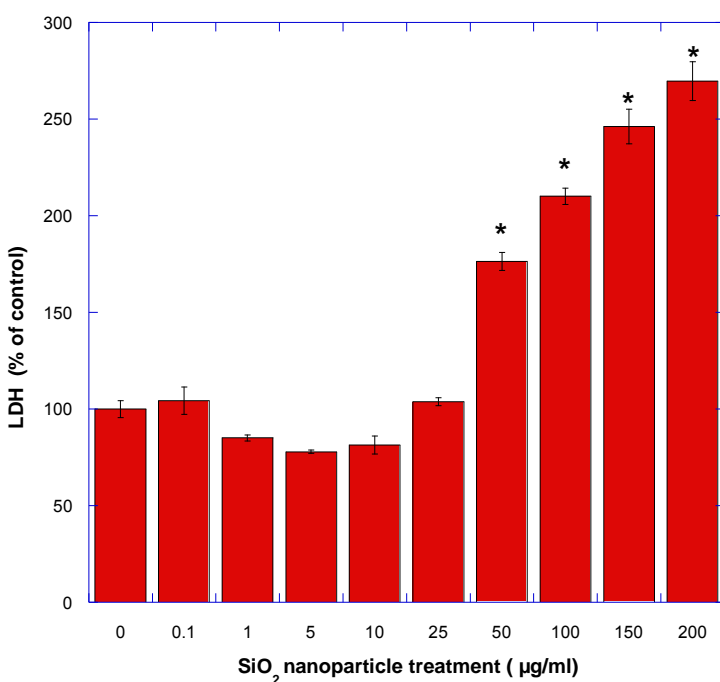


Figure 30. Effect of SiO<sub>2</sub> nanoparticles on inducing lactate dehydrogenase (LDH) release from Schwann cells. \*Values are significantly different from that in control (i.e., untreated) cells: p<0.05.

One of the mechanisms of cell death induced by nanoparticles was found to be necrosis as evident from the lactate dehydrogenase (LDH, a marker of cytoplasmic material) release from cells. The treatment of Schwann cells with silicon dioxide nanoparticles at concentrations higher than 50 µg/ml induced them to significantly release LDH into the surrounding medium, suggesting that the nanoparticles induced necrotic cell damage and death (Fig. 30).

As shown in Fig. 30 above, one of the mechanisms of cell death induced by nanoparticles was found to be necrosis as evident from the LDH release from cells. One possible mechanism that contributed to the necrotic

damage and cell death induced by silicon dioxide nanoparticles might be that of induction of oxidative stress. We investigated this possibility by examining the effect of these nanoparticles on the reduced glutathione (GSH) content of Schwann cells (Fig. 31).

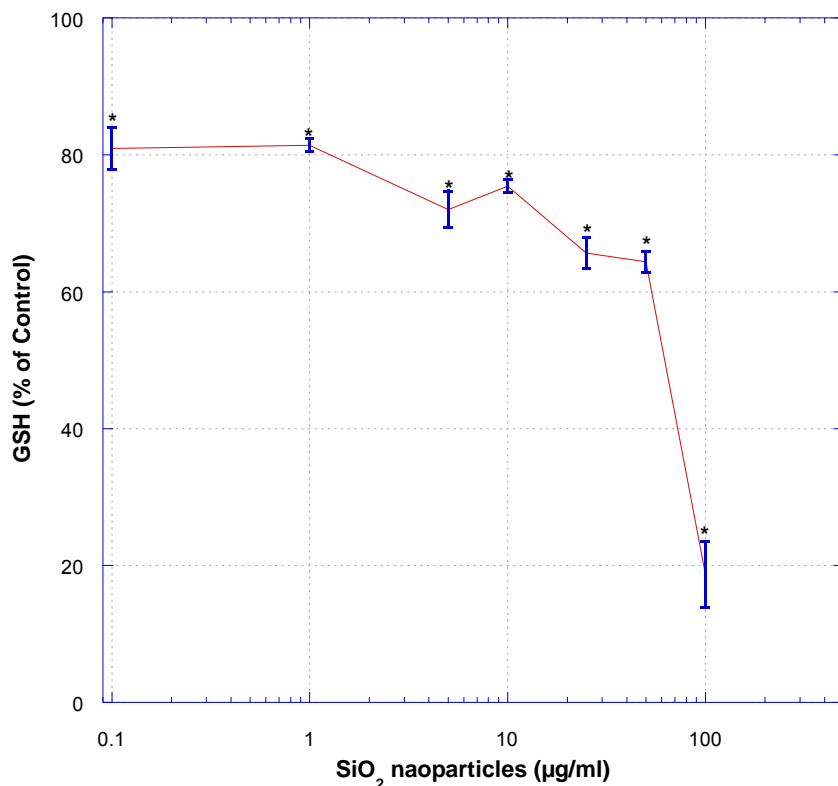


Figure 31. Effect of silicon dioxide nanoparticles on GSH content in Schwann cells. Results are mean  $\pm$  SEM of three separate experiments; \* $p < 0.05$  compared with control values.

As shown in Fig. 31, treatment of Schwann cells with silicon dioxide nanoparticles induced concentration-related decreases in cellular GSH content, suggesting the nanoparticles induced oxidative stress in these cells.

We have also investigated the hypothesis that magnesium oxide (MgO) nanoparticles elicit inflammatory responses in Schwann cells.

MgO nanoparticles induced dose-related decreases in survival of Schwann cells when they were exposed to MgO nanoparticles for 24 hours (Fig. 32). The  $IC_{50}$  of MgO nanoparticles in lowering the survival of Schwann cell was  $\sim 100$   $\mu\text{g/ml}$  (Fig. 32). That initial observation prompted us to monitor the effects of MgO nanoparticles on the morphology of Schwann cells.

We found that as the concentration of MgO nanoparticles was increased, more and more morphological differences between the treated and untreated (i.e., control) Schwann cells were noted (data not shown). When the Schwann cells were treated with the lower levels of the nanoparticles (i.e., 0.1–5  $\mu\text{g/ml}$ ), the polarity of the cells were more pronounced and they appeared to send out more processes. Additionally, at the higher treatment levels (i.e., 5–100  $\mu\text{g/ml}$ ), the nanoparticles induced the cells to swell and round off, suggesting that those cells were possibly undergoing necrosis.



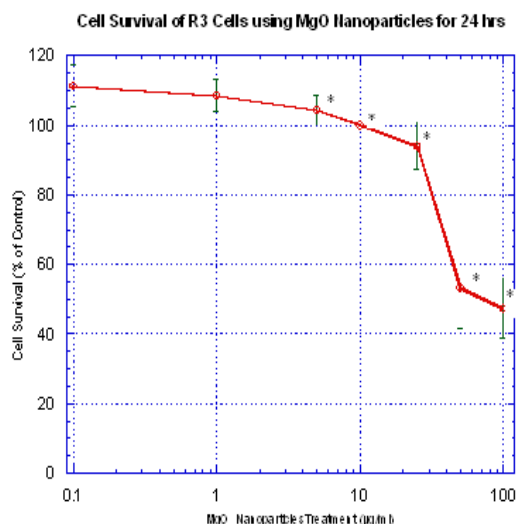


Figure 32. Survival of R3 Schwann cells exposed to MgO nanoparticles for 24 hours (\* $p < 0.05$  versus control, as determined by ANOVA with post-hoc Tukey test).

Morphological changes induced by MgO nanoparticles led us to investigate the possibility of an inflammatory response elicited by the Schwann cells. Inflammatory response is a protective mechanism that most cells exhibit towards an obnoxious stimulus. We therefore examined the expression of inflammatory markers such as interleukin-6 (IL-6) and peroxisome-proliferator activator receptor  $\gamma$  (PPAR $\gamma$ ). IL-6 is a proinflammatory cytokine that protects the cells by eliciting immune response and regulating the transcription of anti-apoptotic genes. On the other hand, PPAR $\gamma$  is a member of nuclear receptor super- family important in regulating many genes relating to glucose metabolism; it has also been shown to have anti-inflammatory actions by regulating cytokine expression.

Our western blot analysis shows Schwann cells treated with MgO nanoparticles for 24 hours exhibited increased expression of both of the markers (data not shown). However, the simultaneous increase in expression of both pro-inflammatory and anti-inflammatory markers in the treated cells is intriguing. This observation prompted us to further examine the expression of these markers in Schwann cells after exposing them to the nanoparticles for 48 hours. The cells so treated did not show any difference in expression of IL-6 and PPAR $\gamma$  compared to those in respective control cells (data not shown), suggesting that the anti-inflammatory effect of PPAR $\gamma$  might have counter-balanced the effects of IL-6. Thus, our results may have some pathophysiological implications in the impact of exposure to MgO nanoparticles on the structure and function of the peripheral nervous system. Our ongoing and future studies aim to further elucidate the mechanism(s) underlying the cytotoxicity and inflammatory effects of MgO nanoparticles in Schwann cells.

All in all, the results of our recent and ongoing studies strongly suggest that nanoparticles may exert differential cytotoxic effects on neural cell types of the peripheral nervous system. As such, our results may assume pathophysiological importance in the environmental health impact of nanoparticles. Obviously, this is an important area that deserves further study.

## **KEY RESEARCH ACCOMPLISHMENTS**

### **Goal 1: EMG Signals and System Identification**

1. Topical contribution:
  - Development of Bayesian filtering techniques for post processing of sEMG signals.
  - Utilization of system identification algorithms for extracting sEMG signal – finger force models, as well as sEMG signal – finger motion models.
  - Development of novel intelligent estimation algorithms using Genetic Algorithms, Particle Swarm, and Tabu Search methods.
  - Development of spatial filtering techniques for use with array sEMG sensors.
  - Zone classification of amputees based on anatomy for finger force and finger motion modeling.
  - Development of novel adaptive model fusion algorithms.
  - Spectral analysis of sEMG signals for characterizing skeletal muscle fatigue.
  - Developed linear and none-linear dynamic model fusion algorithms.
2. Student production:
  - Graduated two PhD students
  - Graduated three MS students
  - Supported one additional PhD and one MS student

## **Goal 2A: Intelligent Control**

- Kinematics, dynamics and control of prosthetic hand with 22 degrees of freedom (DOFs) were conducted.
- A control technique of finite-time linear quadratic optimal control for 14DOFs, five-fingered smart prosthetic hand was developed in MATLAB Simulink with different reference inputs, including constant, ramp, sinusoidal values.
- Fusion of control strategies for 14 DOFs, five-fingered smart prosthetic hand was simulated to grasp an object in 3 dimensional animations.
- A comprehensive literature updated on the topic of control techniques for prosthetic hands was conducted and one book chapter was published.
- Hard control techniques such as feedback linearization, proportional-derivative (PD), proportional-integral-derivative (PID), optimal and adaptive were developed for the 14 DOFs, five-fingered smart prosthetic hand.
- Soft computing techniques such as neural networks (NN), fuzzy logic (FL), adaptive neural-fuzzy inference system (ANFIS), and genetic algorithm (GA) were investigated.
- The fusion of hard and soft control techniques, such as FL+PD and GA+PID, was developed for the five-fingered smart prosthetic hand.

## **Goal 2AB: Real-Time Control**

- Development of new methods for power grasping and precision grasping for fully actuated hands
- Design, Optimization and Control of under-actuated prosthetic hand
- Robust Controller Design for Command Following Controller

## **Goal 2B: Embedded Hierarchical Real-Time Systems**

- The construction of a test bed that integrates the software tool chain and prototype hardware
- The study and experimental set up of a real-time operating system on the embedded processor
- Implementation and various control strategies and test their performance and loading on the microcontroller
- Real-time acquisition and processing of sEMG and sEMG-based algorithms on the microcontroller

### **Goal 3: Robotic Hand**

- Manufacturing and testing of Hand 1 Prototype II, basically a testing device.
- Design of Hand 2 Prototype I, a remotely-actuated prosthetic hand.
- Manufacturing of Hand 2 Prototype I.
- Application of the general kinematic synthesis algorithm for the design of articulated systems for finger and thumb motion.
- Development of a complete design methodology for articulated systems to be used for the design of hand motion, including data capture, kinematic synthesis, optimization of solutions and prototyping.
- Refinement of the process for the camera-based data acquisition system, to recover finger pose from a single camera. Conclusions regarding vision-based precision data capture.

#### **Goal 4: Biocompatibility and Signaling**

- Development of a co-culture model for biocompatibility and other tissue engineering studies and applications
- Development of cell models of peripheral nervous system neural cells consisting of dorsal root ganglion neurons and Schwann cells for biocompatibility and other tissue engineering studies and applications
- Characterization of cell models consisting of dorsal root ganglion neurons and Schwann cells
- Development of “smart” biosensors for tissue engineering and biocompatibility studies and applications
- Characterization of cytotoxicity of silicon dioxide nanoparticles in human neural and non-neural cells
- Elucidation of cell death mechanisms underlying cytotoxic effects induced by silicon dioxide and magnesium oxide nanoparticles in human astrocytoma U87 (astrocytes-like) cells, Schwann cells, and dorsal root ganglion (DRG) neurons
- Initiation of a systematic examination of putative cytotoxicity of metallic oxide nanoparticles

## REPORTABLE OUTCOMES

### A. PUBLICATIONS:

#### Goal 1: EMG Signal Identification

##### Peer Reviewed Journal Publications

1. Anish Sebastian, Parmod Kumar, Marco P. Schoen, “*Modeling surface electromyogram dynamics using Hammerstein-Wiener models with comparison of IIR and spatial filtering techniques*,” International Journal of Circuits, Systems and Signal Processing, Vol. 5(5), pp. 545 – 556, 2011.
2. Anish Sebastian, Parmod Kumar, Marco P. Schoen, “*Spatial filter masks optimization using genetic algorithm and modeling dynamic behavior of sEMG and finger force signals*,” International Journal of Circuits, Systems and Signal Processing Vol. 5(6), pp. 597 – 608, 2011.
3. J. Rafiee, M.A. Rafiee, N. Prause, and M. P. Schoen, “*Wavelet basis functions in biomedical signal processing*,” International Journal of Expert Systems with Applications, Vol. 38(5) pp. 6190-6201, May 2011.
4. J. Rafiee, M.A. Rafiee, F. Yavari, and M. P. Schoen, “*Feature extraction of forearm EMG signals for prosthetics*,” International Journal of Expert Systems with Applications, Vol. 38(4) pp. 4058-4067, April 2011.
5. Parmod Kumar, Chandrasekhar Potluri, Anish Sebastian, Steve Chiu, Alex Urfer, D. Subbaram Naidu, Marco P. Schoen, “*Adaptive Multi Sensor Based Nonlinear Identification of Skeletal Muscle Force*,” WSEAS Transactions on Systems, Vol. 10(9), pp. 1050-1062, October 2010.

##### Peer Reviewed Conference Proceedings:

6. Chandrasekhar Potluri, Madhavi Anugolu, Steve Chiu, Alex Urfer, Marco P. Schoen, D. Subbaram Naidu, “*Fusion of Spectral Models for Dynamic Modeling of sEMG and Skeletal Muscle Force*,” Proceedings of the 34<sup>th</sup> Annual International Conference of the IEEE Engineering in Medicine & biology Society, San Diego, August 28-September 1, 2012.
7. Chandrasekhar Potluri, Madhavi Anugolu, Steve Chiu, Marco P. Schoen, D. Subbaram Naidu, “*A sEMG based Real-time Adaptive Joint angle Estimation and Control for a Prosthetic Hand Prototype*,” Proceedings of the 12<sup>th</sup> WSEAS International Conference on Systems Theory and Scientific Computation (ISTASC '12), Istanbul, Turkey, August 21-23, 2012.
8. Madhavi Anugolu, Chandrasekhar Potluri, Steve Chiu, Member , Alex Urfer, Jim Creelman and Marco P. Schoen, “*A sEMG-skeletal muscle force data fusion based on minimum description length criterion*” Proceedings of the 2012 ICIA World Conference, Las Vegas, July 16-19, 2012.
9. M. Anugolu, C. Potluri, P. Kumar, M. P. Schoen, “*Genetic Algorithm Based Optimization of Kullback Information Criterion: Improved System Identification of Skeletal Muscle Force and sEMG Signals*,” Proceedings of the 2012 IEEE International Instrumentation and Measurement Technology Conference, Graz, Austria, May 2012.
10. Alex Urfer, Jim Creelman, Parmod Kumar, Anish Sebastian, Madhavi Anugolu, and Marco Schoen, “*The Development of a Functional Amputation Residuum Measurement of the Upper Extremity for Potential Myoelectric Prosthesis Use*,” Combined Sections meeting of the American Physical Therapy Association, Chicago, February 8-11, 2012.

11. C. Potluri, M. Anugolu, Y. Yihun, A. Jensen, S. Chiu, M. P. Schoen, D. S. Naidu, "*Optimal Tracking of a sEMG based Force Model for a Prosthetic Hand*," Proceedings of the 33rd Annual International IEEE EMBS Conference, Boston, MA, August 30- September 3, 2011.
12. M. Anugolu, C. Potluri, A. Ilyas, P. Kumar, S. Chiu, N. Devine, A. Urfer, M. P. Schoen, "*A Review on Sensory Feedback for sEMG Based Prosthetic Hands*," Proceedings of the International Conference on Artificial Intelligence, ICAI'11, Las Vegas, NV, July 18-21, 2011.
13. Alexander Urfer, Jim Creelman, Parmod Kumar, Anish Sebastian, Madhavi Anugolu, and Marco P. Schoen, "*The Development of a Functional Amputation Residuum Measurement of the Upper Extremity for Potential Myoelectric Prosthesis Use*," submitted for review, APTA-American Physical Therapy Association's CSM 2012, Tampa FL, February 2 – 13, 2012.
14. Parmod Kumar, Anish Sebastian, Chandrasekhar Potluri, Adnan Ilyas, Madhavi Anugolu, Alex Urfer, Marco P. Schoen, "*Adaptive Finger Angle Estimation from sEMG Data with Multiple Linear and Nonlinear Model Data Fusion*," Proceedings of the WSEAS 10<sup>th</sup> International Conference on Dynamical Systems and Control, Iasi, Rumania, pp. 154 – 159, July 1 -3, 2011.
15. Anish Sebastian, Parmod Kumar, Marco P. Schoen, "*Optimized Spacial Filter Mask using Genetic Algorithm and System Identification for Modeling sEMG and Finger Force Signals*," Proceedings of the WSEAS 10<sup>th</sup> International Conference on Dynamical Systems and Control, Iasi, Rumania, pp. 136 – 141, July 1 -3, 2011.
16. Anish Sebastian, Parmod Kumar, Marco P. Schoen, "*Evaluation of Filtering Techniques applied to surface EMG data and Comparison based on Hammerstein-Wiener Models*," Proceedings of the WSEAS 10<sup>th</sup> International Conference on Dynamical Systems and Control, Iasi, Rumania, pp. 130 – 135, July 1 -3, 2011.
17. P. Kumar, C. Potluri, A. Sebastian, Y. Yihun, A. Ilyas, M. Anugolu, R. Sharma, S. Chiu, J. Creelman, A. Urfer, D.S. Naidu, and M. P. Schoen, "*A Hybrid Adaptive Multi Sensor Data Fusion for Estimation of Skeletal Muscle Force for Prosthetic Hand Control*," International Conference on Artificial Intelligence, ICAI'11, Las Vegas, NV, July 18-21, 2011.
18. P. Kumar, A. Sebastian, J. Creelman, A. Urfer, and M. P. Schoen, "*Spectral Analysis of sEMG Signals to Investigate Skeletal Muscle Fatigue*," Proceedings of the 50<sup>th</sup> IEEE Conference on Decision and Control and European Control Conference, Orlando FL, December 12-15, 2011.
19. C. Potluri, Y. Yihun, M. Anugolu, P. Kumar, M. Anugolu, S. Chiu, M.P. Schoen, D.S. Naidu, "*Implementation of sEMG-Based Real-Time Embedded Adaptive Finger Force Control for Prosthetic Hand*," Proceedings of the 50<sup>th</sup> IEEE Conference on Decision and Control and European Control Conference, Orlando FL, December 12-15, 2011.
20. P. Kumar, A. Sebastian, M. Anugolu, C. Potluri, A. Fassih, Y. Yihun, A. Jensen, Y. Tang, C.-H. Chen, S. Chiu, K. Bosworth, D.S. Naidu, J. Creelman, A. Urfer, and Marco P. Schoen, "*An Adaptive Hybrid Data Fusion Based Identification of Skeletal Muscle Force with ANFIS and Smoothing Spline Curve Fitting*," Proceedings of the 2011 IEEE International Conference on Fuzzy Systems, Taipei, Taiwan, June 27-30, 2011.
21. Parmod Kumar, Chandrasekhar Potluri, Madhavi Anugolu, Anish Sebastian, Steve Chiu, Alex Urfer, D. Subbaram Naidu, Marco P. Schoen, "*An Hybrid Adaptive Data Fusion with Linear and Nonlinear Models for Skeletal Muscle Force Estimation*," Proceedings of the IEEE 5th Cairo International Conference on Biomedical Engineering (CIBEC), Cairo, Egypt, December 16-18, 2010.
22. Parmod Kumar, Chandrasekhar Potluri, Anish Sebastian, Steve Chiu, Alex Urfer, D. Subbaram Naidu, Marco P. Schoen, "*An Adaptive Multi Sensor Data Fusion with Hybrid Nonlinear ARX and Wiener-Hammerstein Models for Skeletal Muscle Force Estimation*," Proceedings of the WSEAS Systems Conference, pp. 186 – 191, July 22-24, 2010, Corfu, Greece.

23. Anish Sebastian, Parmod Kumar, Marco P. Schoen, “*A Study on Hybridization of Particle Swarm and Tabu Search Algorithms for unconstrained Optimization and Estimation Problems*,” Proceedings of the WSEAS Systems Conference, pp. 458 -463, July 22-24, 2010, Corfu, Greece.
24. Parmod Kumar, Nikesh Joshi, Chandrasekhar Potluri, Jensen Alex, Marco P. Schoen, Steve Chiu, “*Genetic Algorithm Running Time Optimization Using OpenMP Parallel Computing*,” Proceedings of The 2010 World Congress in Computer Science Computer Engineering and Applied Computing Conference, Las Vegas, NV, July 12-15, 2010.
25. Anish Sebastian, Parmod Kumar, Marco P. Schoen, Alex Urfer, Jim Creelman, and D. Subbaram Naidu, “*Analysis of EMG-Force Relation Using System identification and Hammerstein-Wiener Models*,” Proceedings of the Dynamic Systems and Control Conference (DSCC), Boston, MA, September 2010.
26. Parmod Kumar, Anish Sebastian, Chandrasekhar Potluri, Alex Urfer, D. Subbaram Naidu, Marco P. Schoen, “*Towards Smart Prosthetic Hand: Adaptive Probability Based Skeletal Muscle Fatigue Model*,” Proceedings of the 32<sup>nd</sup> Annual International Conference of the IEEE Engineering in Medicine and Biology Society, Buenos Aires, Argentina, August 31-September 2010.
27. Chandrasekhar Potluri, Parmod Kumar, Madhavi Anugolu, Alex Urfer, D. Subbaram Naidu, Marco P. Schoen, “*Frequency Domain Surface EMG Sensor Fusion for Estimating Finger Forces*,” Proceedings of the 32<sup>nd</sup> Annual International Conference of the IEEE Engineering in Medicine and Biology Society, Buenos Aires, Argentina, August 31-September 2010.
28. Chandrasekhar Potluri, Parmod Kumar, Madhavi Anugolu, Alex Urfer, Marco P. Schoen, D. Subbaram Naidu, “*sEMG Based Fuzzy Control Strategy with ANFIS Path Planning for Prosthetic Hand*,” Proceedings of the 3<sup>rd</sup> IEEE International Conference on Biomedical Robotics and Biomechatronics, Tokyo, Japan, September 26-30, 2010.



## Goal 2A: Intelligent Control

Portions of goal 2A have been published in four international peer-reviewed conference papers (attachments 2A-1, 2A-2, 2A-5, and 2A-7), one international journal (attachment 2A-3), and one book chapter (attachment 2A-4); two international journal papers (attachments 2A-8 and 2A-9) have been reviewed and two technical reports (attachments 2A-10 and 2A-11) have been completed as follows:

1. C.-H. Chen, D. S. Naidu, and M. P. Schoen. An adaptive control strategy for a five-fingered prosthetic hand. *In the 14<sup>th</sup> World Scientific and Engineering Academy and Society (WSEAS) International Conference on Systems, Latest Trends on Systems (volume II)*, Corfu Island, Greece, July 22-24, pp. 405-410, 2010. (attachment 2A-1)
2. C.-H. Chen and D. S. Naidu. Optimal control strategy for two-fingered smart prosthetic hand. *In Proceedings of the 15<sup>th</sup> International Association of Science and Technology for Development (IASTED) International Conference on Robotics and Applications (RA 2010)*, Cambridge, Massachusetts, USA, November 1-3, pp. 190-196, 2010. (attachment 2A-2)
3. C.-H. Chen, D. S. Naidu, and M. P. Schoen. Adaptive control for a five-fingered prosthetic hand with unknown mass and inertia. *World Scientific and Engineering Academy and Society (WSEAS) Journal on Systems*, Vol. 10, No. 5, pp. 148-161, May 2011. (attachment 2A-3)
4. D. S. Naidu and C.-H. Chen. Automatic control strategies for smart prosthetic hand technology: an overview, book chapter 12, to appear in a book titled “Distributed Diagnosis and Home Healthcare (D<sub>2</sub>H<sub>2</sub>): Volume 2”, American Scientific Publishers, CA, pp. 201-223, 2011. (attachment 2A-4)
5. C.-H. Chen and D. S. Naidu. Fusion of fuzzy logic and PD control for a five-fingered smart prosthetic hand. *In Proceedings of the 2011 IEEE International Conference on Fuzzy Systems (FUZZ-IEEE 2011)*, Taipei, Taiwan, June 27-30, pp. 2108-2115, 2011. (attachment 2A-5 and 2A-6)
6. C.-H. Chen and D. S. Naidu. Hybrid genetic algorithm PID control for a five-fingered smart prosthetic hand. *In Proceedings of the 6th International Conference on Circuits, Systems and Signals (CSS'11)*, Vouliagmeni Beach, Athens, Greece, March 7-9, pp. 57-63, 2012. (attachment 2A-7)
7. C.-H. Chen and D. S. Naidu. A new optimal control strategy for a five-fingered smart prosthetic hand. *Journal of IET Control Theory and Applications*. (Submitted) (attachment 2A-8)
8. C.-H. Chen and D. S. Naidu. Hybrid control strategies for a five-finger smart prosthetic hand. *Journal of Biomedical Signal Processing and Control (Elsevier)*. (Submitted) (attachment 2A-9)
9. P. Ezenwa, “Kinematics, dynamics and control of prosthetic hand with extended degrees of freedom,” M.S. thesis, Measurement and Control Engineering, Idaho State University. (attachment 2A-10)
10. A. Khamis, “Optimal control strategy for smart prosthetic hand,” technical report, Measurement and Control Engineering, Idaho State University, 2012. (attachment 2A-11)

## **Goal 2AB: Real-Time Control**

- Amir Fassih, D.Subbaram Naidu, Steve Chiu, Parmod Kumar, “Robust Control of a Prosthetic Hand Based on a Hybrid Adaptive Finger Angle Estimation”, Wseas Conf. Athen, Greece, March 7-9,2012
- Amir Fassih, D.Subbaram Naidu, Steve Chiu, Parmod Kumar, “Design and Control of an Underactuated Prosthetic Hand”, Wseas Conf. Athen, Greece, March 7-9,2012
- Fassih, D.S. Naidu, S. Chiu, And M.P. Schoen, “Power Grasping of a Prosthetic Hand Based Upon Virtual Spring-Damper Hypothesis”, IASTED Int. Conf. Robotics And Applications, Cambridge, MA, November 1 – 3, 2010
- Fassih, D.S. Naidu, S. Chiu, And M.P. Schoen, “Precision Grasping of a Prosthetic Hand Based on Virtual Spring Damper Hypothesis”, Ieee 5th Cairo International Biomedical Engineering Conference, Cairo, Egypt, Dec 2010
- P. Kumar, C. H. Chen, A. Sebastian, M. Anugolu, C. Potluri, A. Fassih, Y. Yihun, A. Jensen, Y. Tang, S. Chiu, K. Bosworth, “An Adaptive Hybrid Data Fusion Based Identification of Skeletal Muscle Force With Anfis And Smoothing Spline Curve Fitting”, International Conference On Fuzzy Systems, Taipei, Taiwan, June 27 - June 30, 2011.
- Potluri, M. Anugolu, P. Kumar, A. Fassih, P. Yarlagadda, Y. Yihun, And S. Chiu, “Real-Time Seng Acquisition And Processing Using A Pic 32 Microcontroller”, Esa’11 - 9th Int’l Conference On Embedded Systems And Applications, Las Vegas, Nevada, Usa, July 18-21, 2011.

## Goal 2B: Embedded Hierarchical Real-Time Systems

1. **Chandrasekhar Potluri**, Parmod Kumar, Madhavi Anugolu, Alex Urfer, Steve Chiu, D. Subbaram Naidu, and Marco P. Schoen, “*Frequency Domain Surface EMG Sensor Fusion for Estimating Finger Forces*,” 32nd Annual International Conference of the IEEE Engineering in Medicine and Biology Society, Buenos Aires, Argentina, Aug. 31 – Sept. 4, 2010.
2. **Chandrasekhar Potluri**, Parmod Kumar, Jeff Moliter, Madhavi Anugolu, Jensen Alex, Kenyon Hart, and Steve Chiu, “*Multi-Level Embedded Motor Control for Prosthesis*,” *International Conference on Embedded Systems and Applications*, ESA’2010, Las Vegas, Nevada, USA, July 12-15, 2010.
3. **Chandrasekhar Potluri**, Parmod Kumar, Madhavi Anugolu, Steve Chiu, Alex Urfer, Marco P. Schoen, and D. Subbaram Naidu, “*sEMG Based Fuzzy Control Strategy with ANFIS Path Planning For Prosthetic Hand*,” 3rd IEEE RAS &EMBS International Conference on Biomedical Robotics and Biomechatronics, Tokyo, Sept 26-30, 2010.
4. **Chandrasekhar Potluri**, Chandrabanu Vedantam, Shanmuk Anjaneyulu Dasari, Deepak Kumar, Avinash M, Marco P. Schoen, D. Subbaram Naidu, “*Hand Gestures Recognition Based on sEMG Signal Using Wavelet and Pattern Recognition*” International conference on Aerospace Electronics, Communication and Instrumentation (ASECI), Vijayawada, A.P, India, Jan 06-07, 2010.\_
5. **Chandrasekhar Potluri**, Yimesker Yihun, Parmod Kumar, Jeff Molitor, Steve C. Chiu, D. Subbaram Naidu, *Fellow, IEEE*, S.Hossein Mousavinezhad, “*sEMG Based Real-Time Embedded Force Control Strategy for a Prosthetic Hand Prototype*” IEEE International Conference on Electro/Information Technology, Mankato, Minnesota, USA, May 15-17, 2011.
6. **Chandrasekhar Potluri**, Madhavi Anugolu, Yimesker Yihun, Alex Jensen, Steve Chiu *Member, IEEE*, Marco P. Schoen, *Senior Member, IEEE*, and D. Subbaram Naidu, *Fellow, IEEE*. “*Optimal Tracking of a sEMG based Force Model for a Prosthetic Hand*”, 33rd Annual International Conference of the IEEE Engineering in Medicine and Biology Society, Boston, MA, USA, Aug 31- Sep 3, 2011
7. **Chandrasekhar Potluri**, Madhavi Anugolu, Yimesker Yihun, Parmod Kumar, Steve Chiu, *Member, IEEE*, Marco P. Schoen, *Senior Member, IEEE*, D. Subbaram Naidu, *Fellow, IEEE* “*Implementation of sEMG-Based Real-Time Embedded Adaptive Finger Force Control for a Prosthetic Hand*”, IEEE Conference on Decision and Control and European Control Conference (IEEE CDC-ECC), Orlando, Florida, USA, December 12-15, 2011.
8. **Chandrasekhar Potluri**, Madhavi Anugolu, Parmod Kumar, Amir Fassih, Yimesker Yihun, Steve Chiu, and Subbaram Naidu, “*Real-Time sEMG Acquisition and Processing Using a PIC 32 Microcontroller*,” ESA’11 - 9th Int'l Conference on Embedded Systems and Applications, Las Vegas, Nevada, USA, July 18-21, 2011.
9. **Chandrasekhar Potluri**, Madhavi Anugolu, Alex Jensen, Girish Sriram, Shiwei Liu, Steve Chiu, “*PIC 32 Microcontroller Based sEMG Acquisition System and Processing Using Wavelet Transforms*,” ESA’12 - 9th Int'l Conference on Embedded Systems and Applications, Las Vegas, Nevada, USA, July 16-19, 2012.

10. **Chandrasekhar Potluri**, Madhavi Anugolu, Steve Chiu, Alex Urfer, Alba Perez, Marco P. Schoen, D. Subbaram Naidu “Fusion of Spectral Models for Dynamic Modeling of sEMG and Skeletal Muscle Force” submitted to 34th Annual International Conference of the IEEE Engineering in Medicine and Biology Society, San Diego, CA, USA, Aug 28-Sep 1, 2012.

### **Goal 3, Robotic Hand: Manuscripts published or in press:**

Yihun, Y., Bosworth, K. and Perez-Gracia, A., “Design Optimization of Spatial Mechanisms “, *to be submitted to the 2013 ASME IDET Conference*.

Batbold, B., Thomas, F., Yihun, Y. and Perez-Gracia, A., “Approximate Workspace Synthesis for RCCR Linkages”, *to be submitted to the 2013 IFToMM Computational Kinematics conference*.

Simo Serra, E. and **Perez Gracia, A.**, “Kinematic Synthesis Using Tree Topologies”, *Mechanism and Machine Theory*, 2012 (*under review*).

Yihun, Y., Rahman, M.S., and **Perez-Gracia, A.**, “Design of an Exoskeleton as a Finger-Joint Angular Sensor”, *2012 IEEE EMBS Conference, San Diego, CA, August 28-September 1, 2012*.

Yihun, Y., Miklos, R., **Perez-Gracia, A.**, Reinkensmeyer, D.J., Denney, K. and Wolbrecht, E.T., “Single Degree-of-Freedom Exoskeleton Mechanism Design for Thumb Rehabilitation”, *2012 IEEE EMBS Conference, San Diego, CA, August 28-September 1, 2012*.

Scott, K. and **Perez-Gracia, A.**, “Design of a Prosthetic Hand with Remote Actuation”, *2012 IEEE EMBS Conference, San Diego, CA, August 28-September 1, 2012*.

Simo-Serra, E., **Perez-Gracia, A.**, Moon, H. and Robson, N., “Design of Multifingered Robotic Hands for Finite and Infinitesimal Tasks Using Kinematic Synthesis”, *2012 Advances in Robot Kinematics conference*.

**Perez Gracia, A.**, “Synthesis of Spatial RPRP Closed Linkages for a Given Screw System”, *ASME Journal of Mechanisms and Robotics*, 3(2), 2011.

Simo-Serra, E., Moreno-Noguer, F., and **Perez-Gracia, A.**, “Design of Non-anthropomorphic Robotic Hands for Anthropomorphic Tasks”, *accepted at the ASME International Design Engineering Technical Conferences, IDETC 2011, Washington DC, USA, August 29-31, 2011*.

Crawford, A.L., Molitor, J., **Perez Gracia, A.**, and Chiu, S., “Design of a Robotic Hand and Simple EMG Input Controller with a Biologically-Inspired Parallel Actuation System for Prosthetic Applications”, *1st International Conference on Applied Bionics and Biomechanics (ICABB)*, Venice, Italy, October 14-16, 2010.

### **Invited oral presentations:**

Polytechnic University of Catalonia, Barcelona, Spain: “The Smart Prosthetic Hand Project”, presentation at the Equal Opportunities Seminar, February 2011.

#### Goal 4: Biocompatibility and Signaling

Our research has been very productive: to date, we have **9 journal articles, 3 reviews, and 20 conference proceedings papers** published or in press, published **40** abstracts, and given **9 invited oral** and **31** poster presentations (see lists below for details).

##### Journal Articles published or in press:

1. Lai JCK, Ananthakrishnan G, Jandhyam S, Dukhande VV, Bhushan A, Gokhale M, Daniels CK & Leung SW (2010) Treatment of Human Astrocytoma U87 Cells with Silicon Dioxide Nanoparticles Lowers Their Survival and Alters Their Expression of Mitochondrial and Cell Signaling Proteins. *International Journal of Nanomedicine* 5:715-723.
2. Jaiswal AR, Bhushan A, Daniels CK & Lai JCK (2010) A Cell Culture Model for Diabetic Neuropathy Studies. *Journal of the Idaho Academy of Science* 46(1):58-63.
3. Wong YYW, Jaiswal AR, Bhushan A, Leung SW & Lai JCK (2010) Further Elucidation of Neuroprotective Properties of Astrocytoma (Astrocytes-like) Cells. *Journal of the Idaho Academy of Science* 46(1):52-57.
4. Patil PP, Lai MB, Leung SW, Lai JCK & Bhushan A (2010) Differential Cytotoxic Effects of Magnesium Oxide Nanoparticles on Cisplatin-sensitive and Cisplatin-resistant Leukemia Cancer Cells. *Journal of the Idaho Academy of Science* 46(1):70-75.
5. Wright GL, Lai JCK, Chan AWK, Minski MJ, Lim L & Leung SW (2010) Metallomic Distribution in Various Regions of the Brain as Influenced by Dietary Intakes and Their Implications. In *Proceedings of the ISEIS 2010 International Conference on Ecological Informatics and Ecosystem Conservation*, August 27-29, Beijing, China, published in *Procedia Engineering* 01 (2010) 0159-0171.
6. Leung SW, Siddhanti S, Williams B, Chan AWK, Minski MJ, Daniels CK & Lai JCK (2010) Effects of Diet Intake on Metal and Electrolyte Distributions in Various Organs. In *Proceedings of the ISEIS 2010 International Conference on Ecological Informatics and Ecosystem Conservation*, August 27-29, Beijing, China, published in *Procedia Engineering* 01 (2010) 0104-0108.
7. Leung SW, Wang Y & Lai JCK (2011) Biomedical Applications of Modified Carbon Glassy Electrode Sensor with Nanoparticles and Dendrimers. *Sensors & Transducers* (2011) Volume 11, Special Issue, April 2011, pp. 74-82.
8. Gao W, Lai JCK & Leung SW (2012) Functional Enhancement of Chitosan and Nanoparticles in Cell Culture, Tissue Engineering and Pharmaceutical Applications. *Frontiers in Physiology* 3, Article 321, pp. 1-13 [published: 21 August 2012. Doi:10.3389/fphys.2012.00321].
9. Leung SW, Assan D & Lai JCK (2012) Evaluation of Anchoring Materials for Ultra-Sensitive Biosensors Modified with Au Nanoparticles and Enzymes. *Sensors & Transducers Journal*, Volume 15 (Special Issue: Oct. 2012), pp. 59-70.

##### Review Articles published or in press:

1. Bhushan A, Patil PP, Leung SW & Lai JCK (2013) Metallic Nanoparticles in Cancer Imaging and Therapy. In: *CRC Biomedical Engineering Handbook*, 4<sup>th</sup> Edition, CRC Press (in press).
2. Lai JCK & Leung SW (2012) Manganese and Its Interrelations with Other Metal Ions in Health and Disease. In: *Encyclopedia of Metalloproteins* (Uversky VN, Kretsinger RH & Permyakov EA, eds.), Springer (in press).
3. Lai JCK, Jaiswal AR, Lai MB, Jandhyam S, Leung SW & Bhushan A (2013) Toxicity of Silicon Dioxide Nanoparticles in Mammalian Neural Cells. In: *Clinical Nanomedicine — From Bench to Bedside* (Bawa R, Audette GF & Rubinstein I, eds.), Pan Stanford Series in Nanomedicine (Bawa, R, Series Ed.), Volume 1, Pan Stanford Publishing, Singapore (in press).

#### Conference Proceedings Papers published or in press:

1. Jaiswal A, Wong YYW, Bhushan A, Daniels C & Lai JCK (2010) A Noncontact Co-Culture Model of Peripheral Neural Cells for Nanotoxicity, Tissue Engineering and Pathophysiological Studies. Technical Proceedings of the 2010 NSTI Nanotechnology Conference and Expo – Nanotech 2010, Vol. 3 Chapter 8: Environment, Health & Safety, Pages 527-531.
2. Wong YYW, Jaiswal AR, Dukhande VV, Bhushan A, Leung SW & Lai JCK (2010) Elucidation of Neuroprotective Properties of Astrocytoma (Astrocytes-like) Cells in Neural Cell Culture Models *In Vitro*: Applications in Tissue Engineering and Nanotoxicology. Technical Proceedings of the 2010 NSTI Nanotechnology Conference and Expo – Nanotech 2010, Vol. 3 Chapter 8: Environment, Health & Safety, Pages 561-564.
3. Leung SW, Gao W, Gu H, Bhushan A & Lai JCK (2010) Chitosan Membrane in Combinations with Nanoparticles and Adriamycin as a Treatment to Inhibit Glioma Growth and Migration. Technical Proceedings of the 2010 NSTI Nanotechnology Conference and Expo – Nanotech 2010, Vol. 3 Chapter 3: Nano for Biotech, Interfaces & Tissues, Pages 206-209.
4. Leung SW, Wang Y, Gu H & Lai JCK (2010) Biomedical Applications of Modified Carbon Glassy Electrode Sensor with Nanoparticles and Dendrimers. Technical Proceedings of the 2010 NSTI Nanotechnology Conference and Expo – Nanotech 2010, Vol. 3 Chapter 1: Bio Sensors, Diagnostics & Imaging, Pages 122-124.
5. Bhushan A, Patil PP, Bhardwaj V, Lai MB, Daniels CK, Leung SW & Lai JCK (2010) Cross Resistance of Magnesium Oxide Nanoparticles to Cisplatin in Leukemia Cells: Mechanistic Studies. In Seminar Proceedings of Institution of Mechanical Engineers Seminar on Nanotechnology in Medicine and Biotechnology, October 2010, London, UK, Chapt. 5, pp. 1-4.
6. Leung S & Lai J (2011) Advanced Dehydrogenase Biofuel Cell Modified with Highly Branched Polymers and Nanogold Sol-Gel. In Proceedings of 2011 International Conference on Agricultural and Biosystems Engineering (ICABE 2011). Lecture Notes in Information Technology Vols. 3-4, pp. 41-44.
7. Leung S, Williams B, Lai J, Chan A & Minski M (2011) Elemental Analyses in Organ Systems in a Small Animal after Life-Long Controlled Diet. In Proceedings of 2011 International Conference on Agricultural and Biosystems Engineering (ICABE 2011). Lecture Notes in Information Technology Vols. 3-4, pp. 45-48.
8. Leung SW & Lai JCK (2011) Advanced Biofuel Cell Composed of Highly Modified Electrodes for Biomedical Applications. Technical Proceedings of the 2011 NSTI Nanotechnology Conference and Expo – Nanotech 2011, Vol. 3, Chapter 9: Nanotech for Oil, Gas & BioEnergy, pp. 636-639.
9. Jaiswal AR, Lu S, Pfau J, Wong YYW, Bhushan A, Leung SW, Daniels CK & Lai JCK (2011) Effects of Silicon Dioxide Nanoparticles on Peripheral Nervous System Neural Cell Models. Technical Proceedings of the 2011 NSTI Nanotechnology Conference and Expo – Nanotech 2011, Vol. 3, Chapter 7: Environment, Health & Safety, pp. 541 – 544.
10. Wong YYW, Jaiswal A, Dukhande VV, Bhushan A, Leung SW & Lai JCK (2011) New In Vitro Strategy of Astrocytoma (Astrocytes-like) Cells Treated with Pioglitazone (PPARgamma agonist) Offers Neuroprotection Against Nanoparticles-Induced Cytotoxicity. Technical Proceedings of the 2011 NSTI Nanotechnology Conference and Expo – Nanotech 2011, Vol. 3, Chapter 6: Nano Medical Sciences & Neurology, pp. 455 – 458.
11. Jain A, Jaiswal AR, Lu S, Wong YYW, Bhushan A, Leung SW, Daniels CK & Lai JCK (2011) Molecular Effects of Silicon Dioxide Nanoparticles on Cell Survival Signaling of Dorsal Root Ganglion (DRG) Neurons and Schwann Cells. Technical Proceedings of the 2011 NSTI Nanotechnology Conference and Expo – Nanotech 2011, Vol. 3, Chapter 7: Environment, Health & Safety, pp. 545 – 548.
12. Lu S, Jaiswal AR, Wong YYW, Bhushan A, Leung SW, Daniels CK & Lai JCK (2011) Differential Cytotoxic Effects of Titanium Oxide Nanoparticles on Peripheral Nervous System Neural Cells. Technical Proceedings of the 2011 NSTI Nanotechnology Conference and Expo – Nanotech 2011, Vol. 3, Chapter 7: Environment, Health & Safety, pp. 533 – 536.
13. Lai JCK, Gao W & Leung SW (2011) Effects of Chitosan and Nanoparticles on Survival of Schwann Cells and Dorsal Root Ganglion Neurons. Technical Proceedings of the 2011 NSTI Nanotechnology

- Conference and Expo – Nanotech 2011, Vol. 3, Chapter 6: Nano Medical Sciences & Neurology, pp. 440 – 442.
14. Leung SW, Chan A, Minski M & Lai JCK (2011) Comparison of Elemental Distribution in Rat's Brain after Lifelong Treatment with Excessive  $Mn^{2+}$  in Drinking Water and the Health Implications. Proceedings of International Water Convention, Singapore, July 4-8, 2011, Article IWA-6218R1, pp. 1-10.
  15. Wright GL, Lai JCK, Chan A, Minski M & Leung SW (2011) Influence of Metallomic Distribution in Brain by Prolong Consumption of Contaminant in Drinking Water. Proceedings of International Water Convention, Singapore, July 4-8, 2011, Article IWA-6228R1, pp. 1-21.
  16. Gao X, Assan D, Lai JCK & Leung SW (2012) Comparison of Anchoring Materials for High Performance Sensors Modified with Nanoparticles and Enzymes. In Technical Proceedings of the 2012 NSTI Nanotechnology Conference & Expo – Nanotech 2012, Vol. 1, Chapter 1: Nanoscale Materials Characterization, pages 17-20.
  17. Lu, S, Bhushan A, Leung SW, Daniels CK & Lai JCK (2012) Cytotoxic Effects of Four Metallic Oxide Nanoparticles on Dorsal Root Ganglion (DRG) Neurons. In Technical Proceedings of the 2012 NSTI Nanotechnology Conference & Expo – Nanotech 2012, Vol. 3, Chapter 5: Environmental Health & Safety, pages 346-349.
  18. Idikuda VK, Jaiswal AR, Wong YYW, Bhushan A, Leung SW & Lai JCK (2012) Cytotoxicity of Magnesium Oxide Nanoparticles in Schwann Cells. In Technical Proceedings of the 2012 NSTI Nanotechnology Conference & Expo – Nanotech 2012, Vol. 3, Chapter 5: Environmental Health & Safety, pages 342-345.
  19. Lai JCK, Gao W, Bhushan A & Leung SW (2012) Cytotoxic Effects of Short Multi-Wall Carbon Nanotubes in Dorsal Root Ganglion (DRG) Neurons. In Technical Proceedings of the 2012 NSTI Nanotechnology Conference & Expo – Nanotech 2012, Vol. 3, Chapter 5: Environmental Health & Safety, pages 338-341.
  20. Assan D, Gao X, Lai JCK & Leung SW (2012) Surfactant Effect on Intercellular Transport of DNA, Proteins, and Electrolytes. In Technical Proceedings of the 2012 NSTI Nanotechnology Conference & Expo – Nanotech 2012, Vol. 3, Chapter 3: Materials for Drug & Gene Delivery, pages 162-165.

#### **Abstracts published:**

1. Jaiswal A, Wong YYW, Bhushan A, Daniels C & Lai JCK (2010) A Noncontact Co-Culture Model of Peripheral Neural Cells for Nanotoxicity, Tissue Engineering and Pathophysiological Studies. NSTI Nanotechnology Conference and Expo – Nanotech 2010, June 21-25, 2010, Anaheim, CA (in Abstracts Volume).
2. Wong YYW, Jaiswal AR, Dukhande VV, Bhushan A, Leung SW & Lai JCK (2010) Elucidation of Neuroprotective Properties of Astrocytoma (Astrocytes-like) Cells in Neural Cell Culture Models *In Vitro*: Applications in Tissue Engineering and Nanotoxicology. NSTI Nanotechnology Conference and Expo – Nanotech 2010, June 21-25, 2010, Anaheim, CA (in Abstracts Volume).
3. Leung SW, Gao W, Gu H, Bhushan A & Lai JCK (2010) Chitosan Membrane in Combinations with Nanoparticles and Adriamycin as a Treatment to Inhibit Glioma Growth and Migration. NSTI Nanotechnology Conference and Expo – Nanotech 2010, June 21-25, 2010, Anaheim, CA (in Abstracts Volume).
4. Leung SW, Wang Y, Gu H & Lai JCK (2010) Biomedical Applications of Modified Carbon Glassy Electrode Sensor with Nanoparticles and Dendrimers. NSTI Nanotechnology Conference and Expo – Nanotech 2010, June 21-25, 2010, Anaheim, CA (in Abstracts Volume).
5. Wright GL, Lai JCK, Chan AWK, Minski MJ, Lim L & Leung SW (2010) Metallomic Distribution in Various Regions of the Brain as Influenced by Dietary Intakes and Their Implications. ISEIS 2010 International Conference on Environmental Informatics, Beijing, China, August 27-29, 2010 (in Abstracts Volume).
6. Leung SW, Siddhanti S, Williams B, Chan AWK, Minski MJ, Daniels CK & Lai JCK (2010) Effects of Dietary Intake on Metal and Electrolyte Distributions in Various Organs. ISEIS



- 2010 International Conference on Environmental Informatics, Beijing, China, August 27-29, 2010 (in Abstracts Volume).
7. Bhushan A, Patil PP, Bhardwaj V, Lai MB, Daniels CK, Leung SW & Lai JCK (2010) Cross Resistance of Magnesium Oxide Nanoparticles to Cisplatin in Leukemia Cells: Mechanistic Studies. Institution of Mechanical Engineers Seminar on Nanotechnology in Medicine and Biotechnology, October 2010, London, UK (in Program & Abstracts).
  8. Gao W, Lai JCK & Leung SW (2011) Effects of Chitosan on Schwann Cells and Dorsal Root Ganglion Neurons. 53<sup>rd</sup> Annual Symposium of the Idaho Academy of Science, March 31-April 2, 2011, The College of Idaho, Caldwell, ID. Journal of Idaho Academy of Science, 47(1): 59.
  9. Jaiswal AR, Lu S, Bhushan A, Daniels CK, Leung SW & Lai JCK (2011) Toxicity of Nanoparticles: Assessment Using Cells from Peripheral Nervous System. 53<sup>rd</sup> Annual Symposium of the Idaho Academy of Science, March 31-April 2, 2011, The College of Idaho, Caldwell, ID. Journal of Idaho Academy of Science, 47(1): 60.
  10. Wong YYW, Jaiswal AR, Lu S, Dukhande VV, Bhushan A, Daniels CK, Leung SW & Lai JCK (2011) Neuroprotective Role of Pioglitazone, a PPAR $\gamma$  Agonist on Nanoparticles-Induced Cytotoxicity and Stress in Astrocytes-Like U87 Astrocytoma Cells. 53<sup>rd</sup> Annual Symposium of the Idaho Academy of Science, March 31-April 2, 2011, The College of Idaho, Caldwell, ID. Journal of Idaho Academy of Science, 47(1): 73.
  11. Gao X, Assan D, Lai JCK & Leung SW (2011) Anaerobic Biofuel Cell Modified with NanoParticles and Polymers for Biomedical Applications. 53<sup>rd</sup> Annual Symposium of the Idaho Academy of Science, March 31-April 2, 2011, The College of Idaho, Caldwell, ID. Journal of Idaho Academy of Science, 47(1): 74-75.
  12. Kasarla V, Mukka K, Tadinada SM, Wong YYW, Bhushan A, Daniels CK, Leung SW & Lai JCK (2011) Differential Cytotoxic Effects of Zinc Oxide Nanoparticles on S16 Schwann Cells and DRG Neurons. 53<sup>rd</sup> Annual Symposium of the Idaho Academy of Science, March 31-April 2, 2011, The College of Idaho, Caldwell, ID. Journal of Idaho Academy of Science, 47(1): 75.
  13. Tadinada SM, Bhardwaj V, Lai JCK & Bhushan A (2011) Role of Epidermal Growth Factor Receptor in Pancreatic Cancer Resistance. 53<sup>rd</sup> Annual Symposium of the Idaho Academy of Science, March 31-April 2, 2011, The College of Idaho, Caldwell, ID. Journal of Idaho Academy of Science, 47(1): 75-76.
  14. Idikuda V, Singh R, Kumbulla S, Jaiswal AR, Bhushan A, Daniels CK, Leung SW & Lai JCK (2011) Morphological Changes of Schwann Cells after Exposure to Magnesium Oxide Nanoparticles. 53<sup>rd</sup> Annual Symposium of the Idaho Academy of Science, March 31-April 2, 2011, The College of Idaho, Caldwell, ID. Journal of Idaho Academy of Science, 47(1): 76.
  15. Singh MRM, Kumbulla S, Idikuda VK, Jaiswal AR, Bhushan A, Leung SW, Daniels CK & Lai JCK (2011) Neurotoxicity of Magnesium Oxide Nanoparticles as Elicited in Schwann Cells. 53<sup>rd</sup> Annual Symposium of the Idaho Academy of Science, March 31-April 2, 2011, The College of Idaho, Caldwell, ID. Journal of Idaho Academy of Science, 47(1): 77.
  16. Kumbulla S, Idikuda VK, Singh R, Jaiswal AR, Alaydi L, Bhushan A, Leung SW, Daniels CK & Lai JCK (2011) Comparison of Effects of Several Metal-Based Nanoparticles on R3 Schwann Cells. 53<sup>rd</sup> Annual Symposium of the Idaho Academy of Science, March 31-April 2, 2011, The College of Idaho, Caldwell, ID. Journal of Idaho Academy of Science, 47(1): 77-78.
  17. Mukka K, Kasarla V, Tadinada SM, Wong YYW, Bhushan A, Daniels CK, Leung SW & Lai JCK (2011) Exposure of Zinc Oxide and Other Metallic Oxide Nanoparticles Induces Cytotoxicity and Morphological Alterations in Dorsal Root Ganglion Neurons. 53<sup>rd</sup> Annual Symposium of the Idaho Academy of Science, March 31-April 2, 2011, The College of Idaho, Caldwell, ID. Journal of Idaho Academy of Science, 47(1): 78-79.
  18. Jaiswal AR, Lu S, Pfau J, Wong YYW, Bhushan A, Leung SW, Daniels CK & Lai JCK (2011) Effects of Silicon Dioxide Nanoparticles on Peripheral Nervous System Neural Cell Models. NSTI Nanotechnology Conference and Expo – Nanotech 2011, June 13-16, 2011, Boston, MA (in Abstracts Volume).
  19. Lu S, Jaiswal AR, Wong YYW, Bhushan A, Leung SW, Daniels CK & Lai JCK (2011) Differential Cytotoxic Effects of Titanium Oxide Nanoparticles on Peripheral Nervous

- System Neural Cells. NSTI Nanotechnology Conference and Expo – Nanotech 2011, June 13-16, 2011, Boston, MA (in Abstracts Volume).
20. Wong YYW, Jaiswal AR, Dukhande VV, Bhushan A, Leung SW & Lai JCK (2011) New *In Vitro* Strategy of Astrocytoma (Astrocytes-like) Cells Treated with Pioglitazone (PPAR gamma agoist) Offers Neuroprotection Against Nanoparticle-Induced Cytotoxicity. NSTI Nanotechnology Conference and Expo – Nanotech 2011, June 13-16, 2011, Boston, MA (in Abstracts Volume).
  21. Jain A, Jaiswal AR, Lu S, Wong YYW, Bhushan A, Leung SW, Daniels CK & Lai JCK (2011) Molecular Effects of Silicon Dioxide Nanoparticles on Cell Survival Signaling of Dorsal Root Ganglion (DRG) Neurons and Schwann Cells. NSTI Nanotechnology Conference and Expo – Nanotech 2011, June 13-16, 2011, Boston, MA (in Abstracts Volume).
  22. Lai JCK, Gao W & Leung SW (2011) Effects of Chitosan and Nanoparticles on Survival of Schwann Cells and Dorsal Root Ganglion Neurons. NSTI Nanotechnology Conference and Expo – Nanotech 2011, June 13-16, 2011, Boston, MA (in Abstracts Volume).
  23. Lai JCK, Jaiswal AR, Lu S, Pfau J, Wong YYW, Bhushan A, Daniels CK & Leung SW (2011) Differential Cytotoxicity of Silicon Dioxide Nanoparticles on Neural Cells Derived from Peripheral Nervous System. International Conference on Materials for Advanced Technologies, Suntec, June 26-July 1, 2011, Singapore (in Abstracts Volume).
  24. Leung SW, Guo W & Lai JCK (2011) Nanoparticles Modulate the Effects of Chitosan on Survival of Schwann Cells and Dorsal Root Ganglion Neurons. International Conference on Materials for Advanced Technologies, Suntec, June 26-July 1, 2011, Singapore (in Abstracts Volume).
  25. Leung SW, Chan A, Minski M & Lai JCK (2011) Comparison of Elemental Distribution in Rat's Brain after Lifelong Treatment with Excessive  $Mn^{2+}$  in Drinking Water and the Health Implications. International Water Convention, July 4-8, 2011, Singapore (Abstract # IWA-6218-R1).
  26. Leung SW, Chan A, Minski M & Lai JCK (2011) Effects of Lifetime Consumption of Excessive  $Mn^{2+}$  in Drinking Water to Elemental Distribution in Vital Organs. International Water Convention, July 4-8, 2011, Singapore (Abstract #IWA-6243).
  27. Wright GL, Lai JCK, Chan A, Minski M & Leung SW (2011) Influence of Metallomic Distribution in Brain by Prolong Consumption of Contaminant in Drinking Water. International Water Convention, July 4-8, 2011, Singapore (Abstract #IWA-6228R1).
  28. Jaiswal AR, Lu S, Bhushan A, Daniels CK, Leung SW, Lai JC (2011) Silicon Dioxide Nanoparticles Induce Mitochondria-Mediated Cell Damage in Peripheral Neural Cells. Annual Meeting, Society for Neuroscience, November, 2011, Washington, DC (in Abstracts Volume).
  29. Assan D, Gao X, Lai JCK & Leung SW (2012) Characterization of High Performance Sensors Modified with Nanoparticles and Different Enzyme Couplings. Idaho Academy of Science 54<sup>th</sup> Annual Symposium, March 22-24, 2012, University Place, Idaho Falls, ID (in Abstracts volume, p. 9).
  30. VK Idikuda, Jaiswal AR, Wong YYW, Bhushan A, Leung SW & Lai JCK (2012) Magnesium Oxide Nanoparticles Induce Stat-3 Mediated Apoptosis in Schwann Cells. Idaho Academy of Science 54<sup>th</sup> Annual Symposium, March 22-24, 2012, University Place, Idaho Falls, ID (in Abstracts volume, p. 16).
  31. Gao W, Lai JCK, Bhushan A & Leung SW (2012) Cytotoxic Effects of Short Multi-Wall Carbon Nanotubes in Dorsal Root Ganglion (DRG) Neurons. Idaho Academy of Science 54<sup>th</sup> Annual Symposium, March 22-24, 2012, University Place, Idaho Falls, ID (in Abstracts volume, p. 29).
  32. Gao X, Assan D, Lai JCK & Leung SW (2012) Highly Modified Pt Electrode Sensor and Comparison of Performance of the Electrode with Other Sensors Made with Different Anchoring Materials. Idaho Academy of Science 54<sup>th</sup> Annual Symposium, March 22-24, 2012, University Place, Idaho Falls, ID (in Abstracts volume, p. 29).
  33. Lu S, Bhushan A, Leung SW, Daniels CK & Lai JCK (2012) Cytotoxic Effects of Four Metallic Oxide Nanoparticles on Dorsal Root Ganglion (DRG) Neurons. Idaho Academy of

- Science 54th Annual Symposium, March 22-24, 2012, University Place, Idaho Falls, ID (in Abstracts volume, p. 34).
34. Zhang Y, Agharkar V, Lai JCK, Daniels CK, Leung SW & Bhushan A (2012) Short Multi-Wall Carbon Nanotubes Induce Cytotoxicity on Pancreatic Cancer. Idaho Academy of Science 54th Annual Symposium, March 22-24, 2012, University Place, Idaho Falls, ID (in Abstracts volume, p. 38).
  35. Idikuda VK, Jaiswal AR, Wong YYW, Leung SW, Daniels CK & Lai JCK (2012) Magnesium Oxide Nanoparticles Induce Cytotoxic and Proinflammatory Effects in Schwann Cells and DRG Neurons. Experimental Biology 2012, April 21-25, 2012, Convention Center, San Diego, CA (in Abstracts Volume).
  36. Gao X, Assan D, Lai JCK & Leung SW (2012) Comparison of Anchoring Materials for High Performance Sensors Modified with Nanoparticles and Enzymes. NSTI Nanotechnology Conference & Expo – Nanotech 2012, June 18-21, Santa Clara, CA (in Abstracts volume).
  37. Lu, S, Bhushan A, Leung SW, Daniels CK & Lai JCK (2012) Cytotoxic Effects of Four Metallic Oxide Nanoparticles on Dorsal Root Ganglion (DRG) Neurons. NSTI Nanotechnology Conference & Expo – Nanotech 2012, June 18-21, Santa Clara, CA (in Abstracts volume).
  38. Idikuda VK, Jaiswal AR, Wong YYW, Bhushan A, Leung SW & Lai JCK (2012) Cytotoxicity of Magnesium Oxide Nanoparticles in Schwann Cells. NSTI Nanotechnology Conference & Expo – Nanotech 2012, June 18-21, Santa Clara, CA (in Abstracts volume).
  39. Lai JCK, Gao W, Bhushan A & Leung SW (2012) Cytotoxic Effects of Short Multi-Wall Carbon Nanotubes in Dorsal Root Ganglion (DRG) Neurons. NSTI Nanotechnology Conference & Expo – Nanotech 2012, June 18-21, Santa Clara, CA (in Abstracts volume).
  40. Assan D, Gao X, Lai JCK & Leung SW (2012) Surfactant Effect on Intercellular Transport of DNA, Proteins, and Electrolytes. NSTI Nanotechnology Conference & Expo – Nanotech 2012, June 18-21, Santa Clara, CA (in Abstracts volume).

## **Presentations:**

### **A. Invited oral presentations:**

1. Wright GL, Lai JCK, Chan AWK, Minski MJ, Lim L & Leung SW (2010) Metallomic Distribution in Various Regions of the Brain as Influenced by Dietary Intakes and Their Implications. ISEIS 2010 International Conference on Environmental Informatics, Beijing, China, August 27-29, 2010.
2. Leung SW, Siddhanti S, Williams B, Chan AWK, Minski MJ, Daniels CK & Lai JCK (2010) Effects of Dietary Intake on Metal and Electrolyte Distributions in Various Organs. ISEIS 2010 International Conference on Environmental Informatics, Beijing, China, August 27-29, 2010.
3. Bhushan A, Patil PP, Bhardwaj V, Lai MB, Daniels CK, Leung SW & Lai JCK (2010) Cross Resistance of Magnesium Oxide Nanoparticles to Cisplatin in Leukemia Cells: Mechanistic Studies. Institution of Mechanical Engineers Seminar on Nanotechnology in Medicine and Biotechnology, October 2010, London, UK.
4. Leung SW, Guo W & Lai JCK (2011) Nanoparticles Modulate the Effects of Chitosan on Survival of Schwann Cells and Dorsal Root Ganglion Neurons. International Conference on Materials for Advanced Technologies, Suntec, June 26-July 1, 2011, Singapore (in Abstracts Volume).
5. Leung SW, Chan A, Minski M & Lai JCK (2011) Comparison of Elemental Distribution in Rat's Brain after Lifelong Treatment with Excessive  $Mn^{2+}$  in Drinking Water and the Health Implications. International Water Convention, July 4-8, 2011, Singapore (Abstract # IWA-6218-R1).
6. Leung SW, Chan A, Minski M & Lai JCK (2011) Effects of Lifetime Consumption of Excessive  $Mn^{2+}$  in Drinking Water to Elemental Distribution in Vital Organs. International Water Convention, July 4-8, 2011, Singapore (Abstract #IWA-6243).
7. Wright GL, Lai JCK, Chan A, Minski M & Leung SW (2011) Influence of Metallomic Distribution in Brain by Prolong Consumption of Contaminant in Drinking Water. International Water Convention, July 4-8, 2011, Singapore (Abstract #IWA-6228R1).

8. Jaiswal AR, Lu S, Bhushan A, Daniels CK, Leung SW, Lai JC (2011) Silicon Dioxide Nanoparticles Induce Mitochondria-Mediated Cell Damage in Peripheral Neural Cells. Annual Meeting, Society for Neuroscience, November, 2011, Washington, DC (in Abstracts Volume).
9. Lai JCK (2012) Invited Panel Speaker to lead discussion on “Environmental Effects of Nanotechnology,” Idaho Academy of Science 54th Annual Symposium, March 22-24, 2012, University Place, Idaho Falls, ID.

**B. Poster presentations:**

1. Jaiswal A, Wong YYW, Bhushan A, Daniels C & Lai JCK (2010) A Noncontact Co-Culture Model of Peripheral Neural Cells for Nanotoxicity, Tissue Engineering and Pathophysiological Studies. NSTI Nanotechnology Conference and Expo – Nanotech 2010, June 21-25, 2010, Anaheim, CA.
2. Wong YYW, Jaiswal AR, Dukhande VV, Bhushan A, Leung SW & Lai JCK (2010) Elucidation of Neuroprotective Properties of Astrocytoma (Astrocytes-like) Cells in Neural Cell Culture Models *In Vitro*: Applications in Tissue Engineering and Nanotoxicology. NSTI Nanotechnology Conference and Expo – Nanotech 2010, June 21-25, 2010, Anaheim, CA.
3. Leung SW, Gao W, Gu H, Bhushan A & Lai JCK (2010) Chitosan Membrane in Combinations with Nanoparticles and Adriamycin as a Treatment to Inhibit Glioma Growth and Migration. NSTI Nanotechnology Conference and Expo – Nanotech 2010, June 21-25, 2010, Anaheim, CA.
4. Leung SW, Wang Y, Gu H & Lai JCK (2010) Biomedical Applications of Modified Carbon Glassy Electrode Sensor with Nanoparticles and Dendrimers. NSTI Nanotechnology Conference and Expo – Nanotech 2010, June 21-25, 2010, Anaheim, CA.
5. Gao W, Lai JCK & Leung SW (2011) Effects of Chitosan on Schwann Cells and Dorsal Root Ganglion Neurons. 53<sup>rd</sup> Annual Symposium of the Idaho Academy of Science, March 31-April 2, 2011, The College of Idaho, Caldwell, ID. Journal of Idaho Academy of Science, 47(1): 59.
6. Jaiswal AR, Lu S, Bhushan A, Daniels CK, Leung SW & Lai JCK (2011) Toxicity of Nanoparticles: Assessment Using Cells from Peripheral Nervous System. 53<sup>rd</sup> Annual Symposium of the Idaho Academy of Science, March 31-April 2, 2011, The College of Idaho, Caldwell, ID. Journal of Idaho Academy of Science, 47(1): 60.
7. Wong YYW, Jaiswal AR, Lu S, Dukhande VV, Bhushan A, Daniels CK, Leung SW & Lai JCK (2011) Neuroprotective Role of Pioglitazone, a PPAR $\gamma$  Agonist on Nanoparticles-Induced Cytotoxicity and Stress in Astrocytes-Like U87 Astrocytoma Cells. 53<sup>rd</sup> Annual Symposium of the Idaho Academy of Science, March 31-April 2, 2011, The College of Idaho, Caldwell, ID. Journal of Idaho Academy of Science, 47(1): 73.
8. Gao X, Assan D, Lai JCK & Leung SW (2011) Anaerobic Biofuel Cell Modified with NanoParticles and Polymers for Biomedical Applications. 53<sup>rd</sup> Annual Symposium of the Idaho Academy of Science, March 31-April 2, 2011, The College of Idaho, Caldwell, ID. Journal of Idaho Academy of Science, 47(1): 74-75.
9. Kasarla V, Mukka K, Tadinada SM, Wong YYW, Bhushan A, Daniels CK, Leung SW & Lai JCK (2011) Differential Cytotoxic Effects of Zinc Oxide Nanoparticles on S16 Schwann Cells and DRG Neurons. 53<sup>rd</sup> Annual Symposium of the Idaho Academy of Science, March 31-April 2, 2011, The College of Idaho, Caldwell, ID. Journal of Idaho Academy of Science, 47(1): 75.
10. Tadinada SM, Bhardwaj V, Lai JCK & Bhushan A (2011) Role of Epidermal Growth Factor Receptor in Pancreatic Cancer Resistance. 53<sup>rd</sup> Annual Symposium of the Idaho Academy of Science, March 31-April 2, 2011, The College of Idaho, Caldwell, ID. Journal of Idaho Academy of Science, 47(1): 75-76.
11. Idikuda V, Singh R, Kumbulla S, Jaiswal AR, Bhushan A, Daniels CK, Leung SW & Lai JCK (2011) Morphological Changes of Schwann Cells after Exposure to Magnesium Oxide Nanoparticles. 53<sup>rd</sup> Annual Symposium of the Idaho Academy of Science, March 31-April 2, 2011, The College of Idaho, Caldwell, ID. Journal of Idaho Academy of Science, 47(1): 76.
12. Singh MRM, Kumbulla S, Idikuda VK, Jaiswal AR, Bhushan A, Leung SW, Daniels CK & Lai JCK (2011) Neurotoxicity of Magnesium Oxide Nanoparticles as Elicited in Schwann Cells. 53<sup>rd</sup> Annual Symposium of the Idaho Academy of Science, March 31-April 2, 2011, The College of Idaho, Caldwell, ID. Journal of Idaho Academy of Science, 47(1): 77.
13. Kumbulla S, Idikuda VK, Singh R, Jaiswal AR, Alaydi L, Bhushan A, Leung SW, Daniels CK &

- Lai JCK (2011) Comparison of Effects of Several Metal-Based Nanoparticles on R3 Schwann Cells. 53<sup>rd</sup> Annual Symposium of the Idaho Academy of Science, March 31-April 2, 2011, The College of Idaho, Caldwell, ID. Journal of Idaho Academy of Science, 47(1): 77-78.
14. Mukka K, Kasarla V, Tadinada SM, Wong YYW, Bhushan A, Daniels CK, Leung SW & Lai JCK (2011) Exposure of Zinc Oxide and Other Metallic Oxide Nanoparticles Induces Cytotoxicity and Morphological Alterations in Dorsal Root Ganglion Neurons. 53<sup>rd</sup> Annual Symposium of the Idaho Academy of Science, March 31-April 2, 2011, The College of Idaho, Caldwell, ID. Journal of Idaho Academy of Science, 47(1): 78-79.
  15. Jaiswal AR, Lu S, Pfau J, Wong YYW, Bhushan A, Leung SW, Daniels CK & Lai JCK (2011) Effects of Silicon Dioxide Nanoparticles on Peripheral Nervous System Neural Cell Models. NSTI Nanotechnology Conference and Expo – Nanotech 2011, June 13-16, 2011, Boston, MA (in Abstracts Volume).
  16. Lu S, Jaiswal AR, Wong YYW, Bhushan A, Leung SW, Daniels CK & Lai JCK (2011) Differential Cytotoxic Effects of Titanium Oxide Nanoparticles on Peripheral Nervous System Neural Cells. NSTI Nanotechnology Conference and Expo – Nanotech 2011, June 13-16, 2011, Boston, MA (in Abstracts Volume).
  17. Wong YYW, Jaiswal AR, Dukhande VV, Bhushan A, Leung SW & Lai JCK (2011) New *In Vitro* Strategy of Astrocytoma (Astrocytes-like) Cells Treated with Pioglitazone (PPAR gamma agonist) Offers Neuroprotection Against Nanoparticle-Induced Cytotoxicity. NSTI Nanotechnology Conference and Expo – Nanotech 2011, June 13-16, 2011, Boston, MA (in Abstracts Volume).
  18. Jain A, Jaiswal AR, Lu S, Wong YYW, Bhushan A, Leung SW, Daniels CK & Lai JCK (2011) Molecular Effects of Silicon Dioxide Nanoparticles on Cell Survival Signaling of Dorsal Root Ganglion (DRG) Neurons and Schwann Cells. NSTI Nanotechnology Conference and Expo – Nanotech 2011, June 13-16, 2011, Boston, MA (in Abstracts Volume).
  19. Lai JCK, Gao W & Leung SW (2011) Effects of Chitosan and Nanoparticles on Survival of Schwann Cells and Dorsal Root Ganglion Neurons. NSTI Nanotechnology Conference and Expo – Nanotech 2011, June 13-16, 2011, Boston, MA (in Abstracts Volume).
  20. Assan D, Gao X, Lai JCK & Leung SW (2012) Characterization of High Performance Sensors Modified with Nanoparticles and Different Enzyme Couplings. Idaho Academy of Science 54<sup>th</sup> Annual Symposium, March 22-24, 2012, University Place, Idaho Falls, ID (in Abstracts volume, p. 9).
  21. VK Idikuda, Jaiswal AR, Wong YYW, Bhushan A, Leung SW & Lai JCK (2012) Magnesium Oxide Nanoparticles Induce Stat-3 Mediated Apoptosis in Schwann Cells. Idaho Academy of Science 54<sup>th</sup> Annual Symposium, March 22-24, 2012, University Place, Idaho Falls, ID (in Abstracts volume, p. 16).
  22. Gao W, Lai JCK, Bhushan A & Leung SW (2012) Cytotoxic Effects of Short Multi-Wall Carbon Nanotubes in Dorsal Root Ganglion (DRG) Neurons. Idaho Academy of Science 54<sup>th</sup> Annual Symposium, March 22-24, 2012, University Place, Idaho Falls, ID (in Abstracts volume, p. 29).
  23. Gao X, Assan D, Lai JCK & Leung SW (2012) Highly Modified Pt Electrode Sensor and Comparison of Performance of the Electrode with Other Sensors Made with Different Anchoring Materials. Idaho Academy of Science 54<sup>th</sup> Annual Symposium, March 22-24, 2012, University Place, Idaho Falls, ID (in Abstracts volume, p. 29).
  24. Lu S, Bhushan A, Leung SW, Daniels CK & Lai JCK (2012) Cytotoxic Effects of Four Metallic Oxide Nanoparticles on Dorsal Root Ganglion (DRG) Neurons. Idaho Academy of Science 54<sup>th</sup> Annual Symposium, March 22-24, 2012, University Place, Idaho Falls, ID (in Abstracts volume, p. 34).
  25. Zhang Y, Agharkar V, Lai JCK, Daniels CK, Leung SW & Bhushan A (2012) Short Multi-Wall Carbon Nanotubes Induce Cytotoxicity on Pancreatic Cancer. Idaho Academy of Science 54<sup>th</sup> Annual Symposium, March 22-24, 2012, University Place, Idaho Falls, ID (in Abstracts volume, p. 38).
  26. Idikuda VK, Jaiswal AR, Wong YYW, Leung SW, Daniels CK & Lai JCK (2012) Magnesium Oxide Nanoparticles Induce Cytotoxic and Proinflammatory Effects in Schwann Cells and DRG Neurons. Experimental Biology 2012, April 21-25, 2012, Convention Center, San Diego, CA (in Abstracts Volume).
  27. Gao X, Assan D, Lai JCK & Leung SW (2012) Comparison of Anchoring Materials for High Performance Sensors Modified with Nanoparticles and Enzymes. NSTI Nanotechnology

- Conference & Expo – Nanotech 2012, June 18-21, Santa Clara, CA (in Abstracts volume).
28. Lu, S, Bhushan A, Leung SW, Daniels CK & Lai JCK (2012) Cytotoxic Effects of Four Metallic Oxide Nanoparticles on Dorsal Root Ganglion (DRG) Neurons. NSTI Nanotechnology Conference & Expo – Nanotech 2012, June 18-21, Santa Clara, CA (in Abstracts volume).
  29. Idikuda VK, Jaiswal AR, Wong YYW, Bhushan A, Leung SW & Lai JCK (2012) Cytotoxicity of Magnesium Oxide Nanoparticles in Schwann Cells. NSTI Nanotechnology Conference & Expo – Nanotech 2012, June 18-21, Santa Clara, CA (in Abstracts volume).
  30. Lai JCK, Gao W, Bhushan A & Leung SW (2012) Cytotoxic Effects of Short Multi-Wall Carbon Nanotubes in Dorsal Root Ganglion (DRG) Neurons. NSTI Nanotechnology Conference & Expo – Nanotech 2012, June 18-21, Santa Clara, CA (in Abstracts volume).
  31. Assan D, Gao X, Lai JCK & Leung SW (2012) Surfactant Effect on Intercellular Transport of DNA, Proteins, and Electrolytes. NSTI Nanotechnology Conference & Expo – Nanotech 2012, June 18-21, Santa Clara, CA (in Abstracts volume).

## CONCLUSIONS

### Goal 1: EMG Signal Identification

In the first part of this final report on Goal 1 (Chapter 1), the primary research aim was at identifying the most favorable signal processing methodologies to model sEMG-force and sEMG-angle relationships. Here, various types of filters have been tested extensively, from the most basic Butterworth filters to the nonlinear Bayesian filters, for single electrode configurations. The filtered signals were initially modeled using linear and non-linear modeling techniques e.g. output error models (OE), auto regressive with exogenous input models (ARX), nonlinear ARX (NLARX), Box-Jenkins models, to name a few. The estimated force fit values for the actuating sEMG signal was in the range of 30-40% (100% represents a perfect fit between the estimated and actual force). As a result of these poor fit values, optimization of the nonlinear Bayesian filter parameters and the nonlinear Hammerstein-Wiener model order was performed using Genetic Algorithm. The optimization helped improve the model fit percentages significantly (about 20%). We extended the analysis of sEMG-force modeling using a hybrid Particle Swarm Optimization coupled with Tabu Search (PSO-TS) to help improve the speed of the optimization process.

Another study undertaken was to perform data analysis from a large sensor array placed on and around the motor points of the forearm. This study exhaustively analyzed various linear and nonlinear spatial filters. The nonlinear and linear spatial filters (TDD, NDD and NLT, NLTO and NLAFD) did outperform the other filtering methods. The only other filter which had a comparable performance to the spatial filters was the Bessel filter. The spatial filter masks were then modified for optimum estimation of force. Again, a Genetic algorithm was used to optimize the filter masks for various spatial filters. This again led to a significant increase in the fit percentages, but the masks were significantly different than those from the reported literature. We also performed a study on the classification of zones of the arm (degree of amputation) to identify the most favorable locations to place the sEMG sensors. The results obtained were in good agreement with the ideal locations for sEMG measurement from literature.

The issue of skeletal-muscle fatigue is further addressed in phase II of this project, and sEMG – Skeletal-Muscle Force – Skeletal-Muscle Fatigue models are designed for smart prosthesis application. For the skeletal-muscle fatigue, the modeling is done using OE models, modal transformations and curve fitting of the eigenvalues in continuous time. Various possible linear and nonlinear models for the motor point sensor for the ring finger are investigated. sEMG and force data was captured with different experiment design including with a 9-sEMG sensor array and used with Adaptive Neuro Fuzzy Inference System (ANFIS) and Smoothing Spline Curve Fitting. All the approaches used in this research work give better estimation of the skeletal-muscle force of a human arm for prosthetic hand design than previously reported.

## Goal 2A: Intelligent Control

- **22 Degree-of-Freedom Prosthetic Hand:** Kinematics, dynamics and control models of smart prosthetic hand with 22 degrees of freedom (DOFs) were conducted. In our approach, the problem of forward kinematics using the Denavit-Hartenberg (D-H) method was applied to compute the position of the end-effector (fingertip) given the joint variable. This followed by the inverse kinematics which is a little more difficult problem. The inverse kinematics calculates the joint variables given the position of the hand. Based on the kinematic structure, a mathematical model that describes the dynamics of the hand was calculated. These dynamic models were calculated using the Lagrangian and Newton Euler formulations. Hard control strategies such as feedback linearization and proportional integral derivative (PID) control were applied to control the hand based on the kinematic and dynamic models.
- **Optimal Control with Simulink:** A control technique of finite-time linear quadratic optimal control for 14 DOFs, five-fingered smart prosthetic hand was developed in MATLAB Simulink with different reference inputs, including constant, ramp, sinusoidal values. The optimal control was used for feedback linearized dynamics to minimize tracking error. The simulations of this optimal controller showed good performance.
- **3D Simulation:** Fusion of control strategies for 14 degrees of freedom (DOFs), five-fingered smart prosthetic hand was simulated to grasp an object in 3 dimensional animations.
- **Literature Survey:** A comprehensive literature updated on the topic of control techniques for prosthetic hands was conducted and one book chapter was published.
- **Adaptive Control:** An adaptive control strategy for the 14 DOFs, five-fingered smart prosthetic hand with unknown mass and inertia of all the fingers is developed in this work. In modeling, the various links used for the five fingers of the prosthetic hand are shown. A cubic polynomial for the trajectory planning is used. In particular, using a desired orientation for three-link fingers, the forward and inverse kinematics of the prosthetic hand system regarding the analytical solutions between the angular positions of joints and the positions and orientations of the end-effectors (fingertips) have been obtained. The simulations of the resulting adaptive controller with five-fingered prosthetic hand show enhanced performance. This work was published in one international journal.
- **Optimal Control:** This paper addresses a new optimal control strategy for a five-fingered prosthetic hand, to speed up the performance and improve the accuracy, by modifying the performance index with an exponential term. First, the trajectory planning of the joints of each finger is designed by using cubic polynomial. Then the dynamic equations of the prosthetic hand and feedback linearization technique are employed. Next, the optimal control method with modified performance index is applied to the prosthetic hand. Finally, simulations show that the proposed technique provides much faster response with high accuracy compared to adaptive neuro-fuzzy inference system (ANFIS) based inverse kinematics for trajectory planning and PID control. This work has been submitted to *Journal of IET Control Theory and Applications*.
- **Hybrid Control (GA+PID):** A hybrid of soft control technique of ANFIS and genetic algorithm (GA) and hard control technique of proportional-integral-derivative (PID) for a five-fingered, smart prosthetic hand is presented. The ANFIS is used for inverse kinematics and GA is used for tuning the PID parameters with the objective of minimizing the error squared between desired and actual angles of the links of the fingers of the prosthetic hand. Simulation results for all the five fingers with GA-tuned PID controller exhibit superior performance compared to the PID control without GA. This work was published in one international peer-reviewed conference paper.
- **Hybrid Control (FL+PD):** A hybrid of soft control technique of ANFIS and fuzzy logic (FL) and hard control technique of proportional-derivative (PD) for a five-fingered, smart prosthetic hand is presented. The ANFIS is used for inverse kinematics and FL is used for tuning the PD parameters with two input layers (error and error change) using 7 triangular membership functions and 49 fuzzy logic rules.



Simulation results with FL-tuned PD controller exhibit superior performance compared to the PD and PID control alone. This work was published in one international peer-reviewed conference paper and the extended work has been submitted to *Journal of Biomedical Signal Processing and Control (Elsevier)*.

#### **Goal 2B: Embedded Hierarchical Real-Time Systems**

The work under Goal 2B during this Year demonstrated the usability of a fast prototyping test bed for the sEMG acquisition, validation and verification of model-based controller designs. We were also able to study in more details the impact of implementation on the embedded control, including the use of CAN and RTOS. Furthermore, we began our investigation on the modeling and simulation of our embedded control through collaboration with Johns Hopkins University's Applied Physics Laboratory.

### **Goal 3: Robotic Hand**

The main objective of Goal 3 was to develop a prosthetic hand adapted to the findings of the research team. Hand 1 Prototype II is finalized and is considered a good learning experience. The new design, Hand 2, has been developed. It presents a radically different design and overcomes some of the main problems of Hand 1. This hand has been manufactured and is at the assembly stage. We expect the hand to be fully operative by January 2013. The expertise gained and the effort put into it is going to be the base for continuing research in multi-finger hand design, including collaborations for design for grasping and manipulation.

In addition, much insight has been gained in the design process for multi-fingered robotic hands. The methodology developed during this research, which includes a motion capture system, a general, multi-finger kinematic synthesis algorithm, and a link optimization post-processing, will lead to better and more diverse designs of articulated systems to be used to substitute, or together with, the human hand, such as prosthetic hands, partial hand prostheses, exoskeletons and robotic hands for human-robot interaction.

This design framework is to be made freely available as a set of software packages easy to interact together, so that both researchers and developers can benefit from its design flexibility.

#### **Goal 4: Biocompatibility and Signaling**

We have made significant progress in studies specified in Goal 4 of our proposal. In the process of setting up the “Sensor on Cells on Skin Model,” we have identified the three stages we need to undergo to achieve this goal: (i) stage one involves the development of different human and other mammalian cells (including nerve and skin cells) in co-culture; (ii) stage two requires the juxtaposition of cells in relation to the membrane as illustrated in Fig. 1. above (this figure was included in our proposal); and (iii) stage three involves designing the sensor(s) and fitting them into the “sensor on cells on skin model” (as shown in Fig. 1). We have accomplished stages (i) and (ii) by developing the “co-culture” and the “non-contact” cell models and demonstrating that these models can be useful and relevant in facilitating studies to address various mechanistic issues in biocompatibility and other tissue engineering and nanotoxicity research. Furthermore, we have developed new cell models of peripheral nervous systems consisting of dorsal root ganglion neurons and Schwann cells. These models are particularly useful for elucidating nerve degeneration and regeneration. We are currently characterizing these models further. Our extensive literature survey indicates that our approaches are truly novel and will lead to further ground-breaking discoveries because, as we have already discussed above, the whole important issue of how tissue and cellular inflammatory responses are elicited by implant material(s) have not been resolved and is poorly understood. By way of heading towards completing stage (iii), we have developed several “smart” sensors that are pH sensitive and self-assembling with nanoparticles. Thus far, we are using glassy carbon, gold, or silver as anchor material for the sensor electrode. This type of “smart” sensor can be employed to detect many enzymatic and chemical reactions known to occur in different tissues/organs. Thus, we are focusing on the development of biosensors for tissue engineering and biocompatibility studies and related biomedical engineering applications. We also recently noted that some of the sensors we have designed can also be developed into fuel cells and related applications.

One important but as yet poorly characterized facet of biocompatibility pertains to the putative nanotoxicity of nanoparticles and other nanomaterials employed to fabricate artificial implants. As part of our systematic studies to elucidate the cytotoxicity of nanoparticles of metallic oxides that are commonly found in composites in fabricating such implants, we have further characterized the effects of silicon dioxide and magnesium oxide nanoparticles on human neural cells, normal human fibroblasts, dorsal root ganglion neurons, and Schwann cells. We have elucidated some of the cellular and molecular mechanisms underlying the cytotoxicity of these nanoparticles on human and non-human neural cells. These are important advances in nanotoxicity research because of the paucity of literature on the cytotoxicity of nanoparticles of metallic and non-metallic oxides in neural cells. Thus, our findings may have toxicological and other pathophysiological implications on exposure of humans and other mammalian species to such nanoparticles.

## REFERENCES

## Goal 1: EMG Signal Identification

- 1) ISEK Standards : [http://www.isek-online.org/standards\\_emg.html](http://www.isek-online.org/standards_emg.html)
- 2) Mewett, D. T., Nazeran H., Reynolds, K., J., 2001. "Removing power line noise from recorded EMG". *Proceedings of the 23rd Annual EMBS international Conference*.
- 3) Clancy, A. E., Farry, A. K., 2000. "Whitening of the electromyogram to improve amplitude estimation". *IEEE Transactions on Biomedical Engineering*, 47(6), June, pp. 709-719.
- 4) Chan, D. C. A., Englehart, B. K., 2005. "Continuous myoelectric control for powered prostheses using hidden Markov models". *IEEE Transactions on Biomedical Engineering*, 52(1), January, pp. 121-124.
- 5) Chan, H. Y. F., Yang, Y., Lam, F. K., Zhang, Y., Parker, A. P., 2000. "Fuzzy EMG classification for Prosthesis control". *IEEE Transactions on Rehabilitation Engineering*, 8(3), September, pp. 305-311.
- 6) Reaz, I. B. M., Hussain, S. M., Yasin, M. F., 2006. "Techniques of EMG signal analysis: detection, processing, classification and application". *Biomedical Procedures Online*, 8(1), January, pp. 11-35.
- 7) Johnson, T. D., Elashoff, R. M., Harkema S. J., 2003. "Bayesian change-point analysis of electromyographic data: detecting muscle activation patterns and associated applications". *Biostatistics*, 4(1), pp. 143-164.
- 8) Sanger, D. T., 2007. "Bayesian Filtering of Myoelectric signals". *Journal of Neurophysiology*, 97, pp. 1839-1845.
- 9) Dario Farina, Roberto Merletti, Roger M. Enoka, "The extraction of neural strategies from the surface EMG", *Journal of Applied Physiology*, 96, pp. 1486-1495, 2003.
- 10) Hogan N., Mann R W., 1980a. "Myoelectric Signal processing: Optimal estimation applied to electromyography – Part I: Derivation of the optimal myoprocessor". *IEEE Transactions on Biomedical Engineering*, 27:pp. 81-86.
- 11) Hogan N., Mann R W., 1980b. "Myoelectric Signal processing: Optimal estimation applied to electromyography – Part II: Experimental demonstration of optimal myoprocessor performance". *IEEE Transactions on Biomedical Engineering*, 27:pp. 396-410.
- 12) <http://www.mathworks.com/access/helpdesk/help/toolbox/ident/index.html?/access/helpdesk/help/toolbox/ident/gs/bq47jv3-1.html>.
- 13) Ljung, L., 2nd ed., "System Identification: theory for the user". Prentice Hall Information and System Sciences Series, Chap. 1, pp. 1-8.
- 14) Ljung, L., 2nd ed., "System Identification: theory for the user". Prentice Hall Information and System Sciences Series, Chap. 1, pp. 13.
- 15) Ljung, L., 2nd ed., "System Identification: theory for the user". Prentice Hall Information and System Sciences Series, Chap. 5, pp. 140-145.
- 16) [http://www.mathworks.com/access/helpdesk/help/toolbox/ident/index.html?/access/helpdesk/help/toolbox/ident/gs/bq\\_ylq6.html](http://www.mathworks.com/access/helpdesk/help/toolbox/ident/index.html?/access/helpdesk/help/toolbox/ident/gs/bq_ylq6.html)
- 17) Westwick, T. D., Kearney, E. R., 2000. "Identification of a Hammerstein Model of the stretch reflex EMG using separable least squares". *Proceedings of the 22nd Annual EMBS Conference*, July, pp. 1901-1904.
- 18) Dempsey, J. E., Westwick, T. D., 2001. "Identification of a Hammerstein Model of the stretch reflex EMG using cubic splines". *Proceedings of the 23rd Annual EMBS Conference*, October, pp. 1244-1247.
- 19) Chen, C.-H., Bosworth, K. W., and Schoen, M. P., 2007. "Investigation of particle swarm optimization dynamics". In *Proceedings of International Mechanical Engineering Congress and Exposition (IMECE)*.
- 20) Glover, F., "Future paths for Integer programming and Links to Artificial Intelligence", *Computers & Operations Research*, Vol. 5, 1986, pp. 533-549.
- 21) Ramkumar, B., Schoen, M. P., Lin, F., "Application of an Intelligent Hybrid Optimization Technique for Parameter Estimation in the Presence of Colored Noise", *Proceedings of the IMECE*, 2007.
- 22) Higashitami, M., Ishigame, A., Yasuda, K., "Particle Swarm Optimization Considering the Concept of Predator-Prey Behavior", *IEEE Congress on Evolutionary Computation*, 2006, pp. 434-437.
- 23) Clerc, M., "The swarm and the queen: Towards a deterministic and adaptive particle swarm optimization", *Proceedings of the Congress of Evolutionary Computation*, Vol. 3, 1999, pp. 1951-1957.
- 24) Li, X., Cui, J.-F., Qu, J.-X., Yang, S., D., "Energy Transimssion Models Based on Tabu Search and Particle Swarm Hybrid Optimization Algorithm", *J. Cent. South Univ. Technol.* 01-0144-05, 2007.
- 25) Boggs, P.T., Tolle, J.W., "Sequential Quadratic programming, Acta", 1995, No. 4, pp. 1-52.
- 26) Nakano, S., Ishigame, A., Yasuda, K., "Particle Swarm Optimization Based on the Concept of Tabu Search", *IEEE Congress on Evolutionary Computation CEC*, 2007, pp. 3258-3263.

- 27) Eberhart, R.C., Simpson, P.K., Dobbins, R.W., *Computational Intelligence PC Tools.*, Academic Press Professional, 1<sup>st</sup> Edition, 1996.
- 28) Eberhart, R.C., Shi, Y., Particle Swarm Optimization: Developments, Applications and Resources, *Proceedings of the IEEE Congress on Evolutionary Computation*, Vol. 1, 2001, pp. 27-30.
- 29) Shi, Y., Eberhart, R.C., A modified Particle Swarm Optimizer, *Proceedings of the IEEE Congress on Evolutionary Computation*, 1998, pp. 69-73.
- 30) Engelbrecht, A.P., Fundamentals of Computational Swarm Intelligence, *John Wiley & Sons*, 2006.
- 31) Söderström, T., Convergence Properties of Generalized Least Squares Identification Method, *Automatica*, Vol. 10, pp. 617-626, 1974.
- 32) [http://www.geatbx.com/download/GEATbx\\_Intro\\_Algorithmen\\_v38.pdf](http://www.geatbx.com/download/GEATbx_Intro_Algorithmen_v38.pdf) (Genetic and Evolutionary Algorithm Toolbox for Matlab)
- 33) [http://www-optima.amp.i.kyoto-u.ac.jp/member/student/hedar/Hedar\\_files/TestGO\\_files/Page1113.htm](http://www-optima.amp.i.kyoto-u.ac.jp/member/student/hedar/Hedar_files/TestGO_files/Page1113.htm) (Global Optimization by Meta Heuristics)
- 34) <http://www.spatialanalysisonline.com/output/html/Linearspatialfiltering.html>
- 35) Zhou P., and Rymer W. Z., "An evaluation of the utility and limitations of counting motor unit action potentials in the surface electromyogram," *Journal of Neural Engineering*, vol. 1, pp. 238-245, 2004.
- 36) Kaiser J. F., "On a simple algorithm to calculate the 'energy' of a signal", *Proceedings of IEEE ICASSP'90*, Albuquerque, New Mexico, pp. 381-384, April 1990.
- 37) Kaiser J. F., "On Teager's energy algorithm and its generalization to continuous signals", *Proc. 4th IEEE Digital Signal Proc. Workshop*, Mohonk (New Paltz), NY, September 1990.
- 38) Maragos P., Kaiser J. F., and Quatieri T. F., "On amplitude and frequency demodulation using energy operators", *IEEE Transactions on Signal Processing*, Vol. 41, pp. 1532-1550, April 1993.
- 39) Hamila R., Astola J., Alaya Cheikh F., Gabbouj M., and Renfors M., "Teager Energy and the Ambiguity Function", *IEEE International Conference On Image Processing*, Vol. 47, No. 1, pp. 260-262, January 1999.
- 40) Alaya Cheikh F., Hamila R., Gabbouj M. and Astola J., "Impulse Noise Removal In Highly Corrupted Color Images," *Proc. 1996 IEEE International Conference On Image Processing*, Lausanne, Switzerland, Vol. I, pp. 997-1000, September, 1996.
- 41) Astola J., and Kuosmanen P., "Fundamentals of Nonlinear Digital Filtering", *CRC Press LLC*, 1997.
- 42) Urfer A., Creelman J., Kumar Parmod., Sebastian A., Anugolu M., Schoen P. M., "The Development of a Functional Amputation Residuum Measurement of the Upper Extremity for Potential Myoelectric Prosthesis". *Combined Sections Meeting (CSM)*, 2012, Chicago, Illinois.
- 43) <http://www.noraxon.com/downloads/educational.php3>
- 44) S. M. M. Zecca, M. C. Carrozza, & P. Dario, "Control of Multifunctional Prosthetic Hands by Processing the Electromyographic Signal," *Critical Reviews™ in Biomedical Engineering*, vol. 30, no. 4-6, pp. 459-485, 2002.
- 45) C. Castellini, and P. van der Smagt, "Surface EMG in advanced hand prosthetics," *Biological Cybernetics*, vol. 100, no. 1, pp. 35-47, Jan. 2009.
- 46) C. J. De Luca, "The use of surface electromyography in biomechanics," *Journal of Applied Biomechanics*, vol. 13, no. 2, pp. 135-163, May 1997.
- 47) J. V. Basmajian, *Muscles Alive: Their Functions Revealed by Electromyography*, 2 ed., Baltimore: Williams & Wilkins Co., 1967.
- 48) C. J. D. Luca, *Reflections on EMG signal decomposition*, pp. 33-37, Amsterdam, The Netherlands: Elsevier Science, 1989.
- 49) P. G. a. R. Merletti, "Effect of electrode location on surface myoelectric signal variables: a simulation study," in *9th Int. Congress of ISEK 1992*, Florence, Italy, 1992.
- 50) F. Laterza, and G. Olmo, "Analysis of EMG signals by means of the matched wavelet transform," *Electronics Letters*, vol. 33, no. 5, pp. 357-359, Feb. 1997.
- 51) D. Gabor, "Theory of communication," *Journal of the Institute of Electrical Engineers Part III*, vol. 93, pp. 429-457, 1946.
- 52) A. R. I. a. S. S. Asfour, "Continuous wavelet transform application to EMG signals during human gait," in *Conference Record of the Thirty-Second Asilomar Conference on Signals, Systems & Computers*, 1998.,

- Pacific Grove, CA , USA, 1998, pp. 325 - 329
- 53) C. S. Pattichis, and M. S. Pattichis, "Time-scale analysis of motor unit action potentials," IEEE Transactions on Biomedical Engineering, vol. 46, no. 11, pp. 1320-1329, Nov. 1999.
  - 54) D. K. Kumar, N. D. Pah, and A. Bradley, "Wavelet analysis of surface electromyography to determine muscle fatigue," IEEE Transactions on Neural Systems and Rehabilitation Engineering, vol. 11, no. 4, pp. 400-406, Dec. 2003.
  - 55) L. COHEN, "Time-Frequency Distributions-A Review," Proceedings of the IEEE, vol. 77, no. 7, pp. 941 - 981, 1989.
  - 56) W. a. F. Martin, P., "Wigner-Ville spectral analysis of nonstationary processes," IEEE Transactions on Acoustics, Speech and Signal Processing, vol. 33, no. 6, pp. 1461 - 1470, 1985
  - 57) M. G. Amin, Time-frequency spectrum analysis and estimation for nonstationary random processes, p.^pp. 208-232, Melbourne, Australia: Longman Cheshire (AUS), 1992.
  - 58) A. M. S. a. D. L. Jones, "Optimal Kernels for Nonstationary Spectral Estimation," IEEE Transactions on Signal Processing, vol. 43, no. 2, pp. 478-491, 1995.
  - 59) D. a. C. Graupe, William K., "Functional Separation of EMG Signals via ARMA Identification Methods for Prosthesis Control Purposes," IEEE Transactions on Systems, Man and Cybernetics, vol. SMC-5, no. 2, pp. 252 - 259, 1975.
  - 60) M. H. Sherif, "A stochastic model of myoelectric signals for movement pattern recognition in upper limb prostheses," University of California, Los Angeles, 1980, 1980.
  - 61) C. Yitong Zhou, R., and Bekey, G., "Estimation of intramuscular EMG signals from surface EMG signal analysis," in IEEE International Conference on ICASSP'86: Acoustics, Speech, and Signal Processing, Tokyo, Japan 1986, pp. 1805 - 1808
  - 62) Z. W. Hefftner G, and Jaros GG., "The electromyogram (EMG) as a control signal for functional neuromuscular stimulation - Part I: Autoregressive modeling as a means of EMG signature discrimination," IEEE Transactions on Biomedical Engineering, vol. 35, no. 4, pp. 230-237, 1988.
  - 63) L. A. Bernotas, P. E. Crago, and H. J. Chizeck, "A Discrete-Time Model of Electrically Stimulated Muscle," IEEE Transactions on Biomedical Engineering, vol. BME-33, no. 9, pp. 829 - 838, 1986.
  - 64) A. T. a. G. Moser, D., "Identification of nonstationary models with application to myoelectric signals for controlling electrical stimulation of paraplegics," IEEE Transactions on Acoustics, Speech and Signal Processing, vol. 37, no. 5, pp. 713 - 719, 1989.
  - 65) S. Y. Kiryu T, and Ishioka K., "Investigation on parametric analysis of dynamic EMG signals by a muscle-structured simulation model.," IEEE Transactions on Biomedical Engineering, vol. 39, no. 3, pp. 280-288, 1992.
  - 66) A. a. P. Del Boca, D.C., "Myoelectric signal recognition using fuzzy clustering and artificial neural networks in real time," in 1994 IEEE International Conference on Neural Networks, 1994. IEEE World Congress on Computational Intelligence. , Orlando, FL , USA 1994, pp. 3098 - 3103.
  - 67) G. Cheron, J. P. Draye, M. Bourgeois et al., "A dynamic neural network identification of electromyography and arm trajectory relationship during complex movements," IEEE Transactions on Biomedical Engineering, vol. 43, no. 5, pp. 552-558, May. 1996.
  - 68) F. H. Y. Chan, Y. S. Yang, F. K. Lam et al., "Fuzzy EMG classification for prosthesis control," IEEE Transactions on Rehabilitation Engineering, vol. 8, no. 3, pp. 305-311, Sept. 2000.
  - 69) A. Belouchrani, Abed-Meraim, K., Amin, M.G., and Zoubir, A.M., "Joint anti-diagonalization for blind source separation." pp. 2789 - 2792.
  - 70) D. Farina, C. Fevotte, C. Doncarli et al., "Blind separation of linear instantaneous mixtures of nonstationary surface myoelectric signals," IEEE Transactions on Biomedical Engineering, vol. 51, no. 9, pp. 1555-1567, Sept. 2004.
  - 71) Y. M. Kanosue K, Akazawa K, and Fujii K., "The number of active motor units and their firing rates in voluntary contraction of human brachialis muscle.," Japan Journal of Physiology vol. 29, no. 4, pp. 427-443, 1979.
  - 72) R. P., "Intra- and extracellular potential fields of active nerve and muscle fibres. A physico-mathematical analysis of different models.," Thrombosis et diathesis haemorrhagica. Supplementum., vol. 321, pp. 1-168, 1969.
  - 73) N. S. a. S. E., "Simulation of single muscle fibre action potentials.," Medical & Biological Engineering & Computing., vol. 21, no. 2, pp. 158-165, 1983.
  - 74) S. D. a. B. Nandedkar, P.E., "Phase interaction in the compound muscle action potential: application to motor unit estimates," in IEE Colloquium on Neurological Signal Processing, London , UK 1992, pp. 4/1 -

- 75) K. B. Englehart, and P. A. Parker, "Single Motor Unit Myoelectric Signal Analysis with Nonstationary Data," *IEEE Transactions on Biomedical Engineering*, vol. 41, no. 2, pp. 168-180, Feb. 1994.
- 76) Y. T. Zhang, Herzog, W., and Liu, M.M., "A mathematical model of myoelectric signals obtained during locomotion," in *IEEE 17th Annual Conference on Engineering in Medicine and Biology Society*, 1995., Montreal, Que. , Canada 1995, pp. 1403 - 1404
- 77) S. a. N. Karlsson, L., "Real-time system for EMG signal analysis of static and dynamic contractions," in *IEEE 17th Annual Conference on Engineering in Medicine and Biology Society*, 1995., Montreal, Que. , Canada 1995, pp. 1347 - 1348.
- 78) J. Duchene, and J. Y. Hogrel, "A model of EMG generation," *IEEE Transactions on Biomedical Engineering*, vol. 47, no. 2, pp. 192-201, Feb. 2000.
- 79) A. Hamilton-Wright, and D. W. Stashuk, "Physiologically based simulation of clinical EMG signals," *IEEE Transactions on Biomedical Engineering*, vol. 52, no. 2, pp. 171-183, Feb. 2005.
- 80) S. Bouisset, "EMG and muscular force in normal motor activities," in *4th International Congress on EMG*, Brussels, 1973.
- 81) a. B. G. Perry J, "EMG-force relationships in skeletal muscle.," *Critical Reviews in Biomedical Engineering*, vol. 7, no. 1, pp. 1-22, 1981.
- 82) A. J. Fuglevand, D. A. Winter, and A. E. Patla, "Models of Recruitment and Rate Coding Organization in Motor-Unit Pools," *Journal of Neurophysiology*, vol. 70, no. 6, pp. 2470-2488, Dec. 1993.
- 83) A. Seth, and M. G. Pandy, "A neuromusculoskeletal tracking method for estimating individual muscle forces in human movement," *Journal of Biomechanics*, vol. 40, no. 2, pp. 356-366, 2007.
- 84) F. P. De Luca CJ, and Erim Z., "Motor unit control properties in voluntary isometric isotonic contractions.," *Journal of Neurophysiology*, vol. 76, pp. 1503-1516, 1996.
- 85) H. Westerblad, D. G. Allen, and J. Lannergren, "Muscle fatigue: Lactic acid or inorganic phosphate the major cause?," *News in Physiological Sciences*, vol. 17, pp. 17-21, Feb. 2002.
- 86) J. D. Bruton, J. Lannergren, and H. Westerblad, "Effects of CO<sub>2</sub>-induced acidification on the fatigue resistance of single mouse muscle fibers at 28 degrees C," *Journal of Applied Physiology*, vol. 85, no. 2, pp. 478-483, Aug. 1998.
- 87) E. Pate, M. Bhimani, K. Franksskiba et al., "Reduced Effect of pH on Skinned Rabbit PSOAS Muscle Mechanics at High-Temperatures - Implications for Fatigue," *Journal of Physiology-London*, vol. 486, no. 3, pp. 689-694, Aug. 1995.
- 88) H. Westerblad, J. D. Bruton, and J. Lannergren, "The effect of intracellular pH on contractile function of intact, single fibres of mouse muscle declines with increasing temperature," *Journal of Physiology-London*, vol. 500, no. 1, pp. 193-204, Apr. 1997.
- 89) J. S. P. a. A. R. Lind, "The influence of temperature on the amplitude and frequency components of the EMG during brief and sustained isometric contractions," *European Journal of Applied Physiology and Occupational Physiology*, vol. 4, no. 2, pp. 189-200, 1980.
- 90) R. W. Wiseman, T. W. Beck, and P. B. Chase, "Effect of intracellular pH on force development depends on temperature in intact skeletal muscle from mouse," *American Journal of Physiology-Cell Physiology*, vol. 271, no. 3, pp. C878-C886, Sept. 1996.
- 91) A. J. Dahlstedt, A. Katz, and H. Westerblad, "Role of myoplasmic phosphate in contractile function of skeletal muscle: studies on creatine kinase-deficient mice," *Journal of Physiology-London*, vol. 533, no. 2, pp. 379-388, Jun. 2001.
- 92) K. A. Dahlstedt AJ, Wieringa B, and Westerblad H., "Is creatine kinase responsible for fatigue? Studies of isolated skeletal muscle deficient in creatine kinase.," *The Journal of the Federation of American Societies for Experimental Biology (FASEB)*, vol. 14, no. 7, pp. 982-990, 2000.
- 93) A. J. Dahlstedt, and H. Westerblad, "Inhibition of creatine kinase reduces the rate of fatigue-induced decrease in tetanic Ca<sup>2+</sup> (i) in mouse skeletal muscle," *Journal of Physiology-London*, vol. 533, no. 3, pp. 639-649, Jun. 2001.
- 94) M. W. Fryer, V. J. Owen, G. D. Lamb et al., "Effects of Creatine-Phosphate and Pi on Ca<sup>2+</sup> Movements and Tension Development in Rat Skinned Skeletal-Muscle Fibers," *Journal of Physiology-London*, vol. 482, no. 1, pp. 123-140, Jan. 1995.
- 95) A. A. Kabbara, and D. G. Allen, "The role of calcium stores in fatigue of isolated single muscle fibres from the cane toad," *Journal of Physiology-London*, vol. 519, no. 1, pp. 169-176, Aug. 1999.
- 96) D. L. CJ, "Myoelectric manifestations of localized muscular fatigue," *CRC Critical Reviews in Biomedical Engineering*, vol. 11, pp. 251-279, 1984.



- 97) L. Ljung, "Perspectives on system identification," Annual Reviews in Control, vol. 34, no. 1, pp. 1-12, Apr. 2010.
- 98) C. Heij, Ran, André C.M., and Schagen, F. van, Introduction to Mathematical Systems Theory: Linear Systems, Identification and Control, Basel: Birkhäuser Basel, 2007.
- 99) N. I. Corporation, LabVIEW: System Identification Toolkit User Manual, p.^pp. 47-60, Austin, Texas, USA, 2006.
- 100) T. D. Sanger, "Bayesian filtering of myoelectric signals," Journal of Neurophysiology, vol. 97, no. 2, pp. 1839-1845, Feb. 2007.
- 101) V. L. Erik Kral, Viliam Dolinay, and Pavel Varacha, "Usage of PSO Algorithm for Parameters Identification of District HeatingNetwork Simulation Model." pp. 657-659.
- 102) A. Neubauer. pp. 538-543.
- 103) P. K. Anish Sebastian, and Marco P. Schoen, "A Study on Hybridization of Particle Swarm and Tabu SearchAlgorithms for unconstrained Optimization and Estimation Problems." pp. 458-463.
- 104) L. Ljung, System Identification Toolbox: User's Guide, Natick, MA 01760-2098: The MathWorks, Inc., 2010.
- 105) H. C. a. S. Huang, "A Comparative Study on Model Selection and Multiple Model Fusion," in 2005 7th International Conference on Information Fusion (FUSION), Philadelphia, PA., 2005, pp. 820-826.
- 106) A. K. Seghouane, and M. Bekara, "A small sample model selection criterion based on Kullback's symmetric divergence," IEEE Transactions on Signal Processing, vol. 52, no. 12, pp. 3314-3323, Dec. 2004.
- 107) D. S. N. Cheng-Hung Chen, and Marco P. Schoen, "An Adaptive Control Strategy for a Five-Fingered Prosthetic Hand," in The 14th World Scientific and Engineering Academy and Society (WSEAS) International Conference on Systems, Corfu Island, Greece, 2010, pp. 405-410.
- 108) P. Kumar, A. Sebastian, C. Potluri et al., "Towards smart prosthetic hand: Adaptive probability based skeleton muscle fatigue model." pp. 1316 - 1319, 2010.
- 109) P. Kumar, C. Potluri, A. Sebastian, S. Chiu, A. Urfer, D. S. Naidu, and M. P. Schoen, "An Adaptive Multi Sensor Data Fusion with Hybrid Nonlinear ARX and Wiener-Hammerstein Models for Skeletal Muscle Force Estimation ". pp. 186-191.
- 110) L. Ljung, System Identification: Theory for the User, 2/e ed.: Prentice-Hall, Inc., 1998.
- 111) P. Kumar, C. Potluri, M. Anugolu et al., "A hybrid adaptive data fusion with linear and nonlinear models for skeletal muscle force estimation," in 2010 5th Cairo International Biomedical Engineering Conference (CIBEC), Cairo, Egypt, 2010, pp. 9 - 12.
- 112) P. Kumar, C. Potluri, A. Sebastian,, and A. Urfer, S. Chiu, D. S. Naidu, M. P. Schoen, "Adaptive Multi Sensor Based Nonlinear Identification of SkeletalMuscle Force," WSEAS TRANSACTIONS on SYSTEMS, vol. 9, no. 10, pp. 1050-1062, 2010.
- 113) P. Zhou, N. L. Suresh, M. M. Lowery et al., "Nonlinear Spatial Filtering of Multichannel Surface Electromyogram Signals During Low Force Contractions," IEEE Transactions on Biomedical Engineering, vol. 56, no. 7, pp. 1871-1879, Jul. 2009.
- 114) I. B. T. Asli Celikyilmaz, Modeling Uncertainty with Fuzzy Logic: With Recent Theory and Applications, 1 ed., Berlin Heidelberg: Springer-Verlag, 2009.
- 115) J. V. Jairo Espinosa, Vincent Wertz, Fuzzy logic, identification, and predictive control London: Springer-Verlag, 2005.
- 116) MATLAB® Fuzzy Logic Toolbox™ User's Guide, Natick, MA 01760-2098: The MathWorks, Inc., 2010.
- 117) MATLAB® Curve Fitting Toolbox™ User's Guide, Natick, MA 01760-2098: The MathWorks, Inc., 2010.
- 118) J. T. Bingham, and M. P. Schoen, "Characterization of Myoelectric Signals Using System Identification Techniques." pp. 123-127.
- 119) "Standards for Reporting EMG data," Journal of Electromyography and Kinesiology, vol. 9, no. 1, pp. III-IV, 1999.
- 120) J. H. Semmlow, Biosignal and Biomedical Image Processing: MATLAB-Based Applications, pp. 79-162, New York: Marcel Dekker, Inc., 2004.
- 121) H. B. B., The World According to Wavelets, 2 ed., Natick, MA: A.K. Peters, Ltd., 1998.
- 122) Signal Processing Toolbox™ User's Guide, Natick, MA: The MathWorks, Inc., 2010.
- 123) S. L. Marple, Digital Spectral Analysis, p.^pp. 373-378, Englewood Cliffs, NJ: Prentice-Hall, 1987.
- 124) R. Schmidt, "Multiple emitter location and signal parameter estimation," IEEE Transactions on Antennas and Propagation, vol. 34, no. 3, pp. 276 - 280, 1986.
- 125) D. E. D. Don H. Johnson, Array signal processing: concepts and techniques: P T R Prentice Hall, 1993.

- 126) P. Kumar, C. H. Chen, A. Sebastian et al., "An adaptive hybrid data fusion based identification of skeletal muscle force with ANFIS and smoothing spline curve fitting." pp. 932 - 938.
- 127) C. H. C. a. D. S. Naidu, "Hybrid genetic algorithm based PID control for a five-fingered smart prosthetic hand," in The 5th International Conference on Circuits, Systems and Signals (CSS'11), Corfu Island, Greece, July 14-16, 2011.
- 128) C.-H. C. a. D. S. Naidu, "Fusion of Fuzzy Logic and PD Control for a Five-Fingered Smart Prosthetic Hand," in 2011 IEEE International Conference on Fuzzy Systems, Taipei, Taiwan, June 27-30, 2011, pp. 2108-2115.
- 129) C.-H. C. a. D. S. Naidu, "Optimal control strategy for two-fingered smart prosthetic hand," in The 15th International Association of Science and Technology for Development (IASTED) International Conference on Robotics and Applications (RA 2010), Cambridge, Massachusetts, USA, November 1-3, 2010, pp. 190-196.

## Goal 2A: Intelligent Control

- [1]. R. N. Jazar. Theory of applied Robotics, Dynamics and Control. Springer, New York, USA, 2007.
- [2]. John J. Craig. Introduction to robotics, mechanics and control. 2<sup>nd</sup> edition, Addison Wesley.
- [3]. Mason and Salisbury. Robot hand and the mechanics of manipulation. The MIT press Cambridge, Massachusetts, London, England.
- [4]. Kumar, A., and Waldron, K. J., 1981. "The Workspace of a Mechanical Manipulator", ASME J Mech. Design, 103:665-672.
- [5]. Vardy A. Articulated human hand with inter-joint dependency constraints: Computer Science 6755 19898 [<http://www.scs.carleton.ca/~arvardy/software/hand-doc.pdf>].
- [6]. Chen H. Chen. Hybrid Control Strategies for Smart Prosthetic Hand.  
A dissertation submitted in partial fulfillment of the requirements for the degree of Doctor of Philosophy in Engineering and Applied Science College of Engineering, Idaho State University. May 2009
- [7]. Albretch I, Haber J, Seider HP. Construction and Animation of Anatomically Based Human Hand Models. Eurographics/ SIGGRAPH symposium on computer Animation 2003: 98-109.
- [8]. Li S, Xi Z. Measurement of Functional Arm Reach Envelopes for Young Chinese males, Ergonomics 1990, 33: 967-978.
- [9]. Molenbroek JGM. Reach Envelopes of Older adults. In Proceedings of the 42<sup>nd</sup> Annual Meeting of the "Human Factors and Ergonomics Society". Chicago, IL, 1998: 166-170.
- [10]. Bill Goowine. University of Notre Dame. Copyright 2005 by CRC Press LLC.
- [11]. R. J. Scilly. Fundamentals of Robotics, Analysis and Control. Prentice, Hall, Eaglewood cliffs, NJ, 1990.
- [12]. R. Kelly, V. Santibanez, and A. Loria. Control of Robot Manipulators in Joint Space. Springer, Newyork, USA, 2005.
- [13]. B. Siciliano, L. Sciavicco, L. Villiani, and G. Oriolo. Robotics, Modeling, Planning and Control. Springer, Verlay, London, UK, 2009.

## Goal 2AB: Real-Time Control

- [1] Lynette A. Jones and Susan J. Lederman, *Human Hand Function*, New York: Oxford University Press, 2006, pp. 131-149.
- [2] Amir Fassih, D. Subbaram Naidu, Steve Chiu, and Marco P. Schoen, "power grasping of a prosthetic hand based upon virtual spring-damper hypothesis", *Proc. IASTED Int. Conf. Robotics and Applications*, Cambridge, Massachusetts, 2010, pp. 214-220.
- [3] Mohammad Asghar Oskoei, Housheng Hu, "Myoelectric control systems, a survey", *Biomedical Signal Processing and Control*, vol. 2, 2007, pp 275-294.
- [4] Christian Cipriani, Franco Zacccone, Silvestro Micera, Chiara Carrozza, "On the shared control of an emg-controlled prosthetic hand: analysis of user-prosthesis interaction", *IEEE Transaction on Robotics*, vol.24, No1, February 2008.
- [5] Erik D Engeberg, Sanford G. Meek, "Backstepping and sliding mode control hybridized for a prosthetic hand", *IEEE Trans. on Neural Systems and Rehabilitation Engineering*, vol. 17, No.1, February 2009.
- [6] D.E.Whitney, "Resolved motion rate control of manipulators and human prostheses", *IEEE Trans. Man-Machine Syst.*, vol. MMS-10, No.2, 1969, pp.47– 53.
- [7] Y. Nakamura, "Advanced robotics: redundancy and optimization", Addison-Wesley, Reading, MA, 1991.
- [8] N. Dechev, W.L. Cleghron, S. Naumann, Multiplefinger, "Passive adaptive grasp prosthetic hand", *Mechanism and Machine Theory*, vol.36, 2001, pp.1157-1173.
- [9] Ramiero Cabas, Luis Maria Cabas, Carlos Balaguer, "Optimized design of the underactuated robotic hand", *Proceeding of the 2006 IEEE International Conferences on Robotics and Automation*, Orlando, Florida, May 2006.
- [10] Da-Peng Yang, Jing-dong Zhao, Yi-kun Gu, Xin-qing Wang, Nan Li, Li Jiang, Hong Liu, Hai Huang, Da-wei Zhao, "An anthropomorphic robot hand developed based on underactuated mechanism and controlled by EMG signals", *Journal of Bionic Engineering*, vol. 6, 2009, pp 255-263.
- [11] Suguru Arimoto, Masahiro Sekimoto, "Human-like movements of robotic arms with redundant dofs: virtual spring-damper hypothesis to tackle the brenestein problem", *Prec. of IEEE Int. Conf. on Robotics and Automation*, Orlando, Florida, May 2006.
- [12] Jerry Pratt, Chee-Meng Chew, Ann Torres, Peter Dilworth, Gill Pratt, "Virtual model control: an intuitive approach for bipedal locomotion", *The International Journal of Robotics Research*, vol. 20, No. 2, pp. 129-143, February 2001.
- [13] Thomas Wimboeck, Christian Ott, Gerhard Hirzinger, "Passivity-based object-level impedance control for a multifingered hand" *Proceedings of the 2006 IEEE/RSJ, International Conference on Intelligent Robots and Systems*, Beijing, China,2006.
- [14] Lionel Brignel,Thiery Laliberte, Clement Gosselin, "Underactuated robotic hand",Springer 2008.
- [15] Er Bierbaum, M. Rambow, T. Asfour, and R. Dillmann, Grasp affordances from multi-fingered tactile exploration using dynamic potential fields, Humanoids, IEEE Intl. Conference on, 2009, pp. 168 –174.
- [16] Chih-Chung Chang and Chih-Jen Lin, LIBSVM: a library for support vector machines, 2001, Software available at <http://www.csie.ntu.edu.tw/~cjlin/libsvm>.
- [17] Matei Ciocarlie, Claire Lackner, and Peter Allen, Soft finger model with adaptive contact geometry for grasping and manipulation tasks,World Haptics Conference (2007), 219–224.
- [18] Matei T. Ciocarlie and Peter K. Allen, Hand Posture Subspaces for Dexterous Robotic Grasping, *The International Journal of Robotics Research* 28 (2009), no. 7, 851–867.
- [19] C. Ferrari and J. Canny, Planning optimal grasps, *Robotics and Automation*, IEEE Intl. Conference on, May 1992, pp. 2290 –2295.
- [20] C. Goldfeder, M. Ciocarlie, H. Dang, and P.K. Allen, The Columbia grasp database, *Robotics and Automation*, IEEE International Conference on, May 2009, pp. 1710 –1716.

- [21] Nicolas Gorges, Stefan Escalda Navarro, Dirk G'oger, and Heinz W'orn, Haptic object recognition using passive joints and haptic key features, *Robotics and Automation, IEEE International Conference on*, May 2010, pp. 2349 –2355.
- [22] Susan J. Lederman and Roberta L. Klatzky, Hand movements: A window into haptic object recognition, *Cognitive Psychology* 19 (1987), no. 3, 342 – 368.
- [23] Zexiang Li and S. Sastry, Task oriented optimal grasping by multifingered robot hands, *Robotics and Automation, IEEE International Conference on*, 1987, pp. 389–394.
- [24] A. T. Miller and P. K. Allen, Graspit! a versatile simulator for robotic grasping, *Robotics & Automation* 11 (2004), no. 4, 110–122.
- [25] A. Petrovskaya, O. Khatib, S. Thrun, and A.Y. Ng, Bayesian estimation for autonomous object manipulation based on tactile sensors, *Robotics and Automation, IEEE International Conference on*, may. 2006, pp. 707 – 714.
- [26] Mila Popovic, Dirk Kraft, Leon Bodenhagen, Emre Baseski, Nicolas Pugeault, Danica Kragic, Tamim Asfour, and Norbert Kr'uger, A strategy for grasping unknown objects based on co-planarity and colour information, *Robotics and Autonomous Systems* 58 (2010), no. 5, 551 – 565.
- [27] M. Prats, P.J. Sanz, and A.P. del Pobil, Task-oriented grasping using hand preshapes and task frames, *Robotics and Automation, IEEE International Conference on*, april 2007, pp. 1794 –1799.
- [28] Pressure Profile, Robotouch, <http://www.pressureprofile.com/products-robotouch>.
- [29] Ashutosh Saxena, Justin Driemeyer, Justin Kearns, and Andrew Y. Ng, Robotic grasping of novel objects, *Advances in Neural Information Processing Systems* 19 (B. Sch'olkopf, J. Platt, and T. Hoffman, eds.), MIT Press, Cambridge, MA, 2007, pp. 1209–1216.
- [30] Alexander Schneider, J'urgen Sturm, Cyrill Stachniss, Marco Reisert, Hans Burkhardt, and Wolfram Burgard, Object identification with tactile sensors using bag-of-features, *IEEE/RSJ international conference on Intelligent robots and systems*, 2009, pp. 243–248.
- [31] Philip Shilane, Patrick Min, Michael Kazhdan, and Thomas Funkhouser, The princeton shape benchmark, In *Shape Modeling International*, 2004, pp. 167–178.
- [32] Zachary Pezzementi, Erica Jantho, Lucas Estrade, Gregory D. Hager, Characterization and Simulation of Tactile Sensors, *Haptics Symposium*, March 2010.
- [33] Hao Dang, Jonathan Weisz, and Peter K. Allen, Blind Grasping: Stable Robotic Grasping Using Tactile Feedback and Hand Kinematics, *2011 IEEE International Conference on Robotics and Automation*, May 9-13, 2011, Shanghai, China

## Goal 2B: Embedded Hierarchical Real-Time Systems

- [1] N. Dechev, W. L. Cleghorn, and S. Naumann, "Multiple finger, passive adaptive grasp prosthetic hand," *Mechanism and Machine Theory*, 36(2001), pp. 1157-1173.
- [2] H. Kawasaki, T. Komatsu, and K. Uchiyama, "Dexterous Anthropomorphic Robot Hand With Distributed Tactile Sensor: Gifu Hand II," *IEEE/ASME Transactions on Mechatronics*, Vol. 7, No. 3, September 2002, pp. 296-303.
- [3] M. Zecca, S. Micera, M. C. Carrozza, and P. Dario, "Control of Multifunctional Prosthetic Hands by Processing the Electromyographic Signal," *Critical Reviews™ in Biomedical Engineering*, 30(4-6), 2002, pp. 459-485.
- [4] C. Castellini and P. van der Smagt, "Surface EMG in advanced hand prosthetics," *Biological Cybernetics*, (2009) 100, pp. 35-47.
- [5] T. D. Sanger, "Bayesian Filtering of Myoelectric Signals," *J Neurophysiol*, 97, 2007, pp. 1839-1845.
- [6] M. B. I. Reaz, M. S. Hussain and F. Mohd-Yasin, "Techniques of EMG signal analysis: detection, processing, classification and applications," *Biol. Proced. Online*, 2006, 8(1), pp. 11-35.
- [7] E. Kral, L. Vasek, V. Dolinay, P. Varacha, "Usage of PSO Algorithm for Parameter Identification of District Heating Network Simulation Model," *The 14th World Scientific and Engineering Academy and Society (WSEAS) International Conference on Systems*, Corfu Island, Greece, July 22-24, 2010.
- [8] J. Atkins, D. C. Y. Heard, and W. H. Donovan, "Epidemiologic overview of individuals with upper limb loss and their reported research priorities," *J. Prosthet. Orthot.*, vol. 8, no. 1, p. 2, 1996.
- [9] H. Silcox, M. D. Rooks, R. R. Vogel, and L. L. Fleming, "Myoelectric prostheses. A long-term follow-up and a study of the use of alternate prostheses," *J. Bone Joint Surg.*, vol. 75, no. 12, pp. 1781-1789, 1993.
- [10] Reiter R. Eine neue elektrokunsthand Grenzgebiete der Medizin 1948; 4:183.
- [11] M. H. Raibert and J. J. Craig, "Hybrid position and force control of manipulators," *ASME J. Llyn. Syst. Meas. Contr.*, vol. 102, pp. 126-133, June 1981.
- [12] Bashamajian JV, De Luca CJ. *Muscles Alive*. Baltimore, MD: Williams & Wilkins, 1985.
- [13] Shannon CE. "A mathematical theory of communication", *Bell System Techn J* 1948; 27 (379-423): 623-56.
- [14] Johnson RW, Shore JE. "Which is the better entropy expression for speech processing:  $-S \log S$  or  $\log S$ ?" *IEEE Trans Acoust* 1984; ASSP-32: 129-37.
- [15] Pincus SM, Gladstone IM, Ehrenkranz RA. "A regularity statistic for medical data analysis", *J Clin. Monit* 1991; 7: 335-45.
- [16] Bruhn J, Ropcke H, Hoeft A. "Approximate entropy as an electroencephalographic measure of anesthetic drug effect during desflurane anesthesia", *Anesthesiology* 2000; 92: 715-26.
- [17] Bruhn J, Lehmann LE, Ropcke H, Bouillon TW, Hoeft A. "Shannon entropy applied to the measurement of the electroencephalographic effects of desflurane", *Anesthesiology* 2001; 95: 30-5.
- [18] Rezek IA, Roberts SJ. "Stochastic complexity measures for physiological signal analysis", *IEEE Trans Biomed Eng* 1998; 45: 1186-91.
- [19] Inouye T, Shinosaki K, Sakamoto H et al. "Quantification of EEG irregularity by use of the entropy of the power spectrum", *Electroencephalogr Clin. Neurophysiol* 1991; 79: 204-10.
- [20] Dr. Anthony L. Crawford, "Design of a Robotic Hand and Simple EMG Input Controller with a Biologically-Inspired Parallel Actuation System for Prosthetic Applications" ASME2010, IDETC/CIE2010
- [21] Amputee Coalition of America (ACA) National Limb Loss Information, Center (NLLIC) Limb Loss Facts in the United States, <http://www.amputee-coalition.org>, 2005.
- [22] Zinn M, Roth B, Khatib O, and Salisbury JK, "A new actuation approach for human friendly robot design," *Int J Robot Res.* 2004; 23(4-5), pp. 379-398.
- [23] Bien ZZ, and Stefanov D, "Advances in rehabilitation robotics: Human-friendly technologies on movement assistance and restoration for people with disabilities," *Springer, Berlin (Germany)*. 2004.
- [24] T. H. Sueeter, "Control of the Utah/MIT Dexterous hand: Hardware and software hierarchy," *J. Robot. Syst.*, vol. 7, no. 5, pp. 759-790, 1990.
- [25] M. H. Raibert and J. J. Craig, "Hybrid position and force control of manipulators," *ASME J. Llyn. Syst. Meas. Contr.*, vol. 102, pp. 126-133, June 1981.
- [26] Cram, J.R., Kasman G.S., and Holtz J. "Introduction to Surface Electromyography," Aspen Publisher Inc., Gaithersburg, Maryland, 1998.

- [27] Kandel E.R. and Scharztz J.H., "*Principles of Neural Science*," Elsevier/North-Holland, New York, 1981.
- [28] [http://www.isek-online.org/standards\\_emg.html](http://www.isek-online.org/standards_emg.html).
- [29] Karl J. Astrom and Bjorn Writtenmark "*Adaptive Control Second Edition*", Dover Publications, Dec 18, 2008.
- [30] Texas Instruments "SN754410 quadruple half H-driver data sheet" Dallas, Texas, November 1986 and 1995
- [31] Dr. Anthony L. Crawford ,,"Design of a Robotic Hand and Simple EMG Input Controller with a Biologically-Inspired Parallel Actuation System for Prosthetic Applications" ASME2010, IDETC/CIE 2010
- [32] Kutch, J. J., Valero-Cuevas, F. J., "*All muscles are redundant but some are less redundant than others*," 19<sup>th</sup> Annual Meeting of the Society for the Neural Control of Movement, Waikoloa Beach, Hawaii, April 2009.
- [33] "Aca News: National Limb Loss Awareness Month" 2011. Retrieved from <http://www.bocusa.org/aca-news-national-limb-loss-awareness-month>
- [34] Zinn M, Roth B, Khatib O, and Salisbury JK, "A new actuation approach for human friendly robot design," *Int J Robot Res.* 2004; 23(4-5), pp. 379-398.
- [35] Heinzmann J, and Zelinsky J, "A safe-control paradigm for human-robot interaction," *J Intell Robot Syst.* 1999; 25(4): pp. 295-310.
- [36] F.L.Lewis, D.M.Dawson, and C.T. Abdallah, "*Robot Manipulators Control: Second Edition, Revised and Expanded*", New York, NY: Marcel Dekker, Inc., 2004.
- [37] B.Siciliano, L.Sciavicco, L. Villani, and G. Oriolo, "*Robotics: Modelling, Planning and Control*". London, UK: Springer-verlag, 2009.
- [38] R. Kelly, V. Santidanez, and A. Loria, "*Control of Robot Manipulators in Joint Space*", New York, USA, Springer, 2005.
- [39] R.N. Jazar, "*Theory of Applied Robotics, Kinematics, Dynamics, and Control*", New York, USA, Springer 2007.

### Goal 3: Robotic Hand

A.M. Dollar and R. D. Howe, The SDM Hand: A highly adaptive compliant grasper for unstructured environments. *Internat. J. Rbfotics Research*, 2010.

L. Birglen T. Laliberte, and C. Gosselin. *Underactuated Robotic Hands*. Springer, 2008

S. Hirose and YI Umetani, “The development of soft gripper for the versatile robot hand”, *Mechanism and Machine theory*, 13:351-359, 1978.

Balasubramanian, R., Dollar, A.M., “Performance of Serial Underactuated Mechanisms: Number of Degrees of Freedom and Actuators”, *2011 IEEE/RSJ International Conference on Intelligent Robots and Systems September 25-30,2011*.

R.F. Chandler, D.E. Clauser, J. T. McConville, H. M. Reynolds, J. W. Young, “Investigation of inertial properties of the human hand”, *U.S. Department of transportation, Report No. DOT HS-801 430*, pp. 72-79 March 1975.

C. Pylatiuk, S. Shulz, L. Doderlein, “Results of an Internet survey of myoelectric prosthetic hand users”, *Prosthetics and Orthotics International* 2007, vol 31, No. 4. pp. 362-370, 2007.

S. Verrill, “Optimization java package,” 2000. [Online]. Available: <http://www1.fpl.fs.fed.us/optimization.html>

H. Ahsan, “3d computer vision system for hand joint motion calculation,” Ph.D. dissertation, College of Engineering, Idaho State University, Pocatello, ID, USA, 2008.

G. Schweighofer and A. Pinz, “Robust pose estimation from a planar target,” *IEEE Transactions on Pattern Analysis and Machine Intelligence*, pp. 2024–2030, 2006.

Ravi Balasubramanian and Aaron M. Dollar. Performance of Serial Underactuated Mechanisms: Number of Degrees of Freedom and Actuators. *2011 IEEE/RSJ International Conference on Intelligent Robots and Systems*.

Joan Savall, Javier Martin, and Alejo Avello. High Performance Linear Cable Transmission. *Journal of Mechanical Design* June 2008, Vol. 130 / 064501-5

Naoki Saito, Toshiyuki Sato, and Norihiko Saga. Development of Multi-fingered robot hand consists of underactuated fingers for robust object grasping. *ICABB-2010 Venice Italy October 14-16 2010*.

Ravi Balasubramanian and Aaron M. Dollar. A Comparison of Workspace and Force Capabilities between Classes of Underactuated Mechanisms. *2011 IEEE International Conference on Robotices and Automation May 9-13 2011*.

Joseph T. Belter and Aaron M. Dollar. Performance Characteristics of Anthropomorphic Prosthetic Hands. *2011 IEEE International Conference on Rehabilitaion Robotics Rehab Week Zurich 2011*.

Frank Daerden and Dirk Lefeber. Pneumatic Artificial Muscles: actuators for robotics and automation. *Internet Vrije Universiteit Brussel*



#### Goal 4: Biocompatibility and Signaling

Dukhande, V.V., Malthankar-Phatak, G.H., Hugus, J.J., Daniels, C.K. & Lai, J.C.K. (2006) Manganese Induced Neurotoxicity is Differentially Enhanced by Glutathione Depletion in Astrocytoma and Neuroblastoma Cells. *Neurochem Res* 31(11):1349-1357.

Hertz, L., Peng, L. & Lai, J.C.K. (1998) Functional Studies in Cultured Astrocytes. In *Techniques for the Purification, Functional Evaluation and Transplantation of Brain Cells (A Companion to Methods in Enzymology*, Vol. 16) (Rozenal, R. & Chiu, F.-C., eds.), pp. 293-310, Academic, New York, NY.

Isaac, A.O., Kawikova, I., Bothwell, A.L.M., Daniels, C.K. & Lai, J.C.K. (2006) Manganese Treatment Modulates the Expression of Peroxisomal Proliferator Activated Receptors (PPARs) in Astrocytoma and Neuroblastoma Cells. *Neurochem Res* 31(11):1305-1316.

Isaac, A.O., Dukhande, V.V. & Lai, J.C.K. (2007) Metabolic and Antioxidant System Alterations in an Astrocytoma Cell Line Challenged with Mitochondrial DNA Deletion. *Neurochem Res* 32(11):1906-1918.

Lai, J.C.K., Schoen, M.P., Perez Gracia, A., Naidu, D.S. & Leung, S.W. (2007a) Prosthetic Devices: Challenges and Implications of Robotic Implants and Biological Interfaces. In *Proc I Mech E, Vol 221 Part H, J Engineering in Medicine, Special Issue entitled: "Micro and Nano Technologies in Medicine,"* pp 173-183.

Lai, J.C.K., Schoen, M.P., Ebrahimpour, A., Bhushan, A., Daniels, C.K. & Leung, S.W. (2007b) Fast-Response Smart Self-Assembling Biosensors For Biomarker Detection. In *Proceedings of IMECE International Mechanical Engineering Congress and Exposition, November 11-15, 2007, Seattle, Washington*, IMECE2007-42100.

Lai, J.C.K., Lai, M.B., Jandhyam, S., Dukhande, V.V., Bhushan, A., Daniels, C.K. & Leung, S.W. (2008) Exposure to Titanium Dioxide and Other Metallic Oxide Nanoparticles Induces Cytotoxicity on Human Neural Cells and Fibroblasts. *Int J Nanomed* 3(4):533-545.

Lai, J.C.K., Ananthakrishnan, G., Jandhyam, S., Dukhande, V.V., Bhushan, A., Gokhale, M., Daniels, C.K. & Leung, S.W. (2010) Treatment of Human Astrocytoma U87 Cells with Silicon Dioxide Nanoparticles Lowers Their Survival and Alters Their Expression of Mitochondrial and Cell Signaling Proteins. *Int J Nanomed* 5:715-723.

Malthankar, G.V., White, B.K., Bhushan, A., Daniels, C.K., Rodnick, K.J. & Lai, J.C.K. (2004) Differential Lowering by Manganese Treatment of Activities of Glycolytic and Tricarboxylic Acid Cycle Enzymes in Neuroblastoma and Astrocytoma Cells Is Associated with Manganese-Induced Cell Death. *Neurochem. Res.* 29:709-717.

Puli, S., Lai, J.C.K., Edgley, K.L., Daniels, C.K., & Bhushan, A. (2006) Signaling Pathways mediating Manganese-Induced Neurotoxicity in Human Glioblastoma Cells (U87) *Neurochem Res* 31: 1211-1218.

## APPENDICES

# Modeling surface electromyogram dynamics using Hammerstein-Wiener models with comparison of IIR and spatial filtering techniques

ANISH SEBASTIAN, PARMOD KUMAR, MARCO P. SCHOEN

**Abstract**— The national limb loss statistics paints a grim picture. Given the staggering limb loss numbers, the need to develop a “Smart Prosthetic Device” has never been more exigent. Despite years of effort by various government organizations and dedicated work on part of many scientists, we are still quite a ways away from creating the “perfect” prosthetic. Using electromyogram (EMG) signals to control prosthetic devices is and has been in the past, one of the most promising directions for this research. However, most of the control schemes being used, are based on either pre-programming the motion using threshold values of the EMG signal as reference, or using the root-mean-squared values of the EMG signal to actuate the prosthetic device. Using such a control strategy, makes it impossible to capture the underlying dynamics between EMG signals and the intended finger movements and forces. As a result of which the user needs to make an effort to learn to use the device, which can be very exhaustive. We propose to use system identification based dynamic models which are extracted from recorded surface EMG (sEMG) signals and the corresponding finger forces. A key influence on the resulting quality of such models is the filtering methods used for the EMG signals. This paper presents a thorough analysis of spatial filtering and other filtering methods as a possible solution to capture the dynamics of the sEMG signals, and perhaps in the future use these models to implement control schemes which would mimic the intricate force changes for a prosthetic hand. The different filters are compared on the basis of the EMG-finger force model fit percentages, obtained from System Identification using various Non-Linear Hammerstein-Wiener models. The nonlinear spatial filters gave better fit values as compared to the standard filtering techniques.

**Keywords**— Spatial Filtering, Hammerstein-Wiener, Surface Electromyogram (sEMG), System Identification, Sensor Array, Modeling.

Manuscript received June 27, 2011. The research was sponsored by the US Department of Defense; under the award number W81XWH-10-1-0128 awarded and administered by the U.S. Army Medical Research Acquisition Activity, 820 Chandler Street, Fort Detrick MD 21702-5014.

Anish Sebastian is a PhD candidate with the Idaho State University Pocatello, Idaho 83201 USA (e-mail: sebaanis@isu.edu).

Parmod Kumar is a PhD candidate with the Idaho State University Pocatello, Idaho 83201 USA (e-mail: kumaparm@isu.edu)

Marco P. Schoen, Professor, Department of Mechanical Engineering, Colonial Hall 22 Stop 8060 (208) 282-4377 (e-mail: schomarc@isu.edu)

## I. INTRODUCTION

ABOUT 50% of the people who need upper extremity prosthetics do not use them, [1]. This could be due any one of the common following reasons; Lack of a) Dexterity, b) Comfort and c) High Cost. Despite advances in the fields of manufacturing, electronics, signal processing, sensor design, and our understanding of biological signals, we still face a huge challenge designing a prosthetic device. This is due to the fact that such a device has to compete with one that nature has gifted us. A human hand is without doubt the best possible design. For a prosthetic hand, to encompass all of the human hands features and capabilities is as of now still a distant reality. Electromyogram (EMG) signals have been used for quite some time now in the control of prosthesis. The EMG signal is a small voltage signal (in mV), generated by skeletal muscles. This signal carries information of the objective the user would like to execute. Using surface EMG (sEMG) signals, researchers have been able to actuate motors on artificial prosthetic devices. EMG signals can be measured using intramuscular electrodes, needle electrodes, or by placing electrodes on the surface of the skin. The purpose for which the sEMG signal is being recorded generally determines whether it should be measured within the muscle using needle electrodes or surface measurement using electrodes on the skin would suffice. If, the purpose of recording the EMG signal is to look for diseases relating to a particular muscle, one might be better off using needle electrodes. On the other hand, if it is to be used to actuate motors on a prosthetic device, which a user might want to take off and wear without the need of medical supervision, surface EMG would suffice. Measuring the EMG signal on the surface of the skin is also less uncomfortable. This method is generally suited only for superficial muscles. Even though recording sEMG is favorable, it is plagued with many issues, such as crosstalk from firing of multiple motor points in the vicinity of the recording location, which can cause significant corruption of the signal at that site, motion artifacts, and poor signal if the motor unit is not identified correctly, etc. Needle electrodes, on the other hand, require trained medical professionals for appropriate placement of the electrodes in

the muscle. This paper investigates sEMG signals only with the objective to extract intended finger forces. The sEMG-force relationship is modeled using Hammerstein-Wiener models to characterize the dynamics. These models would characterize the controller dynamics for sEMG based prosthetic hands. We look to overcome the crosstalk issue in the measurement by using an array of nine (9) sEMG sensors, and utilizing spatial filters to isolate and improve the quality of the signals at the identified site for EMG recording. The sensor array was placed on the motor unit location, which was identified for the subject using a muscle stimulator. The sensors were then placed around the motor unit to form a 3x3 square matrix. The processed signal was then used for identifying various dynamical models for the prediction of the force, from the recorded sEMG signal, that was generated during various voluntary contractions of the subjects' hand. A comparison of the various outcomes (model fit values computed) from the system identification process, using signal processing techniques stated in the ISEK [2] guidelines and the spatially filtered signals are presented in this paper. The experiments were conducted for long durations also, in order to analyze the effects of the muscle fatigue on the model structures.

## II. PROBLEM FORMULATION

EMG signal should ideally be measured at a motor unit. A motor unit (MU) consists of an  $\alpha$ -motoneuron in the spinal cord and the muscle fiber it innervates. Figure 1 shows the path of the signal from the brain to the muscle.

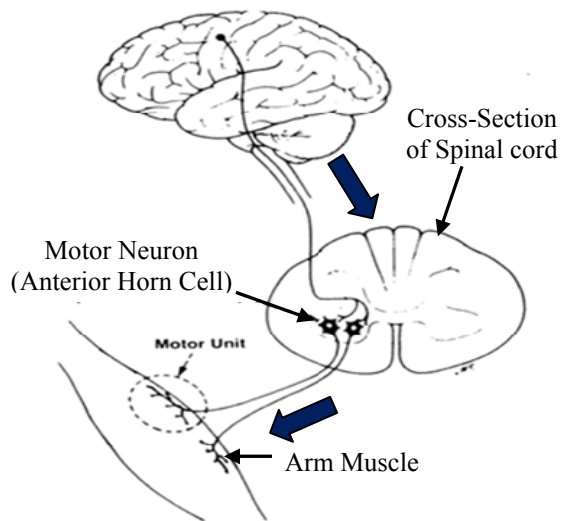


Fig. 1 sEMG signal pathway Brain – Motor Unit [3]

sEMG signals are influenced by multiple factors; physiological and non-physiological factors. The physiological factors are; A) Fiber membrane properties and B) Motor unit properties. Fiber membrane properties are further sub-divided into i) Average muscle fiber conduction velocity, ii) Distribution of motor unit conduction velocities, iii) Distribution of conduction velocities of the fibers within

the motor units and iv) Shape of the intracellular action potentials. Whereas the motor unit properties are subdivided into i) Number of recruited motor units, ii) Distribution of motor unit discharge rates, iii) Statistics and coefficient of variation of discharge rates and iv) Motor unit synchronization.

The non-physiological factors are; A) Anatomic, B) Detection System, C) Geometrical and D) Physical. The anatomic factors include, i) Shape of the volume conductor, ii) Thickness of the subcutaneous tissue layers, iii) tissue inhomogeneities, iv) Distribution of the motor unit territories in the muscle, v) Size of the motor unit territories, f) distribution and the number of fibers in the motor unit territory, vi) Distribution and number of fibers in the motor unit territories, vii) Length of the fibers, viii) Spread of the endplates and tendon junctions within the motor units, and ix) Spread of the innervations zones and tendon regions among motor units. The detection system used also plays an important part in influencing the sEMG measurements. Some of the factors which need to be taken into account, with the detection systems, are i) Skin electrode contact (impedance, noise), ii) Spatial filtering for signal detection, iii) Inter-electrode distance, iv) Electrode size and shape, and v) Inclination of the detection system relative to the muscle fiber orientation, and vi) Location of the electrodes over the muscle. The geometrical factors are, i) Muscle fiber shortening and ii) Shift of the muscle relative to the detection system. And the physical factors are i) Conductivities of the tissue and ii) Amount of crosstalk from nearby muscles [4]. This is not a comprehensive list of all the factors that influence sEMG signals but provides an insight into the complexity that one might encounter while modeling sEMG-force or sEMG-joint angle data. Some of the processing methods implemented for EMG have been mentioned in [5-9]

Since sEMG is plagued by a multitude of issues, as pointed out in the previous paragraph, one cannot approach this problem by realistically trying to account for each of the variables in the measurement, nor can one oversimplify the problem at hand by assuming a simple linear or a non-linear relation between the sEMG signal and the corresponding finger force generated. Hence the approach presented in this paper is to assume a black-box model in order to deduce a suitable relation or model structure for the two signals. This approach has been found to be of merit in our previous studies and has been reported in [10] & [11] to yield satisfactory fits percentages.

## III. PROBLEM SOLUTION

"Spatial filtering" is broadly defined as a method which computes spatial density estimates for events that have been observed at individual locations. These filters are used when there is no a priori curve to fit to a data series. Instead, it relies on nearby or adjacent values to estimate the value at a given point. These filters take out variability in a data set while retaining the local features of data. Spatial filtering is

principally associated with digital image processing. This method may be applied to almost any data in the form of a grid. The most common spatial filters are the low-pass and high-pass spatial filters. These are focal functions whose operation is determined by a kernel or neighborhood of  $N \times N$  cells around each pixel or grid position [12]. Grid cells “covered” by a kernel are multiplied by the matching kernel entry and then the weighted average is calculated and assigned as the value for the central cell,  $G$ . For example, an asymmetric  $3 \times 3$  kernel may look like the one shown in Equation (1), or any combination of the weights. Typically,  $a$ ,  $b$  are positive integers. If  $a=b=1$ , then the kernel provides a simple smoothing or averaging operation. The weights in the kernel can be modified for specific cases or data sets. In any case the weighted average is divided by the sum of the elements of the kernel. Filters of this type are sometimes referred to as low-pass filters.

$$\text{Symmetric Kernel} = \begin{bmatrix} a & a & a \\ a & b & a \\ a & a & a \end{bmatrix}. \quad (1)$$

If the weights in the kernel is similar to the one in Equation (2) and  $a$ ,  $b$ ,  $c$  are positive integers, and if the following,  $b > a > c$ , is true, then the kernel is described as a Gaussian filter which is symmetric but center-weighted.

$$\text{Symmetric Kernel} = \begin{bmatrix} c & a & c \\ a & b & a \\ c & a & c \end{bmatrix}. \quad (2)$$

The filtered grid value ‘ $G$ ’ of an  $m=N \times N$  kernel matrix, with  $C_i$  set of coefficients and  $P_i$  - set of source grid values, is calculated as:

$$G = \frac{\sum_{i=1}^m C_i P_i}{\sum_{i=1}^m C_i} + B, \quad (3)$$

where,  $B$  is often set to 0.  $B$  is a bias term to increase or decrease the resulting value of ‘ $G$ ’. This kernel is also sometimes referred to as the ‘*filter mask*’.

**Linear Spatial Filtering:** Linear spatial filtering would modify the sEMG array data ‘ $f$ ’ by replacing the value at each location with a linear function of the values of nearby data points. Moreover, this linear function is assumed to be independent of the data point locations  $(k, l)$ , where  $(k, l)$  are the indices of the data points in  $f$ , which is represented by a composite data matrix. This kind of operation can be expressed as convolution or correlation. For spatial filtering,

it's often more intuitive to work with correlation. The filtered result  $g(k, l)$  is obtained by centering the mask over pixel  $(k, l)$  and multiplying the elements of  $f$  with the overlapping elements of the mask and then adding them up. In other words, the objective is to amplify the activity of motor unit/s located closest to the recording site (ideally the actual motor location for the particular finger) and reducing the EMG signal generated by other motor units located further away or motor units of other fingers. Other ways to increase the selectivity of surface EMG recordings is by reducing the electrode size (i.e., skin-electrode contact area or inter-electrode distance) [13] and/or by applying temporal filters [14]. More recent work has focused on advances in the design of surface electrode arrays [15-16] to extract single motor unit information from sEMG. A large number of traditional [17-19] and adaptive [20] linear spatial filters have been extensively used to glean more information out of sEMG signals and to understand it much better.

For this paper, the experiments were carried out on a healthy male subject to extract dynamical models describing the relationship between sEMG-force signals. The motor points were located using a Muscle Stimulator, manufactured by Rich-Mar Corporation (model number HV 1100). The motor location of the ring finger was chosen for the experiments. The EMG detection system used was a Delsys, Bagnoli-16 channel EMG (DS-160, S/N-1116). The sensors used for measuring the sEMG action potentials were three pronged DE 3.1 differential surface electrodes. The subjects’ skin was prepared, according to the ISEK standards, before the sensors were placed over the motor point. The electrodes were placed along the muscle fibers (Flexor Digitorum Superficialis) for recording sEMG. Multiple sEMG sensors in an array configuration were mounted on and around the identified motor unit, as shown in Figure 2.

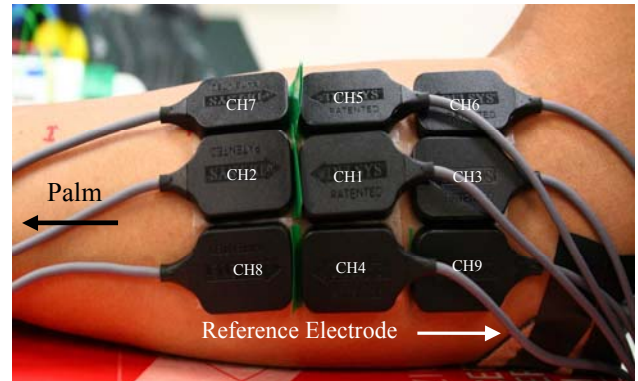


Fig. 2 Experimental Setup – Location of sEMG sensors

The subjects’ hand was placed on a flat surface; the reference electrode was placed on the elbow where there is no sEMG signal. Sensor  $CH1$  was placed on the identified motor unit location.  $CH2$  and  $CH3$  were placed along the muscle fiber in front and behind  $CH1$  respectively. Channels 4-9 were placed in the orientation as shown in Figure 2. Nine different experiments were conducted and the corresponding sEMG

signal was measured simultaneously from all the nine sensors. The force generated by the subject's fingers, for a given motion, was measured using a stress ball with a force sensitive resistor (FSR) mounted on it.

The change in the resistance of the FSR is directly proportional to the force being applied. Figure 3 shows the location of the FSR on the stress ball. Experiments 1 and 2 were used to check for any spurious signals that might be recorded due to the slight angle at which the subjects' hand was held. Experiments 3 to 6 were done using a stress ball with a lesser stiffness as compared to experiments 7, 8 & 9.

Also, a thumb restrain was used for experiments 5-9. The thumb restrain is showed in the Figure 3. The stress ball was changed as we were also interested in looking at the changes in the sEMG signal when fatigue occurs, and also how it would affect the modeling for the relation between force-sEMG using System Identification (SI).

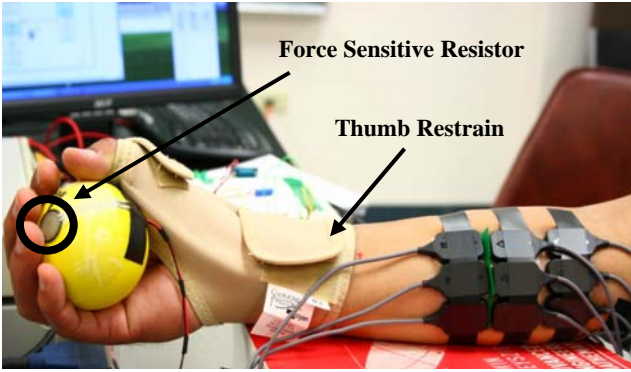


Fig. 3 Force Sensitive Resistor and Thumb Restrain

The linear spatial filters tested in this paper for isolating the motor unit action potentials (MUAPs) are; 1) Longitudinal Single Differential (LSD), 2) Transverse Single Differential (TSD), 3) Longitudinal Double Differential (LDD), 4) Transverse Double Differential (TDD), 5) Normal Double Differential (NDD), 6) Inverse Binomial (IB2) and 7) Inverse Rectangular (IR) Filter. The mask of these filters and the corresponding resultant equations on application of the mask to the grid data obtained from the sEMG array arrangement are given below.

EMG Array Information, **Spatial Filter Mask**

$$\text{LSD} = \begin{bmatrix} sEMG7 & sEMG5 & sEMG6 \\ 0 & 0 & 0 \\ sEMG2 & sEMG1 & sEMG3 \\ -1 & 1 & 0 \\ sEMG8 & sEMG4 & sEMG9 \\ 0 & 0 & 0 \end{bmatrix}$$

Result Equation:  $-sEMG2 + sEMG1$

$$\text{TSD} = \begin{bmatrix} 0 & -1 & 0 \\ 0 & 1 & 0 \\ 0 & 0 & 0 \end{bmatrix} \quad \text{LDD} = \begin{bmatrix} 0 & 0 & 0 \\ -1 & 2 & -1 \\ 0 & 0 & 0 \end{bmatrix}$$

$$\text{TDD} = \begin{bmatrix} 0 & -1 & 0 \\ 0 & 2 & 0 \\ 0 & -1 & 0 \end{bmatrix} \quad \text{NDD} = \begin{bmatrix} 0 & -1 & 0 \\ -1 & 4 & -1 \\ 0 & -1 & 0 \end{bmatrix}$$

*LSD* Equation =  $sEMG1 - sEMG2$ ; *TSD* Equation =  $sEMG1 - sEMG5$ . We can similarly deduce the equations for the other spatial filters.

$$\text{IB2} = \begin{bmatrix} -1 & -2 & -1 \\ -2 & 12 & -2 \\ -1 & -2 & -1 \end{bmatrix} \quad \text{IR} = \begin{bmatrix} -1 & -1 & -1 \\ -1 & 8 & -1 \\ -1 & -1 & -1 \end{bmatrix}$$

In this paper, nonlinear spatial filters have also been discussed these have been reported in literature [21]. These are 1) 1-D Nonlinear Transverse spatial filter (NLT), 2) 1-D Nonlinear Longitudinal spatial filter (NLL), 3) 2-D Nonlinear spatial filter in Two- Orthogonal Directions (NLTOD) and 4) Nonlinear spatial filter in All Four possible Directions (NLAFD). The nonlinear spatial filters use the Teager-Kaiser Energy (TKE) Operator, [22]. This technique is a threshold 'energy' based approach where outliers are first detected and then replaced by their estimated values. This nonlinear operator differs from the common way to calculate the energy of a discrete-time signal as the average sum of its squared magnitudes. The energy of a generating system of a simple oscillation signal was computed as the product of the square of the amplitude and the frequency of the signal. It was found that this nonlinear operator exhibits several attractive features such as simplicity, efficiency and ability to track instantaneously-varying special patterns. Since its introduction, several applications have been derived for one-dimensional [23-24], and two dimensional signal processing [25]. The nonlinear spatial filters with the TKE operator incorporated are given as follows; the general form of nonlinear spatial filter using the (TKE) operator is given in Equation (4);

$$\Psi[x(n)] = x^2(n) - x(n+1)x(n-1) \quad (4)$$

a) 1-D Nonlinear Transverse Spatial Filter (NLT); Equation (5)

$$\Psi_{d,m}[x(m,n)] = x^2(m,n) - x(m-1,n)x(m+1,n) \quad (5)$$

b) 1-D Nonlinear Longitudinal Spatial Filter (NLL); Equation (6)

$$\Psi_{d,n}[x(m,n)] = x^2(m,n) - x(m,n-1)x(m,n+1) \quad (6)$$

c) Nonlinear Spatial Filter in Two Orthogonal Directions (NLTOF): Equation (7)

$$\begin{aligned} \Psi_{d,2}[x(m,n)] &= \Psi_{d,2m}[x(m,n)] + \Psi_{d,n}[x(m,n)] \\ &= 2x^2(m,n) - x(m-1,n)x(m+1,n) - x(m,n-1)x(m,n+1) \end{aligned} \quad (7)$$

d) Nonlinear Spatial Filter in all Four Directions (NLAFD): Equation (8)

$$\begin{aligned} \Psi_{d,4}[x(m,n)] &= 4x^2(m,n) - x(m-1,n)x(m+1,n) \\ &\quad - x(m,n-1)x(m,n+1) - x(m-1,n+1)x(m+1,n-1) \\ &\quad - x(m-1,n-1)x(m+1,n+1) \end{aligned} \quad (8)$$

#### IV. SIMULATION RESULTS

Plots of the raw data gathered are shown in Figure 4. The plots shown in Figure 4 represent the raw data collected from the nine channels of the sensor grid in the same orientation as shows in Figure 2.

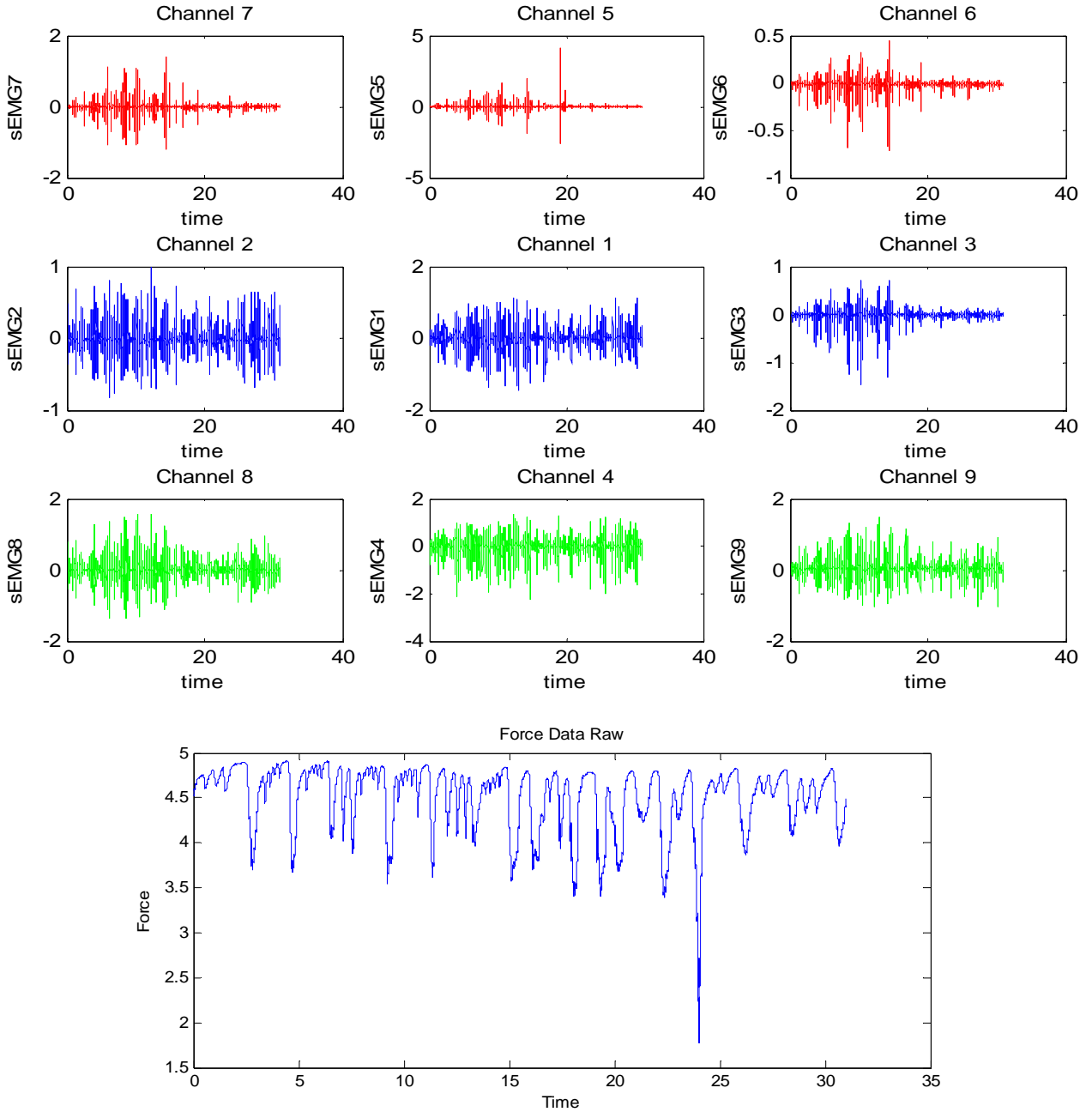


Fig. 4 sEMG Raw Signal Channels 1-9 & the corresponding Force signal



The data shown in Figure 4 is for comparison of the sEMG obtained from various location of the subject's arm. Notice the change especially in the amplitude of the sEMG at Channel 1, 4 & 5. Figure 5 shows the filtered sEMG (location CH1) at the motor point using four (4) IIR filters; 1) Bessel 2) Butterworth, 3) Chebyshev Type I and 4) Chebyshev Type II. The filter characteristics of these 4 filters were in accordance to the ISEK standards.

Figure 6 plots the filtered sEMG signal data from the sensor

array after they were filtered using various spatial filters. In addition to these 11 spatial filters. The relation of sEMG-Force was modeled using Non-Linear Hammerstein-Wiener models. This modeling method has been proven to work in the past [10], [11] in assuming a black-box model structure for the system. In order to model the sEMG-Force relation, the filtered data from the various experiments was split into various four (4) time windows.

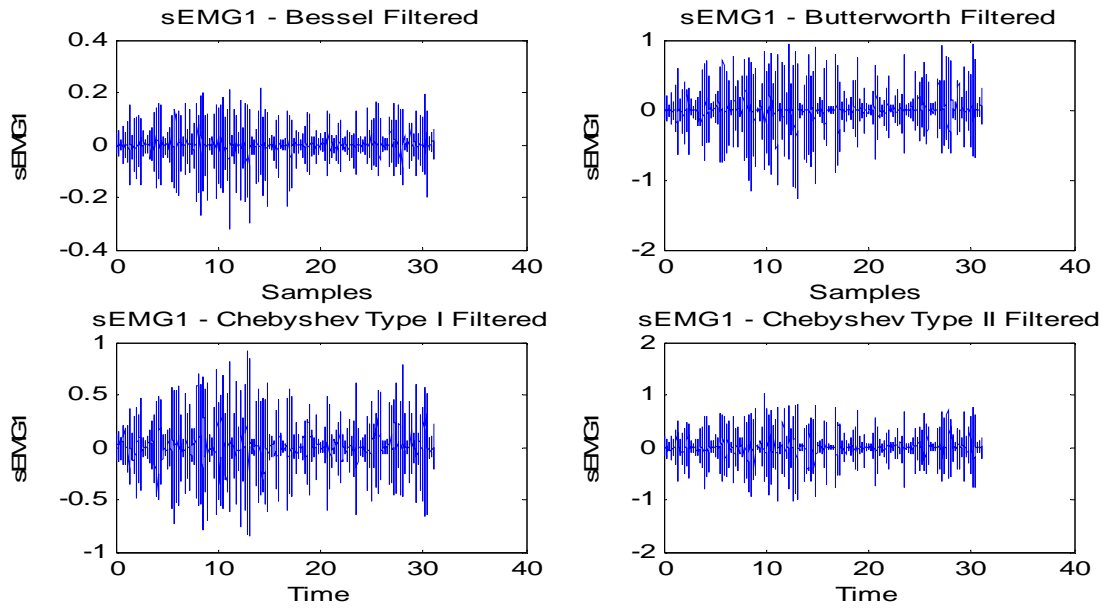


Fig. 5 sEMG1 at Motor Point (CH 1) Filtered using IIR Filters; Bessel, Butterworth, Chebyshev I & Chebyshev II

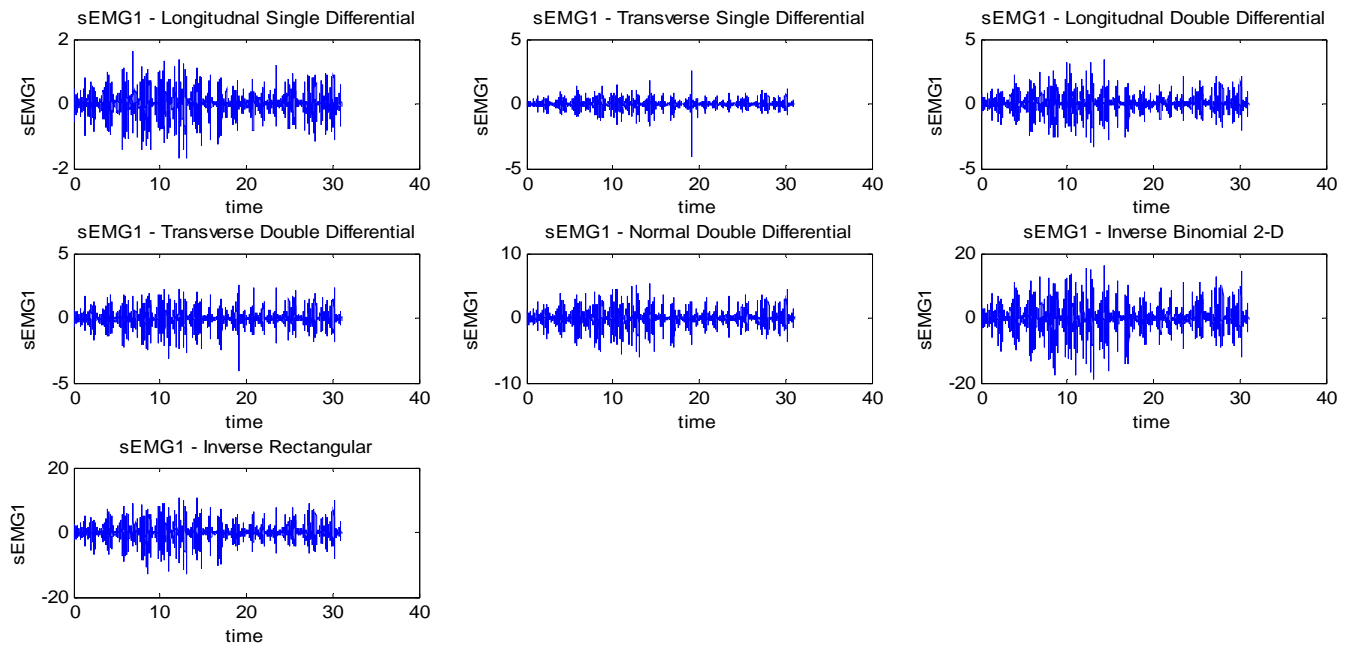


Fig. 6 sEMG1 at Motor Point of Ring Finger (CH 1) Filtered using Linear Spatial Filters; LSD, TSD, LDD, TDD, NDD, IB2 & IR



Equation 9 describes the general Hammerstein-Wiener model structure:

$$w(t) = f((g(t)), \quad b(t) = \frac{B_{j,i}(q)}{F_{j,i}(q)} w(t), \quad y(t) = h(x(t)), \quad (9)$$

where,  $w(t)$  and  $b(t)$  are internal variables,  $w(t)$  has the same dimensions as  $u(t)$  - input, and  $x(t)$  has the same dimensions as  $y(t)$  - output.  $g()$  and  $h()$  are the input and output non-

linearity functions respectively.  $B(q)$  and  $F(q)$  are regression polynomials. The model fit values are computed using Equation (10) as follows;

$$fit = 100 * \frac{1 - \|\hat{y} - y\|}{\|y - \hat{y}\|} \quad (10)$$

where,  $\hat{y}$  is the estimated output by the model.

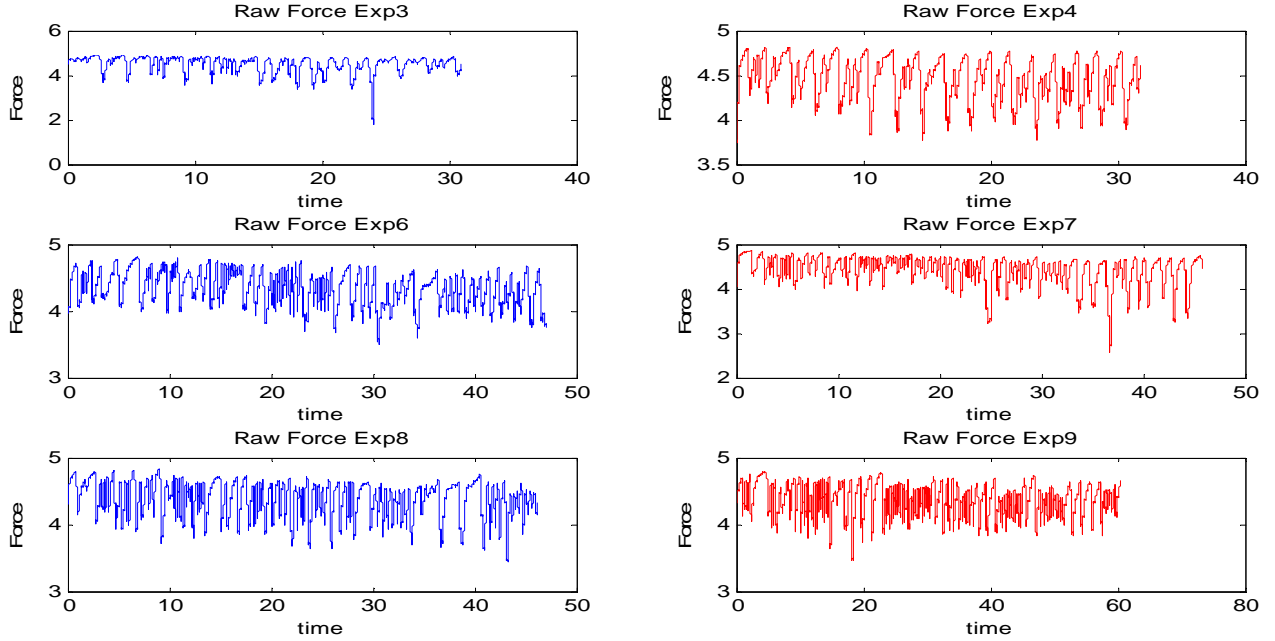


Fig. 7 Variations in Force levels; experiment 3, 4, 6, 7, 8 & 9

The time windows used for estimation and validation of the models were called 'ze' and 'zv' respectively. 'ze' contained 8000 sample points and 'zv' contained data points shifted by 2000 sample points. For example, if 'ze' was a time window between 2-6 seconds i.e. samples 4000-12000, then 'zv' was between 3-7 seconds i.e. 6000-14000 samples. Thus the Hammerstein-Wiener method uses 'ze' to estimate the model structure and based on this information predicts the next 2000 sample points. The data was filtered using the various filters mentioned in the previous sections. We would like to stress once again the point that the force was varied randomly and the subject was in no way trying to achieve maximum voluntary contractions during each cycle. A cycle is defined as the subject starting without any force on the stress ball, squeezing it (to any force level) and then going back to no force. The subject has to keep the finger in contact with the force ball throughout this cycle.

A plot of the variations in force achieved for 6 experiments is shown in Figure 7. The Matlab<sup>TM</sup> code for the Hammerstein-Wiener model is: `nlhw(ze, [na nb nk], ..., ...)`. The modeling was carried out by varying  $n_a$  - the number of past output terms used to predict the current output,  $n_b$  - the

number of past input terms used to predict the current output and  $n_k$  - the delay from input and output in terms of the number of samples for the various Hammerstein-Wiener models.

42 models with variations in  $n_a$  and  $n_b$  were tested while the value of  $n_k$  was kept as 1. The total number of models estimated were 15 (filter types) x 4 (time windows) x 42 models per time window x 4 experiments = 10,080 models. This paper does not list all these models but identifies and reports only the significant results of the analysis.

As an example, for experiment 3, for time window of 2-7 sec, the fit values obtained by varying  $n_a$  between 2-7 and  $n_b$  between 3-9, are shown in Figure 8. Figure 8 contains a lot of information as it shows 49 models fit percentages for each of the IIR and spatial filter types tested. The large variation in the model fit values can be attributed to the fact that the two data sets have poor correlation between one another. The significant result, for this time section, were noted for the Bessel and NLTO filters, these are plotted in Figure 9

The predicted model output plots for these values are shown in Figure 10.

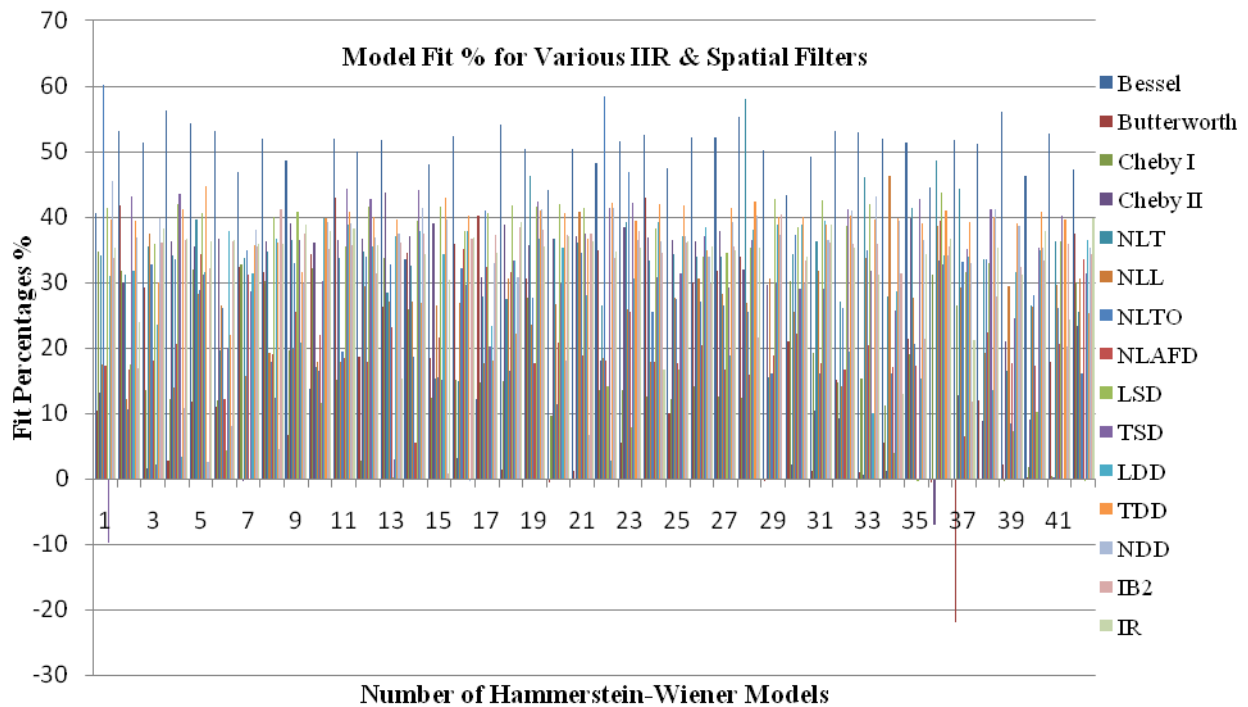


Fig. 8 Fit % for Hammerstein-Wiener Models – Various IIR & Spatial Filters (time window 2-7 sec, exp3)

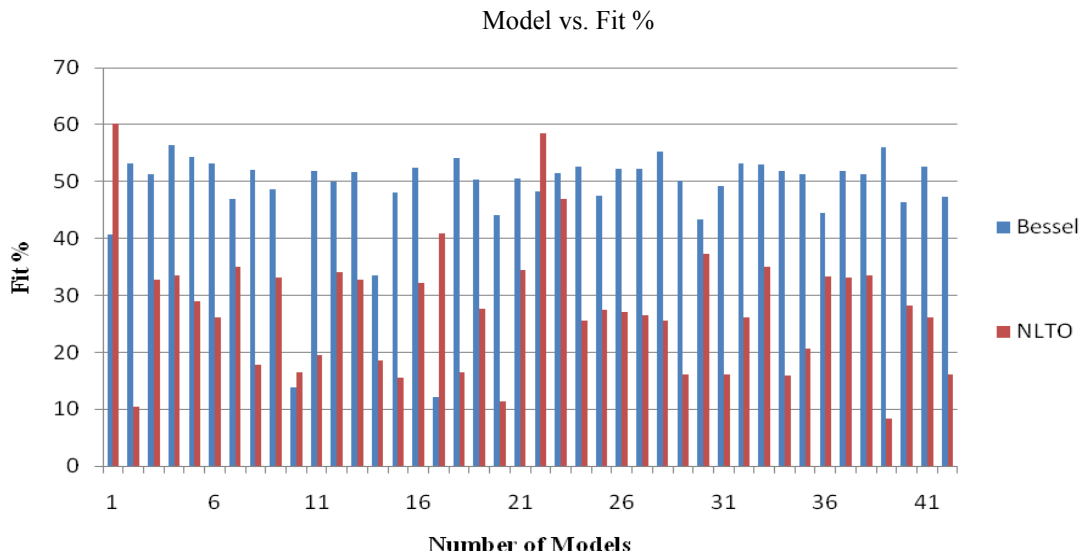


Fig. 9 Fit % for Hammerstein-Wiener Models – Bessel & NLTO (time window 2-7 sec, exp3)

The other filters used also predict the future variations in force but the fit percentages were in the range of 30-48%. A key objective of this research is help develop a control regime which is not based on threshold values of force can incorporate the dynamics in the force. This would help to control the response of the artificial limb to be closer to that of the actual hand. Similarly we tested various models for the other experiments too. Another set of results which gave very

high values of fit was for the later time windows. This case was especially interesting as the subject had fatigued due to the repetitive experiments, but the Hammerstein-Wiener models did successfully capture the variations in the sEMG signal. The Hammerstein-Wiener models performed very well even as the sEMG signal changed and we obtained fit values in the high sixties.

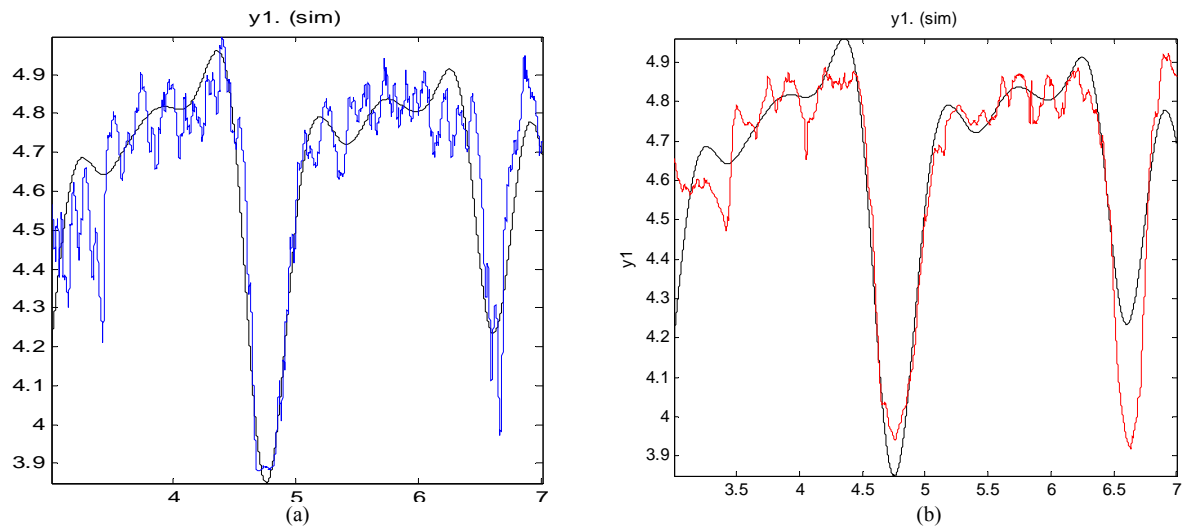


Fig. 10 Measured data (black) a) Bessel (blue) 56.36% and b) NLTO (red) 60.13% for exp 3 time window 2-7seconds.

Figure 11 shows the model fit values obtained for these later data windows. As can be seen from the plots, contrary to our expectations the Hammerstein-Wiener Models performed very well and produced very good fit values.

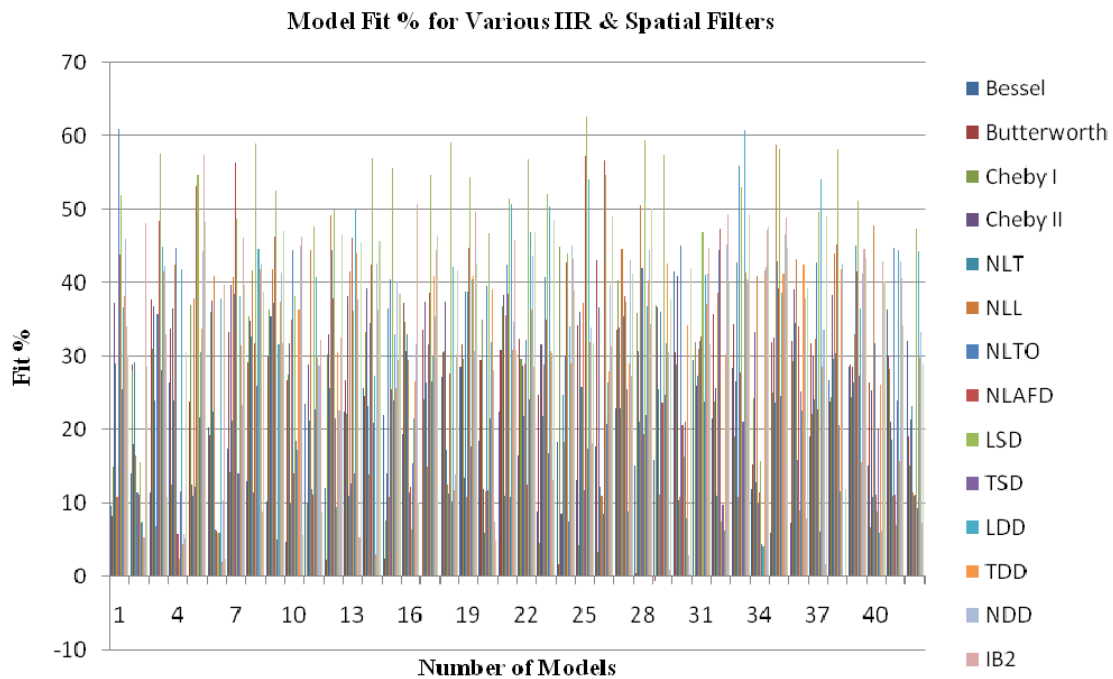


Fig. 11 Fit Values Obtained for Different Hammerstein-Wiener Models – Bessel, NLTO NLT, TDD, NDD, NLAFFD Filters (time window 20-25 sec, exp5)

Figure 12, 13 and 14 shows the model output plots for some of the filters mentioned in Figure 11. The only IIR filter whose performance matched, and in a few cases exceeded, the performance of the linear and the non-linear spatial filters was the Bessel filter. As can be seen from Figure 12 the Bessel

filter modeled the sEMG-force relation to 52.85 % though this is a slightly lower value than the Butterworth filter mentioned, the spread of the model fit values was more consistent in the range of 45-50% as compared to the Butterworth filter which had a far more spread out distribution.

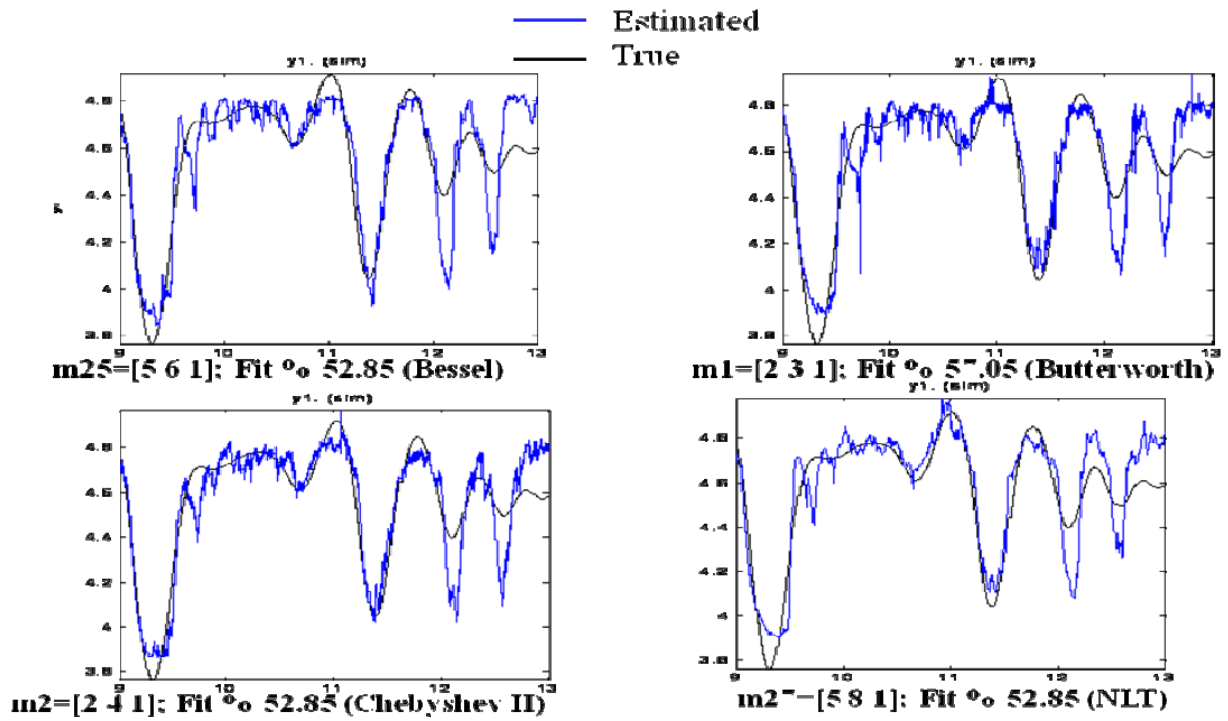


Fig. 12 Measured Data (Black) & Estimated Data (Blue)

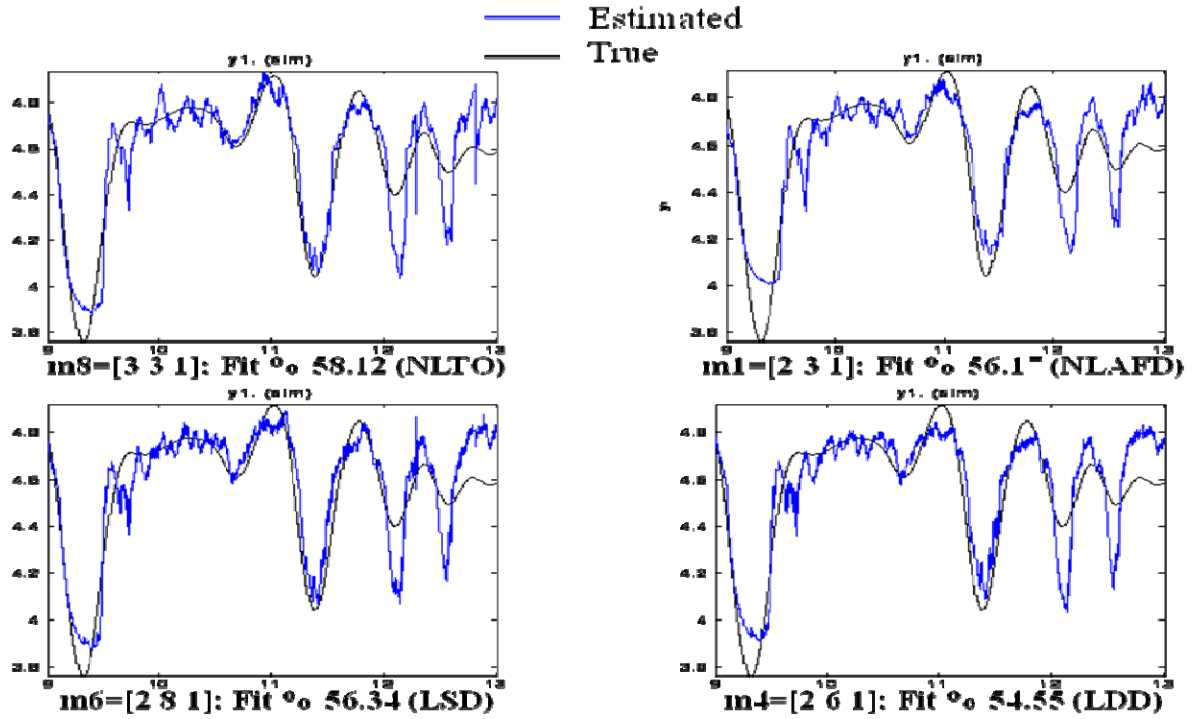


Fig. 13 Measured Data (Black) & Estimated Data (Blue)

## V. CONCLUSION

The Hammerstein-Wiener models worked very well in capturing the dynamics of the force levels for the various experiments conducted. This method of modeling could help

in improving the control over the motors used in prosthetic devices to mimic the actual changes force levels in a real hand. This method also performed very well in the scenarios where the subject did fatigue but the affects were successfully

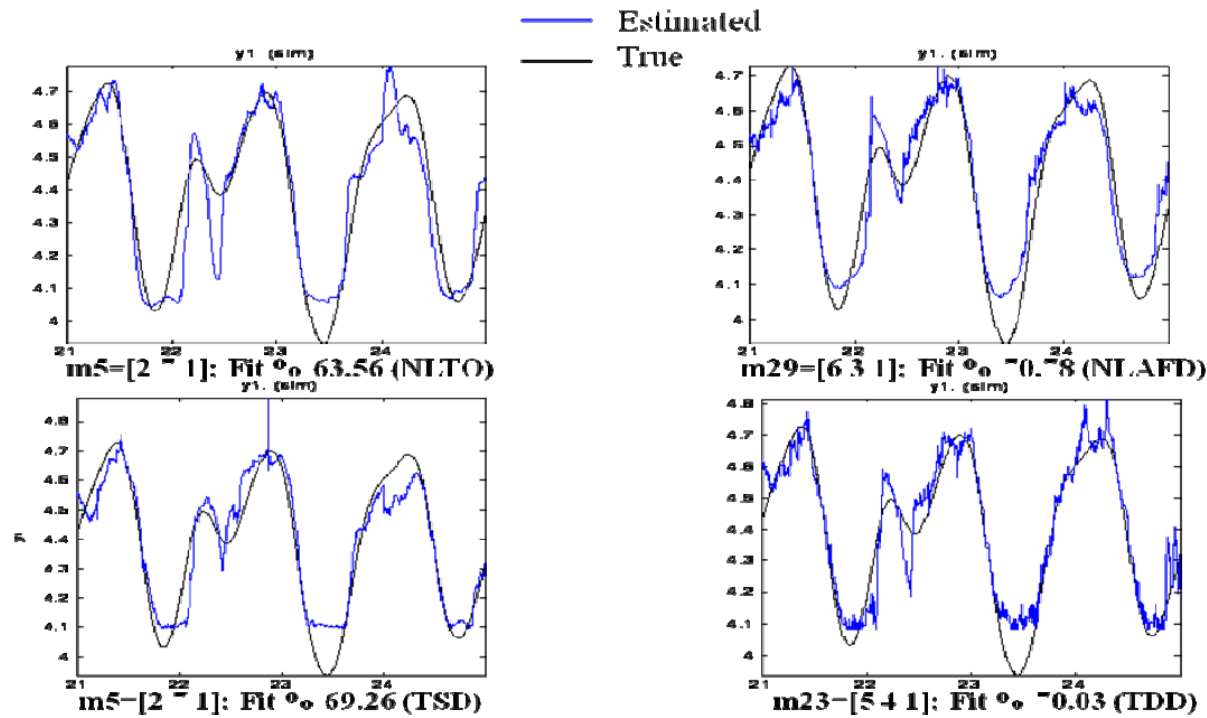


Fig. 14 Measured Data (Black) & Estimated Data (Blue)

modeled by the Hammerstein–Wiener models. The nonlinear and linear spatial filters (TDD, NDD and NLT, NLTO and NLAFD) did outperform the other filtering methods used especially for the later time windows. The only other filter which had a comparable performance to the spatial filters was the Bessel filter. Further investigation into reducing the wide range of the fit values obtained needs to be performed. One of the possible methods to pursue would be to use Genetic Algorithm to optimize the model parameters  $n_a$  and  $n_b$  and also the number of iterations used for the modeling of sEMG-force levels. One of the possible reasons for poor fit values could also be attributed to the model trying to over-fit the data sets.

#### ACKNOWLEDGEMENT

This work was supported by a grant from the Telemedicine Advanced Technology Research Center (TATRC) of the US Department of Defense. The financial support is greatly appreciated.

#### REFERENCES

- [1] <http://www.army.mil/-news/2010/02/24/34906-the-future-of-prosthetics-is-in-your-mind/>
- [2] [http://www.isek-online.org/standards\\_emg.html](http://www.isek-online.org/standards_emg.html)
- [3] <http://www.ott.zynet.co.uk/polio/lincolnshire/library/gawne/images/pandcmfig3.gif>
- [4] Farina, D., Merletti, R., and Enoka, M. R., 2004. "The extraction of neural strategies from the surface EMG". *Journal of Applied Physiology*, 96, pp. 1486-1495.
- [5] Zeghib, A., Palis, F., Tsenov, G., Shoylev, N., Mladenov, V., 2005. "Fuzzy systems and neural networks methods to identify hand and finger movements using surface EMG signals", *ICS'05 Proceedings of the 9th WSEAS International Conference on Systems*, Vouliagmeni, Athens, Greece, July 11-13.
- [6] Hu, X., Ren, X., 2006. "Identification of Surface EMG Signals Using Wavelet Packet Entropy", *Proceedings of the 6th WSEAS International Conference on Wavelet Analysis & Multirate Systems*, Bucharest, Romania, October 16-18, pp. 96-99.
- [7] Zeghib, A., Palis, F., Shoylev, N., Mladenov, V., Mastorakis, N., "Sampling frequency and pass-band frequency effects on Neuromuscular Signals (EMG) Recognition", 2007. *Proceedings of the 6th WSEAS International Conference on Signal Processing, Robotics and Automation*, Corfu Island, Greece, February 16-19, pp. 107-114.
- [8] P. Kumar, C. Potluri, A. Sebastian, S. Chiu, A. Urfer, D. S. Naidu, and M. P. Schoen, "An Adaptive Multi Sensor Data Fusion with Hybrid Nonlinear ARX and Wiener-Hammerstein Models for Skeletal Muscle Force Estimation," *The 14th World Scientific and Engineering Academy and Society (WSEAS) International Conference on Systems*, Corfu Island, Greece, July 22-24, 2010.
- [9] P. Kumar, A. Sebastian, C. Potluri, A. Ilyas, M. Anugolu, A. Urfer, and M. P. Schoen, "Adaptive Finger Angle Estimation from sEMG Data with Multiple Linear and Nonlinear Model Data Fusion," *The 10th World Scientific and Engineering Academy and Society (WSEAS) International Conference on Dynamical Systems and Control*, Iasi, Romania, July 1-3, 2011.
- [10] Sebastian A., Parmod K., Anugolu M., Schoen P. M., Urfer A., Naidu S. D., 2009. "Optimization of Bayesian Filters and Hammerstein-Wiener Models for EMG-Force Signals Using Genetic Algorithm". *Proceedings of the ASME 2009 Dynamic Systems and Control Conference DSCC 2009*.
- [11] Sebastian A., Parmod K., Schoen P. M., Urfer A., Creelman J., Naidu S. D., 2009. "Analysis of EMG-Force relation using System Identification and Hammerstein-Wiener Models". *Proceedings of the ASME 2010 Dynamic Systems and Control Conference DSCC 2010*.
- [12] <http://www.spatialanalysisonline.com/output/html/Linearspatialfiltering.html>
- [13] P. Zhou and W. Z. Rymer, "An evaluation of the utility and limitations of counting motor unit action potentials in the surface electromyogram," *Journal of Neural Engineering*, vol. 1, pp. 238–245, 2004.

- [14] Z. Xu and S. Xiao, "Digital filter design for peak detection of surface EMG," *Journal of Electromyography & Kinesiology*, vol. 10, pp. 275–281, 2000.
- [15] M. J. Zwarts and D. F. Stegeman, "Multichannel surface EMG: Basic aspects and clinical utility," *Muscle Nerve*, vol. 28, pp. 1–17, 2003.
- [16] B. G. Lapatki, J. P. Van Dijk, I. E. Jonas, M. J. Zwarts, and D. F. Stegeman, "A thin, flexible multielectrode grid for high-density surface EMG," *Journal of Applied Physiology*, vol. 96, pp. 327–336, 2004.
- [17] C. Disselhorst-Klug, J. Silny, and G. Rau, "Improvement of spatial resolution in surface-EMG: A theoretical and experimental comparison of different spatial filters," *IEEE Transactions on Biomedical Engineering*, vol. 44, no. 7, pp. 567–574, Jul. 1997.
- [18] D. Farina, E. Schulte, R. Merletti, G. Rau, and C. Disselhorst-Klug, "Single motor unit analysis from spatially filtered surface electromyogram signals. Part I: Spatial selectivity," *Medicine Biology Engineering and Computation*, vol. 41, pp. 330–337, 2003.
- [19] D. Farina, L. Mesin, S. Martina, and R. Merletti, "Comparison of spatial filter selectivity in surface myoelectric signal detection: Influence of the volume conductor model," *Medicine Biology Engineering and Computation*, vol. 42, pp. 114–120, 2004.
- [20] N. Ostlund, J. Yu, and J. S. Karlsson, "Adaptive spatio-temporal filtering of multichannel surface EMG signals," *Medicine Biology Engineering and Computation*, vol. 44, pp. 209–215, 2006.
- [21] P. Zhou, N. L. Suresh, M. Lowery, W. Z. Rymer, "Nonlinear Spatial Filtering of Multichannel Surface Electromyogram Signals During Low Force Contractions", *IEEE Transactions on Biomedical Engineering*, vol. 56, no.7, pp. 1871-1879, July 2009.
- [22] J. F. Kaiser, "On Teager's energy algorithm and its generalization to continuous signals", *Proc. 4th IEEE Digital Signal Proc. Workshop, Mohonk (New Paltz), NY, September 1990*.
- [23] P. Maragos, J. F. Kaiser, and T. F. Quatieri, "On amplitude and frequency demodulation using energy operators", *IEEE Transactions on Signal Processing*, Vol. 41, pp. 1532-1550, April 1993.
- [24] R. Hamila, J. Astola, F. Alaya Cheikh, M. Gabbouj, and M. Renfors, "Teager Energy and the Ambiguity Function", *IEEE International Conference On Image Processing*, Vol. 47, No. 1, pp. 260-262, January 1999.
- [25] F. Alaya Cheikh, R. Hamila, M. Gabbouj And J. Astola, "Impulse Noise Removal In Highly Corrupted Color Images," *Proc. 1996 IEEE International Conference On Image Processing, Lausanne, Switzerland, Vol. I, pp. 997-1000, September, 1996*.

**Anish Sebastian** was born in 1980 and received his B.S. degree in Instrumentation Engineering from Dr. D.Y. Patil College of Engineering in 2002, his M.S. degree in Measurement & Control Engineering from Idaho State University in 2009, and is currently a Ph.D. candidate in the Engineering & Applied Science Program at Idaho State University.

His research interests include development of a Smart Prosthetic Hand, development active flow control to mitigate stall and improve turbine efficiency, radiation therapy for treatment of active nodes in tumors, system identification and control systems. His current research is funded by the Department of Defense (DoD), Telemedicine and Advanced Technology Research Center (TATRC) titled "Smart Prosthetic Hand". He was awarded this research assistantship in 2007. The research being conducted at Idaho State University is on the analysis of surface electromyogram signals (sEMG) in order to establish a relation between the force generated by the fingers while grasping various objects and performing Activities of Daily Living (ADL). From 2005 to 2007 he was a graduate teaching assistant for various departments under the College of Engineering at Idaho State University. Mr Sebastian has 14 publications in all to date in internationally reputed conferences and journals. Mr. Sebastian has also served as a reviewer for various international conferences and journals.

**Parmod Kumar** received his B.S. degree in Marine Engineering from the Marine Engineering & Research Institute, Kolkata, India in 2002, his M.S. degree in Measurement and Control Engineering from Idaho State University in 2009, and expecting to get his Ph.D. in Engineering and Applied Science from Idaho State University by December 2011. Mr. Kumar has worked in Merchant Navy as a Certified Marine Engineer Officer for over four and half years. From 2007 to 2009 he was a graduate teaching assistant and from 2009 to till now he is a graduate research assistant at Measurement and Control Engineering Research Center (MCERC). Mr Kumar has a wide scope of

research interests and published internationally in reputed conferences and journals. Mr Kumar is reviewer for various international conferences and journals. For more details and the list of publications please see the web link <https://sites.google.com/site/parmodkumarms/Home>

**Marco P. Schoen** was born in 1965 and received his B.S. degree in Mechanical Engineering from the Swiss College of Engineering in 1989, his M.E. degree in Mechanical Engineering from Widener University in 1993, and his Ph.D. in Engineering Mechanics from Old Dominion University in 1997. From 1997 to 1998 he was a faculty member at Lake Superior State University and from 1998 to 2001 he served as a faculty to the Mechanical Engineering program at Indiana Institute of Technology. Since 2001 he has been with Idaho State University, where he currently serves as professor and chair for the Department of Mechanical Engineering and as associate director for the Measurement and Control Engineering Research Center (MCERC). His research addresses topics in controls and vibration of biomedical and aerospace systems as well as energy related problems. Schoen has been an associate editor for the *Journal of Dynamic Systems, Measurement and Control*, and a past chair of the Model Identification and Intelligent Systems (MIIS) Technical Committee for the American Society of Mechanical Engineers (ASME).

# Spatial filter masks optimization using genetic algorithm and modeling dynamic behavior of sEMG and finger force signals

ANISH SEBASTIAN, PARMOD KUMAR, MARCO P. SCHOEN

**Abstract** – Electromyography (EMG) signals are widely used for clinical and biomedical applications. One of the rapidly advancing fields of application of EMG is in the control of smart prosthetic devices for rehabilitation purposes. This paper presents the investigation of the use of System Identification (SI) for modeling sEMG-Finger force relation in the pursuit of improving the control of a smart prosthetic hand. Finger force and sEMG data are generated by having the subject perform a number of random motions of the ring finger to simulate various force levels. Post-processing of the sEMG signal is performed using spatial filtering. The linear and nonlinear spatial filters are compared based on the ‘kurtosis’ improvements and also based on the fit values of the models obtained using system identification, in particular the Hammerstein-Wiener models. The results of the modeling using linear spatial filters were found to be in the region of 30-45%, some of these linear spatial filter masks were selected randomly to investigate if there is any improvement in modeling the sEMG-force relation. The spatial filter masks are optimized using a Genetic Algorithm (GA) for two conditions; constrained and unconstrained. The model fit values of the identified models are used as the cost function in the GA optimization scheme. The results are compared to the reported filter mask values in the literature. The unconstrained GA based filter mask values and in some instances the constrained GA based mask values perform better than the filter masks reported in literature in 24 out of the 26 cases tested.

**Keywords**— Spatial Filtering, System Identification, Surface Electromyogram, Sensor Array, Genetic Algorithm, Hammerstein-Wiener Modeling.

## I. INTRODUCTION

IN the United States there are approximately 1.7 million people living with limb loss [1]. It is estimated that one out of every 200 people in the U.S. has had an amputation [2]. An ideal prosthetic hand has to be dexterous; easy to manufacture, must use little power and at the same time, must be of low cost. Building such a prosthetic hand, which can mimic the entire gamut of motions and have the functionality and

dexterity of a human hand exactly, has eluded researchers so far. Most of the hand grasping motions that a prosthetic device would need to perform have been classified by Feix [3]. One of the main strategies used in making a prosthetic hand “user friendly” is to use the electromyogram (EMG) signal to control a prosthetic device. An EMG signal is a small voltage signal (in mV) which is generated by skeletal muscles. EMG signals have a wide range of applications in the fields of medicine (orthopedic, surgery, functional neurology and gait and posture analysis), rehabilitation (post surgery/accident, neurological rehabilitation, physical therapy and active training therapy), ergonomics (risk prevention, ergonomic design, etc.) and sports science (biomechanics, movement analysis, athlete strength training and sports rehabilitation). EMG is measured using fine wire intramuscular electrodes, needle electrodes, or on the surface of the skin over the motor point using surface electrodes. Surface electrodes are quick and easy to apply, do not need medical supervision, cause minimal discomfort and are generally suited for superficial muscles. Needle electrodes on the other hand require trained medical professionals for appropriate placement within the muscle. The study of EMG signals, whether they are recorded using needle sensors or by placing electrodes on the surface of the skin, can provide a window into the fascinating world of how the motors of our body work seamlessly to meet the rigorous demands we place on them. The first investigator of EMG signals is considered to be H. Piper in 1912, [4]. Since then, there have been significant advances in the field of EMG signaling. Now, we have a much better understanding of what information can be derived from EMG signals and the various applications they could be used for. Needle EMG sensors are considered more accurate than surface EMG methods, as they can detect Motor Unit Action Potentials (MUAPs) in a very small volume, as small as a tip of a needle. Nonetheless, surface EMG signals also, are used in a large number of applications. One must be careful though, when drawing “conclusions” using surface EMG signals, [5].

Surface EMG signals have a variety of clinical and engineering applications. Few of the clinical applications include a) kinesiological analysis of movement disorders, b) differentiating types of tremors, myoclonus, and dystonia, c) for evaluating gait and posture disturbances, and for evaluating psychophysical measures of reaction and movement time, [6]. Engineering applications include a)

Manuscript received June 28, 2011. The research was sponsored by the US Department of Defense; under the award number W81XWH-10-1-0128 awarded and administered by the U.S. Army Medical Research Acquisition Activity, 820 Chandler Street, Fort Detrick MD 21702-5014.

Anish Sebastian is a PhD student with the Idaho State University Pocatello, Idaho 83201 USA (e-mail: sebaanis@isu.edu).

Parmod Kumar is a PhD student with the Idaho State University Pocatello, Idaho 83201 USA (e-mail: kumaparm@isu.edu)

Marco P. Schoen, Professor, Department of Mechanical Engineering, Colonial Hall 22 Stop 8060 (208) 282-4377 (e-mail: schomarc@isu.edu)



interpretation of neural control signals for research, [7], b) extraction of command signal for control of prosthetic or robotic devices, [8-10] to name a few.

This paper deals with surface electromyogram signals (sEMG). In the past, multiple methods have been investigated for extracting useful information from EMG signals. Some of these methods include employing low-pass or band-pass filtering; others have also used notch filtering to remove power line noise, [11]. Whitening filters can increase the quality of the amplitude estimates of the sEMG signals, [12]. Other methods include Markov models, [13] and fuzzy logic control, [14] – for classification of EMG, and wavelet processing, [15]. Currently, the accepted standardized method on how EMG signals must be recorded and analyzed is set by the International Society of Electromyography and Kinesiology (ISEK) [16].

The EMG signal is a complicated signal, which is controlled by the nervous system and is dependent on the anatomical and physiological properties of muscles. EMG signal acquires noise while traveling through different tissues. Moreover, the EMG detector, particularly surface electrodes collects signals from different motor units simultaneously which may have been generated through the interaction of

different motor unit signals. sEMG signals are influenced by multiple factors, some of which are; a) shape of the volume conductor, b) the thickness of the subcutaneous tissue layers, c) tissue inhomogeneities, d) distribution of the motor unit territories in the muscle, e) size of the motor unit territories, f) distribution and the number of fibers in the motor unit territory, g) length of the fibers, h) spread of the endplates and tendon junctions within the motor units, and i) spread of the innervations zones and tendon regions among motor units. The type of detection system used also plays an important part in influencing the sEMG measurements. Some of the factors which need to be taken into account, with the detection systems, are a) skin electrode contact (impedance, noise), b) spatial filtering for signal detection, c) inter-electrode distance, d) electrode size and shape, and e) inclination of the detection system relative to the muscle fiber orientation, [17]. Some of the processing methods implemented for EMG processing have been mentioned in [18-22]. Fig. 1 shows the locations where surface EMG electrodes might be placed in the vicinity of a muscle and the underlying anatomy of a muscle.

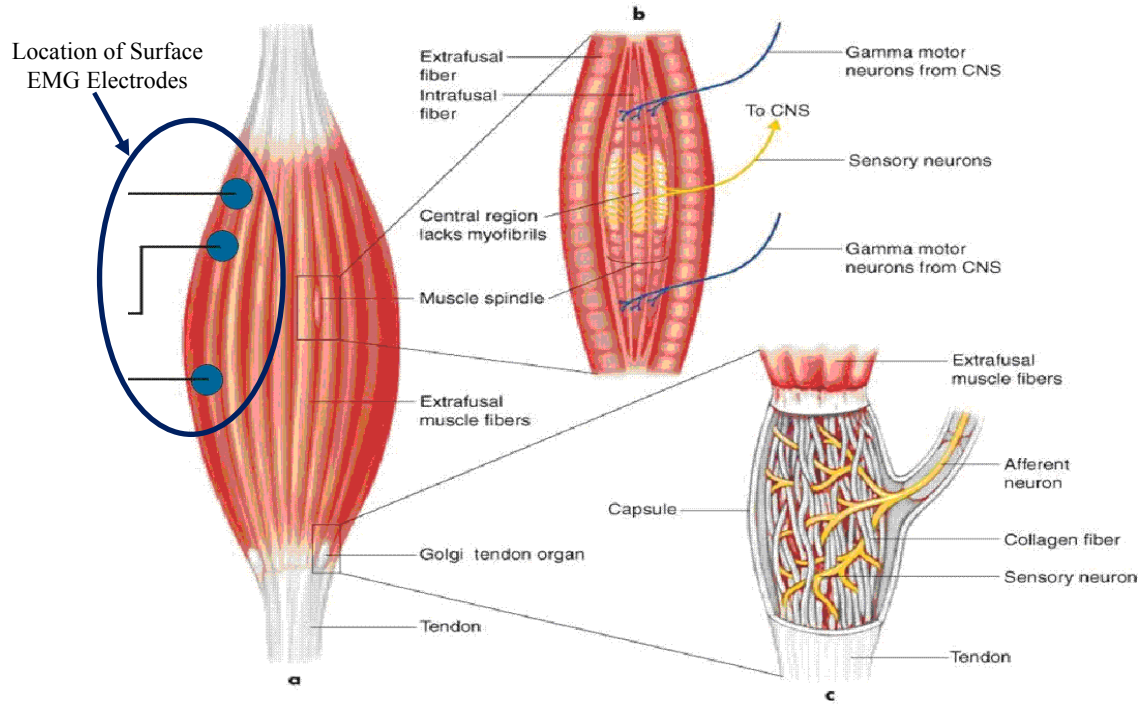


Fig. 1 Muscle anatomy & surface electrodes placement [23]

## II. PROBLEM FORMULATION

Measurement of a surface EMG signal, along with an actual recorded sEMG signal is shown in Fig. 2 (a). This EMG signal was obtained from a healthy male subject. The subject had performed squeezing of a stress ball with a force sensitive resistor (FSR) mounted on it. The change in the resistance of the FSR is correlated to the various force level that the subject

could generate. Fig. 2 (b) shows the sEMG plot and the corresponding change in force for one of the experiments performed. As can be seen the sEMG signal is very noisy, it must have been affected by any of the factors that are mentioned in the previous section. Another important factor that influences sEMG signals is cross-talk from the



neighboring motor units of the muscle. All these factors modify the underlying signal for a given contraction and relaxation of the subject's muscle. Many previous works make different assumptions while modeling the sEMG-force relation; like for example, in the simplest form assuming a linear relation between sEMG & force, developing transfer functions of the hand without including the different factors influencing the sEMG signal or using the root-mean-squared (RMS) value of the sEMG signal in order to formulate simplified models.

In reality it is impossible to account for all the factors influencing the sEMG signal. However, by making some of the assumptions mentioned earlier, one might end up with a

deficient model relating the sEMG-force data. The underlying dynamics of the sEMG signal may be lost in the process of oversimplification. In order to avoid some of these pitfalls our approach is to assume a black-box model to deduce a suitable relation or model structure for the two signals. Here, the modeling of the sEMG-finger force relation is not based on root-mean-square, or average values of the sEMG signal, hence, we facilitate the capture of the dynamical changes in the force levels. Our approach of using Hammerstein-Wiener models has been found to be of merit in our previous studies [24, 25] and have yielded satisfactory fits.

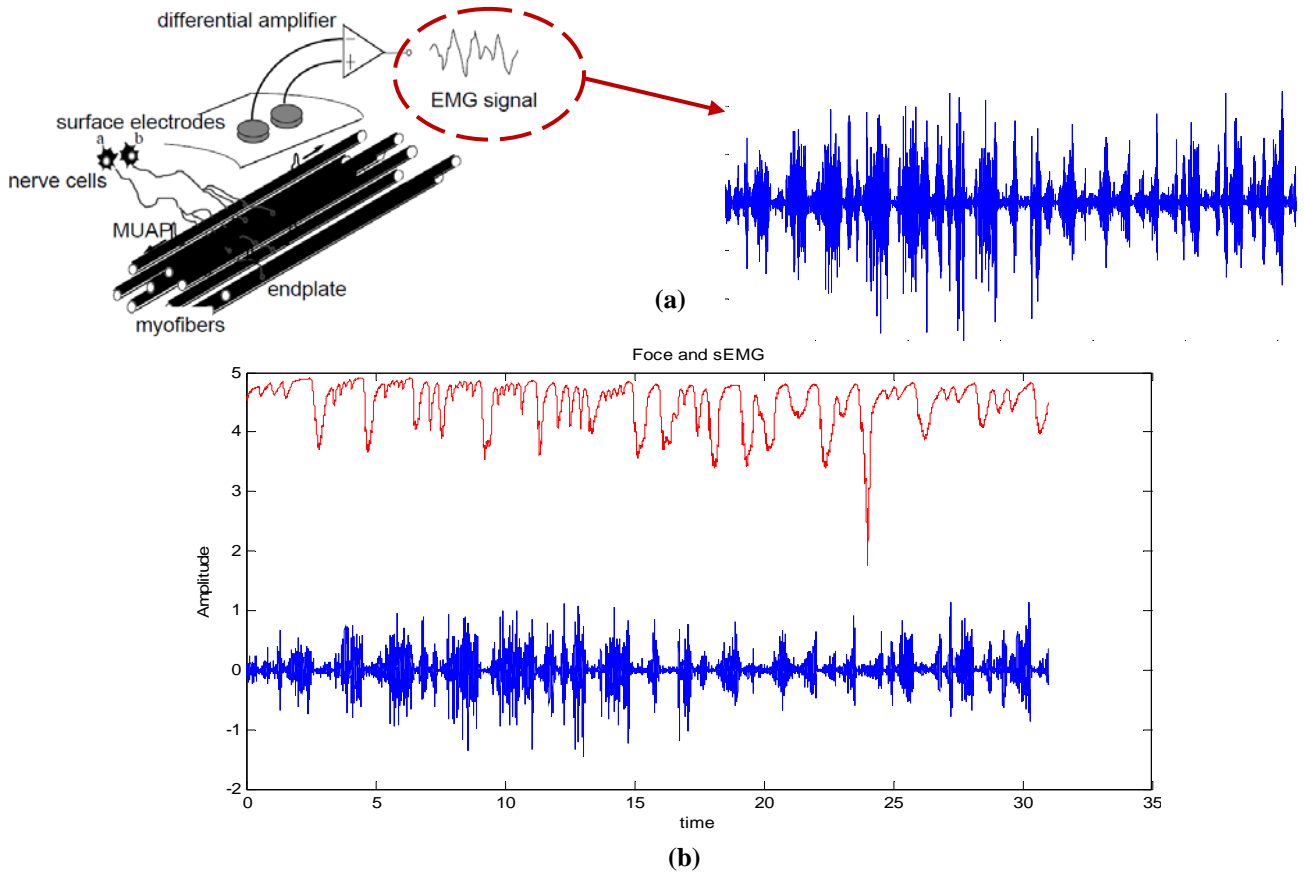


Fig. 2 (a) Measurement of sEMG & actual sEMG from test subject, (b) Force and corresponding sEMG

### III. PROBLEM SOLUTION

The data collected is from a nine (3x3) sensor array and rather than analyzing the data only at the motor unit, we considered using spatial filters. Spatial filtering is a very attractive choice as it can be used to either amplify the signal at the motor unit or extract useful information from the entire grid. "Spatial filtering" is broadly defined as a method which computes spatial density estimates for events that have been observed at individual locations. These filters are used when there is no a priori curve to fit to a data series. Instead, it relies on nearby or adjacent, values to estimate the value at a given

point. The most common spatial filters are the low-pass and high-pass spatial filters. These are focal functions whose operation is determined by a kernel or neighborhood of  $N_x N_y$  cells around each pixel or grid position [26]. Grid cells "covered" by a kernel are multiplied by the matching kernel entry and then the weighted average is calculated and assigned as the value for the central cell,  $G$ . For example, an asymmetric 3x3 kernel may look like the one shown in Equation (1), or any combination of the weights. Typically  $a$ ,  $b$  are positive integers. If  $a=b=1$ , then the kernel provides a simple smoothing or averaging operation. Filters of this type are sometimes referred to as low-pass filters.

$$\text{Symmetric Kernel} = \begin{bmatrix} a & a & a \\ a & b & a \\ a & a & a \end{bmatrix}. \quad (1)$$

The filtered grid value ‘G’ of an  $m=N \times N$  kernel matrix, with  $C_i$  set of coefficients and  $P_i$  - set of source grid values, is calculated as;

$$G = \frac{\sum_{i=1}^m C_i P_i}{\sum_{i=1}^m C_i} + B. \quad (2)$$

where,  $B$  is often set to 0.  $B$  is a bias term to increase or decrease the resulting value of ‘G’. This kernel is also sometimes referred to as the ‘filter mask’. The linear spatial filters tested in this paper are; 1) Longitudinal Single Differential (LSD), 2) Transverse Single Differential (TSD), 3) Longitudinal Double Differential (LDD), 4) Transverse Double Differential (TDD), 5) Normal Double Differential (NDD), 6) Inverse Binomial (IB2) and 7) Inverse Rectangular (IR) Filter. The mask of these filters and the corresponding resultant equations on application of the mask to the grid data obtained from the sEMG array arrangement are given below.

EMG Array Information, **Spatial Filter Mask**

$$\text{LSD} = \begin{bmatrix} sEMG7 & sEMG5 & sEMG6 \\ 0 & 0 & 0 \\ sEMG2 & sEMG1 & sEMG3 \\ -1 & 1 & 0 \\ sEMG8 & sEMG4 & sEMG9 \\ 0 & 0 & 0 \end{bmatrix}$$

Result Equation:  $-sEMG2 + sEMG1$

$$\text{TSD} = \begin{bmatrix} 0 & -1 & 0 \\ 0 & 1 & 0 \\ 0 & 0 & 0 \end{bmatrix}, \quad \text{LDD} = \begin{bmatrix} 0 & 0 & 0 \\ -1 & 2 & -1 \\ 0 & 0 & 0 \end{bmatrix}, \quad \text{TDD} = \begin{bmatrix} 0 & -1 & 0 \\ 0 & 2 & 0 \\ 0 & -1 & 0 \end{bmatrix}$$

*LSD* Equation =  $sEMG1 - sEMG2$ ; *TSD* Equation =  $sEMG1 - sEMG5$ ; we can similarly deduce the equations for the other spatial filters.

$$\text{NDD} = \begin{bmatrix} 0 & -1 & 0 \\ -1 & 4 & -1 \\ 0 & -1 & 0 \end{bmatrix}, \quad \text{IB2} = \begin{bmatrix} -1 & -2 & -1 \\ -2 & 12 & -2 \\ -1 & -2 & -1 \end{bmatrix}, \quad \text{IR} = \begin{bmatrix} -1 & -1 & -1 \\ -1 & 8 & -1 \\ -1 & -1 & -1 \end{bmatrix}$$

In this paper, some nonlinear spatial filters have also been discussed, these have been reported in the literature [27], these are 1) 1-D Nonlinear Transverse spatial filter (NLT), 2) 1-D Nonlinear Longitudinal spatial filter (NLL), 3) 2-D Nonlinear spatial filter in Two- Orthogonal Directions (NLTO) and 4) Nonlinear spatial filter in All Four possible Directions (NLAFD). The Nonlinear Spatial Filters use the Teager-Kaiser Energy (TKE) Operator [28]. This technique is a threshold ‘energy’ based approach where outliers are first

detected and then replaced by their estimated values. General Form of Nonlinear Spatial Filter using the Teager-Kaiser (TKE) operator is given in equation (4), where  $x(n)$  denotes the location of the sensor in the grid;

$$\Psi[x(n)] = x^2(n) - x(n+1)x(n-1). \quad (4)$$

a) 1-D Nonlinear Transverse Spatial Filter (NLT); equation (5)

$$\Psi_{d,m}[x(m,n)] = x^2(m,n) - x(m-1,n)x(m+1,n). \quad (5)$$

where,  $d$ , is the subscript for the dimension, for the 1-D filters it is 1 and  $m$  denotes the longitudinal direction i.e. along the muscle fiber.

b) 1-D Nonlinear Longitudinal Spatial Filter (NLL); equation (6)

$$\Psi_{d,n}[x(m,n)] = x^2(m,n) - x(m,n-1)x(m,n+1). \quad (6)$$

$n$  denotes the transverse direction i.e. perpendicular to the muscle fiber.

c) Nonlinear Spatial Filter in Two Orthogonal Directions (NLTO); equation (7)

$$\begin{aligned} \Psi_{d,2}[x(m,n)] &= \Psi_{d,2m}[x(m,n)] + \Psi_{d,n}[x(m,n)] \\ &= 2x^2(m,n) - x(m-1,n)x(m+1,n) - x(m,n-1)x(m,n+1). \end{aligned} \quad (7)$$

d) Nonlinear Spatial Filter in all Four Directions (NLAFD); equation (8)

$$\begin{aligned} \Psi_{d,4}[x(m,n)] &= 4x^2(m,n) - x(m-1,n)x(m+1,n) \\ &\quad - x(m,n-1)x(m,n+1) - x(m-1,n+1)x(m+1,n-1) \\ &\quad - x(m-1,n-1)x(m+1,n+1). \end{aligned} \quad (8)$$

The experiments were carried out on a healthy male subject. The ring finger motor point was located using a muscle stimulator, manufactured by Rich-Mar Corporation (model number HV 1100). Fig. 3 shows a picture of the Muscle Stimulator used. The EMG detection system used was a Delsys, Bagnoli-16 channel EMG (DS-160, S/N-1116). The sensors used for measuring the surface EMG action potentials were three pronged DE 3.1 differential surface electrodes.



Fig. 3 Muscle stimulator

The material for the contacts of the electrode is 99.9% pure

silver, the contacts are 10mm long, 1mm in diameter and spaced 10mm apart. The subjects' skin was prepared, according to the ISEK standards, before the sensors were placed over the motor point. The electrodes were placed along the muscle fibers (Flexor Digitorum Superficialis) for recording surface EMG. The reference electrode was placed on the elbow where there is no sEMG signal. Nine different experiments were conducted and the corresponding sEMG signal was measured simultaneously from all the nine (9) sensors. The force generated by the subject's fingers, for a given motion, was measured using a stress ball with a force sensitive resistor (FSR) mounted on it. Fig. 4 shows the location of the FSR on the stress ball.

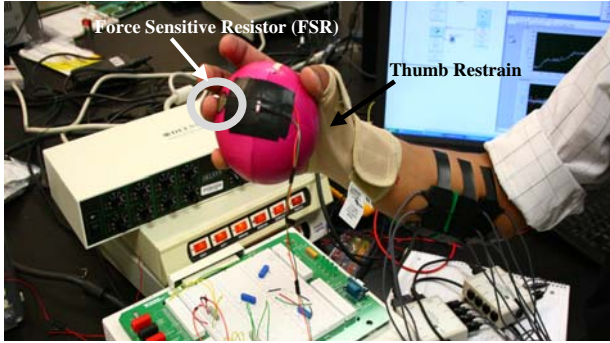


Fig. 4 Force sensitive resistor and thumb restrain

### System Identification

System Identification (SI) has its roots in standard statistical techniques, such as least-squares and maximum likelihood methods, for instance. SI helps the user to build mathematical models of a dynamic system based on measured data. This is done by adjusting the parameters within a given model until its output emulates the measured input in some minimum fashion, [29]. System identification is especially useful for modeling systems that cannot be easily represented in terms of first principles or known physical laws. In this case, one can use SI to perform black-box modeling, where the measured data determines the model structure.

Black-box modeling has the following advantages; 1) the structure and the order of the model need not be known, and 2) many model structures can be estimated and compared, and the best among them can be selected to suit the measured data sets. Systems that can be represented using ordinary difference or differential equations can be modeled using grey-box models. Grey-box models have a known mathematical structure and unknown parameters and they have the following advantages over black-box models; 1) Known constraints can be imposed on the model characteristics, 2) there are fewer model parameters to estimate, 3) coupling between parameters can be defined in the model structure, and 4) in the non-linear case the dynamic equations can be specified dynamically.

The most common system identification models in engineering are Auto-Regressive with eXogenous input (ARX) and Auto-Regressive Moving Average with

eXogenous input (ARMAX). The more recent additions to system identification have been black-box models with a non-linear structure such as Artificial Neural Networks, Fuzzy models and so on.

The most basic relationship between the input and the output of a system can be given by a linear difference equation, [30] such as:

$$y(t) + a_1 y(t-1) + \dots + a_n y(t-n) = b_1 u(t-1) + \dots + b_m u(t-m), \quad (9)$$

where,  $y(t)$  are the input and output of the system at time  $t$  respectively, and  $a_i, b_j$  are the parameters of the system.

$$\theta = [a_1, \dots, a_n, b_1, \dots, b_m]^T, \quad (10)$$

where,  $\theta$  is the parametric vector with coefficients  $a_i$  and  $b_j$ .

$$\phi(t) = [-y(t-1) \dots -y(t-n) u(t-1) \dots u(t-m)]^T, \quad (11)$$

$$\text{then we can write: } y(t) = \phi^T(t) \theta, \quad (12)$$

where,  $\phi(t)$  is the regression vector.

Generally, a model structure is a parameterized mapping from past inputs and outputs  $Z^{t-1}$  to the space of the model outputs, [31]:

$$\hat{y}(t | \theta) = g(\theta, Z^{t-1}), \quad (13)$$

where,  $\hat{y}(t)$  is the predicted output.

In practice most of the systems are nonlinear and the output is a non-linear function of the input variables. However, linear models often sufficiently and accurately describe system dynamics. While modeling a system using grey-box models, the linear and the nonlinear structures can be set using its differential or difference equations. Since linear models are adequate for many situations, it should be tried first to see if the results of the model fit are satisfactory.

It is a possible and a quite common situation where the dynamics of the system can be well described using linear models, but they do not account for any static nonlinearities at the input and/or at the output. This might be the case if the actuators are nonlinear. For example when saturation occurs or when the sensors employed have nonlinear characteristics. A model with a static nonlinearity at the input is called a Hammerstein model. When the nonlinearity is at the output a Wiener model is more appropriate. The combination of the two is then the Hammerstein-Wiener model, [32]. Refer Fig. 5[A] (a) and (b) for Hammerstein and Wiener models respectively. Consider the Hammerstein case where the static nonlinear function  $f(\bullet)$  can be parameterized either in terms of physical parameters, such as saturation point and saturation level, or in black-box terms such as spline-function coefficients. This defines  $f(\bullet, \eta)$ , [31]. If the linear model is given by, the predicted output model will be in the following form:

Equation 14 describes the Hammerstein-Wiener model structure:

$$w(t) = f(g(t)), \quad b(t) = \frac{B_{j,i}(q)}{F_{j,i}(q)} w(t), \quad y(t) = h(x(t)), \quad (14)$$

where,  $w(t)$  and  $b(t)$  are internal variables,  $w(t)$  has the same dimensions as  $u(t)$  - input, and  $x(t)$  has the same dimensions

as  $y(t)$  - output.  $g()$  and  $h()$  are the input and output non-linearity functions respectively.  $B(q)$  and  $F(q)$  are regression polynomials. Fig. 5[A] and 5[B] represent the Hammerstein-Wiener models individually and their combination respectively. The model fit values are computed using Equation 15 as follows;

$$fit = 100 * \frac{1 - \|\hat{y} - y\|}{\|y - \hat{y}\|}. \quad (15)$$

where,  $\hat{y}$  is the estimated output by the model. The linear block is specified using the terms  $n_b$  - the number of zeros plus one,  $n_f$  - the number of poles and  $n_k$  - the delay from the input to the output in terms of the number of samples. The commonly used nonlinear estimators for Hammerstein-Wiener model are, a) Dead Zone, b) Piecewise Linear, c) Saturation, d) Sigmoid Network, and e) Wavelet Network, [32].

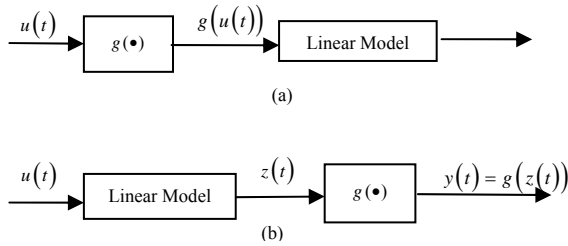


Fig. 5 [A] (a) Hammerstein Model, (b) Wiener Model

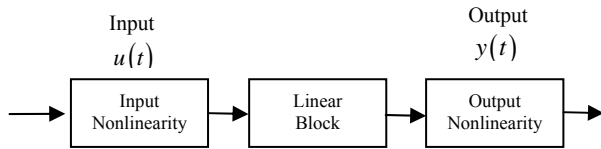


Fig. 5 [B] Hammerstein-Wiener model structure

### Genetic Algorithm (GA)

Genetic Algorithm is a class of evolutionary methods for solving both constrained and unconstrained optimization problems that are based on natural selection. This is the same rule that governs biological systems. In GA, the population of individual solutions is modified repeatedly. A solution is given by a set of parameters (genes) and packaged as a chromosome. Each step or iteration the GA selects individuals (chromosomes) in a fashion that may include some randomness, from a given population, as parents, and uses them to produce offspring for the next generation. Over successive iterations or generations, the population evolves and finally reaches an optimal solution. The steps that make

up GA are as follows:

- 1) Generate a random population of ' $p$ ' chromosomes – these chromosomes carry information of the population and are confined in the feasible solution space.
- 2) Evaluate the objective or fitness function  $f(p)$  for each chromosome.
- 3) Create a new population or offspring from the initial population by using certain rules.

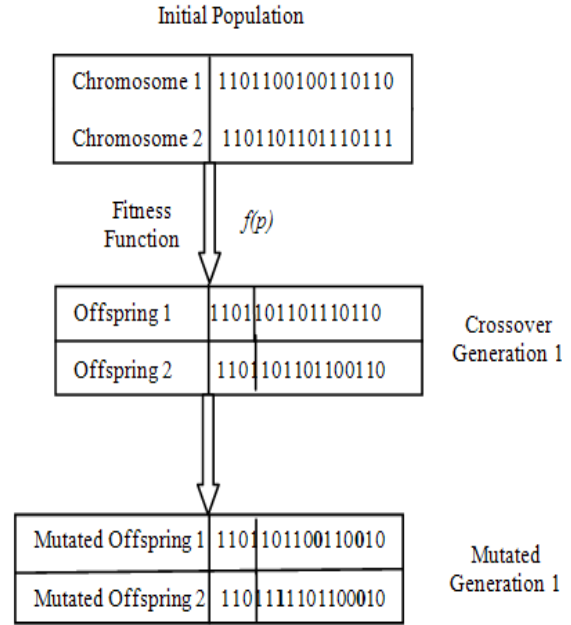


Fig. 6 General steps in a binary genetic algorithm

These rules include a) Selection – selection of two parent chromosomes from the population according to their fitness. b) Crossover – crossover the parents to form new offspring, if no crossover is performed then the offspring is an exact copy of the parents. c) Mutation – involves the changing of a variable in a chromosome or some other change in the original chromosome as defined by the user. d) Acceptance Condition – if offspring satisfies the acceptance condition, include offspring in the new population or else discard. 4) Use the offspring as the parents for the generation of a new population. 5) Continue until the end condition is satisfied. Fig. 6 presents a graphical interpretation of the steps in GA. In this work, GA is used to assist in finding the optimal values of the filter mask for the filtration of the sEMG signal using the various spatial filters. The cost function that the GA tries to minimize, is the model fit obtained from system identification of the sEMG-force data that was collected.

Fig. 7 gives an overview of the method that was followed for this paper.



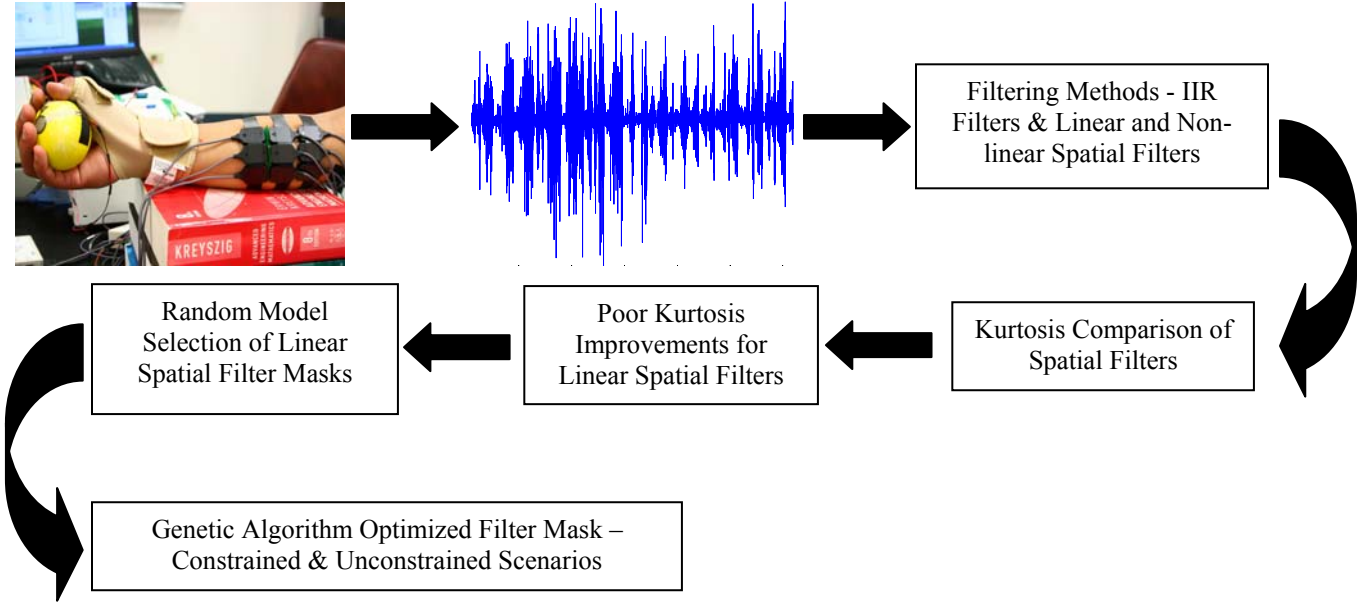


Fig. 7 Overview of the methodology used

#### IV. SIMULATION RESULTS

The results of spatially filtered data for the linear and the nonlinear spatial filters were first compared based on the “Kurtosis” criteria, [27-28]. ‘Kurtosis’ is a measure of whether the data sets are peaked or flat relative to a normal distribution. That is, data sets with high kurtosis tend to have a distinct peak near the mean, decline rather rapidly, and have heavy tails. Data sets with low kurtosis tend to have a flat top near the mean rather than a sharp peak. A uniform distribution would be the extreme case. The mathematical expression for kurtosis is given in Equation 11.

$$Kurt = \frac{E[x^4] - 3(E[x^2])^2}{E[x^2]^2}. \quad (11)$$

Fig. 8 shows the plot obtained for the various filters based on the *kurtosis* measure. The y-axis is the *kurtosis improvements* which is the ratio of the *output* to the *input kurtosis*. It is evident from the plot that the NLT, NLL, NLTO and the NLAFD spatial filters performed very well as compared to the linear spatial filters under investigation. The best *kurtosis improvements* were obtained for experiment 4  $\approx 44$  for the nonlinear spatial filters. The x-axis in Fig. 5 shows the numbers allotted to the various spatial filters investigated. Based on these results we focused our attention to the linear spatial filter masks for experiment 3, which exhibits poor model fit percentages and also low *kurtosis* values. This paper does not investigate the reason for the low *kurtosis* values of the linear spatial filters but only investigates the use of GA to improve the low model fit percentages obtained for experiment 3. The filters were compared based on the model fit values obtained from various Hammerstein-Wiener models.

The Matlab<sup>R</sup> code for the Hammerstein-Wiener model is: `nlhw(ze, [nb nf nk], ..., ...)`. The modeling was carried out by varying  $n_b$  - the number of zeros plus one,  $n_f$  - the number of poles and  $n_k$  - the delay from input and output in terms of the number of samples for the various Hammerstein-Wiener models. In all, 42 models with variations in  $n_a$  and  $n_b$  were tested while the value of  $n_k$  was kept as 1. The total number of models estimated were 7 (filter types) x 4 (time windows) x 42 models per time window = 1,176 models. The time windows used for estimation and validation of the models were called ‘ze’ and ‘zv’ respectively. ‘ze’ contained 8000 sample points and ‘zv’ contained data points shifted by 2000 sample points. For example, if ‘ze’ was a time window between 2-6 seconds i.e. samples 4000-12000, then ‘zv’ was between 3-7 seconds i.e. 6000-14000 samples. These models were computed using the filter masks available in literature. On examining the fit values closely we found them to have large variation from one model order to another. One of the reasons of this could be due to the poor correlation in the estimation and validation data sets, on account of the large variations that were achieved in the force. This paper does not list all these models tested but identifies and reports only the significant results of the analysis. We found that the filters tested performed poorly in the initial time window of 2-7 seconds for experiment 3. Some of the models for this time window were selected and then recomputed using GA to optimize the filter mask with the fitness function being the fit value of an identified model achieved for a given model order.

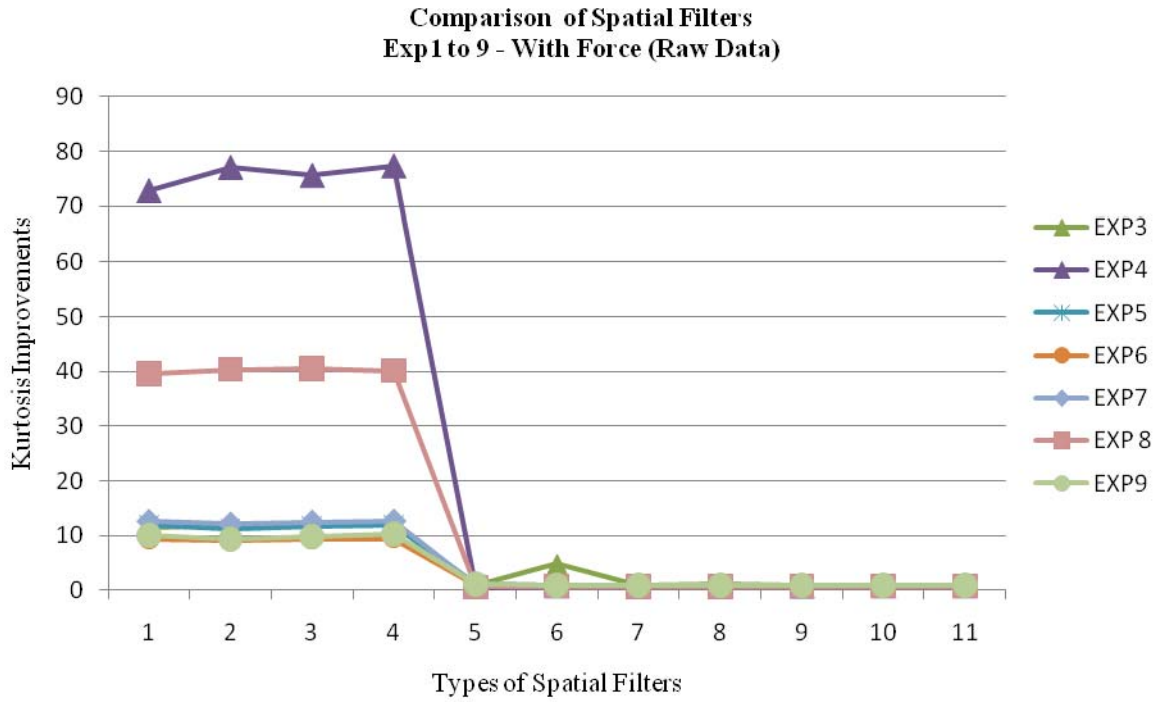


Fig. 8 Kurtosis plots of various filters for exp3 – 9; y-axis numbers are for the various filters tested 1-NLT, 2-NLL, 3-NLTO, 4-NLAFD, 5-LSD, 6-TSD, 7-LDD, 8-TDD, 9-NDD, 10-IB2, and 10- IR

Table 1 shows an example of the fits that were obtained on varying the parameters of the Hammerstein-Wiener model. The highlighted models (and a few other models) were selected randomly to be optimized using GA. We had two scenarios under GA –1) GA Constrained and 2) GA – Unconstrained. The first scenario GA constrained optimized only the mask entry  $a_{22}$  (location of the sEMG sensor on the motor unit). The other entries of the filter mask were then

computed from this optimized value. In the second scenario, GA unconstrained we let GA optimize all the entries for various masks. The GA parameters for optimization were as follows: number of iterations: 50; initial population size Generation 0: 96; population size Generation 1: 48; Number of Chromosomes kept for mating: 24; and mutation rate was set to 4%. Figure 9 shows the difference between the two GA scenarios.

Table 1 Example of System Identification Results Using Filter Mask from Literature – Highlighted Models Optimized using GA

Model Number	$n_a$	$n_b$	$n_k$	LDD	LSD	TDD	TSD	NDD	IB2	IR
m1	2	3	1	31.06	41.39	39.53	-9.685	45.55	33.79	35.38
m2	2	4	1	31.86	17.4	39.36	43.19	36.84	16.88	23.89
m3	2	5	1	23.54	35.94	30.09	2.247	39.78	36.17	38.16
m4	2	6	1	3.266	41.99	41.28	43.46	10.83	36.41	36.7
m5	2	7	1	31.58	40.55	44.65	31.28	2.593	32.26	36.34
m6	2	8	1	37.84	4.259	21.89	20.08	8.036	36.22	36.57
m7	2	9	1	31.42	0.1887	35.78	28.71	38.11	35.54	35.82
m8	3	3	1	36.59	40.04	36.17	12.33	4.478	41.09	35.81
m9	3	4	1	20.74	40.72	31.53	36.57	29.76	37.43	38.76
m10	3	5	1	39.87	11.53	39.83	30.24	39.25	35.15	37.9
⋮	⋮	⋮	⋮	⋮	⋮	⋮	⋮	⋮	⋮	⋮
m40	7	7	1	34.91	10.18	40.79	35.21	35.24	33.42	37.92
m41	7	8	1	0.1127	36.28	39.68	40.26	20.27	35.88	24.32
m42	7	9	1	36.55	-0.412	25.24	31.31	35.4	34.26	39.82

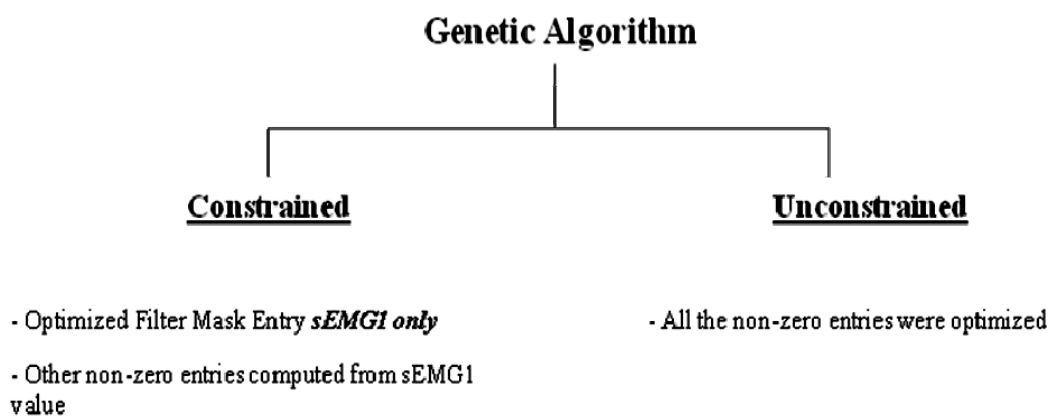


Fig. 9 Two genetic algorithm scenarios tested

Table 2 Results of constrained and unconstrained GA of highlighted models from Table 1

Longitudinal Double Differential (LDD)			
	Fit %		
	From Literature	GA Constrained	GA Unconstrained
m1	31.06	42.8291	61.3475
m6	37.84	53.3134	63.7240
m12	35.54	44.2513	51.7942
m31	39.44	47.0034	60.6489

Longitudinal Single Differential (LSD)			
	Fit %		
	From Literature	GA Constrained	GA Unconstrained
m1	41.39	48.9135	57.9136
m4	41.99	41.5731	60.2369
m8	40.04	40.5924	46.3310
m9	40.72	45.2322	45.4538

Transverse Double Differential (TDD)			
	Fit %		
	From Literature	GA Constrained	GA Unconstrained
m1	39.53	41.5297	59.8055
m5	44.65	49.4667	68.4191
m10	39.83	41.307	63.8523
m15	43.01	43.3466	56.5113

Transverse Single Differential (TSD)			
	Fit %		
	From Literature	GA Constrained	GA Unconstrained
m2	43.19	44.0017	65.9038
m4	43.46	43.0529	58.2755
m11	44.24	39.7867	44.8431
m31	29.1	43.5787	47.6688

Normal Double Differential (NDD)			
	Fit %		
	From Literature	GA Constrained	GA Unconstrained
m1	45.55	53.1512	57.9496
m3	39.87	47.1084	60.7374
m7	38.11	51.8065	60.5535
m11	39.01	46.881	56.1193

Inverse Binomial 2 (IB2)			
	Fit %		
	From Literature	GA Constrained	GA Unconstrained
m1	33.79	38.6076	58.2365
m3	36.17	38.9074	58.1653
m4	36.41	38.9957	55.5179
m8	41.09	47.2971	55.0537

From the results in Table 2 we can see that the optimization of the filter mask using GA worked in almost all the cases chosen. GA without constraints performed significantly better, in most cases, than the filter masks reported in literature and also the mask which we computed using GA, which only optimized the entry ( $a_{22}$ ) i.e. the weight associated with the sEMG signal at the motor unit. This restriction on GA would

leave the filter mask symmetrical. But looking at the results of the GA, we can conclude that the filter mask need not always be symmetrical for analysis of sEMG, especially for data recorded using an array. All the filter masks, with the individual entries of the masks that were obtained after optimization along with the respective fit values are provided in Table 3.

Table 3 Optimized filter masks for constrained and unconstrained GA

Linear Spatial Filter Type	Mask in Literature	GA Optimized Spatial Filter Mask - Constrained	GA Optimized Spatial Filter Mask - Unconstrained
<b>LDD m1</b>	$\begin{bmatrix} 0 & 0 & 0 \\ -1 & 2 & -1 \\ 0 & 0 & 0 \end{bmatrix}$ Fit <b>31.06</b> %	$\begin{bmatrix} 0 & 0 & 0 \\ -6.5 & 13 & -6.5 \\ 0 & 0 & 0 \end{bmatrix}$ Fit <b>42.8912</b> %	$\begin{bmatrix} 0 & 0 & 0 \\ -64.2686 & 23.5033 & -20.8633 \\ 0 & 0 & 0 \end{bmatrix}$ Fit <b>61.3475</b> %
<b>LSD m4</b>	$\begin{bmatrix} 0 & 0 & 0 \\ -1 & 1 & 0 \\ 0 & 0 & 0 \end{bmatrix}$ Fit <b>41.99</b> %	$\begin{bmatrix} 0 & 0 & 0 \\ -2 & 2 & 0 \\ 0 & 0 & 0 \end{bmatrix}$ Fit 41.5731%	$\begin{bmatrix} 0 & 0 & 0 \\ -52.7866 & 54 & 0 \\ 0 & 0 & 0 \end{bmatrix}$ Fit <b>60.2369</b> %
<b>TDD m5</b>	$\begin{bmatrix} 0 & -1 & 0 \\ 0 & 2 & 0 \\ 0 & -1 & 0 \end{bmatrix}$ Fit <b>44.65</b> %	$\begin{bmatrix} 0 & -27 & 0 \\ 0 & 54 & 0 \\ 0 & -27 & 0 \end{bmatrix}$ Fit <b>49.4667</b> %	$\begin{bmatrix} 0 & -41.5561 & 0 \\ 0 & 54.7329 & 0 \\ 0 & -22 & 0 \end{bmatrix}$ Fit <b>68.4191</b> %
<b>TSD m2</b>	$\begin{bmatrix} 0 & -1 & 0 \\ 0 & 1 & 0 \\ 0 & 0 & 0 \end{bmatrix}$ Fit <b>43.19</b> %	$\begin{bmatrix} 0 & -28.5 & 0 \\ 0 & 57 & 0 \\ 0 & 0 & 0 \end{bmatrix}$ Fit <b>44.0017</b> %	$\begin{bmatrix} 0 & -74 & 0 \\ 0 & 89.6214 & 0 \\ 0 & 0 & 0 \end{bmatrix}$ Fit <b>65.9038</b> %
<b>NDD m3</b>	$\begin{bmatrix} 0 & -1 & 0 \\ -1 & 4 & -1 \\ 0 & -1 & 0 \end{bmatrix}$ Fit <b>39.87</b> %	$\begin{bmatrix} 0 & -6.75 & 0 \\ -6.75 & 27 & -6.75 \\ 0 & -6.75 & 0 \end{bmatrix}$ Fit <b>47.1084</b> %	$\begin{bmatrix} 0 & -11.5790 & 0 \\ -46.7773 & 36.9276 & -11.8061 \\ 0 & -70.0491 & 0 \end{bmatrix}$ Fit <b>60.7374</b> %
<b>IB2 m1</b>	$\begin{bmatrix} -1 & -2 & -1 \\ -2 & 12 & -2 \\ -1 & -2 & -1 \end{bmatrix}$ Fit <b>33.79</b> %	$\begin{bmatrix} -0.42 & -0.83 & -0.42 \\ -0.83 & 5 & -0.83 \\ -0.42 & -0.83 & -0.42 \end{bmatrix}$ Fit <b>38.6076</b> %	$\begin{bmatrix} -9.3405 & -85.0222 & -53.7102 \\ -95.4633 & 42 & -30.7811 \\ -28.6087 & -8.2511 & -10.0189 \end{bmatrix}$ Fit <b>58.2365</b> %

## V. CONCLUSION

The linear spatial filter masks as reported in the literature have poor model fit percentages and poor kurtosis improvements. Though the reason for the low *kurtosis* improvements of the linear spatial filters was not investigated here, we optimized the linear spatial filter masks using GA and compared them based on the model fit values achieved. The selected model structure for characterizing the sEMG and finger force data is a Hammerstein-Wiener model. The fit values did improve significantly in the two GA scenarios – GA with and without constraints. The GA without constraints performed better than

the GA with constrains, which brings into focus the possibility that the sEMG signal distribution over the entire grid cannot be assumed to be symmetrically distributed and that the weights associated with the sEMG signal at various locations need to be modified depending on probably the subject and also based on the experimental design. This is in contrast to the reported filter mask in the literature, which are all symmetric. Almost all the filter masks optimized resulted in a significant improvement over the masks reported in literature.



## ACKNOWLEDGEMENT

This work was supported by a grant from the Telemedicine Advanced Technology Research Center (TATRC) of the US Department of Defense. The financial

support is greatly appreciated.

## REFERENCES

- [1] Kathryn Ziegler-Graham, et al., "Estimating the Prevalence of Limb Loss in the United States - 2005 to 2050," Archives of Physical Medicine and Rehabilitation 89: 2008, pp. 422-429.
- [2] Patricia F. Adams, et al., "Current Estimates from the National Health Interview Survey, 1996," Vital and Health Statistics 10:200, 1999.
- [3] <http://enr.isu.edu/FacultyWebpages/alba/documents/PROSTHETIC-HAND-REQUIREMENTS.pdf>
- [4] Piper, H., 1912. "Elektrophysiologie Menschlicher Muskeln". Springer Verlag.
- [5] Merletti, R., Parker, A. P., 1<sup>st</sup> ed., "Electromyography Physiology, Engineering, and Non-Invasive Applications". Chap. 1, pp. xv- xviii.
- [6] Pullman, S. L., Goodin, D. S., Marquinez, A. I., Tabbal, S., Rubin, M., 2000. "Clinical utility of surface EMG". *Neurology*, 55, July, pp. 171-177.
- [7] Merletti, R., Roy, S. H., Kupa, E., Roatta, S., Granata, A., 1999. "Modeling of surface myoelectric signals - part II: model-based signal interpretation". *IEEE Trans Biomed Eng*, 46 (7), July, pp. 821-829
- [8] Meek, S. G., Fetherston, S. J., 1992. "Comparison of signal-to-noise ratio of myoelectric filters for prosthesis control". *J Rehabil Res & Dev*, 29(4), Fall, pp. 9-20.
- [9] Light, C. M., Chappell, P. H., Hudgins, B., Engelhart, K., 2002. "Intelligent multifunction myoelectric control of hand prostheses". *Journal of Medical Engineering & Technology*, 26 (4), pp. 139-146.
- [10] Light, C. M., Chappell, P. H., 2000. "Development of a lightweight and adaptable multiple-axis hand prostheses". *Medical Engineering and Physics*, 22, pp. 679-684.
- [11] Mewett, D. T., Nazeran H., Reynolds, K., J., "Removing power line noise from recorded EMG". Proceedings of the 23rd Annual IEEE/EMBS International Conference, October, 2001, pp. 1-4.
- [12] Clancy, A. E., Farry, A. K., "Whitening of the electromyogram to improve amplitude estimation". *IEEE Transactions on Biomedical Engineering*, 47(6), June 2000, pp. 709-719.
- [13] Chan, D. C. A., Englehart, B. K., "Continuous myoelectric control for powered prostheses using hidden Markov models". *IEEE Transactions on Biomedical Engineering*, 52(1), January 2005, pp. 121-124.
- [14] Chan, H. Y. F., Yang, Y., Lam, F. K., Zhang, Y., Parker, A. P., "Fuzzy EMG classification for Prosthesis control". *IEEE Transactions on Rehabilitation Engineering*, 8(3), September 2000, pp. 305-311.
- [15] Reaz, I. B. M., Hussain, S. M., Yasin, M. F., "Techniques of EMG signal analysis: detection, processing, classification and application". *Biomedical Procedures Online*, 8(1), January 2006, pp. 11-35.
- [16] [http://www.isek-online.org/standards\\_emg.html](http://www.isek-online.org/standards_emg.html)
- [17] Farina, D., Merletti, R., and Enoka, M. R., "The extraction of neural strategies from the surface EMG". *Journal of Applied Physiology*, 96, 2004, pp. 1486-1495.
- [18] Zeghib, A., Palis, F., Tsenov, G., Shoylev, N., Mladenov, V., 2005. "Fuzzy systems and neural networks methods to identify hand and finger movements using surface EMG signals", ICS'05 Proceedings of the 9th WSEAS International Conference on Systems, Vouliagmeni, Athens, Greece, July 11-13.
- [19] Hu, X., Ren, X., 2006. "Identification of Surface EMG Signals Using Wavelet Packet Entropy", Proceedings of the 6th WSEAS International Conference on Wavelet Analysis & Multirate Systems, Bucharest, Romania, October 16-18, pp. 96-99.
- [20] Zeghib, A., Palis, F., Shoylev, N., Mladenov, V., Mastorakis, N., "Sampling frequency and pass-band frequency effects on Neuromuscular Signals (EMG) Recognition", 2007. Proceedings of the 6th WSEAS International Conference on Signal Processing, Robotics and Automation, Corfu Island, Greece, February 16-19, pp. 107-114.
- [21] P. Kumar, C. Potluri, A. Sebastian, S. Chiu, A. Urfer, D. S. Naidu, and M. P. Schoen, "An Adaptive Multi Sensor Data Fusion with Hybrid Nonlinear ARX and Wiener-Hammerstein Models for Skeletal Muscle Force Estimation," The 14th World Scientific and Engineering Academy and Society (WSEAS) International Conference on Systems, Corfu Island, Greece, July 22-24, 2010.
- [22] P. Kumar, A. Sebastian, C. Potluri, A. Ilyas, M. Anugolu, A. Urfer, and M. P. Schoen, "Adaptive Finger Angle Estimation from sEMG Data with Multiple Linear and Nonlinear Model Data Fusion," The 10th World Scientific and Engineering Academy and Society (WSEAS) International Conference on Dynamical Systems and Control, Iasi, Romania, July 1-3, 2011.
- [23] <http://www.tmsi.com/?id=26>
- [24] Sebastian A., Parmod K., Anugolu M., Schoen P. M., Urfer A., Naidu S. D., "Optimization of Bayesian Filters and Hammerstein-Wiener Models for EMG-Force Signals Using Genetic Algorithm". Proceedings of the ASME 2009 Dynamic Systems and Control Conference DSCC 2009.
- [25] Sebastian A., Parmod K., Schoen P. M., Urfer A., Creelman J., Naidu S. D., "Analysis of EMG-Force relation using System Identification and Hammerstein-Wiener Models". Proceedings of the ASME 2010 Dynamic Systems and Control Conference DSCC 2010.
- [26] <http://www.spatialanalysisonline.com/output/html/Linearspatialfiltering.html>
- [27] P. Zhou, N. L. Suresh, M. Lowery, W. Z. Rymer, "Nonlinear Spatial Filtering of Multichannel Surface Electromyogram Signals During Low Force Contractions", *IEEE Transactions on Biomedical Engineering*, vol. 56, no.7, July 2009, pp. 1871-1879.
- [28] J. F. Kaiser, "On a simple algorithm to calculate the 'energy' of a signal", Proceedings of IEEE ICASSP'90, Albuquerque, New Mexico, April 1990, pp. 381-384.
- [29] Ljung, L., 2<sup>nd</sup> ed., "System Identification: theory for the user". Prentice Hall Information and System Sciences Series, Chap. 1, pp. 1-8.
- [30] Ljung, L., 2<sup>nd</sup> ed., "System Identification: theory for the user". Prentice Hall Information and System Sciences Series, Chap. 1, pp. 13.
- [31] Ljung, L., 2<sup>nd</sup> ed., "System Identification: theory for the user". Prentice Hall Information and System Sciences Series, Chap. 5, pp. 140-145.
- [32] [http://www.mathworks.com/access/helpdesk/help/toolbox/ident/index.html?access/helpdesk/help/toolbox/ident/gs/bq\\_yqlq6.html](http://www.mathworks.com/access/helpdesk/help/toolbox/ident/index.html?access/helpdesk/help/toolbox/ident/gs/bq_yqlq6.html)

**Anish Sebastian** received his B.S. degree in Instrumentation Engineering from Dr. D.Y. Patil College of Engineering, India in 2002, his M.S. degree in Measurement & Control Engineering from Idaho State University in 2009, and is currently a Ph.D. candidate in the Engineering & Applied Science Program at Idaho State University.

His research interests include development of a Smart Prosthetic Hand, development active flow control to mitigate stall and improve turbine efficiency, radiation therapy for treatment of active nodes in tumors, system identification and control systems. His current research is funded by the Department of Defense (DoD), Telemedicine and Advanced Technology Research Center (TATRC) titled "Smart Prosthetic Hand". He was awarded this research assistantship in 2007. The research being conducted at Idaho State University is on the analysis of surface electromyogram signals (sEMG) in order to establish a relation between the force generated by the fingers while grasping various objects and performing Activities of Daily Living (ADL). From 2005 to 2007 he was a graduate teaching assistant for various departments under the College of Engineering at Idaho State University. Mr Sebastian has 14 publications in all, to date, in internationally reputed conferences and journals. Mr. Sebastian has also served as a reviewer for various international conferences and journals.

**Parmod Kumar** received his B.S. degree in Marine Engineering from the Marine Engineering & Research Institute, Kolkata, India in 2002, his M.S. degree in Measurement and Control Engineering from Idaho State University

in 2009, and expecting to get his Ph.D. in Engineering and Applied Science from Idaho State University by December 2011. Mr. Kumar has worked in Merchant Navy as a Certified Marine Engineer Officer for over four and half years. From 2007 to 2009 he was a graduate teaching assistant and from 2009 to till now he is a graduate research assistant at Measurement and Control Engineering Research Center (MCERC). Mr Kumar has a wide scope of research interests and published internationally in reputed conferences and journals. Mr Kumar is reviewer for various international conferences and journals. For more details and the list of publications please see the web link <https://sites.google.com/site/parmodkumarms/Home>

**Marco P. Schoen** was born in 1965 and received his B.S. degree in Mechanical Engineering from the Swiss College of Engineering in 1989, his M.E. degree in Mechanical Engineering from Widener University in 1993, and his Ph.D. in Engineering Mechanics from Old Dominion University in 1997. From 1997 to 1998 he was a faculty member at Lake Superior State University and from 1998 to 2001 he served as a faculty to the Mechanical Engineering program at Indiana Institute of Technology. Since 2001 he has been with Idaho State University, where he currently serves as professor and chair for the Department of Mechanical Engineering and as associate director for the Measurement and Control Engineering Research Center (MCERC). His research addresses topics in controls and vibration of biomedical and aerospace systems as well as energy related problems. Schoen has been an associate editor for the Journal of Dynamic Systems, Measurement and Control, and a past chair of the Model Identification and Intelligent Systems (MIIS) Technical Committee for the American Society of Mechanical Engineers (ASME).



Contents lists available at ScienceDirect

## Expert Systems with Applications

journal homepage: [www.elsevier.com/locate/eswa](http://www.elsevier.com/locate/eswa)

## Wavelet basis functions in biomedical signal processing

J. Rafiee<sup>a,\*</sup>, M.A. Rafiee<sup>a</sup>, N. Prause<sup>b</sup>, M.P. Schoen<sup>c</sup><sup>a</sup> Department of Mechanical, Aerospace and Nuclear Engineering, Rensselaer Polytechnic Institute, Troy, NY 12180, USA<sup>b</sup> The Mind Research Network, 1101 Yale Blvd. NE, Albuquerque, NM 87106, USA<sup>c</sup> Measurement and Control Engineering Research Center, College of Engineering, Idaho State University, Pocatello, ID 83201, USA

## ARTICLE INFO

## Keywords:

Biomedical signal processing  
Prosthetics  
Myoelectric control  
Psychophysiology  
Mother wavelet  
EMG  
EEG  
VPA  
Pattern recognition  
Daubechies (db 44)

## ABSTRACT

During the last two decades, wavelet transform has become a common signal processing technique in various areas. Selection of the most similar mother wavelet function has been a challenge for the application of wavelet transform in signal processing. This paper introduces Daubechies 44 (db44) as the most similar mother wavelet function across a variety of biological signals. Three-hundred and twenty four potential mother wavelet functions were selected and investigated in the search for the most similar function. The algorithms were validated by three categories of biological signals: forearm electromyographic (EMG), electroencephalographic (EEG), and vaginal pulse amplitude (VPA). Surface and intramuscular EMG signals were collected from multiple locations on the upper forearm of subjects during ten hand motions. EEG was recorded from three monopolar Ag–AgCl electrodes (Pz, POz, and Oz) during visual stimulus presentation. VPA, a useful source for female sexuality research, were recorded during a study of alcohol and stimuli on sexual behaviors. In this research, after extensive studies on mother wavelet functions, results show that db44 has the most similarity across these classes of biosignals.

Published by Elsevier Ltd.

## 1. Introduction

Biosignal processing has been rapidly developing, increasing the understanding of complex biological processes in a wide variety of areas. Wavelet transform (Daubechies, 1991) is a powerful time-frequency approach which has been applied to multiple domains of biosignal processing, such as EMG (e.g. Englehart, Hudgins, & Parker, 2001), EEG (e.g. Kurt, Sezgin, Akin, Kirbas, & Bayram, 2009; Rosso et al., 2001; Subasi, 2005; Ting, Guo-zheng, Bang-hua, & Hong, 2008), ECG (e.g. Engin, Fedakar, Engin, & Korurek, 2007; Manikandan & Dandapat, 2008; Singh & Tiwari, 2006), VPA (e.g. Rafiee, Rafiee, & Michaelsen, 2009). A significant focus on the application of wavelet transforms (e.g. Englehart et al., 2001; Farina, Lucas, & Doncarli, 2008) has permitted rapid development in the field. However, the selection of the most appropriate mother wavelet to characterize commonalities amongst signals within a given domain is still lacking in biosignal processing. The main contributions to find the optimum basis function can be found in several papers (e.g. Brechet, Lucas, Doncarli, & Farina, 2007; Farina, do Nascimento, Lucas, & Doncarli, 2007; Flanders, 2002; Landolsi, 2006; Lucas, Gaufriau, Pascual, Doncarli, & Farina, 2008; Rafiee & Tse, 2009; Singh & Tiwari, 2006; Tse, Yang, & Tam, 2004).

The mother wavelet function is the main base of wavelet transforms that would permit identification of correlated coefficients across multiple signals. The more similar the mother wavelet function is to the wavelet coefficients across signals, the more precisely the signal of interest can be identified and isolated; hence, identification of a mother wavelet function is of paramount significance.

The Daubechies (db) wavelet functions (Daubechies, 1988) have been applied in several areas with the lower orders (db1 to db20) used most often (Rafiee & Tse, 2009). The few peer-reviewed papers about the application of higher order db refer to Antonino-Daviu, Riera-Guasp, Folch, and Palomares (2006) and Rafiee and Tse (2009) who implemented them for mechanical systems.

This paper focuses on the most similar wavelet basis function matched with complex biosignals such as surface and intramuscular EMG, EEG, and VPA signals (Rafiee, Rafiee, et al., 2009).

## 2. Measures

## 2.1. Surface and intramuscular EMG signals

EMG signals have broad applications in various areas, especially in prosthetics and myoelectric control (Asghari Oskoei & Hu, 2007). The experimental surface and intramuscular EMG signals used in this research have been provided from the Institute of Biomedical Engineering at the University of New Brunswick with a protocol approved by the university's Research Ethics Board (Hargrove, Englehart, & Hudgins, 2007). Two different data acquisition

\* Corresponding author. Address: Department of Mechanical, Aerospace and Nuclear Engineering, Jonsson Engineering Center, Rm. 2049, 110 8th Street, Troy, NY 12180-3590, USA. Tel.: +1 518 276 6351; fax: +1 518 276 6025.

E-mail addresses: [rafiee@rpi.edu](mailto:rafiee@rpi.edu), [krafiee81@gmail.com](mailto:krafiee81@gmail.com) (J. Rafiee).

systems were used to collect surface and intramuscular EMG signals (Hermens et al., 1999). For surface EMG signals, a 16-electrode linear array with interelectrode spacing of 2 cm was used. Each channel was filtered between 10 and 500 Hz and amplified with a gain of 2000. For intramuscular EMG, needles were implanted in the pronator and supinator teres, flexor digitorum sublimis, extensor digitorum communis, flexor and extensor carpi ulnaris. These were used to record information regarding grip, wrist flexion and rotation, and gross movement. These six channels of data were filtered between 10 and 3000 Hz and also amplified with a gain of 2000. These were recorded in six subjects while they performed 10 hand movements for 5 s each, followed by a 2 min resting period. All subjects denied fatigue during these exercises. The location of surface and needle electrodes is depicted in Fig. 1 in a cross section of the forearm. The motions includes forearm pronation, forearm

supination, wrist flexion, wrist extension, wrist abduction, wrist adduction, key grip, chuck grip, hand open, and a rest state.

## 2.2. EEG signals

EEG signals, one of the most complicated biomedical signals, are the variations of electrical potential in the cortex caused by the neuronal activity reflected in electrical potentials at the scalp. EEG offers high time-resolution for changes in mental and physical activity occurring in the brain and has been an investigative tool in such disparate areas as neuroprosthetics, affective psychopathology, diagnosis of nervous diseases, and cognitive models of learning. To illustrate the difference between EEG and EMG signals, their frequency contents are depicted using power spectrum density (see Figs. 2 and 3).

Neuroscan STIM software (Compumedics, Inc.) was used to collect EEG signals, present digitized emotional photographs, and collect physiological data. The EEG signals were recorded from three monopolar Ag–AgCl electrodes which were placed over three mid-line sites (Pz, POz, and Oz) for the purpose of recording visual evoked potentials (see Fig. 4). These locations were chosen to represent visual cortex and provide redundancy. All three-channel analogue EEG signals were converted to digital format through an A/D converter with a sampling rate of 300 Hz, and then amplified by 5000 using a Sensorium, Inc. EPA-6 bioamplifier. The signals were then filtered using a high-pass filter at 10 Hz (12 dB/Octave) and a low-pass filter at 30 Hz (eighth order elliptic). Impedance was maintained below 10 k $\Omega$  by thorough skin preparation, including abrasion. EEG signals recorded in this research have the applications to investigate the relationship of emotion and attention to sexual stimuli and participants' sexual desire levels (Prause, Janssen, & Hetrick, 2007). Participants were seated in a chair and viewed standardized photographs that varied systematically in their emotional content (International Affective Picture System; Center for the Study of Emotion and Attention, 1995). Each stimulus was presented for 6 s with a variable ( $M = 13$  s) inter-trial interval. For the current study, only the data recorded from one subject was used. While spectral density can vary due to individual

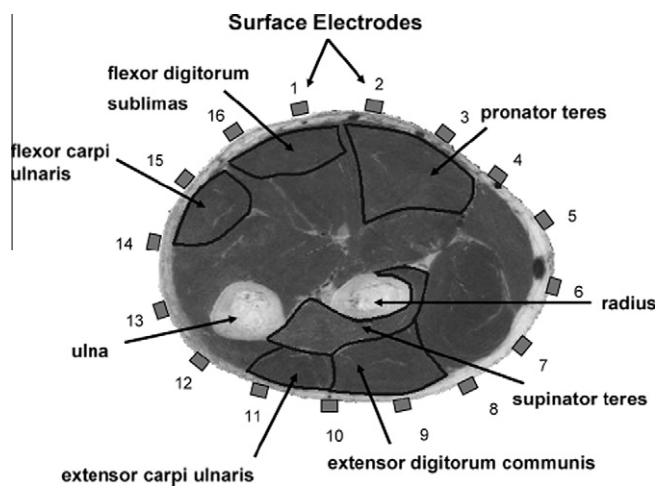


Fig. 1. A cross section of the upper forearm to illustrate the locations of 16 surface electrodes and six needle electrodes. Source: Hargrove, Englehart, & Hudgins, 2007, with permission.

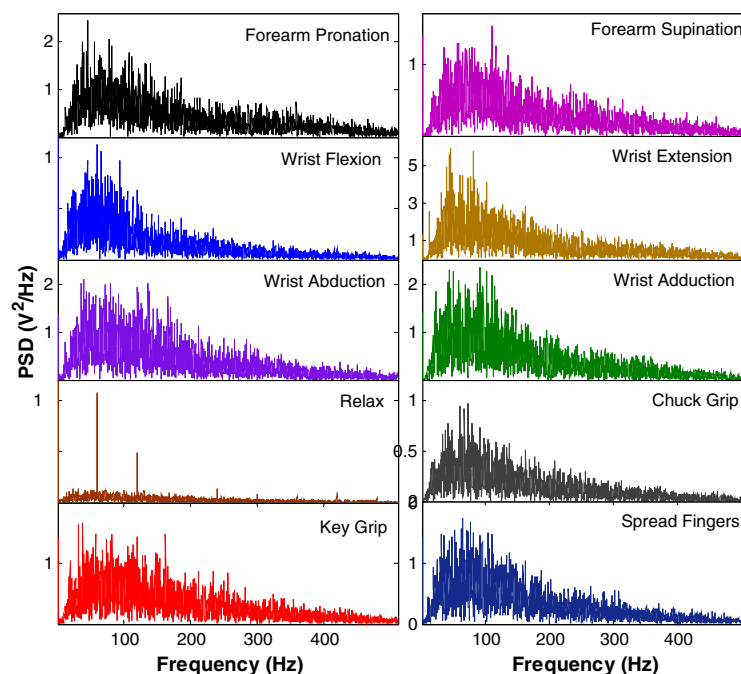


Fig. 2. Power spectrum density ( $V^2/Hz$ ) of surface EMG signals of 10 hand motions recorded from one of the 16 channels of the data acquisition system.

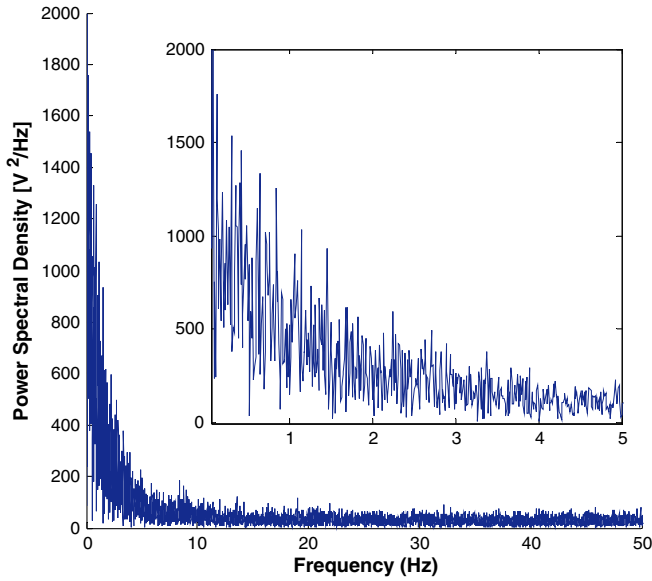


Fig. 3. Power spectrum density ( $V^2/Hz$ ) of EEG signals recorded from one of the three channels of the data acquisition system.

differences and cognitive-affective state, the underlying constant shape of EEG signals was of primary importance in this study and is not expected to vary between subjects.

### 2.3. VPA signals

VPA is one of the most common measure for female sexuality and the application of VPA studies is in a broad variety of gynecology, such as female sexual arousal (Laan, Everaerd, & Evers, 1995), sexual function (Rosen et al., 2000), sexual dysfunction (Basson et al., 2004). The vaginal photoplethysmograph monitors the changes in backscattered light in the vaginal canal to reflect sexual arousal (Prause et al., 2005). An embedded light source, usually infrared, generates a light signal that is reflected back to a receiving photocell. The received signal is interpreted as an index of vasocongestion, although it is likely to reflect several poorly-characterized physiological processes in the vagina (Prause & Janssen, 2005). The signal pulses with heartbeats, which typically are around 60 BPM in the laboratory, and slow waves concordant with breathing rate are evident in many participants, which may be influenced by vaginal canal length.

Two signals are typically extracted: The first is the DC signal, which provides an index of the total amount of blood. The second is the AC signal, abbreviated as VPA, which reflects phasic changes in the vascular walls that result from pressure changes within the vessels. Both signals have been found to be sensitive to responses to erotic stimulation (Geer, Morokoff, & Greenwood, 1974). However, the construct validity of VPA is better established (Laan et

al., 1995) and is used in this study. VPA was collected using the Biopac (Model MP100) data acquisition system. The signal is first band-pass filtered between 0.5 and 30 Hz. The sampling rate was fixed at 80 Hz.

Using PSD, the frequency content of VPA signals are depicted in Fig. 5 for one specific subject. Low-frequency VPA from 20 subjects was recorded in six conditions. Each subject was tested watching a neutral movie followed by an erotic movie with normal blood alcohol levels (BAL), 0.025 BAL, and 0.08 BAL.

### 3. Mother wavelet selection

Wavelet (Daubechies, 1991) is a capable transform with a flexible resolution in both time- and frequency-domains, which can mainly be divided into discrete and continuous forms; the former is faster because of low computational time, but the continuous type is more efficient and reliable because it maintains all information without down-sampling. Continuous wavelet transform of a signal  $s(t) \in L^2(\mathbb{R})$  can be defined as

$$\begin{aligned} CWT(t, \omega) &= \left(\frac{\omega}{\omega_0}\right)^{1/2} \int_{-\infty}^{+\infty} s(t') \psi \left(\frac{\omega}{\omega_0}\right)(t' - t) dt' \\ &= \langle s(t), \psi(t) \rangle \end{aligned} \quad (1)$$

where  $\langle \rangle$  means the inner product of the signal and  $\psi \in L^2(\mathbb{R}) \setminus \{0\}$  which is usually termed the mother wavelet function. The mother wavelet function must satisfy the admissibility condition:

$$0 < c_\psi = 2\pi \int_{-\infty}^{+\infty} |\hat{\psi}(\xi)|^2 \frac{d\xi}{|\xi|} < +\infty \quad (2)$$

and the ratio of  $\omega/\omega_0$  is the scale factor. The mother wavelet is assumed to be centered at time zero and to oscillate at frequency  $\omega_0$ . Essentially, Eq. (1) can be interpreted as a decomposition of the signal  $s(t')$  into a family of shifted and dilated wavelets  $\psi[(\omega/\omega_0)(t' - t)]$ . The wavelet basis function  $\psi[(\omega/\omega_0)(t' - t)]$  has variable width with consideration to  $\omega$  at each time  $t$ , and is wide for small  $\omega$  and narrow for large  $\omega$ . By shifting  $\omega(t')$  at fixed parameter  $\omega$ , the  $(\omega/\omega_0)$ -scale mechanisms in the time response  $s(t')$  can be extracted and localized. Alternatively, by dilating  $\omega(t')$  at a fixed  $t$ , all of the multiscale events of  $s(t')$  at  $t$  can be analyzed according to the scale parameter  $(\omega/\omega_0)$ .

In terms of frequency, low frequencies (high scales) correspond to global information of a signal (that usually spans the entire signal), whereas high frequencies (low scales) correspond to detailed information. In small scales, a temporally localized analysis is done; as the scale increases, the breadth of the wavelet function increases, resulting in analysis with less time resolution but greater frequency resolution. The wavelet functions are band-pass in nature, thus partitioning the frequency axis. In fact, a fundamental property of wavelet functions is that  $c = \Delta f/f$  where  $\Delta f$  is a measure of the bandwidth,  $f$  is the center frequency of the pass-band, and  $c$  is a constant. The wavelet functions may therefore be viewed as a bank of analysis filters with a constant relative pass-band.

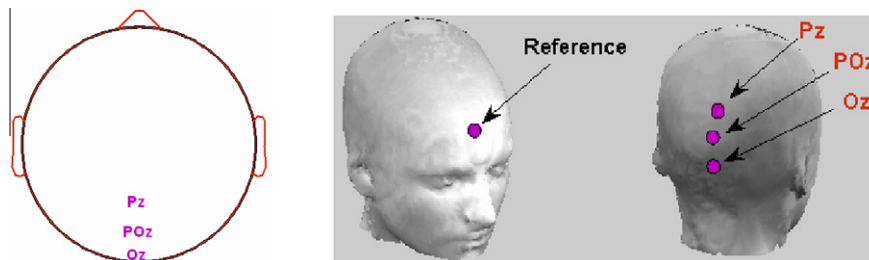


Fig. 4. Channel locations in EEG signals.

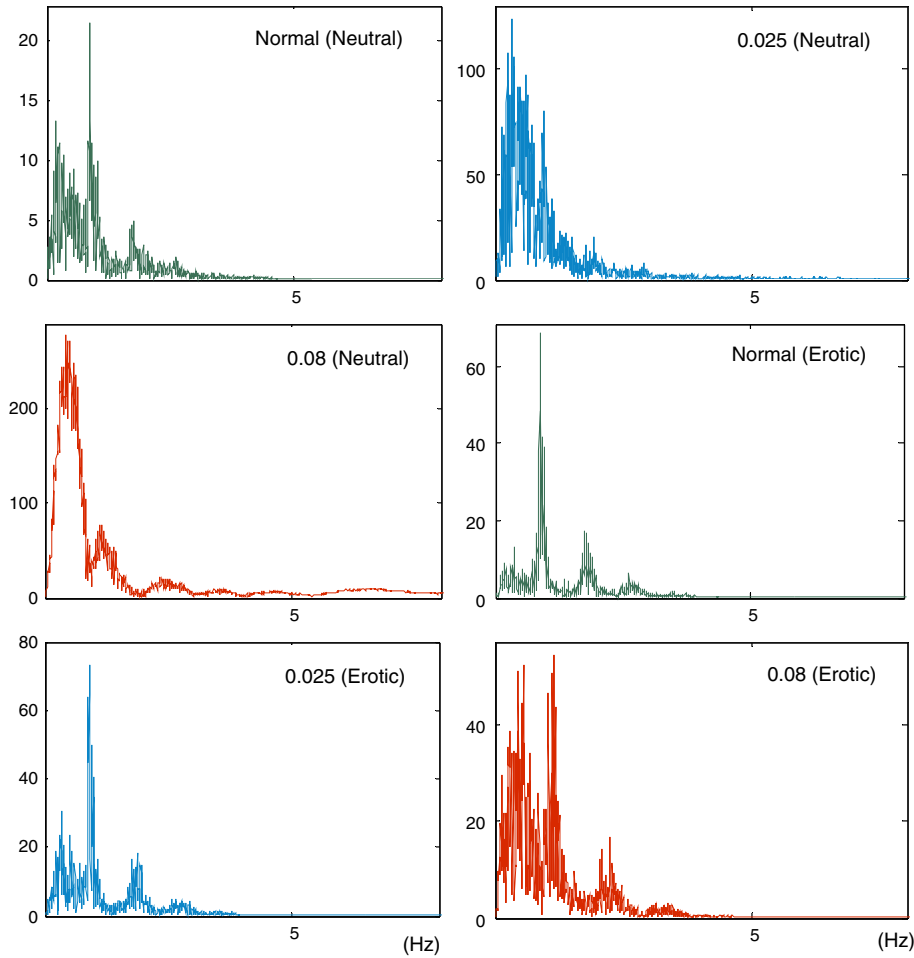


Fig. 5. Power spectrum density ( $V^2/Hz$ ) of VPA recorded in six classes (one specific subject).

The CWT results in continuous wavelet coefficients (CWC), which illustrate how well a wavelet function *correlates* with a specific signal. If the signal has a major frequency component corresponding to a particular scale, then the wavelet at this scale is similar to the signal at the location where this frequency component occurs, regardless of its amplitudes and phases. Correlation is one of the most common statistical measures, and describes the degree of linear dependence between two variables in terms of a coefficient between  $-1$  or  $+1$ . The closer the coefficient is to either  $-1$  or  $+1$ , the stronger the correlation between the two variables. The negative or positive sign of the coefficient indicates the direction of the linear dependence. The coefficient  $0$  implies that the two variables are completely linearly independent of each other.  $\rho_{x,y}$ , the correlation between two random variables  $x$  and  $y$  with expected values  $\mu_x$  and  $\mu_y$  and standard deviations  $\sigma_x$  and  $\sigma_y$  is defined as:

$$\rho_{x,y} = \frac{\text{cov}(x,y)}{\sigma_x \sigma_y} = \frac{E((x - \mu_x)(y - \mu_y))}{\sigma_x \sigma_y}, \quad (3)$$

where  $E$  stands for expected value of the variable and  $\text{cov}$  stands for covariance. As  $E(x) = \mu_x$ ,  $E(y) = \mu_y$  and  $\sigma^2(x) = E(x^2) - E^2(x)$ ,  $\sigma^2(y) = E(y^2) - E^2(y)$ ,  $\rho_{x,y}$  can be defined as:

$$\rho_{x,y} = \frac{E(xy) - E(x)E(y)}{\sqrt{E(x^2) - E^2(x)}\sqrt{E(y^2) - E^2(y)}} \quad (4)$$

In this research, the outcome of the correlation between signal and wavelet basis function (CWC) has been established as the basis for comparing selected mother wavelet functions. Consequently,

to find the most similar mother wavelet to biosignals, mother wavelets from different families including Haar, Daubechies (db), Symlet, Coiflet, Gaussian, Morlet, complex Morlet, Mexican hat, bio-orthogonal, reverse bio-orthogonal, Meyer, discrete approximation of Meyer, complex Gaussian, Shannon, and frequency B-spline families have been analyzed based on CWC and using the following algorithm:

1. *Signal segmentation*: EMG, EEG, VPA signals were segmented to the 256-points, 500-points, 960-points (12 s) windows, respectively as shown in Figs. 6 and 7 for EMG and VPA.
2. One class of recorded data is selected from one channel for one subject for each type of biosignal. The number of subjects is 20, 6, and 1 for VPA, EMG, and EEG, respectively. There are 1, 16, 6, and 3 channels for recording the signals for VPA, surface EMG, intramuscular EMG, and EEG, respectively.
3. One mother wavelet function is selected from 324 candidates. In the fourth decomposition level, CWC of the segmented signals were calculated ( $2^4$  numbers for each segmented signal).
4. Absolute value of CWC in each scale ( $2^4$  scales) was determined using 324 mother wavelets in a segmented signal for each of the 10 hand motions for EMG, as well as each of three specific channels for EEG. Next, the sum of this value in all  $2^4$  scales was determined for 20 EMG segmented signals (signals with the length of 256 points), 50 EEG segmented signals (signals with the length of 500 points), and 15 VPA segmented signals (signals with the length of 960 points). Their average was calculated for each type of signal and called the evaluation criterion (EC) for simplicity and to find the most similar mother



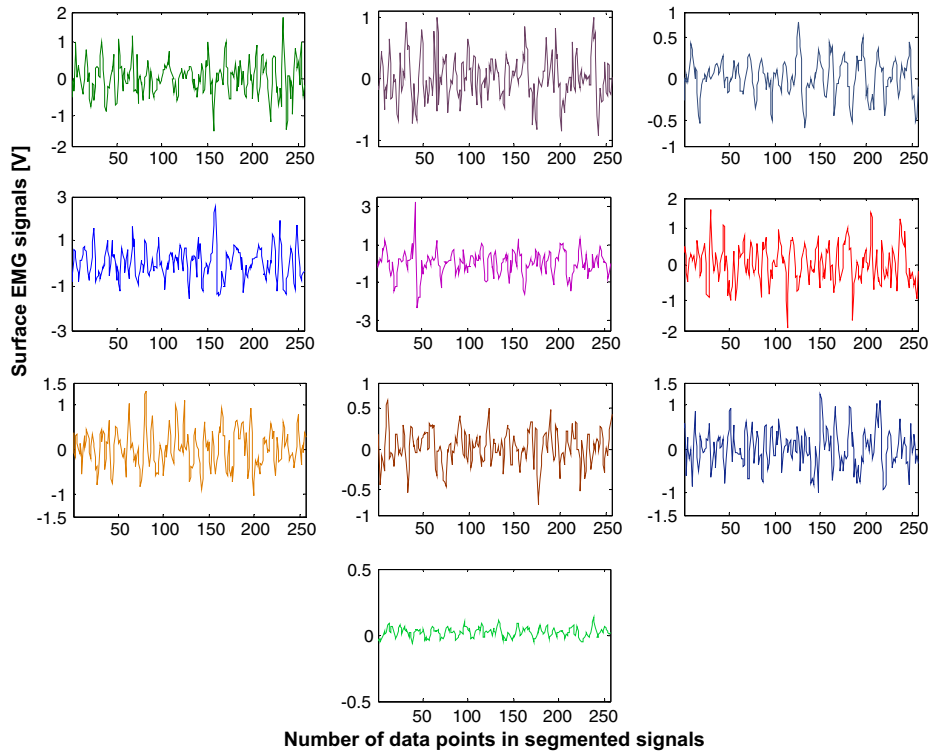


Fig. 6. Segmented surface EMG signals in a 256-points window from one subject performing 10 different hand motions.

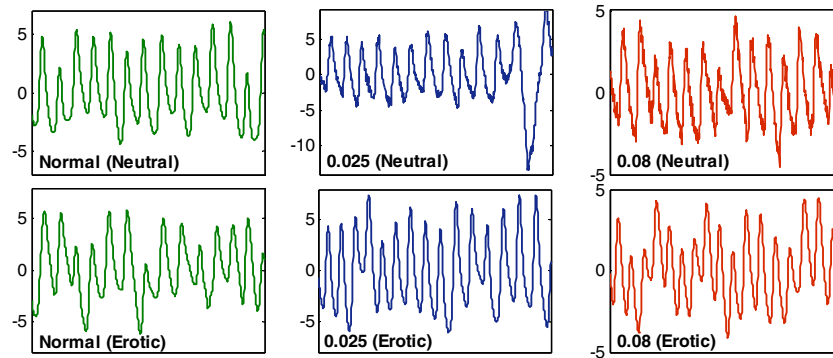


Fig. 7. One segmented VPA in a 960-points window recorded from 6 different classes (X-axis equals to 12 s).

function. Fig. 8 shows the decision-making flow chart to determine the most similar mother wavelet function towards biosignals.

5. Steps 2–4 are repeated until all gathered data is analyzed.

In this research, after running the algorithm, the results are shown that from Daubechies family, db44 is the most similar function for all case studies. Daubechies's functions are orthonormal functions. For any integer  $r$ , the orthonormal basis function (Daubechies, 1988) for  $L^2(\mathbb{R})$  will be determined from the following equation:

$$\phi_{r,j,k}(x) = 2^{j/2} \phi_r(2^j x - k), \quad j, k \in \mathbb{Z} \quad (5)$$

where the function  $\phi_r(x)$  in  $L^2(\mathbb{R})$  has the property that  $\{\phi_r(x - k) | k \in \mathbb{Z}\}$  is an orthonormal sequence in  $L^2(\mathbb{R})$ .  $j$  is the scaling index,  $k$  is the shifting index and  $r$  is the filter index.

$f_j$ , at scale  $2^{-j}$ , of a function  $f \in L^2(\mathbb{R})$  will be defined as follows:

$$f_j(x) = \sum_k \langle f, \phi_{r,j,k} \rangle \phi_{r,j,k}(x). \quad (6)$$

The details or fluctuations are determined by:

$$d_j(x) = f_{j+1}(x) - f_j(x). \quad (7)$$

To analyze these details at a certain scale, the orthonormal basis function,  $\psi_r$ , with similar characteristics to those of above-mentioned  $\phi_r(x)$  has been defined.  $\phi_r(x)$  and  $\psi_r(x)$ , called the father wavelet and the mother wavelet functions, respectively, are the wavelet prototype functions required by the wavelet analysis. Wavelets such as those defined in Eq. (5) are generated from the father or the mother wavelet by changing scale and translation in time (Liang & Que, 2009).

Daubechies' orthonormal basis has the following characteristics:

- $\omega_r$  has the compact support interval  $[0, 2r + 1]$ .
- $\omega_r$  has about  $r/5$  continuous derivatives.

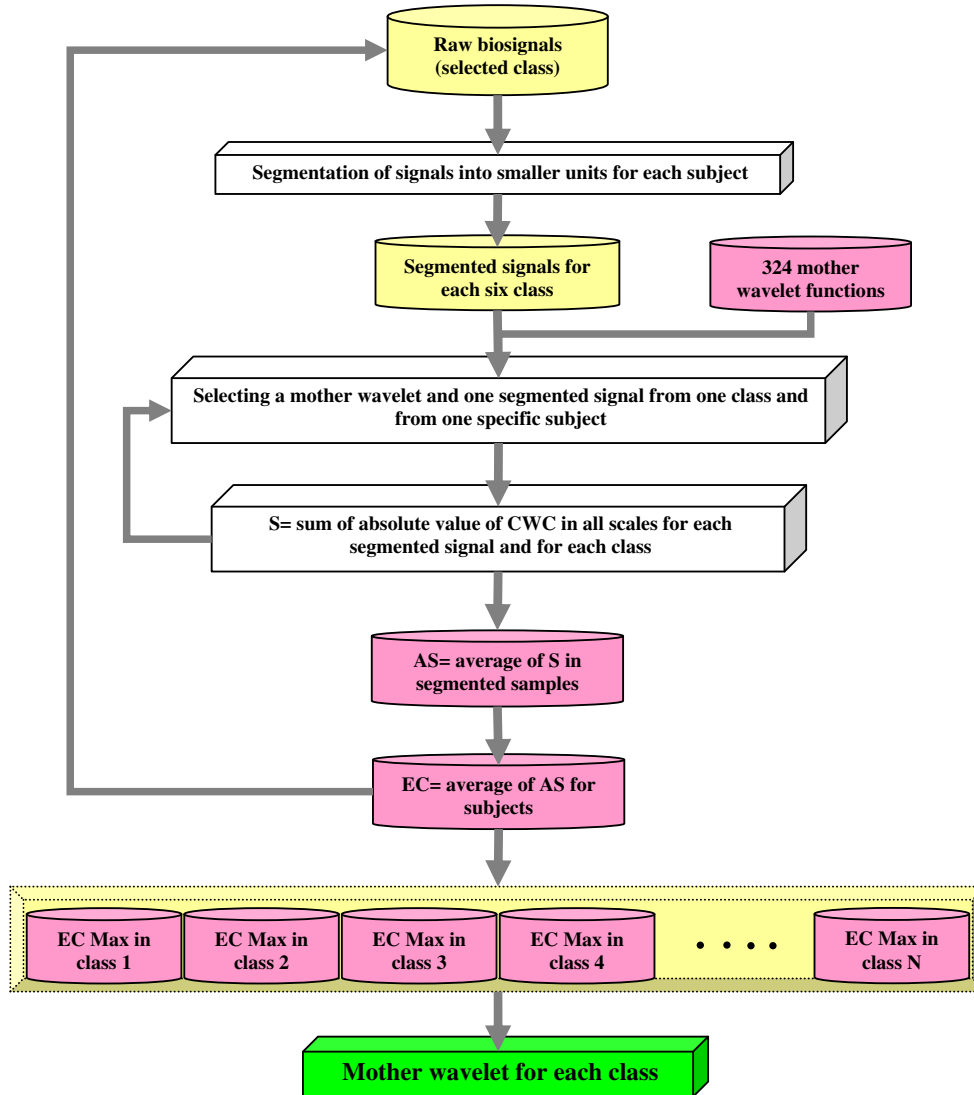


Fig. 8. Searching algorithm to find the most similar mother wavelet based on evaluation criterion (for biosignals).

$$\bullet \int_{-\infty}^{\infty} \psi_r(x) dx = \int_{-\infty}^{\infty} x^r \psi_r(x) dx = 0.$$

Daubechies' wavelets provide appropriate results in signal processing techniques due to the above-mentioned properties. A wavelet function with compact support can be implemented easily by finite length filters. Moreover, the compact support enables spatial domain localization. Since the wavelet basis functions have continuous derivatives, they decompose a continuous function more efficiently while avoiding edge artifacts. Since the mother wavelets are used to characterize details in a signal, they should have a zero integral so that the trend information is stored in the coefficients obtained by the father wavelet. A Daubechies' wavelet representation of a function is a linear combination of the wavelet basis functions. Daubechies' wavelet transforms are usually implemented numerically via quadratic mirror filters. Multiresolution analysis of the trend and fluctuation of a function is implemented by convolving it with a low-pass filter and a high-pass filter that are versions of the same wavelet.

As shown in biosignals, the signal with a sharp spike is properly analyzed by Daubechies' wavelets, because much less energy (or trend) is stored in the high-pass bands. Hence, Daubechies' wave-

lets are ideally suited for natural signals. In general, Daubechies' wavelets with long-length filters give more appropriate energy concentration than those with short-length filters. Therefore, the mentioned reason supports the use of EC to find the most similar function to biosignals. Besides, as illustrated in Fig. 9, db44 is the only Daubechies function with near-symmetric characteristic as well as having sharp spike that would be matched with natural signals.

#### 4. Results and discussion

The result shows that, among all wavelet families considered in Tables 1A–2B (Appendix A), Daubechies 44 (db 44) provides a better fit to the tested biosignals. Figs. 10–12 show the EC across mother wavelet candidates for surface EMG, EEG, and VPA signals, respectively. For example, in Fig. 10, all classes of EMG (for 10 different hand motions) have a peak whose amplitude is greater than those calculated by the other candidate mother wavelets. The peak represents the largest EC which is calculated by db44. The same pattern was achieved for other biosignals. The difference between db44 and the other 323 wavelet functions towards biosignals is



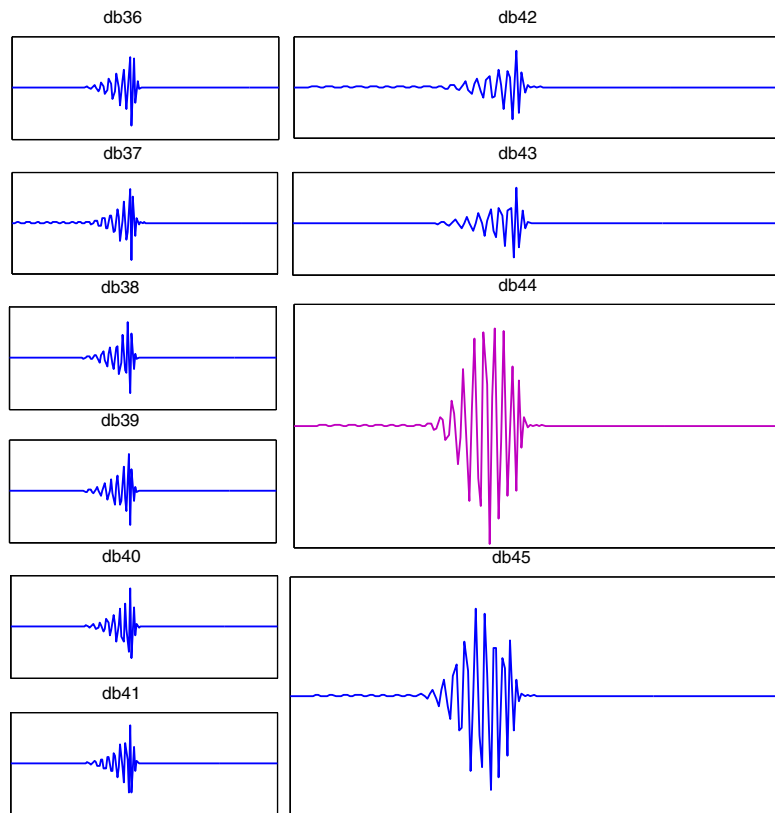


Fig. 9. High-order Daubechies functions.

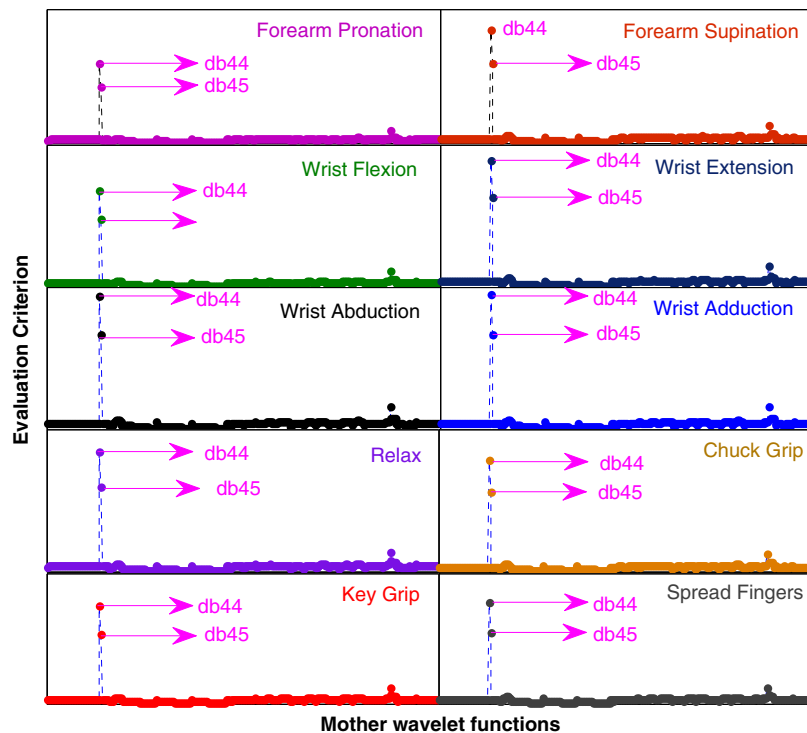


Fig. 10. Evaluation criterion (no unit) across mother wavelet candidate for surface EMG signals recorded from one channels of data acquisition system for 10 hand motions.

noticeable. This would be due to the shape of db functions, which do not change dramatically in low-order Daubechies. Therefore, low order Daubechies have similar performance to the biosignal.

However, in higher order, the difference of functions' shape between two adjacent db functions is more distinct (see Fig. 9). In Fig. 13, the trend of Daubechies family and EC was magnified for

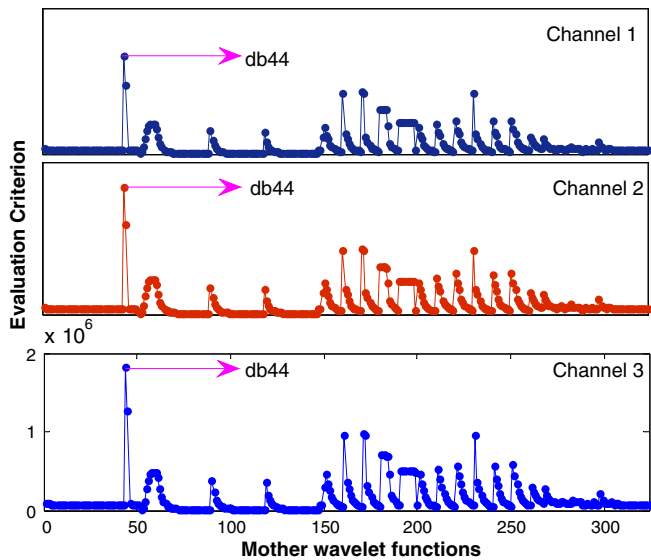


Fig. 11. Evaluation criterion (no unit) across 324 mother wavelet candidates for EEG signals across three channels (Pz, POz, Oz).

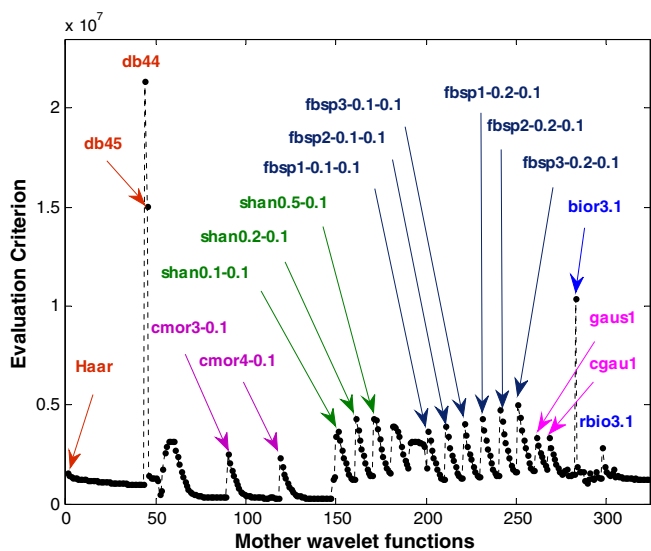


Fig. 12. Evaluation criterion (no unit) vs. mother wavelets for VPA signals recorded from one subject.

Intramuscular EMG signals. As shown, the EC increases slightly in low-order db and decreases slightly for high-order db. This demonstrates that Daubechies functions do not behave dramatically different on the biosignals, while ranging from db1 to db43. It also highlights the likely limitation of the mostly lower order Daubechies that typically are used in prior research. The trend changes dramatically for db44, which cannot be seen in Fig. 13 due to scaling restrictions.

db44 and db45 are the most similar functions as the other 322 functions have pronouncedly poorer performance (similarity). Closer examination of the evaluation criterion (see Figs. 12 and 14) for VPA and intramuscular EMG reveals some variability of fit amongst other function families. To demonstrate the difference between db44 and the other functions, the continuous wavelet coefficients of one of the segmented unit signals using db44 has been

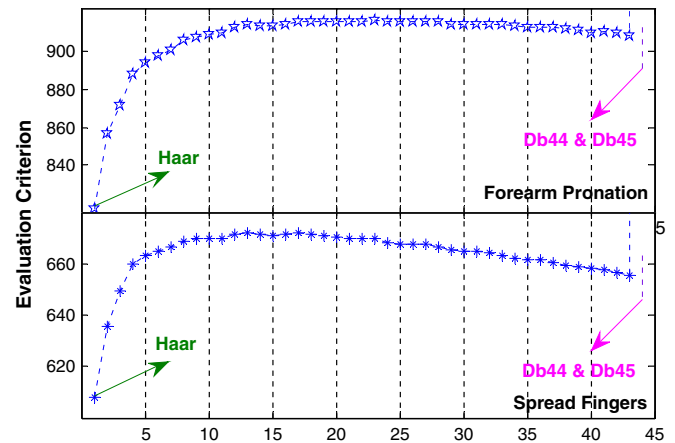


Fig. 13. Trend of Daubechies family vs. evaluation criterion in Intramuscular EMG signals for two motions.

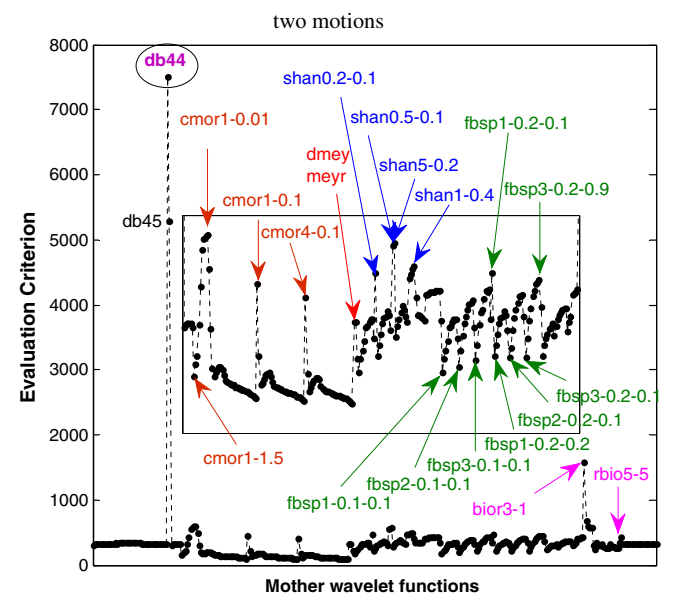
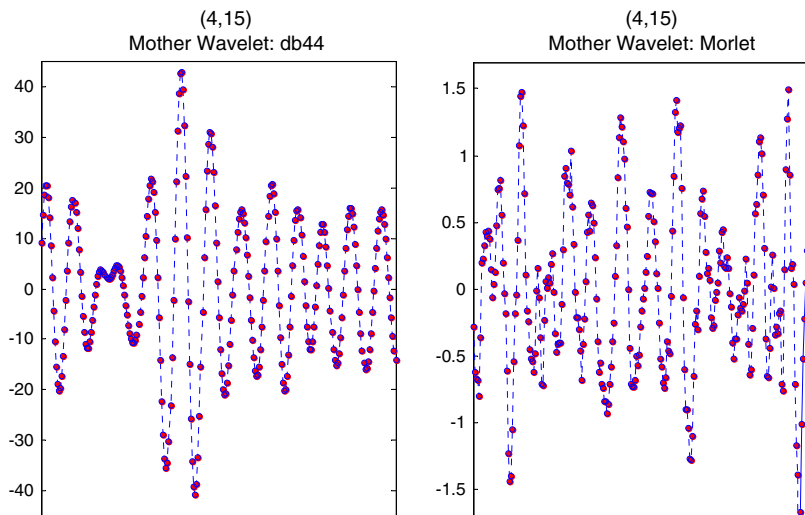


Fig. 14. Evaluation criterion (no unit) vs. mother wavelets for intramuscular EMG signals recorded from one of the six channels of data acquisition system.

compared to those calculated with the Morlet function, which has been used frequently in previous research (see Figs. 15 and 16, see Fig. 17 for decomposition scale) (e.g. Saravanan, Kumar Siddabattuni, & Ramachandran, 2008). The difference between the values of the CWC (Y-axis) calculated by db44 is much higher than those calculated by Morlet function. Moreover, periodic sinusoidal trends also are obvious using the db44. This is a very desirable feature, because it means that periodic behavior can be extracted from biological signals using db44 function. This might be useful for preprocessing biological signals.

Some other complex mother wavelets (in addition to db44 and db45) show high similarity to EEG and VPA signals (e.g. see Fig. 12). After db44 and db45, EEG signals also display some similarity to bior 3.1 and other complex mother wavelets unlike the EMG. However, these differences appear minor and appear due mostly to complex functions with different wavelet center frequency. The center frequency varies simply with the frequency contents of the signals.



**Fig. 15.** CWC of a segmented surface EMG signal calculated using Morlet and Db44 in one specific scale. (Title: scale – see Fig. 17).

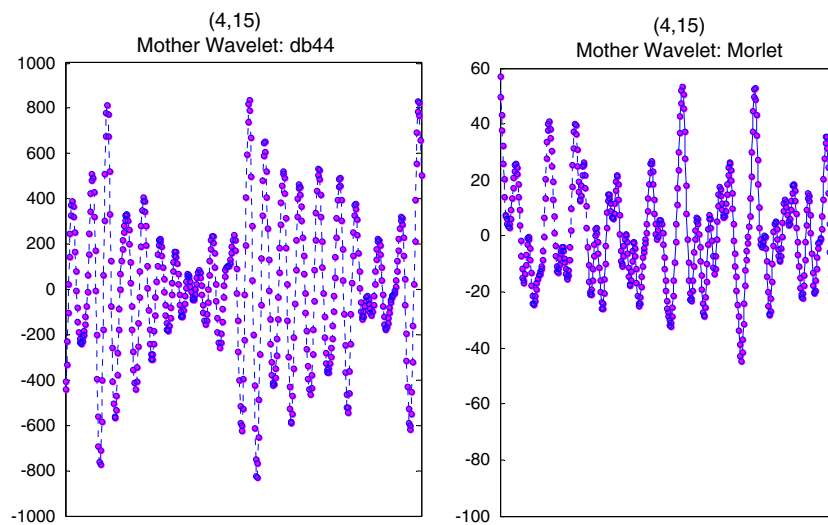


**Fig. 16.** CWC of a segmented EEG signal calculated using Morlet and Db44 in one specific scale. (Title: scale – see Fig. 17).

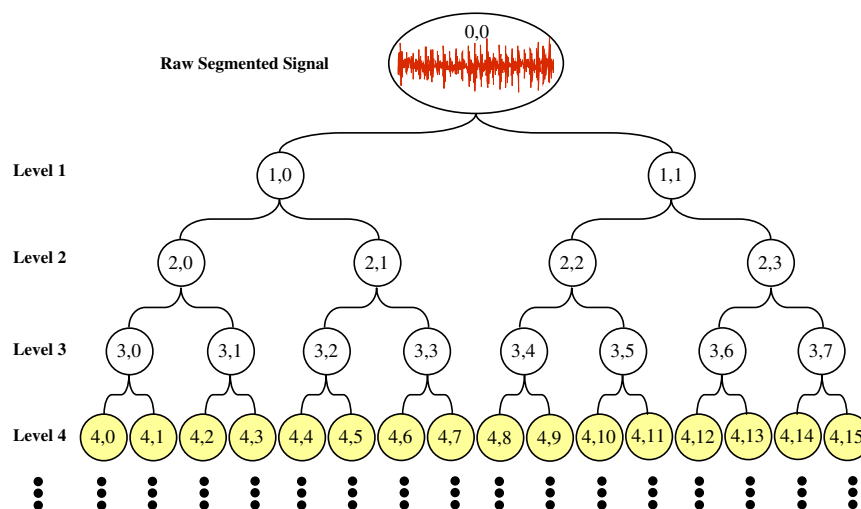


**Fig. 17.** Decomposition tree and the level of decomposition (Rafiee et al., 2010).

**Table 1A**

Studied wavelet families in this research (Rafiee et al., 2010).

No.	Family (short form)	Order
1	Haar (db1)	db 1
2–45	Daubechies(db)	db 2–db 45
46–50	Coiflet (coif)	coif 1–coif 5
51	Morlet (Morl)	morl
52–147	Complex Morlet (cmor Fb-Fc) <sup>a</sup>	Included Table 1B
148	Discrete Meyer (dmey)	dmey
149	Meyer (meyr)	meyr
150	Mexican Hat (mexh)	mexh
151–200	Shannon (Shan Fb-Fc) <sup>a</sup>	Included Table 1B
201–260	Frequency B-Spline (fbps M-Fb- Fc) <sup>a</sup>	Included Table 1B
261–267	Gaussian (gaus)	gaus 1–gaus 7
268–275	Complex Gaussian (cgau)	cgau 1–cgau 8
276–290	Biorthogonal (bior Nr.Nd) <sup>b</sup>	Included Table 1B
291–305	Reverse Biorthogonal (rbio Nr.Nd) <sup>b</sup>	Included Table 1B
306–324	Symlet (sym)	sym 2–sym 20

<sup>a</sup> Fb is a bandwidth parameter, Fc is a wavelet center frequency, and M is an integer order parameter.

<sup>b</sup> Nr and Nd are orders: r for reconstruction/d for decomposition.

## 5. Conclusions

In summary, db44 appears to be the most similar function to EMG, EEG, and VPA signals among 324 mother wavelet functions. Symmetric mother wavelets have been shown more proper results with biosignals in prior research. Daubechies are orthogonal compact support functions and are not symmetric. However, db44 possesses a near-symmetric attribute (see Fig. 9) that well-matched the biosignals. Most biosignals possess sharp spikes that could be appropriately analyzed using Daubechies' wavelets to reflect sharp, asymmetric spikes seen in these signals. These features of db44 suggest that it would be effective for many biosignal processing methods based on the resemblance of the signal and mother wavelet function.

The similarity between signal and mother wavelet function is not always proper for signal processing based on wavelet transform and it is just appropriate for those wavelet-based processing methods based on the resemblance between signals and mother functions.

**Table 1B**

Studied wavelet families in detail (Rafiee et al., 2010).

No	Wave	No	Wave	No	Wave	No	Wave	No	Wave
52	1–1.5	100	3–1.1	148	dmey	196	2–0.6	244	2–0.2–0.4
53	1–1	101	3–1.2	149	meyr	197	2–0.7	245	2–0.2–0.5
54	1–0.5	102	3–1.3	150	mexh	198	2–0.8	246	2–0.2–0.6
55	1–0.3	103	3–1.4	151	0.1–0.1	199	2–0.9	247	2–0.2–0.7
56	1–0.2	104	3–1.5	152	0.1–0.2	200	1–1	248	2–0.2–0.8
57	1–0.1	105	3–1.6	153	0.1–0.3	201	1–0.1–0.1	249	2–0.2–0.9
58	1–0.05	106	3–1.8	154	0.1–0.4	202	1–0.1–0.2	250	2–0.2–1
59	1–0.02	107	3–1.9	155	0.1–0.5	203	1–0.1–0.3	251	3–0.2–0.1
60	1–0.01	108	3–2	156	0.1–0.6	204	1–0.1–0.4	252	3–0.2–0.2
61	2–0.1	109	3–2.1	157	0.1–0.7	205	1–0.1–0.5	253	3–0.2–0.3
62	2–0.2	110	3–2.2	158	0.1–0.8	206	1–0.1–0.6	254	3–0.2–0.4
63	2–0.3	111	3–2.3	159	0.1–0.9	207	1–0.1–0.7	255	3–0.2–0.5
64	2–0.4	112	3–2.4	160	0.1–1	208	1–0.1–0.8	256	3–0.2–0.6
65	2–0.5	113	3–2.5	161	0.2–0.1	209	1–0.1–0.9	257	3–0.2–0.7
66	2–0.6	114	3–2.6	162	0.2–0.2	210	1–0.1–1	258	3–0.2–0.8
67	2–0.7	115	3–2.7	163	0.2–0.3	211	2–0.1–0.1	259	3–0.2–0.9
68	2–0.8	116	3–2.8	164	0.2–0.4	212	2–0.1–0.2	260	3–0.2–1
69	2–0.9	117	3–2.9	165	0.2–0.5	213	2–0.1–0.3	276	1.1
70	2–1	118	3–3	166	0.2–0.6	214	2–0.1–0.4	277	1.3
71	2–1.1	119	4–0.1	167	0.2–0.7	215	2–0.1–0.5	278	1.5
72	2–1.2	120	4–0.2	168	0.2–0.8	216	2–0.1–0.6	279	2.2
73	2–1.3	121	4–0.3	169	0.2–0.9	217	2–0.1–0.7	280	2.4
74	2–1.4	122	4–0.4	170	0.2–1	218	2–0.1–0.8	281	2.6
75	2–1.5	123	4–0.5	171	0.5–0.1	219	2–0.1–0.9	282	2.8
76	2–1.6	124	4–0.6	172	0.5–0.2	220	2–0.1–1	283	3.1
77	2–1.8	125	4–0.7	173	0.5–0.3	221	3–0.1–0.1	284	3.3
78	2–1.9	126	4–0.8	174	0.5–0.4	222	3–0.1–0.2	285	3.5
79	2–2	127	4–0.9	175	0.5–0.5	223	3–0.1–0.3	286	3.7
80	2–2.1	128	4–1	176	0.5–0.6	224	3–0.1–0.4	287	3.9
81	2–2.2	129	4–1.1	177	0.5–0.7	225	3–0.1–0.5	288	4.4
82	2–2.3	130	4–1.2	178	0.5–0.8	226	3–0.1–0.6	289	5.5
83	2–2.4	131	4–1.3	179	0.5–0.9	227	3–0.1–0.7	290	6.8
84	2–2.5	132	4–1.4	180	0.5–1	228	3–0.1–0.8	291	1.1
85	2–2.6	133	4–1.5	181	1–0.1	229	3–0.1–0.9	292	1.3
86	2–2.7	134	4–1.6	182	1–0.2	230	3–0.1–1	293	1.5
87	2–2.8	135	4–1.8	183	1–0.3	231	1–0.2–0.1	294	2.2
88	2–2.9	136	4–1.9	184	1–0.4	232	1–0.2–0.2	295	2.4
89	2–3	137	4–2	185	1–0.5	233	1–0.2–0.3	296	2.6
90	3–0.1	138	4–2.1	186	1–0.6	234	1–0.2–0.4	297	2.8
91	3–0.2	139	4–2.2	187	1–0.7	235	1–0.2–0.5	298	3.1
92	3–0.3	140	4–2.3	188	1–0.8	236	1–0.2–0.6	299	3.3
93	3–0.4	141	4–2.4	189	1–0.9	237	1–0.2–0.7	300	3.5
94	3–0.5	142	4–2.5	190	1–1	238	1–0.2–0.8	301	3.7
95	3–0.6	143	4–2.6	191	2–0.1	239	1–0.2–0.9	302	3.9
96	3–0.7	144	4–2.7	192	2–0.2	240	1–0.2–1	303	4.4
97	3–0.8	145	4–2.8	193	2–0.3	241	2–0.2–0.1	304	5.5
98	3–0.9	146	4–2.9	194	2–0.4	242	2–0.2–0.2	305	6.8
99	3–1	147	4–3	195	2–0.5	243	2–0.2–0.3		

**Table 2A**  
Wavelet families and their specifications.

Property	Haar	Db	Coif	Morl	Cmor	Dmey	Meyr	Mexh
Continuous wavelet transform	✓	✓	✓	✓		✓	✓	✓
Discrete wavelet transform	✓	✓	✓			✓	✓	
Complex CWT					✓			
Compact supported orthogonal	✓	✓	✓					
Compact supported biorthogonal								
Orthogonal analysis	✓	✓	✓				✓	
Biorthogonal analysis	✓	✓	✓				✓	
Symmetry				✓	✓	✓	✓	✓
Near symmetry			✓					
Asymmetry	✓	✓						
Explicit expression	✓			✓	✓			✓

**Table 2B**  
Wavelet families and their specifications.

Property	Shan	Fbsp	Gaus	Cgau	Bior	Rbio	Sym
Continuous wavelet transform			✓		✓	✓	✓
Discrete wavelet transform					✓	✓	✓
Complex CWT	✓	✓		✓			
Compact supported orthogonal					✓		✓
Compact supported biorthogonal						✓	
Orthogonal analysis					✓		✓
Biorthogonal analysis					✓	✓	✓
Symmetry	✓	✓	✓	✓	✓	✓	✓
Near symmetry							
Asymmetry							
Explicit expression	✓	✓	✓	✓	For splines	For splines	

## Acknowledgments

The authors are thankful to Professor Kevin Englehart, associate director of the Institute of Biomedical Engineering at the University of New Brunswick in Canada, for his supporting us with experimental EMG signals used in this research. The authors also acknowledge funding support from the US DARPA (Award No.: W81XWH-07-2-0078) for Idaho State University Smart Prosthetic Hand Technology – Phase I.

## Appendix A

See Tables 1A–2B.

## References

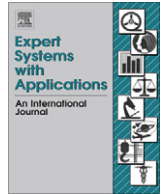
- Antonino-Daviu, J. A., Riera-Guasp, M., Folch, J. R., & Palomares, M. P. M. (2006). Validation of a new method for the diagnosis of rotor bar failures via wavelet transform in industrial induction machines. *IEEE Transactions on Industry Applications*, 42(4).
- Asghari Oskoei, M., & Hu, H. (2007). Myoelectric control systems—A survey. *Biomedical Signal Processing and Control*, 2, 275–294.
- Basson, R., Althof, S., Davis, S., Fugl-Meyer, K., Goldstein, I., Leiblum, S., et al. (2004). Summary of the recommendations on sexual dysfunctions in women. *The Journal of Sexual Medicine*, 1(1), 24–34.
- Brechet, L., Lucas, M. F., Doncarli, C., & Farina, D. (2007). Compression of biomedical signals with mother wavelet optimization and best-basis wavelet packet selection. *IEEE Transactions on Biomedical Engineering*, 54(12).
- Daubechies, I. (1988). Orthonormal bases of compactly supported wavelets. *Communications on Pure and Applied Mathematics*, 41, 909–996.
- Daubechies, I. (1991). Ten lectures on wavelets. CBMS-NSF series in applied mathematics (SIAM).
- Engin, M., Fedakar, M., Engin, E. Z., & Korürek, M. (2007). Feature measurements of ECG beats based on statistical classifiers. *Measurement: Journal of the International Measurement Confederation*, 40(9–10), 904–912.
- Englehart, K., Hudgins, B., & Parker, P. A. (2001). A wavelet-based continuous classification scheme for multifunction myoelectric control. *IEEE Transactions on Biomedical Engineering*, 48(3), 302–311.
- Farina, D., do Nascimento, O. F., Lucas, M. F., & Doncarli, C. (2007). Optimization of wavelets for classification of movement-related cortical potentials generated by variation of force-related parameters. *Journal of Neuroscience Methods*(162), 357–363.
- Farina, D., Lucas, M. F., & Doncarli, C. (2008). Optimized wavelets for blind separation of non-stationary surface myoelectric signals. *IEEE Transactions on Biomedical Engineering*, 55(1).
- Flanders, M. (2002). Choosing a wavelet for single-trial EMG. *Journal of Neuroscience Methods*(116), 165–177.
- Geer, J. H., Morokoff, P., & Greenwood, P. (1974). Sexualarousal in women: The development of a measurement device for vaginal blood volume. *Archives of Sexual Behavior*, 3, 559–564.
- Hargrove, L. J., Englehart, K., & Hudgins, B. (2007). A comparison of surface and intramuscular myoelectric signal classification. *IEEE Transactions on Biomedical Engineering*, 54(5).
- Hermens, H., Freriks, B., Merletti, R., Stegeman, D., Blok, J., Rau, G., et al. (1999). *European recommendations for surface electromyography*. RRD Publisher.
- Kurt, M. B., Sezgin, N., Akin, M., Kirbas, G., & Bayram, M. (2009). The ANN-based computing of drowsy level. *Expert Systems with Applications*, 36(2 Part 1), 2534–2542.
- Laan, E., Everaerd, W., & Evers, A. (1995). Assessment of female sexual arousal: Response specificity and construct validity. *Psychophysiology*, 32, 476–485.
- Landolsi, T. (2006). Accuracy of the split-step wavelet method using various wavelet families in simulating optical pulse propagation. *Journal of the Franklin Institute*(343), 458–467.
- Liang, W., & Que, P.-W. (2009). Optimal scale wavelet transform for the identification of weak ultrasonic signals. *Measurement: Journal of the International Measurement Confederation*, 42(1), 164–169.
- Lucas, M. F., Gaufriau, A., Pascual, S., Doncarli, C., & Farina, D. (2008). Multi-channel surface EMG classification using support vector machines and signal-based wavelet optimization. *Biomedical Signal Processing and Control*(3), 169–174.
- Manikandan, M. S., & Dandapat, S. (2008). Wavelet threshold based TDL and TDR algorithms for real-time ECG signal compression. *Biomedical Signal Processing and Control*, 3(2008), 44–66.
- Prause, N., & Janssen, E. (2005). Blood flow: vaginal photoplethysmography. In I. Goldstein, C. M. Meston, S. Davis, & A. Traish (Eds.), *Textbook of female sexual dysfunction*. London: Taylor & Francis Medical Books.
- Prause, N., Janssen, E., & Hetrick, W. (2007). Attention and emotional responses to sexual stimuli and their relationship to sexual desire. *Archives of Sexual Behavior*, 37(6), 934–949.
- Rafiee, J., Rafiee, M. A., Yavari, F., & Schoen, M. P. (2010). Feature extraction of forearm EMG signals for prosthetics. *Expert System with Applications*. doi:10.1016/j.eswa.2010.09.068.
- Rafiee, J., Rafiee, M. A., & Michaelsen, D. (2009). Female sexual responses using signal processing techniques. *Journal of Sexual Medicine*, 6(11).
- Rafiee, J., & Tse, P. W. (2009). Use of autocorrelation in wavelet coefficients for fault diagnosis. *Mechanical Systems and Signal Processing*, 23, 1554–1572.
- Rosen, R., Brown, C., Heiman, J., Leiblum, S., Meston, C., Shabsigh, R., et al. (2000). The female sexual function index (FSFI): A multidimensional self-report instrument for the assessment of female sexual function. *Journal of Sex and Marital Therapy*, 26(2), 191–208.

- Rosso, O. A., Blanco, S., Yordanova, J., Kolev, V., Figliola, A., Schürmann, M., et al. (2001). Wavelet entropy: A new tool for analysis of short duration brain electrical signals. *Journal of Neuroscience Methods*, 105(1), 65–75.
- Saravanan, N., Kumar Siddabattuni, V. N. S., & Ramachandran, K. I. (2008). A comparative study on classification of features by SVM and PSVM extracted using Morlet wavelet for fault diagnosis of spur bevel gearbox. *Expert Systems with Applications*, 35(3), 1351–1366.
- Singh, B. N., & Tiwari, A. K. (2006). Optimal selection of wavelet basis function applied to ECG signal denoising. *Digital Signal Processing*(16), 275–287.
- Subasi, A. (2005). Automatic recognition of alertness level from EEG by using neural network and wavelet coefficients. *Expert Systems with Applications*, 28(4), 701–711.
- Ting, W., Guo-Zheng, Y., Bang-Hua, Y., & Hong, S. (2008). EEG feature extraction based on wavelet packet decomposition for brain computer interface. *Measurement: Journal of the International Measurement Confederation*, 41(6), 618–625.
- Tse, P. W., Yang, W. X., & Tam, H. Y. (2004). Machine fault diagnosis through an effective exact wavelet analysis. *Journal of Sound and Vibration*(277), 1005–1024.



Contents lists available at ScienceDirect

## Expert Systems with Applications

journal homepage: [www.elsevier.com/locate/eswa](http://www.elsevier.com/locate/eswa)

## Feature extraction of forearm EMG signals for prosthetics

J. Rafiee<sup>a,\*</sup>, M.A. Rafiee<sup>a</sup>, F. Yavari<sup>a</sup>, M.P. Schoen<sup>b</sup><sup>a</sup> Department of Mechanical, Aerospace and Nuclear Engineering, JEC, 110 8th Street, Rensselaer Polytechnic Institute, NY 12180-3590, USA<sup>b</sup> Measurement and Control Engineering Research Center, College of Engineering, Idaho State University, Pocatello, ID, USA

## ARTICLE INFO

## Keywords:

Prosthetics  
 Robotic hand  
 EMG  
 Signal classification  
 Feature extraction  
 Signal processing  
 Mother wavelet

## ABSTRACT

This paper presents a new technique for feature extraction of forearm electromyographic (EMG) signals using a proposed mother wavelet matrix (MWM). A MWM including 45 potential mother wavelets is suggested to help the classification of surface and intramuscular EMG signals recorded from multiple locations on the upper forearm for ten hand motions. Also, a surface electrode matrix (SEM) and a needle electrode matrix (NEM) are suggested to select the proper sensors for each pair of motions. For this purpose, EMG signals were recorded from sixteen locations on the forearms of six subjects in ten hand motion classes. The main goal in classification is to define a proper feature vector able to generate acceptable differences among the classes. The MWM includes the mother wavelets which make the highest difference between two particular classes.

Six statistical feature vectors were compared using the continuous form of wavelet packet transform. The mother wavelet functions are selected with the aim of optimum classification between two classes using one of the feature vectors. The locations where the satisfactory signals are captured are selected from several mounted electrodes. Finally, three ten-by-ten symmetric MWM, SEM, and NEM represent the proper mother wavelet function and the surface and intramuscular selection for recording the ten hand motions.

Published by Elsevier Ltd.

## 1. Introduction

Classification and identification of biosignals (e.g. electromyographic (EMG) (e.g. Farina, Merletti, & Enoka, 2004; Merletti & Lo Conte, 1997; Rasheed, Stashuk, & Kamel, 2008) is still a challenge in several areas. EMG signals are complex due to the non-stationary characteristics and subject dependency of the signals (Aschero & Gizdulich, 2009). EMG signals are generally divided into two main groups: surface and needle EMG signals. Surface EMG signals have attracted remarkable attention in the design and manufacturing of artificial limbs (e.g. Fukuda, Tsuji, Kaneko, & Otsuka, 2003; Silvestro Micera, Sabatini, Dario, & Rossi, 1999). EMG classification is a complicated task since several parameters may effect the EMG signals, e.g. motor unit action potential (MUAP) (e.g. Kallenberg, Preece, Nester, & Hermens, 2009), muscle fatigue (e.g. Vukova, Vydevska-Chichova, & Radicheva, 2008), and force (Clancy, Bertolina, Merletti, & Farina, 2008). Two difficulties in EMG signal classification for prosthetic applications are the selection of electrode locations on the forearm and the extraction of a feature vector able to classify several motions, since the EMG signals are subject dependent. This research addresses these challenges in forearm EMG signals, which is applicable to the manufacturing of

prosthetic hands. However, this research would not be able to address the other significant parameters, such as force, fatigue, and so forth for this application (e.g. Disselhorst-Klug, Schmitz-Rode, & Rau, 2009; Koike & Kawato, 1995; Liu, Herzog, & Savelberg, 1999).

To name a few examples of prior research, Park & Lee (1998) presented a fuzzy-based decision-making system to classify six motions of the six subjects, including elbow flexion and extension, wrist pronation and supination, and in and out humeral rotation. Englehart, Hudgins, Parker, & Stevenson (1999) compared frequency domain and time–frequency methods to preprocess EMG signals and introduced wavelet packet transform with satisfactory results. Englehart, Hudgins, & Parker (2001) applied the combination of wavelet packet and principal component analysis to extract suitable features from myoelectric signals to classify six classes of hand motions. Englehart & Hudgins (2003) also developed a wavelet-based system to control myoelectric signals of four classes of hand motions with high accuracy, low response time, and a user interface control system in 2003. Lowery, Stoykov, Taflave, & Kuiken (2002) presented a finite element method (FEM) model to investigate the effect of skin, muscle, fat, and bone tissue on simulated surface electromyographic (EMG) signals and demonstrated that all aforementioned materials have an effect on EMG signals. Gazzoni, Farina, & Merletti (2004) proposed an ANN-based automatic detection and identification system to pinpoint motor unit action potentials using wavelet transform and artificial neural

\* Corresponding author. Tel.: +1 518 276 6351; fax: +1 518 276 6025.

E-mail addresses: [rafiee@rpi.edu](mailto:rafiee@rpi.edu), [krafiee81@gmail.com](mailto:krafiee81@gmail.com) (J. Rafiee).



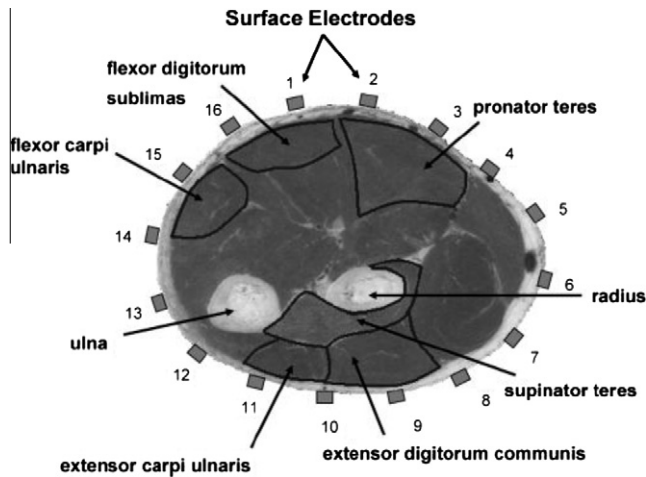


Fig. 1. A cross section of the upper forearm to illustrate the locations of 16 surface electrodes and six needle electrodes (Hargrove et al., 2007, with permission).

network in specific case studies. Sebelius et al. (2005) introduced an ANN-based intelligent system to classify seven hand movements for limited subjects.

In this research, a statistical-based feature extraction system is presented for nine hand motions plus a rest state, including key grip and chuck grip, two motions known for their difficulty in classification.

## 2. Surface and intramuscular EMG signals

In this research, both measures of forearm EMG signals have been collected and processed, although the major goal is surface EMG signal analysis, which is applicable to prosthetics. The experimental surface and intramuscular EMG signals used in this research have been provided by the Institute of Biomedical Engineering at the University of New Brunswick with a protocol approved by the University's Research Ethics Board (Hargrove,

Englehart, & Hudgins, 2007). Two different data acquisition systems were used to collect surface and intramuscular EMG signals (Hermens et al., 1999). For surface EMG signals, a 16-electrode linear array with interelectrode spacing of 2 cm was used (see Fig. 1). Each channel was filtered between 10 and 500 Hz and amplified with a gain of two thousand. Frequency information of surface EMG is shown in Fig. 2 for one subject using power spectrum density (PSD). For intramuscular EMG, needles were implanted in the pronator and supinator teres, flexor digitorum sublimas, extensor digitorum communis, and flexor and extensor carpi ulnaris. These measures were used to record time-domain signals regarding grip, wrist flexion and rotation, and gross movement. These six channels of data were also filtered and amplified (see Fig. 1). These were recorded in six subjects while they performed the ten hand movements for 5 s each, with a 2 min resting period after each exercise. The tests were repeated for each subject, resulting in 10 s of EMG signals per person for each motion. The subjects denied feeling fatigued during these exercises. The studied hand motions includes forearm pronation (FP), forearm supination (FS), wrist flexion (WF), wrist extension (WE), wrist abduction (WAB), wrist adduction (WAD), key grip (KG), chuck grip (CG), spread fingers (SF), and a rest state (RS).

## 3. Wavelet transform

Wavelet transform is being used in broad areas of biosignal processing (e.g. Beck et al., 2005; Cvetkovic, Ubeyli, & Cosic, 2008; Hostens, Seghers, Spaepen, & Ramon, 2004; Kurt, Sezgin, Akin, Kirbas, & Bayram, 2009; Rafiee, Rafiee, Prause, & Schoen, 2009; Subasi, 2005; Tscharnner, 2008; von Tscharnner, 2000; Rafiee, Rafiee, & Michaelsen, 2009). Wavelet transform (Daubechies, 1991) is generally divided into either a discrete and or continuous form (Unser & Aldroubi, 1996). The continuous wavelet transform (CWT) of a signal  $s(t)$  is defined as the integral of the product between the signal  $s(t)$  and the daughter wavelets, which are the time translation and scale expansion/compression versions of a mother wavelet function  $\psi(t)$ . Equivalent to a scalar production, this calculation generates continuous wavelet coefficients CWC ( $a, b$ ), which

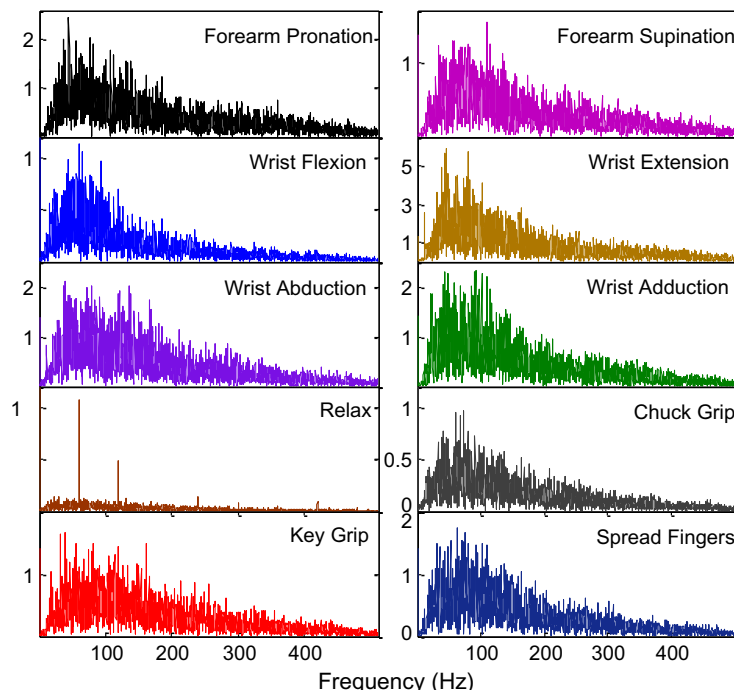


Fig. 2. Power spectrum density (PSD) of surface EMG signals of ten hand motions recorded from one of the 16 channels of the data acquisition system.



determine the similarity between the signal and the daughter wavelets located at position  $b$  (time shifting factor) and positive scale  $a$ :

$$CWC(a, b) = \int_{-\infty}^{+\infty} s(t) \frac{1}{\sqrt{a}} \psi^* \left( \frac{t-b}{a} \right) dt, \quad (1)$$

where  $*$  stands for complex conjugation and  $\psi \in L^2(R) \setminus \{0\}$ . In the frequency domain, Eq. (1) is expressed as:

$$F\{CWC(a, b)\} = \sqrt{a} \Psi^*(a\omega) S(\omega), \quad (2)$$

where  $F\{CWC(a, b)\}$ ,  $\Psi^*(\omega)$ , and  $S(\omega)$  stand for the Fourier transforms of the continuous wavelet coefficients  $CWC(a, b)$ , the signal  $s(t)$ , and the mother wavelet function  $\psi(t)$ , respectively. Eq. (2) shows that a mother wavelet function is a band-pass filter in the frequency domain, and the use of CWC identifies the local features of the signal. According to the theory of Fourier transform, the center frequency of the mother wavelet  $\Psi(a\omega)$  is defined as  $F_0/a$ , given that the center frequency of the  $\Psi(\omega)$  is  $F_0$ . Consequently, extraction of frequency contents from the signal is possible in different scales. In the windowed Fourier transform, the frequency resolution is constant and depends on the width of window. However, wavelet transform offers a rich analysis for a wide variety of window widths as the function of  $a$ . Use of a wide variety of mother wavelet functions, which must satisfy the admissibility condition  $C_\psi$ , is another advantage of wavelet analysis:

$$C_\psi = \int_{-\infty}^{+\infty} \frac{|\Psi(\omega)|^2}{\omega} d\omega < \infty. \quad (3)$$

$C_\psi$  is satisfied if the mean value of the mother wavelet function  $\psi(t)$  is equal to zero and  $\psi(t)$  decays to zero rapidly when  $t \rightarrow \pm\infty$ . If the mother wavelet satisfies the above condition as well as orthogonality, the signal can be reconstructed from wavelet coefficients.

Unlike DWT, CWT operates at any scale and is continuous in terms of shifting. In the calculation of CWC, the mother wavelet is shifted smoothly throughout the analyzed signal/function and gives rich time–frequency information. The main drawback of CWT is that the computation is time-consuming. For signals with low signal to noise ratio, CWT could work better than DWT because DWT down-sampling of the signals can lead to the loss of significant information. Wavelet decomposition of the signals is also divided into two main branches: pyramid and packet decompositions. In both methods, signals are divided into approximation (low frequencies) and detail (high frequencies) in the first level. In the pyramid decomposition, after the first level, only approximations are permitted to be decomposed through higher levels. However, in the packet decomposition both approximation and detail are decomposed into further levels. Therefore, packet decomposition offers rich contents of signals. For EMG signals, the significant frequency contents are achieved in high scales. Continuous wavelet transform, which means continuous shifting

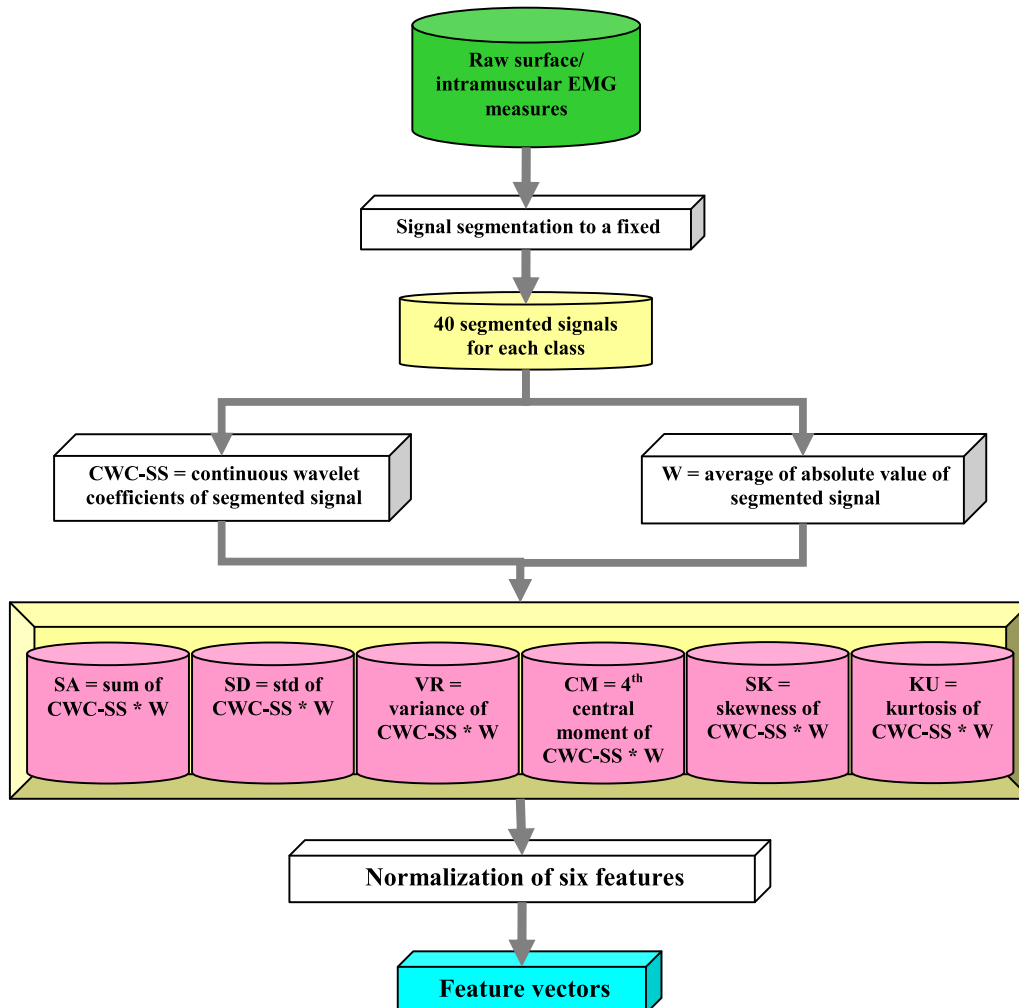


Fig. 3. Feature extraction algorithm.

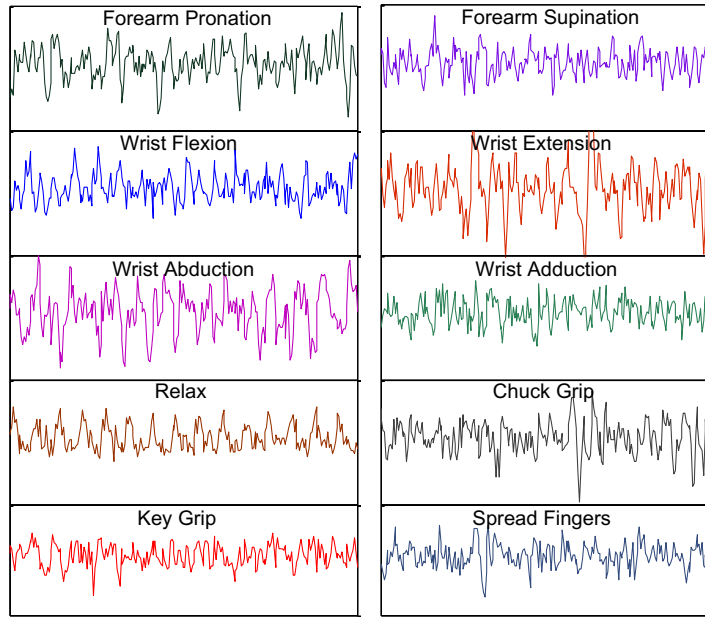


Fig. 4. Segmented surface EMG in a 256-points window from one subject performing 10 hand motions.

through time, is used with packet decomposition in this research. Therefore, CWT converts a one-dimensional signal  $s(t)$  into a matrix of CWC ( $a, b$ ) as follows:

$$\text{CWC}(a, b) = \frac{T_s}{\sqrt{|a|}} \sum_{n=0}^{N-1} \psi^* \left[ \frac{(n-i)T_s}{a} \right] s(nT_s), \quad (4)$$

where  $i = 0, 1, 2, \dots, N$ ,  $T_s$  and  $N$  stand for sampling time and the number of samples, respectively.

In classification, feature vector is defined as a compressed, meaningful vector/matrix possessing the significant information of different classes. In this research, CWC is used for the calculation of feature vectors for EMG signals. The CWC of the signal, itself, is not appropriate as a feature vector because it is computationally expensive. Hence, further processing is needed in order to define a precise and compressed feature vector, which is explained in the next section.

#### 4. Mother wavelet matrix and sensor selection

Selection of the mother wavelet function, a challenge in wavelet transform, was studied in this research by introducing MWM. Prior contributions on mother wavelet functions can be found in literature (e.g. Brechet, Lucas, Doncarli, & Farina, 2007; Farina, do Nascimento, Lucas, & Doncarli, 2007, 2008; Lucas, Gaufriaux, Pascual, Doncarli, & Farina, 2008; Rafiee & Tse, 2009).

Two points regarding the application of mother functions are discussed here. The first concern is the selection of proper mother wavelet function since the application of mother wavelets is problem-dependent. Applicable mother wavelet functions in EMG signal processing could vary depending on the parameters of the problem at hand. If the technique is based on the similarity of the signal to the mother function, then the most important factor is the amplitude of the wavelet coefficient across the signals. The mother functions similar to the signal are not suitable for all wavelet-based approaches. A clear example is the wide application of

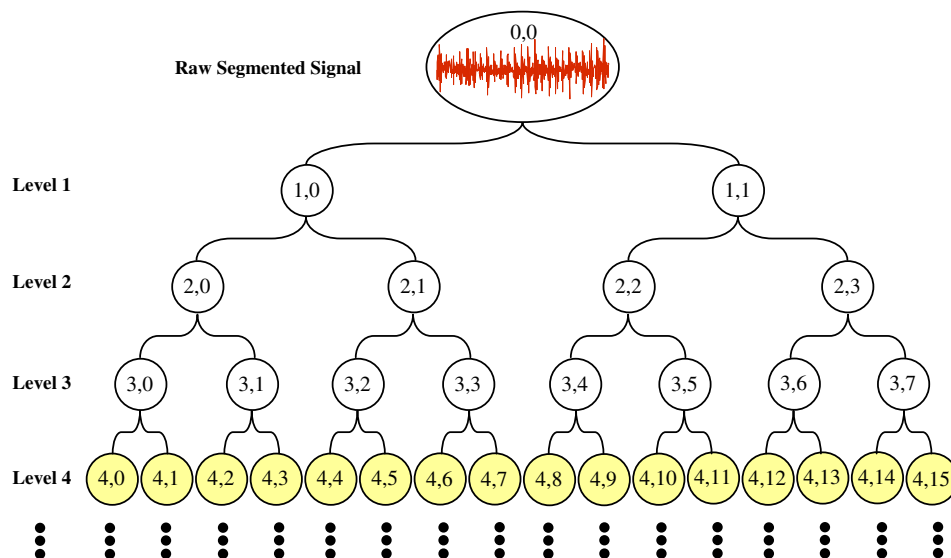


Fig. 5. Decomposition tree and the level of decomposition.

the Haar function, which is dissimilar to the signals but has been introduced as a relatively efficient function in several studies (Subramani, Sahu, & Verma, 2006). In wavelet-based classification systems the mother wavelet functions are related to the problem parameters rather than the shape of signals, unless the method was established based on signal similarity. Another issue in EMG signal classification is the optimal sensor selection. Applicable sensor selection depends on the problem as well. For example, optimal selection of sensors for prosthetic hands to classify six motions is different from those for eight motions. To reduce the computational time for real-time control of a prosthetic hand, the optimal electrodes to be chosen are presented for the ten motions classification by introducing surface electrode matrix (SEM) and needle electrode matrix (NEM) in this research.

First, the feature vector is defined based on the following steps (see flowchart in Fig. 3):

1. Signal segmentation: in this research, surface and intramuscular EMG signals were separately classified for ten hand motions, although intramuscular EMG signals may not be applicable to prosthetics. However, comparisons between surface EMG classification and intramuscular EMG classification may be helpful. After recording EMG signals by means of sixteen electrodes for surface and six electrodes for intramuscular EMG, the raw signals were segmented into the 256-point windows (Hargrove et al., 2007) as shown in Fig. 4 for surface EMG signals. For simplicity, a signal with a length of 256 points is called the segmented signal. Therefore, a matrix of segmented signals ( $16 \times 256$  matrix for surface and a  $6 \times 256$  matrix for intramuscular EMG) can be one input for the control system of prosthetic hand. As mentioned, recorded EMG signals of six subjects were studied. For all ten motions, surface and intramuscular EMG signals were recorded in two separate 5-s exercises for each of six subjects (40 segmented signals for each subject/each hand motion were obtained).
2. In the fourth decomposition level (see Fig. 5), continuous wavelet coefficients of the segmented signals (CWC-SS) were calculated ( $2^4$  scales for each segmented unit signal).
3. The average of the absolute value of the segmented signals ( $1 \times 256$  vector) were calculated for each segmented signal and titled 'weight' ( $W$ ) to construct the feature vector as follows:

$$W = \frac{1}{N} \sum_{i=1}^N |s_i(t)|, \quad (5)$$

where  $N$  is the number of datapoints in each segmented signal (256 in this research).

4. The calculation of feature vectors – six feature vectors are studied in this research:

(✓) Weighted sum of absolute value of CWC-SS (SA) is calculated as the sum of the absolute value of CWC-SS multiplied by the average of the absolute value of the segmented signals (weight).

$$SA(a_{15}, b) = W \left( \sum_{n=1}^N |CWC(a_{15}, b)| \right), \quad (6)$$

where  $a_{15}$  is the scale related to (4, 15) in the decomposition tree (see Fig. 5). Scale selection is another important issue in wavelet analysis. Decomposing the signals into higher scales leads to a greater focus on the frequency domain (Rafiee & Tse, 2009). Nevertheless, computational time in CWT is of paramount significance, and going through high scales makes the computations for the real-time control system of the prosthetic hand difficult. In this research, the fourth level of decomposition has been considered the reasonable level. Based on trial-and-error,  $a_{15}$  represented larger wavelet coefficients, and subsequently the daughter wavelet at this scale is more similar to both classes of EMG signals, which, at that scale, leads to a greater difference in the wavelet coefficient from one motion to another.

(✓) Weighted standard deviation of CWC-SS (SD) is calculated as the standard deviation of CWC-SS multiplied by the average of the absolute value of the segmented signals (weight).

$$SD(a_{15}, b) = W \left( \sqrt{\frac{1}{N-1} \sum_{n=1}^N (CWC_n(a_{15}, b) - \overline{CWC(a_{15}, b)})^2} \right), \quad (7)$$

where:

$$\overline{CWC(a_{15}, b)} = \frac{1}{N} \left( \sum_{n=1}^N CWC_n(a_{15}, b) \right). \quad (8)$$

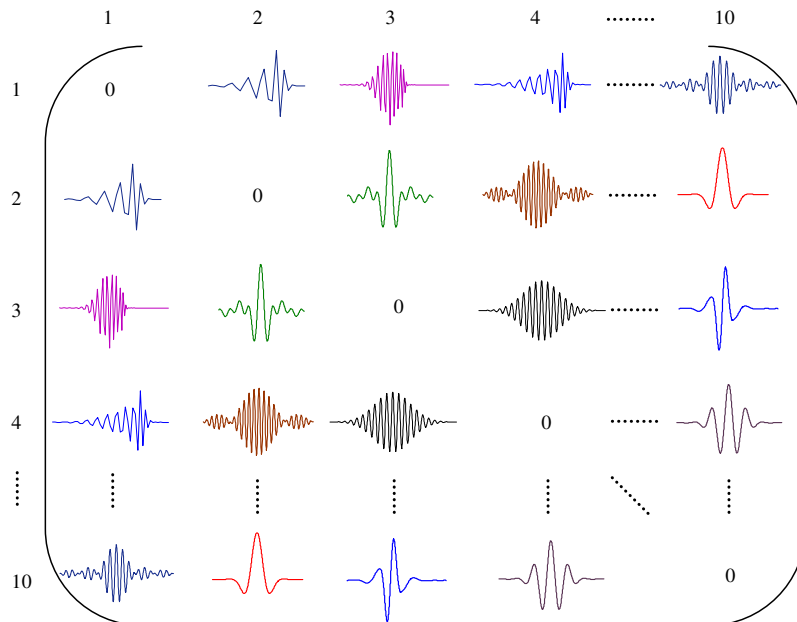


Fig. 6. Schematic of mother wavelet matrix (MWM) (Rafiee et al., 2009).

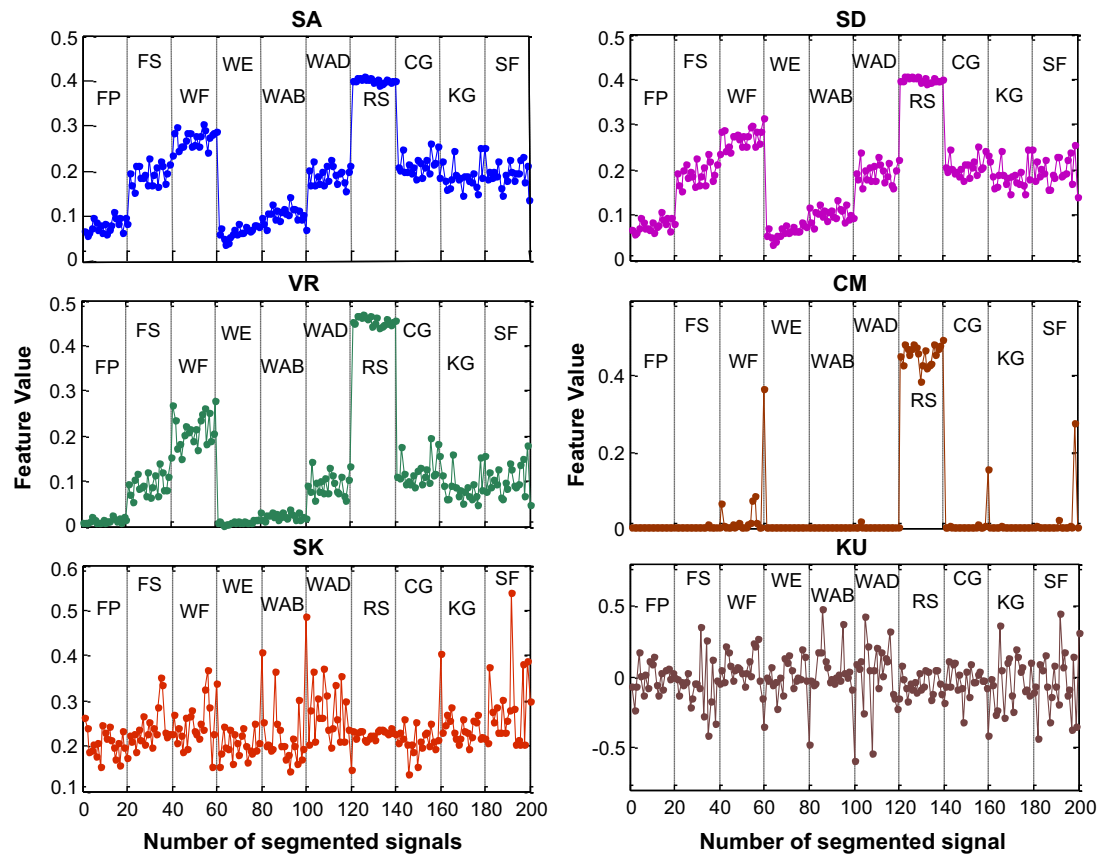


Fig. 7a. Extracted features from surface EMG of one specific subject (sensor 13, scale (4, 15)).

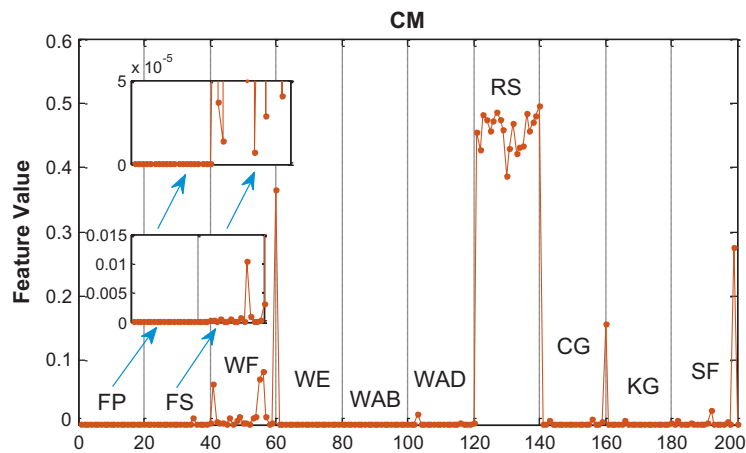


Fig. 7b. CM feature extracted from surface EMG of one specific subject (sensor 13, scale (4, 15)).

0	shan 2-0.8	bior3.1	shan 2-0.9	cmor3-0.2	bior3.1	cmor1-0.3	cmor1-0.3	shan 2-0.8	shan 2-0.9
	0	cmor1-1.5	cmor1-0.5	shan 0.5-0.1	shan 0.5-0.1	shan 0.5-0.1	shan 0.5-0.1	shan 0.5-0.1	shan 0.2-0.1
		0	cmor1-0.5	shan 0.2-0.1	shan 0.2-0.1	shan 0.2-0.1	shan 0.2-0.1	shan 0.2-0.1	shan 0.2-0.1
			0	bior3.1	bior3.1	shan 0.5-0.1	shan 0.5-0.1	bior3.1	bior3.1
				0	0	shan 0.5-0.1	shan 0.5-0.1	shan 0.5-0.1	shan 0.5-0.1
					0	shan 0.2-0.1	shan 0.2-0.1	shan 0.2-0.1	shan 0.2-0.1
						0	cmor1-1.5	rbio3.1	rbio2.6
							0	cmor4-0.1	shan 1-0.9
								0	shan 2-0.5
									0

Fig. 8a. Mother wavelet matrix for surface EMG signals.

0	cmor3-0.3	shan 2-0.9	cmor1-0.05	cmor2-0.3	bior3.1	shan 2-0.5	shan 2-0.5	cmor4-0.2	shan 2-0.5
	0	cmor4-0.2	shan 2-0.5	cmor1-1.5	fbsp2-0.2-0.1	shan 0.5-0.2	shan 1-0.2	shan 2-0.7	shan 1-0.3
		0	'shan 1-0.2	cmor1-1.5	shan 1-0.2	cmor3-0.2	bior3.1	shan 2-0.9	shan 1-0.2
			0	bior3.1	bior3.1	shan 0.2-0.1	shan 0.2-0.1	shan 2-0.9	shan 0.2-0.1
				0	cmor2-2.6	shan 1-0.2	shan 0.5-0.1	shan 2-0.6	shan 1-0.2
					0	shan 0.5-0.1	bior3.1	shan 1-0.1	shan 0.5-0.1
						0	cmor3-0.3	cmor2-2.1	cmor2-2.2
							0	shan 0.5-0.1	bior3.1
								0	cmor2-2.2
									0

Fig. 8b. Mother wavelet matrix for intramuscular EMG signals.

- ✓ Weighted variance of CWC-SS (VR) is calculated as the variance of CWC-SS multiplied by weight, as the last steps for SD and SA are defined.
- ✓ Weighted fourth central moment of CWC-SS (CM) is calculated as the fourth central moment of CWC-SS multiplied by weight. The basic formula is not included for simplicity.
- ✓ Weighted skewness of CWC-SS (SK) is calculated as the skewness of CWC-SS multiplied by weight.
- ✓ Weighted kurtosis of CWC-SS (KU) is calculated as the kurtosis of CWC-SS multiplied by weight.

5. All these features are normalized to make the calculations consistent. SA feature was one of the features showing better classification performance for both surface and intramuscular EMG signals comparing to the others. Therefore, SA was considered the main feature to define the mother wavelet matrix. Schematic of MWM is shown in Fig. 6. In this figure, the horizontal/vertical numbers (1,2,...,10) corresponds to the motions: forearm pronation, forearm supination, wrist flexion, wrist extension, wrist abduction, wrist adduction, rest state, chuck grip, key grip and spread fingers, respectfully.

After selection of the feature, the following procedure is applied to find the MWM, SEM, and NEM:

For each pair of motions the corresponding entity of MWM matrix is the function  $\psi$  that possesses the minimum value for the criterion,  $C(\psi)$ :

$$\forall i, j = 1, \dots, 10 \text{ and } i \neq j, MWM(i, j) = \psi : \min_{\psi} \left( C(\psi) = \frac{1}{L} \sum_{l=1}^L D_l(\psi) \right), \quad (9)$$

where  $L$  is the number of the electrodes, and  $\psi$  is selected from a pool of 324 wavelet basis function (see Tables 1A and 1B)

$$D_l(\psi) = \frac{R_i(\psi) + R_j(\psi)}{|M_i(\psi) - M_j(\psi)|}, \quad (10)$$

where  $R_k(\psi)$  is the range of SA function for all  $k = 1, \dots, N = 240$  segmented signals for  $i^{th}$  motion ( $N = 240$  since there are six subjects and 40 segmented signals for each subject):

$$R_i(\psi) = |\min_k(SA_{ik}(\psi)) - \max_k(SA_{ik}(\psi))|. \quad (11)$$

In Eq. (10),  $M_i(\psi)$  is the average value of SA function for all  $k = 1, \dots, N$  segmented signals for  $i^{th}$  motion:

$$M_i(\psi) = \frac{1}{K} \sum_{k=1}^N SA_{ik}(\psi), \quad (12)$$

where  $SA_{ik}(\psi)$  is the value of SA function for  $i^{th}$  motion and  $k^{th}$  segmented signal calculated by Eq. (6).

By minimizing the value of  $C(\psi)$  and therefore the value of  $D_l(\psi)$  for each pair of motions, the mother wavelet having the less range of feature values for  $N$  segmented signals and more difference between two motions is selected.

The same procedure is considered to calculate MWM for intramuscular EMG signals. After finding MWM matrix, NEM and SEM matrices can be obtained. For each pair of motions, the corresponding entity of SEM matrix is the surface electrode number (see Fig. 1), which has the minimum value of  $D_l(\psi)$  function (Eq. 10) calculated for corresponding mother wavelet extracted from MWM matrix. The same procedure is repeated for EMG intramuscular signals ending up with NEM matrix.

## 5. Results and discussion

In this research, six statistical features are studied for surface and intramuscular EMG signals as shown in Fig. 7a for one specific scale recorded from a specific sensor attached to the arm of one subject. Among the features, SK and KU did not show proper classification for this scale/sensor and neither for the others

	1	2	3	4	5	6	7	8	9	10
1	0	13	15	9	9	5	13	13	6	13
2		0	13	1	12	5	15	9	7	13
3			0	3	9	8	13	9	7	8
4				0	13	15	3	15	6	15
5					0	15	2	2	6	6
6						0	4	9	4	13
7							0	9	6	8
8								0	6	15
9									0	3
10										0

Fig. 9a. Selected sensors within surface electrode matrix (SEM).

	1	2	3	4	5	6	7	8	9	10
1	0	4	4	2	4	6	5	5	6	5
2		0	2	2	1	2	6	3	6	5
3			0	2	1	2	3	1	4	2
4				0	5	6	5	5	6	5
5					0	6	6	5	4	6
6						0	5	1	5	5
7							0	3	4	3
8								0	6	3
9									0	1
10										0

Fig. 9b. Selected intramuscular sensors within needle electrode matrix (NEM).

**Table 1A**  
Studied wavelet families in this research.

No.	Family (short form)	Order
<b>1</b>	Haar (db1)	db 1
<b>2–45</b>	Daubechies (db)	db 2–db 45
<b>46–50</b>	Coiflet (coif)	coif 1–coif 5
<b>51</b>	Morlet (Morl)	morl
<b>52–147</b>	Complex Morlet (cmor Fb–Fc) <sup>a</sup>	Included Table 1B
<b>148</b>	Discrete Meyer (dmey)	dmey
<b>149</b>	Meyer (meyr)	meyr
<b>150</b>	Mexican Hat (mexh)	mexh
<b>151–200</b>	Shannon (Shan Fb–Fc) <sup>a</sup>	Included Table 1B
<b>201–260</b>	Frequency B-Spline (fbps M–Fb–Fc) <sup>a</sup>	Included Table 1B
<b>261–267</b>	Gaussian (gaus)	gaus 1 to gaus7
<b>268–275</b>	Complex Gaussian (cgau)	cgau 1 to cgau8
<b>276–290</b>	Biorthogonal (bior Nr.Nd) <sup>b</sup>	Included Table 1B
<b>291–305</b>	Reverse biorthogonal (rbio Nr.Nd) <sup>b</sup>	Included Table 1B
<b>306–324</b>	Symlet (sym)	sym 2 to sym 20

<sup>a</sup> Fb is a bandwidth parameter, Fc is a wavelet center frequency, M is an integer order parameter.

<sup>b</sup> Nr and Nd are orders: r for reconstruction/d for decomposition.

(see Fig. 7a). The other four features can be useful for forearm EMG signal classification. It is worth mentioning that CM feature shown in Fig. 7a cannot visually show proper classification. However, by zooming on the CM plot, more information may be observed as plotted in Fig. 7b.

Also, mother wavelet matrices (MWM) matched with our experimental data is shown in Figs. 8a and 8b for surface and intra-muscular EMG signals respectfully (see Appendix A, for function detail). As it can be seen from the matrix in Fig. 8a, NEM and SEM have been also depicted in Figs. 9a and 9b for surface EMG dataset used in this research for validation. The numbers in these matrices are referred to the sensor number shown in Fig. 1. As it can be seen in NEM and SEM, sensor number 9, located close to extensor digitorum communis, number 13, located in between extensor and flexor carpi ulnaris, and number 15, close to flexor carpi ulnaris offer more helpful information for feature extraction of the above mentioned ten motions.

The advantages of the proposed technique can be summarized as follows:

**Table 1B**  
Studied wavelet families in detail.

No	Wave	No	Wave	No	Wave	No	Wave	No	Wave
52	1–1.5	100	3–1.1	148	dmey	196	2–0.6	244	2–0.2–0.4
53	1–1	101	3–1.2	149	meyr	197	2–0.7	245	2–0.2–0.5
54	1–0.5	102	3–1.3	150	mexh	198	2–0.8	246	2–0.2–0.6
55	1–0.3	103	3–1.4	151	0.1–0.1	199	2–0.9	247	2–0.2–0.7
56	1–0.2	104	3–1.5	152	0.1–0.2	200	1–1	248	2–0.2–0.8
57	1–0.1	105	3–1.6	153	0.1–0.3	201	1–0.1–0.1	249	2–0.2–0.9
58	1–0.05	106	3–1.8	154	0.1–0.4	202	1–0.1–0.2	250	2–0.2–1
59	1–0.02	107	3–1.9	155	0.1–0.5	203	1–0.1–0.3	251	3–0.2–0.1
60	1–0.01	108	3–2	156	0.1–0.6	204	1–0.1–0.4	252	3–0.2–0.2
61	2–0.1	109	3–2.1	157	0.1–0.7	205	1–0.1–0.5	253	3–0.2–0.3
62	2–0.2	110	3–2.2	158	0.1–0.8	206	1–0.1–0.6	254	3–0.2–0.4
63	2–0.3	111	3–2.3	159	0.1–0.9	207	1–0.1–0.7	255	3–0.2–0.5
64	2–0.4	112	3–2.4	160	0.1–1	208	1–0.1–0.8	256	3–0.2–0.6
65	2–0.5	113	3–2.5	161	0.2–0.1	209	1–0.1–0.9	257	3–0.2–0.7
66	2–0.6	114	3–2.6	162	0.2–0.2	210	1–0.1–1	258	3–0.2–0.8
67	2–0.7	115	3–2.7	163	0.2–0.3	211	2–0.1–0.1	259	3–0.2–0.9
68	2–0.8	116	3–2.8	164	0.2–0.4	212	2–0.1–0.2	260	3–0.2–1
69	2–0.9	117	3–2.9	165	0.2–0.5	213	2–0.1–0.3	276	1.1
70	2–1	118	3–3	166	0.2–0.6	214	2–0.1–0.4	277	1.3
71	2–1.1	119	4–0.1	167	0.2–0.7	215	2–0.1–0.5	278	1.5
72	2–1.2	120	4–0.2	168	0.2–0.8	216	2–0.1–0.6	279	2.2
73	2–1.3	121	4–0.3	169	0.2–0.9	217	2–0.1–0.7	280	2.4
74	2–1.4	122	4–0.4	170	0.2–1	218	2–0.1–0.8	281	2.6
75	2–1.5	123	4–0.5	171	0.5–0.1	219	2–0.1–0.9	282	2.8
76	2–1.6	124	4–0.6	172	0.5–0.2	220	2–0.1–1	283	3.1
77	2–1.8	125	4–0.7	173	0.5–0.3	221	3–0.1–0.1	284	3.3
78	2–1.9	126	4–0.8	174	0.5–0.4	222	3–0.1–0.2	285	3.5
79	2–2	127	4–0.9	175	0.5–0.5	223	3–0.1–0.3	286	3.7
80	2–2.1	128	4–1	176	0.5–0.6	224	3–0.1–0.4	287	3.9
81	2–2.2	129	4–1.1	177	0.5–0.7	225	3–0.1–0.5	288	4.4
82	2–2.3	130	4–1.2	178	0.5–0.8	226	3–0.1–0.6	289	5.5
83	2–2.4	131	4–1.3	179	0.5–0.9	227	3–0.1–0.7	290	6.8
84	2–2.5	132	4–1.4	180	0.5–1	228	3–0.1–0.8	291	1.1
85	2–2.6	133	4–1.5	181	1–0.1	229	3–0.1–0.9	292	1.3
86	2–2.7	134	4–1.6	182	1–0.2	230	3–0.1–1	293	1.5
87	2–2.8	135	4–1.8	183	1–0.3	231	1–0.2–0.1	294	2.2
88	2–2.9	136	4–1.9	184	1–0.4	232	1–0.2–0.2	295	2.4
89	2–3	137	4–2	185	1–0.5	233	1–0.2–0.3	296	2.6
90	3–0.1	138	4–2.1	186	1–0.6	234	1–0.2–0.4	297	2.8
91	3–0.2	139	4–2.2	187	1–0.7	235	1–0.2–0.5	298	3.1
92	3–0.3	140	4–2.3	188	1–0.8	236	1–0.2–0.6	299	3.3
93	3–0.4	141	4–2.4	189	1–0.9	237	1–0.2–0.7	300	3.5
94	3–0.5	142	4–2.5	190	1–1	238	1–0.2–0.8	301	3.7
95	3–0.6	143	4–2.6	191	2–0.1	239	1–0.2–0.9	302	3.9
96	3–0.7	144	4–2.7	192	2–0.2	240	1–0.2–1	303	4.4
97	3–0.8	145	4–2.8	193	2–0.3	241	2–0.2–0.1	304	5.5
98	3–0.9	146	4–2.9	194	2–0.4	242	2–0.2–0.2	305	6.8
99	3–1	147	4–3	195	2–0.5	243	2–0.2–0.3		



1. The number of motions was increased to ten hand motions. Chuck and key grips, which are the complicated motions for classification because of the engagements of several in-depth muscles and complexity of the signals, were studied by the proposed algorithm.
2. The presented features would also be appropriate for training purposes of intelligent classifiers (e.g. Micera, Sabatini, & Dario, 2000; Pandey & Mishra, 2009; Rafiee et al., 2009; Xie, Zheng, Guo, Chen, & Shi, 2009) or to determine rules for fuzzy systems (Chan, Yang, Lam, Zhang, & Parker, 2000).
3. This method was able to find optimal sensors for each pair of motions applicable for classification purposes.

## 6. Conclusions

A method was suggested to extract appropriate features for forearm electromyographic (EMG) signals using a mother wavelet matrix (MWM). After broad investigations on 324 mother wavelet functions, the combination of some mother wavelets ameliorated the EMG signal analysis. Among several installed electrodes on the subjects' forearms, the optimal sensors appropriate for feature extraction were selected in terms of surface electrode matrix (SEM) and a needle electrode matrix (NEM). Six statistical feature vectors were also studied in this research.

## Acknowledgments

The authors would like to offer special thanks to Professor Kevin Englehart, associate director of the Institute of Biomedical Engineering at University of New Brunswick, who supported us with experimental EMG signals used in this research. The authors also acknowledges funding support from the US DARPA (Award Number: W81XWH-07-2-0078) for Idaho State University Smart Prosthetic Hand Technology – Phase I.

## Appendix A

Tables 1A, 1B.

## References

- Aschero, G., & Gizdulich, P. (2009). Denoising of surface EMG with a modified Wiener filtering approach. *Journal of Electromyography and Kinesiology*. doi:10.1016/j.jelekin.2009.02.003.
- Beck, T. W., Housh, T. J., Johnson, G. O., Weir, J. P., Cramer, J. T., Coburn, J. W., et al. (2005). Comparison of Fourier and wavelet transform procedures for examining mechanomyographic and electromyographic frequency versus isokinetic torque relationships. *Electromyography and Clinical Neurophysiology*, 45(2), 93–103.
- Brechet, L., Lucas, M. F., Doncarli, C., & Farina, D. (2007). Compression of biomedical signals with mother wavelet optimization and best-basis wavelet packet selection. *IEEE Transactions on Biomedical Engineering*, 54(12).
- Chan, F. H. Y., Yang, Y.-S., Lam, F. K., Zhang, Y.-T., & Parker, P. A. (2000). Fuzzy EMG classification for prosthesis control. *IEEE Transactions on Rehabilitation Engineering*, 8(3), 305–311.
- Clancy, E. A., Bertolina, M. V., Merletti, R., & Farina, D. (2008). Time- and frequency-domain monitoring of the myoelectric signal during a long-duration, cyclic, force-varying, fatiguing hand-grip task. *Journal of Electromyography and Kinesiology*, 18, 789–797.
- Cvetkovic, D., Ubeyli, E. D., & Cosic, I. (2008). Wavelet transform feature extraction from human PPG, ECG, and EEG signal responses to ELF PEMF exposures: A pilot study. *Digital Signal Processing: A Review Journal*, 18(5), 861–874.
- Daubechies, I. (1991). *Ten lectures on wavelets*. CBMS-NSF series in applied mathematics. Philadelphia, PA: SIAM.
- Disselhorst-Klug, C., Schmitz-Rode, T., & Rau, G. (2009). Surface electromyography and muscle force: Limits in sEMG-force relationship and new approaches for applications. *Clinical Biomechanics*, 24(3), 225–235.
- Englehart, K., & Hudgins, B. (2003). A robust, real-time control scheme for multifunction myoelectric control. *IEEE Transactions on Biomedical Engineering*, 50(7).
- Englehart, K., Hudgins, B., & Parker, P. A. (2001). A wavelet-based continuous classification scheme for multifunction myoelectric control. *IEEE Transactions on Biomedical Engineering*, 48(3), 302–311.
- Englehart, K., Hudgins, B., Parker, P. A., & Stevenson, M. (1999). Classification of the myoelectric signal using time-frequency based representations. *Medical Engineering and Physics*, 21, 431–438.
- Farina, D., do Nascimento, O. F., Lucas, M. F., & Doncarli, C. (2007). Optimization of wavelets for classification of movement-related cortical potentials generated by variation of force-related parameters. *Journal of Neuroscience Methods*, 162, 357–363.
- Farina, D., Lucas, M. F., & Doncarli, C. (2008). Optimized wavelets for blind separation of non-stationary surface myoelectric signals. *IEEE Transactions on Biomedical Engineering*, 55(1).
- Farina, D., Merletti, R., & Enoka, R. M. (2004). The extraction of neural strategies from the surface EMG. *Journal of Applied Physiology*, 96(4), 1486–1495.
- Fukuda, O., Tsuji, T., Kaneko, M., & Otsuka, A. (2003). A human-assisting manipulator teleoperated by EMG signals and arm motions. *IEEE Transactions on Robotics and Automation*, 19(2), 210–222.
- Gazzoni, M., Farina, D., & Merletti, R. (2004). A new method for the extraction and classification of single motor unit action potentials from surface EMG signals. *Journal of Neuroscience Methods*, 136, 165–177.
- Hargrove, L. J., Englehart, K., & Hudgins, B. (2007). A comparison of surface and intramuscular myoelectric signal classification. *IEEE Transactions on Biomedical Engineering*, 54(5).
- Hermens, H., Freriks, B., Merletti, R., Stegeman, D., Blok, J., Rau, G., Disselhorst-Klug, C., et al. (1999). *European recommendations for surface electromyography*. RRD Publisher.
- Hostens, I., Seghers, J., Spaepen, A., & Ramon, H. (2004). Validation of the wavelet spectral estimation technique in Biceps Brachii and Brachioradialis fatigue assessment during prolonged low-level static and dynamic contractions. *Journal of Electromyography and Kinesiology*, 14, 205–215.
- Kallenberg, L. A. C., Preece, S., Nester, C., & Hermens, H. J. (2009). Reproducibility of MUAP properties in array surface EMG recordings of the upper trapezius and sternocleidomastoid muscle. *Journal of Electromyography and Kinesiology*. doi:10.1016/j.jelekin.2008.11.012.
- Koike, Y., & Kawato, M. (1995). Estimation of dynamic joint torques and trajectory formation from surface electromyography signals using a neural network model. *Biological Cybernetics*, 73(4), 291–300.
- Kurt, M. B., Sezgin, N., Akin, M., Kirbas, G., & Bayram, M. (2009). The ANN-based computing of drowsy level. *Expert Systems with Applications*, 36(2 part 1), 2534–2542.
- Liu, M. M., Herzog, W., & Savelberg, H. H. C. M. (1999). Dynamic muscle force predictions from EMG: An artificial neural network approach. *Journal of Electromyography and Kinesiology*, 9(6), 391–400.
- Lowery, M. M., Stoykov, N. S., Taflove, A., & Kuiken, T. A. (2002). A multiple-layer finite-element model of the surface EMG signal. *IEEE Transactions on Biomedical Engineering*, 49(5).
- Lucas, M. F., Gaufriau, A., Pascual, S., Doncarli, C., & Farina, D. (2008). Multi-channel surface EMG classification using support vector machines and signal-based wavelet optimization. *Biomedical Signal Processing and Control*(3), 169–174.
- Merletti, R., & Lo Conte, L. R. (1997). Surface EMG signal processing during isometric contractions. *Journal of Electromyography and Kinesiology*, 7(4), 241–250.
- Micera, S., Sabatini, A. M., & Dario, P. (2000). On automatic identification of upper-limb movements using small-sized training sets of EMG signals. *Medical Engineering and Physics*, 22(8), 527–533.
- Pandey, B., & Mishra, R. B. (2009). An integrated intelligent computing model for the interpretation of EMG based neuromuscular diseases. *Expert Systems with Applications*, 36(5), 9201–9213.
- Park, S. H., & Lee, S. P. (1998). EMG pattern recognition based on artificial intelligence techniques. *IEEE Transactions on Rehabilitation Engineering*, 6(4).
- Rafiee, J., Rafiee, M. A., Prause, N., & Schoen, M. P. (2009). Biorobotics: Optimized biosignal classification using mother wavelet matrix. In *IEEE 35th annual northeast bioengineering conference, harvard-MIT division of health sciences and technology*, Cambridge, MA, USA, April 3–5, 2009. doi:10.1109/NEBC.2009.4967645.
- Rafiee, J., Rafiee, M. A., & Michaelsen, D. (2009). Female sexual responses using signal processing techniques. *The Journal of Sexual Medicine*, 6, 3086–3096.
- Rafiee, J., & Tse, P. W. (2009). Use of autocorrelation of wavelet coefficients for fault diagnosis. *Mechanical Systems and Signal Processing*, 23, 1554–1572.
- Rasheed, S., Stashuk, D. W., & Kamel, M. S. (2008). Diversity-based combination of non-parametric classifiers for EMG signal decomposition. *Pattern Analysis and Applications*, 11(3–4), 385–408.
- Sebelius, F., Eriksson, L., Holmberg, H., Levinsson, A., Lundborg, G., Danielsen, N., et al. (2005). Classification of motor commands using a modified self-organising feature map. *Medical Engineering and Physics*, 27, 403–413.
- Silvestro Micera, S., Sabatini, A. M., Dario, P., & Rossi, B. (1999). A hybrid approach to EMG pattern analysis for classification of arm movements using statistical and fuzzy techniques. *Medical Engineering and Physics*, 21, 303–311.
- Subasi, A. (2005). Automatic recognition of alertness level from EEG by using neural network and wavelet coefficients. *Expert Systems with Applications*, 28(4), 701–711.
- Subramani, P., Sahu, R., & Verma, S. (2006). Feature selection using Haar wavelet power spectrum. *BMC Bioinformatics*, art. no. 432.
- Unser, M., & Aldroubi, A. (1996). A review of wavelets in biomedical applications. *Proceedings of the IEEE* 84 (4), 626–638.
- von Tscharn, V. (2000). Intensity analysis in time-frequency space of surface myoelectric signals by wavelets of specified resolution. *Journal of Electromyography and Kinesiology*, 10, 433–445.

- von Tscharnner, V. (2008). Spherical classification of wavelet transformed EMG intensity patterns. *Journal of Electromyography and Kinesiology*. doi:[10.1016/j.jelekin.2008.07.001](https://doi.org/10.1016/j.jelekin.2008.07.001).
- Vukova, T., Vydevska-Chichova, M., & Radicheva, N. (2008). Fatigue-induced changes in muscle fiber action potentials estimated by wavelet analysis. *Journal of Electromyography and Kinesiology*, 18, 397–409.
- Xie, H.-B., Zheng, Y.-P., Guo, J.-Y., Chen, X., & Shi, J. (2009). Estimation of wrist angle from sonomyography using support vector machine and artificial neural network models. *Medical Engineering and Physics*, 31(3), 384–391.



# Adaptive Multi Sensor Based Nonlinear Identification of Skeletal Muscle Force

PARMOD KUMAR, CHANDRASEKHAR POTLURI, ANISH SEBASTIAN, STEVE CHIU, ALEX  
URFER, D. SUBBARAM NAIDU, and MARCO P. SCHOEN

Measurement and Control Engineering Research Center, College of Engineering  
Idaho State University  
921 South 8<sup>th</sup> Avenue, Stop 8060, Pocatello, Idaho  
USA

{kumaparm, potlchan, sebaanis, chiustev, urfealex, naiduds, schomarc}@isu.edu  
<http://www.isu.edu/~schomarc>

**Abstract:** - Skeletal muscle force and surface electromyographic (sEMG) signals are closely related. Hence, the later can be used for the force estimation. Usually, the location for the sEMG sensors is near the respective muscle motor unit points. EMG signals generated by skeletal muscles are temporal and spatially distributed which results in cross talk that is recorded by different sEMG sensors. This research focuses on modeling muscle dynamics in terms of sEMG signals and the generated muscle force. Here, an array of three sEMG sensors is used to capture the information of the muscle dynamics in terms of sEMG signals and generated muscle force. Optimized nonlinear Half-Gaussian Bayesian filters and a Chebyshev type-II filter are used for the filtration of the sEMG signals and the muscle force signal, respectively. A Genetic Algorithm is used for the optimization of the filter parameters. sEMG and skeletal muscle force is modeled using multi nonlinear Auto Regressive eXogenous (ARX) and Wiener-Hammerstein models with different nonlinearity estimators/classes using System Identification (SI) for three sets of sensor data. An adaptive probabilistic Kullback Information Criterion (KIC) for model selection is applied to obtain the fusion based skeletal muscle force for each sensor first and then for the final outputs from each sensor. The approach yields good skeletal muscle force estimates.

**Key-Words:** - sEMG, ARX, Weiner-Hammerstein, Prosthetic hand, KIC, System Identification,

## 1 Introduction

Aftereffects of the loss of upper limbs are a reduction of functionality and psychological disturbance for the person. According to [1] there are 1.7 million peoples with amputation in the United States and this number is on rise after the Afghanistan and Iraq war in 2003 [2]. Conversely, a prosthetic limb can considerably increase the functionality of an amputee and benefit the person in everyday life.

In the past, there have been various research works towards prosthetic hand design, having similar functionality and appearance as human hand [3-4]. Most of these research works are based on electromyography (EMG). The EMG signal is activated and controlled by the central nervous system, which depends on the flow of specific ions such as sodium ( $Na^+$ ), potassium ( $K^+$ ) and calcium ( $Ca^{++}$ ).

An EMG signal recorded on the surface of the limb is expressed as an electric voltage ranging between -5 and +5 mV. This method is known as surface electromyography (sEMG). sEMG is

utilized as an input to the controller to realize the movements of the prosthesis and force control [5-6]. Past research results show that EMG signal amplitude generally increases with skeletal muscle force. However, this relationship is not always rigid; various factors affect this relationship. EMG signals are a result of the varying motor unit recruitments, crosstalk, and biochemical interaction within the muscular fibres. This makes EMG signals random, complex and dynamic in nature and the control of the prosthesis difficult. Moreover, it changes continuously due to the onset and progression of muscle fatigue which results because of continuous high frequency stimulation or because of titanic stimulation [7]. Synchronization of active motor units along the muscle fibres, and a decrease in conduction velocity are reflected in the EMG signal as an increase of amplitude in time domain and a decrease of medium frequency in frequency domain [7]. All these factors make the relationship between EMG and force nonlinear. Correct interpretation of EMG signal is vital to achieve precise motion and force control of prosthesis.

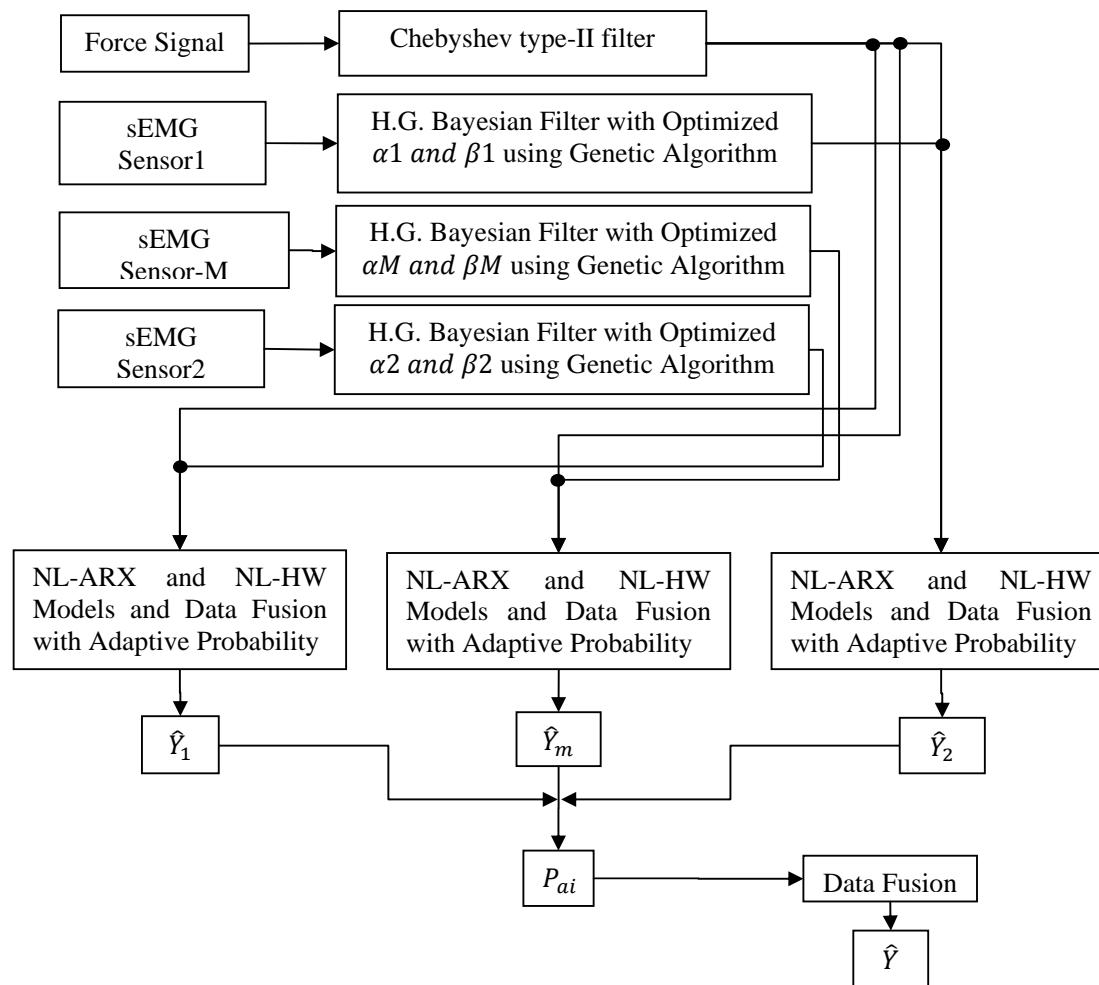


Fig. 1: The Flow Chart for Skeletal Muscle Force Estimation.

The present work presents a novel approach to estimate skeletal muscle force using an adaptive multi-sensor data fusion algorithm with hybrid nonlinear ARX and Wiener-Hammerstein models. Here, an array of three sEMG sensors is used to capture the information of muscle dynamics in terms of sEMG signals. The recorded sEMG signals are filtered utilizing optimized nonlinear Half-Gaussian Bayesian filter parameters, and the skeletal muscle force signal is filtered by using a Chebyshev type-II filter. A simple Genetic Algorithm code is used to optimize the Bayesian filter parameters. Using an input/output approach, the EMG signal measured at the skin surface is considered as input to the skeletal muscle, whereas the resulting hand/finger force constitutes the output. Multi nonlinear ARX and Wiener-Hammerstein models with different nonlinearity

estimators/classes are obtained using SI for three sets of sensor data obtained from the vicinity of a single motor unit. Different nonlinearity estimators/classes are used for nonlinear modeling as they capture the dynamics of the system differently. The outputs of estimated nonlinear models are fused with a probabilistic Kullback Information Criterion (KIC) for model selection and an adaptive probability of KIC. First, the outputs are fused for the same sensor and for different models and then the final outputs from each sensor. The final fused output of three sensors provides good skeletal muscle force estimates.

Fig. 1 shows the flow chart for skeletal muscle force estimation. This paper is structured as follows. First, the experimental set-up, pre-processing and filter parameter optimization for sEMG signals are discussed. Second, nonlinear ARX and Wiener-

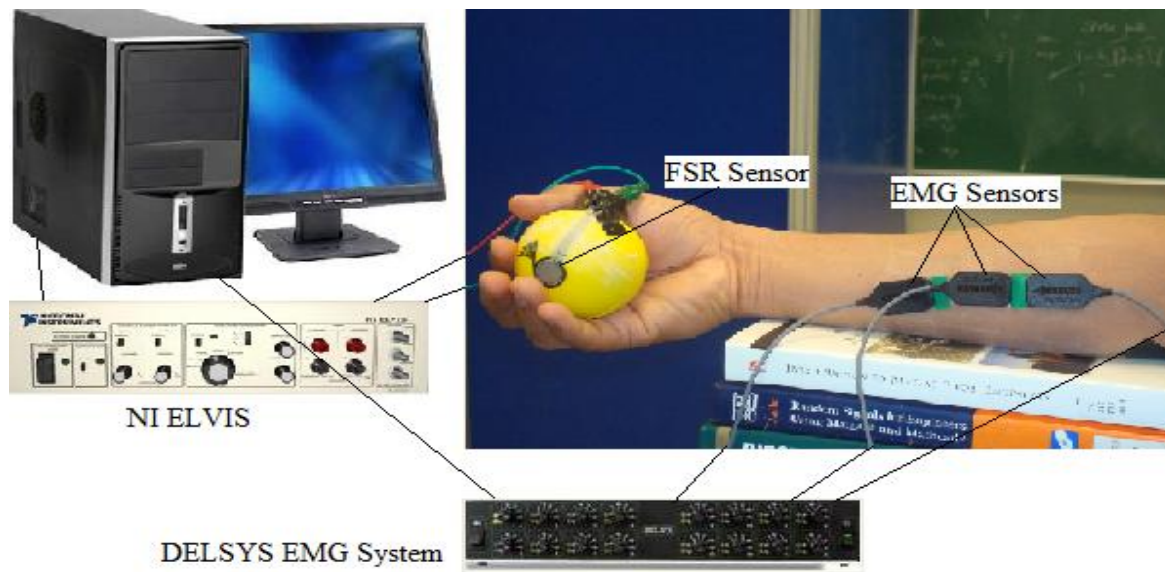


Fig. 2: Experimental Set-Up.

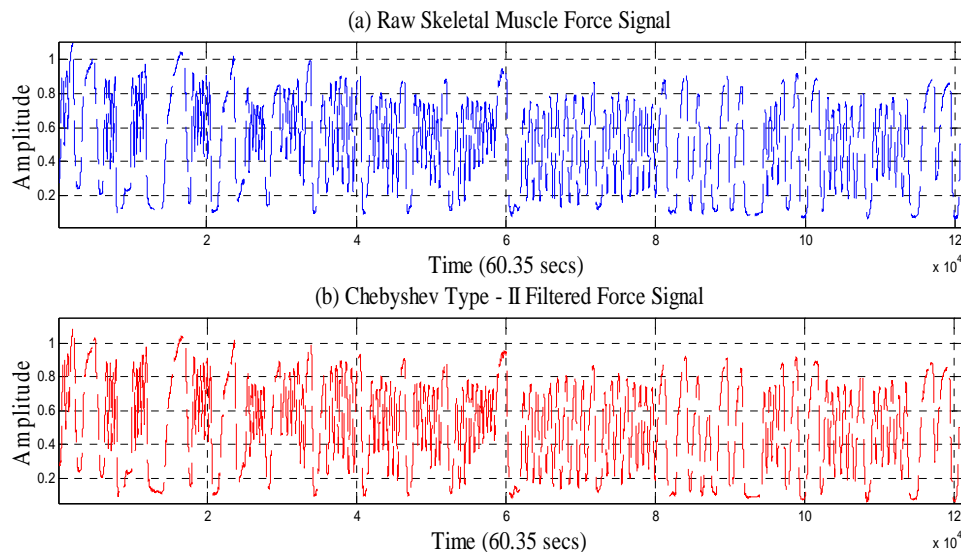


Fig. 3: (a) Raw and (b) Chebyshev Type-II Filtered Skeletal Muscle Force Signals.

Hammerstein modeling is covered. Third, the fusion of various nonlinear model outputs using KIC and adaptive probability of KIC is covered. Finally, the results, discussion and future work are provided followed by a conclusion to summarize the importance of this work.

## 2 Experimental Set-Up and Pre-Processing

The experimental set-up is shown in Fig. 2. Both sEMG and muscle force signals were acquired simultaneously using LabVIEW™ at a sampling rate of 2000 Hz. The sEMG data capturing was aided by a DELSYS® Bagnoli-16 EMG system with DE-2.1 differential EMG sensors. The

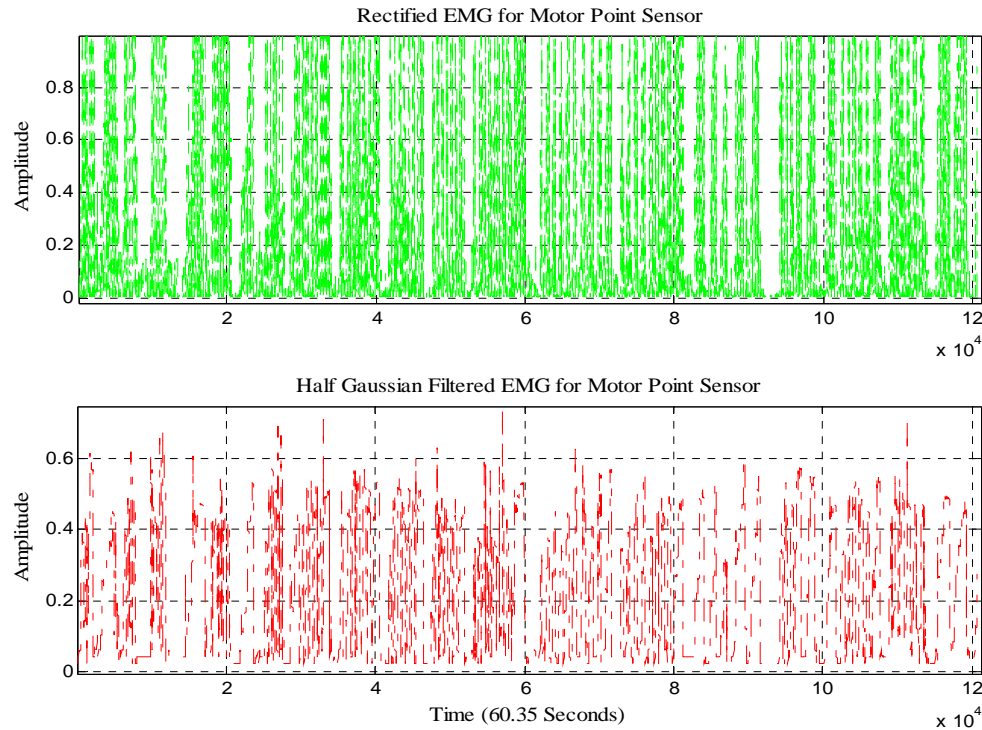


Fig. 4(a): Rectified EMG and Half-Gaussian Filtered EMG Signal for Motor Point Sensor.

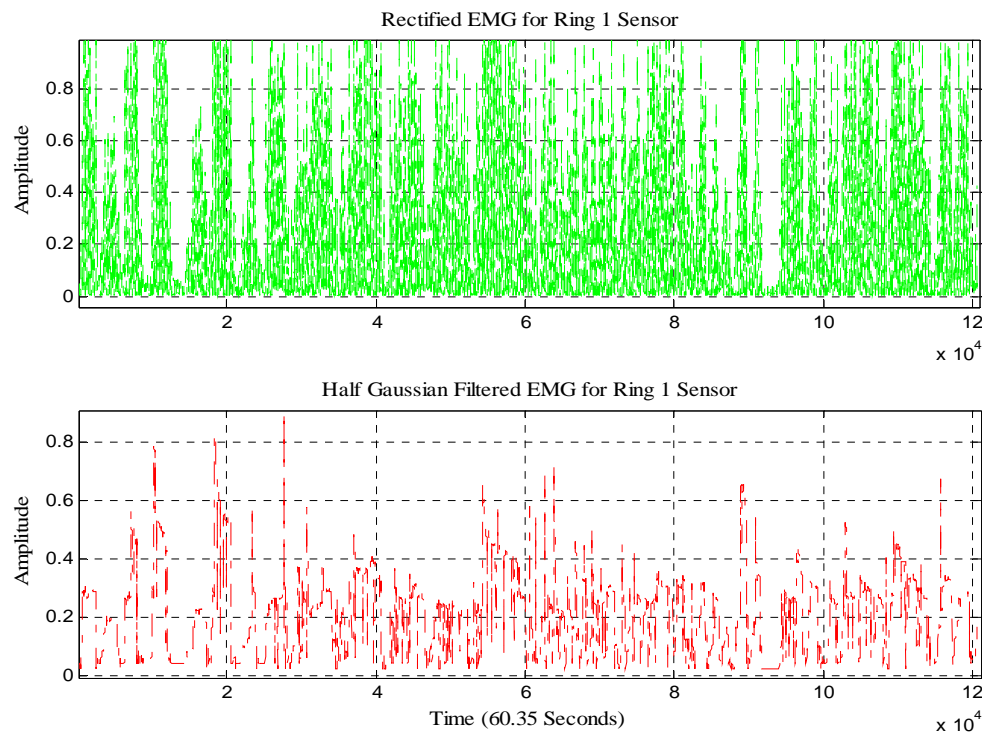


Fig. 4(b): Rectified EMG and Half-Gaussian Filtered EMG Signal for Ring 1 Sensor.

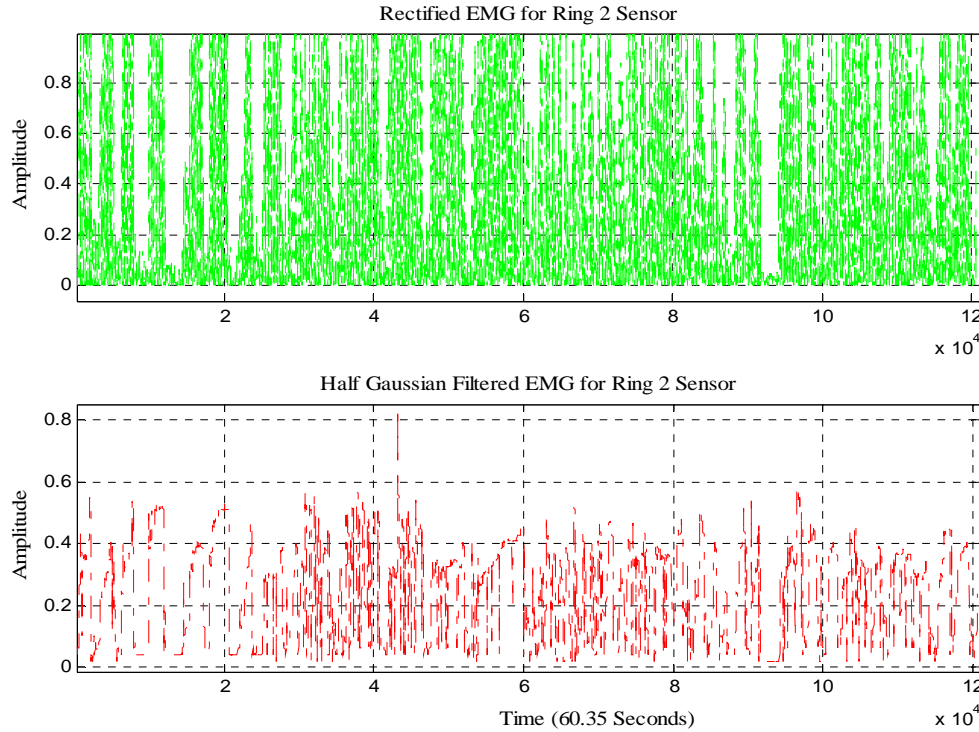


Fig. 4(c): Rectified EMG and Half-Gaussian Filtered EMG Signal for Ring 2 Sensor.

corresponding force data was captured using Interlink Electronics FSR 0.5" circular force sensor. One sEMG sensor was placed on the motor point of the ring finger and two adjacent to the motor point of a healthy subject. Prior to placing the sEMG sensors, the skin surface of the subject was prepared according to International Society of Electrophysiology and Kinesiology (ISEK) protocols. According to previous research, the Bayesian based filtering method yields the most suitable sEMG signals [8]. The nonlinear filter significantly reduces noise and extracts a signal that best describes EMG signals and may permit effective use in prosthetic control. An instantaneous conditional probability density  $P(EMG|x)$  provides the resulting EMG for the latent driving signal  $x$  [8]. The model for the conditional probability of the rectified EMG signal  $emg = |EMG|$  is used in this current estimation algorithm. EMG signals are usually described as amplitude-modulated zero mean Gaussian noise sequence [9]. For the rectified EMG signal, the "Half-Gaussian measurement model" in [8] is given by Equation (1).

$$P(emg|x) = \frac{2 \cdot \exp\left(-\frac{emg^2}{2x^2}\right)}{\sqrt{2\pi}x^2}. \quad (1)$$

The EMG signal is modeled for the conditional probability of the rectified EMG signal as a filtered random process with random rate. The likelihood function for the rate evolves in time according to a Fokker–Planck partial differential equation [8]. The discrete time Fokker–Planck Equation is given by equation (2).

$$p(x, t) \approx \alpha * p(x - \varepsilon, t - 1) + (1 - 2 * \alpha) * p(x, t - 1) + \alpha * p(x + \varepsilon, t - 1) + \beta + (1 - \beta) * p(x, t - 1). \quad (2)$$

Here,  $\alpha$  and  $\beta$  are two free parameters,  $\alpha$  is the expected rate of gradual drift in the signal, and  $\beta$  is the expected rate of sudden shifts in the signal. The unknown driving signal  $x$  is discretized into bins of width  $\varepsilon$ . These two free parameters of the non-linear Half-Gaussian filter model are optimized for the acquired EMG data using elitism based GA. GA belongs to a class of optimization algorithms that are based on observing nature and its corresponding processes to imitate solving complex problems, most often optimization or estimation problems, see [10–12]. A Chebyshev type II low pass filter with a 550 Hz pass frequency is used to filter the force signal. Fig. 3 depicts the raw and Chebyshev type-II low pass filtered force signals. Fig. 4(a), (b) and (c)

show the rectified EMG and Half-Gaussian Filtered EMG signal for three sensors.

### 3 Nonlinear ARX and Wiener-Hammerstein Modeling

In this paper, we are using nonlinear ARX and Wiener-Hammerstein models with different nonlinearity estimators/classes to model three sEMG sensors data as input and skeletal muscle force data as output. The nonlinear ARX model uses a parallel combination of nonlinear and linear blocks [13].

Fig. 5 shows the nonlinear ARX model structure. The nonlinear ARX model uses regressors as variables for nonlinear and linear functions. Regressors are functions of measured input-output data [13]. The predicted output  $\hat{y}(t)$  of a nonlinear model at time  $t$  is given by the general Equation (3):

$$\hat{y}(t) = F(x(t)) \quad (3)$$

where  $x(t)$  represents the regressors,  $F$  is a nonlinear regressor command, which is estimated by nonlinearity estimators/classes [13]. As shown in Fig. 5, the command  $F$  can include both linear and nonlinear functions of  $x(t)$ . Equation (4) gives the description of  $F$ .

$$F(x) = \sum_{k=1}^d \alpha_k \kappa(\beta_k(x - \gamma_k)) \quad (4)$$

where  $\kappa$  is the unit nonlinear command,  $d$  is the number of nonlinearity units, and  $\alpha_k$ ,  $\beta_k$  and  $\gamma_k$  are the parameters of the nonlinearity estimators/classes [13].

The Wiener-Hammerstein model uses one or two static nonlinear blocks in series with a linear block. Structural representation of a nonlinear Wiener-Hammerstein is shown in Fig. 6 [13].

The general Equations (5), (6), and (7) can describe the Wiener-Hammerstein structure [13].

$$w(t) = f(u(t)) \quad (5)$$

$$x(t) = \frac{B_{j,i}(q)}{F_{j,i}(q)} w(t) \quad (6)$$

$$y(t) = h(x(t)). \quad (7)$$

where  $u(t)$  and  $y(t)$  are input and output of the system, respectively,  $f$  and  $h$  are nonlinear functions, which corresponds to input and output nonlinearity, respectively,  $w(t)$  and  $x(t)$  are internal variables, where  $w(t)$  has the same dimensions as  $u(t)$  and  $x(t)$  has the same dimensions as  $y(t)$ , and  $B(q)$  and  $F(q)$  corresponds to the linear dynamic block, these are polynomials in the backward shift operator.

The nonlinearity classes used in this work are Wavenet, Treepartition, Sigmoidnet, Pwlinear, Saturation, and Deadzone. For motor point and ring1 sensors, three nonlinear ARX and four

nonlinear Wiener-Hammerstein models with different nonlinearity estimators/classes are obtained. For ring2 sensor, three nonlinear ARX and five nonlinear Wiener-Hammerstein models with different nonlinearity estimators/classes are obtained. Tables 1, 2 and 3 gives the nonlinearity estimators/classes for different sensors and their corresponding model fit values.

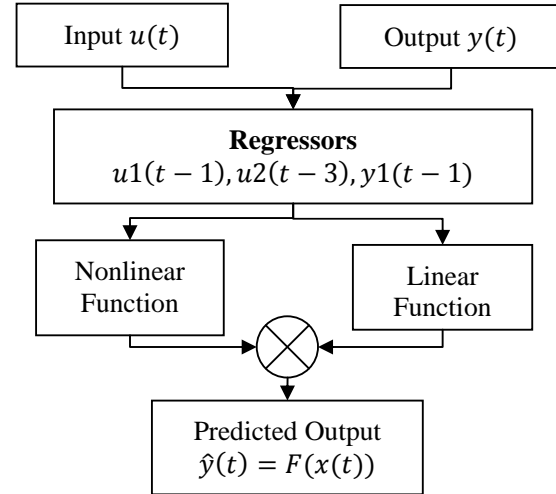


Fig. 5: Nonlinear ARX Model Structure.

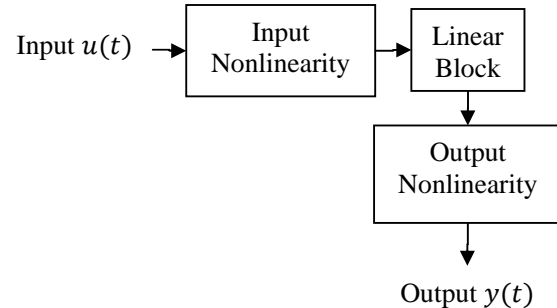


Fig. 6: Nonlinear Wiener-Hammerstein Model Structure.

### 4 Data Fusion and Adaptive KIC Probability

Data fusion of multiple outputs of nonlinear ARX and Wiener-Hammerstein models is done by assigning a particular probability to each individual model [14]. First, the fusion algorithm is applied to the outputs of different nonlinear ARX and Wiener-Hammerstein models for each sensor obtained using different nonlinearity estimators. Second, the fusion algorithm is again applied to the final fusion based

Table 1: Different Nonlinearity Estimators and Model Fit Values for Motor Point Sensor.

S. No.	Model	Nonlinearity Class	Model Fit
1.	<i>nlarx1</i>	Wavenet	24.78 %
2.	<i>nlarx2</i>	Treepartiton	40.46 %
3.	<i>nlarx3</i>	Sigmoidnet	48.75 %
4.	<i>nlhw2</i>	Wavenet	32.38 %
5.	<i>nlhw3</i>	Pwlinear	26.27 %
6.	<i>nlhw4</i>	Saturation	55.16 %
7.	<i>nlhw5</i>	Deadzone	42.45 %

Table 2: Different Nonlinearity Estimators and Model Fit Values for Ring1 Sensor.

S. No.	Model	Nonlinearity Class	Model Fit
1.	<i>nlarx31</i>	Wavenet	-60.76 %
2.	<i>nlarx32</i>	Treepartiton	-52.64 %
3.	<i>nlarx33</i>	Sigmoidnet	-39.36 %
4.	<i>nlhw31</i>	Pwlinear	31.06 %
5.	<i>nlhw32</i>	Sigmoidnet	10.05 %
6.	<i>nlhw33</i>	Saturation	31.57 %
7.	<i>nlhw35</i>	Wavenet	32.36 %

Table 3: Different Nonlinearity Estimators and Model Fit Values for Ring2 Sensor.

S. No.	Model	Nonlinearity Class	Model Fit
1.	<i>nlarx21</i>	Wavenet	-25.12 %
2.	<i>nlarx22</i>	Treepartiton	-22.31 %
3.	<i>nlarx23</i>	Sigmoidnet	-33.65 %
4.	<i>nlhw21</i>	Pwlinear	34.69 %
5.	<i>nlhw22</i>	Sigmoidnet	34.76 %
6.	<i>nlhw23</i>	Saturation	33.3 %
7.	<i>nlhw24</i>	Deadzone	34.94 %
8.	<i>nlhw25</i>	Wavenet	34.89 %

outputs of each sensor; this gives good force estimate. SI model fit value gives the probability for each model, which is given by  $\left[1 - \frac{|Y - \hat{Y}|}{|Y - \bar{Y}|}\right] * 100$ . The model selection criterion used in this paper is KIC. The sum of two directed divergences, which is the measure of the models dissimilarity, is known as Kullback's symmetric or J-divergence [15], as given by Equation (8).

$$KIC(p_i) = \frac{n}{2} \log R_i + \frac{(p_i + 1)n}{n - p_i - 2} - n\psi\left(\frac{n - p_i}{2}\right) + g(n), \quad (8)$$

where  $g(n) = n * \log(n/2)$ .

The following fusion algorithm as given by [14] is applied for data fusion of the outputs of different nonlinear ARX and Wiener-Hammerstein models:

- 1) Identify models  $M_1, M_2, \dots, M_k$  using sEMG data ( $u$ ) as input and force data ( $Y$ ) as output, for  $k$  number of sensors collecting data simultaneously.
- 2) Compute the residual square norm

$$R_i = \|Y - \Phi_i \hat{\Theta}_i\|^2 = \|Y - \hat{Y}\|,$$

where  $\hat{\Theta}_i = \{\Phi_i^T \Phi_i\}^{-1} \Phi_i^T Y$ , and

$$\Phi = \begin{bmatrix} Y_p^T & u_p^T & Y_{p-1}^T & \dots & u_1^T \\ Y_{p+1}^T & u_{p+1}^T & Y_p^T & \dots & u_2^T \\ \vdots & \vdots & \vdots & \ddots & \vdots \\ Y_{n-1}^T & u_{n-1}^T & Y_{n-2}^T & \dots & u_{n-p}^T \end{bmatrix}.$$

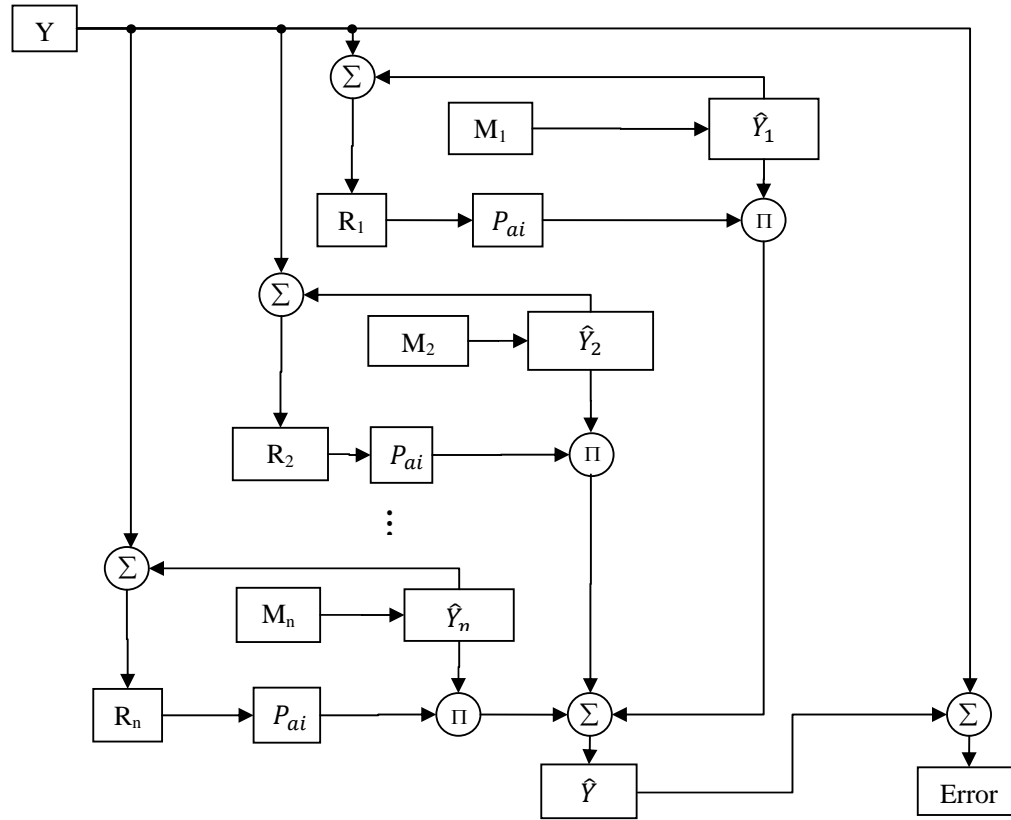


Fig. 7: Data Fusion and Adaptive KIC Probability.

- 3) Calculate the model criteria coefficient using Equation (8).
- 4) Compute the model probability  $p(M_i|Z) = \frac{e^{-l_i}}{\sum_{j=1}^k e^{-l_j}}$ , where  $l$  is model selection criterion, i.e.  $KIC(p_i)$ .
- 5) Compute the fused model output  $\hat{Y}_f = \sum_{i=1}^k p(M_i|Z) \hat{Y}_i$ .
- 6) Compute the overall model from  $\hat{Y}_f$  and force data.

Here all the computation from step 2) to 6) is adaptive i.e. the residual square norm,  $KIC(p_i)$ , model probability  $p(M_i|Z)$ , and fused model output  $\hat{Y}_f$  are being updated with time or for each data point. Fig. 7 shows the flow chart for fusion of outputs and adaptive probability of KIC.

## 5 Results, Discussion and Future Work

This section deals with the results, discussion and future work. The following plots show the nonlinear

(ARX and Wiener-Hammerstein) model and adaptive fusion algorithm based estimated force output for each sensor first and then finally combined adaptive fusion based output for all three sensors. Fig. 8 shows the overlapping plot of the original and adaptive fusion based force output for the motor point sensor. The output is the result of the adaptive fusion algorithm on three nonlinear ARX and four nonlinear Wiener-Hammerstein models for the motor point sensor signal. Fig. 9 shows the overlapping plot of the original and adaptive fusion based force output for ring1 sensor. This output is the result of adaptive fusion algorithm of three nonlinear ARX and four nonlinear Wiener-Hammerstein models for ring1 sensor signal. Fig. 10 shows the overlapping plot of the original and adaptive fusion based force output for ring2 sensor. This output is the result of adaptive fusion algorithm on three nonlinear ARX and five nonlinear Wiener-Hammerstein models for ring2 sensor signal. Fig. 11 shows the overlapping plot of the original and final combined adaptive fusion based force output for motor point, ring1 and ring2 sensors. The output is the result of adaptive fusion algorithm on the final



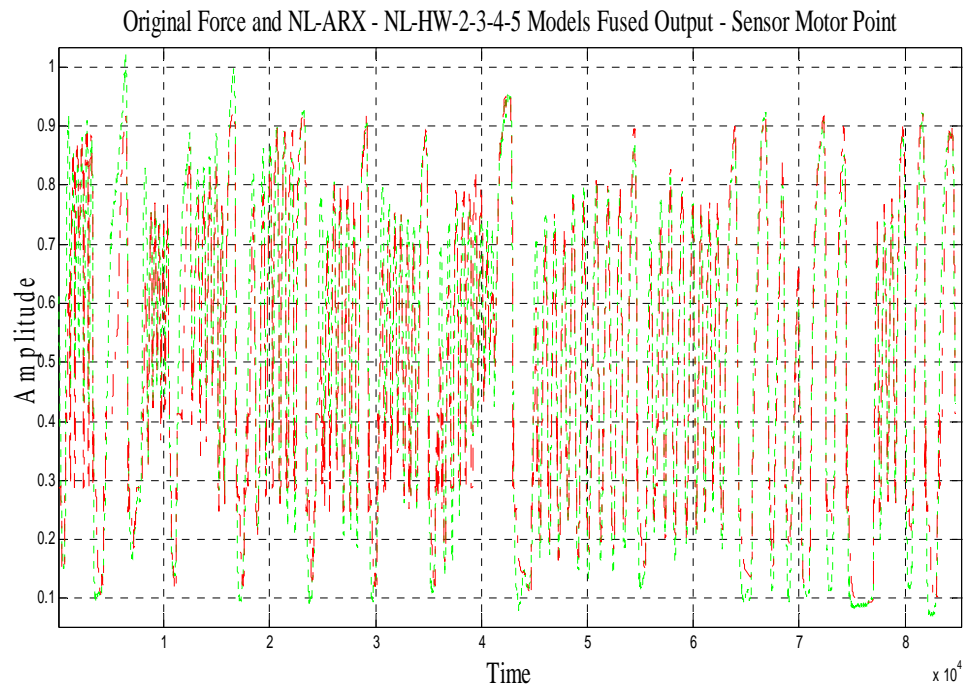


Fig. 8: Original and Fusion Based Output for Motor Point Sensor.

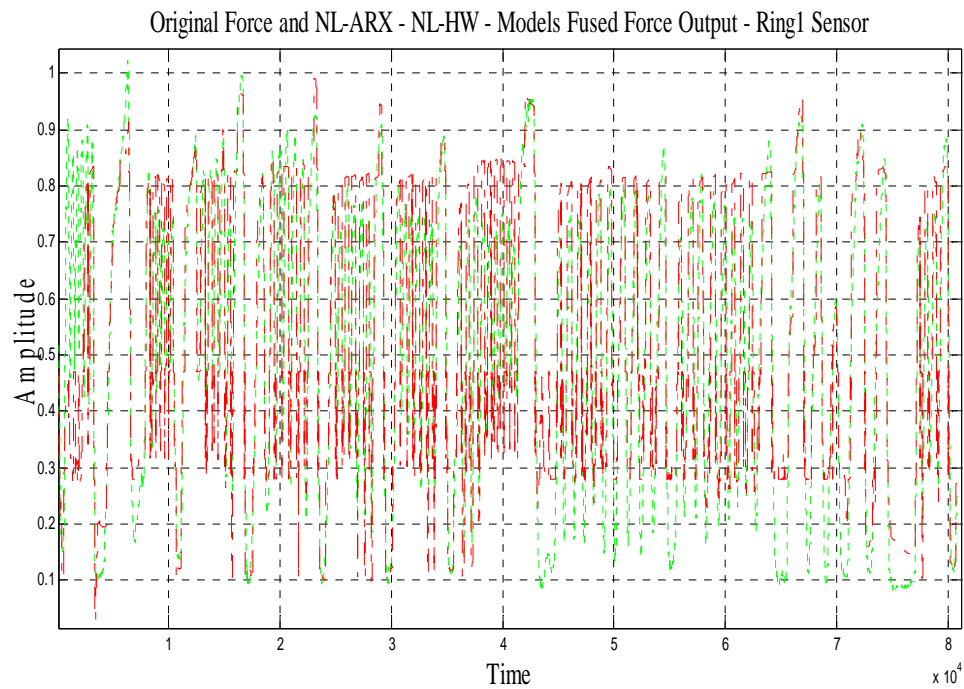


Fig. 9: Original and Fusion Based Output for Ring1 Sensor.

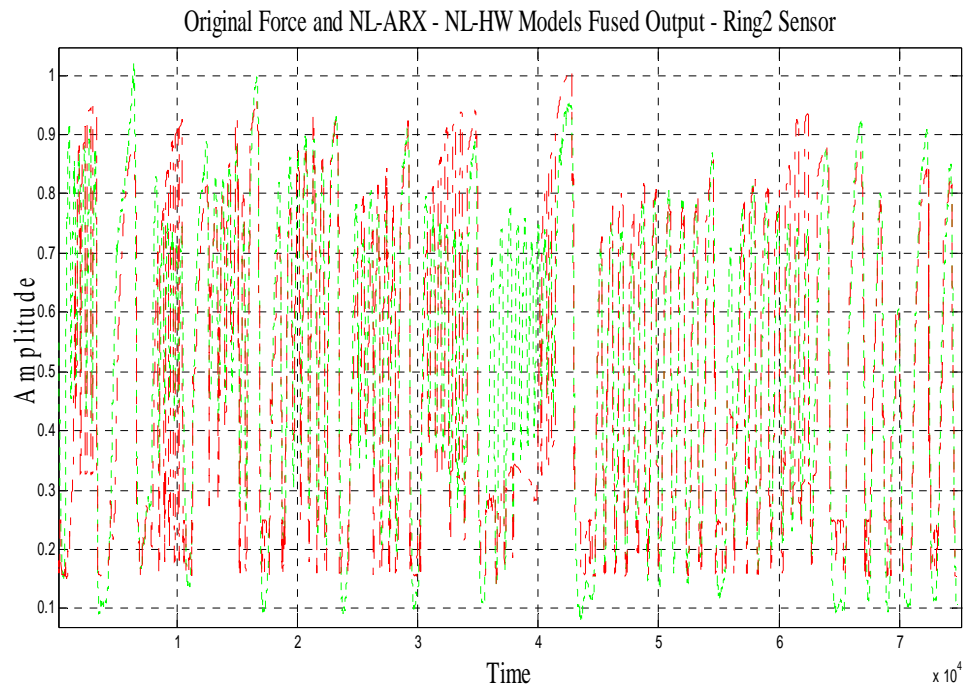


Fig. 10: Original and Fusion Based Output for Ring2 Sensor.

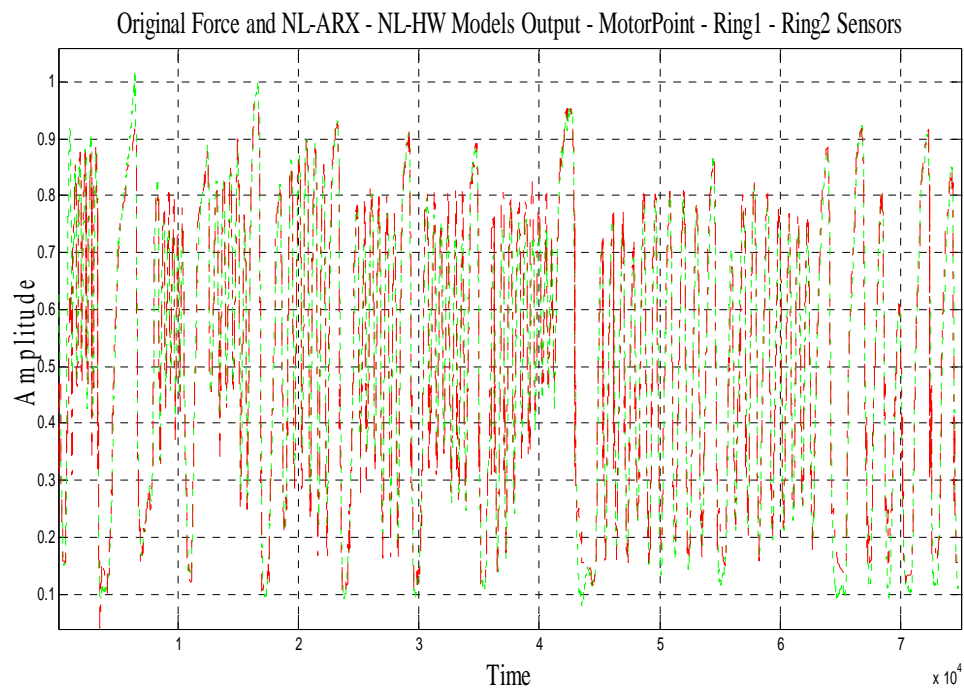


Fig. 11: Final Plot - Original and Fusion Based Output for All Three Sensors.

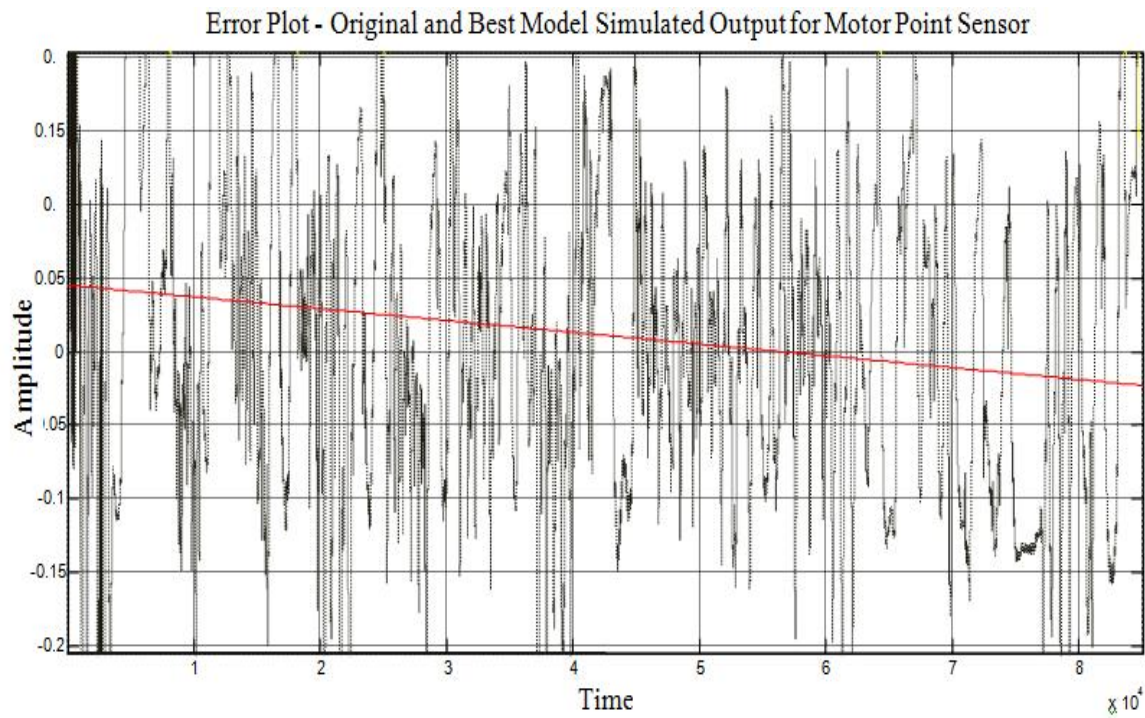


Fig. 12: Error Plot – Original and Best-Estimated Model Output for Motor Point Sensor.

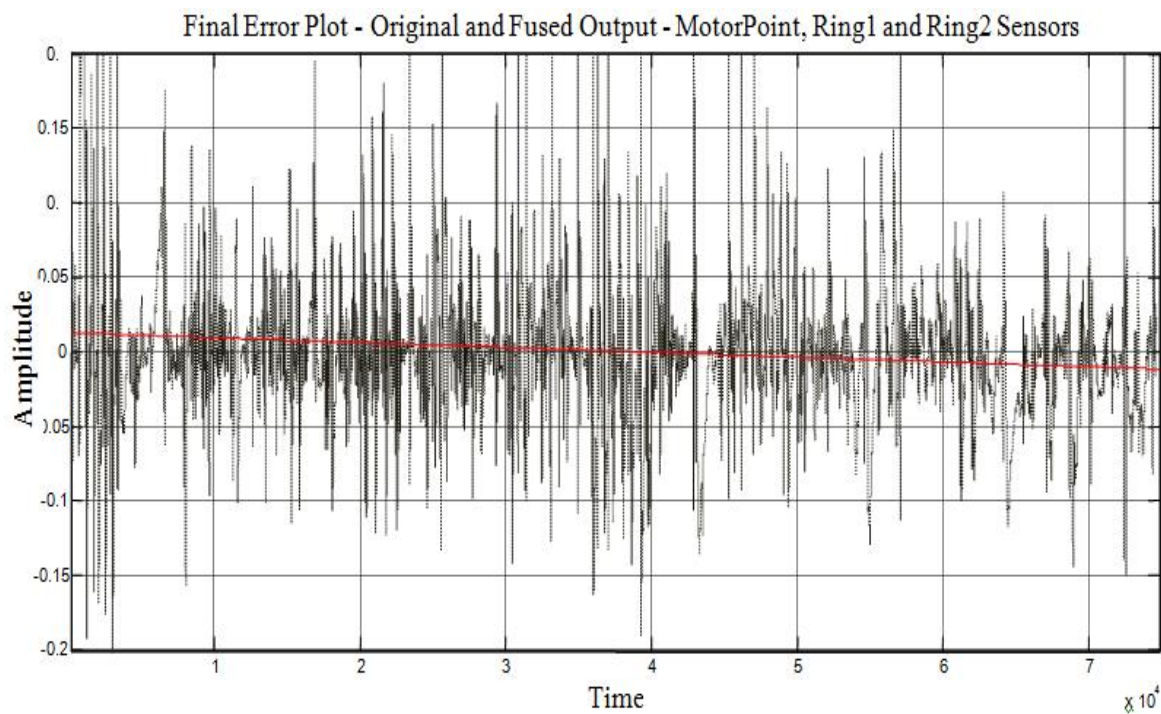


Fig. 13: Final Error Plot – Original and Fusion Based Output for Motor Point, Ring1 and Ring2 Sensors.

outputs of three sensors i.e. motor point, ring1 and ring2 as shown in Fig. 8 to 10. Fig. 11 shows the best skeletal muscle force estimate, which is the result of the multi nonlinear ARX and Wiener-Hammerstein models and an adaptive hybrid data fusion on these nonlinear models. Fig. 12 shows the error plot of the original and best-estimated model output for the motor point sensor.

Fig. 13 shows the error plot of original and final multi nonlinear modeled and adaptive hybrid data fusion based force estimate (results from three sensors, nonlinear modeling and adaptive data fusion algorithm). If we compare Fig. 12 and 13, it is very clear and conspicuous that the error has decreased remarkably and is very close to zero.

Future work will focus on the improvement of the data collection techniques and experimental setup. By using the combination of linear and nonlinear modeling, and adaptive hybrid data fusion, the skeletal muscle force estimate can be improved further. Furthermore, the authors believe that by using different model selection criteria such as Akaike Information Criterion (AIC), Kullback Information Criterion (KIC) and the Bayesian Information Criterion (BIC) together to obtain final skeletal muscle force estimate will give improved results.

## 6 Conclusions

sEMG and force data acquired using three EMG and one common FSR force sensor is modeled using nonlinear SI. Using different nonlinearity estimators/classes, multi nonlinear ARX and Wiener-Hammerstein models are obtained for each sensor. First, the outputs of different models for each sensor are fused with a data fusion algorithm and an adaptive KIC probability. Finally, the fused outputs from each sensor are again fused with same algorithm and adaptive KIC probability. The final estimated force using this technique gives the best estimate. The presented approach can be utilized for controlling prosthetic hands [16].

## Acknowledgement

The research was sponsored by the US Department of the Army, under the award number W81XWH-10-1-0128 awarded and administered by the U.S. Army Medical Research Acquisition Activity, 820 Chandler Street, Fort Detrick MD 21702-5014. The information does not necessarily reflect the position or the policy of the Government, and no official endorsement should be inferred. For purposes of this

article, information includes news releases, articles, manuscripts, brochures, advertisements, still and motion pictures, speeches, trade association proceedings, etc.

## References:

- [1] Kathryn Ziegler-Graham, PhD, et al., Estimating the Prevalence of Limb Loss in the United States - 2005 to 2050, *Archives of Physical Medicine and Rehabilitation*, 89 (2008): 422-429.
- [2] O'Connor, P., Iraq war vet decides to have second leg amputated, *Columbia Missourian*, 2009.
- [3] N. Dechev, W. L. Cleghorn, and S. Naumann, Multiple finger, passive adaptive grasp prosthetic hand, *Mechanism and Machine Theory*, 36(2001), pp. 1157-1173.
- [4] Haruhisa Kawasaki, Tsuneo Komatsu, and Kazunao Uchiyama, Dexterous Anthropomorphic Robot Hand With Distributed Tactile Sensor: Gifu Hand II, *IEEE/ASME Transactions on Mechatronics*, Vol. 7, No. 3, September 2002, pp. 296-303.
- [5] M. Zecca, S. Micera, M. C. Carrozza, and P. Dario, Control of Multifunctional Prosthetic Hands by Processing the Electromyographic Signal, *Critical Reviews™ in Biomedical Engineering*, 30(4-6), 2002, pp. 459-485.
- [6] Claudio Castellini and Patrick van der Smagt, Surface EMG in advanced hand prosthetics, *Biological Cybernetics*, (2009) 100, pp. 35-47.
- [7] C.J. De Luca, Myoelectrical manifestations of localized muscular fatigue in humans, *Crit. Rev. Biomed. Eng.*, 11 (4), 1984, pp. 251-279.
- [8] Terence D. Sanger, Bayesian Filtering of Myoelectric Signals, *J Neurophysiol*, 97, 2007, pp. 1839-1845.
- [9] M. B. I. Reaz, M. S. Hussain and F. Mohd-Yasin, Techniques of EMG signal analysis: detection, processing, classification and applications, *Biol. Proced. Online*, 2006, 8(1), pp. 11-35.
- [10] E. Kral, L. Vasek, V. Dolinay, P. Varacha, Usage of PSO Algorithm for Parameter Identification of District Heating Network Simulation Model, *The 14<sup>th</sup> World Scientific and Engineering Academy and Society (WSEAS) International Conference on Systems*, Corfu Island, Greece, July 22-24, 2010.
- [11] A. Neubaur, The Intrinsic System Model of the Simple Genetic Algorithm with  $\alpha$ -Selection, Uniform Crossover and Bitwise Mutation, *The 14<sup>th</sup> World Scientific and Engineering Academy and Society (WSEAS) International Conference*

- on Systems*, Corfu Island, Greece, July 22-24, 2010.
- [12] A. Sebastian, P. Kumar, M. P. Schoen, A Study on Hybridization of Particle Swarm and Tabu Search Algorithm for Unconstraint Optimization and Estimation, in *The 14<sup>th</sup> World Scientific and Engineering Academy and Society (WSEAS) International Conference on Systems*, Corfu Island, Greece, July 22-24, 2010.
- [13] Lennart Ljung, *System Identification Toolbox<sup>TM</sup> 7 User's Guide*, The MathWorks, Inc., 2010.
- [14] Huimin Chen and Shuqing Huang, A Comparative study on Model Selection and Multiple Model Fusion, *7<sup>th</sup> International Conference on Information Fusion*, 2005, pp. 820-826.
- [15] Abd-Krim Seghouane, Maiza Bekara, and Gilles Fleury, A Small Sample Model Selection Criterion Based on Kullback's symmetric Divergence, *IEEE Transaction on Signal Processing*, 2003, pp. 145-148.
- [16] C. H. Chen, D. S. Naidu, M. P. Schoen, An Adaptive Control Strategy for a Five-Fingered Prosthetic Hand, *The 14<sup>th</sup> World Scientific and Engineering Academy and Society (WSEAS) International Conference on Systems*, Corfu Island, Greece, July 22-24, 2010.

# sEMG Based Fuzzy Control Strategy with ANFIS Path Planning For Prosthetic Hand

Chandrasekhar Potluri, Parmod Kumar, Madhavi Anugolu, Steve Chiu, Alex Urfer, Marco P. Schoen, and D. Subbaram Naidu, *Fellow, IEEE*.

**Abstract**—This paper presents an intelligent adaptive neuro-fuzzy inference system (ANFIS) based fuzzy Mamdani controller for a multifingered prosthetic hand. The objective of the controller is to move the finger joint angles along pre-determined paths representing a grasping motion. The initiation of the grasping task is evaluated via EMG-entropy data, measured at the forearm of the prosthetic user. In addition to the motion control, the finger force is regulated with a Fuzzy logic controller. Simulation results indicate good performance of the proposed controller. Results show that the outputs follow the hand/finger force and given reference trajectory closely.

## I. INTRODUCTION

The design of a prosthetic hand is challenging because of sensing, classification, mechanical, electrical, control and cosmetic issues. Creating a best solution to the user is a big concern in the design of each limb prosthesis. Degree of amputation, residual of motor points for different fingers, and the needs and abilities of the user have to be addressed. Certain degree of adaptation is required for each user. A high degree of customization is required as per the specifics of different users because each has different gender, size, side, and degree of loss. All these differences cause the complexity and challenges in assembly and fitting [1].

In the traditional design, each joint has separate mechanical substitute and requirements. Since a single controller operates the entire prosthesis, the controller has a critical role to play. Depending on the degree of amputation, there are limited numbers of control signals

available. Therefore, designing an efficient control strategy based on these limited inputs for the maximum operating range is a challenging task [1].

Similar to artificial neural networks (ANNs), fuzzy inference systems (FISs) are excellent tools to design human-made systems that can deal with the information processing like a human brain [2, 3].

First, using a set of membership functions (MF), the fuzzy system, fuzzifies inputs to values at interval [0, 1], and then it is inferred by fuzzy logic through rules in the form of IF-THEN. Mamdani fuzzy model uses linguistic models based on the collection of IF-THEN rules. The Mamdani model's fuzzy rule is given by Equation (1).

$$R^i = \text{If } x_1 \text{ is } A_1^i \text{ and } x_2 \text{ is } A_2^i \dots \text{and } x_n \text{ is } A_n^i \text{ then } y^i \text{ is } B^i. \quad (1)$$

where  $R^i (i = 1, 2, \dots, l)$  denotes the  $i^{th}$  fuzzy rule,  $x_j (j = 1, 2, \dots, n)$  is the  $n^{th}$  input,  $y^i$  is the output of the fuzzy rule  $R^i$ , and  $A_1^i, A_2^i, \dots, A_n^i, B^i (i = 1, 2, \dots, l)$  are fuzzy membership functions [3,4].

In this method, a nonlinear system is approximated using several linear systems by decomposing the entire input space into several partial fuzzy spaces and assigning a linear equation to each output. Sugeno-type systems are more suitable to give a precise solution whereas Mamdani-type systems are best suited to obtain a good linguistic interpretability [3,4].

The EMG signal originates because of the neuromuscular activity in the body. Surface electromyographic (sEMG) signals are captured noninvasively and give access to physiological processes responsible for the contraction of muscles. sEMG signal is complicated and dynamic in nature. Apart from instrument characteristics, physiological factors and anatomical properties also affects sEMG signal, which makes it change from person to person. Presently, sEMG signals are the most common input for the design of a controller for prosthetic hand and are in use since 1948 [5]. In past several EMG-based algorithms have been developed and used to enhance the functionality and usability of prosthetic hands [5]. Large number of degrees of freedom, and highly nonlinear coupled dynamics make the control of multi-fingered robotic hand complicated [6]. In addition to the position control, the tactile sensing and force control is also required; this makes it a more complex problem. There has been active research in the area of position and force control of a robotic hand, the typical approach is hybrid position and force control given by [7].

Chandrasekhar Potluri is with Measurement and Control Engineering Research Center (MCERC), College of Engineering, Idaho State University, Pocatello, Idaho 83209, USA (e-mail: potlchan@isu.edu).

Parmod Kumar is with MCERC, College of Engineering, Idaho State University, Pocatello, Idaho 83209, USA (email: kumaparm@isu.edu).

Madhavi Anugolu is with MCERC, College of Engineering, Idaho State University, Pocatello, Idaho 83209, USA (email: anugmadh@isu.edu).

Steve Chiu is with Department of Electrical Engineering and Computer Science, MCERC, Idaho State University, Pocatello, Idaho 83209 USA (email: chiustev@isu.edu).

Alex Urfer is with Department of Physical and Occupational Therapy, Idaho State University, Pocatello, Idaho 83209, USA (email: urfealex@isu.edu).

Marco P. Schoen is with Department of Mechanical and Nuclear Engineering, MCERC, Idaho State University, Pocatello, Idaho 83209, USA (email: schomarc@isu.edu).

D. Subbaram Naidu is with Department of Electrical Engineering and computer science, MCERC, Idaho State University, Pocatello, Idaho 83209 USA (email: naiduds@isu.edu).



A method based on support vector machines is proposed in [9]. This method can detect the opening and closing actions of the human thumb, index and other fingers, which are recorded using EMG. The method was tested and used for the control of the DLR four-finger hand II [10]. Another method given in [11] is called as Tendon-activated pneumatic (TAP) control. TAP hand claims a natural degree of control on force, duration, and coordination of multiple finger movements. An ANFIS based intelligent approach that integrates a real-time learning scheme to identify hand motion commands is proposed in [8]. The common assumption that the instantaneous value of the myoelectric signal contains no information is the bases for most of the commercial myoelectric control systems. Generally, users are trained to stimulate the muscle for a constant level of activation and the prostheses are tuned according to these EMG values. Since, the active modification of recruitment and firing patterns needed to sustain a contraction, so very little temporal structure are present in steady-state EMG signal [12]. The parameters like variance, mean absolute value or Fourier spectrum, median frequency can be used to quantify the amplitude of EMG signal, but usually not sufficient to distinguish between more than two classes of movement.

We are using the entropy values as inputs to design an ANFIS based fuzzy controller for a prosthetic hand. In physical sense, entropy is related to the amount of ‘disorder’ in the system and is proportional to the logarithm of the number of microstates available to a thermodynamic system. Shannon and Weaver in [13] gave the concept of entropy for information theory. Later on Johnson and Shore in [14] used entropy for the power spectrum of a signal. For instance, a signal has an entropy value of zero if its sequential values are alternate of one fixed magnitude and then of another fixed magnitude. A signal with zero entropy value is completely regular and very predictable. In contrast, a signal has higher entropy if a random number generator generates its sequential values. Using entropy, we can visually distinguish a regular signal from an irregular one. Entropy is independent of absolute scales and can be computed by various methods like approximate entropy [15, 16] or Shannon entropy [13, 16, 17] in time domain and spectral entropy [13, 14, 18, 19] in frequency domain.

In this paper, an ANFIS based Mamdani controller is designed for prosthetic hand to control the grasping action. From 11 healthy subjects hand/finger force and sEMG signals were captured for index, middle and ring fingers after detecting the respective motor points using a muscle stimulator. Two experiments were conducted for each subject for grasping a stress ball using power grip. Entropy values are computed for each signal and each person. The non-normalized Shannon entropy is given by Equation (2).

$$E(s) = -\sum_i s_i^2 * \log(s_i^2). \quad (2)$$

where  $s$  is the signal and  $s_i$  the coefficients of  $s$  in an orthonormal basis.

Using these entropy values as input a Mamdani controller is designed. Figure 1 shows the flowchart of grasping action for human hand.

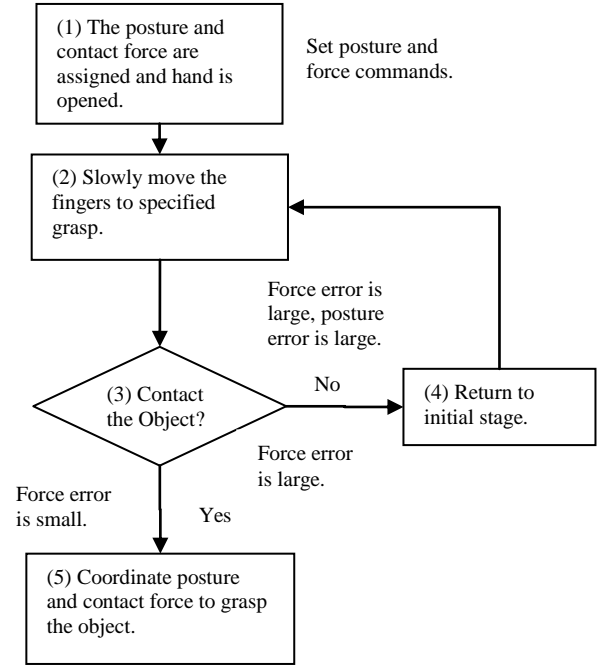


Figure 1: Flowchart of Grasping Action for Human Hand.

## II. EXPERIMENTAL SET-UP AND DATA CAPTURING

Motor point locations for ring, middle, and index finger were detected using muscle stimulator. Three sensors were placed for three motor points of ring, middle and index finger. Prior to placing the EMG sensors, the skin surface of the subject was prepared according to International Society of Electrophysiology and Kinesiology (ISEK) protocols. Two experiments for the power grip of dominant hand of the subject were conducted for ten subjects and EMG signals for all three sensors were acquired simultaneously using DELSYS® Bagnoli-16 EMG system with DE-2.1 differential EMG sensors. The corresponding force data was captured using NI ELVIS with Interlink Electronics FSR 0.5” circular force sensor and Lab VIEW™ 8.2 at a sampling rate of 2000 Hz. The experimental set-up is shown in Figure 2.

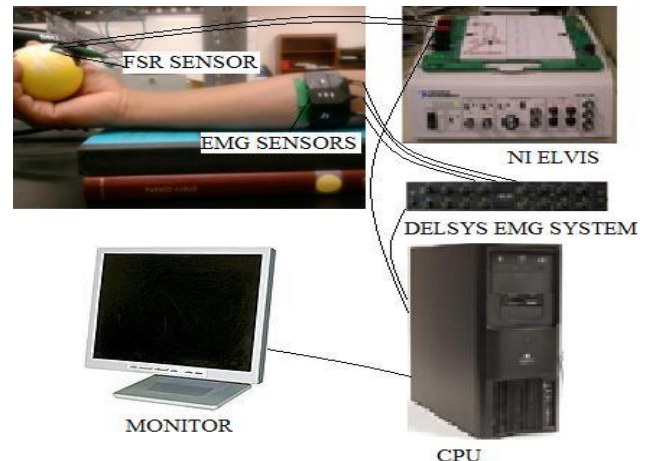


Figure 2: Experimental Set-Up.

### III. PROPOSED DESIGN

In this proposed design, entropy is taken as the threshold value to initiate the motion by the fuzzy controller. The entropy values are extracted from the EMG signals of the index, middle and ring fingers respectively when a power grip is done. Table 1 shows the entropy values for the EMG data taken for 11 different subjects. Ring<sub>1</sub> and Middle<sub>1</sub> in the Table 1 correspond to the entropy of the respective finger right next to its motor point location. Table 2 gives the threshold values. The threshold values are calculated as the difference between the mean and twice the standard deviation. The reason for taking the difference as the threshold value is, that the controller should be initiated even if the sensors are misplaced from the motor units or to eliminate the problems that are caused by the difficulty in identification of motor units in some cases.

Table 1: Entropy values of EMG Signal for Different Fingers.

Index	Ring	Middle	Ring <sub>1</sub>	Middle <sub>1</sub>
2.9792	2.9271	2.1554	2.3994	1.6711
2.6783	3.0008	1.9376	2.3947	1.5346
3.4943	2.9556	3.0277	2.9568	2.6673
3.679	3.1714	2.9268	3.1175	3.0581
3.2110	2.7015	1.9228	2.7997	1.2993
2.8451	2.9429	1.9555	3.0541	1.1095
1.4653	1.5559	3.7151	2.4827	1.6919
1.9371	1.4639	3.6648	3.2785	1.7955
2.7399	3.7132	3.0820	3.0425	2.3929
2.5421	3.5961	2.8593	2.6782	2.2040

Table 2: Threshold values for Index, Ring and Middle Finger EMG Signal.

Index	Ring	Middle
1.3724	1.5176	1.522

In this proposed design, entropy values are used to establish a threshold value for initiation of finger motion. The fuzzy logic determines the correlation between the entropy and the corresponding force. The Mamdani type fuzzy logic is used to in this design. The fuzzy logic implemented in this design has four inputs and two outputs. The inputs for the fuzzy logic are the threshold values for individual finger (index, ring and middle) and the entropy values. The output of the fuzzy logic are the control signals to initiate the motion based on the threshold values and the control signal for the force based on the entropy values. Figure 3 shows the entire rule base for the developed fuzzy logic.

In the Figure 3, columns 1, 2, 3 represent the rules for the sigmoidal membership function of input (i.e.) index, middle and ring fingers respectively and the corresponding threshold values.

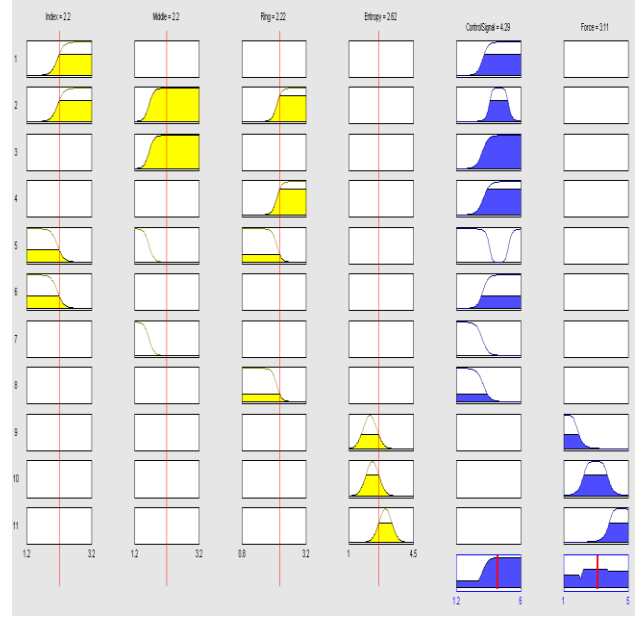


Figure 3: Rules for Fuzzy Logic.

The sigmoidal function enables the initiation of movement for an entropy value, which is greater than or equal to threshold value of individual fingers. 4<sup>th</sup> and 6<sup>th</sup> columns give the rule base for the correlation of entropy with the corresponding force. The entropy range into three levels classifies the force.

The rules for the proposed fuzzy controller are given below:

1. If  $I_i$  is  $I_t$ ,  $M_i$  is  $M_t$ ,  $R_i$  is  $R_t$  then the control signal is power grip close.
2. If  $I_i$  is not  $I_t$ ,  $M_i$  is not  $M_t$  and  $R_i$  is not  $R_t$ , then control signal is power grip open.
3. If  $I_i$  is  $I_t$  then control signal is index finger close.
4. If  $I_i$  is not  $I_t$  then control signal is index finger open.
5. If  $M_i$  is  $M_t$  then control signal is middle finger close.
6. If  $M_i$  is not  $M_t$  then control signal is middle finger open.
7. If  $R_i$  is  $R_t$  then control signal is ring finger close.
8. If  $R_i$  is not  $R_t$  then control signal is ring finger open.
9. If entropy is low, then control signal is low force.
10. If entropy is medium, then the control signal is medium force.
11. If entropy is high, then the control signal is high force.

In the above rules  $I_i$ ,  $M_i$ ,  $R_i$  are the input entropy values and  $I_t$ ,  $M_t$ ,  $R_t$  are the threshold values for individual index, middle and ring fingers respectively.

In conventional work, ANNs was used to detect the recognition of human motor and to control the prosthetic robotic hand/arm in several groups. For instance, Fukuda et al. achieved the EMG control of the prosthetic hand by using the probabilistic NN controller [20].



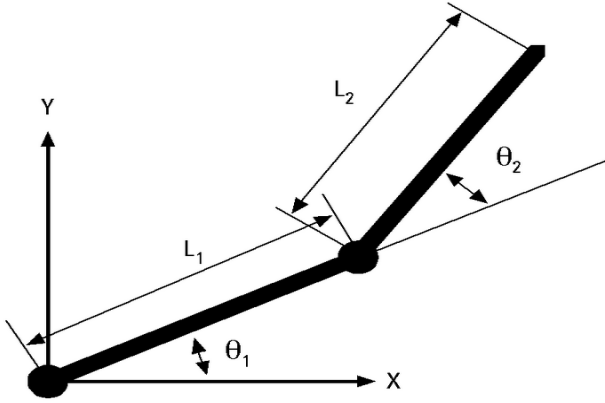


Figure 4: Two-Joint Robotic Arm with Two Angles,  $\theta_1$  and  $\theta_2$ .

After the initiation of movement and the force definition from the fuzzy logic the path planning is done by ANFIS. Inverse kinematics is proposed to achieve the mechatronic design of the arm. This contributes to a two-joint robotic arm with the two angles,  $\theta_1$  is the angle between the reference and the first joint, and  $\theta_2$  the angle between the first arm and the second joint. Figure 4 illustrates the two-joint robotic arm with the two angles,  $\theta_1$  and  $\theta_2$ .

Based on the input-output data, this learning algorithm tunes the membership of fuzzy inference systems. In this paper, the input-output data refers to the coordinate angles, which act as input to ANFIS. The learning algorithm makes the ANFIS to map the coordinates to the angles in its training process. The trained ANFIS network is learned to map the input and output and is ready to be deployed in the large control system solution at the end of the training process. In this proposed design, the first joint is limited to its rotation and is between zero to 90 degrees. Similarly, the second joint has the limited rotation, between zero to 180 degrees.

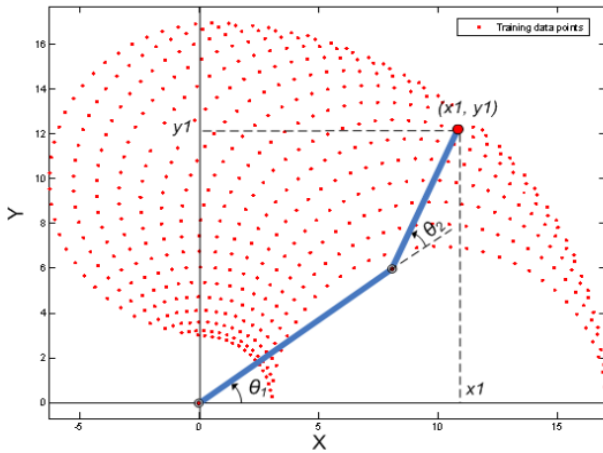


Figure 5: X, Y- coordinates Generated for All Possible  $\theta_1$  and  $\theta_2$  Values.

Figure 5 shows X, Y- data points generated by cycling through different combinations of  $\theta_1$  and  $\theta_2$  and deducing x and y coordinated for each. The ANFIS networks should be able to predict the angles they have to be trained with sample input-output data. The first ANFIS network is trained with X and Y coordinates as input and corresponding  $\theta_1$  value as output. This input-output data is

used to train the first ANFIS network. Similarly, the second ANFIS network is trained with X and Y coordinates as input and corresponding  $\theta_2$  values as output. After the completion of the training process, the ANFIS networks are learned to approximate the angles ( $\theta_1, \theta_2$ ) as a function of coordinates (x, y). The fuzzy approach in ANFIS enables the approximation of the angles for the coordinates that are similar but not exactly, the same as it was trained. The two ANFIS networks are capable of approximating angles for the coordinates that lies between two points that were included in the data set. This allows controller to move the arm smoothly in the allowed space.  $\theta_1$  and  $\theta_2$  values can be deduced mathematically from the x and y coordinates using inverse kinematics formulae. Using this mathematically deduced  $\theta_1$  and  $\theta_2$  values the two ANFIS networks are validated. The inverse kinematics formulae are given in Equations (3) to (8).

$$k_1 = l_1 + l_2 * c_2. \quad (3)$$

$$k_2 = l_2 * s_2. \quad (4)$$

$$\theta_1 d = \tan^{-1} 2(Y, X) - \tan^{-1}(k_2, k_1). \quad (5)$$

$$c_2 = (X^2 + Y^2 - l_1^2 - l_2^2) / (2 * l_1 * l_2). \quad (6)$$

$$s_2 = \sqrt{(1 - c_2^2)}. \quad (7)$$

$$\theta_2 d = \tan^{-1} 2(s_2, c_2). \quad (8)$$

X and Y are the transformed domain specified by vectors x and y into arrays.  $l_1$  and  $l_2$  are length of arm 1 and arm 2 respectively.

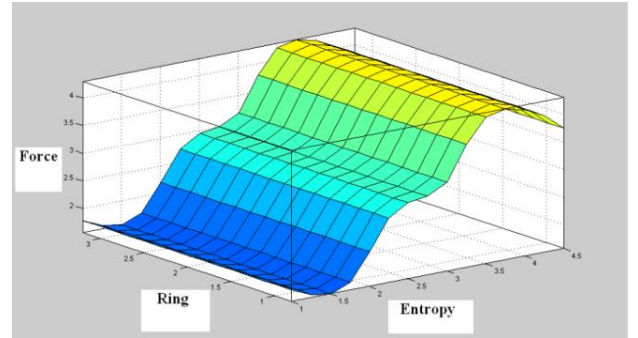


Figure 6: Surface Plot for Entropy and Its Corresponding Force.

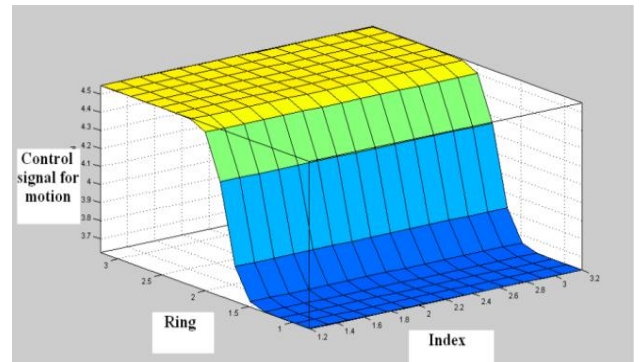


Figure 7: Surface Plot for the Threshold Values for Individual Fingers and the Control Signal for Initiation of Motion.

Figures 6, 7 shows the surface plots of the developed fuzzy logic. Figure 6 deduces the relationship between the entropy and force. The force is a function that correlates

with the entropy classification. Therefore, the fuzzy logic achieves the control for the initiation of motion and force corresponding to entropy.

#### IV. RESULTS

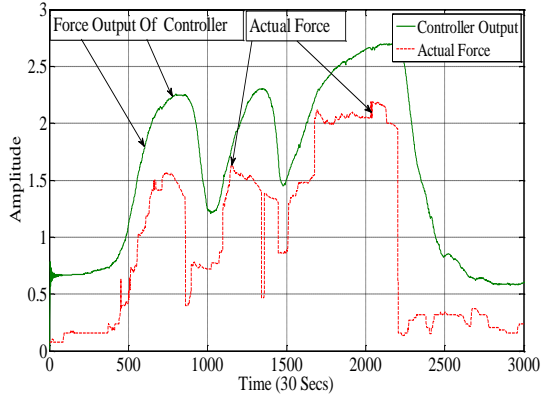


Figure 9: Force Correlation

Force correlation with the entropy of the EMG signal is achieved by the classification of entropy into three sets (i.e.) high, medium and low. Figure 9 shows the controller force that is correlated with the entropy values. It also exhibits the trend with the original force data measured from the FSR while performing the power grip. The amplification of the force is also achieved.

After initiating the finger movements by the fuzzy inference system based on the threshold values, the ANFIS output follows the given reference trajectory. The reference data is generated by applying a bell shaped membership function to the inverse kinematics equations. The output of the ANFIS for eleven training data sets to track the reference data generated is shown in Figure 10. It follows the same path as the reference data. Figure 11 shows the variation of the difference between the generated reference data and the ANFIS output data. From this figure it is evident that the controller is fast since the error is nullified quickly. The training for the ANFIS network is done in such a way that the error converges to zero over time.  $\theta_1 D$  and  $\theta_2 D$  are the deduced  $\theta$  values and are calculated by using the inverse kinematics.  $\theta_1 P$  and  $\theta_2 P$  are predicted from the ANFIS. Figure 12 shows the difference between the deduced and predicted values. The errors are small, which indicates that ANFIS predicts the  $\theta$  values close to deduced ones.

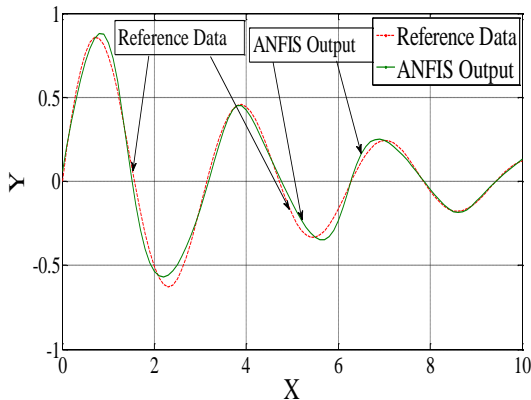


Figure 10: Validation of ANFIS Output.

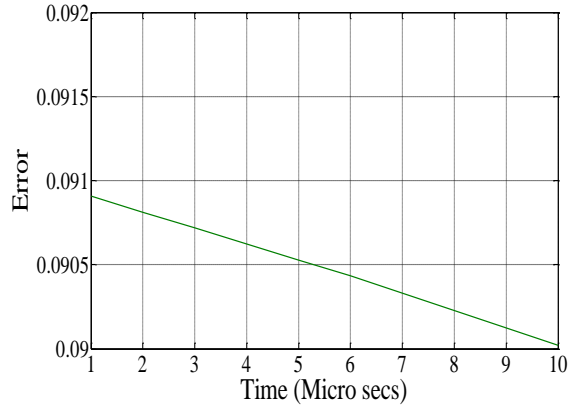


Figure 11: Difference between Reference Data and ANFIS Output Data.

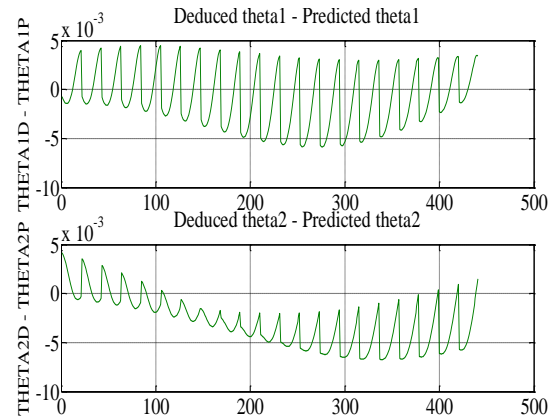


Figure 12: Error between Deduced  $\theta$  and Predicted  $\theta$ .

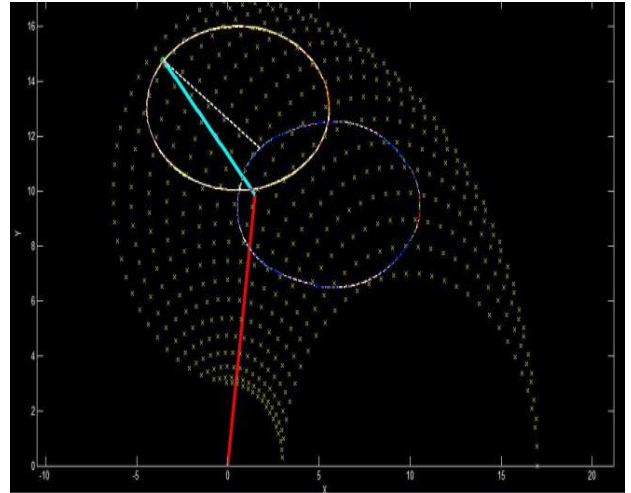


Figure 13: Path Tracking by ANFIS Controller.

The path tracking of the ANFIS to follow an object in the workspace is demonstrated in Figure 12. The object in the figure is the reference trajectory. The tip of the second joint moves along the trajectory. If the object is moved to some other location in the workspace, the tip of the second joint tracks the change and moves along the new trajectory. Hence, the proposed controller initiates the motion through the fuzzy logic with correlation for force and the path planning is achieved by the ANFIS.

## V. CONCLUSION AND FUTURE WORK

An ANFIS based fuzzy controller is designed for a prosthetic hand. Controlled output follows the given reference trajectory very closely, at the same time the error between the deduced and predicted angles are very small. This justifies the accuracy of ANFIS designed fuzzy controller. The designed controller can also track the change of the reference trajectory in the workspace and moves the link to the new trajectory. In addition to the position, the correlation for force is achieved by the fuzzy logic. In the future work we are planning to implement model-based position and force estimation and then the controller design for position and force control.

## ACKNOWLEDGMENT

This work was supported by a grant from the Telemedicine Advanced Technology Research Center (TATRC) – Department of Defence (DoD) and is hereby acknowledged. The support by Anish Sabastian and Jensen Alex is greatly appreciated.

## REFERENCES

- [1] Peter J. Kyberd, Adrian S. Poulton, Leif Sandsjö, Stewe Jonsson, Ben Jones, David Gow, "The ToMPAW Modular Prosthesis: A Platform for Research in Upper-Limb Prosthetics" American Academy of Orthotists and Prosthetists, 2006.
- [2] M. Zecca, S. Micera, M.C. Carrozza, and P. Dario, "Control of Multifunctional Prosthetic Hands by Processing the Electromyographic Signal." *Critical Reviews in Biomedical Engineering*, 30(4-6):459-485, 2002.
- [3] Kosko B. *Fuzzy Engineering*. New York: Prentice Hall, 1996.
- [4] Mitra S, Hayashi Y. Neuro-fuzzy rule generation: Survey in soft computing framework. *IEEE Trans Neural Netw* 2000; 11:748-768.
- [5] Reiter R. Eine neue elektrokunsthand. *Grenzgebiete der Medizin* 1948; 4:183.
- [6] T. H. Sueeter. "Control of the Utah/MIT Dextrous hand: Hardware and software hierarchy," *J. Robot. Syst.*, vol. 7, no. 5, pp. 759-790, 1990.
- [7] M. H. Raibert and J. J. Craig, "Hybrid position and force control of manipulators," *ASME J. Dyn. Syst. Meas. Contr.*, vol. 102, pp. 126-133, June 1981.
- [8] Mahdi Khezri and Mehran Jahed, "Real-time intelligent pattern recognition algorithm for surface EMG signals." *BioMedical Engineering OnLine* December 2007, 6:45.
- [9] Sebastian Bitzer, and Patrick van der Smagt, "Learning EMG control of a robotic hand: Towards Active Prosthesis." *IEEE International Conference on Robotics and Automation*, Orlando, Florida - May 2006.
- [10] J. Butterfass, M. Fischer, and M. Grebenstein, "Design and Experiences with DLR Hand II," in *Proceedings of the World Automation Congress*, 2004.
- [11] William Craelius, Ricki L. Abboudi, and Nicki Ann Newby, "CONTROL OF A MULTI-FINGER PROSTHETIC HAND." *International Conference on Rehabilitation Robotics*, Stanford, CA, 1999.
- [12] Bashamajian JV, De Luca CJ. *Muscles Alive*. Baltimore, MD: Williams & Wilkins, 1985.
- [13] Shannon CE. A mathematical theory of communication. *Bell System Techn J* 1948; 27 (379-423): 623-56.
- [14] Johnson RW, Shore JE. Which is the better entropy expression for speech processing:  $-S \log S$  or  $\log S$ ? *IEEE Trans Acoust* 1984; ASSP-32: 129-37.
- [15] Pincus SM, Gladstone IM, Ehrenkranz RA. A regularity statistic for medical data analysis. *J Clin Monit* 1991; 7: 335-45.
- [16] Bruhn J, Ropcke H, Hoeft A. Approximate entropy as an electroencephalographic measure of anesthetic drug effect during desflurane anesthesia. *Anesthesiology* 2000; 92: 715-26.
- [17] Bruhn J, Lehmann LE, Ropcke H, Bouillon TW, Hoeft A. Shannon entropy applied to the measurement of the electroencephalographic effects of desflurane. *Anesthesiology* 2001; 95: 30-5.
- [18] Rezek IA, Roberts SJ. Stochastic complexity measures for physiological signal analysis. *IEEE Trans Biomed Eng* 1998; 45: 1186-91.
- [19] Inouye T, Shinosaki K, Sakamoto H et al. Quantification of EEG irregularity by use of the entropy of the power spectrum. *Electroencephalogr Clin Neurophysiol* 1991; 79: 204-10.
- [20] O. Fukuda, T. Tsuji, M. Kaneko and A. Otsuka: A Human-Assisting Manipulator Teleoperated by EMG Signals and Arm Motions, *IEEE Transactions on Robotics and Automation*, Vol.19, No.2, pp.210-222, 2003.

# FREQUENCY DOMAIN SURFACE EMG SENSOR FUSION FOR ESTIMATING FINGER FORCES

Chandrasekhar Potluri, Parmod Kumar, Madhavi Anugolu, Alex Urfer, Steve Chiu, D. Subbaram Naidu, *Fellow, IEEE*, and Marco P. Schoen, *Member, IEEE*

**Abstract**— Extracting or estimating skeletal hand/finger forces using surface electro myographic (sEMG) signals poses many challenges due to cross-talk, noise, and a temporal and spatially modulated signal characteristics. Normal sEMG measurements are based on single sensor data. In this paper, array sensors are used along with a proposed sensor fusion scheme that result in a simple Multi-Input-Single-Output (MISO) transfer function. Experimental data is used along with system identification to find this MISO system. A Genetic Algorithm (GA) approach is employed to optimize the characteristics of the MISO system. The proposed fusion-based approach is tested experimentally and indicates improvement in finger/hand force estimation.

## I. INTRODUCTION

The number of people with missing limbs due to combat and non-combat operations in the United States is over 1.2 million according to [1]. The recent wars in Afghanistan and Iraq substantially increased the number of amputees. To date there are no prosthetic devices available at an affordable cost and with the full functionality of a human hand. The need for such a device in these days is becoming more important. There are multiple types of hand prostheses. One of these types is based on measuring sEMG signals to initiate the actuation of the robotic hand. In this paper, surface based EMG sensors are used in order to avoid invasive methods of measuring EMG signals [2]. The major problem in capturing the sEMG signal is cross-talk from different motor units. As a muscle contracts several motor units fire simultaneously and hence make up the EMG signal [3].

Chandrasekhar Potluri is with Measurement and Control Engineering Research Center (MCERC), Idaho State University, Pocatello, Idaho 83201 USA (e-mail: potlchan@isu.edu).

Parmod Kumar is with MCERC, Idaho State University, Pocatello, Idaho 83201 USA (e-mail: kumaparm@isu.edu).

Madhavi Anugolu is with MCERC, Idaho State University, Pocatello, Idaho 83201 USA (e-mail: anugmadh@isu.edu).

Alex Urfer is with Department of Physical and Occupational Therapy, Idaho State University, Pocatello, Idaho 83201 USA (e-mail: urfealex@isu.edu).

Steve Chiu is with Department of Electrical Engineering and Computer Science, MCERC, Idaho State University, Pocatello, Idaho 83201 USA (e-mail: chiustev@isu.edu).

D. Subbaram Naidu is with Department of Electrical Engineering and Computer Science, MCERC, Idaho State University, Pocatello, Idaho 83201 USA (e-mail: naiduds@isu.edu).

Marco P. Schoen is with Department of Mechanical Engineering, MCERC, Idaho State University, Pocatello, Idaho 83201 USA (e-mail: schomarc@isu.edu).

The number of motor units in individual muscles varies from person to person and muscle fatigue begins at the onset of contraction and is ongoing throughout (i.e.) time to contraction failure or reduction in force generating capacity of the muscle. The EMG signal passes through several layers of tissues before reaching the skin surface [3]. This contributes to noise and interference in signal acquisition. The randomness of the EMG signal is an added difficulty in studying it. All of these factors make it rather complex to discriminate the content of the EMG signal against noise and interference. Identification of the content of the EMG signal should focus on the amplitude, frequency and amplitude-frequency content using distinct methods. Since the signal is amplitude modulated and time dependent, it is therefore spatially and temporally frequency encoded [4].

An approach to distinguish the onset of muscle contraction was introduced by Merlo et al. [5]. In their study, the sEMG sensors collect the action potential of individual motor units which are in turn identified by using a continuous wavelet transform. Accuracy of determining the intended force from the EMG signal is improved by using an array sensor. Array sensors use multi-channel EMG electrodes embedded into a small surface area in order to capture the electrical muscle activity from a set of muscles fibers at the skin level. The EMG sensor array approach produces a micro level and a macro level sensor network by utilizing several array sensors at different skin locations of the forearm. An array of micro sensors with the objective to extract signals from one motor unit corresponds to the micro level. The main objective of this arrangement is to use redundant data to infer the hand motion by including cross-talk. Also, a multi-channel methodology is proposed where elements of the sensor array is discarded based on the quality of the signal [6]. A simple sensor fusion scheme to improve the estimated hand/finger force from measured sEMG data based on Bayesian approaches was given [7].

In the following, Genetic Algorithm (GA) is used to accomplish the sensor fusion algorithm [8]. Briefly, GA's are evolutionary algorithms that simulate Darwin's survival of the fittest principle. The initial population of candidate solutions is randomly generated and represented as chromosomes in the form of genes. These chromosomes are evaluated based on an objective function and ranked in terms of its fitness. A subset of the next generation of candidate solutions is selected based on their performance with the objective function. The remaining set of the new generation is generated by a mating process, where the best performing candidate solution comprise the subset of the parents. In

addition to the mating process, a mutation rate is also embedded in the generation of the new population. The mutation rate enables the search for the optimum solution to overcome local minimums and locate the global minimum. This process of selection, mating, and mutation is repeated a number of times until the best performing candidate solution converges to some stationary value. GA's have the capability of overcoming local minima, some additional advantages of a genetic algorithm are the ease with which large numbers of parameters can be handled, the fact that they do not require the traditional approach of taking derivatives, the fact that they result in a set of optimum candidate solutions rather than a single candidate solution, and that they work well with experimental data as well as simulated data.

The approach presented in this paper is based on extracting useful information from all sensors in the array. To infer the intended motion from the sensor array, we propose to use an optimized non-linear filter. Optimization techniques are used as filters to fuse the EMG data from different sensors. The fusion process is done in the frequency domain.

The paper is structured as follows. The experimental set up is given in Section II and Section III provides background on sensor fusion. Section IV details the results and discussion and in the last section some conclusions are provided.

## II. EXPERIMENTAL SET-UP

Experiments were carried out on a healthy male subject in order to collect EMG data from all the sensors corresponding to each individual motor unit. The mchepuotor points of the subject and the appropriated EMG electrode attachment points were identified by using a wet probe point muscle stimulator (Rich-Mar Corporation, model number HV 1100.). For capturing the EMG data from the skin surface, a Delsys, Bagnoli-16 channel EMG, DS-160, S/N-1116 system is used. This capturing system has the capability of internally amplifying and reducing the acquired noise. Pronged DE 2.1 differential surface electrodes are used. For recording EMG at the forearm superficial musculature (flexor digitorum superficialis) electrodes are placed to extract EMG signals. The force data is measured by a force sensitive resistor (FSR). The data acquisition is set to a sampling rate of 2000 samples per second for force and EMG signal data.

## III. SESNOR FUSION BACKGROUND

The sensor fusion process deals with association, correlation and estimation of data from multiple sensors. A data fusion technique, by combining the data from different sensors, enables one to achieve more specific inferences about the measured data. The sEMG sensors pick up the cross-talk from muscle fibers adjacent to motor units. In [7], sensor fusion was done in the time domain, by taking sEMG as input and force signal as the output. They used

combinations of different filters (Butterworth, Chebyshev, Exponential and Half-Gaussian filters) and different information criteria based on Akaike (AIC), Bayesian (BIC), and Kull-back (KIC) and concluded that the KIC criterion with Half Gaussian filtering gives the best EMG-Force model fit.

In the present case, sensor fusion is done in the frequency domain for the sEMG data. Figure 1 depicts the flow diagram of the proposed fusion technique using a simple elitism based GA. The data from the three sensors around the individual motor unit are fused by first rectifying the data and then filtering it using a Half-Gaussian filter. The sEMG data  $u_1, u_2$ , and  $u_3$  from the three sensors and their corresponding force signal is used to identify a dynamical relationship between the sEMG signals and the force signals using System Identification (SI). In this proposed fusion algorithm, SI is achieved by utilizing an Output Error (OE) model first for each individual data set [9]. The OE model structure is given as follows:

$$y(t) = \frac{B(q)}{F(q)}u(t - nk) + e(t), \quad (1)$$

where  $B$ , and  $F$  are the polynomials,  $q$  is shift operator,  $e(t)$  is output error,  $y(t)$  is system output,  $u$  is input,  $nk$  is the system delay and  $t$  is time index.

The corresponding continuous-time model is given by the transfer function.

$$G(s) = \frac{B(s)}{F(s)} = \frac{b_{nb}s^{(nb-1)}b_{nb-1}s^{(nb-2)}+\dots+b_1}{s^{nf}+f_{nf}s^{nf-1}+\dots+f_1}. \quad (2)$$

Similar to the discrete-time case the orders of the numerator and denominator are determined by  $nb$  and  $nf$ . For multi-input systems,  $nb$  and  $nf$  are row vectors.  $b, f$  are the coefficients of the numerator and denominator polynomials respectively.

Based on the poles of the three individual identified OE models, corresponding to each sensor, a MISO transfer function ( $H$ ) is constructed. While the denominators of the respective individual transfer functions (corresponding to each OE model) are transferred over to the new MISO transfer function, the corresponding zeros are found through the use of a GA. Generally GA's can find global optimum points if elitism is used and sufficient number of generations are allowed in the algorithm. This optimization algorithm is rather computationally expensive, but since there was not a computational time requirement, one is free to use GA rather than other intelligent based algorithms. Chromosomes are constructed by designating each zero of a numerator as a gene. Since a discrete time model is utilized, the search area is limited to the unit circle (and the resulting MISO model is decreased to be minimum phase). The number of potential zeros was set to the order of the corresponding denominator because the number of zeros is at most the number of poles (for a causal system, can't predict the future). The objective



function was set as the error squared of the resulting MISO system ( $H$ ) (see appendix) and the recorded force signal.

Here  $H$  is given as,

$$H(s) = \frac{\begin{pmatrix} Z_{1,1}s^n + Z_{1,2}s^{n-1} + \dots + Z_{1,n+1} \\ P_{1,1}s^n + P_{1,2}s^{n-1} + \dots + P_{1,n+1} \\ Z_{2,1}s^n + Z_{2,2}s^{n-1} + \dots + Z_{2,n+1} \\ P_{2,1}s^n + P_{2,2}s^{n-1} + \dots + P_{2,n+1} \\ Z_{3,1}s^n + Z_{3,2}s^{n-1} + \dots + Z_{3,n+1} \\ P_{3,1}s^n + P_{3,2}s^{n-1} + \dots + P_{3,n+1} \end{pmatrix}}{\begin{pmatrix} P_{1,1}s^n + P_{1,2}s^{n-1} + \dots + P_{1,n+1} \\ P_{2,1}s^n + P_{2,2}s^{n-1} + \dots + P_{2,n+1} \\ P_{3,1}s^n + P_{3,2}s^{n-1} + \dots + P_{3,n+1} \end{pmatrix}}, \quad (3)$$

where  $Z$ 's and  $P$ 's are the zeros and poles respectively of individual transfer function and  $n$  is the order of the system.

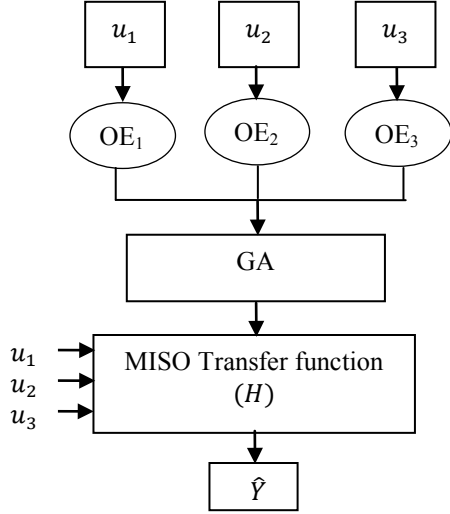


Figure 1: Flow Diagram.

#### IV. RESULTS AND DISCUSSION

The actual force signal from the FSR sensor is filtered using a Chebyshev Type II high pass filter followed by a low pass filter. The EMG signal is rectified and filtered using a Half-Gaussian filter to minimize the noise content. The filter parameters for the Half-Gaussian filter are selected in such a way that the effective EMG signal frequency content is no more than 500 Hz, according to the ISEK standards [10]. Figure 2 shows the results of the fusion based force  $\hat{Y}$  plotted against actual measured force. The predicted force matches the actual force characteristics well. Figure 3 shows the estimated force output, for the individual OE models which were used to construct the fusion model and the actual measured force. It is apparent that the individual force estimates from each OE model do not track the actual force as well as the estimated force from the fused model  $H$ . In particular, the magnitudes are substantially different. While not the most optimal identification was determined, the improvement indicated by the fused model output compared to the individual OE outputs is significant. The output of the fused model fits with peaks of the original force data. Several validation tests for the fused model are done by feeding new data sets to the MISO transfer function ( $H$ ).

Figure 4 and 5 shows the plot between the actual force data and the predicted force data for two representative

validation data sets. The output of the fused model exhibits an 82% fit with the actual force signal.

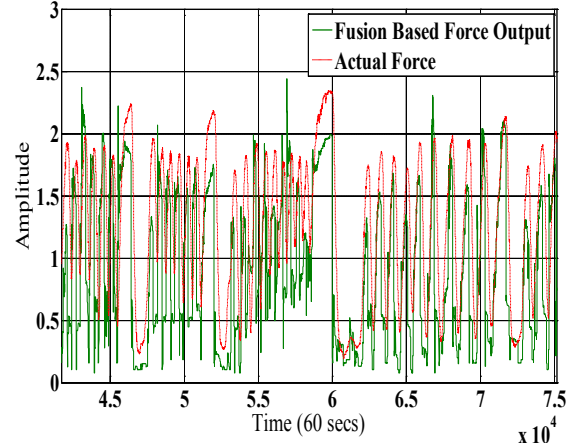


Figure 2 : Final Fused Force Vs. Actual Force.

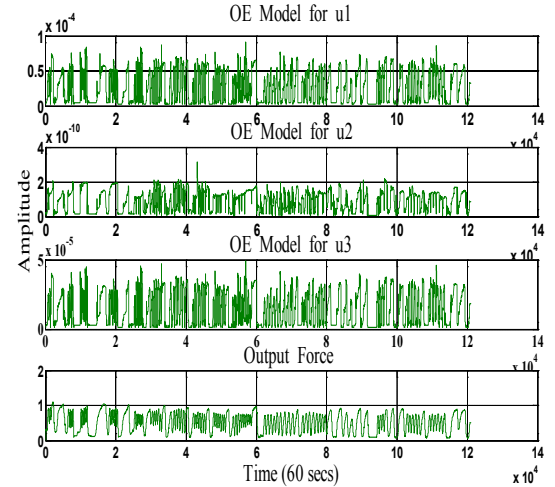


Figure 3: Estimated Force Output for Individual OE Model and the Actual Measured Force.

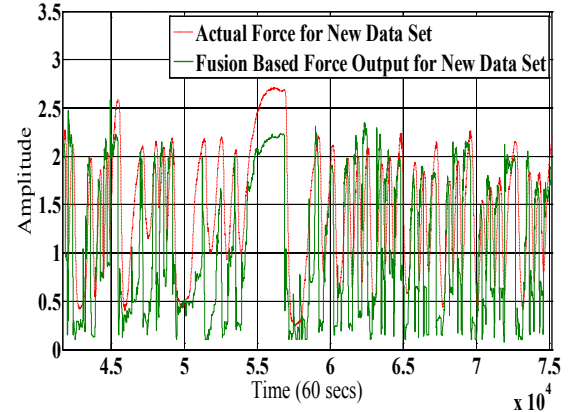


Figure 4: Validation Plot for Data Set-I.

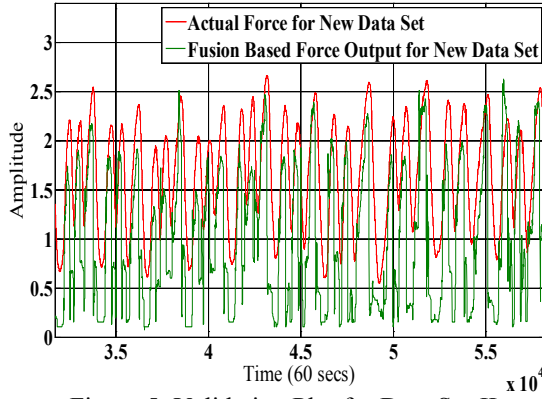


Figure 5: Validation Plot for Data Set-II.

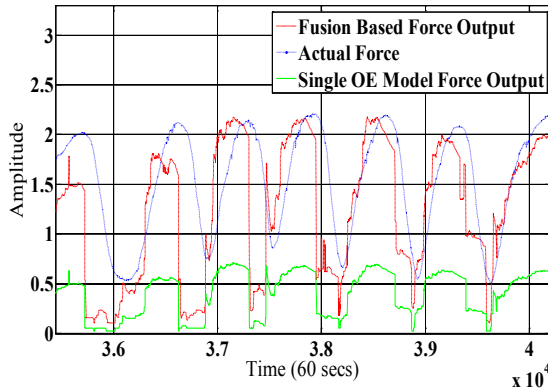


Figure 6: Comparison between Actual, Fusion Based and Single OE Model Output Force.

In order to visualize the improvement achieved with regard to the form of the predicted force, Figure 6 is generated to depict the actual force measured compared to the output of the fused model (predicted force) and the predicted force from one of the OE models used to construct the fused model. The amplitudes were modulated in order to show the different shapes of the wave forms. It is apparent that the fused model output matches the measured finger force better than an individual OE force estimate. While there are some additional higher frequency terms in the estimated finger force, the general trend and lower frequencies are well matched. The higher frequency elements are necessary parts of the MISO model since finger forces can change rather quickly, as indicated in Figure 2.

## V. CONCLUSION

Although better individual models can be inferred using SI under perfect conditions, the proposed fusion algorithm improves the predicted force estimate consistency. The fusion algorithm results in a single MISO transfer function. Cross talk can be reduced by using filtering and in this work a Half-Gaussian filter is used. This also enables the smoothing of the fused signal. Several validation data sets were used to test the proposed fusion algorithm. Compared to single OE model, the proposed fusion-based force model

is in good agreement with that of the actual force. Future work will address the optimization of the SI and the associated experimental conditions in order to arrive at better individual OE models. Also the optimization of the poles and the number of zeros will be undertaken in order to obtain a minimum realization of the MISO system. In addition, the MISO system is an ideal structure to incorporate dynamics related to muscle fatigue, which will be addressed in future work.

## APPENDIX

The resulting MISO transfer function  $H$  is constructed as, From  $u_1$  to output,

$$\frac{s^8 - 3.843s^7 + 7.729s^6 - 10.78s^5 + 10.6s^4 - 7.417s^3 + 3.603s^2 - 0.9795s + 0.1192}{s^8 - 4.028s^7 + 6.325s^6 - 4.121s^5 - 1.545s^4 + 5.87s^3 - 5.433s^2 + 2.28s - 0.3496}$$

From  $u_2$  to output,

$$\frac{s^8 - 4.339s^7 + 9.005s^6 - 12.42s^5 + 12.22s^4 - 8.117s^3 + 3.427s^2 - 0.9134s + 0.1424}{s^8 - 4.028s^7 + 6.325s^6 - 4.121s^5 - 1.545s^4 + 5.87s^3 - 5.433s^2 + 2.28s - 0.3496}$$

From  $u_3$  to output,

$$\frac{s^8 - 3.522s^7 + 6.655s^6 - 8.864s^5 + 8.183s^4 - 5.365s^3 + 2.423s^2 - 0.557s + 0.09585}{s^8 - 4.028s^7 + 6.325s^6 - 4.121s^5 - 1.545s^4 + 5.87s^3 - 5.433s^2 + 2.28s - 0.3496}$$

## ACKNOWLEDGEMENT

The support by a grant from the Telemedicine Advanced Technology Research Center (TATRC) of the U.S. – Department of Defense (DoD) for pursuing this work is hereby acknowledged. Further, the technical help from Dr. Jim Creelman and Mr. Anish Sebastian is greatly appreciated.

## REFERENCES

- [1] Amputee Coalition of America (ACA) National Limb Loss Information, Center (NLLIC) Limb Loss Facts in the United States, <http://www.amputee-coalition.org>, 2005.
- [2] Northrop, R. "Analysis and Application of Analog Electronic Circuits to Biomedical Instrumentation," CRC Press, Boca Raton, Florida, 2004, pp 6-9.
- [3] Cram, J.R., Kasman G.S., and Holtz J. "Introduction to Surface Electromyography," Aspen Publisher Inc., Gaithersburg, Maryland, 1998.
- [4] Kandel E.R. and Schartz J.H., "Principles of Neural Science," Elsevier/North-Holland, New York, 1981.
- [5] Merlo A., Faina D., Merletti R., "A Fast and Reliable Technique for Muscle Activity Detection from Surface EMG Signals," *IEEE Transaction on Biomedical Engineering*, Vol. 50, No. 3, 2003, p. 316- 323.
- [6] Natata K., Adno K., Yamada M., Magatani K., "A Classification Method of Hand Movements using Multi Channel Electrode," *Proceedings of the 27<sup>th</sup> Annual conference IEEE Engineering in Medicine Shanghai, China*, September 1-4, 2005, pp. 2375-2378.
- [7] Madhavi Anugolu, Anish Sebastian, Parmod Kumar, Marco P. Schoen, Alex Urfer, and D. Subbaram Naidu, "Surface EMG Array Sensor Based Model Fusion using Bayesian Approaches for Prosthetic Hands," *Proceedings of the Dynamic Systems and Control Conference (DSCC)*, Hollywood, CA, October 2009.
- [8] R.L. Haupt, and S. E. Haupt, "Practical Genetic Algorithms," John Wiley & Sons, Inc., New York, 1998.
- [9] Jeffrey T. Bingham, and Marco P. Schoen, "Characterization of Myoelectric signals using System Identification Techniques," *IMECE2004*, Anaheim, CA, November 2004.
- [10] [http://www.isek-online.org/standards\\_emg.html](http://www.isek-online.org/standards_emg.html).

# TOWARDS SMART PROSTHETIC HAND: ADAPTIVE PROBABILITY BASED SKELETAN MUSCLE FATIGUE MODEL

Parmod Kumar, Anish Sebastian, Chandrasekhar Potluri, Alex Urfer, D. Subbaram Naidu, *Fellow, IEEE*, and Marco P. Schoen, *Member, IEEE*

**Abstract** - Skeletal muscle force can be estimated using surface electromyographic (sEMG) signals. Usually, the surface location for the sensors is near the respective muscle motor unit points. Skeletal muscles generate a spatial EMG signal, which causes cross talk between different sEMG signal sensors. In this study, an array of three sEMG sensors is used to capture the information of muscle dynamics in terms of sEMG signals. The recorded sEMG signals are filtered utilizing optimized nonlinear Half-Gaussian Bayesian filters parameters, and the muscle force signal using a Chebyshev type-II filter. The filter optimization is accomplished using Genetic Algorithms. Three discrete time state-space muscle fatigue models are obtained using system identification and modal transformation for three sets of sensors for single motor unit. The outputs of these three muscle fatigue models are fused with a probabilistic Kullback Information Criterion (KIC) for model selection. The final fused output is estimated with an adaptive probability of KIC, which provides improved force estimates.

## I. INTRODUCTION

National Limb Loss Information Center [1] reported in 2002 that 1.2 million people live with amputations. Since then, this number is increasing due to ongoing wars in Iraq and Afghanistan. However, prostheses can significantly improve the lives for these people.

Recent research efforts have been active towards creating surface electromyographic (sEMG) based prosthetics for hand amputees. The recorded sEMG signal is used as an input to activate the prosthesis. The central nervous system activates and controls the EMG signals which depend on the flow of specific ions including sodium ( $Na^+$ ), potassium ( $K^+$ ) and calcium ( $Ca^{++}$ ) resulting in the action potentials in nerves and their respective skeletal muscle fibres. A potential difference develops across neuronal membranes because of this ion exchange and this can be measured as an electrical voltage

Parmod Kumar is with Measurement and Control Engineering Research Center (MCERC), College of Engineering, Idaho State University, Pocatello, Idaho 83209, USA (email: kumaparm@isu.edu).

Anish Sebastian is with MCERC, College of Engineering, Idaho State University, Pocatello, Idaho 83209, USA (email: sebaanis@isu.edu).

Chandrasekhar Potluri is with MCERC, College of Engineering, Idaho State University, Pocatello, Idaho 83209, USA (e-mail: potlchan@isu.edu).

Alex Urfer is with Department of Physical and Occupational Therapy, Idaho State University, Pocatello, Idaho 83209, USA (email: urfealex@isu.edu).

D. Subbaram Naidu is with Department of Electrical Engineering, MCERC, Idaho State University, Pocatello, Idaho 83201 USA (email: naiduds@isu.edu).

Marco P. Schoen is with Department of Mechanical Engineering, MCERC, Idaho State University, Pocatello, Idaho 83209, USA (email: schomarc@isu.edu).

change [2]. sEMG signals are collected from the skin as an electric voltage ranging between -5 and +5 mV. The control of the myoelectric-based prosthesis is difficult because of the dynamic nature of the EMG signal [1] due to varying motor unit recruitment, crosstalk, and biochemical interaction within the muscular fibres. In addition, sEMG changes continuously due to the onset and progression of muscle fatigue [1].

Muscle fatigue is complex in nature and results in failure to maintain the required force level [3]. Reasons for fatigue can be the peripheral changes at the muscle level or an inadequate output from the central nervous system to stimulate motoneurons [3]. The amount of force generated, duration of each contraction, and the rest period between two contractions has a direct influence on the muscle fatigue rate [4]. Muscle fibre-type distribution [5], nerve conduction velocity of fatiguing muscles, or even factors within the central nervous system (CNS) affect EMG signals [6]. EMG analysis is a well-accepted method for muscle fatigue assessment [6].

In 1977, L. Lindstrom, R. Kadefors and I. Petersen developed a method that measures the localized muscle fatigue based on the power spectrum analysis using myoelectric signals [7]. This approach permits real-time investigations and can yield statistically based criteria for the occurrence of fatigue. Rate of fatigue development and changes in muscle action potential conduction velocity were used to interpret the findings [7]. Additional recruitment of motor units, synchronization of active motor units along the muscle fibres, and a decrease in conduction velocity are reflected in the EMG signal as an increase of amplitude in time domain and a decrease of medium frequency in frequency domain [8].

The joint analysis method using EMG amplitude and spectrum (JASA) allows distinguishing between the difference of fatigue-induced and force related EMG changes. Simultaneous changes in the EMG amplitude and spectrum are considered in the JASA approach [9]. The JASA principle states that muscle force decreases because of the decrease in EMG amplitude [9]. Fatigue can occur because of continuous high frequency stimulation or because of titanic stimulation. The Flow Chart of the work in this paper is shown in Figure 1.

This paper addresses the issue of skeletal muscle fatigue that is a dynamic phenomenon. The modeling is based on system identification, where mathematical relations are inferred from experimental data. The data consists of sEMG signals and hand/finger force generated by healthy subjects. The recorded three-sEMG signals are filtered using nonlinear Half-Gaussian Bayesian filters



with optimized filter parameters, whereas the skeletal muscle force signal is pre-processed using a Chebyshev type-II filter [1, 10].

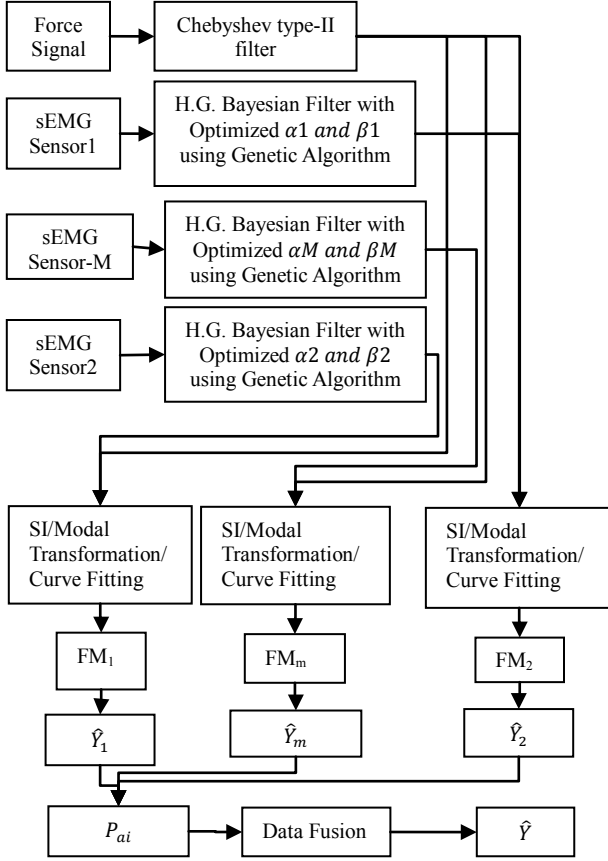


Figure 1: The Flow Chart of the Work in this Paper.

A simple Genetic Algorithm code is used to optimize the Bayesian filter parameters. Using an input/output approach, the EMG signal is the input to the skeletal muscle, and the produced hand/finger force constitutes the output. Three discrete time state-space models are obtained using system identification and modal transformation for three sets of sensors. One sensor is placed at the motor unit of the ring finger of the dominant hand and two sensors are located in its vicinity as shown in Figure 2. The extracted models from the data sets are fused with a probabilistic Kullback Information Criterion (KIC) for model selection. The final fused output is estimated with an adaptive probability of KIC that gives an improved skeletal muscle force estimates.

## II. EXPERIMENTAL SET-UP AND PRE-PROCESSING

Both sEMG and muscle force signals were acquired simultaneously using LabVIEW™ 8.2 at a sampling rate of 2000 Hz. The sEMG data capturing was aided by a DELSYS® Bagnoli-16 EMG system with DE-2.1 differential EMG sensors. The corresponding force data was captured using NI ELVIS with Interlink Electronics FSR 0.5" circular force sensor. The experimental set-up is shown in Figure 2. One sEMG sensor was placed on the

motor point of ring finger and two adjacent to the motor point of a healthy subject. Prior to placing the sEMG sensors, the skin surface of the subject was prepared according to International Society of Electrophysiology and Kinesiology (ISEK) protocols.

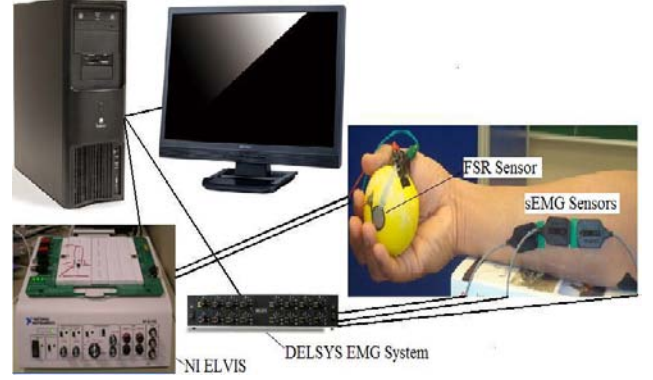


Figure 2: Experimental Set-Up.

The EMG signal is modeled for the conditional probability of the rectified EMG signal as a filtered random process with random rate. The likelihood function for the rate evolves in time according to a Fokker-Planck partial differential Equation [10]. Here,  $\alpha$  and  $\beta$  are two free parameters,  $\alpha$  is the expected rate of gradual drift in the signal, and  $\beta$  is the expected rate of sudden shifts in the signal. These two free parameters of the non-linear ‘‘Half-Gaussian filter model’’ are optimized for the acquired EMG data using an elitism based Genetic Algorithm. A Chebyshev type II low pass filter with a 550 Hz pass frequency is used to filter the force signal.

## III. SYSTEM IDENTIFICATION AND MODAL TRANSFORMATION

An alternative to physically based mathematical modeling is data based ‘system identification (SI)’- that can be applied to different systems where it needs sufficient experimental data [11]. The parametric system identification process yields a dynamical model such as the Auto Regressive with exogenous input (ARX) or Output Error (OE) model, this model gives us the system in mathematical form. In this work, the SI approach is used with the myoelectric signal as the input to the system and as the output is the intended finger/hand force. In this work, we are using an output error (OE) model structure for the modeling of EMG and hand/finger force signals, which has been documented in the literature to perform well for EMG signals among linear parametric models [1]. Each OE model takes the form of Equation (1),

$$y(t) = \frac{B(q)}{F(q)} u(t - n_k) + e(t), \quad (1)$$

where  $t$  is time index,  $y(t)$  is output,  $u(t - n_k)$  is input,  $n_k$  is the delay,  $e(t)$  is the error, and  $B(q)$  and  $F(q)$  are polynomials.

A common OE model is obtained for each sensor data set using one set of model parameters (polynomial order). The OE models then are converted into a state-space formulation. By doing this, the identification properties of

the OE model formulation are preserved and represented in the state-space form. A modal form is computed by using state-space matrices and following transformation:

$$\Lambda = T^{-1}, \Omega = T^{-1}B, \Gamma = CT, \quad (2)$$

where  $T$  is the matrix composed of the eigenvectors of  $A$ ,  $\Lambda, \Omega$  and  $\Gamma$  are corresponding transformations for matrix  $A, B$ , and  $C$ . Matrix  $D$  came out to be a zero matrix for the cases treated in this work. Equation (2) refers to the continuous representation of the identified models. Using the modal form representation for each corresponding data set, the influence of fatigue can be observed by charting the modal coefficients in time for each matrix. For example, the coefficients contained in the transformed matrix  $\Lambda$  can be plotted in the complex  $s$ -plane. This tracking can then be used as the basis for constructing polynomials that connect each element of each matrix in time with the corresponding time stamp. Hence, a fatigue model in state-space description is constructed, where the input is the recorded EMG signal and the output the expected force generated by the hand motion all as a function of time.

#### IV. FUSION OF OUTPUTS AND ADAPTIVE PROBABILITY OF KIC

Multiple model fusion is done by assigning a particular probability to each individual model [12]. These models are obtained using SI for three sEMG sensors for single motor unit. SI model fit value is used to compute the probability for each model. The fit value is given by  $\left[1 - \frac{|Y - \hat{Y}|}{|Y - \bar{Y}|}\right] * 100$ . The model selection criterion used in this paper is Kullback information criterion (KIC), which is an asymmetric measure. The sum of two directed divergences, which is the measure of the models dissimilarity, is known as Kullback's symmetric or J-divergence [13], as given by Equation (3).

$$KIC(p_i) = \frac{n}{2} \log R_i + \frac{(p_i+1)n}{n-p_i-2} - n\psi\left(\frac{n-p_i}{2}\right) + g(n), \quad (3)$$

where  $g(n) = n * \log(n/2)$ .

Following fusion technique is applied for sEMG – force identification models, which is based on [12].

1) Identify OE models  $M_1, M_2, \dots, M_{k1}$  using sEMG data ( $u$ ) as input and force data ( $Y$ ) as output, for  $k1$  number of sensors collecting data simultaneously.

2) Compute the residual square norm

$$R_i = \|Y - \Phi_i \hat{\Theta}_i\|^2 = \|Y - \hat{Y}\|^2,$$

where  $\hat{\Theta}_i = \{\Phi_i^T \Phi_i\}^{-1} \Phi_i^T Y$ , and

$$\Phi = \begin{bmatrix} Y_p^T & u_p^T & Y_{p-1}^T & \dots & u_1^T \\ Y_{p+1}^T & u_{p+1}^T & Y_p^T & \dots & u_2^T \\ \vdots & \vdots & \vdots & \ddots & \vdots \\ Y_{n-1}^T & u_{n-1}^T & Y_{n-2}^T & \dots & u_{n-p}^T \end{bmatrix}.$$

3) Calculate the model criteria coefficient using Equation (3).

4) Compute the model probability  $p(M_i|Z) = \frac{e^{-l_i}}{\sum_{j=1}^{k1} e^{-l_j}}$ ,

where  $l$  is model selection criterion, i.e.  $KIC(p_i)$ .

5) Compute the fused model output  $\hat{Y}_f = \sum_{i=1}^{k1} p(M_i|Z) \hat{Y}_i$ .

6) Compute the overall OE model from  $\hat{Y}_f$  and force data.

Here all the computation from step 2) to step 6) is adaptive i.e. the residual square norm,  $KIC(p_i)$ , model probability  $p(M_i|Z)$ , and fused model output  $\hat{Y}_f$  are being updated with time or for each data point.

#### V. RESULTS, CONCLUSION AND FUTURE WORK

Based on previous research results and after trying different model orders for sEMG/Force data, an optimal model order of  $n_b = 2, n_f = 2, n_k = 1$  is used in this work. Equation (4), (5), and (6) give three resulting discrete time state-space sEMG-Force-Fatigue models for motor point sensor, sensor-1 and sensor-2 respectively.

$$x_m(h+1) = A_m x_m(h) + B_m EMG_m(h);$$

$$\hat{Y}_m(h) = C_m x_m(h) + D_m EMG_m(h). \quad (4)$$

$$x_1(h+1) = A_1 x_1(h) + B_1 EMG_1(h);$$

$$\hat{Y}_1(h) = C_1 x_1(h) + D_1 EMG_1(h). \quad (5)$$

$$x_2(h+1) = A_2 x_2(h) + B_2 EMG_2(h);$$

$$\hat{Y}_2(h) = C_2 x_2(h) + D_2 EMG_2(h). \quad (6)$$

In these case matrices  $D_m, D_1$ , and  $D_2$  are zero matrices, whereas matrices  $A_m, B_m, C_m, A_1, B_1, C_1, A_2, B_2$ , and  $C_2$  are given as:  $A_m = \begin{bmatrix} a_{m1}(t) & 0 \\ 0 & a_{m2}(t) \end{bmatrix}; B_m = \begin{bmatrix} b_{m1}(t) \\ b_{m2}(t) \end{bmatrix};$

$$C_m = [c_{m1}(t) \ c_{m2}(t)]; A_1 = \begin{bmatrix} a_{11} & 0 \\ 0 & a_{12} \end{bmatrix};$$

$$B_1 = \begin{bmatrix} b_{11} \\ b_{12} \end{bmatrix}; C_1 = [c_{11} \ c_{12}]; A_2 = \begin{bmatrix} a_{21}(t) & 0 \\ 0 & a_{22}(t) \end{bmatrix};$$

$$B_2 = \begin{bmatrix} b_{21}(t) \\ b_{22}(t) \end{bmatrix}; \text{ and } C_2 = [c_{21}(t) \ c_{22}(t)]; \text{ where the}$$

elements of matrices  $A_m, B_m, C_m, A_2, B_2$ , and  $C_2$  are function of time and the elements of matrices  $A_1, B_1$ , and  $C_1$  are constants for this particular data set. The time variables  $a_{m1}(t), a_{m2}(t), b_{m1}(t), b_{m2}(t), c_{m1}(t), c_{m2}(t), a_{21}(t), a_{22}(t), b_{21}(t), b_{22}(t), c_{21}(t)$ , and  $c_{22}(t)$  are given by quadratic polynomials obtained by curve fitting the tracked modal transformed coefficients. These time variables are given as:

$$a_{m1}(t) = 0.00026t^2 - 0.033t - 11;$$

$$a_{m2}(t) = -0.0018t^2 + 0.24t - 33;$$

$$b_{m1}(t) = -0.002t^2 + 0.33t + 42;$$

$$b_{m2}(t) = -0.0017t^2 + 0.33t + 25;$$

$$c_{m1}(t) = (3.2 * 10^{-7})t^2 - (4.2 * 10^{-5})t + 0.71;$$

$$c_{m2}(t) = (4.6 * 10^{-8})t^2 - (5.8 * 10^{-6})t - 0.71;$$

$$a_{21}(t) = -(1.2 * 10^{-5})t^2 + 0.0013t - 0.47;$$

$$a_{22}(t) = 0.001t^2 - 0.037t - 35;$$

$$b_{21}(t) = (6.4 * 10^{-6})t^2 - 0.001t + 0.3;$$

$$b_{22}(t) = 0.0023t^2 - 0.12t - 75;$$

$c_{21}(t) = -(1.8 * 10^{-7})t^2 + (6.4 * 10^{-6})t + 0.71$ ; and  $c_{22}(t) = -(2.1 * 10^{-9})t^2 + (2.4 * 10^{-7})t - 0.71$ . Elements of matrices  $A_1$ ,  $B_1$ , and  $C_1$  are constants for this particular data set, they are given as:

$a_{11} = -0.0159$ ;  $a_{12} = -43.1883$ ;  $b_{11} = 0.0090$ ;  $b_{12} = -72.1875$ ;  $c_{11} = 0.7147$ ; and  $c_{12} = -0.7071$ .

The discrete models have a sampling time of  $\Delta t = 0.0005$  seconds. The duration of the final estimated and fused output for three sensors is 37.36 seconds. Figure 3 depicts the probability and 10<sup>th</sup> degree curve fitting for motor point, ring2 and ring1 sensor signals.

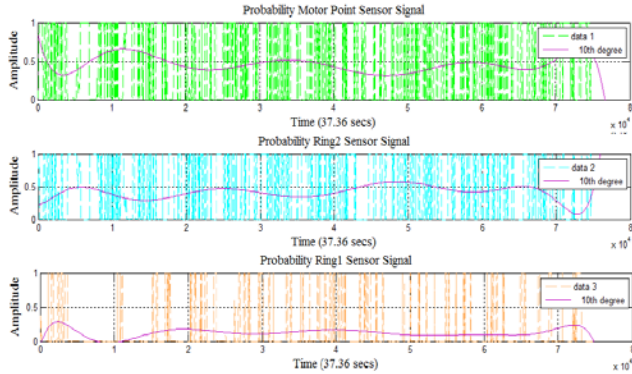


Figure 3: 10<sup>th</sup> Degree Curve Fitting – Probability Motor, Ring2 and Ring1 Sensor Signals.

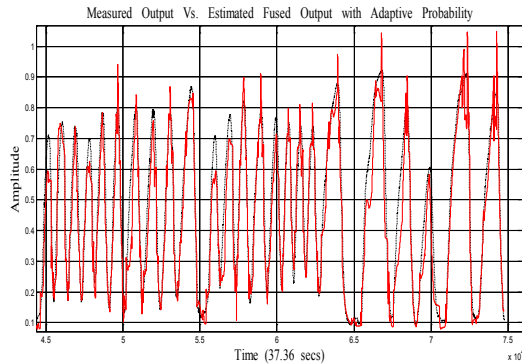


Figure 4: Measured Output Vs. Estimated Fused Output with Adaptive Probability.

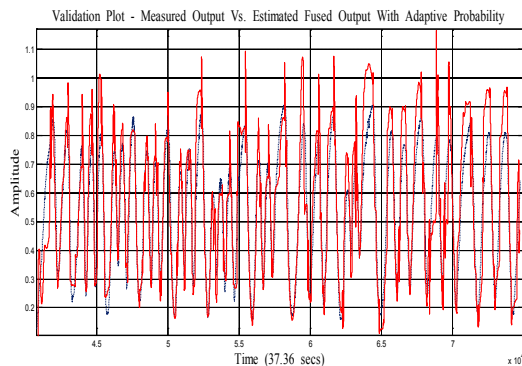


Figure 5: Validation Plot - Measured Vs. Estimated Fused Output with Adaptive Probability.

Figure 4 and Figure 5 shows the measured and estimated fused output, depending on the error between the two later follows the measured signal very closely. This approach identifies a fused fatigue model and estimates an adaptive probability based output that follows the measured output very closely. The outcome of this research can be used to estimate the skeletal muscle force of a human hand for prosthetic hand design, application and improvement.

In future work improvement of the data collection techniques and sEMG sensor design, may lead to improved force estimation.

#### ACKNOWLEDGMENT

This work was supported by a grant from the Telemedicine Advanced Technology Research Center (TATRC) – Department of Defense. The financial support is greatly appreciated.

#### REFERENCES

- [1] Jeffrey T. Bingham and Marco P. Schoen, "Characterization of Myoelectric Signals using System Identification Techniques," *Proceedings of IMECE 2004: 2004 ASME International Mechanical Engineering Congress Anaheim, California*, November 13-19, 2004.
- [2] Northrop, R., *Analysis and application of analogue electronic circuits to biomedical instrumentation*. CRC Press, Boca Raton, Florida, 2004, pp. 6–9.
- [3] S. C. Gandevia, "Spinal and Supraspinal Factors in Human Muscle Fatigue," *Physiological Reviews, American Physiological Society*, 81(4), October 2001.
- [4] B R Bigland-Ritchie, N J Dawson, R S Johansson and O C Lippold, "Reflex origin for the slowing of motoneurone firing rates in fatigue of human voluntary contractions," *Journal of Physiology*, 379, pp. 451-459, 1986.
- [5] Gerdle B, Edstrom M, Rahm M, "Fatigue in the shoulder muscles during static work at two different torque levels," *Clinical Physiology*, 13(5), pp. 469-482, 1993.
- [6] Merletti R, and Lo Conte LR, "Surface EMG signal processing during isometric contractions," *Journal of Electromyography and Kinesiology*, 7(4), pp. 241-250, 1997.
- [7] Finsterer J., "EMG-interference pattern analysis," *J Electromyogr Kinesiol*, 11, pp. 231-246, 2001.
- [8] B. Maton, and D. Gamet, "The fatigability of two agonistic muscles in human isometric voluntary sub maximal contraction: an EMG study. II Motor unit firing rate and recruitment," *Eur. J. Appl. Physiol.*, 58, pp. 369-374, 1989.
- [9] A. Luttmann, M. Jaeger, J. Soekeland, and W. Laurig, "Electromyographical study on surgeons in urology, Part II: Determination of muscular fatigue," *Ergonomics*, 39, pp. 298-313, 1996.
- [10] Terence D. Sanger, "Bayesian Filtering of Myoelectric Signals," *J Neurophysiol* 97, pp. 1839–1845, 2007.
- [11] Lennart Ljung, *System Identification: Theory for the User*. 2nd edition, Printice Hall PTR, 1999, Chap. 1, pp. 1-15.
- [12] H. Chen and S. Huang, "A Comparative study on Model Selection and Multiple Model Fusion," *7<sup>th</sup> International Conference on Information Fusion*, pp. 820-826, 2005.
- [13] Abd-Krim Seghouane, M. Bekara, G. Fleury, "A Small Sample Model Selection Criterion Based on Kullback's symmetric Divergence," *IEEE Transaction*, pp. 145-148, 2003.

# ANALYSIS OF EMG-FORCE RELATION USING SYSTEM IDENTIFICATION AND HAMMERSTEIN-WIENER MODELS

## Anish Sebastian

Measurement and Control Engineering  
Research Center (MCERC)  
Idaho State University, Pocatello,  
Idaho 83209, [sebaanis@isu.edu](mailto:sebaanis@isu.edu)

## Parmod Kumar

MCERC  
Idaho State University, Pocatello,  
Idaho 83209, [kumaparm@isu.edu](mailto:kumaparm@isu.edu)

## Marco P. Schoen

Dept. of Mechanical Engineering,  
MCERC, Idaho State University,  
Pocatello, Idaho 83209,  
[schomarc@isu.edu](mailto:schomarc@isu.edu)

## Alex Urfer

Dept. of Physical and Occupational  
Therapy, Idaho State University,  
Pocatello, Idaho 83209,  
[urfealex@isu.edu](mailto:urfealex@isu.edu)

## Jim Creelman

Dept. of Physical and Occupational  
Therapy, Idaho State University,  
Pocatello, Idaho 83209,  
[creejame@isu.edu](mailto:creejame@isu.edu)

## D. Subbaram Naidu

Dept. of Electrical Engineering,  
MCERC, Idaho State University,  
Pocatello, Idaho 83209,  
[naiduds@isu.edu](mailto:naiduds@isu.edu)

## ABSTRACT

*Surface Electromyographic (sEMG) signals have been exploited for almost a century, for various clinical and engineering applications. One of the most compelling and altruistic applications being, control of prosthetic devices. The study conducted here looks at the modeling of the force and sEMG signals, using nonlinear Hammerstein-Weiner System Identification techniques. This study involved modeling of sEMG and corresponding force data to establish a relation which can mimic the actual force characteristics for a few particular hand motions. Analysis of the sEMG signals, obtained from specific Motor Unit locations corresponding to the index, middle and ring finger, and the force data led to the following deductions; a) Each motor unit location has to be treated as a separate system, (i.e. extrapolation of models for different fingers cannot be done) b) Fatigue influences the Hammerstein-Wiener model parameters and any control algorithm for implementing the force regimen will have to be adaptive in nature to compensate for the changes in the sEMG signal and c) The results also manifest the importance of the design of the experiments that need to be adopted to comprehensively model sEMG and force.*

## NOMENCLATURE

$B_{j,i}(s)$ ,  $F_{j,i}(s)$  Polynomials in the linear block.  
 $b_i, c_i$  Coefficients of polynomials (Hammerstein Model).  
 $fn^*$  Objective function (PSO).  
 $g_i()$  Input nonlinearity function (Hammerstein Model).  
 $g(\bullet)$  Static nonlinear function.

$h()$  Output nonlinearity function.  
 $n_b$  Number of zeros plus one.  
 $n_f$  Number of poles.  
 $n_k$  Delay from the input to the output in terms of the number of samples.  
 $u(t)$  Input to a system.  
 $v(t)$ ,  $w(t)$  Internal variables.  
 $x(t)$  Input nonlinearity (Hammerstein Model).  
 $y(t)$  Output of a system.  
 $\hat{y}(t)$  Predicted or estimated output.  
 $z(t)$  Output linear block (Wiener Model).  
 $x_i^j(t)$  The  $i^{th}$  component position of the  $j^{th}$  particle in time  $t$ .  
 $x_i^{j,lbest}(t)$  The local best position of the  $j^{th}$  particle in generation  $t$ .  
 $x_i^{j,gbest}(t)$  The global best position of the  $j^{th}$  particle in generation  $t$ .  
 $v_i^j(t)$  The  $i^{th}$  component velocity of the  $j^{th}$  particle in time  $t$ .  
 $t$  time.  
 $H$  Physical parameters of non-linear function  $g(\bullet)$ .  
 $\alpha$  Expected rate of gradual drift.  
 $\beta$  Expected rate of sudden shifts in surface EMG.  
 $\varepsilon$  Tolerance.  
 $\theta$  Finite dimensional vector used to parameterize the mapping.

## INTRODUCTION

In spite of all the advances made in the field of biomedical engineering and in the study of biological signals, we still oftentimes find ourselves coming up short in understanding the complexities of the human body. One such field is rehabilitation engineering. The biological signal of interest here is the Surface Electromyogram signal (sEMG). We have come a long way since the first ever study conducted on EMG signals by H. Piper in 1912, [1]. About 50% of the people who need upper extremity prosthetics do not use them, [2] which puts into perspective the research in this area needs to focus on. The ideal scenario would be to mimic the real human hand with all its functionality and dexterity employing sEMG signals. This goal is still far from being realized as of today. EMG signals have been used for quite some time now in the control of prosthetic devices. Simply put, it is analogous to having small voltage signals (in mV), with information of the specific desired objective which can be used to actuate motors, which translate the EMG information into the desired force dynamics.

EMG signals are fairly complex to work with. In order to have a standardized method, on how EMG signals must be recorded and analyzed, the International Society of Electromyography and Kinesiology (ISEK) has a set of guidelines which are widely accepted. These guidelines for reporting EMG data are well documented, [3]. Other signal analysis techniques generally employed include low-pass or band-pass filtering; others have also employed notch filtering to remove power line noise, [4]. Whitening filters have also been employed in order to increase the quality of the amplitude estimates of the surface EMG signals, [5]. Some of the other signal processing methods include using Markov models, [6] and fuzzy logic control, [7] – for classification of EMG, wavelet processing, [8], and Bayesian estimators, [9]. Extensive research has also been carried out in obtaining a relationship between sEMG and force – for example, linear and non-linear sEMG-Force by Wood *et al.*, [10], EMG-Force relationships in skeletal muscles by Jacquelin *et al.*, [11], where a linear relationship was approximately quantified for the middle operating force range during an isometric effort. They also concluded that the presence of any movement, the algebraic relations estimated were not sufficient to describe the relation. Also, considerable attention needs to be given to the data acquisition, the type of electrode, amplification, rectification, sampling, noise filtering etc. as all these elements have an impact on the mathematical formulation of the sEMG-Force relation. The effects of joint position, gravity and recruitment have been studied by Solomonow *et al.*, [12]. The effects of fatigue on EMG-Force relation were investigated by Moxham *et al.*, [13]. Studies investigating the fatigue of motor units in muscles that control the fingers of the hand were carried out by Fuglevand *et al.*, [14]. This study showed that fatigue caused the force-frequency relation to be displaced to higher frequencies. The work reported in this paper is focused on using non-linear System Identification techniques, to come up with a suitable model or combination of models for the sEMG-Force relation. Also

modeling for the effects of fatigue in the sEMG-Force relation is taken into consideration and a guideline is provided on the type of experiments that would be most beneficial to encompass the large number of variables which affects the sEMG signals over time. The results of a number of nonlinear models, used for deducing the sEMG-Force relationship, strongly indicate the need for an adaptive method to be developed to capture the dynamics of the two signals. The results also indicate that the modeling of the sEMG-Force relation should not be extrapolated to different fingers even though the experiments performed were almost the same to obtain very similar force signal patterns. Bayesian filters were also used in analyzing the sEMG signals as they have been shown to be beneficial when using system identification, [15]. Particle Swarm Optimization (PSO) was used to assist in identifying possible trends in the Bayesian filter parameters with the onset of fatigue.

## THEORETICAL BACKGROUND

**EMG, VARIABLES AFFECTING sEMG-FORCE RELATIONSHIP & PREVIOUS RESEARCH:** An EMG signal is an electrical signal which is generated in a muscle contraction and is representative of neuromuscular activity. sEMG signals are measured at motor unit location. A motor unit (MU) consists of an  $\alpha$ -motoneuron in the spinal cord and the muscle fiber it innervates. Many factors influence sEMG signals, some of which are; a) shape of the volume conductor, b) the thickness of the subcutaneous tissue layers, c) tissue inhomogeneities, d) distribution of the motor unit territories in the muscle, e) size of the motor unit territories, f) distribution and the number of fibers in the motor unit territory, g) length of the fibers, h) spread of the endplates and tendon junctions within the motor units, and i) spread of the innervations zones and tendon regions among motor units. The type of detection system used also plays an important part in influencing the sEMG measurements. Some of the factors which need to be taken into account, with the detection systems, are a) skin electrode contact (impedance, noise), b) spatial filtering for signal detection, c) inter-electrode distance, d) electrode size and shape, and e) inclination of the detection system relative to the muscle fiber orientation, [16].

More recent studies suggest poor statistical trends between EMG amplitude and mean power spectral frequency, which indicate limitations in the use of EMG descriptors for fatigue assessment, [17]. Mortiz *et al.* found evidence which supports the hypothesis that the EMG discharge rate variability is a major determinant of the trends in isometric force variability across the working range of a muscle, [18]. Studies also suggest that there is not a significant difference between the EMG-Force relations obtained using intramuscular EMG (iEMG) as compared to sEMG, [19]. Extensive modeling for simulating sEMG signals, detected by surface electrodes, have also been performed, [20]. For the study conducted here, the sEMG signals were filtered using a Chebyshev Type II high pass filter and a Chebyshev Type II low pass filter. The sEMG signals were also filtered using a Bayesian Exponential, and a Half-Gaussian filter similar to the ones described in, [21] and because it has previously been reported in, [15] to yield better fits for non-linear Hammerstein-Wiener modeling.

**Particle Swarm Optimization:** In 1995, a new evolutionary algorithm was developed by J. Kennedy, a social psychologist, and R. Eberhart, known as Particle Swarm Optimization (PSO).



This method is computationally less expensive and has been used in this paper to optimize the Bayesian filter parameters  $\alpha$  and  $\beta$ . Other well established optimization algorithms are; a) Genetic Algorithm (GA) – inspired by biological evolution, is at its core, survival of the fittest. The main drawback of GA being that it is computationally very expensive especially for large search spaces. GA has been paired with many other search methods in order to improve its overall performance. b) Tabu Search on the other hand – which has a set of tabu balls and promising balls or a tabu list which helps it to reduce the search space is not very computationally expensive. Particle swarm optimization has a simple procedure; 1) Defining the input parameters: This includes the swarm size (number of particles of the swarm), maximum number of iterations, the limiting velocity of the particles, the upper and lower bounds of the search space and the stopping tolerance. 2) Initializing the position of the particles – can be randomly assigned using a uniform or normal distribution, [22]. 3) Evaluating the fitness function  $f_n$  (objective function) for the  $j^{th}$  particle. This depends on the cost function, e.g. the local best and the global best values are compared and suitably updated. Moreover, the difference between  $|f_n^*(t) - f_n^*(t-1)|$ , i.e. the current ( $t$ ) and ( $t-1$ ) is compared to the tolerance  $\varepsilon$ . If  $|f_n^*(t) - f_n^*(t-1)| < \varepsilon$ , then stop the loop; otherwise continue. Figures 1 and 2 show the particles of the PSO in the search space and the flow chart of the algorithm respectively.

**System Identification (SI), Nonlinear SI, Hammerstein-Wiener Models:** SI involves modeling, which is, developing a concept or mathematical relation on how the system variables are related. Modeling is divided into three components: 1) Accurately measuring a data set, e.g. the input and output of a system related in the time or the frequency domain. 2) Defining a model structure and 3) A rule by which a model structure can be established from the measured data, such as Least-Squares. Looking closely at these components, the measured data may be recorded during a specifically designed experiment, so that the data carries maximum information, subject to any constraints, [23]. Choice of a model structure is one of the most important and difficult aspects of system identification. Here *a priori* knowledge and engineering intuition coupled with formal properties of the system will prove to be invaluable. Models of systems with some unknown physical parameters can be constructed from basic physical laws and well established relations. These are called *white box* models. Models with unknown physical parameters and a large number of random variables, which cannot be satisfactorily represented by physical laws, are deduced using black box modeling. The third type of model is a gray box model; this represents a compromise and a combination between white and gray box modeling. The third component of modeling is assessment of the model quality and its ability to reproduce the measured data, also known as model validation. The process of System Identification is summarized in Figure 3. Modeling and identification of nonlinear systems is especially challenging, in the sense that the nonlinearity could be in either the input signal, the output signal or in both. If modeling of the system is done using linear and/or non-linear blocks, to represent a system, careful combination of these need to be formulated. In our study, the input is the sEMG and the output is the corresponding force signal generated by the human hand. The system is the particular subject's hand. The sEMG signal is affected by large number of variables, some of which have been mentioned in the EMG section of the theoretical background. The force signals too, are

non-linear, especially as time progresses and the muscle fatigues. It would be very difficult and complicated to take into account all the factors which plague these two signals.

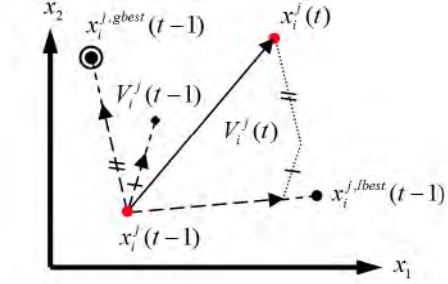


FIGURE 1: PREVIOUS AND UPDATED POSITON OF PARTICLES [22]

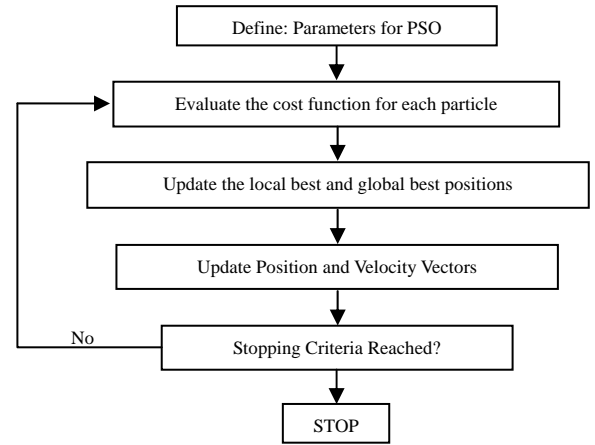


FIGURE 2: PARTICLE SWARM OPTIMIZATION LOOP

So with the assumption that the two signals are non-linear; the modeling for this system can be approached in a general sense. In SI the model structure that has been used previously for capturing the non-linear input and output system dynamics has been the Hammerstein-Wiener model. This modeling method has not been explored, previously, for modeling of sEMG signals and force.

Hammerstein models assume a separation between the non-linearity and the dynamics of the process, [24]. The Hammerstein structure consists of a static non-linear block followed by a linear dynamic block. It is described by the following equations;

$$\begin{aligned} x(t) &= g(u(t)), \\ y(t) &= b_1x(t-1) + \dots + b_mx(t-m) - a_1y(t-1) - \dots - a_my(t-m). \end{aligned} \quad (1)$$

Hammerstein models are popular in the field of control engineering as it is easy to compensate the non-linear process behavior by a controller that implements the inverse static nonlinearity  $g^{-1}(\bullet)$  at its output (if the inverse exists). Another advantage of this model being that the stability is determined solely by the linear part of the model. Any assumption of the structure of the process is very restrictive and can be applied to only a limited class of systems. The static nonlinearity is usually approximated using a polynomial.

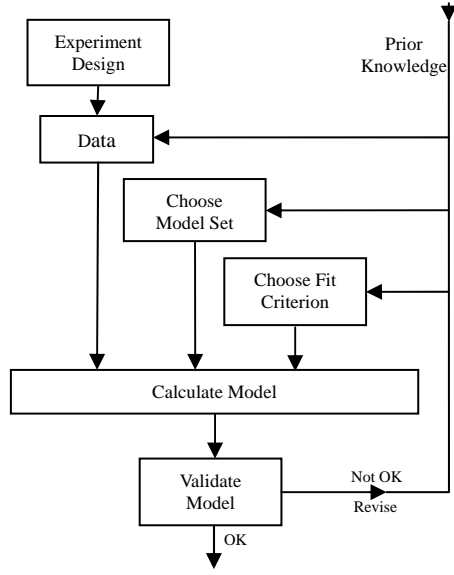


FIGURE 3: SYSTEM IDENTIFICATION LOOP [22]

For systems with multiple inputs the static nonlinearity  $g(\bullet)$  becomes a higher dimensional function, say for  $l = 2$ , and  $m = 2$  Equation (1) becomes;

$$\begin{aligned} x(t) &= c_0 + c_1 u(t) + c_2 u^2(t), \\ y(t) &= b_1 c_0 + b_1 c_1 u(t-1) + b_2 c_0 + b_2 c_1 u(t-2) + \\ &\quad b_1 c_2 u^2(t-1) + b_2 c_2 u^2(t-2) - a_1 y(t-1) - a_2 y(t-2). \end{aligned} \quad (2)$$

The generalized Hammerstein model is constructed by summarizing identical terms and re-parameterizing the model in a manner that yields linear parameters, for example,  $b_1 c_0$  and  $b_2 c_0$  both represent offsets and can be summarized. This leads to Equation (3);

$$\begin{aligned} y(t) &= \theta_1 + \theta_2 u(t-1) + \theta_3 u(t-2) + \\ &\quad \theta_4 y(t-1) + \theta_5 y(t-2) + \theta_6 u^2(t-1) + \theta_7 u^2(t-2). \end{aligned} \quad (3)$$

The Wiener model structure is the Hammerstein model reversed. The linear dynamic block is followed by a static nonlinear block. This yields the equation given in (4)

$$\begin{aligned} x(t) &= b_1 u(t-1) + \dots + b_m u(t-m) - a_1 x(t-1) - \dots - a_l x(t-l), \\ y(t) &= g(x(t)). \end{aligned} \quad (4)$$

Eliminating  $x$  in (4) yields;

$$\begin{aligned} y(t) &= g(b_1 u(t-1) + \dots + b_m u(t-m) \\ &\quad - a_1 g^{-1}(y(t-1)) - \dots - a_l g^{-1}(y(t-l))) \end{aligned} \quad (5)$$

The combination of the two is then, the Hammerstein-Wiener model, [25] as given in Figure 4(a) Hammerstein b) Wiener models and Figure 5 Hammerstein-Wiener model. Consider the Hammerstein case where the static nonlinear function  $g(\bullet)$  can be parameterized either in terms of physical parameters, such as

saturation point and saturation level, or in black-box terms such as spline-function coefficients. This defines  $g(\bullet, \eta)$ . If the linear model is given by  $G(q, \theta)$ , the predicted output model will be in the following form:

$$\hat{y}(t | \theta, \eta) = G(q, \theta) g(u(t), \eta). \quad (6)$$

Equation 7 describes the Hammerstein-Wiener model structure:

$$w(t) = f((g(t))), \quad b(t) = \frac{B_{j,i}(q)}{F_{j,i}(q)} w(t), \quad y(t) = h(x(t)), \quad (7)$$

where,  $w(t)$  and  $b(t)$  are internal variables,  $w(t)$  has the same dimensions as  $u(t)$ , and  $x(t)$  has the same dimensions as  $y(t)$ .

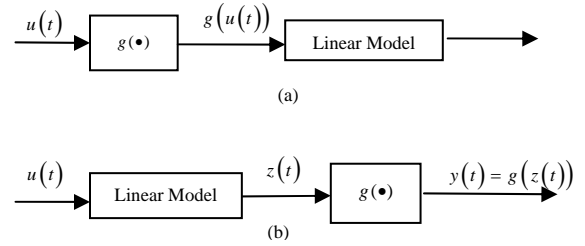


FIGURE 4 (A): A) HAMMERSTEIN MODEL, B) WIENER MODEL

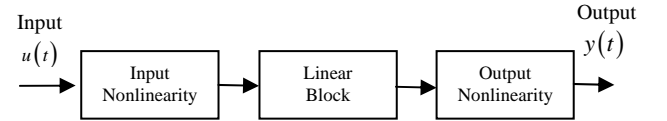


FIGURE 4 (B): HAMMERSTEIN-WIENER MODEL STRUCTURE

The linear block is specified using the terms  $n_b$  - the number of zeros plus one,  $n_f$  - the number of poles and  $n_k$  - the delay from the input to the output in terms of the number of samples. The commonly used nonlinear estimators for Hammerstein-Wiener model are, a) Dead Zone, b) Piecewise Linear, c) Saturation, d) Sigmoid Network, and e) Wavelet Network, [26-28].

## EXPERIMENTAL SETUP

The experiments were carried out on a healthy male subject to extract dynamical models describing the relationship between sEMG-Force signals. The motor points were located using a Muscle Stimulator, manufactured by Rich-Mar Corporation (model number HV 1100). The motor locations of the index, middle and ring fingers were identified and chosen for the experiments. The EMG detection system used was a Delsys, Bagnoli-16 channel EMG (DS-160, S/N-1116), which has internal amplification and noise reduction technology built into it. The sensors used for measuring the surface EMG action potentials are two pronged DE 2.1 differential surface electrodes. The material for the contacts of the electrode is 99.9% pure silver, while the contacts are 10mm long, 1mm in diameter and spaced 10mm apart. The subjects' skin was prepared before the sensors were placed over the motor point, hair around the area was shaved and an alcohol swab was used to clean the skin. Delsys Electrode Interface SC-FO2-3 was used which promotes the quality of the electrical connection between the electrode and the skin, minimizing motion artifacts and line interference. The electrodes

were placed along the muscle fibers (Flexor Digitorum Superficialis) for recording surface EMG. The force was recorded using a force sensitive resistor (FSR) mounted on a stress ball. The data acquisition for the force and the sEMG signals was done at 2000 samples per second and the NI DAQ 6024 E Series boards were used. Experiments were conducted for three fingers, the index, middle and the ring finger. The motions simulated were a) pad to pad grip and b) a power grip, while measuring the force developed by individual fingers. For the ring finger, the motion to generate the force signal was randomized (the levels of force amplitude and frequency varied significantly over one experiment and for all six experiments carried out). This was done in order to have poor correlation between the sEMG-Force signals analyzed for various time windows. For the index and the ring finger four experiments were conducted for each. The motion to generate the force signal was made cyclic in order to have a high correlation between the sEMG-Force signals. Cyclic motion was considered, in this case, to study the effects of fatigue as time progressed on system identification and the Hammerstein-Wiener modeling. Data, for the ring finger (random motion), was collected for 30, 45 and 60 seconds. Data for the middle and index fingers was collected for 30 and 45 seconds. The subject performed a cyclic and random series of flexions and contractions with the ring finger at constant and random speeds. The randomness – as depicted in Figure 5a) – was necessary in order to ensure that the system excited all modes. Figure 5a) shows the output of the random motion raw sEMG signal of the ring finger, 5b) Chebyshev filtered random motion sEMG-Force signals (ring finger), 5c) Half-Gaussian filtered sEMG, and also the data. 5d) cyclic sEMG-Force signals of the middle finger and 5e) cyclic sEMG-Force signals of the index finger. The x-axis in the figures is the number of samples and the y-axis is the amplitude of the sEMG and the force signal in milli-volts. During the experiment all fingers were flexed in order to generate the force and sEMG signal. A result of this there was substantial cross talk in the measurement. This was to simulate closely, a real life situation. The fit values computed for the models uses the relation in equation, (8);

$$\text{fit} = 100 * (1 - \text{norm}(\hat{y} - y) / \text{norm}(y - \text{mean}(y))) \quad (8)$$

## RESULTS AND DISCUSSION

The force signal was filtered using a low pass Butterworth filter using a cutoff frequency of 3Hz. The sEMG signal was also filtered using a Chebyshev Type II high pass filter with the following filter parameters,  $F_{\text{stop}}=60\text{Hz}$ ,  $F_{\text{pass}}=70$ ,  $A_{\text{stop}}=80$ ,  $A_{\text{pass}}=1$ , match=stopband, to remove any line frequencies and followed by a low pass Chebyshev Type II high pass filter with the following filter parameters,  $F_{\text{stop}}=600\text{Hz}$ ,  $F_{\text{pass}}=650$ ,  $A_{\text{stop}}=80$ ,  $A_{\text{pass}}=1$ , match=stopband. This was done since EMG signals have an effective frequency content of not more than 500Hz, according to the ISEK standards, [3].

*Cyclic and Random Data Analysis:* As mentioned earlier, experiments were carried out a) in a cyclic motion, to have a cyclic change in the sEMG and force signal so that the effects of fatigue could be characterized and b) in a random manner (with fatigue induced by repetition) to investigate how the Hammerstein-Wiener model parameters change with time. For the

cyclic case, experiments were conducted on the index and the middle finger, while the ring finger was used for the random case. In all, for the cyclic case four experiments each were conducted on the index and middle finger and the data analyzed.

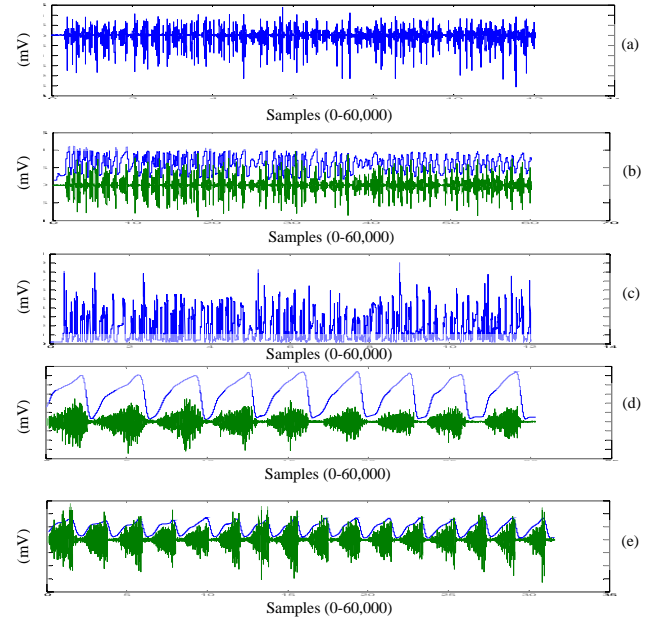


FIGURE 5: A) RANDOM RAW EMG RING FINGER, B) CHEBYSHEV FILTERED EMG AND FORCE (RING FINGER, RANDOM), C) HALF-GAUSSIAN FILTERED EMG (RING), D) CYCLIC EMG-FORCE MIDDLE FINGER, E) CYCLIC EMG-FORCE INDEX FINGER

The sEMG data was filtered using a Chebyshev filter and a Half-Gaussian filter. Hammerstein-Wiener models were tested by varying  $n_b$  and  $n_f$  values for both the cases. The data set was split into smaller windows; an example of the windows used for estimation and validation of the modeling is shown in Table 1, where  $z_e$  is the time interval that was used for the model estimation and  $z_v$  is the time interval used for model validation. A small overlapping time window, with the estimated model is used for the validation model.

In all, the total time intervals for which models and fits were computed for the index finger alone, were 4 (time intervals per experiment) x 4(experiments) x 49 (models per window by varying  $n_b$  and  $n_f$ ) x 2 (filtering methods) = 1,568 different models. This was also repeated for the middle finger (1,568 different models). For the random motion/force variation scenario; 8 (time intervals per experiment) x 7(experiments) x 49 (models per window by varying  $n_b$  and  $n_f$ ) x 2 (filtering methods) x 2 (piecewise linearity function, 5 and 10)= 10,976 different models were analyzed. The time windows for the random case are double the number of intervals for the cyclic case as the correlation between the signals is very poor. The size of the window used for estimation and validation is a very important aspect to be considered in SI.

The window size was varied in order to find the most optimum case which would result in better modeling of the two signals. A detailed analysis of the window size, the signal contained in these individual windows, and their correlation to one another is



required to be able to standardize the modeling process. This aspect is still under investigation.

TABLE 1: MODELING TIME WINDOWS CYCLIC MOTION (INDEX AND MIDDLE FINGERS)

ze (sec)	zv (sec)
0.5-6.5	2.5-8.5
6.5-13.5	9.5-16.5
13.5-19.5	16.5-22.5
17.0-23.0	20.0-26.0

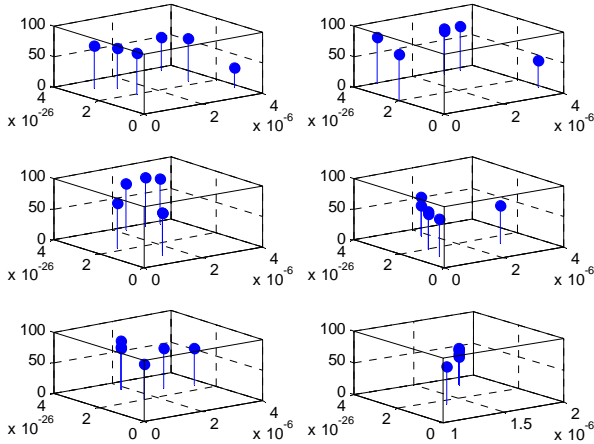


FIGURE 6: RESULTS OF PSO FOR SIX EXPERIMENTS. AXES ARE ALPHA, BETA AND FIT VALUES.

Also, it would not be feasible to show all the results of all the models here, but examples are provided as to how the modeling was affected for the various time intervals and motion/force variations. For the random scenario, PSO was used to investigate a relation between the filter parameters  $\alpha$  and  $\beta$  and to investigate the effect of fatigue on the model outputs. The results of the PSO optimization are summarized in Figure 6. The x axis in the figures are the optimized values of  $\alpha$  for the three different time intervals and the y axis are the optimized values  $\beta$  and the z axis are their respective magnitudes. From the results, it can be concluded that  $\alpha$  values between  $1.5$  to  $2.9 \times 10^{-6}$  and  $\beta$  values between  $2.6$ - $3.7 \times 10^{-26}$  are most likely to give better fits for nonlinear Hammerstein-Wiener models. The model fits obtained initially with PSO were randomly distributed. The fit values for experiment 1 are not very high (this could be due to the limited search space for  $\alpha$  and  $\beta$ ) as compared to the other experiments for the initial time windows, where one would not expect any fatigue. But a trend can be observed that as fatigue sets in towards the last time window (later in the experiment where the subject is experiencing fatigue) of almost all the experiments the fit % dropped, except for experiments 5 and 6 (not shown here) where the fits were relatively high about 67%. This was because the correlation between the signals for these two windows was much higher than the ones for the other experiments. This could indicate that as muscle fatigue increases the recruitment of other motor units was similar and the sEMG obtained for experiments 5 and 6 were similar. As the muscle fatigue increases, it directly deteriorates the input sEMG signals relation to force. This casts a doubt on the effectiveness of the nonlinear blocks in the Hammerstein-Wiener

models investigated. From these results, it could be concluded that a thorough investigation into the existing nonlinear block would be needed and modification of the block may be required to capture the dynamics of fatigue and to compensate for the detrimental effects it has on modeling the sEMG-force signals. Also, the nonlinear block could be substituted for any of the blocks that have been discussed in, [29]. Figure 7 shows some of the results for the index finger nonlinear Hammerstein-Wiener models investigated for the experiments. The red plot is of the signal used for model estimation, the green plot is of the signal used for validation of the model and the blue plot is of the entire data spectrum for that experiment for Figure 7 (a) & (b). Figure 7(c) shows the auto-correlation of the model residuals for the output signal (force).

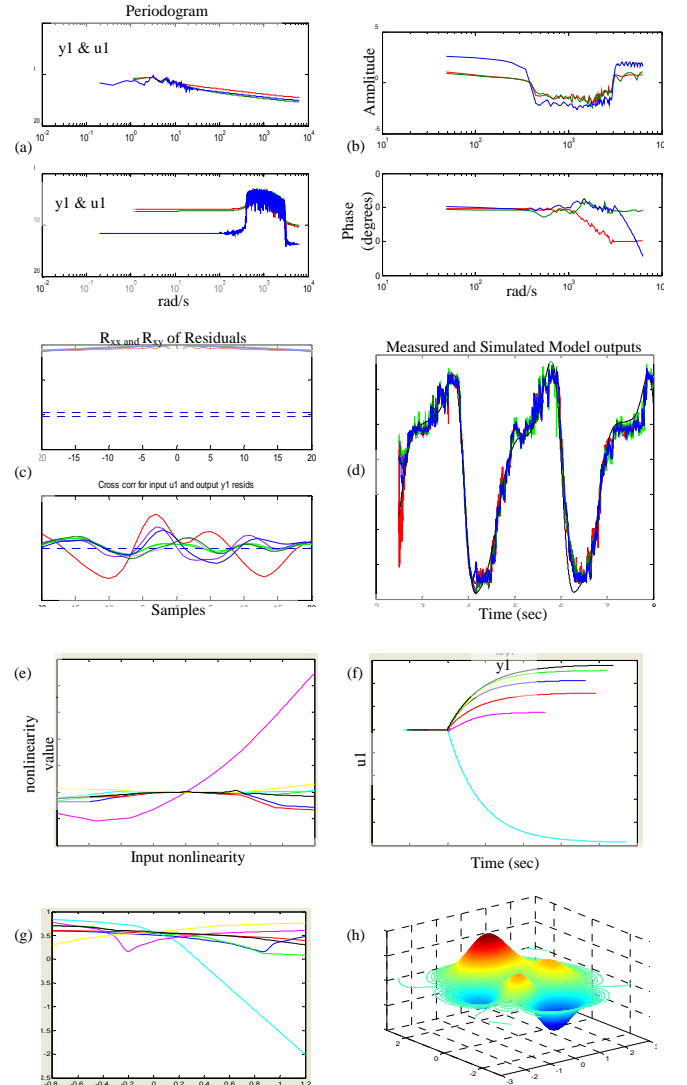


FIGURE 7: A) EMG INDEX FINGER DATA SPECTRUM, B) FREQUENCY CONTENT OF SIGNALS, C) MODEL RESIDUALS AND AUTO-CORRELATION AND CORSS-CORRELATION OF SIGNALS, D) MODEL OUTPUTS, E) INPUT NONLINEARITY, F) LINEAR BLOCK, G) OUTPUT NONLINEARITY, H) CONTOUR PLOT OF MODEL FITS

This figure also plots the cross-correlation of the various models between the input (sEMG) and the residuals of the output (force).

Figure 7 d) shows the results of the measured and the simulated model output signal, for the particular time window. The plots shown here are for the best fit scenarios. For example, nlhw1 with the following model parameters;  $n_b = 2$ ;  $n_f = 3$  and  $n_k = 1$ , with a piecewise linearity function value of 5, gives a fit of 80.51% for the time window 0.5-8.0sec window, which was split into 0.5-6.0 and 2.5-8.0 for model estimation and validation.

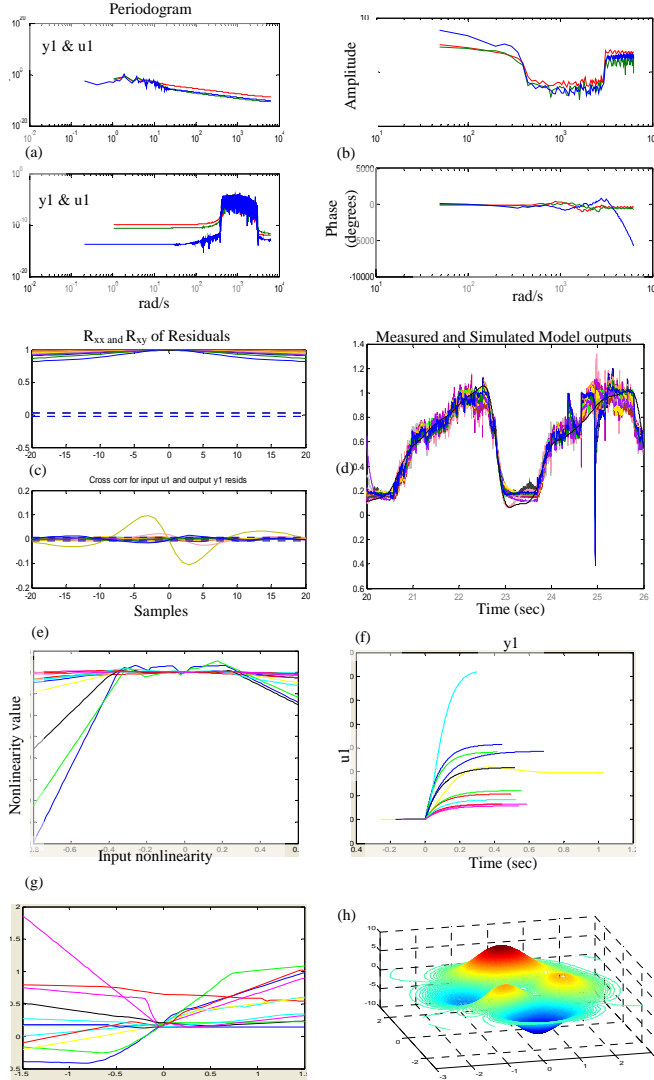


FIGURE 8: A) EMG MIDDLE INGER DATA SPECTRUM, B) FREQUENCY CONTENT OF SIGNALS. C) MODEL RESIDUALS AND AUTO-CORRELATION AND CORSS-CORRELATION OF SIGNALS, D) MODEL OUTPUTS, E) INPUT NONLINEARITY, F) LINEAR BLOCK, G) OUTPUT NONLINEARITY, H) CONTOUR PLOT OF MODEL FITS

The model parameters were varied i.e. various  $n_b$  (from 2-9), and  $n_f$  (from 3-10) were investigated. 7(e), (f) and (g) are the input nonlinearities, the linear block and the output nonlinearity blocks of the Hammerstein-Wiener models. The plot also shows the case where the simulated model failed for a set of parameters (the line

in the input non-linearity which goes across the others). In the linear block plot there are a few lines which have a very large deviation from the others; these too are the cases where the modeling resulted in poor fit values. Figure 9 shows a distribution of the fit values for the various model parameters for a single time window.

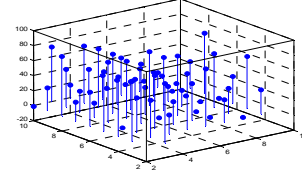


FIGURE 9: DISTRIBUTION OF MODEL PARAMETRS AND THE FIT VALUES (ONE TIME WINDOW)

## CONCLUSION

From the experiments and the Hammerstein-Wiener modeling it can be concluded that, a) the Hammerstein-Wiener models do capture the dynamics of the sEMG-Force data very well for all the three fingers tested (in the range of 65 to 82% model fits). This statement holds true for all the initial time windows in the experiments. But the model fits deteriorate (between 17-25%) as fatigue in the muscle increases. In order, to capture and to account for the changes in the sEMG-force signals due to fatigue, further investigation will be needed into the non-linear block of the model structure. Also, the size of the windows chosen for estimation and validation needs to have a fairly high degree of correlation. For the random motion case, where the force was varied randomly, added analysis of the frequency and amplitude of the two signals was needed. The selection of the size of the window could be automated using correlation coefficients. b) The Half-Gaussian filtering of the sEMG signal, used for modeling, yielded slightly better results than the Chebyshev filtering of sEMG (about 7-12% more). c) A change in the piecewise linearity function in the Hammerstein-Wiener modeling did also have a significant effect on the model fit value. Though a clear trend could not be seen from the results, an adaptive optimization scheme if applied could help in studying the effect of this parameter on the model fits. d) Although the PSO did not offer concrete results about the effect of fatigue on the filter parameters  $\alpha$  and  $\beta$ , it did throw some light on the direction in which the search space for these parameters needs to be further investigated, which could assist in modeling the sEMG-force signals, especially with muscle fatigue.

## ACKNOWLEDGEMENTS

This work was supported by a grant from the Telemedicine Advanced Technology Research Center (TATRC) of the U.S. – Department of Defense (DoD) and is greatly appreciated.

## REFERENCES

1. Piper, H., 1912. "Elektrophysiologie Menschlicher Muskeln". Springer Verlag.

2. <http://www.army.mil/-news/2010/02/24/34906-the-future-of-prosthetics-is-in-your-mind/>
3. [http://www.isek-online.org/standards\\_emg.html](http://www.isek-online.org/standards_emg.html)
4. Mewett, D. T., Nazeran H., Reynolds, K., J., 2001. "Removing power line noise from recorded EMG". *Proceedings of the 23<sup>rd</sup> Annual EMBS international Conference*. Light,
5. Clancy, A. E., Farry, A. K., 2000. "Whitening of the electromyogram to improve amplitude estimation". *IEEE Transactions on Biomedical Engineering*, 47(6), June, pp. 709-719.
6. Chan, D. C. A., Englehart, B. K., 2005. "Continuous myoelectric control for powered prostheses using hidden Markov models". *IEEE Transactions on Biomedical Engineering*, 52(1), January, pp. 121-124.
7. Chan, H. Y. F., Yang, Y., Lam, F. K., Zhang, Y., Parker, A. P., 2000. "Fuzzy EMG classification for Prosthesis control". *IEEE Transactions on Rehabilitation Engineering*, 8(3), September, pp. 305-311.
8. Reaz, I. B. M., Hussain, S. M., Yasin, M. F., 2006. "Techniques of EMG signal analysis: detection, processing, classification and application". *Biomedical Procedures Online*, 8(1), January, pp. 11-35.
9. Johnson, T. D., Elashoff, R. M., Harkema S. J., 2003. "Bayesian change-point analysis of electromyographic data: detecting muscle activation patterns and associated applications". *Biostatistics*, 4(1), pp. 143-164.
10. Woods J. J., Bigland-Ritchie B., 1983. "Linear and non-linear surface EMG/force relationships in human muscles. Anatomical/functional argument for the existence of both". *American Journal of Physical Medicine*, 62(6), December, pp. 287-299.
11. Jacquelin P., George A. B., 1981. "EMG-Force relationships in skeletal muscle". *CRC Critical Reviews in Biomedical Engineering*, 7(1), pp. 1-22.
12. Solomonow M., Guzzi A., Baratta R. Shoji H., D'Ambrosia R., 1986. "EMG-force model of the elbows antagonistic muscle pair. The effect of joint position, gravity and recruitment". *American Journal of Physical Medicine*, 65(5), October, pp. 223-244.
13. Moxham J., Edwards R. H., Aubier M., Troyer De. A., Farkas G., Macklem P.T., Roussos C. 1982. "Changes in EMG power spectrum (high-to-low ratio) with force fatigue in humans". *Journal of Applied Physiology*, 53(5), pp. 1094-1099.
14. Fuglevand J. A., Macefield G. V., Bigland-Ritchie B., 1999. "Force-Frequency and fatigue properties of motor units in muscles that controls digits of the human hand". *The Journal of Neurophysiology*, 81(4), pp. 1717-1729.
15. Sebastian A., Parmod K., Anugolu M., Schoen P. M., Urfer A., Naidu S. D., 2009. "Optimization of Bayesian Filters and Hammerstein-Wiener Models for EMG-Force Signals Using Genetic Algorithm". *Proceedings of the ASME 2009 Dynamic Systems and Control Conference DSCC 2009*.
16. Farina, D., Merletti, R., and Enoka, M. R., 2004. "The extraction of neural strategies from the surface EMG". *Journal of Applied Physiology*, 96, pp. 1486-1495.
17. Clancy A. E., Bertolina V. M., Merletti R., Farina D., 2008. "Time-and frequency-domain monitoring of the myoelectric signal during long-duration, cyclic, force varying, fatiguing hand-grip task". *Journal of Electromyography and Kinesiology*, 18(5), October, pp. 789-797.
18. Mortiz T. C., Barry K. B., Pascoe A. M., Enoka M. R., 2004. "Discharge rate variability in force fluctuations across the working range of a hand muscle". *Journal of Neurophysiology*, 93, December, pp. 2449-2459.
19. Kamavuako N. E., Farina M., Yoshida K., Jensen W., 2009. "Relationship between grasping force and features of single-channel intramuscular EMG signals". *Journal of Neuroscience Methods*, 185(1), December, pp. 143-150.
20. Farina D., Merletti R., 2001. "A novel approach for precise simulation of EMG signal detected by surface electrodes". *IEEE Transactions on Biomedical Engineering*, 48(6), June, pp. 637-646.
21. Sanger, D. T., 2007. "Bayesian Filtering of Myoelectric signals". *Journal of Neurophysiology*, 97, pp. 1839-1845.
22. Chen, C.-H., Bosworth, K. W., and Schoen, M. P., 2007. "Investigation of particle swarm optimization dynamics". In *Proceedings of International Mechanical Engineering Congress and Exposition (IMECE)*.
23. Ljung, L., 2<sup>nd</sup> ed., "System Identification: theory for the user". Prentice Hall Information and System Sciences Series, 1995, Chap. 13, pp. 409-453.
24. Nelles O., "Nonlinear System Identification: From classical approaches to neural networks and fuzzy models". Springer. Chap. 18, pp. 583-586
25. Ljung, L., 2<sup>nd</sup> ed., "System Identification: theory for the user". Prentice Hall Information and System Sciences Series, 1995, Chap. 5, pp. 140-145.
26. [http://www.mathworks.com/access/helpdesk/help/toolbox/ident/index.html?/access/helpdesk/help/toolbox/ident/gs/bq\\_ylq6.html](http://www.mathworks.com/access/helpdesk/help/toolbox/ident/index.html?/access/helpdesk/help/toolbox/ident/gs/bq_ylq6.html)
27. Westwick, T. D., Kearney, E. R., 2000. "Identification of a Hammerstein Model of the stretch reflex EMG using separable least squares". *Proceedings of the 22<sup>nd</sup> Annual EMBS Conference*, July, pp. 1901-1904.
28. Dempsey, J. E., Westwick, T. D., 2001. "Identification of a Hammerstein Model of the stretch reflex EMG using cubic splines". *Proceedings of the 23<sup>rd</sup> Annual EMBS Conference*, October, pp. 1244-1247.
29. Juditsky A., Hjalmarsson H., Benveniste A., Delyon B., Ljung L., 1995. "Nonlinear black-box models in system identification: Mathematical Foundations". *Automatica IFAC*, 31(12), December, pp. 1725-1750.

# Genetic Algorithm Running Time Optimization Using OpenMP Parallel Computing

Parmod Kumar<sup>1</sup>, Nikesh Joshi<sup>2</sup>, Chandrasekhar Potluri<sup>1</sup>, Jensen Alex<sup>1</sup>, Marco P. Schoen<sup>1</sup>, Steve Chiu<sup>2</sup>

<sup>1</sup>Measurement and Control Engineering Research Centre, College of Engineering

<sup>2</sup>Department of Computer Science, College of Engineering

Idaho State University

Pocatello, Idaho, 83209 U.S.A.

<sup>1</sup>kumaparm@isu.edu, <sup>1</sup>potlchan@isu.edu, <sup>1</sup>jensalex@isu.edu, <sup>2</sup>joshnike@isu.edu,  
<sup>1</sup>schomarc@isu.edu, <sup>2</sup>chiustev@isu.edu

## Abstract

*Genetic Algorithm (GA) is biologically motivated evolutionary computation technique used both as search methods for solving problems and for modelling evolutionary systems. GA has been used in a wide variety of optimization tasks, including numerical optimization and combinatorial optimization problems such as circuit design and job shop scheduling. Although there are many problems for which the genetic algorithm can evolve a good solution in reasonable time, there are also problems for which it is inappropriate like the one in which it is important to find the exact global optimum and if the number of iteration increases then that makes the algorithm to take long time. In this work, we are using GA to optimize the parameters of nonlinear Bayesian Filters for electromyographic (EMG) signal. OpenMP is a parallel programming model for shared memory and distributed shared memory multiprocessors. We are using OpenMP on four processors to improve the time of GA optimization for Bayesian Filter parameters.*

**Keywords:** OpenMP, Matlab®, MPI, EMG, GA, Gene, Mother Chromosome, Father Chromosome, Pairing Operator, Mating Operator, Mutation, Population Size.

## 1. Introduction

Principles of natural selection and genetics has been used to deduce some efficient search algorithms, GA is one of them. GA is used in different fields to obtain solutions to different problems, e.g. engineering, science, business and economics [1, 2]. Some of the

applications of GA are in automotive design, engineering design, robotics, evolvable hardware, optimized telecommunication routing, joke and pun generation, bio-mimetic invention, traffic and shipment routing, computer gaming, encryption and code breaking, computer-aided molecular design, gene expression profiling, optimizing chemical kinetic analysis, finance and investment strategies, and marketing and merchandising. Although, for a general problem of normal size, GA is good option to get the optimal solution in appropriate amount of time, whereas for bigger and complex problems GA takes more time to find optimal solution. Researchers have explored different approaches to minimize this computational time and cost and parallel processing came out to be one of the most promising approach.

GA is based on the principle of natural selection. It uses a random search technique to find the optimal solution of a problem by manipulating a population of candidate solutions. To form next generation, GA selects the best solutions from the evaluated population. Good solutions and time to reach them by GA depends on the population size [3, 4], because if the population is too small, then the search space will not be sufficient and it will be difficult to identify good solutions and in case if the population is too big, the GA will waste computational resources processing unnecessary individuals. Each individual in the population has a fitness value, which is a payoff measure that depends on how well the individual solves the problem. Crossover and mutation are the

two operators used by GA to explore the search space, here crossover is primary and mutation is a secondary search operator. The probability of crossover is much higher than the probability of mutation. GA can be stopped based on different conditions, one is predetermined number of generations and function evaluations, second is the average quality of the population get saturated after some number of generations, and the third is when all the individuals are identical, which can only occur when mutation is not used. We are using predetermined number of generations and function evaluations to stop the GA in this research work. The generic GA flow chart is shown in Figure 1.

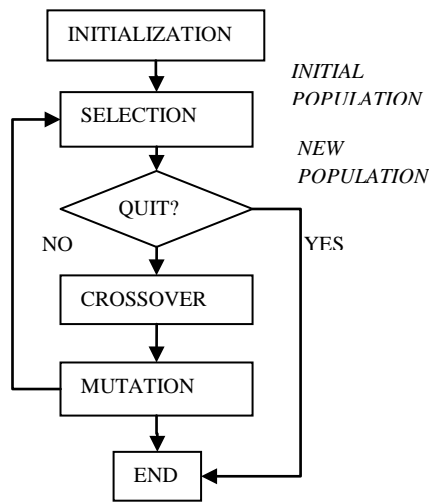


Figure 1: Generic GA Flow Chart.

The time taken by GA is directly proportional to the number of evaluations and generations, more the number of evaluations larger is the time for GA. On the other hand, this time can be minimized by paralleling the GA program on parallel cluster. Most of the parallel programs divide the task in chunks and solve it simultaneously using multiple processors. On a parallel cluster, there are numerous processors, and they share the task, larger the number of processors faster the computation or lesser the time for the completion of the algorithm. In this research work we are using OpenMP parallel programming model and utilizing a cluster of four processors to run the GA and comparing its performance with the single processor in *Matlab*®.

## 2. Background

Most of the parallel programs divide the task into chunks and solve it simultaneously using multiple

processors. Similar approach can be used for GAs in different ways. These approaches can be using a single population, divide the population into several subpopulations, use of massively parallel architecture, or use of fewer multicomputer with fewer and more powerful processing units. Mainly there are three kinds of parallel GAs, and these are (a) global single-population master-slave GAs, (b) single-population fine grained, and (c) multiple-population coarse-grained GAs. The hierarchical parallel GAs combine the multiple demes with master-slave or fine-grained GAs. It has a higher level and a lower level, at higher level they are multiple-deme algorithms and at lower level they are single-population parallel GAs (either master-slave or fine-grained) [1].

The research work in [5] shows a method of parallel GA, in which a global parallel implementation of the conventional GA and a GA with a generation gap, where some part of the population is replaced. The efficiency of global parallel GA is close to 100 % in SIMD (single instruction multiple data) computers by [5]. Four prototypes for parallel GAs are proposed in [6] where the first three are variations of the master-slave GA, and the fourth is a multiple-population GA.

### 2.1 Master-Slave Parallelization

Same as in a simple GA, master-slave GA also have a single panmictic population. Figure 2 shows the schematic of master-slave GA, where the evaluation of fitness is distributed among the slave processors.

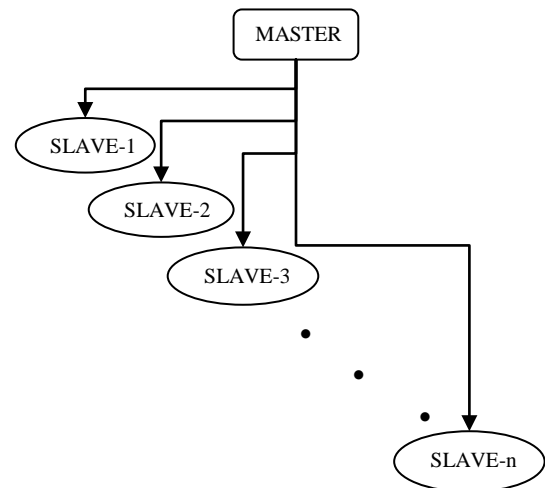


Figure 2: Master-Slave Parallel GA.

The master-slave GA considers full population size for selection and crossover, so it is known as global GA. The master-slave parallelization method for GA

does not change the behavior of the algorithm while the single-population fine grained and multiple-population coarse-grained GA change the way the GA works [1]. The master-slave parallel GA considers all the population for selection, whereas the other parallel GAs considers only a subset of the population. In addition, in the master-slave parallel GA the mating is random, whereas in the other methods mating is restricted to a subset of individuals [1]. Majority of the global parallel GAs are implemented synchronously. If the multiprocessor architecture is of shared memory then each individual processor can share the information, reading and writing without any issue. In contrast, on distributed-memory architecture, the population is stored only at one processor and the master is responsible for sending the individuals to slaves for evaluation, collecting the results and applying GA for next generation. Encore Multimax is a shared-memory computer with 16 processors, a GA is implemented on this to search for efficient timetables for schools in [7]. This research in [7] gave limited speed-up because of the critical path of the program serial code.

In 1993, Abramson, Mills, and Perkins added a distributed-memory machine “Fujitsu AP1000” with 128 processors to the experiments, changed the application to train timetables and modified the code [8]. In this research, the speed-up was significant up to 16 processors and then decreased because of the increase in communication as more processors are added.

Hauser and Männer used global GA on three different parallel processors and got good speed up only on NERV multiprocessor [9]. The speed-up of five using six processors is obtained with a very low communications overhead [9]. The reason of low performance on other processors a SparcServer and a KSR1 is because of the inadequate scheduling of computation threads to processors by the system. All the previous research results shows that the master-slave parallel GAs are easy to implement and very efficient method of parallelization especially when the evaluation needs considerable computations. Additionally the master-slave parallel GAs do not change the search behavior of the GA [1].

### 3. GA In Matlab®

The continuous number GA, which is used in this work, interprets the parameters of a problem as genes, where one set of parameters form a chromosome,  $chromosome = \{gene_1, gene_2, \dots, gene_{N_{par}}\}$ . Since one chromosome corresponds to a candidate solution, its evaluation is done by assessing the numerical value of that solution, which usually referred as the cost. Unlike traditional optimization, the function is not referred to as the cost function but as the fitness function or objective function. Using an initial population size with randomly generated chromosomes, where each gene is generated by a random number generator within the search space, the chromosome will take the dimension of  $R^{N_{par} * population\ size}$ . After evaluating each chromosome cost  $c_i = f(chromosome_i)$ ,  $i = 1, 2, \dots, population\ size$ , the selection operator will select a subset of the chromosomes based on their cost value to survive for the next iteration.

For elitism based GA, the best performing chromosomes always survive. There are two options the population size, a steady-state or a performance based size. The first option maintains a certain number of chromosomes for each iteration – also referred to as a generation; while performance based size, selection sets a minimum criterion for chromosomes to survive. The latter option may cause the algorithm to end prematurely since not minimum criteria (cost value).

*Pairing Operator:* Genetic Algorithm may employ a number of pairing mechanisms. Among them are pairing from top to bottom, where the best performing chromosome is paired with the next best performing chromosome and so on; random pairing, where a uniform distribution is assumed to randomly pick the mother and father chromosome; weighted random pairing where the probability of selection is influenced by the performance of the individual chromosome; and rank weighing, where the probability of selection is influenced by the ranking of chromosome with respect to the others measured again by the performance. In this paper, the pairing is accomplished by determining the cumulative probability for each chromosome is

$$P(n) = \frac{n}{\sum_{i=1}^r i}, \text{ where}$$

$$r = \frac{population\ size - no. of chromosomes\ kept}{2},$$

and  $n$  is the index of chromosomes. Having computed the individual cumulative probabilities  $P(n)$ , the parent chromosomes are now selected by utilizing a

random number generator and indexing this with the cumulative probability. Hence, the best performing chromosome has the best chance of being selected, but also, all chromosomes in the mating pool have a chance of being selected.

*Mating Operator:* In this work, the next generation chromosomes are created from the mother and father chromosome (which were selected as described above) by following equations given as:

$$gene_{new_1} = mother(\alpha) - \beta(mother(\alpha) - father(\alpha)),$$

$gene_{new_2} = father(\alpha) + \beta(mother(\alpha) - father(\alpha))$ ,  
Where,  $\alpha = integer(rand * N_{par})$ ,  
 $\beta = random\ number\ between\ 0 - 1$ , and  $N_{par}$  is number of parameters for complete solution. In this  $\alpha$  can also be viewed as equivalent to the cross-over point utilized in the binary GA. Hence, the offspring (new chromosomes) are found as

$$chrom_{new_1} = (gene_{mother_1}, gene_{mother_2}, \dots, gene_{new_1}, \dots, gene_{dad_{N_{par}}}),$$

and

$$chrom_{new_2} = (gene_{dad_1}, gene_{dad_2}, \dots, gene_{new_2}, \dots, gene_{mother_{N_{par}}}).$$

*Mutation:* Mutation is an important operator that allows the search to escape local minima in order to find better areas on cost surface. Too much mutation will do opposite, i.e. if a chromosome approach an optimum point, it might mutate and be placed at an entirely different location of the cost surface. Mutation is accomplished by randomly changing a gene, i.e. substitute it with a random numbers.

## 4. GA In OpenMP

OpenMP is a parallel programming model, which uses some compiler directives and library routines to express shared-memory parallelism [10]. OpenMP uses Fortran and C++ interfaces, which is a standard feature. OpenMP API is designed and developed by a group, which represents the major vendors of high-performance computing hardware and software. A set of compiler directives is the major part of OpenMP interface. The programmer adds these compiler directives to a sequential program. Programmer

specifies the synchronization points and tells the compiler what parts of the program to execute concurrently. As the directives can be added in an incremental fashion, the OpenMP gives a path and platform for the parallelization of existing software. In contrary, the Pthreads and MPI approaches are library routines. Pthreads and MPI are linked with and called from a sequential program, and the programmer is required to divide the computational work manually [11].

Literature does not show any evidence of the use of OpenMP parallel programming model for GA in specific. This work is using OpenMP to optimize the filter parameters of Bayesian filters using GA technique. The parallel cluster has four processors. The idea of the research is to implement the GA using OpenMP on this four processors cluster and compare the results with the output on *Matlab*<sup>®</sup> on a single processor. The OpenMP parallel programming model is given in Figure 3, where sequential parts and parallel regions are labelled clearly.

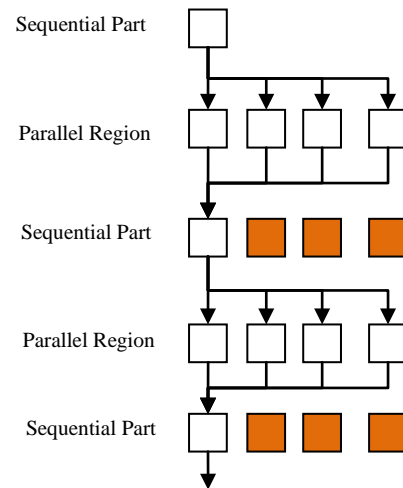


Figure 3: OpenMP Parallel Programming Model.

## 5. Results and Discussions

In this work, we are using GA to optimize the parameters of nonlinear Bayesian Filters for electromyographic (EMG) signal. OpenMP is a parallel programming model for shared memory and distributed shared memory multiprocessors. We are using OpenMP on four processors to improve the time of GA optimization for Bayesian Filter parameters. First *Matlab*<sup>®</sup> is used to run GA on one processor, and the same algorithm is applied on OpenMP parallel processing model using four processors. Two sets of data captured at a sampling rate of 2000Hz are used, first data is for 30 seconds and the second is for 60 seconds. Total simulation time taken by the *Matlab*<sup>®</sup>



and OpenMP is recorded precisely. Following tables shows the results obtained from simulations. Table 1, 2 and 3 shows the *Matlab*<sup>®</sup> simulation results for two different data sets of different lengths.

Table 1: Simulation time for 30 seconds and 60 seconds data sets in *Matlab*<sup>®</sup>.

No. of Iterations	Simulation time seconds – 30 seconds of data set.	Simulation time seconds – 60 seconds of data set.
10,000	7.13	2393.06
15,000	16.95	2403.52
20,000	28.05	2416.66
25,000	42.66	2432.89
30,000	60.61	2452.34
35,000	82.41	2475.94
40,000	108.21	2503.69
45,000	139.35	2535.91
50,000	175.45	2571.72

Table 2: Simulation time for 30 seconds and 60 seconds data sets in *Matlab*<sup>®</sup>.

No. of Iterations	Simulation time seconds – 30 seconds of data set.	Simulation time seconds – 60 seconds of data set.
60,000	208.65	2613.84
70,000	260.67	2741.73
80,000	331.85	2813.34
90,000	428.03	2913.25
100,000	550.89	3039.70

Table 3: Simulation time for 30 seconds and 60 seconds data sets in *Matlab*<sup>®</sup>.

No. of Iterations	Simulation time seconds – 30 seconds of data set.	Simulation time seconds – 60 seconds of data set.
125,000	704.54	3193.36
150,000	943.89	3433.06
175,000	1288.28	3775.16
200,000	1755.77	4236.28

Figures 1, 2 and 3 are graphical representation of the results from the Table 1, 2 and 3 respectively. It is evident from Figure 1, 2 and 3 that CPU time is directly proportional to the data size and number of iterations. Therefore, increase in the data size and the number of iterations results in the increase in CPU time.

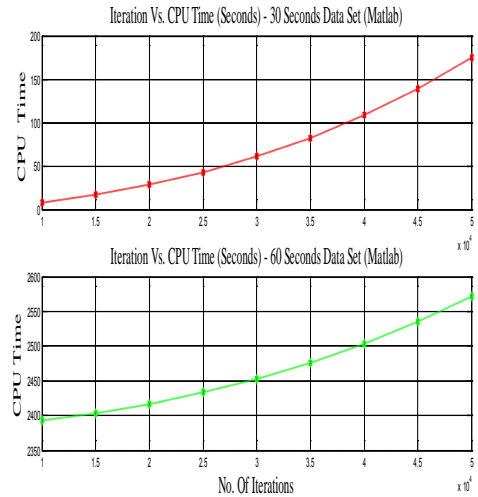


Figure 1: Iterations Vs. CPU Time – Table 1 Data.

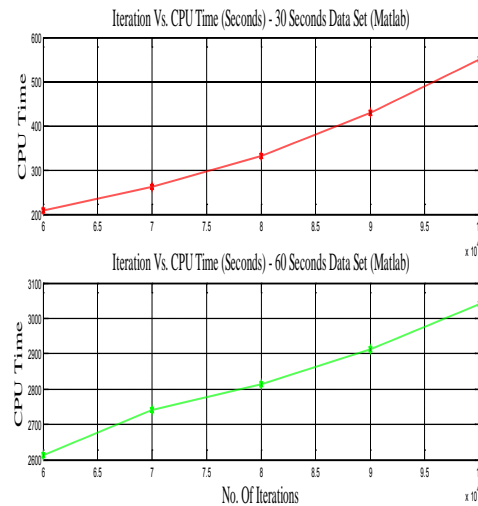


Figure 2: Iterations Vs. CPU Time – Table 2 Data.

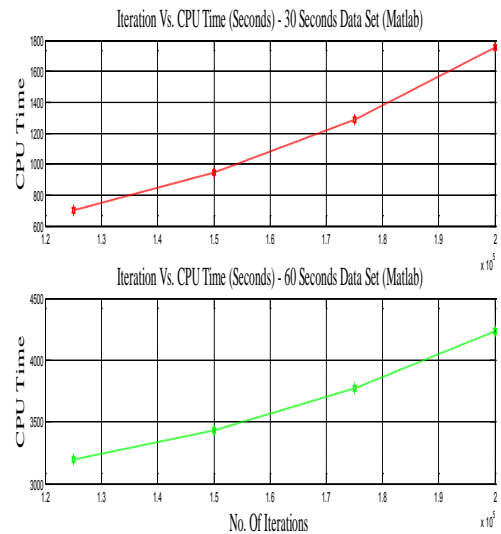


Figure 3: Iterations Vs. CPU Time – Table 3 Data.



## 6. Summary and Future Work

To conclude this work uses the idea of parallel processing and implement GA on OpenMP parallel programming model of four processors. First *Matlab*<sup>®</sup> GA code is converted to C code and then to OpenMP to implement on the parallel cluster. The algorithm is implemented both in OpenMP and *Matlab*<sup>®</sup> for 25, 50, 75 and 100 iterations and the time taken in execution is recorded. As expected the results shows the improvement of time in OpenMP implementation. In future work, similar approach will be applied using MPI and OpenMP and MPI combined for GA and more complex and advanced optimization algorithms.

## Acknowledgement

The authors gratefully acknowledge the support of the Measurement and Control Engineering Research Center (MCERC) and College of Engineering, Idaho State University for using their recourses for this work.

## References

- [1] E. Cantú-Paz, "A survey of parallel genetic algorithms," *Calculateurs Parallèles, Réseaux et Systèmes Répartis*, vol. 10, no. 2, pp. 141–171, 1998.
- [2] GOLDBERG D. E., « Genetic and evolutionary algorithms come of age ». *Communications of the ACM*, vol. 37, n 3, p. 113–119, 1994.
- [3] GOLDBERG D. E., DEB K., CLARK J. H., « Genetic algorithms, noise, and the sizing of populations ». *Complex Systems*, vol. 6, p. 333–362, 1992.
- [4] HARIK G., CANTÚ-PAZ E., GOLDBERG D. E., MILLER B. L., « The gambler's ruin problem, genetic algorithms, and the sizing of populations ». In *Proceedings of 1997 IEEE International Conference on Evolutionary Computation*, p. 7–12, IEEE Press (Piscataway, NJ), 1997.
- [5] BETHKE A. D., « Comparison of Genetic Algorithms and Gradient-Based Optimizers on Parallel Processors: Efficiency of Use of Processing Capacity ». Tech. Rep. No. 197, University of Michigan, Logic of Computers Group, Ann Arbor, MI, 1976.
- [6] GREFENSTETTE J. J., « Parallel adaptive algorithms for function optimization ». Tech. Rep. No. CS-81-19, Vanderbilt University, Computer Science Department, Nashville, TN, 1981.
- [7] ABRAMSON D., ABELA J., « A parallel genetic algorithm for solving the school timetabling problem ». In *Proceedings of the Fifteenth Australian Computer Science Conference (ACSC-15)*, vol. 14, p. 1–11, 1992.
- [8] ABRAMSON D., MILLS G., PERKINS S., « Parallelisation of a genetic algorithm for the computation of efficient train schedules ». *Proceedings of the 1993 Parallel Computing and Transputers Conference*, p. 139–149, 1993.
- [9] HAUSER R., MÄNNER R., « Implementation of standard genetic algorithm on MIMD machines ». In DAVIDOR Y., SCHWEFEL H.-P., MÄNNER R., Eds., *Parallel Problem Solving from Nature, PPSN III*, p. 504–513, Springer-Verlag (Berlin), 1994.
- [10] [Online] Available: <http://www.openmp.org>.
- [11] ENRIQUE A., MARCO T., << Parallelism and Evolutionary Algorithms >>. *IEEE Transactions on Evolutionary Computation*, vol. 6, no. 5, October 2002.

# A Study on Hybridization of Particle Swarm and Tabu Search Algorithms for unconstrained Optimization and Estimation Problems

ANISH SEBASTIAN, PARMOD KUMAR, MARCO P. SCHOEN  
Measurement and Control Engineering Research Center (MCERC)

Idaho State University

921 South 8<sup>th</sup> Ave., Stop 8060, Pocatello, Idaho 83209-8060

UNITED STATES OF AMERICA

[schomarc@isu.edu](mailto:schomarc@isu.edu) <http://www.isu.edu/~schomarc/>

**Abstract:** - This paper presents a short study on the hybridization of a swarm based optimization algorithm with a single agent based algorithm. Swarm based algorithms and single agent based algorithms have each distinct advantages and disadvantages. One goal of the presented work is to combine the concepts of the two different algorithms such that a more effective optimization routine results. In particular, we used a Particle Swarm (PS) based optimization algorithm as basis and induce Tabu Search (TS) based operators. The developed hybrid algorithm is tailored such that it has the capability to adapt to the given cost function during the optimization process. The proposed algorithm is tested on a set of different benchmark problems. In addition, the hybrid algorithm is utilized for solving the estimation problem encountered when colored noise is present and the Least Squares (LS) algorithm has bias problems.

**Key-Words:** - Particle Swarm, Optimization, Tabu Search, Parameter Estimation, Colored Noise

## 1 Introduction

Meta-heuristic approaches such as Particle Swarm Optimization (PSO) and Tabu Search (TS) algorithms have been around for a few years. They present alternative approaches to find optimality for a diverse set of optimization problems, such as estimation and system identification, among others. PSO and TS based approaches stand in contrast to hard computing methods such as gradient based methods by vastly reducing the computational complexity, especially for higher dimensional problems. A key motivation for using these soft-computing algorithms is the ability to escape local optimal points in pursuit of the global optimum during the search process.

PSO was first introduced by Kennedy and Eberhart as a stochastic global optimization routine, [1]. The algorithm searches the cost-surface with a set of individual particles, each representing a solution to the optimization problem. The particles orient themselves via influence components such as inertia, current best solution found by the entire flock, and the particle's best position. TS was presented by Glover, [2], as an iterative optimization procedure that attempts to avoid the shortfalls of the Local Search (LS) algorithm. TS is a single agent algorithm that progresses through the cost surface by creating a set of neighbors (which are potential new locations) and moves to a new location by evaluating these neighbors and comparing them to a

list of previously visited locations. This list, the tabu list, ensures that no cycling will occur and local optimal points are overcome.

Recent efforts in improving PSO and TS have lead to a number of propositions that include concepts from other optimization philosophies. In [3] the authors proposed a TS-Genetic Algorithm based scheme to find best parameter estimates in colored noise environments. Higashitani et al., [4] proposed a predator-prey based PSO. The Constriction Factor Method (CFM) proposed by Clerc [5] reduces the velocity of the particles with duration of the search process in order to facilitate the intensification over the diversification mission with time. Combinations of PSO and TS have also been investigated, such as in [6], where PSO and TS are switched at each step to explore the vicinity of the particles, and in [7] where TS and PSO and sequential quadratic programming are combined. In [8] concepts of TS are used to create two swarms in PSO, one responsible for intensification, the other for diversification.

In this paper, we investigate some elements of the TS algorithm applied to the PSO scheme. In particular we investigate an alternative to the CFM method, where we use the TS concept to adapt the PSO parameters to the given problem using a parallel scheme of hybridization. The paper is organized as follows; Section 2 presents the problem formulation and basic background on PSO and TS.

Section 3 introduces the proposed PSO-TS hybridization algorithm, while Section 4 will present the results.

## 2 Problem Formulation

The optimization problems addressed in this paper are of the unconstrained type. Consider a real valued objective function  $f(\mathbf{x})$  defined on a set  $\mathbf{x} \in S$  in  $\mathbb{R}^n$ . We are tasked to find a point  $\mathbf{x}^*$  corresponding to the value of  $f(\mathbf{x}^*)$  such that

$$f(\mathbf{x}^*) = \min \{f(\mathbf{x}) | \mathbf{x} \in S\} \quad (1)$$

The difficulty of finding such a point arises when  $f(\mathbf{x})$  or the feasible domain  $S$  is non-convex. For such problems, gradient based methods will result in local optimums. Soft computing methods such as PSO and TS allow for an escape from local optimums and the continued search for a better optimum, in the extreme case the global optimum. For PSO algorithms, we consider a set of particles  $p$  and their associated location  $\mathbf{x}^i$  where  $i$  is the index for the particles. The particles explore  $S$  in an incremental fashion. Their position is altered at each step by the following update rule:

$$\mathbf{x}^i(k+1) = \mathbf{x}^i(k) + \mathbf{v}^i(k+1), \quad (2)$$

where,  $k$  is the increment number and  $\mathbf{v}^i$  the velocity associated with the particle, which can be computed as follows:

$$\mathbf{v}^i(k+1) = w\mathbf{v}^i(k) + c_1 r_1 [\mathbf{b}_p^i - \mathbf{x}^i(k)] + c_2 r_2 [\mathbf{b}_g^i - \mathbf{x}^i(k)]. \quad (3)$$

In the velocity update formula,  $\mathbf{b}_p^i$  and  $\mathbf{b}_g^i$  represent the best ever position of the particle  $i$  and the global best position of the swarm up to iteration  $k$ , respectively.  $r_1$  and  $r_2$  are uniformly distributed random numbers between 0 and 1, while  $w$ ,  $c_1$  and  $c_2$  are weighting coefficients that manage the three tendencies of Equation (3). These tendencies – as given by the three terms in the velocity equation – are characterized as: audacious for following your own way; conservative, for going back towards your best previous position; and sheep-like, for being pulled to the best overall position. The weighting coefficients help the balancing act of combining these tendencies in order to be globally efficient. The PSO scheme described so far is rather simple and computationally very efficient, especially when compared to a GA or any gradient based methods. To further this algorithm, a limitation on the maximum value of  $\mathbf{v}$  can be imposed, say  $v_{\max}$ . This type of velocity clamping balances the exploration and intensification and also avoids excessive velocities that are responsible for particles overshooting their targets, [9]. Also, the CFM method can be employed, where the velocity update is modified – reduced – as the search progresses. For this, Equation (3) is altered as follows:

$$\mathbf{v}^i(k+1) = K \times \left[ \mathbf{v}^i(k) + c_1 r_1 (\mathbf{b}_p^i - \mathbf{x}^i(k)) \right] + K \times \left[ +c_2 r_2 (\mathbf{b}_g^i - \mathbf{x}^i(k)) \right] \quad (4)$$

where  $K = \frac{2}{2 - \varphi - \sqrt{\varphi^2 - 4\varphi}}$  and  $\varphi = c_1 + c_2$ , as

given by [5].

The inertia weight  $w$  has a competing purpose to the velocity clamping method [10], and is responsible for balancing the exploration and intensification part of the PSO. In [11] it is also shown that  $w$  is problem dependent. In this paper, we will investigate the option of adapting  $w$  using a TS based scheme such that the PSO algorithm becomes less problem dependent. Besides  $w$ ,  $c_1$  and  $c_2$  control the stochastic influence, analogous to the mutation operator in GA. In [12], it is stated that for most problems one chooses  $c_1 = c_2$ , but the ratio is also problem dependent, i.e. for unimodal problems with smooth surfaces, usually one selects  $c_2 > c_1$ , while for multimodal problems these coefficients are chosen to be  $c_1 > c_2$ . In this paper, we also will investigate the optimization of these coefficients by implementing a TS scheme in parallel to the PSO.

The TS algorithm has the same objective as PSO – given by Equation 1. A TS algorithm employs one candidate point which moves incrementally on  $S$ . The moves between increments are defined by selecting the best update from a set of candidate points. This set is created by forming  $R$   $n$ -dimensional spheres about the current position, and randomly place a point in each section (sphere). These points are evaluated on  $f(\mathbf{x})$  and then compared to a list  $T \in \mathbb{R}^{n \times q}$  of previously visited places. The list length  $q$  basically represents the memory of the algorithm. Around each element in  $T$  a  $n$ -dimensional sphere is created serving as a tabu-ball, where no new solution can be located. The best performing candidate point not violating the restricted spaces given by the  $q$  tabu balls is selected as the new position of the search. An aspiration criterion can be formulated as an escape clause to circumvent the restrictions imposed by the tabu-balls, often in the form of having an improved cost to the current solution. All of the past best solutions are stored in a new list – the promising list, which is assembled as the TS algorithm processes. The optimum of the entries of that list will be used as the final optimal value of the algorithm.

Usually,  $q$ ,  $R$ , and the dimension of the individual  $R$ 's are considered the control parameters of the TS algorithm, which are all problem dependent.

## 3 Problem Solution

The selection of  $w$ ,  $c_1$ , and  $c_2$  have rather large implication on the update of the new velocity vector  $\mathbf{v}^i(k+1)$ , as is illustrated in Fig. 1. Here, the three

influence vectors with regard to the global best solution,  $\mathbf{b}_g^i - \mathbf{x}^i(k)$ , and with regard to the particles best solution  $\mathbf{b}_p^i - \mathbf{x}^i(k)$  as well as the inertia vector  $\mathbf{v}^i(k)$  are depicted for an instant  $k$  and a single particle  $i$ . Each of these vectors are pre-multiplied by  $w$ ,  $c_1$ , and  $c_2$  respectively, resulting into some variation of the vectors, denoted by  $\Delta$  in Fig. 1.

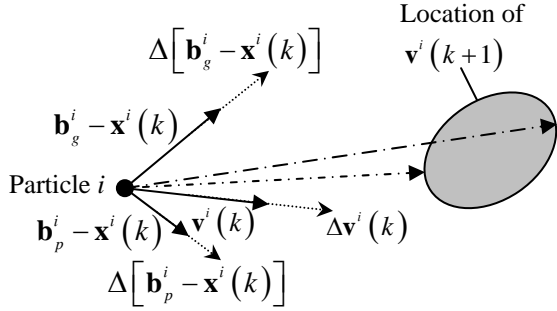


**Fig. 1:** Adaptation of proposed PSO-TS Algorithm.

As stated earlier, these three influence coefficients are problem dependent. In this paper, we propose to find the optimal coefficients by utilizing a TS. This is accomplished by using the variation of the influence vectors to describe a new search area, in which the original cost function  $f(\mathbf{x})$  is prescribed. In Fig. 1, this area is symbolized in the shaded ellipsoid. The best combination of coefficient along with the influence vectors will then determine the velocity update  $\mathbf{v}^i(k+1)$ . This optimization is repeated at each increment. TS lends itself well for this purpose, since it is computationally very efficient. Since  $r_1$  and  $r_2$  are superimposed to the influence coefficients, we will investigate an option where this randomization is suppressed.

Parameter estimation is an important concept in engineering where a mathematical model of a system is identified with the help of input and output signals. The classical Least Squares (LS) algorithm gives an unbiased estimate of the parameters when the system noise is white. A bias result may occur if the residual  $\varepsilon(k) = y(k) - \hat{y}(k)$  is not white, where  $y$  is the system output,  $\hat{y}$  is the estimated output, and  $k$  is the discrete time index. For such instances, one can use a whitening filter, i.e.  $C(q^{-1})\varepsilon(k) = e(k)$ , where  $C(z^{-1})$  is the coefficient polynomial of the whitening filter and  $z^{-1}$  is the backward shift operator. The corresponding cost function for the estimation becomes, [3]:

$$J = \sum e^2(k) = \sum [C(z^{-1})A(z^{-1})y(k) + C(z^{-1})B(z^{-1})u(k)]^2$$
 where,  $u(k)$  is the input sequence,  $A(z^{-1})$  and  $B(z^{-1})$  are the numerator and denominator polynomials of the system transfer function, respectively. As the signal to noise ratio becomes large, the cost function  $J$  may become multimodal. This was shown by Söderström et al. [13]. In order to

obtain the global minimum an intelligent optimization technique needs to be employed. In this paper, we will utilize the proposed hybrid PSO-TS algorithm to such parameter estimation problems with a colored noise environment and compare it to the traditional LS method.

## 4 Simulation Results

The proposed hybrid algorithm is tested on a set of standard optimization benchmark problems, which are listed below:

*Spherical:*  $f(\mathbf{x}) = \sum_{j=1}^n x_j^2$  and

*Quadratic:*  $f(x) = \sum_{j=1}^n \left\{ \sum_{i=1}^j x_j \right\}^2$ ,

where  $x_j \in [-100, 100]$  and  $f(\mathbf{x}^*) = [0, 0]$ .

*Hyperellipsoid:*  $f(\mathbf{x}) = \sum_{j=1}^n j^2 x_j^2$  where  $x_j \in [-1, 1]$

and  $f(\mathbf{x}^*) = [0, 0]$ .

*Bohachevsky 1:*

$f(\mathbf{x}) = x_1^2 + 2x_2^2 - 0.3 \cos(3\pi x_1) - 0.4 \cos(4\pi x_2) + 0.7$

where  $x_j \in [-50, 50]$  and  $f(\mathbf{x}^*) = [0, 0]$ .

*Rastrigin:*  $f(\mathbf{x}) = \sum_{j=1}^n (x_j^2 - 10 \cos(2\pi x_j) + 10)$  where

$x_j \in [-5.12, 5.12]$  and  $f(\mathbf{x}^*) = [0, 0]$ .

*Rosenbrock:*

$$f(\mathbf{x}) = \sum_{j=1}^{n/2} \left[ 100(x_{2j} - x_{2j-1}^2)^2 + (1 - x_{2j-1})^2 \right],$$
 where

$x_j \in [-2.048, 2.048]$  and  $f(\mathbf{x}^*) = [1, 1]$ .

*Haupt & Haupt:*  $f(\mathbf{x}) = x_1 \sin(4x_1) + 1.1x_2 \sin(2x_2)$ ,

where  $x_j \in [0, 10]$  and  $f(\mathbf{x}^*) = [9.0389, 8.6674]$ .

In addition to these benchmark problems, we also will test the proposed algorithm to some parameter estimation problem with a colored noise environment. In particular, we will test the algorithm on one simple model, which is given by Equation 5:

$$y(k) = 0.5y(k-1) - 0.5y(k-2) + u(k) + \varepsilon(k) \quad (5)$$

The simulation was carried out by using the following set of parameters and conditions: uniformly distributed initial locations of particles, number of neighborhoods created at each step for each particle  $R = 25$ , uniform initial velocity of magnitude 1 for all particles,  $p = 40$ ,  $q = 5$ , radius of the  $n$  dimensional Tabu balls:

$r = 0.025(x_{\max} - x_{\min})$ , where  $x_{\max}$  and  $x_{\min}$  are the dimensions of  $S$ , radius of neighborhood  $r_N = 0.5r$ , and radius of promising balls  $r_p = 0.5r_N$ . The PSO portion utilized 100 iterations, while the embedded TS section used 10 iterations. Since randomness is a factor in the used and proposed algorithms, and in order to gain some kind of understanding of consistency, the simulations were carried out 100 times for each cost function listed above.

Table 1 lists the results for the unconstraint optimization problems in comparison with the original PSO algorithm. In this set of simulations,  $r_1$  and  $r_2$  were selected to be uniform random between 0 and 1.

**Table 1:** Simulation results with random  $r$

Cost Function	PSO	Hybrid PSOTS		
		w	w, c1	w, c1c2
Spherical	0.55135	<b>0.17214</b>	<b>0.0555</b>	<b>0.2216</b>
Quadratic	0.50718	<b>0.25637</b>	<b>0.12497</b>	<b>0.1347</b>
Bohachevsky	0.80852	<b>0.17689</b>	<b>0.15473</b>	<b>0.01617</b>
Hperellipsoid	0.03252	<b>0.00436</b>	<b>0.00745</b>	<b>0.00069</b>
Rastrigin	<b>0.07168</b>	0.16678	0.16728	0.16021
Rosenbrock	1.4261	1.43255	1.47011	1.44042
Haupt	12.4736	<b>10.5563</b>	<b>10.5329</b>	<b>11.5222</b>

Table 2 lists the results for the unconstraint optimization problems in comparison with the original PSO algorithm. In this set of simulations,  $r_1$  and  $r_2$  were set equal, at all times, to 1. The proposed hybrid optimization algorithm, regardless of which set of coefficients are optimized, performs significantly better in comparison to the standard PSO for the Hyperellipsoid, the Bohachevsky cost function. For this case too ( $r_1$  and  $r_2$  fixed), the spherical and the quadratic functions produced better results. In both the cases there was no improvement in the Rosenbrock function values and the Rastrigin still showed poor results as compared to the standard PSO algorithm.

**Table 2:** Simulation results with fixed  $r$

Cost Function	PSO	Hybrid PSOTS		
		w	w, c1	w, c1c2
Spherical	0.55135	<b>0.08975</b>	<b>0.19801</b>	<b>0.81325</b>
Quadratic	0.50718	<b>0.31023</b>	<b>0.14124</b>	<b>0.07529</b>
Bohachevsky	0.80852	<b>0.13091</b>	<b>0.20773</b>	<b>0.15158</b>
Hperellipsoid	0.03252	<b>0.01464</b>	<b>0.01736</b>	<b>0.00278</b>
Rastrigin	<b>0.07168</b>	0.13648	0.23206	0.4902
Rosenbrock	1.4261	1.44026	1.44147	<b>1.39044</b>
Haupt	12.4736	<b>10.6342</b>	<b>10.8366</b>	<b>10.8408</b>

The distinction between the characteristics of the cost function and the performance of the proposed algorithm can be made by associating the presented results with unimodal and multimodal cost functions. As listed above, the improved performance given by the proposed hybrid algorithm is found for unimodal cost functions. While the

proposed algorithm does work well for multimodal cost functions, it excels in comparison to the standard PSO algorithm with regard to unimodal functions.

A key objective of this paper is to make the proposed algorithm adaptive in nature to the subjected problem, i.e. cost function. As detailed in Section 2, the choice of the influence coefficients is dependent on the characteristics of the cost surface. The proposed hybrid algorithm optimizes these coefficients as well as the inertia coefficient  $w$  at each iteration. Hence we can plot these coefficients in order to determine if they show adaptation and consistency. This is done in Fig. 2. The plot is a representative characterization of the simulation results obtained for the tested multimodal cost functions. We can recognize that the proposed algorithm adapts fast to the cost function and selects  $c_1 > c_2$  as determined in the literature, indicating that each particle is dominated by its own personal best, and the algorithm is searching wider ranges. The rather non-smooth convergence plot is due to the fact that  $r_1$  and  $r_2$  are kept random and impose a perturbation to the optimal location of the influence coefficients. In comparison, the same plots are generated for some multimodal cost functions, i.e. the Hyperellipsoid in Fig. 3 and Spherical as depicted in Fig. 4. In both cases for the unimodal cost functions, the coefficients move quickly to the case where  $c_2 > c_1$  as given in the literature, but after a few iterations, the weighting is switched and  $c_1 > c_2$ .

This implies that the particles are no longer dominated by the global optimum, but rather by their own personal best performance and try to improve their performances. An explanation for this is found by considering the convergence plot, as detailed in Fig. 5. Here we can see that most of the convergence is achieved after the first few iterations. Once not much improvement is found, the algorithm tries to spread out and search larger regions rather than concentrating to the area dominated by the current global best solution. This adaptation may explain the cause for the improved performance of the proposed algorithm for unimodal functions compared to standard PSO algorithms.

The hybrid algorithm was also tested to estimate the parameters of the system given by Equation (5). The estimated system parameters are given in Table 3 for the two cases a) Random  $r_1$  and  $r_2$  and b) Fixed  $r_1$  and  $r_2$  to unity. In addition, we distinguished two cases where we either computed the instantaneous optimum value of the influence coefficients and the accumulated “averaged” optimum. The variance in the noise was set at 1%, while the input sequence was a white noise sequence with variance of 30%.

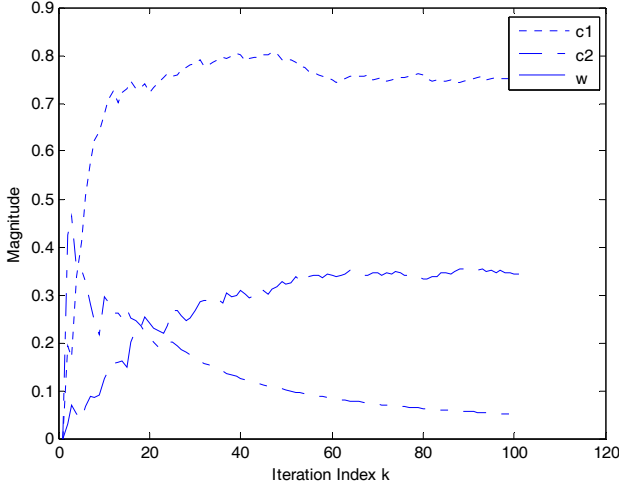


**Fig. 2:** Plot of optimized influence coefficients.

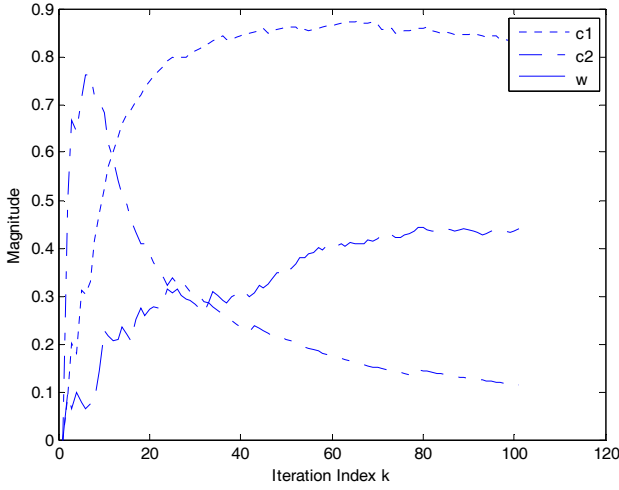


**Fig. 3:** Plot of optimized influence coefficients for Hyperellipsoid cost function.

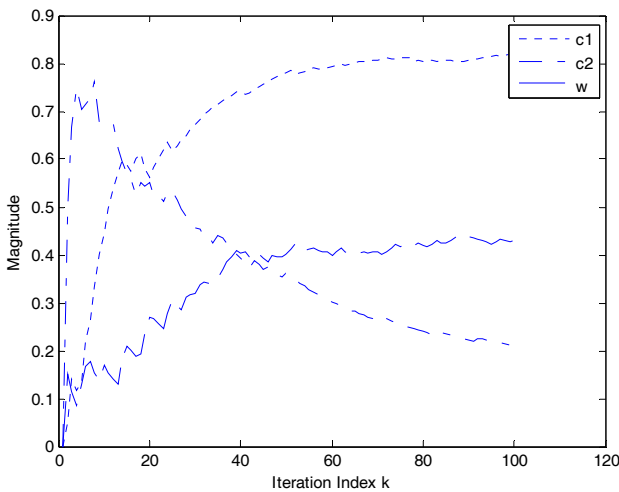


**Fig. 4:** Plot of optimized influence coefficients for the Spherical cost function.

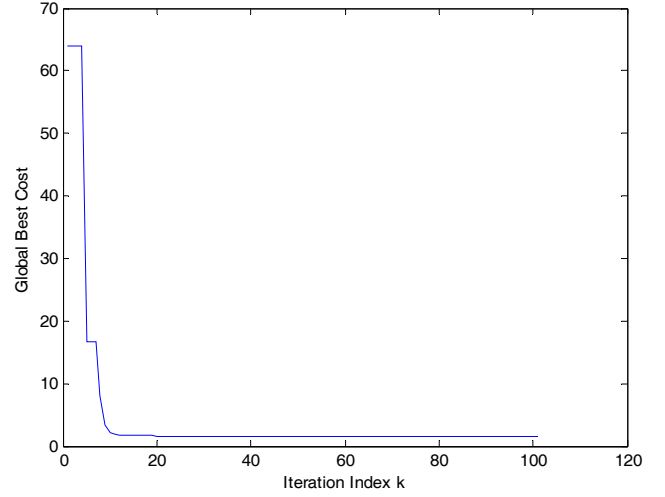


**Fig. 5:** Plot of global best cost vs. iteration index for the Spherical cost function.

**Table 3:** Simulation Results for Estimation

Random			
Accumulative			
w	0.5898	-0.4583	1.0425
w,c1	0.5319	-0.3717	1.1217
w,c1,c2	0.4704	-0.4666	0.8921
Just Optimum			
w	0.5340	-0.5159	1.0025
w,c1	0.5339	-0.5234	1.0550
w,c1,c2	0.4820	-0.4622	1.0110
Fixed			
Accumulative			
w	0.5289	-0.3794	1.0061
w,c1	0.5018	-0.3799	1.0777
w,c1,c2	0.478	-0.4917	0.9182
Just Optimum			
w	0.4707	-0.4827	1.0515
w,c1	0.4797	-0.4397	1.0260
w,c1,c2	<b>0.5074</b>	<b>-0.5164</b>	<b>0.9794</b>

The hybrid algorithm gave the best estimated values of the system parameters for the following combination; Fixed  $r_1$  and  $r_2$ , just optimum,  $w$ ,  $c_1$ ,  $c_2$  optimized, and 40 particles. Table 3 is giving the average values based on 10 sample points. This combination was then used to compare the results of the hybrid algorithm with Least Squares (LS). Table 4 shows the comparison between LS and the proposed hybrid algorithm for various variances in the noise level. The hybrid PSOTS again outperforms the LS method in almost all the cases and in some estimated values. These cases are highlighted in bold italics. Simulation runs, for the hybrid algorithm, for variances 0.05, 0.09, 0.1 and 0.2 were increased from 10 to 30 which gave slightly better results once again in comparison to the LS.

**Table 4:** Comparison Hybrid PSOTS and LS

Simulation Options: Optimized $w, c_1, c_2$ , Fixed $r_1$ and $r_2$ and Just Optimum, Simulation Runs :10	
Hybrid PSOTS	Least Squares
Variance: <b>0.001</b>	
[0.5265,-0.4688,0.9695]	[-0.00640,-0.4238,0.8794]
Variance: <b>0.005</b>	
[0.5256,-0.5206,1.0531]	[0.0005,-0.5050,0.8703]
Variance: <b>0.009</b>	
[0.5289,-0.4394,0.9640]	[0.0640,-0.5395,0.8626]
Variance: <b>0.01</b>	
[0.5074,-0.5164,0.9794]	[0.0208,-0.4711,0.8592]
Variance: <b>0.05</b>	
[0.4183,-0.3988,0.9539]	[0.1354,-0.5345,0.8100]
Variance: <b>0.09</b>	
[0.3300,-0.2699,0.9840]	[0.0981,-0.7102,0.9573]
Variance: <b>0.1</b>	
[0.4035,-0.3056,1.0322]	[0.1276,-0.6684,0.8821]
Variance: <b>0.2</b>	
[0.2952,-0.1684,0.9861]	[0.0418,-0.7096,0.9323]
Variance: <b>0.05</b> , Simulation runs:30	
[0.4476,-0.3844,1.0049]	[0.1354,-0.5345,0.8100]
Variance: <b>0.09</b> , Simulation runs:30	
[0.3852,-0.3505,0.9672]	[0.0981,-0.7102,0.9573]
Variance: <b>0.1</b> , Simulation runs:30	
[0.4129,-0.3550,0.9922]	[0.1276,-0.6684,0.8821]
Variance: <b>0.2</b> , Simulation runs:30	
[0.3072,-0.2769,0.9970]	[0.0418,-0.7096,0.9323]

## 4 Conclusion

In this paper, we propose a hybrid PSO-TS algorithm for optimization of unconstraint cost functions. The algorithm adapts to the underlying cost surface by adjusting the influence coefficients at each step. The proposed algorithm is tested on a series of benchmark problems and showed improved performance for unimodal cost functions. In addition, the hybrid PSO-TS algorithm is tested on one parameter estimation problem where colored noise influence causes bias estimates when the LS algorithm is used. The simulations indicate an improved estimate when the proposed PSO-TS algorithm is used.

## Acknowledgement

This work was supported by a grant from the Telemedicine Advanced Technology Research Center (TATRC) of the US Department of Defense. The financial support is greatly appreciated.

## References:

- [1] Kennedy, J., Eberhart, R., Particle swarm optimization, *Proceedings of the IEEE First International Conference on Neural Networks*, Perth, Australia, 1995, pp. 1942-1948.
- [2] Glover, F., Future paths for Integer programming and Links to Artificial Intelligence, *Computers & Operations Research*, Vol. 5, 1986, pp. 533-549.
- [3] Ramkumar, B., Schoen, M. P., Lin, F., Application of an Intelligent Hybrid Optimization Technique for Parameter Estimation in the Presence of Colored Noise, *Proceedings of the IMECE*, 2007.
- [4] Higashitami, M., Ishigame, A., Yasuda, K., Particle Swarm Optimization Considering the Concept of Predator-Prey Behaviour, *IEEE Congress on Evolutionary Computation*, 2006, pp. 434-437.
- [5] Clerc, M., The swarm and the queen: Towards a deterministic and adaptive particle swarm optimization, *Proceedings of the Congress of Evolutionary Computation*, Vol. 3, 1999, pp. 1951-1957.
- [6] Li, X., Cui, J.-F., Qu, J.-X., Yang, S., D., Energy Transimssion Models Based on Tabu Search and Particel Swarm Hybrid Optimization Algorithm, *J. Cent. South Univ. Technol.* 01-0144-05, 2007.
- [7] Boggs, P.T., Tolle, J.W., Sequential Quadratic programming, *Acta*, 1995, No. 4, pp. 1-52.
- [8] Nakano, S., Ishigame, A., Yasuda, K., Paricle Swarm Optimization Based on the Concept of Tabu Search, *IEEE Congress on Evolutionary Computation CEC 2007*, pp. 3258-3263.
- [9] Eberhart, R.C., Simpson, P.K., Dobbins, R.W., *Computational Intelligence PC Tools.*, Academic Press Professional, 1<sup>st</sup> Edition, 1996.
- [10] Eberhart, R.C., Shi, Y., Particle Swarm Optimization: Developments, Applications and Resources, *Proceedings of the IEEE Congress on Evolutionary Computation*, Vol. 1, 2001, pp. 27-30.
- [11] Shi, Y., Eberhart, R.C., A modified Particle Swarm Optimizer, *Proceedings of the IEEE Congress on Evolutionary Computation*, 1998, pp. 69-73.
- [12] Engelbrecht, A.P., *Fundamentals of Computational Swarm Intelligence*, John Wiley & Sons, 2006.
- [13] Söderström, T., Convergence Properties of Generalized Least Squares Idenfication Method, *Automatica*, Vol. 10, pp. 617-626, 1974.

# An Adaptive Multi Sensor Data Fusion with Hybrid Nonlinear ARX and Wiener-Hammerstein Models for Skeletal Muscle Force Estimation

PARMOD KUMAR, CHANDRASEKHAR POTLURI, ANISH SEBASTIAN, STEVE CHIU, ALEX URFER, D. SUBBARAM NAIDU, and MARCO P. SCHOEN

Measurement and Control Engineering Research Center, College of Engineering  
Idaho State University  
921 South 8<sup>th</sup> Avenue, Stop 8060, Pocatello, Idaho  
USA

[schomarc@isu.edu](mailto:schomarc@isu.edu) <http://isu.edu/~schomarc>

**Abstract:** - Skeletal muscle force can be estimated using surface electromyographic (sEMG) signals. Usually, the sEMG location for the sensors is near the respective muscle motor unit points. Skeletal muscles generate a temporal and spatial distributed EMG signal, which causes cross talk between different sEMG signal sensors. In this paper, an array of three sEMG sensors is used to capture the information of muscle dynamics in terms of sEMG signals and generated muscle force. The recorded sEMG signals are filtered utilizing optimized nonlinear Half-Gaussian Bayesian filter, and a Chebyshev type-II filter prepares the muscle force signal. The filter optimization is accomplished using Genetic Algorithm (GA). Multi nonlinear Auto Regressive eXogenous (ARX) and Wiener-Hammerstein models with different nonlinearity estimators/classes are obtained using system identification (SI) for three sets of sensor data. The outputs of these models are fused with a probabilistic Kullback Information Criterion (KIC) for model selection and an adaptive probability of KIC. First, the outputs are fused for the same sensor and for different models and then the final outputs from each sensor. The final fusion based output of three sensors provides good skeletal muscle force estimates.

**Key-Words:** - sEMG, ARX, Wiener-Hammerstein, KIC, SI, GA

## 1 Introduction

Aftereffects of the loss of upper limbs are a reduction of functionality and psychological disturbance for the person. According to [1] there are 1.7 million peoples with amputation in the United States and this number is on rise after the Afghanistan and Iraq war in 2003 [2]. Conversely, a prosthetic limb can considerably increase the functionality of an amputee and benefit the person in everyday life.

In the past, there have been various research works towards prosthetic hand design, having similar functionality and appearance as human hand [3-4]. Most of these research works are based on electromyography (EMG). The EMG signal is activated and controlled by the central nervous system, which depends on the flow of specific ions such as sodium ( $Na^+$ ), potassium ( $K^+$ ) and calcium ( $Ca^{++}$ ).

An EMG signal recorded on the surface of the limb is expressed as an electric voltage ranging between -5 and +5 mV. This method is known as surface electromyography (sEMG). sEMG is utilized as an input to the controller to realize the movements of the prosthesis and force control [5-6]. Past research results show that EMG signal amplitude generally increases with skeletal muscle force. However, this relationship is not always rigid; various factors affect this relationship.

EMG signals are a result of the varying motor unit recruitments, crosstalk, and biochemical interaction within the muscular fibres. This makes EMG signals random, complex and dynamic in nature and the control of the prosthesis difficult. Moreover, it changes continuously due to the onset and progression of muscle fatigue which results because of continuous high frequency stimulation or because of titanic stimulation [7]. Synchronization of active motor units along the muscle fibres, and a decrease in conduction velocity are reflected in the EMG signal as an increase of amplitude in time domain and a decrease of medium frequency in frequency domain [8]. All these factors make the relationship between EMG and force nonlinear. Correct interpretation of EMG signal is vital to achieve precise motion and force control of prosthesis.

The present work presents a novel approach to estimate skeletal muscle force using an adaptive multi-sensor data fusion algorithm with hybrid nonlinear ARX and Wiener-Hammerstein models. Here, an array of three sEMG sensors is used to capture the information of muscle dynamics in terms of sEMG signals. The recorded sEMG signals are filtered utilizing optimized nonlinear Half-Gaussian Bayesian filter parameters, and the skeletal muscle force signal is filtered by using a Chebyshev type-II filter. A simple Genetic Algorithm





Fokker–Planck partial differential equation [9]. The discrete time Fokker–Planck Equation is given by equation (2).

$$p(x, t-1) \approx \alpha * p(x - \varepsilon, t-1) + (1 - 2 * \alpha) * p(x, t-1) + \alpha * p(x + \varepsilon, t-1) + \beta + (1 - \beta) * p(x, t-1). \quad (2)$$

Here,  $\alpha$  and  $\beta$  are two free parameters,  $\alpha$  is the expected rate of gradual drift in the signal, and  $\beta$  is the expected rate of sudden shifts in the signal. The unknown driving signal  $x$  is discretized into bins of width  $\varepsilon$ . These two free parameters of the non-linear Half-Gaussian filter model are optimized for the acquired EMG data using elitism based GA.

A Chebyshev type II low pass filter with a 550 Hz pass frequency is used to filter the force signal. Fig. 3 depicts the raw and Chebyshev type-II low pass filtered force signals.

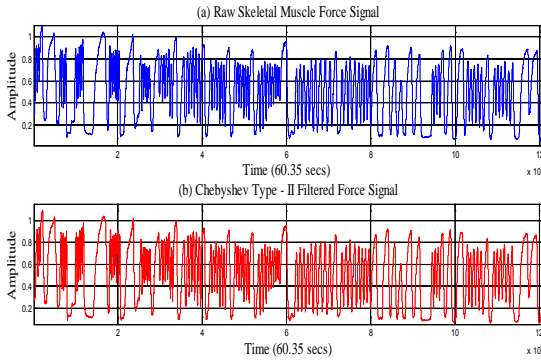


Fig. 3: (a) Raw and (b) Chebyshev Type-II Filtered Skeletal Muscle Force Signals.

### 3 Nonlinear ARX and Wiener-Hammerstein Modeling

In this paper, we are using nonlinear ARX and Wiener-Hammerstein models with different nonlinearity estimators/classes to model three sEMG sensors data as input and skeletal muscle force data as output. The nonlinear ARX model uses a parallel combination of nonlinear and linear blocks [11].

Fig. 4 shows the nonlinear ARX model structure. The nonlinear ARX model uses regressors as variables for nonlinear and linear functions. Regressors are functions of measured input-output data [11]. The predicted output  $\hat{y}(t)$  of a nonlinear model at time  $t$  is given by the general Equation (3):

$$\hat{y}(t) = F(x(t)) \quad (3)$$

where  $x(t)$  represents the regressors,  $F$  is a nonlinear regressor command, which is estimated by nonlinearity estimators/classes [11]. As shown in Fig. 4, the command  $F$  can include both linear and nonlinear functions of  $x(t)$ . Equation (4) gives the description of  $F$ .

$$F(x) = \sum_{k=1}^d \alpha_k \kappa(\beta_k(x - \gamma_k)) \quad (4)$$

where  $\kappa$  is the unit nonlinear command,  $d$  is the number of nonlinearity units, and  $\alpha_k$ ,  $\beta_k$  and  $\gamma_k$  are the parameters of the nonlinearity estimators/classes [11].

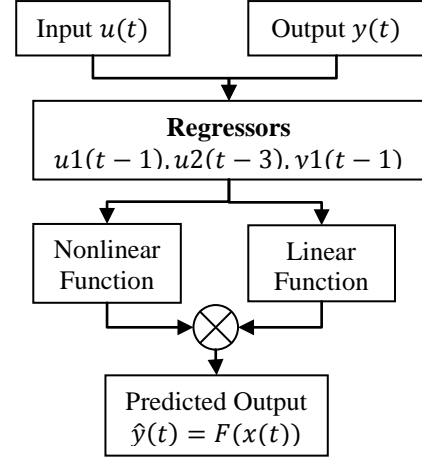


Fig. 4: Nonlinear ARX Model Structure.

The Wiener-Hammerstein model uses one or two static nonlinear blocks in series with a linear block. Structural representation of a nonlinear Wiener-Hammerstein is shown in Fig. 5 [11].

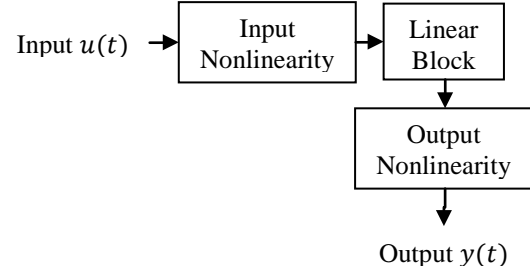


Fig. 5: Nonlinear Wiener-Hammerstein Model Structure.

The general Equations (5), (6), and (7) can describe the Wiener-Hammerstein structure [11].

$$w(t) = f(u(t)) \quad (5)$$

$$x(t) = \frac{B_{j,i}(q)}{F_{j,i}(q)} w(t) \quad (6)$$

$$y(t) = h(x(t)). \quad (7)$$

where  $u(t)$  and  $y(t)$  are input and output of the system, respectively,  $f$  and  $h$  are nonlinear functions, which corresponds to input and output nonlinearity, respectively,  $w(t)$  and  $x(t)$  are internal variables, where  $w(t)$  has the same dimensions as  $u(t)$  and  $x(t)$  has the same dimensions as  $y(t)$ , and  $B(q)$  and  $F(q)$  corresponds to the linear dynamic block, these are polynomials in the backward shift operator.

The nonlinearity classes used in this work are Wavenet, Trepartition, Sigmoidnet, Pwlinear, Saturation, and Deadzone. For motor point and ring1 sensors, three nonlinear ARX and four nonlinear Wiener-Hammerstein models with different nonlinearity

estimators/classes are obtained. For ring2 sensor, three nonlinear ARX and five nonlinear Wiener-Hammerstein models with different nonlinearity estimators/classes are obtained.

## 4 Data Fusion and Adaptive KIC Probability

Data fusion of multiple outputs of nonlinear ARX and Wiener-Hammerstein models is done by assigning a particular probability to each individual model [12]. First, the fusion algorithm is applied to the outputs of different nonlinear ARX and Wiener-Hammerstein models for each sensor obtained using different nonlinearity estimators. Second, the fusion algorithm is again applied to the final fusion based outputs of each sensor; this gives good force estimate. SI model fit value gives the probability for each model, which is given by  $\left[1 - \frac{|Y - \hat{Y}|}{|Y - \bar{Y}|}\right] * 100$ . The model selection criterion used in this paper is KIC. The sum of two directed divergences, which is the measure of the models dissimilarity, is known as Kullback's symmetric or J-divergence [13], as given by Equation (8).

$$KIC(p_i) = \frac{n}{2} \log R_i + \frac{(p_i+1)n}{n-p_i-2} - n\psi\left(\frac{n-p_i}{2}\right) + g(n), \quad (8)$$

where  $g(n) = n * \log(n/2)$ .

The following fusion algorithm as given by [12] is applied for data fusion of the outputs of different nonlinear ARX and Wiener-Hammerstein models:

- 1) Identify models  $M_1, M_2, \dots, M_k$  using sEMG data ( $u$ ) as input and force data ( $Y$ ) as output, for  $k$  number of sensors collecting data simultaneously.
- 2) Compute the residual square norm

$$R_i = \|Y - \Phi_i \hat{\Theta}_i\|^2 = \|Y - \hat{Y}_i\|, \quad \text{where} \\ \hat{\Theta}_i = \{\Phi_i^T \Phi_i\}^{-1} \Phi_i^T Y, \text{ and}$$

$$\Phi = \begin{bmatrix} Y_p^T & u_p^T & Y_{p-1}^T & \dots & u_1^T \\ Y_{p+1}^T & u_{p+1}^T & Y_p^T & \dots & u_2^T \\ \vdots & \vdots & \vdots & \ddots & \vdots \\ Y_{n-1}^T & u_{n-1}^T & Y_{n-2}^T & \dots & u_{n-p}^T \end{bmatrix}.$$

- 3) Calculate the model criteria coefficient using Equation (8).

- 4) Compute the model probability  $p(M_i|Z) = \frac{e^{-l_i}}{\sum_{j=1}^k e^{-l_j}}$ ,

where  $l$  is model selection criterion, i.e.  $KIC(p_i)$ .

- 5) Compute the fused model output  $\hat{Y}_f = \sum_{i=1}^k p(M_i|Z) \hat{Y}_i$ .

- 6) Compute the overall model from  $\hat{Y}_f$  and force data.

Here all the computation from step 2) to 6) is adaptive i.e. the residual square norm,  $KIC(p_i)$ , model probability  $p(M_i|Z)$ , and fused model output  $\hat{Y}_f$  are being updated with time or for each data point. Fig. 6

shows the flow chart for fusion of outputs and adaptive probability of KIC.

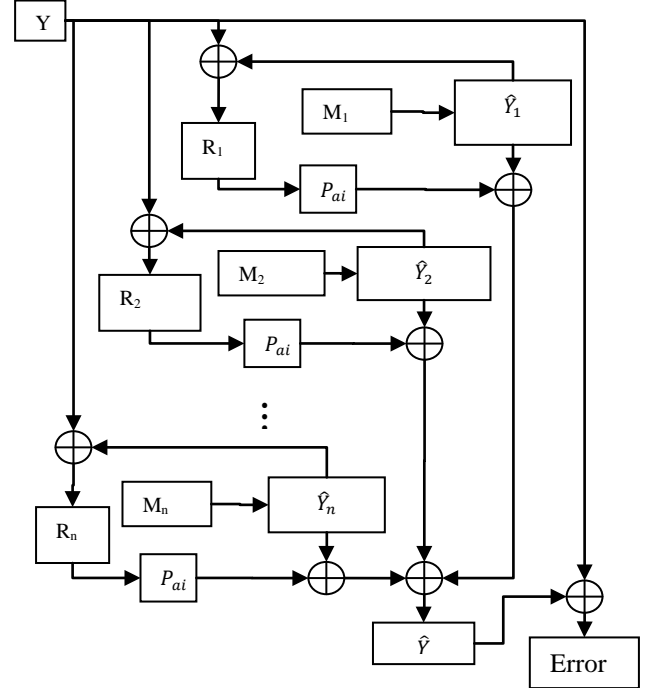


Fig. 6: Data Fusion and Adaptive KIC Probability.

## 5 Results, Discussion and Future Work

This section deals with the results, discussion and future work. The following plots show the nonlinear (ARX and Wiener-Hammerstein) model and adaptive fusion algorithm based estimated force output for each sensor first and then finally combined adaptive fusion based output for all three sensors. Fig. 7 shows the overlapping plot of the original and adaptive fusion based force output for the motor point sensor. The output is the result of the adaptive fusion algorithm on three nonlinear ARX and four nonlinear Wiener-Hammerstein models for the motor point sensor signal.

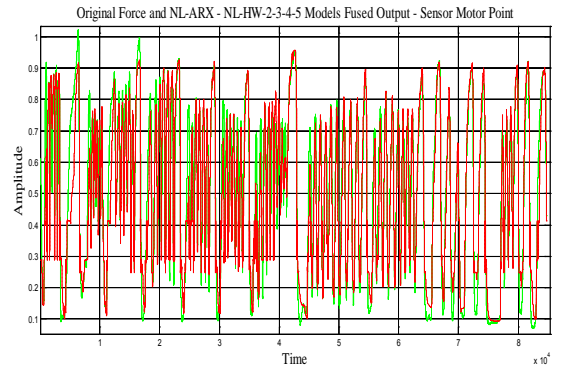


Fig. 7: Original and Fusion Based Output for Motor Point Sensor.

Fig. 8 shows the overlapping plot of the original and adaptive fusion based force output for ring1 sensor. The

output is the result of adaptive fusion algorithm of three nonlinear ARX and four nonlinear Wiener-Hammerstein models for ring1 sensor signal.

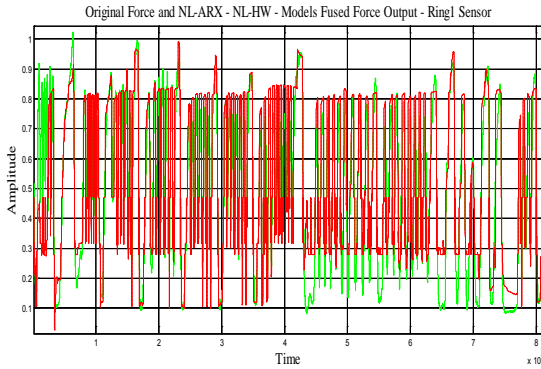


Fig. 8: Original and Fusion Based Output for Ring1 Sensor.

Fig. 9 shows the overlapping plot of the original and adaptive fusion based force output for ring2 sensor. The output is the result of adaptive fusion algorithm on three nonlinear ARX and five nonlinear Wiener-Hammerstein models for ring2 sensor signal.

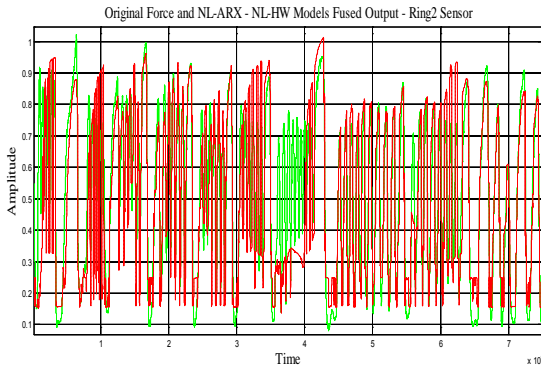


Fig. 9: Original and Fusion Based Output for Ring2 Sensor.

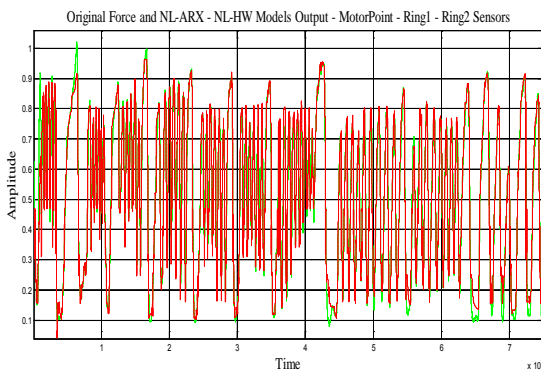


Fig. 10: Final Plot - Original and Fusion Based Output for All Three Sensors.

Fig. 10 shows the overlapping plot of the original and final combined adaptive fusion based force output for

motor point, ring1 and ring2 sensors. The output is the result of adaptive fusion algorithm on the final outputs of three sensors i.e. motor point, ring1 and ring2 as shown in Fig. 7 to 9. Fig. 10 shows the best skeletal muscle force estimate, which is the result of the multi nonlinear ARX and Wiener-Hammerstein models and an adaptive hybrid data fusion on these nonlinear models. Fig. 11 shows the error plot of the original and best-estimated model output for the motor point sensor.

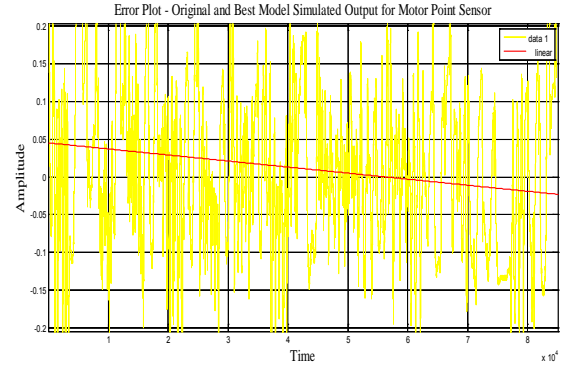


Fig. 11: Error Plot – Original and Best-Estimated Model Output for Motor Point Sensor.

Fig. 12 shows the error plot of original and final multi nonlinear modeled and adaptive hybrid data fusion based force estimate (results from three sensors, nonlinear modeling and adaptive data fusion algorithm). If we compare Fig. 11 and 12, it is very clear and conspicuous that the error has decreased remarkably and is very close to zero.

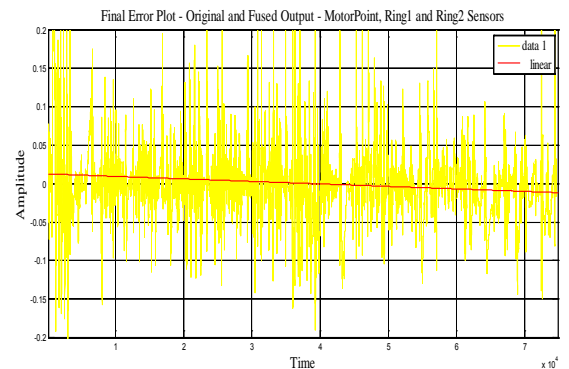


Fig. 12: Final Error Plot – Original and Fusion Based Output for Motor Point, Ring1 and Ring2 Sensors.

Future work will focus on the improvement of the data collection techniques and experimental set-up. By using the combination of linear and nonlinear modeling, and adaptive hybrid data fusion, the skeletal muscle force estimate can be improved further. Furthermore, the authors believe that by using different model selection criteria such as Akaike Information Criterion (AIC), Kullback Information Criterion (KIC) and the Bayesian

Information Criterion (BIC) together to obtain final skeletal muscle force estimate will give improved results.

## 6 Conclusion

sEMG and force data acquired using three EMG and one common FSR force sensor is modeled using nonlinear SI. Using different nonlinearity estimators/classes, multi nonlinear ARX and Wiener-Hammerstein models are obtained for each sensor. First, the outputs of different models for each sensor are fused with a data fusion algorithm and an adaptive KIC probability. Finally, the fused outputs from each sensor are again fused with same algorithm and adaptive KIC probability. The final estimated force using this technique gives the best estimate.

## Acknowledgement

This work was supported by a grant from the Telemedicine Advanced Technology Research Center (TATRC) of the US Department of Defense. The financial support is greatly appreciated.

## References:

- [1] Kathryn Ziegler-Graham, PhD, et al., Estimating the Prevalence of Limb Loss in the United States - 2005 to 2050, *Archives of Physical Medicine and Rehabilitation*, 89 (2008): 422-429.
- [2] O'Connor, P., Iraq war vet decides to have second leg amputated, *Columbia Missourian*, 2009.
- [3] N. Dechev, W. L. Cleghorn, and S. Naumann, *Multiple finger, passive adaptive grasp prosthetic hand*, Mechanism and Machine Theory 36(2001), pp. 1157-1173.
- [4] Haruhisa Kawasaki, Tsuneo Komatsu, and Kazunao Uchiyama, Dexterous Anthropomorphic Robot Hand With Distributed Tactile Sensor: Gifu Hand II, *IEEE/ASME TRANSACTIONS ON MECHATRONICS*, VOL. 7, NO. 3, SEPTEMBER 2002, pp. 296-303.
- [5] M. Zecca, S. Micera, M. C. Carrozza, and P. Dario, Control of Multifunctional Prosthetic Hands by Processing the Electromyographic Signal, *Critical Reviews<sup>TM</sup> in Biomedical Engineering*, 30(4-6), 2002, pp. 459-485.
- [6] Claudio Castellini and Patrick van der Smagt, Surface EMG in advanced hand prosthetics, *Biological Cybernetics*, (2009) 100, pp. 35-47.
- [7] Jeffrey T. Bingham and Marco P. Schoen, Characterization of Myoelectric Signals using System Identification Techniques, *Proceedings of IMECE 2004: 2004 ASME International Mechanical Engineering Congress Anaheim, California*, November 13-19, 2004.
- [8] C.J. De Luca, Myoelectrical manifestations of localized muscular fatigue in humans, *Crit. Rev. Biomed. Eng.*, 11 (4), 1984, pp. 251-279.
- [9] Terence D. Sanger, Bayesian Filtering of Myoelectric Signals, *J Neurophysiol*, 97, 2007, pp. 1839-1845.
- [10] M. B. I. Reaz, M. S. Hussain and F. Mohd-Yasin, Techniques of EMG signal analysis: detection, processing, classification and applications, *Biol. Proced. Online*, 2006, 8(1), pp. 11-35.
- [11] Lennart Ljung, *System Identification Toolbox<sup>TM</sup> 7 User's Guide*, The MathWorks, Inc., 2010.
- [12] Huimin Chen and Shuqing Huang, A Comparative study on Model Selection and Multiple Model Fusion, *7<sup>th</sup> International Conference on Information Fusion*, 2005, pp. 820-826.
- [13] Abd-Krim Seghouane, Maiza Bekara, and Gilles Fleury, A Small Sample Model Selection Criterion Based on Kullback's symmetric Divergence, *IEEE Transaction*, 2003, pp. 145-148.



# AN HYBRID ADAPTIVE DATA FUSION WITH LINEAR AND NONLINEAR MODELS FOR SKELETAL MUSCLE FORCE ESTIMATION

Parmod Kumar, Chandrasekhar Potluri, Madhavi Anugolu, Anish Sebastian, Alex Urfer,

Steve Chiu, D. Subbaram Naidu, *Fellow, IEEE*, and Marco P. Schoen, *Member, IEEE*

**Abstract** – Position and force control are two critical aspects of a prosthesis control. Surface electromyographic (sEMG) signals can be used for skeletal muscle force estimation. In this paper, skeletal muscle is considered as a system and System Identification (SI) is used to model sEMG and skeletal muscle force. The recorded sEMG signal is filtered utilizing optimized nonlinear Half-Gaussian Bayesian filter, and a Chebyshev type-II filter prepares the muscle force signal. The filter optimization is accomplished using Genetic Algorithm (GA). Multi linear and nonlinear models are obtained with sEMG as input and skeletal muscle force as an output. The outputs of these models are fused with a probabilistic Kullback Information Criterion (KIC) for model selection and an adaptive probability of KIC. This approach gives good estimate of the skeletal muscle force.

## I. INTRODUCTION

United States had 1.7 million peoples with amputation [1] and this number is on rise after the Afghanistan and Iraq war in 2003 [2]. Loss of upper limb results in the reduction of functionality and psychological disturbance for the amputee whereas a prosthetic limb can benefit the person in day-to-day life.

Parmod Kumar is with Measurement and Control Engineering Research Center (MCERC), College of Engineering, Idaho State University, Pocatello, Idaho 83209, USA (email: kumaparm@isu.edu).

Chandrasekhar Potluri is with MCERC, College of Engineering, Idaho State University, Pocatello, Idaho 83209, USA (e-mail: potlchan@isu.edu).

Madhavi Anugolu is with MCERC, Idaho State University, Pocatello, Idaho 83201 USA (e-mail: anugmadh@isu.edu).

Anish Sebastian is with MCERC, College of Engineering, Idaho State University, Pocatello, Idaho 83209, USA (email: sebaanis@isu.edu).

Alex Urfer is with Department of Physical and Occupational Therapy, Idaho State University, Pocatello, Idaho 83209, USA (email: urfealex@isu.edu).

Steve Chiu is with Department of Electrical Engineering and Computer Science, MCERC, Idaho State University, Pocatello, Idaho 83201 USA (e-mail: chiustev@isu.edu).

D. Subbaram Naidu is with Department of Electrical Engineering, MCERC, Idaho State University, Pocatello, Idaho 83201 USA (email: naiduds@isu.edu).

Marco P. Schoen is with Department of Mechanical Engineering, MCERC, Idaho State University, Pocatello, Idaho 83209, USA (email: schomarc@isu.edu).

Previous research works [3-4] mainly based on the electromyography (EMG) signals and focus on the prosthetic hand design. The EMG signal recorded at the surface of the limb is known as surface EMG (sEMG) which is an electric voltage ranging between -5 and +5 mV. sEMG can be used to control the position and force of the prosthesis [5-6]. Generally EMG signal amplitude increases with an increase in the skeletal muscle force, however, various factors affect this relationship. Since varying motor unit recruitments, crosstalk, and biochemical interaction within the muscular fibres contributes to generate EMG signals, so EMG signals are random, complex and dynamic in nature. Furthermore, the onset and progression of the muscle fatigue results in the continuous change of EMG signal. Together all of these factors make the relationship between EMG and force nonlinear. Precise control of the prosthesis is critical, so the correct interpretation of EMG signal is important.

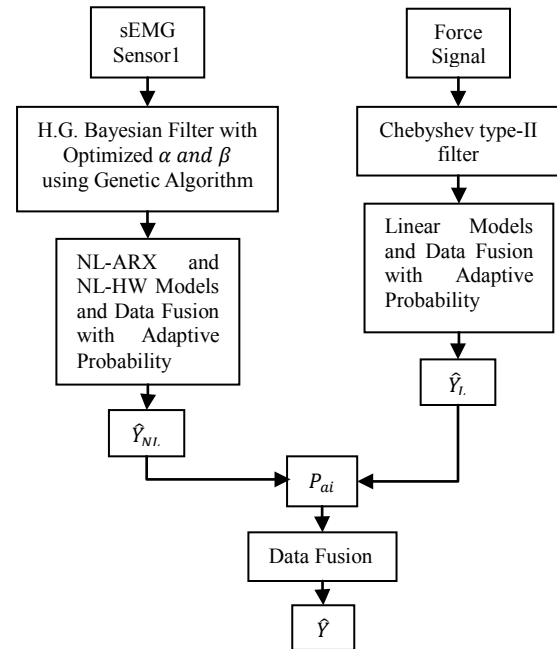


Figure 1: The Flow Chart of the Work in this Paper.

The present work presents a novel approach to estimate skeletal muscle force using an adaptive data fusion algorithm with hybrid multi linear and nonlinear models. The Flow Chart of the work in this paper is shown in figure 1. The recorded sEMG signals are filtered utilizing optimized nonlinear Half-Gaussian Bayesian filter parameters, and the skeletal muscle force signal is filtered by using a Chebyshev type-II filter. A simple Genetic Algorithm code is used to optimize the Bayesian filter parameters. Using an input/output approach, the EMG signal measured at the skin surface is considered as input to the skeletal muscle, whereas the resulting hand/finger force constitutes the output. Multi linear and nonlinear models are obtained using system identification (SI) for the motor point signals as they capture the dynamics of the system differently. The outputs of estimated linear and nonlinear models are fused with a probabilistic Kullback Information Criterion (KIC) for model selection and an adaptive probability of KIC. First, the outputs are fused for the linear models and then for nonlinear models and finally the resultant outputs of linear and nonlinear models are fused together. The final fused output of different linear and nonlinear models gives good skeletal muscle force estimates.

## II. EXPERIMENTAL SET-UP AND PRE-PROCESSING

Data acquisition for EMG and skeletal muscle force is accomplished using LabVIEW™ 8.2 simultaneously at a sampling rate of 2000 Hz. DELSYS® Bagnoli-16 EMG system with DE-2.1 differential EMG sensors is used for sEMG data capturing. However, the corresponding force data was captured using NI ELVIS with Interlink Electronics FSR 0.5" circular force sensor. Figure 2 explains the experimental set-up. One sEMG sensor was placed on the motor point of ring finger and two adjacent to the motor point of a healthy subject. For the experiment, three sEMG sensors were used, but only motor point signal is used for this research work. International Society of Electrophysiology and Kinesiology (ISEK) protocol was followed to capture the sEMG signals.

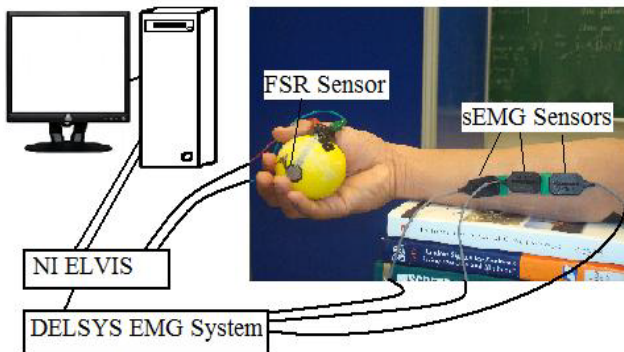


Figure 2: Experimental Set-Up.

To model the sEMG signal, it is assumed that the conditional probability of the rectified EMG signal is a filtered random process with random rate. Fokker–Planck partial differential Equation gives the likelihood function

for the rate evolves in time [7]. In Fokker–Planck partial differential Equation  $\alpha$  and  $\beta$  are two free parameters,  $\alpha$  is the expected rate of gradual drift in the signal, and  $\beta$  is the expected rate of sudden shifts in the signal. Optimization of these two free parameters of the non-linear “Half-Gaussian filter model” of sEMG signal is achieved using an elitism based Genetic Algorithm. Skeletal muscle force signal is filtered with a Chebyshev type II low pass filter.

## III. SYSTEM IDENTIFICATION – LINEAR AND NON-LINEAR MODELING

System Identification (SI) is based on the acquired experimental data and is an alternative to physically based mathematical modeling [8]. A dynamical model such as the Auto Regressive with exogenous input (ARX) or Output Error (OE) gives the system in mathematical form which is the outcome of parametric system identification process. In this work, the SI approach is used with the myoelectric signal as the input to the system and as the output is the intended finger/hand force. In this work, mutli linear and nonlinear models are obtained for the modeling of EMG and hand/finger force signals. Six linear and three nonlinear models are obtained for the motor point sEMG signal. For the linear models Output Error model of order 6, ARX model of order 6, ARMAX model of model order 5, Box-Jenkins model of order 18, State-Space model with subspace method of order 12 and a State-Space model with prediction error/maximum likelihood method of order 12 are obtained using SI. In contrary to these three nonlinear models, nonlinear ARX with nonlinearity estimator as ‘sigmoidnet’ and nonlinear Wiener-Hammerstein models with nonlinearity estimators as ‘piecewise linear - pwnlinear’ and ‘saturation’ are obtained.

Table 3: Linear Models Used and Their Structures.

Linear Model Name	Linear Model Structure
Output Error	$y(t) = \frac{B(q)}{F(q)}u(t - nk) + e(t)$
ARX	$A(q)y(t) = B(q)u(t - n_k) + e(t)$
ARMAX	$A(q)y(t) = B(q)u(t - n_k) + C(q)e(t)$
Box-Jenkins	$y(t) = \frac{B(q)}{F(q)}u(t - nk) + \frac{C(q)}{D(q)}e(t)$
State-Space – subspace method	$x(t + Ts) = Ax(t) + Bu(t) + Ke(t)$ $y(t) = Cx(t) + Du(t) + e(t)$
State-Space – prediction error/maximum likelihood method	$x(t + Ts) = Ax(t) + Bu(t) + Ke(t)$ $y(t) = Cx(t) + Du(t) + e(t)$

For Output Error (OE), Auto Regressive eXogenous (ARX), Autoregressive moving average model with eXogenous inputs (ARMAX), and Box-Jenkins (BJ) models:-  $y$  is output,  $t$  is time,  $B(q)$ ,  $F(q)$ ,  $A(q)$ ,  $C(q)$ ,  $D(q)$ , are polynomials,  $q$  is a backward shift operator,  $u$  is input,  $nk$  and  $n_k$  is delay and  $e$  is error [9].

For State-Space models:-  $x$  is state,  $t$  is time,  $T_s$  is sampling time,  $u$  is input,  $e$  is error,  $A, B, K, C$ , and  $D$  are system matrices, and  $y$  is output [9].

Table 4: Nonlinear Models Used and Their Structures.

Nonlinear Model Name	Nonlinear Model Structure
Nonlinear ARX – Sigmoidnet	$y_p(t) = f(y(t-1), y(t-2), y(t-3), \dots, u(t-1), u(t-2), \dots);$ $f(z) = \frac{1}{e^{-z} + 1} \text{ is sigmoid function.}$
Nonlinear HW – Piecewise Linear – pwlinear	$w(t) = f(u(t)),$ $x(t) = \frac{B_{ji}(q)}{F_{ji}(q)} w(t),$ $y(t) = h(x(t));$ $f \text{ and } h \text{ are piecewise-linear nonlinear estimators.}$
Nonlinear HW – Saturation	$w(t) = f(u(t)),$ $x(t) = \frac{B_{ji}(q)}{F_{ji}(q)} w(t),$ $y(t) = h(x(t));$ $f \text{ and } h \text{ are nonlinear functions which stores the saturation nonlinearity estimators to parameterize the hard limits on the signal value as upper and lower saturation limits.}$

Where  $f$  is a nonlinear function in nonlinear ARX model. Inputs to  $f$  are model regressors.  $y_p(t)$  is the predicted output as a weighted sum of past output values and current and past input values. For nonlinear Hammerstein-Wiener model  $u(t)$  and  $y(t)$  are the inputs and outputs for the system, respectively.  $f$  and  $h$  are nonlinear functions that corresponds to the input and output nonlinearity, respectively.  $w(t)$  and  $x(t)$  are internal variables.  $w(t)$  has the same dimension as  $u(t)$ .  $x(t)$  has the same dimension as  $y(t)$ .  $B(q)$  and  $F(q)$  in the linear dynamic block are polynomials in the backward shift operator. If only the input nonlinearity is present, the model is called the Hammerstein model. If only the output nonlinearity is present, the model is called the Wiener model [9].

#### IV. FUSION OF OUTPUTS AND ADAPTIVE PROBABILITY OF KIC

According to [10] the outputs of multiple models can be fused by assigning a particular probability to each individual model. In this work, we are obtaining multi linear and nonlinear models using SI for the sEMG sensor for the motor unit. The probability of each model is computed using the SI model fit value. Model fit value is given by  $\left[1 - \frac{|Y - \hat{Y}|}{|Y - \bar{Y}|}\right] * 100$ . Kullback information criterion (KIC) that is an asymmetric measure for the model selection is used for this research. Kullback's symmetric or J-divergence is the sum of two directed divergences, which is the measure of the models dissimilarity is given by Equation (1) [11].

$$KIC(p_i) = \frac{n}{2} \log R_i + \frac{(p_i+1)n}{n-p_i-2} - n\psi\left(\frac{n-p_i}{2}\right) + g(n), \quad (1)$$

where  $g(n) = n * \log(n/2)$ .

Based on [10], following fusion technique is applied for sEMG – force identification models.

- 1) Identify OE models  $M_1, M_2, \dots, M_{k1}$  using sEMG data ( $u$ ) as input and force data ( $Y$ ) as output, for  $k1$  number of sensors collecting data simultaneously.
- 2) Compute the residual square norm

$$R_i = \|Y - \Phi_i \hat{\Theta}_i\|^2 = \|Y - \hat{Y}\|^2,$$

where  $\hat{\Theta}_i = \{\Phi_i^T \Phi_i\}^{-1} \Phi_i^T Y$ , and

$$\Phi = \begin{bmatrix} Y_p^T & u_p^T & Y_{p-1}^T & \dots & u_1^T \\ Y_{p+1}^T & u_{p+1}^T & Y_p^T & \dots & u_2^T \\ \vdots & \vdots & \vdots & \ddots & \vdots \\ Y_{n-1}^T & u_{n-1}^T & Y_{n-2}^T & \dots & u_{n-p}^T \end{bmatrix}.$$

- 3) Calculate the model criteria coefficient using Equation (3).

- 4) Compute the model probability  $p(M_i|Z) = \frac{e^{-l_i}}{\sum_{j=1}^{k1} e^{-l_j}}$ ,

where  $l$  is model selection criterion, i.e.  $KIC(p_i)$ .

- 5) Compute the fused model output  $\hat{Y}_f = \sum_{i=1}^{k1} p(M_i|Z) \hat{Y}_i$ .
- 6) Compute the overall OE model from  $\hat{Y}_f$  and force data.

In the above steps all the computation from step 2) to step 6) is adaptive i.e. the residual square norm,  $KIC(p_i)$ , model probability  $p(M_i|Z)$ , and fused model output  $\hat{Y}_f$  are being updated with time or for each data point.

#### V. RESULTS, CONCLUSION AND FUTURE WORK

In this section results, discussion and future work are discussed. Adaptive KIC probability based data fusion algorithm is applied to linear and nonlinear models separately and then combined. Figure 3 and 4 show the results for the linear and nonlinear models respectively. Finally, both linear and nonlinear models are used combined and adaptive KIC probability based data fusion algorithm is applied to obtain the final output that is given by figure 5. Validation of this technique is confirmed with a separate data set. Figure 6 depicts the validation of the proposed technique.



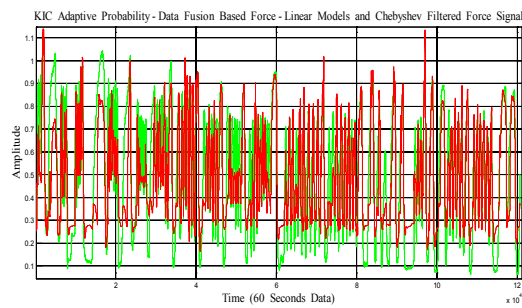


Figure 3: For Linear Models: KIC Adaptive Probability Data Fusion Based Force Vs. Chebyshev Type II Filtered Force.

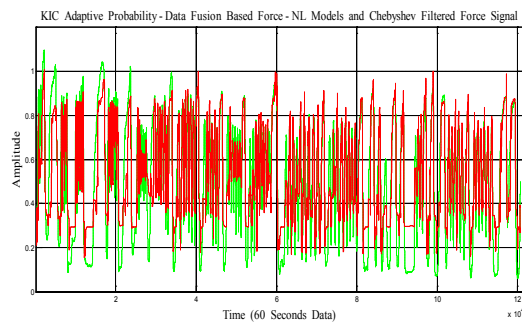


Figure 4: For Nonlinear Models: KIC Adaptive Probability Data Fusion Based Force Vs. Chebyshev Type II Filtered Force.

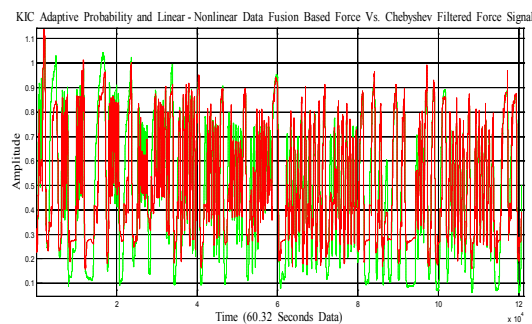


Figure 5: For Linear and Nonlinear Models Combined: KIC Adaptive Probability Data Fusion Based Force Vs. Chebyshev Type II Filtered Force.

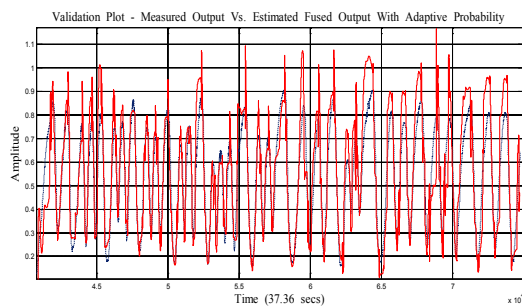


Figure 6: Validation Plot - For Linear and Nonlinear Models Combined: KIC Adaptive Probability Data Fusion Based Force Vs. Chebyshev Type II Filtered Force.

Future work will focus on the improved data collection techniques, use of spatial filters for sEMG signals filtration, and use of multi sensor data with this technique.

#### ACKNOWLEDGMENT

The research was sponsored by the US Department of the Army, under the award number W81XWH-10-1-0128 awarded and administered by the U.S. Army Medical Research Acquisition Activity, 820 Chandler Street, Fort Detrick MD 21702-5014. The information does not necessarily reflect the position or the policy of the Government, and no official endorsement should be inferred. For purposes of this article, information includes news releases, articles, manuscripts, brochures, advertisements, still and motion pictures, speeches, trade association proceedings, etc.

#### REFERENCES

- [1] Kathryn Ziegler-Graham, PhD, et al., Estimating the Prevalence of Limb Loss in the United States - 2005 to 2050, *Archives of Physical Medicine and Rehabilitation*, 89 (2008): 422-429.
- [2] O'Connor, P., Iraq war vet decides to have second leg amputated, *Columbia Missourian*, 2009.
- [3] N. Dechev, W. L. Cleghorn, and S. Naumann, *Multiple finger, passive adaptive grasp prosthetic hand*, Mechanism and Machine Theory 36(2001), pp. 1157-1173.
- [4] Haruhisa Kawasaki, Tsuneo Komatsu, and Kazunao Uchiyama, Dexterous Anthropomorphic Robot Hand With Distributed Tactile Sensor: Gifu Hand II, *IEEE/ASME TRANSACTIONS ON MECHATRONICS*, VOL. 7, NO. 3, SEPTEMBER 2002, pp. 296-303.
- [5] M. Zecca, S. Micera, M. C. Carrozza, and P. Dario, Control of Multifunctional Prosthetic Hands by Processing the Electromyographic Signal, *Critical Reviews™ in Biomedical Engineering*, 30(4-6), 2002, pp. 459-485.
- [6] Claudio Castellini and Patrick van der Smagt, Surface EMG in advanced hand prosthetics, *Biological Cybernetics*, (2009) 100, pp. 35-47.
- [7] Terence D. Sanger, "Bayesian Filtering of Myoelectric Signals," *J Neurophysiol* 97, pp. 1839-1845, 2007.
- [8] Lennart Ljung, *System Identification: Theory for the User*. 2nd edition, Printice Hall PTR, 1999, Chap. 1, pp. 1-15.
- [9] Lennart Ljung, *System Identification Toolbox™ 7 User's Guide*, The MathWorks, Inc., 2010.
- [10] H. Chen and S. Huang, "A Comparative study on Model Selection and Multiple Model Fusion," *7<sup>th</sup> International Conference on Information Fusion*, pp. 820-826, 2005.
- [11] Abd-Krim Seghouane, M. Bekara, G. Fleury, "A Small Sample Model Selection Criterion Based on Kullback's symmetric Divergence," *IEEE Transaction*, pp. 145-148, 2003.

# An Adaptive Hybrid Data Fusion Based Identification of Skeletal Muscle Force with ANFIS and Smoothing Spline Curve Fitting

Parmod Kumar, C. H. Chen, Anish Sebastian,  
Madhavi Anugolu, Chandrasekhar Potluri, Amir  
Fassih, Yimesker Yihun, Alex Jensen, Yi Tang,  
Steve Chiu, Ken Bosworth, D. S. Naidu and Marco

P. Schoen

Measurement and Control  
Engineering Research Center  
College of Science and Engineering  
Idaho State University  
Pocatello, ID 83209, USA

Email: kumaparm@isu.edu, chench@isu.edu,  
sebaanis@isu.edu, anugmadh@isu.edu,  
potlchan@isu.edu, fassamir@isu.edu, yihuyime@isu.edu,  
jensalex@isu.edu, mrtang\_42@hotmail.com,  
chiustev@isu.edu, boswkenn@isu.edu, naiduds@isu.edu,  
schomarc@isu.edu

Jim Creelman and Alex Urfer  
Department of Physical and Occupational Therapy  
Idaho State University  
Pocatello, ID 83209, USA  
Email: creejame@isu.edu, urfealex@isu.edu

**Abstract**—Precise and effective prosthetic control is important for its applicability. Two desired objectives of the prosthetic control are finger position and force control. Variation in skeletal muscle force results in corresponding change of surface electromyographic (sEMG) signals. sEMG signals generated by skeletal muscles are temporal and spatially distributed that result in cross talk between adjacent sEMG signal sensors. To address this issue, an array of nine sEMG sensors is used with a force sensing resistor to capture muscle dynamics in terms of sEMG and skeletal muscle force. sEMG and skeletal muscle force are filtered with a nonlinear Teager–Kaiser Energy (TKE) operator based nonlinear spatial filter and Chebyshev type-II filter respectively. Multiple Takagi-Sugeno-Kang Adaptive Neuro Fuzzy Inference Systems (ANFIS) are obtained using sEMG as input and skeletal muscle force as output. Outputs of these ANFIS systems are fitted with smoothing spline curve fitting. To achieve better estimate of the skeletal muscle force, an adaptive probabilistic Kullback Information Criterion (KIC) for model selection based data fusion algorithm is applied to the smoothing spline curve fitting outputs. Final fusion based output of this approach results in improved skeletal muscle force estimates.

**Keywords** – sEMG; TKE; ANFIS; KIC

## I. INTRODUCTION

In the United States, 1.6 million people lived with amputations during 2005 [1]. This increase reflects on the war effects in Afghanistan and Iraq since 2003 [2]. During the same period of time, the fields of prosthetic design and development research for prosthesis has received increased attention. Precise and timely control of prosthesis is critical for

its applicability, which necessitates the replacement of conventional algorithms by intelligent systems and decision methods. Therefore, a natural means of interface between the user and prosthesis is required. sEMG signals from skeletal muscles are a convenient means for users who do not want to deal with additional surgeries and regular hygiene problems. sEMG signals are simply electric voltages ranging between -5 and +5 [mV] which can be recorded on the skin surface of a hand amputee's forearm. Skeletal muscles generate a base sEMG even without a limb movement which changes with different movements and applied forces. This makes sEMG signals useful for position and force control of prosthesis. Presently available prosthetic hands have no tactile or proprioceptive feedback for grasping and only user's direct vision as a sensory feedback is available for its position control. Afore mentioned reasons cause 30–50% of the upper extremity amputees to choose not to use their prosthetic hand on a regular bases [3-4].

Effective grasping of any object requires the knowledge of force and its feedback. Since the hand amputee uses only sEMG signals collected from skeletal muscles, there is no hand force information directly available. sEMG is a measure of the nervous excitation that ultimately is responsible for activating the skeletal muscles, which in turn generate the finger forces with the help of the link kinematics of human hand. Therefore, a model or estimation scheme is needed for the dynamic estimation of skeletal muscle force from sEMG

signals. There have been numerous efforts in this direction and some of the recent are evident in the research work of [5-10].

The present work proposes a novel scheme of skeletal muscle force identification using sEMG signals. An array of nine sEMG sensors is used to record sEMG signals and skeletal muscle force signals recorded with a force sensing resistor from the arm of a healthy subject, which respectively is explained in detail in Section II and III. Eight Takagi-Sugeno-Kang ANFIS with different membership functions each with a rule base of ten are designed. The training of each ANFIS is done using a hybrid optimization method with zero error tolerance and 40 epochs. Each of the force signals simulated using these ANFIS and measured force signals are applied to a smoothing spline curve fitting method. Figure 1 shows the flow chart of the proposed approach. Final estimated force signal shows good match with the measured signal. This approach is tested on two different data sets of 45 and 60 seconds duration and the results seem promising. The paper is organized in eight sections. Present section follows the experimental set-up and then signal processing, ANFIS modeling, smoothing spline curve fitting, data fusion, results and discussion and conclusion and future work is presented respectively.

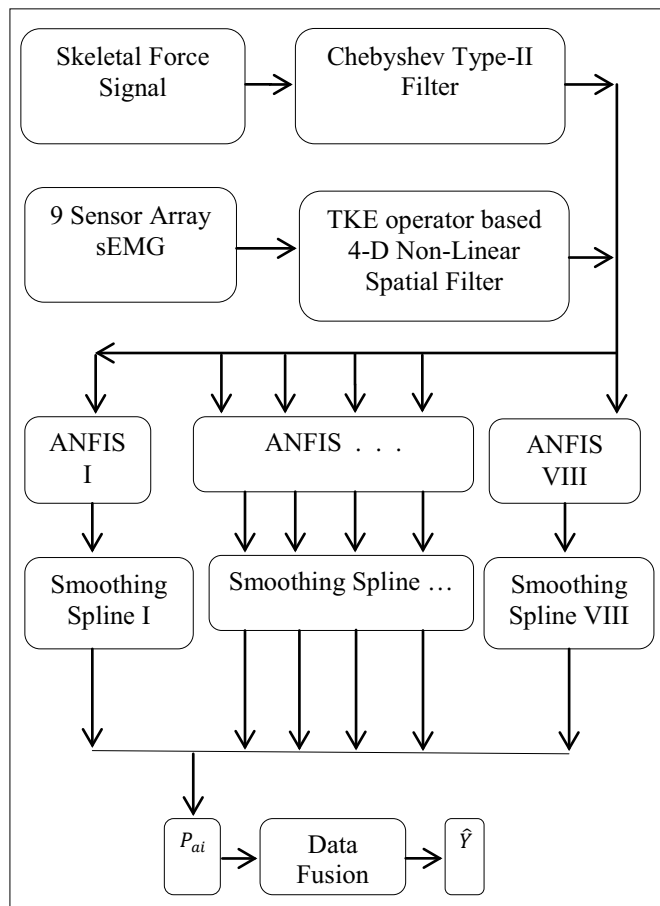


Figure 1. Flow chart of the approach used in this research work.

## II. EXPERIMENTAL SET-UP

Based on the set-up of a sEMG sensor array in [11], an experiment set-up was developed using DELSYS® Bagnoli-16 EMG system with nine DE-3.1 sEMG sensors to capture sEMG signals from skeletal muscles. Here, the array involves nine sensors covering four directional spatial distributions of the sEMG signal. The middle three sEMG sensors were attached directly on the skin surface above the motor point of the flexor digitorum superficialis muscle (FDS) which controls the flexion of the ring finger. Appropriate sEMG electrode attachment point for the flexion of the ring finger was identified using a wet probe muscle stimulator at the FDS (RICH-MAR, HV 1000).

Prior to placing the sEMG sensors, the skin surface of the subject was prepared according to International Society of Electrophysiology and Kinesiology (ISEK) protocols. The thumb movement was restricted in this experiment using a thumb splint. However, the corresponding force data was captured using NI ELVIS™ with Interlink™ Electronics FSR 0.5" circular force sensor. Experimental set-up is shown in Figure 2, where 9 sensors are shown on a healthy subject forearm, holding a stress ball for force measurements. The sEMG and finger force data was collected at a sampling rate of 2000 Hz using LabVIEW™ in conjunction with DELSYS® Bagnoli-16 EMG and NI ELVIS™. With this experimental set-up we conducted several experiments of 30 seconds, 45 seconds and 60 seconds durations.

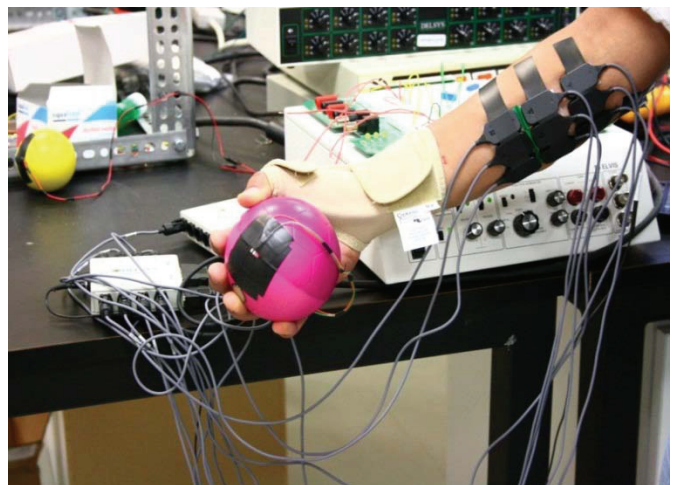


Figure 2. Experiment set-up.

## III. SIGNAL PROCESSING

The recorded sEMG signal is filtered using nonlinear spatial filtering for multichannel surface EMG. As given in [12], this nonlinear spatial filter is derived from “Nonlinear Teager-Kaiser Energy (TKE) Operator.” As given in [11], the

TKE operator in the time domain on sEMG signal is defined by Equation (1).

$$\Psi[x(n)] = x^2(n) - x(n+1) * x(n-1). \quad (1)$$

Here,  $\Psi$  is the TKE operator and  $x(n)$  is the time domain sEMG signal. Based on the TKE operator, the four-dimensional nonlinear spatial filter is given by Equation (2).

$$\Psi_{d,4}[x(m,n)] = 4 * x^2(m,n) - x(m-1,n) * x(m+1,n) - x(m,n-1) * x(m,n+1) - x(m-1,n+1) * x(m+1,n-1) - x(m-1,n-1) * x(m+1,n+1). \quad (2)$$

Figure 3 shows a comparison between the measured and nonlinear spatial filtered sEMG signals.

A Chebyshev type II infinite impulse response (IIR) low pass filter with a 550 Hz pass band frequency is used to filter the skeletal muscle force signal. Figure 4 shows the comparison between the measured and Chebyshev type II filtered skeletal muscle force signal.

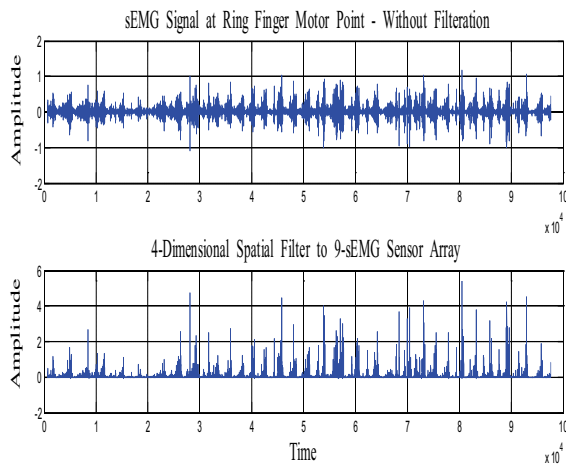


Figure 3. sEMG signal from ring finger.

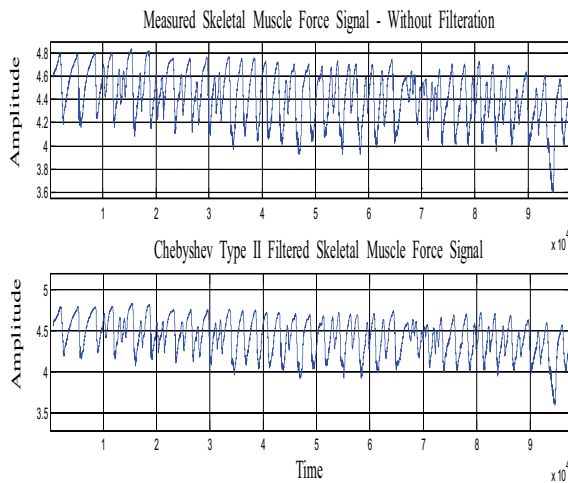


Figure 4. Skeletal muscle force signal from ring finger.

#### IV. ANFIS MODELING

In 1965 professor Lofti A. Zadeh introduced the concept of “Fuzzy Sets”, which are sets with imprecise amplitudes [12]. Dr. Zadeh stated that the “membership” in a fuzzy set is a matter of degree and not a matter of affirmation or denial. For last four decades, this proposal has gained recognition as an important point in the evolution of modern concept of imprecision and uncertainty [12]. This innovation represents a paradigm shift from the classical sets or the crisp sets to “Fuzzy Sets” [12].

Fuzzy set and fuzzy logic theory can be used to capture the natural phenomenon of the imprecision and uncertainty [12]. The membership function is the characteristic of fuzzy set, which is a function whose range is an ordered membership set within the closed unit interval [12].

A crisp set which is a collection of distinct objects is defined in a way to partition objects in a given domain of discourse into two groups: members and non-members [12]. On the other hand, a fuzzy set can be formed by assigning a membership value (which represents the degree to which an object belongs to a fuzzy set) to each object in the interval of 0 to 1 [12]. Fuzzy membership functions can be of different forms such as triangular, trapezoidal, pi, bell and Gaussian form.

Fuzzy Inference System (FIS) in fuzzy logic can be used to model a system which is an inference system based on empirical knowledge based linguistic rules [13]. The fuzzy inference system is composed of five steps: fuzzification of the input variables, application of the fuzzy operator (AND or OR) in the precedent, implication from the precedent to the subsequent, aggregation of the subsequents across the rules, and defuzzification. In the fuzzification process, the membership values coming from quantitative measurements are converted to linguistic values based on the membership functions [13].

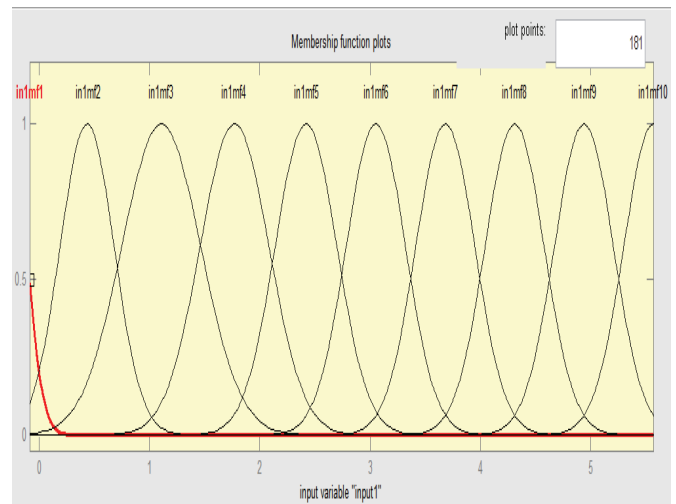


Figure 5. Gaussian membership functions for sEMG.



Figure 5 shows the plot of Gaussian membership functions for fuzzification of sEMG. The process of fuzzification followed by IF .. AND.. THEN ..OR ELSE type control or relation/estimation rules [13]. The output of the rules is computed as a max-min composition [13]. In the defuzzification process, the output of the rules has to be converted to a crisp value [13].

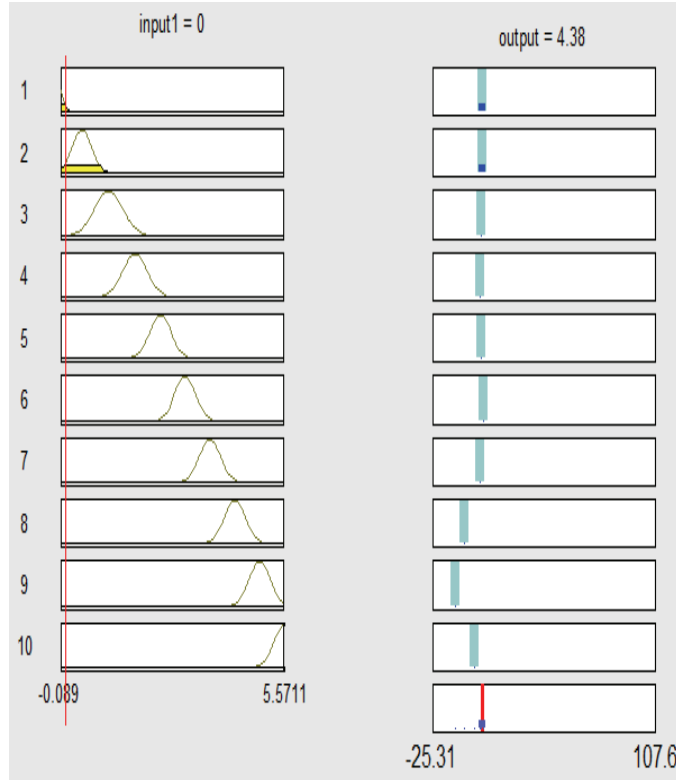


Figure 6. Illustration of ANFIS inference mechanism.

TABLE I. MEMBERSHIP FUNCTIONS

S. No.	Membership Function
1.	Gaussian (GAUSSMF)
2.	Gaussian combination (GAUSS2MF)
3.	Difference between two sigmoidal membership functions (DSIMF)
4.	Generalized bell-shaped (GBELLMF)
5.	Π-shaped (PIMF)
6.	Product of two sigmoidally shaped membership functions (PSIMF)
7.	Trapezoidal-shaped (TRAPMF)
8.	Triangular-shaped (TRIMF)

Using eight different membership functions types we designed eight single-output Sugeno-type adaptive neuro-fuzzy inference systems (ANFIS) using a grid partition on the data. The output membership function in each of these is linear. Each ANFIS has ten rules and connection type is ‘And’ with a weight of 1. For the ‘And’ method ‘product’ and for ‘Or’ method ‘probabilistic’ types are used for each ANFIS. Deffuzification is achieved using weighted average (wtaver) from each rule. Figure 6 shows the rules for ANFIS with Gaussian membership functions and illustrate the ANFIS inference mechanism. The membership functions used are tabulated in Table 1.

A Gaussian function is given by  $f(x; \sigma, c) = e^{\frac{-(x-c)^2}{2\sigma^2}}$  for some real constants  $c$  and  $\sigma > 0$ , and  $e = 2.718$ . Gaussian combination membership function (GAUSS2MF) depends on the  $c$  and  $\sigma$  parameters [14]. The sigmoidal membership function is given as  $f(x; a, c) = \frac{1}{1+e^{-a(x-c)}}$  and depends on the two parameters  $a$  and  $c$ . The difference between two sigmoidal membership function (DSIMF) which is the difference between two sigmoidal functions depends on the four parameters  $a_1, c_1, a_2$ , and  $c_2$  [14]. Generalized bell-shaped membership function (GBELLMF) is given as  $f(x; a, b, c) = \frac{1}{1+|\frac{x-c}{a}|^{2b}}$  and depends on three parameters  $a, b$ , and  $c$  where parameter  $a$  and  $b$  decide the width of the curve and parameter  $c$  locates the center, usually  $b > 0$  [14]. Pi-shaped membership function (PIMF) is given by

$$f(x; a, b, c, d) = \begin{cases} 0, & x \leq a \\ 2 \left( \frac{x-a}{b-a} \right)^2, & a \leq x \leq \frac{a+b}{2} \\ 1 - 2 \left( \frac{x-b}{b-a} \right)^2, & \frac{a+b}{2} \leq x \leq b \\ 1, & b \leq x \leq c \\ 1 - 2 \left( \frac{x-c}{d-c} \right)^2, & c \leq x \leq \frac{c+d}{2} \\ 2 \left( \frac{x-d}{d-c} \right)^2, & \frac{c+d}{2} \leq x \leq d \\ 0, & x \geq d \end{cases}, \quad \text{and}$$

evaluated at the points given by vector  $x$ . The “feet” of the curve is determined by parameters  $a$  and  $d$  whereas parameters  $b$  and  $c$  decides its “shoulders” [14]. The Product of two sigmoidally shaped membership functions (PSIMF) is simply the products of two sigmoidal functions as given before. The trapezoidal shaped membership function (TRAPMF) is given by

$$f(x; a, b, c, d) = \begin{cases} 0, & x \leq a \\ \frac{x-a}{b-a}, & a \leq x \leq b \\ 1, & b \leq x \leq c \\ \frac{d-x}{d-c}, & c \leq x \leq d \\ 0, & d \leq x \end{cases} \quad \text{which depends on}$$

four scalar parameters  $a, b, c$ , and  $d$ . The triangular shaped membership function (TRIMF) is given by

$$f(x; a, b, c) = \begin{cases} 0, & x \leq a \\ \frac{x-a}{b-a}, & a \leq x \leq b \\ \frac{c-x}{c-b}, & b \leq x \leq c \\ 0, & c \leq x \end{cases} \text{ which depends on the}$$

scalar parameters  $a, b$  and  $c$  [14].

## V. SMOOTHING SPLINE CURVE FITTING

MATLAB® Curve Fitting Toolbox™ is a useful tool for fitting curves and surfaces to acquired data [15]. It can be used to do exploratory data analysis, preprocessing and post-processing of the data, comparing candidate models, and for removing outliers [15]. Weights for each smoothing spline curve fit are calculated by subtracting the ANFIS output from the measured skeletal muscle force output. A graphical user interface is used to fit the smoothing spline curve to each output from eight ANFIS with respective weights. Smoothing spline which is a piecewise polynomial computed from a smoothing parameter ( $p$ ) of 0.92 is fitted to each of eight outputs of ANFIS. Smoothing parameter ( $p$ ) is a number between 0 and 1. Change in the value of  $p$  from 0 to 1 results in the change in smoothing spline. For  $p = 0$  the smoothing spline is a least-square straight-line approximation to the data whereas for  $p = 1$  it gives the "natural" cubic spline interpolant to the data [15].

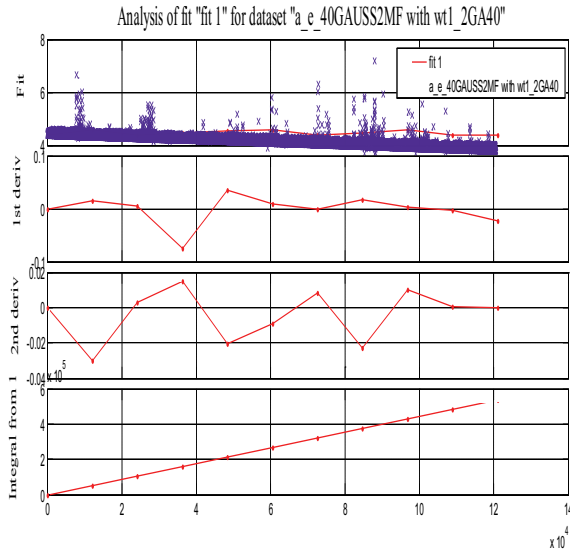


Figure 7. Analysis results for smoothing spline curve fitting to the output of ANFIS with Gaussian membership function.

For the specified weight ( $w_i$ ) and smoothing parameter ( $p$ ) a smoothing spline  $s$  is formed which minimizes the parameter  $J$  given by Equation (3).

$$J = p \sum_i w_i (y_i - s(x_i))^2 + (1 - p) \int \left( \frac{d^2 s}{dx^2} \right)^2 dx, \quad (3)$$

where  $x_i$  and  $y_i$  are predictor and response data respectively. The smoothing parameter  $p$  should be chosen to make the error  $E(s) = \sum_i w_i (y_i - s(x_i))^2$  and roughness  $\int \left( \frac{d^2 s}{dx^2} \right)^2 dx$

small. In this work the smoothing parameter  $p$  is chosen as 0.92 [15]. Figure 7 shows the analysis results for smoothing spline curve fitting to the output of ANFIS with Gaussian membership function.

## VI. DATA FUSION

Data fusion of multiple outputs of smoothing spline curve fittings is done by assigning a particular probability to each individual output [16]. This method gives good estimation of the skeletal muscle force. The goodness of the fit of each smoothing spline output can be measured using System Identification (SI) model fit value which is given by Equation (4).

$$FIT = [1 - |Y - \hat{Y}| / |Y - \bar{Y}|] * 100 \quad (4)$$

In Equation (4)  $Y$  is measured,  $\hat{Y}$  is estimated and  $\bar{Y}$  is mean output signal. The model selection criterion used in this paper is Kullback Information Criterion (KIC) which has shown to perform well for sEMG sensor data fusion [7-10]. The sum of two directed divergences, which is the measure of the models dissimilarity, is known as Kullback's symmetric or J-divergence [17], as given by Equation (5).

$$KIC(p_i) = \frac{n}{2} \log R_i + \frac{(p_i+1)n}{n-p_i-2} - n\psi\left(\frac{n-p_i}{2}\right) + g(n), \quad (5)$$

where  $g(n) = n * \log(n/2)$ .

The fusion algorithm as given by [16] is applied for data fusion of the outputs of eight smoothing spline curve fit outputs which are obtained from eight different ANFIS models:

- (I) Find smoothing spline curve fit outputs  $M_1, M_2, \dots, M_k$  for  $k$  number of outputs.
- (II) Compute the residual square norm

$$R_i = \|Y - \Phi_i \hat{\Theta}_i\|^2 = \|Y - \hat{Y}\|^2, \text{ where } \hat{\Theta}_i = \{\Phi_i^T \Phi_i\}^{-1} \Phi_i^T Y, \text{ and}$$

$$\Phi = \begin{bmatrix} Y_p^T & u_p^T & Y_{p-1}^T & \dots & u_1^T \\ Y_{p+1}^T & u_{p+1}^T & Y_p^T & \dots & u_2^T \\ \vdots & \vdots & \vdots & \ddots & \vdots \\ Y_{n-1}^T & u_{n-1}^T & Y_{n-2}^T & \dots & u_{n-p}^T \end{bmatrix}$$

- (III) Calculate the model criteria coefficient using Equation (5).

- (IV) Compute the model probability  $p(M_i|Z) = \frac{e^{-l_i}}{\sum_{j=1}^{k_1} e^{-l_j}}$ , where

$l$  is model selection criterion, i.e.  $KIC(p_i)$ .

- (V) Compute the fused model output  $\hat{Y}_f = \sum_{i=1}^{k_1} p(M_i|Z) \hat{Y}_i$ .

- (VI) Compute the overall model from  $\hat{Y}_f$  and skeletal muscle force data.

Here all the computation from step (II) to (VI) is adaptive i.e. the residual square norm,  $KIC(p_i)$ , model probability

$p(M_i|Z)$ , and fused model output  $\hat{Y}_f$  are being updated with time or for each data point. Figure 8 shows the flow chart for fusion of outputs and adaptive probability of KIC.

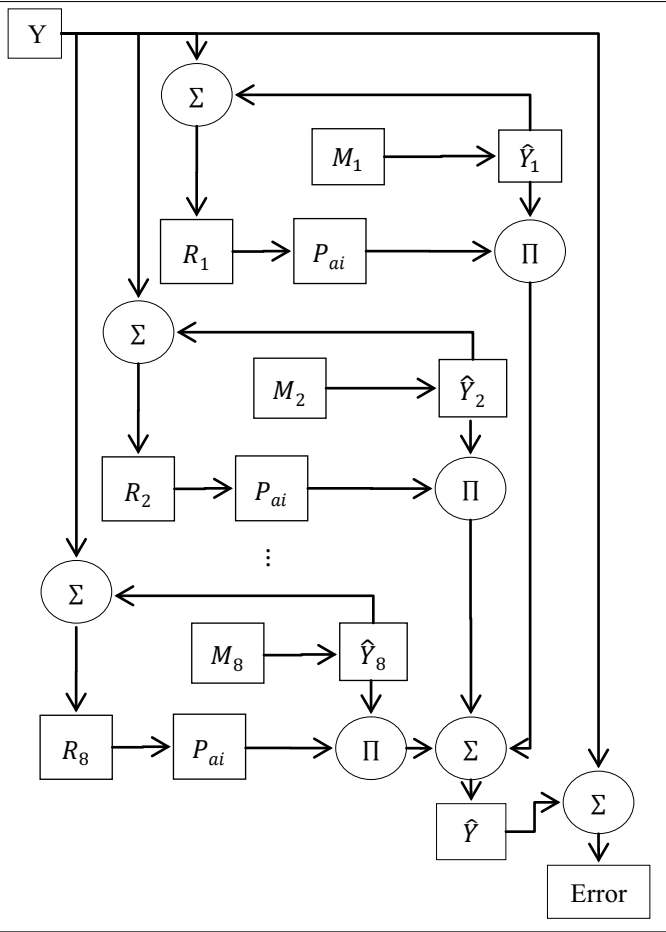


Figure 8. Flow chart for fusion of outputs and adaptive probability.

### VII. RESULTS AND DISCUSSION

The proposed method gives good estimation of the skeletal muscle force. A data set of 45 seconds is used to estimate the output. Figure 9 shows the measured and estimated skeletal muscle force using this method.

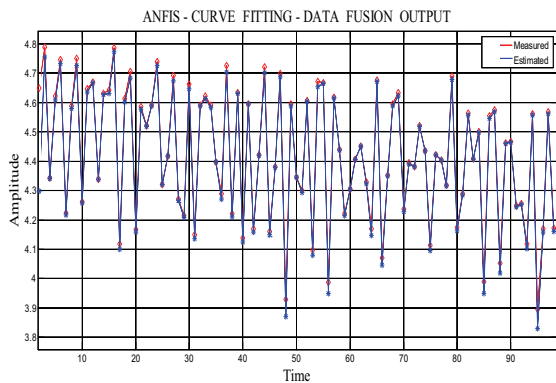


Figure 9. Plot of measured and proposed method estimated skeletal muscle force.

Figures 10 and 11 are the validation plots for 45 seconds and 60 seconds of data sets respectively. All of these three plots show a very close follow up of the measured signal by the estimated signal using this approach. Figure 12 shows the percentage error between the measured force signal and estimated finger force signal for 45 seconds of data set. The percentage error reduced to the lower values and the maximum percentage error value is 1.7 percent. The mean fit value between the measured and estimated output is 91.3 percent.

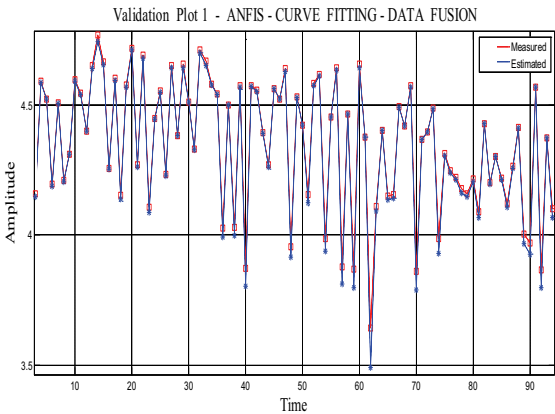


Figure 10. Validation plot 1 using different data set.

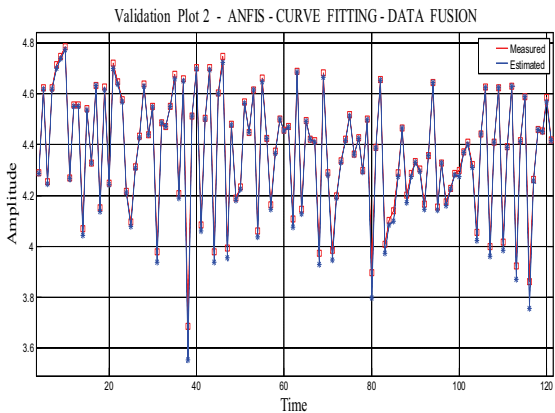


Figure 11. Validation plot 2 using different data set.

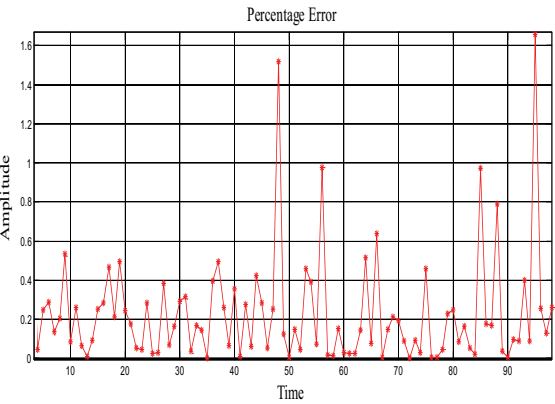


Figure 12. Percentage error plot.

Figure 13 shows the percentage error plot for different data set of 60 seconds duration. Percentage error reduced to lower values and the maximum percentage error value is 3.7 percent. The mean fit value between the measured and estimated output is 40 percent. The mean fit value for another 45 seconds of data set is 73 percent.

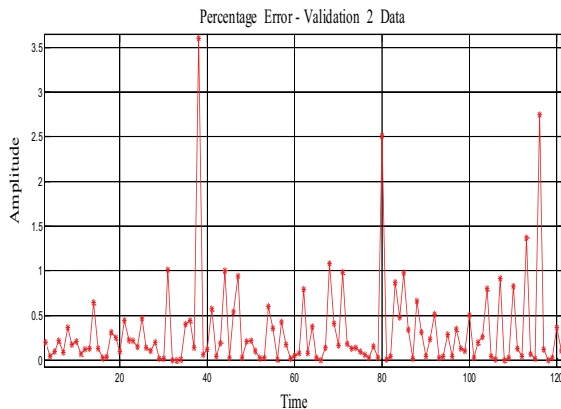


Figure 13. Percentage error plot for 60 seconds data set.

### VIII. CONCLUSION AND FUTURE WORK

Using sEMG and skeletal muscle force as input and output data, eight ANFIS were designed and tested. Output of these ANFIS were fitted with smoothing spline curve fit and resultant outputs were fused using a KIC based data fusion algorithm. This approach has been validated using two separate data sets. Results are promising and show good estimation of skeletal muscle force which can be applied to design, application and improvement of prosthetic hands for amputees.

Future work will address the improvement of data collection techniques, sEMG sensor design, use of this approach for finger angles and stiffness estimation from sEMG signals. Different modeling techniques with this approach and combined probability of different model selection criteria such as Akaike Information Criterion (AIC), Kullback Information Criterion (KIC) and the Bayesian Information Criterion (BIC) together will give improved results.

### ACKNOWLEDGMENT

This research was sponsored by the US Department of the Army, under the award number W81XWH-10-1-0128 awarded and administered by the U.S. Army Medical Research Acquisition Activity, 820 Chandler Street, Fort Detrick MD 21702-5014. The information does not necessarily reflect the position or the policy of the Government, and no official endorsement should be inferred. For purposes of this article, information includes news releases, articles, manuscripts, brochures, advertisements, still and motion pictures, speeches, trade association proceedings, etc.

### REFERENCES

- [1] K. Ziegler-Graham, E. J. MacKenzie, P. L. Ephraim, T. G. Travison, and R. Brookmeyer, "Estimating the Prevalence of Limb Loss in the United States - 2005 to 2050," *Archives of Physical Medicine and Rehabilitation*, vol. 89, pp. 422-429, March 2008.
- [2] P. O'Connor. (2009, February 15). Iraq war vet decides to have second leg amputated [Online]. Available: <http://www.columbiamissourian.com/stories/2009/02/15/soldier-who-lost-leg-iraq-may-lose-other/>
- [3] D. J. Atkins, D. C. Y. Heard, and W. H. Donovan, "Epidemiologic overview of individuals with upper-limb loss and their reported research priorities," *Journal of Prosthetics and Orthotics*, vol. 8, No. 1, pp. 2-11, 1996.
- [4] D. H. Silcox, M. D. Rooks, R. R. Vogel, and L. L. Fleming, "Myoelectric prostheses. A long-term follow-up and a study of the use of alternate prostheses," *The Journal of Bone and Joint Surgery*, vol. 75-A, No. 12, pp. 1781-1789, December 1993.
- [5] P. K. Artemiadis and K. J. Kyriakopoulos, "EMG-based position and force control of a robot arm: Application to teleoperation and orthosis," in *Conf. Rec. 2007 IEEE/ASME Int. Conf. on Advanced Intelligent Mechatronics*, Zurich, pp. 1-6, September 2007.
- [6] P. K. Artemiadis and K. J. Kyriakopoulos, "EMG-Based Position and Force Estimates in Coupled Human-Robot Systems: Towards EMG-Controlled Exoskeletons," in *Experimental Robotics, Springer Tracts in Advanced Robotics*, vol. 54, Berlin Heidelberg: Springer-Verlag, 2009, pp. 241-250.
- [7] P. Kumar, C. Potluri, A. Sebastian, S. Chiu, A. Urfer, D. S. Naidu, and M. P. Schoen, "A Adaptive Multi Sensor Data Fusion with Hybrid Nonlinear ARX and Wiener-Hammerstein Models for Skeletal Muscle Force Estimation," in *Proc. The 14th World Scientific and Engineering Academy and Society (WSEAS) International Conference on Systems*, Corfu Island, Greece, 2010, July 22-24.
- [8] P. Kumar, A. Sebastian, C. Potluri, A. Urfer, D. S. Naidu, and M. P. Schoen, "Towards Smart Prosthetic Hand: Adaptive Probability Based Skeletal Muscle Fatigue Model," in *Conf. Rec. 32nd Annual International Conference of the IEEE Engineering in Medicine and Biology Society*, Buenos Aires, Argentina, Aug. 31 - Sept. 4, 2010.
- [9] P. Kumar, C. Potluri, A. Sebastian, S. Chiu, A. Urfer, D. S. Naidu, and Marco P. Schoen, "Adaptive Multi Sensor Based Nonlinear Identification of Skeletal Muscle Force," *WSEAS Transactions on Systems*, vol. 9, Issue 10, pp. 1051-1062, October 2010.
- [10] P. Kumar, C. Potluri, M. Anugolu, A. Sebastian, J. Creelman, A. Urfer, S. Chiu, D. S. Naidu, and M. P. Schoen, "A Hybrid Adaptive Data Fusion with Linear and Nonlinear Models for Skeletal Muscle Force Estimation," in *Proc. 5th Cairo International Conference on Biomedical Engineering*, Cairo, Egypt, Dec. 16-18, 2010.
- [11] P. Zhou, N. L. Suresh, M. M. Lowery, and W. Z. Rymer, "Nonlinear Spatial Filtering of Multichannel Surface Electromyogram Signals During Low Force Contractions," *IEEE Transactions on Biomedical Engineering*, vol. 56, No. 7, pp. 1871-1879, July 2009.
- [12] A. Celikyilmaz, and I. B. Turksen, *Modeling Uncertainty with Fuzzy Logic: With Recent Theory and Applications*. Berlin Heidelberg: Springer-Verlag, 2009, pp. 11-50.
- [13] J. Espinosa, J. Vandewalle, and V. Wertz, *Fuzzy Logic, Identification and Predictive Control*. Springer-Verlag London Limited, 2005.
- [14] *MATLAB® Fuzzy Logic Toolbox™ User's Guide*. The MathWorks, Inc. 2010.
- [15] *MATLAB® Curve Fitting Toolbox™ User's Guide*. The MathWorks, Inc. 2010.
- [16] H. Chen and S. Huang, "A Comparative study on Model Selection and Multiple Model Fusion," in *Proc. 7th International Conference on Information Fusion*, New Orleans, USA, July 25-28, 2005, pp. 820-826.
- [17] A. K. Seghouane, and M. Bekara, "A Small Sample Model Selection Criterion Based on Kullback's symmetric Divergence," *IEEE Transactions on Signal Processing*, vol. 52, No. 12, pp. 3314-3323, 2004.



# Implementation of sEMG-Based Real-Time Embedded Adaptive Finger Force Control for a Prosthetic Hand

Chandarshekhhar Potluri, Yimesker Yihun, Madhavi Anugolu, Parmod Kumar, Steve Chiu, *Member, IEEE*, Marco P. Schoen, *Senior Member, IEEE*, D. Subbaram Naidu, *Fellow, IEEE*

**Abstract**—This paper presents surface electromyographic (sEMG)-based, real-time Model Reference Adaptive Control (MRAC) strategy for a prosthetic hand prototype. The proposed design is capable of decoding the prerecorded surface electromyographic (sEMG) signal as well as the sensory force feedback from the sensors to control the force of the prosthetic hand prototype using a PIC 32MX360F512L microcontroller. The input sEMG signal is preprocessed using a Half-Gaussian filter and fed to a fusion based Multiple Input Single Output (MISO) skeletal muscle force model. This MISO system provides the estimated finger forces to be produced as input to the prosthetic hand prototype. A simple MRAC method along with a two stage embedded design is used for the force control of the prosthetic hand. The sensed force at the fingertip is fed back to the controller for real-time operation. The data is transmitted to the computer through the universal asynchronous receiver/transmitter (UART) interface of the proposed embedded design. Results show good performance in controlling the finger force as well as shortcomings of the mechanical design of the prosthetic hand prototype to be addressed in future.

## I. INTRODUCTION

In the United States, the number of people with missing

limbs because of combat and non-combat operations is over 1.2 million [1]. The number of amputees has substantially increased due to the recent wars in Afghanistan and Iraq. To date, there has been active research to design a prosthetic hand; however, even today, there are no prosthetic devices available at an affordable cost and with tactile or proprioceptive feedback for grasping [2]. In nonindustrial robotics, ‘rehabilitation robotics’ is an active research area for the last two decades. Rehabilitation robotics is human-centered and addresses a different set of requirements such as mechanical compliance, flexibility, adaptability towards the user, gentleness, safety and, last but not least, humanoid appearance and behavior [3]. Past researches stipulate that human-centered robots must be autonomous with a high level of functionality, pleasure, comfort and ease of use [4]. One interesting domain of rehabilitation robotics is human-machine interface. Human-centered robotics requires a natural means of communication [5], and in the case of electromyographic (EMG) based prosthesis one natural means of interface between the human arm and prosthesis is sEMG itself. The sEMG signals are electrical voltages ranging from -5 to +5 (mV). sEMG signals are always available and their strength and variability depends on different movements and force levels. sEMG signals can be acquired using suitable sensors and can be used as an input to the controller of the hand prosthesis to control the movements and force applied by the fingers. Since, most of the available prostheses employ the users direct vision as a sensory feedback lack in tactile or proprioceptive feedback for grasping [2], and thus half of the upper extremity amputees choose not to use their prosthetic hands on a regular basis [6, 7]. The control of a multi-fingered prosthetic hand is difficult as the human hand is a highly complex and nonlinear system with many degrees of freedom [8]. Past research suggests that the typical approach to the control of a prosthetic hand is to use hybrid position and force control [9]. As sEMG signals are collected from the surface of the skin, the signals pass through numerous tissues before they reaches the surface of the skin and are acquired by the sensors [10]. Hence, they are prone to cross-talk, interference and noise. The sEMG is a temporal and spatially modulated signal [11]. The prediction of skeletal muscle forces corresponding to the sEMG signal is challenging. Usually sEMG measurements are based on single sensor data.

Chandrasekhar Potluri is with Measurement and Control Engineering Research Center (MCERC), Idaho State University, Pocatello, Idaho 83201 USA (e-mail: potlchan@isu.edu).

Yimesker Yihun is with MCERC, College of Engineering, Idaho State University, Pocatello, Idaho 83201, USA (email: yihuyime@isu.edu).

Madhavi Anugolu is with MCERC, Idaho State University, Pocatello, Idaho 83201 USA (email: anugmadh@isu.edu).

Parmod Kumar is with MCERC, Idaho State University, Pocatello, Idaho 83201 USA (email: kumaparm@isu.edu).

Steve Chiu is with Department of Electrical Engineering and Computer Science, MCERC, Idaho State University, Pocatello, Idaho 83209 USA (email: chiustev@isu.edu).

Marco P. Schoen is with Department of Mechanical Engineering, MCERC, Idaho State University, Pocatello, Idaho 83201 USA (email: schomarc@isu.edu).

D. Subbaram Naidu is with Department of Electrical Engineering and Computer Science, MCERC, Idaho State University, Pocatello, Idaho 83201 USA (email: naiduds@isu.edu).

For this work we used an array of three sEMG sensors and a force sensing resistor (FSR) to acquire the EMG signal and the corresponding skeletal muscle force. The data from the three sEMG sensors is fused using a fusion algorithm since, the fusion based force shows a better estimation of skeletal muscle force from the corresponding sEMG signal when compared to single sensor data [12]. In order for this design to accomplish its goals, a real-time embedded control system is essential. Such a system combines the hardware and software components to balance the computational, electrical and mechanical workloads across the system. Also the present work utilizes a real-time MRAC which is implemented on an embedded test bed to control the movements and the force of a prosthetic hand prototype with sensory feedback. The input to the real-time control system is a fusion based force estimate. A two stage embedded platform with a simple MRAC strategy is chosen for the force control of the prosthetic hand prototype. The paper is organized as follows. The present section covers the literature review and introduction, and the next section describes the experimental set-up. These are followed by the proposed design, results and discussion, and conclusion and future work.

## II. EXPERIMENTAL SET-UP

Fig. 1 shows the experimental set-up used to capture sEMG and force signals. The motor points and the appropriated EMG electrode attachment points of the subject were identified by using a wet probe point muscle stimulator (Rich-Mar Corporation, model number HV 1100.). Here we are using an array of three sensors. The sEMG sensor at the center in Fig. 1 is at the motor point while the other two sensors are adjacent to the motor point. sEMG signals are captured from the surface of the skin using DE 2.1 sEMG sensors with a 16-channel DELSYS® Bagnoli EMG system and LabVIEW™. The sEMG signals are acquired at a sampling rate of 2000 samples per second. Prior to placing the sEMG sensors, the skin surface of the subject was prepared according to the International Society of Electrophysiology and Kinesiology (ISEK) protocols [13].

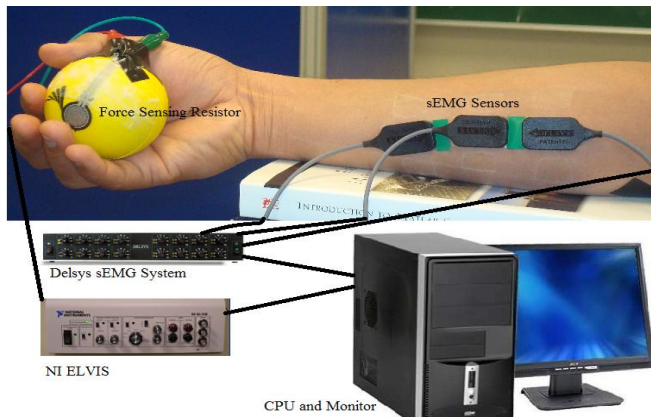


Fig. 1. Experimental Set-Up.

## III. PROPOSED DESIGN

The objective of the embedded system design is for the prosthetic hand fingers to track a force signal as closely as possible. Here, the force signal is inferred from surface EMG (sEMG) signals obtained from the array of the three sEMG sensors located at the arm. The sEMG data is processed by filtering and using a sensor fusion algorithm to facilitate the extraction of the best finger force estimates. Sensor fusion is done in the frequency domain for the sEMG data using a simple elitism based Genetic Algorithm (GA). The data from the three sensors is collected around the corresponding individual motor unit location at the transradial arm location (flexor digitorum superficialis) and before fusing are rectified and filtered using a Half - Gaussian filter, as given by (1).

$$p(EMG|x) = 2 \times \frac{\exp\left(-\frac{EMG^2}{2x^2}\right)}{\sqrt{2\pi}x^2}, \quad (1)$$

where  $p(EMG|x)$  is a conditional probability density function,  $x$  is a latent driving signal.

System identification (SI) is used to identify the dynamical relationship between the sEMG data from the three sensors  $u_1, u_2$ , and  $u_3$  and the corresponding finger force of a healthy male subject. In this fusion algorithm, Output Error (OE) models are used and are constructed for each individual data set. The OE model is given as follows.

$$y(t) = \frac{B(q)}{F(q)}u(t - nk) + e(t), \quad (2)$$

Where  $B$ , and  $F$  are the polynomials,  $q$  is shift operator,  $e(t)$  is output error,  $y(t)$  is system output,  $u$  is input,  $nk$  is the system delay and  $t$  is time index.

Using the three resulting OE models and the fusion algorithm given by [12] a corresponding continuous-time model is constructed as given by the transfer function as

$$G(s) = \frac{B(s)}{F(s)} = \frac{b_{nb}s^{(nb-1)}b_{nb-1}s^{(nb-2)}+\dots+b_1}{s^{nf}+f_{nf}s^{nf-1}+\dots+f_1}, \quad (3)$$

Similar to the discrete-time case  $nb$  and  $nf$  determine the orders of the numerator and denominator. For multi-input systems,  $nb$  and  $nf$  are row vectors.  $b, f$  are the coefficients of the numerator and denominator polynomials respectively.

A MISO transfer function is constructed based on the poles of three individual OE models corresponding to each sensor. GA is used to find the corresponding zeros. The search area is limited to the unit circle, because a discrete time model is used (and the resulting MISO model is decreased to minimum phase). The number of zeros is at most the number of poles. The number of potential zeros is set to the order of the corresponding denominator. The error squared of the resulting MISO system  $H(s)$  (see Appendix)

and the recorded force signal was set as an objective function. The objective function  $f$  is constructed as follows,

$$f = \int_{t_0}^{t_f} (\hat{Y}(t) - Y(t))^2 dt = \int_{t_0}^{t_f} \varphi^2(t) dt, \quad (4)$$

where  $t_0$  and  $t_f$  are the initial and final time values,  $\hat{Y}(t)$  is the fusion model estimated force and  $Y(t)$  is the actual force from the FSR.

The MISO system  $H(s)$  is constructed as follows,

$$H(s) = \begin{pmatrix} \frac{Z_{1,1}s^n + Z_{1,2}s^{n-1} + \dots + Z_{1,n+1}}{P_{1,1}s^n + P_{1,2}s^{n-1} + \dots + P_{1,n+1}} \\ \frac{Z_{2,1}s^n + Z_{2,2}s^{n-1} + \dots + Z_{2,n+1}}{P_{2,1}s^n + P_{2,2}s^{n-1} + \dots + P_{2,n+1}} \\ \frac{Z_{3,1}s^n + Z_{3,2}s^{n-1} + \dots + Z_{3,n+1}}{P_{3,1}s^n + P_{3,2}s^{n-1} + \dots + P_{3,n+1}} \end{pmatrix}, \quad (5)$$

where  $Z$ 's and  $P$ 's are the zeros and poles respectively of the individual transfer function and  $n$  is the order of the system.

Feeding the new data sets to the MISO transfer function ( $H(s)$ ) results in an estimated fusion based force  $\hat{Y}$ .

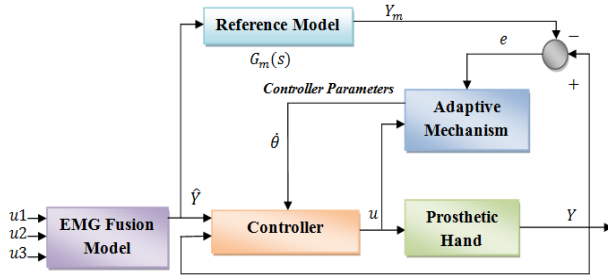


Fig. 2. Block Diagram of Model Reference Adaptive Control (MRAC).

The controller utilized for compensating the dynamics of the prosthetic hand is based on a simple MRAC scheme. During the development of the artificial hand, changes are being undertaken to the mechanical design and drive trains of the hand that affect the dynamics of the finger motion of the prosthesis. In addition, the uncertain characteristics of the kinematic and actuator interaction may lead to different performance than expected. Hence, a simple MRAC controller is devised in order to maintain some performance stability. The controller is given by Fig. 2 where the MIT rule is used for updating the controller parameter  $\theta$ ,

$$\frac{d\theta}{dt} = -\gamma e Y_m. \quad (6)$$

The gain  $\gamma$  is chosen to be 3.0 and the error  $e = Y - Y_m$  is computed by the difference of the model reference output  $Y_m$  and the true output (force generated by the prosthetic hand). The model reference is chosen to be of first order to suppress overshoot and facilitate fast response time, given by

$$G_m(s) = \frac{2}{2s+1}. \quad (7)$$

### Implementation:

The force feedback signal is acquired by a Force Sensitive Resistor (FSR). The FSR is mounted on the fingertip of the prosthetic hand prototype as shown in Fig. 3. A simple MRAC is employed to generate the actual force from the FSR, and make it equal to the model reference output in order to impose a desired dynamical response. The proposed control design is implemented on a PIC 32MX360F512L microcontroller in two stages: “Signal Processing” and “Motor Actuation”. The Signal Processing stage facilitates the execution and implementation of real-time control strategies. A dsPIC block set is used to generate the C code for the PIC 32 from Simulink®. The dsPIC block set generates a .hex file, and this file is imported in MPLAB® to program the PIC 32.

### Signal Processing Stage:

The following modules of the PIC 32 are used for the implementation of the signal processing stage.

- The Analog Input module
- The Digital Output module
- The Output Compare module
- The UART module

The Analog Input module is used for acquiring the sensory feedback force data from the FSR. The PIC 32 has an internal analog to digital converter (ADC) which has a 10-bit resolution so that it can distinguish up to 1024 different voltage values, usually in the range of 0 to 3.3 volts, and it yields 3mV resolution. The Digital Output module of the PIC 32 is used to generate digital control signals based on the selected control strategy to the motor actuation stage. This module detects the changes in the reference/command signal and flips the direction bits between 0 and 1. The motors switch direction accordingly. Depending on the error, a pulse width modulated (PWM) wave with a specific duty cycle is generated by the Output Compare module. The UART module in the PIC 32 is used to transmit the force data from the microcontroller to the PC via serial communication. In this design, a virtual com port was created to feed the data via USB cable to the computer. MATLAB® is used to read the signals from the ports. This enables the user to troubleshoot and see the performance and accuracy of the designed control strategy.

### Motor Actuation Stage:

In this stage, a SN754410 quadruple half-H driver [14] is used to actuate the motor with the corresponding control signal. The PWM wave from the Output Compare module is connected to the pin1 (1, 2EN) of the H driver. The PWM wave enables this H driver. The speed of the motor depends on the duty cycle of the PWM wave from the Output Compare module which is a function of error  $e(t)$ . Therefore the speed of the motor is adjusted based on the

error to achieve desired performance and accuracy. The digital outputs of the PIC 32 microcontroller are connected to the direction pins of the H driver (pins 2 and 7). Switching the digital outputs to 0 and 1 between the pins makes the motor rotate in clockwise and counter-clockwise directions. This controls the finger to maintain the force levels based on the control strategy.  $V_{cc1}$  and  $V_{cc2}$  are connected to the 5V supply of the PIC 32 I/O board. This proposed design was tested on an index finger of a prosthetic hand prototype. Fig. 3 shows the test bed for the proposed design. The Mechanical design of the robotic hand prototype is explained in the following section.

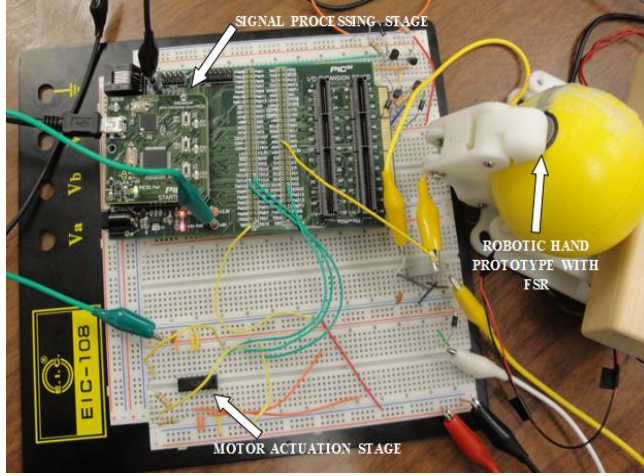


Fig. 3. Embedded Test bed for the proposed design

#### IV. MECHANICAL STRUCTURE OF THE ROBOTIC HAND PROTOTYPE

The prototype finger has three degrees of freedom actuated by two Pololu 35:1 mini metal gear motors. The main characteristic of this robotic hand is its biologically-inspired parallel actuation system, which is based on the behavior/strength space of the Flexor Digitorum Profundus (FDP) and the Flexor Digitorum Superficialis (FDS) muscles [15]. Fig. 4 depicts the strength space of FDS and FDP muscles. The DC motor in the metacarpal phalange of the finger actuates the Proximal Inter Phalangeal (PIP) joint and through the belt transmission system. It also drives the DIP (Distal Inter Phalangeal) joint. The DC motor at the base of the finger actuates the Meta Carpo Phalangeal (MCP) joint as shown in Fig. 5.

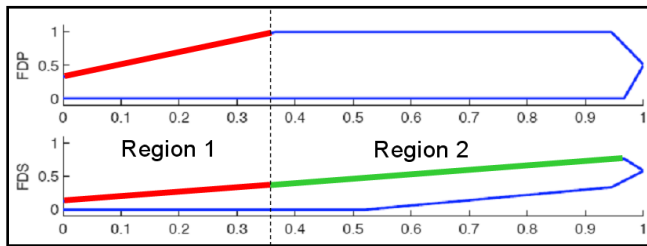


Fig.4. Strength space of FDS and FDP muscles [16]

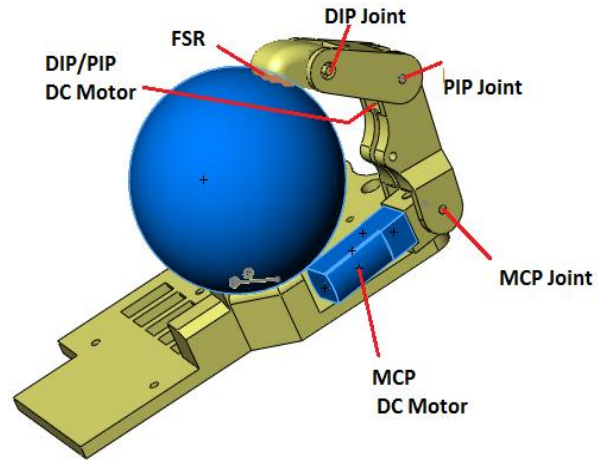


Fig. 5. Actuation scheme for the finger

The DC motors were selected based on their high efficiency (90%) in order to minimize power consumption during more frequently executed tasks (Region 1). An additional criterion is based on the motor's time response, which needs to approximately correspond to the joint speeds of the human hand. Grip force is measured for a number of reasons. For instance, it is typical for real-life gripping scenarios to be recreated to investigate entities such as maximum grip force, and the effects of loading on transmission and range of motions. The requirement to reproduce representative grip conditions means that the force sensor used must not significantly alter the performance characteristics of the grasping action or the operator's ability to use the prosthetic hand prototype. Particularly, in this paper, the Region 1 actuation scheme is considered. In order to sense the normal force applied by the tip of the finger, FSR is attached to the tip of the finger.

#### V. RESULTS AND DISCUSSION

Data is acquired from the microcontroller through UART channel2 of the PIC 32 micro controller by a virtual com port via USB at 57600 baud rate. The data from the microcontroller is converted into unit16 data type before it is transmitted through the UART. The PIC 32 microcontroller is running at 80 million instructions per second (MIPS) with its phase lock loop (PLL) activated. It is running at an external clock frequency of 8MHz with internal scaling enabled. Fig. 6 depicts the experimental results of the proposed design. The prosthetic hand prototype mathematical model is used instead of the actual hand to obtain the simulation based force output to validate the controller performance. The simulation based force output converges to the fusion model estimate  $\hat{Y}$  in approximately 0.9 ms. The simulation based force output exactly matches the fusion model estimated force  $\hat{Y}$  after the convergence. The actual force output from the FSR (i.e.  $Y$ ) closely follows the fusion model estimated force  $\hat{Y}$ . In Fig. 6 there are some instances where the FSR lost contact with the object, as indicated by a sharp drop in the force curve.



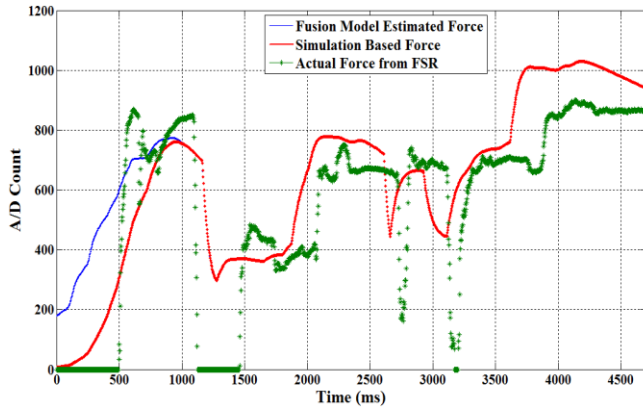


Fig. 6. Fusion based force estimate, simulation based force and actual force from FSR during the grasp.

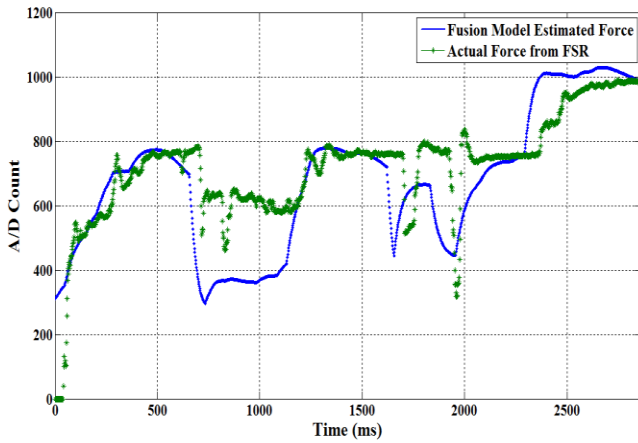


Fig. 7. Fusion based force estimate and actual force from FSR during the grasp (separate experiment).

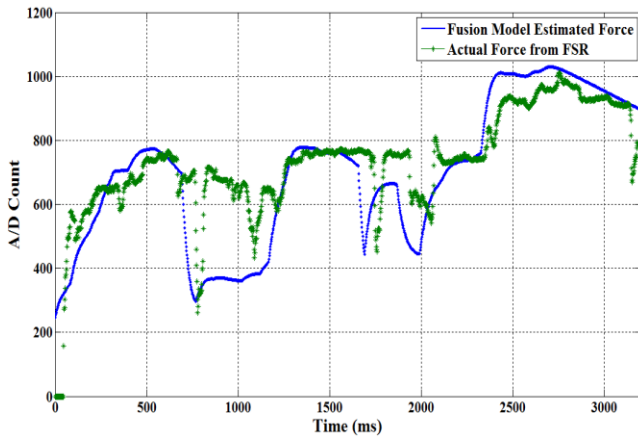


Fig. 8. Fusion based force estimate and actual force from FSR during the grasp (for a repeated experiment).

Fig. 7 shows the fusion model estimated force  $\hat{Y}$  and actual force from the FSR ( $Y$ ) plotted for a separate experiment. In this case, the prosthetic hand prototype is made to maintain a minimum constant force so that the contact between the FSR and the object will not be lost. The same experiment is repeated to test the consistency, and to

make sure that the object is in contact with the FSR throughout the experiment.

Fig. 8 shows the repeated experimental results. The proposed control strategy is tracking the force profile and matching the actual force with the model estimated force ( $\hat{Y}$ ). While conducting the experiments, the following observations were made. The DC motors currently employed have the primary task of moving the prosthetic fingers. As the project is ongoing research, the SMA actuation scheme is not yet implemented because of the slow response of the SMA's, and also SMA's have high relaxation time. Therefore it is difficult to track a randomly changing force profile with a slowly responding actuation system. However, as the hand is designed to use the parallel actuation of these DC motors and SMA's, the DC motors alone cannot produce fusion model estimated force. In this work, the DC motors are solely responsible for the motion and force actuation. Since the DC motors have small gear heads, the usual characteristic of gear driver actuation cores occurs: gear backlash. In addition, the DC motors employed were slow in responding to the changes in the force profile. Hence some gaps were observed in the measured force signal. This indicates that there are instances in which the fingertip loses contact due to backlash and vibration problems. However, the profile of the measured force from the FSR has a similar pattern as the fusion model estimated force ( $\hat{Y}$ ). Thus we can conclude that apart from those mechanical transmission problems the implemented control scheme produced promising results. These problems will be considered in a new prototype design that we are currently developing. It is also evident from Figs. 7 and 8 that the minimum constant force is needed to obtain better contact with the object and to accomplish accuracy in tracking the reference force profile. In order to test the precision of the proposed control strategy, 15 different experiments were conducted. The mean of the Pearson's correlation coefficient (see Appendix) for fusion model estimated force ( $\hat{Y}$ ) and the actual force from the FSR ( $Y$ ) in all the 15 experiments is 0.86. Because of the above mentioned transmission problems and the slow response of the gears, slight variability is observed in the correlation coefficients for the 15 experiments. Hence the difference in tracking the force profile is observed in Figs. 7 and 8. Fig. 9 depicts the validation plot with a different fusion based force estimate  $\hat{Y}$  obtained by feeding a different sEMG signal to the MISO transfer function ( $H(s)$ ). The fusion based force estimate, simulation based force and the actual force from the FSR are all shown in Fig. 9. The same mechanical transmission problems and the slow response of gears are observed in this experiment as well. However, the controller is tracking the force profile and the Pearson's correlation coefficients for fusion model estimated force ( $\hat{Y}$ ) and the actual force from the FSR ( $Y$ ) is 0.84, which is close to other experiments.

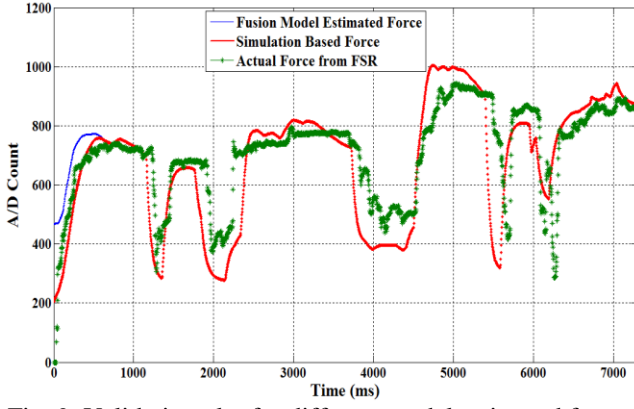


Fig. 9. Validation plot for different model estimated forces.

## VI. CONCLUSION AND FUTURE WORK

A two-stage real-time embedded MRAC strategy was designed for a prosthetic hand prototype. The proposed design gives good performance when tested on a prosthetic hand prototype, based on tracking a reference force profile. This design facilitates the transmission of the data from the microcontroller to the computer. This design enables the control engineer to increase the accuracy and performance of the design by implementing various novel control strategies and also enables fast trouble shooting.

For the future work, we are planning to implement online model-based force estimation along with controller designs that address the above listed mechanical shortcomings for position and force control, using this embedded platform. It will be interesting to acquire the sEMG signal directly from the arm of a healthy subject transmit to our embedded system instead of using prerecorded sEMG signals, which will be investigated as well in the future. Finally, we plan to use the prototype with five fingers.

## APPENDIX

The resulting MISO transfer function  $H(s)$  is constructed as, From  $u_1$  to output,

$$\frac{s^8 - 3.843s^7 + 7.729s^6 - 10.78s^5 + 10.6s^4 - 7.417s^3 + 3.603s^2 - 0.9795s + 0.1192}{s^8 - 4.028s^7 + 6.325s^6 - 4.121s^5 - 1.545s^4 + 5.87s^3 - 5.433s^2 + 2.28s - 0.3496}$$

From  $u_2$  to output,

$$\frac{s^8 - 4.339s^7 + 9.005s^6 - 12.42s^5 + 12.22s^4 - 8.117s^3 + 3.427s^2 - 0.9134s + 0.1424}{s^8 - 4.028s^7 + 6.325s^6 - 4.121s^5 - 1.545s^4 + 5.87s^3 - 5.433s^2 + 2.28s - 0.3496}$$

From  $u_3$  to output,

$$\frac{s^8 - 3.522s^7 + 6.655s^6 - 8.864s^5 + 8.183s^4 - 5.365s^3 + 2.423s^2 - 0.557s + 0.09585}{s^8 - 4.028s^7 + 6.325s^6 - 4.121s^5 - 1.545s^4 + 5.87s^3 - 5.433s^2 + 2.28s - 0.3496}$$

Pearson correlation coefficient is given by,

$$\rho_{X,Y} = \text{corr}(X,Y) = \frac{\text{cov}(X,Y)}{\sigma_X \sigma_Y} = \frac{E[(X - \mu_X)(Y - \mu_Y)]}{\sigma_X \sigma_Y}$$

Where  $X, Y$  are Random Variables,  $\mu_X$  and  $\mu_Y$  are expected values,  $\sigma_X, \sigma_Y$  are standard deviations respectively.  $E$  is expected value operator.

## ACKNOWLEDGMENT

This research was sponsored by the US Department of the Army, under the award number W81XWH-10-1-0128 awarded and administered by the U.S. Army Medical Research Acquisition Activity, 820 Chandler Street, Fort Detrick MD 21702-5014. The information does not necessarily reflect the position or the policy of the Government, and no official endorsement should be inferred. For purposes of this article, information includes news releases, articles, manuscripts, brochures, advertisements, still and motion pictures, speeches, trade association proceedings, etc. Further, the technical help from Dr. Alba Perez and Mr. Alex Jensen is greatly appreciated.

## REFERENCES

- [1] Amputee Coalition of America (ACA) National Limb Loss Information, Center (NLLIC) Limb Loss Facts in the United States, <http://www.amputee-coalition.org>, 2005.
- [2] D.S. Naidu and C.-H. Chen, "Control Strategies for Smart Prosthetic Hand Technology: An Overview", Book Chapter 14, to appear in a book titled, Distributed Diagnosis and Home Healthcare (D2H2): Volume 2, American Scientific Publishers, CA, January 2011.
- [3] Zinn M, Roth B, Khatib O, and Salisbury JK, "A new actuation approach for human friendly robot design," *Int J Robot Res.* 2004; 23(4-5), pp. 379-398.
- [4] Bien ZZ, and Stefanov D, "Advances in rehabilitation robotics: Human-friendly technologies on movement assistance and restoration for people with disabilities," *Springer, Berlin (Germany)*. 2004.
- [5] Heinzmann J, and Zelinsky J, "A safe-control paradigm for human-robot interaction," *J Intell Robot Syst.* 1999; 25(4): pp. 295-310.
- [6] D. J. Atkins, D. C. Y. Heard, and W. H. Donovan, "Epidemiologic overview of individuals with upper limb loss and their reported research priorities," *J. Prosthet. Orthot.*, vol. 8, no. 1, p. 2, 1996.
- [7] D. H. Silcox, M. D. Rooks, R. R. Vogel, and L. L. Fleming, "Myoelectric prostheses. A long-term follow-up and a study of the use of alternate prostheses," *J. Bone Joint Surg.*, vol. 75, no. 12, pp. 1781-1789, 1993.
- [8] T. H. Sueeter, "Control of the Utah/MIT Dextrous hand: Hardware and software hierarchy," *J. Robot. Syst.*, vol. 7, no. 5, pp. 759-790, 1990.
- [9] M. H. Raibert and J. J. Craig, "Hybrid position and force control of manipulators," *ASME J. Llyn. Syst. Meas. Contr.*, vol. 102, pp. 126-133, June 1981.
- [10] Cram, J.R., Kasman G.S., and Holtz J. "Introduction to Surface Electromyography," Aspen Publisher Inc., Gaithersburg, Maryland, 1998.
- [11] Kandel E.R. and Scharzt J.H., "Principles of Neural Science," Elsevier/North-Holland, New York, 1981.
- [12] Potluri C., Kumar P., Anugolu M., Urfer, A.; Chiu S., Naidu D.S., Schoen, "Frequency Domain Surface EMG Sensor Fusion for Estimating Finger Forces," 32nd Annual International Conference of the IEEE Engineering in Medicine and Biology Society, Buenos Aires, Argentina, August 31 - September 4, 2010.
- [13] [http://www.isek-online.org/standards\\_emg.html](http://www.isek-online.org/standards_emg.html).
- [14] Texas Instruments "SN754410 quadruple half H-driver data sheet" Dallas, Texas, November 1986 and 1995
- [15] Dr. Anthony L. Crawford, "Design of a Robotic Hand and Simple EMG Input Controller with a Biologically-Inspired Parallel Actuation System for Prosthetic Applications" ASME2010, IDETC/CIE 2010
- [16] Kutch, J. J., Valero-Cuevas, F. J., "All muscles are redundant but some are less redundant than others," 19<sup>th</sup> Annual Meeting of the Society for the Neural Control of Movement, Waikoloa Beach, Hawaii, April 2009.

# Spectral Analysis of sEMG Signals to Investigate Skeletal Muscle Fatigue

Parmod Kumar, Anish Sebastian, Chandrasekhar Potluri, Yimesker Yihun, Madhavi Anugolu, Jim Creelman, Alex Urfer, D. Subbaram Naidu, *Fellow, IEEE*, and Marco P. Schoen, *Senior Member, IEEE*

**Abstract**— Our recent investigations are focused to develop dynamic models for skeletal muscle force and finger angles for prosthetic hand control using surface electromyographic sEMG as input. Since sEMG is temporal and spatially distributed and is influenced by various factors, muscle fatigue and its related sEMG becomes of importance. This study is an effort to spectrally analyze the sEMG signal during progression of muscle fatigue. The sEMG is captured from the arms of healthy subjects during muscle fatiguing experiments for dynamic and static force levels. Filtered sEMG signal is segmented in five parts with 75% overlap between adjacent segments. The analysis is done using different classical (fast Fourier transform, Welch's averaged modified periodogram), model-based (Yule-Walker, Burg, Covariance and Modified Covariance autoregressive (AR) method), and eigenvector methods (Multiple Signal Classification (MUSIC) and eigenvector spectral estimation method) in frequency domain. Results show that the classical and eigenvector based methods are more sensitive than the model-based methods to fatigue related changes in sEMG signals.

## I. INTRODUCTION

THIS work focuses on the analysis of sEMG signals, which are electric voltages ranging between -5 to +5 mV and investigates the effects of fatigue in the skeletal muscles. The motor units operate as a consequence of the central nervous system control strategies, signal transmission along nerve fibers and across neuromuscular junctions, electrical activation of the muscle fibers organized in elementary motors and, through a chain of complex biochemical events. The productions of the forces acting on the tendons of the agonist and/or antagonist muscles predict bone movement [1]. This mechanism also involves a number of feedback circuits relaying back to the spinal cord and the brain

Manuscript received March 22, 2011. This work was supported in part by the US Department of the Army, under the award number W81XWH-10-1-0128.

Parmod Kumar is with Measurement and Control Engineering Research Center (MCERC), School of Engineering, Idaho State University, Pocatello, Idaho 83209, USA (email: kumaparm@isu.edu).

Anish Sebastian, Chandrasekhar Potluri, Yimesker Yihun, and Madhavi Anugolu are with MCERC, School of Engineering, Idaho State University, Pocatello, Idaho 83209, USA (e-mail: sebaanis@isu.edu, potlchan@isu.edu, yihuyime@isu.edu, anugmadh@isu.edu).

Jim Creelman and Alex Urfer are with Department of Physical and Occupational Therapy, Idaho State University, Pocatello, Idaho 83209, USA (email: creejame@isu.edu, urfealex@isu.edu).

D. Subbaram Naidu is with Department of Electrical Engineering and Computer Science, MCERC, Idaho State University, Pocatello, Idaho 83201 USA (email: naiduds@isu.edu).

Marco P. Schoen is with Department of Mechanical Engineering, MCERC, Idaho State University, Pocatello, Idaho 83209, USA (email: schomarc@isu.edu).

information concerning the length and velocity of shortening of the muscles and the forces acting on the tendons [1]. The EMG signal gives information about the motor points and their controller i.e. the central nervous system [2, 3]. The central nervous system activates and controls the EMG signals which depend on the flow of specific ions including sodium ( $Na^+$ ), potassium ( $K^+$ ) and calcium ( $Ca^{++}$ ) resulting in the action potentials in nerves and their respective skeletal muscle fibers from which EMG signals are derived. Research efforts in the last few decades have focused on the prosthetic design where sEMG is a control input to activate the prosthesis. The sEMG is a dynamic signal with continual change in its pattern and strength and this becomes more complex with the fatigue induced in skeletal muscles.

Failure to maintain the required force level is termed as muscle fatigue, which is a complex phenomenon [4]. Reasons for fatigue can be the result of peripheral changes at the muscle level or an inadequate output from the central nervous system to stimulate motoneurons [4]. Intricacies of muscle fatigue are associated with several aspects where the relative importance of each depends on the fiber type and composition of the contracting muscle(s), as well as the intensity, type, and duration of contraction activity. Muscle cells are the focal points of fatigue and rarely involve the central nervous system or the neuromuscular junction [5]. The amount of force generated, duration of each contraction, and the rest period between two contractions has a direct influence on the muscle fatigue rate [6]. Muscle fiber-type distribution [7, 8], nerve conduction velocity of fatiguing muscles [9, 10], or even central factors within the central nervous system (CNS) will affect motivation to perform activities [11]. The EMG analysis is a well-accepted method for muscle fatigue assessment [8-10, 12-17]. Even though the sEMG has some limitations associated with the skin impedance, electrode placement, and cross-talk, it is used for the estimation of muscle fatigue of different muscles [16, 18, 19].

L. Lindstrom et al. developed a method that measures the localized muscle fatigue based on the power spectrum analysis using myoelectric signals, [20]. This approach permits real-time investigations and can yield statistically based criteria for the occurrence of fatigue. Rate of fatigue development and changes in muscle action potential conduction velocity were used to interpret the findings [20-22]. Additional recruitment of motor units, synchronization

of active motor units along the muscle fibers, and a decrease in conduction velocity is reflected in the EMG signal as an increase of amplitude in time domain and a decrease of medium frequency in frequency domain [23, 24].

The joint analysis method using sEMG amplitude and spectrum (JASA) allows distinguishing between the difference of fatigue-induced and force related EMG changes. Simultaneous changes in the EMG amplitude and spectrum is considered in the JASA approach [25]. According to traditional measurements, the EMG amplitude increases and median frequency (MF) decreases as a result of muscle fatigue [26-28]. Fatigue can occur because of continuous high frequency and tetanic stimulations. Decline in the force magnitude can be attributed to reduced  $Ca^{++}$  release from the sarcoplasmic reticulum (SR), reduced myofibrillar  $Ca^{++}$  sensitivity, or because of reduced maximum  $Ca^{++}$ -activated tension. The main reason of the tension decline with continuous tetanic stimulation is decreased  $Ca^{++}$  release, which is due to impaired action potential propagation in the T tubules. Decrease in pH and increase in inorganic phosphate (Pi) concentration causes reduced  $Ca^{++}$  sensitivity and decline in maximum tension. This is the main contributing factor in decline of force with continual tetanic stimulation [29].

Increase in the inorganic phosphate in the myoplasm ([Pi]myo) results in reduced SR  $Ca^{++}$  release in both skinned and intact fibers. Muscle performance declines with rigorous activities which results in fatigue. Metabolic changes on either the contractile machinery or the activation process are also responsible for the fatigue of muscles. Myofibrillar proteins and activation process both are affected during fatigue with substantial increase in the concentration of inorganic phosphate (Pi) in myoplasm. Further, it has been shown that failure of the sarcoplasmic reticulum (SR) to release  $Ca^{++}$  also contributes to fatigue [30]. During intense exercise of skeletal muscles (less than 20 seconds), cells consume 100 of times more energy than during the rest period. The aerobic capacity of muscle cells falls short on energy demand and anaerobic metabolism must supply the majority of the adenosine triphosphate (ATP) required. Skeletal muscle fatigue results because of the high-intensity exercise. Hence, the anaerobic metabolism pathway results in a decline of contractile functionality [31].

The present work investigates the change in sEMG in frequency domain during skeletal muscle fatigue. The sEMG signals are acquired for multiple subjects for dynamic and static force experiments to induce skeletal muscle fatigue. The sEMG signals are filtered with a nonlinear Teager-Kaiser Energy (TKE) operator-based nonlinear spatial filter [32]. Two sets of dynamic force data are segmented into three and five parts and two sets of static force data are segmented into five parts each. There is a 75% overlap between the two adjacent segments. A number of classical, model-based and eigenvector based spectral estimation techniques are used to study the change in the sEMG signals as a result of muscle fatigue. In classical methods Fast

Fourier transform (FFT) and Welch's averaged modified periodogram methods are used. In case of model-based methods Yule-Walker (Y-W), Burg, Covariance (Cov.) and Modified Covariance (Mcov.) Autoregressive (AR) methods are applied. For eigenvector methods Multiple Signal Classification (MUSIC) and Eigenvector (EIG) spectral estimation methods were selected for processing sEMG signals. Using these spectrum analysis techniques, Power Spectral Density (PSD) estimates and detailed documentations of the sEMG signals were obtained. These methods were compared in terms of their frequency resolution and the effects in determination of skeletal muscle fatigue.

## II. EXPERIMENTAL SET-UP AND PRE-PROCESSING

An experiment set-up was developed using DELSYS® Bagnoli-16 EMG system with nine DE-3.1 sEMG sensors to capture the sEMG signals from skeletal muscles as given in [32]. This arrangement involves nine sensors covering four directional spatial distributions of the sEMG signal. The appropriate motor point of the flexor digitorum superficialis muscle (FDS), which controls the flexion of the ring finger, was identified using a wet probe muscle stimulator at the FDS (RICH-MAR, HV 1000). The middle three sEMG sensors were attached directly on the skin surface above the motor point of the ring finger. Prior to placing the sEMG sensors, the skin surface of the subject was prepared according to International Society of Electrophysiology and Kinesiology (ISEK) protocols [33]. Two different sets of fatigue inducing experiments were conducted using this set-up of sEMG sensors. One experiment using dynamic force variations and another with 50 pounds of static force. For the dynamic force variation we used an Interlink™ Electronics FSR 0.5" circular force sensor on a stress ball and for the static force experiment we used a cable tensionmeter (T5166) by 'Pacific Scientific Company.'

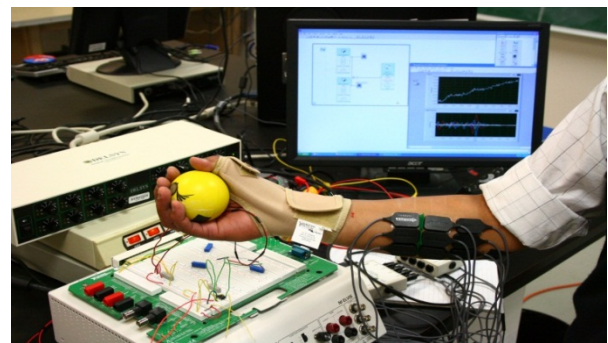


Fig. 1. Experimental set-up for dynamic force levels.

For the dynamic force experiment we restricted the thumb movement using a thumb splint. For the static force experiment we held the force of the dynamometer at 50 pounds and tried to maintain this force level to induce fatigue in skeletal muscles. Force data for dynamic force experiments was captured using NI ELVIS™ with Interlink™ Electronics FSR 0.5" circular force sensor. Experimental set-up is shown in Fig. 1 and 2, where 9 sensors are shown on a healthy subject forearm, holding a



stress ball and a grip tension dynamometer, respectively. The sEMG and finger force data was collected at a sampling rate of 2000 Hz using LabVIEW™ in conjunction with DELSYS® Bagnoli-16 EMG and NI ELVIS™. With these experimental set-ups, we conducted several experiments of 30 seconds, 45 seconds and 60 seconds durations.

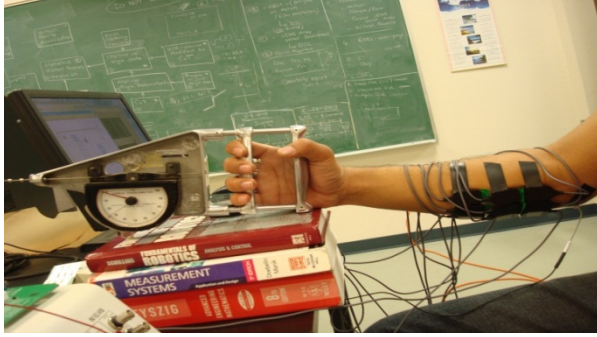


Fig. 2. Experimental set-up for 50 pounds static force levels.

### III. SPECTRAL ESTIMATION METHODS

Signals can be analyzed in the time and frequency domains and in some instances the frequency content of the signal is more useful than the time domain characteristics [34]. Various bio signals such as the heart rate, EMG, EEG, ECG, eye movements, and other motor responses, acoustic heart sounds, and stomach and intestinal sounds, show much richer information in the frequency domain [34]. Spectral analysis is a mathematical prism which finds the frequency content of a waveform by decomposing the signal into its constituent frequencies [34, 35]. There is a wide range of methods for spectral analysis, each having its own benefits and drawbacks. In this research we are using classical methods based on the Fourier transform, modern methods based on the estimation of model parameters, and eigenvector based methods [34] in order to characterize the muscle fatigue occurring in skeletal human muscles, in particular muscles of the forearm. To use the spectral analysis wisely, we need to have an understanding of the spectral features of interests and the best methods to accurately determine those features [34].

#### A. Discrete Fourier Transform (DFT)

DFT which is the computational basis of the spectral analysis transforms the time or space domain data into frequency domain data [36]. The DFT of a vector  $x$  of length  $N$  is given as

$$X(k) = \sum_{j=1}^N x(j) \omega_N^{(j-1)(k-1)}, \quad (1)$$

where  $\omega_N = e^{(-2\pi i)/N}$  is the  $N_{th}$  root of unity [36].

#### B. Welch's averaged modified periodogram method:

As the name suggests, the 'Welch's averaged modified periodogram method' depends on the periodogram of the signal  $\{x(n)_n^N\}$  which is given by Equation (2), [36].

$$\hat{S}_{per}(f) = \frac{1}{N} |\sum_{n=1}^N x(n) \exp(-j2\pi f n)|^2. \quad (2)$$

In Welch method, the signal is segmented into eight parts of equal length with an overlapping ratio of 50% and each part is segmented using a Hamming window as given by Equation (3), [36].

$$w(n) = 0.54 - 0.46 \cos\left(2\pi \frac{n}{N}\right), 0 \leq n \leq N. \quad (3)$$

#### C. Yule-Walker (Y-W) autoregressive (AR) method:

The Yule-Walker autoregressive method, also called the autocorrelation method, estimates the power spectral density (PSD) of the input. This method fits an autoregressive (AR) model to the windowed input data by minimizing the forward prediction error in the least-squares sense. This formulation leads to the Yule-Walker equations, which are solved by Levinson-Durbin recursion [36].

#### D. Burg autoregressive (AR) method:

The Burg autoregressive (AR) method is a parametric spectral estimation method of the signal,  $x$ . The power spectral density is calculated in units of power per radians per sample. This method is based on the minimization of the forward and backward prediction error and on estimation of the reflection coefficients [36].

#### E. Covariance (Cov.) autoregressive (AR) method:

The covariance autoregressive (AR) method uses the covariance algorithm to estimate the parametric spectral density of the signal,  $x$ . Based on causal observation of the input signal, the covariance method minimizes the forward prediction error and fits an AR linear prediction filter model to the signal [36].

#### F. Modified covariance (Mcov.) autoregressive (AR) method:

Modified covariance autoregressive (AR) method estimates the PSD of the signal using the modified covariance method. Based on the causal information of the input signal, the modified covariance method fits an autoregressive (AR) linear prediction filter model to the signal by simultaneously minimizing the forward and backward prediction errors. The spectral estimate returned by this method is the magnitude squared frequency response of the AR model [36].

#### G. Multiple Signal Classification (MUSIC) spectral estimation method:

The MUSIC algorithm estimates the pseudospectrum (in rad/sample) at the corresponding vector of frequencies for the input signal  $x$  [36]. This algorithm uses the estimates of the eigenvectors of a correlation matrix associated with the input signal using Schmidt's eigenspace analysis method [37]. The MUSIC pseudospectrum estimate is given by Equation (4),

$$P_{music}(f) = \frac{1}{e^H(f) (\sum_{k=p+1}^N v_k v_k^H) e(f)} = \frac{1}{\sum_{k=p+1}^N |v_k^H e(f)|^2}, \quad (4)$$

where  $N$  is the dimension of the eigenvectors and  $v_k$  is the  $k$ -th eigenvector of the correlation matrix [36]. The signal subspace has a dimension  $p$  and the eigenvectors  $v_k$  used in the sum corresponds to the smallest eigenvalues and also spans the noise subspace [36]. The vector  $e(f)$  consists of the complex exponentials, so the inner product  $v_k^H e(f)$  amounts to a Fourier transform. To estimate the pseudospectrum, the squared magnitudes are summed for FFT computed for each  $v_k$  [36].

#### H. Eigenvector (EIG) spectral estimation method:

The eigenvector spectral estimation method estimates the pseudospectrum (in rad/sample) at the corresponding vector of frequencies using estimates of the eigenvectors of a correlation matrix associated with the input signal  $x$  [36]. This method estimates the pseudospectrum from a signal or a correlation matrix using a weighted version of the MUSIC algorithm derived from Schmidt's eigenspace analysis method [37, 38]. To find the frequency content of the signal the algorithm performs eigenspace analysis of the signal's correlation matrix. Singular value decomposition is used to compute the eigenvalues and eigenvectors of the signal's correlation matrix [36]. This method computes the pseudospectrum estimate as given by Equation (5).

$$P_{ev}(f) = \frac{1}{(\sum_{k=p+1}^N |v_k^H e(f)|^2) / \lambda_k}, \quad (5)$$

where the eigenvectors have a dimension of  $N$  and  $v_k$  is the  $k$ -th eigenvector of the correlation matrix [36]. The signal subspace has a dimension  $p$  and the eigenvectors  $v_k$  used in the sum corresponds to the smallest eigenvalues and also spans the noise subspace [36]. The vector  $e(f)$  consists of the complex exponentials, so the inner product  $v_k^H e(f)$  amounts to a Fourier transform and to estimate the pseudospectrum, the squared magnitudes are summed for FFT computed for each  $v_k$  [36].

#### I. Selection of Model Orders for Model-Based and Eigenvector Based Methods

Model-based and eigenvector-based methods need to have a specific model order which is an important aspect of the use in these methods. Using the sEMG and force data as input and outputs for three and five sets of the segments for different data sets, we created model structure matrices using 'struc' function in MATLAB®, using 'arxstruc' we compared a model order of 1 to 50<sup>th</sup> with varying delay of 1 to 50 using cross-validation on the second half of the data set. With this approach, it was possible to select the order that gives the best fit for the validation data set.

### IV. RESULTS AND DISCUSSION

sEMG signal changes as a consequence of muscle fatigue [23-28], the amplitude of the PSD of the signal increases and the median frequency shifts towards the lower frequency range [26-28]. In this study, PSDs of the different segments of each sEMG data set were obtained using FFT, Welch's averaged modified periodogram, Yule-Walker, Burg, Covariance, Modified Covariance autoregressive (AR), Multiple Signal Classification (MUSIC), and Eigenvector spectral estimation methods. The objective of this study was to determine preferred methods of signal processing that elevates the sensitivity of muscle fatigue as represented in the PSD of the sEMG signal. An increased sensitivity allows for better modeling of the fatigue phenomena and hence more accurate sEMG models. Ultimately this may lead to better prosthetic control.

Data of two experiments for dynamic force variations was segmented in three and five parts respectively. Each segment is with an overlap of 75% with its adjacent segment. Using

different methods, we computed the PSDs for each segment. For the dynamic force experiments, the maximum value of PSDs of sEMG signal increases with muscle fatigue as time or segment number is increased. The classical methods (FFT and Welch) and eigenvector based methods (MUSIC and Eigenvector (EIG.)) are representing this change well in case of maximum PSD values and show a clear difference.

Table I lists the peak values of the PSDs of five segments using classical and eigenvector based methods for a dynamically varying force experiment. Fig. 3 shows the overlapping plot of PSDs for five segments using the MUSIC algorithm based spectral estimation method. The increase in the maximum PSD value is evident from the 1<sup>st</sup> to the 5<sup>th</sup> segment of the data.

TABLE I  
MAXIMUM VALUE OF PSD FOR CLASSICAL METHODS AND EIGENVECTOR BASED METHODS – DYNAMIC VARYING FORCE – EXPERIMENT 2

Segment No.	Classical-Methods		Eigenvector-Methods	
	FFT	Welch	MUSIC	EIG
1 <sup>st</sup>	4.1e+6	0.0082	371.59	1.0819
2 <sup>nd</sup>	5.09e+6	0.0100	424.43	1.3892
3 <sup>rd</sup>	5.74e+6	0.0111	480.71	1.4132
4 <sup>th</sup>	6.79e+6	0.0133	508.64	1.4936
5 <sup>th</sup>	2.13e+7	0.0379	695.08	10.2118

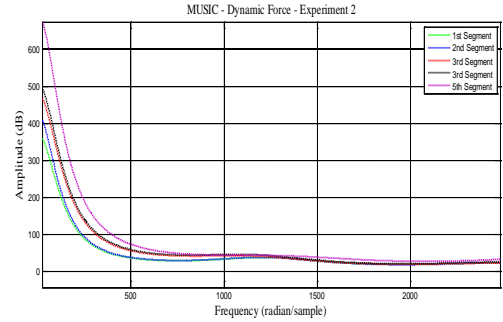


Fig. 3. PSD vs. Frequency Plot for MUSIC Algorithm – Dynamic Force Experiment.

Fig. 4 shows the resulting PSD using the Burg method. Comparing Fig. 3 and 4, the progression of fatigue influence shift in PSDs is evident in both plots. However, the MUSIC algorithm not only shows larger amplitudes, but also a greater relative sensitivity to fatigue.

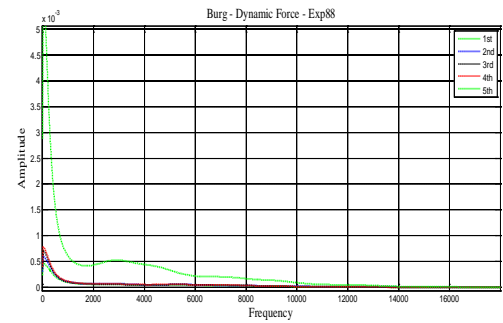


Fig. 4. PSD vs. Frequency Plot for Burg Method – Dynamic Force Experiment.

The rather equal spacing between the lines of the PSD for the MUSIC algorithm compared to the Burg method

indicates a rather more linear relationship of the fatigue progression.

The sEMG data of two experiments for static force (50 pounds) were processed and the maximum PSDs of five segments using classical, model-based, and eigenvector based methods were computed. Data from both the experiments show similar results as the dynamic case. Table II lists the peak values of the PSDs of five segments using classical and eigenvector based methods for static force (50 pounds) for one experiment. Table III lists the maximum values of the PSD for model-based methods: Y-W, Burg, Covariance, and modified covariance.

TABLE II  
MAXIMUM VALUE OF PSD FOR CLASSICAL METHODS – STATIC FORCE – 50 POUNDS - EXPERIMENT 1

Segment No.	Classical-Methods		Eigenvector-Methods	
	FFT	Welch	MUSIC	EIG
1 <sup>st</sup>	1.03e+5	6.81e-5	1413	9.93e-4
2 <sup>nd</sup>	1.80e+5	1.12e-4	1793	16e-4
3 <sup>rd</sup>	3.21e+5	1.80e-4	2296	28e-4
4 <sup>th</sup>	4.25e+5	2.62e-4	3102	37e-4
5 <sup>th</sup>	6.23e+5	3.58e-4	7723	104e-4

TABLE III  
MAXIMUM VALUE OF PSD FOR CLASSICAL METHODS – STATIC FORCE – 50 POUNDS - EXPERIMENT 1

Segment No.	1 <sup>st</sup>	2 <sup>nd</sup>	3 <sup>rd</sup>	4 <sup>th</sup>	5 <sup>th</sup>
Model-Based Methods	7.7e-7	1.3e-6	2.3e-6	3.1e-6	7.81e-6

All of these methods resulted in the same maximum values for each segment. Comparing Table II and III, we recognize the large difference in maximum value between the model-based methods and the corresponding values from the FFT and MUSIC method. Fig. 5 shows the overlapping plot of PSDs for five parts using eigenvector algorithm based spectral estimation method. The increase in the maximum PSD value is evident from the 1<sup>st</sup> to the 5<sup>th</sup> segment of the static force sEMG data.

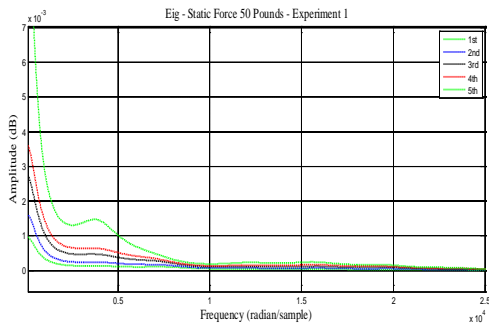


Fig. 5. PSD vs. Frequency Plot for Eigenvector Method – Static Force of 50 Pounds.

The eigenvector method produces a similar characteristic as the MUSIC algorithm and distinguishes itself by also providing a more linear characteristic of the fatigue progression and a greater relative sensitivity. Fig. 6 depicts the PSD generated by using FFT method for the 1<sup>st</sup> and 5<sup>th</sup> segments of a static force experiment. While providing a large maximum value, the FFT method is limited by its own

spectral resolution ( $1/N$ ) and, due to windowing of the finite data set, results into spectral leaking.

All the model-based methods for both dynamic and static force levels produce the same peak values and the same PSD for the corresponding experiment. Since Burg and Y-W methods guarantee stability while the covariance and modified covariance methods have conditions for stability to be satisfied (i.e. min. order must be of certain length of the input frame size), Burg and Y-W should be the preferred methods for sEMG analysis. However, the Burg method is to be preferred if short data sets are used.

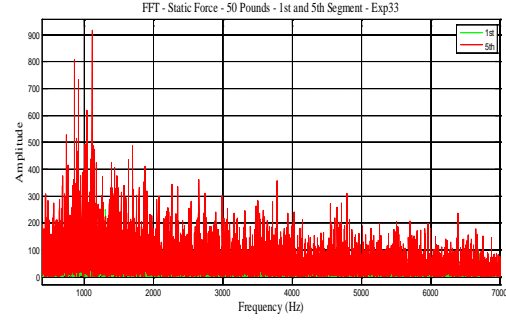


Fig. 6. PSD vs. Frequency Plot for FFT Method – Static Force of 50 Pounds.

Comparing the eigenvector based methods (MUSIC and Eigenvector), both of these methods are frequency estimator techniques based on eigenanalysis of the autocorrelation matrix where the resulting estimate has sharp peaks at the frequencies of interest. The eigenvector method uses inverse eigenvector weighting whereas the MUSIC method uses unity weighting, implying that the eigenvector method gives fewer spurious peaks than the MUSIC algorithm [39]. As seen from the dynamic experiment results, the MUSIC method provides for a better spacing between the segment based PSDs compared to the Burg and eigenvector method. From static experiments, we conclude that all three (MUSIC, Burg, and Eigenvector) methods perform similarly if a linear relationship of the fatigue progression is desired.

## V. CONCLUSION AND FUTURE WORK

This research characterizes muscle fatigue using a PSD representation of different segments of sEMG data. Classical (fast Fourier transform and Welch's averaged modified periodogram), model-based (Y-W, Burg, Cov., and Mcov. autoregressive (AR) method) and eigenvector based methods (MUSIC and EIG. spectral estimation method) are used to compute the PSDs. Classical and eigenvector based methods are more sensitive than the model-based methods for analyzing the fatigue related changes in sEMG signal. However, the MUSIC algorithm provides good maximum value in the PSD as well as a clear distinction between the segmented sEMG data. The latter point is indicative of a relative linear fatigue progression in time for the same case when the MUSIC algorithm is utilized. In the future work these results can be used to design and improve the skeletal muscle 'Force-sEMG-Fatigue' based models [40] for prosthetic design and other rehabilitation research.

## ACKNOWLEDGMENT

This research was sponsored by the US Department of the Army, under the award number W81XWH-10-1-0128 awarded and administered by the U.S. Army Medical Research Acquisition Activity, 820 Chandler Street, Fort Detrick MD 21702-5014. The information does not necessarily reflect the position or the policy of the Government, and no official endorsement should be inferred. For purposes of this article, information includes news releases, articles, manuscripts, brochures, advertisements, still and motion pictures, speeches, trade association proceedings, etc.

## REFERENCES

- [1] R. Merletti, and P. Parker, "ELECTROMYOGRAPHY: Physiology, Engineering, and Noninvasive Applications," John Wiley & Sons, Inc., Hoboken, New Jersey, 2004, ch. 1.
- [2] Merletti, R., D. Farina, M. Gazzoni, A. Merlo, P. Ossola, and A. Rainoldi, "Surface electromyography: A window on the muscle, a glimpse on the central nervous system," *Europa Medicophysica* 37, 57–68 (2001).
- [3] Wolf, W., "The EMG as a window to the brain: signal processing tools to enhance the view," in I. Gath, and G. Inbar, eds., *Advances in processing and pattern analysis of biological signals*, Plenum Press, New York, 1996, pp. 339–356.
- [4] S. C. Gandevia, 2001. "Spinal and Supraspinal Factors in Human Muscle Fatigue". *Physiological Reviews*, American Physiological Society 81(4), October.
- [5] R. H. Fitts, 1994. "Cellular mechanisms of muscle fatigue". *Physiological Reviews*, American Physiological Society, 74, pp. 49–94.
- [6] B R Bigland-Ritchie, N J Dawson, R S Johansson and O C Lippold, 1986. "Reflex origin for the slowing of motoneuron firing rates in fatigue of human voluntary contractions". *Journal of Physiology*, 379, pp. 451–459.
- [7] Gerdle B, Edstrom M, Rahm M, 1993. "Fatigue in the shoulder muscles during static work at two different torque levels". *Clinical Physiology*, 13(5), pp. 469–482.
- [8] Paavo V. Komi, and Per Tesch, 1979. "EMG frequency spectrum, muscle structure, and fatigue during dynamic contractions in man". *European Journal of Applied Physiology*, 42(1), pp. 41–50.
- [9] M. Hagberg, 1981. "Muscular endurance and surface electromyogram in isometric and dynamic exercise". *Journal of Applied Physiology*, 51, pp. 1–7.
- [10] M. Hagberg, 1981. "Electromyographic signs of shoulder muscular fatigue in two elevated arm positions". *American Journal of Physical Medicine*, 60(3), pp. 111–121.
- [11] Enoka RM, 1995. "Morphological features and activation patterns of motor units". *Journal of Clinical Neurophysiology*, 12(6), pp. 538–559.
- [12] L. G. Christova, A. S. Alexabdrov, and B. A. Ishpekova, 1999. "Single motor unit activity pattern in patients with Schwartz-Jampel syndrome". *Journal of Neurology, Neurosurgery and Psychiatry*, 66(2), pp. 252–253.
- [13] Björn Gerdle, Jessica Elert, and Karin Henriksson-Larsén, 1989. "Muscular fatigue during repeated isokinetic shoulder forward flexions in young females". *European Journal of Applied Physiology*, 58(6), pp. 666–673.
- [14] Paula M. Ludewig, and Thomas M. Cook, 1996. "The effect of head position on scapular orientation and muscle activity during shoulder elevation". *Journal of Occupational Rehabilitation*, 6(3), pp. 147–158.
- [15] Merletti R, and Lo Conte LR, 1997. "Surface EMG signal processing during isometric contractions". *Journal of Electromyography and Kinesiology*, 7(4), pp. 241–250.
- [16] T. Moritani, M. Muro and A. Nagata, 1986. "Intramuscular and surface electromyogram changes during muscle fatigue". *Journal of Applied Physiology*, 60(4), pp. 1179–1185.
- [17] J. Bruce Moseley, Frank W. Jobe, Marilyn Pink, Jacquelin Perry, and James Tibone, 1992. "EMG analysis of the scapular muscles during a shoulder rehabilitation program". *The American Journal of Sports Medicine*, 20(2), pp. 128–134.
- [18] D. David Ebaugh, Philip W. McClure, and Andrew R. Karduna, 2006. "Effects of shoulder muscle fatigue caused by repetitive overhead activities on scapulothoracic and glenohumeral kinematics". *Journal of Electromyography and Kinesiology*, 16, pp. 224–235.
- [19] McQuade KJ, Dawson J, and Smidt GL, 1998. "Scapulothoracic muscle fatigue associated with alterations in scapulohumeral rhythm kinematics during maximum resistive shoulder elevation". *The Journal of Orthopedic and Sports Physical Therapy*, 28(2), pp. 74–80.
- [20] L. Lindstrom, R. Kadefors and I. Petersen, 1977. "An electromyographic index for localized muscle fatigue". *Journal of Applied Physiology*, American Physiological Society, 43(4), pp. 750–754.
- [21] Weytjens JLF, and van Steenberghe D, 1984. "The effects of motor unit synchronization on the power spectrum of the electromyogram". *Biol Cybern*, 51, pp. 71–77.
- [22] Finsterer J., 2001. "EMG-interference pattern analysis". *J Electromyogr Kinesiol*, 11, pp. 231–246.
- [23] C.J. De Luca, 1984. "Myoelectrical manifestations of localized muscular fatigue in humans". *Crit. Rev. Biomed. Eng.*, 11 (4), pp. 251–279.
- [24] B. Maton, and D. Gamet, 1989. "The fatigability of two agonistic muscles in human isometric voluntary sub maximal contraction: an EMG study. II Motor unit firing rate and recruitment". *Eur. J. Appl. Physiol.*, 58, pp. 369–374.
- [25] A. Luttmann, M. Ja'ger, J. So'keland, and W. Laurig, 1996. "Electromyographical study on surgeons in urology, Part II: Determination of muscular fatigue". *Ergonomics*, 39, pp. 298–313.
- [26] K. J. Bennie, V.M. Ciriello, P.W. Johnson, and J.T. Dennerlein, 2002. "Electromyographic activity of the human extensor carpi ulnaris muscle changes with exposure to repetitive ulnar deviation". *Eur. J. Appl. Physiol.*, 88, pp. 5–12.
- [27] J. S. Petrofsky, 1979. "Frequency and amplitude analysis of the EMG during exercise on the bicycle ergometer". *Eur. J. Appl. Physiol.*, 41, pp. 1–15.
- [28] Basmajian JV, and DeLuca CJ., 1985. *Muscle alive: their functions reviewed by electromyography*. Williams & Wilkins, Baltimore.
- [29] H. Westerblad, J. A. Lee, J. Lannergren and D. G. Allen, 1991. "Cellular mechanisms of fatigue in skeletal muscle". *AJP - Cell Physiology*, American Physiological Society, 261(2), pp. C195–C209.
- [30] D. G. Allen and H. Westerblad, 2001. "Role of phosphate and calcium stores in muscle fatigue". *Journal of Physiology*, 536.3, pp. 657–665.
- [31] Haken Westerblad, David G. Allen, and Jan Lannergren, 2002. "Muscle Fatigue: Lactic Acid or Inorganic Phosphate the Major Cause?". *News in Physiological Sciences*, The American Physiological Society 17(1), February, pp. 17–21.
- [32] P. Zhou, N. L. Suresh, M. M. Lowery, and W. Z. Rymer, "Nonlinear Spatial Filtering of Multichannel Surface Electromyogram Signals During Low Force Contractions," *IEEE Transactions on Biomedical Engineering*, Vol. 56, No. 7, pp. 1871–1879, July 2009.
- [33] Standards for Reporting EMG data. *Journal of Electromyography and Kinesiology*, February 1999; 9(1): III–IV.
- [34] J. H. Semmlow, "Biosignal and Biomedical Image Processing: MATLAB-Based Applications," Marcel Dekker, Inc., New York, 2004, Ch. 3., pp. 79–162.
- [35] Hubbard B. B., "The World According to Wavelets," 2nd ed., A.K. Peters, Ltd., Natick, MA, 1998.
- [36] "Signal Processing Toolbox™ User's Guide," The MathWorks, Inc., 2010.
- [37] Marple, S.L. *Digital Spectral Analysis*, Englewood Cliffs, NJ, Prentice-Hall, 1987, pp. 373–378.
- [38] Schmidt, R.O., "Multiple Emitter Location and Signal Parameter Estimation," *IEEE® Trans. Antennas Propagation*, Vol. AP-34 (March 1986), pp. 276–280.
- [39] Johnson, D. H. and Dudgeon, D. E., "Array Signal Processing: Concepts and Techniques," Prentice-Hall, Englewood Cliffs, NJ, 1993.
- [40] P. Kumar, A. Sebastian, C. Potluri, A. Urfer, D. S. Naidu, and M. P. Schoen, "Towards Smart Prosthetic Hand: Adaptive Probability Based Skeletal Muscle Fatigue Model," 32nd Annual International Conference of the IEEE Engineering in Medicine and Biology Society, Buenos Aires, Argentina, Aug. 31 – Sept. 4, 2010.

# A Hybrid Adaptive Multi Sensor Data Fusion for Estimation of Skeletal Muscle Force for Prosthetic Hand Control

Parmod Kumar, Chandrasekhar Potluri, Anish Sebastian, Yimesker Yihun, Adnan Ilyas, Madhavi Anugolu, Rohit Sharma, Steve Chiu, Jim Creelman, Alex Urfer, D. Subbaram Naidu, *Fellow IEEE*, and Marco P. Schoen, *Senior Member IEEE*

**Abstract** – *Effective use of upper extremity prostheses depends on the two critical aspects of precise position and force control. Surface electromyographic (sEMG) signals can be used as a control input for the position and force actions related to the prosthesis. In this paper, we use the measured sEMG signals to estimate skeletal muscle force. Further, we consider skeletal muscle as a system and System Identification (SI) is used to model multi-sensor sEMG and skeletal muscle force. The sEMG signals are filtered utilizing optimized nonlinear Half-Gaussian Bayesian filter, and a Chebyshev type-II filter provides the muscle force signal. The filter optimization is accomplished using a Genetic Algorithm (GA). Multi-linear and nonlinear models are obtained with sEMG data as input and skeletal muscle force of a healthy human hand as an output for three sensors. The outputs of these models for three sensors are fused with a probabilistic Kullback Information Criterion (KIC) for model selection and an adaptive probability of KIC. The final fusion based force for multi-sensor sEMG gives improved estimate of the skeletal muscle force.*

**Keywords:** *sEMG, SI, GA, KIC*

## I. INTRODUCTION

In the last decade there have been active research efforts in the field of prosthetics. According to [1] the United States has 1.7 million of amputees and this figure is on the rise since 2003 due to the wars in Afghanistan and Iraq [2].

Manuscript received March 31, 2011. This work was supported in part by the US Department of the Army, under the award number W81XWH-10-1-0128.

Parmod Kumar is with Measurement and Control Engineering Research Center (MCERC), School of Engineering, Idaho State University, Pocatello, Idaho 83209, USA (email: kumaparm@isu.edu).

Chandrasekhar Potluri, Anish Sebastian, Yimesker Yihun, Adnan Ilyas, Madhavi Anugolu, and Rohit Sharma are with MCERC, School of Engineering, Idaho State University, Pocatello, Idaho 83209, USA (e-mail: potlchan@isu.edu, sebaanis@isu.edu, yihuyime@isu.edu, ilyaadna@isu.edu, anugmadh@isu.edu, sharrohi@isu.edu).

Steve Chiu is with Department of Electrical Engineering and Computer Science, MCERC, Idaho State University, Pocatello, Idaho 83201 USA (email: chiustev@isu.edu).

Jim Creelman and Alex Urfer are with Department of Physical and Occupational Therapy, Idaho State University, Pocatello, Idaho 83209, USA (email: creejame@isu.edu, urfealex@isu.edu).

D. Subbaram Naidu is with Department of Electrical Engineering and Computer Science, MCERC, Idaho State University, Pocatello, Idaho 83201 USA (email: naiduds@isu.edu).

Marco P. Schoen is with Department of Mechanical Engineering, MCERC, Idaho State University, Pocatello, Idaho 83209, USA (email: schomarc@isu.edu).

Individuals with upper extremity amputations not only have a reduction in function, but also struggle with numerous psychological issues which may further complicate the appropriate control and use of the prosthesis. Previous research on the prosthetic hand design was mainly based on the electromyography (EMG) signals [3-4]. The EMG signal recorded at the surface of the limb is known as surface EMG (sEMG). The sEMG is an electric voltage ranging between -5 and +5 mV, which reflects the electrical activity associated with voluntary muscle contraction and which has been used to control the position and force of the hand prosthesis [5-6]. The skeletal muscle force and the sEMG signals are related and higher sEMG amplitude generally correlates with greater force production. However, there are various other factors that affect this relationship. The sEMG signals are random, complex and dynamic in nature because of varying motor unit recruitment, crosstalk, and biochemical interaction within the muscular fibers. Hence all these factors contribute towards the nonlinear relationship between the two.

Since sEMG is the control input for the prosthesis, precise control and correct interpretation of the measured sEMG signal is important. In previous works, the authors have published similar work using multi sensor data fusion and Output Error (OE) model and modal transformation [7], and multi sensor data fusion using nonlinear models [8].

The present work is an extension of our previous work [9] where we proposed estimation of the skeletal muscle force using an adaptive data fusion algorithm with hybrid multi linear and nonlinear models. In [9] the sEMG data was based only from measuring the motor point sEMG signal, whereas in the present work we extend this to three sensors for the ring finger of the dominant hand of a healthy male subject. Figure 1 presents the flow chart of the work done in this paper. The sEMG signals are acquired from the forearm of a healthy subject and filtered utilizing Genetic Algorithm (GA) based optimized nonlinear Half-Gaussian Bayesian filter. On the other hand, the skeletal muscle force signal is filtered using a Chebyshev type-II filter. The sEMG is considered as input whereas force signal is considered as an output. Since each model captures the dynamics differently, we obtained multiple linear and nonlinear models using System Identification (SI) for the sEMG data corresponding to the three sensors. First, the outputs of all the linear and nonlinear models from the three sensors are fused separately and then



the resultant three outputs are fused with a probabilistic Kullback Information Criterion (KIC) for model selection and an adaptive probability of KIC. The final fused output using this approach gives improved skeletal muscle force estimates.

The paper is organized as follows, the present section covers the introduction and literature work, which is followed by the description of the experimental set-up and pre-processing, then system identification and linear and nonlinear modeling is discussed, followed by the data fusion algorithm. The paper is concluded by a section with, results and discussions, and followed by the conclusions and future work.

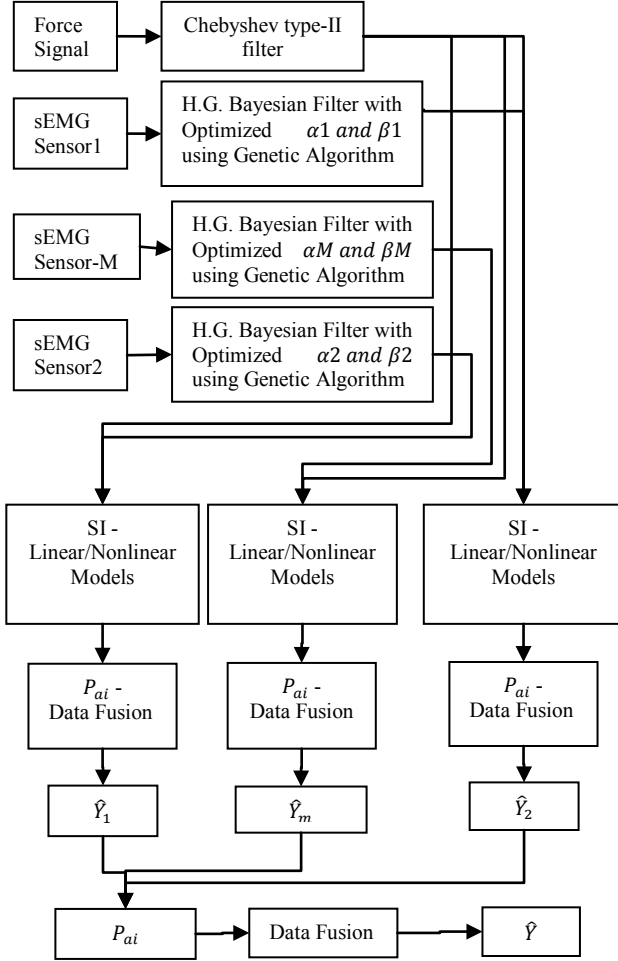


Figure 1. Flow chart for estimation of skeletal muscle force using an adaptive data fusion algorithm.

## II. EXPERIMENTAL SET-UP AND PRE-PROCESSING

The sEMG and skeletal muscle force signals are acquired using LabVIEW™ 8.2 simultaneously at a sampling rate of 2000 Hz. A DELSYS® Bagnoli-16 EMG system with DE-2.1 differential EMG sensors is used for sEMG data capturing. However, the corresponding force data was captured using NI ELVIS with Interlink Electronics FSR 0.5" circular force sensor. The experimental set-up is shown in Figure 2. One

sEMG sensor was placed on the motor point of the ring finger and two adjacent to the motor point of a healthy subject. Skin surface on the forearm of the subject was prepared with the International Society of Electrophysiology and Kinesiology (ISEK) protocol prior to placing sEMG sensors.

The nonlinear Bayesian filter yields good sEMG data and significantly reduces the influence of noise and it also extracts a signal that best describes the EMG signals and may permit effective use in prosthetic control [10]. The sEMG signal can be modeled with the assumption that the conditional probability of the rectified EMG signal is a filtered random process with random rate. The "Half-Gaussian measurement model" for the rectified EMG signal is given by Equation (1), [10].

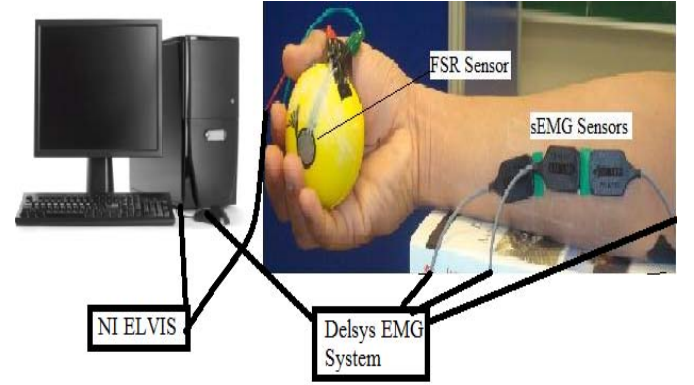


Figure 2. Experimental Set-Up.

$$P(emg|x) = 2 * \exp\left(-\frac{emg^2}{2 * x^2}\right) / (2 * \pi * x^2)^{1/2}. \quad (1)$$

The likelihood function for the rate evolving in time is given by the Fokker–Planck partial differential equation, where the two free parameters in the signal are the expected rate of gradual drift,  $\alpha$  and the expected rate of sudden shifts  $\beta$  [10]. The two free parameters of the sEMG signal are optimized using an elitism based GA. On the other hand the skeletal muscle force signal is filtered with a Chebyshev type II low pass filter.

## III. SYSTEM IDENTIFICATION – LINEAR AND NONLINEAR MODELING

A system can be modeled either by using physics based mathematical models or by System Identification (SI) [11]. Parametric SI gives a dynamic model such as the Auto Regressive with eXogenous input (ARX) or Output Error (OE) of the system in mathematical form. In this research, we use the SI approach to model the two signals. The sEMG is the input to the system and the intended finger/hand force is output. In this work, mutli- linear and nonlinear models are obtained for modeling of sEMG and hand/finger force signals for three sensors for the ring finger of the dominant hand of a healthy subject. Six linear and three nonlinear models are obtained for the motor point sEMG signal, three linear and five nonlinear models are obtained for the ring1 sensor, and six linear and five nonlinear models are obtained for ring2

sensor data. Table I and II gives the structures of linear and nonlinear models respectively.

The model order of the various models used in this work are as follows: linear models for the motor point data, OE model of order 6, ARX model of order 6, ARMAX model of model order 5, Box-Jenkins (BJ) model of order 18, State-Space model with subspace method (N4SID) of order 12 and a State-Space model with prediction error/maximum likelihood method (PEM) of order 12 are obtained using SI. For ring1 sensor (sensor adjacent to the motor point sensor) data OE model of order 17, ARMAX model of order 35 and BJ model of order 11 are obtained. For ring2 sensor (sensor on opposite side of ring1 sensor) data OE model of order 45, ARX model of order 12, ARMAX model of order 17, BJ model of order 14, N4SID model of order 13 and PEM model of order 22 are obtained. Table I gives the structure of all the linear models. In table I  $y$  is output,  $t$  is time,  $B(q)$ ,  $F(q)$ ,  $A(q)$ ,  $C(q)$ ,  $D(q)$ , are polynomials,  $q$  is a backward shift operator,  $u$  is input,  $n_k$  is delay and  $e$  is error [12]. For State-Space models:-  $x$  is state,  $t$  is time,  $T_s$  is sampling time,  $u$  is input,  $e$  is error,  $A, B, K, C$ , and  $D$  are system matrices, and  $y$  is output [12].

TABLE I  
LINEAR MODELS AND THEIR STRUCTURES

Linear Model Name	Linear Model Structure
Output Error	$y(t) = \frac{B(q)}{F(q)}u(t - n_k) + e(t)$
ARX	$A(q)y(t) = B(q)u(t - n_k) + e(t)$
ARMAX	$A(q)y(t) = B(q)u(t - n_k) + C(q)e(t)$
Box-Jenkins	$y(t) = \frac{B(q)}{F(q)}u(t - n_k) + \frac{C(q)}{D(q)}e(t)$
State-Space – subspace method	$\begin{aligned} x(t + Ts) &= Ax(t) + Bu(t) + Ke(t) \\ y(t) &= Cx(t) + Du(t) + e(t) \end{aligned}$
State-Space – prediction error/maximum likelihood method	$\begin{aligned} x(t + Ts) &= Ax(t) + Bu(t) + Ke(t) \\ y(t) &= Cx(t) + Du(t) + e(t) \end{aligned}$

Table II gives the structures of nonlinear models. The nonlinear models for the motor point data are obtained as, the nonlinear ARX with a sigmoidnet nonlinearity estimator, nonlinear Wiener-Hammerstein models with a piecewise linear nonlinearity estimator, and a saturation based estimator. For each ring1 and ring2 signal data sets, five nonlinear Wiener-Hammerstein models with nonlinearity estimators as ‘piecewise linear – pwlinear,’ ‘sigmoidnet,’ ‘saturation,’ ‘deadzone,’ and wavelet network’ are obtained.

In table II  $f$  is a nonlinear function for the nonlinear ARX model. Inputs to  $f$  are model regressors.  $y_p(t)$  is the

predicted output as a weighted sum of past output values and current and past input values. For the nonlinear Hammerstein-Wiener model  $u(t)$  and  $y(t)$  are the inputs and outputs for the system, respectively.  $f$  and  $h$  are nonlinear functions that corresponds to the input and output nonlinearity, respectively.  $w(t)$  and  $x(t)$  are internal variables.  $w(t)$  has the same dimension as  $u(t)$ .  $x(t)$  has the same dimension as  $y(t)$ .  $B(q)$  and  $F(q)$  in the linear dynamic block are polynomials in the backward shift operator. For nonlinear Hammerstein-Wiener model with deadzone nonlinearity estimator,  $F$  is a nonlinear function of  $x$  with the properties given in the table II. For nonlinear Hammerstein-Wiener model with wavelet network as nonlinearity estimator,  $\kappa(s)$  as a wavelet function, and  $\beta_k$  is a row vector such that  $\beta_k(x - \gamma_k)$  is a scalar. If only the input nonlinearity is present, the model is called the Hammerstein model. If only the output nonlinearity is present, the model is called the Wiener model [12].

TABLE II  
NONLINEAR MODELS AND THEIR STRUCTURES

Nonlinear Model Name	Nonlinear Model Structure
Nonlinear ARX – Sigmoidnet	$y_p(t) = f(y(t-1), y(t-2), y(t-3), \dots, u(t-1), u(t-2), \dots);$ $f(z) = \frac{1}{e^{-z} + 1} \text{ is sigmoid function.}$
Nonlinear HW – Piecewise Linear – pwlinear	$w(t) = f(u(t)),$ $x(t) = \frac{B_{ji}(q)}{F_{ji}(q)}w(t),$ $y(t) = h(x(t));$
Nonlinear HW – Sigmoidnet	$y_p(t) = f(y(t-1), y(t-2), y(t-3), \dots, u(t-1), u(t-2), \dots);$ $f(z) = \frac{1}{e^{-z} + 1} \text{ is sigmoid function.}$
Nonlinear HW – Saturation	$w(t) = f(u(t)),$ $x(t) = \frac{B_{ji}(q)}{F_{ji}(q)}w(t),$ $y(t) = h(x(t));$
Nonlinear HW – Deadzone	$y = F(x);$ $a \leq x < b, \quad F(x) = 0$ $x < a, \quad F(x) = x - a$ $x \geq b, \quad F(x) = x - b$
Nonlinear HW – Wavelet Network	$g(x) = \sum_{k=1}^n \alpha_k \kappa(\beta_k(x - \gamma_k))$

#### IV. DATA FUSION ALGORITHM

A data fusion algorithm with an adaptive probability of the Kullback information criterion (KIC) is used to fuse the outputs of different models obtained [13]. Kullback information criterion (KIC) is an asymmetric measure for the model selection. Kullback’s symmetric or J-divergence is the

sum of two directed divergences, which is the measure of the models dissimilarity and given by Equation (2), [14].

$$KIC(p_i) = \frac{n}{2} \log R_i + \frac{(p_i+1)n}{n-p_i-2} - n\psi\left(\frac{n-p_i}{2}\right) + g(n), \quad (2)$$

where  $g(n) = n * \log(n/2)$ .

In this research work, we are obtaining multi- linear and nonlinear models using SI for the sEMG sensor for the ring finger motor unit, and two adjacently placed sensors, ring1 and ring2. The probability of each model is computed using the SI model fit value, which is given by  $[1 - |Y - \hat{Y}|/|Y - \bar{Y}|] * 100$ . The fusion of outputs and adaptive KIC probability is shown in Figure 3 which is followed by the data fusion algorithm.

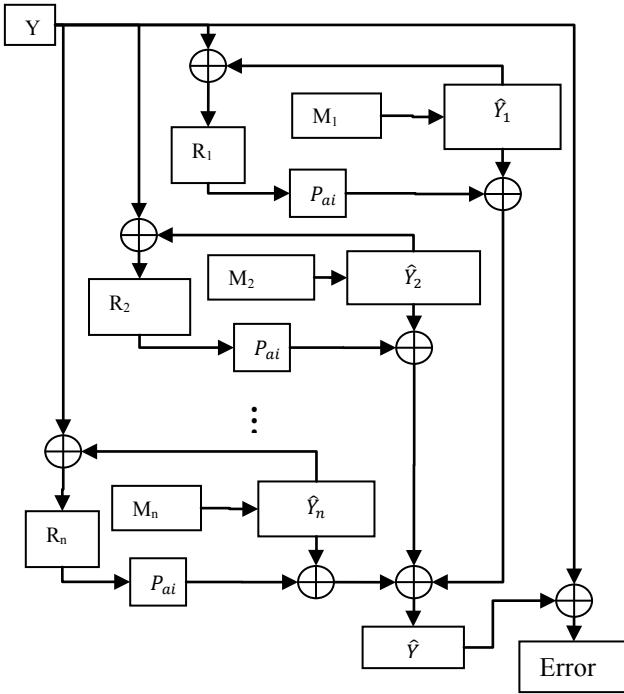


Figure 3. Adaptive KIC Probability Based Data Fusion.

The following fusion algorithm as given by [13] is applied for data fusion of the outputs of different linear and nonlinear models:

- 1) Identify models  $M_1, M_2, \dots, M_k$  using sEMG data ( $u$ ) as input and force data ( $Y$ ) as output, for  $k$  number of sensors collecting data simultaneously.
- 2) Compute the residual square norm

$R_i = \|Y - \Phi_i \hat{\Theta}_i\|^2 = \|Y - \hat{Y}\|$ , where  $\hat{\Theta}_i = \{\Phi_i^T \Phi_i\}^{-1} \Phi_i^T Y$ , and

$$\Phi = \begin{bmatrix} Y_p^T & u_p^T & Y_{p-1}^T & \dots & u_1^T \\ Y_{p+1}^T & u_{p+1}^T & Y_p^T & \dots & u_2^T \\ \vdots & \vdots & \vdots & \ddots & \vdots \\ Y_{n-1}^T & u_{n-1}^T & Y_{n-2}^T & \dots & u_{n-p}^T \end{bmatrix}$$

- 3) Calculate the model criteria coefficient using Equation (2).
- 4) Compute the model probability  $p(M_i|Z) = \frac{e^{-l_i}}{\sum_{j=1}^k e^{-l_j}}$ , where  $l$  is model selection criterion, i.e.  $KIC(p_i)$ .
- 5) Compute the fused model output  $\hat{Y}_f = \sum_{i=1}^k p(M_i|Z) \hat{Y}_i$ .
- 6) Compute the overall model from  $\hat{Y}_f$  and force data.

Here all the computation from step 2) to 6) is adaptive i.e. the residual square norm,  $KIC(p_i)$ , model probability  $p(M_i|Z)$ , and fused model output  $\hat{Y}_f$  are being updated with time or for each data point.

## V. RESULTS AND DISCUSSION

An adaptive KIC probability based data fusion algorithm is applied to linear and nonlinear models separately for the models obtained using three sets of input and output data for three sEMG sensors. First the fusion based output for each sensor is obtained and then the three fusion based outputs from three sEMG sensors are fused to get the improved estimates of the skeletal muscle force. The following plots show the improvement in the force estimates in succession with different sensors separately and then combined. All the plots have the measured skeletal muscle force signal in green and the estimated force signal in red color. Figure 4 is a plot of measured and Chebyshev type II filtered finger force data with the adaptive KIC probability fusion based force for the first sensor named as ring1. The two signals are very clear and the estimated signal shows good follow up of the measured signal. Figure 5 shows the measured and Chebyshev type II filtered skeletal muscle force with the adaptive KIC probability fusion based force signals for the second sensor named as ring2. It is evident that the measured signal has a very close follow up by the estimated signal.

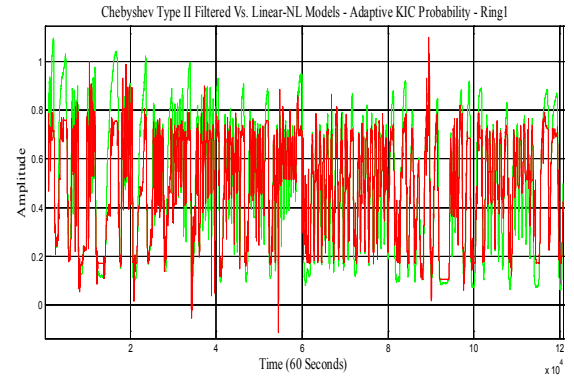


Figure 4. Chebyshev Type II vs. Adaptive KIC Probability Based Force from Linear and Nonlinear Models for Ring1 Sensor.

Figure 6 shows the measured and Chebyshev type II filtered skeletal muscle force with the adaptive KIC probability fusion based force signals for third sensor placed on the motor point of ring finger. The results for this sensor are best among the three based of the used three sensor data and it is evident that the measured signal has a very close follow up by the estimated signal.



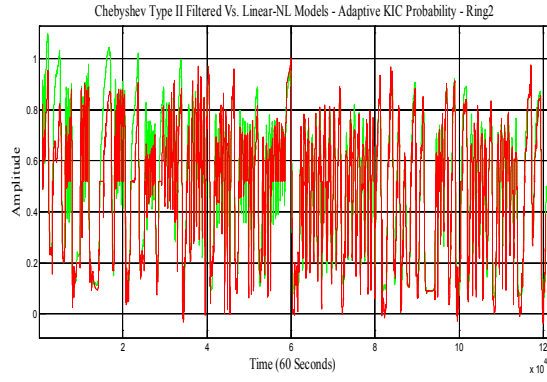


Figure 5. Chebyshev Type II vs. Adaptive KIC Probability Based Force from Linear and Nonlinear Models for Ring2 Sensor.

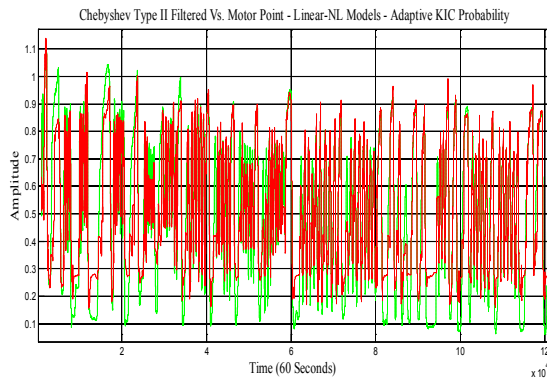


Figure 6. Chebyshev Type II vs. Adaptive KIC Probability Based Force from Linear and Nonlinear Models for Motor Point Sensor.

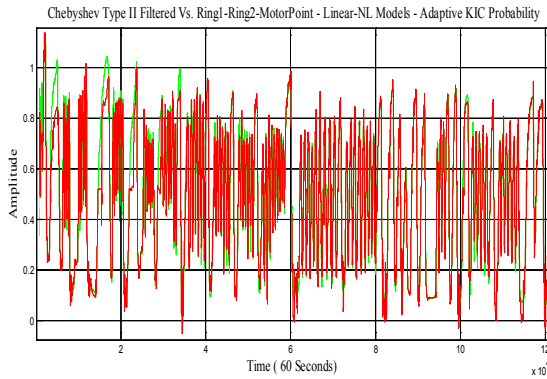


Figure 7. Chebyshev Type II vs. Adaptive KIC Probability Based Force from Linear and Nonlinear Models for Ring1, Ring2 and Motor Point Sensor Combined.

Finally the estimated skeletal muscle force from three sEMG sensors is further fused with adaptive KIC probability based data fusion algorithm. Figure 7 shows the comparison of the measured and Chebyshev type II filter with the final adaptive KIC probability based fusion skeletal muscle force

estimate using three sEMG sensors. The final result for three sensors is the best estimate of skeletal muscle force and it is evident that the measured signal has a very close follow up by the estimated signal.

The results show that there is a decrease in the percentage error from the linear and nonlinear model fusion based separate outputs to the fusion based combined output of linear and nonlinear models combined for all three sensors. However, these results show that there is a 16% improvement in the mean fit value of the motor point signal models with the adaptive KIC probability based data fusion algorithm for multi-sensors (three in this case). Figure 8 and 9 show the validation plots of this approach for two separate sets of sEMG and skeletal muscle force data where green signal is the Chebyshev type II filtered measured force signal and the blue signal is estimated using this approach.

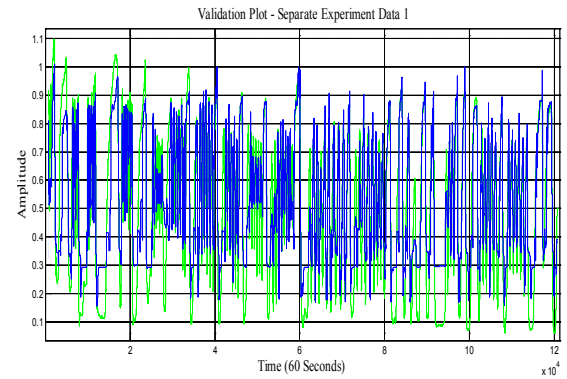


Figure 8. Validation Plot 1 - Chebyshev Type II vs. Estimated Force Signal using Adaptive KIC Probability.

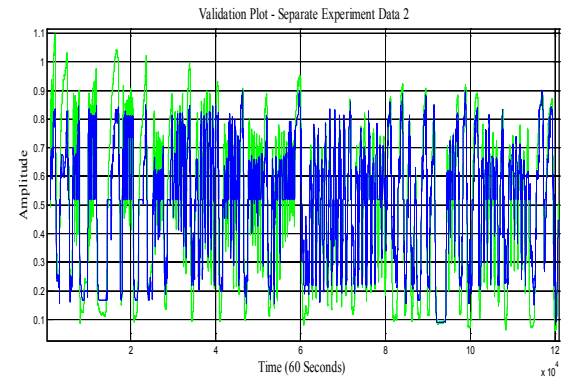


Figure 9. Validation Plot 2 - Chebyshev Type II vs. Estimated Force Signal using Adaptive KIC Probability.

## VI. CONCLUSION AND FUTURE WORK

Different linear and nonlinear models are obtained using system identification (SI) for three sets of data. Linear and nonlinear models' outputs are fused separately for each sensor and then fused together to get the final force estimate for each sensor. The net force estimates for each sensor is then applied with adaptive KIC probability based data fusion algorithm.

The final estimates of the skeletal muscle force gives improved results. Future work will focus on the improved data collection techniques and capturing data at higher sampling rate (6000 samples per second). Also, we would design new model selection criteria using different model selection criteria such as Akaike Information Criterion (AIC), Kullback Information Criterion (KIC) and the Bayesian Information Criterion (BIC).

#### ACKNOWLEDGMENT

This research was sponsored by the US Department of the Army, under the award number W81XWH-10-1-0128 awarded and administered by the U.S. Army Medical Research Acquisition Activity, 820 Chandler Street, Fort Detrick MD 21702-5014. The information does not necessarily reflect the position or the policy of the Government, and no official endorsement should be inferred. For purposes of this article, information includes news releases, articles, manuscripts, brochures, advertisements, still and motion pictures, speeches, trade association proceedings, etc.

#### REFERENCES

- [1] Kathryn Ziegler-Graham, PhD, et al., Estimating the Prevalence of Limb Loss in the United States - 2005 to 2050, *Archives of Physical Medicine and Rehabilitation*, 89 (2008): 422-429.
- [2] O'Connor, P., Iraq war vet decides to have second leg amputated, *Columbia Missourian*, 2009.
- [3] N. Dechev, W. L. Cleghorn, and S. Naumann, Multiple finger, passive adaptive grasp prosthetic hand, *Mechanism and Machine Theory* 36(2001), pp. 1157-1173.
- [4] Haruhisa Kawasaki, Tsuneo Komatsu, and Kazunao Uchiyama, Dexterous Anthropomorphic Robot Hand With Distributed Tactile Sensor: Gifu Hand II, *IEEE/ASME Transactions on Mechatronics*, Vol. 7, No. 3, September 2002, pp. 296-303.
- [5] M. Zecca, S. Micera, M. C. Carrozza, and P. Dario, Control of Multifunctional Prosthetic Hands by Processing the Electromyographic Signal, *Critical Reviews™ in Biomedical Engineering*, 30(4-6), 2002, pp. 459-485.
- [6] Claudio Castellini and Patrick van der Smagt, Surface EMG in advanced hand prosthetics, *Biological Cybernetics*, (2009) 100, pp. 35-47.
- [7] P. Kumar, A. Sebastian, C. Potluri, A. Urfer, D. S. Naidu, and M. P. Schoen, "Towards Smart Prosthetic Hand: Adaptive Probability Based Skeletal Muscle Fatigue Model," 32nd Annual International Conference of the IEEE EMBS Conference, 2010.
- [8] P. Kumar, C. Potluri, A. Sebastian, S. Chiu, A. Urfer, D. S. Naidu, and M. P. Schoen, "An Adaptive Multi Sensor Data Fusion with Hybrid Nonlinear ARX and Wiener-Hammerstein Models for Skeletal Muscle Force Estimation," 14th WSEAS Int. Conf. on Systems, Vol. 1, pp. 186-191, July 2010.
- [9] P. Kumar, C. Potluri, M. Anugolu, A. Sebastian, J. Creelman, A. Urfer, S. Chiu, D. S. Naidu, and M. P. Schoen, "A Hybrid Adaptive Data Fusion with Linear and Nonlinear Models for Skeletal Muscle Force Estimation," 5th Cairo International Conference on Biomedical Engineering, Cairo, Egypt, Dec. 16-18, 2010.
- [10] Terence D. Sanger, Bayesian Filtering of Myoelectric Signals, *J Neurophysiol*, 97, 2007, pp. 1839-1845.
- [11] Lennart Ljung, *System Identification: Theory for the User*. 2nd edition, Prentice Hall PTR, 1999, Chap. 1, pp. 1-15.
- [12] Lennart Ljung, *System Identification Toolbox™ 7 User's Guide*, The MathWorks, Inc., 2010.
- [13] H. Chen and S. Huang, "A Comparative study on Model Selection and Multiple Model Fusion," 7th International Conference on Information Fusion, pp. 820-826, 2005.
- [14] Abd-Krim Seghouane, M. Bekara, G. Fleury, "A Small Sample Model Selection Criterion Based on Kullback's symmetric Divergence," *IEEE Transaction*, pp. 145-148, 2003.

# Optimized spatial filter mask using genetic algorithm and system identification for modeling sEMG and finger force signals

ANISH SEBASTIAN, PARMOD KUMAR, MARCO P. SCHOEN

Measurement and Control Engineering Research Center (MCERC), Idaho State University  
921 South 8<sup>th</sup> Ave., Stop 8060, Pocatello, Idaho 83209-8060

UNITED STATES OF AMERICA

[schomarc@isu.edu](mailto:schomarc@isu.edu) <http://www.isu.edu/~schomarc/>

**Abstract:** - This paper presents the investigation of the use of System Identification (SI) for modeling sEMG-Finger Force relation in the pursuit of improving the control of prosthetic hands. Finger force and sEMG data is generated by having the subject perform a number of random motions of the ring finger to simulate various force levels. Post-processing of the sEMG signal is performed using spatial filtering. The linear and nonlinear spatial filters are compared based on the 'kurtosis' improvements and also are based on the fit values of the models obtained using system identification. Some of the spatial filter masks are optimized using a Genetic Algorithm (GA) for the constrained and unconstrained cases. The resulting model fit value is utilized to serve as the cost function. The results are compared to the reported filter mask values in the literature. The unconstrained GA based filter mask values and in some instances the constrained GA based mask values performed better than the filter masks reported in literature.

**Key-Words:** - Spatial Filtering, System Identification, Surface Electromyogram, Array Sensor, Genetic Algorithm, Hammerstein-Wiener.

## 1 Introduction

In the United States there are approximately 1.7 million people living with limb loss [1]. It is estimated that one out of every 200 people in the U.S. has had an amputation [2]. An ideal prosthetic hand has to be dexterous; easy to manufacture, must use little power and at the same time, must be of low cost. Building such a prosthetic hand, which can mimic the entire gamut of motions and have the functionality and dexterity of a human hand exactly, has eluded researchers so far. One of the main strategies used in making a prosthetic hand "user friendly" is to use the electromyogram (EMG) signal to control a prosthetic device. An EMG signal is a small voltage signal (in mV) which is generated by skeletal muscles. EMG is measured using fine wire intramuscular electrodes, needle electrodes, or on the surface of the skin over the motor point using surface electrodes. Surface electrodes are quick and easy to apply, do not need medical supervision, cause minimal discomfort and are generally suited for superficial muscles. Needle electrodes on the other hand require trained medical professionals for appropriate placement within the muscle. This paper looks only at surface electromyogram signals (sEMG). In the past, multiple methods have been investigated for extracting useful information from EMG signals. Some of these methods include employing low-pass or band-pass filtering; others have also used notch filtering to remove power line noise, [3]. Whitening filters can increase the quality of the amplitude estimates of the sEMG signals, [4]. Other methods include Markov models, [5] and fuzzy logic control, [6] – for classification of EMG,

and wavelet processing, [7]. Currently, the accepted standardized method on how EMG signals must be recorded and analyzed is set by the International Society of Electromyography and Kinesiology (ISEK) [8]. sEMG signals are influenced by multiple factors, some of which are; a) shape of the volume conductor, b) the thickness of the subcutaneous tissue layers, c) tissue inhomogeneities, d) distribution of the motor unit territories in the muscle, e) size of the motor unit territories, f) distribution and the number of fibers in the motor unit territory, g) length of the fibers, h) spread of the endplates and tendon junctions within the motor units, and i) spread of the innervations zones and tendon regions among motor units. The type of detection system used also plays an important part in influencing the sEMG measurements. Some of the factors which need to be taken into account, with the detection systems, are a) skin electrode contact (impedance, noise), b) spatial filtering for signal detection, c) inter-electrode distance, d) electrode size and shape, and e) inclination of the detection system relative to the muscle fiber orientation, [9].

## 2 Problem Formulation

As multiple factors influence sEMG, it is impossible to account for each of these variables while modeling its relation to the force generated. Also, oversimplification of the problem at hand by neglecting some variables, which is a widely used common assumption, will cast doubt over the usefulness of the results of modeling. Our approach is to assume a black-box model in order to deduce a

suitable relation or model structure for the two signals. Here, the modeling of the sEMG-finger force relation is not based on root-mean-square, or average values of the sEMG signal, hence, we facilitate the capture of the dynamical changes in the force levels. Our approach of using Hammerstein-Wiener models has been found to be of merit in our previous studies [10, 11] to yield satisfactory fits.

### 3 Problem Solution

#### Spatial Filtering

The data collected is from a nine (3x3) sensor array and rather than analyzing the data only at the motor unit, we consider using spatial filters. Spatial filtering is a very attractive choice as it can be used to either amplify the signal at the motor unit or extract useful information from the entire grid. "Spatial filtering" is broadly defined as a method which computes spatial density estimates for events that have been observed at individual locations. These filters are used when there is no a priori curve to fit to a data series. Instead, it relies on nearby or adjacent, values to estimate the value at a given point. The most common spatial filters are the low-pass and high-pass spatial filters. These are focal functions whose operation is determined by a kernel or neighborhood of  $N \times N$  cells around each pixel or grid position [12]. Grid cells "covered" by a kernel are multiplied by the matching kernel entry and then the weighted average is calculated and assigned as the value for the central cell,  $G$ . For example, an asymmetric 3x3 kernel may look like the one shown in Equation (1), or any combination of the weights. Typically  $a, b$  are positive integers. If  $a=b=1$ , then the kernel provides a simple smoothing or averaging operation. Filters of this type are sometimes referred to as low-pass filters.

$$\text{Symmetric Kernel} = \begin{bmatrix} a & a & a \\ a & b & a \\ a & a & a \end{bmatrix} \quad (1)$$

The filtered grid value 'G' of an  $m=N \times N$  kernel matrix, with  $C_i$  set of coefficients and  $P_i$  - set of source grid values, is calculated as;

$$G = \frac{\sum_{i=1}^m C_i P_i}{\sum_{i=1}^m C_i} + B \quad (2)$$

Where,  $B$  is often set to 0.  $B$  is a bias term to increase or decrease the resulting value of 'G'. This kernel is also sometimes referred to as the 'filter mask'. The linear spatial filters tested in this paper are; 1) Longitudinal Single Differential (LSD), 2) Transverse Single Differential (TSD), 3) Longitudinal Double Differential (LDD), 4) Transverse Double Differential (TDD), 5) Normal Double Differential (NDD), 6) Inverse Binomial (IB2) and 7) Inverse Rectangular (IR) Filter. The mask of these filters and the corresponding resultant equations on application of the mask to the grid data obtained from the sEMG array arrangement are given below.

EMG Array Information, **Spatial Filter Mask**

$$\text{LSD} = \begin{bmatrix} sEMG7 & sEMG5 & sEMG6 \\ 0 & 0 & 0 \\ sEMG2 & sEMG1 & sEMG3 \\ -1 & 1 & 0 \\ sEMG8 & sEMG4 & sEMG9 \\ 0 & 0 & 0 \end{bmatrix}$$

Result Equation:  $-sEMG2 + sEMG1$

$$\text{TSD} = \begin{bmatrix} 0 & -1 & 0 \\ 0 & 1 & 0 \\ 0 & 0 & 0 \end{bmatrix}; \text{LDD} = \begin{bmatrix} 0 & 0 & 0 \\ -1 & 2 & -1 \\ 0 & 0 & 0 \end{bmatrix}; \text{TDD} = \begin{bmatrix} 0 & -1 & 0 \\ 0 & 2 & 0 \\ 0 & -1 & 0 \end{bmatrix}$$

LSD Equation =  $sEMG1 - sEMG2$ ; TSD Equation =  $sEMG1 - sEMG5$ ; we can similarly deduce the equations for the other spatial filters.

$$\text{NDD} = \begin{bmatrix} 0 & -1 & 0 \\ -1 & 4 & -1 \\ 0 & -1 & 0 \end{bmatrix}; \text{IB2} = \begin{bmatrix} -1 & -2 & -1 \\ -2 & 12 & -2 \\ -1 & -2 & -1 \end{bmatrix}; \text{IR} = \begin{bmatrix} -1 & -1 & -1 \\ -1 & 8 & -1 \\ -1 & -1 & -1 \end{bmatrix}$$

In this paper, some nonlinear spatial filters have also been discussed, these have been reported in the literature [13], these are 1) 1-D Nonlinear Transverse spatial filter (NLT), 2) 1-D Nonlinear Longitudinal spatial filter (NLL), 3) 2-D Nonlinear spatial filter in Two- Orthogonal Directions (NLTO) and 4) Nonlinear spatial filter in All Four possible Directions (NLAFD). The Nonlinear Spatial Filters use the Teager-Kaiser Energy (TKE) Operator [14]. This technique is a threshold 'energy' based approach where outliers are first detected and then replaced by their estimated values. General Form of Nonlinear Spatial Filter using the Teager-Kaiser (TKE) operator is given in equation (4), where  $x(n)$  denotes the location of the sensor in the grid;

$$\Psi[x(n)] = x^2(n) - x(n+1)x(n-1) \quad (4)$$

a) 1-D Nonlinear Transverse Spatial Filter (NLT); equation (5)

$$\Psi_{d,m}[x(m,n)] = x^2(m,n) - x(m-1,n)x(m+1,n) \quad (5)$$

b) 1-D Nonlinear Longitudinal Spatial Filter (NLL); equation (6)

$$\Psi_{d,n}[x(m,n)] = x^2(m,n) - x(m,n-1)x(m,n+1) \quad (6)$$

c) Nonlinear Spatial Filter in Two Orthogonal Directions (NLTO); equation (7)

$$\begin{aligned} \Psi_{d,2}[x(m,n)] &= \Psi_{d,2m}[x(m,n)] + \Psi_{d,n}[x(m,n)] \\ &= 2x^2(m,n) - x(m-1,n)x(m+1,n) - x(m,n-1)x(m,n+1) \end{aligned} \quad (7)$$

d) Nonlinear Spatial Filter in all Four Directions (NLAFD); equation (8)

$$\begin{aligned} \Psi_{d,4}[x(m,n)] &= 4x^2(m,n) - x(m-1,n)x(m+1,n) \\ &\quad - x(m,n-1)x(m,n+1) - x(m-1,n+1)x(m+1,n-1) \\ &\quad - x(m-1,n-1)x(m+1,n+1) \end{aligned} \quad (8)$$

The experiments were carried out on a healthy male subject. The ring finger motor point was located using a Muscle Stimulator, manufactured by Rich-



Mar Corporation (model number HV 1100). The EMG detection system used was a Delsys, Bagnoli-16 channel EMG (DS-160, S/N-1116). The sensors used for measuring the surface EMG action potentials were three pronged DE 3.1 differential surface electrodes. The material for the contacts of the electrode is 99.9% pure silver, the contacts are 10mm long, 1mm in diameter and spaced 10mm apart. The subjects' skin was prepared, according to the ISEK standards, before the sensors were placed over the motor point. The electrodes were placed along the muscle fibers (Flexor Digitorum Superficialis) for recording surface EMG. The reference electrode was placed on the elbow where there is no sEMG signal. Nine different experiments were conducted and the corresponding sEMG signal was measured simultaneously from all the 9 sensors. The force generated by the subject's fingers, for a given motion, was measured using a stress ball with a force sensitive resistor (FSR) mounted on it. Figure 1 shows the location of the FSR on the stress ball.

### System Identification

Equation 9 describes the Hammerstein-Wiener model structure:

$$w(t) = f(g(t)), \quad b(t) = \frac{B_{j,i}(q)}{F_{j,i}(q)} w(t), \quad y(t) = h(x(t)), \quad (9)$$

where,  $w(t)$  and  $b(t)$  are internal variables,  $w(t)$  has the same dimensions as  $u(t)$  - input, and  $x(t)$  has the same dimensions as  $y(t)$  - output.  $g()$  and  $h()$  are the input and output non-linearity functions respectively.  $B(q)$  and  $F(q)$  are regression polynomials.

Figure 2A and 2B represent the Hammerstein-Wiener models individually and their combination respectively. The model fit values are computed using Equation (10) as follows;

$$fit = 100 * \frac{1 - \|\hat{y} - y\|}{\|y - \hat{y}\|} \quad (10)$$

where,  $\hat{y}$  is the estimated output by the model.

The linear block is specified using the terms  $n_b$  - the number of zeros plus one,  $n_f$  - the number of poles and  $n_k$  - the delay from the input to the output in terms of the number of samples. The commonly used nonlinear estimators for Hammerstein-Wiener model are, a) Dead Zone, b) Piecewise Linear, c) Saturation, d) Sigmoid Network, and e) Wavelet Network, [15].

### Genetic Algorithm (GA)

Genetic Algorithm is a class of evolutionary methods for solving both constrained and unconstrained optimization problems that are based on natural selection.

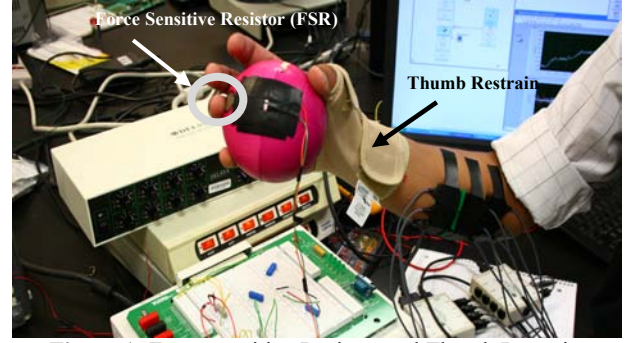


Figure 1: Force sensitive Resistor and Thumb Restrain

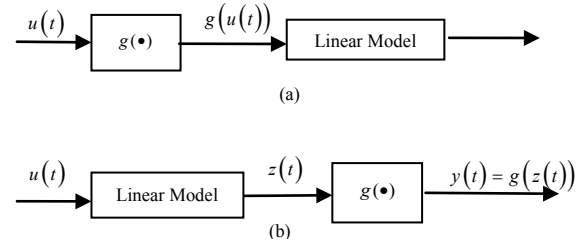


Figure 2A: a) Hammerstein model, b) Wiener model

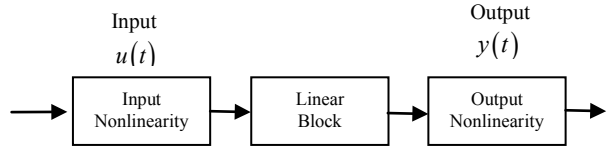
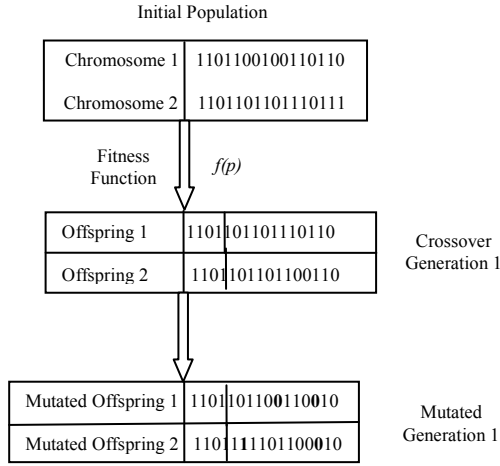


Figure 2B: Hammerstein-Wiener Model Structure

This is the same rule that governs biological systems. In GA, the population of individual solutions is modified repeatedly. A solution is given by a set of parameters (genes) and packaged as a chromosome. Each step or iteration the GA selects individuals (chromosomes) in a fashion that may include some randomness, from a given population, as parents, and uses them to produce offspring for the next generation. Over successive iterations or generations, the population evolves and finally reaches an optimal solution. The steps that make up GA are as follows:

- 1) Generate a random population of ' $p$ ' chromosomes – these chromosomes carry information of the population and are confined in the feasible solution space.
- 2) Evaluate the objective or fitness function  $f(p)$  for each chromosome.
- 3) Create a new population or offspring from the initial population by using certain rules. These rules include a) Selection – selection of two parent chromosomes from the population according to their fitness. b) Crossover – crossover the parents to form new offspring, if no crossover is performed then the offspring is an exact copy of the parents. c) Mutation – involves the changing of a variable in a chromosome or some other change in the original chromosome as defined by the user. d) Acceptance Condition – if offspring satisfies the acceptance condition, include offspring in the new population or else discard. 4) Use the offspring as the parents for the generation of a new population. 5) Continue until the end condition is satisfied. Figure 4 presents

a graphical interpretation of the steps in GA. In this work, GA is used to assist in finding the optimal values of the filter mask for the filtration of the sEMG signal using the various spatial filters. The cost function that the GA tries to minimize, is the model fit obtained from system identification of the sEMG-force data that was collected.



**Figure 4:** General steps in a binary genetic algorithm

## 4 Results

The results of spatially filtered data for the linear and the nonlinear spatial filters were first compared based on the “Kurtosis” criteria, [14]. ‘Kurtosis’ is a measure of whether the data sets are peaked or flat relative to a normal distribution. That is, data sets with high kurtosis tend to have a distinct peak near the mean, decline rather rapidly, and have heavy tails. Data sets with low kurtosis tend to have a flat top near the mean rather than a sharp peak. A uniform distribution would be the extreme case. The mathematical expression for kurtosis is given in Equation 11.

$$Kurt = \frac{E[x^4] - 3(E[x^2])^2}{E[x^2]^2} \quad (11)$$

Figure 5 shows the plot obtained for the various filters based on the kurtosis measure. The y-axis is the kurtosis improvements which is the ratio of the output to the input kurtosis. It is evident from the plot that the NLT, NLL, NLTO and the NLAFFD spatial filters performed very well as compared to the linear spatial filters under investigation. The best kurtosis improvements were obtained for experiment 4  $\approx 44$  for the nonlinear spatial filters. The x-axis in Figure 5 shows the numbers allotted to the various spatial filters investigated. Based on these results we focused our attention to the linear spatial filter masks for experiment 3, which exhibits poor kurtosis values. The filters were compared based on the model fit values obtained from various Hammerstein-Wiener models. The Matlab<sup>R</sup> code for the Hammerstein-Wiener model is: `nlhw(ze, [nb nf nk], ..., ...)`. The modeling was carried out by varying  $n_b$  - the number of zeros plus one,  $n_f$  - the number of poles and  $n_k$  - the delay from input and

output in terms of the number of samples for the various Hammerstein-Wiener models.

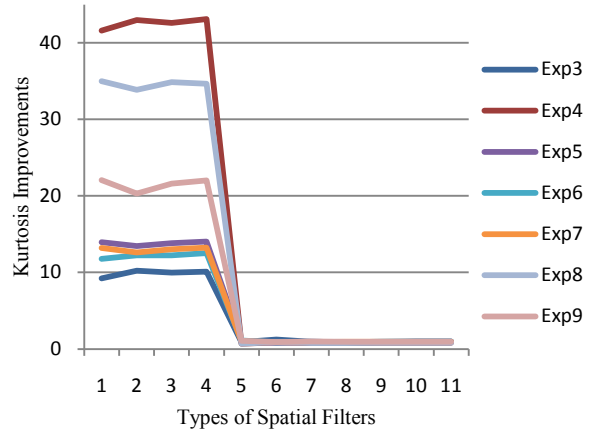


**Figure 5:** Kurtosis plots of various filters for exp3 – y-axis numbers are for the various filters 1-NLT, 2-NLL, 3-NLTO, 4-NLAFFD, 5-LSD, 6-TSD, 7-LDD, 8-TDD, 9-NDD, 10-IB2, 11-IR

In all, 42 models with variations in  $n_a$  and  $n_b$  were tested while the value of  $n_k$  was kept as 1. The total number of models estimated were 7 (filter types) x 4 (time windows) x 42 models per time window = 1,176 models. The time windows used for estimation and validation of the models were called ‘ze’ and ‘zv’ respectively. ‘ze’ contained 8000 sample points and ‘zv’ contained data points shifted by 2000 sample points. For example, if ‘ze’ was a time window between 2-6 seconds i.e. samples 4000-12000, then ‘zv’ was between 3-7 seconds i.e. 6000-14000 samples. These models were computed using the filter masks available in literature. On examining the fit values closely we found them to have large variation from one model order to another. One of the reasons of this could be due to the poor correlation in the estimation and validation data sets, on account of the large variations that were achieved in the force. This paper does not list all these models tested but identifies and reports only the significant results of the analysis. We found that the filters tested performed poorly in the initial time window of 2-7 seconds for experiment 3. Some of the models for this time window were selected and then recomputed using GA to optimize the filter mask with the fitness function being the fit value of an identified model achieved for a given model order. Table 1 shows an example of the fits that were obtained on varying the parameters of the Hammerstein-Wiener model. The highlighted models (and a few other models) were selected randomly to be optimized using GA. We had two scenarios under GA –1) GA Constrained and 2) GA – Unconstrained. The first scenario GA constrained optimized only the mask entry  $a_{22}$  (location of the sEMG sensor on the motor unit). The other entries of the filter mask were then computed from this optimized value. In the second scenario, GA unconstrained we let GA optimize all the entries for

various masks. The GA parameters for optimization were as follows: number of iterations: 50; initial population size Generation 0: 96; population size

Generation 1: 48; Number of Chromosomes kept for mating: 24; and mutation rate was set to 4%.

Model Number	$n_a$	$n_b$	$n_k$	LDD	LSD	TDD	TSD	NDD	IB2	IR
m1	2	3	1	31.06	41.39	39.53	-9.685	45.55	33.79	35.38
m2	2	4	1	31.86	17.4	39.36	43.19	36.84	16.88	23.89
m3	2	5	1	23.54	35.94	30.09	2.247	39.78	36.17	38.16
m4	2	6	1	3.266	41.99	41.28	43.46	10.83	36.41	36.7
m5	2	7	1	31.58	40.55	44.65	31.28	2.593	32.26	36.34
m6	2	8	1	37.84	4.259	21.89	20.08	8.036	36.22	36.57
m7	2	9	1	31.42	-0.1887	35.78	28.71	38.11	35.54	35.82
m8	3	3	1	36.59	40.04	36.17	12.33	4.478	41.09	35.81
m9	3	4	1	20.74	40.72	31.53	36.57	29.76	37.43	38.76
m10	3	5	1	39.87	11.53	39.83	30.24	39.25	35.15	37.9
:	:	:	:	:	:	:	:	:	:	:
m40	7	7	1	34.91	10.18	40.79	35.21	35.24	33.42	37.92
m41	7	8	1	-0.1127	36.28	39.68	40.26	20.27	35.88	24.32
m42	7	9	1	36.55	-0.412	25.24	31.31	35.4	34.26	39.82

**Table 1:** Example of System Identification Results Using Filter Mask from Literature – Highlighted Models Optimized

Longitudinal Double Differential (LDD)				Longitudinal Single Differential (LSD)			
	Fit %				Fit %		
	From Literature	GA Constrained	GA Unconstrained		From Literature	GA Constrained	GA Unconstrained
m1	31.06	42.8291	61.3475	m1	41.39	48.9135	59.8055
m6	37.84	53.3134	33.724	m4	41.99	41.5731	68.4191
m12	35.54	44.2513	51.7942	m8	40.04	40.5924	63.8523
m31	39.44	47.0034	60.6489	m9	40.72	45.2322	56.5113

Transverse Double Differential (TDD)				Transverse Single Differential (TSD)			
	Fit %				Fit %		
	From Literature	GA Constrained	GA Unconstrained		From Literature	GA Constrained	GA Unconstrained
m1	39.53	41.5297	59.8055	m2	43.19	44.0017	65.9038
m5	44.65	49.4667	68.4191	m4	43.46	43.0529	58.2755
m10	39.83	41.307	63.8523	m11	44.24	39.7867	44.8431
m15	43.01	43.3466	56.5113	m31	29.1	43.5787	47.6688

Normal Double Differential (NDD)				Inverse Binomial 2 (IB2)			
	Fit %				Fit %		
	From Literature	GA Constrained	GA Unconstrained		From Literature	GA Constrained	GA Unconstrained
m1	45.55	53.1512	57.9496	m1	33.79	38.6076	58.2365
m3	39.87	47.1084	60.7374	m3	36.17	38.9074	58.1653
m7	38.11	51.8065	60.5535	m4	36.41	38.9957	55.5179
m11	39.01	46.881	56.1193	m8	41.09	47.2971	55.0537

**Table 2:** Results of Constrained and Unconstrained GA of Highlighted Models from Table 1

From the results in Table 2 we can see that the optimization of the filter mask using GA worked in almost all the cases chosen. GA without constraints performed significantly better, in most cases, than the filter masks reported in literature and also the mask which we computed using GA, which only optimized the entry,  $(a_{22})$  i.e. the weight associated with the sEMG signal at the motor unit. This restriction on GA would leave the filter mask symmetrical. But looking at the results of the GA, we can conclude that the filter mask need not always be symmetrical for analysis of sEMG, especially for data recorded using an array. Examples of the filter mask that we obtained for TDD, model m5 and NDD, model 3 spatial filters are given below:

$$\text{TDD} = \begin{bmatrix} 0 & -41.5561 & 0 \\ 0 & 54.7329 & 0 \\ 0 & -22 & 0 \end{bmatrix},$$

$$\text{NDD} = \begin{bmatrix} 0 & -11.5790 & 0 \\ -46.7773 & 36.9276 & -11.8061 \\ 0 & -70.0491 & 0 \end{bmatrix}.$$

## 4 Conclusion

The linear spatial filter masks reported in literature had poor *kurtosis* improvements which we optimized using GA, these were compared based on the model fit values achieved using Hammerstein-Wiener models. The fit values did improve significantly in the two GA scenarios – GA with and without constraints. The GA without constraints performed better than the GA with constraints, which brings into focus the possibility that the sEMG signal distribution over the entire grid cannot be assumed to be symmetrically distributed and that the weights associated with the sEMG signal at various locations need to be modified depending on probably the subject and also based on the experimental design. This is in contrast to the reported filter mask in the literature, which are all symmetric. Almost all the filter masks optimized resulted in a significant improvement over the masks reported in literature.

## Acknowledgement

This work was supported by a grant from the Telemedicine Advanced Technology Research Center (TATRC) of the US Department of Defense. The financial support is greatly appreciated.

## References:

[1] Kathryn Ziegler-Graham, *et al.*, “Estimating the Prevalence of Limb Loss in the United States - 2005 to 2050,” *Archives of Physical Medicine and Rehabilitation* 89: 2008, pp. 422-429.

- [2] Patricia F. Adams, *et al.*, “Current Estimates from the National Health Interview Survey, 1996,” *Vital and Health Statistics* 10:200, 1999.
- [3] Mewett, D. T., Nazaran H., Reynolds, K., J., “Removing power line noise from recorded EMG”. *Proceedings of the 23<sup>rd</sup> Annual IEEE/EMBS International Conference*, October, 2001, pp. 1-4.
- [4] Clancy, A. E., Farry, A. K., “Whitening of the electromyogram to improve amplitude estimation”. *IEEE Transactions on Biomedical Engineering*, 47(6), June 2000, pp. 709-719.
- [5] Chan, D. C. A., Englehart, B. K., “Continuous myoelectric control for powered prostheses using hidden Markov models”. *IEEE Transactions on Biomedical Engineering*, 52(1), January 2005, pp. 121-124.
- [6] Chan, H. Y. F., Yang, Y., Lam, F. K., Zhang, Y., Parker, A. P., “Fuzzy EMG classification for Prosthesis control”. *IEEE Transactions on Rehabilitation Engineering*, 8(3), September 2000, pp. 305-311.
- [7] Reaz, I. B. M., Hussain, S. M., Yasin, M. F., “Techniques of EMG signal analysis: detection, processing, classification and application”. *Biomedical Procedures Online*, 8(1), January 2006, pp. 11-35.
- [8] [http://www.isek-online.org/standards\\_emg.html](http://www.isek-online.org/standards_emg.html)
- [9] Farina, D., Merletti, R., and Enoka, M. R., “The extraction of neural strategies from the surface EMG”. *Journal of Applied Physiology*, 96, 2004, pp. 1486-1495.
- [10] Sebastian A., Parmod K., Anugolu M., Schoen P. M., Urfer A., Naidu S. D., “Optimization of Bayesian Filters and Hammerstein-Wiener Models for EMG-Force Signals Using Genetic Algorithm”. *Proceedings of the ASME 2009 Dynamic Systems and Control Conference DSCC 2009*.
- [11] Sebastian A., Parmod K., Schoen P. M., Urfer A., Creelman J., Naidu S. D., “Analysis of EMG-Force relation using System Identification and Hammerstein-Wiener Models”. *Proceedings of the ASME 2010 Dynamic Systems and Control Conference DSCC 2010*.
- [12] <http://www.spatialanalysisonline.com/output/html/Linearspatialfiltering.html>
- [13] P. Zhou, N. L. Suresh, M. Lowery, W. Z. Rymer, “Nonlinear Spatial Filtering of Multichannel Surface Electromyogram Signals During Low Force Contractions”, *IEEE Transactions on Biomedical Engineering*, vol. 56, no.7, July 2009, pp. 1871-1879.
- [14] J. F. Kaiser, “On a simple algorithm to calculate the ‘energy’ of a signal”, *Proceedings of IEEE ICASSP’90*, Albuquerque, New Mexico, April 1990, pp. 381-384.
- [15] [http://www.mathworks.com/access/helpdesk/help/toolbox/ident/index.html?/access/helpdesk/help/toolbox/ident/gs/bq\\_ylq6.html](http://www.mathworks.com/access/helpdesk/help/toolbox/ident/index.html?/access/helpdesk/help/toolbox/ident/gs/bq_ylq6.html)



# Evaluation of filtering techniques applied to surface EMG data and comparison based on Hammerstein-Wiener models

ANISH SEBASTIAN, PARMOD KUMAR, MARCO P. SCHOEN

Measurement and Control Engineering Research Center (MCERC), Idaho State University

921 South 8<sup>th</sup> Ave., Stop 8060, Pocatello, Idaho 83209-8060

UNITED STATES OF AMERICA

[schomarc@isu.edu](mailto:schomarc@isu.edu) <http://www.isu.edu/~schomarc/>

*Abstract:* - Electromyogram (EMG) signals have been used for control of prosthetic devices in the past. However, most of the control schemes currently used are based on threshold values of the EMG signal as reference to actuate the prosthetic hand. Using such a control strategy, it is not possible to capture the underlying dynamics of the relationship between EMG signals and the intended finger movements and forces. We propose to use system identification based dynamic models which are extracted from recorded EMG signals and the corresponding finger forces. A key influence on the resulting quality of such models is the filtering of the EMG signals. This paper presents a thorough analysis of spatial filtering and other filtering methods. The different filters are compared on the basis of the EMG-finger force model fit values obtained using System Identification using various Non-Linear Hammerstein-Wiener models. The nonlinear spatial filters gave better fit values as compared to the standard filtering techniques.

*Key-Words:* - Spatial Filtering, Hammerstein-Wiener, Surface Electromyogram (sEMG), System Identification, Sensor Array, Modeling.

## 1 Introduction

About 50% of the people who need upper extremity prosthetics do not use them, [1]. This could be due any one of the common following reasons; a) Dexterity, b) Comfort, c) Cost. Despite advances in the fields of manufacturing, electronics, signal processing, sensor design, and our understanding of biological signals, we still face a huge challenge designing a prosthetic device. This is due to the fact that the competition of such a device is with one which nature has gifted us. A human hand is without doubt the best possible design. For a prosthetic hand, to encompass all of the human hands features and capabilities is as of now still a distant reality. Electromyogram (EMG) signals have been used for quite some time now in the control of prosthesis. The EMG signal is a small voltage signal (in mV), generated by skeletal muscles. This signal carries information of the objective the user would like to execute. Using surface EMG (sEMG) signals, researchers have been able to actuate motors on artificial prosthetic devices. EMG signals can be measured using intramuscular electrodes, needle electrodes, or by placing electrodes on the surface of the skin. The purpose for which the sEMG signal is being recorded generally determines whether it should be measured within the muscle using needle electrodes or surface measurement using electrodes on the skin would suffice. If, the purpose of recording the EMG signal is to look for diseases relating to a particular muscle, one might be better off using needle electrodes. On the other hand, if it is to be used to actuate motors on a prosthetic

device, which a user might want to take off and wear without the need of medical supervision, surface EMG would suffice. Measuring the EMG signal on the surface of the skin is also less uncomfortable. This method is generally suited only for superficial muscles. Even though recording (sEMG) is favorable, it is plagued with many issues, such as crosstalk from firing of multiple motor points in the vicinity of the recording location, which can cause significant corruption of the signal at that site, motion artifacts, and poor signal if the motor unit is not identified correctly etc. Needle electrodes, on the other hand, require trained medical professionals for appropriate placement of the electrodes in the muscle. This paper investigates sEMG signals only with the objective to extract intended finger forces. The sEMG-force relationship is modeled using Hammerstein-Wiener models to characterize the dynamics. These models are required to characterize the controller dynamics for sEMG based prosthetic hands. We look to overcome the crosstalk issue in the measurement by using an array of nine (9) sEMG sensors, and utilizing spatial filters to isolate and improve the quality of the signals at the identified site for EMG recording. The sensor array was placed on the motor unit location, which was identified for the subject using an external stimulator. The sensors were then placed around the motor unit to form a 3x3 square matrix. The processed signal was then used for identifying various dynamical models for the prediction of the force, from the recorded sEMG signal, that was generated during various voluntary contractions of the subjects' hand. A comparison of the various

outcomes (model fit values computed) of the system identification process, using signal processing techniques stated in the ISEK [2] guidelines and the spatially filtered signals are presented in this paper. The experiments were conducted for long durations, in order to analyze the effects of the muscle fatigue on the model structures.

## 2 Problem Formulation

EMG signal should ideally be measured at a motor unit. A motor unit (MU) consists of an  $\alpha$ -motoneuron in the spinal cord and the muscle fiber it innervates. sEMG signals are influenced by multiple factors, some of which are; a) shape of the volume conductor, b) the thickness of the subcutaneous tissue layers, c) tissue inhomogeneities, d) distribution of the motor unit territories in the muscle, e) size of the motor unit territories, f) distribution and the number of fibers in the motor unit territory, g) length of the fibers, h) spread of the endplates and tendon junctions within the motor units, and i) spread of the innervations zones and tendon regions among motor units. The type of detection system used also plays an important part in influencing the sEMG measurements. Some of the factors which need to be taken into account, with the detection systems, are a) skin electrode contact (impedance, noise), b) spatial filtering for signal detection, c) inter-electrode distance, d) electrode size and shape, and e) inclination of the detection system relative to the muscle fiber orientation, [3]. Since sEMG is plagued by a multitude of issues, as pointed out in this section, one cannot approach this problem realistically by trying to account for each of the variables in the measurement, nor oversimplify the problem at hand by assuming a simple linear or a non-linear relation between the sEMG signal and the corresponding finger force generated. Hence the approach presented in this paper is to assume a black-box model in order to deduce a suitable relation or model structure for the two signals. This approach has been found to be of merit in our previous studies and has been reported in [4] & [5] to yield satisfactory fits.

## 3 Problem Solution

"Spatial filtering" is broadly defined as a method which computes spatial density estimates for events that have been observed at individual locations. These filters are used when there is no a priori curve to fit to a data series. Instead, it relies on nearby or adjacent values to estimate the value at a given point. These filters take out variability in a data set while retaining the local features of data. Spatial filtering is principally associated with digital image processing. This method may be applied to almost any data in the form of a grid. The most common spatial filters are the low-pass and high-pass spatial filters. These are focal functions whose operation is determined by a kernel or neighborhood of  $N \times N$  cells around each pixel or grid position [6]. Grid cells "covered" by a kernel are multiplied by the matching kernel entry and then the weighted average is calculated and assigned as the value for the central cell,  $G$ . For example, an asymmetric  $3 \times 3$  kernel may look like the one shown in Equation (1),

or any combination of the weights. Typically  $a, b$  are positive integers. If  $a=b=1$ , then the kernel provides a simple smoothing or averaging operation. The weights in the kernel can be modified for specific cases or data sets. In any case the weighted average is divided by the sum of the elements of the kernel. Filters of this type are sometimes referred to as low-pass filters.

$$\text{Symmetric Kernel} = \begin{bmatrix} a & a & a \\ a & b & a \\ a & a & a \end{bmatrix}. \quad (1)$$

If the weights in the kernel is similar to the one in Equation (2) and  $a, b, c$  are positive integers, and if the following,  $b > a > c$ , is true, then the kernel is described as a Gaussian filter which is symmetric but center-weighted.

$$\text{Symmetric Kernel} = \begin{bmatrix} c & a & c \\ a & b & a \\ c & a & c \end{bmatrix}. \quad (2)$$

The filtered grid value ' $G$ ' of an  $m=N \times N$  kernel matrix, with  $C_i$  set of coefficients and  $P_i$  - set of source grid values, is calculated as:

$$G = \frac{\sum_{i=1}^m C_i P_i}{\sum_{i=1}^m C_i} + B, \quad (3)$$

where  $B$  is often set to 0.  $B$  is a bias term to increase or decrease the resulting value of ' $G$ '. This kernel is also sometimes referred to as the '*filter mask*'.

**Linear Spatial Filtering:** Linear spatial filtering would modify the sEMG array data ' $f$ ' by replacing the value at each location with a linear function of the values of nearby data points. Moreover, this linear function is assumed to be independent of the data point locations  $(k, l)$ , where  $(k, l)$  are the indices of the data points in  $f$ , which is represented by a composite data matrix. This kind of operation can be expressed as convolution or correlation. For spatial filtering, it's often more intuitive to work with correlation. The filtered result  $g(k, l)$  is obtained by centering the mask over pixel  $(k, l)$  and multiplying the elements of  $f$  with the overlapping elements of the mask and then adding them up. In other words, the objective is to amplify the activity of motor unit/s located closest to the recording site (ideally the actual motor location for the particular finger) and reducing the EMG signal generated by other motor units located further away or motor units of other fingers. The selectivity of surface EMG recordings can be increased by reducing the electrode size (i.e., skin-electrode contact area or inter-electrode distance) [7] and/or by applying temporal filters [8]. More recent work has focused on advances in the design of surface electrode arrays [9-10] to extract single motor unit information from sEMG. A large number of traditional [11-13] and adaptive [14] linear spatial filters have been extensively used to glean more information out of sEMG signals and to understand it much better.

For this paper, the experiments were carried out on a healthy male subject to extract dynamical models describing the relationship between sEMG-force signals. The motor points were located using a Muscle Stimulator, manufactured by Rich-Mar Corporation (model number HV 1100). The motor

location of the ring finger was chosen for the experiments. The EMG detection system used was a Delsys, Bagnoli-16 channel EMG (DS-160, S/N-1116). The sensors used for measuring the sEMG action potentials were three pronged DE 3.1 differential surface electrodes. The subjects' skin was prepared, according to the ISEK standards, before the sensors were placed over the motor point. The electrodes were placed along the muscle fibers (Flexor Digitorum Superficialis) for recording sEMG. Multiple sEMG sensors in an array configuration were mounted on and around the identified motor unit, as shown in Figure 1. The subjects' hand was placed on a flat surface; the reference electrode was placed on the elbow where there is no sEMG signal. Sensor *CH1* was placed on the identified motor unit location. *CH2* and *CH3* were placed along the muscle fiber in front and behind *CH1* respectively. Channels 4-9 were placed in the orientation as shown in Figure 1. Nine different experiments were conducted and the corresponding sEMG signal was measured simultaneously from all the nine sensors. The force generated by the subject's fingers, for a given motion, was measured using a stress ball with a force sensitive resistor (FSR) mounted on it.

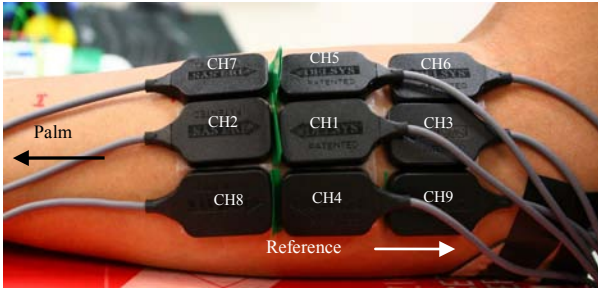


**Figure 1:** Experimental Setup – Location of sEMG sensors

The change in the resistance of the FSR is directly proportional to the force being applied. Figure 2 shows the location of the FSR on the stress ball. Experiments 1 and 2 were used to check for any spurious signals that might be recorded due to the slight angle at which the subjects' hand was held. Experiments 3 to 6 were done using a stress ball with a lesser stiffness as compared to experiments 7, 8 & 9.

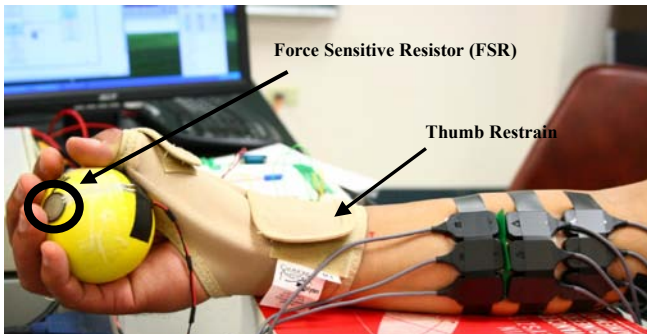


**Figure 2:** Force sensitive Resistor and Thumb Restrain

Also, a thumb restrain was used for experiments 5-9. The thumb restrain is showed in the Figure 2. The stress ball was changed as we were also interested in looking at the change in the sEMG signal when fatigue occurs, and also how it would affect the

modeling for the relation between force-sEMG using System Identification (SI).

The linear spatial filters tested in this paper for isolating the motor unit action potentials (MUAPs) are; 1) Longitudinal Single Differential (LSD), 2) Transverse Single Differential (TSD), 3) Longitudinal Double Differential (LDD), 4) Transverse Double Differential (TDD), 5) Normal Double Differential (NDD), 6) Inverse Binomial (IB2) and 7) Inverse Rectangular (IR) Filter. The mask of these filters and the corresponding resultant equations on application of the mask to the grid data obtained from the sEMG array arrangement are given below.

EMG Array Information, Spatial Filter Mask

$$\text{LSD} = \begin{bmatrix} sEMG7 & sEMG5 & sEMG6 \\ 0 & 0 & 0 \\ sEMG2 & sEMG1 & sEMG3 \\ -1 & 1 & 0 \\ sEMG8 & sEMG4 & sEMG9 \\ 0 & 0 & 0 \end{bmatrix}$$

Result Equation:  $-sEMG2 + sEMG1$

$$\text{TSD} = \begin{bmatrix} 0 & -1 & 0 \\ 0 & 1 & 0 \\ 0 & 0 & 0 \end{bmatrix}; \text{LDD} = \begin{bmatrix} 0 & 0 & 0 \\ -1 & 2 & -1 \\ 0 & 0 & 0 \end{bmatrix}; \text{TDD} = \begin{bmatrix} 0 & -1 & 0 \\ 0 & 2 & 0 \\ 0 & -1 & 0 \end{bmatrix}$$

LSD Equation =  $sEMG1 - sEMG2$ ; TSD Equation =  $sEMG1 - sEMG5$ . We can similarly deduce the equations for the other spatial filters.

$$\text{NDD} = \begin{bmatrix} 0 & -1 & 0 \\ -1 & 4 & -1 \\ 0 & -1 & 0 \end{bmatrix}; \text{IB2} = \begin{bmatrix} -1 & -2 & -1 \\ -2 & 12 & -2 \\ -1 & -2 & -1 \end{bmatrix}; \text{IR} = \begin{bmatrix} -1 & -1 & -1 \\ -1 & 8 & -1 \\ -1 & -1 & -1 \end{bmatrix}$$

In this paper, nonlinear spatial filters have also been discussed these have been reported in literature [15]. These are 1) 1-D Nonlinear Transverse spatial filter (NLT), 2) 1-D Nonlinear Longitudinal spatial filter (NLL), 3) 2-D Nonlinear spatial filter in Two-Orthogonal Directions (NLTO) and 4) Nonlinear spatial filter in All Four possible Directions (NLAFD). The nonlinear spatial filters use the Teager-Kaiser Energy (TKE) Operator, [16]. This technique is a threshold 'energy' based approach where outliers are first detected and then replaced by their estimated values. The nonlinear spatial filters with the TKE operator incorporated are given as follows; The general form of nonlinear spatial filter using the (TKE) operator is given in Equation (4);

$$\Psi[x(n)] = x^2(n) - x(n+1)x(n-1) \quad (4)$$

a) 1-D Nonlinear Transverse Spatial Filter (NLT); Equation (5)

$$\Psi_{d,m}[x(m,n)] = x^2(m,n) - x(m-1,n)x(m+1,n) \quad (5)$$

b) 1-D Nonlinear Longitudinal Spatial Filter (NLL); Equation (6)

$$\Psi_{d,n}[x(m,n)] = x^2(m,n) - x(m,n-1)x(m,n+1) \quad (6)$$

c) Nonlinear Spatial Filter in Two Orthogonal Directions (NLTO): Equation (7)

$$\Psi_{d,2}[x(m,n)] = \Psi_{d,2m}[x(m,n)] + \Psi_{d,n}[x(m,n)] \quad (7)$$

$$= 2x^2(m,n) - x(m-1,n)x(m+1,n) - x(m,n-1)x(m,n+1)$$

d) Nonlinear Spatial Filter in all Four Directions (NLAFD): Equation (8)

$$\begin{aligned} \Psi_{d,4}[x(m,n)] = & 4x^2(m,n) - x(m-1,n)x(m+1,n) \\ & - x(m,n-1)x(m,n+1) - x(m-1,n+1)x(m+1,n-1) \\ & - x(m-1,n-1)x(m+1,n+1) \end{aligned} \quad (8)$$

## 4 Simulation Results

Plots of the raw data gathered are shown in Figure 3. The plots shown in Figure 3 represent the raw data collected from three channels of the grid, Channels 1, 4 & 5.

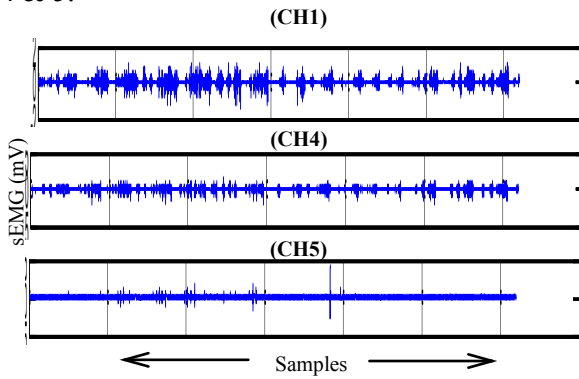


**Figure 3:** sEMG Raw Signal Channels 1, 4 and 5

The data shown above is for comparison of the sEMG obtained from various location of the subject's arm. Notice the change especially in the amplitude of the sEMG at Channel 1, 4 & 5. Figure 4 shows the plot of the filtered sEMG using the various spatial filters. In addition to these 11 spatial filters, the sEMG data was also filtered using 4 other filters – Bessel, Butterworth, Chebyshev Type I and Chebyshev Type II filters. The filter characteristics of these 4 filters were in accordance to the ISEK standards. The relation of sEMG-Force was modeled using Non-Linear Hammerstein-Wiener models. This modeling method has been proven to work in the past [4], [5] in assuming a black-box model structure for the system. In order to model the sEMG-Force relation, the filtered data from the various experiments was split into various four (4) time windows.

Equation 9 describes the general Hammerstein-Wiener model structure:

$$w(t) = f((g(t)), \quad b(t) = \frac{B_{j,i}(q)}{F_{j,i}(q)}w(t), \quad y(t) = h(x(t)), \quad (9)$$

where,  $w(t)$  and  $b(t)$  are internal variables,  $w(t)$  has the same dimensions as  $u(t)$  - input, and  $x(t)$  has the same dimensions as  $y(t)$  - output.  $g()$  and  $h()$  are the input and output non-linearity functions respectively.  $B(q)$  and  $F(q)$  are regression polynomials. The model fit values are computed using Equation (10)

as follows;

$$fit = 100 * \frac{1 - \|\hat{y} - y\|}{\|y - \hat{y}\|} \quad (10)$$

where,  $\hat{y}$  is the estimated output by the model.

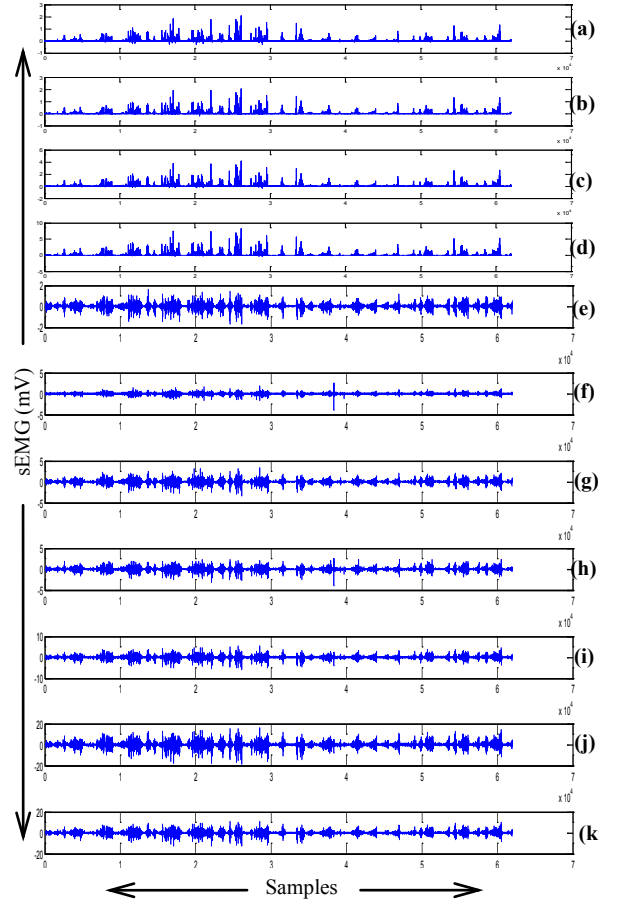
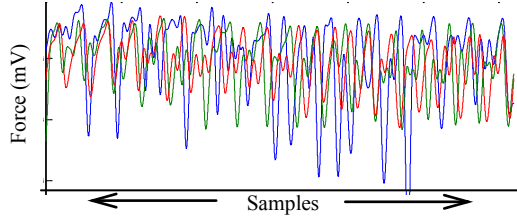


**Figure 4:** Spatially Filtered sEMG at Motor unit Ring Finger a) NLT, b) NLL, c) NLTOD, d) NLAFD, e) LSD, f) TSD, g) LDD, h) TDD, i) NDD, j) IB2, k) IR

The time windows used for estimation and validation of the models were called 'ze' and 'zv' respectively. 'ze' contained 8000 sample points and 'zv' contained data points shifted by 2000 sample points. For example, if 'ze' was a time window between 2-6 seconds i.e. samples 4000-12000, then 'zv' was between 3-7 seconds i.e. 6000-14000 samples. Thus the Hammerstein-Wiener method uses 'ze' to estimate the model structure and based on this information predicts the next 2000 sample points. The data was filtered using the various filters mentioned in the previous sections. We would like to stress once again the point that the force was varied randomly and the subject was in no way trying to achieve maximum voluntary contractions during each cycle. A cycle is defined as the subject starting without any force on the stress ball, squeezing it (to any force level) and then going back to no force. The subject has to keep the finger in contact with the force ball throughout this cycle.

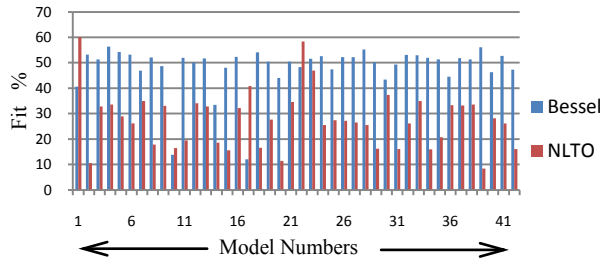


A plot of the variations in force achieved for 3 experiments is shown in Figure 5. The Matlab<sup>TM</sup> code for the Hammerstein-Wiener model is: `nlhw(ze, [na nb nk], ..., ...)`. The modeling was carried out by varying  $n_a$  - the number of past output terms used to predict the current output,  $n_b$  - the number of past input terms used to predict the current output and  $n_k$  - the delay from input and output in terms of the number of samples for the various Hammerstein-Wiener models.



**Figure 5:** Force levels experiment 3 (blue), 5(red) & 7(green)

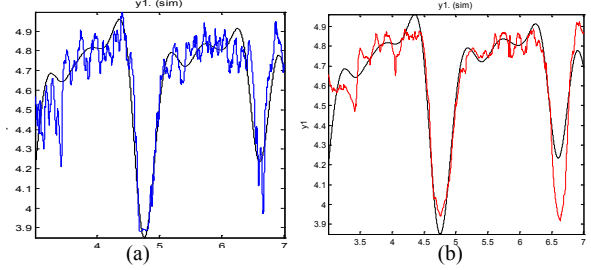
42 models with variations in  $n_a$  and  $n_b$  were tested while the value of  $n_k$  was kept as 1. The total number of models estimated were 15 (filter types) x 4 (time windows) x 42 models per time window x 4 experiments = 10,080 models. This paper does not list all these models but identifies and reports only the significant results of the analysis.



**Figure 6:** Fit % for Hammerstein-Wiener Models – Using Bessel and NLTO Filters (time window 2-7 sec, exp3)

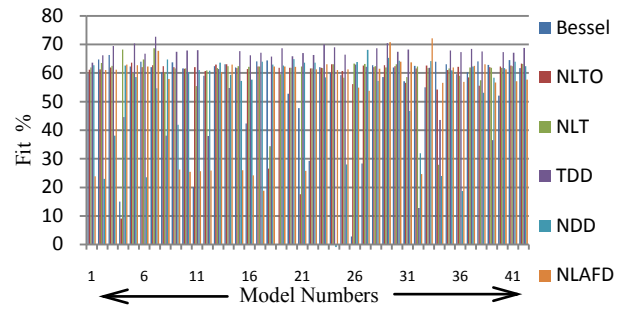
As an example, for experiment 3, for time window of 2-7 sec, the fit values obtained by varying  $n_a$  between 2-7 and  $n_b$  between 3-9, are shown in Figure 6. The fit values ranged from 33-56% for the Bessel filter and from 20-60% for the NLTO filter. The best values obtained for this time window were 56.36% and 60.13% by the Bessel and the NLTO filters respectively. The model output plot for these values is shown in Figure 7. The large variation in the model fit values can be attributed to the fact that the two data sets have poor correlation between one another. The other filters used also predict the future variations in force but the fit percentages were in the range of 30-48%. A key objective of this research is help develop a control regime which in not based on threshold values of force can incorporate the dynamics in the force. This would help to control the response of the artificial limb to be closer to that of the actual hand. Similarly we tested various models for the other experiments too. Another set of results which gave very high values of fit was for

the later time windows. This case was especially interesting as the subject had fatigued due to the repetitive experiments, but the Hammerstein-Wiener models did successfully capture the variations in the sEMG signal. The Hammerstein-Wiener models performed very well and we obtained fit values in the high sixties.



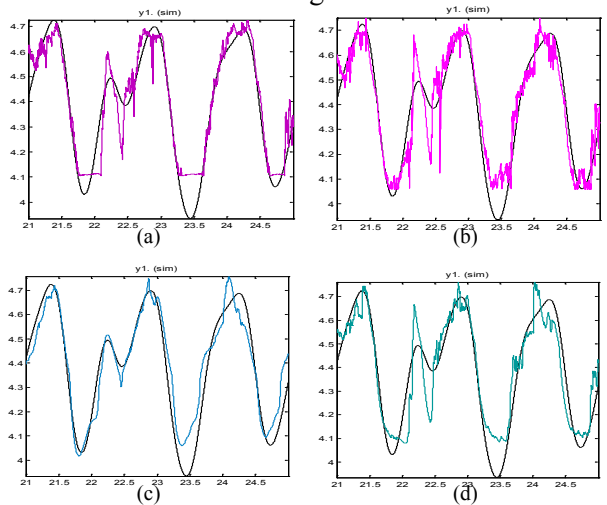
**Figure 7:** Measured data (black) a) Bessel (blue) 56.36% and b) NLTO (red) 60.13% for exp 3 time window 2-7seconds.

Figure 8 shows the model fit values obtained for these later data windows. As can be seen from the plots, contrary to our expectations the Hammerstein-Wiener Models performed very well and produced very good fit values.



**Figure 8:** Fit Values Obtained for Different Hammerstein-Wiener Models – Bessel, NLTO NLT, TDD, NDD, NLAFFD Filters (time window 20-25 sec, exp5)

Figure 9 shows the model output plots for some of the filters mentioned in Figure 8.



**Figure 9:** Measured Data Black – a) TDD (70.28%), b) NDD (68.09%), c) NLT (68.26%), d) NLAFFD (72.16%), Filters

## 4 Conclusion

The Hammerstein-Wiener models worked very well in capturing the dynamics of the force levels for the various experiments conducted. This method of modeling could help in improving the control over the motors used in prosthetic devices to mimic the actual changes force levels in a real hand. This method also performed very well in the scenarios where the subject did fatigue but the affects were successfully modeled by the Hammerstein-Wiener models. The nonlinear and linear spatial filters (TDD, NDD and NLT, NLTO and NLAFFD) did outperform the other filtering methods used especially for the later time windows. The only other filter which had a comparable performance to the spatial filters was the Bessel filter. Further investigation into reducing the wide range of the fit values obtained needs to be performed. One of the possible methods to pursue would be to use Genetic Algorithm to optimize the model parameters  $n_a$  and  $n_b$  and also the number of iterations used for the modeling of sEMG-force levels. One of the possible reasons for poor fit values could also be attributed to the model trying to over-fit the data sets.

## Acknowledgement

This work was supported by a grant from the Telemedicine Advanced Technology Research Center (TATRC) of the US Department of Defense. The financial support is greatly appreciated.

### References:

- [1] <http://www.army.mil/-news/2010/02/24/34906-the-future-of-prosthetics-is-in-your-mind/>
- [2] [http://www.isek-online.org/standards\\_emg.html](http://www.isek-online.org/standards_emg.html)
- [3] Farina, D., Merletti, R., and Enoka, M. R., 2004. "The extraction of neural strategies from the surface EMG". *Journal of Applied Physiology*, 96, pp. 1486-1495.
- [4] Sebastian A., Parmod K., Anugolu M., Schoen P. M., Urfer A., Naidu S. D., 2009. "Optimization of Bayesian Filters and Hammerstein-Wiener Models for EMG-Force Signals Using Genetic Algorithm". *Proceedings of the ASME 2009 Dynamic Systems and Control Conference DSCC 2009*.
- [5] Sebastian A., Parmod K., Schoen P. M., Urfer A., Creelman J., Naidu S. D., 2009. "Analysis of EMG-Force relation using System Identification and Hammerstein-Wiener Models". *Proceedings of the ASME 2010 Dynamic Systems and Control Conference DSCC 2010*.
- [6] <http://www.spatialanalysisonline.com/output/html/Linearspatialfiltering.html>
- [7] P. Zhou and W. Z. Rymer, "An evaluation of the utility and limitations of counting motor unit action potentials in the surface electromyogram," *Journal of Neural Engineering*, vol. 1, pp. 238–245, 2004.
- [8] Z. Xu and S. Xiao, "Digital filter design for peak detection of surface EMG," *Journal of Electromyography & Kinesiology*, vol. 10, pp. 275–281, 2000.
- [9] M. J. Zwarts and D. F. Stegeman, "Multichannel surface EMG: Basic aspects and clinical utility," *Muscle Nerve*, vol. 28, pp. 1–17, 2003.
- [10] B. G. Lapatki, J. P. Van Dijk, I. E. Jonas, M. J. Zwarts, and D. F. Stegeman, "A thin, flexible multielectrode grid for high-density surface EMG," *Journal of Applied Physiology*, vol. 96, pp. 327–336, 2004.
- [11] C. Disselhorst-Klug, J. Silny, and G. Rau, "Improvement of spatial resolution in surface-EMG: A theoretical and experimental comparison of different spatial filters," *IEEE Transactions on Biomedical Engineering*, vol. 44, no. 7, pp. 567–574, Jul. 1997.
- [12] D. Farina, E. Schulte, R. Merletti, G. Rau, and C. Disselhorst-Klug, "Single motor unit analysis from spatially filtered surface electromyogram signals. Part I: Spatial selectivity," *Medicine Biology Engineering and Computation*, vol. 41, pp. 330–337, 2003.
- [13] D. Farina, L. Mesin, S. Martina, and R. Merletti, "Comparison of spatial filter selectivity in surface myoelectric signal detection: Influence of the volume conductor model," *Medicine Biology Engineering and Computation*, vol. 42, pp. 114–120, 2004.
- [14] N. Ostlund, J. Yu, and J. S. Karlsson, "Adaptive spatio-temporal filtering of multichannel surface EMG signals," *Medicine Biology Engineering and Computation*, vol. 44, pp. 209–215, 2006.
- [15] P. Zhou, N. L. Suresh, M. Lowery, W. Z. Rymer, "Nonlinear Spatial Filtering of Multichannel Surface Electromyogram Signals During Low Force Contractions", *IEEE Transactions on Biomedical Engineering*, vol. 56, no.7, pp. 1871-1879, July 2009.
- [16] J. F. Kaiser, "On Teager's energy algorithm and its generalization to continuous signals", *Proc. 4th IEEE Digital Signal Proc. Workshop, Mohonk (New Paltz), NY, September 1990*.

# Adaptive Finger Angle Estimation from sEMG Data with Multiple Linear and Nonlinear Model Data Fusion

PARMOD KUMAR, ANISH SEBASTIAN, CHANDRASEKHAR POTLURI, ADNAN ILYAS,  
MADHAVI ANUGOLU, ALEX URFER, and MARCO P. SCHOEN

Measurement and Control Engineering Research Center, School of Engineering

Idaho State University

921 South 8<sup>th</sup> Avenue, Stop 8060, Pocatello, Idaho

USA

[schomarc@isu.edu](mailto:schomarc@isu.edu) <http://isu.edu/~schomarc>

*Abstract:* - This paper presents a novel approach to control the motion of a smart prosthesis using surface electromyographic (sEMG) signals. Currently, all sEMG based prosthetic hands are controlled based on pre-programmed motion sets, which are initiated when some threshold value of the measured sEMG signal is reached. In this paper, we present an approach that utilizes System Identification (SI) in order to obtain a dynamic finger angle model. Such a model allows for instantaneous control for the finger motions. The algorithm presented relies on an array of nine sEMG sensors. The sEMG and angle data is filtered using a nonlinear Teager–Kaiser Energy (TKE) operator based nonlinear spatial filter and a Chebyshev type-II filter respectively. The filtered signals are smoothed using a smoothing spline curve fitting. The smoothed sEMG data is used as input and the respective smoothed finger angle data is used as output for a system identification routine to obtain multiple linear and nonlinear models. To achieve better estimates of the finger angles, an adaptive probabilistic Kullback Information Criterion (KIC) for model selection based data fusion algorithm is applied to the linear and nonlinear model's outputs. Final fusion based output of this approach results in improved estimates of finger angles.

*Key-Words:* - sEMG, Prosthetics, System Identification, Teager–Kaiser Energy operator, KIC.

## 1 Introduction

The United States had 1.6 million people with amputations during 2005, [1]. This number is continuously on increase due to the ongoing wars in Afghanistan and Iraq, [2]. Hence, one of the prime reasons for the enlarged attention in the field of prosthetic is to facilitate the increased demand for efficiently and highly dexterous prosthesis. Because of the lack of tactile or proprioceptive feedback for grasping in prosthesis, almost 30–50% of the upper extremity amputees choose not to use their prosthetic hand on regular bases [3, 4]. The control of a prosthetic plays a key role in the usefulness and ultimately in the acceptance of the device by a user. Since full dexterity is still out of reach for current prosthetics, the precision and effectiveness of a prosthetics takes on greater value. The controller implemented must be capable of regulating the intended finger forces and finger motion of the artificial hand. The reference value for these outputs is given by the amputee's mind/intention, expressed by the generated surface electromyographic (sEMG) signal of the remaining skeletal arm muscles. In this work, we assume that the amputation is transradial, and hence sufficient muscle mass is accessible for sEMG data acquisition. EMG can be measured on

the surface or by needle electrodes that are injected into the subjects arm. Choosing the sEMG as a control input eliminates the problems associated with surgeries and regular hygiene for the user of implanted electrodes. sEMG signal amplitudes range between -5 and +5 [mV]. The sEMG signal changes with different limb movements and applied forces. This justifies the use of sEMG signals for the position and force control of prosthesis. Current prosthetics using EMG or sEMG sensors utilize this data by computing some threshold value – for example the RMS value – to activate a pre-programmed motion and/or force set of the artificial hand. The resulting motion is only initiated by the user, but not controlled thereafter. This is quite different than what a healthy subject uses to control his/her hand. For non-amputees, the motion of the fingers is controlled at every instance, which allows for complex motion sets to be executed. To mimic this characteristic, we propose to use dynamic models relating sEMG data with finger motion. The potential of such models is obvious from the operational point of view, but also allows the incorporation of muscle fatigue dynamics to be included in the control algorithm [9-13].

Previous research works give different methods to extract the information from the sEMG signals [5]. These methods use wavelet analysis, artificial neural networks, and other feature extraction methods to make use of sEMG for prosthetic control [5]. Research work as reported in [6] presents sEMG as an autoregressive (AR) model with the delayed intramuscular EMG signal as the input. In our work, we rely only on sEMG since no injected electrodes will be used to obtain EMG signals. Hence the task is to develop a model and an estimation scheme for describing the dynamics of the skeletal muscle force and finger angles from the sEMG signals. Some of the recent efforts in this direction are evident in the research work of [7-13].

Present research focus on the dynamic modeling and estimation of the angles of the proximal interphalangeal (PIP) joint of the index finger with the corresponding sEMG signal. An array of nine sEMG sensors is used to record sEMG signals and joint angles are recorded using a wheel potentiometer from the arm of a healthy subject, which respectively is explained in detail in Section 2 and 3. Both the signals are filtered and smoothing spline curve fitted with 0.993 as smoothing parameter. The dynamic modeling is achieved using the approach of System Identification (SI) where smoothed sEMG data is the input and the smoothed joint angle data is the output. Multiple linear and nonlinear models are obtained. To achieve better estimate of the finger angles, an adaptive probabilistic Kullback Information Criterion (KIC) for model selection based data fusion algorithm is applied to the linear and nonlinear models outputs. Final fusion based output of this approach results in improved estimates of finger angles.

## 2 Experimental Set-Up

An experimental set-up is designed to simultaneously acquire the sEMG from the motor point of the index finger and the joint angle of the PIP joint of the index finger. Nine DE-3.1 sEMG sensors of the DELSYS® Bagnoli-16 EMG system are placed in a three-by-three array [14]; the arrangement covers the four directional spatial distributions of the sEMG signal. The middle three sEMG sensors were attached directly on the skin surface above the motor point of the index finger of a healthy subject. Using a 10k-Ohm wheel potentiometer, an angle measurement device is designed to measure the joint angles of the PIP joint of the index finger of a healthy subject. Appropriate sEMG electrode attachment point for the motor point of the index finger was identified using a wet

probe muscle stimulator at the FDS (RICH-MAR, HV 1000).

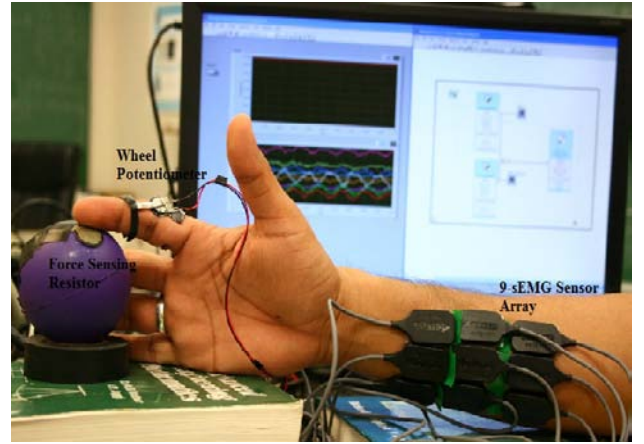


Fig. 1: Experimental Set-Up.

Prior to placing the sEMG sensors, the skin surface of the subject was prepared according to International Society of Electrophysiology and Kinesiology (ISEK) protocols. An Interlink™ Electronics FSR 0.5" circular force sensor on a stress ball is used to press with the movement to introduce some resistance to the movement of the PIP joint of the index finger. Experimental set-up is shown in Fig. 1 where nine sensors are shown on a healthy subject forearm, with an angle measurement device on the PIP joint of the index finger and having a stress ball for force measurements. The various signals are sampled at a rate of 2000 Hz using LabVIEW™ in conjunction with DELSYS® Bagnoli-16 EMG and NI ELVIS™. With this experimental set-up we conducted several experiments of 30 seconds, 45 seconds and 60 seconds durations.

## 3 Signal Pre-Processing

The recorded sEMG signal for the index finger is filtered using nonlinear spatial filtering for nine channel surface EMG. The nonlinear spatial filter is obtained from the "Nonlinear Teager-Kaiser Energy (TKE) Operator," [14]. Equation (1) gives the TKE operator in the time domain on sEMG signal [14].

$$\Psi[x(n)] = x^2(n) - x(n+1) * x(n-1). \quad (1)$$

Here,  $\Psi$  is the TKE operator and  $x(n)$  is the time domain sEMG signal at location  $n$ . The four-directional nonlinear spatial filter can be derived from the TKE operator. Equation (2) gives the four-directional nonlinear spatial filter.

$$\begin{aligned} \Psi_{d,4}[x(m,n)] = & 4 * x^2(m,n) - x(m-1,n) * \\ & x(m+1,n) - x(m,n-1) * x(m,n+1) - \\ & x(m-1,n+1) * x(m+1,n-1) - x(m-1,n- \\ & 1) * x(m+1,n+1). \end{aligned} \quad (2)$$



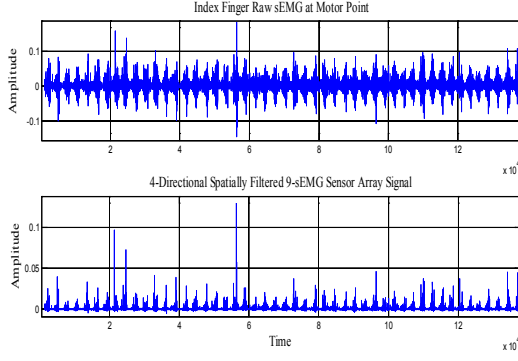


Fig. 2: Raw and Spatially Filtered sEMG Signal from Index Finger.

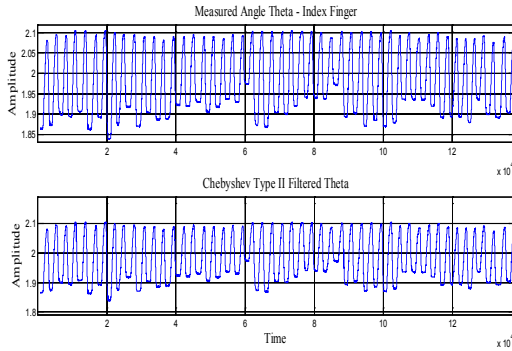


Fig. 3: Raw and Chebyshev Type II Filtered PIP Joint Angle for Index Finger.

Fig. 2 shows a comparison between the measured and nonlinear spatial filtered sEMG signals. A Chebyshev type II infinite impulse response (IIR) low pass filter with a 550 Hz pass band frequency is used to filter the PIP joint angle data. Fig. 3 shows the comparison between the measured and Chebyshev type II filtered skeletal muscle force signal.

#### 4 Smoothing Spline Curve Fitting

Any data can be curve or surface fitted using the MATLAB<sup>®</sup> Curve Fitting Toolbox<sup>™</sup> [15]. Smoothing spline which is a piecewise polynomial computed from a smoothing parameter ( $p$ ) of 0.993 is fitted to the filtered sEMG and angle data. Smoothing parameter ( $p$ ) is a number between 0 and 1. Change in the value of  $p$  from 0 to 1 results in the change in smoothing spline. For  $p = 0$  the smoothing spline is a least-square straight-line approximation to the data, whereas for  $p = 1$  it gives the "natural" cubic spline interpolant to the data [15].

For the specified weight ( $w_i$ ) and smoothing parameter ( $p$ ) a smoothing spline  $s$  is formed which minimizes the parameter  $J$  given by Equation (3).

$$J = p \sum_i w_i (y_i - s(x_i))^2 + (1 - p) \int \left( \frac{d^2 s}{dx^2} \right)^2 dx, \quad (3)$$

where  $x_i$  and  $y_i$  are predictor and response data respectively. The smoothing parameter  $p$  should be chosen to make the error  $E(s) = \sum_i w_i (y_i - s(x_i))^2$  and roughness  $\int \left( \frac{d^2 s}{dx^2} \right)^2 dx$  small. Here in this work the smoothing parameter  $p$  is chosen as 0.993 [15].

#### 5 System Identification

System Identification (SI) is a tool to model a dynamic system based on input-output data [16]. In this research, we use the SI to model two signals which are smoothing spline curve fitted. The sEMG is the input to the system and the intended PIP joint angle is the output. Multiple linear and nonlinear models are obtained for modeling of sEMG and PIP joint angle signals for the index finger of the dominant hand of a healthy subject. Five linear and three nonlinear models are obtained for the input and output data set. Table I and II gives the structures of the linear and nonlinear models respectively.

The model order of the various models used in this work are as follows: linear models for the input and output data set, OE model of order 16, ARX model of order 18, ARMAX model of model order 16, State-Space model with subspace method (N4SID) of order 18 and a State-Space model with prediction error/maximum likelihood method (PEM) of order 12 are obtained using SI. Table I gives the structure of all the linear models. In table I  $y$  is output,  $t$  is time,  $B(q)$ ,  $F(q)$ ,  $A(q)$ ,  $C(q)$ ,  $D(q)$ , are polynomials,  $q$  is a backward shift operator,  $u$  is input,  $n_k$  is delay and  $e$  is error [17]. For State-Space models:-  $x$  is state,  $t$  is time,  $T_s$  is sampling time,  $u$  is input,  $e$  is error,  $A, B, K, C$ , and  $D$  are system matrices, and  $y$  is output [17].

TABLE I  
LINEAR MODELS AND THEIR STRUCTURES

Linear Model Name	Linear Model Structure
Output Error	$y(t) = \frac{B(q)}{F(q)} u(t - n_k) + e(t)$
ARX	$A(q)y(t) = B(q)u(t - n_k) + e(t)$
ARMAX	$A(q)y(t) = B(q)u(t - n_k) + C(q)e(t)$
State-Space – subspace method	$x(t + T_s) = Ax(t) + Bu(t) + Ke(t)$ $y(t) = Cx(t) + Du(t) + e(t)$
State-Space – prediction error/maximum likelihood method	$x(t + T_s) = Ax(t) + Bu(t) + Ke(t)$ $y(t) = Cx(t) + Du(t) + e(t)$

Table II gives the structures of nonlinear models. The nonlinear models for the input and output data set are obtained as, the nonlinear Wiener-Hammerstein models with nonlinearity estimators of ‘piecewise linear – pwlinear,’ ‘sigmoidnet,’ and ‘wavelet network.’

In Table II, for the nonlinear Hammerstein-Wiener model  $u(t)$  and  $y(t)$  are the inputs and outputs for the system, respectively.  $f$  and  $h$  are nonlinear functions that corresponds to the input and output nonlinearity, respectively.  $w(t)$  and  $x(t)$  are internal variables.  $w(t)$  has the same dimension as  $u(t)$ .  $x(t)$  has the same dimension as  $y(t)$ .  $B(q)$  and  $F(q)$  in the linear dynamic block are polynomials in the backward shift operator. For nonlinear Hammerstein-Wiener model with wavelet network as nonlinearity estimator,  $\kappa(s)$  as a wavelet function, and  $\beta_k$  is a row vector such that  $\beta_k(x - \gamma_k)$  is a scalar. If only the input nonlinearity is present, the model is called the Hammerstein model. If only the output nonlinearity is present, the model is called the Wiener model [17].

TABLE II  
NONLINEAR MODELS AND THEIR STRUCTURES

Nonlinear Model Name	Nonlinear Model Structure
Nonlinear HW – Piecewise Linear – pwlinear	$w(t) = f(u(t)),$ $x(t) = \frac{B_{ji}(q)}{F_{ji}(q)} w(t),$ $y(t) = h(x(t));$
Nonlinear HW – Sigmoidnet	$y_p(t) = f(y(t-1), y(t-2), y(t-3), \dots, u(t-1), u(t-2), \dots);$ $f(z) = \frac{1}{e^{-z} + 1}$ is sigmoid function.
Nonlinear HW – Wavelet Network	$g(x) = \sum_{k=1}^n \alpha_k \kappa(\beta_k(x - \gamma_k))$

## 6 Adaptive Data Fusion

Data fusion of multiple outputs of the linear and nonlinear models is done by assigning a particular probability to each individual output [18]. This method gives good estimation of the PIP joint angles. The goodness of the fit of each linear and nonlinear model output can be computed using SI model fit value, which is given by Equation (4).

$$FIT = [1 - |Y - \hat{Y}| / |Y - \bar{Y}|] * 100. \quad (4)$$

In Equation (4)  $Y$  is measured,  $\hat{Y}$  is estimated and  $\bar{Y}$  is mean output signal. The model selection criterion used in this paper is Kullback Information Criterion (KIC) which has shown to perform well for sEMG sensor data fusion [9-13]. The sum of two directed divergences, which is the measure of the

models dissimilarity, is known as Kullback’s symmetric or J-divergence [19], as given by Equation (5).

$$KIC(p_i) = \frac{n}{2} \log R_i + \frac{(p_i+1)n}{n-p_i-2} - n\psi\left(\frac{n-p_i}{2}\right) + g(n), \quad (5)$$

where  $g(n) = n * \log(n/2)$ .

The fusion algorithm as given by [18] is applied for data fusion of the outputs of the linear and nonlinear models obtained using SI:

(I) Find the linear and nonlinear models outputs  $M_1, M_2, \dots, M_k$  for  $k$  number of outputs.

(II) Compute the residual square norm

$$R_i = \|Y - \Phi_i \hat{\Theta}_i\|^2 = \|Y - \hat{Y}\|^2,$$

where  $\hat{\Theta}_i = \{\Phi_i^T \Phi_i\}^{-1} \Phi_i^T Y$ , and

$$\Phi = \begin{bmatrix} Y_p^T & u_p^T & Y_{p-1}^T & \dots & u_1^T \\ Y_{p+1}^T & u_{p+1}^T & Y_p^T & \dots & u_2^T \\ \vdots & \vdots & \vdots & \ddots & \vdots \\ Y_{n-1}^T & u_{n-1}^T & Y_{n-2}^T & \dots & u_{n-p}^T \end{bmatrix}.$$

(III) Calculate the model criteria coefficient using Equation (5).

(IV) Compute the model probability  $p(M_i|Z) = \frac{e^{-l_i}}{\sum_{j=1}^{k1} e^{-l_j}}$ , where  $l$  is model selection criterion, i.e.  $KIC(p_i)$ .

(V) Compute the fused model output  $\hat{Y}_f = \sum_{i=1}^{k1} p(M_i|Z) \hat{Y}_i$ .

(VI) Compute the overall model from  $\hat{Y}_f$  and skeletal muscle force data.

In this algorithm the computation from step (II) to (VI) is adaptive i.e. the residual square norm,  $KIC(p_i)$ , model probability  $p(M_i|Z)$ , and fused model output  $\hat{Y}_f$  are being updated with time or for each data point.

## 7 Results and Discussion

The sEMG signals from the sensor array and angle signals of PIP joint of index finger are filtered; smoothing spline curve fitted and modeled using multiple linear and nonlinear models. First the outputs of linear and nonlinear models are fused separately and then the resultant outputs are fused using an adaptive KIC based probability. This approach gives improved estimates of the finger angles of the PIP joint of the index finger of the dominant hand of a healthy subject. Results are presented in the following figures. Fig. 4 shows the overlapping plot of the measured-curve fitted angle vs. data fusion based angle using linear models. Fig. 5 shows the overlapping plot of the measured-curve

fitted angle vs. data fusion based angle using nonlinear models.

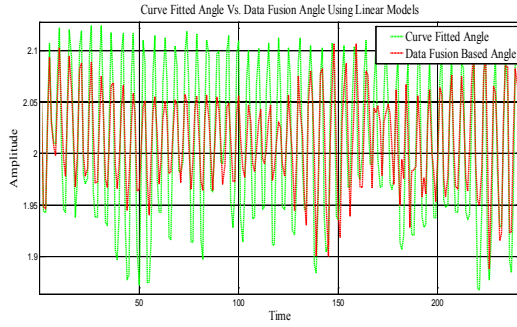


Fig. 4: Curve Fitted Vs. Data Fusion Based Angle Using Linear Models.

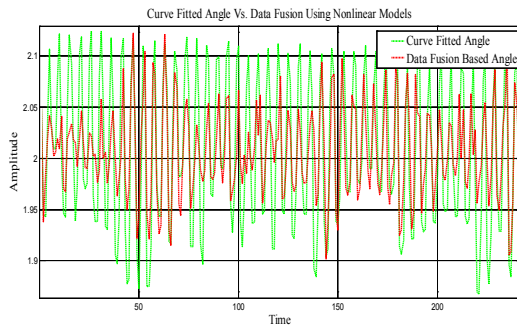


Fig. 5: Curve Fitted Vs. Data Fusion Based Angle Using Nonlinear Models.

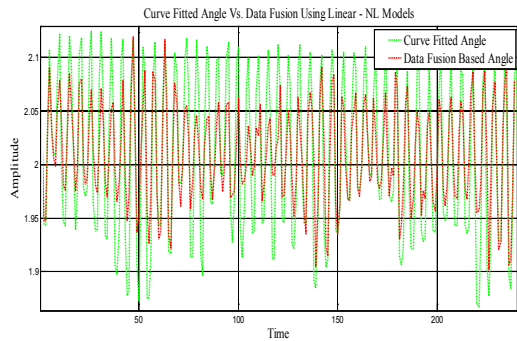


Fig. 6: Curve Fitted Vs. Data Fusion Based Angle Using Linear-Nonlinear Models.

Fig. 6 shows the overlapping plot of the curve fitted angle vs. data fusion based angle using linear-nonlinear models. It is clearly evident that the data fusion based output follows the measured-curve fitted output. Mean percentage error of the linear, nonlinear and linear-nonlinear models data fusion based angles are  $2.5191\text{e-}005$ ,  $-4.5807\text{e-}006$ , and  $8.1167\text{e-}006$  respectively.

Fig. 7 shows the validation plot for a different experimental data where the measured-curve fitted and the linear-nonlinear modeled data fusion based angle signal shows a close follow up. Mean percentage error of the linear, nonlinear and linear-

nonlinear models data fusion based angles are  $2.8202\text{e-}005$ ,  $3.3191\text{e-}005$ , and  $6.8079\text{e-}006$  respectively.

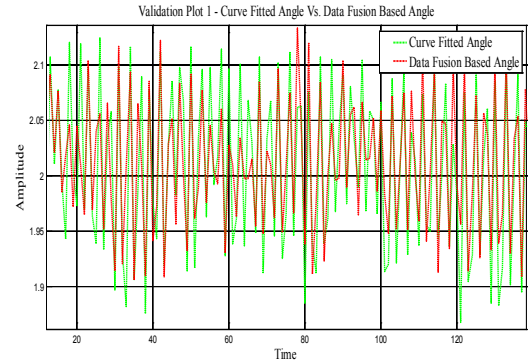


Fig. 7: Validation Plot - Curve Fitted Vs. Data Fusion Based Angle Using Linear-Nonlinear Models.

## 8 Conclusion and Future Work

The dynamic modeling of the filtered and smoothed sEMG and PIP joint angle of the index finger is achieved using SI with sEMG is the input and the joint angle is the output. Multiple linear and nonlinear models are obtained for the input and output data. To achieve a better estimate of the finger angles, an adaptive probabilistic Kullback Information Criterion (KIC) for model selection based data fusion algorithm is applied to the linear and nonlinear models outputs. Final fusion based output of this approach results in improved estimates of finger joint angles. The approach is validated using a different set of experimental data.

As this initial study shows potential in the pursuit of controlling an artificial hand on an instantaneous basis, we will further this work in the future by improving the data collection techniques and optimizing the experimental procedure as well as optimizing the smoothing parameter for the smoothing spline curve fitting.

## Acknowledgement

This research was sponsored by the US Department of the Army, under the award number W81XWH-10-1-0128 awarded and administered by the U.S. Army Medical Research Acquisition Activity, 820 Chandler Street, Fort Detrick MD 21702-5014. The information does not necessarily reflect the position or the policy of the Government, and no official endorsement should be inferred. For purposes of this article, information includes news releases, articles, manuscripts, brochures, advertisements, still and motion pictures, speeches, trade association proceedings, etc.

## References:

- [1] K. Ziegler-Graham, E. J. MacKenzie, P. L. Ephraim, T. G. Travison, and R. Brookmeyer, Estimating the Prevalence of Limb Loss in the United States - 2005 to 2050, *Archives of Physical Medicine and Rehabilitation*, Vol. 89, March 2008, pp. 422-429.
- [2] P. O'Connor. (2009, February 15). Iraq war vet decides to have second leg amputated [Online]. Available: <http://www.columbiamissourian.com/stories/2009/02/15/soldier-who-lost-leg-iraq-may-lose-other/>
- [3] D. J. Atkins, D. C. Y. Heard, and W. H. Donovan, Epidemiologic overview of individuals with upper-limb loss and their reported research priorities, *Journal of Prosthetics and Orthotics*, Vol. 8, No. 1, 1996, pp. 2-11.
- [4] D. H. Silcox, M. D. Rooks, R. R. Vogel, and L. L. Fleming, Myoelectric prostheses. A long-term follow-up and a study of the use of alternate prostheses, *The Journal of Bone and Joint Surgery*, Vol. 75-A, No. 12, December 1993, pp. 1781-1789.
- [5] M. B. I. Reaz, M. S. Hussain and F. Mohd-Yasin, Techniques of EMG signal analysis: detection, processing, classification and applications, *Biological Procedures Online*, Vol. 8, March 2006, pp. 11-35.
- [6] Y. Zhou, R. Chellappa, and G. Bekey, Estimation of intramuscular EMG signals from surface EMG signal analysis, *IEEE International Conference on Acoustics, Speech, and Signal Processing 1986*, Vol. 11, 1986, pp. 1805-1808.
- [7] P. K. Artemiadis and K. J. Kyriakopoulos, EMG-based position and force control of a robot arm: Application to teleoperation and orthosis, in *Conf. Rec. 2007 IEEE/ASME Int. Conf. on Advanced Intelligent Mechatronics*, Zurich, Sept. 2007, pp. 1-6.
- [8] P. K. Artemiadis and K. J. Kyriakopoulos, EMG-Based Position and Force Estimates in Coupled Human-Robot Systems: Towards EMG-Controlled Exoskeletons, in *Experimental Robotics, Springer Tracts in Advanced Robotics*, Vol. 54, Berlin Heidelberg: Springer-Verlag, 2009, pp. 241-250.
- [9] P. Kumar, C. Potluri, A. Sebastian, S. Chiu, A. Urfer, D. S. Naidu, and M. P. Schoen, An Adaptive Multi Sensor Data Fusion with Hybrid Nonlinear ARX and Wiener-Hammerstein Models for Skeletal Muscle Force Estimation, in *Proc. The 14th World Scientific and Engineering Academy and Society (WSEAS) International Conference on Systems*, Corfu Island, Greece, 2010, July 22-24.
- [10] P. Kumar, A. Sebastian, C. Potluri, A. Urfer, D. S. Naidu, and M. P. Schoen, Towards Smart Prosthetic Hand: Adaptive Probability Based Skeletal Muscle Fatigue Model, in *Conf. Rec. 32nd Annual International Conference of the IEEE Engineering in Medicine and Biology Society*, Buenos Aires, Argentina, Aug. 31 – Sept. 4, 2010.
- [11] P. Kumar, C. Potluri, A. Sebastian, S. Chiu, A. Urfer, D. S. Naidu, and Marco P. Schoen, Adaptive Multi Sensor Based Nonlinear Identification of Skeletal Muscle Force, *WSEAS Transactions on Systems*, Vol. 9, Issue 10, October 2010, pp. 1051-1062.
- [12] P. Kumar, C. Potluri, M. Anugolu, A. Sebastian, J. Creelman, A. Urfer, S. Chiu, D. S. Naidu, and M. P. Schoen, A Hybrid Adaptive Data Fusion with Linear and Nonlinear Models for Skeletal Muscle Force Estimation, in *Proc. 5th Cairo International Conference on Biomedical Engineering*, Cairo, Egypt, Dec. 16-18, 2010.
- [13] P. Kumar, C. H. Chen, A. Sebastian, M. Anugolu, C. Potluri, A. Fassih, Y. Yihun, A. Jensen, Y. Tang, S. Chiu, K. Bosworth, D. S. Naidu, M. P. Schoen, J. Creelman and A. Urfer, An Adaptive Hybrid Data Fusion Based Identification of Skeletal Muscle Force with ANFIS and Smoothing Spline Curve Fitting, in *Proc. 2011 IEEE International Conference on Fuzzy Systems*, Taipei, Taiwan, June 27-30, 2011.
- [14] P. Zhou, N. L. Suresh, M. M. Lowery, and W. Z. Rymer, Nonlinear Spatial Filtering of Multichannel Surface Electromyogram Signals During Low Force Contractions, *IEEE Transactions on Biomedical Engineering*, Vol. 56, No. 7, July 2009, pp. 1871-1879.
- [15] *MATLAB® Curve Fitting Toolbox™ User's Guide*. The MathWorks, Inc. 2010.
- [16] L. Ljung, *System Identification: Theory for the User. 2nd edition*, Printice Hall PTR, 1999, Chap. 1, pp. 1-15.
- [17] L. Ljung, *System Identification Toolbox™ 7 User's Guide*, The MathWorks, Inc., 2010.
- [18] H. Chen and S. Huang, A Comparative study on Model Selection and Multiple Model Fusion, in *Proc. 7th International Conference on Information Fusion*, New Orleans, USA, July 25-28, 2005, pp. 820-826.
- [19] A. K. Seghouane, and M. Bekara, A Small Sample Model Selection Criterion Based on Kullback's symmetric Divergence, *IEEE Transactions on Signal Processing*, Vol. 52, No. 12, 2004, pp. 3314-3323.

# A REVIEW ON SENSORY FEEDBACK FOR sEMG BASED PROSTHETIC HANDS

Madhavi Anugolu, Chandrasekhar Potluri, Adnan Ilyas, Parmod Kumar, Steve Chiu, Nancy Devine, Alex Urfer, and Marco P. Schoen, *Senior Member IEEE*

**Abstract**—This paper addresses issues concerning the integration of artificial limbs with amputees. From the reported literature, it is evident that the afferent feedback to prosthetic users can help with their ability to control the device. In addition, incorporation of such a feedback system increases the ownership sensation of amputees with their artificial limbs. This paper includes an overview of research findings on the development of non-invasive sensory feedback (afferent) systems for hand amputees. The reviewed stimulators for the afferent system are based on vibration and electrical systems, and a combination of the two methods.

**Keywords:** sEMG, hand prosthetic, sensory feedback

## I. INTRODUCTION

According to the information provided by the National Limb Loss Information Center, [1], in the year of 2005, 1.6 million persons were living in the United States with the loss of a limb. It is estimated that by the year 2050 this number will more than double to 3.6 million. Hence, prosthetics, such as artificial hands, and their advances in functionality and performance will remain an active research topic.

Madhavi Anugolu is with Measurement and Control Engineering Research Center (MCERC), School of Engineering, Idaho State University, Pocatello, Idaho 83209, USA (email: anugmadh@isu.edu).

Chandrasekhar Potluri is with MCERC, School of Engineering, Idaho State University, Pocatello, Idaho 83209, USA (e-mail: potlchan@isu.edu).

Adnan Ilyas is with Measurement and Control Engineering Research Center (MCERC), School of Engineering, Idaho State University, Pocatello, Idaho 83209, USA (email: ilyaadna@isu.edu).

Parmod Kumar is with Measurement and Control Engineering Research Center (MCERC), School of Engineering, Idaho State University, Pocatello, Idaho 83209, USA (email: kumaparm@isu.edu).

Steve Chiu is with Department of Electrical Engineering and Computer Science, MCERC, Idaho State University, Pocatello, Idaho 83201 USA (email: chiustev@isu.edu).

Nancy Devine is with Department of Physical and Occupational Therapy, Idaho State University, Pocatello, Idaho 83209, USA (email: devinanac@isu.edu).

Alex Urfer is with Department of Physical and Occupational Therapy, Idaho State University, Pocatello, Idaho 83209, USA (email: urfealex@isu.edu).

Marco P. Schoen is with Department of Mechanical Engineering, MCERC, Idaho State University, Pocatello, Idaho 83209, USA (email: schomarc@isu.edu).

Functionality can be achieved by incorporating some kind of a sensory feedback, which allows the user to acquire external information through the artificial hand. Furthermore, the functionality of prosthesis can be improved by using a close to natural control mechanism. Research has shown that the adaptation of the prosthetic arm is conditional to a system that provides distally referred sensations of touch and joint movements [2]. It is postulated that to achieve greater dexterity and performance, prostheses without a sensory feedback system will be obsolete, [3-5]. It was assumed for a long time that the replacement of a natural arm with intelligent prosthetic arm is an impossible task. The main discrepancy lied in the insufficient analysis of the concept of sensory feedback and by not taking into account the knowledge of physiology of kinesthesia [6]. However with the passage of time, and as the technology matured, these factors were taken into account and later formed the base for a modern prosthetic hand. The sensory feedback has opened the new doors to the life of disable subjects compared to the earlier days. By using the sensory feedback, natural ambiances can be provided to the prosthetic hand users. It will help the user to have more control on the hand and can be fully embedded into the work as a normal person without any disability [7].

Sensory feedback can be obtained by the use of different implantable electrodes, such as needle or cuff electrodes. For robotic hands, [8] used this principle to excite the responsible nerves directly. They implanted the electrodes in fascicles of the nerves of amputees. The stimulation through these electrodes gives the feedback information on grip strength and position of the limb. This is not a closed-loop system and has some limitations in terms of optimization.

External sensors and switches are usually used in controlling functional neuromuscular simulation systems (FNS). They pose problems such as donning, and calibration. For implementation artificial sensors are difficult to build and are insufficiently bio compatible. Now-a-days with the advancement of electrical interfacing with nerves and muscles, natural sensors are being considered as an alternative source of feedback and command signals for FNS. For high-level control natural or artificial sensors can equally perform for

decision making methods. Surface electromyography (sEMG) signals are being 1000 times larger than electro neuro organs are easier to measure, but have not provided reliable indicators so far. Characteristics like muscle fatigue are not indicated by these which are in FNS systems [9]. Andrew Y.J. Szeto [10] explained about the electrocutaneous stimulation for sensory communication in rehabilitation engineering. Some procedures for implementing electrotactile displace and generating reliable, pain free sensations with a useful communication bandwidth. This paper presents an overview of what technologies have been developed in recent years and tries to forecast the direction of future research based on the current state of knowledge for advancing sensory feedback based prosthetic hands.

## II BIOLOGICAL BACKGROUND

Some efforts have been made in recent years to address sensory feedback for the prosthetic users, [11]. The sensory feedback system interacting with the prosthetic and sensory cortex needs to be capable of communicating with both systems simultaneously, avoid issues of fatigue, assimilation, as well as be capable of sensing through the mechanical hand various types of signals, such as pressure, texture, temperature, shear forces, and surface conditions. In the following, we present a brief review of the inner workings of sensation through healthy human skin. There are numerous afferent receptors in the human skin to sense different sensation ranging from touch to temperature. In particular, there are cutaneous mechanoreceptors, thermoreceptors, nociceptors, bulboid corpuscles and chemoreceptors.

*Cutaneous Mechanoreceptors* are free nerve endings, sensing touch, pressure, and stretch. They are classified into four main types in the human skin:

1. Ruffini's end organs detect touch, pressure and tension deep in the skin. They are located all over the skin and are rather slowly adapting nerve endings and sensitive to skin stretch. Ruffini's end organs are mainly helpful with sense of and control of finger position and movement; they are also useful for detecting slippage of objects along the surface of the skin. Hence they help control grip force.
2. Meissner's corpuscle (or tactile corpuscle) is a mechanoreceptor (nerve ending). The location of Meissner's corpuscles is the glabrous skin. They detect changes in texture (most sensitive if vibration occurs below or around 50 Hz), are receptive to light touch sensation. Meissner's corpuscles are dynamic

in nature, which results into rapid adaptation to external stimuli.

3. Pacinian corpuscles are fewer in number compared to Meissner and Merkel's discs, but adapt very rapidly. The location of Pacinian corpuscles are in subcutaneous tissue, interosseous membranes. Pacinian corpuscles detect rapid vibrations (about 200-300 Hz). They are nerve endings in the skin which are sensitive to pain and deep pressure (poking), and are also dynamic (adapt to stimuli).
4. Merkel's discs are located in all of the human skin and in hair follicles. Merkel's disc detects sustained touch and pressure and can distinguish shapes and textures. These receptors are good for touch and pressure. Their adaptation rate is rather slow as they are static in nature.

The location of the four mechanoreceptors is shown in Figure 1.

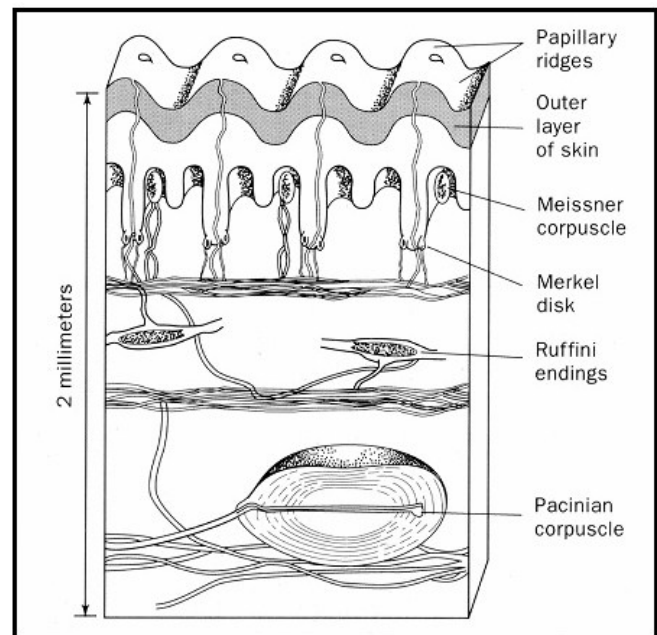


Figure 1: Mechanoreceptors location in human skin [12].

*Thermoreceptors:* are sensory neurons that sense changes in temperature. Heat is sensed through unmyelinated C-fibers, which possess a low conduction velocity. This result into the transmission of sensed information transmitted to the brain within a few seconds. Cold is sensed using C-fibers and thinly myelinated A-delta fibers, which conduct the information to the brain faster (within one second) [8]. For warm receptors, the warming effect is translated into an increase in action potential discharge rate, while cooling results in a decrease of the discharge rate. For



cold receptors this is inverted, where the action potential firing rate is increased when cooling occurs and decreased when warming occurs. There is some literature [13] which notes that above 45°C, some cold receptors also respond with an action potential discharge due to the increased temperature (paradoxical response to heat).

*Cutaneous Nociceptors:* is a skin receptor responsible of detecting damaging stimuli and alarming the system by creating the perception of pain. There are also thermal nociceptors which generate heat pain for temperatures above 42°C.

While healthy subjects have access to all the information gathered by these receptors, individuals with amputations have to relearn how to collect information about an object they touch with the prosthetic. Recent research has shown that sensory feedback of contact information from the prosthetic with its surroundings improves the user's ability to control and adapt to the prosthetic [14]. Currently, most work addressing the inclusion of feedback for the prosthetic user addresses only very basic elements such as tactile feedback about finger pressure.

### III. SENSORY FEEDBACK TYPES

Holmes, [14] addressed the mental representation for sensory inputs of the human body within the brain. This input from the periphery has a strong effect on the perceptual awareness of body parts, natural or appended prosthesis for identifying its own body and for identifying artificial limbs. With sensory inputs, control and handling of the prostheses are improved. Some efforts have been made in recent years to address sensory feedback for the prosthetic users. For example, [15] used electrical stimulation to communicate pressure or position of the prosthesis in order to provide a closed-loop control of the hand. The most successful methods for communicating peripheral inputs were Electrical Surface Simulation (ESS) and Mechanical Surface Simulation (MSS), [16, 17]. Research shows that electro-tactile stimulators allow the distinction of 59 different sensations; the mechanical vibrator is able to transmit 16 different sensations, [18].

Tactile sensors can be split into two types: active and passive. In the general scenario, tactile sensory user interfaces passive touch i.e., stimulation is made passively on the surface of the skin. In some instances, in which when an object needs to be identified active touch comes into picture. This active touch utilizes distinct shapes and texture and encodes this sensory information which helps to identify the object without

visual contact. In the active touch scenario shape encoding is very important, [19].

The tactile sensors can be used with electrical, pneumatic, and electro-mechanical devices. In the following sections the two most prevailing sensory feedback systems are discussed.

#### *Mechanical Stimulation*

In the case of electro-mechanical (vibro tactile) devices, a mechanical vibration or touch is produced and super-positioned onto a healthy skin area with functional mechano-receptors. The vibro tactile displays are classified into two basic types. They are pins and large point contact stimulators, [20].

The pin type vibro tactile displays based on piezoelectric bimorph pins are convenient and simple to use. They are non-invasive with good two point discrimination. These pin types are very good in presenting fine cues for surface texture edge and line detection when used as an array, [21]. In contrast, large contact point stimulators are very simple vibrators that are pressed against the skin surface. They yield much lower resolution when compared to the pin type. But the advantage with these types of simulators is that they can be distributed over large section of the body. Therefore multiple simultaneous cues for surface texture, edge and line detections [22] can be produced.

The mechanical stimulation uses pneumatic devices such as bladders or pockets which can be inflated or deflated, [23]. Hence they create a pulsing sensation that the user can easily feel. These devices can either be attached directly or to other devices that are used to complete the tasks. The main advantages of these pneumatic devices (bladders) – when compared to vibro tactile displays – are localization i.e., they have significantly low interference with the nearby bladders, the pump mechanism can be mounted remotely such that the control devices will require a minor modification. A variety of sensory information of the stimulus can be generated by altering the configuration or shape of these bladders [23, 24].

A number of studies have been conducted using the mechanical vibrator as basis [11, 15, 25, and 26]. This approach generally leads to a higher acceptance rate by the user as well as an increased users' performance (time and efficiency of use). However, there are some limitations with mechanical stimulation, mechanical vibration is limited to 16 sensations when used as a source of sensory feedback, they are bulkier and hard to control, and the pneumatic tactile displays include leak control, and air compressibility issues.

## Electrical stimulation

In order to design better prostheses with vibro tactile feedback, electrical stimulation of the muscles is necessary. By applying the electrical currents paralyzed muscles can be made to contract. These electrically elicited muscle contractions are controlled in such a way that the prosthesis acquires its full functionality. This technique is called “functional electrical stimulation”. There is a lot of ongoing research on FES systems to restore the functionality of the upper and lower extremity prosthesis [27]. *Kajimoto et. al.*[28] used an electrode array with a particular distribution of the electrode’s charge to communicate with the user, the sensation of pressure at the fingertips. Their smart touch prototype consists of optical sensors to capture an image and convert that into tactile information and displays through electrical stimulation. Using an electro-tactile system makes it possible to access seven (7) different classes of mechanoreceptors, two (2) classes of thermo receptors, four (4) classes of nociceptors, and three (3) classes of proprioceptors within the human skin, [28, 29, 30, 31, 32, 33]. To utilize the possible 59 sensations from electrical stimulations, Szeto et. al [32] used electro-tactile stimulations by changing frequency and intensity of the feedback. In [34], the authors used interferential stimulation to transit spatial movement of the hand. Electrical stimulation is described in literature by using voltage-regulated stimulation, [34]. Voltage-regulated systems are sensitive to changes in the amputee’s skin impedance. In reference [35], this problem was addressed by creating a voltage-regulated stimulator with a high frequency biphasic waveform. This approach lead to the avoidance of sensitivity (ability to discriminate objects) drop off. Array sensors have been used successfully for different purposes [36, 37]. As above mentioned, work presented in [28] utilize an electrode array. A rather large array was used by [38], where 144 electrodes are used on a blind person’s tongue in order to provide some spatial awareness of his/her surroundings. Electrode arrays for feedback have numerous advantages and can help tailor the sensory feedback system to the skin area chosen.

## IV CONCLUSION AND FUTURE WORK

In this paper, we addressed issues that concern the integration of artificial limbs to the amputees. There are two systems of note that can be used to structure an afferent system. The two systems are either based on vibration or on electrical stimuli or a combination of the two methods. Electrical Stimulation provides the better

performance compared to the mechanical stimulation, measured by the type and variety of possible sensations generated and perceived by the mechanoreceptors in the human skin. Designing a prosthetic hand with a sensory feedback technique will increase the acceptability by the user of the prosthetic hand and hence the control of the hand, [39, 40].

## ACKNOWLEDGEMENT

This work was supported in part by an internal Career Path Internship grant by Idaho State University. The support is greatly appreciated. The technical support from Dr. D. Subbaram Naidu is greatly appreciated.

## REFERENCES

- [1] Estimating the Prevalence of Limb Loss in the United States- 2005 to 2050 Kathryn Ziegler-Graham, PhD, et al, *Archives of Physical Medicine and Rehabilitation* 89(3):422-429, 2008.
- [2]<http://content.lib.utah.edu/cdm4/document.php?CISOROOT=/ir-main&CISOPTR=43804>.
- [3] J. N. Billock, “*Prosthetic management of complete hand and arm deficiencies*,” in: J.M. Hunter, E.J. MacKin and A.D. Callahan (Eds.), *Rehabilitation of the Hand: Surgery and Therapy*, St. Louis: Mosby-Year Book, 1189-1201, 1995.
- [4] S. Hubbard, “*Myoprosthetic management of the upper limb amputee*,” in: J.M. Hunter, E.J. MacKin and A.D. Callahan (Eds.), *Rehabilitation of the Hand: Surgery and Therapy*, St. Louis: Mosby-Year Book, 1241-1252, 1995.
- [5] G. Lundborg, B. Rosen, K. Lindstrom and S. Lindberg, “*Artificial sensibility based on the use of piezoresistive sensors: preliminary observations*,” *J. Hand Surg. Br.*, 23:620-626, 1998.
- [6] P. Herberts, L. Korner, “*Ideas on Sensory feedback in hand prostheses*”, *Prosthet Orthot Int*, December 1979, vol 3. No. 3 157-162.
- [7][http://www.research.gov/researchportal/appmanager/base/desktop.jsessionid=5JSnNMdMdn5n4vhVrCp32VWlvjJnLsmfdc19DcYbkJd5jrwSQMt!1821093771!1028386895?\\_nfpb=true&\\_windowLabel=awardSummary\\_1&\\_urlType=action&awardSummary\\_1\\_action=selectAwardDetail&awardSummary\\_1\\_id=%2FresearchGov%2FAwardHighlight%2FPublicAffairs%2F16782\\_SensoryFeedbackfromaProstheticHand.html](http://www.research.gov/researchportal/appmanager/base/desktop.jsessionid=5JSnNMdMdn5n4vhVrCp32VWlvjJnLsmfdc19DcYbkJd5jrwSQMt!1821093771!1028386895?_nfpb=true&_windowLabel=awardSummary_1&_urlType=action&awardSummary_1_action=selectAwardDetail&awardSummary_1_id=%2FresearchGov%2FAwardHighlight%2FPublicAffairs%2F16782_SensoryFeedbackfromaProstheticHand.html)
- [8] Christian Antfolk, Christian Balkenius, et al., “*A tactile Display system for Hand prostheses to*



*discriminate pressure and individual finger localization*”

[9] Dhillon, G. S., and Horch K. W., IEEE Trans. Neural Systems and Rehabilitation Engineering, “*Direct neural sensory feedback and control of a prosthetic arm*,” 13(4), pp. 468-472, 2005.

[10] Szeto, A. Y. J., Riso, R., 1990, “*Sensory Feedback using Electrical Stimulation of the Tactile Sense*”, in R.V. Smith and J.H. Leslie, Jr. (Eds.), *Rehabilitation Engineering*, Boca Raton, CRC Press, pp. 29-78.

[11] Cipriani, C. Zacccone, F., Micera, S., Carrozza, M. C., 2008, “*On the Shared Control of an EMG Controlled Prosthetic Hand: Analysis of User-Prosthetics Interaction*,” IEEE Trans. Robotics, 24(1), pp. 170-184.

[12] [http://www.sensorprod.com/news/whitepapers/2006\\_tsa/index.php](http://www.sensorprod.com/news/whitepapers/2006_tsa/index.php)

[13] Darian-Smith, Ian; Johnson KO, LaMotte C, Shigenaga Y, Kenins P, Champness P (1979). “*Warm fibers innervating palmar and digital skin of the monkey: responses to thermal stimuli*.” *Journal of Neurophysiology* 42 (5): 1297–1315.

[14] Holmes, N. P., Spence, C., Cogn. Process, “*The body schema and multisensory representation(s) of peripersonal space*,” 5, 94-105, 2004.

[15] Pylatiuk, C., Kargov, A., Schulz, S., Journal of Prosthetics and Orthotics, “*Design and Evaluation of a Low-Cost Force Feedback System for Myoelectric Prosthetic Hands*,” 18(2), pp. 57-61. 2006a.

[16] G.F. Shannon, “*A comparison of alternative means of providing sensory feedback on upper limb Prostheses*”, Med Biol Eng. 1976 May; 14(3), 289-294.

[17] Geldard, F.A. (1957) Adventures in tactile literacy. Am psycho 115-24.

[18] Kaczmarek, K. A., Webster, J. G., Bach-y-Rita, P., Tompkins, W. J., IEEE Trans. Biomedical Engineering, “*Electro-tactile and vibrotactile display for sensory substitution systems*,” 38, pp. 1-15, 1991.

[19] M. Akamatsu, I.S. MacKenzie, and T. Hasbrouc, “*A Comparison of Tactile, Auditory, and Visual Feedback in a Pointing Task Using a Mouse-Type Device*,” Ergonomics 38, pp. 816-827, 1995.

[20] S. Brewster and L.M. Brown, “*Tactons: Structured Tactile Messages for Non-Visual Information Display*,” Proc. 5th Australasian User Interface Conference (AUIC2004), Dunedin, pp. 15-23, 2004.

[21] J.C. Bliss, M.H. Katcher, C.H. Rogers, R.P. Sheppard, “*Optical-to-tactile image conversion for the blind*,” IEEE Trans. Man-Machine Systems, MMS-11(1), pp. 58-65, 1970.

[22] M. Schroepe, “*Simply Sensational*,” New Scientist, pp. 30-33, June 2, 2001.

[23] M. Enriquez, O. Afonin, B. Yager, and K. Maclean, “*A Pneumatic Tactile Alerting System for the Driving*

*Environment*,” PUI 2001, Workshop on Perceptual/Perceptive User Interfaces, Orlando, FL, November 15-16, 2001.

[24] Lilly Spirkovska, “*Summary on Tactile Interfaces techniques and Systems*, NASA Ames Research Center, September 22, 2004.

[25] Pylatiuk, C., Doederlein, L., Orthopade, “*Bionic Arm prostheses. State of the art in research and development*,” 35(11), pp. 1169-1170, 2006b.

[26] Schulz, A. E., Marasco, P. D., Kuiken, T. A., Brain Research, “*Vibrotactile detection thresholds for chest skin of amputees following targeted reinnervation surgery*,” 1251, pp. 121-129, 2008.

[27] P. Hunter pecham, Jayme S. Knutson, “*Functional electrical simulation for neuromuscular applications*,” Annu. Rev. Biomed.Eng, March 23, 2005.

[28] Kajimoto, H., Kawakami, N., Maeda, T., Inami, M., IEEE Computer Graphics and Applications,” Emerging Technologies, “*SmartTouch: Electric Skin to Touch the Untouchable*”, 24(1), pp. 36-43, 2004.

[29] Kaczmarek, K. A., Webster, J. G., Bach-y-Rita, P., Tompkins, W. J., IEEE Trans. Biomedical Engineering, “*Electro-tactile and vibrotactile display for sensory substitution systems*,” 38, pp. 1-15, 1991.

[30] Kajimoto, H., Kawakami, N., Maeda, T., Tachi, S., Electronics and Communications in Japan, “*Electrocutaneous Display with Receptor Selective Stimulation*”, Part 2, 85(6), pp. 40-49, 2002.

[31] Kajimoto, H., Kawakami, N., Inami, M., Tachi, S., Proceedings of the Annual Conference on Artificial Reality and Tele existence ICAT 99, Virtual Reality Soc. of Japan, “*Tactile feeling Display using Functional Electrical Stimulation*” pp. 107-114, 1999.

[32] Szeto, A. Y. J., Riso, R., in R.V. Smith and J.H. Leslie, Jr. (Eds.), *Rehabilitation Engineering*, Boca Raton, CRC Press, “*Sensory Feedback using Electrical Stimulation of the Tactile Sense*”, pp. 29-78, 1990.

[33] Asamura, N., Yokoyama, N., Shinoda, H., Proceedings IEEE Virtual Reality Conference, “*A Method of Selective Stimulation to Epidermal Skin Receptrots for Realistic Touch Feedback*”, pp. 274-281, 1999.

[34] Navarro, X., Krueger, T., Lago, N., Micera, S., Stieglitz, T., Dario, P., Journal of the Peripheral Nervous System, “*A critical review of interfaces with the peripheral nervous system for the control of neuroprostheses and hybrid bionic systems*”, 10(3), pp. 229-258. 2005.

[35] Hernandez, A., Yokoi, H., Ohnishi, T., a Arai, T., Proceedings of the 9<sup>th</sup> Int. Conf. On Intelligent Autonomous Systems, IOS Press, Tokyo, Japan, “*An f-MRI study of an EMG prosthetic hand biofeedback system*”, pp. 921-929, 2006.

- [36] Chandrasekhar Potluri, Parmod Kumar, Madhavi Anugolu, Alex Urfer, Steve Chiu, D. Subbaram Naidu, and Marco P. Schoen, "*Frequency Domain Surface EMG Sensor Fusion for Estimating Finger Forces*," 32nd Annual International Conference of the IEEE Engineering in Medicine and Biology Society, Buenos Aires, Argentina, Aug. 31 – Sept. 4, 2010.
- [37] Madhavi Anugolu, Anish Sebastian, Parmod Kumar, Marco P. Schoen, Alex Urfer, and D. Subbaram Naidu, "*Surface EMG Array Sensor Based Model Fusion using Bayesian Approaches for Prosthetic Hands*," Proceedings of the Dynamic Systems and Control Conference (DSCC), Hollywood, CA, October 2009.
- [38] Paul Bach-y-Rita, Stephen W. Kercel, Sensort substitution and the human-machine interface, Trends in Cognitive Sciences, Volume 7, Issue 12, December 2003, Pages 541-546.
- [39] Chandrasekhar Potluri, Parmod Kumar, Madhavi Anugolu, Steve Chiu, Alex Urfer, Marco P. Schoen, and D. Subbaram Naidu, "*sEMG Based Fuzzy Control Strategy with ANFIS Path Planning For Prosthetic Hand*," 3rd IEEE RAS &EMBS International Conference on Biomedical Robotics and Biomechatronics, Tokyo, Sept 26-30, 2010
- [40] Chandrasekhar Potluri, Yimesker Yihun, Parmod Kumar, Jeff Molitor, Steve C. Chiu, D. Subbaram Naidu, Fellow, IEEE, S.Hossein Mousavinezhad, "*sEMG Based Real-Time Embedded Force Control Strategy for a Prosthetic Hand Prototype*" IEEE International Conference on Electro/Information Technology, Mankato, Minnesota, USA, May 15-17, 2011.

# Optimal Tracking of a sEMG based Force Model for a Prosthetic Hand

Chandrasekhar Potluri, *Member, IEEE*, Madhavi Anugolu, *Member, IEEE*, YimeskerYihun, Alex Jensen, Steve Chiu, *Member, IEEE*, Marco P. Schoen, *Senior Member, IEEE*, and D. Subbaram Naidu, *Fellow, IEEE*.

**Abstract:** This paper presents a surface electromyographic (sEMG)-based, optimal control strategy for a prosthetic hand. System Identification (SI) is used to obtain the dynamic relation between the sEMG and the corresponding skeletal muscle force. The input sEMG signal is preprocessed using a Half-Gaussian filter and fed to a fusion-based Multiple Input Single Output (MISO) skeletal muscle force model. This MISO system model provides the estimated finger forces to be produced as input to the prosthetic hand. Optimal tracking method has been applied to track the estimated force profile of the Fusion based sEMG-force model. The simulation results show good agreement between reference force profile and the actual force.

## I. INTRODUCTION

Currently there are more than 2 million Americans that have a missing limb. The number of Americans with missing limbs increases 185,000 people a year [1]. As a result of this rising number of people that need prostheses, research is being focused on creating more intuitive prosthetics. There has been active research to design a prosthetic hand. But even today there is no prosthetic hand at an affordable cost with position and tactile force control [2]. It is evident from the past research that the human-centered robotics should be autonomous with a high level of functionality, comfort and ease of use [3]. A natural means of communication is required for human-centered robotics [4], and in the case of electromyographic (EMG) based prostheses, one natural means of interface between the human arm and prosthesis is the surface EMG (sEMG) itself. The EMG signal is present because of the neuromuscular activity in the body. The sEMG signals are captured noninvasively and give access to physiological processes responsible for the contraction of muscles. Since the sEMG signal is amplitude modulated and time

dependent, and dynamic in nature, spatially and temporally frequency encoded [5]. Usually sEMG measurements are based on single sensor data. For this work we used an array of three sEMG sensors and a force sensing resistor (FSR) to acquire the EMG signal and the corresponding skeletal muscle force. The data from the three sEMG sensors are fused using a fusion algorithm to have a better estimation of skeletal muscle force from the corresponding sEMG signal when compared to single sensor data [6].

This paper uses the sEMG-force fusion model as reference profile. A Linear Quadratic Tracking (LQT) technique is employed to the prosthetic hand to track the force profile. This paper is structured as follows. The experimental set up is given in Section II, Section III provides reference force model and Section V provides dynamics of the hand. Section VI details the results and discussion and in the last section some conclusions are provided.

## II. EXPERIMENTAL SET-UP

Experiments were conducted on a right-handed healthy male subject. Using a muscle simulator (Rich-Mar Corporation HV 1100), motor units were marked and sEMG sensors were placed accordingly [6]. One sEMG sensor was placed on the motor point of the subject's ring finger and two sensors were placed at points adjacent to it. Prior to placing the sEMG sensors, the skin surface of the subject was prepared according to International Society of Electrophysiology and Kinesiology (ISEK) protocols [7]. Both sEMG and muscle force signals were acquired simultaneously using LabVIEW™ 8.2 at a sampling rate of 2000 Hz. The sEMG data was captured by a DELSYS® Bagnoli-16 EMG system with DE-2.1 differential EMG sensors. The force information was collected by a NI ELVIS with an Interlink Electronics FSR 0.5" circular force sensor.

## III. REFERENCE FORCE MODEL

In this present work the force signal is extracted from the sEMG signals obtained from the array of the three sEMG sensors located on the arm. The data from the three sensors are collected around the corresponding individual motor unit location at the transradial arm location (flexor digitorum superficialis) and is rectified and filtered using a Half-Gaussian filter given by

$$p(EMG|x) = 2 \times \frac{\exp\left(-\frac{EMG^2}{2x^2}\right)}{\sqrt{2\pi x^2}}, \quad (1)$$

Chandrasekhar Potluri is with Measurement and Control Engineering Research Center (MCERC), College of Engineering, Idaho State University, Pocatello, Idaho 83209, USA (e-mail: potlchan@isu.edu).

Madhavi Anugolu is with MCERC, College of Engineering, Idaho State University, Pocatello, Idaho 83209, USA (email: anugmadh@isu.edu).

YimeskerYihun is with MCERC, College of Engineering, Idaho State University, Pocatello, Idaho 83209, USA (email: yihuyime@isu.edu).

Alex Jensen is with MCERC; is with MCERC, College of Engineering, Idaho State University, Pocatello, Idaho 83209, USA (email: jensalex@isu.edu).

Steve Chiu is with Department of Electrical Engineering and Computer Science, MCERC, Idaho State University, Pocatello, Idaho 83209 USA (email: chiustev@isu.edu).

Marco P. Schoen is with Department of Mechanical Engineering, MCERC, Idaho State University, Pocatello, Idaho 83209, USA (email: schomarc@isu.edu).

D. Subbaram Naidu is with Department of Electrical Engineering and Computer Science, MCERC, Idaho State University, Pocatello, Idaho 83209 USA (email: naiduds@isu.edu).

where  $p(EMG|x)$  is a conditional probability density function,  $x$  is a latent driving signal and  $EMG$  is the rectified signal from the sensors.

The preprocessed sEMG data from the three sensors are fused using a sensor fusion algorithm to facilitate the extraction of the best finger force estimates. Sensor fusion is accomplished in the frequency domain using a simple elitism based Genetic Algorithm (GA). The SI method is used to identify the dynamical relationship between the sEMG data from the three sensors and the corresponding finger force. In this fusion algorithm, Output Error (OE) models are used to achieve the SI. The OE models are constructed for each individual data set. The OE model structure is given as follows.

$$y(t) = \frac{B(q)}{F(q)}u(t - nk) + e(t), \quad (2)$$

Where  $B$  and  $F$  are the polynomials,  $q$  is shift operator,  $e(t)$  is output error,  $y(t)$  is system output,  $u$  is input,  $nk$  is the system delay and  $t$  is time index.

Using the three resulting OE models and the fusion algorithm given by [6], a corresponding continuous-time model is constructed as given by the transfer function as

$$G(s) = \frac{B(s)}{F(s)} = \frac{b_{nb}s^{(nb-1)}b_{nb-1}s^{(nb-2)}+\dots+b_1}{s^{nf}+f_{nf}s^{nf-1}+\dots+f_1}, \quad (3)$$

Similar to the discrete-time case,  $nb$  and  $nf$  determine the orders of the numerator and denominator. For multi-input systems,  $nb$  and  $nf$  are row vectors.  $b, f$  are the coefficients of the numerator and denominator polynomials respectively.

A MISO transfer function is constructed based on the poles of three individual OE models corresponding to each sensor. GA is used to find the corresponding zeros. The search area is limited to the unit circle, because a discrete time model is used (and the resulting MISO model is decreased to minimum phase). The number of zeros is at most the number of poles. The number of potential zeros is set to the order of the corresponding denominator. The square error of the resulting MISO system  $H(s)$  (see Appendix) and the recorded force signal is set as an objective function. The objective function  $f$  is constructed as follows,

$$f = \int_{t_0}^{t_f} (\hat{Y}(t) - Y(t))^2 dt = \int_{t_0}^{t_f} \varphi^2(t) dt, \quad (3)$$

where  $t_0$  and  $t_f$  are the initial and final time values,  $\hat{Y}(t)$  is the fusion model estimated force and  $Y(t)$  is the actual force from the FSR.

The MISO system  $H(s)$  is constructed as follows,

$$H(s) = \begin{pmatrix} \frac{Z_{1,1}s^n + Z_{1,2}s^{n-1} + \dots + Z_{1,n+1}}{P_{1,1}s^n + P_{1,2}s^{n-1} + \dots + P_{1,n+1}} \\ \frac{Z_{2,1}s^n + Z_{2,2}s^{n-1} + \dots + Z_{2,n+1}}{P_{2,1}s^n + P_{2,2}s^{n-1} + \dots + P_{2,n+1}} \\ \frac{Z_{3,1}s^n + Z_{3,2}s^{n-1} + \dots + Z_{3,n+1}}{P_{3,1}s^n + P_{3,2}s^{n-1} + \dots + P_{3,n+1}} \end{pmatrix}, \quad (4)$$

where  $Z$ 's and  $P$ 's are the zeros and poles respectively of the individual transfer function and  $n$  is the order of the system.

Feeding the new data sets to the MISO transfer function ( $H(s)$ ) results in an estimated fusion based force  $\hat{Y}$ .

#### IV. DYNAMICS OF PROSTHETIC HAND

The dynamic equations of motion for the hand are obtained from the Lagrangian approach as [8,9,10,11,12,13]

$$\frac{d}{dt} \left( \frac{\partial \mathcal{L}}{\partial \dot{q}} \right) - \frac{\partial \mathcal{L}}{\partial q} = \tau, \quad (5)$$

where  $\dot{q}$  and  $q$  represent the angular velocity and angle vectors of joints respectively;  $\mathcal{L}$  is the Lagrangian;  $\tau$  is the given torque vector at joints. The Lagrangian  $\mathcal{L}$  is given as

$$\mathcal{L} = T - V, \quad (6)$$

where  $T$  and  $V$  are denoted as kinetic and potential energies respectively. Substituting (6) into (5), we get the following dynamic equations

$$M(q)\ddot{q} + C(q, \dot{q}) + G(q) = \tau, \quad (7)$$

where  $M(q)$  describes the inertia matrix;  $C(q, \dot{q})$  is the coriolis/centripetal vector and  $G(q)$  is the gravity vector. (7) can be written as

$$M(q)\ddot{q} + N(q, \dot{q}) = \tau, \quad (8)$$

where  $N(q, \dot{q}) = C(q, \dot{q}) + G(q)$  represents nonlinear terms.

Feedback linearization technique is used to convert the nonlinear dynamics represented by (8) into a linear state-variable system [8]. In order to obtain the alternative state-space equations of the dynamics, the position/velocity state  $x(t)$  of the joint is defined as

$$x(t) = [q'(t) \ \dot{q}(t)]', \quad (9)$$

and rewriting (8) as,

$$\frac{d}{dt} \dot{q}(t) = -M^{-1}(q(t))[N(q(t), \dot{q}(t)) - \tau(t)] \quad (10)$$

Therefore, from (9) and (10), a linear system in Brunovsky canonical form is obtained and represented as

$$\dot{x}(t) = \begin{bmatrix} 0 & 1 \\ 0 & 0 \end{bmatrix} x(t) + \begin{bmatrix} 0 \\ 1 \end{bmatrix} u(t). \quad (11)$$

The control input vector  $u(t)$  given by

$$u(t) = -M^{-1}(q(t))[N(q(t), \dot{q}(t)) - \tau(t)]. \quad (12)$$

As the prosthetic hand is required to track the desired force profile  $q_d(t)$  described under the reference force model, the tracking error  $e(t)$  is defined as

$$e(t) = q_d(t) - q(t). \quad (13)$$

Here,  $q_d(t)$  is the desired angle vector of the joints and can be obtained by the reference force model [6];  $q(t)$  is the actual angle vector of the joints. Differentiating (13) twice, we get,

$$\dot{e}(t) = \dot{q}_d(t) - \dot{q}(t), \quad \ddot{e}(t) = \ddot{q}_d(t) - \ddot{q}(t). \quad (14)$$

Substituting (10) into (14) gives

$$\ddot{e}(t) = \ddot{q}_d(t) + M^{-1}(q(t))[N(q(t), \dot{q}(t)) - \tau(t)]. \quad (15)$$

From (15) the control function  $u(t)$  can be defined as

$$u(t) = \ddot{q}_d(t) + M^{-1}(q(t))[N(q(t), \dot{q}(t)) - \tau(t)]. \quad (16)$$

This is often called the feedback linearization control law, rewriting (16) as,

$$\tau(t) = M(q(t))[\ddot{q}_d(t) - u(t) + N(q(t), \dot{q}(t))]. \quad (17)$$

Using (14) and (16), the state vector  $x(t) = [e'(t) \dot{e}(t)]'$ , the state-space model can be represented as

$$\dot{x}(t) = \begin{bmatrix} 0 & 1 \\ 0 & 0 \end{bmatrix} x(t) + \begin{bmatrix} 0 \\ 1 \end{bmatrix} u(t). \quad (18)$$

Now, (18) is in the form of a linear system such as

$$\dot{x}(t) = Ax(t) + Bu(t). \quad (19)$$

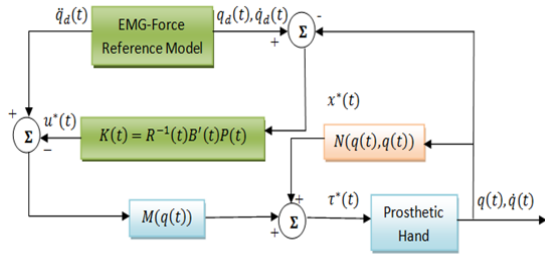


Fig. 1 Block Diagram of Optimal Controller for Prosthetic Hand.

### OPTIMAL TRACKING

Figure 1 shows the block diagram representation of the finite-time linear quadratic optimal controller for the prosthetic hand. The objective of the controller is for the prosthetic hand finger to track optimally the force model.

For the linear system (19), the finite-time linear quadratic optimal control problem can be formulated by defining the performance index  $J$  [14] as

$$J = \frac{1}{2} \int_{t_0}^{t_f} [x'(t) Q(t) x(t) + u'(t) R(t) u(t)] dt \quad (20)$$

where  $Q(t)$  is the error weighted matrix; and  $R(t)$  is the control weighted matrix. The optimal control  $u^*(t)$  is described by

$$u^*(t) = -R^{-1}(t)B'P(t)x^*(t) = -K(t)x^*(t). \quad (21)$$

where  $K(t) = -R^{-1}(t)B'P(t)$  is called Kalman gain and  $P(t)$ , is the solution of the matrix differential Riccati equation (DRE)

$$\dot{P}(t) = -P(t)A - A'P(t) - Q(t) + P(t)BR^{-1}(t)B'P(t) \quad (22)$$

Satisfying the final condition

$$P(t = t_f) = 0. \quad (23)$$

Hence the optimal state  $x^*$  is the solution of

$$\dot{x}^*(t) = [A - BR^{-1}(t)B'P(t)]x^*(t). \quad (24)$$

Therefore, with the optimal control  $u^*(t)$ , the required torque  $\tau^*(t)$  can be calculated by

$$\tau^*(t) = M(q(t))(\ddot{q}_d(t) - u^*(t) + N(q(t), \dot{q}(t))). \quad (25)$$

The torque  $\tau^*(t)$  is converted into force by

$$F_o(t) = \tau^*(t)/L, \quad (26)$$

where  $F_o(t)$  is the total force output of the index finger and  $L$  is the length of the finger. In this present work  $L$  is taken as 2.5 inches.

## VI. RESULTS AND DISCUSSION

Figure 2 shows the fusion model force  $\hat{Y}(t)$  and the force output from the controller  $F_o(t)$ . It is evident that the optimal controller can track the changes in the force profile and follow the trends in reference force profile.

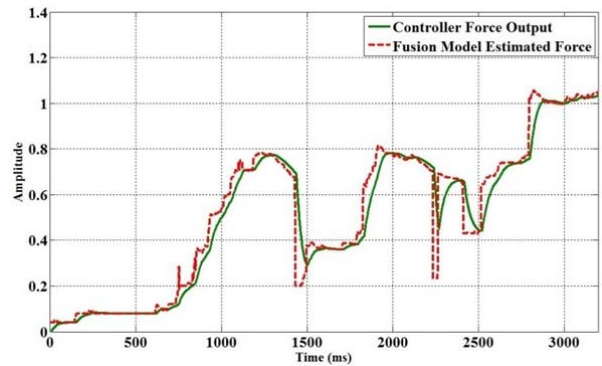


Fig. 2. Fusion Reference Model Force and Actual Force

Figure 3 shows the error between the model force  $\hat{Y}(t)$  and the force output from the controller  $F_o(t)$  for two different sets of results shown in Figs. 2 and 4. This figure shows that the error converged to zero in a very short time and the error is hovering between zero throughout the time interval. In some instances the force output of the controller  $F_o(t)$  cannot track the rapidly changing reference force profile during short intervals. The Pearson correlation coefficient (see Appendix) for the reference

$\hat{Y}(t)$  and controller output force  $F_o(t)$  profile is 0.8714. Figure 4 shows the validation with a different reference force  $\hat{Y}(t)$  profile and it yields 0.8707 correlation, thus showing good agreement between the reference model force and the actual force.

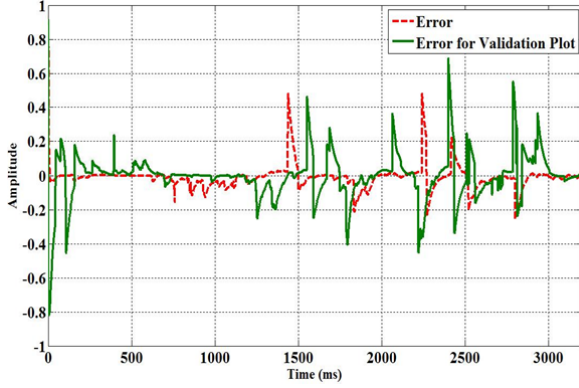


Fig. 3. Error between the Model Force and the Actual Force

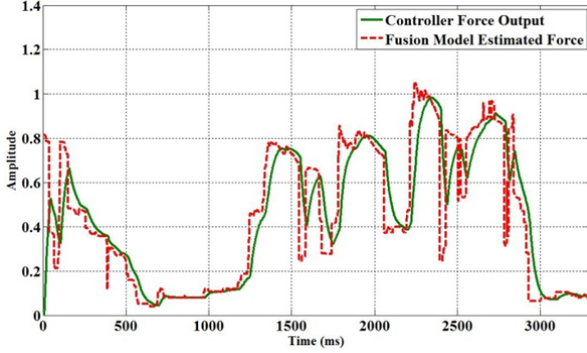


Fig. 4. Validation Plot

## VII. CONCLUSION AND FUTURE WORK

A fusion-based sEMG-force model was utilized to estimate the force profile that a prosthetic hand should track. This fusion enables to get better force estimates than the single sensor data. The dynamics of the hand was obtained and the controller for optimal tracking between the reference model and the hand was designed. The proposed design gives good performance when tested on a prosthetic hand, based on tracking a reference force profile. In future, we plan to implement this proposed control strategy on a micro controller for real time control. It would be interesting to implement both the force and position control using this control strategy. Finally, we plan to use the hand prototype with five fingers.

## APPENDIX

The resulting MISO transfer function  $H(s)$  is constructed as,

From  $u_1$  to output,

$$\frac{s^8 - 3.843s^7 + 7.729s^6 - 10.78s^5 + 10.6s^4 - 7.417s^3 + 3.603s^2 - 0.9795s + 0.1192}{s^8 - 4.028s^7 + 6.325s^6 - 4.121s^5 - 1.545s^4 + 5.87s^3 - 5.433s^2 + 2.28s - 0.3496}$$

From  $u_2$  to output,

$$\frac{s^8 - 4.339s^7 + 9.005s^6 - 12.42s^5 + 12.22s^4 - 8.117s^3 + 3.427s^2 - 0.9134s + 0.1424}{s^8 - 4.028s^7 + 6.325s^6 - 4.121s^5 - 1.545s^4 + 5.87s^3 - 5.433s^2 + 2.28s - 0.3496}$$

From  $u_3$  to output,

$$\frac{s^8 - 3.522s^7 + 6.655s^6 - 8.864s^5 + 8.183s^4 - 5.365s^3 + 2.423s^2 - 0.557s + 0.09585}{s^8 - 4.028s^7 + 6.325s^6 - 4.121s^5 - 1.545s^4 + 5.87s^3 - 5.433s^2 + 2.28s - 0.3496}$$

where  $u_1, u_2, u_3$  are the data from three sensors.

Pearson correlation coefficient is given by,

$$\rho_{X,Y} = \text{corr}(X,Y) = \frac{\text{cov}(X,Y)}{\sigma_X \sigma_Y} = \frac{E[(X - \mu_X)(Y - \mu_Y)]}{\sigma_X \sigma_Y}$$

Where  $X, Y$  are Random Variables,  $\mu_X$  and  $\mu_Y$  are expected values,  $\sigma_X, \sigma_Y$  are standard deviations respectively.  $E$  is expected value operator.

## ACKNOWLEDGMENT

This research was sponsored by the US Department of the Army, under the award number W81XWH-10-1-0128 awarded and administered by the U.S. Army Medical Research Acquisition Activity, 820 Chandler Street, Fort Detrick MD 21702-5014. The information does not necessarily reflect the position or the policy of the Government, and no official endorsement should be inferred. For purposes of this article, information includes news releases, articles, manuscripts, brochures, advertisements, still and motion pictures, speeches, trade association proceedings, etc. Further, the technical help from Dr. Cheng-Hung Chen, Mr. Amir Fassih and Mr. Parmod Kumar is greatly appreciated.

## REFERENCES

- [1] "Aca News: National Limb Loss Awareness Month" 2011. Retrieved from <http://www.bocusa.org/aca-news-national-limb-loss-awareness-month>
- [2] D.S. Naidu and C.-H. Chen, "Control Strategies for Smart Prosthetic Hand Technology: An Overview", Book Chapter 14, to appear in a book titled, Distributed Diagnosis and Home Healthcare (D2H2): Volume 2, American Scientific Publishers, CA, January 2011.
- [3] Zinn M, Roth B, Khatib O, and Salisbury JK, "A new actuation approach for human friendly robot design," *Int J Robot Res.* 2004; 23(4-5), pp. 379-398.
- [4] Heinzmann J, and Zelinsky J, "A safe-control paradigm for human-robot interaction," *J Intell Robot Syst.* 1999; 25(4): pp. 295-310.
- [5] Kandel E.R. and Scharzt J.H., "Principles of Neural Science," Elsevier/North-Holland, New York, 1981.
- [6] Potluri C., Kumar P., Anugolu M., Urfer A., Chiu S., Naidu D.S., and Schoen M, "Frequency Domain Surface EMG Sensor Fusion for Estimating Finger Forces," 32nd Annual International Conference of the IEEE Engineering in Medicine and Biology Society, Buenos Aires, Argentina, August 31 - September 4, 2010.
- [7] [http://www.isek-online.org/standards\\_emg.html](http://www.isek-online.org/standards_emg.html).
- [8] F.L.Lewis, D.M.Dawson, and C.T. Abdallah, "Robot Manipulators Control: Second Edition, Revised and Expanded", New York, NY: Marcel Dekker, Inc., 2004.
- [9] B.Siciliano, L.Sciavicco, L. Villani, and G. Oriolo, "Robotics: Modelling, Planning and Control". London, UK: Springer-verlag, 2009.
- [10] C.-H. Chen, "Hybrid Control Strategies for Smart Prosthetic Hand", Ph.D dissertation, Measurement and Control Engineering, Idaho State University, May 2009.
- [11] R. Kelly, V. Santidanez, and A. Loria, "Control of Robot Manipulators in Joint Space", New York, USA, Springer, 2005.
- [12] R.N. Jazar, "Theory of Applied Robotics, Kinematics, Dynamics, and Control", New York, USA, Springer 2007.
- [13] C-H Chen and D.S.Naidu, "Optimal Control Strategy For Two-Fingered Smart Prosthetic Hand", Proceedings of the IASTED International Conference Robotics and Applications (RA 2010), November 1-3, Cambridge, Massachusetts, USA, 2010.
- [14] D. Naidu, "Optimal Control Systems", Boca Raton, FL, CRC Press, 2003.



# Genetic Algorithm Based Optimization of Kullback Information Criterion: Improved System Identification of Skeletal Muscle Force and sEMG Signals

Madhavi Anugolu

Measurement and Control Engineering  
Research Center(MCERC)  
Idaho State University  
Pocatello, Idaho 83209  
anugmadh@isu.edu

Chandrasekhar Potluri

Measurement and Control Engineering  
Research Center (MCERC)  
Idaho State University  
Pocatello, Idaho 83209  
potlchan@isu.edu

Alex Urfer

Department of Physical and  
Occupational Therapy  
Idaho State University  
Pocatello, Idaho 83209  
urfealex@isu.edu

Jim Creelman

Department of Physical and  
Occupational Therapy  
Idaho State University  
Pocatello, Idaho 83209  
creejame@isu.edu

Parmod Kumar

Nanyang Technological University  
50 Nanyang Avenue, Singapore 639798  
pkumar@ntu.edu.sg

Marco P. Schoen

MCERC  
Department of Mechanical Engineering  
Idaho State University  
Pocatello, Idaho 83209  
schomarc@isu.edu

**Abstract—** This paper focuses on determining the sensitivity of the number of data points used in computing the Kullback Information Criterion (KIC) for the use in sensor data fusion. The primary objective of the sensor fusion is to improve the extraction of dynamic models relating Surface Electromyographic (sEMG) signals with the corresponding skeletal muscle force signals. The proposed approach utilizes a pre-processing of the sEMG data with a Half-Gaussian filter. System Identification techniques are employed to extract a relationship between the sEMG and the skeletal muscle force. In this paper linear and non-linear models are inferred from the fused data to describe the sEMG/force relationship. In order to optimize the number of data points for finding the optimum KIC, a Genetic Algorithm (GA) is used.

**Keywords—**Kullback Information Criterion, Genetic Algorithm, Half-Gaussian filter, Prostheses.

## I. INTRODUCTION

According to the National Limb Loss Information Center analysis; there are two million people with missing upper body limbs living in the United States, [1]. This number is increasing due to ongoing war engagements, and it is estimated that this number will reach 3.6 million by the year 2050. A lot of effort has been placed on research dealing with advanced prosthetic devices. However, up to date there are no prosthetic devices available that mimic the full functionality of a human hand. Moreover, the available prosthetics are rather

costly. There are multiple types of hand prostheses. One of these types is based on measuring surface Electromyographic (sEMG) signals to initiate the actuation of the robotic hand, [2]. Since, sEMG signals are spatially distributed, the sEMG probes will pick up signals from other motor units stemming from different muscle groups. This phenomenon is called crosstalk, which is a major cause for the difficulty in extracting hand finger motion and force intends. EMG signals are generated by the simultaneous firing of several motor units during muscle contraction, [3]. Before reaching the skin surface, the sEMG signal passes through numerous layers of tissues [3], which leads to noise and interference in the signal acquisition. The random nature of the EMG signal represents an added complexity in studying it. All of these issues make it rather complex to distinguish the content of the EMG signal against noise and interference. The content of the EMG signal can be identified based on amplitude, frequency, and amplitude-frequency methods. The EMG signal is time and amplitude modulated as well as spatially and temporally frequency encoded, [4]. In [5] a novel approach was introduced to differentiate the onset of the muscle contraction. In their study, Continuous Wavelet transforms are used to identify the action potential of the individual motor units..

In this work, an array of three sEMG sensors is used to improve the accuracy of the sensed information. The objective is to infer the intended finger force of a transradial hand amputee using sEMG signals collected at the forearm location. Array sensors use multi-channel EMG electrodes which can be embedded into a small surface area in order to capture the

electrical muscle activity from a set of muscles fibers at the skin level.

In [6], a multi-channel methodology is proposed where elements of the sensor array are discarded based on the quality of the signal. In the present work, a sensor fusion is utilized that is based on the Kullback Information Criterion (KIC), System Identification (SI), and a Genetic Algorithm (GA) based optimization scheme.

Contrary to other prosthetic hand designs, in this work, we seek to model the sEMG and finger force relationship in a dynamic fashion. While other smart prosthetics use simple root mean square (RMS) values to initiate a pre-programmed motion and force command set, in this work, we use the measured sEMG signal to infer directly the intended instantaneous fingertip forces. We acquire data using three sEMG sensors and the corresponding skeletal muscle force data with one force sensing resistor (FSR). The forces are generated with the corresponding finger, i.e. the proximal interphalangeal (PIP) joint of the index finger. The sEMG and force data are filtered using a GA based optimized Half-Gaussian Bayesian filter and a Chebyshev Type II filter, respectively. For three sEMG sensors, three Output Error (OE) models of order 6, 6, and 10 and nonlinear Wiener-Hammerstein models of order 10, 10 and 10 are obtained using system identification. The OE model's outputs are fused with a Kullback Information Criterion (KIC) based data fusion. KIC uses a set number of data points to compute the likelihood of the models influence on the output. The authors have not found in the literature a study that indicates what the optimal number of data points is for computing the KIC coefficient. Hence, in this work we utilize a GA based optimization on the number of data points to be used for the computation of the KIC coefficient. The optimization is based on the correlation of the fused model output and the actual finger force. This paper is organized as experimental design, signal pre-processing and system identification, Kullback information criterion, genetic algorithm, results and discussion and conclusion follow this section.

## II. EXPERIMENT DESIGN

To acquire the sEMG signals, experiments are carried out on a healthy male subject in order to collect the data from three sEMG sensors corresponding to one individual motor point and locations in close proximity to this motor point. The motor point on Flexor Digitorum Superficialis (FDS) muscle is identified by using a wet probe point muscle stimulator (Rich-Mar Corporation, model number HV 1100.). For the acquisition of sEMG data from the skin surface, a Delsys<sup>®</sup>, Bagnoli-16 channel EMG system along with DE 2.1 pronged differential surface electrodes is used. The measurement set-up is depicted in Fig. 1. This acquisition system has the capability of amplifying the signal internally and reducing the acquisition noise. The force data is measured by an Interlink<sup>TM</sup> Electronics 0.5" circular FSR. Both the force and sEMG signals are acquired at 2000 samples per second using LabVIEW<sup>TM</sup>.

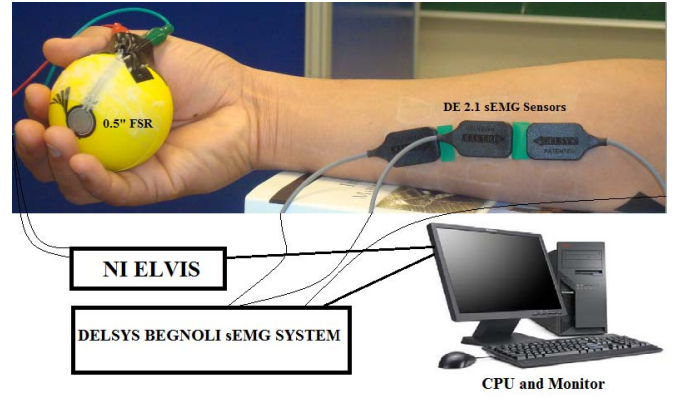


Figure 1. Measurement set-up for acquiring sEMG and fingertip force data.

## III. SIGNAL PRE-PROCESSING AND SYSTEM IDENTIFICATION

The force data is filtered using a low-pass Chebyshev Type II filter, which has a cut off frequency of 550 Hz. Since the Bayesian filters can monitor the rapid changes in the signal, a Bayesian Half-Gaussian filter is used to filter the sEMG data, see Equation (1). A Bayesian filtering method may potentially provide a good EMG signal for classification purposes, [7]. The filter has not been investigated in terms of the use for system identification, where the output forces generated by the hand are modeled based on the measured sEMG data. The Half-Gaussian filter is given by:

$$p(EMG|x) = 2 \frac{\exp\left\{\frac{-EMG^2}{2x^2}\right\}}{\sqrt{2\pi x^2}} \quad (1)$$

where  $p(EMG|x)$  is the conditional probability,  $x$  is the latent driving signal, and EMG is the acquired data. The EMG signal is modeled for the conditional probability of the rectified EMG signal as a filtered random process with random rate. The likelihood function for the rate evolves in time according to a Fokker-Planck partial differential equation, [8]. The discrete time Fokker-Planck equation is given by (2):

$$p(x, t) \approx \alpha p(x - \epsilon, t-1) + (1-2\alpha) p(x, t-1) + \alpha p(x + \epsilon, t-1) + \beta + (1-\beta) p(x, t-1) \quad (2)$$

Here,  $\alpha$  and  $\beta$  are two free parameters, where  $\alpha$  is the expected rate of gradual drift in the signal, and  $\beta$  is the expected rate of sudden shifts in the signal. The unknown driving signal  $x$  is discretized into bins of width  $\epsilon$ . These two free parameters ( $\alpha, \beta$ ) of the non-linear Half-Gaussian filter model are optimized for the acquired EMG data using an elitism based GA.

A system identification technique is used to infer the mathematical relationship between the measured sEMG data and the corresponding finger force data. In this work, both linear parametric models and non-linear models are used. In particular, output error models and Wiener-Hammerstein



models are used. For both of these cases, sEMG data is used as the input and the corresponding collected fingertip force data is the output. The model orders for the various models are selected as 6, 6 and 10 for the three OE models  $M_1, M_2$  and  $M_3$ , corresponding to the each sensor location. For the Wiener-Hammerstein (WH) models, the orders are selected as 10, 10 and 10.

The linear parametric OE model structure is given by

$$y(t) = \frac{B(q)}{F(q)} u(t - n_k) + e(t), \quad (3)$$

where  $y$  is the output vector,  $t$  is the discrete time index,  $B(q)$ ,  $F(q)$ ,  $A(q)$ ,  $C(q)$ , and  $D(q)$  are polynomials,  $q$  is a backward shift operator,  $u$  is the input,  $n_k$  is the delay order, and  $e$  is the error.

The structure of the non-linear Wiener-Hammerstein model is given by Fig 2.

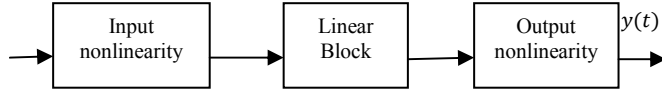


Figure 2. Wiener Hammerstein block diagram.

The linear part of the corresponding equation is given by

$$y_L(t) = \left(\frac{B}{F}\right) u_L(t - n_k) \quad (4)$$

The non-linear equation for a one-dimensional polynomial is given by

$$y = F(x) \quad (5)$$

where ' $F$ ' is a single-variable polynomial function of ' $x$ '.

$$F(x) = c(1)x^n + c(2)x^{n-1} + \dots + c(n)x + c(n+1) \quad (6)$$

The polynomials are estimated using the Matlab® System Identification toolbox. In this process, the collected input and output data are utilized to estimate the corresponding parameters of the assumed model structures (OE and WH) with the predefined model orders. The model orders were selected in a trial-by error approach, observing which combination provides for the best model fit value. This fit value is computed using the following equation:

$$fit = 100 \left[ 1 - \frac{|y - \hat{y}|}{|y - \bar{y}|} \right] \quad (7)$$

where  $\hat{y}$  is the estimated finger force using the identified models, and  $\bar{y}$  is the mean output signal.

The correlation is computed for the actual force and fusion model estimated force. The Pearson correlation coefficient given by [9] is restated below:

$$\rho_{X,Y} = corr(X,Y) = \frac{cov(X,Y)}{\sigma_X \sigma_Y} = \frac{E[(X-\mu_X)(Y-\mu_Y)]}{\sigma_X \sigma_Y} \quad (8)$$

where  $X, Y$  are random variables,  $\mu_X$  and  $\mu_Y$  are expected values,  $\sigma_X, \sigma_Y$  are standard deviations respectively.  $E$  is the expected value operator.

#### IV. KULLBACK INFORMATION CRITERION DATA FUSION

The Kullback Information Criterion (KIC) is a symmetric measure used in this work for the fusion of sEMG sensor array data. Kullback's symmetric or  $J$ -divergence can be used to measure the dissimilarity in models, [10]. The mathematical form of the KIC is given as:

$$KIC(p_i) = \frac{n}{2} \log R_i + \frac{(p_i+1)n}{n-p_i-2} - n\psi\left(\frac{n-p_i}{2}\right) + g(n) \quad (9)$$

where,  $n$  is the number of data points  $p_i$  is the order of the model,  $\psi$  is the digamma function, and  $g(n) = n * \log \frac{n}{2}$ .

After computing the KIC for each of the three models, the following fusion algorithm is utilized in order to get the overall estimated finger force  $\hat{y}$ , [11, 12]:

1. Identify the OE/WH models  $M_1, M_2 \dots M_k$  using sEMG data ( $u$ ) as input and fingertip force data ( $y$ ) as output, for  $k$  number of sEMG sensors.
2. Compute the residual square norm

$$R_i = \|y - \Phi_i \hat{\theta}_i\|^2 = \|y - \hat{y}\|_2 \text{ where } \hat{\theta}_i = \{\Phi_i^T \Phi_i\}^{-1} \Phi_i^T y,$$

$$\text{and } \bar{\Phi} = \begin{bmatrix} y_p^T & u_p^T & y_{p-1}^T & \dots & u_1^T \\ y_{p+1}^T & u_{p+1}^T & y_p^T & \dots & u_2^T \\ \vdots & \vdots & \vdots & \ddots & \vdots \\ y_{n-1}^T & u_{n-1}^T & y_{n-2}^T & \dots & u_{n-p}^T \end{bmatrix}$$

3. Calculate the model criteria coefficient using (9).
4. Compute the model probability as given by

$$p(M_i | Z) = \frac{e^{-l_i}}{\sum_{j=1}^k e^{-l_j}}, \text{ where } l \text{ is the model selection criteria coefficient, i.e. } KIC(p_i).$$

5. Compute the fused model output  $\hat{y}_f = \sum_{i=1}^k p(M_i | Z) \hat{y}_i$

According to the literature, for (9), the standard number of data points,  $n$ , is set to 30. However, there appears to be no investigation on what the optimum value is for achieving a

good fusion output. In this paper, we are interested in finding an optimum value for  $n$  with regard to the identification and fusion results applied to finger force data and sEMG data. In particular, the search for an optimum value is also limited – in order to preserve the computational efficiency – to a range of  $15 \leq n \leq 160$ .

## V. GENETIC ALGORITHM

The objective function for the optimization of the number of data points used in the KIC fusion based algorithm is formulated by the squared accumulative absolute value of the error between the estimated and measured muscle force data and the corresponding correlation between the resulting estimated force  $\hat{y}_f$  and the actual force  $y$ . In particular, the cost function is given by

$$J = \lambda \sum_{i=1}^n |y(t-i) - \hat{y}_f(t-i)|^2 + v(\text{corr}[y, \hat{y}_f]) \quad (8)$$

where,  $\lambda$  and  $v$  are weighting coefficients and  $\text{corr}(\cdot)$  is the correlation function.

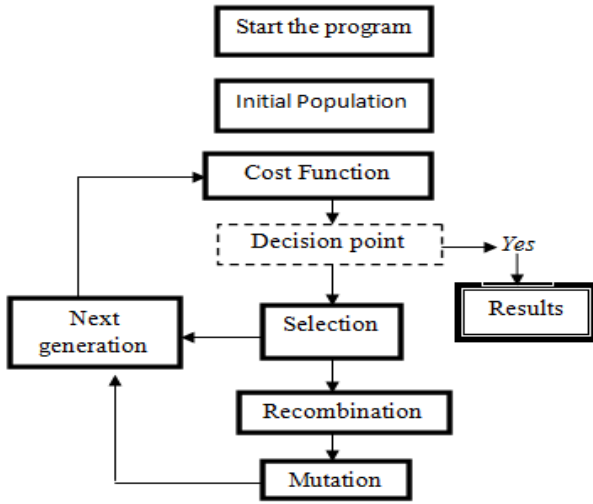


Figure 3. Flow chart representation of a genetic algorithm.

The objective function is used in a elitism based continuous number genetic algorithm. Genetic algorithms are evolutionary algorithms that simulate Darwin's survival of the fittest principle. The initial population of the candidate solutions is randomly generated and represented as chromosomes (where the genes are formed as each parameter of the solution). These chromosomes are evaluated based on an objective function and ranked in terms of its fitness. A subset of the next generation of candidate solutions is selected based on their performance with the objective function. The remaining set of the new generation is produced by a mating process, where the best performing candidate solutions comprise the subset of the parents. In addition to the mating process, a mutation rate is also imbedded in the generation of the new population. The mutation rate enables the search for

the optimum solution to overcome local minimums and locate the global minimum/optimum. This process of selection, mating, and mutation is repeated a number of times until the best performing candidate solution converges to some stationary value. The flow chart representation of the genetic algorithm is shown in Fig. 3.

## VI. RESULTS

Fig. 4 and depicts a sample of collected sEMG data, and the proposed filtering process of the same sEMG data using a Half Gaussian Bayesian filter. Two different sampling frequencies are utilized for the sEMG data collection. Fig. 5 and 6 depict the predicted finger force obtained by using the linear output error model and the actual finger force for the cases of 2000 Hz and 1000 Hz sampling rates. In case of 2000 samples/sec, the correlation between the actual force and estimated force is 91% and the error is 0.0070, where as in case of using 1000 Hz the correlation between the actual force and the estimated force is 86% and the error is 0.0108.

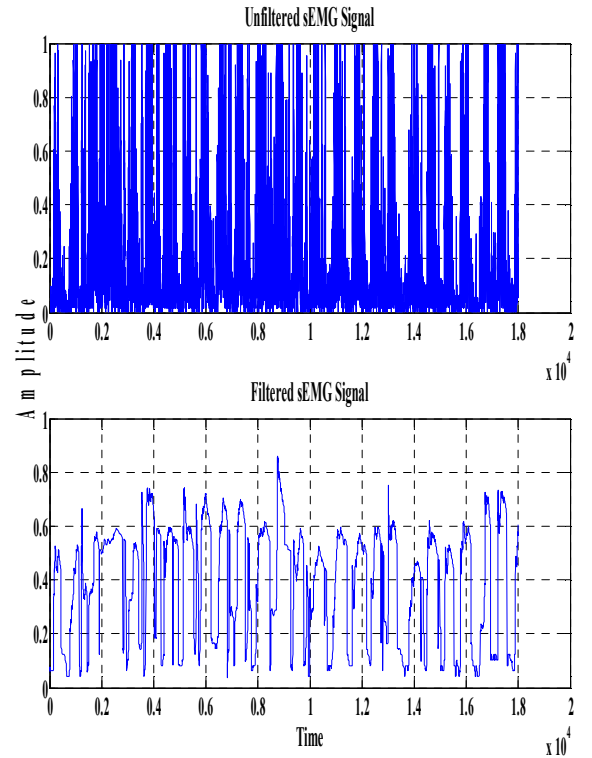


Figure 4. Unfiltered and filtered sEMG data acquired at 2000 sample/sec.

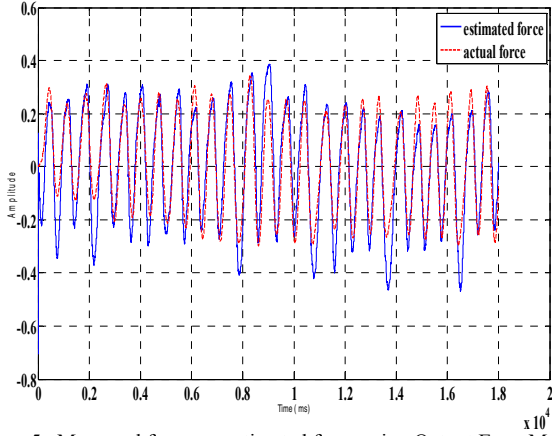


Figure 5. Measured force vs. estimated force using Output Error Models.

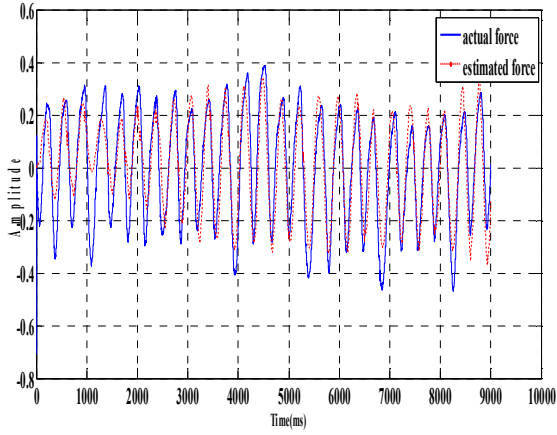


Figure 6. Measured force vs. estimated force for down sampled data using Output Error Models.

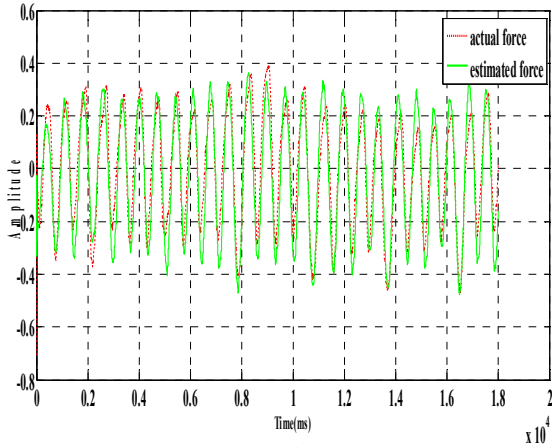


Figure 7. Actual force and fusion model estimated force using non-linear Wiener-Hammerstein model.

For the non-linear Wiener-Hammerstein models, the correlation between the actual force and the estimated force is independent of the sampling rate and is 89% for both cases, 1000 Hz and 2000 Hz.

The literature addressing the use of the KIC for the purpose of data fusion, the number of data points used has been set to some small number, i.e. quite often one finds  $n=30$ . However, there is no analysis existing to support this selection. Using the proposed GA and objective function as defined in Equation 8, and the two model structures to characterize the sEMG relationship to skeletal muscle force, the resulting quality of the extracted OE and WH models is rather insensitive to the number of data points used to compute the KIC. In this paper, the search area has been confined to a range of 145 data points and the conclusions are to be made only for this range. The extended range has not been a topic of this investigation and may hold improved results. However, the computational cost increases substantially with larger numbers of data point for the computation of the KIC, which is reflected in longer computation times, and is impractical for modelling sEMG signals of muscle forces.

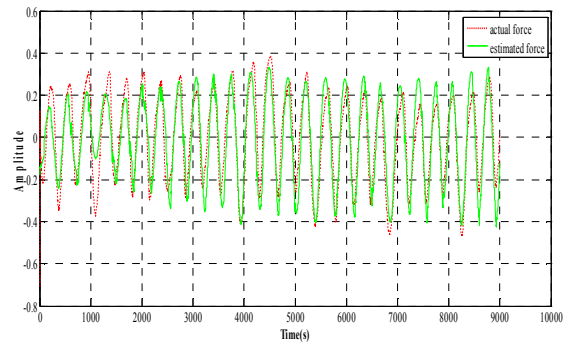


Figure 8. Actual force and fusion model estimated force using non-linear Wiener-Hammerstein model for down sampled data.

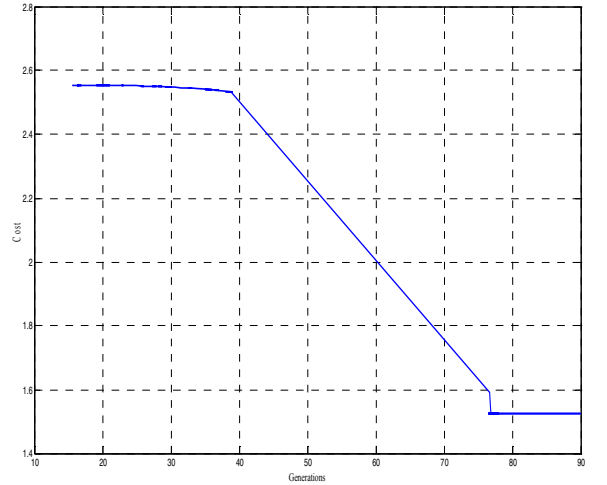


Figure 9. Minimum cost for GA using 100 generations.

The minimum cost as defined by Equation 8 for a GA using 100 generations is shown for each iteration in the Fig. 9

TABLE I. COMPARISON OF OE MODEL PROBABILITY FOR THREE SENSORS

$n$	$pmz1$	$pmz2$	$pmz3$	corr
30	0.0059	0.0059	0.9882	0.9151
50	0.0163	0.0163	0.9673	0.9153
75	0.0311	0.0311	0.8832	0.9155
100	0.0584	0.0584	0.8832	0.9156

For Table I and II,  $pmz1, pmz2, pmz3$  - are the individual probabilities of the models  $M_1, M_2$  and  $M_3$ , corr- stands for the correlation between actual force and estimated force.

TABLE II. COMPARISON OF WH MODEL PROBABILITY FOR THREE SENSORS

$n$	$pmz1$	$pmz2$	$pmz3$	corr
30	0.3502	0.3502	0.2995	0.8869
50	0.3565	0.3565	0.2869	0.8893
75	0.4019	0.4019	0.1962	0.8925
100	0.4273	0.4273	0.1454	0.8928

From Table I and Table II, we can infer that the highest correlation is at the optimum value. However, the sensitivity with respect to the number of data points ' $n$ ' used in the fusion algorithm is minimal. This implies that the selection of the number of data points ' $n$ ' has little influence on the fusion algorithm and can be chosen small in order to preserve computational efficiency.

## VII. CONCLUSION

In summary, this paper is an extension of our previous work in order to find the optimum data points used in computing the KIC for the use in a fusion technique. This addresses a void in the current literature where KIC is used for model probability and model fusion. The optimum number of data points is found in this paper using a GA, with an objective function that incorporates the extracted linear and nonlinear models relating sEMG data and skeletal muscle force data. The sEMG data is pre-processed using a Half-Gaussian filter, where as the linear models are OE models and the non-linear models used in this investigation are WH models. The primary conclusion of this work is that the sensitivity of the number of data points used

in the fusion algorithm is small and hence small numbers can be utilized in order to facilitate computational efficiency.

## ACKNOWLEDGEMENT

This research was sponsored by the US Department of the Army, under the award number W81XWH-10-1-0128 awarded and administered by the U.S. Army Medical Research Acquisition Activity, 820 Chandler Street, Fort Detrick MD 21702-5014. The information does not necessarily reflect the position or the policy of the Government, and no official endorsement should be inferred. For purposes of this article, information includes news releases, articles, manuscripts, brochures, advertisements, still and motion pictures, speeches, trade association proceedings, etc.

## REFERENCES

- [1] Estimating the Prevalence of Limb Loss in the United States - 2005 to 2050, Kathryn Ziegler-Graham, Archives of Physical Medicine and Rehabilitation vol. 89(3), pp 422-429, 2008.
- [2] Northrop R, "Analysis and Application of analog Electronic Circuits to biomedical Instrumentation", CRC Press, Boca Raton, Florida, 2004, pp 6-9.
- [3] J.R. Cram, G.S. Kasman, and J Holtz. "Introduction to Surface Electromyography", Aspen Publisher Inc, Gaithersburg, Maryland, 1998
- [4] E.R. Kandel and J.H., Scharz "Principles of Neural Science", Elsevier/North-Holland, New York, 1981.
- [5] A. Merlo, D Faina and R. Merletti, "A Fast and Reliable Technique for Muscle Activity Detection from Surface EMG Signals", IEEE Transaction on Biomedical Engineering , vol 50(3), pp-316-323, 2003
- [6] K Natata, K Adno, M Yamada, K Magatani, "A Classification Method of Hand Movements using Multi Channel Electrode", Proceedings of the 27<sup>th</sup> Annual conference IEEE Engineering in Medicine, Shanghai, China, September 1-4, 2005, pp.2375-2378
- [7] Terence D. Sanger, "Bayesian Filtering of Myoelectric Signals, 2007, URL <http://jn.physiology.org/cgi/content/abstract/97/2/1839>
- [8] C. Potluri, M. Anugolu, P Kumar, A Fassih, Y. Yihun, S Chiu, D. S. Naidu, " Real-time sEMG acquisition and processing using a PIC 32 Microcontroller", ESA'11 - 9th Int'l Conference on Embedded Systems and Applications, Las Vegas, Nevada, USA, July 18-21, 2011.
- [9] C. Potluri, M. Anugolu, Y Yihun, P. Kumar, S. Chiu, Member, IEEE, M. Schoen, Senior Member, IEEE, D.S. Naidu, Fellow, IEEE "Implementation of sEMG-Based Real-Time Embedded Adaptive Finger Force Control for a Prosthetic Hand", 50<sup>th</sup> International IEEE Conference on Decision and Control and European Control Conference, Orlando, Florida, USA, December 12-15, 2011.
- [10] Abd-Krim Seghouane, M. Bekara and G. Fleury, "A small Sample Model selection Criterion Based on Kullback's symmetric Divergence," IEEE Transaction, 2003, pp 145-148.
- [11] H. chen, S. Huang, "A Comparative study of Model Selectio and Multiple Model Fusion", 7<sup>th</sup> International Conference on Information Fusion, 2005, pp 820-826.
- [12] M. Anugolu, A. Sebastian, P. Kumar, M. Schoen, A. Urfer, and D. S. Naidu, "Surface EMG Array Sensor Based Model Fusion Using Bayesian Approaches For Prosthetic Hands," 2009 ASME Dynamic Systems and Control Conference, Hollywood, California, USA, Oct. 12-14, 2009.

# A sEMG-SKELETAL MUSCLE FORCE DATA FUSION BASED ON MINIMUM DESCRIPTION LENGTH CRITERION

Madhavi Anugolu, Chandrasekhar Potluri, Steve Chiu, Alex Urfer, Jim Creelman and Marco P. Schoen

**Abstract**—This paper provides a method of fusing the sEMG/skeletal muscle force sensor array data using a Minimum Description Length (MDL) data fusion algorithm. The sEMG data and the corresponding skeletal muscle force data are acquired from a test subject. A nonlinear Bayesian Half-Gaussian filter is utilized to filter sEMG data and the skeletal muscle force signal is filtered by using a Chebyshev Type-II filter. A System Identification Technique is employed to derive the mathematical relationship between the sEMG (input) and the skeletal muscle force (output) data. We implemented linear and nonlinear parametric- Auto-Regressive with eXogenous input (ARX), Auto-Regressive Moving Average with eXogenous input (ARMAX), Output Error (OE) and Weiner Hammerstein modeling. The estimated model output from the three sensors are combined by using a probabilistic based Minimum Description Length (MDL) fusion algorithm. The results are thought provoking and the overall fused output has better correlation with the actual force when compared with the individual sensor estimated force.

**Keywords:** sEMG, hand prostheses, data fusion, system identification, minimum description length criterion

## I. INTRODUCTION

In the United States, there are more than 2 million amputees and according to the statistics provided by the National Limb Loss Information Center, this number will reach 3.6 million by 2050 [1].

Madhavi Anugolu is with the Measurement and Control Engineering Research Center (MCERC), School of Engineering, Idaho State University, Pocatello, Idaho 83209, USA (email: anugmadh@isu.edu).

Chandrasekhar Potluri is with the MCERC, School of Engineering, Idaho State University, Pocatello, Idaho 83209, USA (e-mail: potlchan@isu.edu).

Steve Chiu is with the Department of Electrical Engineering and Computer Science, MCERC, Idaho State University, Pocatello, Idaho 83201 USA (email: chiustev@isu.edu).

Jim Creelman is with the Department of Physical and Occupational Therapy, Idaho State University, Pocatello, Idaho 83209, USA (email: creljim@isu.edu).

Alex Urfer is with the Department of Physical and Occupational Therapy, Idaho State University, Pocatello, Idaho 83209, USA (email: urfealex@isu.edu).

Marco P. Schoen is with the Department of Mechanical Engineering, MCERC, Idaho State University, Pocatello, Idaho 83209, USA (email: schomarc@isu.edu).

The etiologies of hand amputations include cardiovascular disease, congenital deformities, nerve injuries, tumors, and trauma [2]. Over the past few decades, numerous research and clinical studies have concentrated on the field of prosthetics. Even today, however, most individuals with upper extremity and hand amputations have difficulty acquiring an affordable prosthesis which allows for good functional hand motion. [3] Due to recent advances in technology, a great interest has emerged in the design of a better hand prosthesis controlled by integrated Electromyographic (EMG) signaling. In general, the EMG signal is a composition of action potentials produced by the electrical activity of the muscle groups. This signal depends on the flow of ions such as sodium ( $\text{Na}^+$ ), calcium ( $\text{Ca}^{++}$ ), and potassium ( $\text{K}^+$ ). These signals can be measured either by inserting the needle electrodes into the muscle tissues or by affixing the surface electrodes to the skin.

In this work, we used surface Electromyographic (sEMG) data since it does not require any surgical monitoring. The sEMG signals can be used in various engineering and clinical applications [4, 5]. One must be careful in analyzing sEMG signal [6]. Especially in engineering application, sEMG can be used to control the position and force of the prosthetic hand [7]. The sEMG signal amplitude varies from person to person and it depends on the applied force. Some other factors like cross-talk from different muscle groups, and biochemical reactions in the muscle fibers influence the sEMG/skeletal muscle force relationship. Therefore, these factors contribute to randomness and complexity of the sEMG signal.

From our particular perspective, it is desirable to combine the data from the array of sensors. So, in this work, we implemented a Minimum Description Length (MDL) criterion to fuse the sEMG/skeletal muscle force data from the three sensors. After collecting the data, the sEMG signals are filtered using a Genetic Algorithm (GA) based nonlinear Bayesian Half-Gaussian filter. The skeletal muscle force data is filtered by using a Chebyshev Type-II filter. Considering the sEMG as input and skeletal muscle force as output, System Identification (SI) technique is utilized to extract the dynamic relationship between the sEMG data and its corresponding skeletal muscle force data. The estimated output models are fused with a probabilistic based Minimum Description Length (MDL) criterion.

## II EXPERIMENTAL DESIGN

For this work, the experiments were conducted on a healthy male subject to acquire the sEMG and its corresponding skeletal muscle force signal. Prior skin preparation was done by following the ISEK standards [8]. A muscle point stimulator manufactured by Richmar Corporation™ was used to identify the muscle motor point. For this particular experiment, the ring finger motor location on the flexor muscle was chosen. Fig. 1 illustrates the experimental design. Three sensors were placed on the skin surface, one on the ring finger flexor digitorum superficialis muscle motor point and the other two adjacent to it. A Delsys Banglo-16, was used to capture the sEMG signal and the Force Sensitive Resistor (FSR) was used to acquire the corresponding skeletal muscle force signals. Both the signals were acquired through LABVIEW at a sampling rate of 2000 sample/sec.

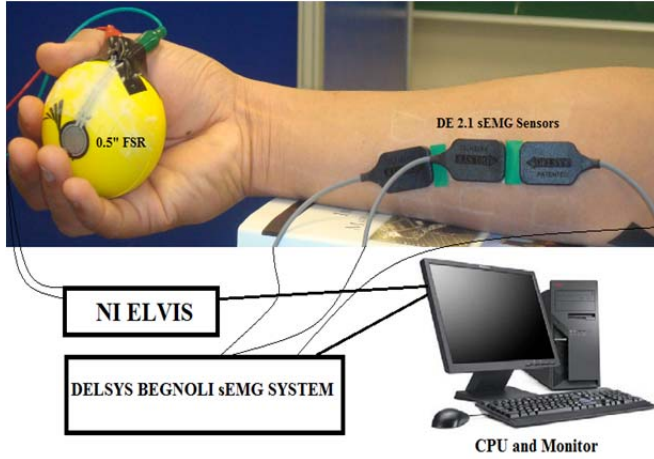


Fig. 1: Experimental Set-up

## III. THEORITICAL BACKGROUND

The sEMG data acquired from the surface of the skin is rectified and filtered using a GA based nonlinear Bayesian Half-Gaussian filter. In our previous work [9] we explored different filters for sEMG filtration. We concluded that the Bayesian Half-Gaussian filter works better when compared to other filters like Butterworth, Chebyshev, Bayesian Poisson. As mentioned earlier, sEMG depends on various factors. The relationship between the actual force and the resulting sEMG after filtration can be given by the conditional probability density function ( $EMG|x$ ). Under the assumption that the conditional probability of the rectified EMG signal is a filtered random process at a random rate the Half-Gaussian filter is given by:

$$p(EMG|x) = 2 \frac{\exp\left\{\frac{-EMG^2}{2x^2}\right\}}{\sqrt{2\pi x^2}}, \quad (1)$$

where  $p(EMG|x)$  is the conditional probability,  $x$  is the latent driving signal, and EMG is the acquired data. According to Fokker-Planck partial differential equation, the likelihood function for the rate evolves in time [10]. The discrete time Fokker-Planck equation is given by (2)

$$p(x, t) \approx \alpha p(x - \varepsilon, t-1) + (1-2\alpha) p(x, t-1) + \alpha p(x + \varepsilon, t-1) + \beta + (1-\beta) p(x, t-1). \quad (2)$$

Here,  $\alpha$  and  $\beta$  are two free parameters, where  $\alpha$  is the expected rate of gradual drift in the signal, and  $\beta$  is the expected rate of sudden shifts in the signal. The unknown driving signal  $x$  is discretized into bins of width  $\varepsilon$ . These two free parameters ( $\alpha, \beta$ ) of the non-linear Half-Gaussian filter model are optimized for the acquired EMG data using an elitism based GA. A Chebyshev Type-II filter with 550 Hz cutoff frequency is used to filter to skeletal muscle force signal.

### Linear and nonlinear System Identification Models:

System Identification uses statistical methods to implement the dynamic relationship between the measured input/output data. This is done by altering the parameters within a given model until its output tracks the measured input, [11]. System identification is an alternative to the physical based modeling [11]. In this work, linear parametric models- Auto-Regressive with eXogenous input (ARX), Auto-Regressive Moving Average with eXogenous input (ARMAX), Output Error (OE) and nonlinear models- Wiener Hammerstein are implemented

The output error model structure is

$$y(t) = \frac{B(q)}{F(q)} u(t - n_k) + e(t) \quad (3)$$

The ARX model is a random process. It predicts the output based on the previous output. Its mathematical notation is given by equation (4)

$$A(q)y(t) = B(q)u(t - n_k) + e(t) \quad (4)$$

Based on the given data, the ARMAX model predicts the future values in a series. The mathematical notation is given by Equation (5). It consists of two parts, the autoregressive part and the moving average part.

$$A(q)y(t) = B(q)u(t - n_k) + C(t)e(t) \quad (5)$$

In Equations (3), (4) and (5),  $y$  is output,  $t$  is time,  $B(q)$ ,  $F(q)$ ,  $A(q)$ ,  $C(q)$ ,  $D(q)$ , are polynomials,  $q$  is a backward shift operator,  $u$  is input,  $nk$  is delay and  $e$  is error

### Nonlinear Wiener Hammerstein

A model with a fixed nonlinearity at the input is called a Hammerstein model. When the nonlinearity is at the output is called a Wiener model. The combination of these both is the Wiener-Hammerstein model, [11]. The structural representation of the Wiener- Hammerstein model is given in Fig. 2, [12]. It consists of two nonlinear blocks with a linear block in series.



Fig. 2: Wiener-Hammerstein model structural representation

The mathematical depiction of the modeling is given by,

$$w(t) = f(u(t)) \quad , \quad (6)$$

$$x(t) = \frac{B_{j,i}(q)}{F_{j,i}(q)} w(t - nk) + e(t) \quad , \quad (7)$$

$$y(t) = h(x(t)) \quad , \quad (8)$$

where  $u(t)$  is the sEMG signal and  $y(t)$  is the skeletal muscle force signal.  $f$  and  $h$  are nonlinear functions,  $w(t)$  and  $x(t)$  are internal variables,  $B_{j,i}(q)$  and  $F_{j,i}(q)$  are polynomials,  $q$  is the back shift operator, and  $e(t)$  is the output error.

### Minimum Description Length (MDL) Criterion

In 1978, the Minimum Description Length (MDL) concept was introduced by Jorma Rissanen [13]. The fundamental idea behind the MDL principle is based on the algorithmic complexity of Solomonoff, Kolmogorov and Chaitin [14]. In this work, we are inspired by [15] and used the Minimum Description Length criterion to fuse the estimated models. It is given by

$$MDL(p_i) = \frac{n}{2} \log(\hat{\sigma}_i^2) + \frac{p_i+1}{2} \log F_i + L_i \quad , \quad (9)$$

where  $F_i = (Y^T Y - R_i) / (p_i \hat{\sigma}_i^2)$ ,

$$L_i = \frac{1}{2} \log\left(\frac{n-p_i}{p_i^3}\right) \quad ,$$

$$\hat{\sigma}_i^2 = R_i / (n - p_i) \quad .$$

Based on [9 and 15], the following fusion algorithm is implemented for sEMG-skeletal muscle models.

1. Identify the models  $M_1, M_2 \dots M_k$  using sEMG data ( $u$ ) as input and fingertip force data ( $y$ ) as output, for  $k$  number of sEMG sensors.
2. Calculate the residual square norm

$$R_i = \|y - \Phi_i \hat{\theta}_i\|^2 = \|y - \hat{y}\|_2^2 \text{ where } \hat{\theta}_i = \{\Phi_i^T \Phi_i\}^{-1} \Phi_i^T y \quad ,$$

$$\text{and } \bar{\Phi} = \begin{bmatrix} y_p^T & u_p^T & y_{p-1}^T & \dots & u_1^T \\ y_{p+1}^T & u_{p+1}^T & y_p^T & \dots & u_2^T \\ \vdots & \vdots & \vdots & \ddots & \vdots \\ y_{n-1}^T & u_{n-1}^T & y_{n-2}^T & \dots & u_{n-p}^T \end{bmatrix}$$

3. Model criteria coefficient is calculated using Equation (9).
4. Compute the model probability as given by

$$p(M_i | Z) = \frac{e^{-l_i}}{\sum_{j=1}^k e^{-l_j}} \quad , \text{ where } l \text{ is the model selection}$$

criteria coefficient, i.e.

5. Compute the fused model output  $\hat{y}_f = \sum_{i=1}^k p(M_i | Z) \hat{y}_i$

## RESULTS AND DISCUSSION

Fig 3. shows the raw sEMG data acquired from the surface of the skin Vs the sEMG filtered data by using Bayesian Half-gaussian filter.

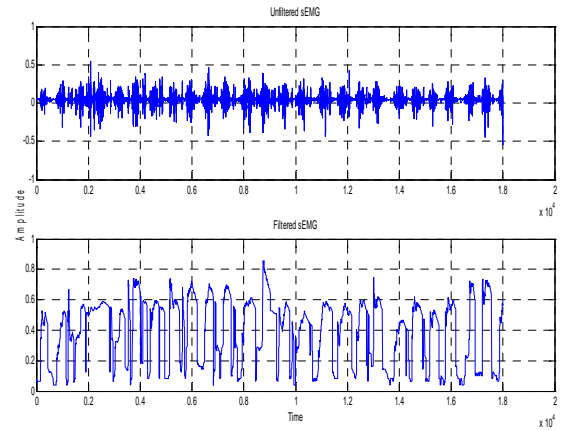


Fig.3: Raw sEMG data Vs filtered Data

Fig. 4 depicts the actual skeletal muscle force data Vs the filtered force data using Chebyshev type-II filter.



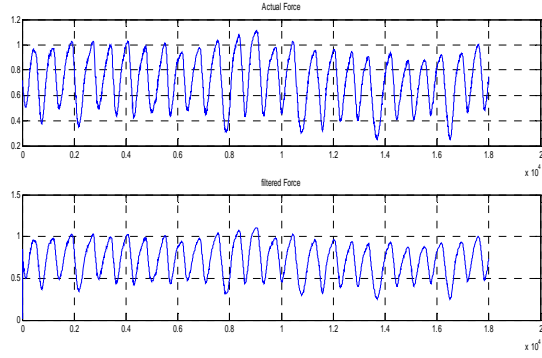


Fig. 4: Actual force and filtered force using Chebyshev Type-II filter

TABLE I: INDIVIDUAL ESTIMATED LINEAR PARAMETRIC MODELS AND THE OVERALL FUSED OUTPUT

SI Models	$M_1$	$M_2$	$M_3$	$\hat{Y}_f$
ARX	12.77	17.57	33.5	43.2
ARMAX	11.6	14.6	35	46.1
OE	54.42	60.39	64.96	75.6

Table I gives the individual estimated model correlation values ( $M_1, M_2, M_3$ ) of the three sensors.  $\hat{Y}_f$  gives the overall fused force correlation values for the linear parametric models. The individual models are computed by using the SI technique - ARX, ARMAX, OE. In all the cases, the values are high for  $M_3$  which is the estimated model output for the sensor placed on the motor unit. All the three models are fused by using the above proposed Minimum Description Length based fusion algorithm. Even though, the fusion algorithm shows improvement in the overall correlation value, the proposed fusion algorithm worked best for the linear Output Error (OE) models.

TABLE II: INDIVIDUAL ESTIMATED NONLINEAR MODELS AND THE OVERALL FUSED OUTPUT

SI Models	$M_1$	$M_2$	$M_3$	$\hat{Y}_f$
WH	52.37	56.8	60.35	70.32

Table II gives the individual estimated nonlinear Wiener Hammerstein models and the overall fused output using a MDL criterion based fusion algorithm. Fig 5 gives the plots of the actual skeletal muscle force and the overall fused output from the MDL fusion algorithm for OE models.

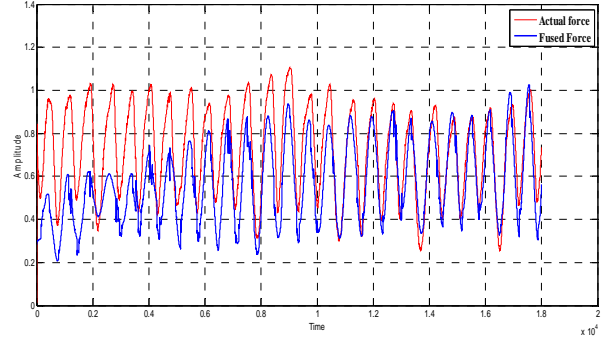


Fig. 5: Actual force and the overall estimated force for the Output Error (OE) Models

## IV CONCLUSION AND FUTURE WORK

In this paper, we addressed a methodology to fuse the sEMG/skeletal muscle force data using a Minimum Description Length (MDL) criterion based fusion algorithm. Compared to the individual estimated models, the fusion-based output is showing improvement in correlation with the actual force.

In the future, we are planning to implement the same criteria for the spectral models [17] and to work on larger data sets and apply this proposed fusion algorithm to them for generalization.

## ACKNOWLEDGEMENT

This research was sponsored by the US Department of the Army, under the award number W81XWH-10-1-0128 awarded and administered by the U.S. Army Medical Research Acquisition Activity, 820 Chandler Street, Fort Detrick MD 21702-5014. The information does not necessarily reflect the position or the policy of the Government, and no official endorsement should be inferred. For purposes of this article, information includes news releases, articles, manuscripts, brochures, advertisements, still and motion pictures, speeches, trade association proceedings, etc. This work was also partially supported in part by an internal Career Path Internship grant by Idaho State University. The support is greatly appreciated.

## REFERENCES

- [1] Estimating the Prevalence of Limb Loss in the United States- 2005 to 2050 Kathryn Ziegler-Graham, PhD, et al, *Archives of Physical Medicine and Rehabilitation* 89(3):422-429, 2008.
- [2] <http://cosmos.ot.buffalo.edu/t2rerc/programs/supplypush/devices.handt.html>
- [3] D.S. Naidu and C.-H. Chen, "Control Strategies for Smart Prosthetic Hand Technology: An Overview", Book Chapter 14, to appear in a book titled, Distributed Diagnosis and



- Home Healthcare (D2H2): Volume 2, American Scientific Publishers, CA, January 2011.
- [4] Pullman, S.L., Goodin, D.S., Marquez, A.I., Tabbal, S., Rubin, M., "Clinical utility of surface EMG", 2000.
  - [5] Light, C.M. Chappell, P.H., "*Development of a lightweight and adaptable multiple-axis hand prosthesis*", Medical Engineering and Physics, 22, pp 679-684, 2000.
  - [6] Merletti, R., Parker, A.P., 1<sup>st</sup> ed., "Electromyography, Physiology Engineering and Non-Invasive Applications", Chapter 1., pp xv-xviii.
  - [7] M. Zecca, S Micera, M.C. Carrozza and P.Daria, "*Control of Multifunctional Prosthetic Hands by Processing the Electromyographic Signal*", Critical reviews in Biomedical Engineering 30 (4-6), pp. 459-485, 2002.
  - [8] [http://www.isek-online.org/standards\\_emg.html](http://www.isek-online.org/standards_emg.html).
  - [9] M. Anugolu, A. Sebastian, P Kumar, M P. Schoen, A Urfer and Naidu DS, "*Surface EMG Array Sensor Based Model Fusion using Bayesian Approaches for Prosthetic Hands*", Proceedings of the Dynamic Systems and Control Conference (DSCC), Hollywood, CA, October 2009.
  - [10] Sanger D.T., "Bayesian Filtering of Myoelectric Signals", Journal of Neurophysiology, 97, pp.1839-1845, 2007
  - [11] Ljung L., 2<sup>nd</sup> ed., "System Identification: Theory for the user", Prentice Hall Information and System Science Series Chapter 1, pp 1-8.
  - [12] Ljung L., 2<sup>nd</sup> ed., "System Identification: Theory for the user", Prentice Hall Information and System Science Series Chapter 5, pp 140-145.
  - [13] Lennart Ljung, system Identification Toolbox 7 User's Guide, the MathWorks, Inc., 2010.
  - [14] J. Rissanen (1978) Modelling by the shortest data description. *Automatica* 14, 465-471.
  - [15] [http://www.scholarpedia.org/article/Minimum\\_description\\_length](http://www.scholarpedia.org/article/Minimum_description_length)
  - [16] Huimin Chen, Shuqing Huang, "A Comparative study on Model Selection and Multiple Model Fusion", 7<sup>th</sup> International Conference on Information Fusion, 2005, PP.820-826.
  - [17] Potluri C., Anugolu M., Chiu S., Urfer A., Perez A., Schoen M., Naidu DS., " *Fusion of Spectral Models for Relating sEMG-Skeletal muscle force data.*, 34<sup>rd</sup> International Conference of the IEEE Engineering in Medicine and Biology Society, San Diego, 2012 ( accepted).

# A sEMG-based Real-time Adaptive Joint angle Estimation and Control for a Prosthetic Hand Prototype

CHANDRASEKHAR POTLURI, MADHAVI ANUGOLU, STEVE CHIU, D. SUBBARAM  
NAIDU, MARCO P. SCHOEN

Measurement and Control Engineering Research Center, School of Engineering  
Idaho State University  
921 South 8<sup>th</sup> Avenue, Stop 8060, Pocatello, Idaho  
USA  
naiduds@isu.edu

*Abstract:* - This paper presents a novel approach of a surface electromyographic (sEMG)-based, real-time Model Reference Adaptive Control (MRAC) strategy for joint angle estimation and control of a prosthetic hand prototype. The proposed design is capable of decoding the pre-recorded sEMG signal as well as the sensory force feedback from the sensors to control the joint angle of the prosthetic hand prototype using a PIC 32MX360F512L microcontroller. The input sEMG signal is rectified, filtered using a Half-Gaussian filter and fed to a Kullback Information Criterion (KIC) based fusion algorithm, which give the overall estimated joint angle (position). This estimated angle is given as input to the prosthetic hand prototype. Then the MRAC along with a two stage proposed embedded design is used for the position control of the prosthetic hand. For the real-time operation, the measured angle data at the joint is fed back to the controller. The data is transmitted to the computer through a universal asynchronous receiver/transmitter (UART) interface of the proposed embedded design. The experimental results in real time show good performance in controlling the angle of the prosthetic hand prototype.

*Key-Words:* - sEMG, Data fusion, Kullback Information Criterion, MRAC, Angle control

## 1 Introduction

For 60 years, there has been active research going on in the area of Prostheses. Due to the unavailability of prosthetic devices with full human hand functionality at an affordable price, more than 30% of upper extremity amputees chose not to use a prosthetic device on regular basis [1, 2]. Besides that, most of the available prosthetic devices do not have tactile or proprioceptive feedback [3]. Previous researchers insisted that human-centered robots must be independent with a great functionality, comfort and ease of use [4]. In rehabilitation robotics, human-machine interface, which requires a natural means of communication, is an interesting domain [5]. The electromyographic (EMG) signal is the electric potential generated by muscles. There are two kinds of EMG signals: Intramuscular (needle) EMG and the Surface EMG (sEMG). Under the assumption that amputation is transradial and which does not require surgery, we relied on sEMG signals in this work whose amplitude ranges from -5 to +5 (mV). sEMG signals are acquired from the surface of the skin, as they penetrate through various tissue layers [6]. Thus, they tend to create cross-talk, interference and noise. The sEMG is a temporally and spatially composed signal [7].

Due to the complexity and nonlinearity of the human hand, the control of a multi-fingered prosthetic hand is a challenging task [8]. From the past research, it is clear that the most widespread approach for controlling the prosthetic hand is by using a position or force control [9]. The challenging task involved in this work is the prediction of the Proximal Inter Phalangeal (PIP) joint angle corresponding to the sEMG signal.

In this paper, we used a three-by-three array of sEMG sensors and a wheel potentiometer device to acquire the EMG signal and the corresponding PIP joint angle. The data from the array of sEMG sensors were fused using a probability based fusion algorithm in order to have a better estimate [10]. A real-time embedded MRAC control system with sensory feedback was implemented to accomplish the goal of this design. Considering the probability based fused joint angle estimate as input to the real-time control system, a two stage embedded platform with a simple MRAC strategy was chosen for the PIP joint angle control of the prosthetic hand prototype.

## 2 Experimental setup

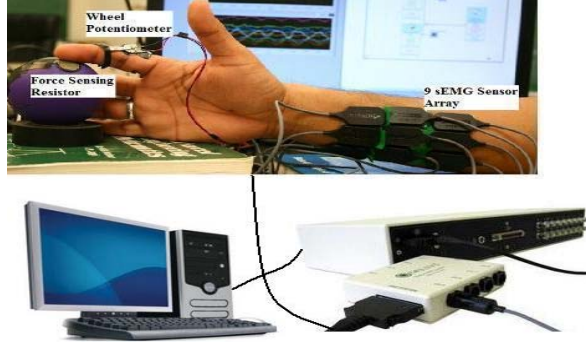


Fig.1: Experimental set-up.

Fig.1. illustrates the experimental design used in this work for capturing the sEMG signal and the corresponding joint angle of the PIP joint of the index finger. Prior to placing the sEMG sensors on the skin surface, the test subject was prepared according to ISEK standards [11]. The motor point was identified by using a wet probe muscle point stimulator (Richmar HV-1000). Nine DE-3.1 sEMG sensors of the DELSYS Bagnoli-16 EMG system were arranged on the skin surface in a three-by-three array. The middle row of sensors was placed on the motor point of the index finger. An angle measurement device was designed using a 10k-Ohm wheel potentiometer shown in Fig.1. It was used to measure the PIP joint angle. Force Sensitive Resistor (FSR) was mounted on the stress ball and was used to measure the force. All the data was acquired at a sampling rate of 2000 samples/sec.

## 3 Proposed Design

The objective of the proposed design is to track a joint angle of the prosthetic hand as closely as possible. Here, the joint angle signal is inferred from the sEMG signals obtained from the array of the sEMG sensors located at the arm.

Sensor fusion is done in the time domain for the sEMG data using a probability based Kullback information criterion (KIC) fusion algorithm. The data from the nine sensors were collected around the corresponding individual motor unit at the transradial arm location (flexor digitorum superficialis) and before fusing the sEMG signals are rectified and filtered using a Half -Gaussian filter, as given by (1).

$$p(EMG|x) = 2 \times \frac{\exp\left(-\frac{EMG^2}{2x^2}\right)}{\sqrt{2\pi x^2}}, \quad (1)$$

where  $p(EMG|x)$  is a conditional probability density function,  $x$  is a latent driving signal.

A System Identification (SI) tool was used to determine the dynamic relationship between the input-output data. The sEMG signal was used as input and the corresponding PIP joint angle as output. In particular, nonlinear Wiener Hammerstein one-dimensional polynomial models were obtained for the sEMG/joint angle data.

The mathematical representation of the modeling is given by,

$$w(t) = f(u(t)) \quad (2)$$

$$x(t) = \frac{B_{ij}(q)}{F_{ij}(q)} w(t - nk) + e(t) \quad (3)$$

$$y(t) = h(x(t)) \quad (4)$$

where  $u(t)$  is the sEMG signal and  $y(t)$  is the PIP joint angle.  $f$  and  $h$  are nonlinear functions,  $w(t)$  and  $x(t)$  are internal variables,  $B_{j,i}(q)$  and  $F_{j,i}(q)$  are polynomials,  $q$  is the back shift operator, and  $e(t)$  is the output error. From (3), the WH model structure utilizes a linear OE model, which is given by,

$$y(t) = \frac{b(q)}{F(q)} u(t - nk) + e(t) \quad (5)$$

where  $nk$  is the system delay and  $t$  is time index

The resulting nine WH models were fused together by using a probabilistic KIC algorithm [12]. It assigns a particular probability to each model [13]. The overall estimated model output and the individual models outputs were compared by using the Pearson's correlation coefficient.

From the previous research, it was shown that the KIC algorithm performs better than the other criteria [10, 12]. KIC is an asymmetric measure of the models' dissimilarity which can be obtained by the sum of the two directed divergences known as J-divergence or Kullback's symmetric [14]. It is given by

$$KIC(p_i) = \frac{n}{2} \log R_i + \frac{(p_i+1)n}{n-p_i-2} - n\psi\left(\frac{n-p_i}{2}\right) + g(n) \quad (6)$$

Where  $g(n) = n^* \log(n/2)$ ,  $\psi$  - digamma function.

The probability based fusion algorithm given by [12, 13] is applied to the nonlinear models obtained by using an SI technique with the following steps:

1: The WH models are obtained by considering the sEMG data  $u(t)$  as input and joint angle  $Y$  as output,

2: Calculate the residual square norm i.e.,  
 $R_i = Y - \Phi_i \hat{\theta}_i = \|Y - \hat{Y}\|$

where  $\hat{\theta}_i = \{\Phi_i^T \Phi_i\}^{-1} \Phi_i^T Y$ , and

$$\Phi = \begin{bmatrix} Y^T & u_{p-1}^T & Y_{p-1}^T & u_1^T \\ Y_{p+1}^T & u_{p+1}^T & Y_p^T & u_2^T \\ \dots & \dots & \dots & \dots \\ Y_{n-1}^T & u_{n-1}^T & Y_{n-2}^T & u_{n-p}^T \end{bmatrix}$$

3: Compute the model criteria coefficients using (6).

4: The model probability can be computed using

$$p(M_i(t) | Z) = \frac{e^{-l_i}}{\sum_{j=1}^k e^{-l_j}}$$

5: The fused model output can be calculated using

$$\hat{Y}_f = \sum_{i=1}^k p(M_i(t) | Z) \hat{Y}_i.$$

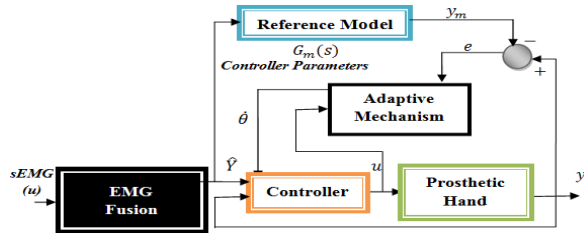


Fig.2: Block diagram representation of Model Reference Adaptive Controller (MRAC)

A simple MRAC based scheme (Fig. 2) is utilized for compensating the dynamics of the prosthetic hand. During the development of the artificial hand, changes were being undertaken to the mechanical design and drive trains of the hand that affect the dynamics of the finger motion of the prosthesis. In addition, the uncertain characteristics of the kinematic and actuator interaction could have led to a different performance than expected. Therefore, a simple MRAC controller was developed in order to maintain some performance stability. For updating the controller parameter  $\theta$ , the MIT rule was used.

$$\frac{d\theta}{dt} = -\gamma e Y_m. \quad (7)$$

According to the MIT rule [15], the gain parameter  $\gamma$  was selected to achieve the desired performance. In this work  $\gamma$  was taken as 3.0 and

the error  $e = Y - Y_m$  was calculated by the difference of the model reference output  $Y_m$  and the actual output (joint angle generated by the prosthetic hand). Different MRAC stability issues were addressed in [14, 15].

### Reference Model Derivation

The dynamic equations of motion for the hand are obtained from the Lagrangian approach as [16]

$$\dot{x}(t) = \begin{bmatrix} 0 & I \\ 0 & 0 \end{bmatrix} x(t) + \begin{bmatrix} 0 \\ I \end{bmatrix} u(t). \quad (8)$$

The control input vector  $u(t)$  was given by

$$u(t) = -M^{-1}(q(t)) [N(q(t), \dot{q}(t)) - \tau(t)]. \quad (9)$$

As the prosthetic hand is required to track the desired angle profile  $q_d(t)$  described under the reference angle model, the tracking error  $e(t)$  is defined as

$$e(t) = q_d(t) - q(t). \quad (10)$$

Here,  $q_d(t)$  is the desired angle vector of the joints and can be obtained by the reference angle model [17];  $q(t)$  is the actual angle vector of the joints. Differentiating (10) twice, we get,

$$\dot{e}(t) = \dot{q}_d(t) - \dot{q}(t), \quad \ddot{e}(t) = \ddot{q}_d(t) - \ddot{q}(t). \quad (11)$$

Substituting  $\dot{q}(t)$  into (11) gives

$$\ddot{e}(t) = \ddot{q}_d(t) + M^{-1}(q(t)) [N(q(t), \dot{q}(t)) - \tau(t)] \quad (12)$$

From (12) the control function  $u(t)$  can be defined as

$$u(t) = \ddot{q}_d(t) + M^{-1}(q(t)) [N(q(t), \dot{q}(t)) - \tau(t)]. \quad (13)$$

This is often called the feedback linearization control law, rewriting (13) as,

$$\tau(t) = M(q(t)) [\ddot{q}_d(t) - u(t) + N(q(t), \dot{q}(t))] \quad (14)$$

Using (11) and (13), the state vector  $x(t) = [e'(t) \dot{e}'(t)]'$ , the state-space model can be represented as

$$\dot{x}(t) = \begin{bmatrix} 0 & I \\ 0 & 0 \end{bmatrix} x(t) + \begin{bmatrix} 0 \\ I \end{bmatrix} u(t). \quad (15)$$

Now, (15) is in the form of a linear system such as

$$\dot{x}(t) = Ax(t) + Bu(t). \quad (16)$$

#### Implementation:

The proposed control design was implemented on a PIC 32MX360F512L microcontroller in two stages: “Signal Processing” and “Motor Actuation”. The Signal Processing stage enables the execution and implementation of real-time control strategies. A dsPIC block set was used to generate the C code for the PIC 32 from Simulink®. The dsPIC block set generates a .hex file, and this file was imported in MPLAB® to program the PIC 32.

#### Signal Processing Stage:

From the many modules available on PIC 32, the following four modules were utilized for the implementation of the signal processing stage: Analog Input Module, Digital Output module, Output Compare module, and URAT module.

The sensory feedback joint angle data from the wheel potentiometer was acquired through the Analog Input module. Based on the selected control strategy for the motor actuation stage, the digital control signals were generated by the Digital Output module of the PIC 32. The changes in the reference/command signal were detected by this module. A pulse width modulated (PWM) wave with a specific duty cycle was generated by the Output Compare module based on the error. The angle data from the microcontroller to the PC was transmitted by the UART module via serial communication. In this particular design, the data was fed to the computer by a virtual com port via USB cable. The signals from the ports were read by MATLAB®.

#### Motor Actuation Stage:

In this stage, the motor was actuated with a SN754410 quadruple half-H driver [18] with the corresponding control signal. This proposed design was tested on the index finger of a prosthetic hand prototype. Fig. 3 shows the test bed for the proposed design.

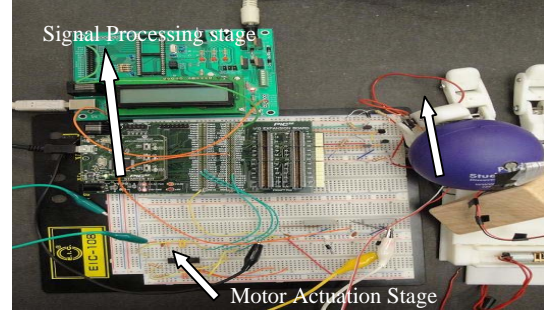


Fig. 3. Embedded Test bed for the proposed design

#### Mechanical structure of the robotic hand prototype:

The prosthetic hand prototype finger has three degrees of freedom stimulated by two Pololu 35:1 mini metal gear motors. Biologically inspired parallel actuation is the main characteristic of this robotic hand prototype. It is based on the behaviour/strength space of the Flexor Digitorum Profundus (FDP) and the Flexor Digitorum Superficialis (FDS) muscles [19]. Using a belt transmission system, the DC motor in the metacarpal phalange of the finger triggers the Proximal Inter Phalangeal (PIP) joint. It also drives the DIP (Distal Inter Phalangeal) joint. The Meta Carpo Phalangeal (MCP) joint is actuated by the DC motor located at the base of the finger as shown in Fig. 4.

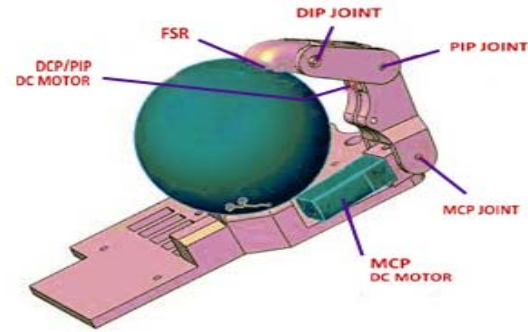


Fig. 4. Finger Actuation Scheme

## 4 Results and Discussion

Data was acquired from the microcontroller through UART channel2 of the PIC 32 micro controller by a virtual com port via USB at a 57600 baud rate. The data from the microcontroller was converted into unit16 data type before it is transmitted through the UART. It ran at an external clock frequency of 8MHz with internal scaling enabled. Fig. 5 depicts the experimental results of the proposed design. The actual angle output from the position sensor (i.e.Y)



closely follows the fusion algorithm estimated angle  $\hat{Y}$ . Fig. 6 shows the fusion estimated angle profile  $\hat{Y}$  and actual angle from the position sensor ( $Y$ ) plotted for a separate experiment. Fig. 7 shows the repeated experimental results. The proposed control strategy was tracking angle profile and matching the actual angle profile with the model estimated angle ( $\hat{Y}$ ).

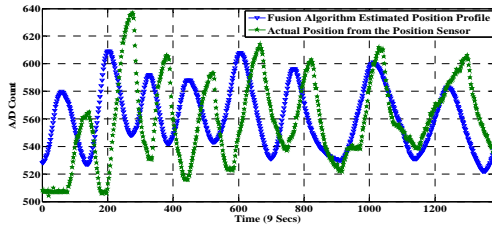


Fig. 5. Fusion based angle estimate and actual angle from angle sensor during the grasp action.

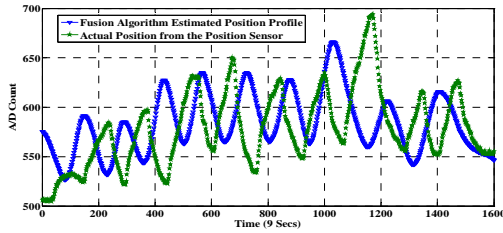


Fig. 6. Fusion based angle estimate and actual angle from angle sensor during the grasp action (for experiment-2).

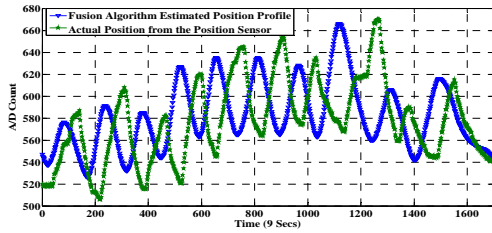


Fig. 7. Fusion based angle estimate and actual angle from angle sensor during the grasp action (for experiment-3).

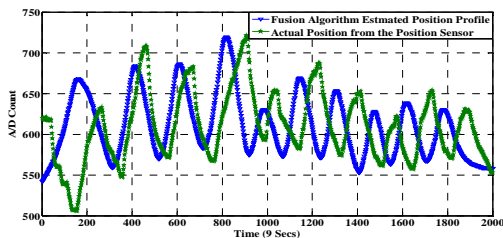


Fig. 8. Validation Plot.

While conducting the experiments, the following observations were made. The DC motors currently employed have the primary task of moving the prosthetic fingers. As the project is on-going, the Shape Memory Alloy (SMA) actuation scheme has

not yet been implemented because of the slow response of the SMA's, and also because SMA's have a long relaxation time. Therefore it is difficult to track a randomly changing angle profile with a slowly responding actuation system. However, as the prosthetic hand prototype is designed to use the parallel actuation of these DC motors and SMA's, the DC motors alone cannot produce a fusion algorithm estimated angle profile.

In this work, the DC motors are solely responsible for motion actuation. Since the DC motors have small gear heads, the usual characteristic of gear driver actuation cores occurs: gear backlash. In addition, the DC motors employed were slow in responding to the changes in the force profile. Hence some gaps and delay were observed in the measured angle signal. However, the profile of the measured angle from the angle sensor has a similar pattern as the fusion algorithm estimated angle ( $\hat{Y}$ ). Thus we can conclude that apart from those mechanical transmission problems, the implemented control scheme produced promising results. These problems will be considered in a new prototype design that we are currently developing.

From the results, it is also evident from Figs. 5, 6 and 7 that the controller is tracking the slow changes in the angle profile very well, where as a small delay was observed while tracking the angle profile. In order to test the precision of the proposed control strategy, 15 different experiments were conducted. The mean of the Pearson's correlation coefficient for the fusion algorithm estimated angle ( $\hat{Y}$ ) and the actual angle from the angle sensor ( $Y$ ) in all the 15 experiments is 0.86. Because of the above mentioned transmission problems and the slow response of the gears, slight variability is observed in the correlation coefficients for the 15 experiments. Hence the difference in tracking the angle profile is observed in Figs. 6 and 7. Fig. 8 depicts the validation plot with a different fusion algorithm angle estimate  $\hat{Y}$  obtained by feeding a different sEMG.

## 5. Conclusion and Future Work

In this paper, based on sEMG signals, we proposed a two-stage real-time embedded MRAC strategy for a prosthetic hand prototype. The proposed design was based on tracking a reference angle profile and it gives good performance when tested on a prosthetic hand prototype. This design enables the transmission of the data from the microcontroller to the

computer. This design allows the control engineer to increase the accuracy and performance of the design by implementing various novel control strategies and also enables fast trouble shooting.

For future work, we are planning to use the above mentioned embedded platform to implement online model-based skeletal muscle angle estimation along with controller designs that address the above listed mechanical shortcomings. It will be valuable to acquire the sEMG signal directly from the arm of a healthy subject and transmit to our embedded system rather than using pre-recorded sEMG signals, which will be investigated as well in the future.

### ACKNOWLEDGMENT

This research was sponsored by the US Department of the Army, under the award number W81XWH-10-1-0128 awarded and administered by the U.S. Army Medical Research Acquisition Activity, 820 Chandler Street, Fort Detrick MD 21702-5014. The information does not necessarily reflect the position or the policy of the Government, and no official endorsement should be inferred. For purposes of this article, information includes news releases, articles, manuscripts, brochures, advertisements, still and motion pictures, speeches, trade association proceedings, etc. Further, the technical help from Dr. Alba Perez and Mr. Alex Jensen is greatly appreciated.

### References:

- [1] <http://www.columbiainmissourian.com/stories/2009/02/15/soldier-who-lost-leg-iraq-may-loseother/>
- [2] D.J. Atkins, D.C. Y. Heard, and W.H. Donovan, "Epidemiologic overview of individuals with upper-limb loss and their reported research priorities", *Journal of Prosthetics and Orthotics*, Vol. 8, NO. 1, 1996, pp- 2-11.
- [3] D.S. Naidu and C.-H. Chen, "Control Strategies for Smart Prosthetic Hand Technology: An Overview", Book Chapter 12, , Distributed Diagnosis and Home Healthcare (D2H2): Volume 2, American Scientific Publishers, CA, January 2011.
- [4] Bien ZZ, and Stefanov D, "Advances in rehabilitation robotics: Human-friendly technologies on movement assistance and restoration for people with disabilities," *Springer, Berlin (Germany)*. 2004.
- [5] Heinzmann J, and Zelinsky J, "A safe-control paradigm for human-robot interaction," *J Intell Robot Syst.* 1999; 25(4): pp. 295-310.
- [6] Cram, J.R., Kasman G.S., and Holtz J. "Introduction to Surface Electromyography," Aspen Publisher Inc., Gaithersburg, Maryland, 1998.
- [7] Kandel E.R. and Scharzt J.H., "Principles of Neural Science," Elsevier/North-Holland, New York, 1981.
- [8] T. H. Sueeter, "Control of the Utah/MIT Dextrous hand: Hardware and software hierarchy," *J. Robot. Syst.*, vol. 7, no. 5, pp. 759-790, 1990.
- [9] M. H. Raibert and J. J. Craig, "Hybrid angle and force control of manipulators," *ASME J. Llyn. Syst. Meas. Contr.*, vol. 102, pp. 126-133, June 1981
- [10] Anugolu M., Sebastian A., Kumar P., Schoen M., Urfer A., Naidu D.S., "Surface EMG array sensor based model fusion using Bayesian approaches for Prosthetic Hand", *Proceeding of the Dynamic Systems and Control Conference*, Hollywood , Ca, October 2009.
- [11] <http://www.isel.online.org/standardsemg.html>.
- [12] Chen H., Huang S., "A Comparative study on Model Selection and Multiple Model Fusion", *7<sup>th</sup> International Conference on Information Fusion*, 2005, PP.820-826.
- [13] Seghouane A.K, Bekara M., Fluery G., " A small Sample Model Selection Criterion based on Kullback's Symmetric Divergence", *IEEE Transaction*, 2003, pp. 145-148.
- [14] Karl J. Astrom and Bjorn Writtenmark "Adaptive Control Second Edition", Dover Publications, Dec 18, 2008.
- [15] Potluri C., Anugolu M., Yihun Y., Kumar P., Chiu S., Schoen M., Naidu D.S., " Implementation of sEMG-based Real-time Embedded Adaptive Finger Force Control for a Prosthetic Hand", *IEEE Conference on Decision and Control and European Control Conference*, Orlando, Florida, USA, Dec 12-15, 2011.
- [16] Potluri C., Anugolu M., Yihun Y., Jensen A., Chiu S., Schoen M., Naidu D.S., " Optimal Tracking of a sEMG based Force Model for a Prosthetic Hand", *33<sup>rd</sup> Annual International Conference of the IEEE Engineering and Medicine and Biology Society*, Boston, Ma, USA, Aug 31-Sep 3, 2011.

- [17] F.L.Lewis, D.M.Dawson, and C.T. Abdallah, "*Robot Manipulators Control: Second Edition, Revised and Expanded*", New York, NY: Marcel Dekker, Inc., 2004.
- [18] Texas Instruments "SN754410 quadruple half H-driver data sheet" Dallas, Texas, November 1986 and 1995
- [19] Dr. Anthony L. Crawford, "Design of a Robotic Hand and Simple EMG Input Controller with a Biologically-Inspired Parallel Actuation System for Prosthetic Application" ASME 2010, IDETC/CIE 2010.



# Fusion of Spectral Models for Dynamic Modeling of sEMG and Skeletal Muscle Force

Chandrasekhar Potluri, *Member, IEEE*, Madhavi Anugolu, *Member, IEEE*, Steve Chiu, *Member, IEEE*, Alex Urfer, Marco P. Schoen, *Senior Member, IEEE*, and D. Subbaram Naidu, *Fellow, IEEE*

**Abstract**— In this paper, we present a method of combining spectral models using a Kullback Information Criterion (KIC) data fusion algorithm. Surface Electromyographic (sEMG) signals and their corresponding skeletal muscle force signals are acquired from three sensors and pre-processed using a Half-Gaussian filter and a Chebyshev Type- II filter, respectively. Spectral models - Spectral Analysis (SPA), Empirical Transfer Function Estimate (ETFE), Spectral Analysis with Frequency Dependent Resolution (SPFRD) - are extracted from sEMG signals as input and skeletal muscle force as output signal. These signals are then employed in a System Identification (SI) routine to establish the dynamic models relating the input and output. After the individual models are extracted, the models are fused by a probability based KIC fusion algorithm. The results show that the SPFRD spectral models perform better than SPA and ETFE models in modeling the frequency content of the sEMG/skeletal muscle force data.

## I. INTRODUCTION

There are approximately 1.7 million people living with an amputation in the United States according to the amputation statistics provided by the National Limb Loss Information Center. It has also been suggested that one out of every 200 people in the U.S. has had an amputation [1]. H. Piper [2] introduced the first investigation into Electro Myographic (EMG) signals in 1921. EMG signals can be used in various applications such as clinical diagnosis, engineering applications, physical therapy, etc. During the past few decades, a wide array of studies have focused on the functionality of various upper extremity prostheses but

investigators have yet to put forth a cost effective prosthesis that truly simulates normal human hand function [3]. The electromyographic (EMG) signal is the primary electrical activity of the skeletal muscles. These signals can be detected either with sensors placed on the surface of the skin or with needle sensors inserted into the muscle tissue. In this work, noninvasive technique is used to acquire the surface electro-myographic (sEMG) signals [4]. During muscle contraction, many motor units are activated at the same time. This contributes to interferences with the sEMG signal and cross talk, which is a major issue in accurate sEMG signal monitoring [5]. The number of motor units in individual muscles varies from person to person. Muscle fatigue begins at the onset of muscle contraction and progressively continues throughout the time of the muscle activation. Fatigue will induce an increase in motor unit recruitment and a decrease in mean medium frequency in the sEMG signal. The sEMG signals pass through numerous layers of tissues before reaching the skin surface [5]. The uncertainty of the sEMG signal presents a special challenge in their analysis. All of these factors increase the complexity of discriminating the content of the EMG signal against noise and interference. Identification of the content of the EMG signal should focus on the amplitude, frequency and amplitude-frequency using distinct methods. As the EMG signal is time dependent and amplitude modulated, it is spatially and temporally frequency encoded [6]. From the literature, it is apparent that sensor data fusion improves the output measurement quality [4]. In [7], a multi-channel grid surface electrode is employed. Using this, the spatial and temporal aspects of time varying potential distribution of the sensors on the skin can be recognized. sEMG data fusion algorithms were designed by the authors using time domain linear Output-Error (OE) models and non-linear Weiner-Hammerstein models in the past [4, 8, 9].

In this work, spectral models - Spectral Analysis (SPA), Empirical Transfer Function Estimate (ETFE), Spectral Analysis with Frequency Dependent Resolution (SPAFDR) –are obtained using sEMG and skeletal muscle force data. Finally, the spectral models are fused using the KIC algorithm for the improved estimation of skeletal muscle force. This paper is structured as follows. The experimental set up is given in Section II and Section III provides the background information for system identification and spectral models. Section IV details the results and discussion and in the last section, some conclusions are provided.

Chandrasekhar Potluri is with Measurement and Control Engineering Research Center (MCERC), Idaho State University, Pocatello, Idaho 83201 USA (e-mail: potlchan@isu.edu).

Madhavi Anugolu is with MCERC, Idaho State University, Pocatello, Idaho 83201 USA (e-mail: anugmadh@isu.edu).

Steve Chiu is with Department of Electrical Engineering and Computer Science, MCERC, Idaho State University, Pocatello, Idaho 83201 USA (email: chiustev@isu.edu).

Alex Urfer is with Department of Physical and Occupational Therapy, Idaho State University, Pocatello, Idaho 83209, (email: urfealex@isu.edu)

Marco P. Schoen is with Department of Mechanical Engineering, MCERC, Idaho State University, Pocatello, Idaho 83201 USA (e-mail: schomarc@isu.edu).

D. Subbaram Naidu is with Department of Electrical Engineering and Computer Science, MCERC, Idaho State University, Pocatello, Idaho 83201 USA (email: naiduds@isu.edu).

## II. EXPERIMENTAL SET-UP

The experiments are conducted on a healthy male subject in order to acquire the sEMG and corresponding skeletal muscle force ( $y_f$ ) signals. First, the skin surface is slightly abraded and cleaned with alcohol swabs and the test subject was prepared by following the ISEK standards [10]. A wet probe point muscle stimulator manufactured by Rich-Mar Corporation (Model number HV-1000) is used to identify the motor point of the flexor digitorum superficialis muscle. An array of three sensors are placed, one on the motor point and the other two adjacent to the motor point. A Delsys Bagnoli-16 channel EMG equipment is used to capture sEMG signal and the related skeletal muscle force ( $y_f$ ) signal is acquired using Force Sensitive Resistor (FSR). Both of the signals are acquired at a sampling rate of 2000 samples/sec for duration of 10 seconds. The sEMG signal is filtered by using a Half-Gaussian filter and the skeletal muscle force signal ( $y_f$ ) is filtered using a Chebyshev Type-II filter whose cut-off frequency is set to 550 Hz [10]. The Half-Gaussian filter is given by:

$$p(EMG|x) = 2 \frac{\exp\left\{-\frac{EMG^2}{2x^2}\right\}}{\sqrt{2\pi x^2}}, \quad (1)$$

where  $p(EMG|x)$  is the conditional probability,  $x$  is the latent driving signal, and EMG is the acquired data.

## III. PROPOSED DESIGN

System Identification (SI) technique is utilized to achieve the dynamic relationship between sEMG and the skeletal muscle force ( $y_f$ ). In [4, 8], sensor fusion is done by combining linear and non-linear time domain SI models. Combinations of different filters (Butterworth, Chebyshev, Exponential and Half-Gaussian filters) and different information criteria based on Akaike (AIC), Bayesian (BIC), and Kull-back (KIC) were used. A KIC criterion with Half Gaussian filtering gives the best EMG/Force model correlation [8]. In this work, spectral models are used to achieve SI. The idea is to capture and model the frequency content of the sEMG signal. Three spectral models of each type i.e. SPA, ETFE and SPAFDR are obtained for the sEMG from the three sensors and the corresponding skeletal muscle force ( $y_f$ ) data. The detailed mathematical structures of the utilized spectral models are given below,

*Spectral Analysis (SPA):*

Consider a linear dynamic system,

$$y(t) = G(q)u(t) + v(t) \quad (2)$$

where  $u(t)$  is the sEMG signal,  $y(t)$ -force signal, and  $G(q)$  is the transfer function which gives the dynamic relationship between sEMG and force.  $G(q)$  is evaluated on the unit circle

$$G(q = e^{j\omega}) \quad (3)$$

where  $\omega$  is a frequency content of the signal. The SPA models are computed as follows,

Computing the covariance's and cross-covariance's from sEMG signal ( $u(t)$ ) and skeletal muscle force signal ( $y_f(t)$ )

$$\hat{R}_y(\tau) = \frac{1}{N} \sum_{t=1}^N y(t+\tau)y(t) \quad (4)$$

$$\hat{R}_u(\tau) = \frac{1}{N} \sum_{t=1}^N u(t+\tau)u(t) \quad (5)$$

$$\hat{R}_{yu}(\tau) = \frac{1}{N} \sum_{t=1}^N y(t+\tau)u(t) \quad (6)$$

Later, the Fourier transforms of the above three equations are computed by using,

$$\hat{\Phi}_y(\omega) = \sum_{\tau=-M}^M \hat{R}_y(\tau)W_M(\tau)e^{-j\omega\tau} \quad (7)$$

$$\hat{\Phi}_u(\omega) = \sum_{\tau=-M}^M \hat{R}_u(\tau)W_M(\tau)e^{-j\omega\tau}, \quad (8)$$

$$\hat{\Phi}_{yu}(\omega) = \sum_{\tau=-M}^M \hat{R}_{yu}(\tau)W_M(\tau)e^{-j\omega\tau}, \quad (9)$$

In (7), (8) and (9)  $W_M(\tau)$  is the Hann window of width  $-M$  to  $M$ . Where  $M$  is a scalar integer that sets the size of the lag window. The frequency-response function  $\hat{G}_N(e^{j\omega})$  and the output noise spectrum  $\hat{\Phi}_v(\omega)$  are computed as,

$$\hat{G}_N(e^{j\omega}) = \frac{\hat{\Phi}_{yu}(\omega)}{\hat{\Phi}_u(\omega)} \quad (10)$$

$$\hat{\Phi}_v(\omega) = \sum_{\tau=-\infty}^{\infty} R_v(\tau)e^{-j\omega\tau} \quad (11)$$

The frequency resolution is calculated by,

$$\zeta = \frac{2\pi}{M} \left( \frac{\text{radians}}{\text{sampling interval}} \right) \quad (12)$$

*Empirical Transfer function Estimate (ETFE)*

The ETFE function of (2) gives the transfer function estimate  $G(e^{j\omega})$  at the frequencies

$$\omega = \left[ \frac{1:N}{N} \right] * \frac{\pi}{T} \quad (13)$$

where  $N = 128$ (default)

$$U_f(\omega) = \sum_{\tau=-M}^M u(\tau)W_M(\tau)e^{-j\omega\tau} \quad (14)$$

$$Y_f(\omega) = \sum_{\tau=-M}^M y(\tau)W_M(\tau)e^{-j\omega\tau} \quad (15)$$

Dividing (15) by (14) and applying the Hann window as in the SPA models, with the length of the range of number of data points yields the frequency-response function  $\hat{G}_N(e^{j\omega})$  and the output noise spectrum  $\hat{\Phi}_v(\omega)$  same as (10) and (11). Both the SPA and ETFE have the same frequency resolution.

*Spectral Analysis with Frequency Dependent Resolution (SPAFRD):*

For the linear dynamic system given in (2) SPAFRD frequency response function returns transfer function estimate  $G(e^{j\omega})$  as well as the spectrum additive noise. The sEMG and the skeletal muscle force data are converted into frequency domain  $U(\omega)$  and  $Y(\omega)$

The frequency domain data are formed as

$$avg \left[ \frac{Y(\omega)conj U(\omega) * U(\omega)conj Y(\omega)}{\omega} \right] \quad (16)$$

with a desired resolution of  $\zeta(k) = 2(w(k+1) - w(k))$

The frequency-response function  $\hat{G}_N(e^{j\omega})$  and the output noise spectrum  $\hat{\Phi}_v(\omega)$  are computed as,

$$\hat{G}_N(e^{j\omega}) = \frac{\hat{\Phi}_{yu}(\omega)}{\hat{\Phi}_u(\omega)} \quad (17)$$

$$\Phi_v(\omega) = \lambda T |H(e^{j\omega T})|^2 \quad (18)$$

*Fusion Algorithm:*

The Kullback Information Criterion (KIC) is a symmetric measure used in this paper for the fusion of spectral data. The mathematical form of the KIC is given as:

$$KIC(p_i) = \frac{n}{2} \log R_i + \frac{(p_i+1)n}{n-p_i-2} - n\psi\left(\frac{n-p_i}{2}\right) + g(n) \quad (19)$$

where,  $n$  is the number of data points  $p_i$  is the order of the model,  $\psi$  is the digamma function, and  $g(n) = n * \log \frac{n}{2}$ .

After calculate the KIC for each of the three models, the following fusion algorithm was used in order to get the overall estimated finger force  $\hat{y}_f$ ,

1. The Spectral models  $M_{f1}, M_{f2} \dots M_{fk}$  are computed using sEMG data ( $u_k$ ) as input and force data ( $y_f$ ) as output, for  $k$  number of sEMG sensors (Where  $k = 3$  in this case).

2. Residual square norm is calculated by

$$R_i = \|y - \Phi_i \hat{\theta}_i\|^2 = \|y - \hat{y}\|_2 \text{ where } \hat{\theta}_i = \{\Phi_i^T \Phi_i\}^{-1} \Phi_i^T y,$$

$$\text{and } \vec{\Phi} = \begin{bmatrix} y_p^T & u_p^T & y_{p-1}^T & \dots \\ & u_{p+1}^T & y_p^T & \dots \\ \vdots & \vdots & \vdots & \ddots & \vdots \\ y_{n-1}^T & u_{n-1}^T & y_{n-2}^T & \dots \end{bmatrix}$$

3. Using (19) model criteria coefficients are computed.

4. The model probability is computed by

$$p(M_{fi}|Z) = \frac{e^{-l_i}}{\sum_{j=1}^k e^{-l_j}}$$

$l$  - Model selection criteria coefficient.

5. Fused output model is computed by,

$$\hat{Y}_f = \sum_{i=1}^k p(M_{fi}|Z) \hat{y}_{fi}$$

#### IV. RESULTS AND DISCUSSION

In order to extract the best working spectral model for the sEMG and skeletal muscle force data three spectral models SPA, ETFE, SPAFDR are constructed based on the sEMG data from the individual sensor and the corresponding skeletal muscle force. The three spectral models of same type are fused using the KIC algorithm resulting in three fusion algorithm estimated force for each spectral model type ( $\hat{Y}_f(SPA)$ ,  $\hat{Y}_f(ETFE)$ ,  $\hat{Y}_f(SPAFDR)$ ). The Pearson's correlation coefficient ( $\rho_{x,y}$ ) in percentage relating the actual force ( $y_f$ ) from the FSR and the fusion algorithm estimated force ( $\hat{Y}_f$ ) for each spectral model is tabulated in Table 1.

TABLE I: COMPARISON OF CORRELATIONS OF INDIVIDUAL MODELS AND THE FUSED OUTPUT FOR SPA, SPAFDR AND ETFE

Models	Correlation ( $\rho_{x,y}$ )			
	( $M_{f1}$ )	( $M_{f2}$ )	( $M_{f3}$ )	Fusion( $\hat{Y}_f$ )
SPA	32.52	29.68	36.19	50.29
SPAFDR	57.61	69.87	65.23	85.68
ETFE	N/A	N/A	N/A	-53.55

It is evident from Table I that SPAFDR models are yielding the better correlation. The ability to choose the frequency resolution in the SPAFDR models allows modeling of the frequency content of the sEMG signals. The inability of SPA and ETFE to model the non-linear frequencies and non-periodic inputs caused them to fail to capture the frequency of a transient sEMG signal.  $M_{f3}$  is constructed from the sensory data located on the motor unit. Therefore it is yielding better correlation than  $M_{f1}$ ,  $M_{f2}$ . It is also clear that the KIC based fusion algorithm improves the skeletal muscle force estimation when compared to individual spectral models.

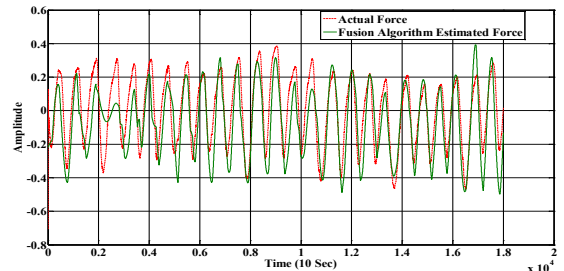


Figure. 1: Actual Force ( $y_f$ ) and the Fusion Algorithm Estimated Force ( $\hat{Y}_f$ ).

Fig. 1 and Fig. 2 shows the actual force ( $y_f$ ) and the fusion algorithm estimated force ( $\hat{Y}_f$ ) from the three SPAFDR models plotted together. The fusion algorithm estimated force follows the trends in the actual force and match up with the actual force.

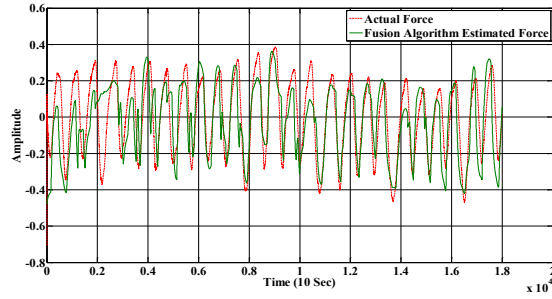


Figure 2: Validation Plot.

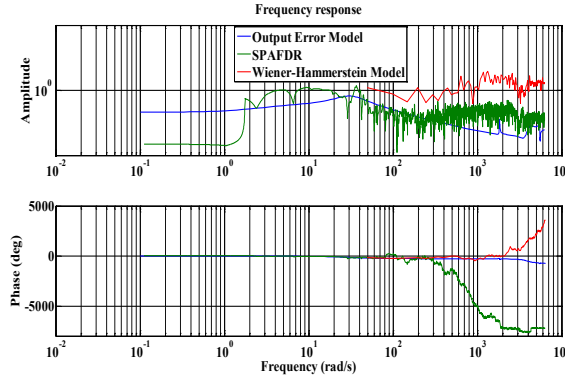


Figure 3: Frequency Response of SPAFDR, Output-Error (OE) and Wiener-Hammerstein Models.

Fig 3 gives the frequency response in comparison with the SPAFDR based fusion force estimate using OE and Wiener-Hammerstein models that were previously developed by the authors [4, 8, 9]. It is interesting that the SPAFDR spectral models are capturing a different band of frequencies when compared to the other two models. This indicates that SPAFDR models are capturing more of the additional information than the time domain OE and Wiener-Hammerstein models. This difference can be due to reasons, such as model order selection, input design for the experiment, etc.

## V. CONCLUSION AND FUTURE WORK

In this work, three different spectral models were analyzed. From the results, it is clear that SPAFDR gives better correlation between the actual force ( $y_f$ ) and the fusion algorithm estimated force ( $\hat{y}_f$ ), when compared to the other two spectral models SPA and ETFE. Since the sEMG is a non-periodic signal, the application of the Hann window and fixed resolution are the possible reasons for the failure of the SPA and ETFE model structures for capturing the characteristics of sEMG/skeletal muscle force signals. In addition, the results imply that the SPAFDR spectral models are capturing the frequencies that are not captured by OE and Wiener-Hammerstein models.

In future we plan to apply wavelet transforms on the sEMG signals to provide a better windowing of the useful frequency content of the sEMG signal. It will also be interesting to fuse both the spectral and the non-linear

models for the improvement of the correlation between actual ( $y_f$ ) and fusion algorithm estimated forces ( $\hat{y}_f$ ).

## ACKNOWLEDGEMENT

This research was sponsored by the US Department of the Army, under the award number W81XWH-10-1-0128 awarded and administered by the U.S. Army Medical Research Acquisition Activity, 820 Chandler Street, Fort Detrick MD 21702-5014. The information does not necessarily reflect the position or the policy of the Government, and no official endorsement should be inferred. For purposes of this article, information includes news releases, articles, manuscripts, brochures, advertisements, still and motion pictures, speeches, trade association proceedings, etc.

## REFERENCES

- [1] [http://www.amputeecoalition.org/fact\\_sheets/amp\\_stats\\_cause.html](http://www.amputeecoalition.org/fact_sheets/amp_stats_cause.html)
- [2] Piper, H., "Electrophysiologie Menschlicher Muskeln", Springer Verlag.
- [3] Potluri C., Yihun Y., Anugolu M., Kumar P., Chiu S., Schoen M., Naidu D.S., "Implementation of sEMG-Based Real-Time Embedded Adaptive Finger Force Control for a Prosthetic Hand", *IEEE Conference on Decision and Control and European Control Conference*, Orlando, Florida, USA, December 12-15, 2011.
- [4] Potluri C., Kumar P., Anugolu M., Urfer, A.; Chiu S., Naidu D.S., Schoen M., "Frequency Domain Surface EMG Sensor Fusion for Estimating Finger Forces," *32nd Annual International Conference of the IEEE Engineering in Medicine and Biology Society*, Buenos Aires, Argentina, August 31 - September 4, 2010.
- [5] Potluri C., Anugolu M., Yihun Y., Jensen A., Chiu S., Schoen M., and Naidu D.S., "Optimal Tracking of a sEMG based Force Model for a Prosthetic Hand", *33rd International Conference of the IEEE Engineering in Medicine and Biology Society*, Boston, 2011.
- [6] Cram, J.R., Kasman G.S., and Holtz J., "Introduction to Surface Electromyography", Aspen Publisher Inc., Gaithersburg, Maryland, 1998.
- [7] Hattori T., Sato T., Minato K., Nakamura H., Yoshida M., "Identification of a single motor unit by grid surface electrodes-A new three dimensional expression of surface EMG", *IEEE/ICME International Conference on Complex Medical Engineering*, 2007.
- [8] Anugolu M., Sebastian A., Kumar P., Schoen M., Urfer A., and Naidu D.S., "Surface EMG array sensor based model fusion using Bayesian approaches for Prosthetic Hands", *Proceeding of the Dynamic Systems and Control Conference*, Hollywood, CA, October 2009.
- [9] Anugolu M., Potluri C., Urfer A., Creelma J., Kumar P., Schoen M., "Genetic Algorithm Based Optimization of Kullback Information Criterion: Improved System Identification of Skeletal Muscle Force and SEMG Signals", *2012 IEEE International Instrumentation and Measurement Technology Conference*, Graz, Austria, May 13-16, 2012.
- [10] [http://www.isek-online.org/standards\\_emg.html](http://www.isek-online.org/standards_emg.html)

## **Optimal Control Strategy for Smart Prosthetic Hand**

### **Summary**

Optimization is a very desirable feature in day-to-day life. We like to work and use our time in an optimum manner, use resources optimally and so on. The subject of optimization is quite general in the sense that it can be viewed in different ways depending on the approach (algebraic or geometric), the interest (single or multiple), the nature of the signals (deterministic or stochastic), and the stage (single or multiple) used in optimization.

This report presents a control technique of finite-time linear quadratic optimal control for five-fingered smart prosthetic hand. The optimal control is used for feedback linearized dynamics to minimize tracking error. This work is different than the work done in [2] as in this work the reference input can be chosen to be constant, ramp, sinusoidal values,...etc. The simulations of this optimal controller showed good performance.

### **Introduction**

Optimal control theory is a mature mathematical discipline with numerous applications in both science and engineering. It is emerging as the computational framework of choice for studying the neural control of movement, in much the same way that probabilistic inference is emerging as the computational framework of choice for studying sensory information processing. Despite the growing popularity of optimal control models, however, the elaborate mathematical machinery behind them is rarely exposed and the big picture is hard to grasp without reading a few technical books on the subject.

The main objective of optimal control is to determine control signals that will cause a plant to satisfy some physical constraints and at the same time (maximize or minimize) a performance index or cost function. We are interested in finding the optimal control  $u^*(t)$  (\* indicates optimal condition) that will drive the plant  $P$  from initial state to final state with some constraints on controls and states and at the same time extremizing the given performance index  $J$ .

The formulation of optimal control problem requires:

1. a mathematical model of the process to be controlled (generally in state variable form),
2. a specification of the performance index, and
3. a statement of boundary conditions and the physical constraints on the states and/or controls.

We can describe a physical plant by a set of linear or nonlinear differential equations.

Classical control design techniques have been successfully applied to linear, time-invariant, single-input, single output (SISO) systems. Typical performance standards are system time response to step or ramp input characterized by rise time, settling time, peak overshoot, and steady state accuracy; and the frequency response of the system characterized by gain and phase margins, and bandwidth.

In modern control theory, the optimal control problem is to find a control which causes the dynamical system to reach a target or follow a state variable (or trajectory) and at the same time extremize a performance index. Performance index in general can be in the form as

$$J = \mathbf{x}'(t_f)\mathbf{F}\mathbf{x}(t_f) + \int_{t_0}^{t_f} [\mathbf{x}'(t)\mathbf{Q}\mathbf{x}(t) + \mathbf{u}'(t)\mathbf{R}\mathbf{u}(t)]dt$$

Where,  $R$  is a positive definite matrix, and  $Q$  and  $F$  are positive semi definite matrices, respectively. Note that the matrices  $Q$  and  $R$  may be time varying. The particular form of this performance index is called quadratic (in terms of the states and controls) form.

In tracking (trajectory following) systems, we require that the output of a system track or follow a desired trajectory in some optimal sense. Thus, we see that this is a generalization of regulator system in the sense that the desired trajectory for the regulator is simply the zero state.

The optimal control  $u(t)$  is given by

$$u^*(t) = -R^{-1}(t)B'P(t)x^*(t) = -K(t)x^*(t)$$

Here,  $K(t)$  is called Kalman gain and  $P(t)$ , the symmetric positive definite matrix is the solution of the matrix differential Riccati equation (DRE)

$$\dot{P}(t) = -P(t)A - A'P(t) - Q(t) + P(t)BR^{-1}(t)B'P(t)$$

Satisfying the final condition:

$$P(t = t_f) = F(t_f)$$

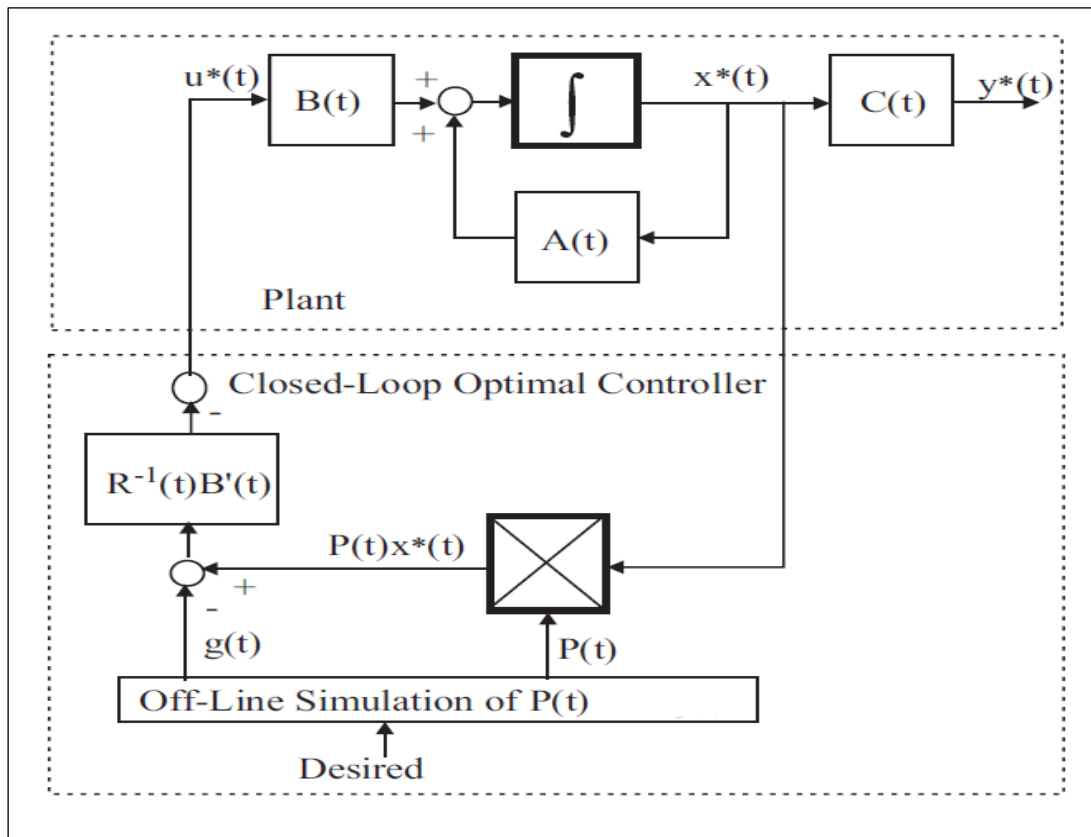
The optimal state  $x^*$  is the solution of:

$$\dot{x}^*(t) = [A - BR^{-1}(t)B'P(t)] x^*(t)$$

And the optimal cost  $J^*$  is

$$J^* = \frac{1}{2}x^{*'}(t)P(t)x^*(t)$$

The optimal tracking system can be summarized in the next figure.



Modeling:

It is necessary to have a mathematical model that describes the dynamic behavior of prosthetic hand for the purpose of designing the control system. Hence, in this section the dynamic equations of hand motion are derived via Lagrangian approach using kinetic energy and potential energy. from Lagrangian approach, dynamic equations of thumb can be obtained as below.

$$\mathbf{M}(\mathbf{q})\ddot{\mathbf{q}} + \mathbf{C}(\mathbf{q}, \dot{\mathbf{q}}) + \mathbf{G}(\mathbf{q}) = \boldsymbol{\tau} - \mathbf{F}_v\dot{\mathbf{q}} - \mathbf{F}_s\text{sign}(\dot{\mathbf{q}}) - \mathbf{J}'\mathbf{F}_{\text{ext}}$$

Where  $\mathbf{M}(\mathbf{q})$  is the inertia matrix;  $\mathbf{C}(\mathbf{q}, \dot{\mathbf{q}})$  is the Coriolis/centripetal vector and  $\mathbf{G}(\mathbf{q})$  is the gravity vector;  $\mathbf{F}_v$  denotes the diagonal positive definite matrix of viscous friction coefficients;  $\mathbf{F}_s$  is a diagonal positive definite matrix and  $\text{sign}(\dot{\mathbf{q}})$  is a vector whose components are given by the sign functions of the single joint velocities;  $\mathbf{J}$  is the Jacobian and  $\mathbf{F}_{\text{ext}}$  denotes the vector of external forces in each direction. It can also be written as:

$$\mathbf{M}(\mathbf{q})\ddot{\mathbf{q}} + \mathbf{N}(\mathbf{q}, \dot{\mathbf{q}}) = \boldsymbol{\tau}$$

Where

$$\mathbf{N}(\mathbf{q}, \dot{\mathbf{q}}) = \mathbf{C}(\mathbf{q}, \dot{\mathbf{q}}) + \mathbf{G}(\mathbf{q}) + \mathbf{F}_v\dot{\mathbf{q}} + \mathbf{F}_s\text{sign}(\dot{\mathbf{q}}) + \mathbf{J}'\mathbf{F}_{\text{ext}}$$

Represents nonlinear terms in  $\mathbf{q}$  and  $\dot{\mathbf{q}}$ .

This work is different than the work done in [2] as in this work the reference input can be chosen to be constant, ramp, sinusoidal values,...etc.

In obtaining the linear system from the original nonlinear system, there has been no state-space transformation. Further, the difficult design of a controller for the original nonlinear system has been transformed into a simple design of a controller for the linear system. If we select the control function  $\mathbf{u}(t)$  to stabilize the linear system and make the tracking error zero, then the nonlinear torque-control will command the prosthetic hand to follow the desired trajectory. The original robotic hand system becomes:

$$\mathbf{M}(\mathbf{q}(t))\ddot{\mathbf{q}}(t) + \mathbf{N}(\mathbf{q}(t), \dot{\mathbf{q}}(t)) = [\mathbf{M}(\mathbf{q}(t))] [\ddot{\mathbf{q}}_d(t) - \mathbf{u}(t)] + \mathbf{N}(\mathbf{q}(t), \dot{\mathbf{q}}(t))$$

Where

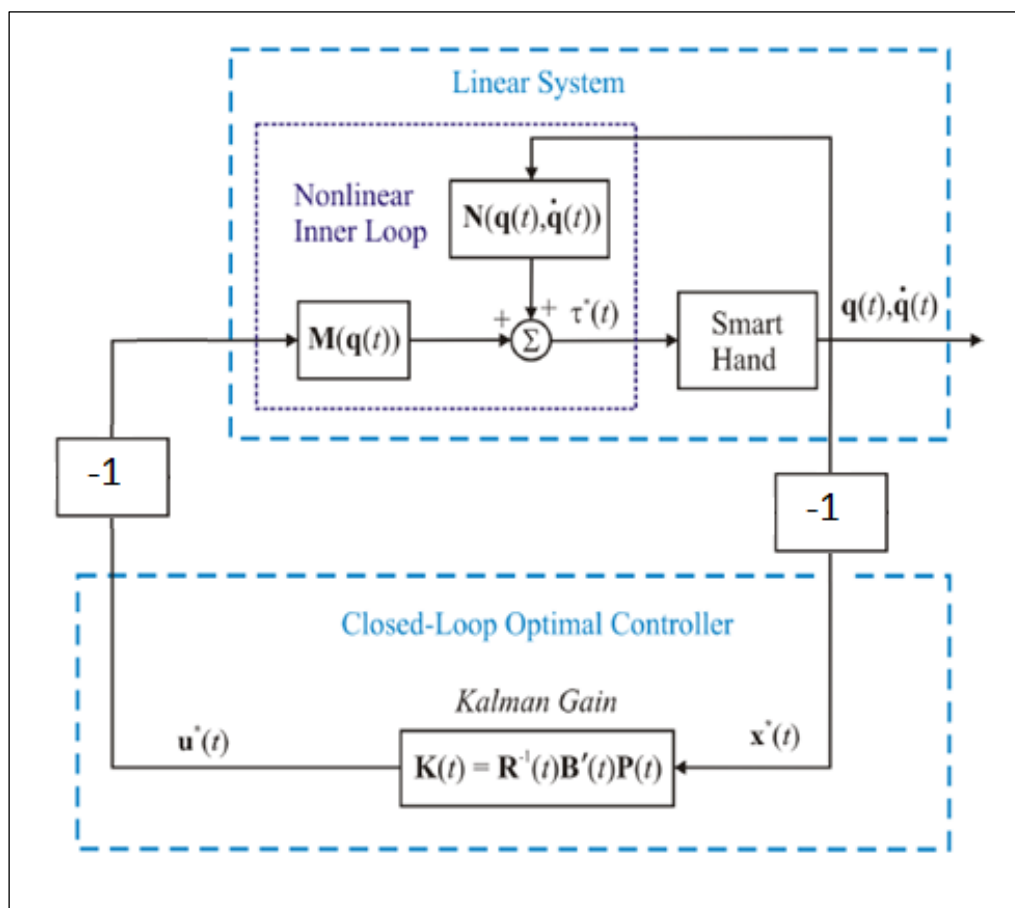
$$\ddot{\mathbf{e}}(t) = \mathbf{u}(t)$$

Therefore, the required torque can be calculated by the optimal control  $\mathbf{u}^*(t)$ .

$$\boldsymbol{\tau}^*(t) = \mathbf{M}(\mathbf{q}(t))(\ddot{\mathbf{q}}_d(t) - \mathbf{u}^*(t)) + \mathbf{N}(\mathbf{q}(t), \dot{\mathbf{q}}(t))$$

The next figure shows the block diagram of a hybrid finite-time linear quadratic optimal controller







Simulation Results:

Optimal control coefficients, A, B, F(tr), R(t) and Q(t) of all fingers are chosen as:

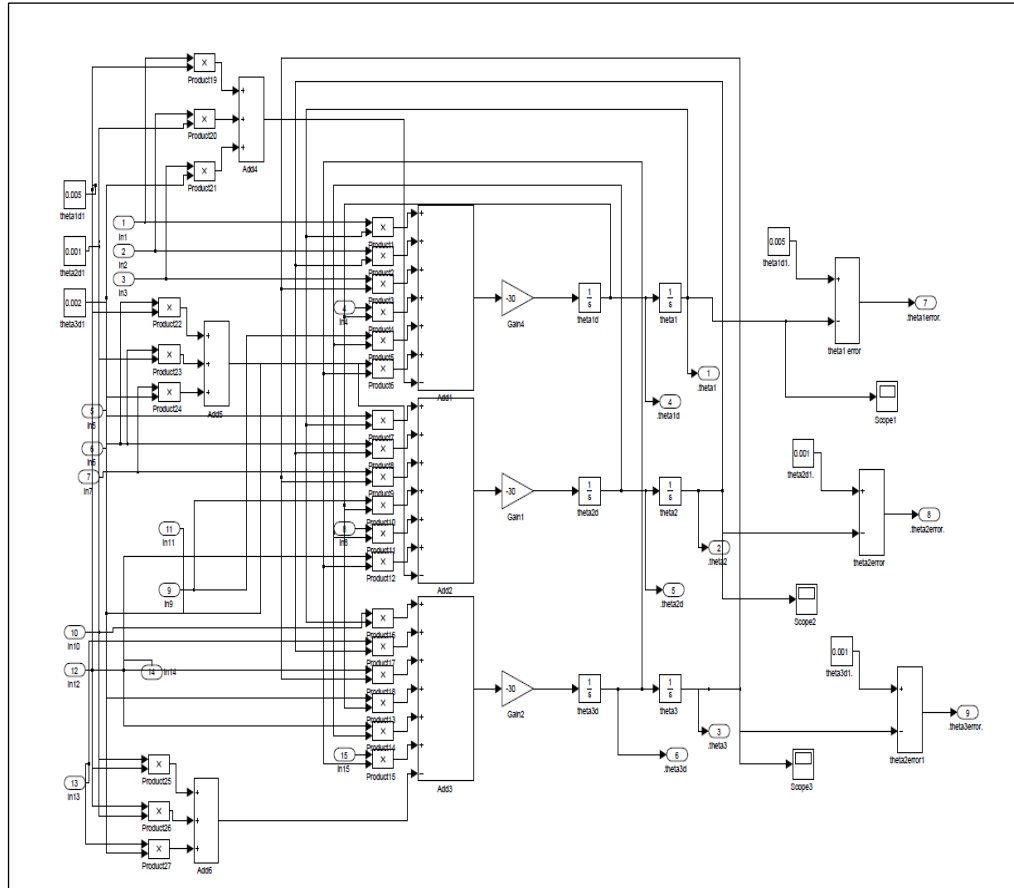
$$A = \begin{bmatrix} 0 & I \\ 0 & 0 \end{bmatrix}, \quad B = \begin{bmatrix} 0 \\ I \end{bmatrix}, \quad F(t_f) = 0, \quad R(t) = \frac{1}{30}I,$$

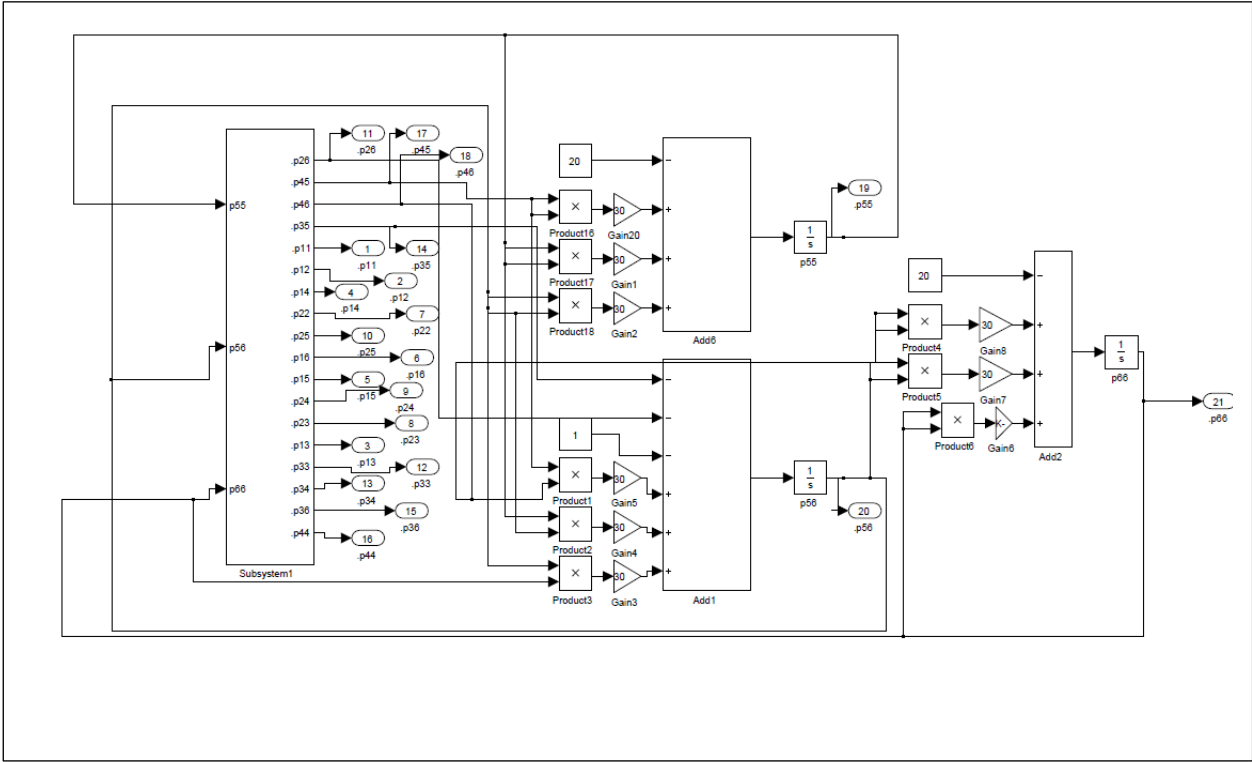
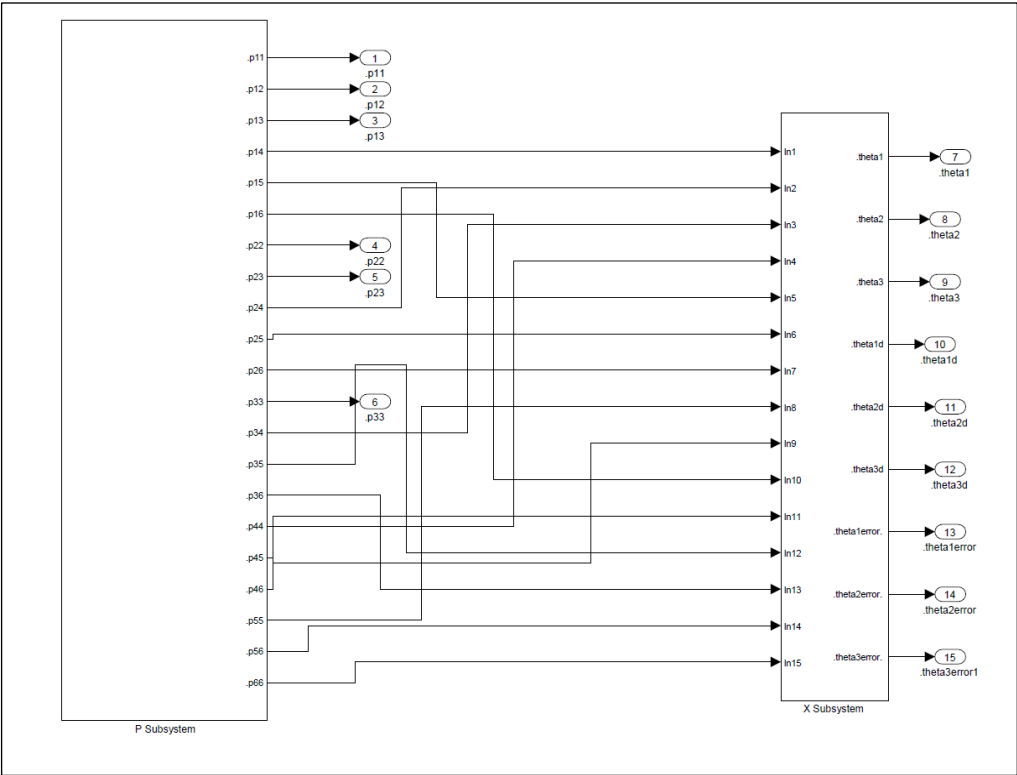
$$Q^t(t) = \begin{bmatrix} Q_{11} & Q_{12} \\ Q_{12} & Q_{22} \end{bmatrix}, \quad Q^j(t) = \begin{bmatrix} Q_{11} & Q_{12} & Q_{13} \\ Q_{12} & Q_{22} & Q_{23} \\ Q_{13} & Q_{23} & Q_{33} \end{bmatrix},$$

$$Q_{11} = \begin{bmatrix} 10 & 2 \\ 2 & 10 \end{bmatrix}, \quad Q_{22} = \begin{bmatrix} 30 & 0 \\ 0 & 30 \end{bmatrix}, \quad Q_{33} = \begin{bmatrix} 20 & 1 \\ 1 & 20 \end{bmatrix},$$

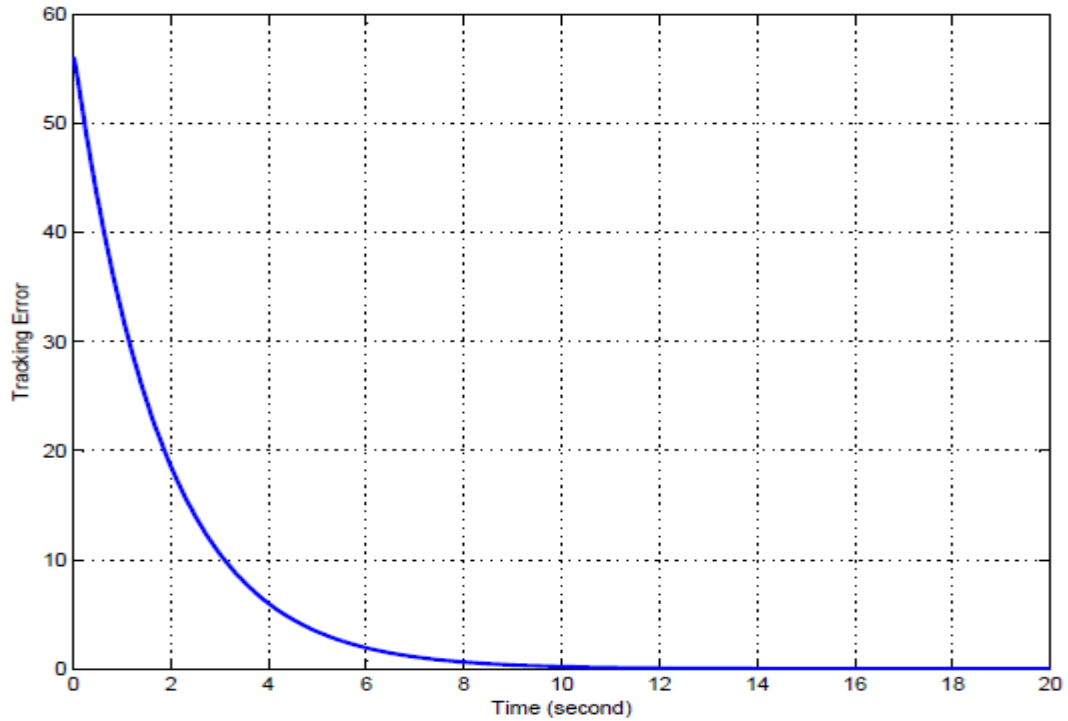
$$Q_{12} = \begin{bmatrix} -4 & 4 \\ 3 & -6 \end{bmatrix}, \quad Q_{13} = \begin{bmatrix} -4 & 4 \\ 3 & -6 \end{bmatrix}, \quad Q_{23} = \begin{bmatrix} -4 & 3 \\ 4 & -6 \end{bmatrix}.$$

The model that is built in Simulink is shown:

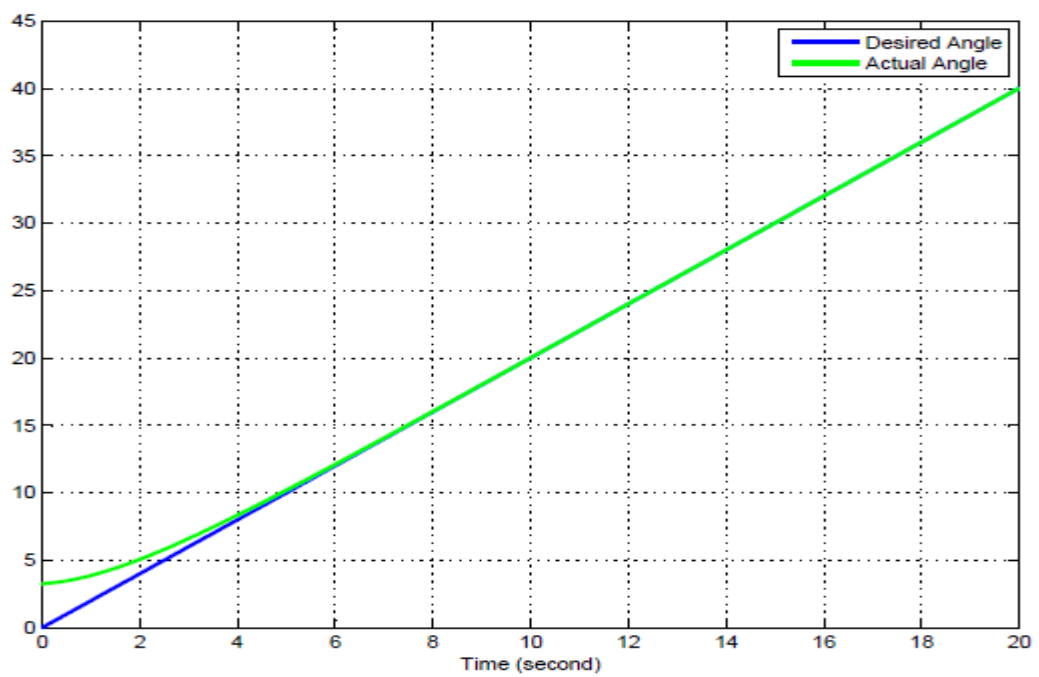




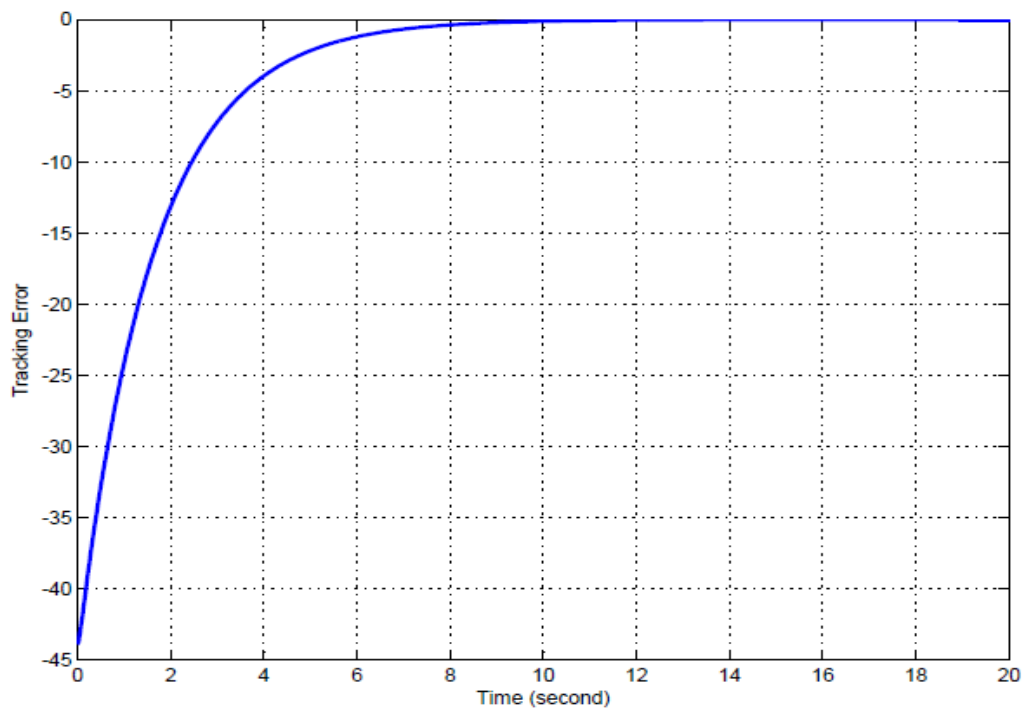
And the next figures shows some study cases to show the designed control method affectivity:



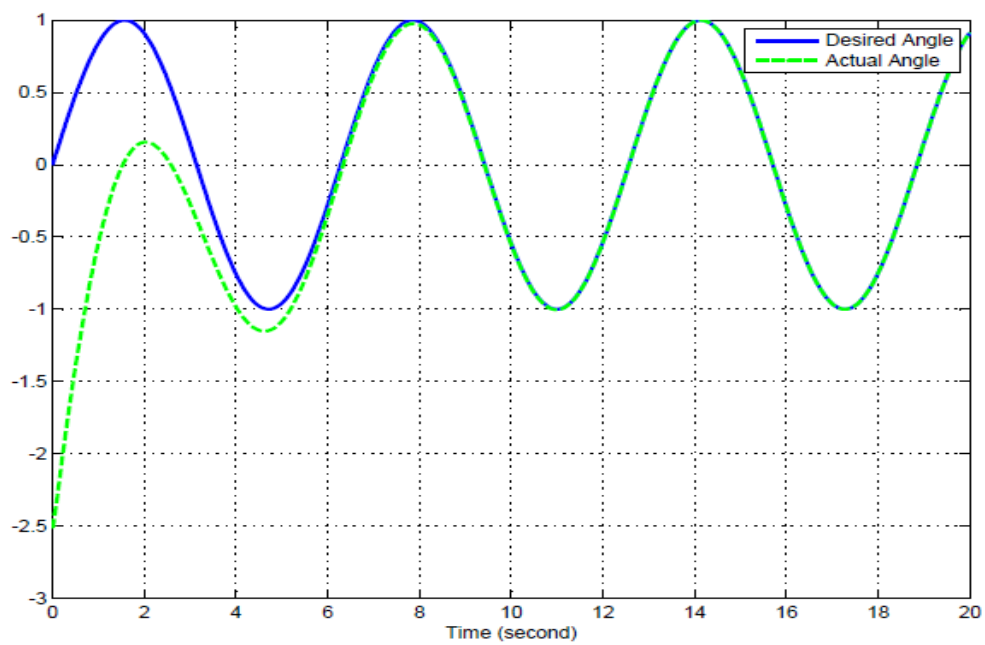
Case 1 tracking error



Case 1 angles



Case 2 tracking error



Case 2 angles

**Conclusion:**

This report presented a control technique of finite-time linear quadratic optimal control for five-fingered smart prosthetic hand. The optimal control used for feedback linearized dynamics to minimize tracking error. This work is different than the work done in [2] as in this work the reference input can be chosen to be constant, ramp, sinusoidal values,...etc. The simulations of this optimal controller showed good performance. This work can be expanded to five fingers hand with 22 degree of freedom

**References:**

- [1] D. Naidu, Optimal Control Systems. Boca Raton, FL: CRC Press, 2003.
- [2] C.-H. Chen, "Hybrid control strategies for smart prosthetic hand," Ph.D. dissertation, Measurement and Control Engineering, Idaho State University, May 2009.
- [3] D. S. Naidu, C.-H. Chen, A. Perez, and M. P. Schoen, "Control strategies for smart prosthetic hand technology: An overview," in Proceedings of the 30th Annual International IEEE EMBS Conference, Vancouver, Canada, August 20-24 2008, pp. 4314–4317.

# Kinematics, Dynamics and Control of Prosthetic Hand with extended Degrees of Freedom

## Abstract

It is obvious to all that the human hand represents a mechanism of the most intricate fashioning and one of great complexity and utility. Its ability to adapt to different surfaces and shapes, touch and grasp objects has made it a versatile tool. But beyond this, it is ultimately correlated with the brain both in the evolution of the specie and the development of the individual.

In this report, we present a virtual hand that closely mimics the human hand. Based on the anatomy of the hand, we designed a hand with 22 degrees of freedom (DOF), with each of the carpometacarpal joints (CMC) having 2 degrees of freedom each and metacarpal joints (MP) and inter-phalangeal (IP) joints having one each. The two degrees of freedom at the CMC joints are non-intersecting and are responsible for the flexion and extension (FE) motion as well as the abduction and adduction motion.. It is important to note that because of the constraint in the range of the abduction adduction motion in the index, middle, ring and small fingers, the workspace is limited.

In our approach, the problem of forward kinematics using the Denavit-Hartenberg (D-H) method was applied to compute the position of the end-effector (fingertip) given the joint variable. This followed by the inverse kinematics which is a little more difficult problem. The inverse kinematics calculates the joint variables given the position of the hand. Based on the kinematic structure, a mathematical model that describes the dynamics of the hand was calculated. These dynamic models were calculated using the Lagrangian and Newton Euler formulations. Hard control strategies such as feedback linearization and proportional integral derivative (PID) control were applied to control the hand based on the kinematic and dynamic models.

## 1.1. Introduction

In robotics terms, the hand can be said to be the end-effector of the human form. Because of its correlation or connection with the brain, it is able to perform tasks like grasping, touching, lifting and so on. Attempts has been made in the past by various researchers to build a prosthetic hand that closely mimics the human hand and various propositions has been made as to the numbers of degrees of freedom the human hand has. Our own virtual model is a 22 degree of freedom smart prosthetic hand that will work with Myo-electric signals from the hand muscles.

## 1.2. Literature

The Human hand consists of connected parts composing kinematic chains so that the hand is highly articulated. At the same time, many constraints among fingers and joints make the hand motion even hard to model. Over the years, there has been an increasing interest in the area of prostheses which lead to the creation of various models. Vardy proposed a 26 degree of freedom (DOF) hand model based on the Danavit-Hartenberg methodology [5]. The model from [5] is in-complete because the wrist was not in-cooperated and the palm was modeled as a seven DOFs articulation whereas in our model, all fingers have the same essential structure, so that the D-H methodology is applied to all fingers. The wrist was modeled as a 2 DOF articulation made up of flexion/extension (FE) and abduction and abduction motion (AA) motions. We placed the global reference frame on the wrist so that the forward kinematics of the finger-tip frame is calculated with respect to the reference frame at the base of the wrist.

In similar model to ours is [6], where the thumb was modeled as two DOFs and the rest of the fingers 3 DOFs. In [6], chen assumed a serial link planer manipulators for all fingers.

## 2. Kinematics

Kinetics being the science of geometry is restricted to a pure geometrical description of motion by means of position, orientation and their time derivatives [1]. The kinematic study of manipulators and their various roles is fundamental to the formation of the equations of motion (dynamics) and control of the manipulator. The manipulator may be thought as a set of bodies connected in a chain by joints [2]. However, for the purpose of deriving the kinematic description of a robot hand, a link is considered as a rigid body which defines the relationship between two neighboring joint axes of a manipulator. To develop a systematic kinematic description and representation of the location of the arms of a robot with respect to a global fixed reference frame G, we utilize the matrix algebra or the Clifford algebra

### 2.1 Robot kinematics using matrix algebra

We model any mechanical system, including robots as a series of rigid link connected by joints. The joints restrict the relative movements of adjacent links and are generally powered and equipped with sensors to control the movements. To apply number synthesis to hand mechanisms, we first define mobility and connectivity. The degrees of freedom of a robot also called mobility are defined as the number of independent parameters needed to specify completely (or within a finite set) the position of everybody in the system at the instant of concern [3]. In order to compute the mobility, we employ the following version of Grubler's formula (Hunt 1978).

$$M \geq \sum f_i + \sum g_j - 6L \quad (2.1)$$

$$M' \geq \sum g_j - 6L \quad (2.2)$$

Where;

$M$  - Mobility of system with finger joints free to move.

$M'$  - Mobility of system with finger joints locked.

$g_j$  - Degrees of freedom of motion at the jth contact point.

$L$ - Number of independent loops in the system

However, for a serial robot, the degrees of freedom are equal to the number of joints multiplied by the mobility allowed by each joint. Once the mobility is defined and the active joints of the hand identified, the two main

problems of kinematic analysis of robot are forward kinematics and inverse kinematics. In the forward kinematics also known as direct kinematics, we define the position of the end-effector as a matrix which is a function of the angles or slides at each joint. If the joint angles are known, the position of the end-effector is completely specified. The inverse kinematic problem which is a more difficult problem is: given the desired position and orientation of the hand relative to the station, how do we compute the set of joint angles which will achieve this result [2].

The solution of forward kinematics defines the workspace of the individual fingers of the hand as well as the hand in general. The workspace can be defined as a set of all possible positions of the end-effector (finger-tip), constructed using all possible values of the joint variables within the range. Note that the position means location plus orientation; the workspace of the robot hand is a six-dimensional subset of the six-dimensional space of rotations and translations.

Several workspace have been defined [4]

- Reachable workspace ( $W_R$ ): Set of all locations of the origin of the fingertip/ hand frame that the robot can reach. It is a three-dimensional subset of the workspace.
- Dexterous workspace ( $W_D$ ): Set of all location of the origin of the end-effector frame that the robot can reach with any orientation. It is useful because the robot has full dexterity in this subspace, which ensures that any task can be performed within it.
- Workspace with constant orientation ( $W_\theta$ ): Set of all locations of the origin of the finger-tip frame that the robot can reach with a specified orientation for the finger-tip.

## 2.2 Forward Kinematics Equations

Consider a rigid body with a fixed reference frame {A} specified as X, Y & Z and another moving body {B}. A possible description of frame {B} with respect to frame {A} is to start with the frame coincident with a known frame {A}. First rotate {B} about  $\hat{Z}_B$  by an angle  $\alpha$ , then rotate about  $\hat{Y}_B$  by an angle  $\beta$  and then rotate about  $\hat{X}_B$  by an angle  $\gamma$ . In this representation, each rotation is performed about an axis of the moving frame {B}, rather than the fixed reference frame {A}. These sets of three rotations are called Euler angles [2]. The Euler angle rotation matrix for XYZ axes are as follows:

$$R_x = \begin{pmatrix} 1 & 0 & 0 \\ 0 & \cos \alpha & -\sin \alpha \\ 0 & \sin \alpha & \cos \alpha \end{pmatrix} \quad (2.2.1)$$

$$R_y = \begin{pmatrix} \cos \beta & 0 & \sin \beta \\ 0 & 1 & 0 \\ -\sin \beta & 0 & \cos \beta \end{pmatrix} \quad (2.2.2)$$

$$R_z = \begin{pmatrix} \cos \theta & -\sin \theta & 0 \\ \sin \theta & \cos \theta & 0 \\ 0 & 0 & 1 \end{pmatrix} \quad (2.2.3)$$



We can represent local transformations from joint to joint using a 4 x 4 homogeneous matrices. The composition of these displacements is given as a result of the displacement from the base to the end-effector. In order to create the local transformations along any chain, we identify the line locating the joint axes,  $S_i$ , and we compute the common normal line  $A_{i,i+1}$  between  $S_{i+1}$ . We consider that the link joining two consecutive joints extends along the common normal line, regardless of its real shape.

We assign local coordinate frames with the z axis along the joints axes and the x axis along the common normal line. Local displacements will take us from local coordinate frame to local coordinate frame, from the base to the end-effector.

### 2.2.1 Denavit-Hartenberg Parameters

In 1995, Denavit and Hartenberg introduced the methodology of 4 x 4 homogeneous matrix transformations to analyze robotic systems, which became a standard tool in robotics [11, 12, 1]. They shaped the local transformations along the chain as screw displacements about z and x axes, dependent on only four parameters. Although a few modifications have been made over the years, the D-H notations we used are similar to Craig [3].

We locate the first local frame with the x axis along the common normal  $A_{12}$ . The origin of the frame is located at the intersection of these two lines. Assume that a general displacement  $[G]$  locates the first local frame with respect to the fixed frame, as shown in fig. 2.1.

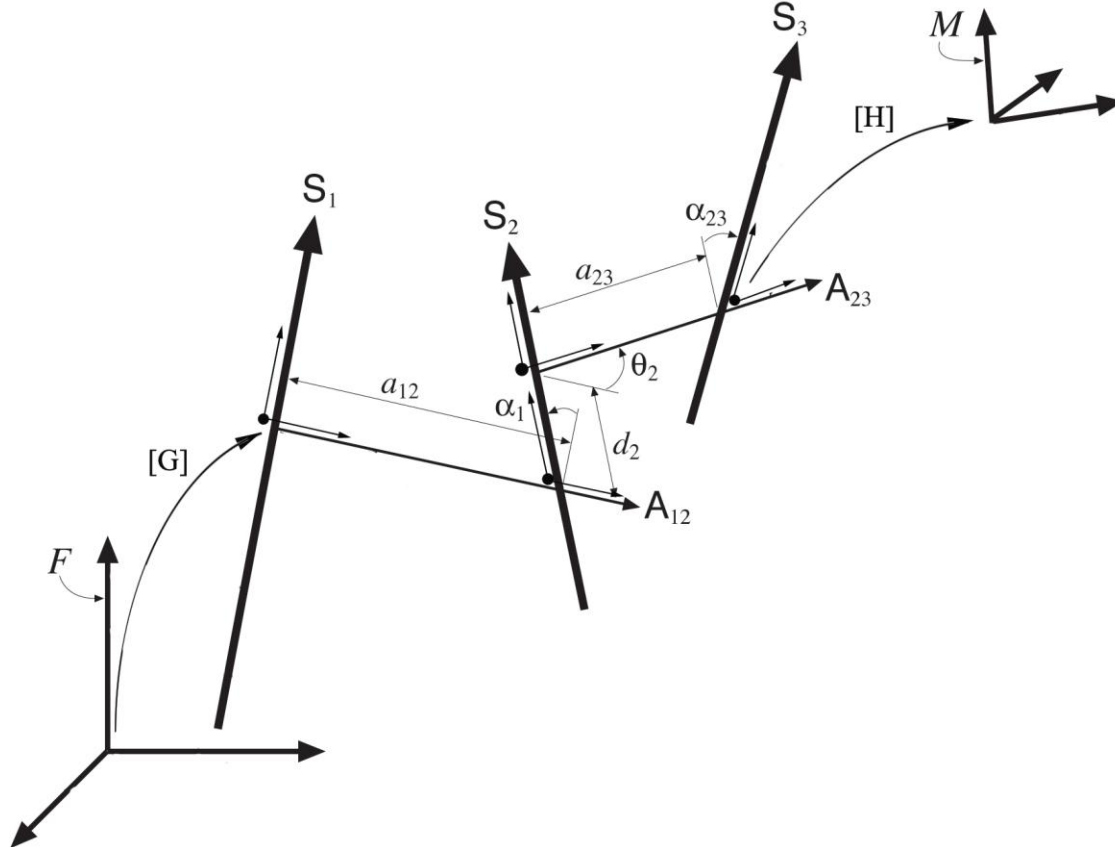


Figure 2.1: Local transformations along the links of a robot

The second local frame has the same x axis but now the z axis is aligned with  $S_2$ , with its origin at the intersection point of these two lines, while the third local frame has same z axis as the second and the line  $A_{23}$  as its x axis. From the local frame attached. Two parameters are needed to transform from local frame to local frame along links: Link twist and link length. This is X-screw displacements. Link twist,  $\alpha_{i-1,i}$ : This defines the relative location of two axes, whose common normal lines are mutually perpendicular and it is measured along this line. Link length,  $a_{i-1,i}$ : This is the distance measured along a line that is mutually perpendicular (common normal) to two axes.

Also, links that are next to each other have a common joint axis between them. The first parameter describes the distance along the common axis from one link to the next. This parameter is called the link offset,  $d_i$ . A second parameter describes the amount of rotation about this common axis between one link and the next. This parameter is called joint angle,  $\theta_i$ .

The human hand consists of connected parts composing kinematical chains so that the hand motion is highly articulated. Various models of the human hand have been created with varying degrees of freedom. The aim of this research is to obtain a model that closely mimics the human hand, as natural as possible. The Kinematical scheme was considered to be consisting of 22 revolute joints linking together the palm and the phalanges as rigid bodies. The Denavit-Hartenberg methodology becomes necessary because we have four open-loop kinematic structure and a high number of degree of freedom (DOF).

### 2.2.2 KINEMATIC SCHEME OF THE HUMAN HAND

The kinematic scheme of the human hand contains the palm and the phalanges as rigid bodies linked by 22 revolute joints. The joint variables for all the fingers are  $q_1$ ,  $q_2$ ,  $q_3$  and  $q_4$ . The kinematic chain structure is the same for the little, ring, middle and index fingers.

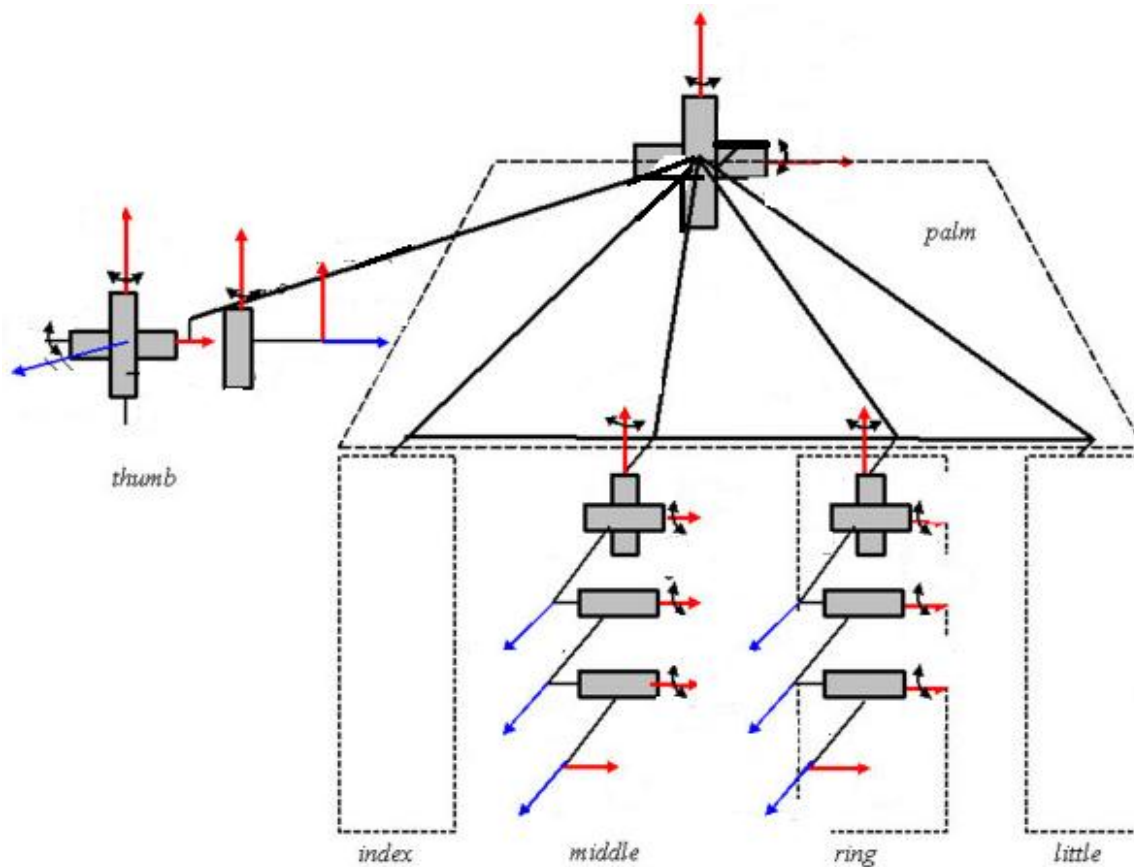


Fig. 2.3 Kinematic scheme of the human hand

### 2.2.3 KINEMATIC MODEL OF THE THUMB

The kinematic properties of the thumb should mimic those of a human thumb. Matching the robotic thumb joints to the anatomic thumb joints creates the proper relative motion between the bones. Working from the wrist up to the thumb tip, the four bones of the thumb are the trapezium carpal, the metacarpal, the proximal phalanx, and the distal phalanx. The three thumb joints are named the carpometacarpal (CMC), metacarpophalangeal (MCP), and interphalangeal (IP) joints, as shown in fig. 1.

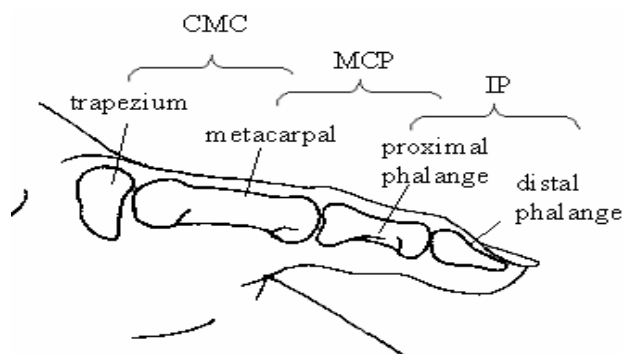


Figure1. Bones and joints of the thumb [11]

Based on the kinematic model described above the resulting location of the axes within the thumb bones are shown in fig. 2.

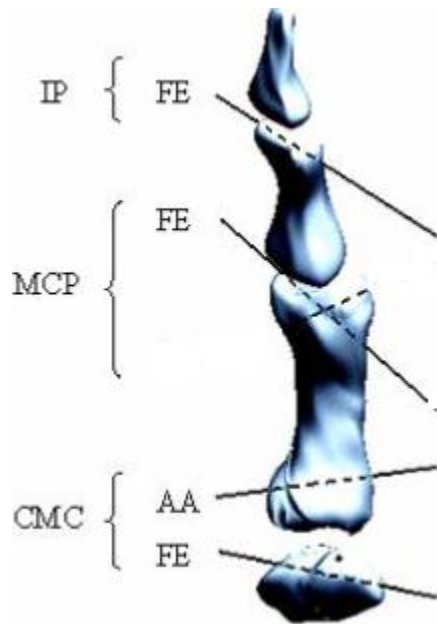


Fig. 2 Kinematic Model of the thumb with four rotational degrees of freedom thumb. [11]

The resulting locations of the axes within the thumb bones are shown in fig. 2. The IP joint FE axis passes through the distal end of the proximal phalanx and is not perpendicular to the sagittal plane of the thumb. The flexion-extension (FE) and the adduction-abduction (AA) rotational degrees of freedom (DOF) at the CMC joint are non-orthogonal and non-intersecting, as shown in figure 2. The FE axis is fixed relative to the trapezium bone at the base of the thumb. However, the anatomy of the interfacing bone surfaces of the trapezium and the thumb metacarpal bones suggests a saddle joint model with two axes that are non-intersecting and non-orthogonal (skew)

### The Four degrees of freedom Thumb

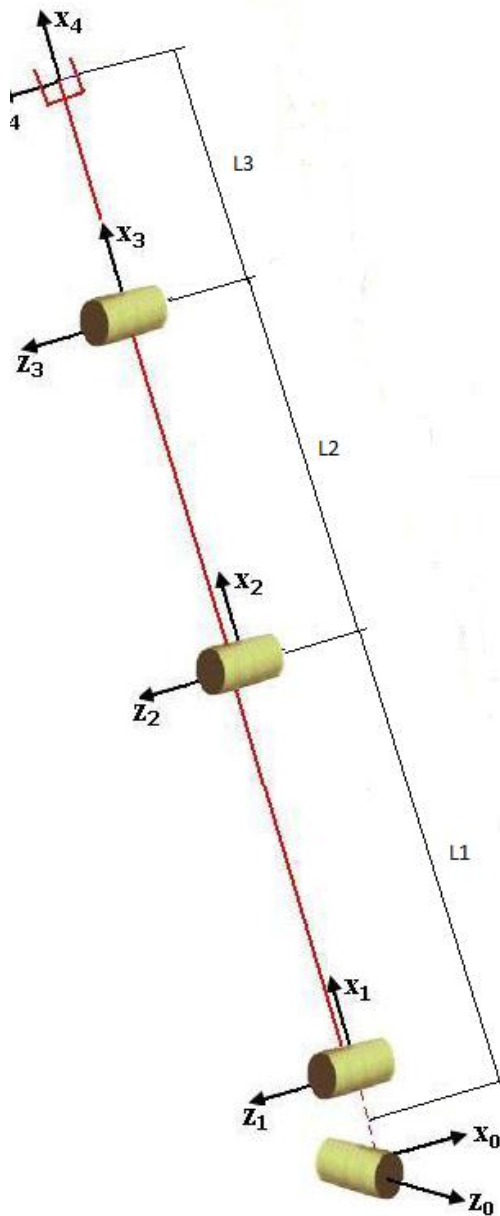


Fig.3 Four-DOF thumb illustration

Figure 1.0 shows the illustration of a four-link thumb.  $L_1$ ,  $L_2$ ,  $L_3$ ,  $L_4$  and  $L_5$  are the link lengths of the respective links;  $S_1$ ,  $S_2$ ,  $S_3$  AND  $S_4$  are the joint axis of the respective joints;  $q_1$ ,  $q_2$ ,  $q_3$ ,  $q_4$ , and  $q_5$  are the twist angles of the respective joints. The orientation of the fingertip (end-effector),  $P(x, y)$  can be obtained using the Denavit-Hartenberg Method. The Denavit-Hartenberg, D-H matrices are obtained by the by the product of the transformations from the origin (fixed frame) to the various local frames and the finger-tip (end-effector frame)

Table 1.0: DH Parameter Table for Four-link shown In Figure 1.1

Link No.	$a_{i-1,i}$	$\alpha_{i-1,i}$	$d_i$	$\theta_i$
1	0	$-\pi/2$	0	$q_1 + \pi/2$
2	$L_2$	0	0	$q_2$
3	$L_3$	0	0	$q_3$
4	$L_4$	0	0	$q_4$

$\alpha_{i-1,i}$  : Twist angle between  $S_{i-1}$  to  $S_i$

$a_{i-1,i}$  : Link length from  $S_{i-1}$  to  $S_i$

$d_i$  : offset

$\theta_i$  : Joint angle between  $A_{i-1,i}$  and  $A_{i+1,i}$

From the DH table for four-link thumb shown in Table 2.0, the transformation matrices

${}^G T_0^t, {}^0 T_1^t, {}^1 T_2^t, {}^2 T_3^t$  and  ${}^3 T_4^t$  can be written as

$${}^G T_0^t = \begin{pmatrix} 1 & 0 & 0 & 0 \\ 0 & 1 & 0 & 0 \\ 0 & 0 & 1 & 0 \\ 0 & 0 & 0 & 1 \end{pmatrix}$$

$${}^0T_1^t = \begin{pmatrix} \cos(q_1^t) & -\sin(q_1^t) & 0 & L_1^t \cos(q_1^t) \\ \sin(q_1^t) & \cos(q_1^t) & 0 & L_1^t \sin(q_1^t) \\ 0 & 0 & 1 & 0 \\ 0 & 0 & 0 & 1 \end{pmatrix}$$

$${}^1T_2^t = \begin{pmatrix} 1 & 0 & 0 & 0 \\ 0 & \cos(q_2^t) & -\sin(q_2^t) & L_2^t \cos(q_2^t) \\ 0 & -\sin(q_2^t) & \cos(q_2^t) & L_2^t \sin(q_2^t) \\ 0 & 0 & 0 & 1 \end{pmatrix}$$

$${}^2T_3^t = \begin{pmatrix} \cos(q_3^t) & -\sin(q_3^t) & 0 & L_3^t \cos(q_3^t) \\ \sin(q_3^t) & \cos(q_3^t) & 0 & L_3^t \sin(q_3^t) \\ 0 & 0 & 1 & 0 \\ 0 & 0 & 0 & 1 \end{pmatrix}$$

$${}^3T_4^t = \begin{pmatrix} \cos(q_4^t) & -\sin(q_4^t) & 0 & L_4^t \cos(q_4^t) \\ \sin(q_4^t) & \cos(q_4^t) & 0 & L_4^t \sin(q_4^t) \\ 0 & 0 & 1 & 0 \\ 0 & 0 & 0 & 1 \end{pmatrix}$$

Here  ${}^G T_0^t$  is the transformation matrix from thumb local base frame (zero) to Global frame.  ${}^0 T_1^t$  Is the transformation matrix from frame 1 to base frame (zero),  ${}^1 T_2^t$  is the transformation matrix from frame 2 to frame 1,

${}^2T_3^t$  is the transformation matrix from frame 3 to frame 2 and  ${}^3T_4^t$  is the transformation matrix from frame 4 to frame 3. The transformation matrix from thumb local frame 4 to global frame  ${}^G T_4^t$  can be written as

$${}^G T_4^t = {}^G T_0^t {}^0 T_1^t {}^1 T_2^t {}^2 T_3^t {}^3 T_4^t$$

#### 2.2.4 The Four degrees of freedom Index finger

The Index, the middle, the ring and the little fingers can be considered to be made up of four links as against the human hand configuration which is made up of three links and three bones (Metacarpal phalangeal MP, Proximal interphalangeal and Distal interphalangeal).

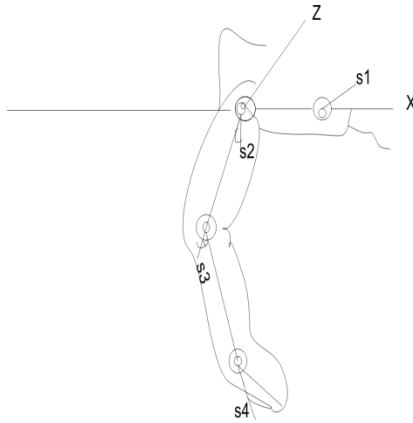


Fig. 4 Configuration of the joints of the index finger

The coordinate of the fingertip,  $P'(X^t, Y^t)$  and the orientation  $\phi^t$  of the thumb finger (t) can be written as

$$X^t = L_1^t c(q_1^t) + L_2^t c(q_{12}^t) + L_3^t c(q_{123}^t) + L_4^t c(q_{1234}^t)$$

$$Y^t = L_1^t s(q_1^t) + L_2^t s(q_{12}^t) + L_3^t s(q_{123}^t) + L_4^t s(q_{1234}^t)$$

$$\phi^t = q_1^t + q_2^t + q_3^t + q_4^t$$



The Homogeneous transformation matrix  ${}^G T_t$  to transform the thumb Local coordinate frame base  $x_0^t - y_0^t - z_0^t$  to the global frame  $x^G - y^G - z^G$  is expressed as a product of two basic homogeneous transformations  $R(X^G, \alpha)$  and  $R(Y^G, \beta)$ .

### 2.3 Inverse Kinematics of 4-Link thumb

As presented in the previous section, the forward kinematics problem of a robot manipulator is to determine the configuration (position and orientation) of the end-effector of the manipulator as a function of the manipulator joint angles. The inverse kinematics problem is to determine the joint angle. The inverse kinematics problem is to determine the joint angles given a desired end-effector configuration. Different approaches to solving the inverse kinematics problem has been studied [10]. The method adopted requires that the number of unknown is the same as that of equations and finally it solves a set of highly non-linear equations. The Newton-Raphson (N-R) method is Implemented for 4 DOFs, 5 DOFs and 6 DOFs, but for some configuration the system of equations will not converge.

The thumb has 4DOFs and to solve the inverse kinematics, we use the theory of robotics [11], where

$${}^G T_4^t = {}^0 T_1^t \bullet {}^1 T_2^t \bullet {}^2 T_3^t \bullet {}^3 T_4^t \quad (2.3.1)$$

and from equation,

$${}^G T_4^t =$$

Where the vector  $d = [d_x d_y d_z]^T$  is a known vector position of the fingertip and each element of the right hand form the equation of transformation matrix:

$${}^G T_4^t = \begin{pmatrix} n_x & 0_x & P_x & d_x \\ n_y & 0_y & P_y & d_y \\ n_z & 0_z & P_z & d_z \\ 0 & 0 & 0 & 1 \end{pmatrix} \quad (2.3.2)$$

$${}^0 T_1^t = \begin{pmatrix} \cos q_1^t & -\cos(\frac{\pi}{2})\sin(q_1^t + \frac{\pi}{2}) & \sin(-\frac{\pi}{2})\sin(q_1^t + \frac{\pi}{2}) & 0 \\ \sin(q_1^t + \frac{\pi}{2}) & \cos(-\frac{\pi}{2})\cos(q_1^t + \frac{\pi}{2}) & -\sin(-\frac{\pi}{2})\cos(q_1^t + \frac{\pi}{2}) & 0 \\ 0 & \sin(-\frac{\pi}{2}) & \cos(-\frac{\pi}{2}) & 0 \\ 0 & 0 & 0 & 1 \end{pmatrix} \quad (2.3.3)$$

$${}^1T_2^t = \begin{pmatrix} \cos q_2^t & -\cos(0)\sin(q_2^t) & \sin(0)\sin(q_2^t) & L_2 \cos(q_2^t) \\ \sin(q_2^t) & \cos(0)\cos(q_2^t) & -\sin(0)\cos(q_2^t) & L_2 \sin(q_2^t) \\ 0 & \sin(0) & \cos(0) & 0 \\ 0 & 0 & 0 & 1 \end{pmatrix} \quad (2.3.4)$$

$${}^2T_3^t = \begin{pmatrix} \cos q_3^t & -\cos(0)\sin(q_3^t) & \sin(0)\sin(q_3^t) & L_3 \cos(q_3^t) \\ \sin(q_3^t) & \cos(0)\cos(q_3^t) & -\sin(0)\cos(q_3^t) & L_3 \sin(q_3^t) \\ 0 & \sin(0) & \cos(0) & 0 \\ 0 & 0 & 0 & 1 \end{pmatrix} \quad (2.3.5)$$

$${}^3T_4^t = \begin{pmatrix} \cos q_4^t & -\cos(0)\sin(q_4^t) & \sin(0)\sin(q_4^t) & L_4 \cos(q_4^t) \\ \sin(q_4^t) & \cos(0)\cos(q_4^t) & -\sin(0)\cos(q_4^t) & L_4 \sin(q_4^t) \\ 0 & \sin(0) & \cos(0) & 0 \\ 0 & 0 & 0 & 1 \end{pmatrix} \quad (2.3.6)$$

The unknown angles are  $q_1^t, q_2^t, q_3^t$  and  $q_4^t$ . We can pre-multiply the equation on both sides for the inverse  $({}^0T_1^t)$  and the equation is now

$$({}^0T_1^t)^{-1} {}^G T_4^t = {}^1T_2^t \bullet {}^2T_3^t \bullet {}^3T_4^t \quad (2.3.7)$$

With the convenient operation, we can see that from the left matrix the element  $[3,4]_L$  is  $-d_x \cos q_1^t - d_y \sin q_1^t$  and for the right hand the element  $[3,4]_R$  is 0. We can assume that  $[3,4]_L = [3,4]_R$  and we calculate the first unknown with

$$\tan q_1^t = -\frac{d_x}{d_y} \quad (2.3.8)$$

The tangent has two solutions with a variation of  $\pi$ , but the thumb has constrained the movement, the range of motion is between  $-13/180\pi$  and  $7/30\pi$  and we only accept one solution within the range of motion. Note that this equation is only for this four DOFs system and its D-H table. We need three more independent equations to find the three unknowns. Following a similar method, the equation can be pre-multiplied for  $({}^1T_2^t)^{-1}$  on both sides and

$$({}^0T_1^t)^{-1}({}^1T_2^t)^{-1} {}^G T_4^t = {}^2T_3^t \bullet {}^3T_4^t \quad (2.3.9)$$

For this equation,  $[1, 4]_L = [1, 4]_R$  and  $[2, 4]_L = [2, 4]_R$ ; from this, we have two equations and three unknowns.

$$d_y \cos q_1^t \cos q_2^t - d_x \cos q_2^t \sin q_1^t - d_z \sin q_2^t - L_1 = L_2 \cos q_3^t + L_3 \cos q_3^t \cos q_4^t - L_3 \sin q_3^t \sin q_4^t \quad (2.3.10)$$

and

$$d_y \cos q_1^t \sin q_2^t + d_x \sin q_2^t \sin q_1^t - d_z \sin q_2^t - L_1 = L_2 \sin q_2^t + L_3 \sin q_3^t \cos q_4^t + L_3 \cos q_3^t \sin q_4^t \quad (2.3.11)$$

We need more equations to pre-multiply for  $({}^2T_3^t)^{-1}$ . The next equation is

$$({}^0T_1^t)^{-1} \bullet ({}^1T_2^t)^{-1} \bullet ({}^2T_3^t)^{-1} \bullet {}^G T_4^t = {}^3T_4^t \quad (2.3.12)$$

With the new equation, we can extract for  $[1, 4]_L = [1, 4]_R$ , as follows

$$\begin{aligned} & -L_1 \cos q_3^t - L_2 - d_z ((\cos q_3^t \sin q_2^t + \cos q_2^t \sin q_3^t + d_y \cos q_1^t ((\cos q_2^t \cos q_3^t - \sin q_2^t \sin q_3^t)) \\ & - d_x \sin q_1 \cos q_2 \cos q_3^t - \sin q_2^t \sin q_3^t = L_3 \cos q_4 \end{aligned} \quad (2.3.13)$$

We have one system of equations with three unknowns. This is a system of non –linear equations and to solve this system of equations, we need some iteration method or applied optimization.

## 2.4. DIFFERENTIAL KINEMATICS

Differential Kinematics establishes the relationship between the linear and angular velocities and accelerations of fingertips and the angular velocities and accelerations of joints by the manipulator geometric Jacobian.

### 2.4.1. Four-link thumb

If we only consider the linear velocities of the fingertip, then the angular velocities and angular accelerations of joints can be obtained by taking the first derivative and second derivative on the finger-tip co-ordinate  $P'(X', Y')C_i$  of the thumb

$$\begin{bmatrix} \dot{X} \\ \dot{Y} \end{bmatrix} = \begin{bmatrix} -L'_1 S(q'_1) - L'_2 S(q'_{12}) - L'_3 S(q'_{123}) - L'_4 S(q'_{1234}) \\ L'_1 C(q'_1) + L'_2 C(q'_{12}) + L'_3 C(q'_{123}) + L'_4 C(q'_{1234}) \end{bmatrix}$$

### 2.4.2. Jacobians

The jacobians, J is a multidimensional form of the derivative. Suppose, for example we have four functions, each of which is a function of four independent variables:

$$Y1 = f1(q1, q2, q3, q4),$$

$$Y2 = f2(q1, q2, q3, q4),$$

$$Y3 = f3(q1, q2, q3, q4),$$

$$Y4 = f4(q1, q2, q3, q4).$$

Now if we wish to calculate the differentials of  $y_i$  as a function of differentials of  $x_j$ , we simply use the chain rule to calculate and we get

$$\partial y_1 = \frac{\partial f_1}{\partial x_1} \delta x_1 + \frac{\partial f_1}{\partial x_2} \delta x_2 + \frac{\partial f_1}{\partial x_3} \delta x_3 + \frac{\partial f_1}{\partial x_4} \delta x_4 ,$$

.

.

$$\partial y_4 = \frac{\partial f_4}{\partial x_1} \delta x_1 + \frac{\partial f_4}{\partial x_2} \delta x_2 + \frac{\partial f_4}{\partial x_3} \delta x_3 + \frac{\partial f_4}{\partial x_4} \delta x_4$$

This again might be written more simply using vector notation as

$$\partial Y = \frac{\partial F}{\partial X}$$

The 6x6 matrix of partial derivatives is what we call the Jacobian, J.

The differential derivative of the coordinate of the points of the finger-tip can be written as

$$\dot{p}^t = J_p^t(q^t) \dot{q}^t$$

The matrices  $\dot{p}^t, \dot{q}^t$  and  $J_p^t(q^t)$  as follows

$$\dot{p}^t = \begin{bmatrix} \dot{X}^t \\ \dot{Y}^t \end{bmatrix} \quad \dot{q}^t = \begin{bmatrix} \dot{q}_1^t \\ \dot{q}_2^t \\ \dot{q}_3^t \\ \dot{q}_4^t \end{bmatrix} \quad q^t = \begin{bmatrix} q_1^t \\ q_2^t \\ q_3^t \\ q_4^t \end{bmatrix}$$

$$J_p^t(q^t) = \begin{bmatrix} -L_1^t S(q_1^t) - L_2^t S(q_{12}^t) - L_3^t S(q_{123}^t) - L_4^t S(q_{1234}^t) \\ {}^t C(q_1^t) + L_2^t C(q_{12}^t) + L_3^t C(q_{123}^t) + L_4^t C(q_{1234}^t) \end{bmatrix}$$

The matrix  $J_p^t(q^t)$  is called a sub-matrix of the geometric jacobian of the thumb. We will only consider the geometric jacobian for the planer location  $P^t(X^t, Y^t)$  and not the orientation, that is, a sub-matrix of the geometric jacobian.

The angular velocities  $\dot{q}_1^t, \dot{q}_2^t, \dot{q}_3^t$  and  $\dot{q}_4^t$  of the joints 1, 2, and 3 are

$$\dot{q}^t = J_p^t \left( \dot{q} \right)^{-1} \dot{P}^t$$

Similarly, the angular accelerations  $\ddot{q}_1^t, \ddot{q}_2^t, \ddot{q}_3^t$  and  $\ddot{q}_4^t$  of the joints 1, 2 and 3 are obtained as

$$\ddot{q}^t = J_p^t \left( \dot{q} \right)^{-1} \left( \ddot{P}^t - \frac{dJ_p^t(q^t)}{dt} \dot{q}^t \right)$$

Where  $\ddot{P}^t$  is the linear acceleration vector of the fingertip.  $\ddot{P}^t$ ,  $\ddot{q}^t$ , and  $\frac{dJ_p^t(q^t)}{dt}$  are denoted as

$$\ddot{P}^t = \begin{bmatrix} \ddot{X}^t \\ \ddot{Y}^t \end{bmatrix}, \quad \ddot{q}^t = \begin{bmatrix} \ddot{q}_1^t \\ \ddot{q}_2^t \\ \ddot{q}_3^t \\ \ddot{q}_4^t \end{bmatrix}$$

$$\frac{dJ_p^t(q^t)}{dt} = \begin{bmatrix} -L_1^t \cos(q_1^t) \dot{q}_1^t - L_2^t \cos(q_{12}^t) \dot{q}_{12}^t - L_3^t \cos(q_{123}^t) \dot{q}_{123}^t - L_4^t \cos(q_{1234}^t) \dot{q}_{1234}^t \\ -L_1^t \sin(q_1^t) \dot{q}_1^t - L_2^t \sin(q_{12}^t) \dot{q}_{12}^t - L_3^t \sin(q_{123}^t) \dot{q}_{123}^t - L_4^t \sin(q_{1234}^t) \dot{q}_{1234}^t \end{bmatrix}$$

### 2.4.3. Finger-tip Workspace

The solutions of the direct kinematics define the workspace of the finger. The workspace can be defined as the set of all possible positions of the finger-tip, constructed using all possible values of joint variables within their range.

Because of the difficulty in visualizing the workspace, several subspaces have been defined

- **Reachable workspace:** This is a set of all locations of the origin of the finger-tip frame that the robot finger can reach. It is a three dimensional subset of the workspace.
- **Dexterous workspace:** Set of all locations of the origin of the finger-tip frame that the robot finger can reach with any orientation. This useful because the robot has full dexterity in this subspace, which ensures that any task can be performed within it
- **Workspace with constant orientation:** Set of all locations of the origin of the end-effector frame that the robot can reach with a specified orientation for the end-effector.

#### 2.4.4. Three-link thumb

The three-link thumb with four degree of freedom is shown in the figure. The red region is the reachable workspace of the thumb. The first, second and third positions (joint angles) are constrained in the ranges of  $[0,90]$ ,  $[-80,0]$  and  $[60,0]$  respectively.

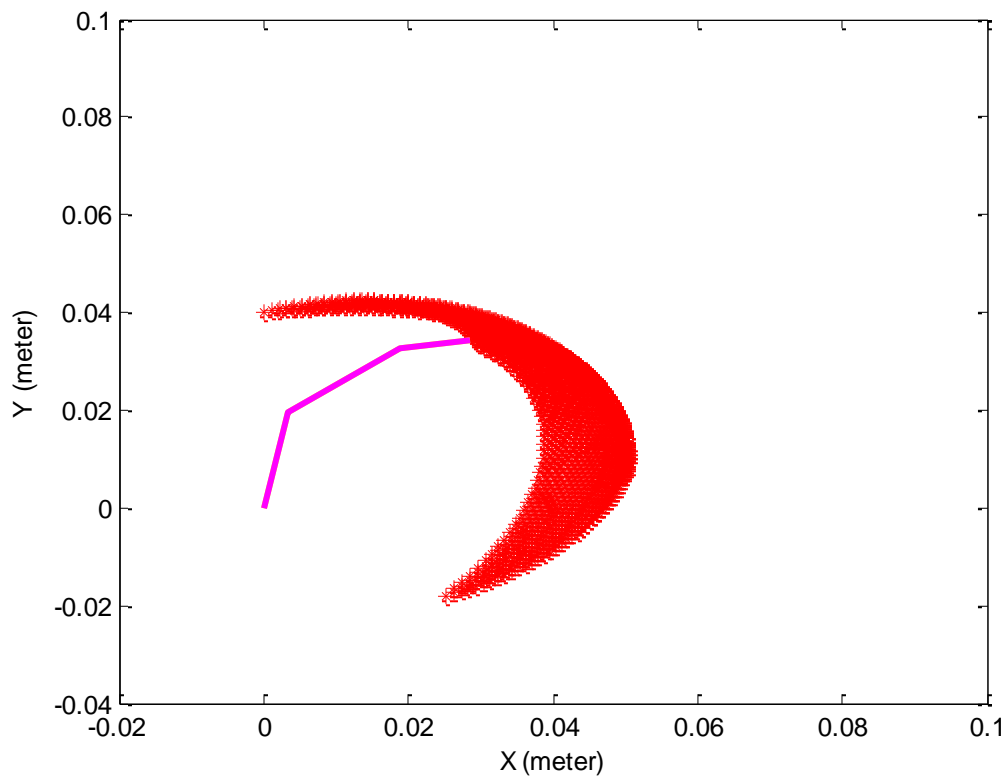


Figure 2.0. Workspace of thumb in Flexion and extension motion

Also for the combined workspace of the thumb and index finger during extension and flexion is show in the figure. The Index finger is constrained within the range  $[0, 90]$ ,  $[0,110]$  and  $[0, 80]$ . In the figure a square shaped object is within the reachable workspace of the thumb-index fingers motion.

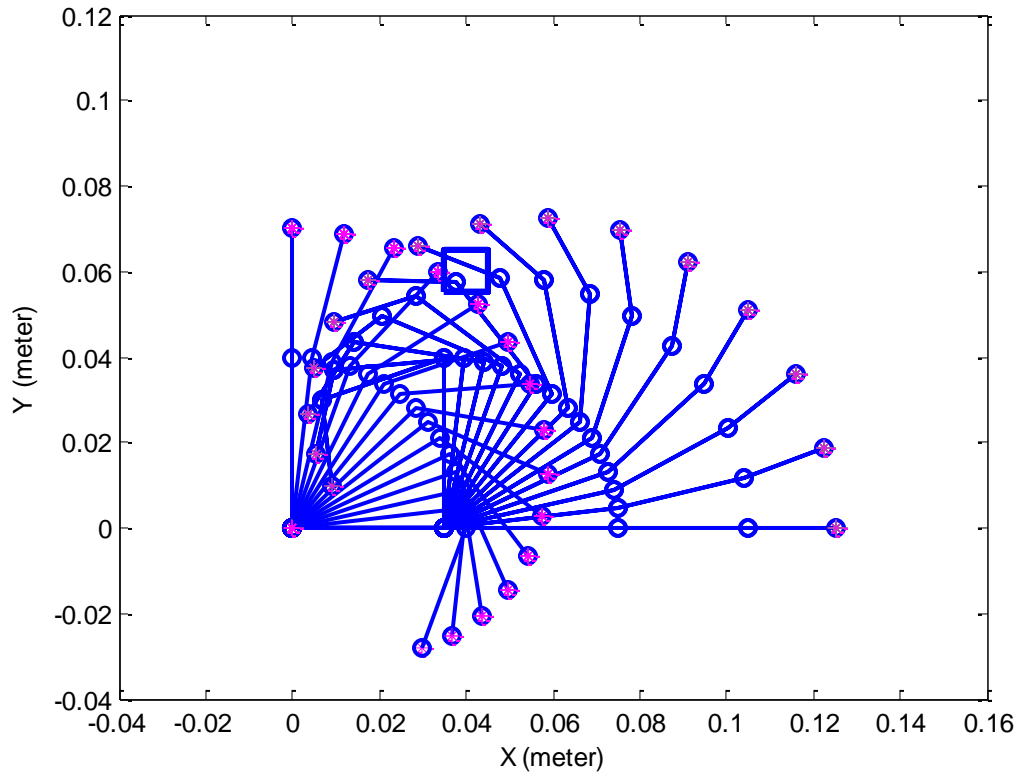


Figure 2.1. Configuration of a Square shaped object within the workspace of a thumb-index finger

### 3. Dynamics

In order to derive a control technique for the prosthetic hand, a mathematical model that describes the dynamic behavior of the hand must be calculated. An ideal model of a 4-link with 4-R finger is studied in this section. It is called ideal because it is assumed that the links are massless and there is no friction. The equation of motion that describes the dynamic behavior of systems can be obtained via Newton's equation of motion or Lagrange's approach. We will use the Lagrange's form of Newton's equation of motion to derive the dynamic equations.

The Lagrangean form of Newton's equation are given by

$$\frac{d}{dt} \left( \frac{\partial L}{\partial \dot{q}} \right) - \frac{\partial L}{\partial q} = Q_r \quad r=1, 2, \dots, n \quad (3.00)$$

Where

$$L = K - V \quad (3.10)$$

Equation (3.10) is called the Lagrangean of the system,  $Q_r$  is the non-potential generalized force; K and V are the potential energy of the n degree of freedom prosthetic hand respectively.



### 3.1. Four-link index finger

The Legrangean equation of the index finger can be expressed as

$$L^i = K^i - V^i. \quad (3.20)$$

Where

$$K^i = \sum_{m=1}^{n=4} \frac{1}{2} m_m^i (\dot{X}_m^2 + \dot{Y}_m^2) \quad (3.30)$$

$$V^i = \sum_{m=1}^{n=4} V^i = \sum_{m=1}^{n=4} M_m^i g Y_m \quad (3.40)$$

Here, n is the number of links of the index finger;  $m_m^i$  is the mass of link m; we take the absolute angle  $\theta_1$  and the relative angles  $\theta_2, \theta_3$  and  $\theta_4$  as the generalized coordinates to express the configuration of the index finger.

The global position of  $m_1, m_2, m_3$  and  $m_4$  are

$$\begin{bmatrix} X_1 \\ Y_1 \end{bmatrix} = \begin{bmatrix} l_1 \cos \theta_1 \\ l_1 \sin \theta_1 \end{bmatrix} \quad (3.50)$$

$$\begin{bmatrix} X_2 \\ Y_2 \end{bmatrix} = \begin{bmatrix} l_1 \cos \theta_1 + l_2 \cos(\theta_1 + \theta_2) \\ l_1 \sin \theta_1 + l_2 \sin(\theta_1 + \theta_2) \end{bmatrix} \quad (3.60)$$

$$\begin{bmatrix} X_3 \\ Y_3 \end{bmatrix} = \begin{bmatrix} l_1 \cos \theta_1 + l_2 \cos(\theta_1 + \theta_2) + l_3 \cos(\theta_1 + \theta_2 + \theta_3) \\ l_1 \sin \theta_1 + l_2 \sin(\theta_1 + \theta_2) + l_3 \sin(\theta_1 + \theta_2 + \theta_3) \end{bmatrix} \quad (3.70)$$

$$\begin{bmatrix} X_4 \\ Y_4 \end{bmatrix} = \begin{bmatrix} l_1 \cos \theta_1 + l_2 \cos(\theta_1 + \theta_2) + l_3 \cos(\theta_1 + \theta_2 + \theta_3) + l_4 \cos(\theta_1 + \theta_2 + \theta_3 + \theta_4) \\ l_1 \sin \theta_1 + l_2 \sin(\theta_1 + \theta_2) + l_3 \sin(\theta_1 + \theta_2 + \theta_3) + l_4 \sin(\theta_1 + \theta_2 + \theta_3 + \theta_4) \end{bmatrix} \quad (3.80)$$

The global velocities of the masses are the time derivative of the global position of the masses.

$$\begin{bmatrix} \dot{X}_1 \\ \dot{Y}_1 \end{bmatrix} = \begin{bmatrix} -l_1 \dot{\theta}_1 \sin \theta_1 \\ l_1 \dot{\theta}_1 \cos \theta_1 \end{bmatrix} \quad (3.90)$$

$$\begin{bmatrix} X_2 \\ Y_2 \end{bmatrix} = \begin{bmatrix} -l_1 \dot{\theta}_1 \sin \theta_1 - l_2 \dot{\theta}_{12} \sin \theta_{12} \\ l_1 \dot{\theta}_1 \cos \theta_1 + l_2 \dot{\theta}_{12} \cos \theta_{12} \end{bmatrix} \quad (3.91)$$

$$\begin{bmatrix} X_3 \\ Y_3 \end{bmatrix} = \begin{bmatrix} -l_1 \dot{\theta}_1 \sin \theta_1 - l_2 \dot{\theta}_{12} \sin \theta_{12} - l_3 \dot{\theta}_{123} \sin \theta_{123} \\ l_1 \dot{\theta}_1 \cos \theta_1 + l_2 \dot{\theta}_{12} \cos \theta_{12} + l_3 \dot{\theta}_{123} \cos \theta_{123} \end{bmatrix} \quad (3.92)$$

$$\begin{bmatrix} X_4 \\ Y_4 \end{bmatrix} = \begin{bmatrix} -l_1 \dot{\theta}_1 \sin \theta_1 - l_2 \dot{\theta}_{12} \sin \theta_{12} - l_3 \dot{\theta}_{123} \sin \theta_{123} - l_4 \dot{\theta}_{1234} \sin \theta_{1234} \\ l_1 \dot{\theta}_1 \cos \theta_1 + l_2 \dot{\theta}_{12} \cos \theta_{12} + l_3 \dot{\theta}_{123} \cos \theta_{123} + l_4 \dot{\theta}_{1234} \cos \theta_{1234} \end{bmatrix} \quad (3.93)$$

The kinetic energy of the finger is made up of the kinetic energy of the masses and is equal to

$$K = K_1 + K_2 + K_3 + K_4$$

$$\begin{aligned}
K := & \frac{m1 \left( L1^2 \sin(\theta1(t))^2 \dot{\theta1}(t)^2 + L1^2 \cos(\theta1(t))^2 \dot{\theta1}(t)^2 \right)}{2} \\
& + \frac{1}{2} \left( m2 \left( L1^2 \sin(\theta1(t))^2 \dot{\theta1}(t)^2 - L2^2 \sin(\theta1(t) \right. \right. \\
& + \left. \left. \theta2(t) \right)^2 \left( \dot{\theta1}(t) + \dot{\theta2}(t) \right)^2 + L1^2 \cos(\theta1(t))^2 \dot{\theta1}(t)^2 \right. \\
& + \left. L2^2 \cos(\theta1(t) + \theta2(t))^2 \left( \dot{\theta1}(t) + \dot{\theta2}(t) \right)^2 \right) \\
& + \frac{1}{2} \left( m3 \left( L1^2 \sin(\theta1(t))^2 \dot{\theta1}(t)^2 - L2^2 \sin(\theta1(t) \right. \right. \\
& + \left. \left. \theta2(t) \right)^2 \left( \dot{\theta1}(t) + \dot{\theta2}(t) \right)^2 - L3^2 \sin(\theta1(t) + \theta2(t) \right. \\
& + \left. \left. \theta3(t) \right)^2 \left( \dot{\theta1}(t) + \dot{\theta2}(t) + \dot{\theta3}(t) \right)^2 + L1^2 \cos(\theta1(t))^2 \dot{\theta1}(t)^2 \right. \\
& + \left. L2^2 \cos(\theta1(t) + \theta2(t))^2 \left( \dot{\theta1}(t) + \dot{\theta2}(t) \right)^2 \right. \\
& + \left. L3^2 \cos(\theta1(t) + \theta2(t) + \theta3(t))^2 \left( \dot{\theta1}(t) + \dot{\theta2}(t) + \dot{\theta3}(t) \right)^2 \right) \\
& + \frac{1}{2} \left( m4 \left( L1^2 \sin(\theta1(t))^2 \dot{\theta1}(t)^2 - L2 \sin(\theta1(t) \right. \right. \\
& + \left. \left. \theta2(t) \right)^2 \left( \dot{\theta1}(t) + \dot{\theta2}(t) \right)^2 + L3^2 \sin(\theta1(t) + \theta2(t) \right. \\
& + \left. \left. \theta3(t) \right)^2 \left( \dot{\theta1}(t) + \dot{\theta2}(t) + \dot{\theta3}(t) \right)^2 + L4^2 \sin(\theta1(t) + \theta2(t) \right. \\
& + \left. \left. \theta3(t) + \theta4(t) \right)^2 \left( \dot{\theta1}(t) + \dot{\theta2}(t) + \dot{\theta3}(t) + \dot{\theta4}(t) \right)^2 \right. \\
& + \left. L1^2 \cos(\theta1(t))^2 \dot{\theta1}(t)^2 + L2^2 \cos(\theta1(t) + \theta2(t))^2 \left( \dot{\theta1}(t) \right. \right. \\
& + \left. \left. \dot{\theta2}(t) \right)^2 + L3^2 \cos(\theta1(t) + \theta2(t) + \theta3(t))^2 \left( \dot{\theta1}(t) + \right. \right. \\
& + \left. \left. \dot{\theta2}(t) + \dot{\theta3}(t) \right)^2 + L4^2 \cos(\theta1(t) + \theta2(t) + \theta3(t) \right. \\
& + \left. \left. \theta4(t) \right)^2 \left( \dot{\theta1}(t) + \dot{\theta2}(t) + \dot{\theta3}(t) + \dot{\theta4}(t) \right)^2 \right)
\end{aligned}$$

The Potential Energy of the manipulator  $V=v1+v2+v3+v4$

$$= m_1 g Y_1 + m_2 g Y_2 + m_3 g Y_3 + m_4 g Y_4$$

$$m_1 g l_1 \sin \theta + m_2 g (l_1 \sin \theta_1 + l_2 \sin \theta_{12}) + m_3 g (l_1 \sin \theta_1 + l_2 \sin \theta_{12} + l_3 \sin \theta_{123})$$

$$+ m_4 g (l_1 \sin \theta_1 + l_2 \sin \theta_{12} + l_3 \sin \theta_{123} + l_4 \sin \theta_{1234}) \quad (3.96)$$

Here  $l_m^i$  is the length of link k;  $\theta_m$  is the angle at joint m and a function of time; g is the acceleration due to gravity.

Therefore the Lagrangean is obtained from equations (3.95) and (3.96) by substituting it in (3.20) . Here  $l_m^i$  is the length of link k;  $\theta_m$  is the angle at joint m and a function of time; g is the acceleration due to gravity.

$$L = K - V$$

$$\begin{aligned}
L := & \frac{m1 (L1^2 \sin(\theta1(t))^2 \dot{\theta1}(t)^2 + L1^2 \cos(\theta1(t))^2 \dot{\theta1}(t)^2)}{2} \\
& + \frac{1}{2} (m2 (L1^2 \sin(\theta1(t))^2 \dot{\theta1}(t)^2 - L2^2 \sin(\theta1(t) \\
& + \theta2(t))^2 (\dot{\theta1}(t) + \dot{\theta2}(t))^2 + L1^2 \cos(\theta1(t))^2 \dot{\theta1}(t)^2 \\
& + L2 \cos(\theta1(t) + \theta2(t))^2 (\dot{\theta1}(t) + \dot{\theta2}(t))^2) \\
& + \frac{1}{2} (m3 (L1^2 \sin(\theta1(t))^2 \dot{\theta1}(t)^2 - L2^2 \sin(\theta1(t) \\
& + \theta2(t))^2 (\dot{\theta1}(t) + \dot{\theta2}(t))^2 - L3^2 \sin(\theta1(t) + \theta2(t) \\
& + \theta3(t))^2 (\dot{\theta1}(t) + \dot{\theta2}(t) + \dot{\theta3}(t))^2 + L1^2 \cos(\theta1(t))^2 \dot{\theta1}(t)^2 \\
& + L2^2 \cos(\theta1(t) + \theta2(t))^2 (\dot{\theta1}(t) + \dot{\theta2}(t))^2 \\
& + L3^2 \cos(\theta1(t) + \theta2(t) + \theta3(t))^2 (\dot{\theta1}(t) + \dot{\theta2}(t) + \dot{\theta3}(t))^2) \\
& + \frac{1}{2} (m4 (L1^2 \sin(\theta1(t))^2 \dot{\theta1}(t)^2 - L2 \sin(\theta1(t) \\
& + \theta2(t))^2 (\dot{\theta1}(t) + \dot{\theta2}(t))^2 + L3^2 \sin(\theta1(t) + \theta2(t) \\
& + \theta3(t))^2 (\dot{\theta1}(t) + \dot{\theta2}(t) + \dot{\theta3}(t))^2 + L4^2 \sin(\theta1(t) + \theta2(t) \\
& + \theta3(t) + \theta4(t))^2 (\dot{\theta1}(t) + \dot{\theta2}(t) + \dot{\theta3}(t) + \dot{\theta4}(t))^2 \\
& + L1^2 \cos(\theta1(t))^2 \dot{\theta1}(t)^2 + L2^2 \cos(\theta1(t) + \theta2(t))^2 (\dot{\theta1}(t) \\
& + \dot{\theta2}(t))^2 + L3^2 \cos(\theta1(t) + \theta2(t) + \theta3(t))^2 (\dot{\theta1}(t) + \\
& \dot{\theta2}(t) + \dot{\theta3}(t))^2 + L4^2 \cos(\theta1(t) + \theta2(t) + \theta3(t) \\
& + \theta4(t))^2 (\dot{\theta1}(t) + \dot{\theta2}(t) + \dot{\theta3}(t) + \dot{\theta4}(t))^2) \\
& - m1 g L1 \sin(\theta1(t)) - m2 g L1 \sin(\theta1(t)) - m2 g L2 \sin(\theta1(t) \\
& + \theta2(t)) - m3 g L1 \sin(\theta1(t)) - m3 g L2 \sin(\theta1(t) + \theta2(t)) \\
& - m3 g L3 \sin(\theta1(t) + \theta2(t) + \theta3(t)) - m4 g L1 \sin(\theta1(t)) \\
& - m4 g L2 \sin(\theta1(t) + \theta2(t)) - m4 g L3 \sin(\theta1(t) + \theta2(t) \\
& + \theta3(t)) - m4 g L4 \sin(\theta1(t) + \theta2(t) + \theta3(t) + \theta4(t))
\end{aligned}$$

$$\frac{\partial L}{\partial \theta_1} = -(m_1 + m_2 + m_3 + m_4) g l_1 \cos \theta_1 - (m_2 + m_3 + m_4) g l_2 \cos(\theta_1 + \theta_2) + (m_2 + m_3 + m_4) g l_2 \cos(\theta_1 + \theta_2) + m_4 g l_4 \cos(\theta_1 + \theta_2 + \theta_3)$$

$$\frac{\partial L}{\partial \dot{\theta}_1} = (m_1 + m_2 + m_3 + m_4) l_1^2 \dot{\theta}_1 - (m_2 + m_3 + m_4) l_2^2 (\dot{\theta}_1 + \dot{\theta}_2) + (m_3 + m_4) l_3^2 (\dot{\theta}_1 + \dot{\theta}_2 + \dot{\theta}_3) + m_4 l_4^2 (\dot{\theta}_1 + \dot{\theta}_2 + \dot{\theta}_3 + \dot{\theta}_4)$$

### 3.2. Dynamics for a 3R Planer Index finger

We can derive a set of recursive equations to relate each link in the coordinate frame attached to the previous link based on the velocity and acceleration kinematics. We may generalize the method of analysis to be suitable for a robot index finger any number of links. The Newton-Euler's equations of motion application in robot dynamics enables us to calculate the joint forces one link at a time starting from the end-effector (finger-tip) link.

The backward Newton-Euler equations of motion for the link (i) in the local coordinate frame  $B_i$  are

$$\begin{aligned}
 F_{i-1} &= \Sigma^i F_{ei} + m_i {}^i a_i \\
 M_{i-1} &= {}^i M_i - \Sigma^i M_{ei} - ({}^i d_{i-1} - {}^i r_i) \times {}^i F_{i-1} \\
 &\quad + ({}^i d_i - {}^i r_i) {}^i F_i + {}^i I_{i0} {}^i \alpha_i + {}^i \omega_i \times {}^i I_{i0} {}^i \omega_i \\
 {}^i n_i &= {}^i d_{i-1} - {}^i r_i \\
 {}^i m_i &= {}^i d_i - {}^i r_i
 \end{aligned}$$

Translational acceleration of link (i) is denoted by  $a_{0i}$  and is measured at the mass center  $C_i$ . Angular acceleration which is the same for all points of a rigid link (i) is denoted by  $\alpha_{0i}$  and is usually shown at the mass center  $C_i$ . The forces,  $F_{i-1}$  and moment  $M_{i-1}$  are the resultant force and moment that link (i) applies to link (i+1) at joint i+1.

When the driving force system ( $F_{i-1}$ , and  $M_{i-1}$ ) is found in frame  $B_i$ , we can transform them to the frame  $B_{i-1}$  and apply the Newton-Euler equation for link (i-1).

$$\begin{aligned}
 {}^{i-1} F_{i-1} &= {}^{i-1} T_i {}^i F_{i-1} \\
 {}^{i-1} M_{i-1} &= {}^{i-1} T_i {}^i M_{i-1}
 \end{aligned}$$

The negative of the converted force system acts as the driven force system ( $F_{i-1}$ , and  $M_{i-1}$ ) for the link (i-1).

### 3.3. Three-link Index finger Dynamics

Fig.

The Torques of the actuators are parallel to the z-axis and are shown to be  $Q_0$ ,  $Q_1$  and  $Q_3$ .

The Newton Euler equations of motion for the first link are

$$\begin{aligned}
 F_0 - F_{01} + M_1 \hat{g} &= M_1 a_{01} \\
 Q_1 - Q_2 + n_{01} \times F_0 - m_{01} \times F_{01} &= I_{01} \alpha_{01}
 \end{aligned} \tag{3.2.1}$$

Equations of motion for the second link are

$$\begin{aligned} F_{01} - F_{02} + M_2 g \hat{j} &= M_2 a_{02} \\ Q_1 - Q_2 + n_{02} \times F_{01} - m_{02} \times F_{02} &= I_{02} \alpha_{02} \end{aligned} \quad (3.2.2)$$

Equations of motion for the third link are

$$\begin{aligned} F_{02} + M_3 g \hat{j} &= M_3 a_{03} \\ Q_2 + n_{03} \times F_{02} &= I_{03} \alpha_{03} \end{aligned} \quad (3.2.3)$$

There are six equations with six unknowns; F0, F1, F2, Q0, Q1 and Q2

However in robot dynamics, actuator torques is usually applied in the control not the joint forces. So we do not necessarily need to find the joint forces. We may eliminate F0, F1 and F2 and reduce the number of equations by half.

Eliminating F2 in equation (3.2.3)

$$Q_2 = I_{03} \alpha_{03} - n_{03} (m_3 a_{03} - m_3 g \hat{j}) \quad (3.2.4)$$

Eliminating F1 and F2 in equation (3.2.2)

$$Q_1 = Q_2 + I_{02} \alpha_{02} + m_{02} \times m_3 (a_{03} - g \hat{j}) - n_{02} (m_2 (a_{02} - g \hat{j}) - m_3 (a_{03} - g \hat{j})) \quad (3.2.5)$$

Eliminating F0 and F1 in equation (3.2.1)

$$Q_0 = Q_1 + I_{01} \alpha_{01} + m_1 \times m_3 (a_{03} - g \hat{j}) - n_{01} (m_1 (a_{01} - g \hat{j}) - m_2 (a_{02} - g \hat{j}) - m_3 (a_{03} - g \hat{j})) \quad (3.2.6)$$

Using MAPLE, the position of Ci and the links' angular velocity and acceleration are calculated. The translational acceleration, a01 at the center of mass of each link is also calculated. Substituting these results in equations (3.2.1), (3.2.2) and (3.2.3), provides the dynamic equations for the 3R robotic finger in appropriate form.

$$\begin{aligned}
Q2 := & \left[ \left[ \frac{1}{2} \left( L3 \cos(\theta1(t) + \theta2(t) + \theta3(t)) m3 \left( \right. \right. \right. \right. \\
& - \frac{L1 \cos(\theta1(t)) \dot{\theta}1(t)^2}{2} - \frac{L1 \sin(\theta1(t)) \ddot{\theta}1(t)}{2} \\
& - \frac{L2 \cos(\theta1(t) + \theta2(t)) (\dot{\theta}1(t) + \dot{\theta}2(t))^2}{2} \\
& - \frac{L2 \sin(\theta1(t) + \theta2(t)) (\ddot{\theta}1(t) + \ddot{\theta}2(t))}{2} \\
& - \frac{L3 \cos(\theta1(t) + \theta2(t) + \theta3(t)) (\dot{\theta}1(t) + \dot{\theta}2(t) + \dot{\theta}3(t))^2}{2} \\
& \left. \left. \left. - \frac{L3 \sin(\theta1(t) + \theta2(t) + \theta3(t)) (\ddot{\theta}1(t) + \ddot{\theta}2(t) + \ddot{\theta}3(t))}{2} \right) \right) \right] \\
& + \frac{1}{2} \left( L3 \sin(\theta1(t) + \theta2(t) + \theta3(t)) m3 \left( \right. \right. \\
& - \frac{L1 \sin(\theta1(t)) \dot{\theta}1(t)^2}{2} + \frac{L1 \cos(\theta1(t)) \ddot{\theta}1(t)}{2} \\
& - \frac{L2 \sin(\theta1(t) + \theta2(t)) (\dot{\theta}1(t) + \dot{\theta}2(t))^2}{2} \\
& + \frac{L2 \cos(\theta1(t) + \theta2(t)) (\ddot{\theta}1(t) + \ddot{\theta}2(t))}{2} \\
& - \frac{L3 \sin(\theta1(t) + \theta2(t) + \theta3(t)) (\dot{\theta}1(t) + \dot{\theta}2(t) + \dot{\theta}3(t))^2}{2} \\
& + \frac{L3 \cos(\theta1(t) + \theta2(t) + \theta3(t)) (\ddot{\theta}1(t) + \ddot{\theta}2(t) + \ddot{\theta}3(t))}{2} \\
& \left. \left. \left. - g L3 \cos(\theta1 + \theta2 + \theta3) \right) \right) \right] \Bigg], \\
& \left[ \begin{array}{c} 0 \\ I3 (\ddot{\theta}1(t) + \ddot{\theta}2(t) + \ddot{\theta}3(t)) \end{array} \right] \Bigg]
\end{aligned}$$

#### 4. Hard Control of the Prosthetic Hand

Control is the science of desired motion. The prescribed motion of a robot is related to the dynamics and kinematics by control. In applying controls, certain optimal indices should be considered to enable the system (device) function optimally. For example performance of task by the prosthesis in the shortest possible time. This is where the concept of path planning for the robotic finger comes into play.

An integral part of robot control is planning the path (path planning) the robot should follow in carrying out specific tasks. Task compliance or constrained motion is critical in situations where the robot comes in contact with obstacles. This could be done in either Cartesian or joint space. Path planning in the joint space appear to be easier compared to Cartesian space.

There are number control algorithms that can be used to control the robotic hand, each of which is best applicable to particular class of robots in a particular task. Some of these control methods are: Feedback linearization or computed torque control, linear control technique, adaptive control, robust control, gain scheduling and also the proportional controls (PI, PD, and PID).

##### 4.1. Feedback Linearization

In feedback linearization or computed torque approach, a control law is defined to obtain a linear differential equation for error command and then use the linear control design technique. An alternate dynamics of a robot finger can be written in the form.

$$Q = D(q)\ddot{q} + H(q, \dot{q}) + G(q) \quad (4.1.1)$$

Where  $q$  is the joint variable vector and  $Q(q, \dot{q}, t)$  is the torques applied at joints. Assume a desired path in joint space is given by twice differentiable function  $q = q_d(t) \in C^2$ . From the dynamics, the desired time history of joints' position, velocity and acceleration are known. Hence, by introducing a computed torque control law, we can control the robot fingers to follow desired path.

$$Q = D(q)(\ddot{q}_d - K_D e - K_P \dot{e}) + H(q, \dot{q}) + G(q) \quad (4.1.2)$$

Where  $e$ , the tracking error is defined as

$$e = q - q_d \quad (4.1.3)$$

$K_D$  and  $K_P$  are constant gain diagonal matrices. The control law is stable and applied as long as all the eigen values of the matrix below have negative real parts.

$$[A] = \begin{pmatrix} 0 & I \\ -K_P & -K_D \end{pmatrix}$$

The idea behind the introduction of a feedback signal is to make the robot fingers' actual path track the desired path. Unlike in the open loop approach, there is always a difference between the robot finger's actual path and the desired path. This is due to non-modeled parameters and also errors in adjustment.



## 4.2. PID CONTROL

The proportional-integral-derivative (PID) control has simple structure and clear physical meanings for the gain. It's a widely accepted control strategy in most industrial robot design. In most cases, feedback loops are controlled using PID algorithm. The main reason why feedback is very important in systems is to be able to attain a set point irrespective of disturbance or any variation in characteristics of any form. The PID control is always designed to correct error(s) between process values and particular desired set point in a system.

Consider the characteristic parameters- Proportional (P), integral (I) and derivative (D) controls as shown in the diagram below is to be applies to the robotic hand (system). The system, S is to be controlled using a controller, C; where C depends on the P, I and D parameters.

Considering the nonlinear equation that are derived from Euler-Lagrange equation (), the control input variable F which represents the torque applied to the robot, is unknown, ( assumed that the considered robot actuators were ideal sources of torques and forces). However it requires a control in the joints to reach a final position. Therefore we use the classical PID law as shown below;

$$F = K_p e + K_i \int_0^t e(\tau) d\tau + K_d \dot{e} \quad (4.2.1)$$

Where  $e = q^d - d$ ,  $q^d$  is the desired joint angle,  $K_p$ ,  $K_i$  and  $K_d$  are the proportional, integral and derivative gains respectively.

### 4.2.1. 4 DOF Index finger

For this experiment, what we want to control with PID is the force applied to the robot to take it to a desired position using as parameter the error between the actual and the desired coordinate. To develop the dynamic model we will consider the index finger configuration shown in figure 3.

Considering the nonlinear equation that are derived from Euler-Lagrange equation (), the control

From equation 4.1.1 we can describe the motion of the system as follows;

$$q = \begin{bmatrix} \theta_1 \\ \theta_2 \\ \theta_3 \\ \theta_4 \end{bmatrix} \quad D(q) = \begin{bmatrix} M_{11} & M_{12} & M_{13} & M_{14} \\ M_{21} & M_{22} & M_{23} & M_{24} \\ M_{31} & M_{32} & M_{33} & M_{34} \\ M_{41} & M_{42} & M_{43} & M_{44} \end{bmatrix} \quad (4.2.2)$$

The matrix entries for D (q), C (q,q) and g(q) can be are obtained from the dynamic equation of a 4DOF thumb obtained in section 3.

Where

$$M_{11} = (M_1 + M_2 + M_3 + M_4) * L_1^2 + (M_2 + M_3 + M_4) * L_2^2 + (M_3 + M_4) * L_3^2 + M_4 * L_4^2 + 2 * (M_2 + M_3 + M_4) * L_1 * L_2 * \cos(x(4)) + 2 * (M_3 + M_4) * L_1 * L_3 * \cos(x(6) + x(7)) + 2 * (M_3 + M_4) * L_2 * L_3 * \cos(x(7)) + 2 * M_4 * L_1 * L_4 * \cos(x(6) + x(7) + x(8)) + 2 * M_4 * L_2 * L_4 * \cos(x(7) + x(8)) + 2 * M_4 * L_3 * L_4 * \cos(x(8))$$

$$\begin{aligned}
M_{22} &= \\
& (M2+M3+M4)*L2^2+(M3+M4)*L3^2+M4*L4^2+2*(M3+M4)*L2*L3*\cos(x(7))+2*M4*L2*L4*\cos(x(7)+x(8))+ \\
& 2*M4*L3*L4*\cos(x(8)) \\
M_{33} &= (M3+M4)*L3^2+M4*L4^2+2*M4*L3*L4*\cos(x(8)) \\
M_{44} &= M4*L4^2 \\
M_{12} &= M_{21} \\
&= (M2+M3+M4)*L2^2+(M3+M4)*L3^2+M4*L4^2+(M2+M3+M4)*L1*L2*\cos(x(6))+(M3+M4)*L1*L3*\cos(x(6) \\
& +x(8))+2*(M3+M4)*L2*L3*\cos(x(7))+M4*L1*L4*\cos(x(6)+x(7)+x(8))+2*M4*L2*L4*\cos(x(7)+x(8))+2*M4*L3 \\
& *L4*\cos(x(8)) \\
M_{13} &= M_{31} \\
&= (M3+M4)*L3^2+M4*L4^2+(M3+M4)*L1*L3*\cos(x(6)+x(7))+(M3+M4)*L2*L3*\cos(x(7))+M4*L1*L4*\cos(x(6) \\
& )+x(7)+x(8))+M4*L2*L4*\cos(x(7)+x(8))+2*M4*L3*L4*\cos(x(8)) \\
M_{14} &= M_{41} = M4*L4^2+M4*L1*L4*\cos(x(6)+x(7)+x(8))+M4*L2*L4*\cos(x(7)+x(8))+M4*L3*L4*\cos(x(8)) \\
M_{23} &= M_{32} = \\
& (M3+M4)*L3^2+M4*L4^2+(M3+M4)*L2*L3*\cos(x(7))+M4*L2*L4*\cos(x(7)+x(8))+2*M4*L3*L4*\cos(x(8)) \\
M_{24} &= M_{42} = M4*L4^2+M4*L2*L4*\cos(x(7)+x(8))+M4*L3*L4*\cos(x(8)) \\
M_{34} &= M_{43} = M4*L4^2+M4*L3*L4*\cos(x(8));
\end{aligned}$$

The Centrifugal force,  $C_i(q, \dot{q})$  are as follows

$$\begin{aligned}
C_1(q, \dot{q}) &= \\
& ((M2+M3+M4)*L1*L2*\sin(x(6))+(M3+M4)*L1*L3*\sin(x(6)+x(7))+M4*L1*L4*\sin(x(6)+x(7)+x(8)))*(2*x(9)*x( \\
& 10)+x(10)^2)+((M3+M4)*L1*L3*\sin(x(6)+x(7)) \\
& +(M3+M4)*L2*L3*\sin(x(7))+M4*L1*L4*\sin(x(6)+x(7)+x(8))+M4*L2*L4*\sin(x(6)+x(8)))*(2*(x(9)*x(11)+x(10) \\
& *x(11))+x(11)^2)+(M4*L1*L4*\sin(x(6)+x(7)+x(8))+M4*L2*L4*\sin(x(7)+x(8))+M4*L3*L4*\sin(x(8)))*(2*(x(9)*x \\
& (12)+x(10)*x(12)+x(11)*x(12))+x(12)^2) \\
C_2(q, \dot{q}) &= -((M3+M4)*L2*L3*\sin(x(7))+M4*L2*L4*\sin(x(7)+x(8)))*(2*(x(9)*x(11)+x(10)*x(11))+x(11)^2)- \\
& (M4*L2*L4*\sin(x(7)+x(8))+M4*L3*L4*\sin(x(8)))*(2*x(9)*x(12)+x(12)^2)- \\
& (M4*L2*L4*\sin(x(7)+x(8))+M4*L3*L4*\sin(x(8)))*2*(x(10)*x(12)+x(11)+x(12)) \\
C_3(q, \dot{q}) &= ((M3+M4)*L2*L3*\sin(x(7))+M4*L2*L4*\sin(x(7)+x(8)))*(2*x(9)*x(10)- \\
& x(10)^2)+(M4*L3*L4*\sin(x(8)))*(2*x(9)*x(12)+2*x(10)*x(12)+2*x(11)*x(12)+x(12)^2)+(M3+M4)*L2*L3*\sin(x( \\
& 7))+(M3+M4)*L1*L3*\sin(x(6)+x(7))+(M4*L1*L4*\sin(x(6)+x(7)+x(8))+M4*L2*L4*\sin(x(7)+x(8)))*x(9)^2; \\
C_4(q, \dot{q}) &= \\
& = (M4*L2*L4*\sin(x(7)+x(8))+M4*L3*L4*\sin(x(8)))*(2*x(9)*x(10)+x(10)^2)+(M4*L3*L4*\sin(x(8)))*(2*(x(9)*x( \\
& 11)+x(10)*x(11))+x(11)^2)+(M4*L1*L4*\sin(x(6)+x(7)+x(8))+M4*L2*L4*\sin(x(7)+x(8))+M4*L3*L4*\sin(x(8)))* \\
& x(9)^2;
\end{aligned}$$

The Vector of gravity torques are as follows

$$\begin{aligned}
g_1(q) &= -(M1+M2+M3+M4)*g*L1*\sin(x(5))-(M2+M3+M4)*g*L2*\sin(x(5)+x(6))- \\
& (M3+M4)*g*L3*\sin(x(5)+x(6)+x(7))-M4*g*L4*\sin(x(5)+x(6)+x(7)+x(8))
\end{aligned}$$

$$g_2(q) = -(M_2 + M_3 + M_4) * g * L_2 * \sin(x(5) + x(6)) - (M_3 + M_4) * g * L_3 * \sin(x(5) + x(6) + x(7)) - M_4 * g * L_4 * \sin(x(5) + x(6) + x(7) + x(8))$$

$$g_3(q) = -(M_3 + M_4) * g * L_3 * \sin(x(5) + x(6) + x(7)) - M_4 * g * L_4 * \sin(x(5) + x(6) + x(7) + x(8))$$

$$g_4(q) = -M_4 * g * L_4 * \sin(x(5) + x(6) + x(7) + x(8))$$

From the system equation, 4.1.1 we can have

$$\ddot{q} = D(q)^{-1} [-C(q, \dot{q}) - g(q)] + \hat{F} \quad (4.2.4)$$

With

$$\hat{F} = D(q)^{-1} F \Leftrightarrow M(q) \hat{F} \quad (4.2.5)$$

The error signals of the system are

$$e(\theta_i) = \theta_{if} - \theta_i \quad (4.2.6)$$

Where  $i$  = joint angle 1 to 4 and  $f$  is the final positions of the joint angles.

Where  $\theta_{if}$  is the final position of joints  $i = 1, 2, 3$  and 4. For the control, the final positions are given by

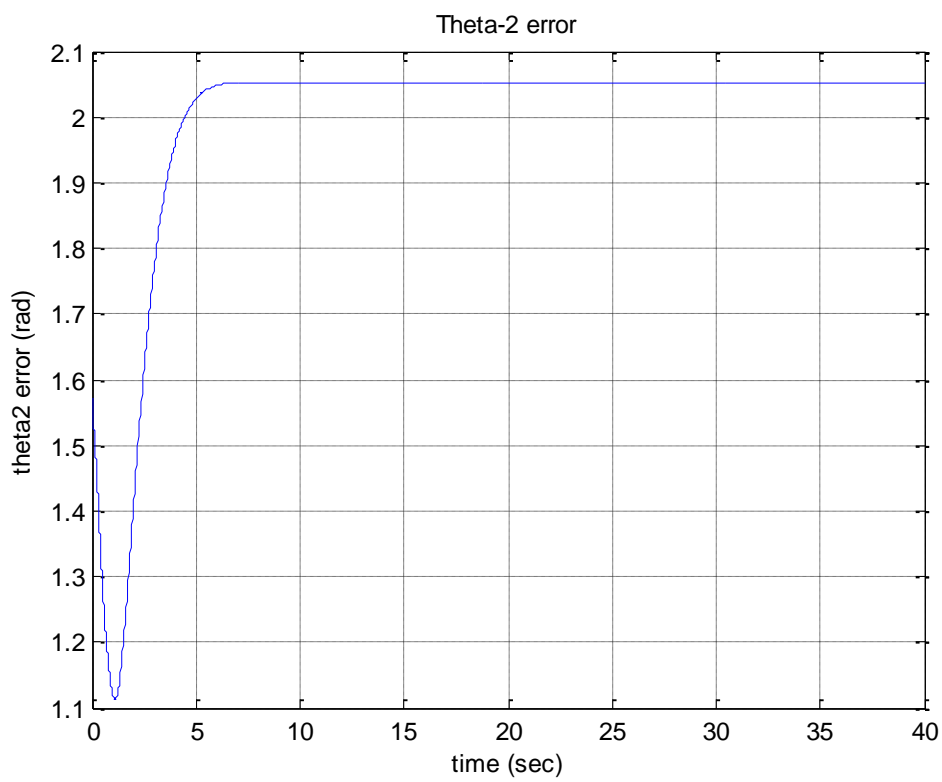
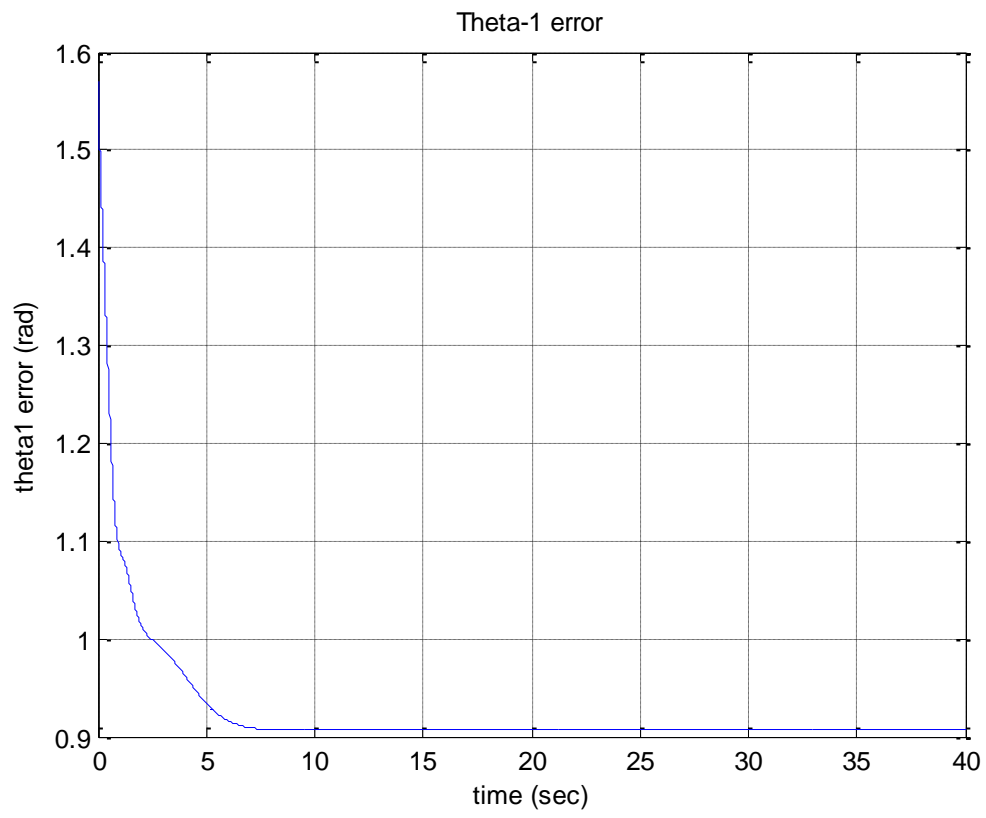
$$\begin{bmatrix} \theta_{1f} \\ \theta_{2f} \\ \theta_{3f} \\ \theta_{4f} \end{bmatrix} = \begin{bmatrix} \pi / 2 \\ \pi / 2 \\ \pi / 4 \\ \pi / 6 \end{bmatrix} \quad (4.2.7)$$

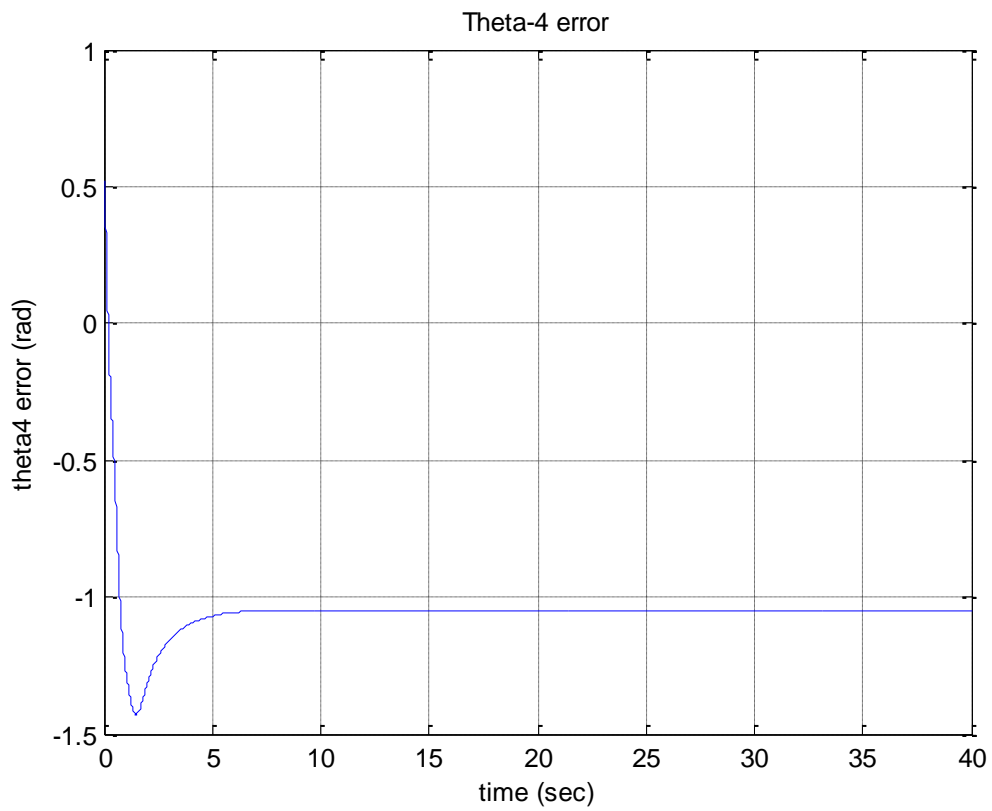
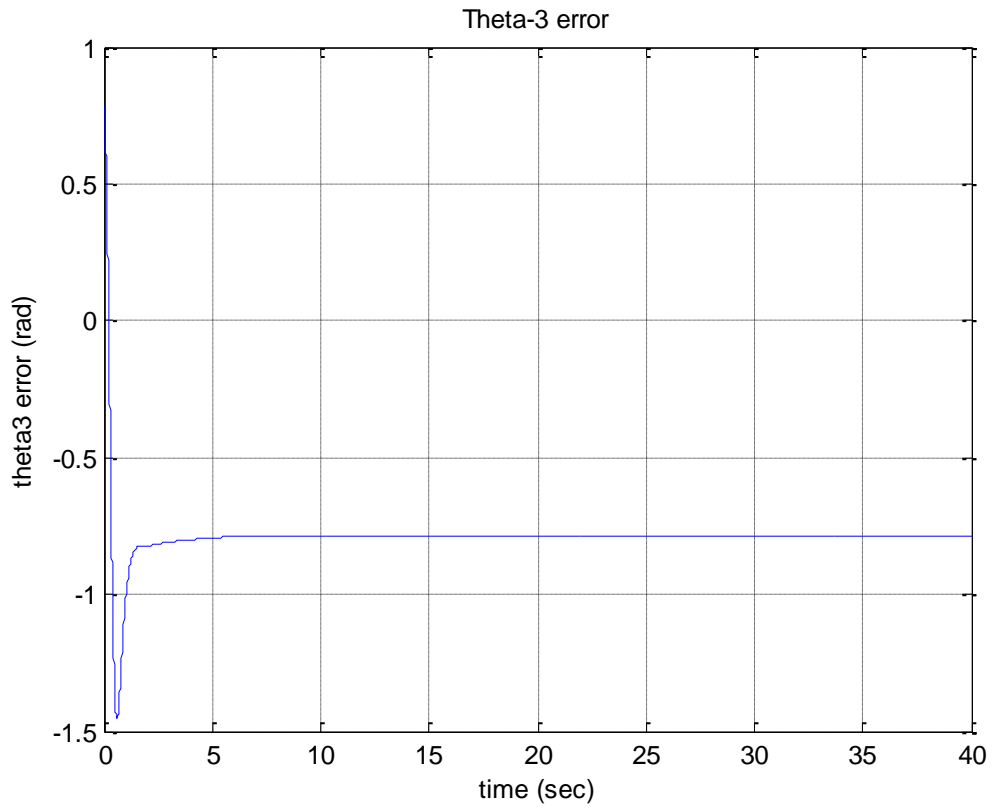
The index finger is considered to be parallel to the x-axis so all initial positions are zero

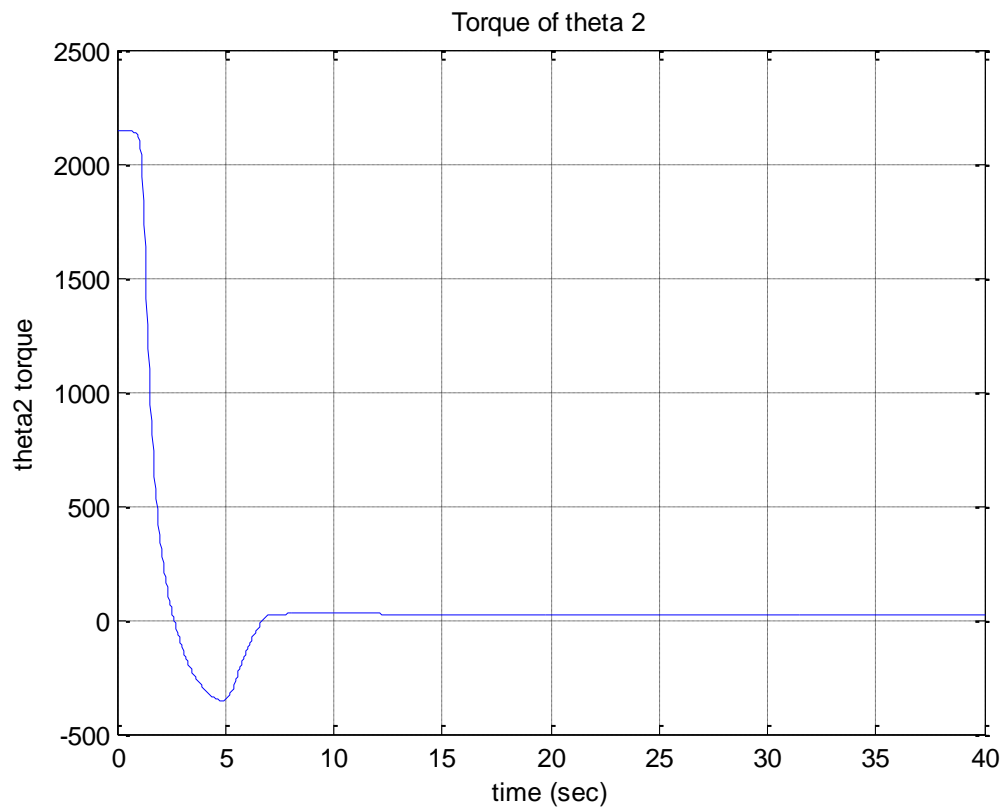
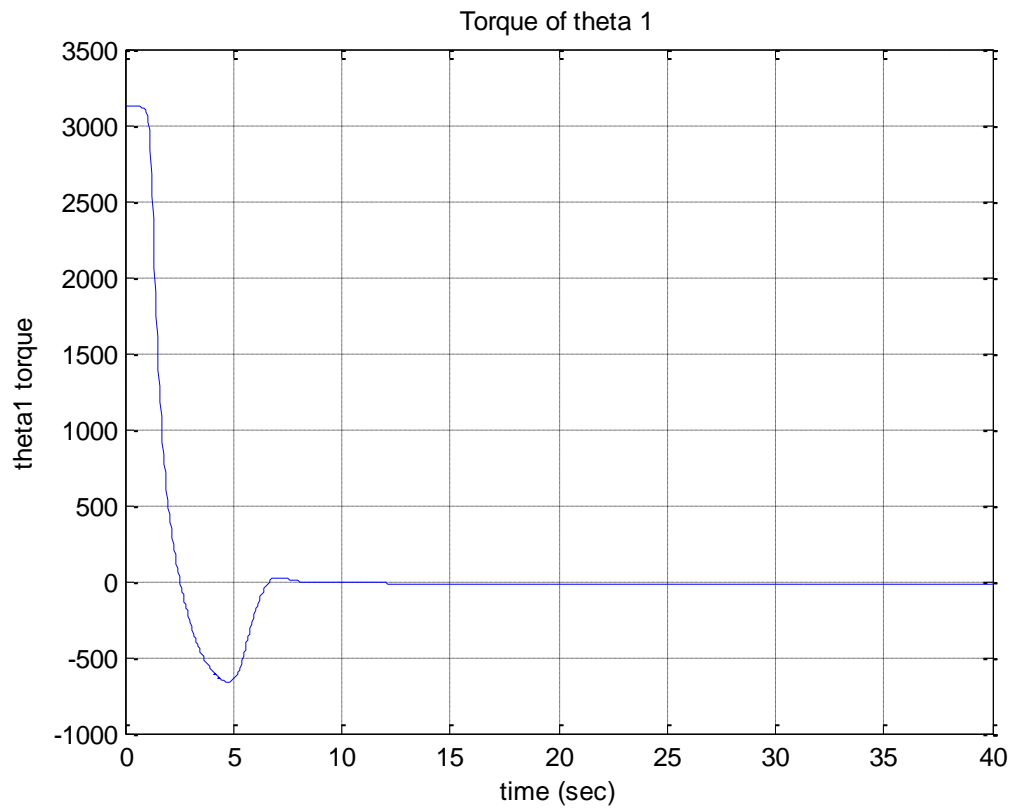
Figures 4.1 and 4.2 are the simulations obtained using the PID controller for a 3DOF thumb. The best performance of the controller parameter where obtained with the following values after considering 3 cases of different PID combinations.

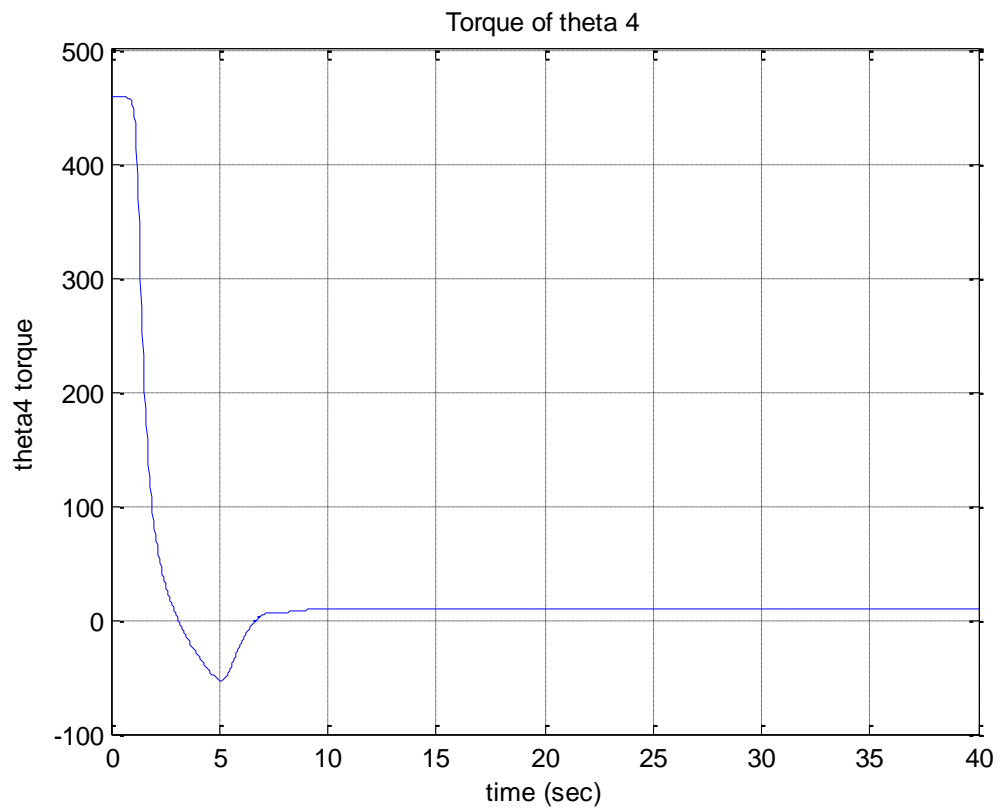
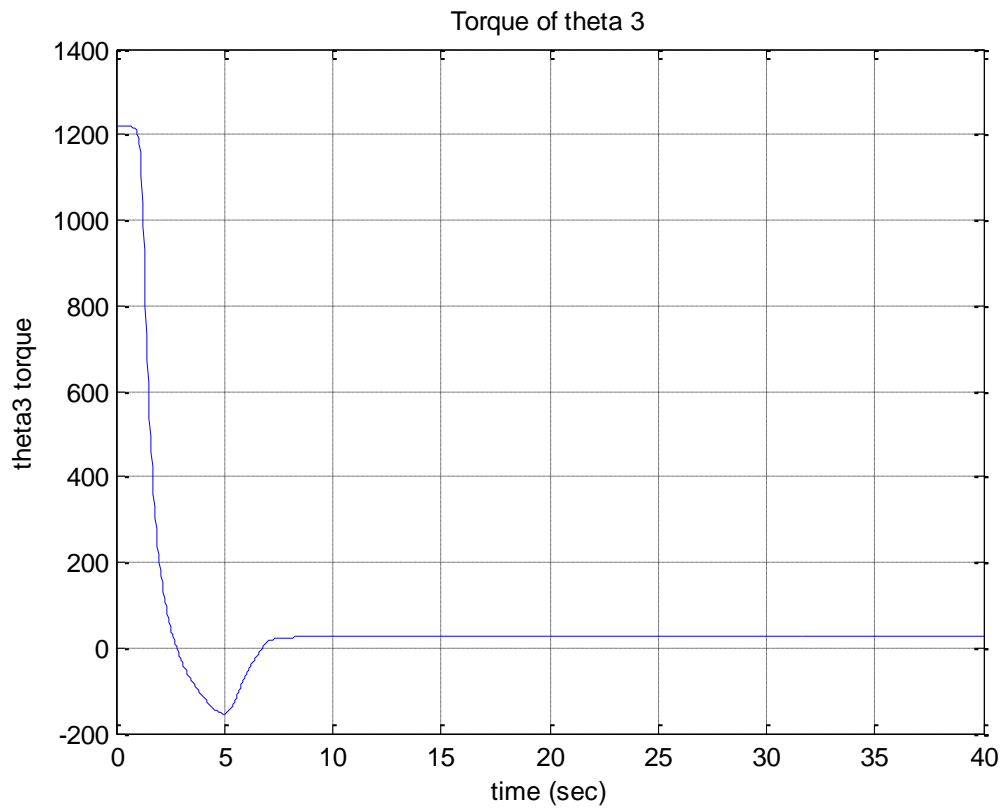
PID PARAMETERS	CASE1	CASE2	CASE3
$K_p$ (1, 2, 3, & 4)	35, 35, 35 & 35	25, 25, 25 & 25	50, 50, 50 & 50
$K_i$ (1, 2, 3, & 4)	10, 13, 17 & 20	20, 23, 27 & 30	15, 20, 35 & 40
$K_d$ (1, 2, 3, & 4)	25, 25, 25 & 25	20, 20, 20 & 20	45, 45, 45 & 45

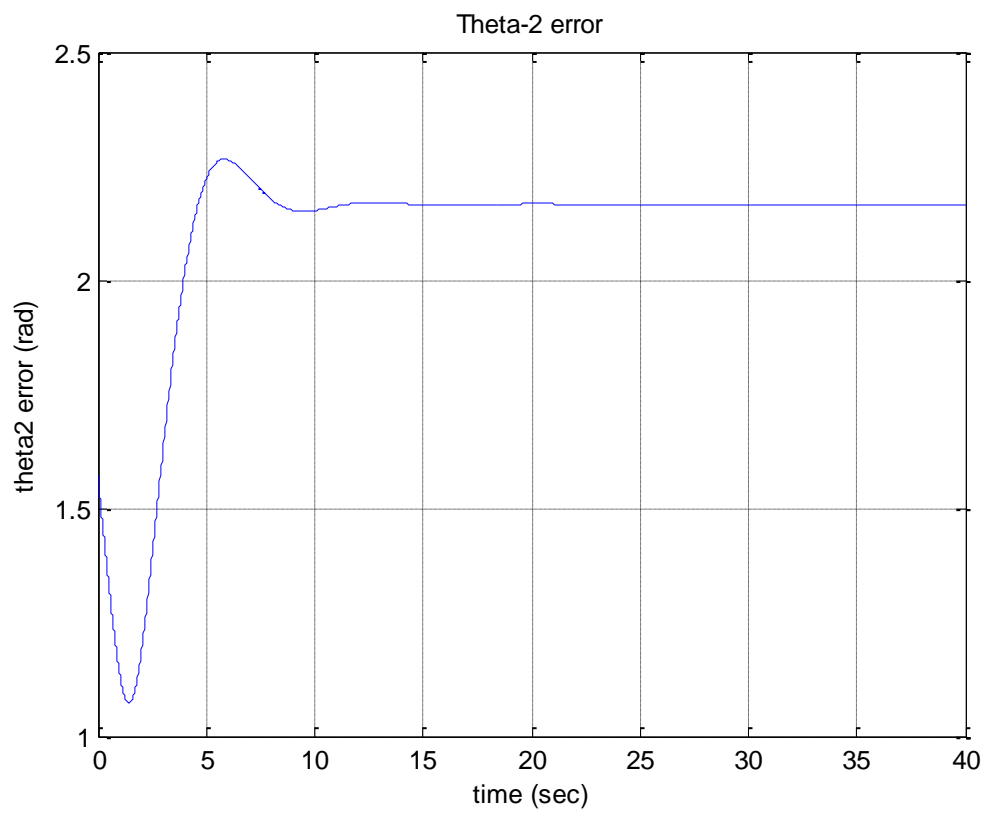
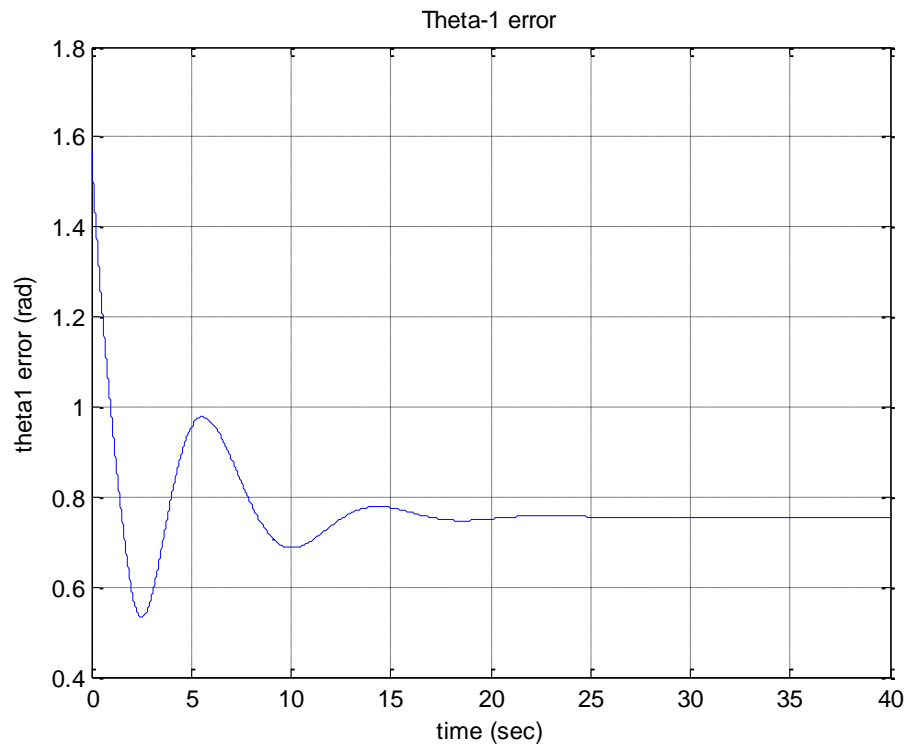
Table 4.1. Three cases of best performance of PID parameters



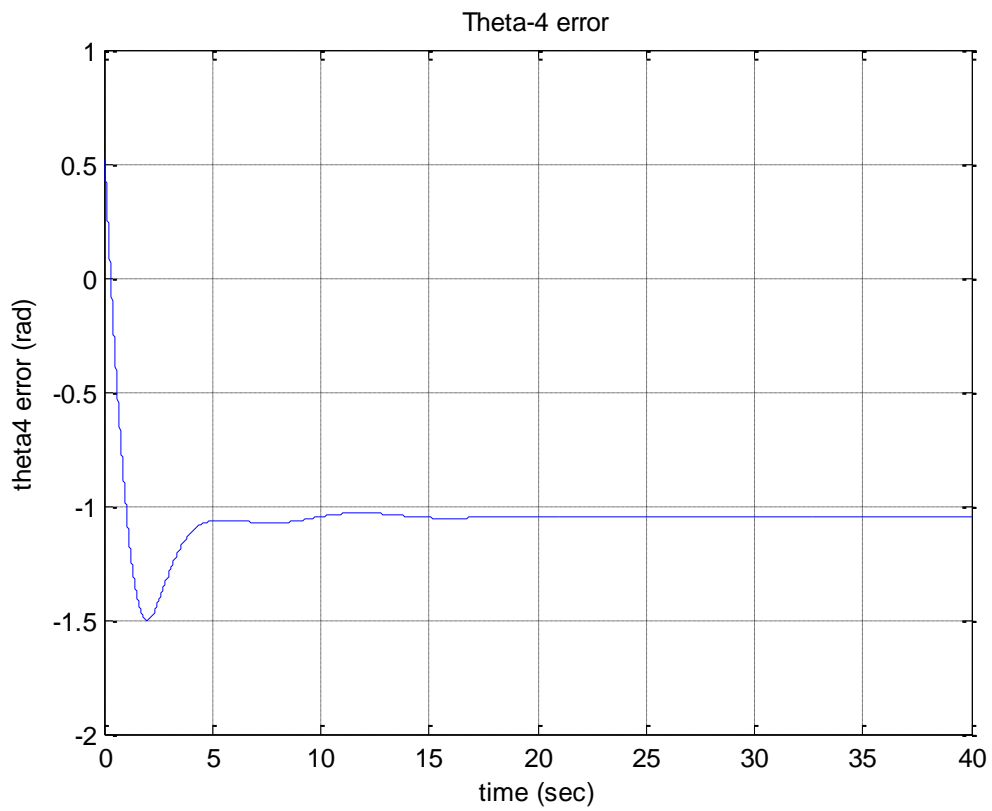
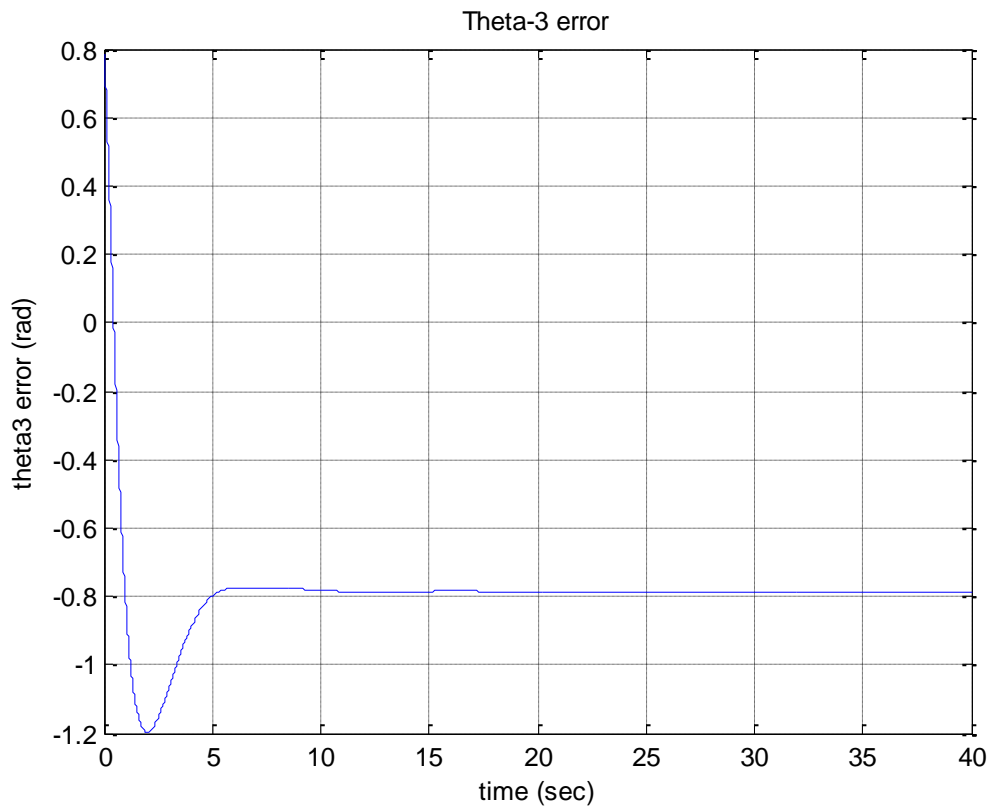


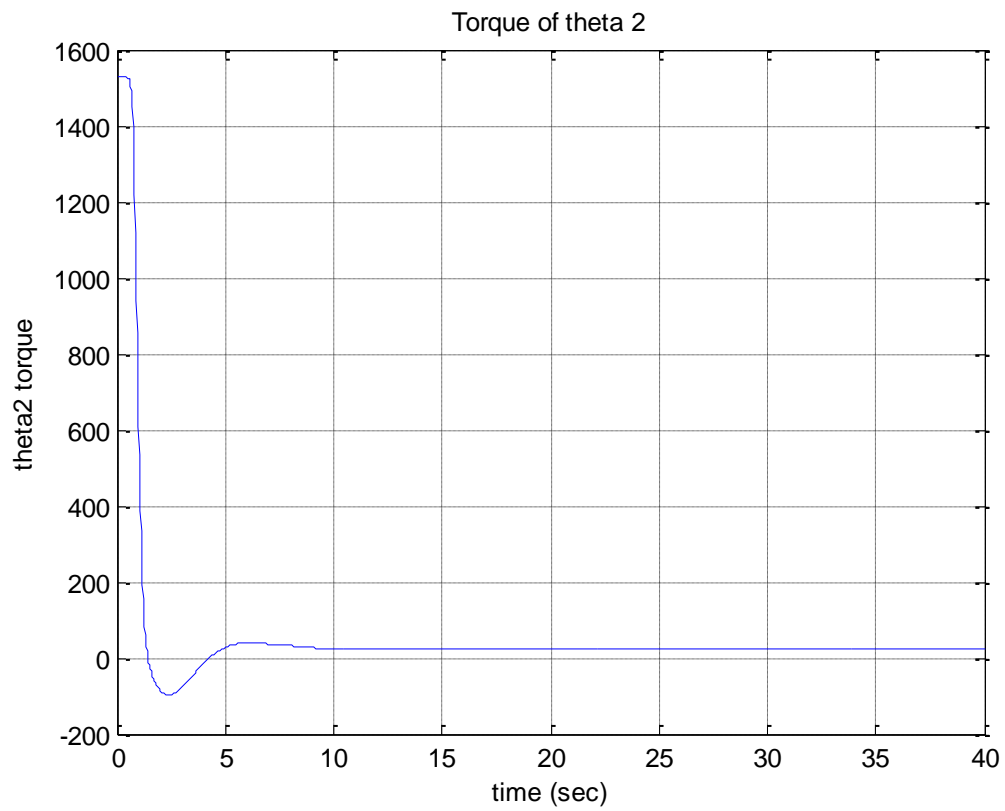
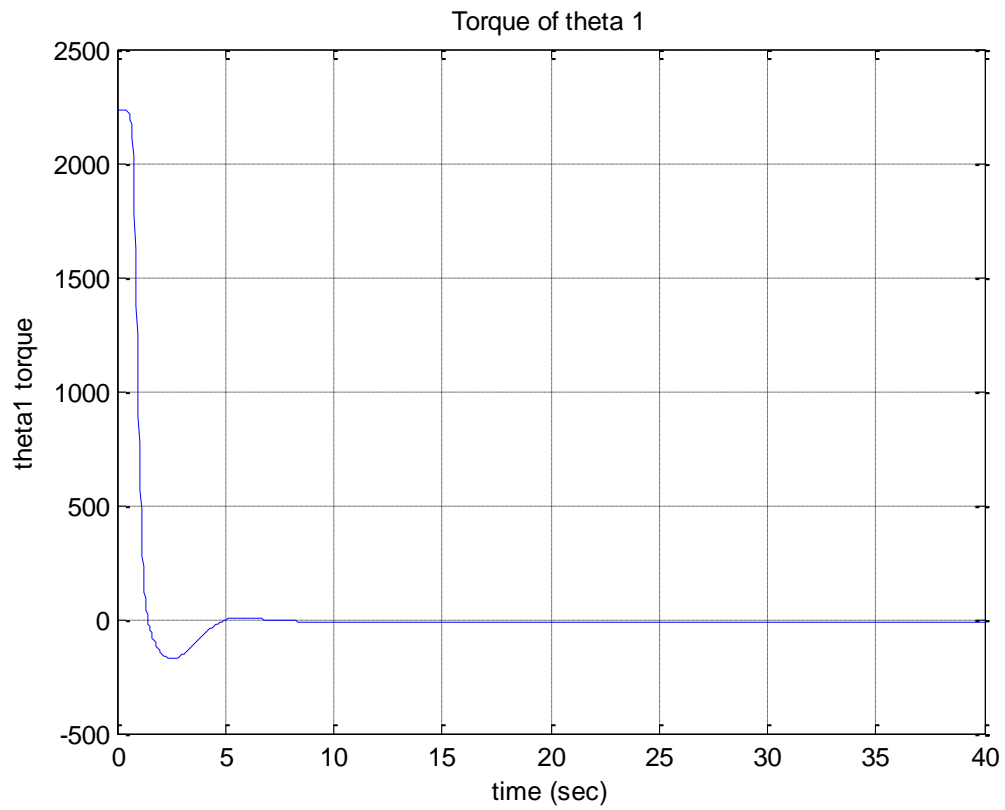


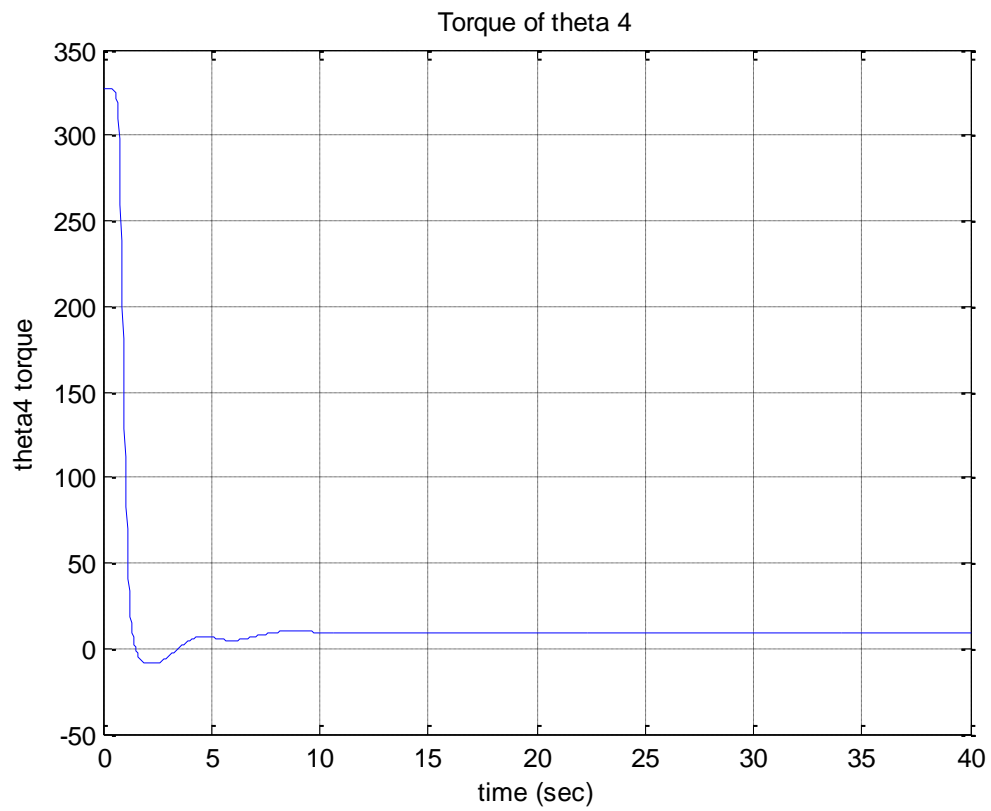
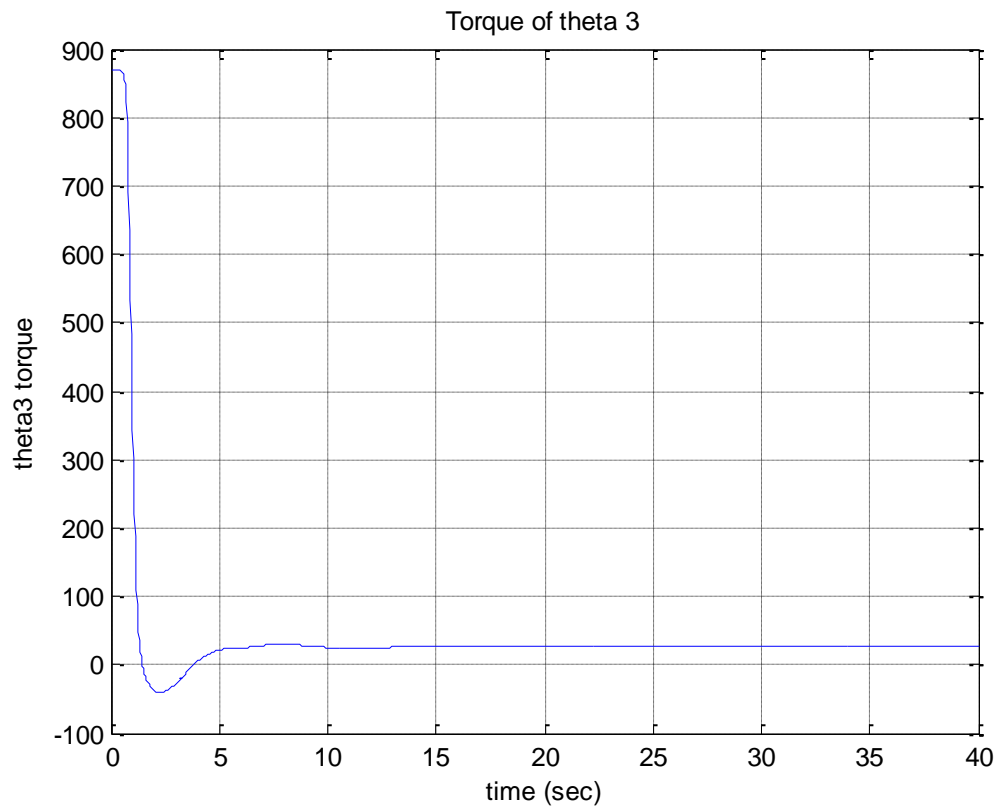


**Graphs of Case 2**

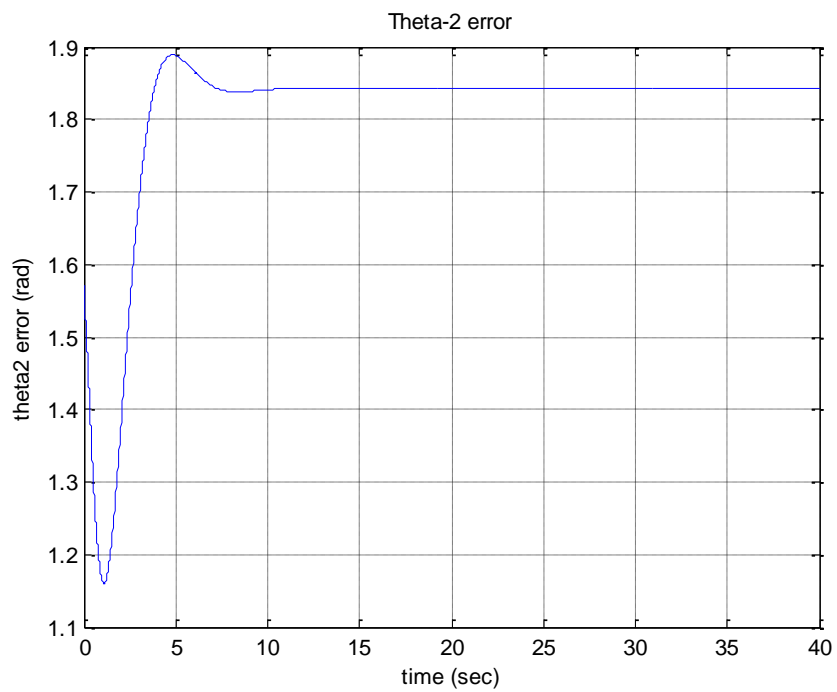
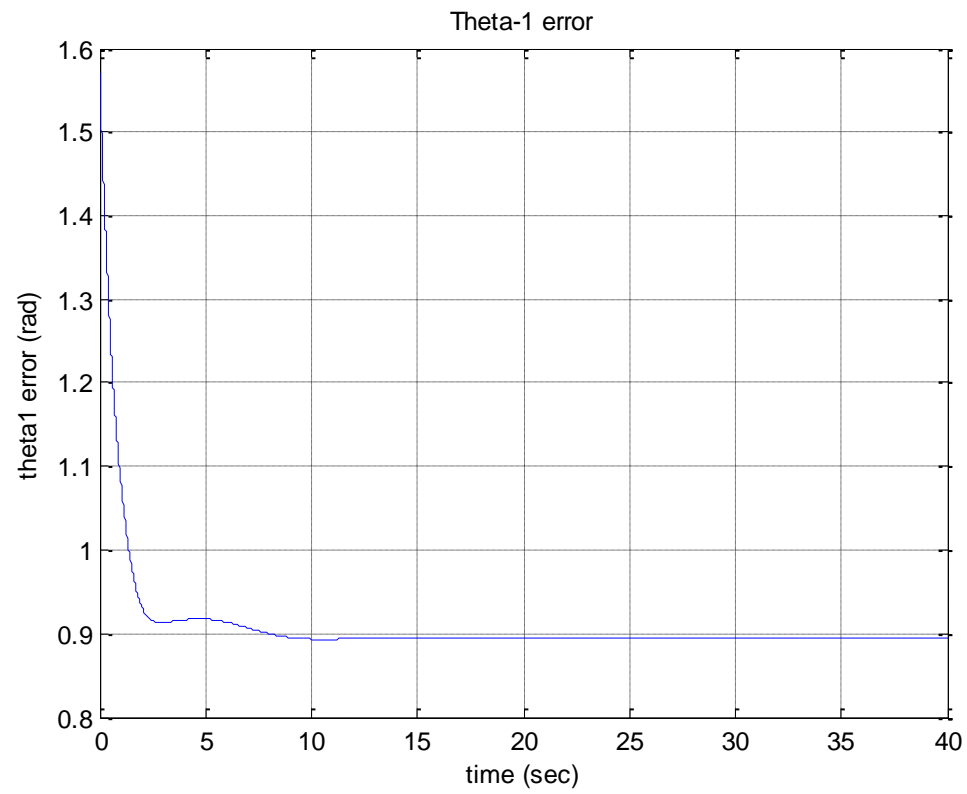


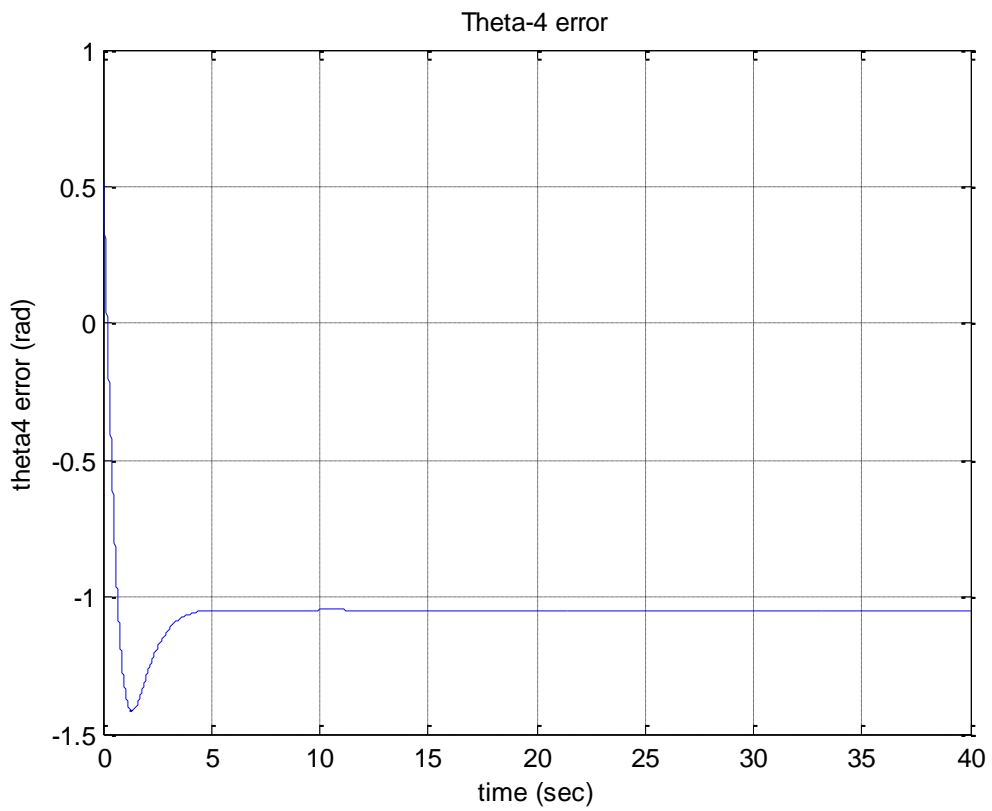
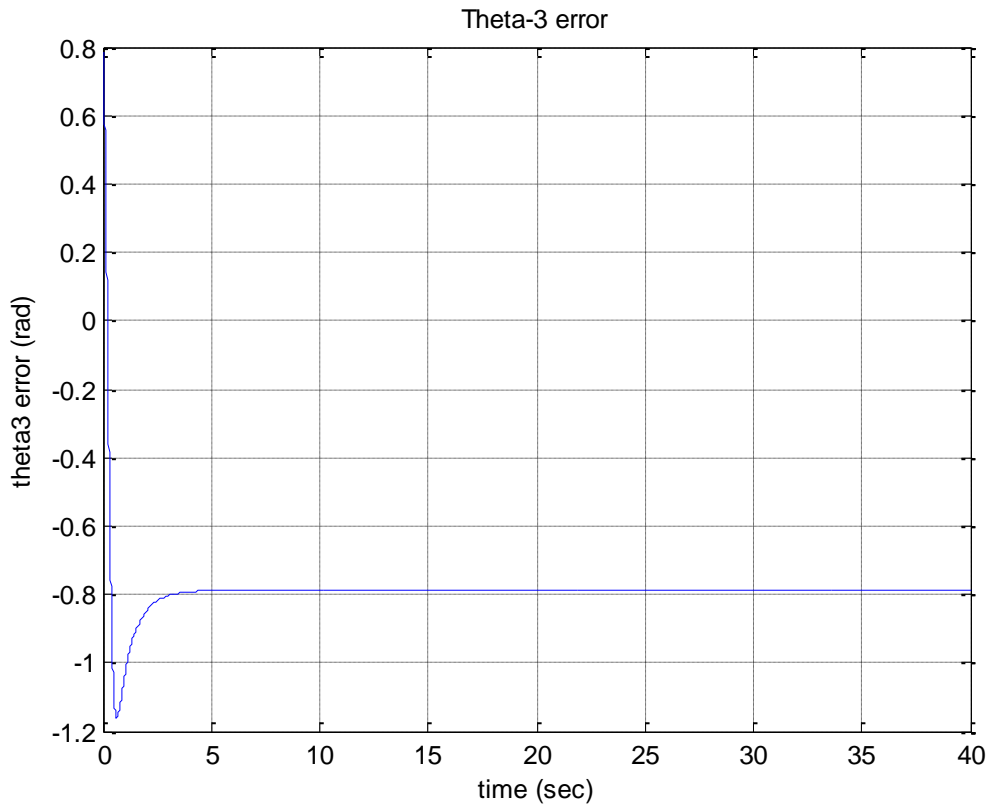


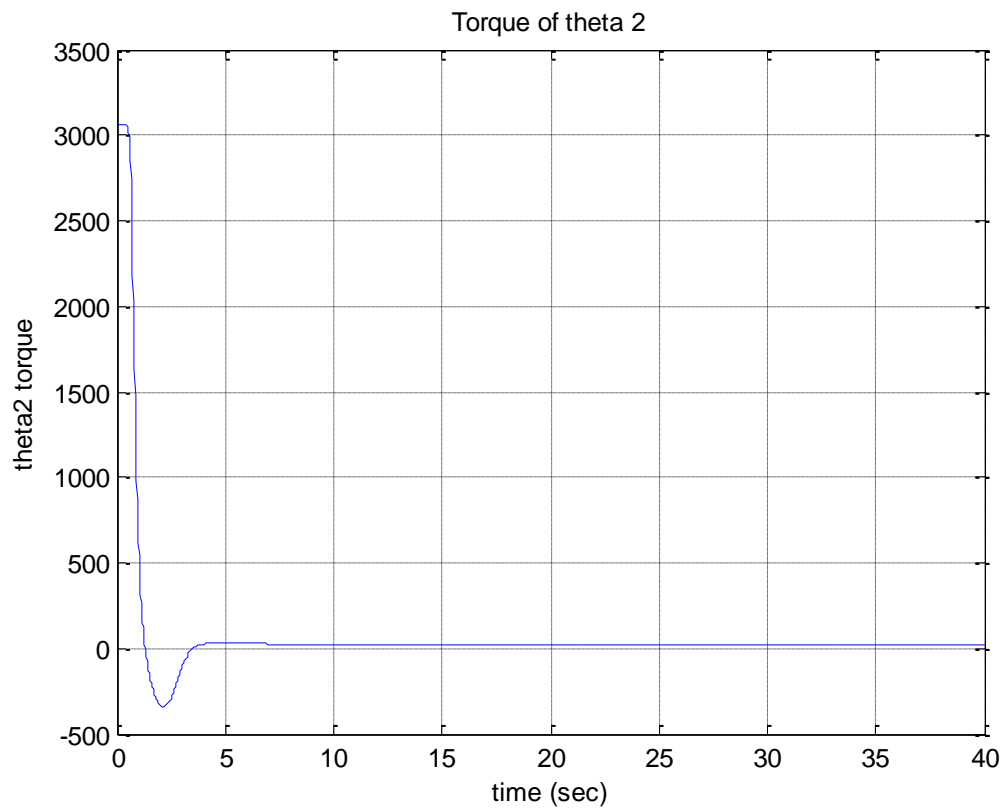
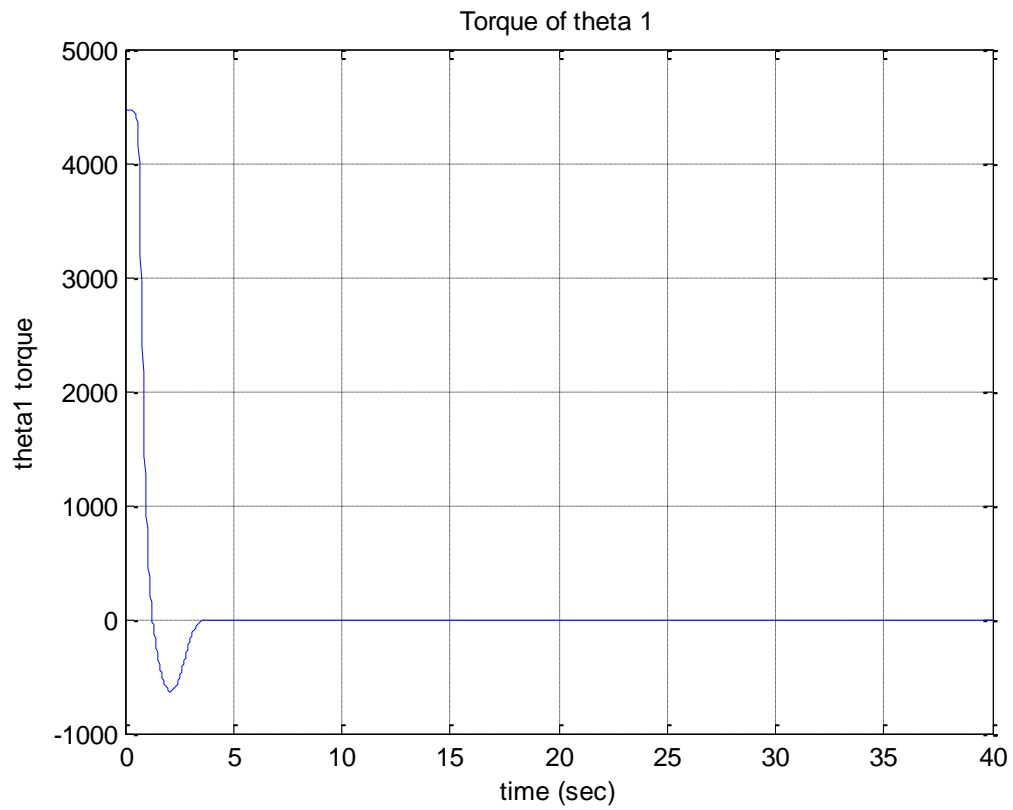


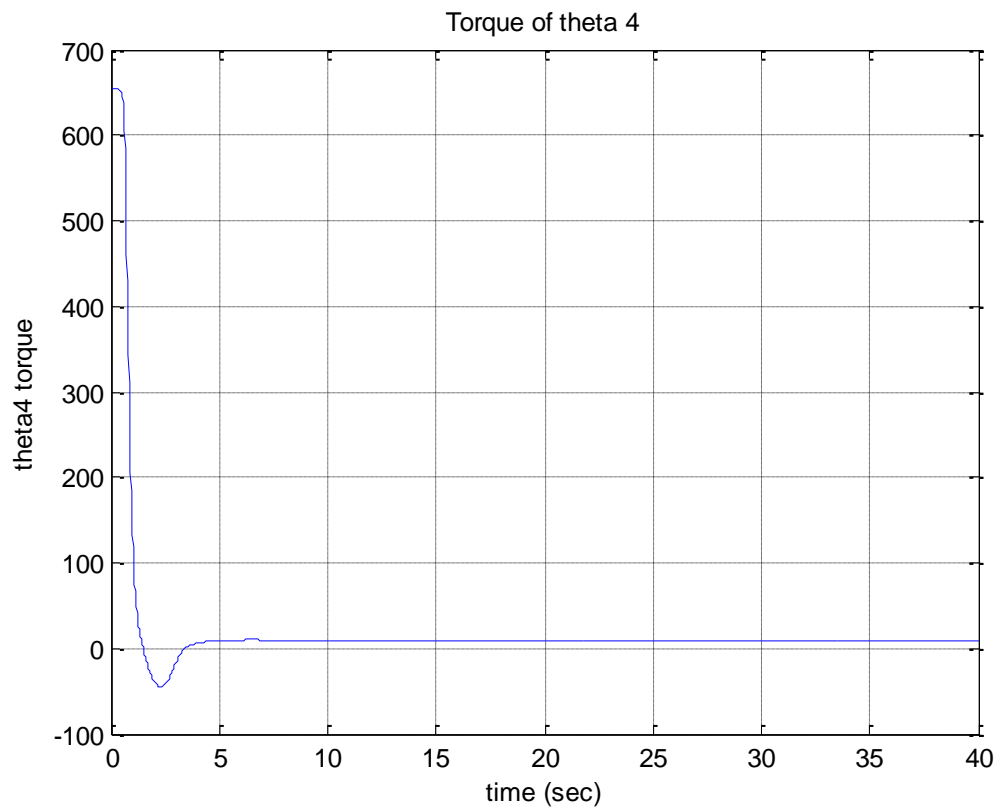
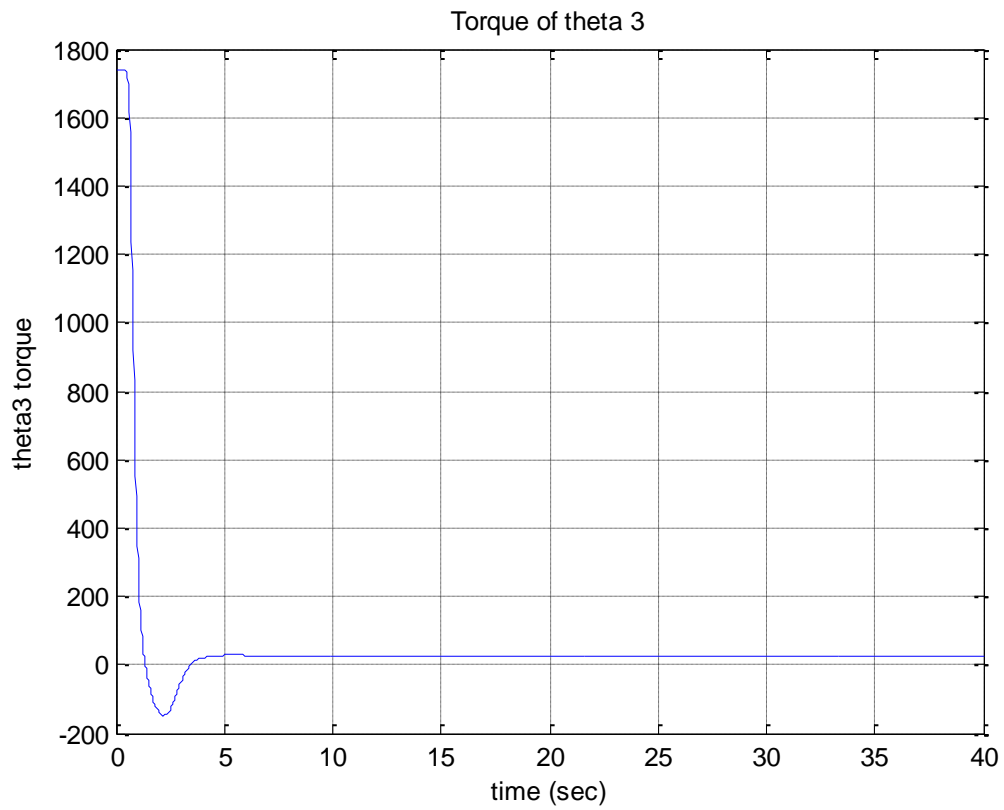


## Graphs of Case 3









## 5. Conclusion

In this report, chapter 1 addressed the problem of kinematics, inverse kinematics and Differential kinematics of the thumb and index finger of a prosthetic hand. These kinematic structures could be applied to the rest of the fingers to form a complete prosthetic hand. In Chapter 3, we derive the dynamic models for a 4 DOFs finger via the Lagrangian convention and the Newton Euler postulations. A Proportional Integral Derivative control strategy was applied to the parameters from the dynamics and simulation results gotten. Our first approach to control the robotic finger arm is by trial and error, the two parameters of the controller will be tuned manually to obtain the best results. The best performance of the controller parameters values were shown in table 4.1 in three different cases.

## Bibliography

- [1]. R. N. Jazar. Theory of applied Robotics, Dynamics and Control. Springer, New York, USA, 2007.
- [2]. John J. Craig. Introduction to robotics, mechanics and control. 2<sup>nd</sup> edition, Addison Wesley.
- [3]. Mason and Salisbury. Robot hand and the mechanics of manipulation. The MIT press Cambridge, Massachusetts, London, England.
- [4]. Kumar, A., and Waldron, K. J., 1981. "The Workspace of a Mechanical Manipulator", ASME J Mech. Design, 103:665-672.
- [5]. Vardy A. Articulated human hand with inter-joint dependency constraints: Computer Science 6755 19898 [http://www.scs.carleton.ca/~arvardy/software/hand-doc.pdf].
- [6]. Chen H. Chen. Hybrid Control Strategies for Smart Prosthetic Hand.  
A dissertation submitted in partial fulfillment of the requirements for the degree of Doctor of Philosophy in Engineering and Applied Science College of Engineering, Idaho State University. May 2009
- [7]. Albretch I, Haber J, Seider HP. Construction and Animation of Anatomically Based Human Hand Models. Eurographics/ SIGGRAPH symposium on computer Animation 2003: 98-109.
- [8]. Li S, Xi Z. Measurement of Functional Arm Reach Envelopes for Young Chinese males, Ergonomics 1990, 33: 967-978.
- [9]. Molenbroek JGM. Reach Envelopes of Older adults. In Proceedings of the 42<sup>nd</sup> Annual Meeting of the "Human Factors and Ergonomics Society". Chicago, IL, 1998: 166-170.
- [10]. Bill Goowine. University of Notre Dame. Copyright 2005 by CRC Press LLC.
- [11]. R. J. Scilly. Fundamentals of Robotics, Analysis and Control. Prentice, Hall, Eaglewood cliffs, NJ, 1990.
- [12]. R. Kelly, V. Santibanez, and A. Loria. Control of Robot Manipulators in Joint Space. Springer, Newyork, USA, 2005.
- [13]. B. Siciliano, L. Sciavicco, L. Villiani, and G. Oriolo. Robotics, Modeling, Planning and Control. Springer, Verlay, London, UK, 2009.





# Hybrid Control Strategies for a Five-Finger Smart Prosthetic Hand

Cheng-Hung Chen\* and D. Subbaram Naidu

*Measurement and Control Engineering Research Center, School of Engineering,  
Idaho State University, 921 S. 8th Ave. Stop 8007, Pocatello, Idaho 83209, USA*

*\*Corresponding Author: chenchen@isu.edu, Tel: 617-388-1509*

---

## Abstract

This paper presents a hybrid controller of soft control techniques, adaptive neuro-fuzzy inference system (ANFIS) and fuzzy logic (FL), and hard control technique, proportional-derivative (PD), for a 14-Degrees-of-Freedom (DoF) five-finger smart prosthetic hand. The ANFIS is used for inverse kinematics of three-link fingers and FL is used for tuning the PD parameters with 2 input layers (error and error rate) using 7 triangular membership functions and 49 fuzzy logic rules. Simulation results with the hybrid of FL-tuned PD controller exhibit superior performance compared to PD, PID or FL control alone.

**Keywords:** Prosthetic Hand, Hybrid Control, Fuzzy Logic, PD Control, Adaptive Neuro-Fuzzy Inference System

---

## 1. Introduction

In the past several decades, prosthetic hands have been developed to replace human hands that can fully operate the various motions, such as holding, moving, grasping, lifting, twisting and so on [1–6], but replacing an artificial hand in all its various functions, appearance, visibility, and weight is still a challenging task [1] due to the extreme complexity of human hands.

Hard computing/control (HC) techniques comprise proportional-derivative (PD) control [7], proportional-integral-derivative (PID) control [8, 9], optimal control [9–12], adaptive control [13–16] etc. with specific applications to prosthetic devices. However, our previous works [7–9, 17] for a smart prosthetic hand showed that PID controller resulted in overshooting and oscillation, which were also demonstrated by Subudhi and Morris [18] and Liu et al. [19].

Soft computing (SC) or computational intelligence (CI) [20] is an emerging field based on synergy and seamless integration of neural networks (NN), fuzzy logic (FL) and optimization methods, such as genetic algorithms (GA) and particle swarm optimization (PSO) [7, 21, 22]. Arslan et al. [23] developed the biomechanical model with a tendon configuration of the 3-Degrees-of-Freedom (DoF) index finger of the human hand and the fuzzy sliding mode controller in which a FL unit tuned the slope of the sliding surface to generate the required tendon forces during closing and opening motion. Kato et al. [24] expressed the reaction of brains to the adaptable prosthetic system for a 13 DOF electromyographic (EMG) signal controlled prosthetic hand with an EMG pattern recognition learning by artificial NN. Kamikawa and Maeno [25] used GA to optimize locations of pivots and grasping force and designed one ultrasonic motor to move 15 compliant joints for an underactuated five-finger prosthetic hand. Khushaba et al. [26] developed a PSO-based method for myoelectrically controlled prosthetic devices.

In hybrid intelligent control strategies, we look at the integrated structure by blending [27, 28] SC techniques and conventional HC techniques. The integration of SC and HC methodologies shown in Figure 1

[Figure 1 about here.]

has the following attractive features [27, 28]:

1. The methodology based on SC can be used, in particular with FL, at upper levels of the overall mission where human involvement and decision making is of primary importance, whereas the HC can be used at lower levels for accuracy, precision, stability and robustness.
2. In another situation using hybrid scheme, a NN of the SC is used to supplement the control provided by a linear, fixed gain controller.
3. Further, the SC-based GA can be used to parameter tuning of a PID controller to achieve good performance and robustness for a wide range of operating conditions.
4. The SC and HC techniques are potentially complementary methodologies.
5. The fusion could solve problems that cannot be solved satisfactorily by using either methodology alone.
6. Novel synergetic combinations of SC and HC lead to high performance, robust, autonomous and cost-effective missions.

Hence, we present the integration or fusion of SC and HC to solve problems that cannot be solved satisfactorily by using either HC or SC methodology alone with specific applications to a smart prosthetic hand.

In this paper, we first consider briefly trajectory planning and kinematics problems associated with a five-finger prosthetic hand. Then, adaptive neuro-fuzzy inference system (ANFIS) is used to solve inverse kinematics problem for three-link fingers (index, middle, ring, and little). Next, the dynamic model of the hand is derived and feedback linearization technique is used to obtain *linear* tracking error dynamics. Then we propose the FL-based PD (hybrid) controller, which uses FL with 7 triangular membership functions in each input/output layer and 49 logic rules to tune PD gain parameters. The resulting overall hybrid system incorporating both soft and hard control techniques is simulated with realistic data for the hand and found the performance to be superior to HC (PD and PID) or SC (FL) alone. Finally, we provide conclusions and future work.

## 2. Modeling

### 2.1. Trajectory Planning and Kinematics

The trajectory planning using cubic polynomial was discussed in our previous work [7, 11, 29, 30] for a two-finger (thumb and index finger) smart prosthetic hand.

Kinematics is the study of geometry in motion and is restricted to a natural geometrical description of motion by the manners, including positions, orientations, and their derivatives (velocities and accelerations) [31]. Forward and inverse kinematics of articulated systems study the analytical relationship between the angular positions of joints and the positions and orientations of the fingertips. A desired trajectory is usually specified in *Cartesian* space and the trajectory controller is easily performed in the *joint* space. Therefore, conversion of Cartesian trajectory planning to the joint space [31] is necessary. Using inverse kinematics, the joint angular positions of each finger need to be obtained from the known fingertip positions. Then the angular velocities and angular accelerations of joints can be obtained from the linear and angular velocities and accelerations of fingertips by differential kinematics. The inverse and differential kinematics of two-link thumb and three-link fingers were discussed in our previous publications [7, 11, 29, 30] for a two-finger (thumb and index finger) smart prosthetic hand.

[Figure 2 about here.]

For five fingers shown in Figure 2,  $X^G$ ,  $Y^G$ , and  $Z^G$  are the three axes of global coordinate. Local coordinate  $x^t$ - $y^t$ - $z^t$  of thumb can be reached by rotating through angles  $\alpha$  and  $\beta$  to  $X^G$  and  $Y^G$  of the global coordinate, subsequently. Local

coordinate  $x^i-y^i-z^i$  of index finger can be obtained by rotating through angle  $\alpha$  to  $X^G$  and then translating a vector  $\mathbf{d}^i$  of the global coordinate; similarly, the local coordinate  $x^j-y^j-z^j$  of middle finger ( $j = m$ ), ring finger ( $j = r$ ), and little finger ( $j = l$ ) can be obtained by rotating through angle  $\alpha$  to  $X^G$  and then translating the vector  $\mathbf{d}^j$  ( $j = m, r$  and  $l$ ) of the global coordinate.

## 2.2. Adaptive Neuro-Fuzzy Inference System (ANFIS)

The inverse kinematics problems for three-link fingers can be solved by using adaptive neuro-fuzzy inference system (ANFIS) method [32] where the input of fuzzy-neuro system is the Cartesian space and the output is the joint space. ANFIS is a fuzzy inference system implemented in the framework of adaptive networks which provides the best optimization algorithm to find parameters in order to fit the data. ANFIS includes *premise parameters*, that defines membership functions, and *consequent parameters*, that defines the coefficients of each output equation. ANFIS tunes the membership function and identifies the coefficients by the backpropagation gradient descent and least-squares methods, respectively. ANFIS uses a hybrid learning algorithm to identify parameters of Sugeno-type fuzzy inference systems for fuzzy modeling procedures to learn information about a data set in order to compute the membership function and track the given input/output data. Figure 3 (a) shows a two input first-order Sugeno fuzzy model with two rules and Figure 3 (b) depicts the equivalent ANFIS structure for all the computation below.

[Figure 3 about here.]

Sugeno-type fuzzy system has the following **Rule Base** [32, 33].

If  $x$  is  $A_1$  and  $y$  is  $B_1$ , then  $f_1 = p_1x + q_1y + r_1$ .

If  $x$  is  $A_2$  and  $y$  is  $B_2$ , then  $f_2 = p_2x + q_2y + r_2$ .

Here,  $x$  and  $y$  are inputs to constitute the premise parameters  $A_1, A_2, B_1$ , and  $B_2$  (Layer 1 in Figure 3 (b)).  $p_i, q_i$ , and  $r_i$  ( $i = 1, 2$ ) are the consequent parameters. We evaluate the rules by choosing *product*  $\prod$  for T-Norm (Layers 2 and 3) which results in

$$w_i = \mu_{A_i}(x) \mu_{B_i}(y), \quad i = 1, 2. \quad (1)$$

Here,  $\mu_{A_i}(x)$  and  $\mu_{B_i}(y)$  are designed fuzzy membership functions. Now after leaving the arguments (Layer 4), we get the output  $f(x, y)$  by **Rule Consequences**.

$$f(x, y) = \frac{w_1(x, y)f_1(x, y) + w_2(x, y)f_2(x, y)}{w_1(x, y) + w_2(x, y)}. \quad (2)$$

$f$  (Layer 5) can be written as

$$\begin{aligned} f &= \frac{w_1 f_1 + w_2 f_2}{w_1 + w_2} \\ &= \bar{w}_1 f_1 + \bar{w}_2 f_2, \end{aligned} \quad (3)$$

where

$$\bar{w}_1 = \frac{w_1}{w_1 + w_2}, \quad \bar{w}_2 = \frac{w_2}{w_1 + w_2}. \quad (4)$$

### 2.3. Dynamics of the Hand

The dynamic equations of hand motion are derived via Lagrangian approach using kinetic energy and potential energy as [30, 31]

$$\frac{d}{dt} \left( \frac{\partial \mathcal{L}(t)}{\partial \dot{\mathbf{q}}(t)} \right) - \frac{\partial \mathcal{L}(t)}{\partial \mathbf{q}(t)} = \boldsymbol{\tau}(t), \quad (5)$$

where  $\mathcal{L}(t)$  is Lagrangian;  $\dot{\mathbf{q}}(t)$  and  $\mathbf{q}(t)$  represent the angular velocity and position vectors of joints, respectively;  $\boldsymbol{\tau}(t)$  is the given torque vector at joints. The Lagrangian  $\mathcal{L}(t)$  can be expressed as

$$\mathcal{L}(t) = T(t) - V(t), \quad (6)$$

where  $T(t)$  and  $V(t)$  denote kinetic and potential energies at time  $t$ , respectively. Substituting (6) into (5), dynamic equations of thumb and all fingers can be obtained as below.

$$\mathbf{M}(\mathbf{q}(t))\ddot{\mathbf{q}}(t) + \mathbf{C}(\mathbf{q}(t), \dot{\mathbf{q}}(t)) + \mathbf{G}(\mathbf{q}(t)) = \boldsymbol{\tau}(t), \quad (7)$$

where  $\mathbf{M}(\mathbf{q}(t))$  is the inertia matrix;  $\mathbf{C}(\mathbf{q}(t), \dot{\mathbf{q}}(t))$  is the Coriolis/centripetal vector and  $\mathbf{G}(\mathbf{q}(t))$  is the gravity vector. Then, (7) can be also written as

$$\mathbf{M}(\mathbf{q}(t))\ddot{\mathbf{q}}(t) + \mathbf{N}(\mathbf{q}(t), \dot{\mathbf{q}}(t)) = \boldsymbol{\tau}(t), \quad (8)$$

where  $\mathbf{N}(\mathbf{q}(t), \dot{\mathbf{q}}(t)) = \mathbf{C}(\mathbf{q}(t), \dot{\mathbf{q}}(t)) + \mathbf{G}(\mathbf{q}(t))$  represents nonlinear terms. The dynamic relations for the two-link thumb and all three-link fingers are detailed in our previous work [30].

### 3. Control Techniques

#### 3.1. Feedback Linearization

The nonlinear dynamics represented by (8) is to be converted into a linear state-variable system using feedback linearization technique [14]. Alternative state-space equations of the dynamics can be obtained by defining the position/velocity state  $\mathbf{x}(t)$  of the joints as

$$\mathbf{x}(t) = [\mathbf{q}'(t) \quad \dot{\mathbf{q}}'(t)]'. \quad (9)$$

Let us repeat the dynamical model and rewrite (8) as

$$\frac{d}{dt}\dot{\mathbf{q}}(t) = -\mathbf{M}^{-1}(\mathbf{q}(t)) [\mathbf{N}(\mathbf{q}(t), \dot{\mathbf{q}}(t)) - \boldsymbol{\tau}(t)]. \quad (10)$$

Thus, from (9) and (10), we can derive a linear system in *Brunovsky canonical form* as

$$\dot{\mathbf{x}}(t) = \begin{bmatrix} \mathbf{0} & \mathbf{I} \\ \mathbf{0} & \mathbf{0} \end{bmatrix} \mathbf{x}(t) + \begin{bmatrix} \mathbf{0} \\ \mathbf{I} \end{bmatrix} \mathbf{u}(t) \quad (11)$$

with its control input vector given by

$$\mathbf{u}(t) = -\mathbf{M}^{-1}(\mathbf{q}(t)) [\mathbf{N}(\mathbf{q}(t), \dot{\mathbf{q}}(t)) - \boldsymbol{\tau}(t)]. \quad (12)$$

Let us suppose the prosthetic hand is required to track the desired trajectory  $\mathbf{q}_d(t)$  described under path generation or tracking. Then, the tracking error  $\mathbf{e}(t)$  is defined as

$$\mathbf{e}(t) = \mathbf{q}_d(t) - \mathbf{q}(t). \quad (13)$$

Here,  $\mathbf{q}_d(t)$  is the *desired* angle vector of joints and can be obtained by trajectory planning [7, 11, 29, 30];  $\mathbf{q}(t)$  is the *actual* angle vector of joints. Differentiating (13) twice, to get

$$\dot{\mathbf{e}}(t) = \dot{\mathbf{q}}_d(t) - \dot{\mathbf{q}}(t), \quad \ddot{\mathbf{e}}(t) = \ddot{\mathbf{q}}_d(t) - \ddot{\mathbf{q}}(t). \quad (14)$$

Substituting (10) into (14) yields

$$\ddot{\mathbf{e}}(t) = \ddot{\mathbf{q}}_d(t) + \mathbf{M}^{-1}(\mathbf{q}(t)) [\mathbf{N}(\mathbf{q}(t), \dot{\mathbf{q}}(t)) - \boldsymbol{\tau}(t)] \quad (15)$$

from which the control function can be defined as

$$\mathbf{u}(t) = \ddot{\mathbf{q}}_d(t) + \mathbf{M}^{-1}(\mathbf{q}(t)) [\mathbf{N}(\mathbf{q}(t), \dot{\mathbf{q}}(t)) - \boldsymbol{\tau}(t)]. \quad (16)$$

This is often called the *feedback linearization* control law, which can also be inverted to express it as

$$\boldsymbol{\tau}(t) = \mathbf{M}(\mathbf{q}(t)) [\ddot{\mathbf{q}}_d(t) - \mathbf{u}(t)] + \mathbf{N}(\mathbf{q}(t), \dot{\mathbf{q}}(t)). \quad (17)$$

Using the relations (14) and (16), and defining state vector  $\mathbf{x}(t) = [\mathbf{e}'(t) \ \dot{\mathbf{e}}'(t)]'$ , the *tracking error dynamics* can be written as

$$\dot{\mathbf{x}}(t) = \begin{bmatrix} \mathbf{0} & \mathbf{I} \\ \mathbf{0} & \mathbf{0} \end{bmatrix} \mathbf{x}(t) + \begin{bmatrix} \mathbf{0} \\ \mathbf{I} \end{bmatrix} \mathbf{u}(t). \quad (18)$$

Note that this is in the form of a *linear* system such as

$$\dot{\mathbf{x}}(t) = \mathbf{A}\mathbf{x}(t) + \mathbf{B}\mathbf{u}(t). \quad (19)$$

### 3.2. Fuzzy Logic-Based PD Hybrid Control

[Figure 4 about here.]

Figure 4 shows the block diagram of the hybrid fuzzy logic-based PD controller for the proposed five-finger prosthetic hand with control signal as

$$\mathbf{u}(t) = -\mathbf{K}_P(t)\mathbf{e}(t) - \mathbf{K}_D(t)\dot{\mathbf{e}}(t) \quad (20)$$

with the proportional  $\mathbf{K}_P(t)$  and derivative  $\mathbf{K}_D(t)$  diagonal gain matrices with time varying. We then rewrite (17) as

$$\begin{aligned} \boldsymbol{\tau}(t) = & \mathbf{M}(\mathbf{q}(t))[\ddot{\mathbf{q}}_d(t) + \mathbf{K}_P(t)\mathbf{e}(t) + \mathbf{K}_D(t)\dot{\mathbf{e}}(t)] + \\ & \mathbf{N}(\mathbf{q}(t), \dot{\mathbf{q}}(t)). \end{aligned} \quad (21)$$

Then we use Mamdani fuzzy inference system to tune the time-varying parameters  $\mathbf{K}_P(t)$  and  $\mathbf{K}_D(t)$  of PD controller. The structural characteristics of proposed fuzzy inference system, which includes two inputs (error  $\mathbf{e}$  and error rate  $\dot{\mathbf{e}}$ ) and one output ( $\mathbf{K}_P$ ). Each input or output layer contains seven triangular membership functions as shown in Figure 5 and 49 logic rules as listed in Table 1.

[Figure 5 about here.]

[Table 1 about here.]

Using 49 logic rules, the output surface  $\mathbf{K}_P$  of fuzzy inference system is generated as shown in Figure 6. Similarly,  $\mathbf{K}_D$  can be computed by the same way.

[Figure 6 about here.]



#### 4. Simulation Results and Discussion

[Figure 7 about here.]

Figure 7 shows that a five-finger prosthetic hand with 14 DoF is grasping a rectangular rod. When thumb and the other four fingers are performing extension/flexion movements, the workspace of fingertips is restricted to the maximum angles of joints. Referring to inverse kinematics, the first and second joint angles of the thumb fingertip are constrained in the ranges of  $[0,90]$  and  $[-80,0]$  (degrees). The first, second, and third joint angles of the other four fingers are constrained in the ranges of  $[0,90]$ ,  $[0,110]$  and  $[0,80]$  (degrees), respectively [34].

Next, we present simulations with PD and PID controllers and fuzzy inference system tuned PD controller for the 14-DOF, five-finger smart prosthetic hand. The parameters of the two-link thumb/three-link fingers were related to desired trajectory [35]. All parameters of the smart prosthetic hand selected for the simulations are given in Table 2 and the side length and length of the target rectangular rod are 0.010 and 0.100 (m), respectively. The relating parameters between the global coordinate and the local coordinates are defined in Table 3 and Figure 2.

[Table 2 about here.]

[Table 3 about here.]

Moreover, each link of all fingers is assumed to be a circular cylinder with the radius ( $R$ ) 0.010 (m), so the inertia  $I_{zzk}^j$  of each link  $k$  of all fingers  $j$  ( $= t, i, m, r$  and  $l$ ) can be calculated as

$$I_{zzk}^j = \frac{1}{4}m_k^j R^2 + \frac{1}{3}m_k^j L_k^{j^2}. \quad (22)$$

All initial actual angles are zero and the diagonal coefficients,  $\mathbf{K_P}$ ,  $\mathbf{K_I}$  and  $\mathbf{K_D}$ , for the PD or PID controller alone are arbitrarily chosen as 100. From the derived dynamic and control models, the control signal  $\mathbf{u}$  and torque  $\boldsymbol{\tau}$  can be calculated after the parameters ( $\mathbf{K_P}$  and  $\mathbf{K_D}$ ) are selected.

[Figure 8 about here.]

Figure 8 shows tracking errors ( $e_1^t$  and  $e_2^t$  on the left column) and desired/actual angles ( $q_1^t$  and  $q_2^t$  on the right column) of joints 1 (the top row) and 2 (the bottom row) for two-link thumb using PD (dash line), PID (dot line), FL (short dash line)

and hybrid of FL and PD (solid line) controllers. The tracking errors for both PD and FL controllers are convergent to zero within 5 seconds without overshooting, but PID controller takes longer (approximate 10 seconds) with overshooting and oscillation. The proposed hybrid control of FL and PD using parameters  $\mathbf{K_P} \in [50, 1000]$  and  $\mathbf{K_D} \in [50, 500]$  provides 5-10 fold faster convergence than PD, PID and FLC alone. FLC includes two inputs (error and error rate) and one output (control signal). To further study whether the parameter range influences tracking errors, we found that the larger the parameter range, the faster the convergent speed for the range  $\mathbf{K_P} \in [50, 2000]$  without additional computational time [36]. These results clearly demonstrate that fusion of soft computing (SC) and hard control (HC) is superior to either HC or SC methodology alone.

[Figure 9 about here.]

The time-variant computed control signals ( $u_1^t$  and  $u_2^t$ ) and torques ( $\tau_1^t$  and  $\tau_2^t$ ) for two-link thumb are shown in Figure 9, suggesting that the proposed hybrid FL-PD controller requires more power (torque) than PD, PID and FL controllers in order to obtain faster convergent tracking errors.

[Figure 10 about here.]

Figure 10 shows tracking errors and desired/actual angles for three-link index finger. As increasing DOFs, PID control still shows overshooting and oscillation but both PD and FL controllers reduce accuracy and convergent speed. However, the hybrid control still shows fast convergence and high accuracy. Similarly, Figures 11, 12 and 13 show similar results of tracking errors for the remaining three-link fingers (middle, ring and little).

[Figure 11 about here.]

[Figure 12 about here.]

[Figure 13 about here.]

Figure 14 shows the animation of hybrid control for a 14-DOF, five-finger smart prosthetic hand in 3D (right upper) and 2D (left upper and bottom). [Note: The animation file (Prosthetic Hand Animation.avi) for Figure 14 is submitted separately along with the manuscript. If you use Adobe Acrobat version 9 (or later), you can directly play the video on this pdf file.]

[Figure 14 about here.]

## 5. Conclusions and Future Work

For a 14-DOF, five-finger smart prosthetic hand, a hybrid control technique involving soft control with adaptive neuro-fuzzy inference system (ANFIS) and fuzzy logic (FL) and hard control with proportional-derivative (PD) was proposed. The ANFIS was used for inverse kinematics and FL was used for tuning the PD parameters with 2 input layers (error and error change) using 7 triangular membership functions and 49 fuzzy logic rules. Simulation results with FL-tuned PD (hybrid) controller showed superior performance compared to hard control or soft computing alone. Work is underway to extend this methodology to a real-time implementation on the prototype of a prosthetic hand.

## Acknowledgment

The research was sponsored by the U.S. Department of the Army, under the award number W81XWH-10-1-0128 awarded and administered by the U.S. Army Medical Research Acquisition Activity, 820 Chandler Street, Fort Detrick, MD 21702-5014, USA. The information does not necessarily reflect the position or the policy of the Government, and no official endorsement should be inferred. For purposes of this article, information includes news releases, articles, manuscripts, brochures, advertisements, still and motion pictures, speeches, trade association proceedings, etc.

## References

- [1] M. Zecca, S. Micera, M. Carrozza, P. Dario, Control of multifunctional prosthetic hands by processing the electromyographic signal, *Critical Reviews<sup>TM</sup> in Biomedical Engineering* 30 (2002) 459–485. (Review article with 96 references).
- [2] J. C. K. Lai, M. P. Schoen, A. Perez-Gracia, D. S. Naidu, S. W. Leung, Prosthetic devices: Challenges and implications of robotic implants and biological interfaces, *Proceedings of the Institute of Mechanical Engineers (IMechE), Part H: Journal of Engineering in Medicine* 221 (2007) 173–183. Special Issue on Micro and Nano Technologies in Medicine.
- [3] L. Zollo, S. Roccella, E. Guglielmelli, M. C. Carrozza, P. Dario, Biomechatronic design and control of an anthropomorphic artificial hand for prosthetic and robotic applications, *IEEE/ASME Transactions on Mechatronics* 12 (2007) 418–429.

- [4] D. S. Naidu, C.-H. Chen, A. Perez, M. P. Schoen, Control strategies for smart prosthetic hand technology: An overview, in: The 30th Annual International Conference of the IEEE Engineering Medicine and Biology Society (EMBS), Vancouver, Canada, pp. 4314–4317.
- [5] S. Micera, J. Carpaneto, S. Raspopovic, Control of hand prostheses using peripheral information, *IEEE Reviews in Biomedical Engineering* 3 (2010) 48–68. (Review article with 161 references).
- [6] D. S. Naidu, C.-H. Chen, Automatic Control Techniques for Smart Prosthetic Hand Technology: An Overview, book chapter 12, to appear in a book titled “Distributed Diagnosis and Home Healthcare (D<sub>2</sub>H<sub>2</sub>): Volume 2”, American Scientific Publishers, California, USA, 2011.
- [7] C.-H. Chen, K. W. Bosworth, M. P. Schoen, S. E. Bearden, D. S. Naidu, A. Perez-Gracia, A study of particle swarm optimization on leukocyte adhesion molecules and control strategies for smart prosthetic hand, in: 2008 IEEE Swarm Intelligence Symposium (IEEE SIS08), St. Louis, Missouri, USA.
- [8] C.-H. Chen, D. S. Naidu, A. Perez-Gracia, M. P. Schoen, Fusion of hard and soft control techniques for prosthetic hand, in: Proceedings of the International Association of Science and Technology for Development (IASTED) International Conference on Intelligent Systems and Control (ISC 2008), Orlando, Florida, USA, pp. 120–125.
- [9] C.-H. Chen, D. S. Naidu, A. Perez-Gracia, M. P. Schoen, A hybrid control strategy for five-fingered smart prosthetic hand, in: Joint 48th IEEE Conference on Decision and Control (CDC) and 28th Chinese Control Conference (CCC), Shanghai, P. R. China, pp. 5102–5107.
- [10] D. Naidu, Optimal Control Systems, CRC Press, Boca Raton, FL, 2003.
- [11] C.-H. Chen, D. S. Naidu, A. Perez-Gracia, M. P. Schoen, A hybrid optimal control strategy for a smart prosthetic hand, in: Proceedings of the ASME 2009 Dynamic Systems and Control Conference (DSCC), Hollywood, California, USA. (No. DSCC2009-2507).
- [12] C.-H. Chen, D. S. Naidu, Optimal control strategy for two-fingered smart prosthetic hand, in: Proceedings of the International Association of Science

and Technology for Development (IASTED) International Conference on Robotics and Applications (RA 2010), Cambridge, Massachusetts, USA, pp. 190–196.

- [13] F. Lewis, S. Jagannathan, A. Yesildirek, *Neural Network Control of Robotic Manipulators and Nonlinear Systems*, Taylor & Francis, London, UK, 1999.
- [14] F. Lewis, D. Dawson, C. Abdallah, *Robot Manipulators Control: Second Edition, Revised and Expanded*, Marcel Dekker, Inc., New York, NY, 2004.
- [15] C.-H. Chen, D. S. Naidu, A. Perez-Gracia, M. P. Schoen, A hybrid adaptive control strategy for a smart prosthetic hand, in: *The 31st Annual International Conference of the IEEE Engineering Medicine and Biology Society (EMBS)*, Minneapolis, Minnesota, USA, pp. 5056–5059.
- [16] C.-H. Chen, D. S. Naidu, M. P. Schoen, An adaptive control strategy for a five-fingered prosthetic hand, in: *The 14th World Scientific and Engineering Academy and Society (WSEAS) International Conference on Systems, Latest Trends on Systems (Volume II)*, Corfu Island, Greece, pp. 405–410.
- [17] C.-H. Chen, M. P. Schoen, K. W. Bosworth, A condensed hybrid optimization algorithm using enhanced continuous tabu search and particle swarm optimization, in: *Proceedings of the ASME 2009 Dynamic Systems and Control Conference (DSCC)*, Hollywood, California, USA. (No. DSCC2009-2526).
- [18] B. Subudhi, A. S. Morris, Soft computing methods applied to the control of a flexible robot manipulator, *Applied Soft Computing* 9 (2009) 149–158.
- [19] F. Liu, H. Chen, Motion control of intelligent underwater robot based on CMAC-PID, in: *Proceedings of the 2008 IEEE International Conference on Information and Automation*, Zhangjiajie, China, pp. 1308–1311.
- [20] A. Konar, *Computational Intelligence: Principles, Techniques and Applications*, Springer-Verlag, Berlin, Germany, 2005.
- [21] C.-H. Chen, K. W. Bosworth, M. P. Schoen, Investigation of particle swarm optimization dynamics, in: *Proceedings of International Mechanical Engineering Congress and Exposition (IMECE) 2007*, Seattle, Washington, USA. (No. IMECE2007-41343).

- [22] C.-H. Chen, K. W. Bosworth, M. P. Schoen, An adaptive particle swarm method to multiple dimensional problems, in: Proceedings of the International Association of Science and Technology for Development (IASTED) International Symposium on Computational Biology and Bioinformatics (CBB 2008), Orlando, Florida, USA, pp. 260–265.
- [23] Y. Z. Arslan, Y. Hacioglu, N. Yagiz, Prosthetic hand finger control using fuzzy sliding modes, *Journal of Intelligent and Robotic Systems* 52 (2008) 121–138.
- [24] R. Kato, H. Yokoi, A. H. Arieta, W. Yub, T. Arai, Mutual adaptation among man and machine by using f-MRI analysis, *Robotics and Autonomous Systems* 57 (2009) 161–166.
- [25] Y. Kamikawa, T. Maeno, Underactuated five-finger prosthetic hand inspired by grasping force distribution of humans, in: Proceedings of the 2008 IEEE/RSJ International Conference on Intelligent Robots and Systems, Nice, France, pp. 717–722.
- [26] R. N. Khushaba, A. Al-Ani, A. Al-Jumaily, Swarm intelligence based dimensionality reduction for myoelectric control, in: Proceedings of the IEEE Conference on Intelligent Sensors, Sensor Networks and Information Processing, Melbourne, Australia, pp. 577–582.
- [27] S. Ovaska, H. VanLandingham, A. Kamiya, Fusion of soft computing and hard computing in industrial applications: An overview, *IEEE Transactions on Systems, Man, and Cybernetics - Part C: Applications and Reviews* 32 (2002) 72–79.
- [28] A. Tettamanzi, M. Tomassini, *Soft Computing: Integrating Evolutionary, Neural, and Fuzzy Systems*, Springer-Verlag, Berlin, Germany, 2001.
- [29] C.-H. Chen, *Hybrid Control Strategies for Smart Prosthetic Hand*, Ph.D. thesis, Measurement and Control Engineering, Idaho State University, 2009.
- [30] C.-H. Chen, D. S. Naidu, M. P. Schoen, Adaptive control for a five-fingered prosthetic hand with unknown mass and inertia, *World Scientific and Engineering Academy and Society (WSEAS) Journal on Systems* 10 (2011) 148–161.

- [31] B. Siciliano, L. Sciavicco, L. Villani, G. Oriolo, *Robotics: Modelling, Planning and Control*, Springer-Verlag, London, UK, 2009.
- [32] J.-S. Jang, C.-T. Sun, E. Mizutani, *Neuro-Fuzzy and Soft Computing: A Computational Approach to Learning and Machine Intelligence*, Prentice Hall PTR, Upper Saddle River, NJ, 1997.
- [33] V. Nandikolla, D. Naidu, Blood glucose regulation for diabetic mellitus using a hybrid intelligent technique, in: *Proceedings of the 2005 ASME International Mechanical Engineering Congress and Exposition (IMECE)*, Orlando, FL, pp. 1–6.
- [34] P. K. Lavangie, C. C. Norkin, *Joint Structure and Function: A Comprehensive Analysis*, Third Edition, F. A. Davis Company, Philadelphia, PA, 2001.
- [35] S. Arimoto, *Control Theory of Multi-fingered Hands: A Modeling and Analytical-Mechanics Approach for Dexterity and Intelligence*, Springer-Verlag, London, UK, 2008.
- [36] C.-H. Chen, D. S. Naidu, Fusion of fuzzy logic and PD control for a five-fingered smart prosthetic hand, in: *In Proceedings of the 2011 IEEE International Conference on Fuzzy Systems (FUZZ-IEEE 2011)*, Taipei, Taiwan, pp. 2108–2115.

## List of Tables

1	A Complete Fuzzy Logic Rule Base . . . . .	16
2	Parameter Selection of the Smart Hand . . . . .	17
3	Parameter Selection of Conversion between Global and Local Co-ordinates . . . . .	18



Table 1: A Complete Fuzzy Logic Rule Base

$\dot{e} \backslash e$	NL	NM	NS	ZR	PS	PM	PL
NL	ZR	ZR	ZR	ZR	VS	S	SM
NM	ZR	ZR	ZR	VS	S	SM	ML
NS	ZR	ZR	VS	S	SM	ML	L
ZR	ZR	VS	S	SM	ML	L	VL
PS	VS	S	SM	ML	L	VL	VL
PM	S	SM	ML	L	VL	VL	VL
PL	SM	ML	L	VL	VL	VL	VL

N: negative; P: positive; ZR: zero; L: large;  
M: medium; S: small; V: very

Table 2: Parameter Selection of the Smart Hand

Parameters	Values
<b>Thumb</b>	
Time $(t_0, t_f)^*$	0, 20 (sec)
Desired Initial Position $(X_0^t, Y_0^t)^{**}$	0.035, 0.060 (m)
Desired Final Position $(X_f^t, Y_f^t)^{**}$	0.0495, 0.060 (m)
Desired Initial Velocity $(\dot{X}_0^t, \dot{Y}_0^t)^*$	0, 0 (m/s)
Desired Final Velocity $(\dot{X}_f^t, \dot{Y}_f^t)^*$	0, 0 (m/s)
Length $(L_1^t, L_2^t)$	0.040, 0.040 (m)
Mass $(m_1^t, m_2^t)$	0.043, 0.031 (kg)
<b>Index Finger</b>	
Desired Initial Position $(X_0^i, Y_0^i)^{**}$	0.065, 0.080 (m)
Desired Final Position $(X_f^i, Y_f^i)^{**}$	0.010, 0.060 (m)
Length $(L_1^i, L_2^i, L_3^i)$	0.040, 0.040, 0.030 (m)
Mass $(m_1^i, m_2^i, m_3^i)$	0.045, 0.025, 0.017 (kg)
<b>Middle Finger</b>	
Desired Initial Position $(X_0^m, Y_0^m)^{**}$	0.065, 0.080 (m)
Desired Final Position $(X_f^m, Y_f^m)^{**}$	0.005, 0.060 (m)
Length $(L_1^m, L_2^m, L_3^m)$	0.044, 0.044, 0.033 (m)
Mass $(m_1^m, m_2^m, m_3^m)$	0.050, 0.028, 0.017 (kg)
<b>Ring Finger</b>	
Desired Initial Position $(X_0^r, Y_0^r)^{**}$	0.065, 0.080 (m)
Desired Final Position $(X_f^r, Y_f^r)^{**}$	0.010, 0.060 (m)
Length $(L_1^r, L_2^r, L_3^r)$	0.040, 0.040, 0.030 (m)
Mass $(m_1^r, m_2^r, m_3^r)$	0.041, 0.023, 0.014 (kg)
<b>Little Finger</b>	
Desired Initial Position $(X_0^l, Y_0^l)^{**}$	0.055, 0.080 (m)
Desired Final Position $(X_f^l, Y_f^l)^{**}$	0.020, 0.060 (m)
Length $(L_1^l, L_2^l, L_3^l)$	0.038, 0.038, 0.030 (m)
Mass $(m_1^l, m_2^l, m_3^l)$	0.041, 0.023, 0.014 (kg)

\*All fingers use same parameters

\*\*All parameters are in local coordinates

Table 3: Parameter Selection of Conversion between Global and Local Coordinates

Parameters	Values
Rotating $\alpha$	90 (deg)
Rotating $\beta$	45 (deg)
Translating $\mathbf{d}^i$	(0.035, 0, 0) (m)
Translating $\mathbf{d}^m$	(0.040, 0, -0.020) (m)
Translating $\mathbf{d}^r$	(0.035, 0, -0.040) (m)
Translating $\mathbf{d}^l$	(0.025, 0, -0.060) (m)

## List of Figures

1	Principle behind Fusion of Soft and Hard Computing . . . . .	21
2	Relationship between Global Coordinate and Local Coordinates: Local coordinate $x^t$ - $y^t$ - $z^t$ of thumb can be reached by rotating through angles $\alpha$ and $\beta$ to $X^G$ and $Y^G$ of global coordinate, sub- sequently. Local coordinate $x^i$ - $y^i$ - $z^i$ of index finger can be ob- tained by rotating through angle $\alpha$ to $X^G$ and then translating a vector $d^1$ of the global coordinate. . . . .	22
3	ANFIS Architecture: (a) A Two Input First-Order Sugeno Fuzzy Model with Two Rules (b) Equivalent ANFIS Structure [32]. The inverse kinematics problems are solved by using adaptive neuro- fuzzy inference system (ANFIS) method where the input of fuzzy- neuro system is Cartesian space and the output is joint space. AN- FIS is a fuzzy inference system implemented in the framework of adaptive networks which provides the best optimization algorithm to find parameters in order to fit the data. . . . .	23
4	Block Diagram of the Proposed Hybrid Fuzzy Logic-Based Proportional- Derivative (PD) Controller for a Five-Finger Prosthetic Hand: Er- rors and error changes are calculated by actual and desired angles, which are based on adaptive neuro-fuzzy inference system (AN- FIS) trajectory planner. Then fuzzy logic controller tunes all pa- rameters of closed-loop PD control so that the required torque of the prosthetic hand nonlinear system is computed by control input. . . . .	24
5	All Membership Functions: Each of Two Inputs (Upper Panel) and One Output (Lower Panel) Uses 7 Triangular Membership Functions . . . . .	25
6	The Output Surface of Fuzzy Inference System with Two Inputs and 49 Logic Rules . . . . .	26
7	Five-Finger Prosthetic Hand Grasping a Rectangular Object . . . .	27
8	Tracking Errors and Desired/Actual Angles of Joints 1 (a,b) and 2 (c,d) for Two-Link Thumb Using PD (dash line), PID (dot line), FL (short dash line) and hybrid of FL and PD (solid line) Controllers . . . . .	28
9	Control Signals and Actuated Torques of Joints 1 (a,b) and 2 (c,d) for Two-Link Thumb Using PD (dash line), PID (dot line), FL (short dash line) and hybrid of FL and PD (solid line) Controllers . . . . .	29

10	Tracking Errors and Desired/Actual Angles of Joints 1 (a,b), 2 (c,d) and 3 (e,f) for Three-Link Index Finger Using PD (dash line), PID (dot line), FL (short dash line) and hybrid of FL and PD (solid line) Controllers . . . . .	30
11	Tracking Errors and Desired/Actual Angles of Joints 1 (a,b), 2 (c,d) and 3 (e,f) for Three-Link Middle Finger Using PD (dash line), PID (dot line), FL (short dash line) and hybrid of FL and PD (solid line) Controllers . . . . .	31
12	Tracking Errors and Desired/Actual Angles of Joints 1 (a,b), 2 (c,d) and 3 (e,f) for Three-Link Ring Finger Using PD (dash line), PID (dot line), FL (short dash line) and hybrid of FL and PD (solid line) Controllers . . . . .	32
13	Tracking Errors and Desired/Actual Angles of Joints 1 (a,b), 2 (c,d) and 3 (e,f) for Three-Link Little Finger Using PD (dash line), PID (dot line), FL (short dash line) and hybrid of FL and PD (solid line) Controllers . . . . .	33
14	Hybrid Control Animation for a Five-Fingered Prosthetic Hand . .	34

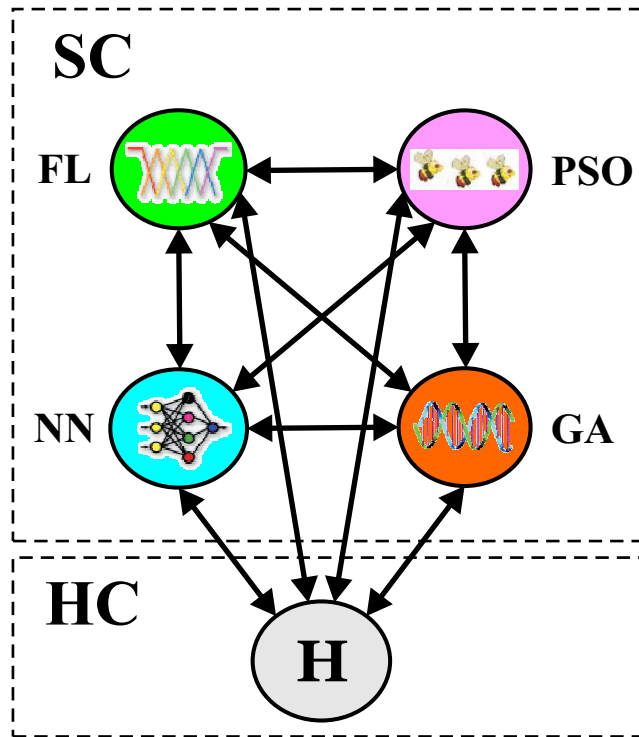


Figure 1: Principle behind Fusion of Soft and Hard Computing

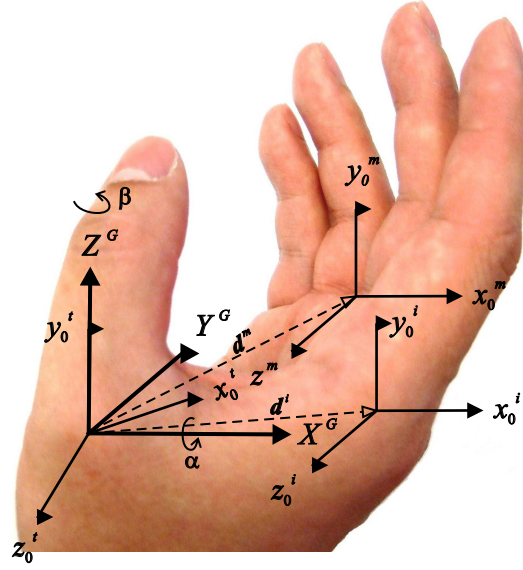


Figure 2: Relationship between Global Coordinate and Local Coordinates: Local coordinate  $x^t$ - $y^t$ - $z^t$  of thumb can be reached by rotating through angles  $\alpha$  and  $\beta$  to  $X^G$  and  $Y^G$  of global coordinate, subsequently. Local coordinate  $x^i$ - $y^i$ - $z^i$  of index finger can be obtained by rotating through angle  $\alpha$  to  $X^G$  and then translating a vector  $d^i$  of the global coordinate.

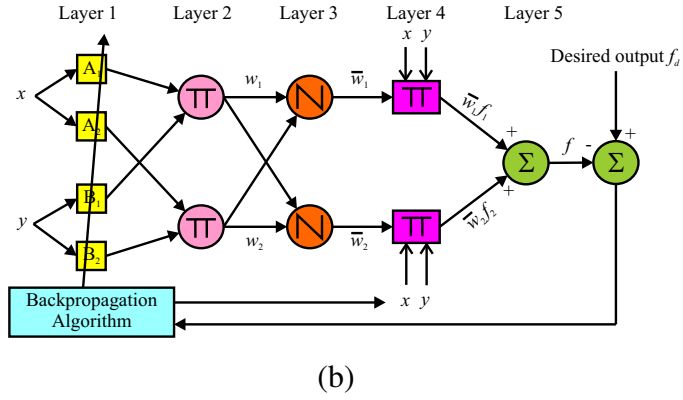
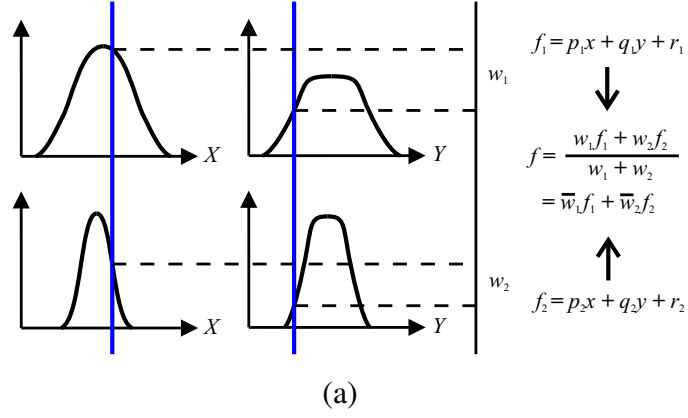


Figure 3: ANFIS Architecture: (a) A Two Input First-Order Sugeno Fuzzy Model with Two Rules (b) Equivalent ANFIS Structure [32]. The inverse kinematics problems are solved by using adaptive neuro-fuzzy inference system (ANFIS) method where the input of fuzzy-neuro system is Cartesian space and the output is joint space. ANFIS is a fuzzy inference system implemented in the framework of adaptive networks which provides the best optimization algorithm to find parameters in order to fit the data.



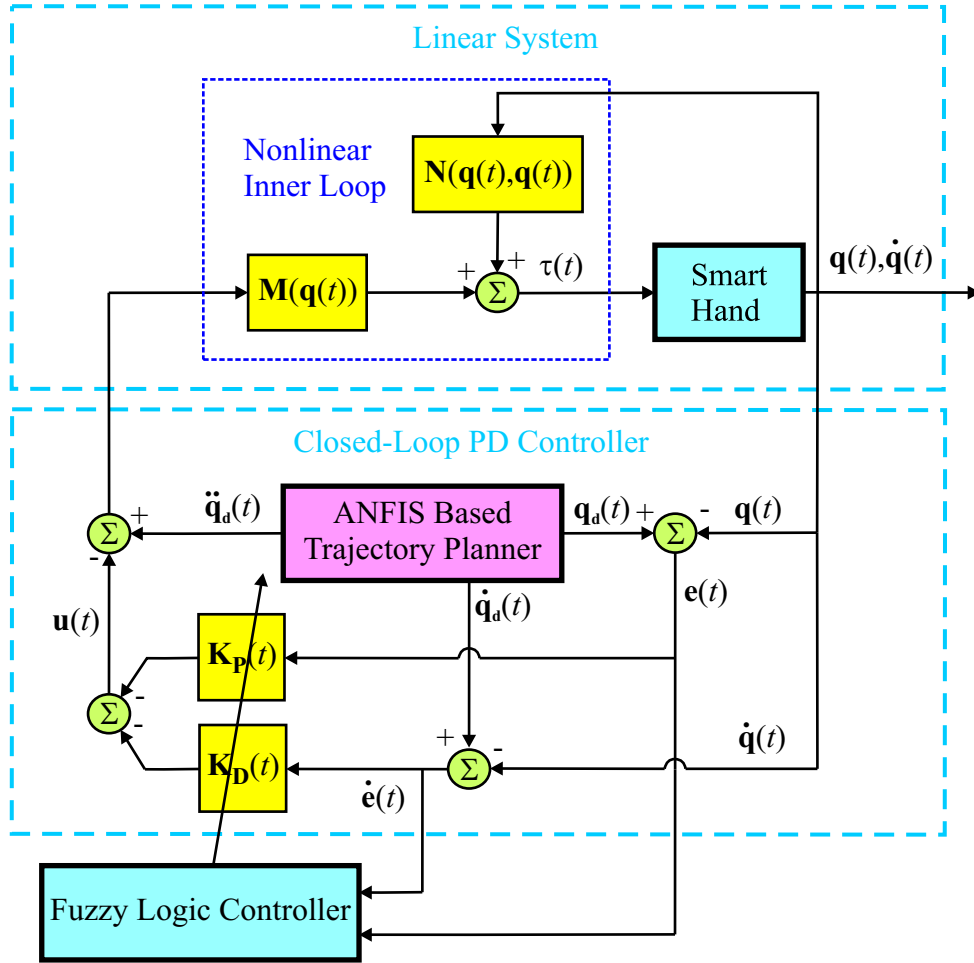


Figure 4: Block Diagram of the Proposed Hybrid Fuzzy Logic-Based Proportional-Derivative (PD) Controller for a Five-Finger Prosthetic Hand: Errors and error changes are calculated by actual and desired angles, which are based on adaptive neuro-fuzzy inference system (ANFIS) trajectory planner. Then fuzzy logic controller tunes all parameters of closed-loop PD control so that the required torque of the prosthetic hand nonlinear system is computed by control input.

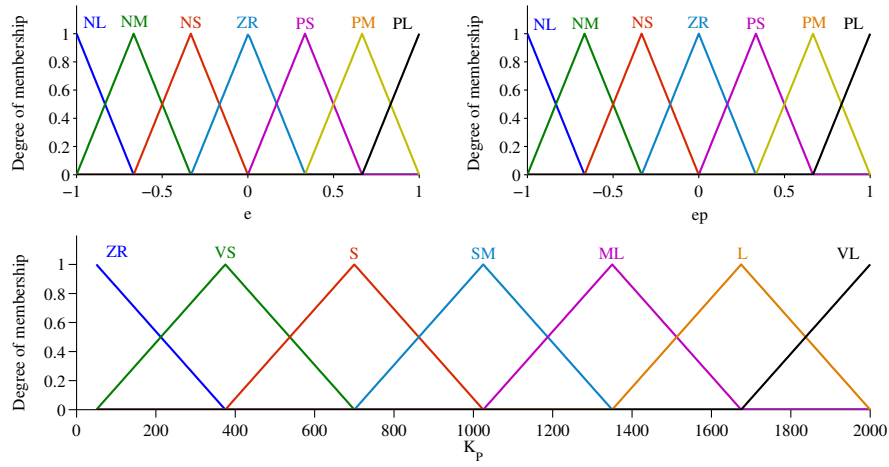


Figure 5: All Membership Functions: Each of Two Inputs (Upper Panel) and One Output (Lower Panel) Uses 7 Triangular Membership Functions

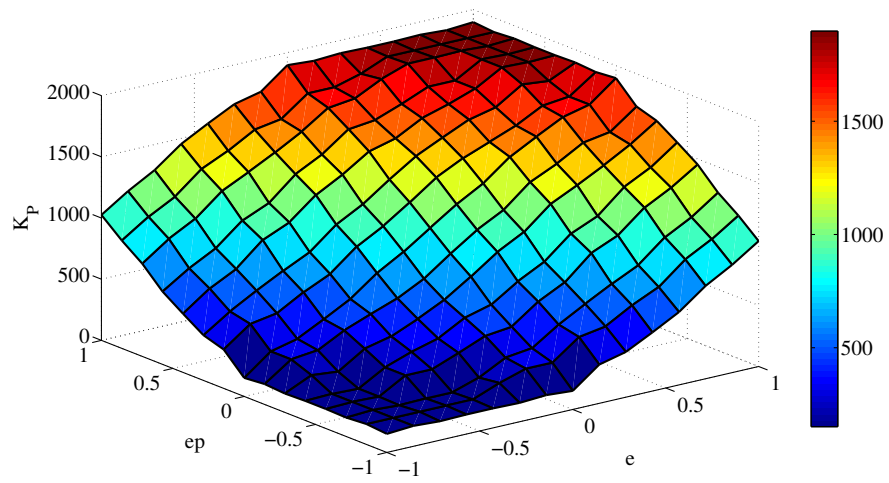


Figure 6: The Output Surface of Fuzzy Inference System with Two Inputs and 49 Logic Rules

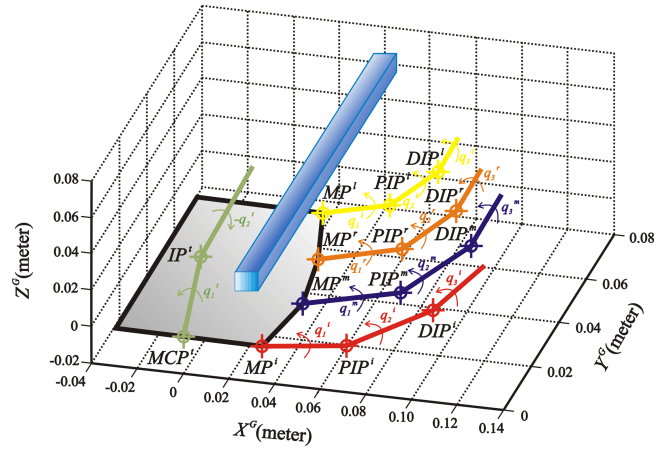
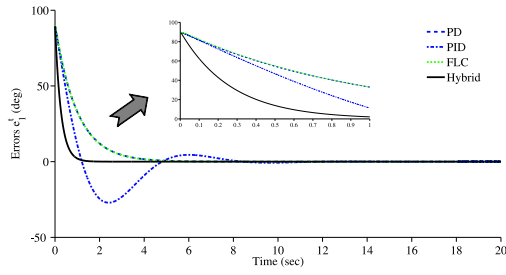
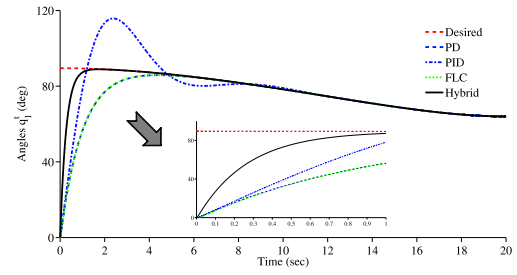


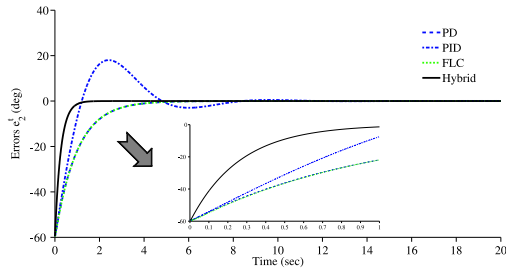
Figure 7: Five-Finger Prosthetic Hand Grasping a Rectangular Object



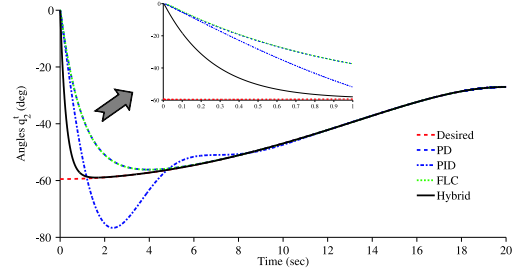
(a)



(b)

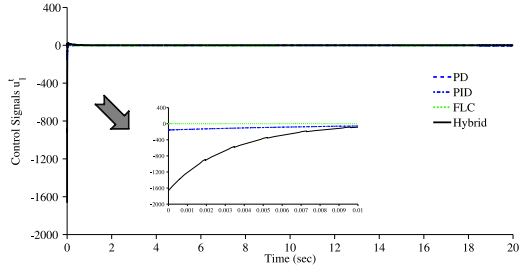


(c)

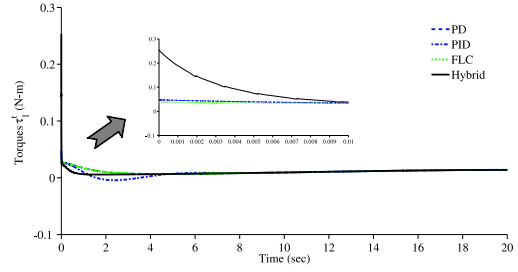


(d)

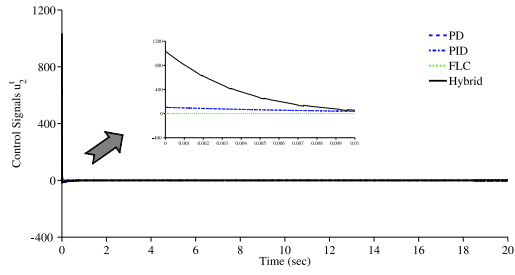
Figure 8: Tracking Errors and Desired/Actual Angles of Joints 1 (a,b) and 2 (c,d) for Two-Link Thumb Using PD (dash line), PID (dot line), FL (short dash line) and hybrid of FL and PD (solid line) Controllers



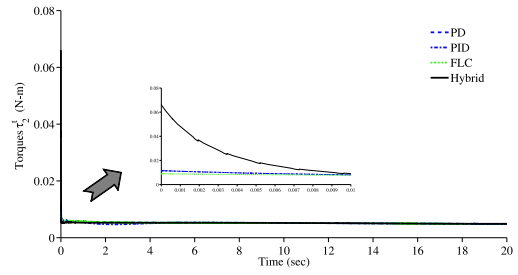
(a)



(b)

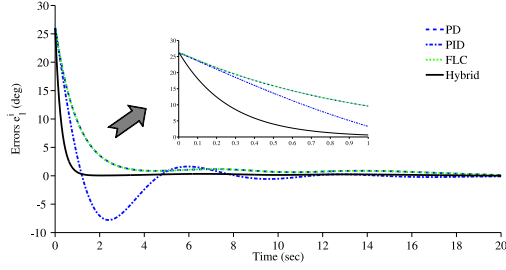


(c)

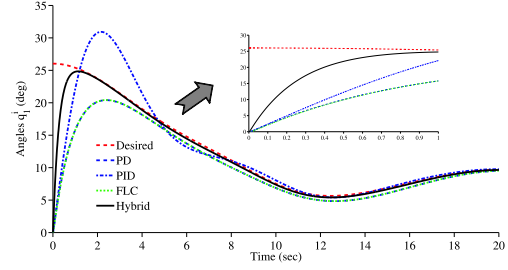


(d)

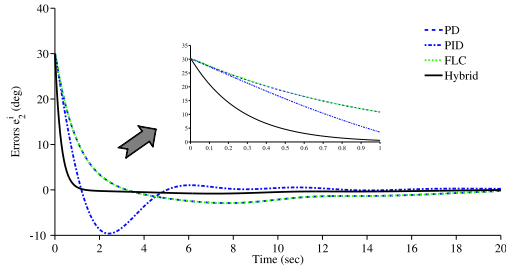
Figure 9: Control Signals and Actuated Torques of Joints 1 (a,b) and 2 (c,d) for Two-Link Thumb Using PD (dash line), PID (dot line), FL (short dash line) and hybrid of FL and PD (solid line) Controllers



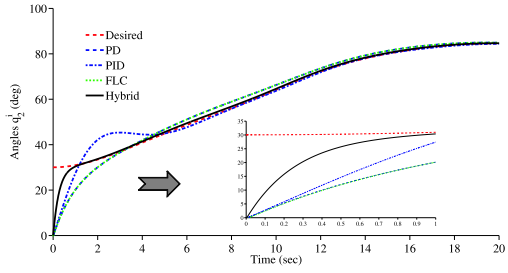
(a)



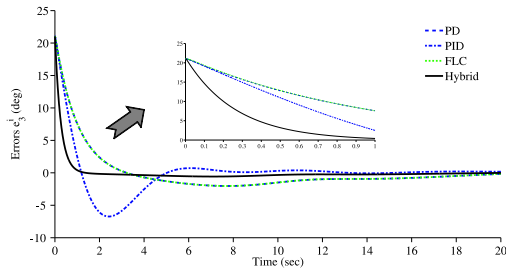
(b)



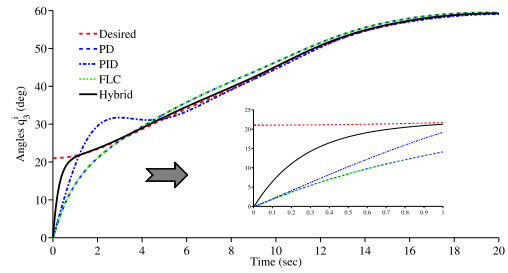
(c)



(d)

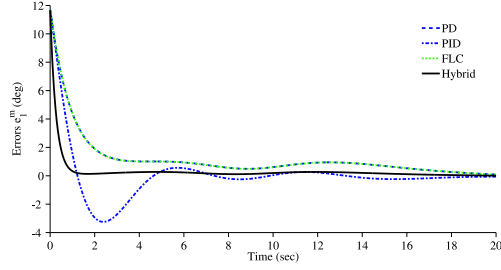


(e)

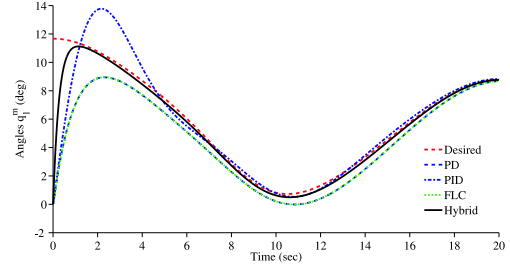


(f)

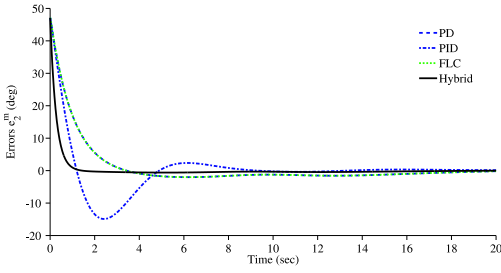
Figure 10: Tracking Errors and Desired/Actual Angles of Joints 1 (a,b), 2 (c,d) and 3 (e,f) for Three-Link Index Finger Using PD (dash line), PID (dot line), FL (short dash line) and hybrid of FL and PD (solid line) Controllers



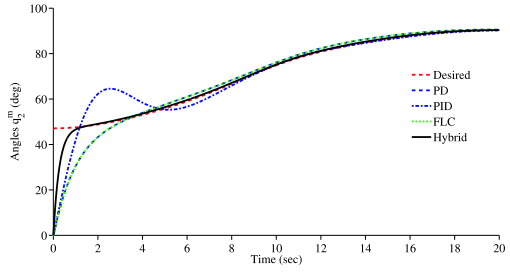
(a)



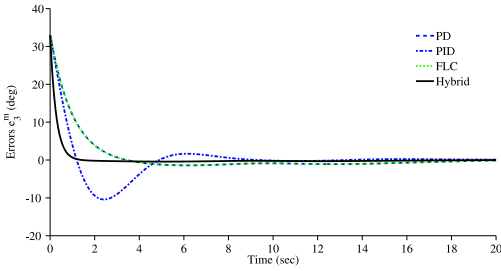
(b)



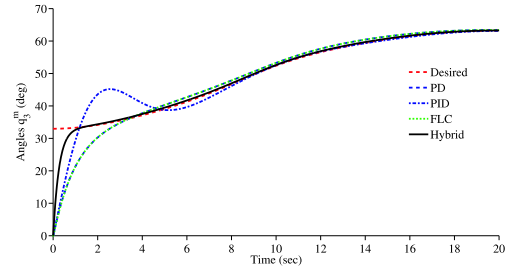
(c)



(d)



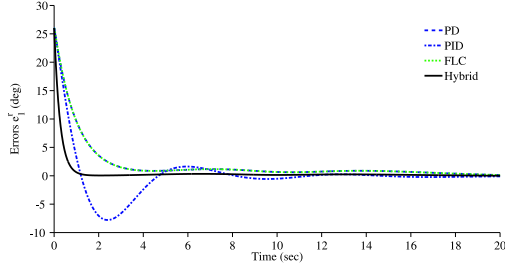
(e)



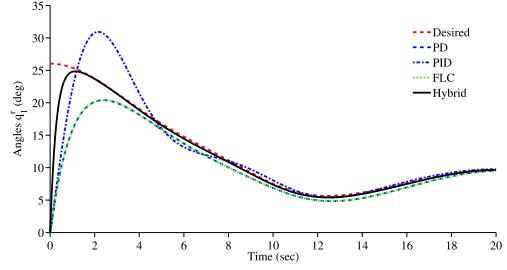
(f)

Figure 11: Tracking Errors and Desired/Actual Angles of Joints 1 (a,b), 2 (c,d) and 3 (e,f) for Three-Link Middle Finger Using PD (dash line), PID (dot line), FL (short dash line) and hybrid of FL and PD (solid line) Controllers

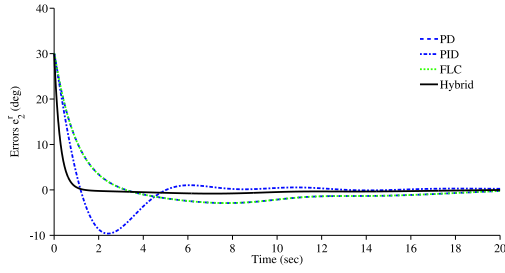




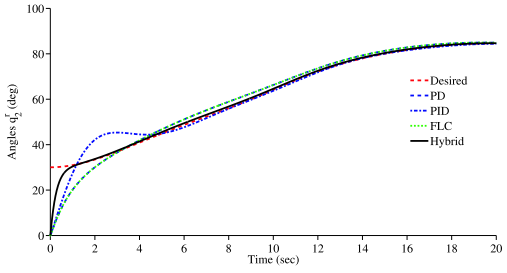
(a)



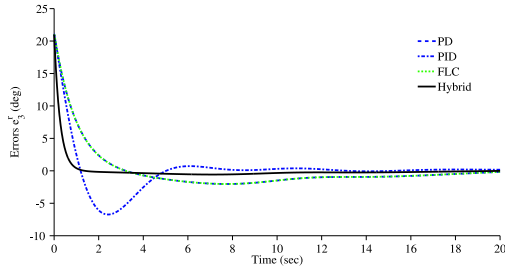
(b)



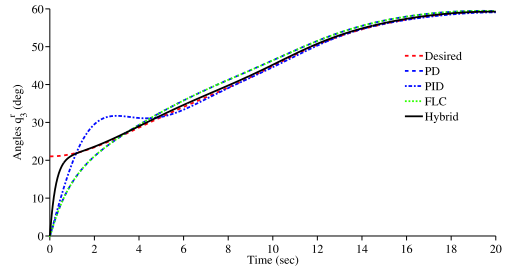
(c)



(d)

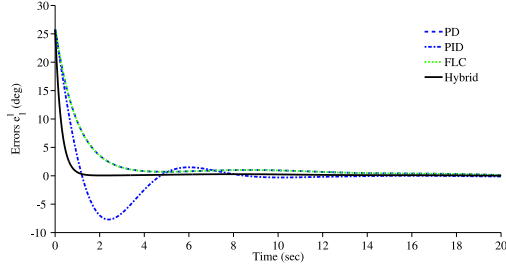


(e)

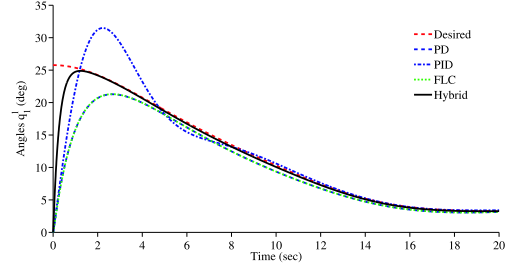


(f)

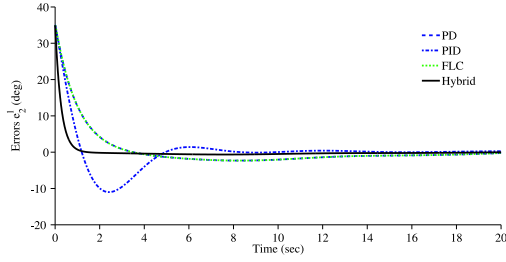
Figure 12: Tracking Errors and Desired/Actual Angles of Joints 1 (a,b), 2 (c,d) and 3 (e,f) for Three-Link Ring Finger Using PD (dash line), PID (dot line), FL (short dash line) and hybrid of FL and PD (solid line) Controllers



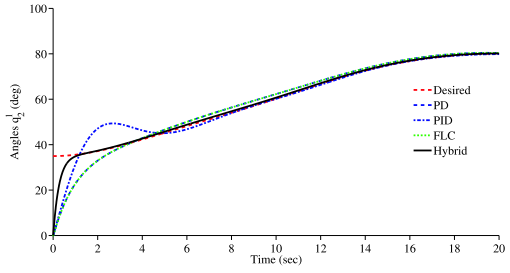
(a)



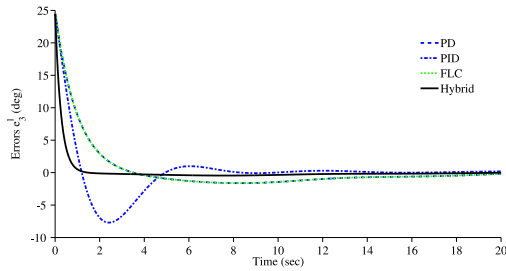
(b)



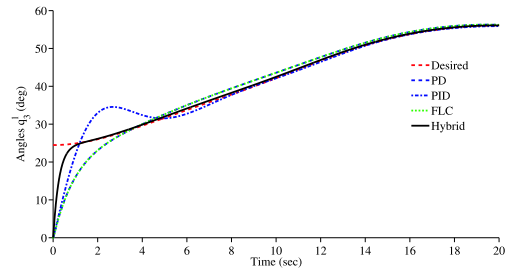
(c)



(d)



(e)



(f)

Figure 13: Tracking Errors and Desired/Actual Angles of Joints 1 (a,b), 2 (c,d) and 3 (e,f) for Three-Link Little Finger Using PD (dash line), PID (dot line), FL (short dash line) and hybrid of FL and PD (solid line) Controllers

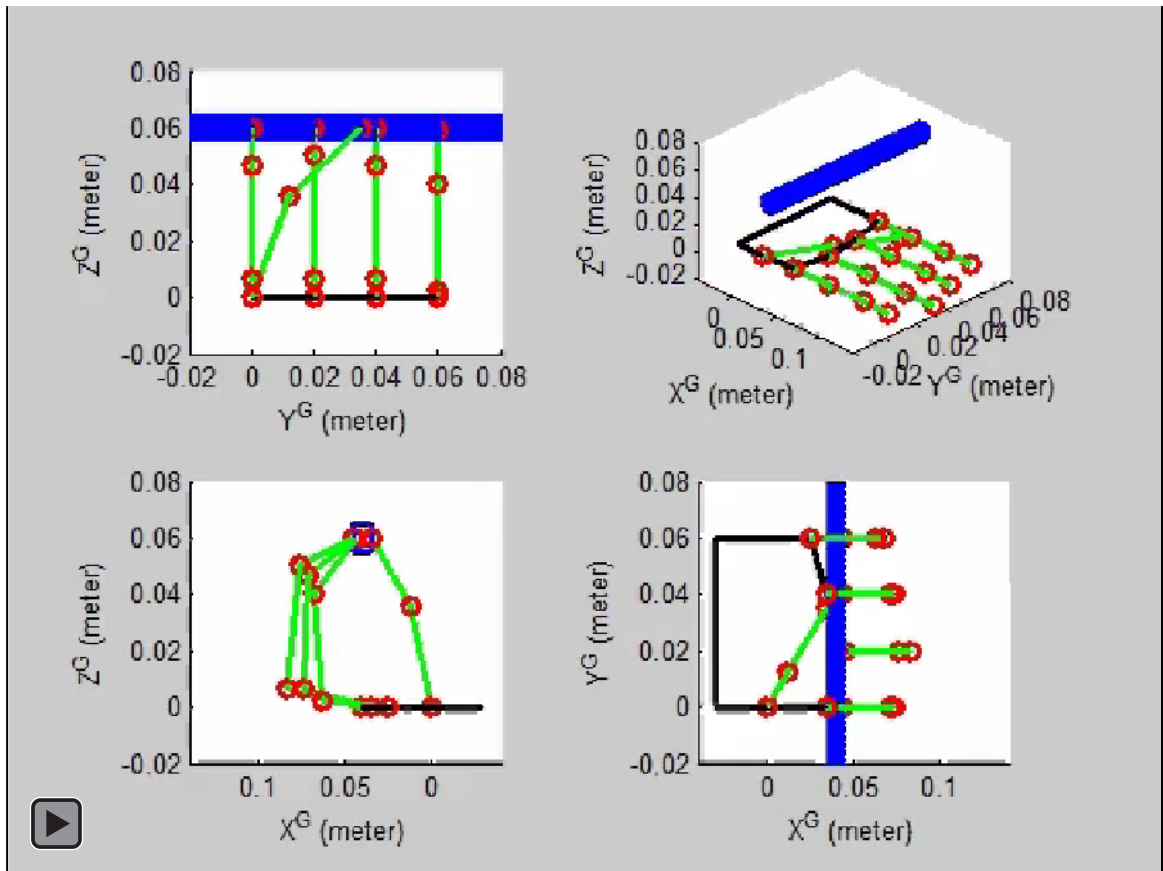


Figure 14: Hybrid Control Animation for a Five-Fingered Prosthetic Hand

# A New Optimal Control Strategy for a Five-Fingered Smart Prosthetic Hand

Cheng-Hung Chen\* and D. Subbaram Naidu

## Abstract

This paper addresses a new optimal control strategy for a five-fingered prosthetic hand, to speed up the performance and improve the accuracy, by modifying the performance index with an exponential term. First, the trajectory planning of the joints of each finger is designed by using cubic polynomial. Then the dynamic equations of the prosthetic hand and feedback linearization technique are employed. Next, the optimal control method with modified performance index is applied to the prosthetic hand. Finally, simulations show that the proposed technique provides much faster response with high accuracy compared to adaptive neuro-fuzzy inference system (ANFIS) based inverse kinematics for trajectory planning and PID control.

## Index Terms

Prosthetic Hand, Optimal Control, Hard Control, PID Control, Trajectory Planning, ANFIS

## I. INTRODUCTION

During the recent wars in Afghanistan and Iraq, “at least 919,967 people have been killed and 1,739,547 people have been seriously wounded” [1]. Further, in the United States, the Amputee Coalition of America (ACA) [2] reports that there are approximately 2 million people living with limb loss, due to combat operations (such as conflicts, wars etc.), and non-combat operations such as accidents, or birth defects. According to a study of the National Health Interview Survey

*Asterisk indicates corresponding author.*

\*Cheng-Hung Chen is with Measurement and Control Engineering Research Center and Department of Biological Sciences, Idaho State University, 921 South 8th Avenue Stop 8007, Pocatello, Idaho 83209, USA (email: chenchen@isu.edu).

D. Subbaram Naidu is with Measurement and Control Engineering Research Center and School of Engineering, Idaho State University, 921 South 8th Avenue Stop 8060, Pocatello, Idaho 83209, USA (email: naiduds@isu.edu).

(NHIS) published by Vital and Health Statistics [3], it is estimated that one out of every 200 people in the U.S. has had an amputation. In other words, about one in every 2,000 new born babies will have limb deficiency and over 3,000 people lose a limb every week in America. By the year 2050, the projected number of Americans living with limb amputation will become 3.6 million [4]. In the past several decades, prosthetic hands have been developed by various researchers in the field [5–10], but reproducing the human hand in all its various functions, appearance, visibility, and weight is still a challenging task [5].

In the research and development of a prosthetic hand using non-invasive techniques, the three basic problems are, first, electromyographic (EMG) signal acquisition, and classification to correspond to various human-like operations or features; second, conversion of EMG feature signals to control signals to input to actuators to operate the prosthetic hand; third, design and building of a prosthetic hand with necessary sensors to operate according to the control signal that corresponds to the EMG signal intended for the particular identified hand operation. Figure 1 shows the schematic diagram of our smart prosthetic hand technology. The overall system, in

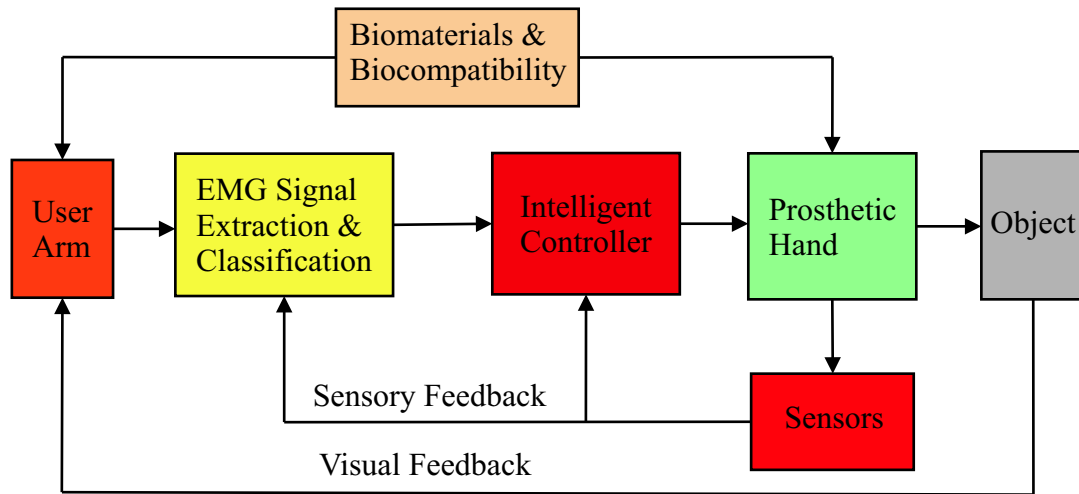


Fig. 1. Schematic diagram of prosthetic hand technology.

brief, consists of EMG signal acquisition from the user arm for surface or implanted electrodes (in the implanted case we focus on biocompatibility based on nano-materials research). The EMG signal is then processed for feature extraction and classification or identification of EMG signal to correspond to different motions of the prosthetic hand. The classified signal is then

used to control the prosthetic hand using actuators and driving mechanisms. This paper focuses on studying the intelligent control strategy.

Soft computing/control (SC) or computational intelligence (CI) [11] is an emerging field based on synergy and seamless integration of neural network (NN), fuzzy logic (FL) and genetic algorithm (GA) and the SC can be used at upper levels of the overall mission where human involvement and decision making is of primary importance. Several SC techniques have been applied to prosthetic hands. Hard computing/control (HC) techniques comprise proportional-integral-derivative (PID) control [12, 13], force-derivative feedback control [14], force-velocity control [15], proportional-derivative (PD) control [16, 17], optimal control [18–21], adaptive control [22–25] etc. with specific applications to prosthetic devices. Unlike SC, HC can be used at lower levels for accuracy, precision, stability and robustness. Recently, the authors conducted an overview of control strategies for prosthetic hands [8, 10]. However, our previous work [19] for a five-fingered smart prosthetic hand showed that PID control results in overshooting and oscillation, which were also demonstrated by Subudhi and Morris [26]. Optimal control can obtain a high performance [19], but requires large computational time. To overcome the overshooting and convergent problems, a novel finite-time optimal control strategy for a 14 degrees of freedom (DOFs) prosthetic hand is precisely the main goal of this work.

In this paper, we first consider briefly kinematics and trajectory planning. The trajectory planning using cubic polynomial employs desired angular positions to avoid inverse kinematics problems. Then the dynamic models of the smart prosthetic hand and feedback linearization technique are briefly introduced. Finally, the new finite-time linear quadratic optimal controllers are investigated using exponential term in the cost function. Simulation results demonstrate the proposed technique giving fast response and high accuracy without increasing computational time for the five-fingered smart prosthetic hand.

## II. MODELING

A normal human hand has 23 DOFs, including 4 DOFs from four fingers (2 at metacarpal-phalangeal [MCP] joint, 1 at proximal phalangeal [PIP] joint and 1 at distal interphalangeal [DIP] joint), 3 DOFs from thumb (2 at MCP joint and 1 at interphalangeal [IP] joint), 2 DOFs from wrist and 2 DOFs from carpometacarpal (CMC) joint [27]. In this work, we model a 14 DOFs, five-fingered prosthetic hand with two-link thumb and the remaining three-link fingers.

$q_1^j$ ,  $q_2^j$  and  $q_3^j$  ( $j = i, m, r$  and  $l$ ) represent the angular positions (or joint angles) of the first joint  $MCP^j$ , second joint  $PIP^j$  and third joint  $DIP^j$  of index, middle, ring and little fingers, respectively;  $q_1^t$  and  $q_2^t$  are the angular positions of the first joint  $MCP^t$  and the second joint  $IP^t$  of thumb ( $t$ ), respectively. In this section, we briefly describe kinematics and trajectory planning problems and dynamics of the hand.

#### A. Kinematics and Trajectory Planning

Kinematics is the study of geometry in motion and it is restricted to a natural geometrical description of motion by the manners, including positions, orientations, and their derivatives (velocities and accelerations). The kinematic descriptions of prosthetic hands are used to derive the fundamental equations for dynamics and control purposes. Forward and inverse kinematics of articulated systems study the analytical relationship between the angular positions of joints and the positions and orientations of fingertips. The forward and inverse kinematics for the two-link thumb and the remaining three-link fingers were derived in our previous work [24]. Also our previous works [19, 23] showed that the adaptive neuro-fuzzy inference system (ANFIS) and GA based trajectory planning take more computational time to solve inverse kinematics, especially for high DOFs problems. To overcome this problem, the present work obtains the desired angular position of each joint using cubic polynomial after the initial and targeted angular positions are determined.

The trajectory planning using cubic polynomial for angular position control is derived for all fingers. A time history of desired ( $d$ ) angular position ( $q_{dk}^j$ ), angular velocity ( $\dot{q}_{dk}^j$ ) and angular acceleration ( $\ddot{q}_{dk}^j$ ) for the joint  $i$  of each finger  $j$  is given as

$$q_{dk}^j(t) = A_{0k} + A_{1k}t + A_{2k}t^2 + A_{3k}t^3, \quad (1)$$

$$\dot{q}_{dk}^j(t) = A_{1k} + 2A_{2k}t + 3A_{3k}t^2, \quad (2)$$

$$\ddot{q}_{dk}^j(t) = 2A_{2k} + 6A_{3k}t, \quad (3)$$

where  $A_{0k}$ - $A_{3k}$  are the undetermined constants of each joint  $k$  and the superscript  $j$  indicates the index of each finger ( $j = t, i, m, r$  and  $l$ ). The relations (1) and (2) for each joint need to satisfy the constraint conditions,  $q_d(t_0)$ ,  $q_d(t_f)$ ,  $\dot{q}_d(t_0)$  and  $\dot{q}_d(t_f)$ , at initial time  $t_0$  and terminal time  $t_f$ . This can be written as

$$\mathbf{T} \mathbf{A} = \mathbf{z}. \quad (4)$$

Here,  $\mathbf{T}$ ,  $\mathbf{A}$  and  $\mathbf{z}$  are

$$\mathbf{T} = \begin{bmatrix} 1 & t_0 & t_0^2 & t_0^3 \\ 1 & t_f & t_f^2 & t_f^3 \\ 0 & 1 & 2t_0 & 3t_0^2 \\ 0 & 1 & 2t_f & 3t_f^2 \end{bmatrix}, \quad (5)$$

$$\mathbf{A} = \begin{bmatrix} A_0 & A_1 & A_2 & A_3 \end{bmatrix}', \quad (6)$$

$$\mathbf{z} = \begin{bmatrix} q_d(t_0) & q_d(t_f) & \dot{q}_d(t_0) & \dot{q}_d(t_f) \end{bmatrix}'. \quad (7)$$

Therefore, the 4 unknown constants,  $A_0$ - $A_3$ , can be computed by  $\mathbf{A} = \mathbf{T}^{-1}\mathbf{z}$  provided  $\mathbf{T}^{-1}$  exists. The notation  $'$  means the transpose.

For the five-fingered hand shown in Figure 2,  $X^G$ ,  $Y^G$ , and  $Z^G$  are the three axes of global

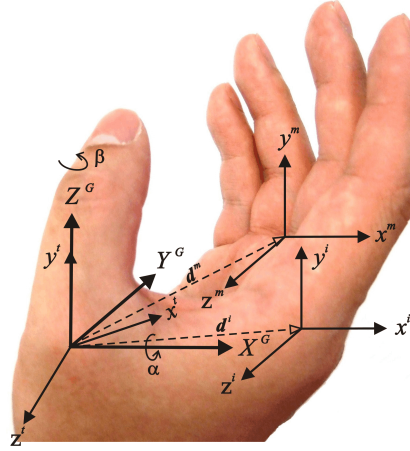


Fig. 2. Relationship between global coordinate and local coordinates.

coordinate system. The local coordinate  $x^t$ - $y^t$ - $z^t$  of thumb can be reached by rotating through angles  $\alpha$  and  $\beta$  to  $X^G$  and  $Y^G$  of the global coordinate, subsequently. The local coordinate  $x^i$ - $y^i$ - $z^i$  of index finger can be obtained by rotating through angle  $\alpha$  to  $X^G$  and then translating the vector  $\mathbf{d}^i$  of the global coordinate; similarly, the local coordinate  $x^j$ - $y^j$ - $z^j$  of middle finger ( $j = m$ ), ring finger ( $j = r$ ), and little finger ( $j = l$ ) can be obtained by rotating through angle  $\alpha$  to  $X^G$  and then translating the vector  $\mathbf{d}^j$  ( $j = m, r$  and  $l$ ) of the global coordinate.



### B. Dynamics of the Hand

The dynamic equations of hand motion are derived via Lagrangian approach using kinetic energy and potential energy as [28]

$$\frac{d}{dt} \left( \frac{\partial \mathcal{L}(t)}{\partial \dot{\mathbf{q}}(t)} \right) - \frac{\partial \mathcal{L}(t)}{\partial \mathbf{q}(t)} = \boldsymbol{\tau}(t), \quad (8)$$

where  $\mathcal{L}(t)$  is Lagrangian;  $\dot{\mathbf{q}}(t)$  and  $\mathbf{q}(t)$  represent the angular velocity and position vectors of joints, respectively;  $\boldsymbol{\tau}(t)$  is the given torque vector at joints. The Lagrangian  $\mathcal{L}(t)$  can be expressed as

$$\mathcal{L}(t) = T(t) - V(t), \quad (9)$$

where  $T(t)$  and  $V(t)$  denote kinetic and potential energies at time  $t$ , respectively. Substituting (9) into (8), dynamic equations of thumb and all fingers can be obtained as below.

$$\mathbf{M}(\mathbf{q}(t))\ddot{\mathbf{q}}(t) + \mathbf{C}(\mathbf{q}(t), \dot{\mathbf{q}}(t)) + \mathbf{G}(\mathbf{q}(t)) = \boldsymbol{\tau}(t), \quad (10)$$

where  $\mathbf{M}(\mathbf{q}(t))$  is the inertia matrix;  $\mathbf{C}(\mathbf{q}(t), \dot{\mathbf{q}}(t))$  is the Coriolis/centripetal vector and  $\mathbf{G}(\mathbf{q}(t))$  is the gravity vector. Then, (10) can be also written as

$$\mathbf{M}(\mathbf{q}(t))\ddot{\mathbf{q}}(t) + \mathbf{N}(\mathbf{q}(t), \dot{\mathbf{q}}(t)) = \boldsymbol{\tau}(t), \quad (11)$$

where  $\mathbf{N}(\mathbf{q}(t), \dot{\mathbf{q}}(t)) = \mathbf{C}(\mathbf{q}(t), \dot{\mathbf{q}}(t)) + \mathbf{G}(\mathbf{q}(t))$  represents nonlinear terms. The dynamic relations for the two-link thumb and all three-link fingers are detailed in our previous work [24].

## III. CONTROL STRATEGIES

### A. Feedback Linearization

The nonlinear dynamics (11) is to be put into a linear state-variable system using feedback linearization technique. Alternative state-space equations of the dynamics can be obtained by defining the angular position/velocity state  $\mathbf{x}(t)$  of the joints as

$$\mathbf{x}(t) = [\mathbf{q}'(t) \quad \dot{\mathbf{q}}'(t)]'. \quad (12)$$

$\mathbf{q}'(t)$  and  $\dot{\mathbf{q}}'(t)$  are the transpose vectors of  $\mathbf{q}(t)$  and  $\dot{\mathbf{q}}(t)$ , respectively. Let us repeat the dynamical model and rewrite (11) as

$$\frac{d}{dt} \dot{\mathbf{q}}(t) = -\mathbf{M}^{-1}(\mathbf{q}(t)) [\mathbf{N}(\mathbf{q}(t), \dot{\mathbf{q}}(t)) - \boldsymbol{\tau}(t)]. \quad (13)$$

Thus, from (12) and (13), we can derive a *linear* system in Brunovsky canonical form as

$$\begin{aligned}\dot{\mathbf{x}}(t) &= \begin{bmatrix} \mathbf{0} & \mathbf{I} \\ \mathbf{0} & \mathbf{0} \end{bmatrix} \mathbf{x}(t) + \begin{bmatrix} \mathbf{0} \\ \mathbf{I} \end{bmatrix} \mathbf{u}(t) \\ &= \mathbf{A}\mathbf{x}(t) + \mathbf{B}\mathbf{u}(t).\end{aligned}\tag{14}$$

with its control input vector given by

$$\mathbf{u}(t) = -\mathbf{M}^{-1}(\mathbf{q}(t)) [\mathbf{N}(\mathbf{q}(t), \dot{\mathbf{q}}(t)) - \boldsymbol{\tau}(t)].\tag{15}$$

Then the required torque of all joints can be calculated by

$$\boldsymbol{\tau}(t) = \mathbf{M}(\mathbf{q}(t))\mathbf{u}(t) + \mathbf{N}(\mathbf{q}(t), \dot{\mathbf{q}}(t)).\tag{16}$$

### B. Linear Quadratic Optimal Control with Tracking System

Our objective is to control the linear system (14) in such a way that the state variable  $\mathbf{x}(t) = [\mathbf{q}'(t) \ \dot{\mathbf{q}}'(t)]'$  tracks the *desired* output  $\mathbf{z}(t) = [\mathbf{q}'_d(t) \ \dot{\mathbf{q}}'_d(t)]'$  as close as possible during the interval  $[t_0, t_f]$  with minimum control energy. For this, let us define the *error* vector as

$$\mathbf{e}(t) = \mathbf{z}(t) - \mathbf{x}(t),\tag{17}$$

and choose the performance index  $J$  [18] as

$$\begin{aligned}J &= \frac{1}{2} \mathbf{e}'(t_f) \mathbf{F}(t_f) \mathbf{e}(t_f) \\ &\quad + \frac{1}{2} \int_{t_0}^{t_f} [\mathbf{e}'(t) \mathbf{Q} \mathbf{e}(t) + \mathbf{u}'(t) \mathbf{R} \mathbf{u}(t)] dt.\end{aligned}\tag{18}$$

We assume that  $\mathbf{F}(t_f)$  and  $\mathbf{Q}$  are symmetric, *positive semidefinite* matrices, and  $\mathbf{R}$  is symmetric, *positive definite* matrix. We use Pontryagin Minimum Principle [18] and then solve the matrix differential Riccati equation (DRE)

$$\dot{\mathbf{P}}(t) = -\mathbf{P}(t)\mathbf{A} - \mathbf{A}'\mathbf{P}(t) + \mathbf{P}(t)\mathbf{B}\mathbf{R}^{-1}\mathbf{B}'\mathbf{P}(t) - \mathbf{Q},\tag{19}$$

with final condition  $\mathbf{P}(t_f) = \mathbf{F}(t_f)$ , and the non-homogeneous vector differential equation

$$\dot{\mathbf{g}}(t) = -[\mathbf{A} - \mathbf{B}\mathbf{R}^{-1}\mathbf{B}'\mathbf{P}(t)]' \mathbf{g}(t) - \mathbf{Q}\mathbf{z}(t),\tag{20}$$

with final condition  $\mathbf{g}(t_f) = \mathbf{F}(t_f)\mathbf{z}(t_f)$ . Then the optimal state  $\mathbf{x}^*(t)$  can be solved from

$$\dot{\mathbf{x}}^*(t) = [\mathbf{A} - \mathbf{B}\mathbf{R}^{-1}\mathbf{B}'\mathbf{P}(t)] \mathbf{x}^*(t) + \mathbf{B}\mathbf{R}^{-1}\mathbf{B}'\mathbf{g}(t)\tag{21}$$

with initial condition  $\mathbf{x}(t_0)$  and optimal control  $\mathbf{u}^*(t)$  is calculated by

$$\mathbf{u}^*(t) = -\mathbf{R}^{-1}\mathbf{B}'\mathbf{P}(t)\mathbf{x}^*(t) + \mathbf{R}^{-1}\mathbf{B}'\mathbf{g}(t). \quad (22)$$

Finally, the optimal required torque  $\tau^*(t)$  is obtained by

$$\tau^*(t) = \mathbf{M}(\mathbf{q}(t))\mathbf{u}^*(t) + \mathbf{N}(\mathbf{q}(t), \dot{\mathbf{q}}(t)). \quad (23)$$

Summarizing, Figure 3 shows the block diagram of a finite-time linear quadratic optimal con-

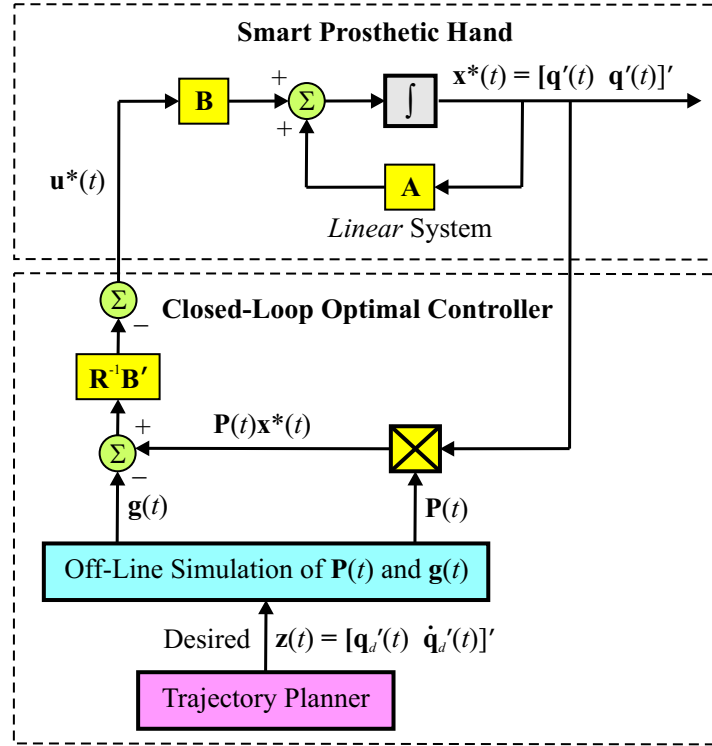


Fig. 3. Block diagram of the linear quadratic optimal controller tracking system for the five-fingered prosthetic hand.

troller tracking system for the prosthetic hand. Use of feedback linearization technique converts the nonlinear dynamics to be linear. Then the closed-loop finite-time linear quadratic optimal controller through Pontryagin Minimum Principle is implemented to track the desired trajectory planning using cubic polynomial.  $\mathbf{P}(t)$  and  $\mathbf{g}(t)$  are computed by solving the matrix differential Riccati and the non-homogeneous vector differential equations with boundary conditions, respectively. Finally, the optimal state  $\mathbf{x}^*(t)$  and optimal control  $\mathbf{u}^*(t)$  are obtained in order to calculate the required torque  $\tau^*(t)$ .

### C. A New Optimal Control with Tracking System

Our previous work [19] shows that the original optimal control can avoid overshooting and oscillation problems and get better results than PID control, but this optimal control method takes execution time when applied to prosthetic hand. To improve the performance of the original optimal controller, we propose to change the performance index  $J$  [18] to include exponential term as

$$\begin{aligned}\hat{J} = & \frac{1}{2}e^{2\alpha t_f}\mathbf{e}'(t_f)\mathbf{F}(t_f)\mathbf{e}(t_f) \\ & + \frac{1}{2}\int_{t_0}^{t_f} e^{2\alpha t} [\mathbf{e}'(t)\mathbf{Q}\mathbf{e}(t) + \mathbf{u}'(t)\mathbf{R}\mathbf{u}(t)] dt\end{aligned}\quad (24)$$

where  $\alpha$  is a positive parameter. We need to find the optimal control which minimizes the new performance index  $\hat{J}$  (24) under the dynamical constraint (14). This problem can be solved by modifying the original system, so the following transformations can be developed as

$$\begin{aligned}\hat{\mathbf{e}}(t) &= e^{\alpha t}\mathbf{e}(t); & \hat{\mathbf{z}}(t) &= e^{\alpha t}\mathbf{z}(t); \\ \hat{\mathbf{x}}(t) &= e^{\alpha t}\mathbf{x}(t); & \hat{\mathbf{u}}(t) &= e^{\alpha t}\mathbf{u}(t).\end{aligned}\quad (25)$$

Then, using the transformations (24), it is easy to see that the *new* system becomes

$$\begin{aligned}\dot{\hat{\mathbf{x}}}(t) &= \frac{d}{dt}\{e^{\alpha t}\mathbf{x}(t)\} = \alpha e^{\alpha t}\mathbf{x}(t) + e^{\alpha t}\dot{\mathbf{x}}(t) \\ &= \alpha\hat{\mathbf{x}}(t) + e^{\alpha t}[\mathbf{A}\mathbf{x}(t) + \mathbf{B}\mathbf{u}(t)] \\ \dot{\hat{\mathbf{x}}}(t) &= (\mathbf{A} + \alpha\mathbf{I})\hat{\mathbf{x}}(t) + \mathbf{B}\hat{\mathbf{u}}(t).\end{aligned}\quad (26)$$

Considering the minimization of the modified system defined by (26) and (24), the new optimal control  $\hat{\mathbf{u}}^*(t)$ , which is similar to (22), is given by

$$\hat{\mathbf{u}}^*(t) = -\mathbf{R}^{-1}\mathbf{B}'\hat{\mathbf{P}}(t)\hat{\mathbf{x}}^*(t) + \mathbf{R}^{-1}\mathbf{B}'\hat{\mathbf{g}}(t) \quad (27)$$

where the matrix  $\hat{\mathbf{P}}(t)$  and the vector  $\hat{\mathbf{g}}(t)$  are, respectively, the solutions of DRE

$$\begin{aligned}\dot{\hat{\mathbf{P}}}(t) &= -\hat{\mathbf{P}}(t)(\mathbf{A} + \alpha\mathbf{I}) - (\mathbf{A}' + \alpha\mathbf{I})\hat{\mathbf{P}}(t) \\ &\quad + \hat{\mathbf{P}}(t)\mathbf{B}\mathbf{R}^{-1}\mathbf{B}'\hat{\mathbf{P}}(t) - \mathbf{Q},\end{aligned}\quad (28)$$

with final condition  $\hat{\mathbf{P}}(t_f) = \mathbf{F}(t_f)$ , and the non-homogeneous vector differential equation

$$\dot{\hat{\mathbf{g}}}(t) = -\left[\mathbf{A} + \alpha\mathbf{I} - \mathbf{B}\mathbf{R}^{-1}\mathbf{B}'\hat{\mathbf{P}}(t)\right]'\hat{\mathbf{g}}(t) - \mathbf{Q}\hat{\mathbf{z}}(t), \quad (29)$$

with final condition  $\hat{\mathbf{g}}(t_f) = \mathbf{F}(t_f)\hat{\mathbf{z}}(t_f)$ . Using the optimal control (27) in the new system (26), we get the optimal closed-loop system as

$$\dot{\mathbf{x}}^*(t) = \left[ \mathbf{A} + \alpha \mathbf{I} - \mathbf{B}\mathbf{R}^{-1}\mathbf{B}'\hat{\mathbf{P}}(t) \right] \mathbf{x}^*(t) + \mathbf{B}\mathbf{R}^{-1}\mathbf{B}'\hat{\mathbf{g}}(t) \quad (30)$$

with initial condition  $\mathbf{x}^*(t_0)$ .

Hence, applying the transformations (26) in the new system (27), the optimal control of the original system (14) and the associated performance measure (24) is given by

$$\begin{aligned} \mathbf{u}^*(t) &= e^{-\alpha t} \hat{\mathbf{u}}^*(t) = -e^{-\alpha t} \mathbf{R}^{-1} \mathbf{B}' \left[ \hat{\mathbf{P}}(t) \mathbf{x}^*(t) - \hat{\mathbf{g}}(t) \right] \\ &= -\mathbf{R}^{-1} \mathbf{B}' \hat{\mathbf{P}}(t) \mathbf{x}^*(t) + e^{-\alpha t} \mathbf{R}^{-1} \mathbf{B}' \hat{\mathbf{g}}(t). \end{aligned} \quad (31)$$

Interestingly, this desired (original) optimal control (31) has the same matrix DRE solutions  $\hat{\mathbf{P}}(t) = \mathbf{P}(t)$  as the optimal control (27) of the new system with  $\hat{\mathbf{g}}(t) = e^{\alpha t} \mathbf{g}(t)$  compared with (31) and (22). We see that the closed-loop optimal control system (30) has eigenvalues with real parts less than  $-\alpha$ . In other words, the state  $\mathbf{x}^*(t)$  approaches zero at least as fast as  $e^{-\alpha t}$ .

#### IV. SIMULATION RESULTS AND DISCUSSION

We present simulations with a PID controller and a new linear quadratic finite-time optimal controller with tracking system for the 14 DOFs, five-fingered smart prosthetic hand in order to grasp a rectangular object as shown in Figure 4.

When thumb and the other four fingers are doing extension/flexion movements, the workspace of fingertips is restricted to the maximum angles of joints. In this work, the first and second joint angles of the thumb are constrained in the ranges of  $[0, 90]$  and  $[-80, 0]$  (degrees) and the first, second, and third joint angles of the other four fingers are constrained in the ranges of  $[0, 90]$ ,  $[0, 110]$  and  $[0, 80]$  (degrees), respectively [29]. All parameters of the smart prosthetic hand selected for the simulations [30] are given in Table I and the side length and length of the targeted rectangular rod are 0.010 and 0.100 (m), respectively. The conversion parameters between the global coordinate and each local coordinate are defined in Table II. The links of all fingers are assumed as circular cylinders with the radius ( $R$ ) 0.010 (m) and the inertia  $I_{zzk}^j$  of each link  $k$  of all fingers  $j$  ( $= t, i, m, r$  and  $l$ ) can be calculated by

$$I_{zzk}^j = \frac{1}{4} m_k^j R^2 + \frac{1}{3} m_k^j L_k^{j^2}. \quad (32)$$

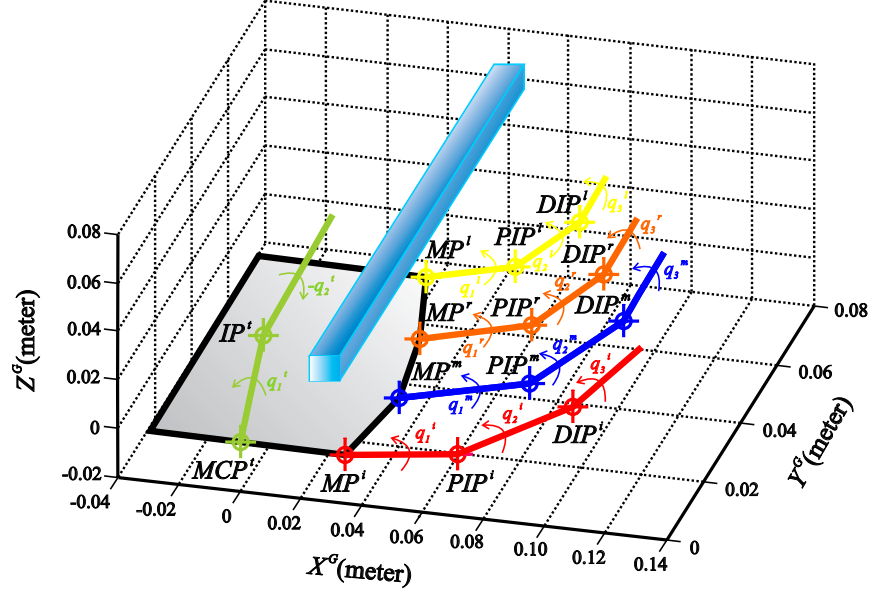


Fig. 4. A 14 degrees-of-freedom (DOFs), five-fingered prosthetic hand with two-link thumb and remaining three-link fingers grasping a rectangular object.

All initial actual angles are zero and the diagonal coefficients,  $K_P$ ,  $K_I$  and  $K_D$ , for the PID controller are *arbitrarily* chosen as 100. As for the coefficients of optimal control,  $A$ ,  $B$ ,  $F(t_f)$ ,  $R$  and  $Q$  of all fingers ( $j = i, m, r$ , and  $l$ ) are chosen as

$$A = \begin{bmatrix} 0 & I \\ 0 & 0 \end{bmatrix}, \quad B = \begin{bmatrix} 0 \\ I \end{bmatrix}, \quad F(t_f) = 0, \quad R = \frac{1}{30}I,$$

$$Q^t = \begin{bmatrix} Q_{11} & Q_{12} \\ Q'_{12} & Q_{22} \end{bmatrix}, \quad Q^j = \begin{bmatrix} Q_{11} & Q_{12} & Q_{13} \\ Q'_{12} & Q_{22} & Q_{23} \\ Q'_{13} & Q'_{23} & Q_{33} \end{bmatrix},$$

$$Q_{11} = \begin{bmatrix} 10 & 2 \\ 2 & 10 \end{bmatrix}, \quad Q_{22} = \begin{bmatrix} 30 & 0 \\ 0 & 30 \end{bmatrix}, \quad Q_{33} = \begin{bmatrix} 20 & 1 \\ 1 & 20 \end{bmatrix},$$

$$Q_{12} = \begin{bmatrix} -4 & 4 \\ 3 & -6 \end{bmatrix}, \quad Q_{13} = \begin{bmatrix} -4 & 4 \\ 3 & -6 \end{bmatrix}, \quad Q_{23} = \begin{bmatrix} -4 & 3 \\ 4 & -6 \end{bmatrix}.$$

To study the performance of the PID and new optimal controllers, Figure 5 and Figure 6

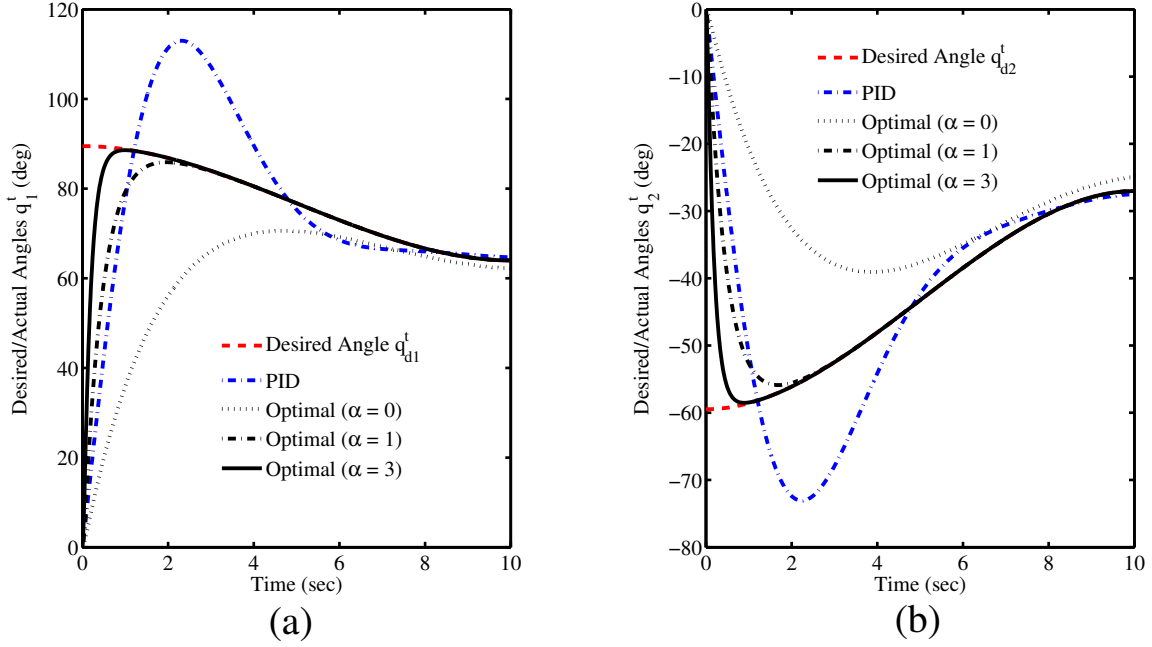


Fig. 5. Desired/actual angular positions of two-link thumb. The actual angles (a)  $q_1^t$  and (b)  $q_2^t$  regulated by PID controller and new optimal controller with the different parameters  $\alpha$  ( $\alpha = 0, 1$ , and  $3$ ) are designed to track the desired angles  $q_{d1}^t$  and  $q_{d2}^t$ .

show desired/actual angles and tracking errors of joints 1 and 2 for two-link thumb, respectively. PID control shows overshooting and oscillation problems. These problems are overcome by original optimal control ( $\alpha = 0$ ), but it takes at least 8 seconds for both joints. The performance is improved by the new optimal controller as the parameter  $\alpha$  increases. In other words, the convergent time is reduced to approximately 1 second as  $\alpha$  equals 3. Similar results are also demonstrated by three-link index finger as shown in Figure 7 and Figure 8. Similar simulations are also made for middle, ring and little fingers.

To investigate the effectiveness of the PID and new optimal controllers, Figure 9 shows that original ( $\alpha = 0$ ) and new optimal controllers ( $\alpha = 0.1, 1$ , and  $10$ ) are significantly more effective (in term of computational time) than PID controller, but there is no significance between the optimal controllers for all three-link fingers, suggesting that the new optimal control with high  $\alpha$  value improves performance without excessive execution time. To further study high DOFs inverse kinematics problems, this work develops desired angles using cubic polynomial to avoid calculating inverse kinematics at every instant of time for all three-link fingers. Figure 9 also shows this modified trajectory planning strategy significantly reduces computational time

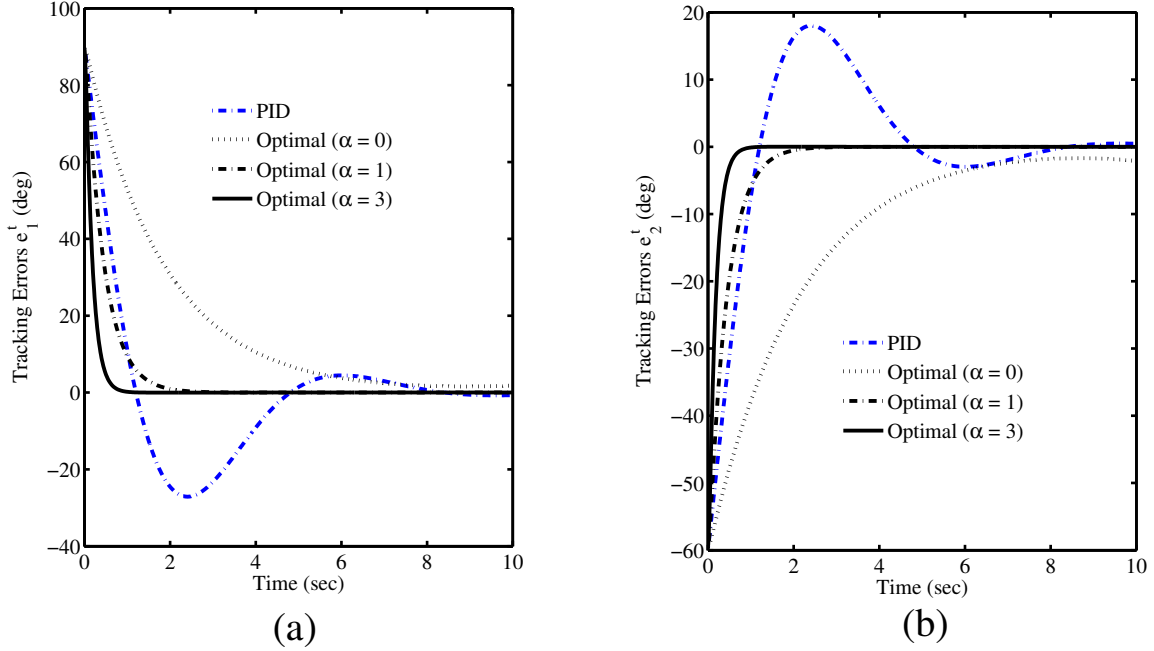


Fig. 6. Tracking errors of two-link thumb. The tracking errors (a)  $e_1^t$  and (b)  $e_2^t$  show that PID controller with arbitrary parameters has overshooting and oscillation problems, which are overcome by proposed new optimal controller with  $\alpha = 0, 1$ , and 3.

compared with ANFIS-based trajectory planning [19, 23] for both PID and optimal controllers. The data was simulated by a laptop with Intel® Core2 Duo CPU at 1.67 GHz.

## V. CONCLUSIONS AND FUTURE WORK

A new optimal control strategy for a 14 DOFs, five-fingered smart prosthetic hand was successfully developed to improve performance, convergence and computational time. A modified trajectory planning strategy using cubic polynomial to track each angular position was designed to avoid computing inverse kinematics at every instant of time. This new optimal control strategy will be tested and validated with real data from surface EMG (sEMG) signals for operation of prosthetic hand devices.

## ACKNOWLEDGMENT

The research was sponsored by the U.S. Department of the Army, under the award number W81XWH-10-1-0128 awarded and administered by the U.S. Army Medical Research Acquisition



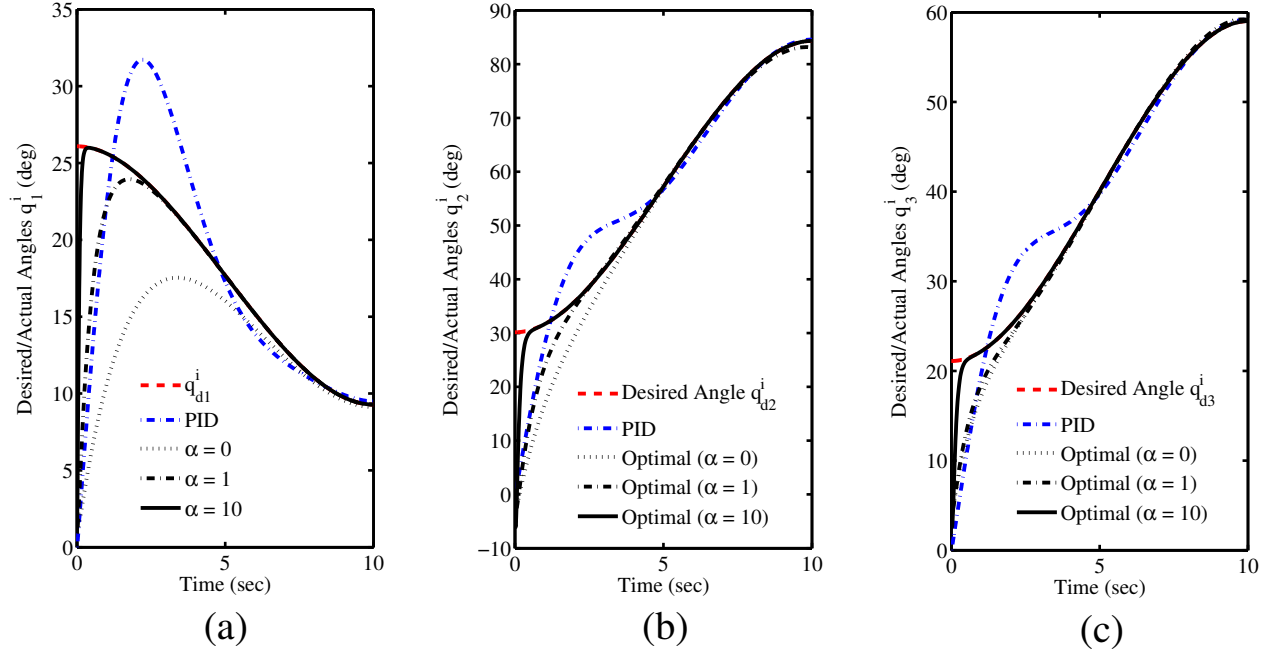


Fig. 7. Desired/actual angular positions of three-link index finger. The actual angles (a)  $q_1^i$ , (b)  $q_2^i$  and (c)  $q_3^i$  regulated by PID controller and new optimal controller with the different parameters  $\alpha$  ( $\alpha = 0, 1$ , and  $10$ ) are designed to track the desired angles  $q_{d1}^i$ ,  $q_{d2}^i$  and  $q_{d3}^i$ , respectively.

Activity, 820 Chandler Street, Fort Detrick, MD 21702-5014, USA. The information does not necessarily reflect the position or the policy of the Government, and no official endorsement should be inferred. For purposes of this article, information includes news releases, articles, manuscripts, brochures, advertisements, still and motion pictures, speeches, trade association proceedings, etc.

## REFERENCES

- [1] "Casualties in Afghanistan & Iraq," <http://www.unknownnews.org/casualties.html>, August 10 2010.
- [2] "Amputee Coalition of America (ACA) National Limb Loss Information Center (NL-LIC) Limb Loss Facts in the United States," <http://www.amputee-coalition.org/Limb-Loss-Awareness/index.php/aboutllam>, March, 10 2011.
- [3] P. F. Adams, G. E. Hendershot, and M. A. Marano, "Current estimates from the national

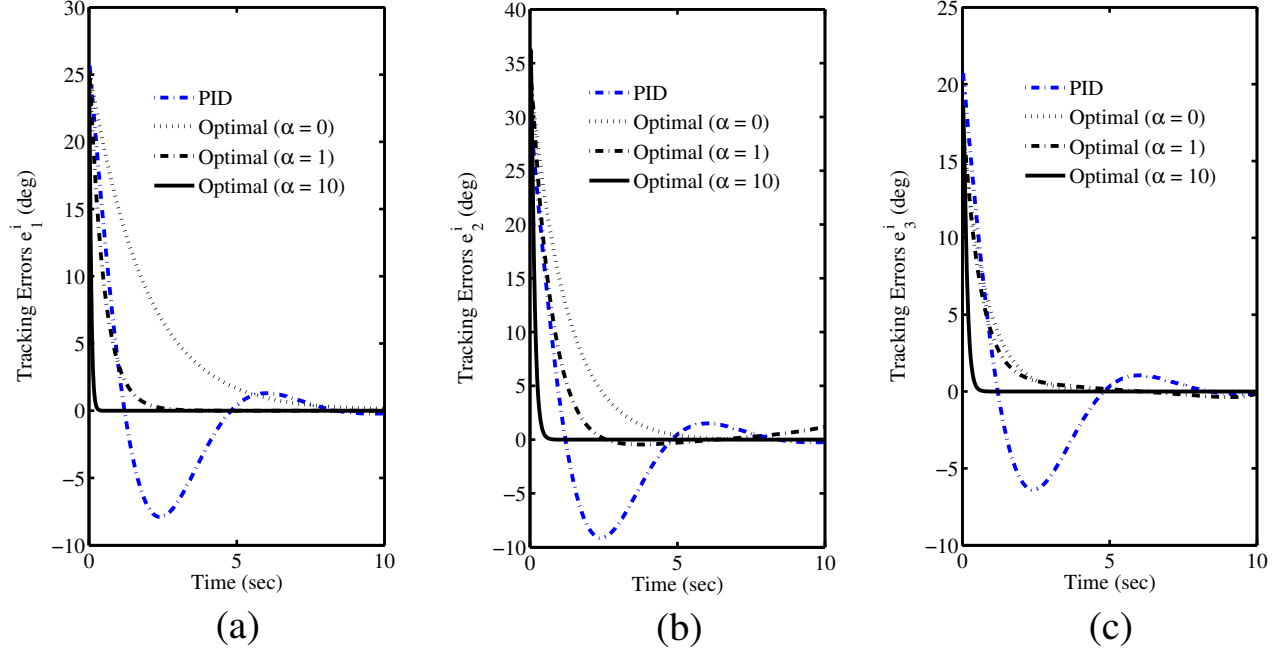


Fig. 8. Tracking errors of three-link index finger. The tracking errors (a)  $e_1^i$ , (b)  $e_2^i$  and (c)  $e_3^i$  show that the new optimal controller acts faster than PID controller as the parameter  $\alpha$  increases.

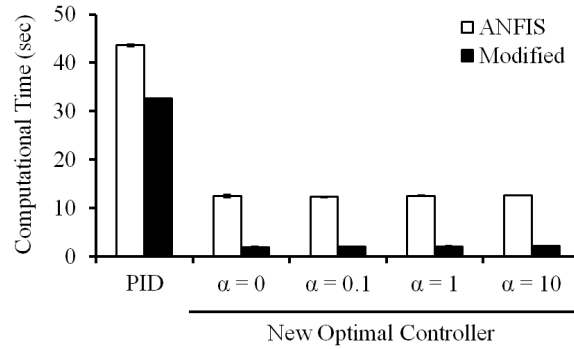


Fig. 9. The new optimal controller and trajectory planning using cubic polynomial without calculating inverse kinematics reduce execution time.

health interview survey, 1996.” *National Center for Health Statistics. Vital and Health Statistics*, vol. 200, no. 10, pp. 1–203, 1999.

- [4] K. Ziegler-Graham, E. J. MacKenzie, P. L. Ephraim, T. G. Travison, and R. Brookmeyer, “Estimating the prevalence of limb loss in the united states: 2005 to 2050,” *Archives of Physical Medicine and Rehabilitation*, vol. 89, pp. 422–429, March 2008.

- [5] M. Zecca, S. Micera, M. Carrozza, and P. Dario, "Control of multifunctional prosthetic hands by processing the electromyographic signal," *Critical Reviews<sup>TM</sup> in Biomedical Engineering*, vol. 30, pp. 459–485, 2002, (Review article with 96 references).
- [6] J. C. K. Lai, M. P. Schoen, A. Perez-Gracia, D. S. Naidu, and S. W. Leung, "Prosthetic devices: Challenges and implications of robotic implants and biological interfaces," *Proceedings of the Institute of Mechanical Engineers (IMechE), Part H: Journal of Engineering in Medicine*, vol. 221, no. 2, pp. 173–183, January 2007, special Issue on Micro and Nano Technologies in Medicine.
- [7] L. Zollo, S. Roccella, E. Guglielmelli, M. C. Carrozza, and P. Dario, "Biomechatronic design and control of an anthropomorphic artificial hand for prosthetic and robotic applications," *IEEE/ASME Transactions on Mechatronics*, vol. 12, no. 4, pp. 418–429, August 2007.
- [8] D. S. Naidu, C.-H. Chen, A. Perez, and M. P. Schoen, "Control strategies for smart prosthetic hand technology: An overview," in *The 30th Annual International Conference of the IEEE Engineering Medicine and Biology Society (EMBS)*, Vancouver, Canada, August 20-24 2008, pp. 4314–4317.
- [9] S. Micera, J. Carpaneto, and S. Raspopovic, "Control of hand prostheses using peripheral information," *IEEE Reviews in Biomedical Engineering*, vol. 3, pp. 48–68, 2010, (Review article with 161 references).
- [10] D. S. Naidu and C.-H. Chen, *Automatic Control Techniques for Smart Prosthetic Hand Technology: An Overview, book chapter 12, to appear in a book titled "Distributed Diagnosis and Home Healthcare (D<sub>2</sub>H<sub>2</sub>): Volume 2"*. California, USA: American Scientific Publishers, 2011.
- [11] A. Konar, *Computational Intelligence: Principles, Techniques and Applications*. Berlin, Germany: Springer-Verlag, 2005.
- [12] C.-H. Chen, K. W. Bosworth, M. P. Schoen, S. E. Bearden, D. S. Naidu, and A. Perez-Gracia, "A study of particle swarm optimization on leukocyte adhesion molecules and control strategies for smart prosthetic hand," in *2008 IEEE Swarm Intelligence Symposium (IEEE SIS08)*, St. Louis, Missouri, USA, September 21-23 2008.
- [13] C.-H. Chen, D. S. Naidu, A. Perez-Gracia, and M. P. Schoen, "Fusion of hard and soft control techniques for prosthetic hand," in *Proceedings of the International Association of*

*Science and Technology for Development (IASTED) International Conference on Intelligent Systems and Control (ISC 2008)*, Orlando, Florida, USA, November 16-18 2008, pp. 120–125.

- [14] E. D. Engeberg and S. G. Meek, “Improved grasp force sensitivity for prosthetic hands through force-derivative feedback,” *IEEE Transactions on Biomedical Engineering*, vol. 55, no. 2, pp. 817–821, 2008.
- [15] E. D. Engeberg, S. G. Meek, and M. A. Minor, “Hybrid force velocity sliding mode control of a prosthetic hand,” *IEEE Transactions on Biomedical Engineering*, vol. 55, no. 5, pp. 1572–1581, 2008.
- [16] R. Okuno, M. Yoshida, and K. Akazawa, “Compliant grasp in a myoelectric hand prosthesis,” *IEEE Engineering in Medicine and Biology Magazine*, vol. 24, no. 2, pp. 48–56, July-August 2005.
- [17] H. K. Kim, S. J. Biggs, D. W. Schloerb, J. M. Carmenta, M. A. Lebedev, M. A. L. Nicolelis, and M. A. Srinivasan, “Continuous shared control for stabilizing reaching and grasping with brain-machine interfaces,” *IEEE Transactions on Biomedical Engineering*, vol. 53, no. 6, pp. 1164–1173, June 2006.
- [18] D. Naidu, *Optimal Control Systems*. Boca Raton, FL: CRC Press, 2003.
- [19] C.-H. Chen, D. S. Naidu, A. Perez-Gracia, and M. P. Schoen, “A hybrid control strategy for five-fingered smart prosthetic hand,” in *Joint 48th IEEE Conference on Decision and Control (CDC) and 28th Chinese Control Conference (CCC)*, Shanghai, P. R. China, December 16-18 2009, pp. 5102–5107.
- [20] C.-H. Chen and D. S. Naidu, “Optimal control strategy for two-fingered smart prosthetic hand,” in *Proceedings of the International Association of Science and Technology for Development (IASTED) International Conference on Robotics and Applications (RA 2010)*, Cambridge, Massachusetts, USA, November 1-3 2010, pp. 190–196.
- [21] D. Vrabie, F. Lewis, and M. Abu-Khalaf, “Biologically inspired scheme for continuous-time approximate dynamic programming,” *Transactions of the Institute of Measurement and Control*, vol. 30, pp. 207–223, 2008.
- [22] F. Lewis, D. Dawson, and C. Abdallah, *Robot Manipulators Control: Second Edition, Revised and Expanded*. New York, NY: Marcel Dekker, Inc., 2004.
- [23] C.-H. Chen, D. S. Naidu, A. Perez-Gracia, and M. P. Schoen, “A hybrid adaptive control

- strategy for a smart prosthetic hand,” in *The 31st Annual International Conference of the IEEE Engineering Medicine and Biology Society (EMBS)*, Minneapolis, Minnesota, USA, September 2-6 2009, pp. 5056–5059.
- [24] C.-H. Chen, D. S. Naidu, and M. P. Schoen, “Adaptive control for a five-fingered prosthetic hand with unknown mass and inertia,” *World Scientific and Engineering Academy and Society (WSEAS) Journal on Systems*, vol. 10, no. 5, pp. 148–161, May 2011.
- [25] F. Lewis, S. Jagannathan, and A. Yesildirek, *Neural Network Control of Robotic Manipulators and Nonlinear Systems*. London, UK: Taylor & Francis, 1999.
- [26] B. Subudhi and A. S. Morris, “Soft computing methods applied to the control of a flexible robot manipulator,” *Applied Soft Computing*, vol. 9, pp. 149–158, 2009.
- [27] R. R. Seeley, T. D. Stephens, and P. Tate, *Anatomy & Physiology, Eighth Edition*. New York, NY: The McGraw-Hill, 2007.
- [28] B. Siciliano, L. Sciavicco, L. Villani, and G. Oriolo, *Robotics: Modelling, Planning and Control*. London, UK: Springer-Verlag, 2009.
- [29] P. K. Lavangie and C. C. Norkin, *Joint Structure and Function: A Comprehensive Analysis, Third Edition*. Philadelphia, PA: F. A. Davis Company, 2001.
- [30] S. Arimoto, *Control Theory of Multi-fingered Hands: A Modeling and Analytical-Mechanics Approach for Dexterity and Intelligence*. London, UK: Springer-Verlag, 2008.

TABLE I  
PARAMETER SELECTION OF THE SMART PROSTHETIC HAND

Parameters	Values
<b>Thumb</b>	
Time Interval $[t_0, t_f]^*$	[0, 10] (sec)
Desired Initial Angle $[q_{d1}^t, q_{d2}^t]^{**}$	[89.48, -59.48] (deg)
Desired Final Angle $[q_{d1}^t, q_{d2}^t]^{**}$	[63.99, -27.04] (deg)
Desired Initial Angular Velocity $[\dot{q}_{d1}^t, \dot{q}_{d2}^t]^*$	[0, 0] (deg/s)
Desired Final Angular Velocity $[\dot{q}_{d1}^t, \dot{q}_{d2}^t]^*$	[0, 0] (deg/s)
Length $[L_1^t, L_2^t]$	[0.040, 0.040] (m)
Mass $[m_1^t, m_2^t]$	[0.043, 0.031] (kg)
<b>Index Finger</b>	
$[q_{d1}^i, q_{d2}^i, q_{d3}^i]$ at $t = t_0^{**}$	[26.09, 30.15, 21.10] (deg)
$[q_{d1}^i, q_{d2}^i, q_{d3}^i]$ at $t = t_f^{**}$	[9.28, 84.32, 59.03] (deg)
$[\dot{q}_{d1}^i, \dot{q}_{d2}^i, \dot{q}_{d3}^i]$ at $t = t_0^*$	[0, 0, 0] (deg/s)
$[\dot{q}_{d1}^i, \dot{q}_{d2}^i, \dot{q}_{d3}^i]$ at $t = t_f^*$	[0, 0, 0] (deg/s)
$[L_1^i, L_2^i, L_3^i]$	[0.040, 0.040, 0.030] (m)
$[m_1^i, m_2^i, m_3^i]$	[0.045, 0.025, 0.017] (kg)
<b>Middle Finger</b>	
$[q_{d1}^m, q_{d2}^m, q_{d3}^m]$ at $t = t_0^{**}$	[26.09, 30.15, 21.10] (deg)
$[q_{d1}^m, q_{d2}^m, q_{d3}^m]$ at $t = t_f^{**}$	[13.34, 84.85, 59.39] (deg)
$[L_1^m, L_2^m, L_3^m]$	[0.044, 0.044, 0.033] (m)
$[m_1^m, m_2^m, m_3^m]$	[0.050, 0.028, 0.017] (kg)
<b>Ring Finger</b>	
$[q_{d1}^r, q_{d2}^r, q_{d3}^r]$ at $t = t_0^{**}$	[26.09, 30.15, 21.10] (deg)
$[q_{d1}^r, q_{d2}^r, q_{d3}^r]$ at $t = t_f^{**}$	[9.28, 84.32, 59.03] (deg)
$[L_1^r, L_2^r, L_3^r]$	[0.040, 0.040, 0.030] (m)
$[m_1^r, m_2^r, m_3^r]$	[0.041, 0.023, 0.014] (kg)
<b>Little Finger</b>	
$[q_{d1}^l, q_{d2}^l, q_{d3}^l]$ at $t = t_0^{**}$	[20.63, 42.11, 29.48] (deg)
$[q_{d1}^l, q_{d2}^l, q_{d3}^l]$ at $t = t_f^{**}$	[2.01, 82.54, 57.78] (deg)
$[L_1^l, L_2^l, L_3^l]$	[0.036, 0.036, 0.027] (m)
$[m_1^l, m_2^l, m_3^l]$	[0.041, 0.023, 0.014] (kg)

\*Same parameters for all fingers

\*\*Used in local coordinates

TABLE II  
PARAMETER SELECTION OF CONVERSION BETWEEN GLOBAL AND LOCAL COORDINATES

Parameters	Values
Rotating $\alpha$	90 (deg)
Rotating $\beta$	45 (deg)
Translating $\mathbf{d}^i$	[0.035, 0, 0] (m)
Translating $\mathbf{d}^m$	[0.040, 0, -0.020] (m)
Translating $\mathbf{d}^r$	[0.035, 0, -0.040] (m)
Translating $\mathbf{d}^l$	[0.025, 0, -0.060] (m)

# Hybrid Genetic Algorithm PID Control for a Five-Fingered Smart Prosthetic Hand

CHENG-HUNG CHEN  
Measurement and Control  
Engineering Research Center  
Department of Electrical Engineering  
and Computer Science  
School of Engineering  
Idaho State University  
Pocatello, ID 83209, USA  
chenchen@isu.edu

D. SUBBARAM NAIDU  
Measurement and Control  
Engineering Research Center  
Department of Electrical Engineering  
and Computer Science  
School of Engineering  
Idaho State University  
Pocatello, ID 83209, USA  
naiduds@isu.edu

**Abstract:** A hybrid of soft control technique of adaptive neuro-fuzzy inference system (ANFIS) and genetic algorithm (GA) and hard control technique of proportional-integral-derivative (PID) for a five-fingered, smart prosthetic hand is presented. The ANFIS is used for inverse kinematics and GA is used for tuning the PID parameters with the objective of minimizing the error squared between desired and actual angles of the links of the fingers of the prosthetic hand. Simulation results for all the five fingers with GA-tuned PID controller exhibit superior performance compared to the PID control without GA.

**Key-Words:** Prosthetic Hand, PID Control, Genetic Algorithm, Adaptive Neuro-Fuzzy Inference System, Hybrid Control

## 1 Introduction

Hard control (HC) methodologies are used at lower levels for accuracy, precision, stability and robustness. HC comprises proportional-derivative (PD) control [1], proportional-integral-derivative (PID) control [2, 3], optimal control [3–6], adaptive control [7–9] etc. with specific applications to prosthetic devices. However, our previous works [1–3, 10] for a smart prosthetic hand showed that PID controller resulted in overshooting and oscillation because the system dynamics are sensitive to the rigidity of the target object and the used gain parameters of PD or PID controller [11].

Soft computing (SC) or computational intelligence (CI) is an emerging field based on synergy and seamless integration of neural networks (NN), fuzzy logic (FL) and optimization methods, such as genetic algorithms (GA), particle swarm (PS) [1, 12, 13], tabu search (TS) [13] and so on. The methodology based on SC can be used at upper levels of the overall mission whereas the HC can be used at lower levels for accuracy, precision, stability and robustness. Hence, we propose the GA-based PID controller to solve problems that cannot be solved satisfactorily by using either HC or SC methodology alone with specific applications to prosthetics.

In this paper, we first consider briefly trajec-

tory planning and kinematics problems. Then, adaptive neuro-fuzzy inference system (ANFIS) is used to solve inverse kinematics problem for three-link fingers (index, middle, ring, and little). Next, the dynamics of the hand is derived and feedback linearization technique is used to obtain linear tracking error dynamics. Then we propose the GA-based PID control, which uses GA to tune all PID parameters by minimizing the tracking errors, for the five-fingered prosthetic hand. The resulting overall hybrid system incorporating both soft and hard control techniques is simulated with practical data for the hand and found to be superior to that using PID alone. We finally provide conclusions and future work.

## 2 Modeling

### 2.1 Trajectory Planning and Kinematics

The trajectory planning using cubic polynomial was discussed in our previous work [1, 2, 5, 8, 9, 14] for a two-fingered (thumb and index finger) smart prosthetic hand. The inverse and differential kinematics of two-link thumb and three-link fingers were discussed in our previous publications [1, 2, 5, 8, 9, 14] for a two-fingered (thumb and index finger) smart prosthetic hand.



For five fingers shown in Figure 1,  $X^G$ ,  $Y^G$ , and

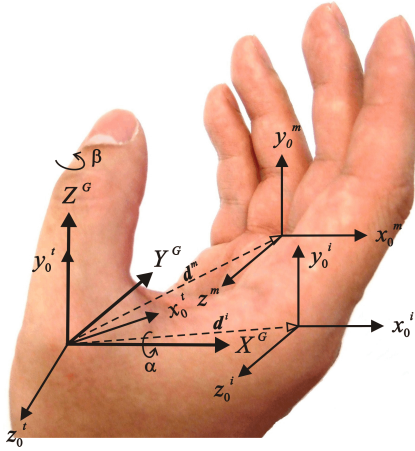


Figure 1: The Relationship between Global Coordinate and Local Coordinates

$Z^G$  are the three axes of the global coordinate. The local coordinate  $x^t$ - $y^t$ - $z^t$  of thumb can be reached by rotating through angles  $\alpha$  and  $\beta$  to  $X^G$  and  $Y^G$  of the global coordinate, subsequently. The local coordinate  $x^i$ - $y^i$ - $z^i$  of index finger can be obtained by rotating through angle  $\alpha$  to  $X^G$  and then translating the vector  $d^i$  of the global coordinate; similarly, the local coordinate  $x^j$ - $y^j$ - $z^j$  of middle finger ( $j = m$ ), ring finger ( $j = r$ ), and little finger ( $j = l$ ) can be obtained by rotating through angle  $\alpha$  to  $X^G$  and then translating the vector  $d^j$  ( $j = m, r$  and  $l$ ) of the global coordinate.

## 2.2 Adaptive Neuro-Fuzzy Inference System (ANFIS)

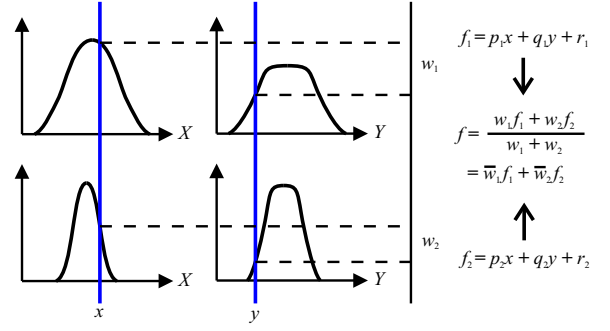
The inverse kinematics problems can be solved by using adaptive neuro-fuzzy inference system (ANFIS) method [15] where the input of fuzzy-neuro system is the Cartesian space and the output is the joint space. ANFIS tunes the membership function and identifies the coefficients by the backpropagation gradient descent and least-squares methods, respectively. Figure 2 (a) shows a two input first-order Sugeno fuzzy model with two rules and Figure 2 (b) depicts the equivalent ANFIS structure for all the computation below. Sugeno-type fuzzy system has the following **Rule Base** [15].

If  $x$  is  $A_1$  and  $y$  is  $B_1$ , then  $f_1 = p_1x + q_1y + r_1$ .

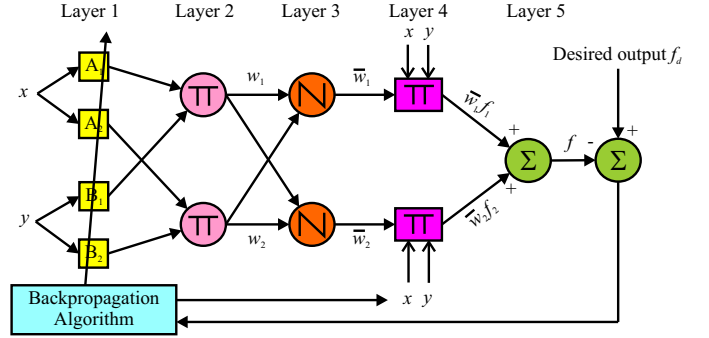
If  $x$  is  $A_2$  and  $y$  is  $B_2$ , then  $f_2 = p_2x + q_2y + r_2$ .

Here,  $x$  and  $y$  are inputs to constitute the premise parameters  $A_1$ ,  $A_2$ ,  $B_1$ , and  $B_2$  (Layer 1 in Figure 2 (b)).  $p_i$ ,  $q_i$ , and  $r_i$  ( $i = 1, 2$ ) are the consequent parameters. We evaluate the rules by choosing *product*  $\prod$  for T-Norm (Layers 2 and 3) which results in

$$w_i = \mu_{A_i}(x) \mu_{B_i}(y), \quad i = 1, 2. \quad (1)$$



(a) A Two Input First-Order Sugeno Fuzzy Model with Two Rules



(b) Equivalent ANFIS Structures

Figure 2: ANFIS Architecture: (a) A Two Input First-Order Sugeno Fuzzy Model with Two Rules (b) Equivalent ANFIS Structure [15]

Here,  $\mu_{A_i}(x)$  and  $\mu_{B_i}(y)$  are designed fuzzy membership functions. Now after leaving the arguments (Layer 4), we get the output  $f(x, y)$  by **Rule Consequences**.

$$f(x, y) = \frac{w_1(x, y)f_1(x, y) + w_2(x, y)f_2(x, y)}{w_1(x, y) + w_2(x, y)}. \quad (2)$$

$f$  (Layer 5) can be written as

$$f = \frac{w_1f_1 + w_2f_2}{w_1 + w_2} = \bar{w}_1f_1 + \bar{w}_2f_2, \quad (3)$$

where

$$\bar{w}_1 = \frac{w_1}{w_1 + w_2}, \quad \bar{w}_2 = \frac{w_2}{w_1 + w_2}. \quad (4)$$

## 2.3 Dynamics of the Prosthetic Hand

The dynamic equations of hand motion are derived via Lagrangian approach using kinetic energy and potential energy as [7, 14, 16] and can be written as below.

$$M(q)\ddot{q} + N(q, \dot{q}) = \tau, \quad (5)$$

where  $M(q)$  is the inertia matrix and  $N(q, \dot{q}) = C(q, \dot{q}) + G(q)$  represents nonlinear terms, including

Coriolis/centripetal vector  $C(\mathbf{q}, \dot{\mathbf{q}})$  and gravity vector  $G(\mathbf{q})$ . The dynamic relations for the two-link thumb and the remaining three-link fingers are quite lengthy and omitted here due to lack of space [14].

### 3 Control Techniques

#### 3.1 Feedback Linearization

The nonlinear dynamics represented by (5) is to be converted into a linear state-variable system using feedback linearization technique [7]. Let us suppose the prosthetic hand is required to track the desired trajectory  $\mathbf{q}_d(t)$  described under path generation or tracking. Then, the tracking error  $\mathbf{e}(t)$  is defined as

$$\mathbf{e}(t) = \mathbf{q}_d(t) - \mathbf{q}(t). \quad (6)$$

Here,  $\mathbf{q}_d(t)$  is the *desired* angle vector of joints and can be obtained by trajectory planning [1, 2, 5, 8, 14];  $\mathbf{q}(t)$  is the *actual* angle vector of joints. Differentiating (6) twice, to get

$$\dot{\mathbf{e}}(t) = \dot{\mathbf{q}}_d(t) - \dot{\mathbf{q}}(t), \quad \ddot{\mathbf{e}}(t) = \ddot{\mathbf{q}}_d(t) - \ddot{\mathbf{q}}(t). \quad (7)$$

Substituting (5) into (7) yields

$$\ddot{\mathbf{e}}(t) = \ddot{\mathbf{q}}_d(t) + \mathbf{M}^{-1}(\mathbf{q}(t)) [\mathbf{N}(\mathbf{q}(t), \dot{\mathbf{q}}(t)) - \boldsymbol{\tau}(t)] \quad (8)$$

from which the control function can be defined as

$$\mathbf{u}(t) = \ddot{\mathbf{q}}_d(t) + \mathbf{M}^{-1}(\mathbf{q}(t)) [\mathbf{N}(\mathbf{q}(t), \dot{\mathbf{q}}(t)) - \boldsymbol{\tau}(t)]. \quad (9)$$

This is often called the *feedback linearization* control law, which can also be inverted to express it as

$$\boldsymbol{\tau}(t) = \mathbf{M}(\mathbf{q}(t)) [\ddot{\mathbf{q}}_d(t) - \mathbf{u}(t)] + \mathbf{N}(\mathbf{q}(t), \dot{\mathbf{q}}(t)). \quad (10)$$

Using the relations (7) and (9), and defining state vector  $\mathbf{x}(t) = [\mathbf{e}'(t) \ \dot{\mathbf{e}}'(t)]'$ , the *tracking error dynamics* in the form of a *linear system* can be written as

$$\dot{\mathbf{x}}(t) = \begin{bmatrix} \mathbf{0} & \mathbf{I} \\ \mathbf{0} & \mathbf{0} \end{bmatrix} \mathbf{x}(t) + \begin{bmatrix} \mathbf{0} \\ \mathbf{I} \end{bmatrix} \mathbf{u}(t). \quad (11)$$

#### 3.2 GA-Based PID Hybrid Control

Figure 3 shows the block diagram of a hybrid GA-based PID controller for the presented five-fingered prosthetic hand with control signal as

$$\mathbf{u}(t) = -\mathbf{K}_P \mathbf{e}(t) - \mathbf{K}_I \int \mathbf{e}(t) dt - \mathbf{K}_D \dot{\mathbf{e}}(t) \quad (12)$$

with the proportional  $\mathbf{K}_P$ , integral  $\mathbf{K}_I$ , and derivative  $\mathbf{K}_D$  diagonal gain matrices. We then rewrite (10) as

$$\begin{aligned} \boldsymbol{\tau}(t) = & \mathbf{M}(\mathbf{q}(t)) [\ddot{\mathbf{q}}_d(t) + \mathbf{K}_P \mathbf{e}(t) + \mathbf{K}_I \int \mathbf{e}(t) dt \\ & + \mathbf{K}_D \dot{\mathbf{e}}(t)] + \mathbf{N}(\mathbf{q}(t), \dot{\mathbf{q}}(t)). \end{aligned} \quad (13)$$

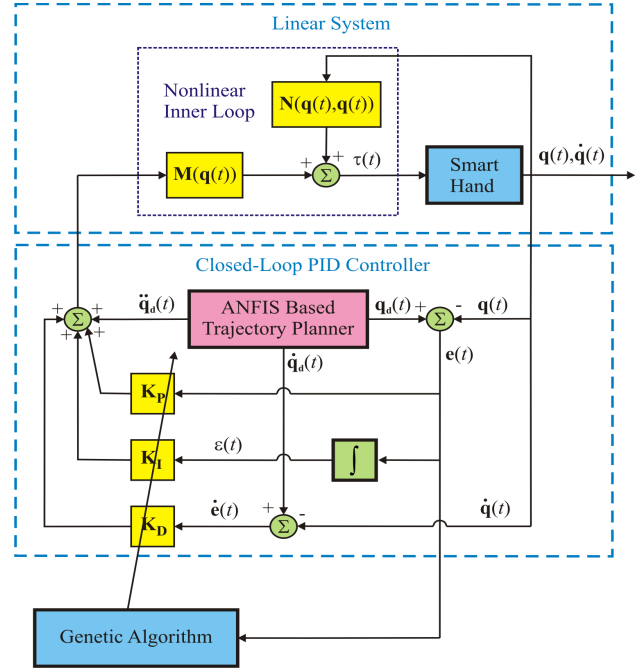


Figure 3: Block Diagram of the Hybrid GA-Based PID Controller for 14-DOF Five-Fingered Prosthetic Hand

Then we use GA to tune all gain coefficients  $\mathbf{K}_P$ ,  $\mathbf{K}_D$  and  $\mathbf{K}_I$  of PID controller. Figure 4 shows the flowchart of GA and the procedure is briefly stated below.

1. Define the GA parameters: include initial population, population at the end of the first generation, number of chromosomes kept for mating, mutation rate, and tolerance  $\epsilon$  so on.
2. Create a homogeneous population: generate  $N$  elements (chromosomes) and  $N$  is the initial population.
3. Evaluate cost (fitness) function of each chromosome: calculate the fitness value of the  $i$ th member in the population.
4. Select mate based on the performance of each gene: create a new population from the current population based on the ranking of the current fitness value, e.g. determine which parents participate in producing offspring for the next generation.
5. Reproduce the generation by crossover: use the single or multiple crossover points to generate new chromosomes that retain the good feature and discard the bad feature.

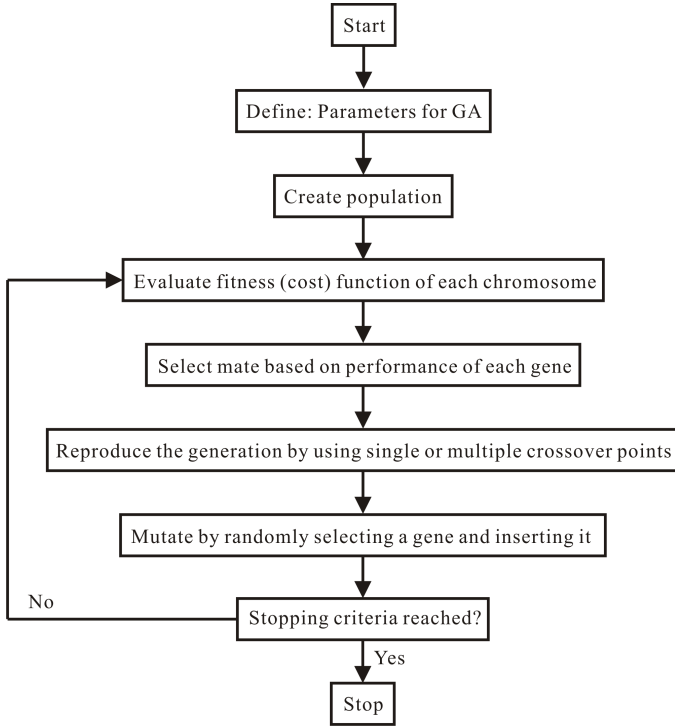


Figure 4: The Flowchart of Genetic Algorithm (GA)

6. Mutate: utilize the mutation rate which can randomly mutate the gene to avoid falling into the local minima area.
7. Repeat steps 3 to 6 until it reaches the maximum number of iterations or stopping condition defined by  $\epsilon$  is satisfied.

## 4 Simulation Results and Discussion

We present simulations with a PID controller and GA-tuned PID controller for the 14 DOFs five-fingered smart prosthetic hand grasping a rectangular object as shown in Figure 5. All parameters of the smart prosthetic hand selected for the simulations are the same as our previous works [3, 9]. All initial actual angles are zero and the diagonal coefficients,  $\mathbf{K}_P$ ,  $\mathbf{K}_I$  and  $\mathbf{K}_D$ , for the PID controller alone are arbitrarily chosen as 100. From the derived dynamic and control models, after the parameters ( $\mathbf{K}_P$ ,  $\mathbf{K}_I$  and  $\mathbf{K}_D$ ) are determined, the torque matrix  $\tau$  can be computed, and then the squared-tracking errors  $e_i^j(t)$  of the joint  $i$  of the finger  $j$  are obtained. Therefore, the total error  $E(t)$ , which is a time-dependent function, can be described as

$$E(t) = \int_{t_0}^{t_f} (e_i^j(t))^2 dt, \quad (14)$$

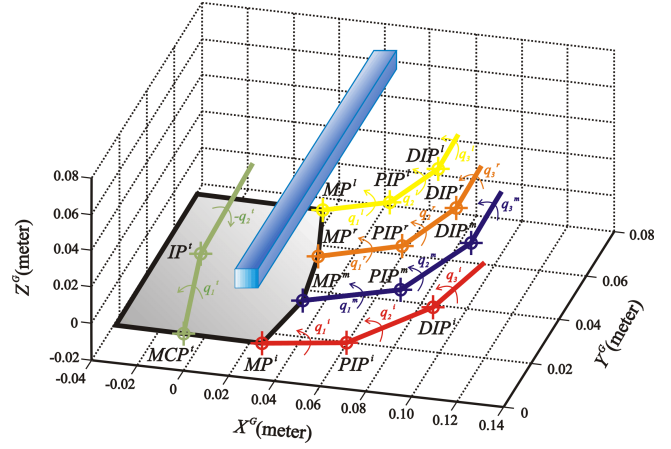


Figure 5: A Five-Finger Prosthetic Hand Grasping a Rectangular Object

where  $t_0$  and  $t_f$  are initial and terminal time, respectively. The tuned diagonal parameters ( $\mathbf{K}_P$ ,  $\mathbf{K}_I$  and  $\mathbf{K}_D$ ) and the total error  $E(t)$  of PID controller by GA are listed in Table 1. To study whether the tuned

Table 1: Parameter Selection of GA-Tuned PID Controller and Computed Total Errors

Fingers	Input			Output
	$\mathbf{K}_P$	$\mathbf{K}_I$	$\mathbf{K}_D$	$E(t)$
Case I	[976,956]	[779,279]	[170,236]	0.3107
Case II	[988,999]	[78,848]	[80,109]	0.1557
Case III	[199,198]	[127,157]	[104,102]	0.8100
Index	[794,398,960]	[960,918,914]	[15,59,242]	0.0465
Middle	[794,398,960]	[960,918,914]	[15,59,242]	0.1003
Ring	[794,398,960]	[960,918,914]	[15,59,242]	0.0465
Little	[794,398,960]	[960,918,914]	[15,59,242]	0.0607

parameter range influences total tracking errors, we design three different cases with altering lower and upper bounds of tuned parameter ranges for two-link thumb. Cases I, II, and III for the thumb represent that the PID parameters  $\mathbf{K}_P$ ,  $\mathbf{K}_I$  and  $\mathbf{K}_D$  are constricted in three different bounded ranges [100,1000], [50,1000], and [100,200], respectively. Figure 6 and Figure 7 show that tracking errors and desired/actual angles of joints 1 and 2 of PID and GA-based PID controllers for Thumb. These simulations show that the large ranges [100,1000] (Case I) and [50,1000] (Case II) provide better results than the PID controller parameters arbitrarily chosen as 100. However, the small range [100,200] (Case III) gives worse result than the PID controller alone. These results suggest that the bigger parameter range, the smaller the total error. Cases I and II explain that GA finds some parameter values  $\in [100,1000]$  and  $[50,100]$  escaping

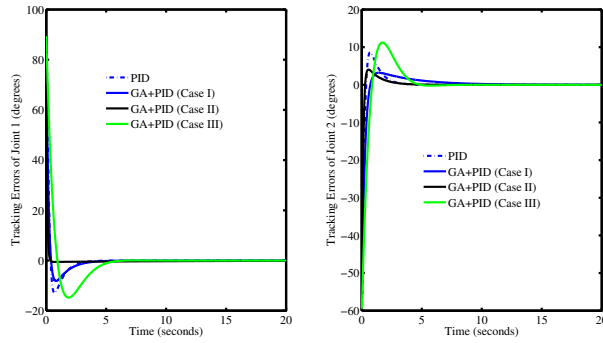


Figure 6: Tracking Errors of Joint 1 (left) and Joint 2 (right) of PID and GA-Based PID Controllers for Thumb

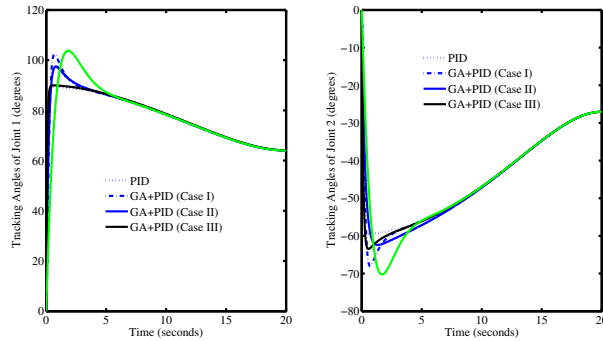


Figure 7: Tracking Angles of Joint 1 (left) and Joint 2 (right) of PID and GA-Based PID Controllers for Thumb

the local minimum area. Case III covers the value 100 in lower bound, but both total error and convergent speed are even worse than PID alone, suggesting that GA performs better for a large range, but is poor for searching on the boundary. To further consider the convergent speed, Case I gives smaller total error, but does not improve its convergent speed when comparing to PID control alone. Yet, Case II gives good total error and convergent speed. Case III gives poor total error and convergent speed. Taken together, these results imply that the global minimum could be located in the ranges [50,100] and [200,1000] and the parameter ranges play an important role in GA tuning. Based on these findings, we use the range [50,1000] for the remaining three-link fingers. Figures 8 to 11 show the simulations of PID and GA-based PID controllers for the remaining three-link fingers.

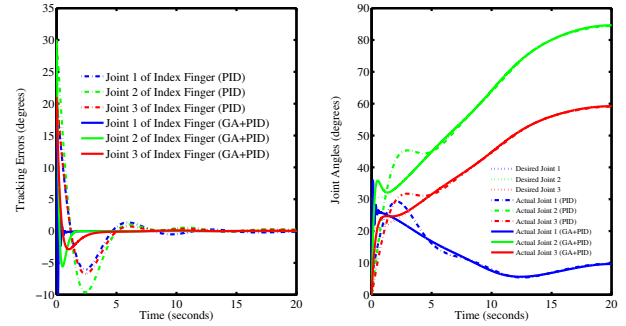


Figure 8: Tracking Errors (left) and Joint Angles (right) of PID and GA-Based PID Controllers for Index Finger

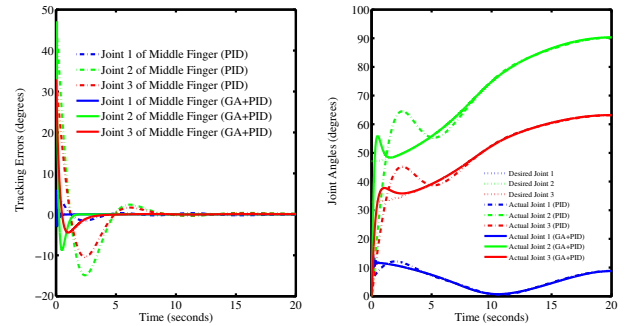


Figure 9: Tracking Errors (left) and Joint Angles (right) of PID and GA-Based PID Controllers for Middle Finger

## 5 Conclusions and Future Work

A hybrid control technique combining soft control with adaptive neuro-fuzzy inference system (ANFIS) and genetic algorithm (GA) and hard control with proportional-integral-derivative (PID) was presented for a five-fingered smart prosthetic hand. The ANFIS is used for inverse kinematics and GA is used for tuning the PID parameters with the objective of minimizing the error squared between desired and actual angles of the links of the fingers. Simulation results for all the five fingers with GA-tuned PID controller showed superior performance compared to the PID control alone. A real-time implementation of this technique on a prototype of a prosthetic hand is planned for future work.

**Acknowledgements:** The research was sponsored by the U.S. Department of the Army, under the award number W81XWH-10-1-0128 awarded and administered by the U.S. Army Medical Research Acquisition Activity, 820 Chandler Street, Fort Detrick, MD 21702-5014. The information does not necessarily

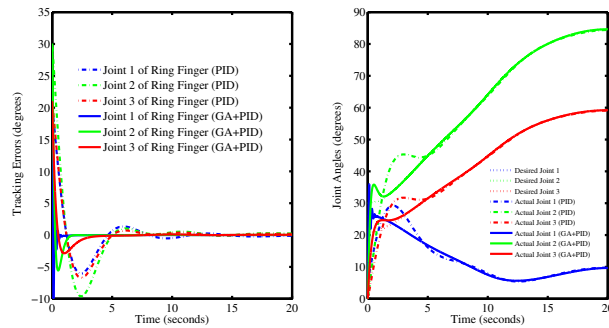


Figure 10: Tracking Errors (left) and Joint Angles (right) of PID and GA-Based PID Controllers for Ring Finger

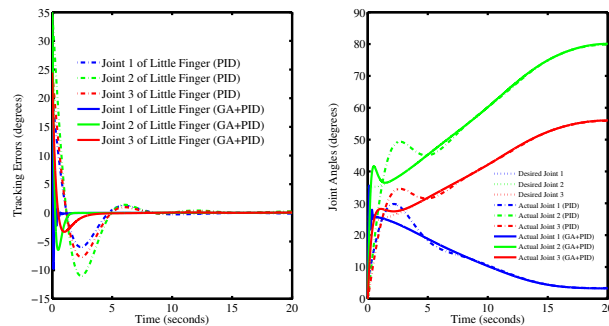


Figure 11: Tracking Errors (left) and Joint Angles (right) of PID and GA-Based PID Controllers for Little Finger

reflect the position or the policy of the Government, and no official endorsement should be inferred. For purposes of this article, information includes news releases, articles, manuscripts, brochures, advertisements, still and motion pictures, speeches, trade association proceedings, etc.

#### References:

- [1] C.-H. Chen, K. W. Bosworth, M. P. Schoen, S. E. Bearden, D. S. Naidu, and A. Perez, "A study of particle swarm optimization on leukocyte adhesion molecules and control strategies for smart prosthetic hand," in *2008 IEEE Swarm Intelligence Symposium (IEEE SIS08)*, St. Louis, Missouri, USA, September 21-23 2008.
- [2] C.-H. Chen, D. S. Naidu, A. Perez, and M. P. Schoen, "Fusion of hard and soft control techniques for prosthetic hand," in *Proceedings of the International Association of Science and Technology for Development (IASTED) International Conference on Intelligent Systems and Control (ISC 2008)*, Orlando, Florida, USA, November 16-18 2008, pp. 120–125.
- [3] C.-H. Chen, D. S. Naidu, A. Perez-Gracia, and M. P. Schoen, "A hybrid control strategy for five-fingered smart prosthetic hand," in *Joint 48th IEEE Conference on Decision and Control (CDC) and 28th Chinese Control Conference (CCC)*, Shanghai, P. R. China, December 16-18 2009, pp. 5102–5107.
- [4] D. Naidu, *Optimal Control Systems*. Boca Raton, FL: CRC Press, 2003.
- [5] C.-H. Chen, D. S. Naidu, A. Perez-Gracia, and M. P. Schoen, "A hybrid optimal control strategy for a smart prosthetic hand," in *Proceedings of the ASME 2009 Dynamic Systems and Control Conference (DSCC)*, Hollywood, California, USA, October 12-14 2009, (No. DSCC2009-2507).
- [6] C.-H. Chen and D. S. Naidu, "Optimal control strategy for two-fingered smart prosthetic hand," in *Proceedings of the International Association of Science and Technology for Development (IASTED) International Conference on Robotics and Applications (RA 2010)*, Cambridge, Massachusetts, USA, November 1-3 2010, pp. 190–196.
- [7] F. Lewis, D. Dawson, and C. Abdallah, *Robot Manipulators Control: Second Edition, Revised and Expanded*. New York, NY: Marcel Dekker, Inc., 2004.
- [8] C.-H. Chen, D. S. Naidu, A. Perez-Gracia, and M. P. Schoen, "A hybrid adaptive control strategy for a smart prosthetic hand," in *The 31st Annual International Conference of the IEEE Engineering Medicine and Biology Society (EMBS)*, Minneapolis, Minnesota, USA, September 2-6 2009, pp. 5056–5059.
- [9] C.-H. Chen, D. S. Naidu, and M. P. Schoen, "An adaptive control strategy for a five-fingered prosthetic hand," in *The 14th World Scientific and Engineering Academy and Society (WSEAS) International Conference on Systems, Latest Trends on Systems (Volume II)*, Corfu Island, Greece, July 22-24 2010, pp. 405–410.
- [10] C.-H. Chen, M. P. Schoen, and K. W. Bosworth, "A condensed hybrid optimization algorithm using enhanced continuous tabu search and particle swarm optimization," in *Proceedings of the*



*ASME 2009 Dynamic Systems and Control Conference (DSCC)*, Hollywood, California, USA, October 12-14 2009, (No. DSCC2009-2526).

- [11] R. Andrecioli and E. D. Engeberg, "Grasped object stiffness detection for adaptive force control of a prosthetic hand," in *Proceedings of the 2010 3rd IEEE RAS and EMBS International Conference on Biomedical Robotics and Biomechatronics (BioRob)*, Tokyo, Japan, September, 26-29 2010, pp. 197–202.
- [12] C.-H. Chen, K. W. Bosworth, and M. P. Schoen, "Investigation of particle swarm optimization dynamics," in *Proceedings of International Mechanical Engineering Congress and Exposition (IMECE) 2007*, Seattle, Washington, USA, November 11-15 2007, (No. IMECE2007-41343).
- [13] C.-H. Chen, K. Bosworth, and M. P. Schoen, "An adaptive particle swarm method to multiple dimensional problems," in *Proceedings of the International Association of Science and Technology for Development (IASTED) International Symposium on Computational Biology and Bioinformatics (CBB 2008)*, Orlando, Florida, USA, November 16-18 2008, pp. 260–265.
- [14] C.-H. Chen, "Hybrid control strategies for smart prosthetic hand," Ph.D. dissertation, Measurement and Control Engineering, Idaho State University, May 2009.
- [15] J.-S. Jang, C.-T. Sun, and E. Mizutani, *Neuro-Fuzzy and Soft Computing: A Computational Approach to Learning and Machine Intelligence*. Upper Saddle River, NJ: Prentice Hall PTR, 1997.
- [16] B. Siciliano, L. Sciavicco, L. Villani, and G. Oriolo, *Robotics: Modelling, Planning and Control*. London, UK: Springer-Verlag, 2009.



# Fusion of Fuzzy Logic and PD Control for a Five-Fingered Smart Prosthetic Hand

Cheng-Hung Chen  
Measurement and Control  
Engineering Research Center  
Department of Biological Sciences  
College of Science and Engineering  
Idaho State University  
Pocatello, ID 83209, USA  
Email: chenchen@isu.edu

D. Subbaram Naidu  
Measurement and Control  
Engineering Research Center  
Department of Electrical Engineering  
School of Engineering  
Idaho State University  
Pocatello, ID 83209, USA  
Email: naiduds@isu.edu

**Abstract**—A hybrid of soft control technique of adaptive neuro-fuzzy inference system (ANFIS) and fuzzy logic (FL) and hard control technique of proportional-derivative (PD) for a five-fingered, smart prosthetic hand is presented. The ANFIS is used for inverse kinematics and FL is used for tuning the PD parameters with two input layers (error and error change) using 7 triangular membership functions and 49 fuzzy logic rules. Simulation results with FL-tuned PD controller exhibit superior performance compared to the PD and PID control alone.

**Index Terms**—Prosthetic Hand, Fuzzy Logic, PD Control, Adaptive Neuro-Fuzzy Inference System, Hybrid Control

## I. INTRODUCTION

During the recent wars in Afghanistan and Iraq, “at least 251,102 people have been killed and 532,715 people have been seriously wounded” [1]. Further, in the United States, the Amputee Coalition of America (ACA) [2] reports that there are approximately 1.9 million people living with limb loss, due to combat operations (such as conflicts, wars etc.), and non-combat operations such as accidents, or birth defects. According to a study of the 1996 National Health Interview Survey (NHIS) published by Vital and Health Statistics [3], it is estimated that one out of every 200 people in the U.S. has had an amputation. In other words, about one in every 2,000 new born babies will have limb deficiency and over 3,000 people lose a limb every week in America. By the year 2050, the projected number of Americans living with limb amputation will become 3.6 million [4]. In the past several decades, prosthetic hands have been developed by various researchers in the field [5]–[9], but reproducing the human hand in all its various functions, appearance, visibility, and weight is still a challenging task [5].

Hard computing/control (HC) techniques are used at lower levels for accuracy, precision, stability and robustness. HC comprises proportional-derivative (PD) control [10], proportional-integral-derivative (PID) control [11], [12], optimal control [12]–[15], adaptive control [16]–[19] etc. with specific applications to prosthetic devices. However, our previous works [10]–[12], [20] for a smart prosthetic hand showed that PID controller resulted in overshooting and oscillation.

Soft computing (SC) or computational intelligence (CI) [21] is an emerging field based on synergy and seamless integration of neural networks (NN), fuzzy logic (FL) and optimization methods, such as genetic algorithms (GA), particle swarm (PS) [10], [22], [23], tabu search (TS) [23] and so on. The methodology based on SC can be used, in particular with FL, at upper levels of the overall mission where human involvement and decision making is of primary importance, whereas the HC can be used at lower levels for accuracy, precision, stability and robustness. Hence, we present the integration of SC and HC to solve problems that cannot be solved satisfactorily by using either HC or SC methodology alone with specific applications to prosthetics.

In this paper, we first consider briefly trajectory planning and kinematics problems associated with a five-fingered prosthetic hand. Then, adaptive neuro-fuzzy inference system (ANFIS) is used to solve inverse kinematics problem for three-link fingers (index, middle, ring, and little). Next, the dynamics of the hand is derived and feedback linearization technique is used to obtain *linear* tracking error dynamics. Then we propose the fuzzy logic-based PD (hybrid) controller, which uses fuzzy logic with 7 triangular membership functions in each input/output layer and 49 logic rules to tune PD gain parameters. The resulting overall hybrid system incorporating both soft and hard control techniques is simulated with practical data for the hand and found the performance to be superior to PD or PID alone. Finally, we provide conclusions and future work.

## II. MODELING

### A. Trajectory Planning and Kinematics

The trajectory planning using cubic polynomial was discussed in our previous work [10], [11], [14], [18], [19], [24] for a two-fingered (thumb and index finger) smart prosthetic hand.

Kinematics is the study of geometry in motion and is restricted to a natural geometrical description of motion by



the manners, including positions, orientations, and their derivatives (velocities and accelerations) [25], [26]. Forward and inverse kinematics of articulated systems study the analytical relationship between the angular positions of joints and the positions and orientations of the fingertips. A desired trajectory is usually specified in *Cartesian* space and the trajectory controller is easily performed in the *joint* space. Therefore, conversion of Cartesian trajectory planning to the joint space [26] is necessary. Using inverse kinematics, the joint angular positions of each finger need to be obtained from the known fingertip positions. Then the angular velocities and angular accelerations of joints can be obtained from the linear and angular velocities and accelerations of fingertips by differential kinematics. The inverse and differential kinematics of two-link thumb and three-link fingers were discussed in our previous publications [10], [11], [14], [18], [19], [24] for a two-fingered (thumb and index finger) smart prosthetic hand.

For five fingers shown in Figure 1,  $X^G$ ,  $Y^G$ , and  $Z^G$  are

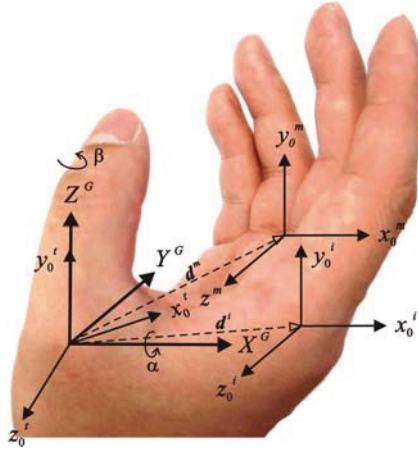


Fig. 1. Relationship between Global Coordinate and Local Coordinates: Local coordinate  $x^t$ - $y^t$ - $z^t$  of thumb can be reached by rotating through angles  $\alpha$  and  $\beta$  to  $X^G$  and  $Y^G$  of global coordinate, subsequently. Local coordinate  $x^i$ - $y^i$ - $z^i$  of index finger can be obtained by rotating through angle  $\alpha$  to  $X^G$  and then translating a vector  $\mathbf{d}^i$  of the global coordinate.

the three axes of global coordinate. Local coordinate  $x^t$ - $y^t$ - $z^t$  of thumb can be reached by rotating through angles  $\alpha$  and  $\beta$  to  $X^G$  and  $Y^G$  of the global coordinate, subsequently. Local coordinate  $x^i$ - $y^i$ - $z^i$  of index finger can be obtained by rotating through angle  $\alpha$  to  $X^G$  and then translating a vector  $\mathbf{d}^i$  of the global coordinate; similarly, the local coordinate  $x^j$ - $y^j$ - $z^j$  of middle finger ( $j = m$ ), ring finger ( $j = r$ ), and little finger ( $j = l$ ) can be obtained by rotating through angle  $\alpha$  to  $X^G$  and then translating the vector  $\mathbf{d}^j$  ( $j = m, r$  and  $l$ ) of the global coordinate.

### B. Adaptive Neuro-Fuzzy Inference System (ANFIS)

The inverse kinematics problems can be solved by using adaptive neuro-fuzzy inference system (ANFIS) method [27] where the input of fuzzy-neuro system is the Cartesian space and the output is the joint space. ANFIS is a fuzzy inference system implemented in the framework of adaptive

networks which provides the best optimization algorithm to find parameters in order to fit the data. ANFIS includes *premise parameters*, that defines membership functions, and *consequent parameters*, that defines the coefficients of each output equation. ANFIS tunes the membership function and identifies the coefficients by the backpropagation gradient descent and least-squares methods, respectively. ANFIS uses a hybrid learning algorithm to identify parameters of Sugeno-type fuzzy inference systems for fuzzy modeling procedures to learn information about a data set in order to compute the membership function and track the given input/output data. Figure 2 (a) shows a two input first-order Sugeno fuzzy model with two rules and Figure 2 (b) depicts the equivalent ANFIS structure for all the computation below. Sugeno-type fuzzy

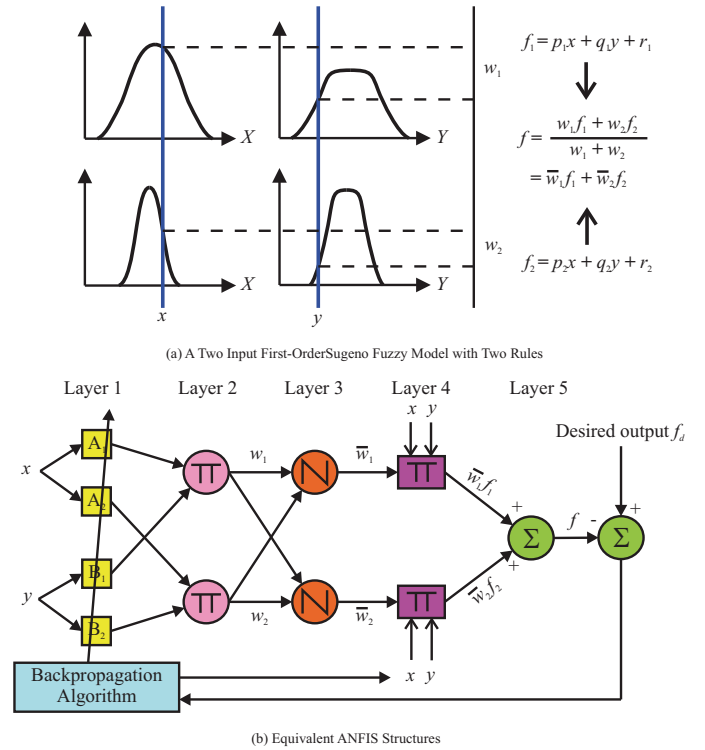


Fig. 2. ANFIS Architecture: (a) A Two Input First-Order Sugeno Fuzzy Model with Two Rules (b) Equivalent ANFIS Structure [27]. The inverse kinematics problems are solved by using adaptive neuro-fuzzy inference system (ANFIS) method where the input of fuzzy-neuro system is the Cartesian space and the output is the joint space. ANFIS is a fuzzy inference system implemented in the framework of adaptive networks which provides the best optimization algorithm to find parameters in order to fit the data.

system has the following **Rule Base** [27]–[31].

If  $x$  is  $A_1$  and  $y$  is  $B_1$ , then  $f_1 = p_1x + q_1y + r_1$ .

If  $x$  is  $A_2$  and  $y$  is  $B_2$ , then  $f_2 = p_2x + q_2y + r_2$ .

Here,  $x$  and  $y$  are inputs to constitute the premise parameters  $A_1, A_2, B_1$ , and  $B_2$  (Layer 1 in Figure 2 (b)).  $p_i, q_i$ , and  $r_i$  ( $i = 1, 2$ ) are the consequent parameters. We evaluate the rules by choosing *product*  $\Pi$  for T-Norm (Layers 2 and 3) which results in

$$w_i = \mu_{A_i}(x) \mu_{B_i}(y), \quad i = 1, 2. \quad (1)$$

Here,  $\mu_{A_i}(x)$  and  $\mu_{B_i}(y)$  are designed fuzzy membership functions. Now after leaving the arguments (Layer 4), we get the output  $f(x, y)$  by **Rule Consequences**.

$$f(x, y) = \frac{w_1(x, y)f_1(x, y) + w_2(x, y)f_2(x, y)}{w_1(x, y) + w_2(x, y)}. \quad (2)$$

$f$  (Layer 5) can be written as

$$\begin{aligned} f &= \frac{w_1 f_1 + w_2 f_2}{w_1 + w_2} \\ &= \bar{w}_1 f_1 + \bar{w}_2 f_2, \end{aligned} \quad (3)$$

where

$$\bar{w}_1 = \frac{w_1}{w_1 + w_2}, \quad \bar{w}_2 = \frac{w_2}{w_1 + w_2}. \quad (4)$$

### C. Dynamics of Hand

The dynamic equations of hand motion are derived via Lagrangian approach using kinetic energy and potential energy as [17], [24]–[26], [32]

$$\frac{d}{dt} \left( \frac{\partial \mathcal{L}}{\partial \dot{\mathbf{q}}} \right) - \frac{\partial \mathcal{L}}{\partial \mathbf{q}} = \boldsymbol{\tau}, \quad (5)$$

where  $\mathcal{L}$  is the Lagrangian;  $\dot{\mathbf{q}}$  and  $\mathbf{q}$  represent the angular velocities and angle vectors of joints, respectively;  $\boldsymbol{\tau}$  is the given torque vector at joints. The Lagrangian  $\mathcal{L}$  can be expressed as

$$\mathcal{L} = T - V, \quad (6)$$

where  $T$  and  $V$  denote kinetic and potential energies, respectively. Substituting (6) into (5), dynamic equations of thumb can be obtained as below.

$$\mathbf{M}(\mathbf{q})\ddot{\mathbf{q}} + \mathbf{C}(\mathbf{q}, \dot{\mathbf{q}}) + \mathbf{G}(\mathbf{q}) = \boldsymbol{\tau}, \quad (7)$$

where  $\mathbf{M}(\mathbf{q})$  is the inertia matrix;  $\mathbf{C}(\mathbf{q}, \dot{\mathbf{q}})$  is the Coriolis/centripetal vector and  $\mathbf{G}(\mathbf{q})$  is the gravity vector. (7) can be also written as

$$\mathbf{M}(\mathbf{q})\ddot{\mathbf{q}} + \mathbf{N}(\mathbf{q}, \dot{\mathbf{q}}) = \boldsymbol{\tau}, \quad (8)$$

where  $\mathbf{N}(\mathbf{q}, \dot{\mathbf{q}}) = \mathbf{C}(\mathbf{q}, \dot{\mathbf{q}}) + \mathbf{G}(\mathbf{q})$  represents nonlinear terms. The dynamic relations for the two-link thumb and the remaining three-link fingers are quite lengthy and omitted here due to lack of space [24], [33], [34].

## III. CONTROL TECHNIQUES

### A. Feedback Linearization

The nonlinear dynamics represented by (8) is to be converted into a linear state-variable system using feedback linearization technique [17]. Alternative state-space equations of the dynamics can be obtained by defining the position/velocity state  $\mathbf{x}(t)$  of the joints as

$$\mathbf{x}(t) = [\mathbf{q}'(t) \quad \dot{\mathbf{q}}'(t)]'. \quad (9)$$

Let us repeat the dynamical model and rewrite (8) as

$$\frac{d}{dt} \dot{\mathbf{q}}(t) = -\mathbf{M}^{-1}(\mathbf{q}(t)) [\mathbf{N}(\mathbf{q}(t), \dot{\mathbf{q}}(t)) - \boldsymbol{\tau}(t)]. \quad (10)$$

Thus, from (9) and (10), we can derive a linear system in *Brunovsky canonical form* as

$$\dot{\mathbf{x}}(t) = \begin{bmatrix} \mathbf{0} & \mathbf{I} \\ \mathbf{0} & \mathbf{0} \end{bmatrix} \mathbf{x}(t) + \begin{bmatrix} \mathbf{0} \\ \mathbf{I} \end{bmatrix} \mathbf{u}(t) \quad (11)$$

with its control input vector given by

$$\mathbf{u}(t) = -\mathbf{M}^{-1}(\mathbf{q}(t)) [\mathbf{N}(\mathbf{q}(t), \dot{\mathbf{q}}(t)) - \boldsymbol{\tau}(t)]. \quad (12)$$

Let us suppose the prosthetic hand is required to track the desired trajectory  $\mathbf{q}_d(t)$  described under path generation or tracking. Then, the tracking error  $\mathbf{e}(t)$  is defined as

$$\mathbf{e}(t) = \mathbf{q}_d(t) - \mathbf{q}(t). \quad (13)$$

Here,  $\mathbf{q}_d(t)$  is the *desired* angle vector of joints and can be obtained by trajectory planning [10], [11], [14], [18], [24];  $\mathbf{q}(t)$  is the *actual* angle vector of joints. Differentiating (13) twice, to get

$$\dot{\mathbf{e}}(t) = \dot{\mathbf{q}}_d(t) - \dot{\mathbf{q}}(t), \quad \ddot{\mathbf{e}}(t) = \ddot{\mathbf{q}}_d(t) - \ddot{\mathbf{q}}(t). \quad (14)$$

Substituting (10) into (14) yields

$$\ddot{\mathbf{e}}(t) = \ddot{\mathbf{q}}_d(t) + \mathbf{M}^{-1}(\mathbf{q}(t)) [\mathbf{N}(\mathbf{q}(t), \dot{\mathbf{q}}(t)) - \boldsymbol{\tau}(t)] \quad (15)$$

from which the control function can be defined as

$$\mathbf{u}(t) = \ddot{\mathbf{q}}_d(t) + \mathbf{M}^{-1}(\mathbf{q}(t)) [\mathbf{N}(\mathbf{q}(t), \dot{\mathbf{q}}(t)) - \boldsymbol{\tau}(t)]. \quad (16)$$

This is often called the *feedback linearization* control law, which can also be inverted to express it as

$$\boldsymbol{\tau}(t) = \mathbf{M}(\mathbf{q}(t)) [\ddot{\mathbf{q}}_d(t) - \mathbf{u}(t)] + \mathbf{N}(\mathbf{q}(t), \dot{\mathbf{q}}(t)). \quad (17)$$

Using the relations (14) and (16), and defining state vector  $\mathbf{x}(t) = [\mathbf{e}'(t) \quad \dot{\mathbf{e}}'(t)]'$ , the *tracking error dynamics* can be written as

$$\dot{\mathbf{x}}(t) = \begin{bmatrix} \mathbf{0} & \mathbf{I} \\ \mathbf{0} & \mathbf{0} \end{bmatrix} \mathbf{x}(t) + \begin{bmatrix} \mathbf{0} \\ \mathbf{I} \end{bmatrix} \mathbf{u}(t). \quad (18)$$

Note that this is in the form of a *linear* system such as

$$\dot{\mathbf{x}}(t) = \mathbf{A}\mathbf{x}(t) + \mathbf{B}\mathbf{u}(t). \quad (19)$$

### B. Fuzzy Logic-Based PD Hybrid Control

Figure 3 shows the block diagram of the hybrid fuzzy logic-based PD controller for the presented five-fingered prosthetic hand with control signal as

$$\mathbf{u}(t) = -\mathbf{K}_P(t)\mathbf{e}(t) - \mathbf{K}_D(t)\dot{\mathbf{e}}(t) \quad (20)$$

with the proportional  $\mathbf{K}_P(t)$  and derivative  $\mathbf{K}_D(t)$  diagonal gain matrices with time varying. We then rewrite (17) as

$$\begin{aligned} \boldsymbol{\tau}(t) &= \mathbf{M}(\mathbf{q}(t)) [\ddot{\mathbf{q}}_d(t) + \mathbf{K}_P(t)\mathbf{e}(t) + \mathbf{K}_D(t)\dot{\mathbf{e}}(t)] + \\ &\quad \mathbf{N}(\mathbf{q}(t), \dot{\mathbf{q}}(t)). \end{aligned} \quad (21)$$

Then we use mamdani fuzzy inference system to tune the time-varying parameters  $\mathbf{K}_P(t)$  and  $\mathbf{K}_D(t)$  of PD controller. Figure 4 shows the structural characteristics of proposed fuzzy inference system, which includes two inputs (error  $\mathbf{e}$  and error change  $\dot{\mathbf{e}}$ ) on the left and one output ( $\mathbf{K}_P$ ) on the right. Each input or output layer contains seven triangular membership

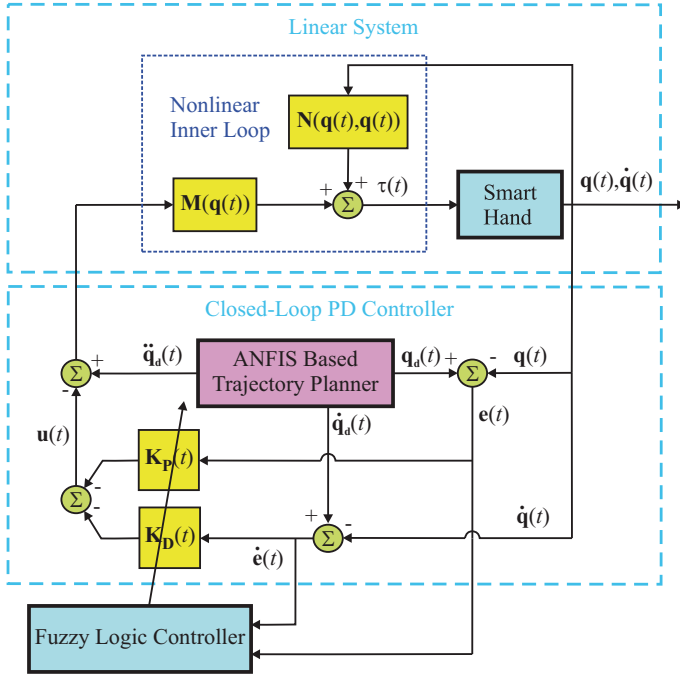


Fig. 3. Block Diagram of the Presented Hybrid Fuzzy Logic-Based Proportional-Derivative (PD) Controller for a Five-Fingered Prosthetic Hand: Errors and error changes are calculated by actual and desired angles, which are based on adaptive neuro-fuzzy inference system (ANFIS) trajectory planner. Then fuzzy logic controller tunes all parameters of closed-loop PD control so that the required torque of the prosthetic hand nonlinear system is computed by control input.

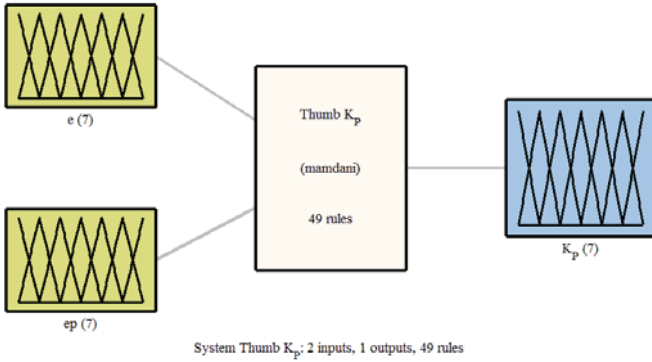


Fig. 4. The Structural Characteristics of Proposed Fuzzy Inference System: Two inputs (error  $e$  and error change  $\dot{e}$ ) on the left and one output (tuned  $K_P$ ) on the right with 49 logic rules

functions as shown in Figure 5 and 49 logic rules as listed in Table I. After using 49 logic rules, the output surface  $K_P$  of fuzzy inference system is generated as shown in Figure 6. Similarly,  $K_D$  can be computed by the same way.

#### IV. SIMULATION RESULTS AND DISCUSSION

Figure 7 shows that a five-fingered prosthetic hand with 14 DOFs is reaching a rectangular rod in order to grasp the object. When thumb and the other four fingers are performing extension/flexion movements, the workspace of fingertips is restricted to the maximum angles of joints. Referring to inverse

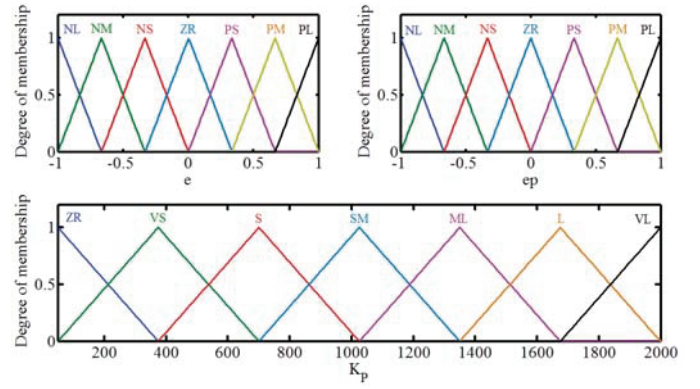


Fig. 5. All Membership Functions: Each of Two Inputs (Upper Panel) and One Output (Lower Panel) Uses 7 Triangular Membership Functions

TABLE I  
A COMPLETE FUZZY LOGIC RULE BASE

$\dot{e} \setminus e$	NL	NM	NS	ZR	PS	PM	PL
NL	ZR	ZR	ZR	ZR	VS	S	SM
NM	ZR	ZR	ZR	VS	S	SM	ML
NS	ZR	ZR	VS	S	SM	ML	L
ZR	ZR	VS	S	SM	ML	L	VL
PS	VS	S	SM	ML	L	VL	VL
PM	S	SM	ML	L	VL	VL	VL
PL	SM	ML	L	VL	VL	VL	VL

N: negative; P: positive; ZR: zero; L: large; M: medium; S: small; V: very

kinematics, the first and second joint angles of the thumb fingertip are constrained in the ranges of  $[0,90]$  and  $[-80,0]$  (degrees). The first, second, and third joint angles of the other four fingers are constrained in the ranges of  $[0,90]$ ,  $[0,110]$  and  $[0,80]$  (degrees), respectively [35].

Next, we present simulations with PD and PID controllers and fuzzy inference system tuned PD controller for the 14 DOFs five-fingered smart prosthetic hand. The parameters of the two-link thumb/three-link fingers [36] were related to desired trajectory. All parameters of the smart prosthetic hand selected for the simulations are given in Table II and the

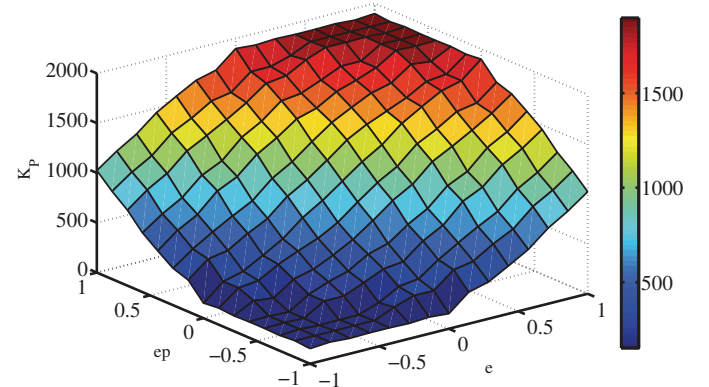


Fig. 6. The Output Surface of Fuzzy Inference System with Two Inputs and 49 Logic Rules

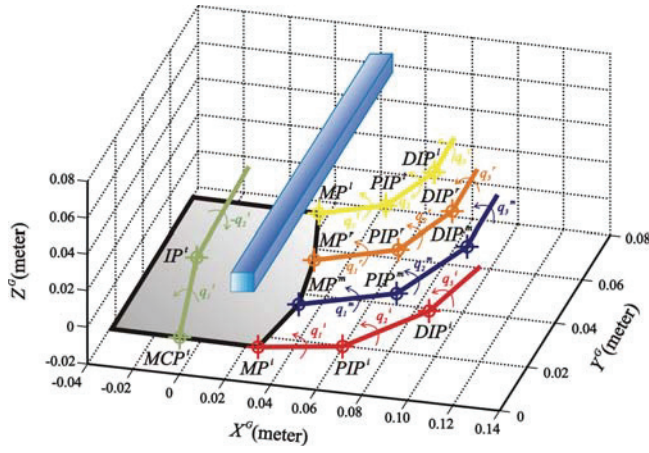


Fig. 7. Five-Fingered Prosthetic Hand Grasping a Rectangular Object

side length and length of the target rectangular rod are 0.010 and 0.100 (m), respectively. The relating parameters between the global coordinate and the local coordinates are defined in Table III. Moreover, in this work, we assumed that each link

TABLE II  
PARAMETER SELECTION OF THE SMART HAND

Parameters	Values
<b>Thumb</b>	
Time ( $t_0, t_f$ )*	0, 20 (sec)
Desired Initial Position ( $X_0^t, Y_0^t$ )**	0.035, 0.060 (m)
Desired Final Position ( $X_f^t, Y_f^t$ )**	0.0495, 0.060 (m)
Desired Initial Velocity ( $\dot{X}_0^t, \dot{Y}_0^t$ )*	0, 0 (m/s)
Desired Final Velocity ( $\dot{X}_f^t, \dot{Y}_f^t$ )*	0, 0 (m/s)
Length ( $L_1^t, L_2^t$ )	0.040, 0.040 (m)
Mass ( $m_1^t, m_2^t$ )	0.043, 0.031 (kg)
<b>Index Finger</b>	
Desired Initial Position ( $X_0^i, Y_0^i$ )**	0.065, 0.080 (m)
Desired Final Position ( $X_f^i, Y_f^i$ )**	0.010, 0.060 (m)
Length ( $L_1^i, L_2^i, L_3^i$ )	0.040, 0.040, 0.030 (m)
Mass ( $m_1^i, m_2^i, m_3^i$ )	0.045, 0.025, 0.017 (kg)
<b>Middle Finger</b>	
Desired Initial Position ( $X_0^m, Y_0^m$ )**	0.065, 0.080 (m)
Desired Final Position ( $X_f^m, Y_f^m$ )**	0.005, 0.060 (m)
Length ( $L_1^m, L_2^m, L_3^m$ )	0.044, 0.044, 0.033 (m)
Mass ( $m_1^m, m_2^m, m_3^m$ )	0.050, 0.028, 0.017 (kg)
<b>Ring Finger</b>	
Desired Initial Position ( $X_0^r, Y_0^r$ )**	0.065, 0.080 (m)
Desired Final Position ( $X_f^r, Y_f^r$ )**	0.010, 0.060 (m)
Length ( $L_1^r, L_2^r, L_3^r$ )	0.040, 0.040, 0.030 (m)
Mass ( $m_1^r, m_2^r, m_3^r$ )	0.041, 0.023, 0.014 (kg)
<b>Little Finger</b>	
Desired Initial Position ( $X_0^l, Y_0^l$ )**	0.055, 0.080 (m)
Desired Final Position ( $X_f^l, Y_f^l$ )**	0.020, 0.060 (m)
Length ( $L_1^l, L_2^l, L_3^l$ )	0.036, 0.036, 0.027 (m)
Mass ( $m_1^l, m_2^l, m_3^l$ )	0.041, 0.023, 0.014 (kg)

\*All fingers use same parameters

\*\*All parameters are in local coordinates

of all fingers is a circular cylinder with the radius ( $R$ ) 0.010 (m), so the inertia  $I_{zzk}^j$  of each link  $k$  of all fingers  $j$  ( $= t, i,$

TABLE III  
PARAMETER SELECTION OF CONVERSION BETWEEN GLOBAL AND LOCAL COORDINATES

Parameters	Values
Rotating $\alpha$	90 (deg)
Rotating $\beta$	45 (deg)
Translating $d^i$	(0.035, 0, 0) (m)
Translating $d^m$	(0.040, 0, -0.020) (m)
Translating $d^r$	(0.035, 0, -0.040) (m)
Translating $d^l$	(0.025, 0, -0.060) (m)

$m, r$  and  $l$ ) can be calculated as

$$I_{zzk}^j = \frac{1}{4}m_k^j R^2 + \frac{1}{3}m_k^j L_k^j{}^2. \quad (22)$$

All initial actual angles are zero and the diagonal coefficients,  $K_P$ ,  $K_I$  and  $K_D$ , for the PD or PID controller alone are arbitrarily chosen as 100. From the derived dynamic and control models, after the parameters ( $K_P$  and  $K_D$ ) are selected, the control signal  $u$  and torque  $\tau$  can be calculated.

Figure 8 shows tracking errors ( $e_1^t$  and  $e_2^t$  on the left

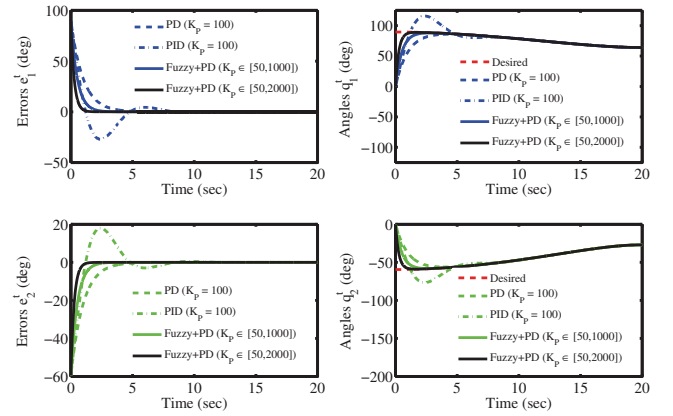


Fig. 8. Tracking Errors (Left) and Desired/Actual Angles (Right) of Joints 1 (Upper) and 2 (Lower) for Two-Link Thumb Using PD (Dash Line), PID (Dot Line) and Fuzzy Logic Based PD (Solid Line) Controllers

column) and desired/actual angles ( $q_1^t$  and  $q_2^t$  on the right column) of joints 1 (the top row) and 2 (the bottom row) for two-link thumb using PD (dash line), PID (dot line) and fuzzy logic based PD (solid line) controllers. The tracking errors for PD control are convergent within 5 seconds without overshooting, but PID control acts longer (approximate 10 seconds) with overshooting and oscillation. The proposed hybrid fuzzy logic PD control using parameters  $K_P \in [50, 1000]$  and  $K_D \in [50, 500]$  provides faster convergence than both PD and PID controllers. To further study whether the parameter range influences tracking errors, we found that the larger parameter range, the faster convergent speed after altering  $K_P \in [50, 2000]$  without additional computational time. We also used fuzzy logic controller with two inputs (error and error rate) and one output (control signal), but the control system could not obtain convergent tracking errors (data not shown). These data suggest that fusion of soft computing (SC) and



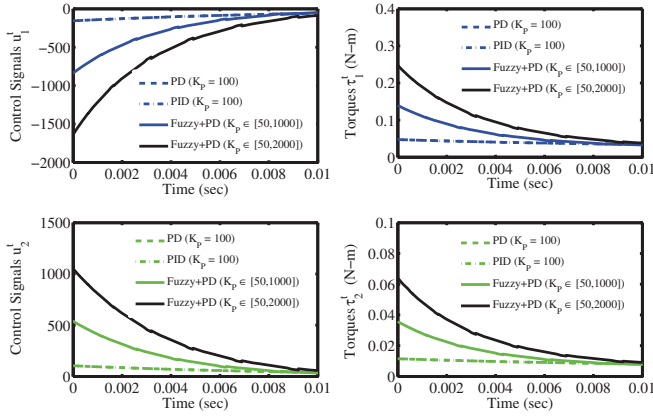


Fig. 9. Control Signals (Left) and Actuated Torques (Right) of Joints 1 (Upper) and 2 (Lower) for Two-Link Thumb Using PD (Dash Line), PID (Dot Line) and Fuzzy Logic Based PD (Solid Line) Controllers in 0.01 Second

hard control (HC) is superior to either HC or SC methodology alone.

The time-variant computed control signals ( $u_1^t$  and  $u_2^t$ ) and torques ( $\tau_1^t$  and  $\tau_2^t$ ) for two-link thumb within the first 0.01 second are shown in Figure 9, suggesting that the presented hybrid fuzzy logic PD controller requires more power (torque) than PD and PID controllers in order to obtain faster convergent tracking errors.

Similarly, Figures 10, 12, 14 and 16 show tracking errors and desired/actual angles for all remaining three-link fingers. Figures 11, 13, 15 and 17 show control signals and torques for the mapping three-link fingers.

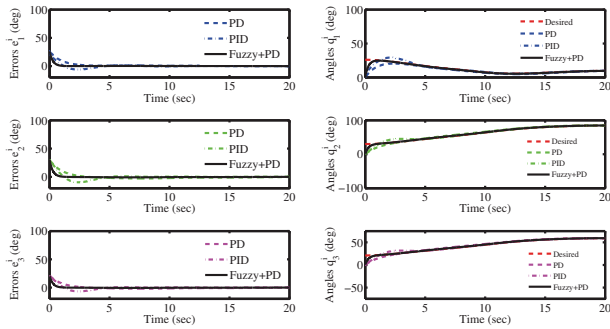


Fig. 10. Tracking Errors (Left) and Desired/Actual Angles (Right) of Joints 1 (Top), 2 (Middle) and 3 (Bottom) for Three-Link Index Finger Using PD (Dash Line), PID (Dot Line) and Fuzzy Logic Based PD (Solid Line) Controllers

## V. CONCLUSIONS AND FUTURE WORK

For a five-fingered smart prosthetic hand, a hybrid control technique involving soft control with adaptive neuro-fuzzy inference system (ANFIS) and fuzzy logic (FL) and hard control with proportional-derivative (PD) was presented. The ANFIS is used for inverse kinematics and FL is used for tuning the PD parameters with two input layers (error and

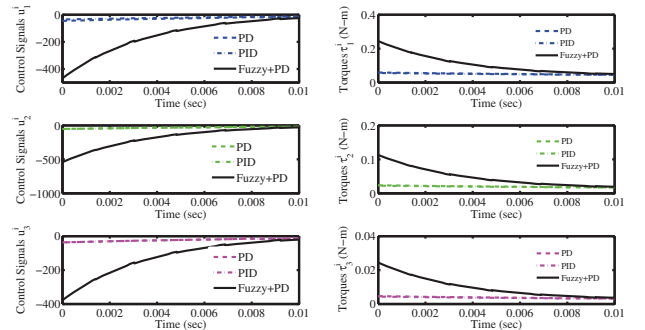


Fig. 11. Control Signals (Left) and Actuated Torques (Right) of Joints 1 (Top), 2 (Middle) and 3 (Bottom) for Three-Link Index Finger Using PD (Dash Line), PID (Dot Line) and Fuzzy Logic Based PD (Solid Line) Controllers in 0.01 Second

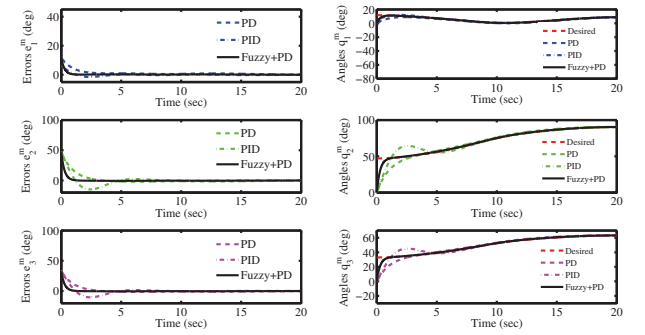


Fig. 12. Tracking Errors (Left) and Desired/Actual Angles (Right) of Joints 1 (Top), 2 (Middle) and 3 (Bottom) for Three-Link Middle Finger Using PD (Dash Line), PID (Dot Line) and Fuzzy Logic Based PD (Solid Line) Controllers

error change) using 7 triangular membership functions and 49 fuzzy logic rules. Simulation results with FL-tuned PD (hybrid) controller showed superior performance compared to the PD and PID control alone. Work is underway to extend this methodology to a real-time implementation on the prototype of a prosthetic hand.

## ACKNOWLEDGMENT

The research was sponsored by the U.S. Department of the Army, under the award number W81XWH-10-1-0128 awarded and administered by the U.S. Army Medical Research Acquisition Activity, 820 Chandler Street, Fort Detrick, MD 21702-5014. The information does not necessarily reflect the position or the policy of the Government, and no official endorsement should be inferred. For purposes of this article, information includes news releases, articles, manuscripts, brochures, advertisements, still and motion pictures, speeches, trade association proceedings, etc.

## REFERENCES

- [1] "Casualties in Afghanistan & Iraq," [www.unknownnews.net](http://www.unknownnews.net), June 5 2006.

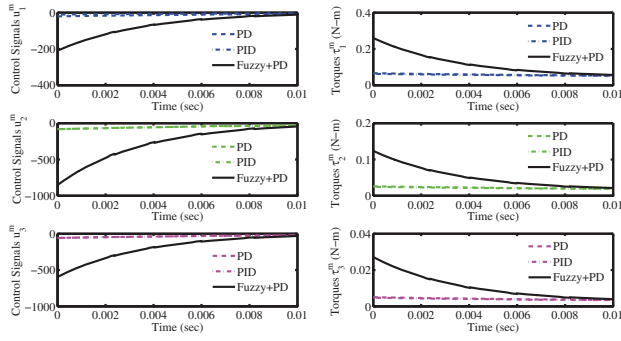


Fig. 13. Control Signals (Left) and Actuated Torques (Right) of Joints 1 (Top), 2 (Middle) and 3 (Bottom) for Three-Link Middle Finger Using PD (Dash Line), PID (Dot Line) and Fuzzy Logic Based PD (Solid Line) Controllers in 0.01 Second

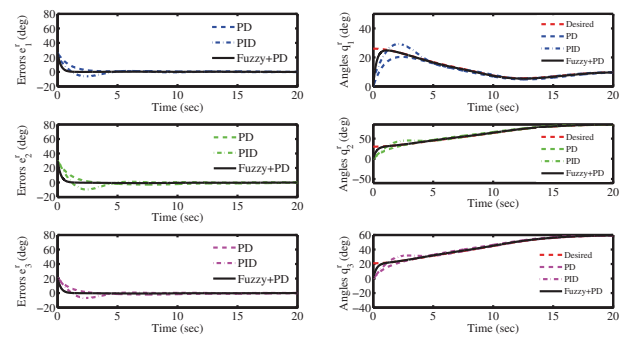


Fig. 14. Tracking Errors (Left) and Desired/Actual Angles (Right) of Joints 1 (Top), 2 (Middle) and 3 (Bottom) for Three-Link Ring Finger Using PD (Dash Line), PID (Dot Line) and Fuzzy Logic Based PD (Solid Line) Controllers

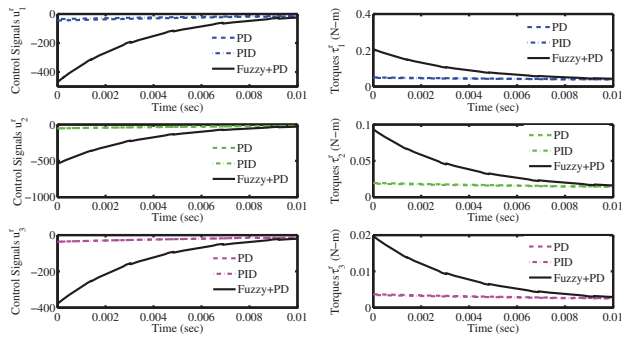


Fig. 15. Control Signals (Left) and Actuated Torques (Right) of Joints 1 (Top), 2 (Middle) and 3 (Bottom) for Three-Link Ring Finger Using PD (Dash Line), PID (Dot Line) and Fuzzy Logic Based PD (Solid Line) Controllers in 0.01 Second

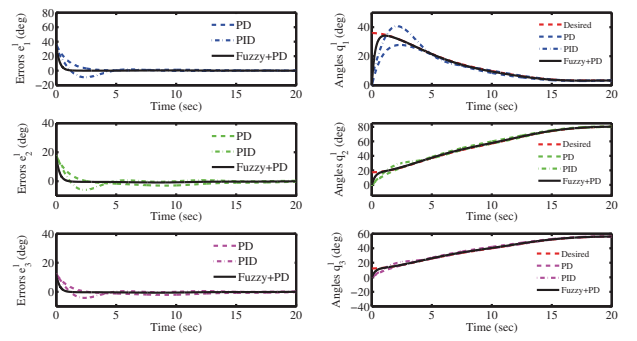


Fig. 16. Tracking Errors (Left) and Desired/Actual Angles (Right) of Joints 1 (Top), 2 (Middle) and 3 (Bottom) for Three-Link Little Finger Using PD (Dash Line), PID (Dot Line) and Fuzzy Logic Based PD (Solid Line) Controllers

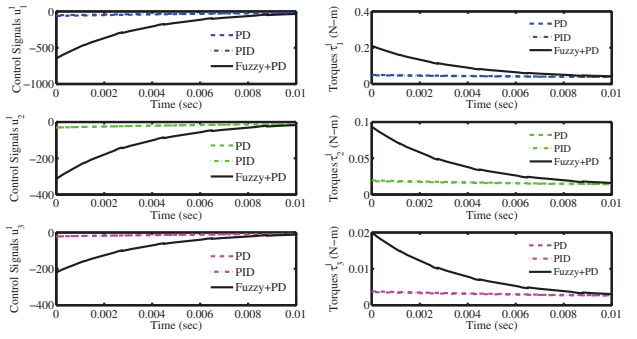


Fig. 17. Control Signals (Left) and Actuated Torques (Right) of Joints 1 (Top), 2 (Middle) and 3 (Bottom) for Three-Link Little Finger Using PD (Dash Line), PID (Dot Line) and Fuzzy Logic Based PD (Solid Line) Controllers in 0.01 Second

- [2] "Amputee Coalition of America (ACA) National Limb Loss Information Center (NLLIC) Limb Loss Facts in the United States," <http://www.amputee-coalition.org>, 2006.
- [3] P. F. Adams, G. E. Hendershot, and M. A. Marano, "Current estimates from the national health interview survey, 1996," *National Center for Health Statistics. Vital and Health Statistics*, vol. 200, no. 10, pp. 1–203, 1999.
- [4] K. Ziegler-Graham, E. J. MacKenzie, P. L. Ephraim, T. G. Travison, and R. Brookmeyer, "Estimating the prevalence of limb loss in the united states: 2005 to 2050," *Archives of Physical Medicine and Rehabilitation*, vol. 89, pp. 422–429, March 2008.
- [5] M. Zecca, S. Micera, M. Carrozza, and P. Dario, "Control of multifunctional prosthetic hands by processing the electromyographic signal," *Critical Reviews<sup>TM</sup> in Biomedical Engineering*, vol. 30, pp. 459–485, 2002, (Review article with 96 references).
- [6] J. C. K. Lai, M. P. Schoen, A. Perez-Gracia, D. S. Naidu, and S. W. Leung, "Prosthetic devices: Challenges and implications of robotic implants and biological interfaces," *Proceedings of the Institute of Mechanical Engineers (IMEchE), Part H: Journal of Engineering in Medicine*, vol. 221, no. 2, pp. 173–183, January 2007, special Issue on Micro and Nano Technologies in Medicine.
- [7] L. Zollo, S. Roccella, E. Guglielmelli, M. C. Carrozza, and P. Dario, "Biomechatronic design and control of an anthropomorphic artificial hand for prosthetic and robotic applications," *IEEE/ASME Transactions on Mechatronics*, vol. 12, no. 4, pp. 418–429, August 2007.
- [8] D. S. Naidu, C.-H. Chen, A. Perez, and M. P. Schoen, "Control strategies for smart prosthetic hand technology: An overview," in *Proceedings of the 30th Annual International IEEE EMBS Conference*, Vancouver, Canada, August 20–24 2008, pp. 4314–4317.
- [9] D. S. Naidu and C.-H. Chen., *Automatic Control Techniques for Smart Prosthetic Hand Technology: An Overview*, book chapter 12, to appear in a book titled "Distributed Diagnosis and Home Healthcare (D2H2): Volume 2". California, USA: American Scientific Publishers, 2011, (in printed).
- [10] C.-H. Chen, K. W. Bosworth, M. P. Schoen, S. E. Bearden, D. S. Naidu, and A. Perez, "A study of particle swarm optimization on leukocyte adhesion molecules and control strategies for smart prosthetic hand," in *2008 IEEE Swarm Intelligence Symposium (IEEE SIS08)*, St. Louis, Missouri, USA, September 21–23 2008.

- [11] C.-H. Chen, D. S. Naidu, A. Perez, and M. P. Schoen, "Fusion of hard and soft control techniques for prosthetic hand," in *Proceedings of the International Association of Science and Technology for Development (IASTED) International Conference on Intelligent Systems and Control (ISC 2008)*, Orlando, Florida, USA, November 16-18 2008, pp. 120-125.
- [12] C.-H. Chen, D. S. Naidu, A. Perez-Gracia, and M. P. Schoen, "A hybrid control strategy for five-fingered smart prosthetic hand," in *Joint 48th IEEE Conference on Decision and Control (CDC) and 28th Chinese Control Conference (CCC)*, Shanghai, P. R. China, December 16-18 2009, pp. 5102-5107.
- [13] D. Naidu, *Optimal Control Systems*. Boca Raton, FL: CRC Press, 2003.
- [14] C.-H. Chen, D. S. Naidu, A. Perez-Gracia, and M. P. Schoen, "A hybrid optimal control strategy for a smart prosthetic hand," in *Proceedings of the ASME 2009 Dynamic Systems and Control Conference (DSCC)*, Hollywood, California, USA, October 12-14 2009, (No. DSCC2009-2507).
- [15] C.-H. Chen and D. S. Naidu, "Optimal control strategy for two-fingered smart prosthetic hand," in *Proceedings of the International Association of Science and Technology for Development (IASTED) International Conference on Robotics and Applications (RA 2010)*, Cambridge, Massachusetts, USA, November 1-3 2010, pp. 190-196.
- [16] F. Lewis, S. Jagannathan, and A. Yesildirek, *Neural Network Control of Robotic Manipulators and Nonlinear Systems*. London, UK: Taylor & Francis, 1999.
- [17] F. Lewis, D. Dawson, and C. Abdallah, *Robot Manipulators Control: Second Edition, Revised and Expanded*. New York, NY: Marcel Dekker, Inc., 2004.
- [18] C.-H. Chen, D. S. Naidu, A. Perez-Gracia, and M. P. Schoen, "A hybrid adaptive control strategy for a smart prosthetic hand," in *The 31st Annual International Conference of the IEEE Engineering Medicine and Biology Society (EMBS)*, Minneapolis, Minnesota, USA, September 2-6 2009, pp. 5056-5059.
- [19] C.-H. Chen, D. S. Naidu, and M. P. Schoen, "An adaptive control strategy for a five-fingered prosthetic hand," in *The 14th World Scientific and Engineering Academy and Society (WSEAS) International Conference on Systems, Latest Trends on Systems (Volume II)*, Corfu Island, Greece, July 22-24 2010, pp. 405-410.
- [20] C.-H. Chen, M. P. Schoen, and K. W. Bosworth, "A condensed hybrid optimization algorithm using enhanced continuous tabu search and particle swarm optimization," in *Proceedings of the ASME 2009 Dynamic Systems and Control Conference (DSCC)*, Hollywood, California, USA, October 12-14 2009, (No. DSCC2009-2526).
- [21] A. Konar, *Computational Intelligence: Principles, Techniques and Applications*. Berlin, Germany: Springer-Verlag, 2005.
- [22] C.-H. Chen, K. W. Bosworth, and M. P. Schoen, "Investigation of particle swarm optimization dynamics," in *Proceedings of International Mechanical Engineering Congress and Exposition (IMECE) 2007*, Seattle, Washington, USA, November 11-15 2007, (No. IMECE2007-41343).
- [23] C.-H. Chen, K. Bosworth, and M. P. Schoen, "An adaptive particle swarm method to multiple dimensional problems," in *Proceedings of the International Association of Science and Technology for Development (IASTED) International Symposium on Computational Biology and Bioinformatics (CBB 2008)*, Orlando, Florida, USA, November 16-18 2008, pp. 260-265.
- [24] C.-H. Chen, "Hybrid control strategies for smart prosthetic hand," Ph.D. dissertation, Measurement and Control Engineering, Idaho State University, May 2009.
- [25] R. N. Jazar, *Theory of Applied Robotics. Kinematics, Dynamics, and Control*. New York, USA: Springer, 2007.
- [26] B. Siciliano, L. Sciavicco, L. Villani, and G. Oriolo, *Robotics: Modelling, Planning and Control*. London, UK: Springer-Verlag, 2009.
- [27] J.-S. Jang, C.-T. Sun, and E. Mizutani, *Neuro-Fuzzy and Soft Computing: A Computational Approach to Learning and Machine Intelligence*. Upper Saddle River, NJ: Prentice Hall PTR, 1997.
- [28] F. Karray and C. De Silva, *Soft Computing and Intelligent Systems Design: Theory, Tools and Applications*. Harlow, England, UK: Pearson Educational Limited, 2004.
- [29] H. Nguyen, N. Prasad, C. Walker, and E. Walker, *A First Course in Fuzzy and Neural Control*. Boca Raton, FL: Chapman & Hall/CRC, 2003.
- [30] V. Nandikolla and D. Naidu, "Blood glucose regulation for diabetic mellitus using a hybrid intelligent technique," in *Proceedings of the 2005 ASME International Mechanical Engineering Congress and Exposition (IMECE)*, Orlando, FL, November 5-11 2005, pp. 1-6.
- [31] V. Nandikolla, "Fusion of hard and soft control techniques in biomedical engineering," Ph.D. dissertation, Measurement and Control Engineering, Idaho State University, Pocatello, Idaho, December 2005, thesis Supervisor: D.S. Naidu.
- [32] R. Kelly, V. Santibanez, and A. Loria, *Control of Robot Manipulators in Joint Space*. New York, USA: Springer, 2005.
- [33] A. Nikoobin and R. Haghighi, "Lyapunov-based nonlinear disturbance observer for serial n-link robot manipulators," *Journal of Intelligent and Robotic Systems*, 2008, (Published online on 11 December 2008).
- [34] Y. Z. Arslan, Y. Hacıoglu, and N. Yagiz, "Prosthetic hand finger control using fuzzy sliding modes," *Journal of Intelligent and Robotic Systems*, vol. 52, pp. 121-138, 2008.
- [35] P. K. Lavangie and C. C. Norkin, *Joint Structure and Function: A Comprehensive Analysis, Third Edition*. Philadelphia, PA: F. A. Davis Company, 2001.
- [36] S. Arimoto, *Control Theory of Multi-fingered Hands: A Modeling and Analytical-Mechanics Approach for Dexterity and Intelligence*. London, UK: Springer-Verlag, 2008.

**CHAPTER 12**

**Automatic Control Techniques for  
Smart Prosthetic Hand  
Technology: An Overview**

**D. Subbaram Naidu, Cheng-Hung Chen**

*Measurement and Controls Engineering Research Center, School of Engineering,  
Idaho State University, Pocatello, Idaho, 83209-8060, USA*

**CONTENTS**

1. Introduction . . . . . 1  
    1.1. Relevance to the Military . . . . . 2  
2. Control Strategies . . . . . 3  
    2.1. Prosthetic Hands . . . . . 3  
    2.2. Chronological Overview . . . . . 4  
    2.3. Main Control Technique Overview Since 2007 . . . . . 11  
    2.4. Revolutionary Prosthesis . . . . . 14  
3. Hybrid Intelligent Control Strategies . . . . . 14  
    3.1. Fusion of Soft and Hard Computing Techniques . . . . . 14  
4. Overview of Research at ISU . . . . . 16  
5. Recent Developments in Neuroprosthetics . . . . . 17  
6. Future Directions . . . . . 17  
References . . . . . 18

**1. INTRODUCTION**

The human hand is considered to be an agent of the human brain and is the most intriguing and versatile appendages of the human body. Over the last several years, attempts have been made to build a prosthetic hand to replace the human hand that fully simulates the various natural/human-like operations of moving, grasping, lifting, twisting and so on. Replicating the human hand in all its various functions is still a challenging task due to its extreme complexity. It has 27 bones, controlled by about 38 muscles to provide the hand with 22 degrees of freedom (DOF) and incorporates about 17,000 tactile units of 4 different units [99, 207]. Parallels between dextrous robot and human hands were explored by studying sensor motor integration in the design and



control of these robots by bringing together experimental psychologists, kinesiologists, computer scientists, and electrical and mechanical engineers.

### 1.1. Relevance to the Military

“In the United States, there are approximately 1.9 million people living with limb loss” due to combat operations (such as conflicts, wars, etc.) and non-combat operations such as accidents, or birth defects, according to the Amputee Coalition of America (ACA) [3]. Further, during the recent wars in Afghanistan and Iraq, “at least 251,102 were killed and 532,715 seriously wounded” [192].

The following documents reveal the intense interest by military in the area of smart prosthetics.

1. First, according to [131], recognizing that “arm amputees rely on old devices” and that the existing technology for arm and hand amputees hasn’t changed significantly in the past six decades, the Defense Department is embarking on a research program to “fund prosthetics research” according to [132] to revolutionize upper-body prosthetics and to develop artificial arms that will “feel, look and perform” like a real arm guided by the central nervous system.
2. According to [55, 56], Bio-Revolution is one of the eight strategic research thrusts that DARPA is emphasizing in response to emerging trends and national security. In particular, the Human Assisted Neural Devices program under Bio-Revolution will have “immediate benefit to injured veterans, who would be able to control prosthetics. . . .” A related area of interest in Bio-Revolution is Cell and Tissue Engineering.
3. Next, according to the Defense Science Office (DSO) of DARPA [57], emerging technologies for combat casualties care with dual-usage for both military and civilian medical care, focus on programs in Revolutionizing Prosthetics, Human Assisted Neural Devices, Biologically Inspired Multi-functional Dynamic Robotics, and so on. In particular, according to [58], “every day one of the most devastating battlefield injuries is loss of a limb . . . at DARPA, the vision of a future is to . . . regain full use of that limb again.”

In research and development of a prosthetic hand using non-invasive techniques, the basic problems are

1. acquiring and classifying electromyographic (EMG) signals to correspond to various human-like operations or features,
2. converting EMG feature signals to control signals to input to actuators to operate the prosthetic hand, and
3. designing and building a prosthetic hand with necessary sensors to operate according to the control signal that corresponds to the EMG signal intended for the particular identified hand operation.

This overview was first prepared in 2006 [138] when the first author and his colleagues at Idaho State University submitted a proposal on *Smart Prosthetic Hand Technology—Phase I of III* to the Telemedicine Advanced Technology Research Center (TATRC), which is the corporate or central laboratory for advanced technology research of the U.S. Army Medical Research and Materiel Command (USAMRMC) of U.S. Department of Defense. Since the proposal was funded by the TATRC in July 2007, the overview has been continuously updated and was then completed in the present form. In this chapter, a chronological overview of the applications of control theory to prosthetic hand is presented. The overview focuses on *hard* computing or control techniques, such as multi-variable feedback, optimal, nonlinear, adaptive and robust, and *soft* computing or control techniques, such as artificial intelligence, neural networks, fuzzy logic, genetic algorithms, and on the *fusion* of hard and soft control techniques. This overview, focusing on recent developments, is intended to supplement the already existing excellent survey articles [50, 112, 207], and is not intended to be an exhaustive survey on this topic. Any omissions of other works is purely unintentional.

## 2. CONTROL STRATEGIES

### 2.1. Prosthetic Hands

Over the last several years artificial hands have been developed by various researchers in the field and some of the prosthetic devices developed are given below (in chronological order) [207, 208]:

1. Russian arm – [108, 128, 177]
2. Waseda hand – [103]
3. Boston arm<sup>a</sup> – [125]
4. UNB hand (University of New Brunswick) – [88, 120, 162]
5. Hanafusa hand – [79]
6. Crossley hand – [51]
7. Okada hand – [146]
8. Utah/MIT hand (University of Utah/Massachusetts Institute of Technology) – [95, 96, 94]
9. JPL/Stanford hand (Jet Propulsion Laboratory/Stanford University) – [167, 195]
10. Minnesota hand – [119]
11. Manus hand – [114, 157]
12. Kobayashi hand – [107]
13. Rovetta hand – [165]
14. UT/RAL hand – [105]
15. Dextrous gripper – [193]
16. Belgrade/USC hand (University of Belgrade/University of Southern California) – [18]
17. Southampton hand (University of Southampton, Southampton, UK) – [111]
18. MARCUS hand (Manipulation And Reaction Control under User Supervision) – [113]
19. Kobe hand (Kobe University, Japan) – [148]
20. Robonaut hand (NASA Johnson Space Center) – [124]
21. NTU hand (National Taiwan University) – [86]
22. Hokkaido hand – [145]
23. DLR hand (Deutschen Zentrums für Luft- und Raumfahrt-German Aerospace Center) – [26, 121]
24. TUAT/Karlsruhe hand (Tokyo University of Agriculture and Technology/University of Karlsruhe) – [74]
25. BUAA hand (Beijing University of Aeronautics and Astronautics) – [209]
26. TBM hand (Toronto/Bloorview MacMillan) – [59]
27. ULRG System (University of Louisiana Robotic Gripper) – [109]
28. Oxford hand – [114]
29. IOWA hand (University of Iowa) – [205]
30. MA-I hand – [182]
31. RCH -1 (ROBO CASA hand 1<sup>b</sup>) – [159]
32. UB hand (University of Bologna) – [123]
33. Ottobock SUVA hand – ([www.ottobock.co.uk](http://www.ottobock.co.uk))
34. Northwestern University system – [72]
35. SKKU Hand II (Sungkyunkwan University, Korea) – [44]
36. Applied Physics Laboratory (APL) at Johns Hopkins University (JHU) – [7, 8, 58]

Some of the commercial web sites for prosthetic devices are:

1. Sensor Hand™ Speed from Otto Bock ([www.ottobock.co.uk](http://www.ottobock.co.uk)),
2. VASI (Variety Ability Systems Inc.), a company of the Otto Boch Group (<http://www.vasi.on.ca/index.html>),

<sup>a</sup>The “Boston Arm,” project involved the Harvard Medical School, Massachusetts General Hospital, the Liberty Mutual Research and Rehabilitation Centers, and M.I.T.

<sup>b</sup>The Italy-Japan joint laboratory for Research on Humanoid and Personal Robotics.



prosthetic limbs was initiated by the US National Academy of Sciences in response to the needs of a large number of casualties in World War II [135]. Researchers reporting in Refs. [16, 203] first proposed the concept of EMG signals for the control of a prosthetic hand for amputees. A proportional (open-loop) control systems in which the amplitude of the hand motor voltage and hence its speed and force measured from strain gauges varies in direct proportion (linearly) to the amplitude of the EMG signal generated by the prosthetic hand, was first reported in Refs. [24, 25]. In addition, the system added force and velocity feedback controls so the users could feel more natural when using this device. An adaptive control scheme was developed by [187] for the Southampton Hand.

#### **1971–79:**

The work reported in Ref. [162] studied the effect of sensory feedback based on semi-conductor strain gauges on either edge of thumb of the prosthetic hand to adjust the stimulus magnitude to target value and avoid dropping or crushing objects for control of a prosthesis and found this acceptable for patients. When the strain gauges received the stimulus, the system amplified and transferred the signals to comparator, and then the comparator modified the range of amplitude of stimulus to the level that the users needed. However, the device with feedback is two or three times larger than the normal hand. A hierarchical method consisting of analytical control theory, such as performance-adaptive self-organizing control algorithm and artificial intelligence using fuzzy automaton, was presented in Ref. [169] to drive a prosthetic hand.

#### **1980–89:**

In providing a historical perspective, the contribution in Ref. [43] presented the status of the closed-loop (feedback) control principles for the application of prosthetic devices. Three concepts relating to supplemental sensory feedback, artificial reflexes, and feedback through control interfaces were discussed, and it was concluded that “we have not moved very far in the last 65 years in the clinical application of these concepts.” A statistical analysis involving the study of zero-crossings, second to fifth moments and correlation functions and pattern classification of EMG signals was given in Ref. [168]. A probabilistic model of the EMG pattern was formulated in the feature space of integral absolute value (IAV) to provide the relation between a command, represented by motion and speed variables and the location and shape of the pattern for real-time control of a prosthetic arm as given in Ref. [118]. Using kinematic relationships for dynamic model of fingers, multi-variable feedback control strategies using pole assignment in frequency domain were employed by [195] to guarantee local stability for controlling one finger of the JPL/Stanford hand. The work in Ref. [195] produced the dynamic models of three fingers (thumb, index, and middle) and three joints first, and then used Laplace transform to work in frequency domain. To get a guaranteed stability of control system, the roots/poles had to be located in the left half plane. Hence, they could get a desired steady movement of fingers by controlling the positions of the roots. The works reported by the groups in Refs. [49, 136] were the first to investigate various aspects such as kinematics, prehensility, dynamics, and control of multi-fingered hands manipulating objects of arbitrary shape in three dimensions.

#### **1990–99:**

Design, implementation, and experimental verification of an improved cybernetic elbow prosthesis was presented in Refs. [1, 2] that mimics the natural limb to both internal (voluntary) inputs from the amputee and external inputs from the environment. The work in Ref. [181] considered a dextrous hand employing a systematic approach to achieve the object stiffness control by actuator position control, tendon tension control, joint torque control, joint stiffness control, and Cartesian fingertip stiffness control. The work in Ref. [174] conducted a survey of 33 patients wearing the proportional myoelectric hand grouped into 3 categories based on previous experience with a terminal device: digital (on-off) myoelectric hand, body-powered terminal device, and no terminal device. The survey results showed that the group of patients having experience with the digital hand “were most impressed with proportionally controlled hand,” because it has the advantages: comfortable, cosmetic acceptance, more natural, superior pinch force

(11–25 lb) compared to voluntary opening (7–8 lb), a greater range of function but less energy, sensory feedback, force feedback, and short below-elbow.

The research work in Ref. [81] developed three tests for evaluation of input-output properties of patient control of neuroprosthetic hand grasp, which can compensate or enrich the function of a damaged peripheral nervous system. The first test was for static input-output properties of the hand grasp, the second one was for control of hand grasp outputs while tracking step and ramp functions, and the final test was to obtain the input-output frequency response of the hand grasp system dynamics to estimate the transfer function using spectral analysis. Each test used visual feedback when the users controlled the grasp force and grasp position tracking of the hand. It was shown in Ref. [89] that the myoelectric signal is not random during the initial phase of muscle contraction thus providing a means of classifying patterns from different contraction types. The means is to establish the 60 records of an isometric contraction of the subjects and then produce some anisometric contraction types, like flexion and extension. This information was useful in designing a new multi-function myoelectric control system using artificial neural networks (ANN) for classifying myoelectric patterns. Additionally, the hidden layer size, segment length, and EMG electrode positions were studied. See related works in Refs. [68, 69, 75, 76] on multi-functional myoelectric control systems using pattern recognition methods for myoelectric signal extraction and classification. The control philosophy of a multi-fingered robotic hands for possible adaptation and use in prosthetics and rehabilitation was discussed in Refs. [90–92] with respect to the Belgrade/USC robot hand [18], called PRESHAPE (Programmable Robotic Experimental System for Hands and Prosthetics Evaluation), which can estimate a system that translates task commands to motor commands using pressure sensors, force sensors and pressure feedback, which is very useful to detect small contact forces.

Using the dynamic model of the nonlinear neuromuscular (motor servo) control system of human finger muscles including mechanical properties (such as viscoelasticity) of the muscle and stretch reflex, a surface-based myoelectrically-controlled biomimetic prosthetic hand (called the Kobe hand) with three fingers (thumb, index and middle fingers) was developed at Kobe University, Japan [148] with a system consisting of an EMG signal processing unit, the dynamic model, a positional control unit, and the prosthetic device. A survey of four important properties—dexterity, equilibrium, stability, and dynamic behavior relating to autonomous multi-fingered robotic hands—was presented [178]. An interesting aspect of this literature survey is a series of tables relating to existing multi-fingered robotic hands, force closure, dexterity in kinematically redundant robotic hands, equilibrium, in robotic grasp, and stability. As reported in Ref. [15], an intelligent prosthesis control system, developed by Animated Prosthetics, consists of two parts: the animation control system (ACS) residing in prosthesis and a remote prosthesis configuration unit (PCU) capable of on/off to variable speed/grip. Dynamic control of two arms to manipulate cooperatively an object with rolling contacts was addressed [170] using a nonlinear feedback control methodology that decouples and linearizes the system.

A sensory control system based on a force sensing resistor (FSR) was developed [191] at The National Institute for Accidents at Work (INAIL), Bologna, Italy, to control the strength of the grip on objects for a commercial prosthetic hand having two main functions: the automatic search for contact with the object and the detection of the object possibly slipping the grip by involuntary feedback (force sensors and slipping sensors). Further, automatic tuning of control parameters of the prostheses was investigated [23] using fuzzy logic expert systems resulting in a software package called the microprocessor controlled arm auto tuning. The automatic tuning software works as follows:

- the client connects the prosthesis hardware
- the program needs both sensor signals as client input the program combines the above qualitative and quantitative information stored in the fuzzy logic database to calculate the prosthesis parameter values
- the program enables the new parameter values to be down-loaded into the prosthesis control system memory.

Dynamic modeling of a robotic hand was proposed [172] using a hybrid approach with a discrete event aspect of grasping and continuous-time part with a variable structure impedance control algorithm. A novel on-line learning method was reported in Ref. [145] for prosthetic hand control based on EMG measurements with a system consisting of three units:

- an analysis unit for generating feature vectors containing useful information for discriminating motions from EMG signals
- an adaptation unit for adapting to the amputee's individual variation and for discriminating motions from the feature vector and at the same time generating the necessary control commands to the prosthetic hand
- a trainer unit for directing the adaptation unit to learn in real time based on the amputee's teaching signal and the feature vector.

In Ref. [191] researchers built a sensory control system based on the force-sensing resistor (FSR) for an upper limb prosthesis and an optical sensor for detecting movement. The prostheses produced were of the "all or nothing" (opening or closing) and proportional control type (the relationship between force and EMG signal is linear). For traditional control, it used voluntary (visual) feedback, but the users had to pay close attention. This work developed an involuntary feedback control that uses two kinds of sensors, strength and slipping sensors. If the prosthesis hand is slipping, the control system can automatically order the actuator of the prosthesis to increase the grip strength. On receiving the EMG signal, the hand begins a closing action and goes on closing until the FSRs produce a signal that is greater than or equal to a "contact threshold" value. Then it stops because the object has been grasped with the required strength of grip. The automatic grip mechanism is very useful in grasping delicate objects.

The investigation in Ref. [130] showed that the proposed neuro-fuzzy classifier known as Abe-Lan network, is able to identify correctly all the EMG signals related to different movements of the human hand. A highly anthropomorphic human hand, called Robonaut Hand consisting of five fingers and fourteen independent degrees of freedom, was built at NASA Johnson Space Center to interface with extra-vehicular activity (EVA) crew interfaces onboard the International Space Station (ISS) [124].

#### 2000–2007:

In Ref. [190], estimating muscular contraction levels of flexors and extensors using neural networks, a new *impedance control* technique [83] was developed to control impedance parameters such as the moment of inertia, joint stiffness, and viscosity of a skeletal muscle model of a prosthetic hand. An overview of dextrous manipulation gave [147] an interesting time-line chart for the development of robotic dextrous manipulation during the period 1960s to 2000. An excellent survey [19] summarizing the evolution and state of the art in the robotic hands focusing mainly on functional requirements of manipulative dexterity, grasp robustness, and human operability. Also, the work in Ref. [126] exploited the nonholonomic character of a pair of bodies with regular rigid surfaces rolling onto each other, to study the constructive controllability algorithm for planning rolling motions for dextrous robot hands. A control system architecture was proposed [133, 134] with a feedforward loop based on EMG measurements consisting of a low-pass filter and neural network to provide the actual torque signal and a feedback loop based on the desired angle consisting of a proportional-derivative (PD) controller to provide the desired torque signal and the error signal between these torques drives the prosthetic hand to achieve the desired angle while the neural network learns based on feedback error.

Peckham et al. [155] studied finger extension, external control, overhead reach, and forearm pronation. For finger extension, they used two electrodes: one placed between the 2nd and 3rd metacarpals and the other between the 3rd and 4th metacarpals. They could provide full extension of the index, long, and ring fingers. For external control, a new form of control was developed by using retained voluntary wrist extension to control grasp opening and closing. Overhead reach can be provided by stimulation of the triceps muscle, so elbow position can be controlled by voluntary activation of biceps as

an antagonist. As for forearm pronation, the main issues are an increased number of stimulus channels to allow stimulation of the finger intrinsic muscles, triceps, and forearm pronator, an implanted control source, bidirectional communication between sensor and body, reduced size, and reduction of all external cables. The work in Ref. [207] presents a review of the traditional methods for control of artificial hands using EMG signals in both clinical and research areas and points out future developments in the control strategy of the prosthetics, in particular advocating neuroprosthesis with biocompatible neural interface for providing sensory feedback to the user leading to electroneurographic (ENG) based control in place of electromyographic (EMG) control.

Collaboration between the University of Southampton and University of New Brunswick (UNB) [120] resulted in a hybrid control system using a multilayer perceptron (MLP) artificial neural network as a classifier of time-domain features set (zero-crossings, mean absolute value, mean absolute slope, and trace length) extracted from myoelectric signals (MES) and a digital signal processor (DSP) controlling the grip pressure of the prosthetic hand without visual feedback (voluntary feedback). Design and development of an underactuated (the number of actuators less than the degrees-of-freedom) mechanism applicable to prosthetic hand was presented in Ref. [127] based on dynamic model of fingers leading to adaptive grasp (that is, being able to conform to the shape of an object held within the hand).

Although an adaptive control scheme was developed [187] for a Southampton Hand, further developments were made in the research first generation [22, 112] producing their IP (intelligent prosthesis) according to Ref. [111]. The investigation [116] provided an evolution of microprocessor-based control systems for prosthetics classified as (based on digital systems), second generation (with low power), and third generation (based on microprocessors and digital signal processors). The work in Ref. [114] conducted a comparison of Oxford and Manus hand prostheses with respect to:

1. hand mechanisms
2. control electronics: EMG analog amplifiers, A/D converters, digital signal processors
3. sensors: force, position and slip sensors based on Hall effect
4. manipulation or control schemes: Oxford hand used Southampton Adaptive Manipulation Scheme consisting of a three-level hierarchical scheme and Manus used a two-level scheme.

The scheme suggested in Ref. [30] consisted of five modules, including an artificial musculoskeletal system, position and force sensors, 3D force sensors, low-level control loop dedicated to control slipping and grasping, and an EMG control unit. Further, the scheme used two semiconductor strain gauges as the force sensor and the sensor in SS496B by Honeywell International, Inc. as the position sensor, which is the linear slider and small magnets. Moreover, the control system receives three signals: activation (EDG used to identify whether there is a movement), direction (SGN decides opening or closing), and amplitude of the movement (AMP controls the seed of the movement in a proportional means). As for the control scheme, it uses a simple proportional open-loop control.

A cylindrical grasp of a cylindrical object and a parallel force/position control is studied by [171] to ensure the stability. The work in Ref. [156] presented a feedback control system for hand prosthesis with elbow control. Using a concept of extended physiological proprioception (EPP) (i.e., using natural physiological sensors), both the work [156] and the investigation in Ref. [6] developed microprocessor-based controllers for upper limb prostheses. A systematic literature review [194] is useful for prosthetic hand, although the survey was done for lower-limb prosthesis. Scherillo et al. [171] developed a procedure to obtain maximum load and contact force distribution for a given grasp task and a parallel force/position control to ensure stability of the grasp. The goal of this control scheme is to specify a set of joint torque inputs so that the desired grasping forces along the constrained directions, and the desired position trajectory along the unconstrained directions are realized.

Several researchers showed [9–11] that sensory feedback signals are obtained for multi-fingered robot hands to perform the function of grasping an object and that dynamic force/torque closure can be constructed without knowing object kinematic parameters and location of the mass center. Further, the convergence of motion of the overall fingers-object system was proved using the concepts of “stability and asymptotic stability on a manifold.” Mechanical design and manipulation (control) issues were addressed [157] for a multi-fingered dextrous hand for upper limb prosthetics using the underactuated kinematics enhancing the performance and providing four grasping modes (cylindrical, precision, hook, and lateral) with just two actuators, one for the thumb and one for the remaining fingers. In particular, the hierarchical control architecture consists of a host (or master) controller for EMG management and definition of grasp set points (for position and torque/force) and three local (or slave) controllers for low-level implementation of stiffness control of the joints. In Ref. [205], design and analysis was presented for a multi-fingered prosthetic hand consisting of a thumb with three joints and the rest of the four fingers having two joints using Haringx and element stiffness models, which enables the location of actuators far away from the hand to a belt around the waist and further enabling actuation and control with relatively high degrees of freedom. Robotic hand MA-I was designed and built [182] at the Institute of Industrial and Control Engineering (IOC) at the Polytechnic University of Catalonia (UPC) with 16 degrees of freedom and the control system consisting of 16 position control loops, independently controlling each of the 16 DC motors. Visual hand motion capture is a multiple-dimension and multiple-objective searching optimization problem and the work reported in Ref. [53] used pose estimation and a motion-tracking scheme with genetic algorithms (GA) embedded particle filter (PF) to navigate visual hand gesture, such as virtual environment and control of a robot arm.

The fabrication of a compliant, under-actuated prosthetic hand (both palm and fingers) molded as a soft polymeric single part for providing *adaptive* grasp was reported [28, 29]. The analysis and synthesis are “so complex and only experimental analysis of the solution adapted validate our works.” It was shown [154] that an object with parallel surfaces in a horizontal plane could be controlled by a pair of robotic fingers to achieve stable grasping, angle and position control without the need for the object parameters or object sensors such as tactile, force, or visual sensors.

At Northwestern University Prosthetics Laboratory (NUPL), the researchers [199, 201] developed multi-function prosthetic hand/arm controller system receiving signals from as many as sixteen implantable myoelectric sensors (IMES) and a heuristic fuzzy logic approach to EMG signal pattern recognition [5, 200]. In particular, fuzzy logic was explored for discriminating between multiple surface EMG control signals and classifying them to user intention. The multi-functional hand mechanism consisted of a three-motor hand (one motor for driving the thumb, one motor for the index finger, and the third motor for the middle, ring and little finger) and a two-motor wrist (one motor for wrist extension/flexion and the other motor for wrist rotation). Further, the research [72] demonstrated that in implementing the extended physiological proprioception (EPP) control for a powered prosthesis, the backlash is determined by the stiffness of the control cable as well as mass located at the distal end of the forearm and that reduction of static friction and backlash in the system could prevent the limit cycle.

It was demonstrated [60] that by implanting electrodes within individual fascicles of peripheral nerve stumps, appropriate, distally referred sensory feedback about joint position and grip force from an artificial arm could be provided to an amputee through stimulation of the severed peripheral nerves, which also provide appropriate signals. It is interesting to note [100] the mechanism, design, and control system of a humanoid-type hand with human-like manipulation capabilities as a part of the development of service robots and the comparison (shown by [101, 158]) of natural and prosthetic hands. In Ref. [211], the EMG motion pattern classifier was developed using a parametric autoregressive (AR) model and Levenberg-Marquardt (LM)-based neural networks to identify three types of motion of thumb, index, and middle fingers to control a five-fingered underactuated prosthetic hand.



The work in Ref. [161] focused on the “optimal” delay as the maximum amount of time from command to hand movement, for a prosthesis controller with a delay of 200 to 400 ms as the range acceptable by users. A bypass prosthesis, called the Prosthetic Hand for Able-Bodied Subjects (PHABS), was developed to allow able-bodied subjects to operate a prosthetic terminal device. The controller is a commercially available Myo-pulse control, which combines pulse width modulation (PWM) and pulse period modulation (PPM) because it provides a linear relation between motor speed and the pulse width and timing of a digital control signal. In addition, it also used a mechanical low-pass filter to smooth the pulse train and movement. If the EMG reaches the threshold, the motor will be turned “on”; otherwise, it will be turned “off.” Furthermore, the experimental controller was created in Matlab’s Simulink and executed using Simulink’s Real Time and XPC Target Toolboxes. Finally, this work summarized seven time-delay sources, including:

1. the time from the intent of movement to the development of EMG
2. the time constant of the analog filters contained in the EMG pre-amplifiers
3. the analog to digital sampling period
4. the time required to collect the EMG signal for feature extraction
5. the time required to perform the EMG signal for feature extraction
6. the time required to execute the pattern recognition on the extracted features
7. the time required to actuate the component

In Ref. [50], a review of the traditional methods of control as well as the current state of new control techniques was provided. A newly developed intelligent flexible hand system with 3 fingers and 10 joints, fitted with a small harmonic drive gear and a high power mini actuator, providing 12 DOF applied to a catching task was developed [117]. The authors [212] developed an EMG-based (using electrodes and torque and angle sensors) prosthetic hand control system composed of a human operator, a five-fingered under-actuated prosthetic hand system, the prosthetic hand controller (with analog-to-digital converters, a digital signal processing (DSP) board, and stepper motors) and visual feedback. In particular, the EMG signals undergo feature extraction and feature classification using neural networks with parametric autoregressive (AR) model and wavelet transforms. In an under-actuated system, there is a lower number of actuators compared to the number of degrees-of-freedom of the system. Further in Ref. [210], a hierarchical control system was proposed with a high-level supervisory controller for implementing the EMG signal acquisition and pattern recognition and also providing a set of commands (for operations such as close, open, position, etc.) to a low-level controller. A sensor-based hybrid control strategy (using normal feedback control based on EMG signals from sensors and feedback to the user) was presented [160] where a digital controller operating from prosthetic signals converts the user grasping intention (EMG signal) into an order to control the prosthesis.

Choi et al. [44] investigated developed a robot hand with tactile sensors (slip sensor and force sensor), called SKKU Hand II, having two functional units: a polyvinylidene fluoride (PVDF)-based slip sensor designed to detect slippage and a thin flexible force sensor that can read the contact force of and geometrical information on the object using a pressure variable resistor ink. A biomechatronic approach to the design and control of an anthropomorphic artificial hand was studied [216] for closing the hand finger while grasping an object using a reference trajectory and using two different versions (joint space and slider space) of proportional-derivative (PD) control system. In particular the artificial hand consists of three under-actuated fingers (index, middle, and thumb), which are actuated by three cable-driven DC motors placed in the lower part of the arm.

Farrell and Weir [71] studied large controller delays created by multi-functional prosthesis controllers. A device called PHABS (Prosthetic Hand for Able Bodied Subjects) was utilized to test the performance of 20 able-bodied subjects on the Box and Block Test. To estimate and compare the performance of prosthetic hands, a functionality index has been proposed [161]. An underwater flexible robot manipulation (called HEU Hand II)

that utilized PBNNIC (position-based neural network impedance control) for the force tracking control was studied in Ref. [129].

This work from [129] developed a dexterous underwater robot hand, called the HEU Hand II. The sensor system mainly includes 12 strain gauges at different locations. When the robot hand is under water, the control system is more complicated because the complete dynamic model is not known exactly. Hence, the control system considers the uncertainty of the robot dynamic model. The controller of the hand force tracking is designed by the PBNNIC scheme. Using biologically-inspired principles for design and control of a bionic robot arm [106], several control approaches were presented such as trajectory planning and optimization based on robot dynamics.

An alternate learning control strategy was proposed [163] based on the working assumptions that both human motor commands and sensory information are passed on in a discrete, episodic manner, quantized in time with a learning algorithm, called S-learning, based on *sequences* arguing against the traditional control approaches due to the highly nonlinear robot's dynamics and large number of degrees of freedom.

In the work in Ref. [206], the first prototype of a five-fingered prosthetic hand fitted with only 3 motors and achieving 20 degrees of freedom was described using a new "strings and springs" mechanism and a continuous wavelet transform (CWT) for extraction of EMG inputs for a feed-forward, back-propagation neural network to recognize the type of grip.

The work in Ref. [215] focuses on the control system of the hand and on the optimization of the hand design. It proposes the control action as proportional to the superficial EMG signals extracted by surface electrodes applied to a couple of antagonistic user's residual muscles. This work first explains designs of the hand prototype, such as biomechatronic design approach, under-actuated artificial hand, 3D CAD model (by ProEngineer) and dynamic analysis (by ANSYS). Second, it builds the model of control system, including the kinetics and dynamics of hand, in PD control in the joint space and slider space with elastic compensation. Third, it validates and optimizes the hand design in four multiple objective problems (or goals). The first two goals are related to the closed-loop control performance and the remaining two goals are part of joint trajectories. It develops the simulation in MATLAB/Simulink. Finally, it compares the experimental results with the simulation.

The dynamic system of a nonlinear flexible robot arm with a tip mass was introduced in Ref. [198]. Here, the proposed intelligent optimal controller, in which the fuzzy neural network controller and robust controller were designed to learn a nonlinear function and compensate the approximation errors respectively, could control the coupling of bending vibration and torsional vibration for the periodic motion. To overcome the traditional fuzzy logic difficulties, such as large rule bases and long training times, researchers [17] proposed a self-learning dynamic fuzzy network (DFN) with dynamic equality constraints to speed up the trajectory calculations for intelligent nonlinear optimal control. For a five-finger under-actuated prosthetic hand with tendon transmission, Cipriani et al. [46] presented a robust controller that implemented two subsequent and different phases, including the pre-shaping of the hand and the involved fingers rapidly closing around the object.

## 2.3. Main Control Technique Overview Since 2007

### 2.3.1. Hard Computing Techniques

1. **PD Controller:** Rong et al. [164] presented one kind of PD controller with feed-forward control based on adaptive theory for 2 DOF direct driven robot with uncertain parameters.
2. **Adaptive Controller:** Cai et al. [27] developed an observer back-stepping adaptive control scheme for a two-link manipulator under unmeasured velocity and uncertain environment. The adaptive velocity observer was designed independently from the state-feedback controller in order to compensate the estimation errors. Seo and Akella [175] derived the novel adaptive control solution involving a new filter

design for the regressor matrix for  $n$  DOF robot manipulator systems. By developing the Fourier series expansion from input reference signals of every joint, Liuzzo and Tomei [122] designed a global output error feedback adaptive learning control for 2 DOF planar robot with uncertain dynamics. To achieve the tracking control objective, Chen et al. [41] proposed an adaptive sliding-mode dynamic controller for wheeled mobile robots with system uncertainties and disturbances to make the real velocity of the wheeled mobile robot reach the desired velocity command.

3. **Robust Controller:** Because of the visco-elastic properties of manipulator links, Torabi and Jahed [189] utilized the loop-shaping method, which can decrease the order of the robust control model of a single-link manipulator examined in time and frequency domains. To enhance control of powered prosthetic hands, Engeberg and Meek [64–67] proposed robust sliding mode, back-stepping, and hybrid sliding mode-back-stepping (HSMBS) parallel force-velocity controllers that enabled the humans to more easily control a fine object by ten able-bodied test subjects. Ziaei et al. [214] developed the modeling, system identification adopting generalized orthonormal basis functions (GOBFs), and robust position and force controllers for single flexible link (SFL) manipulators required to operate the contact motion. Jiang and Ge [97] transformed the nonlinear kinematic models of 3 DOF wheels mobile robot with uncertain disturbance into linear control systems through an approximate linearization algorithm and then designed a partial feedback  $H_\infty$  robust controller through linear matrix inequality (LMI).
4. **Optimal Controller:** Vitiello et al. [196] synthesized the position controller and the Kalman filter to perform the planar movements, such as reaching and catching, of the NEURARM hydraulic piston actuation with nonlinear springs connected on the cable. Vrabie et al. [197] designed an online method via a biological inspired Actor/Critic structure to solve the adaptive optimal continuous-time control problem by the solution of the algebraic Riccati equation without using knowledge of the system internal dynamics. To minimize the positioning time (traveling between two specific points) of an under-actuated 2 DOF robot manipulator restricted to the input constraint and the structural parameter constraint, Cruz-Villar et al. [52] developed a concurrent structure-control redesign method that combined the structural parameters and a bang-bang control law. Duchaine et al. [62] derived the position tracking and velocity control, the dynamic model of the robot, the prediction and control horizons, and the constraints by a general predictive control law and also derived an analytical solution for the optimal control by a computationally-efficient-model-based predictive control scheme for a 6 DOF cable-driven parallel manipulator.
4. **Hierarchical Controller:** Fainekos et al. [70] proposed a hierarchical control law addressing the temporal logic motion planning problem for mobile robots modeled by second order dynamics to track a simpler kinematic model with a globally bounded error, and then solved the new robust temporal logic path planning problem for the kinematic model using automata theory and simple local vector fields.

### 2.3.2. Soft Computing Techniques

1. **Fuzzy Logic:** According to the human anatomy, Arslan et al. [13] developed the biomechanical model with a tendon configuration of the 3 DOF index finger of the human hand. The fuzzy sliding mode controller in which a fuzzy logic unit tuned the slope of the sliding surface was introduced to generate the required tendon forces during closing and opening motions.
2. **Artificial Neural Networks:** Onozato and Maeda [149] utilized two neural networks learning inverse kinematic and inverse dynamic to control the positions of 2 DOF SCARA robot. Aggarwal et al. [4] obtained the neural recordings from rhesus monkeys with three different movements, the flexion/extension of each finger, the rotation of wrist, and dexterous grasps. They also designed the separate decoding filters for each movement by using multilayer feed-forward artificial neural

network (ANN) (implemented in real-time MATLAB/Simulink). An online decentralized neural network control design without deriving the dynamic model for a class of large-scale uncertain robot manipulator systems was proposed by Tan et al. [184]. Kato et al. [104] expressed the reaction of brains to the adaptable prosthetic system for a 13 DOF EMG signal controlled prosthetic hand with an EMG pattern recognition learning by artificial neural networks. In addition, functional magnetic resonance imaging (f-MRI) was used to analyze the reciprocal adaptation between the human brain and the prosthetic hand by the plasticity of the motor and sensory cortex area in brains based on the variations in the phantom upper limb.

3. **Genetic Algorithm:** Marcos et al. [54] proposed the closed-loop pseudo-inverse method with genetic algorithms (CLGA) to minimize the largest joint displacement between two adjacent configurations, the total level of joint velocities, the joint accelerations, the total joint torque, and the total joint power consumption for the trajectory planning of 3 DOF redundant robots. Kamikawa and Maeno [98] used a genetic algorithm to optimize locations of pivots and grasping force and designed one ultrasonic motor to move 15 compliant joints for an under-actuated five-finger prosthetic hand.

### 2.3.3. Hybrid of Soft and Hard Computing Techniques

1. **PID Controller and Robust Controller:** Dieulot and Colas [61] presented a case study of the design of robust parametric methods for flexible axes and an heuristic initial tuning of the PID controller from additional pole placement constraints on the rigid mode.
2. **Adaptive Controller and Robust Controller:** To implement the trajectory tracking mission under the influence of unknown friction and uncertainty, Chen et al. [40] utilized a composite tracking scheme, including the adaptive friction estimation to determine Coulomb friction, viscous friction, and the Stribeck effect and a robust controller to enhance the overall stability and robustness for a 2 DOF planar robot manipulator.
3. **Robust Controller and Optimal Controller:** Huang et al. [87] designed the robust control systems with some uncertainties, including the unknown payload and unknown modeling of objects, and the unknown dynamic parameters, such as the performance index that was optimized by the optimal control method for the space robot to capture unknown objects.
4. **Robust Controller and Fuzzy Logic:** Tootoonchi et al. [188] combined a robust quantitative feedback theory (QFT) designed to follow the desired trajectory tracking with the fuzzy logic controller (FLC) designed to reduce the complexities of the system dynamics for 2 DOF arm manipulator. The control gain of the sliding mode controller tuned according to error states of the system by a fuzzy controller and a moving sliding surface whose slope is dynamically changed by a fuzzy logic algorithm for a 3 DOF spatial robot were presented by Yagiz and Hacıoglu [204].
5. **Robust Controller and Artificial Neural Networks:** Siqueira and Terra [180] developed a neural network-based  $H_\infty$  controller that approximated the uncertain factors of an actual under-actuated cooperative manipulator. They robustly controlled the position and squeeze force errors between the manipulator end-effectors and the object, although one joint was not actuated.
6. **Sliding Mode Controller and Genetic Algorithm:** Chen and Chang [42] utilized the multiple-crossover genetic algorithm to estimate the unknown system parameters and the sliding mode control method to overcome the uncertainty for a two-link robot control.
7. **Sliding Mode Controller and Particle Swarm Optimization:** Salehi et al. [166] used an online particle swarm optimization to tune the parameters of sliding mode control at the contact moments of end effector and unknown environments for the 2 DOF planar manipulator.
8. **Fuzzy Logic and Artificial Neural Networks:** Subudhi and Morris [183] proposed a hybrid fuzzy neural control (HFNC) scheme containing a fuzzy logic controller

and a neural network controller to balance the coupling effects for the multi-link flexible manipulator with both rigid and flexible motions.

9. **Artificial Neural Networks and Particle Swarm Optimization:** Wen et al. [202] addressed the hybrid particle swarm optimization neural network (HPSONN) to compute the pseudo-inverse Jacobian of 2 DOF planar manipulator inverse kinematic control.

## 2.4. Revolutionary Prosthesis

Recently (see the press releases [7, 58]) the Applied Physics Laboratory (APL) of Johns Hopkins University (JHU) in Baltimore, MD, USA received funding for the Revolutionary Prosthesis 2009 program from DARPA (Defense Advanced Research Projects Agency), the U.S. Department of Defense, to “develop a next-generation mechanical arm that mimics the properties and sensory perception of the real thing.” The APL leads an international team of about 30 organizations from Austria, Canada, Germany, Italy, Sweden, and USA. The APL team delivered its first DARPA Limb Proto 1 (see Ref. [8], which “is a complete limb system that also includes a virtual environment used for patient training, clinical configuration, and to record limb movements and control signals during clinical investigations”).

## 3. HYBRID INTELLIGENT CONTROL STRATEGIES

Here we present the recent research activities on hybrid control strategies for a smart prosthetic hand conducted at Idaho State University (ISU). The schematic diagram of the work is shown in Figure 1 (see Refs. [120, 160, 212]). The overall system, in brief, consists of electromyographic (EMG) signal acquisition from the user arm for surface or implanted electrodes (in the implanted case we focus on biocompatibility based on nano-materials research). The EMG signal is then processed for feature extraction and classification or identification of EMG signal to correspond to different motions of the prosthetic hand. The classified signal is then used to control the prosthetic hand using actuators and driving mechanisms. It is to be noted in this proposal that the EMG signal extraction and identification and the control algorithm are investigated using the fusion of soft computing (SC) and hard computing (HC) techniques.

### 3.1. Fusion of Soft and Hard Computing Techniques

Soft computing (SC) or computational intelligence (CI) is an emerging field based on synergy and seamless integration of neural networks (NN), fuzzy logic (FL), and genetic algorithms (GA) [102]. The previous works on prosthetic hands used artificial neural networks [45, 88, 120], fuzzy logic [5, 31, 200], genetic algorithms [73], etc. mostly for EMG signal classification for various movements or functions of the prosthetic hand.

In hybrid intelligent control strategies, we look at the integrated structure by blending [153, 186] soft computing (SC) techniques and conventional hard computing (HC)

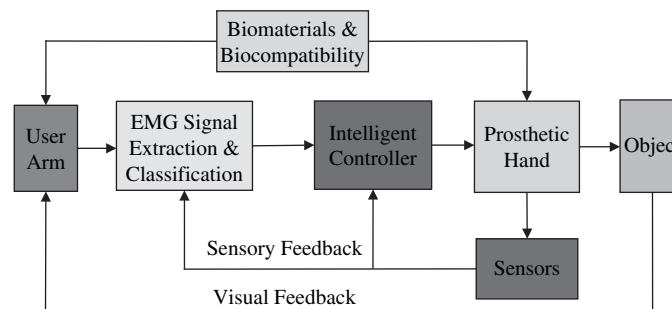


**Figure 1.** Schematic diagram of prosthetic hand technology.

techniques comprising optimal control [140], robust control [213], nonlinear control [110] and/or adaptive control [185] with specific applications to prosthetics.

The integration of SC and HC methodologies shown in Figure 2 has the following attractive features [153, 186]:

1. The methodology based on SC can be used, in particular with fuzzy logic, at upper levels of the overall mission where human involvement and decision making is of primary importance. Whereas, the HC can be used at lower levels for accuracy, precision, stability and robustness.
2. In another situation using a hybrid scheme, a neural network of the SC is used to supplement the control provided by a linear, fixed gain controller for a missile autopilot.
3. Further, the SC-based GA can be used for parameter tuning of a PID controller to achieve good performance and robustness for a wide range of operating conditions.
4. The SC and HC are potentially complementary methodologies.
5. The fusion could solve problems that cannot be solved satisfactorily by using either methodology alone.
6. Novel synergetic combinations of SC and HC lead to high performance, robust, autonomous, and cost-effective missions.

The research at Idaho State University (ISU) focuses on developing intelligent autonomous strategies for EMG signal extraction, analysis, and control of prosthetics by fusion of soft computing techniques comprising NN, FL, and GA [141, 153] and hard computing (HC) techniques. The proposal takes advantage of our in-house research experience with problems in prosthetics [20, 63] in particular, and with problems in biomedical engineering [142, 143] in general.

An overview of nine papers was presented using the techniques in industrial and engineering applications [152]. For the fusion techniques, Sick and Ovaska [179] described a multidimensional categorization scheme in five aspects: the degree of interconnection of soft and hard computing components (fusion grade), the topology of fusion skills (fusion structure), the time when fusion happens (fusion time), the layer of a system architecture (fusion level), and the motivation for the application (fusion incentive). Further, Ovaska et al. [151] classified the fusion techniques into twelve main categories and six supplementary categories.

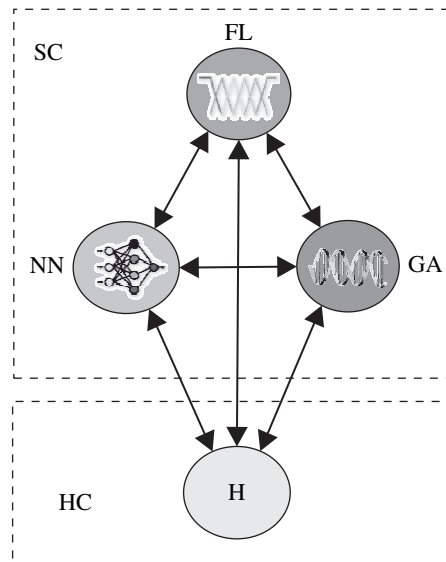


**Figure 2.** Principle behind fusion of soft and hard computing.

#### 4. OVERVIEW OF RESEARCH AT ISU

A chronological overview of the research at Idaho State University is provided below.

A short review by Lai et al. [115] notes the importance of the biological interfaces between robotic implants and other prosthetic devices and notes an interdisciplinary team of biomedical and tissue engineers, and biomaterial and biomedical scientists is needed to work together holistically and synergistically.

In addressing the particle swarm optimization technique, a set of operators for a Particle Swarm Optimization (PSO)-based algorithm is investigated for the purpose of finding optimal values for some of the classical benchmark problems. Particle swarm algorithms are implemented as mathematical operators inspired by the social behaviors of bird flocks and fish schools. In addition, particle swarm algorithms utilize a small number of relatively less complicated rules in response to complex behaviors, such that they are computationally inexpensive in terms of memory requirements and processing time. In particle swarm algorithms, particles in a continuous variable space are linked with neighbors, therefore the updated velocity ~~means~~ particles influence the simulation results. The work presents a statistical investigation on the velocity update rule for continuous variable PS algorithm. In particular, the probability density function influencing the particle velocity update is investigated along with the components used to construct the updated velocity vector of each particle within a flock. The simulation results of several numerical benchmark examples indicate that a small amount of negative velocity is necessary to obtain good optimal values near global optimality [32].

A chronological overview of the applications of control theory to prosthetic hand is presented by Naidu et al. [139] focusing on hard computing or control techniques, such as multi-variable feedback, optimal, nonlinear, adaptive and robust, and soft computing or control techniques, such as artificial intelligence, neural networks, fuzzy logic, genetic algorithms, particle swarm, and on the fusion of hard and soft control techniques. The work [34] presents the PSO algorithm for identifying the rupture force for leukocyte adhesion molecules and the problem of finding the correct control parameters of a robotic hand. Other work at ISU is the fusion of soft computing or control technique of genetic algorithm (GA) and hard computing technique of proportional integral derivative (PID) control with application to prosthetic hand. In particular, an adaptive neuro-fuzzy inference system (ANFIS) is used for inverse kinematics of the three-link index finger, and feedback ~~linearization~~ is used for the dynamics of the hand. The GA is used to find the optimal parameters of the PID controller [35]. An adaptive PSO (APSO) approach based on altering the maximum velocity at each iteration for two thirty-dimensional benchmark problems is used [33].

A hybrid of a soft computing technique of adaptive neuro-fuzzy inference system (ANFIS) and a hard computing technique of adaptive control for a two-dimensional movement of a prosthetic hand with a thumb and index finger was investigated [38]. The results of this hybrid controller, when compared with the PID controller showed enhanced performance. A novel condensed hybrid optimization (CHO) algorithm using enhanced continuous tabu search (ECTS) and the PSO was examined [39]. The proposed CHO algorithm combines the respective strengths of ECTS and the PSO. In particular, the ECTS is utilized to define smaller search spaces that are used in a second stage by the basic PSO to find the respective local optimum. The ECTS covers the global search space by using a TS concept called diversification and then selects the most promising areas in the search space. Once the promising regions in the search space are defined, the proposed CHO algorithm employs another TS concept called intensification in order to search the promising area thoroughly. The proposed CHO algorithm is tested with the multi-dimensional Hyperbolic and Rosenbrock problems. Compared to the other four algorithms, the results indicate that the accuracy and effectiveness of the proposed CHO algorithm were enhanced. Another hybrid of a soft computing technique using the ANFIS and a hard computing or control technique using finite-time linear quadratic optimal control for a two-fingered (thumb and index) prosthetic hand was investigated [37]. In particular, the ANFIS is used for inverse kinematics, and the optimal control is used

to minimize tracking errors utilizing feedback linearized dynamics. The simulations of this hybrid controller, when compared with the proportional-integral-derivative (PID) controller, showed enhanced performance. This work was extended to a five-fingered, three-dimensional prosthetic hand [36].

## 5. RECENT DEVELOPMENTS IN NEUROPROSTHETICS

It is worth noting some of the recent developments in neuroprosthesis [85, 84, 144, 176].

An interesting study was made by Hart et al. [80] on implanted neuroprostheses employing functional electric stimulation (FES) to provide grasp and release to individuals with tetraplegia and comparing three control methods for shoulder position, wrist position, and myoelectric wrist extensors. To improve the control of grasp strength, forearm pronation, and elbow extension to people with spinal cord injury at C5 and C6, the investigation by Peckham et al. [155] developed an advanced neuroprosthesis that includes implanted components, including a 10-channel stimulator, leads, electrodes, and a joint angle transducer, and external components, such as a control unit and transmitter-receiver coil.

A particularly interesting case was reported [48, 78, 150] regarding Jesse Sullivan, who lost both arms in an electrical accident. He could move his bionic arm with his brain—basically rewiring the severed live nerves that control arm and hand movements by redirecting the nerves to pectoral muscles in his chest. Electrodes attached to the chest muscles produce an electrical signal that controls the robotic arm depending upon the nature of muscle movement, which in itself is characterized by “thinking” in the brain what is to be done with arms. However, the demonstrated bionic arm is only a “prototype and for research only.”

More interesting news appeared [47, 82] regarding implantation of an electronic chip into the brain of a quadriplegic man to use a computer to operate a robotic arm.

## 6. FUTURE DIRECTIONS

During the last three decades, investigations have been carried out on the use of EMG signals to develop a prosthetic hand to perform as many functions as possible. However, the use of EMG signals is limited in the number of possible human-like functions with as few electrodes as possible and also for the prosthetic hand to ultimately have a natural “cosmetic” appearance. Further, the EMG signal cannot provide any kind of feedback to the user [207]. One of several possible solutions to overcome the limitations of surface-based EMG approach is neuroprosthesis. Here, we use an interface between the peripheral nervous system (PNS) and the “natural” neural interface to extract, record, and simulate the PNS in a selective way. Further, advances in biocompatible neural interfaces can provide some sensory feedback to the user by stimulating the afferent nerves and allowing motor control of the prosthesis leading to a “natural” EMG-based control. Based on this, two possible ways of controlling prosthetic hands are the simple and non-intrusive EMG-based control and the more complicated, implantable EMG-based control.

In a recent conference of the National Academies *Keck Futures Initiative*, “Smart Prosthetics: Exploring Assistive Devices for Body and Mind,” [12], it was pointed out, “We can make smarter prostheses when we are smarter in integrating state-of-the-art neuroscience with state-of-the-art engineering, medicine, and social science.”

## ACKNOWLEDGMENTS

This overview was first prepared in 2006 when the first author and his colleagues at Idaho State University submitted a proposal on *Smart Prosthetic Hand Technology - Phase I of III* to the Telemedicine Advanced Technology Research Center (TATRC), which is the corporate or central laboratory for advanced technology research of the U.S. Army Medical Research and Materiel Command (USAMRMC) of the U.S. Department of Defense.



Since the proposal was funded by the TATRC in July 2007, the overview has been continuously updated. The financial support from the TATRC is hereby acknowledged. The overview was then completed in the present form in April 2008 while the first author was visiting the School of the Electrical, Electronics and Computer Engineering (EECE) at the University of Western Australia (UWA), Crawley, near Perth, Australia. The financial support for and the excellent hospitality during the visit are gratefully acknowledged.

## REFERENCES

1. C. J. Abu-Haj and N. Hogen, *IEEE Trans. on Biomed. Eng.* 37, 1025 (1990).
2. C. J. Abu-Haj and N. Hogen, *IEEE Trans. on Biomed. Eng.* 37, 1037 (1990).
3. Amputee Coalition of America (ACA) National Limb Loss Information Center (NLLIC) Limb Loss Facts in the United States. <http://www.amputee-coalition.org>, 2006.
4. V. Aggarwal, G. Singhal, J. He, M. H. Schieber, and N. V. Thakor, "30th Ann. Int. IEEE Engi. in Med. and Bio. Soc. Conf. (EMBC 2008)," p. 1703. Vancouver, British Columbia, Canada, August, 2008.
5. A. B. Ajiboye and R. F. ff. Weir, *IEEE Trans. on Neural Sys. and Rehab. Eng.* 13, 280 (2005).
6. H. M. Al-angari, R. F. ff. Weir, C. W. Heckanthurne, and D. S. Childress, *Tech. and Disability* 15, 113 (2003).
7. APL to Lead Team Developing Revolutionary Prosthesis. Press Release: Dated February, 9 2006.
8. Revolutionizing Prosthetics 2009 Team Delivers First DARPA Limb Prototype. Press Release: Dated April 26 2007.
9. S. Arimoto, *Ann. Reviews in Control* 28, 75 (2004).
10. S. Arimoto, "Control Theory of Multi-Fingered Hands: A Modeling and Analytical-Mechanics Approach for Dexterity and Intelligence." Springer-Verlag, London, UK, 2008.
11. S. Arimoto, P. T. A. Nguyen, H.-Y. Han, and Z. Doulgeri, *Robotica* 18, 71 (2000).
12. Arnold and Mabel Beckman Center of the National Academies. "NAKFI: Smart Prosthetics: Exploring Assistive Devices for Body and Mind: Task Group Summaries." Irvine, CA, November 9–11, 2007.
13. Y. Z. Arslan, Y. Hacioglu, and N. Yagiz, *J. Intell. and Robotic Sys.* 52, 121 (2008).
14. D. J. Atkins, D. C. Y. Heard, and W. H. Donovan, *J. Prosth. and Orth.* 8, 2 (1996).
15. D. J. Bak, *Design News* 68 (1997).
16. C. K. Batty, A. Nightingale, and J. Whillis, *J. Bone and Joint Surgery* 37-B, 506 (1955).
17. Y. Becerikli, Y. Oysal, and A. F. Konar, *IEEE Trans. on Neural Networks* 15, 383 (2004).
18. G. A. Bekey, R. Tomovic, and I. Zeljkovic, "Dextrous Robot Hands" (S. T. Venkataraman and T. Iberall, Eds.), p. 136. Springer-Verlag, New York, NY, 1990.
19. A. Bicchi, *IEEE Trans. on Robotics and Automation* 16, 652 (2000), (Summary article with 191 references).
20. J. T. Bingham and M. P. Schoen, "Proc. of the 2004 ASME Int. Mech. Eng. Congress and Exposition (IMECE)," p. 123. Anaheim, CA, November, 2004.
21. L. Birglen, T. Laliberte, and C. Gosselin, "Underactuated Robotic Hands." Springer Tracts in Advanced Robotics, Springer-Verlag, Berlin, Germany, 2008.
22. Blatchford intelligent prosthesis. <http://www.blatchford.co.uk>, 1994.
23. C. Bonivento and A. Davalli, *J. Rehab. Res. & Dev.* 35, 294 (1998).
24. A. H. Bottomley, *The J. Bone and Joint Surgery* 47-B, 411 (1965).
25. A. H. Bottomley, G. Kingshill, P. Robert, D. Styles, P. H. Jilbert, J. W. Birtill, and J. R. Truscott, Prosthetic hand with improved control system for activation by electromyogram signals, Technical report, National Research Development Corporation, London, UK, December 1968, US Patent 3418662.
26. J. Butterfass, M. Grebenstein, H. Liu, and G. Hirzinger, "Proc. of the IEEE Int. Conf. on Robotics and Automation," p. 109. 2001.
27. J. Cai, X. Ruan, and X. Li, "2008 Int. Conf. on Intell. Computation Tech. and Auto. (ICICTA 2008)," p. 404. Changsha, Hunan, China, October, 2008.
28. M. C. Carrozza, G. Cappiello, G. Stellan, F. Zacccone, F. Vecchi, S. Micera, and P. Dario, "Proc. of the IEEE/RSJ Int. Conf. on Intell. Robots and Systems," p. 1271. August, 2005.
29. M. C. Carrozza, B. Massa, S. Micera, R. Lazzarini, and M. Zecca, *IEEE/ASME Trans. on Mechatronics* 7, 108 (2002).
30. M. C. Carrozza, F. Vecchi, F. Sebastiani, G. Cappiello, S. Roccella, M. Zecca, R. Lazzarini, and P. Dario, "Proc. of the 2003 IEEE Int. Conf. on Robotics & Automation," p. 2230. September, 2003.
31. F. H. Y. Chan, Y.-S. Yang, F. K. Lam, Y.-T., Zhang, and P. A. Parker, *IEEE Trans. on Rehab. Eng.* 8, 305 (2000).
32. C.-H. Chen, K. W. Bosworth, and M. P. Schoen, "Proc. of Int. Mech. Eng. Cong. and Exposition (IMECE) 2007," Seattle, Washington, USA, November, 2007 (No. IMECE2007-41343).
33. C.-H. Chen, K. W. Bosworth, and M. P. Schoen, "Proc. of the Int. Assoc. of Sci. and Tech. for Dev. (IASTED) Int. Symp. on Computational Bio. and Bioinformatics (CBB 2008)," p. 260. Orlando, Florida, USA, November, 2008.
34. C.-H. Chen, K. W. Bosworth, M. P. Schoen, S. E. Bearden, D. S. Naidu, and A. Perez, "2008 IEEE Swarm Intelligence Symp. (IEEE SIS08)," St. Louis, Missouri, USA, September, 2008.
35. C.-H. Chen, D. S. Naidu, A. Perez, and M. P. Schoen, "Proc. of the Int. Assoc. of Sci. and Tech. for Dev. (IASTED) Int. Conf. on Intell. Sys. and Control (ISC 2008)," p. 120. Orlando, Florida, USA, November, 2008.

36. C.-H. Chen, D. S. Naidu, A. Perez-Gracia, and M. P. Schoen, "The 48th IEEE Conf. on Dec. and Control (CDC) and 28th Chinese Control Conf. (CCC)," Shanghai, P. R. China, December, 2009 (Accepted).
37. C.-H. Chen, D. S. Naidu, A. Perez-Gracia, and M. P. Schoen, "Proc. of ASME 2009 Dynamic Sys. and Cont. Conf. (DSCC)," Hollywood, California, USA, October, 2009 (Accepted).
38. C.-H. Chen, D. S. Naidu, A. Perez-Gracia, and M. P. Schoen, "The 31st Ann. Int. Conf. of the IEEE Eng. Med. and Bio. Soc. (EMBC)," Minneapolis, Minnesota, USA, September, 2009 (Accepted).
39. C.-H. Chen, M. P. Schoen, and K. W. Bosworth, "Proc. of ASME 2009 Dynamic Sys. and Cont. Conf. (DSCC)," Hollywood, California, USA, October, 2009 (Accepted).
40. C.-Y. Chen, M. H.-M. Cheng, C.-F. Yang, and J.-S. Chen, "The 3rd Int. Conf. on Innovative Computing Info. and Cont. (IICIC '08)," p. 422. Dalian, Liaoning, China, June, 2008.
41. C.-Y. Chen, T.-H. S. Li, Y.-C. Yeh, and C.-C. Chang, *Mechatronics* 19, 156 (2009).
42. J. L. Chen and W.-D. Chang, *Expert Systems with Applications* 36, 4154 (2009).
43. D. S. Childress, *J. Annals of Biomed. Eng.* 8, 293 (1980), (45 references).
44. B. Choi, S. Lee, H. R. Choi, and S. Kang, "Proc. of the 2006 IEEE/RSJ Int. Conf. on Intel. Robots and Sys.," p. 3779. Beijing, China, October, 2006.
45. C. I. Christodoulu and C. S. Pattichis, *IEEE Trans. on Biomed. Eng.* 46, 169 (1999).
46. C. Cipriani, F. Zaccane, G. Stellin, L. Beccai, G. Cappiello, M. C. Carrozza, and P. Dario, "Proc. 2006 IEEE Int. Conf. on Robotics and Auto. (ICRA 2006)," p. 2111. Orlando, Florida, USA, May, 2006.
47. CNN-News: Brain chip heralds neurotech dawn, July 17, 2006.
48. CNN-News: Bionic arm provides hope for amputees, September 14, 2006.
49. A. A. Cole, J. E. Hauser, and S. S. Sastry, *IEEE Trans. on Auto. Cont.* 34, 398 (1989).
50. D. P. J. Cotton, A. Cranny, P. H. Chappell, N. M. White, and S. P. Beeby, "Proc. of the Insti. of Measurement and Cont. UK ACC Cont. 2006 Symp.," p. 211. 2006.
51. E. F. R. Crossley and F. G. Umholtz, *J. Mech. and Machine Theory* 12, 85 (1977).
52. C. A. Cruz-Villar, J. Alvarez-Gallegos, and M. G. Villarreal-Cervantes, *Mechatronics* 19, 178 (2009).
53. J. Cui and Z. Sun, "Proc. of the Sixth IEEE Int. Conf. on Auto. Face and Gesture Recog. (FGR'04)," p. 729. May, 2004.
54. M. da G. Marcos, J. A. T. Machado, and T.-P. Azevedo-Perdicoulis, *Comm. in Nonlinear Sci. and Numer. Simul.* 14, 2858 (2009).
55. Director of Defense Advanced Research Projects Agency (DARPA) Presentation to Subcommittee on Terrorism, Unconventional Threats and Capabilities, House Armed Services Committee, US House of Representatives - Bridging the Gap. Press Release: Dated March 25, 2004.
56. Director of Defense Advanced Research Projects Agency (DARPA): Bridging The Gap Powered by Ideas. Press Release, February (2005).
57. Director of Defense Advanced Research Projects Agency (DARPA): Defense Sciences Office (2006).
58. DARPA - News Release: DARPA Initiates Revolutionary Prosthetic Programs. Press Release: Dated February 8, 2006.
59. N. Dechev, W. L. Cleghorn, and S. Naumann, *Mech. and Machine Theory* 36, 1157 (2001).
60. G. S. Dhillon and K. W. Horch, *IEEE Trans. on Neural Sys. and Rehab. Eng.* 13, 468 (2005).
61. J.-Y. Dieulot and F. Colas, *Mechatronics* 19, 269 (2009).
62. V. Duchaine, S. Bouchard, and C. M. Gosselin, *IEEE/ASME Trans. on Mechatronics* 12, 570 (2007).
63. K. Duraisamy, O. Isebor, A. Perez, M. P. Schoen, and D. S. Naidu, "Proc. of the First IEEE/RAS-EMBS 2006 Int. Conf. on Biomed. Robotics and Biomechanics," p. 1135. Pisa, Italy, February, 2006.
64. E. D. Engeberg and S. G. Meek, "Proc. of the 2008 IEEE/RSJ Int. Conf. on Intell. Robots and Sys.," p. 1940. Nice, France, September, 2008.
65. E. D. Engeberg and S. G. Meek, *IEEE Trans. on Biomed. Eng.* 55, 817 (2008).
66. E. D. Engeberg and S. G. Meek, *IEEE Trans. on Neural Sys. and Rehab. Eng.* 17, 70 (2009).
67. E. D. Engeberg, S. G. Meek, and M. A. Minor, *IEEE Trans. on Biomed. Eng.* 55, 1572 (2008).
68. K. Englehart and B. Hudgins, *IEEE Trans. on Biomed. Eng.* 50, 848 (2003).
69. K. Englehart, B. Hudgins, and A. D. C. Chan, *Tech. and Disability* 15, 95 (2003).
70. G. E. Fainekos, A. Girard, H. Kress-Gazit, and G. J. Pappas, *Automatica* 45, 343 (2009).
71. T. R. Farrell and R. F. Weir, *IEEE Trans. on Neural Sys. and Rehab. Eng.* 15, 111 (2007).
72. T. R. Farrell, R. F. Weir, C. W. Heckathorne, and D. S. Childress, *J. Rehab. Res. & Dev.* 42, 327 (2005).
73. J. J. Fernandez, K. A. Farry, and J. B. Cheatham, "Proc. of the First Ann. Conf. of Genetic Prog.," p. 1754. 2000.
74. N. Fukaya, S. Toyama, T. Asfour, and R. Diffmann, "Proc. of the 2000 IEEE/RSJ Int. Conf. on Intell. Robots and Sys.," p. 1. Stanford, CA, July, 1996.
75. D. Graupe, R. W. Liu, and G. S. Moschytz, "Proc. of the 27th IEEE Conf. on Dec. and Cont.," p. 343. Austin, TX, December, 1988.
76. D. Graupe, J. Magnussen, and A. A. Beex, *IEEE Trans. on Auto. Cont.* 23, 538 (1978).
77. R. A. Grupen, T. C. Henderson, and I. D. McMammon, *Int. J. Robotics Res.* 8, 38 (1989).
78. P. Guinnessy, *Physics Today* 59, 24 (2006).
79. H. Hanafusa and H. Asada, "Robot Motion: Planning and Control" (M. Brady, J. M. Hollerbach, T. L. Johnson, T. Lozano-Pérez, and M. T. Mason, Eds.), p. 322. MIT Press, Cambridge, MA, 1977.
80. R. L. Hart, K. L. Kilgore, and P. H. Peckham, *IEEE Trans. on Rehab. Eng.* 6, 208 (1998).
81. A. E. Hines, N. E. Owens, and P. E. Crago, *IEEE Trans. on Biomed. Eng.* 39, 610 (1992).

82. L. R. Hochberg, M. D. Serruya, G. M. Friebs, A. Mukand, M. Saleh, A. H. Caplan, A. Branner, D. Chen, R. D. Penn, and J. P. Donoghue, *Nature* 442, 164 (2006).
83. N. Hogan, *Trans. of ASME, J. Dynamic Sys., Measurement, and Cont.* 107, 1 (1985).
84. K. W. Horch and G. S. Dhillon, "Neuroprosthesis: Theory and Practice." World Scientific, River Edge, NJ, 2004.
85. K. W. Horch and G. S. Dhillon, "Proc. of the First IEEE/RAS-EMBS 2006 Int. Conf. on Biomed. Robotics and Biomechanics," p. 1. Pisa, Italy, February, 2006.
86. H. Huang and C. Chen, "Proc. of the 1999 IEEE Int. Conf. on Robotics & Automation," p. 2392. Detroit, MI, May, 1999.
87. P. Huang, J. Yan, J. Yuan, and Y. Xu, "Proc. of the 2007 Int. Conf. on Infor. Acquis. (ICIA '07)," p. 397. Jeju City, Korea, July, 2007.
88. B. S. Hudgins, A Novel Approach to Multifunctional Myoelectric Control of Prosthesis, Ph.D. Thesis, University of New Brunswick, Fredericton, Canada, 1991.
89. B. S. Hudgins, P. Parker, and R. N. Scott, *IEEE Trans. on Biomed. Eng.* 40, 82 (1993).
90. T. Iberall, G. Sukhatme, D. Beattie, and G. A. Bekey, "Proc. of the Rehab. Eng. and Assist. Tech. Soc. of N. Amer. (RESNA)," p. 12. Los Vegas, NV, June, 1993.
91. T. Iberall, G. Sukhatme, D. Beattie, and G. A. Bekey, "Proc. of the 1994 IEEE Int. Conf. on Robotics and Automation," p. 1753. San Diego, CA, May, 1994.
92. T. Iberall, G. Sukhatme, D. Beattie, and G. A. Bekey, "Proc. of the 1993 IEEE/RSJ Int. Conf. on Intell. Robots and Sys.," p. 824. Yokohama, Japan, July, 1993.
93. T. Inoue and S. Hirai, "Mechanics and Control of Soft-Fingered Manipulation." Springer, New York, NY, 2009.
94. E. Iversen, H. H. Sears, and S. C. Jacobsen, *IEEE Cont. Sys. Mag.* 25, 16 (2005).
95. S. C. Jacobsen, D. F. Knutti, R. T. Johnson, and H. H. Sears, *IEEE Trans. on Biomed. Eng.* BME-29, 249 (1982).
96. S. C. Jacobsen, J. E. Wood, D. F. Knutti, K. B. Biggers, and E. K. Iversen, "Robotics Research: The Second International Symposium" (H. Hanafusa and H. Inoue, Eds.), p. 301. MIT Press, Cambridge, MA, 1985.
97. W. Jiang and W. Ge, "2008 IEEE Conf. on Robotics, Auto. and Mechatronics (RAM 2008)," p. 1108. Chengdu, China, September, 2008.
98. Y. Kamikawa and T. Maeno, "Proc. of the 2008 IEEE/RSJ Int. Conf. on Intel. Robots and Sys.," p. 717. Nice, France, September, 2008.
99. E. R. Kandel and J. H. Scharf, "Principles of Neural Science," 3rd Edition. Elsevier/North-Holland, New York, NY, 1985.
100. A. Kargov, T. Asfour, C. Pylatiuk, R. Oberle, H. Klosek, S. Schulz, K. Regenstein, G. Bretthauer, and R. Dillmann, "9th Int. Conf. Rehab. Robotics (ICORR)," p. 182. Chicago, IL, June-July 2005.
101. A. Kargov, C. Pylatiuk, J. Martin, S. Schulz, and L. Derlein, *Disability and Rehab.* 26, 705 (2004).
102. F. O. Karray and C. De Silva, "Soft Computing and Intelligent Systems Design: Theory, Tools and Applications." Pearson Educational Limited, Harlow, England, UK, 2004.
103. I. Kato, E. Okazaki, H. Kikuchi, and K. Iwanami, "Digest of 7th ICMBE," p. 367. 1967.
104. R. Kato, H. Yokoi, A. H. Arieta, W. Yub, and T. Arai, *Robotics and Auto. Sys.* 57, 161 (2009).
105. J. J. Kim, D. R. Blythe, D. A. Penny, and A. A. Goldenberg, "Proc. of the IEEE Conf. on Robotics and Auto.," p. 1590. Raleigh, NC, March, 1987.
106. S. Klug, O. von Stryk, and B. Mohl, "The First IEEE/RAS-EMBS Int. Conf. on Biomed. Robo. and Biomechanics," p. 450. Pisa, Italy, February, 2006.
107. H. Kobayashi, *J. Robotic Res.* 1, 3 (1985).
108. A. E. Koblinski, "Proc. of First IFAC," p. 619. Moscow, USSR, 1960.
109. R. Kolluru, K. P. Valavanis, P. Kimon, S. Smith, and N. Tsourveloudis, *Trans. of the Instit. of Measurement & Cont.* 24, 65 (2002).
110. M. Krstic, I. Kanellakopoulos, and P. Kokotović, "Nonlinear and Adaptive Control Design." John Wiley & Sons, New York, NY, 1995.
111. P. Kyberd and P. H. Chappell, *J. Rehab. Res. & Dev.* 31, 326 (1994).
112. P. Kyberd, P. H. Chappell, and D. Gow, *Tech. and Disability* 15, 57 (2003).
113. P. J. Kyberd, O. E. Holland, P. H. Chappell, S. Smith, R. Tregidgo, P. J. Bagwell, and M. Snaith, *IEEE Trans. on Rehab. Eng.* 3, 70 (1995).
114. P. J. Kyberd and J. L. Pons, "Proc. of the 2003 IEEE Int. Conf. on Robotics and Auto.," p. 3231. Taipei, Taiwan, September 2003.
115. J. C. K. Lai, M. P. Schoen, A. Perez-Gracia, D. S. Naidu, and S. W. Leung, *Proc. of the Insti. of Mech. Eng. (IMechE), Part H: J. Eng. in Med.* 221, 173 (2007). Special Issue on Micro and Nano Technologies in Medicine.
116. C. Lake and J. M. Miguelez, *Tech. and Disability* 15, 63 (2003).
117. X.-T. Le, W.-G. Kim, B.-C. Kim, S.-H. Han, J.-G. Ann, and Y.-H. Ha, "Proc. of the SICE-ICASE Int. Joint Conf.," p. 1. Bexco, Busan, Korea, October, 2006.
118. S. Lee and G. N. Saridis, *IEEE Trans. on Auto. Cont.* 29, 290 (1984).
119. D. Lian, S. Peterson, and M. Donath, "Proc. of the 13th Int. Symp. on Indus. Robots," p. 18.91. 1983.
120. C. M. Light, P. H. Chappell, B. Hudgins, and K. Engelhart, *J. Med. Eng. & Tech.* 26, 139 (2002).
121. H. Liu, J. Butterfass, S. Knoch, P. Meusel, and G. Hirzinger, *IEEE Cont. Sys. Mag.* 19, 47 (1999).
122. S. Liuzzo and P. Tomei, *Int. J. Adapt. Control Signal Process.* 23, 97 (2009).
123. F. Lotti, P. Tiezzi, G. Vassura, L. Biagiotti, G. Palli, and C. Melchiorri, "Proc. of the 2005 IEEE Int. Conf. on Robotics and Auto.," p. 4488. Barcelona, Spain, April, 2005.

124. C. S. Lovchik and M. A. Diftler, "Proc. of the IEEE Int. Conf. on Robotics and Auto.," p. 907. May, 1999.
125. R. W. Mann and S. D. Reimers, *IEEE Trans. on Man-Machine Sys.* MMS-11, 110 (1970).
126. A. Marigo and A. Bicchi, *IEEE Trans. on Auto. Control* 45, 1586 (2000).
127. B. Massa, S. Roccella, M. C. Carrozza, and P. Dario, "Proc. of the 2002 IEEE Int. Conf. on Robotics and Auto.," p. 3374. Washington, DC, May, 2002.
128. D. S. McKenzie, *The J. Bone and Joint Surg.* 47, 418 (1965).
129. Q. Meng, H. Wang, P. Li, L. Wang, and Z. He, "Proc. of the 2006 IEEE Int. Conf. on Mechatronics and Auto.," p. 1477. Luoyang, China, June, 2006.
130. S. Micera, A. M. Sabatini, P. Dario, and B. Rossi, *Med. Eng. Physics* 21, 303 (1999).
131. D. Moniz, Arm Amputees Rely on Old Devices, USA Today, 10-06-2005, June 2005.
132. D. Moniz, Military to Fund Prosthetics Research, USA Today, 10-06-2005, June 2005.
133. S. Morita, T. Kondo, and K. Ito, "Proc. of the 2001 ICRA/IEEE Int. Conf. on Robotics and Auto.," p. 1477. Seoul, Korea, May, 2001.
134. S. Morita, K. Shibata, X. Z. Zheng, and K. Ito, "Proc. of the 2000 IEEE/RSJ Int. Conf. on Intel. Robots and Sys.," p. 389. Takamatsu, Japan, October–November, 2000.
135. E. F. Murphy and A. B. Wilson, "Biomedical Engineering Systems" (M. Clynes and J. H. Milsum, Eds.), p. 489. McGraw-Hill, New York, NY, 1970.
136. R. M. Murray, Z. Li, and S. S. Sastry, "A Mathematical Introduction to Robotic Manipulation." CRC Press, Boca Raton, FL, 1994.
137. A. Muzumdar, Ed., "Powered Upper Limb Prostheses Control, Implementation and Clinical Application." Springer-Verlag, New York, NY, 2004.
138. D. S. Naidu, Control strategies for prosthetic hand technology. Technical report, Measurement and Control Engineering Research Center, Idaho State University, Pocatello, ID, November 2006. (Over 100 references).
139. D. S. Naidu, C.-H. Chen, A. Perez, and M. P. Schoen, "Proc. of the 30th Ann. Int. IEEE EMBS Conf.," p. 4314. Vancouver, Canada, August, 2008.
140. D. S. Naidu, "Optimal Control Systems." CRC Press, Boca Raton, FL, 2003.
141. D. S. Naidu, Intelligent Control Systems. Graduate Course Class Notes, 2007.
142. D. S. Naidu and V. K. Nandikolla, "Proc. of the Auto. Cont. Conf. (ACC)," p. 1575. Portland, OR, June, 2005.
143. V. K. Nandikolla and D. S. Naidu, "Proc. of the 2005 ASME Int. Mech. Eng. Congress and Exposition (IMECE)," p. 1. Orlando, FL, November, 2005.
144. X. Navarro, T. B. Krueger, N. Lago, S. Micera, T. Stieglitz, and P. Dario, *J. the Peripheral Nervous Sys.* 10, 229 (2005). (Review article with over 300 references).
145. D. Nishikawa, W. Yu, H. Yokoi, and Y. Kakazu, *Electronics and Communications in Japan (Part III: Fundamental Electronic Science)* 84, 35 (2001). (Translated from Denshi Joho Tsushin Gakkai Ronbunshi, Vol. J82-D-II, No. 9, September 1999, pp. 1510–1519).
146. T. Okada, *IEEE Trans. on Sys., Man, and Cybernetics* 12, 289 (1982).
147. A. M. Okamura, N. Smaby, and M. R. Cutkosky, "Proc. of the IEEE Int. C2000 Conf. on Robotics and Auto.," p. 255. San Francisco, CA, April, 2000 (52 references).
148. R. Okuno, M. Yoshida, and K. Akazawa, "1996 4th Int. Workshop on Adv. Motion Cont.," p. 103. Mie, Japan, March, 1996.
149. K. Onozato and Y. Maeda, "The Soc. of Instrument and Cont. Eng. (SICE) Ann. Conf. 2007," p. 1031. Kagawa University, Takamatsu, Japan, September, 2007.
150. K. Oppenheim, Jess Sullivan powers robotic arms with his mind, CNN, March 23, 2006.
151. S. J. Ovaska, A. Kamiya, and Y. Chen, *IEEE Trans. on Sys., Man, and Cybernetics—Part C: Appl. and Reviews* 36, 439 (2006).
152. S. J. Ovaska and H. F. VanLandingham, *IEEE Trans. on Sys., Man, and Cybernetics—Part C: Appl. and Rev.* 32, 69 (2002).
153. S. J. Ovaska, H. F. VanLandingham, and A. Kamiya, *IEEE Trans. on Sys., Man, and Cybernetics—Part C: Appl. and Rev.* 32, 72 (2002).
154. R. Ozawa, S. Arimoto, S. Nakamura, and J.-H. Bae, *IEEE Trans. on Robotics* 21, 965 (2005).
155. P. H. Peckham, K. L. Kilgore, M. W. Keith, A. M. Bryden, N. Bhadra, and F. W. Montague, *The J. Hand Surgery* 27A, 265 (2002).
156. D. H. Plettenburg and J. L. Herder, *Tech. and Disability* 15, 85 (2003).
157. J. L. Pons, E. Rocon, R. Ceres, D. Reynaerts, B. Saro, S. Levin, and W. Van Moorleghe, *Autonomous Robots* 16, 143 (2004).
158. C. Pylatiuk, S. Mounier, A. Kargov, S. Schulz, and G. Bretthauer, "Proc. of the 26th Ann. Int. Conf. of the IEEE EMBS," p. 4260. San Francisco, CA, September, 2004.
159. S. Roccella, M. C. Carrozza, G. Cappeello, M. Zecca, H. Miwa, K. Itoh, and M. Matsumoto, "Proc. of the 2004 IEEE/RSJ Int. Conf. on Intel. Robots and Sys.," p. 266. Sendai, Japan, September–October, 2004.
160. L. E. Rodriguez-Cheu and A. Casals, "Proc. of the The First IEEE/RAS-EMBS 2006 Int. Conf. on Biomed. Robotics and Biomechatronics," p. 607. Pisa, Italy, February, 2006.
161. L. E. Rodriguez-Cheu, A. Casals, A. Cuxart, and A. Parra, "2005 IEEE/RSJ Int. Conf. on Intel. Robots and Sys. (IROS)," p. 541. August, 2005.
162. T. A. Rohland, *Med. and Bio. Eng.* 12, 300 (1975).
163. B. Rohrer and S. Hulet, "Proc. of the The First IEEE/RAS-EMBS 2006 Int. Conf. on Biomed. Robotics and Biomechatronics," p. 57. Pisa, Italy, February, 2006.

164. P. X. Rong, Z. J. He, C. D. Zong, and N. Liu, "2008 Int. Conf. on Intel. Computation Tech. and Auto. (ICICTA 2008)," p. 298. Changhsa, Hunan, China, October, 2008.
165. A. Rovetta, "Proc. of the IEEE Conf. on Robotics and Auto.," p. 1060. St. Louis, Missouri, March, 1983.
166. M. Salehi, G. R. Vossoughi, M. Vajedi, and M. Brooshaki, "Proc. of the 2008 IEEE Int. Conf. on Info. and Auto.," p. 458. Zhangjiajie, China, June, 2008.
167. J. K. Salisbury, Kinematic and Force Analysis of Articulated Hands, Ph.D. Thesis, Stanford University, Stanford, CA, 1982.
168. G. N. Saridis and T. P. Gootee, *IEEE Trans. on Biomed. Eng.* BME-29, 403 (1982).
169. G. N. Saridis and H. E. Stephanou, *IEEE Trans. on Sys., Man and Cybernetics* 7, 407 (1977).
170. N. Sarkar, X. Yun, and V. Kumar, *IEEE Trans. on Robotics and Auto.* 13, 364 (1977).
171. P. Scherillo, B. Siciliano, L. Zollo, M. C. Carrozza, E. Guglielmelli, and P. Dario, "Proc. of the 2003 IEEE/ASME Int. Conf. on Adv. Intell. Mechatronics (AIM 2003)," p. 920. 2003.
172. T. Schlegl and M. Buss, "Proc. of the 1998 IEEE Int. Conf. on Robotics and Auto.," p. 3026. Leuven, Belgium, May, 1998.
173. R. N. Scott and P. A. Parker, *J. Med. Eng. & Tech.* 12, 143 (1988).
174. H. H. Sears and J. Shaperman, *Amer. J. Phys. Med. & Rehab.* 70, 20 (1991).
175. D. Seo and M. R. Akella, *Sys. & Cont. Lett.* 58, 304 (2009).
176. K. Shenoy, Toward High-Performance Neural Control of Prosthetic Devices. Technical Report, Stanford University, Stanford, CA, May (2007).
177. E. D. Sherman, *Canadian Med. Assoc. J. (CMAJ)* 91, 1268 (1964).
178. K. B. Shimoga, *The Int. J. Robotics Res.* 15, 230 (1996), (Survey article with over 130 references).
179. B. Sick and S. J. Ovaska, "2005 IEEE Mid-Summer Workshop on Soft Computing in Ind. Appl.," p. 57. Espoo, Finland, June, 2005.
180. A. A. G. Siqueira and M. H. Terra, *Cont. Eng. Practice* 17, 418 (2009).
181. G. P. Starr, *IEEE Trans. on Robotics and Auto.* 6, 342 (1990).
182. R. Suárez and P. Grosch, "Proc. of the Intel. Manipulation and Grasping," p. 91. Genova, 2004.
183. B. Subudhi and A. S. Morris, *Applied Soft Computing* 9, 149 (2009).
184. K. K. Tan, S. Huang, and T. H. Lee, *Automatica* 45, 161 (2009).
185. G. Tao, Ed., "Adaptive Control Design and Analysis." Wiley-Interscience, New York, NY, 2003.
186. A. Tettamanzi and M. Tomassini, "Soft Computing: Integrating Evolutionary, Neural, and Fuzzy Systems." Springer-Verlag, Berlin, Germany, 2001.
187. R. W. Todd, Adaptive Control of a Human Prosthesis, Ph.D. Thesis, University of Southampton, Southampton, UK, 1969.
188. A. A. Tootoonchi, M. R. Gharib, and Y. Farzaneh, "2008 IEEE Conf. on Robotics, Auto. and Mechatronics (RAM 2008)," p. 649. Chengdu, China, September, 2008.
189. M. Torabi and M. Jahed, "Tenth Int. Conf. on Computer Modeling and Simulation (UKSIM 2008)," p. 685. Cambridge, UK, April, 2008.
190. T. Tsuji, O. Fukuda, H. Shigeyoshi, and M. Kaneko, "Proc. of the 2000 IEEE/RSJ Int. Conf. on Intel. Robots and Systems," p. 377. Takamatsu, Japan, 2000.
191. A. Tura, C. Lamberti, A. Davalii, and R. Sacchetti, *J. Rehab. Res. & Dev.* 35, 14 (1998).
192. Casualties in Afganistan & Iraq. [www.unknownnews.net](http://www.unknownnews.net), June 5 2006.
193. H. Van Brussel, B. Santoso, and D. Reynaerts, "Proc. of the NASA Conf. on Space Telerobotics," p. 89. Pasadena, CA, January/February, 1989.
194. H. van der Linde, C. J. Hofstad, A. C. H. Geurts, K. Postema, J. H. B. Geertzen, and J. van Limbeek, *J. Rehab. Res. & Dev.* 41, 555 (2004). (Review article with 91 references).
195. S. T. Venkataraman and T. E. Djaferis, "Proc. of the IEEE Int. Conf. on Robotics and Auto.," p. 77. 1987.
196. N. Vitiello, E. Cattin, S. Roccella, F. Giovacchini, F. Vecchi, M. C. Carrozza, and P. Dario, "Proc. of the 2007 IEEE/RSJ Int. Conf. on Intel. Robots and Systems," p. 1852. San Diego, California, USA, October–November, 2007.
197. D. Vrabie, F. Lewis, and M. Abu-Khalaf, *Trans. of the Inst. of Measurement and Cont.* 30, 207 (2008).
198. R.-J. Wai and M.-C. Lee, *IEEE Trans. on Indust. Elect.* 51, 201 (2004).
199. R. F. Weir, Direct Muscle Attachment as a Control Input for a Position-Servo Prosthesis Controller, Ph.D. Thesis, Northwestern University, Evanston, IL, 1995.
200. R. F. Weir and A. B. Ajiboye, "Proc. of the 25th Ann. Int. Conf. of IEEE EMBS," p. 17. Cancun, Mexico, September, 2003.
201. R. F. Weir, P. R. Troyk, G. DeMichele, and D. Kerns, "Proc. of the 25th IEEE Eng. in Med. and Bio. 27th Ann. Conf.," p. 7337. Shanghai, China, September, 2005.
202. X. Wen, D. Sheng, and J. Huang, "A Hybrid Particle Swarm Optimization for Manipulator Inverse Kinematics Control," Lecture Notes in Computer Science, Vol. 5226. Springer-Verlag, Berlin, Heidelberg, 2008.
203. N. Wiener, "Cybernetics or Cont. and Comm. in the Animal and the Machine." MIT Press, Cambridge, MA, 1948; 2nd Edition, 1961.
204. N. Yagiz and Y. Hacioglu, *Math. and Computer Modelling* 49, 114 (2009).
205. J. Yang, E. P. Pitarch, K. Abdel-Malek, A. Patrick, and L. Lindkvist, *Mechanism and Machine Theory* 39, 555 (2004).
206. J. Žajdlík, "Proc. of the 2006 Int. Conf. on Intel. Eng. Systems," p. 202. 2006.
207. M. Zecca, S. Micera, M. C. Carrozza, and P. Dario, *Crit. Rev.<sup>TM</sup> in Biomed. Eng.* 30, 459 (2002). (Review article with 96 references).

- 208. M. Zecca, S. Roccella, G. Cappiello, K. Ito, K. Imanishi, H. Miwa, C. Carrozza, P. Dario, and A. Takamishi, From the human hand to a humanoid hand: Biologically-inspired approach for the development of robo-casa hand #1. Technical report, 3ARTS Lab, Scuola Superiore Sant Anna, Pisa, Italy, 2006.
- 209. Y. Zhang, Z. Han, H. Zhang, X. Shang, T. Wang, and W. Guo, "Proc. of the 2001 IEEE Int. Conf. on Robotics and Auto.," p. 2517. Seoul, Korea, May, 2001.
- 210. D. W. Zhao, L. Jiang, H. Huang, M. H. Jin, H. G. Cai, and H. Liu, "Proc. of the 2006 IEEE Int. Conf. on Robotics and Biomimetics," p. 1. Kunming, China, December, 2006.
- 211. J. Zhao, Z. Xie, L. Jiang, H. G. Cai, H. Liu, and G. Hirzinger, "Proc. of the 2005 IEEE Int. Conf. on Robotics and Auto.," p. 1. Barcelona, Spain, April, 2005.
- 212. J. Zhao, Z. Xie, L. Jiang, H. G. Cai, H. Liu, and G. Hirzinger, "Proc. of the First IEEE/RAS-EMBS 2006 Int. Conf. on Biomed. Robot. and Biomechatronics," p. 995. Pisa, Italy, February, 2006.
- 213. K. Zhou and J. C. Doyle, "Essentials of Robust Control." Prentice Hall, Upper Saddle River, NJ, 1998.
- 214. K. Ziaei, L. Ni, and D. W. L. Wang, *Cont. Eng. Prac.* 17, 329 (2009).
- 215. L. Zollo, S. Roccella, E. Guglielmelli, M. C. Carrozza, and P. Dario, *IEEE/ASME Trans. on Mechatronics* 12, 418 (2007).
- 216. L. Zollo, S. Roccella, R. Tucci, B. Siciliano, E. Guglielmelli, M. C. Carrozza, and P. Dario, "Proc. of the First IEEE/RAS-EMBS 2006 Int. Conf. on Biomed. Robo. and Biomechatronics," p. 402. Pisa, Italy, February, 2006.

# Adaptive Control for a Five-Fingered Prosthetic Hand with Unknown Mass and Inertia

CHENG-HUNG CHEN<sup>1,2</sup>, D. SUBBARAM NAIDU<sup>1,3</sup>, MARCO P. SCHOEN<sup>1,4</sup>

<sup>1</sup>Measurement and Control Engineering Research Center

<sup>2</sup>Department of Biological Sciences

<sup>3</sup>Department of Electrical Engineering

<sup>4</sup>Department of Mechanical Engineering

School of Engineering, Idaho State University

921 S. 8th Avenue, Pocatello, ID 83209, USA

{chenchen; naiduds; schomarc}@isu.edu

**Abstract:** An adaptive control strategy for the 14 degrees of freedom (DOFs), five-fingered smart prosthetic hand with unknown mass and inertia of all the fingers is developed in this work. In modeling, the various links used for the five fingers of the prosthetic hand are shown. A cubic polynomial for the trajectory planning is used. In particular, using a desired orientation for three-link fingers, the forward and inverse kinematics of the prosthetic hand system regarding the analytical solutions between the angular positions of joints and the positions and orientations of the end-effectors (fingertips) have been obtained. The simulations of the resulting adaptive controller with five-fingered prosthetic hand show enhanced performance.

**Key-Words:** adaptive control, prosthetic hand, hard control, five finger hand, feedback linearization, trajectory planning

## 1 Introduction

Due to the extreme complexity of human hand that has 27 bones, controlled by about 38 muscles to provide the hand with 22 degrees of freedom (DOFs), and incorporates about 17,000 tactile units of 4 different units, reproducing the human hand in all its various functions and appearance is still a challenging task [1]. Prosthetic hands have been built to replace human hands that can fully operate the various motions, such as holding, moving, grasping, lifting, twisting and so on [1–6]. However, about 35% of the users do not regularly use their prosthetic hands because of several reasons, including poor functionality of the presently available prosthetic hands and psychological problems. Thus, designing and developing an artificial hand which can “mimic the human hand as closely as possible” both in functionality and appearance can overcome these problems.

Hard computing/control (HC) techniques are used at lower levels for accuracy, precision, stability and robustness. HC comprises proportional-derivative (PD) control [7], proportional-integral-derivative (PID) control [8–11], optimal control [9, 12–14], adaptive control [15–17], robust control [18], etc. with specific applications to prosthetic devices. However, our previous work [16] for a two-fingered (thumb and index finger) prosthetic hand showed that

adaptive controller can overcome overshooting and oscillation. However, a five-fingered prosthetic hand with adaptive control technique has not been developed yet.

In this work, we first describe briefly the trajectory planning problem, human hand anatomy and the inverse kinematics for two-link thumb and the remaining three-link fingers (index, middle, ring and little). Next, the dynamics of the prosthetic hand is derived and feedback linearization technique is used to obtain linear tracking error dynamics. Then the adaptive controller is designed to minimize the tracking error. The simulation results show that the five-fingered prosthetic hand with the proposed adaptive controller can grasp an object without overshooting and oscillation. The last section provides conclusions and future work.

## 2 Modeling

### 2.1 Human Hand Anatomy

Figure 1 (a) shows a normal human hand composed of thumb ( $t$ ), index ( $i$ ), middle ( $m$ ), ring ( $r$ ), little ( $l$ ) fingers and palm. The wrist is located between the forearm and the hand and consists of eight carpal bones organized in two rows of proximal (movable) and dis-



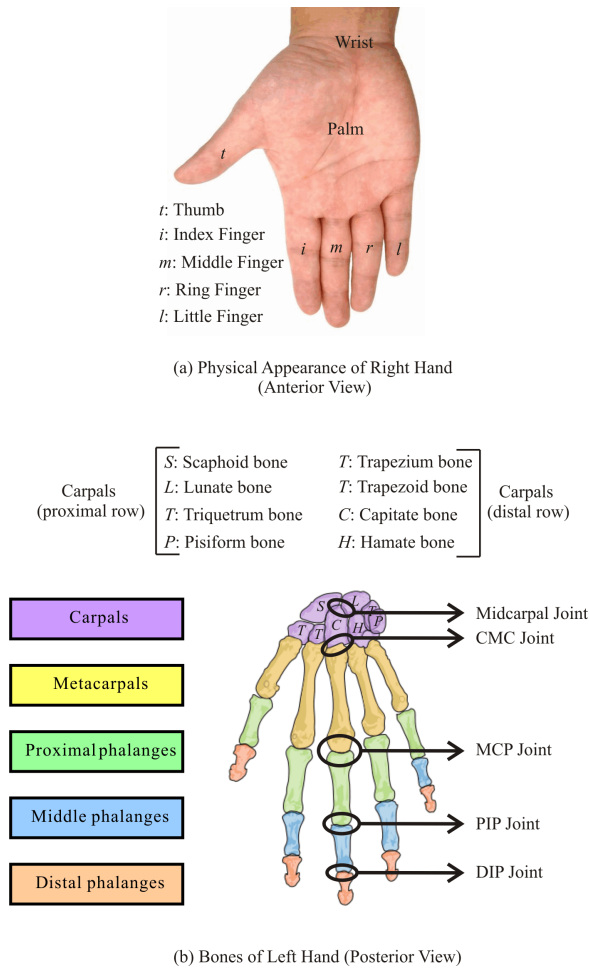


Figure 1: Human Wrist and Hand: (a) Physical Appearance of Right Hand (Anterior View): A human hand has thumb, index, middle, ring and little fingers, palm and wrist. (b) Bones of Left Hand (Posterior View): A human hand has 27 bones, including 5 distal phalanges, 4 middle phalanges, 5 proximal phalanges, 5 metacarpals and 8 carpals.

tal (immovable) carpal bones as shown in Figure 1 (b) [19]. The proximal row (top) of carpal bones from lateral to medial is the Scaphoid, Lunate, Triquetrum and Pisiform; the distal row (bottom) of carpal bones from medial to lateral has the Hamate, Capitate, Trapezoid and Trapezium. The hand is composed of five Metacarpals and five Digits. The metacarpals produce a curve, so the palm is concave in the resting position. The five digits contain one thumb ( $t$ ) and four fingers, e.g. index ( $i$ ), middle ( $m$ ), ring ( $r$ ), and little ( $l$ ) fingers, respectively. The thumb has two bones, Proximal phalanx and Distal phalanx. Each finger consists of three bones, Proximal phalanx, Middle phalanx and Distal phalanx. In this work, we assumed that the palm is fixed, the thumb has two links (proximal pha-

lanx and distal phalanx), and each finger has three links (proximal phalanx, middle phalanx and distal phalanx).

Synovial joints are formed at the surface of relative motion between two bones. The joints of thumb and four fingers contain two saddle-shaped articulating surfaces between two bones and can be classified as saddle joints. Index, middle, ring, and little fingers include three revolute joints in order to do the angular movements (Figure 1 (b)). Metacarpal-phalangeal (MCP) joint is located between metacarpal and proximal phalange bones; proximal and distal interphalangeal (PIP and DIP) joints separate the phalangeal bones. Thumb contains metacarpal-phalangeal (MCP) and interphalangeal (IP) joints [19]. For a human hand, each finger has 4 DOFs (2 at MCP joint, 1 at PIP joint and 1 at DIP joint), thumb has 3 DOFs (2 at MCP joint and 1 at IP joint), wrist has 2 DOFs and carpometacarpal (CMC) joint has 2 DOFs. In this work, we model 14 DOFs, five-fingered prosthetic hand with two-link thumb and remaining three-link fingers.  $q_1^j$ ,  $q_2^j$  and  $q_3^j$  ( $j = i, m, r$  and  $l$ ) represent the angular positions (or joint angles) of the first joint  $MCP^j$ , the second joint  $PIP^j$  and the third joint  $DIP^j$  of index, middle, ring and little fingers, respectively;  $q_1^t$  and  $q_2^t$  are the angular positions of the first joint  $MCP^t$  and the second joint  $IP^t$  of thumb ( $t$ ), respectively.

## 2.2 Trajectory Planning

The trajectory planning using cubic polynomial for fingertip position control was discussed in our previous work [5,7,8,13,16] for a two-fingered (thumb and index finger) smart prosthetic hand. For three-link fingers, we present the same technique for fingertip orientation control. A time history of desired ( $d$ ) fingertip orientation ( $\phi$ ) and its differentiation ( $\dot{\phi}$  and  $\ddot{\phi}$ ) is given as

$$\phi_d^j(t) = \omega_0 + \omega_1 t + \omega_2 t^2 + \omega_3 t^3, \quad (1)$$

$$\dot{\phi}_d^j(t) = \omega_1 + 2\omega_2 t + 3\omega_3 t^2, \quad (2)$$

$$\ddot{\phi}_d^j(t) = 2\omega_2 + 6\omega_3 t, \quad (3)$$

where  $\omega_0$ - $\omega_3$  are undetermined constants and the superscript  $j$  indicates the index of each finger ( $j = i, m, r$  and  $l$ ). The relations (1) and (2) need to satisfy the constraint conditions at initial time  $t_0$  and final time  $t_f$ . This can be written as

$$\mathbf{T} \mathbf{\Omega} = \mathbf{\Phi}. \quad (4)$$



Here, the matrices  $\mathbf{T}$ ,  $\mathbf{\Omega}$ , and  $\mathbf{\Phi}$  are

$$\mathbf{T} = \begin{bmatrix} 1 & t_0 & t_0^2 & t_0^3 \\ 0 & 1 & 2t_0 & 3t_0^2 \\ 1 & t_f & t_f^2 & t_f^3 \\ 0 & 1 & 2t_f & 3t_f^2 \end{bmatrix}, \quad (5)$$

$$\mathbf{\Omega} = [\omega_0 \ \omega_1 \ \omega_2 \ \omega_3]', \quad (6)$$

$$\mathbf{\Phi} = [\phi_0^j \ \phi_0^j \ \phi_f^j \ \phi_f^j]'. \quad (7)$$

Therefore, the 4 unknown constants,  $\omega_0$ - $\omega_3$ , can be computed by  $\mathbf{\Omega} = \mathbf{T}^{-1}\mathbf{\Phi}$ . The notation  $'$  means the transpose.

### 2.3 Kinematics

Kinematics is the study of geometry in motion and is restricted to a natural geometrical description of motion by the manners, including positions, orientations, and their derivatives (velocities and accelerations) [20, 21]. Forward and inverse kinematics of articulated systems study the analytical relationship between the angular positions of joints and the positions and orientations of the end-effectors (fingertips). A desired trajectory is usually specified in Cartesian space and the trajectory controller is easily performed in the joint space. Hence, conversion of Cartesian trajectory planning to the joint space [21] is necessary. Using inverse kinematics, the joint angular positions of each finger need to be obtained from the known fingertip positions. Then the angular velocities and angular accelerations of joints can be obtained from the linear and angular velocities and accelerations of fingertips by differential kinematics. The kinematic descriptions of prosthetic hands are used to derive the fundamental equations for dynamics and control purposes. The following subsections introduce forward and inverse kinematics for the two-link thumb and the remaining three-link fingers and then three-dimensional five-fingered prosthetic hand will be described [5, 7, 8, 13, 16].

#### 2.3.1 Forward Kinematics

Figure 2 shows the illustration of two-link thumb.  $L_1^t$  and  $L_2^t$  are the lengths of the links 1 and 2 of the thumb ( $t$ ), respectively;  $q_1^t$  and  $q_2^t$  are the angular positions (or called angles) of joints 1 and 2 of the thumb. Using Denavit-Hartenberg (DH) method [20–23], the fingertip coordinate  $\mathbf{P}^t(X^t, Y^t)$  of the thumb can be obtained by DH transformation matrices. The fingertip coordinate  $\mathbf{P}^t(X^t, Y^t)$  of the thumb ( $t$ ) and the ori-

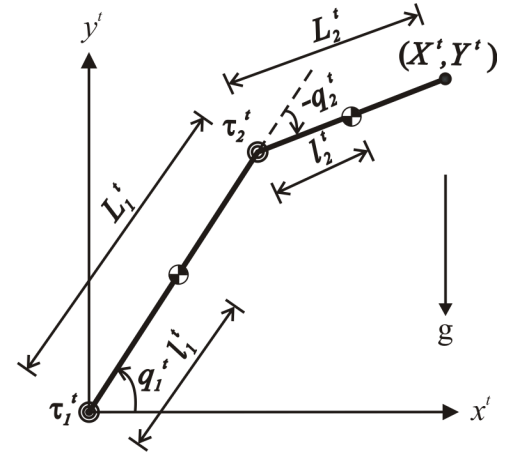


Figure 2: Two-Link Thumb Illustration: The fingertip coordinate  $(X^t, Y^t)$  can be derived by forward kinematics.  $L_1^t$  and  $L_2^t$  are the lengths of the links 1 and 2, respectively;  $q_1^t$  and  $q_2^t$  are the angles of joints 1 and 2;  $\tau_1^t$  and  $\tau_2^t$  are the torques of the joints 1 and 2.

entation  $\phi^t$  of the fingertip frame can be described as

$$\begin{aligned} X^t &= L_1^t \cos(q_1^t) + L_2^t \cos(q_1^t + q_2^t), \\ Y^t &= L_1^t \sin(q_1^t) + L_2^t \sin(q_1^t + q_2^t), \\ \phi^t &= q_1^t + q_2^t. \end{aligned} \quad (8)$$

Figure 3 shows the illustration of three-link index fin-

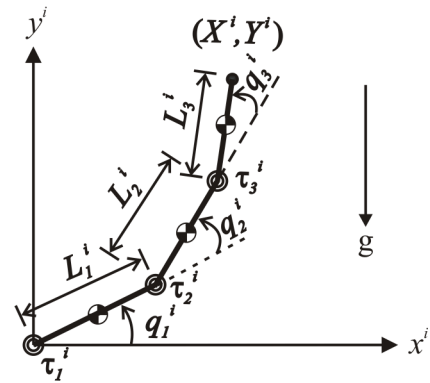


Figure 3: Three-Link Index Finger Illustration: The fingertip coordinate  $(X^i, Y^i)$  can be obtained by forward kinematics.  $L_1^i$ ,  $L_2^i$ , and  $L_3^i$  are the lengths of the links 1, 2, and 3, respectively;  $q_1^i$ ,  $q_2^i$ , and  $q_3^i$  are the angles of the joints 1, 2, and 3;  $\tau_1^i$ ,  $\tau_2^i$  and  $\tau_3^i$  are the torques of the joints 1, 2, and 3.

ger.  $L_1^i$ ,  $L_2^i$ , and  $L_3^i$  are the lengths of the links 1, 2 and 3 of the index finger ( $i$ ), respectively;  $q_1^i$ ,  $q_2^i$ , and  $q_3^i$  are the angles of the joints 1, 2, and 3 of the index finger. Similarly, using DH method, the fingertip coordinate  $\mathbf{P}^i(X^i, Y^i)$  and the orientation  $\phi^i$  of the index

finger ( $i$ ) can be written as

$$\begin{aligned} X^i &= L_1^i \cos(q_1^i) + L_2^i \cos(q_1^i + q_2^i) \\ &\quad + L_3^i \cos(q_1^i + q_2^i + q_3^i), \\ Y^i &= L_1^i \sin(q_1^i) + L_2^i \sin(q_1^i + q_2^i) \\ &\quad + L_3^i \sin(q_1^i + q_2^i + q_3^i), \\ \phi^i &= q_1^i + q_2^i + q_3^i. \end{aligned} \quad (9)$$

### 2.3.2 Inverse Kinematics

The joint angular positions of each finger can be deduced as following. The sum of squared (8) is written as

$$X^{t2} + Y^{t2} = L_1^{t2} + L_2^{t2} + 2L_1^t L_2^t \cos(q_2^t). \quad (10)$$

Rearranging (10), we can get the equation below.

$$\cos(q_2^t) = \frac{X^{t2} + Y^{t2} - L_1^{t2} - L_2^{t2}}{2L_1^t L_2^t}. \quad (11)$$

Choosing the *elbow up* configuration, the angle  $q_2^t$  of the joint 2 can be obtained from

$$q_2^t = -\cos^{-1} \left( \frac{X^{t2} + Y^{t2} - L_1^{t2} - L_2^{t2}}{2L_1^t L_2^t} \right). \quad (12)$$

Notice that in this paper, all positive angles are defined counterclockwise. When choosing the *elbow up* configuration, the angle  $q_2^t$  is clockwise, so the sign of  $q_2^t$  is negative. Figure 4 is the geometric illustration of

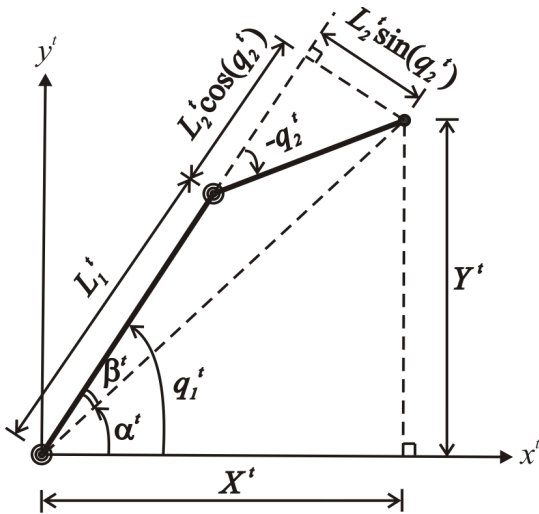


Figure 4: Geometric Illustration of Two-Link Thumb two-link thumb (elbow up). Based on the geometry, we can get two triangular relations below

$$\tan(\alpha^t) = \frac{Y^t}{X^t}, \tan(\beta^t) = -\frac{L_2^t \sin(q_2^t)}{L_1^t + L_2^t \cos(q_2^t)}. \quad (13)$$

Accordingly, the angles  $\alpha^t$  and  $\beta^t$  can be gained as

$$\begin{aligned} \alpha^t &= \tan^{-1} \left( \frac{Y^t}{X^t} \right), \\ \beta^t &= -\tan^{-1} \left( \frac{L_2^t \sin(q_2^t)}{L_1^t + L_2^t \cos(q_2^t)} \right). \end{aligned} \quad (14)$$

Then, by the summation of (14), the angle  $q_1^t$  of the joint 1 can be determined as

$$q_1^t = \tan^{-1} \left( \frac{Y^t}{X^t} \right) - \tan^{-1} \left( \frac{L_2^t \sin(q_2^t)}{L_1^t + L_2^t \cos(q_2^t)} \right). \quad (15)$$

Hence, the expression of the joint angles  $q_2^t$  and  $q_1^t$  of the thumb is given in (12) and (15), respectively.

The local coordinate  $P_2^i(X_2^i, Y_2^i)$  of the joint 2 of the index finger can be obtained as

$$X_2^i = X^i - L_3^i \cos(\phi^i), Y_2^i = Y^i - L_3^i \sin(\phi^i). \quad (16)$$

Choosing the *elbow down* configuration, the angles  $q_2^i$  and  $q_1^i$  can be obtained as

$$\begin{aligned} q_2^i &= \cos^{-1} \left( \frac{X_2^{i2} + Y_2^{i2} - L_1^{i2} - L_2^{i2}}{2L_1^i L_2^i} \right), \\ q_1^i &= \tan^{-1} \left( \frac{Y^i}{X^i} \right) - \tan^{-1} \left( \frac{L_2^i \sin(q_2^i)}{L_1^i + L_2^i \cos(q_2^i)} \right). \end{aligned} \quad (17)$$

Then we can get the angle  $q_3^i$  of the joint 3 as

$$q_3^i = \phi^i - q_1^i - q_2^i. \quad (18)$$

The orientation  $\phi^i$  can be designed by trajectory planning in Section 2.2.

For the five-fingered hand shown in Figure 5,  $X^G$ ,  $Y^G$ , and  $Z^G$  are the three axes of the global coordinate. The local coordinate  $x^t$ - $y^t$ - $z^t$  of thumb can be reached by rotating through angles  $\alpha$  and  $\beta$  to  $X^G$  and  $Y^G$  of the global coordinate, subsequently. The local coordinate  $x^i$ - $y^i$ - $z^i$  of index finger can be obtained by rotating through angle  $\alpha$  to  $X^G$  and then translating the vector  $d^i$  of the global coordinate; similarly, the local coordinate  $x^j$ - $y^j$ - $z^j$  of middle finger ( $j = m$ ), ring finger ( $j = r$ ), and little finger ( $j = l$ ) can be obtained by rotating through angle  $\alpha$  to  $X^G$  and then translating the vector  $d^j$  ( $j = m, r$  and  $l$ ) of the global coordinate.

### 2.4 Dynamics of Hand

The dynamic equations of hand motion are derived via Lagrangian approach using kinetic energy and potential energy as [5, 15, 20, 21, 23]

$$\frac{d}{dt} \left( \frac{\partial \mathcal{L}}{\partial \dot{\mathbf{q}}} \right) - \frac{\partial \mathcal{L}}{\partial \mathbf{q}} = \boldsymbol{\tau}, \quad (19)$$

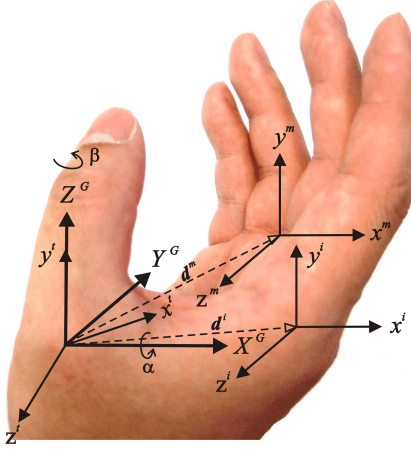


Figure 5: Relationship between Global Coordinate and Local Coordinates: Local coordinate  $x^t-y^t-z^t$  of thumb can be reached by rotating through angles  $\alpha$  and  $\beta$  to  $X^G$  and  $Y^G$  of global coordinate, subsequently. Local coordinate  $x^i-y^i-z^i$  of index finger can be obtained by rotating through angle  $\alpha$  to  $X^G$  and then translating a vector  $d^i$  of the global coordinate.

where  $\mathcal{L}$  is the Lagrangian;  $\dot{\mathbf{q}}$  and  $\mathbf{q}$  represent the angular velocities and angle vectors of joints, respectively;  $\boldsymbol{\tau}$  is the given torque vector at joints. The Lagrangian  $\mathcal{L}$  can be expressed as

$$\mathcal{L} = T - V, \quad (20)$$

where  $T$  and  $V$  denote kinetic and potential energies, respectively. Substituting (20) into (19), dynamic equations of thumb can be obtained as below.

$$\mathbf{M}(\mathbf{q})\ddot{\mathbf{q}} + \mathbf{C}(\mathbf{q}, \dot{\mathbf{q}}) + \mathbf{G}(\mathbf{q}) = \boldsymbol{\tau}, \quad (21)$$

where  $\mathbf{M}(\mathbf{q})$  is the inertia matrix;  $\mathbf{C}(\mathbf{q}, \dot{\mathbf{q}})$  is the Coriolis/centripetal vector and  $\mathbf{G}(\mathbf{q})$  is the gravity vector. (21) can be also written as

$$\mathbf{M}(\mathbf{q})\ddot{\mathbf{q}} + \mathbf{N}(\mathbf{q}, \dot{\mathbf{q}}) = \boldsymbol{\tau}, \quad (22)$$

where  $\mathbf{N}(\mathbf{q}, \dot{\mathbf{q}}) = \mathbf{C}(\mathbf{q}, \dot{\mathbf{q}}) + \mathbf{G}(\mathbf{q})$  represents non-linear terms. The dynamic relations for the two-link thumb and the three-link index finger are described in Appendix A [5, 24, 25].

### 3 Control Techniques

#### 3.1 Feedback Linearization

The nonlinear dynamics represented by (22) is to be converted into a linear state-variable system using feedback linearization technique [15]. Alternative state-space equations of the dynamics can be obtained by defining the position/velocity state  $\mathbf{x}(t)$  of

the joints as

$$\mathbf{x}(t) = [\mathbf{q}'(t) \quad \dot{\mathbf{q}}'(t)]'. \quad (23)$$

$\mathbf{q}'(t)$  and  $\dot{\mathbf{q}}'(t)$  are the transpose vectors of  $\mathbf{q}(t)$  and  $\dot{\mathbf{q}}(t)$ , respectively. Let us repeat the dynamical model and rewrite (22) as

$$\frac{d}{dt}\dot{\mathbf{q}}(t) = -\mathbf{M}^{-1}(\mathbf{q}(t)) [\mathbf{N}(\mathbf{q}(t), \dot{\mathbf{q}}(t)) - \boldsymbol{\tau}(t)]. \quad (24)$$

Thus, from (23) and (24), we can derive a linear system in *Brunovsky canonical form* as

$$\dot{\mathbf{x}}(t) = \begin{bmatrix} \mathbf{0} & \mathbf{I} \\ \mathbf{0} & \mathbf{0} \end{bmatrix} \mathbf{x}(t) + \begin{bmatrix} \mathbf{0} \\ \mathbf{I} \end{bmatrix} \mathbf{u}(t) \quad (25)$$

with its control input vector given by

$$\mathbf{u}(t) = -\mathbf{M}^{-1}(\mathbf{q}(t)) [\mathbf{N}(\mathbf{q}(t), \dot{\mathbf{q}}(t)) - \boldsymbol{\tau}(t)]. \quad (26)$$

Let us suppose the prosthetic hand is required to track the desired trajectory  $\mathbf{q}_d(t)$  described under path generation or tracking. Then, the tracking error  $\mathbf{e}(t)$  is defined as

$$\mathbf{e}(t) = \mathbf{q}_d(t) - \mathbf{q}(t). \quad (27)$$

Here,  $\mathbf{q}_d(t)$  is the *desired* angle vector of joints and can be obtained by trajectory planning [5, 7, 8, 13, 16];  $\mathbf{q}(t)$  is the *actual* angle vector of joints. Differentiating (27) twice, to get

$$\dot{\mathbf{e}}(t) = \dot{\mathbf{q}}_d(t) - \dot{\mathbf{q}}(t), \quad \ddot{\mathbf{e}}(t) = \ddot{\mathbf{q}}_d(t) - \ddot{\mathbf{q}}(t). \quad (28)$$

Substituting (24) into (28) yields

$$\ddot{\mathbf{e}}(t) = \ddot{\mathbf{q}}_d(t) + \mathbf{M}^{-1}(\mathbf{q}(t)) [\mathbf{N}(\mathbf{q}(t), \dot{\mathbf{q}}(t)) - \boldsymbol{\tau}(t)] \quad (29)$$

from which the control function can be defined as

$$\mathbf{u}(t) = \ddot{\mathbf{q}}_d(t) + \mathbf{M}^{-1}(\mathbf{q}(t)) [\mathbf{N}(\mathbf{q}(t), \dot{\mathbf{q}}(t)) - \boldsymbol{\tau}(t)]. \quad (30)$$

This is often called the *feedback linearization* control law, which can also be inverted to express it as

$$\boldsymbol{\tau}(t) = \mathbf{M}(\mathbf{q}(t)) [\ddot{\mathbf{q}}_d(t) - \mathbf{u}(t)] + \mathbf{N}(\mathbf{q}(t), \dot{\mathbf{q}}(t)). \quad (31)$$

Using the relations (28) and (30), and defining state vector  $\bar{\mathbf{x}}(t) = [\mathbf{e}'(t) \quad \dot{\mathbf{e}}'(t)]'$ , the *tracking error dynamics* can be written as

$$\dot{\bar{\mathbf{x}}}(t) = \begin{bmatrix} \mathbf{0} & \mathbf{I} \\ \mathbf{0} & \mathbf{0} \end{bmatrix} \bar{\mathbf{x}}(t) + \begin{bmatrix} \mathbf{0} \\ \mathbf{I} \end{bmatrix} \mathbf{u}(t). \quad (32)$$

Note that this is in the form of a *linear* system such as

$$\dot{\bar{\mathbf{x}}}(t) = \mathbf{A}\bar{\mathbf{x}}(t) + \mathbf{B}\mathbf{u}(t). \quad (33)$$

### 3.2 Adaptive Control Technique

The tracking error  $e(t)$  and the filtered tracking error  $r(t)$  are defined as

$$e(t) = q_d(t) - q(t), \quad (34)$$

$$r(t) = \dot{e}(t) + \Lambda e(t). \quad (35)$$

Here,  $q_d(t)$  is the *desired* angle vector of joints;  $q(t)$  is the *actual* angle vector of joints;  $\Lambda = \text{diag}(\lambda_1, \lambda_2, \dots, \lambda_n)$  is the positive-definite diagonal gain matrix. The filtered error (35) ensures stability of the overall system so that the tracking error (34) is bounded. Figure 6 shows the block diagram of the adaptive controller. Here, the filtered signal  $r(t)$  is derived from the tracking error  $e(t)$  and the trajectory planner and is fed to the adaptive controller of the prosthetic hand. Differentiating and substituting

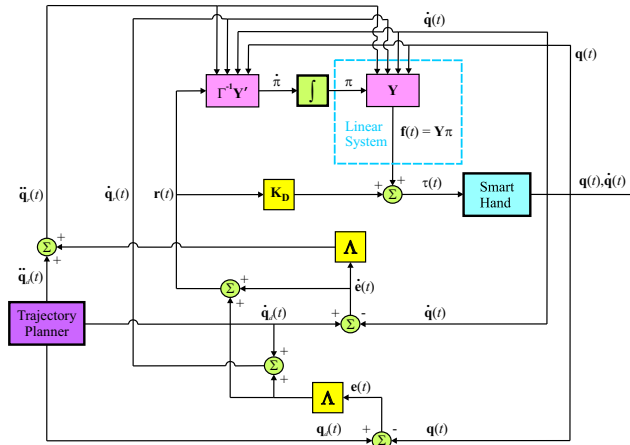


Figure 6: Block Diagram of the Adaptive Controller for a Five-Fingered Prosthetic Hand: Tracking errors  $e(t)$  are calculated by actual angles  $q(t)$  and desired angles  $q_d(t)$ , which are based on trajectory planner. Then filtered tracking errors  $r(t)$  are computed by error changes and the parameters  $\Lambda$  multiplying errors. The required torque  $\tau(t)$  of the prosthetic hand non-linear system is computed by the nonlinear term  $f(t)$  and the gain  $K_D$  multiplying the filtered tracking errors.

(35) into (21) gives the dynamic equation in terms of the filtered error  $r(t)$  as

$$M(q(t))\dot{r}(t) = -C_m(q(t), \dot{q}(t))r(t) + f(t) - \tau(t), \quad (36)$$

where  $C(q(t), \dot{q}(t)) = C_m(q(t), \dot{q}(t))\dot{q}(t)$  and the nonlinear term  $f(t)$  can be defined as

$$\begin{aligned} f(t) &= M(q(t))(\ddot{q}_d(t) + \Lambda\dot{e}(t)) + G(q(t)) + \\ &\quad C_m(q(t), \dot{q}(t))(\dot{q}_d(t) + \Lambda e(t)) + \tau_{dis}, \\ &= Y\pi. \end{aligned} \quad (37)$$

Here,  $\tau_{dis}$  is the unknown disturbance.  $Y$  is a regression matrix of known robot functions and  $\pi$  is a vector of unknown parameters [26]. The regression matrix  $Y$  and the unknown parameter vector  $\pi$  of two-link thumb and three-link index finger are given in Appendix B [5]. The torque vector  $\tau(t)$  can be calculated by

$$\tau(t) = f(t) + K_D r(t). \quad (38)$$

The unknown parameter rate vector  $\dot{\pi}$  can be updated by

$$\dot{\pi} = \Gamma^{-1}Y'r(t) \quad (39)$$

where  $\Gamma$  is a tuning parameter diagonal matrix.

## 4 Simulation Results and Discussion

Figure 7 shows that five-fingered prosthetic hand with

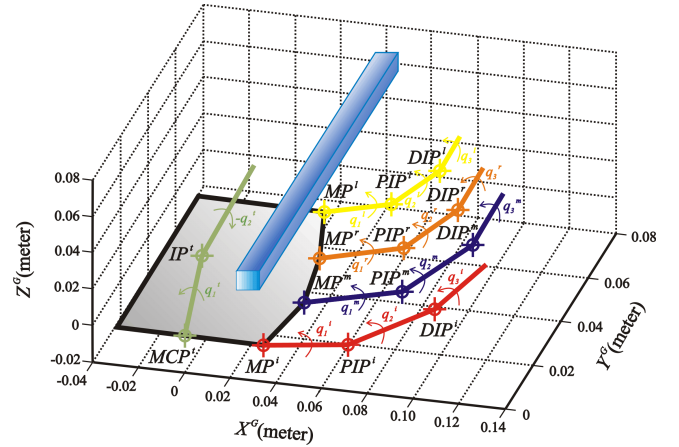


Figure 7: Five-Fingered Prosthetic Hand Grasping a Rectangular Object

14 DOFs is reaching a rectangular rod in order to grasp the object. When thumb and the other four fingers are performing extension/flexion movements, the workspace of fingertips is restricted to the maximum angles of joints. Referring to inverse kinematics, the first and second joint angles of the thumb fingertip are constrained in the ranges of  $[0,90]$  and  $[-80,0]$  (degrees). The first, second, and third joint angles of the other four fingers are constrained in the ranges of  $[0,90]$ ,  $[0,110]$  and  $[0,80]$  (degrees), respectively [27].

Next, we present simulations with an adaptive controller for the 14 DOFs five-fingered smart prosthetic hand. The parameters of the two-link thumb/three-link fingers [28] were related to desired trajectory. All parameters of the smart prosthetic hand selected for the simulations are given in Table 1 and the side length and length of the target rectangular rod

are 0.010 and 0.100 (m), respectively. All initial actual angles are zero. The relating parameters between the global coordinate and the local coordinates are defined in Table 2. Besides, in this work, we assumed

Table 1: Parameter Selection of the Smart Hand

Parameters	Values
<b>Thumb</b>	
Time ( $t_0, t_f$ )*	0, 20 (sec)
Desired Initial Position**	0.035, 0.060 (m)
Desired Final Position**	0.0495, 0.060 (m)
Desired Initial Velocity*	0, 0 (m/s)
Desired Final Velocity*	0, 0 (m/s)
Length	0.04, 0.04 (m)
<b>Index Finger</b>	
Desired Initial Position**	0.065, 0.080 (m)
Desired Final Position**	0.010, 0.060 (m)
Desired Initial $\phi_0$ ***	75 (deg)
Desired Final $\phi_f$ ***	160 (deg)
Desired Initial $\dot{\phi}_0$ ***	0 (m/s)
Desired Final $\dot{\phi}_f$ ***	0 (m/s)
Length	0.04, 0.04, 0.03 (m)
<b>Middle Finger</b>	
Desired Initial Position**	0.065, 0.080 (m)
Desired Final Position**	0.005, 0.060 (m)
Length	0.04, 0.04, 0.03 (m)
<b>Ring Finger</b>	
Desired Initial Position**	0.065, 0.080 (m)
Desired Final Position**	0.010, 0.060 (m)
Length	0.04, 0.04, 0.03 (m)
<b>Little Finger</b>	
Desired Initial Position**	0.055, 0.080 (m)
Desired Final Position**	0.020, 0.060 (m)
Length	0.04, 0.04, 0.03 (m)

\*All fingers use same parameters

\*\*Local coordinates

\*\*\*All 3-link fingers use same parameters

that each link of all fingers is a circular cylinder with the radius ( $R$ ) 0.010 (m), so the inertia  $I_{zzk}^j$  of each link  $k$  of all fingers  $j$  ( $= t, i, m, r$  and  $l$ ) can be calculated as

$$I_{zzk}^j = \frac{1}{4}m_k^j R^2 + \frac{1}{3}m_k^j L_k^{j^2}. \quad (40)$$

Figure 8, Figure 10, Figure 12, Figure 14 and Figure 16 show the tracking errors of thumb, index, middle, ring, and little fingers for the proposed five-fingered smart prosthetic hand, respectively. Figure 9, Figure 11, Figure 13, Figure 15 and Figure 17 show

Table 2: Parameter Selection of the Conversion from Global to Local Coordinates

Parameters	Values
Rotating $\alpha$	90 (deg)
Rotating $\beta$	45 (deg)
Translating $d^i$	(0.035, 0, 0) (m)
Translating $d^m$	(0.040, 0, -0.020) (m)
Translating $d^r$	(0.035, 0, -0.040) (m)
Translating $d^l$	(0.025, 0, -0.060) (m)

the desired/actual angles of thumb, index, middle, ring, and little fingers for the proposed five-fingered smart prosthetic hand, respectively. The observation that all tracking errors dramatically drop within one second and are less than one degree after convergence provides the evidence that the adaptive controller for the 14-DOFs prosthetic hand enhances performance. The other observation that after convergence, all three-link fingers show more unstable errors than two-link thumb suggests that the more DOFs increase the difficulty of the adaptive controller without knowing the mass and inertia of the links of all fingers.

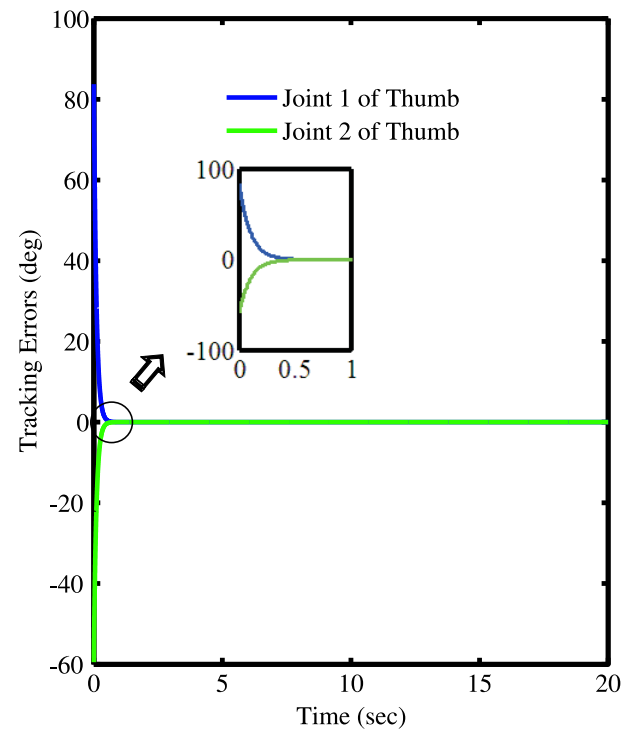


Figure 8: Tracking Errors of Adaptive Controller for Two-Link Thumb



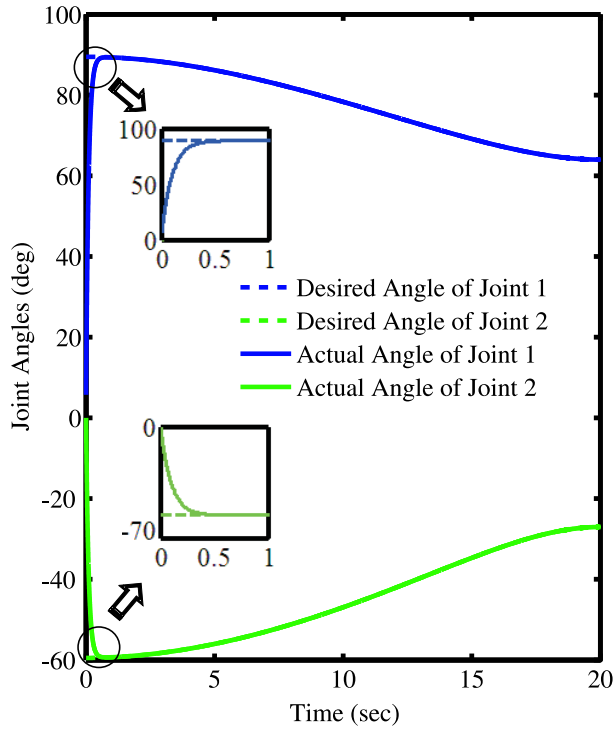


Figure 9: Tracking Angles of Adaptive Controller for Two-Link Thumb

## 5 Conclusions and Future Work

An adaptive control strategy was developed for the 14 degrees of freedom (DOFs), five-fingered smart prosthetic hand with unknown mass and inertia of all the fingers. Further, the forward and inverse kinematics of the system regarding the analytical relationship between the angular positions of joints and the positions and orientations of the end-effectors (fingertips), was obtained using a desired orientation for three-link fingers. The simulations of the resulting adaptive controller showed good agreement between the reference and the actual trajectories. Work is in progress for developing an adaptive/robust controller for the five fingered hand with 14-DOFs.

**Acknowledgments:** The research was sponsored by the U.S. Department of the Army, under the award number W81XWH-10-1-0128 awarded and administered by the U.S. Army Medical Research Acquisition Activity, 820 Chandler Street, Fort Detrick, MD 21702-5014. The information does not necessarily reflect the position or the policy of the Government, and no official endorsement should be inferred. For purposes of this article, information includes news releases, articles, manuscripts, brochures, advertisements, still and motion pictures, speeches, trade association proceedings, etc.

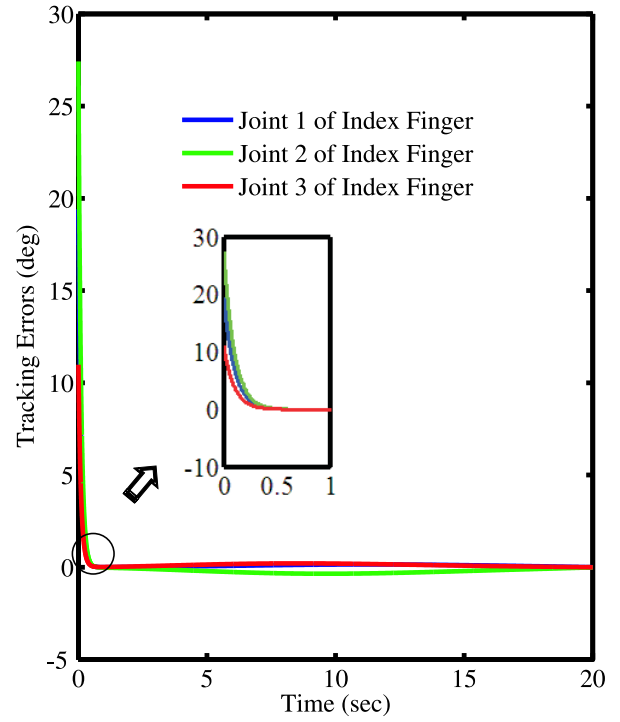


Figure 10: Tracking Errors of Adaptive Controller for Three-Link Index Finger

## Appendix A: Dynamic Equations of Two-link Thumb and Three-link Index Finger

The dynamic equations of thumb in (21) can be rewritten as below.

$$\begin{bmatrix} M_{11}^t & M_{12}^t \\ M_{21}^t & M_{22}^t \end{bmatrix} \begin{bmatrix} \ddot{q}_1^t \\ \ddot{q}_2^t \end{bmatrix} + \begin{bmatrix} C_1^t \\ C_2^t \end{bmatrix} + \begin{bmatrix} G_1^t \\ G_2^t \end{bmatrix} = \begin{bmatrix} \tau_1^t \\ \tau_2^t \end{bmatrix}. \quad (41)$$

Here,

$$\begin{aligned} M_{11}^t &= 2m_2^t L_1^t l_2^t \cos(q_2^t) + m_1^t l_1^{t^2} + m_2^t L_1^{t^2} + m_2^t l_2^{t^2} + I_{zz1}^t + I_{zz2}^t, \\ M_{12}^t &= m_2^t L_1^t l_2^t \cos(q_2^t) + m_2^t l_2^{t^2} + I_{zz2}^t, \\ M_{21}^t &= M_{12}^t, \\ M_{22}^t &= m_2^t l_2^{t^2} + I_{zz2}^t, \end{aligned} \quad (42)$$

$$\begin{aligned} C_1^t &= -2m_2^t L_1^t l_2^t \sin(q_2^t) \dot{q}_1^t \dot{q}_2^t - m_2^t L_1^t l_2^t \sin(q_2^t) \dot{q}_2^t \dot{q}_2^t, \\ C_2^t &= m_2^t L_1^t l_2^t \sin(q_2^t) \dot{q}_1^t \dot{q}_1^t - m_2^t L_1^t l_2^t \sin(q_2^t) \dot{q}_1^t \dot{q}_2^t, \end{aligned} \quad (43)$$

$$\begin{aligned} G_1^t &= g(m_1^t l_1^t \cos(q_1^t) + m_2^t L_1^t \cos(q_1^t) + m_2^t l_2^t \cos(q_1^t + q_2^t)), \\ G_2^t &= g m_2^t l_2^t \cos(q_1^t + q_2^t), \end{aligned} \quad (44)$$

$\tau_1^t$  and  $\tau_2^t$  are the given torques at the joints 1 and 2, respectively;  $l_k^t$  is the distance between the end of previous link and the center of mass of link  $k$ ;  $L_k^t$  is the length of link  $k$ ;  $q_k^t$  is the angle at joint  $k$  and a function of time;  $g$  is the acceleration due to gravity; the diagonal elements  $I_{mnk}^t$  ( $k = 1, 2$ ),  $m = n$  are called polar moments of inertia.

Similarly, dynamic equations of index finger in

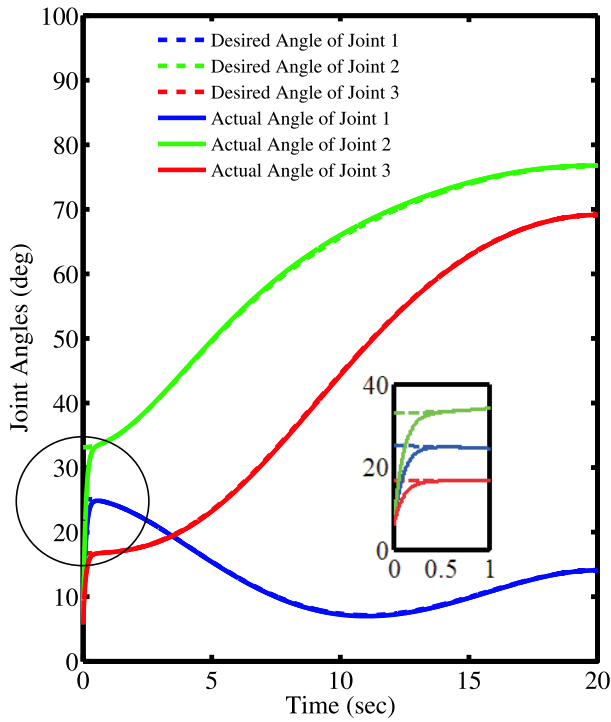


Figure 11: Tracking Angles of Adaptive Controller for Three-Link Index Finger

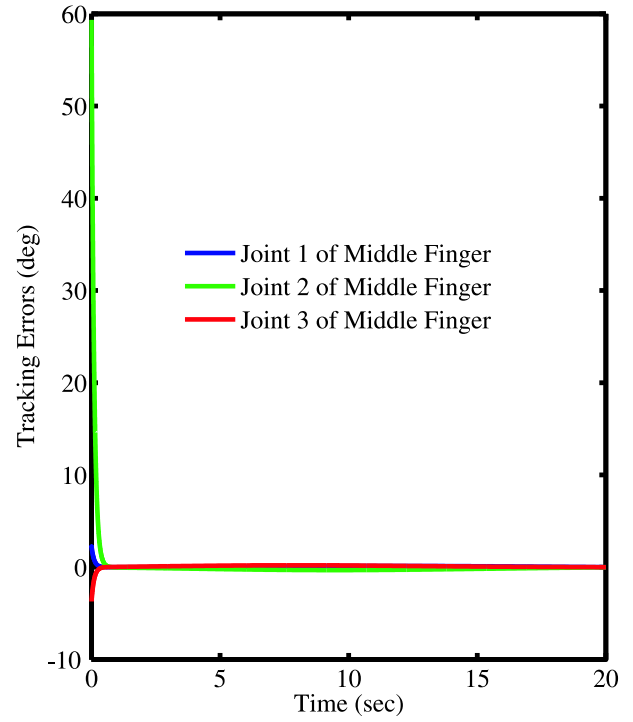


Figure 12: Tracking Errors of Adaptive Controller for Three-Link Middle Finger

(21) can be also obtained as

$$\begin{bmatrix} \tau_1^i \\ \tau_2^i \\ \tau_3^i \end{bmatrix} = \begin{bmatrix} M_{11}^i & M_{12}^i & M_{13}^i \\ M_{21}^i & M_{22}^i & M_{23}^i \\ M_{31}^i & M_{32}^i & M_{33}^i \end{bmatrix} \begin{bmatrix} \ddot{q}_1^i \\ \ddot{q}_2^i \\ \ddot{q}_3^i \end{bmatrix} + \begin{bmatrix} C_1^i \\ C_2^i \\ C_3^i \end{bmatrix} + \begin{bmatrix} G_1^i \\ G_2^i \\ G_3^i \end{bmatrix}. \quad (45)$$

Here,

$$\begin{aligned} M_{11}^i &= 2m_2^i L_1^i l_2^i \sin(q_1^i) \sin(q_1^i + q_2^i) \\ &\quad + 2m_2^i L_1^i l_2^i \cos(q_1^i) \cos(q_1^i + q_2^i) \\ &\quad + 2m_3^i L_1^i L_2^i \sin(q_1^i) \sin(q_1^i + q_2^i) \\ &\quad + 2m_3^i L_1^i L_2^i \cos(q_1^i) \cos(q_1^i + q_2^i) \\ &\quad + 2m_3^i L_1^i l_3^i \sin(q_1^i) \sin(q_1^i + q_2^i + q_3^i) \\ &\quad + 2m_3^i L_1^i l_3^i \cos(q_1^i) \cos(q_1^i + q_2^i + q_3^i) \\ &\quad + 2m_3^i L_2^i l_3^i \sin(q_1^i + q_2^i) \sin(q_1^i + q_2^i + q_3^i) \\ &\quad + 2m_3^i L_2^i l_3^i \cos(q_1^i + q_2^i) \cos(q_1^i + q_2^i + q_3^i) \\ &\quad + m_1^i l_1^2 + m_2^i L_1^2 + m_2^i l_2^2 \\ &\quad + m_3^i L_1^2 + m_3^i L_2^2 + m_3^i l_3^2 \\ &\quad + I_{zz1}^i + I_{zz2}^i + I_{zz3}^i, \\ M_{12}^i &= m_2^i L_1^i l_2^i \sin(q_1^i) \sin(q_1^i + q_2^i) \\ &\quad + m_2^i L_1^i l_2^i \cos(q_1^i) \cos(q_1^i + q_2^i) \\ &\quad + 2m_3^i L_2^i l_3^i \sin(q_1^i + q_2^i) \sin(q_1^i + q_2^i + q_3^i) \\ &\quad + 2m_3^i L_2^i l_3^i \cos(q_1^i + q_2^i) \cos(q_1^i + q_2^i + q_3^i) \\ &\quad + m_3^i L_1^i L_2^i \sin(q_1^i) \sin(q_1^i + q_2^i) \\ &\quad + m_3^i L_1^i L_2^i \cos(q_1^i) \cos(q_1^i + q_2^i) \end{aligned}$$

$$\begin{aligned} &\quad + m_3^i L_1^i l_3^i \sin(q_1^i) \sin(q_1^i + q_2^i + q_3^i) \\ &\quad + m_3^i L_1^i l_3^i \cos(q_1^i) \cos(q_1^i + q_2^i + q_3^i) \\ &\quad + m_2^i l_2^2 + m_3^i L_2^2 + m_3^i l_3^2 + I_{zz2}^i + I_{zz3}^i, \\ M_{13}^i &= m_3^i L_1^i l_3^i \sin(q_1^i) \sin(q_1^i + q_2^i + q_3^i) \\ &\quad + m_3^i L_1^i l_3^i \cos(q_1^i) \cos(q_1^i + q_2^i + q_3^i) \\ &\quad + m_3^i L_2^i l_3^i \sin(q_1^i + q_2^i) \sin(q_1^i + q_2^i + q_3^i) \\ &\quad + m_3^i L_2^i l_3^i \cos(q_1^i + q_2^i) \cos(q_1^i + q_2^i + q_3^i) \\ &\quad + m_3^i l_3^2 + I_{zz3}^i, \end{aligned} \quad (46)$$

$$\begin{aligned} M_{21}^i &= M_{12}^i, \\ M_{22}^i &= 2m_3^i L_2^i l_3^i \sin(q_1^i + q_2^i) \sin(q_1^i + q_2^i + q_3^i) \\ &\quad + 2m_3^i L_2^i l_3^i \cos(q_1^i + q_2^i) \cos(q_1^i + q_2^i + q_3^i) \\ &\quad + m_2^i l_2^2 + m_3^i L_2^2 + m_3^i l_3^2 + I_{zz2}^i + I_{zz3}^i, \\ M_{23}^i &= m_3^i L_2^i l_3^i \sin(q_1^i + q_2^i) \sin(q_1^i + q_2^i + q_3^i) \\ &\quad + m_3^i L_2^i l_3^i \cos(q_1^i + q_2^i) \cos(q_1^i + q_2^i + q_3^i) \\ &\quad + m_3^i l_3^2 + I_{zz3}^i, \end{aligned} \quad (47)$$

$$\begin{aligned} M_{31}^i &= M_{13}^i, \quad M_{32}^i = M_{23}^i, \\ M_{33}^i &= m_3^i l_3^2 + I_{zz3}^i. \end{aligned} \quad (48)$$

$$\begin{aligned} G_1^i &= g(m_1^i l_1^i \cos(q_1^i) + m_2^i L_1^i \cos(q_1^i) + m_3^i L_1^i \cos(q_1^i) \\ &\quad + m_1^i l_2^i \cos(q_1^i + q_2^i) + m_3^i L_2^i \cos(q_1^i + q_2^i) \\ &\quad + m_3^i l_3^i \cos(q_1^i + q_2^i + q_3^i)), \\ G_2^i &= g(m_2^i l_2^i \cos(q_1^i + q_2^i) + m_3^i L_2^i \cos(q_1^i + q_2^i) \\ &\quad + m_3^i l_3^i \cos(q_1^i + q_2^i + q_3^i)), \\ G_3^i &= g(m_3^i l_3^i \cos(q_1^i + q_2^i + q_3^i)). \end{aligned} \quad (49)$$

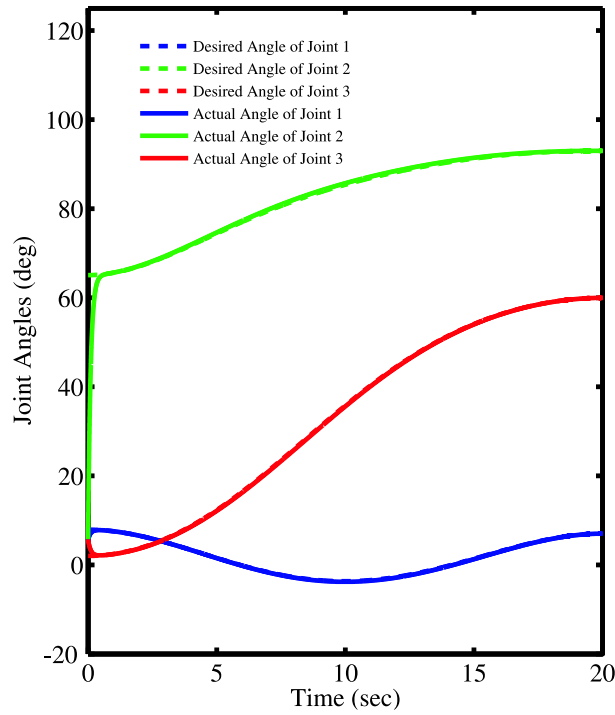


Figure 13: Tracking Angles of Adaptive Controller for Three-Link Middle Finger

$$\begin{aligned}
 C_1^i = & (2m_2^i L_1^i l_2^i \sin(q_1^i) \cos(q_1^i + q_2^i) - 2m_2^i L_1^i l_2^i \cos(q_1^i) \sin(q_1^i + q_2^i) \\
 & + 2m_3^i L_1^i L_2^i \sin(q_1^i) \cos(q_1^i + q_2^i) - 2m_3^i L_1^i L_2^i \cos(q_1^i) \sin(q_1^i + q_2^i) \\
 & + 2m_3^i L_1^i l_3^i \sin(q_1^i) \cos(q_1^i + q_2^i + q_3^i) - 2m_3^i L_1^i l_3^i \cos(q_1^i) \sin(q_1^i + q_2^i + q_3^i)) \times \left( \frac{\partial q_1^i}{\partial t} \right) \left( \frac{\partial q_2^i}{\partial t} \right) \\
 & + (2m_3^i L_1^i l_3^i \sin(q_1^i) \cos(q_1^i + q_2^i + q_3^i) - 2m_3^i L_1^i l_3^i \cos(q_1^i) \sin(q_1^i + q_2^i + q_3^i) \\
 & + 2m_3^i L_2^i l_3^i \sin(q_1^i + q_2^i) \cos(q_1^i + q_2^i + q_3^i) - 2m_3^i L_2^i l_3^i \cos(q_1^i + q_2^i) \sin(q_1^i + q_2^i + q_3^i)) \times \left( \frac{\partial q_1^i}{\partial t} \right) \left( \frac{\partial q_3^i}{\partial t} \right) \\
 & + (2m_3^i L_1^i l_3^i \sin(q_1^i) \cos(q_1^i + q_2^i + q_3^i) - 2m_3^i L_1^i l_3^i \cos(q_1^i) \sin(q_1^i + q_2^i + q_3^i) \\
 & + 2m_3^i L_2^i l_3^i \sin(q_1^i + q_2^i) \cos(q_1^i + q_2^i + q_3^i) - 2m_3^i L_2^i l_3^i \cos(q_1^i + q_2^i) \sin(q_1^i + q_2^i + q_3^i)) \times \left( \frac{\partial q_2^i}{\partial t} \right) \left( \frac{\partial q_3^i}{\partial t} \right) \\
 & + (m_2^i L_1^i l_2^i \sin(q_1^i) \cos(q_1^i + q_2^i) - m_2^i L_1^i l_2^i \cos(q_1^i) \sin(q_1^i + q_2^i) \\
 & + m_3^i L_1^i L_2^i \sin(q_1^i) \cos(q_1^i + q_2^i) - m_3^i L_1^i L_2^i \cos(q_1^i) \sin(q_1^i + q_2^i) \\
 & + m_3^i L_1^i l_3^i \sin(q_1^i) \cos(q_1^i + q_2^i + q_3^i) - m_3^i L_1^i l_3^i \cos(q_1^i) \sin(q_1^i + q_2^i + q_3^i)) \times \left( \frac{\partial q_2^i}{\partial t} \right) \left( \frac{\partial q_3^i}{\partial t} \right) \\
 & + (m_3^i L_1^i l_3^i \sin(q_1^i) \cos(q_1^i + q_2^i + q_3^i) - m_3^i L_1^i l_3^i \cos(q_1^i) \sin(q_1^i + q_2^i + q_3^i) \\
 & + m_3^i L_2^i l_3^i \sin(q_1^i + q_2^i) \cos(q_1^i + q_2^i + q_3^i) - m_3^i L_2^i l_3^i \cos(q_1^i + q_2^i) \sin(q_1^i + q_2^i + q_3^i)) \times \left( \frac{\partial q_3^i}{\partial t} \right) \left( \frac{\partial q_3^i}{\partial t} \right),
 \end{aligned}$$

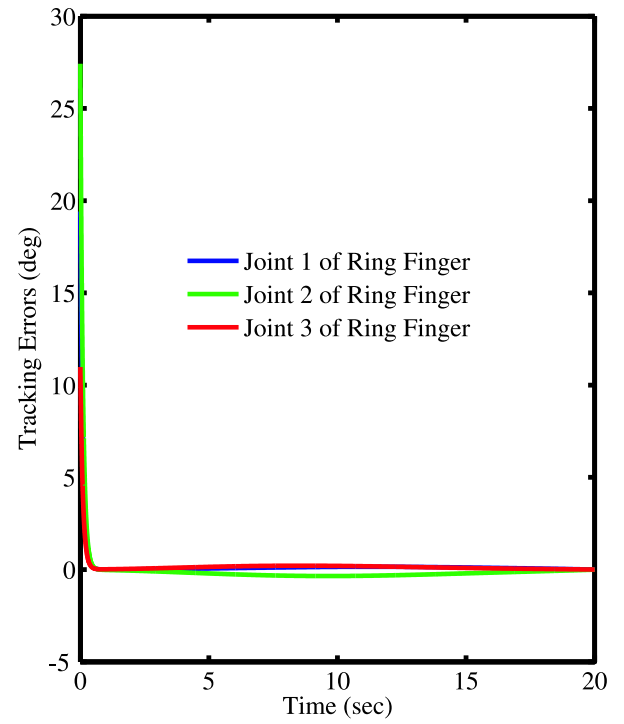


Figure 14: Tracking Errors of Adaptive Controller for Three-Link Ring Finger

$$\begin{aligned}
 C_2^i = & (m_2^i L_1^i l_2^i \sin(q_1^i) \cos(q_1^i + q_2^i) - m_2^i L_1^i l_2^i \cos(q_1^i) \sin(q_1^i + q_2^i) \\
 & + m_3^i L_1^i L_2^i \sin(q_1^i) \cos(q_1^i + q_2^i) - m_3^i L_1^i L_2^i \cos(q_1^i) \sin(q_1^i + q_2^i) \\
 & + m_3^i L_1^i l_3^i \sin(q_1^i) \cos(q_1^i + q_2^i + q_3^i) - m_3^i L_1^i l_3^i \cos(q_1^i) \sin(q_1^i + q_2^i + q_3^i)) \times \left( \frac{\partial q_1^i}{\partial t} \right) \left( \frac{\partial q_2^i}{\partial t} \right) \\
 & + (2m_3^i L_2^i l_3^i \sin(q_1^i + q_2^i) \cos(q_1^i + q_2^i + q_3^i) - 2m_3^i L_2^i l_3^i \cos(q_1^i + q_2^i) \sin(q_1^i + q_2^i + q_3^i)) \times \left( \frac{\partial q_1^i}{\partial t} \right) \left( \frac{\partial q_3^i}{\partial t} \right) \\
 & + (2m_3^i L_2^i l_3^i \sin(q_1^i + q_2^i) \cos(q_1^i + q_2^i + q_3^i) - 2m_3^i L_2^i l_3^i \cos(q_1^i + q_2^i) \sin(q_1^i + q_2^i + q_3^i)) \times \left( \frac{\partial q_2^i}{\partial t} \right) \left( \frac{\partial q_3^i}{\partial t} \right) \\
 & + (-m_2^i L_1^i l_2^i \sin(q_1^i) \cos(q_1^i + q_2^i) + m_2^i L_1^i l_2^i \cos(q_1^i) \sin(q_1^i + q_2^i) \\
 & - m_3^i L_1^i L_2^i \sin(q_1^i) \cos(q_1^i + q_2^i) + m_3^i L_1^i L_2^i \cos(q_1^i) \sin(q_1^i + q_2^i) \\
 & - m_3^i L_1^i l_3^i \sin(q_1^i) \cos(q_1^i + q_2^i + q_3^i) + m_3^i L_1^i l_3^i \cos(q_1^i) \sin(q_1^i + q_2^i + q_3^i)) \times \left( \frac{\partial q_1^i}{\partial t} \right) \left( \frac{\partial q_1^i}{\partial t} \right) \\
 & + (m_3^i L_2^i l_3^i \sin(q_1^i + q_2^i) \cos(q_1^i + q_2^i + q_3^i) - m_3^i L_2^i l_3^i \cos(q_1^i + q_2^i) \sin(q_1^i + q_2^i + q_3^i)) \times \left( \frac{\partial q_3^i}{\partial t} \right) \left( \frac{\partial q_3^i}{\partial t} \right),
 \end{aligned}$$

(50)



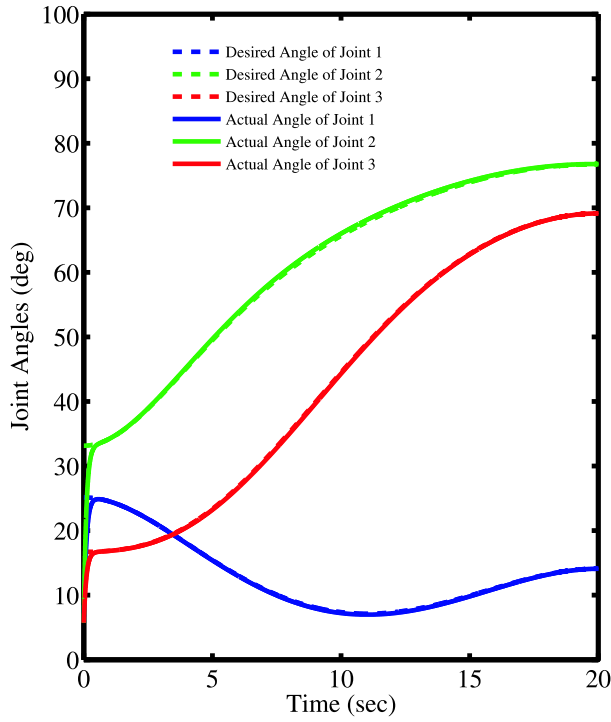


Figure 15: Tracking Angles of Adaptive Controller for Three-Link Ring Finger

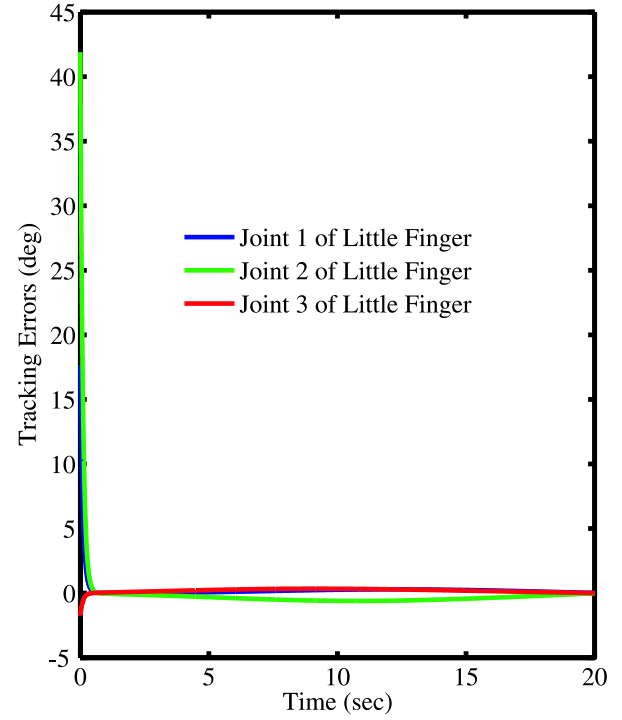


Figure 16: Tracking Errors of Adaptive Controller for Three-Link Little Finger

$$\begin{aligned}
 C_3^i = & (2m_3^i L_2^i l_3^i \cos(q_1^i + q_2^i) \sin(q_1^i + q_2^i + q_3^i) \\
 & - 2m_3^i L_2^i l_3^i \sin(q_1^i + q_2^i) \cos(q_1^i + q_2^i + q_3^i)) \times \\
 & \left( \frac{\partial q_1^i}{\partial t} \right) \left( \frac{\partial q_2^i}{\partial t} \right) \\
 & + (m_3^i L_1^i l_3^i \sin(q_1^i) \cos(q_1^i + q_2^i + q_3^i) \\
 & - m_3^i L_1^i l_3^i \cos(q_1^i) \sin(q_1^i + q_2^i + q_3^i) \\
 & + (m_3^i L_2^i l_3^i \sin(q_1^i + q_2^i) \cos(q_1^i + q_2^i + q_3^i) \\
 & - m_3^i L_2^i l_3^i \cos(q_1^i + q_2^i) \sin(q_1^i + q_2^i + q_3^i)) \times \\
 & \left( \frac{\partial q_1^i}{\partial t} \right) \left( \frac{\partial q_3^i}{\partial t} \right) \\
 & + (m_3^i L_2^i l_3^i \sin(q_1^i + q_2^i) \cos(q_1^i + q_2^i + q_3^i) \\
 & - m_3^i L_2^i l_3^i \cos(q_1^i + q_2^i) \sin(q_1^i + q_2^i + q_3^i)) \times \\
 & \left( \frac{\partial q_2^i}{\partial t} \right) \left( \frac{\partial q_3^i}{\partial t} \right) \\
 & + (m_3^i L_1^i l_3^i \cos(q_1^i) \sin(q_1^i + q_2^i + q_3^i) \\
 & - m_3^i L_1^i l_3^i \sin(q_1^i) \cos(q_1^i + q_2^i + q_3^i) \\
 & + m_3^i L_2^i l_3^i \cos(q_1^i + q_2^i) \sin(q_1^i + q_2^i + q_3^i) \\
 & - m_3^i L_2^i l_3^i \sin(q_1^i + q_2^i) \cos(q_1^i + q_2^i + q_3^i)) \times \\
 & \left( \frac{\partial q_1^i}{\partial t} \right) \left( \frac{\partial q_1^i}{\partial t} \right) \\
 & + (m_3^i L_2^i l_3^i \cos(q_1^i + q_2^i) \sin(q_1^i + q_2^i + q_3^i) \\
 & - m_3^i L_2^i l_3^i \sin(q_1^i + q_2^i) \cos(q_1^i + q_2^i + q_3^i)) \times \\
 & \left( \frac{\partial q_2^i}{\partial t} \right) \left( \frac{\partial q_2^i}{\partial t} \right). \quad (51)
 \end{aligned}$$

## Appendix B: Regression Matrix $\mathbf{Y}$ and Unknown Parameter Vector $\boldsymbol{\pi}$

In Section 3.2, the regression matrix  $\mathbf{Y}^t$  and the unknown parameter vector  $\boldsymbol{\pi}^t$  of two-link thumb can be expressed as

$$\begin{aligned}
 \mathbf{Y}^t &= \begin{bmatrix} Y_{11}^t & Y_{12}^t & Y_{13}^t & Y_{14}^t \\ Y_{21}^t & Y_{22}^t & Y_{23}^t & Y_{24}^t \end{bmatrix}, \\
 \boldsymbol{\pi}^t &= [m_1^t \ m_2^t \ I_{zz1}^t \ I_{zz2}^t]'.
 \end{aligned}$$

where

$$\begin{aligned}
 Y_{11}^t &= l_1^t l_1^t (\ddot{q}_{d1} + \lambda_1 \dot{e}_1) + g l_1^t C_1, \\
 Y_{12}^t &= (2L_1^t l_2^t C_2 + L_1^t L_1^t + l_2^t l_2^t) (\ddot{q}_{d1} + \lambda_1 \dot{e}_1) \\
 &\quad + (L_1^t l_2^t C_2 + l_2^t l_2^t) (\ddot{q}_{d2} + \lambda_2 \dot{e}_2) \\
 &\quad - L_1^t l_2^t S_2 \dot{q}_2 (\dot{q}_{d1} + \lambda_1 \dot{e}_1) \\
 &\quad - L_1^t l_2^t S_2 (\dot{q}_1 + \dot{q}_2) (\dot{q}_{d2} + \lambda_2 \dot{e}_2) + g l_2^t C_{12}, \\
 Y_{13}^t &= \ddot{q}_{d1} + \lambda_1 \dot{e}_1, \\
 Y_{14}^t &= \ddot{q}_{d1} + \lambda_1 \dot{e}_1 + \ddot{q}_{d2} + \lambda_2 \dot{e}_2, \\
 Y_{21}^t &= Y_{23}^t = 0, \\
 Y_{22}^t &= (L_1^t l_2^t C_2 + l_2^t l_2^t) (\ddot{q}_{d1} + \lambda_1 \dot{e}_1) + l_2^t l_2^t (\ddot{q}_{d2} + \lambda_2 \dot{e}_2) \\
 &\quad + L_1^t l_2^t S_2 \dot{q}_1 (\dot{q}_{d1} + \lambda_1 \dot{e}_1) \\
 &\quad - L_1^t l_2^t S_2 \dot{q}_1 (\dot{q}_{d2} + \lambda_2 \dot{e}_2) + g l_2^t C_{12}, \\
 Y_{24}^t &= \ddot{q}_{d1} + \lambda_1 \dot{e}_1 + \ddot{q}_{d2} + \lambda_2 \dot{e}_2, \\
 C_1 &= \cos(q_1^t), C_2 = \cos(q_2^t), \\
 S_2 &= \sin(q_2^t), C_{12} = \cos(q_1^t + q_2^t).
 \end{aligned}$$

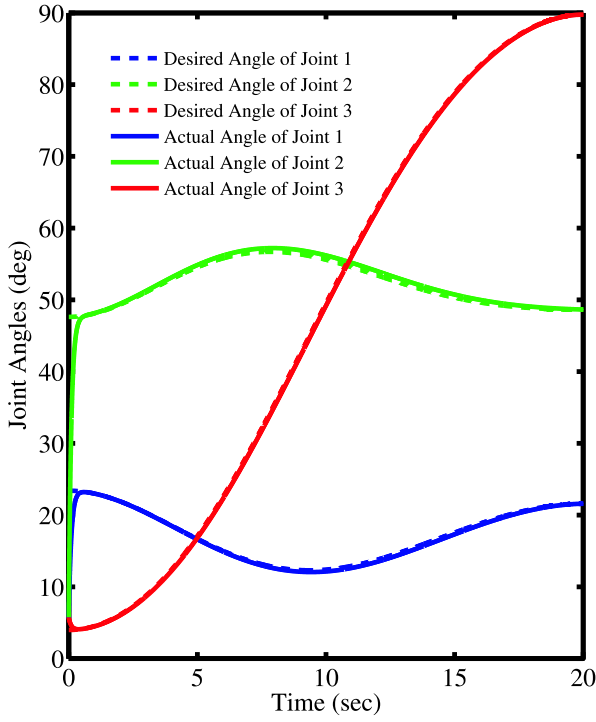


Figure 17: Tracking Angles of Adaptive Controller for Three-Link Little Finger

Similarly, the regression matrix  $\mathbf{Y}^i$  and the unknown parameter vector  $\pi^i$  of three-link index finger can be written as

$$\mathbf{Y}^i = \begin{bmatrix} Y_{11}^i & Y_{12}^i & Y_{13}^i & Y_{14}^i & Y_{15}^i & Y_{16}^i \\ Y_{21}^i & Y_{22}^i & Y_{23}^i & Y_{24}^i & Y_{25}^i & Y_{26}^i \\ Y_{31}^i & Y_{32}^i & Y_{33}^i & Y_{34}^i & Y_{35}^i & Y_{36}^i \end{bmatrix},$$

$$\pi^i = [m_1^i \ m_2^i \ m_3^i \ I_{zz1}^i \ I_{zz2}^i \ I_{zz3}^i]'$$

Here,

$$\begin{aligned} Y_{11}^i &= l_1^i l_1^i (\ddot{q}_{d1} + \lambda_1 \dot{e}_1) + g l_1^i C_1 + g l_2^i C_{12}, \\ Y_{12}^i &= (2L_1^i l_2^i S_1 S_{12} + 2L_1^i l_2^i C_1 C_{12} + L_1^i l_1^i + l_2^i l_2^i)(\ddot{q}_{d1} + \lambda_1 \dot{e}_1) \\ &\quad + (L_1^i l_2^i S_1 S_{12} + L_1^i l_2^i C_1 C_{12} + l_2^i l_2^i)(\ddot{q}_{d2} + \lambda_2 \dot{e}_2) + g L_1 C_1 \\ &\quad + (L_1^i l_2^i S_1 C_{12} - L_1^i l_2^i C_1 S_{12}) \dot{q}_1 (\dot{q}_{d2} + \lambda_2 \dot{e}_2) \\ &\quad + (L_1^i l_2^i S_1 C_{12} - L_1^i l_2^i C_1 S_{12}) \dot{q}_2 (\dot{q}_{d1} + \lambda_1 \dot{e}_1) \\ &\quad + (L_1^i l_2^i S_1 C_{12} - L_1^i l_2^i C_1 S_{12}) \dot{q}_2 (\dot{q}_{d2} + \lambda_2 \dot{e}_2), \\ Y_{13}^i &= (2L_1^i L_2^i S_1 S_{12} + 2L_1^i L_2^i C_1 C_{12} + 2L_1^i l_3^i S_1 S_{123} \\ &\quad + 2L_1^i l_3^i C_1 C_{123} + 2L_2^i l_3^i S_{12} S_{123} + 2L_2^i l_3^i C_{12} C_{123} \\ &\quad + L_1^i L_1^i + L_2^i L_2^i + l_3^i l_3^i)(\ddot{q}_{d1} + \lambda_1 \dot{e}_1) \\ &\quad + (2L_2^i l_3^i S_{12} S_{123} + 2L_2^i l_3^i C_{12} C_{123} + L_1^i L_2^i S_1 S_{12} \\ &\quad + L_1^i L_2^i C_1 C_{12} + L_1^i l_3^i S_1 S_{123} + L_1^i l_3^i C_1 C_{123} \\ &\quad + L_2^i L_2^i + l_3^i l_3^i)(\ddot{q}_{d2} + \lambda_2 \dot{e}_2) \\ &\quad + (L_1^i l_3^i S_1 S_{123} + L_1^i l_3^i C_1 C_{123} + L_2^i l_3^i S_{12} S_{123} \\ &\quad + L_2^i l_3^i C_{12} C_{123} + l_3^i l_3^i)(\ddot{q}_{d3} + \lambda_3 \dot{e}_3) \\ &\quad + g L_1 C_1 + g L_2 C_{12} + g l_3 C_{123} \\ &\quad + (L_1^i L_2^i S_1 C_{12} - L_1^i L_2^i C_1 S_{12}) \dot{q}_1 (\dot{q}_{d2} + \lambda_2 \dot{e}_2) \end{aligned}$$

$$\begin{aligned} &+ (L_1^i L_2^i S_1 C_{12} - L_1^i L_2^i C_1 S_{12}) \dot{q}_2 (\dot{q}_{d1} + \lambda_1 \dot{e}_1) \\ &+ (L_1^i l_3^i S_1 C_{123} - L_1^i l_3^i C_1 S_{123}) \dot{q}_1 (\dot{q}_{d2} + \lambda_2 \dot{e}_2) \\ &+ (L_1^i l_3^i S_1 C_{123} - L_1^i l_3^i C_1 S_{123}) \dot{q}_2 (\dot{q}_{d1} + \lambda_1 \dot{e}_1) \\ &+ (L_1^i l_3^i S_1 C_{123} - L_1^i l_3^i C_1 S_{123}) \dot{q}_3 (\dot{q}_{d1} + \lambda_1 \dot{e}_1) \\ &+ (L_2^i l_3^i S_{12} C_{123} - L_2^i l_3^i C_{12} S_{123}) \dot{q}_1 (\dot{q}_{d3} + \lambda_3 \dot{e}_3) \\ &+ (L_2^i l_3^i S_{12} C_{123} - L_2^i l_3^i C_{12} S_{123}) \dot{q}_3 (\dot{q}_{d1} + \lambda_1 \dot{e}_1) \\ &+ (L_1^i l_3^i S_1 C_{123} - L_1^i l_3^i C_1 S_{123}) \dot{q}_2 (\dot{q}_{d3} + \lambda_3 \dot{e}_3) \\ &+ (L_1^i l_3^i S_1 C_{123} - L_1^i l_3^i C_1 S_{123}) \dot{q}_3 (\dot{q}_{d2} + \lambda_2 \dot{e}_2) \\ &+ (L_2^i l_3^i S_{12} C_{123} - L_2^i l_3^i C_{12} S_{123}) \dot{q}_2 (\dot{q}_{d3} + \lambda_3 \dot{e}_3) \\ &+ (L_2^i l_3^i S_{12} C_{123} - L_2^i l_3^i C_{12} S_{123}) \dot{q}_3 (\dot{q}_{d2} + \lambda_2 \dot{e}_2) \\ &+ (L_1^i L_2^i S_1 C_{12} - L_1^i L_2^i C_1 S_{12}) \dot{q}_2 (\dot{q}_{d2} + \lambda_2 \dot{e}_2) \\ &+ (L_1^i l_3^i S_1 C_{123} - L_1^i l_3^i C_1 S_{123}) \dot{q}_2 (\dot{q}_{d2} + \lambda_2 \dot{e}_2) \\ &+ (L_1^i l_3^i S_1 C_{123} - L_1^i l_3^i C_1 S_{123}) \dot{q}_3 (\dot{q}_{d3} + \lambda_3 \dot{e}_3) \\ &+ (L_2^i l_3^i S_{12} C_{123} - L_2^i l_3^i C_{12} S_{123}) \dot{q}_3 (\dot{q}_{d3} + \lambda_3 \dot{e}_3), \end{aligned}$$

$$Y_{14}^i = \ddot{q}_{d1} + \lambda_1 \dot{e}_1,$$

$$Y_{15}^i = \ddot{q}_{d1} + \lambda_1 \dot{e}_1 + \ddot{q}_{d2} + \lambda_2 \dot{e}_2,$$

$$Y_{16}^i = \ddot{q}_{d1} + \lambda_1 \dot{e}_1 + \ddot{q}_{d2} + \lambda_2 \dot{e}_2 + \ddot{q}_{d3} + \lambda_3 \dot{e}_3,$$

$$Y_{21}^i = Y_{24}^i = Y_{31}^i = Y_{32}^i = Y_{34}^i = Y_{35}^i = 0,$$

$$\begin{aligned} Y_{22}^i &= (L_1^i l_2^i S_1 S_{12} + L_1^i l_2^i C_1 C_{12} + l_2^i l_2^i)(\ddot{q}_{d1} + \lambda_1 \dot{e}_1) \\ &\quad + l_2^i l_2^i (\ddot{q}_{d2} + \lambda_2 \dot{e}_2) + g l_2 C_{12} \\ &\quad + (L_1^i l_2^i S_1 C_{12} - L_1^i l_2^i C_1 S_{12}) \dot{q}_2 (\dot{q}_{d1} + \lambda_1 \dot{e}_1) \\ &\quad + (L_1^i l_2^i C_1 S_{12} - L_1^i l_2^i S_1 C_{12}) \dot{q}_1 (\dot{q}_{d1} + \lambda_1 \dot{e}_1), \\ Y_{23}^i &= (2L_2^i l_3^i S_{12} S_{123} + 2L_2^i l_3^i C_{12} C_{123} + L_1^i L_2^i S_1 S_{12} \\ &\quad + L_1^i L_2^i C_1 C_{12} + L_1^i l_3^i S_1 S_{123} + L_1^i l_3^i C_1 C_{123} \\ &\quad + L_2^i L_2^i + l_3^i l_3^i)(\ddot{q}_{d1} + \lambda_1 \dot{e}_1) + (2L_2^i l_3^i S_{12} S_{123} \\ &\quad + 2L_2^i l_3^i C_{12} C_{123} + L_2^i L_2^i + l_3^i l_3^i)(\ddot{q}_{d2} + \lambda_2 \dot{e}_2) \\ &\quad + (L_2^i l_3^i S_{12} S_{123} + L_2^i l_3^i C_{12} C_{123} + l_3^i l_3^i)(\ddot{q}_{d3} + \lambda_3 \dot{e}_3) \\ &\quad + g L_2 C_{12} + g l_3 C_{123} \\ &\quad + (L_1^i L_2^i S_1 C_{12} - L_1^i L_2^i C_1 S_{12}) \dot{q}_1 (\dot{q}_{d2} + \lambda_2 \dot{e}_2) \\ &\quad + (L_1^i l_3^i S_1 C_{123} - L_1^i l_3^i C_1 S_{123}) \dot{q}_1 (\dot{q}_{d2} + \lambda_2 \dot{e}_2) \\ &\quad + (L_2^i l_3^i S_{12} C_{123} - L_2^i l_3^i C_{12} S_{123}) \dot{q}_1 (\dot{q}_{d3} + \lambda_3 \dot{e}_3) \\ &\quad + (L_2^i l_3^i S_{12} C_{123} - L_2^i l_3^i C_{12} S_{123}) \dot{q}_3 (\dot{q}_{d1} + \lambda_1 \dot{e}_1) \\ &\quad + (L_2^i l_3^i S_{12} C_{123} - L_2^i l_3^i C_{12} S_{123}) \dot{q}_2 (\dot{q}_{d3} + \lambda_3 \dot{e}_3) \\ &\quad + (L_2^i l_3^i S_{12} C_{123} - L_2^i l_3^i C_{12} S_{123}) \dot{q}_3 (\dot{q}_{d2} + \lambda_2 \dot{e}_2) \\ &\quad + (L_1^i L_2^i S_1 C_{12} - L_1^i L_2^i C_1 S_{12}) \dot{q}_1 (\dot{q}_{d1} + \lambda_1 \dot{e}_1) \\ &\quad + (L_1^i l_3^i S_1 C_{123} - L_1^i l_3^i C_1 S_{123}) \dot{q}_1 (\dot{q}_{d1} + \lambda_1 \dot{e}_1) \\ &\quad + (L_2^i l_3^i S_{12} C_{123} - L_2^i l_3^i C_{12} S_{123}) \dot{q}_3 (\dot{q}_{d3} + \lambda_3 \dot{e}_3), \end{aligned}$$

$$Y_{25}^i = \ddot{q}_{d1} + \lambda_1 \dot{e}_1 + \ddot{q}_{d2} + \lambda_2 \dot{e}_2,$$

$$Y_{26}^i = \ddot{q}_{d1} + \lambda_1 \dot{e}_1 + \ddot{q}_{d2} + \lambda_2 \dot{e}_2 + \ddot{q}_{d3} + \lambda_3 \dot{e}_3,$$

$$\begin{aligned} Y_{33}^i &= (L_1^i l_3^i S_1 S_{123} + L_1^i l_3^i C_1 C_{123} + L_2^i l_3^i S_{12} S_{123} \\ &\quad + L_2^i l_3^i C_{12} C_{123} + l_3^i l_3^i)(\ddot{q}_{d1} + \lambda_1 \dot{e}_1) \\ &\quad + (L_2^i l_3^i S_{12} S_{123} + L_2^i l_3^i C_{12} C_{123} + l_3^i l_3^i)(\ddot{q}_{d2} + \lambda_2 \dot{e}_2) \\ &\quad + l_3^i l_3^i (\ddot{q}_{d3} + \lambda_3 \dot{e}_3) + g l_3 C_{123} \\ &\quad + (L_2^i l_3^i S_{12} S_{123} - L_2^i l_3^i S_{12} C_{123}) \dot{q}_1 (\dot{q}_{d2} + \lambda_2 \dot{e}_2) \\ &\quad + (L_2^i l_3^i S_{12} S_{123} - L_2^i l_3^i S_{12} C_{123}) \dot{q}_2 (\dot{q}_{d1} + \lambda_1 \dot{e}_1) \\ &\quad + (L_1^i l_3^i S_1 C_{123} - L_1^i l_3^i C_1 S_{123}) \dot{q}_1 (\dot{q}_{d3} + \lambda_3 \dot{e}_3) \\ &\quad + (L_2^i l_3^i S_{12} C_{123} - L_2^i l_3^i C_{12} S_{123}) \dot{q}_1 (\dot{q}_{d3} + \lambda_3 \dot{e}_3) \\ &\quad + (L_2^i l_3^i S_{12} C_{123} - L_2^i l_3^i C_{12} S_{123}) \dot{q}_2 (\dot{q}_{d3} + \lambda_3 \dot{e}_3) \\ &\quad + (L_1^i l_3^i S_1 C_{123} - L_1^i l_3^i C_1 S_{123}) \dot{q}_1 (\dot{q}_{d1} + \lambda_1 \dot{e}_1) \end{aligned}$$

$$\begin{aligned}
& + (L_2^i l_3^i C_{12} S_{123} - L_2^i l_3^i S_{12} C_{123}) \dot{q}_1 (\dot{q}_{d1} + \lambda_1 e_1) \\
& + (L_2^i l_3^i C_{12} S_{123} - L_2^i l_3^i S_{12} C_{123}) \dot{q}_2 (\dot{q}_{d2} + \lambda_2 e_2), \\
Y_{36}^i &= \ddot{q}_{d1} + \lambda_1 \dot{e}_1 + \ddot{q}_{d2} + \lambda_2 \dot{e}_2 + \ddot{q}_{d3} + \lambda_3 \dot{e}_3, \\
C_1 &= \cos(q_1^i), C_{12} = \cos(q_1^i + q_2^i), \\
S_1 &= \sin(q_1^i), S_{12} = \sin(q_1^i + q_2^i), \\
C_{123} &= \cos(q_1^i + q_2^i + q_3^i), \\
S_{123} &= \sin(q_1^i + q_2^i + q_3^i).
\end{aligned}$$

## References:

- [1] M. Zecca, S. Micera, M. Carrozza, and P. Dario, "Control of multifunctional prosthetic hands by processing the electromyographic signal," *Critical Reviews<sup>TM</sup> in Biomedical Engineering*, vol. 30, pp. 459–485, 2002, (Review article with 96 references).
- [2] J. C. K. Lai, M. P. Schoen, A. Perez-Gracia, D. S. Naidu, and S. W. Leung, "Prosthetic devices: Challenges and implications of robotic implants and biological interfaces," *Proceedings of the Institute of Mechanical Engineers (IMEchE), Part H: Journal of Engineering in Medicine*, vol. 221, no. 2, pp. 173–183, January 2007, special Issue on Micro and Nano Technologies in Medicine.
- [3] L. Zollo, S. Roccella, E. Guglielmelli, M. C. Carrozza, and P. Dario, "Biomechatronic design and control of an anthropomorphic artificial hand for prosthetic and robotic applications," *IEEE/ASME Transactions on Mechatronics*, vol. 12, no. 4, pp. 418–429, August 2007.
- [4] D. S. Naidu, C.-H. Chen, A. Perez, and M. P. Schoen, "Control strategies for smart prosthetic hand technology: An overview," in *Proceedings of the 30th Annual International IEEE EMBS Conference*, Vancouver, Canada, August 20–24 2008, pp. 4314–4317.
- [5] C.-H. Chen, "Hybrid control strategies for smart prosthetic hand," Ph.D. dissertation, Measurement and Control Engineering, Idaho State University, May 2009.
- [6] D. S. Naidu and C.-H. Chen, *Automatic Control Techniques for Smart Prosthetic Hand Technology: An Overview, book chapter 12, to appear in a book titled "Distributed Diagnosis and Home Healthcare (D2H2): Volume 2"*. California, USA: American Scientific Publishers, 2011, (in printing).
- [7] C.-H. Chen, K. W. Bosworth, M. P. Schoen, S. E. Bearden, D. S. Naidu, and A. Perez, "A study of particle swarm optimization on leukocyte adhesion molecules and control strategies for smart prosthetic hand," in *2008 IEEE Swarm Intelligence Symposium (IEEE SIS08)*, St. Louis, Missouri, USA, September 21–23 2008.
- [8] C.-H. Chen, D. S. Naidu, A. Perez, and M. P. Schoen, "Fusion of hard and soft control techniques for prosthetic hand," in *Proceedings of the International Association of Science and Technology for Development (IASTED) International Conference on Intelligent Systems and Control (ISC 2008)*, Orlando, Florida, USA, November 16–18 2008, pp. 120–125.
- [9] C.-H. Chen, D. S. Naidu, A. Perez-Gracia, and M. P. Schoen, "A hybrid control strategy for five-fingered smart prosthetic hand," in *Joint 48th IEEE Conference on Decision and Control (CDC) and 28th Chinese Control Conference (CCC)*, Shanghai, P. R. China, December 16–18 2009, pp. 5102–5107.
- [10] P. Dostalek, L. Pekar, V. Vasek, and J. Dolinay, "Microcontroller based self-tuning digital pid controller," in *The 14th World Scientific and Engineering Academy and Society (WSEAS) International Conference on Systems, Latest Trends on Systems (Volume I)*, Corfu Island, Greece, July 22–24 2010, pp. 248–251.
- [11] L. Macku and D. Samek, "Two step, pid and model predictive control applied on fed batch process," in *The 14th World Scientific and Engineering Academy and Society (WSEAS) International Conference on Systems, Latest Trends on Systems (Volume II)*, Corfu Island, Greece, July 22–24 2010, pp. 470–473.
- [12] D. Naidu, *Optimal Control Systems*. Boca Raton, FL: CRC Press, 2003.
- [13] C.-H. Chen, D. S. Naidu, A. Perez-Gracia, and M. P. Schoen, "A hybrid optimal control strategy for a smart prosthetic hand," in *Proceedings of the ASME 2009 Dynamic Systems and Control Conference (DSCC)*, Hollywood, California, USA, October 12–14 2009, (No. DSCC2009-2507).
- [14] C.-H. Chen and D. S. Naidu, "Optimal control strategy for two-fingered smart prosthetic hand," in *Proceedings of the International Association of Science and Technology for Development (IASTED) International Conference on Robotics*

and Applications (RA 2010), Cambridge, Massachusetts, USA, November 1-3 2010, pp. 190–196.

- [15] F. Lewis, D. Dawson, and C. Abdallah, *Robot Manipulators Control: Second Edition, Revised and Expanded*. New York, NY: Marcel Dekker, Inc., 2004.
- [16] C.-H. Chen, D. S. Naidu, A. Perez-Gracia, and M. P. Schoen, “A hybrid adaptive control strategy for a smart prosthetic hand,” in *The 31st Annual International Conference of the IEEE Engineering Medicine and Biology Society (EMBS)*, Minneapolis, Minnesota, USA, September 2-6 2009, pp. 5056–5059.
- [17] C.-H. Chen, D. S. Naidu, and M. P. Schoen, “An adaptive control strategy for a five-fingered prosthetic hand,” in *The 14th World Scientific and Engineering Academy and Society (WSEAS) International Conference on Systems, Latest Trends on Systems (Volume II)*, Corfu Island, Greece, July 22-24 2010, pp. 405–410.
- [18] M. Bakosova, A. Vasickaninova, and M. Kar-saiova, “Robust static output feedback stabilization of an exothermic chemical reactor with input constraints,” in *the 14th World Scientific and Engineering Academy and Society (WSEAS) International Conference on Systems, Latest Trends on Systems (Volume I)*, Corfu Island, Greece, July 22-24 2010, pp. 341–346.
- [19] R. R. Seeley, T. D. Stephens, and P. Tate, *Anatomy & Physiology, Eighth Edition*. New York, NY: The McGraw-Hill, 2007.
- [20] R. N. Jazar, *Theory of Applied Robotics. Kinematics, Dynamics, and Control*. New York, USA: Springer, 2007.
- [21] B. Siciliano, L. Sciavicco, L. Villani, and G. Ori-olo, *Robotics: Modelling, Planning and Control*. London, UK: Springer-Verlag, 2009.
- [22] R. Schilling, *Fundamentals of Robotics: Analysis and Control*. Englewood Cliffs, NJ: Prentice Hall, 1990.
- [23] R. Kelly, V. Santibanez, and A. Loria, *Control of Robot Manipulators in Joint Space*. New York, USA: Springer, 2005.
- [24] A. Nikoobin and R. Haghighi, “Lyapunov-based nonlinear disturbance observer for serial n-link robot manipulators,” *Journal of Intelligent and Robotic Systems*, 2008.
- [25] Y. Z. Arslan, Y. Hacioglu, and N. Yagiz, “Prosthetic hand finger control using fuzzy sliding modes,” *Journal of Intelligent and Robotic Systems*, vol. 52, pp. 121–138, 2008.
- [26] F. Lewis, S. Jagannathan, and A. Yesildirek, *Neural Network Control of Robotic Manipulators and Nonlinear Systems*. London, UK: Taylor & Francis, 1999.
- [27] P. K. Lavangie and C. C. Norkin, *Joint Structure and Function: A Comprehensive Analysis, Third Edition*. Philadelphia, PA: F. A. Davis Company, 2001.
- [28] S. Arimoto, *Control Theory of Multi-fingered Hands: A Modeling and Analytical-Mechanics Approach for Dexterity and Intelligence*. London, UK: Springer-Verlag, 2008.

# OPTIMAL CONTROL STRATEGY FOR TWO-FINGERED SMART PROSTHETIC HAND

**Cheng-Hung Chen**

Measurement and Control  
Engineering Research Center  
Department of Biological Sciences  
College of Science and Engineering  
Idaho State University  
Pocatello, Idaho 83209, USA  
Email: chenchen@isu.edu

**D. Subbaram Naidu**

Measurement and Control  
Engineering Research Center  
Department of Electrical Engineering  
School of Engineering  
Idaho State University  
Pocatello, Idaho 83209, USA  
Email: naiduds@isu.edu

## ABSTRACT

This paper addresses the optimal control for a two-fingered (thumb and index finger) prosthetic hand. To speed up the performance and improve the accuracy, we modified the performance index by including an exponential term. First, we developed the differential kinematics for a serial  $n$ -link revolute-joint planar manipulator to computer the angular velocities and angular accelerations of each finger. Further, the trajectory planning of the orientation was designed by using cubic polynomial. Simulations show that the proposed technique provides fast action with high accuracy and 30-fold faster than ANFIS or GA based trajectory planning.

## KEY WORDS

Prosthetic Hand, Optimal Control, Stability, ANFIS

## 1 Introduction

Hard control (HC) techniques comprise proportional-integral-derivative (PID) control [1–3], optimal control [4–6], adaptive control [7–9] etc. with specific applications to prosthetic devices. However, our previous works [2,3] for smart prosthetic hand showed that PID controller results in overshooting and oscillation. Optimal controller can obtain a high performance [5,6]. However, this control technique takes time to be convergent. To overcome the overshooting and convergent problems, studying the stability of the optimal controller is precisely the main goal of this work. In addition, the adaptive neuro-fuzzy inference system (ANFIS) and genetic algorithm (GA) based trajectory planning [5,6,10] take much time to train the neural layers, especially for high degree-of-freedom (DOF) problems. To improve the performance, it is also the goal of this paper.

In this paper, we first consider briefly forward kinematics and inverse kinematics for a serial  $n$ -link revolute-joint planar manipulator and two-link thumb and three-link index finger, respectively. Then, by using differential kinematics, the angular velocities and angular accelerations of a serial  $n$ -link revolute-joint planar manipulator are derived.

Moreover, the trajectory planning of the orientation is designed by using cubic polynomial. The dynamic models of the smart prosthetic hand and linearization technique were briefly introduced. Finally, the stability of finite-time linear quadratic optimal controller are investigated by changing cost function  $J$ . The simulation results show the presented technique can be fast convergence and hold the high performance for the two-fingered smart prosthetic hand.

## 2 Modeling

Forward and inverse kinematics of articulated systems study the analytical relationship between the angular positions of joints and the positions and orientations of the end-effectors (fingertips). A desired trajectory is usually specified in *Cartesian* space and the trajectory controller is easily performed in the *joint* space. Hence, conversion of Cartesian trajectory planning to the joint space [11] is necessary. Using inverse kinematics, the joint angular positions of each finger need to be obtained from the known fingertip positions. Then the angular velocities and angular accelerations of joints can be obtained from the linear and angular velocities and accelerations of fingertips (end-effectors) by differential kinematics. The inverse kinematics of two-link thumb and three-link fingers were discussed in our previous publications [2,3,6,10,12] for a two-fingered (thumb and index finger) smart prosthetic hand. Here, we derive the general form of forward and differential kinematics for a serial  $n$ -link revolute-joint planar manipulator.

### 2.1 Forward Kinematics

Figure 1 shows the illustration of a serial  $n$ -link revolute-joint planar manipulator.  $L_i$  is the length of the link  $i$  and  $q_i$  is the angle of the joint  $i$  ( $i = 1, 2, \dots, n$ ).  $\tau_i$  is the actuator of the joint  $i$ . The position  $\mathbf{P}_n (X_n, Y_n)$  of the end-effector and the orientation  $\phi_n$  of the end-effector frame have been

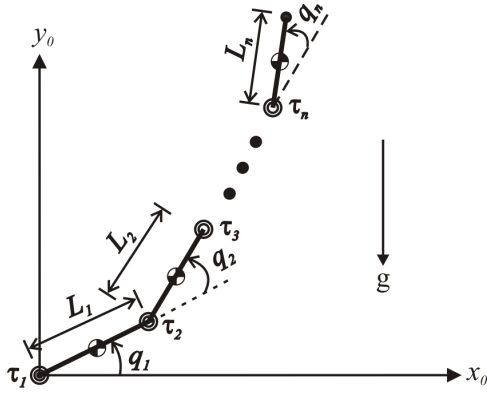


Figure 1. Illustration of a Serial  $n$ -Link Revolute-Joint Planar Manipulator

derived [12] as

$$\begin{aligned} X_n &= \sum_{j=1}^n L_j \cos \left( \sum_{i=1}^j q_i \right), \\ Y_n &= \sum_{j=1}^n L_j \sin \left( \sum_{i=1}^j q_i \right), \\ \phi_n &= \sum_{i=1}^n q_i. \end{aligned} \quad (1)$$

## 2.2 Inverse Kinematics

### 2.2.1 Two-Link Thumb

As shown in Figure 2, thumb is assumed as the two-link ( $n = 2$ ) finger and the other four fingers, such as index finger, middle finger, ring finger, and little finger, are considered as three-link fingers. Hence, the angular positions, angular velocities, and angular accelerations of each finger can be deduced as follows. According to equation (1), the

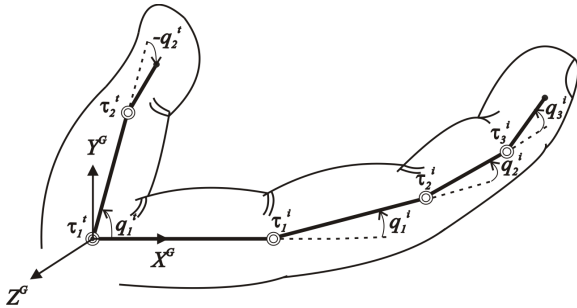


Figure 2. Schematic Diagram of Thumb and Index Finger

fingertip coordinate  $(X^t, Y^t)$  of thumb ( $t$ ) can be described

as

$$X^t = L_1^t \cos(q_1^t) + L_2^t \cos(q_1^t + q_2^t), \quad (2)$$

$$Y^t = L_1^t \sin(q_1^t) + L_2^t \sin(q_1^t + q_2^t). \quad (3)$$

Here  $L_1^t$  and  $L_2^t$  are the lengths of the links 1 and 2 of the thumb, respectively;  $q_1^t$  and  $q_2^t$  are the angular positions (or called angles) of joints 1 and 2 of the thumb. Choosing the *elbow up* configuration, the angle  $q_2^t$  of the joint 2 can be obtained from [11]

$$q_2^t = -\cos^{-1} \left( \frac{X^{t^2} + Y^{t^2} - L_1^{t^2} - L_2^{t^2}}{2L_1^t L_2^t} \right). \quad (4)$$

Notice that in this paper, all positive angles are defined counterclockwise. When choosing the *elbow up* configuration, the angle  $q_2^t$  is clockwise, so the sign of  $q_2^t$  is negative. Based on the geometry, we can get

$$q_1^t = \tan^{-1} \left( \frac{Y^t}{X^t} \right) - \tan^{-1} \left( \frac{L_2^t \sin(q_2^t)}{L_1^t + L_2^t \cos(q_2^t)} \right). \quad (5)$$

### 2.2.2 Three-Link Index Finger

Figure 3 shows the illustration of three-link ( $n = 3$ ) index

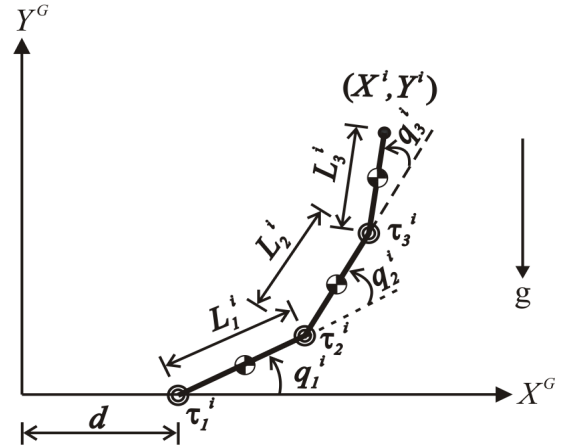


Figure 3. Three-Link Index Finger Illustration

finger.  $d$  is the distance between the global ( $G$ ) frame and index finger ( $i$ ) local frame base (zero);  $L_1^i$ ,  $L_2^i$ , and  $L_3^i$  are the lengths of the links 1, 2 and 3 of the index finger ( $i$ ), respectively;  $q_1^i$ ,  $q_2^i$ , and  $q_3^i$  are the angles of the joints 1, 2, and 3 of the index finger. Using *Denavit-Hartenberg* (DH) [11–15] transformation matrices, the fingertip (end-effector) coordinate  $\mathbf{P}^i (X^i, Y^i)$  and the orientation  $\phi^i$  of the index finger ( $i$ ) can be written as

$$\begin{aligned} X^i &= d + L_1^i \cos(q_1^i) + L_2^i \cos(q_1^i + q_2^i) + L_3^i \cos(\phi^i), \\ Y^i &= L_1^i \sin(q_1^i) + L_2^i \sin(q_1^i + q_2^i) + L_3^i \sin(\phi^i), \\ \phi^i &= q_1^i + q_2^i + q_3^i. \end{aligned} \quad (6)$$

The local coordinate  $\mathbf{P}_2^i (X_2^i, Y_2^i)$  of the joint 2 can be obtained as

$$\begin{aligned} X_2^i &= X^i - L_3^i \cos(\phi^i) - d, \\ Y_2^i &= Y^i - L_3^i \sin(\phi^i). \end{aligned} \quad (7)$$

Choosing the *elbow down* configuration, the angles  $q_2^i$  and  $q_1^i$  can be obtained as

$$q_2^i = \cos^{-1} \left( \frac{X_2^{i2} + Y_2^{i2} - L_1^{i2} - L_2^{i2}}{2L_1^i L_2^i} \right),$$

$$q_1^i = \tan^{-1} \left( \frac{Y^i}{X^i} \right) - \tan^{-1} \left( \frac{L_2^i \sin(q_2^i)}{L_1^i + L_2^i \cos(q_2^i)} \right). \quad (8)$$

Then we can get the angle  $q_3^i$  of the joint 3 as

$$q_3^i = \phi^i - q_1^i - q_2^i. \quad (9)$$

### 2.3 Differential Kinematics

The *linear* velocity  ${}^0\dot{\mathbf{P}}_n$  and *angular* velocity  ${}^0\boldsymbol{\omega}_n$  of the origin of the end-effector frame are linear relations to the joint angular velocities  $\dot{\mathbf{q}}$  [12]. The *linear* relation represents the differential kinematics equation and can be expressed as

$${}^0\mathbf{V}_n = \mathbf{J}(\mathbf{q}) \dot{\mathbf{q}}. \quad (10)$$

Here,  ${}^0\mathbf{V}_n = [{}^0\dot{\mathbf{P}}_n \ {}^0\boldsymbol{\omega}_n]'$  is the  $(6 \times 1)$  end-effector velocity vector.  $\mathbf{J}(\mathbf{q}) = [\mathbf{J}_P(\mathbf{q}) \ \mathbf{J}_O(\mathbf{q})]'$  is the  $(6 \times n)$  geometric Jacobian matrix of a serial  $n$ -link revolute-joint planar manipulator; both position Jacobian  $\mathbf{J}_P(\mathbf{q})$  and orientation Jacobian  $\mathbf{J}_O(\mathbf{q})$  are the  $(3 \times n)$  matrices which contribute the joint angular velocities  $\dot{\mathbf{q}}$  to the linear velocity  ${}^0\dot{\mathbf{P}}_n$  and angular velocity  ${}^0\boldsymbol{\omega}_n$  of the end-effector, respectively. The entry  $J_{ij}$  ( $i, j \in N$ ) of the geometric Jacobian  $\mathbf{J}(\mathbf{q})$  in (10) can be rewritten as

$$J_{ij} = \begin{cases} -\sum_{j=1}^n L_j \sin \left( \sum_{k=1}^j q_k \right) & \text{if } i = 1, j \in [1, 6]; \\ \sum_{j=1}^n L_j \cos \left( \sum_{k=1}^j q_k \right) & \text{if } i = 2, j \in [1, 6]; \\ 0 & \text{if } i \in [3, 5], j \in [1, 6]; \\ 1 & \text{if } i = 6, j \in [1, 6]. \end{cases}$$

Then, the angular velocities  $\dot{\mathbf{q}}$  can be written as

$$\dot{\mathbf{q}} = \mathbf{J}^{-1}(\mathbf{q}) {}^0\mathbf{V}_n. \quad (11)$$

Similarly, the angular accelerations  $\ddot{\mathbf{q}}$  can be obtained as

$$\ddot{\mathbf{q}} = \mathbf{J}^{-1}(\mathbf{q}) \left( {}^0\mathbf{A}_n - \dot{\mathbf{J}}(\mathbf{q})\dot{\mathbf{q}} \right). \quad (12)$$

Here,  ${}^0\mathbf{A}_n = [{}^0\ddot{\mathbf{P}}_n \ {}^0\ddot{\boldsymbol{\alpha}}_n]'$  is the  $(6 \times 1)$  end-effector acceleration vector, including linear acceleration  ${}^0\ddot{\mathbf{P}}_n$  and angular acceleration  ${}^0\ddot{\boldsymbol{\alpha}}_n$ . The differential Jacobian  $\dot{\mathbf{J}}(\mathbf{q})$  can be

also written as

$$\dot{J}_{ij} = \begin{cases} -\sum_{j=1}^n L_j \cos \left( \sum_{k=1}^j q_k \right) \left( \sum_{k=1}^j \dot{q}_k \right) & \text{if } i = 1, j \in [1, 6]; \\ -\sum_{j=1}^n L_j \sin \left( \sum_{k=1}^j q_k \right) \left( \sum_{k=1}^j \dot{q}_k \right) & \text{if } i = 2, j \in [1, 6]; \\ 0 & \text{if } i \in [3, 6], j \in [1, 6]. \end{cases}$$

### 2.4 Trajectory Planning

The trajectory planning using cubic polynomial for fingertip position control was discussed in our previous work [2, 3, 6, 10, 12] for a two-fingered (thumb and index finger) smart prosthetic hand. For the three-link index finger, we present the same technique for fingertip orientation control. A time history of desired ( $d$ ) fingertip orientation ( $\phi$ ) and its differentiation ( $\dot{\phi}$  and  $\ddot{\phi}$ ) is given as

$$\phi_d^j(t) = \omega_0 + \omega_1 t + \omega_2 t^2 + \omega_3 t^3, \quad (13)$$

$$\dot{\phi}_d^j(t) = \omega_1 + 2\omega_2 t + 3\omega_3 t^2, \quad (14)$$

$$\ddot{\phi}_d^j(t) = 2\omega_2 + 6\omega_3 t, \quad (15)$$

where  $\omega_0$ - $\omega_3$  are undetermined constants and the superscript  $j$  indicates the index of each finger ( $j = i, m, r$  and  $l$ ). The relations (13) and (14) need to satisfy the constraint conditions at initial time  $t_0$  and final time  $t_f$ . This can be written as

$$\mathbf{T} \boldsymbol{\Omega} = \boldsymbol{\Phi}. \quad (16)$$

Here, the matrices  $\mathbf{T}$ ,  $\boldsymbol{\Omega}$ , and  $\boldsymbol{\Phi}$  are

$$\mathbf{T} = \begin{bmatrix} 1 & t_0 & t_0^2 & t_0^3 \\ 0 & 1 & 2t_0 & 3t_0^2 \\ 1 & t_f & t_f^2 & t_f^3 \\ 0 & 1 & 2t_f & 3t_f^2 \end{bmatrix}, \quad (17)$$

$$\boldsymbol{\Omega} = [\omega_0 \ \omega_1 \ \omega_2 \ \omega_3]', \quad (18)$$

$$\boldsymbol{\Phi} = [\phi_0^j \ \dot{\phi}_0^j \ \phi_f^j \ \dot{\phi}_f^j]'. \quad (19)$$

Therefore, the 4 unknown constants,  $\omega_0$ - $\omega_3$ , can be computed by  $\boldsymbol{\Omega} = \mathbf{T}^{-1}\boldsymbol{\Phi}$ .

### 2.5 Dynamics of Hand

The dynamic equations of hand motion are derived via Lagrangian approach using kinetic energy and potential energy as [8, 11, 12, 14, 15]

$$\frac{d}{dt} \left( \frac{\partial \mathcal{L}}{\partial \dot{\mathbf{q}}} \right) - \frac{\partial \mathcal{L}}{\partial \mathbf{q}} = \boldsymbol{\tau}, \quad (20)$$

where  $\mathcal{L}$  is the Lagrangian;  $\dot{\mathbf{q}}$  and  $\mathbf{q}$  represent the angular velocity and angle vectors of joints, respectively;  $\boldsymbol{\tau}$  is the given torque vector at joints. The Lagrangian  $\mathcal{L}$  can be expressed as

$$\mathcal{L} = T - V, \quad (21)$$



where  $T$  and  $V$  denote kinetic and potential energies, respectively. Substituting (21) into (20), dynamic equations can be obtained as below.

$$\mathbf{M}(\mathbf{q})\ddot{\mathbf{q}} + \mathbf{C}(\mathbf{q}, \dot{\mathbf{q}}) + \mathbf{G}(\mathbf{q}) = \boldsymbol{\tau}, \quad (22)$$

where  $\mathbf{M}(\mathbf{q})$  is the inertia matrix;  $\mathbf{C}(\mathbf{q}, \dot{\mathbf{q}})$  is the Coriolis/centripetal vector and  $\mathbf{G}(\mathbf{q})$  is the gravity vector. (22) can be also written as

$$\mathbf{M}(\mathbf{q})\ddot{\mathbf{q}} + \mathbf{N}(\mathbf{q}, \dot{\mathbf{q}}) = \boldsymbol{\tau}, \quad (23)$$

where  $\mathbf{N}(\mathbf{q}, \dot{\mathbf{q}}) = \mathbf{C}(\mathbf{q}, \dot{\mathbf{q}}) + \mathbf{G}(\mathbf{q})$  represents nonlinear terms. The dynamic relations for the two-link thumb and the three-link index finger are quite lengthy and omitted here due to lack of space [12, 16, 17].

### 3 Control Techniques

#### 3.1 Feedback Linearization

The nonlinear dynamics represented by (23) is to be converted into a linear state-variable system using feedback linearization technique [8]. Alternative state-space equations of the dynamics can be obtained by defining the position/velocity state  $\mathbf{x}(t)$  of the joints as

$$\mathbf{x}(t) = [\mathbf{q}'(t) \quad \dot{\mathbf{q}}'(t)]'. \quad (24)$$

Let us repeat the dynamical model and rewrite (23) as

$$\frac{d}{dt}\dot{\mathbf{q}}(t) = -\mathbf{M}^{-1}(\mathbf{q}(t)) [\mathbf{N}(\mathbf{q}(t), \dot{\mathbf{q}}(t)) - \boldsymbol{\tau}(t)]. \quad (25)$$

Thus, from (24) and (25), we can derive a linear system in *Brunovsky canonical form* as

$$\dot{\mathbf{x}}(t) = \begin{bmatrix} \mathbf{0} & \mathbf{I} \\ \mathbf{0} & \mathbf{0} \end{bmatrix} \mathbf{x}(t) + \begin{bmatrix} \mathbf{0} \\ \mathbf{I} \end{bmatrix} \mathbf{u}(t) \quad (26)$$

with its control input vector given by

$$\mathbf{u}(t) = -\mathbf{M}^{-1}(\mathbf{q}(t)) [\mathbf{N}(\mathbf{q}(t), \dot{\mathbf{q}}(t)) - \boldsymbol{\tau}(t)]. \quad (27)$$

Let us suppose the prosthetic hand is required to track the desired trajectory  $\mathbf{q}_d(t)$  described under path generation or tracking. Then, the tracking error  $\mathbf{e}(t)$  is defined as

$$\mathbf{e}(t) = \mathbf{q}_d(t) - \mathbf{q}(t). \quad (28)$$

Here,  $\mathbf{q}_d(t)$  is the *desired* angle vector of joints and can be obtained by trajectory planning [2, 3, 6, 10, 12];  $\mathbf{q}(t)$  is the *actual* angle vector of joints. Differentiating (28) twice, to get

$$\dot{\mathbf{e}}(t) = \dot{\mathbf{q}}_d(t) - \dot{\mathbf{q}}(t), \quad \ddot{\mathbf{e}}(t) = \ddot{\mathbf{q}}_d(t) - \ddot{\mathbf{q}}(t). \quad (29)$$

Substituting (25) into (29) yields

$$\ddot{\mathbf{e}}(t) = \ddot{\mathbf{q}}_d(t) + \mathbf{M}^{-1}(\mathbf{q}(t)) [\mathbf{N}(\mathbf{q}(t), \dot{\mathbf{q}}(t)) - \boldsymbol{\tau}(t)] \quad (30)$$

from which the control function can be defined as

$$\mathbf{u}(t) = \ddot{\mathbf{q}}_d(t) + \mathbf{M}^{-1}(\mathbf{q}(t)) [\mathbf{N}(\mathbf{q}(t), \dot{\mathbf{q}}(t)) - \boldsymbol{\tau}(t)]. \quad (31)$$

This is often called the *feedback linearization* control law, which can also be inverted to express it as

$$\boldsymbol{\tau}(t) = \mathbf{M}(\mathbf{q}(t)) [\ddot{\mathbf{q}}_d(t) - \mathbf{u}(t)] + \mathbf{N}(\mathbf{q}(t), \dot{\mathbf{q}}(t)). \quad (32)$$

Using the relations (29) and (31), and defining state vector  $\mathbf{x}(t) = [\mathbf{e}'(t) \quad \dot{\mathbf{e}}'(t)]'$ , the *tracking error dynamics* can be written as

$$\dot{\mathbf{x}}(t) = \begin{bmatrix} \mathbf{0} & \mathbf{I} \\ \mathbf{0} & \mathbf{0} \end{bmatrix} \mathbf{x}(t) + \begin{bmatrix} \mathbf{0} \\ \mathbf{I} \end{bmatrix} \mathbf{u}(t). \quad (33)$$

Note that this is in the form of a *linear* system such as

$$\dot{\mathbf{x}}(t) = \mathbf{A}\mathbf{x}(t) + \mathbf{B}\mathbf{u}(t). \quad (34)$$

#### 3.2 Finite-Time Linear Quadratic Optimal Control

Figure 4 shows the block diagram of finite-time linear

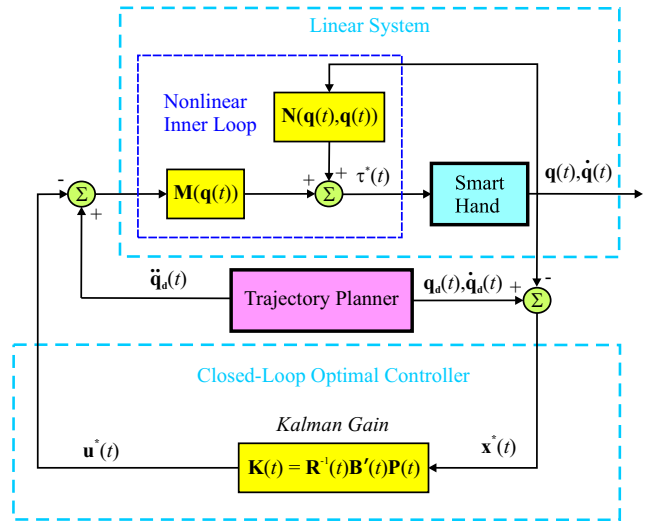


Figure 4. Block Diagram of Hybrid Optimal Controller for Prosthetic Hand

quadratic optimal controller for prosthetic hand. For the linear system (34), we can formulate the well-known finite-time linear quadratic optimal control problem by defining a performance index  $J$  [4] such as

$$J = \frac{1}{2} \mathbf{x}'(t_f) \mathbf{F}(t_f) \mathbf{x}(t_f) + \frac{1}{2} \int_{t_0}^{t_f} [\mathbf{x}'(t) \mathbf{Q}(t) \mathbf{x}(t) + \mathbf{u}'(t) \mathbf{R}(t) \mathbf{u}(t)] dt \quad (35)$$

where the terminal cost matrix  $\mathbf{F}(t_f)$  and the error weighted matrix  $\mathbf{Q}(t)$  are positive *semidefinite* matrices, respectively; the control weighted matrix  $\mathbf{R}(t)$  is a positive *definite* matrix. The optimal control  $\mathbf{u}^*(t)$  is given by

$$\mathbf{u}^*(t) = -\mathbf{R}^{-1}(t) \mathbf{B}' \mathbf{P}(t) \mathbf{x}^*(t) = -\mathbf{K}(t) \mathbf{x}^*(t). \quad (36)$$



Here,  $\mathbf{K}(t) = \mathbf{R}^{-1}(t)\mathbf{B}'\mathbf{P}(t)$  is called *Kalman gain* and  $\mathbf{P}(t)$ , the symmetric *positive definite* matrix (for all  $t \in [t_0, t_f]$ ), is the solution of the matrix differential Riccati equation (DRE)

$$\dot{\mathbf{P}}(t) = -\mathbf{P}(t)\mathbf{A} - \mathbf{A}'\mathbf{P}(t) - \mathbf{Q}(t) + \mathbf{P}(t)\mathbf{B}\mathbf{R}^{-1}(t)\mathbf{B}'\mathbf{P}(t) \quad (37)$$

satisfying the *final* condition

$$\mathbf{P}(t = t_f) = \mathbf{F}(t_f). \quad (38)$$

The optimal state  $\mathbf{x}^*$  is the solution of

$$\dot{\mathbf{x}}^*(t) = [\mathbf{A} - \mathbf{B}\mathbf{R}^{-1}(t)\mathbf{B}'\mathbf{P}(t)] \mathbf{x}^*(t). \quad (39)$$

Therefore, the required torque  $\boldsymbol{\tau}^*(t)$  can be calculated by the optimal control  $\mathbf{u}^*(t)$ .

$$\boldsymbol{\tau}^*(t) = \mathbf{M}(\mathbf{q}(t))(\ddot{\mathbf{q}}_d(t) - \mathbf{u}^*(t)) + \mathbf{N}(\mathbf{q}(t), \dot{\mathbf{q}}(t)). \quad (40)$$

### 3.3 The Stability of Finite-Time Optimal Control

Our previous work [5, 6, 12] shows optimal control can avoid overshooting and get better results than PID control, but the regular optimal control takes time to be convergent. To study the convergent stability of the optimal control, we modify the performance index  $J$  [4] as

$$J = \frac{1}{2}\mathbf{x}'(t_f)\mathbf{F}(t_f)\mathbf{x}(t_f) + \frac{1}{2}\int_{t_0}^{t_f} e^{2\alpha t} [\mathbf{x}'(t)\mathbf{Q}(t)\mathbf{x}(t) + \mathbf{u}'(t)\mathbf{R}(t)\mathbf{u}(t)] dt, \quad (41)$$

where  $\alpha$  is a positive parameter. To find the optimal control which minimizes the performance index (41) under the dynamical constraint (34). This problem can be solved by changing the previous system, so the following transformations can be developed as

$$\hat{\mathbf{x}}(t) = e^{\alpha t}\mathbf{x}(t); \quad \hat{\mathbf{u}}(t) = e^{\alpha t}\mathbf{u}(t). \quad (42)$$

Then, using the transformations (42), it is easy to see that the *modified* system becomes

$$\begin{aligned} \dot{\hat{\mathbf{x}}}(t) &= \frac{d}{dt}\{e^{\alpha t}\mathbf{x}(t)\} = \alpha e^{\alpha t}\mathbf{x}(t) + e^{\alpha t}\dot{\mathbf{x}}(t) \\ &= \alpha\hat{\mathbf{x}}(t) + e^{\alpha t}[\mathbf{A}\mathbf{x}(t) + \mathbf{B}\mathbf{u}(t)] \\ \dot{\hat{\mathbf{x}}}(t) &= (\mathbf{A} + \alpha\mathbf{I})\hat{\mathbf{x}}(t) + \mathbf{B}\hat{\mathbf{u}}(t). \end{aligned} \quad (43)$$

Considering the minimization of the modified system (43) and the performance index (41), we see that the optimal control [4] is given by

$$\hat{\mathbf{u}}^*(t) = -\mathbf{R}^{-1}\mathbf{B}'\bar{\mathbf{P}}\hat{\mathbf{x}}^*(t) = -\bar{\mathbf{K}}\hat{\mathbf{x}}^*(t), \quad (44)$$

where  $\bar{\mathbf{K}} = \mathbf{R}^{-1}\mathbf{B}'\bar{\mathbf{P}}$  and the matrix  $\bar{\mathbf{P}}$  is the positive definite, symmetric solution of the algebraic Riccati equation

$$\bar{\mathbf{P}}(\mathbf{A} + \alpha\mathbf{I}) + (\mathbf{A}' + \alpha\mathbf{I})\bar{\mathbf{P}} - \bar{\mathbf{P}}\mathbf{B}\mathbf{R}^{-1}\mathbf{B}'\bar{\mathbf{P}} + \mathbf{Q} = 0. \quad (45)$$

Using the optimal control (44) in the modified system (43), we get the optimal closed-loop system as

$$\dot{\hat{\mathbf{x}}}^*(t) = (\mathbf{A} + \alpha\mathbf{I} - \mathbf{B}\mathbf{R}^{-1}\mathbf{B}'\bar{\mathbf{P}})\hat{\mathbf{x}}^*(t). \quad (46)$$

Hence, applying the transformations (43) in the modified system (44), the optimal control of the original system (34) and the associated performance measure (41) is given by

$$\begin{aligned} \mathbf{u}^*(t) &= e^{-\alpha t}\hat{\mathbf{u}}^*(t) = -e^{-\alpha t}\mathbf{R}^{-1}\mathbf{B}'\bar{\mathbf{P}}e^{\alpha t}\mathbf{x}^*(t) \\ &= -\mathbf{R}^{-1}\mathbf{B}'\bar{\mathbf{P}}\mathbf{x}^*(t) = -\bar{\mathbf{K}}\mathbf{x}^*(t). \end{aligned} \quad (47)$$

We see that the closed-loop optimal control system (46) has eigenvalues with real parts less than  $-\alpha$ . In other words, the state  $\mathbf{x}^*(t)$  approaches zero at least as fast as  $e^{-\alpha t}$ .

## 4 Simulation Results and Discussion

Referring to inverse kinematics, Figure 5 exhibits that the

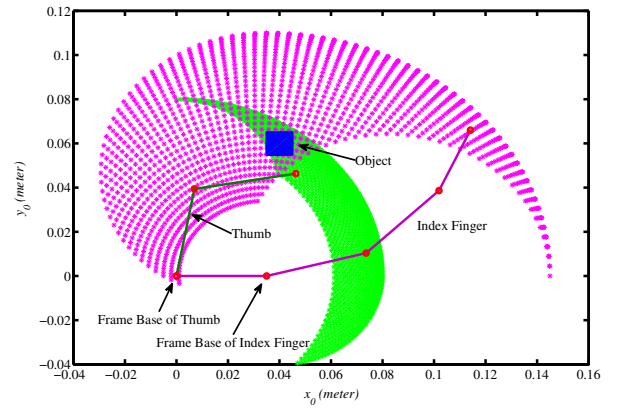


Figure 5. The Fingertip Workspace of Thumb and Index Finger and a Square Object

fingertip workspace of the thumb and index finger. We present simulations with the stability of optimal controller for the two-link thumb and three-link index finger of a smart prosthetic hand. All used parameters are the same to our previous work [6]. The initial and final orientation  $\phi_0$  and  $\phi_f$  are 75 and 160 degrees, respectively. Figure 6 displays the tracking errors and desired/actual angles of thumb for the smart prosthetic hand by using the presented optimal controller with the stability ( $\alpha = 0, 0.1$ , and 1). Figure 7 to Figure 9 are the tracking errors and desired/actual angles of index finger for the smart prosthetic hand ( $\alpha = 0, 1$ , and 10). To compare with the original system ( $\alpha = 0$ ), these results demonstrate that the presented optimal controller behaves fast convergent and accurate as the stability  $\alpha$  increases. For the three-link index finger, we design the orientation  $\phi$  to calculate the angular positions via inverse kinematics. To compare with our previous works [5,6,10,12] by using adaptive neuro-fuzzy inference system (ANFIS) and genetic algorithm (GA), the simulations show that the presented method is not time consuming.

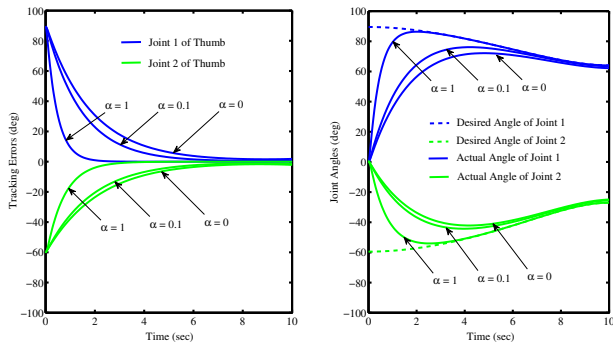


Figure 6. Tracking Errors (left) and Joint Angles (right) of Thumb for Optimal Control with the Stability ( $\alpha = 0, 0.1$ , and 1)

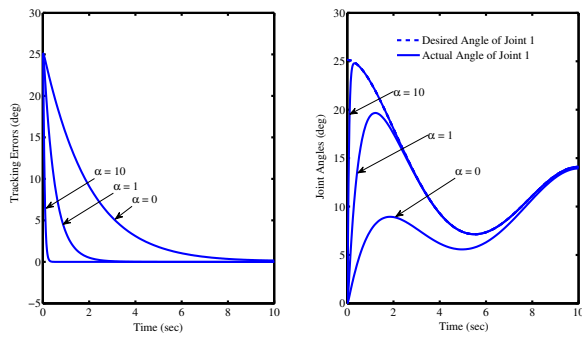


Figure 7. Tracking Errors (left) and Joint 1 Angles  $q_1^i$  (right) of Index Finger for Optimal Control with the Stability ( $\alpha = 0, 1$ , and 10)

## 5 Conclusion and Future Work

This paper developed the differential kinematics for a serial  $n$ -link revolute-joint planar prosthetic hand to compute the angular velocities and angular accelerations of each finger. Then, the cubic polynomial function was designed to track the orientation  $\phi$  in order to calculate inverse kinematics and differential kinematics. To make the optimal controller fast acting, the performance index  $J$  included an exponential term. The simulation results demonstrated a 30-fold increase in fast response compared to ANFIS or GA based trajectory planning [6]. Work is underway to extend this methodology to five-fingered, three-dimensional prosthetic hand.

## Acknowledgments

The research was sponsored by the U.S. Department of the Army, under the award number W81XWH-10-1-0128 awarded and administered by the U.S. Army Medical Research Acquisition Activity, 820 Chandler Street, Fort Detrick, MD 21702-5014. The information does not neces-

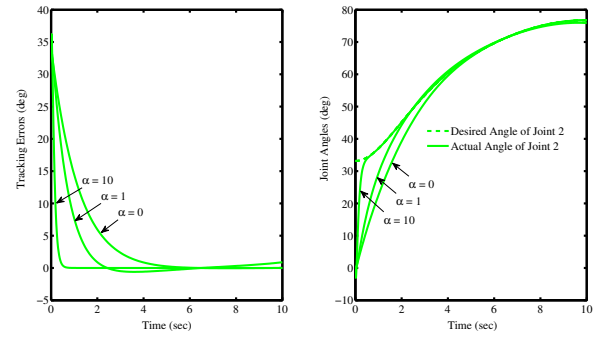


Figure 8. Tracking Errors (left) and Joint 2 Angles  $q_2^i$  (right) of Index Finger for Optimal Control with the Stability ( $\alpha = 0, 1$ , and 10)

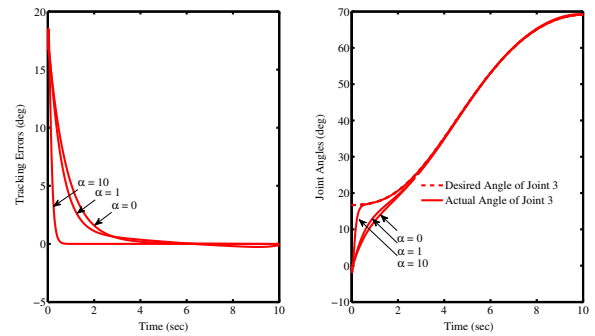


Figure 9. Tracking Errors (left) and Joint 3 Angles  $q_3^i$  (right) of Index Finger for Optimal Control with the Stability ( $\alpha = 0, 1$ , and 10)

sarily reflect the position or the policy of the Government, and no official endorsement should be inferred. For purposes of this article, information includes news releases, articles, manuscripts, brochures, advertisements, still and motion pictures, speeches, trade association proceedings, etc.

## References

- [1] B. Subudhi and A. S. Morris, "Soft computing methods applied to the control of a flexible robot manipulator," *Applied Soft Computing*, vol. 9, pp. 149–158, 2009.
- [2] C.-H. Chen, K. W. Bosworth, M. P. Schoen, S. E. Bearden, D. S. Naidu, and A. Perez, "A study of particle swarm optimization on leukocyte adhesion molecules and control strategies for smart prosthetic hand," in *2008 IEEE Swarm Intelligence Symposium (IEEE SIS08)*, St. Louis, Missouri, USA, September 21-23 2008.

- [3] C.-H. Chen, D. S. Naidu, A. Perez, and M. P. Schoen, "Fusion of hard and soft control techniques for prosthetic hand," in *Proceedings of the International Association of Science and Technology for Development (IASTED) International Conference on Intelligent Systems and Control (ISC 2008)*, Orlando, Florida, USA, November 16-18 2008, pp. 120–125.
- [4] D. Naidu, *Optimal Control Systems*. Boca Raton, FL: CRC Press, 2003.
- [5] C.-H. Chen, D. S. Naidu, A. Perez-Gracia, and M. P. Schoen, "A hybrid control strategy for five-fingered smart prosthetic hand," in *Joint 48th IEEE Conference on Decision and Control (CDC) and 28th Chinese Control Conference (CCC)*, Shanghai, P. R. China, December 16-18 2009, pp. 5102–5107.
- [6] C.-H. Chen, D. Naidu, A. Perez-Gracia, and M. P. Schoen, "A hybrid optimal control strategy for a smart prosthetic hand," in *Proceedings of the ASME 2009 Dynamic Systems and Control Conference (DSCC)*, Hollywood, California, USA, October 12-14 2009, (No. DSCC2009-2507).
- [7] F. L. Lewis, S. Jagannathan, and A. Yesildirek, *Neural Network Control of Robotic Manipulators and Non-linear Systems*. London, UK: Taylor & Francis, 1999.
- [8] F. L. Lewis, D. M. Dawson, and C. T. Abdallah, *Robot Manipulators Control: Second Edition, Revised and Expanded*. New York, NY: Marcel Dekker, Inc., 2004.
- [9] C.-H. Chen, D. S. Naidu, and M. P. Schoen, "An adaptive control strategy for a five-fingered prosthetic hand," in *The 14th World Scientific and Engineering Academy and Society (WSEAS) International Conference on Systems, Latest Trends on Systems (Volume II)*, Corfu Island, Greece, July 22-24 2010, pp. 405–410.
- [10] C.-H. Chen, D. S. Naidu, A. Perez-Gracia, and M. P. Schoen, "A hybrid adaptive control strategy for a smart prosthetic hand," in *The 31st Annual International Conference of the IEEE Engineering Medicine and Biology Society (EMBS)*, Minneapolis, Minnesota, USA, September 2-6 2009, pp. 5056–5059.
- [11] B. Siciliano, L. Sciavicco, L. Villani, and G. Oriolo, *Robotics: Modelling, Planning and Control*. London, UK: Springer-Verlag, 2009.
- [12] C.-H. Chen, "Hybrid control strategies for smart prosthetic hand," Ph.D. dissertation, Measurement and Control Engineering, Idaho State University, May 2009.
- [13] R. J. Schilling, *Fundamentals of Robotics: Analysis and Control*. Englewood Cliffs, NJ: Prentice Hall, 1990.
- [14] R. Kelly, V. Santibanez, and A. Loria, *Control of Robot Manipulators in Joint Space*. New York, USA: Springer, 2005.
- [15] R. N. Jazar, *Theory of Applied Robotics. Kinematics, Dynamics, and Control*. New York, USA: Springer, 2007.
- [16] A. Nikoobin and R. Haghighi, "Lyapunov-based non-linear disturbance observer for serial n-link robot manipulators," *Journal of Intelligent and Robotic Systems*, 2008, (Published online on 11 December 2008).
- [17] Y. Z. Arslan, Y. Hacioglu, and N. Yagiz, "Prosthetic hand finger control using fuzzy sliding modes," *Journal of Intelligent and Robotic Systems*, vol. 52, pp. 121–138, 2008.

# An Adaptive Control Strategy for a Five-Fingered Prosthetic Hand

CHENG-HUNG CHEN  
Measurement and Control  
Engineering Research Center  
Dept. of Biological Sciences  
Idaho State University  
Pocatello, ID 83209  
USA  
chenchen@isu.edu

D. SUBBARAM NAIDU  
Measurement and Control  
Engineering Research Center  
Dept. of Electrical Engineering  
Idaho State University  
Pocatello, ID 83209  
USA  
naiduds@isu.edu

MARCO P. SCHOEN  
Measurement and Control  
Engineering Research Center  
Dept. of Mechanical Engineering  
Idaho State University  
Pocatello, ID 83209  
USA  
schomarc@isu.edu

**Abstract:** In this paper, an adaptive control strategy is developed for the 14 degrees of freedom (DOFs), five-fingered smart prosthetic hand with unknown mass and inertia of all the fingers. In particular, the forward and inverse kinematics of the system regarding the analytical relationship between the angular positions of joints and the positions and orientations of the end-effectors (fingertips) have been obtained using a desired orientation for three-link fingers. The simulations of the resulting adaptive controller with five-fingered prosthetic hand show enhanced performance.

**Key-Words:** adaptive control, prosthetic hand, hard control, five finger hand, feedback linearization, trajectory planning

## 1 Introduction

Due to the extreme complexity of human hand, that has 27 bones, controlled by about 38 muscles to provide the hand with 22 degrees of freedom (DOFs), and incorporates about 17,000 tactile units of 4 different units, reproducing the human hand in all its various functions and appearance is still a challenging task [1]. Prosthetic hands have been built to replace human hands that can fully operate the various motions, such as holding, moving, grasping, lifting, twisting and so on [1–5]. However, about 35% of the users do not regularly use their prosthetic hands because of several reasons, including poor functionality of the presently available prosthetic hands and psychological problems. Thus, designing and developing an artificial hand which can “mimics the human hand as closely as possible” both in functionality and appearance can overcome these problems.

Hard computing/control (HC) techniques can be used at lower levels for accuracy, precision, stability and robustness. HC comprises proportional-integral-derivative (PID) control [6], optimal control [7, 8], adaptive control [9–11] etc. with specific applications to prosthetic devices. However, our previous work [11] for a two-fingered, thumb and index finger, prosthetic hand showed that adaptive controller can overcome overshooting and oscillation. However, a five-fingered prosthetic hand with adaptive control technique has not been developed yet.

In this work, we first describe briefly the trajec-

tory planning problem, human hand anatomy and the inverse kinematics for two-link thumb and the remaining three-link fingers (index, middle, ring and little). Next, the dynamics of the prosthetic hand is derived and feedback linearization technique is used to obtain *linear* tracking error dynamics. Then the adaptive controller is designed to minimize the tracking error. The simulation results show that the five-fingered prosthetic hand with the presented adaptive controller can grasp an object without overshooting and oscillation. Conclusions and future work are provided in the last section.

## 2 Modeling

### 2.1 Trajectory Planning and Inverse Kinematics

The trajectory planning using cubic polynomial was discussed in our previous work [5, 6, 11, 12] for a two-fingered (thumb and index finger) smart prosthetic hand. Figure 1 shows that index finger, middle finger, ring finger and little finger contain three revolute joints in order to do the angular movements. Metacarpal-phalangeal (MCP) joint is located between metacarpal and proximal phalange bone; proximal and distal interphalangeal (PIP and DIP) joints separate the phalangeal bones. Thumb contains metacarpal-phalangeal (MCP) and interphalangeal (IP) joints. In this work,  $q_1^j$ ,  $q_2^j$  and  $q_3^j$  repre-

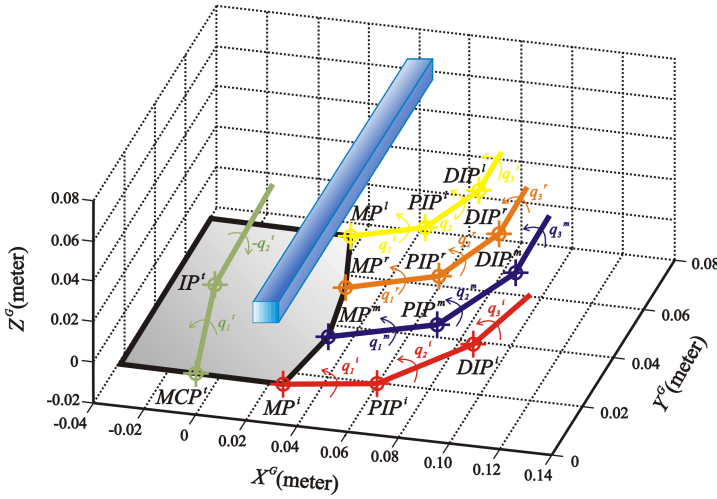


Figure 1: The Joints of Five-Finger Prosthetic Hand Reaching a Rectangular Rod

sent the angular positions (or joint angles) of the first joint  $MCP^j$ , the second joint  $PIP^j$  and the third joint  $DIP^j$  of index finger ( $j = i$ ), middle finger ( $j = m$ ), ring finger ( $j = r$ ) and little finger ( $j = l$ ), respectively;  $q_1^t$  and  $q_2^t$  are the angular positions of the first joint  $MCP^t$  and the second joint  $IP^t$  of thumb ( $t$ ).

Forward and inverse kinematics of articulated systems study the analytical relationship between the angular positions of joints and the positions and orientations of the end-effectors (fingertips). A desired trajectory is usually specified in *Cartesian* space and the trajectory controller is easily performed in the *joint* space. Hence, to convert Cartesian trajectory planning to the joint space [13] is necessary. Using inverse kinematics, the joint angular positions of each finger need to be obtained from the known fingertip positions (*joint space*). Then the angular velocities and angular accelerations of joints can be obtained from the linear and angular velocities and accelerations of fingertips (end-effectors) by the *geometric Jacobian*. As shown in Figure 2,  $X^G$ ,  $Y^G$ , and  $Z^G$  are the three axes of the global coordinate. The local coordinate  $x^t$ - $y^t$ - $z^t$  of the thumb can be reached by rotating through angles  $\alpha$  and  $\beta$  to  $X^G$  and  $Y^G$  of the global coordinate, subsequently. The local coordinate  $x^i$ - $y^i$ - $z^i$  of index finger can be obtained by rotating through angle  $\alpha$  to  $X^G$  and then translating the vector  $d^i$  of the global coordinate; similarly, the local coordinate  $x^j$ - $y^j$ - $z^j$  of middle finger ( $j = m$ ), ring finger ( $j = r$ ), and little finger ( $j = l$ ) can be obtained by rotating through angle  $\alpha$  to  $X^G$  and then translating the vector  $d^j$  ( $j = m, r$  and  $l$ ) of the global coordinate. The inverse kinematics of two-link thumb and three-link fingers was discussed in our previous publications [5,6,11,12] for

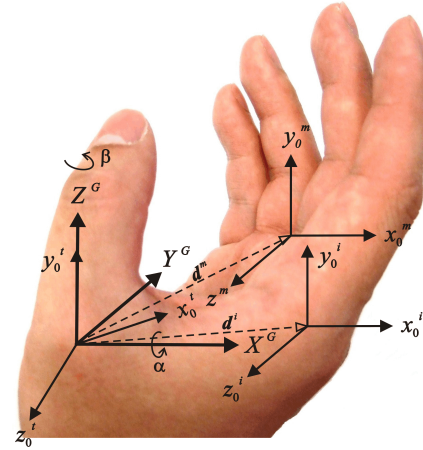


Figure 2: The Definition of Global Coordinate and Local Coordinates

a two-fingered (thumb and index finger) smart prosthetic hand.

## 2.2 Dynamics of Hand

The dynamic equations of hand motion are derived via Lagrangian approach using kinetic energy and potential energy as [5]

$$\frac{d}{dt} \left( \frac{\partial \mathcal{L}}{\partial \dot{\mathbf{q}}} \right) - \frac{\partial \mathcal{L}}{\partial \mathbf{q}} = \boldsymbol{\tau}, \quad (1)$$

where  $\mathcal{L}$  is the Lagrangian;  $\dot{\mathbf{q}}$  and  $\mathbf{q}$  represent the angular velocity and angle vectors of joints, respectively;  $\boldsymbol{\tau}$  is the given torque vector at joints. The Lagrangian  $\mathcal{L}$  can be expressed as

$$\mathcal{L} = T - V, \quad (2)$$

where  $T$  and  $V$  denote kinetic and potential energies, respectively. Substitute (2) into (1) and dynamic equations of thumb can be obtained as below.

$$\mathbf{M}(\mathbf{q})\ddot{\mathbf{q}} + \mathbf{C}(\mathbf{q}, \dot{\mathbf{q}}) + \mathbf{G}(\mathbf{q}) = \boldsymbol{\tau}, \quad (3)$$

where  $\mathbf{M}(\mathbf{q})$  is the inertia matrix;  $\mathbf{C}(\mathbf{q}, \dot{\mathbf{q}})$  is the Coriolis/centripetal vector and  $\mathbf{G}(\mathbf{q})$  is the gravity vector. (3) can be also written as

$$\mathbf{M}(\mathbf{q})\ddot{\mathbf{q}} + \mathbf{N}(\mathbf{q}, \dot{\mathbf{q}}) = \boldsymbol{\tau}, \quad (4)$$

where  $\mathbf{N}(\mathbf{q}, \dot{\mathbf{q}}) = \mathbf{C}(\mathbf{q}, \dot{\mathbf{q}}) + \mathbf{G}(\mathbf{q})$  represents nonlinear terms. The dynamic relations for the two-link thumb and the remaining three-link fingers are quite lengthy and omitted here due to lack of space [5].



### 3 Control Techniques

#### 3.1 Feedback Linearization

The nonlinear dynamics represented by (4) is to be converted into a linear state-variable system by finding a transformation using feedback linearization technique [10]. Alternative state-space equations of the dynamics can be obtained by defining the position/velocity state  $\mathbf{x}(t)$  of the joints as

$$\mathbf{x}(t) = [\mathbf{q}(t)' \quad \dot{\mathbf{q}}(t)']'. \quad (5)$$

Let us repeat the dynamical model and rewrite (4) as

$$\frac{d}{dt}\dot{\mathbf{q}}(t) = -\mathbf{M}(\mathbf{q}(t))^{-1} [\mathbf{N}(\mathbf{q}(t), \dot{\mathbf{q}}(t)) - \boldsymbol{\tau}(t)]. \quad (6)$$

Thus, from (5) and (6), we can derive a linear state-variable equation in *Brunovsky canonical form* as

$$\dot{\mathbf{x}}(t) = \begin{bmatrix} \mathbf{0} & \mathbf{I} \\ \mathbf{0} & \mathbf{0} \end{bmatrix} \mathbf{x}(t) + \begin{bmatrix} \mathbf{0} \\ \mathbf{I} \end{bmatrix} \mathbf{u}(t) \quad (7)$$

with its control input vector given by

$$\mathbf{u}(t) = -\mathbf{M}(\mathbf{q}(t))^{-1} [\mathbf{N}(\mathbf{q}(t), \dot{\mathbf{q}}(t)) - \boldsymbol{\tau}(t)]. \quad (8)$$

Let us suppose the prosthetic hand is required to track the desired trajectory  $\mathbf{q}_d(t)$  described under path generation or tracking. Then, the tracking error  $\mathbf{e}(t)$  is defined as

$$\mathbf{e}(t) = \mathbf{q}_d(t) - \mathbf{q}(t). \quad (9)$$

Here,  $\mathbf{q}_d(t)$  is the *desired* angle vector of joints and can be obtained by trajectory planning [5, 6, 11, 12];  $\mathbf{q}(t)$  is the *actual* angle vector of joints. Differentiating (9) twice, to get

$$\dot{\mathbf{e}}(t) = \dot{\mathbf{q}}_d(t) - \dot{\mathbf{q}}(t), \quad \ddot{\mathbf{e}}(t) = \ddot{\mathbf{q}}_d(t) - \ddot{\mathbf{q}}(t). \quad (10)$$

Substituting (6) into (10) yields

$$\ddot{\mathbf{e}}(t) = \ddot{\mathbf{q}}_d(t) + \mathbf{M}(\mathbf{q}(t))^{-1} [\mathbf{N}(\mathbf{q}(t), \dot{\mathbf{q}}(t)) - \boldsymbol{\tau}(t)] \quad (11)$$

from which the control function can be defined as

$$\mathbf{u}(t) = \ddot{\mathbf{q}}_d(t) + \mathbf{M}(\mathbf{q}(t))^{-1} [\mathbf{N}(\mathbf{q}(t), \dot{\mathbf{q}}(t)) - \boldsymbol{\tau}(t)]. \quad (12)$$

This is often called the *feedback linearization* control law, which can also be inverted to express it as

$$\boldsymbol{\tau}(t) = \mathbf{M}(\mathbf{q}(t)) [\ddot{\mathbf{q}}_d(t) - \mathbf{u}(t)] + \mathbf{N}(\mathbf{q}(t), \dot{\mathbf{q}}(t)). \quad (13)$$

Using the relations (10) and (12), and defining state vector  $\mathbf{x}(t) = [\mathbf{e}(t)' \quad \dot{\mathbf{e}}(t)']'$ , the *tracking error dynamics* can be written as

$$\dot{\mathbf{x}}(t) = \begin{bmatrix} \mathbf{0} & \mathbf{I} \\ \mathbf{0} & \mathbf{0} \end{bmatrix} \mathbf{x}(t) + \begin{bmatrix} \mathbf{0} \\ \mathbf{I} \end{bmatrix} \mathbf{u}(t). \quad (14)$$

Note that this is in the form of a *linear* system such as

$$\dot{\mathbf{x}}(t) = \mathbf{A}\mathbf{x}(t) + \mathbf{B}\mathbf{u}(t). \quad (15)$$

#### 3.2 Adaptive Control Technique

The tracking error  $\mathbf{e}$  and the filtered tracking error  $\mathbf{r}$  are defined as

$$\mathbf{e} = \mathbf{q}_d - \mathbf{q}, \quad (16)$$

$$\mathbf{r} = \dot{\mathbf{e}} + \boldsymbol{\Lambda}\mathbf{e}. \quad (17)$$

Here,  $\mathbf{q}_d$  is the *desired* angle vector of joints;  $\mathbf{q}$  is the *actual* angle vector of joints;  $\boldsymbol{\Lambda}$  is the positive-definite diagonal gain matrix. The filtered error (17) ensures stability of the overall system so that the tracking error (16) is bounded. Figure 3 shows the block diagram of the adaptive controller. Here, the filtered signal  $\mathbf{r}(t)$  is derived from the tracking error  $\mathbf{e}(t)$  and the trajectory planner and is fed to the adaptive controller of the prosthetic hand.

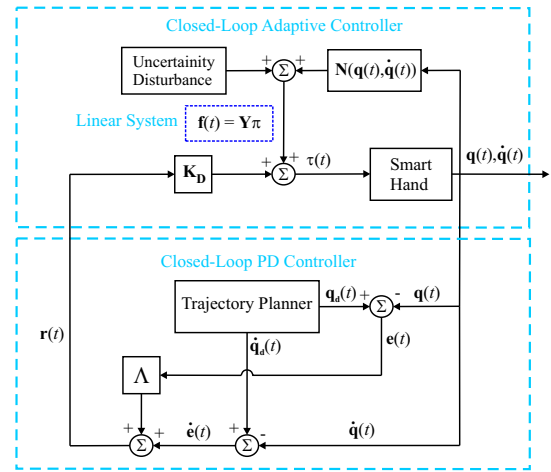


Figure 3: Block Diagram of Adaptive Control Technique

Differentiating and substituting (17) into (3) gives the dynamic equation in terms of the filtered error  $\mathbf{r}$  as

$$\mathbf{M}(\mathbf{q})\dot{\mathbf{r}} = -\mathbf{C}_m(\mathbf{q}, \dot{\mathbf{q}})\mathbf{r} + \mathbf{f} - \boldsymbol{\tau} \quad (18)$$

where  $\mathbf{C}(\mathbf{q}, \dot{\mathbf{q}}) = \mathbf{C}_m(\mathbf{q}, \dot{\mathbf{q}})\dot{\mathbf{q}}$  and the nonlinear term  $\mathbf{f}$  can be defined as

$$\begin{aligned} \mathbf{f} &= \mathbf{M}(\mathbf{q})(\ddot{\mathbf{q}}_d + \boldsymbol{\Lambda}\dot{\mathbf{e}}) + \mathbf{C}_m(\mathbf{q}, \dot{\mathbf{q}})(\dot{\mathbf{q}}_d + \boldsymbol{\Lambda}\mathbf{e}) \\ &\quad + \mathbf{G}(\mathbf{q}) + \boldsymbol{\tau}_{dis} \\ &= \mathbf{Y}\boldsymbol{\pi}. \end{aligned} \quad (19)$$

Here, the regression matrix  $\mathbf{Y}$  is a matrix of known robot functions and  $\boldsymbol{\pi}$  is a vector of unknown parameters [9]. The regression matrix  $\mathbf{Y}$  and the unknown parameter vector  $\boldsymbol{\pi}$  of two-link thumb and three-link index finger are expressed in [5]. The torque vector  $\boldsymbol{\tau}$  can be calculated by

$$\boldsymbol{\tau} = \mathbf{Y}\boldsymbol{\pi} + \mathbf{K}_D\mathbf{r}. \quad (20)$$

The unknown parameter rate vector  $\dot{\pi}$  can be updated by

$$\dot{\pi} = \Gamma^{-1} \mathbf{Y}' \mathbf{r} \quad (21)$$

where  $\Gamma$  is a tuning parameter diagonal matrix.

## 4 Simulation Results and Discussion

When thumb and the other four fingers are doing extension/flexion movements, the workspace of fingertips is restricted to the maximum angles of joints. Referring to inverse kinematics, the first and second joint angles of the thumb fingertip are constrained in the ranges of  $[0,90]$  and  $[-80,0]$  (degrees). The first, second, and third joint angles of the other four fingers are constrained in the ranges of  $[0,90]$ ,  $[0,110]$  and  $[0,80]$  (degrees), respectively [14]. Next, we present simulations with an adaptive controller for the 14 DOFs five-fingered smart prosthetic hand. The parameters of the two-link thumb/three-link index finger [15] were related to desired trajectory. All parameters of the smart prosthetic hand selected for the simulations are given in Table 1 and the side length and length of the target rectangular rod are 0.010 and 0.100 (m), respectively. The relating parameters between the global coordinate and the local coordinates are defined in Table 2. Besides, all links are assumed as a circular cylinder with the radius ( $R$ ) 0.010 (m), so the inertia  $I_{zzk}^j$  of each link  $k$  of each finger  $j$  ( $j = t, i, m, r, \text{ and } l$ ) can be calculated as

$$I_{zzk}^j = \frac{1}{4} m_k^j R^2 + \frac{1}{3} m_k^j L_k^{j2}. \quad (22)$$

All initial actual angles are zero.

Figure 4 to Figure 8 are the tracking errors and desired/actual angles of thumb, index finger, middle finger, ring finger, and little finger for the proposed five-fingered smart prosthetic hand.

## 5 Conclusions and Future Work

An adaptive control strategy was developed for the 14 degrees of freedom (DOFs), five-fingered smart prosthetic hand with unknown mass and inertia of all the fingers. Further, the forward and inverse kinematics of the system regarding the analytical relationship between the angular positions of joints and the positions and orientations of the end-effectors (fingertips), was obtained using a desired orientation for three-link fingers. The simulations of for the resulting adaptive controller with five-fingered prosthetic hand showed good agreement between the reference and the actual trajectories. Work is in progress for developing an

Table 1: Parameter Selection of the Smart Hand

Parameters	Values
<b>Thumb</b>	
Time ( $t_0, t_f$ )*	0, 20 (sec)
Desired Initial Position**	0.035, 0.060 (m)
Desired Final Position**	0.0495, 0.060 (m)
Desired Initial Velocity*	0, 0 (m/s)
Desired Final Velocity*	0, 0 (m/s)
Length	0.04, 0.04 (m)
<b>Index Finger</b>	
Desired Initial Position**	0.065, 0.080 (m)
Desired Final Position**	0.010, 0.060 (m)
Length	0.04, 0.04, 0.03 (m)
<b>Middle Finger</b>	
Desired Initial Position**	0.065, 0.080 (m)
Desired Final Position**	0.005, 0.060 (m)
Length	0.04, 0.04, 0.03 (m)
<b>Ring Finger</b>	
Desired Initial Position**	0.065, 0.080 (m)
Desired Final Position**	0.010, 0.060 (m)
Length	0.04, 0.04, 0.03 (m)
<b>Little Finger</b>	
Desired Initial Position**	0.055, 0.080 (m)
Desired Final Position**	0.020, 0.060 (m)
Length	0.04, 0.04, 0.03 (m)

\*All fingers use same parameters

\*\*Local coordinates

adaptive/robust controller for the five fingered hand with 14-DOFs.

**Acknowledgements:** The financial support for this research from the Telemedicine Advanced Technology Research Center (TATRC) of the U.S. Department of Defense (DoD) is gratefully acknowledged.

### References:

- [1] M. Zecca, S. Micera, M. Carrozza, and P. Dario, "Control of multifunctional prosthetic hands by processing the electromyographic signal," *Critical Reviews<sup>TM</sup> in Biomedical Engineering*, vol. 30, pp. 459–485, 2002, (Review article with 96 references).
- [2] J. C. K. Lai, M. P. Schoen, A. Perez-Gracia, D. S. Naidu, and S. W. Leung, "Prosthetic devices: Challenges and implications of robotic implants and biological interfaces," *Proceedings of the Institute of Mechanical Engineers*

Table 2: Parameter Selection of the Relation between Global and Local Coordinates

Parameters	Values
$\alpha$	90 (degrees)
$\beta$	45 (degrees)
$d^i$	(0.035, 0, 0) (m)
$d^m$	(0.040, 0, -0.020) (m)
$d^r$	(0.035, 0, -0.040) (m)
$d^l$	(0.025, 0, -0.060) (m)

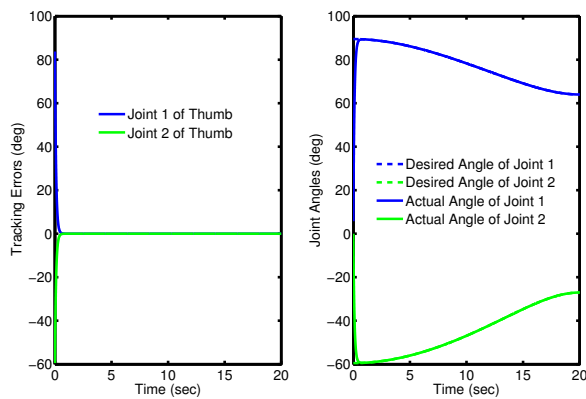


Figure 4: Tracking Errors (left) and Joint Angles (right) for Adaptive Controller of Thumb

(*IMechE*), Part H: *Journal of Engineering in Medicine*, vol. 221, no. 2, pp. 173–183, January 2007, special Issue on Micro and Nano Technologies in Medicine.

- [3] L. Zollo, S. Roccella, E. Guglielmelli, M. C. Carrozza, and P. Dario, “Biomechatronic design and control of an anthropomorphic artificial hand for prosthetic and robotic applications,” *IEEE/ASME Transactions on Mechatronics*, vol. 12, no. 4, pp. 418–429, August 2007.
- [4] D. S. Naidu, C.-H. Chen, A. Perez, and M. P. Schoen, “Control strategies for smart prosthetic hand technology: An overview,” in *Proceedings of the 30th Annual International IEEE EMBS Conference*, Vancouver, Canada, August 20–24 2008, pp. 4314–4317.
- [5] C.-H. Chen, “Hybrid control strategies for smart prosthetic hand,” Ph.D. dissertation, Measurement and Control Engineering, Idaho State University, May 2009.
- [6] C.-H. Chen, D. S. Naidu, A. Perez, and M. P. Schoen, “Fusion of hard and soft control techniques for prosthetic hand,” in *Proceedings of*

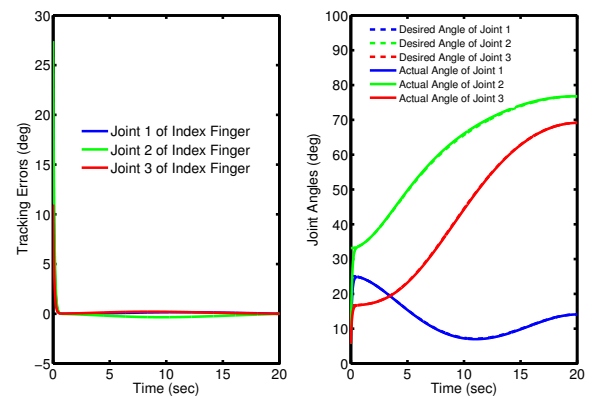


Figure 5: Tracking Errors (left) and Joint Angles (right) for Adaptive Controller of Index Finger

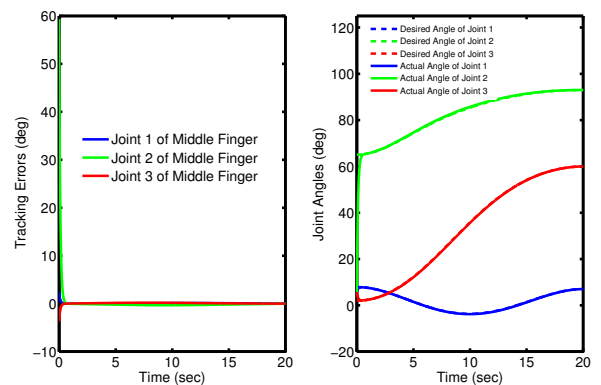


Figure 6: Tracking Errors (left) and Joint Angles (right) for Adaptive Controller of Middle Finger

*the International Association of Science and Technology for Development (IASTED) International Conference on Intelligent Systems and Control (ISC 2008)*, Orlando, Florida, USA, November 16–18 2008, pp. 120–125.

- [7] D. Naidu, *Optimal Control Systems*. Boca Raton, FL: CRC Press, 2003.
- [8] C.-H. Chen, D. S. Naidu, A. Perez-Gracia, and M. P. Schoen, “A hybrid control strategy for five-fingered smart prosthetic hand,” in *Joint 48th IEEE Conference on Decision and Control (CDC) and 28th Chinese Control Conference (CCC)*, Shanghai, P. R. China, December 16–18 2009, pp. 5102–5107.
- [9] F. Lewis, S. Jagannathan, and A. Yesildirek, *Neural Network Control of Robotic Manipulators and Nonlinear Systems*. London, UK: Taylor & Francis, 1999.



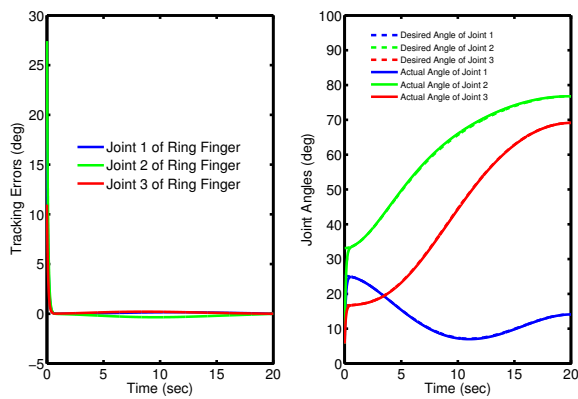


Figure 7: Tracking Errors (left) and Joint Angles (right) for Adaptive Controller of Ring Finger

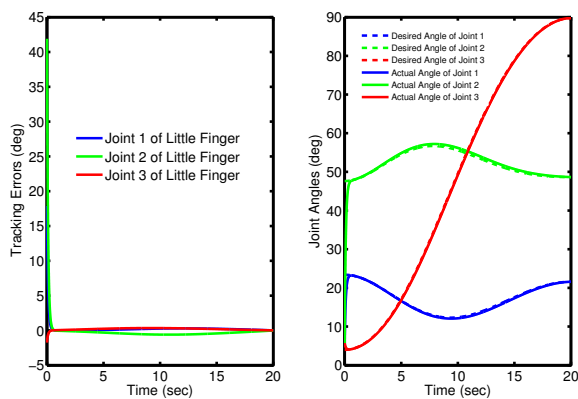


Figure 8: Tracking Errors (left) and Joint Angles (right) for Adaptive Controller of Little Finger

- [13] B. Siciliano, L. Sciavicco, L. Villani, and G. Oriolo, *Robotics: Modelling, Planning and Control*. London, UK: Springer-Verlag, 2009.
- [14] P. K. Lavangie and C. C. Norkin, *Joint Structure and Function: A Comprehensive Analysis, Third Edition*. Philadelphia, PA: F. A. Davis Company, 2001.
- [15] S. Arimoto, *Control Theory of Multi-fingered Hands: A Modeling and Analytical-Mechanics Approach for Dexterity and Intelligence*. London, UK: Springer-Verlag, 2008.

[10] F. Lewis, D. Dawson, and C. Abdallah, *Robot Manipulators Control: Second Edition, Revised and Expanded*. New York, NY: Marcel Dekker, Inc., 2004.

[11] C.-H. Chen, D. S. Naidu, A. Perez-Gracia, and M. P. Schoen, "A hybrid adaptive control strategy for a smart prosthetic hand," in *The 31st Annual International Conference of the IEEE Engineering Medicine and Biology Society (EMBS)*, Minneapolis, Minnesota, USA, September 2-6 2009, pp. 5056–5059.

[12] C.-H. Chen, D. Naidu, A. Perez-Gracia, and M. P. Schoen, "A hybrid optimal control strategy for a smart prosthetic hand," in *Proceedings of the ASME 2009 Dynamic Systems and Control Conference (DSCC)*, Hollywood, California, USA, October 12-14 2009, (No. DSCC2009-2507).

# Design and Control of an Underactuated Prosthetic Hand

AMIR FASSIH, D.SUBBARAM NAIDU, STEVE CHIU, PARMOD KUMAR

School of Engineering  
Idaho State University  
921 S. 8<sup>th</sup> Ave, Pocatello, Idaho  
U.S.A  
fassamir@isu.edu

*Abstract:* The robotic hands can be divided into two major groups: fully-actuated and underactuated hands. In fully-actuated hands all the joints have separate motors, while in underactuated hands the number of motors is less than number of degrees of freedom. The underactuated hands can adapt to the object shape by use of their mechanical design while they have less functionality. A relationship between forces and displacement is found through virtual work method. Based on this relationship an analytical approach is used to optimize hand based on two criteria: isotopic force and maximum chance of stable grasping. A PD type of controller is designed for this class of hands and the functionality of designed hand is compared with fully actuated hand using virtual spring damper hypothesis.

*Key-Words:* Prosthetic Hand, Underactuated, Virtual Spring Damper, Control, Comparison Analysis, Grasping

## 1 Introduction

Human hand is one of the most important and complex parts of the body, which has the ability to handle different tasks. The ultimate goal of robotic hand is to achieve the functionality of a human hand. In the past three decades, there have been numerous investigations to achieve dexterity and ability of human hand, especially in the fields of humanoid robotics and prosthetic hand [1-6]. In spite of all these advances in this field, the current state of research on prosthetic hands is far from that objective of achieving the functionality of human hand. Commercially available prosthetic hands have very limited functionality and they are just simple grippers. The present research on prosthetic hands involves complex control schemes to achieve the most important functions of the hand [7-8].

There are two main categories of robotic hands including fully actuated and underactuated mechanism. In underactuated mechanisms the number of actuators is less than their degree of freedom. These mechanisms are widely used in prosthetic hands because of two useful properties: the first advantage is less weight due to less actuator which is used in their design and the second advantage is easier control method.

In fully actuated hands all joints are active. In this type of hands many control methods require the

knowledge of the shape of the object. For humans this information is available by visual feedback from eyes, while in case of a prosthetic hand this visual information is not directly available for hand controller, and the only available information is electromyographic (EMG) signal related to patient's arm muscle activities. However, normally the EMG signal is not available for all individual joints and besides, due to measurement noise, accessing high quality EMG signal is hard [10]. Moreover, using EMG signal to control all the movements requires lot of attention during grasping and leads to fatigue for the amputees [11]. Hence it is required for prosthetic hand to be semi-autonomous which means a part of command information will be provided by the EMG signal and the rest of the required command should be provided automatically by hand controller.

Defining finger trajectory without the knowledge of shape of object to be grasped is a challenging task for many path planning techniques. For multi DOFs robots there are two common methods for trajectory planning which are "inverse kinematic" and "inverse dynamic" [12-15]. Both these methods require object shape and are based on solving optimization problem which requires high computation, hence they are hard to implement for real-time applications.

To avoid solving the path planning problem in our previous paper [2] we developed a control method based on “virtual spring damper hypothesis” for power grasping. The “virtual spring-damper hypothesis” is introduced by Arimoto *et al.* to control arm movement. This method is based on the use of Jacobian matrix to relate task space movement to joint space. In [20] it is shown that any kind of force can be defined between two points and the other study [2] shows that use of spring-damper forces will result in human like movement. From physiological point of view, human skilled multi-joint reaching movement has these characteristics that :

- 1) endpoint trajectory become a quasi-straight line and less variable
- 2) velocity profiles of the endpoint has a bell-shape
- 3) joint trajectories are rather variable from trial to trial [2].

In this paper, design and optimization of an underactuated mechanism is investigated. Then a control method is developed for this type of hands. Later on the functionality of this hand is compared with functionality of fully actuated hands using virtual spring damper hypothesis.

## 2 Force Analysis of Underactuated Finger

A two phalanx finger is considered in Fig.2. The input torque  $T_i$  is applied to the link  $a$  which transmits the torque to the whole finger through phalanges. A rotational spring with force  $T$  is located at  $O$  which moves the phalanx back to its original position in absence of external force. The closing process is shown in Fig 2. Providing a mechanical limit can help in order to make pretension for the spring to prevent undesirable motion of the second phalanx and also hyper-flexion of the finger.

To obtain the static model between inputs and outputs of the finger the virtual work principle is used. Equating the input and output virtual powers results

$$t^T \omega_i = f^T v \quad (1)$$

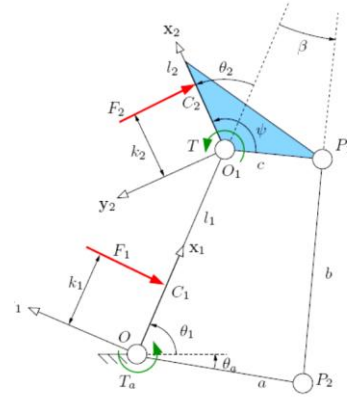


Fig.1. Underactuated hand model and exerted forces

Where  $t$  is the input torque vector exerted by the actuator and the spring,  $\omega_i$  is the rotational velocity vector,  $f$  is the vector of contact forces, and  $v$  is the velocity of the contact points along the normal vector of each phalanx. Contact forces are assumed to be normal to the phalanges and without friction. Each element in the above equation can be expressed as

$$t = \begin{bmatrix} T_i \\ T = -k\Delta\theta_2 \end{bmatrix} \quad (2)$$

$$\omega_i = \begin{bmatrix} \dot{\theta}_1 \\ \dot{\theta}_2 \end{bmatrix} \quad (3)$$

$$f = \begin{bmatrix} f_1 \\ f_2 \end{bmatrix} \quad (4)$$

$$v = \begin{bmatrix} v_{C1}^T y_1 \\ v_{C2}^T y_2 \end{bmatrix} \quad (5)$$

The normal velocities of the contact point can be expressed as a Jacobian matrix  $J_T$  and the derivatives of the phalanx joint coordinates which is a natural choice, as  $v = J_T \dot{\theta}$  or

$$\begin{bmatrix} v_{C1}^T y_1 \\ v_{C2}^T y_2 \end{bmatrix} = \begin{bmatrix} k_1 & 0 \\ k_2 + l_1 \cos \theta_1 & k_2 \end{bmatrix} \begin{bmatrix} \dot{\theta}_1 \\ \dot{\theta}_2 \end{bmatrix} \quad (6)$$

Through differential calculus, one also can relate vector  $\omega_i$  to the derivatives of the phalanges joint coordinates defined previously with an actuation Jacobian matrix  $J_A$  as  $\dot{\theta} = J_A \omega_a$  or

$$\begin{bmatrix} \dot{\theta}_1 \\ \dot{\theta}_2 \end{bmatrix} = \begin{bmatrix} X & Y \\ 0 & 1 \end{bmatrix} \begin{bmatrix} \dot{\theta}_i \\ \dot{\theta}_2 \end{bmatrix} \quad (7)$$

where  $X=1$  and

$$Y = \frac{c[l_1 \sin(\theta_2 - \psi) - a \sin(\theta_1 - \theta_a + \theta_2 - \psi)]}{a[l_1 \sin(\theta_1 - \theta_a) + c \sin(\theta_1 - \theta_a + \theta_2 - \psi)]} \quad (8)$$

Finally, one obtains

$$f = J_T^{-T} J_A^{-T} t \quad (9)$$

which is the equation that provides a practical relationship between the actuator torque and contact forces. If the spring contribution is neglected the analytical expression are rather simple linear functions of the actuator torque,

$$f_1 = \frac{(k_2 - h \cos \theta_2) l_1}{a k_1 k_2 (\cot \beta \cos \alpha_1 + \sin \alpha_1)} T_a \quad (10)$$

$$f_2 = \frac{h}{a k_2 (\cot \beta \cos \alpha_1 + \sin \alpha_1)} T_a \quad (11)$$

where  $h = c(\cos(\theta_2 - \psi) - \sin(\theta_2 - \psi) \cot \beta)$  is the distance between point  $O_1$  and the intersection of lines  $(OO_1)$  and  $(P_1P_2)$ . Also,  $\alpha_1$  is the angle between link  $a$  and the first phalanx. It can be shown that

$$\cot \beta \cos \alpha_1 + \sin \alpha_1 = \frac{\sin X}{\sin \beta} \quad (12)$$

where  $X$  is the angle between links  $a$  and  $b$ .

## 4 Design Optimization

After obtaining the forces equation two consideration form the guidelines for design parameters selection: first grasp should be stable which means ejection should be prevented and differences between the phalanx forces should be minimum possible value. In ejection phenomena the finger slide and push the object out instead of a secure grasping. To prevent ejection the exerted forces by each phalanx to the object should be positive. It is also desirable that forces at each phalanx to be close to their mean value and force distribute evenly between phalanxes which is referred to as force isotropy. So the conditions which should be satisfied can be expressed as:

$$\begin{cases} f_1 = f_2 \\ f_1 > 0 \text{ and } f_2 > 0 \end{cases} \quad (13)$$

In order to have force isotropy it is necessary that forces by each phalanx are equal, but forces are function of contact position and  $\theta_2$  angle hence it is a local property. Therefore if the object moves these conditions are not true anymore. However in this

case, another step is necessary since  $h$  is a function of the design parameters and the angle  $\theta_2$ . Furthermore, many design variables are available to satisfy the latter equation, namely  $a$ ,  $b$ ,  $c$ , and  $d$ .

For instance, if one chooses  $a = b$ , a known  $c$  (e.g. resulting from minimal distance considerations) and  $\psi = \frac{\pi}{2}$ ,  $a$  is completely defined as

$$a = \frac{2 l_1 c \sin \theta_2 + c^2 + l_1^2 \sqrt{A}}{2B} \quad (14)$$

with ,

$$A = (C - 1)((C - 1)c^2 + 2cCl_1 \sin \theta_2) + C^2 l_1^2 \quad (15)$$

$$B = -c^2 + Cc^2 - l_1 c \sin \theta_2 + 2Cl_1 c \sin \theta_2 + Cl_1^2 \quad (16)$$

$$C = -K\theta_2 + \frac{k_2}{k_2 + l_1 \cos \theta_2 + k_1} \quad (17)$$

The above mentioned relationship can be used in order achieving isotropic design. However, the isotropic property is not very robust with respect to design parameters, so it suggests using the following method.

If one obtains an isotropic and therefore stable design for a particular contact set  $(k_1, k_2, \theta_2)$ , it may be of interest that the finger is also robust with respect to ejection around this isotropic point, in order to ensure that a deviation from this configuration does not lead to an unstable grasp. The final aim is to guaranty stability for all grasps if possible and satisfy certain “quality” based indices like the isotropy. An index that can be used to ensure the grasp stability, even if the proximal contact is lost, is:

$$\mu = \frac{\int_W \delta(k_2, \theta_2) dk_2 d\theta_2}{\int_W dk_2 d\theta_2} \quad (18)$$

Where  $\delta(k_2, \theta_2)$  is a Kronecker-like symbol for characterizing the stability of the contact situation:

$$\delta(k_2, \theta_2) = \begin{cases} 1 & \text{if the final grasp is stable} \\ 0 & \text{otherwise} \end{cases} \quad (19)$$

This index is the ratio between the stable and unstable areas in the grasp-state plane of the finger. Contour plots of the index  $\mu$  is illustrated in Fig. 2 for a mechanically actuated finger. The optimal design parameter values can be obtained using the following plot. In our design equal lengths are considered for both phalanxes ( $l_2/l_1=1$ ), so the optimal value for  $c/a$  is around 0.6 .

## 5 Control Method

The control is aimed at exploiting the main properties of underactuation to perform motion tasks close to reference angles obtained by EMG signal. The ordinary task considered for design and development of the motion control law is the finger preshaping for the palmer grasp of a cylindrical object.

Kinematic coupling among the joints is related by the relation

$$x_s = l_1\theta_1 + l_2(\theta_1 + \theta_2) \quad (20)$$

$$\ddot{x}_s = l_1\ddot{\theta}_1 + l_2(\ddot{\theta}_1 + \ddot{\theta}_2) \quad (21)$$

where  $x$  is endpoint position,  $l_1$  and  $l_2$  are link lengths, and  $\theta_1, \theta_2$  are angle between links (Fig.1).

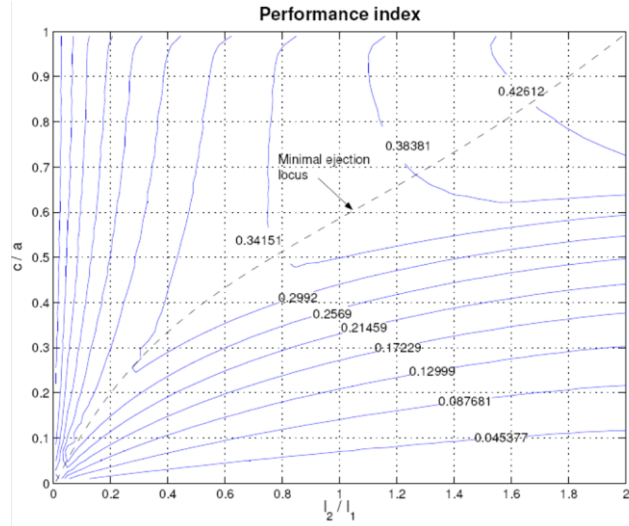


Fig.2. Performance index for linkage driven 2 phalanx underactuated hand

### 5.1 PD Control in the joint space with elastic compensation

Dynamic relation (20) and (21) is used to actively control the first joint and passively move the second joint. The proposed control law is a modified version of the standard *PD* control in the joint space with gravity compensation and is expressed as

$$T_a = K_p\tilde{\theta} - K_D\dot{\theta} + g(\theta) + T_e \quad (22)$$

where  $\tilde{\theta} = \theta_D - \theta$  is the joint position error defined as the difference between the reference set point  $\theta_D$  and the current joint angle  $\theta$ ,  $g(\theta)$  is the estimation of joint gravitational torque, and  $K_p$  and  $K_D$  are the diagonal gain matrices for the proportional and derivative control actions, respectively. In addition to the standard *PD* control plus gravity compensation, an elastic term is introduced in order to compensate for the preload spring located between phalanxes joint.

The joint elastic torque is expressed as  $T_e = k\Delta\theta_2$ .

For fully actuated hand based on our previous paper [2] we used a controller which simulates effect of virtual elements. These virtual elements are dampers at each joint and a spring-damper attached to tip of the finger and the other side moves along a semi-circle. Using this method the hand can grasp an object which is located inside the semi-circle. The virtual elements are shown in Fig.3.

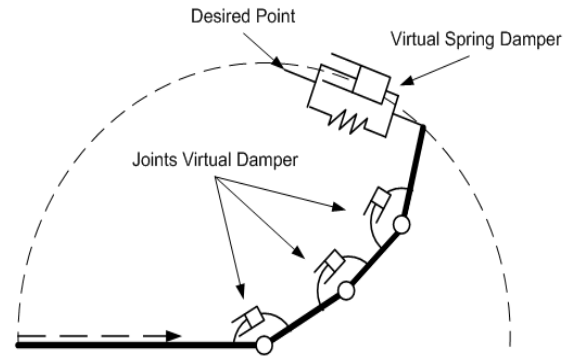


Fig.3. Virtual Elements Used for Control of Fullyactuated Hand

## 6 Numerical Simulations

Based on results of optimal design a model of two phalanx finger is made in Adams multi-body dynamic modelling software linked with Matlab and Simulink software to implement the controller. Both phalanxes have the equal length and  $c/a$  ratio is 0.6 based on optimal design analysis. Torsion spring is located between two phalanxes. The revolute joint is located at joints and a motor is moving the finger which is shown by round arrow. A circular object is chosen to be grasped and the proposed controller is used to control finger movement.

By applying the control algorithm to the mechanism the finger can grasp the object. The grasping sequence is shown in Fig. 3.

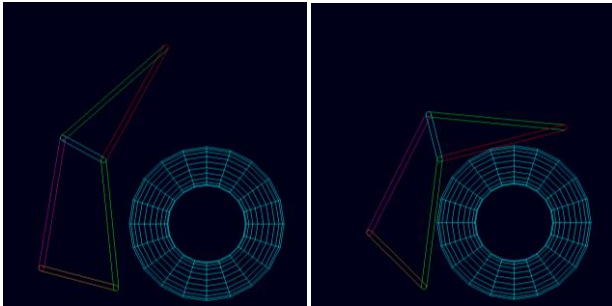


Fig. 4. The grasping sequence of a circular object by underactuated hand

The finger tip angle respect to horizontal plane is shown in Fig. 5. It starts from 90 degree and after first phalanx has contact with the object the rate of change of angle is changed.

Angle between two phalanxes is shown in Fig. 5. The angle starts from 180 degree and gradually changes until second phalanx touches the object.

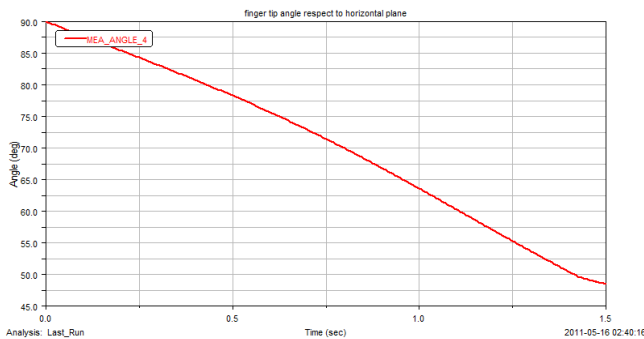


Fig. 5. Finger tip angle respect to horizontal plane for underactuated hand

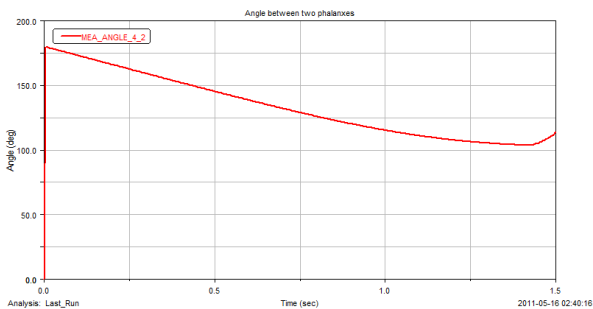


Fig.6. Angle between two phalanxes for underactuated hand

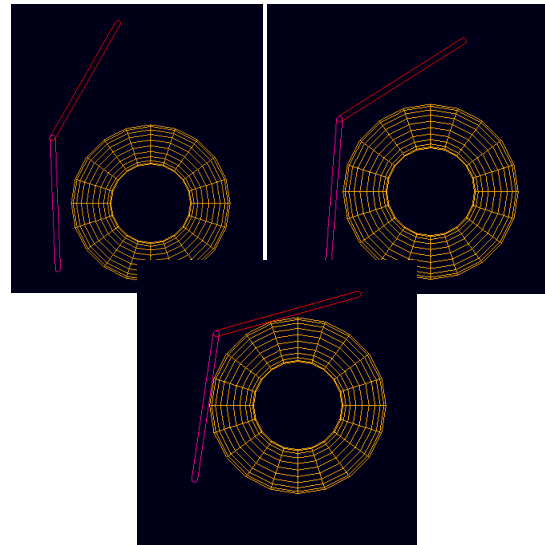


Fig. 7. The grasping sequence of a circular object by a fully actuated hand

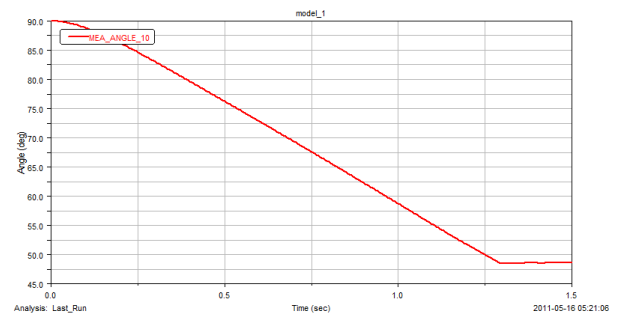


Fig.8. Finger tip angle respect to horizontal plane for fully actuated hand

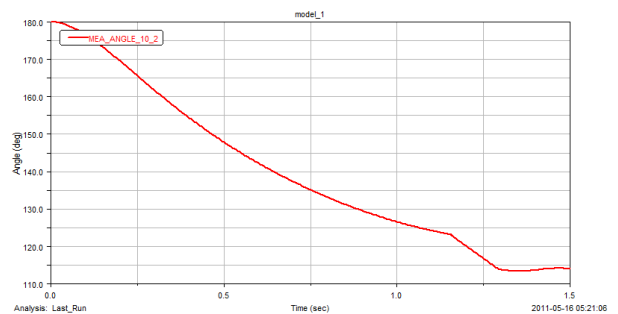


Fig.9. Angle between two phalanxes for fully actuated hand

Two general design which are fully actuated and underactuated and appropriate control methods for each of them are provided for prosthetic hand. In order to compare the functionality of these two methods a fully actuated finger with the same dimension and with a similar object to grasp is simulated. Power grasping algorithm which described before is used in order to control the movement. The sequence of movement is shown in Fig. 6. The finger tip angle respect to horizontal plane is shown in Fig. 7 and the angle between two joints is shown in Fig. 8. As we can see both methods are capable to perform grasping and the graphs are very similar for both methods.

## Conclusion

In this paper two type of hand which are fully actuated and underactuated hand studied. Appropriate control methods are provided for precision and power grasping for fully actuated hand. For underactuated hand the optimal design condition derived and tested. Appropriate controller for hand movement proposed and tested through numerical simulation. Two methods of power grasping, based on fully actuated and underactuated hand compared and the results were close which means both method are capable of providing secure grasp for prosthetic hand.

## References:

- [1] Lynette A. Jones and Susan J. Lederman, *Human Hand Function*, New York: Oxford University Press, 2006, pp. 131-149.
- [2] Amir Fassih, D. Subbaram Naidu, Steve Chiu, and Marco P. Schoen, "power grasping of a prosthetic hand based upon virtual spring-damper hypothesis", *Proc. IASTED Int. Conf. Robotics and Applications*, Cambridge, Massachusetts, 2010, pp. 214-220.
- [3] Amir Fassih, D. Subbaram Naidu, Steve Chiu, and Marco P. Schoen, "precision grasping of a prosthetic hand based upon virtual spring-damper hypothesis", *Proc. IEEE 5th Cairo International Biomedical Engineering Conference, Cairo, Egypt, Dec 2010*.
- [4] Mohammad Asghar Oskooei, Housheng Hu, "Myoelectric control systems, a survey", *Biomedical Signal Processing and Control*, vol. 2, 2007, pp 275-294.
- [5] Christian Cipriani, Franco Zaccane, Silvestro Micera, Chiara Carrozza, "On the shared control of an emg-controlled prosthetic hand: analysis of user-prosthesis interaction", *IEEE Transaction on Robotics*, vol.24, No1, February 2008.
- [6] Erik D Engeberg, Sanford G. Meek, "Backstepping and sliding mode control hybridized for a prosthetic hand", *IEEE Trans. on Neural Systems and Rehabilitation Engineering*, vol. 17, No.1, February 2009.
- [7] D.E. Whitney, "Resolved motion rate control of manipulators and human prostheses", *IEEE Trans. Man-Machine Syst.*, vol. MMS-10, No.2, 1969, pp.47- 53.
- [8] Y. Nakamura, "Advanced robotics: redundancy and optimization", Addison-Wesley, Reading, MA, 1991.
- [9] N. Dechev, W.L. Cleghorn, S. Naumann, Multiplefinger, "Passive adaptive grasp prosthetic hand", *Mechanism and Machine Theory*, vol.36, 2001, pp.1157-1173.
- [10] Ramiero Cabas, Luis Maria Cabas, Carlos Balaguer, "Optimized design of the underactuated robotic hand", *Proceeding of the 2006 IEEE International Conferences on Robotics and Automation*, Orlando, Florida, May 2006.
- [11] Da-Peng Yang, Jing-dong Zhao, Yi-kun Gu, Xin-qing Wang, Nan Li, Li Jiang, Hong Liu, Hai Huang, Da-wei Zhao, "An anthropomorphic robot hand develeoped based on underactuated mechanism and controlled by EMG signals", *Journal of Bionic Engineering*, vol. 6, 2009, pp 255-263.
- [12] Suguru Arimoto, Masahiro Sekimoto, "Human-like movements of robotic arms with redundant dofs: virtual spring-damper hypothesis to tackle the brenestein problem", *Prec. of IEEE Int. Conf. on Robotics and Automation*, Orlando, Florida, May 2006.
- [13] Jerry Pratt, Chee-Meng Chew, Ann Torres, Peter Dilworth, Gill Pratt, "Virtual model control: an intuitive approach for bipedal locomotion", *The International Journal of Robotics Research*, vol. 20, No. 2, pp. 129-143, February 2001.
- [14] Thomas Wimboeck, Christian Ott, Gerhard Hirzinger, "Passivity-based object-level impedance control for a multifingered hand" *Proceedings of the 2006 IEEE/RSJ, International Conference on Intelligent Robots and Systems*, Beijing, China, 2006.
- [15] Lionel Brignel, Thierry Laliberte, Clement Gosselin, "Underactuated robotic hand", Springer 2008.

# Robust Control of a Prosthetic Hand Based on a Hybrid Adaptive Finger Angle Estimation

AMIR FASSIH, D.SUBBARAM NAIDU, STEVE CHIU, PARMOD KUMAR

School of Engineering  
Idaho State University  
921 S. 8<sup>th</sup> Ave, Pocatello, Idaho  
U.S.A  
fassamir@isu.edu

*Abstract:* - This paper presents a robust control approach to control the movement of a prosthetic hand based on an estimation of the finger angles using surface electromyographic (sEMG) signals. All the available prosthesis uses the motion control strategy which is pre-programmed get initiated when some threshold value of the measured sEMG signal is reached for a particular motion set. Here we use a novel approach to model the finger angle which utilizes System Identification (SI) techniques. The dynamic model obtained allows the instantaneous control for the finger motions. sEMG data is acquired using an array of nine sensors and the corresponding finger angle is acquired using a finger angle measuring device and a data glove. A nonlinear Teager–Kaiser Energy (TKE) operator based nonlinear spatial filter is used to filter sEMG data whereas the angle data is filtered using a Chebyshev type-II filters. An EMG-angle estimation model is proposed then the estimated angles are used to control movement of a prosthetic hand using a robust approach which can deal with modeling uncertainty. The overall performance of the prosthetic hand are measured based on numerical simulation. The resulting fusion based output of this approach plus the robust controller gives improved the prosthetic hand motion control.

*Key-Words:* Robotics, Control, Prosthetics, Robust Control, sEMG, Finger Angle Model, System Identification.

## 1 Introduction

over 1.6 million people were reported to have amputations during 2005 in the United States, [1]. The ongoing wars in the Afghanistan and Iraq results in the continuously increase of this number, [2]. This makes it important to have an efficient and dexterous prosthesis that can improve the daily lives of the amputees. Currently available prosthesis lacks the tactile or proprioceptive feedback for grasping which makes the 30-50% of the upper extremity amputees not to use their prosthesis [3, 4]. One of the most important aspects of the prosthesis is to have a good control for the daily life tasks which is a prime factor to make the amputee to accept the device for regular use. There is lots of work need to be done before we reach to have a fully dexterous hand and the precise and effective control is of high demand. The prosthetic hand need to be able to have good control for the intended finger angle sand forces to perform a certain task. The input signal for the control of the prosthesis is the surface electromyographic (sEMG) which is originates from the mind of the amputee. The sEMG signals can be

acquired from skeletal muscles on the residual part of the upper extremity. In this work, we assume that the amputation is transradial, and hence sufficient muscle mass is accessible for sEMG data acquisition. There are two types of EMG electrodes available for use, one that needs to be imbedded in the muscle mass i.e. needle electrodes and the others are the surface electrodes. This makes the sEMG an obvious choice as a control input signal because it eliminates the problems associated with surgeries and regular hygiene for the user of implanted electrodes. sEMG signal is an electric voltage signal with amplitude ranging between -5 and +5 [mV]. The sEMG signals are highly dynamic in nature which changes with different limb movements and required/applied forces for these movements and other tasks. The issue of muscle fatigue makes the sEMG signal further intricate. Therefore to have prosthesis with good control of hand/finger positions, required forces and at the same time that can compensate for the issue of muscle fatigue, the sEMG seems to be the best choice. Almost all of the currently available prosthetics using EMG or sEMG



sensors and compute some threshold value of this signal – for example the RMS value – to activate a pre-programmed motion and/or force set of the artificial prosthetic hand. The user only initiates the resulting motion/force, but the further control is not available which is quite different than what a healthy subject uses to control his/her hand. The natural hand of a non-amputee executes the complex motion sets by controlling the motion of the fingers at every instance in time. To mimic this characteristic of the natural hand, we propose to use dynamic models relating sEMG data with finger movement. The potential of such models is obvious from the operational point of view, but also allows the incorporation of muscle fatigue dynamics to be included in the control algorithm [9-13].

The control algorithm of a prosthetic hand can be divided into two parts. The first part is extracting information from sEMG signal to find the intended motion, and the second part is using this command signal to control a robotic hand.

Previously there have been numerous efforts to extract the useful information the sEMG signals [5]. Some of these methods are based on the wavelet analysis, artificial neural networks, and other feature extraction methods to make use of sEMG for prosthetic control [5]. sEMG is presented as an autoregressive (AR) model with the delayed intramuscular EMG signal as the input in the research work of [6]. In our work, we rely only on sEMG since no injected electrodes will be used to obtain EMG signals. Hence the task is to develop a model and an estimation scheme for describing the dynamics of the skeletal muscle force and finger angles from the sEMG signals. Some of the recent efforts in this direction are evident in the research work of [7-13].

Present research focus on the dynamic modeling and estimation of the angles of the proximal interphalangeal (PIP) joint of the index and the middle finger with the corresponding sEMG signal and Robust Control design for prosthetic hand to follow this signal. Two different systems and experimental set-ups are used to acquire the data for the index and middle finger angles and the corresponding sEMG signals. For the index finger data an array of nine sEMG sensors is used to record sEMG signals and joint angles are recorded using a wheel potentiometer from the arm of a healthy subject. For the middle finger data an array of three sensors is used to record sEMG signals and joint angles are recorded using a NODNA X-IST

## 2 EMG Angle Estimation Model

The filtered sEMG and angle data is smoothed with a smoothing-spline curve fitting. Smoothing spline is a piecewise polynomial computed from a smoothing parameter ( $p$ ) of 0.993 is fitted to the filtered sEMG and angle data. Smoothing parameter ( $p$ ) is a number between 0 and 1. By varying the value of  $p$  from 0 to 1 we can change the smoothing spline. For  $p = 0$  the smoothing spline is a least-square straight-line approximation to the data, whereas for  $p = 1$  it gives the "natural" cubic spline interpolant to the data [1]. Smoothing spline  $s$  is designed for a specific weight ( $w_i$ ) and smoothing parameter and minimizes the function  $J$ , which is given as:

$$J = p \sum_i w_i (y_i - s(x_i))^2 + (1 - p) \int \left( \frac{d^2 s}{dx^2} \right)^2 dx, \quad (1)$$

where  $x_i$  and  $y_i$  are predictor and response data respectively. By choosing a suitable value of the smoothing parameter  $p$  we make the error  $E(s) = \sum_i w_i (y_i - s(x_i))^2$  and roughness  $\int \left( \frac{d^2 s}{dx^2} \right)^2 dx$  small. In our case we took the smoothing parameter  $p$  as 0.993 [1].

Both the filtered and smoothed sEMG and angle data (input and output) are used to make model by applying System Identification (SI) techniques. The sEMG is the input to the system and the intended PIP joint angle is the output. Multiple linear and nonlinear models are obtained for modeling of sEMG and PIP joint angle signals for the index finger of the dominant hand of a healthy subject. Five linear and three nonlinear models are obtained for the input and output data set.

The model order of the various models used in this work are as follows: linear models for the input and output data set, OE model of order 16, ARX model of order 18, ARMAX model of model order 16, State-Space model with subspace method (N4SID) of order 18 and a State-Space model with prediction error/maximum likelihood method (PEM) of order 12 are obtained using SI, [2].

The nonlinear models for the input and output data set are obtained as, the nonlinear Wiener-Hammerstein models with nonlinearity estimators of 'piecewise linear – pwlinear,' 'sigmoidnet,' and 'wavelet network,' [2].

All these linear and nonlinear models are simulated and the simulated output i.e. estimated angle data and the measured angle data is used in an adaptive data fusion based algorithm to obtain the final fusion based output. The final fusion based output is used as a control signal to design a controller which controls the angles of the joint of the two link robot. Results are presented in the following parts. Fig. 1 shows the measured and data fusion based angle signal. This signal is used as a control input for the controller.

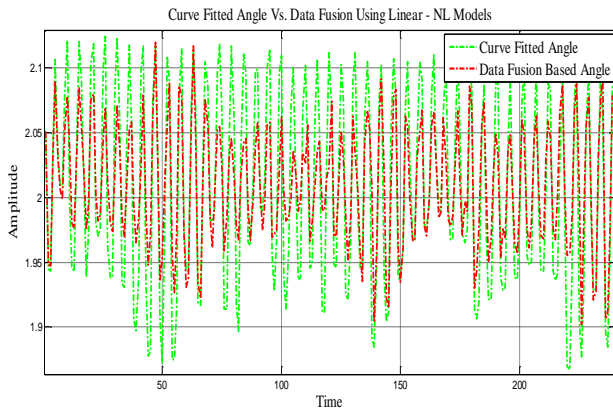


Fig. 7: Curve Fitted Vs. Data Fusion Based Angle Using Linear-Nonlinear Models.

### 3 Prosthetic Hand Control

The controller performance of a prosthetic hand is relying on two factors. Accurate intention estimation model and powerful control algorithm to which use the command signal from the estimation model and provide accurate movement for robotic part of the hand. The later part good performance requires the consideration of efficient dynamic models and sophisticated control approaches. Traditionally, control law is designed based on a good understanding of system model and parameters. Thus, a detailed and correct model of a robotic hand is needed for this approach [21, 22].

A finger can be considered as a 3 link robot, while in extracting the model for angle estimation, the PIP joint (the second) angle is considered, the third link angle normally has about 70% of the second joint angle and the first link angle is not considered in this research. As a result a two-link planar robot is

considered as a plant to investigate the control approach performance.

A dynamic model can be derived from the general Lagrange equation method. The modeling of a two-link planar nonlinear robotic system with assumption of only masses in the two joints can be found in the literature, e.g., [3, 4]. However, in practice, the robot arms have their mass distributed along their arms, not only masses in the joints as assumed. Thus, it is desired to develop a detailed model for two-link planar robotic systems with the mass distributed along the arms. We present a new detailed consideration of any mass distributions along robot arms in addition to the joint mass. Moreover, it is also necessary to consider numerous uncertainties in parameters and modeling. Thus, robust control, robust adaptive control and learning control become important when knowledge of the system is limited. We need robust stabilization of uncertain robotic systems and furthermore robust performance of these uncertain robotic systems. Robust stabilization problem of uncertain robotic control systems has been discussed in [21-24] and many others. Also, adaptive control methods have been discussed in [21,23] and many others. Because the closed-loop control system pole locations determine internal stability and dominate system performance, such as time responses for initial conditions, papers [26,28] consider a robust pole clustering in vertical strip on the left half s-plane to consider robust stability degree and degree of coupling effects of a slow subsystem (dominant model) and the other fast subsystem (non-dominant model) in a two-time-scale system. A control design method to place the system poles robustly within a vertical strip has been discussed in [22, 23], especially [24] for robotic systems. However, as mentioned above, for accurate prosthetic hand control there is a need of a detailed and practical two-link planar robotic system modeling with the practically distributed robotic arm mass for control.

Therefore a practical and detailed two-link planar robotic systems modeling and a robust control design for this kind of nonlinear robotic systems with uncertainties considered for robust control approach with both  $H_\infty$  disturbance rejection and robust pole clustering in a vertical strip. The design approach is based on the new developing two-link planar robotic system models, nonlinear control compensation, a linear quadratic regulator theory and Lyapunov stability theory.

## 4 Modeling of Prosthetic Hand Systems

The dynamics of a rigid revolute robot manipulator can be described as the following nonlinear differential equation [21, 22, 24]:

$$F_c = M(q)\ddot{q} + V(q, \dot{q})\dot{q} + N(q, \dot{q}) \quad (2)$$

$$N(q, \dot{q}) = G(q) + F_d\dot{q} + F_s(\dot{q}) \quad (3)$$

where  $M(q)$  is an  $n \times n$  inertial matrix,  $V(q, \dot{q})$  an  $n \times n$  matrix containing centrifugal and coriolis terms,  $G(q)$  an  $n \times 1$  vector containing gravity terms,  $q(t)$  an  $n \times 1$  joint variable vector,  $F_c$  an  $n \times 1$  vector of control input functions (torques, generalized forces),  $F_d$  an  $n \times n$  diagonal matrix of dynamic friction coefficients, and  $F_s(\dot{q})$  an  $n \times 1$  Nixon static friction vector.

However, the dynamics of the robotic system (2,3) in detail is needed for designing the angle control, i.e., especially, what matrices  $M(q)$ ,  $V(q, \dot{q})$  and  $G(q)$  are.

Consider a two-link planar robotic system representing the prosthetic hand finger in Fig. 8, where the system has its joint mass  $m_1$  and  $m_2$  of joints 1 and 2, respectively, robot arms mass  $m_{1r}$  and  $m_{2r}$  distributed along arms 1 and 2 with their lengths  $l_1$  and  $l_2$ , generalized coordinates  $q_1$  and  $q_2$ , i.e., their rotation angles,  $q = [q_1, q_2]$ , control torques (generalized forces)  $f_1$  and  $f_2$ ,  $F_c = [f_1, f_2]$ .

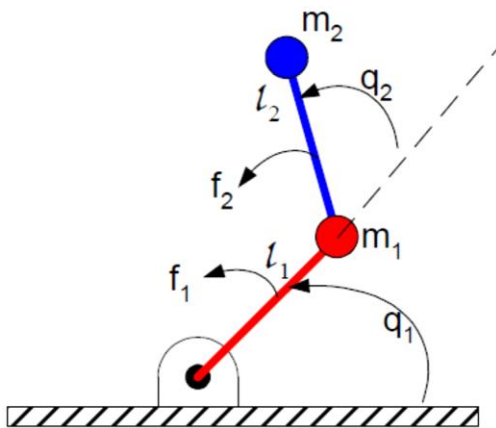


Fig 8- A two link robot system representing prosthetic hand

## 5 Robust Control

In view of possible uncertainties, the terms in (2,3) can be decomposed without loss of any generality into two parts, i.e., one is known parts and another is unknown perturbed parts as follows [22, 23]:

$$M = M_0 + \Delta M, \quad N = N_0 + \Delta N, \quad V = V_0 + \Delta V \quad (4)$$

where  $M_0$ ,  $N_0$ ,  $V_0$  are known parts,  $\Delta M$ ,  $\Delta N$ ,  $\Delta V$  are unknown parts. Then, the models in previous section can be used not only for the total uncertain robotic systems with uncertain parameters, but also for a known part with their nominal parameters of the systems.

Following [24], we develop the torque control law as two parts as follows:

$$F_c = M_0(q)\ddot{q}_d + V_0(q, \dot{q})\dot{q} + N_0(q, \dot{q}) - M_0(q)u \quad (5)$$

where the first part consists of the first three terms in the right side of (5), the second part is the term of  $u$  that is to be designed for the desired disturbance rejection and pole clustering,  $q_d$  is the desired

trajectory of  $q$ , however, the coefficient matrices are with all nominal parameters of the system. Define

an error between the desired  $q_d$  and the actual  $q$  as:

$$e = q_d - q \quad (6)$$

From (2) and (4)–(6), it yields:

$$\ddot{e} = M^{-1}(q)[\Delta M(q)\ddot{q}_d + \Delta V(q, \dot{q})\dot{q} + \Delta N(q, \dot{q}) + M_0(q)u] = w + E\dot{e} + Fu + u \quad (7)$$

$$E = -M^{-1}(q)\Delta V(q, \dot{q}),$$

$$F = -M^{-1}(q)\Delta M(q),$$

$$w = -F\ddot{q}_d - E\dot{q}_d + M^{-1}\Delta N \quad (8)$$

From [24], we can have the fact that their norms are bounded:

$$\|w\| < \delta_w, \quad \|E\| < \delta_e, \quad \|F\| < \delta_f \quad (9)$$

Then, it leads to the state space equation as:

$$\dot{x} = Ax + Bu + B[0 \ E]x + BFu + Bw \quad (10)$$

$$\mathbf{x} = \begin{bmatrix} \mathbf{e} \\ \dot{\mathbf{e}} \end{bmatrix} = [\mathbf{e}_1 \ \mathbf{e}_2 \ \dot{\mathbf{e}}_1 \ \dot{\mathbf{e}}_2]', \quad (11)$$

$$\mathbf{A} = \begin{bmatrix} 0 & \mathbf{I} \\ 0 & 0 \end{bmatrix}, \quad \mathbf{B} = \begin{bmatrix} 0 \\ \mathbf{I} \end{bmatrix} \quad (12)$$

The last three terms denote the total uncertainties in the system. The desired trajectory  $\mathbf{q}_d$  for manipulators to follow is to be bounded functions of time. Its corresponding velocity  $\dot{\mathbf{q}}_d$  and acceleration  $\ddot{\mathbf{q}}_d$ , as well as itself  $\mathbf{q}_d$ , are assumed to be within the physical and kinematic limits of manipulators. They may be conveniently generated by a model of the type:

$$\ddot{\mathbf{q}}_d(t) + \mathbf{K}_v \dot{\mathbf{q}}_d(t) + \mathbf{K}_p \mathbf{q}_d(t) = \mathbf{r}(t) \quad (13)$$

where  $\mathbf{r}(t)$  is a 2-dimensional driving signal and the matrices  $\mathbf{K}_v$  and  $\mathbf{K}_p$  are stable.

The design objective is to develop a state feedback control law for control  $\mathbf{u}$  in (7) as

$$\mathbf{u}(t) = \mathbf{K}\mathbf{x}(t) \quad (14)$$

such that the closed-loop system:

$$\dot{\mathbf{x}} = (\mathbf{A} - \mathbf{BK} + \mathbf{B}[0 \ \mathbf{E}] - \mathbf{BFK})\mathbf{x} + \mathbf{B}\mathbf{w} \quad (15)$$

has its poles robustly lie within a vertical strip  $\Omega$ :

$$\lambda(\mathbf{A}_c) \in \Omega = \{s = x + jy \mid -\alpha_2 < x < -\alpha_1 \leq 0\} \quad (16)$$

and a  $\delta$ -degree disturbance rejection from the disturbance  $\omega$  to the state  $\mathbf{x}$ , i.e.,

$$\|\mathbf{T}_{\mathbf{x}\mathbf{w}}(s)\|_\infty = \|(s\mathbf{I} - \mathbf{A}_c)^{-1}\mathbf{B}\|_\infty \leq \delta \quad (17)$$

$$\mathbf{A}_c + \mathbf{A} - \mathbf{BK} + \mathbf{B}[0 \ \mathbf{E}] - \mathbf{BFK} \quad (18)$$

we derive the following robust control law to achieve this objective is discussed in [20,24].

Consider prosthetic hand uncertain system (15) with (2)–(18) where the unstructured perturbations in (8) with the norm bounds in (9), the disturbance

rejection index  $\delta \geq 0$  in (17), the vertical strip  $\Omega$  in (16) and a matrix  $\mathbf{Q} > 0$ .

With the selection of the adjustable scalars  $\varepsilon_1$  and  $\varepsilon_2$ , i.e.,

$$(1 - \delta_f)/\delta_e > \varepsilon_1 > 0, (1 - \delta_f - \varepsilon_1 \delta_e)\delta > \varepsilon_2 > 0 \quad (19)$$

there always exists a matrix  $\mathbf{P} > 0$  satisfying the following Riccati equation:

$$\mathbf{A}'_{\alpha_1} \mathbf{P} + \mathbf{P} \mathbf{A}_{\alpha_1} - \left(1 - \delta_f - \varepsilon_1 \delta_e - \frac{\varepsilon_2}{\delta}\right) \mathbf{P} \mathbf{B} \mathbf{B}' \mathbf{P} + \left(\frac{\delta_e}{\varepsilon_1}\right) \mathbf{I} + \left(\frac{1}{\varepsilon_2 \delta}\right) \mathbf{I} + \mathbf{Q} = 0 \quad (20)$$

where

$$\mathbf{A}_{\alpha_1} = \mathbf{A} + \alpha_1 \mathbf{I} = \begin{bmatrix} \alpha_1 \mathbf{I}_2 & \mathbf{I}_2 \\ 0 & \alpha_1 \mathbf{I}_2 \end{bmatrix} \quad (21)$$

Then, a robust pole-clustering and disturbance rejection control law in (7) and (14) to satisfy (17)

and (18) for all admissible perturbations  $\mathbf{E}$  and  $\mathbf{F}$  in (11) is as:

$$\mathbf{u} = -\mathbf{K}\mathbf{x} = -\mathbf{r}\mathbf{B}'\mathbf{P}\mathbf{x} \quad (22)$$

if the gain parameter  $\mathbf{r}$  satisfies the following two conditions:

$$(i) \quad \mathbf{r} \geq 0.5 \text{ and} \quad (23)$$

$$(ii) \quad 2\alpha_2 \mathbf{P} + \mathbf{A}' \mathbf{P} + \mathbf{P} \mathbf{A} - \left(\frac{\delta_e}{\varepsilon_1}\right) \mathbf{I} - [2\mathbf{r}(1 + \delta_f) + \varepsilon_1 \delta_e] \mathbf{P} \mathbf{B} \mathbf{B}' \mathbf{P} > 0 \quad (24)$$

Proof for the approach is provided in [24].

It is also noticed that:

$$\mathbf{B} \mathbf{B}' = \begin{bmatrix} 0 & 0 \\ 0 & \mathbf{I}_2 \end{bmatrix} \quad (25)$$

It is evident that condition (i) is for the  $\alpha_1$  degree stability and  $\delta$  degree disturbance rejection, and condition (ii) is for the  $\alpha_2$  degree decay, i.e., the left vertical bound of the robust pole-clustering.

There is always a solution for relative stability and disturbance rejection in this form. It is because the Riccati equation (20) guarantees a positive definite solution matrix  $\mathbf{P}$ , and thus there exists a Lyapunov function to guarantee the robust stability of the closed loop uncertain robotic systems. The nonlinear compensation part in (7) has a similar function to a feedback linearization.

## 6 Numerical Simulation

Based on the proposed control approach, a two link robot is modeled considering uncertainties. Then the input signal from sEMG-Angle estimation model is used as reference signal to the plant and the performance is evaluated.

The system parameters are: link mass:  $m_2 = m_2 = 0.05\text{Kg}$ , lengths  $l_1 = l_2 = 0.03\text{m}$ , angular positions  $q_1, q_2(\text{rad})$ , applied, torques  $f_1, f_2(\text{Nm})$ .

The initial states are set as  $q_1(0) = q_2(0) = 0$ , and  $\dot{q}_1(0) = \dot{q}_2(0) = 0$ . The parametric uncertainties are assumed to satisfy (11) with  $\delta_f = 0.05$ ,  $\delta_e = 0.4$ ,  $\delta_n = 0.1$ . Select the adjustable parameters  $\varepsilon_1 = 0.01$ ,  $\varepsilon_2 = 0.01$  from (19), disturbance rejection index  $\delta = 0.1$ , the relative stability index  $\alpha_1 = 0.1$ , and the left bound of vertical strip  $\alpha_2 = 2000$  since we want a fast response. We solved the Riccati equation (20)

to get the solution matrix P and the gain matrix as:

$$P = \begin{bmatrix} 12693I_2 & 1584I_2 \\ 1584I_2 & 1643I_2 \end{bmatrix}$$

$$K = rB'P = [950I_2 \ 985I_2]$$

Numerical simulation is done in Matlab software. For the plant the above mentioned parameters is used. Two sets of simulation are done. In the first simulation nominal plant is used and for the second simulation the perturbed model considering uncertainty is tested. The input signal for both simulations is measured angles from the above mentioned experiments from PIP joint. For the third joint the 70% of the measured angle of PIP joint used which is a good estimate of that signal.

The system response with nominal plant and perturbed plant to the input signal respectively are shown in Fig. 9 and Fig. 10. As it is shown the input and output signals are close and system is capable of following the command signal with sufficient accuracy. Obviously the system has a better performance in case of nominal plant compare to the perturbed model in which the uncertainties are applied.

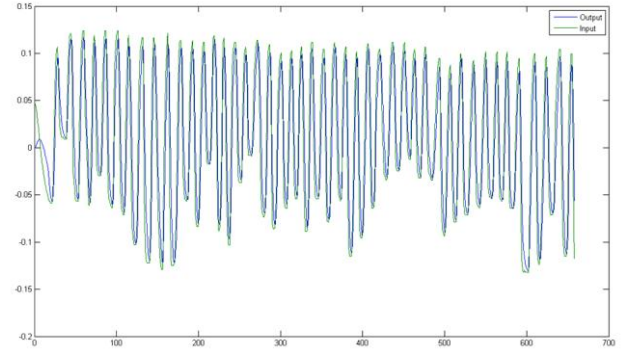


Fig. 9- System response to the nominal plant

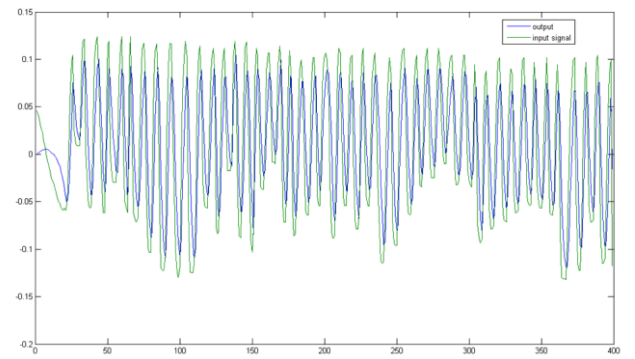


Fig. 9- System response to the perturbed plant

## 7 Conclusion

The dynamic modeling of the filtered and smoothed sEMG and PIP joint angle of the index and middle finger is achieved using SI with sEMG as the input and the joint angle as the output. Multiple linear and nonlinear models are obtained for the input and output data. To achieve a better estimate of the finger angles, an adaptive probabilistic Kullback Information Criterion (KIC) for model selection based data fusion algorithm is applied to the linear and nonlinear models outputs. The estimation method is mixed with a robust control algorithm for a two link robot to show the performance and functionality of the prosthetic hand.

As this initial study shows potential in the pursuit of controlling an artificial hand on an instantaneous basis, we will further this work in the future by improving the data collection techniques and optimizing the experimental procedure as well as using other advanced control techniques as adaptive control.

## References:

- [1] K. Ziegler-Graham, E. J. MacKenzie, P. L. Ephraim, T. G. Travison, and R. Brookmeyer, Estimating the Prevalence of Limb Loss in the United States - 2005 to 2050, *Archives of Physical Medicine and Rehabilitation*, Vol. 89, March 2008, pp. 422-429.
- [2] P. O'Connor. (2009, February 15). Iraq war vet decides to have second leg amputated [Online]. Available:<http://www.columbiamissourian.com/stories/2009/02/15/soldier-who-lost-leg-iraq-may-lose-other/>
- [3] D. J. Atkins, D. C. Y. Heard, and W. H. Donovan, Epidemiologic overview of individuals with upper-limb loss and their reported research priorities, *Journal of Prosthetics and Orthotics*, Vol. 8, No. 1, 1996, pp. 2-11.
- [4] D. H. Silcox, M. D. Rooks, R. R. Vogel, and L. L. Fleming, Myoelectric prostheses. A long-term follow-up and a study of the use of alternate prostheses, *The Journal of Bone and Joint Surgery*, Vol. 75-A, No. 12, December 1993, pp. 1781-1789.
- [5] M. B. I. Reaz, M. S. Hussain and F. Mohd-Yasin, Techniques of EMG signal analysis: detection, processing, classification and applications, *Biological Procedures Online*, Vol. 8, March 2006, pp. 11-35.
- [6] Y. Zhou, R. Chellappa, and G. Bekey, Estimation of intramuscular EMG signals from surface EMG signal analysis, *IEEE International Conference on Acoustics, Speech, and Signal Processing* 1986, Vol. 11, 1986, pp. 1805-1808.
- [7] P. K. Artemiadis and K. J. Kyriakopoulos, EMG-based position and force control of a robot arm: Application to teleoperation and orthosis, in *Conf. Rec. 2007 IEEE/ASME Int. Conf. on Advanced Intelligent Mechatronics*, Zurich, Sept. 2007, pp. 1-6.
- [8] P. K. Artemiadis and K. J. Kyriakopoulos, EMG-Based Position and Force Estimates in Coupled Human-Robot Systems: Towards EMG-Controlled Exoskeletons, in *Experimental Robotics*, Springer Tracts in Advanced Robotics, Vol. 54, Berlin Heidelberg: Springer-Verlag, 2009, pp. 241-250.
- [9] P. Kumar, C. Potluri, A. Sebastian, S. Chiu, A. Urfer, D. S. Naidu, and M. P. Schoen, An Adaptive Multi Sensor Data Fusion with Hybrid Nonlinear ARX and Wiener-Hammerstein Models for Skeletal Muscle Force Estimation, in *Proc. The 14th World Scientific and Engineering Academy and Society (WSEAS) International Conference on Systems*, Corfu Island, Greece, 2010, July 22-24.
- [10] P. Kumar, A. Sebastian, C. Potluri, A. Urfer, D. S. Naidu, and M. P. Schoen, Towards Smart Prosthetic Hand: Adaptive Probability Based Skeletal Muscle Fatigue Model, in *Conf. Rec. 32nd Annual International Conference of the IEEE Engineering in Medicine and Biology Society*, Buenos Aires, Argentina, Aug. 31 – Sept. 4, 2010.
- [11] P. Kumar, C. Potluri, A. Sebastian, S. Chiu, A. Urfer, D. S. Naidu, and Marco P. Schoen, Adaptive Multi Sensor Based Nonlinear Identification of Skeletal Muscle Force, *WSEAS Transactions on Systems*, Vol. 9, Issue 10, October 2010, pp. 1051-1062.
- [12] P. Kumar, C. Potluri, M. Anugolu, A. Sebastian, J. Creelman, A. Urfer, S. Chiu, D. S. Naidu, and M. P. Schoen, A Hybrid Adaptive Data Fusion with Linear and Nonlinear Models for Skeletal Muscle Force Estimation, in *Proc. 5th Cairo International Conference on Biomedical Engineering*, Cairo, Egypt, Dec. 16-18, 2010.
- [13] P. Kumar, C. H. Chen, A. Sebastian, M. Anugolu, C. Potluri, A. Fassih, Y. Yihun, A. Jensen, Y. Tang, S. Chiu, K. Bosworth, D. S. Naidu, M. P. Schoen, J. Creelman and A. Urfer, An Adaptive Hybrid Data Fusion Based Identification of Skeletal Muscle Force with ANFIS and Smoothing Spline Curve Fitting, in *Proc. 2011 IEEE International Conference on Fuzzy Systems*, Taipei, Taiwan, June 27-30, 2011.
- [14] P. Zhou, N. L. Suresh, M. M. Lowery, and W. Z. Rymer, Nonlinear Spatial Filtering of Multichannel Surface Electromyogram Signals During Low Force Contractions, *IEEE Transactions on Biomedical Engineering*, Vol. 56, No. 7, July 2009, pp. 1871-1879.
- [15] *MATLAB® Curve Fitting Toolbox™ User's Guide*. The MathWorks, Inc. 2010.
- [16] L. Ljung, *System Identification: Theory for the User*. 2nd edition, Printice Hall PTR, 1999, Chap. 1, pp. 1-15.
- [17] L. Ljung, *System Identification Toolbox™ 7 User's Guide*, The MathWorks, Inc., 2010.
- [18] H. Chen and S. Huang, A Comparative study on Model Selection and Multiple Model Fusion, in *Proc. 7th International Conference on Information Fusion*, New Orleans, USA, July 25-28, 2005, pp. 820-826.
- [19] A. K. Seghouane, and M. Bekara, A Small Sample Model Selection Criterion Based on Kullback's symmetric Divergence, *IEEE Transactions on Signal Processing*, Vol. 52, No. 12, 2004, pp. 3314-3323.
- [20] Shield B. Lin and Sheng-Guo Wang, Robust control design for two-link nonlinear robotic system, *Advances in robot manipulators Addison-Wesley (Publishing Company, Inc., New York, 2008)*
- [21] J.J.Craig, *Adaptive control of mechanical manipulators*, Addison-Wesley (Publishing Company, Inc., New York, 1988).
- [22] J.H. Kaloust, & Z. Qu, Robust guaranteed cost control of uncertain nonlinear robotic system using mixed minimum time and quadratic performance index, *Proc. 32nd IEEE Conf. on Decision and Control*, 1993, 1634-1635.
- [23] J. Kaneko, A robust motion control of manipulators with parametric uncertainties and random disturbances, *Proc. 34rd IEEE Conf. on Decision and Control*, 1995, 1609-1610.
- [24] R.L. Tummala, *Dynamics and Control – Robotics*, in *The Electrical Engineering Handbook*, Ed. by R.C. Dorf, (2nd ed., CRC Press with IEEE Press, Boca Raton, FL, 1997, 2347).



# POWER GRASPING OF A PROSTHETIC HAND BASED UPON VIRTUAL SPRING-DAMPER HYPOTHESIS

Amir Fassih, D. Subbaram Naidu, Steve Chiu, and Marco P. Schoen  
Measurement and Control Engineering Research Center, Idaho State University  
921 South 8th Ave, Stop 8060, Pocatello, Idaho  
USA  
fassamir@isu.edu, naiduds@isu.edu, chiustev@isu.edu, and schomarc@isu.edu

## ABSTRACT

A control scheme for achieving object power grasping by a prosthetic hand is proposed. The control scheme is based on defining virtual spring-damper between finger tip and desired point, and a semi circular path for finger tip. It is shown that the suggested control scheme provides satisfactory performance in power grasping of prosthetic hand, without the need for additional complexity regarding equations for inverse kinematics, or inverse dynamics, and the information on tactile or force sensing or even object shape.

## KEY WORDS

Medical Robotics, Control, Power Grasping, Prosthetic Hand Control.

## 1. Introduction

Human hand is one of the most important and complex parts of the body, which has the ability to handle different tasks. The ultimate goal of robotic hand is to achieve the functionality of a human hand. In the past three decades, there have been numerous investigations to achieve dexterity and ability of human hand, especially in the fields of humanoid robotics and prosthetic hand [1-6]. In spite of all these advances in this field, the current state of research on prosthetic hands is far from that objective of achieving the functionality of human hand. Commercially available prosthetic hands have very limited functionality and they are just simple grippers. The present research on prosthetic hands involves complex control schemes to achieve the most important functions of the hand [7-8].

Grasping can be categorized into two main groups: precision and power grasping. In precision grasping the object is held by tips of the fingers, while in power grasping, the whole the finger is active and in contact with the object [9]. Many research works addressed the precision grasping problem [12-15] mainly because of the well-established techniques for control of end effector; however the problem of power grasping is not studied in depth.

Many control methods require the knowledge of the shape of the object. For humans this information is available by

visual feedback from eyes, while in case of a prosthetic hand this visual information is not directly available for hand controller, and the only available information is electromyographic (EMG) signal related to patient's arm muscle activities. However, normally the EMG signal is not available for all individual joints and besides, due to measurement noise, accessing high quality EMG signal is hard [10]. Moreover, using EMG signal to control all the movements requires lot of attention during grasping and leads to fatigue for the amputees [11]. Hence it is required for prosthetic hand to be semi-autonomous which means a part of command information will be provided by the EMG signal and the rest of the required command should be provided automatically by hand controller.

Defining finger trajectory without the knowledge of shape of object to be grasped is a challenging task for many path planning techniques. For multi DOFs robots there are two common methods for trajectory planning which are "inverse kinematic" and "inverse dynamic" [12-15]. Both these methods require object shape and are based on solving optimization problem which requires high computation, hence they are hard to implement for real-time applications.

To avoid solving the path planning problem for prosthetic hands, many researchers advocated under-actuated mechanisms, which are capable of adapting to object shape mechanically and without additional computation [16-18]. In these mechanisms, the number of actuators are less than the DOFs, and because of less actuators they have less weight. However fewer actuators result in less functionality, because fingers joints can't move independently.

Arimoto et al. [19] used "virtual spring-damper hypothesis" for control of robotic arm-hand systems. A similar method called "virtual model control" is also suggested by J.Pratt et al. [20] used for walking robots, and it is based on defining virtual forces between two points. Both methods are based on the use of Jacobian matrix to relate task space movement to joint space. In [20] it is shown that any kind of force can be defined between two points and the other study [19] shows that use of spring-damper forces will result in human like movement. From physiological point of view, human skilled multi-joint reaching movement has these

characteristics that 1) endpoint trajectory become a quasi-straight line and less variable, 2) velocity profiles of the endpoint has a bell-shape, and 3) joint trajectories are rather variable from trial to trial [19].

In this paper, a new control scheme is proposed that can efficiently address the problem of power grasping without complete knowledge of the shape of the object which may be called “blind power grasping” for prosthetic hand. The proposed method is based on the works by Arimoto et al. [19] using virtual spring-damper (VSD) hypothesis used for control of robotic arm-hand systems. In our paper, we use the above mentioned hypothesis, in particular for the power grasping of a prosthetic hand. In this method, we define a virtual spring-damper between finger tip and desired point for control of movement of fingers. Further, in this method there is no need to introduce any performance indices to solve inverse kinematics uniquely and Jacobian pseudo-inverse or inverse dynamics which are common methods to define trajectories of redundant DOFs robots. Besides, in the present method, there is no need for any information on tactile or force sensing. The paper is organized as follows. In Section 2 modeling of prosthetic hand is discussed, Section 3 covers virtual spring damper method. Section 4 describes control strategy. Section 5 analyzes the efficiency of the proposed control scheme using numerical simulation. Finally, conclusion and discussion are presented in section 6.

## 2. Modeling of Prosthetic Hand

In this control method, controller is not derived directly from dynamic model of the system. Kinematics equation and Jacobian matrix are the required for controller design.

A model of a robotic hand system is shown in Fig.1. The model consists of a finger with 3DOF which represents three joints of a finger and palm.

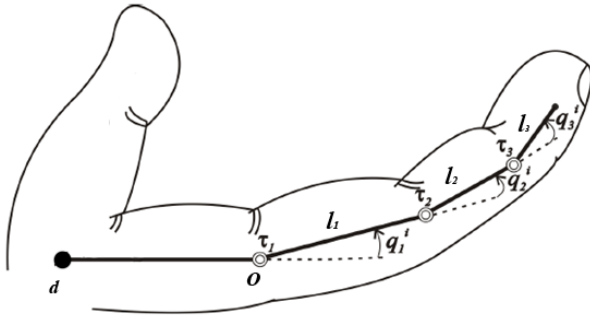


Fig. 1: Model of a Robotic Hand System.

In this paper we assume the following:

- 1- Movement of both finger and object are confined to a two dimensional horizontal plane, and therefore there is no gravity effect.
- 2- The object is assumed to be initially stable in its position.

- 3- The initial movement toward object is handled by amputee, so the hand is close enough to the object before grasping.

The position of the tip of the finger is evaluated as (see Figure 1):

$$x = l_1 \cos q_1 + l_2 \cos(q_1 + q_2) + l_3 \cos(q_1 + q_2 + q_3) \quad (1)$$

$$y = l_1 \sin q_1 + l_2 \sin(q_1 + q_2) + l_3 \sin(q_1 + q_2 + q_3) \quad (2)$$

where,  $l_1$ ,  $l_2$ , and  $l_3$  are lengths of each finger and  $q_1$ ,  $q_2$ , and  $q_3$  are angles of each corresponding joint.

Based on above equation the Jacobian matrix is as:

$$J = \begin{bmatrix} j_{11} & j_{12} & j_{13} \\ j_{21} & j_{22} & j_{23} \end{bmatrix}, \quad (3)$$

$$j_{11} = -l_1 \sin q_1 - l_2 \sin(q_1 + q_2) - l_3 \sin(q_1 + q_2 + q_3), \quad (4)$$

$$j_{12} = -l_2 \sin(q_1 + q_2) - l_3 \sin(q_1 + q_2 + q_3), \quad (5)$$

$$j_{13} = -l_3 \sin(q_1 + q_2 + q_3), \quad (6)$$

$$j_{21} = l_1 \cos q_1 + l_2 \cos(q_1 + q_2) + l_3 \cos(q_1 + q_2 + q_3), \quad (7)$$

$$j_{22} = l_2 \cos(q_1 + q_2) + l_3 \cos(q_1 + q_2 + q_3), \quad (8)$$

$$j_{23} = l_3 \cos(q_1 + q_2 + q_3). \quad (9)$$

$$j_{23} = l_3 \cos(q_1 + q_2 + q_3). \quad (10)$$

## 3. Virtual Spring-Damper Method

“Virtual model control” is a motion control scheme that uses simulations of virtual components to generate desired joint torques [20]. These joints produce the same effect that the virtual elements placed on robot would have created; hence they create the illusion that these virtual elements are connected to the real robot. Virtual elements can be any kind of real physical elements such as springs, dampers, gravity fields, nonlinear fields or any other components.

Virtual model control was proposed by J. Pratt et al [20] for biped walking robot. In a study by Arimoto [19] on robotic hand arm system, it is shown that using a virtual spring damper between robot end effector and desired point, and virtual dampers at each joint, human like movement can be achieved.

For power grasping by a prosthetic hand, one of the best options is the use of Virtual Spring-Damper (VSD) hypothesis. Some benefits of VSD control scheme are that it has a simple structure and requires relatively less computation. Besides, it doesn't need inverse dynamics to precisely define the robot movement. Thus, we use spring set points instead of commanded movement and robot automatically adapts its shape. Since finger joints at prosthetic hand work as virtual dampers, which is sensitive to velocity and not to position, they don't have a forced shape, instead just finger tip follow a defined path as will be discussed more in control strategy section.

The joint torques to virtual forces is given by:



$$\tau = J^T F, \quad (11)$$

where  $\tau$  is the torque, and  $F$  is the force due to virtual spring damper given as

$$F = -(\xi\sqrt{k}\dot{x} + k\Delta x), \quad (12)$$

and

$$\tau_{spring-damper} = -J^T(\xi\sqrt{k}\dot{x} + k\Delta x), \quad (13)$$

where  $k$  represents the stiffness of the virtual spring,  $\Delta x$  is distance between finger tip and desired point, and  $\xi$  is the damping ratio. The damping force is defined at each joint as

$$\tau_{joints damping} = -C\dot{q}, \quad (14)$$

where,  $C$  denotes a diagonal positive definite matrix as follows:

$$C = \xi_0 \text{diag}(c_1, \dots, c_n). \quad (15)$$

Hence control signal would be sum of these two terms

$$u = -C\dot{q} - J^T(q)(\xi\sqrt{k}\dot{x} + k\Delta x). \quad (16)$$

Higher values of  $k$  result in more accurate and faster response to the desired point and higher  $C$  provides more stability. Thus  $k$  and  $C$  are chosen as design variables.

#### 4. Control Strategy

Virtual spring-damper hypothesis is suitable for point to point control. Defining the desired trajectory as a semicircle (in order to have a full grasp of the object) given by,

$$x_d = (l_1 + l_2 + l_3) \cos(t), \quad (17)$$

$$y_d = (l_1 + l_2 + l_3) \sin(t), \quad (18)$$

Where  $t$  is proportional to EMG signal which is scaled to change between  $0 < t < \pi$ .

As shown in Fig. 2, after passing this semi-circle, finger tip goes toward center to make a tighter grasping. This is achieved by defining a desired point close to center.

As mentioned earlier, the goal is not exactly following the defined path. If the object is big, due to contact of hand and object, it would be impossible to follow exact path and following this path is just to achieve grasping.

Fig. 3 illustrates the physical counterparts of the virtual forces for control strategy and Fig. 4 shows structure of the proposed control system. As shown, the command force comes from EMG signal, and controller provides the movement for hand which has dynamic interaction with the object.

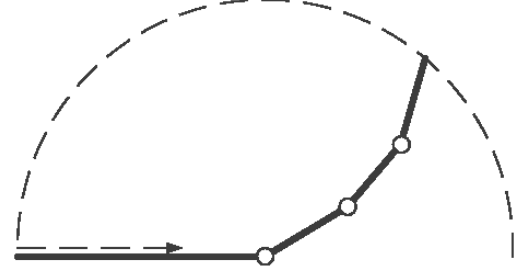


Fig. 2: Semi-Circle Path of Finger Tip

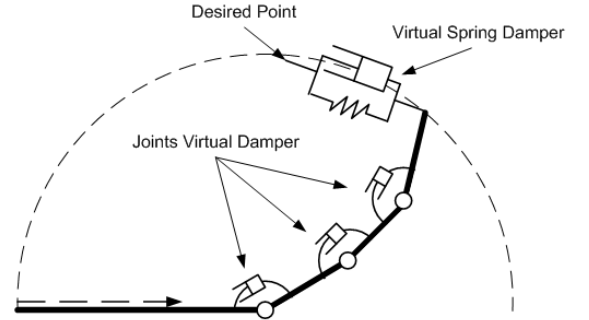


Fig 3: Physical Counterparts of the Virtual Forces

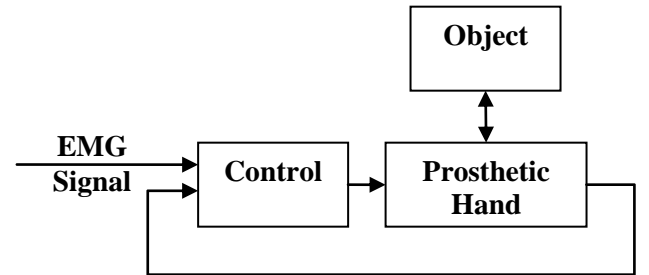


Fig. 4: Control Diagram of Prosthetic Hand System

#### 5. Numerical Simulation

In order to show the effectiveness of the proposed control strategy, numerical simulations were conducted to grasp three different objects, based on the physical parameters of a hand system and objects summarized in Table 1.

In order to simulate dynamics of the hand and interaction with object, Adams software is used. This software is a multi-body analysis simulation program that solves the rigid body dynamic equilibrium equations and directly interfaces with Matlab/Simulink software in order to implement controller. The contact between object and hand is modeled and three sets of simulations with different objects are performed. In all three simulations

the same control strategy is used which shows controller can handle grasping without information about physical parameters of object. Fingers and objects are assumed to be rigid. In these simulations the EMG signal is assumed to increase linearly with time.

Table 1. Parameters used for simulation

Index finger link 1	5 cm
Index finger link 2	2.5 cm
Index finger link 3	2.5 cm
Damping at joints	0.01 kg/s
Virtual damping ratio ( $c$ )	1
Virtual spring stiffness ( $k$ )	50 N/m
Rectangular object width	3 cm
Circular object radius	3 cm
Star shape object outer radius	2 cm

## 5.1 Simulation One

For first simulation a rectangular (cubic) object is used, and as mentioned earlier the movement is restricted to 2D movement. Object is not moving initially. Hand starts movement from open finger configuration. The hand positions at 1 second time interval are shown. Fig. 5 shows finger tip angle with respect to palm. As it is shown in Fig. 6 the grasping is accomplished successfully.

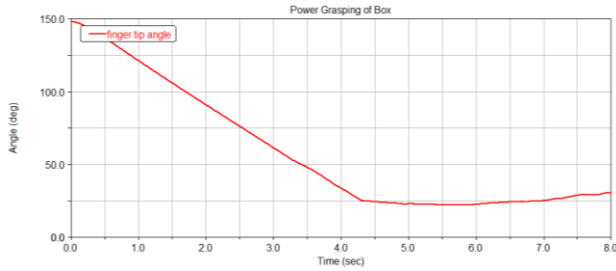


Fig. 5: Finger's Tip Angle at Rectangular Object Grasping

## 5.2 Simulation Two

For the second simulation a glass (circular object) is used. The control parameters are identical to previous simulation.

As shown in Fig. 7 the grasping is done successfully and the hand positions for 1 second time interval are depicted. Similarly the finger tip angle respect to palm is shown in Fig. 8.

Regardless of object shape, by use of proposed control scheme the hand can successfully grasp objects.

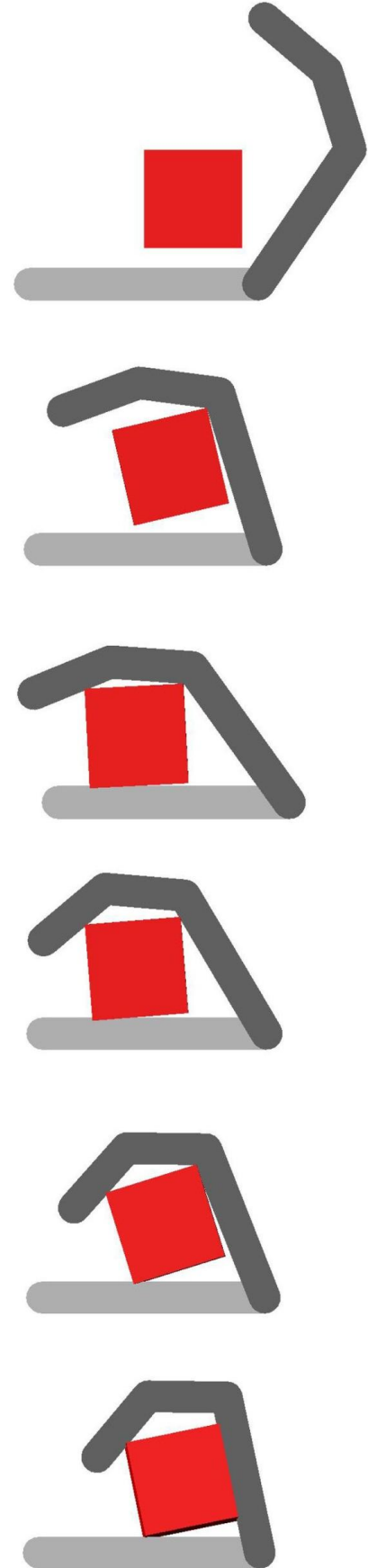
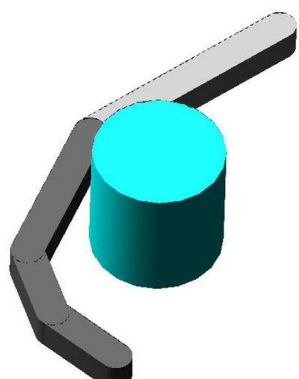
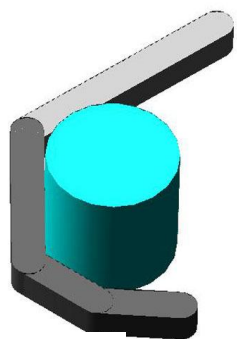


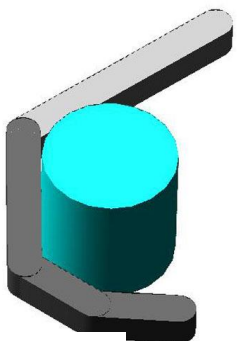
Fig. 6: Rectangular Object Grasping (1 Sec Intervals)



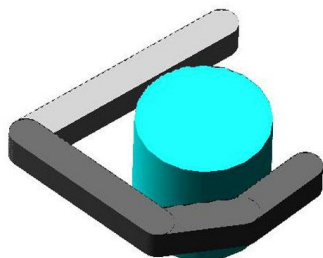
(a)



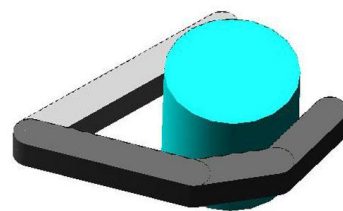
(b)



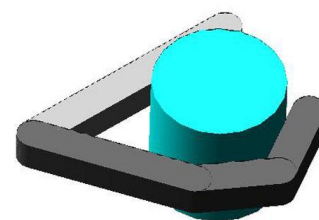
(c)



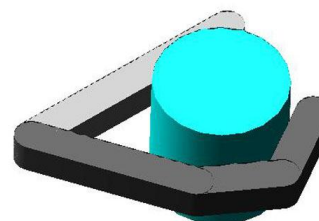
(d)



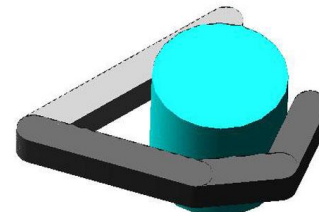
(e)



(f)



(g)



(h)

Fig. 7 (a-h) : Grasping of a Glass (1 sec. Intervals)

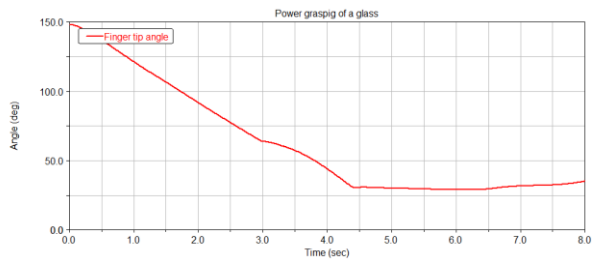


Fig. 8: Finger's Tip Angle at Grasping a Glass

### 5.3 Simulation Three

For the third simulation a star shape object is used. The control parameters are identical to previous simulation. As shown in Fig. 9 the grasping is done successfully and the hand positions for 1 second time interval are illustrated. Final position of grasping in 3D (isometric) view is depicted in Fig. 10. Similarly the finger tip angle respect to palm is shown in Fig. 11. The complicated shape of object shows that controller is able to handle grasp for wide variety of objects, without information of object shape.

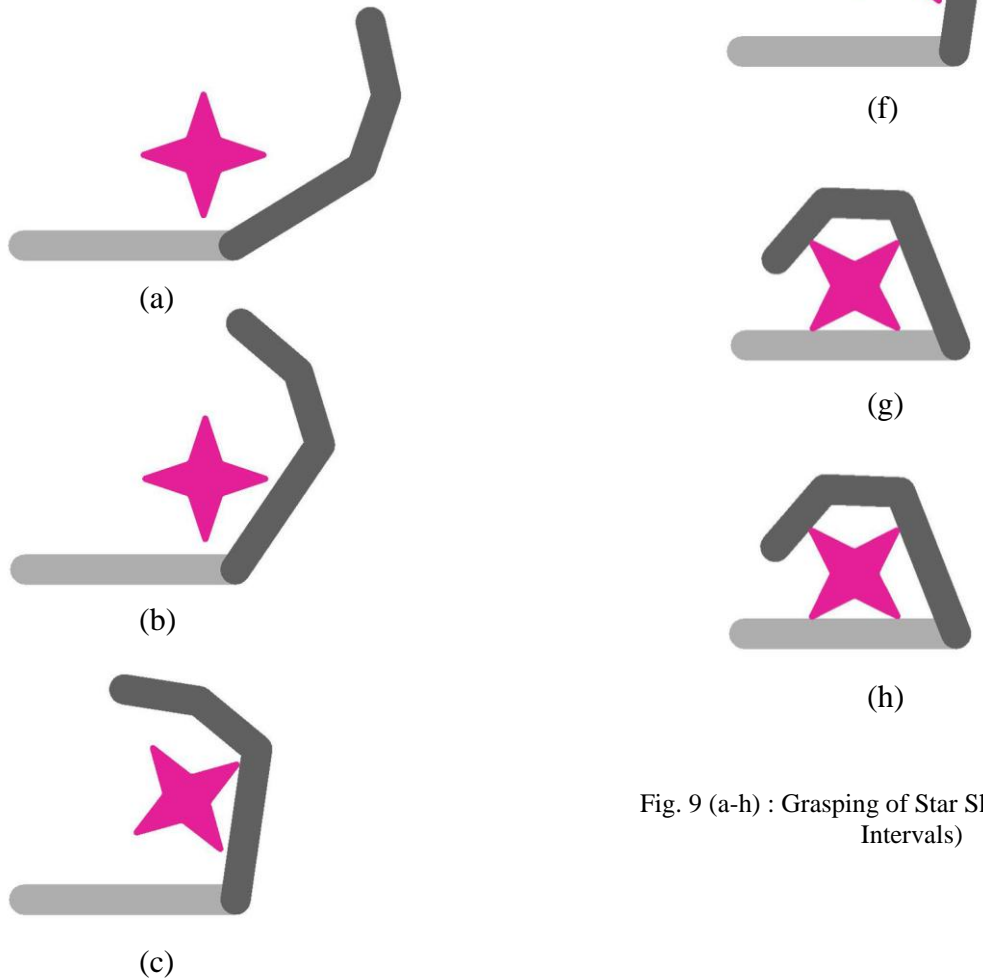


Fig. 9 (a-h) : Grasping of Star Shape Object (1 sec. Intervals)

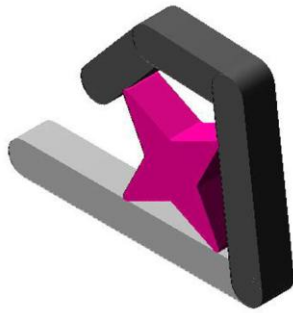


Fig. 10 : 3D (Isometric) View of Star Shape Object After Grasping

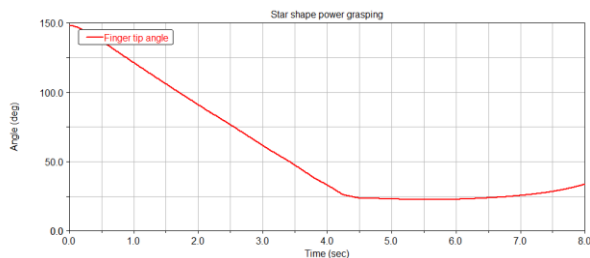


Fig. 11: Finger's Tip Angle at Star Shape Object Grasping

## 6. Conclusion

In this paper a control scheme for achieving object power grasping by a prosthetic hand was proposed. The control scheme was based on defining virtual spring-damper between finger tip and desired point, as well as, damping at finger joints, and a semi circular path for finger tip. It was shown through three sets of numerical simulations for different objects that the proposed control scheme can effectively be used for power grasping of prosthetic hand. It is shown that regardless of object shape proposed control method is successful for wide variety of situations. The proposed method did not rely on complex equations of inverse kinematics, or inverse dynamic and hence this method is better suitable for real-time applications. The immediate future investigation is the application of the proposed method to precision grasping of prosthetic hand.

## Acknowledgements

The research was sponsored by the US Department of the Army, under the award number W81XWH-10-1-0128 awarded and administered by the U.S. Army Medical Research Acquisition Activity, 820 Chandler Street, Fort Detrick MD 21702-5014. The information does not necessarily reflect the position or the policy of the

Government, and no official endorsement should be inferred. For purposes of this article, information includes news releases, articles, manuscripts, brochures, advertisements, still and motion pictures, speeches, trade association proceedings, etc.

## References

- [1] Z. Li, P. Hsu, and S. Sastry, Grasping and Coordinated Manipulation by a Multifingered Robot Hand," *J. of Robotics Research*, Vol. 8, No. 4, 1989, pp. 33-50.
- [2] T. Yoshikawa and K. Nagai, Manipulating and Grasping Forces in Manipulation by Multifingered Robot Hands, *IEEE Trans. on Robotics and Automation*, Vol. 7, No. 1, 1991, pp. 67-77.
- [3] A. M. Okamura, N. Smaby, and M. R. Cutkosky, An Overview of Dexterous Manipulation, *Proc. of the 2000 IEEE Int. Conf. on Robotics and Automation*, San Francisco, CA, April 2000, pp. 255-262.
- [4] S. C. Jacobsen, E. K. Iversen, D. F. Knutti, and R. T. Johnson, Design of the Utah/MIT Dexterous Hand, *Proc. of the 1986 IEEE Int. Conf. on Robotics and Automation*, San Francisco, April, 1986, pp. 96-102.
- [5] M. V. Weghe, M. Rogers, M. Weissert, and Y. Matsuoka, The ACT Hand: Design of the Skeletal Structure, *Proc. of the 2004 IEEE Int. Conf. on Robotics & Automation*, New Orleans, LA, USA, April 26-May 1, 2004, pp. 3375-3379.
- [6] M. Higashimori, H. Jeong, I. Ishii, M. Kaneko, A. Namiki, and M. Ishikawa, A New Four-fingered Robot Hand with Dual Turning Mechanism, *Proc. of the 2005 IEEE Int. Conf. on Robotics & Automation*, Barcelona, Spain, April 18-22, 2005, pp.2690-2695.
- [7] Erik D Engeberg, Sanford G. Meek, Backstepping and Sliding Mode Control Hybridized for a Prosthetic Hand, *IEEE Transaction on Neural Systems and Rehabilitation Engineering*, Vol. 17, No.1, February 2009.
- [8] Lorendana Zollo, Stefano Rocella, Eugenio Guglielmelli, M. Chiara Carrozza, Paolo Dario, Biomechatronic Design and Control of an Anthropomorphic Artificial Hand for Prosthetic and Robotic Application, *IEEE/ASME Transaction on Mechatronics*, Vol.12, No.4, August 2007.
- [9] Lynette A. Jones and Susan J. Lederman, *Human Hand Function*, Oxford University Press, New York, 2006, pp. 131-149.
- [10] Mohammad Asghar Oskoei, Housheng Hu, Myoelectric control systems, A survey, *Biomedical Signal Processing and Control*, Vol. 2, 2007, pp 275-294.
- [11] Christian Cipriani, Franco Zaccane, Silvestro Micera, Chiara Carrozza, On the Shared Control of an EMG-Controlled Prosthetic Hand: Analysis of User-Prosthesis Interaction, *IEEE Transaction on Robotics*, Vol.24, No1, February 2008.
- [12] D.E.Whitney, Resolved motion rate control of manipulators and human prostheses, *IEEE Trans. Man-Machine Syst.*, Vol.MMS-10, No.2, 1969, pp.47- 53.

- [13] Y. Nakamura, *Advanced Robotics: Redundancy and Optimization*, Addison-Wesley, Reading, MA, 1991.
- [14] T. Yoshikawa, M. Brady and R. Paul Eds. Analysis and control of robot manipulators with redundancy, in *Robotics Research: The 1st Int. Symp.*, Cambridge, MA: MIT Press, 1984, pp.735–747.
- [15] J.M. Hollerbach and K.C. Suh, Redundancy resolution of manipulators through torque optimization, *IEEE J. of Robotics and Automation*, Vol.RA-3, No.4, 1987, pp. 308–316.
- [16] N. Dechev, W.L. Cleghron, S. Naumann, Multiplefinger, Passive Adaptive Grasp Prosthetic Hand, *Mechanism and Machine Theory*, Vol.36, 2001, pp.1157-1173.
- [17] Ramiero Cabas, Luis Maria Cabas, Carlos Balaguer, Optimized Design of the Underactuated Robotic Hand, *Proceeding of the 2006 IEEE International Conferences on Robotics and Automation*, Orlando, Florida, May 2006.
- [18] Da-Peng Yang, Jing-dong Zhao, Yi-kun Gu, Xinqing Wang, Nan Li, Li Jiang, Hong Liu, Hai Huang, Dawei Zhao, An Anthropomorphic Robot Hand Develeoped Based on Underactuated Mechanism and Controlled by EMG Signals, *Journal of Bionic Engineering*, Vol. 6, 2009, pp 255-263.
- [19] Suguru Arimoto, Masahiro Sekimoto, Human-like Movements of Robotic Arms with Redundant DOFs: Virtual Spring-Damper Hypothesis to Tackle the Brenestein Problem, *Preceding of the 2006 IEEE International Conference on Robotics and Automation*, Orlando, Florida, May 2006.
- [20] Jerry Pratt, Chee-Meng Chew, Ann Torres, Peter Dilworth, Gill Pratt, Virtual Model Control: An Intuitive Approach for Bipedal Locomotion, *The International Journal of Robotics Research*, Vol. 20, No. 2, pp. 129-143, February 2001.

# Precision Grasping of a Prosthetic Hand Based on Virtual Spring Damper Hypothesis

Amir Fassih, D. Subbaram Naidu, *Fellow*, Steve Chiu, *Member* and Marco P. Schoen, *Member, IEEE*

**Abstract**— A control strategy for achieving object precision grasping by a prosthetic hand is proposed. The control strategy is based on defining virtual spring-damper between two finger tips and damping force at each finger joint. It is shown that the proposed control strategy provides a satisfactory performance in precision grasping of a prosthetic hand, without the need for additional complexity regarding equations for inverse kinematics, or inverse dynamics, and the information on tactile or force sensing or even object shape.

## I. INTRODUCTION

HUMAN hand is one of the most important and complex parts of the body, which has the ability to handle different tasks. Loss of hand can highly affect the quality of life; hence there is a high demand among amputees for prosthetic hands. The goal is to design an anthropomorphic prosthetic hand which is capable to be controlled through mind and has functionality close to normal human hand. The muscle movements in humans are controlled by electromyographic (EMG) signal which comes from brain to the body. In case of a lower hand amputee the remaining part of muscles are capable to measure EMG and through it find the subject's intention.

Grasping can be categorized into two main groups: precision and power grasping. In precision grasping the object is held by tips of the fingers, while in power grasping, the whole finger is active and in contact with the object [1]. Our previous work [2] addressed the problem of power grasping and here we study the problem of precision grasping of a prosthetic hand.

Many control methods require the knowledge of the shape of the object. For humans this information is available by visual feedback from eyes, while in case of a prosthetic hand this visual information is not directly available for hand controller, and the only available information is electromyographic (EMG) signal related to patient's arm muscle activities. However, normally the EMG signal is not available for all individual joints and besides, due to measurement noise, accessing high quality EMG signal is hard [3]. Moreover, using EMG signal to control all the movements requires lot of attention during grasping and leads to fatigue for the amputees [4]. Hence it is required for prosthetic hand to be semi-autonomous which means a part

of command information will be provided by the EMG signal and the rest of the required command should be provided automatically by hand controller.

Defining finger trajectory without the knowledge of shape of object to be grasped is a challenging task for many path planning techniques. For multi DOFs robots there are two common methods for trajectory planning which are "inverse kinematics" and "inverse dynamics" [5]-[7]. Both these methods require object shape and are based on solving optimization problem which requires high computation, hence they are hard to implement for real-time applications.

To avoid solving the path planning problem for prosthetic hands, many researchers advocated under-actuated mechanisms, which are capable of adapting to object shape mechanically and without additional computation [8]-[10]. In these mechanisms, the number of actuators is less than the DOFs, and because of less number of actuators they have less weight. However fewer actuators result in less functionality, because fingers joints can't move independently.

Arimoto *et al.* [11] used "virtual spring-damper hypothesis" for control of robotic arm-hand systems. A similar method called "virtual model control" is also suggested by J.Pratt *et al.* [12] used for walking robots, and it is based on defining virtual forces between two points. Both methods are based on the use of Jacobian matrix to relate task space movement to joint space. In [12] it is shown that any kind of force can be defined between two points and the other study [11] shows that use of spring-damper forces will result in human like movement. From physiological point of view, human skilled multi-joint reaching movement has these characteristics: 1) endpoint trajectory become a quasi-straight line and less variable, 2) velocity profiles of the endpoint has a bell-shape, and 3) joint trajectories are rather variable from trial to trial [11].

In this paper, a new control scheme is proposed that can efficiently address the problem of precision grasping without complete knowledge of the shape of the object which may be called "blind precision grasping" for prosthetic hand. The proposed method is based on the works by Arimoto *et al.* [11] using virtual spring-damper (VSD) hypothesis for control of robotic arm-hand systems. In our paper, we use the above mentioned hypothesis, in particular for the precision grasping of a prosthetic hand. In this method, we define a virtual spring-damper between finger tip and desired point for control of movement of fingers. Further, in this method there is no need to introduce any performance indices to solve inverse kinematics uniquely

Manuscript received August 25, 2010. The research was sponsored by the US Department of the Army, under the award number W81XWH-10-1-0128 awarded and administered by the U.S. Army Medical Research Acquisition Activity, 820 Chandler Street, Fort Detrick MD 21702-5014.

Authors are with School of Engineering, Idaho State University, 921 S, 8<sup>th</sup> Ave, Pocatello, Idaho, ID 83209 USA (e-mail : naiduds@isu.edu).

and Jacobian pseudo-inverse or inverse dynamics which are common methods to define trajectories of redundant DOFs robots. Besides, in the present method, there is no need for any information on tactile or force sensing.

The paper is organized as follows. In Section 2 modeling of prosthetic hand is discussed, Section 3 covers virtual spring damper method. Section 4 describes control strategy. Section 5 analyzes the efficiency of the proposed control scheme using numerical simulation. Finally, conclusion and discussion are presented in section 6.

## II. MODELING OF PROSTHETIC HAND

In this control method, controller is not designed based on dynamic model of the system. Instead, kinematics equation and Jacobian matrix are used for controller design.

A model of a robotic hand system is shown in Fig.1. The model consists of a finger with 3DOF which represents three joints of index finger, palm and a finger with 2DOF which represents thumb.

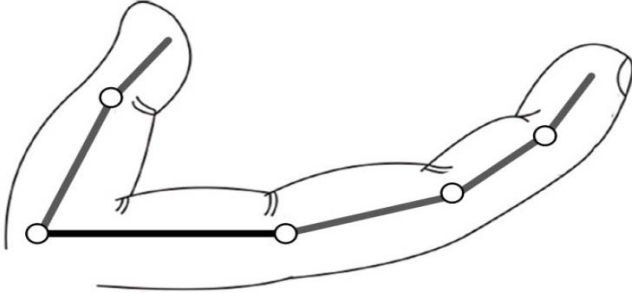


Fig. 1. Schematic of a robotic hand system

In this paper we assume the following:

- 1) Movement of both finger and object are confined to a 2 dimensional horizontal plane, and therefore there is no gravity effect.
- 2) The object is assumed to be initially stable in its position.
- 3) The initial movement toward object is handled by amputee, so the hand is close enough to the object before grasping.

The position of the tip of index fingers is evaluated as (see Fig. 1):

$$x_i = l_{i1} \cos q_{i1} + l_{i2} \cos(q_{i1} + q_{i2}) + l_{i3} \cos(q_{i1} + q_{i2} + q_{i3}), \quad (1)$$

$$y_i = l_{i1} \sin q_{i1} + l_{i2} \sin(q_{i1} + q_{i2}) + l_{i3} \sin(q_{i1} + q_{i2} + q_{i3}), \quad (2)$$

where,  $l_{i1}$ ,  $l_{i2}$ , and  $l_{i3}$  are lengths of index finger and  $q_{i1}$ ,  $q_{i2}$ , and  $q_{i3}$  are angles of each corresponding joint. Similarly the position of thumb finger is evaluated as:

$$x_t = l_{t1} \cos q_{t1} + l_{t2} \cos(q_{t1} + q_{t2}), \quad (3)$$

$$y_t = l_{t1} \sin q_{t1} + l_{t2} \sin(q_{t1} + q_{t2}), \quad (4)$$

where,  $l_{t1}$  and  $l_{t2}$  are lengths of thumb finger and  $q_{t1}$  and  $q_{t2}$ , are angles of corresponding joints.

Based on above equation the Jacobian matrix for index finger is as:

$$J_i = \begin{bmatrix} \frac{\partial x}{\partial q_{i1}} & \frac{\partial x}{\partial q_{i2}} & \frac{\partial x}{\partial q_{i3}} \\ \frac{\partial y}{\partial q_{i1}} & \frac{\partial y}{\partial q_{i2}} & \frac{\partial y}{\partial q_{i3}} \end{bmatrix}, \quad (5)$$

and Jacobian for thumb finger is as:

$$J_t = \begin{bmatrix} \frac{\partial x}{\partial q_{t1}} & \frac{\partial x}{\partial q_{t2}} \\ \frac{\partial y}{\partial q_{t1}} & \frac{\partial y}{\partial q_{t2}} \end{bmatrix}. \quad (6)$$

## III. VIRTUAL SPRING DAMPER METHOD

Virtual model control was first proposed by J. Pratt *et al* [12] for biped walking robot. This method is a motion control scheme that uses simulations of virtual components to generate desired joint torques [12]. These joints produce the same effect that the virtual elements placed on robot would have created; hence they create the illusion that these virtual elements are connected to the real robot. Virtual elements can be any kind of real physical elements such as springs, dampers, gravity fields, nonlinear fields or any other components. In a study by Arimoto [11] on robotic hand arm system, it is shown that using a virtual spring damper between robot end effector and desired point, and virtual dampers at each joint, human like movement can be achieved.

For precision grasping by a prosthetic hand, one of the best options is the use of Virtual Spring-Damper (VSD) hypothesis. Some benefits of VSD control scheme are that it has a simple structure and requires relatively less computation. Besides, it doesn't need inverse dynamics to precisely define the robot movement. Thus, we use spring set points instead of commanded movement and robot automatically adapts its shape. Since finger joints at prosthetic hand work as virtual dampers, which is sensitive to velocity and not to position, they don't have a forced shape, instead just finger tip follow a defined path as will be discussed more in control strategy section.

The joint torques to virtual forces is given by:

$$\tau = J^T F, \quad (7)$$

where  $\tau$  is the torque, and  $F$  is the force due to virtual spring damper given as

$$F = -(\xi\sqrt{k}\dot{x} + k\Delta x), \quad (8)$$

and

$$\tau_{spring-damper} = -J^T (\xi\sqrt{k}\dot{x} + k\Delta x), \quad (9)$$

where  $k$  represents the stiffness of the virtual spring,  $\Delta x$  is distance between finger tip and desired point, and  $\xi$  is the damping ratio. The damping force is defined at each joint as



$$\tau_{joints\ damping} = -C\dot{q}, \quad (10)$$

where,  $C$  denotes a diagonal positive definite matrix as follows:

$$C = \xi_0 \text{diag}(c_1, \dots, c_n). \quad (11)$$

Hence control signal would be sum of these two terms:

$$u = -C\dot{q} - J^T(q)(\xi\sqrt{k}\dot{x} + k\Delta x). \quad (12)$$

#### IV. CONTROL STRATEGY

Virtual spring-damper hypothesis is suitable for point to point control. In precision grasping two approaches can be considered. 1) Defining a virtual spring damper between fingers tip and geometrical center of the object, which requires information about the object position and shape, and this information is not available in case of a prosthetic hand for the controller which is used in [13] 2) Defining a virtual spring damper between tips of two fingers, then fingers attract together and grasp the object in between, without exact knowledge of object position and shape. In this case the amputee should place the hand close to the object and in appropriate position. Besides, a virtual damper force is considered at each finger joint. The latter method is used and physical counterpart of virtual forces are depicted at Fig. 2.

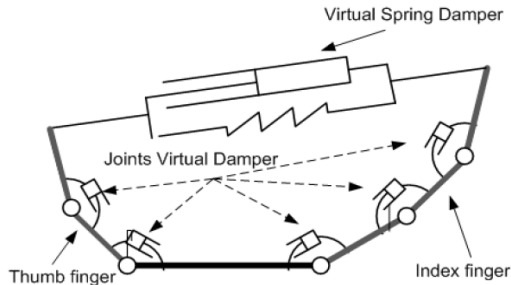


Fig. 2. Physical counterparts of the virtual forces

Higher values of  $k$  (virtual spring stiffness) results in faster movement of fingers as well as, higher grasping force. Thus by defining  $k$  proportional to EMG signal, amputee have control over speed of movement and grasping force. The damping coefficient of finger joints, can change the final shape of fingers. The joints with lower damping tends to move more, while higher damped joints move more. The appropriate values of damping are evaluated based on trial and error to reach positions close to normal hand and they are held constant for further simulations.

#### V. NUMERICAL SIMULATION

In order to show the effectiveness of the proposed control strategy, numerical simulations were conducted to grasp two

different objects, based on the physical parameters of a hand system and objects summarized in Table I.

The Adams software which is multi-body dynamic simulation software is used for numerical analysis. The software is capable to conduct information between Matlab/Simulink software environment, hence the plant is modeled by Adams and controller is implemented in Matlab/Simulink.

TABLE I  
PARAMETERS USED FOR SIMULATION

Parameter	Value
index finger link 1 length	5 cm
index finger link 2 length	2.5 cm
index finger link 3 length	2.5 cm
thumb finger link 1 length	4 cm
thumb finger link 2 length	3 cm
distance between thumb and index	6 cm
damping at joints	0.01 kg/s
virtual damping ratio	1
virtual spring stiffness	50 N/m
rectangular object width	2 cm
circular object radius	2 cm

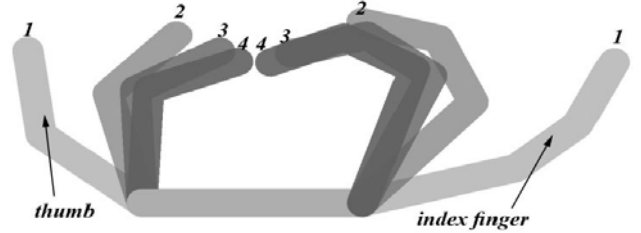


Fig. 3. Finger movements in 4 different position (0.25 sec. intervals)

For first simulation, two fingers are modeled without any object in between. As shown in Fig. 3, two fingers come together, and final position is close to normal hand coordination.

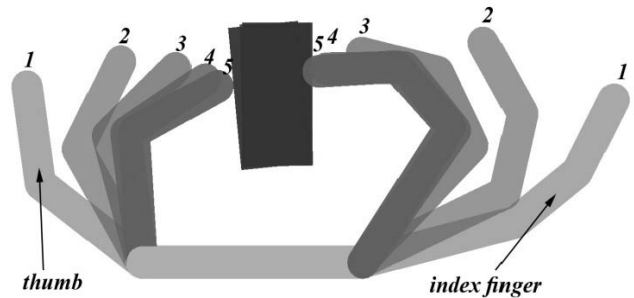


Fig. 4. Rectangular object grasping (0.25 sec intervals)

For the second simulation, a rectangular object is chosen to be grasped. The object is free to move in 2 dimensional plane, and contact and friction force are simulated between finger tip and the object. The object is placed at arbitrary final position of previous experiment. The finger movement at 0.25 sec time intervals and finger tip angles relative to palm are shown respectively in Figs. 4 and 5.

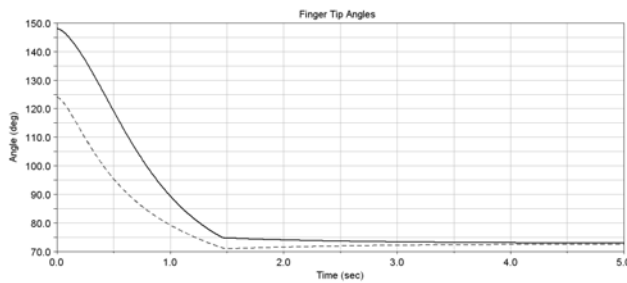


Fig. 5. Finger tips angle at rectangular object grasping (index finger solid line and thumb finger dashed line)

As it is shown after contact with object at approximately 1.5 second the angles are not changing much. The small changes are due to object movements toward left.

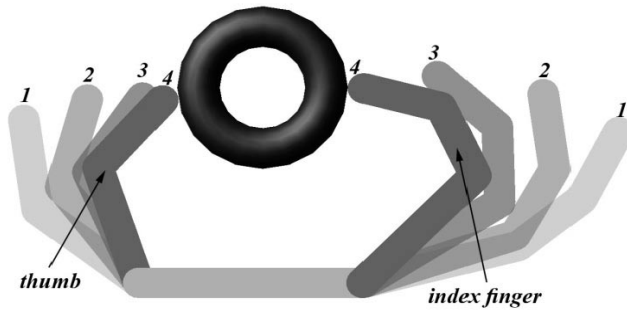


Fig. 6. Circular object grasping (0.25 sec intervals)

For third simulation a round object is selected. The object is not subjected to any constrain in 2 dimensional plane. The contact and friction force are defined between object and finger tip. The virtual spring coefficient which is proportional to EMG signal is assumed to be constant. Almost after 1 sec, the fingers contacted with the object. The finger movement at 0.25 sec time intervals and finger tip angles relative to palm are shown respectively in Figs. 6 and 7.

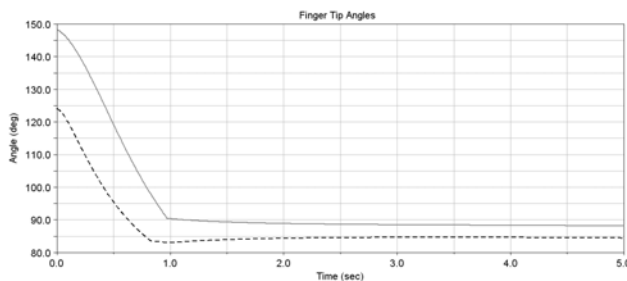


Fig. 7. Finger tips angle at circular object grasping (index finger solid line and thumb finger dashed line)

Appropriate object position and friction force between fingers and object are important parameters that help successful grasping. For the case of a round object if the object has inappropriate position or friction is not enough, the grasping might be unstable, but guaranteed successful grasping under all conditions require information about object shape and position which are not available for case of a prosthetic hand hence this control strategy is appropriate for most of the daily activities.

## VI. CONCLUSION

Based on virtual spring damper hypothesis, a control strategy for precision grasping of a prosthetic hand was proposed. The controller doesn't require extensive computation of inverse kinematic or inverse dynamics to describe finger movement and hence the method is appropriate for real-time applications. The control strategy is independent of object shape or force and contact sensor. By numerical simulation, the capability and effectiveness of control strategy are shown. The same strategy was used for two different objects and grasping was successful.

The future work will focus on precision grasping by gravity cancelation and analysis in three-dimensional space and experimental implementation with EMG signals.

## REFERENCES

- [1] Lynette A. Jones and Susan J. Lederman, *Human Hand Function*, New York: Oxford University Press, 2006, pp. 131-149.
- [2] Amir Fassih, D. Subbaram Naidu, Steve Chiu, and Marco P. Schoen, "power grasping of a prosthetic hand based upon virtual spring-damper hypothesis", *Proc. IASTED Int. Conf. Robotics and Applications*, Cambridge, Massachusetts, 2010, pp. 214-220.
- [3] Mohammad Asghar Oskooei, Housheng Hu, "Myoelectric control systems, a survey", *Biomedical Signal Processing and Control*, vol. 2, 2007, pp 275-294.
- [4] Christian Cipriani, Franco Zaccane, Silvestro Micera, Chiara Carrozza, "On the shared control of an emg-controlled prosthetic hand: analysis of user-prosthesis interaction", *IEEE Transaction on Robotics*, vol.24, No1, February 2008.
- [5] Erik D Engeberg, Sanford G. Meek, "Backstepping and sliding mode control hybridized for a prosthetic hand", *IEEE Trans. on Neural Systems and Rehabilitation Engineering*, vol. 17, No.1, February 2009.
- [6] D.E. Whitney, "Resolved motion rate control of manipulators and human prostheses", *IEEE Trans. Man-Machine Syst.*, vol. MMS-10, No.2, 1969, pp.47- 53.
- [7] Y. Nakamura, "Advanced robotics: redundancy and optimization", Addison-Wesley, Reading, MA, 1991.
- [8] N. Dechev, W.L. Cleghorn, S. Naumann, Multiplefinger, "Passive adaptive grasp prosthetic hand", *Mechanism and Machine Theory*, vol.36, 2001, pp.1157-1173.
- [9] Ramiero Cabas, Luis Maria Cabas, Carlos Balaguer, "Optimized design of the underactuated robotic hand", *Proceeding of the 2006 IEEE International Conferences on Robotics and Automation*, Orlando, Florida, May 2006.
- [10] Da-Peng Yang, Jing-dong Zhao, Yi-kun Gu, Xin-qing Wang, Nan Li, Li Jiang, Hong Liu, Hai Huang, Da-wei Zhao, "An anthropomorphic robot hand developed based on underactuated mechanism and controlled by EMG signals", *Journal of Bionic Engineering*, vol. 6, 2009, pp 255-263.
- [11] Suguru Arimoto, Masahiro Sekimoto, "Human-like movements of robotic arms with redundant dofs: virtual spring-damper hypothesis to tackle the brenestein problem", *Prec. of IEEE Int. Conf. on Robotics and Automation*, Orlando, Florida, May 2006.
- [12] Jerry Pratt, Chee-Meng Chew, Ann Torres, Peter Dilworth, Gill Pratt, "Virtual model control: an intuitive approach for bipedal locomotion", *The International Journal of Robotics Research*, vol. 20, No. 2, pp. 129-143, February 2001.
- [13] Thomas Wimboeck, Christian Ott, Gerhard Hirzinger, "Passivity-based object-level impedance control for a multifingered hand" *Proceedings of the 2006 IEEE/RSJ, International Conference on Intelligent Robots and Systems*, Beijing, China, 2006.

# REAL-TIME sEMG ACQUISITION AND PROCESSING USING A PIC 32 MICROCONTROLLER

Chandrasekhar Potluri, Madhavi Anugolu, Parmod Kumar, Amir Fassih, Pavan Yarlagadda, Yimesker Yihun, and Steve Chiu, *Member, IEEE*.

**Abstract** – This paper presents a novel approach for the signal acquisition and processing using an embedded platform. A PIC 32 microcontroller is used to acquire Surface Electromyographic (sEMG) signals and the corresponding skeletal muscle force signal for the respective motor point in this case the ring finger of the dominant hand of a healthy subject. The data is acquired by MATLAB®/SIMULINK®. Both sEMG and force signals are acquired at a rate of 2000 samples per sec. The acquired sEMG data is filtered using three different types of nonlinear Bayesian filter, Exponential, Poisson, and Half-Gaussian filter and the force signal is filtered using a Chebyshev type II filter. The data acquired from the PIC 32 and embedded test bed are compared with the standard LabVIEW™ data acquisition system using these three filters and Half-Gaussian filter with DE 3.1 electrodes gives the best results.

## I. INTRODUCTION

Human body is one of the most complex and intricate system available. In the same way the human body signals such as sEMG are quite complex and challenging to understand. To aid the peoples with upper extremity amputations there has been an active research in the field of upper limb prosthesis. Loss of upper extremity brings a reduction in functions to amputees and also struggle with numerous psychological issues which may further complicate the appropriate control and use of the prosthesis. Research work in [1] and [2] was mainly based on the electromyography (EMG) signals. The EMG signal is a naturally available and can be recorded at the surface of the limb which is known as surface EMG (sEMG).

Chandrasekhar Potluri is with MCERC, School of Engineering, Idaho State University, Pocatello, Idaho 83209, USA (email : potlchan@isu.edu).

Madhavi Anugolu is with MCERC, School of Engineering, Idaho State University, Pocatello, Idaho 83209, USA (email : anugmadh@isu.edu).

Parmod Kumar is with Measurement and Control Engineering Research Center (MCERC), School of Engineering, Idaho State University, Pocatello, Idaho 83209, USA (email: kumaparm@isu.edu).

Amir Fassih is with Measurement and Control Engineering Research Center (MCERC), School of Engineering, Idaho State University, Pocatello, Idaho 83209, USA (email: fassamir@isu.edu).

Pavan Yarlagadda is with Measurement and Control Engineering Research Center (MCERC), School of Engineering, Idaho State University, Pocatello, Idaho 83209, USA (email: yarlpava@isu.edu).

Yimesker Yihun is with MCERC, School of Engineering, Idaho State University, Pocatello, Idaho 83209, USA (e-mail: yihuyime@isu.edu).

Steve Chiu is with Department of Electrical Engineering and Computer Science, MCERC, Idaho State University, Pocatello, Idaho 83201 USA (email: chiustev@isu.edu).

The sEMG is simply an electric voltage ranging between -5 and +5 mV, which is a result of the electrical activity associated with voluntary muscle contraction. This made the sEMG signal of great use for the position and force control of the hand prosthesis [3, 4].

Since the skeletal muscle force and the sEMG signals are related and an increase force production results in the increased sEMG activity. Therefore the latter is used as a control input to realize force and motion control of a prosthetic hand. This makes the precise interpretation of the sEMG signal an essential task.

In today's research environment the embedded systems have become pervasive and as research advances, more and more functions of analog circuits are being realized by microcontrollers, Analog to Digital Converters (ADCs) and Digital to Analog Converters (DACs). In a modern control system, embedded system and control performs most of the data acquisition, processing and control functions. To realize the excellent system performance we need to have a well-designed embedded control which can deals with widely varying operating conditions. For robust, fast, precise and consistent high performance, the embedded system should be designed carefully and in balance. In case of a prosthetic hand we need to have a real-time embedded control system that performs the desired force and motion control [5-7].

Present work is a step in this direction where the authors explore the PIC 32 microcontroller as an embedded platform to simultaneously acquire the sEMG and skeletal muscle force. sEMG sensors are placed on the ring finger motor point of the dominant hand of a healthy subject and the subject is asked to squeeze a stress ball which has a force sensing resistor attached to it. The data is simultaneously captured using the PIC 32 embedded platform with MATLAB®/SIMULINK® real-time workshop (RTW) and regular NI LabVIEW™ data acquisition. Both sEMG and force data is captured at 2000 Hz. The sEMG signal is filtered using three different types of nonlinear Bayesian filters, Exponential, Poisson, and Half-Gaussian filter and the corresponding skeletal muscle force is filtered by a Chebyshev type-II filter [8]. Among these three different types of filters the Half-Gaussian filter is giving the best results [8-14].

The paper is organized as follows: present section followed by the 'Experimental Set-Up,' then the 'Signal Pre-Processing,' 'Proposed Design,' 'Results and Discussion,' are presented. The paper is concluded with the section of 'Conclusion and Future Work.'

## II. EXPERIMENTAL SET-UP

Using a muscle stimulator the motor point for the ring finger of the dominant hand of a healthy subject are marked. Prior to placing the sEMG sensors, the skin surface of the subject was prepared according to International Society of Electrophysiology and Kinesiology (ISEK) protocols. Different sets of experiments are conducted with DE 2.1 and DE 3.1 DELSYS® Bagnoli sEMG sensors. One sensor was placed on top of the motor point location and two sensors were placed next to the motor point. Subject is asked to squeeze the stress ball with the ring finger which has a 0.5 inch force sensing resistor from Interlink™ Electronics. The sEMG and skeletal muscle force signals were acquired using the 16-channel DELSYS® Bagnoli sEMG and NI ELVIS™ respectively. Similar experimental set-up was designed using a PIC 32 embedded platform where the sEMG and the force data is acquired using this platform. Both the data are captured at a sampling frequency of 2000Hz. Fig. 1 and 2 show the two experimental set-ups.



Fig. 1. Experimental Set-Up with NI ELVIS and DELSYS® EMG System.

## III. SIGNAL PRE-PROCESSING

Previous research work [15] shows that the Bayesian based filtering method yields the most suitable sEMG signals. These nonlinear filters significantly reduce noise and extract a signal that best describes EMG signals and can be effective for prosthetic hand signal processing. The latent driving signal  $x$  results in the EMG which can be computed using an instantaneous conditional probability  $P(EMG|x)$ , [15]. Research work in [16] describes EMG signal as amplitude-modulated zero mean Gaussian noise sequence. This estimation algorithm uses the model of the conditional probability of the rectified EMG signal  $emg = |EMG|$ , [15].

Equation (1) gives an “Exponential Measurement Model” for the rectified EMG signal [15].

$$P(emg|x) = \frac{\exp(\frac{-emg}{x})}{x}. \quad (1)$$

Equation (2) gives a “Poisson Measurement Model” for the rectified EMG signal [15].

$$P(emg|x) \approx x^n \frac{\exp^{-x}}{n!}. \quad (2)$$

In equation (2)  $n$  is the number of events. Equation (3) presents the “Half-Gaussian measurement model” for the rectified EMG signal [15].

$$P(emg|x) = \frac{2 \cdot \exp(\frac{-emg^2}{2x^2})}{\sqrt{(2\pi x^2)}}. \quad (3)$$

The model for the conditional probability of the rectified EMG is a filtered random process with random rate and the likelihood function for the rate evolves in time according to a Fokker–Planck partial differential equation [15]. The discrete time Fokker–Planck Equation is given by Equation (4).

$$p(x, t-) \approx \alpha * p(x - \varepsilon, t - 1) + (1 - 2 * \alpha) * p(x, t - 1) + \alpha * p(x + \varepsilon, t - 1) + \beta + (1 - \beta) * p(x, t - 1) \quad (4)$$

In the Equation (4)  $\alpha$  and  $\beta$  are two free parameters, where  $\alpha$  is the expected rate of gradual drift and  $\beta$  is the expected rate of sudden shift in the signal [15]. The latent driving signal  $x$  is discretized into bins of  $\varepsilon$ . An elitism based Genetic Algorithm (GA) is used to optimize these free parameters of the non-linear Half-Gaussian filter model. GA is an optimization algorithm which is based on observing nature and its corresponding processes to imitate solving complex problems, most often optimization or estimation problems, see [17-19]. Skeletal muscle force signal from FSR is filtered utilizing a Chebyshev type II low pass filter with a 550 Hz pass band frequency.

## IV. PROPOSED DESIGN

In this proposed design the analog input and the UART modules of the PIC 32 are used for the acquisition and transmission of the sEMG signals. The outputs from the DELSYS® Bagnoli system are connected to the analog input channels of the PIC 32 micro controller. In this present work the signal from the motor unit (middle sensor) is acquired and pre-processed. The sEMG signal and the corresponding skeletal muscle force are acquired at 2000 samples per second. A dsPIC blockset is used to generate the C code for the PIC32 from SIMULINK®. The dsPIC blockset generates a ‘.hex’ file, and this file is imported by MPLAB® to program the PIC32. The Analog Input module is used for reading the sEMG and the corresponding skeletal muscle force data. The PIC32 has an internal analog to digital converter (ADC) which has a 10-bit resolution so that it can distinguish up to 1024 different voltages, usually in the range of 0 to 3.3 volts, and it yields 3mV resolution. The UART module in the PIC32 is used to transmit the signals from the microcontroller to the PC using serial communication. In this design, a virtual ‘com port’ is created to feed the data via USB cable to the computer. MATLAB® is used to read the signals from the

ports. The acquisition system using the PIC 32 micro controller is shown in the Fig. 2.

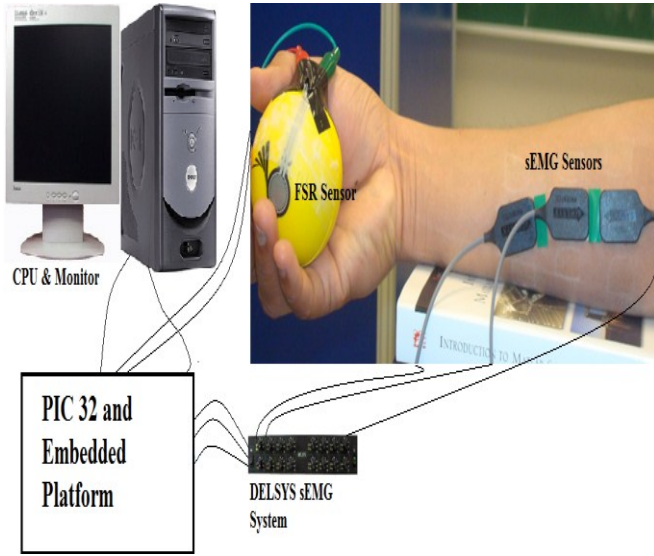


Fig. 2. Experimental Set-Up with PIC 32 Embedded Platform and DELSYS® EMG System.

## V. RESULTS AND DISCUSSION

sEMG and the corresponding skeletal muscle force data is acquired from the microcontroller through UART channel 2 of the PIC32MX360F512L by a virtual com port via USB at 57600 baud rate. The data from the microcontroller is converted into uint16 data before it is transmitted through the UART. The PIC32 microcontroller is running at 80 million instructions per second (MIPS) with its phase lock loop (PLL) activated. It is running at an external clock frequency of 8 MHz with internal scaling enabled. Fig. 3 and 4 show the sEMG signal acquired by the proposed acquisition system using DE 2.1 electrodes. Fig. 5 and 6 show the sEMG signals acquired by the proposed acquisition system using DE 3.1 electrodes. These acquired signals are processed using the Half-Gaussian filter.

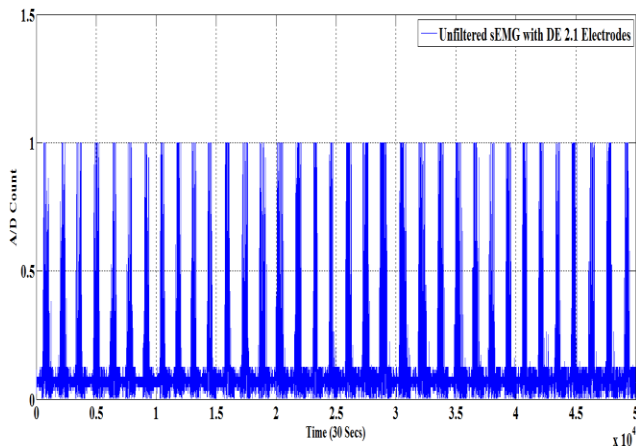


Fig. 3. Unfiltered sEMG Signal from the Proposed Acquisition System Using DE 2.1 Electrodes.

The following experiment is repeated several times to check the consistency and the accuracy of the proposed acquisition system. Fig. 7 and 8 show the validation for the proposed acquisition system for repeated experiments using DE 2.1 and DE 3.1 electrodes. It is evident from the Fig. 6 that the DE 3.1 electrodes are giving good results when compared to DE 2.1 results.

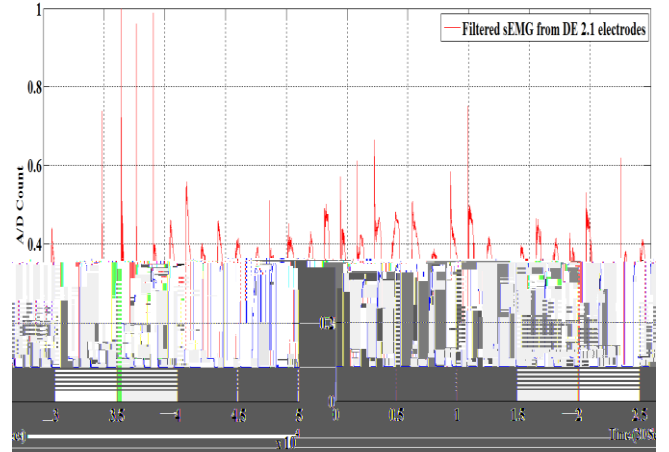


Fig. 4. Filtered sEMG Signal from the Proposed Acquisition System Using DE 2.1 Electrodes.

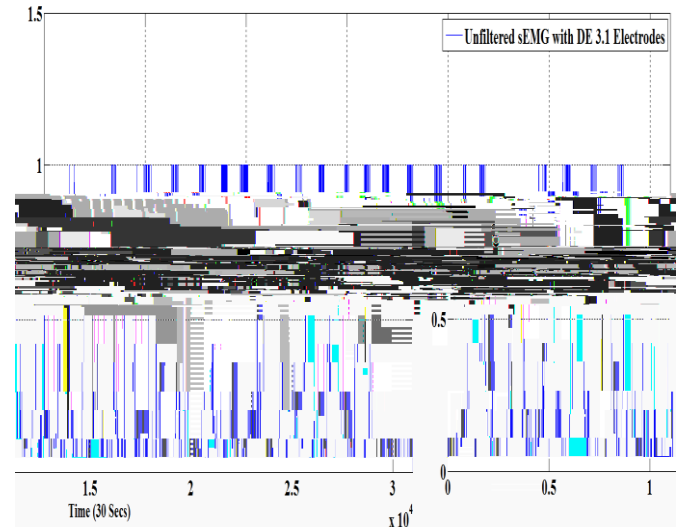


Fig. 5. Unfiltered sEMG Signal from the Proposed Acquisition System Using DE 3.1 Electrodes.

The sEMG signals acquired from the proposed acquisition system using DE 3.1 electrodes are in good correlation with the sEMG signals acquired from the standard acquisition system. The sEMG signals and the corresponding skeletal muscle force acquired from the standard acquisition system are given in Fig. 9 and 10. Since the sEMG is a random signal corrupted with noise it is hard to achieve the same correlation every time.

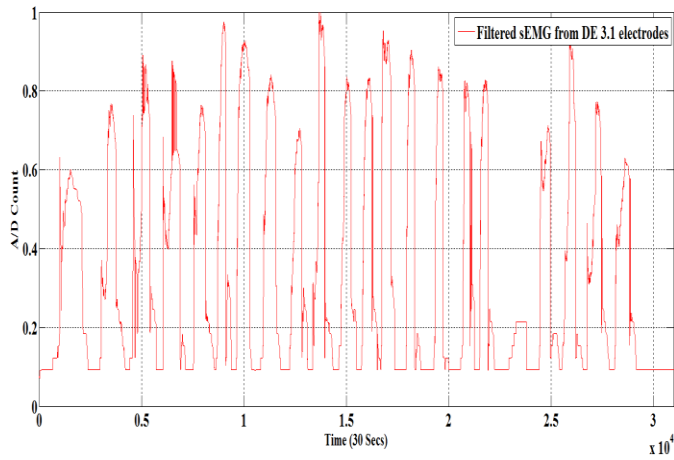


Fig. 6. Filtered sEMG Signal from the Proposed Acquisition System Using DE 3.1 Electrodes.

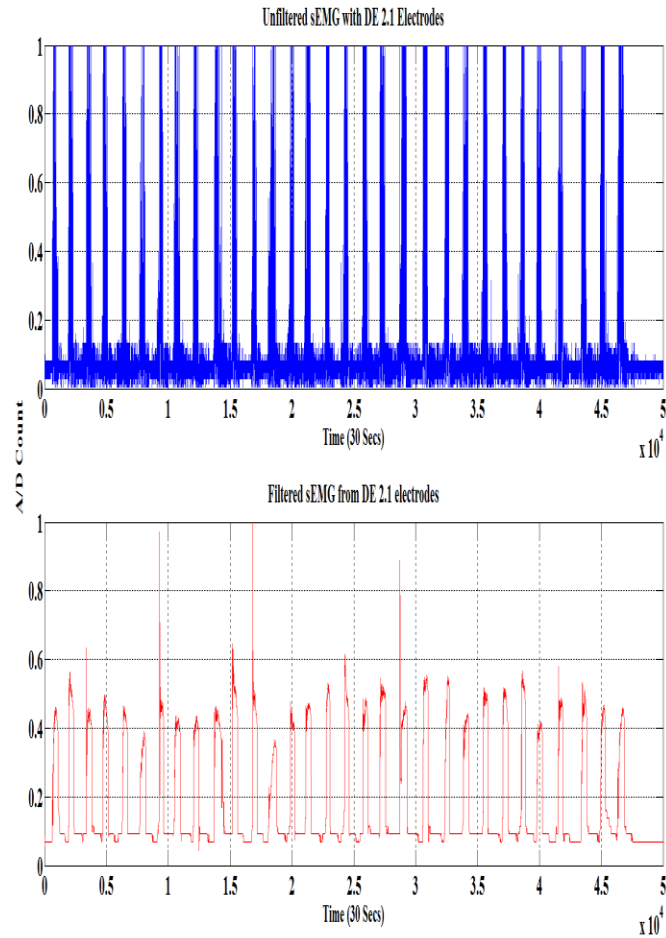


Fig. 7. sEMG Signal from the Proposed Acquisition System Using DE 2.1 Electrodes with Repeated Experiment.

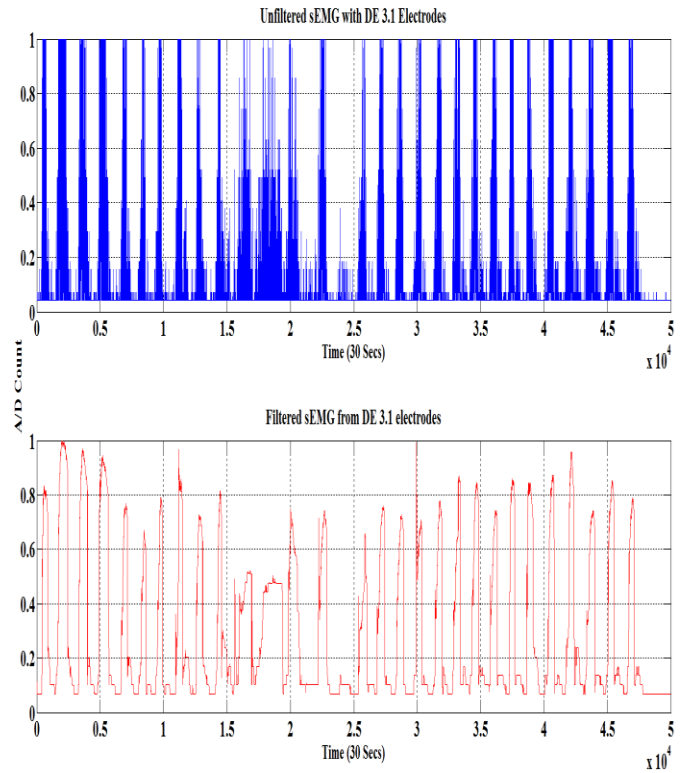


Fig. 8. sEMG Signal from the Proposed Acquisition System Using 3.1 Electrodes with Repeated Experiment.

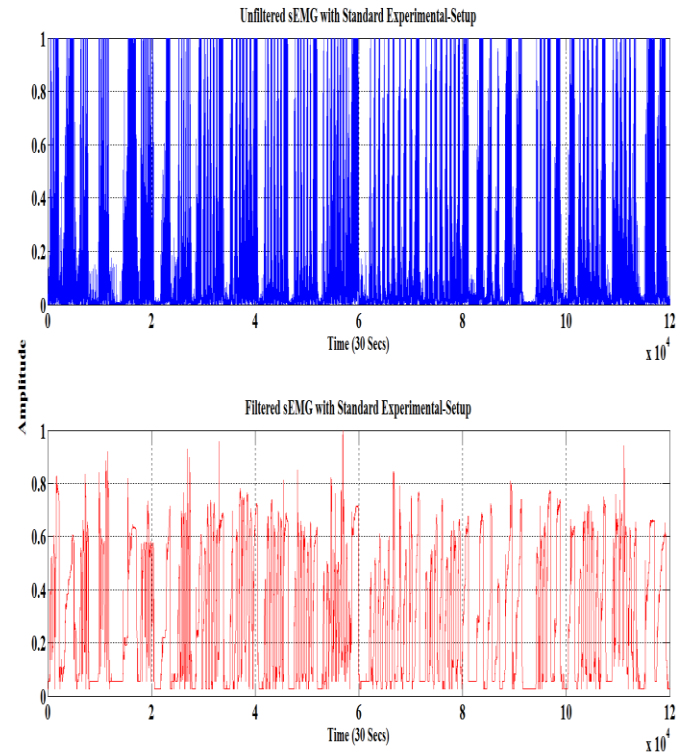


Fig. 9. sEMG Signal from the Standard Acquisition System.



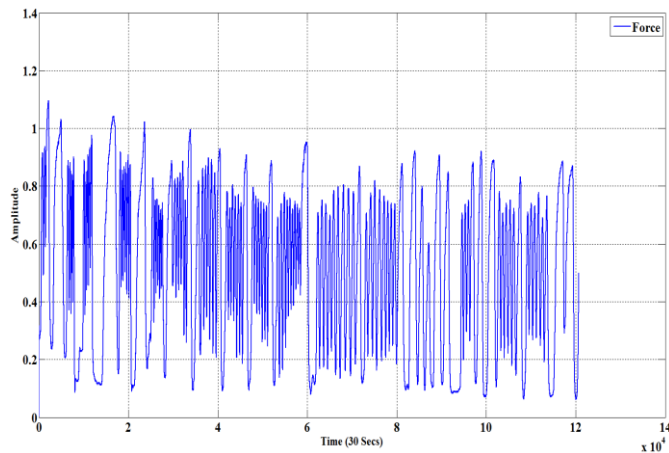


Fig. 10. Filtered Force Signal from the Standard Acquisition System.

## VI. CONCLUSION AND FUTURE WORK

A real-time sEMG acquisition system was designed for the control of the robotic hand prototype. The proposed design gives good performance when compared with the standard EMG acquisition system. Comparison between DE 2.1 and the DE 3.1 electrodes is done and the DE 3.1 electrodes are giving good results. This proposed acquisition system facilitates the transmission of the data from the microcontroller to the computer. This enables the user to compare the accuracy and performance of the acquisition system. Investigation was done on various other filters and finally Half-Gaussian filter with DE 3.1 electrodes is giving good results.

For future work we are planning to implement real time model-based force estimation and along with controller design for position and force control, based on this embedded platform [20, 21]. It will be interesting to acquire signals from the three sensors and then make a comparison between the standard and the proposed acquisition system. Finally, we plan to implement the Acquisition and control for a five fingered prototype.

## ACKNOWLEDGMENT

This research was sponsored by the US Department of the Army, under the award number W81XWH-10-1-0128 awarded and administered by the U.S. Army Medical Research Acquisition Activity, 820 Chandler Street, Fort Detrick MD 21702-5014. The information does not necessarily reflect the position or the policy of the Government, and no official endorsement should be inferred. For purposes of this article, information includes news releases, articles, manuscripts, brochures, advertisements, still and motion pictures, speeches, trade association proceedings, etc. Further, the technical help from Dr. D. Subbaram Naidu and Dr. Marco P. Schoen is greatly appreciated.

## REFERENCES

- [1] N. Dechev, W. L. Cleghorn, and S. Naumann, "Multiple finger, passive adaptive grasp prosthetic hand," *Mechanism and Machine Theory*, 36(2001), pp. 1157-1173.
- [2] H. Kawasaki, T. Komatsu, and K. Uchiyama, "Dexterous Anthropomorphic Robot Hand With Distributed Tactile Sensor: Gifu Hand II," *IEEE/ASME Transactions on Mechatronics*, Vol. 7, No. 3, September 2002, pp. 296-303.
- [3] M. Zecca, S. Micera, M. C. Carrozza, and P. Dario, "Control of Multifunctional Prosthetic Hands by Processing the Electromyographic Signal," *Critical Reviews™ in Biomedical Engineering*, 30(4-6), 2002, pp. 459-485.
- [4] C. Castellini and P. van der Smagt, "Surface EMG in advanced hand prosthetics," *Biological Cybernetics*, (2009) 100, pp. 35-47.
- [5] C. Potluri, P. Kumar, J. Molitor, M. Anugolu, A. Jensen, K. Hart, and S. Chiu, "Multi-Level Embedded Motor Control for Prosthesis," *International Conference on Embedded Systems and Applications, ESA'2010*, Las Vegas, Nevada, USA, July 12-15, 2010.
- [6] C. Potluri, P. Kumar, M. Anugolu, S. Chiu, A. Urfer, M. P. Schoen, and D. S. Naidu, "sEMG Based Fuzzy Control Strategy with ANFIS Path Planning For Prosthetic Hand," *3rd IEEE RAS & EMBS International Conference on Biomedical Robotics and Biomechatronics*, Tokyo, Sept 26-30, 2010.
- [7] C. Potluri, Y. Yihun, P. Kumar, J. Molitor, S. Chiu, D. S. Naidu, and S. H. Mousavinezhad, "sEMG Based Real-Time Embedded Force Control Strategy for a Prosthetic Hand Prototype" *IEEE International Conference on Electro/Information Technology*, Mankato, Minnesota, USA, May 15-17, 2011.
- [8] M. Anugolu, A. Sebastain, P. Kumar, M. P. Schoen, A. Urfer, and D. S. Naidu, "Surface EMG Array Sensor Based Model Fusion Using Bayesian Approaches for Prosthetic Hands," *2009 ASME Dynamic Systems and Control Conference*, Hollywood, California, USA, Oct. 12-14, 2009.
- [9] C. Potluri, P. Kumar, M. Anugolu, A. Urfer, S. Chiu, D. S. Naidu, and M. P. Schoen, "Frequency Domain Surface EMG Sensor Fusion for Estimating Finger Forces," *32nd Annual International Conference of the IEEE Engineering in Medicine and Biology Society*, Buenos Aires, Argentina, Aug. 31 - Sept. 4, 2010.
- [10] P. Kumar, A. Sebastian, C. Potluri, A. Urfer, D. S. Naidu, and M. P. Schoen, "Towards Smart Prosthetic Hand: Adaptive Probability Based Skeletal Muscle Fatigue Model," *32nd Annual International Conference of the IEEE Engineering in Medicine and Biology Society*, Buenos Aires, Argentina, Aug. 31 - Sept. 4, 2010.
- [11] P. Kumar, C. Potluri, A. Sebastian, S. Chiu, A. Urfer, D. S. Naidu, and M. P. Schoen, "An Adaptive Multi Sensor Data Fusion with Hybrid Nonlinear ARX and Wiener-Hammerstein Models for Skeletal Muscle Force Estimation," *The 14th World Scientific and Engineering Academy and Society (WSEAS) International Conference on Systems*, Corfu Island, Greece, July 22-24, 2010.
- [12] P. Kumar, C. Potluri, A. Sebastian, S. Chiu, A. Urfer, D. S. Naidu, and M. P. Schoen, "Adaptive Multi Sensor Based Nonlinear Identification of Skeletal Muscle Force," *WSEAS Transactions on Systems*, Issue 10, Volume 9, October 2010, pp. 1051-1062, 2010.
- [13] P. Kumar, C. Potluri, M. Anugolu, A. Sebastian, J. Creelman, A. Urfer, S. Chiu, D. S. Naidu, and M. P. Schoen, "A Hybrid Adaptive Data Fusion with Linear and Nonlinear Models for Skeletal Muscle Force Estimation," *5th Cairo International Conference on Biomedical Engineering*, Cairo, Egypt, Dec. 16-18, 2010.
- [14] P. Kumar, C. Potluri, A. Sebastian, Y. Yihun, A. Ilyas, M. Anugolu, R. Sharma, S. Chiu, J. Creelman, A. Urfer, D. S. Naidu, and M. P. Schoen, "A Hybrid Adaptive Multi Sensor Data Fusion for Estimation of Skeletal Muscle Force for Prosthetic Hand Control," *The 2011 International Conference on Artificial Intelligence, ICAI'11*, Las Vegas, Nevada, USA, July 18-21, 2011.
- [15] T. D. Sanger, "Bayesian Filtering of Myoelectric Signals," *J Neurophysiol*, 97, 2007, pp. 1839-1845.
- [16] M. B. I. Reaz, M. S. Hussain and F. Mohd-Yasin, "Techniques of EMG signal analysis: detection, processing, classification and applications," *Biol. Proced. Online*, 2006, 8(1), pp. 11-35.
- [17] E. Kral, L. Vasek, V. Dolinay, P. Varacha, "Usage of PSO Algorithm for Parameter Identification of District Heating Network Simulation Model," *The 14th World Scientific and Engineering Academy and Society (WSEAS) International Conference on Systems*, Corfu Island, Greece, July 22-24, 2010.

- [18] A. Neubaur, "The Intrinsic System Model of the Simple Genetic Algorithm with  $\alpha$ -Selection, Uniform Crossover and Bitwise Mutation," *The 14th World Scientific and Engineering Academy and Society (WSEAS) International Conference on Systems*, Corfu Island, Greece, July 22-24, 2010.
- [19] A. Sebastian, P. Kumar, M. P. Schoen, "A Study on Hybridization of Particle Swarm and Tabu Search Algorithm for Unconstraint Optimization and Estimation," in *The 14th World Scientific and Engineering Academy and Society (WSEAS) International Conference on Systems*, Corfu Island, Greece, July 22-24, 2010.
- [20] C. Potluri, Y. Yihun, M. Anugolu, P. Kumar, S. Chiu, M. P. Schoen, and D. S. Naidu, "Implementation of sEMG-Based Real-Time Embedded Adaptive Finger Force Control for a Prosthetic Hand", submitted to *IEEE CDC*, 2011.
- [21] C. Potluri, M. Anugolu, Y. Yihun, A. Jensen, S. Chiu, M. P. Schoen, and D. S. Naidu, "Optimal Tracking of a sEMG based Force Model for a Prosthetic Hand," submitted to *IEEE EMBS*, 2011.



# A sEMG-based Real-time Adaptive Joint angle Estimation and Control for a Prosthetic Hand Prototype

CHANDRASEKHAR POTLURI, MADHAVI ANUGOLU, STEVE CHIU, D. SUBBARAM  
NAIDU, MARCO P. SCHOEN

Measurement and Control Engineering Research Center, School of Engineering  
Idaho State University  
921 South 8th Avenue, Stop 8060, Pocatello, Idaho  
USA  
naiduds@isu.edu

**Abstract:** - This paper presents a novel approach of a surface electromyographic (sEMG)-based, real-time Model Reference Adaptive Control (MRAC) strategy for joint angle estimation and control of a prosthetic hand prototype. The proposed design is capable of decoding the pre-recorded sEMG signal as well as the sensory force feedback from the sensors to control the joint angle of the prosthetic hand prototype using a PIC 32MX360F512L microcontroller. The input sEMG signal is rectified, filtered using a Half-Gaussian filter and fed to a Kullback Information Criterion (KIC) based fusion algorithm, which give the overall estimated joint angle (position). This estimated angle is given as input to the prosthetic hand prototype. Then the MRAC along with a two stage proposed embedded design is used for the position control of the prosthetic hand. For the real-time operation, the measured angle data at the joint is fed back to the controller. The data is transmitted to the computer through a universal asynchronous receiver/transmitter (UART) interface of the proposed embedded design. The experimental results in real time show good performance in controlling the angle of the prosthetic hand prototype.

**Key-Words:** - Prosthetic Hand, sEMG, Data fusion, Kullback Information Criterion, MRAC, Angle control

## 1 Introduction

For 60 years, there has been active research going on in the area of Prostheses. Due to the unavailability of prosthetic devices with full human hand functionality at an affordable price, more than 30% of upper extremity amputees chose not to use a prosthetic device on regular basis [1, 2]. Besides that, most of the available prosthetic devices do not have tactile or proprioceptive feedback [3]. Previous researchers insisted that human-centered robots must be independent with a great functionality, comfort and ease of use [4]. In rehabilitation robotics, human-machine interface, which requires a natural means of communication, is an interesting domain [5]. The electromyographic (EMG) signal is the electric potential generated by muscles. There are two kinds of EMG signals: Intramuscular (needle) EMG and the Surface EMG (sEMG). Under the assumption that amputation is transradial and which does not require surgery, we relied on sEMG signals in this work whose amplitude ranges from -5 to +5 (mV). sEMG signals are acquired from the surface of the skin, as they penetrate through various tissue layers [6]. Thus, they tend to create cross-talk, interference and noise. The sEMG is a temporally and spatially composed signal [7].

Due to the complexity and nonlinearity of the human hand, the control of a multi-fingered prosthetic hand is a challenging task [8]. From the past research, it is clear that the most widespread approach for controlling the prosthetic hand is by using a position or force control [9]. The challenging task involved in this work is the prediction of the Proximal Inter Phalangeal (PIP) joint angle corresponding to the sEMG signal.

In this paper, we used a three-by-three array of sEMG sensors and a wheel potentiometer device to acquire the EMG signal and the corresponding PIP joint angle. The data from the array of sEMG sensors were fused using a probability based fusion algorithm in order to have a better estimate [10]. A real-time embedded MRAC control system with sensory feedback was implemented to accomplish the goal of this design. Considering the probability based fused joint angle estimate as input to the real-time control system, a two stage embedded platform with a simple MRAC strategy was chosen for the PIP joint angle control of the prosthetic hand prototype.

## 2 Experimental setup

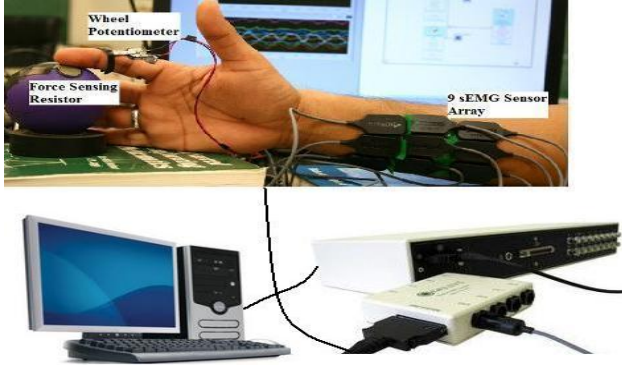


Fig.1: Experimental set-up.

Fig.1. illustrates the experimental design used in this work for capturing the sEMG signal and the corresponding joint angle of the PIP joint of the index finger. Prior to placing the sEMG sensors on the skin surface, the test subject was prepared according to ISEK standards [11]. The motor point was identified by using a wet probe muscle point stimulator (Richmar HV-1000). Nine DE-3.1 sEMG sensors of the DELSYS Bagnoli-16 EMG system were arranged on the skin surface in a three-by-three array. The middle row of sensors was placed on the motor point of the index finger. An angle measurement device was designed using a 10k-Ohm wheel potentiometer shown in Fig.1. It was used to measure the PIP joint angle. Force Sensitive Resistor (FSR) was mounted on the stress ball and was used to measure the force. All the data was acquired at a sampling rate of 2000 samples/sec.

## 3 Proposed Design

The objective of the proposed design is to track a joint angle of the prosthetic hand as closely as possible. Here, the joint angle signal is inferred from the sEMG signals obtained from the array of the sEMG sensors located at the arm.

Sensor fusion is done in the time domain for the sEMG data using a probability based Kullback information criterion (KIC) fusion algorithm. The data from the nine sensors were collected around the corresponding individual motor unit at the transradial arm location (flexor digitorum superficialis) and before fusing the sEMG signals are rectified and filtered using a Half -Gaussian filter, as given by (1).

$$p(EMG|x) = 2 \times \frac{\exp\left(-\frac{EMG^2}{2x^2}\right)}{\sqrt{2\pi x^2}}, \quad (1)$$

where  $p(EMG|x)$  is a conditional probability density function,  $x$  is a latent driving signal.

A System Identification (SI) tool was used to determine the dynamic relationship between the input-output data. The sEMG signal was used as input and the corresponding PIP joint angle as output. In particular, nonlinear Wiener Hammerstein one-dimensional polynomial models were obtained for the sEMG/joint angle data.

The mathematical representation of the modeling is given by,

$$w(t) = f(u(t)) \quad (2)$$

$$x(t) = \frac{B_{i,j}(q)}{F_{i,j}(q)} w(t - nk) + e(t) \quad (3)$$

$$y(t) = h(x(t)) \quad (4)$$

where  $u(t)$  is the sEMG signal and  $y(t)$  is the PIP joint angle.  $f$  and  $h$  are nonlinear functions,  $w(t)$  and  $x(t)$  are internal variables,  $B_{j,i}(q)$  and  $F_{j,i}(q)$  are polynomials,  $q$  is the back shift operator, and  $e(t)$  is the output error. From (3), the WH model structure utilizes a linear OE model, which is given by,

$$y(t) = \frac{b(q)}{F(q)} u(t - nk) + e(t) \quad (5)$$

where  $nk$  is the system delay and  $t$  is time index

The resulting nine WH models were fused together by using a probabilistic KIC algorithm [12]. It assigns a particular probability to each model [13]. The overall estimated model output and the individual models outputs were compared by using the Pearson's correlation coefficient.

From the previous research, it was shown that the KIC algorithm performs better than the other criteria [10, 12]. KIC is an asymmetric measure of the models' dissimilarity which can be obtained by the sum of the two directed divergences known as J-divergence or Kullback's symmetric [14]. It is given by

$$KIC(p_i) = \frac{n}{2} \log R_i + \frac{(p_i+1)n}{n-p_i-2} - n\psi\left(\frac{n-p_i}{2}\right) + g(n) \quad (6)$$

Where  $g(n) = n \log(n/2)$ ,  $\psi$  - digamma function.

The probability based fusion algorithm given by [12, 13] is applied to the nonlinear models obtained by using an SI technique with the following steps:

1: The WH models are obtained by considering the sEMG data  $u(t)$  as input and joint angle  $Y$  as output,

2: Calculate the residual square norm i.e.,  $R_i = Y - \Phi_i \hat{\theta}_i = \|Y - \hat{Y}\|$

where  $\hat{\theta}_i = \{\Phi_i^T \Phi_i\}^{-1} \Phi_i^T Y$ , and

$$\Phi = \begin{bmatrix} Y^T & u_{p-1}^T & Y_{p-1}^T & u_1^T \\ Y_{p+1}^T & u_{p+1}^T & Y_p^T & u_2^T \\ \dots & \dots & \dots & \dots \\ Y_{n-1}^T & u_{n-1}^T & Y_{n-2}^T & u_{n-p}^T \end{bmatrix}$$

3: Compute the model criteria coefficients using (6).

4: The model probability can be computed using

$$p(M_i(t) | Z) = \frac{e^{-l_i}}{\sum_{j=1}^k e^{-l_j}}$$

5: The fused model output can be calculated using

$$\hat{Y}_f = \sum_{i=1}^k p(M_i(t) | Z) \hat{Y}_i.$$

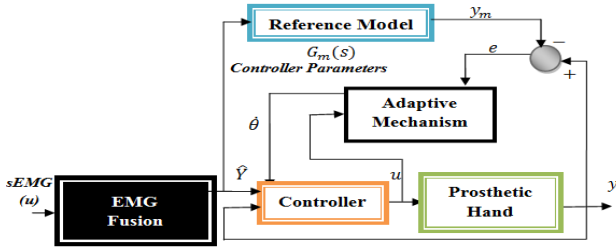


Fig.2: Block diagram representation of Model Reference Adaptive Controller (MRAC)

A simple MRAC based scheme (Fig. 2) is utilized for compensating the dynamics of the prosthetic hand. During the development of the artificial hand, changes were being undertaken to the mechanical design and drive trains of the hand that affect the dynamics of the finger motion of the prosthesis. In addition, the uncertain characteristics of the kinematic and actuator interaction could have led to a different performance than expected. Therefore, a simple MRAC controller was developed in order to maintain some performance stability. For updating the controller parameter  $\theta$ , the MIT rule was used.

$$\frac{d\theta}{dt} = -\gamma e Y_m. \quad (7)$$

According to the MIT rule [15], the gain parameter  $\gamma$  was selected to achieve the desired performance. In this work  $\gamma$  was taken as 3.0 and

the error  $e = Y - Y_m$  was calculated by the difference of the model reference output  $Y_m$  and the actual output (joint angle generated by the prosthetic hand). Different MRAC stability issues were addressed in [14, 15].

#### Reference Model Derivation

The dynamic equations of motion for the hand are obtained from the Lagrangian approach as [16]

$$\dot{x}(t) = \begin{bmatrix} 0 & I \end{bmatrix} x(t) + \begin{bmatrix} 0 \\ I \end{bmatrix} u(t). \quad (8)$$

The control input vector  $u(t)$  was given by

$$u(t) = -M^{-1}(q(t)) [N(q(t), \dot{q}(t)) - \tau(t)]. \quad (9)$$

As the prosthetic hand is required to track the desired angle profile  $q_d(t)$  described under the reference angle model, the tracking error  $e(t)$  is defined as

$$e(t) = q_d(t) - q(t). \quad (10)$$

Here,  $q_d(t)$  is the desired angle vector of the joints and can be obtained by the reference angle model [17];  $q(t)$  is the actual angle vector of the joints. Differentiating (10) twice, we get,

$$\dot{e}(t) = \dot{q}_d(t) - \dot{q}(t), \quad \ddot{e}(t) = \ddot{q}_d(t) - \ddot{q}(t). \quad (11)$$

Substituting  $\dot{q}(t)$  into (11) gives

$$\ddot{e}(t) = \ddot{q}_d(t) + M^{-1}(q(t)) [N(q(t), \dot{q}(t)) - \tau(t)] \quad (12)$$

From (12) the control function  $u(t)$  can be defined as

$$u(t) = \ddot{q}_d(t) + M^{-1}(q(t)) [N(q(t), \dot{q}(t)) - \tau(t)]. \quad (13)$$

This is often called the feedback linearization control law, rewriting (13) as,

$$\tau(t) = M(q(t)) [\ddot{q}_d(t) - u(t) + N(q(t), \dot{q}(t))] \quad (14)$$

Using (11) and (13), the state vector  $x(t) = [e'(t) \dot{e}(t)]'$ , the state-space model can be represented as

$$\dot{x}(t) = \begin{bmatrix} 0 & 1 \\ 0 & 0 \end{bmatrix} x(t) + \begin{bmatrix} 0 \\ 1 \end{bmatrix} u(t). \quad (15)$$

Now, (15) is in the form of a linear system such as

$$\dot{x}(t) = Ax(t) + Bu(t). \quad (16)$$

#### Implementation:

The proposed control design was implemented on a PIC 32MX360F512L microcontroller in two stages: “Signal Processing” and “Motor Actuation”. The Signal Processing stage enables the execution and implementation of real-time control strategies. A dsPIC block set was used to generate the C code for the PIC 32 from Simulink®. The dsPIC block set generates a .hex file, and this file was imported in MPLAB® to program the PIC 32.

#### Signal Processing Stage:

From the many modules available on PIC 32, the following four modules were utilized for the implementation of the signal processing stage: Analog Input Module, Digital Output module, Output Compare module, and URAT module.

The sensory feedback joint angle data from the wheel potentiometer was acquired through the Analog Input module. Based on the selected control strategy for the motor actuation stage, the digital control signals were generated by the Digital Output module of the PIC 32. The changes in the reference/command signal were detected by this module. A pulse width modulated (PWM) wave with a specific duty cycle was generated by the Output Compare module based on the error. The angle data from the microcontroller to the PC was transmitted by the UART module via serial communication. In this particular design, the data was fed to the computer by a virtual com port via USB cable. The signals from the ports were read by MATLAB®.

#### Motor Actuation Stage:

In this stage, the motor was actuated with a SN754410 quadruple half-H driver [18] with the corresponding control signal. This proposed design was tested on the index finger of a prosthetic hand prototype. Fig. 3 shows the test bed for the proposed design.

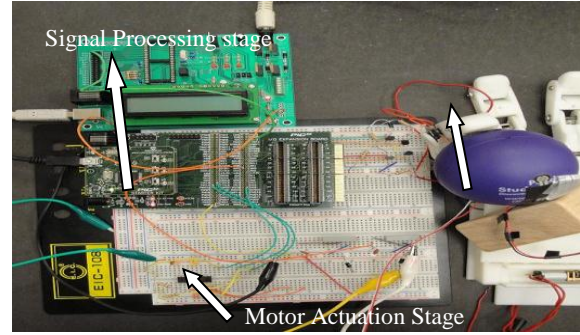


Fig. 3. Embedded Test bed for the proposed design

#### Mechanical structure of the robotic hand prototype:

The prosthetic hand prototype finger has three degrees of freedom stimulated by two Pololu 35:1 mini metal gear motors. Biologically inspired parallel actuation is the main characteristic of this robotic hand prototype. It is based on the behaviour/strength space of the Flexor Digitorum Profundus (FDP) and the Flexor Digitorum Superficialis (FDS) muscles [19]. Using a belt transmission system, the DC motor in the metacarpal phalange of the finger triggers the Proximal Inter Phalangeal (PIP) joint. It also drives the DIP (Distal Inter Phalangeal) joint. The Meta Carpo Phalangeal (MCP) joint is actuated by the DC motor located at the base of the finger as shown in Fig. 4.

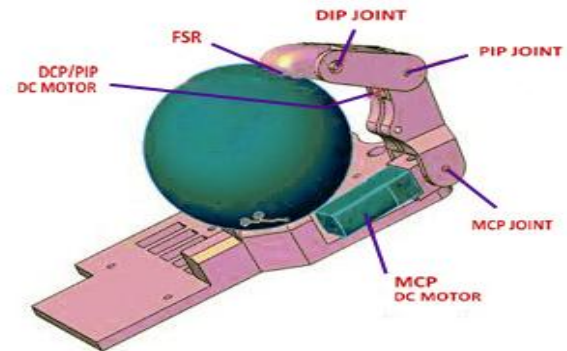


Fig. 4. Finger Actuation Scheme

## 4 Results and Discussion

Data was acquired from the microcontroller through UART channel2 of the PIC 32 micro controller by a virtual com port via USB at a 57600 baud rate. The data from the microcontroller was converted into unit16 data type before it is transmitted through the UART. It ran at an external clock frequency of 8MHz with internal scaling enabled. Fig. 5 depicts the experimental results of the proposed design. The actual angle output from the position sensor (i.e.Y)



closely follows the fusion algorithm estimated angle  $\hat{Y}$ . Fig. 6 shows the fusion estimated angle profile  $\hat{Y}$  and actual angle from the position sensor ( $Y$ ) plotted for a separate experiment. Fig. 7 shows the repeated experimental results. The proposed control strategy was tracking angle profile and matching the actual angle profile with the model estimated angle ( $\hat{Y}$ ).

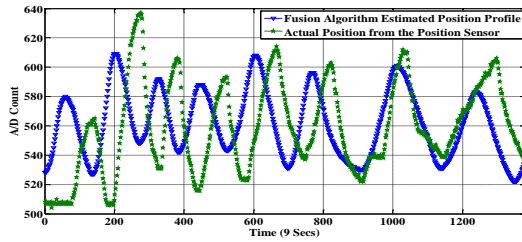


Fig. 5. Fusion based angle estimate and actual angle from angle sensor during the grasp action.

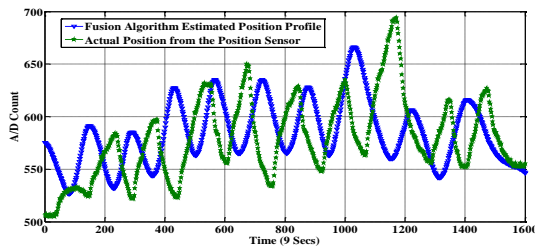


Fig. 6. Fusion based angle estimate and actual angle from angle sensor during the grasp action (for experiment-2).

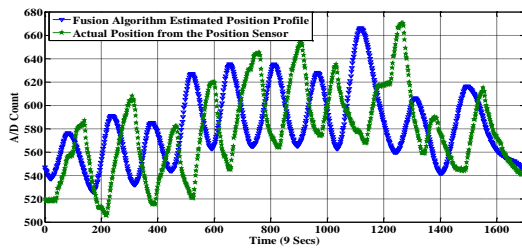


Fig. 7. Fusion based angle estimate and actual angle from angle sensor during the grasp action (for experiment-3).

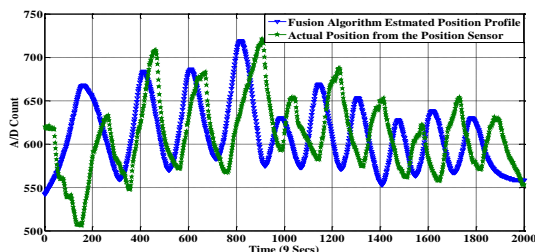


Fig. 8. Validation Plot.

While conducting the experiments, the following observations were made. The DC motors currently employed have the primary task of moving the prosthetic fingers. As the project is on-going, the Shape Memory Alloy (SMA) actuation scheme has

not yet been implemented because of the slow response of the SMA's, and also because SMA's have a long relaxation time. Therefore it is difficult to track a randomly changing angle profile with a slowly responding actuation system. However, as the prosthetic hand prototype is designed to use the parallel actuation of these DC motors and SMA's, the DC motors alone cannot produce a fusion algorithm estimated angle profile.

In this work, the DC motors are solely responsible for motion actuation. Since the DC motors have small gear heads, the usual characteristic of gear driver actuation cores occurs: gear backlash. In addition, the DC motors employed were slow in responding to the changes in the force profile. Hence some gaps and delay were observed in the measured angle signal. However, the profile of the measured angle from the angle sensor has a similar pattern as the fusion algorithm estimated angle ( $\hat{Y}$ ). Thus we can conclude that apart from those mechanical transmission problems, the implemented control scheme produced promising results. These problems will be considered in a new prototype design that we are currently developing.

From the results, it is also evident from Figs. 5, 6 and 7 that the controller is tracking the slow changes in the angle profile very well, where as a small delay was observed while tracking the angle profile. In order to test the precision of the proposed control strategy, 15 different experiments were conducted. The mean of the Pearson's correlation coefficient for the fusion algorithm estimated angle ( $\hat{Y}$ ) and the actual angle from the angle sensor ( $Y$ ) in all the 15 experiments is 0.86. Because of the above mentioned transmission problems and the slow response of the gears, slight variability is observed in the correlation coefficients for the 15 experiments. Hence the difference in tracking the angle profile is observed in Figs. 6 and 7. Fig. 8 depicts the validation plot with a different fusion algorithm angle estimate  $\hat{Y}$  obtained by feeding a different sEMG.

## 5. Conclusion and Future Work

In this paper, based on sEMG signals, we proposed a two-stage real-time embedded MRAC strategy for a prosthetic hand prototype. The proposed design was based on tracking a reference angle profile and it gives good performance when tested on a prosthetic hand prototype. This design enables the transmission of the data from the microcontroller to the

computer. This design allows the control engineer to increase the accuracy and performance of the design by implementing various novel control strategies and also enables fast trouble shooting.

For future work, we are planning to use the above mentioned embedded platform to implement online model-based skeletal muscle angle estimation along with controller designs that address the above listed mechanical shortcomings. It will be valuable to acquire the sEMG signal directly from the arm of a healthy subject and transmit to our embedded system rather than using pre-recorded sEMG signals, which will be investigated as well in the future.

### ACKNOWLEDGMENT

This research was sponsored by the US Department of the Army, under the award number W81XWH-10-1-0128 awarded and administered by the U.S. Army Medical Research Acquisition Activity, 820 Chandler Street, Fort Detrick MD 21702-5014. The information does not necessarily reflect the position or the policy of the Government, and no official endorsement should be inferred. For purposes of this article, information includes news releases, articles, manuscripts, brochures, advertisements, still and motion pictures, speeches, trade association proceedings, etc. Further, the technical help from Dr. Alba Perez and Mr. Alex Jensen is greatly appreciated.

### References:

- [1] <http://www.columbiainmissourian.com/stories/2009/02/15/soldier-who-lost-leg-iraq-may-loseother/>
- [2] D.J. Atkins, D.C. Y. Heard, and W.H. Donovan, "Epidemiologic overview of individuals with upper-limb loss and their reported research priorities", *Journal of Prosthetics and Orthotics*, Vol. 8, NO. 1, 1996, pp- 2-11.
- [3] D.S. Naidu and C.-H. Chen, "Control Strategies for Smart Prosthetic Hand Technology: An Overview", Book Chapter 12, , Distributed Diagnosis and Home Healthcare (D2H2): Volume 2, American Scientific Publishers, CA, January 2011.
- [4] Bien ZZ, and Stefanov D, "Advances in rehabilitation robotics: Human-friendly technologies on movement assistance and restoration for people with disabilities," *Springer, Berlin (Germany)*. 2004.
- [5] Heinzmann J, and Zelinsky J, "A safe-control paradigm for human-robot interaction," *J Intell Robot Syst.* 1999; 25(4): pp. 295-310.
- [6] Cram, J.R., Kasman G.S., and Holtz J. "Introduction to Surface Electromyography," Aspen Publisher Inc., Gaithersburg, Maryland, 1998.
- [7] Kandel E.R. and Scharzt J.H., "*Principles of Neural Science*," Elsevier/North-Holland, New York, 1981.
- [8] T. H. Sueeter, "Control of the Utah/MIT Dextrous hand: Hardware and software hierarchy," *J. Robot. Syst.*, vol. 7, no. 5, pp. 759-790, 1990.
- [9] M. H. Raibert and J. J. Craig, "Hybrid angle and force control of manipulators," *ASME J. Llyn. Syst. Meas. Contr.*, vol. 102, pp. 126-133, June 1981
- [10] Anugolu M., Sebastian A., Kumar P., Schoen M., Urfer A., Naidu D.S., "Surface EMG array sensor based model fusion using Bayesian approaches for Prosthetic Hand", *Proceeding of the Dynamic Systems and Control Conference*, Hollywood , Ca, October 2009.
- [11] <http://www.isel.online.org/standardsemg.html>.
- [12] Chen H., Huang S., "A Comparative study on Model Selection and Multiple Model Fusion", *7<sup>th</sup> International Conference on Information Fusion*, 2005, PP.820-826.
- [13] Seghouane A.K, Bekara M., Fluery G., " A small Sample Model Selection Criterion based on Kullback's Symmetric Divergence", *IEEE Transaction*, 2003, pp. 145-148.
- [14] Karl J. Astrom and Bjorn Wittenmark "*Adaptive Control Second Edition*", Dover Publications, Dec 18, 2008.
- [15] Potluri C., Anugolu M., Yihun Y., Kumar P., Chiu S., Schoen M., Naidu D.S., " Implementation of sEMG-based Real-time Embedded Adaptive Finger Force Control for a Prosthetic Hand", *IEEE Conference on Decision and Control and European Control Conference*, Orlando, Florida, USA, Dec 12-15, 2011.
- [16] Potluri C., Anugolu M., Yihun Y., Jensen A., Chiu S., Schoen M., Naidu D.S., " Optimal Tracking of a sEMG based Force Model for a Prosthetic Hand", *33<sup>rd</sup> Annual International Conference of the IEEE Engineering and Medicine and Biology Society*, Boston, Ma, USA, Aug 31-Sep 3, 2011.
- [17] F.L.Lewis, D.M.Dawson, and C.T. Abdallah, "*Robot Manipulators Control: Second Edition, Revised and Expanded*", New York, NY: Marcel Dekker, Inc., 2004.
- [18] Texas Instruments "SN754410 quadruple half H-driver data sheet" Dallas, Texas, November 1986 and 1995
- [19] Dr. Anthony L. Crawford,"Design of a Robotic Hand and Simple EMG Input Controller with a Biologically-Inspired Parallel Actuation System for Prosthetic Application" ASME 2010, IDETC/CIE 2010.

# Optimal Tracking of a sEMG based Force Model for a Prosthetic Hand

Chandrasekhar Potluri, Madhavi Anugolu, YimeskerYihun, Alex Jensen, Steve Chiu *Member, IEEE*, Marco P. Schoen, *Senior Member, IEEE*, and D. Subbaram Naidu, *Fellow, IEEE*.

**Abstract:** This paper presents a surface electromyographic (sEMG)-based, optimal control strategy for a prosthetic hand. System Identification (SI) is used to obtain the dynamic relation between the sEMG and the force. The input sEMG signal is preprocessed using a Half-Gaussian filter and fed to a fusion-based Multiple Input Single Output (MISO) skeletal muscle force model. This MISO system model provides the estimated finger forces to be produced as input to the prosthetic hand. Optimal tracking method has been applied to track the estimated force profile of the Fusion based sEMG-force model. The simulation results show good agreement between reference force profile and the actual force.

## I. INTRODUCTION

Currently there are more than 2 million Americans that have a missing limb. The number of Americans with missing limbs increases 185,000 people a year [1]. As a result of this rising number of people that need prostheses, research is being focused on creating more intuitive prosthetics. There has been active research to design a prosthetic hand. But even today there is no prosthetic hand at an affordable cost with position and tactile force control [2]. It is evident from the past research that the human-centered robotics should be autonomous with a high level of functionality, comfort and ease of use [3]. A natural means of communication is required for human-centered robotics [4], and in the case of electromyographic (EMG) based prostheses, one natural means of interface between the human arm and prosthesis is the surface EMG (sEMG) itself. The EMG signal is present because of the neuromuscular activity in the body. The sEMG signals are captured noninvasively and give access to physiological processes responsible for the contraction of muscles. Since the sEMG signal is amplitude modulated and time dependent, and dynamic in nature, spatially and

temporally frequency encoded [5]. Usually sEMG measurements are based on single sensor data. For this work we used an array of three sEMG sensors and a force sensing resistor (FSR) to acquire the EMG signal and the corresponding skeletal muscle force. The data from the three sEMG sensors is fused using a fusion algorithm to have a better estimation of skeletal muscle force from the corresponding sEMG signal when compared to single sensor data [6].

This paper uses the sEMG-force fusion model as reference profile. A Linear Quadratic Tracking (LQT) technique is employed to the prosthetic hand to track the force profile. This paper is structured as follows. The experimental set up is given in Section II, Section III provides reference force model and Section V provides dynamics of the hand. Section VI details the results and discussion and in the last section some conclusions are provided.

## II. EXPERIMENTAL SET-UP

Experiments were conducted on a right-handed healthy male subject. Using a muscle simulator (Rich-Mar Corporation HV 1100), motor units were marked and sEMG sensors were placed accordingly [6]. One sEMG sensor was placed on the motor point of the subject's ring finger and two sensors were placed at points adjacent to it. Prior to placing the sEMG sensors, the skin surface of the subject was prepared according to International Society of Electrophysiology and Kinesiology (ISEK) protocols [7]. Both sEMG and muscle force signals were acquired simultaneously using LabVIEW™ 8.2 at a sampling rate of 2000 Hz. The sEMG data was captured by a DELSYS® Bagnoli-16 EMG system with DE-2.1 differential EMG sensors. The force information was collected by a NI ELVIS with an Interlink Electronics FSR 0.5" circular force sensor.

## III. REFERENCE FORCE MODEL

In this present work the force signal is extracted from the sEMG signals obtained from the array of the three sEMG sensors located on the arm. The data from the three sensors is collected around the corresponding individual motor unit location at the transradial arm location (flexor digitorum superficialis) and is rectified and filtered using a Half-Gaussian filter given by

$$p(EMG|x) = 2 \times \frac{\exp\left(-\frac{EMG^2}{2x^2}\right)}{\sqrt{2\pi x^2}}, \quad (1)$$

Chandrasekhar Potluri is with Measurement and Control Engineering Research Center (MCERC), College of Engineering, Idaho State University, Pocatello, Idaho 83209, USA (e-mail: potlchan@isu.edu).

Madhavi Anugolu is with MCERC, College of Engineering, Idaho State University, Pocatello, Idaho 83209, USA (email: anugmadh@isu.edu).

YimeskerYihun is with MCERC, College of Engineering, Idaho State University, Pocatello, Idaho 83209, USA (email: yihuyime@isu.edu).

Alex Jensen is with MCERC; is with MCERC, College of Engineering, Idaho State University, Pocatello, Idaho 83209, USA (email: jensalex@isu.edu).

Steve Chiu is with Department of Electrical Engineering and Computer Science, MCERC, Idaho State University, Pocatello, Idaho 83209 USA (email: chiustev@isu.edu).

Marco P. Schoen is with Department of Mechanical Engineering, MCERC, Idaho State University, Pocatello, Idaho 83209, USA (email: schomarc@isu.edu).

D. Subbaram Naidu is with Department of Electrical Engineering and Computer Science, MCERC, Idaho State University, Pocatello, Idaho 83209 USA (email: naiduds@isu.edu).

where  $p(EMG|x)$  is a conditional probability density function,  $x$  is a latent driving signal.

The preprocessed sEMG data from the three sensors is fused using a sensor fusion algorithm to facilitate the extraction of the best finger force estimates. Sensor fusion is accomplished in the frequency domain using a simple elitism based Genetic Algorithm (GA). The SI method is used to identify the dynamical relationship between the sEMG data from the three sensors and the corresponding finger force. In this fusion algorithm, Output Error (OE) models are used to achieve the SI. The OE models are constructed for each individual data set. The OE model structure is given as follows.

$$y(t) = \frac{B(q)}{F(q)}u(t - nk) + e(t), \quad (2)$$

Where  $B$ , and  $F$  are the polynomials,  $q$  is shift operator,  $e(t)$  is output error,  $y(t)$  is system output,  $u$  is input,  $nk$  is the system delay and  $t$  is time index.

Using the three resulting OE models and the fusion algorithm given by [6], a corresponding continuous-time model is constructed as given by the transfer function as

$$G(s) = \frac{B(s)}{F(s)} = \frac{b_{nb}s^{(nb-1)}b_{nb-1}s^{(nb-2)}+\dots+b_1}{s^{nf}+f_{nf}s^{nf-1}+\dots+f_1}, \quad (3)$$

Similar to the discrete-time case,  $nb$  and  $nf$  determine the orders of the numerator and denominator. For multi-input systems,  $nb$  and  $nf$  are row vectors.  $b, f$  are the coefficients of the numerator and denominator polynomials respectively.

A MISO transfer function is constructed based on the poles of three individual OE models corresponding to each sensor. GA is used to find the corresponding zeros. The search area is limited to the unit circle, because a discrete time model is used (and the resulting MISO model is decreased to minimum phase). The number of zeros is at most the number of poles. The number of potential zeros is set to the order of the corresponding denominator. The error squared of the resulting MISO system  $H(s)$  (see Appendix) and the recorded force signal is set as an objective function. The objective function  $f$  is constructed as follows,

$$f = \int_{t_0}^{t_f} (\hat{Y}(t) - Y(t))^2 dt = \int_{t_0}^{t_f} \phi^2(t) dt, \quad (3)$$

where  $t_0$  and  $t_f$  are the initial and final time values,  $\hat{Y}(t)$  is the fusion model estimated force and  $Y(t)$  is the actual force from the FSR.

The MISO system  $H(s)$  is constructed as follows,

$$H(s) = \begin{pmatrix} \frac{Z_{1,1}s^n + Z_{1,2}s^{n-1} + \dots + Z_{1,n+1}}{P_{1,1}s^n + P_{1,2}s^{n-1} + \dots + P_{1,n+1}} \\ \frac{Z_{2,1}s^n + Z_{2,2}s^{n-1} + \dots + Z_{2,n+1}}{P_{2,1}s^n + P_{2,2}s^{n-1} + \dots + P_{2,n+1}} \\ \frac{Z_{3,1}s^n + Z_{3,2}s^{n-1} + \dots + Z_{3,n+1}}{P_{3,1}s^n + P_{3,2}s^{n-1} + \dots + P_{3,n+1}} \end{pmatrix}, \quad (4)$$

where  $Z$ 's and  $P$ 's are the zeros and poles respectively of the individual transfer function and  $n$  is the order of the system.

Feeding the new data sets to the MISO transfer function ( $H(s)$ ) (See Appendix) results in an estimated fusion based force  $\hat{Y}$ .

#### IV. DYNAMICS OF PROSTHETIC HAND

The dynamic equations of motion for the hand are obtained from the Lagrangian approach as [8,9,10,11,12, 13]

$$\frac{d}{dt} \left( \frac{\partial \mathcal{L}}{\partial \dot{q}} \right) - \frac{\partial \mathcal{L}}{\partial q} = \tau, \quad (5)$$

Where  $\dot{q}$  and  $q$  represent the angular velocity and angle vectors of joints respectively;  $\mathcal{L}$  is the Lagrangian;  $\tau$  is the given torque vector at joints. The Lagrangian  $\mathcal{L}$  is given as

$$\mathcal{L} = T - V, \quad (6)$$

Where  $T$  and  $V$  are denoted as kinetic and potential energies respectively. Substituting (6) into (5), we get the following dynamic equations

$$M(q)\ddot{q} + C(q, \dot{q}) + G(q) = \tau, \quad (7)$$

Where  $M(q)$  describes the inertia matrix;  $C(q, \dot{q})$  is the coriolis/centripetal vector and  $G(q)$  is the gravity vector. (7) can be written as

$$M(q)\ddot{q} + N(q, \dot{q}) = \tau, \quad (8)$$

where  $N(q, \dot{q}) = C(q, \dot{q}) + G(q)$  represents nonlinear terms.

Feedback linearization technique is used to convert the nonlinear dynamics represented by (8) into a linear state-variable system [8]. In order to obtain the alternative state-space equations of the dynamics, the position/velocity state  $x(t)$  of the joint is defined as

$$x(t) = [q'(t) \ \dot{q}'(t)]', \quad (9)$$

and rewriting (8) as

$$\frac{d}{dt} \dot{q}(t) = -M^{-1}(q(t)) [N(q(t), \dot{q}(t)) - \tau(t)] \quad (10)$$

Therefore, from (9) and (10), a linear system in Brunovsky canonical form is obtained and represented as

$$\dot{x}(t) = \begin{bmatrix} 0 & I \\ 0 & 0 \end{bmatrix} x(t) + \begin{bmatrix} 0 \\ I \end{bmatrix} u(t). \quad (11)$$

The control input vector  $u(t)$  given by

$$u(t) = -M^{-1}(q(t)) [N(q(t), \dot{q}(t)) - \tau(t)]. \quad (12)$$

As the prosthetic hand is required to track the desired force profile  $q_d(t)$  described under the reference force model, the tracking error  $e(t)$  is defined as



$$e(t) = q_d(t) - q(t). \quad (13)$$

Here,  $q_d(t)$  is the desired angle vector of the joints and can be obtained by the reference force model [6];  $q(t)$  is the actual angle vector of the joints. Differentiating (13) twice, we get,

$$\dot{e}(t) = \dot{q}_d(t) - \dot{q}(t), \quad \ddot{e}(t) = \ddot{q}_d(t) - \ddot{q}(t). \quad (14)$$

Substituting (10) into (14) gives

$$\ddot{e}(t) = \ddot{q}_d(t) + M^{-1}(q(t))[N(q(t), \dot{q}(t)) - \tau(t)] \quad (15)$$

From (15) the control function  $u(t)$  can be defined as

$$u(t) = \ddot{q}_d(t) + M^{-1}(q(t))[N(q(t), \dot{q}(t)) - \tau(t)]. \quad (16)$$

This is often called the feedback linearization control law, rewriting (16) as,

$$\tau(t) = M(q(t))[\ddot{q}_d(t) - u(t) + N(q(t), \dot{q}(t))]. \quad (17)$$

Using (14) and (16), the state vector  $x(t) = [e'(t) \dot{e}'(t)]'$ , the state-space model can be represented as

$$\dot{x}(t) = \begin{bmatrix} 0 & I \\ 0 & 0 \end{bmatrix} x(t) + \begin{bmatrix} 0 \\ I \end{bmatrix} u(t). \quad (18)$$

Now, (18) is in the form of a linear system such as

$$\dot{x}(t) = Ax(t) + Bu(t). \quad (19)$$

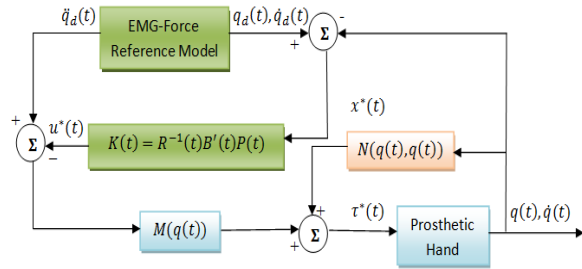


Fig. 1. Block Diagram of Optimal Controller for Prosthetic Hand.

### OPTIMAL TRACKING

Figure 1 shows the block diagram representation of the finite-time linear quadratic optimal controller for the prosthetic hand. The objective of the controller is for the prosthetic hand finger to track optimally the force model.

For the linear system (19), the finite-time linear quadratic optimal control problem can be formulated by defining the performance index  $J$  [14] as

$$J = \frac{1}{2} \int_{t_0}^{t_f} [x'(t) Q(t) x(t) + u'(t) R(t) u(t)] dt \quad (20)$$

where  $Q(t)$  is the error weighted matrix; and  $R(t)$  is the control weighted matrix. The optimal control  $u^*(t)$  is

described by

$$u^*(t) = -R^{-1}(t)B'P(t)x^*(t) = -K(t)x^*(t). \quad (21)$$

where  $K(t) = -R^{-1}(t)B'P(t)$  is called Kalman gain and  $P(t)$ , is the solution of the matrix differential Riccati equation (DRE)

$$\dot{P}(t) = -P(t)A - A'P(t) - Q(t) + P(t)BR^{-1}(t)B'P(t) \quad (22)$$

Satisfying the final condition

$$P(t = t_f) = 0. \quad (23)$$

Hence the optimal state  $x^*$  is the solution of

$$\dot{x}^*(t) = [A - BR^{-1}(t)B'P(t)]x^*(t). \quad (24)$$

Therefore, with the optimal control  $u^*(t)$ , the required torque  $\tau^*(t)$  can be calculated by

$$\tau^*(t) = M(q(t))(\ddot{q}_d(t) - u^*(t)) + N(q(t), \dot{q}(t)). \quad (25)$$

The torque  $\tau^*(t)$  is converted into force by

$$F_o(t) = \tau^*(t)/L, \quad (26)$$

Where  $F_o(t)$  is the force and  $L$  is the length of the finger.

## VI. RESULTS AND DISCUSSION

Figure 2 shows the fusion model force  $\hat{Y}(t)$  and the force output from the controller  $F_o(t)$ . It is evident that the optimal controller can track the changes in the force profile and follow the trends in reference force profile.

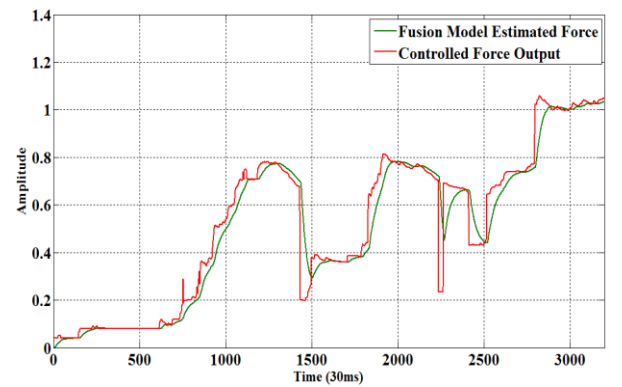


Fig. 2. Fusion Reference Model Force and Actual Force

Figure 3 shows the error between the model force  $\hat{Y}(t)$  and the force output from the controller  $F_o(t)$  for two different sets of results shown in Figs. 2 and 4. This figure shows that the error converged to zero in a very short time and the error is hovering between zero throughout the time interval. In some instances the force output of the controller  $F_o(t)$  cannot track the rapidly changing reference force profile during short intervals. The Pearson correlation coefficient (see Appendix) for the reference

$\hat{Y}(t)$  and controller output force  $F_o(t)$  profile is 0.8714. Figure 4 shows the validation with a different reference force  $\hat{Y}(t)$  profile and it yields 0.8707 correlation, thus showing good agreement between the reference model force and the actual force.

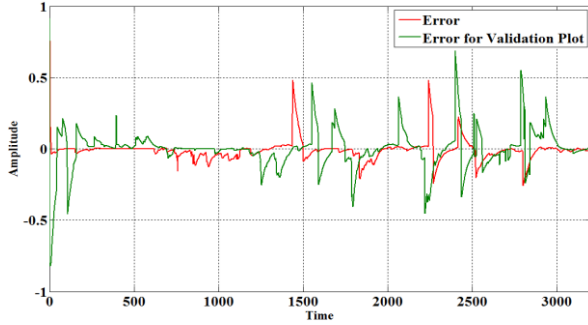


Fig. 3. Error Between the Model Force and the Actual Force

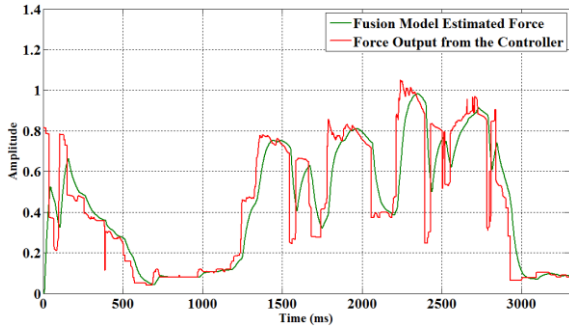


Fig. 4. Validation Plot.

## VII. CONCLUSION AND FUTURE WORK

A fusion-based sEMG-force model was utilized to estimate the force profile that a prosthetic hand should track. This fusion enables to get better force estimates than the single sensor data. The dynamics of the hand was obtained and the controller for optimal tracking between the reference model and the hand was designed. The proposed design gives good performance when tested on a prosthetic hand, based on tracking a reference force profile. In future, we plan to implement this proposed control strategy on a micro controller for real time control. It would be interesting to implement both the force and position control using this control strategy. Finally, we plan to use the hand prototype with five fingers.

## APPENDIX

The resulting MISO transfer function  $H(s)$  is constructed as,

From  $u_1$  to output,

$$\frac{s^8 - 3.843s^7 + 7.729s^6 - 10.78s^5 + 10.6s^4 - 7.417s^3 + 3.603s^2 - 0.9795s + 0.1192}{s^8 - 4.028s^7 + 6.325s^6 - 4.121s^5 - 1.545s^4 + 5.87s^3 - 5.433s^2 + 2.28s - 0.3496}$$

From  $u_2$  to output,

$$\frac{s^8 - 4.339s^7 + 9.005s^6 - 12.42s^5 + 12.22s^4 - 8.117s^3 + 3.427s^2 - 0.9134s + 0.1424}{s^8 - 4.028s^7 + 6.325s^6 - 4.121s^5 - 1.545s^4 + 5.87s^3 - 5.433s^2 + 2.28s - 0.3496}$$

From  $u_3$  to output,

$$\frac{s^8 - 3.522s^7 + 6.655s^6 - 8.864s^5 + 8.183s^4 - 5.365s^3 + 2.423s^2 - 0.557s + 0.09585}{s^8 - 4.028s^7 + 6.325s^6 - 4.121s^5 - 1.545s^4 + 5.87s^3 - 5.433s^2 + 2.28s - 0.3496}$$

Pearson correlation coefficient is given by,

$$\rho_{X,Y} = \text{corr}(X,Y) = \frac{\text{cov}(X,Y)}{\sigma_X \sigma_Y} = \frac{E[(X - \mu_X)(Y - \mu_Y)]}{\sigma_X \sigma_Y}$$

Where  $X, Y$  are Random Variables,  $\mu_X$  and  $\mu_Y$  are expected values,  $\sigma_X, \sigma_Y$  are standard deviations respectively.  $E$  is expected value operator.

## ACKNOWLEDGMENT

This research was sponsored by the US Department of the Army, under the award number W81XWH-10-1-0128 awarded and administered by the U.S. Army Medical Research Acquisition Activity, 820 Chandler Street, Fort Detrick MD 21702-5014. The information does not necessarily reflect the position or the policy of the Government, and no official endorsement should be inferred. For purposes of this article, information includes news releases, articles, manuscripts, brochures, advertisements, still and motion pictures, speeches, trade association proceedings, etc. Further, the technical help from Dr. Cheng-Hung Chen, Mr. Amir Fassih and Mr. Parmod Kumar is greatly appreciated.

## REFERENCES

- [1] "Aca News: National Limb Loss Awareness Month" 2011. Retrieved from <http://www.bocusa.org/aca-news-national-limb-loss-awareness-month>
- [2] D.S. Naidu and C.-H. Chen, "Control Strategies for Smart Prosthetic Hand Technology: An Overview", Book Chapter 14, to appear in a book titled, Distributed Diagnosis and Home Healthcare (D2H2): Volume 2, American Scientific Publishers, CA, January 2011.
- [3] Zinn M, Roth B, Khatib O, and Salisbury JK, "A new actuation approach for human friendly robot design," *Int J Robot Res.* 2004; 23(4-5), pp. 379-398.
- [4] Heinzmann J, and Zelinsky J, "A safe-control paradigm for human-robot interaction," *J Intell Robot Syst.* 1999; 25(4): pp. 295-310.
- [5] Kandel E.R. and Scharz J.H., "Principles of Neural Science," Elsevier/North-Holland, New York, 1981.
- [6] Potluri C., Kumar P., Anugolu M., Urfer, A.; Chiu S., Naidu D.S., Schoen, "Frequency Domain Surface EMG Sensor Fusion for Estimating Finger Forces," 32nd Annual International Conference of the IEEE Engineering in Medicine and Biology Society, Buenos Aires, Argentina, August 31 - September 4, 2010.
- [7] [http://www.isek-online.org/standards\\_emg.html](http://www.isek-online.org/standards_emg.html).
- [8] F.L.Lewis, D.M.Dawson, and C.T. Abdallah, "Robot Manipulators Control: Second Edition, Revised and Expanded", New York, NY: Marcel Dekker, Inc., 2004.
- [9] B.Siciliano, L.Sciavicco, L. Villani, and G. Oriolo, "Robotics: Modelling, Planning and Control". London, UK: Springer-verlag, 2009.
- [10] C-H. Chen, "Hybrid Control Strategies for Smart Prosthetic Hand", Ph.D dissertation, Measurement and Control Engineering, Idaho State University, May 2009.
- [11] R. Kelly, V. Santidanez, and A. Loria, "Control of Robot Manipulators in Joint Space", New York, USA, Springer, 2005.
- [12] R.N. Jazar, "Theory of Applied Robotics, Kinematics, Dynamics, and Control", New York, USA, Springer 2007.
- [13] Cheng-Hung Chen, D. Subbaram Naidu, "Optimal Control Strategy For Two-Fingered Smart Prosthetic Hand", Proceedings of the IASTED International Conference Robotics and Applications(RA 2010), November 1-3, Cambridge, Massachusetts, USA, 2010.
- [14] D. Naidu, "Optimal Control Systems", Boca Raton, FL, CRC Press, 2003.

# sEMG Based Real-Time Embedded Force Control Strategy For a Prosthetic Hand Prototype

Chandrasekhar Potluri, Yimesker Yihun, Parmod Kumar, Jeff Molitor, Steve C. Chiu, S. Hossein Mousavinezhad and D. Subbaram Naidu, *Fellow, IEEE*.

**Abstract** — This paper presents a real-time force control strategy for a prosthetic hand. The proposed design is capable of decoding the prerecorded surface electromyographic (sEMG) signal as well as the sensory force feedback from the sensors to control the force of the prosthetic hand prototype. The input sEMG signal is preprocessed using a Half-Gaussian filter with optimized parameters and Chebyshev type II filter. Entropy of the sEMG signal is used as a threshold value to establish the correlation between the sEMG signal and the skeletal muscle force. A simple proportional integral controller along with a two-stage embedded design is used for the force control of the prosthetic hand. The results are transmitted to the computer through the universal asynchronous receiver/ transmitter (UART) interface of the proposed embedded design. The results demonstrate good performance in controlling the force of the prosthetic hand.

## I. INTRODUCTION

In the field of rehabilitation, one of the most interesting topics of research is human-machine interface. In case of prosthesis design, development and control, the sEMG signals play a vital role which is a natural means of interface between the human arm and prosthesis. The sEMG signals are electrical voltages ranging from -5 to +5 (mV) which can be recorded on the human arm using suitable sensing

elements. The base sEMG signal is always available and this signal changes with the movements of different fingers and applied force for different tasks. This is the reason that sEMG signals are very useful and can be input signals for the controller of hand prosthesis to control the movements and force applied by the fingers. There has been active research work to design a prosthetic hand, but even today we do not have a prosthetic hand with tactile or proprioceptive feedback for grasping [1]. Most of these prostheses only use the direct vision of the user as a sensory feedback for the position control. This is why 30–50% of upper extremity amputees choose not to use their prosthetic hands on a regular basis [2-3]. Thus far, several EMG-based algorithms have been developed and used to enhance the functionality and usability of prosthetic hands [4]. Since the human hand is a highly complex and nonlinear system with a large number of degrees of freedom, the control of a multi-fingered prosthetic hand is complicated [5]. Previously there has been active research in the area of position and force control of a prosthetic hand, and the typical approach is to use hybrid position and force control [6]. By contrast, this proposed research work focuses on the design of an embedded control system that can control the movements and force of a smart prosthetic hand with sensory feedback. The input to this embedded control system is the entropy of the input sEMG signal. Steady state sEMG signals have little temporal structure and actively modify the recruitment and firing patterns needed to sustained contraction [7]. The sEMG signal amplitude can be quantified using variance, mean absolute value, Fourier spectrum and median frequency. But these techniques are not usually sufficient to distinguish between more than two classes of movements.

Embedded systems have become pervasive and as research advances, more and more functions of analog circuits are being realized by microcontrollers, Analog to Digital Converters (ADCs) and Digital to Analog Converters (DACs). In a modern control system, embedded control addresses most control functions. A well designed embedded control system can give excellent system performance under widely varying operating conditions. For robust and consistent high performance, the embedded system should be designed carefully and in balance. In this particular case we need to have a real-time embedded control system that performs the desired tasks.

Chandrasekhar Potluri is with Measurement and Control Engineering Research Center (MCERC), School of Engineering, Idaho State University, Pocatello, Idaho 83209, USA (e-mail: potlchan@isu.edu).

Yimesker Yihun is with MCERC, School of Engineering, Idaho State University, Pocatello, Idaho 83209, USA (email: yihuyime@isu.edu).

Parmod Kumar is with MCERC, School of Engineering, Idaho State University, Pocatello, Idaho 83209, USA (email: kumaparm@isu.edu).

Jeff Molitor is with MCERC, School of Engineering, Idaho State University, Pocatello, Idaho 83209, USA (email: molijeff@isu.edu).

Steve C. Chiu is with Department of Electrical Engineering and Computer Science, MCERC, Idaho State University, Pocatello, Idaho 83209 USA (email: chiustev@isu.edu).

S. Hossein Mousavinezhad is with Department of Electrical Engineering and computer science, MCERC, Idaho State University, Pocatello, Idaho 83209 USA (email: mousseye@isu.edu).

D. Subbaram Naidu is with Department of Electrical Engineering and computer science, MCERC, Idaho State University, Pocatello, Idaho 83209 USA (email: naiduds@isu.edu).

In this present work we are using the Shannon entropy values of sEMG signals as inputs to design a proportional integral (PI) controller to control the force of a prosthetic hand prototype. Force feedback is acquired using a Force Sensing Resistor (FSR) which is compared with stored force signals. The sEMG signal is filtered through a Half-Gaussian filter with optimized parameters; the force signal is filtered using a Chebyshev type-II filter.

In physics, entropy is related to the amount of disorder in a system, and is proportional to the logarithm of the number of microstates available to a thermodynamic system. The concept of entropy for information theory is given by Shannon and Weaver [8], and Johnson and Shore [9], who used entropy for the power spectrum of a signal. For instance, a signal has an entropy value of zero if its sequential values alternate between one fixed magnitude and another fixed magnitude. A signal with zero entropy value is completely regular and very predictable. In contrast, a signal has higher entropy if a random number generates its sequential values. Thus, using entropy, we can visually distinguish a regular signal from an irregular one. Since entropy is independent of the absolute scales, it can be computed by methods such as approximate entropy [10, 11] or Shannon entropy [8, 12, 13] in the time domain, and spectral entropy [8, 9, 14, 15] in the frequency domain. The non-normalized Shannon entropy is given by Equation (1).

$$E(s) = -\sum_i s_i^2 * \log(s_i^2), \quad (1)$$

where  $s$  is the signal and  $s_i$  are the coefficients of  $s$  in an orthonormal basis.

The threshold values of the entropy are used to initiate the movement of the DC motors, which is the reference for the controller. The details are specified in the Proposed Design section. Our results demonstrate good performance by the proposed design. This paper is organized as follows. Section II addresses Experimental Set-Up, Section III gives Proposed Design, Section IV has Mechanical Structure of the Robotic Hand Prototype, Results and Discussion are given in Section V. and finally some conclusion and future work are given in Section VI.

## II. EXPERIMENTAL SET-UP

Ten healthy subjects volunteered for our experiments. A muscle stimulator was used to detect the motor points for index, middle and ring fingers. The sEMG and skeletal muscle force signals were acquired using the 16-channel DELSYS® BagnolisEMG and NI ELVIS™ respectively. DE 2.1 sEMG sensors and a stress ball with a 0.5 inches circular as force sensing resistor (FSR) from Interlink™ Electronics was used to acquire the force signals. Prior to placing the sEMG sensors, the skin surface of the subject was prepared according to the International Society of Electrophysiology and Kinesiology (ISEK) protocols. Both the signals were acquired in LabVIEW™ at a rate of 2000 Hz. The experimental set-up is shown in Fig. 1, where a healthy

subject is hooked-up with sEMG sensors and is squeezing the stress ball to generate the skeletal muscle force, which in turn affects the sEMG signals. Several experiments with different durations were conducted for each subject.

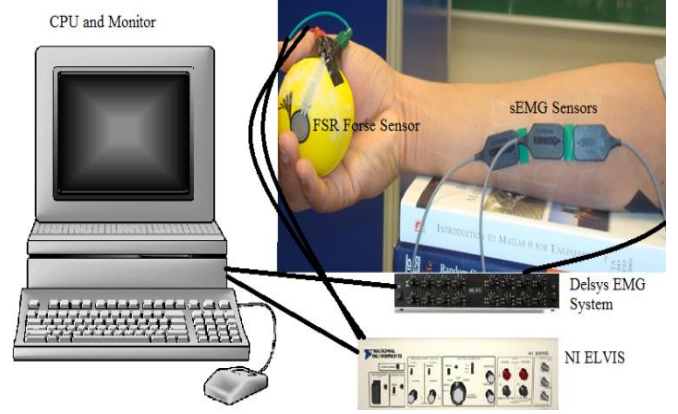


Fig. 1. Experimental set-up.

## III. PROPOSED DESIGN

For our proposed design, entropy values of the sEMG signals were calculated and taken as threshold values to initiate the motion. Entropy values were extracted from sEMG of the index, middle and ring fingers respectively for a power grasping action. The entropy values of the sEMG data for 10 different subjects are tabulated in Table 1, where Ring<sub>1</sub> and Middle<sub>1</sub> correspond to the Shannon entropy of the respective finger right next to its motor unit location.

TABLE 1  
ENTROPY VALUES OF sEMG SIGNALS FOR THREE FINGERS

Index	Ring	Middle	Ring <sub>1</sub>	Middle <sub>1</sub>
2.9792	2.9271	2.1554	2.3994	1.6711
2.6783	3.0008	1.9376	2.3947	1.5346
3.4943	2.9556	3.0277	2.9568	2.6673
3.679	3.1714	2.9268	3.1175	3.0581
3.2110	2.7015	1.9228	2.7997	1.2993
2.8451	2.9429	1.9555	3.0541	1.1095
1.4653	1.5559	3.7151	2.4827	1.6919
1.9371	1.4639	3.6648	3.2785	1.7955
2.7399	3.7132	3.0820	3.0425	2.3929
2.5421	3.5961	2.8593	2.6782	2.2040

Threshold values are tabulated in Table 2. The threshold values are calculated as the difference between the mean and twice the standard deviation.

TABLE 2  
SHANNON ENTROPY THRESHOLD VALUES FOR INDEX, RING,  
AND MIDDLE FINGER sEMG SIGNALS.

Index	Ring	Middle
1.3724	1.5176	1.522

In this design, the threshold values establish a correlation between the sEMG and the corresponding force required for the power grasp of an object. C.Potluri *et. al* [16] explained about the correlation between sEMG entropy threshold values and skeletal muscle forces. These threshold values are fed as the reference or a set point to the controller. The signal flow representation of the proposed design is depicted as a block diagram in Fig. 2.

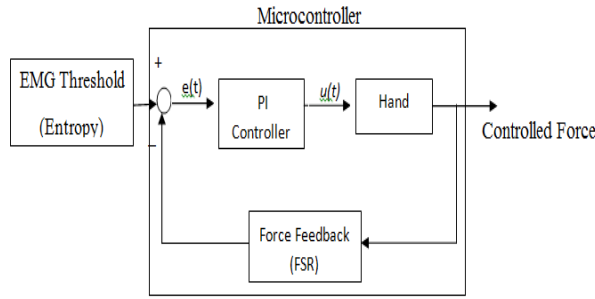


Fig. 2. Block diagram of the proposed design.

The force feedback signal is acquired by a force sensitive resistor (FSR). The FSR is mounted on the fingertip of the prosthetic hand prototype as shown in Fig. 4. The error  $e(t)$  is computed as the difference between the reference value and the actual force from the FSR. A proportion-integral (PI) controller is employed to generate the actual force from the FSR, and make it equal to the reference force in order to reduce the error  $e(t)$  to zero. The PI control action is given below in Equation (2).

$$u(t) = K_p * e(t) + K_i \int_0^t e(\tau) d\tau, \quad (2)$$

Where  $u(t)$  is the control signal,  $K_p$  is the proportional gain, and  $K_i$  is the integral gain.  $e(t)$  is the error and  $\tau$  is the dummy integration variable. Gain parameters  $K_p$  and  $K_i$  are tuned using the Ziegler-Nichols method in MATLAB®.

Our proposed design was implemented on a PIC32 microcontroller in two stages: "Signal Processing" and "Motor Actuation". The Signal Processing stage facilitates the implementation of real-time control strategies. A dsPIC blockset was used to generate the C code for the PIC32 from Simulink®. The dsPIC blockset generates a .hex file, and this file is imported by MPLAB® to program the PIC32.

### Signal Processing Stage

We used the following modules of the PIC32 as a part of implementing our control strategies:

- The Analog Input module
- The Digital Output module
- The Output Compare module
- The UART module

The Analog Input module was used for reading the sEMG and sensory feedback data. The PIC32 has an internal analog to digital converter (ADC) which has a 10-bit resolution so that it can distinguish up to 1024 different voltages, usually in the range of 0 to 3.3 volts, and it yields 3mV resolution. A real-time control strategy was developed using the threshold value of the entropy of sEMG data as a reference or set point. The difference between the threshold of the sEMG entropy and the FSR feedback was fed in to the PI control loop to reduce the error to zero. The Digital Output module of the PIC32 was used to generate digital control signals. Depending on the error, a pulse width modulated (PWM) wave with a specific duty cycle was generated in the Output Compare module. The UART module in the PIC32 was used to transmit the signals from the microcontroller to the PC via serial communication. In this design, a virtual com port was created to feed the data via USB cable to the computer. MATLAB® was used to read the signals from the ports. This enables the user to troubleshoot and see the performance of the designed control strategy.

### Motor Actuation Stage

In this stage, a SN754410 quadruple half-H driver is used to actuate the motor with the corresponding control signal. Fig. 3 shows the schematic of the pin configuration of the half-H driver.

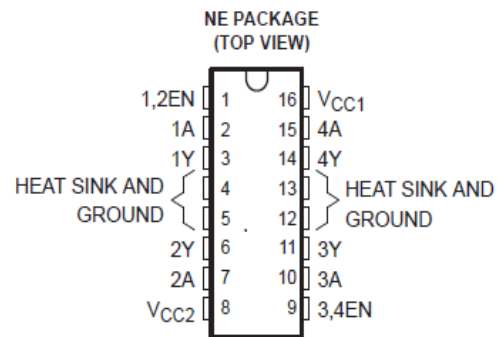


Fig. 3. Pin configuration of quadruple half-H driver [17].



The PWM signal from the Output Compare module was connected to pin1 (1, 2EN) of the H driver. The PWM wave enables this H driver. The speed of the motor depends on the duty cycle of the PWM wave from the Output Compare module, which is a function of  $e(t)$ . The digital outputs of the PIC32 microcontroller are connected to the direction pins of the H driver (pins 2 and 7). Switching the digital outputs to 0 and 1 between the pins will makes the motor rotate in clockwise and counter-clockwise directions.  $V_{cc1}$  and  $V_{cc2}$  are connected to the 5V supply of the PIC32 I/O board. This proposed design was tested on an index finger of a prosthetic hand prototype. Fig. 4 shows the test bed for the proposed design. Mechanical design of the robotic hand prototype is explained in the following section.

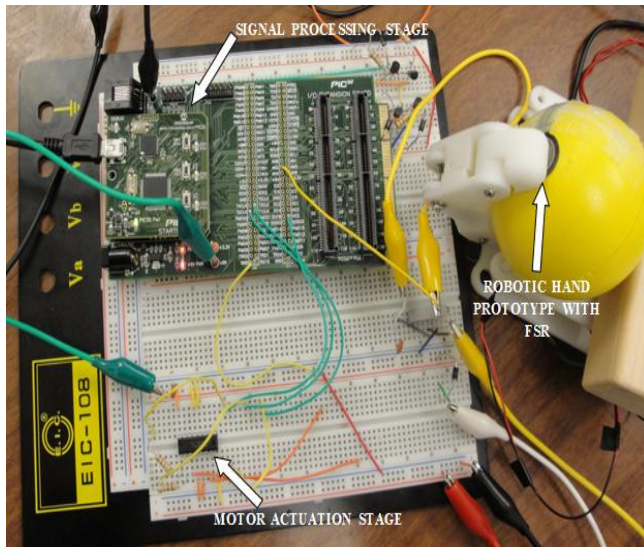


Fig. 4. Test bed for the proposed design.

#### IV. MECHANICAL STRUCTURE OF THE ROBOTIC HAND PROTOTYPE

The robotic hand prototype finger has three degrees of freedom, and is actuated by two Pololu 35:1 mini metal gear motors and a bevel gear transmission system. The main characteristic of this prototype is its biologically-inspired parallel actuation system based on the behavior/strength space of the "Flexor Digitorum Profundus (FDP)" and the "Flexor Digitorum Superficialis (FDS)" muscles as explained in Fig. 5. However this research work focuses on the "Region 1" actuation system and it is interfacing with a microcontroller. Region 1 is populated by the more frequent dexterous tasks, whereas "Region 2" is populated by the less frequent and more strength-based tasks for which an additional parallel actuation system is provided as discussed in [18].

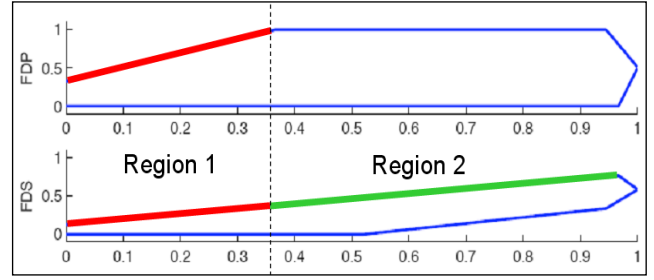


Fig. 5. Strength space of FDS and FDP muscles [19].

In our design, the movements associated with Region 1 are achieved by 2 DC motors. The motor in the metacarpal phalange of the finger actuates the PIP (Proximal Inter Phalangeal) joint and the motor at the base of the finger actuates the MCP (Meta Carpo Phalangeal) joint, as shown in Fig. 6. As the main objective of this work is to interface and control the two motors with a microcontroller, we have not considered the belt transmission system shown in Fig. 6, which is designed to drive the DIP (Distal Inter Phalangeal) joint as well.

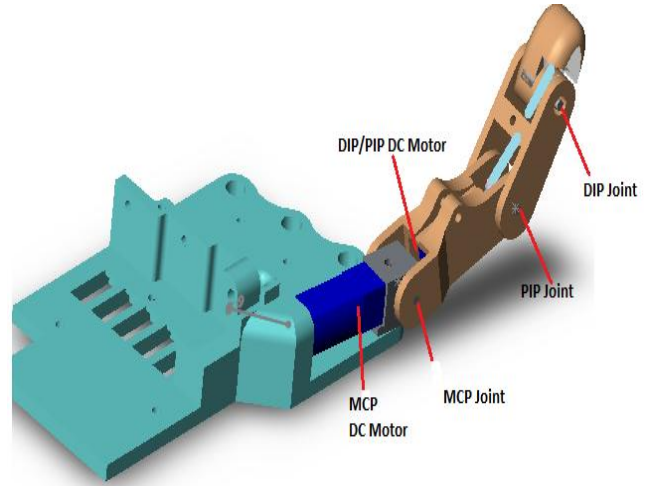


Fig.6. Region 1 Actuation scheme for the finger.

#### V. RESULTS AND DISCUSSION

Results are acquired from the microcontroller through UART channel 2 of the PIC32 by a virtual com port via USB at 57600 baud rate. The data from the microcontroller is converted into unit16 data before it is transmitted through the UART. The PIC32 microcontroller is running 80 million instructions per second (MIPS) with its phase lock loop (PLL) activated. It is running at an external clock frequency of 8MHz with internal scaling enabled.

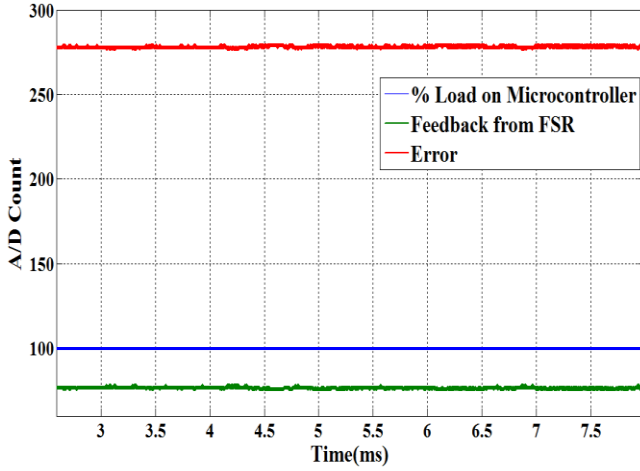


Fig. 7. Feedback force and error before grasp.

Fig. 7. Depicts the feedback force from the FSR, and the error  $e(t)$  before the grasp. As there is no contact between the object and the hand, the force is low and ideally it should be zero. However, because the PIC32's analog to digital conversion provides a high resolution, it shows some value even when the object is not in contact.

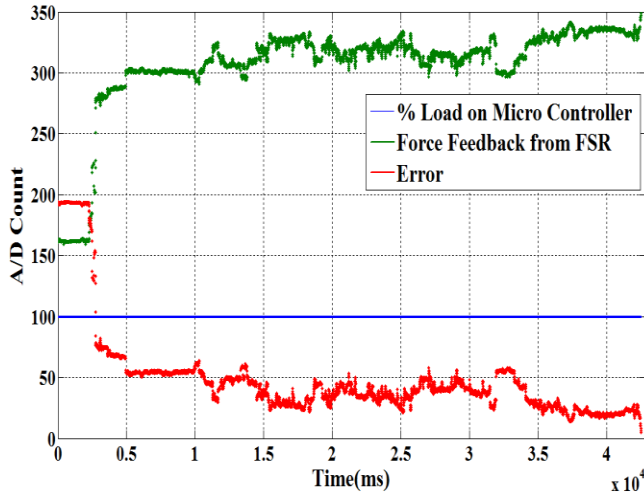


Fig. 8. Feedback force and error after grasp.

Fig. 8 depicts the feedback force from the FSR plotted against the error  $e(t)$  during the grasp. The error  $e(t)$ , i.e. the difference between the reference force from the sEMG threshold value and the actual force feedback from the FSR, is almost zero. From Fig. 8, it is also evident that the actual force from the FSR is almost equal to the reference force value that is established from the sEMG threshold value, as the error approaches zero. Fig. 9 shows the computational load on the microcontroller while performing this grasp. It indicates that the microcontroller completed the computation in approximately 12 ms. The rest is handed over to the I/O blocks of the microcontroller and the motor actuation stage.

This result suggests an extensible design for increased load on the processing by the embedded system.

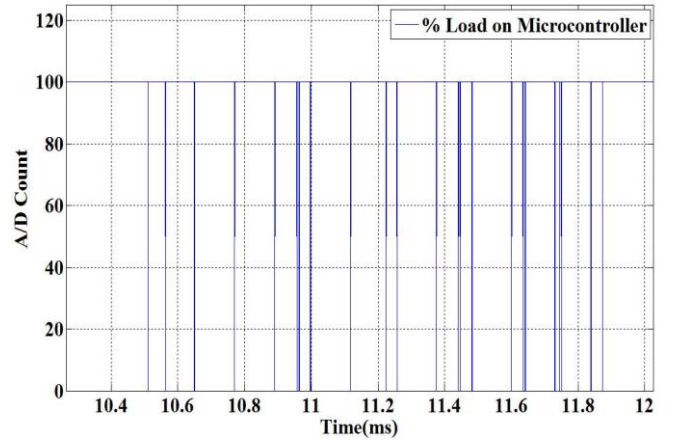


Fig.9. Computational load on the PIC32 during the grasp

## VI. CONCLUSION AND FUTURE WORK

A two-stage real-time control strategy was designed for a robotic hand prototype. The proposed design gives good performance when tested on a prosthetic hand prototype, and at the same time the error between the reference force and the actual force from the sensors is very small and approaches zero. This design facilitates the transmission of the data from the microcontroller to the computer. This enables the user to increase the accuracy and performance of the design by implementing various novel control strategies and also enables quick trouble shooting.

For future work we are planning to implement model-based force estimation and along with controller design for position and force control, based on this embedded platform. It will be interesting to acquire the sEMG signal directly from the arm of a healthy subject to our embedded system instead of using prerecorded sEMG signals, which will be investigated. Finally, we plan to use the prototype with five fingers.

## ACKNOWLEDGMENT

This research is sponsored by the US Department of Defense Army Research, under award W81XWH-10-1-0128 and administered by the U.S. Army Medical Research Acquisition Activity, 820 Chandler Street, Fort Detrick MD 21702-5014. The information does not necessarily reflect the position or the policy of the Government, and no official endorsement should be inferred. For purposes of this article, information includes news releases, articles, manuscripts, brochures, advertisements, still/motion pictures, speeches, trade association proceedings, etc. The support by Madhavi Anugolu and Dr. Marco P. Schoen is greatly appreciated.

## REFERENCES

- [1] D.S. Naidu and C.-H. Chen, "Control Strategies for Smart Prosthetic Hand Technology: An Overview", Book Chapter 14, to appear in a book titled, Distributed Diagnosis and Home Healthcare (D2H2): Volume 2, American Scientific Publishers, CA, January 2011
- [2] D. J. Atkins, D.C.Y. Heard, and W.H. Donovan, "Epidemiologic overview of individuals with upper limb loss and their reported research priorities," *J. Prosthet. Orthot.*, vol. 8, no. 1, p. 2, 1996.
- [3] D. H. Silcox, M. D. Rooks, R. R. Vogel, and L. L. Fleming, "Myoelectric prostheses. A long-term follow-up and a study of the use of alternate prostheses," *J. Bone Joint Surg.*, vol. 75, no. 12, pp. 1781–1789, 1993.
- [4] Reiter R. *Eineneueelektrokunsthand. Grenzgebiete der Medizin* 1948; 4:183.
- [5] T. H. Sueeter, "Control of the Utah/MIT Dextrous hand: Hardware and software hierarchy," *J. Robot. Syst.*, vol. 7, no. 5, pp. 759-790, 1990.
- [6] M. H. Raibert and J. J. Craig, "Hybrid position and force control of manipulators," *ASME J. Llyn. Syst. Meas. Contr.*, vol. 102, pp. 126-133, June 1981.
- [7] Bashamajian JV, De Luca CJ. *Muscles Alive*. Baltimore, MD: Williams & Wilkins, 1985.
- [8] Shannon CE. "A mathematical theory of communication", *Bell System Techn J* 1948; 27 (379-423): 623-56.
- [9] Johnson RW, Shore JE. "Which is the better entropy expression for speech processing:  $-S \log S$  or  $\log S$ ?" *IEEE Trans Acoust* 1984; ASSP-32: 129-37.
- [10] Pincus SM, Gladstone IM, Ehrenkranz RA. "A regularity statistic for medical data analysis", *J Clin Monit* 1991; 7: 335-45.
- [11] Bruhn J, Ropcke H, Hoeft A. "Approximate entropy as an electroencephalographic measure of anesthetic drug effect during desflurane anesthesia", *Anesthesiology* 2000; 92: 715-26.
- [12] Bruhn J, Ropcke H, Hoeft A. "Approximate entropy as an electroencephalographic measure of anesthetic drug effect during desflurane anesthesia", *Anesthesiology* 2000; 92: 715-26.
- [13] Bruhn J, Lehmann LE, Ropcke H, Bouillon TW, Hoeft A. "Shannon entropy applied to the measurement of the electroencephalographic effects of desflurane", *Anesthesiology* 2001; 95: 30-5.
- [14] Rezek IA, Roberts SJ. "Stochastic complexity measures for physiological signal analysis", *IEEE Trans Biomed Eng* 1998; 45: 1186—91.
- [15] Inouye T, Shinosaki K, Sakamoto H et al. "Quantification of EEG irregularity by use of the entropy of the power spectrum", *Electroencephalogr Clin Neurophysiol* 1991; 79: 204-10.
- [16] Chandrasekhar Potluri, Parmod Kumar, Madhavi Anugolu, "sEMG Based Fuzzy Control Strategy with ANFIS path planning For prosthetic Hand", *Proceedings of the 2010 3<sup>rd</sup> IEEE RAS & EMBS International Conference on Biomedical Robotics and Bio mechatronics*, The University of Tokyo, Tokyo, Japan September 26-29, 2010.
- [17] Texas Instruments "SN754410 quadruple half H-driver data sheet" Dallas, Texas, November 1986 and 1995.
- [18] Dr. Anthony L. Crawford, "Design of a Robotic Hand and Simple EMG Input Controller with a Biologically-Inspired Parallel Actuation System for Prosthetic Applications" ASME 2010, IDETC/CIE 2010
- [19] Kutch, J. J., Valero-Cuevas, F. J., "All muscles are redundant but some are less redundant than others," poster presentation for USC Viterbi School of Engineering Brain-Body Dynamics Lab.



# Optimal Tracking of a sEMG based Force Model for a Prosthetic Hand

Chandrasekhar Potluri, Madhavi Anugolu, YimeskerYihun, Alex Jensen, Steve Chiu *Member, IEEE*, Marco P. Schoen, *Senior Member, IEEE*, and D. Subbaram Naidu, *Fellow, IEEE*.

**Abstract:** This paper presents a surface electromyographic (sEMG)-based, optimal control strategy for a prosthetic hand. System Identification (SI) is used to obtain the dynamic relation between the sEMG and the force. The input sEMG signal is preprocessed using a Half-Gaussian filter and fed to a fusion-based Multiple Input Single Output (MISO) skeletal muscle force model. This MISO system model provides the estimated finger forces to be produced as input to the prosthetic hand. Optimal tracking method has been applied to track the estimated force profile of the Fusion based sEMG-force model. The simulation results show good agreement between reference force profile and the actual force.

## I. INTRODUCTION

Currently there are more than 2 million Americans that have a missing limb. The number of Americans with missing limbs increases 185,000 people a year [1]. As a result of this rising number of people that need prostheses, research is being focused on creating more intuitive prosthetics. There has been active research to design a prosthetic hand. But even today there is no prosthetic hand at an affordable cost with position and tactile force control [2]. It is evident from the past research that the human-centered robotics should be autonomous with a high level of functionality, comfort and ease of use [3]. A natural means of communication is required for human-centered robotics [4], and in the case of electromyographic (EMG) based prostheses, one natural means of interface between the human arm and prosthesis is the surface EMG (sEMG) itself. The EMG signal is present because of the neuromuscular activity in the body. The sEMG signals are captured noninvasively and give access to physiological processes responsible for the contraction of muscles. Since the sEMG signal is amplitude modulated and time dependent, and dynamic in nature, spatially and

temporally frequency encoded [5]. Usually sEMG measurements are based on single sensor data. For this work we used an array of three sEMG sensors and a force sensing resistor (FSR) to acquire the EMG signal and the corresponding skeletal muscle force. The data from the three sEMG sensors is fused using a fusion algorithm to have a better estimation of skeletal muscle force from the corresponding sEMG signal when compared to single sensor data [6].

This paper uses the sEMG-force fusion model as reference profile. A Linear Quadratic Tracking (LQT) technique is employed to the prosthetic hand to track the force profile. This paper is structured as follows. The experimental set up is given in Section II, Section III provides reference force model and Section V provides dynamics of the hand. Section VI details the results and discussion and in the last section some conclusions are provided.

## II. EXPERIMENTAL SET-UP

Experiments were conducted on a right-handed healthy male subject. Using a muscle simulator (Rich-Mar Corporation HV 1100), motor units were marked and sEMG sensors were placed accordingly [6]. One sEMG sensor was placed on the motor point of the subject's ring finger and two sensors were placed at points adjacent to it. Prior to placing the sEMG sensors, the skin surface of the subject was prepared according to International Society of Electrophysiology and Kinesiology (ISEK) protocols [7]. Both sEMG and muscle force signals were acquired simultaneously using LabVIEW™ 8.2 at a sampling rate of 2000 Hz. The sEMG data was captured by a DELSYS® Bagnoli-16 EMG system with DE-2.1 differential EMG sensors. The force information was collected by a NI ELVIS with an Interlink Electronics FSR 0.5" circular force sensor.

## III. REFERENCE FORCE MODEL

In this present work the force signal is extracted from the sEMG signals obtained from the array of the three sEMG sensors located on the arm. The data from the three sensors is collected around the corresponding individual motor unit location at the transradial arm location (flexor digitorum superficialis) and is rectified and filtered using a Half-Gaussian filter given by

$$p(EMG|x) = 2 \times \frac{\exp\left(-\frac{EMG^2}{2x^2}\right)}{\sqrt{2\pi x^2}}, \quad (1)$$

Chandrasekhar Potluri is with Measurement and Control Engineering Research Center (MCERC), College of Engineering, Idaho State University, Pocatello, Idaho 83209, USA (e-mail: potlchan@isu.edu).

Madhavi Anugolu is with MCERC, College of Engineering, Idaho State University, Pocatello, Idaho 83209, USA (email: anugmadh@isu.edu).

YimeskerYihun is with MCERC, College of Engineering, Idaho State University, Pocatello, Idaho 83209, USA (email: yihuyime@isu.edu).

Alex Jensen is with MCERC; is with MCERC, College of Engineering, Idaho State University, Pocatello, Idaho 83209, USA (email: jensalex@isu.edu).

Steve Chiu is with Department of Electrical Engineering and Computer Science, MCERC, Idaho State University, Pocatello, Idaho 83209 USA (email: chiustev@isu.edu).

Marco P. Schoen is with Department of Mechanical Engineering, MCERC, Idaho State University, Pocatello, Idaho 83209, USA (email: schomarc@isu.edu).

D. Subbaram Naidu is with Department of Electrical Engineering and Computer Science, MCERC, Idaho State University, Pocatello, Idaho 83209 USA (email: naiduds@isu.edu).

where  $p(EMG|x)$  is a conditional probability density function,  $x$  is a latent driving signal.

The preprocessed sEMG data from the three sensors is fused using a sensor fusion algorithm to facilitate the extraction of the best finger force estimates. Sensor fusion is accomplished in the frequency domain using a simple elitism based Genetic Algorithm (GA). The SI method is used to identify the dynamical relationship between the sEMG data from the three sensors and the corresponding finger force. In this fusion algorithm, Output Error (OE) models are used to achieve the SI. The OE models are constructed for each individual data set. The OE model structure is given as follows.

$$y(t) = \frac{B(q)}{F(q)}u(t - nk) + e(t), \quad (2)$$

Where  $B$ , and  $F$  are the polynomials,  $q$  is shift operator,  $e(t)$  is output error,  $y(t)$  is system output,  $u$  is input,  $nk$  is the system delay and  $t$  is time index.

Using the three resulting OE models and the fusion algorithm given by [6], a corresponding continuous-time model is constructed as given by the transfer function as

$$G(s) = \frac{B(s)}{F(s)} = \frac{b_{nb}s^{(nb-1)}b_{nb-1}s^{(nb-2)}+\dots+b_1}{s^{nf}+f_{nf}s^{nf-1}+\dots+f_1}, \quad (3)$$

Similar to the discrete-time case,  $nb$  and  $nf$  determine the orders of the numerator and denominator. For multi-input systems,  $nb$  and  $nf$  are row vectors.  $b, f$  are the coefficients of the numerator and denominator polynomials respectively.

A MISO transfer function is constructed based on the poles of three individual OE models corresponding to each sensor. GA is used to find the corresponding zeros. The search area is limited to the unit circle, because a discrete time model is used (and the resulting MISO model is decreased to minimum phase). The number of zeros is at most the number of poles. The number of potential zeros is set to the order of the corresponding denominator. The error squared of the resulting MISO system  $H(s)$  (see Appendix) and the recorded force signal is set as an objective function. The objective function  $f$  is constructed as follows,

$$f = \int_{t_0}^{t_f} (\hat{Y}(t) - Y(t))^2 dt = \int_{t_0}^{t_f} \phi^2(t) dt, \quad (3)$$

where  $t_0$  and  $t_f$  are the initial and final time values,  $\hat{Y}(t)$  is the fusion model estimated force and  $Y(t)$  is the actual force from the FSR.

The MISO system  $H(s)$  is constructed as follows,

$$H(s) = \begin{pmatrix} \frac{Z_{1,1}s^n + Z_{1,2}s^{n-1} + \dots + Z_{1,n+1}}{P_{1,1}s^n + P_{1,2}s^{n-1} + \dots + P_{1,n+1}} \\ \frac{Z_{2,1}s^n + Z_{2,2}s^{n-1} + \dots + Z_{2,n+1}}{P_{2,1}s^n + P_{2,2}s^{n-1} + \dots + P_{2,n+1}} \\ \frac{Z_{3,1}s^n + Z_{3,2}s^{n-1} + \dots + Z_{3,n+1}}{P_{3,1}s^n + P_{3,2}s^{n-1} + \dots + P_{3,n+1}} \end{pmatrix}, \quad (4)$$

where  $Z$ 's and  $P$ 's are the zeros and poles respectively of the individual transfer function and  $n$  is the order of the system.

Feeding the new data sets to the MISO transfer function ( $H(s)$ ) (See Appendix) results in an estimated fusion based force  $\hat{Y}$ .

#### IV. DYNAMICS OF PROSTHETIC HAND

The dynamic equations of motion for the hand are obtained from the Lagrangian approach as [8,9,10,11,12, 13]

$$\frac{d}{dt} \left( \frac{\partial \mathcal{L}}{\partial \dot{q}} \right) - \frac{\partial \mathcal{L}}{\partial q} = \tau, \quad (5)$$

Where  $\dot{q}$  and  $q$  represent the angular velocity and angle vectors of joints respectively;  $\mathcal{L}$  is the Lagrangian;  $\tau$  is the given torque vector at joints. The Lagrangian  $\mathcal{L}$  is given as

$$\mathcal{L} = T - V, \quad (6)$$

Where  $T$  and  $V$  are denoted as kinetic and potential energies respectively. Substituting (6) into (5), we get the following dynamic equations

$$M(q)\ddot{q} + C(q, \dot{q}) + G(q) = \tau, \quad (7)$$

Where  $M(q)$  describes the inertia matrix;  $C(q, \dot{q})$  is the coriolis/centripetal vector and  $G(q)$  is the gravity vector. (7) can be written as

$$M(q)\ddot{q} + N(q, \dot{q}) = \tau, \quad (8)$$

where  $N(q, \dot{q}) = C(q, \dot{q}) + G(q)$  represents nonlinear terms.

Feedback linearization technique is used to convert the nonlinear dynamics represented by (8) into a linear state-variable system [8]. In order to obtain the alternative state-space equations of the dynamics, the position/velocity state  $x(t)$  of the joint is defined as

$$x(t) = [q'(t) \ \dot{q}'(t)]', \quad (9)$$

and rewriting (8) as

$$\frac{d}{dt} \dot{q}(t) = -M^{-1}(q(t)) [N(q(t), \dot{q}(t)) - \tau(t)] \quad (10)$$

Therefore, from (9) and (10), a linear system in Brunovsky canonical form is obtained and represented as

$$\dot{x}(t) = \begin{bmatrix} 0 & I \\ 0 & 0 \end{bmatrix} x(t) + \begin{bmatrix} 0 \\ I \end{bmatrix} u(t). \quad (11)$$

The control input vector  $u(t)$  given by

$$u(t) = -M^{-1}(q(t)) [N(q(t), \dot{q}(t)) - \tau(t)]. \quad (12)$$

As the prosthetic hand is required to track the desired force profile  $q_d(t)$  described under the reference force model, the tracking error  $e(t)$  is defined as

$$e(t) = q_d(t) - q(t). \quad (13)$$

Here,  $q_d(t)$  is the desired angle vector of the joints and can be obtained by the reference force model [6];  $q(t)$  is the actual angle vector of the joints. Differentiating (13) twice, we get,

$$\dot{e}(t) = \dot{q}_d(t) - \dot{q}(t), \quad \ddot{e}(t) = \ddot{q}_d(t) - \ddot{q}(t). \quad (14)$$

Substituting (10) into (14) gives

$$\ddot{e}(t) = \ddot{q}_d(t) + M^{-1}(q(t))[N(q(t), \dot{q}(t)) - \tau(t)] \quad (15)$$

From (15) the control function  $u(t)$  can be defined as

$$u(t) = \ddot{q}_d(t) + M^{-1}(q(t))[N(q(t), \dot{q}(t)) - \tau(t)]. \quad (16)$$

This is often called the feedback linearization control law, rewriting (16) as,

$$\tau(t) = M(q(t))[\ddot{q}_d(t) - u(t) + N(q(t), \dot{q}(t))]. \quad (17)$$

Using (14) and (16), the state vector  $x(t) = [e'(t) \dot{e}'(t)]'$ , the state-space model can be represented as

$$\dot{x}(t) = \begin{bmatrix} 0 & I \\ 0 & 0 \end{bmatrix} x(t) + \begin{bmatrix} 0 \\ I \end{bmatrix} u(t). \quad (18)$$

Now, (18) is in the form of a linear system such as

$$\dot{x}(t) = Ax(t) + Bu(t). \quad (19)$$

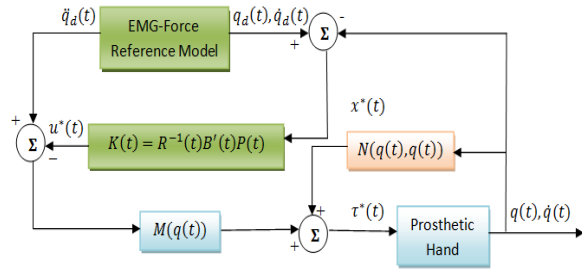


Fig. 1. Block Diagram of Optimal Controller for Prosthetic Hand.

### OPTIMAL TRACKING

Figure 1 shows the block diagram representation of the finite-time linear quadratic optimal controller for the prosthetic hand. The objective of the controller is for the prosthetic hand finger to track optimally the force model.

For the linear system (19), the finite-time linear quadratic optimal control problem can be formulated by defining the performance index  $J$  [14] as

$$J = \frac{1}{2} \int_{t_0}^{t_f} [x'(t) Q(t) x(t) + u'(t) R(t) u(t)] dt \quad (20)$$

where  $Q(t)$  is the error weighted matrix; and  $R(t)$  is the control weighted matrix. The optimal control  $u^*(t)$  is

described by

$$u^*(t) = -R^{-1}(t)B'P(t)x^*(t) = -K(t)x^*(t). \quad (21)$$

where  $K(t) = -R^{-1}(t)B'P(t)$  is called Kalman gain and  $P(t)$ , is the solution of the matrix differential Riccati equation (DRE)

$$\dot{P}(t) = -P(t)A - A'P(t) - Q(t) + P(t)BR^{-1}(t)B'P(t) \quad (22)$$

Satisfying the final condition

$$P(t = t_f) = 0. \quad (23)$$

Hence the optimal state  $x^*$  is the solution of

$$\dot{x}^*(t) = [A - BR^{-1}(t)B'P(t)]x^*(t). \quad (24)$$

Therefore, with the optimal control  $u^*(t)$ , the required torque  $\tau^*(t)$  can be calculated by

$$\tau^*(t) = M(q(t))(\ddot{q}_d(t) - u^*(t)) + N(q(t), \dot{q}(t)). \quad (25)$$

The torque  $\tau^*(t)$  is converted into force by

$$F_o(t) = \tau^*(t)/L, \quad (26)$$

Where  $F_o(t)$  is the force and  $L$  is the length of the finger.

## VI. RESULTS AND DISCUSSION

Figure 2 shows the fusion model force  $\hat{Y}(t)$  and the force output from the controller  $F_o(t)$ . It is evident that the optimal controller can track the changes in the force profile and follow the trends in reference force profile.

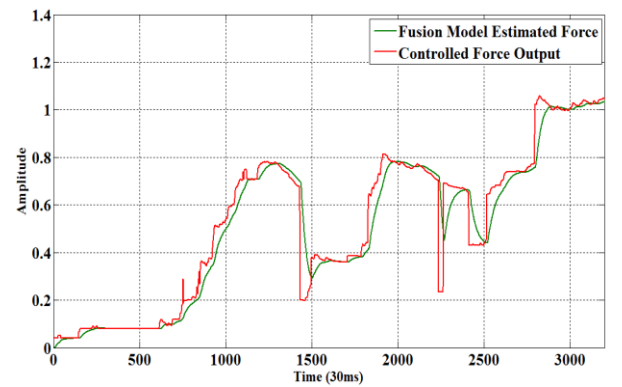


Fig. 2. Fusion Reference Model Force and Actual Force

Figure 3 shows the error between the model force  $\hat{Y}(t)$  and the force output from the controller  $F_o(t)$  for two different sets of results shown in Figs. 2 and 4. This figure shows that the error converged to zero in a very short time and the error is hovering between zero throughout the time interval. In some instances the force output of the controller  $F_o(t)$  cannot track the rapidly changing reference force profile during short intervals. The Pearson correlation coefficient (see Appendix) for the reference

$\hat{Y}(t)$  and controller output force  $F_o(t)$  profile is 0.8714. Figure 4 shows the validation with a different reference force  $\hat{Y}(t)$  profile and it yields 0.8707 correlation, thus showing good agreement between the reference model force and the actual force.

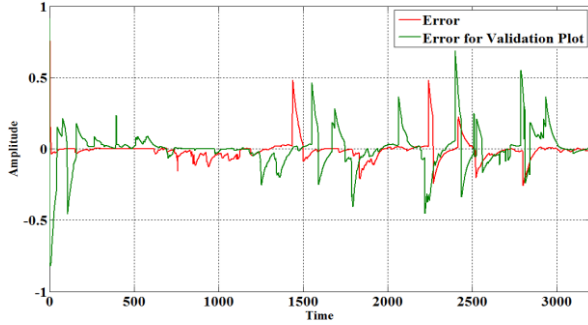


Fig. 3. Error Between the Model Force and the Actual Force

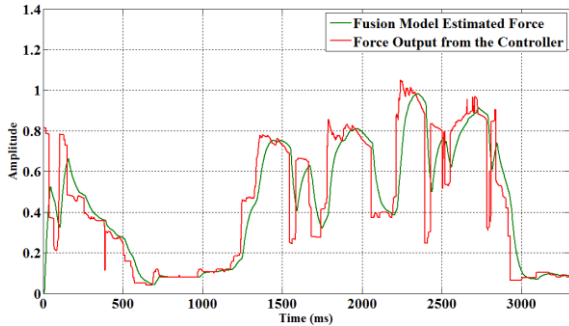


Fig. 4. Validation Plot.

## VII. CONCLUSION AND FUTURE WORK

A fusion-based sEMG-force model was utilized to estimate the force profile that a prosthetic hand should track. This fusion enables to get better force estimates than the single sensor data. The dynamics of the hand was obtained and the controller for optimal tracking between the reference model and the hand was designed. The proposed design gives good performance when tested on a prosthetic hand, based on tracking a reference force profile. In future, we plan to implement this proposed control strategy on a micro controller for real time control. It would be interesting to implement both the force and position control using this control strategy. Finally, we plan to use the hand prototype with five fingers.

## APPENDIX

The resulting MISO transfer function  $H(s)$  is constructed as,

From  $u_1$  to output,

$$\frac{s^8 - 3.843s^7 + 7.729s^6 - 10.78s^5 + 10.6s^4 - 7.417s^3 + 3.603s^2 - 0.9795s + 0.1192}{s^8 - 4.028s^7 + 6.325s^6 - 4.121s^5 - 1.545s^4 + 5.87s^3 - 5.433s^2 + 2.28s - 0.3496}$$

From  $u_2$  to output,

$$\frac{s^8 - 4.339s^7 + 9.005s^6 - 12.42s^5 + 12.22s^4 - 8.117s^3 + 3.427s^2 - 0.9134s + 0.1424}{s^8 - 4.028s^7 + 6.325s^6 - 4.121s^5 - 1.545s^4 + 5.87s^3 - 5.433s^2 + 2.28s - 0.3496}$$

From  $u_3$  to output,

$$\frac{s^8 - 3.522s^7 + 6.655s^6 - 8.864s^5 + 8.183s^4 - 5.365s^3 + 2.423s^2 - 0.557s + 0.09585}{s^8 - 4.028s^7 + 6.325s^6 - 4.121s^5 - 1.545s^4 + 5.87s^3 - 5.433s^2 + 2.28s - 0.3496}$$

Pearson correlation coefficient is given by,

$$\rho_{X,Y} = \text{corr}(X,Y) = \frac{\text{cov}(X,Y)}{\sigma_X \sigma_Y} = \frac{E[(X - \mu_X)(Y - \mu_Y)]}{\sigma_X \sigma_Y}$$

Where  $X, Y$  are Random Variables,  $\mu_X$  and  $\mu_Y$  are expected values,  $\sigma_X, \sigma_Y$  are standard deviations respectively.  $E$  is expected value operator.

## ACKNOWLEDGMENT

This research was sponsored by the US Department of the Army, under the award number W81XWH-10-1-0128 awarded and administered by the U.S. Army Medical Research Acquisition Activity, 820 Chandler Street, Fort Detrick MD 21702-5014. The information does not necessarily reflect the position or the policy of the Government, and no official endorsement should be inferred. For purposes of this article, information includes news releases, articles, manuscripts, brochures, advertisements, still and motion pictures, speeches, trade association proceedings, etc. Further, the technical help from Dr. Cheng-Hung Chen, Mr. Amir Fassih and Mr. Parmod Kumar is greatly appreciated.

## REFERENCES

- [1] "Aca News: National Limb Loss Awareness Month" 2011. Retrieved from <http://www.bocusa.org/aca-news-national-limb-loss-awareness-month>
- [2] D.S. Naidu and C.-H. Chen, "Control Strategies for Smart Prosthetic Hand Technology: An Overview", Book Chapter 14, to appear in a book titled, Distributed Diagnosis and Home Healthcare (D2H2): Volume 2, American Scientific Publishers, CA, January 2011.
- [3] Zinn M, Roth B, Khatib O, and Salisbury JK, "A new actuation approach for human friendly robot design," *Int J Robot Res.* 2004; 23(4-5), pp. 379-398.
- [4] Heinzmann J, and Zelinsky J, "A safe-control paradigm for human-robot interaction," *J Intell Robot Syst.* 1999; 25(4): pp. 295-310.
- [5] Kandel E.R. and Scharz J.H., "Principles of Neural Science," Elsevier/North-Holland, New York, 1981.
- [6] Potluri C., Kumar P., Anugolu M., Urfer, A.; Chiu S., Naidu D.S., Schoen, "Frequency Domain Surface EMG Sensor Fusion for Estimating Finger Forces," 32nd Annual International Conference of the IEEE Engineering in Medicine and Biology Society, Buenos Aires, Argentina, August 31 - September 4, 2010.
- [7] [http://www.isek-online.org/standards\\_emg.html](http://www.isek-online.org/standards_emg.html).
- [8] F.L. Lewis, D.M. Dawson, and C.T. Abdallah, "Robot Manipulators Control: Second Edition, Revised and Expanded", New York, NY: Marcel Dekker, Inc., 2004.
- [9] B. Siciliano, L. Sciacivico, L. Villani, and G. Oriolo, "Robotics: Modelling, Planning and Control". London, UK: Springer-verlag, 2009.
- [10] C.-H. Chen, "Hybrid Control Strategies for Smart Prosthetic Hand", Ph.D dissertation, Measurement and Control Engineering, Idaho State University, May 2009.
- [11] R. Kelly, V. Santidanez, and A. Loria, "Control of Robot Manipulators in Joint Space", New York, USA, Springer, 2005.
- [12] R.N. Jazar, "Theory of Applied Robotics, Kinematics, Dynamics, and Control", New York, USA, Springer 2007.
- [13] Cheng-Hung Chen, D. Subbaram Naidu, "Optimal Control Strategy For Two-Fingered Smart Prosthetic Hand", Proceedings of the IASTED International Conference Robotics and Applications (RA 2010), November 1-3, Cambridge, Massachusetts, USA, 2010.
- [14] D. Naidu, "Optimal Control Systems", Boca Raton, FL, CRC Press, 2003.

# A sEMG-based Real-time Adaptive Joint angle Estimation and Control for a Prosthetic Hand Prototype

CHANDRASEKHAR POTLURI, MADHAVI ANUGOLU, STEVE CHIU, D. SUBBARAM  
NAIDU, MARCO P. SCHOEN

Measurement and Control Engineering Research Center, School of Engineering  
Idaho State University  
921 South 8<sup>th</sup> Avenue, Stop 8060, Pocatello, Idaho  
USA  
naiduds@isu.edu

**Abstract:** - This paper presents a novel approach of a surface electromyographic (sEMG)-based, real-time Model Reference Adaptive Control (MRAC) strategy for joint angle estimation and control of a prosthetic hand prototype. The proposed design is capable of decoding the pre-recorded sEMG signal as well as the sensory force feedback from the sensors to control the joint angle of the prosthetic hand prototype using a PIC 32MX360F512L microcontroller. The input sEMG signal is rectified, filtered using a Half-Gaussian filter and fed to a Kullback Information Criterion (KIC) based fusion algorithm, which give the overall estimated joint angle (position). This estimated angle is given as input to the prosthetic hand prototype. Then the MRAC along with a two stage proposed embedded design is used for the position control of the prosthetic hand. For the real-time operation, the measured angle data at the joint is fed back to the controller. The data is transmitted to the computer through a universal asynchronous receiver/transmitter (UART) interface of the proposed embedded design. The experimental results in real time show good performance in controlling the angle of the prosthetic hand prototype.

**Key-Words:** - Prosthetic Hand, sEMG, Data fusion, Kullback Information Criterion, MRAC, Angle control

## 1 Introduction

For 60 years, there has been active research going on in the area of Prostheses. Due to the unavailability of prosthetic devices with full human hand functionality at an affordable price, more than 30% of upper extremity amputees chose not to use a prosthetic device on regular basis [1, 2]. Besides that, most of the available prosthetic devices do not have tactile or proprioceptive feedback [3]. Previous researchers insisted that human-centered robots must be independent with a great functionality, comfort and ease of use [4]. In rehabilitation robotics, human-machine interface, which requires a natural means of communication, is an interesting domain [5]. The electromyographic (EMG) signal is the electric potential generated by muscles. There are two kinds of EMG signals: Intramuscular (needle) EMG and the Surface EMG (sEMG). Under the assumption that amputation is transradial and which does not require surgery, we relied on sEMG signals in this work whose amplitude ranges from -5 to +5 (mV). sEMG signals are acquired from the surface of the skin, as they penetrate through various tissue layers [6]. Thus, they tend to create cross-talk, interference and noise. The sEMG is a temporally and spatially composed signal [7].

Due to the complexity and nonlinearity of the human hand, the control of a multi-fingered prosthetic hand is a challenging task [8]. From the past research, it is clear that the most widespread approach for controlling the prosthetic hand is by using a position or force control [9]. The challenging task involved in this work is the prediction of the Proximal Inter Phalangeal (PIP) joint angle corresponding to the sEMG signal.

In this paper, we used a three-by-three array of sEMG sensors and a wheel potentiometer device to acquire the EMG signal and the corresponding PIP joint angle. The data from the array of sEMG sensors were fused using a probability based fusion algorithm in order to have a better estimate [10]. A real-time embedded MRAC control system with sensory feedback was implemented to accomplish the goal of this design. Considering the probability based fused joint angle estimate as input to the real-time control system, a two stage embedded platform with a simple MRAC strategy was chosen for the PIP joint angle control of the prosthetic hand prototype.

## 2 Experimental setup

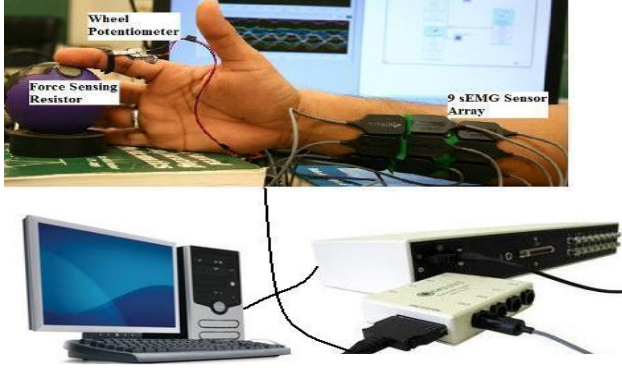


Fig.1: Experimental set-up.

Fig.1. illustrates the experimental design used in this work for capturing the sEMG signal and the corresponding joint angle of the PIP joint of the index finger. Prior to placing the sEMG sensors on the skin surface, the test subject was prepared according to ISEK standards [11]. The motor point was identified by using a wet probe muscle point stimulator (Richmar HV-1000). Nine DE-3.1 sEMG sensors of the DELSYS Bagnoli-16 EMG system were arranged on the skin surface in a three-by-three array. The middle row of sensors was placed on the motor point of the index finger. An angle measurement device was designed using a 10k-Ohm wheel potentiometer shown in Fig.1. It was used to measure the PIP joint angle. Force Sensitive Resistor (FSR) was mounted on the stress ball and was used to measure the force. All the data was acquired at a sampling rate of 2000 samples/sec.

## 3 Proposed Design

The objective of the proposed design is to track a joint angle of the prosthetic hand as closely as possible. Here, the joint angle signal is inferred from the sEMG signals obtained from the array of the sEMG sensors located at the arm.

Sensor fusion is done in the time domain for the sEMG data using a probability based Kullback information criterion (KIC) fusion algorithm. The data from the nine sensors were collected around the corresponding individual motor unit at the transradial arm location (flexor digitorum superficialis) and before fusing the sEMG signals are rectified and filtered using a Half -Gaussian filter, as given by (1).

$$p(EMG|x) = 2 \times \frac{\exp\left(-\frac{EMG^2}{2x^2}\right)}{\sqrt{2\pi x^2}}, \quad (1)$$

where  $p(EMG|x)$  is a conditional probability density function,  $x$  is a latent driving signal.

A System Identification (SI) tool was used to determine the dynamic relationship between the input-output data. The sEMG signal was used as input and the corresponding PIP joint angle as output. In particular, nonlinear Wiener Hammerstein one-dimensional polynomial models were obtained for the sEMG/joint angle data.

The mathematical representation of the modeling is given by,

$$w(t) = f(u(t)) \quad (2)$$

$$x(t) = \frac{B_{i,j}(q)}{F_{i,j}(q)} w(t - nk) + e(t) \quad (3)$$

$$y(t) = h(x(t)) \quad (4)$$

where  $u(t)$  is the sEMG signal and  $y(t)$  is the PIP joint angle.  $f$  and  $h$  are nonlinear functions,  $w(t)$  and  $x(t)$  are internal variables,  $B_{j,i}(q)$  and  $F_{j,i}(q)$  are polynomials,  $q$  is the back shift operator, and  $e(t)$  is the output error. From (3), the WH model structure utilizes a linear OE model, which is given by,

$$y(t) = \frac{b(q)}{F(q)} u(t - nk) + e(t) \quad (5)$$

where  $nk$  is the system delay and  $t$  is time index

The resulting nine WH models were fused together by using a probabilistic KIC algorithm [12]. It assigns a particular probability to each model [13]. The overall estimated model output and the individual models outputs were compared by using the Pearson's correlation coefficient.

From the previous research, it was shown that the KIC algorithm performs better than the other criteria [10, 12]. KIC is an asymmetric measure of the models' dissimilarity which can be obtained by the sum of the two directed divergences known as J-divergence or Kullback's symmetric [14]. It is given by

$$KIC(p_i) = \frac{n}{2} \log R_i + \frac{(p_i+1)n}{n-p_i-2} - n\psi\left(\frac{n-p_i}{2}\right) + g(n) \quad (6)$$

Where  $g(n) = n \cdot \log(n/2)$ ,  $\psi$  - digamma function.

The probability based fusion algorithm given by [12, 13] is applied to the nonlinear models obtained by using an SI technique with the following steps:



1: The WH models are obtained by considering the sEMG data  $u(t)$  as input and joint angle  $Y$  as output,

2: Calculate the residual square norm i.e.,  $R_i = Y - \Phi_i \hat{\theta}_i = \|Y - \hat{Y}\|$

where  $\hat{\theta}_i = \{\Phi_i^T \Phi_i\}^{-1} \Phi_i^T Y$ , and

$$\Phi = \begin{bmatrix} Y^T & u_{p-1}^T & Y_{p-1}^T & u_1^T \\ Y_{p+1}^T & u_{p+1}^T & Y_p^T & u_2^T \\ \dots & \dots & \dots & \dots \\ Y_{n-1}^T & u_{n-1}^T & Y_{n-2}^T & u_{n-p}^T \end{bmatrix}$$

3: Compute the model criteria coefficients using (6).

4: The model probability can be computed using

$$p(M_i(t) | Z) = \frac{e^{-l_i}}{\sum_{j=1}^k e^{-l_j}}$$

5: The fused model output can be calculated using

$$\hat{Y}_f = \sum_{i=1}^k p(M_i(t) | Z) \hat{Y}_i.$$

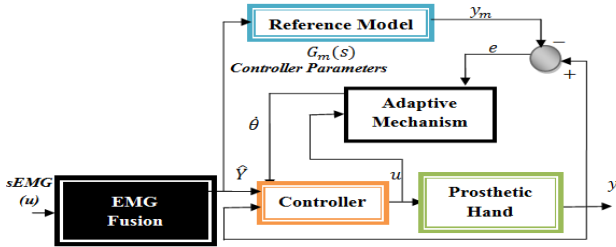


Fig.2: Block diagram representation of Model Reference Adaptive Controller (MRAC)

A simple MRAC based scheme (Fig. 2) is utilized for compensating the dynamics of the prosthetic hand. During the development of the artificial hand, changes were being undertaken to the mechanical design and drive trains of the hand that affect the dynamics of the finger motion of the prosthesis. In addition, the uncertain characteristics of the kinematic and actuator interaction could have led to a different performance than expected. Therefore, a simple MRAC controller was developed in order to maintain some performance stability. For updating the controller parameter  $\theta$ , the MIT rule was used.

$$\frac{d\theta}{dt} = -\gamma e Y_m. \quad (7)$$

According to the MIT rule [15], the gain parameter  $\gamma$  was selected to achieve the desired performance. In this work  $\gamma$  was taken as 3.0 and

the error  $e = Y - Y_m$  was calculated by the difference of the model reference output  $Y_m$  and the actual output (joint angle generated by the prosthetic hand). Different MRAC stability issues were addressed in [14, 15].

### Reference Model Derivation

The dynamic equations of motion for the hand are obtained from the Lagrangian approach as [16]

$$\dot{x}(t) = \begin{bmatrix} 0 & I \end{bmatrix} x(t) + \begin{bmatrix} 0 \\ I \end{bmatrix} u(t). \quad (8)$$

The control input vector  $u(t)$  was given by

$$u(t) = -M^{-1}(q(t)) [N(q(t), \dot{q}(t)) - \tau(t)]. \quad (9)$$

As the prosthetic hand is required to track the desired angle profile  $q_d(t)$  described under the reference angle model, the tracking error  $e(t)$  is defined as

$$e(t) = q_d(t) - q(t). \quad (10)$$

Here,  $q_d(t)$  is the desired angle vector of the joints and can be obtained by the reference angle model [17];  $q(t)$  is the actual angle vector of the joints. Differentiating (10) twice, we get,

$$\dot{e}(t) = \dot{q}_d(t) - \dot{q}(t), \quad \ddot{e}(t) = \ddot{q}_d(t) - \ddot{q}(t). \quad (11)$$

Substituting  $\dot{q}(t)$  into (11) gives

$$\ddot{e}(t) = \ddot{q}_d(t) + M^{-1}(q(t)) [N(q(t), \dot{q}(t)) - \tau(t)] \quad (12)$$

From (12) the control function  $u(t)$  can be defined as

$$u(t) = \ddot{q}_d(t) + M^{-1}(q(t)) [N(q(t), \dot{q}(t)) - \tau(t)]. \quad (13)$$

This is often called the feedback linearization control law, rewriting (13) as,

$$\tau(t) = M(q(t)) [\ddot{q}_d(t) - u(t) + N(q(t), \dot{q}(t))] \quad (14)$$

Using (11) and (13), the state vector  $x(t) = [e'(t) \dot{e}'(t)]'$ , the state-space model can be represented as

$$\dot{x}(t) = \begin{bmatrix} 0 & 1 \\ 0 & 0 \end{bmatrix} x(t) + \begin{bmatrix} 0 \\ 1 \end{bmatrix} u(t). \quad (15)$$

Now, (15) is in the form of a linear system such as

$$\dot{x}(t) = Ax(t) + Bu(t). \quad (16)$$

#### Implementation:

The proposed control design was implemented on a PIC 32MX360F512L microcontroller in two stages: “Signal Processing” and “Motor Actuation”. The Signal Processing stage enables the execution and implementation of real-time control strategies. A dsPIC block set was used to generate the C code for the PIC 32 from Simulink®. The dsPIC block set generates a .hex file, and this file was imported in MPLAB® to program the PIC 32.

#### Signal Processing Stage:

From the many modules available on PIC 32, the following four modules were utilized for the implementation of the signal processing stage: Analog Input Module, Digital Output module, Output Compare module, and URAT module.

The sensory feedback joint angle data from the wheel potentiometer was acquired through the Analog Input module. Based on the selected control strategy for the motor actuation stage, the digital control signals were generated by the Digital Output module of the PIC 32. The changes in the reference/command signal were detected by this module. A pulse width modulated (PWM) wave with a specific duty cycle was generated by the Output Compare module based on the error. The angle data from the microcontroller to the PC was transmitted by the UART module via serial communication. In this particular design, the data was fed to the computer by a virtual com port via USB cable. The signals from the ports were read by MATLAB®.

#### Motor Actuation Stage:

In this stage, the motor was actuated with a SN754410 quadruple half-H driver [18] with the corresponding control signal. This proposed design was tested on the index finger of a prosthetic hand prototype. Fig. 3 shows the test bed for the proposed design.

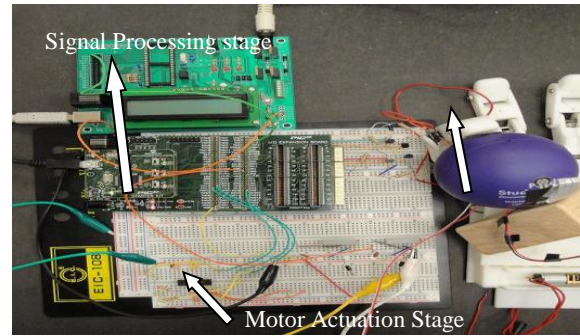


Fig. 3. Embedded Test bed for the proposed design

#### Mechanical structure of the robotic hand prototype:

The prosthetic hand prototype finger has three degrees of freedom stimulated by two Pololu 35:1 mini metal gear motors. Biologically inspired parallel actuation is the main characteristic of this robotic hand prototype. It is based on the behaviour/strength space of the Flexor Digitorum Profundus (FDP) and the Flexor Digitorum Superficialis (FDS) muscles [19]. Using a belt transmission system, the DC motor in the metacarpal phalange of the finger triggers the Proximal Inter Phalangeal (PIP) joint. It also drives the DIP (Distal Inter Phalangeal) joint. The Meta Carpo Phalangeal (MCP) joint is actuated by the DC motor located at the base of the finger as shown in Fig. 4.

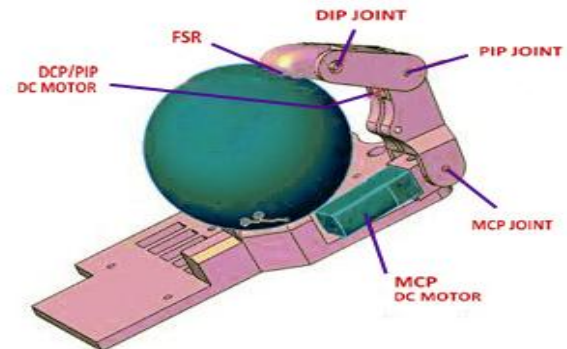


Fig. 4. Finger Actuation Scheme

## 4 Results and Discussion

Data was acquired from the microcontroller through UART channel2 of the PIC 32 micro controller by a virtual com port via USB at a 57600 baud rate. The data from the microcontroller was converted into unit16 data type before it is transmitted through the UART. It ran at an external clock frequency of 8MHz with internal scaling enabled. Fig. 5 depicts the experimental results of the proposed design. The actual angle output from the position sensor (i.e.Y)



closely follows the fusion algorithm estimated angle  $\hat{Y}$ . Fig. 6 shows the fusion estimated angle profile  $\hat{Y}$  and actual angle from the position sensor ( $Y$ ) plotted for a separate experiment. Fig. 7 shows the repeated experimental results. The proposed control strategy was tracking angle profile and matching the actual angle profile with the model estimated angle ( $\hat{Y}$ ).

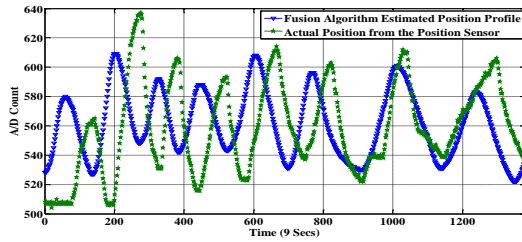


Fig. 5. Fusion based angle estimate and actual angle from angle sensor during the grasp action.

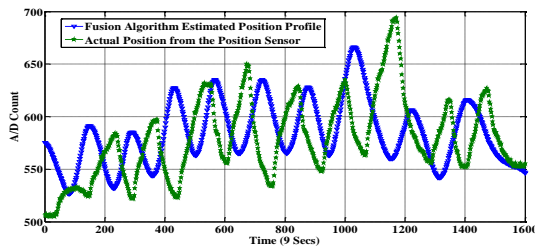


Fig. 6. Fusion based angle estimate and actual angle from angle sensor during the grasp action (for experiment-2).

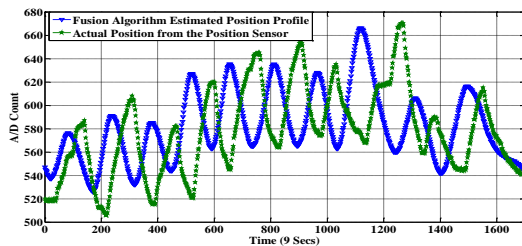


Fig. 7. Fusion based angle estimate and actual angle from angle sensor during the grasp action (for experiment-3).

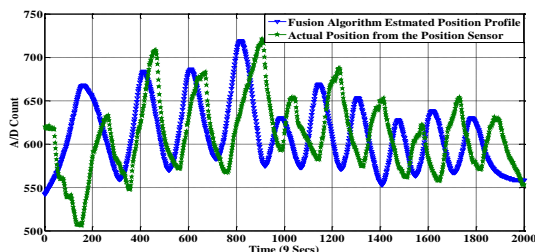


Fig. 8. Validation Plot.

While conducting the experiments, the following observations were made. The DC motors currently employed have the primary task of moving the prosthetic fingers. As the project is on-going, the Shape Memory Alloy (SMA) actuation scheme has

not yet been implemented because of the slow response of the SMA's, and also because SMA's have a long relaxation time. Therefore it is difficult to track a randomly changing angle profile with a slowly responding actuation system. However, as the prosthetic hand prototype is designed to use the parallel actuation of these DC motors and SMA's, the DC motors alone cannot produce a fusion algorithm estimated angle profile.

In this work, the DC motors are solely responsible for motion actuation. Since the DC motors have small gear heads, the usual characteristic of gear driver actuation cores occurs: gear backlash. In addition, the DC motors employed were slow in responding to the changes in the force profile. Hence some gaps and delay were observed in the measured angle signal. However, the profile of the measured angle from the angle sensor has a similar pattern as the fusion algorithm estimated angle ( $\hat{Y}$ ). Thus we can conclude that apart from those mechanical transmission problems, the implemented control scheme produced promising results. These problems will be considered in a new prototype design that we are currently developing.

From the results, it is also evident from Figs. 5, 6 and 7 that the controller is tracking the slow changes in the angle profile very well, where as a small delay was observed while tracking the angle profile. In order to test the precision of the proposed control strategy, 15 different experiments were conducted. The mean of the Pearson's correlation coefficient for the fusion algorithm estimated angle ( $\hat{Y}$ ) and the actual angle from the angle sensor ( $Y$ ) in all the 15 experiments is 0.86. Because of the above mentioned transmission problems and the slow response of the gears, slight variability is observed in the correlation coefficients for the 15 experiments. Hence the difference in tracking the angle profile is observed in Figs. 6 and 7. Fig. 8 depicts the validation plot with a different fusion algorithm angle estimate  $\hat{Y}$  obtained by feeding a different sEMG.

## 5. Conclusion and Future Work

In this paper, based on sEMG signals, we proposed a two-stage real-time embedded MRAC strategy for a prosthetic hand prototype. The proposed design was based on tracking a reference angle profile and it gives good performance when tested on a prosthetic hand prototype. This design enables the transmission of the data from the microcontroller to the

computer. This design allows the control engineer to increase the accuracy and performance of the design by implementing various novel control strategies and also enables fast trouble shooting.

For future work, we are planning to use the above mentioned embedded platform to implement online model-based skeletal muscle angle estimation along with controller designs that address the above listed mechanical shortcomings. It will be valuable to acquire the sEMG signal directly from the arm of a healthy subject and transmit to our embedded system rather than using pre-recorded sEMG signals, which will be investigated as well in the future.

### ACKNOWLEDGMENT

This research was sponsored by the US Department of the Army, under the award number W81XWH-10-1-0128 awarded and administered by the U.S. Army Medical Research Acquisition Activity, 820 Chandler Street, Fort Detrick MD 21702-5014. The information does not necessarily reflect the position or the policy of the Government, and no official endorsement should be inferred. For purposes of this article, information includes news releases, articles, manuscripts, brochures, advertisements, still and motion pictures, speeches, trade association proceedings, etc. Further, the technical help from Dr. Alba Perez and Mr. Alex Jensen is greatly appreciated.

### References:

- [1] <http://www.columbiainmissourian.com/stories/2009/02/15/soldier-who-lost-leg-iraq-may-loseother/>
- [2] D.J. Atkins, D.C. Y. Heard, and W.H. Donovan, "Epidemiologic overview of individuals with upper-limb loss and their reported research priorities", *Journal of Prosthetics and Orthotics*, Vol. 8, NO. 1, 1996, pp- 2-11.
- [3] D.S. Naidu and C.-H. Chen, "Control Strategies for Smart Prosthetic Hand Technology: An Overview", Book Chapter 12, , Distributed Diagnosis and Home Healthcare (D2H2): Volume 2, American Scientific Publishers, CA, January 2011.
- [4] Bien ZZ, and Stefanov D, "Advances in rehabilitation robotics: Human-friendly technologies on movement assistance and restoration for people with disabilities," *Springer, Berlin (Germany)*. 2004.
- [5] Heinzmann J, and Zelinsky J, "A safe-control paradigm for human-robot interaction," *J Intell Robot Syst.* 1999; 25(4): pp. 295-310.
- [6] Cram, J.R., Kasman G.S., and Holtz J. "Introduction to Surface Electromyography," Aspen Publisher Inc., Gaithersburg, Maryland, 1998.
- [7] Kandel E.R. and Scharzt J.H., "*Principles of Neural Science*," Elsevier/North-Holland, New York, 1981.
- [8] T. H. Sueeter, "Control of the Utah/MIT Dextrous hand: Hardware and software hierarchy," *J. Robot. Syst.*, vol. 7, no. 5, pp. 759-790, 1990.
- [9] M. H. Raibert and J. J. Craig, "Hybrid angle and force control of manipulators," *ASME J. Llyn. Syst. Meas. Contr.*, vol. 102, pp. 126-133, June 1981
- [10] Anugolu M., Sebastian A., Kumar P., Schoen M., Urfer A., Naidu D.S., "Surface EMG array sensor based model fusion using Bayesian approaches for Prosthetic Hand", *Proceeding of the Dynamic Systems and Control Conference*, Hollywood , Ca, October 2009.
- [11] <http://www.isel.online.org/standardsemg.html>.
- [12] Chen H., Huang S., "A Comparative study on Model Selection and Multiple Model Fusion", *7<sup>th</sup> International Conference on Information Fusion*, 2005, PP.820-826.
- [13] Seghouane A.K, Bekara M., Fluery G., " A small Sample Model Selection Criterion based on Kullback's Symmetric Divergence", *IEEE Transaction*, 2003, pp. 145-148.
- [14] Karl J. Astrom and Bjorn Wittenmark "*Adaptive Control Second Edition*", Dover Publications, Dec 18, 2008.
- [15] Potluri C., Anugolu M., Yihun Y., Kumar P., Chiu S., Schoen M., Naidu D.S., " Implementation of sEMG-based Real-time Embedded Adaptive Finger Force Control for a Prosthetic Hand", *IEEE Conference on Decision and Control and European Control Conference*, Orlando, Florida, USA, Dec 12-15, 2011.
- [16] Potluri C., Anugolu M., Yihun Y., Jensen A., Chiu S., Schoen M., Naidu D.S., " Optimal Tracking of a sEMG based Force Model for a Prosthetic Hand", *33<sup>rd</sup> Annual International Conference of the IEEE Engineering and Medicine and Biology Society*, Boston, Ma, USA, Aug 31-Sep 3, 2011.
- [17] F.L.Lewis, D.M.Dawson, and C.T. Abdallah, "*Robot Manipulators Control: Second Edition, Revised and Expanded*", New York, NY: Marcel Dekker, Inc., 2004.
- [18] Texas Instruments "SN754410 quadruple half H-driver data sheet" Dallas, Texas, November 1986 and 1995
- [19] Dr. Anthony L. Crawford,"Design of a Robotic Hand and Simple EMG Input Controller with a Biologically-Inspired Parallel Actuation System for Prosthetic Application" ASME 2010, IDETC/CIE 2010.

# Kinematic Synthesis of Multi-fingered Robotic Hands for Finite and Infinitesimal Tasks

E. Simo-Serra, A. Perez-Gracia, H. Moon and N. Robson

**Abstract** In this paper we present a novel method of designing multi-fingered robotic hands using tasks composed of both finite and infinitesimal motion. The method is based on representing the robotic hands as a kinematic chain with a tree topology. We represent finite motion using Clifford algebra and infinitesimal motion using Lie algebra to perform finite dimensional kinematic synthesis of the multi-fingered mechanism. This allows tasks to be defined not only by displacements, but also by the velocity and acceleration at different positions for the design of robotic hands. The additional information enables an increased local approximation of the task at critical positions, as well as contact and curvature specifications. An example task is provided using an experimental motion capture system and we present the design of a robotic hand for the task using a hybrid Genetic Algorithm/Levenberg-Marquadt solver.

**Key words:** kinematic synthesis, multi-fingered grippers, Clifford and Lie algebra.

## 1 Introduction

The design of end-effector robotic tools has traditionally taken place in an application-oriented fashion within the framework of the mechanical design theory [7]. Among the rich variety of robotic end-effectors, those generally defined as robotic hands are considered suited not only for grasping, but also for dexterous manipulation. We can

---

E. Simo-Serra  
Institut de Robòtica i Informàtica Industrial (CSIC-UPC) e-mail: esimo@iri.upc.edu  
A. Perez-Gracia  
Idaho State university, Pocatello, Idaho 83209 e-mail: perealba@isu.edu  
H. Moon  
Texas A&M University, College Station, TX 77843 e-mail: hsmoon@neo.tamu.edu  
N. Robson  
Texas A&M University, College Station, TX 77843 e-mail: ninarobson@tamu.edu

define a multi-fingered robotic hand as an end-effector in which the base, or palm, spans several serial chains in a tree-like structure.

There are a great variety of designs for robotic hands. Some designs mimic the human hand and exhibit a high number of degrees of freedom, [1] and [15]; others are designed for specific applications [4] and may or not be anthropomorphic [5].

Most of the designs have been oriented either towards maximum anthropomorphism or towards optimizing grasping, manipulability or workspace size. A good review on the efforts toward kinematic hand design can be found in [6]. As robotic hands become more common in industrial applications and human environments, it makes sense to think that their design will become more task-oriented. Soto Martell and Gini [14] expose the need for a task-based design process for robotic hands.

The use of kinematic synthesis for the design of the multi-fingered robotic hand has been applied to individual fingers, see [2]. We believe that the reason why dimensional synthesis has been scarcely applied to robotic hand design is because of the lack of a method that takes a multi-fingered task as the input and outputs a multi-fingered design.

In this paper, we extend the work presented in [13] by combining it with the results on kinematic synthesis for infinitesimal positions [8, 9] and expressing the kinematics using the Clifford algebra of dual quaternions [10]. Note that mechanical linkages are traditionally synthesized by specifying a task, consisting of a number of positions that the end-effector has to move through, with the goal of determining the design parameters, i.e. fixed and moving pivot locations, as well as the size of the linkage. The difference between the traditional design of mechanical linkages and the current design with contact direction, used in this research, is basically in the task, which consists not only of positions, but velocities and accelerations compatible with contact and curvature specifications between the end-effector/fingers and the object to be grasped. In comparison to the traditional synthesis techniques, these velocities and accelerations yield to a more complicated system of position, velocity and acceleration design equations, as well as more complicated trajectory planning techniques.

As an example, we apply this methodology to the design of a multi-fingered hand for operating a door knob. The motivation for this design arose from an individual, who is confined to a wheel chair after an accident. He has limited movement and weakness in his hands, making it difficult for him to grasp doorknobs at his workspace. The synthesis presented here is the first step towards developing assistive manipulation devices.

## 2 Infinitesimal Kinematics

The generic screw  $S$  for a twist can be represented as an element of the Lie algebra  $se(3)$  [12],

$$S = \lambda (\mathbf{s}; \mathbf{r} \times \mathbf{s} + h\mathbf{s}) = \lambda (\mathbf{s}; \mathbf{s}^0 + h\mathbf{s}) = (\omega; \mathbf{v}) \in se(3) \quad (1)$$

where  $\mathbf{s}, \mathbf{r}, \boldsymbol{\omega}, \mathbf{v} \in \mathbb{R}^3$  with  $\mathbf{s} \cdot \mathbf{s} = 1$ ,  $\mathbf{s}^0 = \mathbf{r} \times \mathbf{s}$  and  $\lambda, h \in \mathbb{R}$ .

The relative velocities between a pair of rigid bodies form one-dimensional subalgebras of the Lie algebra  $se(3)$  [11]. The most generic subalgebra is generated by the screw or helical joint  $S$  which becomes a revolute joint  $S_R = (\mathbf{s}; \mathbf{s}^0)$  with  $h = 0$  or a prismatic joint  $S_P = (0; \mathbf{s})$  with the screw axis at infinity. The binary operation of the Lie algebra is the Lie bracket, which can be expanded for screws as,

$$[S_1, S_2] = [(\boldsymbol{\omega}_1; \mathbf{v}_1), (\boldsymbol{\omega}_2; \mathbf{v}_2)] = (\boldsymbol{\omega}_1 \times \boldsymbol{\omega}_2; \boldsymbol{\omega}_1 \times \mathbf{v}_2 + \mathbf{v}_1 \times \boldsymbol{\omega}_2) \quad (2)$$

The velocity of the end-effector for a serial articulated chain with  $n$  joints in a given configuration can be written as [12],

$$\frac{d\mathbf{P}}{dt} = \dot{\mathbf{P}} = \sum_{i=1}^n \dot{\theta}_i S_i \quad (3)$$

where  $\dot{\mathbf{P}} = (\boldsymbol{\omega}; \mathbf{v})$  with  $\boldsymbol{\omega}$  being the angular velocities and  $\mathbf{v}$  being the Cartesian velocities. The screws  $S_i$  represent the infinitesimal screws of each joint.

The infinitesimal screws can be transformed to an instantaneous position from a reference position using the Clifford algebra conjugation action,

$$S_i^k = \left( e^{\frac{\Delta\hat{\theta}_{i-1}^k}{2} S_{i-1}^k} \right) S_i \left( e^{\frac{\Delta\hat{\theta}_{i-1}^k}{2} S_{i-1}^k} \right)^* = \left( \prod_{j=1}^{i-1} e^{\frac{\Delta\hat{\theta}_j^k}{2} S_j} \right) S_i \left( \prod_{j=1}^{i-1} e^{\frac{\Delta\hat{\theta}_j^k}{2} S_j} \right)^* \quad (4)$$

where  $\Delta\hat{\theta}_i^k = \hat{\theta}_i^k - \hat{\theta}_i^r$  with  $\hat{\theta}_i^r$  is the joint parameter in the reference configuration and  $S_i^k$  is the  $i$ -th screw in a serial chain at position  $k$ .

The velocity of a joint  $j$  in a chain is written as the derivative of a finite screw [3],

$$\frac{dS_j}{dt} = \dot{S}_j = \sum_{i=1}^{j-1} \dot{\theta}_i [S_i, S_j] \quad (5)$$

Cross terms and the non-commutation of the derivation operator must be taken into account as seen by differentiating each velocity component of (3) using the chain rule. This can be expanded to obtain the acceleration of the end-effector,

$$\frac{d^2\mathbf{P}}{dt^2} = \ddot{\mathbf{P}} = \frac{d}{dt} \dot{\mathbf{P}} = \sum_{i=1}^n (\ddot{\theta}_i S_i + \dot{\theta}_i \dot{S}_i) = \sum_{i=1}^n \ddot{\theta}_i S_i + \sum_{i=1}^{n-1} \dot{\theta}_i \sum_{j=i+1}^n \dot{\theta}_j [S_i, S_j] \quad (6)$$

where  $\ddot{\mathbf{P}} = (\boldsymbol{\alpha}; \mathbf{a})$  with  $\boldsymbol{\alpha}$  being the angular accelerations and  $\mathbf{a}$  being the Cartesian accelerations.

The approach is general in the sense that the chain rule can be successively applied to obtain higher derivatives if necessary.

### 3 Design Equations for Tree Topologies

Tree topologies can be seen as many different serial chains that share a number of common joints. The equations can be written as for serial chains, but the task definition will vary with the topology. The finite motion of a joint can be expressed using the exponential map of a screw  $S$ . This can be expressed using the unit element of the Clifford even subalgebra of the projective space  $Cl^+(0, 3, 1)$  or dual quaternion,

$$e^{\frac{\hat{\theta}}{2}S} = (\cos \frac{\theta}{2} - \frac{d}{2} \sin \frac{\theta}{2} \varepsilon) + (\sin \frac{\theta}{2} + \frac{d}{2} \cos \frac{\theta}{2} \varepsilon)S = \cos \frac{\hat{\theta}}{2} + \sin \frac{\hat{\theta}}{2}S. \quad (7)$$

where  $\varepsilon$  is the dual unit such that  $\varepsilon^2 = 0$ .

For a serial chain with  $n$  joints, the forward kinematics of a serial chain can be written relative to a reference configuration of the serial chain,

$$\hat{Q}(\Delta \hat{\theta}) = \prod_{i=1}^n e^{\frac{\Delta \hat{\theta}_i}{2} S_i} = \prod_{i=1}^n (\cos \frac{\Delta \hat{\theta}_i}{2} + \sin \frac{\Delta \hat{\theta}_i}{2} S_i) \quad (8)$$

where  $\Delta \hat{\theta}_i = \hat{\theta}_i - \hat{\theta}_0$  with  $\hat{\theta}_0$  being the joint parameters of the reference configuration.

For a task composed of finite positions, the relative forward kinematics can be compared to the relative motion from the reference configuration to each position  $\hat{P}_{1k} = \hat{P}_k \hat{P}_1^{-1}$  [10],

$$\hat{P}_{1k} = \prod_{i=1}^n e^{\frac{\Delta \hat{\theta}_i^k}{2} S_i}, \quad k = 2, \dots, m_p \quad (9)$$

where  $m_p$  is the number of positions considered and  $\Delta \hat{\theta}_i^k = \hat{\theta}_i^k - \theta_i^1$ , with  $k = 1$  being the reference configuration.

For a task with velocities, we can use (3) to write,

$$\dot{P}_k = \sum_{i=1}^n \dot{\theta}_i^k S_i^k, \quad k = 1, \dots, m_v \quad (10)$$

where  $\dot{P}_k$  is the absolute velocity information for a given position  $k$  in the form  $(\omega; \mathbf{v})$ . The instantaneous joint screw axis  $S_i^k$  can be calculated from (4).

The same procedure can be applied to acceleration to obtain from (6),

$$\ddot{P}_k = \sum_{i=1}^n \ddot{\theta}_i^k S_i^k + \sum_{i=1}^{n-1} \dot{\theta}_i^k \sum_{j=i+1}^n \dot{\theta}_j^k [S_i^k, S_j^k], \quad k = 1, \dots, m_a \quad (11)$$

where  $\ddot{P}_k$  is the absolute acceleration for a given position  $k$  in the form  $(\alpha; \mathbf{a})$ .

The velocity and acceleration equations can be seen as additional pose information that reduce the number of poses needed. Counting the number of independent unknowns  $n_x$  and independent equations  $n_f$  we obtain,

$$n_x = n_s + n_j(m_p + m_v + m_a - 1) \quad (12)$$

$$n_f = n_c + n_d(m_p + m_v + m_a - 1) \quad (13)$$

where  $n_s$  is the number of independent structural parameters,  $n_j$  the number of joint degrees of freedom,  $n_c$  the number of independent constraints and  $n_d$  the degrees of freedom of the end-effector motion. The number of positions, velocities and accelerations are given by  $m_p$ ,  $m_v$  and  $m_a$  respectively. If we consider  $m = m_p + m_v + m_a$  we obtain the familiar formula [10],

$$m = \frac{n_s - n_c}{n_d - n_j} + 1 \quad (14)$$

## 4 Experimental Set up and Task Specification

Since the first step in our synthesis technique is related to choosing a specific task, the kinematic task selected for the design is the operation of a standard door knob. In order to define this kinematic task, the door knob grasping and turning movement was performed, from a start to end spatial locations. During the movement, the subject emulates the opening of the door motion with an apparatus shown in Fig. 1a. The upper limb kinematics at specific points of interest are captured by a 3D Motion Capture System (Vicon, OMG Plc., UK), available in our Human Interactive Robotics Lab at Texas A&M University.

Three infrared cameras track the position of each marker relative to a predefined global coordinate frame, with a sampling rate of 100 *Hz*. Five moving frames are defined at the: elbow, wrist, and tip of thumb, tip of index and tip of middle fingers, respectively. Fig. 1b shows the marker attachment. To only synthesize the motion of the forearm, the positions chosen were transformed from absolute positions  $\hat{P}_i$  to positions local to the elbow  $\hat{P}_{ij} = \hat{P}_j^{-1}\hat{P}_i$  with  $\hat{P}_j$  is the position of the elbow. For velocities this can be written as  $\dot{P}_{ij} = \dot{P}_i - \dot{P}_j$ .

The obtained positions and velocities were then used as a task for the kinematic synthesis of the multi-fingered robotic hand. The kinematic specification consists

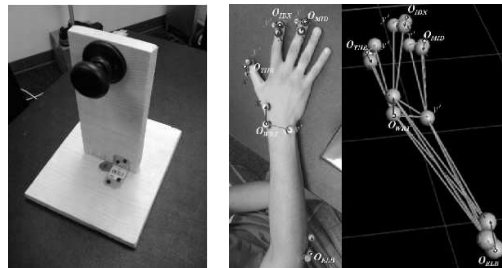


**Fig. 1** 1a The experimental apparatus for emulating the door knob task and 1b the kinematic model configured in the 3D Motion Capture System.

(a)

(b)

of set of three spatial displacements defined by  $\hat{P}_k = (\boldsymbol{\psi}_k, \mathbf{d}_k), k = 1, 2, 3$ , and the associated angular and linear velocities  $\dot{P}_k = (\omega_k; \mathbf{v}_k), k = 1, 2$  in two of the positions for each fingertip.

## 5 Solving Numerically

The solver used is an updated version of the kinematic synthesis solver for tree structures [13] updated to support the design equations (10) and (11). The solver is composed of a Genetic Algorithm (GA) paired with a Levenberg-Marquadt (LM) local optimizer. For more details on the solving approach see [13].

The full equation system for a multi-fingered robot with  $b$  fingers formed by  $n$  revolute joints can be defined directly by manipulation of the design equations,

$$\mathbf{F}(\mathbf{S}, \Delta \hat{\boldsymbol{\theta}}, \dot{\boldsymbol{\theta}}, \ddot{\boldsymbol{\theta}}) = \begin{pmatrix} \hat{P}_{1k} - \prod_{i=1}^{n_c} e^{\frac{\Delta \hat{\theta}_i^k}{2}} S_{i,c}, & k = 2, \dots, m_p \\ & c = 1, \dots, b \\ \dot{P}_k - \sum_{i=1}^{n_c} \dot{\theta}_i^k S_{i,c}^k, & k = 1, \dots, m_v \\ & c = 1, \dots, b \\ \ddot{P}_k - \left( \sum_{i=1}^{n_c} \ddot{\theta}_i^k S_{i,c}^k + \sum_{i=1}^{n_c-1} \dot{\theta}_i^k \sum_{j=i+1}^{n_c} \dot{\theta}_j^k [S_{i,c}^k, S_{j,c}^k] \right), & k = 1, \dots, m_a \\ & c = 1, \dots, b \end{pmatrix} \quad (15)$$

where  $b$  is the number of branches or fingers,  $n_c$  is the number of joints for a branch  $c$ ,  $n$  is the total number of joints in the structure and  $S_{i,c}^k$  are the instantaneous axis of the joint  $i$  in the branch  $c$  for the frame  $k$  calculated by (4). A valid mechanism is said to be found when  $\mathbf{F}(\mathbf{S}, \Delta \hat{\boldsymbol{\theta}}, \dot{\boldsymbol{\theta}}, \ddot{\boldsymbol{\theta}}) = \mathbf{0}$ .

## 6 Results

The kinematic structure of the hand consists of a three degree of freedom palm+wrst complex (RRR), and three fingers, each of which is modeled as a two degree of freedom RR kinematic chain as seen in Fig. 2a. This structure was chosen for the kinematic synthesis of the task as it has fewer degrees of freedom than the human hand while having an non-fractional number of required samples. As this paper does not deal with structural synthesis, a pre-determined topology is used. No additional constraints were placed on the structure. For this kinematic structure with 9 revolute joints, a total of  $m = 5$  samples are needed as obtained from (14).

The experimental task consists of many hundreds of frames of which  $m_p = 3$  were selected. For two of them velocity information was also used providing  $m_v = 2$ . Due to the nature of the door-knob opening task, the accelerations, related to curvature constraints (i.e. sliding motion of the fingers along the door-knob) are fairly small in comparison to the other task specifications and were not taken into



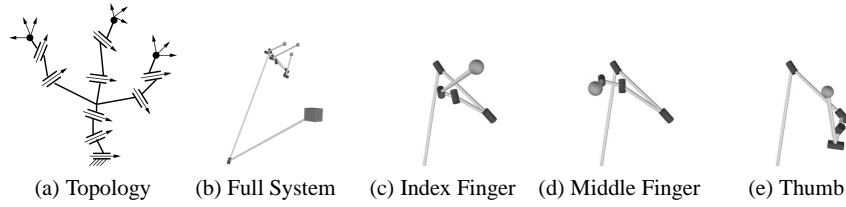


Fig. 2: The topology used and overview of a solution mechanism found.

account. Therefore, our task consists of positions, prescribed at the point where the fingers need to grasp the door knob, and velocities, describing the contact of the fingers with the door knob. The resulting equation system has 90 unknowns and 102 equations of which only 72 are independent. A set of 50 solutions was obtained taking an average of 18.06 minutes per solution and needing an average of 13.76 generations per solution with a population of 100 entities.

A selected solution mechanism of the doorknob task can be seen in Fig. 2. The thick joint axes are connected by thinner lines at the intersections of the common normals of the joints and the joint axes. The origin is represented by using a square and the end-effectors are represented by using spheres. This solution shown is more compact than the human hand as all the joints except one are grouped together and is able to perform the same task as the human hand. It was observed that generally the solutions have a similarity between the index and middle finger, while the thumb has a different shape, which is similar to how the human hand is designed.

## 7 Conclusions

This paper presents a novel dimensional synthesis methodology for articulated systems with a tree structure using additional constraints such as velocity and acceleration. It also presents a new design for numerically solving kinematic systems using these new constraints, adding upon the previous work of numerically solving tree structures with kinematic synthesis. The addition of velocity, acceleration and other derivatives at the positions allows a better local approximation of the task motion, as well tasks with contact and curvature specifications.

For the selected knob-operating task, a tree-like robot with three two-jointed fingers has been designed. Kinematic synthesis is just one step in the design process, one that allows you to create innovative candidates fitted for the kinematic tasks under consideration. Enough solutions have been found to suggest that a method to analyze and rank those needs to be a part of the design process. These results show that the dimensional synthesis of robotic multi-fingered hands is possible. In addition, multi-fingered hands appear not to be redundant when a task involving several fingers is to be performed.

**Acknowledgements** This work is partially supported by the Spanish Ministry of Science and Innovation under project DPI2010-18449.

## References

- [1] Borst, C., Fischer, M., Haidacher, S., Liu, H., Hirzinger, G.: DLR Hand II: Experiments and experiences with an anthropomorphic hand. In: ICRA (2003)
- [2] Ceccarelli, M., Nava Rodriguez, N., Carbone, G.: Design and Tests of a Three Finger Hand with 1-DOF Articulated Fingers. *Robotica* **24**, 183–196 (2006)
- [3] Cervantes-Sánchez, J.J., Rico-Martínez, J.M., González-Montiel, G., González-Galván, E.J.: The differential calculus of screws: Theory, geometrical interpretation, and applications. *Proc. of the Institution of Mechanical Engineers, Part C: Journal of Mechanical Engineering Science* **223**(6), 1449–1468 (2009)
- [4] Chalon, M.e.a.: Dexhand : a space qualified multi-fingered robotic hand. In: ICRA (2011)
- [5] Dai, J.S., Wang, D., Cui, L.: Orientation and workspace analysis of the multi-fingered metamorphic hand-metahand. *Trans. Rob.* **25**, 942–947 (2009)
- [6] Grebenstein, M., Chalon, M., Hirzinger, G., Siegwart, R.: A method for hand kinematics design. 7 billion perfect hands. In: ICABB (2010)
- [7] Mason, M., Srinivasa, S., Vazquez, A., Rodriguez, A.: Generality and simple hands. *International Journal of Robotics Research* (2010)
- [8] Patarinsky Robson, N., McCarthy, J.M.: Kinematic Synthesis With Contact Direction and Curvature Constraints on the Workpiece. In: IDETC (2007)
- [9] Patarinsky Robson, N., McCarthy, J.M.: Synthesis of a Spatial SS Serial Chain for a Prescribed Acceleration Task. In: World Congress in Mechanism and Machine Science (IFTOMM). Besancon, France (2007)
- [10] Perez-Gracia, A., McCarthy, J.M.: Kinematic synthesis of spatial serial chains using clifford algebra exponentials. *Proc. of the Institution of Mechanical Engineers, Part C: Journal of Mechanical Engineering Science* **220**(7), 953–968 (2006)
- [11] Rico, J.M., Gallardo, J., Ravani, B.: Lie algebra and the mobility of kinematic chains. *Journal of Robotic Systems* **20**(8), 477–499 (2003)
- [12] Selig, J.M.: *Geometric Fundamentals of Robotics* (Monographs in Computer Science). SpringerVerlag (2004)
- [13] Simo-Serra, E., Moreno-Noguer, F., Perez-Gracia, A.: Design of non-anthropomorphic robotic hands for anthropomorphic tasks. In: IDETC (2011)
- [14] Soto Martell, J., Gini, G.: Robotic hands: Design review and proposal of new design process. *World Academy of Science, Engineering and Technology* **26** (2007)
- [15] Ueda, J., Kondo, M., Ogasawara, T.: The multifingered naist hand system for robot in-hand manipulation. *Mechanism and Machine Theory* **45**(2), 224–238 (2010)

# KINEMATIC SYNTHESIS USING TREE TOPOLOGIES

Edgar Simo-Serra<sup>a</sup>, Alba Perez-Gracia<sup>b,\*</sup>

<sup>a</sup>*Institut de Robotica i Informatica Industrial (CSIC-UPC), Llorens i Artigas 4-6, 08028  
Barcelona, Spain*

<sup>b</sup>*Department of Mechanical Engineering, Idaho State University, Pocatello, Idaho 83209,  
USA*

---

## Abstract

*This paper presents a methodology for describing and synthesizing articulated systems with multiple end-effectors, such as those occurring in multi-fingered hands. The articulated system is represented as a rooted tree graph. Graph and synthesis theories are applied to determine when exact synthesis can be performed on the tree structures by considering all the possible subgraphs and the subgroup of motion of each subgraph. Two examples of tree topologies are presented and studied in detail.*

*Keywords:* kinematic synthesis, graph theory, tree articulated systems

---

## 1. Introduction

Kinematic synthesis theory, in which an articulated system is designed to meet certain motion specifications, has been applied to planar open and closed linkages and spatial serial chains. For dimensional synthesis of planar linkages see [1, 2, 3, 4]. Dimensional synthesis of spatial articulated systems has targeted mostly serial chains [5, 6, 7, 8, 9] due to the complexity of the problem [10], and has been applied, to some extent, to parallel robots [11, 12].

Recent developments in type or structural synthesis [13, 14] highlight the importance of a systematic classification for the linkage type in the synthesis process, which is based on graph theory. Graph theory has for long been used

---

\*Corresponding author. Phone number 001 208 2825655

*Email addresses:* esimo@iri.upc.edu (Edgar Simo-Serra), perealba@isu.edu (Alba Perez-Gracia)

for the analysis of linkages, see early research by Huang and Soni [15], and Freudenstein and Maki [16], and more recently Tsai [17] and Mruthyunjaya [18]. Chuang and Lee [19] use structural synthesis for the design of finger mechanisms.

This paper focuses on the dimensional synthesis problem, in particular exact dimensional synthesis, applied to articulated systems with a tree structure. A tree-structured articulated system has a base (a grounded link), some common joints, and multiple end-effectors, each one of them corresponding to a separate branch.

There has been some work done mainly in the analysis of tree structures. Selig [20] cites tree-structured mechanisms and models them as rooted trees following [21]. His work includes basic definitions and its application for the kinematic and dynamic analysis. Chen et al. [22] perform the analysis of tree-type geometries for applications in modular robots; Song and Amato [23] apply the analysis of tree-like articulated systems to folding. Jain [24] uses tree graphs for the dynamic analysis of multi-body systems; tree-systems also appear describing dynamic systems in Garcia de Jalon [25]. Tree articulated systems and their graph representation are also studied in [26] for the analysis and control, where they are named forking linkages. Tischler et al. [27, 28] apply graph theory for the structural synthesis of kinematic chains with applications to robot hands.

Even though very few literature is devoted to them when compared to their serial or parallel counterparts, tree articulated systems are widely used in robotic multi-fingered hands; locomotive structures for mobile robots could also be modeled as tree-like systems.

In this case, the design of multi-fingered robotic grippers is the primary application for the kinematic synthesis of tree topologies. The advantage of having a methodology for the kinematic synthesis of a set of fingers is the possibility of defining manipulation and grasping actions for the whole hand. Aside from underactuated robotic hands (see [29] for a review and [30] for recent results), which present little dexterity, the design of robotic hands has been performed from an anthropomorphic point of view. See recent reviews for different applications in [31, 32]. In addition to this, there is some development in the design of modular fingers able to perform certain grasping actions, which are later integrated in the hand. See for instance the work by Dai and Wang [33]. With the development of a theory for the use of kinematic synthesis in tree topologies, we aim to create a tool for new designs that can be applied, for instance, in many areas of human-robot interaction.

In this paper, we present a theory and methodology for the dimensional synthesis of articulated systems with a tree topology. Taking as input data a finite set of rigid-body positions for each of the multiple end-effectors, we perform dimensional synthesis for the tree-structured kinematic chain. This is modeled using rooted tree graphs. A first step to be performed is the substitution of kinematic chains in order to obtain a compact rooted graph. This graph must be checked to see if it is solvable. If not, an equivalent graph must be found.

For the resulting solvable rooted tree graph, the forward kinematics equations of relative displacements for each serial chain are computed using dual quaternions. The synthesis of spatial serial chains for up to five degrees of freedom using this technique was developed in [34]. In this case, each serial chain corresponds to one branch, including the common joints. The dependency among the different serial chains allows to extend the exact synthesis to articulated systems with a high number of degrees of freedom and to tasks defined by a high number of positions.

The set of design equations for all serial chains are solved simultaneously. We must point out the high dimension and degree of the obtained system of equations, which normally require a numerical solver. As a last step, the solution is used to dimension the substituted kinematic chains.

This method has been applied to two examples. The first one is a possible application to a multi-fingered robotic hand, for which numerical solutions have been found [35]. The second example is a simple PR-(R,P) tree structure, which can be solved analytically and is used to illustrate the process.

## 2. Rooted Tree Graph Representation

Articulated systems with a tree topology can be modeled using graph theory. This allows for a compact representation of the structure, the identification of key paths in the system and the realization of some operations that help simplify the synthesis process.

Tsai [17] established a methodology to represent mechanisms with graphs. It consists of representing the joints as edges and the links as the vertices. For the kinematic synthesis, the mechanisms is to be represented always as a rooted graph. The root vertex will be considered to be fixed with respect to the reference system.

We shall denote a rooted connected graph representing a kinematic structure as  $G(V,E)$ , with a set of  $v$  vertices  $V$  and a set of  $e$  edges  $E$  connecting

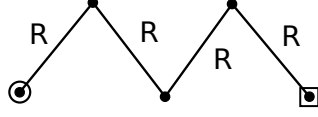


Figure 1: Graph representation of a 4R manipulator where the circle represents the root and the square represents the end-effector.

the vertices. The vertices represent the rigid bodies and the edges represent the joints connecting adjacent bodies. Besides the root vertex, a number of vertices will be given the special characteristic of being considered end-effectors.

A graph representing a 4R manipulator can be seen in Fig. 1. There are four edges representing the four revolute joints. The root vertex is marked with a circle around the point and the end-effector is represented by a square around the point.

In tree topologies, a vertex will be connected to several edges for spanning branches. The degree of a vertex is the number of edges that are connected to it, which in this case would be equivalent to the number of joints connected to it.

### 2.1. Contraction

After constructing the initial graph representing a linkage we shall proceed to contract the graph. The graph is contracted so that each edge represents the set of joints of a kinematic serial chain instead of an individual kinematic joint.

The 4R manipulator seen in Fig. 1 would be contracted to a single edge representing the serial chain of four revolute joints connecting the root vertex and the end-effector vertex. Contraction removes all vertices with a degree of 2; notice that all vertices with a degree of 1 that are not the root vertex are end-effectors.

### 2.2. Setting the Root Node

The special characteristic of the root node is that it indicates that the rigid body associated with it is immobile in the reference system. Essentially it marks the fixed reference system. However, the root node can be set at any other end-effector by performing a transformation. If we consider the

positions  $\mathbf{P}_i$  associated to the end-effector  $i$  where  $i = 1$  is the root node, then the transformation of the root from  $i = 1$  to  $i = j$  is,

$$\mathbf{P}_i^* = \mathbf{P}_j^{-1} \mathbf{P}_i \quad (1)$$

where  $\mathbf{P}_i^*$  would be the new end-effector positions relative to the new root.

Changing the root node can be useful for solving particular systems as it will be seen in the examples.

### 2.3. Rooted Graphs for Tree Topologies

Let  $T(V, E)$  be a contracted rooted tree graph, with a set of  $v$  vertices  $V$  and a set of  $e$  edges  $E$ , obtained from a rooted connected graph  $G(V_r, E_r)$  that represents a kinematic structure. We assume that there are no loops in the contracted rooted tree graph. For synthesis purposes, loops can be substituted with equivalent serial chains in a process called *reduction*, which is explained in Section 5. Then the following relations exist:

1.  $e = v - 1$
2. Between any two vertices  $i$  and  $j$  where  $i \neq j$  there exists only one path.
3. The only vertices with a degree of 1 will be either the graph root or an end-effector.
4. There are no vertices with a degree of 2.

## 3. Forward Kinematics for Tree Topologies

The forward kinematics for a serial kinematic chain can be written using the representation-agnostic exponential map [36],

$$\hat{Q}(\hat{\theta}) = \left( \prod_{i=1}^n e^{\frac{\hat{\theta}_i}{2} \mathbf{S}_i} \right) \hat{g} \quad (2)$$

where  $\hat{\theta} = \theta + \epsilon d$  and  $\hat{g}$  is the transformation from the reference system to the end-effector at the zero or reference configuration, and the  $\mathbf{S}_i$  are the positions of the joint axes at the zero configuration.

The term  $\hat{g}$  can be eliminated by considering the forward kinematics of relative displacements with respect to this reference configuration, measured from the fixed frame,

$$\hat{Q}(\Delta\hat{\theta}) = \prod_{i=1}^n e^{\frac{\Delta\hat{\theta}_i}{2}S_i} \quad (3)$$

where  $\Delta\hat{\theta} = \theta - \theta_0 + \epsilon(d - d_0)$  with  $\theta_0$  and  $d_0$  being the values of the joint parameters at the reference configuration.

For a linkage with a tree topology, a set of forward kinematics equations can be written for each of the branches, considering the common joints in all of them,

$$\hat{Q}_i(\Delta\hat{\theta}) = \underbrace{\prod_{j=1}^{k_i} e^{\frac{\Delta\hat{\theta}_j}{2}S_j}}_{\text{common}} \underbrace{\prod_{j=k_i+1}^{n_i} e^{\frac{\Delta\hat{\theta}_{i,j}}{2}S_{i,j}}}_{\text{branch}}, \quad i = 1, \dots, b \quad (4)$$

where the number of common joints for a given branch  $i$  is indicated by  $k_i$ , and the number of end-effectors, or branches, is indicated by  $b$ . Each branch or serial chain has a total of  $n_i$  joints, counting the common ones.

#### 4. Linkage Locus Space

For the most general case in Eqn. (4), where the joint axes can be arbitrarily positioned in space, it is important to define the minimum subgroup of  $SE(3)$  able to contain the full motion of each end-effector as generated by the motion of the joints defining its serial chains.

For a given serial chain with  $n$  joint axes  $S_i$ , the workspace of relative motion can be defined as,

$$W = \left\{ \mathbf{w} \mid \prod_{i=1}^n e^{\frac{\Delta\hat{\theta}_i}{2}S_i} - \mathbf{w} = 0, \quad \forall \hat{\theta} \right\} \quad (5)$$

However, for performing synthesis we have to consider an extended version of the workspace, the potential workspace of a generic mechanism topology,



as opposed to the particular workspace of a specific mechanism. In order to define where the generic mechanism topology lies, we define the Linkage Locus Space.

Let  $\$J^*$  be the smallest subalgebra of  $\mathfrak{se}(3)$  containing all the possible infinitesimal mechanical liaison [37] between two rigid bodies of a serial chain. In general, this is calculated for consecutive rigid bodies separated by a joint. However, in the case of having constraints defined by relationships between joint parameters for two or more consecutive rigid bodies in a serial chain, this cannot be calculated as the mechanical liaison of individual joints.

For example  $\$P^*$  would be the smallest subalgebra that contains all possible infinitesimal mechanical liaisons of the form

$$S_P = \lambda(0; \mathbf{s}) \quad (6)$$

which in this case would be

$$\$P^* = \mathbb{R}^3 \quad (7)$$

We can consider the most general form of joint as the helicoidal joint which has the form of

$$S_H = \lambda(\mathbf{s}; \mathbf{r} \times \mathbf{s} + h\mathbf{s}) \quad (8)$$

which in this case would have, as smallest subalgebra containing its generic version,

$$\$H^* = \mathfrak{se}(3) \quad (9)$$

Special relationships can also be considered using explicit calculation. As an example, the case of a revolute joint followed by a cylindric joint forming an RC chain, where both joints have the same rotation axis with opposite angles, such that if the revolute joint rotates  $\theta$ , the cylindric joint rotates  $-\theta$ . In this case individually each joint would be,

$$S_R = \theta(\mathbf{s}; \mathbf{r}_R \times \mathbf{s}) \quad (10)$$

$$S_C = -\theta(\mathbf{s}; \mathbf{r}_C \times \mathbf{s}) + d(0; \mathbf{s}) \quad (11)$$

with  $\theta$  and  $d$  being the joint parameters.

When we consider all the elements generated by the RC subchain we obtain,

$$W_{RC} = \left\{ \mathbf{w} \mid e^{\frac{\Delta\hat{\theta}_R}{2}} \mathbf{S}_R e^{\frac{\Delta\hat{\theta}_C}{2}} \mathbf{S}_C - \mathbf{w} = 0, \quad \forall \hat{\boldsymbol{\theta}} \right\} \quad (12)$$

which when expanded is found to have the form

$$\mathbf{S}_{RC} = (0; \theta(\mathbf{r}_R \times \mathbf{s} - \mathbf{r}_C \times \mathbf{s}) + d\mathbf{s}) \quad (13)$$

The smallest subalgebra of  $\mathfrak{se}(3)$  containing all possible joints of the form  $\mathbf{S}_{RC}$  in this case would be the same as for  $\mathbb{S}_P$  or  $\mathbb{R}^3$ .

Now we can consider the entire chain and define the Linkage Locus Space  $\mathcal{L}$  as the smallest subalgebra of  $\mathfrak{se}(3)$  corresponding to the smallest subgroup containing the generic workspace for the given topology as

$$\mathbf{S} = \left\{ \mathbf{w} \mid \prod_{i=1}^n e^{\frac{\Delta\hat{\theta}_i}{2}} \mathbf{S}_i - \mathbf{w} = 0, \quad \forall \hat{\boldsymbol{\theta}}, \forall \mathbf{S}_i \in \mathbb{S}_i^* \right\} \quad (14)$$

This can be calculated directly by finding the smallest subalgebra that contains  $\mathbf{S}$  or, given all the subalgebras of all the joints of the serial chain, by using the closure of subalgebras

$$\mathcal{L} = \mathbb{S}_1^* \odot \mathbb{S}_2^* \odot \cdots \odot \mathbb{S}_n^* \quad (15)$$

*Proof.* We can begin by expanding  $\mathbf{w}$  by using the well-known Campbell-Baker-Hausdorf series

$$\begin{aligned}
\log(\mathbf{w}) &= \log\left(\prod_{i=1}^n e^{\frac{\Delta\hat{\theta}_i}{2}S_i}\right) \\
&= \frac{\Delta\hat{\theta}_1}{2}S_1 + \frac{\Delta\hat{\theta}_2}{2}S_2 + \cdots + \frac{\Delta\hat{\theta}_n}{2}S_n + \\
&\quad \frac{1}{8}(\Delta\hat{\theta}_1\Delta\hat{\theta}_2[S_1, S_2]\Delta\hat{\theta}_1\Delta\hat{\theta}_3[S_1, S_3] + \cdots) + \\
&\quad \frac{1}{96}(\Delta\hat{\theta}_1^2\Delta\hat{\theta}_2[S_1, [S_1, S_2]] + \\
&\quad \Delta\hat{\theta}_1\Delta\hat{\theta}_2^2[S_1, [S_1, S_3]] + \cdots) + \cdots
\end{aligned} \tag{16}$$

The closure of subalgebras from Eqn. (15) can be seen to be the vector subspace containing all the finite Lie products of the form

$$\mathfrak{L} = \langle S_1 S_2 \cdots S_n [S_1, S_2] \cdots [S_1, [S_1, S_2]] \cdots \rangle \tag{17}$$

It is straight forward to see that we can find a linear combination of Eqn. (17) for each element of  $\log(\mathbf{w})$  in the form of

$$\left(\frac{\Delta\hat{\theta}_1}{2} \frac{\Delta\hat{\theta}_2}{2} \cdots \frac{\Delta\hat{\theta}_n}{2} \frac{\Delta\hat{\theta}_1\Delta\hat{\theta}_2}{8} \frac{\Delta\hat{\theta}_1\Delta\hat{\theta}_3}{8} \cdots\right) \tag{18}$$

From this we can deduce that

$$\log(\mathbf{w}) \in \mathfrak{L}, \quad \forall \mathbf{w} \in S \tag{19}$$

and thus

$$\log(S) \leq \mathfrak{L} \tag{20}$$

$\log(S)$  is closed under the Lie bracket and is thus a subalgebra of  $\mathfrak{se}(3)$ . For simplicity let us take two arbitrary elements of  $\log(S)$  in the form of

$$X = X_1 + X_2 + \cdots + X_n + \frac{1}{2}[X_1, X_2] + \cdots \tag{21}$$

The Lie bracket of two elements, which we shall denote as  $X$  and  $X^*$  respectively, can be expanded as

$$\begin{aligned}
& [X_1 + X_2 + \cdots + X_n + \frac{1}{2}[X_1, X_2] + \cdots, \\
& X_1^* + X_2^* + \cdots + X_n^* + \frac{1}{2}[X_1^*, X_2^*] + \cdots] = \\
& [X_1, X_1^*] + [X_1, X_2^*] + \cdots + [X_2, X_1^*] + \cdots + \\
& \frac{1}{2}([X_1, X_2], X_1^* + [X_1, X_2], X_2^* + \cdots) + \cdots
\end{aligned} \tag{22}$$

where each element in the summation belongs to  $\mathfrak{L}$ .

It is straight forward to see that the subalgebras  $\mathfrak{S}_i^*$  are also contained in  $\log(\mathbf{S})$ . As  $\mathfrak{L}$  is the smallest subalgebra containing all  $\mathfrak{S}_i^*$ ,  $\log(\mathbf{S})$  contains all  $\mathfrak{S}_i^*$  and  $\log(\mathbf{S}) \leq \mathfrak{L}$  we can establish that

$$\log\left(\prod_{i=1}^n e^{\mathfrak{S}_i^*}\right) = \log(\mathbf{S}) = \mathfrak{L} = \mathfrak{S}_1^* \odot \mathfrak{S}_2^* \odot \cdots \odot \mathfrak{S}_n^* \tag{23}$$

□

Therefore, in order to calculate  $\dim(\mathbf{S})$  it is possible to instead calculate  $\dim(\mathfrak{L})$  by means of iteratively adding successive higher order Lie bracket of each subalgebra  $\mathfrak{S}_i^*$  until all the Lie brackets are linear products of the previously found Lie brackets.

As shown in the next section, we can use the expressions developed here in order to define the dimension of the space in which all possible mechanisms of a given topology can be found. This is important for both being able to define a task that is feasible for a given topology and also in order to be able to determine when exact synthesis can be performed.

## 5. Reduced Tree Topology for Exact Synthesis

The main objective of the reduction is to find a tree graph equivalent to the graph of the mechanism for performing exact kinematic synthesis. At the end of the process, the remaining serial chains or edges must have a finite number of solutions for dimensional synthesis, while keeping the motion constraints of the original mechanism. An example of a complex

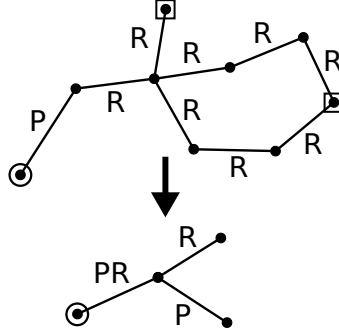


Figure 2: Reduction of a complex kinematic structure with a Sarrus linkage to a tree graph.

graph representing a kinematic structure being contracted and reduced to a rooted tree graph can be seen in Fig. 2.

In the case of open-loop chains the process is simple. The mobility of the loops can be calculated by the CKG equation

$$F = \lambda(n - j - 1) + \sum_{i=1}^j f_i \quad (24)$$

where  $F$  is the number of degrees of freedom of the mechanism,  $\lambda = \dim(W)$  [11] is the number of allowed degrees-of-freedom of the space in which the end-effector moves,  $n$  is the number of links,  $j$  is the number of joints and  $f_i$  is the degrees of freedom of the joint  $i$ .

However, this mobility does not take into account the actual structure of the workspace. With a mobility of 4 the workspace could be redundantly defined as would be the case of four prismatic joints. Therefore the dimension of the linkage locus space must be studied.

The number of redundant degrees-of-freedom  $r$  of a serial mechanism be calculated by,

$$r = \sum_{k=i}^j f_k - \dim(\mathcal{L}) \quad (25)$$

where  $f_k$  denotes the number of degrees of freedom of joint  $k$ .

If  $r > 0$  the mechanism is considered to have redundant degrees-of-freedom. For a given relative transformation there will be an entire subspace of joint parameters that will perform the transformation. These mechanisms are not suitable for exact kinematic synthesis as there will be a subspace of solutions and not a finite number of solutions.

Chains without redundant degrees-of-freedom that can move anywhere in the Linkage Locus space  $\mathcal{L}$  may also have subspaces of solutions. The degrees-of-freedom can be represented as the ordered screw surface  $\$$  of a mechanism topology as

$$\begin{aligned}\$ &= [ \$^*_1 \$^*_2 \cdots \$^*_n ] \\ &= \$^*_1 \oplus \$^*_2 \oplus \cdots \oplus \$^*_n\end{aligned}\tag{26}$$

In order for the kinematic synthesis to have a finite number of solutions the kinematic chain must comply with,

$$\dim(\$) < \dim(\mathcal{L})\tag{27}$$

Combining the two conditions we obtain the combined condition that the serial chains must comply with to be able to perform exact kinematic synthesis,

$$\sum_{k=i}^j f_k = \dim(\$) < \dim(\mathcal{L})\tag{28}$$

Additionally, the special euclidean group  $SE(3)$  is formed by  $SO(3) \ltimes \mathbb{R}^3$ , with  $\mathbb{R}^3$  being a normal subgroup. The Lie bracket of any vector from the subspace of  $\mathfrak{se}(3)$  with any vector of  $\mathbb{R}^3$  belongs to  $\mathbb{R}^3$ . In order to perform exact kinematic synthesis,  $\mathbb{R}^3$  must not be a subspace of the ordered screw surface,

$$\mathbb{R}^3 \notin \$\tag{29}$$

The special orthogonal group  $SO(3)$  is not a normal subgroup of  $SE(3)$  and does not have this issue. The only case in which  $\mathfrak{so}(3) \in \$$  would be

a spherical joint  $S$  centered on the origin would be represented by  $(\mathbf{s}_1; 0) + (\mathbf{s}_2; 0) + (\mathbf{s}_3; 0)$ . This mechanism would not be suitable for exact synthesis of the joint orientations. However, spherical joints are only defined by the center point of the joint. Thus, a spherical joint centered on the origin would have no structural parameters and would be suitable for exact synthesis.

Kinematic serial chains that either fully determine the Linkage Locus space  $\mathfrak{L}$  or have redundant degrees-of-freedom must be substituted by other chains that preserve  $\mathfrak{L}$  while having a finite number of kinematic synthesis solutions. This can be seen as solving for a more constrained problem in order to obtain intermediate positions, which are then used to solve the original problem, albeit it will not have a finite number of solutions.

The process of substituting serial chains not suitable for exact kinematic synthesis is not straightforward when there are many constraints applied to the kinematic chain. For simple cases such as the 4P serial chain it is simple to see that it must be substituted for the 2P serial chain, which shares the  $\mathfrak{L} = \mathbb{R}^3$  Linkage Locus space with no redundant degrees of freedom.

### 5.1. Parallel Mechanism Equivalence

To be able to convert the graph to a tree graph the loops must be substituted for non-loop equivalent. We must refer to the study of the mobility of single-loop kinematic chains done by Rico and Ravani [37] for a more in depth study of types of kinematic loops.

Kinematic loops can be split into two paths corresponding to the clockwise and counterclockwise path between the two rigid bodies. In order to study the mobility, the intersection of the subalgebras corresponding to both paths must be analyzed. Depending on the class of the loops, different steps must be taken to substitute the loop for a non-loop equivalent.

Trivial kinematic loops are the simplest to handle. In this case the intersection is either the clockwise or counterclockwise path of the loop. We shall call the path that is the intersection the dominant path and remove the other path, as the restrictions imposed by the dominant path are in fact what are determining the workspace of the mechanism.

Exceptional kinematic loops have an intersection of subalgebras that is not trivial and is not equal to neither path. The exceptional kinematic chain loop can be substituted for this subalgebra corresponding to the intersection which may not always have a simple equivalence. Fanghella and Galletti [38] were the first to find many equivalences of intersections using group theory. Some of these have been converted to use Lie algebra by Rico and Ravani

[37]. However, finding the equivalent open kinematic chain is not always a simple task depending on the mobility class of the loop.

Kinematic chains with partitioned mobility can be removed from the graph, that is the edge representing the chain can be removed and both vertices merged into a single one, as they do not have relative motion.

The remaining cases which correspond to the paradoxical of class 1 and 2 kinematic chains must be handled on a case-to-case basis as there is no general solution.

This process is to be repeated until there are no loops in the graph and it becomes a tree graph. The equivalent serial chains also need to comply with the serial chain requirements from Eqn. (28).

The reduction of a Sarrus linkage to an equivalent prismatic joint [39] can be seen in Fig. 2. The Sarrus linkage is formed by two 3R branches with a set of constraints that give it the same workspace as a single prismatic joint. The problem can then be solved considering the Sarrus linkage to be a prismatic joint. Afterwards the motion of the prismatic joint can be used to generate a Sarrus joint.

## 6. Kinematic Synthesis

In this paper the focus is on the exact dimensional kinematic synthesis for a finite set of positions. Dimensional kinematic synthesis seeks to find the location and orientation of all joint axes in order for each of the end-effectors to perform a given set of displacements. In this section an overview of the process for serial chains will be reviewed and in the next chapter it shall be extended to tree topologies.

### 6.1. Design Equations

Using the relative forward kinematics from Eqn. (3), we can then write the design equations for a serial kinematic chain to reach  $m$  finite positions as,

$$\hat{P}_{1j} = \prod_{i=1}^n e^{\frac{\Delta \hat{\theta}_i^j}{2} \mathbf{S}_i}, \quad j = 2, \dots, m \quad (30)$$

where  $j = 1$  is considered the reference configuration and  $\hat{P}_{1j} = \hat{P}_j \hat{P}_1^{-1}$ .

This creates a set of design equations that can be solved for the unknown joint axes (denoted here as structural parameters) and joint variables in order to reach the set of relative displacements  $\hat{P}_{1j}$ .



Besides the design equations, additional equations can be added. For example, relationships between joint axes would be represented as additional constraints  $c$ . These functions can either be considered as a decrease in the number of structural parameters or separately as additional functions when analyzing the number of positions needed for kinematic synthesis.

Furthermore, the design equations can be modified to handle velocities and accelerations as done in [40].

### 6.2. The Synthesis Task

To be able to create the synthesis design equations from Eqn. (30) we must be able to define the number of variables and equations in the system. We shall distinguish two types of variables: structural and joint parameters. Joint parameters are those variables parameterizing the motion about the joints, and depend on the number of end-effector poses. The total number of variables  $n_x$  will be,

$$n_x = (m - 1)n_j + n_s \quad (31)$$

where  $m$  is the number of task positions,  $n_j = \dim(\mathcal{J})$  is the number of joint variables and  $n_s$  is the number of structural parameters.

We shall also distinguish two types of equations: design equations and constraints. The design equations come from Eqn. (30) and depend on the number of end-effector positions, while here we assume that the constraints do not. The total number of independent equations  $n_f$  will be,

$$n_f = (m - 1)d + c \quad (32)$$

where  $d = \dim(\mathcal{L})$  and  $c$  is the number of constraints.

For the system to have a finite number of solutions  $n_x = n_f$  must be imposed for the task. From there we can obtain the number of absolute positions needed,

$$m = \frac{n_s - c}{d - n_j} + 1 \quad (33)$$

where we assume all the equations are independent.

Table 1: Design parameters for different serial chains

Linkage	$n_j$	$n_s$	$d$	$m$	$m^R$	$m^T$	$\mathcal{L}$
P	1	2	3	2	1	2	$\mathbb{R}^3$
R	1	4	6	$1\frac{4}{5}$	2	3	$SE(3)$
H	1	5	6	2	2	$3\frac{1}{2}$	$SE(3)$
C	2	4	6	2	2	5	$SE(3)$
T	2	5	6	$2\frac{1}{4}$	5	6	$SE(3)$
E	3	2	6	$1\frac{2}{3}$	2	$\infty$	$SE(3)$
S	3	3	6	2	$\infty$	$\infty$	$SE(3)$
PP	2	2	3	3	1	3	$\mathbb{R}^3$
RP	2	6	6	$2\frac{1}{2}$	2	7	$SE(3)$
RR	2	8	6	3	5	9	$SE(3)$
PPR	3	6	6	3	2	$\infty$	$SE(3)$
PRP	3	8	6	$3\frac{2}{3}$	2	$\infty$	$SE(3)$
PRR	3	10	6	$4\frac{1}{3}$	5	$\infty$	$SE(3)$
RRR	3	12	6	5	$\infty$	$\infty$	$SE(3)$

This leaves us with the calculation of the number of structural parameters  $n_s$ . While this may seem like a simple task, it is not always straight forward. Generally any unconstrained screw joint as the one in Eqn.(8) will have 7 parameters:  $h \in \mathbb{R}$ ,  $\mathbf{s} \in \mathbb{R}^3$  and  $\mathbf{s}^0 \in \mathbb{R}^3$  with two constraints  $\mathbf{s} \cdot \mathbf{s} = 1$  and  $\mathbf{s} \cdot \mathbf{s}^0 = 0$ , which we consider to be 5 independent parameters. An unconstrained general revolute joint has 4 parameters as  $h = 0$ . An unconstrained general prismatic joint has 2 parameters as they can be represented by lines at infinity with the form  $(0; \mathbf{s})$  with  $\mathbf{s} \cdot \mathbf{s} = 0$ .

Table 1 shows various sets of kinematic chains. The constraints are considered implicitly as part of the structural parameters  $n_s$ . Different combinations of joints and constraints can modify the number of parameters. A striking example would be that two general prismatic joints PP have a total of 2 parameters and not 4 as expected. This happens whenever two prismatic joints are consecutive in a kinematic serial chain, as their joint axes do not appear individually in the design equations, but always as a cross product.

There is no general rule for calculating the number of structural parameters  $n_s$ . However, the design equations Eqn. (30) can always be expanded and checked for variable dependencies.

### 6.3. Task Degeneration

The  $m$  design equations obtained using Eqn. (33) are not necessarily independent. In fact it is possible for the system of equations to degenerate into two subsystems where one is overdetermined and the other has an infinite number of solutions.

We can split the special euclidean group  $SE(3)$  into its two subgroups using the semi-direct product,  $SE(3) = SO(3) \ltimes \mathbb{R}^3$ . The same technique used to obtain Eqn. (33) can be used to determine the number of rotations needed for the change of orientation of the system. The equations corresponding to motion in  $SO(3)$  as treated separately. Thus, the number of variables  $n_x^R$  will be,

$$n_x^R = (m^R - 1)n_j^R + n_s^R \quad (34)$$

where  $m^R$  is the number of orientations,  $n_j^R$  the number of joints with a revolute component and  $n_s^R$  the number of structural parameters for the rotations.

The number of independent equations corresponding to rotations,  $n_f^R$ , can be defined by,

$$n_f^R = (m^R - 1)d^R + c^R \quad (35)$$

where  $d^R = \dim(\mathcal{L} \cap \mathfrak{so}(3))$  and  $c^R$  is the number of constraints affecting the rotational parameters in the design equations.

We can now define the number of independent orientations  $m^R$  needed to fully define the rotational component of design equations by making  $n_x^R = n_f^R$ ,

$$m^R = \frac{n_s^R - c^R}{d^R - n_j^R} + 1 \quad (36)$$

If  $m^R \in \mathbb{Q}^+$  there will be a limit on the number of independent orientations in the screw system that can be defined. If  $m^R < m$ , the orientation of

the positions in the task can no longer be fully arbitrary, and  $m - m^R$  orientations will be dependent on the arbitrary  $m^R$  rotations. It is important to remark that this only can happen when  $n_j^R < d^R$ .

A similar counting can be done for the translational component of  $SE(3)$ . However,  $\mathbb{R}^3$  is a normal subgroup of  $SE(3)$  and thus the equations can not be decoupled. Following the same process as Eqn. (33) and Eqn. (36) we obtain,

$$m^T = \frac{n_s - c}{d^T - n_j} + 1 \quad (37)$$

where  $d^T = \dim(\mathfrak{L} \cap \mathbb{R}^3)$ .

As can be seen from Eqn. (37), the translational part depends on all the parameters and variables while only providing  $d^T$  independent equations. A serial mechanism will be solvable using only translational information if  $m^T \in \mathbb{Q}^+$ , which can only happen in systems with one or two single degree-of-freedom joints.

The important result is that for systems where  $m^R < m$  and  $m^T \notin \mathbb{Q}^+$ , they will not be solvable for arbitrary positions. The positions need to be generated taking into account the limitations of the mechanism in  $SO(3)$  to have a finite number of solutions. This can be problematic when designing for certain topologies.

#### 6.4. Defining Tasks

When defining a task we can identify three different scenarios with  $m \in \mathbb{Q}^+$  depending on the topology of the mechanism to be synthesized.

1. When  $m^R \geq m$  and  $m \in \mathbb{Q}^+$  the kinematic chain is fully solvable for  $m$  arbitrary spatial positions. Additionally if  $m^T \in \mathbb{Q}^+$ , the kinematic chain can be solved for only locations and space without considering orientations.
2. When  $m^R < m$  and  $m, m^R, m^T \in \mathbb{Q}^+$  the kinematic chain can still be solved for arbitrary spatial positions. However, only  $m^R$  positions may contain arbitrary rotations. An additional  $m^T = \frac{dm - d^R m^R}{d}$  positions with only arbitrary translational component will have to be defined.
3. When  $m^R < m$ ,  $m, m^R \in \mathbb{Q}^+$  and  $m^T \notin \mathbb{Q}^+$  the rotational component will be solvable for the mechanism. However, the translational part will not have a finite number of solutions. This type of topology can not be

used to perform exact kinematic synthesis for arbitrary positions. It is still possible to solve for finite solutions if the task is generated within  $\mathfrak{L}$  in such a way that the rotational part is not overdetermined, yet still possible to obtain the joint parameters for each position.

In all other situations the single kinematic chain will not have a finite number of solutions.

## 7. Tree Kinematic Synthesis

Once we have obtained a contracted tree graph representing a kinematic structure we can proceed to perform exact rigid body synthesis for a finite number of task positions. For this, it is necessary to calculate the number of positions needed for all the end-effectors to fully determine the kinematic structure and thus to have a finite number of solutions.

Following similar methodology as with serial kinematic chains we shall assign constraints to all vertices, degrees-of-freedom to all end-effector vertices, joint variables to all edges, and structural parameters to all edges. In the case of the degrees-of-freedom and joint variables, which depend on the number of relative positions  $(m - 1)$ , we shall only represent the coefficient multiplying  $(m - 1)$ . This will allow us to use matrices to simplify the equations. The constraints are a design parameter and thus are known.

### 7.1. Design Equations

The design equations for tree systems are the same design equations for serial chains from Eqn. (30) applied to all branches at the same time. This can be written as,

$$\hat{P}_{1j}^i = \underbrace{\prod_{j=1}^{k_i} e^{\frac{\Delta\hat{\theta}_j^k}{2} S_j}}_{\text{common}} \underbrace{\prod_{j=k_i+1}^{n_i} e^{\frac{\Delta\hat{\theta}_{i,j}^k}{2} S_{i,j}}}_{\text{branch}} \quad \begin{array}{l} i = 1, \dots, b \\ k = 2, \dots, m \end{array} \quad (38)$$

where the number of common joints is indicated by  $k_i$  and the number of end-effectors is indicated by  $b$ .

The definition of the task for the design equations is similar to what is done in the previous section. Due to having multiple end-effectors, tasks become sets of displacements for all end-effectors. However, in the case of tree topologies more care must be taken to avoid task degeneration. This is explained in detail in the next section.

## 7.2. Solving Substitutions

If the tree structure has had substitutions of parallel or serial kinematic chains, once the reduced rooted tree graph has been solved, the substitutions can be undone and the solution used to create constraints allowing the substituted chain to be solved.

The substituted serial chains will have both rigid bodies on either side determined. It is then possible to consider one of the rigid bodies a reference and consider the other rigid body as the end-effector of the chain with a motion equivalent to the relative motion between both rigid bodies. However, as the substitution was done to obtain a finite number of solutions, there will be subspaces of solutions. Equation (30) can be applied to perform the synthesis of the subspace.

In the case of substituted parallel chains, each branch can be treated as a separate individual serial chain and can be solved using the same procedure used for the substituted serial chains.

## 8. Matrix Representation

In this section we will outline how to use matrix notation for tree topologies in order to perform exact kinematic synthesis. The main advantage to this approach is it is an exhaustive approach when testing for degeneration within the tree structure which makes it inadequate for exact synthesis. As a reminder, we are considering the mechanism to be in the rooted tree graph representation with  $v$  vertices,  $e$  edges and  $b$  branches.

We can construct the  $e \times b$  reduced end-effector path matrix  $[\tilde{T}]$  by constructing a  $e \times (v - 1)$  path matrix  $[T]$  and eliminating all columns that do not correspond to an end-effector. The path matrix is defined as,

$$[T] = \begin{matrix} & \text{vertex } j \\ & \begin{bmatrix} t_{1,1} & t_{1,2} & \cdots & t_{1,v-1} \\ t_{2,1} & t_{2,2} & \cdots & t_{2,v-1} \\ \vdots & \vdots & \ddots & \vdots \\ t_{e,1} & t_{e,2} & \cdots & t_{e,v-1} \end{bmatrix} \\ \text{edge } i & \end{matrix} \quad (39)$$

where,

$$t_{i,j} = \begin{cases} 1 & \text{if edge } i \text{ lies on the path originating at the root,} \\ & \text{and terminating at the vertex } j \\ 0 & \text{otherwise.} \end{cases} \quad (40)$$

We can also construct the  $e \times (v - 1)$  reduced incidence matrix  $[\tilde{B}]$  as,

$$[\tilde{B}] = \begin{matrix} & \text{edge } j \\ \begin{bmatrix} b_{1,1} & b_{1,2} & \cdots & b_{1,e} \\ b_{2,1} & b_{2,2} & \cdots & b_{2,e} \\ \vdots & \vdots & \ddots & \vdots \\ b_{v-1,1} & b_{v-1,2} & \cdots & b_{v-1,e} \end{bmatrix} & \text{vertex } i \end{matrix} \quad (41)$$

where,

$$\tilde{b}_{i,j} = \begin{cases} 1 & \text{if vertex } i \text{ is connected to edge } j \\ 0 & \text{otherwise.} \end{cases}, \quad (42)$$

We can use the matrix representation of the graph to work with and define the conditions for exact kinematic synthesis. For this purpose we will define vectors to represent the number of joint degrees-of-freedom and structural parameters for the edges and the number of degrees-of-freedom and constraints of the nodes.

### 8.1. Task Sizing using Matrices

In order to be able to perform exact kinematic synthesis, the global system must be solvable. This is analogous to what is done with simple serial chains. However, in this case, the criteria is only necessary but not sufficient for exact synthesis due to the appearance of subgraphs, which will be discussed in the next subsection.

The number edge unknowns will be represented using  $e \times 1$  vectors and will be denoted as  $\mathbf{D}_j^e$  for joint degrees-of-freedom and  $\mathbf{D}_s^e$  for structural parameters,

$$n_x = ((m - 1)\mathbf{D}_j^e + \mathbf{D}_s^e)^T \mathbf{E} \quad (43)$$

where  $\mathbf{E}$  are the edges in the graph considered.

The number node equations will be represented using  $b \times 1$  vectors and will be denoted as  $\mathbf{D}_{ee}^n$  for the end-effector degrees-of-freedom and  $\mathbf{D}_c^n$  for the constraints of the end-effectors,

$$n_f = ((m-1)\mathbf{D}_{ee}^n + \mathbf{D}_c^n)^T \mathbf{B} \quad (44)$$

where  $\mathbf{B}$  are the vertices in the graph considered.

In order for the system to have a finite number of solutions  $n_f = n_x$  must be imposed, from which we can obtain the number positions  $m$  needed for exact synthesis,

$$m = \frac{(\mathbf{D}_s^e)^T \mathbf{E} - (\mathbf{D}_c^n)^T \mathbf{B}}{(\mathbf{D}_{ee}^n)^T \mathbf{E} - (\mathbf{D}_j^e)^T \mathbf{B}} + 1 \quad (45)$$

where if  $m \notin \mathbb{Q}^+$  the system will be unsolvable. However, this criteria is necessary, but not sufficient for the system to be solvable.

Additionally, as seen in Section 6.3 for serial chains, care must be taken with the subgroups  $SO(3)$  and  $\mathbb{R}^3$  of  $SE(3)$ . This can be done by defining the number of positions needed for the rotational part  $m^R$  of the mechanism as

$$m^R = \frac{(\mathbf{D}_s^{eR})^T \mathbf{E} - (\mathbf{D}_c^{nR})^T \mathbf{B}}{(\mathbf{D}_{ee}^{nR})^T \mathbf{E} - (\mathbf{D}_j^{eR})^T \mathbf{B}} + 1 \quad (46)$$

$$(47)$$

where the supraindex  $^R$  denotes that we only consider the number of equations or variables that affect the  $SO(3)$  component of the design equations (30).

The criteria is then exactly the same as defined for serial chains in Section 6.4, although translation-only tasks have not been covered as they are of little or no interest for tree topologies due to the limitation of only one or two joint per serial chain.

## 8.2. Subgraphs

It is sometimes possible to find subgraphs within the tree graph representing a kinematic structure that are solvable individually. These subgraphs



will generally need a different amount of end-effector positions to solve and will always end in a smaller equation system size when performing exact kinematic synthesis. However, if subgraphs exist within the system, not all end-effectors will necessarily need the same number of positions. This is because for a given number of positions calculated by Eqn. (45), it may so happen that a subgraph becomes overdetermined.

An interesting effect of this is that it only allows for tree kinematic structures where all chains from the root to end-effector have more or equal mobility than needed to reach the entire subalgebra of the end-effector. If any kinematic chain has less mobility than needed to reach the subalgebra of the end-effector it will always form a subgraph that is solvable separately. Figure 3 presents an example of a graph with solvable subgraphs.

For this subsection we shall consider a system to be solvable for a given task with  $m$  positions, if there is a finite number of mechanisms, given a specific topology, that can comply exactly with the task positions.

A sufficient, but not necessary condition for the system to be solvable is that it must have no proper solvable subgraphs that is, subgraphs that comply with  $m \in \mathbb{Q}^+$  using Eqn. (45). In order to check for this condition, all possible proper subgraphs must be tested. This can be expressed using the reduced path matrix,

$$\mathbf{E}_i = [\tilde{T}] \tilde{\mathbf{B}}_i^{ee} \Big|_{[>0]} \quad (48)$$

where  $\tilde{\mathbf{B}}_i^{ee}$  is a  $b \times 1$  vector representing the end-effectors considered for a given subgraph  $i$ . The Iverson bracket  $[> 0]$  is used to denote that elements of the  $\mathbf{E}$  vector should be either be 1 if  $> 0$  or 0 otherwise. There are  $2^b - 2$  possible subgraphs for any given tree graph representing a reduced kinematic structure, excluding both the full graph and the null graph.

Given the  $\mathbf{E}_i$  corresponding to the edges in a subgraph we can calculate the  $\mathbf{B}_i$  nodes in the subgraphs by,

$$\mathbf{B}_i = [\tilde{B}] \mathbf{E}_i \quad (49)$$

This criteria is sufficient, but not necessary. While it does always generate the smallest system size for performing exact synthesis, it increases the number of end-effector positions needed. A more lax criteria can be used instead, where we consider cases where the subgraphs are separately solvable.

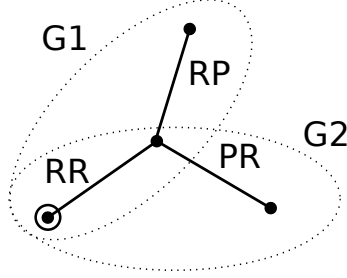


Figure 3: Both branches with fewer than  $\dim(\mathfrak{L}) = 6$  joints form subgraphs G1 and G2 that are solvable separately.

For each subgraph  $i$ , Eqn. (45) can be used to calculate the number of positions needed for exact synthesis of the subgraph,

$$m_i = \frac{(\mathbf{D}_s^e)^T \mathbf{E}_i - (\mathbf{D}_c^n)^T \mathbf{B}_i}{(\mathbf{D}_{ee}^n)^T \mathbf{E}_i - (\mathbf{D}_j^e)^T \mathbf{B}_i} + 1 \quad (50)$$

A necessary and sufficient criteria for determining the solvability of a graph is, given the number of positions  $m$  needed for exact synthesis of the subgraph, for all proper subgraphs  $i$  in the graph

$$m \leq m_i, \text{ if } m_i \in \mathbb{Q}^+ \quad (51)$$

Additionally, as in the general case, we must consider  $SO(3)$  and  $\mathbb{R}^3$  separately. Given a number of rotational components of the  $m$  positions, denoted as  $m^R$ , we obtain the additional criteria

$$m^R \leq m_i^R, \text{ if } m_i^R \in \mathbb{Q}^+ \quad (52)$$

where  $m_i^R$  are the number of frames needed to solve only the rotation part of the mechanism.

If this criteria isn't met, then the subgraph  $i$  where either  $m > m_i$  or  $m^R > m_i^R$  becomes overdetermined while other kinematic chains become underdetermined. The system of equations for exact kinematic synthesis is no longer guaranteed to have any solutions when same number of task positions is defined for each end-effector. In this case, the system will not be solvable.

### 8.3. Solvable Rooted Tree Graph

**Definition** Let  $T$  be a contracted rooted tree graph representing a kinematic structure and  $S$  be the set of subgraphs of  $T$ .  $T$  will be called *solvable* for a finite number of independent positions if,

1.  $m \in \mathbb{Q}^+$
2.  $m \leq m_i, \forall m_i \in \mathbb{Q}^+, i \in S$
3.  $m^R \leq m_i^R, \forall m_i^R \in \mathbb{Q}^+, i \in S$

The advantage of solving a tree with subgraphs is that the workspace can be defined by lesser number of positions of all end-effectors at the same time. However, the dimension of the equation system will always be larger than solving the smallest subgraph first and using the results to solve other subgraphs and eventually the entire graph.

## 9. Examples

For the notation of contracted rooted kinematic trees we shall use hyphens to indicate serial links and parenthesis to indicate parallel links.

### 9.1. Anthropomorphic Hand Model Subgraphs

Previous presented work performed kinematic synthesis on an anthropomorphic hand model with 5 fingers and a total of 26 revolute joints [35] and the first mention of kinematic tree topologies. However, the lack of the formal methods for exact kinematic synthesis of tree topologies led to this work on synthesis of tree topologies. We can now revisit the anthropomorphic hand model using the new tools for synthesis.

The anthropomorphic hand model is organized as a 3R-(4R,4R,5R,5R,5R) tree, where the wrist is considered to have 3 revolute joints which are common to the five fingers. The index and middle fingers have 4 revolute joints, while the third finger, fourth finger and thumb have 5 revolute joints. This gives a total of 26 revolute joints. There are not any constraints besides the implicit constraints of the joints.

The contraction of the individual joints in this case is trivial as there are no closed loops and all serial chains are formed by revolute joints. The contracted graph can be seen in Fig. 4 and has had all the edges and vertices labelled. It is also easy to see that in this case there is no edge with 6 or

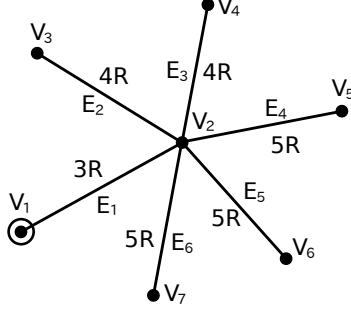


Figure 4: Rooted tree graph of an anthropomorphic hand model.

more revolute joints, which is a necessary, but not sufficient condition for the structure to be solvable if there are no additional constraints.

As the system is formed entirely by revolute joints it is straightforward to assign the  $6 \times 1$  vectors associated with the joint degrees-of-freedom  $\mathbf{D}_j^e$  and the structural parameters  $\mathbf{D}_s^e$ ,

$$\mathbf{D}_j^e = [3 \ 4 \ 4 \ 5 \ 5 \ 5]^T \quad (53)$$

$$\mathbf{D}_s^e = [12 \ 16 \ 16 \ 20 \ 20 \ 20]^T, \quad (54)$$

as revolute joints have 4 structural parameters associated to them.

The same can be done with the vertices, which are  $5 \times 1$  vectors associated to the end-effector degrees-of-freedom  $\mathbf{D}_{ee}^n$  and constraints  $\mathbf{D}_c^n$ ,

$$\mathbf{D}_{ee}^n = [6 \ 6 \ 6 \ 6 \ 6]^T \quad (55)$$

$$\mathbf{D}_c^n = [0 \ 0 \ 0 \ 0 \ 0]^T \quad (56)$$

Notice that in this case all end-effectors have a Synthesis Locus space  $\mathfrak{L} = \mathfrak{se}(3)$  and no additional constraints.

We can now check the number of positions needed for the entire system for performing exact kinematic synthesis. This is done by using Eqn. (45) with all the edges and branches,

$$\begin{aligned}
\mathbf{E} &= [1 \ 1 \ 1 \ 1 \ 1 \ 1] \\
\mathbf{B} &= [1 \ 1 \ 1 \ 1 \ 1] \\
m &= \frac{26 \cdot 4 - 0}{6 \cdot 5 - 26} + 1 = 27
\end{aligned} \tag{57}$$

Additionally we must check the rotational components by first calculating the system that interacts with the  $SO(3)$ ,

$$\mathbf{D}_j^{eR} = [3 \ 4 \ 4 \ 5 \ 5 \ 5]^T \tag{58}$$

$$\mathbf{D}_s^{eR} = [6 \ 8 \ 8 \ 10 \ 10 \ 10]^T \tag{59}$$

$$\mathbf{D}_{ee}^{nR} = [3 \ 3 \ 3 \ 3 \ 3]^T \tag{60}$$

$$\mathbf{D}_c^{nR} = [0 \ 0 \ 0 \ 0 \ 0]^T \tag{61}$$

Now using Eqn. (47) the number of rotation positions  $m^R$  needed considering only the rotational component can be computed as

$$m^R = \frac{26 \cdot 2 - 0}{3 \cdot 5 - 26} + 1 = -\frac{41}{11} \tag{62}$$

As  $m = 27 \in \mathbb{Q}^+$  and  $m = -\frac{41}{11} \notin \mathbb{Q}^+$  we can see the system meets another necessary, but not sufficient condition to be solvable. For it to be solvable we need that all the subgraphs comply with Eqn. (51). This can be done by first determining the reduced path matrix  $[\tilde{T}]$  and the reduced incidence matrix  $[\tilde{B}]$ . The path matrix consists on the edges that lay on the path to a given node. This is relative to the rote node, which for this example is  $V_1$ . Thus the reduced path matrix can be written as,

$$[\tilde{T}] = \begin{matrix} & \begin{matrix} V_3 & V_4 & V_5 & V_6 & V_7 \end{matrix} \\ \begin{matrix} E_1 \\ E_2 \\ E_3 \\ E_4 \\ E_5 \\ E_6 \end{matrix} & \begin{bmatrix} 1 & 1 & 1 & 1 & 1 \\ 1 & 0 & 0 & 0 & 0 \\ 0 & 1 & 0 & 0 & 0 \\ 0 & 0 & 1 & 0 & 0 \\ 0 & 0 & 0 & 1 & 0 \\ 0 & 0 & 0 & 0 & 1 \end{bmatrix} \end{matrix} \tag{63}$$

where we can see there are no columns for neither  $V_1$  nor  $V_2$  as they are not end-effectors and have been eliminated.

The reduced incidence matrix  $[\tilde{B}]$  is

$$[\tilde{B}] = \begin{matrix} & E_1 & E_2 & E_3 & E_4 & E_5 & E_6 \\ \begin{matrix} v_2 \\ v_3 \\ v_4 \\ v_5 \\ v_6 \\ v_7 \end{matrix} & \begin{bmatrix} 1 & 1 & 1 & 1 & 1 & 1 \\ 0 & 1 & 0 & 0 & 0 & 0 \\ 0 & 0 & 1 & 0 & 0 & 0 \\ 0 & 0 & 0 & 1 & 0 & 0 \\ 0 & 0 & 0 & 0 & 1 & 0 \\ 0 & 0 & 0 & 0 & 0 & 1 \end{bmatrix} \end{matrix} \quad (64)$$

where we can see that there is no first row for the root vertex  $V_1$ .

Now the end-effectors must be iterated on using Eqn. (48) to construct the edges leading to the end-effectors and Eqn. (49). There are in general  $2^b - 2$  possible subgraphs. However, in this case there are symmetries as many branches are the same leading to many equivalent subgraphs. For single branches they can be studied using the single serial chain equation from Eqn. (33) and in this case it is easy to see that all branches need a negative number positions. Therefore none of these subgraphs are solvable systems.

Next we can consider the two branches with 4 revolute joints (index and middle finger),

$$\tilde{\mathbf{B}}_6^{ee} = [1 \ 1 \ 0 \ 0 \ 0]^T \quad (65)$$

The system has the following edges,

$$\begin{aligned} \mathbf{E}_6 &= [\tilde{T}] \tilde{\mathbf{B}}_6^{ee} \Big|_{[>0]} = [2 \ 1 \ 1 \ 0 \ 0 \ 0]^T \Big|_{[>0]} \\ &= [1 \ 1 \ 1 \ 0 \ 0 \ 0]^T \end{aligned} \quad (66)$$

and the following vertices,

$$\mathbf{B}_6 = [\tilde{B}] \mathbf{E}_6 = [1 \ 1 \ 1 \ 1 \ 0 \ 0 \ 0]^T \quad (67)$$

Table 2: All solvable subgraphs of the anthropomorphic hand model

Subgraph	$b$	$r$	$m$	$n_f = n_x$
3R-(4R,4R,5R,5R,5R)	5	26	27	780
3R-(4R,5R,5R,5R)	4	22	45	1056
3R-(4R,4R,5R,5R)	4	21	29	672
3R-(4R,5R,5R)	3	17	69	1224
3R-(4R,4R,5R)	3	16	33	576
3R-(4R,4R)	2	11	45	528

We can see graphically from Fig. 4 that the system indeed has the edges  $E_1, E_2, E_3$  and vertices  $V_1, V_2, V_3, V_4$ . The value  $m_6$  can be calculated by Eqn. (50),

$$m_6 = \frac{4 \cdot 11 - 0}{6 \cdot 2 - 11} + 1 = 45 \quad (68)$$

Additionally  $m_6^R$  can be calculated as,

$$m_6 = \frac{2 \cdot 11 - 0}{3 \cdot 2 - 11} + 1 = -\frac{17}{5} \quad (69)$$

We can clearly see that  $m_6^R \notin \mathbb{Q}^+$  and  $m_6 = 45 \geq m = 27$ , therefore subgraph is solvable. This process has to be continued for all the possible subgraph, and if all possible subgraphs meet the criteria we will say that the graph is solvable. Through continuing we can obtain the results from Table 2. From this we can see that all the possible subgraphs were found in [35] and that the entire system is solvable. It is also important to note that as all the end-effectors have  $\mathfrak{L} = \mathfrak{se}(3)$  and  $\mathfrak{L} \cap \mathfrak{so}(3) = \mathfrak{so}(3)$ , all  $m$  positions defined in the task can have arbitrary orientation and location. This is generally true for all unconstrained pure revolute-joint systems that are solvable.

Now that the task specifications have been defined for the mechanism, synthesis can be performed for a specific task, consisting of  $m$  spatial positions, by solving the design equations from Eqn. (38). In our previous work [35, 40] we have employed a numerical optimization scheme based on genetic

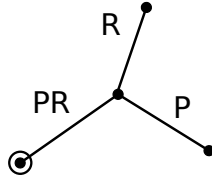


Figure 5: Rooted tree graph of the RP-(R,P) mechanism.

algorithm and Levenberg-Marquadt minimization that has been proven to be successful at finding solutions representing different mechanisms that can perform the task.

### 9.2. Algebraic PR-(R,P)

The PR-(R,P) consists of two common joints, one prismatic and one revolute, that fork into two branches, one being a revolute joint and the other a prismatic joint as seen in Fig. 5. In this case, we have two subgraphs which would be the PRR mechanism and the PRP mechanism. To decrease the global equation system size either subgraph can be solved individually and then the results would be used to solve the remaining joint. However, this requires more task positions for the first branch solved than for the remaining joint. Heterogeneous numbers of positions for each end-effector are generally not desired.

The direct method for solving this would be to use the general design equations and a numerical solver such as a Levenberg-Marquadt optimizer, solving for all branches at once. From Eqn. (45) we can count the number of positions needed for all possible chains which are shown in Table 1. The PRR chain needs  $m = 3$  positions, the PRP needs  $m = 3\frac{1}{2}$  positions and the entire system needs  $m = 2\frac{1}{2}$  positions. As we can see the entire system needs fewer positions than either branch.

We must now look at the rotational component following Eqn. (47). We see that the PRR chain needs  $m^R = 5$  positions, the PRP needs  $m^R = 2$  position and the entire system would also need  $m^R = 2$  positions. We can see clearly that in the case of the PRP chain, we are being limited to only two positions with a rotational component. As explained in Section 6.4, when  $m^R < m$ , the number of position orientations is being limited by  $m^R$ . Therefore when defining the task, some additional positions without orientation information will have to be added.



Table 3: Solvability of the different subgraphs of the PR-(R,P) mechanism

Subgraph	$m$	$m^R$	$m^T$	Comments
PR-(R,P)	$2\frac{1}{2}$	2	7	Full system, rotational and translational components solvable
PRR	3	5	$\infty$	Full system and rotational component solvable
PRP	$3\frac{1}{2}$	2	$\infty$	Only rotational component solvable $m^R < m$ and $m^T \notin \mathbb{Q}^+$

In order to make sure the system is still solvable, we must also check the limit of translations  $m^T$  for all subgraphs. For the PRR and PRP chain we obtain  $m^T = \infty$ , while for the entire system we obtain  $m^T = 7$ . This indicates that only the entire system is solvable for only translations and additionally that the PRP subgraph is only solvable using rotational components. The results of the solvability are summed up in Table 3.

Being a simple mechanism it can also be solved algebraically. For solving algebraically we can avoid the divide and conquer approach by first considering the kinematic chain from one end-effector to another. This can be thought of as changing the root node to one of the end effectors and then solving a subgraph. The forward kinematics of both branches can be written as,

$$\hat{S}_P^c(d^c)\hat{S}_R^c(\theta^c)\hat{S}_R(\theta) = \hat{P}_{PRR} \quad (70)$$

$$\underbrace{\hat{S}_P^c(d^c)\hat{S}_R^c(\theta^c)}_{\text{common}} \underbrace{\hat{S}_P(d)}_{\text{branch}} = \underbrace{\hat{P}_{PRP}}_{\text{pose}} \quad (71)$$

By considering the kinematic chain from one end-effector to another we can eliminate the common joints and consider the kinematic chain,

$$\hat{S}_P(d)^{-1}\hat{S}_R(\theta) = \hat{P}_{PRP}^{-1}\hat{P}_{PRR} \quad (72)$$

where  $\hat{S}_P(d)^{-1}$  is equivalent to  $\hat{S}_P(-d)$ . This is analogous to making the end-effector at the end of the P edge the root of the system and solving the subgraph formed by the PR branch in the new tree graph.

This can be solved algebraically and gives a single solution [41]. Given the solution the position of the rigid body connecting the common branches can be solved as a serial chain,

$$\hat{S}_P^c(d^c)\hat{S}_R^c(\theta^c) = \hat{P}_{PRP}\hat{S}_P(-d) \quad (73)$$

which also has a single solution. Furthermore the entire system has a single solution.

Therefore the problem can be treated as two separate PR chains and solved individually. If we look at the number of positions each PR chain needs we see it is  $m = 2\frac{1}{2}$  and is coincidentally the same as the number of positions needed for the entire system. The procedure to solve is the same as in [42].

As  $m = 2\frac{1}{2} \notin \mathbb{N}^+$  we can not define completely arbitrary positions. Due to the fact that  $m^R = 2$  and  $m^T = 7$ , we realize that in order to solve the entire system, half a position can correspond to only the translation information of a position. Which would mean we would have to define 3 translation positions, where 2 additionally have orientation information, to perform kinematic synthesis. This gives us a single relative rotation and 2 relative translations. If we were to define more than 2 orientations, the rotational component of the system would be overdetermined. The positions can thus be defined as,

$$\begin{aligned} \hat{P}_{12} &= \hat{P}_{PRP}^{-1}\hat{P}_{PRR}\Big|_{12} = s_{12}^w + \mathbf{b}_{12} + \epsilon(s_{12}^{w0} + \mathbf{b}_{12}^0) \\ \hat{P}_{13} &= \hat{P}_{PRP}^{-1}\hat{P}_{PRR}\Big|_{13} = s_{12}^w + \mathbf{b}_{12} + \epsilon(s_{13}^{w0} + \mathbf{b}_{13}^0) \end{aligned} \quad (74)$$

where we can see they share the same orientation.

From the relative rotation we can determine R joint orientation  $\mathbf{g}$  and angles  $\boldsymbol{\theta}$  as,

$$\mathbf{g} = \frac{\mathbf{b}_{12}}{\|\mathbf{b}_{12}\|}, \quad \tan \boldsymbol{\theta} = \frac{\|\mathbf{b}_{1i}\|}{s_{1i}^w}, \quad i = 2, 3 \quad (75)$$

The dual part can then be solved for the remaining 2 relative translations to obtain the moment of the line  $\mathbf{g}^0$  and the P joint orientation  $\mathbf{h}$  with,

$$\mathbf{g}^0 = \mathbf{b}_{1i}^0 - \frac{d_{1i}}{2}(\cos \frac{\theta_{1i}}{2}\mathbf{h} + \sin \frac{\theta_{1i}}{2}\mathbf{g} \times \mathbf{h}), \quad i = 2, 3 \quad (76)$$

by imposing  $\|\mathbf{h}\| = 1$  and,

$$\frac{s_{12}^{w0}}{\frac{d_{12}}{2} \sin \frac{\theta_{12}}{2}} = \frac{s_{13}^{w0}}{\frac{d_{13}}{2} \sin \frac{\theta_{13}}{2}} \quad (77)$$

This characterizes the RP joint formed by the two end-effector edges. With  $d_{1i}$  and  $\mathbf{h}$  known, the relative transformation from the end-effector of the P joint to the vertex between the PR chain and the P joint can be calculated to obtain two new relative transformations,

$$\begin{aligned} \hat{S}_{12}^c &= \hat{P}_{PRP} \hat{S}_P(-d) \Big|_{12} = s_{12}^{wc} + \mathbf{b}_{12}^c + \epsilon(s_{12}^{w0c} + \mathbf{b}_{12}^{0c}) \\ \hat{S}_{13}^c &= \hat{P}_{PRP} \hat{S}_P(-d) \Big|_{13} = s_{13}^{wc} + \mathbf{b}_{13}^c + \epsilon(s_{13}^{w0c} + \mathbf{b}_{13}^{0c}) \end{aligned} \quad (78)$$

The procedure follows as before where we determine the new system using Eqn. (75) and Eqn. (76), obtaining all the joint variables and structural parameters of the system.

The entire system gives a single unique solution for a set of 3 translation positions with 2 rotation positions for each end-effector. The method for solving the RP-(R,P) kinematic structure is not general as not all kinematic structures can be split into two non-overlapping substructures that can be solved with the same number of task positions. However, this example shows a novel methodology that can be used on many structures.

## 10. Conclusions

In this paper we presented a methodology for the kinematic synthesis of articulated systems with a tree structure, which has applications on the design of articulated multi fingered hands and locomotion systems, among others. The design process follows existing techniques for the dimensional synthesis of spatial linkages, however, in the design of tree-like topologies specific issues appear that are explored and solved here.

The method is based on representing the tree as a rooted graph and performing reduction operations in order to simplify the initial topology. The forward kinematics equations for each of the serial chains forming the tree articulated system are stated and equated to a set of task positions, and conditions for the solvability of the whole tree and individual subgraphs or

branches of the tree are derived. The inclusion of tree articulated systems among possible candidate topologies for the design process allows to extend dimensional synthesis to systems with a high number of degrees of freedom and more complex motion tasks.

## References

- [1] R. Hartenberg, J. Denavit, Kinematic Synthesis of Linkages, McGraw-Hill, 1964.
- [2] B. Roth, Finite position theory applied to mechanism synthesis, Journal of Applied Mechanics 34 (1967) 599–605.
- [3] G. N. Sandor, A. G. Erdman, Advanced Mechanism Design: Analysis and Synthesis, Vol. 2, Prentice-Hall, Englewood Cliffs, NJ, 1984.
- [4] C. Suh, C. Radcliffe, Kinematics and Mechanisms Design, John Wiley, 1978.
- [5] P. Chen, B. Roth, Design equations for finitely and infinitesimally separated position synthesis of binary link and combined link chains, ASME Journal of Engineering for Industry 91 (1967) 209–219.
- [6] E. Lee, C. Mavroidis, Geometric design of 3r manipulators for reaching four end-effector spatial poses, The International Journal of Robotics Research 23(3) (2004) 247–254.
- [7] J. M. McCarthy, Geometric Design of Linkages, Springer-Verlag, New York, first edition, 2000.
- [8] G. Sandor, K. Bishopp, On a general method of spatial kinematic synthesis by means of a stretch-rotation tensor', Journal of Engineering for Industry 91 (1969) 115–122.
- [9] H. Su, J. M. McCarthy, L. T. Watson, Generalized linear product homotopy algorithms and the computation of reachable surfaces, ASME Journal of Computers and Information Science and Engineering 4(3) (2004) 226–235.
- [10] M. L. Husty, M. Pfurner, H.-P. Schrocker, K. Brunnthaler, Algebraic methods in mechanism analysis and synthesis, Robotica 25 (2007) 661–675.

- [11] J. Angeles, Spatial Kinematic Chains. Analysis, Synthesis, Optimization, Springer-Verlag, New York, 1982.
- [12] J. Merlet, D. Daney, Dimensional synthesis of parallel robots with a guaranteed given accuracy over a specific workspace, in: Proc. of the 2005 International Conference on Robotics and Automation, Barcelona, Spain, pp. 942–947.
- [13] G. Gogu, Structural Synthesis of Parallel Robots. Part 1: Methodology, Springer, first edition, 2007.
- [14] J. M. Herve, The lie group of rigid body displacements, a fundamental tool for mechanism design, Mechanism and Machine Theory 34 (1999) 717–730.
- [15] M. Huang, A. Soni, Application of linear and nonlinear graphs in structural synthesis of kinematic chains, Journal of Engineering for Industry (1973) 525–532.
- [16] F. Freudenstein, E. R. Maki, The creation of mechanisms according to kinematic structure and function, Journal of Environment and Planning 6 (1979) 375–391.
- [17] L. W. Tsai, Mechanism Design: Enumeration of Kinematic Structures According to Function, CRC Press, Boca Raton, 2001.
- [18] T. Mruthyunjaya, Kinematic structure of mechanisms revisited, Mechanism and Machine Theory 38 (2003) 279–320.
- [19] C. Chuang, J. Lee, Topological synthesis of underactuated passively adaptive finger mechanisms, in: Proc. of the 13th World Congress in Mechanism and Machine Science, Guanajuato, Mexico,.
- [20] J. M. Selig, Geometric Fundamentals of Robotics (Monographs in Computer Science), Springer-Verlag, 2004.
- [21] N. Biggs, Discrete Mathematics, 1985.
- [22] I. Chen, G. Yang, I. Kang, Numerical inverse kinematics for modular reconfigurable robots, Journal of Robotic Systems 16(4) (1999) 213–225.

- [23] G. Song, N. Amato, A motion-planning approach to folding: from paper craft to protein folding, *IEEE Transactions on Robotics and Automation* 20(1) (2004) 60–71.
- [24] A. Jain, Graph-theory roots of spatial operators for kinematics and dynamics, in: *Proc. of the 2010 International Conference on Robotics and Automation*, Anchorage, Alaska, USA,, pp. 2745–2750.
- [25] J. Garcia de Jalon, E. Bayo, *Kinematic and Dynamic Simulation of Multibody Systems: The Real-Time challenge*, Springer-Verlag, 1994.
- [26] S. Stramigioli, *Modeling and IPC control of interactive mechanical systems - A coordinate-free approach*, volume LNCIS 266, Springer, 2001.
- [27] C. Tischler, A. Samuel, K. Hunt, Kinematic chains for robot hands - 1. orderly number synthesis, *Mechanism and Machine Theory* 30(8) (1995) 1193–1215.
- [28] C. Tischler, A. Samuel, K. Hunt, Kinematic chains for robot hands ii: Kinematic constraints, classification, connectivity and actuation, *Mechanism and Machine Theory* 30(8) (1995) 1217–1239.
- [29] L. Briglen, T. Laliberte, C. Gosselin, *Underactuated Robotic Hands*, Springer, 2008.
- [30] A. Ciocarlie, P. Allen, Data-driven optimization for underactuated robotic hands, in: *Proc. of the 2010 International Conference on Robotics and Automation*, Anchorage, Alaska, USA,, pp. 1292–1299.
- [31] J. Belter, A. Dollar, Performance characteristics of anthropomorphic prosthetic hands, in: *Proceedings of the 2011 IEEE International Conference on Rehabilitation Robotics*, pp. 921–927.
- [32] L. Biagiotti, F. Lotti, C. Melchiorri, G. Vassura, How Far is the Human Hand? A Review of Anthropomorphic Robotic End-effectors. Internal report, Technical Report, Universita di Bologna, 2004.
- [33] J. Dai, D. Wang, Geometric analysis and synthesis of the metamorphic robotic hand, *ASME Journal of Mechanical Design* 129 (2007) 1191–1197.

- [34] A. Perez Gracia, J. M. McCarthy, The kinematic synthesis of spatial serial chains using clifford algebra exponentials, Proceedings of the Institution of Mechanical Engineers, Part C, Journal of Mechanical Engineering Science 220(7) (2006) 953–968.
- [35] E. Simo-Serra, F. Moreno-Noguer, A. Perez-Gracia, Design of Non-Anthropomorphic Robotic Hands for Anthropomorphic Tasks, in: Proc. of the 2011 ASME International Design Engineering Technical Conferences, Washington D.C., USA,.
- [36] R. M. Murray, Z. Li, S. S. Sastry, A Mathematical Introduction to Robotic Manipulation, CRC Press, Inc., Boca Raton, FL, 1994.
- [37] J. M. Rico, J. Gallardo, B. Ravani, Lie algebra and the mobility of kinematic chains, Journal of Robotic Systems 20 (2003) 477–499.
- [38] P. Fanghella, C. Galletti, Metric relations and displacement groups in mechanism and robot kinematics, Journal of Mechanical Design 117 (1995) 470–478.
- [39] J. M. Rico, B. Ravani, On calculating the degrees of freedom or mobility of overconstrained linkages: Single-loop exceptional linkages, Journal of Mechanical Design 129 (2007) 301–311.
- [40] E. Simo-Serra, A. Perez-Gracia, H. Moon, N. Robson, Design of Multi-fingered Robotic Hands for Finite and Infinitesimal Tasks using Kinematic Synthesis, in: Advances in Robot Kinematics (ARK).
- [41] A. Perez, Dual Quaternion Synthesis of Constrained Robotic Systems, Ph.D. thesis, University of California - Irvine, 2003.
- [42] A. Perez-Gracia, Synthesis of spatial rprp closed linkages for a given screw system, ASME Journal of Mechanisms and Robotics 3(2) (2011).

### Figure captions

- Figure 1: Graph representation of a 4R manipulator where the circle represents the root and the square represents the end-effector.
- Figure 2: Reduction of a complex kinematic structure with a Sarrus linkage to a tree graph.
- Figure 3: Both branches with fewer than  $\dim(\mathcal{L}) = 6$  joints form subgraphs G1 and G2 that are solvable separately.
- Figure 4: Rooted tree graph of an anthropomorphic hand model.
- Figure 5: Rooted tree graph of the RP-(R,P) mechanism.

### Table captions

- Table 1: Design parameters for different serial chains.
- Table 2: All solvable subgraphs of the anthropomorphic hand model.
- Table 3: Solvability of the different subgraphs of the PR-(R,P) mechanism.



## Tables

Table 1: Design parameters for different serial chains

Linkage	$n_j$	$n_s$	$d$	$m$	$m^R$	$m^T$	$\mathcal{L}$
P	1	2	3	2	1	2	$\mathbb{R}^3$
R	1	4	6	$1\frac{4}{5}$	2	3	$SE(3)$
H	1	5	6	2	2	$3\frac{1}{2}$	$SE(3)$
C	2	4	6	2	2	5	$SE(3)$
T	2	5	6	$2\frac{1}{4}$	5	6	$SE(3)$
E	3	2	6	$1\frac{2}{3}$	2	$\infty$	$SE(3)$
S	3	3	6	2	$\infty$	$\infty$	$SE(3)$
PP	2	2	3	3	1	3	$\mathbb{R}^3$
RP	2	6	6	$2\frac{1}{2}$	2	7	$SE(3)$
RR	2	8	6	3	5	9	$SE(3)$
PPR	3	6	6	3	2	$\infty$	$SE(3)$
PRP	3	8	6	$3\frac{2}{3}$	2	$\infty$	$SE(3)$
PRR	3	10	6	$4\frac{1}{3}$	5	$\infty$	$SE(3)$
RRR	3	12	6	5	$\infty$	$\infty$	$SE(3)$

Table 2 : All solvable subgraphs of the anthropomorphic hand model

Subgraph	$b$	$r$	$m$	$n_f = n_x$
3R-(4R,4R,5R,5R,5R)	5	26	27	780
3R-(4R,5R,5R,5R)	4	22	45	1056
3R-(4R,4R,5R,5R)	4	21	29	672
3R-(4R,5R,5R)	3	17	69	1224
3R-(4R,4R,5R)	3	16	33	576
3R-(4R,4R)	2	11	45	528

Table 3: Solvability of the different subgraphs of the PR-(R,P) mechanism

Subgraph	$m$	$m^R$	$m^T$	Comments
PR-(R,P)	$2\frac{1}{2}$	2	7	Full system, rotational and translational components solvable
PRR	3	5	$\infty$	Full system and rotational component solvable
PRP	$3\frac{1}{2}$	2	$\infty$	Only rotational component solvable $m^R < m$ and $m^T \notin \mathbb{Q}^+$

## Figures

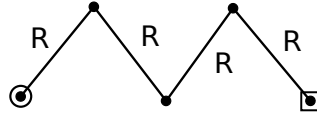


Figure 1: Graph representation of a 4R manipulator where the circle represents the root and the square represents the end-effector.

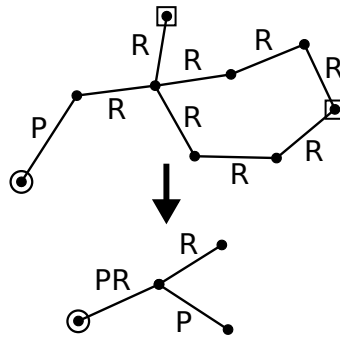


Figure 2: Reduction of a complex kinematic structure with a Sarrus linkage to a tree graph.

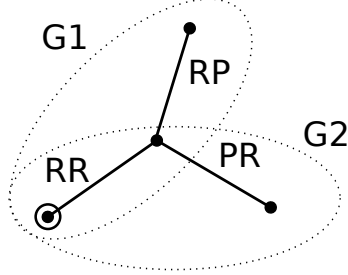


Figure 3: Both branches with fewer than  $\dim(\mathcal{L}) = 6$  joints form subgraphs G1 and G2 that are solvable separately.

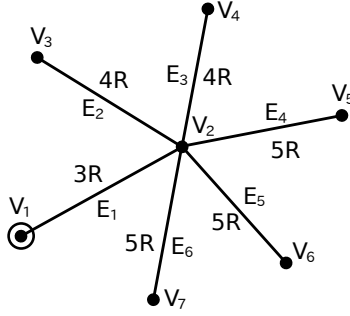


Figure 4 : Rooted tree graph of an anthropomorphic hand model.

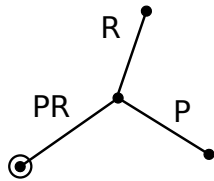


Figure 5: Rooted tree graph of the RP-(R,P) mechanism.

# Single Degree-of-Freedom Exoskeleton Mechanism Design for Thumb Rehabilitation\*

Yimesker Yihun, Robert Miklos, Alba Perez-Gracia,<sup>1</sup>  
David J. Reinkensmeyer<sup>2</sup>, Keith Denney and Eric T. Wolbrecht<sup>3</sup>

**Abstract**—This paper presents the kinematic design of a spatial, 1-degree-of-freedom closed linkage to be used as an exoskeleton for thumb motion. Together with an already-designed finger mechanism, it forms a robotic device for hand therapy. The goal for the exoskeleton is to generate the desired grasping and pinching path of the thumb with one degree of freedom, rather than using a system actuating all its joints independently. In addition to the path of the thumb, additional constraints are added in order to control the position and size of the exoskeleton, reducing physical and sensory interference with the user.

## I. INTRODUCTION

Robotic devices have been shown to be capable of automating the strenuous and repetitive nature of movement therapy after stroke or other neurological injury (for an introduction, see [1], [2]). Additionally, robotic devices give scientists a new investigative tool for recording progress during movement training and for determining the factors that promote functional recovery. Of particular interest is the ability to design, implement, and test assistive control strategies. Many different control strategies have been developed (see review: [3]). The most promising approaches fall into the assist-as-needed category, where an attempt is made to vary the level of assistance to match the impairment level of the patient. For example, [4] presents an assist-as-needed controller that learns a model of the patients abilities while simultaneously reducing assistance when the patient performs well. The result is a robotic device that can help patients complete movements but continuously challenges them to try. The efficacy of these and other control strategies has been documented ([5], [6], [7]) but it remains unclear what specific controller characteristics increase patient learning during therapy.

Proper evaluation of assist-as-needed control strategies is dependent upon the abilities of the robotic device. Ideally, the device would be able to apply any force at any speed at any location along the movement trajectory. In practice,

this is impossible, but can be approached in a robotic device by keeping apparent inertia and friction low, and the controllable force bandwidth high. To achieve these features, we are developing an exoskeleton device for the fingers and thumb, with the actuators mounted along the forearm where their effect on device inertia is minimized. In addition, the actuators are high-speed, low-friction linear motors, which allows for high-bandwidth control. These characteristics have not been fully achieved in previous robotic hand and wrist devices, including end-effector, glove, and exoskeleton type devices ([8], [9], [10]).

The device presented in this paper is obtained following a new methodology for the design of exoskeletons. Traditionally, exoskeletons are designed so that they try to align with the human joint axes of motion [8]. This assumes that the location of the axis can be accurately known, and in addition, that such a fixed axis exists for the range of motion of the joint or set of joints, which is not always the case. A clear example of complex kinematic modeling is the thumb, for which precise detection methods such as MRI segmentation [11] show that considering fixed rotational axes, especially for the CMC joint, is not a good approximation; see also [12]. Using the methodology described in this paper, based on kinematic synthesis, it is not necessary to know the geometry of the hand, but rather to have a description of its motion at the point of attachment.

To meet the design needs for the rehabilitation application described above, a lightweight single-degree-of freedom mechanism has been selected for following the paths of the thumb during simple pinch and grasping movements. The complete exoskeleton device consists of two separate single degree-of-freedom exoskeleton mechanisms: one for finger curling motions, whose design was presented in [13], and one for thumb motions, presented in this paper. The resulting robot will be able to assist in common, naturalistic finger and thumb motions. As such, the therapy delivered should translate to a wide range of functional tasks, even if the degrees-of-freedom of the robot are minimal.

The linkage to perform the thumb motion was selected among several single-degree-of-freedom spatial closed linkages with four to six links, with a single end-effector for controlling the orientation and position of the proximal phalanx of the thumb. In this approach, the mechanism will be actuated with a single actuator, and so the design of the mechanism is responsible for appropriately shaping the thumb motion. In addition, the designed mechanism is confined to the back of the hand, so as to minimize sensory

\*This work was partially supported by Grant Number NIH-R01HD062744-01 from NCHHD, and by the US Department of the Army, award number W81XWH-10-1-0128 awarded and administered by the U.S. Army Medical Research Acquisition Activity. The content is solely the responsibility of the authors.

<sup>1</sup>Dept. of Mechanical Engineering, Idaho State University, Pocatello, ID, USA. yihuyime@isu.edu, mikrobe@isu.edu, perealba@isu.edu

<sup>2</sup>Departments of Mechanical and Aerospace Engineering, Anatomy and Neurobiology, and Biomedical Engineering, University of California, Irvine, Irvine, CA, USA. dreinken@uci.edu

<sup>3</sup>Department of Mechanical Engineering, University of Idaho, Moscow, ID, USA. kmdenney@gmail.com, ewolbrec@uidaho.edu

feedback interference, and to allow the mechanism to be manufactured with minimal size. This combined with the intended location of the actuators will allow the device to be constructed with low apparent inertia.

## II. THUMB MECHANISM DESIGN

### A. Design objectives

The human thumb presents a complex 3D motion that can be modeled, depending on the needed accuracy, with three to four degrees of freedom, and using variable joint axes. For this project, the targeted task of the thumb is a single spatial path going from index pinching to contacting the tip of the fingers. We postulate that it is still possible to use simplified, low-dof linkages for assisting in this motion. We focus on a set of closed, spatial overconstrained and non-overconstrained four-bar to six-bar linkages with low mobility that present the desired characteristics for this application, see [14] and [15]. The spatial mechanism is to be attached to the proximal phalanx of the thumb. The goal is to find a single-dof mechanism whose path is as close to the experimental thumb path as possible, while complying with additional size and placement constraints.

### B. Thumb data

The method is based on synthesizing a linkage to follow as closely as possible experimental paths of the human thumb. The thumb data was acquired using a Vicon motion tracking system. The set up we used had eight infrared cameras set around the room, primarily for larger applications; however it worked very well for the hand motions. The markers that are used with the system are small white balls that reflect the inferred light. We used arrays with the markers placed 1.25 inches apart making it easy to collect data in the three dimensions. In order to assess the exact location of the fixed link with respect to the hand, additional sets of sensors are placed on the arm, see Figure 1



Fig. 1. Markers placed in the thumb and data capture setup

The several experimental paths so obtained were separated for clarity; Figure 2 shows one typical point path, seen from the reference frame of the motion capture system.

For the design of spatial motion, it is sometimes advantageous to work with relative displacements. Each relative displacement expresses a motion of the thumb from a reference configuration, taken as the thumb position at the first frame. Each displacement can be modeled as an axis, plus a rotation about and a translation along the axis. We encode this information as a *screw*, where the screw axis is the axis of the displacement and the pitch is the ratio of translation to rotation for that displacement.

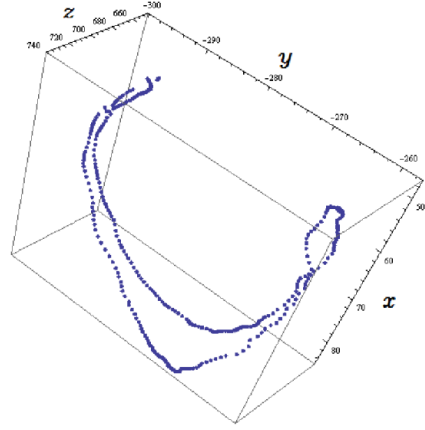


Fig. 2. Thumb's proximal phalanx point path

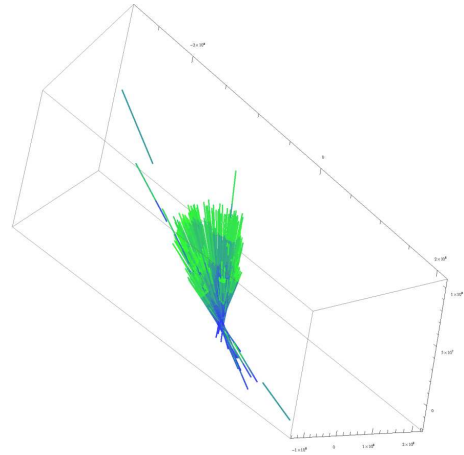


Fig. 3. Thumb's proximal phalanx path: screw surface of relative screw axes

Figure 3 shows the displacements of the thumb's proximal phalanx path as screw axes with a pitch, where the screw lengths are proportional to the pitch. The screw axes of the displacements with their pitches generate a *screw hypersurface*. This representation has all the information of the motion except for the value of the rotation, which can be calculated independently.

### C. Mechanism Selection

In order to accomplish simplicity together with spatial motion under a one-degree-of-freedom system, an initial set of closed spatial linkages with four to six links and standard revolute (R), prismatic (P) and cylindrical (C) joints has been selected. Some of these linkages are overconstrained, while others are trivial linkages, all of them with mobility equal to one [14], [15]. Figure 4 shows the topology of the spatial CCCC linkage (a linkage with four cylindrical joints); candidate linkages with four links are particular cases of this one, obtained by making some of the joint variables ( $\theta_i, r_i$ ) constant.

Similarly, the closed, spatial CCC-CCC linkage can be seen as the general case for the six-bar candidate linkages, see Figure 5. In particular, the following four-bar linkages:

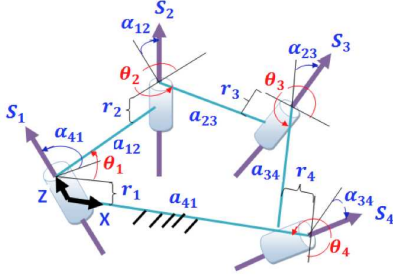


Fig. 4. A spatial 4-bar CCCC linkage

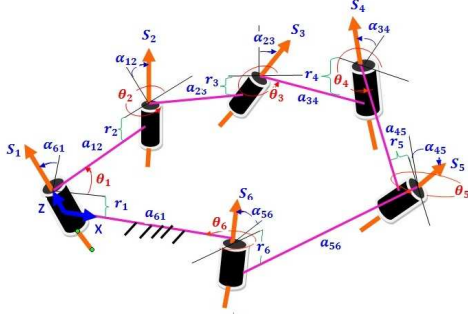


Fig. 5. A spatial 6-bar CCCCCC linkage

RC-CC, RP-RP, RR-RR, and the following six-bar linkage: CRR-RRR were selected as candidates. Here, the dash separating joints indicates where the end-effector, or attachment to the thumb, is being placed.

In order to assess the suitable topology for the thumb linkage, the workspace of relative displacements has been analyzed for each of these linkages. Figure 6 shows a typical workspace for the candidate linkage.

From inspection of the workspace shape, the candidate linkages to be used for dimensional synthesis are the RR-RR, the RC-CC and the CRR-RRR. The RRRR is an overconstrained linkage, while the other two present trivial mobility equal to one.

Among the properties of these linkages that are useful for our application we can cite the 1-dof motion, requiring only one actuator, and topological simplicity while creating a complex motion. In addition, overconstrained linkages have other advantages, such as inherent structural rigidity.

#### D. Mechanism Design Equations

In this section, the design equations corresponding to the CRR-RRR mechanism are presented. The reason to do so is that it turned out to give the most fitted mechanisms for the task.

Let us consider the closed CRR-RRR linkage as two serial chains, CRR and RRR, joined at their end-effectors. The axes are labeled as shown in Figure 5, starting at the fixed C joint and going around up to the final fixed R joint. For every joint  $i$ , let  $S_i = s_i + \epsilon s_i^0$  be the joint axis, with rotation  $\theta_i$ , and slide (for the C joint only)  $d_i$ . We express the forward

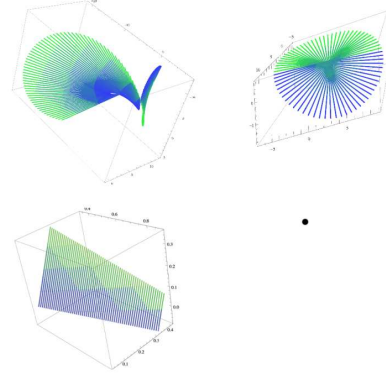


Fig. 6. Workspaces of the CCCR, the RRRR, the RPRP linkages

kinematics equations of the CRR and RRR chains using dual quaternions [16],

$$\begin{aligned} \hat{Q}_{CRR}(\Delta\hat{\theta}_1, \Delta\theta_2, \Delta\theta_3) &= \prod_{i=1}^3 \left( \cos \frac{\Delta\hat{\theta}_i}{2} + \sin \frac{\Delta\hat{\theta}_i}{2} S_i \right) \\ \hat{Q}_{RRR}(\Delta\theta_6, \Delta\theta_5, \Delta\theta_4) &= \prod_{i \in \{6,5,4\}} \left( \cos \frac{\Delta\theta_i}{2} + \sin \frac{\Delta\theta_i}{2} S_i \right) \end{aligned} \quad (1)$$

where  $\Delta\hat{\theta}_i = \Delta\theta_i + \epsilon\Delta d_i$  is the dual angle, and all  $d_i = 0$  except  $d_1$  corresponding to the cylindrical joint. The forward kinematics so expressed represent the set of relative displacements of the chain with respect to a reference configuration.

In order to create the design equations, we minimize the distance between the displacements captured in Section II.B. and the displacements of the candidate chain. We perform dimensional synthesis, that is, the goal is to find the location and dimensions of the mechanism that performs approximately the task.

The design equations are created by equating the forward kinematics of the mechanism to each of the discrete positions obtained from the motion capture. If we denote each finite displacement of the thumb as  $\hat{P}^i$ , we can create the relative displacements with respect to the first position of the thumb,  $\hat{P}^{1i} = \hat{P}^i(\hat{P}^1)^{-1}$ , to yield design equations

$$\begin{aligned} \hat{Q}_{CRR}(\Delta\hat{\theta}_1^i, \Delta\theta_2^i, \Delta\theta_3^i) &= \hat{P}^{1i}, \\ \hat{Q}_{RRR}(\Delta\theta_6^i, \Delta\theta_5^i, \Delta\theta_4^i) &= \hat{P}^{1i}, \quad i = 2, \dots, m. \end{aligned} \quad (2)$$

In these equations, the variables we are interested in are what we call the *structural variables*, which are the Plucker coordinates of the joint axes  $S_i = s_i + \epsilon s_i^0$  at the reference configuration. In addition, the optimization process outputs the angles of the chains in order to reach the thumb displacements.

To complete the system of equations in (2), we impose size constraints on the mechanism so that it can be attached to the

lower arm and with reasonable dimensions. In particular, for the six-link CRR-RRR mechanism, we add the constraints of distance between both fixed axes and also between the fixed axes and the thumb,

$$\begin{aligned} S_1 \cdot S_6 &= \cos \alpha + \epsilon a \sin \alpha \\ S_1 \cdot P^1 &= \cos \beta + \epsilon b \sin \beta \end{aligned} \quad (3)$$

where  $P^1$  is the screw axis of the first thumb position, and we fix the distance between the axes along the common normal,  $a$ , to a value between 50mm and 150mm, and the distance between the thumb attachment and the coupler axes,  $b$ , to similar values.

#### E. Implementation of the Design Equations

Ten positions were selected from the thumb path, and the first frame was taken as the reference configuration. Each forward kinematics equality is composed of 8 equations, and forward kinematics are written for both serial chains composing the mechanism. This gives a total of 144 nonlinear equations. In addition, we have the constraints of (3). Overall, we have 147 equations.

The variables to solve for are the Plucker coordinates of the axes, that is, six parameters per axis, and the joint variables to reach each thumb position. The total is 97 unknowns.

The equations were solved using a Levenberg-Marquardt nonlinear, unconstrained solver implemented in Java. This is based on public domain MINPACK routines, translated from FORTRAN to Java by Steve Verrill [17].

### III. RESULTS

The best results were obtained for the CRR-RRR mechanism. One of the sets of ten equally-spaced positions selected from the thumb data can be seen in Figure 9. The equations were run 14 times for three different sets of positions chosen from the thumb frames. The distance to the desired path has been optimized by minimizing the distance at each step. The overall error of the function was smaller than 0.03, and it took a variable amount of time, from a few minutes to a few hours, to find solutions. For these 14 runs, 14 considerably different solutions were found.

Out of these 14 solutions, 2 linkages were selected because of their overall dimensions and placement on the hand. Figure 7 shows the SolidWorks model of those solutions, named candidate I and II.

As overall solution, we selected the mechanism with the best combination of fit to the path, dimensions and placement. Due to the potentially very large number of solutions for this problem, not all the solution space has been searched and hence we cannot assume that the selected candidate is the optimal one, but rather an acceptable one.

Figures 8 and 9 present the actual motion of the linkage as compared to the thumb path and design poses. Even though there is some small divergence in the paths, we must point out that it is of the order of the variability of the several paths observed in the motion capture data, rendering an overall motion that is within the normal thumb actuation.

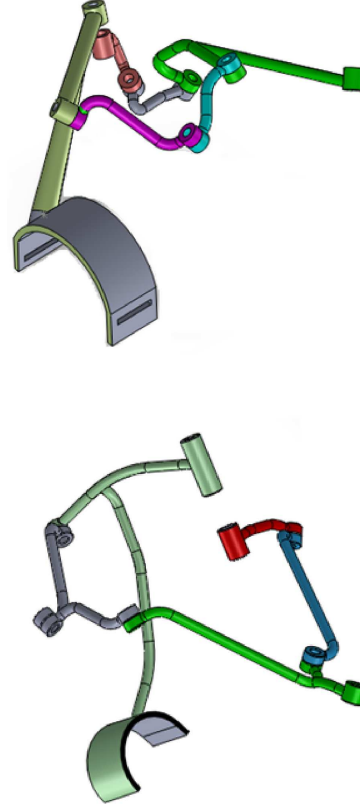


Fig. 7. The two solutions selected for prototyping

Rapid prototypes have been built in order to assess the manufacturing and to better design the hand attachment and compatibility with the finger exoskeleton. Figure 10 shows one of the prototype linkages mounted on the hand.

### IV. CONCLUSIONS AND FUTURE WORK

This paper presents a task-oriented design methodology for exoskeletons. Previous work targeted planar motion, while this paper focuses on the application to spatial motion. In particular, we apply the methodology to develop a 1-dof thumb exoskeleton for rehabilitation. The kinematic design is followed by a detailed mechanical design and prototyping.

The main advantage of this method with respect to previous exoskeleton designs is that it does not need any assumption about location and type of joints in the subject; the exoskeleton is going to follow the path that is selected as task regardless of the skeleton structure that generates it. This allows for the creation of new and innovative exoskeleton designs. The high number of solutions obtained mean more choices for the designer regarding placement, size, and inertia of the exoskeleton.

The final designs presented in this paper have been tested for the desired path and the results seem to be acceptable. The placement of the mechanism on the lower arm and close to the wrist is also according to specifications.

The next step is the force analysis of the mechanism. This is important because of the spatiality of the linkage, and will allow us to determine the best joint to place the actuator.



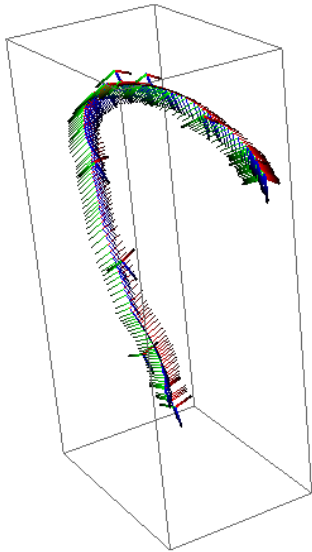


Fig. 8. One of the thumb paths (thin frames) with superimposed linkage path (thick lines)

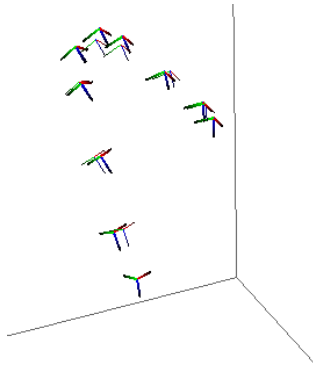


Fig. 9. Comparison between design positions (thin lines) and linkage positions (thick lines)

Future research for the mechanism optimization includes identifying a small subset of structural variables that, when modified, will produce a new mechanism to track a similar path created by a slightly different thumb. In a fashion similar to [18], this will allow the mechanism to be re-configured to varying subject sizes.

## REFERENCES

- [1] E. M. Frick and J. L. Alberts, "Combined use of repetitive task practice and an assistive robotic device in a patient with subacute stroke," *Physical Therapy*, vol. 86(10), pp. 1378–1386, 2006.
- [2] D. J. Reinkensmeyer, J. A. Galvez, L. Marchal, E. T. Wolbrecht, and J. E. Bobrow, "Some key problems for robot-assisted movement therapy research: A perspective from the university of california at irvine," in *Proc. 10th IEEE Intl. Conf. on Rehabilitation Robotics*, ASME, Ed., Noordwijk, The Netherlands, 2007, pp. 1009–1015.
- [3] L. M. Crespo and D. J. Reinkensmeyer, "Review of control strategies for robotic movement training after neurologic injury," *J. Neuroeng. Rehabil.*, vol. submitted, 2008.
- [4] E. T. Wolbrecht, D. J. Reinkensmeyer, and J. E. Bobrow, "Optimizing compliant, model-based robotic assistance to promote neurorehabilitation," *IEEE Transactions Neural Systems and Rehabilitation Engineering*, vol. 16, pp. 286–297, 2008.

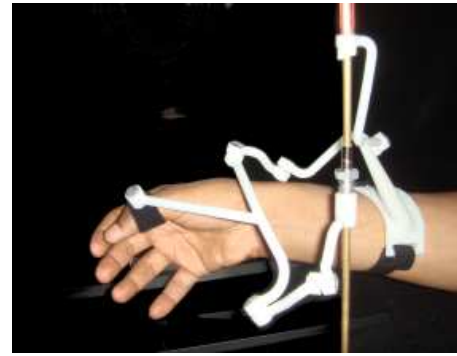


Fig. 10. One prototype attached to the thumb

- [5] B. R. Brewer, S. K. McDowell, and L. C. Worthen-Chaudhari, "Post-stroke upper extremity rehabilitation: a review of robotic systems and clinical results," *Top. Stroke Rehabil.*, vol. 14, pp. 22–44, 2007.
- [6] H. I. Krebs, S. Mernoff, S. E. Fasoli, R. Hughes, J. Stein, and N. Hogan, "A comparison of functional and impairment-based robotic training in severe to moderate chronic stroke: a pilot study," *NeuroRehabilitation*, vol. 23, pp. 81–87, 2008.
- [7] J. Mehrholz, T. Platz, J. Kugler, and M. Pohl, "Electromechanical and robot-assisted arm training for improving arm function and activities of daily living after stroke," *Cochrane Database Syst. Rev.*, vol. 4, p. CD006876, 2008.
- [8] S. Balasubramanian, J. Klein, and E. Burdet, "Robot-assisted rehabilitation of hand function," *Curr. Opin. Neurol.*, vol. 23(6), pp. 661–670, 2010.
- [9] S. Ito, H. Kawasakia, Y. Ishigureb, M. Natsumec, T. Mouria, and Y. Nishimotod, "A design of fine motion assist equipment for disabled hand in robotic rehabilitation system," *J. Franklin Inst.*, vol. doi:10.1016/j.jfranklin.2009.02.009, 2009.
- [10] T. Worsnopp, M. Peshkin, J. Colgate, and D. Kamper, "An actuated finger exoskeleton for hand rehabilitation following stroke," in *Proc. 10th IEEE Intl. Conf. on Rehabilitation Robotics*, Noordwijk, The Netherlands, 2007, pp. 896–901.
- [11] G. Stillfried and P. van der Smagt, "Movement model of a human hand based on magnetic resonance imaging (mri)," in *Proceedings of the 1st Int. Conf. on Applied Bionics and Biomechanics*, Venice, Italy, October 14–16,, 2010.
- [12] M. Chalon, M. Grebenstein, T. Wimbock, and G. Hirzinger, "The thumb: Guidelines for a robotic design," in *Proc. of the 2010 Int. Conf. on Intelligent Robots and Systems*, Taipei, Taiwan, October 18–22, 2010.
- [13] E. Wolbrecht, D. Reinkensmeyer, and A. Perez-Gracia, "Single degree-of-freedom exoskeleton mechanism design for finger rehabilitation," in *Proceedings of the ICORR 2011: Int. Conference on Rehabilitation Robotics*, June 29–July 1, 2011, Zurich, Switzerland, 2011.
- [14] K. Waldron, "A study of overconstrained linkage geometry by solution of closure equations - part ii- four-bar linkages with lower pair joints other than screw joints," *Mechanism and Machine Theory*, vol. 8, pp. 233–247, 1973.
- [15] L.-W. Tsai, *Enumeration of Kinematic Structures According to Function*. CRC Press, 2000.
- [16] A. Perez Gracia and J. M. McCarthy, "The kinematic synthesis of spatial serial chains using clifford algebra exponentials," *Proceedings of the Institution of Mechanical Engineers, Part C, Journal of Mechanical Engineering Science*, vol. 220(7), pp. 953–968, 2006.
- [17] S. Verrill, "Optimization java package," 2000. [Online]. Available: <http://www1.fpl.fs.fed.us/optimization.html>
- [18] D. Sands, A. Perez-Gracia, J. McCormack, and E. Wolbrecht, "Design method for a reconfigurable mechanisms for finger rehabilitation," in *Proceedings of the 2010 IASTED Robotics and Applications Conference*, November 1–3, 2010, Cambridge, Massachusetts, USA, 2010.

# Design of an Exoskeleton as a Finger-Joint Angular Sensor \*

Yimesker Yihun, Md Shamim N. Rahman and Alba Perez-Gracia<sup>1</sup>

**Abstract**—Estimation of joint angles for human joints is important for many applications in Bioengineering. Most of the existing angular joint sensors rely on the assumption of the knowledge of the type of motion and location of the joint. This paper presents a new design for the measurement of finger joint angular motion. The design presented here consists of an exoskeleton, designed to fit the finger motion, in which we can relate the angular displacement of its links to the change in orientation of the phalanx under consideration. Unlike other designs, the exoskeleton does not need any information about the actual anatomy and dimensions of the hand in order to provide with the angular information. The design is to be used in myoelectrical signal identification.

## I. INTRODUCTION

Accurate hand pose tracking and finger joint measurements are important research topics in bioengineering fields for different applications; the design of exoskeleton and prosthetic devices and the implementation of control algorithms are a few of those. Almost all currently available prosthetics using EMG or sEMG sensors compute some threshold value for the corresponding finger joint positions [1]. In most cases, models are obtained with the smoothed sEMG data as input and the respective smoothed finger angle data as output. The dynamic model obtained allows the instantaneous control of the finger motions. For these and other reasons, to relate the surface EMG signals to the finger motion, and also for gesture recognition, researchers have been using data gloves and expensive infrared sensors [2]. These devices tend to be expensive and affected by noise; in the case of glove devices, the fitting greatly influences the measurement error [3]. In addition, the accuracy of the result depends on a faithful underlying hand model, which is a complex problem on its own [4]. This paper presents a novel approach to estimate the finger joint-angles that can be applied for modeling of surface electromyography (sEMG) signals.

The approach presented here is based on creating an exoskeleton device, which can be attached to the hand, that links in a one-to-one relation the angular pose of the phalanx under consideration to the relative angle between two links of the exoskeleton. This relative angle is easy to sense in an accurate and inexpensive fashion. The exoskeleton design follows the approach of [5] and [6].

In order to design the exoskeleton, a camera vision system is used to track the hand motion. Non-contact technologies

are mostly vision-based or use infrared or magnetic technologies. Most of the focus in single-camera tracking has been with detecting the region of interest (ROI) of the hand. Some research has attempted to create simplified hand models through markerless detection [7], [8]. Work has also been done using markers [8] and multi camera systems [9]. In this research we are using a marker-based detection technique to get information about the finger motion.

Using the vision information as an input, the kinematic synthesis of the mechanism is performed to obtain the exoskeleton-based joint angle sensor. After that, a sensitivity analysis is performed in order to decide the location of the sensor. The linkage analysis yields the angular relation between the sensed angle and the limb orientation.

## II. FINGER EXOSKELETON DESIGN

It is important to notice that the internal structure of the hand -the skeleton- is not a part of the exoskeleton mechanism. The mid phalanx of the finger is attached to the coupler of the linkage, as indicated in Figure 1, and the whole mechanism is placed on the dorsal carpal of the hand. The exoskeleton is designed for the coupler to follow a task motion -in this case, the motion of the phalanx. The exoskeleton mechanism is designed to be light and have a smooth motion over the range of the finger, so to minimize dynamic loading effects on the signal under study. An angular potentiometer is to be attached to one of the joints of the linkage, and the sensed angle is to be related to the angle of the coupler with respect to the fixed link.

Type synthesis, the selection of the topology of the mechanism to be used as exoskeleton, is a first step in the design process. For this sensor, the approach has been to try to use the simplest mechanism possible, for decreased complexity, weight and inertia on the finger. The planar four-bar mechanism was tried first, but it was not successful due to the interference of the links with the finger and the dorsal part of the hand in all designs. The six-bar linkage is the next simplest one. It allows positioning the links away from the finger so that no interference appears, while matching the planar 1-dof motion of the single finger joint. Thus, a planar, single-dof six-bar linkage (see Figure 6) has been selected as the exoskeleton topology.

## III. FINGER INPUT DATA

The experimental approach to get the data is based on the principle that the pose of a calibrated camera can be uniquely determined from a minimum of four coplanar but non-collinear points. Thus, two squares attached to the proximal phalanges and to the dorsal part of the carpal are used as

\*This work was supported by the US Department of the Army, award number W81XWH-10-1-0128 awarded and administered by the U.S. Army Medical Research Acquisition Activity. The content is solely the responsibility of the authors.

<sup>1</sup>Dept. of Mechanical Engineering, Idaho State University, Pocatello, ID, USA. yihuyime@isu.edu, rahmmd2@isu.edu, perealba@isu.edu

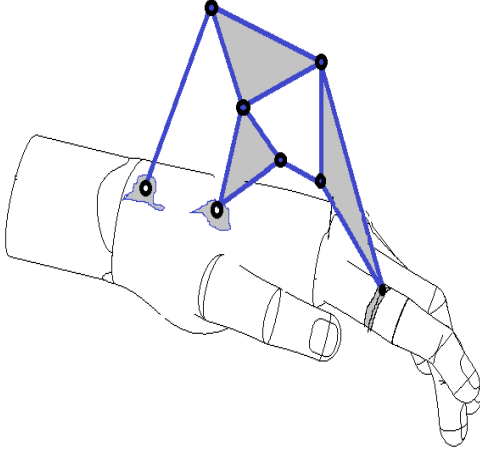


Fig. 1. Schematic drawing of the exoskeleton on the index finger

shown in Figure 3. Then the index finger is moved to its different positions/reaches. While moving the index finger, different frames are captured using a Dragonfly 2 camera from GreyPoint, with a Fujinon 1:1.4/9mm lens, interfaced with a computer using LabVIEW. The LabVIEW program captures and saves multiple images into the hard disk [10]. Once the frames are saved, sample frames from different orientation of the index finger are selected for processing.

In order to compute pose for 3D to 2D correspondences of a planar target, the algorithm used is based on Hager and Schweighofer [11]. The algorithm is customized to obtain a set of task positions from a video stream of a hand moving with markers. As it is clearly visible on the figure, the square on the dorsal carpal is used as a reference position, as the relative position between this square and the fixed joint of the mechanism is always constant while the index finger is moving.

The markers are used to estimate the pose, which consists of the position and orientation of the finger. An important aspect of this setup is the geometry of the markers. The geometry of a marker affects directly its performance and usability in computer vision applications. The design used by this project is a simple white square with a smaller black square inside as shown in Figure 3. It gives four sharp visible corners that form a perfect square to be used to find the 3D pose of the marker. Figure 5 shows a properly detected marker. It is important for these markers to be completely rigid for accurate pose estimation. For detection of the candidate points the Harris corner and edge detector algorithm [12] is used. To get a better result in both the detection and pose recovery, image segmentation is also performed so that the square corners are visible enough to be detected as shown in Figure 5. The overall methodology to design the exoskeleton-based sensor is shown in Figure 2.

The 3D pose recovery algorithm can map 3D reference points from the 2D image coordinates. It takes a set of non-collinear 3D coordinates of reference points  $P_i = (x_i, y_i, z_i)^t, i = 1, \dots, n, n \geq 3$ . These points can be expressed in an object-centered reference frame. The corresponding

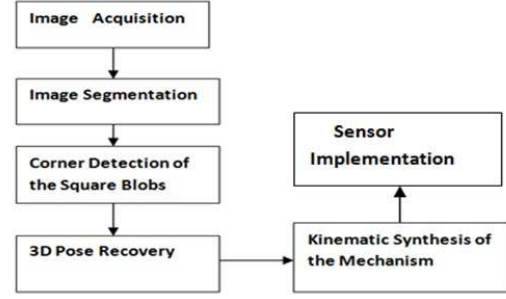


Fig. 2. The methodology adopted to design the exoskeleton based position sensor



Fig. 3. The captured image of the index finger with the square blobs on it

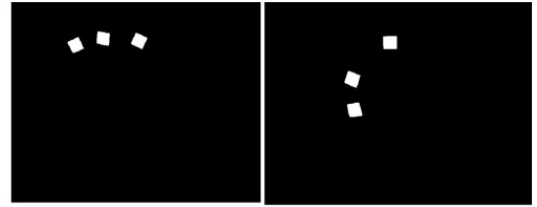


Fig. 4. The index finger movement and the square blobs

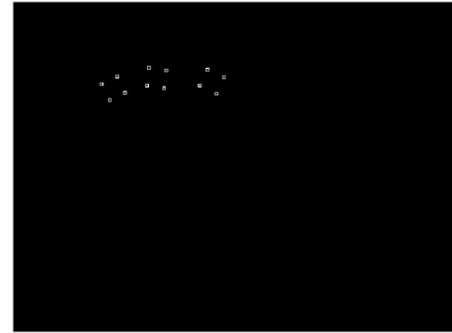


Fig. 5. Corner detection of one frame done by Harris corner detection

camera-space coordinates are  $q_i = (x'_i, y'_i, z'_i)^t$ . These two points are related by the rigid transformation

$$q_i = RP_i + t, \quad (1)$$

where  $R$  and  $t$  are the rotation matrix and translation vector respectively. Using this approach we obtain a transformation matrix  $T_{pi}$  for each position of the target point (the point from the square at the proximal phalanx) with respect to the camera and we also obtained  $T_{ci}$  (the point from the square at the carpal) with respect to the camera. In order to reference locally all movements of the target point, we use coordinate

transformation as  $T_{cp} = T_{ci}^{-1}T_{pi}$ . After getting  $T_{cp}$ , the transformation from the reference frame at the carpal to the proximal phalange, the design equations are formulated based on the candidate mechanism.

#### IV. EXOSKELETON DESIGN EQUATIONS

For this application, the desired mechanism is required to do two things: firstly, it should follow the trajectories described by the collected data; and secondly, there should be a one-to-one correspondence between the orientation of the MIP joint of the finger to one of the joints of the mechanism.

The six-bar linkage is the simplest closed, 1-dof planar linkage able to follow the collected trajectories accurately. On the other hand, being a simple, one-dof linkage, the relationships between all its angles and the driving joint angle are well known and can be related to the angle of the coupler and the MIP joint.

The variables defined for the six-bar mechanism are shown in Figure 6, where  $\theta_1, \theta_2, \theta_3, \theta_4$  and  $\theta_5$  are the joint angles and the remaining parameters (i.e.,  $s_{1x}, s_{1y}, s_{4x}, s_{4y}, a, l_1, l_2, l_3, l_4, l_5, b_1, b_2, \alpha, \gamma$  and  $\delta$ ) are the structural variables of the mechanism. Compared with the more common four-bar mechanisms, six-bar mechanisms have more design variables, therefore with an appropriate design, six-bar mechanisms can adapt to a wider number of motions.

Using the variables defined in Figure 6, the forward kinematic equations for a planar six-bar mechanism are defined as [13], [14]

$$\begin{aligned}
& s_{1x} + l_1 \cos(\theta_1) + l_2 \cos(\theta_1 + \theta_2 + \gamma) + \\
& \quad a \cos(\theta_1 + \theta_2 + \gamma + \theta_3 + \alpha) - P_x = 0 \\
& s_{1y} + l_1 \sin(\theta_1) + l_2 \sin(\theta_1 + \theta_2 + \gamma) + \\
& \quad a \sin(\theta_1 + \theta_2 + \gamma + \theta_3 + \alpha) - P_y = 0 \\
& s_{1x} + l_1 \cos(\theta_1) + b_2 \cos(\theta_1 + \theta_2) - \\
& \quad (s_{4x} + b_2 \cos(\theta_4 + \delta)) = 0 \\
& s_{1y} + l_1 \sin(\theta_1) + b_2 \sin(\theta_1 + \theta_2) - \\
& \quad (s_{4y} + b_2 \sin(\theta_4 + \delta)) = 0 \\
& s_{1x} + l_1 \cos(\theta_1) + l_2 \cos(\theta_1 + \theta_2 + \gamma) + \\
& \quad l_3 \cos(\theta_1 + \theta_2 + \gamma + \theta_3) - (l_5 \cos(\theta_4 + \theta_5) + \\
& \quad l_4 \cos(\theta_4) + s_{4x}) = 0 \\
& s_{1y} + l_1 \sin(\theta_1) + l_2 \sin(\theta_1 + \theta_2 + \gamma) + \\
& \quad l_3 \sin(\theta_1 + \theta_2 + \gamma + \theta_3) - (l_5 \sin(\theta_4 + \theta_5) + \\
& \quad l_4 \sin(\theta_4) + s_{4y}) = 0.
\end{aligned} \tag{2}$$

From the set up we can also identify the following angular relation

$$\theta_1 + \theta_2 + \gamma + \theta_3 + \alpha + \beta - \varphi = 0. \tag{3}$$

The equations given above in (2) and (3) were used to determine the trajectory that point  $P$  and its attached frame would follow through the operation of the mechanism. The axis shown in Figure 6 indicates the angle  $\varphi$  is the same as the one of the MIP joint of the finger.

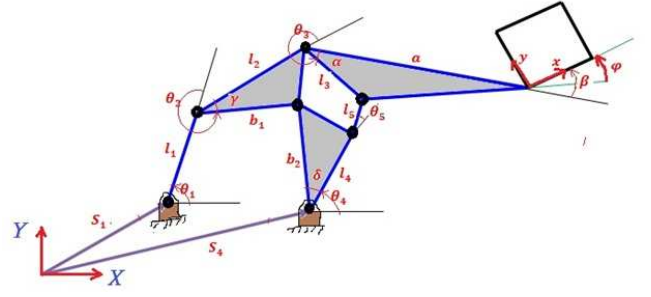


Fig. 6. The six-bar linkage with variables used

Nine positions are selected from the index finger trajectory. The end-effector location at the coupler link yields two equations, and the loop equations account for four equations for each position. This gives a total of 52 nonlinear equations. In addition, we have 9 angular equations; overall, we have 63 equations. The total variables to be found are 61 in total. Some auxiliary equations are added to limit the size of some key links in the linkage.

The equations are solved using a Levenberg-Marquardt nonlinear, unconstrained solver implemented in Java. This is based on public domain MINPACK routines, translated from FORTRAN to Java by Steve Verrill [15].

The process yields many solutions. Each solution took an average of 7.5 minutes on a 2.2GHz Intel Core i7. We solved several times, in groups of 50 runs, out of which approximately 3 solutions were acceptable each time. The acceptability was defined in terms of position on the hand, overall dimensions and hand interference. The accepted candidates were modeled using CAD software in order to select the final design.

#### V. ANGULAR MEASUREMENT

From the design of the mechanism it is shown that the angle  $\varphi$  corresponds to the orientation of the MIP joint of the finger. Thus, using (3) we can get the value of  $\varphi$  for every finite displacement of the finger in terms of the angles  $\theta_1, \theta_2, \gamma, \theta_3, \alpha$  and  $\beta$ . Here  $\alpha, \gamma$  and  $\beta$  are constants, and  $\theta_1, \theta_2$  and  $\theta_3$  are the joint variables, which can be expressed in terms of one of them (for instance  $\theta_1$ ),

$$\varphi^i = \theta_1^i + \theta_2^i + \theta_3^i + \alpha + \beta + \gamma, \tag{4}$$

where  $i$  corresponds to any single measurement of the angle.

We use 4, together with the constraint relations between the joint angles [13] that give  $\theta_2^i = f(\theta_1^i)$  and  $\theta_3^i = f(\theta_1^i)$ .

Therefore, the only variable that we need to measure is  $\theta_1$ . Since one of our objectives is to come up with a cost-effective sensing device, a resistive potentiometer is selected to be mounted on that joint of the six-bar mechanism to measure  $\theta_1$ . Similarly, relations can be found to place the sensor at any other joints.

#### VI. SENSITIVITY ANALYSIS

The selection of the sensed angle is based on calculating the relative variation of each angle with respect to the MIP

joint angle  $\varphi$ . If possible, the sensor should be mounted on the joint that presents a higher sensitivity, defined as the ratio of change of the measured angle with respect to the change in the joint angle.

For this sensor,  $\theta_1$  has been selected as the sensed variable, due to the sensitivity analysis and also for accessibility in mounting and reading the sensor.

Figure 7 shows part of the motion in which a constant angular velocity of  $1.5\text{rad/sec}$  is applied to joint1  $\theta_1$  and the change of the angular position of each joint has been compared. From this figure we can deduce that all the other joint angles i.e  $\theta_2$ ,  $\theta_3$  and  $\theta_4$  have smaller angular changes than  $\theta_1$  and  $\theta_5$ . The angular velocity ratio has been calculated and it is shown in Figure 8 for the angle  $\theta_1$ . For mounting the potentiometer, we found that  $\theta_1$  is more convenient. The potentiometer is mounted as shown in Figure 9.

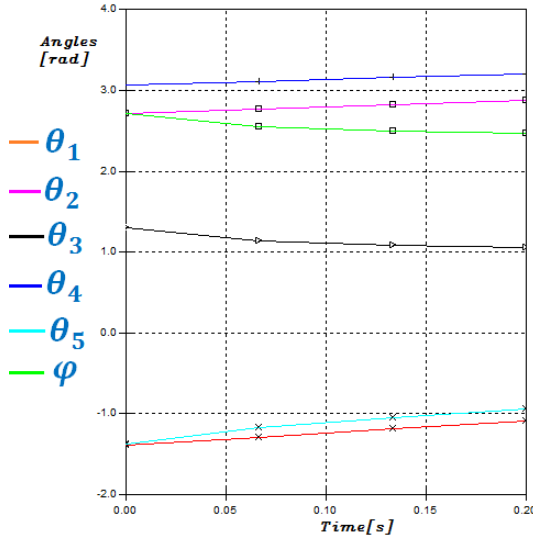


Fig. 7. The angular positions as a function of time

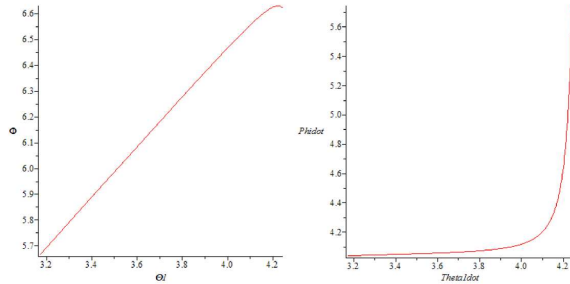


Fig. 8. Sensitivity analysis for  $\theta_1$

## VII. RESULTS

The candidate designs were ranked considering size, mechanism placement and overall structure. The selected design is optimized and modeled as shown in Figure 10. The design parameters of the selected six-bar linkage are shown in Table I (angles in radians and lengths in millimeters).

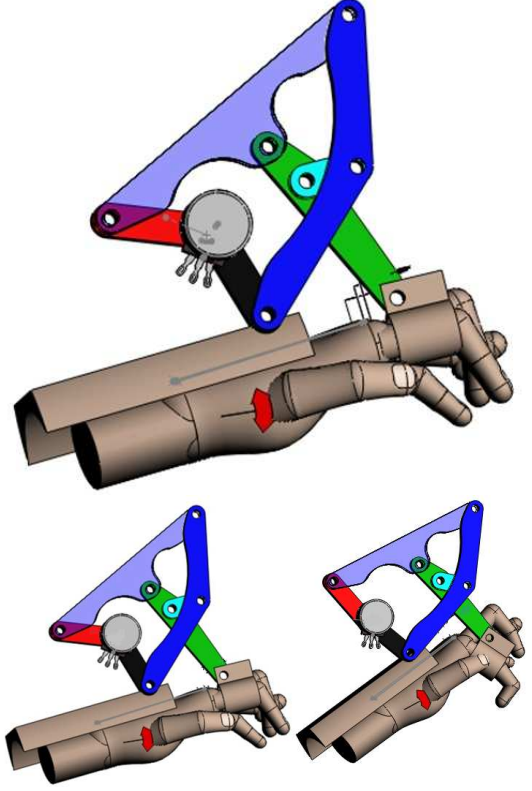


Fig. 9. The exoskeleton and the sensor on the hand, at two different configurations

TABLE I  
EXOSKELETON DIMENSIONS

$s_1$	(46.34, -94.63)
$s_4$	(-30.49, -57.91)
$a$	-77.66
$l_1$	-40.01
$l_2$	-68.46
$l_3$	20.00
$l_4$	-68.46
$l_5$	20.00
$b_1$	-122.58
$b_2$	-122.57
$\gamma$	-0.27
$\alpha$	3.04
$\delta$	0.28
$\beta$	2.27

A rapid prototype has been built in order to further assess the performance of the sensor and it is shown in Figure 11. The final product will be made from aluminum and the estimated total cost for several joints, including machining, is within hundreds of dollars. We believe that this sensor will be cheaper than other sensors such as data gloves, magnetic, and infrared sensors, which cost in the order of thousands of dollars.

## VIII. CONCLUSIONS

In this paper we present the development of a simple and cost-effective mechanism for the estimation of the angles of the Metacarpal interphalangeal (MIP) joint of the index



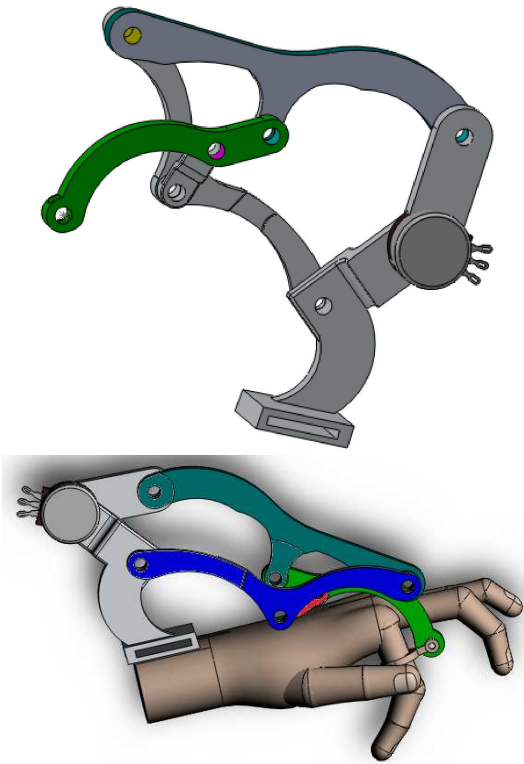


Fig. 10. CAD model of the selected linkage

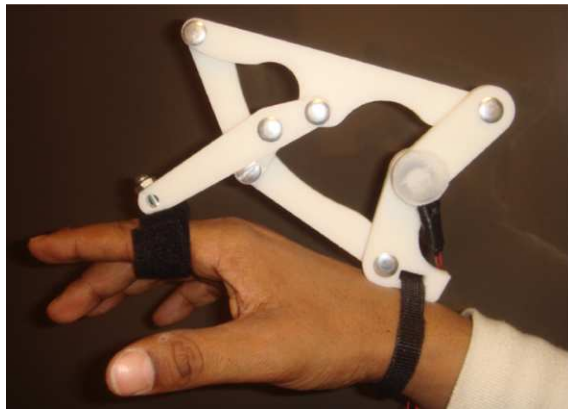


Fig. 11. Initial prototype of the selected linkage

finger. The design strategy includes vision system and image processing coupled with kinematic synthesis techniques.

The main advantage of this method is that it does not need any assumption about location and type of joints in the subject; the exoskeleton is going to follow the trajectory that is selected as task regardless of the skeleton structure that generates it. This allows for the creation of new and innovative exoskeleton-based position sensors which can help for EMG and position modeling in the grasp and control study. The application of image-processing techniques and use of a six-bar mechanism and a simple potentiometer grants a cheap, effective sensing device. The high number of solutions obtained means more choices for the designer

regarding placement and size of the exoskeleton.

Future research includes the dynamic analysis of the device and estimation of resolution, noise and possible loading effects on the sensed signal, as well as extension to other joints of the hand.

## REFERENCES

- [1] P. K. Artemiadis and K. J. Kyriakopoulos, "Emg-based position and force control of a robot arm: Application to teleoperation and orthosis," in *int Conf. Rec. 2007 IEEE/ASME Int. Conf. on Advanced Intelligent Mechatronics*, Zurich,, October 10-13, 2004, 2007.
- [2] E. A. Matthias Rehm, Nikolaus Bee, "Wave like an egyptian - accelerometer based gesture recognition for culture specific interactions," in *British Computer Society*, 2007.
- [3] M. Kolsch and M. Turk, "Fast 2d hand tracking with flocks of features and multi-cue integration," in *Computer Vision and Pattern Recognition Workshop*, May 27-June 2004, 2004.
- [4] G. Stillfried and P. van der Smagt, "Movement model of a human hand based on magnetic resonance imaging (mri)," in *Proceedings of the 1st Int. Conf. on Applied Bionics and Biomechanics*, Venice, Italy, October 14-16,, 2010.
- [5] D. Sands, A. Perez-Gracia, J. McCormack, and E. Wolbrecht, "Design method for a reconfigurable mechanisms for finger rehabilitation," in *Proceedings of the 2010 IASTED Robotics and Applications Conference*, November 1 3, 2010, Cambridge, Massachusetts, USA, 2010.
- [6] E. Wolbrecht, D. Reinkensmeyer, and A. Perez-Gracia, "Single degree-of-freedom exoskeleton mechanism design for finger rehabilitation," in *Proceedings of the ICORR 2011: Int. Conference on Rehabilitation Robotics*, June 29-July 1, 2011, Zurich, Switzerland, 2011.
- [7] Z. Hang, R. Qiuqi, and C. Houjin, "A new approach of hand tracking based on integrated optical low analyse," in *Signal processing (ICSP), 2010 IEEE 10th International Conference on*, Oct 2010, 2010, pp. 1194–1197.
- [8] A. A. Lasenby, "Motion capture with constrained inverse kinematics for real-time hand tracking," in *Communications, control and Signal processing (ISCCSP)*, 2010, pp. 1–5.
- [9] T. K., "Remarks on robust extraction of hand's silhouette for 3d hand motion capture system," in *Industrial Electronics, 2009 (IECON 09), Annual Conference of IEEE*, 2009, pp. 326–2331.
- [10] H. Ahsan, "3d computer vision system for hand joint motion calculation," Ph.D. dissertation, College of Engineering, Idaho State University, Pocatello, ID, USA, 2008.
- [11] G. Schweighofer and A. Pinz, "Robust pose estimation from a planar target," *IEEE Transactions on Pattern Analysis and Machine Intelligence*, pp. 2024–2030, 2006.
- [12] C. H. Stephens and M., "A combined corner and edge detector," in *the 4th Alvy Vision conference*, 1988, pp. 147–151.
- [13] J. M. McCarthy and G. Soh, *Geometric Design of Linkages*, 2nd ed. New York: Springer-Verlag, 2010.
- [14] C. W. Wampler, "Solving the kinematics of planar mechanisms," in *1998 ASME Design Engineering Technical Conferences, Sept 13-16, 1998*, Atlanta, Georgia, USA, 1998.
- [15] *Optimization java package*, 2000, program library long writeup W5013[Online]. Available <http://www1.fpl.fs.fed.us/optimization.html>.

# Exact/approximate Workspace Synthesis for RCCR linkages

Batchimeg Batbold, Federico Thomas, Yimesker Yihun and Alba Perez-Gracia

**Abstract** A tool for the exact kinematic synthesis of a given workspace is especially needed when designing closed linkages. In these cases, finite-position synthesis cannot ensure smoothness of motion between task positions. In order to keep the simplicity of the finite-position synthesis approach but without having to rely on big optimization methods, here we describe the workspace of relative displacements as a set of screws using Parkin's definition of pitch. The workspace can then be seen as a line bundle called screw surface. The screw surface is then characterized by a number of screws which are used to generate the whole surface, and in turn to perform dimensional synthesis. The methodology is here applied to the overconstrained RCCR closed linkage.

## 1 Introduction

NOTE TO AUTHORS: Here I just literally copied the intro from my RPRP paper. This part needs to be upgraded and adapted to the RCCR case. Synthesis of parallel robots has focused mainly on type or structural synthesis, using group theory, screw theory, or geometric methods, see for instance [9], [2], [7]. Dimensional synthesis examples exist, mainly for optimizing performance indices [13], [14], [16] or for reachable workspace sizing [1], [18], [6]; see also [19] for a comprehensive approach.

The dimensional synthesis of spatial serial chains for a prescribed set of positions can be used for the design of parallel robots by synthesizing all supporting legs for the same set of positions. There are a few examples of finite-position dimensional synthesis of parallel robots in the literature, most of them doing partial synthesis.

---

Batchimeg Batbold and Federico Thomas  
Institut de Robotica i Informatica Industrial (CSIC-UPC), e-mail: name@email.address

Yimesker Yihun and Alba Perez Gracia  
Department of Mechanical Engineering, Idaho State University e-mail: name@email.address

Wolbrecht et al. [27] perform synthesis of 3-RRS, 4-RRS and 5-RRS symmetric parallel manipulators; Kim and Tsai [17] and Rao [23] solve the partial kinematic synthesis of a 3-RPS parallel manipulator. This method has been successfully applied mainly to special parallel systems with imposed symmetry. In general, the method does not allow the control of the final trajectory of the parallel system; in the most extreme cases, it may yield a system with negative mobility, that can be assembled at each task positions but cannot be driven from task position to task position.

The kinematic mapping is used for the synthesis of planar and spherical linkages in order to state design equations and to provide a tool for visualizing the workspace and trajectories of the linkage. See Ravani and Roth [24] and more recent applications by Hayes [8], Schröcker [25] and Wu and Ge [28]. For spatial motion, Study's kinematic mapping is used to obtain simplified equations for analysis and synthesis, see Husty et al. [15] and [5]. However, the kinematic image for the spatial motion is a six-dimensional quadric and that makes the visualization of workspaces and trajectories difficult for the designer.

In this paper, the workspace of the linkage is visualized as a set of finite screws corresponding to the set of finite displacements of the end-effector. One interesting question is whether the finite-screw surfaces generated by a set of task positions can give any information for the synthesis of parallel robots and, in particular, of some overconstrained closed linkages. Using Parkin's definition for pitch [20], the screws corresponding to finite displacements of some linkages can form screw systems. Huang [10] showed that the single RR chain forms a finite screw system of third order; however, the set of finite displacements of the coupler of the Bennett linkage form a cylindroid, which is a general 2-system of screws [11]. Baker [4] has also studied the motion of the Bennett linkage. Perez and McCarthy [21] used two arbitrary displacements to generate the cylindroid of finite screws associated to the Bennett linkage in order to perform dimensional synthesis.

In this paper, the focus is on the simplest of the overconstrained linkages, the closed spatial RPRP linkage. This linkage is one of the Delassus linkages, later studied by Waldron [26] and Baker [3]. Recently, Huang [12] has shown that the set of screws corresponding to displacements of this linkage forms a 2-screw system. We use this result in order to synthesize RPRP linkages with positive mobility and for a given shape of the screw system of relative displacements. In order to do so, we state the design equations using the Clifford algebra of dual quaternions [22]. The dual quaternion expression can be easily related to the screw system and it is also used to assign the magnitude to the screws in order to obtain the correspondence between the screw system and the trajectory of the end-effector. The design yields a single RPRP linkage.



## 2 The Workspace of Finite Screws

Given the forward kinematics for an articulated system, we can define the workspace as the set of finite displacements obtained when giving values to all active joint variables within their ranges. If the forward kinematics used is that of relative motion from a reference configuration, giving values to the active joint variables we obtain the workspace of relative displacements. Each of these displacements can be as a rotation about and a translation along a screw axis.

The relative rotations can hence be expressed as screws with a magnitude and a pitch. While for infinitesimal screws the pitch is defined in a fairly universal way, for finite screws several pitch definitions can be found. For the purpose of this research, Parkin's definition of pitch [20] is used. When using this pitch, the screws corresponding to finite displacements of some linkages can form linear systems of screws, which are called screw systems. However some other definitions of pitch exist that handle the inherent nonlinearity of finite displacements in a different way.

Parkin's definition of pitch appears naturally from the expression of the forward kinematics equations using the Clifford algebra  $\mathcal{C}l_{0,3,1}$ , also known as dual quaternions. For an introduction to the use of dual quaternions in robot kinematics, see [22].

The Plücker coordinates  $S = (\mathbf{s}, \mathbf{c} \times \mathbf{s})$  of a line can be identified with the Clifford algebra element  $S = \mathbf{s} + \varepsilon \mathbf{c} \times \mathbf{s}$ , with  $\varepsilon^2 = 0$ . Similarly, a screw  $J$  becomes the element  $J = (1 + \mu \varepsilon)S$ , where  $\mu$  is the pitch. Using the Clifford product we can compute the exponential of the screw  $\frac{\theta}{2}J$ ,

$$e^{\frac{\theta}{2}J} = \left(\cos \frac{\theta}{2} - \frac{d}{2} \sin \frac{\theta}{2} \varepsilon\right) + \left(\sin \frac{\theta}{2} + \frac{d}{2} \cos \frac{\theta}{2} \varepsilon\right)S = \cos \frac{\hat{\theta}}{2} + \sin \frac{\hat{\theta}}{2}S. \quad (1)$$

The exponential of a screw defines a unit dual quaternion, which can be identified with a relative displacement from an initial position to a final position in terms of a rotation around and a slide along axis  $S$ .

For a serial chain with  $n$  joints, in which each joint can rotate an angle  $\theta_i$  and slide a distance  $d_i$ , around and along the axis  $S_i$ ,  $i = 1, \dots, k$ , the forward kinematics of relative displacements (with respect to a reference position) can be expressed as the composition of Clifford algebra elements corresponding to the motion of each joint. Let  $\theta_0$  and  $\mathbf{d}_0$  be the joint parameters of this chain when in the reference configuration, so we have  $\Delta\hat{\Theta} = (\Theta - \Theta_0 + (\mathbf{d} - \mathbf{d}_0)\varepsilon)$ . Then, the movement from this reference configuration is defined by

$$\hat{D}(\Delta\hat{\Theta}) = \cos \frac{\hat{\Psi}}{2} + \sin \frac{\hat{\Psi}}{2}S = e^{\frac{\Delta\hat{\theta}_1}{2}S_1} e^{\frac{\Delta\hat{\theta}_2}{2}S_2} \dots e^{\frac{\Delta\hat{\theta}_k}{2}S_k}. \quad (2)$$

Notice that it is immediate to find the screw axis of the relative displacement  $S$  from this expression. If we concentrate now on that part of the forward kinematics that contains the screw axis, we can easily obtain a magnitude and a pitch,

$$\sin \frac{\hat{\Psi}}{2} S = \left( \sin \frac{\Psi}{2} + \varepsilon \frac{t}{2} \cos \frac{\Psi}{2} \right) S = \sin \frac{\Psi}{2} \left( 1 + \varepsilon \frac{\frac{t}{2}}{\tan \frac{\Psi}{2}} \right) S, \quad (3)$$

so that we can see the relative workspace as a set of screw axes with magnitude  $\sin \frac{\Psi}{2}$  and Parkin's pitch  $\frac{t/2}{\tan \frac{\Psi}{2}}$ . It turns out that, for the case of finite displacements, the value of the magnitude is unique and can be calculated using the scalar part of the forward kinematics, which yields a nonlinear relation. See [12] for details.

As a conclusion, the workspace of relative displacements can be expressed as a set of unit screws plus a scalar magnitude equation. It turns out that this set of screws form linear systems of screws (screw systems) for several well-known linkages. However, most of the linkages have a workspace which cannot be expressed as a screw system, but rather as a screw surface of a certain degree. We will denote this as the finite-screw workspace of the linkage.

We can derive a general formula for the expression of the finite-screw workspace if we develop the forward kinematics equations in Eq.(2). The Clifford product of screw transformations about each axis can be collected as a linear combination of the joint axes plus products of joint axes as follows,

$$\hat{D}(\Delta \hat{\Theta}) = \cos \frac{\hat{\Psi}}{2} + \sin \frac{\Psi}{2} \left( 1 + \varepsilon \frac{\frac{t}{2}}{\tan \frac{\Psi}{2}} \right) S = [\hat{Id} \ \hat{S}_1 \ \dots \ \hat{S}_k \ \hat{S}_1 \hat{S}_2 \ \dots \ \hat{S}_1 \dots \hat{S}_k] \hat{V}, \quad (4)$$

where the dual vector  $\hat{V}$  contains products of the joint variables. For a closed chain, the relations among those joint variables may simplify the expression of the linear combination.

### 3 Classification of Screw Surfaces

NOTE TO AUTHORS: Futuristic section... the idea here is to see if we can derive some property of the screw surface just by looking at its parameterized expression (for instance, determine whether it is linear... So far, the way I have determined linearity is by calculating the determinant to see the dimension of the space that the appropriate number of screws generate, and then the linear combination. For instance, if I know that a linkage has 1 dof, then I check whether 3 arbitrary screws of the workspace have dimension two. Then I see if the linear combination of two screws is another screw of the workspace. Now to move to higher dimensions and quadratic workspaces, we need a more clever way of doing it.

### 4 The Closed RCCR Linkage

There closed RC-CR linkage is overconstrained and able to move with one degree of freedom [26] when the cylindrical (C) and revolute (R) joints of each pair are

parallel, while both pairs are skew one to each other. The geometry of the closed linkage can be seen in Figure ?? and Figure ??.

#### 4.1 The overconstrained RC-CR linkage

In order to prove the above statement, let us start calculating the mobility. The mobility of this spatial four-bar linkage, assuming that the axes are arbitrarily positioned, is, using CKG formula, equal to zero. However it is possible to obtain a one-dof linkage for some special geometry.

The geometric features and the joint variable functions can be derived, for instance, by equating the forward kinematics of both RC serial chains at their end-effector. According to the coordinate frame shown in Figure ??, and assuming parallel axes, that is,  $\alpha_1 = \alpha_3 = 0$ , the forward kinematics of chain 1-2 is,

$$[D_{12}] = \begin{bmatrix} c(\theta_1 + \theta_2) & -s(\theta_1 + \theta_2)c\alpha_2 & s(\theta_1 + \theta_2)s\alpha_2 & a_2c(\theta_1 + \theta_2) + a_1c\theta_1 \\ s(\theta_1 + \theta_2) & c(\theta_1 + \theta_2)c\alpha_2 & -c(\theta_1 + \theta_2)s\alpha_2 & a_2s(\theta_1 + \theta_2) + a_1s\theta_1 \\ 0 & s\alpha_2 & c\alpha_2 & R_1 + r_2 \\ 0 & 0 & 0 & 1 \end{bmatrix}, \quad (5)$$

where  $s$  and  $c$  stand for the  $\sin$  and  $\cos$  functions respectively.

The forward kinematics of the second half of the linkage is given by

$$[D_{43}] = \begin{bmatrix} c(\theta_3 + \theta_4) & s(\theta_3 + \theta_4) & 0 & -a_3c\theta_4 - a_4 \\ -s(\theta_3 + \theta_4)c\alpha_4 & c(\theta_3 + \theta_4)c\alpha_4 & s\alpha_4 & (r_3 + R_4)s\alpha_4 + a_3s\theta_4c\alpha_4 \\ s(\theta_3 + \theta_4)s\alpha_4 & -c(\theta_3 + \theta_4)s\alpha_4 & c\alpha_4 & (r_3 + R_4)c\alpha_4 - a_3s\theta_4s\alpha_4 \\ 0 & 0 & 0 & 1 \end{bmatrix}, \quad (6)$$

Some geometrical constraints and angular relations are obtained from equating these two transformations,

$$\begin{aligned} \cos \alpha_2 &= \cos \alpha_4 \implies \alpha_4 = \pm \alpha_2, \\ \cos(\theta_1 + \theta_2) &= \pm 1, \quad \sin(\theta_1 + \theta_2) = 0 \implies \theta_2 = n * \pi - \theta_1, \\ \cos(\theta_3 + \theta_4) &= \pm 1, \quad \sin(\theta_3 + \theta_4) = 0 \implies \theta_3 = n * \pi - \theta_4, \end{aligned} \quad (7)$$

which indicate that the directions of the fixed joints are parallel to the directions of the moving joints, with opposite rotation angles. We can also derive the following joint variable relations:

$$\begin{aligned}
\theta_4 &= \pm \arccos\left(\frac{\pm a_2 - a_4 - a_1 \cos \theta_1}{a_3}\right) \\
r_3 &= \frac{a_1 \sin \theta_1 - a_3 \cos \alpha_4 \sin \theta_4 - R_4 \sin \alpha_4}{\sin \alpha_4} \\
r_2 &= \frac{a_1 \cos \alpha_4 \sin \theta_1 - a_3 \sin \theta_4 - R_1 \sin \alpha_4}{\sin \alpha_4}
\end{aligned} \tag{8}$$

## 4.2 The Workspace of Finite Displacements of the RC-CR Linkage

If we apply the conditions in Eqs. (7) and (8) with one of the signs, we can compute the workspace of the linkage as all possible transformations obtained when giving values to the actuated joint variable (in this case selected as the angle  $\theta_1$ ). We are considering the particular case of an RC-CR linkage located with respect to the fixed frame as shown in Figure ??.

$$[D_{12}] = \begin{bmatrix} 1 & 0 & 0 & a_1 \cos \theta_1 - a_2 \\ 0 & -\cos \alpha_2 & \sin \alpha_2 & a_1 \sin \theta_1 \\ 0 & \sin \alpha_2 & \cos \alpha_2 & (a_1 \cos \alpha_4 \sin \theta_1 - a_3 \sin \theta_4) / \sin \alpha_4 \\ 0 & 0 & 0 & 1 \end{bmatrix}. \tag{9}$$

Notice that the RC-CR linkage has a constant-orientation workspace.

In particular, we are interested in the workspace of relative displacements with respect to a reference configuration. The reference configuration can be arbitrarily selected, and the joint variables are now increments from the reference configuration, that is,  $\Delta r_2 = r_2 - r_{20}$ , and  $\Delta \theta_i = \theta_i - \theta_{i0}$ . Now we are going to start using dual quaternions to define the displacements, as they give a simpler expression with an easier geometric interpretation. We obtain the following expression:

$$\hat{D}_{12} = \begin{Bmatrix} 0 \\ 0 \\ 0 \\ 1 \end{Bmatrix} + \varepsilon \begin{Bmatrix} a_1(\cos^2 \frac{\Delta \theta_1}{2} - \sin^2 \frac{\Delta \theta_1}{2} - \cos \frac{\Delta \theta_1}{2}) \\ a_1(\cos \frac{\Delta \theta_1}{2} \sin \frac{\Delta \theta_1}{2} (2(\cos^2 \frac{\Delta \theta_1}{2} - \sin^2 \frac{\Delta \theta_1}{2}) - 1) \\ \frac{\Delta r_2}{2} \\ 0 \end{Bmatrix} \tag{10}$$

Here again we can observe that the relative displacements have zero rotation.

In order to find the workspace of relative displacements for an arbitrarily-located, RC-CR linkage, we write its forward kinematics in dual quaternion form,

$$\hat{D} = \hat{R}(\Delta \theta_1) \hat{C}(\Delta \theta_2, \Delta r_2) = 1 + \varepsilon \frac{1}{2} (\Delta r_2 \mathbf{s}_1 + (\cos \Delta \theta_1 + 1)(\mathbf{c}_2 - \mathbf{c}_1) - \sin \Delta \theta_1 (\mathbf{c}_2 - \mathbf{c}_1)) \tag{11}$$

where  $\hat{R}(\Delta \theta_1)$  is a rotation about an axis with Plucker coordinates  $\mathbf{S}_1$ , and  $\hat{C}(\Delta \theta_2, \Delta r_2)$  is a rotation and a translation about and along an axis with Plucker coordinates  $\mathbf{S}_2$ .

Both axes share the same direction  $\mathbf{s}_1$ , and the points  $\mathbf{c}_1$  and  $\mathbf{c}_2$  are any points on the axes along a common normal line.

NOTE TO AUTHORS: Now what we need to do is to add the expression of  $r_2$  in this, in order to have everything as a function of  $\theta_1$ . For doing so, remember that the formula for the angular relation is for absolute angles, while these are relative. That is not important for linear relations, but for cos we need to apply the cosine of the difference of angles formula. We need to keep working on it.

## 5 Dimensional Synthesis for the RCCR Linkage

In the previous section we have proved that the workspace of the RCCR linkage is a constant-orientation one. Hence, the synthesis problem for this linkage reduces to a point-path synthesis problem. The point-path synthesis problem is stated as follows: given an initial point  $\mathbf{P}_1$  (which we will use as reference configuration), relative displacements of the RC-CR chain will move this point to the rest of task points  $\mathbf{P}_2, \mathbf{P}_3, \dots, \mathbf{P}_n$ .

The action of the chain on this point can be calculated using the conjugation in the Clifford algebra. If the forward kinematics of relative displacements of Eq.(11) is denoted by  $\hat{D} = 1 + \varepsilon \mathbf{d}$ , then

$$\mathbf{P}_i = \hat{D} \hat{P}_1 \hat{D}^*, \quad i = 2, \dots, n, \quad (12)$$

where  $\hat{P}_1 = (1 + \varepsilon \mathbf{P}_1)$  is the dual quaternion expression of the point  $\mathbf{P}_1$ , and the conjugation yields

$$(1 + \varepsilon \frac{1}{2} \mathbf{d})(1 + \varepsilon \mathbf{P}_1)(1 + \varepsilon \frac{1}{2} \mathbf{d}) = 1 + \varepsilon (\mathbf{P}_1 + \mathbf{d}) \quad (13)$$

Let us consider first the case of the serial RC chain in which the values of  $\theta_1$  and  $r_2$  are not constrained. This results in  $3(n-1)$  design equations, with the structural variables  $\mathbf{s}_1$  and  $\mathbf{a} = \mathbf{c}_2 - \mathbf{c}_1$  and the values of the joint variables  $r_2$  and  $\theta_1$  for each point, which is a total of  $4 + 2(n-1)$  unknowns. Simply equating these two values we obtain that we can define up to  $n = 5$  point-positions in order to do exact point-path synthesis.

In the case of the RC chain belonging to the movable RC-CR linkage, we have only one joint variable and hence the number of unknowns is  $4 + (n-1)$ . The maximum number of points we can define for exact point-path synthesis is  $n = 3$ .

NOTE TO AUTHORS: Here we have an example of the first case,  $r_2$  and  $\theta_1$  independent, but not of the second one because we don't have the expression worked out yet. We need to do so.

## 6 The workspace of the RC-CR linkage as a screw surface

## 7 Synthesis for the RC-CR workspace

## 8 Conclusions

bal bal bal

## References

1. Affi, Z., Romdhane, L., Maalej, A.: Dimensional synthesis of a 3-translational-dof in-parallel manipulator for a desired workspace. *European Journal of Mechanics, A / Solids* **23**, 311–324 (2004)
2. Angeles, J.: The qualitative synthesis of parallel manipulators. In: C. Gosselin, I. Ebert-Uphoff (eds.) *Proceedings of the WORKSHOP on Fundamental Issues and Future Research Directions for Parallel Mechanisms and Manipulators*. October 3-4, 2002, Quebec City, Quebec, Canada (2002)
3. Baker, J.E.: The delassus linkages. In: *Proc. of the 4th World Congress on the Theory of Machines and Mechanisms*, p. 4549. Newcastle upon Tyne, England, (1975)
4. Baker, J.E.: On the motion geometry of the bennett linkage. In: *Proc. 8th Internat. Conf. on Engineering Computer Graphics and Descriptive Geometry*, pp. 433–437. Austin, Texas, USA, (1998)
5. Brunthaler, K.: Synthesis of 4r linkages using kinematic mapping. Ph.D. thesis, Institute for Basic Sciences and Engineering, University of Innsbruck, Innsbruck, Austria (2006)
6. Chablat, D., Wenger, P.: Architecture optimization of a 3-dof parallel mechanism for machining applications, the orthoglide. *IEEE Transactions on Robotics and Automation* **19**(3), 403–410 (2003)
7. Gogu, G.: *Structural Synthesis of Parallel Robots. Part 1: Methodology*, first edn. Springer (2007)
8. Hayes, M.J.D., Luu, T., Chang, X.W.: Kinematic mapping application to approximate type and dimension synthesis of planar mechanisms. In: J. Lenarcic, C. Galletti (eds.) *On Advances in Robot Kinematics*. Kluwer Academic Publisher (2004)
9. Herve, J.M.: The lie group of rigid body displacements, a fundamental tool for mechanism design. *Mechanism and Machine Theory* **34**, 717–730 (1999)
10. Huang, C.: On the finite screw system of the third order associated with a revolute-revolute chain. *ASME Journal of Mechanical Design* **116**, 875–883 (1994)
11. Huang, C.: The cylindroid associated with finite motions of the bennett mechanism. In: *Proceedings of the ASME Design Engineering Technical Conferences*. 1996, Irvine, CA, USA (1996)
12. Huang, C.: Linear property of the screw surface of the spatial rprp linkage. *ASME Journal of Mechanical Design* **128**, 581–586 (2006)
13. Huang, T., Li, M., Zhao, X.M., Mei, J., Chetwynd, D.G., Hu, S.J.: Conceptual design and dimensional synthesis for a 3-dof module of the trivariant - a novel 5-dof reconfigurable hybrid robot. *IEEE Transactions on Robotics* **21**(3), 449–456 (2005)
14. Huang, T., Zhanxian, L., Li, M., Chetwynd, D.G., Gosselin, C.M.: Conceptual design and dimensional synthesis of a novel 2-dof translational parallel robot for pick-and-place operations. *AMSE Journal of Mechanical Design* **126**, 449–455 (2004)
15. Husty, M.L., Pfurner, M., Schrockner, H.P., Brunthaler, K.: Algebraic methods in mechanism analysis and synthesis. *Robotica* **25**, 661–675 (2007)

16. Kim, H.S., Tsai, L.W.: Design optimization of a cartesian parallel manipulator. *ASME Journal of Mechanical Design* **125**, 43–51 (2003)
17. Kim, H.S., Tsai, L.W.: Kinematic synthesis of a spatial 3-rps parallel manipulator. *ASME Journal of Mechanical Design* **125**, 92–97 (2003)
18. Kosinska, A., Galicki, M., Kedzior, K.: Design and optimization of parameters of delta-4 parallel manipulator for a given workspace. *Journal of Robotic Systems* **20**(9), 539–548 (2003)
19. Merlet, J.P.: Optimal design of robots. In: *Proceedings of Robotics: Science and Systems*. June, 2005, Cambridge, USA (2005)
20. Parkin, I.A.: A third conformation with the screw systems: Finite twist displacements of a directed line and point. *Mechanism and Machine Theory* **27**, 177–188 (1992)
21. Perez, A., McCarthy, J.M.: Dimensional synthesis of bennett linkages. *ASME Journal of Mechanical Design* **125**(1), 98–104 (2003)
22. Perez Gracia, A., McCarthy, J.M.: The kinematic synthesis of spatial serial chains using clifford algebra exponentials. *Proceedings of the Institution of Mechanical Engineers, Part C, Journal of Mechanical Engineering Science* **220**(7), 953–968 (2006)
23. Rao, N.M., Rao, K.M.: Dimensional synthesis of a 3-rps parallel manipulator for a prescribed range of motion of spherical joints. *Mechanism and Machine Theory* **44**, 477–486 (2009)
24. Ravani, B., Roth, B.: Motion synthesis using kinematic mappings. *ASME Journal of Mechanisms, Transmissions and Automation in Design* **105**(3), 460–467 (1983)
25. Schrocker, H.P., Husty, M.L., McCarthy, J.M.: Kinematic mapping based assembly mode evaluation of planar four-bar mechanisms. *AMSE Journal of Mechanical Design* **129**, 924–929 (2007)
26. Waldron, K.J.: A study of overconstrained linkage geometry by solution of closure equations - part ii- four-bar linkages with lower pair joints other than screw joints. *Mechanism and Machine Theory* **8**, 233–247 (1972)
27. Wolbrecht, E., Su, H.J., Perez, A., McCarthy, J.M.: Geometric design of symmetric 3-rrs constrained parallel platforms. In: *ASME (ed.) Proceedings of the 2004 ASME International Mechanical Engineering Congress and Exposition*. November 13–19, 2004, Anaheim, California, USA (2004)
28. Wu, J., Purwar, A., Ge, Q.J.: Interactive dimensional synthesis and motion design of planar 6r single-loop closed chains via constraint manifold modification. *ASME Journal of Mechanisms and Robotics* **2**(3) (2010)

## DETC2013/MESA-12345

### DRAFT:OPTIMIZATION OF SPATIAL CLOSED LINKAGE MECHANISMS USING HYBRID GA

**Yimesker Yihun**

Department of Mechanical Engineering Department of Mechanical Engineering Department of Mechanical Engineering  
Idaho State University Idaho State University Idaho State University  
Pocatello, Idaho,USA Pocatello, Idaho,USA Pocatello, Idaho,USA  
Email: yimeyihu@isu.edu Email: boswkenn@isu.edu Email:perealba@isu.edu

**Ken Bosworth**

**Alba Perez-Gracia**

#### ABSTRACT

*In a finite- position synthesis of a closed linkage spatial mechanisms, obtaining a smoother motion between task positions is difficult due to a number of conflicting objectives and constraints. In this paper, In order to keep the simplicity of the usual synthesis techniques, we have developed a methodology to Optimize spatial mechanisms by obtaining the best results for a group of design variables which will meet constraints including dimension, restricted region and force transmission. The evaluation is expressed by means of an objective function that has to meet certain restrictions or requirements to minimize the overall dimensions. For illustration, the methodology is applied to a spatial, CRR-RRR, 1-degree-of-freedom closed linkage to be used as an exoskeleton for thumb motion. The algorithm is implemented on the exoskeleton to consider additional constraints to control the position and size of the exoskeleton, and reducing physical and sensory interference. The Exoskeleton is optimized by using two nonlinear constrained optimization algorithms namely, Genetic algorithm (GA) and gradient-based minimization. The Methodology implemented in this paper allow and help to interactively monitor and control objectives and constraints, which will yield practical solutions to realistic spatial mechanism design problems.*

#### INTRODUCTION

In exact synthesis, the number of positions to be reached are limited by the number of structural variables in the design. Af-

ter that maximum number, any other position will be only approximated by the linkage. Designers use different optimization methods to design a higher number of task positions. To mention some of the Optimization methods used in Mechanism design one of the simplest one is Least-square technique with vector geometric and functional equations as it is described in [1], it is a straightforward method to state equations but it has many more equations than needed. Its problems can be summarized as: overdimensioned set of equations, no condition for same-assembly trajectory included in set of equations, degenerate cases may appear. Least-square technique with assembly constraints, many authors have used this methodology, for instance [2] and [3]. See also [4]. The method is designed to accommodate slight nonassembly in the solutions (which translates, once the linkage is assembled, in some error in reaching the positions). The numerical problem appears when the assembly conditions are exact constraints of the optimization process, as they may not be able to hold for all positions. Some researchers use a method with a modification of the previous two methods, in which we use the constraints between angles to reduce the number of angular variables to a minimum. It requires the analysis of the linkage, which is easy for the 4-bar linkage but more complicated to generalize. Many authors have used the loop equation method, but following the equations can be expressed in different ways. For instance, [5], whose work has been extended for a six-bar linkage by [6]. Also in [7], and [8]. There are other interesting approaches for the synthesis of linkages for instance, workspace optimization [9]; geometric constraint programming [10]; topol-



ogy optimization [11]; genetic algorithms ([12], [13]); others, especially used for optimization of more complicated linkages ([14], [15], [16]). Kinematic mapping is another method of Optimization, which is basically the mapping of the minimum parameters that define the motion with an algebraic meaning, as coordinates of a three-dimensional space (six-dimensional space in the case of spatial motion) creating a given manifold. This method, started by Ravani and Roth [17], has a relatively small group of followers, maybe because of the more complicated math involved. It can be related to the dual quaternion method for spatial linkages. See [18], [19]. In this paper the optimization is performed based on two nonlinear constrained optimization algorithms namely, Genetic algorithm (GA) and gradient-based minimization. The GA creates a grid of iterative points and keeps only those under a certain value with respect to the previous iteration, then the output from the GA is used as an input for the gradient-based minimization to get into a global minimum point. This approach of exoskeleton optimization allow and help to interactively monitor and control objectives and constraints. In the following section, the optimization approach is illustrated on a spatial, CRR-RRR, 1-degree-of-freedom closed linkage to be used as an exoskeleton for thumb motion

## THE OPTIMIZATION APPROACH

The kinematic synthesis of a spatial mechanism performed in many ways for a desired task. The algorithm implemented here is to consider additional constraints for controlling the position and size of the spatial mechanisms. The Optimization starts from the screw axes of the mechanism expressed in Plucker coordinates. The main principle of the design is based on the principle that moving a joint along the screw axis will not affect the motion of the end effector. However, the force transmission and higher derivatives of the mechanism may change. Hence, by defining control design variables on each screw axis objective functions and constraints are formulated. Size constraint, better force transmission and avoidance of restricted regions in the work space of the mechanism are three major issues in the design of a spatial mechanisms. The methodology adopted here, considered those three conditions. For illustration purpose the constrained region is modeled as a cylindrical surface however it can be spherical or any other geometrical shape.

## OPTIMIZATION OF CRR-RRR SPATIAL MECHANISM USED AS SN EXOSKELETON FOR THUMB MOTION

The dual quaternion synthesis approach has been implemented in the design of spatial mechanism of CRR-RRR. This mechanism was designed to be used as an exoskeleton device for thumb motion [1]. The mechanism has a single degree of freedom, which can be listed as one of the advantages of the mechanism which requires a single actuator yet gives 3D complex motion.

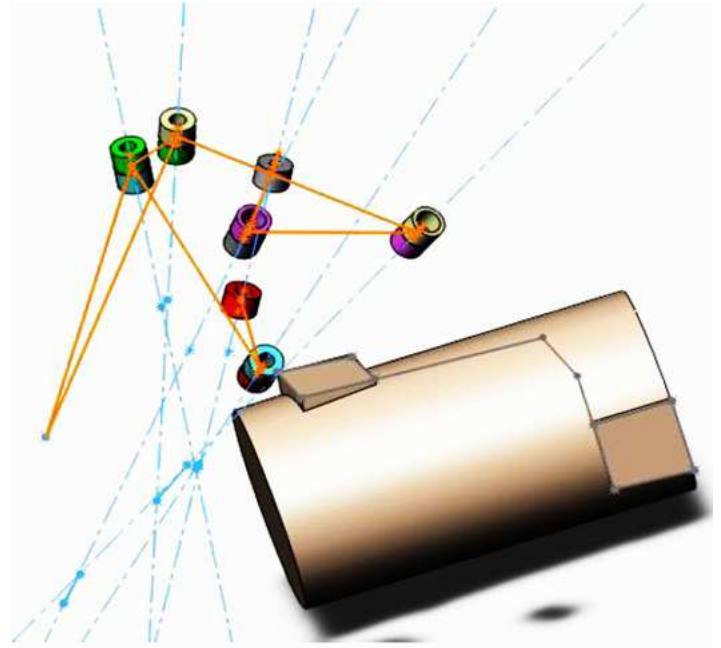


FIGURE 1. Caption for Manuoapt

The goal for the exoskeleton is to generate the desired grasping and pinching path of the thumb with one degree of freedom, rather than using a system actuating all its joints independently. In addition to the path of the thumb, additional constraints are added in order to control the position, size of the exoskeleton and reducing physical and sensory interference with the user. The kinematic synthesis alone had 147 nonlinear equations and 97 variables which makes it challenging to add more constraints. The synthesis gave a mechanism which can follow the desired trajectory however it may be over sized and interfered with a restricted region as. Therefore, it is found that additional optimization is necessary. To start with such process, a CAD model for manual adjustment has been created as shown in Figure 1. It works by plotting the screw axes obtained from the synthesis and then adjusting the link size and orientation by moving joint points. This procedure can give a mechanism which is out of the constrained region, however it is time taking and do not give the optimized solution as well. Therefore considering the size and the constraints, an optimization problem has been developed and solved using genetic algorithm coupled with fmincon through the hybrid optimization algorithm option in Matlab. The procedure and the technique implemented here can also be applied for other problems too. the mechanism is required to be compact while preserving its function.

**Optimization problem formulation:** The design objective considered here is the minimization of the total link length

needed for the mechanism . In this stage ,the link dimensions were optimized by converting them into a single combined objective function. The problem has a number of geometrical constraints.To formulate the objective function for minimizing the overall length of the mechanism, The parameters shown in the Figure 2 are used where  $S_i$ , are the screw axes obtained from the mechanism synthesis expressed in dual quaternion form .  $C_i$ , are the points on  $S_i$  at which the line from the origin and  $S_i$  are perpendicular . $P_i k$  and  $P_i(k+1)$  are two arbitrary points on axis  $S_i$ .  $t_{ik}$  and  $t_{i(k+1)}$  are corresponding distances of  $P_{ik}$  and  $P_{i(k+1)}$  from the point  $C_i$  respectively

$$S_i = s_i + \varepsilon s_i^0 \quad (1)$$

$$C_i = \frac{(s_i) \times (s_i^0)}{(s_i) \cdot (s_i)} \quad (2)$$

Then  $P_{ik}$  and  $P_{i(k+1)}$  are expressed with respect to  $C_i$  as follow.

$$\begin{aligned} P_{ik} &= C_i + t_{ik}(s_i) \\ P_{i(k+1)} &= C_i + t_{i(k+1)}(s_i) \end{aligned} \quad (3)$$

The objective function formulated to minimize the distance between points in the same axis as well as the links between each axis.  $F$  is a nonlinear function with twelve variables in it.

$$F = \sum [(P_{i(k+1)} - P_{ik}) \cdot (P_{i(k+1)} - P_{ik}) + (P_{(i+1)k} - P_{i(k+1)}) \cdot (P_{(i+1)k} - P_{i(k+1)})] \quad (4)$$

**Constraint Functions:** (i) The distance between  $P_{ik}$  and  $P_{i(k+1)}$  is set to be greater than or equal to a constant value  $d$ , this will help for latter construction of joints and ease of assembly of the mechanism .This results six linear equality constraints.

$$\begin{aligned} (P_{i(k+1)} - P_{ik}) &\geq d \\ (t_{i(k+1)} - t_{ik}) &\geq d \end{aligned} \quad (5)$$

(ii) Space constraints: as a requirement the mechanism should not interfere with the hand. For the convenience of analysis the hand has been represented or modeled as a cylindrical region with radius  $R_c$  and the axis of the cylinder through points  $P_{c1}$  and  $P_{c2}$  as shown in the Figure 3. The constraint functions are defined in such a way that the 3D points of the mechanism joint

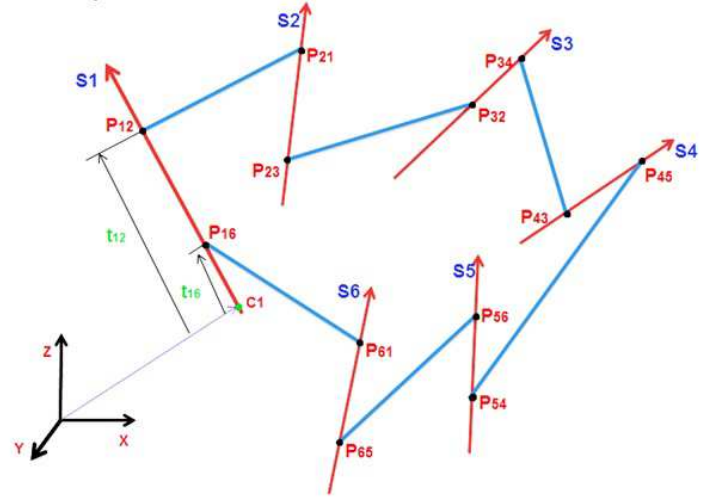


**FIGURE 2.** THE SCREW AXES OF CRR-RRR MECHANISM

should stay out of the cylinder . The unit vector along the cylinder axis is defined as Equation (6).

$$V_c = (P_{c2} - P_{c1}) / \sqrt{[(P_{c2} - P_{c1}) \cdot (P_{c2} - P_{c1})]} \quad (6)$$

If any of the mechanism joint points represented by  $P_{mi}$ , the distance of  $P_{mi}$  with respect to the point  $P_{c1}$  along  $V_c$  is represented by  $L_{mc}$  as Equation (7).

$$L_{mc} = (P_{mi} - P_{c1}) \cdot V_c \quad (7)$$

Since the CRR-RRR mechanism has six axes and twelve points (joints) we have a total of twelve nonlinear constraint functions for this space constraint, each of them defined as Equation (8).

$$(P_{mi} - P_{c1}) \cdot (P_{mi} - P_{c1}) - L_{mc}^2 \geq R_c^2 \quad (8)$$

(iii) Link length constraints , as the final mechanism is required to be compact in size ,this constraint is necessary . Considering manufacturability and compactness the minimum and maximum link lengths have been set 20mm and 150mm respectively for this particular mechanism. Therefore, the constraint functions for this case are defined as Equation (9). This gives a total of twelve nonlinear constraints.

$$\begin{aligned} (P_{(i+1)k} - P_{i(k+1)}) \cdot (P_{(i+1)k} - P_{i(k+1)}) &\geq (20)^2 \\ (P_{(i+1)k} - P_{i(k+1)}) \cdot (P_{(i+1)k} - P_{i(k+1)}) &\geq (150)^2 \end{aligned} \quad (9)$$

Considering all the constraints and the objective function , the optimization problem involves twelve decision variables ,

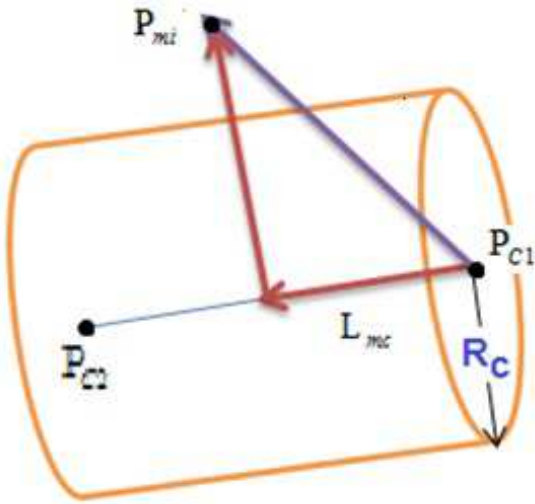


**FIGURE 3.** RESTRICTED REGION REPRESENTED BY A CYLINDRICAL SURFACE

one nonlinear objective functions , six linear inequality constraints and twenty four nonlinear constraints. Each variable also bounded within a lower and an upper limit. The nonlinearity in the objective function over the constraints provide the main difficulty in solving the problem. A set of randomly generated solutions over the above mentioned variable bounds indicate that about only one in  $10^5$  solutions is feasible. Such a severity of the feasible region makes the problem even more difficult to solve. In the following section the optimization method and simulation results are presented for one particular solution.

Consider one of the solution obtained through the synthesis of CRR-RRR, figure 4. The screw axis in plucker coordinate are given in the Table. The Black colors are the links of the mechanism, whereas the colored lines represent the screw axes i.e red= $S_1$ , blue= $S_2$  etc. where the cylinder represents the hand with which the mechanism should not interfere. As we can see , some of the joints are in the hand or in the restricted region(the cylinder) and the link sizes are also not controlled, ranges from very small to a very large one. Both of them are not acceptable in terms of compactness , manufacturability and assembly point of view. Therefore, a post processing of the design results was found necessary.

After the applying the genetic algorithm based on the objective function and constraints defined above the link lengths become  $L_{p12}, L_{p23}, L_{p34}, L_{p45}, L_{p56}, L_{p61} = 107.091, 119.521, 140.557, 71.2734, 103.12, 125.262$ . the solution satisfies all the constraints, as we can see in the Figure 5 the space constraint is also satisfied. The result obtained was further refined by using a hybrid genetic algorithm approach. Here the above solution has been given as an initial value for the nonlinear gradient optimization. The re-

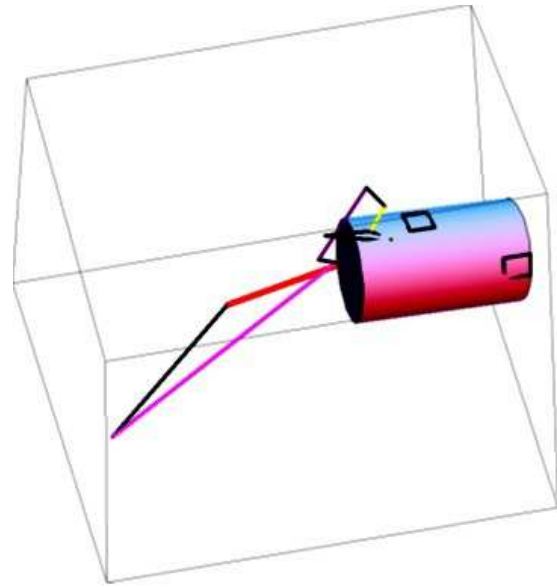


**FIGURE 4.** MECHANISM OBTAINED THROUGH SYNTHESIS

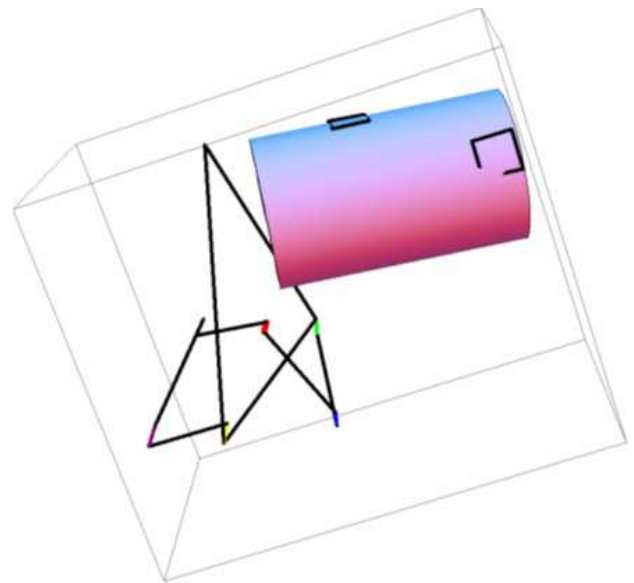


**FIGURE 5.** MECHANISM OBTAINED THROUGH GA

sult obtained is shown in Figure 6. The link lengths are  $L_{p12}, L_{p23}, L_{p34}, L_{p45}, L_{p56}, L_{p61} = 74.9468, 37.5481, 94.2339, 48.6024, 39$  which is a more optimized one and still satisfies the constraints.

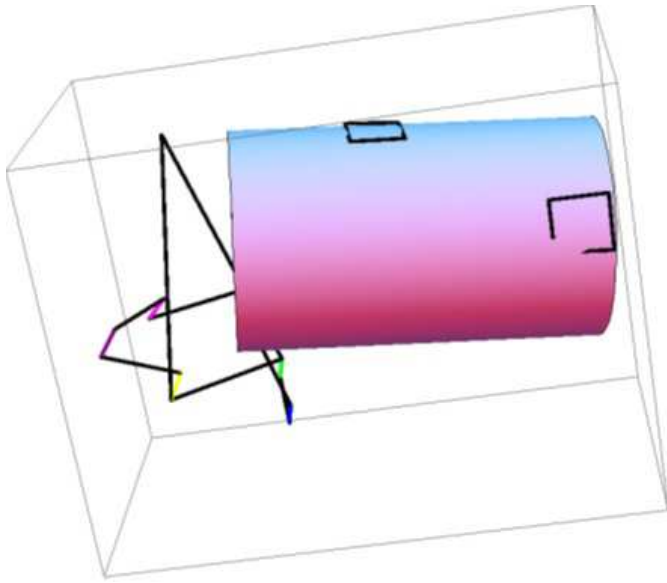


**FIGURE 6.** MECHANISM OBTAINED THROUGH A HYBRID OPTIMIZATION METHOD

## CONCLUSIONS

## ACKNOWLEDGMENT

This work is partially supported by the US department of Army, award number W81XWH-10-1-0128 awarded and administered by the US Army Medical Research Acquisition Activity. The content is solely the authors' responsibility.

## REFERENCES

- [1] de Jalon, G., and Bayo, 1994. *Kinematic and Dynamic Simulation of Multibody Systems*. Springer-Verlag.
- [2] Minaar, Tortorelli, and Snyman, 2001. "On nonassembly in the optimal dimensional synthesis of planar mechanisms". *Structural Multidisciplinary Optimization*, **21**, pp. 345–354.
- [3] Jensen, and Hansen, 2006. "Dimensional synthesis of spatial mechanisms and the problem of non-assembly". *Multibody System Dynamics*, **15**, pp. 107–133.
- [4] Hansen, 2002. "Synthesis of mechanisms using time-varying dimensions". *Multibody System Dynamics*, **7**, pp. 127–144.
- [5] Hobson, and Torfason, 1975. "Computer optimization of polycentric prosthetic knee mechanisms". *Bulletin of Prosthetic Research*, **10**, pp. 187–201.
- [6] et al, J., 2003. "Kinematic and dynamic performance of prosthetic knee joint using six-bar mechanism". *Rehabilitation Research and Development*, **40**, pp. 39–48.
- [7] Yao, and Angeles, 2000. "Computation of all optimum dyads in the approximate synthesis of planar linkages for rigid-body guidance". *Mechanism and Machine Theory*, **35**, pp. 1065–1078.
- [8] Shen, Q., Al-Smadi, Y., Martin, P., Russell, K., and Sodhi, R., 2009. "An extension of mechanism design optimization for motion generation". *Mechanism and Machine Theory*, **44**, pp. 1759–1767.
- [9] Arsenault, M., and Boudreau, R., 2004. "The synthesis of three- degree-of-freedom planar parallel mechanisms with revolute joints (3-rrr) for an optimal singularity-free workspace". *Robotic Systems*, **21**(5), pp. 259–274.
- [10] E.C. Kinzel, J. S., and Pennock, G., 2006. "Kinematic synthesis for finitely separated positions using geometric constraint programming". *Mechanism and Machine Theory*, **128**, pp. 1070–1079.
- [11] Pedersen, C. B. W., Fleck, N. A., and Ananthasuresh, G. K., 2006. "Design of a compliant mechanism to modify an actuator characteristic to deliver a constant output force". *ASME Journal of Mechanical Design*, **128**, pp. 1101–1112.
- [12] Cabrera, J., Simon, A., and Prado, M., 2002. "Optimal synthesis of mechanisms with genetic algorithms". *Mechanism and Machine Theory*, **37**, p. 11651175.
- [13] Acharyya, S., and Mandal, M., 2009. "Performance of eas for four-bar linkage synthesis". *Mechanism and Machine Theory*, **44**, pp. 1784–1794.
- [14] Shieh, W.-B. and Tsai, L., and Azarm, S., 1997. "Design and optimization of a one-degree-of-freedom six-bar leg mechanism for a walking machine". *Journal of Robotic Systems*, **14**(12), pp. 871–880.
- [15] Nokleby, S., and Podhorodeski, R., 2006. "Optimization-based synthesis of grashof geared five-bar mechanisms". *ASME Journal of Mechanical Design*, **138**, pp. 529–534.
- [16] Zhou, H., 2009. "Dimensional synthesis of adjustable path generation linkages using the optimal slider adjustment". *Mechanism and Machine Theory*.
- [17] Ravani, B., and Roth, B., 1983. "Motion synthesis using kinematic mappings". *ASME Journal of Mechanism, Transmissions, and Automation in Design*, **105**, p. 460467.
- [18] Hong, and Erdman, 2005. "A method for adjustable planar and spherical four-bar linkage synthesis". *ASME Journal of Mechanical Design*, **127** (3), pp. 456–463.
- [19] Hayes, M., Luu, T., and Chang, X.-W., 2004. "Kinematic mapping application to approximate type and dimension synthesis of planar mechanisms". In *Advances in Robot Kinematics*, J. Lenarcic and C. Galletti, eds., Kluwer Academic Publishers, pp. 41–48.

# Synthesis of Spatial RPRP Closed Linkages for a Given Screw System

**Alba Perez-Gracia**

Institut de Robòtica i Informàtica Industrial (IRI) UPC/CSIC  
Llorens i Artigas, 4-6, 08028 Barcelona, Spain;  
And: College of Science and Engineering  
Idaho State University  
921 S. 8th Ave., Pocatello, ID 83209, USA.  
Email: aperez@iri.upc.edu

*The dimensional synthesis of spatial chains for a prescribed set of positions can be applied to the design of parallel robots by joining the solutions of each serial chain at the end effector. This design method does not provide with the knowledge about the trajectory between task positions and, in some cases, may yield a system with negative mobility. These problems can be avoided for some overconstrained but movable linkages if the finite screw system associated to the motion of the linkage is known. The finite screw system defining the motion of the robot is generated by a set of screws, which can be related to the set of finite tasks positions traditionally used in the synthesis theory. The interest of this paper lies in presenting a method to define the whole workspace of the linkage as the input task for the exact dimensional synthesis problem. This method is applied to the spatial RPRP closed linkage, for which one solution exists.*

## Nomenclature

- S Line or dual vector, defined using Plücker coordinates.
- s Vector
- $\hat{S}$  Quaternion or dual quaternion
- $\hat{w}$  Dual number
- [M] Matrix

## 1 Introduction

Synthesis of parallel robots has focused mainly on type or structural synthesis, using group theory, screw theory, or geometric methods, see for instance [1], [2], [3]. Dimensional synthesis examples exist, mainly for optimizing performance indices [4], [5], [6] or for reachable workspace sizing [7], [8], [9]; see also [10] for a comprehensive approach.

The dimensional synthesis of spatial serial chains for a prescribed set of positions can be used for the design of parallel robots by synthesizing all supporting legs for the same set of positions. There are a few examples of finite-position dimensional synthesis of parallel robots in the lit-

erature, most of them doing partial synthesis. Wolbrecht et al. [11] perform synthesis of 3-RRS, 4-RRS and 5-RRS symmetric parallel manipulators; Kim and Tsai [12] and Rao [13] solve the partial kinematic synthesis of a 3-RPS parallel manipulator. This method has been successfully applied mainly to special parallel systems with imposed symmetry. In general, the method does not allow the control of the final trajectory of the parallel system; in the most extreme cases, it may yield a system with negative mobility, that can be assembled at each task positions but cannot be driven from task position to task position.

The kinematic mapping is used for the synthesis of planar and spherical linkages in order to state design equations and to provide a tool for visualizing the workspace and trajectories of the linkage. See Ravani and Roth [14] and more recent applications by Hayes [15], Schröcker [16] and Wu and Ge [17]. For spatial motion, Study's kinematic mapping is used to obtain simplified equations for analysis and synthesis, see Husty et al. [18] and [19]. However, the kinematic image for the spatial motion is a six-dimensional quadric and that makes the visualization of workspaces and trajectories difficult for the designer.

In this paper, the workspace of the linkage is visualized as a set of finite screws corresponding to the set of finite displacements of the end-effector. One interesting question is whether the finite-screw surfaces generated by a set of task positions can give any information for the synthesis of parallel robots and, in particular, of some overconstrained closed linkages. Using Parkin's definition for pitch [20], the screws corresponding to finite displacements of some linkages can form screw systems. Huang [21] showed that the single RR chain forms a finite screw system of third order; however, the set of finite displacements of the coupler of the Bennett linkage form a cylindroid, which is a general 2-system of screws [22]. Baker [23] has also studied the motion of the Bennett linkage. Perez and McCarthy [24] used two arbitrary displacements to generate the cylindroid of finite screws associated to the Bennett linkage in order to perform dimen-



sional synthesis.

In this paper, the focus is on the simplest of the over-constrained linkages, the closed spatial RPRP linkage. This linkage is one of the Delassus linkages, later studied by Waldron [25] and Baker [26]. Recently, Huang [27] has shown that the set of screws corresponding to displacements of this linkage forms a 2-screw system. We use this result in order to synthesize RPRP linkages with positive mobility and for a given shape of the screw system of relative displacements. In order to do so, we state the design equations using the Clifford algebra of dual quaternions [28]. The dual quaternion expression can be easily related to the screw system and it is also used to assign the magnitude to the screws in order to obtain the correspondence between the screw system and the trajectory of the end-effector. The design yields a single RPRP linkage.

## 2 Clifford Algebra Equations for the Synthesis

The approach used in this paper for stating design equations is based on the method of Lee and Mavroidis [29]. They equate the forward kinematics of a serial chain to a set of goal displacements and consider the Denavit-Hartenberg parameters as variables. A more efficient formulation for our purposes consists of stating the forward kinematics of relative displacements using the even Clifford subalgebra of the projective space  $C^+(P^3)$ , also known as dual quaternions [28].

The Plücker coordinates  $S = (s, c \times s)$  of a line can be identified with the Clifford algebra element  $S = s + \epsilon c \times s$ , with  $\epsilon^2 = 0$ . Similarly, a screw  $J$  becomes the element  $J = (1 + \mu\epsilon)S$ , where  $\mu$  is the pitch. Using the Clifford product we can compute the exponential of the screw  $\frac{\theta}{2}J$ ,

$$e^{\frac{\theta}{2}J} = \left( \cos \frac{\theta}{2} - \frac{d}{2} \sin \frac{\theta}{2} \epsilon \right) + \left( \sin \frac{\theta}{2} + \frac{d}{2} \cos \frac{\theta}{2} \epsilon \right) S = \cos \frac{\hat{\theta}}{2} + \sin \frac{\hat{\theta}}{2} S. \quad (1)$$

The exponential of a screw defines a unit dual quaternion, which can be identified with a relative displacement from an initial position to a final position in terms of a rotation around and a slide along an axis.

### 2.1 Forward Kinematics

For a serial chain with  $n$  joints, in which each joint can rotate an angle  $\theta_i$  and slide a distance  $d_i$ , around and along the axis  $S_i$ ,  $i = 1, \dots, n$ , the forward kinematics of relative displacements (with respect to a reference position) can be expressed as the composition of Clifford algebra elements corresponding to the motion of each joint. Let  $\vec{\theta}_0$  and  $\vec{d}_0$  be the joint parameters of this chain when in the reference configuration, so we have  $\vec{\Delta\theta} = (\vec{\theta} - \vec{\theta}_0 + (\vec{d} - \vec{d}_0)\epsilon)$ . Then, the movement from this reference configuration is defined by

$$\begin{aligned} \hat{Q}(\vec{\Delta\theta}) &= e^{\frac{\Delta\hat{\theta}_1}{2} S_1} e^{\frac{\Delta\hat{\theta}_2}{2} S_2} \dots e^{\frac{\Delta\hat{\theta}_n}{2} S_n} = \left( \cos \frac{\Delta\hat{\theta}_1}{2} + \sin \frac{\Delta\hat{\theta}_1}{2} S_1 \right) \\ &\quad \left( \cos \frac{\Delta\hat{\theta}_2}{2} + \sin \frac{\Delta\hat{\theta}_2}{2} S_2 \right) \dots \left( \cos \frac{\Delta\hat{\theta}_n}{2} + \sin \frac{\Delta\hat{\theta}_n}{2} S_n \right). \end{aligned} \quad (2)$$

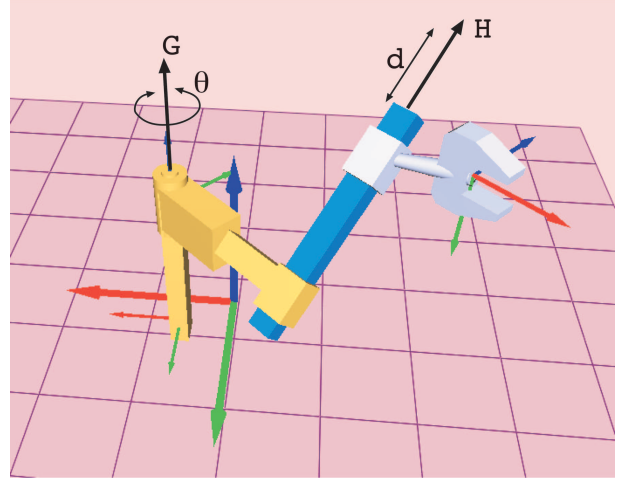


Fig. 1. The RP serial chain

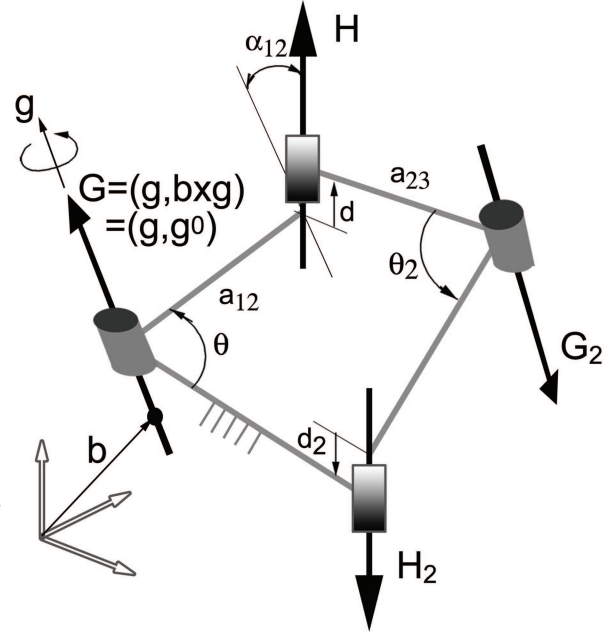


Fig. 2. The RPRP closed linkage

The RPRP linkage has a mobility  $M = -2$  using the Kutzbach-Gruebler formula; however, for certain dimensions of the links, it moves with one degree of freedom. Waldron [25] shows that the RPRP linkage will have positive mobility only if both revolute joints are parallel, and the directions of the prismatic joints are symmetric with respect to the plane containing the revolute joints.

The RPRP linkage can be seen as a serial RP chain and a serial PR chain joined at their end-effectors. The RP serial chain consists of a revolute joint followed by a prismatic joint. Figure 1 shows the RP serial chain and Figure 2 shows a sketch of the RPRP linkage with its axes. In the PR serial chain, the order of the joints in the chain is switched.

For both the RP and PR serial chains, let  $G = g + \epsilon g^0$  be the revolute joint axis, with rotation  $\theta$ , and  $H = h + \epsilon h^0$  the prismatic joint axis, with slide  $d$ . Notice that, for synthesis

purposes, the location of the slider, given by  $\mathbf{h}^0$ , is irrelevant. The Clifford algebra forward kinematics equations for the RP chain are

$$\begin{aligned}\hat{Q}_{RP}(\Delta\theta, \Delta d) &= (\cos \frac{\Delta\theta}{2} + \sin \frac{\Delta\theta}{2} \mathbf{G})(1 + \epsilon \frac{\Delta d}{2} \mathbf{H}) \\ &= (\cos \frac{\Delta\theta}{2} + \sin \frac{\Delta\theta}{2} \mathbf{g}) + \epsilon (\frac{\Delta d}{2} \cos \frac{\Delta\theta}{2} \mathbf{h} + \\ &\quad \sin \frac{\Delta\theta}{2} \mathbf{g}^0 + \frac{\Delta d}{2} \sin \frac{\Delta\theta}{2} (\mathbf{g} \times \mathbf{h} - \mathbf{g} \cdot \mathbf{h})).\end{aligned}\quad (3)$$

For the PR chain, the only difference is a negative sign in the cross product. In Eq. (3), the angle and slide are measured from a reference configuration.

## 2.2 Design Equations and Counting

Given a set of  $m$  task positions expressed as relative displacements,  $\hat{P}_{1j} = \cos \frac{\Delta\hat{\phi}_{1j}}{2} + \sin \frac{\Delta\hat{\phi}_{1j}}{2} \mathbf{P}_{1j}$ ,  $j = 2, \dots, m$ , we equate them to the forward kinematics equations in Eq. (2),

$$\hat{P}_{1j} = e^{\frac{\Delta\hat{\theta}_{1j}}{2} S_1} e^{\frac{\Delta\hat{\theta}_{2j}}{2} S_2} \dots e^{\frac{\Delta\hat{\theta}_{nj}}{2} S_n}, \quad j = 2, \dots, m \quad (4)$$

in order to create the design equations.

The result is  $8(m-1)$  design equations. The design variables that determine the dimensions of the chain are the  $n$  joint axes  $S_i$ ,  $i = 1, \dots, n$ , in the reference configuration. In addition, the equations contain the  $n(m-1)$  pairs of joint parameters  $\Delta\hat{\theta}_{ij} = \Delta\theta_{ij} + \Delta d_{ij}\epsilon$ , which are also unknown.

For the RP (and similarly for the PR) serial chain, the design equations are

$$\hat{Q}_{RP}(\Delta\theta^j, \Delta d^j) = \hat{P}_{1j}, \quad j = 2, \dots, m. \quad (5)$$

The counting of independent equations and unknowns defines the maximum number of arbitrary positions  $m$  that can be reached, based only on the type and number of joints of the serial chain, see [30] for details. Consider a serial chain with  $r$  revolute and  $p$  prismatic joints. The maximum number of task positions is given by

$$m = \frac{3r + p + 6}{6 - (r + p)}. \quad (6)$$

For serial chains with less than three revolute joints, the structure of semi-direct product of the composition of displacements needs to be considered, and the maximum number of rotations  $m_R$  needs to be calculated too. Assuming that the orientations are given and that both the directions of the revolute joints and the angles to reach the task orientations are known, we can count, in a similar fashion, the number of translations  $m_T$  that the chain can be defined for.

$$m_R = \frac{3+r}{3-r}, \quad m_T = \frac{2r+p+3}{3-p}. \quad (7)$$

In order to determine the maximum number of task positions for the RP and PR chains, we apply Eq. (6) to obtain  $m = 2.5$  task positions. Additional information is obtained using Eq. (7) to compute  $m_R = 2$  task rotations, and  $m_T = 3$  task translations. Hence, we can define one arbitrary relative displacement and a second relative displacement whose orientation is not general.

## 3 Screw System for the RPRP Linkage

In the context of this paper, a finite-screw surface is a ruled surface in which the lines with their associated pitch correspond to relative displacements. A screw surface will be a screw system if it is closed under addition and scalar multiplication, that is, if every screw of the set can be written as a linear combination of screws belonging to it.

### 3.1 The finite Screw System Generated by the Motion of the RPRP Linkage

The linear combination of two arbitrary screws representing relative displacements form a 2-system known as the cylindroid, which turns out to be the manifold for the relative displacements of the closed 4R linkage. Huang [27], by intersecting the 3-systems associated with the finite displacements of the RP and PR dyads, shows that the screw surface of the closed RPRP linkage forms a 2-system of a special type, the fourth special type according to Hunt [31], also known as 2-IB [32]. The screws of this system are parallel, coplanar screws whose pitches vary linearly with their distance.

The screw system corresponding to the RPRP linkage can be obtained in a quite straightforward way by using the composition of relative displacements at each joint, as expressed in Eq.(3). Let us denote the resulting displacements

$$\begin{aligned}\hat{Q}_{RP}(\Delta\theta, \Delta d) &= \cos \frac{\Delta\psi}{2} + \sin \frac{\Delta\psi}{2} S_{RP} = \\ &= (\cos \frac{\Delta\psi}{2} - \epsilon \frac{\Delta t}{2} \sin \frac{\Delta\psi}{2}) + \sin \frac{\Delta\psi}{2} (1 + \epsilon \frac{\Delta t}{2 \tan \frac{\Delta\psi}{2}}) S_{RP},\end{aligned}\quad (8)$$

where  $\Delta\psi$  and  $\Delta t$  are the angle about and slide along the screw axis  $S_{RP}$  of the resulting relative displacement. Expand the product in Eq.(3) and separate the dual scalar and the dual vector part, so that

$$\begin{aligned}\cos \frac{\Delta\psi}{2} - \epsilon \frac{\Delta t}{2} \sin \frac{\Delta\psi}{2} &= \cos \frac{\Delta\theta}{2} - \epsilon \frac{\Delta d}{2} \sin \frac{\Delta\theta}{2} \mathbf{G} \cdot \mathbf{H} \\ \sin \frac{\Delta\psi}{2} (1 + \epsilon \frac{\Delta t}{2 \tan \frac{\Delta\psi}{2}}) S_{RP} &= \\ \sin \frac{\Delta\theta}{2} \mathbf{G} + \epsilon \frac{\Delta d}{2} \cos \frac{\Delta\theta}{2} \mathbf{H} + \epsilon \frac{\Delta d}{2} \sin \frac{\Delta\theta}{2} \mathbf{G} \times \mathbf{H}.\end{aligned}\quad (9)$$

For studying the screw system, we are only interested in the dual-vector part of Eq.(9), which defines the lines with their associated pitch.

The resulting screw is parameterized by joint variables  $\Delta\theta$  of the revolute joint and  $\Delta d$  corresponding to the prismatic joint. We denote the expression in Eq.(9) as the *finite kinematic generator* of the screw system. In the case of finite displacements, the screw systems correspond to subspaces of a projective space, and so we take the unit screws as representatives by dividing the dual vector of Eq.(9) by  $\sin \frac{\Delta\psi}{2}$ . From the real part of the first equation in (9) we can see that  $\sin \frac{\Delta\psi}{2} = \pm \sin \frac{\Delta\theta}{2}$ , so that

$$\pm(1 + \varepsilon \frac{\frac{\Delta\psi}{2}}{\tan \frac{\Delta\psi}{2}})S_{RP} = G + \varepsilon \frac{\frac{\Delta d}{2}}{\tan \frac{\Delta\theta}{2}}H + \varepsilon \frac{\Delta d}{2}G \times H. \quad (10)$$

If we give values to the joint variables  $\Delta\theta$  and  $\Delta d$ , we will generate a screw surface of dimension 3 of a special type, in which all the screws have parallel directions.

It is easy to show that the set of screws generated by the motion of the RP serial chain is indeed a screw system, that is, closed under addition and multiplication by scalar. Generate two unit screws  $S_1$  and  $S_2$  using Eq.(10) and perform the linear combination with real constants  $k_1$  and  $k_2$ . We normalize the resulting screw by dividing by  $k_1 + k_2$  to obtain

$$\begin{aligned} (1 + \varepsilon \frac{\frac{\Delta\psi_3}{2}}{\tan \frac{\Delta\psi_3}{2}})S_3 &= \frac{1}{k_1 + k_2}(k_1 S_1 + k_2 S_2) \\ &= \mathbf{g} + \varepsilon(\mathbf{g}^0 + \varepsilon \frac{\frac{\Delta d_c}{2}}{\tan \frac{\Delta\theta_c}{2}}\mathbf{h} + \varepsilon \frac{\Delta d_c}{2}\mathbf{g} \times \mathbf{h}), \end{aligned} \quad (11)$$

where

$$\begin{aligned} \Delta d_c &= \frac{k_1}{k_1 + k_2}\Delta d_1 + \frac{k_2}{k_1 + k_2}\Delta d_2, \\ \tan \frac{\Delta\theta_c}{2} &= \frac{k_1 \frac{\Delta d_1}{2} + k_2 \frac{\Delta d_2}{2}}{k_1 \frac{\frac{\Delta\theta_1}{2}}{\tan \frac{\Delta\theta_1}{2}} + k_2 \frac{\frac{\Delta\theta_2}{2}}{\tan \frac{\Delta\theta_2}{2}}}, \end{aligned} \quad (12)$$

hence the linear combination belongs to the screw system generated by the relative motion of the RP chain. Next is to calculate the dimension of this screw system. Notice that the direction of all unit screws generated is equal to  $\mathbf{g}$ , then we just need to look at the dimension of the dual part. Generate three screws with values  $\Delta\theta_i$  and  $\Delta d_i$ ,  $i = 1, 2, 3$ . For the three vectors corresponding to the dual part to be linearly independent, the determinant of the column vector matrix must be different from zero. We obtain the value for the determinant

$$\begin{aligned} \det([S_i^0]) &= \mathbf{g} \cdot \mathbf{h} \quad \mathbf{g}^0 \cdot \mathbf{h} (\frac{\frac{\Delta d_1}{2}}{\tan \frac{\Delta\theta_1}{2}} (\frac{\Delta d_3}{2} - \frac{\Delta d_2}{2}) + \\ &\quad \frac{\frac{\Delta d_2}{2}}{\tan \frac{\Delta\theta_2}{2}} (\frac{\Delta d_1}{2} - \frac{\Delta d_3}{2}) + \frac{\frac{\Delta d_3}{2}}{\tan \frac{\Delta\theta_3}{2}} (\frac{\Delta d_2}{2} - \frac{\Delta d_1}{2})), \end{aligned} \quad (13)$$

which is different from zero when the angle  $\theta$  and the slide  $d$  are independent, except for special parallel or perpendicular arrangements of the joints. Hence, a maximal set of independent screws has cardinality 3.

In order to generate the screw system of the RPRP linkage, we impose the motion constraint relations between the joint variables. The conditions are derived in [27] from the closure equations of the linkage, to obtain

$$\begin{aligned} d &= d_2, \\ \theta &= \pm(\theta_2 - \pi), \\ \frac{\tan \frac{\theta}{2}}{d} &= \frac{\sin \alpha_{12}}{a_{12} \pm a_{23}} = k, \end{aligned} \quad (14)$$

where the twist angle  $\alpha_{12}$  and link lengths  $a_{12}$ ,  $a_{23}$  are shown in Figure 2; the angles  $\theta$ ,  $\theta_2$  and slides  $d$ ,  $d_2$ , also shown in Figure 2, have to be measured according to the convention [27] from the previous common normal line. The plus/minus sign corresponds to folded and unfolded linkages. For our purposes, only the third condition is needed. It is important to notice that this condition applies to absolute values of the joint variables, measured from the previous common normal line as stated before.

In order to use this relation, substitute  $\Delta d = d - d_0$ ,  $\Delta\theta = \theta - \theta_0$  to apply Eq.(14) so that the resulting expression depends only on  $d$ , for instance. For all possible values of the slide  $d$ , this generates a 2-IB system of screws [31, 32]. This can be checked numerically by generating 6 random screws and computing the rank of the matrix that has the screws as columns. In this case, the rank is 2. It can also be shown that when the third condition in Eq.(14) holds, the determinant in Eq.(13) is equal to zero.

The unit screws of the system can be related to spatial displacements if we add the value of the magnitude of the screw. For finite displacement screws, the value of the magnitude related to each screw is unique; this is due to the fact that finite screw systems are projective subspaces [33]. The information about the magnitude corresponding to each screw can be extracted from the scalar part of the dual quaternion product in Eq.(9). This equation relates the rotation associated to the resulting screw,  $\Delta\psi$ , to the joint variables of the kinematic chain. For the RPRP chain, this yields  $\sin \frac{\Delta\psi}{2} = \pm \sin \frac{\Delta\theta}{2}$  as noted before.

Figure 3 illustrates the nonlinear relation between the screws generated by an RPRP closed chain and the corresponding set of absolute positions of the end effector (for those positions we assume that the reference configuration is the identity). We use as values for the linkage those of an example from [27].

### 3.2 The Finite Screw System Generated as a Linear Combination of Two Screws

It has been shown that the relative displacements of the RPRP chain generate a 2-IB finite screw system. By definition, this same screw system can be generated as the linear combination of two screws with same direction and arbitrary



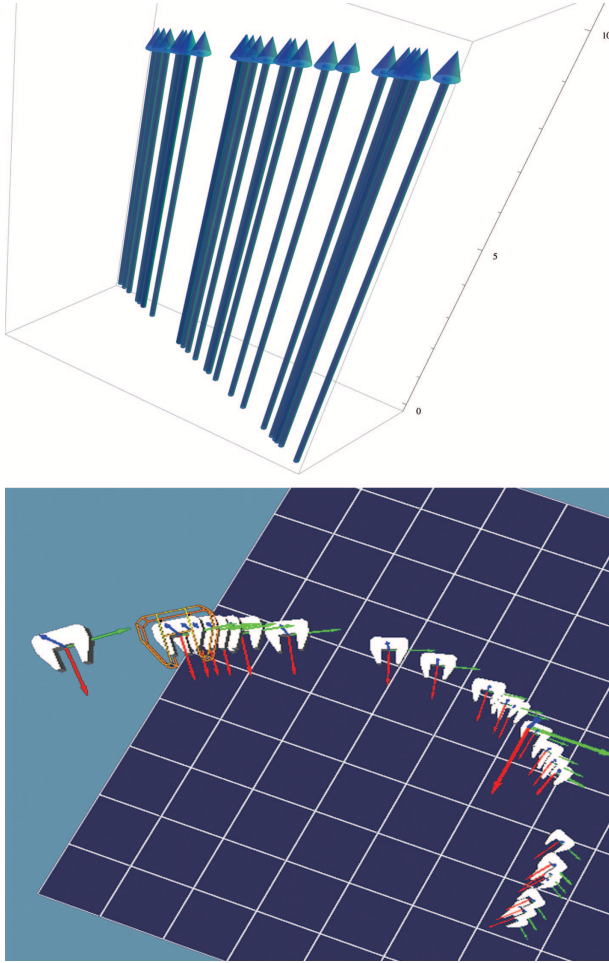


Fig. 3. Screw system generated by the RPRP linkage, above; corresponding absolute displacements, below

location and (possibly) finite pitches. From a synthesis point of view, the key is that this coincides with the results of the counting in section 2.2. The task positions defined for the synthesis of the RP (or PR) chain are two relative displacements with same direction and, in general, finite pitches.

The screw system is characterized by the pitch distribution as a linear function of the distance between screws along a common normal. In this derivation we can parameterize the results as a function of the angle  $\theta$  or the slide  $d$ .

Consider the screw  $S_{RP} = (1 + \varepsilon p)S_{RP}^0 = \mathbf{s}_{RP} + \varepsilon \mathbf{s}_{RP}^0$ . The pitch is obtained by computing  $p = \frac{\mathbf{s}_{RP} \cdot \mathbf{s}_{RP}^0}{\mathbf{s}_{RP} \cdot \mathbf{s}_{RP}}$  in Eq.(10),

$$p = \frac{1 + k^2 dd_0}{2k} \mathbf{g} \cdot \mathbf{h} = \frac{1}{2k} (1 + \tan \frac{\theta_0}{2} \tan \frac{\theta}{2}) \mathbf{g} \cdot \mathbf{h}. \quad (15)$$

For two screws  $S_A$  and  $S_B$ , the difference in the pitches is given by

$$p_B - p_A = \frac{kd_0 \mathbf{g} \cdot \mathbf{h}}{2} (d_B - d_A) = \frac{\tan \frac{\theta_0}{2} \mathbf{g} \cdot \mathbf{h}}{2k} (\tan \frac{\theta_B}{2} - \tan \frac{\theta_A}{2}) \quad (16)$$

The distance between two screws along the common normal is calculated by finding the perpendicular point on

the axis,  $\mathbf{c}_{RP} = \frac{\mathbf{s}_{RP} \times \mathbf{s}_{RP}^0}{\mathbf{s}_{RP} \cdot \mathbf{s}_{RP}^0}$  and computing the norm of the difference for two of them,

$$\begin{aligned} \mathbf{c}_B - \mathbf{c}_A &= (\frac{kd_0}{2} \mathbf{g} \times \mathbf{h} + \frac{1}{2} (\mathbf{g} \mathbf{g} \cdot \mathbf{h} - \mathbf{h} \mathbf{h})) (d_B - d_A) \\ &= \frac{1}{2k} (\tan \frac{\theta_0}{2} \mathbf{g} \times \mathbf{h} + \mathbf{g} \mathbf{g} \cdot \mathbf{h} - \mathbf{h} \mathbf{h}) (\tan \frac{\theta_B}{2} - \tan \frac{\theta_A}{2}), \end{aligned} \quad (17)$$

and

$$\begin{aligned} \|\mathbf{c}_B - \mathbf{c}_A\| &= \frac{1}{2} |d_B - d_A| \sqrt{\sin^2 \alpha_{12} (1 + d_0^2 k^2)} \\ &= \frac{1}{2} (\tan \frac{\theta_B}{2} - \tan \frac{\theta_A}{2}) \sqrt{\frac{\sin^2 \alpha_{12}}{k^2 \cos^2 \frac{\theta_0}{2}}} \end{aligned} \quad (18)$$

The slope of the (linear) pitch distribution is computed as

$$K = \frac{p_B - p_A}{\|\mathbf{c}_B - \mathbf{c}_A\|}, \quad (19)$$

and for the RPRP chain we can simplify the expression to

$$K = \pm \frac{\cos \alpha_{12}}{\sqrt{d_0^2 \sin^2 \alpha_{12} + (a_{12} + a_{23})^2}} d_0 = \pm \frac{\cos \alpha_{12}}{\sin \alpha_{12}} \sin \frac{\theta_0}{2}. \quad (20)$$

Notice that the slope is constant and depends on the initial configuration. The sign is negative if  $d_B < d_A$  or if  $\tan \frac{\theta_B}{2} < \tan \frac{\theta_A}{2}$ .

The screw system is related to the displacement of the RPRP linkage by computing the distribution of the magnitude with respect to the known pitch, distance and magnitude of the screws  $S_A$  and  $S_B$  used to define the distribution. Consider the magnitude of the screws as  $m = \sin \frac{\Delta \psi}{2} = \pm \sin \frac{\Delta \theta}{2}$ . Knowing the magnitude and pitch of screws  $S_A$  and  $S_B$ , we can solve for the magnitude  $m_C$  of a screw  $S_C$  using Eq.(18)

$$m_C = \pm \sin \frac{\Delta \theta_C}{2} = \frac{X}{\sqrt{1 + X^2}}, \quad (21)$$

where the factor  $X$  is simplified using Eq.(15) to (20) to

$$X = \frac{\|\mathbf{c}_B - \mathbf{c}_A\| p_A \tan \frac{\Delta \theta_A}{2} - \|\mathbf{c}_C - \mathbf{c}_A\| (p_A \tan \frac{\Delta \theta_A}{2} \pm p_B \tan \frac{\Delta \theta_B}{2})}{\|\mathbf{c}_B - \mathbf{c}_A\| p_C} \quad (22)$$

The positive and negative signs in the expression of  $X$  correspond to the sign of the  $\tan \frac{\theta_B}{2} - \tan \frac{\theta_A}{2}$  factor.

### 3.3 Defining the Kinematic Task as a Finite Screw System

It is now possible to define the screw system as the input task for the dimensional synthesis of the RPRP closed chain.

As a linear subspace, it is easy to shape the task at our convenience. Once we have a satisfactory screw system, any two screws from it can be selected to perform the dimensional synthesis and to obtain a finite number of solutions (in this case, just one).

We have several strategies for shaping the screw system. For instance, we can define a first relative displacement,  $\hat{S}_{12} = \cos \frac{\Delta\psi}{2} + \sin \frac{\Delta\psi}{2} (\mathbf{s}_{12} + \epsilon \mathbf{s}_{12}^0)$ . The rotation axis of the displacement,  $\mathbf{s}_{12}$  is common to both  $\hat{S}_{12}$  and the second relative displacement. We set  $\mathbf{s}_{12} = \mathbf{s}_{13}$  and select a rotation angle to define the relative rotation  $\hat{s}_{13}$ .

We can then set the slope of the pitch distribution in order to shape the screw system. The pitch for the finite displacement screws is [20]

$$p_{1i} = \frac{\frac{\Delta t_{1i}}{2}}{\tan \frac{\Delta\psi_{1i}}{2}}, \quad (23)$$

directly calculated from the dual quaternion using  $p_{1i} = \frac{\mathbf{s}_{1i} \cdot \mathbf{s}_{1i}^0}{\mathbf{s}_{1i} \cdot \mathbf{s}_{1i}}$ . Similarly, a point on the screw axis is calculated as

$$\mathbf{c}_{1i} = \frac{\mathbf{s}_{1i} \times \mathbf{s}_{1i}^0}{\mathbf{s}_{1i} \cdot \mathbf{s}_{1i}}. \quad (24)$$

Define the slope of the distribution as  $K = \frac{p_{13} - p_{12}}{\|\mathbf{c}_{13} - \mathbf{c}_{12}\|}$ , according to Eq.(20). If we set the value of  $K$ , we can solve for  $\Delta t_{13}$  in order to define the pitch of the second relative displacement, the location of its screw axis being defined. This is one possible way of defining the screw system. Converting from this to absolute displacements we can easily check whether the trajectory for the synthesis is acceptable.

Any other strategy to basically define a triangle in space can be used. The purpose of this is to have a better control on the shape of the trajectory of the linkage than the one given by just two separate finite positions.

#### 4 Dimensional Synthesis of the RPRP Linkage for a Prescribed Screw System

The synthesis of the RP, and similarly, PR chains, is simple and yields one solution. In general, the task positions are expressed as relative displacements  $\hat{Q}_{1i} = \hat{Q}_i \hat{Q}_1^{-1}$  with respect to the first task position  $\hat{Q}_1$ . For the RP or PR chains, the maximum number of task positions that we can define is  $i = 3$ , as explained in section 2.2. Given an arbitrary relative displacement  $\hat{Q}_{12} = (q_{12}^w + \mathbf{q}_{12}) + \epsilon(q_{12}^{w0} + \mathbf{q}_{12}^0)$  and a second displacement  $\hat{Q}_{13} = (q_{13}^w + \mathbf{q}_{13}) + \epsilon(q_{13}^{w0} + \mathbf{q}_{13}^0)$  such that both have same direction and a given pitch distribution, we equate them to the forward kinematics in Eq.(3). We can solve for the direction of the revolute joint  $\mathbf{g}$  and the rotation angles,

$$\mathbf{g} = \frac{\mathbf{q}_{12}}{\|\mathbf{q}_{12}\|}, \quad \tan \frac{\Delta\theta_{1i}}{2} = \frac{\|\mathbf{q}_{1i}\|}{q_{1i}^w}, \quad i = 2, 3. \quad (25)$$

The equations corresponding to the dual part are linear in the moment of the revolute joint,  $\mathbf{g}^0$ ,

$$\mathbf{g}^0 = \frac{1}{\sin \frac{\Delta\theta_{1i}}{2}} \left( \mathbf{q}_{1i}^0 - \frac{\Delta d_{1i}}{2} \left( \cos \frac{\Delta\theta_{1i}}{2} \mathbf{h} + \sin \frac{\Delta\theta_{1i}}{2} \mathbf{g} \times \mathbf{h} \right) \right), \quad i = 1, 2. \quad (26)$$

Equating the solution of  $\mathbf{g}^0$  for both relative displacements, we can solve linearly for  $\mathbf{h}$  as a function of the slides  $\Delta d_{12}$ ,  $\Delta d_{13}$ . The relation between the slides is given by the pitch condition,

$$\frac{q_{12}^{w0}}{\frac{\Delta d_{12}}{2} \sin \frac{\Delta\theta_{12}}{2}} = \frac{q_{13}^{w0}}{\frac{\Delta d_{13}}{2} \sin \frac{\Delta\theta_{13}}{2}} \quad (27)$$

Imposing  $\|\mathbf{h}\| = 1$ , we can solve for the slides to obtain one solution. Using the same process, we can solve for the PR serial chain.

## 5 Examples

Two examples are presented below. The first one is performed to check the method, while for the second one, a fully general task is used.

### 5.1 First Example

In this first case, the two relative displacements are generated using the RP chain presented in Huang [27]. In this example, the revolute joint is located at the origin and the prismatic joint is located along the  $x$  direction with a twist angle of  $\alpha_{12} = \pi/5$  and link length  $a_{12} = 5$ . We use the loop condition in Eq.(14) and random values for the slide to generate the set of relative displacements of the corresponding RPRP closed chain. From those, we randomly select two displacements, the ones in Table 1.

Table 1. Goal relative displacements for the RP and PR chains, Huang's example

---


$$(0, 0, -0.05, 0.99) + \epsilon(0.02, 0.37, -0.51, -0.03)$$

$$(0, 0, -0.34, 0.94) + \epsilon(0.80, 2.23, -3.08, -1.10)$$


---

The resulting screw system is shown in Figure 4, where the length of each screw is proportional to its pitch. Also the corresponding trajectory of absolute displacements, considering the reference position as the identity, is shown in same Figure.

Using the synthesis procedure explained in Section 4, we obtain the RP and PR chains of Table 2. Notice that they coincide with the values given in [27], which means this is a folded RPRP overconstrained movable linkage. Figure 5 shows the linkage reaching some of the positions. Notice that the shape of the coupler link attached to the end effector depends on the position chosen as reference configuration.

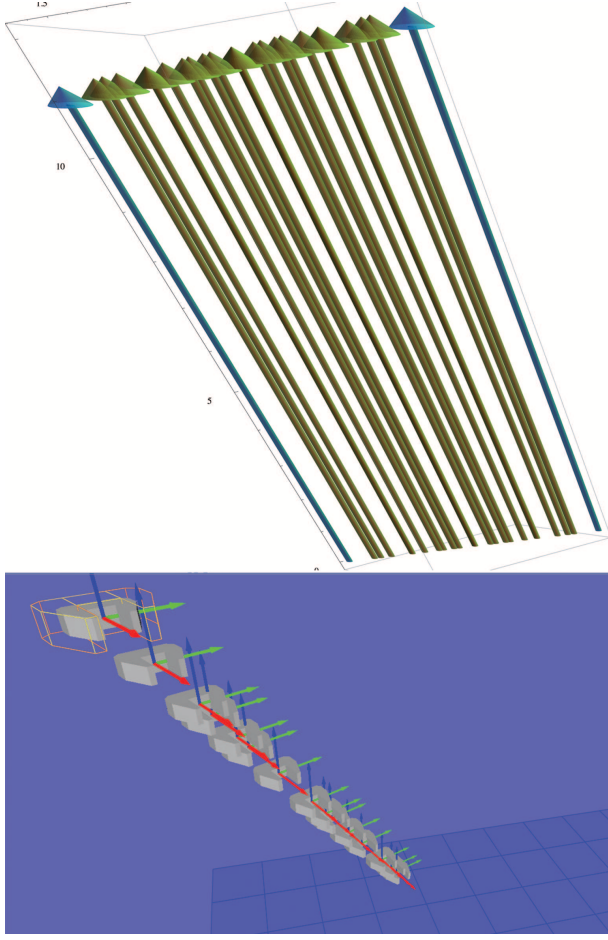


Fig. 4. Above, screw system generated by  $S_{12}$  and  $S_{13}$  (shown as first and last screws); below, corresponding absolute displacements with reference displacement being the identity

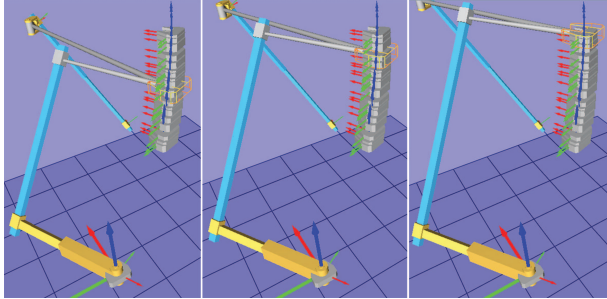


Fig. 5. RPRP linkage reaching three positions of the trajectory

## 5.2 Second example

For the second example, the dual quaternions in Table 3 have been generated as explained.  $\hat{S}_{12}$  has been randomly generated, while the rotation in  $\hat{S}_{13}$  is such that it belongs to the workspace of the chain.

We set the location of the second screw axis of the relative displacement with a point  $\mathbf{p}_{13} = (0.083, 2.159, -3.226)$ , randomly generated. Then we choose a value for the slope of the pitch distribution,  $K = 0.480$ , which allows us to create the second relative displacement.

The resulting screw system is shown in Figure 6, where

Table 2. Joint axes for the RPRP linkage at the reference configuration, Example 1

Chain	Revolute joint G	Prismatic joint $\mathbf{h}$
RP axes	$\begin{Bmatrix} 0 + 0\epsilon \\ 0 + 0\epsilon \\ 1 + 0\epsilon \end{Bmatrix}$	$\begin{Bmatrix} 0 \\ 0.59, \\ -0.81 \end{Bmatrix}$
RP Joint vars.	$\theta_{12} = -5.7$ $\theta_{13} = -39.4$	$d_{12} = 1.27$ $d_{13} = 8.08$
PR axes	$\begin{Bmatrix} 0 + 5.38\epsilon \\ 0 + 13.0\epsilon \\ -1 + 0\epsilon \end{Bmatrix}$	$\begin{Bmatrix} -0.42 \\ -0.42 \\ -0.81 \end{Bmatrix}$
PR Joint vars.	$\theta_{12} = 5.7$ $\theta_{13} = 39.4$	$d_{12} = 1.27$ $d_{13} = 8.08$

Table 3. Goal relative displacements for the RP and PR chains

$$(0.46, -0.13, -0.56, -0.67) + \epsilon(1.66, 0.34, -0.02, 1.08)$$

$$(0.13, -0.04, -0.17, 0.98) + \epsilon(0.02, -0.57, -0.92, -0.18)$$

the length of each screw is proportional to its pitch. The corresponding trajectory of absolute displacements, considering the reference position as the identity, is shown in Figure 7.

We obtain one solution for the RPRP linkage, specified in Table 4 as the Plücker coordinates of the axes and the joint variables to reach the positions.

Again, the dimensions form an overconstrained movable RPRP linkage. Figure 8 shows the chain reaching three displacements along the trajectory, considering the reference displacement as the identity.

## 6 Conclusions

This paper presents the exact workspace synthesis of an overconstrained closed linkage, the RPRP. The knowledge of the screw system that corresponds to the finite displacements of the linkage is used to generate the workspace of the linkage, which in turn ensures that the solutions of the synthesis of the RP and PR serial chains can be assembled to create a movable system. The counting of the maximum number of positions for the finite-position synthesis of the serial chain turns out to fully define the finite screw system of the linkage. This provides an easy method to shape the whole trajectory of the RPRP linkage as an input for the synthesis process. Even though the method targets the whole motion of the linkage, the synthesis equations need to be stated only at

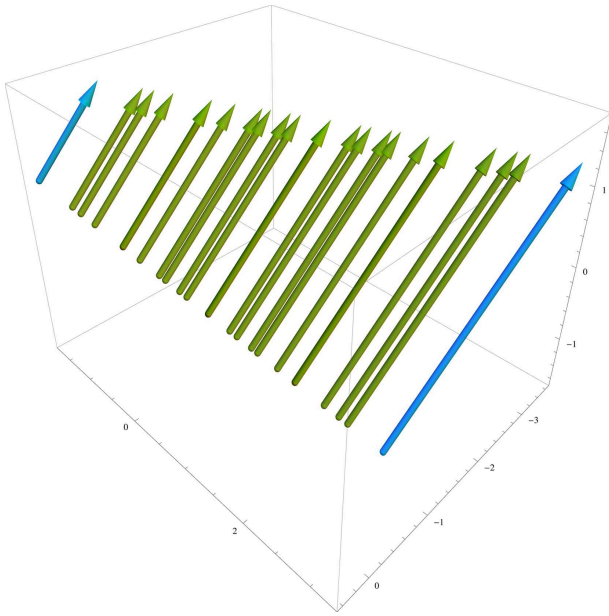


Fig. 6. Screw system generated by  $S_{12}$  and  $S_{13}$  (first and last screws)

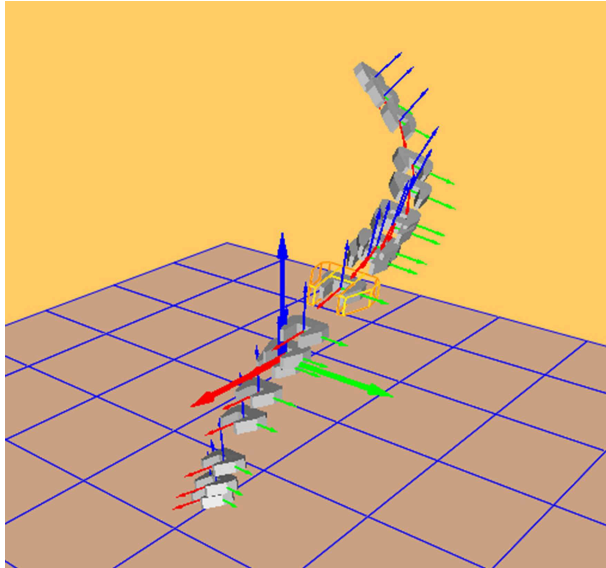


Fig. 7. The RPRP end-effector task trajectory

the task positions used to generate the linear combination of screws, hence the finite-position synthesis equations can still be used. The method yields a single RPRP linkage.

#### Acknowledgements

This work is supported by a Ramon y Cajal Research Fellowship from the Spanish Ministry of Science and Innovation.

#### References

- [1] Herve, J. M., 1999. "The lie group of rigid body displacements, a fundamental tool for mechanism design".

Table 4. Joint axes for the RPRP linkage at the reference configuration, Example 2

Chain	Revolute joint G	Prismatic joint $\mathbf{h}$
RP axes	$\begin{Bmatrix} -0.62 - 0.44\epsilon \\ 0.18 - 3.17\epsilon \\ 0.76 + 0.39\epsilon \end{Bmatrix}$	$\begin{Bmatrix} -0.09 \\ 0.89 \\ 0.44 \end{Bmatrix}$
RP Joint vars.	$\theta_{12} = -264.5$ $\theta_{13} = -25.2$	$d_{12} = 5.30$ $d_{13} = -3.05$
PR axes	$\begin{Bmatrix} 0.62 + 2.32\epsilon \\ -0.18 - 1.83\epsilon \\ -0.76 + 2.31\epsilon \end{Bmatrix}$	$\begin{Bmatrix} -0.27 \\ 0.06 \\ -0.96 \end{Bmatrix}$
PR Joint vars.	$\theta_{12} = 264.5$ $\theta_{13} = 25.2$	$d_{12} = -5.30$ $d_{13} = 3.05$

*Mechanism and Machine Theory*, **34**, pp. 717–730.

- [2] Angeles, J., 2002. "The qualitative synthesis of parallel manipulators". In *Proceedings of the WORKSHOP on Fundamental Issues and Future Research Directions for Parallel Mechanisms and Manipulators*, C. Gosselin and I. Ebert-Uphoff, eds.
- [3] Gogu, G., 2007. *Structural Synthesis of Parallel Robots. Part 1: Methodology*, first ed. Springer.
- [4] Huang, T., Li, M., Zhao, X. M., Mei, J., Chetwynd, D. G., and Hu, S. J., 2005. "Conceptual design and dimensional synthesis for a 3-dof module of the trivariant - a novel 5-dof reconfigurable hybrid robot". *IEEE Transactions on Robotics*, **21**(3), pp. 449–456.
- [5] Huang, T., Zhanxian, L., Li, M., Chetwynd, D. G., and Gosselin, C. M., 2004. "Conceptual design and dimensional synthesis of a novel 2-dof translational parallel robot for pick-and-place operations". *AMSE Journal of Mechanical Design*, **126**, pp. 449–455.
- [6] Kim, H. S., and Tsai, L.-W., 2003. "Design optimization of a cartesian parallel manipulator". *ASME Journal of Mechanical Design*, **125**, pp. 43–51.
- [7] Affi, Z., Romdhane, L., and Maalej, A., 2004. "Dimensional synthesis of a 3-translational-dof in-parallel manipulator for a desired workspace". *European Journal of Mechanics, A / Solids*, **23**, pp. 311–324.
- [8] Kosinska, A., Galicki, M., and Kedzior, K., 2003. "Design and optimization of parameters of delta-4 parallel manipulator for a given workspace". *Journal of Robotic Systems*, **20**(9), pp. 539–548.
- [9] Chablat, D., and Wenger, P., 2003. "Architecture optimization of a 3-dof parallel mechanism for machining applications, the orthoglide". *IEEE Transactions on Robotics and Automation*, **19**(3), pp. 403–410.
- [10] Merlet, J.-P., 2005. "Optimal design of robots". In



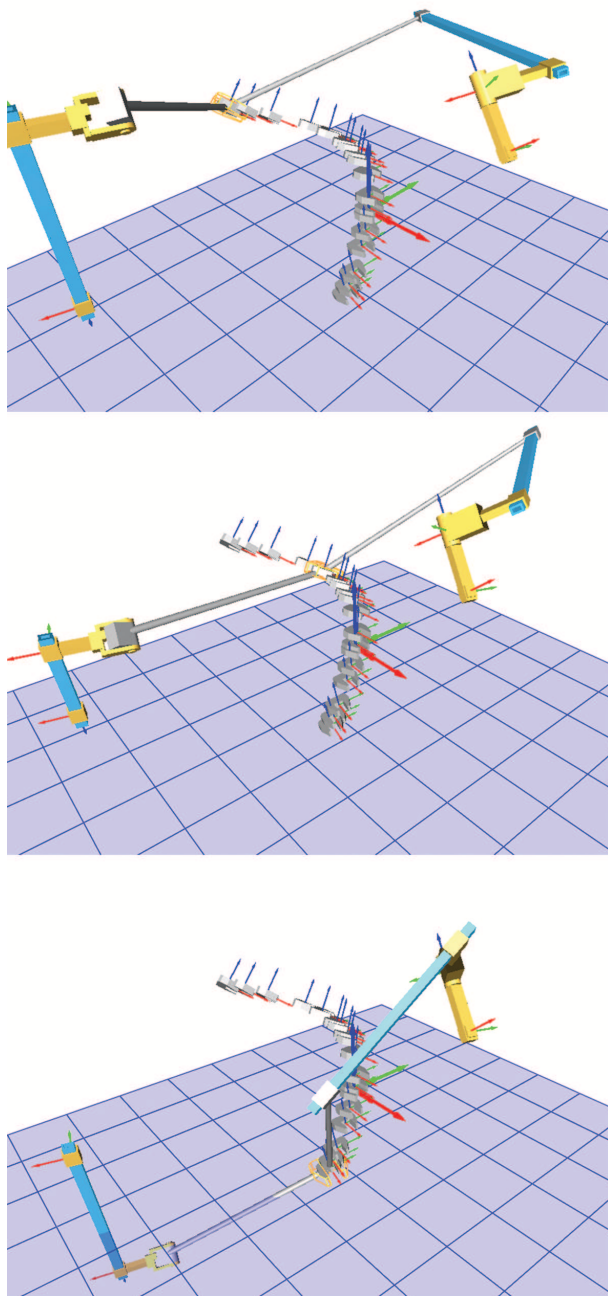


Fig. 8. The RPRP linkage reaching three positions along the trajectory

Proceedings of Robotics: Science and Systems.

- [11] Wolbrecht, E., Su, H.-J., Perez, A., and McCarthy, J. M., 2004. "Geometric design of symmetric 3-rrs constrained parallel platforms". In Proceedings of the 2004 ASME International Mechanical Engineering Congress and Exposition, ASME, ed.
- [12] Kim, H. S., and Tsai, L.-W., 2003. "Kinematic synthesis of a spatial 3-rps parallel manipulator". *ASME Journal of Mechanical Design*, **125**, pp. 92–97.
- [13] Rao, N. M., and Rao, K. M., 2009. "Dimensional synthesis of a 3-rps parallel manipulator for a prescribed range of motion of spherical joints". *Mechanism and*

*Machine Theory*, **44**, pp. 477–486.

- [14] Ravani, B., and Roth, B., 1983. "Motion synthesis using kinematic mappings". *ASME Journal of Mechanisms, Transmissions and Automation in Design*, **105**(3), pp. 460–467.
- [15] Hayes, M. J. D., Luu, T., and Chang, X. W., 2004. "Kinematic mapping application to approximate type and dimension synthesis of planar mechanisms". In *On Advances in Robot Kinematics*, J. Lenarcic and C. Gallietti, eds., Kluwer Academic Publisher.
- [16] Schrockner, H.-P., Husty, M. L., and McCarthy, J. M., 2007. "Kinematic mapping based assembly mode evaluation of planar four-bar mechanisms". *ASME Journal of Mechanical Design*, **129**, pp. 924–929.
- [17] Wu, J., Purwar, A., and Ge, Q. J., 2010. "Interactive dimensional synthesis and motion design of planar 6r single-loop closed chains via constraint manifold modification". *ASME Journal of Mechanisms and Robotics*, **2**(3).
- [18] Husty, M. L., Pfurner, M., Schrockner, H.-P., and Brunthaler, K., 2007. "Algebraic methods in mechanism analysis and synthesis". *Robotica*, **25**, pp. 661–675.
- [19] Brunthaler, K., 2006. "Synthesis of 4r linkages using kinematic mapping". PhD thesis, Institute for Basic Sciences and Engineering, University of Innsbruck, Innsbruck, Austria.
- [20] Parkin, I. A., 1992. "A third conformation with the screw systems: Finite twist displacements of a directed line and point". *Mechanism and Machine Theory*, **27**, pp. 177–188.
- [21] Huang, C., 1994. "On the finite screw system of the third order associated with a revolute-revolute chain". *ASME Journal of Mechanical Design*, **116**, pp. 875–883.
- [22] Huang, C., 1996. "The cylindroid associated with finite motions of the bennett mechanism". In Proceedings of the ASME Design Engineering Technical Conferences.
- [23] Baker, J. E., 1998. "On the motion geometry of the bennett linkage". In Proc. 8th Internat. Conf. on Engineering Computer Graphics and Descriptive Geometry, pp. 433–437.
- [24] Perez, A., and McCarthy, J. M., 2003. "Dimensional synthesis of bennett linkages". *ASME Journal of Mechanical Design*, **125**(1), pp. 98–104.
- [25] Waldron, K. J., 1972. "A study of overconstrained linkage geometry by solution of closure equations - part ii- four-bar linkages with lower pair joints other than screw joints". *Mechanism and Machine Theory*, **8**, pp. 233–247.
- [26] Baker, J. E., 1975. "The delassus linkages". In Proc. of the 4th World Congress on the Theory of Machines and Mechanisms, p. 4549.
- [27] Huang, C., 2006. "Linear property of the screw surface of the spatial rprp linkage". *ASME Journal of Mechanical Design*, **128**, pp. 581–586.
- [28] Perez Gracia, A., and McCarthy, J. M., 2006. "The kinematic synthesis of spatial serial chains using clifford algebra exponentials". *Proceedings of the Institu-*

*tion of Mechanical Engineers, Part C, Journal of Mechanical Engineering Science*, **220(7)**, pp. 953–968.

- [29] Lee, E., and Mavroidis, C., 2002. “Solving the geometric design problem of spatial 3r robot manipulators using polynomial homotopy continuation”. *ASME Journal of Mechanical Design*, **124(4)**, pp. 652–661.
- [30] Perez, A., and McCarthy, J. M., 2004. “Dual quaternion synthesis of constrained robotic systems”. *ASME Journal of Mechanical Design*, **126(3)**, pp. 425–435.
- [31] Hunt, K. H., 1978. *Kinematic Geometry of Mechanisms*. , Oxford University Press.
- [32] Zlatanov, D., Agrawal, S., and Gosselin, C. L., 2005. “Convex cones in screw spaces”. *Mechanism and Machine Theory*, **40**, pp. 710–727.
- [33] Huang, C., Sugimoto, K., and Parkin, I., 2008. “The correspondence between finite screw systems and projective spaces”. *Mechanism and Machine Theory*, **43**, pp. 50–56.

# Design of a Prosthetic Hand with Remote Actuation\*

Kurt Scott, Alba Perez-Gracia

**Abstract**— One of the main issues of prosthetic hands is to be able to fulfill all the specifications about speed, torque, weight and inertia while placing all the components within the prosthetic hand. This is especially true when full dexterity is required in the prosthesis. In this paper, a new design for a prosthetic hand is presented, which uses remote actuation in order to satisfy most of those requirements. The actuators are to be located in the back of the subject and the transmission is implemented via cables. Other characteristics of this new prosthetic hand include torque limitation and the possibility of switching between underactuated and fully actuated functions.

## I. INTRODUCTION

The design of robotic prosthetic hands is a very active field of research. Recent research has focused on finding better actuation systems [1-4], integrating some compliance in the design [5-8], and generating better control strategies or input signals [8-10]. In addition to this, newer mechanical designs of fingers and hands are also being developed [5,6,11,12,13,14]. Some robotic hands that could be used for prosthetics are in an advanced design stage, such as DLR hand, i-Limb hand, Shadow hand, and fluidhand [2]. However, a prosthetic hand with all the properties desired by the users [15, 16] has yet to be achieved.

The main reason for the current state of hand prostheses is the complexity associated with the human hand, with its many actuators and sensors, which makes use of forearm muscles, nervous system, and body's energy generation system. Fitting all needed components within the physical size of the hand requires a degree of miniaturization that is still to be achieved.

There are two primary designs that are commonly used to specify how a robotic hand is actuated. Using one actuator for each degree of freedom produces a fully-actuated system. This approach allows maximum dexterity and manipulation, but often results in a bulky design requiring complex control algorithms and elaborate sensor modules for each degree of freedom. Underactuated systems, which require fewer actuators, have been known to adapt to variable environmental conditions without the use of sensors [17], [18], [19]. This approach simplifies the control algorithms by sacrificing hand function, strength, and the ability for the hand to adapt to the user.

The human hand has an average weight of 400 grams [20] (distal to the wrist and not including the forearm extrinsic muscles). However, prosthetic terminal devices of similar weight have been described as being too heavy by users [21]. This is primarily because the attachment methods between the prosthesis and the user compound the effects of the weight in the terminal device. Although researchers are currently working to alleviate attachment problems through the use of integrated attachment mechanisms, the weight of the prosthesis is a key contributor to interface discomforts and user fatigue [22].

In this paper, we explore two specific problems associated with robotic prosthetics: 1) the ability for the robot to adapt to the user and 2) the reduction in weight on ergonomics.

Our solution uses a remote-actuation, hybrid design, with an external multi-degree-of-freedom actuating system that can be switched from coupled actuation to full actuation.

A key performance of this hybrid design is to produce power grasps that passively make contact at multiple points, thereby providing the user the ability to apply the desired force on the object from multiple contact points. Due to the limited number of actuators and the uncertainty in object location and shape, the coupled actuation must be designed to minimize situations in which not all links make contact with the object.

It is expected that the flexibility associated with this design will allow for a better adaptation to the many different types of amputees.

## II. MECHANICAL DESIGN

### A. Hand Structure

The overall shape and size of the hand is based on the average human hand. This includes five fingers and a thumb that are attached to a fixed palm. Revolute joints make up the 10 degrees of freedom for the interphalangeal (IP) joints of the fingers and IP and MCP joints of the thumb. Universal joints are used in the Metacarpals of each finger (MCP joints) and the CMC joint of the thumb, as well as the combination of flexion-extension and abduction-adduction of the wrist. These joints make up the other 12 degrees of freedom in this design. Joint actuation is created by a cable system that converts actuator rotational motion to linear motion and that back to rotational motion in the joint.

\* This work was partially supported by Grant Number NIH-R01HD062744-01 from NCHHD, and by the US Department of the Army, award number W81XWH-10-1-0128 awarded and administered by the U.S. Army Medical Research Acquisition Activity. The content is solely the responsibility of the authors.

K. Scott and A. Perez-Gracia are with the Department of Mechanical Engineering, Idaho State University, Pocatello, ID, USA (e-mail: scotkurt@isu.edu, perealba@isu.edu).

To achieve the desired motion in a lightweight, durable construction, the hand components are made from thin gauge stainless steel. Individual links that makeup each finger and the thumb are created by bending thin gauge sheet metal into a tube like section that allow the finger pulleys, cables, and cable conduit to be discreetly hidden inside.

The palm of the hand is constructed in a similar fashion using shaped sheet metal as an external shell. Consecutive links are connected with 3 mm axle shafts that pass through ball bearings creating the revolute and universal joints. To drive the joint motion, 0.039 diameter Teflon-coated cables pass through 0.100 diameter cable conduit as it is roughed through each finger to the palm and then out to actuators located away from the hand. *Figure 1* shows the joint arrangement.

### B. Joint Actuation

The linear actuation design in this paper operates with the use of a pull-pull cable system. Each joint is controlled by two cables that pass through cable conduits, from the actuator to the joint pulley. The actuator's rotational motion causes the pulley on the actuator to release cable on one side and draw cable in on the other. This results in a rotation of the joint pull and ultimately a rotation of the joint. In reverse fashion when the actuator rotates in the reverse direction the opposite cable is drawn or pulled in causing a tension in the cable and a reverse rotation of the joint pulley and the joint.

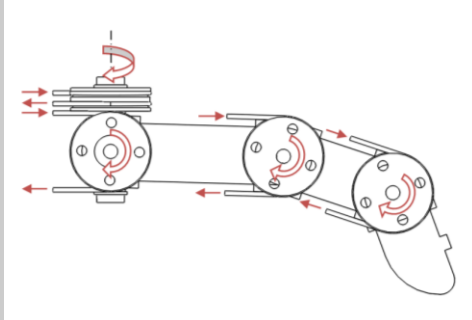


Figure 1: Finger Pulleys

This simple design is repeated for the Distal, Proximal, and Metacarpal joints of each finger and the thumb. However the metacarpal joints on each finger and the thumb are universal joints and add a second degree of freedom and a second pull-pull actuation cable system to the joint, see Figure 2.

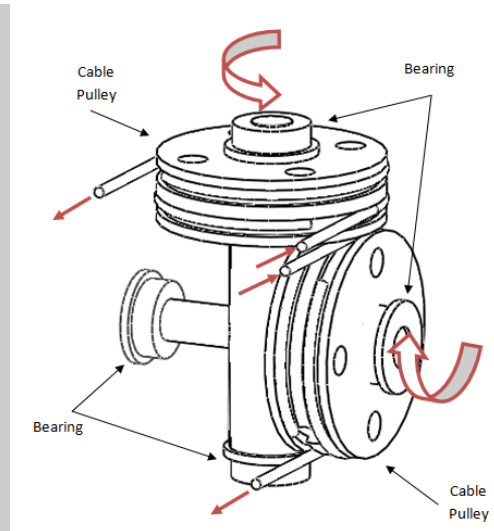


Figure 2: Metacarpal Universal Joint

The 2-dof wrist joint is also a universal joint, but a third rotational degree is added to allow hand pronation/supination. This results in 23 degrees of freedom. Because of the fact that the distal IP joints of a human hand on average are 70% coupled to the Proximal IP joints, the distal joint and the proximal joint of this design are actuated with one actuator resulting in a coupled motion for each finger. This coupling reduces the total independent degrees of freedom down to 19.

The cable conduit that is used to route the cable to the specific joint is a Bowden cable design and provides compression strength that is usually provided by the bones in the human hand. This allows thinner material to be used in the construction of the fingers and palm reduction weight that is felt by the user. The cables act as tendons that in this case are connected to actuators instead of mussels. A cable passing through a cable conduit can be seen in Figure 3. Notice that two cables are needed for each degree of freedom.



Figure 3: Cable conduit

## III. ACTUATION SENSING

### A. Faulhaber Actuation

To minimize the overall weight seen by the user, the actuators that control the hand motion are to be placed remotely, in an operational backpack. This allows actuators to be sized based on output power instead of overall



dimensions. The power unit that is used to power both the control system and the actuators can also benefit from this design.



Figure 4: Faulhaber Gearmotor and Encoder

For each degree of freedom a Faulhaber Gear Motor and Encoder (Figure 4) will be used to drive the 19 active degrees of freedom. The windings have an overall resistance of 11 ohm, which means the motor will draw 0.55 amps at 6V if stalled. The motor has a peak efficiency of 74%. The no-load motor speed is 13,400 RPM at 6V but will be slower with a gearhead attached. **Error! Reference source not found.** shows the output shaft that connects to the actuator drive pulley. Resulting forces caused by tension in the cables will pass through the actuator mounting screws to the actuator mounting plate, then to the cable conduit.

The dual-channel encoder is similar to an HEM encoder that accepts a 4.5v to 15v. To measure only RPM or distance, the encoder has two channels, one of them providing one high pulse per revolution of the motor. There will be 141 high pulses per revolution of the gearshift, or about 2.55 degrees of final output rotation per pulse. To increase resolution or to measure rotation direction, the microcontroller can watch both channels A and B. The output of the encoder is very clean, see Figure 5.

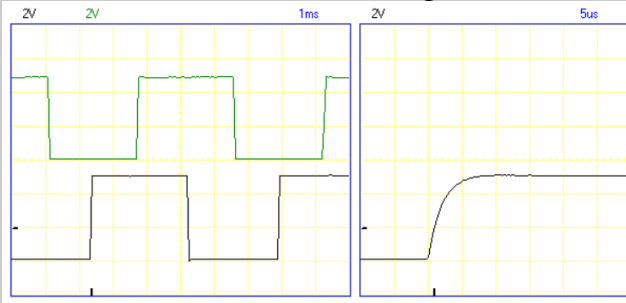


Figure 5: Oscilloscope trace of two channel encoder

To connect the gear motors to the individual finger pulleys, the pull-pull system described above is to be utilized. The routing of the individual cable conduits is yet to be developed.

### B. Pressure Sensing

To provide tough/strength of grasp sensing in the hand, the actuator utilizes a variable resistance sensor. This sensor provides feedback to the controller of the torque being applied by the actuator to the finger. In simple control

layouts the input voltage for the motor would pass through the variable resistor controlling the speed and stopping signal based on the spring constant. In more complicated controls this resistive signal would provide the force input that will allow one finger to provide more force than another and possibly create motion of object that have already been grasp.

This sensor is constructed by connecting a variable resistor to the drive hub and the motor pulley. A torsion spring connects the motor pulley to the drive hub. When force increased due to object contact, this force is carried through the actuation cables to the motor pulley and then into the torsion spring. As the spring stores this energy it allows the motor pulley to rotate on the drive hub and change the resistance in the variable resistor. This change in resistance provides feedback to the motor controller on the strength of grasp that the robot is producing. This sensor also provides a buffer to jerk that would otherwise be produced in the actuation system during grasp contact. A diagram of this sensor is shown in Figure 6.

One of the main benefits of using this type of tough/strength sensing is it allows for contact to be sensed no matter where it occurs on the robotic hand. Pressure sensors located at the tips of each finger have been used to provide similar sensing however if object contact does not happen in the unit normal direction this force can be misinterpreted by the sensor.

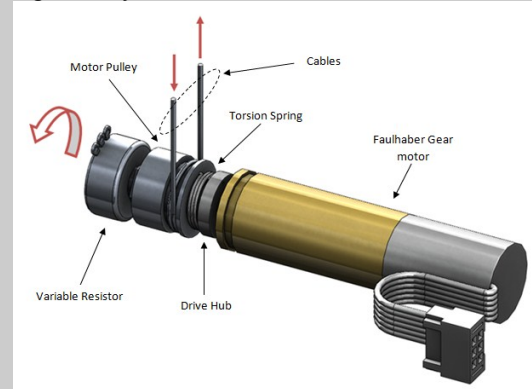


Figure 6: Pressure Sensor

## IV. MOTION ANALYSIS

Because this design does not incorporate complex coupling linkages, the kinematics of the fingertip positions is relatively simple. Let  $R_1$ ,  $R_2$  and  $R_3$  be the lengths of the phalanges and  $\theta_1$  to  $\theta_4$  be the joint angles for the four finger joints. The pose of the fingertip (point B) respect to point A can be expressed as a transformation, where the orientation of the fingertip is given by the quaternion

$$q = \begin{pmatrix} \sin\left(\frac{\theta_1}{2}\right) \sin\left(\frac{\theta_2 + \theta_3 + \theta_4}{2}\right) \\ \sin\left(\frac{\theta_1}{2}\right) \cos\left(\frac{\theta_2 + \theta_3 + \theta_4}{2}\right) \\ \cos\left(\frac{\theta_1}{2}\right) \sin\left(\frac{\theta_2 + \theta_3 + \theta_4}{2}\right) \\ \cos\left(\frac{\theta_1}{2}\right) \cos\left(\frac{\theta_2 + \theta_3 + \theta_4}{2}\right) \end{pmatrix} \quad (1)$$

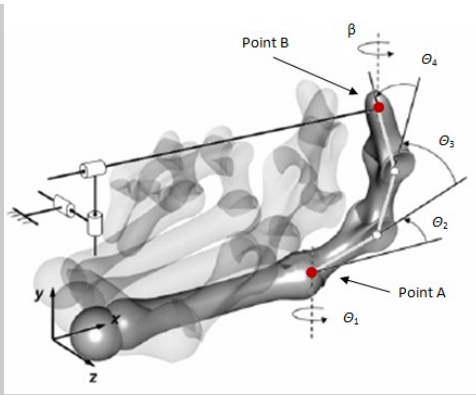


Figure 7: Joint notation

The location of point B referenced from point A is given by the vector

$$P_B = \begin{bmatrix} \cos(\theta_1)(R_1 \cos(\theta_2) + R_2 \cos(\theta_2 + \theta_3) - (2(R_1 + R_2) + R_3) \cos(\theta_2 + \theta_3 + \theta_4)) \\ R_1 \sin(\theta_2) + R_2 \sin(\theta_2 + \theta_3) - (2(R_1 + R_2) + R_3) \sin(\theta_2 + \theta_3 + \theta_4) \\ \sin(\theta_1)(-R_1 \cos(\theta_2) - R_2 \cos(\theta_2 + \theta_3) + (2(R_1 + R_2) + R_3) \cos(\theta_2 + \theta_3 + \theta_4)) \end{bmatrix}$$

Since  $\theta_1$ ,  $\theta_2$ , and  $\theta_3$  joints are controlled by their own independent actuator and  $\theta_3$  and  $\theta_4$  are coupled 1:1, the pose of the finger can be quickly determined.

## V. PROTOTYPE

The prototype will be created using a sheet metal laser. Thin gauge stainless and sheet metal flat patterns created in Solidworks® CAD software (Figure 8) will allow each link in the hand to be created with an interlocking design that minimizes weight and maintains strength. This design also allows for simple maintains on the joint pulleys, cables, and cable conduits by allowing access to these areas without major disassembly.

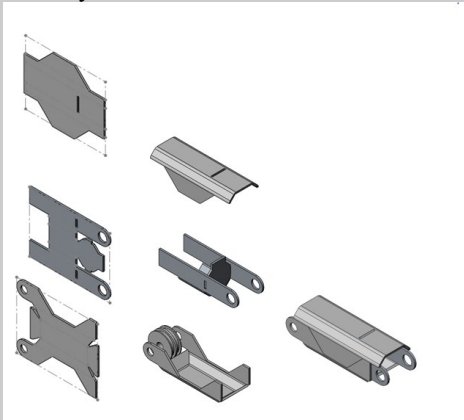


Figure 8: Sheet Metal Construction

The remaining palm and wrist of the hand will be constructed in similar fashion. Formed sheet metal stainless steel plates are joined together to form the bearing carrier for each metacarpal universal joint. The thumb of the hand is constructed the like each finger and connected to the palm plates with internal sheet metal bearing carriers. Structural strange of the system is achieved after all components are

connected. This included the access plates that are used to maintain the actuation cables. Actuators for each degree of motion are mounted to a common mounting plate that is located in an operational backpack. A general layout of the actuators can be found in Figure 9.

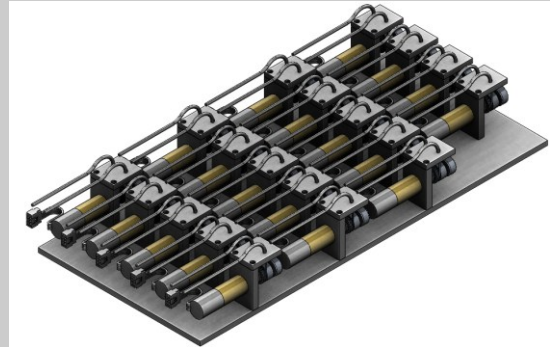


Figure 9: Remote Actuation

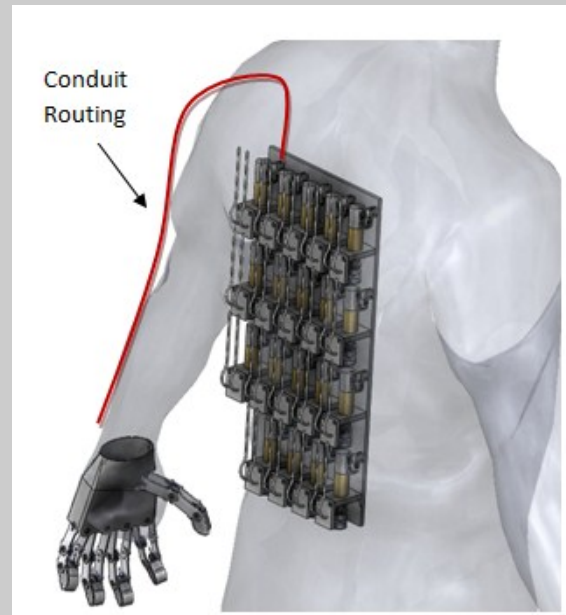


Figure 10: Conduit Layout

Cable conduit runs connect the robotic hand to the remote actuators that are located in the operational backpack. These conduit runs will attach the outside of the operators arm and follow the arm down to the hand similar to the sleeve on a shirt.

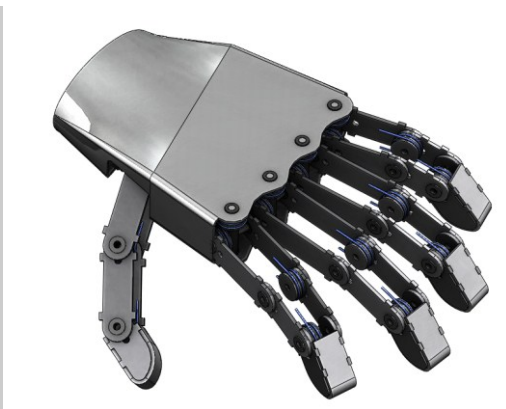


Figure 11: General Layout

The prototype is currently being built and will be used for testing the design.

## VI. CONCLUSIONS

This paper presents a new design for a prosthetic hand. The design is based on remote actuation of electric DC motors via cables. This type of construction and design shifts the weight of the hand from the end of the prosthesis to a localized point closer to the center of mass of the user. This shift in weight is intended to reduce strain and fatigue on the operator during normal daily activities.

Future work includes the detailed modeling and simulation of the design, and the assembly and testing of the prototype.

## REFERENCES

- [1] Fite,K.,Withrow,T.,Shen,Z.,Wait,K.,Mitchell,J.,Goldfarb,M., "A Gas-Actuated Anthropomorphic Prosthesis for Transhumeral Amputees," *IEEE Transactions on Robotics*, 24(1):159:169, 2008.
- [2] Pylatiuk,C.,Schulz,S.,Kargov,A.,Bretthauer,G.,"Two Multiarticulated Hydraulic Hand Prostheses," *Artificial Organs*, 28(11),980:986, 2004.
- [3] Yamono, I., and Maeno, T., "Five-fingered Robot Hand using Ultrasonic Motors and Elastic Elements," *Proc. of the 2005 IEEE International Conference on Robotics and Automation*, Barcelona, Spain, April 2006.
- [4] Andrianesis, K., Tzes, A., "Design of an Anthropomorphic Prosthetic Hand Driven by Shape Memory Alloy Actuators," *Proceedings of the 2nd Biennial IEEE/RAS-EMBS International Conference on Biomedical Robotics and Biomechatronics*, Scottsdale, AZ, USA, October 19-22, 2008.
- [5] Dollar, A.M.,and Howe,R.D., "Joint coupling design of underactuated grippers", *Proc. of the ASME 2006 International Design Engineering Technical Conferences and Computers and Information in Engineering Conference*, September 10-13, 2006, Philadelphia, PA, USA.
- [6] Carrozza, M., Cappiello, G., Stellin, G., Zacccone, F., Vecchi, F., Micera, S., Dario, P., "A Cosmetic Prosthetic Hand with Tendon Driven Under- Actuated Mechanism and Compliant Joints: Ongoing Research and Preliminary Results," *Proc. of the 2005 IEEE International Conference on Robotics and Automation*, April 2005, Barcelona, Spain.
- [7] Vanderniepen, I., VanHam, R., VanDamme, M., Lefeber, D., "Design of a powered elbow orthosis for orthopaedic rehabilitation using compliant actuation," *Proc. of the 2nd Biennial IEEE/RAS- EMBS International Conference on Bimedical Robotics and Biomechatronics*, October 19-22, 2008, Scottsdale, AZ, USA.
- [8] Zollo, L., Roccella, S., Guglielmelli, E., Carrozza, M., Dario, P., "Biomechatronic Design and Control of an Anthropomorphic Artificial Hand for Prosthetic and Robotic Applications," *IEEE/ASME Transactions on Mechatronics*, Vol. 12, No. 4, August 2007.
- [9] Engeberg, E.D., Meek,S., "Improved Grasp Force Sensitivity for Prosthetic Hands Through Force-Derivative Feedback," *IEEE Transactions on Biomedical Engineering*, Vol. 55, No. 2, February 2008.
- [10] Cipriani, C., Zacccone, F., Micera,S., Carrozza,M., "On the Shared Control of an EMG-Controlled Prosthetic Hand: Analysis of User-Prosthesis Interaction," *IEEE Transactions on Robotics*, Vol. 24, No. 1, February 2008.
- [11] Chuan, Ch-W., and Lee, J.-J., "Topological Synthesis of Underactuated Passively Adaptive Finger Mechanisms", *13<sup>th</sup> World Congress in Mechanism and Machine Science*, Guajanato, Mexico, June 19-25, 2011.
- [12] Chalon, M., Grebenstein, M., and Hirzinger, G., "The thumb : guidelines for a robotic design", *IROS 2010*, pp. 5886-5893.
- [13] Grebenstein, M., Hirzinger, G., Siegart, "Antagonistically Driven Finger Design for the Anthropomorphic DLR Hand Arm System", *Humanoids 2010*, p. 609 - 616.
- [14] Ceccarelli, M., Nava Rodriguez, N.E., Carbone, G., "Design and tests of a three finger hand with 1-DOF articulated fingers", *Robotica*, 24:183-196, 2006.
- [15] Grebenstein, M., Chalon, M., Hirzinger, G., Siegart, R., "Seven Billion Perfect Hand Kinematics; A Kinematics Synthesis Method", *Int. Conf. on Applied Bionics and Biomechanics*, 2010.
- [16] Bicchi, A., "Hands for dexterous manipulation and robust grasping: a difficult road toward simplicity", *IEEE Transactions on Robotics and Automation*, 16(6):652-662, 2000.
- [17] A.M. Dollar and R. D. Howe, The SDM Hand: A highly adaptive compliant grasper for unstructured environments. *Internat. J. Rbfotics Research*, 2010.
- [18] L. Birglen T. Laliberte, and C. Gosselin. *Underactuated Robotic Hands*. Springer, 2008
- [19] S. Hirose and Yl Umetani, "The development of soft gripper for the versatile robot hand", *Mechanism and Machine theory*, 13:351-359, 1978.
- [20] Balasubramanian, R., Dollar, A.M., "Performance of Serial Underactuated Mechanisms: Number of Degrees of Freedom and Actuators", *2011 IEEE/RSJ International Conference on Intelligent Robots and Systems September 25-30, 2011*.
- [21] R.F. Chandler, D.E. Clauser, J. T. McMeonville, H. M. Reynolds, J. W. Young, "Investigation of inertial properties of the human hand", *U.S. Department of transportation, Report No. DOT HS-801 430*, pp. 72-79 March 1975.
- [22] C. Pylatiuk, S. Shulz, L. Doderlein, "Results of an Internet survey of myoelectric prosthetic hand users", *Prosthetics and Orthotics International* 2007, vol 31, No. 4. pp. 362-370, 2007.

## DETC2011/MECH-47818

### DESIGN OF NON-ANTHROPOMORPHIC ROBOTIC HANDS FOR ANTHROPOMORPHIC TASKS

**Edgar Simo-Serra**

Institut de Robòtica i Informàtica Ind.  
(CSIC-UPC)  
Llorens i Artigas, 4-6  
08028 Barcelona, Spain  
Email: esimo@iri.upc.edu

**Francesc Moreno-Noguer**

Institut de Robòtica i Informàtica Ind.  
(CSIC-UPC)  
Llorens i Artigas, 4-6  
08028 Barcelona, Spain  
Email: fmoreno@iri.upc.edu

**Alba Perez-Gracia\***

Institut de Robòtica i Informàtica Ind.  
(CSIC-UPC)  
Llorens i Artigas, 4-6  
08028 Barcelona, Spain  
And: College of Science and Engineering  
Idaho State University  
Pocatello, Idaho 83209  
Email: aperez@iri.upc.edu

#### ABSTRACT

*In this paper, we explore the idea of designing non-anthropomorphic multi-fingered robotic hands for tasks that replicate the motion of the human hand. Taking as input data a finite set of rigid-body positions for the five fingertips, we develop a method to perform dimensional synthesis for a kinematic chain with a tree structure, with five branches that share three common joints.*

*We state the forward kinematics equations of relative displacements for each serial chain expressed as dual quaternions, and solve for up to five chains simultaneously to reach a number of positions along the hand trajectory. This is done using a hybrid global numerical solver that integrates a genetic algorithm and a Levenberg-Marquardt local optimizer.*

*Although the number of candidate solutions in this problem is very high, the use of the genetic algorithm allows us to perform an exhaustive exploration of the solution space to obtain a set of solutions. We can then choose some of the solutions based on the specific task to perform. Note that these designs match the task exactly while generally having a finger design radically different from that of the human hand.*

#### NOMENCLATURE

- $b$  Number of kinematic chains branches.
- $n$  Number of joints.
- $m$  Number of end-effector positions for all branches considered.
- $\epsilon$  Dual unit such that  $\epsilon^2 = 0$ .
- $\mathbf{v}$  A vector.
- $\hat{Q}$  A dual quaternion.
- $S$  Plücker coordinates of a line:  $S = \mathbf{s} + \epsilon \mathbf{s}^0$

#### INTRODUCTION

There are many applications for which a robotic system is needed to work in human environments and to perform tasks that are designed for the human hand. In most cases, the solution adopted for grasping and manipulation consists of anthropomorphic robotic hands, which imitate to a certain extent the topology and joint location of the human hand. See [1] for a review of applications and concept definition.

It is difficult to match the complexity of the human hand, commonly accepted to have 26 degrees of freedom when counting the motion at the wrist and the pronation/supination of the forearm. The anthropomorphic design must include a complex mechanical system, actuation and sensing in a small space [2].

---

\*Address all correspondence to this author.

In order to reduce complexity, current designs limit the active degrees of freedom, through simplification of the mechanical structure or by designing underactuated hands. The design of simplified grippers limits the tasks of the robotic end-effector to some grasping and manipulation actions. Pairing these designs with some degree of underactuation and compliance, it is then possible to perform robust grasping of objects of unknown shape. Dollar and Howe [3] present a simplified, underactuated design for reliable grasping. Ciocarlie and Allen [4] optimize an underactuated, non-anthropomorphic gripper for performing a series of grasps from a database. A more thorough review on underactuated hands can be found in [5].

In order to perform some of the more complex functions of the human hand (not only grasping and manipulation, but also perception through surface exploration), it seems that an end-effector with several independently-actuated fingers may be needed. There are many examples of anthropomorphic robotic hands, see for instance [6] for a relatively recent review. However, for complex multi-fingered designs, it may not be necessary that the robotic fingers mimic those of the human hand in order to perform human-like tasks. We want to explore these alternative designs with the use of kinematic synthesis.

These alternate designs may have multiple applications. One possible usage is on the design of exoskeletons. These exoskeletons move the finger tips exactly like a human hand, while being able to be mounted on a hand without interfering with the hand's movement. Another application is the improvements of existing designs. Solutions can be chosen with additional criteria like equal distribution of joint velocities for a given task or location criteria for the joint axes. This can allow, for instance, designs optimized for particular actuators.

Kinematic design of robotic hands has focused on the design of individual motion of fingers or parts of the hand. Dai and Wang [7] use kinematic synthesis to design a spherical mechanism to act as the palm of a metamorphic hand. Van Varseveld and Bone [8] designed a finger mechanism for a non-anthropomorphic dexterous hand. Walker *et al.* [9] also design planar linkages for the fingers of a non-anthropomorphic, dexterous hand. Schafer and Dillman [10] present the kinematic design of a humanoid robotic wrist.

In this paper, we develop a method for the design of a full non-anthropomorphic multi-fingered robotic hand for tasks that replicate the motion of the human hand at the fingertips. Taking as input data a finite set of rigid-body positions for the human fingertips, we perform dimensional synthesis for a kinematic chain with a tree structure, with three common joints and five branches. As a whole, the process entails the simultaneous solution of up to five serial chains, two of them having four independent joints and three of them with five independent joints, plus three common joints for all of them. The total degrees of freedom of the non-anthropomorphic hand design is 26, similar to the human hand.

We state the forward kinematics equations of relative displacements for each serial chain expressed as dual quaternions, and solve for all five chains simultaneously to reach a number of positions along the hand trajectory. The synthesis of spatial serial chains for up to five degrees of freedom using this technique was developed in [11]. We use a similar methodology together with a hybrid global numeric solver, composed of a genetic algorithm paired with a Levenberg-Marquardt local optimizer. For the tree-like kinematic structure, a high number of positions can be defined to perform exact synthesis, obtaining a good approximation for the desired trajectory.

Finding the complete solution set for the synthesis of complex kinematic chains is an unsolved problem. Only dyads, such as the RR kinematic chain [12, 13], and some triads with particular characteristics [14], have been fully studied. Even the 3R kinematic chain has not been completely solved with a closed algebraic expression [15]. The complexity of a tree-like kinematic chain with a total of 26 revolute joints, and our numerical results, lead to believe that there will be a very large amount of solutions. This is an issue that has been found before even for simpler kinematic chains, see [14]. In order to deal with this, additional constraints may be added to help in the selection of the final design, depending on the task. We present two of the solutions for a hand task that was synthetically generated. The designs exactly match the task while having a finger design radically different from that of the human hand.

## KINEMATIC HAND MODEL

The human hand has 5 fingers formed by 14 joints. These joints are created at the contact surface of the 27 major bones forming the hand. The joints do not exactly match the motion of a classical lower pair, and some of them present more than one degree of freedom. However, they can be modeled fairly precisely using only simple revolute kinematic joints. The axes of these revolute joints do not necessarily have to intersect within the same joint.

The full hand can be modeled using a total of 26 joints if we consider the wrist and the pronation/supination of the forearm to be formed by 3 revolute joints. The index and middle finger have 4 revolute joints, while the third, fourth and thumb have 5 revolute joints. The dimensions are taken from the literature [16, 17]. The skeleton can be represented by drawing the common normals of the joint axes as shown in Fig. 1.

## Hand Task Generation

The task is defined as a series of finite positions (locations and orientations) for each finger tip, created by assigning a set of joint variables to the kinematic model. The range of motion of each joint varies greatly among the population and it is therefore impossible to assign a precise range to each joint. In this paper,



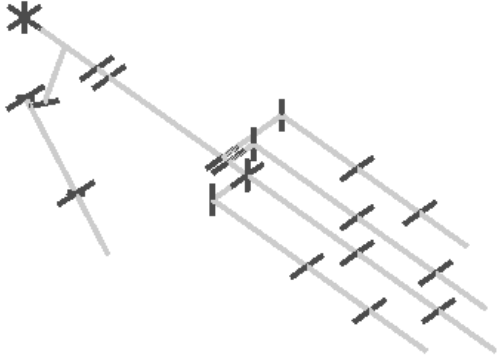


**FIGURE 1:** HAND SKELETON USED TO GENERATE POSITIONS.

**TABLE 1:** JOINT ANGLES USED TO GENERATE THE TRAJECTORY.

Chain	Hand task revolute joint limits $[\theta_{min}-\theta_{max}]$
Common	$[-90^\circ, 90^\circ], [-90^\circ, 90^\circ], [-90^\circ, 90^\circ]$
Index	$[-10^\circ, 90^\circ], [-10^\circ, 10^\circ], [0^\circ, 100^\circ], [0^\circ, 90^\circ]$
Middle	$[-10^\circ, 90^\circ], [-10^\circ, 10^\circ], [0^\circ, 100^\circ], [0^\circ, 90^\circ]$
Third	$[-10^\circ, 10^\circ], [0^\circ, 20^\circ], [-10^\circ, 10^\circ], [0^\circ, 100^\circ], [0^\circ, 90^\circ]$
Fourth	$[-10^\circ, 10^\circ], [0^\circ, 20^\circ], [-10^\circ, 10^\circ], [0^\circ, 100^\circ], [0^\circ, 90^\circ]$
Thumb	$[-25^\circ, 25^\circ], [-25^\circ, 25^\circ], [-10^\circ, 10^\circ], [0^\circ, 70^\circ], [-10^\circ, 85^\circ]$

we will evaluate our solver using synthetically generated trajectories. These trajectories are generated from random positions within the joint angle ranges defined in Table 1 to simplify the convergence of the solver.

## KINEMATIC SYNTHESIS

The goal of the dimensional kinematic synthesis is to find the location and orientation of a set of joint axes able to perform a given motion, where the number and type of joints are pre-defined. This is also known as the motion-to-form problem in which we are given a motion, defined by a sequence of end-effector positions, as an input and must calculate the form as a set of joints and angles that can perform the motion. In this paper, we follow the original idea of [18] of using the forward kinematics equations of the kinematic chain, but formulated as relative

displacements and expressed as dual quaternions, see [11] for a complete description of this approach.

The input data for the synthesis are the  $m - 1$  relative transformations  $\hat{P}_{1j} = \cos \frac{\Delta\hat{\theta}_{1j}}{2} + \sin \frac{\Delta\hat{\theta}_{1j}}{2} P_{1j}$ ,  $j = 2, \dots, m$ , defining the task; the output are the Plücker coordinates  $S_i = \mathbf{s}_i + \varepsilon \mathbf{s}_i^0 = \mathbf{s}_i + \varepsilon \mathbf{c}_i \times \mathbf{s}_i$ ,  $i = 1, \dots, n$ , of the  $n$  joints that define the kinematic chain at a reference configuration, and also the  $j = 2, \dots, m$  sets of joint variables  $\Delta\hat{\theta}_j = \theta_{1j} - \theta_{11} + \varepsilon(d_{1j} - d_{11})$ ,  $i = 1, \dots, n$ , used to reach the task positions, measured from the reference configuration  $\hat{\theta}_1 = \theta_{11} + \varepsilon d_{11}$ ,  $i = 1, \dots, n$ .

## Forward Kinematics

We can represent each individual branch of a tree-like topology as an individual kinematic serial chain, which shares a number of joints with other branches. Given a kinematic serial chain with  $n$  joints, we can write the kinematics equations using the product of exponentials of the screws corresponding to the joint axes, as described in [19]. In this paper, instead of calculating the exponentials using matrix algebra, we do the exponentials for the Clifford even subalgebra of the projective space, in which the unit elements, also known as dual quaternions, express spatial displacements. The exponential of a screw represented by the Clifford algebra element  $J = (1 + \mu\varepsilon)S$  of axis  $S$ , where  $\mu$  is the pitch relating the slide  $d$  and the rotation  $\theta$  along and about the screw, yields a finite displacement,

$$e^{\frac{\theta}{2}J} = \left(\cos \frac{\theta}{2} - \frac{d}{2} \sin \frac{\theta}{2} \varepsilon\right) + \left(\sin \frac{\theta}{2} + \frac{d}{2} \cos \frac{\theta}{2} \varepsilon\right) S \\ = \cos \frac{\hat{\theta}}{2} + \sin \frac{\hat{\theta}}{2} S. \quad (1)$$

For a serial chain with  $n$  joints, in which each joint can rotate an angle  $\theta_i$  and slide a distance  $d_i$ , around and along the axis  $S_i$ ,  $i = 1, \dots, n$ , we calculate the forward kinematics of relative displacements (with respect to an arbitrary reference configuration),

$$\hat{Q}(\Delta\hat{\theta}) = e^{\frac{\Delta\hat{\theta}_1}{2} S_1} e^{\frac{\Delta\hat{\theta}_2}{2} S_2} \dots e^{\frac{\Delta\hat{\theta}_n}{2} S_n} \\ = \left(\cos \frac{\Delta\hat{\theta}_1}{2} + \sin \frac{\Delta\hat{\theta}_1}{2} S_1\right) \dots \left(\cos \frac{\Delta\hat{\theta}_n}{2} + \sin \frac{\Delta\hat{\theta}_n}{2} S_n\right), \quad (2)$$

where  $\Delta\hat{\theta} = \theta_j - \theta_1 + \varepsilon(\mathbf{d}_j - \mathbf{d}_1)$  contains the joint variables, as relative values with respect to the joint parameters of the chain  $\theta_1$  and  $\mathbf{d}_1$  when in the reference configuration.

## Synthesis Design Equations

The dimensioning of the articulated system has to be done so that the forward kinematics equations in Eqn. (2) can reach all

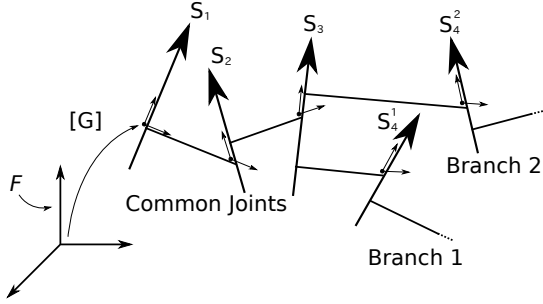


FIGURE 2: TOPOLOGY OF THE KINEMATIC CHAIN.

the desired task positions  $\hat{P}_{1j}$ ,

$$\hat{P}_{1j} = e^{\frac{\Delta\hat{\theta}_{1j}}{2}S_1} e^{\frac{\Delta\hat{\theta}_{2j}}{2}S_2} \dots e^{\frac{\Delta\hat{\theta}_{nj}}{2}S_n}, \quad j = 2, \dots, m \quad (3)$$

where  $j = 1$  is reserved for the reference configuration.

This results in  $8(m-1)$  design equations, considering the fact that we are using dual quaternions which have 8 components. The design variables that determine the dimensions of the chain are the  $n$  joint axes  $S_i$ ,  $i = 1, \dots, n$ , in the reference configuration. In addition, the equations contain the  $n(m-1)$  pairs of joint parameters  $\Delta\hat{\theta}_{ij} = \Delta\theta_{ij} + \varepsilon\Delta d_{ij}$ , which are also unknown.

## NON-ANTHROPOMORPHIC HAND SYNTHESIS

In this paper, we are interested in the synthesis of robotic grippers for human-hand tasks. We do not impose any explicit limitation on the link dimensions or placement. The resulting design should be able to perform a given human-hand task while having a non-anthropomorphic aspect.

### System Topology

As input topology, we define a tree-like kinematic chain with three common joints in series at the base, connected to five serial chains arranged in parallel, two of them with four degrees of freedom and three of them with five degrees of freedom. This structure follows the generally accepted joint arrangement of the human hand plus the wrist motion. Figure 2 shows the topology of the kinematic chain to be synthesized.

Note that, to our knowledge, no previous approach has addressed the synthesis of tree-like structures. In addition, tree topologies can also be used to represent pure serial topologies, when there is only one branch, and loop topologies, when end-effectors of multiple branches are placed at the same position.

### Design Equations

We state the design equations by adapting Eqn. (3) to our particular topology. For each one of the serial chains in the parallel arrangement we state a set of design equations, to obtain the total system of equations

$$\begin{aligned} \hat{P}_{1j}^k &= e^{\frac{\Delta\hat{\theta}_{1j}}{2}S_1} e^{\frac{\Delta\hat{\theta}_{2j}}{2}S_2} e^{\frac{\Delta\hat{\theta}_{3j}}{2}S_3} e^{\frac{\Delta\hat{\theta}_{4j}^k}{2}S_4^k} \dots e^{\frac{\Delta\hat{\theta}_{7j}^k}{2}S_7^k}, \quad k \in \{1, 2\}, \\ \hat{P}_{1j}^k &= \underbrace{e^{\frac{\Delta\hat{\theta}_{1j}}{2}S_1} e^{\frac{\Delta\hat{\theta}_{2j}}{2}S_2} e^{\frac{\Delta\hat{\theta}_{3j}}{2}S_3}}_{\text{common}} \underbrace{e^{\frac{\Delta\hat{\theta}_{4j}^k}{2}S_4^k} \dots e^{\frac{\Delta\hat{\theta}_{8j}^k}{2}S_8^k}}_{\text{individual}}, \quad k \in \{3, 4, 5\}, \\ &\quad j = 2, \dots, m. \end{aligned} \quad (4)$$

Here  $k$  identifies the kinematic chain and  $j = 2, \dots, m$  is the index of the task position. The fingers are denoted by: index,  $k = 1$ ; middle,  $k = 2$ ; third,  $k = 3$ ; fourth,  $k = 4$  and thumb,  $k = 5$ .

Each of the five serial chains, taken individually, has a total of seven or eight degrees of freedom, depending on the finger it corresponds to. Even though the exact dimensional synthesis does not apply to serial chains with six or more degrees of freedom, by having three common degrees of freedom we are able to state the design equations of the system as a whole.

Notice that even though each individual finger has more than six degrees of freedom, the tree-like architecture is not kinematically redundant when defining the motion of several branches at the same time.

### KINEMATIC SOLVER

In order to deal with the large system of equations presented in the previous section, the selected solver aims to minimize the error in Eqn. (4) for each kinematic chain. In principle, problems with selection of the metric does not apply to this case, as we are targeting exact synthesis.

The objective of the solver is to perform general inverse kinematics, that is, adjust both joint angles and joint axes to follow a motion. However, by making the joint axes constant it can also perform inverse kinematics.

### Objective Functions

Given a vector  $v = \{4, 4, 5, 5, 5\}$  with the number of independent joints for each finger, the design equations from Eqn. (4) can be written as a set of unconstrained functions,

$$\hat{F}_j^k(\mathbf{S}^k, \Delta\hat{\theta}_j^k) = \underbrace{\prod_{i=1}^3 e^{\frac{\Delta\hat{\theta}_{ij}}{2}S_i}}_{\text{common}} \underbrace{\prod_{i=4}^{3+v_k} e^{\frac{\Delta\hat{\theta}_{ij}^k}{2}S_i^k}}_{\text{individual}} - \hat{P}_{1j}^k, \quad \begin{matrix} j = 2, \dots, m \\ k = 1, \dots, 5 \end{matrix} \quad (5)$$

where we can separate the product of the common joints from the individual joints that belong to each branch.

The global objective of the solver is to solve the design equations defined in Eqn. (4). This can be written as,

$$\sum_{j=2}^m \sum_{k=1}^5 |\hat{F}_j^k(\mathbf{S}^k, \Delta \hat{\theta}_j^k)| = 0 \quad (6)$$

In order to avoid falling into local minima we will use a hybrid solver composed of both a genetic algorithm and a Levenberg-Marquadt optimizer.

Genetic algorithms behave better with defined positive maximization objective functions. We can convert Eqn. (6) to a minimization function and invert it to obtain,

$$\underset{\mathbf{S}, \Delta \hat{\theta}}{\text{maximize}} \quad \left( \sum_{j=2}^m \sum_{k=1}^5 |\hat{F}_j^k(\mathbf{S}^k, \Delta \hat{\theta}_j^k)| \right)^{-1} \quad (7)$$

which we can see is defined positive if the domain of Eqn. (5) is finite. This single function is also known as the fitness function.

For the Levenberg-Marquadt local optimizer we use the minimizing least squares objective function,

$$\underset{\mathbf{S}, \Delta \hat{\theta}}{\text{minimize}} \quad \sum_{j=2}^m \sum_{k=1}^5 \hat{F}_j^k(\mathbf{S}^k, \Delta \hat{\theta}_j^k)^2 \quad (8)$$

## Dimension of the Equation Set

The equations and variables in the objective functions Eqn. (5) are not all linearly independent. The equations are formed by unit dual quaternions  $\hat{Q} = \hat{q} + \varepsilon \hat{q}^0$  which have a dimension of eight, but are subject to the two implicit constraints  $\hat{q}\hat{q}^* = 1$  and  $\hat{q} \cdot \hat{q}^0 = 0$ , which reduce the independent dimension of the dual quaternion to 6. Similarly, only four of the six Plücker components of each line are independent as they are subject to the two implicit constraints  $\|\mathbf{s}\| = 1$  and  $\mathbf{s} \cdot \mathbf{s}^0 = 0$ . The number of variables  $x$  and independent variables  $x^0$  can be written as,

$$\begin{aligned} x &= n(6 + (m - 1)) \\ x^0 &= n(4 + (m - 1)) \end{aligned} \quad (9)$$

The number of equations  $f$  and independent equations  $f^0$  can be written as,

$$\begin{aligned} f &= 8b(m - 1) \\ f^0 &= 6b(m - 1) \end{aligned} \quad (10)$$

An important question remaining is how many task positions  $m$  are required for the system to have a finite number of solutions, see [20] for details. This can be obtained by imposing  $f^0 = x^0$  and solving to obtain,

$$m = \frac{4n}{6b - n} + 1 \quad (11)$$

The number of task positions obtained is the amount needed to have a finite solution for non-degenerate tree topologies. Non-degenerate tree topologies are those where no kinematic chain segment, that is the smallest kinematic serial chain from an end-effector to a fork or from the origin to a fork, has fewer than 6 degrees-of-freedom and that no serial chain from the origin to an end effector has fewer joints than the largest kinematic chain segment from a fork to an end-effector. Degenerate tree topologies have redundant equations and thus Eqn. (10) is no longer valid.

More task positions can be provided although this over-determines the system. If the system is overdetermined by task positions from the same workspace it will still have solutions, otherwise an exact match will generally not exist. Overdetermined systems can lead to problems of convergence and much slower performance.

Applying Eqn. (11) to our model with  $b = 5$  branches and  $n = 26$  revolute joints, three of them being shared by all the branches, we obtain that we can solve exactly for a task defined by  $m = 27$  finite positions for each finger. This gives a total of 156 structural parameters and 676 joint variables for our set of equation.

## Solver Implementation

Note that the complexity of the problem that we are trying to solve is especially challenging. However, the use of Clifford algebra allows reducing the number of equations and variables, compared to a matrix-based approach. In particular, we represent the entire equation system with only 832 input variables between both structural and joint variables. This is a reduction of 33% in the number of variables compared to using homogeneous matrix, only considering the 3x4 submatrix containing the rotation and translation information.

Genetic algorithms have already been used in many kinematic problems [21, 22]. The genetic algorithm performs an exhaustive exploration of the solution space in order find a solution.



However, due to complexity of the system a pure genetic algorithm would have convergence problems past a certain fitness. This problem was overcome by reducing the solution space used by the genetic algorithm to only the local minima. This converts the solution space from a continuous domain to a discrete finite domain that improves the behaviour of the genetic algorithm. The local minima are found by a Levenberg-Marquardt optimizer.

The genetic algorithm chromosomes consist of sets of variables that belong to the full solution space. After being generated they are then converged to a local minima. This local optimization is also computed when chromosomes are crossed or mutated to ensure each chromosome always represents a local minima of the search space.

The fitness is calculated as the inverse of the sum of the error as seen in Eqn. (7). This makes the fitness a continuous positive function, which allows the usage of roulette-wheel selection when choosing pairs from the genetic algorithm population to crossover. It also converts the genetic algorithm to a maximization problem. The crossover rate is kept low to encourage diversity in the population, since the strong convergence is provided by the Levenberg-Marquardt optimizer.

To avoid explicit constraints the chromosomes are generated in the proximity of the ideal kinematic solution. This plays the role of a soft limit for the possible shapes of the robotic hand. However, it is not unusual for the Levenberg-Marquardt minimizer to move far from the generation space and find extremely non-anthropomorphic solutions.

The solver is executed until the fitness surpasses the value of  $10^{10}$  at which it is considered to have arrived to a solution. The error is attributed to the imprecision in the computer representation of real numbers.

### Kinematic Subsystems

It is worth noting that it is possible to solve a subsystem of the full kinematic chain tree. These subsystems are independently solvable as long as they have a finite number of task positions  $m$  needed for a finite number of solutions. To have  $m \in \mathbb{Q}^+$  the subsystem must satisfy the following inequality,

$$6b - r > 0 \quad (12)$$

which is obtained from imposing  $m > 0$  in Eqn. (11). Table 2 shows all the possible subsystems of the hand model that can be solved.

The most interesting configurations to solve are the 5 kinematic chains at once, to minimize the needed positions, and the configuration with only two 4R branches to reduce the amount of variables needed. The two 4R branches are the index and middle

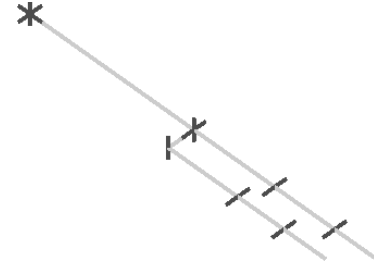


**FIGURE 3: TOPOLOGY OF THE SOLVABLE (4R, 4R) FINGERS SUBSYSTEM.**

**TABLE 2: SOLVABLE SYSTEMS OF EQUATIONS FOR DIFFERENT COMBINATIONS OF CHAINS.**

$b$	$r$	$x$	$f$	$m$	Notes
5	26	832	1092	27	Full model
4	22	1100	1452	45	(5R, 5R, 5R, 4R) fingers
4	21	714	938	29	(5R, 5R, 4R, 4R) fingers
3	17	1258	1666	69	(5R, 5R, 4R) fingers
3	16	608	800	33	(5R, 4R, 4R) fingers
2	11	550	726	45	(4R, 4R) fingers
1	5	130	170	21	5R finger, common solved
1	4	56	72	9	4R finger, common solved

fingers and can be seen in Fig. 3. Afterwards, the remaining fingers can be solved individually as the common revolute joints are now identified. There are also other systems that can be solved that are a compromise between the number of positions and the number of variables needed.

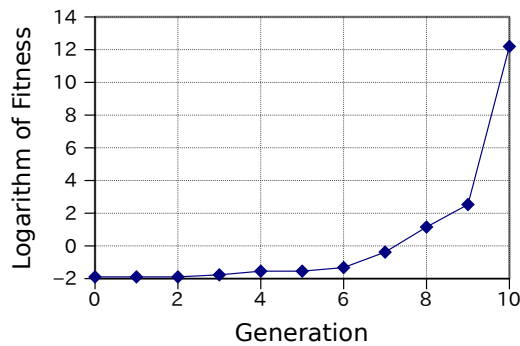
### RESULTS

It is very important for the solver to converge that the end-effector positions, for all branches describing the task, do not follow an equation for the movement. This can lead to implicit equations that can lower the dimension of the system so that Eqn. (11) no longer guarantees a finite number of solutions. It is also important for the difference between end-effector positions to be large to aid in the solver convergence, and that all the joints present movement in the generated task.

The algorithm presented in this paper has a parallel nature and can be adjusted to run on supercomputers or other distributed computing systems to increase the calculation speed. This is due to the nature of the genetic algorithm which forms part of the

**TABLE 3: SOLVER EXECUTION INFORMATION.**

Solution	Generations	Time (hours)
1	13	20.8
2	5	20.5
3	10	16.5
4	12	85.0

**FIGURE 4: CONVERGENCE OF A SOLVER EXECUTION.**

hybrid solver presented.

We have obtained best results when using a population size of 100 for the genetic algorithm. This is much lower than what would be expected to be needed for a pure genetic algorithm for an equation system of this size. The crossover rate was set at 0.2 while the mutation rate was set extremely high at 0.5. This is due to the fact that our hybrid solver uses a Levenberg-Marquadt optimizer which provides the strong convergence. Therefore the genetic algorithm must explore as much of the solution space as possible and not focus on local convergence.

Runtime information can be found in Table 3 for the various solutions found. These results were obtained on an Intel® Core™ i7-870 CPU running at 2.93 GHz. The solver was using all 4 cores of the CPU by using 5 threads for the local optimization of the chromosomes, which is the slowest part of the algorithm. An example of the solver's converge can be seen in Fig. 4.

We present two example solutions that can be seen in Fig. 5 and Fig. 6. The non-anthropomorphic solutions are rendered on top of the anthropomorphic skeleton used to generate the data, and both are drawn as joint axes linked along their common normal lines. The anthropomorphic skeleton is represented by thick gray lines while the non-anthropomorphic solution is represented using thinner green lines.

## CONCLUSIONS

In this paper we have presented a method for the kinematic synthesis of tree-like articulated systems, with an application in the design of a robot to perform human-hand tasks. To our knowledge this is the first time kinematic synthesis has been applied to tree topologies. This methodology allows obtaining non-anthropomorphic designs that can perform an anthropomorphic finite-position task exactly, while having a very different joint distribution and motion. These designs have applications in exoskeleton design, as they could be mounted on the hand without physically interfering with it.

The presented methodology is not limited to anthropomorphic tasks and hand models. It can be applied to generic serial, loop and tree topologies of articulated systems, making the solver a powerful tool.

Our hybrid solver has managed to successfully find solutions to kinematic synthesis problems much larger than previously considered. This has been accomplished by using Clifford algebra to provide a more compact system of equations that is then solved by the application of both meta-heuristics and classical math optimization.

From the dimensional synthesis point of view, an interesting result is that, due to the tree structure, we can perform exact synthesis for general serial chains with more than five degrees of freedom. We may conclude from this that, despite common believe that the human wrist/hand is a redundant mechanical system, it may not be so when we consider a task in which several fingers must act.

The dimensional synthesis for articulated systems like the one presented here, with a high number of joints, yields many solutions. A good selection process is required in order to choose a solution from the pool of candidates. For instance, for the application presented in this paper, additional constraints could be imposed either in the solving process or in the post-processing phase in order to find a suitable design. Among others, we can cite size or location restrictions for exoskeletons mounted on the human hand, or dexterity conditions at given configurations for manipulation in human environments. Future work will take into consideration possible link collisions that may be present in some of the solutions of the kinematic synthesis.

In order for the designs to be able to perform realistic human tasks, not only fingertip positions, but also fingertip forces and infinitesimal motion need to be considered. Future work will focus on including task velocities and accelerations in order to define grasping actions.

## ACKNOWLEDGMENT

This work is partially supported by the Spanish Ministry of Science and Innovation under projects DPI2010-18449, Consolider Ingenio 2010 CSD2007-00018, and a Ramon y Cajal

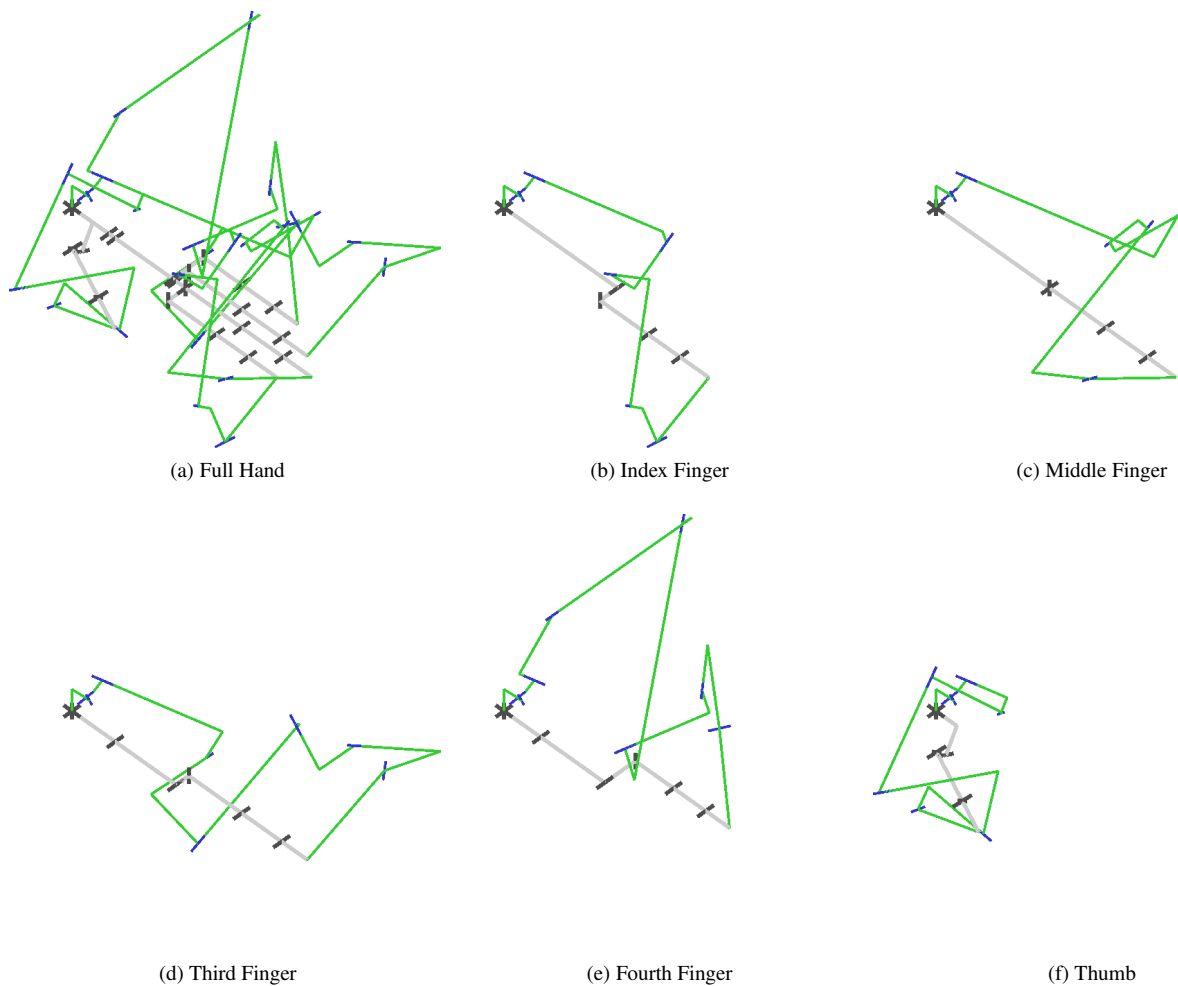


**FIGURE 5: OVERVIEW OF A SOLUTION FOUND.**

Research Fellowship. Also by the EU project GARNICS FP7-247947.

## REFERENCES

- [1] Siciliano, B., and Khatib, O., 2008. *Handbook of Robotics*. Springer, Berlin.
- [2] Soto Martell, J., and Gini, G., 2007. "Robotic hands: Design review and proposal of new design process". *World Academy of Science, Engineering and Technology*, **26**.
- [3] Dollar, A., and Howe, R., 2007. "Simple, robust autonomous grasping in unstructured environments". In Proc. of the 2007 International Conference on Robotics and Automation, pp. 4693–4700.
- [4] Ciocarlie, A., and Allen, P., 2010. "Data-driven optimization for underactuated robotic hands". In Proc. of the 2010 International Conference on Robotics and Automation, pp. 1292–1299.
- [5] Briglen, L., Laliberte, T., and Gosselin, C., 2008. *Under-actuated Robotic Hands*. Springer.
- [6] Biagiotti, L., Lotti, F., Melchiorri, C., and Vassura, G., 2004. How far is the human hand? a review of anthropomorphic robotic end-effectors. internal report. Tech. rep., Universita di Bologna.
- [7] Dai, J., and Wang, D., 2007. "Geometric analysis and synthesis of the metamorphic robotic hand". *ASME Journal of Mechanical Design*, **129**, pp. 1191–1197.
- [8] van Varseveld, R., and Bone, G., 1999. "Design and implementation of a lightweight, large workspace non-anthropomorphic dexterous hand". *ASME Journal of Mechanical Design*, **121**.
- [9] Ramos, A., Gravagne, I., and Walker, I., 1999. "Goldfin-

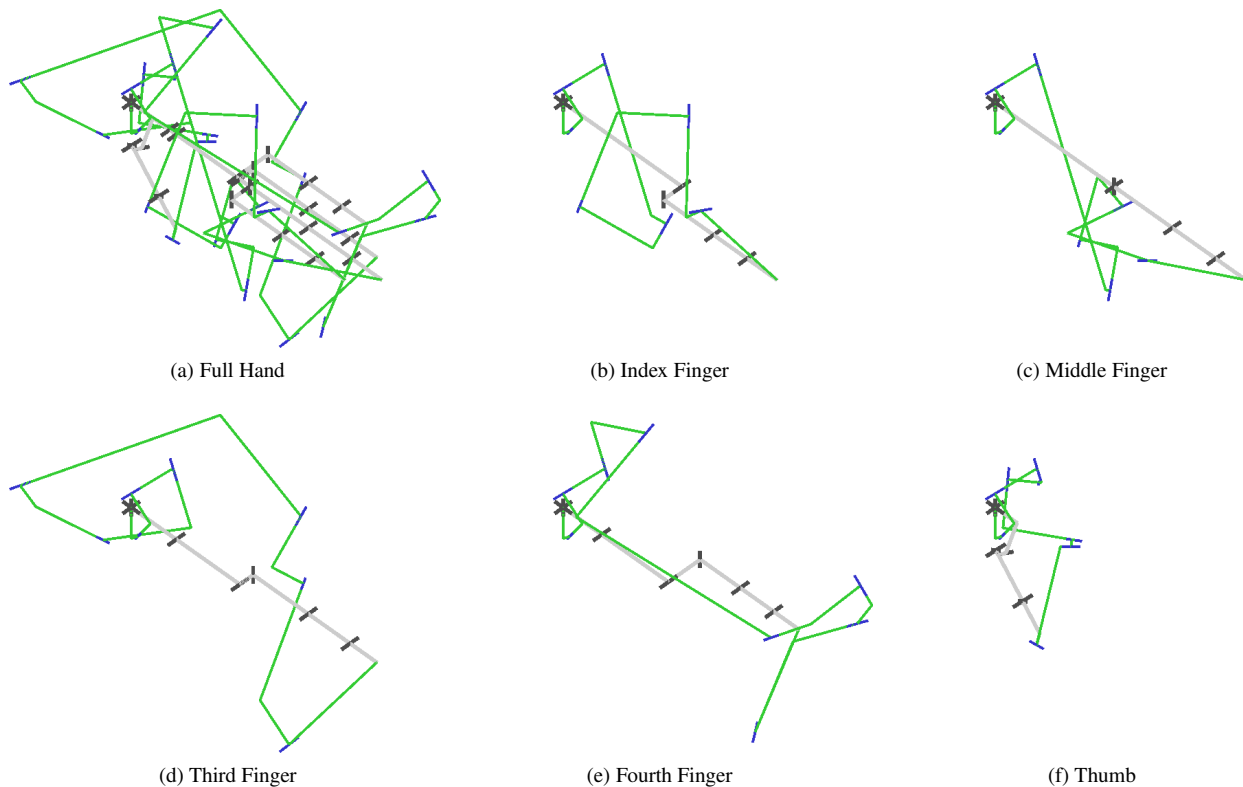


**FIGURE 6: OVERVIEW OF A SECOND SOLUTION FOUND.**

- ger: A non-anthropomorphic, dextrous robot hand". In Proceedings of the 1999 IEEE International Conference on Robotics and Automation.
- [10] Schaffer, C., and Dillmann, R., 2001. "Kinematic design of a humanoid robot wrist". *Journal of Robotic Systems*, **18**(12), pp. 747–754.
- [11] Perez Gracia, A., and McCarthy, J. M., 2006. "The kinematic synthesis of spatial serial chains using clifford algebra exponentials". *Proceedings of the Institution of Mechanical Engineers, Part C, Journal of Mechanical Engineering Science*, **220**(7), pp. 953–968.
- [12] Perez, A., and McCarthy, J. M., 2003. "Dimensional synthesis of bennett linkages". *ASME Journal of Mechanical Design*, **125**(1), pp. 98–104.
- [13] Brunthaler, K., 2006. "Synthesis of 4r linkages using kinematic mapping". PhD thesis, Institute for Basic Sciences and Engineering, University of Innsbruck, Innsbruck, Austria.
- [14] Su, H., McCarthy, J. M., and Watson, L. T., 2004. "Generalized linear product homotopy algorithms and the computation of reachable surfaces". *ASME Journal of Computers and Information Science and Engineering*, **4**(3), pp. 226–235.
- [15] Lee, E., Mavroidis, C., and Merlet, J. P., 2004. "Five precision point synthesis of spatial rrr manipulators using interval analysis". *ASME Journal of Mechanical Design*, **126**(5), pp. 842–850.
- [16] Fadi J. Bejjani, J. M. F. L., 1989. *Basic Biomechanics of the Musculoskeletal System*. Lea & Febiger, ch. Biomechanics of the hand, pp. 275–304.
- [17] Chang, L., and Matsuoka, Y., 2006. "A kinematic thumb model for the act hand". In Robotics and Automation, 2006. ICRA 2006. Proceedings 2006 IEEE International Conference on, pp. 1000–1005.
- [18] Lee, E., and Mavroidis, C., 2002. "Solving the geometric design problem of spatial 3r robot manipulators using polynomial homotopy continuation". *ASME Journal of Mechanical Design*, **124**(4), pp. 652–661.
- [19] Murray, R. M., Li, Z., and Sastry, S. S., 1994. *A Mathematical Introduction to Robotic Manipulation*. CRC Press, Inc., Boca Raton, FL.
- [20] Perez, A., and McCarthy, J. M., 2004. "Dual quaternion synthesis of constrained robotic systems". *ASME Journal of Mechanical Design*, **126**(3), pp. 425–435.

- [21] Chocron, O., and Bidaud, P., 1997. “Evolutionary algorithms in kinematic design of robotic systems”. In Intelligent Robots and Systems, 1997. IROS '97., Proceedings of the 1997 IEEE/RSJ International Conference on, Vol. 2, pp. 1111 –1117 vol.2.
- [22] Yang, Y., Peng, G., Wang, Y., and Zhang, H., 2007. “A new solution for inverse kinematics of 7-dof manipulator based on genetic algorithm”. In Automation and Logistics, 2007 IEEE International Conference on, pp. 1947 –1951.

# Treatment of human astrocytoma U87 cells with silicon dioxide nanoparticles lowers their survival and alters their expression of mitochondrial and cell signaling proteins

James CK Lai<sup>1</sup>  
Gayathri Ananthakrishnan<sup>1,2</sup>  
Sirisha Jandhyam<sup>1</sup>  
Vikas V Dukhande<sup>1</sup>  
Alok Bhushan<sup>1</sup>  
Mugdha Gokhale<sup>1</sup>  
Christopher K Daniels<sup>1</sup>  
Solomon W Leung<sup>3</sup>

<sup>1</sup>Department of Biomedical and Pharmaceutical Sciences, College of Pharmacy and Biomedical Research Institute, <sup>2</sup>Department of Health and Nutrition Sciences, Kasiska College of Health Professions, <sup>3</sup>Department of Civil and Environmental Engineering, College of Engineering and Biomedical Research Institute, Idaho State University, Pocatello, ID, USA

Correspondence: Solomon W Leung  
Department of Civil and Environmental Engineering, College of Engineering and Biomedical Research Institute, Idaho State University, Pocatello, ID, USA  
Email leunsolo@isu.edu

**Abstract:** Recent evidence suggests silicon dioxide micro- and nanoparticles induce cytotoxic effects on lung cells. Thus, there is an increasing concern regarding their potential health hazard. Nevertheless, the putative toxicity of nanoparticles in mammalian cells has not yet been systematically investigated. We previously noted that several metallic oxide nanoparticles exert differential cytotoxic effects on human neural and nonneural cells. Therefore, we hypothesized that silicon dioxide nanoparticles induce cytotoxicity in U87 cells by lowering their survival by decreasing cell survival signaling and disturbing mitochondrial function. To investigate this hypothesis, we determined the activities of the key mitochondrial enzymes, citrate synthase and malate dehydrogenase, in astrocytoma U87 cells treated with silicon dioxide nanoparticles. In addition, we studied the expression of the mitochondrial DNA-encoded proteins, cytochrome C oxidase II and nicotinamide adenine dinucleotide (NADPH) dehydrogenase subunit 6, and cell signaling pathway protein extracellular signal-regulated kinase (ERK) and phosphorylated ERK in treated U87 cells. The activated form of ERK controls cell growth, differentiation, and proliferation. In parallel, we determined survival of U87 cells after treating them with various concentrations of silicon dioxide nanoparticles. Our results indicated that treatment with silicon dioxide nanoparticles induced decreases in U87 cell survival in a dose-related manner. The activities of citrate synthase and malate dehydrogenase in treated U87 cells were increased, possibly due to an energetic compensation in surviving cells. However, the expression of mitochondrial DNA-encoded cytochrome C oxidase subunit II and NADH dehydrogenase subunit 6 and the cell signaling protein ERK and phosphorylated ERK were altered in the treated U87 cells, suggesting that silicon dioxide nanoparticles induced disruption of mitochondrial DNA-encoded protein expression, leading to decreased mitochondrial energy production and decreased cell survival/proliferation signaling. Thus, our results strongly suggest that the cytotoxicity of silicon dioxide nanoparticles in human neural cells implicates altered mitochondrial function and cell survival/proliferation signaling.

**Keywords:** cytotoxicity, silicon dioxide nanoparticles, mitochondrial enzyme, extracellular signaling regulated kinase, cell signaling, neural cells

## Introduction

According to the Environmental Protection Agency, exposure to nanomaterials can occur during the manufacturing or production process, and also has the potential to pollute the environment,<sup>1</sup> in this case the occupational environment. A case in point is exposure to silicon dioxide nanoparticles because silicon dioxide, including a range of its particle sizes, is being used in cosmetics, food,<sup>2</sup> and drug formulations.<sup>3</sup>

In general, silicon dioxide is viewed as a nontoxic substance and its industrial applications are numerous.<sup>2–4</sup> Nevertheless, there have been reports, at least in the last two decades, that silicon dioxide particles are not as harmless as they were previously assumed to be.

When the size of silicon dioxide is above the micrometer scale (ie,  $>1\ \mu\text{m}$ ), it appears to be benign to human, insects, and microorganisms. However, diatomaceous earth, which contains more than 85% of amorphous silicon dioxide, is used as insecticide in dust form,<sup>4</sup> but its toxicity to insects is not well defined. When the size of silicon dioxide is in the micrometer scale and below, several toxic effects have been observed in humans and animals. Most noticeable is the disease of silicosis in humans,<sup>5</sup> resulting from prolonged exposure to crystalline silica dust, and similar symptoms have also been reported in rats.<sup>5</sup> Thus far, silicon dioxide toxicity reports have been almost exclusively on particle sizes at the micrometer scale, and mostly concerning pulmonary injuries or lung inflammation.<sup>5,6</sup> Few studies have been conducted on silicon dioxide at the nanometer scale,<sup>5,6</sup> and even fewer studies so far reported have been conducted with human cells.

In macroscopic sizes, silicon dioxide is not known to be cytotoxic.<sup>2,3,5,6</sup> However, a recent study demonstrated that exposure of amorphous spherical silicon dioxide nanoparticles of different sizes induced decreases in viability of human endothelial cells, an expression of their cytotoxicity which was apparently dependent on their particle size.<sup>7</sup> Nevertheless, few, if any, studies have examined the putative cytotoxic effects of silicon dioxide nanoparticles on human neural cells.

There was an early study indicating that silica particles (in the micrometer and nanometer ranges) when introduced into the brains of rats and mice induced an inflammatory response in brain astrocytes and macrophages, and the degeneration of some adjacent axons and axon terminals, as elucidated by light and electron microscopy.<sup>8</sup> Furthermore, silicon and aluminum were found to be co-localized in the central region of senile plaque cores in the cortex of patients with senile dementia of the Alzheimer type,<sup>9</sup> and the accumulated silicon and aluminum appeared to be localized, at least in part, in lipofuscin granules in the brains of patients who died with Alzheimer's disease.<sup>10</sup> Consequently, these early studies<sup>8–10</sup> suggest that silicon dioxide nanoparticles may exert cytotoxic effects on neural cells.

We recently found that exposure to titanium dioxide and two other metallic oxide (namely, ZnO and MgO) nanoparticles induced differential cytotoxicity on human neural cells.<sup>11</sup> Because of our recent findings<sup>11</sup> and the increasing evidence that a variety of nanoparticles (including silicon

dioxide-containing nanoparticles) can cross the blood–brain barrier,<sup>12,13</sup> we initiated this study to investigate the putative cytotoxic effect(s) of silicon dioxide nanoparticles on human neural cells. In particular, we focused on investigation of the putative cytotoxic effects of these nanoparticles on mitochondrial function and survival cell signaling in human astrocytoma U87 cells that are astrocyte-like in view of the fact that they are good models of astrocytes normally found in the brain *in vivo*<sup>14,15</sup> and that astrocytes in the brain are functionally coupled to endothelial cells and hence the functions of the blood–brain barrier.<sup>16,17</sup>

Because of the aforementioned considerations, we hypothesized that silicon dioxide nanoparticles induce cytotoxicity in U87 cells by disturbing mitochondrial function and by lowering cell survival via decreasing cell survival signaling. To investigate our hypothesis, we determined the effects of treatment with various concentrations of silicon dioxide nanoparticles on the activities of two key mitochondrial enzymes, ie, citrate synthase and malate dehydrogenase, and expression of the mitochondrial DNA-encoded proteins, cytochrome oxidase subunit II and NADH dehydrogenase subunit 6, and the cell survival signaling pathway protein ERK and phosphorylated ERK in U87 cells.

## Materials and methods

### Materials

Silicon dioxide nanoparticles (size 12 nm) were purchased from STREM Chemicals, Newburyport, MA. Dulbecco's modified Eagle's medium (DMEM) and other chemicals were purchased from Sigma-Aldrich (St. Louis, MO). U87 cells were obtained from American Type Culture Collection (Manassas, VA).

### Cell culture

Human U87 astrocytoma cells were cultured using DMEM supplemented with 10% (v/v) fetal bovine serum and antimycotic solution. The cells were maintained in a 75 cm<sup>2</sup> flask containing 20 mL medium, incubated at 37°C in a CO<sub>2</sub> incubator. When the cells reached 70%–80% confluency, they were harvested either by scraping or trypsinization and transferred to other flasks.

### Preparation of stock suspension of silicon dioxide nanoparticles

The silicon dioxide nanoparticles stock suspension was first prepared by suspending 50 mg of silicon dioxide nanoparticles in a 100 mL conical flask containing sterile phosphate-buffered saline. The suspension was then placed



in a magnetic stirrer to allow the mixture to stir continuously at room temperature before further dilutions were made from the stock (which was being continuously stirred) to be used at specified concentrations and then mixed for use in treating cells.

### MTT assay to assess cell viability

Cells were seeded (2000 cells/well) onto a 96-well plate and allowed to attach to the bottom of each well (inner diameter 0.6 cm) for an hour. Silicon dioxide nanoparticles were then added at specified concentrations (0.1–100  $\mu\text{g/mL}$ ) to each well containing 0.2 mL with the cells attached at the bottom and mixed. The plates so prepared were incubated for 48 hours at 37°C. MTT dye was then added to each well and the plate incubated for another four hours at 37°C. The purple crystals formed in cells were dissolved using dimethyl sulfoxide and the absorbance of the resultant material in the wells was measured at 567 nm using the microplate reader as described previously.<sup>11</sup>

### Determination of mitochondrial enzyme activity

The U87 cells were cultured in DMEM in 75 cm<sup>2</sup> flasks. When the cells were 70%–80% confluent, silicon dioxide nanoparticle treatments were initiated. The mitochondrial function of the untreated and treated U87 cells was assessed by measuring activities of two tricarboxylic acid cycle enzymes, citrate synthase and malate dehydrogenase, in U87 cells treated with silicon dioxide nanoparticles at 0, 25, 50, or 100  $\mu\text{g/mL}$  by previously published methods.<sup>18</sup> The untreated U87 cells served as the control. Citrate synthase and malate dehydrogenase activity in cell homogenates was measured at 412 nm and 340 nm, respectively, using an ultraviolet-VIS spectrophotometer.<sup>18</sup>

### Western blot analysis

Expression of the mitochondrial DNA-encoded proteins, NADPH dehydrogenase subunit 6 and cytochrome C oxidase subunit II, and the cell signaling proteins ERK and phosphorylated ERK were determined by Western blot analysis. The U87 cells treated with or without (ie, control) silicon dioxide nanoparticles were collected and homogenized in a buffer containing 5 mM HEPES and 250 mM sucrose, along with protease inhibitors as described previously.<sup>15</sup> Protein content of the homogenates was then determined using the bicinchoninic acid technique with a microplate reader.<sup>11</sup> Briefly, equal amounts of protein from the samples were loaded onto the lanes of the gels, and the proteins were separated

by polyacrylamide gel electrophoresis and transferred to a polyvinylidene fluoride membrane.<sup>19</sup> Monoclonal antibodies against the respective proteins were then used to probe the proteins of interest. The polyvinylidene fluoride membrane containing the target protein was then developed using the chemiluminescence technique on an X-ray film to assess the extent of expression of respective proteins.<sup>19</sup>

### Assessment of cellular morphology

The morphology of the U87 cells, treated with silicon dioxide nanoparticles for 48 hours at 37°C using specified concentrations, were compared with that of the control or untreated U87 cells by using bright field light microscopy. The images were obtained using a Leica light microscope at 400 $\times$  magnification (Leica DM IRB; Leica, Bannockburn, IL) equipped with a digital camera (Leica DFC 300FX; Leica).<sup>15</sup>

### Statistical analysis

Data analysis was performed employing one way ANOVA followed by Dunnett's post hoc test using SPSS software (SPSS Inc., Chicago, IL). All data reported are mean  $\pm$  SEM of three individual experiments. Statistical significance was set at  $P < 0.05$ .

## Results

### Effect of nanoparticles on human U87 astrocytoma cell survival

To determine the effect of silicon dioxide nanoparticles on cell survival, U87 cells were exposed to silicon dioxide nanoparticles for 48 hours at concentrations ranging from 0.1 to 100  $\mu\text{g/mL}$ . At lower treatment concentrations, from 0.1 to 10  $\mu\text{g/mL}$ , the nanoparticles did not affect viability of the U87 cells (Figure 1). However, at treatment concentrations of 25  $\mu\text{g/mL}$  and higher, silicon dioxide nanoparticles induced concentration-related decreases in survival of U87 cells.

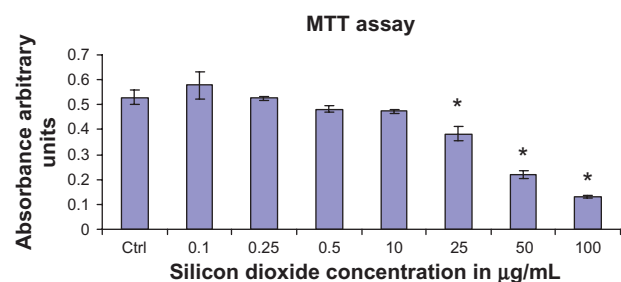


**Figure 1** Effect of treatment with silicon dioxide nanoparticles on survival of human astrocytoma U87 cells. U87 cells were treated at specified concentrations of silicon dioxide nanoparticles for 48 hours. Values were the mean  $\pm$  SEM of at least three separate experiments; CTRL represented the untreated (ie, control) U87 cells; \* $P < 0.05$  versus control cells.



At the highest treatment level of 100  $\mu\text{g/mL}$ , less than 30% of the cells survived (Figure 1).

## Effect on mitochondrial function in human U87 astrocytoma cells

Because cell survival critically depends on mitochondrial functions being maintained at a normal physiologic level, we determined the effect of silicon dioxide nanoparticles on mitochondrial function in U87 cells by monitoring the activities of citrate synthase and malate dehydrogenase.<sup>18</sup> Both enzymes are nuclear DNA-encoded; these enzyme proteins are synthesized in the endoplasmic reticulum and then imported into the mitochondrial matrix compartment.

At treatment concentrations of 25–100  $\mu\text{g/mL}$  for 48 hours, silicon dioxide nanoparticles induced dose-related increases in citrate synthase activities in U87 cells (Figure 2). On the other hand, although at the same concentrations the nanoparticles also induced significantly increased activity in malate dehydrogenase in U87 cells, the increases were not dose-related (Figure 3). Using the same nanoparticle concentrations for treatment of U87 cells, there was a dose-related decrease in cell survival (Figure 1), and it is likely that the remaining surviving U87 cells were compensating by upregulation of citrate synthase and, to a less extent, malate dehydrogenase, so as to maintain their energy production via tricarboxylic acid cycle metabolism for survival.

## Effects of nanoparticles on mitochondrial DNA-encoded and cell signaling protein expression

Because silicon dioxide nanoparticles induced dose-related decreases in survival of U87 cells at concentrations of

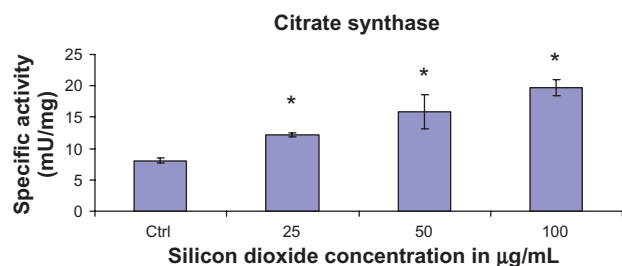


**Figure 2** Effect of treatment with silicon dioxide nanoparticles on specific activities of citrate synthase in human astrocytoma U87 cells. U87 cells were treated at specified concentrations of silicon dioxide nanoparticles for 48 hours. Then the activities of citrate synthase in the homogenates of treated and untreated (ie, control, ctrl) U87 cells were determined as described in Materials and methods; the activities of citrate synthase were expressed per mg of homogenate protein as specific activities. The specific activities values were the mean  $\pm$  SEM of at least three separate experiments; ctrl represented the value in untreated U87 cell homogenate; \* $P < 0.05$  versus that of control cells.

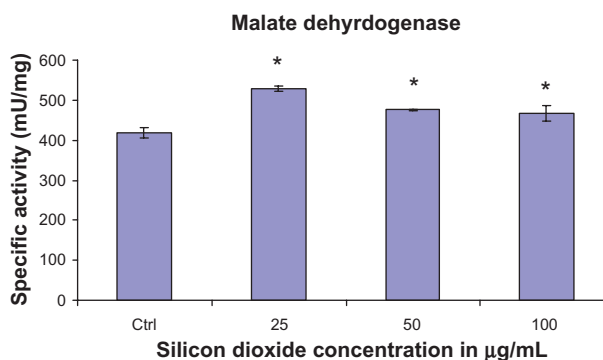


**Figure 3** Effect of treatment with silicon dioxide nanoparticles on specific activities of malate dehydrogenase in human astrocytoma U87 cells. U87 cells were treated at specified concentrations of silicon dioxide nanoparticles for 48 hours. Then the activities of malate dehydrogenase in the homogenates of treated and untreated (ie, control, ctrl) U87 cells were determined as described in Materials and methods; the activities of malate dehydrogenase were expressed per mg of homogenate protein as specific activities. The specific activity values were the mean  $\pm$  SEM of at least three separate experiments; ctrl represented the value in untreated U87 cell homogenate; \* $P < 0.05$  versus that of control cells.

25–100  $\mu\text{g/mL}$  over 48 hours (Figure 1), we investigated the possibility that these decreases in survival can be attributed to the nanoparticle-induced alterations in expression of mitochondrial DNA-encoded and cell signaling proteins (Figures 4–6).

At treatment concentrations of 25–100  $\mu\text{g/mL}$  for 48 hours, silicon dioxide nanoparticles induced dose-related decreases in the expression of cytochrome C oxidase subunit II and NADH dehydrogenase subunit 6 (two mitochondrial DNA-encoded peptides) in U87 cells (Figures 4 and 5). These results strongly suggested treatment with silicon dioxide nanoparticles altered the normal functioning of the mitochondrial genome in U87 cells. A likely consequence

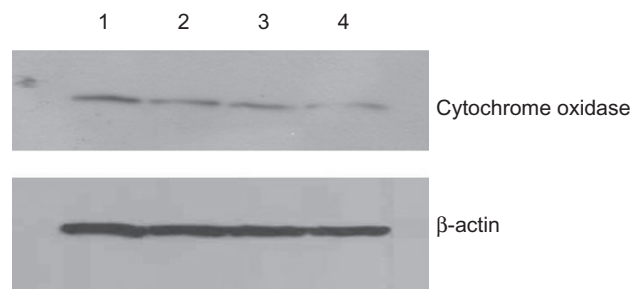


**Figure 4** Effect of treatment with silicon dioxide nanoparticles on expression of cytochrome oxidase subunit II in human astrocytoma U87 cells. U87 cells were treated at specified concentrations of silicon dioxide nanoparticles for 48 hours. Then cell lysates of treated and untreated (ie, control) U87 cells were prepared as described in Materials and methods. The expression of cytochrome oxidase subunit II, encoded by mitochondrial DNA, was determined by Western blot analysis using  $\beta$ -actin as the loading control: Lane 1, lysate of untreated or control U87 cells; lane 2, lysate of U87 cells treated with silicon dioxide nanoparticles at 25  $\mu\text{g/mL}$ ; lane 3, lysate of U87 cells treated with silicon dioxide nanoparticles at 50  $\mu\text{g/mL}$ ; lane 4, lysate of U87 cells treated with silicon dioxide nanoparticles at 100  $\mu\text{g/mL}$ . The blots were from a typical experiment. Two other experiments yielded essentially the same trend of results.

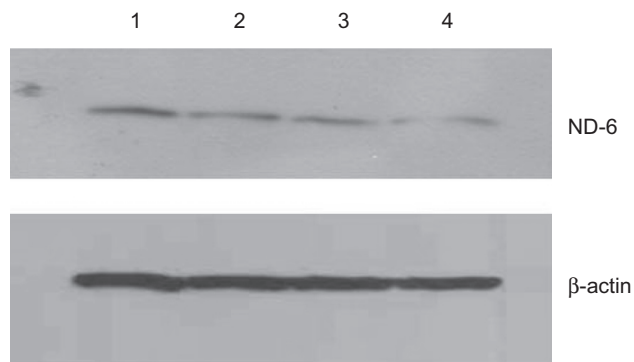


**Figure 5** Effect of treatment with silicon dioxide nanoparticles on expression of nicotinamide adenine dinucleotide (NADH) dehydrogenase subunit 6 in human astrocytoma U87 cells. U87 cells were treated at specified concentrations of silicon dioxide nanoparticles for 48 hours. Then cell lysates of treated and untreated (ie, control) U87 cells were prepared as described in Materials and methods. The expression of NADH dehydrogenase subunit 6, encoded by mitochondrial DNA, was determined by Western blot analysis using  $\beta$ -actin as the loading control: Lane 1, lysate of untreated or control U87 cells; lane 2, lysate of U87 cells treated with silicon dioxide nanoparticles at 25  $\mu$ g/mL; lane 3, lysate of U87 cells treated with silicon dioxide nanoparticles at 50  $\mu$ g/mL; lane 4, lysate of U87 cells treated with silicon dioxide nanoparticles at 100  $\mu$ g/mL. The blots were from a typical experiment. Two other experiments yielded essentially the same trend of results.

of this effect is impairment in the mitochondrial electron transport chain in U87 cells. Indeed, the nanoparticle-induced disruption of mitochondrial respiratory chain structure and function may be one cause of energy failure that ultimately led to the death of U87 cells.

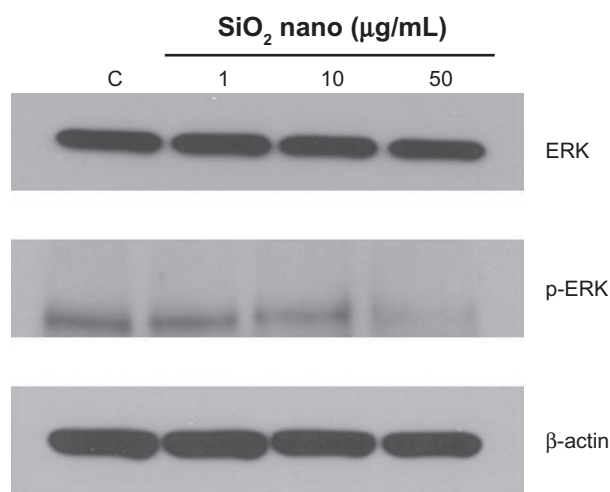


**Figure 6** Effect of treatment with silicon dioxide nanoparticles on expression of extracellular signal regulated kinase (ERK) and phosphorylated ERK (p-ERK) in human astrocytoma U87 cells. U87 cells were treated at specified concentrations of silicon dioxide nanoparticles for 48 hours. Then cell lysates of treated and untreated (ie, control) U87 cells were prepared as described in Materials and methods. The expression of ERK and phosphorylated ERK was determined by Western blot analysis using  $\beta$ -actin as the loading control: Lane marked C, lysate of untreated or control U87 cells; lane marked 1, lysate of U87 cells treated with silicon dioxide nanoparticles at 1  $\mu$ g/mL; lane marked 10, lysate of U87 cells treated with silicon dioxide nanoparticles at 10  $\mu$ g/mL; lane marked 50, lysate of U87 cells treated with silicon dioxide nanoparticles at 50  $\mu$ g/mL. The blots were from a typical experiment. Two other experiments yielded essentially the same trend of results.

Other than their effect of depressing the mitochondrial respiratory chain, thereby decreasing oxidative phosphorylation, treatment of U87 cells with silicon dioxide nanoparticles could also lower survival of U87 cells through altering cell signaling pathway(s) that regulate(s) cell survival and proliferation.<sup>20</sup> We therefore investigated this possibility by examining the effect of these nanoparticles on expression of ERK and phosphorylated ERK proteins. We observed that when U87 cells were treated with silicon dioxide nanoparticles 1–50  $\mu$ g/mL for 48 hours, the protein expression of phosphorylated ERK showed a dose-related decrease, while that of ERK protein remained essentially unchanged (Figure 6), suggesting that a lowering of this cell survival/proliferation signaling mechanism could, at least in part, account for the dose-related decrease in U87 cell survival induced by these nanoparticles.

### Effect on morphology of U87 cells

To ascertain whether or not treatment of U87 cells with silicon dioxide nanoparticles led to any gross changes in their morphology, we examined the cells under bright field light microscopy (Figure 7). We observed that as we exposed U87 cells to increasing concentrations of silicon dioxide nanoparticles higher than 25  $\mu$ g/mL, the cells became more and more enlarged and swollen, suggesting that they assumed a pathologic appearance (Figure 7).

### Discussion

Few, if any, recent studies have addressed the cytotoxic effects of silicon dioxide nanoparticles in neural cells. As far as we are aware, ours is the first to report the cytotoxic effects of silicon dioxide nanoparticles on human astrocytoma U87 cells and some of the underlying subcellular mechanisms. Consistent with our hypothesis that silicon dioxide nanoparticles induce cytotoxicity in U87 cells by disturbing mitochondrial function and by lowering cell survival via decreasing cell survival signaling, we found that treatment with silicon dioxide nanoparticles induced concentration-related lowering of protein expression of the mitochondrial DNA-encoded cytochrome C oxidase subunit II and NADH dehydrogenase subunit 6, two key components of the mitochondrial respiratory chain, and phosphorylated ERK, a key cell survival/proliferation signaling molecule in U87 cells. It is noteworthy that we found those changes in protein expression at concentrations of silicon dioxide nanoparticles that correlated with those inducing concentration-related decreases in survival of U87 cells.

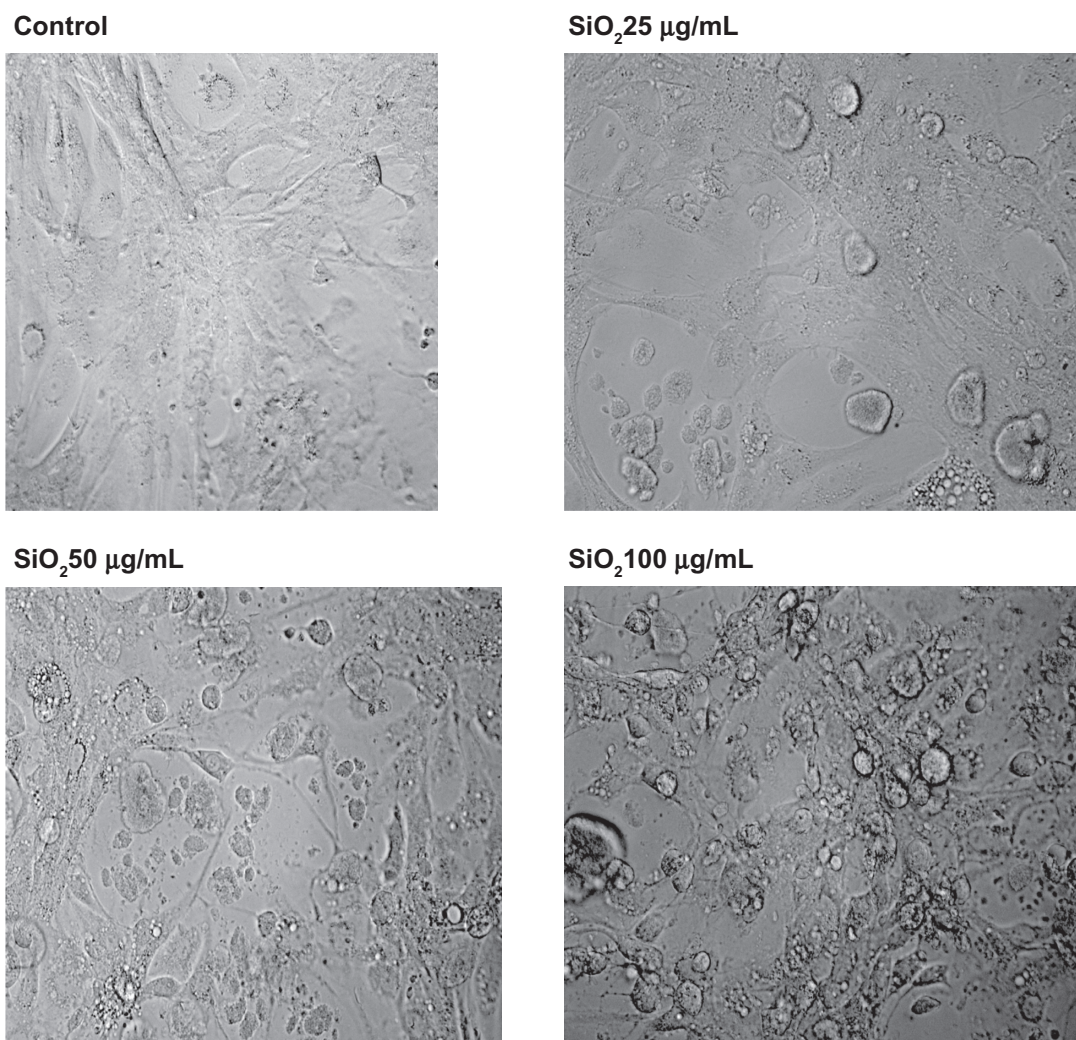


**Figure 7** Effect of treatment with silicon dioxide nanoparticles on the morphology of human astrocytoma U87 cells. U87 cells were treated at specified concentrations of silicon dioxide nanoparticles for 48 hours. Then the morphology of treated and untreated (ie, control) U87 cells were assessed using bright field light microscopy at 400 × magnification as described in Materials and methods. The photomicrographs shown were representative of those obtained in several studies.

As emphasized earlier, the initial rationale for focusing our studies on U87 cells was that few studies have addressed the putative cytotoxic effects of silicon dioxide nanoparticles on neural cells, especially those from the human brain. More importantly, not only do astrocytes have many physiologic roles (eg, metabolic trafficking, neurotransmitter cycling, protecting neurons from pathophysiologic assaults),<sup>15,21,22</sup> they also play pathophysiologic roles in disease states (eg, neuroinflammation in neurodegenerative diseases such as Alzheimer's disease and Parkinson's disease).<sup>22</sup> Furthermore, it is relevant to note that although U87 are neurotumor cells, they possess many of the "normal" physiologic characteristics of astrocytes detected in primary cultures of astrocytes and astrocytes in the brain *in vivo*.<sup>14,15</sup> Thus, U87 cells constitute a good model system *in vitro* for brain astrocytes.<sup>14,15</sup> Consequently, we have

employed U87 cells as a model system to elucidate the putative cytotoxicity of nanoparticles on neural cells in a systematic manner.<sup>11</sup>

One neurotoxic effect of a neurotoxicant, such as manganese, is via a lowering of cell survival/proliferation signaling molecule expression, leading ultimately to death of neural cells.<sup>20</sup> Consistent with this observation is our finding in this study that treatment of U87 cells with increasing concentrations of silicon dioxide nanoparticles induced a dose-related decrease in protein expression of phosphorylated ERK (Figure 6), one important cell survival/proliferation signaling molecule.<sup>20</sup> This effect correlated quite well with the dose-related decrease in survival of these cells (Figure 1) and alterations in their morphology (Figure 7) induced by the nanoparticles. Moreover, we also found that in U87 cells treated in the same nanoparticle dose



range, there was a concentration-related decrease in protein expression of mitochondrial DNA-encoded cytochrome C oxidase subunit II and NADH dehydrogenase subunit 6 (Figures 4 and 5).

Our present findings that exposure of human astrocytoma U87 cells to silicon dioxide induced dose-related decreases in cell survival and alteration of their mitochondrial structure and function (Figures 1–6) are similar to those of Chen et al<sup>23</sup> who demonstrated that exposure of human brain microvascular endothelial cells to aluminum oxide nanoparticles induced decreased viability of those cells, alteration in their mitochondrial membrane potential, and a lowering of their tight junction protein expression. Consequently, in this context, our finding that silicon dioxide nanoparticles induced a dose-related lowering of the expression of cytochrome C oxidase subunit II and NADH dehydrogenase subunit 6 is of pathophysiologic importance and interest in several respects. Because these two peptides are structural components of the mitochondrial respiratory chain complexes IV and I, respectively, and have key functional roles in that respiratory chain,<sup>24</sup> decreased expression of these peptides induced by the nanoparticles likely results in dysfunction in the mitochondrial respiratory chain and oxidative phosphorylation, leading ultimately to decreased adenosine triphosphate synthesis. Consequently, the decreased expression of the two mitochondrial DNA-encoded peptides could likely contribute to decreasing U87 cell survival induced by silicon dioxide nanoparticles through necrotic cell death as a result of energy failure.<sup>11</sup> This conclusion is certainly consistent with our observation that the U87 cells assumed an increasingly swollen appearance, a hallmark of necrosis, as we increased their treatment levels of silicon dioxide nanoparticles (Figure 7). The decreased expression of cytochrome C oxidase subunit II and NADH dehydrogenase subunit 6 peptides induced by the nanoparticles could reflect the effect of the nanoparticles on altering communication between the mitochondrial genome and the nuclear genome, decreasing mitochondrial peptide synthesis, disruption of protein targeting to mitochondria, and/or a combination of these mechanisms. The nanoparticle-induced decrease in protein expression of the two peptides could also result from the overall effect of the nanoparticles on survival/proliferation signaling in U87 cells. Clearly, these are novel but mechanistically relevant possibilities that deserve further investigation.

Unlike the downregulation of the protein expression of mitochondrial DNA-encoded cytochrome C oxidase subunit II and NADH dehydrogenase subunit 6, and the

survival/proliferation signaling molecule phosphorylated ERK, treatment of U87 cells with silicon dioxide nanoparticles induced concentration-related increases in the activity of citrate synthase and malate dehydrogenase, both of which are located in the mitochondrial matrix (Figures 2 and 3). Because the increases in citrate synthase and malate dehydrogenase activity were observed at nanoparticle concentrations that also induced dose-related decreases in U87 cell survival (Figure 1), one possible, and likely, explanation for the increased citrate synthase and malate dehydrogenase activity is that the surviving cells were showing compensatory/adaptive mechanisms involving upregulation of tricarboxylic acid cycle enzymes in the mitochondrial matrix of surviving or dying cells, or both, in the face of downregulation of mitochondrial DNA-encoded respiratory chain components, such as cytochrome C oxidase subunit II and NADH dehydrogenase subunit 6. Consequently, this upregulation of tricarboxylic acid cycle enzymes may offset (or compensate for) the effect on mitochondrial energetics through the downregulation of respiratory chain components induced by the nanoparticles. Only future studies can elucidate whether this mechanistic possibility is tenable because they are beyond the scope of the present study.

Because ours is the first study to report on the cytotoxic effects of silicon dioxide nanoparticles on human neural cells, only a few comparisons can be made with the effects of silicon dioxide nanoparticles on neural and peripheral cell types because the literature in this area of research is rather scant.<sup>11</sup> For example, Napierska et al<sup>7</sup> demonstrated exposure of human endothelial cells to amorphous spherical silicon dioxide nanoparticles induced decreases in their viability and this effect was apparently dependent on their particle size. Several groups had also shown that silicon dioxide nanoparticles decreased viability of some peripheral human and other mammalian cell types.<sup>5,25,26</sup> Thus, recent reports,<sup>5,7,25,26</sup> as well as the findings of this study, are in accord in emphasizing that silicon dioxide nanoparticles induces decreased viability of a variety of human and other mammalian cell types. Nevertheless, more systematic studies are required to elucidate fully the molecular mechanisms underlying the cytotoxicity of these nanoparticles.

As we discussed previously, one early study indicated that when silicon nanoparticles were introduced directly into the brains of rats and mice, they induced an inflammatory response in brain astrocytes.<sup>8</sup> Furthermore, silicon was found in senile plaque cores and in lipofuscin granules in the cortex of patients who died of Alzheimer's disease.<sup>9,10</sup>

In view of these earlier findings,<sup>8–10</sup> because astrocytes play important roles in neuroinflammation,<sup>22</sup> and U87 cells constitute a good cell model for astrocytes, the results of this study may have pathophysiologic implications in the inflammation in astrocytes in Alzheimer's disease in particular and in neuroinflammation in general. Thus, the mechanistic connection between the inflammatory response in Alzheimer's disease, neuroinflammation, and the cytotoxic effects of silicon dioxide nanoparticles in neural cells merits further investigation.

## Conclusion

This study is the first to report on the cytotoxic effects of silicon dioxide nanoparticles on human astrocytoma U87 cells, and some of the underlying subcellular mechanisms. Consistent with our hypothesis, we found that treatment with silicon dioxide nanoparticles induced concentration-related lowering of protein expression in the mitochondrial DNA-encoded cytochrome C oxidase subunit II and NADH dehydrogenase subunit 6, two key components of the mitochondrial respiratory chain, and phosphorylated ERK, a key cell survival/proliferation signaling molecule in U87 cells. We also noted those changes in protein expression induced by silicon dioxide nanoparticles correlated with concentration-related decreases in survival of U87 cells induced by the nanoparticles. On the other hand, we observed upregulation of citrate synthase and malate dehydrogenase, two key tricarboxylic acid cycle enzymes. Those changes were likely compensatory/adaptive mechanism of dying and/or surviving U87 cells. Thus, our findings may assume pathophysiologic importance in neuroinflammation and Alzheimer's disease and in the environmental health impact of human exposure to these nanoparticles. This is obviously a worthwhile area for further study.

## Acknowledgments

Our studies were supported by a US Army Medical Research and Materiel Command Project Grant (Contract W81XWH-07-2-0078) and National Institutes of Health Grant P20 RR016454 from the Idaho Idea Biomedical Research Excellence Program of the National Center for Research Resources. JCKL and GA contributed equally to this work.

## Disclosure

The authors report no conflicts of interest in this work.

## References

- Environmental Protection Agency. Draft Nanomaterial Research Strategy. Available at: ([http://epa.gov/ncsr/nano/publications/nano\\_strategy\\_012408.pdf](http://epa.gov/ncsr/nano/publications/nano_strategy_012408.pdf)). Accessed August 3, 2010.
- Martin KR. The chemistry of silica and its potential health benefits. *J Nutr Health Aging*. 2007;11:94–97.
- Jonat S, Hasenzahl S, Gray A, Schmidt PC. Influence of compacted hydrophobic and hydrophilic colloidal silicon dioxide on tableting properties of pharmaceutical excipients. *Drug Dev Ind Pharm*. 2005;31:687–696.
- Ulrichs C, Krause F, Rockscht T, et al. Electrostatic applications of inert silica dust based insecticides onto plant surfaces. *Commun Agric Appl Biol Sci*. 2006;71:171–178.
- Sayes CM, Reed KL, Warheit DB. Assessing toxicity of fine and nanoparticles: Comparing in vitro measurements to in vivo pulmonary toxicity profiles. *Toxicol Sci*. 2007;97:163–180.
- Adams LK, Lyon DY, McIntosh A, Alvarez PJ. Comparative toxicity of nano-scale TiO<sub>2</sub>, SiO<sub>2</sub>, and ZnO water suspensions. *Water Sci Technol*. 2006;54:327–334.
- Napierska D, Thomassen LC, Rabolli V, et al. Size-dependent cytotoxicity of monodisperse silica nanoparticles in human endothelial cells. *Small*. 2009;5:846–853.
- Rees S, Cragg B. Is silica involved in neuritic (senile) plaque formation? *Acta Neuropathol*. 1983;59:31–40.
- Candy JM, Oakley AE, Klinowski J, et al. Aluminosilicates and senile plaque formation in Alzheimer's disease. *Lancet*. 1986;1:354–357.
- Takutake S, Oyanagi S. Accumulation of aluminium and silicon in lipofuscin granules. *Gerontology*. 1995;41 Suppl 2:131–144.
- Lai JC, Lai MB, Jandhyam S, et al. Exposure to titanium dioxide and other metallic oxide nanoparticles induces cytotoxicity on human neural cells and fibroblasts. *Int J Nanomedicine*. 2008;3:533–545.
- Kim JS, Yoon T-J, Yu KN, et al. Toxicity and tissue distribution of magnetic nanoparticles in mice. *Toxicol Sci*. 2006;89:338–347.
- Sharma HS, Hussain S, Schlager J, et al. Influence of nanoparticles on blood-brain barrier permeability and brain edema formation in rats. *Acta Neurochir Suppl*. 2010;106:359–364.
- Malthankar GV, White BK, Bhushan A, et al. Differential lowering by manganese treatment of activities of glycolytic and tricarboxylic acid (TCA) cycle enzymes investigated in neuroblastoma and astrocytoma cells is associated with manganese-induced cell death. *Neurochem Res*. 2004;29:709–717.
- Dukhande VV, Malthankar-Phatak GH, Hugus JJ, et al. Manganese induced neurotoxicity is differentially enhanced by glutathione depletion in astrocytoma and neuroblastoma cells. *Neurochem Res*. 2006;31:1349–1357.
- Haseloff RE, Blasig IE, Bauer H-C, Bauer H. In search of the astrocytic factor(s) modulating blood-brain barrier functions in brain capillary endothelial cells in vitro. *Cell Mol Neurobiol*. 2005;25:25–39.
- Liebner S, Plate KH. Differentiation of the brain vasculature: The answer came blowing by the Wnt. *J Angiogenesis Res*. 2010;2:1–10.
- Clark JB, Lai JCK. Glycolytic, tricarboxylic acid cycle, and related enzymes in brain. In: Boulton AA, Baker GB, Butterworth RF (editors). *NeuroMethods Vol 11*. Clifton, NJ: Humana Press; 1989:233–281.
- Isaac AO, Dukhande VV, Lai JCK. Metabolic and antioxidant system alterations in an astrocytoma cell line challenged with mitochondrial DNA deletion. *Neurochem Res*. 2007;32:1906–1918.
- Puli S, Lai JCK, Edgley KL, et al. Signaling pathways mediating manganese-induced neurotoxicity in human glioblastoma cells (U87). *Neurochem Res*. 2006;31:1211–1218.
- Faharani R, Pina-Benabou MH, Kyrozis A, et al. Alterations in metabolism and gap junction protein expression may determine the role of astrocytes as “Good Samaritans” or executioners. *Glia*. 2005;50:351–361.

22. Sofroniew MV, Vinters HV. Astrocytes: Biology and pathology. *Acta Neuropathol.* 2010;119:7–35.
23. Chen L, Yokel RA, Hennig B, Toborek M. Manufactured aluminum oxide nanoparticles decrease expression of tight junction proteins in brain vasculature. *J Neuroimmune Pharmacol.* 2008;3:286–295.
24. Heales SJR, Gegg ME, Clark JB. Oxidative phosphorylation: Structure, function, and intermediary metabolism. *Int Rev Neurobiol.* 2002; 53:25–56.
25. Lin W, Huang YW, Zhou XD, Ma Y. In vitro toxicity of silica nanoparticles in human lung cancer cells. *Toxicol Appl Pharmacol.* 2006;217:252–259.
26. Adili A, Crowe S, Beaux II FM, et al. Differential cytotoxicity exhibited by silica nanowires and nanoparticles. *Nanotoxicology.* 2008;2:1–8.

### International Journal of Nanomedicine

### Publish your work in this journal

The International Journal of Nanomedicine is an international, peer-reviewed journal focusing on the application of nanotechnology in diagnostics, therapeutics, and drug delivery systems throughout the biomedical field. This journal is indexed on PubMed Central, MedLine, CAS, SciSearch®, Current Contents®/Clinical Medicine,

Submit your manuscript here: <http://www.dovepress.com/international-journal-of-nanomedicine-journal>

Journal Citation Reports/Science Edition, EMBase, Scopus and the Elsevier Bibliographic databases. The manuscript management system is completely online and includes a very quick and fair peer-review system, which is all easy to use. Visit <http://www.dovepress.com/testimonials.php> to read real quotes from published authors.

Dovepress

## **A Cell Culture Model for Diabetic Neuropathy Studies**

Ashvin R. Jaiswal<sup>1</sup>, Alok Bhushan, Christopher K. Daniels and  
James C.K. Lai<sup>2</sup>

Department of Biomedical and Pharmaceutical Sciences,  
College of Pharmacy, and Biomedical Research Institute,  
Idaho State University, Pocatello, ID 83209, USA

Fax: 208-282-4305;

Tel: 208-282-2275;

email: [lai@pharmacy.isu.edu](mailto:lai@pharmacy.isu.edu)

<sup>1</sup>Presenting author.

<sup>2</sup>Corresponding author.

## **A Cell Culture Model for Diabetic Neuropathy Studies**

### **Abstract :**

Diabetic neuropathy is one of the most severe complications of chronic diabetes. Though several theories exist, the pathophysiology of the disease is poorly understood. We have therefore developed an *in vitro* model to elucidate its underlying pathophysiologic mechanisms. We believe our model allows us to gain new insights into such mechanisms. Moreover, our model improves on existing primary culture models because the latter change with passage number and have limited life-span. We hypothesize that high glucose treatment induces oxidative stress and decreases GSH level, ultimately leading to apoptosis in dorsal root ganglion (DRG) neurons and Schwann cells. Results of our ongoing studies suggest exposure of DRG neurons to high levels of glucose (e.g., 45 & 60 mM), conditions that favor increased ROS generation, decrease their survival, eventually leading to cell death whereas in co-culture, Schwann cells help protect DRG neurons and enhance their survival. Other studies are in progress to further characterize our cell model. Thus, results of our ongoing studies are consistent with the notion that our cell model is appropriate for investigation of diabetic neuropathy.

**Keywords:** Cell Culture Model, Diabetic Neuropathy, Neurodegeneration

### **Introduction:**

Diabetes is the disease of high blood glucose and according to the American Diabetic Association, 23.6 million people (8% of United States populations) have diabetes. Diabetic neuropathy is one of the most severe complications of diabetes, an



inflammatory condition in which the nerves in the extremities of the body become damaged, ultimately resulting in death of nerve cells (Brownlee 2001, Figueroa-Romero et al. 2008, Leininger et al. 2006). It affects more than 60% of diabetic population (Figueroa-Romero et al. 2008). Some of the serious complications of nerve damage as a result of diabetes include loss of sensation or pain in limbs, adverse effects on digestion, decreased sexual response, and urinary tract infection. Half of the foot amputations in the United States constitute the consequence of diabetic neuropathy. There is little advancement in the management and treatment of diabetic neuropathy because it is very difficult to predict and monitor nerve cell damage.

Various *in vivo* and *in vitro* models mimicking closely or approximately the diabetic pathologies in humans have been devised to investigate pathophysiological mechanisms of the disease. Each model has its own advantages and limitations. *In vivo* models are preferred in elucidating the etiology of the disease and for testing the efficacy of potential therapies. However, limitations of *in vivo* models include inability to tightly control their glycemic status and the fact that these models do not lend themselves readily for use in investigating the pathophysiology of the disease at the cellular and molecular levels (Apfel 2006).

Unlike *in vivo* models, *in vitro* models of diabetes in general and diabetic neuropathy in particular allow investigations of pathophysiological/pathogenic mechanisms at the cellular and molecular levels (Sango et al. 2006). For example, these models permit the examination of effects of high glucose on neurons in a controlled environment (Sango et al. 2006). Nevertheless, there is no *in vitro* cell model available whereby one could study the long-term exposure of dorsal root ganglion

(DRG) neurons and/or Schwann cells to high and pathologic levels of glucose. To address this need for such model(s), we have been systematically developing different co-culture models of DRG neurons and Schwann cells because the DRG neurons *in vivo* are always surrounded by Schwann cells and Schwann cells protect them from any damage or cell death (Vincent et al. 2005). We hypothesize that immortalized cell culture models using DRG neurons, Schwann cells and their co-cultures can be productively employed to elucidate the pathophysiological and/or pathogenic mechanisms of diabetic neuropathy. This study was initiated to investigate our hypothesis.

#### **Materials and Methods:**

**Cell Cultures.** The immortalized DRG neurons were a gift from Dr. Ahmet Hoke's laboratory at Johns Hopkins University (Baltimore, MD, USA) (Chen et al. 2007). The rat Schwann cell line was obtained from ATCC (Manassas, VA, USA). These cells and their co-culture were cultured in DMEM (Sigma; St Louis, MO, USA) supplemented with 10% (v/v) fetal bovine serum (FBS), 1% (w/v) sodium pyruvate, 0.292 g/l L-glutamine, 1.5 g/l sodium bicarbonate, 1% (v/v) anti-mycotic and various specified concentrations (5-45 mM) of glucose.

**Cell Survival (MTT) Assay.** 8000-10000 DRG neurons or Schwann cells were seeded per well in a 48-well plate in a medium with a normal or high glucose concentration. After incubation at 37°C for 48 hours, 50 µl of MTT (5 mg/ml in PBS) reagent was added to each well. After incubation for another 4 hours, the medium was removed gently and the cellular reaction product was extracted in 200 µl DMSO. Then the optical density of

contents of each well was measured in a plate reader at 570 nm. The absorbance was proportional to the number of live cells previously present in each well.

**Reactive Oxygen Species (ROS) Assay.** Cells in a medium with normal or high glucose were incubated at 37°C for 48 hours and then 200 µl of H<sub>2</sub>DCF dye (10 µM in PBS) was added to each well. After another 45 minutes, the medium was removed gently and 200 µl of PBS was added in each well. The fluorescence output in each well was measured in the plate reader set at 489 nm excitation-521 nm emission in the fluorescence mode. The fluorescence output corresponded to the ROS produced by cells present in each well and was normalized with respect to cellular protein, which was determined using the BCA Protein Assay Kit.

**Glutathione (GSH) Assay.** GSH in cell homogenates was measured using Ellman's reagent (5,5'-dithiobis-(2-nitrobenzoic acid) or DTNB) as described previously (Dukhande et al. 2006).

**Co-culture of DRG neurons and Schwann cells.** Our co-culture model closely mimics the physiological conditions of DRG neurons & Schwann cells because Schwann cells always surround DRG neurons *in vivo* and protect them from pathophysiological assaults. DRG neurons & Schwann cells were cultured at 37°C and 5% CO<sub>2</sub> in Dulbecco's Modified Eagle's Medium supplemented with 10% FBS and counted using a Coulter counter after 24 hours or at about 60-70 % confluence. DRG neurons were seeded on a Corning Costar 24-well plate. Schwann cells were then seeded on a Millipore hanging cell culture insert (pore size 0.4 µm) on a separate plate and then introduced to a DRG neuron-containing well after 4 hours to achieve the co-culture condition. DRG neurons (co-cultured with Schwann cells) were exposed to various

levels of glucose for specified periods and their survival determined employing the cell survival assay.

**Statistical analysis of results.** Statistical significance of experimental results was analyzed with one-way ANOVA followed by Dunnett's post-hoc test using SPSS 17 software package, with a minimum significance level set at  $p < 0.05$ .

### **Results and Discussion:**

Diabetic neuropathy affects the peripheral nervous system (PNS) the most: dorsal root ganglion (DRG) neurons in PNS are especially susceptible to high glucose-induced cell damage and/or death. Therefore, we used DRG neurons to develop a cell culture model for diabetic neuropathy and have begun to characterize it. When we exposed DRG neurons to various glucose levels, we noted that these cells survived best at 25 mM of glucose (Fig. 1), a level higher than the physiological level of 5.5 mM. Relevant to our finding (Fig. 1) is the observation of Izawa et al. (2009) who found that lactate produced by Schwann cells may be a fuel for DRG neuronal energy metabolism.

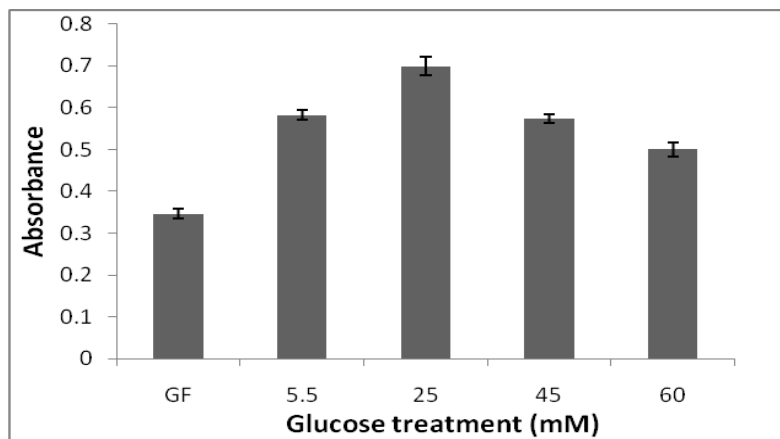


**Fig. 1 Survival of DRG Neurons after 24-hour Exposure to Different Glucose Concentrations.**

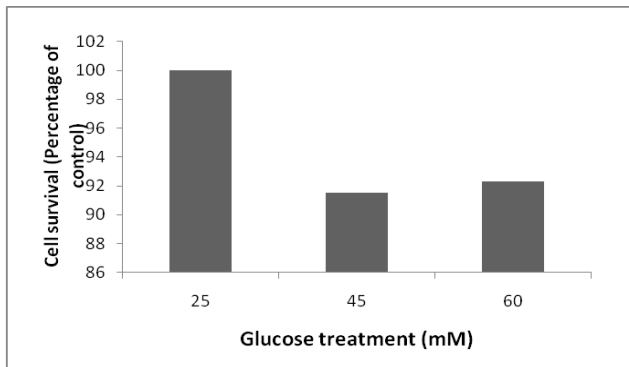


**Fig. 2 Survival of DRG Neurons after exposure to high glucose for 24 hours.**  
(\* $p < 0.05$  compare to 25 mM of glucose)

Schwann cells usually surround DRG neurons *in vivo*, provide them with glycolytic intermediates (Miller et al. 2002) and protect them from pathophysiological assaults. Consistent with this notion is our observation that both cell types survived better in co-culture than when they were cultured alone (data not shown). Furthermore, when DRG neurons are cultured alone, they need more glucose because of the absence of the glycolytic intermediates normally supplied to them by Schwann cells (Miller et al. 2002). Based on the above considerations and our finding that DRG neurons showed optimal survival with 25 mM glucose (Figs. 1 and 2), we employed 25 mM of glucose as a control parameter when DRG neurons and Schwann cells are cultured separately and 5.5 mM of glucose as a physiological control when we co-cultured them.

Exposure of neural cells to high glucose increases reactive oxygen species (ROS) production, a by-product of glucose metabolism and marker of diabetic neuropathy (Vincent et al. 2005). Consistent with this notion is our finding that ROS production by DRG neurons was increased when they were exposed to glucose level higher than 25

mM (Fig. 3). Clearly the mechanisms underlying the increased ROS production by DRG neurons in high glucose merit further elucidation.

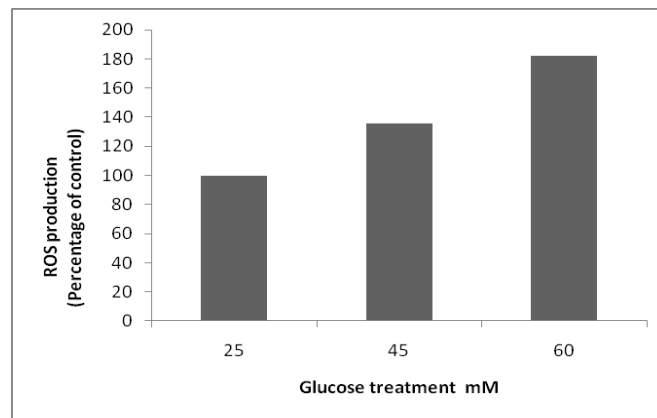


**Fig. 3 ROS Production by DRG Neurons after Exposures to High Glucose Concentrations**

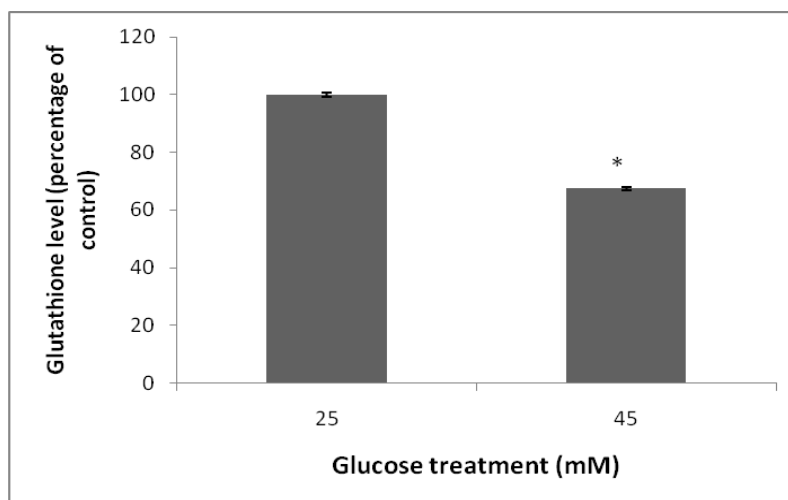


**Fig. 4 Changes in Glutathione Level in Schwann Cells after Exposure to High Glucose for 24 hr (\*p<0.05 compare to 25 mM of glucose)**

Because glial cells in brain have a protective role on neurons (Dukhande et al. 2006), we investigated the possibility that under the stress of exposure to high glucose, Schwann cells may produce less glutathione (antioxidant) thereby decreasing their

ability to protect DRG neurons. We exposed Schwann cells to high glucose and measured their glutathione content. Consistent with this hypothesis is our finding that exposure to high glucose induced decreases in glutathione in Schwann cells compared to their levels when treated with 25 mM of glucose (Fig. 4).

In conclusion, results from this study strongly suggest our model is suitable for systematic investigation of mechanisms underlying pathophysiology and pathogenesis of diabetic neuropathy. Thus, these results (and those to be obtained in our ongoing studies) provide additional insights into cellular and molecular mechanisms relevant to diabetic neuropathy and as such may be implicated not only in this disease but also in other chronic diseases such as Alzheimer's disease and Parkinson's disease.

#### **Acknowledgements:**

We thank Dr. Ahmed Hoke (Johns Hopkins University School of Medicine) for his generous gift of DRG neurons. Our study was supported, in part, by an USAMRMC Project Grant (Contract #W81XWH-07-2-0078), and NIH Grant #P20 RR016454 from the Idaho INBRE Program of the National Center for Research Resources.

#### **References:**

- Apfel SC. 2006. Diabetic neuropathy models: Are they relevant? *Drug Discovery Today: Disease Models* 3: 397-402.
- Brownlee M. 2001. Biochemistry and molecular cell biology of diabetic complications. *Nature* 414: 813-820.
- Chen W, Mi R, Haughey N, Oz M, Höke A. 2007. Immortalization and characterization of a nociceptive dorsal root ganglion sensory neuronal line. *Journal of the Peripheral Nervous System* 12: 121-130.

Dukhande VV, Malthankar-Phatak GH, Hugus JJ, Daniels CK & Lai JCK 2006. Manganese-Induced Neurotoxicity is Differentially Enhanced by Glutathione Depletion in Astrocytoma and Neuroblastoma Cells. *Neurochemical Research* 31: 1349-1357.

Figuerola-Romero C, Sadidi M, Feldman E. 2008. Mechanisms of disease: The oxidative stress theory of diabetic neuropathy. *Reviews in Endocrine & Metabolic Disorders* 9: 301-314.

Izawa Y, Takahashi S, Suzuki N. 2009. Pioglitazone enhances pyruvate and lactate oxidation in cultured neurons but not in cultured astroglia. *Brain Research* 1305: 64-73.

Leininger GM, Edwards JL, Lipshaw MJ, Feldman EL. 2006. Mechanisms of Disease: mitochondria as new therapeutic targets in diabetic neuropathy. *Nat Clin Pract Neuro* 2: 620-628.

Miller KE, Richards BA, Kriebel RM. 2002. Glutamine-, glutamine synthetase-, glutamate dehydrogenase- and pyruvate carboxylase-immunoreactivities in the rat dorsal root ganglion and peripheral nerve. *Brain Research* 945: 202-211.

Sango K, Saito H, Takano M, Tokashiki A, Inoue S, Horie H. 2006. Cultured Adult Animal Neurons and Schwann Cells Give Us New Insights into Diabetic Neuropathy. *Current Diabetes Reviews* 2: 169-183.

Vincent AM, McLean LL, Backus C, Feldman EL. 2005. Short-term hyperglycemia produces oxidative damage and apoptosis in neurons. *FASEB J* 19(6): 638-640.



## **Further Elucidation of Neuroprotective Properties of Astrocytoma (Astrocytes-like) Cells**

Yin Yin Wendy Wong<sup>1</sup>, Ashvin R. Jaiswal<sup>2</sup>, Alok Bhushan<sup>2</sup>, Solomon W. Leung<sup>3</sup>, and James C.K. Lai<sup>4</sup>

<sup>1</sup>Presenting author: Department of Biomedical & Pharmaceutical Sciences, College of Pharmacy, and Biomedical Research Institute, Idaho State University, Pocatello, ID 83209, USA

<sup>2</sup>Department of Biomedical & Pharmaceutical Sciences, College of Pharmacy, and Biomedical Research Institute, Idaho State University, Pocatello, ID 83209, USA

<sup>3</sup>Department of Civil and Environmental Engineering, College of Engineering, and Biomedical Research Institute, Idaho State University, Pocatello, ID 83209, USA

<sup>4</sup>Corresponding author: Department of Biomedical and Pharmaceutical Sciences, College of Pharmacy, and Biomedical Research Institute, Idaho State University, Pocatello, ID 83209, USA Fax: 208-282-4305; Tel: 208-282-2275; email: [lai@pharmacy.isu.edu](mailto:lai@pharmacy.isu.edu)

## **Further Elucidation of Neuroprotective Properties of Astrocytoma (Astrocytes-like) Cells**

### **Abstract:**

Astrocytes protect neurons against various assaults although the underlying pathophysiological and molecular mechanisms are poorly understood. Therefore, we have continued to develop cell models *in vitro* to further investigate the putative neuroprotective properties of astrocyte-like astrocytoma cells. We hypothesized that different stress factors can elicit and/or enhance the neuroprotective effects of astrocytes through the activation of astrocytic survival signaling and alteration of astroglial function. Employing cell models involving astrocytes-like U87 astrocytoma and neurons-like SK-N-SH cells, results of our previous and ongoing studies suggest that U87 cells protect SK-N-SH cells against cytotoxicity due to oxidative stress. Other ongoing studies target the putative neuroprotective effect(s) of U87 cells due to alterations of cell signaling and/or other astroglial function(s). Thus, our results may have implications for the pathophysiology of neuroprotection.

**Keywords:** Astrocytes; neuroprotection; astroglial function; U87 astrocytes-like astrocytoma cells; SK-N-SH neurons-like neuroblastoma cells

### **Introduction:**

Astrocytes (non-neuronal, glial cells) in the brain are known to play important roles in protecting neurons (nerve cells) against various assaults although the

underlying mechanisms are incompletely understood (Sofroniew et al. 2010). Well known chronic neurodegenerative diseases, such as Alzheimer's disease (AD) and Parkinson's disease (PD), are correlated with neuronal cell death, which involves many factors alone or in combination (Przedborski et al. 2003). Among all neurodegenerative diseases, significant attention has been given to Alzheimer's disease (AD), following by Parkinson's disease (PD) (Przedborski et al. 2003). While the signs and symptoms of AD affect such patients' quality of life, the conditions that lead to memory loss and death of neurons in this disease state are not yet defined. AD remains one of the top ten leading causes of death in the elderly population in the United States and it is referred as the progressive and irreversible neurodegenerative disorder in human brain (Chung, 2009). Current therapy predominantly treats AD symptoms and, at best, helps the disease from worsening as there is no known cure available for AD. Hence, there is an urgent need to better understand how astrocytes exert their protective effects on neurons. Once the mechanisms for astrocyte-mediated neuronal protection are elucidated, one can design treatment strategies to prevent the occurrence of accelerated neuronal loss in neurodegenerative diseases such as AD and PD.

Our project seeks to examine the underlying neuroprotective properties offered by astrocytes to protect neurons employing a cell model system *in vitro*. We have therefore developed cell model systems to investigate cytotoxic and inflammatory mechanisms associated with induction of neuronal cell damage and cell death (Malthankar et al. 2004, Dukhande et al. 2006, Wang et al. 2008). We have previously shown that U87 astrocytoma and SK-N-SH neuroblastoma cells constitute good model systems for astrocytes and neurons, respectively, *in vitro* because of their close

functional resemblance to normal astrocytes and neurons and that U87 cells protect SK-N-SH cells from several pathological assaults (Malthankar et al. 2004, Dukhande et al. 2006). We therefore hypothesized that different stress factors (e.g. oxidative stress and nutrient depletion) can elicit and/or enhance the neuroprotective effects of astrocytes through the activation of astrocytic signaling and alteration of astroglial function. In this study, we have investigated this hypothesis further.

## **Materials and Methods:**

### **Cell culture**

The human astrocytoma (U87) and neuroblastoma (SK-N-SH) cell lines were obtained from (ATCC; Manassas, VA, USA) and cultured in Minimum Essential Medium (MEM) supplemented with 10% (v/v) fetal bovine serum (Atlanta Biologicals; Lawrenceville, GA), 1% (w/v) sodium pyruvate (Sigma Aldrich; St Louis, MO), 0.292 g/L L-glutamine (Sigma), 1.5g/L sodium bicarbonate (Sigma) and 1% (v/v) antimycotic (Atlanta Biologicals). Cells were maintained at 37°C and 5% (v/v) CO<sub>2</sub> as described previously (Malthankar et al. 2004, Dukhande et al. 2006).

### **Treatment of U87 cells**

The U87 cells were cultured in T-75 tissue culture flasks until ~50% confluent in 20 ml of 10% FBS MEM medium. Then the medium was discarded and changed with 20 ml of 5% FBS-MEM medium and the cells incubated for 24 hours. After that, the medium was replaced with 20 ml of medium without FBS and the cells incubated for an additional 24 hours. Cells were treated with 5mM L-sulfoximine buthionine (BSO), or 20nM pioglitazone (PZ) or a combination of both frugs at the same concentrations. At

the end of another 24 hours of incubation, the media were first removed and frozen with liquid nitrogen immediately. The cells were collected subsequently and both cells and media collected were kept at -80°C until used for experiments.

### **Cell Survival (MTT) assay**

The neuroprotective properties of U87 cells on SK-N-SH cells were determined in different combinations of regular media (RM) and conditioned media (CM) collected from U87 cells cultured (see above) with RC/CM ratios of 100/0, 70/30, 50/50, 40/60, 30/70, and 0/100. 5000 SK-N-SH cells were seeded per well in a 48-well plate. After 48 hours of incubation at 37°C, 50 µl thiazolyl blue tetrazolium bromide (MTT) (5 mg/ml in PBS) reagent was added to each well. The medium in each well was removed after 4 hours at 37°C and the purple formazan crystals formed were solubilized using DMSO. Optical densities (OD) of the contents of the wells were read in a plate reader at 570 nm; the OD corresponded to the proportion of live cells in each well (Dukhande et al. 2006).

### **Western Blot Analysis**

Western blot analysis was used to assess protein expression in cell lysates to determine the effects of media, BSO and PZ. 10% SDS-PAGE gel electrophoresis was performed as described by Dukhande et al. (2006). The separated proteins were probed with anti-glutamine synthetase and anti-glial fibrillary acidic protein antibodies and then visualized using chemiluminescence detection kit with  $\beta$ -actin as the loading control.

### **Statistical Analysis of Data**

Statistical significance of experimental results was analyzed with one-way ANOVA followed by Tukey's post-hoc test with a minimum significance level set at  $p < 0.05$  using Kaleidagraph 4.0 software package.

## **Results and Discussion:**

Being a selective inhibitor of glutathione (a naturally-occurring antioxidant) synthesis, L-buthionine sulfoximine (BSO) is used to induce oxidative stress in cells. Pioglitazone (PZ), a peroxisome proliferator activated receptor gamma (PPAR $\gamma$ ) agonist, is used to block the inflammation which is usually unregulated in AD (Yamagishi 2000, Syversen et al. 2009). Consequently, we designed studies whereby we could use BSO and PZ to further elucidate the putative protective mechanism(s) on neurons-like SK-N-SH cells derived from conditioned media in which astrocytes-like U87 cells had been exposed to BSO or PZ or a combination of both drugs.

Serum depletion and drug treatment for U87 cell cultures were prepared as shown the flow chart below (Fig. 1). U87 cells cultured in medium containing 10% FBS were used as control (not shown in Fig. 1). Medium containing 0% FBS were defined as serum free (SF) medium.

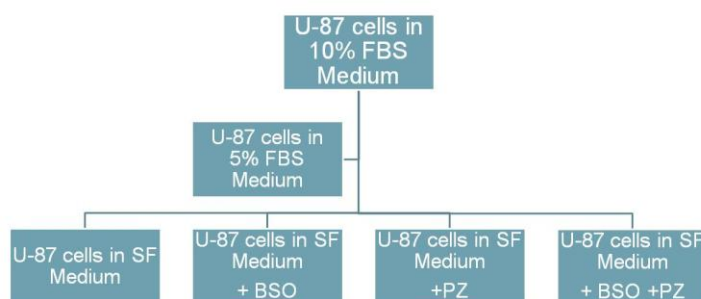


Figure 1. Experimental design of U87 cells treated with BSO, PZ or in combination.

Because oxidative and other environmental stresses can induce morphological and function changes/adaption in astrocytes *in vivo* and in culture, we employed light microscopy (by taking photomicrographs at 100x magnification) to examine the effects

of BSO treatment and FBS depletion to induce oxidative and environmental stress, respectively, on U87 cells and assess the effects of PZ treatment thereon.

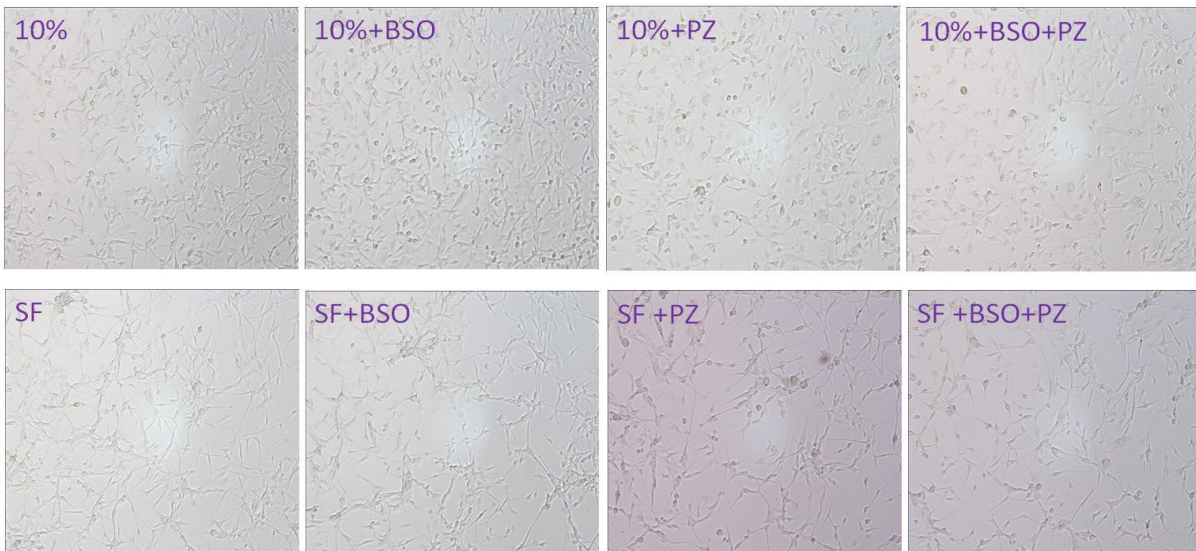


Figure.2 Treatment-induced cellular morphology changes in U87 cells (100X magnification).

In Figure 2, the top panel of photomicrographs shows U87 cells cultured in 10% FBS medium treated with or without drug or drug combination while those of the bottom panel represents U87 cells cultured in serum-deprived (SF) medium treated with or without drug or drug combination. In general, the photomicrographs revealed that treatment with SF medium induced U87 cells to extend multipolar processes. Moreover, treatment of U87 cells with or without drug treatment led to further changes in cellular morphology (e.g., extension of processes and shape changes) in addition to that noted in the U87 cells cultured in SF medium. Clearly, these observations raise interesting mechanistic questions that need to be addressed further: we were able to address two of these issues (see below) while others are beyond the scope of this study.

GFAP is an established marker for astrocytes: its altered expression is associated with changes in astroglial morphology. Thus, we employed Western blot to determine if the morphological changes in U87 cells exposed to SF medium with and

without BSO/PZ treatment were also associated with changes in glial fibrillary acid protein (GFAP) expression. GFAP expression was increased when U87 cells were cultured in SF medium compared to those cultured in 10% FBS medium, suggesting a correlation between changes its expression and cellular morphology (data not shown).

A key detoxification enzyme in astrocytes, glutamine synthetase (GS) can detoxify the excitotoxins glutamate and ammonia and its expression is modulated by changes in the surroundings of astrocytes. However, employing Western blot analysis we found little, if any, changes of GS expression in U87 cells exposed to the conditions employed (data not shown).

Growth factors and neuronal survival enhancers are putatively released into the medium by astrocytes to protect their surrounding neurons. To further investigate this neuroprotective mechanism, we collected media in which we grew U87 cells under the conditions specified in Figure 1 above and assessed their ability to influence survival of SK-N-SH cells employing the MTT cell survival assay (Fig. 3). Our results suggested that exposure of SK-N-SH cells to various combinations of SF media allowed them to survive better than when cultured in 10% FBS medium (control condition) alone (Fig. 3). Specifically, we found that exposure to PZ enhanced this protective effect, even under conditions of oxidative stress.

In conclusion, results from this study suggest changes in cell morphology of astrocytes-like U87 cells in various environmental conditions (e.g., serum deprivation & oxidative stress) can be correlated with up-regulation of GFAP in U87 cells.



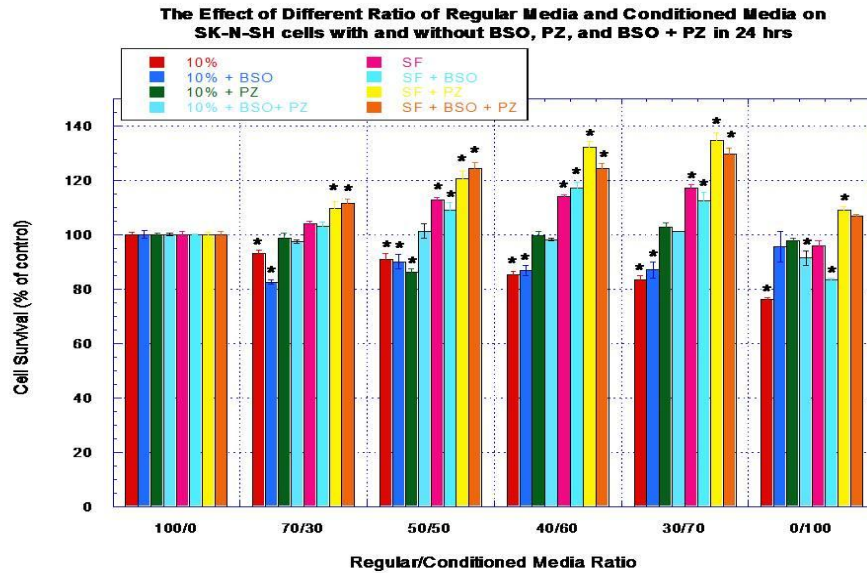


Figure 3. Treatment effects on SK-N-SH cell survival.

Our findings also suggest that conditioned medium has the ability to enhance the survival of neurons-like SK-N-SH cells and PZ treatment modulates this effect. Thus, our results provide additional evidence that our cell model can be productively employed to further elucidate the putative neuroprotective mechanisms of astrocytes. As such they assume pathophysiological importance in neuronal survival/death mechanisms in neurodegenerative diseases such as AD and PD. Clearly, this is an area that merits further study.

#### **Acknowledgment:**

Our studies were supported by NIH RO1 NS054038-01A1 subaward #A06474 and USAMRMC Project Grant (Contract #W81XWH-07-2-0078).

## **References:**

- Chung S. 2009. Aberrant phosphorylation in the pathogenesis of Alzheimer's disease. *BMB Rep.* 42(8): 467-474.
- Dukhande VV, Malthankar-Phatak GH, Hugus JJ, Daniels CK, Lai JCK. 2006. Manganese induced neurotoxicity is differentially enhanced by glutathione depletion in astrocytoma and neuroblastoma cells. *Neurochem Res.* 31(11):1349-1357.
- Malthankar GV, White BK, Bhushan A, Daniels CK, Rodnick KJ, Lai JCK. 2004. Differential lowering by manganese treatment of activities of glycolytic and tricarboxylic acid cycle enzymes in neuroblastoma and astrocytoma cells is associated with manganese-induced cell death. *Neurochem Res.* 29:709-717.
- Przedborski S, Vila M, Jackson-Lewis V. 2003. Neurodegeneration: What is it and where are we? *Journal of Clinical Investigation.* 111(1): 3-10.
- Sofroniew M V, Vinters H V. 2010. Astrocytes: biology and pathology. *Acta Neuropathol.* 119:7-35.
- Syversen, U., Stunes, A K, Gustafsson, B I. et al. 2009. Different skeletal effects of the peroxisome proliferator activated receptor (PPAR)  $\alpha$  agonist fenofibrate and the PPAR $\gamma$  agonist pioglitazone. *BMC Endocrine Disorders.* 9:10
- Wang Y-H, Jandhyam S, Dukhande VV, Gao WJ, Gu H-Y, Lai MB, Leung SW, Lai JCK. 2008. A co-culture model for nanotoxicity and tissue engineering studies. In *Technical Proceedings of the 2008 Nanotechnology Conference and Trade Show; Volume 2, Chapter 2: Environment, Health & Toxicology*, pp. 164-167.
- Yamagishi S. 2010. Protective role of PPAR $\gamma$  agonists against cardiovascular disease. *Nippon Rinsho.* 68(2): 307-11.

**Differential Cytotoxic Effects of Magnesium oxide Nanoparticles on Cisplatin Sensitive and Cisplatin Resistant Leukemia Cancer Cells**

Prathamesh P. Patil<sup>1,3</sup>, Maria B. Lai<sup>1,3</sup>, Solomon W. Leung<sup>2,3</sup>, James C.K. Lai<sup>1,3</sup>, and Alok Bhushan<sup>1,3</sup>

<sup>1</sup>Department of Biomedical & Pharmaceutical Sciences, College of Pharmacy;

<sup>2</sup>Department of Civil and Environmental Engineering, College of Engineering; and

<sup>3</sup>Biomedical Research Institute,

Idaho State University, Pocatello, ID 83209-8334

Address for correspondence:

Alok Bhushan

Department of Biomedical and Pharmaceutical Sciences

College of Pharmacy

Idaho State University

Pocatello, ID 83209-8334

Phone: 208-282-4408

Fax: 208-282-4482

Email:abhushan@pharmacy.isu.edu

## **Differential Cytotoxic Effects of Magnesium oxide Nanoparticles on Cisplatin Sensitive and Cisplatin Resistant Leukemia Cancer Cells**

### **Abstract:**

Magnesium oxide (MgO) has many applications in pharmaceutical, cosmetic and food industry. It has been extensively used in these industries for decades. Magnesium oxide is used in preparation of antacid, laxatives and mineral supplements. It is also used in cosmetics in preparation of sunscreens, toothpastes and dental cements. Earlier studies from our laboratory have characterized the effects of different metal oxide nanoparticles on normal fibroblast cells and cancer cells. In this study, we compared the cytotoxicity of magnesium oxide nanoparticles on murine leukemia cells (L1210) and cisplatin resistant sub line (L1210/DDP). We found that magnesium oxide nanoparticles exhibit differential cytotoxicity in L1210 and L1210/DDP leukemia cells. Our results also suggested that cisplatin resistant cancer cells were cross resistant to MgO nanoparticles. These findings may assume pathophysiologic importance in elucidation of mechanisms underlying anti-cancer drug resistance and may aid future discovery of anti-cancer drugs.

**Key Words:** cancer, resistance, nanoparticles, leukemia

### **Introduction:**

Approaches to treat cancers include surgery, chemotherapy and radiation therapy. Conventional chemotherapeutic agents like cisplatin, methotrexate, and 5-fluorouracil are used extensively in the treatment of a variety of cancers. One major reason for the failure of chemotherapy is resistance to primary chemotherapeutic agents used in

treatment (Gottesman *et al.* 2002). Certain cancers, which develop resistance to primary cancer chemotherapeutic agent(s), also develop cross resistance to other unrelated chemotherapeutic agents (Bhushan *et al.* 1999).

Several mechanisms contribute to the development of resistance in cancers. Some of the mechanisms include increased efflux of the drug out of the cancer cell, decreased influx of into the cancer cell, and increase in altered cellular targets (Siddik *et al.* 2003, Liu *et al.* 2009). Other studies implicate the involvement of altered cellular signaling in the development of resistance to chemotherapy in cancer cells.

Overcoming cancer drug resistance is a major hindrance in effective use of chemotherapeutic drugs to treat cancers. Development of resistance in cancer cells is the major cause of failure of chemotherapy in treatment of cancer (Giaccone *et al.* 1996). Better understanding of the drug resistance mechanisms is necessary so that novel strategies can be devised for more effective treatment of cancer. In this study, we use a novel approach to target resistance in cancer by using metal-based nanomaterials.

Metallic nanoparticles are a subtype of nanoparticles which comprise of nanoparticles made from metals and their compounds (e.g., titanium dioxide, zinc oxide, MgO, gold, silver). The use of nanomaterials provides new technology and approaches to develop drugs for treatment of diseases. The metallic nanoparticles differ from their bulk counterparts in several properties like magnetic, surface electric, and their optical properties owing to their small size. These properties make metallic nanoparticles suitable candidates for developing treatment therapies and diagnostic and imaging agents (Bhattacharya *et al.* 2008).

Work in our laboratory emphasizes the biological and toxicological effects of nanomaterials. Previous studies from our laboratory have examined the effects of different metallic nanoparticles on neurotumor cells and normal human fibroblasts. We found while zinc oxide and titanium oxide nanoparticles induced high cytotoxicity in normal fibroblasts, magnesium oxide nanoparticles exhibited comparatively low cytotoxicity on these cells even at high concentrations (Lai *et al.* 2008). Because MgO nanoparticles exhibited low cytotoxicity on normal fibroblasts, we selected them to determine if they could be used to overcome drug resistance in cisplatin resistant leukemia cancer cells. If resistant cells are susceptible to nanoparticles in influencing their proliferation, we can exploit this putative effect to develop novel ways to overcome anti-cancer drug resistance.

**Materials and Methods:** MgO nanopowder (Sigma-Aldrich Cat no: 549649, 50 nm particle size nanopowder) was dispersed in 100 ml of sterile saline in a sealed conical flask and stirred at ambient temperature for four hours prior to be diluted to the specified concentrations for treatment of cells. McCoy's 5A medium was purchased from Sigma-Aldrich. Mouse polyclonal antibodies for Akt and Erk, respectively, were obtained from Santa Cruz Biotechnology.

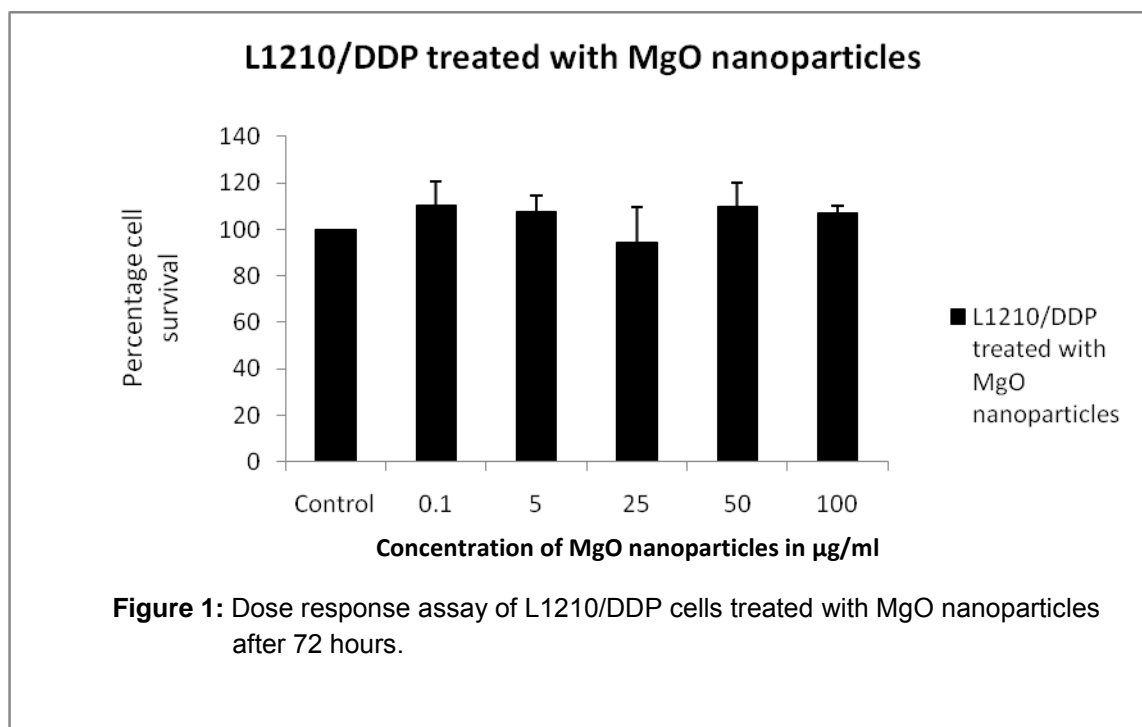
**Cells and Culture Conditions:** L1210 murine leukemia cells were purchased from Sigma-Aldrich and maintained under sterile conditions at 37°C and 5 % CO<sub>2</sub> in McCoy's 5A supplemented with 10% (v/v) horse serum. The L1210/DDP murine leukemia cells were obtained as a subline of L1210 cells resistant to cisplatin and were maintained under sterile conditions at 37°C and 5% CO<sub>2</sub> in McCoy's 5A supplemented with 10% (v/v) fetal bovine serum.

**Dose Response Assay:** L1210 and L1210/DDP cells were split at equal density in each well of 24-well plates. Cells in each well were treated with specified concentrations of MgO nanoparticles (ranging from 0.1 µg/ml to 100 µg/ml) for 72 hours at 37°C. After 72 hours, an aliquot was used for counting using a Z2 Beckman coulter counter.

**Western Blot Analysis:** L1210 cells were treated with various concentrations of MgO nanoparticles (10, 25, 50, or 100 µg/ml) for 72 hours. After treating the cells with MgO nanoparticles, cell lysates were prepared using the lysis buffer (1% (v/v) Triron X-100, 10 mM Tris base pH 7.6, 5 mM EDTA, 50 mM sodium chloride, 30 mM sodium pyrophosphate, 50 mM sodium fluoride, 0.1% (w/v) sodium azide, 50 mM phenyl methyl sulphonyl fluoride, 0.5 mg/ml aprotinin, 2.5 mg/ml leupeptin, and 100 mM sodium orthovanadate in distilled water, pH 7.6). BioRad reagents (Bradford assay) were used to determine the protein concentration. 25 µg of protein sample was loaded onto the wells in the sodium dodecyl sulphate polyacrylamide gel. The proteins separated by gel electrolysis were transferred to polyvinylidene fluoride membrane (PVDF), blocked (5% (w/v) Tris buffered saline with 0.01% (v/v) Tween or TBST in no-fat powdered milk). After washing, the blots were incubated in 1:500 primary antibody solution prepared in 5% bovine serum albumin (BSA) in distilled water. Membranes were washed and treated with the secondary antibody and developed using chemiluminescence kit (Pierce biotechnology, Rockford, Illinois), as recommended by the manufacturer. The blots were analyzed for the levels of Akt, pAkt, Erk and pErk. The scans were digitized using Unscan-it-gel 6.1 software

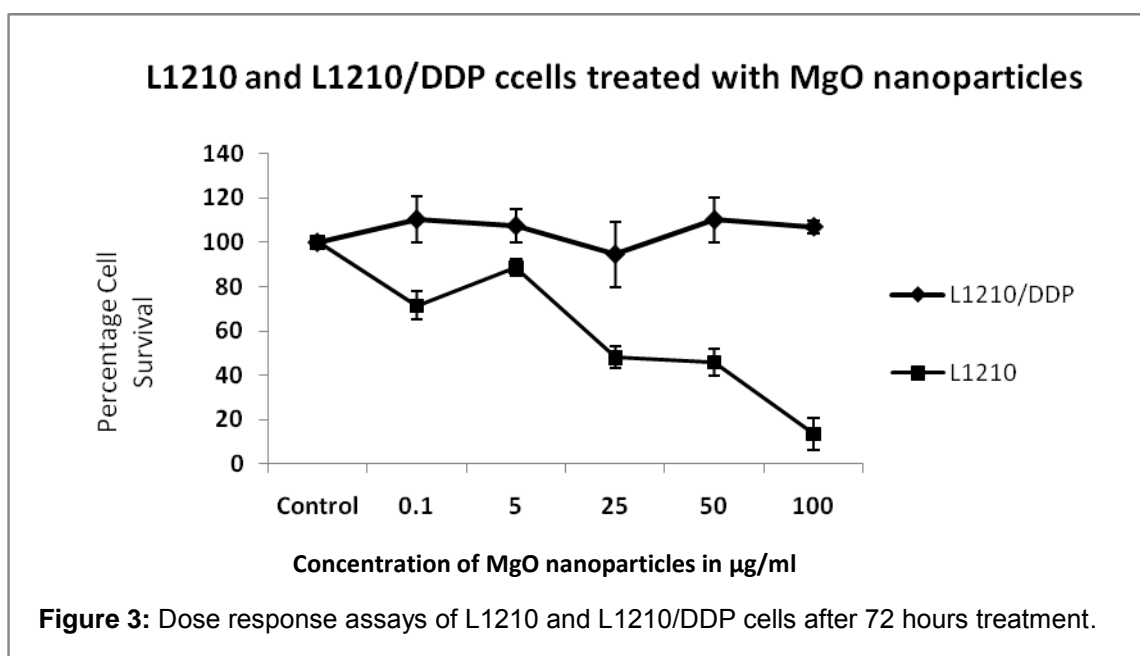
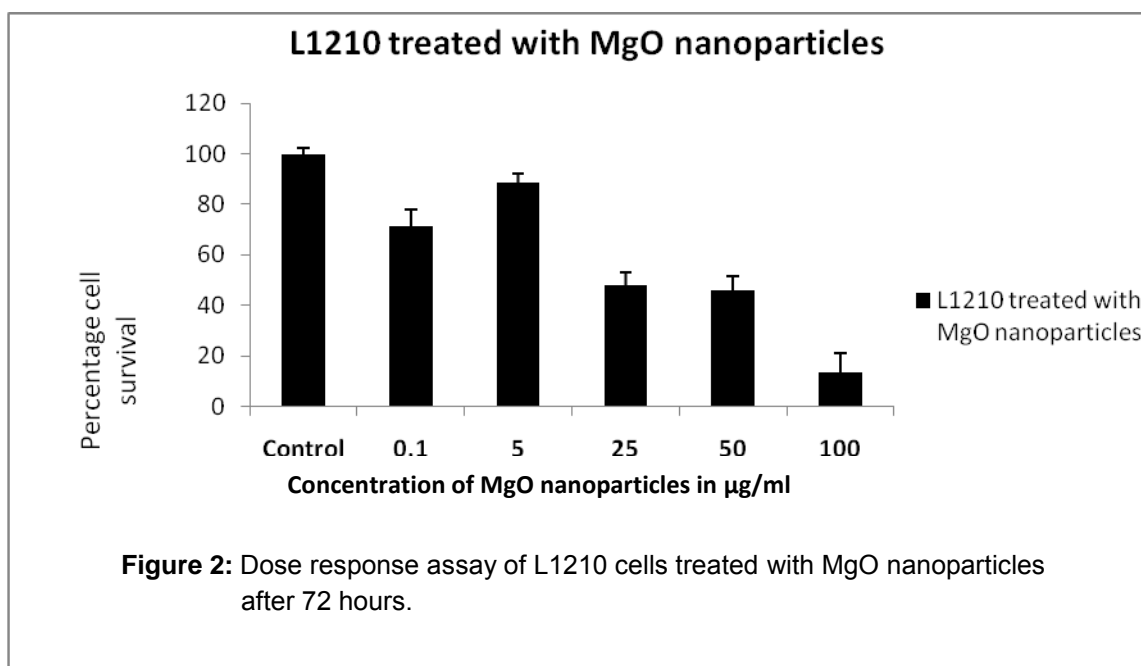
**Results:**

**Dose Response Studies:** L1210 and L1210/DDP cells were treated with different concentrations of magnesium oxide nanoparticles for 72 hours. The dose response studies were performed following the procedure described above.



The results revealed that at the concentrations employed, MgO nanoparticles did not exert any cytotoxic effect on L1210/DDP cells after 72 hours treatment (Figure 1). By contrast, MgO nanoparticles did exert some cytotoxic effects on L1210 cells after 72 hours treatment (Figure 2). When the effects of MgO nanoparticles on the two cell lines were compared (Figure 3), it was evident that the resistant L1210/DDP cells was not susceptible to the cytotoxicity of the nanoparticles at the concentrations used while the sensitive L1210 cells showed dose-related decrease in survival upon treatment with the nanoparticles.





**Akt and Erk expression:** We performed western blot analysis to assess the change in expression of cell signaling elements like Akt, pAkt, Erk and pErk in L1210 cells after MgO nanoparticles treatment using a procedure described above. Our results showed that the expression of pAkt and pErk in these cells decreases when treated with increasing concentrations of MgO nanoparticles (Figure 4).

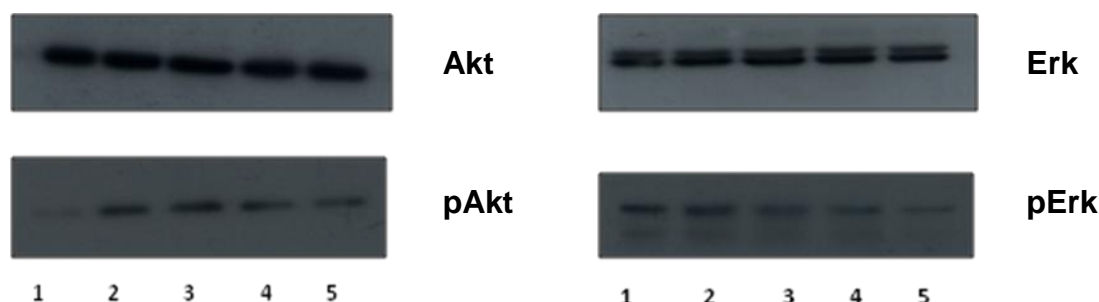


**Figure 4:** Western Blot Analysis of the effect of MgO nanoparticels on expression of AKT, pAKT, Erk and pErk in L1210 cells. In the above figure 1,2,3,4 and 5 represent the protein expression levels at control, 10 µg/ml, 25 µg/ml, 50 µg/ml and 100 µg/ml treatment of MgO nanoparticles.

In future we will examine the effects of these nanoparticles on expression of other cell signaling proteins like multiple drug resistance associated protein.

**Discussion:** The major reason for the failure of cancer chemotherapy is the development of resistance to chemotherapy in cancer cells. Few drug resistance mechanisms for cisplatin, which contribute to cisplatin resistance, include increase in intracellular glutathione, increase in MRP protein expression, and increase in DNA repair mechanisms. Despite these suggested mechanisms, a definitive mechanism for cisplatin drug resistance remains to be demonstrated. In our laboratory, we are developing a novel approach towards using metal-based nanoparticles in overcoming cancer drug resistance.

Although magnesium oxide nanoparticles did not overcome drug resistance in L1210/DDP cells, our results from the dose-response studies showed that the cisplatin resistant L1210/DDP leukemia cancer cells are cross resistant to MgO nanoparticles. We also observe that cisplatin sensitive leukemia cells are sensitive to MgO nanoparticles. These observations suggest that L1210/DDP may have similar mechanisms of drug resistance for cisplatin and for MgO nanoparticles.

Altered expression of signal transduction pathways are known to play a role in drug resistance. Our analysis of cell signaling proteins like Akt, pAkt, Erk and pErk by western blot analysis showed that the MgO nanoparticles decreased the expression of phosphorylated forms of Akt and Erk in the sensitive cell line. The decrease in the levels of phosphorylated forms of Akt and Erk with increasing concentrations of MgO nanoparticles in L1210 cells is highly suggestive of down-regulation of pathways leading to cellular proliferation and other processes critical for cancer progression. Clearly, this is an important area that merits further investigation.

**Acknowledgements:** Our study was supported, in part, by an USAMRMC Project Grant (Contract #W81XWH-07-2-0078), University Research Grant FY 2002-2009 and NIH P20RR016454.

**References:**

1. Bhattacharya, R., Mukherjee, P. (2008) Biological properties of “naked” metal nanoparticles. *Adv. Drug Deliv. Rev.* 60(11), 1289-306.
2. Bhushan, A., Hacker, M.P., Tritton T.R. (1999) Collateral methotrexate resistance in cisplatin-selected murine leukemia cells. *Braz. J. Med. Biol. Res.* 32, 827-33.
3. Giaccone, G., Pinedo H.M., (1996) Drug resistance. *Oncologist*, 1(1&2), 82-87.
4. Gottesman, M.M. (2002) Mechanisms of cancer drug resistance. *Annu. Rev. Med.* 53, 615-27.
5. Kartalou, M., Essigmann, J.M., (2001) Mechanisms of resistance to cisplatin. *Mutat Res.*, 478(1-2), 23-43.
6. Lai, J. C., Lai, M.B., Jandhyam, S., Dukhande, V.V, Bhushan, A., Daniels,C.K., Leung, S.W., (2008) Exposure to titanium dioxide and other metallic oxide

nanoparticles induces cytotoxicity on human neural cells and fibroblasts. *Int. J. Nanomedicine*, 3(4), 533–545.

7. Liu, F.S. (2009) Mechanisms of chemotherapeutic drug resistance in cancer therapy-A quick review *Taiwan J. Obstet. Gynecol.* 48(3), 239-244.
8. Siddik, Z.H. (2003) Cisplatin: mode of cytotoxic action and molecular basis of resistance. *Oncogene*, 22(47), 7265-79.

## ***Metallic Nanoparticles in Cancer Imaging and Therapy***

\*Alok Bhushan Ph.D., \*Prathamesh P. Patil B.Pharm., M.S., \*\*Solomon W. Leung Ph.D., and  
\*James C.K. Lai Ph.D.

\*Department of Biomedical & Pharmaceutical Sciences, College of Pharmacy and Biomedical  
Research Institute, Idaho State University, Pocatello, ID 83209, USA.

\*\*Department of Civil & Environmental Engineering, School of Engineering, College of Science  
& Engineering and Biomedical Research Institute, Idaho State University, Pocatello, ID 83209,  
USA.

Correspond Author: Dr. Alok Bhushan, Department of Biomedical & Pharmaceutical Sciences,  
College of Pharmacy, 921 S 8<sup>th</sup> Avenue, Stop 8288, Pocatello, ID 83209; Fax: 208-282-4482;  
Tel: 208-282-4408; email:abhushan@pharmacy.isu.edu

### Contents

1. Introduction
2. Applications of metallic nanoparticles in cancer imaging
3. Applications of metallic nanoparticles in cancer therapy
4. Conclusions and future directions

**Abstract** Use of nanoparticles in cancer diagnosis, detection, and therapy is rapidly gaining impetus. This review focuses on the recent advances in the applications of metallic nanoparticles in cancer imaging and therapy. In particular, we discuss the uses of iron oxide nanoparticles, gadolinium-based nanoparticles, and multimodal metallic nanoparticles in cancer imaging and detection. Subsequently, we discuss the applications of several types of cancer therapies based on the use of metallic nanoparticles. The latter applications include: metallic nanoparticles in photodynamic therapy, in hyperthermia therapy, and in neutron capture therapy as well as surface-modified metallic nanoparticles in cancer therapy. Despite the possibility that advances in biomedical applications of such nanoparticles may ultimately lessen the suffering of cancer patients and improve their prospects for survival, we raise a strong note of caution regarding the safety of clinical use of metallic nanoparticles because of their putative or demonstrated toxicity.

**Key Words:** Metallic nanoparticles; cancer imaging; cancer therapy

## **1. Introduction**

The diverse applications of nanotechnology in biomedical research and development have escalated exponentially in the last decade. This generalization is particularly pertinent when one considers the use of nanomaterials in the development of targeted drug delivery systems [1]. In light of growing interests in this and related areas, this review aims to highlight and discuss the recent and current advances of applications of one class of nanoparticles, namely metallic nanoparticles, in cancer imaging and therapy.

## **2. Applications of Metallic Nanoparticles in Cancer Imaging**

Although various other techniques (e.g., X-ray imaging, CT-Scans, ultrasound imaging) exist, this review focuses on the current use of metallic nanoparticles (including iron oxide nanoparticles such as nanoparticles of super paramagnetic iron oxides (SPIO) and ultrasmall superparamagnetic iron oxides (USPIO), gadolinium nanoparticles, and manganese nanoparticles) in magnetic resonance imaging (MRI) in the detection and staging of cancer [2].

### **2.1 Iron Oxide Nanoparticles**

Two subtypes of iron oxide nanoparticles are employed in the MRI applications — colloidal iron oxide nanoparticles and USPIO.

#### **Colloidal Iron Oxide Nanoparticles**

Colloidal iron oxides, also called superparamagnetic iron oxide (SPIO) nanoparticles constitute the first generation iron oxide nanoparticles and are comprised of colloidal iron oxides. Prepared by one-step alkaline precipitation of iron oxides (average size ~75 nm), they are stabilized by addition of polymers [3, 4].

Blood half life of SPIO nanoparticles is short because they are rapidly phagocytosed by mononuclear phagocyte system (MPS), leading to their accumulation in normal tissues but not in tumors [5]. This differential localization of phagocytosed SPIO nanoparticles facilitates the noninvasive and easy detection of tumors in the body by MRI.

SPIO nanoparticles have been successfully administered orally for imaging of the gastrointestinal tract [6]. Ferumoxsil (Lumirem) (i.e., SPIO nanoparticles coated with silicone) is approved for detecting cancer metastasis to the liver [7]. SPIO nanoparticles-enhanced MRI is superior to helical CT to detect liver metastases in candidates for hepatic resection [8] and superior to ultrasound and CT in detecting focal hepatic lesions and suspected cancer lesions [9].

Additionally, SPIO nanoparticles-enhanced MRI scans proved to be beneficial in planning surgeries of squamous cell carcinoma of head and neck [10].

Ferucarbotran (Resovist), another SPIO formulation, is currently under Phase III clinical trials in USA for detection of liver neoplasms. Ferumoxide (Endorem, Feridex) is an FDA-approved MRI contrasting agent for detection of neoplastic lesions in liver neoplasms.

### **Ultrasmall Superparamagnetic Iron Oxide (USPIO) Nanoparticles**

The second generation iron oxide nanoparticles, USPIO nanoparticles are smaller in size (<50 nm): consequently, their circulating half life is increased, thereby enabling them to permeate through the vascular endothelium and reach the interstitium and the lymph nodes [11]. In the lymph nodes, USPIO nanoparticles are rapidly phagocytosed by lymphocytes: their differential accumulation in lymph nodes gives rise to a contrast in the imaging of normal versus metastatic lymph tissues using MRI.

Staging of cancer is essential for planning its treatment. In contrast to the current less precise techniques of CT and ultrasound, MRI using ferumoxtran-10 can identify the spread of cancer to lymph nodes with better sensitivity and specificity [12]. MRI using USPIO nanoparticles helps identify patients requiring salvage radiation therapy after prostatectomy [13]. USPIO nanoparticles (i.e., ferumoxytol-10)-enhanced MRI potentially can detect brain tumors [14].

## **2.2 Gadolinium**

For some time, gadolinium chelates have been used as a MRI contrast agent [15]. Recently gadolinium-based nanoparticles have been introduced into these MRI applications. Gadolinium oxide nanoparticles with fluorescence probes have been synthesized for use as contrast agents for MRI and fluorescence imaging [16]. Silica nanoparticles loaded with gadolinium have been used to detect nasopharyngeal cancer in nude mice [17]. Gadolinium dendrimers are being researched



for their efficiency as MRI contrast agents: the efficiency of gadolinium delivery depends upon the type of dendrimer used. Comparative study of gadolinium delivery to lymph nodes using polyamidoamine (PMAM) and diaminobutane (DAB) dendrimers showed that PMAM dendrimers were the more efficient in delivering gadolinium to the lymph nodes [18], thereby demonstrating their potential use in detecting lymph node involvement of tumors by MRI imaging [19]. However, the drawback associated with the use of PMAM dendrimers labeled with gadolinium is the intrinsic toxicity associated with PMAM and gadolinium [20, 21].

### **2.3 Multimodal Metallic Nanoparticles**

Multi-modal imaging is sensitive, specific and yields more information than single-probe imaging. Multimodal metallic nanoparticles consist of magnetic nanoparticles as the core to which different functional moieties are tagged. The functional moieties can be fluorescence probes for fluorescence image analysis, antibodies for targeting a particular group of cells, or biomarker and radionucleotides for PET imaging [22]. For example, polysialic acid (PSA) is a cancer biomarker for neuroblastoma. HmenB1 antibody tagged with magnetic iron oxide nanoparticles having a dye doped silica core (for fluorescence imaging) can target PSA, thereby facilitating the detection of neuroblastoma in rats [23]. Similarly, iron oxide nanoparticles tagged with a fluorescence probe have been investigated for breast cancer detection in nude mice [24].

It is important to note that the current research trend on applications of metallic nanoparticles in cancer imaging strongly suggests that such applications can be coupled to or employed in conjunction with applications of metallic nanoparticles in cancer therapy.

### **3. Application of Metallic Nanoparticles in Cancer Therapy**

Conventional cancer therapies include chemotherapy, radiation therapy, and surgery. These therapies have limitations that decrease their efficacy: anti-cancer drugs exhibit adverse effects

on normal cells and cross-resistance to other anti-cancer drugs [25] and radiation therapy also show deleterious side effects [26]. Thus, improved cancer therapies are needed. Metallic nanoparticles have demonstrated potential in several experimental cancer therapies, including photodynamic therapy (PDT), hyperthermia therapy (HT), neutron capture therapy (NCT), and surface-modified metallic nanoparticles for drug delivery or anti-proliferative activity [27].

### **3.1 Metallic Nanoparticles in Photodynamic Therapy**

Photodynamic therapy (PDT) generally exploits a photosensitive compound that is subsequently activated using an external light source to kill the cancer cells [28]. When photons from the light source are incident upon the photosensitive material, the photosensitive drug is excited and produces reactive oxygen species that damage the cancer cells. Choice of the photosensitive compound depends upon the location of the tumor in the body [29,30].

Gold nanoparticles conjugated with epidermal growth factor receptor (EGFR) antibodies can induce cancer cell death after irradiation with light in the near-infrared (NIR) range. The conjugation of anti-EGFR antibodies to spherical gold nanoparticles facilitates their selective accumulation in cancer cells that over-express EGFR receptors [30]. The temperatures achieved upon NIR irradiation of gold nanoparticles *in vitro* were 70<sup>0</sup> - 80<sup>0</sup> C [31].

A comparison of the photothermal destruction of malignant cancer cells using gold nanoparticles with different surface dimensions and core material revealed that the efficiency of gold nanoparticles was dependent on the photothermal conversion efficiency and dimensions of nanoparticles [32]. Moreover, gold nanoshells can be used effectively for photodynamic therapy in cancer [33] and Au-Ag nanorods functionalized with aptamer exhibit specificity of these nanorods and their use for PDT in treating cancer [34].

The advantages of PDT include: 1) it is a noninvasive technique for killing cancer cells; 2) it induces tumor regression prior to surgery; and 3) it can target tumors located at inoperable areas (e.g., trachea). The main disadvantages of PDT therapy include, but are not limited to: 1) it uses near-IR light of limited power; 2) it does not penetrate more than 1 cm deep into the tissue; and 3) PDT therapy induces reddening or inflammation of the target tissue.

### **3.2 Metallic nanoparticles in Hyperthermia Therapy**

Hyperthermia therapy (HT) is effected by exposing the cancerous tissues to high temperatures of up to 42-43<sup>0</sup>C leading to damage or killing of cancer cells. Unlike PDT, where a light source is used to induce rise in target temperatures, HT utilizes radiofrequency, ultrasound, or microwave for raising the target temperatures [35]. HT is a conjugate therapy employed when the tumors are nonresponsive to chemotherapy and radiation therapy.

Conventional HT employing heating sources like microwave, radiofrequency or ultrasound is non-specific [36]. Metallic nanoparticles can help overcome this drawback: thus, the use of magnetic nanoparticles in HT was proposed [37]. Therapeutic potentials of iron oxide nanoparticulate formulations are being actively assessed in HT [38].

Use of magnetic iron oxide nanoparticles for HT is called “Magnetic Fluid Hyperthermia” (MFH) [39]. When iron oxide nanoparticles (dimensions < 10 nm) are subjected to an alternating external magnetic field, the heat so generated ultimately damages cancer cells. An *in vitro* and *in vivo* study demonstrated this MFH effect of Fe<sub>2</sub>O<sub>3</sub> nanoparticles in cultured liver cancer cells and in xenograph liver cancers [40]. Similarly, MFH effect of dextran coated iron oxide and that of silane-coated nanoparticles were studied in normal and cancerous human cells *in vitro*: the consequent hyperthermia induced cytotoxicity in cancer cells [41]. Furthermore, conjugating iron oxide nanoparticles with folate, which binds to its receptors expressed by cancer cells, is

effective in inducing hyperthermia within the cancer cells [42]. MFH effect of  $\text{Fe}_2\text{O}_3$ , in combination with arsenic trioxide, was noted in human cervical cancer cells [43] and Au nanoparticles produced marked hyperthermia in gastrointestinal cancer cells *in vitro* [44].

Despite their utility in inducing hyperthermia, a major drawback of this application is that the temperature generated thus inside cells is difficult to control. A new class of magnetic nanoparticles, manganite perovskites show promise to overcome this limitation. The curie temperatures ( $42^0 - 43^0\text{C}$ ) of silver-doped manganite perovskites enable isothermal heating [45].

### **3.3 Metallic Nanoparticles in Neutron Capture Therapy**

Neutron capture therapy utilizes a stable nuclide delivered to the tumor cells. Upon irradiation with neutrons, the stable nucleus produces ionizing radiations [46]. Boron Neutron capture therapy (BNCT) is a form of radiotherapy which utilizes neutron beam and boron-10: irradiation with neutron rays induces boron to form lithium and alpha rays. Although BNCT using boron-10 was investigated for treating glioblastoma multiforme [47], progress of BCNT in cancer treatment has been slow because few tumor-selective boron-containing drugs exist and the neutron beams employed are of the low-energy type [48, 49].

Use of gadolinium for NCT was recognized over two decades ago. Gadolinium emits gamma rays when irradiated with neutrons [50]. Currently, gadolinium nanoparticles (Gd-NP) are being investigated for their application in NCT [51]. A comparison of Gd-NP and gadolinium solution revealed that Gd-NP showed significant accumulation and tumor growth suppression in cancer cells as compared to gadolinium solution [52]. Gd-NP can also target cancer cells by attaching to Gd-NP ligands or antibodies specific to the cancer cells. By attaching folate to the surface of Gd-NP, the uptake of Gd-NP into cancer cells *in vitro* and *in vivo* is enhanced [46, 53].

### **3.4 Surface-modified metallic nanoparticles in cancer therapy**

Another type of application of metallic nanoparticles in cancer therapy exploits the intrinsic properties of the nanoparticles. That silver has been extensively commercialized in applications as anti-microbial agents [54] prompted investigations of anti-proliferative effect of silver nanoparticles on human glioblastoma cells [55]. Though the underlying mechanisms are incompletely understood, some researchers believe this anti-proliferative effect is attributable to oxidative stress induced by Ag nanoparticles [56]. Radioactive gold nanoparticles coated with gum arabica glycoprotein show promising results in targeting and treating prostate cancer: the nanoparticles passed through tumor vasculature to induce decrease in tumor volume [57].

One adverse effect of radiation therapy is its deleterious effects on normal cells. Cerium oxide nanoparticles have demonstrated selective radio-protective effect on normal cells [58]. For example, UV exposure of normal and tumor breast cells pretreated with cerium oxide nanoparticles induced more deaths in cancer cells compared to normal cells. Although the radio protective effect of nanoceria in normal cells is not understood, some researchers hypothesize this effect is due to superoxide dismutase enzyme mimetic activity of nanoceria [59].

Gadolinium endohedral metallofullerenol nanoparticles have exhibited high anti-tumor activity in mice bearing liver tumors [60]. Gadolinium endohedral metallofullerenol nanoparticles owe their anti-tumor activity to their ability to scavenge reactive oxygen species [61, 62]. Metallic nanoparticles of motexafin gadolinium also have similar antioxidant properties. Clinical studies have indicated that they can prevent metastasis of cancer to brain when administered to patients in early stages of non-small cell lung cancer (NSCLC) [63, 64].

Metallic nanoparticles have improved the delivery of chemotherapeutic drugs, specifically at the tumor site. Metallic nanoparticles like iron oxide nanoparticles which have magnetic properties

can be targeted to the tumor site under the influence of external magnetic field [65]. For example, employing iron oxide nanoparticles as carriers for chemotherapeutic drugs such as doxorubicin and camptothecin resulted in improved therapeutic efficacy of these drugs in decreasing tumor size in rat cancer xenograft model [66].

#### **4. Conclusions and Future Directions**

The current rapid and explosive advances of nanotechnology herald a new age in cancer diagnosis and therapy. In this review, we have only highlighted the seminal roles of metallic nanoparticles in cancer imaging and therapy. Clearly one should appreciate the advances we have discussed above constitute only a small fraction of the applications of nanotechnology in cancer imaging and therapy. However, limitation of space does not allow us to even mention other important advances unrelated to the use of metallic nanoparticles.

Although mortality rates due to cancer have shown decreases in the recent two decades, cancer is still the leading cause of disease-related deaths in USA. The advances in development of newer cancer imaging and therapies based on metallic nanoparticles may help in early detection of cancer and thus contribute to decreasing deaths due to cancer. Various cancer imaging and therapies based on use of metallic nanoparticles are at different stages of preclinical and clinical development. Iron oxide nanoparticles, zinc oxide nanoparticles, gold nanoparticles, silver nanoparticles, and cerium oxide nanoparticles have tremendous potentials to be developed as novel diagnostic and therapeutic agents in cancer.

Enhanced cancer biomarker and genetic mutation detection techniques would help in identifying individuals at high risk for developing cancer. In this context, multi-functional metallic nanoparticles show exciting therapeutic potentials and these are currently under development for cancer therapy to be clinically applied in the near future. Metallic nanoparticles can be

engineered to enhance the efficacy of current diagnostic and imaging techniques in cancer. Furthermore, cancer therapies utilizing metallic nanoparticles as targeting vehicles for drug delivery, and other allied therapies using metallic nanoparticles would also play key roles in clinical management of cancer in the next decade.

Understandably, the advances of the biomedical applications of metallic nanoparticles discussed above strongly suggest that the clinical applications of such nanoparticles may ultimately lessen the suffering of cancer patients and improve their prospects for survival. Nevertheless, we cannot help but inject a strong note of caution here. As the ubiquitous and diverse applications of nanotechnology have become almost uncontrollable phenomena, humans are increasingly exposed to nanoparticles and other nanomaterials although the health effects and environmental impact of their exposure have not been systematically assessed and are therefore largely unknown [67]. Moreover, recent advances in understanding the putative toxicity of nanoparticles and other nanomaterials [67-72] indicate that in developing metallic nanoparticles for cancer imaging and therapy, one needs to consider, and fully investigate in parallel, the putative toxicity of such nanoparticles prior to even adopting them for pre-clinical trial.

## **References**

1. Arruebo M, Fernández-Pacheco R, Ibarra MR, Santamaría J. Magnetic nanoparticles for drug delivery. *Nanotoday* 2007;3:22-32.
2. Bonnemain B. Superparamagnetic agents in magnetic resonance imaging: physicochemical characteristics and clinical applications. *J Drug Target* 1998; 6:167-174.
3. Qiu J, Yang R, Li M, Jiang. Preparation and characterization of porous ultrafine Fe<sub>2</sub>O<sub>3</sub> particles. *N Mater Res Bull* 2005; 40:1968-1975.

4. Babes L, Denizot B, Tanguy G, Le Jeune JJ, Jallet P. Synthesis of Iron Oxide Nanoparticles Used as MRI Contrast Agents: A Parametric Study. *J Colloid Interface Sci* 1999;212:474-482.
5. Pouliquen D, Le Jeune, JJ, Perdrisot R, Ermias A, Jallet P. Iron oxide nanoparticles for use as an MRI contrast agent: pharmacokinetics and metabolism. *Magn Reson Imaging* 1991; 9: 275-255.
6. Rubin D.L., Muller HH, Young SW, Hunke WA, Gorman WG. Optimization of an oral gastrointestinal contrast agent for magnetic resonance imaging. *Invest Radiol* 1994;29: 81-86.
7. Kubaska S, Sahani DV, Hahn PF, Halpern E. Dual contrast enhanced magnetic resonance imaging of liver with superparamagnetic iron oxide followed by gadolinium for lesion detection and characterization. *Clin Radiol* 2001;56:410-415.
8. Ward J, Robinson PJ, Guthrie, JA, Downing S, Wilson D. Liver metastases in candidates for hepatic resection: comparison of helical CT and gadolinium- and SPIOs – enhanced MR imaging. *Radiol* 2005;237:170-180.
9. Shah AJ, Parsons B, Pope I, Callaway M, Finch-Jones MD, Thomas MG. The clinical impact of magnetic resonance imaging in diagnosing focal hepatic lesions and suspected cancer. *Clin Imaging* 2009;33:209-212.
10. Mack MG, Balzer JO, Straub R, Eichler K, Vogl TJ, Superparamagnetic iron oxide enhanced MR imaging of head and neck lymphnodes. *Radiology* 2002;222:239-244.
11. Iannone A, Magin RL, Walczak T, Fedrico M, Swartz HM, Tomasi A. Blood clearance of dextran magnetite particles determined by a noninvasive *in vivo* ESR method. *Magn Reson Med* 1991;22:435-442.



12. Tatsumi Y, Tanigawa N, Nishimura H, Nomura E, Mabuchi H, Matsuki M, Narabayashi I. Preoperative diagnosis of lymph node metastasis in gastric cancer by magnetic resonance imaging with ferumoxtran-10. *Gastric Cancer* 2006;9:120-128.
13. Ross RW., Zietman AL, Xie W, Coen JJ, Dahl DM, Shipley WU, Kaufman DS, Islam T, Guimaraes AR, Weissleder R, Harisinghani M. Lymphotropic nanoparticle-enhanced magnetic resonance imaging (LNMRI) identifies occult lymph node metastases in prostate cancer patients prior to salvage radiation therapy. *Clin Imaging* 2009; 33:301-305.
14. Neuwelt EA, Varallyay CG, Manninser S, Solymosi D, Haluska M, Hunt MA. The potential of ferumoxytol nanoparticle magnetic resonance imaging, perfusion, and angiography in central nervous system malignancy: A pilot study. *Neurosurgery* 2007; 60:601-612.
15. Sitharaman B, Kissell KR, Hartman KB, Tran LA, Baikarov A, Rusakova I, Sun Y, Khant HA, Ludtke SJ, Chiu W, Laus S, Tóth E, Helm L, Merbach AE, Wilson LJ. Superparamagnetic gadonanotubes are high-performance MRI contrast agents. *Chem Commun (Camb)* 2005;31:3915-3917.
16. Bridot JL, Faure AC, Laurent S, Rivière C, Billotey C, Hiba B, Janier M, Josserand V, Coll JL, Elst LV, Muller R, Roux S, Perriat P, Tillement O. Hybrid gadolinium oxide nanoparticles: multimodal contrast agents for in vivo imaging. *J Am Chem Soc* 2007;129:5076-5084.
17. Liu LZ, Guo GJ, Zeng MS, Lü YC, Liu XW, Cui CY, Wu PH, Li L. [Gadolinium-loaded nanoparticle as a novel molecular imaging contrast agent for magnetic resonance imaging] *Zhonghua Yi Xue Za Zhi*. 2007;87:240-243.
18. Kobayashi H, Kawamoto S, Bernardo M, Brechbiel MW, Knopp MV, Choyke PL. Delivery of gadolinium-labeled nanoparticles to the sentinel lymph node: Comparison of the sentinel node

visualization and estimations of intra-nodal gadolinium concentration by the magnetic resonance imaging. *J Controlled Release* 2006;111:343-351.

19. Kobayashi H, Kawamoto S, Sakai Y, Choyke PL, Star RA, Brechbiel MW, Sato N, Tagaya Y, Morris JC, Waldmann TA. Lymphatic drainage imaging of breast cancer in mice by micro-magnetic resonance lymphangiography using a nano-size paramagnetic contrast agent. *J Natl Cancer Inst* 2004;96:703-708.

20. Xu R, Wang Y, Wang X, Jeong EK, Parker DL, Lu ZR. In Vivo evaluation of a PAMAM-cystamine-(Gd-DO3A) conjugate as a biodegradable macromolecular MRI contrast agent. *Exp Biol Med (Maywood)* 2007;232:1081-1089.

21. Perazella MA. Gadolinium-contrast toxicity in patients with kidney disease: nephrotoxicity and nephrogenic systemic fibrosis. *Curr Drug Saf* 2008;3:67-75.

22. Cheon J, Lee JH. Synergistically integrated nanoparticles as multimodal probes for nanobiotechnology. *Acc Chem Res* 2008;41:1630-1640.

23. Lee JH, Jun YW, Yeon SI, Shin JS, Cheon J. Dual-mode nanoparticle probes for high-performance magnetic resonance and fluorescence imaging of neuroblastoma. *Angew Chem Int Ed Engl* 2006;45:8160-8162.

24. Shan L, Wang S, Sridhar R, Bhujwalla ZM, Wang PC. Dual Probe with Fluorescent and Magnetic Properties for Imaging Solid Tumor Xenografts. *Mol Imaging* 2007;6:85-95.

25. Assaraf YG. The role of multidrug resistance efflux transporters in antifolate resistance and folate homeostasis. *Drug Resist Updat* 2006;9:227-246.

26. Al-Mefty O, Kersh JE, Routh A, Smith RR. The long-term side effects of radiation therapy for benign brain tumors in adults. *J Neurosurg* 1990;73:502-512.

27. Liang S, Wang Y, Yu J, Zhang C, Xia J, Yin D. Surface modified superparamagnetic iron oxide nanoparticles: as a new carrier for bio-magnetically targeted therapy. *J Mater Sci Mater Med* 2007;18:2297-2302.
28. Dolmans D, Fukumara D, Jain RK. Photodynamic therapy for cancer. *Nature Rev Cancer* 2003;3:380-387.
29. Wilson BC. Photodynamic therapy for cancer: Principles. *Can. J. Gastroenterol* 2002;16:393-396.
30. Huang X, El-Sayed, IH, Qian W, El-Sayed MA. Cancer cell imaging and photothermal therapy in near IR region by using gold nanorods. *J Am Chem Soc* 2006; 128:2115-2120.
31. Huang X, Jain PK, El-Sayed IH, El-Sayed MA. Determination of the minimum temperature required for selective photothermal destruction of cancer cells with the use of immunotargeted gold nanoparticles. *Photochem Photobiol* 2006; 82:412-417.
32. Fong, YC, Chen TC, Chen SY. Comparative efficiencies of photothermal destruction of malignant cells using antibody cells using antibody-coated silica@Au nanoshells, hollow Au/Ag nanospheres and Au nanorods. *Nanotechnology* 2009;20:425104.
33. Gobin AM, Lee MH, Halas NJ, James WD, Drezek RA, West JL. Near-Infrared resonant nanoshells for combined optical imaging and photothermal cancer therapy. *Nano Lett* 2007;7:1929-1934.
34. Huang YF, Sefah K, Bamrungsap S, Chang HT, Tan W. Selective photothermal therapy for mixed cancer cells using aptamer-conjugated nanorods. *Langmuir* 2008;24:11860-11865.
35. Diederich CV. Thermal ablation and high-temperature thermal therapy: overview of technology and clinical implementation. *Int J Hyperthermia* 2005;21(8):745-753.

36. Kong G, Braun RD, Dewhirst MW. Hyperthermia enables tumor-specific nanoparticle delivery: effect of particle size. *Cancer Res* 2000;60:4440-4445.
37. Gilchrist R K. Selective Inductive Heating of Lymph. *Ann Surg* 1957;146(4): 596–606.
38. Xie J, Huang J, Li X, Sun S, Chen X. Iron oxide nanoparticle platform for biomedical applications. *Curr Med Chem*. 2009;16(10):1278-1294.
39. Latorre M, Rinaldi C. Applications of magnetic nanoparticles in medicine: magnetic fluid hyperthermia. *P R Health Sci J* 2009;28:227-238.
40. Therapeutic effect of  $\text{Fe}_2\text{O}_3$  nanoparticles combined with magnetic fluid hyperthermia on cultured liver cancer cells and xenograft liver cancers. *J Nanosci Nanotechnol* 2005;5:1185-1192.
41. Jordan A, Scholz R, Wust P, Schirra H, Schiestel T, Schmidt H, Felix R. Endocytosis of dextran and silan-coated magnetite nanoparticles and the effect of intracellular hyperthermia on human mammary carcinoma cells in vitro. *J Magnetism and Magnetic Materials* 1999; 94:185-196.
42. Sonvico F, Mornet S, Vasseur S, Dubernet C. Folate-conjugated iron oxide nanoparticles for solid tumor targeting as potential specific magnetic hyperthermia mediators: synthesis, physicochemical characterization and, in vitro experiments. *Bioconjugate Chem* 2005;16:1181-1188.
43. Du Y, Zhang D, Liu H, Lai R. Thermochemotherapy effect of nanosized  $\text{As}_2\text{O}_3/\text{Fe}_3\text{O}_4$  complex on experimental mouse tumors and its influence on the expression of CD44v6, VEGF-C and MMP-9. *BMC Biotechnol* 2009; 9:84.

44. Ganon CJ, Patra CR, Bhattacharya R, Mukherjee P, Curley SA. Intracellular gold nanoparticles enhance non-invasive radiofrequency thermal destruction of human gastrointestinal cancer cells. *J Nanobiotechnol* 2008;6:2.
45. Melnikov OV, Gorbenko Y, Markelova MN, Kaul AR, Atsarkin VA. Ag-doped manganite nanoparticles: New materials for temperature-controlled medical hyperthermia. *J Biomed Mater Res A* 2008;91(4):1048-1055.
46. Oyewumi MO, Mumper RJ. Engineering tumor-targeted gadolinium hexanedione nanoparticles for potential application in neutron capture therapy. *Bioconjugate Chem* 2002;13:1328-1335.
47. Yamamoto T, Nakai K, Matsumura A. Boron neutron capture therapy for glioblastoma. *Cancer Lett* 2008;262(2):143-152.
48. Barth, RF. Boron neutron capture therapy at the crossroads: challenges and opportunities. *Appl Radiat Isot* 2009;67(7-8 Suppl):S3-S6.
49. Barth RF. A critical assessment of boron neutron capture therapy: an overview. *J Neuro-Oncol* 2003;62:1-5.
50. Martin RF, D'Cunha G, Pardee M, Allen BJ. Induction of DNA double-strand breaks by <sup>157</sup>Gd neutron capture. *Pigment Cell Res* 1989;2:330-332.
51. Tokumitsu H, Ichikawa H, Fukumori Y. Chitosan-gadopentetic acid complex nanoparticles for gadolinium neutron-capture therapy of cancer: preparation by novel emulsion-droplet coalescence technique and characterization. *Pharm Res* 1999;16:1830-1835.
52. Shikata F, Tokumitsu H, Ichikawa H, Fukumori Y. In vitro cellular accumulation of gadolinium incorporation into chitosan nanoparticles designed for neutron-capture therapy of cancer. *Eur J BioPharm* 2002;53:57-63.

53. Oyewumi MO, Yokel RA, Coakley T, Mumper RJ. Comparison of cell uptake, biodistribution and tumor retention of folate and PEG-coated gadolinium nanoparticles in tumor bearing mice. *J Control Release* 2004;95:613-626.
54. Percival SL, Bowler P.G., Dolman J. Antimicrobial activity of silver containing dressing on wound microorganisms using in vitro biofilm model. *Int Wound J.* 2007;4:186-191.
55. Rahman MF, Wang J, Patterson TA, Saini UT, Robinson BL, Newport GD, Murdock R.C, Schlager JJ, Hussain SM, Ali SF. Expression of genes related to oxidative stress in the mouse brain after exposure to silver nanoparticles. *Toxicol Lett* 2009;187:15-21.
56. AshaRani PV, Hande MP, Valiyaveetil S. Anti-proliferative activity of silver nanoparticles. *BMC Cell Biology* 2009;10:65.
57. Chanda N, Kan P, Watkinson LD, Shukla R, Zambre A. *et al.* Radioactive gold nanoparticles in cancer therapy: therapeutic efficacy studies of GA-198AuNP nanoconstruct in prostate tumor-bearing mice. *Nanomed* 2010;6(2):201-209.
58. Tarnuzzer RW, Colon J, Patil S, Seal S. Vacancy Engineered Ceria Nanostructures for protection from Radiation-Induced cellular damage. *Nano Lett* 2005;5:2573-2577.
59. Heckert EG, Karakoti AS, Seal Sudipta, Self WT. The role of cerium redox state in the SOD mimetic activity of nanoceria. *Biomaterials* 2008;29:2705-2709.
60. Chen C, Xing G, Wang J, Zhao Y, Li B, Tang J, Jia G, Wang T, Sun J, Xing L, Yuan H, Gao Y, Meng H, Chen Z, Zhao F, Chai Z, Fang X. Multihydroxylated [Gd@C82(OH)22]n nanoparticles: antineoplastic activity of high efficiency and low toxicity. *Nano Lett* 2005;5:2050-2057.

61. Wang J, Chen C, Li B, Yu H, Zhao Y, Sun J, Li Y, Xing G, Yuan H., Tang J, Chen Z, Meng H, Gao Y, Ye C, Chai Z, Zhu C., Ma B, Fang X, Wan L. Anti-oxidative function and biodistribution of [Gd@C82(OH)22]n nanoparticles in tumor-bearing mice. *Biochem Pharmacol* 2006;71:872-881.
62. Yin JJ, Lao F, Meng J, Fu PP, Zhao Y, Xing G, Gao X, Sun B, Wang PC, Chen C, Liang XJ. Inhibition of tumor growth by endohedral metallofullerenol nanoparticles optimized as reactive oxygen species scavenger. *Mol Pharmacol* 2008;74:1132-1140.
63. Thomas SR, Khuntia D. Motexafin gadolinium injection for the treatment of brain metastases in patients with non-small cell lung cancer. *Int J Nanomed* 2007;2:79-87.
64. Mehta MP, Shapiro WR, Phan SC, Gervais R, Carrie C, Chabot P, Patchell RA. Motexafin gadolinium combined with prompt whole brain radiotherapy prolongs time to neurologic progression in non-small-cell lung cancer patients with brain metastases: results of a phase III trial. *Int J Radiat Oncol Biol Phys* 2009;73:1069-1076.
65. C. Alexiou, Jurgons R., Schmid R, Hilpert A, Bergemann C, Parak F, Iro H In vitro and in vivo investigations of targeted chemotherapy with magnetic nanoparticles. *Journal of Magnetism and Magnetic Materials* 2005;293:389-393.
66. Munnier E, Cohen-Jonathan S, Linassier C, Douziech-Eyrolles L, Marchais H, Soucé M, Hervé K, Dubois P, Chourpa I. Novel method of doxorubicin-SPION reversible association for magnetic drug targeting. *Int J Pharm* 2008;363:170-176.
67. Lai JCK, Schoen MP, Perez Gracia A, Naidu DS & Leung SW. Prosthetic devices: challenges and implications of robotic implants and biological interfaces: In: *Proc I Mech E, Vol 221 Part H, J Engineering in Medicine, Special Issue entitled: "Micro and Nano Technologies in Medicine"*; 2007, p 173-183.

68. Aghargar VA, Bhushan A, Lai JCK, Daniels CK. Cytotoxic Effects of Short Multiwall Carbon Nanotubes: In: Technical Proceedings of the 2008 Nanotechnology Conference and Trade Show, Volume 2, Chapter 2: Environment, Health & Toxicology; 2008, p. 122-125.
69. Jandhyam S, Lai MB, Dukhande VV, Bhushan A, Daniels CK, Leung SW, Lai JCK. Silicon dioxide nanoparticles exert dissimilar cytotoxic effects on mammalian cell types: In: Technical Proceedings of the 2008 Nanotechnology Conference and Trade Show, Volume 2, Chapter 2: Environment, Health & Toxicology; 2008, p. 126-129.
70. Lai MB, Jandhyam S, Dukhande VV, Bhushan A, Daniels CK, Leung SW, Lai JCK. Differential cytotoxicity of metallic oxide nanoparticles in mammalian cells: In: Technical Proceedings of the 2008 Nanotechnology Conference and Trade Show, Volume 2, Chapter 2: Environment, Health & Toxicology; 2008, p. 130-133.
71. Lai JCK, Lai MB, Jandhyam S, Dukhande VV, Bhushan A, Daniels CK, Leung SW. Exposure to titanium dioxide and other metallic oxide nanoparticles induce cytotoxicity on human neural cells and fibroblasts. *Int J Nanomed* 2008;3:533-545.
72. Lai JCK, Ananthakrishnan G, Jandhyam S, Dukhande VV, Bhushan A, Gokhale M, Daniels CK, Leung SW. Treatment of human astrocytoma U87 cells with silicon dioxide nanoparticles lowers their survival and alters their expression of mitochondrial and cell signaling proteins. *Int J Nanomed* 2010;5:715-723.



# A Noncontact Co-Culture Model of Peripheral Neural Cells for Nanotoxicity, Tissue Engineering and Pathophysiological Studies

A.R. Jaiswal<sup>\*</sup>, Yin Yin W. Wong<sup>\*\*</sup>, Alok Bhushan<sup>\*\*\*</sup>, Christopher K. Daniels<sup>\*\*\*\*</sup> and James C.K. Lai<sup>\*\*\*\*\*</sup>

<sup>\*</sup>Department of Biomedical and Pharmaceutical Sciences, College of Pharmacy, and Biomedical Research Institute, Idaho State University, Pocatello, ID 83209, USA Fax: 208-282-4305; Tel: 208-705-2447

<sup>\*\*</sup>Department of Biomedical & Pharmaceutical Sciences, College of Pharmacy, and Biomedical Research Institute, Idaho State University, Pocatello, ID 83209, USA Fax: 208-282-4305; Tel: 469-463-5139, email: [wongyin@pharmacy.isu.edu](mailto:wongyin@pharmacy.isu.edu)

<sup>\*\*\*</sup>Department of Biomedical & Pharmaceutical Sciences, College of Pharmacy, and Biomedical Research Institute, Idaho State University, Pocatello, ID 83209, USA Fax: 208-282-4305; Tel: 208-282-4408, email: [abhushan@pharmacy.isu.edu](mailto:abhushan@pharmacy.isu.edu)

<sup>\*\*\*\*</sup>Department of Biomedical & Pharmaceutical Sciences, College of Pharmacy, and Biomedical Research Institute, Idaho State University, Pocatello, ID 83209, USA Fax: 208-282-4305; Tel: 208-282-3324, email: [cdaniels@pharmacy.isu.edu](mailto:cdaniels@pharmacy.isu.edu)

<sup>\*\*\*\*\*</sup>Corresponding author: Department of Biomedical & Pharmaceutical Sciences, College of Pharmacy, and Biomedical Research Institute, Idaho State University, Pocatello, ID 83209, USA Fax: 208-282-4305; Tel: 208-282-2275, E-mail: [lai@pharmacy.isu.edu](mailto:lai@pharmacy.isu.edu)

## ABSTRACT

Cell culture models *in vitro* have long served as tools for the elucidation of cellular and molecular mechanisms of diseases. Recently these versatile models have gained wide acceptance in toxicology and tissue engineering research. Although these models are not exactly the same as the models *in vivo*, they facilitate mechanistic insights pertaining to a particular cell type. Nevertheless, co-cultures of two different but functionally complementary cell types provide structural and functional perspectives single-cell-type models do not. We have initiated a systematic development of this model type employing dorsal root ganglion (DRG) neurons and Schwann cells. Our first model involves non-contact co-cultures of Schwann cells and DRG neurons employing the hanging cell culture insert. The results from our studies to date demonstrate that our non-contact co-culture model is suitable for both high throughput and mechanistic studies in nanotoxicological and pathophysiological research.

**Keywords:** Co-culture model, DRG neurons, Schwann cells, nanotoxicology, tissue engineering, pathophysiology.

## Topic:

## 1 INTRODUCTION

The aim of our studies is to systematically develop and characterize cell culture models of neural cells of the peripheral nervous system *in vitro* for nanotoxicological and pathophysiological research. Once such models are developed, they may have wide applications in tissue engineering research. The need for such models is derived from the fact that the peripheral nervous system is most susceptible for the development of neuropathy. Some examples of peripheral neuropathies include drug-(chemotherapy) induced neuropathy [1], disease-induced neuropathy (e.g., diabetes) [2], immune and inflammatory neuropathies, inherited and genetic neuropathies, and other neuropathies induced by toxicity.

The applications of nanomaterials, including nanoparticles, have been increasing exponentially in the last decade and have infiltrated diverse fields. Once they enter the body by inhalation or other routes, nanoparticles may be toxic to one or more organ systems [3]. However, the toxicity of nanoparticles in mammals, especially humans, has not been systematically studied although there is increasing concern about the environmental and health impact of exposure to nanoparticles of different types [4].

Consequently, we have systematically initiated a series of studies to elucidate the putative cytotoxicity of nanoparticles in various mammalian cell types [4]. For example, once recent study of ours noted that several metal oxide (including titanium and zinc oxides) nanoparticles exert differential cytotoxic effects on human neural cells in cell model systems *in vitro* [4].

There have been, however, extremely few cell model systems developed employing peripheral neural cell types for nanotoxicological and tissue engineering studies. We have therefore initiated a systematic development of this type of models employing Schwann cells and dorsal root ganglion (DRG) neurons. The first model we have developed involved a non-contact co-culture model of Schwann cells and DRG neurons using the hanging cell culture insert. Thus, this type of co-culture cell systems, consisting of two distinctly different but functionally complementary cell types, provide structural and functional perspectives that single-cell-type models do not.

We hypothesized that non-contact co-culture model of Schwann cells and DRG neurons can be useful in elucidating the putative toxic effects of various nanoparticles on the peripheral nervous system. Furthermore, the putative cytotoxic effects of nanoparticles could also influence/disrupt the cell-to-cell communications between the two cell types. To test our hypothesis, we have initially characterized the Schwann cells the DRG neurons in monotypic or single-cell-type cultures. In our ongoing studies, employing our new co-culture, non-contact model, we have recently demonstrated that the survival of DRG neurons is increased when co-cultured with Schwann cells in this construct. In this study, we compare the putative cytotoxic effects of SiO<sub>2</sub> and TiO<sub>2</sub> nanoparticles on dorsal root ganglion (DRG) neurons and Schwann cells employing established cytotoxicity testing [5-8]. Furthermore, we are investigating the putative toxic effect of these nanoparticles on interaction(s) between DRG neurons and Schwann cells in non-contact co-culture.

## 2 MATERIALS AND METHODS

### 2.1 Cells and Culture Conditions

The immortalized DRG neurons were a gift from Dr. Ahmet Hoke's Laboratory at Johns Hopkins University (Baltimore, MD, USA)[9]. The rat Schwann cell line was obtained from ATCC (Manassas, VA, USA). These cells and their co-culture were cultured in DMEM (Sigma; St Louis, MO, USA) supplemented with 10% (v/v) fetal bovine serum (FBS), 1% (w/v) sodium pyruvate, 0.292 g/l L-glutamine, 1.5 g/l sodium bicarbonate, 1% (v/v) anti-mycotic and various specified concentrations (5-45 mM) of glucose.

### 2.2 Co-culture Model System

DRG neurons were cultured on a Corning Costar 24-well plate. Schwann cells were then seeded on a Millipore hanging cell culture insert (pore size 0.4  $\mu$ m) on a separate plate and then introduced to a DRG neuron-containing well after 4 hours to achieve the co-culture condition [7]. DRG neurons (co-cultured with Schwann cells) were exposed to various concentrations of SiO<sub>2</sub> nanoparticles for specified periods and their survival determined employing the cell survival assay.

### 2.3 Cell Survival (MTT) Assay

DRG neurons or Schwann cells were seeded per well in a 48-well plate in DMEM with specified concentrations of SiO<sub>2</sub> nanoparticles. After incubation at 37°C for 24 or 48 hours, 50  $\mu$ l of MTT (5 mg/ml in PBS) reagent was added to each well. After incubation for another 4 hours, the medium was removed gently and the cellular reaction product was solubilized in 200  $\mu$ l DMSO. Then the optical density of the contents of each well was measured in a plate reader at 570 nm [4]. The absorbance corresponds to live cells present in each well [4].

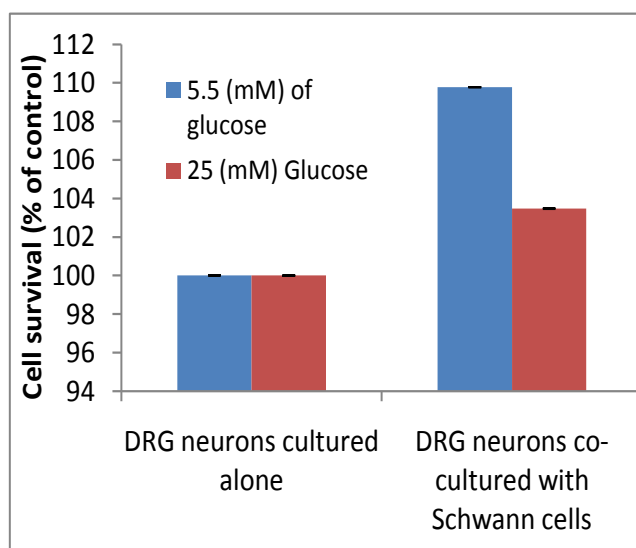


Figure 1: Co-cultures of DRG neurons and Schwann cells using hanging cell culture inserts (non-contact co-culture). Values are mean  $\pm$  SEM of 2-3 determinations. DRG neurons cells treated with SiO<sub>2</sub> nanoparticles for 24 hours are marked with blue line and those treated for 48 hrs are marked with red line.

### 2.4 Cellular morphology

DRG neurons, Schwann cells and their co-culture was treated with SiO<sub>2</sub> specified concentration for 24 and 48 hours at 37°C as described above and bright field images were acquired by using a Leica light microscope (Leica DM IRB, Bannockburn, IL, USA) equipped with a digital camera (Leica DFC 300FX) [4].

## 2.5 Statistical analysis of results

Statistical significance of experimental results was analyzed with one-way ANOVA followed by Dunnett's post-hoc test with a minimum significance level set at  $p < 0.05$  using the SPSS 17 software package.

## 3 RESULTS AND DISCUSSION

We are the first to employ dorsal root ganglion (DRG) neurons and Schwann cells to develop co-culture models *in vitro* because DRG neurons are the most susceptible nerve cells to developing pathologies in peripheral neuropathy. We have characterized the two cell types individually with respect to their optimum glucose requirement and activities of enzymes important in modulation of glutamate-glutamine cycling (e.g., glutamine synthetase) that is part of the metabolic and functional inter-dependence between DRG neurons and Schwann cells known to occur *in vivo* (data not shown). We have also studied the protein expression of various apoptosis-related proteins such as BCL-2, BCL-XL, BAX and cytochrome C in the two cell types (data not shown).

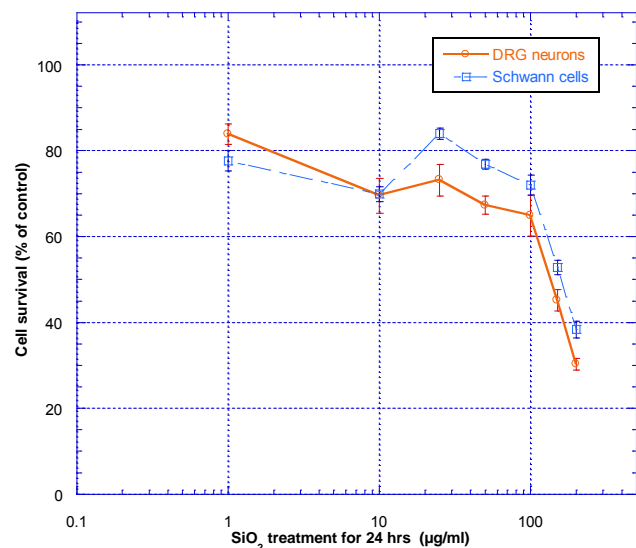


Figure 2: Effects of SiO<sub>2</sub> nanoparticles on DRG neurons and Schwann cells. Values are mean  $\pm$  SEM of 12 determinations and replicate experiments show the same trend. DRG neurons and Schwann cells treated with SiO<sub>2</sub> nanoparticles for 24 hours are marked red and blue, respectively. treated with SiO<sub>2</sub> nanoparticles for 24 hrs are marked with blue line.

To our knowledge, we are the first to determine, in this study, the putative cytotoxic effects of SiO<sub>2</sub> and TiO<sub>2</sub> nanoparticles on neural cells of the peripheral nervous system (i.e., DRG neurons and Schwann cells).

As shown in Figure 2, treatment of DRG neurons or Schwann cells for 24 hours with SiO<sub>2</sub> induced a dose-related decreases in survival of those cells when we progressively increased the concentrations of the nanoparticles from 1 to 200  $\mu$ M, with IC<sub>50</sub> values of  $\sim$ 150  $\mu$ M (Figure 2). At the highest concentration employed, less than 40% of the cells survived (Figure 2).

Because we had previously noted that TiO<sub>2</sub> nanoparticles exerted differential cytotoxic effects on central nervous system neural cells [4], we have investigated the possibility that these nanoparticles may also exert cytotoxic effects on neural cells from the peripheral nervous system. As shown in Figure 3, our ongoing studies indicate that treatment with TiO<sub>2</sub> nanoparticles in the dose range so far employed (0.1 to 20  $\mu$ M) appeared to lower the survival of both DRG neurons and Schwann cells: the effects seemed somewhat dose-related. Moreover, the Schwann cells appeared to be more susceptible to the effect of TiO<sub>2</sub> nanoparticles, suggesting they may exert differential effects on the neural cells of the peripheral nervous system.

We have also employed light microscopy to examine the effects of nanoparticles on DRG neurons and Schwann cells and assess the effects of SiO<sub>2</sub> and TiO<sub>2</sub> nanoparticles thereon (data not shown). In general, the photomicrographs revealed that treatment with the nanoparticles induced dose-related changes in cellular morphology consistent with the nanoparticle-induced progressive decrease in cell viability (Figures 2 and 3).

As we have previous noted, treatment with TiO<sub>2</sub> nanoparticles induced dose-related increases in cell death of human central neural cells, marked by apoptosis, and necrosis, and an as yet uncharacterized cell death mechanism that appeared to be a mixture of apoptosis and necrosis [4]. Thus, the results of our ongoing studies with the peripheral nervous system neural cells such as DRG neurons and Schwann cells appear to show some similarity to those we obtained with central neural cells [4]. The DRG neurons and Schwann cells appear also to be susceptible to the cytotoxic effects of SiO<sub>2</sub> and TiO<sub>2</sub> nanoparticles. As we have indicated earlier, we are also determining the cell death mechanisms underlying the cytotoxic effects of SiO<sub>2</sub> and TiO<sub>2</sub> nanoparticles on DRG neurons and Schwann cells. Clearly, this is an important area that merits further study.

## 4 CONCLUSIONS

Thus, the results from our studies to date as well as those from our ongoing studies demonstrate that our non-contact co-culture model is highly suitable for both high throughput and mechanistic studies in nanotoxicological and tissue engineering research. Moreover, this model is also relevant for the investigation of mechanistic issues associated with peripheral diabetic neuropathy and other disease states of the peripheral nervous system.

## 6 REFERENCES

1. Chrissa, S. and A. Kyritsis, Cancer Chemotherapy and Pharmacology, 2009. **63**: p. 761–767.
2. Brownlee, M., *Biochemistry and molecular cell biology of diabetic complications*. Nature, 2001. **414**(6865): p. 813-820.
3. Cha K E and M. H, Journal of microbiology and biotechnology, Sep 2007. **17**(9): p. 1573-8.
4. James C K Lail, et al., International Journal of Nanomedicine, Decmber 2008. **3**(4).
5. Malthankar, G., et al., Neurochemical Research, 2004. **29**(4): p. 709-717.
6. Malthankar GV, White BK, and B. A, Neurochemistry Research, 2004. **29**: p. 709–17.
7. Puli S, Lai JCK, and Edgley KL, Neurochemistry Research, 2006. **31**: p. 1211–8.
8. Dukhande, V., et al., . Neurochemical Research, 2006. **31**(11): p. 1349-1357.
9. Lai JCK, Nguyen JV, and W. BK, Mol Biol Cell 1999. **10**(Suppl): p. 445a.
10. Chen, W., et al., Journal of the Peripheral Nervous System, 2007. **12**(2): p. 121-130.

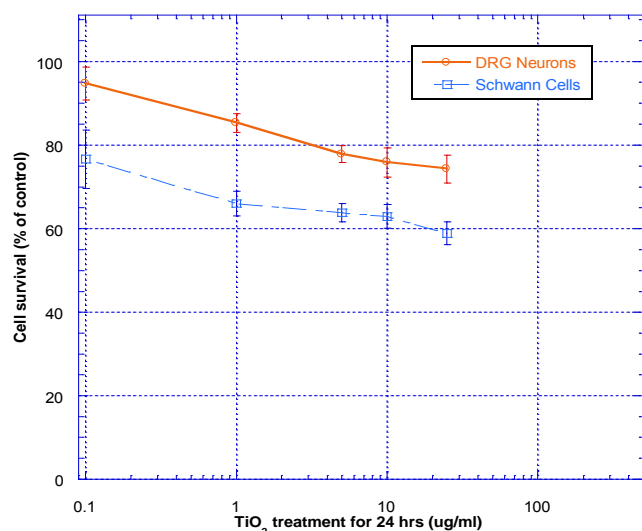


Figure 3: Effects of TiO<sub>2</sub> nanoparticles on DRG neurons or Schwann cells. Values are mean  $\pm$  SEM of 12 determinations and replicate experiments show the same trend. DRG neurons and Schwann cells treated with TiO<sub>2</sub> nanoparticles for 24 hours are marked red and blue, respectively.

Results of our present and ongoing studies have confirmed that neural cells of the peripheral nervous system, similar to their counter parts in the central nervous system, are also susceptible to the cytotoxicity of SiO<sub>2</sub> and TiO<sub>2</sub> nanoparticles. Thus, these results are consistent with our hypothesis that our non-contact co-culture model of Schwann cells and DRG neurons can be useful to study toxic effects of various nanoparticles on peripheral nervous system.

The results of this and our ongoing studies suggest that nanoparticles may exert differential cytotoxic effects on neural cell types of the peripheral nervous system. As such, our results may assume pathophysiological importance in the environmental health impact of nanoparticles. Obviously, there is an important area that deserves further study.

## 5 ACKNOWLEDGEMENT

We thank Dr. Ahmed Hoke (Johns Hopkins University School of Medicine) for his generous gift of DRG neurons. Our study was supported, in part, by an USAMRMC Project Grant (Contract #W81XWH-07-2-0078), and NIH Grant #P20 RR016454 from the Idaho INBRE Program of the National Center for Research Resources.

# Elucidation of Neuroprotective Properties of Astrocytoma (Astrocytes-like) Cells in Neural Cell Culture Models *In Vitro*: Applications in Tissue Engineering and Nanotoxicology

Y.Y.W. Wong<sup>\*</sup>, A.R. Jaiswal<sup>\*\*</sup>, V.V. Dukhande<sup>\*\*\*</sup>, A. Bhushan<sup>\*\*\*\*</sup>, S.W. Leung<sup>\*\*\*\*\*</sup> and J.C.K. Lai<sup>\*\*\*\*\*</sup>

<sup>\*</sup>Presenting author: Department of Biomedical & Pharmaceutical Sciences, College of Pharmacy, and Biomedical Research Institute, Idaho State University, Pocatello, ID 83209, USA Fax: 208-282-4305; Tel: 469-463-5139, email: [wongyin@pharmacy.isu.edu](mailto:wongyin@pharmacy.isu.edu)

<sup>\*\*</sup>Department of Biomedical & Pharmaceutical Sciences, College of Pharmacy, and Biomedical Research Institute, Idaho State University, Pocatello, ID 83209, USA Fax: 208-282-4305; Tel: 208-705-2447, email: [jaisashv@pharmacy.isu.edu](mailto:jaisashv@pharmacy.isu.edu)

<sup>\*\*\*</sup>Department of Molecular and Cellular Biochemistry, College of Medicine, University of Kentucky, Lexington, KY 40536-0509, USA Fax: 859-257-2283; Tel: 208-315-3370, email: [vikas.dukande@gmail.com](mailto:vikas.dukande@gmail.com)

<sup>\*\*\*\*</sup>Department of Biomedical & Pharmaceutical Sciences, College of Pharmacy, and Biomedical Research Institute, Idaho State University, Pocatello, ID 83209, USA Fax: 208-282-4305; Tel: 208-282-4408, email: [abhushan@pharmacy.isu.edu](mailto:abhushan@pharmacy.isu.edu)

<sup>\*\*\*\*\*</sup>Department of Civil and Environmental Engineering, College of Engineering, and Biomedical Research Institute, Idaho State University, Pocatello, ID 83209, USA Fax: 208-282-4538; Tel: 208-282-2524; email: [leunsolo@isu.edu](mailto:leunsolo@isu.edu)

<sup>\*\*\*\*\*</sup>Corresponding author: Department of Biomedical and Pharmaceutical Sciences, College of Pharmacy, and Biomedical Research Institute, Idaho State University, Pocatello, ID 83209, USA Fax: 208-282-4305; Tel: 208-282-2275; email: [lai@pharmacy.isu.edu](mailto:lai@pharmacy.isu.edu)

## ABSTRACT

Evidence is accumulating that cell culture models *in vitro* facilitate high throughput and mechanistic studies in tissue engineering. Astrocytes are known to protect neurons against pathophysiological assaults *in vivo* and *in vitro* although the underlying mechanisms are not fully understood. Previously, we investigate several of the putative neuroprotective properties of astrocytes in cell culture model. Those studies led us to hypothesize that different stress factors can elicit and/or enhance the neuroprotective effects of astrocytes through the activation of astrocytic signaling and alteration of astroglial function. The results of this study suggest that U87 (astrocytes-like) astrocytoma cells exert some protective effects on SK-N-SH (neurons-like) neuroblastoma cells against pathophysiological assaults (e.g., oxidative stress) under several sets of culture conditions not previously studied. Thus, our results may have pathophysiological implications in neuroprotection

and implications and applications in tissue engineering and nanotoxicological research.

**Key Words:** Cell culture models; human neural cells; U87 astrocytes-like astrocytoma cells; neuroprotection; tissue engineering; nanotoxicology

## Topic Area:

## 1. INTRODUCTION

There is increasing evidence that cell model systems *in vitro* play vital roles in recent tissue engineering research. The additional structural and functional perspectives of co-culture cell systems *in vitro* start to gain prominence over

single cell type cell systems because unlike the latter, the former more closely resemble cell types in a tissue/organ *in vivo*.

Astrocytes (non-nerve, glial cells) in the brain play important roles in protecting neurons (nerve cells) against various assaults; yet, the cellular and molecular mechanisms underlying this protection is far more being understood [1]. Among the research on further elucidating such mechanisms, more efforts appear to center on commonly known neurodegenerative diseases such as Alzheimer's disease (AD), followed by Parkinson's disease (PD) [2]. AD is a progressive and irreversible neurodegenerative disorder in human brain leading to key symptoms of memory loss [3]. No known cure is available for AD as current therapy primarily treats AD symptoms and presents them from worsening. Thus, there is an urgent need to better understand how astrocytes exert their protective effects on neurons in a co-culture cell system *in vitro*. Once this protection is elucidated, then one could design treatment strategies and/or tissue engineering application to prevent the occurrence of accelerated neuronal loss in neurodegenerative diseases such as AD and PD.

Our project seeks to examine the underlying neuroprotective properties offered by astrocytes to protect neurons, employing a co-culture cell model system *in vitro*. We have been developing several model systems to investigate putative cytotoxic and inflammatory mechanisms associated with induction of neuronal cell damage and cell death [4-6]. Our previously data have shown that U87 astrocytoma and SK-N-SH neuroblastoma cells constitute good co-culture model systems for astrocytes and neurons, respectively, *in vitro* because of their close functional resemblance to normal astrocytes and neurons and that U87 cells protect SK-N-SH cells from several pathological assaults [4-5]. We therefore hypothesized that different stress factors can elicit and/or enhance the neuroprotective effects of astrocytes through the activation of astrocytic signaling and alteration of astroglial function. In this study, we have investigated this hypothesis further.

## 2. MATERIALS AND METHODS

### 2.1 Cell culture of U87 and SK-N-SH cells

The human astrocytoma (U87) and neuroblastoma (SK-N-SH) cell lines were obtained from (ATCC; Manassas, VA, USA) and cultured in MEM supplemented with 10% (v/v) fetal bovine serum (Atlanta Biologicals; Lawrenceville, GA), 1% (w/v) sodium pyruvate (Sigma Aldrich; St Louis, MO), 0.292 g/L L-glutamine (Sigma), 1.5g/L sodium bicarbonate (Sigma) and 1% (v/v) antimycotic (Atlanta Biologicals; Lawrenceville, GA). Cells were maintained at 37°C and 5% (v/v) CO<sub>2</sub> as described previously [4-5].

### 2.2 Treatment of U87 cells

The U87 cells were cultured in T-75 tissue culture flasks to ~50% confluent in 20 ml of 10% FBS-containing MEM medium. Then the medium was discarded and changed to 20 ml of 5% FBS-containing medium and the cells incubated for 24 hours. After that, the medium was replaced with 20 ml of medium containing 0% FBS and the cells incubated for an additional 24 hours. Cells were treated L-sulfoximine buthionine (BSO), or pioglitazone (PZ) or a combination of both. At the end of another 24 hours of incubation, the media were removed and frozen with liquid nitrogen immediately. The cell pellet was collected and both cell pellet and media collected were kept at -80°C until used for experiments.

### 2.3 Cell Survival (MTT) assay

The neuroprotective properties of U87 cells on SK-N-SH cells were determined in different combinations of regular medium (RM) and conditioned medium (CM) collected from U87 cells cultured under various conditions (see above). RC/CM ratio of 100/0, 70/30, 50/50, 40/60, 30/70, and 0/100 were used. SK-N-SH cell survival after the treatments was assessed employing the MTT assay [5].

### 2.4 Western Blot Analysis

Western blot analysis was employed to assess protein expression in cell lysates to determine the effects of media, BSO and PZ. SDS-PAGE electrophoresis was performed as previously described [7]. The separated proteins were visualized using chemiluminescence detection kit while  $\beta$ -actin was the loading control.

## 3. RESULTS AND DISCUSSION

Our culture model consists of U87 (astrocytes-like) cells and medium collected from U87 cells cultured under specified conditions to grow SK-N-SH (neurons-like) cells. This is a new modified co-culture strategy to allow the characterization of putative "protective factors" secreted by U87 cells to protect SK-N-SH cells in a non-contact cell culture setup. In addition, we can characterize the putative structural and functional properties of U87 cells under the different specified conditions.

A selective inhibitor of glutathione (naturally-occurring antioxidant) synthesis, L-buthionine sulfoximine (BSO), is used to induce oxidative stress in cells. A peroxisome proliferator activated receptor gamma (PPAR $\gamma$ ) agonist, Pioglitazone (PZ), is used to block the inflammation which is usually unregulated in AD [8,9]. We have designed studies whereby we could utilize BSO and PZ in addition to serum depletion to further elucidate the putative protective mechanism(s) of U87 cells on neurons-like SK-N-SH cells. Serum depletion and drug treatment for U87 cell cultures were prepared as shown in the flow chart below (Fig. 1).



U87 cells cultured in medium containing 10% FBS were used as control (not shown in Fig. 1). Medium containing 0% FBS were defined as serum free (SF) medium.

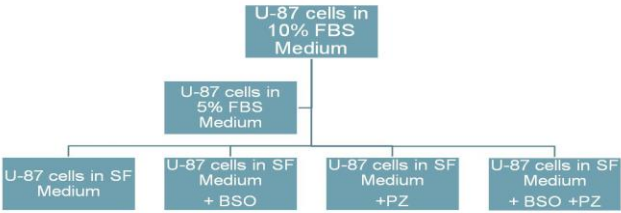


Figure 1. Experimental design of U87 cells treated with BSO, PZ or in combination. The U87 cells were grown to ~50% confluent in 10%-FBS containing medium and subsequently discarded and changed to 5% FBS-containing medium and incubated for 24 hours. After that, the medium was replaced with medium containing 0% FBS and incubated for an additional 24 hours. Cells were treated BSO or PZ or a combination of both for another 24 hours of incubation.

Morphological and functional changes/adaption in astrocytes *in vivo* and *in vitro* is known to associate with oxidative and other environmental stresses. We employed light microscopy to examine the effects of BSO treatment and FBS depletion to induce oxidative and environmental stress, respectively, on U87 cells and assess the effects of PZ treatment thereon.

employed western blot to determine if the morphological changes in U87 cells exposed to SF medium with and without BSO/PZ treatment were seen also associated with changes in GFAP expression. An increased GFAP expression was observed when U87 cells were cultured in SF medium compared to those cultured in 10% FBS medium (data not shown), suggesting a correlation between changes in cellular morphology and GFAP expression.

Growth factors and neuronal survival enhancers are putatively released into the medium by astrocytes to protect their surrounding neurons. To investigate this possibility, we collected media in which we grew U87 cells under the conditions specified in Figure 1 above and assessed their ability to influence survival of SK-N-SH cells. Our results suggested that exposure of SK-N-SH cells to various combinations of SF media allowed them to survive better than when cultured in 10% FBS medium (control condition) alone (Fig. 3). Moreover, exposure to PZ enhanced this protective effect, even under conditions of oxidative stress.

### 4. CONCLUSIONS

When taken together, our results suggest astrocytes-like U87 cells changed their cell shape and morphology when cultured under serum-free media with and without drug treatment. Those morphological changes correlated with upregulation of GFAP in such cells.

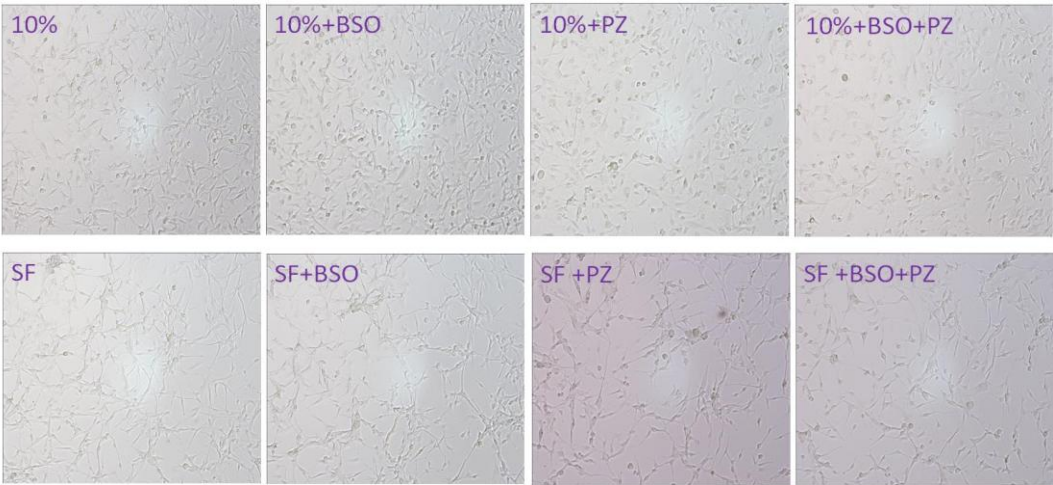


Figure. 2 Treatment-induced cellular morphology changes in U87 cells (100X magnification). Top panel of photomicrographs represents U87 cells cultured in 10% FBS medium treated with or without drug or drug combination while those of the bottom panel represents U87 cells cultured in serum-depleted (SF) medium treated with or without drug or drug combination.

Treatment with SF medium induced U87 cells to put out multipolar processes and the other treatments accentuated this effect (Fig. 2). Clearly, these observations raise interesting mechanistic questions that need to be addressed further (see below).

Glial fibrillary acid protein (GFAP) is a well-known and classical marker for astrocytes: its altered expression is associated with changes in astroglial morphology. Thus, we

Moreover, exposure of SK-N-SH cells to various combinations of SF media allowed them to survive better than when cultured in 10% FBS medium (control condition) alone and exposure to PZ enhanced this protective effect, even under conditions of oxidative stress. Thus, our results provide additional evidence that our cell model can be productively employed to further elucidate the putative neuroprotective mechanisms of astrocytes. As such they assume pathophysiological importance in neuronal

survival/death mechanisms in AD and PD. Clearly, this is an area that merits further study, especially in tissue engineering and nanotoxicological research and applications.

**5. ACKNOWLEDGMENTS**

This study was supported by an USAMRMC Project Grant (Contract #W81XWH-07-2-0078), NIH Grant #P20 RR016454 from the Idaho INBRE Program of the National Center for Research Resources.

**REFERENCES**

[1] Sofroniew M V, Vinters H V. Astrocytes: biology and pathology. *Acta Neuropathol.* 119:7-35,2010.

[2] Przedborski S, Vila M, Jackson-Lewis V. Neurodegeneration: What is it and where are we? *Journal of Clinical Investigation.* 111(1): 3-10, 2003.

[3] Chung S. Aberrant phosphorylation in the pathogenesis of Alzheimer’s disease. *BMB Rep.* 42(8): 467-474, 2009.

[4] Malthankar GV, White BK, Bhushan A, Daniels CK, Rodnick KJ, Lai JCK. Differential lowering by manganese treatment of activities of glycolytic and tricarboxylic acid cycle enzymes in neuroblastoma and astrocytoma cells is

associated with manganese-induced cell death. *Neurochem Res.* 29:709-717, 2004.

[5] Dukhande VV, Malthankar-Phatak GH, Hugus JJ, Daniels CK, Lai JCK. Manganese induced neurotoxicity is differentially enhanced by glutathione depletion in astrocytoma and neuroblastoma cells. *Neurochem Res.* 31(11):1349-1357, 2006.

[6] Wang Y-H, Jandhyam S, Dukhande VV, Gao WJ, Gu H-Y, Lai MB, Leung SW, Lai JCK. A co-culture model for nanotoxicity and tissue engineering studies. In *Technical Proceedings of the 2008 Nanotechnology Conference and Trade Show; Volume 2, Chapter 2: Environment, Health & Toxicology*, pp. 164-167, 2008.

[7] Isaac AO, Kawikova I, Bothwell ALM, Daniels CK & Lai JCK. Manganese Treatment Modulates the Expression of Peroxisomal Proliferator Activated Receptors (PPARs) in Astrocytoma and Neuroblastoma Cells. *Neurochem. Res.* 31(11):1305-1316, 2006.

[8] Yamagishi S. Protective role of PPARgamma agonists against cardiovascular disease. *Nippon Rinsho.* 68(2): 307-11, 2010.

[9] Syversen, U., Stunes, A K, Gustafsson, B I. et al. Different skeletal effects of the peroxisome proliferator activated receptor (PPAR)  $\alpha$  agonist fenofibrate and the PPAR $\gamma$  agonist pioglitazone. *BMC Endocrine Disorders.*; 9:10,2009.

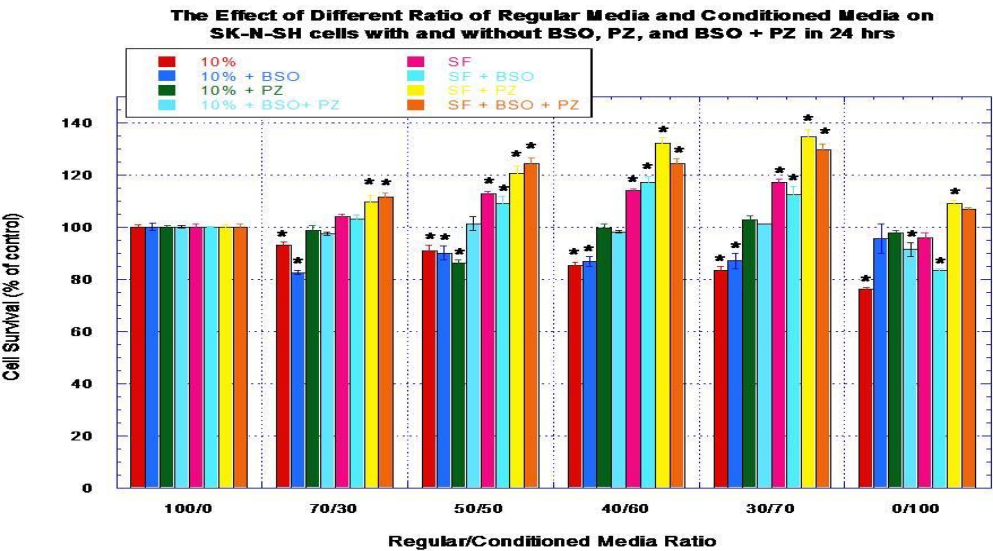


Figure 3. Treatment effects on SK-N-SH cell survival with different regular/conditioned media combination (see Fig. 1). SK-N-SH cells cultured in 10% FBS served as the control. Values are expressed as % of the control and are given as mean  $\pm$  SEM of separate determinations. \* $p$ <0.05 versus control.



# Chitosan Membrane in Combinations with Nanoparticles and Adriamycin as a Treatment to Inhibit Glioma Growth and Migration

S. W. Leung\*, W. Gao\*\*, H. Gu\*\*\*, A. Bhushan\*\*\*\*, and J.C.K. Lai\*\*\*\*\*

\*Corresponding author, Civil and Environmental Engineering Department, College of Engineering and Biomedical Research Institute, Idaho State University, Pocatello, ID 83209, USA Fax: 208-282-4538; tel: 208-282-2524; email: [leunsolo@isu.edu](mailto:leunsolo@isu.edu)

\*\*Civil and Environmental Engineering Department, College of Engineering, Idaho State University, Pocatello, ID 83209, USA, email: [gaowenj@isu.edu](mailto:gaowenj@isu.edu)

\*\*\*School of Public Health, Nantong University, Nantong, Jiangsu, 226007, P. R. China, email: [hygu@ntu.edu.cn](mailto:hygu@ntu.edu.cn)

\*\*\*\*Biomedical & Pharmaceutical Sciences Department and Biomedical Research Institute, Idaho State University, Pocatello, ID 83209, USA, email: [adhushan@pharmacy.isu.edu](mailto:adhushan@pharmacy.isu.edu)

\*\*\*\*\*Biomedical & Pharmaceutical Sciences Department and Biomedical Research Institute, Idaho State University, Pocatello, ID 83209, USA, email: [lai@pharmacy.isu.edu](mailto:lai@pharmacy.isu.edu)

## ABSTRACT

Chitosan exhibits antimicrobial activities through its interaction(s) with microbial cell surface thereby altering their gene expression and cellular function, leading to cell death. Nanometal particles exert many effects not previously expected on biological systems and thus can be explored for diverse biomedical applications. Our previous and on-going studies indicate that U87 cells cultured on chitosan film/membrane exhibited significantly slower growth and proliferation kinetics compared to U87 cells cultured alone. In this study we tested the hypothesis that the inhibitory effect of chitosan is enhanced if combined with nanometals and adriamycin, a common anticancer drug. Our results showed that combinations of metal nanoparticles, adriamycin and chitosan induced decreased survival of U87 glioma cells at different rates, more marked than those with chitosan alone. Thus, our results have pathophysiological implications in inhibiting human brain glioma invasion and migration.

**Key words:** Chitosan, nanoparticles, adriamycin, cancer therapy, U87 cells

## 1 INTRODUCTION

Chitosan, a polysaccharide biopolymer that combines a unique set of physicochemical and biological properties has increasingly gained popularity in biomedical applications [1, 2]. Our previous and on-going studies indicate that U87 cells (human brain glioblastoma cell line) cultured on chitosan film/membrane exhibit significantly slower growth and proliferation kinetics compared to U87 cells cultured in the absence of chitosan film/membrane [3]. Chitosan exhibits antimicrobial activities through its interaction(s) with microbial cell surface thereby altering their gene expression and cellular function and leading to cell death [4].

Nanometal particles, such as nanosilver, nanogold, are important material being utilized frequently. Recent studies of nanometal particles have revealed many properties that were not previously expected in biological systems and thus can be explored for various applications in biomedicine, such as tissue engineering [5] and wound dressing [6].

In this study, we hypothesized that the inhibitory effect of chitosan would be greatly modulated if we combine chitosan with nanometals and adriamycin, a common drug for cancer therapy. Similar treatments with a different cancer (PANC-1, human pancreatic cancer cell line) and normal cells (BJ, human fibroblast cell line) were also used to investigate this hypothesis.

## 2 MATERIALS AND METHODS

### 2.1 Materials

Human astrocytoma (astrocytes-like) U87 cells, human pancreatic PANC-1 cells and human fibroblast BJ cells were obtained from ATCC (Manassas, VA, USA). Chitosan (from crab shells, minimum 85% deacetylated), thiazolyl blue tetrazolium bromide (MTT), dimethyl sulfoxide (DMSO) and adriamycin were purchased from Sigma-Aldrich (St Louis, MO, USA). Fetal bovine serum (FBS) was obtained from Atlanta Biologicals (Lawrenceville, GA, USA). tetrachloroauric (III) acid ( $\text{HAuCl}_4 \cdot 3\text{H}_2\text{O}$ ), trisodium citrate ( $\text{C}_6\text{H}_5\text{Na}_3\text{O}_7 \cdot 2\text{H}_2\text{O}$ ) and silver nitrate ( $\text{AgNO}_3$ ) were purchased from Fisher Scientific (Pittsburgh, PA, USA). Other chemicals were of analytical grade and were usually from Sigma-Aldrich (St. Louis, MO, USA) unless otherwise stated.

### 2.2 The Preparation of Nanosilver, Nanogold Particles

To prepare nanosilver,  $\text{AgNO}_3$  and  $\text{C}_6\text{H}_5\text{Na}_3\text{O}_7 \cdot 2\text{H}_2\text{O}$  solutions were filtered through a  $0.22 \mu\text{m}$  microporous membrane filter, and nanosilver was prepared according to the literature [7] by adding  $\text{C}_6\text{H}_5\text{Na}_3\text{O}_7 \cdot 2\text{H}_2\text{O}$  solution to boiling  $\text{AgNO}_3$  aqueous solution.

To prepare nanogold,  $\text{HAuCl}_4 \cdot 3\text{H}_2\text{O}$  and  $\text{C}_6\text{H}_5\text{Na}_3\text{O}_7 \cdot 2\text{H}_2\text{O}$  solutions also need to be filtered through a  $0.22 \mu\text{m}$  microporous membrane filter prior to use. Nanogold was prepared according to the literature [8] by adding  $\text{C}_6\text{H}_5\text{Na}_3\text{O}_7 \cdot 2\text{H}_2\text{O}$  solution to boiling  $\text{HAuCl}_4 \cdot 3\text{H}_2\text{O}$  aqueous solution.

## 2.3 Cell Culture

Chitosan membrane was prepared as described previously [3]. A certain amount of nanosilver or nanogold solution was added into each well of 24-well culture plates in which a sterile chitosan membrane had already been placed. After 12 hours, nanosilver or nanogold solution was aspirated and sterile phosphate-buffered saline (PBS) was added into each well to wash the membrane.

U87 cells were seeded with equal density in each well of the 24-well plates and cultured in an incubator at  $37^\circ\text{C}$  and 5 %  $\text{CO}_2$  in modified Eagle's medium (MEM) supplemented with 10% fetal bovine serum (FBS). Adriamycin with a final concentration of  $0.1 \mu\text{M}$  was added after cells were seeded. Culture of PANC-1 cells and BJ cells were similar with U87 cells whereas PANC-1 cells were grown in the RPMI 1640 medium.

## 2.4 MTT Assay

Cell survival and growth was determined using the MTT assay [9]. Cells (U87, PANC-1, and BJ) were cultured in 24-well plates as described in the preceding subsection. At the end of the incubation period (4, 7, 10, or 14 days), MTT dye (0.5%, w/v, in PBS) was added to each well and the plates were incubated for an additional 4 hours at  $37^\circ\text{C}$ . The purple-colored insoluble formazan crystals in viable cells were dissolved using dimethyl sulfoxide, and the subsequent

absorbance of the content of each well was measured at 570 nm using a Bio-Tek Synergy HT Plate Reader (Winooski, VT, USA) [10].

## 2.5 Statistical Analysis of Data

Results are presented as mean  $\pm$  standard error of the mean (S.E.M.) of 6 determinations in each experiment.

## 3 RESULTS AND DISCUSSION

As shown in Figure 1, all the treatments induced decrease in cell survival of U87 cells. There were apparent differences in the effects exerted by different treatments. After being treated for 14 days, chitosan with nanosilver and  $0.1 \mu\text{M}$  adriamycin was the most effective. This may enable lower doses of adriamycin to be used, with reduced toxicity. Chitosan with nanogold and  $0.1 \mu\text{M}$  adriamycin was the second most effective; chitosan alone was the least effective. Chitosan with nanosilver showed greater effect than chitosan with nanogold. Therefore, these results provided some support for our hypothesis that a combination of chitosan with nanometals and adriamycin was more effective than chitosan or adriamycin alone or chitosan with nanometals.

As shown in Figure 2, all the treatments showed an inhibitory effect on cell survival of PANC-1 cells. Similarly, after being treated for 14 days, chitosan with nanosilver and  $0.1 \mu\text{M}$  adriamycin was the most effective; chitosan alone was the least effective. However, the effect was stronger on PANC-1 cells than on U87 cells. Compared with U87 cells, PANC-1 cells were considerably more sensitive to the effects of adriamycin alone.

Figure 3 showed the effect of different treatments on the survival of BJ cells. Chitosan with nanosilver and  $0.1 \mu\text{M}$  adriamycin was the most effective, the same as U87 cells and PANC-1 cells. By day 14, however, there was no significant difference in the survival rate of cells treated with chitosan alone and chitosan with nanogold and untreated (control).

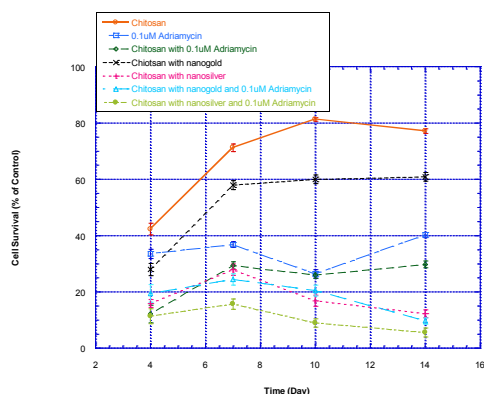


Figure 1: Effect of chitosan, chitosan/nanosilver, chitosan/nanogold and adriamycin on survival of U87 cells. Red circles: chitosan; Black cross signs: chitosan with nanogold; Blue squares:  $0.1 \mu\text{M}$  adriamycin; Green squares: chitosan with  $0.1 \mu\text{M}$  adriamycin; Red plus signs: chitosan with nanosilver; Blue triangles: chitosan with nanogold and adriamycin; Dark green circles: chitosan with nanosilver and  $0.1 \mu\text{M}$  adriamycin. At the end of the specified incubation time, cell survival and growth was determined using the MTT assay. Values are the mean  $\pm$  SEM.

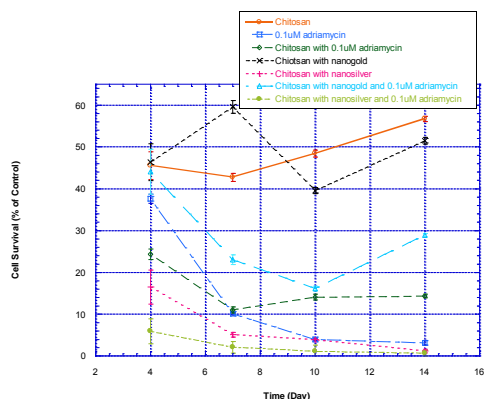


Figure 2: Effect of chitosan, chitosan/nanosilver, chitosan/nanogold and adriamycin on survival of PANC-1 cells. Red circles: chitosan; Black cross signs: chitosan with nanogold; Blue triangles: chitosan with nanogold and adriamycin; Green squares: chitosan with 0.1  $\mu$ M adriamycin; Blue squares: 0.1  $\mu$ M adriamycin; Red plus signs: chitosan with nanosilver; Dark green circles: chitosan with nanosilver and 0.1  $\mu$ M adriamycin. At the end of the specified incubation time, cell survival and growth was determined using the MTT assay. Values are the mean  $\pm$  SEM.

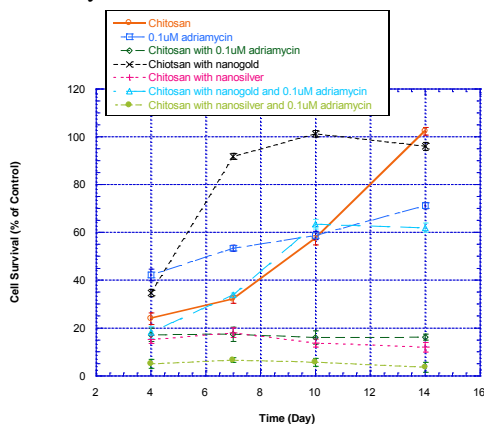


Figure 3: Effect of chitosan, chitosan/nanosilver, chitosan/nanogold and adriamycin on survival of BJ cells. Red circles: chitosan; Black cross signs: chitosan with nanogold; Blue squares: 0.1  $\mu$ M adriamycin; Blue triangles: chitosan with nanogold and adriamycin; Green squares: chitosan with 0.1  $\mu$ M adriamycin; Red plus signs: chitosan with nanosilver; Dark green circles: chitosan with nanosilver and 0.1  $\mu$ M adriamycin. At the end of the specified incubation time, cell survival and growth was determined using the MTT assay. Values are the mean  $\pm$  SEM.

## 4 CONCLUSIONS

Our previous and ongoing studies demonstrate that combinations of metal nanoparticles, adriamycin and chitosan induced cell death at different rates, with reference to U87 cells cultured in the absence of chitosan and with chitosan alone. Chitosan with nanosilver and 0.1  $\mu$ M adriamycin showed the greatest cell survival reduction on all three cell lines. Chitosan with nanosilver showed greater effect than chitosan with nanogold. Taken together, these results suggest potentials for pathophysiological applications in inhibition of human brain glioma migration and invasion and in treatment of pancreatic cancer.

## 5 ACKNOWLEDGMENTS

Our studies were supported by a DOD USAMRMC Project Grant (Contract #W81XWH-07-2-0078).

## REFERENCES

- [1] Li Z, Cen L, Zhao L, Cui L, Liu W, Cao YL, "Preparation and evaluation of thiolated chitosan scaffolds for tissue engineering," *Journal of Biomedical Materials Research Part A*, 92A (3): 973 – 978, 2010.
- [2] Wilson B, Samanta MK, Santhi K, Kumar KPS, Ramasamy M, Suresh B, "Chitosan nanoparticles as a new delivery system for the anti-Alzheimer drug tacrine," *Nanomedicine: Nanotechnology, Biology and Medicine*, 6(1):144-152, 2010.
- [3] Gao WJ, Wang YH, Gu HY, Jandhyam S, Dukhande VV, Lai MB, Leung SW, Bhushan A, Lai JCK, "Chitosan Film/Membrane as a Surface to Alter Brain Glioma Growth and Migration," In *Proceeding of the 12<sup>th</sup> NSTI (Nano Science and Technology Institute) Nanotech*, Houston, USA, Volume 2, pp. 302-305, 2009.
- [4] Raafat D, Bargen K, Haas A, Sahl H, "Insights into the mode of action of chitosan as an antibacterial compound," *Appl Environ Microbiol*, 74(12):3764-3773, 2008.
- [5] Zhang Y, He H, Gao WJ, Lu SY, Liu Y, Gu HY, "Rapid adhesion and proliferation of keratinocytes on the gold colloid/chitosan film scaffold," *Materials Science and Engineering C*, 29(3): 908-912, 2009.

- [6] Lu SY, Gao WJ, Gu HY, "Construction, application and biosafety of silver nanocrystalline chitosan wound dressing," *Burns*, 34 (5): 623–628, 2008.
- [7] Kamat PV, Flumiani M, Hartland GV, "Picosecond Dynamics of Silver Nanoclusters. Photoejection of Electrons and Fragmentation," *J. Phys. Chem. B*, 102(17): 3123-3128, 1998.
- [8] Turkevich J, Stevenson PC, Hillier J, "A study of the nucleation and growth processes in the synthesis of colloidal gold," *Discuss. Faraday Soc.*, 11: 55-75, 1951.
- [9] Mossman T, "Rapid colorimetric assay for cellular growth and survival: Application to proliferation and cytotoxicity assays," *Journal of Immunological Methods*, 65(1-2): 55-63, 1983.
- [10] Dukhande VV, Malthankar-Phatak GH, Hugus JJ, Daniels CK, Lai JCK, "Manganese induced neurotoxicity is differentially enhanced by glutathione depletion in astrocytoma and neuroblastoma cells," *Neurochem Res.*, 31(11): 1349-1357, 2006.

# Biomedical Applications of Modified Carbon Glassy Electrode Sensor with Nanoparticles and Dendrimers

S. W. Leung<sup>1</sup>, Y. Wang<sup>2</sup>, H. Gu<sup>3</sup>, and J.C.K. Lai<sup>4</sup>

<sup>1</sup>Corresponding author, Civil and Environmental Engineering Department, College of Engineering and Biomedical Research Institute, Idaho State University, Pocatello, ID 83209, USA Fax: 208-282-4538; tel: 208-282-2524; email: leunsolo@isu.edu

<sup>2</sup>Civil and Environmental Engineering Department, College of Engineering, Idaho State University, Pocatello, ID 83209, USA

<sup>3</sup>School of Public Health, Nantong University, Nantong, Jiangsu, 226007, P. R. China.

<sup>4</sup>College of Pharmacy and Biomedical Research Institute, Idaho State University, Pocatello, ID 83209, USA

## ABSTRACT

In our previous reports, we studied the development of biosensor platform that are capable of measuring biometabolites and environmental sensitive species, such as peroxide and nitrate/nitrate, to concentration in the order of ppb (parts per billion) or lower.

In our more recent development, we modified our platform with dendrimers to enhance its performance. Zero and second generation of dendrimers were coated on the surface of a carbon glassy platform electrode modified with GDH (glutamate dehydrogenase) and it was used to measured ammonium, a common biometabolite, at near neutral pH that is common for normal bioactivities.

The resulting electrode was tested with ammonium concentrations ranged from 0.002 to 0.3  $\mu\text{M}$  with satisfactory results. Measurements at lower concentrations had better resolution than at higher concentrations and it is believed that the lower concentration limit can be better than the tested lower limit at 0.002  $\mu\text{M}$ . Performance of the modified carbon glassy electrode was compared with other glassy electrodes that were modified differently, and the results will be reported.

The biosensor platform thus far was proven to be versatile and can be used in many biomedical and environmental applications.

**Key words:** biosensor, nanoparticle, GDH, ammonium, electrode, PAMAM

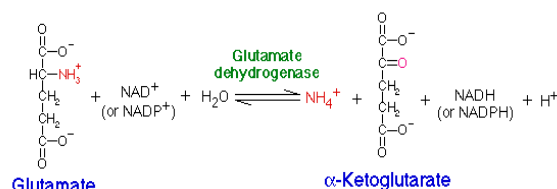
## 1 INTRODUCTION

In the past several years, our research group has been developing a platform for biosensor construction that are capable of detecting target species that are in nano and subnanomolar levels [1, 2].

In this study, we were developing a biosensor that can measure ammonia at submicromolar levels that cannot be detected by commercial ammonia electrodes or wet chemistry method easily.

### 1.1 Theory

As shown in the following equation, glutamate and  $\text{NAD}^+$  can be hydrolyzed to form  $\alpha$ -keto glutarate,  $\text{NADH}$ , and ammonium ion with the enzyme, glutamate dehydrogenase. The equilibrium constant is in favor of the formation of glutamate and thus the reverse reaction is faster kinetically.



For many biological reactions, the end product or metabolite is ammonium, accumulation of high concentration of ammonium is toxic to the body. Environmentally, ammonium is a byproduct of many industrial processes, uncontrolled discharges of ammonium will lead to harmful consequence to the environment. Our goal here was to develop a sensor device that can measure ammonium ion at the lowest concentrations possible, its utilities can be in biomedical or environmental applications. Hence, it is the reverse of the reaction as shown above (glutamate formation) that we utilized.



## 2 MATERIALS AND METHODS

### 2.1 Materials

L-glutamic dehydrogenase (from bovine liver, solution in 50% glycerol) (GDH) was purchased from Sigma-Aldrich (St. Louis, MO, USA), the concentration of GDH is 28 mg protein/ml, and 46 units/mg. Cysteamine, polyamidoamine dendrimer generation 0 (PAMAM 0), polyamidoamine dendrimer generation 2<sup>nd</sup> (PAMAM 2<sup>nd</sup>), and  $\alpha$ -keto glutarate,  $\text{AuCl}_3\text{HCl}\cdot 4\text{H}_2\text{O}$  (Au %> 48%) and  $\text{Na}_3\text{citrate}$  were purchased from Sigma. All the other chemicals were of analytical grade or highest grade available. All the experiments were carried out under deoxygenated condition in 0.1 M phosphate buffer solution.

### 2.2 Electrode Preparation

The cleaned glassy carbon electrode was first immersed in 0.1 M cysteamine solution in darkness. The resulting monolayer-modified electrode was rinsed thoroughly with twice-distilled water and soaked in water. Then, it was dipped into the colloidal gold. The gold colloid–cysteamine-modified electrode was dipped into the l-glutamate dehydrogenase (GDH) solution (pH 7.4) (or GDH solution containing NADH). In such a way, a GDH (/NADH) gold colloid–cysteamine-modified glassy carbon electrode was obtained.

In case that both cysteamine and PAMAM were coated onto electrodes, the cleaned glassy carbon electrode was first immersed in cysteamine solution, the resulting electrode was dipped into the PAMAM solution. The gold colloid–cysteamine/PAMAM-modified electrode was dipped into the GDH solution (pH 7.4) (or GDH solution containing NADH). In such a way, a GDH (/NADH) gold colloid–cysteamine/PAMAM-modified glassy carbon electrode was obtained.

### 2.3 Nanoparticles Solution Preparations

Nanoparticles Au was prepared by reacting  $\text{HAuCl}_4$  with citric acid [2].

### 2.4 Detections

UV-VIS spectrophotometry was carried out by an Agilent diodearray spectrophotometer; cyclic voltammetry was conducted by using a Gamry 600 Potentiostat. Voltammetric potential was measured against a saturated chloride electrode (SCE).

## 3 RESULTS AND DISCUSSION

### 3.1 Stability of Electrodes

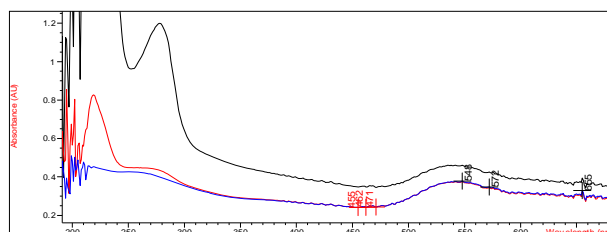


Figure 1. Cysteamine-PAMAM-Au-GDH coated on plastic UV-VIS cell with permanent absorption peak at 278 nm. Various lines indicated concentration differences.

As shown in Figure 1, PAMAMs can be attached to cysteamine to enhance the available sites for the electrons transfer between reactions, in this case, ammonium and  $\alpha$ -keto glutarate, therefore increase the detection lower limit.

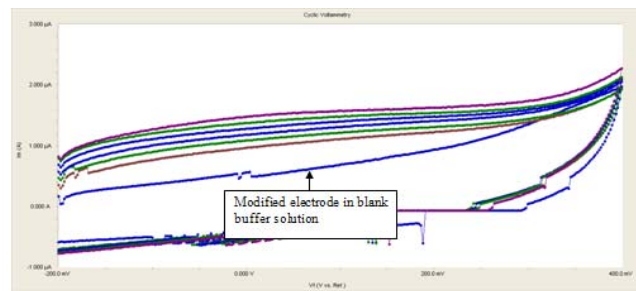


Figure 2. Cyclic voltammograms (i/v) of gold colloid-cysteamine/PAMAM\_2<sup>ND</sup>-modified glassy carbon electrode measured from -0.2 to 0.4 V for the measurement of  $\text{NH}_4^+$ , the lowest concentration was 2 nM.

Figure 2 shows the cyclic voltammograms of various ammonium concentrations measured by the modified glassy carbon electrode, the lowest concentration was 2 nM. As indicated in the voltammogram in the reductive curves (upper lines), there was a big gap (current difference) between the blank (of buffer solution) and the first reductive curve (2 nM). Therefore, it is possible that the modified electrode can measure ammonium concentrations down to subnanomolar levels.

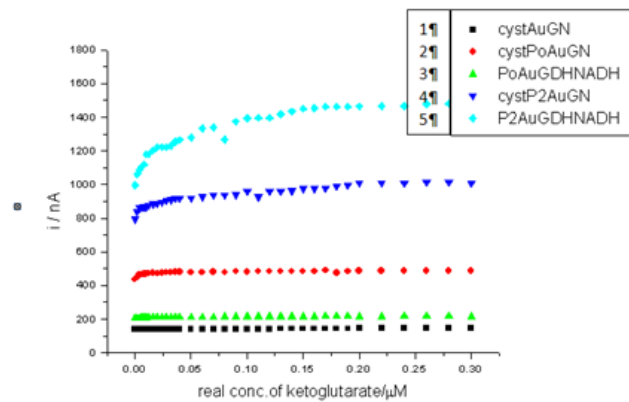


Figure 3. Performance differences of the glassy carbon electrode modified by different materials: 1. Modified with cysteamine-Au-GDH/NADH; 2. Cysteamine /PAMAM\_0-Au-GDH/NADH; 3. PAMAM\_0-Au-GDH/NADH; 4. Cysteamine /PAMAM\_2<sup>nd</sup>-Au-GDH/NADH; 5. PAMAM\_2<sup>nd</sup>-Au-GDH/NADH.

Figure 3 shows that there were distinctive current differences for the reaction of ammonium and  $\alpha$ -keto glutarate when the electrode was modified by different

materials. From the stand point of detection, within the five modifications, sensor coated with second generation of PAMAM would have the highest sensitivity (current vs. concentration). The results were conceivably due to the higher branching property of PAMAM<sub>2<sup>nd</sup></sub>.

## **4 CONCLUSIONS**

We successfully modified our glassy carbon electrode biosensor platform [2] for ammonium detection; we further modified the sensor platform with PAMAMs and the detection lower limit was enhanced. This highly modified electrode can detect ammonium concentrations down to 2 nM, or lower. The low detection limit of this biosensor is far more superior to most available methods, more research is needed for noise reduction and the stability of the electrode.

## **5 ACKNOWLEDGMENT**

This study was supported by an USAMRMC Project Grant (Contract #W81XWH-07-2-0078).

## **REFERENCES**

- [1] S. W. Leung, Y. Wang, H. Gu, and J.C.K. Lai, "Characterization and Applications of Modified Gold Electrode Sensor with Nanoparticles", in Technical Proceedings of the 2009 Nanotechnology Conference and Trade Show, Volume 2: Chapter 4: Biosensors and Diagnostics, pp. 233-235.
- [2] J.C.K. Lai, Y. Wang, W. Gao, H. Gu, and S. W. Leung, "Performance Comparisons of Nanoparticle Modified Sensor Electrodes for the Detection of Nitrite and Peroxide", in Technical Proceedings of the 2009 Nanotechnology Conference and Trade Show, Volume 2: Chapter 4: Biosensors and Diagnostics, pp. 233-235.

## Metallomic Distribution in Various Regions of the Brain as Influenced by Dietary Intakes and Their Implications

G.L. Wright<sup>a</sup>, J.C.K. Lai<sup>b</sup>, A.W.K. Chan<sup>c</sup>, M.J. Minski<sup>c</sup>, L. Lim<sup>d</sup> and S.W. Leung<sup>e,\*</sup>

<sup>a</sup>*Civil and Environmental Engineering Department, College of Engineering, Idaho State University, Pocatello, ID 83209, USA*

<sup>b</sup>*Biomedical & Pharmaceutical Sciences Department, College of Pharmacy and Biomedical Research Institute, Idaho State University, Pocatello, ID 83209, USA*

<sup>c</sup>*Imperial College Reactor Centre, University of London, Silwood Park, Ascot, Berks., SL5 7PY, UK*

<sup>d</sup>*University College London, Institute of Neurology, University of London, London WCIN 1P3, UK*

<sup>e</sup>*Corresponding author: Civil and Environmental Engineering Department, and Biomedical Research Institute, Idaho State University, Pocatello, ID 83209, USA*

---

**Abstract.** Lifelong exposure to environmental factors can influence the risk of developing diseases according to recent research findings. Environmental stresses ultimately leading to neuronal cell death have been hypothesized as the causes of the increased occurrence in developing Alzheimer's and Parkinson's disease. Our daily diet is considered to be one of the most important environmental factors that can seriously affect the development and proper functions of the brain. Depending on the concentrations, metals and electrolytes can pose some health concerns, especially for a prolonged consumption period. For example, it was reported that excess amounts of iron, zinc and copper in the human brain may cause oxidative damage and protein aggregation; the neurotoxicity induced by these metals may lead to cerebral and/or cerebellar degeneration. Other reports showed that there were differences in concentrations of five different elements (aluminum, zinc, copper, manganese, and iron) between normal human brain and brains of patients with Alzheimer's disease. In this study, we investigated 30 elements, including electrolytes, and how dietary intake on a life-time basis would affect their concentrations and distributions in various regions of the rat brain (hypothalamus, cerebellum, pons and medulla, striatum, mid-brain, cerebral cortex, and hippocampus) and discussed their health implications. Information matrices of these 30 different elements (mostly metals) and their distributions in various regions of the rat brain were analyzed as a function of normal dietary intake at different ages during development. Our results showed that metallomic distribution in various regions of the rat brain is age-related. The results may help researchers to identify possible links between daily dietary intake of metals and electrolytes and diseases associated with aging (e.g., Alzheimer's and Parkinson's disease) and suggest such metallomic distributions may be used as neurological biomarkers of exposure to heavy metals.

*Key words:* Brain; elements; metals; electrolytes; distribution; metallomic; neurological; diseases

---

### 1. Introduction

Many of the metals around us are essential for life, but others are known to be highly toxic; even the essential metals can be toxic when their intakes are too high. For example, metals such as chromium, cobalt, copper, manganese, and zinc are essential for life. But, an excess intake of these essential metals can induce toxicity. Some metals such as arsenic, cadmium, lead, mercury, and vanadium, which are found throughout our environment, are toxic to humans and other animals. Some of these toxic metals are even capable of forming covalent bonds with carbon, resulting in metal-organic transformations. This type of transformation affects the mobility and toxicity of the element. Elements can come from naturally-occurring processes such as volcanoes, water, bacterial activity, and also from anthropogenic sources such as automobile exhaust, agricultural fertilizers, industrial activities, and many other sources. It has been shown that in highly industrialized areas, the exposure to metallic elements is extremely high [1].

Being a specialized organ of the body, the brain metabolizes and accumulates metals as part of its normal development and function. But in a rich metal environment, loss of metalloproteins and loss of defense against oxidative stress caused by one or more of the heavy metals could be responsible for neurodegenerative disorders such as Parkinson's disease (PD) and Alzheimer's disease (AD) [2]. The intake of these metals occurs via ingestion

---

\* Solomon W. Leung. Tel.: +1-208-282-2524; fax: +1-208-282-4538.  
E-mail address: leunsolo@isu.edu



of metal-containing food and water, and/or through inhaling metal-contaminated air. The elemental distributions in the different brain regions appear to vary for each element. Some of these metallic elements are known to increase or decrease in brains of humans with a neurodegenerative disorder.

The following are some of the more studied elements in brain; other elements are also found in brain, but research on the latter group has been scant. Although many metals are normally found in brain, over-accumulation of metals may lead to health problems. Moreover, an unbalanced increase or decrease could cause a major functional change and lead to a neurodegenerative disorder even though the underlying molecular mechanisms are largely unknown.

#### Aluminum

Aluminum (Al) is one of the more widely distributed metals in the environment. Approximately 8% of the earth's crust is Al. The exposure of Al normally occurs through air, food, and water [3]. The brain contains approximately 1% of the body's total Al; however, Al has no known function in normal mammalian brain.

During the life-span of a normal human brain, its Al levels appear to increase around age 40, and then plateau at about age 70. The Al levels then begin to increase again from age 80 to 90. The globus pallidus (GP), substantia nigra (SN) and the nucleus ruber appear to be the highest Al levels in the normal human brain [4]. The levels of Al increase in the grey matter in patients with dialysis encephalopathy [5]. Also, Al accumulations in the brain have been found to increase in patients with renal failure. Following oral exposure to this metal, retention of Al was reported in the hippocampus. This region of the brain is rich in cholinergic neurons. These and other observations suggest that Al has neurotoxic properties. Furthermore, following chronic exposure, Al has been shown to accumulate in all regions of the rat brain. There is evidence of a relationship between the high levels of Al and increased risk of neurodegenerative disorders, including AD and PD [3].

#### Calcium

Calcium (Ca) is the fifth most abundant element found in the earth's crust. Ca occurs most commonly in sedimentary rocks in the minerals calcite, dolomite, and gypsum. Ca is essential for life in most living organisms, including humans. Ca has been shown to be elevated in the brains of patients with AD: it concentrates in the amyloid plaques. These plaques are one of the neuropathological hallmarks of AD. However, PSAPP mice (a mouse model of AD) appear to accumulate less Ca in their plaques compared to their surrounding brain tissue [6].

#### Chromium

Chromium (Cr) is also found in the earth's crust and is mined as chromite ore. Because of chromium's high corrosion resistance and hardness, it is added to nickel to create stainless steel: this is the most common application of Cr. It is also used in dyes and pigments, as a gasoline additive, and in the tanning of leather. The pathophysiological role of Cr has not been elucidated. However, Cr has been shown to moderately increase in the parietal cortex of patients with AD when compared to that in normal brain [7].

#### Copper

Copper (Cu), like most elements, is mined from the earth's crust. Furthermore, Cu is recycled. Cu is commonly used in electrical applications, piping, many household products (e.g., sinks, plumbing, pots), architectural applications, coin-making, and chemical applications. Cu has been found to be vital in human and plant life. Cu is introduced into the body mostly via food intake. Some foods that are high in Cu are oysters, beef or lamb liver, Brazil nuts, cocoa, black pepper, lobster, sunflower seeds, green olives, avocados, and wheat bran. The brain contains approximately 7.3% of the total body Cu supply.

Cu has been an extensively studied metal in the brain [8]. In a normal brain, Cu is distributed in similar ways in the central and subcortical white matter of the cerebellum of both young and old brains; however, the periphery of the dentate nucleus is rich in Cu [2]. The higher Cu concentrations are mostly found in the cortex and hippocampus [8]. A normal aging brain has been shown to have increased Cu levels, especially in the substantia nigra and in some cerebellar regions [4]. However, when the levels of Cu in the cortex and hippocampus increase, Wilson's disease is said to result [9]. In AD, there is an abnormal brain Cu distribution, with large amounts in the amyloid plaques but a deficiency in the neighboring brain tissue. Other researchers also reported Cu to increase in the senile plaques [4]. These findings suggest the involvement of Cu in AD is multifactorial and complex.

#### Iron

Iron (Fe) is one of the most common metals found in everyday use. Fe makes up about 5% of the earth's crust. The earth's core is believed to consist largely of an iron-nickel alloy constituting 35% of the mass of the earth as a whole. Because of this distribution, Fe is thought to be the most abundant element on earth. Some popular food stuffs rich in Fe include red meat, fish, poultry, beans, vegetables, black-eye peas, wheat, and cereals.

Fe is another extensively studied metal in brain. Fe is necessary for normal brain function (e.g., in learning and memory) [10]. In a normal brain, Fe is distributed in similar ways in central and subcortical white matter of the cerebellum of both young and old brains; in the cerebellar cortex, there are high Fe levels, and the periphery of the dentate nucleus is also rich in Fe [2]. Fe appears to increase rapidly in the young brain and then remains stable until the later years; increases in Fe in the substantia nigra and globus pallidus have been reported [4]. Regions where brain Fe is high include substantia nigra, globus pallidus, red nucleus, caudate nucleus, and the putamen [11].

Like Cu and Ca, Fe has been shown to be elevated in brains of patients with AD. Elevated Fe is found in the amyloid plaques [6]. Fe is also moderately increased in the parietal cortex in AD patients [7]. In patients with Attention Deficit Hyperactivity Disorder (ADHD), Fe has been shown to increase in the substantia nigra [12].

#### Manganese

Manganese (Mn) is found in the earth's crust and in seawater. It is often found with Fe. Some of the more common usages of Mn are in steel, aluminum alloys, alkaline batteries, coins, and pigments. Some popular foods that contain Mn include tea, spinach, grains, rice, eggs, nuts, olive oil, green beans, and fish.

The majority of the human body's Mn is found in liver and kidneys; nevertheless, Mn is an important element for normal brain development and function [13]. In the aging brain, Mn has been shown to redistribute itself in different brain regions, including hypothalamus, thalamus, and corpus callosum [4]. High brain Mn concentrations are related to PD. There has been much research indicating that human striatum, globus pallidus, and substantia nigra show increases in Mn levels and are thought to be target sites for Mn neurotoxicity. The globus pallidus and pituitary glands are other regions where Mn preferentially accumulates. High exposures to Mn result in increases in Mn in the olfactory epithelium and olfactory bulb [14]. It is noteworthy that Mn levels in the cerebellum are similar in AD and normal brains while Mn increases in the parietal cortex of AD brains [7].

#### Magnesium

Magnesium (Mg) is the 8<sup>th</sup> most abundant element in the earth's crust and is found also in seawater. Mg is commonly used in structural building materials, automotive parts, electronic devices, aerospace construction, photography, and fireworks. Mg is an essential metal in human and plant life [13]. Human Mg deficiency has been linked to the development of asthma, ADHD, and osteoporosis. Foods that are high in Mg include spices, nuts, cereals, coffee, cocoa, tea, and vegetables. In neurodegenerative disorders such as AD and PD, Mg does not appear to play a major role. For example, Mg levels in the cerebellum and parietal cortex do not differ between patients with AD and normal humans [7].

#### Mercury

Mercury (Hg) is found in deposits throughout the world, mostly as cinnabar (a common ore of Hg). The more common uses of Hg are in barometers, thermometers, dental products (e.g., fillings), and electrical equipment (e.g., computers, telephones, etc.) [15]. Exposures to Hg most commonly occur from the consumption of marine species [1]. Other exposures to Hg may be from exhaust of coal-burning power plants, cement production, batteries, and gold production. The role of Hg in neurological diseases such as AD and PD has been controversial. Hg can cross the blood-brain and blood-placental barriers. It is then retained by the brain for years [16]. Hg tends to accumulate in lipid-rich regions of the brain. Human exposure to Hg usually results in kidney and neurological disorders [15].

#### Potassium & Rubidium

Potassium (K) occurs in nature as an ionic salt and is essential for humans and other animals. It is found dissolved in seawater and in other minerals. Some common food sources of K include orange juice, potatoes, bananas, avocados, tomatoes, broccoli, apricots, and many other fruits.

Rubidium (Rb) is not essential for humans, but is readily taken up by the body. It is found commonly mixed in with other elements, especially K. Rb is found in some plants as well. Some common uses of Rb are in fireworks, lasers, chemical applications, and electronic transmission. Rb is found in some brain tumors.

Exposure to K and Rb is not known to cause neurodegenerative disorders. For example, the concentrations of K and Rb are similar between AD and control brains [1; 7].

#### Sodium

Sodium (Na) is an essential element for humans and other animals. It is found in nature as a compound only; the most common forms are salt deposits. The most common form of Na that we know and use is sodium chloride, table salt. It does have many other industrial uses as well. Over- or under-exposure to Na has not been shown to cause neurological disorders. Nevertheless, Na has been shown to increase every brain region in AD patients [1].

#### Zinc

Zinc (Zn) is naturally found in the earth's crust and in seawater. It is normally found with Fe and Cu deposits. Zn is commonly used in batteries, production of brass, bronze, rubber, in pigments, fire retardant, nuclear weapons, automobile engines, and agricultural fungicides. The most common food source of Zn is red meats.

Zn is another essential element in mammals. Zn is distributed in similar ways in the central and subcortical white matter of both young and old brains; the interior of the dentate nucleus and the cerebellar cortex contain high levels of Zn [2]. The regions of the normal brain rich in Zn include the hippocampus, amygdala, and the cortex. As the brain ages, its Zn distribution changes, just in the regions mentioned above. Nevertheless, little or no decrease in brain Zn has been reported in aging humans or rats [4]. Zn is found to be elevated in human amyloid plaques while PSAPP mice (an AD mouse model that does not show neurodegeneration) only had a 29% increase of Zn in their plaques compared to the Zn in brain tissue surrounding the plaques [6]. The potential role of Zn as a cofactor in the pathogenesis of AD was strengthened when Zn enrichment was found in senile plaques and a Zn elevation in the neuropil of AD patients as compared to those in control individuals [4].

Of the 90 plus naturally-occurring elements, 26 are known to be essential for humans and animals [17]. These consist of 11 major elements or macro-elements. They are: C, H, O, N, S, Ca, P, K, Na, Cl, and Mg. Fifteen elements are known as trace elements or micro-nutrients. They include: Fe, Zn, Cu, Mn, Ni, Co, Mo, Se, Cr, I, F, Sn, Si, V, and As. The molecular bases for the essential element selection and rejection have not been elucidated, however. Major elements, such as Na, K, Ca, and Mg, are required for bodily functions such as body fluid buffer, active transport, ionic balance, electrical transmission, tissue development as well as the composition of body fluids and structures. Trace elements act primarily as catalyst in enzyme systems in cells where they serve a wide range of functions from weak ionic effects to highly specific associations such as metalloenzymes. In addition, the protein-metal interactions may increase the stability of the protein moiety to metabolic turnover.

In this study, we investigated 30 elements (including electrolytes) and how dietary intake on a life-time basis would affect their concentration and distribution in various regions of the rat brain (hypothalamus, cerebellum, pons and medulla, striatum, mid-brain, cerebral cortex, and hippocampus) and discussed their health implications. The 30 elements of interests were: Al, As, Ba, Br, Ca, Cd, Cl, Co, Cr, Cu, F, Fe, Hg, I, K, La, Mg, Mn, Mo, Na, Rb, S, Sb, Sc, Se, Si, Sm, Sr, V, and Zn. In the past, research has primarily focused on the effects of different elements on the brain and the neurological disorders they may cause. None of those studies, however, have examined simultaneously as many elements in a single study as we have presented here. The objective of this paper is to characterize the levels of major and selected trace elements in various regions of the rat brain during several critical stages of development. Because during the first 8-9 days of age postnatal, the rat hippocampus is extremely difficult to visually distinguish from the overlying cerebral cortex, we had included the hippocampus tissue together with the cerebral cortex for analysis in the case of 5-day-old tissue samples. The four postnatal age groups of rats we have studied include the following:

- I. 5 days old;
- II. 10 days old;
- III. 22/23 days old; and
- IV. 120 days old (i.e., adult).

While humans and rats are not identical neurologically and physiologically, there are more similarities between the two species as far as brain structure and functions are concerned. The four stages of the postnatal development of the rat chosen in this study closely parallel the postnatal development of humans. As our well being is largely impacted by the environment we are living in, dietary intake is definitely a major factor that posts a long-term effect on our health. This paper provides some insight into how our diet and pollutants in our diet may affect our neurological health. Consequently, our experimental results may allow us to take some preventative measures in determining how best to optimize and gauge our dietary intake of major and trace elements for the betterment of our health.

## **2. Experimental Methods**

Wistar rats of the Porton strain (Animal Breeding Unit, Carshalton, Surrey, U.K.) bred in the Institute of Neurology, University of London, U.K. were used. All animals were kept on a 12-hour light/12-hour dark cycle with free access to food and water. Elemental concentrations in the rat food pellets had been determined (Table 1 below).

Table 1. Elemental Concentration of rat food pellet.

Element	Concentration (in mg/g)
Ca	6.39 ± 1.68
Cl	2.31 ± 0.49
Fe	0.25 ± 0.05
K	5.36 ± 0.95
Mg	1.17 ± 0.32
Na	1.48 ± 0.32
	Concentration (in µg/g)
Al	98.06 ± 8.05
Br	10.57 ± 2.26
Co	0.20 ± 0.04
Cr	1.50 ± 0.44
Cu	7.21 ± 2.12
F	ND(5.00)
Hg	ND (0.25)
I	ND (0.50)
Mn	49.34 ± 8.65
Mo	2.80 ± 0.45
Se	ND (0.25)
Rb	12.73 ± 2.61
V	ND (0.50)
Zn	47.73 ± 4.11

Thirty trace and major elements in different brain regions of rats at the four different age groups (i.e., I through IV as defined above) were analyzed by instrumental neutron activation analysis (INAA) [18]. The samples were irradiated by thermal neutrons using three different sets of conditions depending on the nuclear characteristics of the elements of interest [18]. Not all 30 elements were reported in the results because those not reported herein were either below the detection limits of our INAA technique [18] or the elements were not retained by the brain tissue. All values listed are mean ± S.D.; ND = not detectable, and values in brackets are the maximum elemental concentrations present in the diet.

As already noted above, in age group I, the hippocampal tissue had been included in the cerebral cortex and analyzed as such.

All the standard materials and samples for INAA were freeze-dried and pelleted. Dried samples (rat brain regions) were homogenized using a Glen Creston polystyrene ball-mill and pelleted. Other details of standard and sample preparations were as described previously [18; 19].

Standards and samples were irradiated in a 100 KW 'Consort' Reactor Mark II at the Imperial College Reactor Centre. Irradiated standards and samples were then analyzed for their elemental contents by gamma ray spectrometry using various Ge(Li) detectors and ND6600 Multichannel Analyzer (Nuclear Data Inc., Schaumburg, Illinois, USA). Details of the elemental determinations were described in the methodology paper by Chan et al. (1983).

All laboratory chemicals used were of analytical grade (BDH Chemicals Limited, U.K.) and single element standards of trace elements were obtained from AAS (Ventron Division, Limited, U.K.); other elemental standards for F, Cl, Br, and P were obtained from Hopkin and Williams Chemical Ltd., U.K. Water for solution preparations and feeding was double-distilled.

### 3. Results

#### Cerebellum

The cerebellum is the “cauliflower-shaped” region of the brain located in the lower part of the brain next to the brain stem. The cerebellum controls movement, balance, and coordination. More recent evidence suggests that it plays roles in regulations of emotions and memory and learning. Figure 1 shows the elemental distributions in the cerebellum during rat postnatal development.

It can be noted from Figure 1 that the levels of different elements generally show a decreasing trend as the cerebellum develops and reaches adulthood: this trend may reflect the gradual closing of the blood-brain barrier between age 10 days through weanling and beyond. However, research on elemental distributions in cerebellum during development has been minimal: some of the more studied elements include magnesium, rubidium, and sodium.

Magnesium levels in the parietal cortex in AD patients do not differ from those in normal controls [7]. Similarly, rubidium levels in AD brains do not differ from those in control brains [1]. Consequently, the age-related changes in magnesium and rubidium levels in the cerebellum may not have good predictive value of neurological diseases in later life. On the other hand, the sodium levels in the rat cerebellum decreases during the latter half of postnatal development as they approach the adult level. On the other hand, sodium levels in every regions of the human brain are significantly higher in the AD patients than those in control subjects [1]. These results taken together suggest that dietary intake of sodium may have some relevance in the causation and/or progression of AD.

#### Cerebral Cortex

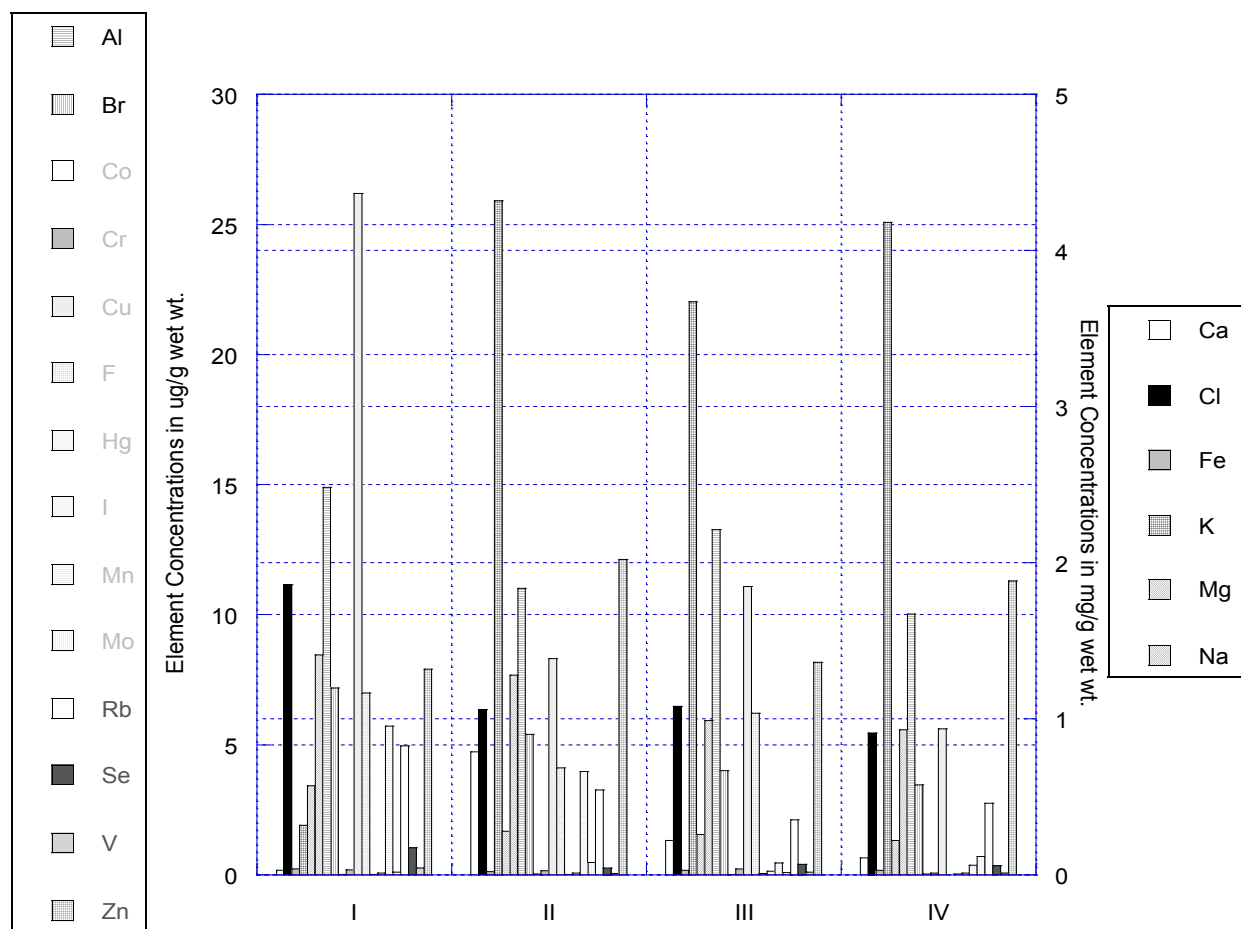


Fig. 1. Element Concentrations of Rat Cerebellum at Different Development Stages.

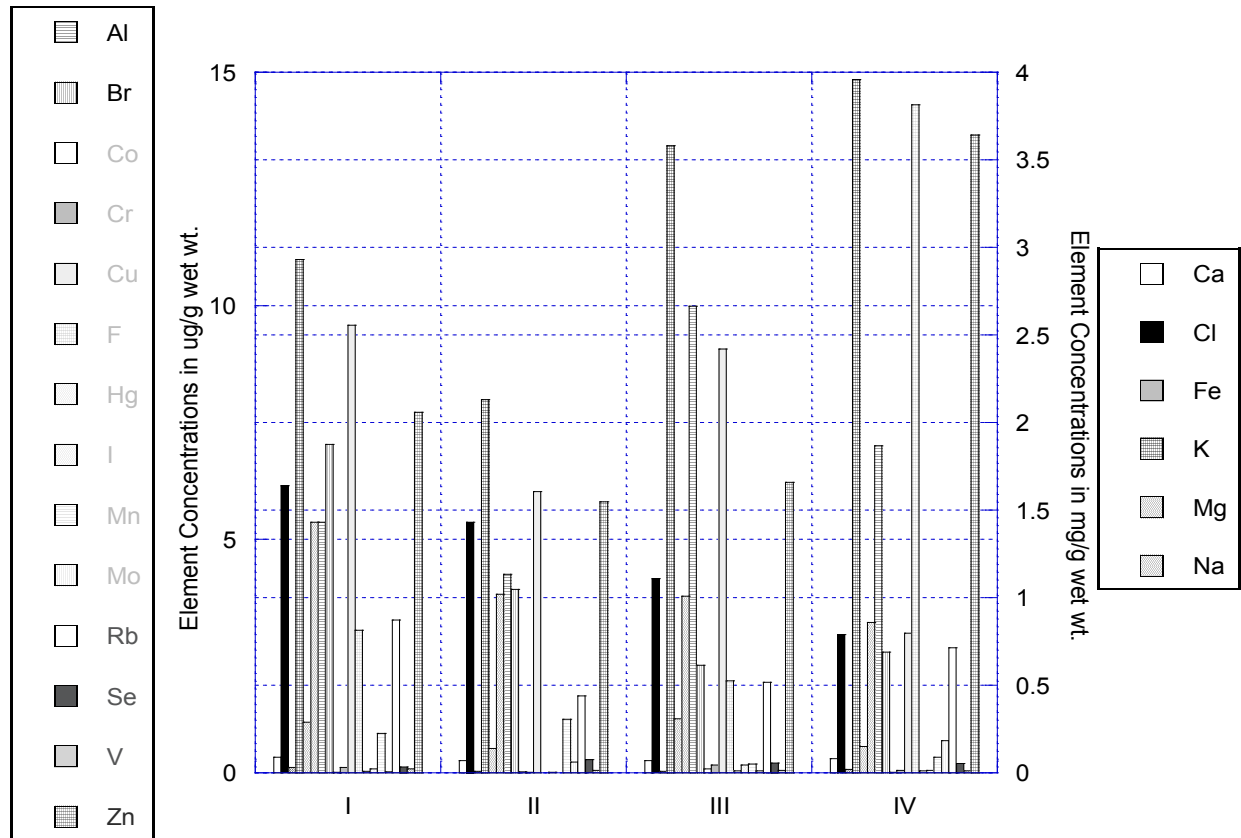


Fig. 2. Element Concentration of Rat Cerebral-Cortex at Different Developmental Stages

The cerebral cortex is responsible for all intellectual and other higher functions such as thinking, voluntary movements, language, reasoning, and perception. Figure 2 shows the elemental distributions in the cerebral cortex during postnatal development till adulthood. It can be gleaned from the results shown in Figure 2 that on average, about half of the concentrations of different elements increase with increasing age while about half of the levels of the other elements decrease as age advances toward adulthood.

Several elements in the human cerebral cortex have received more attention recently; they are described in further details in the following:

Even though the physiological role of aluminum (Al) in brain has not been identified, it is accumulated in the cerebral cortex of the rat as it matures to adulthood: presumably, this accumulation reflects dietary intake (Figure 2). Consequently, increasing brain accumulation of Al, which is known to be neurotoxic, could induce neurological problem(s) in the long term. For example, Al shows significantly higher level in the parietal cortex in AD patients compared to those in control individuals [7]. Similarly, Al accumulation in brain and other tissues, including bone, liver, and kidney, has also been shown to accompany renal failure [3].

Calcium (Ca) levels in the rat cerebral cortex do not markedly change during postnatal development (Figure 2). On the other hand, one of the pathological hallmarks of Alzheimer's disease (AD) is the accumulation of amyloid plaques between nerve cells (i.e., neurons) in different parts of human brain including cerebral cortex. Ca levels in human amyloid plaques in AD are elevated. Consistent with the latter observation is the finding that, in PSAAP mice (a mouse model of AD, which shows plaques but little neurodegeneration), Ca accumulation in their plaques is less than those in the surrounding brain tissue [6]. Consequently, age-related accumulation of Ca in this brain region could potentially serve as marker for the likelihood of developing neurodegeneration as age advances.

Chromium (Cr) shows a moderate increase in parietal cortex of AD patients compared to those in control subjects [7]. In rat cerebral cortex, Cr levels increase from day 10 to day 22/23 and thereafter decrease as adulthood is reached (Figure 2). Nevertheless, relations between brain Cr levels and neurological diseases have not been firmly established.

Copper (Cu) in amyloid plaques in AD is elevated [4]. In PSAAP mice (a mouse model of AD, which shows plaques but less neurodegeneration) Cu accumulation in their plaques is less than those in the surrounding brain tissue [6]. Consequently, increasing Cu accumulation in cerebral cortex as age advances can potentially herald the onset of neurological problems.

The magnesium (Mg) levels in rat cerebral cortex fluctuate during development and level off toward adulthood (Figure 2). Mg levels in parietal cortex and cerebellum in AD patients do not differ from those in control subjects. Taken together, these observations suggest Mg to be more predictor of neurological problems as age advances.

Manganese (Mn) shows significantly higher levels in the parietal cortex of AD patients compared to those in control subjects [7]. However, cerebellar Mn levels in AD are similar to those in control subjects [7]. Figure 2 shows that Mn levels in cerebral cortex of the rat show a general trend of decrease as its age increases. Nonetheless, whether this is a generalized trend of an essential element remains to be established.

Potassium (K) concentrations in the AD brain appear to be similar to those in control brain, especially in the regions examined [1]. K generally shows a trend of age-related increases in the rat cerebral cortex (Figure 2), perhaps reflecting increases in cellular material because intracellular K is higher than extracellular K.

Sodium (Na) levels in the rat cerebral cortex decrease with increasing age (Figure 2), reflecting the closing of the blood-brain barrier thereby excluding the entry of extracellular Na into cells. On the other hand, Na levels in every region of the AD brain are higher than corresponding levels in control brain [1]. Consequently, age-related increases in brain sodium may be considered at least a partial predictor of age-related neurological problems.

Zinc (Zn) is elevated in the amyloid plaques in AD and PSAPP mice (an AD mouse model that shows little or no neurodegeneration) only had a 29% increase of Zn in their plaques compared to the Zn in brain tissue surrounding the plaques [6]. By contrast, Zn levels in the rat cerebral cortex markedly increase between age 22/23 days and adulthood suggesting that the increase is associated with tissue growth. However, the increase in brain Zn during brain aging may be more predictive of onset and/or presence of neurological problems [6].

#### Hippocampus

The hippocampus is located deep within the temporal lobe and is part of the limbic system. This brain region is responsible for learning and formation of long-term memory. Figure 3 shows the elemental distributions in the rat hippocampus at different stages during postnatal development. We discuss below the elements that were emphasized in several recent reports.

Following oral exposure of rats to aluminum (Al), its retention has been noted in the hippocampus as occurs in other brain regions: rat hippocampal Al levels increase markedly after 10 days of age (Figure 3). In patients with PD, elevated Al levels have been found in several brain regions including the hippocampus, which is rich in cholinergic neurons [3]. Consequently, chronic accumulation of Al in this brain region over a life-span may lead to the development of neurodegenerative diseases such as PD because of Al is known to be neurotoxic.

Potassium (K) levels in the rat hippocampus increase from age day 10 till adulthood, likely reflecting the increase in cellular material during this developmental period (Figure 3). However, in the brain regions examined in AD, brain K remains essentially unchanged compared with corresponding levels in control subjects [1], suggesting that brain K may not be a good indicator of the likelihood of developing neurological diseases such as AD.

Rubidium (Rb) levels in rat hippocampus fluctuate between age day 10 and adulthood (Figure 3). However, Rb levels in the AD brain do not differ from those in control brain [1] suggesting that Rb levels in brain may not be a good predictor neurodegenerative diseases such as AD.

Sodium (Na) levels in the rat hippocampus decrease between ages day 10 and day 22/23 and level off at adulthood (Figure 3). However, Na levels in every part of the AD brain examined are higher than corresponding levels in the control brain [1].

#### Hypothalamus

The hypothalamus is located at the interior of the brain under the thalamus. It controls body temperature, emotion, thirst, hunger, appetite, digestion, and sleep. Figure 4 shows the elemental distributions in rat hypothalamus in the four developmental stages we have investigated. Even though this brain region is known to accumulate a variety of metals, their precise functional significance remains to be fully elucidated. Only few functionally important changes during development can be commented on (Figure 4).

The electrolytes in this rat brain region show fluctuating trends in the four age groups investigated, partly reflecting the closing of the blood-brain barrier. For example, sodium (Na) and chlorine (Cl) levels significant decrease in the first 22/23 days postnatal. On the other hand potassium (K) levels markedly increase between day 5 and day 10 postnatal.

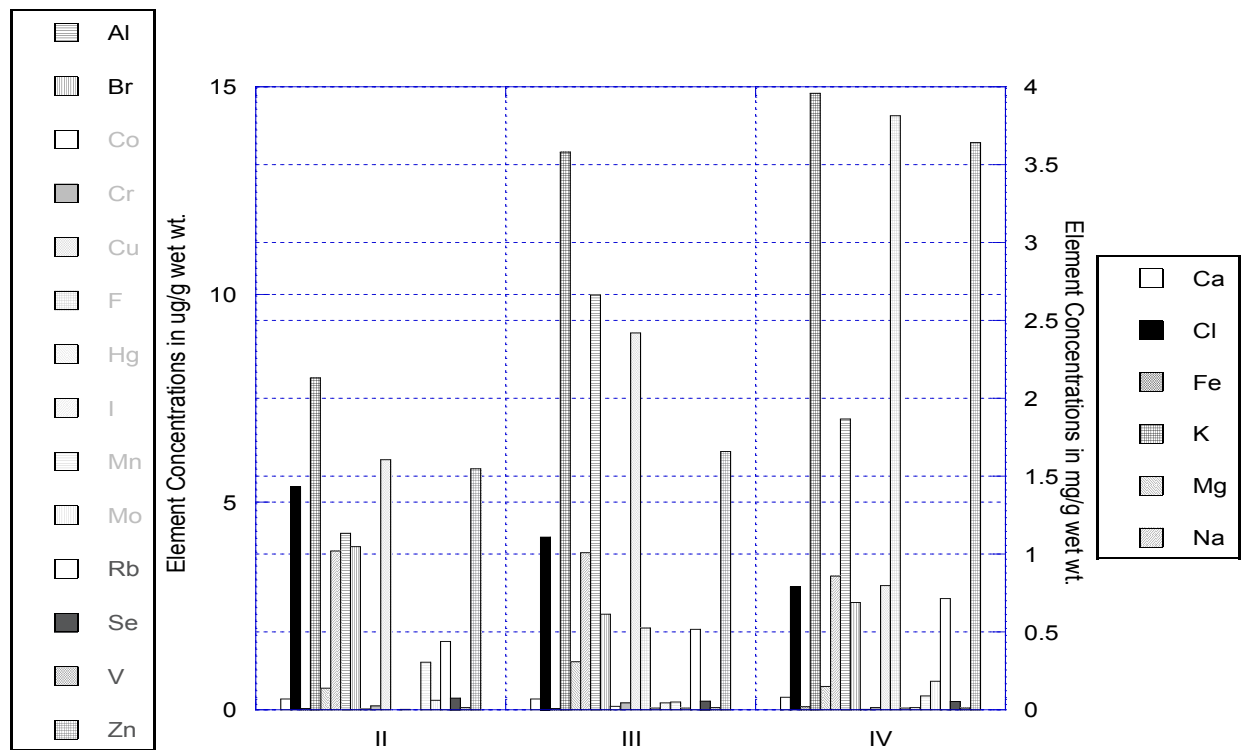


Fig. 3. Elemental Concentrations of Rat Hippocampus at Different Developmental Stages

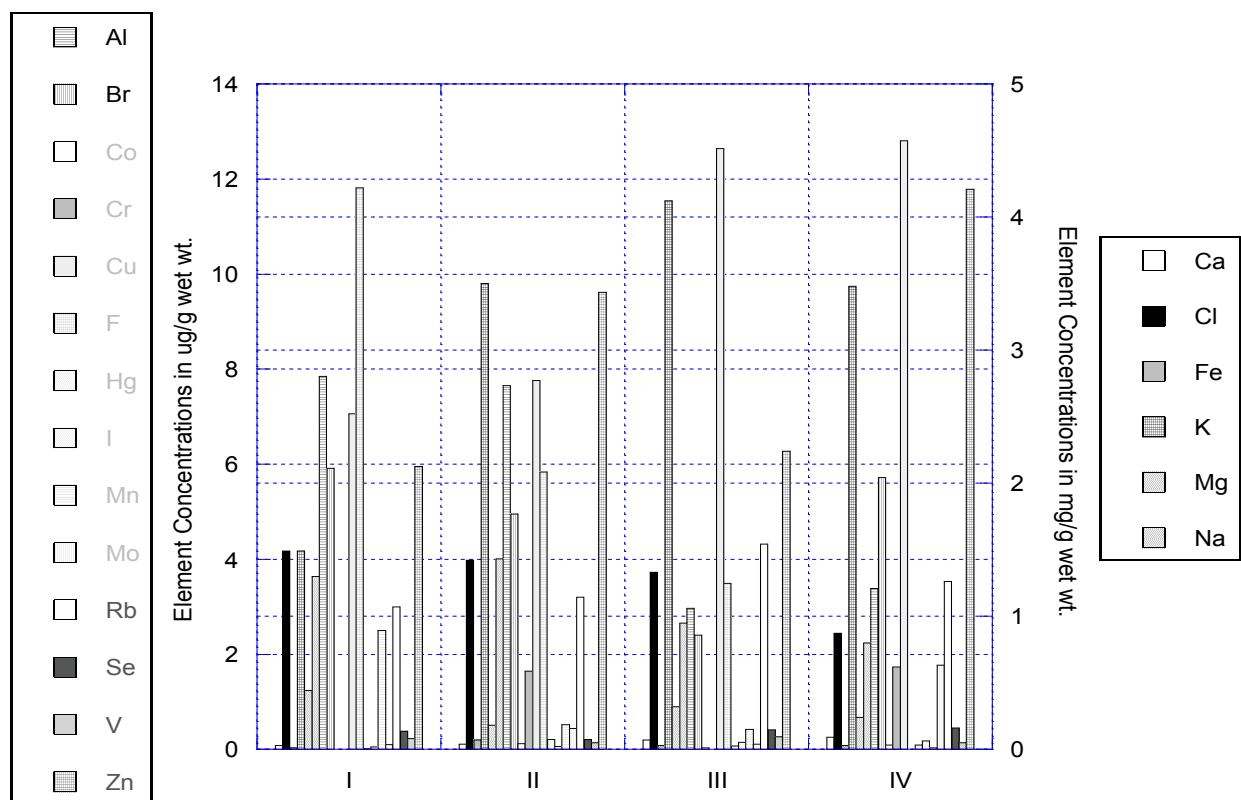


Fig. 4. Element Concentrations of Rat Hypothalamus at Different Developmental Stages



Although they show some age-related fluctuations, the essential trace elements copper (Cu), selenium (Se), and zinc (Zn) levels in the rat hypothalamus significantly increase between postnatal age 5 and adulthood (Figure 4). At present, one can only speculate about the functional significance of the postnatal increases of these essential metals in the rat hypothalamus because of the absence of relevant studies.

#### Mid-Brain

As its name implies, the mid-brain is located in the middle of the brain above the brain stem. The mid-brain generally acts as a relay station for both sensory and spinal cord signals and passes them on to the limbic system and the cortical areas. Figure 5 shows the elemental distributions in the rat mid-brain in the four age groups we have investigated. In the rat mid-brain, the levels of both major and trace elements studied show age-related fluctuations that differ from those in the rat cerebral cortex or hippocampus. However, the relevance of these fluctuations in the mid-brain to neurological diseases remains to be elucidated.

#### Pons and Medulla

Situated immediately below the mid-brain, pons and medulla constitute the brain stem which is connected to the spinal cord. Key functions of pons include motor control and sensory analysis and signal relay between the mid-brain and spinal cord. The medulla is known to be responsible for maintaining heart and breathing rates. Figure 6 shows the elemental distributions in the rat pons and medulla in the four age groups we have investigated. Most major and trace elements show age-related decreases in their levels in rat pons and medulla as adulthood approaches (Figure 6). Overall, the accumulation of metals in this brain region is not as quantitatively marked as those in the other brain regions, possibly due to the fact that this brain region is full of fiber tracts rather cell bodies. Moreover, the physiological significance of the distributions of metals in this brain region is still poorly understood.

#### Striatum

The striatum constitutes the sub-cortical parts of the forebrain: it includes the substantia nigra and the globus pallidus. Among its best known function is its role in the planning and modulation of movement pathways as well as roles in other cognitive functions. Figure 7 shows the elemental distributions in the rat striatum in the four age groups we have investigated. We discuss below the elements that were emphasized in several recent reports.

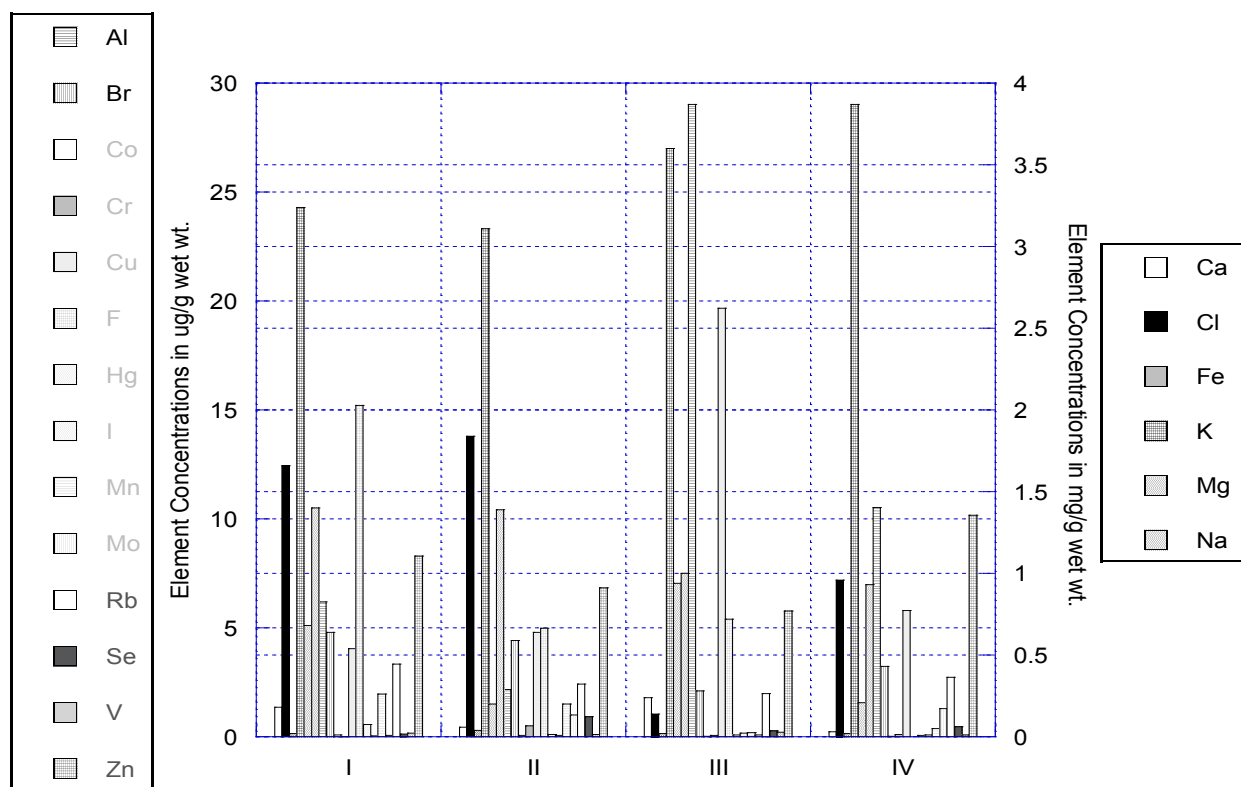


Fig. 5. Element Concentrations of Rat Mid-Brain at Different Developmental Stages

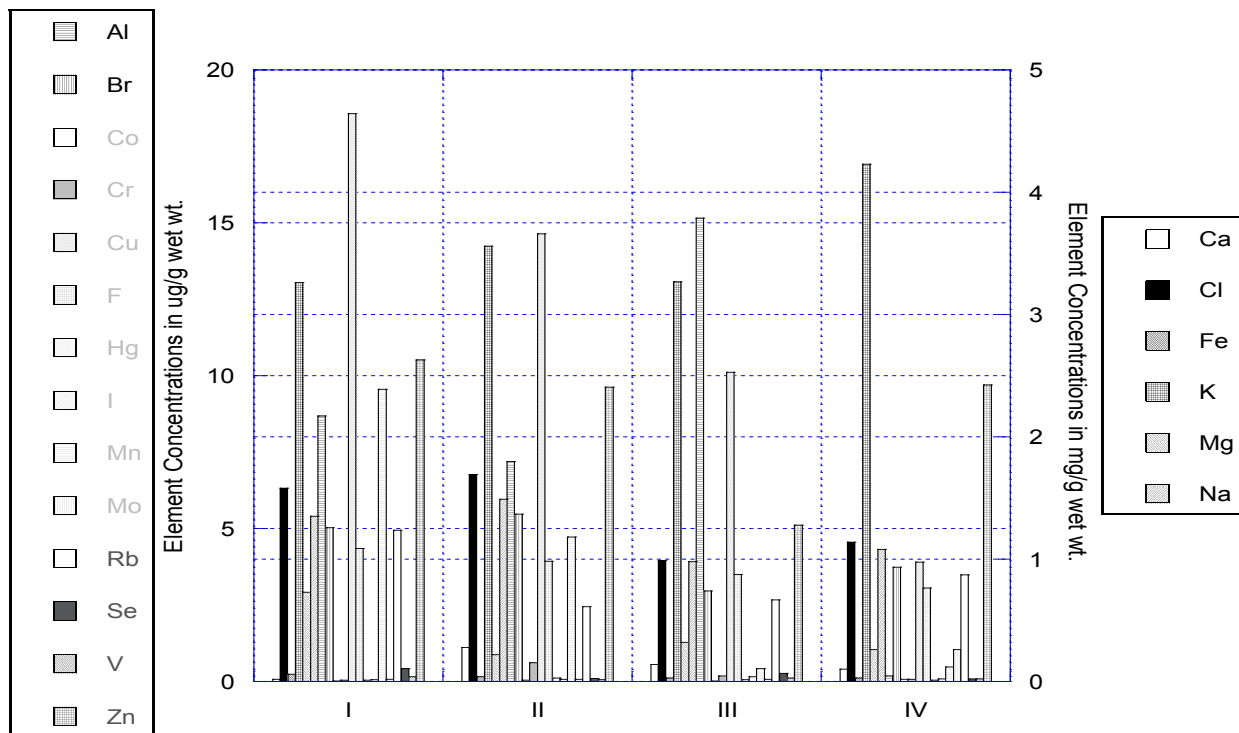


Fig. 6. Element Concentrations of Rat Pons & Medulla at Different Developmental Stages

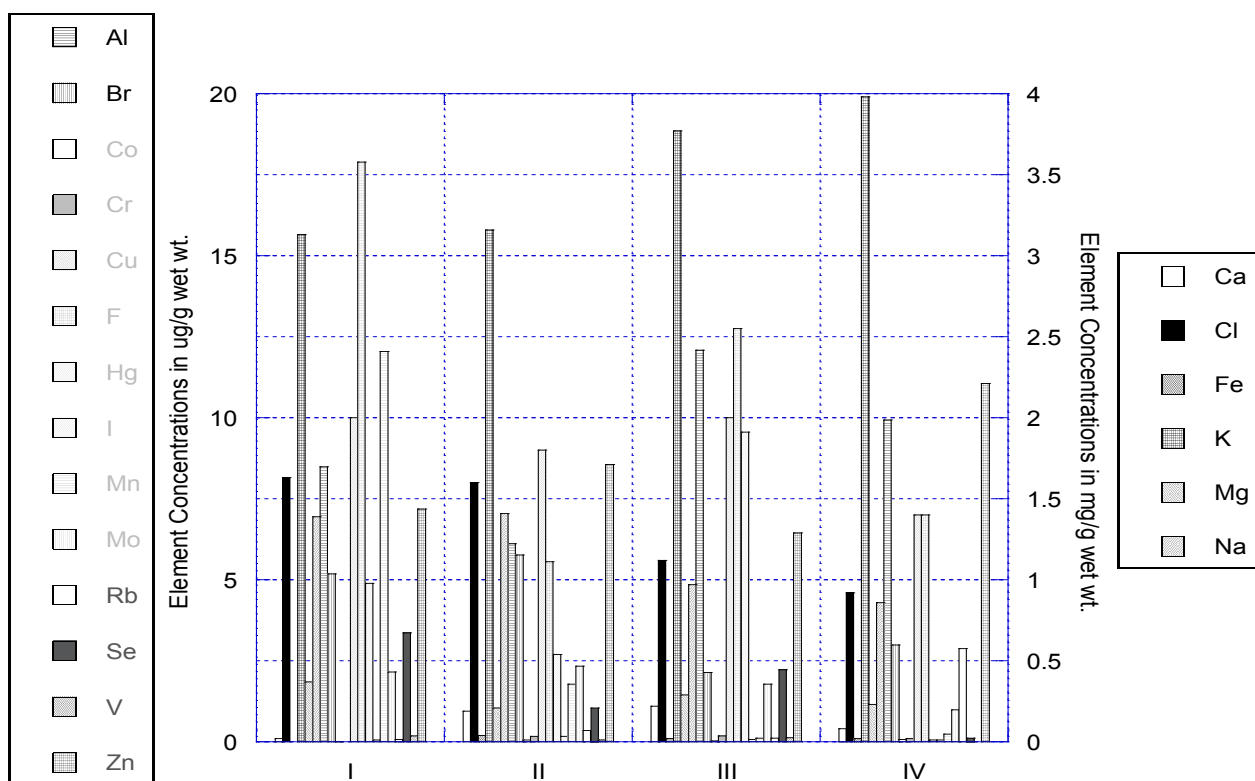


Fig. 7. Element Concentrations of the Striatum Different Developmental Stages

There is recent evidence that iron (Fe) plays a role in the consolidation of long-term memory. Brain Fe distribution overlaps with that of dopaminergic neurons. In rodent models of neurological disorders, Fe levels in the substantia nigra and basal ganglia increase. Because of those observations, increased striatal Fe has been suggested to be responsible for neuronal cell. Furthermore, Fe accumulates in brain as a function of age [19]. In rat striatum, Fe levels decrease between ages 10 days and 22/23 days and level off thereafter (Figure 7).

Brain Fe is highest in the substantia nigra, globus pallidus, red nucleus, caudate nucleus, and putamen. Increased brain Fe has been found in several neurodegenerative disorders although it has not been defined as the main cause [21]. Fe level in the substantia nigra increases in PD but total Fe in the substantia nigra zona reticulata does not change in either PD or AD [11]. Thus, these findings suggest that over accumulation of iron in striatum may lead to development of neurodegenerative diseases such as PD and AD and sources of Fe exposure could be environmental and dietary. However, it remains to be determined if the elevated Fe levels antedate injury of pigmented neurons or constitute a consequence of neuronal degeneration because the increased Fe in the substantia nigra may contribute to oxidative damage to neurons. Nevertheless, most brain Fe is stored in an inactive form bound to intracellular ferritin, which is thought to be mainly localized in microglia and oligodendroglia. Clearly, additional studies are needed to clearly delineate the pathophysiological role of Fe in neurodegenerative diseases.

Chronic manganese (Mn) toxicity in human induces signs and symptoms that closely resemble those noted in PD. There is a great deal of evidence that human striatum, globus pallidus, and substantia nigra show preferential increases in Mn and are believed to be the primary sites associated with Mn neurotoxicity. Moreover, exposure to high Mn leads to elevation of Mn levels in olfactory epithelium and olfactory bulb [14].

In every region of the brain examined, brain sodium (Na) is increased in AD compared with corresponding levels in control subjects [1]. On the other hand, Na levels in rat striatum decrease during postnatal development. Taken together, these observations suggest that high Na accumulation in brain may lead to pathological states and sources of the Na could be environmental and/or dietary in origin.

#### 4. Conclusions

Our results strongly suggest that the metallomic distributions in various regions of the rat brain change markedly during the different stages of postnatal development. In conjunction with the reports in the literature, our findings also suggest that brain regional metallomic distribution can be influenced by dietary intake of metals and other elements and may pathophysiological implications in several key neurodegenerative diseases such as Parkinson's disease and Alzheimer's disease. A metallomic distribution model of various regions of the rat brain can be developed based on ours experimental results and statistical analysis. However, much remains to be discovered regarding the brain functional significance of metallomic distribution during development.

#### Acknowledgements

This study was partially supported a USAMRMC Project Grant (Contract #W81XWH-07-2-0078).

#### References

- [1] Belavaria, C., Andresi, E., Molnar, Z., and Bertalan, E. (2005) Determination of Alkali Metals in Control and AD Brain Samples by Different Techniques. *Microchemical Journal*, 79(1-2), 367-373.
- [2] Popescu, B. F. G., Robinson, C. A., Rajput, A., Rajput, A. H., Harder, S. L., and Nichol, H.. (2009) Iron, Copper, and Zinc Distribution of the Cerebellum. *Cerebellum*, 8(2), 74-79.
- [3] Kumar, V., and Gill, K. D.. (2009) Aluminium Neurotoxicity; Neurobehavioural and Oxidative Aspects. *Archives of Toxicology*, 83(11), 965-978.
- [4] Bolognin, S., Messori, L., and Zatta, P. (2009) Metal Ion Physiopathology in Neurodegenerative Disorders. *Neuromolecular Medicine*, 11(4), 223-238.
- [5] Schafer, U., and Jahreis, G. (2006) Exposure, Bioavailability, Distribution, and Excretion of Aluminum and its Toxicological Relevance to Humans. *Trace Elements and Electrolytes*, 23(3), 162-172.
- [6] Leskovjan, A. C., Lanzirrotti, A., and Miller, L. M. (2009) Amyloid Plaques in PSAPP Mice Bind Less Metal Than Plaques in Human Alzheimer's Disease. *Neuroimage*, 47(4), 1215-1220.

- [7]Srivastava, RAK., and Jain, JC. (2002) Scavenger Receptor Class B Type I Expression and Elemental Analysis in Cerebellum and Parietal Cortex Regions of the Alzheimer's Disease Brain. *Journal of the Neurological Sciences*, 196(1-2), 45-52.
- [8]Hung, YH., Bush, AI, and Cherny, RA. (2010) Copper in the Brain and Alzheimer's Disease. *Journal of Biological Inorganic Chemistry*, 15(1), 61-76.
- [9]Zhang, L., Lichtmanegger, J., Summer, K. H., Webb, S., Pickering, I. J., and George, G. N. (2009) Tracing Copper-Thiomolybdate Complexes in Prospective Treatment for Wilson's Disease. *Biochemistry*, 48(5), 891-897.
- [10] Gerlach, M., Benshachar, D., Riederer, P., and Youdim, MBH. (1994) Altered Brain Metabolism of Iron as a Cause of Neurodegenerative Diseases. *Journal of Neurochemistry*, 63(3), 793-807.
- [11]Kienzl, E., Puchinger, L., Jellinger, K., Linert, W., Stachelberger, H., and Jameson, R.F. (1995) The Role of Transition Metals in the Pathogenesis of Parkinson's Disease. *Journal of the Neurological Sciences*, 134, 69-78.
- [12] Berg D., Gelach M., Youdim, MBH., Double, KL., Zecca, L., Riederer, P., and Becker, G. (2001) Brain Iron Pathways and Their Relevance to Parkinson's Disease. *Journal of Neurochemistry*, 79(2), 225-236.
- [13] Yokel, RA. (2009) Manganese Flux Across the Blood-Brain Barrier. *Neuromolecular Medicine*, 11(4), 297-310.
- [14] Dorman, DC, Struve, MF, Wong, BA, Dye, JA, and Robertson, ID. (2006) Correlation of Brain Magnetic Resonance Imaging Changes with Pallidal Manganese Concentration in Rhesus Monkeys Following Subchronic Manganese Inhalation. *Toxicological Sciences*, 92(1), 219-227.
- [15] Florea, AM, and Busselberg, D. (2006) Occurrence, Use, and Potential Toxic Effects of Metals and Metal Compounds. *Biometals*, 19(4) 419-427.
- [16] Rooney, JPK. (2007) The Role of Thiols, Dithiols, Nutritional Factors and Interacting Ligands in the Toxicology of Mercury. *Toxicology*, 234(3), 145-156.
- [17] Underwood, E.J. (1977) Trace Elements in Animal Nutrient. Academic Press.
- [18] Chan, A.W.K., Minski, M.J., Lai, J.C.K. (1983) An Application of Neutron Activation Analysis to Small Biological Samples: Simultaneous Determination of Thirty Elements in Rat brain Regions. *Journal of Neuroscience Methods*, 7(4), 317-328.
- [19] Chan, A.W.K. and Minski, M. J. (1981) U. L. R. C. Internal Report (RES/36), p 37-39.
- [20] de Lima, MNM, Laranja, DC, Caldana, F, Graziotin, MM, Garcia, VA, Dal-Pizzol, F., Bromberg, E., and Schroder, N. (2005) Selegiline Protects Against Recognition Memory Impairment Induced by Neonatal Iron Treatment. *Experimental Neurology*, 196(1), 177-183.
- [21]Lee, DW., and Anderson, JK. (2010) Iron Elevations in the Aging Parkinsonian Brain: A Consequence of Impaired Iron Homeostasis. *Journal of Neurochemistry*, 112(2), 332-339.

## Effects of Diet Intakes on Metal and Electrolyte Distributions in Vital Organs

S. W. Leung<sup>a,\*</sup>, S. Siddhanti<sup>b</sup>, B. Williams<sup>b</sup>, A.W. K. Chan<sup>c</sup>, M.K. Minski<sup>c</sup>, C.K. Daniels<sup>d</sup>, J.C.K. Lai<sup>d</sup>

<sup>a</sup>Corresponding author: Civil and Environmental Engineering Department, and Biomedical Research Institute, Idaho State University, Pocatello, ID 83209, USA

<sup>b</sup>Civil and Environmental Engineering Department, College of Engineering, Idaho State University, Pocatello, ID 83209, USA

<sup>c</sup>Imperial College Reactor Centre, University of London, Silwood Park, Ascot, Berks., SL5 7PY, UK

<sup>d</sup>Biomedical & Pharmaceutical Sciences Department, College of Pharmacy and Biomedical Research Institute, Idaho State University, Pocatello, ID 83209, USA

---

**Abstract.** The intake and concentration of metals and electrolytes from our diet are believed to be affecting our general health, in particular, the proper functions of vital organs. For example, in addition to other genetic and environmental factors, consuming water with high alkalinity for prolonged time is suspected to lead to diseases such as kidney stone. Evidence has been accumulating that excessive metal intakes would lead to organ failures. Once absorbed, minerals and electrolytes can travel freely throughout the body, and distribute at key organ systems such as the brain, lung, kidney, etc. By conducting experiments with animal models (e.g., rats), it is possible to not only determine where the organ distribution of various matrices of elements and minerals but also correlate such matrices with the overall physiological and behavioral status of such models. In this study, information matrices of 30 different elements (including heavy metals and some electrolytes) and their distributions in various vital organs (e.g., brain, lung, kidney, liver, heart, spleen, and uterus) were analyzed as a function of normal dietary intake at adulthood (120 days old). An elemental (metal and electrolyte) distribution model was then formulated based on experimental results. The study has high impact to our understanding of how environmental health would affect our well being. This study would also provide insights on how our diet would affect the accumulations of unwanted elements, such as heavy metals, in our vital organs. The results may help researchers and health practitioner to identify possible links between daily diet (metals and electrolytes) and diseases, and may also lead to a better understanding of diseases associated with aging such as Alzheimer's and Parkinson's diseases, and other neurological disorders.

*Key words:* Brain organs; elements; metals; distributions; diseases; diet; environment

---

### 1. Introduction

Since the era of industrial evolution, living conditions for humans have improved drastically; with the consequence of better living conditions and less physical activities, we are facing other aspects of health issues such as obesity and hyper immune responses (allergy). In modern living, considerable attention has been paid to dietary intake or supplement due to health concerns. On the other hand, involuntarily consumption of unwanted chemicals and preservatives via processed food and polluted water is also possible. One such example would be consumption of drinking water from sources that are laden with soluble ions and heavy metals. This occurs quite frequently for those that are living in rural areas with no treatment system for their drinking water in developing countries.

Attempts in understanding the homeostasis of different elements in brain and other major organs fell short significantly due to the vast complexity of mechanisms involved [1]. What cause this complexity are the multiple factors that can affect the dynamics of biological functions. For examples, an element of different compounds (chloride versus phosphate) would have various uptake rates by the body [2] and the uptake rate of elements in solution by the digestive system was proven to be faster than in food stuffs. Elemental accumulations are not solely related to exposure but likely have more to do with impairment of the relevant homeostasis mechanism [3]; conversely, a Cu deficiency in mice were able to be corrected by supplementation of Cu in drinking water [4],

---

\* Solomon W. Leung. Tel.: +1-208-282-2524; fax: +1-208-282-4538.

E-mail address: leunsolo@isu.edu

2003). In addition, larger sample size is needed to observe statistical significance in the small changes over life time exposure [5]. Such constraint creates a vast obstacle to conduct research, and the hurdle is more difficult if human subjects are involved.

Currently, the understanding of homeostasis mechanisms for accumulation and control of individual element in our body is very limited; hence, the influence of elements with similar properties to each other is practically non-existent. However, results of Zn replacing Cu in a competitive homeostasis mechanism in rat's brain were recently reported by Maynard et al. [5]. Therefore, it can be concluded that our understanding of elemental homeostasis mechanisms in our body systems is still in the pioneer stage, and opportunities for further research and development are widely untouched.

There are chemicals (vitamins, for example) and elements needed to maintain proper bodily functions; in this study, we focused on the essence of major and selected trace elements and how these elements accumulated in our major organs. The major organs are: brain, lung, kidney, liver, heart, spleen, and uterus. Information matrices of 30 different elements (including heavy metals and some electrolytes) that were fed to rats as part of a regular diet were obtained from the seven major organs and analyzed. Measurements of the elements from the adult rats (120 days old) were compared with information obtained from healthy Japanese males [6]. A linear distribution model based on experimental results and statistical analysis for the elemental accumulations in the major organs was then developed to relate the accumulation ratio between rats and humans taking their respective regular diet. This model can be used as an assessment tool to evaluate elemental homeostasis in different organs for the initial screening of potential health issues and diseases.

## 2. Experimental Methods

The 30 elements included in this study were: Al, As, Ba, Br, Ca, Cd, Cl, Co, Cr, Cu, F, Fe, Hg, I, K, La, Mg, Mn, Mo, Na, Rb, S, Sb, Sc, Se, Si, Sm, Sr, V, and Zn. Analytical measurements of the elements from the organs of adult (120 days old) Wistar rats and diet pellets that were used to feed the rats were reported in a parallel paper at the same conference (Metallomic Distribution in Various Regions of the Brain as Influenced by Dietary Intakes and Their Implications) [7].

Information from the organs of healthy Japanese males was abstracted from Katoh et al. [5]: The data were collected from 64 persons ranging from 6 to 82 years of age with a mean age of 42 years. These data were assumed to be representatives of healthy humans regardless of race.

## 3. Results

### 3.1 Concentration of Elemental Accumulations with Rats

Table 1 tabulates the elemental concentrations obtained from 7 major organs of the rats which were feed with regular food pellets. Out of the 30 elements of interest, only 20 elements were detectable within the measurement limit by instrumental neutron activation analysis (INAA). This implies that either the concentrations of other (undetectable) elements were too low for the analytical method, or the organs did not retain those elements significantly. The latter observation was especially obvious for the brain that showed only 15 measureable elements.

Table 1. Measurements of elemental concentrations for the seven major organs. Noted that concentrations of the first 6 elements (above Al) were in mg/g of wet weight and concentrations of the rest of the elements were in  $\mu\text{g/g}$  of wet weight. ND indicates not detectable.

Element	Liver	Lung	Heart	Heart	Spleen	Uterus	Brain
Ca	0.05	0.08	0.16	0.04	0.06	0.09	0.054
Cl	1.01	1.39	1.35	0.8	0.94	1.99	0.95
Fe	0.28	0.14	0.1	0.1	1.06	0.09	0.019
K	3.6	1.94	2.15	2.39	3.61	2.35	2.677
Mg	0.24	0.11	0.14	0.15	0.19	0.22	0.103
Na	0.64	1.12	1.11	0.76	0.57	1.62	0.957

Al	6.57	3.98	4.13	5.68	7.17	3.43	5.87
Br	4.67	10.49	7.76	4.3	4.96	12.53	1.91
Co	0.1	0.03	0.22	0.04	0.05	0.02	0.011
Cr	0.05	0.06	0.44	0.33	0.13	0.58	ND
Cu	5.41	2.53	10.39	5.33	3.79	2.9	2.1
F	2.41	2.82	4.95	2.46	ND	6.15	ND
Hg	0.12	0.02	0.53	0.01	0.2	0	ND
I	0.06	0.05	0.08	0.05	ND	0.12	ND
Mn	2.76	0.2	0.78	0.32	0.35	0.19	0.51
Mo	1.11	1.37	0.61	0.28	0.61	0.71	ND
Rb	16.27	4.38	5.04	3.9	5.79	4.54	2.66
Se	1.26	0.4	1.54	0.39	0.72	0.44	0.64
V	0.08	0.01	0.1	0.07	0.04	0.08	ND
Zn	41.13	16.98	24.56	16.05	17.34	15.85	10.79

### 3.2 Elemental Accumulations in Human Organs

Similar to Table 1, Table 2 shows the corresponding elemental accumulations in 6 organs that were collected by Katoh et al. [6] and Magalhaes et al. [8]. Discussions with the brain is excluded from this paper but are discussed in a parallel study [7] due to the complexity of the brain. Katoh et al. have collected 21 elements of which 15 elements are common with the elements from the rat's study in Table 1. Magalhaes et al. have collected fewer elements, Table 2 only shows those that are of interested in this study. However, Magalhaes et al. also compared elemental concentrations of health tissues with cancerous tissues of the same individuals. It should be noted that samples of Magalhaes et al. were expressed in  $\mu\text{g/g}$  of dry weight instead of wet weight, but this relative weight ratio should be compatible for both approaches.

Table 2. Elemental concentrations of various organs reported by Katoh et al. [6], the concentrations were in  $\mu\text{g/g}$  of wet weight except as noted. \*The elemental concentrations of uterus were abstracted from Magalhaes et al. [8] with samples of German origin, concentrations were reported as  $\mu\text{g/g}$  of dry weight, except otherwise specified.

Element	Liver	Lung	Kidney	Heart	Spleen	Uterus*
Al	11.3	130	10.4	11.4	12.5	
As( $\text{ng/g}$ )	300	560	400	250	380	
Br	12.2	48.6	40.9	16.7	25.6	19
Ca	208	585	529	291	335	1590
Cd	16.7	4	237	1.2	5.4	
Cl( $\text{mg/g}$ )	4.2	10.1	10.9	5	6.7	
Co( $\text{ng/g}$ )	173	123	69	70	31	
Cs( $\text{ng/g}$ )	69	88	120	113	77	
Cu	32.2	14.2	15.4	18	7.3	4
Fe	837	987	430	257	1400	59
K( $\text{mg/g}$ )	9.4	9.9	10.4	15.5	15.9	0.571
La( $\text{ng/g}$ )	285	311	64	32	650	
Mg	678	565	711	1070	729	
Mn	5.58	1.17	4.92	1.63	0.82	

Mo	2.1	1.37	1.55	0.69	0.96	
Na(mg/g)	4.2	10.4	10.7	5.7	5	
Rb	22.3	15.9	17	20.1	22	
Sb(ng/g)	52	242	69	16	49	
Sc(ng/g)	5	26	4	5	5	
Se	1.87	1.3	3.86	1.37	1.61	
Zn	228	62	238	126	83	40

### 3.3 Normalized Elemental Distribution Ratio in Various Organs between Rats and Humans

A normalized elemental distribution ratio can be obtained by dividing the concentration of an element in a rat organ by the concentration in the same human organ. Figure 1 shows the normalized elemental distribution ratio for the 6 organs and 15 elements that were common in our work and that of Katoh et al. [6]. As shown in Figure 1, the elemental distributions (homeostasis) for the 15 elements in the 6 major organs fit rather consistently in general. For examples, Na and Cl have nearly the same distribution ratio for all 6 organs, K is almost as consistent except for concentration in the uterus. This may be due to diet difference between rats and humans, or the difference is a factor of physiological/genetic origin; a proper explanation of the observation remains to be determined. In general, Co has the widest spread in distribution among organs.

The distribution model can be used to predict physiological development from rat (animal) to human. An abnormally high or low concentration of elements in organs can be a prelude of organ malfunction and/or cancer development. For example, samples of cancerous uterus tissue had 1.6 time the concentration of K when compared with that of normal uterus tissue from the same individual [8]. However, the general direction of increase or decrease in elemental concentration of cancerous tissue is not always the same for different elements and organs. The approach of normalized distribution ratios developed in this study can be used to find the general direction of elemental distribution of disease tissues, although there are genetic difference between rats and humans.

## 4. Conclusions

A normalized elemental distribution model is developed by comparing elemental measurements of the same organ in rats and humans. The model can be used to predict disease tissues based on their elemental measurements and to determine how well we can absorb elemental nutrients from food. This study has high impact on our understanding of how environmental health would affect our well being. This study would provide insights on how our diet would affect the accumulations of unwanted elements, such as heavy metals, in our vital organs. The results may help researchers and health practitioner to identify possible links between daily diet (metals and electrolytes) and diseases, and may also lead to a better understanding of diseases associated with aging such as Alzheimer's and Parkinson's diseases, and other neurological disorders.

## Acknowledgment

This study was partially supported by NIH Grant P20RR16454 from the INBRE program of the National Center for Research Resources and USAMRMC Project Grant (Contract #W81XWH-07-2-0078).

## References

- [1] Pardridge, W. Blood-brain barrier drug targeting: the future of brain drug development. *Molecular Interventions*, **2003**;3(2):90-105
- [2] Anderson, J.G., Fordahl, S.C., Cooney, P.T., Weaver, T.L., Colyer, C.L., and Erikson, K.M. Manganese exposure alters extracellular GABA, GABA receptor and transporter protein and mRNA levels in the developing rat brain. *Neurotoxicology*, **2008**;29(6) ;1044-53
- [3] Bolognin, S., Messori, L., and Zatta, P. Metal ion physiopathology in neurodegenerative disorders. *Neuromolecular Medicine*, **2009**;11(4):223-38



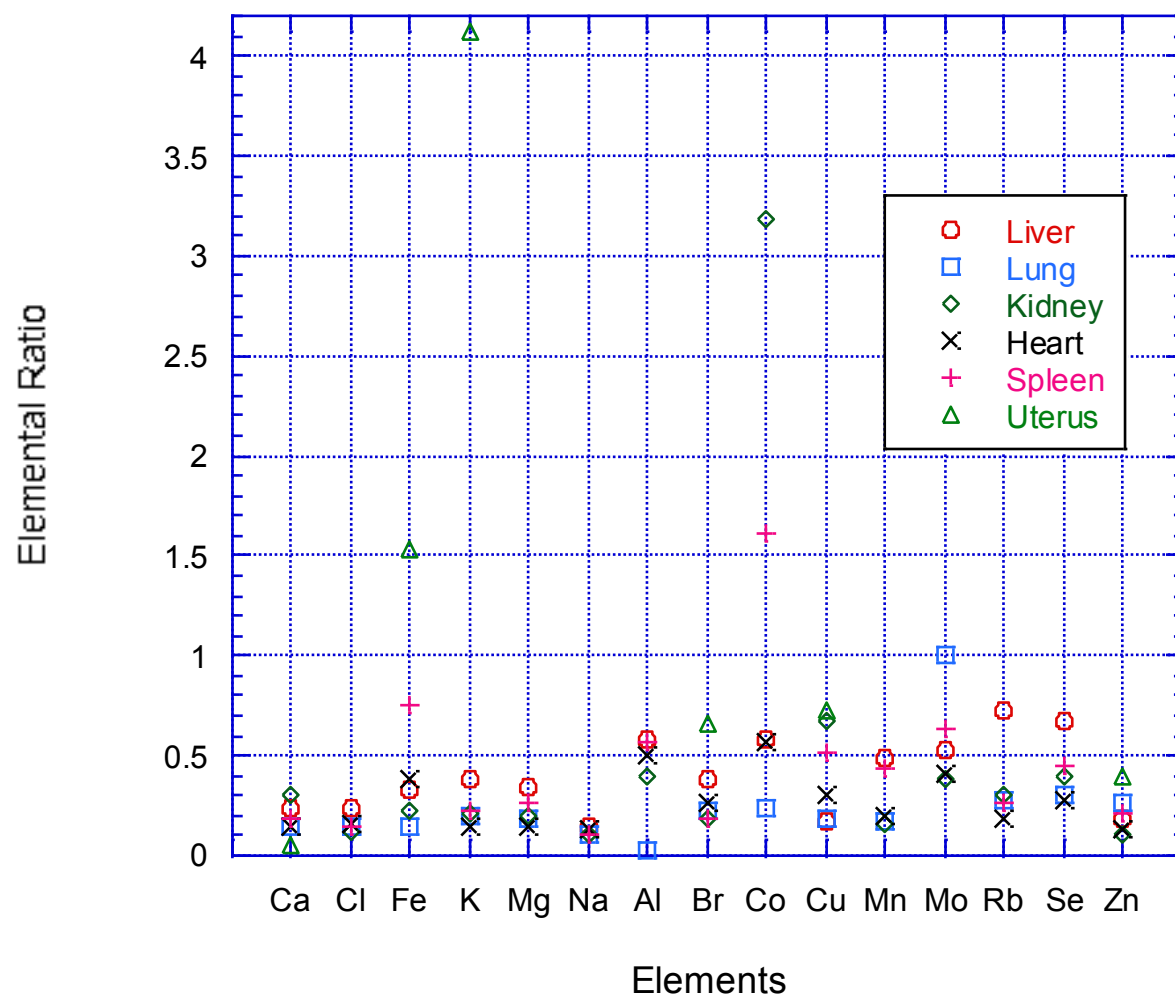


Fig. 1. Elemental concentration ratio of rat versus human for 6 major organs.

[4] Bayer T.A., Schafer S., Simons A., Kemmling A., Kamer T., Tepest R. et al. Dietary Cu stabilizes brain superoxide dismutase 1 activity and reduces amyloid abeta production in APP23 transgenic mice. *Proc Natl Acad Sci USA* **2003**;100(24):14187–92

[5] Maynard, C.J., Cappai, R., Volitakis, I., Laughton, K.M., Masters, C.L., Bush, A.I. et al. Chronic exposure to high levels of zinc or copper has little effect on brain metal homeostasis or a beta accumulation in transgenic APP-C100 mice. *Cellular and Molecular* **2009**;29(5):757-67

[6] Katoh, Y., Sato, T., and Yamamoto, Y. Determination of multielement concentration in normal human organs for the Japanese. *Biological Trace Element Research* **2002**;90:57-70

[7] Wright, G., Lai, J. C. K., Chan, A.W.K., Minski, M.J., Lim, L., Leung, S. W. Metallomic distribution in various regions of the brain as influenced by dietary intakes and their implications. (ISEIS 100321), in proceedings of ISEIS 2010 International Conference on Environmental Informatics, **2010**, in press.

[8] Magalhaes, T., von Bohlen, A., Carvalho, M.L., Becker, M. Trace elements in human cancerous and healthy tissues from the same individual: A comparative study by TXRF and EDXRF. *Spectrochimica Acta Part B* **2006**;61:1185–3.

# Cross Resistance of Magnesium Oxide Nanoparticles to Cisplatin in Leukemia Cells: Mechanistic Studies

By Alok Bhushan PhD, Prathamesh P Patil BPharm MS, Vikas Bhardwaj BPharm, Maria B Lai BS, Christopher K Daniels PhD, Solomon W Leung\* PhD, and James CK Lai PhD

Department of Biomedical and Pharmaceutical Sciences, College of Pharmacy, Idaho Biomedical Research Institute, Idaho State University, Pocatello, Idaho, USA and \*College of Engineering, Idaho State University, Pocatello, Idaho 83209, USA

## 1. INTRODUCTION

The failure of cancer chemotherapy can be attributed to two major factors. The two major reasons are toxic effects of the drugs and secondly the resistance to the chemotherapeutic agents used in treatment of cancer. Although the design of the drugs is to get rid of cancer cells in the body, the normal cells also are exposed to the anti-cancer drugs resulting in toxic effects. The challenge to specifically target cancer cells continues and there have been many drugs designed and are now in use for specific cancer cells. Several drugs like herceptin and gleevec are in use in clinic with improvement of survival (1, 2). It becomes difficult to treat cancer when few of the cells in tumors acquire the ability to adapt to the toxic environment of the drugs that are used in chemotherapy (3). For the past 25 years, many laboratories around the world have focused efforts to unravel the mechanisms that contribute to the emergence of resistance in cancer. The hallmark of resistance was the discovery of P-glycoprotein by Dr. Victor Ling. P-glycoprotein was found to be an active transporter and pumped drugs outside the cells (4). This in turn decreased the intracellular concentration resulting in adaptation of cancer cells to toxic environment. A downside of this overexpression of P-glycoprotein was that it imparted cross resistance to several structurally unrelated drugs (5). Since the discovery of P-glycoprotein, several proteins have been identified which result in resistance in cancer. Multidrug Resistant related Proteins (MRPs) belong to a family of ATP cassette and about 7 MRPs have been identified with different substrate affinity (6). Studies in our laboratories have focused on many drug resistant cells from leukemias, sarcomas, multiple myelomas, breast cancer and pancreatic cancers. We have shown that cisplatin selected methotrexate resistant cells have a 66 kD protein that in its unphosphorylated state fails to transport the drug inside the leukemia cells resulting in resistance. Our studies with sarcoma cells selected for resistance to adriamycin has increased expression of c-fos indicating a role of this transcription factor in anthracycline resistance (7, 8, 9). Breast cancer cells resistant to adriamycin have higher expression of IL6 receptor (10). Studies with dexamethasone resistant multiple myeloma cells show changes in intracellular signaling. In addition, 5-fluorouracil resistant pancreatic cells have upregulated levels of mitogenic and drug metabolizing enzyme (unpublished data). All these findings from our laboratories indicate that resistance is a complex phenomenon and differs in different cell lines as well as mechanisms vary depending upon the exposure of the chemotherapeutic agent.

We took a different approach by utilizing nano materials to study the effect on various cancer cells. We exposed Leukemia cells and its subline that was selected for resistance to cisplatin as well as pancreatic cancer cells selected for resistance to 5-fluorouracil to MnO and ZnO nanoparticles that range in size from 30-80nm. The rationale of these studies was to determine if the resistant cells differ in sensitivity to nano particles and if the cellular signaling pathways were altered differentially in these cell lines. The data will provide us with information if cells resistant to anticancer drugs respond differently to nanoparticles so that we may design drugs using nanomaterials to specifically target resistant cells.

## **2. CYTOTOXICITY OF METALLIC OXIDE NANOPARTICLES AND THE UNDERLYING SIGNALING MECHANISMS**

Nanomaterials have been increasingly used in industrial applications (e.g., drug delivery, additives to drugs and cosmetics). Because of their wide use, occupational exposure to nanomaterials and nanoparticles may pose as health risks. Recent studies have suggested that exposure to nanoparticles may induce cytotoxic effects in some mammalian cell types although these effects have not been systematically investigated (11).

In a series of studies, we tested the hypothesis that titanium oxide, magnesium oxide, and zinc oxide nanoparticles exert differential cytotoxic effects on human astrocytoma (U87) cells and human fibroblasts (HFF-1). Because the effects of such nanoparticles on human neural cells are unknown, we have determined the putative cytotoxic effects of these nanoparticles on human astrocytes-like astrocytoma U87 cells and compared their effects on normal human fibroblasts. We found that TiO<sub>2</sub> micro- and nanoparticles induced cell death on both human cell types in a concentration-related manner. We further noted that ZnO nanoparticles were the most effective, TiO<sub>2</sub> nanoparticles the second most effective, and MgO nanoparticles the least effective in inducing cell death in U87 cells. The cell death mechanisms underlying the effects of TiO<sub>2</sub> micro- and nanoparticles on U87 cells include apoptosis, necrosis, and possibly apoptosis-like and necrosis-like cell death types. Thus, our findings may have toxicological and other pathophysiological implications on exposure of humans and other mammalian species to metallic oxide nanoparticles. Furthermore, we are of the opinion that these mechanisms can be exploited to induce the death of cancer cells thereby enhancing the process of new anti-cancer drug discovery (11).

## **3. CYTOTOXIC EFFECTS OF METALLIC OXIDE NANOPARTICLES AND DRUG RESISTANCE MECHANISMS**

In this study, we determined the effect of MgO nanoparticles on murine leukemia cancer cells (L1210 cells) and a subline selected for resistance to cisplatin (L/DDP cells). The magnesium oxide nanoparticles showed differential effect on cell survival using different methods of assays. We further determined the effect of MgO on various cells signaling proteins (Akt, p-Akt and Erk and p-Erk) in L1210 and LDDP cells after magnesium oxide nanoparticles treatment. Our results indicate that the treatment with MgO nanoparticles increased the expression of p-Akt and decrease the expression of p-Erk expression in L1210 and L1210/DDP cells. The treatment of nanoparticles showed no effect on the level of expression of Erk and Akt in these cells indicating that the treatment of cells with MgO nanoparticles decreased activation of erk pathway but increased activation of Akt.

We further examined the expression of downstream transcription factors (c-fos and c-jun) as they are altered due to erk signaling. The western blot analysis shows that MgO nanoparticles decreased the expression of c-fos in L1210 and LDDP cancer cells. Expression of c-jun in L1210 cells showed some increase at treatment concentration of 25µg/ml. In L1210/DDP cells, the level of c-fos reduced in dose-related manner, however the level of c-jun was undetected.

## **4. CONCLUSIONS**

We have presented an overview of our studies on anti-cancer drug resistance mechanisms as well as ongoing systematic studies of the nanotoxicity of metallic oxide nanoparticles. Our ongoing studies also

suggest that resistant cancer cells may exhibit cross-resistant to the cytotoxic effects of metallic oxide nanoparticles. The latter effects appear to be mediated by cell survival/proliferation signaling mechanisms. Clearly these are important and novel areas of anti-cancer drug discovery. As such they merit further investigation. We are currently pursuing these exciting new dormains of nanomedicine and nanocancer research.

## 5. ACKNOWLEDEMENTS

Our studies were supported by an USAMRMC Project Grant (Contract #W81XWH-07-2-0078) and NIH Grant #P20 RR016454 from the Idaho INBRE Program of the National Center for Research Resources.

## 6. REFERENCES

- 1) Arnold K. After 30 years of laboratory work, a quick approval for STI571 (2001). *J Natl Cancer Inst.* 4;93(13):972.
- 2) Miller JL. Progress in breast cancer treatment: prevention, new therapies come to forefront (1998). *Am J Health Syst Pharm.* 15;55(22):2326, 2328, 2330.
- 3) Gottesman MM. Mechanisms of cancer drug resistance (2002). *Annu Rev Med.* 53:615-27.
- 4) Juranka PF, Zastawny RL, Ling V. P-glycoprotein: multidrug-resistance and a superfamily of membrane-associated transport proteins (1989). *FASEB J.* 1989 3(14):2583-92.
- 5) Goda K, Bacsó Z, Szabó G. Multidrug resistance through the spectacle of P-glycoprotein (2009). *Curr Cancer Drug Targets.* ;9(3):281-97.
- 6) Toyoda Y, Hagiya Y, Adachi T, Hoshijima K, Kuo MT, Ishikawa T. MRP class of human ATP binding cassette (ABC) transporters: historical background and new research directions (2008). *Xenobiotica.* 38(7-8):833-62.
- 7) Bhushan A, Abramson R, Chiu JF, Tritton TR. Expression of c-fos in human and murine multidrug-resistant cells (1992). *Mol Pharmacol.* 42(1):69-74.
- 8) Bhushan A, Wroblewski D, Xuan Y, Tritton TR, Hacker MP. Correlation of altered tyrosine phosphorylation with methotrexate resistance in a cisplatin-resistant subline of L1210 cells (1996). *Biochem Pharmacol.* 1996 Feb 23;51(4):477-82.
- 9) Wroblewski DH, Bhushan A, Xuan Y, Brinton BT, Tritton TR, Hacker MP. Investigations on the mechanisms of methotrexate resistance in a cisplatin-resistant L1210 murine leukemia cell subline (1996). *Cancer Chemother Pharmacol.* 37(4):337-42.
- 10) Conze D, Weiss L, Regen PS, Bhushan A, Weaver D, Johnson P, Rincón M. Autocrine production of interleukin 6 causes multidrug resistance in breast cancer cells (2001). *Cancer Res.* 2001 Dec 15;61(24):8851-8.
- 11) Lai JC, Lai MB, Jandhyam S, et al. 2008. Exposure to titanium dioxide and other metallic oxide nanoparticles induces cytotoxicity on human neural cells and fibroblasts (2008). *Int J Nanomed,* 3, 533-545.

# Advanced Dehydrogenase Biofuel Cell Modified with Highly Branched Polymers and Nano Gold Sol-Gel

Solomon Leung

Civil and Environmental Engineering Department  
Idaho State University  
Pocatello, Idaho, 83209, USA  
leunsolo@isu.edu

James Lai

Biomedical and Pharmaceutical Sciences Department  
Idaho State University  
Pocatello, Idaho, 83209, USA  
Lai@pharmacy.isu.edu

**Abstract** – Highly branched polymers and nano Au particles sol-gel were used to construct an enzymatic biofuel cell system. The anode and cathode of this biofuel cell modified with the sol-gel were characterized. The sol-gel was very effective in anchoring and stabilizing lactate dehydrogenase (LDH) and glutamate dehydrogenase (GDH), the enzymes used in the biofuel cell system. This sol-gel modification would enable further enzymatic biofuel cell development that was not possible due to rapid deterioration of enzymes.

**Keywords** - LDH; GDH; nanoparticle; biofuel cell; PAMAM

## I. INTRODUCTION

Biochemical fuel cell drew heavy popularity among scientist and engineers in the early 1960s but the commercialization of it was not realized due to technical difficulties and the availability of inexpensive petroleum energy [1]. However, the recent energy crisis and the development of micro circuitry reiterate the interest of biofuel cell; with the aid of nano technology, biofuel cell has leapfrogged to a new horizon. In addition to the conventional application of waste conversion to energy recycling concept, the micro and nano technology enable the concept of biofuel cell to directly extract energy from organisms and plants [2, 3].

Our research group has started a biofuel fuel cell initiative, the objective of this initiative is to develop a biofuel cell system that is non-toxic and biological compatible that can be employed in a natural environment or human body. In this paper, we are reporting an enzymatic biofuel cell system that was constructed with electrodes that were enhanced with polymer and nanogold particles sol-gel that can be implanted into our body as power source for biomedical devices such as pacemaker and insulin pump; this cell/battery can be modified to generate electrical current to be utilized at point of generation or stored as battery power. The energy source or reactants were lactate,  $\alpha$ -ketoglutarate, and ammonia that are all existing in our body or as parts of our body fluid.

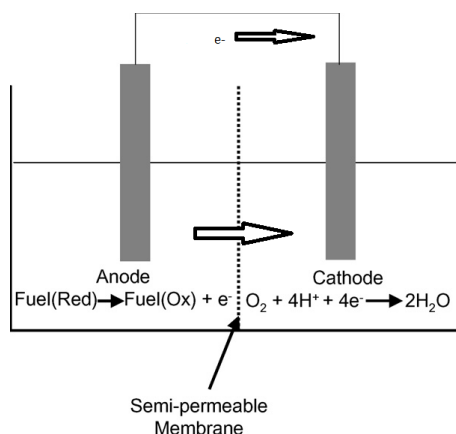
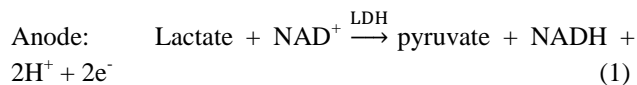


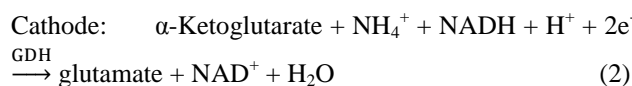
Fig. 1 A typical fuel cell, products of fuel cell reactants (fuel oxidants) can migrate to the cathode side through the semi-permeable membrane to complete the overall fuel cell reactions.

For our biofuel cell system, the anodic half-cell was made by an Au electrode coated with lactate dehydrogenase (LDH) submerged in solution containing lactate and nicotinamide adenine dinucleotide (NAD<sup>+</sup>), thus, for the anodic half reaction:



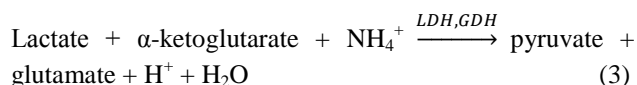
As lactate was oxidized into pyruvate in the anode, the oxidative potential,  $E_0'$  (25 °C), would be 0.19 V.

The cathodic half-cell was made by a glassy carbon electrode (GCE) coated with glutamate dehydrogenase (GDH) submerged in solution containing ammonia and reduced nicotinamide adenine dinucleotide (NADH), the cathodic half reaction was:



As  $\alpha$ -ketoglutarate was reduced into glutamate in the cathode, it generated a reductive potential,  $E_0'$  (25 °C), of -0.14 V.

Combining (1) and (2), the total potential for the fuel cell with the anode and cathode above was 0.05 V (per mole). In general, biological reactions in nature do not release large amount of energy for each reaction step to preserve energy utilization efficiency. The overall reaction for the biofuel cell thus was [4]:



Since the  $\Delta E_0'$  of (3) was greater than 0, the reaction was spontaneous and would proceed as written from left to right.

## II. MATERIALS AND METHOD

### A. Electrodes

Gold electrode had diameter of 0.3 cm and the GCE had diameter of 0.35 cm, they both were purchased from Tianjin Aida Heng Sheng Co, Tianjin, China.

### B. Electrode Preparation

1). Anode: A clean gold electrode was immersed in 0.1 M cysteamine solution for 2 hours in the dark, then it was dipped into colloidal gold nanoparticles for 24 hours, finally the electrode was dipped into LDH solution for 20 hours before it was used for testing. This was a LDH-Au-cysteamine (sol-gel)-modified Au anode as shown in Fig. 2. LDH was embedded in the Au sol-gel matrix which also enabled electronic transfer.

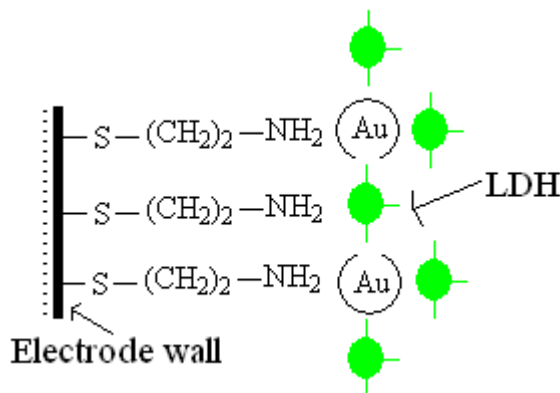


Fig. 2. A gold anode modified with cysteamine, Au nanoparticles (sol-gel) and LDH.

2). Cathode: Several combinations of polymers (poly(amido amine) (PAMAM) of 0<sup>th</sup> and 2<sup>nd</sup> generation, and cysteamine) with GDH and nanogold particles were tested for their efficacies to enable the reductive reaction as in (2). A cleaned glassy carbon electrode was first immersed in 0.1 M cysteamine (or PAMAM) solution in darkness. The resulting monolayer-modified electrode was rinsed thoroughly with twice-distilled water and

soaked in water. Then, it was dipped into the colloidal gold. The gold colloid-cysteamine-modified cathode was dipped into the l-glutamate dehydrogenase (GDH) solution (pH 7.4) (or GDH solution containing NADH). In such a way, a GDH (/NADH) gold colloid-cysteamine (or PAMAM)-modified glassy carbon cathode was obtained.

For cathode that both cysteamine and PAMAM were coated, the cleaned glassy carbon electrode was first immersed in cysteamine solution, the resulting electrode was dipped into the PAMAM solution. Then, it was dipped into the colloidal gold. The gold colloid-cysteamine/PAMAM-modified electrode was dipped into the GDH solution (pH 7.4) (or GDH solution containing NADH). In such a way, a GDH (/NADH) gold colloid-cysteamine/PAMAM-modified glassy carbon electrode was obtained

### C. Nanoparticles Solution Preparations

Nanoparticles Au was prepared by reacting HAuCl<sub>4</sub> with citric acid [5].

All chemical reagents used in this study were analytical grade or the highest grade available, water was double deionized distilled water. All the experiments were carried out under deoxygenated condition in 0.1 M phosphate buffer solution. All enzymes and biochemicals were purchased from Sigma-Aldrich Chemical Co, St. Louis, MO, USA.

### D. Detections

UV-VIS spectrophotometry was carried out by an Agilent diodearray spectrophotometer when needed; cyclic voltammetry was conducted by using a Gamry 600 Potentiostat. Voltammetric potential was measured against a saturated chloride electrode (SCE).

## III. RESULTS AND DISCUSSIONS

### A. Anodic half-cell

Fig. 3 shows the oxidative responses of the modified Au electrode with nanogold particles, cysteamine and LDH. As seen, the characteristic peak of lactate conversion to pyruvate was detected at 250 mV and the accumulative current increased linearly with added lactate instantaneously [6]. It verified that the modified anodic electrode was functioning as expected in (1).

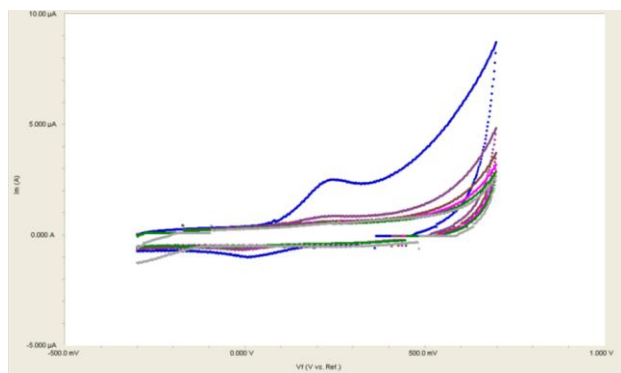


Fig. 3 Voltammetric responses of an Au electrode coated with cysteamine, Au nanoparticles, and LDH at pH 8. Responses were stepwise additions of lactate at  $1.0 \times 10^{-4}$  mol/ml with linear current increments (oxidative peaks) at 250 mV.

### B. Cathodic half-cell

Fig. 4 is the UV-VIS spectrum PAMAM-Au-GDH coated on a plastic cuvette that has no absorption in the UV-VIS range, the same procedures used to modify the cathode. As shown, PAMAM and Au have strong absorption at 278 and 548 nm, respectively. The red and blue line were absorption of the same coating after numerous rinses that indicated the self-assembling coating was stable, although some PAMAM were released after the initial rinses.

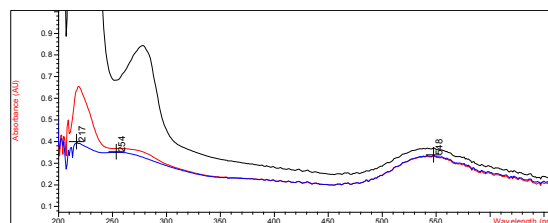


Fig. 5 is the reductive response of a GCE modified with 2<sup>nd</sup> generation of PAMAMs, nanogold particles, and GDH. The cathodic half-cell reaction functioned more efficiently at lower concentrations of  $\alpha$ -ketoglutarate and became less effective as the accumulative concentration of  $\alpha$ -ketoglutarate was higher ( $>0.025$  mM). This could be an effect of saturation that the nanoAu particles could only support a limited amount of GDH for the conversion of  $\alpha$ -ketoglutarate to glutamate. An alternative explanation is that some PAMAM was released by the Au sol-gel that resulted in less conversion efficiency. This also supported the general speculation that the Au sol-gel can only support a finite amount of “sorbed” molecules per unit of Au molecule. The near linear current versus  $\alpha$ -

ketoglutarate relationship appeared to support this observation.

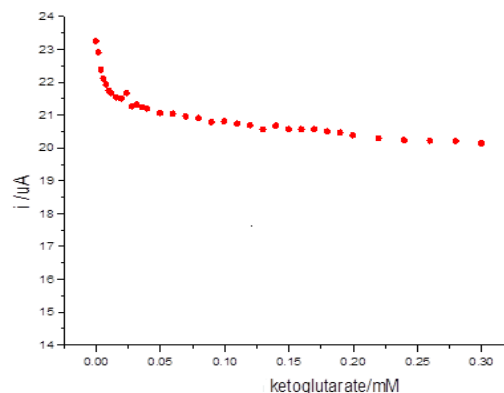


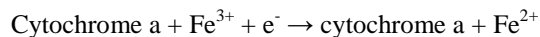
Fig. 5. Reductive responses of a glassy carbon electrode modified with PAMAM, Au nanoparticle and GDH measured at 0.7 V in solution of ammonia and  $\alpha$ -ketoglutarate.

For the PAMAM-Au-GDH cathodic half-cell, the voltammetric responses of (3) at 0.7 V was shown in Fig. 5, the total current measured was  $3.11 \mu\text{A}$ ; Considering the electrode surface area of  $0.0962 \text{ cm}^2$  (diameter of 0.35 cm) and reactants consumption of 0.3 mM, thus the current density ( $\text{A}/\text{cm}^2$ ) would be  $32.3 \mu\text{A}/\text{cm}^2$  and the current generated from the reaction was  $10.4 \text{ mA/M}$ .

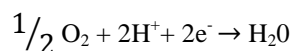
It was observed that with the different combinations of cysteamine and PAMAMs, polymers with the most branched structure would support the sol-gel nanogold structure with the most efficiency to anchor the embedded enzymes (LDH and GDH, for examples) for the enzymatic conversions [6]. In addition, this sol-gel structure on the electrodes could stabilize the enzymes that normally would easily decompose rapidly once they are in diluted solution, which was the case in our electrode preparation. Our anode and cathode performed repeatedly consistently as they were freshly prepared even after they were stored submerged in distilled water at  $4^\circ\text{C}$  for 2 weeks. A stable and cost effective enzymatic system is very important for the realization of using enzymatic biofuel cell for practical applications.

Our biofuel cell system would generate a relative low potential (0.05V), but the reactants are all readily available from our body which make it closer to reality for the system to be implanted into our body as power source for biomedical devices. If this concept of enzymatic biofuel cell is to be employed to extract energy from an industrial waste containing high energy that is normally discarded, such as waste from potato processing

plant and cheese factory, then a more potential favorable redox reaction route should be chosen[7]. For example, the current cathode with (2) has a negative potential, one can choose a cathode made with cytochrome a that has a positive potential as shown in the following:



that will produce a reductive potential of 0.29 V per mole at 25 °C. Another half reaction with high positive potential:



produces a reductive potential of 0.816 V [8].

#### IV. CONCLUSIONS

An enzymatic biofuel cell system consisted of anode and cathode modified with enzymes, highly branched polymers, and Au nanoparticles sol-gel was constructed and characterized. This enzymatic biofuel cell concept can be used to generate power for various biomedical and environmental applications, depending on the available energy sources. The energy sources also dictate the enzyme systems to be used, which could be a limiting factor for biofuel cell. The highly branched polymers and nanogold particles sol-gel proved to be effective in anchoring and stabilizing the enzymes used in the biofuel cell and should be explored further in the development of a practical biofuel cell system.

#### ACKNOWLEDGMENT

This study was supported by a DOD USAMRMC Project Grant (Contract #W81XWH-07-2-0078).

#### References

- [1] Dieter Sell, "Bioelectrochemical Fuel Cells", in *Biotechnology: Special Processes*, 2nd ed., vol. 10, H. Rehm and G. Reed, Eds., New York, Wiley and Sons, 2008, pp. 1-21.
- [2] V. Flexer and N. Mano, "From Dynamic Measurements of Photosynthesis in a Living Plant to Sunlight Transformation into Electricity, ". *Analytical Chemistry*, vol 82, Apr. 2010, pp.1444-1449, doi: 10.1021/ac902537h.
- [3] P. Cinquin, C. Gondran, F. Giroud, S. Mazabrard, A. Pellissier, F. Boucher, J.Alcaraz, K. Gorgy, F. Lenouvel, S. Mathé, P. Porcu, and S. Cosnier, "A Glucose BioFuel Cell Implanted in Rats," 2010, PLoS ONE 5(5): e10476. doi:10.1371/journal.pone.0010476.
- [4] Clarence Suelter and Larry Kricka, *Methods of Biochemical Analysis*, Volume 36, Bioanalytical Applications of Enzymes. New York, NY, Wiley and Sons, 1992.
- [5] J. Lai, Y. Wang, W. Gao, H. Gu, and S. Leung, "Performance Comparisons of Nanoparticle Modified Sensor Electrodes for the Detection of Nitrite and Peroxide", Technical Proceedings of the

2009 Nanotechnology Conference and Expo, volume 2: chapter 4: Biosensors and Diagnostics, NSTI, pp. 233-235.

- [6] J. Cheng, J. Di, J. Hong, K. Yao, Y. Sun, J. Zhuang, Q. Xu, H. Zheng, and S. Bi, "The Promotion Effect of Titania Nanoparticles on the Direct Electrochemistry of Lactate Dehydrogenase Sol-Gel Modified Gold Electrode," *Talanta*, vol 76, Sep 2008, pp. 1065-1069.
- [7] K. Rabaey and W. Verstraete, "Microbial Fuel Cells: Novel Biotechnology for Energy Generation", *TRENDS in Biotechnology*, vol 23, Jun 2005, pp. 291-298.
- [8] Harry Clark, Standard Reduction Potentials, <http://www.jesuitnola.org/upload/clark/refs/tables.html>



# Elemental Analyses in Organ Systems in a Small Animal after Life-Long Controlled Diet

Solomon Leung and Brad Williams

*Civil and Environmental Engineering Department  
Idaho State University  
Pocatello, Idaho, 83209, USA*

leunsolo@isu.edu

James Lai

*Biomedical and Pharmaceutical Sciences Department  
Idaho State University  
Pocatello, Idaho, 83209, USA*

lai@pharmacy.edu.edu

Alex Chan and Margret Minski

*Imperial College Reactor Centre  
University of London  
Silwood Park, SL5 7PY Ascot, Berks, UK*

lai@pharmacy.edu.edu

**Abstract** – The intake and concentration of metals and electrolytes from our diet are believed to be affecting our general health, in particular, the proper functions of vital organs. Other than genetic factors and environmental stresses, evidence has been accumulating that excessive metal intakes would lead to organ failure. Once absorbed, minerals and electrolytes can travel freely within the body, and deposit at key organ systems such as the brain, lung, kidney, etc. By conducting experiments with an established systematic animal model (e.g., rats), it is possible to determine the elemental distribution matrices within the organs, as well as to correlate such matrices with the overall physiological and behavioral status of the animal. In this study, rats were used as the testing animal with a controlled diet for their entire lifetime. Information matrices of 30 different elements (including heavy metals and electrolytes) associated with their distributions in various vital organs including brain, lung, kidney, liver, heart, spleen, and uterus were analyzed as a function of age at 5, 10, 23, and 120 days old. In addition, how excessive Mn intakes would affect the accumulation of other elements was also studied. It was found that the excessive Mn intakes would greatly affect the accumulation of most metals and electrolytes from the intake diet, although the diet only contained trace amount of some of these elements. For example, excessive amount of Hg was found in kidney issue compared to control sample. This multidimensional analysis of elemental accumulations in major organs provided groundbreaking information in our understanding of how dietary intakes, including pollutants, can directly affect our physiological condition and general health.

**Keywords** - *Metals, electrolytes, distribution, Mn, diet, accumulation.*

## I. INTRODUCTION

In the contemporary society, considerable attention has been paid to dietary intake or supplement due to health concerns. On the other hand, involuntarily consumption of unwanted chemicals and preservatives via processed foods and polluted water is also inevitable depending on the lifestyle and available resources of individuals; one such example would be consumption of

drinking water source that is laden with soluble ions and heavy metals. This occurs quite frequently for those that are living in rural areas with no treatment system for their drinking water in developing countries.

Attempts in understanding the homeostasis of different elements in brain and other major organs fell short significantly due to the vast complexity of the mechanisms involved [1]. What cause this complexity are the multiple factors that can affect the dynamics of biological functions, and often these factors are not apparent until the advanced age of an animal. In addition, larger sample size is needed to observe statistical significance in the small changes over life time exposure [2]. Such constraint creates a vast obstacle to conduct research, and the hurdle is more difficult if human subject is involved, making studying such factors prohibitively costly.

There are chemicals and elements that we need to maintain proper bodily functions: in this study, we focused on the essence of major and selected trace elements and how these elements accumulated in our major organs. The major organs are: brain, lung, kidney, liver, heart, spleen, and uterus. Information matrices of 30 different elements (including heavy metals and some electrolytes) that were fed to rats as part of a regular diet were obtained from the seven major organs and analyzed. The 30 elements of interests were: Al, As, Ba, Br, Ca, Cd, Cl, Co, Cr, Cu, F, Fe, Hg, I, K, La, Mg, Mn, Mo, Na, Rb, S, Sb, Sc, Se, Si, Sm, Sr, V, and Zn.

Also, we investigated how intake of an excessive contaminant, such as a heavy metal ion ( $Mn^{2+}$ ) in this study, would alter the accumulation of all other elements and electrolytes in the vital organs over the lifetime of the rats, that would directly affect the proper functions of these organs.

## II. EXPERIMENTATION

Wistar rats of the Porton strain (Animal Breeding Unit, Carshalton, Surrey, U.K.) bred in the Institute of Neurology, University of London, U.K. were used. All

animals were kept on a 12-hour light/12-hour dark cycle with free access to food and water. Elemental concentrations in the rat food pellets have been determined as shown in Table 1 below.

TABLE I. Elemental Concentration of rat food pellet.

Element	Concentration (in mg/g)
Ca	6.39 ± 1.68
Cl	2.31 ± 0.49
Fe	0.25 ± 0.05
K	5.36 ± 0.95
Mg	1.17 ± 0.32
Na	1.48 ± 0.32
Concentration (in µg/g)	
Al	98.06 ± 8.05
Br	10.57 ± 2.26
Co	0.20 ± 0.04
Cr	1.50 ± 0.44
Cu	7.21 ± 2.12
F	ND(5.00)
Hg	ND (0.25)
I	ND (0.50)
Mn	49.34 ± 8.65
Mo	2.80 ± 0.45
Se	ND (0.25)
Rb	12.73 ± 2.61
V	ND (0.50)
Zn	47.73 ± 4.11

Thirty trace and major elements in different organs of rats at four different age groups (5, 10, 23, and 120 days) were analyzed by instrumental neutron activation analysis (INAA) [3]. The samples were irradiated by thermal neutrons using three different sets of conditions depending on the nuclear characteristics of the elements of interest. Not all 30 elements were reported in the results because those not reported herein were either below the detection limits of the INAA technique [3] or the element concentrations were not high enough in the samples (food pellets or organ) for detection.

All the standard materials and samples for INAA were freeze-dried and pelleted. Dried samples were homogenized using a Glen Creston polystyrene ball-mill and pelleted. Other details of standard and sample preparations were as described previously [3, 4].

Standards and samples were irradiated in a 100 KW 'Consort' Reactor Mark II at the Imperial College Reactor

Centre. Irradiated standards and samples were then analyzed for their elemental contents by gamma ray spectrometry using various Ge (Li) detectors and ND 6600 Multichannel Analyzer (Nuclear Data Inc., Schaumburg, Illinois, USA). Details of the elemental determinations were described in the methodology paper by Chan et al. [3].

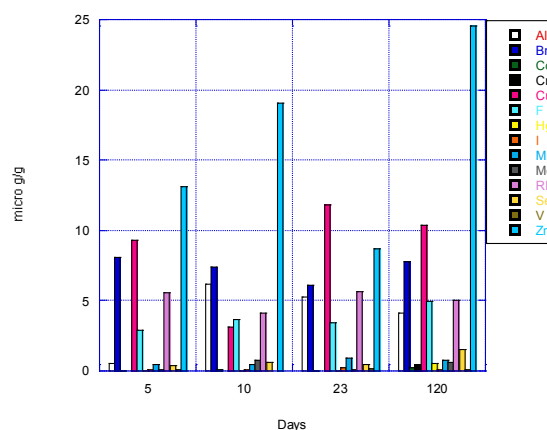
All laboratory chemicals used were of analytical grade (BDH Chemicals Limited, U.K.) and single element standards of trace elements were obtained from AAS (Ventron Division, Limited, U.K.); other elemental standards for F, Cl, Br, and P were obtained from Hopkin and Williams Chemical Ltd., U.K. Water for solution preparations and feeding was double-distilled.

The three concentrations of  $Mn^{2+}$  fed to the rats via drinking water were 1, 10, and 20 mg/ml.

### III. RESULTS AND DISCUSSIONS

As shown in Fig. 1, there were only 20 elements detectable from the kidney tissue of the rats out of the 30 elements of interest. The rest of elements were either under the detectable limit of INAA, or the kidney did not retain these elements: As, Ba, Cd, La, S, Sb, Sc, Si, Sm, Sr. Notes that some of the undetectable elements from the food pellets showed up in the kidney tissue (such as F, Hg, I, Se, and V) which indicated that the elements would accumulate with time and the amounts would also depend on the organs, thus their functions.

Some elements increased with time (age); many elements would decrease slightly or level off with age, these variations were also organ dependent.



(a)

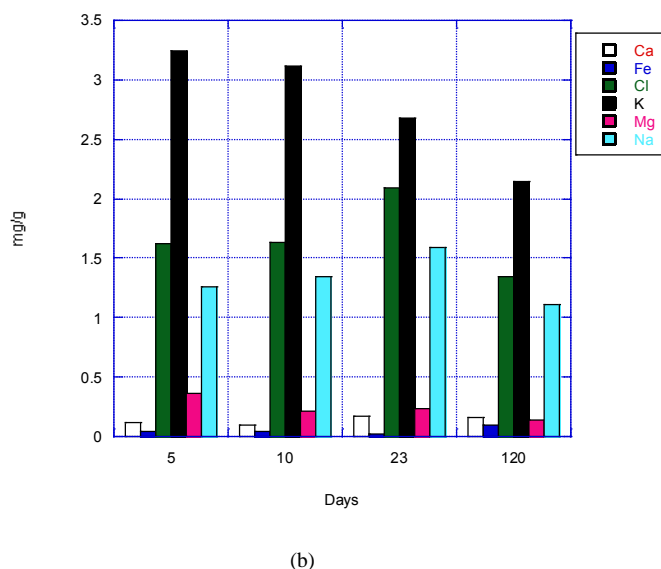


Fig.1 Elemental concentrations of rats' kidney at different developmental stages of 5, 10, 23, and 120 days. (a) The weight of elements in  $\mu\text{g/g}$  of organ in wet weight; (b). weight of elements in  $\text{mg/g}$  of organ in wet weight.

It was found that  $\text{Mn}^{2+}$  intake would definitely affect the retention of other elements in the major organs. Fig. 2 shows the fractional changes of different elements in the kidney tissue when 3 different concentrations of  $\text{Mn}^{2+}$  were fed to 120 days old rats, as compared to the 120 days old control without excessive  $\text{Mn}^{2+}$ . The intake of excessive Mn increased the accumulation of most heavy metals. More noticeably, it also increased the accumulation of I and Hg, and decreased the retention of Se and V, all of which were not detectable in the food pellet. Therefore, if we consume an excessive amount of an heavy metal (for example, Mn) for a lengthy period, it is likely that the total toxicity would be synergistically increase due to increased accumulation of other heavy metals induced by the excessive Mn. This synergistic effect has been observed consistently in all the organs we studied.

#### IV. CONCLUSIONS

Retention of elements from diet intake was found to be age and organ dependent. Excessive intake of a heavy metal can induce synergistic toxicity due to increased accumulation of other heavy metals presented in the diet, although the concentrations of these metals may be at trace level.

#### ACKNOWLEDGMENT

This study was supported by a DOD USAMRMC Project Grant (Contract #W81XWH-07-2-0078).

#### REFERENCES

- [1] W. Pardridge, "Blood-Brain Barrier Drug Targeting: The Future of Brain Drug Development," *Molecular Interventions*, vol 3, Feb 2003, pp. 90-105.
- [2] C. Maynard, R. Cappai, I. Volitakis, K. Laughton, C. Masters, A. Bush. et al. "Chronic Exposure to High Levels of Zinc or Copper Has Little Effect on Brain Metal Homeostasis or a Beta Accumulation in Transgenic APP-C100 Mice," *Cellular and Molecular*, vol 29, May 2009, pp. 757-67.
- [3] A. Chan, M. Minski, and J. Lai, (1983) "An Application of Neutron Activation Analysis to Small Biological Samples: Simultaneous Determination of Thirty Elements in Rat brain Regions," *Journal of Neuroscience Methods*, vol 7, Apr 1983, pp. 317-328.
- [4] A. Chan and M. Minski, U. L. R. C. Internal Report (RES/36), 1981, pp. 37-39.

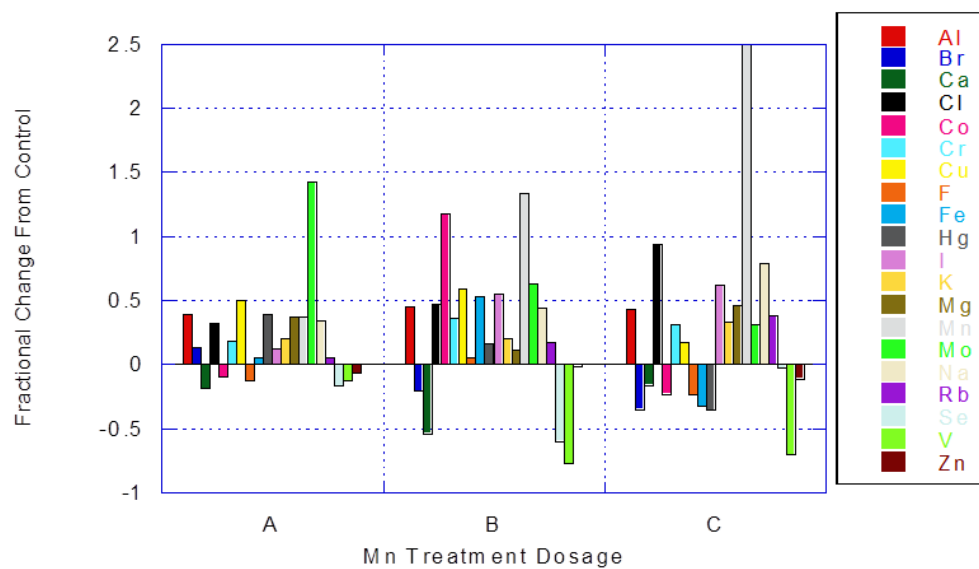
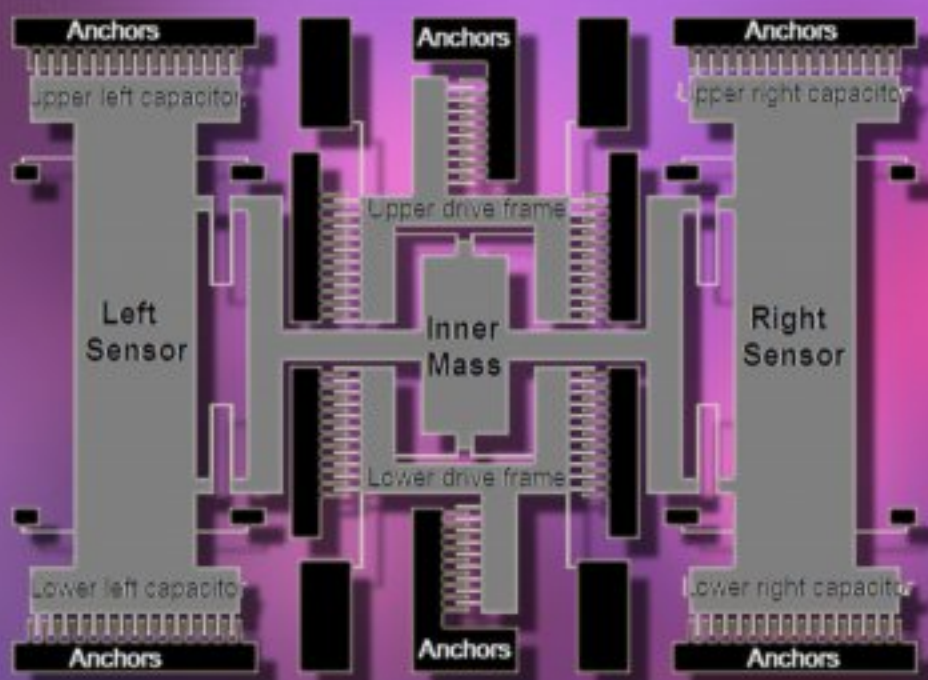


Fig. 2. Different concentration treatments with  $Mn^{2+}$  in water with % changes in adult kidney relative to control adult level: A.) Life-long treatment with 1 mg/ml of  $Mn^{2+}$ ; B.) 10 mg/ml of  $Mn^{2+}$ ; C.) 20 mg/ml of  $Mn^{2+}$ .

ISSN 1726-5749

# SENSORS & TRANSDUCERS

vol. 11  
Special  
**4 / 11**



## MEMS & NEMS: Devices and Technologies

International Frequency Sensor Association Publishing





# Sensors & Transducers

Volume 11, Special Issue,  
April 2011

www.sensorsportal.com

ISSN 1726-5479

**Editors-in-Chief:** professor Sergey Y. Yurish, tel.: +34 696067716, fax: +34 93 4011989, e-mail: editor@sensorsportal.com

**Guest Editor:** Jason Moore, NASA Langley Research Center, USA, e-mail: jason.p.moore@nasa.gov

## Editors for Western Europe

Meijer, Gerard C.M., Delft University of Technology, The Netherlands  
Ferrari, Vittorio, Università di Brescia, Italy

## Editor South America

Costa-Felix, Rodrigo, Inmetro, Brazil

## Editor for Eastern Europe

Sachenko, Anatoly, Ternopil State Economic University, Ukraine

## Editors for North America

Datskos, Panos G., Oak Ridge National Laboratory, USA  
Fabien, J. Josse, Marquette University, USA  
Katz, Evgeny, Clarkson University, USA

## Editor for Asia

Ohyama, Shinji, Tokyo Institute of Technology, Japan

## Editor for Asia-Pacific

Mukhopadhyay, Subhas, Massey University, New Zealand

## Editorial Advisory Board

Abdul Rahim, Ruzairi, Universiti Teknologi, Malaysia  
Ahmad, Mohd Noor, Northern University of Engineering, Malaysia  
Annamalai, Karthigeyan, National Institute of Advanced Industrial Science and Technology, Japan  
Arcega, Francisco, University of Zaragoza, Spain  
Arguel, Philippe, CNRS, France  
Ahn, Jae-Pyoung, Korea Institute of Science and Technology, Korea  
Arndt, Michael, Robert Bosch GmbH, Germany  
Ascoli, Giorgio, George Mason University, USA  
Atalay, Selcuk, Inonu University, Turkey  
Atghiaee, Ahmad, University of Tehran, Iran  
Augutis, Vyantas, Kaunas University of Technology, Lithuania  
Avachit, Patil Lalchand, North Maharashtra University, India  
Ayes, Aladdin, De Montfort University, UK  
Azamimi, Azian binti Abdullah, Universiti Malaysia Perlis, Malaysia  
Bahreyni, Behraad, University of Manitoba, Canada  
Baliga, Shankar, B., General Motors Transnational, USA  
Baolian, Ye, Zhengzhou University, China  
Barford, Lee, Agilent Laboratories, USA  
Barlingay, Ravindra, RF Arrays Systems, India  
Basu, Sukumar, Jadavpur University, India  
Beck, Stephen, University of Sheffield, UK  
Ben Bouzid, Sihem, Institut National de Recherche Scientifique, Tunisia  
Benachaiba, Chellali, Universitaire de Bechar, Algeria  
Binnie, T. David, Napier University, UK  
Bischoff, Gerlinde, Inst. Analytical Chemistry, Germany  
Bodas, Dhananjay, IMTEK, Germany  
Borges Carval, Nuno, Universidade de Aveiro, Portugal  
Bousbia-Salah, Mounir, University of Annaba, Algeria  
Bouvet, Marcel, CNRS – UPMC, France  
Brudzewski, Kazimierz, Warsaw University of Technology, Poland  
Cai, Chenxin, Nanjing Normal University, China  
Cai, Qingyun, Hunan University, China  
Campanella, Luigi, University La Sapienza, Italy  
Carvalho, Vitor, Minho University, Portugal  
Cecelja, Franjo, Brunel University, London, UK  
Cerdà Belmonte, Judith, Imperial College London, UK  
Chakrabarty, Chandan Kumar, Universiti Tenaga Nasional, Malaysia  
Chakravorty, Dipankar, Association for the Cultivation of Science, India  
Changhai, Ru, Harbin Engineering University, China  
Chaudhari, Gajanan, Shri Shivaji Science College, India  
Chavali, Murthy, N.I. Center for Higher Education, (N.I. University), India  
Chen, Jiming, Zhejiang University, China  
Chen, Rongshun, National Tsing Hua University, Taiwan  
Cheng, Kuo-Sheng, National Cheng Kung University, Taiwan  
Chiang, Jeffrey (Cheng-Ta), Industrial Technol. Research Institute, Taiwan  
Chiriac, Horia, National Institute of Research and Development, Romania  
Chowdhuri, Arijit, University of Delhi, India  
Chung, Wen-Yaw, Chung Yuan Christian University, Taiwan  
Corres, Jesus, Universidad Publica de Navarra, Spain  
Cortes, Camilo A., Universidad Nacional de Colombia, Colombia  
Courtois, Christian, Université de Valenciennes, France  
Cusano, Andrea, University of Sannio, Italy  
D'Amico, Arnaldo, Università di Tor Vergata, Italy  
De Stefano, Luca, Institute for Microelectronics and Microsystem, Italy  
Deshmukh, Kiran, Shri Shivaji Mahavidyalaya, Barshi, India  
Dickert, Franz L., Vienna University, Austria  
Diegue, Angel, University of Barcelona, Spain  
Dimitropoulos, Panos, University of Thessaly, Greece  
Ding, Jianning, Jiangsu Polytechnic University, China

Djordjevic, Alexandar, City University of Hong Kong, Hong Kong  
Donato, Nicola, University of Messina, Italy  
Donato, Patricio, Universidad de Mar del Plata, Argentina  
Dong, Feng, Tianjin University, China  
Drljaca, Predrag, Intersema Sensoric SA, Switzerland  
Dubey, Venketesh, Bournemouth University, UK  
Enderle, Stefan, Univ. of Ulm and KTB Mechatronics GmbH, Germany  
Erdem, Gursan K. Arzum, Ege University, Turkey  
Erkmen, Aydan M., Middle East Technical University, Turkey  
Estelle, Patrice, Insa Rennes, France  
Estrada, Horacio, University of North Carolina, USA  
Faiz, Adil, INSA Lyon, France  
Fericean, Sorin, Balluff GmbH, Germany  
Fernandes, Joana M., University of Porto, Portugal  
Francioso, Luca, CNR-IMM Institute for Microelectronics and Microsystems, Italy  
Francis, Laurent, University Catholique de Louvain, Belgium  
Fu, Weiling, South-Western Hospital, Chongqing, China  
Gaura, Elena, Coventry University, UK  
Geng, Yanfeng, China University of Petroleum, China  
Gole, James, Georgia Institute of Technology, USA  
Gong, Hao, National University of Singapore, Singapore  
Gonzalez de la Rosa, Juan Jose, University of Cadiz, Spain  
Granel, Annette, Goteborg University, Sweden  
Graff, Mason, The University of Texas at Arlington, USA  
Guan, Shan, Eastman Kodak, USA  
Guillet, Bruno, University of Caen, France  
Guo, Zhen, New Jersey Institute of Technology, USA  
Gupta, Narendra Kumar, Napier University, UK  
Hadjiloucas, Sillas, The University of Reading, UK  
Haider, Mohammad R., Sonoma State University, USA  
Hashsham, Syed, Michigan State University, USA  
Hasni, Abdelhafid, Bechar University, Algeria  
Hernandez, Alvaro, University of Alcalá, Spain  
Hernandez, Wilmar, Universidad Politecnica de Madrid, Spain  
Homentcovschi, Dorel, SUNY Binghamton, USA  
Horstman, Tom, U.S. Automation Group, LLC, USA  
Hsiai, Tzung (John), University of Southern California, USA  
Huang, Jeng-Sheng, Chung Yuan Christian University, Taiwan  
Huang, Star, National Tsing Hua University, Taiwan  
Huang, Wei, PSG Design Center, USA  
Hui, David, University of New Orleans, USA  
Jaffrezic-Renault, Nicole, Ecole Centrale de Lyon, France  
Jaime Calvo-Galleg, Jaime, Universidad de Salamanca, Spain  
James, Daniel, Griffith University, Australia  
Janting, Jakob, DELTA Danish Electronics, Denmark  
Jiang, Liudi, University of Southampton, UK  
Jiang, Wei, University of Virginia, USA  
Jiao, Zheng, Shanghai University, China  
John, Joachim, IMEC, Belgium  
Kalach, Andrew, Voronezh Institute of Ministry of Interior, Russia  
Kang, Moonho, Sunmoon University, Korea South  
Kaniusas, Eugenijus, Vienna University of Technology, Austria  
Katake, Anup, Texas A&M University, USA  
Kausel, Wilfried, University of Music, Vienna, Austria  
Kavasoglu, Nese, Mugla University, Turkey  
Ke, Cathy, Tyndall National Institute, Ireland  
Khelfaoui, Rachid, Université de Bechar, Algeria  
Khan, Asif, Aligarh Muslim University, Aligarh, India  
Kim, Min Young, Kyungpook National University, Korea South  
Ko, Sang Choon, Electronics. and Telecom. Research Inst., Korea South



**Kockar, Hakan**, Balikesir University, Turkey  
**Kong, Ing**, RMIT University, Australia  
**Kotulska, Malgorzata**, Wroclaw University of Technology, Poland  
**Kratz, Henrik**, Uppsala University, Sweden  
**Kumar, Arun**, University of South Florida, USA  
**Kumar, Subodh**, National Physical Laboratory, India  
**Kung, Chih-Hsien**, Chang-Jung Christian University, Taiwan  
**Lacnjevac, Caslav**, University of Belgrade, Serbia  
**Lay-Ekuakille, Aime**, University of Lecce, Italy  
**Lee, Jang Myung**, Pusan National University, Korea South  
**Lee, Jun Su**, Amkor Technology, Inc. South Korea  
**Lei, Hua**, National Starch and Chemical Company, USA  
**Li, Genxi**, Nanjing University, China  
**Li, Hui**, Shanghai Jiaotong University, China  
**Li, Xian-Fang**, Central South University, China  
**Li, Yuefa**, Wayne State University, USA  
**Liang, Yuanchang**, University of Washington, USA  
**Liawruangrath, Saisunee**, Chiang Mai University, Thailand  
**Liew, Kim Meow**, City University of Hong Kong, Hong Kong  
**Lin, Hermann**, National Kaohsiung University, Taiwan  
**Lin, Paul**, Cleveland State University, USA  
**Linderholm, Pontus**, EPFL - Microsystems Laboratory, Switzerland  
**Liu, Aihua**, University of Oklahoma, USA  
**Liu Changgeng**, Louisiana State University, USA  
**Liu, Cheng-Hsien**, National Tsing Hua University, Taiwan  
**Liu, Songqin**, Southeast University, China  
**Lodeiro, Carlos**, University of Vigo, Spain  
**Lorenzo, Maria Encarnacio**, Universidad Autonoma de Madrid, Spain  
**Lukaszewicz, Jerzy Pawel**, Nicholas Copernicus University, Poland  
**Ma, Zhanfang**, Northeast Normal University, China  
**Majstorovic, Vidosav**, University of Belgrade, Serbia  
**Marquez, Alfredo**, Centro de Investigacion en Materiales Avanzados, Mexico  
**Matay, Ladislav**, Slovak Academy of Sciences, Slovakia  
**Mathur, Prafull**, National Physical Laboratory, India  
**Maurya, D.K.**, Institute of Materials Research and Engineering, Singapore  
**Mekid, Samir**, University of Manchester, UK  
**Melnyk, Ivan**, Photon Control Inc., Canada  
**Mendes, Paulo**, University of Minho, Portugal  
**Mennell, Julie**, Northumbria University, UK  
**Mi, Bin**, Boston Scientific Corporation, USA  
**Minas, Graca**, University of Minho, Portugal  
**Moghavvemi, Mahmoud**, University of Malaya, Malaysia  
**Mohammadi, Mohammad-Reza**, University of Cambridge, UK  
**Molina Flores, Esteban**, Benemérita Universidad Autónoma de Puebla, Mexico  
**Moradi, Majid**, University of Kerman, Iran  
**Morello, Rosario**, University "Mediterranea" of Reggio Calabria, Italy  
**Mounir, Ben Ali**, University of Sousse, Tunisia  
**Mulla, Imtiaz Sirajuddin**, National Chemical Laboratory, Pune, India  
**Nabok, Aleksey**, Sheffield Hallam University, UK  
**Neelamegam, Periasamy**, Sastra Deemed University, India  
**Neshkova, Milka**, Bulgarian Academy of Sciences, Bulgaria  
**Oberhammer, Joachim**, Royal Institute of Technology, Sweden  
**Ould Lahoucine, Cherif**, University of Guelma, Algeria  
**Pamidighanta, Sayanu**, Bharat Electronics Limited (BEL), India  
**Pan, Jisheng**, Institute of Materials Research & Engineering, Singapore  
**Park, Joon-Shik**, Korea Electronics Technology Institute, Korea South  
**Penza, Michele**, ENEA C.R., Italy  
**Pereira, Jose Miguel**, Instituto Politecnico de Seteбал, Portugal  
**Petsev, Dimiter**, University of New Mexico, USA  
**Pogacnik, Lea**, University of Ljubljana, Slovenia  
**Post, Michael**, National Research Council, Canada  
**Prance, Robert**, University of Sussex, UK  
**Prasad, Ambika**, Gulbarga University, India  
**Prateepasen, Asa**, Kingmoungut's University of Technology, Thailand  
**Pullini, Daniele**, Centro Ricerche FIAT, Italy  
**Pumera, Martin**, National Institute for Materials Science, Japan  
**Radhakrishnan, S.**, National Chemical Laboratory, Pune, India  
**Rajanna, K.**, Indian Institute of Science, India  
**Ramadan, Qasem**, Institute of Microelectronics, Singapore  
**Rao, Basuthkar**, Tata Inst. of Fundamental Research, India  
**Raoof, Kosai**, Joseph Fourier University of Grenoble, France  
**Reig, Candid**, University of Valencia, Spain  
**Restivo, Maria Teresa**, University of Porto, Portugal  
**Robert, Michel**, University Henri Poincare, France  
**Rezazadeh, Ghader**, Urmia University, Iran  
**Royo, Santiago**, Universitat Politècnica de Catalunya, Spain  
**Rodriguez, Angel**, Universidad Politécnica de Cataluña, Spain  
**Rothberg, Steve**, Loughborough University, UK  
**Sadana, Ajit**, University of Mississippi, USA  
**Sadeghian Marnani, Hamed**, TU Delft, The Netherlands  
**Sandacci, Serghei**, Sensor Technology Ltd., UK  
**Schneider, John K.**, Ultra-Scan Corporation, USA  
**Sengupta, Deepak**, Advance Bio-Photonics, India  
**Shah, Kriyang**, La Trobe University, Australia  
**Sapozhnikova, Ksenia**, D.I.Mendeleyev Institute for Metrology, Russia  
**Saxena, Vibha**, Bhabha Atomic Research Centre, Mumbai, India  
**Seif, Selemanni**, Alabama A & M University, USA  
**Seifter, Achim**, Los Alamos National Laboratory, USA  
**Silva Girao, Pedro**, Technical University of Lisbon, Portugal  
**Singh, V. R.**, National Physical Laboratory, India  
**Slomovitz, Daniel**, UTE, Uruguay  
**Smith, Martin**, Open University, UK  
**Soleymanpour, Ahmad**, Damghan Basic Science University, Iran  
**Somani, Prakash R.**, Centre for Materials for Electronics Technol., India  
**Srinivas, Talabattula**, Indian Institute of Science, Bangalore, India  
**Srivastava, Arvind K.**, NanoSonix Inc., USA  
**Stefan-van Staden, Raluca-Ioana**, University of Pretoria, South Africa  
**Sumriddetchka, Sarun**, National Electronics and Computer Technology Center, Thailand  
**Sun, Chengliang**, Polytechnic University, Hong-Kong  
**Sun, Dongming**, Jilin University, China  
**Sun, Junhua**, Beijing University of Aeronautics and Astronautics, China  
**Sun, Zhiqiang**, Central South University, China  
**Suri, C. Raman**, Institute of Microbial Technology, India  
**Sysoev, Victor**, Saratov State Technical University, Russia  
**Szewczyk, Roman**, Industrial Research Inst. for Automation and Measurement, Poland  
**Tan, Ooi Kiang**, Nanyang Technological University, Singapore  
**Tang, Dianping**, Southwest University, China  
**Tang, Jaw-Luen**, National Chung Cheng University, Taiwan  
**Teker, Kasif**, Frostburg State University, USA  
**Thirunavukkarasu, I.**, Manipal University Karnataka, India  
**Thumbavanam Pad, Kartik**, Carnegie Mellon University, USA  
**Tian, Gui Yun**, University of Newcastle, UK  
**Tsiantos, Vassilios**, Technological Educational Institute of Kaval, Greece  
**Tsigara, Anna**, National Hellenic Research Foundation, Greece  
**Twomey, Karen**, University College Cork, Ireland  
**Valente, Antonio**, University, Vila Real, - U.T.A.D., Portugal  
**Vanga, Raghav Rao**, Summit Technology Services, Inc., USA  
**Vaseashta, Ashok**, Marshall University, USA  
**Vazquez, Carmen**, Carlos III University in Madrid, Spain  
**Vieira, Manuela**, Instituto Superior de Engenharia de Lisboa, Portugal  
**Vigna, Benedetto**, STMicroelectronics, Italy  
**Vrba, Radimir**, Brno University of Technology, Czech Republic  
**Wandelt, Barbara**, Technical University of Lodz, Poland  
**Wang, Jiangping**, Xi'an Shiyong University, China  
**Wang, Kedong**, Beihang University, China  
**Wang, Liang**, Pacific Northwest National Laboratory, USA  
**Wang, Mi**, University of Leeds, UK  
**Wang, Shinn-Fwu**, Ching Yun University, Taiwan  
**Wang, Wei-Chih**, University of Washington, USA  
**Wang, Wensheng**, University of Pennsylvania, USA  
**Watson, Steven**, Center for NanoSpace Technologies Inc., USA  
**Weiping, Yan**, Dalian University of Technology, China  
**Wells, Stephen**, Southern Company Services, USA  
**Wolkenberg, Andrzej**, Institute of Electron Technology, Poland  
**Woods, R. Clive**, Louisiana State University, USA  
**Wu, DerHo**, National Pingtung Univ. of Science and Technology, Taiwan  
**Wu, Zhaoyang**, Hunan University, China  
**Xiu Tao, Ge**, Chuzhou University, China  
**Xu, Lisheng**, The Chinese University of Hong Kong, Hong Kong  
**Xu, Sen**, Drexel University, USA  
**Xu, Tao**, University of California, Irvine, USA  
**Yang, Dongfang**, National Research Council, Canada  
**Yang, Shuang-Hua**, Loughborough University, UK  
**Yang, Wuqiang**, The University of Manchester, UK  
**Yang, Xiaoling**, University of Georgia, Athens, GA, USA  
**Yaping Dan**, Harvard University, USA  
**Ymeti, Aurel**, University of Twente, Netherlands  
**Yong Zhao**, Northeastern University, China  
**Yu, Haihu**, Wuhan University of Technology, China  
**Yuan, Yong**, Massey University, New Zealand  
**Yufera Garcia, Alberto**, Seville University, Spain  
**Zakaria, Zulkarnay**, University Malaysia Perlis, Malaysia  
**Zagnoni, Michele**, University of Southampton, UK  
**Zamani, Cyrus**, Universitat de Barcelona, Spain  
**Zeni, Luigi**, Second University of Naples, Italy  
**Zhang, Minglong**, Shanghai University, China  
**Zhang, Qintao**, University of California at Berkeley, USA  
**Zhang, Weiping**, Shanghai Jiao Tong University, China  
**Zhang, Wenming**, Shanghai Jiao Tong University, China  
**Zhang, Xueji**, World Precision Instruments, Inc., USA  
**Zhong, Haoxiang**, Henan Normal University, China  
**Zhu, Qing**, Fujifilm Dimatix, Inc., USA  
**Zorzano, Luis**, Universidad de La Rioja, Spain  
**Zourob, Mohammed**, University of Cambridge, UK

# Contents

Volume 11  
Special Issue  
April 2011

[www.sensorsportal.com](http://www.sensorsportal.com)

ISSN 1726-5479

## Research Articles

- Piezoresistive Sensors Development Using Monolithic CMOS MEMS Technology**  
*A. Chaehoi, M. Begbie, D. Weiland, D. O'Connell and S. Ray* ..... 1
- A Fully Symmetric and Completely Decoupled MEMS-SOI Gyroscope**  
*Abdelhameed Sharaf, Sherif Sedky, Mohamed Serry, Amro Elshurafa, Mahmoud Ashour and S. E.-D. Habib*..... 10
- Surface Acoustic Wave Strain Sensor Model**  
*William Wilson, Gary Atkinson*..... 23
- Pb(Zr,Ti)O<sub>3</sub> (PZT) Thin Film Sensors for Fully-Integrated, Passive Telemetric Transponders**  
*Richard X. Fu, Ryan C. Toonen, Eric H. Ngo, Melanie W. Cole Samuel G. Hirsch, Mathew P. Ivill, Clifford W. Hubbard* ..... 34
- Low Cost Three-Dimensional Anemometer for High Spatial Resolution Wind Profiling**  
*John Hirano and David Garmire*..... 43
- Mechanical Robustness of FPA in a-Si Microbolometer with Fine Pitch**  
*Hee Yeoun Kim, Kyoung Min Kim, Byeong Il Kim, Won Soo Jang, Tae Hyun Kim and Tai Young Kang*..... 56
- Point-Mass Model for Nano-Patterning Using Dip-Pen Nanolithography (DPN)**  
*Seok-Won Kang and Debjyoti Banerjee*..... 64
- Biomedical Applications of Modified Carbon Glassy Electrode Sensor with Nanoparticles and Dendrimers**  
*Solomon W. Leung, Yuanhong Wang and James C. K. Lai* ..... 74

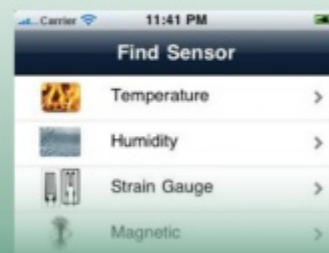
## Mobile Advertising Solutions for Sensor Industry: How to reach 80,000+ addressable mobile audiences?



An industry first Smartphone mobile advertising solution for sensors manufacturers and distributors



**50% OFF**  
for limited time interval



Create your account today and use a **discount coupon code Is10001** to start advertising your sensors now:  
[https://www.lesensor.com/sensor/Profiles/CreateNewAccount.aspx?sensor\\_portal=Is10001](https://www.lesensor.com/sensor/Profiles/CreateNewAccount.aspx?sensor_portal=Is10001)



# Call for Books Proposals

Sensors, MEMS, Measuring instrumentation, etc.

International Frequency Sensor Association Publishing



## Benefits and rewards of being an IFSA author:

### 1) Royalties.

Today IFSA offers most high royalty in the world: you will receive 50 % of each book sold in comparison with 8-11 % from other publishers, and get payment on monthly basis compared with other publishers' yearly basis.

### 2) Quick Publication.

IFSA recognizes the value to our customers of timely information, so we produce your book quickly: 2 months publishing schedule compared with other publishers' 5-18-month schedule.

### 3) The Best Targeted Marketing and Promotion.

As a leading online publisher in sensors related fields, IFSA and its Sensors Web Portal has a great expertise and experience to market and promote your book worldwide. An extensive marketing plan will be developed for each new book, including intensive promotions in IFSA's media: journal, magazine, newsletter and online bookstore at Sensors Web Portal.

### 4) Published Format: pdf (Acrobat).

When you publish with IFSA your book will never go out of print and can be delivered to customers in a few minutes.

You are invited kindly to share in the benefits of being an IFSA author and to submit your book proposal or/and a sample chapter for review by e-mail to [editor@sensorsportal.com](mailto:editor@sensorsportal.com). These proposals may include technical references, application engineering handbooks, monographs, guides and textbooks. Also edited survey books, state-of-the art or state-of-the-technology, are of interest to us.



## International Frequency Sensor Association



**International Frequency Sensor Association (IFSA)** is a professional association, created with the aim to encourage the researches and developments in the area of quasi-digital and digital smart sensors and transducers.

**IFSA Membership is open to all organizations and individuals worldwide who have a vested interest in promoting or exploiting smart sensors and transducers and are able to contribute expertise in areas relevant to sensors technology.**

More than 600 members from 63 countries world-wide including ABB, Analog Devices, Honeywell, Bell Technologies, John Deere, Endevco, IMEC, Keller, Mazda, Melexis, Memsis, Motorola, PCB Piezotronics, Philips Research, Robert-Bosch GmbH, Sandia Labs, Yokogawa, NASA, US Navy, National Institute of Standard & Technology (NIST), National Research Council, etc.



For more information about IFSA membership, visit  
<http://www.sensorsportal.com>

Authors are encouraged to submit article in MS Word (doc) and Acrobat (pdf) formats by e-mail: [editor@sensorsportal.com](mailto:editor@sensorsportal.com)  
Please visit journal's webpage with preparation instructions: <http://www.sensorsportal.com/HTML/DIGEST/Submission.htm>

## Biomedical Applications of Modified Carbon Glassy Electrode Sensor with Nanoparticles and Dendrimers

<sup>1</sup>Solomon W. LEUNG, <sup>2</sup>Yuanhong WANG and <sup>3</sup>James C. K. LAI

<sup>1</sup>Civil and Environmental Engineering Department, School of Engineering and Biomedical Research Institute, Idaho State University, Pocatello, ID 83209, USA  
Tel.: 1-208-282-2524, fax: 1-208-283-4538

<sup>2</sup>Civil and Environmental Engineering Department, School of Engineering, Idaho State University, Pocatello, ID 83209, USA

<sup>3</sup>College of Pharmacy and Biomedical Research Institute, Idaho State University, Pocatello, ID 83209, USA

<sup>1</sup>E-mail: leunsolo@isu.edu

*Received: 13 December 2010 /Accepted: 15 March 2011 /Published: 5 April 2011*

---

**Abstract:** We previously reported the development of a biosensor platform that is capable of measuring biometabolites and environmental sensitive species, such as peroxide and nitrate/nitrite, to concentrations in the order of ppb (parts per billion) or lower. In this investigation, we modified our platform with dendrimers to enhance its performance. Zero and second generation of dendrimers were coated on the surface of a carbon glassy electrode which was then modified with l-glutamate dehydrogenase (GDH) and  $\alpha$ -keto glutarate. The resulting electrode was tested with ammonium solutions, concentrations ranged from 2 to 300 nM at pH 7.4; the results were satisfactory. Measurements at lower concentrations had better resolution than at higher concentrations and it is believed that the measurement limit can be lower than 2 nM. This biosensor platform was proven to be versatile and can be employed as a platform for ultrasensitive detecting devices in many biomedical and environmental applications. *Copyright* © 2011 IFSA.

**Keywords:** Biosensor, GDH, Ammonium, Glassy carbon electrode, PAMAM.

---

### 1. Introduction

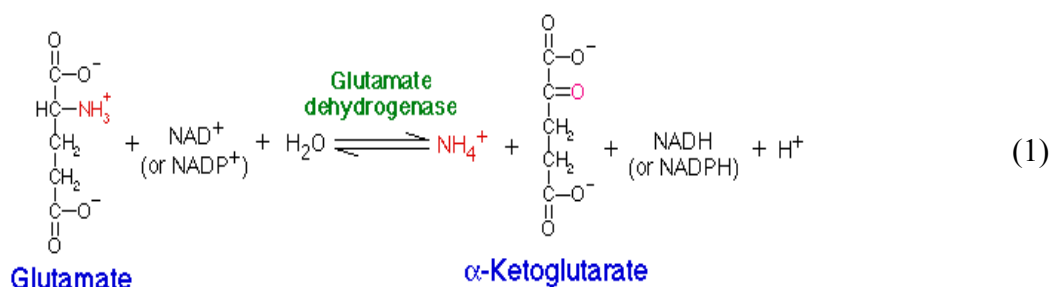
In the past several years, our research group has been developing a platform for biosensor construction that is capable of detecting target species that are in nano and subnanomolar levels [1, 2]. This sensor

platform is based on an Au electrode modified with sol-gel Au colloid and biocatalyst that is specific to the chemical species to be detected, the Au colloid comprises nano-size Au particles and cysteamine which binds strongly on the surface of the metal electrode and provide stable linkage with the nano gold particles and biocatalysts. Thus far, biometabolites and environmental sensitive chemicals such as nitrite/nitrate and peroxide were successfully detected at level of nM and below with this sensor platform.

In this study, we were developing another biosensor platform that can be used to measure biometabolites and environmental sensitive chemicals based on a non-metal glassy carbon electrode modified with sol-gel Au colloid that is similar to the sensor platform mentioned previously, except the binding polymer would be a dendrimer (polyamidoamine, PAMAM) instead of cysteamine. A dendrimer was chosen to be the linker between the electrode and Au particles/catalysts because of its low toxicity and highly branched structure that presumably can provide more anchoring sites for the Au particles and catalysts. Thus, the dendrimer can enhance the performance of the sensor platform. However, PAMAM does not have an S atom in the molecular structure and may not bind as well on the electrode's wall thus would be less durable. Performance of using cysteamine and dendrimer as a linker for the same sensor platform was compared in this study and the stability and durability of the sensor would be investigated. Ammonia, which is a major biometabolite and environmental sensitive chemical, was used as the surrogate chemical to be tested by this sensor platform [3].

### 1.1. Theory

As shown in the following Equation (1), glutamate and nicotinamide adenine dinucleotide ( $\text{NAD}^+$ ) can be hydrolyzed to form  $\alpha$ -keto glutarate,  $\beta$ -nicotinamide adenine dinucleotide reduced (NADH), and ammonium ion with the enzyme, glutamate dehydrogenase (GDH). The equilibrium constant is in favor of the formation of glutamate and thus the reverse reaction is faster kinetically [4].



For many biological reactions, the end product or metabolite is ammonium; accumulation of a high concentration of ammonium is toxic to the body. Environmentally, ammonium is a byproduct of many industrial processes, uncontrolled discharges of ammonium will lead to harmful consequence to the environment. Our goal here was to develop a sensor device that is nontoxic and can measure the ammonium ion at the lowest concentration possible; its utilities can be found in many biomedical or environmental applications. Hence, it is the reverse reaction as shown above (glutamate formation) that we utilized in this study; however, the same sensor can be used to detect  $\alpha$ -keto glutarate or glutamate with a slight alternation of the measuring approach. Measurements of these chemical species mentioned above that were reported in literature were mostly in the range of mM [5-7]. It should be noted that the motivation of this study was to develop a sensor that can measure low concentration of the target species, more specifically, it is to relate the current measurements exerted by the reacting species in a solution (with characteristics peaks of oxidation and/or reduction) by cyclic voltammetry

to concentrations of the species, rather than to determine the reaction kinetics of the measuring species of which in many instances are already known.

## **2. Materials and Methods**

### **2.1. Materials**

L-glutamic dehydrogenase (GDH, from bovine liver, solution in 50 % glycerol) was purchased from Sigma-Aldrich (St. Louis, MO, USA), the concentration of GDH was 28 mg protein/mL, and 46 units/mg. Cysteamine, polyamidoamine dendrimer generation 0 (PAMAM\_0), polyamidoamine dendrimer generation 2<sup>nd</sup> (PAMAM\_2),  $\alpha$ -keto glutarate,  $\beta$ -nicotinamide adenine dinucleotide reduced disodium salt hydrate (NADH),  $\text{AuCl}_3\text{HCl} \cdot 4\text{H}_2\text{O}$  (Au % > 48 %) and  $\text{Na}_3\text{citrate}$  were purchased from Sigma. All the other chemicals were of analytical grade or highest grade available.

### **2.2. Electrode Preparation**

The cleaned glassy carbon electrode (GCE) was first immersed in 0.1 M cysteamine solution in darkness. The resulting monolayer-modified electrode was rinsed thoroughly with twice-distilled water and soaked in distilled water. Then, it was dipped into the colloidal gold. The gold colloid–cysteamine-modified electrode was dipped into the l-glutamate dehydrogenase (GDH) solution (pH 7.4) (or GDH solution containing NADH). In such a way, a GDH (or GDH/NADH) gold colloid–cysteamine-modified glassy carbon electrode was obtained (GCE cysteamine-Au-GDH or cysteamine-Au-GDH/NADH).

For electrode that was modified by PAMAM only, either PAMAM\_0 or PAMAM\_2 was used in place of cysteamine, these resulting electrodes were termed GCE PAMAM\_0 or PAMAM\_2-Au-GDH or GDH/NADH. In cases that both cysteamine and PAMAM were coated onto electrodes, the cleaned glassy carbon electrode was first immersed in cysteamine solution, the resulting electrode was dipped into the PAMAM solution (PAMAM\_0 or PAMAM\_2). The gold colloid–cysteamine/PAMAM-modified electrode was dipped into the GDH solution (pH 7.4) (or GDH solution containing NADH). In such a way, a GDH (or GDH/NADH) gold colloid–cysteamine/PAMAM-modified glassy carbon electrode was obtained (GCE cysteamine/PAMAM\_0 or PAMAM\_2-Au-GDH or GDH/NADH).

### **2.3. Nanoparticles Solution Preparations**

Nanoparticles Au was prepared by reacting  $\text{HAuCl}_4$  with citric acid [2].

### **2.4. Detections**

UV-VIS spectrophotometry was carried out by an Agilent diode-array spectrophotometer (Agilent Model 8453); cyclic voltammetry was conducted by using a Gamry 600 Potentiostat. Voltammetric potential was measured against a saturated chloride electrode (SCE). The experimental setup of the cyclic voltammetry is shown in Fig. 1.



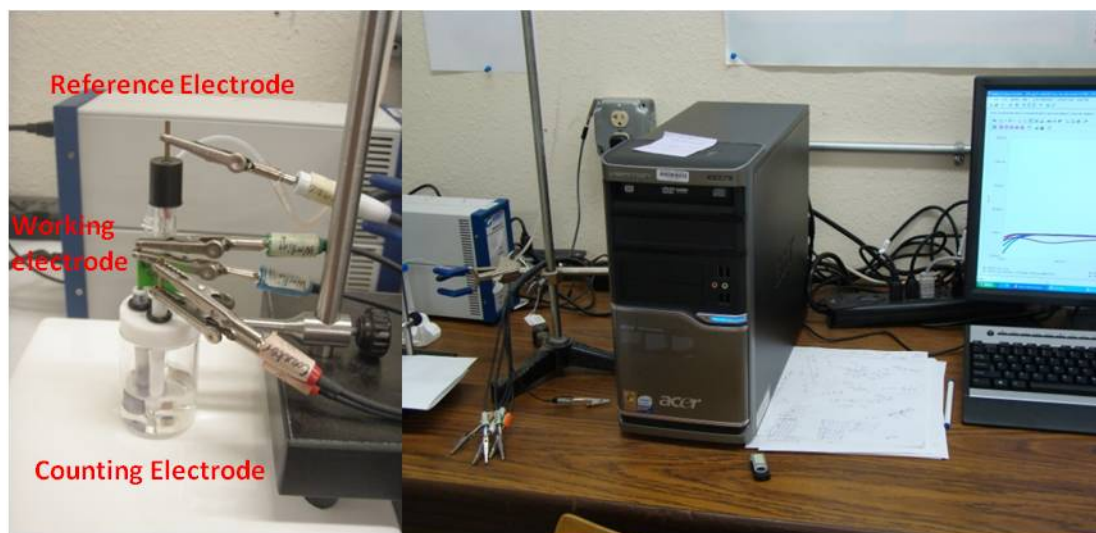


**Fig. 1.** Cyclic voltammetry and the sensor measurement cell.

## 2.5. Experimental Procedures

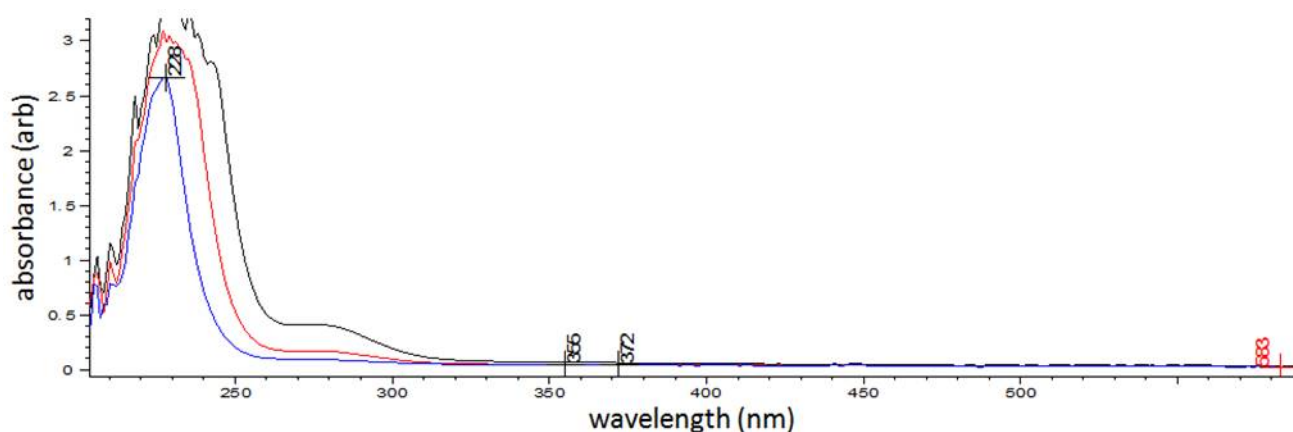
For all experiments, the measurement cell contained 5 mL of 2.5 mM of NADH, then a combined solution of  $\alpha$ -keto glutarate and  $\text{NH}_4^+$  was injected into the reaction cell for measurement periodically, at 60 second intervals; injection volume varied from 10 to 1500  $\mu\text{L}$  depending on the concentration required. The concentration of  $\alpha$ -keto glutarate solution was  $1 \times 10^{-6}$  mol/L,  $\text{NH}_4^+$  was  $1 \times 10^{-6}$  mol/L. All experiments were conducted at pH 7.4 in a 0.1 M phosphate buffer solution under deoxygenated condition and all solutions were prepared with double deionized distilled water.

Measurement of current ( $i$ ) with time was usually at about 700 mV (vs. SCE) for the reduction reaction and at near 2.0 mV for the oxidation reaction. The resulting concentrations of  $\alpha$ -keto glutarate and  $\text{NH}_4^+$  in the reaction cell ranged from 2 to 300 nM after each injection unless otherwise stated.

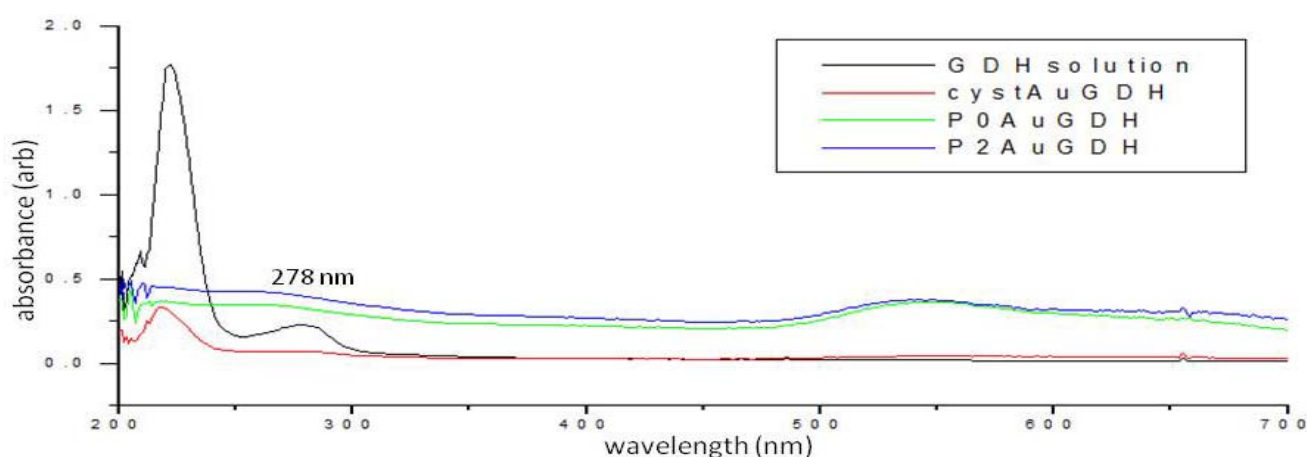
## 3. Results and Discussion

### 3.1. Identification of PAMAM Binding with GDH in Sol-Gel Au Colloid

Fig. 2(a) shows the UV-VIS spectrum of PAMAM\_2 solution at various concentrations. PAMAM's in general have major absorption peak at 227 nm, but a minor peak also appears at 278 nm. The peak at 278 disappears at dilute concentration as shown in blue in Fig. 2(a). GDH solution has similar spectrum as PAMAM\_2 except that its absorptivity is less intense at 278, as shown in black in Fig. 2(b). Fig. 2(b) also shows the spectra of a plastic cuvette (made for UV-VIS range) coated with cysteamine-Au-GDH, PAMAM\_0-Au-GDH, and PAMAM\_2-Au-GDH in red, green, and blue, respectively. The peak at near 548 nm is associated with Au particles. The peak at 227 nm would nearly disappear for the coating (sol-gel colloid) containing cysteamine (red line) after the cuvette was rinsed with deionized water numerous times, but a small peak at 278 nm would remain, that was believed to be a combined cluster layer of cysteamine and GDH situated in the Au colloid. The same can be observed if rinsing was done with the PAMAM's coating, however, the remaining cluster peak at 278 nm was much larger and the Au peak at 548 nm was accordingly higher. Hence, it can be reasoned from the magnitude of the absorbance at 278 nm that PAMAM's can bind better with the Au nanoparticles and GDH to form a colloid attached onto the electrode surface than cysteamine with Au nanoparticles and GDH in this self-assembly process.



(a)



(b)

**Fig. 2.** UV-VIS spectra of PAMAM\_2 and other sensor materials coated on an UV-VIS cuvette: (a) Spectra of PAMAM\_2 solutions at various concentrations, characteristic peaks of PAMAM's are at 227 and 278 nm. At lower concentration, as shown in blue, PAMAM\_2 only has absorption peak at 227 nm; (b) Spectrum of GDH solution and spectra of an UV-VIS plastic cuvette coated with cysteamine-Au-GDH, PAMAM\_0-Au-GDH, and PAMAM\_2-Au-GDH in black, red, green, and blue, respectively.

### 3.2. Voltammetric Responses of the Modified GCE's for $\text{NH}_4^+$ Detection

We have explored several combinations of sol-gel Au colloids for the sensor development to detect ammonia, these combinations were: Cysteamine/PAMAM\_0-Au-GDH, cysteamine/PAMAM\_2-Au-GDH, cysteamine/PAMAM\_0-Au-GDH/NADH, and cysteamine/PAMAM\_2-Au-GDH/NADH. We have carried out a wide-range of ammonia concentrations from 2 nM to 300 nM with all the GCE's modified with different sol-gel Au colloid combinations in order to determine the champion performer. Trial measurements of the electrodes indicated that two distinguish characteristic peaks could be used to relate proportionally the concentrations of ammonia with heights of current peaks: a reductive peak at near 700 mV and an oxidative peak at 2 mV. Fig. 3 in the following is the voltammograms for the ammonia measurements generated by using a GCE modified with PAMAM\_2-Au-GDH. The blue voltammogram is measurement of the blank in phosphate buffer solution. It should be noted that the reductive peaks at 700 mV shifted to higher positive voltage with increase of ammonia concentrations. The oxidative peaks at about 2 mV were also detected but were not obviously observed from the figure.

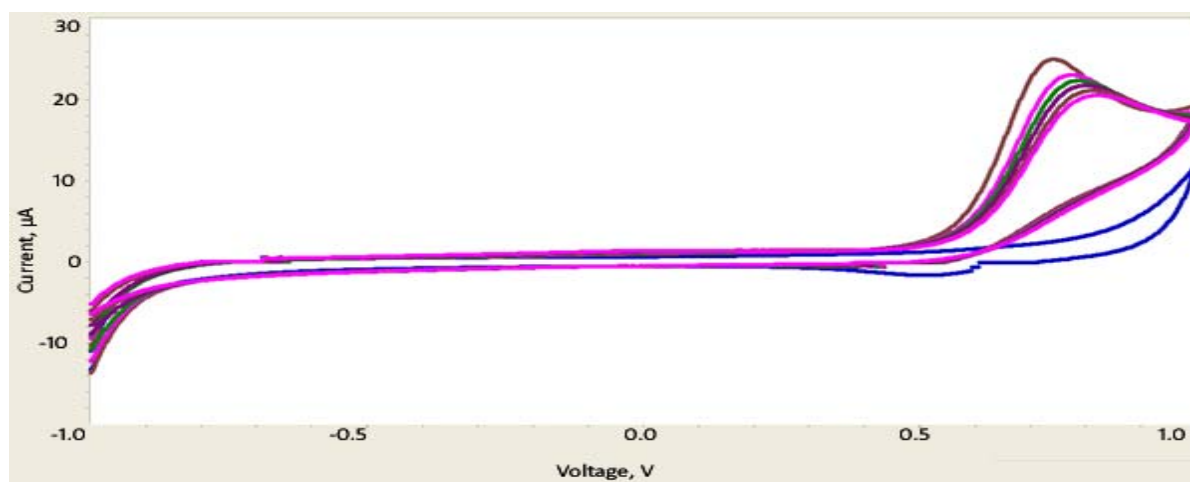
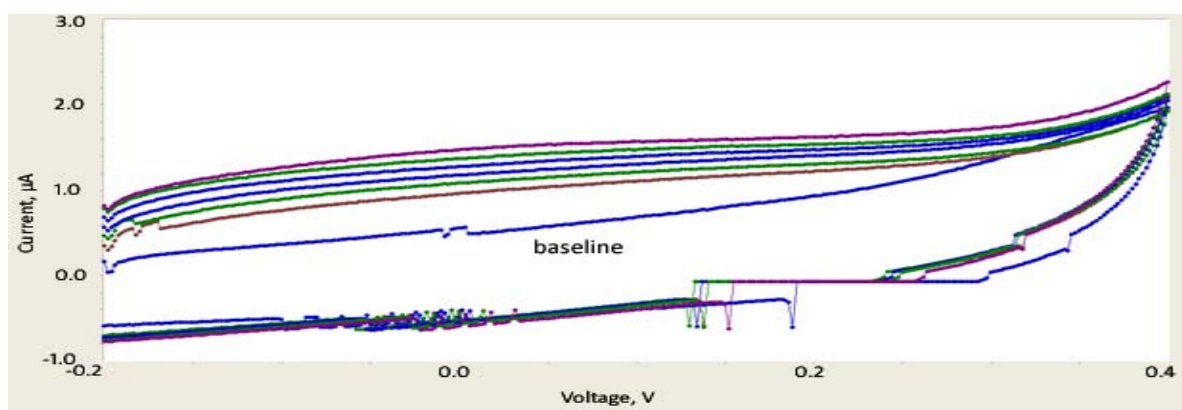


**Fig. 3.** Cyclic voltammograms of reaction of  $\text{NH}_4^+$  with  $\alpha$ -keto glutarate at pH 7.4 for concentrations from 2 to 300 nM.

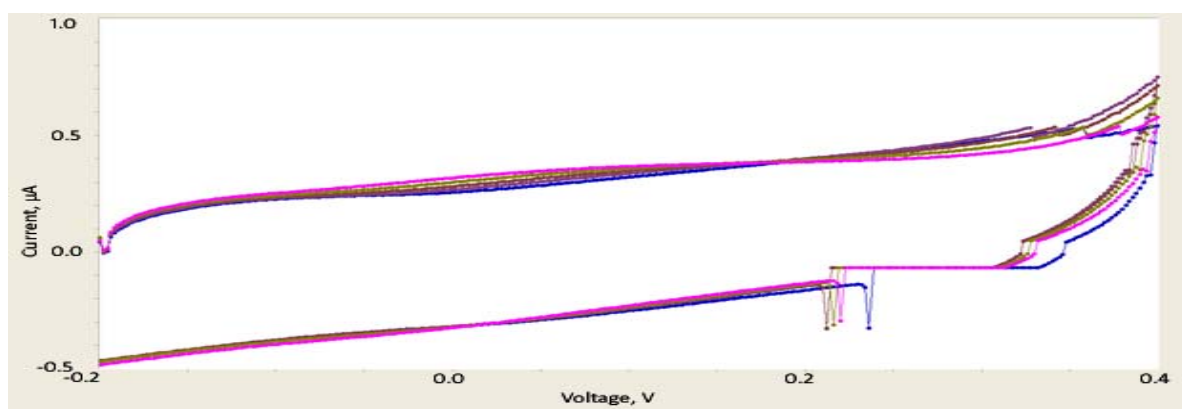
Overall, GCE modified with either PAMAM\_0 or PAMAM\_2-Au- GDH/NADH worked best for the detection of ammonia with  $\alpha$ -keto glutarate, although there was no significant detection advantage by using the more branched PAMAM\_2 in the sensor preparation. Detection of  $\text{NH}_4^+$  concentrations can be better demonstrated by using the oxidative peaks at 2 mV. Voltammograms of the oxidative peaks at 2 mV of the ammonia reaction with  $\alpha$ -keto glutarate using GCE modified by PAMAM\_2-Au-GDH/NADH and cysteamine-Au-GDH are shown in Fig. 4 (a) and Fig. 4 (b) respectively.

As shown in Fig. 4(a), there was about 0.45  $\mu\text{A}$  difference between the blank buffer solution (in blue) and the measurement of 2 nM  $\text{NH}_4^+$  solution (in brown), which indicated that the sensor platform is capable of measuring  $\text{NH}_4^+$  concentration to subnanomolar level. Fig. 4(b) is the voltammograms of the same solutions, but current increments of the oxidative peaks were relatively small, which indicates that the PAMAM\_2-Au-GDH/NADH modification makes a more superior sensor for low ammonia concentration detection. The more efficient of NADH oxidation in the system could also be attributed, at least partially, by the direct binding of NADH with GDH in the Au colloid.

Fig. 5 shows the amperometric responses measured by 5 sensors using the same platform with different modifications for the reaction of  $\text{NH}_4^+$  with  $\alpha$ -keto glutarate at 2 mV for concentrations ranged from 2 to 300 nM. It can be observed that there were two near linear regions that can be explored to be used for sensor design: a sensitive region at concentrations less than 20 nM, and a relatively less sensitive region at concentrations larger than 40 nM. One may conclude that this non-metal biosensor platform is ideal for making sensor for ammonia detection at extremely low concentrations (>20 nM). It is unclear at this time about the mechanisms why the modified GCE's become less sensitive at the higher concentration region, it is conceivable that there is a limited quantity of Au colloid attached to the GCE surface and its ability to transfer electrons is saturated and hence turns inefficient at higher concentration.



(a)



(b)

**Fig. 4.** (a) Cyclic voltammograms of PAMAM\_2-Au-GDH/NADH modified GCE for detection of  $\text{NH}_4^+$  at pH 7.4., concentrations of  $\text{NH}_4^+$  varied from 2 to 300 nM. The bottom reduction line in blue was measurement for a blank. (b) Same measurements with a GCE modified with cysteamine-Au-GDH.

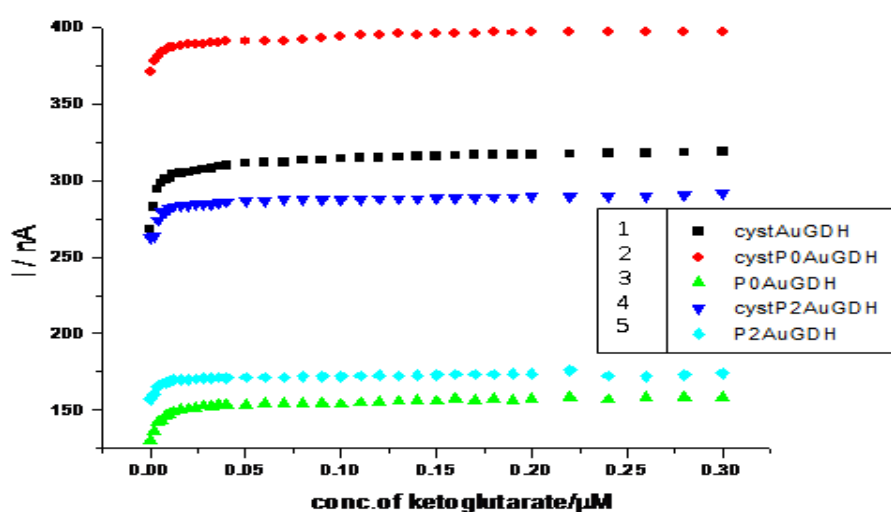


**Fig. 5.** Amperometric responses of ammonia reaction with  $\alpha$ -keto glutarate from 5 different GCE sensors modified with similar platform materials: black is cysteamine-Au-GDH, red is cysteamine/PAMAM\_0-Au-GDH, green is PAMAM\_0-Au-GDH, blue is cysteamine/PAMAM\_2-Au-GDH, light blue is PAMAM\_2-Au-GDH.



### 3.2. Reproducibility and Stability of the Modified GCE's

An ideal sensor platform should be able to generate measurements that are reproducible and the system is stable with time, thus the measurements are consistent and reliable. Fig. 6 (a) shows the 50 cyclic responses of a typical modified GCE in the same ammonia solution. It can be seen that some deterioration occurred (as shown by the characteristic peaks at near 700 mV) after the 50 cycles but the results are relatively consistent. Fig. 6 (b) shows the amperometric responses of a GCE modified by PAMAM\_0-Au-GDH/NADH at 2.0 mV after 2 weeks stored inside a refrigerator at 4 °C, the responses are nearly identified with the same trend, the measurements indicated that the sol-gel Au colloid stabilized the GDH/NADH within the cluster and prevented the bioenzyme/biochemical from deteriorating. It is well known that these bioenzyme/biochemical are very unstable, especially under dilute concentrations as they were in this study. These results demonstrated that the biosensor platform has reasonable reproducibility and stability.

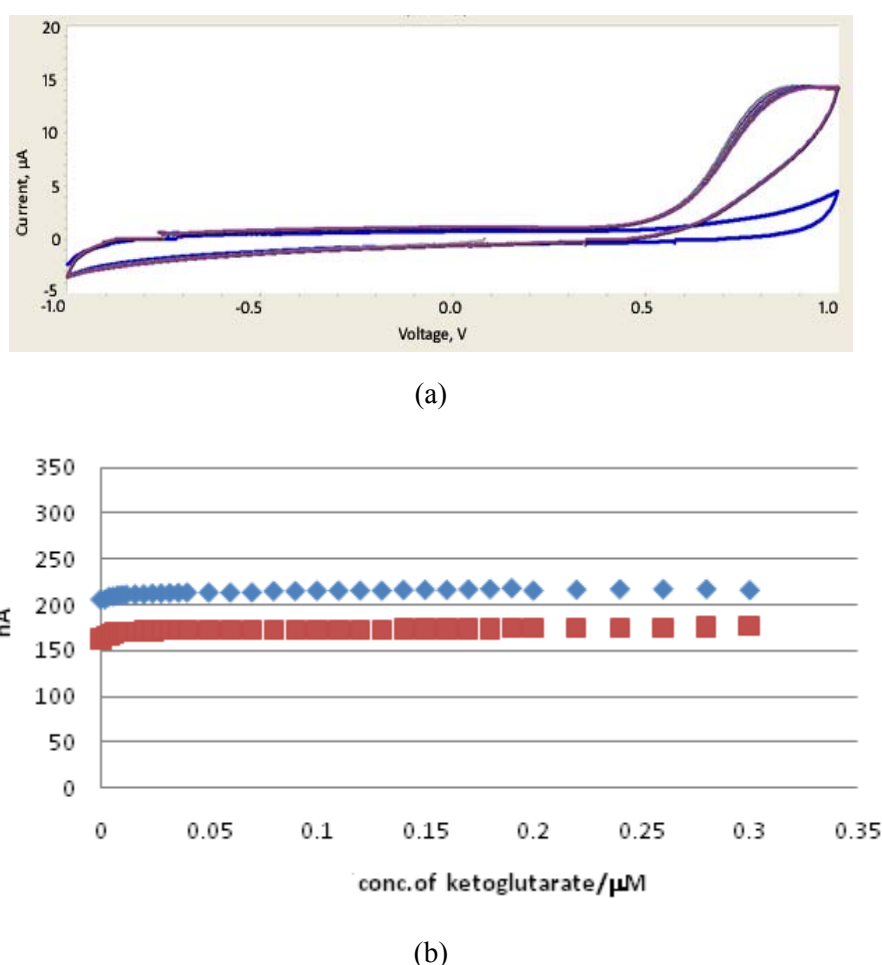


**Fig. 6.** (a) Voltammograms of a modified GCE with 50 measurement cycles of the same solution; (b) Amperometric responses of a GCE modified by PAMAM\_0-Au-GDH/NADH at 1.8 mV, before (blue) and after (red) 2 weeks stored inside a refrigerator at 4 °C.

## 4. Conclusions

We successfully modified our glassy carbon electrode biosensor platform [2] for ammonium detection; we further modified the sensor platform with PAMAMs and the detection lower limit was enhanced. This highly modified electrode can detect ammonium concentrations down to 2 nM or lower. The low detection limit of this biosensor is far more superior than most available detection methods in the

public domain. This biosensor platform can be modified to be used for many measurement applications in biomedical and environmental field that require high sensitivity at low concentrations. Currently, the challenge of biosensor development is not in finding the right enzymes or conjugate reactions (Equation (1)) that govern the particular species to be detected, it is the portability, stability, and noise reduction that demand further research and development.

## Acknowledgement

This study was supported by an USAMRMC Project Grant (Contract #W81XWH-07-2-0078).

## References

- [1]. S. W. Leung, Y. Wang, H. Gu, J. C. K. Lai, Characterization and Applications of Modified Gold Electrode Sensor with Nanoparticles, in *Proceedings of the 2009 Nanotechnology Conference and Trade Show*, Vol. 2, Chapter 4: Biosensors and Diagnostics, 2009, pp. 233-235.
- [2]. J. C. K. Lai, Y. Wang, W. Gao, H. Gu, S. W. Leung, Performance Comparisons of Nanoparticle Modified Sensor Electrodes for the Detection of Nitrite and Peroxide, in *Proceedings of the 2009 Nanotechnology Conference and Trade Show, Volume 2: Chapter 4: Biosensors and Diagnostics*, 2009, pp. 233-235.
- [3]. Y. Wang, L-glutamate Dehydrogenase Modified Biosensor Based with Gold Nanoparticles, M. S. Project Report, *Idaho State University*, Pocatello, Idaho, 2009.
- [4]. P. Belenky, K. L. Bogan, C. Brenner,  $\text{NAD}^+$  Metabolism in Health and Disease, *Trends in Biochemical Sciences*, Vol. 32, Issue 1, 2007, pp. 12-19.
- [5]. A. K. Basu, P. Chattopadhyay, U Roychudhuri, Runu Chakraborty, A biosensor Based on Co-Immobilized L-glutamate Oxidase and L-glutamate Dehydrogenase for Analysis of Monosodium Glutamate in Food, *Biosensors and Bioelectronics*, Vol. 21, 2006, pp. 1968-1972.
- [6]. K. Riedel, J. Huth, M. Kuehn, P. Liebs, Amperometric Determination of Ammonium ions with a Microbial Sensor, *Journal of Chemical Technology & Biotechnology*, Vol. 47, Issue 2, 1990, pp. 109-116.
- [7]. N. Pasco, C. Jeffries, Q. Davies, A. J. Downard, A. D. Roddick-Lanzilotta, L. Gorton, Characterisation of a Thermophilic L-glutamate Dehydrogenase Biosensor for Amperometric Determination of L-glutamate by Flow Injection Analysis, *Biosensors & Bioelectronics*, Vol. 14, 1999, pp. 171-178.

2011 Copyright ©, International Frequency Sensor Association (IFSA). All rights reserved.  
(<http://www.sensorsportal.com>)

## BioMEMS 2010

Yole's BioMEMS report 2010-2015

IFSA offers  
a SPECIAL PRICE

### Microsystems Devices Driving Healthcare Applications

**The BioMEMS 2010 report** is a robust analysis of the Micro Devices with the most advances to develop solutions for vital bio-medical applications. The devices considered are:

Pressure sensors

Silicon microphones

Accelerometers

Gyroscopes

Optical MeMs and image sensors

Microfluidic chips

Microdispensers for drug delivery

Flow meters

Infrared temperature sensors

Emerging MeMs (rfID, strain sensors, energy harvesting)

Also addressed are the regulation aspects for medical device development.

<http://www.sensorsportal.com/HTML/BioMEMS.htm>





## The Third International Conference on Bioinformatics, Biocomputational Systems and Biotechnologies

### BIOTECHNO 2011

May 22-27, 2011 - Venice, Italy



#### Tracks:

##### A. Bioinformatics, chemoinformatics, neuroinformatics and applications

- Bioinformatics
- Advanced biocomputation technologies
- Chemoinformatics
- Bioimaging
- Neuroinformatics

##### B. Computational systems

- Bio-ontologies and semantics
- Biocomputing
- Genetics
- Molecular and Cellular Biology
- Microbiology

##### C. Biotechnologies and biomanufacturing

- Fundamentals in biotechnologies
- Biodevices
- Biomedical technologies
- Biological technologies
- Biomanufacturing



#### Important deadlines:

Submission (full paper)	January 10, 2011
Notification	February 20, 2011
Registration	March 5, 2011
Camera ready	March 20, 2011

<http://www.iaria.org/conferences2011/BIOTECHNO11.html>



## The Seventh International Conference on Networking and Services

### ICNS 2011

May 22-27, 2011 - Venice, Italy



#### Important deadlines:

Submission (full paper)	January 10, 2011
Notification	February 20, 2011
Registration	March 5, 2011
Camera ready	March 20, 2011

<http://www.iaria.org/conferences2011/ICNS11.html>

#### Tracks:

- ENCOT: Emerging Network Communications and Technologies
- COMAN: Network Control and Management
- SERVI: Multi-technology service deployment and assurance
- NGNUS: Next Generation Networks and Ubiquitous Services
- MPQSI: Multi Provider QoS/SLA Internetworking
- GRIDNS: Grid Networks and Services
- EDNA: Emergency Services and Disaster Recovery of Networks and Applications
- IPv6DFI: Deploying the Future Infrastructure
- IPDy: Internet Packet Dynamics
- GOBS: GRID over Optical Burst Switching Networks



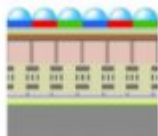
## CMOS Image Sensors Technologies & Markets - 2010 Report

**Disruptive technologies are paving the way  
to the future of digital imaging industry !**

**IFSA offers  
a SPECIAL PRICE**

Image sensors have come a long way since the first introduction of CCD sensor technology in the 1990's. They made a big jump in the 2000's with the introduction of CMOS sensor technology which gave birth to the low-cost, high volume camera phone market. Image sensors are now part of our everyday life: from cell-phone cameras, to notebook webcams, digital cameras, video camcorders to security & surveillance systems. In the future, new markets are also emerging such as sensors for medical applications, automotive security features, but also gaming and home TV webcams ... The reason why we are now releasing our first report on the CMOS image sensor industry is that we feel that we are at an historic turning point for this young, but still maturing industry.

[http://www.sensorsportal.com/HTML/CMOS\\_Image\\_Sensors.htm](http://www.sensorsportal.com/HTML/CMOS_Image_Sensors.htm)







The Second International Conference  
on Sensor Device Technologies and Applications

## SENSORDEVICES 2011

August 21-27, 2011 - French Riviera, France



**Important deadlines:**

Submission deadline	April 10, 2011
Notification	April 30, 2011
Registration	May 15, 2011
Camera ready	May 22, 2011

**Tracks:**

- Sensor devices
- Photonics
- Infrared
- Ultrasonic and Piezosensors
- Sensor device technologies
- Sensors signal conditioning and interfacing circuits
- Medical devices and sensors applications
- Sensors domain-oriented devices, technologies, and applications
- Sensor-based localization and tracking technologies

<http://www.iaria.org/conferences2011/SENSORDEVICES11.html>



The Fifth International Conference on Sensor  
Technologies and Applications

## SENSORCOMM 2011

August 21-27, 2011 - French Riviera, France



**Important deadlines:**

Submission deadline	April 10, 2011
Notification	April 30, 2011
Registration	May 15, 2011
Camera ready	May 22, 2011

**Tracks:**

- APASN: Architectures, protocols and algorithms of sensor networks
- MECSN: Energy, management and control of sensor networks
- RASQOFT: Resource allocation, services, QoS and fault tolerance in sensor networks
- PESMOSN: Performance, simulation and modelling of sensor networks
- SEMOSN: Security and monitoring of sensor networks
- SECSED: Sensor circuits and sensor devices
- RIWISN: Radio issues in wireless sensor networks
- SAPSN: Software, applications and programming of sensor networks
- DAIPSN: Data allocation and information in sensor networks
- DISN: Deployments and implementations of sensor networks
- UNWAT: Under water sensors and systems
- ENOPT: Energy optimization in wireless sensor networks

<http://www.iaria.org/conferences2011/SENSORCOMM11.html>



The Fourth International Conference on Advances  
in Circuits, Electronics and Micro-electronics

## CENICS 2011

August 21-27, 2011 - French Riviera, France



**Important deadlines:**

Submission deadline	April 10, 2011
Notification	April 30, 2011
Registration	May 15, 2011
Camera ready	May 22, 2011

**Tracks:**

- Semiconductors and applications
- Design, models and languages
- Signal processing circuits
- Arithmetic computational circuits
- Microelectronics
- Electronics technologies
- Special circuits
- Consumer electronics
- Application-oriented electronics

<http://www.iaria.org/conferences2011/CENICS11.html>



## Guide for Contributors

---

### Aims and Scope

*Sensors & Transducers Journal* (ISSN 1726-5479) provides an advanced forum for the science and technology of physical, chemical sensors and biosensors. It publishes state-of-the-art reviews, regular research and application specific papers, short notes, letters to Editor and sensors related books reviews as well as academic, practical and commercial information of interest to its readership. Because of it is a peer reviewed international journal, papers rapidly published in *Sensors & Transducers Journal* will receive a very high publicity. The journal is published monthly as twelve issues per year by International Frequency Sensor Association (IFSA). In addition, some special sponsored and conference issues published annually. *Sensors & Transducers Journal* is indexed and abstracted very quickly by Chemical Abstracts, IndexCopernicus Journals Master List, Open J-Gate, Google Scholar, etc. Since 2011 the journal is covered and indexed (including a Scopus, Embase, Engineering Village and Reaxys) in Elsevier products.

### Topics Covered

Contributions are invited on all aspects of research, development and application of the science and technology of sensors, transducers and sensor instrumentations. Topics include, but are not restricted to:

- Physical, chemical and biosensors;
- Digital, frequency, period, duty-cycle, time interval, PWM, pulse number output sensors and transducers;
- Theory, principles, effects, design, standardization and modeling;
- Smart sensors and systems;
- Sensor instrumentation;
- Virtual instruments;
- Sensors interfaces, buses and networks;
- Signal processing;
- Frequency (period, duty-cycle)-to-digital converters, ADC;
- Technologies and materials;
- Nanosensors;
- Microsystems;
- Applications.

### Submission of papers

Articles should be written in English. Authors are invited to submit by e-mail [editor@sensorsportal.com](mailto:editor@sensorsportal.com) 8-14 pages article (including abstract, illustrations (color or grayscale), photos and references) in both: MS Word (doc) and Acrobat (pdf) formats. Detailed preparation instructions, paper example and template of manuscript are available from the journal's webpage: <http://www.sensorsportal.com/HTML/DIGEST/Submission.htm> Authors must follow the instructions strictly when submitting their manuscripts.

### Advertising Information

Advertising orders and enquires may be sent to [sales@sensorsportal.com](mailto:sales@sensorsportal.com) Please download also our media kit: [http://www.sensorsportal.com/DOWNLOADS/Media\\_Kit\\_2011.pdf](http://www.sensorsportal.com/DOWNLOADS/Media_Kit_2011.pdf)



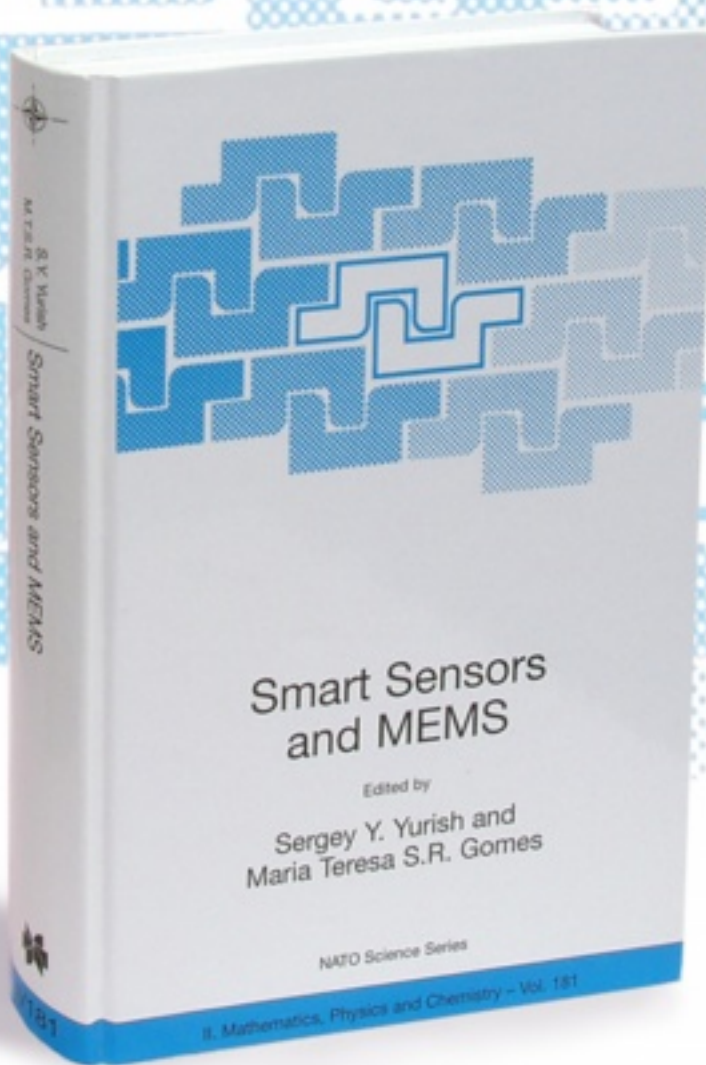
# Smart Sensors and MEMS

Edited by

Sergey Y. Yurish and  
Maria Teresa S.R. Gomes

The book provides an unique collection of contributions on latest achievements in sensors area and technologies that have made by eleven internationally recognized leading experts ...and gives an excellent opportunity to provide a systematic, in-depth treatment of the new and rapidly developing field of smart sensors and MEMS.

The volume is an excellent guide for practicing engineers, researchers and students interested in this crucial aspect of actual smart sensor design.



**Kluwer Academic Publishers**

Order online:

[www.sensorsportal.com/HTML/BOOKSTORE/Smart\\_Sensors\\_and\\_MEMS.htm](http://www.sensorsportal.com/HTML/BOOKSTORE/Smart_Sensors_and_MEMS.htm)

**[www.sensorsportal.com](http://www.sensorsportal.com)**

## Chapter 30

# TOXICITY OF SILICON DIOXIDE NANOPARTICLES IN MAMMALIAN NEURAL CELLS

James C. K. Lai, PhD<sup>1</sup>, Ashvin R. Jaiswal, MS<sup>1</sup>, Maria B. Lai, MS<sup>1</sup>, Sirisha Jandhyam, MS<sup>1</sup>, Solomon W. Leung, PhD<sup>2</sup>, and Alok Bhushan, PhD<sup>1</sup>

<sup>1</sup>*Department of Biomedical and Pharmaceutical Sciences, College of Pharmacy, and Biomedical Research Institute, Idaho State University, Pocatello, ID 83209*

<sup>2</sup>*Department of Civil and Environmental Engineering, School of Engineering, College of Science and Engineering and Biomedical Research Institute, Idaho State University, Pocatello, ID 83209*

### KEY WORDS

silicon dioxide nanoparticles; toxicity in neural cells; cytotoxicity of nanoparticles; neurons; astrocytes; dorsal root ganglion neurons; Schwann cells; central and peripheral nervous system

## 1.1 INTRODUCTION

In a recent draft document, the US Environmental Protection Agency (EPA) has emphasized that exposure to nanomaterials can occur during their fabrication or production process because the materials can pollute the environment [1]. Environmental exposure of humans to silicon dioxide has been increasing because of escalating use of silicon dioxide, including a range of its particle sizes, in cosmetics, food, and drug formulations [2,3]. Although silicon dioxide has been considered to be a comparatively nontoxic substance, research in the last two decades has revealed that silicon dioxide particles are not as harmless as they were previously assumed to be.

In sizes above the micrometer range (i.e.,  $> 1 \mu\text{m}$ ), silicon dioxide appears to be benign to humans, insects, and microorganisms. However, silicon dioxide particles of sizes smaller than  $1 \mu\text{m}$  can exert toxic effects in humans and animals. For example, silicosis is a disease found both in humans and rats: the underlying silicon dioxide toxicity is due to prolonged exposure to crystalline silica dust,

leading to pulmonary injuries or lung inflammation [4,5]. Because silicon dioxide nanoparticles can readily cross the blood-brain barrier (see below), they can penetrate into the nervous system and exert their toxicity on neural cells. This review therefore focuses on discussing the effects of silicon dioxide nanoparticles on neural cells both *in vivo* and *in vitro*. Three recent reviews [6-8] cover the toxicity of these particles in peripheral tissues and cell types: readers are referred to those for effects of silicon dioxide nanoparticles on non-neural cell types and other aspects not covered in this review.

## 1.2 NANOPARTICLES CAN CROSS THE BLOOD-BRAIN BARRIER

The blood-brain barrier (BBB) constitutes an effective barrier to exclude undesirable and/or toxic substances in the circulation from entering the central nervous system, including the brain. In this context, for targeting therapeutic agents to the brain, one needs to devise mechanism(s) whereby this restriction of the BBB is overcome or by-passed. Consequently, various studies on employing nanoparticles to assist with drug delivery or delivery of genetic material to advance gene therapy have concluded that nanoparticles can cross the BBB [9,10]. For example, Kim et al. [9] synthesized silica-overcoated magnetic nanoparticles containing rhodamine B isothiocyanate within a silica shell of controllable thickness (MNPs@SiO<sub>2</sub>(RITC)): in that study they employed particles with 50-nm thickness. They administered those particles intraperitoneally into mice for four weeks and were able to detect the nanoparticles in the brains of those mice. Their study [9] clearly demonstrated that such nanoparticles can penetrate the BBB.

Nanoparticles have also been employed to achieve neuron-specific delivery of genetic material to advance gene therapy of various neurological disorders. For example, Zang et al. [11] employed 85-nm PEGylated immunoliposome (containing antibodies to the rat transferrin receptor) to deliver tyrosine hydroxylase (TH) expression plasmid to normalize TH activity in the striatum in a rat model of experimental parkinsonism induced by 6-hydroxydopamine. Their results demonstrated that intravenously-administered immunoliposomes containing the TH expression plasmid could cross the BBB giving rise to increased striatal TH activity in the TH-transfected rats [11]. Thus, their findings suggested that the immunoliposomes crossed the BBB via the transvascular route [11]. In addition to the transvascular route, nanoparticles can also cross the BBB after they have induced alterations in BBB permeability and induced cerebral edema [10].



### 1.3 TOXICITY OF SILICON DIOXIDE NANOPARTICLES IN MAMMALIAN NEURAL CELLS

The toxicity of silicon dioxide nanoparticles in mammalian neural cells is discussed below from three perspectives: (i) environmental health impact of exposure to silicon dioxide nanoparticles, (ii) toxicity of the nanoparticles in mammalian neural cells *in vivo*, and (iii) toxicity of the nanoparticles in mammalian neural cells *in vitro*.

#### 1.3.1 *Environmental health impact of exposure to silicon dioxide nanoparticles*

As has already been alluded to above, the ever increasing use of silicon dioxide, including a range of its particles sizes, in cosmetics, food, drug formulations, and numerous other industrial applications [2,3,12] has raised some concerns regarding the environmental health impact of human exposure to silicon dioxide particles, especially nanoparticles [12]. Because nanoparticles, including silicon dioxide nanoparticles, can cross the BBB (see above), their accumulation in significant quantities in the central nervous system can induce deleterious effects on neural cells, thereby disturbing the normal functions of such cells and even inducing neurodegeneration. The findings of three early studies provide some support for the notion that accumulation of silicon dioxide nanoparticles in brain could lead to neurodegeneration [13-15]. Silica micro- and nanoparticles, when introduced into the brains of rats and mice, induced inflammatory responses in brain astrocytes and macrophages and degeneration of axons and axon terminals adjacent to the astrocytes [13]. Silicon and aluminum were noted to be co-localized in the central region of senile plaque cores in the cortex of patients with senile dementia of the Alzheimer type [14]. Moreover, the accumulated silicon and aluminum appeared to be found, at least in part, in lipofuscin granules in the brains of patients who died with Alzheimer's disease [15].

#### 1.3.2 *Toxicity in vivo of silicon dioxide nanoparticles in mammalian neural cells*

There have been very few studies on the toxicity of silicon dioxide nanoparticles *in vivo* on mammalian neural cells. Nevertheless, the results of the few studies are quite revealing and allow us to make two tentative generalizations. (i) Silicon dioxide nanoparticles can cross the BBB: one consequence of such particles being able to cross the BBB is that they could, at least potentially, exert undesirable effects on neural cells in the central nervous system. (ii) Most of the toxic effects of silicon nanoparticles *in vivo* on neural cells are similar to, if not identical with, the effects of such nanoparticles noted in neural cells *in vitro* (see below). Thus, this generalization points to the utility of employing neural cell models *in vitro* to screen for the toxicity of various types of silicon dioxide nanoparticles and the importance of employing such models to elucidate the cellular and molecular

mechanisms underlying the cytotoxicity of silicon dioxide nanoparticles. Nevertheless, it is noteworthy that cytotoxicity of these nanoparticles in neural cells cannot be easily and readily investigated employing animal models in studies *in vivo*. We will briefly discuss how the findings of the few studies on toxicity of silicon dioxide nanoparticles on neural cells *in vivo* have led us to formulate the two generalizations above.

In their study to investigate toxicity and tissue distribution of silica-overcoated magnetic nanoparticles in mice, Kim et al. [9] synthesized silica-overcoated magnetic nanoparticles containing rhodamine B isothiocyanate within a silica shell of controllable thickness (MNPs@SiO<sub>2</sub>(RITC)). They employed MNPs@SiO<sub>2</sub>(RITC) with 50-nm thickness and administered those particles intraperitoneally into mice for four weeks and were able to detect the nanoparticles in the brains of those mice. Furthermore, using an immunocytochemical approach and employing the dorsal cochlear nucleus as a representative example of whole brain localization, they were able to show that MNPs@SiO<sub>2</sub>(RITC) co-localized with a well-characterized neuronal marker, NeuN. Based on their observations, Kim et al. concluded that the silica nanoparticles (MNPs@SiO<sub>2</sub>(RITC)) could cross the BBB, enter neurons, but do not alter the permeability of the BBB [9]. Nevertheless, they did not detect any gross abnormal histopathological lesions in several organs, including brain, kidney, liver, testis, uterus, lung, heart and spleen, in mice four weeks after intraperitoneally injection of MNPs@SiO<sub>2</sub>(RITC) into the mice at 25, 50 or 100 mg/kg [9]. Consequently, Kim et al. [9] concluded such silica nanoparticles can penetrate the BBB and enter neurons without apparently altering their normal function, suggesting that the silica-overcoated nanoparticles at the doses employed were apparently not toxic to neurons. The findings and conclusions of Kim et al. [9] are in sharp contrasts with those of a more recent study by Wu et al. [16].

Wu et al. [16] examined the effects of intranasal exposure of adult rats to silica nanoparticles (20 µg per rat daily for 1 or 7 days). They reported intranasal instillation of silicon dioxide nanoparticles into rats, especially for seven days, significantly increased levels of silicon dioxide nanoparticles in several brain regions monitored, with the rank order: olfactory bulb > striatum ≥ hippocampus > brain stem > cerebellum > frontal cortex [16]. Evidently, after intranasal administration, silicon dioxide nanoparticles were able to cross the BBB and became differentially accumulated within seven days in several key brain regions, especially in olfactory bulb, striatum, and hippocampus. Because of their importance in several neurodegenerative diseases, Wu et al. further examined the effects of these nanoparticles on key parameters concerned with oxidative stress, inflammatory response(s), and neurotransmitter metabolism [16]. They noted that the striatum was more vulnerable than the hippocampus to the toxic effects of silicon dioxide nanoparticles in terms of changes in these parameters subsequent to the accumulation of such nanoparticles in the two brain regions.

Specifically, in rats exposed to silicon dioxide nanoparticles for seven consecutive days, their striatal levels of hydrogen peroxide, a by-product of reactive oxygen species (ROS) generation, and MDA, a marker and end-product of lipid peroxidation, were significantly increased while striatal level of reduced glutathione (GSH) was significantly decreased; however, striatal SOD, an important antioxidant enzyme, was unchanged [16]. By contrast, in the hippocampus of rats intranasally instilled with silicon dioxide nanoparticles for seven consecutive days, only MDA levels were increased [16]. Thus, their findings strongly suggested that intranasal exposure of adult rats to silicon dioxide nanoparticles selectively induces oxidative stress in their striatum: Wu et al. also confirmed that the nanoparticles can, and do, induce oxidative stress *in vitro* in PC12 cells, which constitute a model of dopaminergic neurons (see Table 1 and the next subsection below).

Wu et al. [16] also observed that intranasal instillation of silicon dioxide nanoparticles into adult rats for seven consecutive days resulted in differential changes in inflammatory responses in the striatum (but not in the hippocampus) of the treated rats. They detected significantly higher striatal levels of TNF- $\alpha$ , IL-1 $\beta$ , and IL6 in the treated rats: both TNF- $\alpha$  and IL-1 $\beta$  are pro-inflammatory cytokines, whose release leads to the stimulation of expression of IL-6 and IL-8. Along with the selective changes in the striatal levels of cytokines associated with inflammatory response(s) induced by intranasal exposure of rats to silicon dioxide nanoparticles for seven days, Wu et al. [16] also discerned a significant decrease (by ~25%) in striatal dopamine level in the treated rats whereas their hippocampal glutamate level was not significantly altered. Animal models revealed that dopamine depletion in the striatum is associated with movement disorders [16] that were reminiscent of that in Parkinson's disease. Consequently, their findings led Wu et al. [16] to conclude that exposure to silicon nanoparticles exerts a negative impact on the striatum and dopaminergic neurons and may pose a risk for neurodegenerative diseases. In view of the interesting observations and conclusion of Wu et al. [16], we would like to propose that accumulation and toxicity of silicon dioxide nanoparticles in the striatum may serve as a model system for parkinsonism and Parkinson's disease. Clearly, this is a research area that merits further investigation.

Despite the interesting differential changes in striatum and to a much lesser extent in the hippocampus induced by intranasal instillation of silicon dioxide nanoparticles noted by Wu et al. [16], those researchers did not detect any noticeable changes in the general behavior of the treated rats. Nevertheless, Wu et al. [16] cautioned that more extensive and specialized neurobehavioral testing is needed to clearly delineate whether or not exposure of rats *in vivo* to silicon dioxide nanoparticles definitely results in functional behavioral changes [16].

### 1.3.3 Toxicity *in vitro* of silicon dioxide nanoparticles in mammalian neural cells

**The need for cell models *in vitro* to screen cytotoxicity of nanoparticles in neural cells.** Until recently, few, if any, studies have addressed the cytotoxicity of nanoparticles in neural cells. We were the first to propose the importance of developing neural cell models *in vitro* to facilitate the high throughput screening of the putative toxicity of nanoparticles in various neural cell types [12, 17-32].

Initially we developed several types of neural cell models *in vitro* consisting of human astrocytoma U87 cells and human neuroblastoma SK-N-SH cells for high throughput screening of the putative toxicity of nanomaterials, including nanoparticles [12, 17-24]. Even though U87 and SK-N-SH cells are neurotumor cells, they are good models *in vitro* for astrocytes and neurons, respectively, because there is good evidence that the structure and functions of U87 and SK-N-SH cells closely resemble their counterparts in normal brain, [17-24, 26]. We have initiated a series of studies to systematically examine the putative cytotoxic effects of nanoparticles of metallic and non-metallic oxides in astrocytes and neurons employing U87 (astrocytes-like) and SK-N-SH (neurons-like) cells [12, 17-26]. We have also modified the “standard” cell survival (i.e., MTT) assay so that the assay can be used to assess the effects of nanoparticles on cell survival with improved accuracy by minimizing the interference by nanoparticles in the assay [22,23].

We have further developed several types of co-culture models of astrocytes and neurons employing U87 and SK-N-SH cells to facilitate mechanistic elucidation of the protection by astrocytes conferred on neurons against agents (including toxic nanoparticles) that induce neurodegeneration [20-22, 26,30].

Table 1. *In vitro* studies of nanosilica toxicity in neural cells

Silica form (Size)	Cells Used (Exposure time in hours)	Endpoints and Findings	Ref.
Colloidal SiO <sub>2</sub> -NP (25 nm)	SK-N-SH U87 (48)	<ul style="list-style-type: none"> <li>- ↓ cell survival (significant decrease at 25, 50, 100 µg/ml)</li> <li>- ↑ LDH release</li> <li>- ↑ cell survival when co-cultured with U87 cells</li> <li>- Altered cellular morphology</li> </ul>	[17,18, 20]
Mesoporous Nanomaterials MCM-41 (5-30 nm ) <ul style="list-style-type: none"> <li>• AP-T</li> <li>• MP-T</li> </ul> Spherical silica nanoparticles SiO <sub>2</sub> (5-30 nm )	SK-N-SH (24)	<ul style="list-style-type: none"> <li>- Cytotoxicity of nanoparticles MCM-41&gt;MP-T&gt;AP-T ≈ SiO<sub>2</sub> (cytotoxicity of nanoparticles in descending order of toxicity)</li> <li>- More adsorptive surface area of the particle resulted in higher toxicity</li> </ul>	[33]
Amorphous SiO <sub>2</sub> -NP (50 & 70 nm)	SK-N-SH , N2a (4)	<ul style="list-style-type: none"> <li>- Internalized nanoparticles into the cytoplasm and localized in nuclei</li> <li>- Induced aberrant clusters of protein aggregates in the nucleoplasm</li> </ul>	[35]

Table 1. *In vitro* studies of nanosilica toxicity in neural cells (cont.)

Silica form (Size)	Cells Used (Exposure time in hours)	Endpoints and Findings	Ref.
Mesoporous nanomaterials (MSNs) <ul style="list-style-type: none"> <li>•MCM-41</li> <li>•SBA-15</li> </ul> Solid-cored Silica microsphere (SMS) (300 - 350 nm)	SK-N-SH (3, 24 and 51)	<ul style="list-style-type: none"> <li>- SBA-15 inhibitory effect on cell survival at 50 and 100 µg/mL and cytotoxic at 200 µg/mL (3 hr) recovery in cell viability (27 hr and 51 hr)</li> <li>- MCM-41 toxicity during the short exposure (3 hr) recovery in cell viability ( 51 hr) except at 200 µg/mL</li> <li>- SMS not toxic except at 200 µg/mL ( 3 hr) toxic (27 hr and 51 hr) functionalization of amine group decreases toxicity</li> </ul>	[34]
Si-NP (prepared by sol gel method) (150-200 nm)	primary culture of rat microglia (24)	<ul style="list-style-type: none"> <li>- Internalization by microglia at all concentrations tested</li> <li>- Not cytotoxic and did not alter phagocytosis</li> <li>- ↑ in intracellular production of ROS and RNS</li> <li>- ↑ IL-1β level</li> <li>- ↓ TNF-α gene expression</li> <li>- ↑ COX-2 gene expression at 36.4 µg/ml</li> </ul>	[36]

Table 1. *In vitro* studies of nanosilica toxicity in neural cells (cont.)

Silica form (Size)	Cells Used (Exposure time in hours)	Endpoints and Findings	Ref.
Colloidal SiO <sub>2</sub> -NP (25 nm)	U87 (48)	<ul style="list-style-type: none"> <li>- ↓ cell survival (significant decrease at 25, 50, 100 µg/ml)</li> <li>- ↑ citrate synthase and malate dehydrogenase activities</li> <li>- ↓ expression of cytochrome C oxidase subunit II, ↓ expression of NADH dehydrogenase subunit 6 and ↓ expression of phosphorylated ERK</li> <li>- Cells became more enlarged and swollen</li> </ul>	[12]
SiO <sub>2</sub> -NP 15 nm (92 nm with FBS protein)	PC12 (24)	<ul style="list-style-type: none"> <li>- ↓ cell survival, ↑ LDH release,</li> <li>- Oxidative stress               <ul style="list-style-type: none"> <li>↑ ROS production, ↑ MDA, ↓ GSH and ↓ SOD activity</li> </ul> </li> <li>- Rounded shaped and reduced length of extended neurites</li> <li>- Apoptosis               <ul style="list-style-type: none"> <li>double stained with PI- and FITC-labeled annexin V</li> <li>↓ the expression of bcl2, ↑ the expression of p53, p21, p-p53, Gadd45 and bax</li> </ul> </li> <li>- Cell cycle arrest at 100 and 200 µg/ml</li> </ul>	[16]

Table 1. *In vitro* studies of nanosilica toxicity in neural cells (cont.)

Silica form (Size)	Cells Used (Exposure time in hours)	Endpoints and Findings	Ref.
Colloidal SiO <sub>2</sub> -NP (25 nm)	Schwann cells (R3), DRG neurons (50B11) (36 and 48)	<ul style="list-style-type: none"> <li>- ↓ cell survival DRG neurons &lt; Schwann cells</li> <li>- Internalized nanoparticles (Schwann cells and DRG neurons)</li> <li>- Enlarged and swollen nuclei (Schwann cells and DRG neurons)</li> <li>- Oxidative stress Schwann cells ↓ GSH and ↓ Mn-SOD (R3) DRG neurons Multi-phasic effect on GSH and ↑ Mn-SOD</li> <li>- ↓ expression of NADH dehydrogenase subunit 6 and ↑ expression of succinate dehydrogenase fc subunit</li> <li>- ↓ expression of p-ERK (Schwann cells and DRG neurons)</li> <li>- Did not change the expression of ERK</li> </ul>	[28,31, 37]

Abbreviations: COX-2, cyclooxygenase 2; DRG, dorsal root ganglion; FITC, fluorescein isothiocyanate; GSH, reduced glutathione; IL, interleukin; LDH, lactate dehydrogenase; MDA, malondialdehyde (end product of lipid peroxidation); N2a, mouse neuroblastoma cell line; NMR, nuclear magnetic resonance; PC12, pheochromocytoma cells; PI, propidium iodide; Ref., references; RNS, reactive nitrogen species; ROS, reactive oxygen species; SEM, scanning electron microscopy; SiO<sub>2</sub>-NP, silicon dioxide nanoparticles; SK-N-SH, human neuroblastoma cell line; TEM, transmission electron microscopy; TNF, tumor necrosis factor; U87, human astrocytoma cell line; XRD, X-ray diffraction.



Because the putative cytotoxic effects of nanoparticles of metallic and non-metallic oxides in neural cells of the peripheral nervous system (PNS) are unknown, we have recently developed cell models *in vitro* consisting of Schwann cells and dorsal root ganglion (DRG) neurons to facilitate the systematic investigation of the effects of such nanoparticles on the PNS [27-29, 31,32]. The results of our recent and ongoing studies clearly demonstrate that our cell models *in vitro* constitute excellent cell culture models for elucidating pathophysiological mechanisms of agents (including nanoparticles) that can induce peripheral neuropathy [27-29,31,32].

The results of our previous and ongoing studies clearly demonstrate that the cell models we have developed allow the systematic and mechanistic investigations of putative cytotoxicity of nanoparticles of metallic and non-metallic oxides in neural cells derived from both the central and the peripheral nervous systems [12, 17-32]. Furthermore, they also strongly suggest that our models can be applied to screen the cytotoxicity of nanomaterials other than nanoparticles of metallic and non-metallic oxides in neural cells of central and peripheral nervous systems [12, 17-32]. We will discuss in the next subsection the findings of our studies and compare them with those of other researchers.

**Cellular and molecular mechanisms underlying the cytotoxicity *in vitro* of silicon dioxide nanoparticles in neural cells.** The results of the studies to date concerning the cytotoxicity *in vitro* of silicon dioxide nanoparticles in neural cells are summarized and compared as shown in Table 1.

We were the first to initiate a series of studies to systematically investigate the cytotoxic mechanisms of silicon dioxide nanoparticles on mammalian (including human) neural cells [12,17,18,20,22]. Our initial finding that silicon dioxide nanoparticles induced cytotoxicity on human neuroblastoma SK-N-SH (neurons-like) and human astrocytoma U87 (astrocytes-like) cells by lowering their survival [17] prompted us to further elucidate the mechanisms underlying the cytotoxicity of silicon dioxide nanoparticles in neurals cells [12,18]. Necrosis appeared to be one cytotoxic effect induced by the nanoparticles in both SK-N-SH (neurons-like) and U87 (astrocytes-like) cells as indicated by the increases in lactate dehydrogenase (LDH) release from the cells into the surrounding medium (Table 1) [17,18]. The dose-related changes in cellular morphology in U87 and SK-N-SH cells induced by silicon dioxide nanoparticles paralleled the dose-related decreases in the survival of those cells induced by the nanoparticles [17,18]. Interestingly, when SK-N-SH (neurons-like) cells were co-cultured on a monolayer of U87 (astrocytes-like) cells and exposed to silicon dioxide nanoparticles, the survival of both cell types was improved compared to the survival of both cell types when they were cultured alone as monotypic culture and exposed to silicon dioxide nanoparticles (Table 1) [20].

We investigated further the cytotoxic mechanisms underlying the dose-related decreases in survival of U87 cells induced by silicon dioxide nanoparticles [12]. We found the activities of citrate synthase and malate dehydrogenase in nanoparticles-treated U87 cells were increased, possibly due to an energetic compensation in surviving cells (Table 1) [12]. By contrast, the expression of mitochondrial DNA-encoded cytochrome C oxidase subunit II and NADH dehydrogenase subunit 6 and the cell signaling protein phosphorylated ERK (p-ERK) was altered in the nanoparticles-treated U87 cells (Table 1) [12]. Thus, we were the first to report on the effects of silicon dioxide nanoparticles on expression of mitochondrial DNA-encoded protein and on expression of cell survival signaling protein (i.e., ERK) [12]. Our findings suggest that silicon dioxide nanoparticles induces disruption of mitochondrial DNA-encoded protein expression, leading to decreased mitochondrial energy production in U87 cells; the nanoparticles also induced decreases in cell survival/proliferation signaling in those cells [12].

Different types of nanosilica particles exert dissimilar cytotoxic effects on neural cells. Di Pasqua et al. [33] and Tao et al. [34] demonstrated that mesoporous silica (MCM 41) nanoparticles are more toxic to SK-N-SH cells compared to spherical silica (including silicon dioxide) nanoparticles (Table 1). They also found that functional groups on silica nanoparticles play major roles in determining the toxicity of silica nanoparticles: for example, grafting aminopropyl group(s) on mesoporous silica nanoparticles decreased the cytotoxicity of MCM-41 in SK-N-SH cells [33]. Thus, it is imperative to consider whether or not and how the surface of the nanoparticles may influence their properties while selecting nanosilica for biomedical and biotechnological applications.

In elegant studies *in vitro*, Chen and von Mikecz [35] demonstrated that amorphous silica nanoparticles (50 & 70 nm) entered several cell types including neuronal cells (i.e., N2a and SK-N-SH cells), translocated into their nuclei, and altered nuclear functions in a matter of hours (Table 1) [35]. However, silica particles of sizes between 200 nm and 5  $\mu$ m neither penetrated into the nuclei nor modified nuclear function and architecture of the cells [35]. Furthermore, this group noted that once they penetrated into the nuclei of the cells, silica nanoparticles with an average diameter of 50 nm induced the formation of aberrant protein aggregates in their nuclei [35]. The protein aggregates, whose formation was induced by the silica nanoparticles, contained essential components of nuclear protein machines such as coactivators of transcription, unmutated polyQ proteins, and members of the ubiquitin proteasome systems (UPS) [35]. Their interesting observations led von Mikecz and co-workers to propose that the components of the UPS are recruited to silica-nanoparticles-induced nuclear inclusions to break down aggregated proteins [35]. Moreover, even when silica nanoparticles did not alter cell viability or enhance cell death, silica nanoparticles induced repression of gene expression, ultimately leading to decreased cellular replication and irreversible inhibition of cell proliferation [35].

This group of researchers therefore concluded that through the induction of intranuclear protein aggregation that contains proteins with polyQ stretches, silica nanoparticles trigger a subnuclear pathology that closely mimics molecular events characteristic of formation of insoluble protein inclusions in neurodegenerative aggregation diseases [35]. Chen and von Mikecz further advocated that “silica nanoparticles have emerged as excellent tools for proof-of-principle studies, in this case, establishment of cell-based models for degenerative protein aggregation diseases” [35].

Silicon dioxide nanoparticles can induce alterations in mitochondrial oxidative metabolism and induce oxidative stress. For example, silicon dioxide nanoparticles induced cell death in U87 (astrocytes-like) cells by disturbing their mitochondrial function (Table 1) [12]. Wu et al. [16] observed that treatment of PC12 cells (a model of dopaminergic neurons *in vitro*) with silicon dioxide nanoparticles led to increased LDH release, enhanced ROS production, increased MDA production but decreased levels of GSH and SOD, and ultimately decreased cell survival [16]. Additionally, their mechanistic studies with PC12 cells also revealed that at doses higher than 50 µg/mL, the number of apoptotic PC12 cells increased markedly [16]. They attributed this apoptotic effect induced by silicon dioxide nanoparticles to the G2/M cell cycle arrest in conjunction with increased protein expression of p53, phospho-p53 (p-p53), p21, Gadd45, and bax, but decreased protein expression of bcl-2 because both p21 and Gadd45 are proteins that are down-stream from p53 in regulating cell cycle whereas the increase in bax/bcl-2 ratio favors apoptosis [16]. Along with those observations, they also found that silicon dioxide nanoparticles induced decreases in dopamine levels and expression of tyrosine hydroxylase (TH, a rate-limiting enzyme in dopamine synthesis) [16]. (However, the authors erroneously stated that silicon dioxide nanoparticles upregulated the expression of TH in dose-dependent manner [see Ref. 16, p. 4485].) Interestingly, and relevant to this discussion of the mechanistic actions of silicon dioxide nanoparticles on neural cells, the findings of Wu et al. in PC12 cells *in vitro* (i.e., enhanced ROS production, increased MDA production but decreased levels of GSH and dopamine) confirmed what they observed in the striatum of rats after intranasal instillation of silicon dioxide nanoparticles into those rats *in vivo* [16]. Consequently, their parallel studies *in vivo* and *in vitro* strongly suggest that many – if not most – of the mechanisms underlying the cytotoxicity of silicon dioxide nanoparticles in neural cells *in vitro* may also occur in the cytotoxicity of silicon dioxide nanoparticles in neural cells *in vivo* [16].

The effects of silica nanoparticles in primary cultures of rat microglia *in vitro* [36] appear to somewhat differ from the effects of these nanoparticles in PC12 cells *in vitro* [16] and in the rat striatum after intranasal instillation of the nanoparticles *in vivo* [16]. Choi et al. [36] were the first to observe that over a 24-hour period, exposure of rat microglial cells in primary culture *in vitro* to silica nanoparticles resulted in the entry of nanoparticles into those cells via endocytosis and other

nanoparticle uptake mechanisms [36]. Similar to the effects of silicon dioxide nanoparticles in PC12 cells *in vitro* [36] and to the same effects in the rat striatum after intranasal instillation of the nanoparticles *in vivo* [16], Choi et al. also noted that these nanoparticles induce oxidative stress in rat microglial cells *in vitro* by enhancing their production of ROS and reactive nitrogen species (RNS) and altering their expression of proinflammatory genes (i.e., increase in COX-2 but decrease in tumor necrosis factor- $\alpha$  expression) (Table 1) [36]. However, even at the highest treatment concentration of 40,000 nanoparticles per  $\mu\text{L}$  (i.e., 7.28  $\mu\text{g/mL}$ ) for 24 hours, silica nanoparticles did not significantly lower the survival of microglial cells *in vitro* [36]. Nevertheless, Choi et al. [36] did suggest that continuous production of ROS by microglia induced by the silica nanoparticles could induce deleterious effects on neurons in their vicinity and the dysfunction induced by the nanoparticles may not allow the microglia to sustain neuronal health.

Because the putative cytotoxic effects of silicon dioxide nanoparticles in neural cells in the peripheral nervous system (PNS) are largely unknown, we have employed our *in vitro* model of Schwann cells to systematically investigate the putative cytotoxicity of silicon dioxide nanoparticles on neural cells derived from the PNS [25,27,28,31,37]. We are the first to report on the effects of silicon dioxide nanoparticles on neural cells in the PNS [28,37]. Results of our ongoing studies have demonstrated that silicon dioxide nanoparticles exerted cytotoxic effect on Schwann cells by lowering their survival (Table 1) [28,37]. Light microscopic examination revealed that treatment of Schwann cells with the nanoparticles induced dose-related changes in cellular morphology, consistent with the nanoparticles-induced progressive decrease in cell viability and increase in uptake of nanoparticles. Furthermore, employing flow cytometry, we noted the cytotoxicity of silicon dioxide nanoparticles could be attributed, at least in part, to the uptake of the nanoparticles by Schwann cells [28,37]. Treatment with silicon dioxide nanoparticles also induced increased LDH release, decreased glutathione level, and altered morphology and expression of Mn-superoxide dismutase, NADH dehydrogenase subunit 6, and succinate dehydrogenase in Schwann cells [28,37]. Thus, our findings are compatible with the observation that silicon dioxide nanoparticles induce decreases in survival of neural cells derived from the central nervous system and the decreases in cell survival can be attributed, at least in part, to the nanoparticles-induced oxidative stress [12,16,28,36,37].

The effects of silicon dioxide nanoparticles on dorsal root ganglion (DRG) neurons, an *in vitro* model of DRG neurons in PNS *in vivo* [27-29, 31,32], only show a few similarities to those noted in the Schwann cells *in vitro* (Table 1). Treatment of silicon dioxide nanoparticles altered the morphology of DRG neurons: their nuclei were swollen and their processes decreased in number and they became rounded whereas untreated DRG neurons were spindle-shaped [28-37]. Treatment of DRG neurons with silicon dioxide nanoparticles did not induce any necrotic cell damage or necrotic cell death at concentrations from 0.1 to 150

µg/mL but induced oxidative stress by decreasing glutathione levels (Table 1) [28,37]. Nevertheless, when we treated DRG neurons with the nanoparticles at the highest concentration employed (i.e., 200 µg/mL), they showed significant increases in LDH release into the surrounding medium, suggesting that the nanoparticles did induce necrotic damage and/or cell death in DRG neurons at that concentration [28,37]. Thus, the results of our current and ongoing studies strongly suggest that silicon dioxide nanoparticles induce differential effects on neural cells in the PNS.

#### 1.4 PATHOPHYSIOLOGICAL IMPLICATIONS OF TOXICITY OF SILICON DIOXIDE NANOPARTICLES IN MAMMALIAN NEURAL CELLS

Even though, to date, the literature on the effects of silicon dioxide nanoparticles on mammalian neural cells is rather limited, the results of published and ongoing studies appear to coalesce into a recognizable pattern (see Tables 1) which allows us to draw some tentative generalizations regarding pathophysiological implications of toxicity of silicon dioxide nanoparticles in mammalian neural cells. However, in this review, we can only very briefly discuss four such generalizations.

(i) Because silicon dioxide nanoparticles can readily cross the blood-brain barrier (BBB) (also see section 1.2 above), once the nanoparticles penetrate into the central (or for that matter, the peripheral) nervous system, they can directly influence neural cells therein. Consequently, whether the effects of silicon dioxide nanoparticles on neural cells are deleterious critically depends on the extent of the accumulation of the nanoparticles in the nervous tissue.

(ii) Evidence is accumulating that silicon dioxide nanoparticles appear to exert differential effects on neural cells. It is well recognized that glial cells protect neurons from a variety of pathophysiological assaults [26,30]. Therefore, it is conceivable that in addition to the direct cytotoxic effect on neurons exerted by silicon dioxide nanoparticles, the nanoparticles can exert indirect toxic effects on neurons through their actions on glial cells, ultimately compromising the ability of glial cells to maintain neuronal health and well being.

(iii) As alluded to above (see subsections 1.3.2 and 1.3.3 above), silicon and aluminum were found to be co-localized in the cores of senile plaques in the cortex of Alzheimer's disease (AD) patients [14] and accumulated silicon and aluminum were also found in lipofuscin granules in patients who died of AD [15]. Moreover, when directly introduced into the brains of rats and mice *in vivo*, silica nanoparticles induced inflammatory responses in astrocytes and degeneration of axons and axon terminals in the vicinity of the astrocytes [13]. These early observations [13-15], together with more recent reports (see Table 1) of toxic effects of silicon dioxide nanoparticles on mammalian neural cells *in vivo* and *in vitro*, strongly suggest that the neurotoxicity of silicon dioxide

nanoparticles may assume pathophysiological and perhaps even pathogenetic importance in neurodegenerative diseases such as Alzheimer's disease.

(iv) We have mentioned earlier that their important findings led Wu et al. [16] to conclude exposure to silicon dioxide nanoparticles exerts negative health impact on the striatum in general and on dopaminergic neurons in particular and may therefore pose a risk for neurodegenerative diseases. Our review of the literature on toxicity of silicon dioxide nanoparticles in mammalian neural cells has also prompted us to propose that accumulation and toxicity of silicon dioxide nanoparticles in the striatum may serve as a model system for parkinsonism and Parkinson's disease. Furthermore, Chen, von Mikecz and their associates [35] elegantly demonstrated that upon entering neural cells, silicon dioxide nanoparticles can enter their nuclei and induce the formation of aberrant protein aggregates therein. Because such aberrant protein aggregates are highly reminiscent of those noted in the brain in neurodegenerative diseases, Chen and von Mikecz [35] therefore proposed that "silica nanoparticles have emerged as excellent tools for proof-of-principle studies, in this case, establishment of cell-based models for degenerative protein aggregation diseases."

## 1.5 CONCLUSIONS AND PROSPECTS FOR FUTURE RESEARCH

In this concise review, we have summarized and discussed the literature on the toxicity of silicon dioxide nanoparticles on mammalian neural cells *in vivo* and *in vitro*. Despite the fact that, to date, the studies published in this literature are rather limited in number, a clear and consistent "picture" is slowly emerging regarding the mechanisms underlying the toxicity of silicon dioxide nanoparticles in neural cells. As we have emphasized earlier, one major reason why this literature is scant is that until recently, there was a lack of suitable cell models *in vitro* for high throughput screening of the cytotoxicity of silicon dioxide nanoparticles — and for the matter the cytotoxicity of nanoparticles in general — in mammalian neural cells. We were the first to develop neural cell models *in vitro* consisting of various neural cell types derived from both the central and the peripheral nervous systems so as to allow the high throughput screening of the cytotoxicity of silicon dioxide nanoparticles in mammalian neural cells [12, 17-32].

Based on a critical review of the literature as well as current and ongoing studies, we can tentatively arrive at the following conclusions. (i) Far from being harmless, silicon dioxide nanoparticles can and do induce differential cytotoxicity on mammalian neural cells. (ii) Some of the recognized mechanisms underlying the toxicity of silicon dioxide nanoparticles in neural cells include, but are not limited to, oxidative stress, inflammatory responses, necrotic damage and cell death, apoptosis, formation of aberrant nuclear protein aggregates and

altered mitochondrial metabolism. (iii) Perhaps the most interesting and also intriguing conclusion is that silicon dioxide nanoparticles can serve as versatile tools for elucidating pathophysiological and molecular mechanisms underlying neurodegenerative diseases such as Alzheimer's disease and Parkinson's disease. Moreover, our current and ongoing studies also strongly suggest that these nanoparticles can also be fruitfully exploited to elucidate mechanisms underlying peripheral neuropathy.

As evident from this concise review, there are still much to be discovered concerning the toxicity of silicon dioxide nanoparticles in mammalian neural cells. The availability of various models *in vitro* consisting of various neural cell types derived from both the central as well as the peripheral nervous system greatly facilitate both the high throughput screening of the cytotoxicity of silicon dioxide nanoparticles and systematic investigation of the underlying cellular and molecular mechanisms. Clearly, these are interesting and exciting areas that merit further and systematic investigation.

## 1.6 STATEMENT OF DISCLOSURE/CONFLICTS OF INTEREST

The authors declare that they have no conflict of interest and have no affiliations or financial involvement with any organization or entity discussed in this chapter. This includes employment, consultancies, honoraria, grants, stock ownership or options, expert testimony, patents (received or pending) or royalties. No writing assistance was utilized in the production of this manuscript and the authors have received no payment for preparation of this chapter. The findings and conclusions here reflect the current views of the authors. They should not be attributed, in whole or in part, to the organizations with which they are affiliated, nor should they be considered as expressing an opinion with regard to the merits of any particular company or product discussed herein. Nothing contained herein is to be considered as the rendering of legal advice.

## 1.7 AUTHOR BIOGRAPHIES

**James C.K. Lai** is Professor of Pharmacology and Toxicology, Department of Biomedical and Pharmaceutical Sciences, and Associate Director, Biomedical Research Institute, Idaho State University, Pocatello, Idaho. He received his B.Sc. (Honors.) degree in Microbiology from Cardiff University, Wales in 1970, his M.Sc. degree in Neurocommunications from University of Birmingham, England in 1971, and his Ph.D. degree in Biochemistry from University of London, England in 1975. Prior to joining to Idaho State University in 1991, Dr. Lai had

held faculty appointments at Albert Einstein College of Medicine, Bronx, NY and Cornell Medical College, New York, NY. From 1985 to 1990, he was an Editorial Board Member of *Neurotoxicology*; from 1993 to 1996, he was the Associate Editor of *Pharmacy Case Review*; from 1990 to 2010, he was an Editorial Board Member of *Metabolic Brain Disease*; and from 1995 to 2008, he was an Editorial Board Member of *Neurochemical Research*. His long-standing research interests include Neuroscience, Neurotoxicology, and Regulation of Brain Metabolism. In the last decade, he has also worked on Nanoscience, Nanopharmacology, and Nanotoxicology as well as Cancer Pharmacology and Anti-Cancer Drug Discovery. He has published over 190 journal articles, reviews, and book chapters in these and related areas.

**Ashvin R. Jaiswal** is currently engaged in contract research in biomedical sciences in the Boston area. He received a Bachelor of Pharmacy degree (First Division) from the Amravanti University, Amravanti, India in 2004 and a M.S. degree in Pharmaceutical Sciences in 2011 from Idaho State University College of Pharmacy. He has developed cell culture models *in vitro* of the peripheral nervous system consisting of Schwann cells and dorsal root ganglion (DRG) neurons and employed them to investigate cytotoxicity of silicone dioxide nanoparticles in neural cells; he has also employed the cell models to investigate some of the pathophysiological mechanisms underlying peripheral neuropathy, especially diabetic neuropathy. His publications include 8 journal articles, a review chapter, and 10 abstracts.

**Maria B. Lai** is presently a Ph.D. student in the Department of Molecular, Cellular, and Developmental Biology at the University of Colorado at Boulder. She received her B.S. degree in Microbiology in 2009 from Idaho State University and her M.S. degree in Pharmaceutical Sciences in 2011 from Idaho State University College of Pharmacy. From 2005 to 2011 she worked on several research projects including, but not limited to, cytotoxicity of manganese in tumor cells, toxic mechanisms of nanoparticles of metallic and non-metallic oxides in neural and non-neural cancer cells, effects of statins on hepatocellular carcinoma and pancreatic cancer cells, and anti-cancer drug discovery. Her publications in these and related areas include 13 journal papers, 1 book chapter, and 41 abstracts.

**Sirisha Jandhyam** is currently looking for research opportunities to continue her career. She received her Bachelor of Pharmacy degree in 2003 from Andhra University, India and her M.S. degree in Pharmaceutical Sciences in 2008 from Idaho State University College of Pharmacy. Her M.S. thesis research was on the cytotoxicity of metallic and non-metallic oxide nanoparticles. She also has additional research experience working on cancer pharmacology. Her publications include 11 journal papers, 1 book chapter, and 13 abstracts.

**Solomon W. Leung** is Professor in Department of Civil and Environmental Engineering, School of Engineering, College of Science and Engineering, Idaho



State University and the coordinator of Environmental Engineering program at Idaho State University. He received his Ph.D. in Civil and Environmental Engineering in 1989 from University of Iowa; he also has a M.S. in Chemical Engineering and a B.A. in Chemistry from the University of Iowa. His research interests include physicochemical treatment processes, particularly chemical oxidations applied to the treatment of soils and groundwater, disinfection and by-products generation in water and wastewater, environmental systems modeling, environmental risk assessment, biotechnology, and nanotechnology. In the last 10 years, Dr. Leung has researched extensively in biomedical applications of nanotechnology, biosensors, and nanotoxicology. He has published 90 peer-reviewed journal articles, proceedings and book chapters, and given more than 140 presentations in regional, national, and international conferences. Dr. Leung is also a registered Professional Engineer (P.E.) in the State of Idaho.

**Alok Bhushan** is Professor in Department of Biomedical and Pharmaceutical Sciences, College of Pharmacy at Idaho State University in Pocatello. Dr. Bhushan received his B. Sc. (Honors) and M. Sc. degree in chemistry from University of Delhi, India. He received his Ph.D. in Biochemistry from Punjab Agricultural University, India. He was a post-doctoral fellow at Johns Hopkins School of Medicine, Medical University of South Carolina and University of Vermont. He has held faculty positions at Department of Pharmacology, School of Medicine, University of Vermont and Department of Biomedical and Pharmaceutical Sciences, College of Pharmacy, Idaho State University. He has over 10 years of experience in Pharmacy education. He successfully completed the Academic Fellows Leadership Program (AFLP) at AACCP. He has been trained to serve as site evaluator for accreditation by ACPE and has had the opportunity to be a site evaluator. Dr. Bhushan's areas of interest include cancer pharmacology and signal transduction focused on treatment and prevention. His research areas are 1) understanding mechanisms to block glioblastoma invasion in brain and synthesis of novel agents that target the process of invasion; 2) understanding the mechanism of the role of isoflavones in preventing breast and oral cancer; 3) pharmacology of nanomaterials; 4) natural drug discovery for prevention and treatment of cancer; and 5) characterization and cloning of a novel reduced folate transporter which plays role in methotrexate and cisplatin resistance. Dr. Bhushan has over 75 journal articles and reviews to his credit. He has served as major advisor to several Ph.D. and Master's students at Idaho State University.

### Acknowledgment

Our studies were supported by a US Army Medical Research and Material Command Project Grant (Contract W81XWH-07-2-0078).

## References

1. US Environmental Protection Agency. Draft nanomaterial research strategy. Available at: ([http://epa.gov/ncer/nano/publications/nano\\_strategy\\_012408.pdf](http://epa.gov/ncer/nano/publications/nano_strategy_012408.pdf)). [Accessed August 3, 2010.]
2. Martin, K.R. (2007). The chemistry of silica and its potential health benefits. *Journal of Nutrition and Health in Aging* **11**:94-97.
3. Jonat, S., Hasenzahl, S., Gray, A., and Schmidt, P.C. (2005). Influence of compacted hydrophobic and hydrophilic colloidal silicon dioxide on tableting properties of pharmaceutical excipients. *Drug Development in Industrial Pharmacy* **31**:687-696.
4. Sayes, C.M., Reed, K.L., and Warheit, D.B. (2007). Assessing toxicity of fine and nanoparticles: comparing in vitro measurements to in vivo pulmonary toxicity profiles. *Toxicological Science* **97**:163-180.
5. Adams, L.K., Lyon, D.Y., McIntoch, A., and Alvarez, P.J. (2006). Comparative toxicity of nano-scale TiO<sub>2</sub>, SiO<sub>2</sub>, and ZnO water suspensions. *Water Science and Technology* **54**: 327-334.
6. Lewinski, N., Colvin, V., and Drezek, R. (2008). Cytotoxicity of nanoparticles. *small* **4**(1):26-49.
7. Barik, T.K., Sahu, B., and Swain, V. (2008). Nanosilica – from medicine to pest control. *Parasitology Research* **103**:253-258.
8. Napierska, D., Thomassen, L.C.J., Lison, D., Martens, J.A., and Hoet, P.H. (2010). The nanosilica hazard: another variable entity. *Particle & Fibre Toxicology* **7**:39-71.
9. Kim, J.S., Yoon, T.-J., Yu, K.N., Kim, B.G., Park, S.J., et al. (2006). Toxicity and tissue distribution of magnetic nanoparticles in mice. *Toxicological Science* **89**(1):338-347.
10. Sharma, H.S., Hussain, S., Schlager, J., Ali, S.F., and Sharma, A. (2010). Influence of nanoparticles on blood-brain barrier permeability and brain edema formation in rats. *Acta Neurochirurgica Supplement* **106**:359-364.
11. Zang, Y., Calon, F., Zhu, C. Boado, R.J., and Pardridge, W.M. (2003). Intravenous nonviral gene therapy causes normalization of striatal tyrosine hydroxylase and reversal of motor impairment in experimental parkinsonism. *Human Gene Therapy* **14**(1):1-12.
12. Lai, J.C.K., Ananthakrishnan, G., Jandhyam, S., Dukhande, V.V., Bhushan, A., et al. (2010). Treatment of human astrocytoma U87 cells with silicon dioxide nanoparticles lowers their survival and alters their expression of mitochondrial and cell signaling proteins. *International Journal of Nanomedicine* **5**:715-723.
13. Rees, S., and Cragg, B. (1983). Is silica involved in neuritic (senile) plaque formation? *Acta Neuropathologica* **59**:31-40.
14. Candy, J.M., Oakley, A.E., Klinowski, J., Carpenter, T.A., Perry, R.H., et al. (1986). Aluminosilicates and senile plaque formation in Alzheimer's disease. *Lancet* **I**(8477):354-357.
15. Takutake, S., and Oyanagi, S. (1995). Accumulation of aluminium and silicon in lipofuscin granules. *Gerontology* **41 Suppl. 2**:131-144.
16. Wu, J., Wang, C., Sun, J., and Xue, Y. (2011). Neurotoxicity of silica nanoparticles: brain localization and dopaminergic neurons damage pathways. *ACS Nano* **5**(6):4476-4489.

17. Lai, J.C.K., Lai, M.B., Edgley, K.L., Bhushan, A., Dukhande, V.V., et al. (2007). Silicon dioxide nanoparticles can exert cytotoxic effects on neural cells. *Technical Proceedings of 2007 Nanotechnology Conference and Trade Show, Volume 2, Chapter 8: Bio Materials and Tissues*:741-743.
18. Jandhyam, S., Lai, M.B., Dukhande, V.V., Bhushan, A., Daniels, C.K., et al. (2008). Silicon dioxide nanoparticles exert dissimilar cytotoxic effects on mammalian cell types. *Technical Proceedings of 2008 Nanotechnology Conference and Trade Show, Volume 2, Chapter 2: Environment, Health and Toxicology*:126-129.
19. Lai, M.B., Jandhyam, S., Dukhande, V.V., Bhushan, A., Daniels, C.K., et al. (2008). Differential cytotoxicity of metallic oxide nanoparticles in mammalian cells. *Technical Proceedings of 2008 Nanotechnology Conference and Trade Show, Volume 2, Chapter 2: Environment, Health and Toxicology*:130-133.
20. Wang, Y.-H., Jandhyam, S., Dukhande, V.V., Gao, W.J., Gu, H.-Y., et al. (2008). A co-culture model for nanotoxicity and tissue engineering studies. *Technical Proceedings of 2008 Nanotechnology Conference and Trade Show, Volume 2, Chapter 2: Environment, Health and Toxicology*:164-167.
21. Gao, W.J., Dukhande, V.V., Jandhyam, S., Wang, Y.-H., Gu, H.-Y., et al. (2008). A non-contact culture model for investigating cell signaling and nanotoxicity. *Techn. Proc. 2008 Nanotechnology Conference and Trade Show, Volume 2, Chapter 2: Environment, Health and Toxicology*:172-175.
22. Lai, J.C.K., Jandhyam, S., Lai, M.B., Dukhande, V.V., Bhushan, A., et al. (2008). Cytotoxicity of metallic oxide nanoparticles: new insights into methodological problems and advances in elucidation of underlying mechanisms. *Proceedings of 12<sup>th</sup> WMSCI 2008, Orlando, FL, USA, Volume II*:10-15.
23. Lai, J.C.K., Lai, M.B., Jandhyam, S., Dukhande, V.V., Bhushan, A., et al. (2008). Exposure to titanium dioxide and other metallic oxide nanoparticles induces cytotoxicity on human neural cells and fibroblasts. *International Journal of Nanomedicine* **3**(4):533-545.
24. Lai, M.B., Jandhyam, S., Dukhande, V.V., Bhushan, A., Daniels, C.K., et al. (2009). Cytotoxicity of metallic oxide nanoparticles in human neural and non-neural cells. *Technical Proceedings of 2009 Nanotechnology Conference and Trade Show, Volume 2, Chapter 3: Nano Medicine*:135-138.
25. Jaiswal, A., Wong, Y.Y.W., Bhushan, A., Daniels, C.K., and Lai, J.C.K. (2010). A noncontact co-culture model of peripheral neural cells for nanotoxicity, tissue engineering and pathophysiological studies. *Technical Proceedings of 2010 NSTI Nanotechnology Conference and Expo – Nanotech 2010, Vol. 3 Chapter 8: Environment, Health and Safety*:527-531.
26. Wong, Y.Y.W., Jaiswal, A.R., Dukhande, V.V., Bhushan, A., Leung, S.W., et al. (2010). Elucidation of neuroprotective properties of astrocytoma (astrocytes-like) cells in neural cell culture models *in vitro*: applications in tissue engineering and nanotoxicology. *Technical Proceedings of 2010 NSTI Nanotechnology Conference and Expo – Nanotech 2010, Vol. 3 Chapter 8: Environment, Health and Safety*:561-564.
27. Jaiswal, A.R., Bhushan, A., Daniels, C.K., and Lai, J.C.K. (2010). A cell culture model for diabetic neuropathy studies. *Journal of Idaho Academy of Science* **46**(1):58-63.
28. Jaiswal, A.R., Lu, S., Pfau, J., Wong, Y.Y.W., Bhushan, A., et al. (2011). Effects of silicon dioxide nanoparticles on peripheral nervous system neural cell models. *Technical Proceedings of 2011 NSTI Nanotechnology Conference and Expo – Nanotech 2011, Vol. 3, Chapter 7: Environment, Health and Safety*:541-544.

29. Lu, S., Jaiswal, A.R., Wong, Y.Y.W., Bhushan, A., Leung, S.W., et al. (2011). Differential cytotoxic effects of titanium oxide nanoparticles on peripheral nervous system neural cells. *Technical Proceedings of 2011 NSTI Nanotechnology Conference and Expo – Nanotech 2011, Vol. 3, Chapter 7: Environment, Health and Safety*:533–536.
30. Wong, Y.Y.W., Jaiswal, A.R., Dukhande, V.V., Bhushan, A., Leung, S.W., et al. (2011). New *in vitro* strategy of astrocytoma (astrocytes-like) cells treated with pioglitazone (PPAR gamma agonist) offers neuroprotection against nanoparticle-induced cytotoxicity. *Technical Proceedings of 2011 NSTI Nanotechnology Conference and Expo – Nanotech 2011, Vol. 3, Chapter 6: Nano Medical Sciences and Neurology*:455–458.
31. Jain, A., Jaiswal, A.R., Lu, S., Wong, Y.Y.W., Bhushan, A., et al. (2011). Molecular effects of silicon dioxide nanoparticles on cell survival signaling of dorsal root ganglion (DRG) neurons and Schwann cells. *Technical Proceedings of 2011 NSTI Nanotechnology Conference and Expo – Nanotech 2011, Vol. 3, Chapter 7: Environment, Health and Safety*:545–548.
32. Lai, J.C.K., Gao, W., and Leung, S.W. (2011). Effects of chitosan and nanoparticles on survival of Schwann cells and dorsal root ganglion neurons. *Technical Proceedings of 2011 NSTI Nanotechnology Conference and Expo – Nanotech 2011, Vol. 3, Chapter 6: Nano Medical Sciences and Neurology*:440–442.
33. Di Pasqua, A.J., Sharma, K.K., Shi, Y.L., Toms, B.B., Ouellette, W., et al. (2008). Cytotoxicity of mesoporous silica nanomaterials, *Journal of Inorganic Biochemistry* **102**(7):1416–1423.
34. Tao, Z., Toms, B.B., Goodisman, J., and Asefa, T. (2009). Mesoporosity and functional group dependent endocytosis and cytotoxicity of silica nanomaterials. *Chemical Research and Toxicology* **22**:1869–1880.
35. Chen, M., and von Mikecz, A. (2009). Nanoparticle-induced cell culture models for degenerative protein aggregation diseases. *Inhalation Toxicology* **21**(S1):110–114.
36. Choi, J., Zheng, Q., Katz, H.E., and Guilarte, T.R. (2010). Silica-based nanoparticle uptake and cellular response by primary microglia. *Environmental Health Perspectives* **118**(5):589–595.
37. Jaiswal, A.R. (2011). Cytotoxicity of silicon dioxide nanoparticles in peripheral nervous system neural cell. M.S. Thesis, Idaho State University, Pocatello, ID.

## Metadata of the chapter that will be visualized online

Chapter Title	Mn and Its Interrelation with Other Metal Ions in Health and Disease		
Copyright Year	2012		
Copyright Holder	Springer Science+Business Media, LLC		
Corresponding Author	Family Name		
	Particle		
	Given Name		
	Suffix		
	Division/Department	Department of Biomedical & Pharmaceutical	
	Organization/University		
	Street		
	City		
	State		
	Postcode		
	Country		
	Phone		
	Email		
	Author	Family Name	
Particle			
Given Name		.	
Suffix			
Division/Department			
Organization/University			
City			
State			
Postcode			
Country			
Email			

## Mn and Its Interrelation with Other Metal Ions in Health and Disease

James C. K. Lai<sup>1</sup> and Solomon W. Leung<sup>2</sup>

<sup>1</sup>Department of Biomedical & Pharmaceutical Sciences, College of Pharmacy and Biomedical Research Institute, Idaho State University, Pocatello, ID, USA

<sup>2</sup>Department of Civil & Environmental Engineering, School of Engineering, College of Science and Engineering and Biomedical Research Institute, Idaho State University, Pocatello, ID, USA

### Synonyms

Interdependence between manganese and other metal ions; Manganese-metal ion interactions

### Definition

Manganese and its interrelation with other metal ions in health and disease refers to how the level and metabolism of manganese in an organ are related to the levels and metabolism of other metal ions in the same organ in a healthy individual and how disease states exert modulatory effects on such interrelations.

### Introduction

To understand the “state of the art” regarding manganese (Mn) and its interrelation with other metal ions in health and disease, one needs to appreciate the

advantages and the limitations of the approaches that critically drive the advances of this multidisciplinary field. As have been emphasized earlier, “Ideally, if one can demonstrate directly the mechanisms that causally link the metabolism of manganese to those of other metals, then one can define the physiological . . . situations or conditions that show *interdependence* between Mn and other metal ions. However, largely because of methodological limitations as well as limitations of experimental approaches, the data in the literature and those of ongoing studies are better or more accurately defined as depicting the *interrelations* between Mn and other metal ions. This conceptual distinction should be borne in mind when one assesses the advances in the topic areas to be discussed. . .” (Lai et al. 2000).

The scope of this entry is limited to a summary discussion of the interrelations between Mn and other elements after chronic exposure of animals or humans to Mn because distributions of ► [Mn in brain](#) regions and in peripheral organs usually reflect chronic rather than acute exposure to this metal. Several aspects of this topic not covered in this entry because of space limitations have been discussed in some detail in one or another of our previous publications (Chan et al. 1983; Lai et al. 1984, 1985a, c, 1999, 2000; Leung et al. 2011; Wright et al. 2011).

### Interdependence Between Manganese and Other Metals in Absorption

Because manganese (Mn) is an essential trace metal, intake of this metal is usually via food intake and intake via the drinking water (Underwood 1977; Lai

et al. 1984, 2000). Respiratory exposure of Mn to humans is rare except under poorly controlled industrial environments such as manganese mining, steel mills, and metal soldering in a confined space. Consequently, the major findings to date employing animal models concerning the interdependence between Mn and other metals are centered upon intestinal absorption and subsequent organ distribution. Several generalizations are evident: intestinal Mn absorption depends on dietary iron (Fe). Low-dietary Fe enhances Mn absorption whereas high-dietary Fe lowers Mn absorption (Lai et al. 1985c, 2000). Similarly, high-dietary Mn intake results in lowered Fe absorption (Lai et al. 1985c, 2000). Furthermore, inclusion of essential and nonessential trace metals in the drinking water of rats and mice can alter accumulation of essential trace metals (including Mn) in their peripheral organs (see Lai et al. 2000 for discussion).

## Interrelations Between Manganese and Other Metals in Several Peripheral Organs

A developmental rat model had been developed so that the organ distribution of multiple metals and other elements could be systematically analyzed based on dietary intake. Furthermore, by exposing rats in utero to manganese (added as the chloride form in the drinking water) and continuously until they were employed for analysis, the effects of Mn on the distributions of other trace metals and electrolytes in various organs during development and aging can be systematically investigated employing versatile techniques such as instrumental neutron activation analysis (INAA) (Chan et al. 1983; Lai et al. 1984, 1999, 2000). Those series of studies constitute the largest and most complete sets of data in the Mn-metal interaction literature (Chan et al. 1983; Lai et al. 1985a, 1985c, 1999, 2000; Leung et al. 2011; Wright et al. 2011).

The relative distribution of trace metals in different peripheral organs subsequent to their intestinal absorption reflects the amount of metal-binding molecules (e.g., proteins and nucleic acids) in each organ and the organ's storage capacity (Lai et al. 2000). In rats, the rank order of the relative abundance of trace metals in peripheral organs is  $\text{Fe} \gg \text{Zn} > \text{Cu} > \text{Al} > \text{Mn} > \text{Se}$ . The rank order of Fe level in peripheral organs is  $\text{spleen} \gg \text{liver} > \text{lung} > \text{heart} \approx \text{kidney}$ . The rank order of Zn level is  $\text{liver} \gg \text{kidney} > \text{spleen} \approx \text{lung} \approx \text{heart}$ .

The rank order of Cu level is  $\text{kidney} \gg \text{liver} \approx \text{heart} > \text{spleen} > \text{lung}$ . The rank order of Mn level is  $\text{liver} \gg \text{kidney} \gg \text{spleen} \approx \text{heart} > \text{lung}$  whereas that for Se is  $\text{kidney} \geq \text{liver} > \text{spleen} > \text{lung} = \text{heart}$ . However, the rank order of the level of the nonessential metal Al is  $\text{spleen} > \text{liver} > \text{heart} > \text{kidney} \approx \text{lung}$ .

In adult (i.e., 120-day-old) rats, chronic Mn treatment induces dose-related differential elevation in Mn in heart, kidney, spleen, and liver (Lai et al. 1985c, 2000). Associated with the differential elevation of Mn in the peripheral organs is a shift in the patterns of organ distribution of trace metals (Lai et al. 1985c, 2000). For example, in Mn-treated rats, Fe levels are increased in spleen and lung whereas Zn level is decreased in liver and Cu level is decreased in spleen, compared to corresponding levels in untreated rats (Lai et al. 1985c, 2000). However, the organ distributions of several other metals are also affected by chronic manganese exposure. (Because of space limitation, those findings will not be discussed here: see Lai et al. 1985c, 2000 for additional details.)

Based on the findings discussed above, two generalizations can be arrived at: (1) Dietary intake of trace metals and electrolytes and their subsequent organ distribution is under regulatory control even though the mechanisms mediating the control are far from being understood. (2) Increasing the levels of Mn in dietary intake (e.g., via addition of manganese salt in the drinking water) ultimately alters the patterns of organ distribution of trace metals.

## Regional Differences in Distribution of Trace Metals in Brain

In the adult rat, whole brain levels of trace metals differ and the rank order of levels of several trace metals is  $\text{Fe} > \text{Zn} > \text{Al} > \text{Cu} > \text{Se} \approx \text{Mn}$  (Lai et al. 1985c, 2000). Additionally, brain levels of several trace metals (e.g., Fe, Cu, Mn, and Se) are altered in the aged rat brain compared to the corresponding levels in the young adult rat brain (Lai et al. 1985c, 2000). On the other hand, each trace metal has its own, almost unique, brain regional distribution.

In development, various regions of the mammalian brain undergo structural changes concomitant with increases in glial cell numbers and migrations of growing and maturing neurons (Lai et al. 2000). Although

not yet fully understood, these developmental structural and cellular changes ultimately give rise to each trace metal exhibiting its characteristic regional distribution in the adult brain (Lai et al. 1985c, 2000). For example, in the adult rat, Fe level is higher in hippocampus, hypothalamus, pons and medulla, and cerebellum than in midbrain, striatum, and cerebral cortex. Zn level is higher in hippocampus and cerebral cortex than in the other regions whereas Cu level is highest in hypothalamus, intermediate in striatum, midbrain, and cerebellum but lowest in hippocampus, pons and medulla, and cerebral cortex. Se level is highest in hippocampus, midbrain, and hypothalamus, intermediate in cerebellum and cerebral cortex, but lowest in striatum and pons and medulla. Mn level is highest in midbrain, cerebellum, and pons and medulla, intermediate in cerebral cortex and hypothalamus, but lowest in striatum and hippocampus. The level of the nonessential trace metal, Al, unlike those of the essential metals (e.g., Fe, Zn, Cu, Mn, Se) is lower in cerebral cortex than those in other regions.

Distributions of electrolytes are also somewhat different from those of trace metals (Lai et al. 1985c, 2000). In the adult rat, Ca level is lower in cerebral cortex and midbrain than in the other regions. Mg level is also lower in cerebral cortex than those in other regions.

## Interrelations Between Manganese and Other Metals in Brain

To facilitate the investigation of the interrelations between manganese and other trace metals and electrolytes in brain and other organs, a model of chronic and life-span exposure of rats to manganese had been developed (Lai et al. 1984, 1985b). Chronic Mn exposure was carried out by adding  $\text{MnCl}_2 \cdot 4\text{H}_2\text{O}$  into the drinking water given to the rats. Four groups of rats were studied: the control group was given just the double-distilled water; group A was given 1 mg of  $\text{MnCl}_2 \cdot 4\text{H}_2\text{O}$  per mL of double-distilled water; group B was given 10 mg of  $\text{MnCl}_2 \cdot 4\text{H}_2\text{O}$  per mL of double-distilled water; and group C was given 20 mg of  $\text{MnCl}_2 \cdot 4\text{H}_2\text{O}$  per mL of double-distilled water (Lai et al. 1984, 1985b). The rats were exposed to Mn in utero via their mothers' circulation; postnatally, they were exposed to Mn via their mothers' milk; and from around weaning (i.e., 21/22 days postnatal) onward,

they were directly exposed to Mn in the drinking water (Lai et al. 1984, 1985b). When the rats attained full adulthood (i.e., at 120 days of age), they were euthanized and their organ removed (Lai et al. 1984, 1985b). Each rat brain was dissected into the following seven regions: cerebellum, cerebral cortex, hippocampus, hypothalamus, midbrain, pons and medulla, and striatum (Lai et al. 1984, 1985b). The contents of trace metals and other elements in each brain region were determined employing instrumental neutron activation analysis (INAA) (Chan et al. 1983; Lai et al. 1985c, 1999, 2000). By combining the versatile technique of INAA with the animal model of chronic and life-span exposure to Mn, a comprehensive metallomic database had been collected of levels of trace metals and other essential and nonessential elements in all the brain regions in the four groups of rats (one control and three Mn-treated groups, namely, A, B, and C) (Chan et al. 1983; Lai et al. 1985c, 1999, 2000). The data were taken from the comprehensive metallomic database and then analyzed so as to allow the interpretation of how Mn can interact with trace and major elements in discrete rat brain regions (Leung et al. 2011; Wright et al. 2011). The level of each trace metal or element in each brain region in the Mn-treated rat was compared with the corresponding level (set as 100%) in the same region in the untreated (i.e., control) rat and the difference ranked as % increase or % decrease relative to the value in the control animal. For ease of visual comparison, the rank orders of increases or decreases of levels were color-coded (Tables 1 and 2) (Leung et al. 2011; Wright et al. 2011).

As evident from the rank-order patterns of the regional distributions of trace metals (Table 1) and electrolytes (Table 2) in the seven brain regions in the rats treated with the three doses of Mn, several generalizations regarding how Mn interacts with other trace metals and other elements can be arrived at. (1) Because the distributions of trace metals and other elements in the adult rat brain show region-specific differences, their patterns of distribution in the untreated normal rat brain are significantly altered by Mn treatment and such alterations can be generally correlated with the dose of Mn administered (Tables 1 and 2). (2) Mn treatment leads to selective, region-specific increases in the accumulation of some trace and major elements (Tables 1 and 2). (3) Mn treatment results in selective, region-specific decreases in the accumulation of other trace and major elements



(Tables 1 and 2). (4) By contrast, Mn treatment gives rise to both increases and decreases in the accumulation of some other trace and major elements, and these fluctuations in their accumulation are dependent on both brain region in question and the dose of Mn administered (Tables 1 and 2).

As may be expected, upon chronic Mn treatment, Mn levels show the largest region-specific increases among all the trace metals that were investigated and showed increases (Table 1). Among the trace metals examined showing region-specific increases in their levels induced by Mn treatment, the rank order of their relative changes compared with each other is  $Mn > Hg > Cu > Se$  (Table 1). Because all these trace metals are neurotoxic when taken in excess, this finding suggests that increased brain regional Mn accumulation consequent to Mn treatment results in increased regional accumulation of Hg (a nonessential toxic metal), Cu, and Se, ultimately leading to a cumulative toxicity due to all three metals and perhaps even neurodegeneration.

Among the trace metals and other elements showing region-specific decreases in their levels induced by Mn treatment, the rank order of their relative changes compared with each other is  $F > V > Br > Al > Mo$  (Table 1). The functional roles of F, V, Br, and Mo in mammalian brain are poorly defined. Nevertheless, Al, a nonessential trace metal in mammals, is known to be neurotoxic (Lai et al. 2000). Thus, this finding suggests that Mn accumulation consequent to Mn treatment induces region-specific decreases in Al accumulation, leading to a lowering of neurotoxicity due to Al.

Among the trace metals and other elements showing region-specific fluctuations (i.e., both trends of increases and decreases) in their levels induced by Mn treatment, the rank order of their relative changes compared with each other is  $Cr > Zn > Co > Rb > I$  (Table 1). The functional roles of Cr, Rb, and I in mammalian brain are not defined. Zn is an essential trace metal: its decreases and increases in brain regional accumulation induced by Mn treatment could lead to, respectively, deficiency and toxicity states (Lai et al. 2000). On the other hand, the only known role of Co in mammals is that it is a component in vitamin B12 and is required in ultra-trace quantities. However, it is neurotoxic when taken in excess. Thus, the decreases and increases in brain regional accumulation of Co induced by Mn treatment could give rise

to, respectively, vitamin B12 deficiency and Co neurotoxicity.

Brain Fe level approaches those of major elements and electrolytes such as Ca (Lai et al. 1985c, 2000). Fe interacts with Mn in intestinal absorption (see above); thus, consistent with this notion is the observation that in Mn-treated rats, the largest increase in Fe levels are noted in hypothalamus, striatum, and cerebellum (Table 2), and these are the same regions that show the highest accumulation of Mn (Table 1). Because Fe is neurotoxic when taken and/or accumulated in excess, this observation suggests that the increase in Fe accumulation could accentuate the neurotoxicity of the accumulated Mn, possibly leading to enhanced neurodegeneration (Lai et al. 2000).

Similar to Fe, two electrolytes (namely, Na and Cl) show region-specific increases in their levels induced by Mn treatment, the rank order of their relative changes compared with each other is  $Fe > Na > Cl$  (Table 2). This finding suggests that increases in Na and Cl accumulation induced by Mn treatment could result in altered ionic balance in neural cells.

Unlike the trace metals, none of the electrolytes exhibit predominantly region-specific decreases in their levels induced by Mn treatment (Table 2).

Three other electrolytes exhibit region-specific fluctuations (i.e., both trends of increases and decreases) in their levels induced by Mn treatment, the rank order of their relative changes compared with each other is  $Ca > K > Mg$  (Table 2). It is interesting to note that Mn treatment results in increased Ca accumulation in midbrain, pons and medulla, and striatum but decreased accumulation in cerebellum and hippocampus (Table 2), suggesting in Mn-treated rats, midbrain, pons and medulla, and striatum are the regions that are prone to calcification and Ca-mediated neurodegeneration (Lai et al. 2000). On the other hand, the Mn-treatment-induced fluctuations in regional K may lead to altered neuronal excitability and conduction, while the fluctuations in regional Mg could result in some alterations in key protein functions (e.g., receptor-gated ion channels and protein kinases) in which Mg plays important roles.

In addition to the findings discussed above, chronic and life-span Mn treatment also modulates on the region-specific distributions of trace metals and electrolytes during development and aging. Some of those findings have been discussed previously and will not

be reiterated here (see Lai et al. 1985c, 1999, 2000 for detailed discussion).

Taken together, the region-specific interactions between Mn and other trace metals and other elements (Tables 1 and 2) may have pathophysiological implications in neurodegenerative and other neurological diseases (see below).

### Interrelations Between Manganese and Other Metals in Brain in Human Health and Diseases

While Mn can interact with trace elements (e.g., F, V, Br, Al, Mo) leading to region-specific decreases in their accumulation, the health impact of the Mn-induced decreases is largely unknown as the functional roles of these trace elements in brain, with the exception of Al, are unknown. Of some health concern are the Mn interactions where brain regional levels of trace metals become increased: these trace metals include Mn, Hg, Cu, Se, Fe, and Zn. The available evidence suggests that the accumulation of these metals may have pathophysiological implications in several neurodegenerative and other neurological diseases and the implications are briefly summarized below.

High brain levels of Mn, Ca, and Al are found in Alzheimer's disease (AD). In AD patients, plasma levels of Al, Cd, Hg, and Se are increased (see Lai et al. 2000 for discussion). Fe is also elevated in multiple regions of the AD brain. Fe in the cores and rims of senile plaques of amygdala of AD patients is elevated and Fe (like Cu and Zn) can accelerate aggregation of  $\beta$ -amyloid peptide, a hallmark of AD neuropathology (see Lai et al. 2000 for discussion). Additionally, Zn level is increased in different regions of the AD brain (see Lai et al. 2000 for discussion). Consequently, Fe, Zn, Al, and Cu have been proposed to be responsible for inducing cell death, especially neuronal cell death, in the AD brain because of (a) formation of reactive oxygen species, (b) other metal-mediated cytotoxic effects, or (c) a combination of mechanisms (see Lai et al. 2000 for discussion).

Chronic  $\blacktriangleright$  Mn toxicity in humans shows signs and symptoms that are reminiscent of those noted in Parkinson's disease (PD) and dystonia (Lai et al. 2000). Some but not all studies have demonstrated an increased brain level of Mn in PD. However, increased

levels of Fe and Zn are found in the substantia nigra of PD patients.

In several neurological diseases other than AD and PD, brain metabolism of Mn and other metals are also disturbed. Pick's disease is associated with increases in brain Mn, Fe, and Na and decreases in brain Cr and Se. In amyotrophic lateral sclerosis (ALS) brain, levels of Al and Ca are elevated. These findings suggest Mn may interact with other metals in Pick's disease and in ALS (see Lai et al. 2000 for discussion).

In some metabolic encephalopathies (e.g., dialysis encephalopathy, chronic renal failure without dialysis, and hepatic coma), brain Al is elevated. Thus, Al neurotoxicity is implicated in these encephalopathies. There is also good evidence that Mn level is elevated in globus pallidus of patients with liver cirrhosis, thereby implicating  $\blacktriangleright$  Mn in brain in hepatic encephalopathy (see Lai et al. 2000 for discussion).

### Conclusions and Prospects for Future Investigation

There have been significant advances in our understanding of manganese and its interrelations with other metal ions in health and disease. The advances in the last 25 years have been built upon the skillful exploitation of the versatile technique of instrumental neutron activation analysis (INAA) in conjunction with a rat model of chronic and life-span exposure to Mn in constructing and assembling a comprehensive metallomic database containing the distributions of over 20 trace and major elements in seven discrete brain regions and in multiple peripheral organs in rats during their life span (i.e., from early postnatal development until aging). This comprehensive database also contains the distributions of some 20 trace and major elements in seven discrete brain regions and in multiple peripheral organs in rats continuously exposed to three doses of Mn over their life span. The gradual mining and analyses of selected sets of data within this comprehensive metallomic database have allowed us to arrive at a number of fundamental conclusions as to how Mn interacts with other trace and major elements in various regions of the rat brain and in various peripheral organs.

- (1) Mn interacts with multiple trace elements (especially Fe) in the process of intestinal absorption.
- (2) Each trace and major element has its own, almost

unique, brain regional distribution. (3) The patterns of distributions of trace and major elements in the untreated rat brain show region-specific differences, and these patterns are significantly altered by Mn treatment in an approximately dose-related manner. (4) The patterns of brain regional distributions of trace and major elements in the adult rats and the modulations by chronic Mn treatments thereon have implications in health and disease, especially in regard to several neurodegenerative (e.g., Alzheimer's disease and Parkinson's disease) and other neurological diseases. (5) However, the cellular and molecular mechanisms underlying how Mn interacts with other trace and major elements in brain and other organs are almost totally unknown. (6) Nevertheless, the continued mining and systematic analyses of discrete segments of the comprehensive metallomic database are beginning to facilitate the formulation of discrete, testable hypotheses regarding such cellular and molecular mechanisms and lead to novel and productive research. Thus, these endeavors promise to break new grounds in our understanding of how trace and major elements interact in biological systems.

**Acknowledgments** We wish to acknowledge the contributions of Drs. Alex W.K. Chan and Margaret J. Minski (now retired), both formerly of Imperial College, University of London, UK, and Dr. Louis Lim of Institute of Neurology, University of London, UK, and their role in either designing or producing or supporting the creation of the comprehensive metallomic database. JCK Lai wishes to thank the Worshipful Company of Pewterers, London, UK, for their generous support to allow him to initiate the project and create the metallomic database. We thank Mr. G.L. Wright for his timely help with mining and analyzing some sets of the data. This study is supported, in part, by a US Army Medical Research and Material Command Project Grant (Contract W81XWH-07-2-0078).

## Cross-References

- Mn in Brain
- Mn Toxicity

## References

- Chan AWK, Minski MJ, Lai JCK (1983) An application of neutron activation analysis to small biological samples: simultaneous determination of thirty elements in rat brain regions. *J Neuro Method* 7:17–328
- Lai JCK, Leung TKC, Lim L (1984) Differences in the neurotoxic effects of manganese during development and aging: some observations on brain regional neurotransmitter and non-neurotransmitter metabolism in a developmental rat model of chronic manganese encephalopathy. *Neurotoxicology* 5:37–48
- Lai JCK, Chan AWK, Minski MJ, Lim L (1985a) Roles of metal ions in brain development and aging. In: Gabay S, Harris J, Ho BT (eds) *Metal ions in neurology and psychiatry*. Alan Liss, New York
- Lai JCK, Leung TKC, Lim L (1985b) Effects of metal ions on neurotransmitter function and metabolism. In: Gabay S, Harris J, Ho BT (eds) *Metal ions in neurology and psychiatry*. Alan Liss, New York
- Lai JCK, Chan AWK, Minski MJ, Leung TKC, Lim L, Davison AN (1985c) Application of instrumental neutron activation analysis to the study of trace metals in brain and metal toxicity. In: Gabay S, Harris J, Ho BT (eds) *Metal ions in neurology and psychiatry*. Alan Liss, New York
- Lai JCK, Minski MJ, Chan AWK, Leung TKC, Lim L (1999) Manganese mineral interactions in brain. *Neurotoxicology* 20:433–444
- Lai JCK, Minski MJ, Chan AWK, Lim L (2000) Interrelations between manganese and other metal ions in health and disease. In: Sigel A, Sigel H (eds) *Metal ions in biological systems*, vol 37. Marcel Dekker, New York
- Leung SW, Chan A, Minski M, Lai JCK (2011) Comparison of elemental distribution in rat's brain after lifelong treatment with excessive  $Mn^{2+}$  in drinking water and the health implications. In: *Proceedings of international water convention*, Singapore, 4–8 July 2011, Article IWA-6218R1, pp 1–10
- Underwood EJ (1977) *Trace elements in human and animal nutrition*, 4th edn. Academic, New York
- Wright GL, Lai JCK, Chan A, Minski M, Leung SW (2011) Influence of metallomic distribution in brain by prolong consumption of contaminant in drinking water. *Proceedings of International Water Convention*, Singapore, 4–8 July 2011, Article IWA-6228R1, pp 1–21

t1.1 **Mn and Its Interrelation with Other Metal Ions in Health and Disease, Table 1** Changes in levels of trace metals and other elements in brain regions in adult female rats after chronic treatment with Mn compared with corresponding levels in untreated (i.e., control) rats. The Mn-treated groups consisted of group A (1 mg of  $\text{MnCl}_2 \cdot 4\text{H}_2\text{O}$  per mL of double-distilled water), group B (10 mg of  $\text{MnCl}_2 \cdot 4\text{H}_2\text{O}$  per mL of double-distilled water), and group C (20 mg of  $\text{MnCl}_2 \cdot 4\text{H}_2\text{O}$  per mL of double-distilled water). The data were derived from the comprehensive metallomic database. The level of each trace metal or element in each brain region in the Mn-treated rat was compared with the corresponding level (set as 100%) in the same region in the untreated (i.e., control) rat and the difference ranked as % increase or % decrease relative to the value in the control animal. For ease of visual comparison, the rank orders of increases or decreases of levels were color-coded as follows: Those levels showing % higher than corresponding values in control rats were color-coded as: *red*, 0–25%; *purple*, 25–50%; and *brown*, >50%. Those levels showing % decrease compared with corresponding values in control rats were color-coded as: *yellow*, 0% to –25%; *green*, –25% to –50%; and *blue*, >–50%. Those levels that were the same as corresponding values in control rats were coded in *black* and those levels that were not detectable (i.e., below the limits of detection) by the INAA technique were not color-coded (i.e., *white*)

	Elements																				
Region	Al			Br			Co			Cr			Cu			F			Hg		
	A	B	C	A	B	C	A	B	C	A	B	C	A	B	C	A	B	C	A	B	C
Cerebellum	Red	Yellow	Yellow	Green	Green	Blue	Brown	Red	Yellow	Purple	Green	Blue	Red	Red	Red				Brown	Blue	Green
Cerebral Cortex	Red	Yellow	Green	Green	Red		Green	Green				Brown			Brown				Green	Purple	
Hippocampus	Brown			Blue		Blue	Yellow		Purple	Yellow			Red	Red	Yellow				Brown		Brown
Hypothalamus	Yellow	Yellow		Green	Green							Brown	Purple	Purple	Purple				Red		Red
Midbrain		Purple	Red	Green	Red	Blue	Brown		Blue				Purple	Purple	Purple	Yellow	Red	Red	Blue	Brown	
Pons & Medulla	Red	Red	Yellow	Yellow	Green	Green	Yellow	Green	Green	Brown			Brown	Brown	Purple				Red		Brown
Striatum																					

	Elements																				
Region	I			Mn			Mo			Rb			Se			V			Zn		
	A	B	C	A	B	C	A	B	C	A	B	C	A	B	C	A	B	C	A	B	C
Cerebellum	Green	Green	Green	Green	Red	Red	Yellow	Brown	Red	Yellow	Red	Red	Brown	Brown	Brown	Green	Red	Yellow	Red	Purple	Yellow
Cerebral Cortex	Purple	Purple	Yellow	Red			Red	Yellow	Green	Yellow	Red	Yellow	Red	Yellow	Green		Brown	Black	Red	Red	Red
Hippocampus	Yellow								Blue				Red	Red	Red			Green	Yellow	Red	Yellow
Hypothalamus	Blue		Blue				Purple	Yellow		Purple	Red	Red		Yellow	Brown	Purple	Yellow	Blue	Brown	Brown	Yellow
Midbrain	Green		Green				Blue	Red	Green	Red	Purple	Red	Purple	Purple	Blue	Yellow	Black	Red	Red	Red	Yellow
Pons & Medulla	Blue			Red						Purple		Green		Brown			Red	Yellow	Red	Yellow	Green
Striatum	Yellow	Red					Yellow			Purple		Red	Brown	Brown			Red		Purple	Brown	

t2.1 **Mn and Its Interrelation with Other Metal Ions in Health and Disease, Table 2** Changes in levels of iron and electrolytes in brain regions in adult female rats after chronic treatment with Mn compared with corresponding levels in untreated (i.e., control) rats. The Mn-treated groups consisted of group A (1 mg of  $\text{MnCl}_2 \cdot 4\text{H}_2\text{O}$  per mL of double-distilled water), group B (10 mg of  $\text{MnCl}_2 \cdot 4\text{H}_2\text{O}$  per mL of double-distilled water), and group C (20 mg of  $\text{MnCl}_2 \cdot 4\text{H}_2\text{O}$  per mL of double-distilled water). The data were derived from the comprehensive metallomic database. The level of each trace metal or element in each brain region in the Mn-treated rat was compared with the corresponding level (set as 100%) in the same region in the untreated (i.e., control) rat and the difference ranked as % increase or % decrease relative to the value in the control animal. For ease of visual comparison, the rank orders of increases or decreases of levels were color-coded as follows: Those levels showing % higher than corresponding values in control rats were color-coded as: *red*, 0–25%; *purple*, 25–50%; and *brown*, >50%. Those levels showing % decrease compared with corresponding values in control rats were color-coded as: *yellow*, 0% to –25%; *green*, –25% to –50%; and *blue*, >–50%. Those levels that were the same as corresponding values in control rats were coded in *black* and those levels that were not detectable (i.e., below the limits of detection) by the INAA technique were not color-coded (i.e., *white*)

Region	Elements																	
	Ca			Cl			Fe			K			Mg			Na		
	A	B	C	A	B	C	A	B	C	A	B	C	A	B	C	A	B	C
<i>Cerebellum</i>	green	yellow	green	red	red	red	brown	brown	red	red	red	yellow	yellow	yellow	yellow	red	red	red
<i>Cerebral Cortex</i>	yellow	red	yellow	red	red	red	red	red	red	red	red	red	red	blue	red	red	red	red
<i>Hippocampus</i>	green	green	green	yellow	yellow	yellow	brown	purple	yellow	red	red	red	yellow	green	green	red	yellow	red
<i>Hypothalamus</i>	green	red	green	purple	purple	purple	brown	brown	purple	purple	purple	red	red	red	red	purple	purple	purple
<i>Midbrain</i>	brown	brown	brown	red	red	red	purple	red	red	purple	red	red	yellow	yellow	yellow	red	red	red
<i>Pons &amp; Medulla</i>	red	brown	red	yellow	yellow	yellow	purple	brown	yellow	yellow	yellow	yellow	yellow	yellow	green	blue	green	green
<i>Striatum</i>	red	purple	purple	red	red	red	purple	brown	brown	red	red	red	red	red	red	purple	red	red

## Chapter 30

# TOXICITY OF SILICON DIOXIDE NANOPARTICLES IN MAMMALIAN NEURAL CELLS

James C. K. Lai, PhD<sup>1</sup>, Ashvin R. Jaiswal, MS<sup>1</sup>, Maria B. Lai, MS<sup>1</sup>, Sirisha Jandhyam, MS<sup>1</sup>, Solomon W. Leung, PhD<sup>2</sup>, and Alok Bhushan, PhD<sup>1</sup>

<sup>1</sup>*Department of Biomedical and Pharmaceutical Sciences, College of Pharmacy, and Biomedical Research Institute, Idaho State University, Pocatello, ID 83209*

<sup>2</sup>*Department of Civil and Environmental Engineering, School of Engineering, College of Science and Engineering and Biomedical Research Institute, Idaho State University, Pocatello, ID 83209*

### KEY WORDS

silicon dioxide nanoparticles; toxicity in neural cells; cytotoxicity of nanoparticles; neurons; astrocytes; dorsal root ganglion neurons; Schwann cells; central and peripheral nervous system

## 1.1 INTRODUCTION

In a recent draft document, the US Environmental Protection Agency (EPA) has emphasized that exposure to nanomaterials can occur during their fabrication or production process because the materials can pollute the environment [1]. Environmental exposure of humans to silicon dioxide has been increasing because of escalating use of silicon dioxide, including a range of its particle sizes, in cosmetics, food, and drug formulations [2,3]. Although silicon dioxide has been considered to be a comparatively nontoxic substance, research in the last two decades has revealed that silicon dioxide particles are not as harmless as they were previously assumed to be.

In sizes above the micrometer range (i.e.,  $> 1 \mu\text{m}$ ), silicon dioxide appears to be benign to humans, insects, and microorganisms. However, silicon dioxide particles of sizes smaller than  $1 \mu\text{m}$  can exert toxic effects in humans and animals. For example, silicosis is a disease found both in humans and rats: the underlying silicon dioxide toxicity is due to prolonged exposure to crystalline silica dust,

leading to pulmonary injuries or lung inflammation [4,5]. Because silicon dioxide nanoparticles can readily cross the blood-brain barrier (see below), they can penetrate into the nervous system and exert their toxicity on neural cells. This review therefore focuses on discussing the effects of silicon dioxide nanoparticles on neural cells both *in vivo* and *in vitro*. Three recent reviews [6-8] cover the toxicity of these particles in peripheral tissues and cell types: readers are referred to those for effects of silicon dioxide nanoparticles on non-neural cell types and other aspects not covered in this review.

## 1.2 NANOPARTICLES CAN CROSS THE BLOOD-BRAIN BARRIER

The blood-brain barrier (BBB) constitutes an effective barrier to exclude undesirable and/or toxic substances in the circulation from entering the central nervous system, including the brain. In this context, for targeting therapeutic agents to the brain, one needs to devise mechanism(s) whereby this restriction of the BBB is overcome or by-passed. Consequently, various studies on employing nanoparticles to assist with drug delivery or delivery of genetic material to advance gene therapy have concluded that nanoparticles can cross the BBB [9,10]. For example, Kim et al. [9] synthesized silica-overcoated magnetic nanoparticles containing rhodamine B isothiocyanate within a silica shell of controllable thickness (MNPs@SiO<sub>2</sub>(RITC)): in that study they employed particles with 50-nm thickness. They administered those particles intraperitoneally into mice for four weeks and were able to detect the nanoparticles in the brains of those mice. Their study [9] clearly demonstrated that such nanoparticles can penetrate the BBB.

Nanoparticles have also been employed to achieve neuron-specific delivery of genetic material to advance gene therapy of various neurological disorders. For example, Zang et al. [11] employed 85-nm PEGylated immunoliposome (containing antibodies to the rat transferrin receptor) to deliver tyrosine hydroxylase (TH) expression plasmid to normalize TH activity in the striatum in a rat model of experimental parkinsonism induced by 6-hydroxydopamine. Their results demonstrated that intravenously-administered immunoliposomes containing the TH expression plasmid could cross the BBB giving rise to increased striatal TH activity in the TH-transfected rats [11]. Thus, their findings suggested that the immunoliposomes crossed the BBB via the transvascular route [11]. In addition to the transvascular route, nanoparticles can also cross the BBB after they have induced alterations in BBB permeability and induced cerebral edema [10].

### 1.3 TOXICITY OF SILICON DIOXIDE NANOPARTICLES IN MAMMALIAN NEURAL CELLS

The toxicity of silicon dioxide nanoparticles in mammalian neural cells is discussed below from three perspectives: (i) environmental health impact of exposure to silicon dioxide nanoparticles, (ii) toxicity of the nanoparticles in mammalian neural cells *in vivo*, and (iii) toxicity of the nanoparticles in mammalian neural cells *in vitro*.

#### 1.3.1 *Environmental health impact of exposure to silicon dioxide nanoparticles*

As has already been alluded to above, the ever increasing use of silicon dioxide, including a range of its particles sizes, in cosmetics, food, drug formulations, and numerous other industrial applications [2,3,12] has raised some concerns regarding the environmental health impact of human exposure to silicon dioxide particles, especially nanoparticles [12]. Because nanoparticles, including silicon dioxide nanoparticles, can cross the BBB (see above), their accumulation in significant quantities in the central nervous system can induce deleterious effects on neural cells, thereby disturbing the normal functions of such cells and even inducing neurodegeneration. The findings of three early studies provide some support for the notion that accumulation of silicon dioxide nanoparticles in brain could lead to neurodegeneration [13-15]. Silica micro- and nanoparticles, when introduced into the brains of rats and mice, induced inflammatory responses in brain astrocytes and macrophages and degeneration of axons and axon terminals adjacent to the astrocytes [13]. Silicon and aluminum were noted to be co-localized in the central region of senile plaque cores in the cortex of patients with senile dementia of the Alzheimer type [14]. Moreover, the accumulated silicon and aluminum appeared to be found, at least in part, in lipofuscin granules in the brains of patients who died with Alzheimer's disease [15].

#### 1.3.2 *Toxicity in vivo of silicon dioxide nanoparticles in mammalian neural cells*

There have been very few studies on the toxicity of silicon dioxide nanoparticles *in vivo* on mammalian neural cells. Nevertheless, the results of the few studies are quite revealing and allow us to make two tentative generalizations. (i) Silicon dioxide nanoparticles can cross the BBB: one consequence of such particles being able to cross the BBB is that they could, at least potentially, exert undesirable effects on neural cells in the central nervous system. (ii) Most of the toxic effects of silicon nanoparticles *in vivo* on neural cells are similar to, if not identical with, the effects of such nanoparticles noted in neural cells *in vitro* (see below). Thus, this generalization points to the utility of employing neural cell models *in vitro* to screen for the toxicity of various types of silicon dioxide nanoparticles and the importance of employing such models to elucidate the cellular and molecular



mechanisms underlying the cytotoxicity of silicon dioxide nanoparticles. Nevertheless, it is noteworthy that cytotoxicity of these nanoparticles in neural cells cannot be easily and readily investigated employing animal models in studies *in vivo*. We will briefly discuss how the findings of the few studies on toxicity of silicon dioxide nanoparticles on neural cells *in vivo* have led us to formulate the two generalizations above.

In their study to investigate toxicity and tissue distribution of silica-overcoated magnetic nanoparticles in mice, Kim et al. [9] synthesized silica-overcoated magnetic nanoparticles containing rhodamine B isothiocyanate within a silica shell of controllable thickness (MNPs@SiO<sub>2</sub>(RITC)). They employed MNPs@SiO<sub>2</sub>(RITC) with 50-nm thickness and administered those particles intraperitoneally into mice for four weeks and were able to detect the nanoparticles in the brains of those mice. Furthermore, using an immunocytochemical approach and employing the dorsal cochlear nucleus as a representative example of whole brain localization, they were able to show that MNPs@SiO<sub>2</sub>(RITC) co-localized with a well-characterized neuronal marker, NeuN. Based on their observations, Kim et al. concluded that the silica nanoparticles (MNPs@SiO<sub>2</sub>(RITC)) could cross the BBB, enter neurons, but do not alter the permeability of the BBB [9]. Nevertheless, they did not detect any gross abnormal histopathological lesions in several organs, including brain, kidney, liver, testis, uterus, lung, heart and spleen, in mice four weeks after intraperitoneally injection of MNPs@SiO<sub>2</sub>(RITC) into the mice at 25, 50 or 100 mg/kg [9]. Consequently, Kim et al. [9] concluded such silica nanoparticles can penetrate the BBB and enter neurons without apparently altering their normal function, suggesting that the silica-overcoated nanoparticles at the doses employed were apparently not toxic to neurons. The findings and conclusions of Kim et al. [9] are in sharp contrasts with those of a more recent study by Wu et al. [16].

Wu et al. [16] examined the effects of intranasal exposure of adult rats to silica nanoparticles (20 µg per rat daily for 1 or 7 days). They reported intranasal instillation of silicon dioxide nanoparticles into rats, especially for seven days, significantly increased levels of silicon dioxide nanoparticles in several brain regions monitored, with the rank order: olfactory bulb > striatum ≥ hippocampus > brain stem > cerebellum > frontal cortex [16]. Evidently, after intranasal administration, silicon dioxide nanoparticles were able to cross the BBB and became differentially accumulated within seven days in several key brain regions, especially in olfactory bulb, striatum, and hippocampus. Because of their importance in several neurodegenerative diseases, Wu et al. further examined the effects of these nanoparticles on key parameters concerned with oxidative stress, inflammatory response(s), and neurotransmitter metabolism [16]. They noted that the striatum was more vulnerable than the hippocampus to the toxic effects of silicon dioxide nanoparticles in terms of changes in these parameters subsequent to the accumulation of such nanoparticles in the two brain regions.

Specifically, in rats exposed to silicon dioxide nanoparticles for seven consecutive days, their striatal levels of hydrogen peroxide, a by-product of reactive oxygen species (ROS) generation, and MDA, a marker and end-product of lipid peroxidation, were significantly increased while striatal level of reduced glutathione (GSH) was significantly decreased; however, striatal SOD, an important antioxidant enzyme, was unchanged [16]. By contrast, in the hippocampus of rats intranasally instilled with silicon dioxide nanoparticles for seven consecutive days, only MDA levels were increased [16]. Thus, their findings strongly suggested that intranasal exposure of adult rats to silicon dioxide nanoparticles selectively induces oxidative stress in their striatum: Wu et al. also confirmed that the nanoparticles can, and do, induce oxidative stress *in vitro* in PC12 cells, which constitute a model of dopaminergic neurons (see Table 1 and the next subsection below).

Wu et al. [16] also observed that intranasal instillation of silicon dioxide nanoparticles into adult rats for seven consecutive days resulted in differential changes in inflammatory responses in the striatum (but not in the hippocampus) of the treated rats. They detected significantly higher striatal levels of TNF- $\alpha$ , IL-1 $\beta$ , and IL6 in the treated rats: both TNF- $\alpha$  and IL-1 $\beta$  are pro-inflammatory cytokines, whose release leads to the stimulation of expression of IL-6 and IL-8. Along with the selective changes in the striatal levels of cytokines associated with inflammatory response(s) induced by intranasal exposure of rats to silicon dioxide nanoparticles for seven days, Wu et al. [16] also discerned a significant decrease (by ~25%) in striatal dopamine level in the treated rats whereas their hippocampal glutamate level was not significantly altered. Animal models revealed that dopamine depletion in the striatum is associated with movement disorders [16] that were reminiscent of that in Parkinson's disease. Consequently, their findings led Wu et al. [16] to conclude that exposure to silicon nanoparticles exerts a negative impact on the striatum and dopaminergic neurons and may pose a risk for neurodegenerative diseases. In view of the interesting observations and conclusion of Wu et al. [16], we would like to propose that accumulation and toxicity of silicon dioxide nanoparticles in the striatum may serve as a model system for parkinsonism and Parkinson's disease. Clearly, this is a research area that merits further investigation.

Despite the interesting differential changes in striatum and to a much lesser extent in the hippocampus induced by intranasal instillation of silicon dioxide nanoparticles noted by Wu et al. [16], those researchers did not detect any noticeable changes in the general behavior of the treated rats. Nevertheless, Wu et al. [16] cautioned that more extensive and specialized neurobehavioral testing is needed to clearly delineate whether or not exposure of rats *in vivo* to silicon dioxide nanoparticles definitely results in functional behavioral changes [16].

### 1.3.3 Toxicity *in vitro* of silicon dioxide nanoparticles in mammalian neural cells

**The need for cell models *in vitro* to screen cytotoxicity of nanoparticles in neural cells.** Until recently, few, if any, studies have addressed the cytotoxicity of nanoparticles in neural cells. We were the first to propose the importance of developing neural cell models *in vitro* to facilitate the high throughput screening of the putative toxicity of nanoparticles in various neural cell types [12, 17-32].

Initially we developed several types of neural cell models *in vitro* consisting of human astrocytoma U87 cells and human neuroblastoma SK-N-SH cells for high throughput screening of the putative toxicity of nanomaterials, including nanoparticles [12, 17-24]. Even though U87 and SK-N-SH cells are neurotumor cells, they are good models *in vitro* for astrocytes and neurons, respectively, because there is good evidence that the structure and functions of U87 and SK-N-SH cells closely resemble their counterparts in normal brain, [17-24, 26]. We have initiated a series of studies to systematically examine the putative cytotoxic effects of nanoparticles of metallic and non-metallic oxides in astrocytes and neurons employing U87 (astrocytes-like) and SK-N-SH (neurons-like) cells [12, 17-26]. We have also modified the “standard” cell survival (i.e., MTT) assay so that the assay can be used to assess the effects of nanoparticles on cell survival with improved accuracy by minimizing the interference by nanoparticles in the assay [22,23].

We have further developed several types of co-culture models of astrocytes and neurons employing U87 and SK-N-SH cells to facilitate mechanistic elucidation of the protection by astrocytes conferred on neurons against agents (including toxic nanoparticles) that induce neurodegeneration [20-22, 26,30].

Table 1. *In vitro* studies of nanosilica toxicity in neural cells

Silica form (Size)	Cells Used (Exposure time in hours)	Endpoints and Findings	Ref.
Colloidal SiO <sub>2</sub> -NP (25 nm)	SK-N-SH U87 (48)	<ul style="list-style-type: none"> <li>- ↓ cell survival (significant decrease at 25, 50, 100 µg/ml)</li> <li>- ↑ LDH release</li> <li>- ↑ cell survival when co-cultured with U87 cells</li> <li>- Altered cellular morphology</li> </ul>	[17,18, 20]
Mesoporous Nanomaterials MCM-41 (5-30 nm ) <ul style="list-style-type: none"> <li>• AP-T</li> <li>• MP-T</li> </ul> Spherical silica nanoparticles SiO <sub>2</sub> (5-30 nm )	SK-N-SH (24)	<ul style="list-style-type: none"> <li>- Cytotoxicity of nanoparticles MCM-41&gt;MP-T&gt;AP-T ≈ SiO<sub>2</sub> (cytotoxicity of nanoparticles in descending order of toxicity)</li> <li>- More adsorptive surface area of the particle resulted in higher toxicity</li> </ul>	[33]
Amorphous SiO <sub>2</sub> -NP (50 & 70 nm)	SK-N-SH , N2a (4)	<ul style="list-style-type: none"> <li>- Internalized nanoparticles into the cytoplasm and localized in nuclei</li> <li>- Induced aberrant clusters of protein aggregates in the nucleoplasm</li> </ul>	[35]

Table 1. *In vitro* studies of nanosilica toxicity in neural cells (cont.)

Silica form (Size)	Cells Used (Exposure time in hours)	Endpoints and Findings	Ref.
Mesoporous nanomaterials (MSNs) <ul style="list-style-type: none"> <li>•MCM-41</li> <li>•SBA-15</li> </ul> Solid-cored Silica microsphere (SMS) (300 - 350 nm)	SK-N-SH (3, 24 and 51)	<ul style="list-style-type: none"> <li>- SBA-15 inhibitory effect on cell survival at 50 and 100 µg/mL and cytotoxic at 200 µg/mL (3 hr) recovery in cell viability (27 hr and 51 hr)</li> <li>- MCM-41 toxicity during the short exposure (3 hr) recovery in cell viability ( 51 hr) except at 200 µg/mL</li> <li>- SMS not toxic except at 200 µg/mL ( 3 hr) toxic (27 hr and 51 hr) functionalization of amine group decreases toxicity</li> </ul>	[34]
Si-NP (prepared by sol gel method) (150-200 nm)	primary culture of rat microglia (24)	<ul style="list-style-type: none"> <li>- Internalization by microglia at all concentrations tested</li> <li>- Not cytotoxic and did not alter phagocytosis</li> <li>- ↑ in intracellular production of ROS and RNS</li> <li>- ↑ IL-1β level</li> <li>- ↓ TNF-α gene expression</li> <li>- ↑ COX-2 gene expression at 36.4 µg/ml</li> </ul>	[36]

Table 1. *In vitro* studies of nanosilica toxicity in neural cells (cont.)

Silica form (Size)	Cells Used (Exposure time in hours)	Endpoints and Findings	Ref.
Colloidal SiO <sub>2</sub> -NP (25 nm)	U87 (48)	<ul style="list-style-type: none"> <li>- ↓ cell survival (significant decrease at 25, 50, 100 µg/ml)</li> <li>- ↑ citrate synthase and malate dehydrogenase activities</li> <li>- ↓ expression of cytochrome C oxidase subunit II, ↓ expression of NADH dehydrogenase subunit 6 and ↓ expression of phosphorylated ERK</li> <li>- Cells became more enlarged and swollen</li> </ul>	[12]
SiO <sub>2</sub> -NP 15 nm (92 nm with FBS protein)	PC12 (24)	<ul style="list-style-type: none"> <li>- ↓ cell survival, ↑ LDH release,</li> <li>- Oxidative stress               <ul style="list-style-type: none"> <li>↑ ROS production, ↑ MDA, ↓ GSH and ↓ SOD activity</li> </ul> </li> <li>- Rounded shaped and reduced length of extended neurites</li> <li>- Apoptosis               <ul style="list-style-type: none"> <li>double stained with PI- and FITC-labeled annexin V</li> <li>↓ the expression of bcl2, ↑ the expression of p53, p21, p-p53, Gadd45 and bax</li> </ul> </li> <li>- Cell cycle arrest at 100 and 200 µg/ml</li> </ul>	[16]

Table 1. *In vitro* studies of nanosilica toxicity in neural cells (cont.)

Silica form (Size)	Cells Used (Exposure time in hours)	Endpoints and Findings	Ref.
Colloidal SiO <sub>2</sub> -NP (25 nm)	Schwann cells (R3), DRG neurons (50B11) (36 and 48)	<ul style="list-style-type: none"> <li>- ↓ cell survival DRG neurons &lt; Schwann cells</li> <li>- Internalized nanoparticles (Schwann cells and DRG neurons)</li> <li>- Enlarged and swollen nuclei (Schwann cells and DRG neurons)</li> <li>- Oxidative stress Schwann cells ↓ GSH and ↓ Mn-SOD (R3) DRG neurons Multi-phasic effect on GSH and ↑ Mn-SOD</li> <li>- ↓ expression of NADH dehydrogenase subunit 6 and ↑ expression of succinate dehydrogenase fc subunit</li> <li>- ↓ expression of p-ERK (Schwann cells and DRG neurons)</li> <li>- Did not change the expression of ERK</li> </ul>	[28,31, 37]

Abbreviations: COX-2, cyclooxygenase 2; DRG, dorsal root ganglion; FITC, fluorescein isothiocyanate; GSH, reduced glutathione; IL, interleukin; LDH, lactate dehydrogenase; MDA, malondialdehyde (end product of lipid peroxidation); N2a, mouse neuroblastoma cell line; NMR, nuclear magnetic resonance; PC12, pheochromocytoma cells; PI, propidium iodide; Ref., references; RNS, reactive nitrogen species; ROS, reactive oxygen species; SEM, scanning electron microscopy; SiO<sub>2</sub>-NP, silicon dioxide nanoparticles; SK-N-SH, human neuroblastoma cell line; TEM, transmission electron microscopy; TNF, tumor necrosis factor; U87, human astrocytoma cell line; XRD, X-ray diffraction.

Because the putative cytotoxic effects of nanoparticles of metallic and non-metallic oxides in neural cells of the peripheral nervous system (PNS) are unknown, we have recently developed cell models *in vitro* consisting of Schwann cells and dorsal root ganglion (DRG) neurons to facilitate the systematic investigation of the effects of such nanoparticles on the PNS [27-29, 31,32]. The results of our recent and ongoing studies clearly demonstrate that our cell models *in vitro* constitute excellent cell culture models for elucidating pathophysiological mechanisms of agents (including nanoparticles) that can induce peripheral neuropathy [27-29,31,32].

The results of our previous and ongoing studies clearly demonstrate that the cell models we have developed allow the systematic and mechanistic investigations of putative cytotoxicity of nanoparticles of metallic and non-metallic oxides in neural cells derived from both the central and the peripheral nervous systems [12, 17-32]. Furthermore, they also strongly suggest that our models can be applied to screen the cytotoxicity of nanomaterials other than nanoparticles of metallic and non-metallic oxides in neural cells of central and peripheral nervous systems [12, 17-32]. We will discuss in the next subsection the findings of our studies and compare them with those of other researchers.

**Cellular and molecular mechanisms underlying the cytotoxicity *in vitro* of silicon dioxide nanoparticles in neural cells.** The results of the studies to date concerning the cytotoxicity *in vitro* of silicon dioxide nanoparticles in neural cells are summarized and compared as shown in Table 1.

We were the first to initiate a series of studies to systematically investigate the cytotoxic mechanisms of silicon dioxide nanoparticles on mammalian (including human) neural cells [12,17,18,20,22]. Our initial finding that silicon dioxide nanoparticles induced cytotoxicity on human neuroblastoma SK-N-SH (neurons-like) and human astrocytoma U87 (astrocytes-like) cells by lowering their survival [17] prompted us to further elucidate the mechanisms underlying the cytotoxicity of silicon dioxide nanoparticles in neurals cells [12,18]. Necrosis appeared to be one cytotoxic effect induced by the nanoparticles in both SK-N-SH (neurons-like) and U87 (astrocytes-like) cells as indicated by the increases in lactate dehydrogenase (LDH) release from the cells into the surrounding medium (Table 1) [17,18]. The dose-related changes in cellular morphology in U87 and SK-N-SH cells induced by silicon dioxide nanoparticles paralleled the dose-related decreases in the survival of those cells induced by the nanoparticles [17,18]. Interestingly, when SK-N-SH (neurons-like) cells were co-cultured on a monolayer of U87 (astrocytes-like) cells and exposed to silicon dioxide nanoparticles, the survival of both cell types was improved compared to the survival of both cell types when they were cultured alone as monotypic culture and exposed to silicon dioxide nanoparticles (Table 1) [20].



We investigated further the cytotoxic mechanisms underlying the dose-related decreases in survival of U87 cells induced by silicon dioxide nanoparticles [12]. We found the activities of citrate synthase and malate dehydrogenase in nanoparticles-treated U87 cells were increased, possibly due to an energetic compensation in surviving cells (Table 1) [12]. By contrast, the expression of mitochondrial DNA-encoded cytochrome C oxidase subunit II and NADH dehydrogenase subunit 6 and the cell signaling protein phosphorylated ERK (p-ERK) was altered in the nanoparticles-treated U87 cells (Table 1) [12]. Thus, we were the first to report on the effects of silicon dioxide nanoparticles on expression of mitochondrial DNA-encoded protein and on expression of cell survival signaling protein (i.e., ERK) [12]. Our findings suggest that silicon dioxide nanoparticles induces disruption of mitochondrial DNA-encoded protein expression, leading to decreased mitochondrial energy production in U87 cells; the nanoparticles also induced decreases in cell survival/proliferation signaling in those cells [12].

Different types of nanosilica particles exert dissimilar cytotoxic effects on neural cells. Di Pasqua et al. [33] and Tao et al. [34] demonstrated that mesoporous silica (MCM 41) nanoparticles are more toxic to SK-N-SH cells compared to spherical silica (including silicon dioxide) nanoparticles (Table 1). They also found that functional groups on silica nanoparticles play major roles in determining the toxicity of silica nanoparticles: for example, grafting aminopropyl group(s) on mesoporous silica nanoparticles decreased the cytotoxicity of MCM-41 in SK-N-SH cells [33]. Thus, it is imperative to consider whether or not and how the surface of the nanoparticles may influence their properties while selecting nanosilica for biomedical and biotechnological applications.

In elegant studies *in vitro*, Chen and von Mikecz [35] demonstrated that amorphous silica nanoparticles (50 & 70 nm) entered several cell types including neuronal cells (i.e., N2a and SK-N-SH cells), translocated into their nuclei, and altered nuclear functions in a matter of hours (Table 1) [35]. However, silica particles of sizes between 200 nm and 5  $\mu$ m neither penetrated into the nuclei nor modified nuclear function and architecture of the cells [35]. Furthermore, this group noted that once they penetrated into the nuclei of the cells, silica nanoparticles with an average diameter of 50 nm induced the formation of aberrant protein aggregates in their nuclei [35]. The protein aggregates, whose formation was induced by the silica nanoparticles, contained essential components of nuclear protein machines such as coactivators of transcription, unmutated polyQ proteins, and members of the ubiquitin proteasome systems (UPS) [35]. Their interesting observations led von Mikecz and co-workers to propose that the components of the UPS are recruited to silica-nanoparticles-induced nuclear inclusions to break down aggregated proteins [35]. Moreover, even when silica nanoparticles did not alter cell viability or enhance cell death, silica nanoparticles induced repression of gene expression, ultimately leading to decreased cellular replication and irreversible inhibition of cell proliferation [35].

This group of researchers therefore concluded that through the induction of intranuclear protein aggregation that contains proteins with polyQ stretches, silica nanoparticles trigger a subnuclear pathology that closely mimics molecular events characteristic of formation of insoluble protein inclusions in neurodegenerative aggregation diseases [35]. Chen and von Mikecz further advocated that “silica nanoparticles have emerged as excellent tools for proof-of-principle studies, in this case, establishment of cell-based models for degenerative protein aggregation diseases” [35].

Silicon dioxide nanoparticles can induce alterations in mitochondrial oxidative metabolism and induce oxidative stress. For example, silicon dioxide nanoparticles induced cell death in U87 (astrocytes-like) cells by disturbing their mitochondrial function (Table 1) [12]. Wu et al. [16] observed that treatment of PC12 cells (a model of dopaminergic neurons *in vitro*) with silicon dioxide nanoparticles led to increased LDH release, enhanced ROS production, increased MDA production but decreased levels of GSH and SOD, and ultimately decreased cell survival [16]. Additionally, their mechanistic studies with PC12 cells also revealed that at doses higher than 50 µg/mL, the number of apoptotic PC12 cells increased markedly [16]. They attributed this apoptotic effect induced by silicon dioxide nanoparticles to the G2/M cell cycle arrest in conjunction with increased protein expression of p53, phospho-p53 (p-p53), p21, Gadd45, and bax, but decreased protein expression of bcl-2 because both p21 and Gadd45 are proteins that are down-stream from p53 in regulating cell cycle whereas the increase in bax/bcl-2 ratio favors apoptosis [16]. Along with those observations, they also found that silicon dioxide nanoparticles induced decreases in dopamine levels and expression of tyrosine hydroxylase (TH, a rate-limiting enzyme in dopamine synthesis) [16]. (However, the authors erroneously stated that silicon dioxide nanoparticles upregulated the expression of TH in dose-dependent manner [see Ref. 16, p. 4485].) Interestingly, and relevant to this discussion of the mechanistic actions of silicon dioxide nanoparticles on neural cells, the findings of Wu et al. in PC12 cells *in vitro* (i.e., enhanced ROS production, increased MDA production but decreased levels of GSH and dopamine) confirmed what they observed in the striatum of rats after intranasal instillation of silicon dioxide nanoparticles into those rats *in vivo* [16]. Consequently, their parallel studies *in vivo* and *in vitro* strongly suggest that many – if not most – of the mechanisms underlying the cytotoxicity of silicon dioxide nanoparticles in neural cells *in vitro* may also occur in the cytotoxicity of silicon dioxide nanoparticles in neural cells *in vivo* [16].

The effects of silica nanoparticles in primary cultures of rat microglia *in vitro* [36] appear to somewhat differ from the effects of these nanoparticles in PC12 cells *in vitro* [16] and in the rat striatum after intranasal instillation of the nanoparticles *in vivo* [16]. Choi et al. [36] were the first to observe that over a 24-hour period, exposure of rat microglial cells in primary culture *in vitro* to silica nanoparticles resulted in the entry of nanoparticles into those cells via endocytosis and other

nanoparticle uptake mechanisms [36]. Similar to the effects of silicon dioxide nanoparticles in PC12 cells *in vitro* [36] and to the same effects in the rat striatum after intranasal instillation of the nanoparticles *in vivo* [16], Choi et al. also noted that these nanoparticles induce oxidative stress in rat microglial cells *in vitro* by enhancing their production of ROS and reactive nitrogen species (RNS) and altering their expression of proinflammatory genes (i.e., increase in COX-2 but decrease in tumor necrosis factor- $\alpha$  expression) (Table 1) [36]. However, even at the highest treatment concentration of 40,000 nanoparticles per  $\mu\text{L}$  (i.e., 7.28  $\mu\text{g/mL}$ ) for 24 hours, silica nanoparticles did not significantly lower the survival of microglial cells *in vitro* [36]. Nevertheless, Choi et al. [36] did suggest that continuous production of ROS by microglia induced by the silica nanoparticles could induce deleterious effects on neurons in their vicinity and the dysfunction induced by the nanoparticles may not allow the microglia to sustain neuronal health.

Because the putative cytotoxic effects of silicon dioxide nanoparticles in neural cells in the peripheral nervous system (PNS) are largely unknown, we have employed our *in vitro* model of Schwann cells to systematically investigate the putative cytotoxicity of silicon dioxide nanoparticles on neural cells derived from the PNS [25,27,28,31,37]. We are the first to report on the effects of silicon dioxide nanoparticles on neural cells in the PNS [28,37]. Results of our ongoing studies have demonstrated that silicon dioxide nanoparticles exerted cytotoxic effect on Schwann cells by lowering their survival (Table 1) [28,37]. Light microscopic examination revealed that treatment of Schwann cells with the nanoparticles induced dose-related changes in cellular morphology, consistent with the nanoparticles-induced progressive decrease in cell viability and increase in uptake of nanoparticles. Furthermore, employing flow cytometry, we noted the cytotoxicity of silicon dioxide nanoparticles could be attributed, at least in part, to the uptake of the nanoparticles by Schwann cells [28,37]. Treatment with silicon dioxide nanoparticles also induced increased LDH release, decreased glutathione level, and altered morphology and expression of Mn-superoxide dismutase, NADH dehydrogenase subunit 6, and succinate dehydrogenase in Schwann cells [28,37]. Thus, our findings are compatible with the observation that silicon dioxide nanoparticles induce decreases in survival of neural cells derived from the central nervous system and the decreases in cell survival can be attributed, at least in part, to the nanoparticles-induced oxidative stress [12,16,28,36,37].

The effects of silicon dioxide nanoparticles on dorsal root ganglion (DRG) neurons, an *in vitro* model of DRG neurons in PNS *in vivo* [27-29, 31,32], only show a few similarities to those noted in the Schwann cells *in vitro* (Table 1). Treatment of silicon dioxide nanoparticles altered the morphology of DRG neurons: their nuclei were swollen and their processes decreased in number and they became rounded whereas untreated DRG neurons were spindle-shaped [28-37]. Treatment of DRG neurons with silicon dioxide nanoparticles did not induce any necrotic cell damage or necrotic cell death at concentrations from 0.1 to 150

µg/mL but induced oxidative stress by decreasing glutathione levels (Table 1) [28,37]. Nevertheless, when we treated DRG neurons with the nanoparticles at the highest concentration employed (i.e., 200 µg/mL), they showed significant increases in LDH release into the surrounding medium, suggesting that the nanoparticles did induce necrotic damage and/or cell death in DRG neurons at that concentration [28,37]. Thus, the results of our current and ongoing studies strongly suggest that silicon dioxide nanoparticles induce differential effects on neural cells in the PNS.

#### 1.4 PATHOPHYSIOLOGICAL IMPLICATIONS OF TOXICITY OF SILICON DIOXIDE NANOPARTICLES IN MAMMALIAN NEURAL CELLS

Even though, to date, the literature on the effects of silicon dioxide nanoparticles on mammalian neural cells is rather limited, the results of published and ongoing studies appear to coalesce into a recognizable pattern (see Tables 1) which allows us to draw some tentative generalizations regarding pathophysiological implications of toxicity of silicon dioxide nanoparticles in mammalian neural cells. However, in this review, we can only very briefly discuss four such generalizations.

(i) Because silicon dioxide nanoparticles can readily cross the blood-brain barrier (BBB) (also see section 1.2 above), once the nanoparticles penetrate into the central (or for that matter, the peripheral) nervous system, they can directly influence neural cells therein. Consequently, whether the effects of silicon dioxide nanoparticles on neural cells are deleterious critically depends on the extent of the accumulation of the nanoparticles in the nervous tissue.

(ii) Evidence is accumulating that silicon dioxide nanoparticles appear to exert differential effects on neural cells. It is well recognized that glial cells protect neurons from a variety of pathophysiological assaults [26,30]. Therefore, it is conceivable that in addition to the direct cytotoxic effect on neurons exerted by silicon dioxide nanoparticles, the nanoparticles can exert indirect toxic effects on neurons through their actions on glial cells, ultimately compromising the ability of glial cells to maintain neuronal health and well being.

(iii) As alluded to above (see subsections 1.3.2 and 1.3.3 above), silicon and aluminum were found to be co-localized in the cores of senile plaques in the cortex of Alzheimer's disease (AD) patients [14] and accumulated silicon and aluminum were also found in lipofuscin granules in patients who died of AD [15]. Moreover, when directly introduced into the brains of rats and mice *in vivo*, silica nanoparticles induced inflammatory responses in astrocytes and degeneration of axons and axon terminals in the vicinity of the astrocytes [13]. These early observations [13-15], together with more recent reports (see Table 1) of toxic effects of silicon dioxide nanoparticles on mammalian neural cells *in vivo* and *in vitro*, strongly suggest that the neurotoxicity of silicon dioxide

nanoparticles may assume pathophysiological and perhaps even pathogenetic importance in neurodegenerative diseases such as Alzheimer's disease.

(iv) We have mentioned earlier that their important findings led Wu et al. [16] to conclude exposure to silicon dioxide nanoparticles exerts negative health impact on the striatum in general and on dopaminergic neurons in particular and may therefore pose a risk for neurodegenerative diseases. Our review of the literature on toxicity of silicon dioxide nanoparticles in mammalian neural cells has also prompted us to propose that accumulation and toxicity of silicon dioxide nanoparticles in the striatum may serve as a model system for parkinsonism and Parkinson's disease. Furthermore, Chen, von Mikecz and their associates [35] elegantly demonstrated that upon entering neural cells, silicon dioxide nanoparticles can enter their nuclei and induce the formation of aberrant protein aggregates therein. Because such aberrant protein aggregates are highly reminiscent of those noted in the brain in neurodegenerative diseases, Chen and von Mikecz [35] therefore proposed that "silica nanoparticles have emerged as excellent tools for proof-of-principle studies, in this case, establishment of cell-based models for degenerative protein aggregation diseases."

## 1.5 CONCLUSIONS AND PROSPECTS FOR FUTURE RESEARCH

In this concise review, we have summarized and discussed the literature on the toxicity of silicon dioxide nanoparticles on mammalian neural cells *in vivo* and *in vitro*. Despite the fact that, to date, the studies published in this literature are rather limited in number, a clear and consistent "picture" is slowly emerging regarding the mechanisms underlying the toxicity of silicon dioxide nanoparticles in neural cells. As we have emphasized earlier, one major reason why this literature is scant is that until recently, there was a lack of suitable cell models *in vitro* for high throughput screening of the cytotoxicity of silicon dioxide nanoparticles — and for the matter the cytotoxicity of nanoparticles in general — in mammalian neural cells. We were the first to develop neural cell models *in vitro* consisting of various neural cell types derived from both the central and the peripheral nervous systems so as to allow the high throughput screening of the cytotoxicity of silicon dioxide nanoparticles in mammalian neural cells [12, 17-32].

Based on a critical review of the literature as well as current and ongoing studies, we can tentatively arrive at the following conclusions. (i) Far from being harmless, silicon dioxide nanoparticles can and do induce differential cytotoxicity on mammalian neural cells. (ii) Some of the recognized mechanisms underlying the toxicity of silicon dioxide nanoparticles in neural cells include, but are not limited to, oxidative stress, inflammatory responses, necrotic damage and cell death, apoptosis, formation of aberrant nuclear protein aggregates and

altered mitochondrial metabolism. (iii) Perhaps the most interesting and also intriguing conclusion is that silicon dioxide nanoparticles can serve as versatile tools for elucidating pathophysiological and molecular mechanisms underlying neurodegenerative diseases such as Alzheimer's disease and Parkinson's disease. Moreover, our current and ongoing studies also strongly suggest that these nanoparticles can also be fruitfully exploited to elucidate mechanisms underlying peripheral neuropathy.

As evident from this concise review, there are still much to be discovered concerning the toxicity of silicon dioxide nanoparticles in mammalian neural cells. The availability of various models *in vitro* consisting of various neural cell types derived from both the central as well as the peripheral nervous system greatly facilitate both the high throughput screening of the cytotoxicity of silicon dioxide nanoparticles and systematic investigation of the underlying cellular and molecular mechanisms. Clearly, these are interesting and exciting areas that merit further and systematic investigation.

## 1.6 STATEMENT OF DISCLOSURE/CONFLICTS OF INTEREST

The authors declare that they have no conflict of interest and have no affiliations or financial involvement with any organization or entity discussed in this chapter. This includes employment, consultancies, honoraria, grants, stock ownership or options, expert testimony, patents (received or pending) or royalties. No writing assistance was utilized in the production of this manuscript and the authors have received no payment for preparation of this chapter. The findings and conclusions here reflect the current views of the authors. They should not be attributed, in whole or in part, to the organizations with which they are affiliated, nor should they be considered as expressing an opinion with regard to the merits of any particular company or product discussed herein. Nothing contained herein is to be considered as the rendering of legal advice.

## 1.7 AUTHOR BIOGRAPHIES

**James C.K. Lai** is Professor of Pharmacology and Toxicology, Department of Biomedical and Pharmaceutical Sciences, and Associate Director, Biomedical Research Institute, Idaho State University, Pocatello, Idaho. He received his B.Sc. (Honors.) degree in Microbiology from Cardiff University, Wales in 1970, his M.Sc. degree in Neurocommunications from University of Birmingham, England in 1971, and his Ph.D. degree in Biochemistry from University of London, England in 1975. Prior to joining to Idaho State University in 1991, Dr. Lai had

held faculty appointments at Albert Einstein College of Medicine, Bronx, NY and Cornell Medical College, New York, NY. From 1985 to 1990, he was an Editorial Board Member of *Neurotoxicology*; from 1993 to 1996, he was the Associate Editor of *Pharmacy Case Review*; from 1990 to 2010, he was an Editorial Board Member of *Metabolic Brain Disease*; and from 1995 to 2008, he was an Editorial Board Member of *Neurochemical Research*. His long-standing research interests include Neuroscience, Neurotoxicology, and Regulation of Brain Metabolism. In the last decade, he has also worked on Nanoscience, Nanopharmacology, and Nanotoxicology as well as Cancer Pharmacology and Anti-Cancer Drug Discovery. He has published over 190 journal articles, reviews, and book chapters in these and related areas.

**Ashvin R. Jaiswal** is currently engaged in contract research in biomedical sciences in the Boston area. He received a Bachelor of Pharmacy degree (First Division) from the Amravanti University, Amravanti, India in 2004 and a M.S. degree in Pharmaceutical Sciences in 2011 from Idaho State University College of Pharmacy. He has developed cell culture models *in vitro* of the peripheral nervous system consisting of Schwann cells and dorsal root ganglion (DRG) neurons and employed them to investigate cytotoxicity of silicone dioxide nanoparticles in neural cells; he has also employed the cell models to investigate some of the pathophysiological mechanisms underlying peripheral neuropathy, especially diabetic neuropathy. His publications include 8 journal articles, a review chapter, and 10 abstracts.

**Maria B. Lai** is presently a Ph.D. student in the Department of Molecular, Cellular, and Developmental Biology at the University of Colorado at Boulder. She received her B.S. degree in Microbiology in 2009 from Idaho State University and her M.S. degree in Pharmaceutical Sciences in 2011 from Idaho State University College of Pharmacy. From 2005 to 2011 she worked on several research projects including, but not limited to, cytotoxicity of manganese in tumor cells, toxic mechanisms of nanoparticles of metallic and non-metallic oxides in neural and non-neural cancer cells, effects of statins on hepatocellular carcinoma and pancreatic cancer cells, and anti-cancer drug discovery. Her publications in these and related areas include 13 journal papers, 1 book chapter, and 41 abstracts.

**Sirisha Jandhyam** is currently looking for research opportunities to continue her career. She received her Bachelor of Pharmacy degree in 2003 from Andhra University, India and her M.S. degree in Pharmaceutical Sciences in 2008 from Idaho State University College of Pharmacy. Her M.S. thesis research was on the cytotoxicity of metallic and non-metallic oxide nanoparticles. She also has additional research experience working on cancer pharmacology. Her publications include 11 journal papers, 1 book chapter, and 13 abstracts.

**Solomon W. Leung** is Professor in Department of Civil and Environmental Engineering, School of Engineering, College of Science and Engineering, Idaho

State University and the coordinator of Environmental Engineering program at Idaho State University. He received his Ph.D. in Civil and Environmental Engineering in 1989 from University of Iowa; he also has a M.S. in Chemical Engineering and a B.A. in Chemistry from the University of Iowa. His research interests include physicochemical treatment processes, particularly chemical oxidations applied to the treatment of soils and groundwater, disinfection and by-products generation in water and wastewater, environmental systems modeling, environmental risk assessment, biotechnology, and nanotechnology. In the last 10 years, Dr. Leung has researched extensively in biomedical applications of nanotechnology, biosensors, and nanotoxicology. He has published 90 peer-reviewed journal articles, proceedings and book chapters, and given more than 140 presentations in regional, national, and international conferences. Dr. Leung is also a registered Professional Engineer (P.E.) in the State of Idaho.

**Alok Bhushan** is Professor in Department of Biomedical and Pharmaceutical Sciences, College of Pharmacy at Idaho State University in Pocatello. Dr. Bhushan received his B. Sc. (Honors) and M. Sc. degree in chemistry from University of Delhi, India. He received his Ph.D. in Biochemistry from Punjab Agricultural University, India. He was a post-doctoral fellow at Johns Hopkins School of Medicine, Medical University of South Carolina and University of Vermont. He has held faculty positions at Department of Pharmacology, School of Medicine, University of Vermont and Department of Biomedical and Pharmaceutical Sciences, College of Pharmacy, Idaho State University. He has over 10 years of experience in Pharmacy education. He successfully completed the Academic Fellows Leadership Program (AFLP) at AACCP. He has been trained to serve as site evaluator for accreditation by ACPE and has had the opportunity to be a site evaluator. Dr. Bhushan's areas of interest include cancer pharmacology and signal transduction focused on treatment and prevention. His research areas are 1) understanding mechanisms to block glioblastoma invasion in brain and synthesis of novel agents that target the process of invasion; 2) understanding the mechanism of the role of isoflavones in preventing breast and oral cancer; 3) pharmacology of nanomaterials; 4) natural drug discovery for prevention and treatment of cancer; and 5) characterization and cloning of a novel reduced folate transporter which plays role in methotrexate and cisplatin resistance. Dr. Bhushan has over 75 journal articles and reviews to his credit. He has served as major advisor to several Ph.D. and Master's students at Idaho State University.

### Acknowledgment

Our studies were supported by a US Army Medical Research and Material Command Project Grant (Contract W81XWH-07-2-0078).



## References

1. US Environmental Protection Agency. Draft nanomaterial research strategy. Available at: ([http://epa.gov/ncer/nano/publications/nano\\_strategy\\_012408.pdf](http://epa.gov/ncer/nano/publications/nano_strategy_012408.pdf)). [Accessed August 3, 2010.]
2. Martin, K.R. (2007). The chemistry of silica and its potential health benefits. *Journal of Nutrition and Health in Aging* **11**:94-97.
3. Jonat, S., Hasenzahl, S., Gray, A., and Schmidt, P.C. (2005). Influence of compacted hydrophobic and hydrophilic colloidal silicon dioxide on tableting properties of pharmaceutical excipients. *Drug Development in Industrial Pharmacy* **31**:687-696.
4. Sayes, C.M., Reed, K.L., and Warheit, D.B. (2007). Assessing toxicity of fine and nanoparticles: comparing in vitro measurements to in vivo pulmonary toxicity profiles. *Toxicological Science* **97**:163-180.
5. Adams, L.K., Lyon, D.Y., McIntoch, A., and Alvarez, P.J. (2006). Comparative toxicity of nano-scale TiO<sub>2</sub>, SiO<sub>2</sub>, and ZnO water suspensions. *Water Science and Technology* **54**: 327-334.
6. Lewinski, N., Colvin, V., and Drezek, R. (2008). Cytotoxicity of nanoparticles. *small* **4**(1):26-49.
7. Barik, T.K., Sahu, B., and Swain, V. (2008). Nanosilica – from medicine to pest control. *Parasitology Research* **103**:253-258.
8. Napierska, D., Thomassen, L.C.J., Lison, D., Martens, J.A., and Hoet, P.H. (2010). The nanosilica hazard: another variable entity. *Particle & Fibre Toxicology* **7**:39-71.
9. Kim, J.S., Yoon, T.-J., Yu, K.N., Kim, B.G., Park, S.J., et al. (2006). Toxicity and tissue distribution of magnetic nanoparticles in mice. *Toxicological Science* **89**(1):338-347.
10. Sharma, H.S., Hussain, S., Schlager, J., Ali, S.F., and Sharma, A. (2010). Influence of nanoparticles on blood-brain barrier permeability and brain edema formation in rats. *Acta Neurochirurgica Supplement* **106**:359-364.
11. Zang, Y., Calon, F., Zhu, C. Boado, R.J., and Pardridge, W.M. (2003). Intravenous nonviral gene therapy causes normalization of striatal tyrosine hydroxylase and reversal of motor impairment in experimental parkinsonism. *Human Gene Therapy* **14**(1):1-12.
12. Lai, J.C.K., Ananthakrishnan, G., Jandhyam, S., Dukhande, V.V., Bhushan, A., et al. (2010). Treatment of human astrocytoma U87 cells with silicon dioxide nanoparticles lowers their survival and alters their expression of mitochondrial and cell signaling proteins. *International Journal of Nanomedicine* **5**:715-723.
13. Rees, S., and Cragg, B. (1983). Is silica involved in neuritic (senile) plaque formation? *Acta Neuropathologica* **59**:31-40.
14. Candy, J.M., Oakley, A.E., Klinowski, J., Carpenter, T.A., Perry, R.H., et al. (1986). Aluminosilicates and senile plaque formation in Alzheimer's disease. *Lancet* **I**(8477):354-357.
15. Takutake, S., and Oyanagi, S. (1995). Accumulation of aluminium and silicon in lipofuscin granules. *Gerontology* **41 Suppl. 2**:131-144.
16. Wu, J., Wang, C., Sun, J., and Xue, Y. (2011). Neurotoxicity of silica nanoparticles: brain localization and dopaminergic neurons damage pathways. *ACS Nano* **5**(6):4476-4489.

17. Lai, J.C.K., Lai, M.B., Edgley, K.L., Bhushan, A., Dukhande, V.V., et al. (2007). Silicon dioxide nanoparticles can exert cytotoxic effects on neural cells. *Technical Proceedings of 2007 Nanotechnology Conference and Trade Show, Volume 2, Chapter 8: Bio Materials and Tissues*:741-743.
18. Jandhyam, S., Lai, M.B., Dukhande, V.V., Bhushan, A., Daniels, C.K., et al. (2008). Silicon dioxide nanoparticles exert dissimilar cytotoxic effects on mammalian cell types. *Technical Proceedings of 2008 Nanotechnology Conference and Trade Show, Volume 2, Chapter 2: Environment, Health and Toxicology*:126-129.
19. Lai, M.B., Jandhyam, S., Dukhande, V.V., Bhushan, A., Daniels, C.K., et al. (2008). Differential cytotoxicity of metallic oxide nanoparticles in mammalian cells. *Technical Proceedings of 2008 Nanotechnology Conference and Trade Show, Volume 2, Chapter 2: Environment, Health and Toxicology*:130-133.
20. Wang, Y.-H., Jandhyam, S., Dukhande, V.V., Gao, W.J., Gu, H.-Y., et al. (2008). A co-culture model for nanotoxicity and tissue engineering studies. *Technical Proceedings of 2008 Nanotechnology Conference and Trade Show, Volume 2, Chapter 2: Environment, Health and Toxicology*:164-167.
21. Gao, W.J., Dukhande, V.V., Jandhyam, S., Wang, Y.-H., Gu, H.-Y., et al. (2008). A non-contact culture model for investigating cell signaling and nanotoxicity. *Techn. Proc. 2008 Nanotechnology Conference and Trade Show, Volume 2, Chapter 2: Environment, Health and Toxicology*:172-175.
22. Lai, J.C.K., Jandhyam, S., Lai, M.B., Dukhande, V.V., Bhushan, A., et al. (2008). Cytotoxicity of metallic oxide nanoparticles: new insights into methodological problems and advances in elucidation of underlying mechanisms. *Proceedings of 12<sup>th</sup> WMSCI 2008, Orlando, FL, USA, Volume II*:10-15.
23. Lai, J.C.K., Lai, M.B., Jandhyam, S., Dukhande, V.V., Bhushan, A., et al. (2008). Exposure to titanium dioxide and other metallic oxide nanoparticles induces cytotoxicity on human neural cells and fibroblasts. *International Journal of Nanomedicine* **3**(4):533-545.
24. Lai, M.B., Jandhyam, S., Dukhande, V.V., Bhushan, A., Daniels, C.K., et al. (2009). Cytotoxicity of metallic oxide nanoparticles in human neural and non-neural cells. *Technical Proceedings of 2009 Nanotechnology Conference and Trade Show, Volume 2, Chapter 3: Nano Medicine*:135-138.
25. Jaiswal, A., Wong, Y.Y.W., Bhushan, A., Daniels, C.K., and Lai, J.C.K. (2010). A noncontact co-culture model of peripheral neural cells for nanotoxicity, tissue engineering and pathophysiological studies. *Technical Proceedings of 2010 NSTI Nanotechnology Conference and Expo – Nanotech 2010, Vol. 3 Chapter 8: Environment, Health and Safety*:527-531.
26. Wong, Y.Y.W., Jaiswal, A.R., Dukhande, V.V., Bhushan, A., Leung, S.W., et al. (2010). Elucidation of neuroprotective properties of astrocytoma (astrocytes-like) cells in neural cell culture models *in vitro*: applications in tissue engineering and nanotoxicology. *Technical Proceedings of 2010 NSTI Nanotechnology Conference and Expo – Nanotech 2010, Vol. 3 Chapter 8: Environment, Health and Safety*:561-564.
27. Jaiswal, A.R., Bhushan, A., Daniels, C.K., and Lai, J.C.K. (2010). A cell culture model for diabetic neuropathy studies. *Journal of Idaho Academy of Science* **46**(1):58-63.
28. Jaiswal, A.R., Lu, S., Pfau, J., Wong, Y.Y.W., Bhushan, A., et al. (2011). Effects of silicon dioxide nanoparticles on peripheral nervous system neural cell models. *Technical Proceedings of 2011 NSTI Nanotechnology Conference and Expo – Nanotech 2011, Vol. 3, Chapter 7: Environment, Health and Safety*:541-544.

29. Lu, S., Jaiswal, A.R., Wong, Y.Y.W., Bhushan, A., Leung, S.W., et al. (2011). Differential cytotoxic effects of titanium oxide nanoparticles on peripheral nervous system neural cells. *Technical Proceedings of 2011 NSTI Nanotechnology Conference and Expo – Nanotech 2011, Vol. 3, Chapter 7: Environment, Health and Safety*:533–536.
30. Wong, Y.Y.W., Jaiswal, A.R., Dukhande, V.V., Bhushan, A., Leung, S.W., et al. (2011). New *in vitro* strategy of astrocytoma (astrocytes-like) cells treated with pioglitazone (PPAR gamma agonist) offers neuroprotection against nanoparticle-induced cytotoxicity. *Technical Proceedings of 2011 NSTI Nanotechnology Conference and Expo – Nanotech 2011, Vol. 3, Chapter 6: Nano Medical Sciences and Neurology*:455–458.
31. Jain, A., Jaiswal, A.R., Lu, S., Wong, Y.Y.W., Bhushan, A., et al. (2011). Molecular effects of silicon dioxide nanoparticles on cell survival signaling of dorsal root ganglion (DRG) neurons and Schwann cells. *Technical Proceedings of 2011 NSTI Nanotechnology Conference and Expo – Nanotech 2011, Vol. 3, Chapter 7: Environment, Health and Safety*:545–548.
32. Lai, J.C.K., Gao, W., and Leung, S.W. (2011). Effects of chitosan and nanoparticles on survival of Schwann cells and dorsal root ganglion neurons. *Technical Proceedings of 2011 NSTI Nanotechnology Conference and Expo – Nanotech 2011, Vol. 3, Chapter 6: Nano Medical Sciences and Neurology*:440–442.
33. Di Pasqua, A.J., Sharma, K.K., Shi, Y.L., Toms, B.B., Ouellette, W., et al. (2008). Cytotoxicity of mesoporous silica nanomaterials, *Journal of Inorganic Biochemistry* **102**(7):1416–1423.
34. Tao, Z., Toms, B.B., Goodisman, J., and Asefa, T. (2009). Mesoporosity and functional group dependent endocytosis and cytotoxicity of silica nanomaterials. *Chemical Research and Toxicology* **22**:1869–1880.
35. Chen, M., and von Mikecz, A. (2009). Nanoparticle-induced cell culture models for degenerative protein aggregation diseases. *Inhalation Toxicology* **21**(S1):110–114.
36. Choi, J., Zheng, Q., Katz, H.E., and Guilarte, T.R. (2010). Silica-based nanoparticle uptake and cellular response by primary microglia. *Environmental Health Perspectives* **118**(5):589–595.
37. Jaiswal, A.R. (2011). Cytotoxicity of silicon dioxide nanoparticles in peripheral nervous system neural cell. M.S. Thesis, Idaho State University, Pocatello, ID.

## Metadata of the chapter that will be visualized online

Chapter Title	Mn and Its Interrelation with Other Metal Ions in Health and Disease
Copyright Year	2012
Copyright Holder	Springer Science+Business Media, LLC
Corresponding Author	Family Name
	Particle
	Given Name
	Suffix
	Division/Department
	Organization/University
	Street
	City
	State
	Postcode
	Country
	Phone
	Email
Author	Family Name
	Particle
	Given Name
	Suffix
	Division/Department
	Organization/University
	City
	State
	Postcode
	Country
	Email

## Mn and Its Interrelation with Other Metal Ions in Health and Disease

James C. K. Lai<sup>1</sup> and Solomon W. Leung<sup>2</sup>

<sup>1</sup>Department of Biomedical & Pharmaceutical Sciences, College of Pharmacy and Biomedical Research Institute, Idaho State University, Pocatello, ID, USA

<sup>2</sup>Department of Civil & Environmental Engineering, School of Engineering, College of Science and Engineering and Biomedical Research Institute, Idaho State University, Pocatello, ID, USA

### Synonyms

Interdependence between manganese and other metal ions; Manganese-metal ion interactions

### Definition

Manganese and its interrelation with other metal ions in health and disease refers to how the level and metabolism of manganese in an organ are related to the levels and metabolism of other metal ions in the same organ in a healthy individual and how disease states exert modulatory effects on such interrelations.

### Introduction

To understand the “state of the art” regarding manganese (Mn) and its interrelation with other metal ions in health and disease, one needs to appreciate the

advantages and the limitations of the approaches that critically drive the advances of this multidisciplinary field. As have been emphasized earlier, “Ideally, if one can demonstrate directly the mechanisms that causally link the metabolism of manganese to those of other metals, then one can define the physiological . . . situations or conditions that show *interdependence* between Mn and other metal ions. However, largely because of methodological limitations as well as limitations of experimental approaches, the data in the literature and those of ongoing studies are better or more accurately defined as depicting the *interrelations* between Mn and other metal ions. This conceptual distinction should be borne in mind when one assesses the advances in the topic areas to be discussed. . .” (Lai et al. 2000).

The scope of this entry is limited to a summary discussion of the interrelations between Mn and other elements after chronic exposure of animals or humans to Mn because distributions of ► [Mn in brain](#) regions and in peripheral organs usually reflect chronic rather than acute exposure to this metal. Several aspects of this topic not covered in this entry because of space limitations have been discussed in some detail in one or another of our previous publications (Chan et al. 1983; Lai et al. 1984, 1985a, c, 1999, 2000; Leung et al. 2011; Wright et al. 2011).

### Interdependence Between Manganese and Other Metals in Absorption

Because manganese (Mn) is an essential trace metal, intake of this metal is usually via food intake and intake via the drinking water (Underwood 1977; Lai

et al. 1984, 2000). Respiratory exposure of Mn to humans is rare except under poorly controlled industrial environments such as manganese mining, steel mills, and metal soldering in a confined space. Consequently, the major findings to date employing animal models concerning the interdependence between Mn and other metals are centered upon intestinal absorption and subsequent organ distribution. Several generalizations are evident: intestinal Mn absorption depends on dietary iron (Fe). Low-dietary Fe enhances Mn absorption whereas high-dietary Fe lowers Mn absorption (Lai et al. 1985c, 2000). Similarly, high-dietary Mn intake results in lowered Fe absorption (Lai et al. 1985c, 2000). Furthermore, inclusion of essential and nonessential trace metals in the drinking water of rats and mice can alter accumulation of essential trace metals (including Mn) in their peripheral organs (see Lai et al. 2000 for discussion).

### Interrelations Between Manganese and Other Metals in Several Peripheral Organs

A developmental rat model had been developed so that the organ distribution of multiple metals and other elements could be systematically analyzed based on dietary intake. Furthermore, by exposing rats in utero to manganese (added as the chloride form in the drinking water) and continuously until they were employed for analysis, the effects of Mn on the distributions of other trace metals and electrolytes in various organs during development and aging can be systematically investigated employing versatile techniques such as instrumental neutron activation analysis (INAA) (Chan et al. 1983; Lai et al. 1984, 1999, 2000). Those series of studies constitute the largest and most complete sets of data in the Mn-metal interaction literature (Chan et al. 1983; Lai et al. 1985a, 1985c, 1999, 2000; Leung et al. 2011; Wright et al. 2011).

The relative distribution of trace metals in different peripheral organs subsequent to their intestinal absorption reflects the amount of metal-binding molecules (e.g., proteins and nucleic acids) in each organ and the organ's storage capacity (Lai et al. 2000). In rats, the rank order of the relative abundance of trace metals in peripheral organs is  $\text{Fe} \gg \text{Zn} > \text{Cu} > \text{Al} > \text{Mn} > \text{Se}$ . The rank order of Fe level in peripheral organs is  $\text{spleen} \gg \text{liver} > \text{lung} > \text{heart} \approx \text{kidney}$ . The rank order of Zn level is  $\text{liver} \gg \text{kidney} > \text{spleen} \approx \text{lung} \approx \text{heart}$ .

The rank order of Cu level is  $\text{kidney} \gg \text{liver} \approx \text{heart} > \text{spleen} > \text{lung}$ . The rank order of Mn level is  $\text{liver} \gg \text{kidney} \gg \text{spleen} \approx \text{heart} > \text{lung}$  whereas that for Se is  $\text{kidney} \geq \text{liver} > \text{spleen} > \text{lung} = \text{heart}$ . However, the rank order of the level of the nonessential metal Al is  $\text{spleen} > \text{liver} > \text{heart} > \text{kidney} \approx \text{lung}$ .

In adult (i.e., 120-day-old) rats, chronic Mn treatment induces dose-related differential elevation in Mn in heart, kidney, spleen, and liver (Lai et al. 1985c, 2000). Associated with the differential elevation of Mn in the peripheral organs is a shift in the patterns of organ distribution of trace metals (Lai et al. 1985c, 2000). For example, in Mn-treated rats, Fe levels are increased in spleen and lung whereas Zn level is decreased in liver and Cu level is decreased in spleen, compared to corresponding levels in untreated rats (Lai et al. 1985c, 2000). However, the organ distributions of several other metals are also affected by chronic manganese exposure. (Because of space limitation, those findings will not be discussed here: see Lai et al. 1985c, 2000 for additional details.)

Based on the findings discussed above, two generalizations can be arrived at: (1) Dietary intake of trace metals and electrolytes and their subsequent organ distribution is under regulatory control even though the mechanisms mediating the control are far from being understood. (2) Increasing the levels of Mn in dietary intake (e.g., via addition of manganese salt in the drinking water) ultimately alters the patterns of organ distribution of trace metals.

### Regional Differences in Distribution of Trace Metals in Brain

In the adult rat, whole brain levels of trace metals differ and the rank order of levels of several trace metals is  $\text{Fe} > \text{Zn} > \text{Al} > \text{Cu} > \text{Se} \approx \text{Mn}$  (Lai et al. 1985c, 2000). Additionally, brain levels of several trace metals (e.g., Fe, Cu, Mn, and Se) are altered in the aged rat brain compared to the corresponding levels in the young adult rat brain (Lai et al. 1985c, 2000). On the other hand, each trace metal has its own, almost unique, brain regional distribution.

In development, various regions of the mammalian brain undergo structural changes concomitant with increases in glial cell numbers and migrations of growing and maturing neurons (Lai et al. 2000). Although

not yet fully understood, these developmental structural and cellular changes ultimately give rise to each trace metal exhibiting its characteristic regional distribution in the adult brain (Lai et al. 1985c, 2000). For example, in the adult rat, Fe level is higher in hippocampus, hypothalamus, pons and medulla, and cerebellum than in midbrain, striatum, and cerebral cortex. Zn level is higher in hippocampus and cerebral cortex than in the other regions whereas Cu level is highest in hypothalamus, intermediate in striatum, midbrain, and cerebellum but lowest in hippocampus, pons and medulla, and cerebral cortex. Se level is highest in hippocampus, midbrain, and hypothalamus, intermediate in cerebellum and cerebral cortex, but lowest in striatum and pons and medulla. Mn level is highest in midbrain, cerebellum, and pons and medulla, intermediate in cerebral cortex and hypothalamus, but lowest in striatum and hippocampus. The level of the nonessential trace metal, Al, unlike those of the essential metals (e.g., Fe, Zn, Cu, Mn, Se) is lower in cerebral cortex than those in other regions.

Distributions of electrolytes are also somewhat different from those of trace metals (Lai et al. 1985c, 2000). In the adult rat, Ca level is lower in cerebral cortex and midbrain than in the other regions. Mg level is also lower in cerebral cortex than those in other regions.

## Interrelations Between Manganese and Other Metals in Brain

To facilitate the investigation of the interrelations between manganese and other trace metals and electrolytes in brain and other organs, a model of chronic and life-span exposure of rats to manganese had been developed (Lai et al. 1984, 1985b). Chronic Mn exposure was carried out by adding  $\text{MnCl}_2 \cdot 4\text{H}_2\text{O}$  into the drinking water given to the rats. Four groups of rats were studied: the control group was given just the double-distilled water; group A was given 1 mg of  $\text{MnCl}_2 \cdot 4\text{H}_2\text{O}$  per mL of double-distilled water; group B was given 10 mg of  $\text{MnCl}_2 \cdot 4\text{H}_2\text{O}$  per mL of double-distilled water; and group C was given 20 mg of  $\text{MnCl}_2 \cdot 4\text{H}_2\text{O}$  per mL of double-distilled water (Lai et al. 1984, 1985b). The rats were exposed to Mn in utero via their mothers' circulation; postnatally, they were exposed to Mn via their mothers' milk; and from around weaning (i.e., 21/22 days postnatal) onward,

they were directly exposed to Mn in the drinking water (Lai et al. 1984, 1985b). When the rats attained full adulthood (i.e., at 120 days of age), they were euthanized and their organ removed (Lai et al. 1984, 1985b). Each rat brain was dissected into the following seven regions: cerebellum, cerebral cortex, hippocampus, hypothalamus, midbrain, pons and medulla, and striatum (Lai et al. 1984, 1985b). The contents of trace metals and other elements in each brain region were determined employing instrumental neutron activation analysis (INAA) (Chan et al. 1983; Lai et al. 1985c, 1999, 2000). By combining the versatile technique of INAA with the animal model of chronic and life-span exposure to Mn, a comprehensive metallomic database had been collected of levels of trace metals and other essential and nonessential elements in all the brain regions in the four groups of rats (one control and three Mn-treated groups, namely, A, B, and C) (Chan et al. 1983; Lai et al. 1985c, 1999, 2000). The data were taken from the comprehensive metallomic database and then analyzed so as to allow the interpretation of how Mn can interact with trace and major elements in discrete rat brain regions (Leung et al. 2011; Wright et al. 2011). The level of each trace metal or element in each brain region in the Mn-treated rat was compared with the corresponding level (set as 100%) in the same region in the untreated (i.e., control) rat and the difference ranked as % increase or % decrease relative to the value in the control animal. For ease of visual comparison, the rank orders of increases or decreases of levels were color-coded (Tables 1 and 2) (Leung et al. 2011; Wright et al. 2011).

As evident from the rank-order patterns of the regional distributions of trace metals (Table 1) and electrolytes (Table 2) in the seven brain regions in the rats treated with the three doses of Mn, several generalizations regarding how Mn interacts with other trace metals and other elements can be arrived at. (1) Because the distributions of trace metals and other elements in the adult rat brain show region-specific differences, their patterns of distribution in the untreated normal rat brain are significantly altered by Mn treatment and such alterations can be generally correlated with the dose of Mn administered (Tables 1 and 2). (2) Mn treatment leads to selective, region-specific increases in the accumulation of some trace and major elements (Tables 1 and 2). (3) Mn treatment results in selective, region-specific decreases in the accumulation of other trace and major elements

(Tables 1 and 2). (4) By contrast, Mn treatment gives rise to both increases and decreases in the accumulation of some other trace and major elements, and these fluctuations in their accumulation are dependent on both brain region in question and the dose of Mn administered (Tables 1 and 2).

As may be expected, upon chronic Mn treatment, Mn levels show the largest region-specific increases among all the trace metals that were investigated and showed increases (Table 1). Among the trace metals examined showing region-specific increases in their levels induced by Mn treatment, the rank order of their relative changes compared with each other is  $Mn > Hg > Cu > Se$  (Table 1). Because all these trace metals are neurotoxic when taken in excess, this finding suggests that increased brain regional Mn accumulation consequent to Mn treatment results in increased regional accumulation of Hg (a nonessential toxic metal), Cu, and Se, ultimately leading to a cumulative toxicity due to all three metals and perhaps even neurodegeneration.

Among the trace metals and other elements showing region-specific decreases in their levels induced by Mn treatment, the rank order of their relative changes compared with each other is  $F > V > Br > Al > Mo$  (Table 1). The functional roles of F, V, Br, and Mo in mammalian brain are poorly defined. Nevertheless, Al, a nonessential trace metal in mammals, is known to be neurotoxic (Lai et al. 2000). Thus, this finding suggests that Mn accumulation consequent to Mn treatment induces region-specific decreases in Al accumulation, leading to a lowering of neurotoxicity due to Al.

Among the trace metals and other elements showing region-specific fluctuations (i.e., both trends of increases and decreases) in their levels induced by Mn treatment, the rank order of their relative changes compared with each other is  $Cr > Zn > Co > Rb > I$  (Table 1). The functional roles of Cr, Rb, and I in mammalian brain are not defined. Zn is an essential trace metal: its decreases and increases in brain regional accumulation induced by Mn treatment could lead to, respectively, deficiency and toxicity states (Lai et al. 2000). On the other hand, the only known role of Co in mammals is that it is a component in vitamin B12 and is required in ultra-trace quantities. However, it is neurotoxic when taken in excess. Thus, the decreases and increases in brain regional accumulation of Co induced by Mn treatment could give rise

to, respectively, vitamin B12 deficiency and Co neurotoxicity.

Brain Fe level approaches those of major elements and electrolytes such as Ca (Lai et al. 1985c, 2000). Fe interacts with Mn in intestinal absorption (see above); thus, consistent with this notion is the observation that in Mn-treated rats, the largest increase in Fe levels are noted in hypothalamus, striatum, and cerebellum (Table 2), and these are the same regions that show the highest accumulation of Mn (Table 1). Because Fe is neurotoxic when taken and/or accumulated in excess, this observation suggests that the increase in Fe accumulation could accentuate the neurotoxicity of the accumulated Mn, possibly leading to enhanced neurodegeneration (Lai et al. 2000).

Similar to Fe, two electrolytes (namely, Na and Cl) show region-specific increases in their levels induced by Mn treatment, the rank order of their relative changes compared with each other is  $Fe > Na > Cl$  (Table 2). This finding suggests that increases in Na and Cl accumulation induced by Mn treatment could result in altered ionic balance in neural cells.

Unlike the trace metals, none of the electrolytes exhibit predominantly region-specific decreases in their levels induced by Mn treatment (Table 2).

Three other electrolytes exhibit region-specific fluctuations (i.e., both trends of increases and decreases) in their levels induced by Mn treatment, the rank order of their relative changes compared with each other is  $Ca > K > Mg$  (Table 2). It is interesting to note that Mn treatment results in increased Ca accumulation in midbrain, pons and medulla, and striatum but decreased accumulation in cerebellum and hippocampus (Table 2), suggesting in Mn-treated rats, midbrain, pons and medulla, and striatum are the regions that are prone to calcification and Ca-mediated neurodegeneration (Lai et al. 2000). On the other hand, the Mn-treatment-induced fluctuations in regional K may lead to altered neuronal excitability and conduction, while the fluctuations in regional Mg could result in some alterations in key protein functions (e.g., receptor-gated ion channels and protein kinases) in which Mg plays important roles.

In addition to the findings discussed above, chronic and life-span Mn treatment also modulates on the region-specific distributions of trace metals and electrolytes during development and aging. Some of those findings have been discussed previously and will not



be reiterated here (see Lai et al. 1985c, 1999, 2000 for detailed discussion).

Taken together, the region-specific interactions between Mn and other trace metals and other elements (Tables 1 and 2) may have pathophysiological implications in neurodegenerative and other neurological diseases (see below).

### Interrelations Between Manganese and Other Metals in Brain in Human Health and Diseases

While Mn can interact with trace elements (e.g., F, V, Br, Al, Mo) leading to region-specific decreases in their accumulation, the health impact of the Mn-induced decreases is largely unknown as the functional roles of these trace elements in brain, with the exception of Al, are unknown. Of some health concern are the Mn interactions where brain regional levels of trace metals become increased: these trace metals include Mn, Hg, Cu, Se, Fe, and Zn. The available evidence suggests that the accumulation of these metals may have pathophysiological implications in several neurodegenerative and other neurological diseases and the implications are briefly summarized below.

High brain levels of Mn, Ca, and Al are found in Alzheimer's disease (AD). In AD patients, plasma levels of Al, Cd, Hg, and Se are increased (see Lai et al. 2000 for discussion). Fe is also elevated in multiple regions of the AD brain. Fe in the cores and rims of senile plaques of amygdala of AD patients is elevated and Fe (like Cu and Zn) can accelerate aggregation of  $\beta$ -amyloid peptide, a hallmark of AD neuropathology (see Lai et al. 2000 for discussion). Additionally, Zn level is increased in different regions of the AD brain (see Lai et al. 2000 for discussion). Consequently, Fe, Zn, Al, and Cu have been proposed to be responsible for inducing cell death, especially neuronal cell death, in the AD brain because of (a) formation of reactive oxygen species, (b) other metal-mediated cytotoxic effects, or (c) a combination of mechanisms (see Lai et al. 2000 for discussion).

Chronic  $\blacktriangleright$  Mn toxicity in humans shows signs and symptoms that are reminiscent of those noted in Parkinson's disease (PD) and dystonia (Lai et al. 2000). Some but not all studies have demonstrated an increased brain level of Mn in PD. However, increased

levels of Fe and Zn are found in the substantia nigra of PD patients.

In several neurological diseases other than AD and PD, brain metabolism of Mn and other metals are also disturbed. Pick's disease is associated with increases in brain Mn, Fe, and Na and decreases in brain Cr and Se. In amyotrophic lateral sclerosis (ALS) brain, levels of Al and Ca are elevated. These findings suggest Mn may interact with other metals in Pick's disease and in ALS (see Lai et al. 2000 for discussion).

In some metabolic encephalopathies (e.g., dialysis encephalopathy, chronic renal failure without dialysis, and hepatic coma), brain Al is elevated. Thus, Al neurotoxicity is implicated in these encephalopathies. There is also good evidence that Mn level is elevated in globus pallidus of patients with liver cirrhosis, thereby implicating  $\blacktriangleright$  Mn in brain in hepatic encephalopathy (see Lai et al. 2000 for discussion).

### Conclusions and Prospects for Future Investigation

There have been significant advances in our understanding of manganese and its interrelations with other metal ions in health and disease. The advances in the last 25 years have been built upon the skillful exploitation of the versatile technique of instrumental neutron activation analysis (INAA) in conjunction with a rat model of chronic and life-span exposure to Mn in constructing and assembling a comprehensive metallomic database containing the distributions of over 20 trace and major elements in seven discrete brain regions and in multiple peripheral organs in rats during their life span (i.e., from early postnatal development until aging). This comprehensive database also contains the distributions of some 20 trace and major elements in seven discrete brain regions and in multiple peripheral organs in rats continuously exposed to three doses of Mn over their life span. The gradual mining and analyses of selected sets of data within this comprehensive metallomic database have allowed us to arrive at a number of fundamental conclusions as to how Mn interacts with other trace and major elements in various regions of the rat brain and in various peripheral organs.

- (1) Mn interacts with multiple trace elements (especially Fe) in the process of intestinal absorption.
- (2) Each trace and major element has its own, almost

433 unique, brain regional distribution. (3) The patterns of  
434 distributions of trace and major elements in the  
435 untreated rat brain show region-specific differences,  
436 and these patterns are significantly altered by Mn treat-  
437 ment in an approximately dose-related manner. (4) The  
438 patterns of brain regional distributions of trace and  
439 major elements in the adult rats and the modulations  
440 by chronic Mn treatments thereon have implications in  
441 health and disease, especially in regard to several neu-  
442 rodegenerative (e.g., Alzheimer's disease and  
443 Parkinson's disease) and other neurological diseases.  
444 (5) However, the cellular and molecular mechanisms  
445 underlying how Mn interacts with other trace and  
446 major elements in brain and other organs are almost  
447 totally unknown. (6) Nevertheless, the continued min-  
448 ing and systematic analyses of discrete segments of the  
449 comprehensive metallomic database are beginning to  
450 facilitate the formulation of discrete, testable hypoth-  
451 eses regarding such cellular and molecular mecha-  
452 nisms and lead to novel and productive research.  
453 Thus, these endeavors promise to break new grounds  
454 in our understanding of how trace and major elements  
455 interact in biological systems.

456 **Acknowledgments** We wish to acknowledge the contributions  
457 of Drs. Alex W.K. Chan and Margaret J. Minski (now retired),  
458 both formerly of Imperial College, University of London, UK,  
459 and Dr. Louis Lim of Institute of Neurology, University of  
460 London, UK, and their role in either designing or producing or  
461 supporting the creation of the comprehensive metallomic data-  
462 base. JCK Lai wishes to thank the Worshipful Company of  
463 Pewterers, London, UK, for their generous support to allow  
464 him to initiate the project and create the metallomic database.  
465 We thank Mr. G.L. Wright for his timely help with mining and  
466 analyzing some sets of the data. This study is supported, in part,  
467 by a US Army Medical Research and Material Command Project  
468 Grant (Contract W81XWH-07-2-0078).

## 469 Cross-References

- 470 ► [Mn in Brain](#)
- 471 ► [Mn Toxicity](#)

## References

- 472 Chan AWK, Minski MJ, Lai JCK (1983) An application of  
473 neutron activation analysis to small biological samples: 474  
475 simultaneous determination of thirty elements in rat brain  
476 regions. *J Neuro Method* 7:17–328 477
- Lai JCK, Leung TKC, Lim L (1984) Differences in the neuro-  
478 toxic effects of manganese during development and aging: 479  
480 some observations on brain regional neurotransmitter and  
481 non-neurotransmitter metabolism in a developmental rat  
482 model of chronic manganese encephalopathy. 483  
484 *Neurotoxicology* 5:37–48 485
- Lai JCK, Chan AWK, Minski MJ, Lim L (1985a) Roles of metal  
486 ions in brain development and aging. In: Gabay S, Harris J,  
487 Ho BT (eds) *Metal ions in neurology and psychiatry*. Alan  
488 Liss, New York 489
- Lai JCK, Leung TKC, Lim L (1985b) Effects of metal ions  
490 on neurotransmitter function and metabolism. In: Gabay S,  
491 Harris J, Ho BT (eds) *Metal ions in neurology and psychiatry*.  
492 Alan Liss, New York 493
- Lai JCK, Chan AWK, Minski MJ, Leung TKC, Lim L, Davison AN  
494 (1985c) Application of instrumental neutron activation analysis  
495 to the study of trace metals in brain and metal toxicity. In: Gabay  
496 S, Harris J, Ho BT (eds) *Metal ions in neurology and psychiatry*.  
497 Alan Liss, New York 498
- Lai JCK, Minski MJ, Chan AWK, Leung TKC, Lim L (1999)  
499 Manganese mineral interactions in brain. *Neurotoxicology*  
500 20:433–444 501
- Lai JCK, Minski MJ, Chan AWK, Lim L (2000) Interrelations  
502 between manganese and other metal ions in health and dis-  
503 ease. In: Sigel A, Sigel H (eds) *Metal ions in biological*  
504 systems, vol 37. Marcel Dekker, New York 505
- Leung SW, Chan A, Minski M, Lai JCK (2011) Comparison of  
506 elemental distribution in rat's brain after lifelong treatment  
507 with excessive  $Mn^{2+}$  in drinking water and the health impli-  
508 cations. In: *Proceedings of international water convention*,  
509 Singapore, 4–8 July 2011, Article IWA-6218R1, pp 1–10 510
- Underwood EJ (1977) *Trace elements in human and animal*  
511 nutrition, 4th edn. Academic, New York 512
- Wright GL, Lai JCK, Chan A, Minski M, Leung SW (2011) Influ-  
513 ence of metallomic distribution in brain by prolong consump-  
514 tion of contaminant in drinking water. *Proceedings of*  
515 *International Water Convention*, Singapore, 4–8 July 2011,  
516 Article IWA-6228R1, pp 1–21 517

t1.1 **Mn and Its Interrelation with Other Metal Ions in Health and Disease, Table 1** Changes in levels of trace metals and other elements in brain regions in adult female rats after chronic treatment with Mn compared with corresponding levels in untreated (i.e., control) rats. The Mn-treated groups consisted of group A (1 mg of  $\text{MnCl}_2 \cdot 4\text{H}_2\text{O}$  per mL of double-distilled water), group B (10 mg of  $\text{MnCl}_2 \cdot 4\text{H}_2\text{O}$  per mL of double-distilled water), and group C (20 mg of  $\text{MnCl}_2 \cdot 4\text{H}_2\text{O}$  per mL of double-distilled water). The data were derived from the comprehensive metallomic database. The level of each trace metal or element in each brain region in the Mn-treated rat was compared with the corresponding level (set as 100%) in the same region in the untreated (i.e., control) rat and the difference ranked as % increase or % decrease relative to the value in the control animal. For ease of visual comparison, the rank orders of increases or decreases of levels were color-coded as follows: Those levels showing % higher than corresponding values in control rats were color-coded as: *red*, 0–25%; *purple*, 25–50%; and *brown*, >50%. Those levels showing % decrease compared with corresponding values in control rats were color-coded as: *yellow*, 0% to –25%; *green*, –25% to –50%; and *blue*, >–50%. Those levels that were the same as corresponding values in control rats were coded in *black* and those levels that were not detectable (i.e., below the limits of detection) by the INAA technique were not color-coded (i.e., *white*)

	Elements																				
Region	Al			Br			Co			Cr			Cu			F			Hg		
	A	B	C	A	B	C	A	B	C	A	B	C	A	B	C	A	B	C	A	B	C
Cerebellum																					
Cerebral Cortex																					
Hippocampus																					
Hypothalamus																					
Midbrain																					
Pons & Medulla																					
Striatum																					

	Elements																				
Region	I			Mn			Mo			Rb			Se			V			Zn		
	A	B	C	A	B	C	A	B	C	A	B	C	A	B	C	A	B	C	A	B	C
Cerebellum																					
Cerebral Cortex																					
Hippocampus																					
Hypothalamus																					
Midbrain																					
Pons & Medulla																					
Striatum																					

t2.1 **Mn and Its Interrelation with Other Metal Ions in Health and Disease, Table 2** Changes in levels of iron and electrolytes in brain regions in adult female rats after chronic treatment with Mn compared with corresponding levels in untreated (i.e., control) rats. The Mn-treated groups consisted of group A (1 mg of  $\text{MnCl}_2 \cdot 4\text{H}_2\text{O}$  per mL of double-distilled water), group B (10 mg of  $\text{MnCl}_2 \cdot 4\text{H}_2\text{O}$  per mL of double-distilled water), and group C (20 mg of  $\text{MnCl}_2 \cdot 4\text{H}_2\text{O}$  per mL of double-distilled water). The data were derived from the comprehensive metallomic database. The level of each trace metal or element in each brain region in the Mn-treated rat was compared with the corresponding level (set as 100%) in the same region in the untreated (i.e., control) rat and the difference ranked as % increase or % decrease relative to the value in the control animal. For ease of visual comparison, the rank orders of increases or decreases of levels were color-coded as follows: Those levels showing % higher than corresponding values in control rats were color-coded as: *red*, 0–25%; *purple*, 25–50%; and *brown*, >50%. Those levels showing % decrease compared with corresponding values in control rats were color-coded as: *yellow*, 0% to –25%; *green*, –25% to –50%; and *blue*, >–50%. Those levels that were the same as corresponding values in control rats were coded in *black* and those levels that were not detectable (i.e., below the limits of detection) by the INAA technique were not color-coded (i.e., *white*)

Region	Elements																	
	Ca			Cl			Fe			K			Mg			Na		
	A	B	C	A	B	C	A	B	C	A	B	C	A	B	C	A	B	C
<i>Cerebellum</i>	green	yellow	green	red	red	red	brown	brown	red	red	red	yellow	yellow	yellow	yellow	red	red	red
<i>Cerebral Cortex</i>	yellow	red	yellow	red	red	red	red	red	red	red	red	red	red	blue	red	red	red	red
<i>Hippocampus</i>	green	green	green	yellow	yellow	yellow	brown	purple	yellow	red	red	red	yellow	green	green	red	yellow	red
<i>Hypothalamus</i>	green	red	green	purple	purple	purple	brown	brown	purple	purple	purple	red	red	red	red	purple	purple	purple
<i>Midbrain</i>	brown	brown	brown	red	red	red	purple	red	red	purple	red	red	yellow	yellow	yellow	red	red	red
<i>Pons &amp; Medulla</i>	red	brown	red	yellow	yellow	yellow	purple	brown	yellow	yellow	yellow	yellow	yellow	yellow	green	blue	green	green
<i>Striatum</i>	red	purple	purple	red	red	red	purple	brown	brown	red	red	red	red	red	red	purple	red	red

# Comparison of Elemental Distribution in Rat's Brain after Lifelong Treatment with Excessive Mn<sup>2+</sup> in Drinking Water and the Health Implications

G.L. Wright<sup>a</sup>, J.C.K. Lai<sup>b</sup>, A.W.K. Chan<sup>c</sup>, M.J. Minski<sup>c</sup>, L. Lim<sup>d</sup> and S.W. Leung<sup>e,\*</sup>

<sup>a</sup>Civil and Environmental Engineering Department, College of Engineering, Idaho State University, Pocatello, ID 83209, USA

<sup>b</sup>Biomedical & Pharmaceutical Sciences Department, College of Pharmacy and Biomedical Research Institute, Idaho State University, Pocatello, ID 83209, USA

<sup>c</sup>Imperial College Reactor Centre, University of London, Silwood Park, Ascot, Berks., SL5 7PY, UK

<sup>d</sup>University College London, Institute of Neurology, University of London, London WC1N 1P3, UK

<sup>e</sup>Corresponding author: Civil and Environmental Engineering Department, and Biomedical Research Institute, Idaho State University, Pocatello, ID 83209, USA

---

**Abstract.** Lifelong exposure to environmental factors can influence the risk of developing diseases; environmental stresses can ultimately lead to cell death and have been thought to be the cause of many neurological diseases. Our daily diet is one of the important environmental factors that can seriously affect the development and proper function of the brain. In this study, we investigated how 30 elements and electrolytes that were consumed in a regular diet over a lifetime would affect the distribution of these elements in the brain of rats. We also investigated how excessive concentrations of contaminant in drinking water, such as Mn, may affect the accumulation of elements in the brain. Our results indicated that increased consumption of Mn would enhance the retention of heavy metals such Hg and Se in the brain and is believed to be pivotal in many neurological disorders such as Parkinson's and Alzheimer's disease.

*Key words:* Brain; heavy metals; electrolytes; distribution; metallomic; neurological diseases

---

## Acknowledgement

The project is funded in part by a DOD USAMRMC Project Grant (Contract #W81WH-07-2-0078)

## 1. Introduction

Many of the metals around us are essential for life, but others are known to be highly toxic; even the essential metals can be toxic when their intakes are too high. For example, metals such as chromium, cobalt, copper, manganese, and zinc are essential for life. But, an excess intake of these can be toxic. Some metals such as arsenic, cadmium, lead, mercury, and even vanadium (which are found all throughout our environment) are toxic to humans. Some of these toxic metals are even capable of forming covalent bonds with carbon, which result in metal-organic transformation. This transformation affects the mobility and toxicity of the element. Exposure to metal exists all around us. Elements come from natural processes such as volcanoes, water, bacterial activity, and also from anthropogenic sources such as automobile exhaust, agricultural fertilizers, industrial activities, and many other sources. It has been shown that in highly industrialized areas the exposure to elements is extremely high.

The brain is a specialized organ of the body that metabolizes and accumulates metals as part of its normal function. But in a rich metal environment, loss of metalloproteins and loss of defense against oxidative stress caused by one or more of these metals could be responsible for neurodegeneration disorders such as Parkinson's disease (PD) and Alzheimer's disease (AD). The intake of these metals occurs by ingestion of food, water, and inhaling the air. The elemental distribution in the different brain regions vary for each element. Some of these elements are even known to increase or decrease in brains that have a neurodegenerative disorder.

## Elements Studied

Of the 90 plus naturally-occurring elements, 26 are known to be essential for humans and animals (Underwood, 1977). These consist of 11 major elements or macro-elements. They are: C, H, O, N, S, Ca, P, K, Na, Cl, and Mg.

Fifteen elements are known as trace elements or micro-nutrients. They include: Fe, Zn, Cu, Mn, Ni, Co, Mo, Se, Cr, I, F, Sn, Si, V, and As. The molecular bases for the essential element selection and rejection have not been elucidated, however. Major elements, such as Na, K, Ca, and Mg, are required for bodily functions such as body fluid buffer, active transport, ionic balance, electrical transmission, and tissue development as well as the composition of body fluids and structures. Trace elements act primarily as a catalyst in enzyme systems in cells where they serve a wide range of functions from weak ionic effects to highly specific associations such as metalloenzymes. In addition, the protein-metal interactions may increase the stability of the protein moiety to metabolic turnover.

The following are some of the more studied elements discussed in this paper. Others do exist, but not much has been done with them in research. As it can be seen metals are found normally in the brain, but too much of them is not a good thing. An increase/decrease could cause a major change and lead to a neurological disorder.

### *Calcium*

Calcium (Ca) is the fifth most abundant element found in the earth's crust. Ca occurs most commonly in sedimentary rocks in the minerals calcite, dolomite, and gypsum. Ca is essential for life in most living organisms, including humans. Ca has been shown to be elevated in the brains of patients with AD: it concentrates in the amyloid plaques. These plaques are one of the neuropathological hallmarks of AD. However, PSAPP mice (a mouse model of AD) appear to accumulate less Ca in their plaques compared to their surrounding brain tissue (Belavaria et al, 2005).

### *Copper*

Copper (Cu), like most elements, is mined from the earth's crust. Furthermore, Cu is recycled. Cu is commonly used in electrical applications, piping, many household products (e.g., sinks, plumbing, and pots), architectural applications, coin-making, and chemical applications. Cu has been found to be vital in human and plant life. Cu is introduced into the body mostly via food intake. Some foods that are high in Cu are oysters, beef or lamb liver, brazil nuts, cocoa, black pepper, lobster, sunflower seeds, green olives, avocados, and wheat bran. The brain contains approximately 7.3% of the total body Cu supply.

Cu has been an extensively studied metal in the brain (Popescu et al, 2009). In a normal brain, Cu is distributed in similar ways in the central and subcortical white matter of the cerebellum of both young and old brains; however, the periphery of the dentate nucleus is rich in Cu (Zhang et al, 2009). The higher Cu concentrations are mostly found in the cortex and hippocampus (Popescu et al, 2009). A normal aging brain has been shown to have increased Cu levels, especially in the substantia nigra and in some cerebellar regions (Bolognin et al, 2009). However, when the levels of Cu in the cortex and hippocampus increase, Wilson's disease is said to result (Gerlach et al, 1994). In AD, there is an abnormal brain Cu distribution, with large amounts in the amyloid plaques but a deficiency in the neighboring brain tissue. Other researchers also reported Cu to increase in the senile plaques (Bolognin et al, 2009). These findings suggest the involvement of Cu in AD is multifactorial and complex.

### *Iron*

Iron (Fe) is one of the most common metals found in everyday use. Fe makes up about 5% of the earth's crust. The earth's core is believed to consist largely of an iron-nickel alloy constituting 35% of the mass of the earth as a whole. Because of this distribution, Fe is thought to be the most abundant element on earth. Some popular food items rich in Fe include red meat, fish, poultry, beans, vegetables, black-eyed peas, wheat, and cereals.

Fe is another extensively studied metal in the brain. Fe is necessary for normal brain function (e.g., in learning and memory) (Kienzl et al, 1995). In a normal brain, Fe is distributed in similar ways in central and subcortical white matter of the cerebellum of both young and old brains; in the cerebellar cortex, there are high Fe levels, and the periphery of the dentate nucleus is also rich in Fe (Zhang et al, 2009). Fe appears to increase rapidly in the young brain and then remains stable until the later years; increases in Fe in the substantia nigra and globus pallidus have been reported (Bolognin et al, 2009). Regions where brain Fe is high include substantia nigra, globus pallidus, red nucleus, caudate nucleus, and the putamen (Leskovjan et al, 2009).

Like Cu and Ca, Fe has been shown to be elevated in brains of patients with AD. Elevated Fe is found in the amyloid plaques (Belavaria et al, 2005). Fe is also moderately increased in the parietal cortex in AD patients (Srivastava et al, 2002). In patients with Attention Deficit Hyperactivity Disorder (ADHD), Fe has been shown to increase in the substantia nigra (Berg et al, 2001).

### *Magnesium*

Magnesium (Mg) is the 8<sup>th</sup> most abundant element in the earth's crust and is found also in seawater. Mg is commonly used in structural building materials, automotive parts, electronic devices, aerospace construction, photography, and fireworks. Mg is an essential metal in human and plant life (Yokel et al., 2009). Human Mg deficiency has been linked to the development of asthma, ADHD, and osteoporosis. Foods that are high in Mg include spices, nuts, cereals, coffee, cocoa, tea, and vegetables. In neurodegenerative disorders such as AD and PD, Mg does not appear to play a major role. For example, Mg levels in the cerebellum and parietal cortex do not differ between patients with AD and normal humans (Srivastava et al., 2002).

### *Manganese*

Manganese (Mn) is found in the earth's crust and in seawater. It is often found with Fe. Some of the more common usages of Mn are in steel, aluminum alloys, alkaline batteries, coins, and pigments. Some popular foods that contain Mn include tea, spinach, grains, rice, eggs, nuts, olive oil, green beans, and fish.

The majority of the human body's Mn is found in liver and kidneys; nevertheless, Mn is an important element for normal brain development and function (Yokel et al., 2009). In the aging brain, Mn has been shown to redistribute itself in different brain regions, including hypothalamus, thalamus, and corpus callosum (Bolognin et al., 2009). High brain Mn concentrations are related to PD. There has been much research indicating that human striatum, globus pallidus, and substantia nigra show increases in Mn levels and are thought to be target sites for Mn neurotoxicity. The globus pallidus and pituitary glands are other regions where Mn preferentially accumulates. High exposures to Mn results in increases in Mn in the olfactory epithelium and olfactory bulb (Dorman et al., 2006). It is noteworthy that Mn levels in the cerebellum are similar in AD and normal brains while Mn increases in the parietal cortex of AD brains (Srivastava et al., 2002).

### *Potassium*

Potassium (K) occurs in nature as an ionic salt and is essential for humans and other animals. It is found dissolved in seawater and in other minerals. Some common food sources of Potassium include orange juice, potatoes, bananas, avocados, tomatoes, broccoli, apricots, and many other fruits.

Exposure to Potassium is not known to cause neurodegenerative disorders. For example, the concentrations of Potassium are similar between AD and control brains (Hung, 2010; Leskovjan, 2009).

### *Sodium*

Sodium (Na) is considered an essential element for human life. It is found in nature as a compound and never alone, just Na. The most common way it is found is in salt deposits. The most common form of sodium that we know and use is sodium chloride, table salt. It does have other uses as well. Over or under exposure to sodium has not yet been shown to cause neurological disorders. It has been noted that sodium has been shown to increase in every part of the brain in AD patients.

### **What Was Done**

In the past, research has been done on the effects of the different elements on the brain and the neurological disorders that they may cause. None though, have looked into as many metals that will be presented here at one time. Also, manganese has not yet been deployed at different stages in a developing rat brain.

In this study, we investigated 30 elements (including electrolytes) and how dietary intake on a life-time basis would affect their concentration and distribution in various regions of the rat brain (hypothalamus, cerebellum, pons and medulla, striatum, mid-brain, cerebral cortex, and hippocampus) and discussed their health implications. The 30 elements of interest were: Al, As, Ba, Br, Ca, Cd, Cl, Co, Cr, Cu, F, Fe, Hg, I, K, La, Mg, Mn, Mo, Na, Rb, S, Sb, Sc, Se, Si, Sm, Sr, V, and Zn. In the past, research has primarily focused on the effects of different elements on the brain and the neurological disorders they may cause. None of those studies, however, have examined simultaneously as many elements in a single study as we have presented here. The objective of this paper is to characterize the levels of major and selected trace elements in various regions of the rat brain during several critical stages of development. Because during the first 8-9 days of age postnatal, the rat hippocampus is extremely difficult to visually distinguish from the overlying cerebral cortex, we had included the hippocampus tissue together with the cerebral cortex for analysis in the case of 5-day-old tissue samples. The four postnatal age groups of rats we have studied include the following:

- I. 5 days old;
- II. 10 days old;
- III. 22/23 days old; and
- IV. 120 days old (i.e., adult).

When manganese was administered, the following levels were added to the drinking water (This will be the same nomenclature used on the Figures):

Control: 120 days old adult female Wistar rat (Porton Strain)

A group: Life-long manganese treatment with 1 mg/ml  $\text{Mn}^{2+}$  in drinking water

B group: Life-long manganese treatment with 10 mg/ml  $\text{Mn}^{2+}$  in drinking water

C group: Life-long manganese treatment with 20 mg/ml  $\text{Mn}^{2+}$  in drinking water

As our well being is largely impacted by the environment we are living in, dietary intake is definitely a major factor that posts a long-term effect on our health. This paper provides some insight into how our diet and pollutants in our diet may affect our neurological health. Consequently, our experimental results may allow us to take some preventative measures in determining how best to optimize and gauge our dietary intake of major and trace elements for the betterment of our health.

## Humans vs. Rats

While humans and rats are not identical neurologically and physiologically, there are more similarities between the two species as far as brain structure and functions are concerned. The four stages of the postnatal development of the rat chosen in this study closely parallel the postnatal development of humans.

## 2. Experimental Methods

Wistar rats of the Porton strain (Animal Breeding Unit, Carshalton, and Surrey, U.K.) bred in the Institute of Neurology, University of London, United Kingdom were used. All animals were kept on a 12-hour light/12-hour dark cycle with free access to food and water. Elemental concentrations in the rat food pellets had been determined (Table 1 below).

**Table 1** Elemental Concentration of Rat Food Pellet

Element	Concentration (in mg/g)
Ca	$6.39 \pm 1.68$
Cl	$2.31 \pm 0.49$
Fe	$0.25 \pm 0.05$
K	$5.36 \pm 0.95$
Mg	$1.17 \pm 0.32$
Na	$1.48 \pm 0.32$
	Concentration (in $\mu\text{g/g}$ )
Al	$98.06 \pm 8.05$
Br	$10.57 \pm 2.26$
Co	$0.20 \pm 0.04$
Cr	$1.50 \pm 0.44$
Cu	$7.21 \pm 2.12$
F	ND(5.00)
Hg	ND (0.25)
I	ND (0.50)
Mn	$49.34 \pm 8.65$



Mo	2.80 ± 0.45
Se	ND (0.25)
Rb	12.73 ± 2.61
V	ND (0.50)
Zn	47.73 ± 4.11

Thirty trace and major elements in different brain regions of rats at the four different age groups (i.e., I through IV as defined above) were analyzed by instrumental neutron activation analysis (INAA) (Chan et al., 1983). The samples were irradiated by thermal neutrons using three different sets of conditions depending on the nuclear characteristics of the elements of interest (Chan et al., 1983). Not all 30 elements were reported in the results because those not reported herein were either below the detection limits of our INAA technique (Chan et al., 1983) or the elements were not retained by the brain tissue. All values listed are mean  $\pm$  S.D.; ND = not detectable, and values in brackets are the maximum elemental concentrations present in the diet.

As already noted above, in age group I, the hippocampus tissue had been included in the cerebral cortex and analyzed as such.

All the standard materials and samples for INAA were freeze-dried and pelleted. Dried samples (rat brain regions) were homogenized using a Glen Creston polystyrene ball-mill and pelleted. Other details of standard and sample preparations were as described previously (Chan, 1981; Lee, 2010).

Standards and samples were irradiated in a 100 KW ‘Consort’ Reactor Mark II at the Imperial College Reactor Centre. Irradiated standards and samples were then analyzed for their elemental contents by gamma ray spectrometry using various Ge(Li) detectors and ND6600 Multichannel Analyzer (Nuclear Data Inc., Schaumburg, Illinois, USA). Details of the elemental determinations were described in the methodology paper by Chan et al. (1983).

All laboratory chemicals used were of analytical grade (BDH Chemicals Limited, U.K.) and single element standards of trace elements were obtained from AAS (Ventron Division, Limited, U.K.); other elemental standards for F, Cl, Br, and P were obtained from Hopkin and Williams Chemical Ltd., U.K. Water for solution preparations and feeding was double-distilled.

### 3. Manganese

For some experiments, manganese was added to the rat’s water. The purpose was to study the effects the manganese had on the other elements that were in the brain. The results of this will be shown later. A brief description of manganese was given above, but do to the extent of discussion with manganese a more detailed description is needed.

Manganese was first discovered by Johan G. Gahn in 1774 by reduction of the dioxide with carbon. The name, manganese, comes from the Latin word ‘magnes,’ which means magnet. Manganese is a gray-white, brittle, hard, metal. Pure manganese exists in four allotropic forms. The metal makes up approximately 0.1% of the Earth’s crust. This makes it the 12<sup>th</sup> most abundant element found in the Earth’s crust. The metal is used extensively to produce a variety alloys, such as steel. In fact without manganese steel would be said not to exist. It is also used in pigments, cell batteries, and can be added as an additive in gasoline to increase the octane rating. (Manganese et al., 2008)

Manganese is also known to be an important element in our daily diet. The metal helps the body convert protein and fat to energy. Some other benefits of manganese are a reduction in fatigue levels, help improve memory, prevent the incidence and severity of osteoporosis, promote normal bone growth, and help to maintain healthy nervous, immune, and reproductive systems. (Manganese, 2005) In our diet we can find manganese in plants and animals. These foods include avocados, nuts, seaweed, tea, raisins, spinach, pineapple, blueberries, beans, whole grains, and other green leafy vegetables.

In the body, the largest manganese quantities are found in bones, liver, kidney, and pancreases. One interesting thing to note about manganese in the body is that decreasing levels of manganese are tied with increasing levels of iron. This leads us to believe that manganese absorption is tied to iron absorption. Currently there is no recommended dietary allowance of manganese, but it has been shown that 2.5 – 5.0 milligrams is safe for humans 11 years old and older. However, not enough manganese can lead to manganese deficiencies. These deficiencies can include seizures, convulsions, eye problems, heart disorders, high cholesterol, memory loss, osteoporosis, contractions, hypertension, and atherosclerosis. (Manganese, 2005) Too much manganese is rare due to the fact that manganese is one of the least toxic trace minerals in the body. However, exposure to high manganese levels has been recorded and linked to impaired motor skills and cognitive disorders. A fatal dose is said to be 10 grams. When Manganese is abnormally concentrated in the brain, especially in the basal ganglia (composed of the striatum), neurological disorders could result due to high concentrations. (Amano et al, 2004)

#### **4. Results**

Table 6 and Figure 3b show the elemental concentration distribution for the brain as a whole as an adult (120 days) and old (750 days). Table 6 is in mg/g and µg/g. Ca, Cl, Fe, K, Mg, and Na are in mg/g while the others are in µg/g. This is the same for Figure 3a as well. The amount of manganese added to the water, for the old treated, was 1 mg/ml. Both the table and the figure display the same information, just in different formats. In Table 6, the percentages shown are found by dividing the control (120 days) with the old control (720 days) and the old treated. Figure 3b shows an enlarged scale of 3a to clarify what happens on the lower concentration levels. No information is available on a breakdown of the different parts of the older brain as shown before for the younger brains.

#### **Comparison of Older Brains**

The following describes what is being shown in the table and figure below. An emphasis has been placed on the older (750 days) brains.

From both the table and figure it can be seen that a majority of the elements decrease as the brain increases in age. This is seen especially with manganese and selenium. It has been shown that high levels of Mn have been found in AD and PD brains. (Dorman et al, 2006) Maybe the decrease shown is the body's way of decreasing the levels of Mn naturally. Selenium is important in humans for cellular function. In large doses it is toxic. Large doses are considered to be greater than 4000 micrograms per day. This can lead to selenosis. Selenium deficiency is extremely rare in humans. This is probably due to the fact that selenium is found in many foods that humans consume such as meat, fish, eggs, nuts, and mushrooms.

The elements that do increase dramatically are calcium, copper, and iron. Without calcium, the brain could age more quickly than normal and it could lead to the inability to make quick judgments. As people age the ability to make quick judgments does decrease so the increase in calcium could be a good thing. As was stated in previous sections many regions of the brain have been shown to have abnormal copper distributions during AD and high accumulations have been related to Wilson's disease. High accumulations of copper in the brain have been shown to be the primary cause of Wilson's disease (Gerlach et al, 1994). Increased brain iron has been found in several neurodegenerative disorders although it has not been defined as the main cause (Lee et al, 2010). Lower levels of iron in the brain could help decrease the chance of neurodegenerative disorders (This has not been proven in research).

When manganese is added to the water it can be seen that a majority of the elements decrease when compared to the control and old control. This is seen especially in selenium. This decrease in selenium can be a good thing but, as mentioned above, selenium is important for cellular function. Calcium, copper, and iron are greater than the control (120 days) although, are not as high as the old control. The possible effects of the higher concentrations were discussed above.

	Elements													
Type	Al	Br	Ca	Cl	Co	Cu	Fe	K	Mg	Mn	Na	Se	Rb	Zn
Old Control														
Old Treated														

**Table 6** Comparison of Adult Brain to Old Brain in Table Format

Key:  
 Above Control      Under Control  
 0 to 25% red      0 to -25% yellow  
 25 to 50% purple      -25% to -50% green  
 > 50% brown      < 50% blue

In Figure 3a the abbreviations that are used are the following:

AC: Adult Control (120 days old)

OC: Old Control (750 days old)

OT: Old Treated (750 days old) - Life-long manganese treatment with 1 mg/ml  $Mn^{2+}$  in drinking water

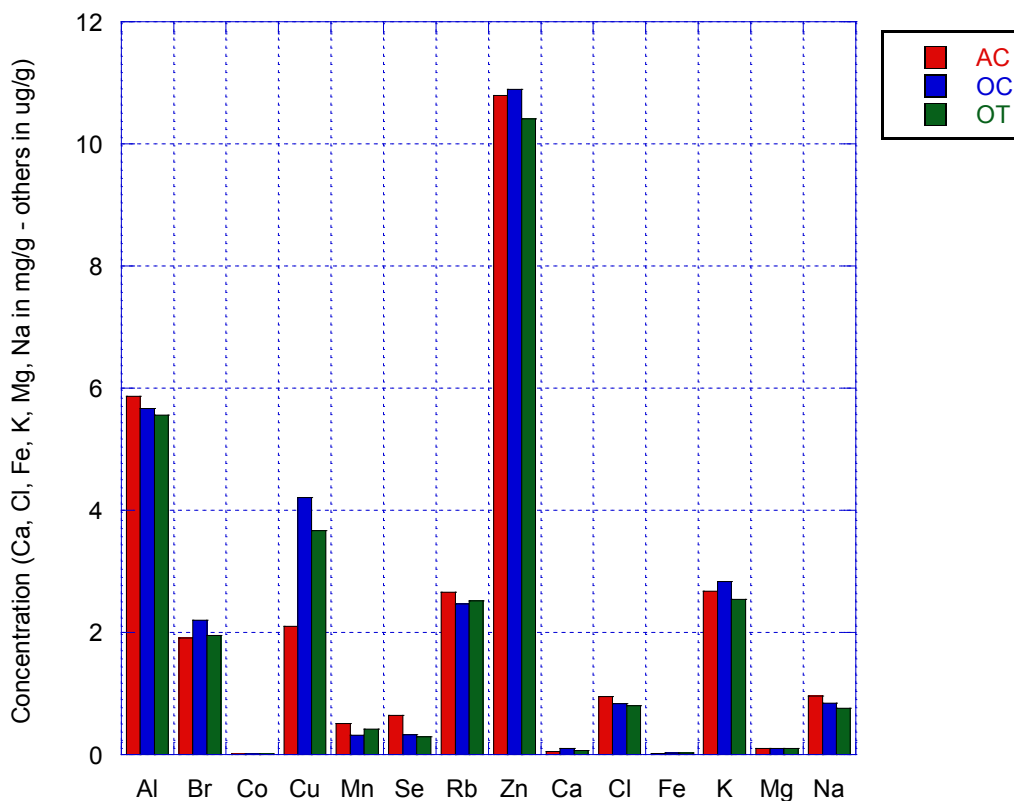


**Figure 3a** Comparison of Adult Brain to Old Brain

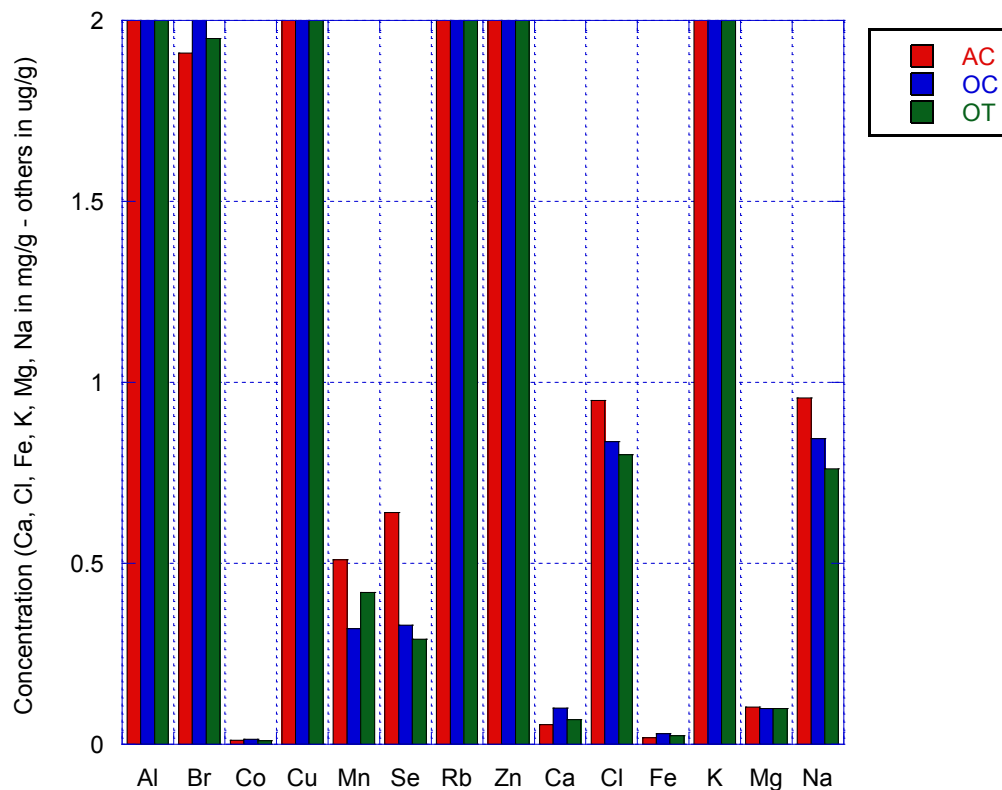


**Figure 3b** Same as Figure 3a, with enlarged scale

## 5. Conclusion

Our results strongly suggest that the metallomic distributions in the rat brain change markedly during the latter years of life. In conjunction with the reports in the literature, our findings also suggest that brain regional metallomic distribution can be influenced by dietary intake of metals and other elements and may contain pathophysiological implications in several key neurodegenerative diseases such as Parkinson's disease and Alzheimer's disease. This is especially seen when the manganese was added to the water of the rats.

Our results also show that as the brain ages it dispenses of the metals and electrolytes that could cause harm to the brain. This is especially seen in the levels of manganese. However on the flip side the brain also adds to the essential elements that are needed for brain development and memory. This is seen in the levels of calcium.

There are, though, some elements that the brain does not deal with, but should. An example of this is shown in copper. The levels of copper increased as the brain aged and copper is shown to be one of the primary causes of Wilson's disease. The added levels of manganese in the water did help lower the copper levels. However, much more research needs to be done to see if this would actually help.

A metallomic distribution model of various regions of the rat brain can be developed based on our experimental results and statistical analysis. Nevertheless, much remains to be discovered regarding the brain functional significance of metallomic distribution during development.

## References

- Amano, R., Tarohda, T., Yamamoto, M. (2004) Regional Distribution of Manganese, Iron, Copper, and Zinc in the rate brain during development. *Anal Bioanal Chemical*, 380, 240-246.
- Belavaria, C., Andresi, E., Molnar, Z., and Bertalan, E. (2005) Determination of Alkali Metals in Control and AD Brain Samples by Different Techniques. *Microchemical Journal*, 79(1-2), 367-373.

- Berg D., Gelach M., Youdim, MBH., Double, KL., Zecca, L., Riederer, P., and Becker, G. (2001) Brain Iron Pathways and Their Relevance to Parkinson's Disease. *Journal of Neurochemistry*, 79(2), 225-236.
- Bolognin, S., Messori, L., and Zatta, P. (2009) Metal Ion Physiopathology in Neurodegenerative Disorders. *Neuromolecular Medicine*, 11(4), 223-238.
- Chan, A.W.K. and Minski, M. J. (1981) U. L. R. C. Internal Report (RES/36), p 37-39.
- Chan, A.W.K., Minski, M.J., Lai, J.C.K. (1983) An Application of Neutron Activation Analysis to Small Biological Samples: Simultaneous Determination of Thirty Elements in Rat brain Regions. *Journal of Neuroscience Methods*, 7(4), 317-328.
- Dorman, DC, Struve, MF, Wong, BA, Dye, JA, and Robertson, ID. (2006) Correlation of Brain Magnetic Resonance Imaging Changes with Pallidal Manganese Concentration in Rhesus Monkeys Following Subchronic Manganese Inhalation. *Toxicological Sciences*, 92(1), 219-227
- Gerlach, M., Benshachar, D., Riederer, P., and Youdim, MBH. (1994) Altered Brain Metabolism of Iron as a Cause of Neurodegenerative Diseases. *Journal of Neurochemistry*, 63(3), 793-807.
- Grobstein, Paul. Brain Sizes. (2001) *Serendip*. <<http://serendip.brynmawr.edu/bb/kinser/Int3.html>> 20 September 2010.
- Hung, YH., Bush, AL, and Cherny, RA. (2010) Copper in the Brain and Alzheimer's disease. *Journal of Biological Inorganic Chemistry*, 15(1), 61-76.
- Kienzl, E., Puchinger, L., Jellinger, K., Linert, W., Stachelberger, H., and Jameson, R.F. (1995) The Role of Transition Metals in the Pathogenesis of Parkinson's disease. *Journal of the Neurological Sciences*, 134, 69-78.
- Lee, DW., and Anderson, JK. (2010) Iron Elevations in the Aging Parkinsonian Brain: A Consequence of Impaired Iron Homeostasis. *Journal of Neurochemistry*, 112(2), 332-339.
- Leskovjan, A. C., Lanzirotti, A., and Miller, L. M. (2009) Amyloid Plaques in PSAPP Mice Bind Less Metal Than Plaques in Human Alzheimer's Disease. *Neuroimage*, 47(4), 1215-1220.
- Manganese. (2005) *vitaminstuff.com*. <<http://www.vitaminstuff.com/mineral-manganese.html>> 7 September 2010.
- Manganese Element Facts. (2008) *Chemicool.com*. <<http://www.chemicool.com/elements/manganese.html>> 7 September 2010
- Popescu, B. F. G., Robinson, C. A., Rajput, A., Rajput, A. H., Harder, S. L., and Nichol, H.. (2009) Iron, Copper, and Zinc Distribution of the Cerebellum. *Cerebellum*, 8(2), 74-79.
- Srivastava, RAK., and Jain, JC. (2002) Scavenger Receptor Class B Type I Expression and Elemental Analysis in Cerebellum and Parietal Cortex Regions of the Alzheimer's disease Brain. *Journal of the Neurological Sciences*, 196(1-2), 45-52.
- Underwood, E.J. (1977) Trace Elements in Animal Nutrient. Academic Press.
- Yokel, RA. (2009) Manganese Flux Across the Blood-Brain Barrier. *Neuromolecular Medicine*, 11(4), 297-310.
- Zhang, L., Lichtmanegger, J., Summer, K. H., Webb, S., Pickering, I. J., and George, G. N. (2009) Tracing Copper-Thiomolybdate Complexes in Prospective Treatment for Wilson's Disease. *Biochemistry*, 48(5), 891-897.

# Influence of Metallomic Distribution in Brain by Prolonged Consumption of Contaminants in Drinking Water

G.L. Wright<sup>a</sup>, J.C.K. Lai<sup>b</sup>, A.W.K. Chan<sup>c</sup>, M.J. Minski<sup>c</sup>, L. Lim<sup>d</sup> and S.W. Leung<sup>e,\*</sup>

<sup>a</sup>*Civil and Environmental Engineering Department, College of Engineering, Idaho State University, Pocatello, ID 83209, USA*

<sup>b</sup>*Biomedical & Pharmaceutical Sciences Department, College of Pharmacy and Biomedical Research Institute, Idaho State University, Pocatello, ID 83209, USA*

<sup>c</sup>*Imperial College Reactor Centre, University of London, Silwood Park, Ascot, Berks., SL5 7PY, UK*

<sup>d</sup>*University College London, Institute of Neurology, University of London, London WC1N 1P3, UK*

<sup>e</sup>*Corresponding author: Civil and Environmental Engineering Department, and Biomedical Research Institute, Idaho State University, Pocatello, ID 83209, USA*

---

**Abstract.** Lifelong exposure to environmental factors can influence the risk of developing diseases; environmental stresses can ultimately lead to cell death and have been thought to be the cause of many neurological diseases. Our daily diet is one of the important environmental factors that can seriously affect the development and proper function of the brain. In this study, we investigated how 30 elements and electrolytes that were consumed in a regular diet over a lifetime would affect the distribution of these elements in seven regions of the brain of rats. We also investigated how excessive concentrations of contaminant in drinking water, such as Mn, may affect the accumulation of elements in the brain. Our results indicated that increased consumption of Mn would enhance the retention of heavy metals such as Hg and Se in the brain that is believed to be pivotal in many neurological disorders such as Parkinson's and Alzheimer's disease.

*Key words:* Brain; heavy metals; electrolytes; distribution; metallomic; neurological diseases

---

## Acknowledgement

The project is funded in part by a DOD USAMRMC Project Grant (Contract #W81WH-07-2-0078)

## 1. Introduction

Many of the metals around us are essential for life, but others are known to be highly toxic; even the essential metals can be toxic when their intakes are too high. For example, metals such as chromium, cobalt, copper, manganese, and zinc are essential for life. But, an excess intake of these can be toxic. Some metals such as arsenic, cadmium, lead, mercury, and even vanadium (which are found all throughout our environment) are toxic to humans. Some of these toxic metals are even capable of forming covalent bonds with carbon, which result in metal-organic transformation. This transformation affects the mobility and toxicity of the element. Exposure to metal exists all around us. Elements come from natural processes such as volcanoes, water, bacterial activity, and also from anthropogenic sources such as automobile exhaust, agricultural fertilizers, industrial activities, and many other sources. It has been shown that in highly industrialized areas the exposure to elements is extremely high.

The brain is a specialized organ of the body that metabolizes and accumulates metals as part of its normal function. But in a rich metal environment, loss of metalloproteins and loss of defense against oxidative stress caused by one or more of these metals could be responsible for neurodegeneration disorders such as Parkinson's disease (PD) and Alzheimer's disease (AD). The intake of these metals occurs by ingestion of food, water, and inhaling the air. The elemental distribution in the different brain regions vary for each element. Some of these elements are even known to increase or decrease in brains that have a neurodegenerative disorder.

## Elements Studied

Of the 90 plus naturally-occurring elements, 26 are known to be essential for humans and animals (Underwood, 1977). These consist of 11 major elements or macro-elements. They are: C, H, O, N, S, Ca, P, K, Na, Cl, and Mg. Fifteen elements are known as trace elements or micro-nutrients. They include: Fe, Zn, Cu, Mn, Ni, Co, Mo, Se, Cr,

I, F, Sn, Si, V, and As. The molecular bases for the essential element selection and rejection have not been elucidated, however. Major elements, such as Na, K, Ca, and Mg, are required for bodily functions such as body fluid buffer, active transport, ionic balance, electrical transmission, and tissue development as well as the composition of body fluids and structures. Trace elements act primarily as catalyst in enzyme systems in cells where they serve a wide range of functions from weak ionic effects to highly specific associations such as metalloenzymes. In addition, the protein-metal interactions may increase the stability of the protein moiety to metabolic turnover.

The following are some of the more studied elements. Others do exist, but not much has been done with them in research. As it can be seen metals are found normally in the brain, but too much of them is not a good thing. An increase/decrease could cause a major change and lead to a neurological disorder.

### *Aluminum*

Aluminum (Al) is one of the more widely distributed metals in the environment. Approximately 8% of the earth's crust is Al. The exposure of Al normally occurs through air, food, and water (Kuman & Gill, 2009). The brain contains approximately 1% of the body's total Al; however, Al has no known function in normal mammalian brain.

During the life-span of a normal human brain, its Al levels appear to increase around age 40, and then plateau at about age 70. The Al levels then begin to increase again from age 80 to 90. The globus pallidus (GP), substantia nigra (SN) and the nucleus ruber appear to be the highest Al levels in the normal human brain (Bolognin ect, 2009). The levels of Al increase in the grey matter in patients with dialysis encephalopathy (Schafer ect, 2006). Also, Al accumulations in the brain have been found to increase in patients with renal failure. Following oral exposure to this metal, retention of Al was reported in the hippocampus. This region of the brain is rich in cholinergic neurons. These and other observations suggest that Al has neurotoxin properties. Furthermore, following chronic exposure, Al has been shown to accumulate in all regions of the rat brain. There is evidence of a relationship between the high levels of Al and increased risk of neurodegenerative disorders, including AD and PD (Kuman & Gill, 2009).

### *Arsenic*

Arsenic (As) is found in the soil and can be transferred to water sources from the soil. Arsenic is introduced into the body by drinking contaminated water or consuming marine species (known to be high in arsenic). Arsenic is also found in wood preservatives, in the production of semiconductors and glass, and in pesticides.

Arsenic is known to induce damage to brain cells. The metal is noted to pass from the maternal to fetal tissue across the transplacental barrier. Arsenic is known to cause disturbances in lipid peroxidation, generation of nitric oxide, reactive oxygen species, and apoptosis. (Florea ect, 2006)

### *Boron*

Boron (B) is normally found in the soil. The semiconductor industry uses boron as a dopant, while boron is also used in light structural materials (e.g. fiberglass), insecticides, preservatives, and reagent for chemical synthesis. Boron is essential for plant growth. The lack of boron can cause deficiencies in plants while too much boron can be toxic to the plants. Boron is also necessary for the health of rats.

In research, boron's physiological role in humans has not yet been fully studied. It is known that Boron is shown to moderately increase in the parietal cortex of the brain in AD brains when compared to normal brains. (Srivastava ect, 2002)

### *Calcium*

Calcium (Ca) is the fifth most abundant element found in the earth's crust. Ca occurs most commonly in sedimentary rocks in the minerals calcite, dolomite, and gypsum. Ca is essential for life in most living organisms, including humans. Ca has been shown to be elevated in the brains of patients with AD: it concentrates in the amyloid plaques. These plaques are one of the neuropathological hallmarks of AD. However, PSAPP mice (a mouse model of AD) appear to accumulate less Ca in their plaques compared to their surrounding brain tissue (Belavaria ect, 2005).

### *Carbon*

Carbon is best known as graphite, diamond, or amorphous carbon. Carbon is also found in coal, gas, and oil reserves. Carbon is present in all known life forms; and in the human body, carbon is the second most abundant element by mass after oxygen.

It was not found the role of Carbon in neurologic disorders. Carbon has been noted to be about half its normal values in the AD brains when compared to normal brains. (Dorman et al, 2006)

### *Cadmium*

Cadmium is produced mainly as a byproduct from mining, smelting, and refining sulfide ores of zinc. Cadmium is used in nickel-cadmium batteries and cadmium telluride solar panels. The use of cadmium has been decreasing due to its high toxicity and carcinogenicity. There are many environmental and health concerns associated with cadmium. Traces of cadmium naturally occur in phosphate, and have been shown to transmit in food through fertilizer applications.

Cadmium (Cd) has been found to not be essential to the human body. Cadmium has been found though to be in the initiation of cancer and the progression of cancer. No research was found on cadmium studies in the brain. (Hung et al, 2010)

### *Chromium*

Chromium (Cr) is also found in the earth's crust and is mined as chromite ore. Because of chromium's high corrosion resistance and hardness, it is added to nickel to create stainless steel: this is the most common application of Cr. It is also used in dyes and pigments, as a gasoline additive, and in the tanning of leather. The pathophysiological role of Cr has not been elucidated. However, Cr has been shown to moderately increase in the parietal cortex of patients with AD when compared to that in normal brains (Srivastava et al, 2002).

### *Copper*

Copper (Cu), like most elements, is mined from the earth's crust. Furthermore, Cu is recycled. Cu is commonly used in electrical applications, piping, many household products (e.g., sinks, plumbing, and pots), architectural applications, coin-making, and chemical applications. Cu has been found to be vital in human and plant life. Cu is introduced into the body mostly via food intake. Some foods that are high in Cu are oysters, beef or lamb liver, brazil nuts, cocoa, black pepper, lobster, sunflower seeds, green olives, avocados, and wheat bran. The brain contains approximately 7.3% of the total body Cu supply.

Cu has been an extensively studied metal in the brain (Popescu et al, 2009). In a normal brain, Cu is distributed in similar ways in the central and subcortical white matter of the cerebellum of both young and old brains; however, the periphery of the dentate nucleus is rich in Cu (Zhang et al, 2009). The higher Cu concentrations are mostly found in the cortex and hippocampus (Popescu et al, 2009). A normal aging brain has been shown to have increased Cu levels, especially in the substantia nigra and in some cerebellar regions (Bolognin et al, 2009). However, when the levels of Cu in the cortex and hippocampus increase, Wilson's disease is said to result (Gerlach et al, 1994). In AD, there is an abnormal brain Cu distribution, with large amounts in the amyloid plaques but a deficiency in the neighboring brain tissue. Other researchers also reported Cu to increase in the senile plaques (Bolognin et al, 2009). These findings suggest the involvement of Cu in AD is multifactorial and complex.

### *Iron*

Iron (Fe) is one of the most common metals found in everyday use. Fe makes up about 5% of the earth's crust. The earth's core is believed to consist largely of an iron-nickel alloy constituting 35% of the mass of the earth as a whole. Because of this distribution, Fe is thought to be the most abundant element on earth. Some popular food items rich in Fe include red meat, fish, poultry, beans, vegetables, black-eye peas, wheat, and cereals.

Fe is another extensively studied metal in the brain. Fe is necessary for normal brain function (e.g., in learning and memory) (Kienzl et al, 1995). In a normal brain, Fe is distributed in similar ways in central and subcortical white matter of the cerebellum of both young and old brains; in the cerebellar cortex, there are high Fe levels, and the periphery of the dentate nucleus is also rich in Fe (Zhang et al, 2009). Fe appears to increase rapidly in the young brain and then remains stable until the later years; increases in Fe in the substantia nigra and globus pallidus have been reported (Bolognin et al, 2009). Regions where brain Fe is high include substantia nigra, globus pallidus, red nucleus, caudate nucleus, and the putamen (Leskovjan et al, 2009).

Like Cu and Ca, Fe has been shown to be elevated in brains of patients with AD. Elevated Fe is found in the amyloid plaques (Belavaria et al, 2005). Fe is also moderately increased in the parietal cortex in AD patients



(Srivastava et al., 2002). In patients with Attention Deficit Hyperactivity Disorder (ADHD), Fe has been shown to increase in the substantia nigra (Berg et al., 2001).

### *Lead*

Lead (Pb) is one of the oldest and most studied environmental toxins. Lead paints in old houses remain a common source of exposure. Lead though is also found in building materials, glass, batteries, gasoline additives, and many others sources. Too much lead is not a good thing.

Lead is known to be very toxic to the brain. Lead poisoning has been linked to memory and learning deficit. Lead-exposure is found in the cerebral cortex, cerebellum, and the hippocampus. Lead can also cause brain damage in children even at low exposure levels. (Florea et al., 2006)

### *Magnesium*

Magnesium (Mg) is the 8<sup>th</sup> most abundant element in the earth's crust and is found also in seawater. Mg is commonly used in structural building materials, automotive parts, electronic devices, aerospace construction, photography, and fireworks. Mg is an essential metal in human and plant life (Yokel et al., 2009). Human Mg deficiency has been linked to the development of asthma, ADHD, and osteoporosis. Foods that are high in Mg include spices, nuts, cereals, coffee, cocoa, tea, and vegetables. In neurodegenerative disorders such as AD and PD, Mg does not appear to play a major role. For example, Mg levels in the cerebellum and parietal cortex do not differ between patients with AD and normal humans (Srivastava et al., 2002).

### *Manganese*

Manganese (Mn) is found in the earth's crust and in seawater. It is often found with Fe. Some of the more common usages of Mn are in steel, aluminum alloys, alkaline batteries, coins, and pigments. Some popular foods that contain Mn include tea, spinach, grains, rice, eggs, nuts, olive oil, green beans, and fish.

The majority of the human body's Mn is found in liver and kidneys; nevertheless, Mn is an important element for normal brain development and function (Yokel et al., 2009). In the aging brain, Mn has been shown to redistribute itself in different brain regions, including hypothalamus, thalamus, and corpus callosum (Bolognin et al., 2009). High brain Mn concentrations are related to PD. There has been much research indicating that human striatum, globus pallidus, and substantia nigra show increases in Mn levels and are thought to be target sites for Mn neurotoxicity. The globus pallidus and pituitary glands are other regions where Mn preferentially accumulates. High exposures to Mn result in increases in Mn in the olfactory epithelium and olfactory bulb (Dorman et al., 2006). It is noteworthy that Mn levels in the cerebellum are similar in AD and normal brains while Mn increases in the parietal cortex of AD brains (Srivastava et al., 2002).

### *Mercury*

Mercury (Hg) is found in deposits throughout the world, mostly as cinnabar (a common ore of Hg). The more common uses of Hg are in barometers, thermometers, dental products (e.g., fillings), and electrical equipment (e.g., computers, telephones, etc.) (Florea et al., 2006). Exposures to Hg most commonly occur from the consumption of marine species (Cannino et al., 2008). Other exposures to Hg may be from exhaust of coal-burning power plants, cement production, batteries, and gold production. The role of Hg in neurological diseases such as AD and PD has been controversial. Mercury can cross the blood-brain and blood-placental barriers. It is then retained by the brain for years (Rooney et al., 2007). Mercury tends to accumulate in lipid-rich regions of the brain. Human exposure to Hg usually results in kidney and neurological disorders (Florea et al., 2006).

### *Platinum*

Platinum (Pt) is mostly found in today's environment in catalytic converters of cars, jewelry, laboratory equipment, and electrical contacts. Once platinum is soluble it can contaminate the water, soil, sediments, and animals, which in turn contaminate food. (Florea et al., 2006)

The role of platinum was not found in neurologic disorders. One thing to note about platinum is that platinum drugs cisplatin, carboplatin and oxaliplatin are the most useful anticancer agents available. (Florea et al., 2006) The side effects of these drugs have not been related to neurological disorders.

### *Nickel*

The large majority of nickel comes from nickel mines; the rest come from byproducts from other mining activities. Because nickel is corrosion-resistant it is commonly used in the manufacture of coins, magnets, batteries, and household utensils.

Exposure to nickel as a gas ( $\text{Ni}(\text{CO})_4$ ) is highly toxic to humans. Other nickel exposure to humans occurs in miners, pierced ears, and the items themselves that are made of nickel. Once nickel is exposed to the human brain it becomes well retained in the tissues even after long periods of time. (Zhang et al, 2009) Not much has been done to study the effects of this. (Florea et al, 2006)

### *Potassium & Rubidium*

Potassium (K) occurs in nature as an ionic salt and is essential for humans and other animals. It is found dissolved in seawater and in other minerals. Some common food sources of K include orange juice, potatoes, bananas, avocados, tomatoes, broccoli, apricots, and many other fruits.

Rubidium (Rb) is not essential for humans, but is readily taken up by the body. It is found commonly mixed in with other elements, especially K. Rb is found in some plants as well. Some common uses of Rb are in fireworks, lasers, chemical applications, and electronic transmission. Rb is found in some brain tumors.

Exposure to K and Rb is not known to cause neurodegenerative disorders. For example, the concentrations of K and Rb are similar between AD and control brains (Hung, 2010; Leskovjan, 2009).

### *Sodium*

Sodium (Na) is considered an essential element for human life. It is found in nature as a compound and never alone, just Na. The most common way it is found is in salt deposits. The most common form of sodium that we know and use is sodium chloride, table salt. It does have other uses as well. Over or under exposure to sodium has not yet been shown to cause neurological disorders. It has been noted that sodium has been shown to increase in every part of the brain in AD patients.

### *Silicon*

Silicon is the second most abundant element found in the Earth's crust, right after oxygen. It is found in the form of quartz (silicon dioxide). The most common place is in gold mines and volcanic exhalations. Silicon is used primarily in semiconductor devices (microchips), glasses, ceramics, cements, and as a sealing agent,

Exposure to silicon has not yet shown to cause neurological disorders. It has been noted that silicon has shown higher concentration in the parietal cortex of AD brains. (Srivastava et al, 2002)

### *Tellurium*

Tellurium is one of the rarest elements found in the Earth crust. It is most often found in gold mining. Tellurium is used in alloys (steel and copper) to improve machinability, solar panels, and in semiconductors.

Exposure to tellurium has not yet shown to cause neurological disorders. It has been noted that tellurium has been shown to have increases in the parietal cortex of the brain in AD patients when compared to normal brains. (Srivastava et al, 2002)

### *Tin*

Tin (Sn) is not found naturally by itself in nature. It is extracted from a compound, cassiterite. This is usually found with granite rocks. One of the most common ways to mine tin is by dredging. Tin is commonly used as a coating for iron to prevent corrosion and solder. Because tin is not highly toxic it is coated over iron to create tin cans, which are used to store food. Tin foil is also used in the household as well to wrap food.

Exposure to tin has not yet shown to cause neurological disorders. It has been noted that tin has been shown to have increases in the parietal cortex of the brain in AD patients when compared to normal brains. (Srivastava et al, 2002)

### *Zinc*

Zinc (Zn) is naturally found in the earth's crust and in seawater. It is normally found with Fe and Cu deposits. Zn is commonly used in batteries, production of brass, bronze, rubber, in pigments, fire retardant, nuclear weapons, automobile engines, and agricultural fungicides. The most common food source of Zn is red meats.

Zn is another essential element in mammals. Zn is distributed in similar ways in the central and subcortical white matter of both young and old brains; the interior of the dentate nucleus and the cerebellar cortex contain high

levels of Zn (Zhang et al, 2009). The regions of the normal brain rich in Zn include the hippocampus, amygdala, and the cortex. As the brain ages, its Zn distribution changes, just in the regions mentioned above. Nevertheless, little or no decrease in brain Zn has been reported in aging humans or rats (Bolognin et al, 2009). Zn is found to be elevated in human amyloid plaques while PSAPP mice (an AD mouse model that does not show neurodegeneration) only had a 29% increase of Zn in their plaques compared to the Zn in brain tissue surrounding the plaques (Belavaria et al, 2005). The potential role of Zn as a cofactor in the pathogenesis of AD was strengthened when Zn enrichment was found in senile plaques and a Zn elevation in the neuropil of AD patients as compared to those in control individuals (Bolognin et al, 2009).

### **What Was Done**

In the past, research has been done on the effects of the different elements on the brain and the neurological disorders that they may cause. None though, have looked into as many metals that will be presented here at one time. Also, manganese has not yet been deployed at different stages in a developing rat brain.

In this study, we investigated 30 elements (including electrolytes) and how dietary intake on a life-time basis would affect their concentration and distribution in various regions of the rat brain (hypothalamus, cerebellum, pons and medulla, striatum, mid-brain, cerebral cortex, and hippocampus) and discussed their health implications. The 30 elements of interest were: Al, As, Ba, Br, Ca, Cd, Cl, Co, Cr, Cu, F, Fe, Hg, I, K, La, Mg, Mn, Mo, Na, Rb, S, Sb, Sc, Se, Si, Sm, Sr, V, and Zn. In the past, research has primarily focused on the effects of different elements on the brain and the neurological disorders they may cause. None of those studies, however, have examined simultaneously as many elements in a single study as we have presented here. The objective of this paper is to characterize the levels of major and selected trace elements in various regions of the rat brain during several critical stages of development. Because during the first 8-9 days of age postnatal, the rat hippocampus is extremely difficult to visually distinguish from the overlying cerebral cortex, we had included the hippocampus tissue together with the cerebral cortex for analysis in the case of 5-day-old tissue samples. The four postnatal age groups of rats we have studied include the following:

- I. 5 days old;
- II. 10 days old;
- III. 22/23 days old; and
- IV. 120 days old (i.e., adult).

When manganese was administered, the following levels were added to the drinking water (This will be the same nomenclature used on the Figures):

Control: 120 days old adult female Wistar rat (Porton Strain)

A group: Life-long manganese treatment with 1 mg/ml  $Mn^{2+}$  in drinking water

B group: Life-long manganese treatment with 10 mg/ml  $Mn^{2+}$  in drinking water

C group: Life-long manganese treatment with 20 mg/ml  $Mn^{2+}$  in drinking water

As our well being is largely impacted by the environment we are living in, dietary intake is definitely a major factor that posts a long-term effect on our health. This paper provides some insight into how our diet and pollutants in our diet may affect our neurological health. Consequently, our experimental results may allow us to take some preventative measures in determining how best to optimize and gauge our dietary intake of major and trace elements for the betterment of our health.

### **Humans vs. Rats**

While humans and rats are not identical neurologically and physiologically, there are more similarities between the two species as far as brain structure and functions are concerned. The four stages of the postnatal development of the rat chosen in this study closely parallel the postnatal development of humans.

## **2. Experimental Methods**

Wistar rats of the Porton strain (Animal Breeding Unit, Carshalton, and Surrey, U.K.) bred in the Institute of Neurology, University of London, United Kingdom were used. All animals were kept on a 12-hour light/12-hour

dark cycle with free access to food and water. Elemental concentrations in the rat food pellets had been determined (Table 1 below).

**Table 1** Elemental Concentration of Rat Food Pellet

Element	Concentration (in mg/g)
Ca	6.39 ± 1.68
Cl	2.31 ± 0.49
Fe	0.25 ± 0.05
K	5.36 ± 0.95
Mg	1.17 ± 0.32
Na	1.48 ± 0.32
	Concentration (in µg/g)
Al	98.06 ± 8.05
Br	10.57 ± 2.26
Co	0.20 ± 0.04
Cr	1.50 ± 0.44
Cu	7.21 ± 2.12
F	ND(5.00)
Hg	ND (0.25)
I	ND (0.50)
Mn	49.34 ± 8.65
Mo	2.80 ± 0.45
Se	ND (0.25)
Rb	12.73 ± 2.61
V	ND (0.50)
Zn	47.73 ± 4.11

Thirty trace and major elements in different brain regions of rats at the four different age groups (i.e., I through IV as defined above) were analyzed by instrumental neutron activation analysis (INAA) (Chan et al, 1983). The samples were irradiated by thermal neutrons using three different sets of conditions depending on the nuclear characteristics of the elements of interest (Chan et al, 1983). Not all 30 elements were reported in the results because those not reported herein were either below the detection limits of our INAA technique (Chan et al, 1983) or the elements were not retained by the brain tissue. All values listed are mean ± S.D.; ND = not detectable, and values in brackets are the maximum elemental concentrations present in the diet.

As already noted above, in age group I, the hippocampus tissue had been included in the cerebral cortex and analyzed as such.

All the standard materials and samples for INAA were freeze-dried and pelleted. Dried samples (rat brain regions) were homogenized using a Glen Creston polystyrene ball-mill and pelleted. Other details of standard and sample preparations were as described previously (Chan, 1981; Lee, 2010).

Standards and samples were irradiated in a 100 KW 'Consort' Reactor Mark II at the Imperial College Reactor Centre. Irradiated standards and samples were then analyzed for their elemental contents by gamma ray spectrometry using various Ge(Li) detectors and ND6600 Multichannel Analyzer (Nuclear Data Inc., Schaumburg, Illinois, USA). Details of the elemental determinations were described in the methodology paper by Chan et al. (1983).

All laboratory chemicals used were of analytical grade (BDH Chemicals Limited, U.K.) and single element standards of trace elements were obtained from AAS (Ventron Division, Limited, U.K.); other elemental standards for F, Cl, Br, and P were obtained from Hopkin and Williams Chemical Ltd., U.K. Water for solution preparations and feeding was double-distilled.

### 3. Manganese

For some experiments, manganese was added to the rat's water. The purpose was to study the effects the manganese had on the other elements that were in the brain. The results of this will be shown later. A brief description of manganese was given above, but do to the extent of discussion with manganese a more detailed description is needed.

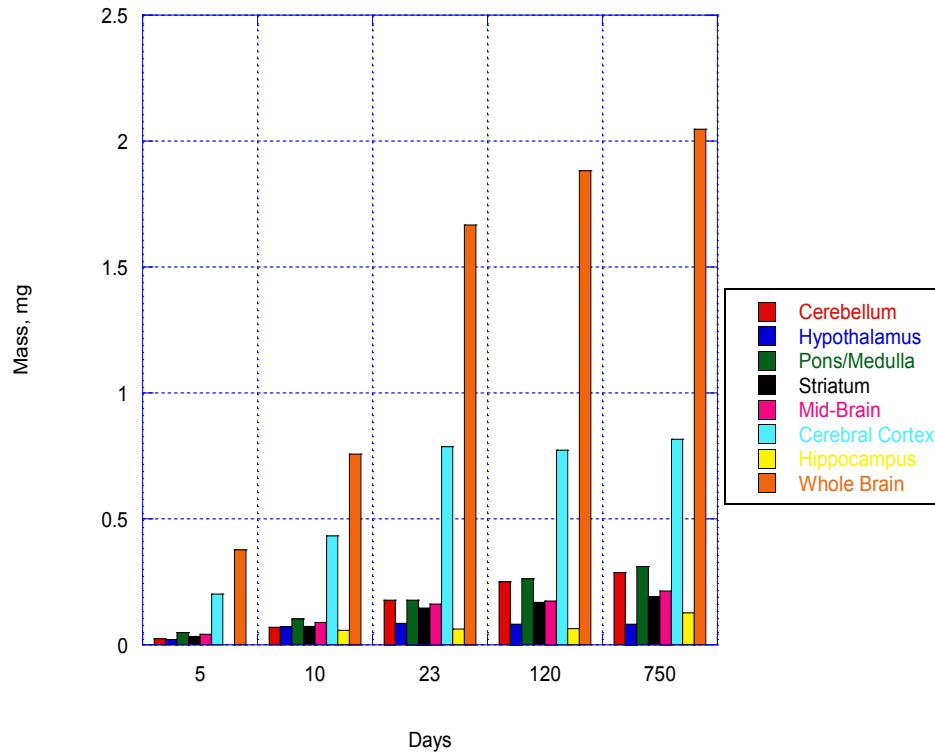
Manganese was first discovered by Johan G. Gahn in 1774 by reduction of the dioxide with carbon. The name, manganese, comes from the Latin word 'magnes,' which means magnet. Manganese is a gray-white, brittle, hard, metal. Pure manganese exists in four allotropic forms. The metal makes up approximately 0.1% of the Earth's crust. This makes it the 12<sup>th</sup> most abundant element found in the Earth's crust. The metal is used extensively to produce a variety alloys, such as steel. In fact without manganese steel would be said not to exist. It is also used in pigments, cell batteries, and can be added as an additive in gasoline to increase the octane rating. (Manganese ect, 2008)

Manganese is also known to be an important element in our daily diet. The metal helps the body convert protein and fat to energy. Some other benefits of manganese is a reduction in fatigue levels, help improve memory, prevent the incidence and severity of osteoporosis, promote normal bone growth, and helps to maintain healthy nervous, immune, and reproductive systems. (Manganese, 2005) In our diet we can find manganese in plants and animals. These foods include avocados, nuts, seaweed, tea, raisins, spinach, pineapple, blueberries, beans, whole grains, and other green leafy vegetables.

In the body the largest manganese quantities are found in bones, liver, kidney, and pancreases. One interesting thing to note about manganese in the body is that decreasing levels of manganese are tied with increasing levels of iron. This leads to believe that manganese absorption is tied to iron absorption. Currently there is no recommended dietary allowance or manganese, but it has been shown that 2.5 – 5.0 milligrams is safe for humans 11 years old and older. However, not enough manganese can lead to manganese deficiencies. These deficiencies can include seizures, convulsions, eye problems, heart disorders, high cholesterol, memory loss, osteoporosis, contractions, hypertension, and atherosclerosis. (Manganese, 2005) Too much manganese is rare due to the fact that manganese is one of the least toxic trace minerals in the body. However, exposure to high manganese levels has been recorded and linked to impaired motor skills and cognitive disorders. A fatal dose is said to be 10 grams. When Manganese is abnormally concentrated in the brain, especially in the basal ganglia (composed of the striatum), neurological disorders could result due to high concentrations. (Amano ect, 2004)

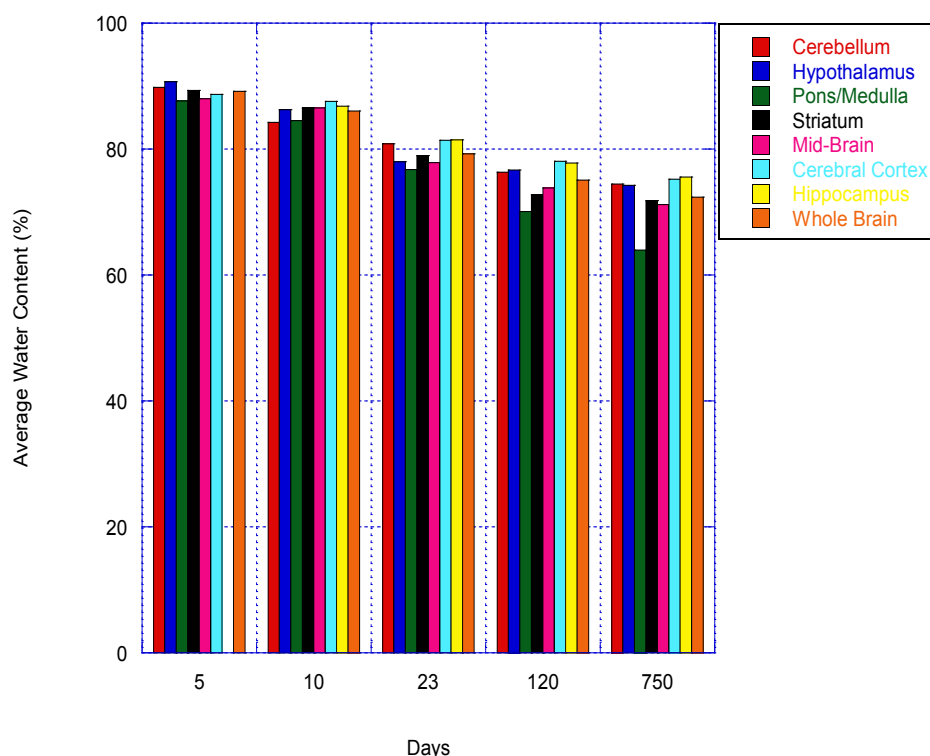
### 4. Results

Figure 1 shows the average mass of the rat brain tissues at different aging stages with no influence of treatment. It can be seen that as the rat ages the weight of its brain increases. A similar process for the human brain happens as well. A newborn human brain weighs 350-400 grams ( $350 - 400 \times 10^3$  mg), while the average adult human brain is about 1,300-1,400 grams ( $1.3 - 1.4 \times 10^6$  mg). This is approximately two percent of the human's overall mass. An average rat brain weighs approximately 0.4 grams. However, even though the human brain weighs more than the rat brain, the brain to body weight ratio is the same, 1/40 (Grobstein ect, 2001). The increase in mass in both the human and rat brain is likely due to the accumulation of different elements in the brain. This is normal because we do accumulate different elements from our food, water, and environment throughout our daily lives.



**Figure 1** Average Mass of Control Rat Brain Tissues at Different Aging Stages

Figure 2 shows the average water content of the brain tissues at different aging stages with no influence of treatment. Here it can be seen that the brain loses water as it ages. This shows that the extra mass that the brain gains as it ages is due to the elements (solid objects), not water accumulation. The average human brain is actually approximately 85% water. According to research, as humans age their percentage of water content decreases. A newborn may have as much as 75% of its weight composed of water. But, this progressively decreases as that new born ages. Most of this decrease does occur during the first 10 years. Also, one interesting thing to note is that obese humans have less water than thin people do. This is due to the fact that fat has less water in it than muscle does (Grobstein et al, 2001). Therefore, Figure 2 makes sense for a human as well as for a rat.



**Figure 2** Average Water Content (%) of Control Rat Tissues at Different Aging Stages

Later in the paper it will be seen that the elements are measured by wet weight. It should be noted that the cerebral cortex and the hippocampus were measured separately in both Figure 1 and Figure 2. It will be noted in the paper if the cerebral cortex and hippocampus were measured together or apart. In the early stages of development it was difficult to separate the sections of the brain and get reasonable results.

### Various Levels of Manganese

Tables 2 and 3 show the elemental concentration in the rats after 120 days when administered different levels of manganese in their drinking water. Table 2 is in mg/g while Table 3 is in  $\mu\text{g/g}$ . Both figures display the same information, just with different elements. The following is a description for each of the sections of the brain and their relationship to Tables 2 and 3.

#### *Cerebellum*

The cerebellum is the cauliflower-shaped section of the brain located in the lower part of the brain next to the brain stem. The cerebellum controls movement, balance, posture, and coordination. It is also thought to control emotions as well.

It can be seen that, on average, element concentrations fluctuate as when administered different doses of the manganese. This can be seen in elements such as copper, potassium, and zinc. As discussed above, for some elements this could be good while others not so good. For example, sodium levels were found to be higher in patients with AD and in our figures below the sodium levels actually increased for all doses of manganese administered. We do not know the levels that could cause AD, however an increase may not be good. Sodium though has not been found in research to be the leading cause of AD; however sodium may have some relevance in the causation and/or progression of AD.

#### *Cerebral Cortex*

The cerebral cortex is located on the outer surface of the brain. The cerebral cortex is responsible for all intellectual functioning such as thinking, voluntary movements, language, reasoning, and perception.

It can be seen that on average manganese helps lower the elemental concentrations in the cerebral cortex, especially at the higher levels of manganese. This is especially seen in Fluorine. Fluorine was not discussed above because it is not one of the more studied elements in the cerebral cortex, so there is a lack of information on it. A couple things to note about fluorine overdose and its effects on the brain are that it causes a reduction in lipid content and nicotinic acetylcholine receptors, increased uptake of aluminum, and the formation of beta-amyloid plaques. These beta-amyloid plaques are a classic brain abnormality in AD. (Connett, 2011) From this we want a lower fluorine level in the brain and this can be achieved from groups A and B.

Another element known to play a part in the formation of AD is calcium. In Table 2 the levels of calcium vary. The low and high levels of manganese decrease the calcium in the cerebral cortex. As stated above one of the pathological hallmarks of Alzheimer's disease (AD) is the accumulation of amyloid plaques between nerve cells (i.e., neurons) in different parts of the human brain including the cerebral cortex. Ca levels in human amyloid plaques in AD are elevated. Maybe lower levels of calcium could affect the amyloid plaques makeup, thus changing the effect of AD.

### *Hippocampus*

The hippocampus is located deep within the temporal lobe in front of the limbic system. The hippocampus is responsible for storing memories and is involved with learning as well. It can be seen that on average manganese helps lower the elemental concentrations in the hippocampus. This is most noticeable at the higher levels of manganese.

One element that it does not decrease is Fluorine, the levels increase. This is not a good thing because high levels of fluorine have been known to cause damage to the hippocampus (Connett, 2011). Another element that does not decrease is copper. Copper increases with every dose of manganese administered. Copper is essential to a healthy brain, however some research has indicated that excess copper in the brain can lead to Huntington's disease. Increased levels of iron are also said to play a part in Huntington's disease as well (Miller, 2007). In Table 2, the lower levels of manganese increase the iron while the higher levels decrease the iron levels.

### *Hypothalamus*

The hypothalamus is located in the internal portion of the brain under the thalamus. It is part of the limbic system. The hypothalamus controls body temperature, emotions, thirst, hunger, appetite, digestion and sleep. From research it appears that the hypothalamus is one of the least studied areas of the brain. Here it shows that about half the elements increase while the rest decrease in Table 2 and 3.

One interesting element is aluminum. At group A (1mg/ml of manganese) the level of aluminum spikes while at the other doses, aluminum decreases. In AD aluminum levels have been shown to increase, though not necessarily in the hypothalamus. This is shown in the cerebral cortex and hippocampus as stated under their sections. Other interesting ones are copper and zinc. At the same doses they do the same thing. For example at A and B they increase while at C they decrease. This could possibly show that there is a copper-zinc balance in the hypothalamus like there is in the cerebellum. Without more research one can only speculate.

### *Midbrain*

The midbrain is located in the middle of the brain in front of the frontal lobes above the pons. The mid-brain is responsible for breathing, and reflexes. On average it appears that a majority of the elements appear to increase with the dosage of manganese. There is not a particular dosage of manganese that appears to increase or decrease the elements for one another.

Some of the more interesting elements are copper and manganese. The copper concentration increased with every dosage of manganese that was administered. According to research, high accumulations of copper have been found in patients with Alzheimer's and Wilsons. Whether or not this is true, the cause is yet to be determined. However an increased copper content in any section of the brain may not be a good thing.

The manganese concentration also increased with every dosage of manganese that was administered. An increase of manganese in the mid-brain is believed to be a primary target site for manganese neurotoxicity. It has



also been shown that high levels of Mn have been found in AD brains. In Table 3, it is shown that levels of manganese drop off as the brain ages. If there is more manganese in the brain to start with, the levels may not necessarily drop off. More research here would be needed. However, these high levels of manganese are unwanted in the mid-brain.

### *Pons & Medulla*

The pons is located between the medulla and the midbrain. The medulla is located between the pons and spinal cord. The pons is responsible for motor control and sensory analysis while the medulla is responsible for maintaining vital body functions such as the heart-rate and breathing. Here each element appears to be their own. Some increase with the manganese at different levels while others decrease. The different levels of manganese also cause different concentrations as well. Some of the more interesting ones are copper and iron.

As more manganese is added the higher the copper concentrations go. This is not necessarily a good thing because, as stated above, high accumulation of copper in the brain has been found in patients with Wilson's disease. The last thing we want to do is add more of an element that could be a factor in a neurological disorder. We are not saying that copper is the cause of Wilson's disease.

With iron, the manganese does not seem to affect the iron concentrations except at group B (10 mg/ml of Mn). As mentioned in other sections of the brain, rich iron content has been found in patients with Parkinson's disease. However if the body does not have enough iron it cannot produce enough red blood cells and the brain will not get the oxygen that it needs to survive. Low iron levels in the brain in young people have even been said to possibly cause neurological disorders, such as poor memory.

### *Striatum*

The striatum is located in the forebrain. It is in the sub-cortical section of the forebrain. The striatum includes the substantia nigra and the globus pallidus. The striatum is responsible for modulation and planning of movement pathways (communication of brain parts) and other cognitive processes. It appears that on average the elemental concentrations decrease with the manganese dosages. There are some exceptions though. Some of these exceptions are manganese and selenium.

The manganese levels increase with over dosage. This would make sense, due to the fact that we are giving the rats more manganese. This extra manganese is not necessarily a good thing because, as discussed above, chronic manganese toxicity in humans induces signs and symptoms that closely resemble those noted in PD. There is also a great deal of evidence that human striatum show preferential increases in Mn and is believed to be one of the primary sites associated with Mn neurotoxicity (Dorman et al, 2006).

Selenium is one of the least studied elements in the brain. In Table 3, it can be seen that every level of manganese caused the concentration of selenium to increase. In the other sections of the brain it was mentioned that high or low levels of selenium have been known to cause any problems, mainly neurological problems. Selenium toxicity is not well known. You do not achieve this from just eating or drinking, but by some type of supplement. Selenium is necessary for boosting the immune system to help prevent disease. Some have even argued that selenium can help to prevent some types of cancer and Parkinson's disease. This is a controversial issue though (Selenium, 2011).

**Table 2** Different Levels of Manganese Compared to the Control

	Elements																	
Region	Ca			Cl			Fe			K			Mg			Na		
	A	B	C	A	B	C	A	B	C	A	B	C	A	B	C	A	B	C
Cerebellum																		
Cerebral Cortex																		
Hippocampus																		
Hypothalamus																		
Midbrain																		
Pons & Medulla																		
Striatum																		

**Table 3** Different Levels of Manganese Compared to the Control

	Elements																				
Region	Al			Br			Co			Cr			Cu			F			Hg		
	A	B	C	A	B	C	A	B	C	A	B	C	A	B	C	A	B	C	A	B	C
Cerebellum																					
Cerebral Cortex																					
Hippocampus																					
Hypothalamus																					
Midbrain																					
Pons & Medulla																					
Striatum																					

	Elements																				
Region	I			Mn			Mo			Rb			Se			V			Zn		
	A	B	C	A	B	C	A	B	C	A	B	C	A	B	C	A	B	C	A	B	C
Cerebellum																					
Cerebral Cortex																					
Hippocampus																					
Hypothalamus																					
Midbrain																					
Pons & Medulla																					
Striatum																					

Key:

Above Control      Under Control

0 to 25% red      0 to -25% yellow

25 to 50% purple      -25% to -50% green

> 50% brown      < 50% blue

No data white

Same Black

## Developmental Stages

Tables 4 and 5 show the elemental concentration distribution for the various brain regions at different developmental stages when compared to the control. Table 4 is in mg/g while Table 5 is in µg/g. Both figures display the same information, just with different elements. The following is a description for each of the sections of the brain and their relationship to Tables 4 and 5.

### Cerebellum

It can be seen from Tables 4 and 5, that on average, the concentration of the different elements decreases as time goes on. There was no influence of treatment in Tables 4 and 5. Some of the more studied elements in the cerebellum are the following:

Copper appears to be evenly distributed in both younger and older brains in both the central and subcortical white matter of the cerebellum. The presence of copper in the white matter of the cerebellum is not unexpected because copper, iron, and zinc are essential for myelin synthesis, structure, and maintenance with oligodendrocytes being the main iron repository cells in the brain. Out of all the metals, copper is entirely protein bound. There is little or no free copper present in cells and only trace amounts of the copper leach from formalin-fixed tissues (Zhang et al., 2009). In Tables 4 and 5, it can be seen that the copper concentrations drop off dramatically after 5 days and then fluctuates slightly for the rest of the developmental stages.

Magnesium levels in the parietal cortex in AD patients do not differ from those in normal controls (Srivastava et al., 2002). The Magnesium levels in Table 4 drop off slightly after 5 days old and then remain constant for the rest of the developmental stages. Similarly, rubidium levels in AD brains do not differ from those in control brains (Cannino et al., 2008). Rubidium also has the same pattern in the rats as did magnesium. Consequently, the age-related changes in magnesium and rubidium levels in the cerebellum may not be good predictive values of neurological diseases in later life. On the other hand, the sodium levels in the rat cerebellum decrease during the latter half of postnatal development as they approach the adult level. On the other hand, sodium levels in every region of the human brain are significantly higher in the AD patients than those in control subjects (Cannino et al., 2008). These results taken together suggest that dietary intake of sodium may have some relevance in the causation and/or progression of AD. Interestingly though the levels of sodium appear only to slightly decrease throughout the developmental stages in Table 4.

Zinc has also been shown to be rich in the cerebellar gray and white matter. The subcortical white matter of the cerebellum has been shown to be the highest. This area of the brain though has a delicate zinc/copper balance. This balance must be maintained because zinc toxicity has been linked to multiple sclerosis and cerebellar demyelinating lesions. (Zhang et al., 2009) Zinc can be seen to fluctuate throughout the developmental stages in Table 5. Interestingly though the copper and zinc concentrations are not the same. This questions whether there is a zinc/copper balance. There is always either more copper or more zinc. The two are never equal.

Some elements are studied together due to the fact that they are normally found together. In the cerebellum these elements include the following: Iron and zinc have similar levels in both younger and older brains but have higher levels in the subcortical white matter than in the central white matter. Chromium, copper, iron, nickel, and zinc have been found to be retained in fixed tissues, such as the cerebellum, even after long periods of storage. (Iron, chromium, and copper all remain low and relatively constant throughout the developmental stages.) However, other elements such as arsenic, cadmium, magnesium, rubidium, and sodium have been shown to leach out of fixed tissues over time (Zhang et al., 2009). It has not been shown if this affects other element concentrations in the brain. (As shown in Table 5, Rubidium decreases up until 22/23 days and then begins to increase again.)

### *Cerebral Cortex*

It can be seen from Tables 4 and 5, that on average, about half of the concentrations of the different elements increase while the other half decrease as time goes on. Several elements in the human cerebral cortex have received more attention recently; they are described in further details in the following:

Consequently, increasing brain accumulation of Al, which is known to be a neurotoxin, could induce neurological problem(s) in the long term. For example, Al shows a significantly higher level in the parietal cortex in AD patients compared to those in control individuals (Srivastava et al., 2002). Similarly, Al accumulation in brain and other tissues, including bone, liver, and kidney, has also been shown to accompany renal failure (Kuman & Gill, 2009). Even though the physiological role of aluminum in the brain has not been identified, in Table 5, Aluminum decreases through 10 days old and then spikes up at 22/23 days old and then decreases for the rest of the developmental stages. This shows that as the rat matures it accumulates aluminum and then is depleted of it in its older years, as suggested in the research. This accumulation also reflects dietary intake of the rat.

Calcium (Ca) levels in the rat's cerebral cortex do not markedly change during postnatal development (Table 4). On the other hand, one of the pathological hallmarks of Alzheimer's disease (AD) is the accumulation of amyloid plaques between nerve cells (i.e., neurons) in different parts of human brains including the cerebral cortex. Ca levels in human amyloid plaques in AD are elevated. Consistent with the latter observation is the finding that, in

PSAAP mice (a mouse model of AD, which shows plaques but little neurodegeneration), Ca accumulation in their plaques is less than those in the surrounding brain tissue (Belavaria et al, 2005). Consequently, age-related accumulation of Ca in this brain region could potentially serve as a marker for the likelihood of developing neurodegeneration as age advances.

Chromium (Cr) shows a moderate increase in the parietal cortex of AD patients compared to those in control subjects (Srivastava et al, 2002). In rats cerebral cortex, Cr levels increase from day 10 to day 22/23 and thereafter decrease as adulthood is reached (Table 5). Nevertheless, relations between brain Cr levels and neurological diseases have not been firmly established.

Copper (Cu) in amyloid plaques in AD is elevated (Bolognin et al, 2009). In PSAAP mice (a mouse model of AD, which shows plaques but less neurodegeneration) Cu accumulation in their plaques is less than those in the surrounding brain tissue (Belavaria et al, 2005). Consequently, increasing Cu accumulation in cerebral cortex as age advances can potentially herald the onset of neurological problems. **In Error! Reference source not found.** Table 5 the copper varies dramatically as the brain ages.

The magnesium (Mg) levels in rats cerebral cortex fluctuates during development and levels off toward adulthood (Table 4). Mg levels in parietal cortex and cerebellum in AD patients do not differ from those in control subjects. Taken together, these observations suggest Mg to be more of a predictor of neurological problems as age advances.

Manganese (Mn) shows significantly higher levels in the parietal cortex of AD patients compared to those in control subjects (Srivastava et al, 2002). However, cerebellar Mn levels in AD are similar to those in control subjects (Srivastava et al, 2002). Table 5 shows that Mn levels in cerebral cortex of the rat show a general trend of decreasing as its age increases. Nonetheless, whether this is a generalized trend of an essential element remains to be established.

Potassium (K) concentrations in the AD brain appear to be similar to those in the control brain, especially in the regions examined (Cannino et al, 2008), such as the cerebral cortex. K generally shows a trend of age-related increases in the rat cerebral cortex (Table 4), perhaps reflecting increases in cellular material because intracellular K is higher than extracellular K.

Sodium (Na) levels in the rat cerebral cortex decreases with increasing age (Table 4), reflecting the closing of the blood-brain barrier thereby excluding the entry of extracellular Na into cells. On the other hand, Na levels in every region of the AD brain are higher than corresponding levels in the control brain (Cannino et al, 2008). Consequently, age-related increases in brain sodium may be considered at least a partial predictor of age-related neurological problems.

Zinc (Zn) is elevated in the amyloid plaques in AD. In PSAPP mice (an AD mouse model that shows little or no neurodegeneration), there was only a 29% increase of Zn in their plaques compared to the Zn in brain tissue surrounding the plaques (Belavaria et al, 2005). By contrast, Zn levels in the rat cerebral cortex markedly increased between age 22/23 days and adulthood suggesting that the increase is associated with tissue growth. However, the increase in brain Zn during brain aging may be more predictive of onset and/or presence of neurological problems (Belavaria et al, 2005).

### *Hippocampus*

Developmental stage I is not listed in tables 4 or 5 for the hippocampus due to the fact that it can be found with the cerebral cortex. During the early stages it is difficult to separate the hippocampus and cerebral cortex.

In research, the following has been determined about the following elements:

Following oral exposure of rats to aluminum (Al), its retention has been noted in the hippocampus as occurs in other brain regions: rat hippocampus Al levels increase markedly after 10 days of age (Table 5). In patients with PD, elevated Al levels have been found in several brain regions including the hippocampus, which is

rich in cholinergic neurons. This suggests that Al could have neurotoxin properties. Al has also been detected in both the senile plaques and neurofibrillary tangle bearing neurons in the brain of AD patients. This leads us to believe that Al may play a part in AD. (Kuman & Gill, 2009) One thing to note though is that a number of studies have shown the cognitive impairments that follow Al exposure do not have consistent results. This suggests that Al has different properties in the brain that we still do not understand. Consequently, chronic accumulation of Al in this brain region over a life-span may lead to the development of neurodegenerative diseases such as PD because Al is known to be a neurotoxin.

Copper concentrations have been identified in the hippocampus, but have not been extensively researched, just mentioned. The brain does maintain a tight regulation of brain copper transport because copper is essential to the integrity of a healthy brain. In Table 5, the copper concentrations increase towards maturity and then drop off once the rat has reached adulthood.

Potassium (K) levels in the rat hippocampus increase from age day 10 till adulthood, likely reflecting the increase in cellular material during this developmental period (Table 4). However, in the brain regions examined in AD, brain K remains essentially unchanged compared with corresponding levels in control subjects (Cannino et al, 2008), suggesting that brain K may not be a good indicator of the likelihood of developing neurological diseases such as AD.

Rubidium (Rb) levels in rat hippocampus fluctuate between age day 10 and adulthood (Table 5). However, Rb levels in the AD brain do not differ from those in the control brain (Cannino et al, 2008) suggesting that Rb levels in the brain may not be a good predictor for neurodegenerative diseases such as AD.

Sodium (Na) levels in the rat hippocampus decrease between ages day 10 and day 22/23 and level off at adulthood (Table 4). However, Na levels in every part of the AD brain examined are higher than corresponding levels in the control brain (Cannino et al, 2008).

### *Hypothalamus*

The electrolytes in this rat brain region show fluctuating trends in the four age groups investigated, partly reflecting the closing of the blood-brain barrier. For example, sodium (Na) and chlorine (Cl) levels significantly decrease in the first 22/23 days postnatal. On the other hand potassium (K) levels markedly increase between day 5 and day 10 postnatal. (Shown in Table 4.)

Although they show some age-related fluctuations, the essential trace elements copper (Cu), selenium (Se), and zinc (Zn) levels in the rat hypothalamus significantly increase between postnatal age 5 days and adulthood (Table 5). At present, one can only speculate about the functional significance of the postnatal increases of these essential metals in the rat hypothalamus because of the absence of relevant studies.

### *Midbrain*

After reviewing different texts, the following can be said about the different elements located in the midbrain:

Chlorine, iron, bromine, cobalt, chromium, mercury, iodine, manganese, molybdenum, selenium, and vanadium all follow the same pattern while all the other elements vary in accumulation. Overall accumulation of metals in the brain stem does not appear to be major. All elements appear to level off at adulthood or die off all together, as shown in Tables 4 and 5. This may be one of the reasons why the brain stem has not been noted in papers related to brain diseases. The midbrain makes up a piece of the brain stem, while the pons and medulla make up the rest.

One of the more interesting elements that stand out is copper. In the midbrain, copper is high at 22/23 days but drops off dramatically afterwards. Many of the sections of the brain have been shown to have abnormal copper distributions during AD and high accumulations have been related to Wilson's disease. High accumulations of copper in this section of the brain have not been noted or have not been a problem.

Another interesting element is calcium. In the midbrain, calcium is high in the young brains and then decreases off as the brain ages. This could suggest that calcium is adding in the process of the growth and development of the brain. Calcium is required in the brain for electrical signals. Without it, the brain could age more quickly than normal. Other failures could lead to the inability to make quick judgments, 'short circuit' messages in the brain which could cause involuntary movement, and other issues.

Iron though has been shown to increase in the substantia nigra (SN – located in the midbrain) in patients with Parkinson's disease. It still remains to be known whether this is a cause of PD. Ultrasound studies do argue that iron plays an important part forming the pathogenesis of PD. PD does cause disturbances with iron uptake, storage, post-transcriptional control, and intracellular metabolism. An imbalance of any of these could cause cell death. However iron-related oxidative stress could promote  $\alpha$ -synuclein aggregation. This links the important role of iron with some of the hallmarks of PD. (Berg et al, 2001) Brain iron is found to be highest in the substantia nigra. (Leskovic et al, 2009) The iron levels in Table 4 remain constant throughout the entire developmental stages for the rat.

Manganese increases in the mid-brain are believed to be primary target sites for manganese neurotoxicity. It has also been shown that high levels of Mn have been found in AD brains. (Dorman et al, 2006) As stated above, the manganese appears to level off at adulthood or die off all together, as shown in Table 5.

Sodium levels in every part of the brain are shown to be significantly higher in AD patients compared to normal brains (Belavaria et al, 2005). In Table 4 it can be seen that the sodium levels actually decrease in the mid-brain as the brain ages.

#### *Pons & Medulla*

After reviewing different texts, the following has been found out about the Pons & Medulla relating to Tables 4 and 5:

One of the more interesting elements that stand out is copper. In the pons and medulla copper decreases slowly as the brain ages. Many of the sections of the brain have been shown to have abnormal copper distributions during AD and high accumulations have been related to Wilson's disease. High accumulations of copper in the brain have been shown to be the primary cause of Wilson's disease. Copper chelating therapy is one possible treatment for Wilson's (Gerlach et al, 1994). In Table 5 it can be seen that the levels of copper decrease throughout the entire developmental stages. Something (diet or environmental conditions) must be what is causing the copper to spike and cause Wilson's disease.

Another interesting element is calcium. In the pons and medulla, calcium increases up to 10 days and then levels off as the brain ages (See Table 4). Calcium is required in the brain for electrical signals. Without it, the brain could age more quickly than normal. Other failures could lead to the inability to make quick judgments, 'short circuit' messages in the brain, which could cause involuntary movement, and other issues.

Sodium levels in every part of the brain are shown to be significantly higher in AD patients compared to normal brains (Belavaria et al, 2005). In Table 4 the sodium levels fluctuate in the pons and medulla as the brain ages.

Most major and trace elements show age-related decreases in their levels in rat pons and medulla as adulthood approaches. Overall, the accumulation of metals in this brain region is not as quantitatively marked as those in the other brain regions, possibly due to the fact that this brain region is full of fiber tracts rather than cell bodies. Moreover, the physiological significance of the distributions of metals in this brain region is still poorly understood.

#### *Striatum*

In research the following has been determined about these elements in the striatum:

There is recent evidence that iron (Fe) plays a role in the consolidation of long-term memory. Brain Fe distribution overlaps with that of dopaminergic neurons. In rodent models of neurological disorders, Fe levels in the substantia nigra and basal ganglia increase. Because of those observations, increased striatal Fe has been suggested to be responsible for neuronal cell. Furthermore, Fe accumulates in the brain as a function of age (Chan et al, 1981). In rat striatum, Fe levels decrease between ages 10 days and 22/23 days and level off thereafter (Table 4).

Brain Fe is highest in the substantia nigra, globus pallidus, red nucleus, caudate nucleus, and putamen. Increased brain Fe has been found in several neurodegenerative disorders although it has not been defined as the main cause (Lee et al, 2010). Fe level in the substantia nigra increases in PD but total Fe in the substantia nigra zona reticulata does not change in either PD or AD (Leskovjan et al, 2009). Thus, these findings suggest that an over accumulation of iron in striatum may lead to development of neurodegenerative diseases such as PD and AD and sources of Fe exposure could be environmental and dietary. However, it remains to be determined if the elevated Fe levels antedate injury of pigmented neurons or constitute a consequence of neuronal degeneration because the increased Fe in the substantia nigra may contribute to oxidative damage to neurons. Nevertheless, most brain Fe is stored in an inactive form bound to intracellular ferritin, which is thought to be mainly localized in microglia and oligodendroglia. Clearly, additional studies are needed to delineate the pathophysiological role of Fe in neurodegenerative diseases.

Chronic manganese (Mn) toxicity in humans induces signs and symptoms that closely resemble those noted in PD. There is a great deal of evidence that human striatum, globus pallidus, and substantia nigra show preferential increases in Mn and are believed to be the primary sites associated with Mn neurotoxicity. Moreover, exposure to high Mn leads to elevation of Mn levels in olfactory epithelium and olfactory bulb (Dorman et al, 2006). The concentration of manganese decreases dramatically after 5 days old and never increases. This is shown in Table 5.

In every region of the brain examined, brain sodium (Na) is increased in AD compared with corresponding levels in control subjects (Cannino et al, 2008). On the other hand, Na levels in rat striatum decrease during postnatal development (See Table 4). Taken together, these observations suggest that high Na accumulation in the brain may lead to pathological states and sources of the Na could be environmental and/or dietary in origin.

**Table 4** Different Development Stages Compared to Control

	Elements																	
Region	Ca			Cl			Fe			K			Mg			Na		
	I	II	III	I	II	III	I	II	III	I	II	III	I	II	III	I	II	III
Cerebellum																		
Cerebral Cortex																		
Hippocampus																		
Hypothalamus																		
Midbrain																		
Pons & Medulla																		
Striatum																		
Whole Brain																		

**Table 5** Different Development Stages Compared to Control

Region	Elements																							
	Al			Br			Co			Cr			Cu			F			Hg					
	I	II	III	I	II	III	I	II	III	I	II	III	I	II	III	I	II	III	I	II	III	I	II	III
Cerebellum																								
Cerebral Cortex																								
Hippocampus																								
Hypothalamus																								
Midbrain																								
Pons & Medulla																								
Striatum																								
Whole Brain																								

Region	Elements																							
	I			Mn			Mo			Rb			Se			V			Zn					
	I	II	III	I	II	III	I	II	III	I	II	III	I	II	III	I	II	III	I	II	III	I	II	III
Cerebellum																								
Cerebral Cortex																								
Hippocampus																								
Hypothalamus																								
Midbrain																								
Pons & Medulla																								
Striatum																								
Whole Brain																								

Key:  
 Above Control      Under Control  
 0 to 25% red      0 to -25% yellow  
 25 to 50% purple      -25% to -50% green  
 > 50% brown      < 50% blue  
 No data white  
 Same Black

## 5. Conclusion

Our results strongly suggest that varying the elemental intake can have an effect on the metallomic distributions in the various regions of the rat brain. The results also show, that on average, the higher supplemental element produce the same results as the lower supplemental element. This shows that the body has a way of regulating the elements on its own, as was mentioned with some elements in the above discussion. However, as shown in the above tables in this section when you have added a large amount the body does not regulate as well. You can see by comparing adding a small amount to adding a larger amount of manganese.

Our results also strongly suggest that the metallomic distributions in various regions of the rat brain change markedly during the different stages of postnatal development. This suggests that as the body ages it depletes or adds the elements that are necessary for growth and living. However, if we alter from our diet and increase the consumption of certain elements, the body may not handle this correctly and neurodegenerative diseases may form, as was shown in the above section.

In summary, our findings and along with reports in the literature, suggest that brain regional metallomic distribution can be influenced by dietary intake of metals and other elements and may cause pathophysiological implications in several key neurodegenerative diseases such as Parkinson's disease and Alzheimer's disease. A metallomic distribution model of various regions of the rat brain can be developed based on our experimental results and statistical analysis. However, much remains to be discovered regarding the brains functional significance of metallomic distribution during development.

## References

Amano, R., Tarohda, T., Yamamoto, M. (2004) Regional Distribution of Manganese, Iron, Copper, and Zinc in the rate brain during development. *Anal Bioanal Chemical*, 380, 240-246.



- Belavaria, C., Andresi, E., Molnar, Z., and Bertalan, E. (2005) Determination of Alkali Metals in Control and AD Brain Samples by Different Techniques. *Microchemical Journal*, 79(1-2), 367-373.
- Berg D., Gelach M., Youdim, MBH., Double, KL., Zecca, L., Riederer, P., and Becker, G. (2001) Brain Iron Pathways and Their Relevance to Parkinson's Disease. *Journal of Neurochemistry*, 79(2), 225-236.
- Bolognin, S., Messori, L., and Zatta, P. (2009) Metal Ion Physiopathology in Neurodegenerative Disorders. *Neuromolecular Medicine*, 11(4), 223-238.
- Cannino, Giuseppe, Ferruggia, Elisa, Luparello, Claudio, and Rinaldi, Anna Maria. (2008) Effects of Cadmium Chloride on Some Mitochondria-Related Activity and Gene Expression of Human MDA-MB231 Breast Tumor Cells. *Journal of Inorganic Biochemistry*, 102(8), 1668-1676.
- Chan, A.W.K. and Minski, M. J. (1981) U. L. R. C. Internal Report (RES/36), p 37-39.
- Chan, A.W.K., Minski, M.J., Lai, J.C.K. (1983) An Application of Neutron Activation Analysis to Small Biological Samples: Simultaneous Determination of Thirty Elements in Rat brain Regions. *Journal of Neuroscience Methods*, 7(4), 317-328.
- Connett, Michael. Fluoride & the Brain. (2011) *Fluoride Action Network*. <<http://www.fluoridealert.org/health/brain/>> 27 September 2010.
- Dorman, DC, Struve, MF, Wong, BA, Dye, JA, and Robertson, ID. (2006) Correlation of Brain Magnetic Resonance Imaging Changes with Pallidal Manganese Concentration in Rhesus Monkeys Following Subchronic Manganese Inhalation. *Toxicological Sciences*, 92(1), 219-227.
- Florea, AM, and Busselberg, D. (2006) Occurrence, Use, and Potential Toxic Effects of Metals and Metal Compounds. *Biometals*, 19(4) 419-427.
- Gerlach, M., Benshachar, D., Riederer, P., and Youdim, MBH. (1994) Altered Brain Metabolism of Iron as a Cause of Neurodegenerative Diseases. *Journal of Neurochemistry*, 63(3), 793-807.
- Grobstein, Paul. Brain Sizes. (2001) *Serendip*. <<http://serendip.brynmawr.edu/bb/kinser/Int3.html>> 20 September 2010.
- Hung, YH., Bush, AL, and Cherny, RA. (2010) Copper in the Brain and Alzheimer's disease. *Journal of Biological Inorganic Chemistry*, 15(1), 61-76.
- Kienzl, E., Puchinger, L., Jellinger, K., Linert, W., Stachelberger, H., and Jameson, R.F. (1995) The Role of Transition Metals in the Pathogenesis of Parkinson's disease. *Journal of the Neurological Sciences*, 134, 69-78.
- Kumar, V., and Gill, K. D. (2009) Aluminum Neurotoxicity; Neurobehavioral and Oxidative Aspects. *Archives of Toxicology*, 83(11), 965-978.
- Lee, DW., and Anderson, JK. (2010) Iron Elevations in the Aging Parkinsonian Brain: A Consequence of Impaired Iron Homeostasis. *Journal of Neurochemistry*, 112(2), 332-339.
- Leskovjan, A. C., Lanzirrotti, A., and Miller, L. M. (2009) Amyloid Plaques in PSAPP Mice Bind Less Metal Than Plaques in Human Alzheimer's Disease. *Neuroimage*, 47(4), 1215-1220.
- Manganese. (2005) *vitaminstuff.com*. <<http://www.vitaminstuff.com/mineral-manganese.html>> 7 September 2010.
- Manganese Element Facts. (2008) *Chemicool.com*. <<http://www.chemicool.com/elements/manganese.html>> 7 September 2010.
- Miller, Marsha. Copper in the HD Brain. (2007) <<http://hdlighthouse.org/research/brain/updates/1382copper.php>> 28 September 2010.
- Popescu, B. F. G., Robinson, C. A., Rajput, A., Rajput, A. H., Harder, S. L., and Nichol, H.. (2009) Iron, Copper, and Zinc Distribution of the Cerebellum. *Cerebellum*, 8(2), 74-79.
- Rooney, JPK. (2007) The Role of Thiols, Dithiols, Nutritional Factors and Interacting Ligands in the Toxicology of Mercury. *Toxicology*, 234(3), 145-156.
- Schafer, U., and Jahreis, G. (2006) Exposure, Bioavailability, Distribution, and Excretion of Aluminum and its Toxicological Relevance to Humans. *Trace Elements and Electrolytes*, 23(3), 162-172.
- Selenium. (2011) *The George Mateljan Foundation*. <<http://www.whfoods.com/genpage.php?dbid=95&tname=nutrient>> 28 September 2010.
- Srivastava, RAK., and Jain, JC. (2002) Scavenger Receptor Class B Type I Expression and Elemental Analysis in Cerebellum and Parietal Cortex Regions of the Alzheimer's disease Brain. *Journal of the Neurological Sciences*, 196(1-2), 45-52.
- Underwood, E.J. (1977) Trace Elements in Animal Nutrient. Academic Press.
- Yokel, RA. (2009) Manganese Flux Across the Blood-Brain Barrier. *Neuromolecular Medicine*, 11(4), 297-310.
- Zhang, L., Lichtmannegger, J., Summer, K. H., Webb, S., Pickering, I. J., and George, G. N. (2009) Tracing Copper-Thiomolybdate Complexes in Prospective Treatment for Wilson's Disease. *Biochemistry*, 48(5), 891-897.

## Appendix 31. List of published Abstracts:

1. Jaiswal A, Wong YYW, Bhushan A, Daniels C & Lai JCK (2010) A Noncontact Co-Culture Model of Peripheral Neural Cells for Nanotoxicity, Tissue Engineering and Pathophysiological Studies. NSTI Nanotechnology Conference and Expo – Nanotech 2010, June 21-25, 2010, Anaheim, CA (in Abstracts Volume).

**Abstract.** Cell culture models *in vitro* have long serve as tools for the elucidation of the cellular and molecular mechanisms underlying the pathophysiology of diverse diseases. More recently these versatile model systems have permeated into the fields of toxicology and tissue engineering. Their attraction and utility for use in investigations in toxicology and tissue engineering appear to derive from the fact such model systems are particularly suitable for high throughput and mechanistic studies. Although these models do not exactly simulate the cellular architecture in tissues and organs *in vivo*, they have been well accepted for studies employing a single cell type. Their limitations notwithstanding, they facilitate gaining unique mechanistic insights regarding the role of a particular cell type, a position not easily attainable employing whole organ/tissue studies.

On the other hand, co-culture cell systems consisting of two distinctly different but functionally complementary cell types provide structural and functional perspectives that single-cell-type models do not offer. Consequently, there is a need for the development for more such model systems and applied them to nanotoxicological and tissue engineering studies. Our group have been emphasized the necessity of developing a variety of cell model systems using neural cells. We have recently demonstrated some of the utilities of such model systems in nanotoxicological and tissue engineering studies.

There have been, however, few cell model systems developed employing peripheral neural cell types for nanotoxicological and tissue engineering studies. We have therefore initiated a systematic development of this type of model systems using dorsal root ganglion (DRG) neurons and Schwann cells. The first model we have developed involved a non-contact co-culture model of Schwann cells and DRG neurons employing the hanging cell culture insert. Initially, we have partially characterized the DRG neurons and Schwann cells in single-cell-type cultures. In ongoing studies employing our new co-culture, non-contact model, we demonstrated that the cell survival of DRG neurons increased when co-cultured with Schwann cells in this construct. Thus, the results from our studies to date as well as those from our ongoing studies demonstrate that our non-contact co-culture model is highly suitable for both high throughput and mechanistic studies in nanotoxicological and tissue engineering research. Clearly this model is also germane for the investigation of mechanistic issues associated with peripheral diabetic neuropathy and other disease states of the peripheral nervous system.

2. Wong YYW, Jaiswal AR, Dukhande VV, Bhushan A, Leung SW & Lai JCK (2010) Elucidation of Neuroprotective Properties of Astrocytoma (Astrocytes-like) Cells in Neural Cell Culture Models *In Vitro*: Applications in Tissue Engineering and Nanotoxicology. NSTI Nanotechnology Conference and Expo – Nanotech 2010, June 21-25, 2010, Anaheim, CA (in Abstracts Volume).

**Abstract.** Evidence is accumulating that cell culture models *in vitro* facilitate high throughput and mechanistic studies in tissue engineering. More recently, our group as well as other researchers have developed several cell models for the systematic investigation of molecular mechanisms underlying the putative cytotoxicity of nanoparticles and other nanomaterials. These and other studies have drawn wide-spread interest in the possible environmental and occupational health impact of nanoparticles and other nanomaterials.

As part of a continuing effort to further develop and characterize cell models for cellular and molecular mechanistic studies, we have extended our previous investigation employing neural cell models because most studies have traditionally employed peripheral cell types but not neural cells.

Astrocytes are known to protect neurons against pathophysiological assaults *in vivo* and *in vitro* although the underlying mechanisms are not fully understood. We have previously developed several cell culture models *in vitro* to systematically investigate several of the putative neuroprotective properties of astrocytes. For example, we have previously shown U-87 (astrocytes-like) astrocytoma cells afford SK-N-SH (neurons-like) neuroblastoma cells against several pathophysiological assaults such as oxidative stress induced by depletion of cellular glutathione.

Based on the results of our previous studies, we hypothesized that different stress factors can elicit and/or enhance the neuroprotective effects of astrocytes through the activation of astrocytic signaling and alteration of astroglial function. We have initiated a series of studies employing our cell models to test this hypothesis. The results of our ongoing studies demonstrate that U-87 (astrocytes-like) astrocytoma cells provide SK-N-SH (neurons-like) neuroblastoma cells against pathophysiological assaults (e.g., oxidative stress) under several sets of culture conditions not previously studied. Other studies are in progress to further elucidate the cellular and molecular mechanisms underlying these protective effects proffered by U-87 (astrocytes-like) astrocytoma cells to SK-N-SH (neurons-like) neuroblastoma cells. Thus, our results may have pathophysiological implications in neuroprotection but also implications and applications in tissue engineering and nanotoxicological research.

3. Leung SW, Gao W, Gu H, Bhushan A & Lai JCK (2010) Chitosan Membrane in Combinations with Nanoparticles and Adriamycin as a Treatment to Inhibit Glioma Growth and Migration. NSTI Nanotechnology Conference and Expo – Nanotech 2010, June 21-25, 2010, Anaheim, CA (in Abstracts Volume).

**Abstract.** Our previous and on-going studies indicated that U87 cells cultured on chitosan film/membrane exhibited significantly slower growth and proliferation kinetics compared to U87 cells cultured in the absence of chitosan film/membrane. Chitosan exhibits anti-microbial activities through its interaction(s) with microbial cell surface thereby altering their gene expression and cellular function and leading to cell death. Recent studies of nanometal particles have revealed many properties that were not previously expected in biological systems and thus can be explored for various applications in biomedical applications. In this study, we hypothesized that the inhibitory effect of chitosan would be greatly modulated if we combine chitosan with nanometals and adriamycin, a common drug for cancer therapy. Our results showed that combinations of metal nanoparticles, adriamycin and chitosan induced cell death at different rates, with reference to U87 cells cultured in the absence of chitosan and with chitosan alone. The results showed potentials for pathophysiological applications to inhibit human brain glioma migration and invasion. Results of similar treatments with different cancer and normal cells will also be presented.

4. Leung SW, Wang Y, Gu H & Lai JCK (2010) Biomedical Applications of Modified Carbon Glassy Electrode Sensor with Nanoparticles and Dendrimers. NSTI Nanotechnology Conference and Expo – Nanotech 2010, June 21-25, 2010, Anaheim, CA (in Abstracts Volume).

**Abstract.** In our previous reports, we studied the development of biosensor platform that are capable of measuring biometabolites and environmental sensitive species, such as peroxide and nitrate/nitrite, to concentration in the order of ppb (parts per billion) or lower. In our more recent development, we modified our platform with dendrimers to enhance its performance. Zero and second generation of dendrimers were coated on the surface of a carbon glassy platform electrode modified with GDH (glutamate dehydrogenase) and it was used to measure ammonium, a common biometabolite, at near neutral pH that is common for normal bioactivities.

The resulting electrode was tested with ammonium concentrations ranged from 0.002 to 0.3  $\mu\text{M}$  with satisfactory results. Measurements at lower concentrations had better resolution than at higher concentrations and it is believed that the lower concentration limit can be better than the tested lower limit at 0.002  $\mu\text{M}$ . Performance of the modified carbon glassy electrode was compared with other glassy electrodes that were modified differently, and the results will be reported.

The biosensor platform thus far was proven to be versatile and can be used in many biomedical and environmental applications.

5. Wright GL, Lai JCK, Chan AWK, Minski MJ, Lim L & Leung SW (2010) Metallomic Distribution in Various Regions of the Brain as Influenced by Dietary Intakes and Their Implications. ISEIS 2010 International Conference on Environmental Informatics, Beijing, China, August 27-29, 2010 (in Abstracts Volume).

**Abstract.** Lifelong exposure to environmental factors can influence the risk of developing diseases according to recent research findings. Environmental stresses ultimately leading to neuronal cell death have been hypothesized as the causes of the increased occurrence in developing Alzheimer's and Parkinson's disease. Our daily diet is considered to be one of the most important environmental factors that can seriously affect the development and proper functions of the brain. Depending on the concentrations, metals and electrolytes can post some health concerns, especially for a prolonged consumption period. For example, it was reported that excess amounts of iron, zinc and copper in the human brain may cause oxidative damage and protein aggregation; the neurotoxicity induced by these metals may lead to cerebral and/or cerebellar degeneration. Other reports showed that there were differences in concentrations of five different elements (aluminum, zinc, copper, manganese, and iron) between normal human brain and brains of patients with Alzheimer's disease. In this study, we investigated 30 elements, including electrolytes, and how dietary intake on a life-time basis would affect their concentrations and distributions in various regions of the rat brain (hypothalamus, cerebellum, pons and medulla, striatum, mid-brain, cerebral cortex, and hippocampus) and discussed their health implications. Information matrices of these 30 different elements (mostly metals) and their distributions in various regions of the rat brain were analyzed as a function of normal dietary intake at different ages during development. Our results showed that metallomic distribution in various regions of the rat brain is age-related. The results may help researchers to identify possible links between daily dietary intake of metals and electrolytes and diseases associated with aging (e.g., Alzheimer's and Parkinson's disease) and suggest such metallomic distributions may be used as neurological biomarkers of exposure to heavy metals.

6. Leung SW, Siddhanti S, Williams B, Chan AWK, Minski MJ, Daniels CK & Lai JCK (2010) Effects of Dietary Intake on Metal and Electrolyte Distributions in Various Organs. ISEIS 2010 International Conference on Environmental Informatics, Beijing, China, August 27-29, 2010 (in Abstracts Volume).

**Abstract.** The intake and concentration of metals and electrolytes from our diet are believed to be affecting our general health, in particular, the proper functions of vital organs. For example, in addition to other genetic and environmental factors, consuming water with high alkalinity for prolonged time is suspected to lead to diseases such as kidney stone. Evidence has been accumulating that excessive metal intakes would lead to organ failures. Once absorbed, minerals and electrolytes can travel freely throughout the body, and distribute at key organ systems such as the brain, lung, kidney, etc. By conducting experiments with animal models (e.g., rats), it is possible to not only determine where the organ distribution of various matrices of elements and minerals but also correlate such matrices with the overall physiological and behavioral status of such models. In this study, information matrices of 30 different elements (including heavy metals and some electrolytes) and their distributions in various vital organs (e.g., brain, lung, kidney, liver, heart, spleen, and uterus) were analyzed as a function of normal dietary intake at adulthood (120 days old). An elemental (metal and electrolyte) distribution model was then formulated based on

experimental results. The study has high impact to our understanding of how environmental health would affect our well being. This study would also provide insights on how our diet would affect the accumulations of unwanted elements, such as heavy metals, in our vital organs. The results may help researchers and health practitioner to identify possible links between daily diet (metals and electrolytes) and diseases, and may also lead to a better understanding of diseases associated with aging such as Alzheimer's and Parkinson's diseases, and other neurological disorders.

7. Bhushan A, Patil PP, Bhardwaj V, Lai MB, Daniels CK, Leung SW & Lai JCK (2010) Cross Resistance of Magnesium Oxide Nanoparticles to Cisplatin in Leukemia Cells: Mechanistic Studies. Institution of Mechanical Engineers Seminar on Nanotechnology in Medicine and Biotechnology, October 2010, London, UK (in Program & Abstracts).

**Abstract.** We have presented an overview of our studies on anti-cancer drug resistance mechanisms as well as ongoing systematic studies of the nanotoxicity of metallic oxide nanoparticles. Our ongoing studies also suggest that resistant cancer cells may exhibit cross-resistance to the cytotoxic effects of metallic oxide nanoparticles. The latter effects appear to be mediated by cell survival/proliferation signaling mechanisms. Clearly these are important and novel areas of anti-cancer drug discovery. As such they merit further investigation. We are currently pursuing these exciting new domains of nanomedicine and nanocancer research.

8. Gao W, Lai JCK & Leung SW (2011) Effects of Chitosan on Schwann Cells and Dorsal Root Ganglion Neurons. 53<sup>rd</sup> Annual Symposium of the Idaho Academy of Science, March 31-April 2, 2011, The College of Idaho, Caldwell, ID. Journal of Idaho Academy of Science, 47(1): 59.

**Abstract.** Chitosan has been studied as a scaffolding material for nerve regeneration due to its biocompatible nature. Current cell models involving primary cultures of peripheral nervous system (PNS) neural cells used to investigate the interactions between neural cells and chitosan have significant limitations because primary cultures of PNS neural cells have a very limited life-span. In this study, we have overcome such limitations by employing immortalized Schwann cells (S16) and genetically-modified dorsal root ganglion (DRG) neurons (50B11), which have much longer life-span when cultured *in vitro*. We have elucidated some of the effects of chitosan on the growth of these two cell types by employing the MTT assay. Results of our on-going studies suggested that chitosan had no effects on the growth rate of Schwann cells up to two weeks. However, chitosan appeared to exert a small inhibitory effect on the growth rate of DRG neurons. These findings suggested that chitosan is more biocompatible with Schwann cells than with DRG neurons. We therefore conclude that chitosan has good biocompatibility in PNS neural cells and may have some potential to be a suitable scaffolding material to support nerve regeneration and repair.

9. Jaiswal AR, Lu S, Bhushan A, Daniels CK, Leung SW & Lai JCK (2011) Toxicity of Nanoparticles: Assessment Using Cells from Peripheral Nervous System. 53<sup>rd</sup> Annual Symposium of the Idaho Academy of Science, March 31-April 2, 2011, The College of Idaho, Caldwell, ID. Journal of Idaho Academy of Science, 47(1): 60.

**Abstract.** The diverse applications of nanomaterial, including nanoparticles, have been increasing exponentially in the last decade. Once they enter the body, nanoparticles may be toxic to one or more organs. However, the toxicity of nanoparticles in mammals has not been systematically studied although there is increasing concern about their environmental and health impact. We have systematically elucidated the putative cytotoxicity of nanoparticles of silicon dioxide (SiO<sub>2</sub>) and titanium dioxide (TiO<sub>2</sub>) in various cell types. Here, we investigated the putative toxicity of the nanoparticles in peripheral nervous system employing cell culture models of Schwann cells and dorsal root ganglion (DRG) neurons. The results from our ongoing studies demonstrate treatment with SiO<sub>2</sub> or TiO<sub>2</sub> nanoparticles induced increases in reactive oxygen species production, decreases in cell survival, increases in lactate dehydrogenase release and changes in cellular morphology. The results from flow cytometer and microscopic observation show that there is internalization of the nanoparticles by Schwann cells. Thus, results of our ongoing studies are consistent with the hypothesis that SiO<sub>2</sub> and TiO<sub>2</sub> nanoparticles are cytotoxic to cells of the peripheral nervous system and may have health impact on environmental exposure to such nanoparticles.

10. Wong YYW, Jaiswal AR, Lu S, Dukhande VV, Bhushan A, Daniels CK, Leung SW & Lai JCK (2011) Neuroprotective Role of Pioglitazone, a PPAR $\gamma$  Agonist on Nanoparticles-Induced Cytotoxicity and Stress in Astrocytes-Like U87 Astrocytoma Cells. 53<sup>rd</sup> Annual Symposium of the Idaho Academy of Science, March 31-April 2, 2011, The College of Idaho, Caldwell, ID. Journal of Idaho Academy of Science, 47(1): 73.

**Abstract.** Evidence has been accumulating that nanoparticles have been increasingly employed in diverse industrial applications. Nevertheless, the health impact of exposure to nanoparticles has not been fully assessed. Recent studies from our and other laboratories suggest that exposure to nanoparticles induces cytotoxic and inflammatory responses in lung tissue and cells from both central and peripheral nervous systems. To systematically investigate molecular mechanisms underlying the putative cytotoxicity of nanoparticles, we have developed several cell models *in vitro* for high throughput studies. For example, we have previously shown that astrocytes-like U87 astrocytoma cells can offer neuroprotection to neurons-like SK-N-SH neuroblastoma cells in the co-culture paradigm. In the presented studies, we have tested the hypothesis that nanoparticles-induced cytotoxic stress can elicit and/or enhance the neuroprotective effects of astrocytes through the activation of astrocytic signaling and alteration of astroglial function. Results from our ongoing studies provide some support for this hypothesis. Furthermore, the neuroprotection proffered by the astrocytoma cells may be enhanced in the presence of pioglitazone, a peroxisome proliferator-activated receptors  $\gamma$  (PPAR $\gamma$ ) agonist. Consequently, our results may have pathophysiological implications in neuroprotection and nanotoxicological research.

11. Gao X, Assan D, Lai JCK & Leung SW (2011) Anaerobic Biofuel Cell Modified with NanoParticles and Polymers for Biomedical Applications. 53<sup>rd</sup> Annual Symposium of the Idaho Academy of Science, March 31-April 2, 2011, The College of Idaho, Caldwell, ID. Journal of Idaho Academy of Science, 47(1): 74-75.

**Abstract.** Highly branched polymers and nano Au particles sol-gel were used to construct an enzymatic biofuel cell used in an anaerobic system. The anode and cathode of this biofuel cell were modified with polymers and sol-gel that effectively stabilized the enzymes, lactate dehydrogenase (LDH) and glutamate dehydrogenase (GDH) that were essential for converting body substrates to energy and metabolic products. This sol-gel modification would enable further enzymatic biofuel cell development that was not possible due to rapid deterioration of enzymes that are necessary for all biochemical reactions. The anaerobic biofuel cell can be the power source for biomedical devices such as pacemaker and insulin pump that are imbedded in the body; this “build-in” biofuel cell can avoid many problems associated with external power source.

12. Kasarla V, Mukka K, Tadinada SM, Wong YYW, Bhushan A, Daniels CK, Leung SW & Lai JCK (2011) Differential Cytotoxic Effects of Zinc Oxide Nanoparticles on S16 Schwann Cells and DRG Neurons. 53<sup>rd</sup> Annual Symposium of the Idaho Academy of Science, March 31-April 2, 2011, The College of Idaho, Caldwell, ID. Journal of Idaho Academy of Science, 47(1): 75.

**Abstract.** Nanoparticles are increasing employed in drug delivery and targeting although their putative toxicity is incompletely understood. Our previously observation that several metallic oxide nanoparticles exert cytotoxic effects on human neural and non-neural cells prompted us to hypothesize that zinc oxide (ZnO) nanoparticles exert cytotoxicity on Schwann cells and dorsal root ganglion (DRG) neurons by decreasing their survival. To investigate this hypothesis, we determined the survival of S16 Schwann cells and DRG neurons after treating them with various concentrations of ZnO nanoparticles for 48 hours. Our results indicated that treatment with ZnO nanoparticles decreased their cell survival in a dose-related manner. Furthermore, DRG neurons were more susceptible to cytotoxicity of ZnO nanoparticles than S16 Schwann cells. Consequently, there is an urgent need to identify the mechanisms underlying the differential cytotoxicity of ZnO nanoparticles in these cell types. Nevertheless, our results may have pathophysiological implications in toxicity of ZnO nanoparticles in peripheral nervous system.

13. Tadinada SM, Bhardwaj V, Lai JCK & Bhushan A (2011) Role of Epidermal Growth Factor Receptor in Pancreatic Cancer Resistance. 53<sup>rd</sup> Annual Symposium of the Idaho Academy of Science, March 31-April 2, 2011, The College of Idaho, Caldwell, ID. Journal of Idaho Academy of Science, 47(1): 75-76.

**Abstract.** Pancreatic cancer (PC) is one of the most aggressive cancers with a dismally low survival rate of 4-5%. The reasons for the low PC patients' survival rate are: late diagnosis and highly metastatic and drug resistant nature of PC. Two drugs of the anti-metabolite class, gemcitabine (GEM) and 5-fluorouracil (5FU), have been approved for the treatment of PC; however, the cancer cells soon acquire resistance against these drugs rendering them ineffective. In this study, we determined the role of epidermal growth factor receptor (EGFR) and its downstream signaling molecules in drug resistant characteristics of PC cells. We hypothesized that modulation of EGFR activity affects the cytotoxicity of GEM and 5FU providing the PC cells with drug resistant characteristics. We selected GEM and 5FU resistant cell lines and found that the levels of activated EGFR were altered in them compared to their parent cells. In addition, the resistant cells were differentially sensitive to gefitinib. Thus, the resistant cells can serve as models to better understand the mechanisms of drug resistance in PC and may be helpful in developing new therapies for targeting drug-resistant PC cells.

14. Idikuda V, Singh R, Kumbulla S, Jaiswal AR, Bhushan A, Daniels CK, Leung SW & Lai JCK (2011) Morphological Changes of Schwann Cells after Exposure to Magnesium Oxide Nanoparticles. 53<sup>rd</sup> Annual Symposium of the Idaho Academy of Science, March 31-April 2, 2011, The College of Idaho, Caldwell, ID. Journal of Idaho Academy of Science, 47(1): 76.

**Abstract.** Schwann cells are the supportive cells of neurons in the peripheral nervous system (PNS) and interact with them in myelin production and axonal regeneration. Moreover, the processes extended by Schwann cells serve to guide regenerating nerves to their target organ. This study focuses on examining the morphological changes of cultured Schwann cells after exposing them to magnesium oxide nanoparticles. Results of ongoing studies suggest that treatment with the nanoparticles modulate on this mechanism of Schwann cells. However, we noted the Schwann cells extended maximum number of processes when treated with 0.1-1 µg/ml of the nanoparticles whereas at higher exposure concentrations, Schwann cells and their nuclei appeared to be swollen and their survival decreased. Our results are the first to report on morphological changes of these cells when exposed to magnesium oxide nanoparticles and as such may have pathophysiological implications of exposure of the PNS to the nanoparticles.

15. Singh MRM, Kumbulla S, Idikuda VK, Jaiswal AR, Bhushan A, Leung SW, Daniels CK & Lai JCK (2011) Neurotoxicity of Magnesium Oxide Nanoparticles as Elicited in Schwann Cells. 53<sup>rd</sup> Annual Symposium of the Idaho Academy of Science, March 31-April 2, 2011, The College of Idaho, Caldwell, ID. Journal of Idaho Academy of Science, 47(1): 77.

**Abstract.** Nanoparticles have found wide usage in semiconductors, robotics, pharmaceuticals and medical sciences. However, because of their diverse and ever-increasing applications, their potential environmental impact and health risk have become prominent issues to be addressed. Nevertheless, the health effects of exposure to nanoparticles are poorly understood. Our ongoing study constitutes part of a systematic elucidation of putative toxicity of nanoparticles in the peripheral nervous system (PNS). Schwann cells are the principal glia of the PNS and play significant roles in supporting neurons, the conduction of nerve impulses, and nerve development and regeneration. We monitored the putative cytotoxicity of magnesium oxide (MgO) nanoparticles in Schwann cells employing the MTT (cell survival) assay and found that survival of Schwann cells decreased when exposed to the nanoparticles in a dose- and time-related manner. Thus, results of our ongoing study suggest that MgO nanoparticles can exert some neurotoxicity on PNS as detected in Schwann cells in culture and may have toxicological implications in environmental exposure to such nanoparticles.

16. Kumbulla S, Idikuda VK, Singh R, Jaiswal AR, Alaydi L, Bhushan A, Leung SW, Daniels CK & Lai JCK (2011) Comparison of Effects of Several Metal-Based Nanoparticles on R3 Schwann Cells. 53<sup>rd</sup> Annual Symposium of the Idaho Academy of Science, March 31-April 2, 2011, The College of Idaho, Caldwell, ID. Journal of Idaho Academy of Science, 47(1): 77-78.

**Abstract.** The increased use of nanotechnology in everyday life raises questions regarding the health impact of nanoparticles. Because the toxicity of various nanoparticles in mammalian cells has not been elucidated, our ongoing study focuses on comparing the toxicity of several metal-based and non-metal-based nanoparticles on the peripheral nervous system (PNS). We exposed R3 Schwann cells, a major PNS neural cell type, to magnesium oxide (MgO), silicon dioxide (SiO<sub>2</sub>), titanium oxide (TiO<sub>2</sub>) and zinc oxide (ZnO) nanoparticles for 24, 36 and 48 hours

and monitored their cell survival. We found that MgO, SiO<sub>2</sub>, TiO<sub>2</sub> and ZnO nanoparticles induced cell death in R3 Schwann cells in a dose- and time-related manner. Furthermore, comparison of the effects of these nanoparticles reveals that TiO<sub>2</sub> and ZnO nanoparticles are more toxic to R3 Schwann cells compared to the other nanoparticles investigated. Thus, our results may have implications in pathophysiology of metal-based nanoparticles in PNS neural cells and in the environmental exposure to these metal-based nanoparticles.

17. Mukka K, Kasarla V, Tadinada SM, Wong YYW, Bhushan A, Daniels CK, Leung SW & Lai JCK (2011) Exposure of Zinc Oxide and Other Metallic Oxide Nanoparticles Induces Cytotoxicity and Morphological Alterations in Dorsal Root Ganglion Neurons. 53<sup>rd</sup> Annual Symposium of the Idaho Academy of Science, March 31-April 2, 2011, The College of Idaho, Caldwell, ID. Journal of Idaho Academy of Science, 47(1): 78-79.

**Abstract.** The use of nanoparticles in industrial applications has been expanding and accelerating in the last two decades. Nevertheless, the occupational and health impact from the exposure to such nanoparticles is poorly understood. We previously detected the cytotoxic effects of several metallic oxides nanoparticles in central nervous system neural cells *in vitro*. Because the cytotoxic effects of the nanoparticles on the peripheral nervous system (PNS) are unknown, we developed a PNS cell model *in vitro* consisting of dorsal root ganglion (DRG) neurons to study the effects of the nanoparticles. We exposed these cells to various concentrations of metallic oxides nanoparticles and observed that their survival decreased as the treatment levels increased. Among those studied, Zinc oxide (ZnO) nanoparticles were the most effective in lowering survival of DRG neurons and in inducing morphological changes in these neurons. Thus, our results have implications in the pathophysiology of cytotoxicity of metallic oxides nanoparticles in peripheral neurons. Clearly, the molecular mechanisms underlying the cytotoxicity of ZnO nanoparticles merit further investigation.

18. Jaiswal AR, Lu S, Pfau J, Wong YYW, Bhushan A, Leung SW, Daniels CK & Lai JCK (2011) Effects of Silicon Dioxide Nanoparticles on Peripheral Nervous System Neural Cell Models. NSTI Nanotechnology Conference and Expo – Nanotech 2011, June 13-16, 2011, Boston, MA (in Abstracts Volume).

**Abstract.** As cautioned by the US Environmental Protection Agency, exposure to nanomaterials can occur during their manufacture or production: these industrial processes also may potentially give rise to environmental pollution of such materials. Thus, a case in point is the exposure to silicon dioxide (SiO<sub>2</sub>) nanoparticles because SiO<sub>2</sub> – including a range of its particle sizes – is increasingly being used in cosmetics, food, and drug formulations. SiO<sub>2</sub> was generally regarded as a non-toxic substance in view of its numerous industrial applications. Nevertheless, there have been reports that SiO<sub>2</sub> particles are not as harmless as they were assumed to be. Consequently, the need is increasing to examine the biocompatibility of SiO<sub>2</sub> particles ranging from the micro- to the nanometer sizes.

There is increasing evidence that cell model systems *in vitro* facilitate the high through-put screening of putative toxicity of a variety of nanomaterials, including nanoparticles. However, until recently, most of such cell models consisted of non-neural cells such as lung, skin, and liver cells. Because of the paucity of the literature on employing neural cell types to elucidate the putative cytotoxicity of nanomaterials, we began developing several human neural cell model systems (e.g., the astrocytes-like U87 astrocytoma and neurons-like SK-N-SH neuroblastom cells) to systematically investigate the putative cytotoxicity of metallic and non-metallic oxide nanoparticles. Our previous studies demonstrated that the nanoparticles of several metallic and non-metallic oxides, including SiO<sub>2</sub>, exert differential cytotoxic effects on our models. Nevertheless, as far as we are aware, the putative cytotoxicity of these nanoparticles on neural cells derived from the peripheral nervous system (PNS) has not been reportedly studied.

We have recently developed two neural cell models derived from the PNS, namely dorsal root ganglion (DRG) neurons and Schwann cells. Our systematic studies have indicated that the two *in vitro* cell models are suitable not only for elucidating the pathophysiological mechanisms underlying diabetic neuropathy but also for nanotoxicology and tissue engineering studies.

Because the putative cytotoxic effects of metallic and non-metallic oxide nanoparticles in PNS neural cells are largely unknown, we have employed our *in vitro* models of DRG neurons and Schwann cells to systematically investigate the putative cytotoxicity of nanoparticles of several metallic and non-metallic oxides. Results of our ongoing studies have revealed that SiO<sub>2</sub> nanoparticles exert differential cytotoxic effects on DRG neurons and



Schwann cells by lowering their survival. Furthermore, employing the flow cytometry, we noted the cytotoxicity of SiO<sub>2</sub> nanoparticles in the two cell models *in vitro* could be attributed, at least in part, to the uptake of the nanoparticles by the two cell types. Clearly, these interesting cytotoxic mechanisms underlying the effects of the nanoparticles in the cell models merit further investigation.

All in all, results of our ongoing studies strongly suggest that the DRG neurons and Schwann cells constitute excellent cell model systems *in vitro* for high-throughput screen of cytotoxicity of nanoparticles in PNS neural cells. Moreover, they may have pathophysiological implications in how exposure to SiO<sub>2</sub> nanoparticles impacts on the structure and function of the peripheral nervous system.

19. Lu S, Jaiswal AR, Wong YYW, Bhushan A, Leung SW, Daniels CK & Lai JCK (2011) Differential Cytotoxic Effects of Titanium Oxide Nanoparticles on Peripheral Nervous System Neural Cells. NSTI Nanotechnology Conference and Expo – Nanotech 2011, June 13-16, 2011, Boston, MA (in Abstracts Volume).

**Abstract.** Evidence has been accumulating that titanium dioxide (TiO<sub>2</sub>) has been employed in increasing number of a variety of industrial applications including, but not limited to, production of paper, plastics, cosmetics and paints. Because many of such applications require fine grade or dust of TiO<sub>2</sub>, that requirement strongly imply that significant amounts of TiO<sub>2</sub> employed in the applications are in the form of micro- and nanoparticles. Thus, these ever-increasing applications of TiO<sub>2</sub> in diverse industries raise the distinct possibility of elevating the occupational and other environmental exposure of TiO<sub>2</sub> micro- and nanoparticles to humans and other species. Nevertheless, the health impact of exposure to TiO<sub>2</sub> nanoparticles has not been fully assessed despite recent evidence suggesting that such exposure induces inflammatory responses in lung tissue and cells.

In a recent study, we have demonstrated that treatment with TiO<sub>2</sub> micro- or nanoparticles induce cell death in human astrocytes-like U87 astrocytoma cells and in normal human fibroblasts in a concentration-related manner. In particular, these particles appeared to induce in U87 cells a cell death mode that exhibited both the characteristics of apoptosis and necrosis. Thus, our earlier findings suggest both TiO<sub>2</sub> micro- and nanoparticles may pose health hazards to humans when exposed to them. Moreover, our previous study constituted part of a systematic program of developing cell models *in vitro* consisting of the astrocytes-like U87 astrocytoma and neurons-like SK-N-SH neuroblastoma cells to elucidate the putative cytotoxicity of nanomaterials, including nanoparticles.

Our previous findings in human neural cells derived from the central nervous system also prompted us to consider the distinct possibility that exposure of neural cells derived from the peripheral nervous system (PNS) to nanomaterials such as metallic and non-metallic oxide nanoparticles may induce cytotoxicity in PNS neural cells. However, such effects in the PNS neural cells have not been reportedly studied. We have, therefore, developed two PNS neural cell models *in vitro* consisting of dorsal root ganglion (DRG) neurons and Schwann cells to allow the systematic investigation of cytotoxicity of such nanoparticles in PNS neural cells.

Our on-going studies indicate that treatment with TiO<sub>2</sub> nanoparticles induced differential cytotoxic effects on DRG neurons and Schwann cells. Treatment with the nanoparticles lowered the survival of both DRG neurons and Schwann cells in a dose- and time-related manner. Moreover, we found that DRG neurons were more sensitive to the effect of the nanoparticles than Schwann cells. Other studies are in progress to further characterize such effects of the nanoparticles. Thus, our findings may have pathophysiological implications in the impact of exposure to TiO<sub>2</sub> nanoparticles on the structure and function of the PNS.

20. Wong YYW, Jaiswal AR, Dukhande VV, Bhushan A, Leung SW & Lai JCK (2011) New *In Vitro* Strategy of Astrocytoma (Astrocytes-like) Cells Treated with Pioglitazone (PPAR gamma agonist) Offers Neuroprotection Against Nanoparticle-Induced Cytotoxicity. NSTI Nanotechnology Conference and Expo – Nanotech 2011, June 13-16, 2011, Boston, MA (in Abstracts Volume).

**Abstract.** Among *in vitro* cell culture models, co-cultures gained attention with accumulating evidence showing their capacity for high throughput studies and mechanistic investigation in tissue engineering research. Recently, we and others have developed several cell models for the investigation of the molecular mechanisms underlying the cytotoxicity of nanoparticles of several metallic and non-metallic oxides. These important findings have raised the awareness for the need to derive a set of strategies whereby critical mammalian cell types (e.g., neural cells) can be protected from the cytotoxicity induced by nanoparticles and other nanomaterials.

As part of our response to the need to devise a strategy to protect critical cell types against the cytotoxicity induced by nanomaterials, we have continued to develop cell models *in vitro* to further elucidate and exploit the putative neuroprotective properties of astrocytes-like astrocytoma cells. Previously, we demonstrated the neuroprotection offered by astrocytoma cells to neuroblastoma cells in the direct co-culture milieu. For example, we have shown U-87 (astrocytes-like) astrocytoma cells confer protection to SK-N-SH (neurons-like) neuroblastoma cells against several pathophysiological assaults such as oxidative stress induced by depletion of cellular glutathione and inhibition of glycolysis mediated by iodoacetate or 3-bromopyruvate.

Apart from the protection against pathophysiological assaults, we have also demonstrated that the addition of peroxisome proliferator-activated receptor- $\gamma$  agonist pioglitazone in the culture medium can amplify the neuroprotective properties of astrocytoma cells conferred on SK-N-SH cells against manganese toxicity. This study aims to further determine and identify the neuroprotective properties of astrocytes conferred on neurons employing a novel *in vitro* co-culture model.

U87 astrocytoma and SK-N-SH neuroblastoma cells have been shown to constitute good model systems *in vitro* for astrocytes and neurons due to their close functional resemblance to normal astrocytes and neurons, respectively. Based on the results of our previous studies, the present studies have tested the hypothesis that nanoparticle-induced cytotoxic stress can elicit and/or enhance the neuroprotective effects of astrocytes through the activation of astrocytic signaling and alteration of astroglial function. Furthermore, the neuroprotection can be enhanced in the presence of pioglitazone. Thus, our results may have pathophysiological implications in neuroprotection research but also implication and application in nanotoxicological research.

21. Jain A, Jaiswal AR, Lu S, Wong YYW, Bhushan A, Leung SW, Daniels CK & Lai JCK (2011) Molecular Effects of Silicon Dioxide Nanoparticles on Cell Survival Signaling of Dorsal Root Ganglion (DRG) Neurons and Schwann Cells. NSTI Nanotechnology Conference and Expo – Nanotech 2011, June 13-16, 2011, Boston, MA (in Abstracts Volume).

**Abstract.** Dorsal root ganglion (DRG) neurons of the peripheral nervous system (PNS) become damaged in diabetic and other forms of neuropathy: the pathophysiological changes can induce a variety of major and minor complications in patients with such neuropathies. The molecular mechanisms underlying the pathophysiology of peripheral neuropathies have not been fully elucidated and, in many cases, have yet to be determined. Our limited understanding of such pathophysiological mechanisms in molecular terms is largely attributable to (i) the inherent limitation of animal models *in vivo* and their inaccessibility to mechanistic probing and (ii) the limited life-span of primary culture models of DRG neurons and Schwann cells *in vitro* rendering them unsuitable for more chronic studies.

To meet the need for suitable cell culture models *in vitro* of PNS neural cells that allow long-term studies, we have developed unique PNS neural cell culture models *in vitro* consisting of immortalized DRG neurons and Schwann cells. Schwann cells are oligodendroglial cells of the PNS and function to nourish and protect DRG neurons *in vivo*. They surround DRG neurons and this interaction is important in protecting the neurons from degeneration. Our previous and on-going studies strongly suggest that our PNS neural cell models constitute good model systems and allow the probing of molecular mechanisms underlying peripheral nerve damage and dysfunction consequent to diabetic neuropathy, and chemically-induced peripheral neuropathy.

In our previous studies we found that silicon dioxide (SiO<sub>2</sub>) nanoparticles induce differential cytotoxic effects in neurons-like SK-N-SH neuroblastoma and astrocytes-like U87 astrocytoma cells. However, the putative cytotoxicity of SiO<sub>2</sub> nanoparticles in neural cells derived from the PNS is unknown. Thus, a systematic investigation of the putative cytotoxicity of SiO<sub>2</sub> nanoparticles in PNS neural cells not only will elucidate how exposure to such nanoparticles may impact on the structure and function of the PNS but also will shed light on pathophysiological and related molecular mechanisms underlying chemically-induced peripheral neuropathy. Therefore, we hypothesized that SiO<sub>2</sub> nanoparticles induce differential cytotoxicity in DRG neurons and Schwann cells.

Because little is known regarding the cell survival signaling in both DRG neurons and Schwann cells, especially when cultured *in vitro*, we have determined the expression of proteins involved in cell survival in these two cell models and the effects of treatment with SiO<sub>2</sub> nanoparticles thereon. Results of our on-going studies show that both cultured DRG neurons and Schwann cells express detectable levels of ERK and p-ERK, which are signaling proteins known to be important in regulating cell survival/proliferation. Moreover, exposure of the two PNS neural cell types to SiO<sub>2</sub> nanoparticles (1, 25, 50  $\mu$ g/mL) for 48 hours induced alterations in their expression of

p-ERK. Other studies are in progress to determine the effects of the nanoparticles on cell survival signaling mechanisms other than ERK.

Our results suggest one mechanism underlying the cytotoxicity of SiO<sub>2</sub> nanoparticles in PNS neural cell types may be via disturbing their cell survival signaling. These findings have functional and pathophysiological implications in cell survival signaling in PNS neural cells and in chemically-induced peripheral neuropathy.

22. Lai JCK, Gao W & Leung SW (2011) Effects of Chitosan and Nanoparticles on Survival of Schwann Cells and Dorsal Root Ganglion Neurons. NSTI Nanotechnology Conference and Expo – Nanotech 2011, June 13-16, 2011, Boston, MA (in Abstracts Volume).

**Abstract.** Ideally, a promising alternative for the repair of substantive peripheral nerve injuries is the bioartificial nerve graft, comprised of biocompatible materials pre-seeded with neuronal supporting cells, such as Schwann cells. In practice, the optimal bioartificial nerve graft has yet to be realized. Nevertheless, several groups of biocompatible materials have been tested for their suitability for fabricating the bioartificial nerve graft. In this context, chitosan has been studied as a candidate material for nerve regeneration due to its biocompatible nature. Additionally, nanometal particles, which are known to exert certain beneficial effects not previously expected on biological systems, are also introduced into the construct and/or modification of the bioartificial nerve graft.

Schwann cells play key roles in development and regeneration of peripheral neurons. However, the molecular mechanisms underlying these functional roles of Schwann cells are poorly understood. Because current cell models for investigating the mechanisms underlying nerve degeneration and regeneration have significant limitations because such models involve primary cultures of peripheral nervous system (PNS) neural cells that have very limited life-span. Consequently, to overcome such limitations, we have employed immortalized Schwann cells (S16) and dorsal root ganglion (DRG) neurons (50 B 11) to develop PNS neural cell models *in vitro* suitable for nerve degeneration and regeneration studies. Results of our on-going studies strongly suggest that our cell models are suitable and can be employed to attain such a goal.

Because chitosan has been considered as having the potential to be a candidate material suitable for application in nerve regeneration, we have set out to test the hypothesis that chitosan in combination with nanometal particles can be a platform for further developing the ideal bioartificial nerve graft as the effects of chitosan or nanometal particles on PNS neural cells are largely unknown.

We have therefore systematically examined the effects of chitosan film or chitosan in combination with nanometal particles (nanogold or nanosilver particles) on the growth of Schwann cells (S16) and DRG neurons (50 B 11). Results of our on-going studies strongly suggest that chitosan and chitosan in combination with nanogold particles have no effects on the growth kinetics of Schwann cells. However, chitosan, and in particular, chitosan in combination with nanogold appeared to exert a small negative impact on the growth kinetics of DRG neurons. These findings suggest that chitosan and chitosan in combination with nanogold particles are more biocompatible with Schwann cells than with DRG neurons. On the other hand, chitosan in combination with nanosilver particles depressed the growth kinetics of both Schwann cells and DRG neurons. Thus, in the context of this type of application, nanosilver particles are much less biocompatible compared to nanogold particles. Consequently, our results suggest that chitosan film and chitosan in combination with nanogold particles may have significant potential to be further developed as suitable biocompatible materials for the fabrication of the ideal bioartificial nerve graft. Clearly, this is an interesting “tissue engineering problem” for further investigation.

23. Lai JCK, Jaiswal AR, Lu S, Pfau J, Wong YYW, Bhushan A, Daniels CK & Leung SW (2011) Differential Cytotoxicity of Silicon Dioxide Nanoparticles on Neural Cells Derived from Peripheral Nervous System. International Conference on Materials for Advanced Technologies, Suntec, June 26-July 1, 2011, Singapore (in Abstracts Volume).

## **Abstract.**

## **Introduction.**

Nanomaterials, including nanoparticles, have been increasingly employed in a variety of industries: thus, their accelerating industrial applications raise some concerns regarding health risks due to occupational and/or other environmental exposure to these materials. Nevertheless, the putative environmental toxicity of nanomaterials is unknown [1,2]. There is increasing evidence that cell model systems *in vitro* facilitate the high through-put screening of putative toxicity of a variety of nanomaterials, including nanoparticles, although the use of neural cell types in such studies have been extremely limited [1,2]. We have developed several human neural cell models (e.g., the astrocytes-like U87 astrocytoma and neurons-like SK-N-SH neuroblastom cells) to systematically investigate the putative cytotoxicity of metallic and non-metallic oxide nanoparticles [1,2]. Employing the models, we found the nanoparticles of several metallic and non-metallic oxides, including SiO<sub>2</sub>, exerted differential cytotoxic effects on U87 and SK-N-SH cells [1,2]. Because the putative cytotoxicity of these nanoparticles on neural cells derived from the peripheral nervous system (PNS) is unknown, we have developed two neural cell models derived from the PNS, namely dorsal root ganglion (DRG) neurons and Schwann cells and employed them to systematically investigate the putative cytotoxicity of nanoparticles of several metallic and non-metallic oxides [3].

## **Materials and Methods.**

DRG neurons and Schwann cells were cultured as previously described [3]. Both types were treated with SiO<sub>2</sub> nanoparticles at specified concentrations at 37°C for 36 hours. Then the survival of the treated and untreated (i.e., control) cells were determined by the MTT assay as previously described [3].

## **Results and Discussion.**

Results of our ongoing studies strongly suggest that treatment with SiO<sub>2</sub> nanoparticles (1 to 200 µg/mL) exerted differential cytotoxic effects on PNS neural cells and that Schwann cells, which are prominent glial cells of the PNS, were more susceptible than DRG neurons to the effect of SiO<sub>2</sub> nanoparticles. That Schwann cells are susceptible to the cytotoxicity of SiO<sub>2</sub> nanoparticles is consistent with our previous finding that these nanoparticles also exert cytotoxicity on U87 astrocytoma (astrocytes-like) cells [2].

In studies employing the flow cytometry, we noted the cytotoxicity of SiO<sub>2</sub> nanoparticles in the two cell models *in vitro* could be attributed, at least in part, to cellular uptake of the nanoparticles.

Our results strongly suggest that the DRG neurons and Schwann cells constitute excellent cell model systems *in vitro* for high-throughput screen of cytotoxicity of nanoparticles in PNS neural cells. Furthermore, our results may have pathophysiological implications in how exposure to SiO<sub>2</sub> nanoparticles impacts on the structure and function of the peripheral nervous system.

## **Acknowledgement.**

This study was supported by an USAMRMC Project Grant (Contract #W81XWH-07-2-0078).

## **References**

1. Lai JCK, Lai MB, Jandhyam S, Dukhande VV, Bhushan A, Daniels CK & Leung SW (2008) Exposure to Titanium Dioxide and Other Metallic Oxide Nanoparticles Induces Cytotoxicity on Human Neural Cells and Fibroblasts. *Int. J. Nanomed.* 3(4):533-545.
2. Lai JCK, Ananthakrishnan G, Jandhyam S, Dukhande VV, Bhushan A, Gokhale M, Daniels CK & Leung SW (2010) Treatment of Human Astrocytoma U87 Cells with Silicon Dioxide Nanoparticles Lowers Their Survival and Alters Their Expression of Mitochondrial and Cell Signaling Proteins. *Int J Nanomed* 5:715-723.
3. Jaiswal AR, Bhushan A, Daniels CK & Lai JCK (2010) A Cell Culture Model for Diabetic Neuropathy Studies. *Journal of the Idaho Academy of Science* 46(1):58-63.
24. Leung SW, Guo W & Lai JCK (2011) Nanoparticles Modulate the Effects of Chitosan on Survival of Schwann Cells and Dorsal Root Ganglion Neurons. *International Conference on Materials for Advanced Technologies*, Suntec, June 26-July 1, 2011, Singapore (in Abstracts Volume).

**Abstract.** Chitosan has been investigated as a candidate material for nerve regeneration applications due to its

biocompatible nature. On the other hand, nanometal particles, which are known to exert certain beneficial effects not previously expected on biological systems, are also considered as part of the composite material for the construct and/or modification of the bioartificial nerve graft. Nevertheless, how these putatively biocompatible materials may interact with the neural cell types derived from the peripheral nervous system (PNS) is largely unknown because of the lack of appropriate cell models. Consequently, to overcome such limitations, we have employed immortalized Schwann cells (S16) and dorsal root ganglion (DRG) neurons (50 B 11) to develop PNS neural cell models *in vitro*. Results of our on-going studies strongly suggest our cell models are suitable for a variety of tissue engineering applications, especially in the *in vitro* setting. We have therefore systematically investigated the effects of chitosan film or chitosan in combination with nanometal particles (nanogold or nanosilver particles) on the growth of Schwann cells (S16) and DRG neurons (50 B 11). Our results demonstrated chitosan and chitosan in combination with nanogold particles exerted no effects on the growth kinetics of Schwann cells. However, chitosan, and in particular, chitosan in combination with nanogold appeared to mildly inhibit the growth kinetics of DRG neurons. These findings indicate chitosan and chitosan in combination with nanogold particles are more biocompatible with Schwann cells than with DRG neurons. By contrast, chitosan in combination with nanosilver particles depressed the growth kinetics of both Schwann cells and DRG neurons. Consequently, our results prompted us to conclude that chitosan film and chitosan in combination with nanogold particles may have significant potential to be further developed as suitable biocompatible materials for fabricating the ideal bioartificial nerve graft.

25. Leung SW, Chan A, Minski M & Lai JCK (2011) Comparison of Elemental Distribution in Rat's Brain after Lifelong Treatment with Excessive  $Mn^{2+}$  in Drinking Water and the Health Implications. International Water Convention, July 4-8, 2011, Singapore (Abstract # IWA-6218-R1).

**Abstract.** Lifelong exposure to environmental factors can influence the risk of developing diseases; environmental stresses can ultimately lead to cell death and have been thought to be the cause of many neurological diseases. Our daily diet is one of the important environmental factors that can seriously affect the development and proper function of the brain. In this study, we investigated how 30 elements and electrolytes that were consumed in a regular diet over a lifetime would affect the distribution of these elements in the brain of rats. We also investigated how excessive concentrations of contaminant in drinking water, such as Mn, may affect the accumulation of elements in the brain. Our results indicated that increased consumption of Mn would enhance the retention of heavy metals such as Hg and Se in the brain and is believed to be pivotal in many neurological disorders such as Parkinson's and Alzheimer's disease.

26. Leung SW, Chan A, Minski M & Lai JCK (2011) Effects of Lifetime Consumption of Excessive  $Mn^{2+}$  in Drinking Water to Elemental Distribution in Vital Organs. International Water Convention, July 4-8, 2011, Singapore (Abstract #IWA-6243).

**Abstract.** Diet is one of the major environmental factors that can have serious effect on our well-being in health. The knowledge of how elements and electrolytes are accumulated in our body through diet ingestion is not well understood, especially over a prolonged period. A recent study has shown that a cancer patient was having intracellular heavy metal accumulations within lymph nodes, bone marrow, and liver. In this study, we investigated the distributions of 30 metals and electrolytes that were consumed in a regular diet over a lifetime in liver, lung, heart, spleen, and kidney of healthy adult rats; we further compared the elemental distributions in these vital organs with aged rats that were treated with excessive  $Mn^{2+}$  in the drinking water. Our results showed that there were differences in elemental accumulations with age, the differences were element and organ specific. Prolonged consumption of excessive  $Mn^{2+}$  also affected elemental accumulations within organs.

27. Wright GL, Lai JCK, Chan A, Minski M & Leung SW (2011) Influence of Metallomic Distribution in Brain by Prolong Consumption of Contaminant in Drinking Water. International Water Convention, July 4-8, 2011, Singapore (Abstract #IWA-6228R1).

**Abstract.** Lifelong exposure to environmental factors can influence the risk of developing diseases; environmental stresses can ultimately lead to cell death and have been thought to be the cause of many neurological diseases. Our daily diet is one of the important environmental factors that can seriously affect the development and proper function of the brain. In this study, we investigated how 30 elements and electrolytes that were consumed in a regular diet over a lifetime would affect the distribution of these elements in seven regions of the brain of rats. We also investigated how excessive concentrations of contaminant in drinking water, such as Mn, may affect the accumulation of elements in the brain. Our results indicated that increased consumption of Mn would enhance the retention of heavy metals such as Hg and Se in the brain that is believed to be pivotal in many neurological disorders such as Parkinson's and Alzheimer's disease.

28. Jaiswal AR, Lu S, Bhushan A, Daniels CK, Leung SW, Lai JC (2011) Silicon Dioxide Nanoparticles Induce Mitochondria-Mediated Cell Damage in Peripheral Neural Cells. Annual Meeting, Society for Neuroscience, November, 2011, Washington, DC (in Abstracts Volume).

**Abstract.** The diverse applications of nanoparticles in many fields have been increasing exponentially in the last decade. Once they enter the body by inhalation or other routes, nanoparticles may be toxic to one or more organ systems: thus, exposure to these nanoparticles may induce health hazards. Nevertheless, the effects of their exposure on the nervous system have not been elucidated. We have therefore initiated systematic studies to elucidate the putative cytotoxicity of nanoparticles on peripheral nervous system, employing in vitro cell models consisting of Schwann cells and dorsal root ganglion (DRG) neurons. We have examined the effects of silicon dioxide nanoparticles on DRG neurons and Schwann cells. The results from our ongoing studies demonstrate that treatment of DRG neurons and Schwann cells with silicon dioxide nanoparticles induced a decrease in cell survival and increase in lactate dehydrogenase release from cells. The treatment also induced oxidative stress and altered mitochondrial genome function. The results from flow cytometry and microscopy suggest there is internalization of the nanoparticles by Schwann cells. Thus, results of our ongoing studies indicate silicon dioxide nanoparticles induce cytotoxicity in neural cells of the peripheral nervous system and as such may assume pathophysiological importance.

29. Assan D, Gao X, Lai JCK & Leung SW (2012) Characterization of High Performance Sensors Modified with Nanoparticles and Different Enzyme Couplings. Idaho Academy of Science 54<sup>th</sup> Annual Symposium, March 22-24, 2012, University Place, Idaho Falls, ID (in Abstracts volume, p. 9).

**Abstract.** The idea of directly coupled enzyme electrodes to measure low concentrations of specific chemical species, such as glucose and peroxide, has existed for decades. The recent euphoria of nanotechnology has elevated the development of these fourth generation bionanosensors to another horizon by using highly modified direct enzyme-electrode couplings with nanoparticles. These bionanosensors can detect target species below parts per billion (ppb) almost instantly.

In our research group, we investigated the performance of electrode sensors fabricated with different biocomposite materials, including the coupling enzyme for a specific target chemical; this chemical can be organic or inorganic, such as a metabolite, biomarker, or environmental pollutant. Materials for the biocomposite layer consist of polymers, metal nanoparticles, and enzyme for the coupling reaction which enables the high sensitivity of detection.

In this report, LDH (Lactate dehydrogenase), GDH (Glutamate dehydrogenase), and Hemoglobin were the enzymes used to fabricate these high performance electrode sensors. Various metabolites and environmental pollutants were used to characterize the selectivity and sensitivity of these sensors at pH 7.0. Concentration levels down to  $10^{-12}$  M were tested.

30. VK Idikuda, Jaiswal AR, Wong YYW, Bhushan A, Leung SW & Lai JCK (2012) Magnesium Oxide Nanoparticles Induce Stat-3 Mediated Apoptosis in Schwann Cells. Idaho Academy of Science 54<sup>th</sup> Annual Symposium, March 22-24, 2012, University Place, Idaho Falls, ID (in Abstracts volume, p. 16).

**Abstract.** Abstract. Diverse applications of metal oxide nanoparticles in various industries have been accelerating in the last decade. Magnesium oxide (MgO) nanoparticles have been employed in ceramics, and as adhesive and additive in chemical raw materials, leading to their increased human exposure, thereby posing potential health hazards. Because cytotoxicity of MgO nanoparticles in neural cells derived from the peripheral nervous system is unknown, we have investigated the effects of MgO nanoparticles on Schwann cells. Our results indicated treatment with MgO for 24 hours induced dose-related cytotoxicity in Schwann cells. Moreover, such treatment also induced distinct morphological changes in Schwann cells leading us to investigate the hypothesis that these nanoparticles elicit inflammatory responses in Schwann cells. Consistent with this hypothesis was our finding that the nanoparticles induced enhanced expression of cytokines such as IL-6 and PPAR gamma. We then investigated the mode of cell death in Schwann cells; our preliminary results show that the cells undergo Stat3 mediated apoptosis 48 hours after treatment with the MgO nanoparticles. Thus, our finding may have pathophysiological implications in toxicity of MgO nanoparticles in neural cells derived from the peripheral nervous system.

31. Gao W, Lai JCK, Bhushan A & Leung SW (2012) Cytotoxic Effects of Short Multi-Wall Carbon Nanotubes in Dorsal Root Ganglion (DRG) Neurons. Idaho Academy of Science 54th Annual Symposium, March 22-24, 2012, University Place, Idaho Falls, ID (in Abstracts volume, p. 29).

**Abstract.** Carbon nanotubes (CNTs) have found their way into diverse industrial and biomedical applications due to their unique physico-chemical properties. Their escalating uses in industries result in enhanced occupational human exposure to CNTs. However, the human health hazard of exposure to CNTs has not been assessed. Furthermore, the effects of CNTs on the nervous system and/or neural cells are virtually unknown. In this study, we have investigated the putative cytotoxic effects of both functionalized (i.e., carboxylated and hydroxylated) and non-functionalized short multi-wall carbon nanotubes (SMWCNTs) on dorsal root ganglion (DRG) neurons, an excellent model *in vitro* of neurons derived from the peripheral nervous system (PNS). We found that SMWCNTs induced concentration-related decreases in survival and growth of DRG neurons, the non-functionalized ones being more cytotoxic than the functionalized ones, especially at the higher concentrations. Treatment of DRG neurons with non-functionalized SMWCNTs induced necrotic damage and/or cell death in the neurons and decreased their expression of phospho-Akt. Thus, our results may have pathophysiological implications in how exposure to SMWCNTs impacts on the structure and function of the PNS.

32. Gao X, Assan D, Lai JCK & Leung SW (2012) Highly Modified Pt Electrode Sensor and Comparison of Performance of the Electrode with Other Sensors Made with Different Anchoring Materials. Idaho Academy of Science 54th Annual Symposium, March 22-24, 2012, University Place, Idaho Falls, ID (in Abstracts volume, p. 29).

**Abstract.** In our research group, we are developing high performance biosensors that are based on electrodes modified with sol-gel nanoparticles that bind with different enzymes which can couple with different redox species for the enzymatic reactions. Depending on the enzymes, the corresponding enzymatic reactions are very selective and sensitive; in recent development, the detection is almost instantaneous.

In previous studies, we reported the performance of electrode sensors that were fabricated with non-toxic biocomposite materials anchored on various conductive materials. The biocomposite materials are layers of polymer(s), nanoparticles, and enzyme(s) that are self-assembled on the surface of the conductive anchor; the anchoring materials are Ag, Au, and glassy carbon. Aside from the variations of the biocomposite layers, performance of the electrode and the linking layer (linker) connecting between the electrode surface and the enzyme(s) where redox reactions take place.

In this study, we investigated the performance of an electrode sensor consisted of the identical composite biomaterial as previously reported but was anchored with Pt. Characteristic peaks that can be used for speciation detection were identified. Performance of the electrode sensor was optimized and compared with other electrode sensors.

33. Lu S, Bhushan A, Leung SW, Daniels CK & Lai JCK (2012) Cytotoxic Effects of Four Metallic Oxide Nanoparticles on Dorsal Root Ganglion (DRG) Neurons. Idaho Academy of Science 54th Annual Symposium, March 22-24, 2012, University Place, Idaho Falls, ID (in Abstracts volume, p. 34).

**Abstract.** Metallic oxide nanoparticles are extensively used in diverse industries due to their unusual but exploitable physico-chemical properties. Consequently, the environmental exposure of humans to these nanoparticles is accelerating. However, the health impact of exposure to such nanoparticles are poorly understood. We found nanoparticles of several metallic and non-metallic oxides exerted differential cytotoxic effects on human U87 astrocytoma and SK-N-SH neuroblastoma cells. Because such effects in neural cells from the peripheral nervous system (PNS) are unknown, we developed PNS neural cell models *in vitro* — dorsal root ganglion (DRG) neurons and Schwann cells — to investigate such effects. Our results suggested that the nanoparticles investigated induced concentration- and time-related decreases in survival of DRG neurons and they exerted differential effects on their expression of p-AKT and p-ERK. Thus, our findings may have pathophysiological implications in the impact of exposure to such nanoparticles on the PNS.

34. Zhang Y, Agharkar V, Lai JCK, Daniels CK, Leung SW & Bhushan A (2012) Short Multi-Wall Carbon Nanotubes Induce Cytotoxicity on Pancreatic Cancer. Idaho Academy of Science 54th Annual Symposium, March 22-24, 2012, University Place, Idaho Falls, ID (in Abstracts volume, p. 38).

**Abstract.** Pancreatic cancer is one of the most aggressive types of cancers with poor prognosis and low survival rate. Thus, it is imperative to find effective treatments for this cancer. Carbon nanotubes (CNTs) constitute one novel and important nanomaterial extensively investigated for potential biomedical applications. Previous studies have shown that CNTs could be utilized as drug delivery vehicles and diagnostic agents. In our laboratory, we have shown that short multi-wall carbon nanotubes (SMWCNTs) can induce cytotoxicity on several cancers. SMWCNTs treatments induced decreased expression of signaling proteins associated with cancer cell survival and/or proliferation. However, the putative cytotoxicity of SMWCNTs on pancreatic cancer is unknown. Thus, we hypothesized that SMWCNTs can induce cytotoxicity on PANC1 cells in a dose-related manner employing cell survival assays. Results of ongoing studies provide some support for this hypothesis. Other studies are in progress to determine the cell survival/proliferation mechanisms underlying such cytotoxicity effects. Our findings may have implications of cytotoxicity of SMWCNTs in pancreatic cells and in designing therapies for pancreatic cancer.

35. Idikuda VK, Jaiswal AR, Wong YYW, Leung SW, Daniels CK & Lai JCK (2012) Magnesium Oxide Nanoparticles Induce Cytotoxic and Proinflammatory Effects in Schwann Cells and DRG Neurons. Experimental Biology 2012, April 21-25, 2012, Convention Center, San Diego, CA (in Abstracts Volume).

**Abstract.** Applications of metal oxide nanoparticles in diverse fields have been accelerating in the last decade. For example, magnesium oxide (MgO) nanoparticles have been employed in ceramics, and as adhesive and additive in chemical raw materials, leading to their increased human exposure, thereby posing potential health hazards. We have therefore investigated the hypothesis that MgO nanoparticles exert differential cytotoxic effects on neural cells in the peripheral nervous system employing cell models consisting of Schwann cells and dorsal root ganglion neurons (DRG) *in vitro*. Results of our ongoing studies revealed MgO nanoparticles exerted differential effects on lowering the survival of Schwann cells and DRG neurons. Along with their morphological changes, we also found the nanoparticles induced differential dose-related increases in expression of markers of inflammatory responses such as IL-6 and PPAR- $\gamma$  in the two neural cell types. Thus, our results suggest that MgO nanoparticles can induce differential cytotoxic effects and elicit inflammatory responses in Schwann cells and DRG neurons and as such may have implications in health hazard of human exposure to the nanoparticles.

36. Gao X, Assan D, Lai JCK & Leung SW (2012) Comparison of Anchoring Materials for High Performance Sensors Modified with Nanoparticles and Enzymes. NSTI Nanotechnology Conference & Expo – Nanotech 2012, June 18-21, Santa Clara, CA (in Abstracts volume).

**Abstract.** We have previously developed some of the most sensitive biosensors/electrodes modified by Au nanoparticles and enzymes that are capable of detecting concentration levels below ppb. These sensors were fabricated with composite layers of nanomaterials and enzymes anchored on conductive but non-reactive materials, such as glassy carbon Au, Ag, and Pt. Performance of these sensors varies depending on the anchoring materials



and as well as the composition of the biocomposite materials. In this report, we investigated the performance of sensors fabricated with identical biocomposite materials and procedures, except the anchoring conductive materials. The anchoring materials were glassy carbon, Pt, Au and Ag; the biocomposite layer consisted of polymer/Au nanoparticles/enzyme. The enzymes in the biocomposite layers are essential for the target species detection with which enable the coupling (detection) reactions occur. The enzymes used in this study were LDH, GDH, and hemoglobin. The specific target species for the detection included lactate, NO<sub>2</sub><sup>-</sup>, peroxide, and NH<sub>4</sub><sup>+</sup>. We also tested different combinations of the biocomposite layers for optimal performance of the sensors/electrodes. The testing solutions were buffered with 0.1 M of phosphate at pH 7.0.

37. Lu, S, Bhushan A, Leung SW, Daniels CK & Lai JCK (2012) Cytotoxic Effects of Four Metallic Oxide Nanoparticles on Dorsal Root Ganglion (DRG) Neurons. NSTI Nanotechnology Conference & Expo – Nanotech 2012, June 18-21, Santa Clara, CA (in Abstracts volume).

**Abstract.** Metallic oxide nanoparticles have diverse applications in a variety of industries because of their unusual but exploitable physico-chemical and other properties. Consequently, the exposure of humans to these nanoparticles is increasing, especially in the occupational environmental settings. Even though the health impact of exposure to such nanoparticles has not been fully assessed, there is recent evidence based on studies employing animal models suggesting that such exposure may induce differential toxicity in various organs. These findings notwithstanding, the cytotoxic effects of metallic oxide nanoparticles on neural cells are still poorly understood.

We have launched a series of studies to systematically investigate the cytotoxic effects of nanoparticles of metallic and non-metallic oxides in human and other mammalian neural and non-neural cell types. We found that such nanoparticles exerted differential cytotoxic effects on human astrocytes-like U87 astrocytoma and human neurons-like SK-N-SH neuroblastoma cells. Their toxic effects were concentration- and time-dependent. Ours were among the small number of studies that reported on the cytotoxic effects of nanoparticles of metallic and non-metallic oxides in human and other mammalian neural cells from the central nervous system. However, even less is known regarding the putative cytotoxicity of such nanoparticles in neural cells derived from the peripheral nervous system (PNS).

Because the putative cytotoxicity of nanoparticles of metallic and non-metallic oxides in neural cells derived from the PNS has not been reportedly studied, we have developed two PNS neural cell models *in vitro* consisting of dorsal root ganglion (DRG) neurons and Schwann cells to facilitate the systematic investigation of the putative cytotoxicity of such nanoparticles in PNS neural cells.

We have investigated the putative cytotoxic effects of nanoparticles of anatase TiO<sub>2</sub>, rutile TiO<sub>2</sub>, Fe<sub>2</sub>O<sub>3</sub> and ZnO in dorsal root ganglion (DRG) neurons. Results of our ongoing studies revealed that the nanoparticles investigated induced concentration- and time-related decreases in survival of DRG neurons. The rank order of the potency of the four types of metallic oxide nanoparticles in inducing decreases in survival of DRG neurons was: ZnO nanoparticles > anatase TiO<sub>2</sub> nanoparticles > rutile TiO<sub>2</sub> nanoparticles ≈ Fe<sub>2</sub>O<sub>3</sub> nanoparticles.

To further elucidate the molecular mechanisms underlying the cytotoxic effects of the nanoparticles investigated, we have assessed the expression signaling molecules known to be important in regulating cell survival and/or proliferation, namely AKT and p-AKT and ERK and p-ERK in DRG neurons treated with the nanoparticles. Results of our ongoing studies revealed that treatment with the four types of nanoparticles investigated exerted differential effects on the expression of p-AKT and p-ERK proteins in DRG neurons. Other studies are ongoing to further elucidate these and other related molecular mechanisms underlying the cytotoxic effects of the four types of nanoparticles. Thus, our findings may have pathophysiological implications in the impact of exposure to such nanoparticles on the structure and function of the PNS.

38. Idikuda VK, Jaiswal AR, Wong YYW, Bhushan A, Leung SW & Lai JCK (2012) Cytotoxicity of Magnesium Oxide Nanoparticles in Schwann Cells. NSTI Nanotechnology Conference & Expo – Nanotech 2012, June 18-21, Santa Clara, CA (in Abstracts volume).

**Abstract.** Diverse applications of metal oxide nanoparticles in various industries have been accelerating in the last decade. Magnesium oxide (MgO) nanoparticles have been employed in ceramics, and as adhesive and additive in chemical raw materials, leading to their increased human exposure, thereby posing potential health hazards. Because cytotoxicity of MgO nanoparticles in neural cells derived from the peripheral nervous system is unknown, we have investigated the effects of MgO nanoparticles on Schwann cells. Our results indicated treatment with MgO nanoparticles for 24 hours induced dose-related cytotoxicity in Schwann cells. Moreover, such treatment also induced distinct morphological changes in Schwann cells leading us to investigate the hypothesis that these nanoparticles elicit inflammatory responses in Schwann cells. Consistent with this hypothesis was our finding that the nanoparticles induced enhanced expression of cytokines such as IL-6. Thus, our findings may have pathophysiological implications in toxicity of MgO nanoparticles in neural cells derived from the peripheral nervous system.

39. Lai JCK, Gao W, Bhushan A & Leung SW (2012) Cytotoxic Effects of Short Multi-Wall Carbon Nanotubes in Dorsal Root Ganglion (DRG) Neurons. NSTI Nanotechnology Conference & Expo – Nanotech 2012, June 18-21, Santa Clara, CA (in Abstracts volume).

**Abstract.** Because of their unique physico-chemical properties, carbon nanotubes (CNTs) have found their way into diverse industrial and biomedical applications, including but not limited to fabrication of sensors, electrodes, catalysts, actuators, transistors and capacitors. Their escalating uses in multiple industries result in humans being more and more exposed to CNTs, especially in the workplace where they are found. However, the human health hazard of exposure to CNTs has not been assessed even though there have been recent studies employing animal models indicating that various types of CNTs can induce toxicity to different organs and tissues. Nevertheless, the effects of CNTs on the nervous system and/or neural cells are virtually unknown.

We have initiated a series of studies to systematically investigate the putative cytotoxicity of a variety of nanomaterials, including CNTs. Because the putative neurotoxicity of CNTs has not been reportedly studied, we have developed several neural cell models *in vitro* to facilitate such cytotoxicity studies. In this study, we have investigated the putative cytotoxic effects of both functionalized and non-functionalized short multi-wall carbon nanotubes (SMWCNTs).

We have examined the effects two functionalized, namely carboxylated and hydroxylated, SMWCNTs as well as non-functionalized SMWCNTs on dorsal root ganglion (DRG) neurons, which constitute an excellent model *in vitro* of neurons derived from the peripheral nervous system (PNS). We hypothesized that treatment with CNTs induces a dose-related decrease in the viability of DRG neurons and functionalization of CNTs modulates the cytotoxicity profile of CNTs.

Our results demonstrated that treatment with SMWCNTs induced concentration-related decreases in survival and growth of DRG neurons, the non-functionalized ones being more cytotoxic than the functionalized ones, especially at the higher treatment concentrations. Treatment of DRG neurons with non-functionalized SMWCNTs enhanced their release of lactate dehydrogenase into the medium, suggesting that SMWCNTs induced necrotic damage and/or cell death in DRG neurons. Moreover, treatment of DRG neurons with non-functionalized SMWCNTs resulted in their decreased expression of phospho-Akt, a known signal of cell survival and proliferation. Thus, ours is the first study that demonstrates SMWCNTs are cytotoxic to neural cells. Furthermore, our results may have pathophysiological implications in how exposure to SMWCNTs impact on the structure and function of the PNS.

40. Assan D, Gao X, Lai JCK & Leung SW (2012) Surfactant Effect on Intercellular Transport of DNA, Proteins, and Electrolytes. NSTI Nanotechnology Conference & Expo – Nanotech 2012, June 18-21, Santa Clara, CA (in Abstracts volume).

**Abstract.** Surfactants play a key role on bodily functions at molecular level, such as cell signaling and signal transmission. Their importance in cell survival is well recognized, but the surfactant effect on intermolecular/interfacial mass transport is not well understood and the available information of the subject is very limited quantitatively. In this report, we systemically studied the effect of surfactants on intercellular transport of DNA, proteins, and some key electrolytes with an artificial cellular system constructed with a semipermeable membrane. The permeabilities of these biomolecules and electrolytes across the semipermeable membranes in the artificial cell system were measured. Results of this study provide quantitative understanding of intermolecular interfacial mass transport that is important in the design of many fore-coming applications of biotechnology.